To view these Proceedings online, visit
https://www.nemre.nnsa.doe.gov/review2005

2005

Proceedings of the 27th Seismic Research Review:
Ground-based Nuclear Explosion Monitoring Technologies

Vol. I

Proceedings of the 27th Seismic Research Review: Ground-based Nuclear Explosion Monitoring Technologies

September 20–22, 2005

Rancho Mirage, California

Volume I

Seismic Regional Characterization and Wave Propagation
Seismic Event Detection and Location
Seismic Identification and Source Characterization

Approved for Public Release; further dissemination unlimited.

National Nuclear Security Administration

AIR FORCE RESEARCH LABORATORY

LA-UR-05-6407

Acknowledgements

The National Nuclear Security Administration (NNSA) and the Air Force Research Laboratory (AFRL) gratefully acknowledge the important contributions of the following people for their work to produce the ***Proceedings of the 27th Seismic Research Review: Ground-based Nuclear Explosion Monitoring Technologies.***

Authors of papers for excellent research, good technical content, and willing cooperation in electronic submission.

Dr. Anton M. Dainty, Mr. Robert J. Raistrick, Dr. Frederick R. Schult, AFRL/VSBYE, and ***Ms. Doris Richards***, ESC/PAM, for review and clearance of abstracts and papers related to AFRL contracts.

Dr. Mark T. Woods, Air Force Technical Applications Center (AFTAC)/TTR, for review and clearance of abstracts and papers related to AFTAC contracts.

Mr. John J. Dwyer, AFTAC/CTI, for review of abstracts and papers related to AFTAC contracts.

Ms. Sabrina Fletcher, Lawrence Livermore National Laboratory (LLNL), for assistance in ensuring that the CDs could be read on a variety of platforms and for burning, labeling, and jacketing the CDs.

Ms. Jody Benson and Ms. Eileen Patterson, Los Alamos National Laboratory (LANL), for supplementary technical editing of papers.

Mr. Marvin A. Wetovsky, LANL, for overall coordination of the Proceedings development and for technical editing of abstracts and papers.

Ms. Deidré A. Plumlee, LANL, for final composition of Proceedings covers.

Mr. Geoff G. Miller and Mr. Rodger P. Lilyestrand, LANL, for classification review of compiled papers.

Information Management Group, LANL, for color printing and binding of the hard copies.

Ms. Ruth N. Robichaud, LANL, for design and artwork of the CD label.

Ms. Leslie A. Casey, NNSA, for review and clearance of abstracts and papers related to NNSA contracts and for NNSA managerial and financial support of the Proceedings.

Dr. Joseph C. Wehlburg, NNSA/SNL, for technical review of abstracts and papers.

Dr. Leigh S. House, NNSA/LANL, for technical review of abstracts and papers.

Mr. William L. Andre, Space and Missile Defense Command (SMDC), for review and clearance of abstracts and papers related to SMDC contracts.

Ms. Mary L. Girven, Sandia National Laboratories (SNL), for making everyone's job easier with web-based technology for abstract and paper submission, on-line review and approval tools, and creation of the master files for the hardcopy, CD, and website versions of the Proceedings.

Ms. Guadalupe (Lupe) Massoth, SNL, for providing assistance to Mary Girven on troubleshooting web related problems.

Dr. David B. Harris, LLNL; ***Mr***. ***Phillip E. Harben,*** LLNL; ***Mr. Julio Aguilar-Chang,*** LANL; ***Mr. Ward L. Hawkins,*** LANL; ***Dr***. ***Steve R. Taylor***, LANL; ***Dr. Dale N. Anderson***, Pacific Northwest National Laboratory (PNNL); ***Dr. Harry S. Miley,*** PNNL; ***Mr. J. Mark Harris,*** SNL; ***Mr. Preston B. Herrington,*** SNL; and ***Dr. Christopher J. Young***, SNL, for a myriad of internal management and technical reviews of NNSA abstracts and papers.

Table of Contents - Volume I

1. Seismic Regional Characterization and Wave Propagation 1

1-01 **Ammon, C., M. Kosarian, R. Herrmann, M. Pasyanos, W. Walter, W. Sevilla, and G. Randall**
Simultaneous Inversion of Receiver Functions and Surface-Wave Dispersion Measurements for Lithospheric Structure Beneath Asia and North Africa 3

1-02 **Bungum, H., N. Maercklin, O. Ritzmann, J. Faleide, C. Weidle, A. Levshin, J. Schweitzer, W. Mooney, and S. Detweiler**
Development of a Three-Dimensional Velocity Model for the Crust and Upper Mantle in the Greater Barents Sea Region 13

1-03 **Cong, L. and B. Mitchell**
Regional Variation of Rayleigh-wave Attenuation in Southern Asia Predicted from New Maps of Lg Coda Q and Its Frequency Dependence at 1 Hz 23

1-04 **Harris, D., F. Ringdal, E. Kremenetskaya, S. Mykkeltveit, D. Rock, N. Maercklin, J. Schweitzer, T. Hauk, and J. Lewis**
Ground Truth Collection for Mining Explosions in Northern Fennoscandia and Northwestern Russia 31

1-05 **Herrmann, R., Y. Jeon, W. Walter, and M. Pasyanos**
Seismic Source and Path Calibration in the Korean Peninsula, Yellow Sea and Northeast China 42

1-06 **Lay, T., X. Xie, X. Yang, S. Taylor, and W. Phillips**
Development of Regional Phase Tomographic Attenuation Models for Eurasia 52

1-07 **Mackey, K., K. Fujita, H. Hartse, L. Steck, and R. Stead**
Seismic Characterization of Northeast Asia and Analysis of the Neva Peaceful Nuclear Explosions 61

1-08 **Martin, R., M. Krasovec, S. Romer, M. Toksöz, H. Kuleli, L. Gulen, and E. Vergino**
The Caucasus Seismic Information Network Study and Its Extension into Central Asia 71

1-09 **Minaya, E. and P. Aliaga**
Anomalous Recording of Earthquakes Occuring in Central Andes of Bolivia 79

1-10 **Mooney, W. and S. Detweiler**
Continuing Analysis of Earth Structure and Ground Truth Data from the Middle East 88

1-11 **Morozov, I., E. Morozova, S. Smithson, and I. Kadurin**
Nuclear-Explosion Profiles for Seismic Calibration of Northern Eurasia 98

1-12 **Morozov, I., H. Li, H. Zheng, and S. Smithson**
Observations and Modeling of Frequency-Dependent Lg Coda from Peaceful Nuclear Explosions 104

1-13 **Morozov, I., W. Phillips, and I. Kadurin**
Magnitude-Yield and Travel-Time Calibration of Northern Eurasia Using Deep Seismic Sounding Datasets 113

1-14 **Myers, S., J. Wagoner, L. Preston, K. Smith, and S. Larsen**
The Effect of Realistic Geologic Heterogeneity on Local and Regional P/S Amplitude Ratios Based on Numerical Simulations 123

1-15 **Ni, X., W. Chan, R. Wagner, W. Walter, and E. Matzel**
Source and Propagation Characteristics of Explosive and Other Seismic Sources 133

1-16 **Pasyanos, M., W. Walter, H. Tkalcic, G. Franz, R. Gok, and A. Rodgers**
Geophysical Model Applications for Monitoring 142

1-17 **Pulliam, J. and M. Sen**
Assessing Uncertainties in Waveform Modeling of the Crust and Upper Mantle 152

1-18 **Ritzwoller, M., N. Shapiro, M. Pasyanos, G. Bensen, and Y. Yang**
Short Period Surface Wave Dispersion Measurements from Ambient Seismic Noise in North Africa, the Middle East, and Central Asia 161

1-19 **Rodgers, A., P. Bodin, L. Malagnini, K. Mayeda, and A. Akinci**
Source and Path Effects on Regional Phases in India from Aftershocks of the January 26, 2001, Bhuj Earthquake 171

1-20 **Rodi, W. and D. Reiter**
Development of a Joint Regional Body and Surface Wave Tomography Method 178

1-21 **Romanowicz, B., M. Panning, and A. Kim**
Calibration of 3D Upper Mantle Structure in Eurasia Using Regional and Teleseismic Full Waveform Seismic Data 189

1-22 **Sandvol, E., E. Zor, J. Xie, and B. Mitchell**
High-Resolution Tomographic Mapping of Regional Phase Q in the Middle East 196

1-23 **Stevens, J., J. Given, G. Baker, and H. Xu**
Development of Surface-Wave Dispersion and Attenuation Maps and Improved Methods for Measuring Surface Waves 205

1-24 **Tibuleac, I., A. Stroujkova, J. Bonner, and K. Mayeda**
Predicting Explosion-Generated Sn and Lg Coda Using Synthetic Seismograms 214

1-25 **Toksöz, M., R. Van der Hilst, Y. Sun, and C. Li**
P and S Wave Velocity Structure of the Crust and Upper Mantle Under China and Surrounding Areas from Body and Surface Wave Tomography 222

1-26 **van der Lee, S., A. Rodgers, M. Flanagan, M. Pasyanos, F. Marone, and B. Romanowicz**
Towards a Comprehensive Seismic Velocity Model for the Broader Africa-Eurasia Collision Region, to Improve Nuclear Explosion Monitoring 232

1-27 **Xie, J., D. Schaff, and Y. Liu**
Tomographic Mapping of Lg Q in Eastern Eurasia 242

1-28 **Xie, X., T. Lay, and R. Wu**
Near-Source Energy Partitioning for Regional Waves in 2D and 3D Models, Contributions of S-to-Lg and P-to-Lg Scattering* 249

1-29 **Yang, X., A. Lowry, A. Levshin, and M. Ritzwoller**
Toward a Rayleigh Wave Attenuation Model for Eurasia and Calibrating a New M_S Formula 259

1-30 **Zhang, H., C. Thurber, and X. Song**
High-Resolution Seismic Velocity and Attenuation Structure of the Sichuan-Yunnan Region, Southwest China, Using Seismic Catalog and Waveform Data 266

2. Seismic Event Detection and Location 277

2-01 **Antolik, M., J. Erickson, M. Tinker, K. Hutchenson, G. Kraft, and L. Owiesny**
A Priori Empirical Calibration for Multiple-Event Location Methods 279

2-02 **Bondár, I., B. Kohl, E. Bergman, K. McLaughlin, H. Israelsson, Y. Kung, P. Piraino, and E. Engdahl**
Global Ground Truth Data Set with Waveform and Improved Arrival Data 289

2-03 **Bondár, I., K. McLaughlin, and H. Israelsson**
Improved Event Location Uncertainty Estimates 299

2-04 **Brazier, R., M. Benoit, Y. Park, A. Nyblade, and M. Pasyanos**
Ground Truth Events, Magnitude Scale, Velocity Models and Travel Time Correction Surfaces for Northeastern Africa 308

2-05 **Brooks, B., F. Gomez, E. Sandvol, and L. Frazer**
Ground Truth of African and Eastern Mediterranean Shallow Seismicity Using SAR Interferomtery and Gibbs Sampling Inversion 318

2-06 **Carlson, D., K. Kane, F. Schult, S. Ballard, C. Young, and D. Anderson**
Utilizing Prior Information for Depth to Improve Seismic Event Discrimination 327

2-07 **Engdahl, E., E. Bergman, S. Myers, and F. Ryall**
Improved Ground Truth in Southern Asia Using In-Country Data, Analyst Waveform Review and Advanced Algorithms 332

2-08 **Fisk, M. and S. Myers**
Ground-Truth Event Locations Using Cross-Correlated Seismic Phases and Satellite Imagery 342

2-09 **Hipp, J., S. Ballard, M. Chang, and L. Jensen**
Representing Kriged Travel Time Correction Surfaces with Optimal Tessellations 352

2-10 **Kim, W., P. Richards, D. Schaff, F. Waldhauser, and J. Zhang**
Evaluation of Cross-Correlation Methods on a Massive Scale for Accurate Relocation of Seismic Events 362

2-11 **Monsalve, G., A. Sheehan, T. de la Torre, C. Rowe, and M. Begnaud**
Ground Truth in Central Asia from In-Country Networks 372

2-12 **Myers, S., G. Johannesson, and W. Hanley**
Multiple-Event Location Using the Markov-Chain Monte Carlo Technique 383

2-13 **Reeves, P., S. Ballard, J. Hipp, C. Young, D. Myers, and B. Ammons**
Improved Representation and Calculation of Base Model Travel Times Using the Parametric Grid Library 393

2-14 **Reiter, D. and A. Stroujkova**
Improved Depth-Phase Detection at Regional Distances 403

2-15 **Ringdal, F., S. Gibbons, and D. Harris**
Adaptive Waveform Correlation Detectors for Arrays: Algorithms for Autonomous Calibration 413

2-16 **Ringdal, F., S. Gibbons, T. Kvaerna, V. Asming, Y. Vinogradov, S. Mykkeltveit, and J. Schweitzer**
Research in Regional Seismic Monitoring 423

2-17 **Rodi, W.**
Error Analysis in the Joint Event Location/Seismic Calibration Inverse Problem 433

2-18 **Saikia, C., H. Thio, D. Helmberger, G. Ichinose, and C. Ji**
Ground Truth Locations Using Synergy Between Remote Sensing and Seismic Methods—Application to Chinese and North African Earthquakes 443

2-19 **Salzberg, D., K. Votaw, and M. Marshall**
Seismic Source Locations and Parameters for Sparse Networks by Matching Observed Seismograms to Semi-Empirical Synthetic Seismograms 454

2-20 **Shumway, R.**
Advances in Mixed Signal Processing for Regional and Teleseismic Arrays 463

2-21 **Steck, L., W. Phillips, C. Rowe, M. Begnaud, K. Mackey, K. Fujita, and H. Hartse**
Pn Tomography and Location in Eurasia 471

2-22 **Yang, T., Y. Shen, and X. Yang**
Crustal and Mantle Structure Beneath Eastern Eurasia from Finite Frequency Seismic Tomography (FFST) 479

3. Seismic Identification and Source Characterization 489

3-01 **Anderson, D., D. Carlson, G. Kraft, F. Schult, S. Taylor, and W. Walter**
Event Identification Framework for Teleseismic and Regional Discriminants 491

3-02 **Arrowsmith, M., S. Arrowsmith, B. Stump, and M. Hedlin**
Discrimination of Small Events Using Regional Waveforms: Application to Seismic Events in the US and Russia 498

3-03 **Bonner, J., D. Russell, D. Harkrider, D. Reiter, and R. Herrmann**
Application of a Time-Domain, Variable-Period Surface Wave Magnitude Measurement Procedure at Regional and Teleseismic Distances 509

3-04 **Bonner, J., B. Stump, M. Leidig, X. Yang, R. Zhou, T. Kim, W. Walter, A. Velasco, C. Hayward, D. Baker, C. Edwards, S. Harder, H. Hooper, T. Glenn, C. Zeiler, R. Gok, J. Britton, and J. Lewkowicz**
Source Phenomenology Experiments in Arizona 519

3-05 **Bungum, H., T. Kvaerna, S. Mykkeltveit, N. Maercklin, M. Roth, K. Aastebol, D. Harris, and S. Larsen**
Energy Partitioning for Seismic Events in Fennoscandia and NW Russia 529

3-06 **Fisk, M., T. Lay, and S. Taylor**
Modeling and Empirical Research on Energy Partitioning of Regional Seismic Phases used for Explosion Monitoring 539

3-07 **Gitterman, Y., V. Pinsky, and A. Hofstetter**
Using Ground Truth Explosions for Studying Seismic Energy Generation and Partitioning into Various Regional Phases 550

3-08 **Hong, T. and J. Xie**
Source Array Analysis on the Composition of Regional Waves from Balapan Explosions in the Near-Source Region 561

3-09 **Hooper, H., I. Tibuleac, M. Pasyanos, and J. Bonner**
Improving M_S Estimates by Calibrating Variable Period Magnitude Scales at Regional Distances 570

3-10 **Leidig, M., J. Bonner, R. Hansen, V. Romanovsky, S. Brown, R. Martin, and J. Lewkowicz**
Possible Effects of Frozen Rock on Explosive Coupling 580

3-11 **Mayeda, K., L. Malagnini, W. Phillips, W. Walter, D. Dreger, and P. Morasca**
2-D Path Corrections for Local and Regional Coda Waves: A Test of Transportability 587

3-12 **Murphy, J., B. Barker, and J. Sultanov**
A Scaling Analysis of Frequency Dependent Energy Partition for Local and Regional Seismic Phases from Explosions 597

3-13 **Patton, H. and W. Phillips**
Regional Magnitude Research Supporting Broad-Area Monitoring of Small Seismic Events 606

3-14 **Rautian, T., V. Khalturin, W. Phillips, and P. Richards**
Explosion Source Phenomena Using Soviet Test Era Waveform Data 612

3-15 **Richardson, E., A. Nyblade, W. Walter, K. Mayeda, and L. Lowe**
Seismic Source Characterization and Energy Partitioning from In-Mine and Regional Broadband Data in South Africa 622

3-16 **Saikia, C., K. Mayeda, L. Zhu, and R. Herrmann**
Developing Multiple-Frequency Discriminants for Use with Regional Coda-Amplitude Measurements 632

3-17 **Sammis, C. and R. Biegel**
Seismic Radiation from Explosions in Frozen Crystalline Rock 642

3-18 **Srinivasan, C., C. Sivakumar, and R. Gupta**
Source Parameters of Seismic Events in a Coal Mine in India 653

3-19 **Stevens, J., G. Baker, H. Xu, and T. Bennett**
The Physical Basis of the Explosion Source and Generation of Regional Seismic Phases 663

3-20 **Taylor, S., H. Patton, X. Yang, and M. Maceira**
Regional Event Identification Research in Eastern Asia 673

3-21 **Toksöz, M., S. Chi, Y. Zhang, E. Sze, and R. Lu**
Characterization of an Explosion Source in a Complex Medium by Modeling and Wavelet Domain Inversion 683

3-22 **Walter, W., K. Mayeda, R. Gok, A. Rodgers, A. Sicherman, T. Hickling, D. Dodge, E. Matzel, M. Ganzberger, and V. Parker**
Regional Seismic Discrimination Optimization With and Without Nuclear Test Data: Western U.S. Examples 693

3-23 **Zhou, R., B. Stump, C. Hayward, Z. Yang, and Y. Chen**
Study of Regional Broadband Waves from Earthquakes and Man-induced Events in NE China 704

Seismic Regional Characterization and Wave Propagation

SIMULTANEOUS INVERSION OF RECEIVER FUNCTIONS AND SURFACE-WAVE DISPERSION MEASUREMENTS FOR LITHOSPHERIC STRUCTURE BENEATH ASIA AND NORTH AFRICA

Charles J. Ammon[1], Minoo Kosarian[1], Robert B. Herrmann[2], Michael E. Pasyanos[3], William R. Walter[3], Winchelle Sevilla[1], and George Randall[4]

Penn State University[1], Saint Louis University[2], Lawrence Livermore National Laboratory[3], and Los Alamos National Laboratory[4]

Sponsored by Air Force Research Laboratory
and
National Nuclear Security Administration
Office of Nonproliferation Research and Engineering
Office of Defense Nuclear Nonproliferation

Contract Nos. DE-FC03-02SF22498[1], DTRA01-02-C-0038[2], W-7405-ENG-48[3], and W-7405-ENG-36[4]

ABSTRACT

This paper reports on initial investigations into the seismic structure of the lithosphere in the Middle East and North Africa (MENA) using surface waves and receiver functions. Collections of prior work in the region and computing receiver functions for use in the joint inversion have been initiated. Critical to the joint inversion are surface-wave dispersion information localized to approximately the same region sampled by receiver functions. We continue to improve our surface-wave dispersion model of Western Eurasia and North Africa. We have developed group velocity maps at 2-degree resolution for both Love and Rayleigh waves from 10- to 100-second periods. The model shows excellent relationship to tectonic structure and group velocity variations correlate well with orogenic zones, cratons, sedimentary basins, and rift zones. We have recently implemented a variable-resolution tomography and have pushed the resolution of the model down to 1-degree in areas with sufficient density sampling. We plan to present information on the complexity of receiver structure at many permanent sites in the region and several illustrative inversions for lithospheric structure. We have examined receiver functions at over 200 stations in Eurasia and North Africa and have inverted about 160 using dispersion measurement from global and regional tomographic models. We will present a comparison of crustal thickness and Poisson's ratio estimates for the crust beneath these stations as well as several examples of the joint receiver function surface-wave modeling methodology.

OBJECTIVES

Our objectives are the construction of shear-velocity profiles for regions surrounding broad-band seismic stations throughout Eurasia and central and north Africa (Figure 1). Application of the technique in the region provides an opportunity to revise models of the crust and upper mantle structure throughout the region and to exploit the global and regional work of previous seismic verification research (e.g., Pasyanos et al., 2001; Ritzwoller & Levshin, 1998, Larson and Ekstrom, 2001). The resulting shear-velocity models provide a single structure consistent with a range of observations and which can be tested as a tool for the construction of mode isolation filters that can help improve surface-wave magnitude estimates. We also plan to explore the possibility of adding additional data to our inversions of receiver functions and surface-wave dispersion. The diverse seismic activity throughout the region will facilitate cross-validation of the mode isolation filters with simple empirical filters constructed using larger events with adequate signal-to-noise ratios.

Estimating Subsurface Shear Velocities

Subsurface geology generally has a broad wavenumber spectrum containing spatially localized broadband-wavenumber changes in velocity near Earth's major geologic boundaries and smooth low-wavenumber variations in regions of relatively uniform geologic structure. Access to the full spectrum of earth structure requires that we exploit signals that span a wide frequency range and that are sensitive to the entire spectrum of heterogeneity. Surface-waves, travel times, and direct-wave amplitudes, for example, are sensitive to smooth variations in earth structure; reflected and converted waves are sensitive to velocity contrasts. Combining seismic data in joint inversions is an obvious approach to improve estimates of earth structure. To successfully combine data in an inversion, we must ensure that all the data are sensitive to the same (or related) physical quantities and that they sample or average structure over comparable length scales. Advances in surface-wave tomography have provided an opportunity to combine localized surface-wave dispersion estimates with other data such as P- and S-wave receiver functions.

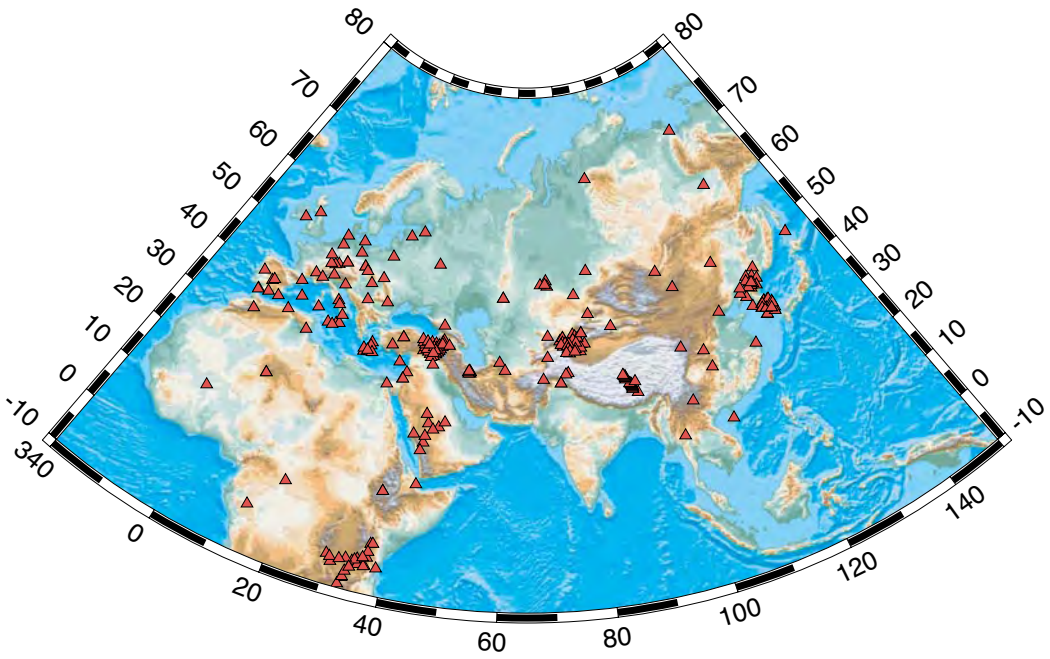

Figure 1. Available permanent and temporary three-component seismic stations in the research area. The data include all readily available permanent and temporary network stations.

Surface-wave dispersion measurements are sensitive to broad averages, or low wavenumber components of earth structure. They provide valuable information on the absolute seismic shear velocity but are relatively insensitive to sharp, high-wavenumber velocity changes. Generally surface-wave inversions must be constrained using a particular layer parameterization (e.g., near-surface, upper-crust, lower crust, mantle lid, deep mantle), resembling an *a priori* model, or substantially smoothed to stabilize earth-structure estimation. Despite these drawbacks, surface-wave dispersion values contain important constraints on the subsurface structure, and the general increase in depth sensitivity with period allows an intuitive understanding of their constraints on structure. Additionally, modeling dispersion values facilitate a broadband inversion by reducing the dominance of Airy phases, which pose problems when constructing broad-band misfit norms to model seismograms directly. Perhaps most important for our application is the ability to localize Earth's dispersion properties using seismic tomography. The idea is now well established and global dispersion models exist for a broad range of frequencies (e.g., Larson and Ekström, 2001; Stevens et al., 2001). The localization of dispersion allows us to isolate the variations in properties spatially and global models of surface-wave dispersion exist and are readily available for application to other studies such as the proposed work.

Receiver functions are time series computed from three-component body-wave seismograms, which show the relative response of Earth structure near the receiver (e.g., Langston, 1979). Source, near-source structure, and mantle propagation effects are removed from the seismograms using a deconvolution that sacrifices P-wave information for the isolation of near-receiver effects (Langston, 1979; Owens et al., 1984; Ammon, 1991; Cassidy, 1992). Receiver function waveforms are a composite of P-to-S (or S-to-P) converted waves that reverberate within the structure near the seismometer. Modeling the amplitude and timing of those reverberating waves can supply valuable constraints on the underlying geology. In general, the receiver functions sample the structure over a range of 10's of kilometers from the station in the direction of wave approach (the specific sample width depends on the depth of the deepest contrast). Stations sited near geologic boundaries can produce different responses for different directions. Recent innovations in receiver function analysis include more detailed modeling of receiver function arrivals from sedimentary basin structures (e.g. Clitheroe et al., 2000), anisotropic structures (e.g. Levin and Park, 1997; Savage 1998), estimation of Poisson's ratio (e.g. Zandt et al., 1995; Zandt and Ammon, 1995; Zhu and Kanamori, 2000, Ligorría, 2000), reflection-like processing of array receiver functions (e.g. Chevrot and Girardin, 2000; Ryberg and Weber, 2000) and joint inversions (e.g. Özalaybey et al., 1997; Du and Foulger, 1999; Julia et al., 2000).

Ammon and Zandt (1993) used surface-wave dispersion observations to try and distinguish between competing models of the Mojave desert, but Özalaybey et al., (1997) pioneered a formal, joint inversion of these data. They nicely illustrated the value of even a limited band of dispersion values to help reduce the trade-off between crustal thickness and velocity inherent in receiver function analyses. Specifically, they used Rayleigh-wave phase velocities in the 20–25 second period range to help produce stable estimates of crustal thickness in the northern and central Basin & Range. The limited bandwidth did not permit resolution of details in the crust and they limited their inversion (or at least their interpretation) to depths above 40 km. More recent authors have exercised the approach and combined the data with additional *a priori* model constraints (Du and Foulger, 1999; Julia et al., 2000). Recent accomplishments in global and regional tomography now provide a more complete band of dispersion measurements to combine with receiver functions that allow us to improve the resolution of earlier works.

Our joint inversion method is similar to that of Özalaybey et al. (1997) except that we use jumping, smoothness, and constraints to include as much *a priori* information into the inversion as is available. We combine the receiver function and surface-wave observations into a single algebraic equation and account for their different physical units and equalize their importance in the misfit norm by weighting each data set by an estimate of the uncertainty in the observations and the number of data. We also append smoothness constraints and *a priori* model constraints on the deepest part of the model. Although we cannot resolve fine details in the deep upper mantle, these regions can impact our results since surface-wave dispersion values at intermediate and longer periods are somewhat sensitive to this deeper structure. We believe that it is important to have a reasonable basement structure so that our results are more consistent with global models. We extend our models to about 500–700 km to insure this consistency. The resulting inversion equations are

$$\begin{bmatrix} \sqrt{\frac{\mathbf{p}}{\mathbf{w_s}^2}}\mathbf{D_s} \\ \sqrt{\frac{\mathbf{q}}{\mathbf{w_r}^2}}\mathbf{D_r} \\ \sigma\Delta \\ \mathbf{W} \end{bmatrix} \cdot \mathbf{m_{i+1}} = \begin{bmatrix} \sqrt{\frac{\mathbf{p}}{\mathbf{w_s}^2}}\mathbf{r_s} \\ \sqrt{\frac{\mathbf{q}}{\mathbf{w_r}^2}}\mathbf{r_r} \\ 0 \\ 0 \end{bmatrix} + \begin{bmatrix} \sqrt{\frac{\mathbf{p}}{\mathbf{w_s}^2}}\mathbf{D_s} \\ \sqrt{\frac{\mathbf{q}}{\mathbf{w_r}^2}}\mathbf{D_r} \\ 0 \\ 0 \end{bmatrix} \cdot \mathbf{m_i} + \begin{bmatrix} 0 \\ 0 \\ 0 \\ \mathbf{W} \end{bmatrix} \cdot \mathbf{m_a} \qquad (1)$$

where $\mathbf{p}$, $\mathbf{q} = 1 - \mathbf{p}$, σ, and $\mathbf{W}$ are weights that control the relative importance of receiver functions, dispersion values, smoothness, and *a priori* model constraints in the norm minimized during the inversion. The data comprise the vectors $\mathbf{r_s}$ and $\mathbf{r_r}$, and the partial derivatives fill the matrices $\mathbf{D_r}$ and $\mathbf{Ds}$. The matrix Δ is a finite-difference stencil that "computes" model roughness, and the matrix $\mathbf{W}$ is a layer-dependent weight that is used to insure the model blends smoothly into the *a priori* model, $\mathbf{m_a}$, at depth. The values of $\mathbf{w_s}$ and $\mathbf{w_r}$ are equal to the product of the number of points in the dispersion curve and receiver functions and the variance of the observations.The second term on the right is added to create the "jumping" inversion scheme (e.g., Constable et al., 1987; Ammon et al., 1990) and allows us to solve for (and constrain) the shear-velocity models as opposed to shear-velocity correction vectors. Equation (1) is solved in a least-squares sense for the model, $\mathbf{m_{i+1}}$, starting with an initial model $\mathbf{m}_0$. The procedure generally converges in a few iterations.

RESEARCH ACCOMPLISHED

Tomographic Imaging of Group-Velocity Variations

We have performed a large-scale study of surface wave group velocity dispersion across Western Eurasia and North Africa (Pasyanos, 2002). This study expands the coverage area northwards relative to previous work (Pasyanos et al., 2001), which covered only North Africa and the Middle East. As a result, we have increased by about 50% the number of seismograms examined and group velocity measurements made. We have now made good quality dispersion measurements for more than 10,000 Rayleigh wave and 6,000 Love wave paths, and have incorporated measurements from several other researchers into the study. We use a conjugate gradient method to perform a group velocity tomography. We have improved our inversion from the previous study by adopting a variable smoothness (Pasyanos, 2002). This technique allows us to go to higher resolution where the data allow without producing artifacts. Our current results include both Love and Rayleigh wave inversions across the region for periods from 10 to 100 seconds. Figure 2 shows inversion results for Rayleigh waves at a period of 35 seconds. Short period group velocities are sensitive to slow velocities associated with large sedimentary features such as the Russian Platform, Mediterranean Sea, and Persian Gulf. Intermediate periods are sensitive to differences in crustal thickness, such as those between oceanic and continental crust or along orogenic zones. At longer periods, we find fast velocities beneath cratons and slow upper mantle velocities along rift systems and the Tethys Belt.

Receiver-Function Estimation

The first step in the project is the selection of target stations and the computation of receiver functions at those stations. To begin, we have a selected a subset of permanent stations that have relatively long recording histories and thus will have substantial data already available. More recently installed stations and operating temporary stations will be added later in the project. Data processed at the time this report was written are shown in Figure 1. We have included all available temporary and permanent stations within central and northern Africa and across much of Eurasia. We have investigated 213 stations: 35 in Africa, 79 in the Middle East, 54 stations in southern Europe, and 45 in eastern Asia.

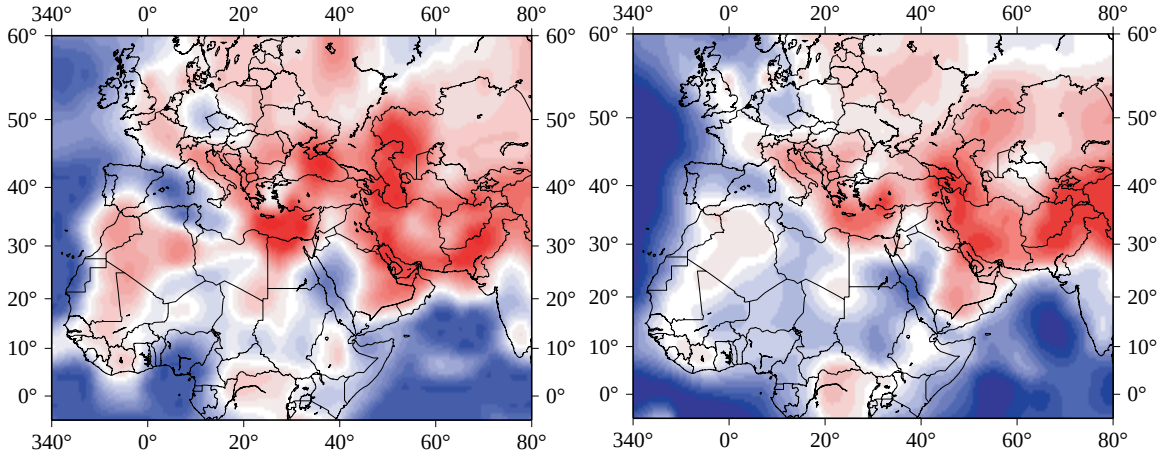

Figure 2. Tomographic imaging results for the Middle East, North Africa, and western Europe. The left diagram shows the lateral group velocity variations in 35-second period Love waves. The map on the right shows the corresponding variations in 35-second period Rayleigh waves. Color scales are relative: blue is fast, red is slow.

Poisson's Ratio and Crustal Thickness Estimation

As a first step in the receiver function analysis we use the receiver function stacking method of Zhu and Kanamori (2000) to estimate the crustal thickness and Vp/Vs velocity ratio (or Poisson's ratio). The stacking method makes a rather limiting assumption of a uniform crust but the analysis provides good estimates of these quantities when the structure is relatively simple. The estimated values of Poisson's ratios can be used in subsequent inversions which require some assumed value of bulk crustal Poisson's ratio. We summarize our results in Figure 3. Although it is difficult to just cluster regions of the continent into simple classifications, we follow Zandt and Ammon (1995) and separate our data into tectonic-age based groups with the exception of Tibet, which we keep as a separate subset of the Mesozoic-Cenozoic regions. Our results are similar to those of Zandt and Ammon (1995) with the exception that our larger survey of shields (including Archean shields) does not show an unusually high Poisson's ratio as was suggested in the earlier data set. Only 7 stations are common to both studies, so the differences are a sampling result. Interestingly, we see no differences between Archean and Proterozoic shields.

Crustal thickness estimates agree on average with the global crustal model 2.0, but at times the differences are significant (greater than 5 km). The mean difference between our results and Crust 2.0 is about 1 km and the standard deviation of the differences is about 7 km, which is larger than the resolution we have on stations with stable receiver functions (probably between 2.5 and 5 km). The crustal thicknesses agree better when we rank our estimates using the complexity of the observed receiver functions.

The Joint Inversion of Receiver Functions and Surface-Wave Dispersion Curves

The receiver function is sensitive to velocity transitions and vertical travel times, surface-wave dispersion measurements are sensitive to averages of the velocities, and relatively insensitive to sharp velocity contrasts. The complementary nature of the signals makes them ideal selections for joint study because they can fill in resolution gaps of each data set. Ammon and Zandt (1993) pointed this out in a study of the Landers region of southern California (although for their specific case, available observations were unsuitable to resolve subtle features in the lower crust) and Özalaybey et al. (1997) and Last et al. (1997) have performed complementary analyses of surface-wave dispersion and receiver functions and Du and Foulger (1999) and Julia et al. (2000) implemented joint inversions of these data types. The mechanics of the inversion are relatively simple since partial derivatives of dispersion observations (Herrmann, 1995) and receiver functions waveforms (e.g., Randall, 1989, Ammon et. al, 1990) can be

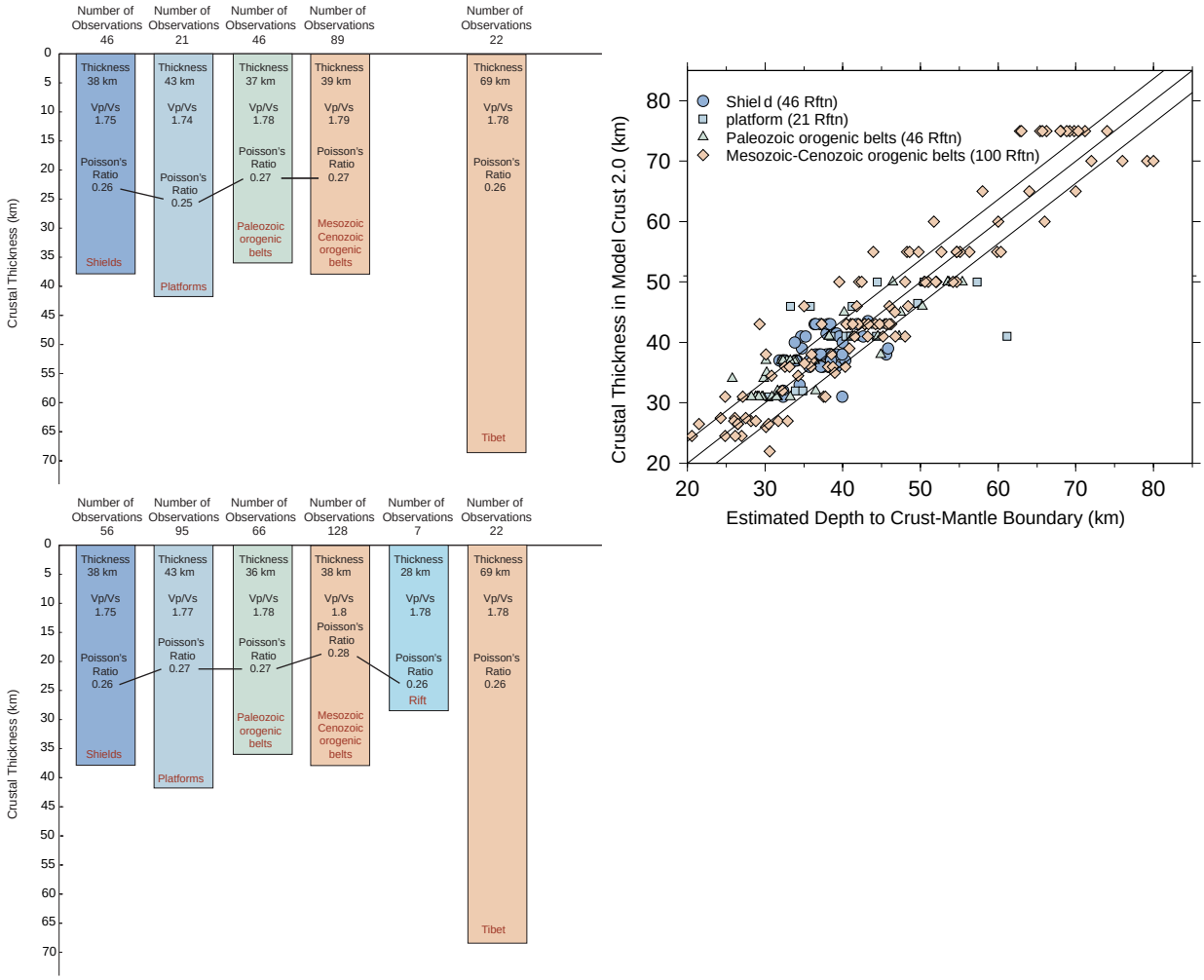

Figure 3. Comparison of crustal thickness estimated with receiver functions in our recent work versus tectonic affiliation. (Top Left) results from this work that include 224 observations; some stations had interpretable receiver functions from more than one azimuth. (Bottom Left) A composite of measurements made during this project and values from the literature. The primary difference is in the platform regions. One would expect a decrease in Poisson's ratio from shield to platform, where the primary geologic difference is in the sediment cover, which tends to lower the Poisson's ratio values. (Top Right) Comparison of crustal thickness estimates from this study and the model Crust 2.0. The results correlate well to first order. Most differences are less than 5 km. Largest differences occur in regions of rapid variations in crustal thickness, where the smooth Crust 2.0 averages across a number of receiver function observation points.

calculated quickly and accurately. Ammon et al. (2004) presented a number of examples, here we present a single example to illustrate the procedure.

An Example Combined Inversion, Station PUGE, Tanzania

We illustrate the ideas with an example. In Figure 4 we present the results of the inversion of PUGE receiver functions with the Rayleigh-wave group-velocity dispersion values from Pasyanos and Walter (2002) combined with phase velocities digitized from Weeraratne et al. (2003). The fit to the Pasyanos and Walter (2002) dispersion curve is very good and the general fit to the phase-velocities is good. The phase velocities are slightly under-predicted for the shorter periods and over-predicted for the longest periods. The long-period over-prediction is a result of our constraints that the deepest part of the model match that of the Prelimninary Reference Earth Model (PREM). Relax-

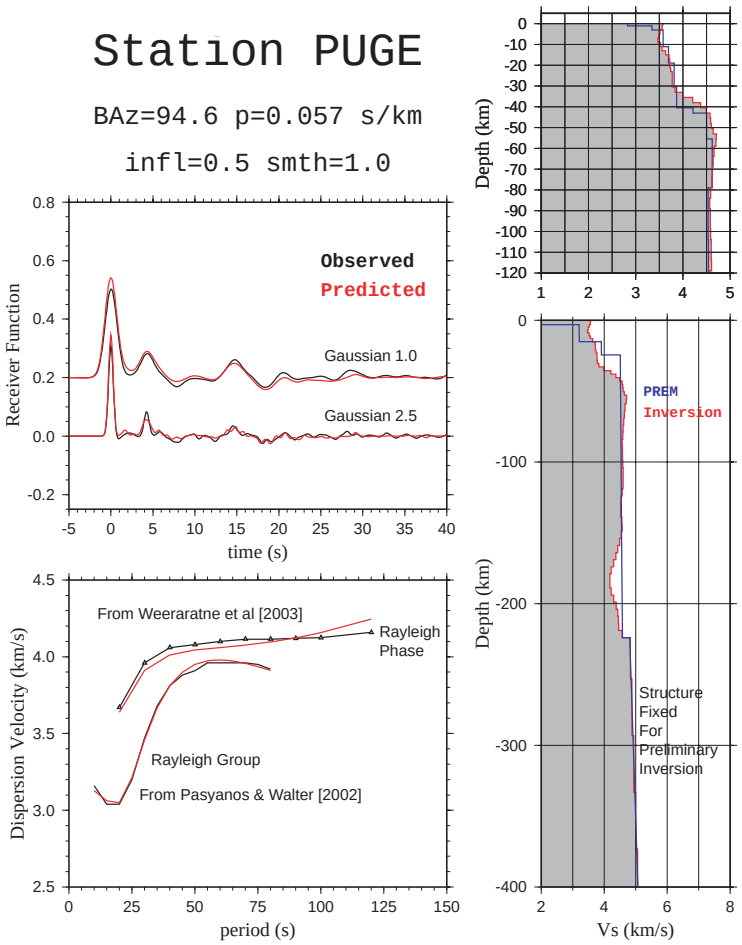

Figure 4. Inversion results for station PUGE using dispersion curves from Pasyanos and Walter (2002) & Weeeratne et al., (2003). The back azimuth and ray parameter of the incoming P-wave are shown at the top. The influence parameter was 0.5, which balances the weight between the receiver functions and dispersion values, and the smoothness weight was 1.0. The observed and predicted receiver functions in two bandwidths are shown in the upper left, the observed and predicted dispersion curves in the lower left, and the resulting models are shown on the right. The deep structure is constrained to transition smoothly into the PREM - the data have little sensitivity for detailed absolute velocities below approximately 100-150 km.

ing that assumption would allow the low velocities to extend deeper than 220 km and reduce the deepest average shear-velocity to match the phase velocity. The difference at the shorter periods represents a fundamental difference between the group and phase-velocities. One explanation may be the smoothing of the group velocities has resulted in an artificially lower estimate, very slightly inconsistent with the phase velocities. The receiver functions are very well modeled and produce the relatively smooth crust-mantle transition and crustal thickness (provided with the absolute velocity information from the surface-wave information). The model has a relatively simple crust, consistent with earlier results, and the crust-mantle transition about 7.5 km thick (this could be an intermediate layer at the base of the crust). The mantle structure includes a lid with a thickness of approximately 100 km underlain by a region of low velocities. These velocities are low compared with other shields - consistent with the results of Weeraratne et al (2003). Although the lid is fast at shallow depths, consistent with regional propagation *(*e.g., Nyblade and Brazier, 2002; Langston et al., 2002) the model lid is also thinner than usual for an Archean shield.

CONCLUSIONS AND RECOMMENDATIONS

Our work is concluding nicely. We are refining the results and assessing model performance for waveform matching. In addition to the shear-velocity models, which can act like borehole constraints for smoothed tomography models, our survey has identified a number of seismic stations with exceedingly complicated near-receiver structures that may have an impact on amplitude measurements at those stations.

ACKNOWLEDGEMENTS

We thank P. Wessel and W. H. F. Smith (1991), the authors of GMT for producing easy-to-use, quality software for making maps and charts. We obtained all the data shown in the report through the Incorporated Research Institutions for Seismology Data Management Center.

REFERENCES

Ammon, C. J., G. E. Randall, and G. Zandt (1990), On the non-uniqueness of receiver function inversions, *J. Geophys. Res.* 95: 15303-15318.

Ammon, C. J. (1991), The isolation of receiver effects from teleseismic P waveforms, *Bull. Seism. Soc. Am.* 81: 2504-2510.

Ammon, C. J., and G. Zandt (1993), The receiver structure beneath the southern Mojave Block, *Bull. Seism. Soc. Am.* 83: 737-755.

Ammon, C. J., M. Kosarian, R. B. Herrmann, M. E. Pasyanos, W. R. Walter, and H. Tkalcic (2004), Simultaneous inversion of receiver functions, multi-mode dispersion, and travel-time tomography for lithospheric structure beneath the Middle East and North Africa, in *Proceedings of the 26th Seismic Research Review: Trends in Nuclear Explosion Monitoring*, LA-UR-04-5801, Vol. 1, pp. 17-28.

Cassidy, J. F. (1992), Numerical experiments in broadband receiver function analysis, *Bull. Seismol. Soc. Am.* 82: 1453-1474.

Chevrot, S., and N. Girardin (2000), On the detection and identification of converted and reflected phases from receiver functions, *Geophys. J. Int.* 141: (3), 801-808.

Clitheroe, G., O. Gudmundsson, and B. L. N. Kennett (2000), Sedimentary and upper crustal structure of Australia from receiver functions, *Australian Journal of Earth Sciences* 47: (2), 209-216.

Constable, S. C., R.L. Parker, and C. G. Constable (1987), Occam's inversion: A practical algorithm for generating smooth models from electromagnetic sounding data, *Geophysics* 52: 289-300.

Du, Z .J. and G. R. Foulger (1999), The crustal structure beneath the northwest fjords, Iceland, from receiver functions and surface waves, *Geophys. J. Int.* 139: 419-432.

Herrmann, R. B., *Computer Programs in Seismology*, (1995), St. Louis University, St. Louis, MO.

Julia, J., C. J. Ammon, R. B. Herrmann, and A. M. Correig (2000), Joint Inversion of receiver function and surface-wave dispersion observations, *Geophys. J. Int.* 143: 99-112.

Kikuchi, M., and H. Kanamori, Inversion of complex body waves (1982), *Bull. Seism. Soc. Am.*, 72, 491-506, 1982.

Langston, C.A. (1979), Structure under Mount Rainier, Washington, inferred from teleseismic body waves, *J. Geophys. Res.*, 84, 4749-4762.

Langston, C. A., A. A. Nyblade, and T. J. Owens (2002), Regional wave propagation in Tanzania, East Africa, *J. Geophys. Res.* 107: 1-18.

Larson, E. W. F. and G. Ekström (2001), Global Models of Group Velocity, *Pure and Applied Geophys.* 158: 1377-1399.

Last, R. J., A. A. Nyblade, C. A. Langston, and T. J. Owens (1997), Crustal structure of the East African Plateau from receiver functions and Rayleigh wave phase velocities, *J. Geophys. Res*. 102: 24469-24483.

Levin, V., and J. Park (1997), Crustal anisotropy in the Ural Mountains from teleseismic receiver functions, *Geophysical Research Letters* 24: (11), 1283-1286.

Ligorría, J.P. (2000), An Investigation of the Crust-Mantle Transition Beneath North America and the Bulk Composition of the North American Crust, *Ph.D. Thesis, Saint Louis University,* 261 pages.

Ligorría, J. P. and C. J. Ammon (1999), Iterative deconvolution and receiver function estimation, *Bull. Seismol. Soc. Am.* 89: 1395-1400.

Myers, S. C., and S. L. Beck (1994), Evidence for a local crustal root beneath the Santa Catalina metamorphic core complex, Arizona, *Geology* 22: 223-226.

Nyblade, A. A. and R. A. Brazier (2002), Precambrian lithospheric controls on the development of the East African rift system, *Geology* 30: 755-758.

Owens, T. J., G. Zandt, and S. R. Taylor (1984), Seismic evidence for an ancient rift beneath the Cumberland Plateau, Tennessee: A detailed analysis of broadband teleseismic P waveforms, *J. Geophys. Res.* 89: 7783-7795.

Özalaybey, S., M. K. Savage, A. F. Sheehan, J. N. Louie, and J. N. Brune (1997), Shear-wave velocity structure in the northern Basin and Range Province from the combined analysis of receiver functions and surface waves, *Bull. Seismol. Soc. Am.* 87: 183-199.

Park, J. and V. Levin (2000), Receiver functions from multiple-taper spectral correlation estimates, *Bull. Seismol. Soc. Am.* 90: (6), 1507-1520.

Pasyanos, M. E., W. R. Walter, and S.E. Hazler (2001), A Surface wave dispersion study of the Middle East and North Africa for Monitoring the Comprehensive Nuclear-Test-Ban Treaty, *Pure and Applied Geophys* 158: 1445-1474.

Pasyanos, M. E., and W. R. Walter, Crust and upper-mantle structure of North Africa, Europe and the Middle East from inversion of surface waves, *Geophys. J. Int.* 149: 463-481, 2002.

Pasyanos, M.E. (2002), A Variable-resolution surface wave dispersion Study of Western Eurasia and North Africa, submitted to *Journal of Geophysical Research*.

Ritzwoller, M. H. and A. L. Levshin (1998), Eurasian surface wave tomography: Group velocities, *J. Geophys. Res.* 103: 1839-1878.

Ryberg, T., and M. Weber (2000), Receiver function arrays; a reflection seismic approach, *Geophys. J. Int.* 141: (1), 1-11.

Savage, M.K. (1998), Lower crustal anisotropy or dipping boundaries? Effects on receiver functions and a case study in New Zealand, *J. Geophys. Res.* 103: (7), 15069-15087.

Stevens, J. L. and K. L. McLaughlin (2001), Optimization of Surface Wave Identification and Measurement, *Pure and Applied Geophys*. 158: 1547-1582

Su, W., R. L. Woodward, and A. M. Dziewonski (1994), Degree 12 model of shear velocity heterogeneity in the mantle, *Nature* 99: 6945-6980.

Weeraratne, D.S., D.W. Forsyth, K.M. Fischer, and A.A. Nyblade, Evidence for an upper mantle plume beneath the Tanzanian craton from Rayleigh wave tomography, *J. Geophys. Res.*, 2002JB002273R, 2003.

Wessel, P. and W. H. F. Smith (1991), Free software helps map and display date, EOS, *Trans. of Am. Geophys. Union*, 72: 441-445.

Zandt, G., and C. J. Ammon (1995), Continental Crustal composition constrained by measurements of crustal Poisson's ratio, *Nature* 374: 152-154.

Zandt, G., S.C. Myers, and T.C. Wallace (1995), Crust and mantle structure across the Basin and Range-Colorado Plateau boundary at 37 degrees N latitude and implications for Cenozoic extensional mechanism, *J. Geophys. Res.* 100: (6), 10529-10548.

Zhu, L., and H. Kanamori (2000), Moho depth variation in Southern California from teleseismic receiver functions, *J. Geophys. Res.* 105: (2), 2969-2980.

DEVELOPMENT OF A THREE-DIMENSIONAL VELOCITY MODEL FOR THE CRUST AND UPPER MANTLE IN THE GREATER BARENTS SEA REGION

Hilmar Bungum[1,2], Nils Maercklin[1], Oliver Ritzmann[2], Jan Inge Faleide[2,1], Christian Weidle[2], Anatoli Levshin[3], Johannes Schweitzer[1], Walter D. Mooney[4], and Shane T. Detweiler[4].

NORSAR[1], University of Oslo[2], University of Colorado[3], and United States Geological Service[4]

Sponsored by National Nuclear Security Administration
Office of Nonproliferation Research and Engineering
Office of Defense Nuclear Nonproliferation

Contract Nos. DE-FC52-03NA99508[1], DE-FC52-03NA99509[2], and DE-FC52-03NA99531[4]

ABSTRACT

We have compiled a 3D seismic velocity model for the crust and upper mantle in the greater Barents Sea region including northern Scandinavia, Svalbard, Novaya Zemlya, the Kara Sea and the Kola-Karelia regions. While the general motivation for developing this model is basic geophysical research, a more specific goal is to create a model for research on the identification and location of small seismic events in the study region, and for operational use in locating and characterizing seismic events in the study region.

The observational basis for the velocity model are previous, crustal-scale 2D seismic reflection and refraction profiles, and passive seismological recordings, supplemented by potential field data to provide additional constraints on the crustal structure. The model is defined at grid tiles spaced every 50 km, and each tile is represented by up to two sedimentary and three crystalline crustal layers (plus water and ice). For crustal regions not constrained by primary velocity data, we developed an interpolation scheme based on several defined geological provinces that are characterized by individual tectono-sedimentary histories. The interpolation utilizes the observed strong correlation between sediment and crystalline crustal thickness within continental provinces. For comparison, an alternative interpolation approach applies a continuous curvature gridding algorithm within each of the provinces.

To provide a complete lithospheric model, we complemented the crustal model with an upper mantle velocity model based on surface wave inversion, thereby covering depths essential for P_n and S_n travel time modeling. As an extension to the previously existing data set, we recently retrieved a large amount of surface wave data recorded or excited in the European Arctic during the last three decades. The merged surface wave data set will enable us to refine the upper mantle velocity structure in the study region significantly. Preliminary group velocity maps for Rayleigh and Love waves reflect large-scale geological structures and demonstrate lateral velocity variations in the mantle.

Validation of our velocity model includes travel time modeling and relocation of seismic events. For this purpose we compiled a set of Ground Truth (GT) events comprising chemical and nuclear explosions, and natural earthquakes. Phase arrival times of multiple events at some sites provide timing error estimates at some stations. With the GT events we obtain a rather good P_n and S_n ray coverage in the main target region. Besides the comparison of observed and modeled travel times along selected transects, we have computed source-specific station corrections (SSSCs) from our 3D model.

The crustal velocity models are also evaluated by comparison of predicted gravity fields with the observed free-air gravity. To model the gravity field, we used standard velocity-density relationships for crustal rock types and the density structure of the upper mantle from previous studies. The inferred gravity fields both reflect and exaggerate the basic geological features. Accomplishments so far have been concerned with implementation of a forward modeling procedure and software development needed to support the complex 3D model structure. The forward modeling is done in order to reduce the misfit between observed and modeled gravity and finally to supplement our crustal velocity model with a density distribution.

OBJECTIVE

The principal objective of this study is to compile a 3D seismic velocity model of the crust and upper mantle for the Barents Sea, Novaya Zemlya, Kara Sea and Kola-Karelia regions (see Figure 1). The general motivation for developing this higher-resolution model is basic geophysical research as well as seismic verification. The goal is to provide a model useful both for further research on the detection, location and identification of small events in the study region, and for operational use in locating and characterizing seismic events in the region including event discrimination for nuclear test monitoring. Along with the development of the model, a calibration and validation program is executed, aimed both at quality controlling the model through comparisons between observed and synthetic travel times, and at investigating the potential improvements in terms of event locations.

RESEARCH ACCOMPLISHED

The observational basis for the velocity model are previous, crustal-scale 2D seismic reflection and refraction profiles, and passive seismological recordings, supplemented by potential field data to provide additional constraints on the crustal structure. The model is defined at grid tiles spaced every 50 km, and each tile is represented by up to two sedimentary and up to three crystalline crustal layers, plus water and ice (Bungum et al., 2004, 2005). Mantle velocities are described as continuous velocity-depth profiles at each tile.

For crustal regions not constrained by primary velocity data we developed two interpolation methods and currently evaluate both resulting models. The first utilizes sediment-to-total crustal thickness relationships to infer Moho-depth, hereafter called *db* (depth-to-basement) model, while the second model is constructed by continuous curvature gridding of the Moho-depth entries of our compiled database, called *sg* (surface gridding) model. Both models are still under evaluation (see section on density modeling), and a decision a decision on which model to use for the final 3D model has not been made. Generally we would like to keep both models open for updates and new database entries. As an example, Figure 1 shows the Moho depths determined for the target area, based on the *db* interpolation scheme, and with an equal spaced grid with a node distance of 50 km. Due to a limited extension of the used depth-to-basement map, fundamental for this model, the Moho map terminates at 80.5°N.

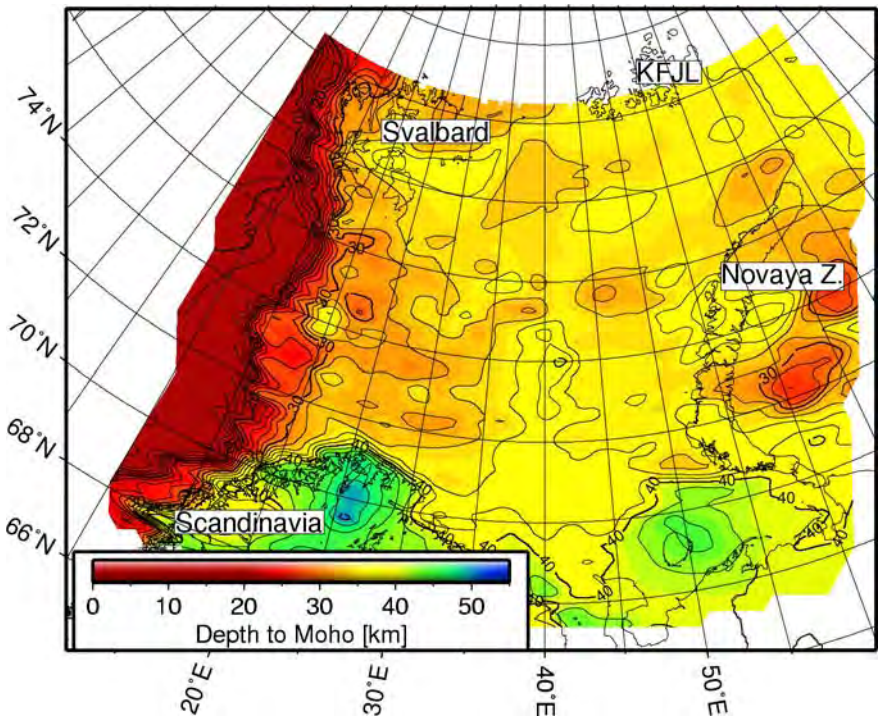

Figure 1.
Moho depth map for the main target area in the greater Barents Sea region. The depths are taken from the crustal model based on thickness relations (the so-called *db* model), and the contour interval is 2 km. KFJL, Kaiser Franz Josef Land.

The *db* interpolation method described above produces a consistent and smooth model that relates to the local extensional tectonic setting, but it does not completely preserve velocity and layer thickness data at constrained tiles. Therefore, as an alternative interpolation method, we also applied horizontal continuous curvature gridding of velocities and layer thicknesses within each of the geologic provinces (*sg* model).

To provide a complete lithospheric model, we complemented the crustal models with an upper mantle velocity structure derived from surface wave dispersion data (Shapiro & Ritzwoller, 2002), thereby covering depths sufficient for tracing far-regional wave paths. An ongoing study uses an extended surface wave data set to refine the upper mantle structure significantly.

Surface wave tomography

Existing global and regional tomographic models have limited resolution in the European Arctic due to the small number of seismic stations, low regional seismicity, and limited knowledge of the crustal structure. More recently, however, more seismic stations have been, permanently or temporarily, installed in and around this region. Many of these new recordings are, however, not accessible via the international data centers but only by direct request to the different station operators.

In this part of the project, we have extensively searched for larger events with observable surface wave radiation that occurred in or around the area of interest. Searching back to the early 1970s, we were able to retrieve Rayleigh and Love wave observations from the data archives at NORSAR, University of Bergen, University of Helsinki, the Kola Science Center in Apatity, the Geological Survey of Denmark, and the data centers IRIS and GEOFON. In these data archives, not yet analyzed Rayleigh- or Love-wave data were found for more than 200 seismic events (earthquakes and nuclear explosions). From these records group velocities of Rayleigh and Love waves were measured in the period range 10-150 s using the package for Frequency-Time Analysis developed at the University of Colorado (Ritzwoller & Levshin, 1998). After several cleaning procedures, the new measurements were combined with the existing set of group velocity measurements provided by the Center for Imaging the Earth's Interior at the Colorado University (CU; see Levshin et al., 2001). Only paths completely inside the cell [50-90°N, 60°W-60°E] were selected, such that the entire data set consists of paths within the same regional frame.

To demonstrate the amount of new surface wave observations, we compare in Table 1 the number of newly analyzed Rayleigh and Love wave observations with the number of the preselected set of data from University of Colorado (CU) that generously were made available to the project. Obviously, the new data set increased ray density and consequently the resolution of the planned tomography. In particular for short period data, the number of rays crossing the target area was increased by more than 200% for Rayleigh waves and close to 200% for Love waves. For longer periods (i. e., $T > 80$ s), the ratio of added data significantly drops since large seismic events, necessary to generate long period radiation, are very rare in this region.

All group velocity observations were inverted into group velocity maps (Barmin et al., 2001). In all cases, we inverted the combined data set of newly acquired and analyzed data and preselected CU data. From the cluster analysis (Ritzwoller and Levshin, 1998) the rms of the group velocity measurements in the considered period range for the new data set was estimated as 0.010-0.015 km/s for Rayleigh waves and 0.015-0.025 km/s for Love waves. As a first result, we present in Figure 2 group velocity maps for Rayleigh waves at three different periods: 16, 25, and 40 s. To illustrate the newly achieved, high path density, we also present in Figure 2 all paths of the newly acquired data set for respective periods. The Rayleigh wave group velocity maps (right panels), derived from the combined data base, show the lateral deviation of the group velocities from the average velocity in percent. Note that these deviations are up to ±36% for Rayleigh waves with a period of 16 s. This reflects the strong lateral heterogeneity of the Earth's crust in this region, which changes between the mid-oceanic ridge system (white line on the map), thick sedimentary basins in the Barents Sea, and old continental shields.

The next step will be the inversion of all group velocity maps (Love and Rayleigh waves) into a 3D shear velocity model for the whole region (Shapiro & Ritzwoller, 2002). As additional constraints the thickness of the sedimentary layer and the Moho depth, as they are derived during this project (Figure 1) will be included in the inversion. The result should yield a new, robust 3D model of the velocities in the upper mantle beneath the greater Barents Sea region down to about 100 km.

Table 1: Number of newly analyzed regional Rayleigh and Love wave observations with respect to their signal periods, compared to the initial data base made available from the University of Colorado (CU).

Period [s]	Rayleigh Waves			Love Waves		
	Number of New Data	Total Number of Data	Data Increase [%]	Number of New Data	Total Number of Data	Data Increase [%]
14	773	1072	259	354	546	184
16	1073	1526	237	529	802	194
18	1313	1898	224	635	958	197
20	1453	2124	217	687	1064	182
25	1642	2447	204	733	1184	163
30	1655	2488	199	697	1206	137
35	1522	2342	186	626	1119	127
40	1343	2138	169	508	971	110
45	1115	1863	149	397	823	93
50	953	1656	136	295	672	78
60	625	1245	101	154	461	50
70	384	925	71	64	289	28
80	211	684	45	36	194	23
90	106	509	26	25	138	22
100	81	425	24	11	80	16
125-200	50	548	10	6	59	11

Ground truth events

Validation of our velocity model includes forward modeling of observed body wave travel times and relocation of seismic events. For this purpose we compiled a set of reference events with known or well-located epicenters, referred to as Ground Truth (GT) events. Bungum et al. (2004) showed an initial set of potential GT events in the greater Barents Sea region comprising mainly natural events, but also some presumed mining explosions in northern Fennoscandia and on the Kola peninsula. Most of these events were used in studies by Hicks et al. (2004), and they are plotted as circles in Figure 3. The color-code of each event corresponds to the area of the respective location error ellipse using a 1D regional velocity model (BAREY; Schweitzer & Kennett, 2002).

We extended the initial database with reference events published by Bondár et al. (2004). All events in this database are classified already into GT levels, where GT*X* denotes *X* km maximum location error. Selected events from this database are plotted in Figure 3 with a color-code corresponding to the assigned GT level. These events comprise nuclear explosions in northwestern Russia and Novaya Zemlya (all red stars) as well as mining explosions and calibration shots in Fennoscandia and Kola. Besides events and stations, Figure 3 shows also all available P wave travel paths. The distribution of available S wave paths is only slightly poorer.

Although the majority of events collected at NORSAR (circles in Figure 3) have rather small location errors, many of these events would not pass formal GT*X* acceptance criteria (see e.g. Bondár et al., 2004). This is mainly due to the poor station coverage in the region, resulting often in a rather large maximum azimuthal gap, and the lack of a sufficient number of short-distance observations. However, seismic array recordings were used here, which provide additional constraints (azimuth and slowness) for the event location.

To get an estimate for timing of phase reading errors of events taken from Bondár et al. (2004), we have analyzed the consistency of travel times from many events at the same site. For example, station KHE (Kaiser Franz Josef Land; see Figure 3) recorded several of the Soviet nuclear explosions classified as GT1. Especially in this rather poorly constrained model region, accurate timing is mandatory for both the origin times and the arrival times at the station. Theoretically, the travel times of all recorded nuclear tests on the same site on Novaya Zemlya should be the same, but in fact, excluding outliers, we observe a scatter of about 2 s around the mean, i.e. the scatter is in the same range as the travel time residuals of our 3D model relative to a 1D regional model. The same observation applies to station KBS on Svalbard. Since the observed travel times from exactly the same events scatter much less (less than 0.5 s) at the stations APA and KEV (Kola peninsula), both in a similar distance range from the source as KHE and KBS, we conclude that the time variations are related to the stations. Taking a mean travel time at those stations might be most appropriate when comparing observed and modeled times.

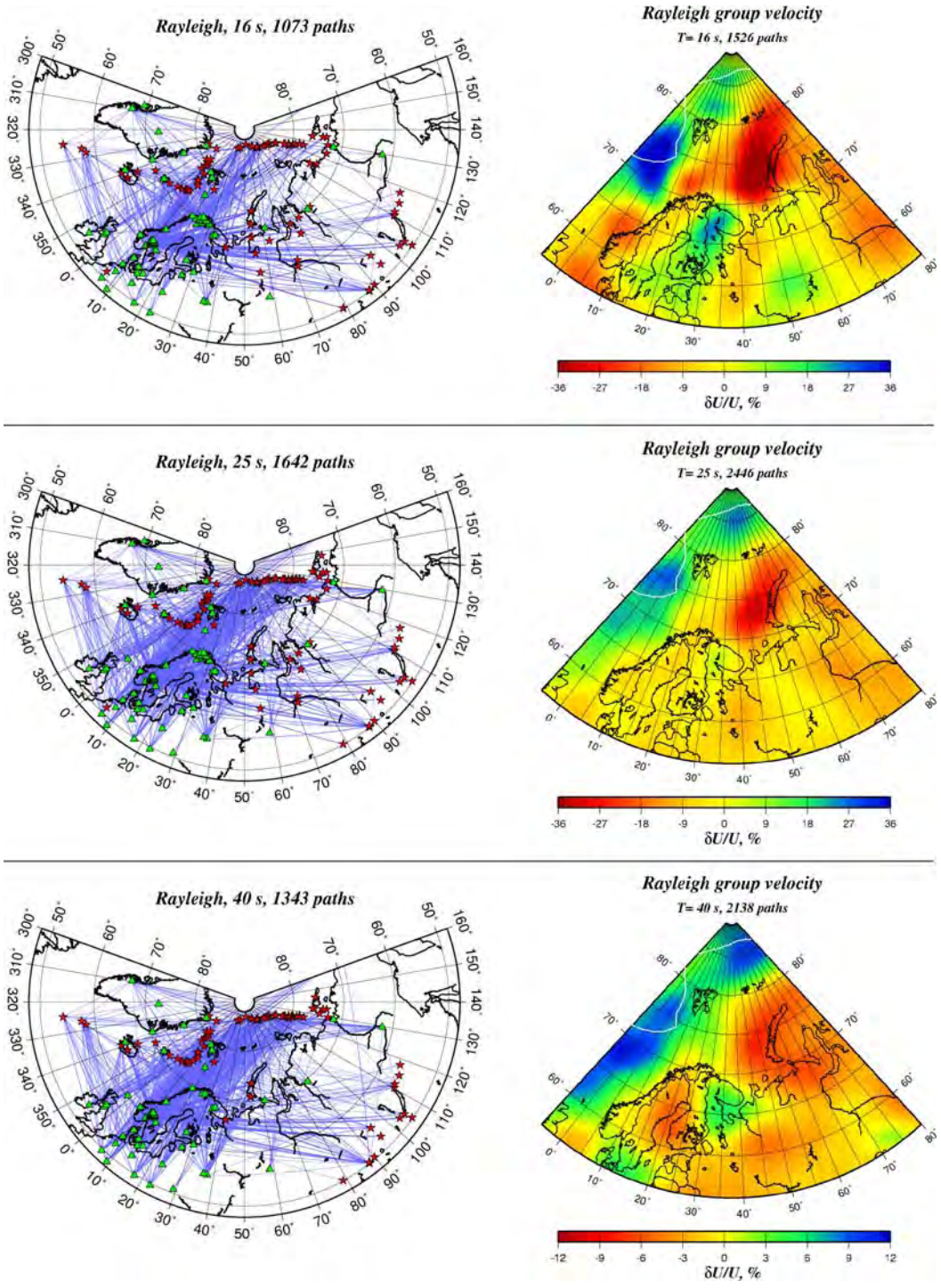

Figure 2. Ray paths (left) of newly analyzed Rayleigh waves (stations as green triangles, events as red stars), and the group velocities inverted with the whole data set (right), including also the initial data base from University of Colorado (CU), for different signal periods.

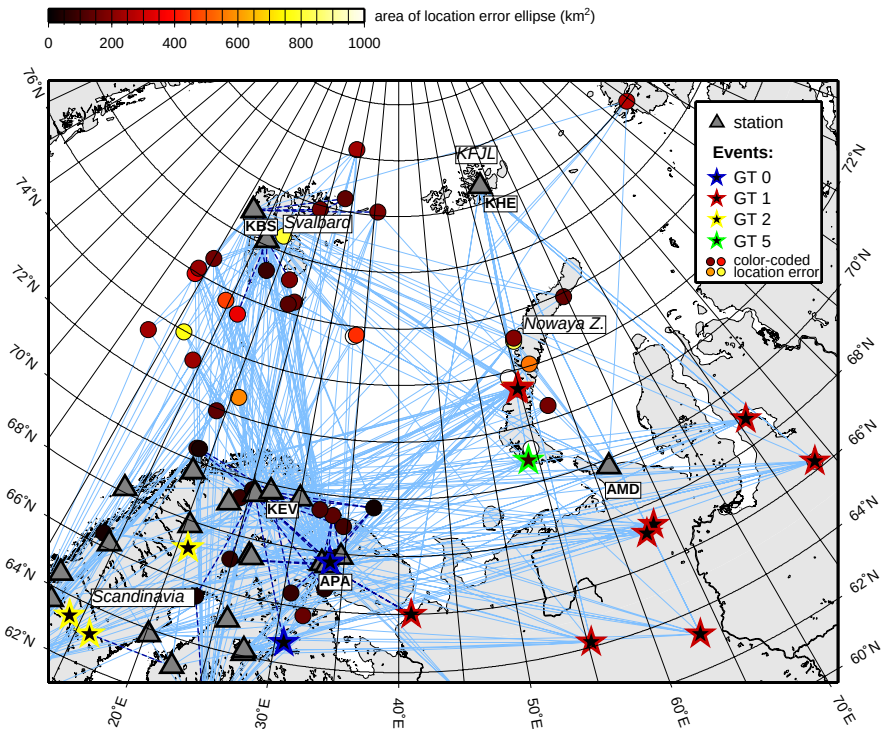

Figure 3.
Ground Truth events (circles, stars), seismic stations (triangles), and P_n (light blue) and P_g (dark blue, dashed) travel paths. Events collected at NORSAR are shown as circles with color-coded location error (Hicks et al., 2004; see also Bungum et al., 2004), whereas the events taken from Bondár et al. (2004) are plotted as stars with colors indicating their respective GT levels. The black circle near 69.6°N. 37.6°E is the Kursk explosion on August 12, 2000.

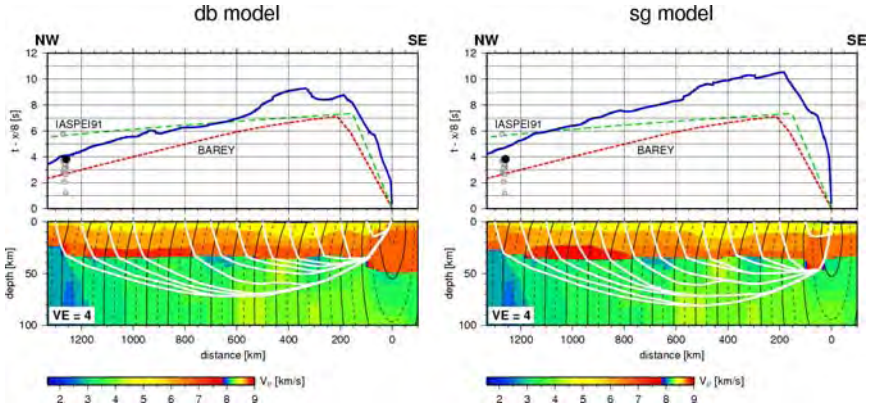

Figure 4.
Velocity transects from central Novaya Zemlya to station KBS (Svalbard) with superimposed rays (white) and wave fronts (solid black, spaced every 10 s). The interpolation method used to construct the crustal model is given at the top. Dashed travel time curves (top panels) correspond to 1D reference models, and the solid blue curve to the respective 3D model.

Figure 4 compares both crustal velocity models, i.e. the *db* model based on thickness relations (left) and the *sg* model from surface gridding (right), in terms of travel times. The example transect extends from the NZ test site mentioned above to the station KBS on Svalbard (Figure 3). The observed P_n travel times recorded at KBS (circles) are shown together with the calculated travel times continuously along the transect for both of our 3D models and the 1D reference models (IASPEI91 and BAREY). The average slope of the mantle phases of the travel time curves of our models and the BAREY model are very similar, according to similar upper mantle seismic velocities. On the other hand, our models reveal a nearly constant offset, i.e. later arrivals, compared to the 1D model. And moreover, small and local undulations along the P_n travel time curves show the regional differences between our two models (note profile section between km 200 and 400) and between our models and the reference models.

The case study shown in Figure 4 illustrates two issues: Firstly, it exemplifies the regional sensitivity of our compiled crustal models (not mantle) compared to the simple(r) 1D models. Not only large sedimentary basin structures (km 300) cause significant travel time delays but also local jumps in basement topography may result in 500 ms delay (km

950). Secondly, the absolute travel time between the source and the receiver may be modeled with a good fit, but the relevant elements for this calculation are the crustal columns below the source and receiver and the upper mantle model. Thus forward travel time modeling is confined to the limited amount of recorded events and the mantle structure along the path. Travel time modeling with the entire set of events derives a mean fit to all recorded travel times. The comparison between both models (*db*, *sg*) will most probably derive the more suitable model for fitting the recent set of recorded events.

Density modeling

Density modeling provides two important results that may be applied to the present velocity model. Firstly, it derives the requested density structure which is essential for later seismic wave field modeling using FE or FD techniques to study e.g. source characteristics. Secondly, density modeling works as a test for both models, since we can compare and link the induced gravity fields to the observed gravity. Further, software was developed using a grid search method in order determine the density field that fits best the observed gravity field. The final relationship between seismic velocity and density reveals basic physical rock properties and allows further discrimination of rock types and sheds lights on the geological evolution.

1. Getting the density structure from the seismic velocity field.

In order to derive an initial density model from the compiled seismic velocity models relationships established by Birch (1961) and Nafe & Drake (1957) for sedimentary rocks and Christensen & Mooney (1995) for continental crystalline rocks were used for conversion. Seismic wave velocity in an isotropic medium depends firstly on the atomic mass and material density, and secondly (in real rock formations) also on the given p/T field. Therefore, the results of the referred authors show a significant scatter around the mean density value for any crustal rocks. The scatter decreases with increasing seismic observation wavelengths which is almost large in the included crustal studies. Our chosen model construction shows (up to five) major crustal levels, or regional geological units so that we expect to narrow the scatter of possible densities significantly. The mean density for sedimentary rocks is taken from Barton's (1986) review of the earlier publications. The non-linear velocity-density regressions of Christensen & Mooney (1995) were utilized to infer a depth-dependent density field for crystalline rocks with respect to an underlying mantle.

2. Comparison of the theoretical and observed gravity fields

The calculation of the induced gravity of an arbitrarily shaped 3D body is rather complex and involves volume integration. We have taken into account the fact that our seismic velocity models are too complex in terms of the total number of bodies at the 1330/1490 nodes (the *db* and *sg* interpolation schemes, respectively). Every node bears a combination of a water layer, up to 5 crustal bodies and up to 35 mantle levels (Shapiro & Ritzwoller, 2002) depending on the desired depth of the density model. As the gravity field above a single grid node is influenced by all masses (or bodies) in the surrounding of the observation point, the local gravity field becomes a stack of contributions from all surrounding bodies. These bodies are rectangularly shaped prisms on an equal-spaced grid. Therefore, we used Plouff's (1976) derivation of the integration term for a single rectangular prism, i.e. the summation of the responses from all corners of the prism multiplied by the prism density and gravity constant. In Figure 6 we present a calculation that incorporates the gravity effect of the 50x50 km wide bodies below the observation point, considered to be a good first approximation to the complete field inferred from all bodies of the model.

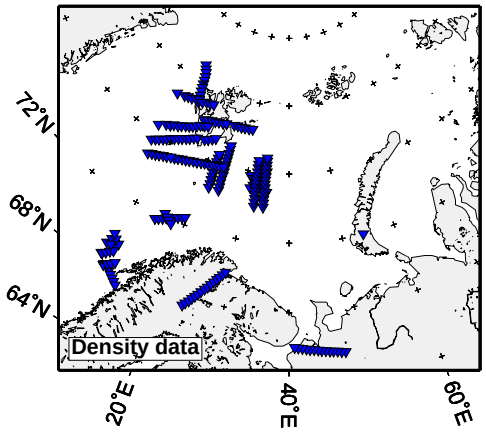

Figure 5. Location map of 2D wide-angle seismic transects in the Barents Sea region for which crustal densities have been modeled using measured layer boundaries and P wave velocities.

Local studies of the density structure along 2D seismic velocity transects are only available from modern OBS experiments (Figure 5). The data distribution is too insufficient to construct an independent density model from the data-

base as it was accomplished for seismic velocities. In order to built a uniform density model these results were not entered in the initial converted model. The density distribution of the upper mantle is given by the surface wave model of Shapiro & Ritzwoller (2002). The mantle density structure is kept fixed during all subsequent modeling steps.

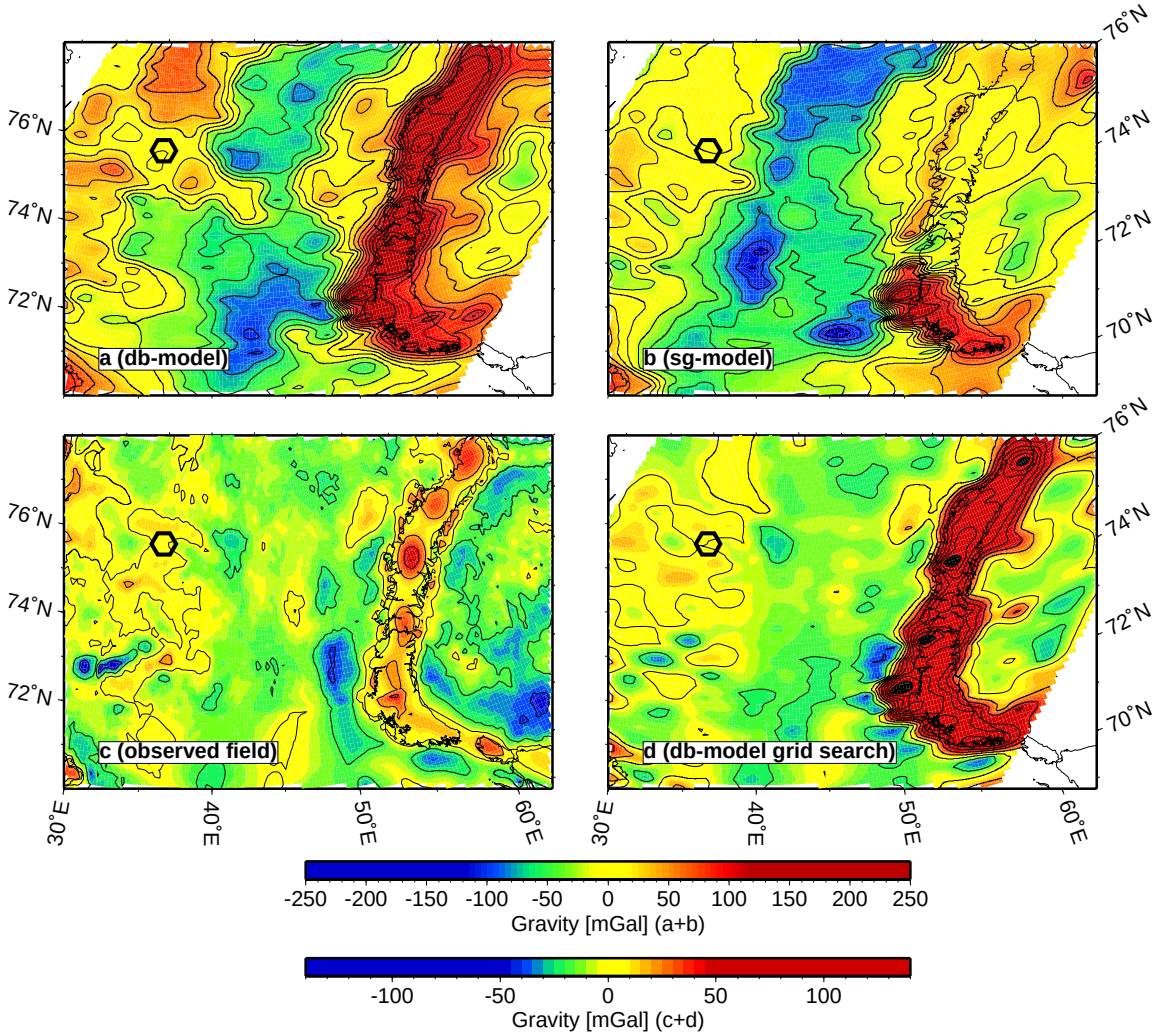

Figure 6. Density modeling results. (a) Gravity field inferred from the recent version of model *db*. (b) Gravity field inferred from the recent *sg* model. The lower gravity in northern Novaya Zemlya in (b) is due to the connection of the thick sedimentary sections in the Barents- and Kara Seas across Novaya Zemlya. (c) Observed gravity field (taken from Arctic Gravity Project, 2002). Note the different color scales for a/b and c/d. The black hexagon marks the reference location used for tying the calculated gravity fields (free-air anomaly = 0 mgal). (d) Gravity field inferred from the recent version of model *db* after applying the grid search algorithm to upper and lower sediment densities (partly also upper crystalline crust). West of Novaya Zemlya a good match to the observed field (c) could be achieved. To enhance the match on Novaya Zemlya and the Kara Sea, the grid search has to be extended to crystalline crustal rocks.

Figures 6a and 6b shows the calculated fields for the models *db* and *sg*, respectively. A major difference between the gravity effects of the models occurs in the northern part of Novaya Zemlya (NZ). The depth-to-basement compilation shows only a thin sedimentary cover onshore NZ. Therefore the shallow, higher-density crystalline rocks contribute significantly to the gravity field. The second model (b) is derived by surface gridding and shows a considerably lower gravity field across northern NZ. Thick sedimentary sections occur on both sides of NZ in the Barents and Kara Seas and are interpolated across NZ; an advantage of *db* model is that incorporates depth-to-basement information. The *sg* model shows more extreme values within the eastern Barents Sea sedimentary basins (blue shade). Both models

exaggerate the basic geological features, such as sedimentary basins or basement horsts. Interestingly these structures are well defined by analyzing regional seismic data of the region but have no pronounced expression in the observed field (Figure 6c).

3. Forward modeling (grid search) of the density structure

The gravity fields shown in Figure 6a and 6b clearly image the geological units that are present in the model region or, the depth-to-basement relief while the observed field is rather smooth. As mentioned earlier, the velocity-density relations used for model conversion all show a significant spread around the mean value taken here. The velocity of a single layer of a grid node is a mean velocity: during the calculation all compatible layers stored in the database (sediments or crystalline crust; seismic velocity above, between or below given thresholds) are used to stack the one-way travel times and the thicknesses of these layers to infer the seismic velocity for a single final model layer. This sustains the one-way travel times of the input models. Since the range of seismic velocities of crystalline crustal rocks in the continental domain is narrow, the mean seismic velocity is very close to all of the input layer velocities. Instead, the bandwidth of velocity of sedimentary rocks is very large and may range from 3.0-6.5 (7.0?) km/s for the lower sediments. Thus, the mean velocities have large standard deviations (σ<0.67). We expect therefore the velocity-density conversion for the upper and lower sedimentary layers to be a likely cause of the mismatches to the observed gravity field, because a series of layers with different densities and depths (or distances to an observation point) is 'gathered' to a single prism in the model.

We therefore programmed a grid search algorithm to adjust the densities of the upper and lower sediment within a given uncertainty range. According to Barton's (1986) review the spread in density increases drastically towards low seismic velocities (±0.3 g/cm^3) and is moderate to low within rocks of higher velocity (±0.1-0.2 g/cm^3). Therefore the grid search is limited to a maximum deviation of ±0.2 g/cm^3 for upper sediments and ±0.13 g/cm^3 for lower sediments (~60%). The search is further performed from the top to the bottom layers (upper, lower sediment, upper crystalline crust etc.) until a reasonable fit to the observed gravity is given. Due to our regional study of the crust and mantle a residual of ±5 mgal is regarded as a good fit. As some provinces do not reveal both upper and lower sediments, the underlying crystalline layers were altered to obtain a good fit. Figure 6d shows the gravity field inferred by the adjusted 'db' model. A good fit is achieved compared to the observed field (Figure 6c), disregarding Novaya Zemlya where no thicker sediment layers are present. Although the gravity field is inferred only from model prisms directly below, clear trends in the grid search are observed. For example, sediment densities in the eastern Barents Basin are obviously too low and were increased after the grid search. This result fits to the enormous depths of these basins (up to 20 km) which may result in high compaction and the increase of the regional density. Future work will include the comparison between the adjusted models, *db* and *sg*, respectively. The magnitude of necessary adjustments might be an indicator for the quality of the input velocity model.

CONCLUSIONS AND RECOMMENDATIONS

At this stage, when we are well into the second year of this two-year study, the 50x50 km 3D model for the crust in the greater Barents Sea region is in the final stages of preparation. We have, however, developed this model through two different approaches for interpolation in areas with less primary data coverage, namely (1) an interpolation scheme using geological background information, i.e. depth-to-basement (*db*) data outside data base information, and (2) an interpolation scheme (called *sg*) using a full mathematical approach, i.e. continuous curvature or surface gridding (*sg*) of data base information. The two approaches give results that differ only at a more detailed level, but since the question of which one to use is methodologically interesting they will both for some time continue to be evaluated against new data. To this end the density modeling work reported on here has been essential, since this allows us to compare and link the induced gravity fields from the two models to the observed gravity. However, at the end of the project only one model will be presented as the 'final' one.

Since last year (Bungum et al., 2004) significant developments have been achieved also in terms of an improved upper mantle model. Large amounts of new 10-150 s surface wave (Rayleigh and Love) data have been collected and analyzed, improving in particular the regional coverage in the lower period ranges. The group velocity observations have been inverted into group velocity maps, combining new and old data. The next step will be to invert the Rayleigh and Love wave group velocities into a 3D shear velocity model for the greater Barents Sea region, constrained

by the already established Moho depths and crustal velocities. This will cover depths down to about 100 km and thereby also many of the regional S_n and P_n ray paths essential for improved event locations.

In order to evaluate the potential event location improvements from the new 3D model we have also established a new data base of (GT) events in the region. However, since the availability of recording stations has been limited, many of these events would not pass formal GT acceptance criteria. Our analysis has also shown that there are timing errors on some of the stations that have recorded the earlier nuclear explosions from Novaya Zemlya. Even so, essential comparisons between observed and computed travel times have already been conducted.

REFERENCES

Barmin, M. P., M. H. Ritzwoller, and A. L. Levshin (2001), A fast and reliable method for surface wave tomography, *Pure Appl. Geophys.* 158: 1351-1375.

Barton, P. J. (1986), Comparision of deep reflection and refraction studies in the North Sea, in Barazangi, M. and L. D. Brown (eds.), Reflection seismology; a global perspective, *Geodynamic Series* 13: 297-300.

Birch, F. (1961), The velocity of compressional waves in rocks to 10 kilobars (Part II), *J. Geophys. Res.* 66: 2199-2224.

Bondár, I, E. R. Engdahl, X. Yang, H. A. A. Ghalib, A. Hofstetter, V. Kirichenko, R. Wagner, I. Gupta, G. Ekström, E. Bergman, H. Israelsson, and K. McLaughin (2004), Collection of a reference event set for regional and teleseismic calibration, *Bull. Seis. Soc. Am.* 94: 1528–1545.

Bungum, H., O. Ritzmann, N. Maercklin, J. I. Faleide, W. D. Mooney, and S. T. Detweiler (2005), Three-dimensional model for the crust and upper mantle in the Barents Sea region, in *Eos. Trans. Am Geophys. Union*, 86: 160–161.

Bungum, H., O. Ritzmann, J. I. Faleide, N. Maercklin, J. Schweitzer, W. D. Mooney, S. T. Detweiler, and W. S. Leith (2004), Development of a three-dimensional velocity model for the crust and upper mantle in the Barents Sea, Novaya Zemlya and Kola-Karelia regions, in *Proceedings of the 26th Seismic Research Review: Trends in Nuclear Explosion Monitoring*, Vol. 1, pp. 50-60.

Christensen, N. I. and W. D. Mooney (1995), Seismic velocity structure and composition of the continental crust: A global view, *J. Geophys. Res.* 100: 9761-9788.

Hicks, E. C., T. Kværna, S. Mykkeltveit, J. Schweitzer, and F. Ringdal (2004), Travel-times and attenuation relations for regional phases in the Barents Sea region, *Pure Appl. Geophys.* 161: 1–19.

Levshin, A. L., M. H. Ritzwoller, M. P. Barmin, A. Villaseñor, and C. A. Padgett (2001), New constraints on the arctic crust and uppermost mantle: surface wave group velocities, P_n, and S_n, *Phys. Earth Planet. Int.*, 123: 185-204.

Nafe, J. E. and C. L. Drake (1957), Variation with depth in shallow and deep water marine sediments of porosity, density and velocities of compressional- and shear waves, *Geophysics*, 22(3): 523-552.

Plouff, D. (1976), Gravity and magnetic fields of polygonal prisms and application to magnetic terrain corrections, *Geophysics* 41: 727-741.

Ritzwoller, M. H. and A. L. Levshin (1998), Eurasian surface wave tomography: Group velocities, *J. Geophys. Res.* 103: 4839-4878.

Schweitzer, J. and B.L.N. Kennett (2002), Comparison of location procedures – The Kara Sea event of 16 August 1997, Semiannual Technical Summary, NORSAR Sci. Rep., No. 1-2002, Kjeller, Norway.

Shapiro, N. M. and M. H. Ritzwoller (2002), Monte-Carlo inversion for a global shear velocity model of the crust and upper mantle, *Geophys. J. Int.* 151: 88-105.

REGIONAL VARIATION OF RAYLEIGH-WAVE ATTENUATION IN SOUTHERN ASIA PREDICTED FROM NEW MAPS OF LG CODA Q AND ITS FREQUENCY DEPENDENCE AT 1 HZ

Lianli Cong[1] and Brian J. Mitchell[2]

Yunnan University[1] and Saint Louis University[2]

Sponsored by Air Force Research Laboratory

Contract No. FA8718-04-C-0021

ABSTRACT

In order to ascertain whether of not seismic stations in low-Q regions, such as southern Eurasia, can detect small nuclear events and earthquakes, it is important to develop maps that show how Q varies regionally. In addition, in order to test the usefulness of seismic discriminants we must quantify the frequency dependence of Q and its variation from region to region. Toward those goals, we have (1) developed new continent-wide maps of Lg coda Q and its frequency dependence at 1 Hz (Q_o and η respectively) with lower standard errors and improved resolution compared to earlier maps and (2) have used the new sets of Q_o and η values to estimate how Rayleigh-wave attenuation varies through selected regions of Eurasia.

Our new maps of Q_o and η cover virtually all of Eurasia but they concentrate especially on five regions where data coverage was absent or poor in earlier work. Those regions are southeastern China with new Q values for 165 new event-station pairs, India and the Himalaya with 269 new values, northeastern Siberia with 387 new values, Spain with 79 new values and southeast Asia with 43 new values. The maps provide new coverage throughout much of those five regions as well as much improved coverage in their peripheral portions. We have developed maps of standard errors for all determinations and maps of point spreading functions in selected regions in order to provide a measure of our ability to resolve features on the maps. Q_o is relatively high, up to 700 or more, in most cratonic regions but low than expected in the Arabian craton (300 – 450), the Siberian trap portion of the Siberian Platform (~450) and the Deccan trap portion of the Indian Platform (450-650). It is generally low throughout the Tethysides orogenic belt but there too it displays substantial regional variations (150 – 400).

In our studies of Rayleigh-wave attenuation coefficients (γ_R) and their regional variation for various periods across southern Eurasia, we have assumed that the values of Q_o and η obtained from Lg coda can be used to infer values of shear-wave Q (Q_μ) and its frequency dependence (ζ) with suitably chosen empirical scaling factors. We have tested this assumption for several crustal shear-wave Q models, one for the Arabian Peninsula, one for the Turkish/Iranian Plateaus and seven for China where determinations of Rayleigh-wave attenuation and Lg coda Q information are both available. We find that the relations $Q_\mu \sim Q_o$ at all depths and $\zeta = 0.8\eta$ for the depth range 0-40 km and $\zeta = 0.5\eta$ for depths greater than 40 km provide realistic estimates for γ_R in the period range 5 – 70 s. Throughout southern Asia γ_R at a period of 10s varies roughly between 0.3×10^{-3} and 1.7×10^{-3} km^{-1}, at a period of 20 s varies between 0.2×10^{-3} and 0.9×10^{-3} km^{-1}, and at 50s varies between about 0.06×10^{-3} and 0.30×10^{-3} km^{-1}. Rayleigh-wave attenuation coefficients at 10s period are very sensitive to thick accumulations of sediments but that sensitivity is lost at 50s periods where variations in attenuation are due largely to regional variations in shear-wave Q in deeper crystalline rock.

OBJECTIVES

Seismic Q is an important parameter that affects how rapidly various seismic waves attenuate with distance as they travel through the Earth. Its value can vary both spatially and with frequency. The overall purpose of our research is to better understand details of those variations throughout southern Asia and how they might affect our ability to detect waves generated by small seismic events, to estimate magnitudes and yields of those events, and to determine if they are explosions or earthquakes. To improve understanding in those areas we have focused on two specific objectives. Our first objective has been to expand and improve previously published maps of regional variations of Lg coda Q across Eurasia with emphasis on regions where path coverage was too sparse to obtain reliable and high-resolution results. Our second objective has been to use those new maps of Lg coda Q and its frequency dependence at 1 Hz (Q_o and η, respectively) to develop maps of Rayleigh-wave attenuation coefficients for various periods (10-50s) throughout southern Asia.

RESEARCH ACCOMPLISHED

Lg coda Q data and their processing

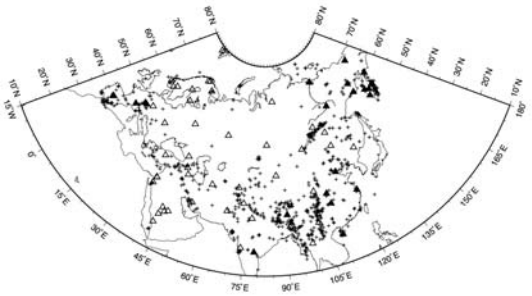

Figure 1. Earthquakes and stations used in this study. + signs denote earthquakes. Open circles denote stations used in Mitchell et al. (1997) and closed circles denote stations for new data.

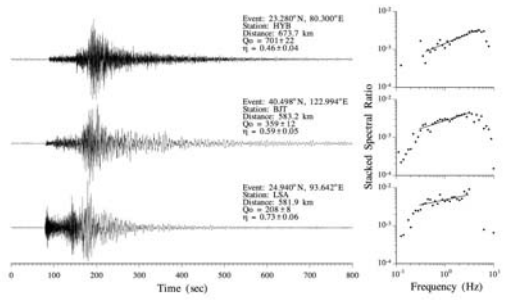

Figure 2. Seismograms (left) recorded for source-station paths for which Q_o decreases from top to bottom. SSRs (right) provide determinations of both Q_o and η.

Figure 1 presents a map of the earthquakes and recording stations used in this study. Data from 27 stations on the map are new to this study and provide recordings of Lg coda from 943 earthquake-station pairs. The new determinations, when combined with 440 from Mitchell et al., (1997) yield a total of 1383 determinations for both Q_o and η. The new data provide new coverage for northeastern Siberia, where the largest gap previously existed, for Spain and for southeastern Asia. In addition, we achieved much improved coverage in northeastern China, southeastern China, and India.

Three examples of seismograms that include Lg and its coda for Eurasian paths appear in Figure 2. Measured values of Q_o decrease from top bottom in the figure. The top trace is for a relatively high-Q (701) path to station HYB in India, the bottom trace is for a low-Q (208) path to station LSA in Tibet and the middle trace is from a path to station BJT in northern China where Q (359) is intermediate between the other two. The traces show a progression of decreasing predominant coda frequencies and decreasing amplitudes with decreasing Q value.

Stacked spectral ratio (SSR) plots (Xie and Nuttli, 1988) appear to the right of each trace. Portions of all three traces form an approximate straight line on a log-log plot that can be fit by least squares. The value and slope of the best-fitting line at 1 Hz yield, respectively, values for Q_o and η from which we invert to obtain tomographic maps as described in the following section.

Mapping Q_o and η variations – Method

A discussion of the inversion method for mapping Q_o and

η appears, in detail, in Xie and Mitchell (1990), and more briefly, in Mitchell et al. (1997). The method assumes that the area occupied by the scattered energy of recorded Lg coda can be approximated by an ellipse with the source at one focus and the recording station at the other, as was shown theoretically by Malin (1978) to be the case for single scattering.

The process utilizes a back-projection algorithm for producing tomographic images of Q_o and η over a broad region using a number (N_d) of Q_o or η values determined from observed ground motion. Figure 3 shows the ellipses corresponding to all event-station pairs that we used in Eurasia. The inversion process assumes that each ellipse approximates the spatial coverage of scattered energy comprising late Lg coda. The areas of the ellipses vary with the lag time of the Lg coda components and will be larger for later times. The ellipses in the figure are plotted for maximum lag times used in the determination of Q_o and η. It is best to have as much overlap of ellipses as possible to obtain redundancy that is beneficial in the inversion process.

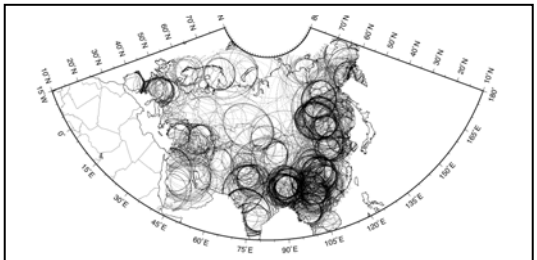

Figure 3. Assumed sampling patterns for late Lg coda. The ellipses represent areas sampled at maximum lapse times used in the analysis of each seismogram.

We divided Eurasia into N_c cells with dimensions 3^o by 3^o, based upon theoretical resolution. over which Q_o will have constant value. The Q_n value for each trace signifies the areal average of the cells covered by its corresponding ellipse. If the area over which the ellipse for the nth trace overlaps the m^{th} cell is s_{mn} then

$$\frac{1}{Q_n} = \frac{1}{S_n}\sum_{m=1}^{N_c}\frac{S_{mn}}{Q_m} + \varepsilon_n \qquad n = 1,2,\ldots,N_d \qquad (1)$$

where

$$S_n = \sum_{j=1}^{N_c} S_{jn} \qquad (2)$$

and ε is the residual due to the errors in the measurement and modeling of Lg coda. Back-projection, or the Algebraic Reconstruction Technique [Gordon, 1974] has been applied in several tomographic mappings of seismic velocity (e.g. McMechan, 1983; Humphreys and Clayton, 1988] and is convenient for our purposes.

A tomographic map of the frequency dependence of Lg coda Q at 1 Hz is obtained using the Q_o and η values for the N_d traces to estimate Lg coda Q at another frequency which we take to be 3 Hz. The 3-Hz values become Q_n in equation (1) and an inversion yields a map of Lg coda Q at 3 Hz. A map of the frequency dependence of Lg coda Q is then obtained using

$$\eta = \frac{1}{\ln 3}\ln\left[\frac{Q(f)_{3\,Hz}}{Q_o}\right] \qquad (3)$$

For the back-projection process it is convenient to use the "point spreading function" (*psf*) suggested by Humphreys and Clayton [1988] as a measure of resolution. It is obtained constructing a model in which Q^{-1} is unity in a cell of interest and zero in all other cells. Average Q_o is determined for all elliptical areas in Figure 3 for that model. An inversion of those synthetic data yields the *psf* pertaining to the region surrounding the selected cell. The area and falloff with distance from the central cell provides an estimate of resolution.

The effect that random noise included in Lg coda has on images of Q_o and η can be tested empirically using the sample standard error in Q_n caused by randomness of the SSRs [Xie and Nuttli, 1988]. If the standard error of Q_n is denoted by δQ_n, n = 1, 2,…N_d, and if we assume that δQ_n gives a good measure of the absolute value of real error preserved in the Q_n measurements, we can construct a number of noise series whose m^{th} member has an absolute value equal to δQ_n and a sign that is chosen randomly. The n^{th} term of the noise series is added to Q_n and the sums of the two series are then inverted to obtain a new Q_m image from which the original one is subtracted to yield an error

estimate of the Q_n values. Since the sign of δQ_n was chosen by a random binary generator, it is important to repeat the process several times and obtain an average error estimate.

New Q_o and η maps

Figures 4 and 5 are new continent-wide maps of Q_o and η for Eurasia. They differ from earlier continent-wide maps (Mitchell et al., 1997) by providing new coverage for northeastern Siberia, Spain, southern India and southeast Asia. In addition they provide much improved data coverage for several regions, including southeastern China, northeastern China, northern India and portions of northern Asia.

The broad-scale features of the new Q_o map are virtually the same as those of Mitchell et al. (1997) for regions where there is common coverage. These include low values (150 – 400) throughout, and extending slightly north of,

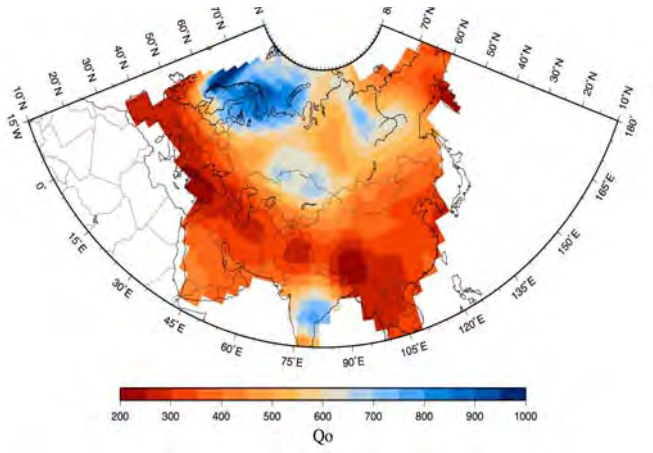

Figure 4. Lg coda *Q* at 1 Hz (Q_o) for Eurasia. Each cell is 3^o x 3^o in area.

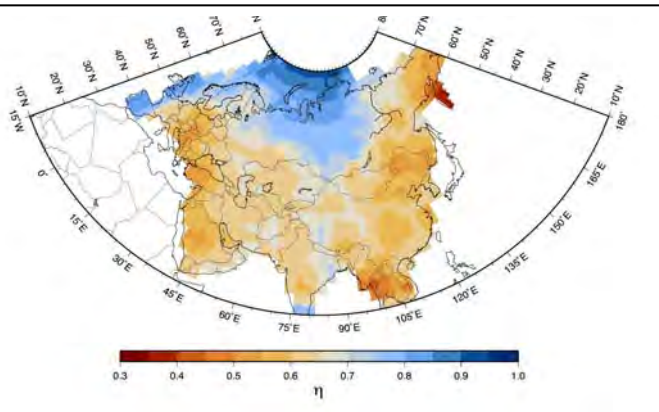

Figure 5. Frequency dependence of Lg coda *Q* at 1 Hz (η) for Eurasia. Each cell is 3^o x 3^o in area.

the Tethysides orogenic belt, the active region resulting from the collision of the Afro/Arabian and Indian plates with Europe and Asia, and significantly higher values (as high as 950 or more) throughout most of the stable northern portions of Eurasia. There are, however, some unexpected results including relatively low values in central Siberia, and the Arabian Peninsula that were reported by Mitchell et al. (1997). The present study differs from

Mitchell et al. (1997) by finding lower than expected values in the British Isles and by showing four regions of very low Q that appear to be associated with concentrated seismic activity in western Turkey, Pakistan and northern India, southern China and Kamchatka. These apparently anomalous values are consistent with our previous suggestion that seismic *Q* values in the crust of continents in any region are proportional to the time that has elapsed since the most recent tectonic or orogenic activity there (Mitchell and Cong, 1998).

Q_o is relatively high, 700 - 900 or more, in most cratonic regions in northern Eurasia but is surprisingly low in the Arabian craton (300 – 450), the Siberian trap portion of the Siberian Platform (~450) and the Deccan trap portion of the Indian Platform (450-650). It is generally low throughout the tectonically active Tethysides orogenic belt but there too it displays substantial regional variations (150 – 400).

Figure 5 presents the distribution of η, the frequency dependence of Lg coda Q at 1 Hz. Since its determination requires the differencing of Q_o values at two frequencies, the uncertainties in mapped values η are much higher than for Q_o. η values are generally higher (0.7 – 0.9) in regions where Q_o is high (e.g., northern Eurasia and southern India) and are low (e.g. most of southern and eastern Eurasia) where Q_o is low. The opposite relation occurs in Spain and the British Isles, where Q_o is low and η is high. It is possible that systematic errors in the differencing process for determining η are high in that region.

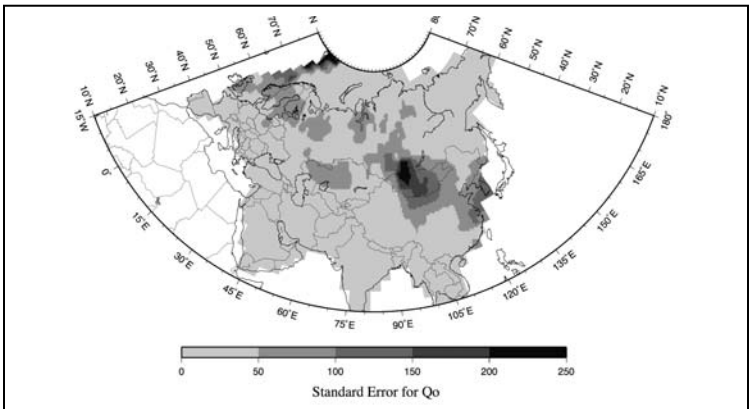

Figure 6. Standard errors for Q_o.

Figures 6 is a map of standard error values for Q_o. Q_o The errors range between 0 and 50 throughout most of Eurasia but lie between 50 and 100 is a few places, and is quite high in regions to the southwest of Lake Baikal and in the northwestern corner of the map. The high standard errors near Lake Baikal coincide with a region that stood out as being laterally anomalous in a study of shear-wave Q variation (Jemberie and Mitchell, 2004). The pattern of η standard error variation is generally similar to that of Q_o, being between 0.0 and 0.1 throughout most of the continent and between 0.1 and 0.2 in most other places. It is again higher to the southwest of Lake Baikal and in the northwestern-most corner of the map.

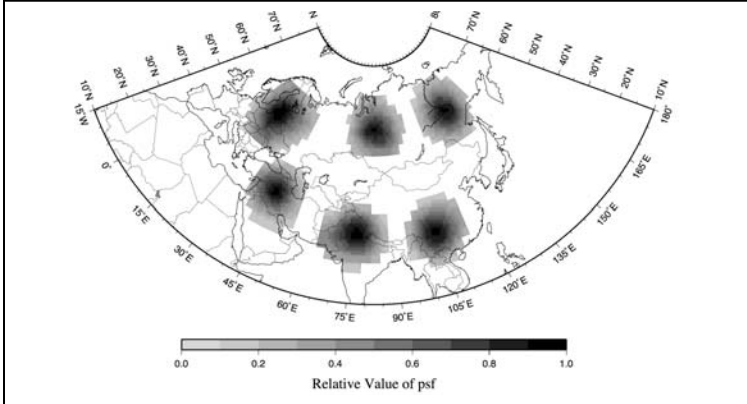

Figure 7. Point spreading function (*psf*) plots for six selected cells.

The *psf* patterns for six selected cells appear in Figure 7. They indicate that our ability to resolve features across Eurasia is about the same everywhere. Assigning numbers to this resolvability is somewhat subjective, depending upon what we choose as a fraction of the maximum value that is assumed to denote resolvability but appears to indicate that we can resolve features between about 600 and 900 km in most regions. This marks a significant improvement over resolution in Mitchell et al.(1997) where the *psf*'s in some regions, especially where coverage was much poorer, was greater than 1500 km or more.

Rayleigh-wave attenuation estimates in southern Asia – Methodology

We used the values of Q_o and η for Lg coda at 1 Hz to estimate Rayleigh-wave attenuation at periods of 10, 20 and 50 s for all of southern Asia. We assumed that the values of Q_o in Figure 4 represent average values of shear-wave Q (Q_μ) for the crust everywhere in that region. We then developed an empirical relation between η values in Figure 5 and the frequency dependence (ζ) of shear-wave Q (Q_μ) in order to compute Rayleigh-wave attenuation coefficients produced by inferred Q_μ models of the crust. To do that we used observed Rayleigh-wave attenuation coefficients for regions where they are available to Rayleigh-wave attenuation coefficients values that are theoretically predicted by the Q_o and η values for the same regions in Figures 4 and 5. Both types of information are available for the Arabian Peninsula and Turkish/Iranian Plateaus (Cong and Mitchell, 1998), as well as seven regions of China (Jemberie and Mitchell, 2004). One example comparison of observed and computed attenuation coefficients appears in Figure 8 for the Iran/Turkey Plateaus. We found that using the relations $\zeta = 0.8\eta$ for the depth range 0-40 km and $\zeta = 0.5\eta$ for depths greater than 40 km provided realistic estimates for γ_R over the period range 10-70 s for most regions of southern Asia.

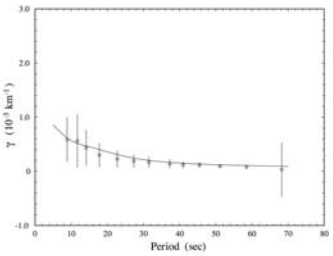

Figure 8. Rayleigh-wave attenuation coefficients calculated for a shear-wave Q model of the Arabian Peninsula in which $Q_\mu = Q_o$, $\zeta = 0.8\eta$ for depths less than 40 km and $\zeta = 0.5\eta$ for depths greater than 40 km (solid line). These are compared with Rayleigh-wave attenuation coefficients obtained from two-station measurements in the same region.

Maps of Rayleigh-wave attenuation estimates for southern Asia

Figures 9, 10, and 11 present predicted Rayleigh-wave attenuation coefficient values for periods of 10, 20 and 50 s, respectively. At a period of 10 s Rayleigh-wave attenuation coefficients vary between about 0.3 x 10^{-3} and 1.7 x 10^{-3} km^{-1}, while at 20 s they vary between about 0.2 x 10^{-3} and 0.9 x 10^{-3} km^{-1}, and at 50 s they vary between about 0.06 x 10^{-3} and 0.30 x 10^{-3} km^{-1}. The patterns of Rayleigh-wave attenuation are generally similar to the patterns of Q_o variation in Figure 4, but important differences occur, mainly because of variations in the frequency dependence of shear-wave Q used to calculate the Rayleigh-wave attenuation maps.

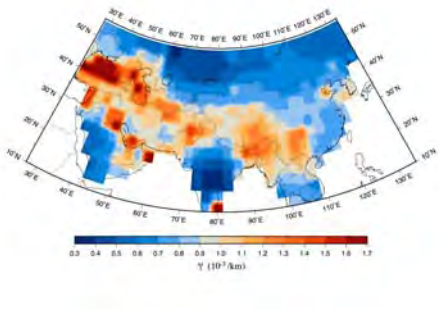

Figure 9. Predicted Rayleigh-wave attenuation coefficient values at a period of 10 s.

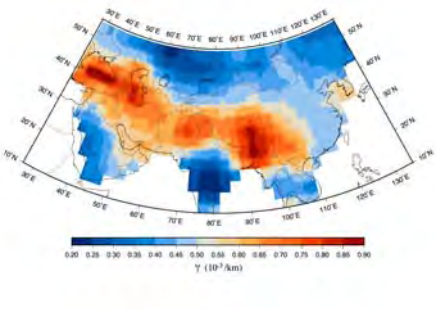

Figure 10. Predicted Rayleigh-wave attenuation coefficient values at a period of 20 s.

Rayleigh-wave attenuation is especially sensitive to accumulations of thick sediments in regions such as the Black Sea and Persian Gulf. At longer and longer periods there is less and less correlation with sediments but greater sensitivity to anelasticity in the crystalline crust. The highest attenuation at 50 s period occurs as a striking large circular region in the southeastern Tibetan Plateau, a region previously found to be highly attenuative for Lg coda (Mitchell et al., 1997) and extremely attenuative for direct Lg (Xie, 2002).

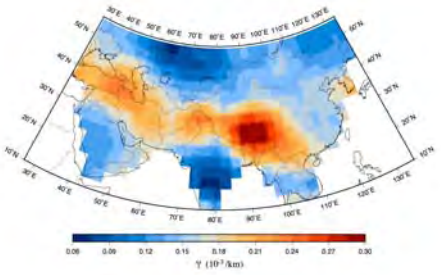

Figure 11. Predicted Rayleigh-wave attenuation coefficient values at a period of 50 s.

CONCLUSIONS AND RECOMMENDATIONS

New maps of Lg coda Q and its frequency dependence at 1 Hz (Q_o and η, respectively) for virtually all of Eurasia show order of magnitude variations that certainly need to be accounted for in determinations of yield and in implementing many discrimination methods. The variations clearly reflect past tectonic activity, with lowest values being in regions of present or recent tectonic and/or orogenic activity. The maps of Q_o and η values allow the construction of Rayleigh-wave attenuation coefficient maps at various frequencies, assuming that the value of the frequency-dependence parameter remains constant over a wide frequency range. These new maps show that thick accumulations of sediment have a large effect on 10 s Rayleigh-wave amplitudes, but little effect on the amplitudes at 50s.

Studies of the frequency dependence of Q are still rudimentary and much work in this area remains to be done. The usefulness of our maps of Rayleigh-wave attenuation depend strongly on how well the frequency dependence of Lg coda *Q* near 1 Hz frequency has been determined and on our assumption that its value does not change between 1 Hz and surface-wave frequencies. We recommend that systematic studies of that parameter be conducted from frequencies near 10 Hz down to intermediate-range surface-wave frequencies.

ACKNOWLEDGMENTS

We thank Jack Xie for making his codes for the SSR method of processing and for tomographic mapping of Q_o and η available to us. The maps in this paper were prepared using GMT version 3.0 developed by Paul Wessel and H.F. Smith.

REFERENCES

Cong, L. and B. J. Mitchell (1998), Seismic velocity and Q structure of the Middle Eastern crust and upper mantle from surface-wave dispersion and attenuation, *Pure Appl. Geophys.* 153: 503-538.

Gordon, R. (1974), A tutorial on ART, *IEEE Trans. Nucl. Sci.* NS-21: 78-93.

Humphreys, E. and R. W. Clayton (1988), Adaptation of back projection tomography to seismic travel time problems, *J. Geophys. Res.* 93: 1073-1086.

Jemberie, A. L. and B. J. Mitchell (2004), Shear-wave Q structure and its lateral variation in the crust of China and surrounding regions, *Geophys. J. Int.* 157: 363-380.

Malin, P. E. (1978), A first-order scattering solution for modeling lunar and terrestrial seismic coda, *Ph.D. dissertation,* Princeton Univ., Princeton, NJ.

McMechan, G. A. (1983), Seismography in boreholes, *Geophys. J.R. Astr. Soc*. 74: 601-612.

Mitchell, B.J., Y. Pan, J. Xie, and L. Cong (1997), Lg coda variation across Eurasia and its relation to crustal evolution, *J. Geophys. Res.* 102: 22767-22779.

Mitchell, B.J., and L. Cong (1998), Lg coda Q and its relation to the structure and evolution of continents: A global perspective, *Pure Appl. Geophys.* 153: 655-663.

Xie, J. (2002), Lg Q in the eastern Tibetan Plateau, *Bull. Seism. Soc. Am.* 92: 871-876.

Xie, J., and O.W. Nuttli (1998), Interpretation of high-frequency coda at large distances: Stochastic modeling and method of inversion, *Geophy. J.* 95: 579-595.

Xie, J., and B.J. Mitchell (1990), A back-projection method for imaging large-scale lateral variations of Lg coda Q with application to continental Africa, *Geophys. J. Int*. 100: 161-181.

GROUND TRUTH COLLECTION FOR MINING EXPLOSIONS IN NORTHERN FENNOSCANDIA AND NORTHWESTERN RUSSIA

Dave B. Harris[1], Frode Ringdal[2], Elena O. Kremenetskaya[3], Svein Mykkeltveit[2], Donald W. Rock[1], Nils Maercklin[2], Johannes Schweitzer[2], Teresa F. Hauk[1], and Jon P. Lewis[1]

Lawrence Livermore National Laboratory[1], NORSAR[2], and Kola Regional Seismological Center[3]

Sponsored by National Nuclear Security Administration
Office of Nonproliferation Research and Engineering
Office of Defense Nuclear Nonproliferation

Contract Nos. W-7405-Eng-48[1] and DE-FC52-01SF22420[2]

ABSTRACT

We concluded comprehensive ground truth collection at the Khibiny, Olenegorsk, Kovdor, and Zapolyarnyi mines, and have basic information on 2,052 explosions. In the past two years we used this ground truth information to extract waveform data from the ARCES array and a number of regional stations (KEV, LVZ, APA) as well as from six stations that we deployed along two lines stretching between the Khibiny Massif mines and the region around the ARCES array. We calculated P/S ratios using the Seismic Array in Northern Norway (ARCES) array data for many of these events comprising several source types (compact underground explosions, underground ripple-fired explosions, surface ripple-fired explosions). We found that the P/S ratios of small compact underground explosions in mines of the Khibiny Massif are systematically lower than the P/S ratios of large ripple-fired surface explosions. We had anticipated that smaller underground shots would appear more like single well-coupled explosions, thus having higher P/S ratios than large ripple-fired explosions. A possible explanation for this phenomenon is that the compact underground explosions in these mines are designed to fracture and drop a large quantity of ore from the ceiling of a horizontal shaft. The potential energy released by the falling ore may express as shear wave energy, which may be considerably greater than the (P wave) energy released directly by the explosive.

We concluded the deployment of the six stations along the Khibiny-ARCES lines this past summer; this year we are examining the data from these stations to see how P/S ratios vary with range from the source. We have an update on the P/S ratio analysis contrasting different source types, with the addition of an analysis of range dependence using data from the temporary stations.

The portable stations were redeployed in the fall of 2004 to the Kiruna and Malmberget underground mines in northern Sweden. The stations deployed in Malmberget also record events from the surface mining operations at the Aitik mine, located some 15 km from Malmberget mine. The data from these stations will allow comparisons of seismic waveforms resulting from different types of shooting practices at different locations within the mines. These stations will provide ground truth on a large number of explosions at these mines allowing future analyses of the dependence of discriminants on source type, possibly assessing the portability of results obtained with the Khibiny explosion observations.

OBJECTIVE(S)

This year the project had 3 principal objectives:

1. Complete assembly of a comprehensive mining explosion database of waveforms from permanent network stations in the region and the temporary Khibiny-ARCES line stations.

2. Operate temporary stations at the iron mines of Kiruna and Malmberget in Sweden for ground truth collection and near-source event waveform characterization.

3. Continue preliminary analysis of the variation of regional discriminants with source-receiver range and source type.

RESEARCH ACCOMPLISHED

Database assembly

By late June 2005, we had assembled a comprehensive database of ground truth information and waveforms for the 2,052 ground truth explosions identified in the Kola Peninsula. The waveforms have been collected from the six temporary stations (Figure 1) described in the next section, as well as the ARCES array, broadband stations KEV and LVZ, and the Apatity array and broadband station (APA). This database is an outstanding resource for studying general propagation effects with range, and the performance of detectors, location algorithms, discriminants, and magnitude-yield relations for a wide range of explosion types.

Completion of the Khibiny-ARCES temporary lines deployment

Our deployment of temporary stations in Finnmark, Norway and Finland was concluded in September 2004. The stations were recovered then for shipment to Sweden. Figure 2 shows the periods of operation of the temporary stations. Difficult access to the stations compounded by some equipment failures led to significant down times.

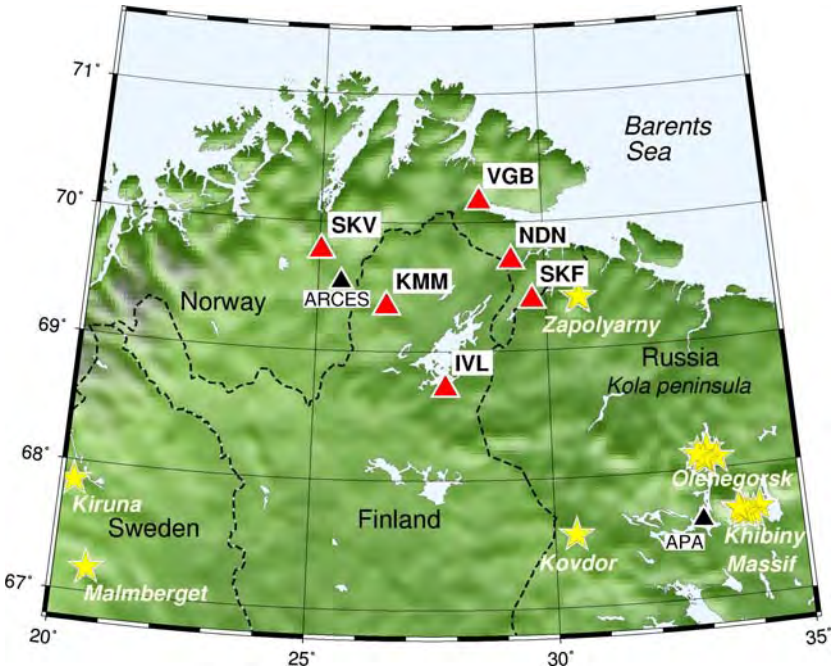

Figure 1. The deployment of six temporary three-component stations in Finnmark, Norway and Finland was concluded in early September 2004. The stations (shown as red triangles) had GS-13 sensors and 24-bit Reftek recorders.

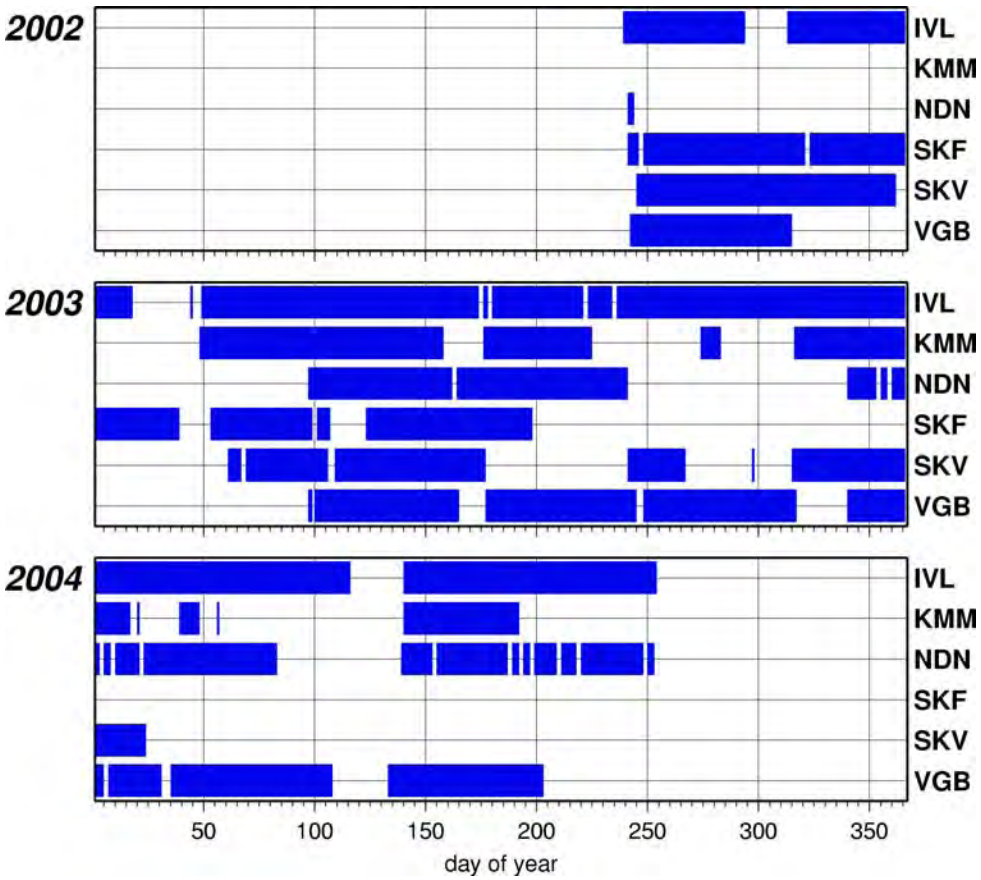

Figure 2. Periods of operation (blue bars) for the six stations in the temporary line deployments. We extended the deployment at no cost from one year to two years to assure collection of an adequate amount of data. The temporary deployment had significant amounts of down-time, due to difficulties in retrieving data and maintaining stations in high arctic conditions.

Consequently, we extended the period of operation by a year at no cost to the Department of Energy (DOE) to achieve an adequate collection of data.

Operation of temporary stations at the Swedish mines at Kiruna and Malmberget

The six LLNL Reftek field recorders that had been deployed in Finnmark in northern Norway and in Finland until September 2004 were redeployed to northern Sweden in the beginning of October 2004. The recorders are deployed around two iron mines operated by Swedish company LKAB. One of these mines, at Kiruna, is the largest underground iron mine in the world. The second, at Malmberget, exploits multiple iron ore deposits some 75 kilometers SSE of Kiruna. Figure 3 shows the locations of the mines and the temporary stations, and Figure 4 shows the time periods for which data are available following our first collection trip.

Three three-component stations (KPN, MJR, STR) were deployed around Malmberget (Figure 5) in a triangle spanning an aperture of about 1.5 kilometers. These stations use S6000 sensors; the recorders operate in trigger mode, recording 60 seconds of data per trigger at 250 samples per second with a 10-second pre-event noise window.

Two small arrays were deployed at Kiruna, one in the basement of a laboratory building of the LKAB mine, and the second in the basement of a hotel 1.2 km to the east of the first array (Figure 6, upper right). These arrays each consist of one S6000 three-component sensor and three geophones. The aperture of the first array is about 60 meters and that of the second is 30 meters. The S6000 in the second array is collocated with one of the geophones allowing direct comparison of the responses of the two types of sensors. A third station (ALN) was set up in Puoltsa about 20 kilometers WSW of Kiruna (Figure 6, lower right). This station is placed roughly midway between a fault and the

mine. We hope to observe small earthquakes on the fault and mining explosions at approximately the same distance, enabling discriminant studies at local distances and small magnitudes. This fault is one of the more active faults in northern Fennoscandia and is thought to be driven by elastic rebound following the melting of the continental ice sheet. The sensors at this station consist of a three-component set of GS-13 seismometers.

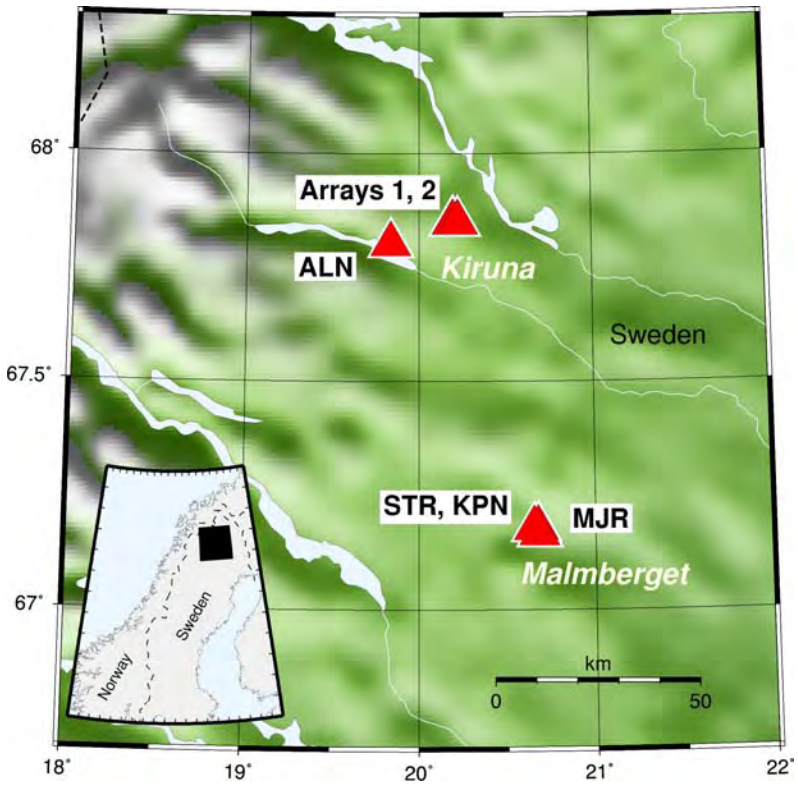

Figure 3. Following completion of our deployment in Finnmark and Finland, we redeployed the field recorders with a variety of sensors to the vicinity of the iron mines at Kiruna and Malmberget in Sweden. One three-component station with GS-13 seismometers was deployed to the west of Kiruna roughly midway between a fault and the mine.

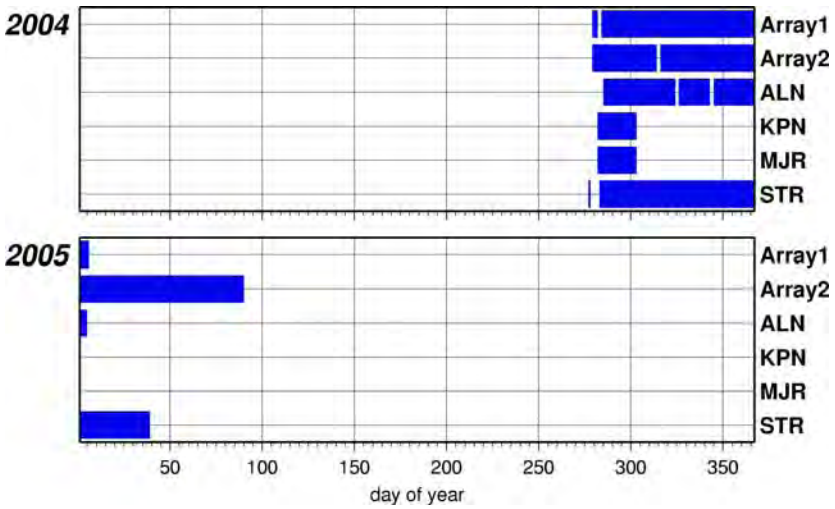

Figure 4. Periods of operation (blue bars) for the stations around the Kiruna and Malmberget mines. Additional data have been recorded but not yet collected from the field recorders.

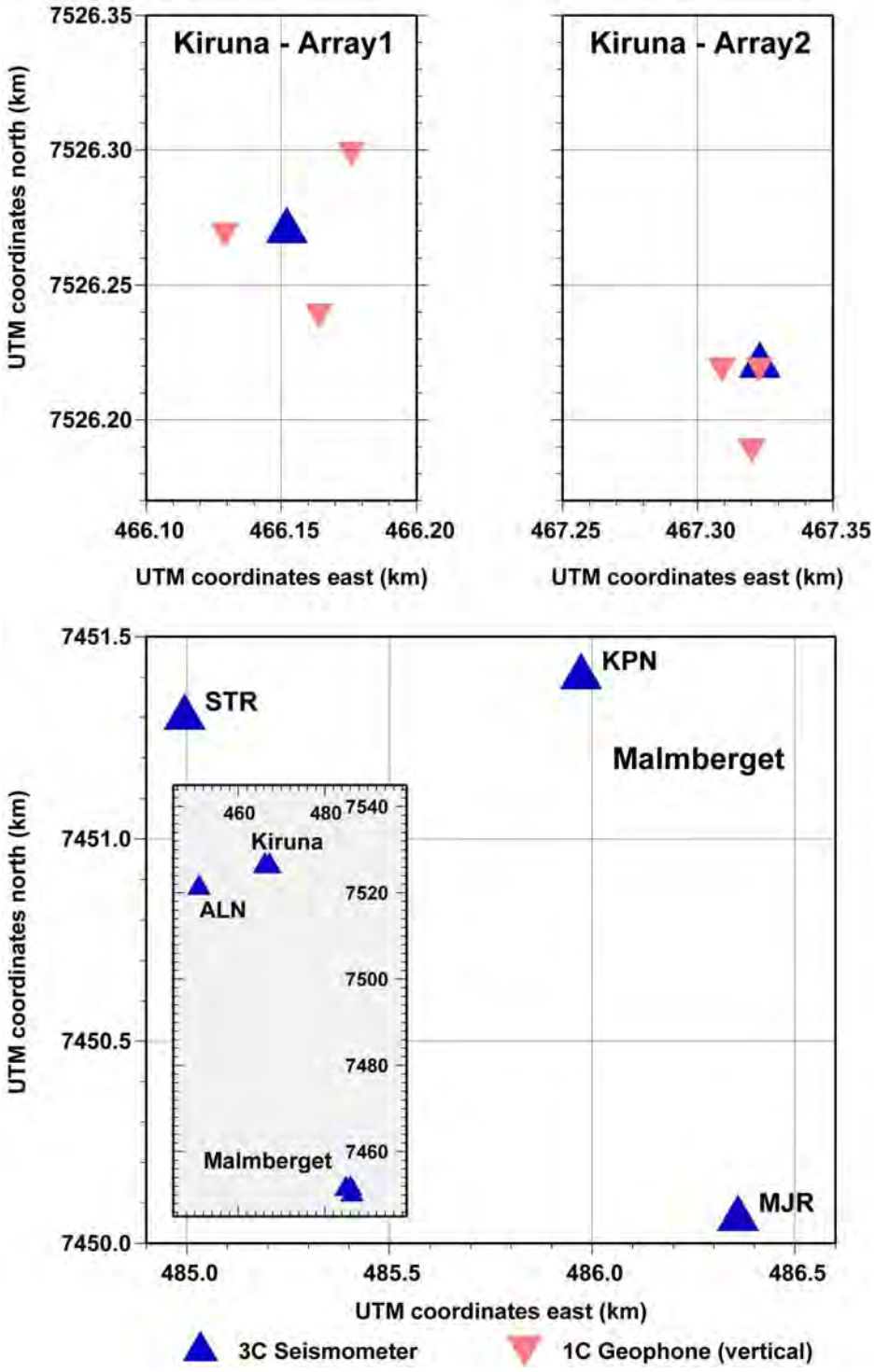

Figure 5. Detail of the deployments at the Kiruna and Malmberget iron mines. Two small arrays were deployed at Kiruna and three three-component stations were deployed at Malmberget.

Initial data collections (Figure 7) have provided observations of rockbursts and production explosions at very close ranges (~ 1 kilometer) at the Kiruna and Malmberget mines. These observations suggest that rockbursts and explosions have different spectral content (Figure 7). At this range, phase ratio discriminants may not be feasible,

since even direct P and direct S are not well separated. It appears that spectral ratio discriminants, or more generally, spectral shape discriminants may have potential.

The mines of Sweden offer an opportunity to examine the portability of observations made at ARCES in previous years [Harris et al., 2004] (and examined in the next section) that compact underground explosions have smaller Pn/Lg ratios than adjacent surface ripple-fired explosions. The mine at Aitik is approximately 17 km southeast of the Malmberget mine, and conducts weekly, large ripple fired explosions that may be compared to the underground explosions at Malmberget. The stations deployed at Malmberget, and the relationship developed with LKAB will provide ground truth information essential to that comparison.

Figure 6. Photographs of Kiruna and Malmberget deployments. The historic surface mine is apparent as the gap in the hill in the photograph at top left. Today the ore is mined underground. The collocated S6000 and geophone in array 2 at Kiruna are shown in the upper right photograph. A typical Malmberget deployment in the basement of a private home is shown at lower left. Station ALN is shown at lower right.

Regional discriminant analysis

We have continued analysis of P/S discriminants using data from ARCES and temporary station IVL. This year we recalculated Pn/Lg and calculated Pn/Sn ratios for compact underground explosions at the Kirovsk mine and surface ripple-fired explosions at the Central mine using data from ARA0. The mines are adjacent and about 410 kilometers from the ARCES. Histograms of the Pn/Lg ratios in five frequency bands (2-4, 4-6, 6-8, 8-10 and 10-12 Hertz) are

shown in Figure 8 for the two types of explosions and display a distinct low bias for the compact undergournd explosions relative to the surface explosions. This bias is most pronounced in the 4-6 and 6-8 Hertz bands, though noticeable in the 2-4 and 10-12 Hertz bands. In previous years we speculated that this bias may be due to differences in the style of the explosions. The compact underground explosions are designed to drop the roofs of adits, while the surface explosions fracture rock into rubble in-place. Energy from the underground events may be dominated by rockfall rather than by the explosion itself, and may be richer in shear waves as a consequence.

Figure 9 shows Pn/Sn ratios for the same suites of explosions. The pattern is similar here in the 4-6, 6-8 and 8-10 Hertz band, though not in the 2-4 Hertz band. These results suggest that the difference in sources is observed similarly independent of the take-off angle of the shear energy from the source.

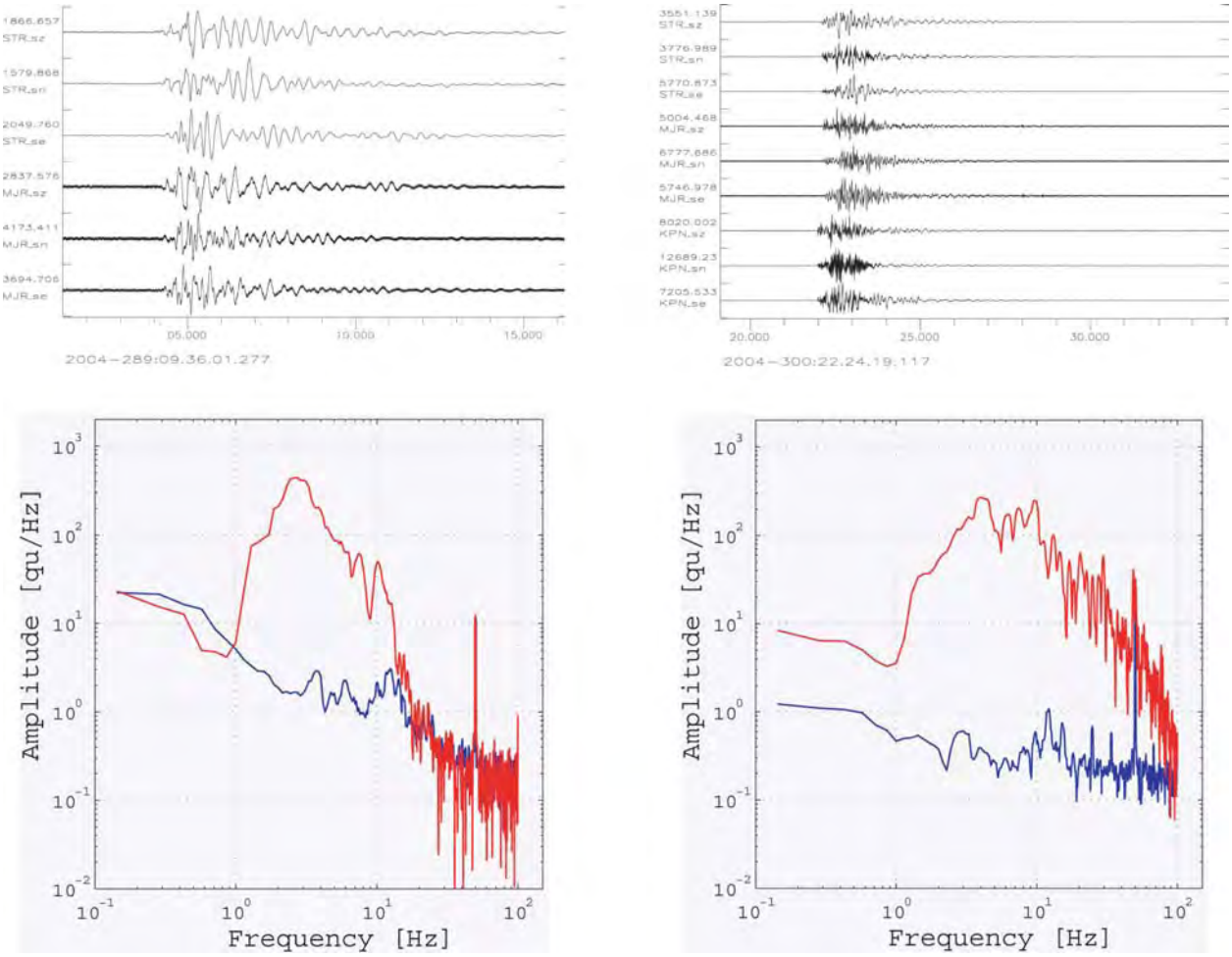

Figure 7. Waveforms and spectra for a rockburst (left) and an explosion (right) in the Malmberget mine recorded by local station STR demonstrate the much higher frequency content of explosions. The rockburst was observed at a range of about 1 kilometer. The signal spectra are shown in red and pre-event noise spectra are shown in blue. Both are uncorrected for instrument response.

With its good recording history IVL also offers many observations of the Khibiny explosions. Pn and Lg phases (but not Sn) are sufficiently distinct at this range to allow amplitude measurements to be made. However, the histograms of Pn/Lg ratios (Figure 10) do not show the same pattern for the two shot types as at ARA0. Since IVL and ARA0 are roughly on the same backazimuth from the Khibiny mines, this difference suggests strong distance and/or site dependencies in the Pn/Lg ratios, which should be better quantified and removed before final conclusions are drawn about biases between source types. Frequency- and phase-dependent path and site corrections for phase amplitudes

could be derived from MDAC calibrations using the earthquakes in the region. Given the relative scarcity of earthquakes in Fennoscandia and northwest Russia, it may be desirable to develop such corrections directly from mining explosions. This is a research topic given the considerable complexity of the explosion sources. Possibly two-station techniques could be employed to minimize the effects of the source in estimating path and site corrections.

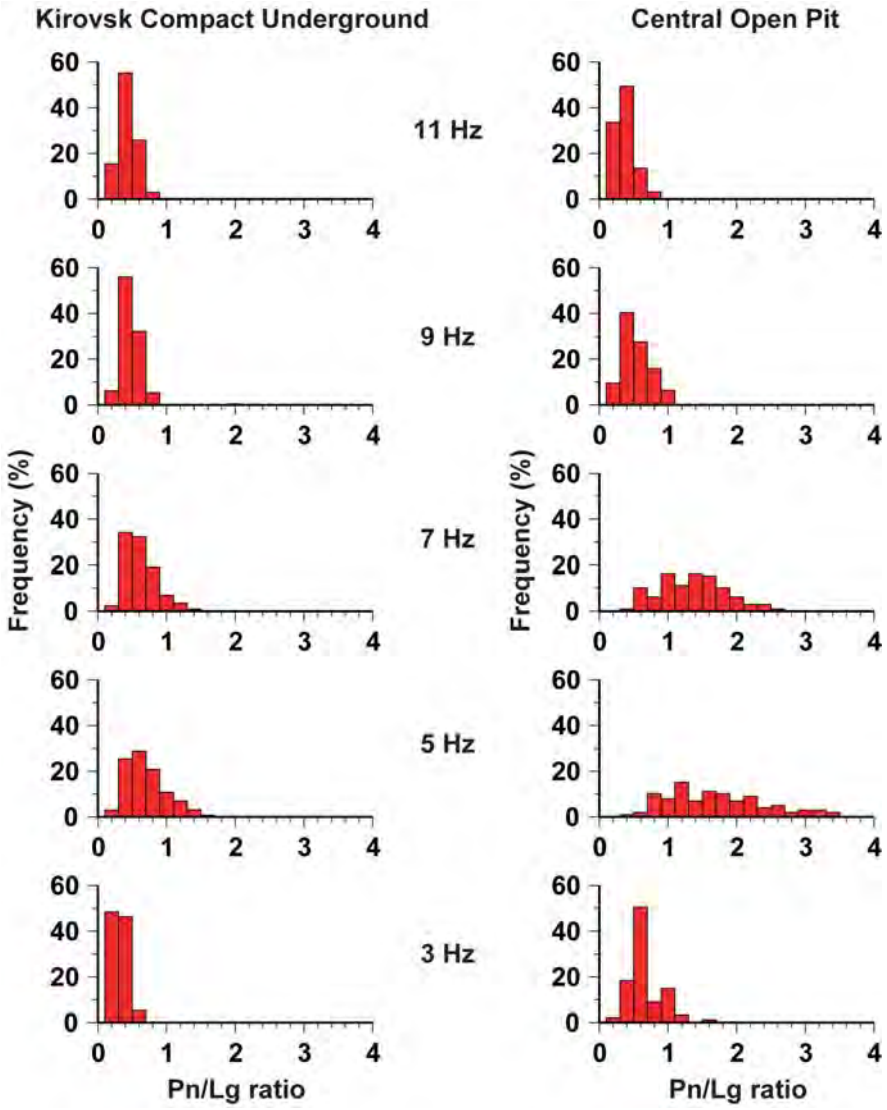

Figure 8. Histograms of Pn/Lg ratios observed at station ARA0 of the ARCES array demonstrate that, at this station, compact underground explosions typically have smaller Pn/Lg ratios than surface ripple-fired explosions. The two mines examined here are adjacent in the Khibiny Massif and at an approximate range of 410 kilometers from ARA0. The ratios are displayed in five frequency bands with bandwidths of two Hz and labeled by their center frequencies. The differences in the distributions are most pronounced in the 4-6 and 6-8 Hz bands, but significant in the 2-4 Hz band.

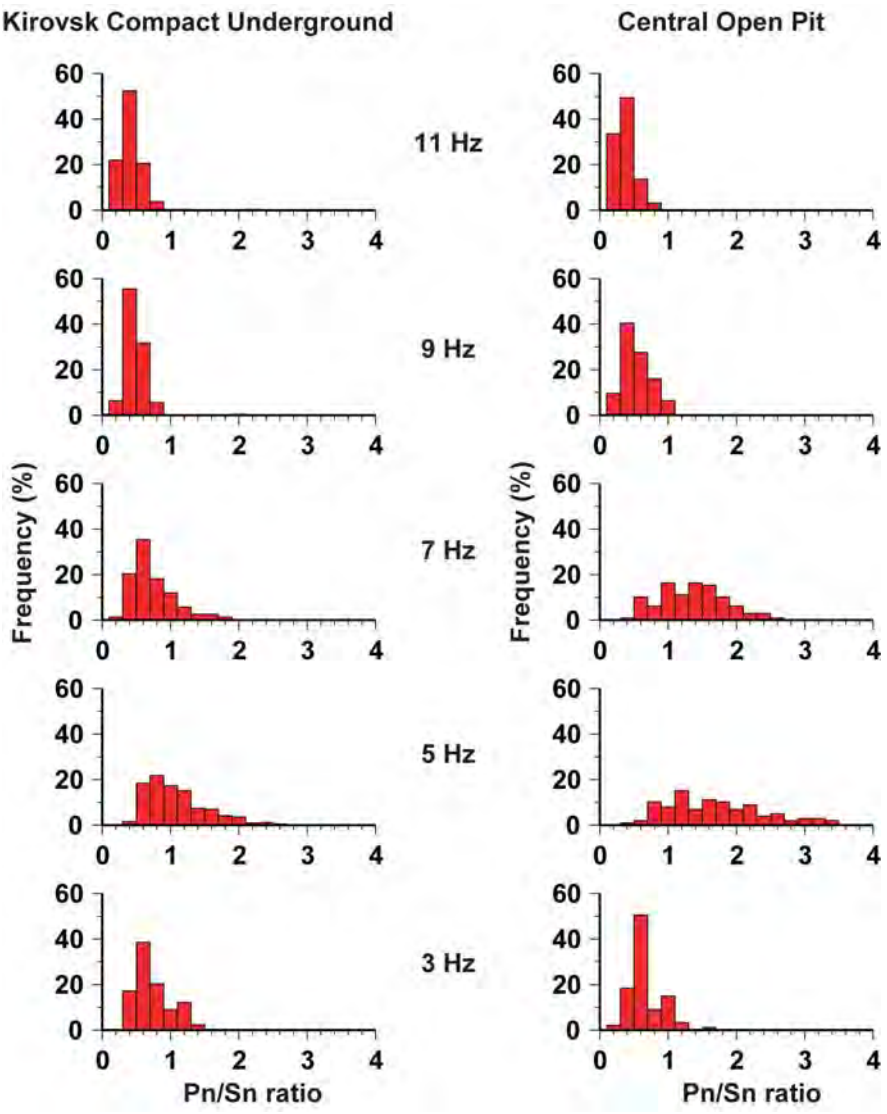

Figure 9. Pn/Sn ratios observed at station ARA0 also display significant differences in the 4-6 and 6-8 Hertz bands. The compact underground explosions have the smaller Pn/Sn ratios in these bands.

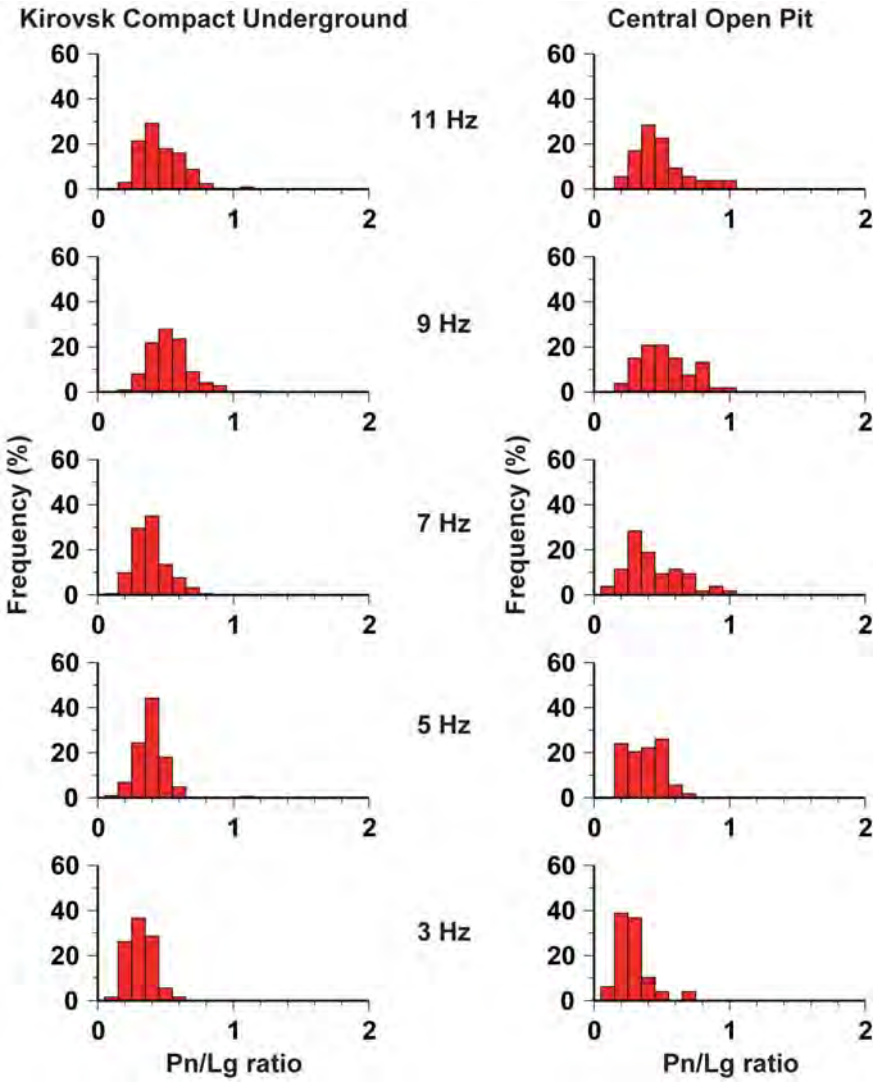

Figure 10. Pn/Lg ratios observed at temporary station IVL. This station is much closer (280 km) to the mines of the Khibiny Massif, but still outside of the Pn/Pg crossover. The Pn/Lg ratios for the compact underground explosions at this station show little or no tendency to be smaller than the surface ripple-fired ratios.

CONCLUSIONS AND RECOMMENDATIONS

We conclude that we have assembled a valuable data set for examining the relative excitation of different seismic phases and discriminants by several types of mining explosions. Initial examination of the data has revealed significant differences in P/S ratios observed by the ARCES array for distinct types of mining explosions conducted in the Khibiny mine group, which may be linked to the different ways that ore is moved by the explosions in surface and underground mines. We recommend that a number of additional analyses be conducted on the data.

1. Development of path/station corrections allowing comparison of explosions at different ranges from a station and among different observing stations. Such corrections should be used to sort out whether the variations in P/S discriminants among different explosion types are due to different source mechanisms.
2. Conduct a comparison (using ARCES and other stations) of the underground explosions at Malmberget and the surface ripple-fired explosions at Aitik to determine whether the P/S variations observed for compact underground explosions and surface ripple-fired explosions at the Khibiny mines are reproduced for a different source region.

3. Examine the behavior of the same (path corrected) discriminants for earthquakes in the region.

4. Examine the performance of spectral shape and spectral ratio discriminants for rockbursts and explosions at local distances using data from close-in sensors. Such data are being collected in the vicinity of Kiruna and Malmberget mines as this project concludes.

REFERENCE

Harris, D., F. Ringdal, E. Kremenetskaya, S. Mykkeltveit, D. Rock, J. Schweitzer, T. Hauk, and J. Lewis (2004), Ground-Truth collection for mining explosions in Northern Fennoscandia and Russia, in *Proceedings of the 26th Seismic Research Review*: *Trends in Nuclear Explosion Monitoring*, LA-UR-04-5801, Vol. 1, pp. 73-82

SEISMIC SOURCE AND PATH CALIBRATION IN THE KOREAN PENINSULA, YELLOW SEA, AND NORTHEAST CHINA

Robert B. Herrmann[1], Young-Soo Jeon[1], William R. Walter[2], and Michael E. Pasyanos[2]

Saint Louis University[1] and Lawrence Livermore National Laboratory[2]

Sponsored by National Nuclear Security Administration
Office of Nonproliferation Research and Engineering
Office of Defense Nuclear Nonproliferation

Contract Nos. DE-FC52-04NA25539[1] and W-7405-ENG-48[2]

ABSTRACT

This paper focuses on the determination of seismic source parameters for earthquakes in the region surrounding the northern Yellow Sea. Broadband waveform data from the Incorporated Research Institutions for Seismology (IRIS) and the Korean Meteorological Administration (KMA) stations are used to determine moment magnitudes, source depths and focal mechanisms for these earthquakes. The seismic moments are required to calibrate the magnitude and distance amplitude corrections (MDAC) procedure for the region. The current database consists of events in northeastern China and Korea. After initial data acquisition, efforts were directed toward defining better regional models for the required theoretical Green's functions. For the events recorded in the 500 - 1000 km distance range, the regional waveforms are used to refine the initial model. For events recorded at shorter distance, especially those in Korea recorded by the KMA and the Korean Institute of Geology and Mining (KIGAM) networks, an initial reconciliation between “joint inversion of surface-wave dispersion and receiver function” models and local waveforms was prototyped to define a generic Korean crustal velocity model. Efforts are underway to acquire a continuous broadband data stream from Korea.

OBJECTIVE(S)

This effort addresses the specific problem of understanding seismic wave propagation and sources in the broad region surrounding the Korean Peninsula, the Yellow Sea and northeastern China – the region encompassing the latitudes 30 – 50 N and the longitudes 115-135 E. The unifying feature of the studies undertaken is the use of broadband waveforms . Aspects of the effort include surface-wave dispersion measurements and waveform based source parameter determination. The results of the effort will be calibrated moments and depths for ground truth catalogs and a refined crustal velocity model for use in detailed waveform analyses of regional events.

RESEARCH ACCOMPLISHED

Initial efforts were directed at the determination of earthquake source parameters whose moment magnitudes are key to calibrating MDAC for regional phases. In addition, a subset of the events studied are sufficiently constrained to permit an evaluation of candidate crustal velocity models for improved source parameter determination.

Initial Source Parameter Determination

The determination of earthquake source parameters uses two methodologies described in the Computer Programs in Seismology – 3.30 package (CPS3.30) (Herrmann and Ammon, 2002): fitting surface-wave spectral amplitude radiation patterns and broadband waveforms. The data used for Korean earthquakes are available in miniSEED from the KMA website http://www.kmaneis.go.kr/depth04_1.htm with event locations given at http://www.kmaneis.go.kr/eng/eng02.htm. Following a new event, miniSEED data are downloaded from the KMA website for all velocity sensor and accelerometer traces, converted to seismic analysis code (SAC) and deconvolved to ground velocity. Multiple filter analysis is applied to the broadband waveforms to determine the spectral amplitudes of the fundamental mode Love and Rayleigh waves. Using surface-wave eigenfunctions of the Central U.S. (CUS) model, a grid search over strike, dip, rake and depth is made for the best fitting focal mechanism; the ambiguity of fault strike and pressure and tension quadrants is resolved by comparison with bandpass filtered waveforms and/or very sharp first motion data.

Direct waveform inversion proceeds by rotating the three component deconvolved seismograms to radial, transverse and vertical components, picking the P-wave first arrival for trace alignment, the determination of the passband for the search, followed by a similar grid search. The CPS3.30 package introduced an efficient time shifting operation to overcome imperfect source parameters and the effects of an approximate crustal model. Both source determination techniques are applied because of different sensitivity to depth and because of the negative effects of ground noise when working with earthquakes with magnitudes of less than 4.0.

Table 1 and Figure 1 present the current catalog source mechanisms for the region. These earthquakes are characterized by a maximum compressive stress axis (Zoback, 1992) oriented E to ENE. With the exception of one normal faulting mechanism, the focal mechanisms are predominantly strike-slip with some thrust faulting.

The CUS model was initially used because precomputed Green's functions were available. Surprisingly the CUS model did very well in matching waveforms. A Korea specific model is being developed so that the preliminary source parameters can be refined; it is expected that the source parameters will not change signifiicantly.

Evaluation of Joint Inversion Crustal Velocity Models for Korea

Although the CUS crustal velocity model adequately modeled earthquake waveforms out to 300 km, it is not a Korea specific model basically because the depth to the Moho in the CUS model is 40 km and joint inversion of receiver functions and surface-wave dispersion for Korea indicates a crustal thickness on the order of 30 km. The utility of the CUS model lies in the fact that its upper crustal shear-wave velocities seem to be those required to define the observed surface-wave signal in the 10 – 30 period band.

Figure 2 shows the phase and group velocity dispersion data used for the joint inversion. At long periods, the Rayleigh-wave group and phase velocity values include tomographic values estimated by Harvard and Lawrence Livermore National Laboratory (LLNL). The majority of Rayleigh wave phase velocity values are obtained from a p-omega stack of teleseismic surface waves crossing the Korean peninsula. For periods of less than 10 seconds, the p-omega stack was applied to the May 29, 2004 regional earthquake signal. Rayleigh wave group velocity values for

periods of less than 10 seconds and Love group velocity values result from the application of multiple filter analysis to broadband signals of local and regional earthquakes. A tabulation of the data sets used for various joint inversions of receiver functions at Seoul National University (SNU) is given in Table 2.

Figure 3 presents the shear-wave velocity models corresponding to the various joint inversions together with the starting model, *START/start.mod*, and the reference CUS model, *CUS/dcsuq.mod*. The deeper parts of the starting and CUS models are the AK135 structure. The joint inversion models indicate a sharp Moho at a depth of about 28-30 km. The upper 1 km is characterized by a lower velocity, overlying an almost constant velocity upper crustal layer. The middle crust has a transitional velocity structure at about 15 km to an 8 km thick constant velocity layer. The upper mantle may show evidence of a low velocity zone. Except for the INVSNU inversion which was constrained by few dispersion data, the upper 10 km of the joint inversion models are similar to the CUS model. This may explain the usefulness of the CUS model for source inversion of local and regional events.

Each of the models presented is affected by the nature of the individual dispersion data sets used. The use of short period group velocity dispersion from an analysis of earthquakes at distances < 400 km, is affected by the signal spectrum and the fact that there is not a large number of wavelengths between the source and unknown origin time bias.

To visualize the consequences of these different models, a waveform inversion, with time shifts, is run for the April 26, 2004 earthquake. This earthquake was selected because of its relatively large size and because of its location on the peninsula, surrounded by KMA stations. Thus the epicenter is well constrained.

Table 3 presents the waveform inversion grid search results for three of the crustal velocity models used. A comparison of observed and predicted traces is given in Figure 4. Fits were made for the 0.02 – 0.15 Hz frequency band, and a distance dependent weighting was applied. The agreement between the observed and predicted waveforms in Figure 4 are good, although some subtle differences are seen. Comparison of the ULJ traces at 143 km, indicates that although the P-wave arrival may align, the surface-wave pulse is typically predicted later. The problem of origin time is tied up with the velocity model, but not necessarily with depth because the surface wave pulse broadens as source depth increases. It is difficult to choose among the two Korea based models, but it is comforting that a joint-inversion model using phase velocity dispersion in the 5 – 175 second period band can form the basis for waveform inversion. The application of this model at greater distances awaits data from similarly well costrained earthquakes.

Further Evaluation of Joint Inversion Crustal Velocity Models for Korea

A new technique for investigating upper crustal structure is described in a number of papers (Campillo and Paul, 2003; Shapiro et al., 2005; Ritzwoller et al., 2005). Wapenaar (2004) used the elastic wave representation theorem to provide a theoretical understanding of the procedure. Basically, noise segments of different seismograph stations are cross-correlated and stacked the result of which is a pulse that corresponds to the Green's function between the two stations for a surface application of force. The observed pulse is shaped by the power spectrum of the loading function causing the signal (Wapanaar, 2004). To avoid biases due to large amplitude signals, especially teleseisms, the favored technique is to apply a one-bit operator to the traces followed by a cross-correlation. This non-linear operation has the side effect of yielding a signal with a very peaked spectrum, which makes the determination of the group velocities difficult. We used an alternative non-linear operator. The entire series is analyzed in one-hour chunks, which are then whitened to yield a flat amplitude spectrum. Cross-correlations are then applied, and the hourly cross-correlations are stacked.

Through cooperative efforts with KMA and researchers at Seoul National University, we have acquired 83 days of continuous 20 Hz broadband data from 12 stations of the KMA network. Initial determination of inter-station Green's functions looks promising. Figure 5 shows the Rayleigh wave group velocities (orange) estimated from 50 of the 66 possible inter-station pairs. These are compared to the theoretical dispersion of the CUS and the t5.invSNU.CVEL models. The variability in dispersion along these paths is similar to that shown in Figure 2 from local earthquake data. We noted that individual dispersion curves seem shifted along the period axis with respect to one another. If we assume that a single layer over a halfspace is an adequate model for the short periods, then the layer thickess could vary by ±20 – 30 % over the southern half of the Korean peninsula. The comparison also shows that the joint inversion model can provide information about very shallow velocity structure.

CONCLUSIONS AND RECOMMENDATIONS

This study focuses on the related determination of seismic event source parameters and crustal velocity models. The testing of crustal models derived from receiver functions and surface-wave dispersion provides confidence in those models. The recent acquisition of continuous broadband waveform data from the Korean Meteorological Administration introduces new possibilities for defining the crustal velocity structure of the study area.

The initial evaluation of the technique for determining interstation Green's functions from the cross-correlation of ground noise looks promising. The path coverage should permit a unique determination of upper crustal velocities for the southern part of the Korean Peninsula. Access to more data is required to push the analysis toward longer periods and to extend the region of study outward. Since this is a new technique, the robustness of the dispersion results must be studied in detail.

ACKNOWLEDGEMENTS(S)

This work has benefited significantly from cooperation with Dr. Dukkee Lee of KMRI, Dr. Kiehwa Lee an, Mr. Kwang-Hyun Cho and Mr. Hyun-Jae Yoo of Seoul National University.

REFERENCE(S)

Campillo, M., and A. Paul (2003). Long-range correlations in the diffuse seismic coda, *Science* 299: 547-549.

Herrmann, R. B. (1979). Surface-wave focal mechanisms for eastern North American earthquakes with tectonic implications, *J. Geophys. Res.* 84: 3543-3552.

Herrmann, R. B., and C. J. Ammon (2002). Computer Programs in Seismology – 3.30: Source inversion, available at URL: http://www.eas.slu.edu/People/RBHerrmann/CPS330.html, 99pp.

Ritzwoller, M.H., N.M. Shapiro, M.E. Pasyanos, G.D. Bensen, and Y. Yang (2005), Short period surface wave dispersion measurements from the ambient seismic noise in North Africa, the Middle East, and Central Asia, in current Proceedings.

Shapiro, N.M. M. Campillo, L. Stehly, and M.H. Ritzwoller, High resolution surface wave tomography from ambient seismic noise, Science, 307: (5715), 1615-1618, 11 March 2005.

Wapenaar, K. (2004). Retrieving the elastodynamic Green's function of an arbitrary inhomogeneous medium by cross correlation, *PRL* 93: 254301, 4pp.

Zoback, M. L., (1992). First and second-order patterns of stress in the lithosphere: The World Stress Map Project. *J. Geophys. Res*. 97: B8, 11703-11728.

Table 1. Focal mechanism parameters for events plotted in Figure 1.

EVENT	LAT (N)	LON (E)	H (km)	Strike	Dip	Rake	Mw
20001209	36.46	130.04	11	185	65	75	4.06
20011121	36.72	128.28	9	115	55	35	3.44
20011124	36.74	129.87	10	315	65	20	3.79
20020317	37.99	124.53	7	180	65	-120	3.72
20020708	35.85	129.76	11	125	75	10	3.63
20020723	35.57	122.18	19	120	70	25	4.9
20021209	38.86	127.26	6	295	90	-25	3.69
20030109	37.4	124.2	5	355	65	-170	3.85
20030322	34.96	124.39	14	30	80	-170	4.83
20030330	37.57	123.57	13	25	80	-155	4.61
20031012	36.95	126.51	9	25	75	-175	3.8
20030609	36	123.6	16	305	75	15	3.98
20030415	36.44	126.17	9	300	35	50	3.3
20040105	38.7	125.1	7	135	60	25	3.25
20040426	35.8	128.2	10	150	60	50	3.64
20040529	36.67	129.94	10	160	65	65	5.1
20040601	37.2	130	19	215	70	-145	3.71
20041216	41.8	127.94	8	40	70	-155	3.97

Table 2. Details of joint inversion runs showing dispersion period range and number of observations

Inversion	Number RFTN's	Rayleigh Wave Phase Velocity	Rayleigh Wave Group Velocity	Love Wave Phase Velocity	Love Wave Group Velocity
INVSNU	39	12 – 40 s (5)	10 - 70 s (21)	–	–
nnINVSNU	39	9 – 234 (362)	10 – 200 (46)	–	–
ttt.INVSNU	39	9 – 234 (371)	10 – 200 (65)	–	–
tttt.INVSNU	39	9 – 234 (497)	15 – 175 (495)	–	–
t4.INVSNU	39	9 – 234 (371)	1.2 – 200 (122)	–	1.2 – 36 (62)
t5.INVSNU	39	4 – 234 s (411)	1 – 175 s (222)	4.6 – 12 (33)	5 – 30 (31)
t5.invSNU.CVEL	39	4 – 234 s (411)	-	4.6 – 12 (33)	–

Table 3. Grid search results for the April 26, 2004 earthquake.

Model	H (km)	Strike	Dip	Rake	Mw	Fit
CUS	12	140	70	40	3.64	0.8088
T4.INVSNU	10	140	70	40	3.55	0.7801
T5.invSNU.CVEL	11	140	70	45	3.59	0.7748

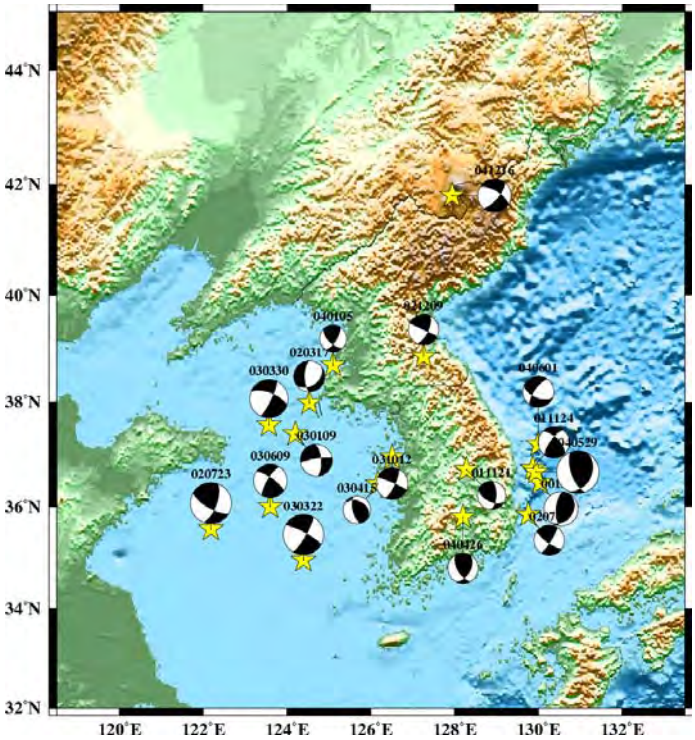

Figure 1. Plots of focal mechanisms in the current catalog.

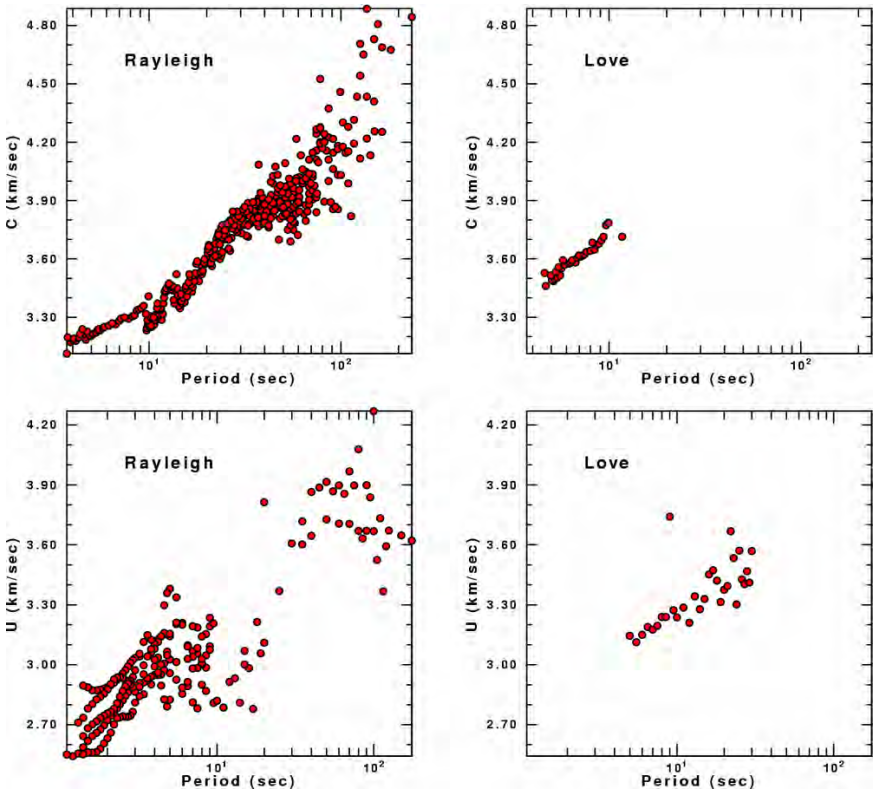

Figure 2. Dispersion values used for the t5.INVSNU and t5.inv SNU.CVEL joint inversions.

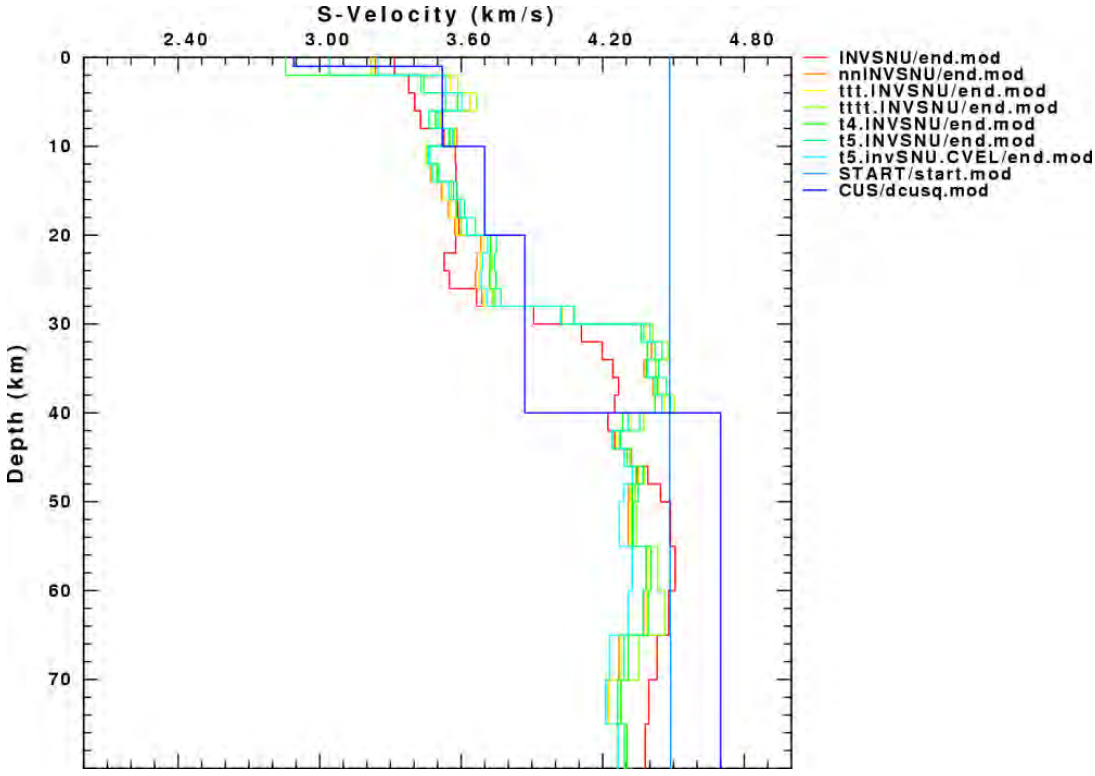

Figure 3. Comparison of models used for synthetics. START/start.mod is the starting model.

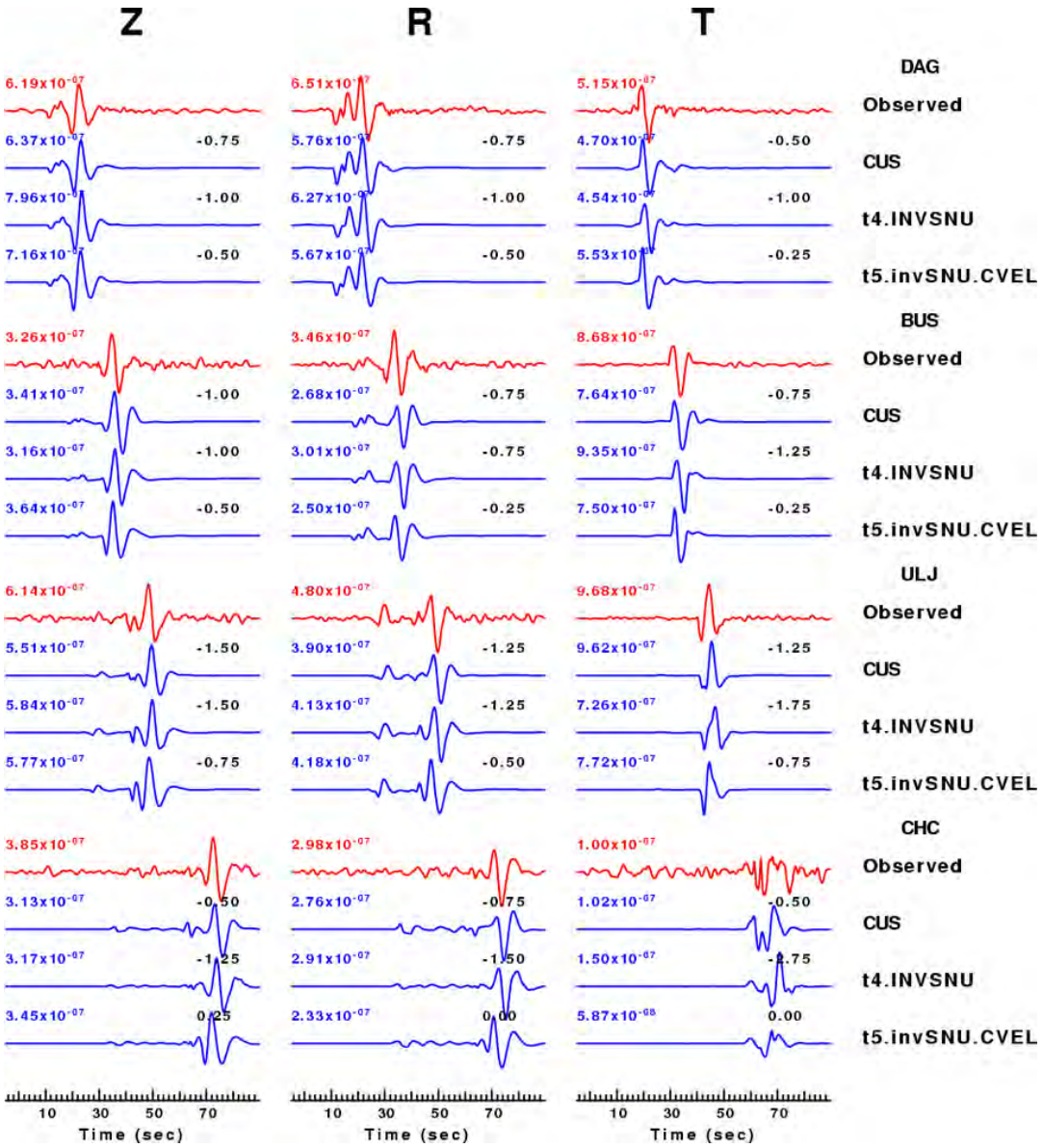

Figure 4. Comparison of observed and predicted filtered waveforms at selected stations of the KMA network for the 26 APR 2004 earthquake. The epicentral distances to the stations DAG, BUS, ULJ and CHC are 62, 104, 143 and 217 km, respectively. The observed traces are plotted in red. The number adjacent to each predicted trace is the time shift in seconds required for maximum correlation. The traces for each component of a station are plotted to the same scale. All traces start 5 seconds before and continue to 90 seconds after the origin time, and are bandpass filtered using a 3-pole high pass Butterworth at 0.02 Hz followed by a 3-pole low pass Butterworth filter at 0.15 Hz. The peak filtered amplitudes in meters/sec is indicated.

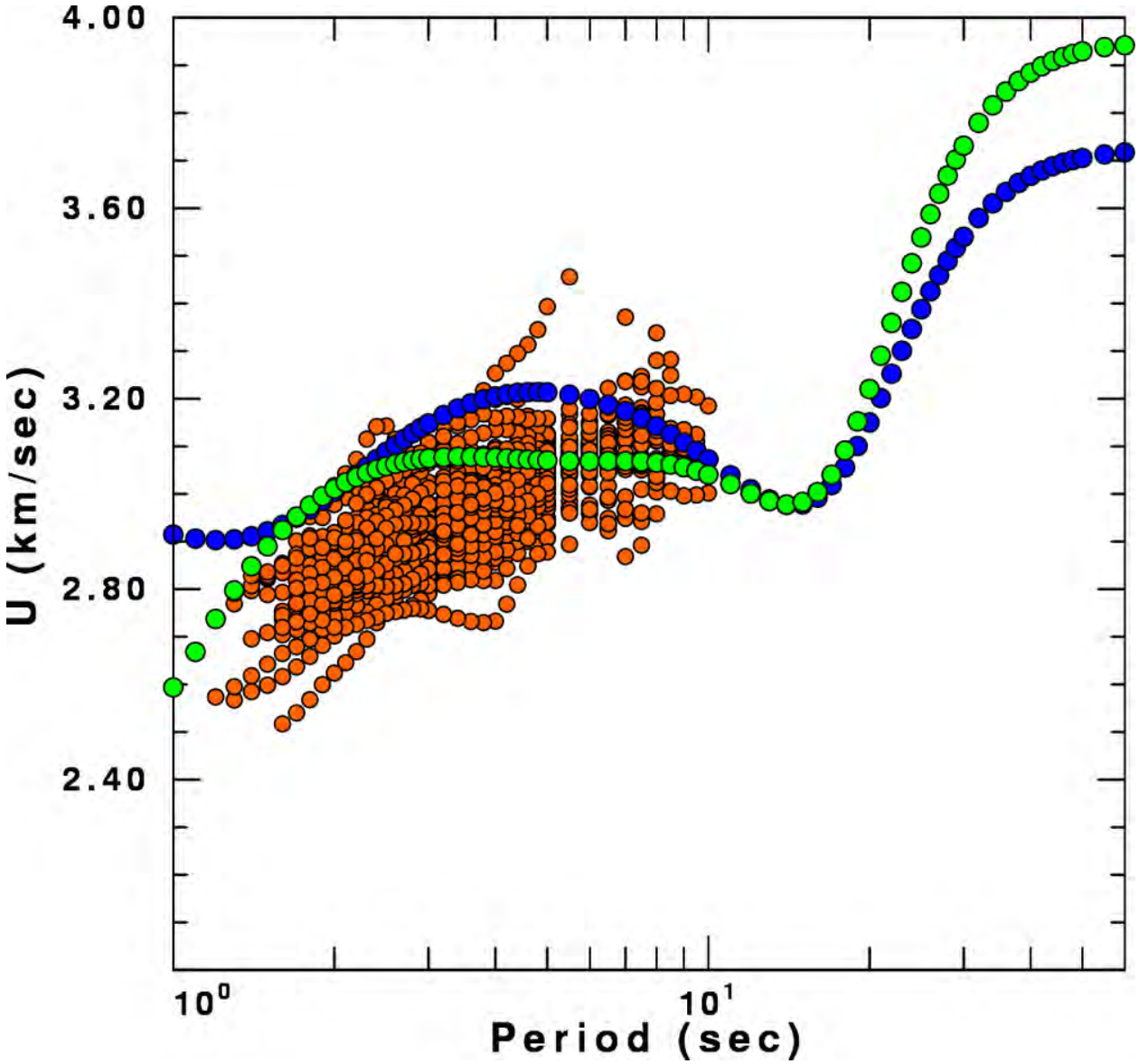

Figure 5. Comparison of interstation group velocities for station pairs in the Korean peninsula (orange) with theoretical dispersion for the CUS model (green) and t5.invSNU.CVEL (blue)

DEVELOPMENT OF REGIONAL PHASE TOMOGRAPHIC ATTENUATION MODELS FOR EURASIA

Thorne Lay[1], Xiao-Bi Xie[1], Xiaoning (David) Yang[2], Steven R. Taylor[2], and W. Scott Phillips[2]

Los Alamos National Laboratory[1] and University of California, Santa Cruz[2]

Sponsored by National Nuclear Security Administration
Office of Nonproliferation Research and Engineering
Office of Defense Nuclear Nonproliferation

Contract Nos. DE-FC52-05NA26606[1] and W-7405-ENG-36[2]

ABSTRACT

The national laboratories are currently calibrating regional seismic discriminants for Eurasia. The Magnitude and Distance Amplitude Correction (MDAC) (Taylor and Hartse, 1998; Taylor et al., 2002, Walter and Taylor, 2002) is being used to correct amplitudes for discriminants. The MDAC methodology corrects regional seismic amplitudes by assuming physically based propagation and earthquake source models. Regional phase attenuation models at 1 Hz developed by Los Alamos National Laboratory (LANL) are currently being used in eastern Asia to perform MDAC corrections. In other regions, one-dimensional Q models are used. These tomographic models need to be extended to all of Eurasia to improve nuclear explosion monitoring capabilities to wider areas. We are expanding existing 1 Hz regional phase (Pn, Pg, Sn, Lg) tomographic attenuation models for Eurasia. The models will be integrated into the National Nuclear Security Administration (NNSA) Knowledge Base and will be used in the MDAC station calibration for development of regional seismic discriminants. Accurately accounting for regional phase geometrical spreading is critical for development of useful anelastic attenuation models, particularly for upper mantle diving waves (Pn and Sn). The MDAC approach currently uses a simple representation of regional phase geometrical spreading that performs well between local to near-regional (200–400 km) and far-regional to teleseismic transition zone regions (< 16–18^{o}). In order to seamlessly tie regional MDAC to local and teleseismic distances, it is important to devise strategies to account for geometrical effects in these transition zone regions. We will focus our work on the 1 Hz Pn phase and examine whether combined empirical and model-based approaches can be used to improve geometric spreading corrections in different geophysical regions. As is well known, Pn is an extremely important phase in seismic event identification and the goal of this work is to improve its efficacy. One of the questions we hope to answer is whether it is adequate to continue to use the simple formulation currently used supplemented by amplitude tomography and possibly station-centric amplitude kriging or could a set of model-based corrections be formed from geophysical models being compiled for Eurasia as part of the NNSA program. The metric to be used to test these different methodologies would be event classification error rates using the extensive ground truth dataset compiled by the NNSA laboratories.

OBJECTIVES

The project has the following research objectives:

- Develop regional phase (Pn, Pg, Sn, Lg) tomographic attenuation maps for Eurasia at 1 Hz.
- Develop combined empirical/model-based approaches for representation of 1 Hz Pn (and Sn) wave geometrical spreading factors at transition zone regions (local to regional and far regional to teleseismic).

RESEARCH ACCOMPLISHED

Bayesian Attenuation Tomography

We have added the ability to incorporate Bayesian attenuation tomography to the MDAC methodology (Tarantola, 1987; Taylor et al., 2003). Tomographic results from prior studies can be used or built upon using a Bayesian approach that accounts for inadequacies of the assumption of a constant Q_0 for a large region. The advantages of a Bayesian approach to tomography are that large-scale and high-resolution tomographic models available from other well-accepted studies can be used as prior background models. The resulting refined tomographic model blends into these prior background models. Moreover, the error budget is well established in a Bayesian framework. We assume a general linear Gaussian (least squares) model, where the covariance matrix is partitioned into data and prior model components. Uncertain data are naturally down-weighted, and certain model components will be subject to small perturbations.

An advantage of the Bayesian approach to tomography is that the posterior model will blend into the prior background model. The prior model can be a well-accepted global model that can contain constraints from detailed studies in specific regions. For example, Xie (2002) included results from PASSCAL experiments within Tibet that suggest attenuation within the plateau is greater than that calculated using data crossing the entire plateau (which may be due to a data censoring problem discussed below). Additionally, Fan and Lay (2002) suggest that apparent blockage of Lg in Tibet may be due to strong crustal attenuation in northern Tibet, although blockages are known to exist elsewhere (e.g., Baumgardt, 1990; Zhang and Lay, 1995). In the study of Taylor et al. (2003), we used the Eurasia Lg coda Q model and associated errors of Mitchell et al. (1997) as the prior attenuation and covariance model **(**Equation 13).

Figure 1 shows an example of a 1 Hz Lg tomographic Q model for eastern Asia that blends into the *a priori* Eurasian Lg coda Q model of Mitchell et al. (1997). The eastern Asia model was computed using 2^o cells (as opposed to 3^o cells for the Mitchell model) because of the addition of many more amplitude measurements and stations. Subsequent high-resolution models have been developed having 1^o cells.

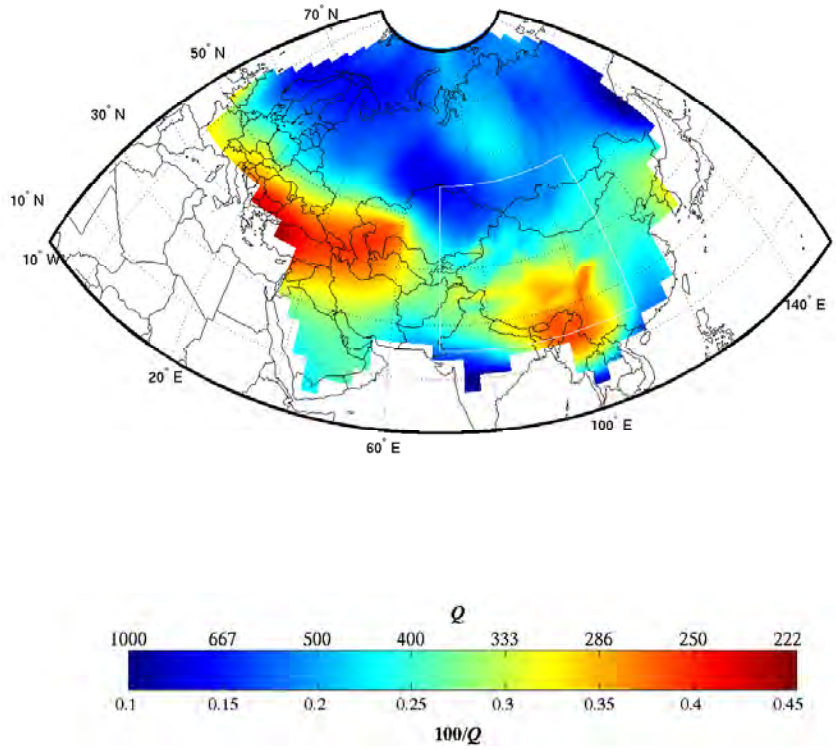

Figure 1. Two degree attenuation tomography map for 1 Hz Lg of Figure 2 (white outline) blending into 3 degree Lg coda Q map of Mitchell et al. (1997).

An alternative approach using the Bayesian framework is to perform a two-stage inversion as suggested by Yang et al., (2004; Figure 2), where the *a priori* model comes from a coarse grid tomographic model using interstation amplitude ratios. The results will then be used as the *a priori* in the single-station amplitude inversion to obtain the final attenuation model. Of course, many effects common to both stations, such as Mw drop out resulting in more stable measurements.

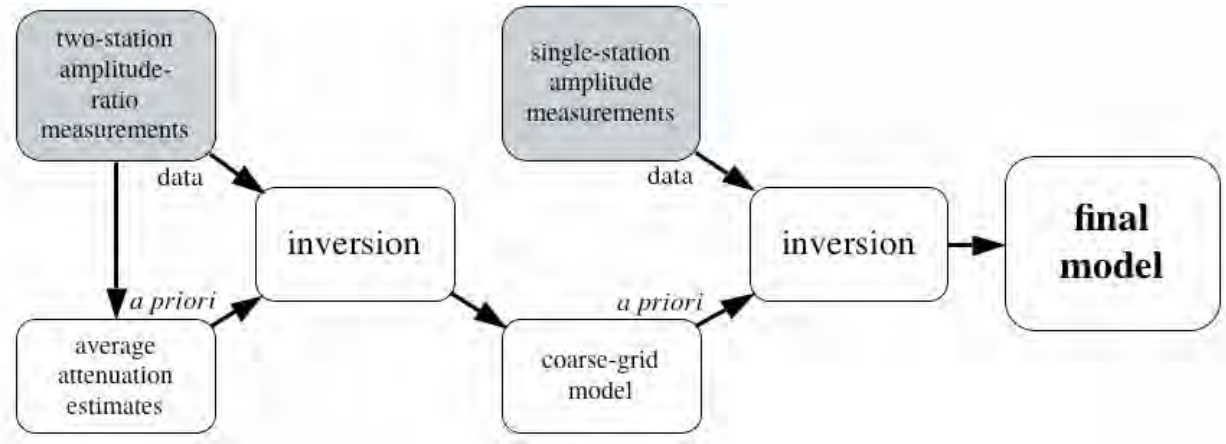

Figure 2. Flowchart of the two-stage tomographic inversion.

Amplitude tomography provides only an approximation to the propagation effects a seismic wave may experience. It is well known that there exist significant tradeoffs between geometric spreading and attenuation. For example, geometric spreading factors for Pn can vary with range and frequency, depending on the velocity structure (e.g., Sereno and Given, 1990). In contrast, Yang (2002) found that Lg geometrical spreading is independent of frequency

for a wide range of velocity models. Thus, the emphasis of this study will be to examine effects of crust and upper mantle structure on the transition zone distances of local to regional (e.g. Pg to Pn) and far-regional to teleseismic (Pn to teleseismic P) at 1 Hz. This far-regional to teleseismic transition is important for making a seamless tie between regional and teleseismic discriminants.

Upper mantle velocity structure plays an important role in determining the complexity of far-regional and near-teleseismic waveforms. In general, a low-velocity zone (LVZ) exists between about 100–200 km depth. Below the LVZ, *P*- and *S*-wave velocities increase smoothly through the upper mantle, to a depth of approximately 410 km. The mantle transition zone, between about 400–700 km depth contains discontinuities near 410 km and 660 km, where the velocities increase rapidly. Plots of the IASP91 (Kennett and Engdahl, 1991) and JB (Jeffreys and Bullen, 1958) velocity structures for the mantle and the transition zone are shown in Figure 3. These discontinuities cause *triplications* in the travel time curve, as shown in Figure 4. Although these regions are often referred to as the 410- and 660-km discontinuities, their exact depths vary from region to region.

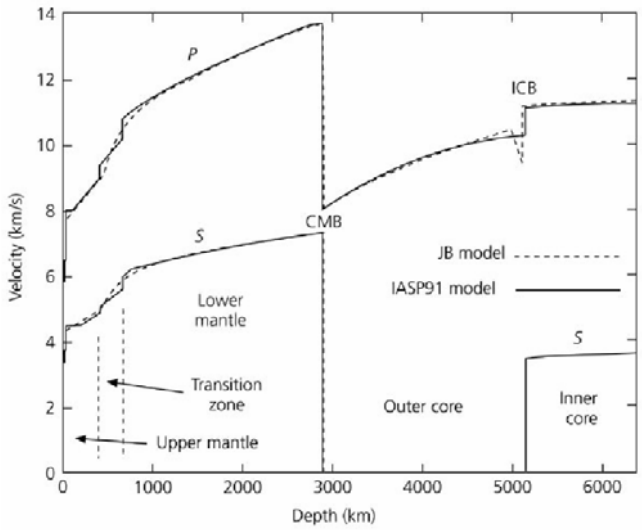

Figure 3. P- and S-wave velocity models for the earth showing the sharp discontinuities in the upper mantle transition zone (from Stein and Wysession, 2002).

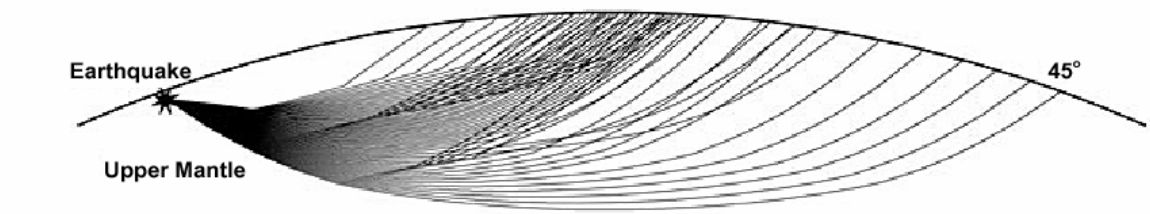

Figure 4. Illustration of the effects of triplication on ray paths between 17° to 23° epicentral distance (from Stein and Wysession, 2002).

Many of the regional monitoring methodologies currently employed, such as kriged amplitude and travel-time correction surfaces, were developed for regions *in between* the *Pn-Pg* and the *Pn-P* crossover distances, leaving two important distance ranges uncalibrated in terms of realistic physical models that explain the observed effects of triplication, phase blockage, and lateral heterogeneity. The latter of these distance ranges is at far-regional/near-teleseismic distances (13° to 30°), where the crossover occurs between *Pn* to *P* as the first arrival on seismograms. At this distance, *P*-waves bottom between the Moho and 660 km. Accurate velocity models are required for the region of interest in order to identify the phase as *Pn*, *P*, *Pdiff*, *PP*, their shear-wave equivalents, and possible precursors, and to accurately locate events, which can be very problematic given a small event recorded on a sparse

network. Perhaps the only way to correctly identify each phase is through accurate travel-time prediction and/or improved array processing. In addition, triplication can result in a focusing of the *P*- and *S*-wave energy, resulting in anomalous amplitudes, incorrect magnitude estimates, and inaccurate phase ratio discriminant performance.

As discussed above, the MDAC method was originally developed for distances between the *Pg*-*Pn* crossover (< 5°) and the *Pn*-*P* crossover (> 17°). One of the objectives of this proposal is to use the information gathered in studies of transition-zone amplitude anomalies observed at regional arrays to extend MDAC outside of its currently defined distance range. As a first step, we will investigate the geometrical spreading term in Equation 1 which is defined following Street et al. (1975) with a critical distance R_o within which the spreading is spherical and beyond which it decays as distance to the power η

$$G(R) = \begin{cases} \dfrac{1}{R} & \text{where} \quad R < R_o \\ \dfrac{1}{R_o}\left(\dfrac{R_o}{R}\right)^{\eta} & \text{where} \quad R \geq R_o \end{cases} \qquad (1)$$

This formulation accounts for the crustal waveguide effect on some phases, such as *Pg* and *Lg*. For upper mantle phases *Pn* and *Sn*, we can set R_o to a small number (e.g., 1 km). Because MDAC is a station-centric amplitude correction method, the simple frequency-independent geometric spreading correction is going to be inadequate at transition-zone distances for *P* (and *S*) waves. Additionally, geometric spreading factors for a particular phase can vary with range and frequency depending on the velocity structure (e.g., Sereno and Given, 1990). The geometric spreading can be particularly affected at transition-zone distances where triplications occur. This is illustrated in Figure 5, which shows kriged 1 Hz *Pn* amplitude residuals calculated using a simple geometric spreading model normalized for source amplitude from station LZH. From this figure it can be seen that amplitudes show a distinctive ringed pattern moving outward from LZH. In particular, there is a change in amplitudes from low to high of 0.1 to 0.2 magnitude units out at approximately the 20-degree transition region. This suggests that a simple geometric spreading representation such as that used in Equation 1 can only match amplitude decay to the first order for *Pn*. Using the phase arrival database and the mapped amplitude variations for each station relative to the MDAC model, we will work to extend MDAC to the far-regional distance range. As part of this task, UCSC and LANL will investigate improved geometric spreading representations that capture the phenomenology of the *Pg* to *Pn* and *Pn* to teleseismic *P* transition zones.

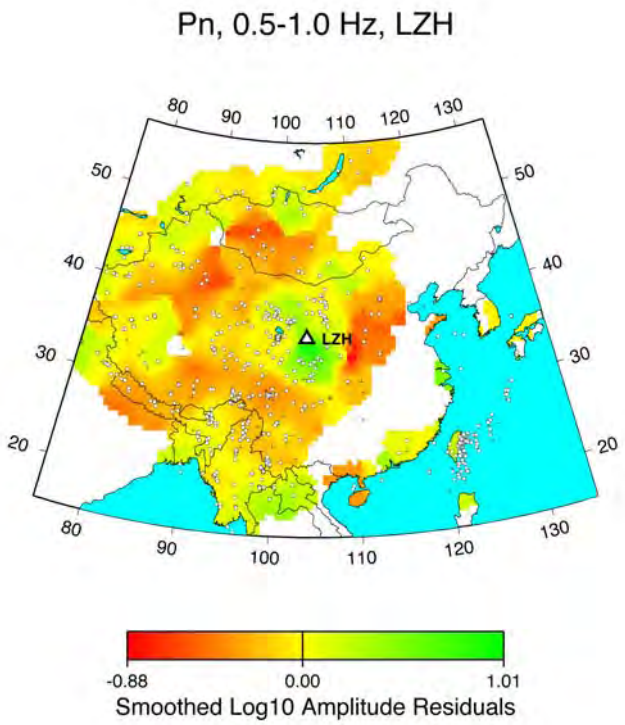

Figure 5. Kriged 1 Hz Pn amplitude residuals normalized for source amplitude from station LZH (Lanzhou, China).

Additionally, phase blockage can occur over relatively short distances in the absence of any anelastic effects (e.g., McNamara et al., 1996; Rapine et al., 1997). Station-centric kriged amplitude correction surfaces on top of the tomographic models may assist in identifying blocked paths (e.g., Phillips, 1999; Rodgers et al., 1999) as well as deficiencies in geometrical spreading representations.

Waveform Data Collection

We are currently requesting and assembling waveform data from the Incorporated Research Institute for Seismology (IRIS) Data Management Center (DMC) and LANL Database to prepare for phase picking and amplitude measurement. We have selected about 100 broadband and short-period stations in the region for the data collection. Figure 6 shows the distribution of the stations. We have removed some stations from the initial selection because of their proximity to each other (< 2º).

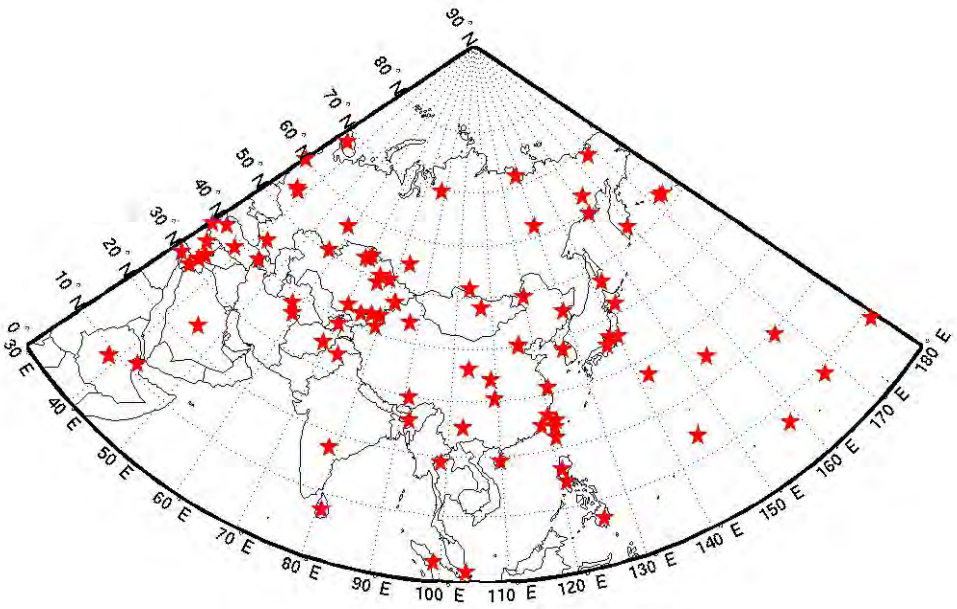

Figure 6. Station distribution for the data collection.

Figure 7 plots the seismic events that we initially selected for our data requests. These are events that occurred between 1975 and 2004, have magnitudes of 3 or larger and have depths of 50 km or shallower. From the histogram in the figure, we can see severe event clustering along the West Pacific Rim. These event clusters would potentially bias the path coverage for our later inversion. To decluster the events, we divided the whole region into 1-by-1º cells and required that the number of events in each cell be no more than one. Events in each cell were ranked based on their magnitudes and the number of stations that might have recorded the events (estimated from source-receiver distances and operation status of the stations). Although the area of the cells is different for different latitudes, the difference becomes significant only when we approach the North Pole, where the events are so scattered that we did not want to remove too many events in this region anyway. Additional criteria, such as a source-receiver distance of 4000 km or shorter, etc., are imposed in formulating the data requests. A total of 3796 events were selected. Figure 7 shows the distribution of final event selection that was used in the data request. Depending on the actual number and quality of waveforms that we obtain, we will reevaluate our criteria and make adjustments to relax some of the criteria if necessary.

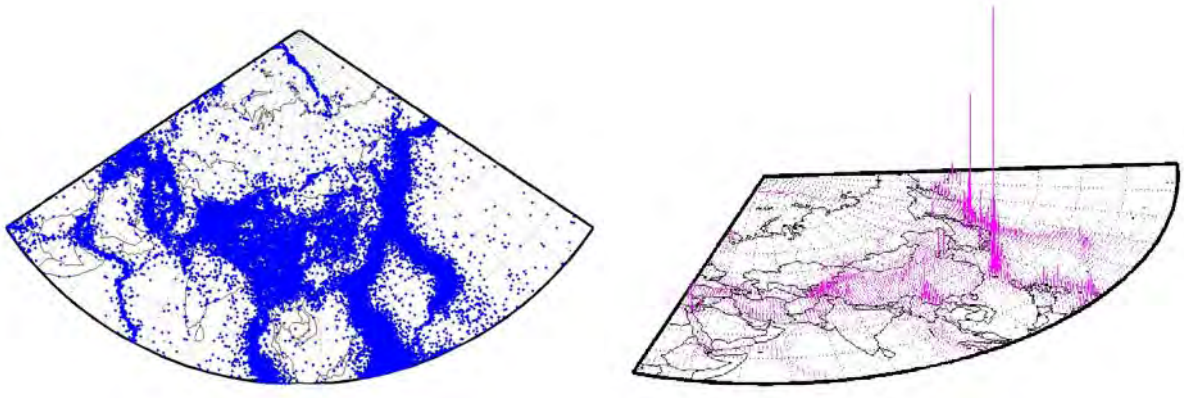

Figure 7. Events that passed initial selection criteria of magnitude and depth. The plot on the right is a three-dimensional histogram of the number of events in each 1-by-1º cell.

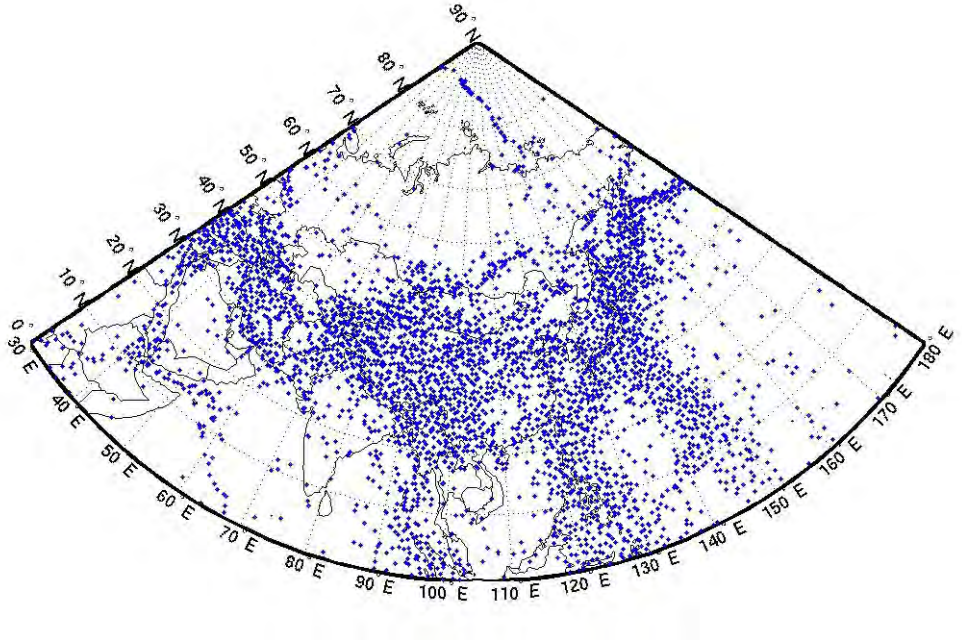

Figure 8. Final event selection used in the data collection. The distribution is much more uniform compared to Figure 7.

CONCLUSIONS AND RECOMMENDATIONS

Underlying geophysical calibration is important for development and improvement of regional seismic discriminants. MDAC amplitude corrections used to develop regional discriminants are critically dependent on such parameters as attenuation and geometrical spreading. This work will address methods to address these issues through a blend of empirical and theoretical techniques.

REFERENCES

Baumgardt, D.R., Investigation of teleseismic Lg blockage and scattering using regional arrays, *Bull. Seism. Soc. Am.*, 80, 2261–2281, 1990.

Fan, G. and T. Lay (2002), Characteristics of Lg attenuation in the Tibetan Plateau, *J. Geophys. Res.* 107: (B10), 2256, doi:10.1029/2001JB000804.

Jeffreys, H. and K. E. Bullen (1958), *Seismological Tables*, British Association for the Advancement of Science, Gray Milne Trust, Office of the British Association, Burlington House, London, England.

Kennett, B. L. N., and E. R. Engdahl (1991), Travel times for global earthquake location and phase identification, *Geophys. J. Int.* 105, 429–465.

McNamara, D.E., T.J Owens, and W.R. Walter, Propagation characteristics of Lg across the Tibetan Plateau, *Bull. Seism. Soc. Am.* 86: 457–469, 1996.

Mitchell, B.J., Y.Pan, J. Xie (1997), and L. Cong, Lg coda Q variation across Eurasia and its relation to crustal evolution, *J. Geophys. Res.* 102: (22),767–22,779.

Phillips, W. S. (1999), Empirical path corrections for regional-phase amplitudes, *Bull. Seism. Soc. Am.* 89: 384-393.

Rapine, R. R. J. F. Ni, and T. M Hearn (1997), Regional wave propagation in China and its surrounding regions, *Bull. Seism. Soc. Am.* 87: 1622–1636.

Rodgers, A. J., W. R. Walter, C. A. Schultz, S. C. Myers, and T. Lay (1999), A comparison of methodologies for representing path effects on regional P/S discriminants, *Bull. Seism. Soc. Am.* 89: 394–408.

Sereno, T. J. and J. W. Given (1990), Pn attenuation for a spherically symmetric earth model, *Geophys. Res. Lett.* 17, 1141–1144.

Stein, S. and M. Wysession (2002), *An Introduction to Seismology, Earthquakes and Earth Structure*, Blackwell Science, Inc.

Street, R., R. Herrmann, and O. Nuttli (1975), Spectral characteristics of the Lg wave generated by central United States earthquakes, *Geophys. J. R. Astron. Soc.* 41: 51–63.

Tarantola, A. (1987), *Inverse Problem Theory*, Elsevier Science, Amsterdam, The Netherlands.

Taylor, S. R., and H. E. Hartse (1998), A procedure for estimation of source and propagation amplitude corrections for regional seismic discriminants, *J. Geophys. Res.* 103: 2781–2789.

Taylor, S. R., A. A. Velasco, H. E. Hartse, W. S. Phillips (2002), W.R. Walter, and A.J. Rodgers, Amplitude corrections for regional seismic discriminants, *Pure. App. Geophys. 159*: 623–650.

Taylor, S. R., X. Yang and W. S. Phillips (2003). Bayesian Lg attenuation tomography applied to eastern Asia, *Bull. Seism. Soc. Am.* 93: 795–803.

Walter, W. R. and S. R. Taylor (2002), A revised Magnitude and Distance Amplitude Correction (MDAC2) procedure for regional seismic discriminants: Theory and testing at NTS, Los Alamos National Laboratory document LA-UR-02-1008.

Yang, X., A numerical investigation of Lg geometrical spreading, *Bull. Seism. Soc. Am.* 92, 3067–3079, 2002.

Yang, X., S.R. Taylor, and H.J. Patton (2004), 20-sec Rayleigh-wave attenuation tomography for central and southeast Asia, *J. Geophys. Res*. 109 B12.

Xie, J. (2002), Lg Q in the eastern Tibetan Plateau, *Bull. Seism. Soc. Am.* 92: 871–876.

Zhang, T., and T. Lay (1995), Why the Lg phase does not traverse oceanic crust, *Bull. Seism. Soc. Am.* 85 1665–1678.

SEISMIC CHARACTERIZATION OF NORTHEAST ASIA AND ANALYSIS OF THE NEVA PEACEFUL NUCLEAR EXPLOSIONS

Kevin G. Mackey[1], Kazuya Fujita[1], Hans E. Hartse[2], Lee K. Steck[2], and Richard J. Stead[2]

Michigan State University[1] and Los Alamos National Laboratory[2]

Sponsored by National Nuclear Security Administration
Office of Nonproliferation Research and Engineering
Office of Defense Nuclear Nonproliferation

Contract Nos. DE-FC52-2004NA25540[1] and W-7405-ENG-36[2]

ABSTRACT

Twelve peaceful nuclear explosions (PNEs) were detonated in the Yakutsk region of Russia in the 1970s and 1980s. In July and August 1987, three PNEs were detonated south of the village of Tas-Yuryakh in southwest Yakutia, in an attempt to increase oil production (Neva-2 and -3) and construct an underground oil storage facility (Neva-4) in the region. These explosions were recorded across the Yakutsk regional seismic network (event-station distances of between about 750 and 1400 km), but none of these data (origin parameters, arrival times and amplitudes) were ever published in either regional or international seismic bulletins. We present and interpret this previously unpublished Yakutsk data, including our new analysis of seismograms.

From analysis of the regional Neva PNE seismic data we find Pn and Pg velocities of 8.31 km/s and 6.16 km/s, respectively, and Sn and Sg velocities of 4.70 km/s and 3.59 km/s, respectively. These velocities are primarily valid for the eastern Siberian Platform, and are consistent with earlier studies.

Comparison between various Pg/Sg amplitude ratios of the Neva PNEs and those of regional earthquakes show that for a given distance or K-class (source size), the ratio is larger for explosions, and the best discriminants use only horizontal component Pg/Sg ratios. Neva-4 was detonated in salt, and plots closer to tectonic earthquakes than the Neva-2 and -3 PNEs, which may have implications for other discrimination scenarios. We also found that the Yakutsk network discrimination results, which were obtained using analog data, essentially match our previous results for the Neva explosion data recorded digitally at station HIA, China. Hence, the analog data from Yakutia can be used to demonstrate transportibility of discriminants to regions where no digital data from nuclear explosions exist.

Additional work we have undertaken over this past year include (1) compilation of a station book of northeastern Russia seismic stations including all obtainable station information and yearly instrument calibration curves; (2) a comprehensive analysis of all focal mechanisms that have been generated, reported, or published for continental eastern Russia with special emphasis placed on data source, data quality, and mechanism reliability; and (3) continued origin, arrival, and amplitude information to our Siberia seismicity database.

OBJECTIVES

The transportability of regional discriminants is an especially interesting topic as no new nuclear explosions have occurred in Asia for several years. We have analyzed previously unavailable seismic information from historic events to study crustal velocity models and to investigate regional discriminants in Yakutia. Our objective is to demonstrate that our previously estimated velocity models are valid and to demonstrate that analog amplitude data can be utilized to transport discriminants to a new region.

RESEARCH ACCOMPLISHED

Neva PNE Background Information

In July and August 1987, three PNEs were detonated south of the village of Tas-Yuryakh in southwest Yakutia, Russia, (Figures 1 and 2) in an attempt to increase oil production (Neva-2 and -3) and construct an underground oil storage facility (Neva-4) in the region (Fujita, 1995). These explosions were recorded across the Yakutsk regional seismic network, but none of the data were ever published in either international bulletins or Soviet regional seismic bulletins. However, the seismograms were analyzed and the data recorded in the Yakutsk network internal bulletin. Here we present and interpret previously unpublished Yakutsk data.

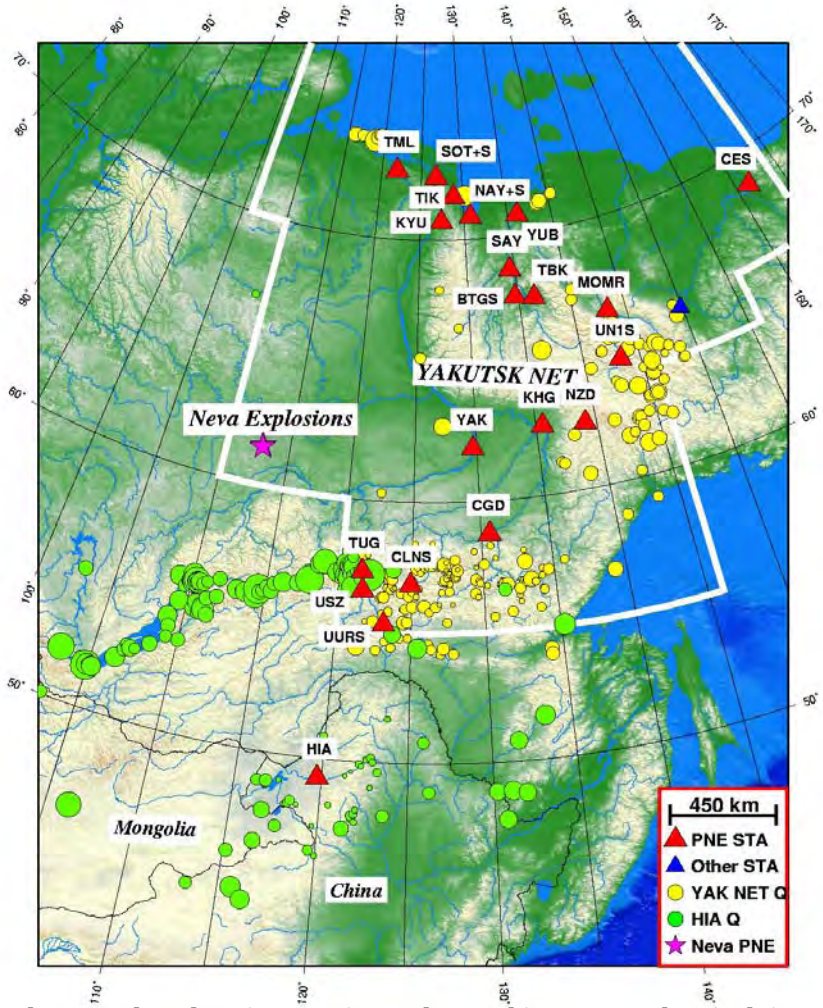

Figure 1. Yakutsk Network and station HIA in northeast China. We used arrival time and amplitude information from the Neva-2, -3, and -4 PNEs to conduct travel time and discrimination analysis for the stations shown in red. Yellow circles represent earthquakes recorded by the Yakutsk Network and green circles are earthquakes recorded digitally at HIA.

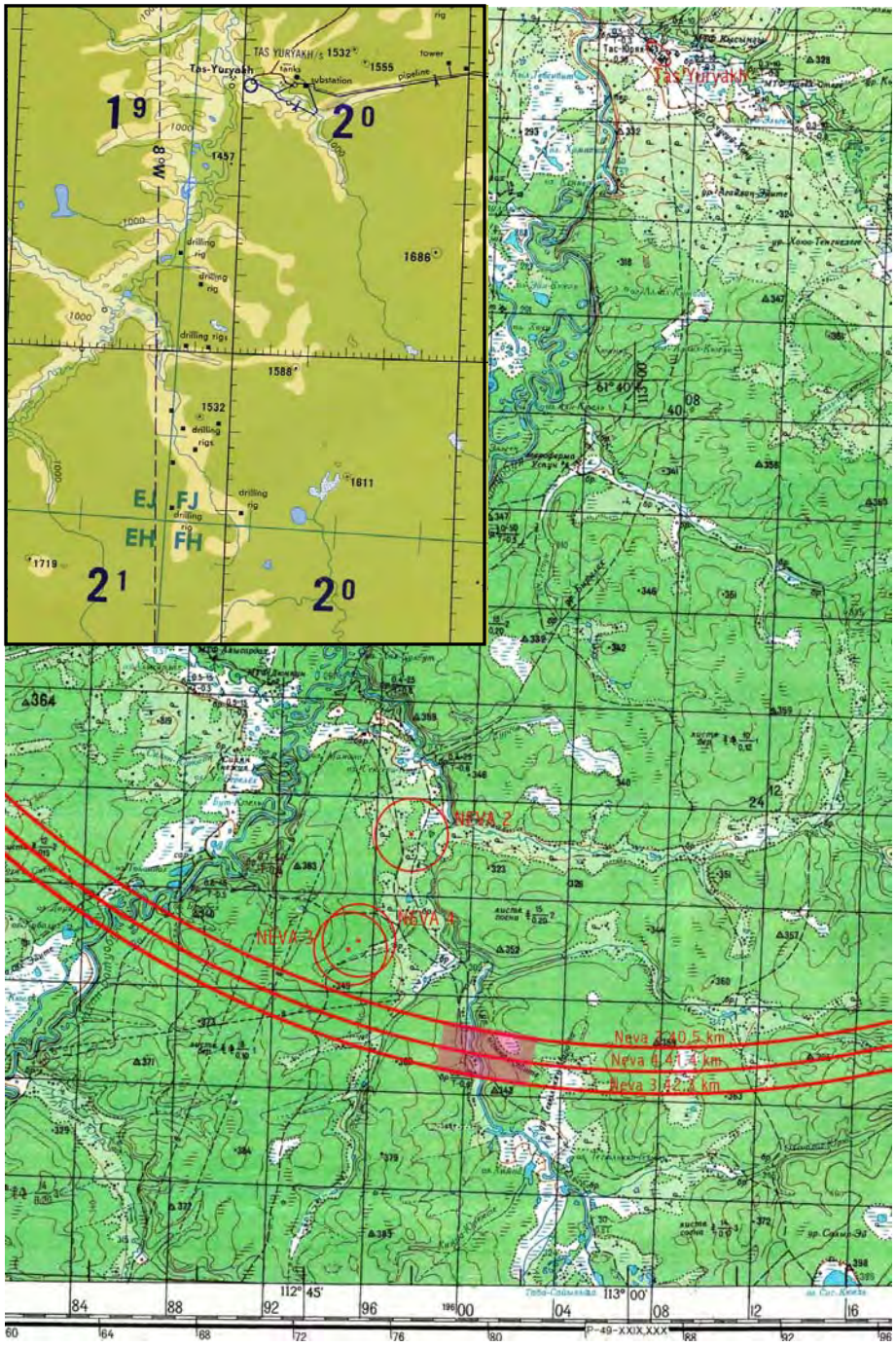

Figure 2. Tas'Yuryakh region showing the probable locations of the Neva PNEs. The inset covers the same geographic region as the main map and shows the locations of the oil fields associated with the Neva PNEs. The large map shows arcs representing the reported linear distances from the town to each PNE, with the shaded region the most likely area of detonation based on association with oil wells. Circled dots represent International Seismological Centre (ISC) seismically determined locations for the events. Grid line spacing represents approximately 4 km.

The general setting of the Neva -2, -3 and -4 PNEs, as well as a discussion of other PNEs in Yakutia and the Tas-Yuryakh region, can be found in Fujita (1995). Several locations have been reported for the Neva-2, -3 and -4 PNEs, including both instrumental and descriptive, though there seems to be no reported ground truth location.

Sultanov et al. (1999) report geodetically determined coordinates for many Soviet PNEs, but they report only seismic locations for the Neva explosions. Table 1 lists the various published locations of the events. Burtsev (1993) describes the events as having taken place south of Tas-Yuryakh in the basin of the Telgespit River. Specific parameters and locations being Neva-2 (13 kt in Borehole 68 at 1526.6-m depth in dolomite, 40.5 km south), Neva-3 (13 kt in Borehole 61 at 1515.2-m depth in dolomite, 42.3 km south), and Neva-4 (3.2 kt in Borehole 101 at 815.3-m depth in salt, 41.4 km south; Burtsev [1993], Mikhailova [1994]).

Table 1. PNE determinations

DATE	TIME	LAT.	LONG	DEPTH	MAG.	REF.
Neva-2						
19870706	23 59 46.00( )	60.3000	115.9000	5.6	mb	HFS
19870706	23 59 56.70( )	61.5010	112.8030	0.0	5.1 mb	NEIC
19870706	23 59 59.90( )	61.5000	113.2000	.		PEK
19870707	00 00 00.00( )	61.5000	112.4000	0.0	5.2 mb	NAO
19870707	00 00 00.00( )	61.5000	112.8500	1.502	5.1 mb	SUL*
19870706	23 59 56.93(0.2)	61.5014	112.8252	0.0	5.1 mb	ISC
Neva-3						
19870724	01 59 55.70( )	61.5000	112.7000	4.5	MS	PEK
19870724	01 59 56.80( )	61.4780	112.7530	0.0	5.1 mb	NEIC
19870724	02 00 00.00( )	61.5000	112.4000	0.0	5.2 mb	NAO
19870724	02 00 00.00( )	61.4500	112.8000	1.515	5.1 mb	SUL*
19870724	02 00 09.00( )	62.7000	112.7000	5.3	mb	HFS
19870724	01 59 56.93(0.2)	61.4574	112.7819	0.0	5.1 mb	ISC
Neva-4						
19870812	01 29 44.00( )	60.1000	116.4000	5.5	mb	HFS
19870812	01 29 55.90( )	61.5000	113.1000			PEK
19870812	01 29 56.80( )	61.4550	112.7600	0.0	5.0 mb	NEIC
19870812	01 30 00.00( )	61.5000	112.4000	0.0	4.9 mb	NAO
19870812	01 30 00.50( )	61.4500	112.8000	0.815	5.0 mb	SUL*
19870812	01 29 57.05(0.2)	61.4592	112.7887	0.0	5.0 mb	ISC

*Sultanov et al., 1999

We checked both instrumental and descriptive locations for consistency on U.S. air navigation charts (1:500,000 scale; tactical pilotage chart [TPC] D-7A; Figure 2 inset) and Soviet military topographic maps (1:200,000 scale; P-49-XXIII, XXVI;
Figure 2). Comparison of the ISC determined epicenters to the most likely location of the explosions based on cited distances and locations of oil drill rigs (see Figure 2) suggest the ISC locations are 8–10 km to the northeast. However, it is unclear if the distances given from Tas-Yuryakh are driving distances (road) or linear (as the crow flies). Given the historic difficulty in the use of accurate maps and/or coordinates in the Soviet Union, it would have been difficult to calculate an accurate linear distance. Overall, it is reasonable to consider that the distances from Tas-Yuryakh cited in Burtsev (1993) to be driving distances. Hence, the actual locations of the PNEs would be closer to Tas-Yuryakh and closer to the reported ISC epicenters. Overall, given the uncertainties involved in determining a ground truth location based on the location descriptions and available maps, the instrumental ISC determined epicenters appear to be sufficiently accurate to be useful in a basic seismic velocity study.

Travel Time Summary

We acquired seismograms from several Yakutsk network stations that recorded the 1987 Neva PNEs. Using the seismograms, we re-analyzed the arrival time picks for the southern Yakutsk stations, as well as northern stations. Our re-association of arrivals are depicted in Figure 3, along with travel-time curves that use ISC epicenter and origin time. Regressions calculated for Pg and Sg velocities assume an origin (0, 0) intercept.

By combining all new and corrected phase associations from the Neva-2, -3, and -4 PNEs and using the instrumentally determined ISC epicenter and origin time, we estimated best fitting velocities for P, Pg, S, and Sg

phases (Figure 3). The velocities determined primarily reflect the seismic velocities of the eastern Siberian Platform, as all or most of each path is within it. The Pg (6.158 km/s) and Sg (3.594 km/s) velocities determined are consistent with the Pg and Sg velocities determined by a grid search method that obtained the best fitting crustal velocities for locating earthquakes (Figure 4; Mackey et al., 2003). In the study of Mackey et al. (2003), the Siberian Platform has elevated seismic velocities, averaging about 6.2 for Pg and 3.6 km/s for Sg, relative to other regions of eastern Russia. The similar elevated crustal velocities determined here from the Neva PNEs lend validation to the Mackey et al. (2003) model.

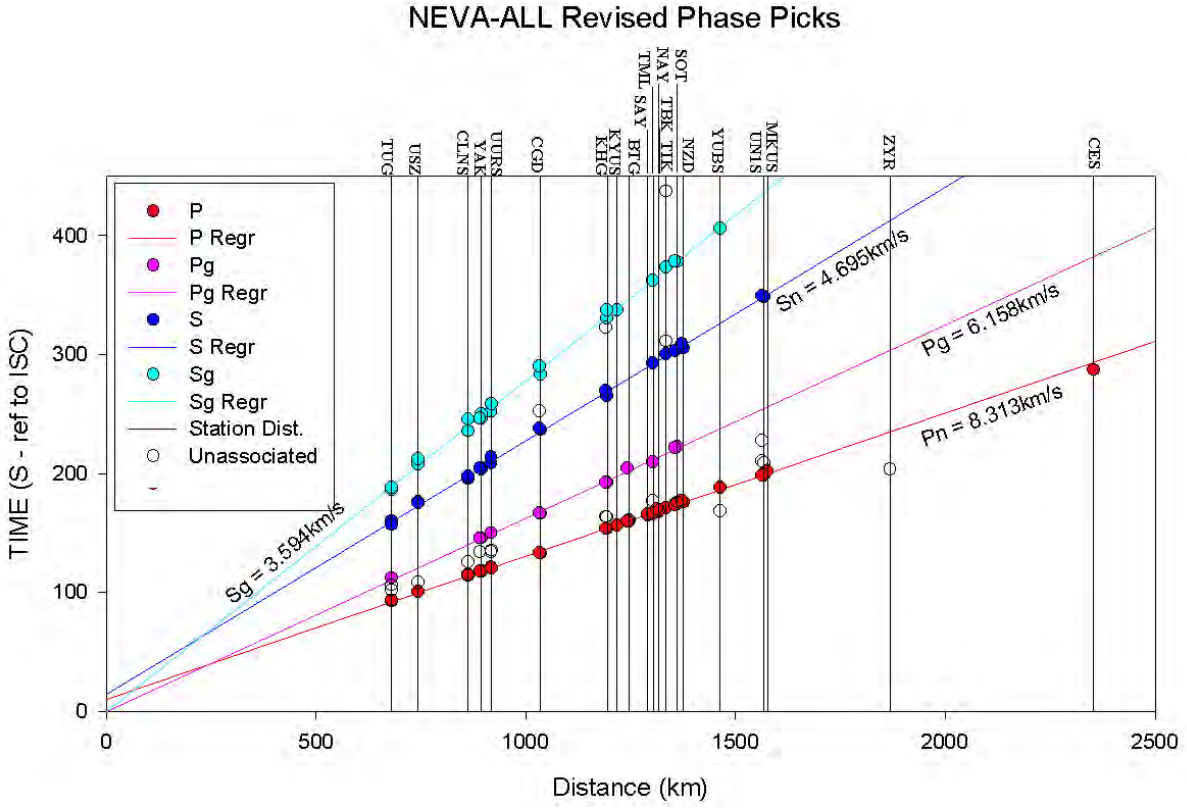

Figure 3. Travel time curves based on the NEVA PNEs.

Explosion Discrimination

Amplitudes from the Yakutsk network stations are available in the Yakutsk bulletin for the Neva PNEs, as are amplitudes for local and regional earthquakes. For the Neva-2 and -3 events, we reread amplitudes from available seismograms. We calculated amplitudes from our measurements following the standard operating procedures used in the Yakutsk network. Amplitudes are calculated by measuring the maximum peak to trough distance for a given phase. The measured amplitude is then divided by 2, and again divided by the station magnification in thousands. The resulting value is then reported as microns. Frequency of the arrival is not taken into account. Amplitudes for the Neva-4 PNE and some stations for Neva-2 and -3 were taken from the unpublished Yakutsk data bulletin.

To test discriminants, we also utilized amplitude data from several earthquakes that occurred across Yakutia in the 1980s and early 1990s (yellow circles, Figure 1). For earthquakes, we only selected amplitudes from stations that had also reported amplitudes for the PNEs. Unfortunately, because of analysis procedures used in the Yakutsk network, the Yakutsk bulletin does not list northern station amplitudes for southern region earthquakes, which restricts the available earthquake data at greater distances. PNE amplitudes are often three-component for P phases (Pn and Pg) and S (Sn and Sg) phases. Following the convention in our Russian data, we refer to Sg rather than Lg for the crustal S phase.

Using the available amplitudes, we formed various Pg/Sg ratios for the Neva PNE's and earthquakes. We tested vertical component discriminants (PgZ/SgH, Figure 5) and several other combinations of vertical and horizontal

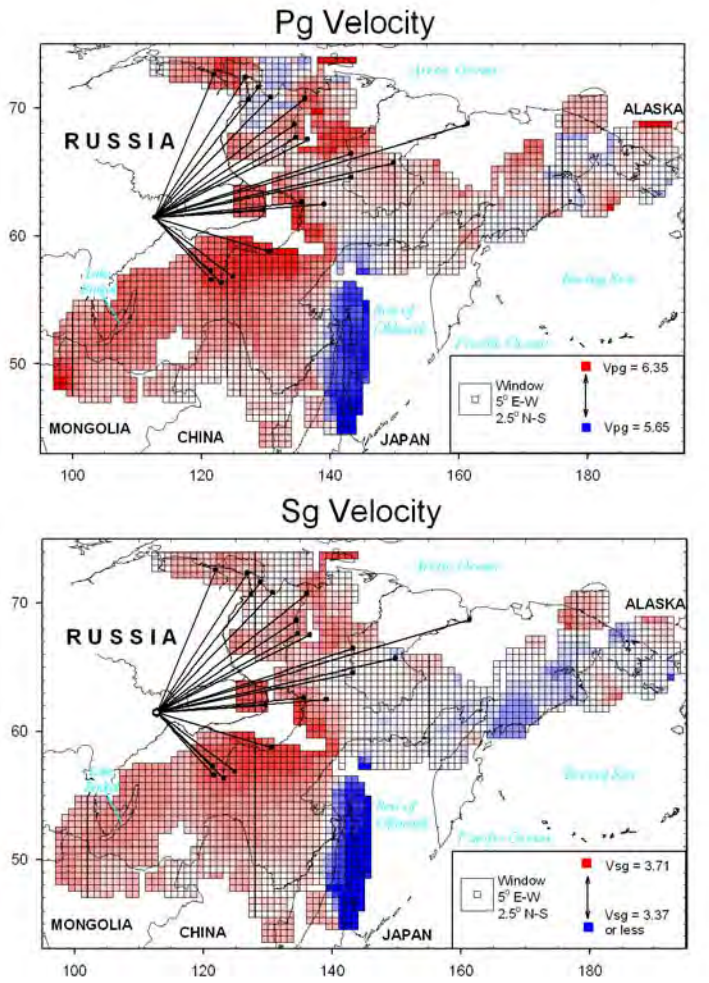

Figure 4. Velocity model of northeast Russia determined by Mackey et al. (2003). Elevated crustal velocities associated with the Siberian Platform determined in this model are consistent with velocities found in this study.

component ratios. Note that we show ratios from all stations, not just a single station in Figure 5. For each ratio type tested, we estimated a ratio-distance linear trend using only the earthquake data, and then removed that trend from both the earthquake and the explosion ratios. Figure 5A shows uncorrected ratios versus distances, and 5B shows the uncorrected ratios versus magnitude. Figures 5C and 5D show the corrected ratios versus distance and magnitude, respectively. In general, all combinations of amplitudes read from vertical and horizontal components form ratios that perform similarly to those in Figure 5A–C, though ratios using only horizontal amplitudes are slightly better.

Overall, regardless of components used, separation of the earthquake and explosion populations is quite good, especially considering that the amplitudes are measured from analog records without instrument corrections or band pass filtering, and the earthquakes are from such a broad geographic area. This separation is consistent with other Asian event discrimination studies (Hartse et al., 1997; Hartse, 2000). For comparison to discrimination performance of these same 3 PNEs using digital data, we show results from Hartse (2000) in Figure 5E and Figure 5F where he used HIA data and bandpass-filtered the waveforms prior to amplitude measurement. Clearly, the analog data have demonstrated that the regional Pg/Sg discriminant can be transported to northeastern Asia.

It is interesting to note that the amplitude ratios from Neva-4 are somewhat different. We find that the Pg/Sg ratios for Neva-4 plot roughly between the trends of ratios from the earthquakes and Neva-2 and -3 explosions (see Figures 5A and 5C). Neva-4 is also unusual in that the reported magnitudes are nearly identical (Neva-4 m_b 5.0 and Neva-2 and -3 m_b 5.1), even though Neva-4 was much smaller (3.2 kt) than Neva-2 and -3 (both 13 kt; see Table 1).

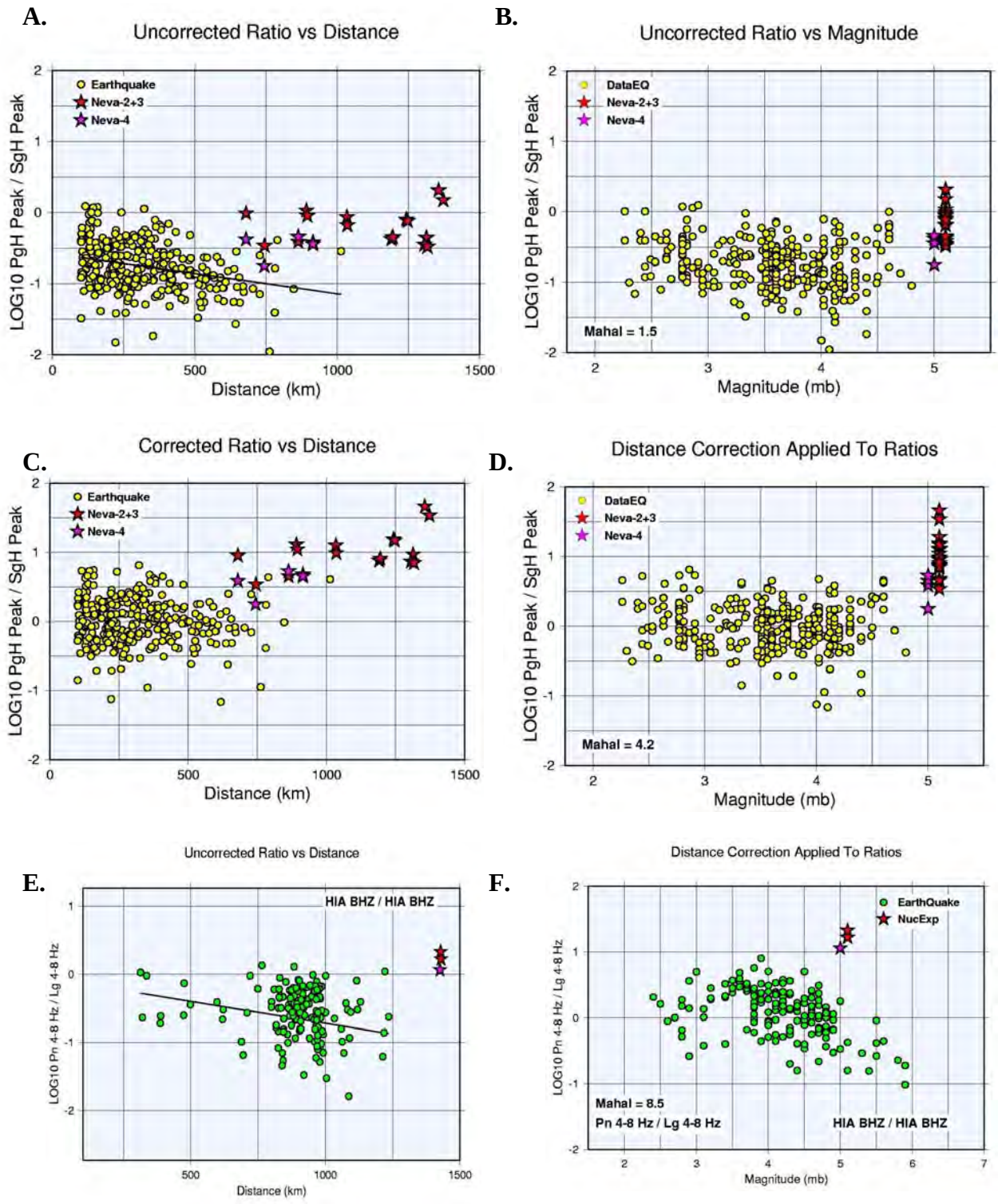

Figure 5. (A-D) Discrimination plots using PgH/SgH amplitude ratios of the Neva PNEs and tectonic earthquakes derived from analog stations in the Yakutsk network. Distance corrections are applied to C and D. (E, F). Discrimination plots between the Neva PNEs and earthquakes using digital data recorded at station Hialar (HIA) in China. The Hialar data were filtered to find the optimum frequency band for discrimination. A distance correction is applied to F.

Although the Neva-4 explosion was shallower (815.3 m) than Neva-2 (1526 m) and Neva-3 (1515.2 m; Fujita, 1995) all were overburied; thus, we do not believe that this is a result of depth of burial. The differences in Pg/Sg amplitude ratios and magnitudes between Neva-2 and -3 and Neva-4 may be explained by the type of rock in which the explosions took place. Neva-4 occurred in salt, while Neva-2 and -3 occurred in dolomite (Fujita, 1995). This suggests that seismic energy was better coupled for the nuclear explosion in salt, which may affect yield estimation. Also, nuclear explosions in salt may generate larger S-waves relative to P-waves when compared to other types of rock, thus plotted Pg/Sg amplitude ratios will appear closer to tectonic earthquakes than other nuclear explosions.

Despite the fact that this brief discrimination study is based on analog data, it is important that we observe separation between nuclear explosion and earthquake populations based on P/S amplitudes for the eastern Siberian Platform because little regional nuclear explosion data are available from the area. This study also confirms that it is possible to conduct discrimination studies using historic Soviet regional station data. Specifically, all of the Yakutsk network stations used here operated either SKM, VEGIK, or SM-3 short period seismometers recorded on photopaper.

Other Research

We have begun compilation of two major data sets, the first being a complete inventory of seismic stations that have operated in eastern Russia, and the second being a compilation of all focal mechanisms that have been determined for the study area. Both data sets are being compiled in a loose leaf format so that additions and corrections can easily be made without the need to reprint the entire document. Both documents are based on published Russian and western literature, discussions with Russian seismologists, and our own personal observations or studies.

Station Book

The seismic station inventory consists of one or more pages per station and includes information on station codes (formal and informal), site information (including maps), station history, instrumentation, response curves for the instruments, and other known information about the station, such as noise levels, type of recording, etc. A sample page is presented in Figure 6.

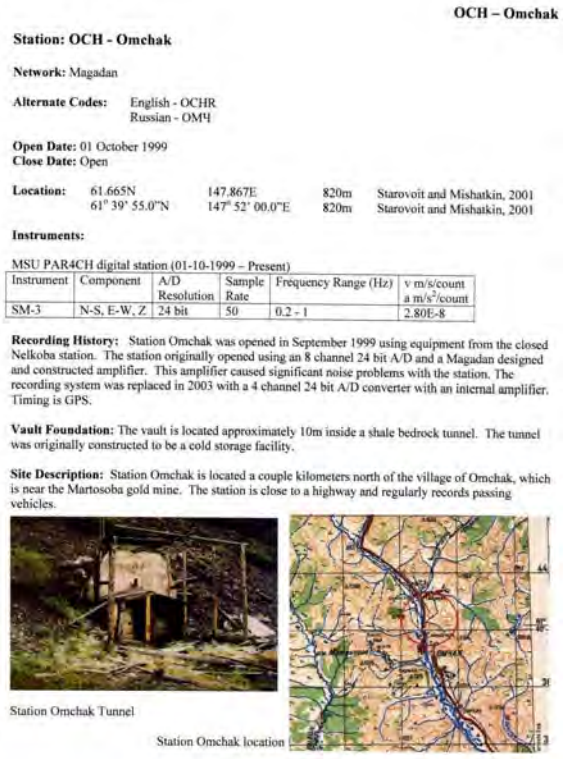

OCH – Omchak

Station: OCH - Omchak

Network: Magadan

Alternate Codes: English - OCHR
Russian - ОМЧ

Open Date: 01 October 1999
Close Date: Open

Location:

61.665N		147.867E	820m	Starovoit and Mishatkin, 2001
61° 39' 55.0"N		147° 52' 00.0"E	820m	Starovoit and Mishatkin, 2001

Instruments:

MSU PAR4CH digital station (01-10-1999 – Present)

Instrument	Component	A/D Resolution	Sample Rate	Frequency Range (Hz)	v m/s/count a m/s²/count
SM-3	N-S, E-W, Z	24 bit	50	0.2 - 1	2.80E-8

Recording History: Station Omchak was opened in September 1999 using equipment from the closed Nelkoba station. The station originally opened using an 8 channel 24 bit A/D and a Magadan designed and constructed amplifier. This amplifier caused significant noise problems with the station. The recording system was replaced in 2003 with a 4 channel 24 bit A/D converter with an internal amplifier. Timing is GPS.

Vault Foundation: The vault is located approximately 10m inside a shale bedrock tunnel. The tunnel was originally constructed to be a cold storage facility.

Site Description: Station Omchak is located a couple kilometers north of the village of Omchak, which is near the Martosoba gold mine. The station is close to a highway and regularly records passing vehicles.

Station Omchak Tunnel

Station Omchak location

Figure 6. Sample page from the Station inventory.

Coordinates, and locations on maps, have been taken from the best possible information, including site visits. Response curve information is taken primarily from those published in Russian operational bulletins (e.g., the instrument supplement to *Materialy po Seismichnost' Sibiri*). Photographs of the station are provided when available, and were primarily taken by the senior author. Station history information has been compiled not only from the published literature but in discussions with station operators. In many cases, stations have been moved over their lifetime even though the same station code (and even station coordinates!) has been maintained. Station locations are shown on Soviet military topographic maps of 1:200,000 scale (U.S. TPCs and maps at other scales have been used when necessary or available). Information detail varies somewhat by station; for the exact locations of some temporary stations are poorly known. So far we have completed the inventory for the Magadan and Yakutsk seismic networks. This inventory will continue to be updated and expanded in the future.

Focal Mechanism Compilation

We have also started compiling a listing and analysis of focal mechanisms which have been determined for continental eastern Russia (see Figure 7). To date, the compilation has been completed for the Stanovoi, Amur, and Chersky seismic regions. These compilations include all known focal mechanisms reported in the published Russian and western literature, along with unpublished mechanisms determined by the Michigan State group over the past 20 years. Focal mechanisms are given as strike, dip, and rake for both nodal planes. The source and the method (data sources) used are tabulated. Where available, a figure showing the data used is included when mechanisms have been determined using P-wave first motions, Rayleigh wave radiation patterns, or synthetic seismograms. For many Russian computer grid-search determined mechanisms, no figure is available. Based on these data, the mechanisms have been qualified as "Poorly Constrained" or "Unknown" (no data available to judge). Mechanisms that appear reasonably well constrained are not qualified and interpretation is left to the user. A "preferred solution" has been selected (which need not be well constrained) when multiple solutions are available. Typographical errors in various publications, errors arising from reversed sign conventions and projections, and other inconsistencies are noted where they have been identified. Additional comments are included which note other citations of the solution, problems in the original or secondary sources, major inconsistencies, and problems with orthogonality of the nodal planes.

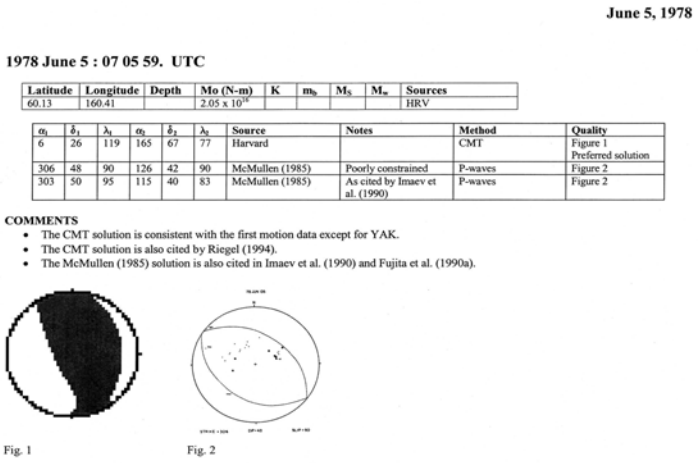

June 5, 1978

1978 June 5 : 07 05 59. UTC

Latitude	Longitude	Depth	Mo (N-m)	K	m_b	M_S	M_w	Sources
60.13	160.41		2.05×10^{18}					HRV

α_1	δ_1	λ_1	α_2	δ_2	λ_2	Source	Notes	Method	Quality
6	26	119	165	67	77	Harvard		CMT	Figure 1 Preferred solution
306	48	90	126	42	90	McMullen (1985)	Poorly constrained	P-waves	Figure 2
303	50	95	115	40	83	McMullen (1985)	As cited by Imaev et al. (1990)	P-waves	Figure 2

COMMENTS

- The CMT solution is consistent with the first motion data except for YAK.
- The CMT solution is also cited by Riegel (1994).
- The McMullen (1985) solution is also cited in Imaev et al. (1990) and Fujita et al. (1990a).

Fig. 1 Fig. 2

Figure 7. Sample page from focal mechanism compilation.

CONCLUSIONS AND RECOMMENDATIONS

Separation between nuclear explosion and earthquake populations based on P/S amplitudes are observed in analog data from the Neva explosion sequence in the southeastern Siberian Platform. Our work also confirms that it is possible to conduct discrimination studies using historic Soviet regional station data. The next step is to determine whether similar discriminants are applicable to industrial and chemical explosions which occur in mining districts in eastern Russia. A large quantity of amplitude information is available in the MSU database; however, considerable filtering of the data set will be required before analyzing the smaller industrial explosions.

Enhanced quality control of the Michigan State University data set and improvement of station parameters continue and production of a usable, adaptable, station book is underway. This information will assist in identifying problem or abnormal stations as well as improving travel times and velocity models. We are also working on a focal mechanism compilation for eastern Russia, which will provide baseline information on regional tectonics and the ambient stress regime.

REFERENCES

Burtsev, I. S., Ed. (1993), *Radiatsionnoe zagryaznenie territorii Respubliki Sakha (Yakutia): Problemy radiatsionnoi bezopasnosti*. Yakutsk, Russia: Ministerstvo Zdravookhraneniya Respubliki Sakha (Yakutia), (in Russian).

Fujita, K., 1995. Peaceful Nuclear Explosions in the Sakha Republic (Yakutia), Russia, *Seismol. Res. Lett.* 66: (3): 20–24.

Hartse, H. E., S. R. Taylor, W. S. Phillips, and G. E. Randall (1997), A Preliminary Study of Regional Seismic Discrimination in Central Asia with Emphasis on Western China, *Bull. Seismol. Soc. Am.* 87: 551–568.

Hartse, H. E., Regional Seismic Event Discrimination in Siberia, 2000, in *Proceedings of the 22nd Annual DoD/DOE Seismic Research Symposium: Planning for Verification of and Compliance with the Comprehensive Nuclear-Test-Ban Treaty (CTBT)*, Vol. 2, pp. 137-146.

Mackey, K. (1999), Seismological Studies in Northeast Russia. Ph.D. thesis, Michigan State University, East Lansing, xxiii, +326 pp.

Mackey, K. G., K. Fujita, L. K. Steck, and H. E. Hartse (2003), Seismic Regionalization in Eastern Russia, in *Proceedings of the 25th Seismic Research Review—Nuclear Explosion Monitoring: Building the Knowledge Base*, LA-UR-03-6029, Vol. 1, pp. 73–82.

Mackey, K. and K. Fujita (2001), Seismicity Characterization and Structure Velocity of Northeast Russia, NERSP Report # 8, Michigan State University, Department of Geological Sciences, East Lansing.

Mikhailova, V. N., Ed. (1994) Yadernye Zzryvy v SSSR, vyp. 4, Mirnoe Ispol'zovanie Podzemnykh Yadernykh Vzryvov, VNIPIpromtekhnologii, Moscow (in Russian).

Sultanov, D. D, J. R. Murphy, and K. D. Rubinstein (1999), A Seismic Source Summary for Soviet Peaceful Nuclear Explosions, *Bull. Seismol. Soc. Am.* 89*:* 640–647.

THE CAUCASUS SEISMIC INFORMATION NETWORK STUDY AND ITS EXTENSION INTO CENTRAL ASIA

Randolph Martin[1], Mary L. Krasovec[1], Spring Romer[1], M. Nafi Toksöz[2], Sadi Kuleli[2], Levent Gulen[2], and Eileen S. Vergino[3]

New England Research[1]
Earth Resources Laboratory, Massachusetts Institute of Technology[2]
Lawrence Livermore National Laboratory[3]

Sponsored by National Nuclear Security Administration
Office of Nonproliferation Research and Engineering
Office of Defense Nuclear Nonproliferation

Contract Nos. DE-AC52-04NA25612 and DE-AC52-03NA99600

ABSTRACT

The Caucasus Seismic Information Network (CauSIN) and the Central Asian Seismic Research Initiative (CASRI) are collaborative projects to build a database of geological, geophysical, and seismic information and to use crustal modeling techniques to create a model to aid in seismic monitoring from the Caucasus to China.

Over the past year we have expanded our database in several ways. We obtained and evaluated regional scale geological maps that cover the Central Asian and Caucasus region. We conducted fieldwork to check the accuracy of the maps. This fieldwork will continue along portions of the Georgian Borjomi-Kazbegi fault during the summer of 2005, with the addition of geophysical surveys including gravity and magnetics.

Our extended collection of seismic data now includes data from Turkey and phase arrival times from local networks in the Caucasus which we have combined with data from the International Seismic Center (ISC) and ground truth events (both earthquakes and explosions) from the U. S. Army Space and Missile Defense Command (SMDC) Research Program. This combined database has been checked for station and event overlaps. Most events are being relocated with the aid of data from local networks. Finally, waveform data from both historical and current events are continually being gathered at Lawrence Livermore National Laboratory (LLNL).

The travel time database has been used for 1D crustal inversions in the Caucasus region. New 1D models will be input to 3D crustal tomography. Due to the political situation in many of the Central Asian countries, communication with scientists in these countries has been limited. Meetings with our Central Asian colleagues during the CauSIN meeting in Vermont in June 2004, and at the CauSIN/CASRI joint meeting in Istanbul in January 2005, have been very important for establishing a good working relationship for data collection in Central Asia.

OBJECTIVES

The primary goal of these projects is to develop a database of geology, tectonics, and seismicity in the Caucasus and Central Asian regions (shown in Figure 1).

With this new database, we will be able to improve earthquake locations and identify potential "ground truth" (GT) events. The dense network, calibration events (mining and quarry blasts), improved models, and better location algorithms (including multiple-event grid search, and double difference) will improve the event locations. Scientists at collaborating countries are assisting with this task, since improved locations will aid in the identification of active faults.

With the ground truth events to serve as validation, we will obtain a detailed crust/upper mantle structure in the Caucasus, eastern Turkey, northwestern Iran, and Central Asia, using data from local seismic stations as well as GSN and other stations operated as part of the national networks. The model will incorporate the extensive geological and geophysical data (e.g., surface seismic reflection profiles, gravity maps) as well as the seismic data.

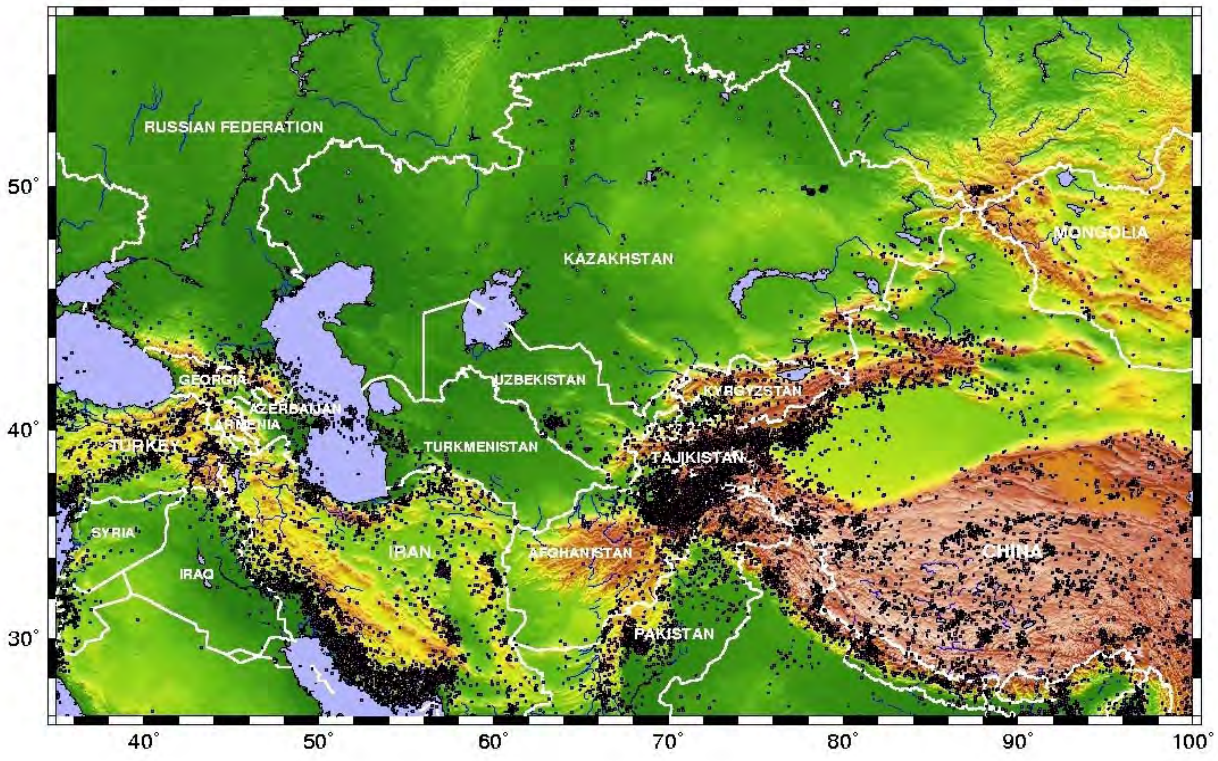

Figure 1. CauSIN and CASRI project area political boundaries and seismicity (USGS).

RESEARCH ACCOMPLISHED

Geology and Tectonics

The goal of the CauSIN and CASRI projects is to produce a seamless tectonic, geological and geophysical model of the Caucasus and Central Asia.

The active tectonics of Central Asia is a consequence of the continental collision and the continuing continental convergence between the Indian and the Eurasian plates. Our approach to reveal the large-scale active tectonics of Asia is to utilize satellite imagery and a few ground truth studies, augmented by the synthesis of the existing Russian and Chinese geological and geophysical data in the mid-seventies (Molnar and Tapponnier, 1975; Tapponnier and Molnar, 1976, 1979). The active tectonic pattern of Asia obtained in these studies (Figure 1) was interpreted as deformation in a rigidly indented rigid-plastic solid, where India is analogous to the indenter and the delineated great strike-slip faults, such as Altyn, Tagh, Kunlun, Sagaing, Red River, Herat, and Quetta-Chaman that correspond to slip lines. Along these slip lines, major continental blocks such as Tibet escape laterally away from the continental collision front.

Within this general tectonic setting, the CASRI project countries, namely Kazakhstan, Uzbekistan, Kyrgyzstan, and Tajikistan, are situated in one of the world's most rapidly deforming continental regions, because the leading tip of the indenting Indian Plate has penetrated furthest into the Eurasian plate in the Hindu Kush-Pamir region (Figures 1 and 2).

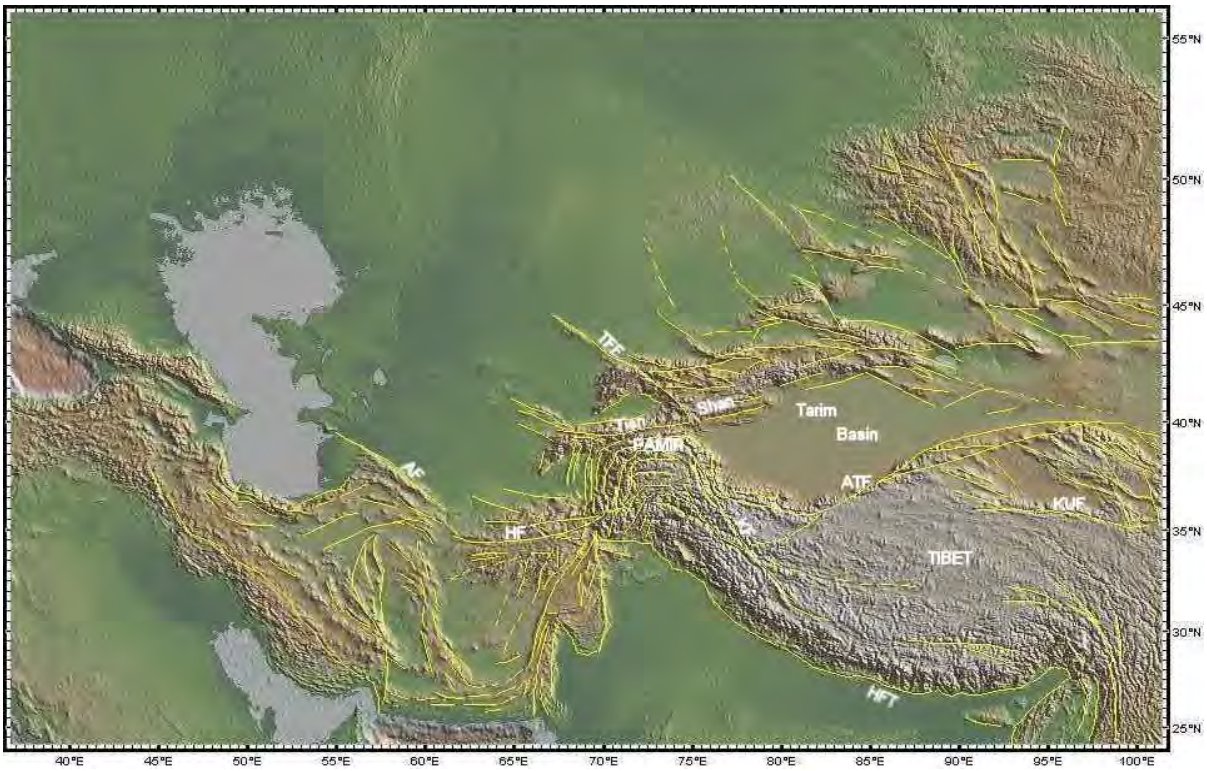

Figure 2. Preliminary tectonic lineament map of Central Asia. Only the major fault zones have been delineated in this figure in order to avoid clutter.

Some prominent faults in this region have been delineated within the scope of the CASRI project using the newly acquired Shuttle Radar Topographic Mission (SRTM) data (Figure 2). The SRTM data is much superior compared to satellite imagery, because it is not affected with cloud cover, and the 3-arc second resolution provides excellent morphological detail of the earth's surface. Furthermore, the capability of artificially illuminating the SRTM data with varying illumination angles and azimuths provides unprecedented advantage to do structural analysis.

Comparison of the previous tectonic maps of the region (e.g. Tapponnier and Molnar, 1979) and Figure 2 indicates that much more tectonic information can be obtained using the high resolution SRTM data compared with the satellite imagery. In fact, some of the delineated faults either have not been mapped previously, or if mapped, the existing data have not been published in the English literature. One of the tasks to be accomplished in the next phase of the CASRI project is to unearth the existing data through active collaboration with our colleagues from the CASRI countries, and to initiate new field excursions to collect structural data in the field and verify those newly delineated fault zones.

Recently acquired GPS data provide important constraints on the nature of the continental deformation in Central Asia (Abdrakhmatov et al., 1996; Reigber et al., 2001; Wang et al., 2001), indicating that the ongoing N-S convergence between the Indian and the Eurasian plates is taken up within a zone of more than 2000 km all the way from the Himalayan Frontal Trust to the mountain ranges of Mongolia. GPS data suggest that 18 mm/yr of convergence is taken up with shortening within the Himalayas, while in the Central Tien Shan the active shortening reaches values up to 13 ± 2 mm/yr. It is also suggested that the rigid Tarim Block rotates clockwise 0.8º/Myr with respect to stable Siberia about a pole located at 96ºE and 43.5ºN (Reigber et al., 2001).

Figure 3 shows a recent geological map compilation covering the CauSIN and CASRI regions. This geological map was originally compiled by Tingdong et al. (1997), and it was published by the Geological Publishing House, Beijing, China, in a scale of 1:5,000,000 as the Geological Map of Asia and Europe. In the original map an equal-area oblique zenithal projection was used with density of graticule: $\Delta\lambda=\Delta\Phi=5°$, Central Meridian: 85ºE, Projection Center: 85ºE - 40ºN. To make it compatible with other datasets, we converted the map into a Lambert Equal area projection (Figure 3). Availability of this geological map is invaluable for the CAUSIN and CASRI projects, because it saves significant amount of time and money.

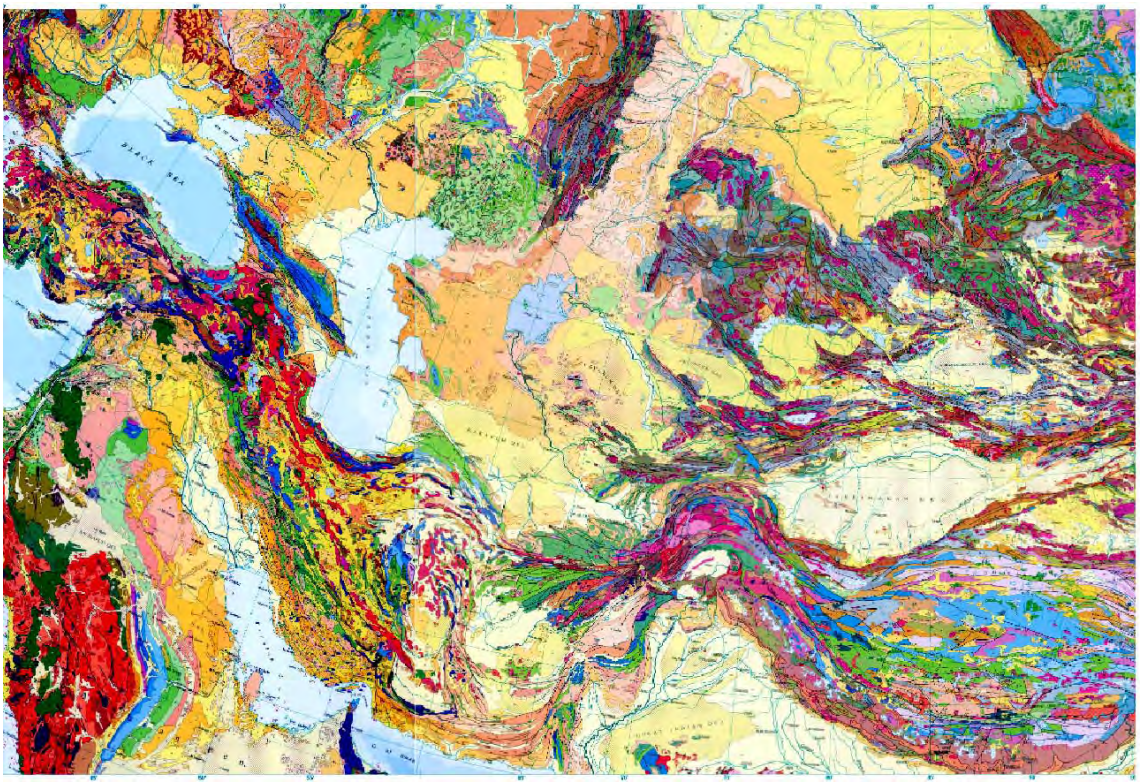

Figure 3. Geological map compilation of the CauSIN and the CASRI regions.

The seismicity data (M > 5) over the last 30 years (Figure 1) show that the Hindu Kush-Pamir and Tien Shan regions are seismically very active. Numerous seismological studies have established that faults in this region are

predominantly trust faults that indicate the overall N-S shortening of the Asian continental crust. Some notable exceptions are the strike-slip Talas-Fergano, Altyn-Tagh, Karakoram, Kunlun, Herat, and Quetta-Chaman faults. The sideways escape of continental blocks is accommodated along these major strike-slip fault zones. Also, the faults that form the western and eastern flanks of the Pamir and Hindu Kush region are oblique-slip faults with significant strike-slip components.

Event Catalog, Phase and Waveform Data

Compiling a comprehensive catalog of seismic events in the Caucasus and Central Asia is a primary objective of these projects. Investigators from LLNL, NER and MIT met with seismologists from the Caucasus and Central Asian countries in the January 2005 in Istanbul to consolidate plans for this effort. We are compiling phase arrival times and waveform data for selected events. The ISC, SMDC, and IRIS data will be used as the backbone of our database which will be supplemented with data from local networks in Georgia, Azerbaijan, Armenia, Kazakhstan, Uzbekistan, Kyrgyzstan, and Tajikistan.

Digital waveform data is important for validating velocity/attenuation models and seismic wave propagation characteristics of the region. We are collecting waveform data of selected events from local/regional network stations, as well as other established databases.

The integration of local data to the general database requires an extensive selection and relocation process. The data from Azerbaijan, shown in Figure 4, is an example. In the general catalog (Figure 4), most epicenters fall on a coarse grid. Recent events, recorded by and located with the aide of expanded national networks, show a better distribution. Relocation of old and recent events will improve epicenters and their association with tectonic features.

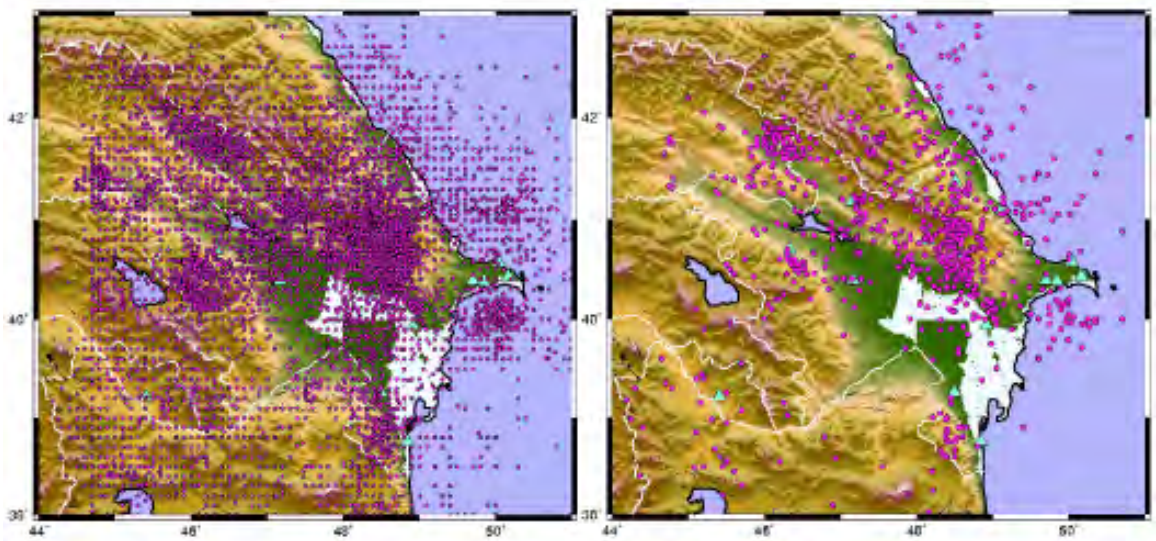

Figure 4. Epicenters in the Azerbaijan catalog. Left: For the period 1900 to 2004. Right: Relocated events in 2002 and 2003.

Near Real Time Data

One important aspect of both projects is to collect data from events in each country in near real-time. It will be useful if they could collect the data and post it in a timely fashion. Over the past several years we have requested data for a number of recent events in Turkey and Iran. Although the participants are cooperative, it takes days or more to get the data from the field and transmit it to us. For the remainder of these projects, we'll be working to improve reporting, publishing, and posting both phase picks and waveforms for regional events recorded on their local networks. An example of data for an earthquake in Iran (2-22-05, Mw = 6.4), recorded in Kazakhstan and Georgia, is shown in Figures 5a and 5b; the epicenter, stations locations, raypaths, and seismograms are presented. Additional data for this and other events in Iran and eastern Turkey are presently being submitted. With continued

effort and upgrading of the local networks, it is realistic to expect data within days so that timely analysis can be performed on significant events.

Seismic Velocity Structure

Analysis of seismic data will be used to produce a 3D structure of the region. To obtain the starting model for the 3D tomography, we use VELEST (Kissling, 1993), a 1D joint inversion program that simultaneously solves for event locations, station delays, and a 1D earth model. The starting models are based on the Crust 2.0 (Bassin et al., 2000) model. Figure 6 shows event locations and the 1D velocity profiles. In Figure 6 (left), both ISC and final VELEST locations are shown. In Figure 6b (right), 1D velocity profiles for each of 15 iterations are shown. The greatest variation in the final models is in the depth range of 0-20 kilometers, which is not unexpected given that we are using a 1D model in a region with much lateral variation, from continental crust in the central Caucasus to oceanic crust in the Caspian and Black Seas.

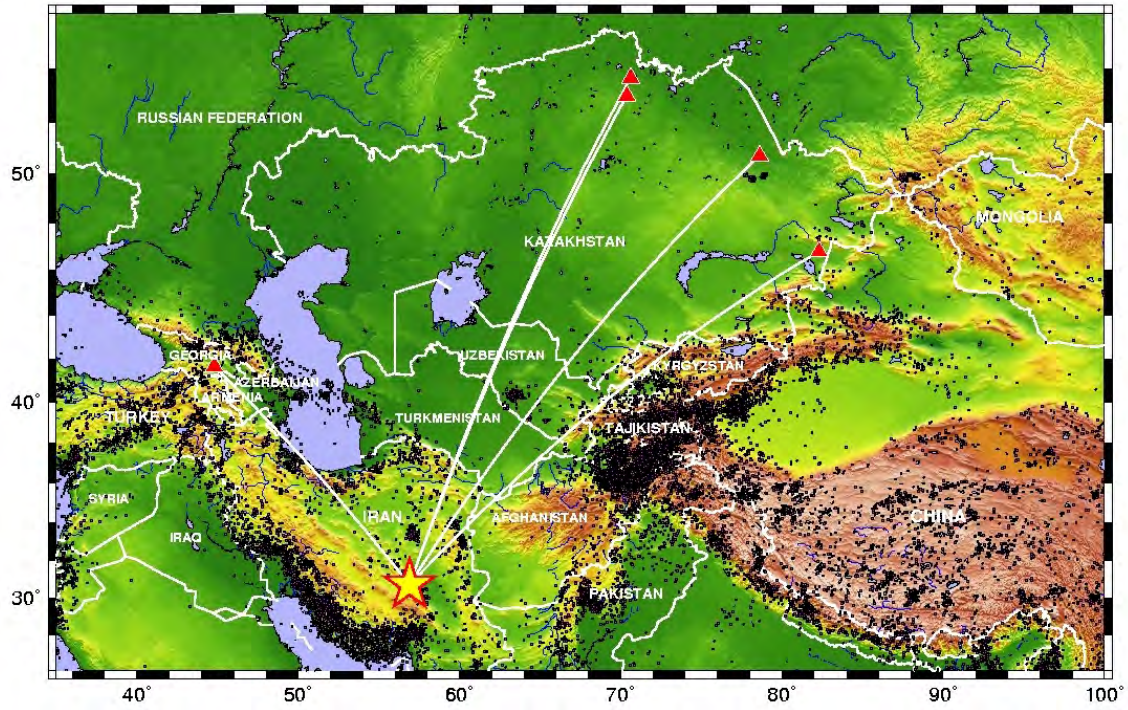

Figure 5a. Iran 2/22/05 earthquake location (yellow/red star). We are continuing our effort to make data from moderate to large events available to all participants in the study soon after the events happen. So far we have collected waveform recordings from one station in Georgia and four stations in Kazakhstan.

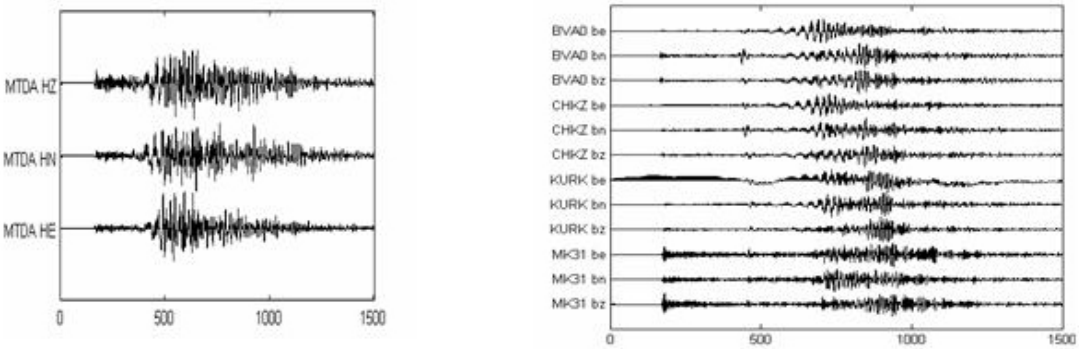

Figure 5b. Traces from stations in Georgia (left) and Kazakhstan (right) for the Iran 02/22/05 earthquake.

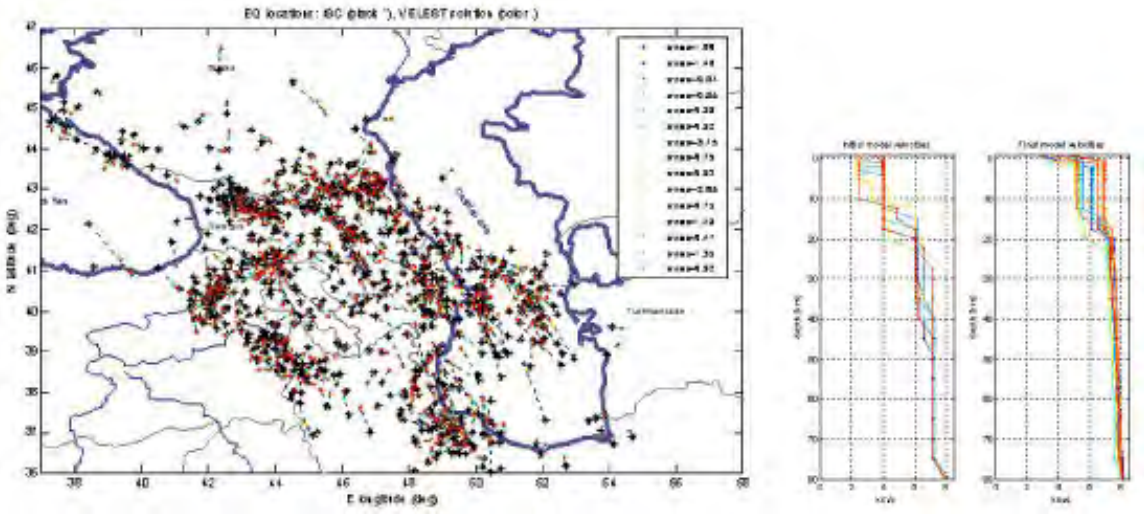

Figure 6. VELEST location/inversions of the Caucasus data. Left: Dashed lines connect the ISC locations (black *) and the VELEST final location. Right: 1D velocity profiles for 15 iterations.

CONCLUSIONS AND RECOMMENDATIONS

Progress is being made in collecting and evaluating data from regional events collected on local networks in the Caucases and Central Asia for the database. We selected 100 earthquakes recorded in the Caucasus for detailed study as part of the CauSIN project. A similar approach was adopted for the CASRI project. Events occurring within the region are particularly important to constrain crustal models. Furthermore, as additional broadband stations are added in the Caucasus and Central Asia and existing stations are upgraded more comprehensive data will be available.

Based on the additional regional data, and a number of ground truth events, we are refining our 1-D crustal models. The 3-D crustal models for the Caucasus and Central Asia will be developed. Using these crustal models, we will relocate critical events to delineate active faults. This is particularly important for identifying hazards and locating events in the regions. Based on refined locations, updated fault and tectonic maps will be completed.

ACKNOWLEDGMENTS

Dina Hunt from LLNL collected and organized data from the Caucasus into a coherent database.

L. Gulen thanks the GIS Services Team members at MIT: Anne Graham, Lisa Sweeney, and Daniel Sheehan for help in map projection conversions.

REFERENCES

Abdrakhmatov, K.Y. et al. (1996), Relatively recent construction of the Tien Shan inferred from GPS measurements of present day crustal deformation rates, *Nature*, 384: 450-453.

Bassin, C., G. Laske, and G. Masters (2000), The current limits of resolution for surface wave tomography in North America, *EOS Trans AGU*, 81: F897.

International Seismological Centre (2001), *On-line Bulletin*, http://www.isc.ac.uk/Bull, Internatl. Seis. Cent., Thatcham, United Kingdom.

Kissling, E., W.L. Ellsworth, D. Eberhart-Phillips, and U. Kradolfer (1994), Initial reference models in local earthquake tomography, *J. Geophys. Res.* 99: 19635-19646.

Molnar, P. and P. Tapponnier, P. (1975), Cenozoic tectonics of Asia, *Science, 189*, 419-426.

Reigber, C. et al., (2001), New space geodetic constraints on the distribution of deformation in Central Asia, Earth *Planet. Sci. Lett.* 191: 157-165.

Tapponnier, P. and P. Molnar, P. (1976), Slip-line field theory and large-scale continental tectonics, *Nature* 264: 319-324.

Tapponnier, P. and P. Molnar, P. (1979), Active faulting and Cenozoic tectonics of the Tien Shan, Mongolia, and Baykal regions, *J. Geophys. Res.* 84: 3425-3459.

Tingdong, L. et al. (1997), Geological Map of Asia and Europe (Scale: 1:5,000,000), Geological Publishing House, Beijing, China.

Wang, Q. et al. (2001), Present-day crustal deformation in China constrained by Global Positioning System measurements, Science, 294, 574-577.

ANOMALOUS RECORDING OF EARTHQUAKES OCCURRING IN THE CENTRAL ANDES OF BOLIVIA

Estela Minaya R. and Percy Aliaga H.

Observatorio San Calixto

Sponsored by the Air Force Research Laboratory

Contract No. FA8718-04-C-0062

ABSTRACT

To improve the location method of earthquakes occurred in the Central Andes of Bolivia, an automatic location model was proposed, developed on the basis of Red Neuronal in Radial Base Function; a second test was applied: Wavelet's method with the WDEN function (Aliaga, 2002; Minaya et al., 2003). Due to the signal complexity several processes were applied, such as WAVEDEC and WRMCOEF functions (MatLab), signal normalization and optimization to reduce the run time duration of the process as the signal needed to be adjusted (with left-to-right movements). The signals were introduced in the Neuronal Network. The final result of the process was successful up to a 78% rate in 36 seismic events.

The functionality of the model was proved by increasing the amount of samples from 36 to 83 earthquakes that occurred in the same region (central part of Bolivia). Once the model was applied the results were not satisfactory, mainly due to the presence of several phases among phases P and S and including the phases observed after phase S. These results obey to the complex structure of the crust under the Central Andes of Bolivia.

The 83 seismic signals split into four zones according to their waveform (envelope), and subsequently in sub-groups according to their specific characteristics that may be correlated to the geology, tectonic structures, crust structures, and status of the stress present at the study zone.

The analysis will continue in order to study the anomalous phases between P and S waves, and those that are recorded after the S wave, along with profiles balance to verify structures than could originate that anomalous phase. Once this research is finished, the automatic localization model will be applied.

OBJECTIVE

To improve the Neural Network Wavelet (NNW) Model to automatically locate earthquakes occurred in the Central Andes in Bolivia, applying other Matlab® functions when performing this step.

RESEARCH PERFORMED

ANALYSIS 1. Validation of the NNW model

In order to verify and to improve the results obtained with the NNW model, we selected events 2, 7, and 14, their waveform and location were correlated with events 3, 8, and 15 respectively, (circle, Figure 1). The same occurs for events 11, 18, 20, and 23, (in triangles, Figure 1) that display correlation with event 30 (Figure 1, closed square) without any correlation in location and waveform, thus the deficiency in results. Figure 1 shows locations obtained with the Geiger method after those previously obtained with the NNW. For the events with best results, (circles, Figure 1, Table 1) their final localization is noted in the triangle; for example, we remember that for event 7 the acceptable result with the NNW model is event 8, from which it inherits its localization parameters (latitude, length, and depth), and when we applied the Geiger method, the localization is close to both. This procedure is applied to the rest of the events analyzed in this stage.

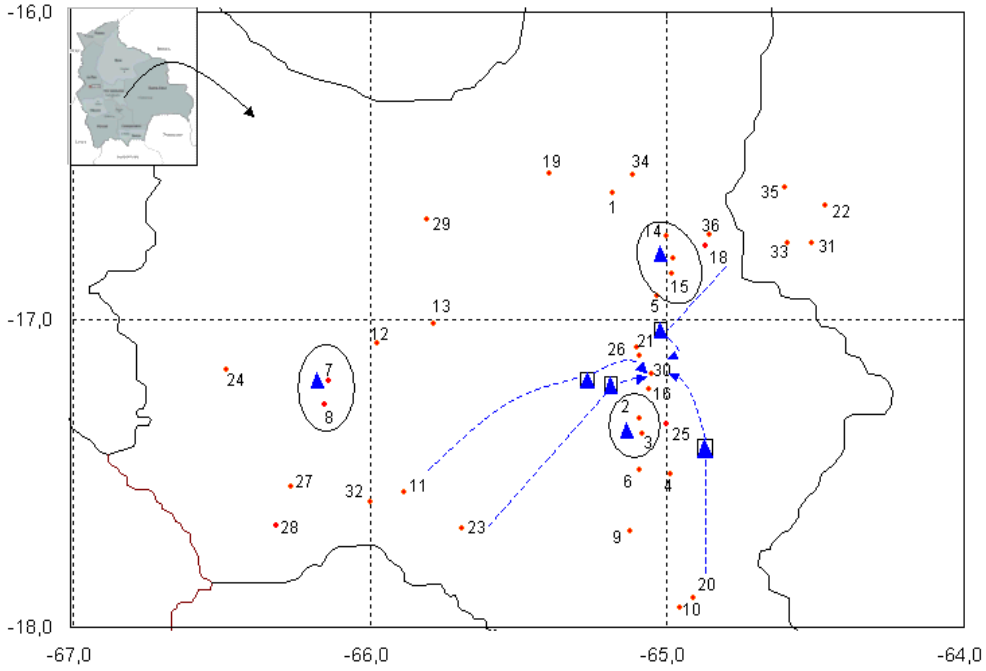

Figure 1. Localization obtained with the Geiger method, in regard to the preliminary localization

Table 1. Locations obtained with the Geiger method for events 2, 7, 11, 14, 18, 20, and 23.

	Original location				Final location			Difference in location		
No.	**No.**	**Lat. (°)**	**Lon. (°)**	**Dep. (km)**	**Lat. (°)**	**Lon. (°)**	**Dep. (km)**	**Lat. (°)**	**Lon. (°)**	**Dep. (km)**
2	3	-17.369	-65.083	65.00	-17.365	-65.139	54.00	0,004	0,056	11.00
7	8	-17.275	-66.154	40.00	-17.210	-66.185	45.00	0,065	0,031	5.00
11	30	-17.178	-65.052	35.00	-17.185	-65.371	20.00	0,007	0,319	15.00
14	15	-16.851	-64.985	31.00	-16.800	-65.051	8.00	0,051	0,066	23.00
18	30	-17.178	-65.052	35.00	-17.036	-65.025	8.00	0,142	0,027	17.00
20	30	-17.178	-65.052	35.00	-17.452	-64.933	49.00	0,274	0,119	14.00
23	30	-17.178	-65.052	35.00	-17.203	-65.271	55.00	0,025	0,219	20.00

As we remember, the parameter of event 30 (Figure 1) is the same for events 11, 18, 20, and 23. Consequently, they inherit their parameters of localization and when applying the Geiger method a new locations for events 11 18, 20, and 23 are obtained, (Figure 1, framed triangle). It should be remarked that data event 30 data have influenced the located events final result. Consequently, results are not acceptable.

To analyze the events with deficient results (11, 18, 20, and 23) a verification of original signs has been made with events that were close. For example, in Figure 1 the event 11 is in the same zone as events 23, 27, 28, and 32, and not in the same zone as event 30. In Figure 2 it is shown that event 11 does not correlate to the events of the same zone, like the characteristics of the analyzed events. Therefore, it would not be possible to obtain a positive result for this event. The opposite goes for events 23 and 32, which apparently have similar waveforms and locations.

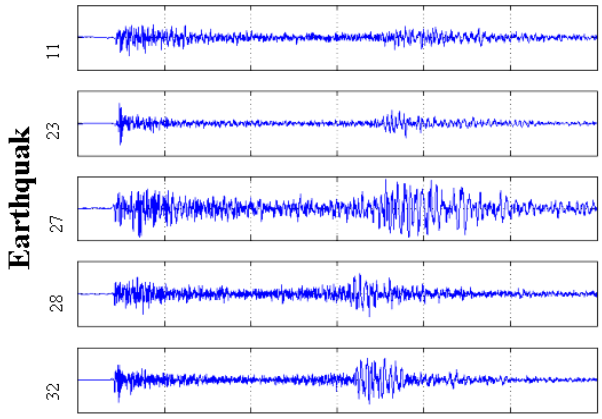

Figure 2. Signals of events 11, 23, 27, 28 y 32 located in the same area but with a difference in waveforms.

ANALYSIS 2. Wden Function

The variations obtained applying the WDEN function affected the results of the Neural Network, as differences between signal amplitude in regard to each other were made in parallel.

In order to justify the invalidity of the WDEN function, a complex signal displaying amplitude variations is analyzed, corresponding to an earthquake occurred in Peru and registered in the station BBOE occurred on 22/08/2000 (Figure 3). A duration of 120 seconds was considered for each event. The original signal and the transformed one after applying the WDEN function are shown in Figure 3. The cause of this variation is due to the WDEN function that executes the convolution product and the algorithm of soft-thresholding. The WDEN function obtains zeros at the beginning of the Pn phase and in some points of the signal, when making several decompositions, which is shown with the overlay of the transformed and original signals, Figure 3. This is the reason it is difficult to use the Wden function. The weighting of some values in the coda of the transformed signal are more marked that others, giving estimations that do not work for signal models. In order to solve this problem it is necessary to apply the Transformed Wavelets so that the coda of the transformed signal is approximated, and some values are not emphasized.

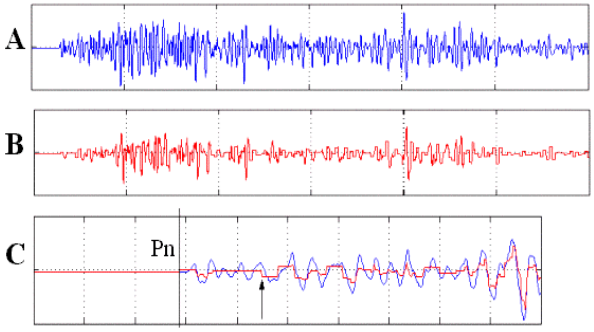

Figure 3. Event occurred on 22/08/2000, the original signal (A), transformed (B) and (C) overlay of original signal (blue) and transformed (red), the line on phase Pn and the arrow show the variation of signals when the WDEN function is applied.

ANALYSIS 3. Wavelets Transformed in the Neural Network

In this analysis the objective is to apply Wavelet Transform and a Neural Network to a sample of 36 earthquakes.

The Wavelet Transform allows a better management of WAVEDEC and WRMCOEF functions (MatLab, 1999), in view that the Neural Network gets better results if the signal pattern is generic, not detailed. The procedure corresponds to a sequential methodology according to the process that must be realized by the transformation.

Step 1: An interval should be considered at the beginning and end of the signal in each event.

Step 2: The main idea is not to plan the events on a map and group them, but to classify them according to their likeness between signals.

This classification according to similarity is not only made with signal filtering, or with filters as the Fast Transformed Fourier, or algorithms of reduction of the Wavelet noise (soft-thresholding), that provide the identification of phases in the coda if the signal, allowing a grouping of events according to their characteristics, but hen this is applied to the Neural Network, the classification made by comparisons results in “details,” which is not advisable. The Discreet Wavelet Transform is applied to the waveform signal, that allows the modeling of a signal as “generics” for regions that have their own peculiarities.

Step 3: Once the transformation is done event by event a cutting of the signal is made from a new "beginning," defined by the Haar Wavelet up to the end of coda, as it is observed in the Figure 4. When the Wavelet is applied to the beginning of the Pn phase in the original signal, it is “moved” towards the right approximately an average of 1.30 seconds, which does not affect the MSE value to a great extent.

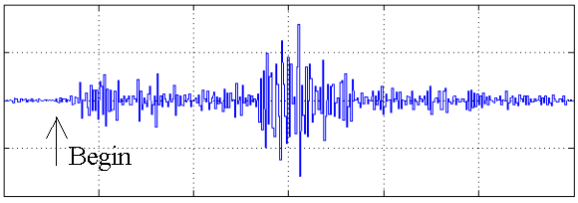

Figure 4. Beginning defined by the transformed Haar Wavelets.

Step 4: In order to test the functionality with the Wavelets and Neural Network, an event is taken from the 36 total events, to classify it with the 35 remaining events, and successively perform the same process with each one of the 35 events.

The data in Table 2 shows the results obtained once the Wavelets and the Neural Network were applied giving a rate of 64% that corresponds to acceptable results.

ANALYSIS 4. Signal Transform and Cropping

After the transformation of the 36 signals, an entrance signal is taken and at least one training signal, repeating this process with the remaining events. In the next step the cropping of the signal is made, that consists of the selection of only one common beginning for the signals that are being treated, the Pn will, be called “Pn assumed,” as it is in Figure 5, for two transformed signals (events 7 and 8, Table 2).

The cropping made in the transformed signal coincides with the Pn phase of the original signal (Figure 6). Nevertheless in some cases the Pn phase is

assumed after the Pn phase of the original signal (Figure 7). This happens when the amplitude of the beginning of the original signal is small and comes near zero, when applying the transformed one.

.

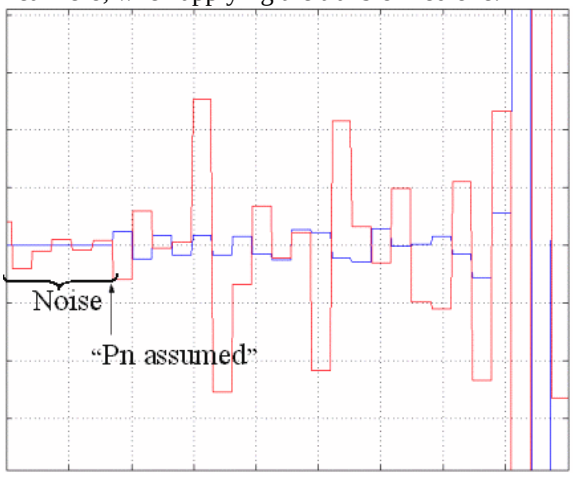

Figure 5. Cutting selection a common beginning for events 7 (blue) and 8 (red)

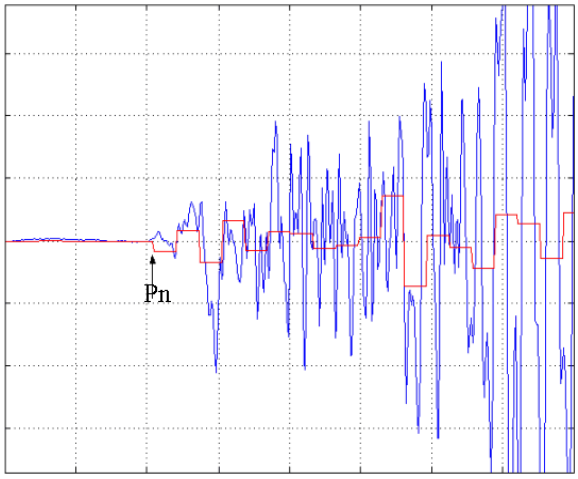

Figure 6. Original signal (blue), Transformed signal (red), both phases (original Pn and "Pn" assumed) coincides, event 17 Table 2.

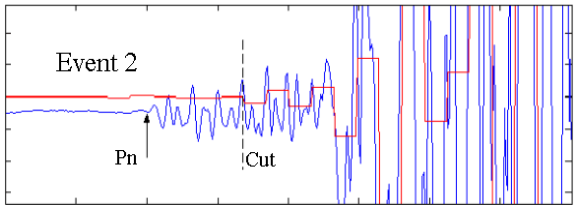

Figure 7. Cutting after the Pn phase is shown in an overlaid picture of the original signal (blue) and transformed signal (red).

Transformed Signal Normalized

Normalization of the transformed signals may be considered as a waiting room for the adjustment of the Neural Network.

Step 1: Once the cropped transformed signals are obtained, they take initial values from zero, followed of by positive and negative values (Figure 4) and then absolute values are obtained (Figure 8).

Step 2: 80 seconds are taken from the beginning of the cropping because in this time period, the characteristics of the region could be recorded.

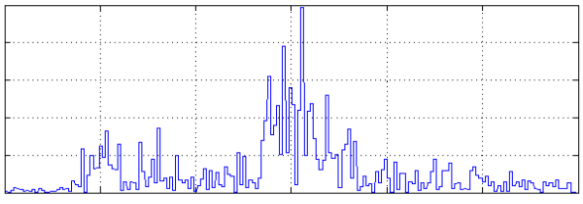

Figure 8. Absolute transformed signal of event 1.

Step 3: For each one of the 36 transformed signals, the maximum threshold is found. Then the minimum threshold is chosen, so that normalization of the signals is made with the minimum threshold.

Step 4: The maximum thresholds are divided by the minimum threshold, these are values to be standardized. Later the signal is standardized dividing each point by that value. Once these steps conclude, the signal transformed is obtained and the 36 events are standardized, with approximate characteristics but without details of the phases of coda of the signals, that at the time of applying the neural network are not considerable.

The results of this analysis gave a rate of 61% successful when the signal is transformed and normalized (Table 2). the normalization is the cause of reduction of the percentage of successes, because it allows the comparison of signals of equal amplitude, a situation that is not possible when there are earthquakes of different magnitudes, for example between earthquakes with magnitudes 3 and 5. Consequently, normalization of signals is a necessary process.

ANALYSIS 5. Optimization and Adjustment

In this analysis two processes are introduced to improve the Neural Network results, but before doing the adjustment process, one first step is necessary to improve the values of Neural Network: optimization.

Optimization

The signals have a duration of 80 seconds that correspond to 4000 points. The adjustment of those points and Neural Network to obtain the MSE are executed in an excessive period of time. Due to this situation the signal was reduced from 4000 to 125 points. As the decomposition of level 5 is used, it is possible to reduce the signal taking a value of32 points each conserving the signal waveform (Figure 9). An optimized signal is shown in Figure 10 with the absolute values of the amplitude. It should be noted that when this process is made it tends to lose some beginnings of the transformed signal, because their amplitude comes near to zero.
A second step is necessary make an adjustment to the signal. In this process the points are moved from the left to the right.

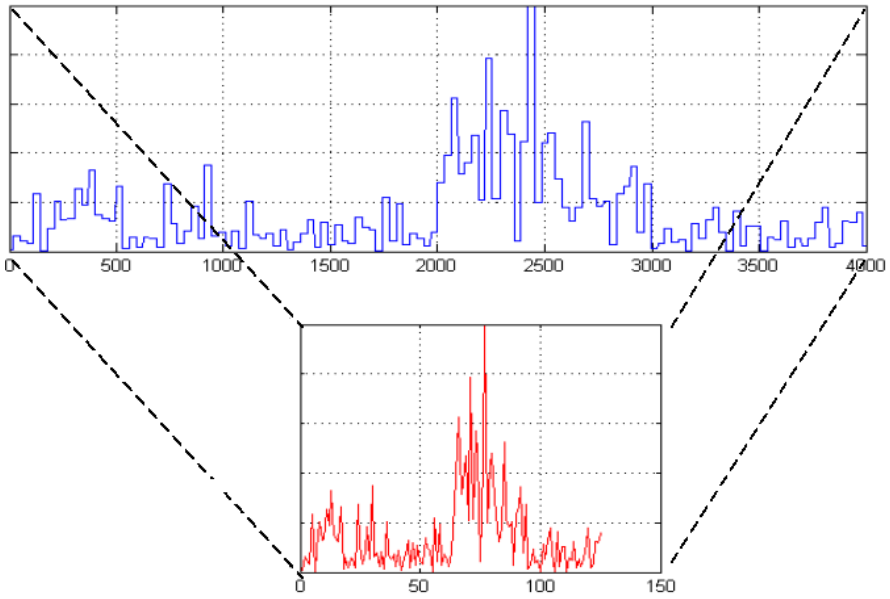

Figure 9. Reduction of size of event 1, from its transformed signal of 4000 points to an optimised signal of 125 points.

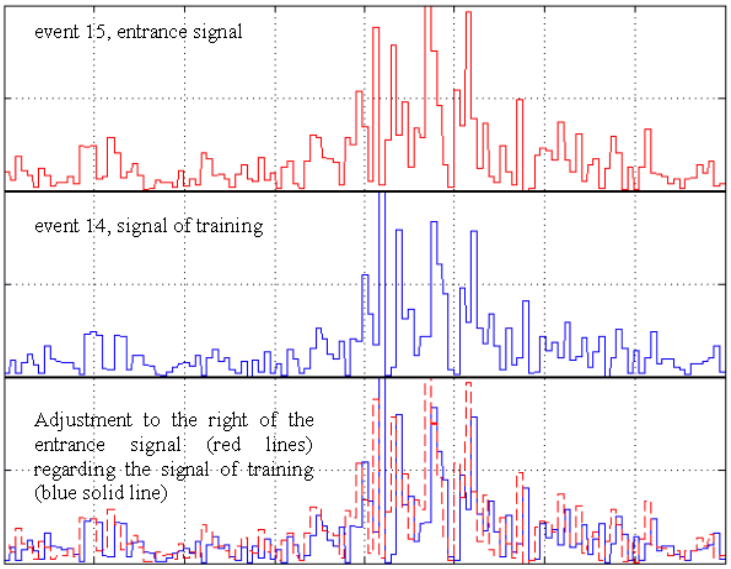

Figure 10. Adjustment process between events 15 and 14, Table 2.

Adjustment

In Figure 10, an example of the adjustment process is shown. Event 15 was considered like the input signal and event 14 like the signal of training, whose maximum thresholds are out of phase (lower part of Figure 10). Event 15 is shown by dashed lines, which will be adjusted by moving it to the right, so that the maximum thresholds agree with the maximum thresholds of event 14.

The example described allows observation of the difference of the result with analysis 4. Event 15 is associated with event 34, whereas in this analysis its relation is with event 14, obtaining a similar result as with the initial analysis. In order to be able to fit an optimized signal, it is necessary to know which points are moved at the beginning and at the end of the signal. These tests were made taking into account the movement of the points to the left and to the right. This is if the movement to the left eliminated a point, and it was duplicated one point, to maintain duration of the signal.

The result using the movement of 10 points (left and right), concludes that it is better to consider movements of 3 points (in both ends). Consequently, the positive results reach 78% (Table 2). This is acceptable. Notice that the percentage with respect to the results to analysis 4 has improved the locations. For example, event 5, with analysis 4 gave event 22 and with new analysis gave event 18. The same happens with events 1, 13, 14, 15, 16, 17, 22, 24, 28, 33, and 36.

ANALYSIS 6. New Validation

A new validation of the process is realized incrementing the data from 36 to 83 seismic events, the results were not successful. The principal cause should be because signals are complex; several probable phases are observed among phases Pn and Sn. In addition, an evaluation of the waveform was performed looking for the details registered in that interval. The results permitted division of the region of study into four zones according to their general characteristics (Figure 11) and each of them was subdivided according the details more relevant.

The four zones apparently keep more relation with general geology of the region and the subdivisions have direct relation with Tectono- Stratigraphic dominions. They are been studied and will allow us to get more information about the actual deformation that causes this superficial seismic activity in the region. This analysis is relevant to determine the relation of the complex crust with anomalous phases observed in earthquakes with epicenters in the Central Andes (the anomalous phases would not correspond to phases normally registered). The importance of this situation is due to the fact that the seismic activity of the region of study is only in the crust (without proofs in the surface). The intermediate seismic activity (depths about 300 km to 400 km), that corresponds to the Nazca Plate is absent.

CONCLUSIONS AND RECOMMENDATIONS

The results obtained with different analysis performed to improve the Automatic Locate Model using Wavelets and Neuronal Network are summarized as follows:

The test to validate the Model, on the basis of correlation among seismic signals according to waveform and position, permitted the detection of expected results. Several cases were deficient due to the similarity among signals was not effective at either location.

The WDEN function determines the details of the signal, in the coda of the phase Pn, generating zeros before the same phase, in other points of the signal, and highlighting the amplitude of others. Aspects that do not favour the results when is applied to the Neuronal Network since this uses generic signals and no detailed signals.

For the above, the WDEN function is discarded and the application of Wavelet Discrete Transform is introduced, using WAVEDEC and WRMCOEF functions, and modelling generic signals necessary for the Neuronal Network.

Other artifices are needed in the models that permit a best development in Neuronal Network process. One of these is cutting the signal because some signals register emerging beginnings that can be mixed up

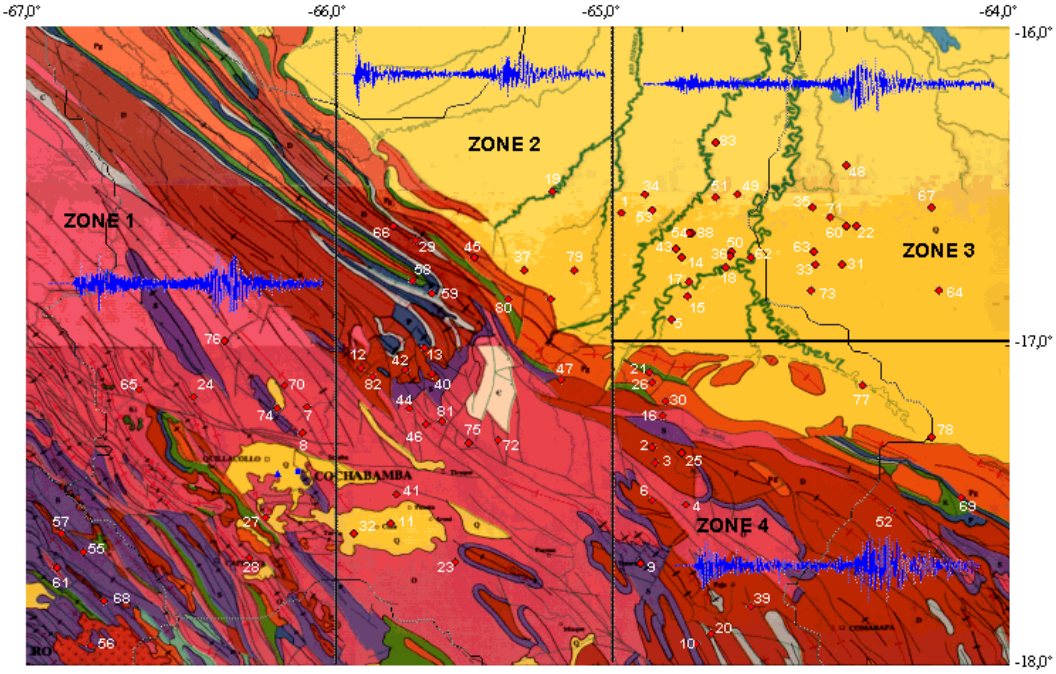

Figure 11. Study region with the geological and structural map, division in four zones according to their waveform, 83 seismic events (red dots) and temporal station (blue triangles).

Table 2. Results of the analyses

Event No.	Date (dd/mm/yy)	Hour (HH:MM:SS.mm)	Lat. (°)	Lon. (°)	Dep.(km)	MI	Analysis 3	Analysis 4	Analysis 5
1	16/01/00	10:55:11.775	-16.588	-65.183	65.00	3.32	19	2	36
2	20/01/00	23:05:39.860	-17.323	-65.091	65.00	4.13	3	14	18
3	21/01/00	03:35:16.869	-17.369	-65.083	65.00	4.19	2	25	2
4	21/01/00	05:34:56.200	-17.502	-64.990	16.06	3.14	6	6	21
5	24/02/00	23:28:59.762	-16.921	-65.032	15.00	3.48		22	18
6	25/02/00	11:02:57.937	-17.489	-65.093	45.00	3.51	4	34	18
7	07/03/00	03:57:30.910	-17.197	-66.140	16.95	3.71	8	8	8
8	07/03/00	03:59:36.234	-17.275	-66.154	40.00	3.57	7	32	32
9	21/03/00	00:22:12.273	-17.687	-65.125	65.00	3.52	6	25	1
10	22/03/00	19:47:53.374	-17.907	-64.913	30.00	3.18	20	34	22
11	29/03/00	21:50:00.221	-17.559	-65.887	20.00	3.14		27	25
12	04/04/00	06:31:32.980	-17.076	-65.978	50.00	3.76	8	7	32
13	25/04/00	23:21:28.667	-17.013	-65.786	42.00	3.71	29	27	29
14	03/05/00	11:19:09.060	-16.730	-65.000	10.00	3.10	15	18	15
15	03/05/00	15:44:17.249	-16.851	-64.985	31.00	3.28	14	34	14
16	05/05/00	01:41:16.831	-17.224	-65.060	30.00	3.69	21	1	26
17	07/05/00	07:43:58.882	-16.803	-64.978	8.00	4.16	18	26	18
18	24/05/00	09:16:37.859	-16.761	-64.869	10.00	3.75	17	14	22

Event No.	Date (dd/mm/yy)	Hour (HH:MM:SS.mm)	Lat. (°)	Lon. (°)	Dep.(km)	MI	Analysis 3	Analysis 4	Analysis 5
19	03/06/00	15:36:49.793	-16.523	-65.397	25.00	3.20	1	33	33
20	14/07/00	01:06:52.358	-17.936	-64.956	30.00	3.61		18	21
21	28/07/00	18:57:09.935	-17.089	-65.102	15.00	3.56	16	26	36
22	29/07/00	13:30:02.771	-16.628	-64.468	10.00	3.13		5	36
23	16/08/00	13:33:06.738	-17.680	-65.692	65.00	3.09		13	33
24	22/08/00	19:52:28.232	-17.165	-66.485	51.00	3.02		12	8
25	25/08/00	19:43:32.564	-17.338	-65.001	40.00	3.08	26	30	36
26	08/09/00	05:23:24.860	-17.118	-65.090	15.00	3.06	25	21	36
27	15/09/00	19:38:23.284	-17.542	-66.267	21.00	3.81		7	13
28	20/09/00	04:47:15.985	-17.669	-66.314	65.00	3.40		11	27
29	21/09/00	05:06:07.212	-16.676	-65.810	23.99	3.31	12	12	8
30	27/09/00	03:06:03.683	-17.178	-65.052	35.00	3.26	25	34	18
31	01/10/00	09:34:52.154	-16.750	-64.512	50.00	3.70		34	21
32	03/10/00	15:00:43.571	-17.592	-65.997	65.00	3.35		8	8
33	03/10/00	17:46:26.885	-16.750	-64.593	65.00	3.19		19	36
34	12/11/00	05:44:50.738	-16.529	-65.115	20.00	3.26	1	30	26
35	30/11/00	15:44:54.595	-16.570	-64.604	65.00	3.83		22	18
36	04/12/00	06:30:10.883	-16.724	-64.856	30.00	3.05		30	22

with noise. Normalization is applied because the signals of the sample do not have the same magnitude, but this application showed that can be a complex wave in many cases. The last step permits the adjustment of the signal, especially when there is a small displacement in the same point of the signals. Optimization was introduced to reduce the run time of the process.

Finally, a new test was made increasing the sample from 36 to 83 earthquakes that occurred at the same zone, but the process was deficient, and results confirm that the analysis of the waveform is not enough. Also, the signal cannot be considered generic due to the complexity of the presence of these anomalous phases registered in many of the seismic events of the sample.

Individual characteristics are associated with geological, tectonic structures observed in several cortical continental structures as those present in the Central Andes. These characteristics correspond to the details that are not admissible in the process of the Neural Network but now must be considered in the model.

According to those characteristics of detail, the region of study was split into four zones correlated to geology in general: each zone was subdivided in groups according to special natures of earthquakes analyzed that would be related directly with the Tecto – Stratigraphic domains and sub-domains, which must be related to the complex crust present underneath the Central Andes.

The analysis will continue to obtain a structure that could explain the origin of the anomalous phases that correspond to characteristics and details observed in the coda of earthquakes that occurred in the Central Andes.

This process will have to apply to each one of the stations of the seismic network because these are on places with different structures to prove if any of those anomalous phases originate by the structure under the station.

Finally, other functions will have to be introduced in the Automatic Location Model on the basis of the results obtained this analysis.

The objective of Wavelets and the Neural Network methodology is to obtain one previous localization, and later to apply the Geiger localization method in order to complete the cycle of the model of localization.

REFERENCES

Aliaga, H. P. (2002), Modelo de Localización Sísmica con Parámetros Sismológicos Aplicando la Red Neuronal con Funciones de Base Radial y la Metodología de Geiger, *Tesis Universidad Catolica Boliviana*, La Paz –Bolivia.

MatLab (1999), *The MathWorks, Inc.*, MatLab 5.3 release notes, Chapter 34.

Minaya E., P. Aliaga, G. Avila, C. Condori, and A. Córdova (2003), Neural network and wavelets model in seismic location for the Central Andes of Bolivia, in *Proceedings of the 25th Seismic Research Review—Nuclear Explosion Monitoring: Building the Knowledge Base*, LA-UR-03-6029, Vol. 1, pp. 248-258.

CONTINUING ANALYSIS OF EARTH STRUCTURE AND GROUND TRUTH DATA FROM THE MIDDLE EAST

Walter D. Mooney and Shane Detweiler

U.S. Geological Survey

Sponsored by National Nuclear Security Administration
Office of Nonproliferation Research and Engineering
Office of Defense Nuclear Nonproliferation

Contract No. DE-AI04-98AL66517

ABSTRACT

Middle Eastern countries have a very high level of seismic activity. For this reason, there are a large number of seismic networks in operation, and data from these networks have provided details of the crustal structure of the region. One such network, the Tehran Telemetry Seismic Network (TTSN), consists of twelve stations and is located around the city of Tehran. Nearly two years of local data are available from this array, and these data yield estimates of crustal thickness based on receiver function analysis. These results consistently show a crustal thickness of 44 – 50 km. This value is about 12 km thicker than has been measured in eastern Turkey, and 9 km greater than the global average for stable platform regions. The 45 km crustal thickness near Tehran is almost exactly the same as the 46 – 48 km thickness reported from receiver function analysis from the central Zagros mountains. The apparent uniformity of the crustal thickness implies that mountain building has only recently started in the region, and the crust beneath the Zagros mountains has not been appreciably thickened by compression. Despite the platform-like crustal structure, we find evidence that the upper mantle Pn velocity is lower than the typical value of 8.1 km/s. The relocated earthquakes of Engdahl et al. (2004) show a consistent pattern of longer (by several seconds) Pn travel times compared with the predictions of the global seismic velocity model ak135. The Pn velocity observations are confirmed by a new tomographic model that shows variation in seismic velocities in the uppermost mantle across the Middle East. The zone of low upper mantle velocity coincides with the region of high seismic activity, which indicates that the mantle anomaly is related to active tectonic processes.

OBJECTIVES

The structure of the crust and upper mantle of the Middle East is highly heterogeneous. We have integrated seismic and non-seismic data from this region to determine the properties of the crust and sub-crustal lithosphere. Available data and results include seismic networks data, receiver functions from permanent and temporary stations, Pn travel time residuals from regional earthquakes, seismic tomographic models, and recently-obtained strong motion waveform data. Our results allow us to compare crustal signatures across the region and to provide better-constrained velocity models for event locations.

RESEARCH ACCOMPLISHED

We have continued our existing program of collecting high-quality seismic data from the Middle East by capitalizing on newly-established research relations between the United States Geological Survey (USGS) and leading research institutions in the Middle East and overseas Middle Eastern scientists. These data include some local and regional phase and waveform data (especially strong motion waveforms). We also possess several hundred digital records from a regional 1500-station strong motion network.

These new research opportunities evolved as seismic hazards in the Middle East came to international attention following the devastating earthquake in the city of Bam, Iran, on December 26th, 2003. That event killed over 30,000 inhabitants and left 85 percent of the city in ruins, and has reignited efforts to study seismic events in the Middle East. In addition to the Bam earthquake, the Middle East has a long history of large-magnitude seismic events. The Tabas-e-Golshan earthquake of September 1978, and the Rudbar-Tarom earthquake of June 1990, are additional examples of strong earthquakes in the last 25 years. These type of events are extremely useful as ground truth data. We have obtained strong motion records from numerous events with magnitude greater than 5.0 that have occurred in the past ten years.

To record these regional events, a 1,500-station digital strong motion array has been built in the Middle East, and we have obtained 1813 high-quality digital strong motion records and associated meta-data for numerous events of varying size. Our work focuses on the larger magnitude (>M=6) events that have six or more records distributed over all azimuths.

The distribution of seismological stations and lack of national catalogs of events has limited the study of seismicity to a catalog of events published by international agencies such as the International Seismological Centre (ISC) and the USGS. Threshold magnitude of reporting of about 3.5 and poor location and depth accuracy for moderate and small events have been obstacles for realistic and quantitative assessments of seismicity in this region. Only recently have there been attempts to acquire better depth estimates by waveform modeling (e.g., Maggi et al., 2000) and improved locations (Engdahl et al., 1998, 2004). Although the installation of the National Broadband Network (Iran) and some regional telemetry networks commenced in the mid 1990's, there have been no concerted efforts towards preparation of a seismic catalog. Therefore, seismicity studies on a nation-wide or regional scale still rely heavily on information from international monitoring.

Two important scientific groups that conduct seismic research in the Middle East are the International Institute for Earthquake Engineering Seismology (IIEES) and the Geophysical Institute (GIUT) of the University of Tehran. The IIEES operates eleven broadband and many strong motion instruments. The GIUT operates more than 40 short-period digital stations, distributed into eight seismic networks. Management is within the National Center of Seismic Networks. The 12-station short period telemetered array around Tehran uses state-of-the-art Canadian Nanometrics equipment. This network is fully operational, and it provides the opportunity for obtaining excellent ground truth data. The IIEES has been making efforts to reach out internationally, and has hosted a series of international meetings in seismology and earthquake engineering. Table 1 lists the permanent seismic networks in our area of study which are also shown in Figures 1a-b.

Table 1. Five Permanent Networks
1. Broadband Network (11 stations)
There are presently 11 broadband seismic stations operating in our region of interest (Figure. 1a). The equipment consists of Guralp (CMG3T) sensors and Guralp 25 bit data loggers. The seismographs record continuously at the station sites. Selected time windows, on request of the analyzing seismologists, are sent to the central recording station in Tehran, IIEES, via satellite (VSAT).
2. Tehran Telemetry Seismic Network (12 stations)
The 12 station Tehran Telemetry network (Figure 1a) consists of short period seismographs connected to central recording station via telemetry. The recording is done on a triggering basis. Data available outside of Iran consist of teleseismic events with magnitude greater than 5.7 for the time period of 1996-2001 and local data for a period of over 22 months.
3. Azarbaijan Telemetry Seismic Network (8 stations)
The 8 stations of the Azarbaijan Telemetry network (Figure 1a) consist of short period seismographs connected to central recording station via telemetry. The recording is done on a triggering basis. Data available consists of two months of recording.
4. Iran Long Period Array (ILPA, 7 stations)
The seven stations of the ILPA (Figure 1a) consist of short period and long period borehole sensors located south and west of Tehran and transmits continuous data to a central recording station in Tehran. Available data consists of three years of long period and 17 months of short period recordings.
5. Strong Motion Network (ISMN, ~1500 stations)
The Iran Strong Motion Network (Figure 1b) in its present form consists of about 1500 stations. Digital waveforms for a large number of main shock and aftershock earthquakes in the Middle East have been obtained by the USGS-Menlo Park.

Although the identification and mapping of active faults in the Middle East have a long history (e.g. Berberian, 1976, 1977; Jackson and McKenzie, 1984; Baker et al., 1993; Jackson et al., 1995), the regional tectonics are poorly understood. In the face of poor locations of earthquakes and lack of slip measurements in the field, it is difficult to accurately associate earthquakes with known faults. To discriminate between earthquakes and suspected man-made events at teleseismic distances, such information is of paramount importance.

In the Zagros Mountains (Figure 2), a general absence of surface faulting further complicates this picture and leaves us to rely solely on seismological data. In the absence of terrestrial geodetic data, Jackson et al. (1995) used the modified method of Haines and Holt (1993) to construct a velocity field based on strain rate data obtained from scalar moment tensors of earthquakes. A major breakthrough has been the deployment of global positioning system (GPS) instruments in the late 1990's for a series of measurements. The results (e.g, Nilforoushan et al., 2003; Vernant et al., 2004) depict strain rates across the study area and show that north-south shortening from Arabia to Eurasia is about 2-2.5 cm/year less than previously estimated by global plate tectonic models (Figure 2), and that the transition between the Makran subduction zone and the Zagros system is sharp. The transition between the two regimes is accommodated along faults bordering the Lut Block.

The installation of new broadband stations and Incorporated Research Institutions for Seismology (IRIS) temporary deployments in Saudi Arabia and Turkey has resulted in a new series of tomographic imaging of Pn, Sn, Lg, and Q values across the Arabian, Eurasian, and African plates (e.g., Sandvol et al., 2001; Al-Damegh et al., 2004; Al-Lazaki et al., 2004). Earlier the Lg and Q values for the region were based primarily on the work of Jih and Lynnes (1993) (who expanded upon the earlier work of Nuttli (1980), Kadinsky-Cade et al. (1981) and the pioneering work of Asudeh (1982)) on Pn velocity mapping across the region. Recent findings show that Central Iran is, in contrast to the Caspian Block and Arabian Shield, characterized by low Pn velocities (< 8.1 km/s; e.g., Al-Damegh et al., 2004; Al-Lazaki et al., 2004) (Figure 3). According to these studies, the region also shows inefficiency for Sn propagation, compared with neighboring Arabia and Eurasia. These fundamental structural differences have further been confirmed by recent and ongoing body wave tomography studies (e.g., Alinaghi et al., 2004) showing that the Arabian and Eurasian plates generally have higher P- and S-wave velocities than other regions of the Middle East. Hearn and Ni (1994) and Rodgers et al. (1999) have noted that Sn propagation is very weak near the IRIS ABTK (Turkmenistan) station.

Our opportunity to calculate a crustal and upper-mantle model for the Middle East using seismic tomography is due to the work recently completed by (Engdahl et al., 2004). Their work was based on a careful analysis of phase arrival times reported to the International Seismic Summary (ISS), the International Seismological Centre (ISC), and the USGS. This effort has resulted in the relocation of nearly 2,000 earthquakes that occurred in the study area during the period 1909-2004 (Figure 4). The "EHB" methodology of Engdahl et al. (1998) was applied, and special attention was given to focal depths. The "EHB" method uses phase arrival times of P, S, PKP and depth phases (pP, sP, and pwP) with the 1-D Earth model Ak135 (Kennett and Engdahl, 1991). In general, the relocated earthquakes of Engdahl et al. (2004) show a consistent pattern of longer (by several seconds) Pn travel times compared with the predictions of the global velocity model ak135. These authors estimate the uncertainties in "EHB" locations to be 10-15 km owing to lateral heterogeneities in the Earth's structure. Previous studies of the seismicity of the region include the work of Maggi et al. (2000), who used synthetic seismographs to model P- and SH-waveforms. The uncertainties in "EHB" depths are estimated to be 10 km, in comparison with 4 km for the depth estimates derived from an analysis using synthetic seismograms.

There are numerous limitations to performing the inversions using only regional phase data. For example, such a tomographic inversion would mainly provide estimates of only regional crustal thickness and Pn velocity. However, since there are several independent estimates of crustal thickness of the region (e.g., Doloei and Roberts, 2003; Hatzfeld et al., 2003), it is possible to fix the initial crustal model based on these estimates in order to obtain a better constraint on lateral variations in Pn velocity. In addition, some phase data, which provide valuable regional travel time constraints are available for local stations. Also useful are data from a number of temporary deployments of broadband seismographs (e.g., East Turkey, 1999-2001, Turkmenistan, 1992-1994, Saudi Arabia, 1995-1997).

Some limited phase data has been obtained from the Tehran Telemetry Seismic Network (TTSN). This 12-station, short period digital network (Figure 1a) has been in operation in its present configuration since the mid-1990s. Teleseismic waveform data from this network has previously been released to overseas Iranian nationals for use in tomographic and receiver function studies. For example, in order to determine the crustal structure beneath the array, some 129 teleseismic waveforms recorded between 1997 and 2001 were compiled at the GeoForshungsZentrum (GFZ) in Potsdam, Germany. Receiver functions determined from these data have shown clear P-to-S conversions from the Moho ranging in time from 5.4 s (station QOM) to 6.3 s (station MHD), corresponding to depths of approximately 44 km to 50 km, respectively. A mid-crustal boundary is evident at ~20 km depth, and the Vp/Vs ratio appears to be close to 1.76, a rather typical value for the crust.

The Iran strong motion network has grown steadily over the past decade and consists of more than 1,500 stations. The instrumentation is mainly SMA-1 and SSA-2 Kinemetrics recorders. Analog recorders were replaced by digital recorders following the 1990 Manjil earthquake. Instruments are concentrated in the Zagros fault zone where seismicity levels are very high (Figures 2 and 4), and in the Tehran region where the population density is highest.

An example of strong motion data is provided by the data recorded from the Mw = 6.0 Golestan village earthquake of 28 February 1997, located SW of the city of Ardebil. (Approximate event location: 38º N by 48º E; Figure 5) We have 16 local strong motion records for this event within the distance range of 20 km to 150 km (city names: Haris, Nir, Niaragh, Razi, Ardebil (2 stations), Astara, Bilehsavar, Meshkinsharahr, Germi, Hir, Mianeh, Namin, Sarein, Khalkhal, and Karigh; Figure 5). Peak acceleration is 0.6 g recorded at a distance of 25 km. Data quality is very high, as can be seen in two examples (Figure 6). Although a surface rupture was not identified for this event, the focal mechanism determined by IIEES indicates that the causative fault was most likely an extension of the well-known Bozghosh fault (Figure 5). Additional examples of waveform data from other seismic events are shown in Figure 7.

Automatic moment tensor inversion of Middle Eastern earthquakes at teleseismic distances, which is done routinely by agencies such as Harvard and USGS, has been limited to large events (M > 5.5 and beyond). Although automatic determination of moderate earthquakes is becoming more and more a routine process, the uncertainties involved make the results not very useful for seismotectonic investigations, where we must determine the association of events with known active faults. For moderate and small events, inaccuracies concerning location, depth, and nodal planes render the events unfit for ascertaining their significance or possible association with known active faults versus suspected nuclear test events.

This work is responsive to the goals of (1) determining regional 3D Earth structure in the Middle East, and (2) collecting high-quality seismic data for reference events and determining source parameters using waveforms for a specific area of interest (the Middle East). Temporary deployments of seismological stations across the region (e.g. Tatar et al., 2004; Hatzfeld et al., 2003; Figure 2) have provided new insights into lithospheric structures and seismicity. These ongoing studies have provided the first body wave tomographic results which not only delineate large-scale tectonic structures, but provide better-constrained velocity models for event locations.

CONCLUSIONS AND RECOMMENDATIONS

Seismic velocities in the crust and uppermost mantle vary across the Middle East. The zone of low upper mantle velocity coincides with regions of high seismic activity, indicating that the mantle anomaly is related to tectonic processes. To enhance the existing catalog of moment tensor inversions, systematic waveform inversions at local (strong motion data), regional and teleseismic distances, should continue to be developed. This would provide more reliable estimates of source parameters. For local and regional distances, we recommend using Dreger's method (Time-Domain Moment Tensor INVerse Code, release 2002) which evaluates the complete waveform inversion for seismic moment tensor. This is a "tried and true" method and has been used extensively in the past. In this process we have relied heavily on data from the Iran Strong Motion Network (Fig. 1b), however it has been shown (D. Dreger, pers. comm., 2004) that using IRIS stations in neighboring countries produce promising results. At teleseismic distances a number of revisited earthquakes prove that waveform inversion can provide better constraints, vital for seismotectonic studies (Berberian et al., 1999). Therefore, we perform waveform inversions using both locally recorded strong motion data and teleseismic data using Nabelek's approach (Nabelek, 1984).

REFERENCES

Al-Damegh, K., Sandvol, E., Al-Lazki, A. and Barazangi, M., (2004), Regional seismic wave propagation (Lg and Sn) and Pn attenuation in the Arabian Plate and surrounding regions, *Geophys. J. Int*. 157: 775-795.

Alinaghi, A., Koulakov, I., and Thybo, H., (2004), Tomographic images of the crust and upper mantle in Iran from regional and teleseismic P and S body waves, Abstract, EGU Meeting, Nice, France.

Al-Lazaki, A.I., Sandvol, E., Seber, D., Barazangi, M., Turkelli, N., and Mohamad, R., 2004. Pn tomographic imaging of mantle lid velocity and anisotropy at the junction of the Arabian, Eurasian, and African plates, *Geophy. J. Int*. 157: 775-795.

Asudeh, I., 1982. Pn velocities beneath Iran, Earth Planet. *Sci. Lett*. 61: 136 142.

Baker, C., Jackson, J. and Priestley, K., 1993. Earthquakes on the Kazerun Line in the Zagros Mountains of Iran: strike-slip faulting within a fold and-thrust belt, *Geophys. J. Int*., 115, 41-61.

Berberian, M., Jackson, J.A., Qorashi, M., Khatib, M.M., Priestley, K., Talebian, M. and Ghafuri-Ashtiani, M., 1999. The 1997 May 10 Zirkuh (Qa'enat) earthquake (Mw 7.2): faulting along the Sistan suture zone of eastern Iran, *Geophys. J. Int*. 136: 671-694.

Berberian, M., 1976. Contribution to the seismotectonics of Iran (Part II), Geol. Survey Iran, Report no. 39.

Berberian, M., 1977. Contribution to the seismotectonics of Iran (Part III), Geol. Survey Iran, Report no. 40.

Doloei, J., and Roberts, R., 2003. Crust and uppermost mantle structure of Tehran region from analysis of teleseismic P-waveform receiver functions, *Tectonophysics*, 364: 115-133.

Engdahl, E.R., van der Hilst, R. and Buland, R., 1998. Global teleseismic earthquake relocation with improved travel times and procedures for depth determination, *Bull. Seis. Soc. Am*. 88: 722-743.

Engdahl, E.R., Bergman, E.A., Meyers, S.C., and Ryall, F., 2004. Improved ground truth in southern Asia using in-country data, analyst waveform review and advanced algorithms, in *Proceedings of the 26th Seismic Research Review: Trends in Nuclear Explosion Monitoring*, LA-UR-04-5801, Vol. 1, pp. 257-266.

Haines, A.J., and Holt, W.E., 1993. A procedure for obtaining the complete horizontal motions within zones of distributed deformation from the inversion of strain rate data, *J. Geophys. Res*. 98: 12057-12082.

Hatzfeld, D., Tatar, M., Preistley, K., and Ghafory-Ashtiani, M., 2003, Seismological constraints on the crustal structure beneath the Zagros Mountain belt (Iran), *Geophys. J. Int*. 155: 403-410.

Hearn, T. M., and Ni, J.F. 1994. Pn velocities beneath continental collision zones: the Turkish-Iranian Plateau: *Geophys. J. Int*. 117: 273-283.

Jackson, J., Haines, J., and Holt, W., 1995. The accommodation of Arabia-Eurasia plate convergence in Iran, *J. Geophys. Res*. 100: 15205-15219.

Jackson, J. and McKenzie, D., 1984. Active tectonics of the Alpine-Himalayan belt between western Turkey and Pakistan, *Geophys. J. Roy. Astr. Soc*. 77: 185-264.

Jih, R. S., and Lynnes, C.S. 1993. Regional Lg Q variation in Iranian plateau and its implication for mb (Lg) determination, Phillips Lab report PL-TR-93- 2003 (TGAL-93-Ol), p. 13-37.

Kadinsky-Cade, K., M. Barazangi, J. Oliver, and Isacks, B. 1981. Lateral variations of high-frequency seismic wave propagation at regional distances across the Turkish and Iranian plateaus. *J. Geophys. Res*. 86: 9377-9376.

Kennett, B.L.N. and Engdahl, E.R., 1991. Traveltimes for global earthquake location and phase identification, *Geophys. J. Int*. 105: 429-465.

Maggi, A., Jackson, J.A., Priestley, K. and Baker, C., 2000. A re-assessment of focal depth distributions in southern Iran, the Tien Shan and northern India: do earthquakes really occur in the continental mantle?, *Geophys. J. Int*. 143: 629-661.

Nabelek, J., 1984. Determination of earthquake source parameters from inversion of body waves, PhD thesis, Massachusetts Institute of Technology.

Nilforoushan, F., Masson, F., Vernant, P., Vigny, C., Martinod, J., Abbassi, M., Nankali, H., Hatzfeld, D., Bayer, R., Tavakoli, F., Ashtiani, A., Doerflinger, E., Daignieres, M., Collard, P., and Chery, J., 2003. GPS networks monitors the Arabia-Eurasia collision deformation in Iran, *J. Geodyn*. 77: 411-422.

Nuttli, O. W., 1980. The excitation and attenuation of seismic crustal phases, *Bull. Seism. Soc. Am*. 70: 469-485.

Rodgers, A. J., Walter, W.R., Zhang, Y.S., Mellors, R.J. and Al-Amri, A.M.S. 1999. Lithospheric structure of the Arabian shield and platform from complete regional waveform modeling and surface wave group velocities, Geophys. *J. Int*. 138: 871-878.

Sandvol, E., Al-Damegh, K., Calvert, A., Seber, D., Barazangi, M., Mohamad, R., Gok, R., Turkelli, N. and Gurbuz, C., 2001. Tomographic imaging of observed regional wave propagation in the Middle East, *Pure Appl. Geophys*. 158: 1121-1163.

Tatar, M., Hatzfeld, D., and Ghafori-Ashtiany, M., 2004. Tectonics of the Central Zagros (Iran) deduced from microearthquake seismicity, *Geophys J*. Int. 156: 255-266.

Vernant, Ph., Nilforoushan, F., Hatzfeld, D., Abbassi, M.R., Vigny, C., Masson, F., Nankali, H., Martinod, J., Asttiani, A., Bayer, R., Tavakoli, F., and Chery, J., 2004, Present-day crustal deformation and plate kinematics in the Middle East constrained by GPS measurements in Iran and northern Oman, *Geophys. J. Int.* 157: 381-398.

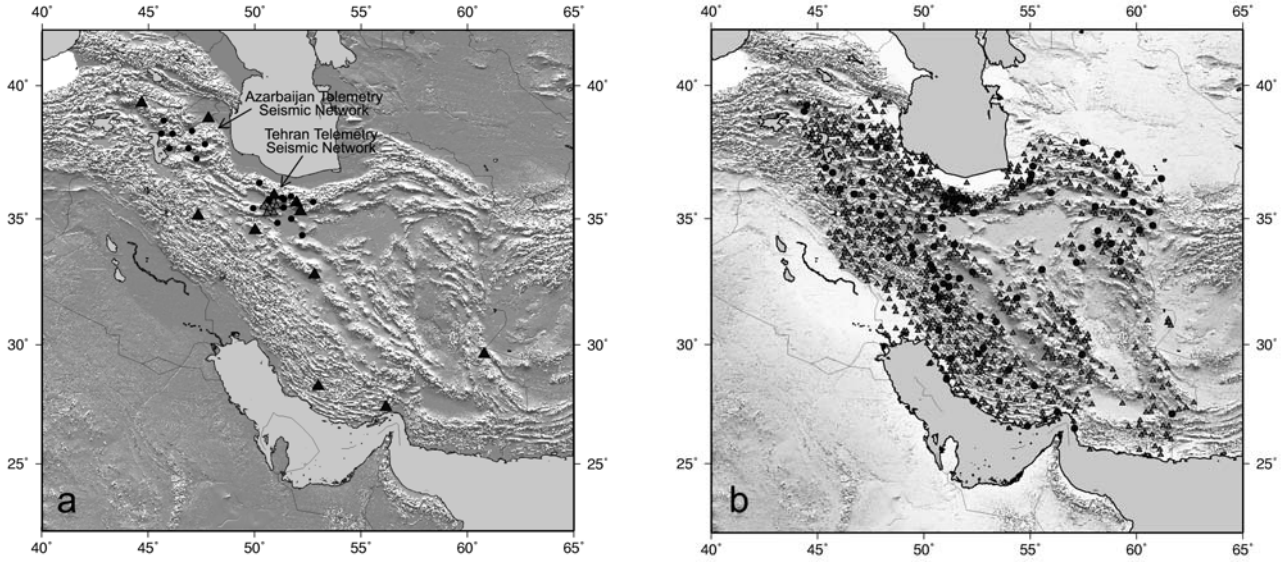

Figure 1. a) Distribution of stations of the Iran Broadband Network (black triangles), the short-period stations of Tehran and Tabriz (Azarbaijan Province) (black circles), and stations of the Iranian Long Period Array (grey triangles). b) Distribution of stations of the Iran Strong Motion Network (ISMN) with about 1000 stations. The triangles represent SSA2 digital Kinemetrics instruments whereas the circles are SMA-1 analog recorders.

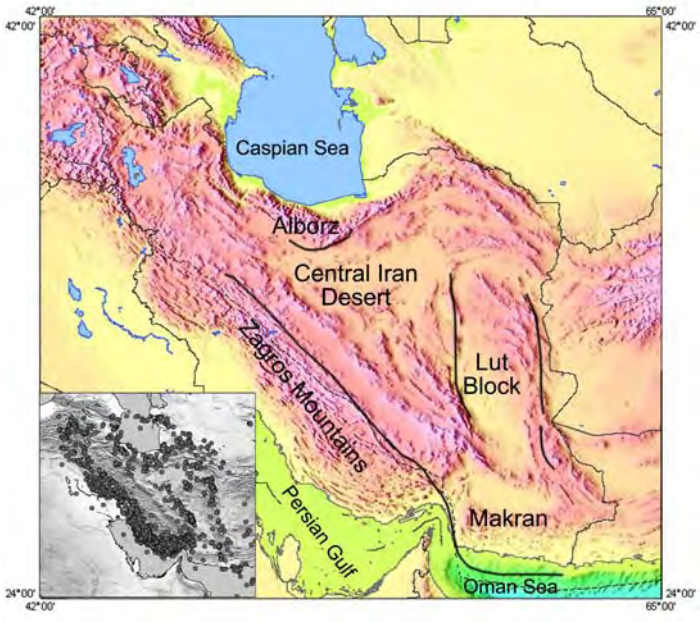

Figure 2. Tectonic province map of Iran showing the Zagros and Alborz mountains, the Lut block, and the Makran subduction zone. Inset shows significant seismic events in Iran (for detailed seismicity see Figure 4).

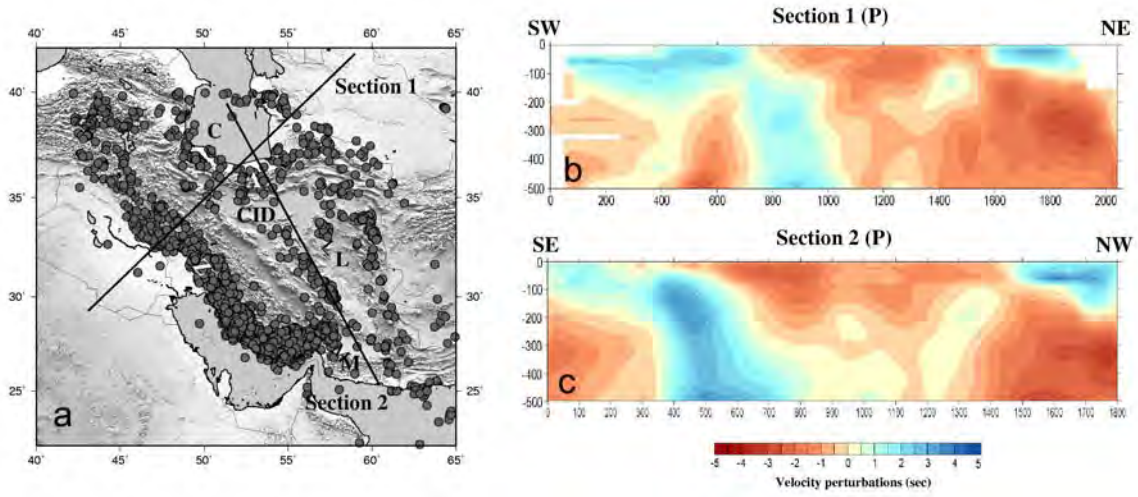

Figure 3. Instrumental Seismicity of Iran (a) for time period of 1964-2002 (updated catalog of Engdahl et al, 1998). The seismicity is concentrated mainly along Zagros Mountains (Z) extending from northwest to southeast, along Alborz Mountains (A) which lie adjacent to the southern shore of the aseismic southern Caspian Block (C). The borders separating the Lut Block (L) from the rather aseismic Central Iranian Desert (CID) and Afghanistan are marked by seismicity along major strike-slip faults. The Makran (where the oceanic plate of the Oman Sea subducts under the Iranian Plateau) is almost aseismic. (b and c) show the latest results of P-wave tomography using Iranian earthquakes along two sections 1 and 2 crossing the Zagros and Makran, respectively (Alinaghi et al., 2004). Central Iran is characterized by low velocity whereas the Caspian Block is a high-velocity domain.

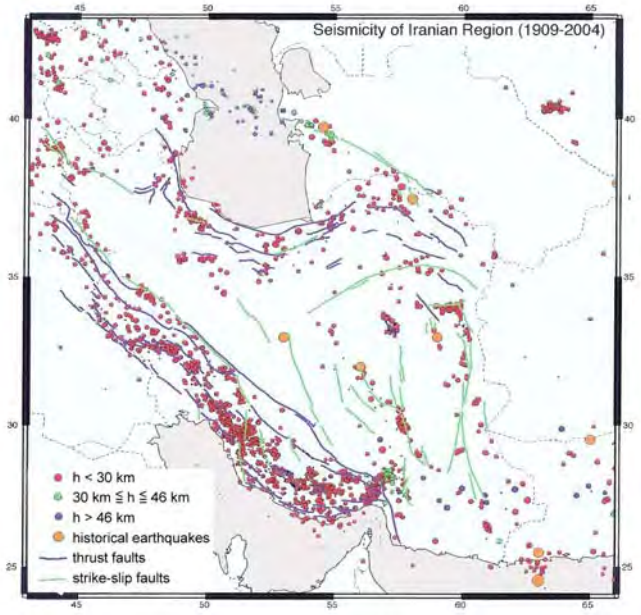

Figure 4. Detailed seismicity of Iran from 1909 to 2004. Note the majority of seismic events occur in the Alborz and Zagros mountains. Hypocentral depths are given as are orientations of faults.

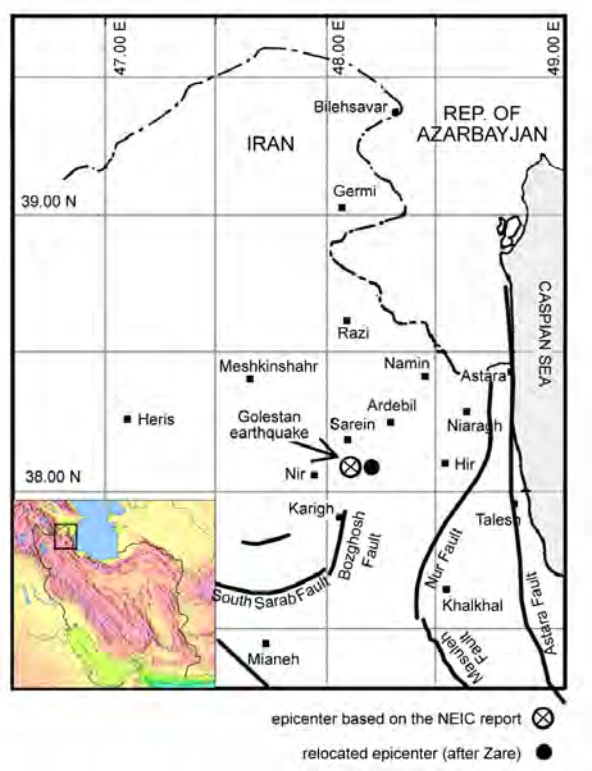

Figure 5. Location map of the Mw=6.0 Golestan earthquake for which we have high-quality strong motion data (see Figure 6). Sixteen local strong motions records are available for this event. Peak ground acceleration is 0.6 g recorded at 25 km distance.

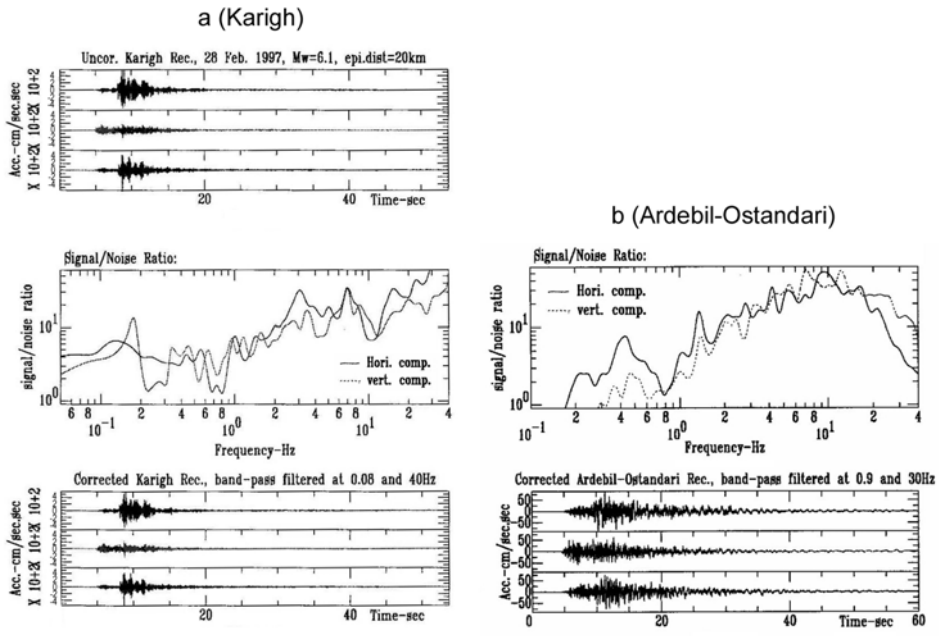

Figure 6. Strong motion waveforms for the Mw=6.0 Golestan earthquake recorded at Karigh (a) and Ardebil (b) see figure 5 for location. Data quality is very high. Additional data are shown in Figure 7.

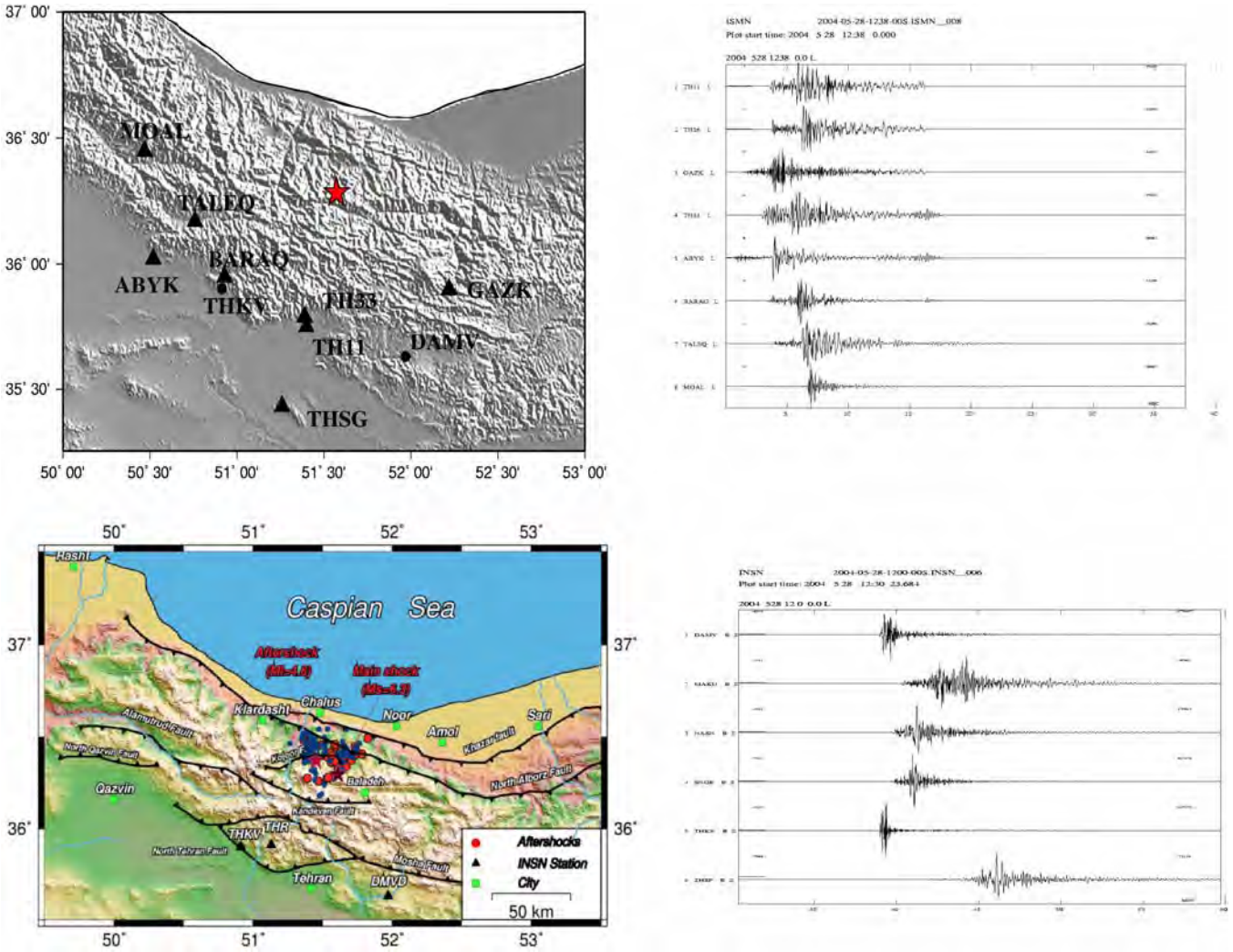

Figure 7. Samples of data from the Baladeh earthquake of 28 May, 2004 (M=6.2) in northern Iran. The top right panel shows waveforms from some representative stations of the ISMN (filled triangles in top left map). The bottom right panel are waveform data from six representative stations of the Iran broadband network (two of the stations are shown in the top left map as filled circles). The bottom left map shows the distribution of aftershocks as have been recorded by a temporary network of ten stations deployed by IIEES, Iran.

NUCLEAR-EXPLOSION PROFILES FOR SEISMIC CALIBRATION OF NORTHERN EURASIA

Igor B. Morozov[1,2], Elena A. Morozova[2], Scott B. Smithson[2], and Igor N. Kadurin[3]

University of Saskatchewan[1], University of Wyoming[2], and Center GEON[3]

Sponsored by Air Force Research Laboratory

Contract No. DTRA01-01-C-0081

ABSTRACT

In a four-year project, the University of Wyoming, in cooperation with the Center for Geophysical and Geoecological Studies (GEON) in Moscow, Russia, is preprocessing and organizing digital data from several unique long-range Deep Seismic Sounding (DSS) profiles using Peaceful Nuclear Explosions (PNEs).The data are being digitized from the original field tapes by GEON, quality-checked, edited, reformatted, and transferred to the Incorporated Research Institutions for Seismology (IRIS). As a result of this effort, seismic data from nine major DSS projects using 22 PNEs and several hundred chemical explosions are becoming broadly available for seismological and nuclear test monitoring research. To date, complete sets of records from the projects BAZALT, BATHOLITH, CRATON, KIMBERLITE, RIFT, RYBY, and QUARTZ have been delivered to IRIS. Project METEORITE is planned for delivery later this year.

DSS PNE profiles were recorded by GEON (the Special Geophysical Expedition at the time) from the early 1970s through late 1980s using 200-400 three-component analog instruments deployed in a grid of lines traversing most of the territory of the Former USSR. Each profile recorded 2-4 PNEs and several dozen chemical explosions at the same receiver locations. Long listening times of up to ~600 sec after the first arrival allowed recording of the secondary phases (S, Lg, Pg, Rg) critical for nuclear test monitoring. The energies of the PNEs ($m_b \approx 5$) were sufficient for reliable recordings beyond 3000 km, including consistent reflections from the mantle transition zone and several reflections from the core-mantle boundary. Chemical explosions of 5-12 tons yielded reflections from ~100-km depths and were recorded to 300-600-km distance.

DSS PNE data represents an unparalleled source of seismic information about the detailed structure of the upper mantle down to 400-800 km depth. Longer-offset recordings from some PNEs (QUARTZ-4, BATHOLITH-1, CRATON-1) show reflections from the core-mantle boundary. The PNE data sets cover an intermediate distance range (between 0-3200 km) and bridge the gap between controlled-source, earthquake-, and nuclear-explosion monitoring seismology. Dense, linear systems of DSS PNE observations lead to unusually detailed models of the crust and uppermost mantle over 4000-km long geotraverses. For regional seismic calibration, these datasets provide virtually the only dense three-component recordings of regional phases in aseismic regions of Northern Eurasia.

OBJECTIVES

From the mid-1970s and to the time of the break up of the Soviet Union, Russian scientists carried out an unparalleled program for Deep Seismic Sounding (DSS) of the territory of this vast country. In the course of this program they acquired a network of dense, linear, long-range, three-component profiles using large conventional and Peaceful Nuclear Explosions (PNEs). Fortunately for seismic nuclear test monitoring that emerged at about the time the DSS PNE program ended, these profiles systematically covered much of the aseismic parts of Northern Eurasia that would be difficult to calibrate by other means. These historic data provide unique opportunities to study seismic nuclear discrimination techniques and regional wave propagation through complex lithospheric structures.

The objective of this four-year project, which is currently near its end, was to complete digitization, verify, edit and make the key part of the unique collection of DSS PNE datasets broadly available to the monitoring and research communities.

RESEARCH ACCOMPLISHED

The data were being digitized at Center GEON, Moscow, and pre-processed and edited at the University of Wyoming. After nearly four years of this effort, the data processed and archived at IRIS currently include 18 PNEs and 522 chemical explosions recorded in eleven major seismic projects (Figure 1). The project is near completion, and only the METEORITE dataset (including 4 PNEs) remains to be delivered in November 2005. As a result of this effort, the broad seismological and seismic monitoring communities are obtaining a set of digital recordings of a large number of nuclear explosions recorded across a variety of propagation paths to the distances of ~3000 km.

DSS PNE data have been widely recognized as an unparalleled source of seismic information about the detailed structure of the upper mantle down to 400- to 800-km depths (e.g., Ryaboy, 1989; Kozlovsky, 1990; Morozova et al., 1999). PNE yields of ~7 – 23 kton provided reliable seismic recording throughout the full recording ranges (Figure 2). Several PNE record sections (BATHOLITH, CRATON-1, and QUARTZ-4) show reflections from the Earth's core. On a typical PNE profile, 3 – 4 nuclear explosions were recorded at up to 400 of three-component seismograph stations with nominal spacing of 10 to 15 km. About 50 – 80 chemical explosions (typically, each 3000 – 5000 kg, with some shots up to 15000 kg) per profile were also recorded to enable interpretation of crustal and uppermost mantle structures. The locations, depths, yields, and times of the PNEs, and characterizations of the source media were reported by Sultanov et al. (1999).

PNE data sets of the DSS program cover an intermediate distance range between 0 and 3200 km bridging the gap between the conventional controlled source, earthquake, and nuclear–explosion-monitoring seismology. Dense, linear systems of PNE and chemical explosions profiles cross a variety of contrasting tectonic structures in Northern Eurasia and result in unusually detailed models of the crust and uppermost mantle over 4000-km long geotraverses (Yegorkin, 1992; Pavlenkova, 1996). Some of the recent interpretations were performed by Egorkin and Mikhaltsev (1990), Mechie et al. (1993, 1997), Cipar et al. (1993), Priestley et al., (1994), Ryberg et. al. (1995, 1996), Schueller et al., (1997), Lorenz et al. (1997), Morozov et al. (1998a), and Morozova et al. (1999). These datasets also provide virtually the only dense three-component recordings of regional phases in aseismic regions of Northern Eurasia. Some of our recent results related to nuclear test monitoring were presented in Morozov (1998b), Morozov and Smithson (2000, 2002), and Morozov et al. (2005). One of the most spectacular PNE records from PBE QUARTZ-4 that received most attention in the past decade and which led to a number of far-reaching conclusions (some of them highly controversial) about the detailed structure of the upper mantle is shown in Figure 2.

Our current project schedule is shown in the table below. To date, we are on schedule for deliveries to IRIS and AFRL, although the chemical-profile data from project METEORITE were seriously delayed by GEON due to a series of unforeseen circumstances. Regardless of the delay with chemical-explosion data from METEORITE, we anticipate that its PNEs will be delivered to IRIS and AFRL as planned.

Table 1. Updated planned and actual data delivery schedule as of September, 2005.

#	Data set	Raw data delivery from GEON to UWyo (months)		Edited and reduced data delivered to IRIS DMS (months)	
		planned	*Actual*	*planned*	*actual*
1	QUARTZ	-	-	12/2001	12/2002
2	CRATON	02/2002	10/2002	08/2002	11/2002
3	KIMBERLITE	05/2002	11/2002	11/2002	11/2002,10/2003(chemical)
4	RIFT	08/2002	11/2002	05/2003	10/2003
5	RUBY	02/2003	02/2003	10/2003	02/2004
6	AGATE (5 profiles)	08/2003	07/2003	05/2004	06/2004
7	BATHOLITH-1 (3 profiles)	10/2003	12/2003	11/2004	12/2004
8	BATHOLITH-2** (4 profiles)	03/2004	12/2003	11/2004	12/2004
9	BAZALT-1** (3 profiles)	06/2004	01/2004	06/2005	07/2005
10	BAZALT-2 **(2 profiles)	10/2004	09/2004	06/2005	07/2005
11	METEORITE	03/2005*		11/2005	

*Only chemical explosion data sets need to be delivered to UWYO. Delivery delayed.
**Only chemical explosions used in these projects.

CONCLUSIONS AND RECOMMENDATIONS

The newly available PNE and chemical-explosion datasets from eleven major Russian seismic projects should boost research on seismic calibration of the region and on transportable seismic discriminants in Northern Asia. Greater availability of the unique PNE recordings would foster current research on several NNSA, AFRL, and DOE-sponsored nuclear test monitoring projects and facilitate extension of such research in the future. In addition, from a broader scientific perspective, the digitized DSS recordings and models of the upper mantle could also provide ideal reference and calibration data sets for the detailed structure of the upper mantle targeted by US Array.

REFERENCES

Cipar, J., K. F. Priestley, A. V. Egorkin, and N. I. Pavlenkova (1993), The Yamal Peninsula-Lake Baikal deep seismic sounding profile, *Geophys. Res. Lett*. 20: (15), 1631-1634.

Egorkin, A. V. and A. V. Mikhaltsev (1990), The Results of Seismic Investigations along Geotraverses, in *Super-Deep Continental Drilling and Deep Geophysical Sounding*, K. Fuchs, Y. A. Kozlovsky, A. I. Krivtsov and M. D. Zoback (Eds.), Springer, Berlin, 111-119.

Kozlovsky, Y. A. (1990), The USSR Integrated Program of Continental Crust Investigations and Studies of the Earth's Deep Structure under the Globus Project, in *Super-Deep Continental Drilling and Deep Geophysical Sounding*, Fuchs K., Kozlovsky Y. A., Krivtsov A. I. and Zoback M. D. (Eds.), Springer, Berlin, 90-103.

Lorenz, F., F. Wenzel, and J. Mechie (1997), Lateral heterogeneity implications from 2-D nuclear-seismic travel-time inversion, in: Fuchs, K. (Ed.) Upper mantle heterogeneities from active and passive seismology, pp. 237-248, *Kluwer Academic Publ*., Dordrecht.

Mechie, J., A. V. Egorkin, K. Fuchs, T. Ryberg, L. Solodilov, and F. Wenzel (1993), P-wave velocity structure beneath northern Eurasia from long-range recordings along the profile Quartz, *Phys. Earth Planet Inter*. 79: 269-286.

Mechie, J., A. V. Egorkin, L. Solodilov, K. Fuchs, F. Lorenz, and F. Wenzel (1997), Major features of the mantle velocity structure beneath northern Eurasia from long-range seismic recordings of peaceful nuclear explosions, in: Fuchs, K. (Ed.) Upper mantle heterogeneities from active and passive seismology, pp. 33-50, *Kluwer Academic Publ*., Dordrecht.

Morozov, I. B. (2001), Comment on “High-frequency wave propagation in the uppermost mantle” by T. Ryberg and F. Wenzel, *J. Geophys. Res*. 106: 30,715-30,718.

Morozov, I. B., and S. B. Smithson (2000), Coda of long-range arrivals from nuclear explosions, *Bull. Seism. Soc. Am.* 90: 929-939.

Morozov, I. B., and Smithson, S. B. (2002), Imaging crustal structure along refraction profiles using multicomponent recordings of first-arrival coda, *Bull. Seismol. Soc. Am.* 98: (8), 3080-3086.

Morozov, I. B., E. A. Morozova, and S. B. Smithson, (1998a), On the nature of the teleseismic Pn phase observed in the recordings from the ultra-long range profile "Quartz", Russia, *Bull. Seismol. Soc. Am*. 88: (1), 62-73.

Morozov, I. B., E. A. Morozova, S. B. Smithson, and L. N. Solodilov. (1998b), 2-D image of seismic attenuation beneath the Deep Seismic Sounding profile "Quartz", Russia, *Pure and Applied Geoph*. 153: 311-348.

Morozov, I. B., E. A. Morozova, S. B. Smithson, P. G. Richards, V. I. Khalturin, and L. N. Solodilov (2005), 3-D first-arrival regional calibration model of northern Eurasia, *Bull. Seismol. Soc. Am*., 95: (3), 951-964, doi:10.1785/0120030173.

Morozova, E. A., I. B. Morozov, S. B. Smithson, and L. N Solodilov (1999), Heterogeneity of the uppermost mantle beneath the ultra-long range profile "Quartz," Russian Eurasia, *J. Geophys. Res.*, 104 (B9), 20,329-20,348.

Pavlenkova, N. I., (1996), General features of the uppermost mantle stratification from long-range seismic profiles, *Tectonophysics* 264: 261-278.

Priestley, K. F., J. Cipar, A. Egorkin, and N. I. Pavlenkova (1994), Upper-mantle velocity structure beneath the Siberian Platform, *Geophysical Journal International* 118: (2), 369-378.

Ryaboy, V. (1989), Upper mantle structure studies by explosion seismology in the USSR, Delphic Associates, 138 pp.

Ryberg, T., F. Wenzel, J. Mechie, A. Egorkin, K. Fuchs, and L. Solodilov (1996), Two-dimensional velocity structure beneath Northern Eurasia derived from the super long-range seismic profile Quartz, *Bull. Seismol. Soc. Am*. 86: 857-867.

Ryberg, T., K. Fuchs, A. V. Egorkin, and L. Solodilov (1995), Observations of high-frequency teleseismic *Pn* on the long-range Quartz profile across northern Eurasia, *J. Geophys. Res.* 100: 18151-18163.

Schueller, W., I. B. Morozov, and S. B. Smithson (1997), Crustal and uppermost mantle velocity structure of northern Eurasia along the profile Quartz, *Bull. Seismol. Soc. Am.* 87: 414-426.

Sultanov, D. D., J. R. Murphy, and Kh. D. Rubinstein (1999), A seismic source summary for Soviet Peaceful Nuclear Explosions, *Bull. Seism. Soc. Am.*: 89: 640-647.

Yegorkin, A. V. (1992), Crustal structure along seismic geotraverses, International Geology Review, 34 (4), 345-362.

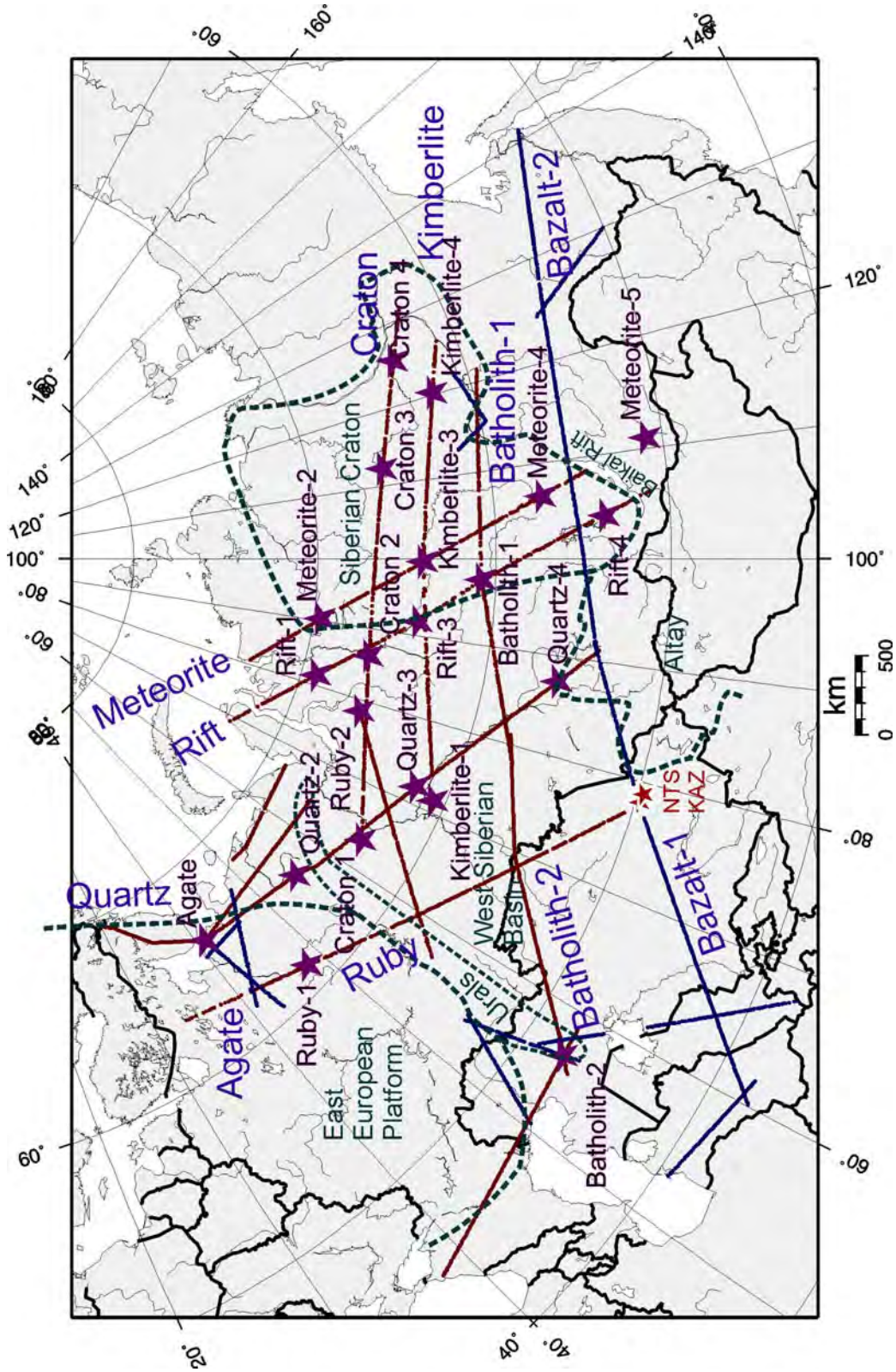

Figure 1 Eleven DSS PNE projects of this project (blue labels). With the exception for project METEORITE, all data were already delivered to IRIS and AFRL. The coordinates and other parameters of the PNEs used in these profiles were reported by Sultanov et al. (1999). Major tectonic units are indicated in green. Note the extent of systematic, continuous profiling, with PNEs (labeled stars) detonated at the nodes of a 2-D recording grid. Small brown circles are PNE recording stations, and blue circles are chemical-explosion recording stations. Project RUBY also recorded two Semipalatinsk nuclear test site explosions (red).

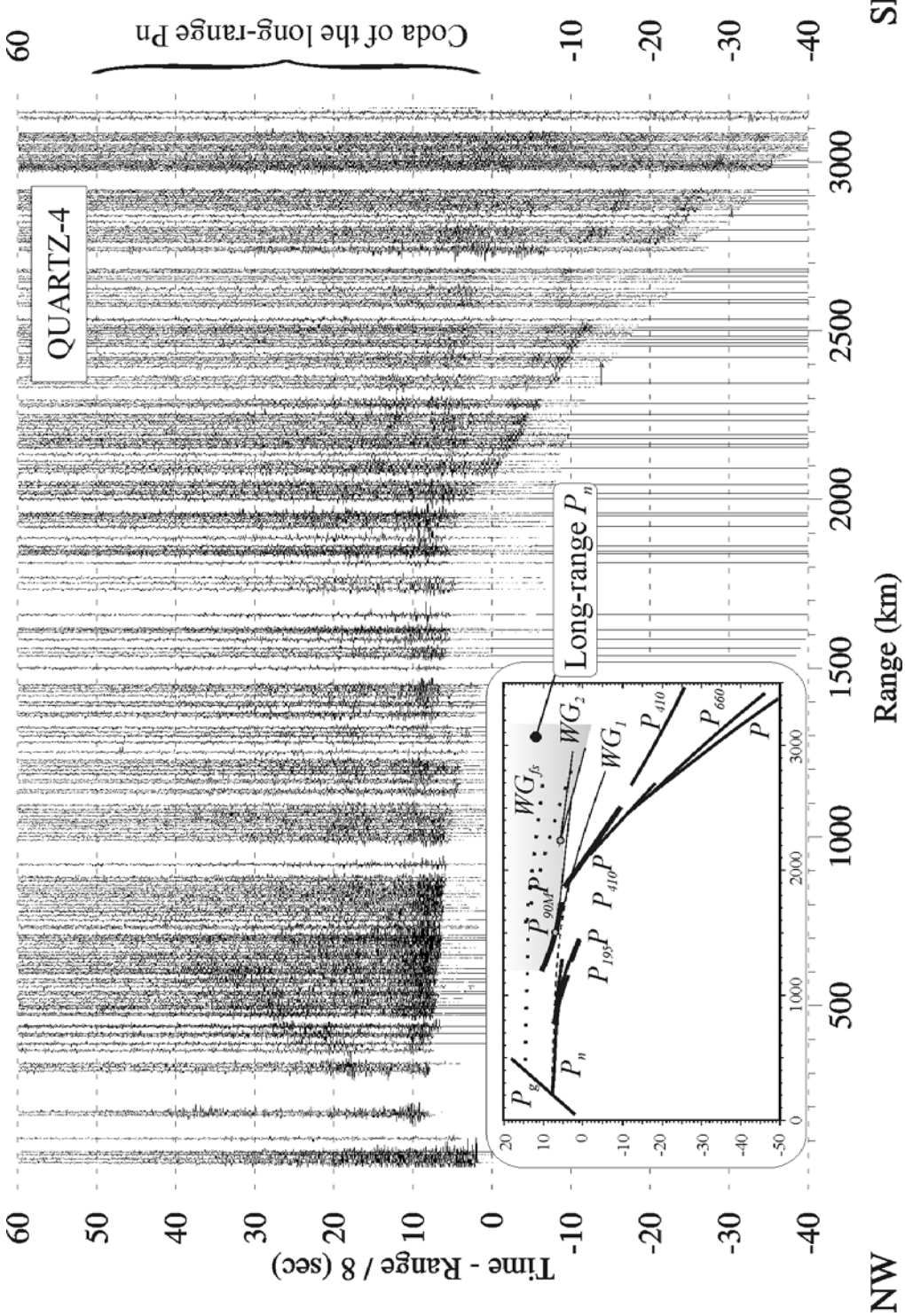

Figure 2. Vertical-component record from PNE QUARTZ-4 (Figure 1). Inset shows a sketch of seismic phases identified in the wavefield. Note the free-surface and Moho *P*-wave multiples (*PP*, or whispering-gallery modes) labeled WG_{fs} and *WG*, respectively. These phases were interpreted as caused by strong scattering within the uppermost mantle (Ryberg et al., 1995); however, in our interpretation, they are more likely to be the *PP* caused by a strong velocity gradient and mantle layering beneath the East European platform and the southern part of the West Siberian Basin (Morozov, 2001). Also, note the ~5-s gap in the first arrival caused by interpreted mantle low-velocity zone characteristic of the East European Platform and SW Western Siberia (Morozova et al., 1999). Both of these observations have significant implications for nuclear test monitoring along NW-SE paths across the East European Platform.

OBSERVATIONS AND MODELING OF FREQUENCY-DEPENDENT Lg CODA FROM PEACEFUL NUCLEAR EXPLOSIONS

Igor B. Morozov,[1] Hongyan Li,[2] Haishan Zheng,[1] and Scott B. Smithson[2]

University of Saskatchewan[1] and University of Wyoming[2]

Sponsored by Air Force Research Laboratory

Contract No. DTRA01-01-C-0057[1]

ABSTRACT

Coda amplitude decay of regional arrivals from peaceful nuclear explosions (PNEs) could be used for characterization of crustal properties critical for seismic monitoring. In particular, as coda waves at 0.5–10 Hz are believed to predominantly consist of scattered shear waves, coda analysis could provide information about *Lg* attenuation and scattering from crustal heterogeneities. Digital recordings of 21 reversed PNEs, recorded by 200–400 three-component instruments within 0–3000 km range in northern Eurasia enable coda amplitude measurements to provide valuable information for understanding *Lg* propagation in the region. In this report, we focus on the analysis of the observed frequency dependence of *Lg* coda and ongoing efforts for its modeling.

A striking observation from comparative analysis of the PNEs is the difference of *Lg* coda decay characters across the study area. Within the East European Platform and south-west West Siberian Basin (profile QUARTZ), *Lg* coda amplitude decays exhibit clear frequency dependence that was previously described by frequency-dependent coda quality factor $Q \approx 350_f^{0.13}$ (*f* is the frequency). By contrast, within the Siberian Craton (profile KIMBERLITE), the coda exhibits a constant decay rate for all frequencies, which would correspond to *Q* nearly proportional to frequency. However, we argue that such a strong frequency dependence of *Q* could actually be due to a non–frequency-dependent coda attenuation process associated with geometric spreading and leakage of the energy from the crust (e.g., by refraction). The modified coda amplitude decay relation thus becomes

$$\frac{d \log A}{dt} \approx -\gamma - \frac{\pi f}{Q} ,$$

where γ is the coda geometric spreading factor. Notably, when using this form, γ remains constant (≈ 0.003 s^{-1}) for the entire region, and $Q \approx 4\ 70$ for QUARTZ and $Q = \infty$ for KIMBERLITE. Very low attenuation within the Siberian Craton is also indicated by *Pg* propagating to unusual distances of 1600–1700 km. An additional advantage of using the above expression is that *Q* can now be viewed as frequency-independent.

Our modeling effort targets realistic, three-component phase amplitudes and codas produced by a distant PNE source. Currently, method and algorithm development and testing are underway. Simulations will be performed using a combination of three-dimensional (3D) visco-elastic finite-difference and 3D cylindrical screen propagator modeling. The finite-difference scheme will be utilized in the vicinities of the source and receivers, while the screen propagator will be used to propagate the energy to regional distances. The codes are parallelized using the Parallel Virtual Machine and implemented on two Beowulf clusters. Both codes are parts of an integrated seismic processing system, allowing tight integration of the models and providing a powerful user interface. When complete, this modeling package will provide the means for testing the above model of geometrical spreading and also to invert the *Lg Q* and *Lg* coda amplitude decay data for crustal attenuation.

OBJECTIVES

High-frequency regional phases used in CTBT monitoring (*Lg*, *Pg*, *Pn*, *Sn*) travel through the crust and the upper mantle and are therefore sensitive to the effects of these highly heterogeneous parts of the Earth. Large bodies of densely sampled observations and realistic modeling are required for understanding the properties of these phases and predicting their propagation across contrasting tectonic structures. In northern Eurasia, despite the paucity of its natural seismicity, such analysis is facilitated by the availability of dense regional phase recordings along the refraction lines of the Deep Seismic Sounding program, many of them using PNEs (Figure 1). In this project, we analyze PNE recordings for the purposes of regional seismic calibration. The general objectives of this study are as the following:

1) Gathering empirical data on amplitude and spectral characteristics of the regional phases in DSS PNE records, in their relation to the tectonic and geological structures.

2) Using numerical modeling, establishing semiempirical relationships between the in situ crustal properties and the observed wavefield characteristics. Among these characteristics, we are particularly interested in the quality factor, *Q*, describing attenuation of seismic waves.

In particular, in this report, we focus on observations and interpretation of frequency dependence of *Lg* coda *Q* and preliminary results of modeling aimed at elucidation of *Lg* coda *Q* properties.

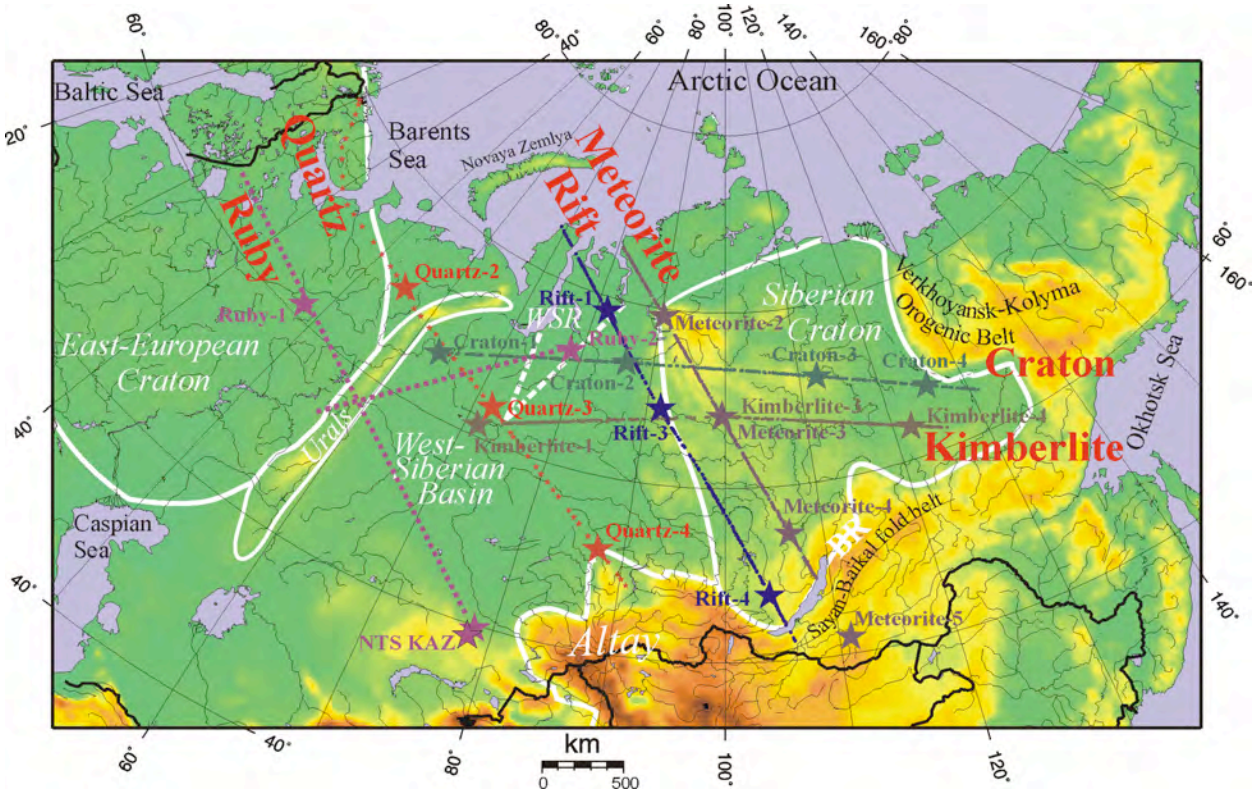

Figure 1. Location of PNE profiles used in this study shown on the background of topography of northern Eurasia. Large labeled stars indicate nuclear explosion locations, and small stars indicate the chemical explosions. For profile QUARTZ, small dots show chemical explosions; for other profiles, they show individual station locations. Two lines of project RUBY are shown schematically. White lines show major tectonic features (WSR, West Siberian Rift; BR, Baikal Rift), and color represents the topography (Zonenshain, 1990).

RESEARCH ACCOMPLISHED

Geometrical-spreading corrected vs. frequency-dependent coda Q

Measurements of the frequency-dependent quality factor, $Q(f)$, often results in Q increasing with frequency, which is conventionally expressed as a power law,

$$Q(f) = Q_0 \left(f / f_0 \right)^{\eta} , \quad (1)$$

where f_0 is a reference frequency often taken equal 1 Hz. Both Q_0 and exponent η are assumed constant within the frequency range of interest, and thus relation (1) essentially represents fitting a two-parameter dependence to the observations of Q made at a set of selected frequencies. The power-law dependence appears to be generally dictated by convenience and represents a suitable parameterization in most cases. From several *Lg* Q and *Lg* coda Q studies, the frequency-dependence parameters η typically range from ~0.1 to near 1.0 (e.g., Nuttli, 1973; Mitchell, 1975; Frankel, 1991; Benz et al., 1997; Mitchell et al., 1997, 1998; McNamara, 2001; Erickson et al., 2004). General correlation to tectonics appears to suggest that active tectonic regions are characterized by low Q_0 and high η, while stable cratons are characterized by higher Q_0 and lower η (Erickson et al., 2004).

An initial attempt for application of the above conclusion to the region and frequency band of DSS profiles led to similar observations (Morozov and Smithson, 2000). Measurements of *Lg* coda Q at frequencies ~2 and 5 Hz from PNE QUARTZ-4 in the Mezenskaya Depression (near the position of PNE QUARTZ-2 in Figure 1) resulted in the values of $Q_1 = 350$ (at $f_0 = 1$ Hz) and $\eta = 0.13$ in relation (1) (Figure 2; Morozov and Smithson, 2000). The somewhat low Q_0 value was explained by the influence of thick sediments within the depression, and low η appears in agreement with the stable East European Platform.

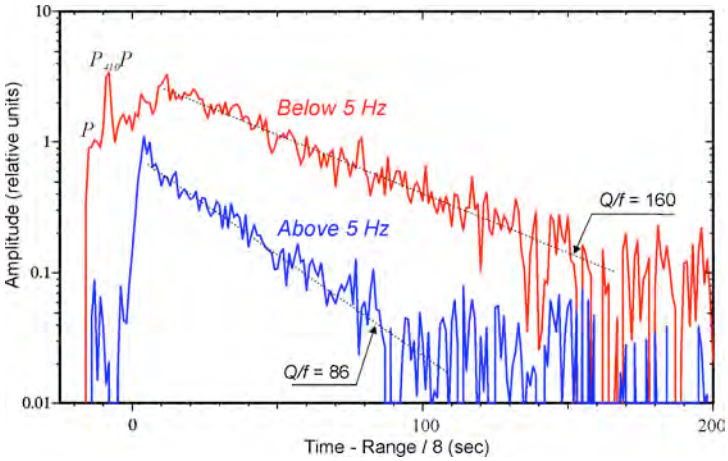

Figure 2. Amplitude-time decay for *Lg* coda from PNE QUARTZ-4, measured near the position of PNE QUARTZ-2 (Figure 1). Note the increasing amplitude decay rate with frequency; this increase is indicative of seismic attenuation. The *Q/f* values measured from the slopes are given in the labels.

Similar measurements using the records from profiles KIMBERLITE and METEORITE in Siberia lead to strikingly different results. From the unusual efficiency of *Pg* propagation within the Siberian Craton, crustal Q was expected to be relatively high (Figure 3). In addition, travel-time modeling of QUARTZ profile (Figure 1) also suggested a simpler, layered crustal structure with little Moho topography within the West Siberian Basin as compared to the northern parts of the East European Platform (Shueller et al., 1997; Morozova et al., 1999). However, the logarithm of *Lg* coda amplitude measured from PNE KIMBERLITE-3 at a station within the Siberian craton shows an approximately frequency-independent decay (Figure 4). When interpreted in terms of the usual assumption of correctly compensated geometrical spreading of the coda (Morozov and Smithson, 2000), this decay is entirely due to the coda Q:

$$\log A_{coda}(f,t) = const - \frac{\pi f}{Q(f)} t = const - \frac{\pi}{Q_0} f^{1-\eta} t \ . \quad (2)$$

To account for the frequency-independent decay rate in relation (2), $Q(f)$ should be proportional to the frequency, corresponding to $\eta \approx 1$ in power law (1). Q_0 can be estimated as ~200 for *Lg* coda and 400 for the S-wave coda, both values appearing surprisingly low for this cratonic area and in disagreement with other observations.

The observations above suggest that the interpretation of the frequency dependence of Q could be reconsidered, at least for strong ($\eta \approx 1$) frequency dependences, in the DSS frequency band (~1–10 Hz), or within the area of this

study. Note that the strong frequency dependence of Q arising from formula (2) is observed for the entire KIMBERLITE profile (Figure 5) and not only at the location presented in Figure 4.

High $h \approx 1$ values in relation (1) imply that attenuation is quickly reduced with frequency. Liu et al. (1976) showed that linear visco-elastic rheology based on a "generalized standard linear solid" could explain frequency-dependent intrinsic attenuation observed during wave propagation through Earth materials. However, laboratory measurements are carried out at significantly higher frequencies and shorter wavelengths than those of the seismic waves considered here. At short-period seismic scales (100–10000 m), pervasive crustal and upper-mantle heterogeneity creates a complex interplay of numerous rheologies and could result in completely different properties. In particular, the presence of an attenuating component (e.g., water or small fouls) would reduce the inferred high Q at higher frequencies. Moreover, for coda waves bouncing within the crustal waveguide, scattering should be the primary contributor to their attenuation. For scattering, attenuation decreasing with frequency would mean that the total volume of scatterers drops nearly linearly at smaller scale lengths. Although this could be possible, it still appears unlikely that heterogeneities within the West Siberian Basin and Siberian Craton become progressively less abundant as their sizes reduce. Typically, scaling laws suggest increasing representation of heterogeneities (e.g., faults and topographic features) at smaller scales.

Accepting the above conjecture that high h could in fact be observed where Q is very high, we note that the frequency-independent amplitude decay should not be related to the attenuation defined as an energy dissipation process proportional to the number of wave cycles (that is, to f_t). Instead, if coda amplitude decay with time includes a purely geometrical component, it could be approximated by the following relation:

$$\log A_{coda}(f,t) = const - \left(\gamma + \frac{\pi f}{Q}\right)t \cdot \qquad (3)$$

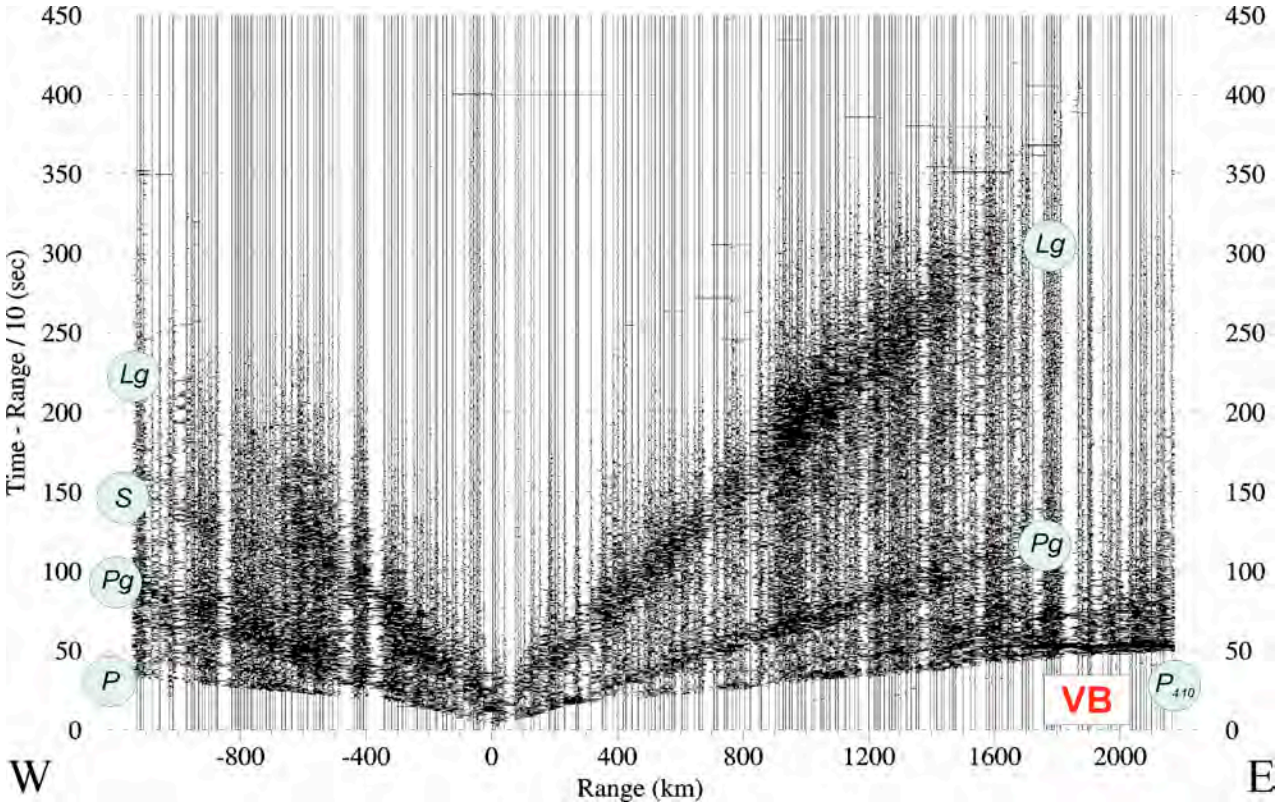

Figure 3. Vertical-component records from PNE CRATON-2 (Figure 1). Note the unusually strong propagation of *Pg* to ~1700 km from the shot, quickly attenuating within the Viluy basin (VB). Such high propagation efficiency suggests high crustal *Q*, at least in the eastern part of the profile.

Here, γ describes an effective geometrical spreading process. Amplitude decaying with scattering time and independent of the frequency could correspond, for example, to leaking of the wave energy out of the *Pg*/*Lg* waveguide as the multiple-reflected waves bounce within it (Gutenberg, 1955). Note that the exponential relation for $A_{coda} \propto \exp(-\gamma t)$ is primarily dictated by the convenience of working in the (t, log$A$) plane. With significant measurement errors inherent in attenuation measurements, other frequency-independent expressions could be defined, yet in practice, they could hardly be distinguished from form (3).

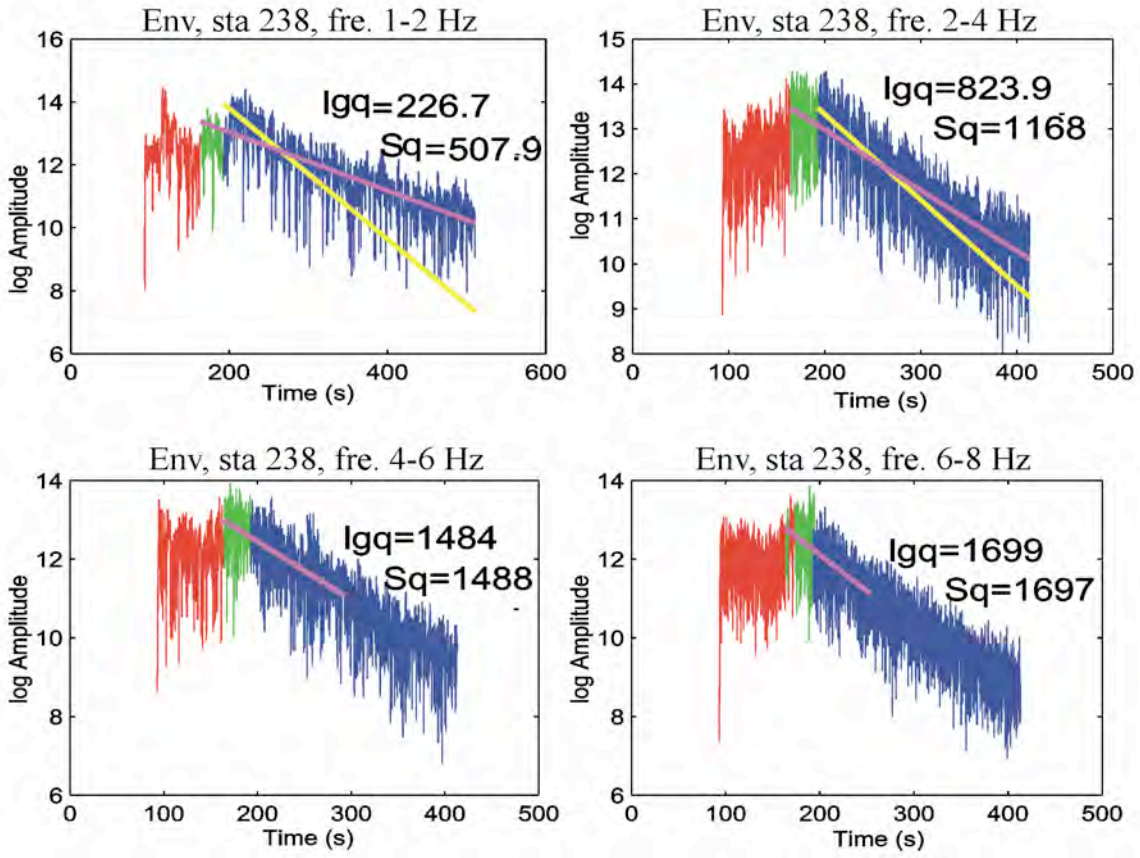

Figure 4. Amplitude envelope of vertical-component record from station 238 from PNE KIMBERLIE-3 filtered within frequency bands of 1–2, 2–4, 4–6, and 6–8 Hz (labeled). Estimated coda *Q* for the S-wave and *Lg* coda windows are indicated. Note that these *Q* values quickly increase with frequency. Also note that at the same time, temporal slopes of log (amplitudes) appear to be independent on the frequency bands.

With a single constant Q, expression (3) represents another two-parameter relation for $\log A_{coda}(f,t)$, which is an alternative to (2). Although Q could also be theoretically considered as frequency-dependent in formula (3), distinguishing this dependence from the effect of γ appears highly problematic with the available data. Thus, in a minimalistic approach, we view the form (3) with a single and constant Q as a viable alternative to frequency-dependent $Q(f)$ for the DSS PNE data. Potential extrapolation of this conjecture to other situations will still need to be examined in the future.

Within the accuracy of fitting relations (2) or (3) to the typical data, both of them apparently could be used interchangeably. Thus, the dependence (3) with $Q = \tilde{Q}$, when recast in the form (2), would lead to frequency-dependent attenuation with

$$\eta = -\log_f \left(\frac{\gamma}{f_{ref}} + \frac{\pi}{\tilde{Q}} \right), \quad (4)$$

where the reference frequency f_{ref} could be selected within the frequency band. This shows that $\eta = 0$ for $\gamma = 0$ and $\eta \rightarrow 1$ when $Q \rightarrow \infty$. A high γ (steep geometric coda amplitude decay, as possibly caused by strong crustal folding and rough Moho) would thus explain the low Q_0 and high η observed in active tectonic areas.

Using the dependence (3) instead of (2) to fit QUARTZ-4 (Figure 2) and KIMBERLITE-3 (Figure 4) observations reveals that, for both datasets, the geometrical factor is the same, $\gamma \approx 0.003$ s^{-1}, with $Q \approx 470$ for QUARTZ and $Q = \infty$ for KIMBERLITE. In agreement with the observations of unusually efficiently propagating *Pg* within the Siberian Craton, its crust shows very low attenuation. Close geometrical factors both east and west of the Uralian belt (Figure 1) could also be expected, as crustal structure remains generally similar on both sides. As another hypothesis, it appears that crustal thickness could be the primary factor controlling the values of γ. With increasing crustal thickness, the number of reverberations required to form a crustal-guided phase at a given distance would decrease, leading to lower values of geometrical attenuation γ.

If confirmed by further analysis of the DSS PNE and other data, the above observations could have several important implications for seismic calibration and nuclear test monitoring. First, as frequency dependence of Q trades off with geometrical spreading, it is important to eliminate this uncertainty before correlating the resulting parameters with the geological structures or looking for portable attributes. Equation (3) removes this trade-off by defining the geometrical spreading as a frequency-independent part of signal attenuation with time (distance). This could allow local measurements of geometrical spreading by spectral analysis of coda waves. The resulting spreading parameter γ could be regionalized and correlated with geology.

The second potential advantage from using form (3) arises from the stability of the geometrical exponent γ suggested by the present observations. If γ is confirmed to be stable or correlated with the crustal thickness, it could be used as a useful and transportable calibration parameter. Robust regional values of geometrical spreading could be utilized to correct the observed coda Q values. Moreover, because of their frequency independence, the resultant coda Q values also may have a better chance of being transportable between different frequency bands, types of observations, and geographic regions.

In most practical cases, removal of the $\gamma \leftrightarrow Q(f)$ trade-off would leave us with only frequency-independent Q in relation (3). The advantage of this point of view would be in freeing Q measurements from reliance on independent determinations of geometrical spreading, which are the critical part of most attenuation measurements (Benz et al., 1997). Note that because of their using band-limited data without explicitly enforcing frequency-independence, geometrical spreading estimates may also turn out to be effectively dependent on the frequency. In addition, (γ.Q) parameterization is also closer to and should be consistent with attenuation measurements using spectral ratio

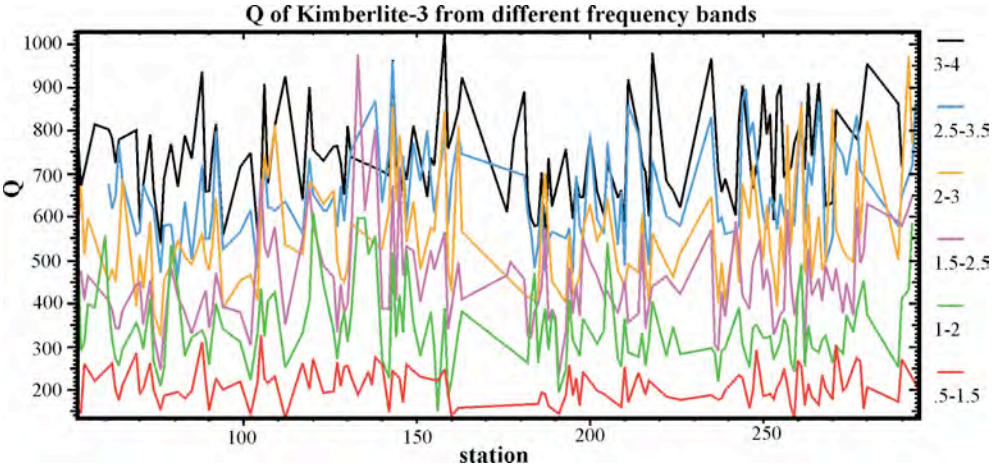

Figure 5. *Lg* coda *Q* of PNE KIMBERLITE-3 measured across the profile within several frequency bands (labeled on the right). Despite the scatter in the *Lg Q* values, *Q* consistently increases with frequency.

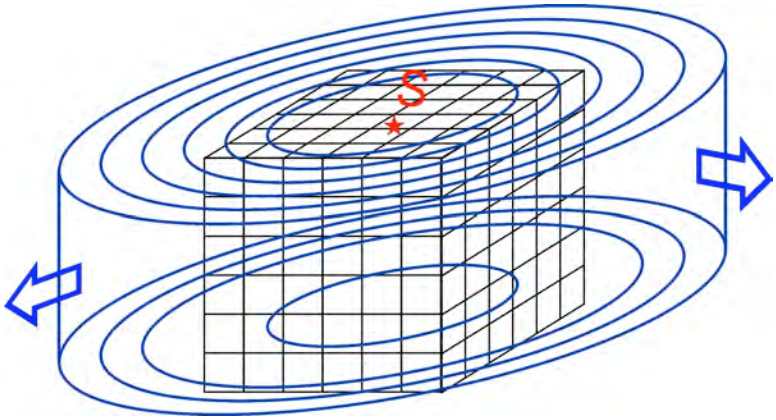

Figure 6. Schematic illustration of our 3D numerical wavefield simulation scheme. First, in the near-source region, the wavefield is modeled using a 3D visco-elastic finite-difference simulator (cubic grid). This field is propagated to regional distances using a modification of the Generalized Complex Screen Propagator method (blue cylindrical surfaces; Wu, et al., 2000).

techniques (which eliminate the absolute amplitude effects and rely on spectral slopes, thereby typically also producing frequency-independent *Q* estimates insensitive to the geometrical spreading).

Lg and coda modeling in 3D

Modeling short-period seismic phases in realistic crustal structures at regional distances is another key component of this project. Code development is still in progress, and here we only summarize the key ideas of the approach. We utilize parallel cluster computer systems (10- and 66-processor) to implement a hybrid 3D finite-difference (FD) and finite-element (FE) modeling scheme (Figure 6).

The near-source region is modeled using a parallel visco-elastic finite difference program based on the fourth-order finite-differencing scheme by Bohlen (2002). Compared with Bohlen's code, we use a different parallelization scheme (the Parallel Virtual Machine instead of the Message Passing Interface), an extensive user interface allowing us to build complexly structured models, more general periodic boundary conditions, and free-surface boundary conditions with arbitrary topography. The code has been integrated into our seismic processing system (Morozov and Smithson, 1997; Chubak and Morozov, in review), adding many options for user interaction with the code and for data and model visualizations.

Farther away from the source, full 3D FD simulations become impractical because of excessive demand on computational resources, and we switch to an efficient Generalized Screen Propagator (GSP) scheme first developed by Wu et al. (2000). However, unlike the original two-dimensional (2D) implementation (Wu et al., 2000, and references therein), we introduce the following new requirements to our screen propagator: (1) it should operate in 3D, and therefore the screens become cylindrical (Figure 6); (2) surface topography, the Moho depth, and the key crustal boundaries (such as the top of the basement) are explicitly included in the model and are allowed to vary; and (3) we allow for arbitrary velocity/density variations with depth and also their slow variations with propagation radius. This GSP scheme is therefore fundamentally different from that by Wu et al. (2000) and requires a different implementation. Owing to the structural complexity of the model, the finite element (FE) method apparently represents the most sitable approach to responding to the above requirements.

The FE scheme is formulated as follows. In variational formulation (see Aki and Richards, 2002, Chapter 7.3), solution of the wave propagation problem is reduced to finding a stationary point of a functional sometimes called Action,

$$A[\mathbf{u}] = \int d^3\mathbf{r} L(\dot{\mathbf{u}}, \mathbf{u}), \tag{5}$$

where **u** is the displacement field, the dot denotes the time derivative, and the Lagrangian *L*() is the difference of the kinetic and potential energy densities. For an isotropic medium,

$$L(\dot{\mathbf{u}},\mathbf{u}) = \frac{1}{2}\rho \dot{u}_i \dot{u}_i - \left[\frac{1}{2}\lambda(\varepsilon_{ii})^2 + \mu\varepsilon_{ij}\varepsilon_{ij}\right], \quad (6)$$

where ε is the strain tensor. Because the model is independent of the time variable, different Fourier harmonics do not interfere with each other, and in the frequency domain, (6) becomes

$$L(\dot{\mathbf{u}},\mathbf{u}) = -\frac{\omega^2}{2}\rho u_i u_i - \left[\frac{1}{2}\lambda(\varepsilon_{ii})^2 + \mu\varepsilon_{ij}\varepsilon_{ij}\right]. \quad (7)$$

The problem reduces to maximization of the integral (5) by finding the appropriate spatial distribution of **u** for each frequency ω. The Rayleigh-Ritz method achieves this by first approximating the wavefield by a linear combination of basis functions,

$$\mathbf{u}(\mathbf{r}) = c_i \boldsymbol{\phi}_i(\mathbf{r}). \quad (8)$$

The basis functions are chosen to satisfy the boundary conditions (zero normal traction at the free surface and radiation condition at the bottom of the model). In our case, for each screen, we associate the basis functions with a grid of points in depth, z, and azimuth, θ, so that

$$\boldsymbol{\phi}_{k,n,l} = J_0(kr)s_n(z)s_l(\theta), \quad (9)$$

where k is the radial wavenumber, J_0 is the zero-order Bessel function, and $s()$ are linear spline functions centered at node (n, l) respectively in the (z,θ) cylindrical surface. With the use of functional basis (8), action (5) becomes a quadratic form,

$$A[\mathbf{u}] = c_i A_{ij} c_j, \quad (10)$$

where A_{ij} is a sparse and symmetrical matrix. The key assumption of this GSP method, as with the method by Wu et al. (2000), is the preservation of the wavenumber between the screens (matrix A is thus approximately diagonal in k), so that, along with ω, k could be considered an integral of motion during the maximization. This approximation reduces the set of unknowns to one two-dimensional (2D) grid per screen, and the screens can be spaced relatively sparsely, making numerical maximization of (5) a tractable problem. The resulting matrix problem (10) can be solved by an iterative technique, such as conjugate gradients or LSQR. Because of the independent spoliations with different (ω, k), the method can be parallelzed in a straightforward manner.

CONCLUSIONS AND RECOMMENDATIONS

Analysis of the frequency-dependent *Lg* coda *Q* from several DSS PNE profiles in northern Eurasia indicates significant differences in attenuation properties between the East European Platform and the West Siberian Basin and the Siberian Craton. A consistent interpretation arises from abandoning the traditional $Q(f) = Q_0 f^{-\eta}$ model in favor of the model utilizing regionally-variable geometrical spreading and frequency-independent attenuation. In this model, the geometrical spreading is consistent between the two studied areas, and the attenuation appears to be very low within the Siberian Craton, in agreement with other observations.

If confirmed by further analysis, these observations could have several important implications for seismic calibration and nuclear test monitoring:

1) It would allow more consistent and reliable measurements of geometrical spreading and *Q*.
2) The geometrical exponent γ is likely to be stable or correlated with the crustal thickness, in which cases it could be used as a useful and transportable calibration parameter.
3) Because of their frequency independence, the resultant coda *Q* values also may also be better transportable between different the frequency bands, types of observations, and geographic regions.

In numerical modeling, we described a comprehensive hybrid parallel 3D finite-difference and finite-element screen propagator method that should allow simulations of short-period wavefields to regional distances, with an account of

the topography of the free surface, of the Moho, and of the key intracrustal boundaries. The method should also be able to handle depth and lateral velocity variations. Finally, the method is currently being implemented in an integrated seismic processing package that will provide uniform model parameterization, input/output, and visualization.

REFERENCES

Aki, K. and P. G. Richards (2002), *Quantitative Seismology*, 2nd Ed. Sausalito, CA: University Science Books.

Benz, H., A. Frankel, and D. Boore (1997), Regional *Lg* Attenuation in the Continental United States, *Bull. Seis. Soc. Am.* 87: 600–619.

Bohlen, T. (2002), Parallel 3-D Viscoelastic Finite Difference Seismic Modelling, *Comput. Geosciences* 28: 887–899.

Chubak, G. and I. B. Morozov, (in review), Integrated Software Framework for Processing of Geophysical Data, *Comput. Geosciences*.

Erickson, D., D. E. McNamara, and H. Benz (2005), Frequency-Dependent *Lg Q* within the Continental United States, *Bull. Seism. Soc. Am.* 94: 1630–1643.

Frankel, A. (1991), Mechanism of Seismic Attenuation in the Crust: Scattering and Inelasticity in New York State, South Africa, and Southern California, *J. Geophys. Res*. 96: 17441–17457.

Gutenberg, B. (1955), Channel Waves within Earth's Crust, *Geophysics* 20: 283–294.

Liu, H. P., D. L. Anderson, and H. Kamamori (1976), Velocity Dispersion due to Anelasticity: Implications for Seismology and Mantle Composition, *Geoph. J. Roy. Astr. Soc.* 47: 41–58.

McNamara, D. E. (2000), Frequency-Dependent *Lg* Attenuation in South-Central Alaska, *Geophys. Res. Lett.* 27: 3949–3952.

Mitchell, B. (1975), Regional Rayleigh Wave Attenuation in North America, *J. Geophys. Res.* 80: 4904–4916.

Mitchell, B. J. and L. Cong (1998), *Lg* coda Q and Its Relation to the Structure and Evolution of Continents: A Global Perspective, *Pure Appl. Geophys.* 153: 655–663.

Mitchell, B. J., Y. Pan, J. Xie, and L. Cong (1997), *Lg* Coda Q Variation across Eurasia and Its Relation to Crustal Evolution, *J. Geophys. Res.* 102: 22767–22779.

Morozov, I. B., and S. B. Smithson (2000), Coda of Long-Range Arrivals from Nuclear Explosions, *Bull. Seism. Soc. Am.* 90: 929–939.

Morozov, I. B. and S. B. Smithson, (1997), A New System for Multicomponent Seismic Processing, *Comput. Geosciences* 23: 689–696.

Morozova, E. A., I. B. Morozov, S. B. Smithson, and L. N. Solodilov (1999), Heterogeneity of the Uppermost Mantle beneath the Ultra-Long Range Profile "Quartz," Russian Eurasia, *J. Geophys. Res.* 104 (B9): 20, 329–330, 348.

Nuttli, O. (1973), Seismic Wave Attenuation and Magnitude Relations for Eastern North America, *J. Geophys. Res.* 78: 87–885.

Schueller, W., I. B. Morozov, and S. B. Smithson (1997), Crustal and Uppermost Mantle Velocity Structure of Northern Eurasia along the Profile Quartz, *Bull. Seism. Soc. Am.* 87: 414–426.

Wu, R.-S., S. Jin, and X.-B. Xie (2000), Energy Partition and Attenuation of *Lg* Waves by Numerical Simulation Using Screen Propagators, *Phys. Earth. Planet. Inter*. 120: 227–243.

Zonenshain L. P., M. I. Kuzmin, and B. M. Natapov (1990), *Geology of the USSR: A Plate Tectonic Synthesis*. Washington, DC: American Geophysical Union.

MAGNITUDE-YIELD AND TRAVEL-TIME CALIBRATION OF NORTHERN EURASIA USING DEEP SEISMIC SOUNDING DATASETS

Igor B. Morozov[1], W. Scott Phillips[2], and Igor. N. Kadurin[3]

University of Saskatchewan[1], Los Alamos National Laboratory[2], and Center GEON[3]

Sponsored by National Nuclear Security Administration
Office of Nonproliferation Research and Engineering
Office of Defense Nuclear Nonproliferation

Contract Nos. DE-FC52-05NA26609[1] and W-7405-ENG-36[2]

ABSTRACT

This study continues our analysis of digital seismograms from chemical and peaceful nuclear explosions (PNEs) of the Russian Deep Seismic Sounding (DSS) program that have recently become available. In this new project, we are extending this analysis to

- Obtaining ground truth source parameters (charge types, sizes, and other relevant information) of ~500 chemical explosions used in 11 major projects of the DSS program;
- Obtaining and digitizing regional and local earthquakes recorded by the DSS PNE profiles for their use as empirical Green's functions in coda magnitude calibration;
- Coda magnitude analysis for DSS chemical and nuclear explosions;
- Derivation of empirical magnitude (apparent coda source spectra) yield relationships for small (m_b ~1-3) explosion events in Northern Eurasia;
- Study of transportability of the coda source-yield relationship over a broad area and a variety of emplacement conditions based on PNE data and extrapolating the relationship to smaller, chemical yields;
- Examination of the variability of the derived coda calibration parameters, attenuation in particular, along and across the profiles; correlating this variability with geology and tectonics of the area;
- Derivation of a P-wave travel-time calibration model for Northern Eurasia with an unusually well constrained and detailed crustal and uppermost mantle structure based on the chemical explosion data. Using this model, derive sample Source Specific Station corrections (SSSC) for an IMS station (e.g., BRVK) and developing a methodology for its enhancement, and comparing with previous SSSC to assess importance of additional data.

As a result of this effort, we plan to produce a large calibration dataset of stable magnitudes and test magnitude-yield relations for a broad, largely aseismic, and critical portion of Northern Eurasia. Coda calibration will bridge the gap between central Asia and the European Arctic and provide additional calibration information to further work in that area.

OBJECTIVES

From mid-1970s to 1990, Russian scientists carried out an extensive program for DSS of the territory of this the Soviet Union. The program resulted in the acquisition of a network of densely sampled, long-range, three-component profiles using large conventional and peaceful nuclear explosions (PNEs). Currently, an effort (sponsored by AFRL contract DTRA01-01-C-0081 and NSF Grant EAR-0092744) for digitizing these datasets and preserving them in modern digital formats in IRIS (Incorporated Research Institutions for Seismology) and AFRL is underway, with 22 PNEs and 522 chemical explosions archived to date. DSS PNE profiles covered much of the aseismic parts of Northern Eurasia and are now receiving growing attention in their application to seismic calibration and nuclear test monitoring in Northern Asia. In this new project, we plan to derive two types of new calibration information from these datasets

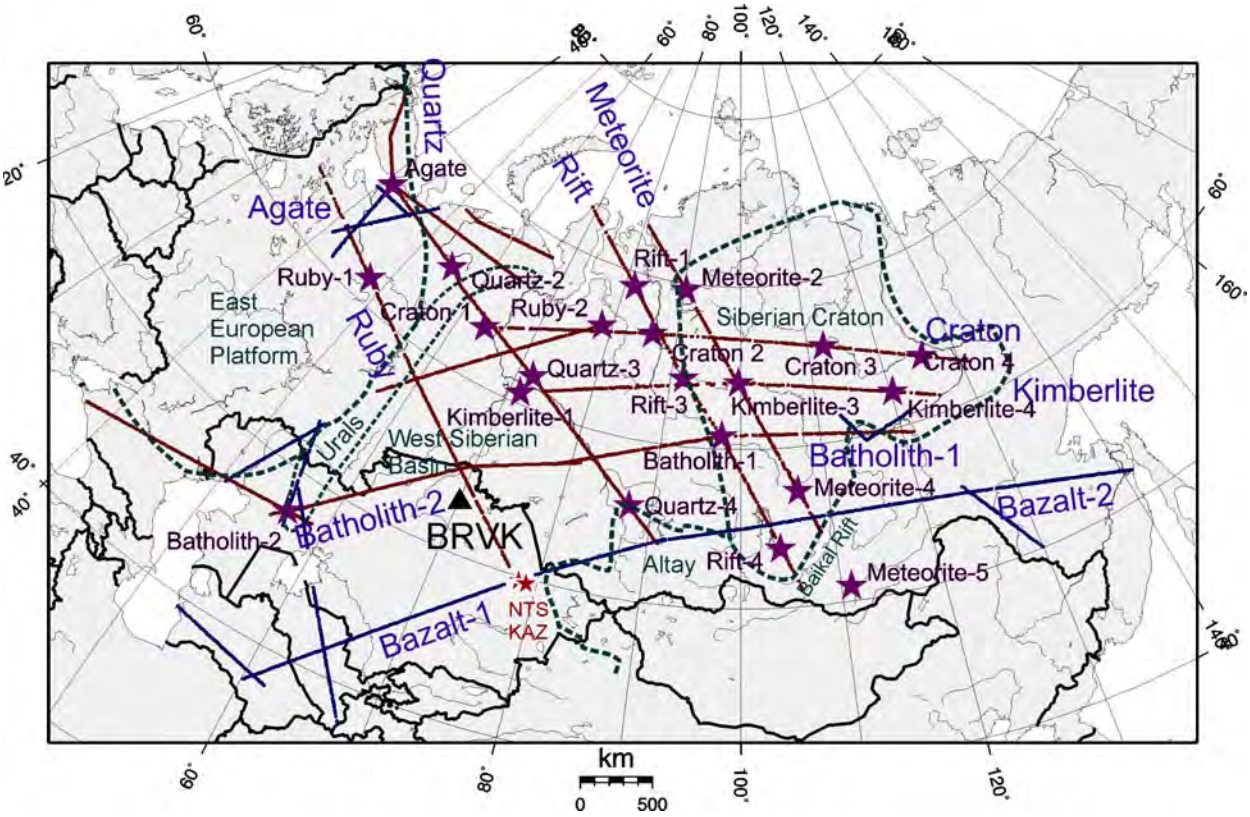

Figure 1. Location map of DSS PNE projects of this project. Projects are labeled in blue, and labeled purple stars show the PNEs. The dataset also includes two Semipalatinsk nuclear test site explosions (red). Parameters of the PNEs were reported by Sultanov et al (1999). Major tectonic units are indicated in green. Small brown circles (mostly appearing as lines at station spacing of 10-15 km) are PNE recording stations, and blue circles are chemical-explosion recording stations. Each profile also contains from 30 to 150 chemical explosions. Borovoye IMS station is also indicated (BRVK).

The primary objective of this study is to derive stable and transportable regional magnitudes of smaller events. The importance of using chemical explosions would be to study the magnitude (seismic amplitude corrected for distance and attenuation) versus yield relationships for smaller events and over a broad area. Smaller events of $m_b < 3.0$ are critical for nuclear test monitoring yet they are poorly represented in cratonic parts of Northern Eurasia, where most of calibration data come from PNEs and large mining explosions (Conrad et al., 2001). Depending on their explosion efficiency; DSS chemical shots should range, in terms of coda magnitudes, from ~1.0 to ~2.5 (Brocher, 2003). As the shots were designed for refraction seismic profiling (e.g., many of them shot in water reservoirs), they are likely to lie on the higher-efficiency end of the magnitude spectrum. Therefore, utilizing the chemical DSS datasets should help extrapolating magnitude calibration results to smaller yields.

Use of redundant recordings from over 500 shots should allow us to better account for path and site terms and derive coda magnitude estimates. High-efficiency DSS shots, even those conducted in water, are likely to produce strong *S* waves created through mode conversions on the base of the weathering layer or reservoir bottom. We will examine the amplitudes and the resulting magnitudes for stability and transportability, and also collect a comprehensive database on phase amplitude ratios at local distances. The coda work will be performed using standard techniques common to the NNSA laboratories that will allow integration with the Knowledge Base, as well as direct comparison with yield studies in other regions to test transportability. A useful side benefit of the work will be an extension of absolute coda calibration from central Asia to the European Arctic, where coda calibration performed by the Lawrence Livermore National Laboratory (LLNL) group relies on a small number of reference earthquakes to obtain absolute levels.

Improvement of travel-time calibration of the region is the second key objective of this research. Several thousand reliable travel-time picks from chemical shots along the DSS PNE lines (Figure 1) will further constrain the crustal velocities, which can then be incorporated into the Source Specific Station Correction (SSSC) tables used for accurate event locations. Improved SSSCs could be derived by incorporation of the chemical-explosion *P*- and *S*-wave travel times into regionalized travel-time models (e.g., Conrad et al., 2001) or into the 3-D apparent-velocity models derived in our recent analysis of the DSS PNEs (Morozov et al., 2005). In addition, based on the detailed, reversed travel-time coverage of the crust along the profiles, we will derive statistical models of the *P*-wave travel-times in the region. Such travel-time statistics could be incorporated into kriging used for IMS station calibration.

RESEARCH ACCOMPLISHED

As the project is in its initial stage, we summarize the key planned approaches, and results of preliminary investigations below.

1) Coda calibration

Coda magnitudes have significantly improved stability (by a factor of 3-5 in interstation scatters of magnitude estimates; Mayeda et al., 2003) compared to body-wave and short-window coda magnitudes. For this reason, we will emphasize coda calibration as our primary approach to source spectra and magnitude estimation. However, apart from the "coda modeling" step below, the following discussion also applies to body-wave amplitudes, which can be treated similarly.

Based on various assumptions about the stochastic properties of the crust and the nature of coda waves, several coda models have been proposed (e.g., Aki and Chouet, 1975; Sato and Fehler, 1998). However, in practice, with virtually any coda model, additional *ad hoc* distance and spectral corrections are required to obtain earthquake moment-rate spectra (Mayeda and Walter, 1996; Phillips et al., 2004). We will thus rely on an empirical procedure endeavoring to capture the key features of coda scattering phenomena by specifying a set of parameters that are adjusted by (typically) nonlinear fitting procedures. Such a coda calibration method is based on the following coda envelope model (modified after Mayeda et al., 2003):

$$A(t, f, r) = W_0(f) S(f) P(r, f) A_{shape}(t - t_0), \qquad (1)$$

where $W_0(f)$ is the *S*-wave source amplitude, $S(f)$ is the recording site response including the S-wave to coda scattering transfer function, $P(f,r)$ represents the effects of propagation (spreading, scattering, and absorption), $A_{\text{shape}}(t\text{-}t0,f,r)$ is the temporal signal shape function (coda, or a broadening pulse for body waves), t is the time, t_0 is the time of the *S*-wave peak envelope at the receiver, r is the source-receiver distance, and f is the frequency.

The procedure to separate the various factors in the expression above includes (1) band-pass filtering to form narrowband envelopes; (2) measurement of the moveout velocities of the peak S-, Lg- or surface-wave amplitudes (depending on band); (3) fitting empirical synthetics for the observed shapes of coda envelopes; (4) empirical distance corrections, including tomography for laterally varying attenuation; (5) empirical Green's function corrections to obtain relative spectral shapes; and (6) tying the relative spectra to independently determined seismic moment. This procedure accounts for propagation, site, differing coda composition (Lg, surface waves) in each band, and the efficiency of coda generation. As a result, the method provides stable and unbiased spectra and derived magnitude estimates (Mayeda et al., 2003). Results are the moment rate spectra for earthquakes and the apparent coda source spectra for explosions, with the term "apparent" indicating the possible inclusion of near source effects, including coupling, shear transfer function and near source path that are not experienced by the earthquakes used to calibrate the coda.

We will apply standard National Nuclear Security Administration (NNSA) coda calibration techniques in order to remain consistent with work performed by other laboratories (e.g., Mayeda et al., 2003). However, several critical steps deserve additional attention in the coda calibration procedure above and the dense sampling of the DSS data sets should prove valuable. For example, the measurement of the moveout velocity of the peak (step 2) as a function of distance, is typically performed on manually determined peak times that show significant scatter. This scatter could result from the broad peaks that are occasionally observed, or from systematic propagation factors, such as variable velocity or variable modal composition of the peak arrival along different paths. The dense spacing of receivers along a common path will allow us to watch the development of envelope peaks with distance, and whether or not the variation is random or systematic will be quickly obvious. This could lead to application of two-dimensional group velocity maps for determining envelope peaks as an enhancement to current coda techniques.

In addition, the coda shape modeling (step 3) could be critical in the derivation of the "true" (pre-coda) *S*-wave amplitude (Morozov and Smithson, 2000). Several heuristic coda decay models can be employed, such as a superposition of power and exponential decays (the standard NNSA coda shape model, Mayeda et al., 2003):

$$A_{shape}(t) \equiv A_{coda}(t) \propto H(t) t^{-\gamma(r,f)} e^{-b(r,f)t}, \tag{2}$$

where γ and b control the short and long time range, frequency- and distance-dependent coda amplitude decay behavior, respectively, and $H()$ is the Heaviside step function. For the dependence of γ on distance, Mayeda et al. (2003) used a hyperbolic three-parameter expression,

$$\gamma(r) = \gamma_0 - \frac{\gamma_1}{\gamma_2 + r}, \tag{3}$$

and a similar expression for b. An undesirable property of the form $A_{coda}(t)$ above is the trade-off between γ and b making its interpretation and formal least-squares fitting problematic. Morozov and Smithson (2000) used another empirical model representing the record as a superposition of an *S*-wave onset of finite duration and its exponential coda (Figure 2):

$$P(t - t^0) = \begin{cases} 0, & t < t^0, \\ \lambda P^0 \tau \exp\left[-\beta(t - t^0)\right], & t \geq t^0. \end{cases} \tag{4}$$

We will try the above, or other similar forms in our analysis. This will better separate direct wave and coda portions of the envelope, which is currently done by specifying *ad hoc* minimum offset start times for all distances for a given band in the coda calibration.

Distance correction (step 4 above) is critical for obtaining low interstation magnitude scatter and consequently (eventually) stable discriminants. Many heuristic dependencies for distance dependence of *S*-wave amplitudes can be used, such as (Mayeda et al., 2003),

$$P(r, f) = \frac{1}{1 + \left(\frac{r}{R_0(f)}\right)^{p(f)}}, \tag{5}$$

where R_0 is the characteristic distance at which the which the amplitude starts to decrease (typically, 20-100 km), and p is the far-offset effective attenuation factor (including geometrical spreading and other effects). In another model, the path effect is decomposed into a combination of predefined geometrical spreading and an attenuation-related path integral (e.g. Phillips et al., 2004),

$$P(r, f) = G(r) e^{-\int \frac{\pi f}{vQ} dl} \tag{6}$$

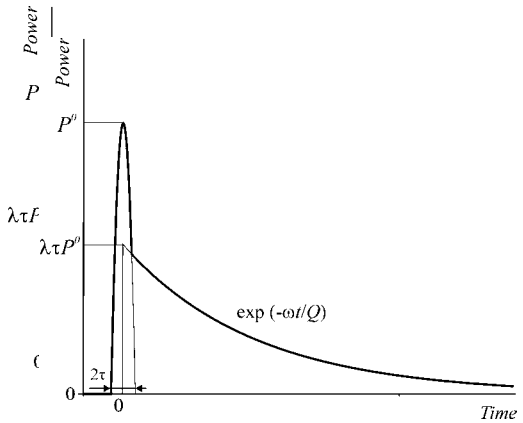

Figure 2. Coda model by Morozov and Smithson (2000). The trace power envelope is represented by a superposition of a finite-bandwidth primary pulse of power P_0 and duration 2τ, followed by its coda of relative amplitude $\lambda\tau$.

where G represents geometrical spreading. Instead of the (R_0,p) parameters above, this path correction for all paths is characterized by a common spatial grid of values of {$Q(f)$}. This tomographic approximation, adopted at LANL, is preferable if significant variation of regional extents of coverage (such as between the PNEs and chemical shots), or significant spatial or azimuthal variations are expected, as in this study. As an additional possibility, parameters controlling the frequency-independent geometric spreading $G(r)$ could also be included into the tomography. The dense DSS sampling at long and short distances, including chemical shots at short distances, will allow the separation of spreading and attenuation effects.

The strength of DSS datasets is in their linearity and high recording density (10-15 km station spacings) with numerous sources recorded by groups of stations. At the same time, DSS absolute recording amplitudes may have not been well calibrated, in combination with unknown site and path effects. Utilizing the redundancy of recordings, this lack of absolute calibration could be overcome by forming distance-, coda shape-, and site response-corrected source amplitudes:

$$W_0(f) = \frac{A(t, f, r)}{S(f)P(r, f)A_{coda}(t - t_0)}, \qquad (7)$$

for every frequency f. In this expression, $S(f)$ is associated with every receiver, $W_0(f)$ – with every shot, and $P(r,f)$ is controlled by the parameters {Q} varying along the profile. Finally, the requirement:

$$W_0(f) = const$$

for all records from the same shot, leads to an overdetermined (tomographic) inverse problem.

The long-range PNE and short-range chemical path effects may or may not be consistent with each other. Physically, the question is whether or not crustal *S* and *Lg* and their associated coda sample the same portions (depths) of the crust. If they do, we could use one *Q* model along the profile for all data, if not, we will have to calibrate the chemical-shot (presumably shallow) and PNE ("deep") *Q* models separately. This could be an important result of this study, giving us further insight into coda calibration for a wide range of distances that will be difficult to obtain from traditional data sets.

The objective of the final coda calibration steps (5-6) above is to compensate for the frequency-dependent site effects, including the *S*-wave to coda scattering amplitudes and shift to absolute units. This is normally achieved by using small earthquakes as empirical Green's functions and large reference events with independently determined moments. For this study, we will use several PNEs recorded at permanent stations and whose apparent coda source spectra have been obtained as part of the LANL coda calibration effort. As an example, from our preliminary investigations, records from PNEs Meteorite-2, 3, and 4, Kimberlite-3, Batholith-1, Rift-3 and 4, Quartz-4, and Ruby-1 (Figure 1) are present in the Borovoye station archive available at LANL. Additionally, PNE profiles recorded a number of local and regional earthquakes that could also be used to calibrate, or at minimum, to validate

the absolute source spectra. Digitization and obtaining these earthquake records together with the corresponding location and magnitude information is an important part of GEON's contribution to the present project. This will provide redundancy to a critical calibration step.

Magnitude-yield analysis will be used to relate the seismic efficiency to source conditions (Brocher, 2003). According to our present knowledge, many of the chemical shots, particularly in the hard-to-access areas of Siberia, were conducted in lakes or other water reservoirs. This mode of detonation results in the best source coupling, and thus the resulting events should fall on the higher-magnitude envelope in the yield-magnitude cross-plots (Brocher, 2003). For purposes of studying yield transportability, we will simply compare apparent coda source amplitude in various bands to yield, rather than compare magnitude to yield.

2) Travel-time mapping and regional reference model for building SSSCs

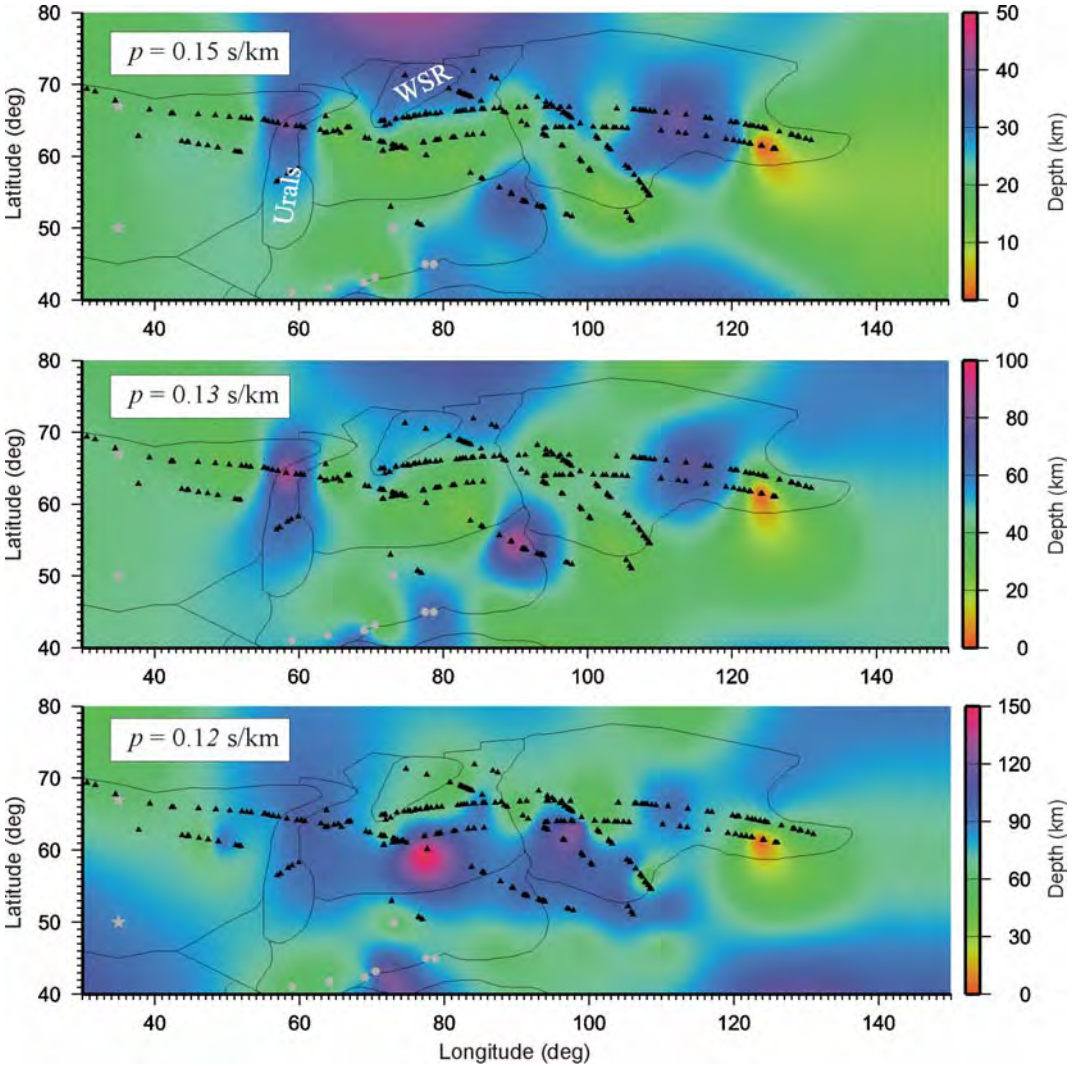

Figure 3. Slices at three values of apparent slowness, *p*, through the 3-D travel-time calibration model, as labeled. The model uses only DSS PNE times constrained with several additional regional travel-time curves (with Baltic Shield and Kazakhstan) and was derived in a straightforward, single-pass procedure (cf. Morozov et al. 2005). In this study, travel times picked from ~500 additional DSS chemical explosion records will greatly improve the shallow part of this model.

Depending on the way travel times are parameterized and associated with surface locations, numerous interpolation schemes can be devised for them, and it is important to choose the one reflecting the fundamental character of the surface-to-surface refraction travel-time problem. In addition, an optimal interpolation scheme should include scalability allowing incorporation of additional data as it becomes available and thereby attaining high accuracy and detail of travel-time prediction. In traditional travel-time regionalization, the regional travel-time dependencies are usually combined using a heuristic interpolation rule, such as (Bondár et al., 2001; Yang et al., 2001):

$$t(S,R) = \frac{\sum_i L_i t_i(d_{SR})}{d_{SR}}, \qquad (8)$$

where S is the source, R is the receiver (both assumed to be located close to the surface), L_i is the length of the great-arc segment connecting S and R and lying within the i-th region, and $d_{SR} = \sum_i L_i$ is the total source-receiver distance. With this rule, the scalability criterion above cannot be met, principally because the travel times vary systematically with offsets and cannot be directly associated with locations. In consequence, the rule above can only be used (and works reasonably well) when the number of regions is small, offsets are large, and crustal variability does not need to be reproduced. However, with the detailed travel times available from additional PNEs and hundreds of DSS chemical explosions distributed over the area (Figure 1), we would need a more accurate and detailed interpolation scheme, and founded on fundamental physical principles of refraction.

Our "regionless" calibration scheme results in a continuous, 3-D travel-time "cube" and was successfully applied to DSS PNE travel times (Morozov et al., 2005). The idea of the method is as follows. Unlike travel times determined along extended subsurface paths, the velocity structure *is* naturally associated with geographical and depth coordinates and therefore it can be spatially interpolated. Thus, by contrast to the formula above, our travel-time mapping is performed through interpolation of an effective "velocity structure" rather than of the travel times themselves. Schematically, this method can be presented as a series of three transformations:

$$t(r)|_{L_i} \xrightarrow{1)\ \tau-p} \tau(p)|_{L_i} \xrightarrow{2)\ HWT} \Delta z(p)|_{L_i} \xrightarrow{3)\ Interpolation} \Delta z(p)|_{(x,y)} \qquad (9)$$

Here, i=1…N counts the observed travel-time curves, L_i is the great arc connecting the source and receiver, r is the range (source-receiver distance), approximated along the great arc, $t(r)$ is the observed travel time, p is the ray parameter, $\tau(p)$ is the delay (intercept) time (e.g., Buland and Chapman, 1983), x and y are the spatial (geographic) coordinates, and Δz is the layer thickness in the resulting 3-D apparent-velocity model. The Herglotz-Wiechert transform (HWT) is used to encode the $\tau(p)$ dependences into the equivalent "apparent velocity columns" $\Delta z(p)$ that are further spatially interpolated to yield a 3-D model cube, $\Delta z(p|x,y)$ (Figure 3).

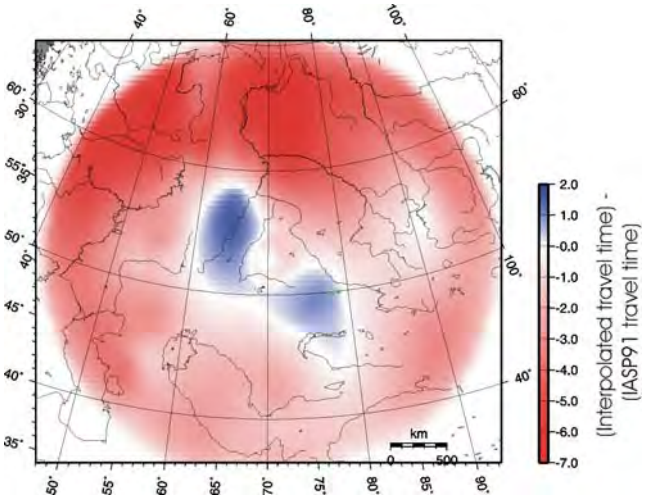

Figure 4. SSSC for station BRVK (Kazakhstan) predicted from DSS PNE travel times alone (Figure 3).

The essential improvement offered by this method as compared to traditional regionalization is its ability to accommodate realistic velocity structure and any volume of input data, similarly to 3-D velocity tomography. On the other hand, compared to tomography, this method is simple, free from uncertainties of the inversion, performed in one "downward" pass and does not require regularization. Finally, using a simple 1.5D ray tracing, this model can be used to quickly generate the Source-Specific Station Corrections (SSSC) for any location, as illustrated in Figure 4 for station BRVK.

Similar to the coda calibration model above (Figure 2), the 1.5D $\tau(p)$ parameterization of the first-arrival travel times separates the contributions from the near- (site terms) and long-range (path terms) propagation. Without such a separation in the previous work, fine-scale variations that are really site effects may have been effectively mapped into the deeper structures.

In this study, we will use the first-arrival travel times picked from all chemical explosions to augment the apparent-velocity model of Northern Eurasia (Figure 3). Even with limited sampling from 19 PNEs, the model already reproduces the key characteristics of the regional travel times in the area. With addition of several hundred of travel time curves from the chemical DSS shots, this model will account for the crustal variability and reproduce the associated travel times significantly more accurately.

Even after its enhancement from all DSS travel times, the travel-time model in Figure 3 would still not account for the near-source and receiver effects in the vicinities of the sources and receivers not included in its derivation. However, the model already represents a far better regional reference model then IASP91, and it can be additional fine-tuned by its use as a regional background and utilizing additional ground truth events in standard SSSC calibration procedures, such as kriging (Myers and Schultz, 2000). Note that the analysis of detailed DSS travel times could be the key source of quantitative information on the travel-time correlation functions for kriging, as described below.

Testing SSSC sensitivity to additional data

To assess the improvement from the use of detailed chemical-shot travel times, we will compute the travel times from all the available DSS shots to a selected point in the model, such as the IMS station Borovoye, and subtract from them the travel times predicted by the IASP91 model, by the existing SSSCs (such as derived by the Group II Location Calibration Consortium; Conrad et al., 2001), or by our current PNE-based SSSC (Figure 4). The resulting distributions of travel-time residuals would provide quantitative estimates of the significance of short-scale (~50-100-km) crustal variability for travel-time prediction. These estimates would be further developed in much more comprehensive statistical sampling of SSSC uncertainty.

Statistical modeling of SSSC travel-time variability

The 3-D apparent-velocity travel-time model above (Figure 3) has the ability to correctly separate the shallow (short-range) and deep (long-range) travel time patterns and also to incorporate the complete structural complexity of the region. Its resolution will only be limited by the available travel-time data concentrated along the linear DSS profiles (Figure 1). In the broader area between and outside the profiles, no detailed travel-time information is available yet a good guidance on the main features of crustal structure is still available. In order to assess the potential effects of such imperfectly known crustal and upper-mantle heterogeneity on the resulting SSSCs, we will utilize the following statistical sampling approach.

First, for each profile, we will extract its corresponding the $\Delta z(p|x,y)$ model out of our 3-D cube and examine its correlation with the available regional summary models (Figure 3). It is likely that in the vicinities of the profiles, the summary models would have to be adjusted to satisfy the detailed DSS travel times. Further, we will extract p- and geographically-dependent statistics of the values $\Delta z(p|x,y)$ (mean values, variances, correlation lengths, or othe parameters of probability distribution functions). This analysis would yield quantitative, ray parameter- dependent (and equivalently, range-dependent) statistical characterization of the spatial variability of the travel times within the region.

With the statistics of the (apparent-)velocity structure characterized, we would use the modified apparent-velocity

models (Figure 3) to build the average crustal structure and simulate a representative number (several thousand) of random realizations. We will further compute SSSC for BRVK, or for other stations of interest, in each of these realizations and compile statistics (mean, autocorrelation functions, and PDFs) on each of them. As a result, this should yield a direct, objective, quantitative, detailed, range and regionally-variant, and (in principle) non-Gaussian, measure of statistical SSSC variability based on the integrated analysis of two comprehensive, complementary datasets.

CONCLUSIONS AND RECOMMENDATIONS

As a result of this effort using a large database of digital seismograms from chemical and PNEs of the DSS program, we will produce a large calibration dataset of stable and transportable magnitudes and magnitude-yield relations for a vast and largely aseismic, which is critical for seismic monitoring in this part of Northern Eurasia. We also anticipate extending absolute coda calibration from central Asia to the European Arctic, where the LLNL coda group could take advantage of the additional calibration information, presumably through constraints from events common to both networks (most likely a PNE recorded at NORSAR).

REFERENCES

Aki, K. and B. Chouet (1975), Origin of coda waves: source, attenuation, and scattering effects, *J. Geophys. Res.* 80: 3: 322-3, 342.

Bondár, I., and V. Ryaboy (1997), Regional travel-time tables for the Baltic Shield region, Technical Report CMR-97/24.

Bondár, I., X. Yang, R. North, and C. Romney (2001), Location calibration data for the CTBT monitoring at the Prototype International Data Center, Pageoph Technical Volumes, Monitoring of the Comprehensive Nuclear Test-Ban Treaty: Source Location, F. Ringdal and B. Kennett (editors), *Pure Appl. Geophys.* 158: 19-34.

Brocher, T. M. (2003), Detonation charge size versus coda magnitude relations in California and Nevada, *Bull. Seism. Soc. Am.* 93: (5), 2089-2105.

Buland, R, and Chapman, C. H. (1983), The computation of seismic travel times, *Bull. Seism. Soc. Am*. 73: 1271-1302.

Conrad, C., Cormier, V., Fisk, M., Ichinose, G., Khalturin, V. I., Kim, W.-Y., Morozov, I., Morozova, E., Richards, P. G., Saikia, C., Shaff, D., and Waldhauser, F., (2001), Annual Technical report: Seismic Location Calibration of 30 International Monitoring System Stations in Eastern Asia, DTRA, Contracts No. DTRA01-00-C-0029, DTRA01-00-C-0031, DTRA01-00-C-0033.

Mayeda, K., A. Hofstetter, J. L. O'Boyle, and W. R. Walter (2003), Stable and transportable regional magnitudes based on coda-derived moment-rate spectra, *Bull. Seism. Soc. Am*. 99: (1), 224-239.

Mayeda, K., and W. R. Walter (1996). Moment, energy, stress drop, and souirce spectra of western United States earthquakes from regional coda envelopes, *J. Geophys. Res.* 101: 11195-11208.

Morozov, I. B., and Smithson, S. B. (2000), Coda of long-range arrivals from nuclear explosions, BSSA, 90, 929-939.

Morozov, I. B., E. A. Morozova, S. B. Smithson, P. G. Richards, V. I. Khalturin, and L. N. Solodilov (2005), 3-D first-arrival regional calibration model of northern Eurasia, *Bull. Seismol. Soc. Am* 95: (3), 951-964, doi:10.1785/0120030173.

Myers, S. C., and Schultz, C. A. (2000), Improving sparse network seismic location with Bayesian kriging and teleseismically constrained calibration events, *Bull. Seism. Soc. Am*. 90: 1, 199-211.

Phillips, W.S., H.J. Patton, S.R. Taylor, H.E. Hartse, and R.E. Randall (2004), Calibration for coda based magnitude and yield, in the *26th Seismic Research Review: Trends in Nuclear Explosion Monitoring*, LA-UR-04-5801, Vol. 1, pp. 449-456.

Sato, H., and M. Fehler (1998), *Seismic Wave Propagation and Scattering in the Heterogeneous Earth*, Springer-Verlag, New York.

Sultanov, D. D., J. R. Murphy, and Kh. D. Rubinstein (1999), A seismic source summary for Soviet Peaceful Nuclear Explosions, *Bull. Seism. Soc. Am*. 89: 640-647.

Yang, X., I. Bondár, K. McLauglin, R. North, and W. Nagy (2001), Path-dependent regional phase travel-time corrections for the International Monitoring system in North America, *Bull. Seism. Soc. Am*. 91: 1831-1850.

THE EFFECT OF REALISTIC GEOLOGIC HETEROGENEITY ON LOCAL AND REGIONAL P/S AMPLITUDE RATIOS BASED ON NUMERICAL SIMULATIONS

Stephen C. Myers[1], Jeffery Wagoner[1], Leiph Preston[2], Ken Smith[2], and Shawn Larsen[1]

Lawrence Livermore National Laboratory[1] and University of Nevada at Reno[2]

Sponsored by National Nuclear Security Administration
Office of Nonproliferation Research and Engineering
Office of Defense Nuclear Nonproliferation

Contract Nos. W-7405-ENG-48[1] and DE-FC03-02SF22656[2]

ABSTRACT

Regional seismic discriminants based on high-frequency P/S ratios reliably distinguish between earthquakes and explosions. However, P/S discriminants in the 0.5 to 3 Hz band (where the signal-to-noise ratio [SNR] can be highest) rarely perform well, with similar ratios for earthquake and explosion populations. Variability in discriminant performance has spawned numerous investigations into the generation of S-waves from explosions. Several viable mechanisms for the generation of S-waves from explosions have been forwarded, but most of these mechanisms do not explain observations of frequency-dependent S-wave generation. Recent studies have focused on the effect of near-source scattering to explain the frequency-dependence of both S-wave generation and P/S discriminant performance. In this study we investigate near-source scatter through numerical simulation with a realistic geological model.

We have constructed a realistic, three-dimensional (3D) earth model of the southern basin and range. This regional model includes detailed constraints at the Nevada Test Site (NTS) based on extensive geologic and geophysical studies. Gross structure of the crust and upper mantle is taken from regional surface-wave studies. Variations in crustal thickness are based on receiver function analysis and a compilation of reflection/refraction studies. Upper-crustal constraints are derived from geologic maps and detailed studies of sedimentary basin geometry throughout the study area. The free surface is based on a 10-m digital elevation model (DEM) at NTS, and a 60-m DEM elsewhere. The model extends to a depth of 150 km, making it suitable for simulations at local and regional distances.

Our simulation source is based on the 1993 non-proliferation experiment (NPE) explosion at NTS. This shot was well recorded, offering ample validation data. Our validation tests include measures of long-period waveform fit and relative amplitude measurements for P and S phases. Our primary conclusion is that near-source topography and geologic complexity in the upper crust strongly contributed to the generation of S-waves from the NPE shot. When either geologic heterogeneity or topography is removed from the model, simulated amplitudes of regional S-waves are diminished. We also find that deeper sources scatter less energy off of topography and upper-crustal structures, resulting in diminished S-wave amplitudes with increasing source depth.

OBJECTIVE

Regional monitoring relies heavily on comparisons of P- and S-phase amplitudes (Pomeroy et al., 1982; Walter et al., 1995). Further, widely used methods of determining magnitude make use of Lg and Lg coda amplitudes (e.g., Nuttli, 1986; Mayeda and Walter, 1996; Patton, 2001), and regional S-phases often add important arrival-time observations to limited, small-magnitude data sets used for location (Denny and Stull, 1994; Mayeda and Waltr, 1996; Myers et al., 1999).

Most investigators agree that appreciable energy from the explosions is converted to S-waves near the source, but the dominant P-to-S transfer mechanism is not agreed upon. Several physically reasonable transfer mechanisms are proposed, including P-to-S conversion at the free surface, spall, scattering of short-period surface waves, tectonic release, and rock-damage (e.g., Vogfjord, 1997; Day and Mclaughlin, 1991; Gupta et al., 1992; Wallace et al., 1985; Johnson and Sammis, 2001). Each mechanism fits a subset of observations, and each mechanism, with the exception of surface-wave scattering, is understood from first principles. Currently, the Rg-to-S mechanism is represented by an empirical transfer function (e.g., Gupta et al., 1992; Patton, 2001).

This project aims to study the physical process of near-source scattering to establish a fundamental understanding of this phenomenon. Our recent progress is in the area of model construction, and subsequent numerical experiments on the effect of near-source topography and event depth are presented below.

RESEARCH ACCOMPLISHED

In previous years of this project, we developed a detailed upper-crustal model centered on the 1993 NPE shot (Figure 1). The rationale for centering on the NPE is discussed in the subsection, “Model validation using NPE observations.” The local model is 20 km on a side (including depth), and construction of the model leverages the extensive Lawrence Livermore National Laboratory (LLNL) database of geological and geophysical information that includes mapping, bore-hole logs, seismic surveys, and gravity surveys (e.g., Healey et al., 1963). Much of LLNL’s geological database is unpublished. The local model is imbedded in a regional model that will allow simulations to distances of interest.

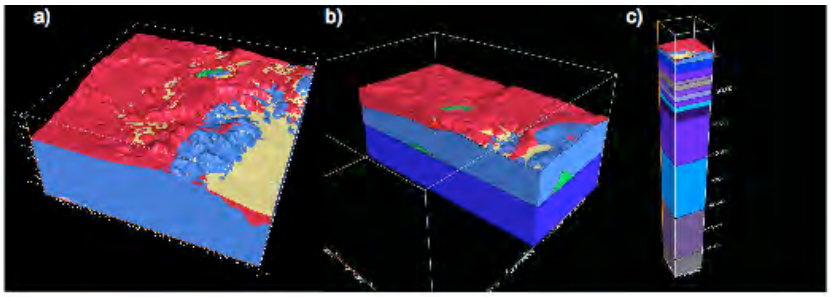

Figure 1. Local model around NPE shot determined from detailed geologic and geophysical studies. (a) The entire local model. (b) Cross section through the NPE shot. (c) Local model merged into a lithospheric velocity stack.

We have made considerable advances this year in the regional model (Figure 2). The default velocity structure continues to be a one-dimensional (1D) model based on work of Patton and Taylor (1984). Variations to the default model are based on the geographic specifics of published studies. The current version of the model includes variations in upper-crustal structure based on regional geologic maps of Nevada, Utah, California, and Arizona. We assume that crystalline rocks are continuous into the lower crust and that basin depths are proportional to the magnitude of local gravity anomalies (e.g., Blakely et al., 1997). The lower crustal velocities and Moho depth are modified based on the work of Zandt et al. (1994) and Mooney et al. (1998). Minor modifications to mantle velocities are based on refraction profiles summarized in Mooney et al. (1998). In specific areas we have incorporated tomographic studies, such as Biasi (2005) and Preston et al. (2005).

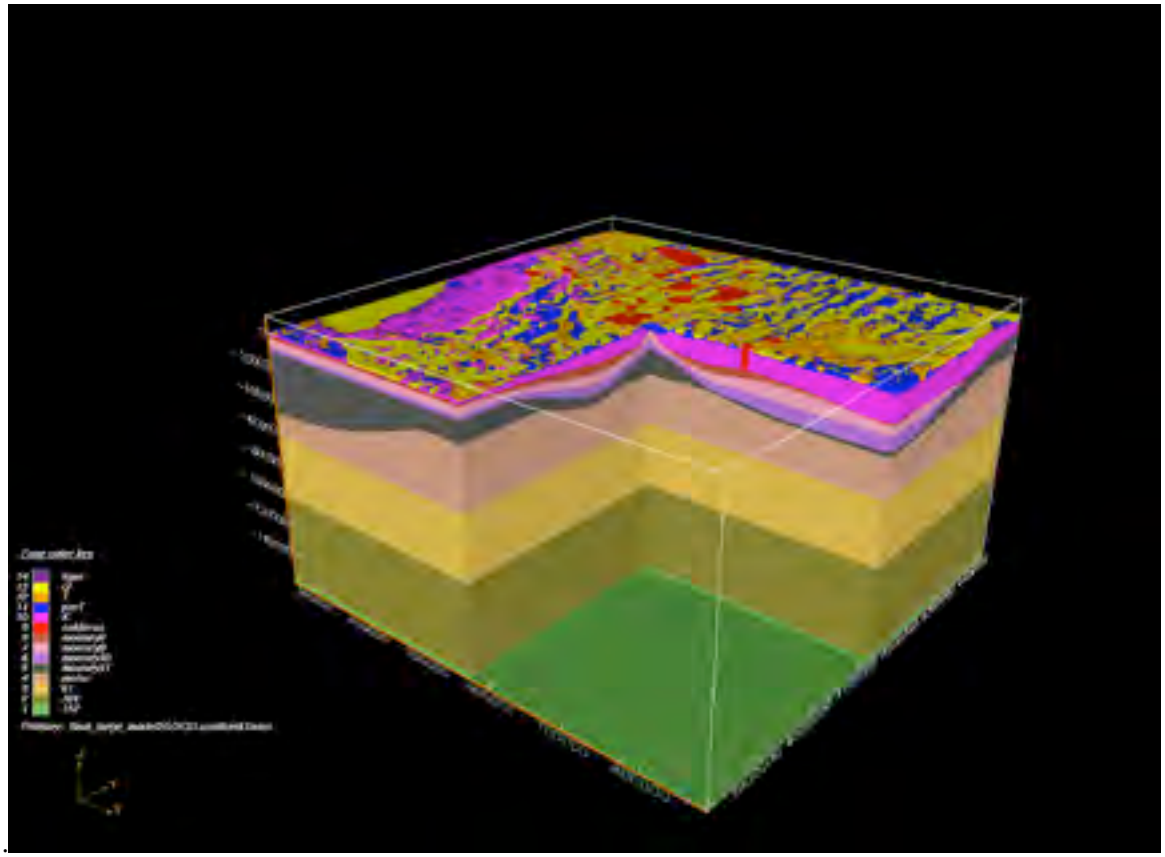

Figure 2. Regional geologic model centered on NTS. The model extends into California (to the left) and Utah and Arizona (to the right). The model is a compilation of geologic mapping; seismic profiles, receiver functions, and tomography; and gravity modeling for basin structure.

Model validation using NPE observations

We use the E3D code of Larson and Grieger (1998) for seismic simulations. E3D is a full elastic code that allows the input of a general geologic structure, including the free surfaces. All of our simulations use a grid spacing of 60 m, which enables interpretation to 3 or 4 Hz.

Our numerical simulations are based on the 1993 NPE. The NPE was a 1-kiloton chemical explosion at NTS. NPE details and research reports can be found in Denny and Stull. (1994). Figure 3 shows the extensive network of stations that recorded the NPE. We have compiled all these recordings to validate our model. We begin with the local recordings, which we used both to validate the near-source model and to estimate the NPE moment tensor.

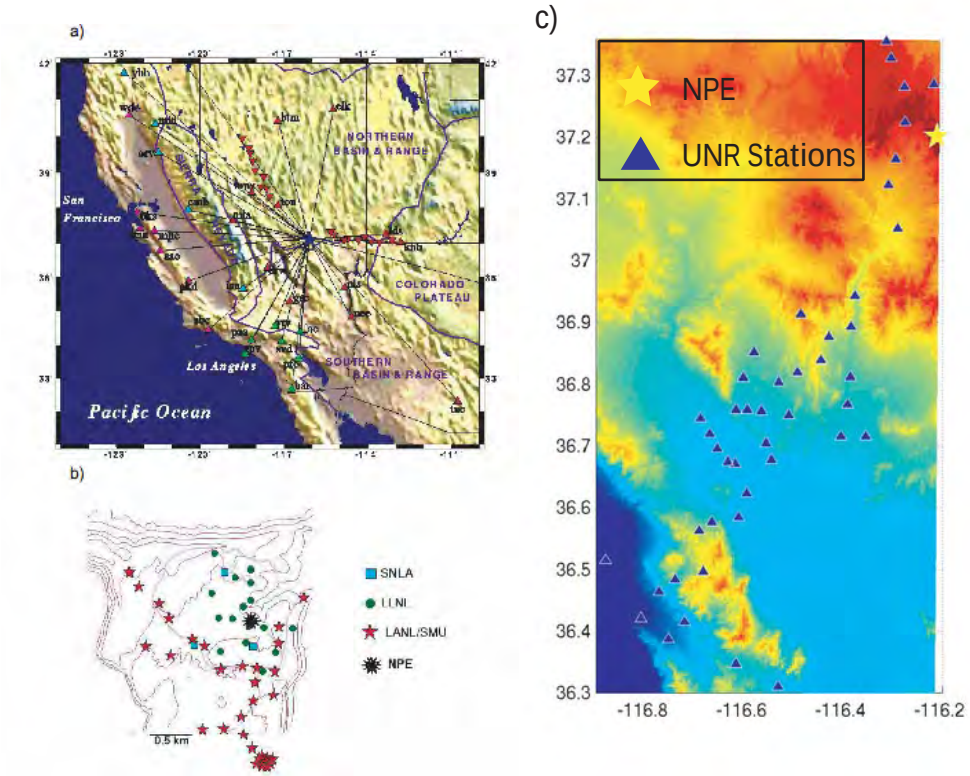

Figure 3:Stations with recordings of the NPE shot. We have compiled waveforms from all of these stations.

Figure 4 shows an example waveform (black) from a station that is approximately 2 km from the NPE. Simulations (red) with combinations of isotropic (Figure 4 a,b) and CLVD (Figure 4 c,d) moment tensors and topographic free surface (Figure 4 a,c) and flat free surface (Figure 4 b,d) are compared with the data. It is clear that the isotropic source in a model that includes the topographic free surface is the best fit to the data. Comparisons with other local data (not shown) are similar, and we conclude that the NPE is best modeled as an isotropic source.

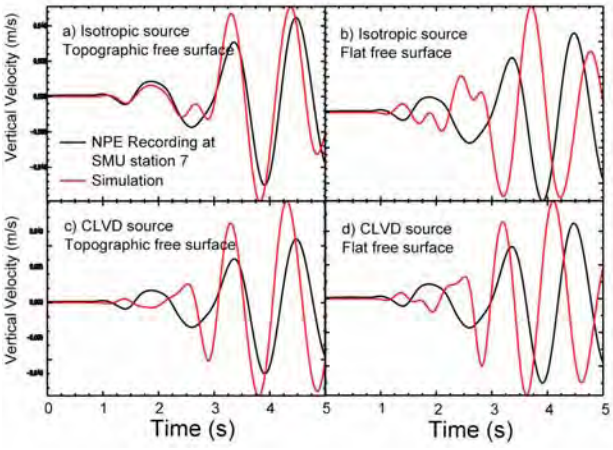

Figure 4. Recorded (black) and simulated (red) displacement seismograms for the NPE shot. These 3-dimensional simulations make use of the local NPE model (see above). Event-station distance is approximately 2 km. a) simulation with isotropic moment tensor and free surface based on digital elevation model (DEM). b) Simulation with isotropic source and flat free surface. c) Simulation with compensated linear vector dipole (CLVD) moment tensor with DEM free surface. d) Simulation with CLVD moment tensor and flat free surface. The NPE is best modeled as an isotropic source. Simulation with a realistic free surface is essential to match the data.

We also conclude that simulations that include the frequencies of interest (up to 3-4 Hz) must include a realistic topographic model.

Figure 5 is an example of our regional validation effort, which is on-going. In this example we use the temporary, broadband (STS-2 sensor) deployment fielded by the University of Arizona. The cross section is color coded to P-wave velocity, which was taken from our regional 3-dimensional model. The upper crust is characterized by Paleozoic sedimentary rocks, which are interrupted by low-velocity basins. Velocity in the mid- and lower crust primarily increases with depth, but we include minor lateral variation in velocity as well has changes in Moho depth based on the work of Zandt et al. (1995). The interface between light and dark red in the lower quarter of the cross section is the Moho. We have superimposed a snap shot of the seismic wavefield on the cross section to demonstrate the complexity that results from this relatively simple model.

The traces shown in Figure 5 compare recorded (black) and synthetic (red) velocity seismograms. Both velocity and synthetic records are band passed between 0.7 Hz and 3 Hz. Amplitudes are normalized because geometric spreading in the 2-dimensional synthetics is incorrect. In general, the comparison of observed and synthetic data is favorable. The degree of waveform complexity is nearly identical, and it would be difficult to tell which trace is real based on simple inspection. The relative amplitudes of the real and synthetic waveforms are also in good agreement (with the notable exception of sta 8, where synthetic amplitudes after the first arrival are too large). Although the phase is matched in many instances (particularly the first arrival), we cannot claim to have simulated phase reliably. Nonetheless, the overall agreement between observed and synthetic data is very good, especially considering that the model was not directly derived from the data.

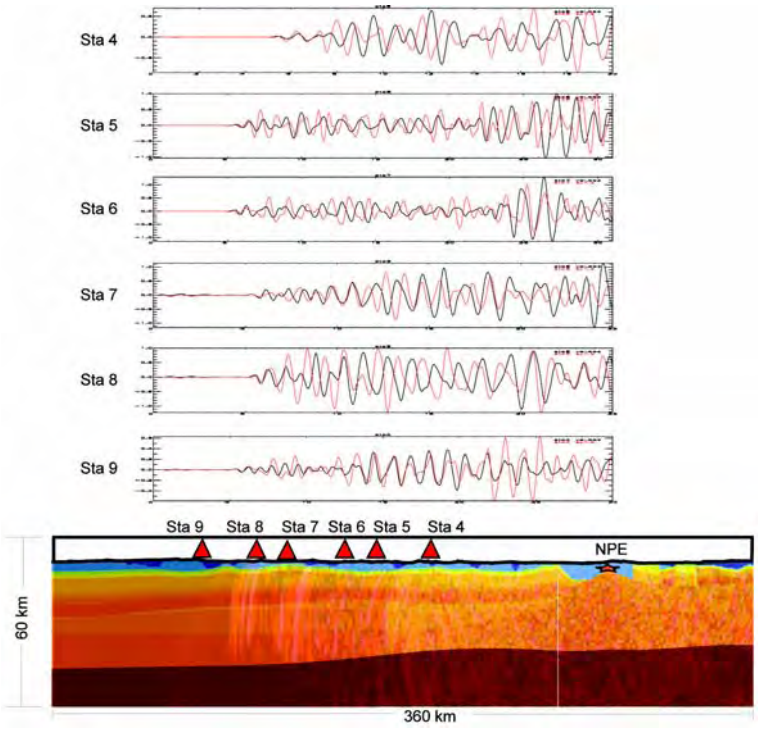

Figure 5. Model validation with regional seismic simulations of the U. Arizona broadband deployment (line extending east from NPE in Figure 3). West is to the right. Lower cross-section shows a snap shot of the seismic wavefield overlain on a P-wave velocity. The transition from red to near black in the lower quarter of the cross section is the Moho. The cross section and waveform are for the station 9 simulation. A separate 2-dimensional simulation was made for each of the stations to account for azimuth variations in structure. The upper traces are vertical velocity recordings of the NPE between 0.7 Hz and 3 Hz (black) with synthetics (red) for comparison. Amplitudes are normalized. Note that the time windows for the different stations are not synchronized. The general character of the observed seismograms is duplicated by the synthetics, suggesting that the regional model is a reasonable rendition of true structure.

The effect of topography on P/S ratios

Figure 6 is a map-view snap shot of a local simulation with and without topography (note that these are the same simulation that produced the synthetic seismograms in Figure 4 a,b). The topographic elevation at the NPE epicenter is used as the reference elevation for the flat free surface simulations. Topography that lies below that reference has surface velocity extended to the level of the reference; topography that extends above the reference is truncated at the reference level. Figure 6 shows that local topography immediately imparts disorder (scattering) into the wavefield.

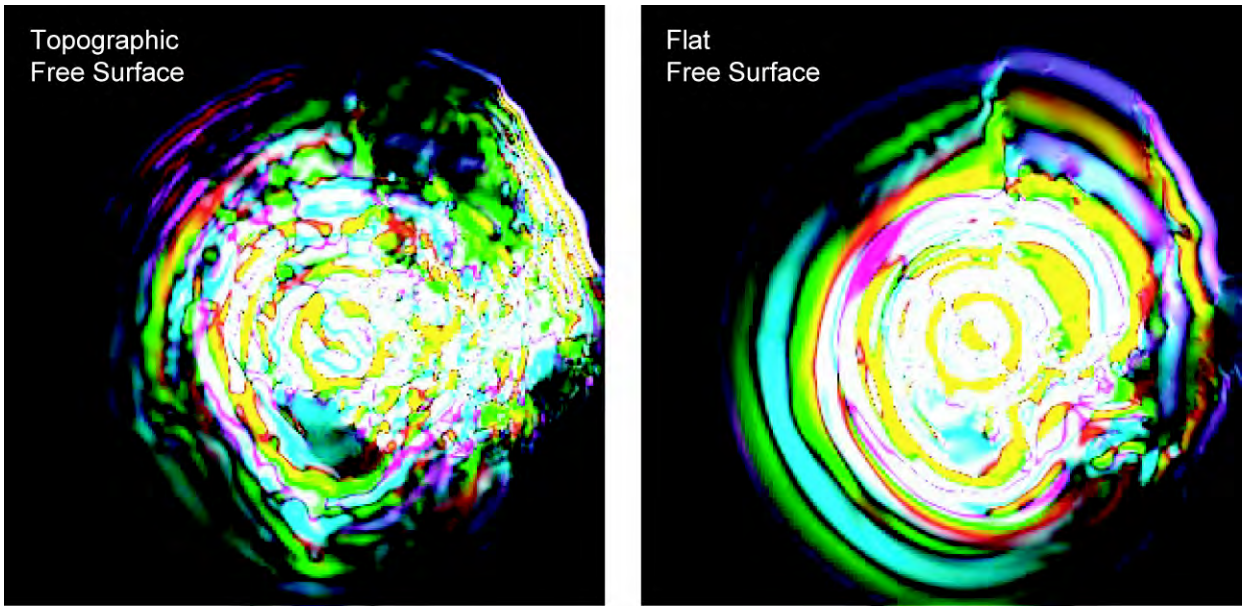

Figure 6. Map view of simulations with topographic free surface based on a digital elevation model (left) and flat free surface (right). Red, magenta and blue colors are P-waves. Green and yellow colors are S-waves. The map views shown above are 20 km on a side. Images are snap shots at approximately 5.5 seconds after event origin time and are at the lowest topographic elevation in the model. Detailed geologic structure from local mapping and geophysical studies is included in both simulations. Inclusion of realistic topography complicates the wave field considerably with appreciably more scattering.

Figure 7 shows synthetic spectra and seismograms of P-potential and S-potential at approximately 5 km from the source (Taken from the simulations shown in Figure 4). In all cases the S-potential exceeds the P-potential, which is presumably the result of free surface effects. However, the real topographic free surface results in a frequency-dependent P/S ratio. In fact the P/S ratio is significantly decreased at frequencies close to 1 Hz. Although these results are preliminary, the qualitative similarity in the frequency dependence of observed P/S ratios (mentioned in the Objectives section) and the synthetic P/S ratios for simulations that include real topography is suggestive. Further testing and rigor will determine whether topographic scattering is the primary mechanism for S-waves in the 1 Hz band.

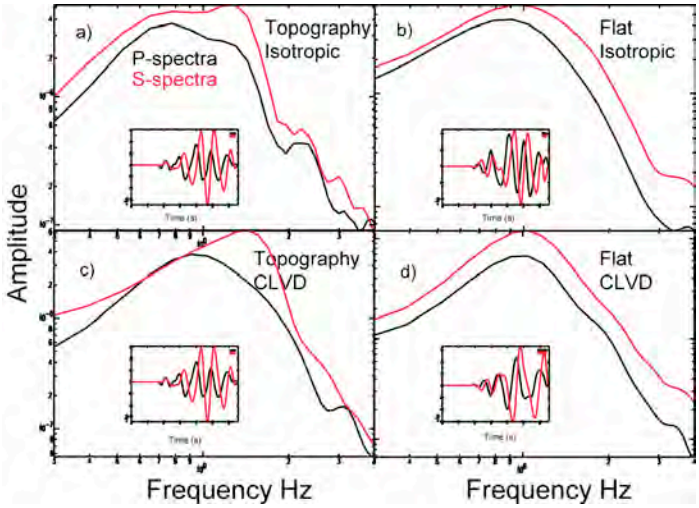

Figure 7. P (black) and S (red) displacement spectra and seismograms for simulations of the NPE shot (simulations shown in Figure 4). These 3-dimensional simulations make use of the local NPE model (see above). The inset seismograms are P-potential (black) and S-potential (red) for a location approximately 5 km from the source. The spectra are derived from P and S potential seismograms. (a) Simulation with isotropic moment tensor and free surface based on DEM. (b) Simulation with isotropic source and flat free surface. (c) Simulation with CLVD moment tensor with DEM free surface. (d) Simulation with CLVD moment tensor and flat free surface. Both isotropic and CLVD moment tensors produce a distinctly frequency-dependent P/S ratio.

The effect of source depth on P/S ratios

Results presented above suggest that near-source scattering, particularly scattering off of the free surface, boosts the amplitude of radiated S-waves at the expense of P-wave amplitudes. We test this hypothesis by comparing the simulation of a shallow source with a simulation of a deep (mid-crustal) source (Figure 8). Near-source heterogeneity for the shallow source (upper-crustal structure and topography) is considerable. Near-source heterogeneity for the deep source, where velocity is changing smoothly with depth, is minor. In both instances the source is isotropic (explosion) with the same moment. The model is approximately 300 km wide and 150 km deep. Some artifacts from reflections off of the side of the model are evident, but these artifacts do not muddle the overall picture.

The difference between the shallow- and deep-source simulations is striking. For the shallow source, S-waves grow to large amplitudes within seconds. The large S-waves radiate from the source in all directions. Therefore, S-waves are observed to propagate at steep angles into the mantle (and could propagate to teleseismic distances), as well as at shallow angles into the crustal waveguide to regional distances. For the deep source, S-waves are all but absent until the P-wave enters the upper crust. Notable conversion to S-waves does occur, but the S-wave amplitudes are significantly smaller than they are for the shallow source. Much of the S-wave energy is trapped in the upper crust, forming a P-coda. S-energy that escapes local, upper-crustal structures (e.g., basins) is reflected downward at steep angles. Therefore, the majority of the S-energy that escapes the upper crust is transmitted into the mantle, and little energy is trapped in the crustal waveguide.

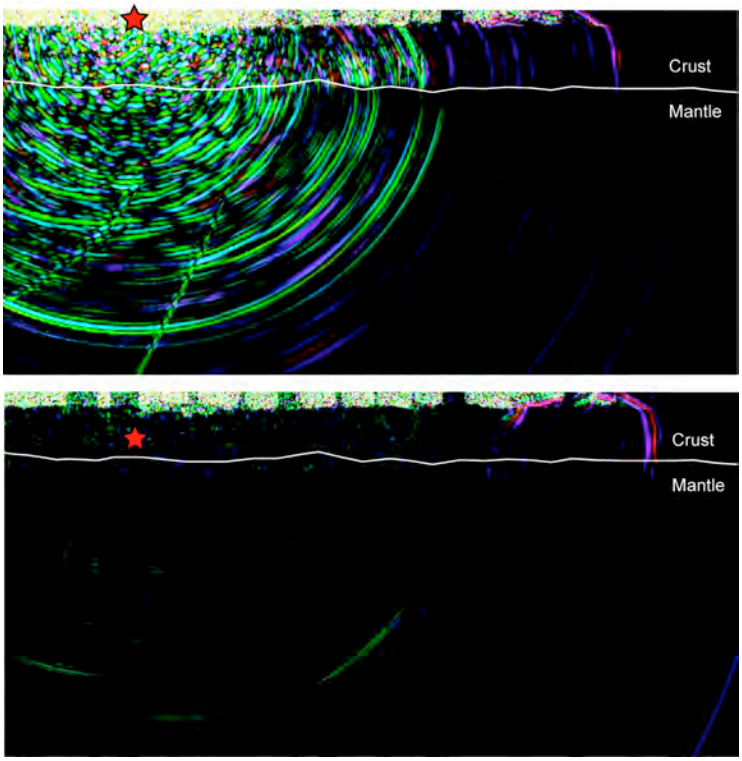

Figure 8. Regional 2D simulation showing the difference between a shallow source (upper panel) and a deep source (lower panel). The red star shows the source location. The model is approximately 300 km wide and 150 km deep. Both snapshots are at approximately 75 s after the source origin time. The shallow source generates vastly more S-waves (green and yellow) than the deeper source. The intensity of Pg (red and blue crustal phase on the right side of each panel) is greater for the deeper source.

CONCLUSIONS AND RECOMMENDATIONS

We have constructed a regional model centered on the NTS based on published and unpublished studies. The starting point of the regional model is a 1D model that is based on surface-wave studies. We include significant 3D modifications to the 1D model based on receiver function, refraction, reflection, and gravity studies. The regional model includes a detailed upper-crustal model centered on the NPE explosion. This local model is constrained by geologic maps, borehole data, and geophysical studies at the NTS. The local model is seamlessly imbedded into a regional model to enable realistic simulations of NTS sources to regional distance.

Validation of the model is based on recordings and simulations of the NPE shot. Validation of the local model is complete and the model reliably predicts local NPE waveforms. Validation of the regional model is ongoing, and we are reliably predicting the character of regional waveforms (i.e., arrival times and relative amplitudes of regional phases). However, accurate prediction of the full waveform (including phase) is spotty.

Local 3D simulations demonstrate that topographic scattering is an important source of S-wave generation for the NPE. We find that topographic scattering peaks S-wave amplitudes at approximately 1 Hz, which is in agreement with observations in many instances (at NTS and other locales). Topographic scattering produces a disordered wavefield and scatters energy in all directions. Simulations with a flat free surface produce S-waves, but little frequency dependence is observed.

Regional simulations demonstrate that a shallow NPE source produces appreciable S-waves that radiate at a large range of slownesses. For shallow sources, S-waves generated through structural and topographic scattering propagate in all directions. This means that the S-wave propagate at steep angles into the mantle (and would

presumably continue to teleseismic distance) as well as into the regional waveguide to form Sn and/or Lg. When the equivalent NPE source is placed in the mid-crust, S-wave generation is significantly diminished. S-waves are generated as the P-wave traverses the upper crust and reflects off of the topographic free surface, but S-waves that escape the upper crust travel at steep angles and are largely transmitted into the mantle.

ACKNOWLEDGEMENTS

We acknowledge the LLNL containment program for generous access to its extensive database of geologic and geophysical studies at NTS. We also would like to thank Glenn Biasi and Walter Mooney for providing regional geophysical information.

REFERENCES

Blakely, R. J., R. C. Jachens, J. P. Calzia, and V. E. Langenheim (1997), Cenozoic Basins of the Death Valley Extended Terrain as Reflected in Regional-Scale Gravity Anomalies, in Wright, L.A. and B.W. Troxel, Eds., Cenozoic Basins of the Death Valley Region, *Geol. Soc. Am. Special Paper* 333.

Biasi, G. (2005), Mantle Lithospheric Clues to Walker Lane Evolution, 2005 Seismological Society of America spring meeting, Incline, NV.

Day, S. and K. Mclaughlin (1991), Seismic Source Representations for Spall, *Bull. Seismol. Soc. Am*. 81: 191–201.

Denny, M. D. and S. P. Stull, Eds. (1994), *Proceedings of the Symposium on the Non-Proliferation Experiment (NPE): Results and Implications for Test Ban Treaties*, Lawrence Livermore National Laboratory CONF-9404100.

Glenn L. and S. Myers (1997). Depth of Burial Experiment at Balapan, in *Proceedings of the International Symposium on Monitoring and Discrimination of Underground Nuclear Explosions and Earthquakes*, Lawrence Livermore National Laboratory UCRL-JC-1283 13: 229–235.

Gupta, I. N., W. W. Chan, and R. A. Wagner (1992), A Comparison of Regional Phases from Underground Nuclear Explosions at East Kazakh and Nevada Test Site, *Bull. Seismol. Soc. Am*. 82: 352–382.

Gupta, I. N., T. R. Zhang, and R. A. Wagner (1997), Low Frequency Lg from NTS and Kazakh Nuclear Explosions—Observations and Interpretations, *Bull. Seismol. Soc. Am*. 87, 1115–1125.

Healey, D. L. and Miller, C. H. (1963), Gravity Survey of the Gold Meadows Stock, Nevada Test Site, Nye County, Nevada, USGS Technical Letter NTS-40.

Jih, R. S. (1995), Numerical Investigation of Relative Contribution of Rg Scattering and Incomplete Dissipation to Lg Excitation, in *Proceedings of the 17th Seismic Research Symposium on Monitoring a Comprehensive Test Ban Treaty*, PL-TR-95-2108, 1: pp. 401–410.

Johnson, L. R. and C. G. Sammis (2001), Effects of Rock Damage on Seismic Waves Generated by Explosions, *Pageoph* 158: 1869-–908.

Larsen, S. C. and C. A. Schultz, ELAS3D: 2D/3D Elastic Finite-Eifference Wave Propagation Code, LLNL internal report, 18.

Larsen, S. and J. Grieger (1998), Elastic Modeling Initiative, Part III: 3-D Computational Modeling, in *Proceedings of the Society of Exploration Geophysicists International Conference* 68: pp. 1803–1806.

Levander, A. R. (1988), Fourth-Order Finite-Difference P-SV Seismograms, *Geophysics* 53: 1425–1436

Mayeda, K. and W. Walter (1996). Moment, Energy, Stress Drop, and Source Spectra of Western United States Earthquakes from Regional Coda Envelopes, *J. Geophys. Res*. 101: 11,195–11,208.

Myers, S. C., W. R. Walter, K. Mayeda, and L. Glenn (1999), Observations in Support of Rg Scattering as a Source for Explosion S Waves: Regional and Local Recordings of the 1997 Kazakhstan Depth of Burial Experiment, *Bull. Seismol. Soc. Am*. 89: 544–549.

Myers, S. C., D. B. Harris, M. L. Anderson, W. L. Rodi, W. R. Walter, M. P. Flanagan, and F. Ryall, LLNL Location and Detection Research 2003, in *Proceedings of the 25th Seismic Research Review—Nuclear Explosion Monitoring: Building the Knowledge Base*, LA-UR-03-6029, 1: pp. 259–268.

Mooney, W., G. Laske, G. Masters (1998), Crust 5.1: A Global Crustal Model at 5 × 5 Degrees, *J. Geophys. Res*. 103: 727–747.

Nuttli, O. W. (1986), Yield Estimates of Nevada Test Site Explosions Obtained from Seismic Lg Waves, *J. Geophys. Res*. 91: 2137–2151.

Patton, H. J. and S. R. Taylor (1984), Q-Structure of the Basin and Range from Surface Waves, *J. Geophys. Res*. 89 (NB8): 6929–6940.

Patton, H. J. (2001), Regional Magnitude Scaling, Transportability, and Ms:mb Discrimination at Small Magnitudes, *Pageoph* 158: 1951–2015.

Pomeroy, P., W. Best, and T. McEvilly (1982), Test Ban Treaty Verification with Regional Data—A Review, *Bull. Seismol. Soc. Am*. 72: S89–S129.

Preston, L., K. Smith, and D. von Seggern (2005), 3D Velocity Structure of the Yucca Mountain, 2005 Seismological Society of America Meeting, Incline, NV.

Stevens, J. L., G. E. Baker, H. Xu, T. J. Bennett, N. Rimer, and S. M. Day (2004), The Physical Basis of Lg Generated by Explosion Sources, in *Proceedings of the 26th Seismic Research Review: Trends in Nuclear Explosion Monitoring*, LA-UR-04-5801.

United States Geological Survey (1983), Geologic and Geophysical Investigations of Climax Stock Intrusive, Nevada, USGS Open-File Report 83-377.

Vogfjord, K. (1997), Effect of Explosion Depth and Earth Structure on the Excitation of Lg Waves: S* Revisited, *Bull. Seismol. Soc. Am*. 87: 1100–1114.

Walter, W., K, Mayeda, and H. Patton (1995), Phase and Spectral Ratio Discrimination between NTS Earthquakes and Explosions, Part I: Empirical Observations, *Bull. Seismol. Soc. Am*. 85: 1050–1067.

Walter, W. R., K. Mayeda, and H. J. Patton, Regional Seismic Observations of the Non-Proliferation Experiment at the Livermore NTS Network, in *Proceedings of the Symposium on The Non-Proliferation Experiment (NPE): Results and Implications for Test Ban Treaties*, M. D. Denny and S. P. Stull, Eds.

Whitney, J. W. and W.R. Keefer, Geologic and Geophysical Characterization Studies of Yucca Mountain, Nevada, a Potential High-Level Radioactive-Waste Repository, *USGS Digital Data Series* 58.

Wu, R. S., X. B. Xie, Z. Ge, and T. Lay (2004), Quantificating Source Excitation and Path Effects for High Fequency Regional Waves, in *Proceedings of the 26th Seismic Research Review: Trends in Nuclear Explosion Monitoring*, LA-UR-04-5801.

Zandt, G., S. C. Myers, and T. C. Wallace (1995), Crust and Mantle Structure across the Basin and Range—Colorado Plateau at 37° North Latitude and Implications for Cenozoic Extension Mechanism, *J. Geophys. Res*. 100: 10,592–10,548.

SOURCE AND PROPAGATION CHARACTERISTICS OF EXPLOSIVE AND OTHER SEISMIC SOURCES

Xiaoxi Ni[1], Winston Chan[1], Robert Wagner[1], William Walter[2], and Eric Matzel[2]

Multimax, Inc.[1] and Lawrence Livermore National Laboratory[2]

Sponsored by National Nuclear Security Administration
Office of Nonproliferation Research and Engineering
Office of Defense Nuclear Nonproliferation

Contract No. DE-AC52-04NA25538[1] and W-7405-ENG-48[2]

ABSTRACT

Understanding of the source and propagation characteristics of seismic events of different types, including earthquakes, explosions, and mining-induced events is essential for successful discrimination of nuclear explosions. We are compiling a data set of mining related seismic events in east Eurasia. Natural earthquake data in the same region are also collected for a comparison study between mining related events and earthquakes. The ground-truth data set will provide a unique and valuable resource for monitoring research. We will use the data set to investigate the source and propagation characteristics of seismic sources of different types, including mine blasts, tremors, collapses, and earthquakes. We will use various seismological techniques, including spectral analysis and waveform modeling to conduct the investigation. The research will improve our understanding of the S-wave excitation and propagation characteristics of chemical explosions and other source types.

OBJECTIVES

The objective of this study is to build a ground-truth database of mining related seismic events, including mine blasts, mine tremors, and mine collapses, along with natural earthquakes in east Eurasia. We will use this unique data set to study the source and propagation characteristics of seismic events of different source types. The research will improve our understanding of the source and propagation characteristics of seismic events of explosives and other source types and our abilities to discriminate and monitor nuclear explosions with ground-based systems.

RESEARCH ACCOMPLISHED

Methodology

In the past 20 years significant advances have been made in small magnitude discrimination using regional body waves. In particular measurements that use high-frequency (> 4 Hz) regional phase (Pn, Pg, Sn, Lg) amplitude ratios can discriminate earthquakes from nuclear and contained chemical explosions in many different parts of the world (Taylor et al. 1988; Dysart and Pulli 1990; Baumgardt and Young 1990; Kim et al. 1993; Walter et al. 1995; Taylor 1996; Fisk et al. 1996; Hartse et al. 1997; Rodgers and Walter 2002, and many others). A factor undermining our confidence in using these discriminants in uncalibrated regions is the large variation in performance for the different regions where they have been tested. For example, some regional discriminant ratios such as low- to high-frequency spectral ratios in P and S phases work well at the Nevada Test Site but not at Eurasia test sites (e.g., Taylor and Denny 1991; Walter et al. 1995). The key unresolved issue is the lack of a firm physical basis for these discriminants.

The dense local to near regional distance data from east Eurasia, with both earthquake and mining sources, provide a unique data set to investigate some of these issues. In particular we will examine: 1) S-wave excitation and propagation in distance and azimuth from both earthquakes and mine seismicity (blasts, tremors, and collapses); 2) differences and similarities between fairly contained chemical explosions and those more distributed in space and time; and 3) issues of wave amplitude and frequency evolution during propagation from local to regional distances as interactions with basin, crustal and uppermost mantle structure take place.

The physical basis for the generation of S wave from nuclear explosions has remained a central issue in monitoring research for many years. Physically sound models of S-wave energy from explosions include tectonic release, rock cracking, spall, P to S conversion at the free surface and Rg to S scattering (e.g., Wallace 1991, Johnson and Sammis 2001, Day and McLaughlin 1991, Vogfjord 1997, Gupta et al. 1992). Recent observational evidence from the 1997 Kazakh depth of burial experiment points to Rg-to S scattering as a major source of S-waves (Myers et al. 1999) from explosions. However the relative importance of these mechanisms and their dominant frequency contributions is not clear. We will measure body wave amplitudes at the stations and utilize the independent information on the mine blast source characteristics to examine these possible mechanisms of explosion S-wave generation.

In many regions of the world, the only seismically recorded explosions are those from mine blasts. In such regions there have been studies discriminating the two (e.g., Baumgardt and Young 1990, Walter et al. 1997), but the application to nuclear explosion monitoring remains complex. While the equivalence between single contained chemical and nuclear explosions was demonstrated during the 1993 Non-Proliferation Experiment (Denny and Stull 1994), the relationship between the more complex mining explosions and nuclear blasts is more complicated. Because mine blasts come in a great variety of configurations in time, space, containment, and mass displacement, the relationship between discrimination performance for the three types of events— nuclear explosion, mining explosion, and earthquake— is not straightforward. For this study we will have some independent information about blasting practices for some of the mining shots. We will use this information to study the relationship between mine blasting practice and discrimination for east Eurasia. We will compare these results with ongoing efforts to study explosion phenomenology through experiments such as the 2003 Arizona Source Phenomenology Experiment (Bonner et al. 2003).

Much of the existing work on body wave discriminants has been at regional distances. The performance of discriminants such as high frequency P to S ratio at local distances is much less well characterized. In particular, it is known that body waves undergo very large amplitude variations over their first few hundred kilometers of propagation as they interact with local basin structure, crustal layering, Moho reflections, and uppermost mantle refractions. In preliminary study of earthquake and mine blast discrimination using high frequency P/S ratios in

Israel, Walter et al. (1997) noted that some stations at local distances showed good separation between event types and others did not. They attributed some of this effect to local propagation issues. With the coincidence of earthquake and mine blast source types and dense distance and azimuthal coverage, we will use the east Eurasia data to examine these issues. Specifically, we will measure instrument corrected local and regional amplitudes at a range of frequencies to study discriminantion performance as a function of distance, azimuth and relationship to crustal structure.

Data Collection and Processing

We initiated the project by investigating seismicities, including natural earthquakes and mining events in the studied region. East Eurasia is a region with vast mine resources as well as frequent earthquakes. Mining-induced seismic events occur frequently in many areas all over the region. There are over 3,500 seismic events reported by the regional seismic networks from 2001 to 2003 in the region (Figure 1). Valuable seismic data on mine related seismic events as well as earthquakes have been collected and archived for the region in data repositories such as IRIS, IDC, etc.

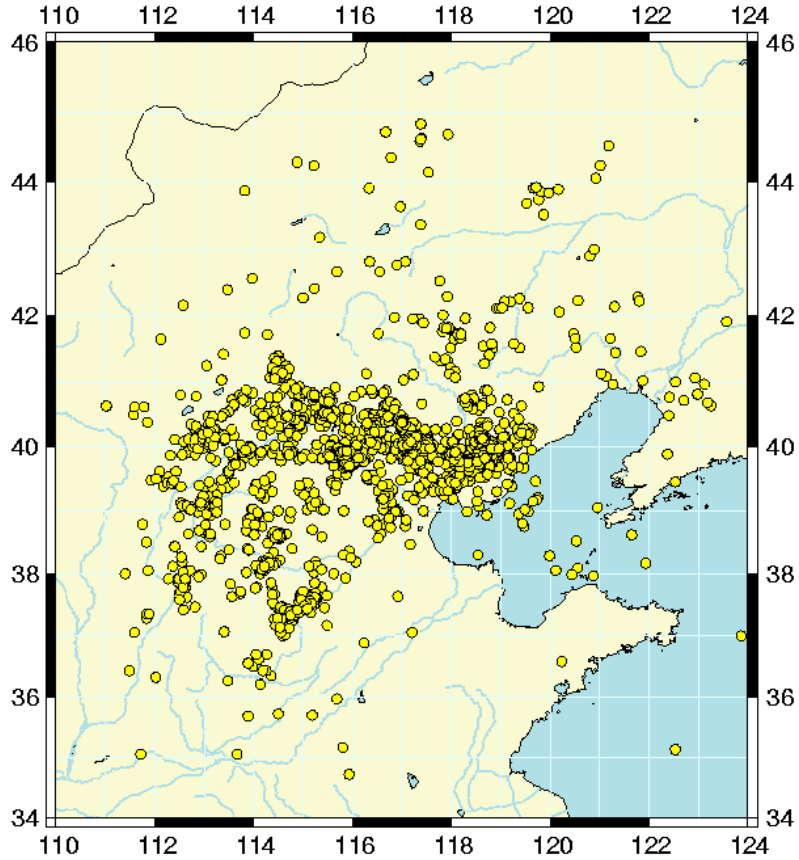

Figure 1. Over 3,500 seismic events recorded in east Eurasia from 2001 to 2003.

At data processing centers of the regional seismic networks in east Eurasia, data analysts routinely single out suspicious explosions based on characteristics of waveform, such as arrival onset, surface wave development, etc. Among the over 3,500 seismic events recorded from 2001 to 2003, more than 1,800 events are classified as possible mine blasts. The seismic stations in the regional seismic networks are equipped with very-broad-band seismographs with a bandwidth from 120 s to 20 Hz, broadband seismographs from 20s to 20Hz, and short-period seismographs in boreholes from 1 to 20Hz (Figure 2). The instruments have GPS timing, a 24-bit recording module, and a dynamic range greater than 130dB.

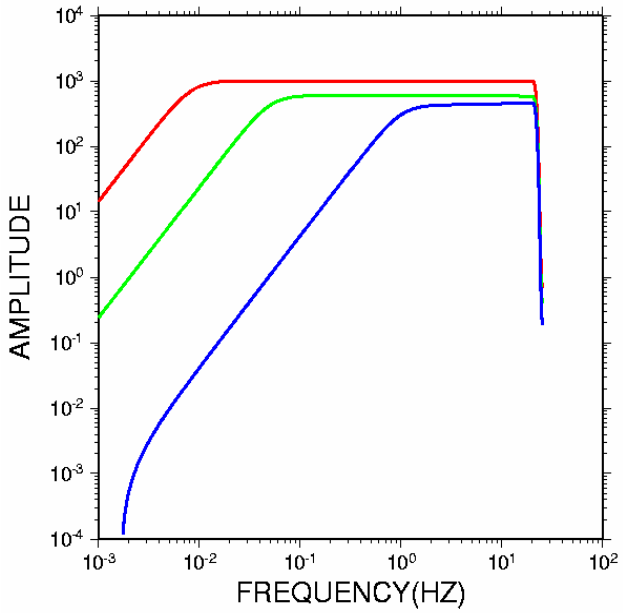

Figure 2. Instrument responses of the very-broad-band (red), broad-band (green) and short-period (blue) seismographs in the regional seismic networks in east Eurasia.

The waveform data are archived in SEED format. Figure 3 shows the vertical components of a possible mine blast that occurred on June 15, 2002. Figure 4 represents the vertical components for a magnitude 4.7 earthquake on May 18, 2002 in the nearby region. Initial observation reveals distinctive characteristics of the two different types of seismic events. We are in the process classifying and validating the raw data, making phase identification and measurement, and will perform discrimination studies in the next phase.

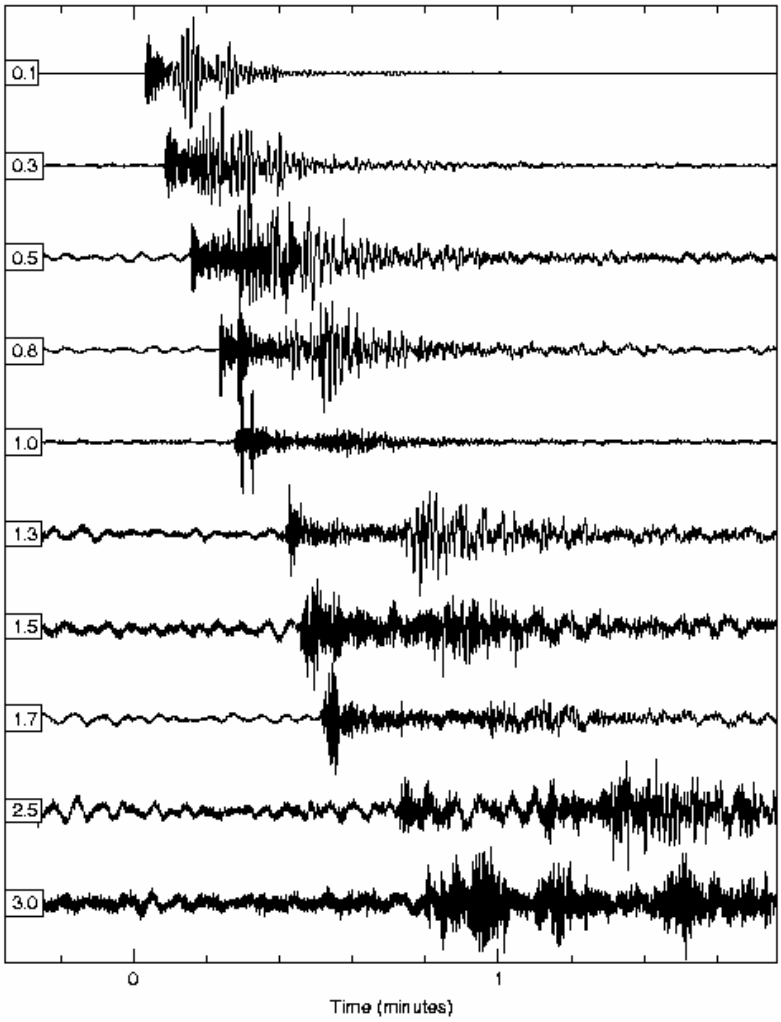

Figure 3. Vertical components of a possible mining blast recorded by regional seismic networks in east Eurasia on June 15, 2002. The numbers at the beginning of each trace indicate epicentral distance in kilometers.

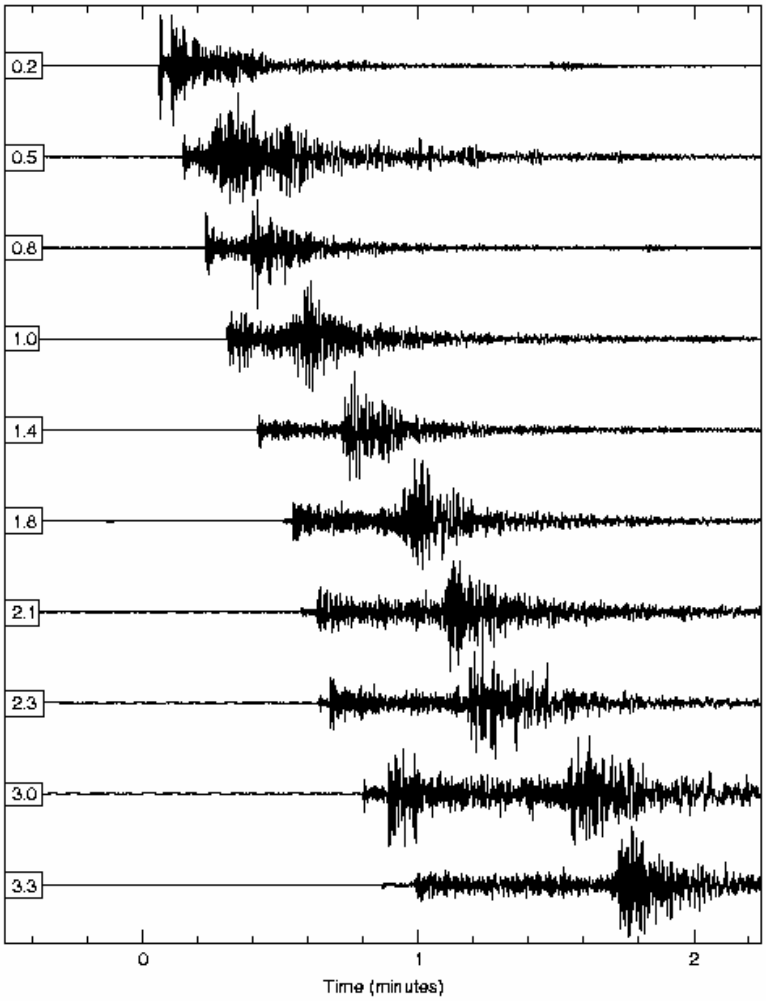

Figure 4. As a comparison with the possible mining blast in Figure 3, this panel shows the vertical components of a magnitude 4.7 earthquake recorded by the same networks on May 18, 2002. The numbers at the beginning of each trace indicate epicentral distance in kilometers.

Preliminary Results

In a preliminary look at the behavior of the regional body wave amplitudes in this region we have collected waveform data through IRIS from the CDSN station BJT. We focus on data within a few hundred kilometers of the station to look at local to regional effects. We selected about 23 earthquakes with magnitudes greater than 4.0 from the United States Geological Survey Preliminary Determination of Epicenters (USGS PDE) catalog and about 19 presumed mine blasts with magnitudes between 3 and 4. For each event we windowed the Pg and Lg phases using group velocity windows of about 6.0 to 5.0 km/s for Pg and 3.6 to 3.0 km/s for Lg. Windows were slightly adjusted by hand in order to best capture each phase. We then formed log averaged raw spectral amplitudes in the 2–4 and 6–8 Hz bands and examined some possible discriminant measures as a function of distance. Many studies have identified high-frequency P/S ratios as possible discriminants. In the top of Figure 5, we see that at 2–4 Hz the populations are quite intermixed but at 6–8 Hz we see some reasonable separation, although some of the mine blast signals are weak and fall below our signal to noise threshold of 2. At the bottom of the plot we look at low- to high-frequency spectral ratios and see some trend in the earthquake with distance. Looking at events at the same distance range, we see some separation in populations, but we have not yet corrected for source size effects, which may enhance the separation. Mine blasts can be different from single fired explosions, such as being relatively richer in S-waves leading to different discrimination behavior than nuclear explosions (see for example Walter et al. and Bonner et al. this Proceedings). In future work we will expand our dataset and analysis over the region to look at discrimination behavior with distance and source type.

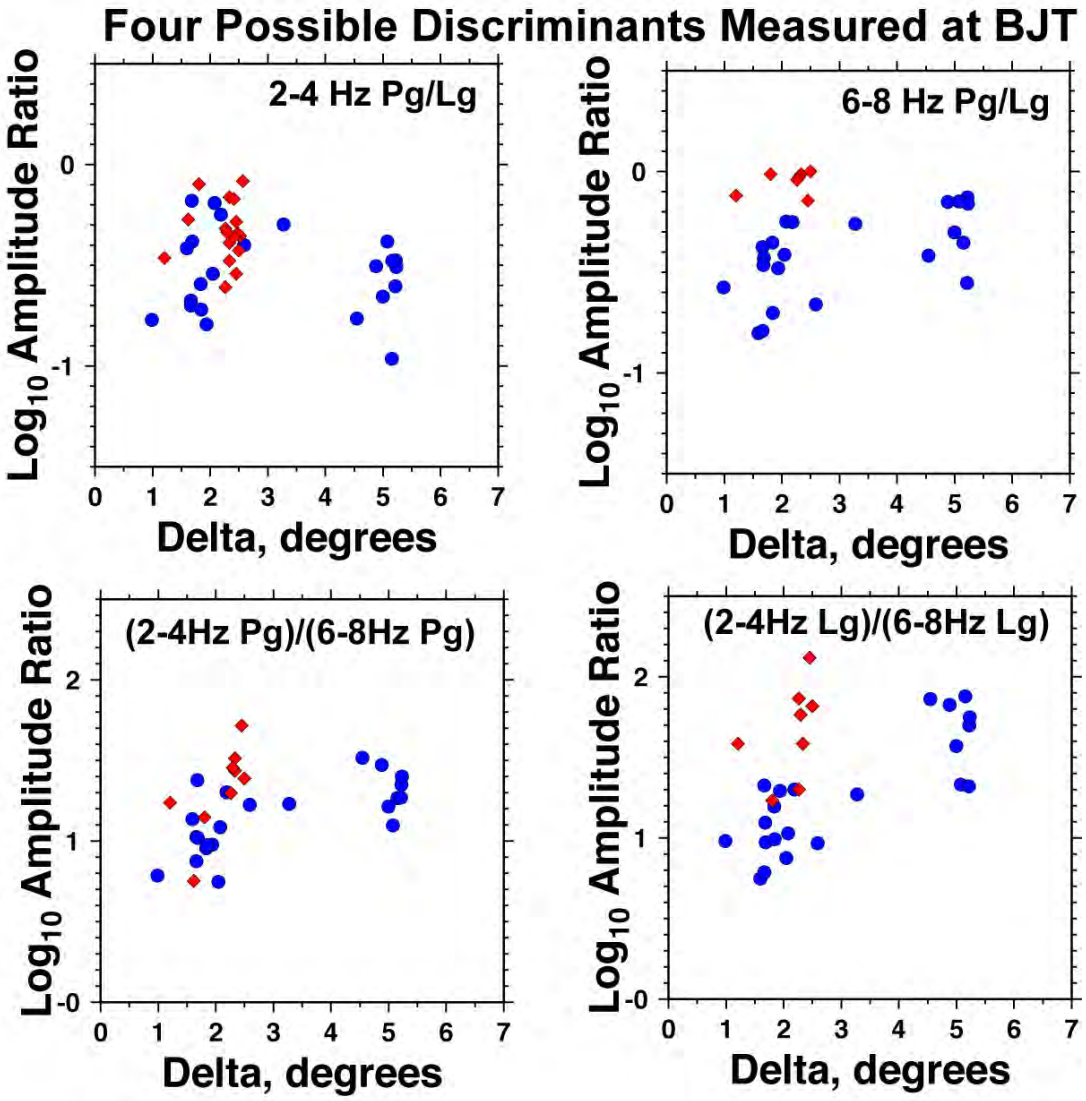

Figure 5. This plot shows four possible local-to-regional body wave amplitude ratio measures that have previously shown some ability to discriminate earthquakes from explosions (e.g., Walter et al. 1995). Earthquakes are shown as blue circles and presumed mine blasts as red diamonds. The two measures on the right hand side show some separation between the means of the populations, the log amplitude ratios are plotted versus distance, and no attenuation or source corrections have been applied.

CONCLUSIONS AND RECOMMENDATIONS

The current project is in the early stages. We have collected ground-truth data for seismic events of different sources including mine blasts, tremors, collapses, and natural earthquakes in east Eurasia. Digital waveform data from regional seismic networks in the region have been collected and archived. This data set will serve as a unique resource for the study of source and propagation characteristics of explosives and other seismic sources. In the next phase of the project, we shall conduct spectral analysis, discrimination studies and waveform modeling on the waveform data and investigate the S-wave excitation and propagation characteristics of different seismic sources.

REFERENCES

Baumgardt, D. R. and G. B. Young (1990), Regional seismic wave form discriminants and case-based event identification using regional arrays, *Bull. Seism. Soc. Am.* 80: 1874-1892.

Bonner, J., I. Orrey, and A. Rosca (2002). Modeling short-period surface waves from small explosions at the Shagan Test Site, in *Proceedings of the 24th Seismic Research Review—Nuclear Explosion Monitoring: Innovation and Integration*, LA-UR-02-5048: Vol. 1, pp. 488-497.

Bonner, J., B. Stump, W. Walter, D. pearson, C. Hayward, A. Velasco, D. Baker, C. Edwards, J. Lewkowicz, S. Harder, T. Wallace, S. Russell, M. Leidig, and S. Myers (2003). Planning source phenomenology experiments in Arizona, in *Proceedings of the 25th Seismic Research Review – Nuclear Explosion Monitoring: Building the Knowledge Base,* LA-UR-03-6029, Vol. 1, pp. 363–372.

Bowers, D. and W. R. Walter (2002), Discriminating between large mine collapses and explosions using teleseismic P-waves, *Pure Appl. Geophys*, 159, 803–830.

Chan, W. and X. Ni (1999). Collection and Analysis of Seismic and Ground-truth Information in Northeastern China, in *Proceedings of the 21st Seismic Research Symposium: Technologies for Monitoring The Comprehensive Nuclear -Test-Ban Treaty*, LA-UR-99-4700, Vol. 1, pp. 27–39.

Chan, W. and X. Ni (2000). Tomographic Inversion of 3-D Crustal Structure and Relocation of Earthquakes in Northeast China, *EOS, TRANS. Am. Geophys. Union* 81: (19): Suppl., p. 323, May. 9.

Chan, W., W. Jiao, R. Wagner, and I. Gupta (2001). Regional Seismic Database for Southwest China, in *Proceedings of the 23rd Seismic Research Symposium: Worldwide Monitoring of Nuclear Explosions*, LA-UR-01-4454, Vol. 1, pp. 21–29.

Day, S. and K. McLaughlin, (1991). Seismic source representations for spall, *Bull. Seism. Soc. Am.*, 81, 191-201.

Denny, M. D., and S. P. Stull (1994). Proceedings of the Symposium on The Non-Proliferation Experiment (NPE): Results and Implications for Test Ban Treaties, Rockville Maryland; Lawrence Livermore National Laboratory.

Dysart, P. S. and J. J. Pulli (1990), Regional seismic event classification at the NORESS array: seismological measurements and the use of trained neural networks, *Bull. Seism. Soc. Am.*, 80, 1910–1933.

Fisk, M. D., H. L. Gray, and G. D. McCartor (1996), Regional event discrimination without transporting thresholds, *Bull. Seism. Soc. Am*. 86: 1545-1558.

Guo, B., Q. Liu, J. Chen, and S. Li (2002), Test of epicenter determination of microearthquakes recorded by the Digital Seismic Network in Capital Circle, *Seism. and Geol.* 24 (3): 453–460.

Gupta, I. N., W. W. Chan, and R. A. Wagner (1992), A comparison of regional phases from underground nuclear explosions at East Kazakh and Nevada test sites, *Bull. Seism. Soc. Am*. 82: 352–382.

Hartse, H., S. R. Taylor, W. S. Phillips, and G. E. Randall (1997), A preliminary study of regional seismic discrimination in Central Asia with an emphasis on Western China, *Bull. Seism. Soc. Am*. 87, 551–568.

Hedlin, M. A.H. (1998). Identification of mining blasts at all regional distances using low-frequency seismic signals, in *Proceedings of 20th Annual Seismic Research Symposium on Monitoring A Comprehensive Test Ban Treaty (CTBT)*, Vol. 1, pp. 570-579.

Johnson, L.R., and C.G. Sammis, (2001), Effects of rock damage on seismic waves generated by explosions, *Pageoph* 158: 1869–1908.

Kim, W.-Y., D. W. Simpson, and P. G. Richards (1993), Discrimination of earthquakes and explosions in eastern United States using regional high-frequency data, *Geophys. Res. Lett.* 20: 1507–1510.

Liu X., P. Sheng, L. Zhang and Y. Li (2003). Using method of energy linearity in wavelet transform to distinguish explosion or collapse from nature earthquake, *NW Seismol. J.* 25 (3): 204–209.

Myers, S. C., W. R. Walter, K. Mayeda and L. Glenn (1999), Observations in support of Rg scattering as a source for explosion S waves: regional and local recordings of the Kazakhstan depth of burial experiment, *Bull. Seism. Soc. Am.* 89: 544–549.

Pechmann, J. C., W. R. Walter, S. J. Nava, and W. J. Arabasz (1995), The February 3, 1995 M_L 5.1 seismic event in the trona mining district of southwestern Wyoming, *Seism. Res. Lett.*, 66: 25–34.

Rodgers, A. J. and W. R. Walter (2002), Seismic discrimination of the May 11, 1998 Indian Nuclear Test with short-period regional data from Station NIL (Nilore, Pakistan), *Pure. App. Geophys*. 159: 679–700.

Stump, B., C. Hayward and R. Zhou (2002). A comparative study of natural and man-induced seismicity in the Yanqing-Huailai Basin and the Haicheng Area, *Proceedings of the 24th Seismic Research Review—Nuclear Explosion Monitoring: Innovation and Interation*, LA-UR-02-5048, Vol. 1, pp. 192–199.

Taylor, S. R., N. W. Sherman and M. D. Denny (1988). Spectral discrimination between NTS explosions and western United States earthquakes at regional distances, *Bull. Seism. Soc. Am.* 78: 1563–1579.

Taylor, S. R. and M. D. Denny (1991). An analysis of spectral differences between Nevada Site and Shagan River nuclear explosions, *J. Geophys. Res*. 96: 6237–6245.

Taylor, S. (1996), Analysis of high-frequency Pg/Lg ratios from NTS explosions and Western U.S. earthquakes, *Bull. Seism. Soc. Am.* 86: 1042–1053.

Vogfjord, K. (1997), Effects of explosion depth and earth structure on the excitation of Lg waves: S* revisited, *Bull Seism. Soc. Am.* 87: 1100.

Wallace, T. C. (1991), Body wave observations of tectonic release, in *Explosion Source Phenomenology* edited by Taylor, S. R., H. J. Patton, and P. G. Richards, *Am. Geophys. Union Geophys. Monog*. 65: 161-170.

Walter, W. R., K. M. Mayeda and H. J. Patton, (1995), Phase and spectral ratio discrimination between NTS earthquakes and explosions, part I: empirical observations, *Bull. Seism. Soc. Am.* 85: 1050-1067.

Walter, W. R., D. B. Harris, and S. C. Myers (1997), Seismic discrimination between earthquakes and explosions in the Middle East and North Africa, in *Proceedings of the 19th Seismic Research Symposium on Monitoring a Comprehensive Test Ban Treaty, Defense Special Weapons Agency Report*, pp. 459-468.

Xia, A. and X. Liu (2002), Recognition of artificial explosion and earthquake using the records at the Urumqi Digital Telemetry Seismic Station, *Inland Earthquake* 16 (4): 337-345.

Yamamoto, J., L. Quintanar, C.J. Rebollar and Z. Jimenez (2002), Source characteristics and propagation effects of the Puebla, Mexico, Earthquake of 15 June 1999, *Bull. Seism. Soc. Am.* 92 (6): 2126-2138.

Yang, X. (1998). Mineseis - A Matlab GUI Program to Calculate Synthetic Seismograms from a Linear, Multi-shot Blast Source Model, in *Proceedings of 20th Annual Seismic Research Symposium on Monitoring A Comprehensive Test Ban Treaty (CTBT)*,755-764.

Zhang, S.Q., J. P. Wu, and L. B. Xia, (1997), On non-natural earthquake sources, in Advances of China Seismological Research, (Editor: Y. T. Chen) Beijing, China.

Zhuang, C. (1999). Technical structures of the Capital Region Digital Telemetric Seismic Network, *Seismol. Geomagn. Obs. Res.*20 (5): 23-27.

GEOPHYSICAL MODEL APPLICATIONS FOR MONITORING

Michael E. Pasyanos, William R. Walter, Hrvoje Tkalcic,
Gregory A. Franz, Rengin Gok, and Arthur J. Rodgers

Lawrence Livermore National Laboratory

Sponsored by National Nuclear Security Administration
Office of Nonproliferation Research and Engineering
Office of Defense Nuclear Nonproliferation

Contract No. W-7405-ENG-48

ABSTRACT

Geophysical models constitute an important component of calibration for nuclear explosion monitoring. We will focus on four major topics and their applications: 1) surface wave models, 2) receiver function profiles, 3) regional tomography models, and 4) stochastic geophysical models. First, we continue to improve upon our surface wave model by adding more paths. This has allowed us to expand the region to all of Eurasia and into Africa, increase the resolution of our model, and extend results to even shorter periods (7 sec). High-resolution models exist for the Middle East and the Yellow Sea and Korean Peninsula (YSKP) region. The surface wave results can be inverted either alone, or in conjunction with other data, to derive models of the crust and upper mantle structure. One application of the group velocities is to construct phase-matched filters in combination with regional surface-wave magnitude formulas to improve the mb:Ms discriminant and extend it to smaller magnitude events. Next, we are using receiver functions, in joint inversions with the surface waves, to produce profiles directly under seismic stations throughout the region. In the past year, we have been focusing on deployments throughout the Middle East, including the Arabian Peninsula and Turkey. By assembling the results from many stations, we can see how regional seismic phases are affected by complicated upper mantle structure, including lithospheric thickness and anisotropy. The next geophysical model item, regional tomography models, can be used to predict regional travel times such as Pn and Sn. The times derived by the models can be a background model for empirical measurements or, where these don't exist, simply used as is. Finally, we have been exploring methodologies such as Markov Chain Monte Carlo (MCMC) to generate data-driven stochastic models. We have applied this technique to the YSKP region using surface-wave dispersion data, body wave travel time data, receiver functions, and gravity data. The models can be used to predict a number of geophysical measurements, including waveforms that can be generated using techniques such as finite difference and spectral element modeling.

OBJECTIVE

The objective of regional-scale geophysical models is to improve predictions for the location and identification of regional seismic events by improving the resolution in comparison to global-scale models. As such, we wish to provide models of the highest possible resolution that can used to reliably derive parameters such as body wave travel times, group velocity dispersion, waveforms, etc. In addition, the models should convey proper uncertainty estimates which can be mapped into uncertainties in the derived products.

Geophysical models can take a number of forms. Much interest in *a priori* models has been made in the monitoring community in recent years and several of them have been constructed by various groups for different regions. Examples include the WINPAK model (Johnson and Vincent, 2002) for India and Pakistan, the WENA model (Pasyanos et al., 2004) for Western Eurasia and North Africa, as well as the various consortia models. These models can serve as background values for travel time correction surfaces and other derived parameters. This can be particularly important in aseismic regions, which might only have a limited number of empirical measurements. These models can also serve as an integrated geophysical repository for research community results.

In this paper, however, we will not be discussing *a priori* geophysical models, but rather concentrate on several other types of geophysical models. The focus in this paper is to outline some of the other model types, and focus as much as possible on their applications to monitoring. The first that we consider are surface-wave models. By themselves, these stand-alone models can be used to construct phase-matched filters, which can improve weak surface wave signal and calculate regionally determined M_S. In addition, they can be used either alone or in conjunction with other data to construct 3-D velocity models of the lithosphere. A second type is receiver functions, which are a reliable way of obtaining the local velocity structure near a station from teleseismic events. While the results are only applicable to the limited portions of our model area covered by seismic stations, they are important to constrain precisely because they represent the structure at the station locations. Regional tomography models, such as those for upper mantle head-waves Pn and Sn, can be used to predict regional travel times. We present our results from stochastic models, which are data-driven models generated using a Markov Chain Monte Carlo (MCMC) technique. This method combines a priori information with geophysical data from multiple sources (and varying sensitivities) to produce models that are most consistent with the constraints. Finally, all of the methods can be used to evaluate some of the aforementioned a priori geophysical models.

RESEARCH ACCOMPLISHED

Surface Wave Models

Over the past several years, Lawrence Livermore National Laboratory (LLNL) has been developing surface wave models in Eurasia for nuclear explosion monitoring (Pasyanos et al., 2001; Pasyanos, 2005). Dispersion measurements are made using multiple narrow-band filters on deconvolved displacement data from the LLNL Seismic Research Knowledge Base (SRKB). We continue to improve upon our surface wave model by adding more paths, generally by taking advantage of new data sets, but also by revisiting stations with more recent events. Most recently, we have added measurements from stations in Eastern Europe, Central Asia, Africa, and the Indian Ocean, including several the Incorporated Research Institutions for Seismology program tht manages seismic equipment (PASSCAL) deployments.

To date, over 100,000 seismograms have been analyzed to determine the individual group velocities of 7-150 second Rayleigh and Love waves. Overall, we have made good quality dispersion measurements for 30,000 Rayleigh and 20,000 Love wave paths. We then tomographically invert these measurements to produce group velocity maps for Love and Rayleigh waves. A conjugate gradient method is used for the tomography.

The group velocity models continue to improve in several ways. First, with more measurements, we have been able to expand the region of coverage to all of Eurasia and into Africa. By increasing the density of coverage in existing regions, we have increased the resolution of our model. Finally, we have been able to provide more reliable maps at short periods, expanding the frequency coverage down to a 7-second period. With the group velocities, we are able to resolve structural features associated with the tectonics of the region. Short period surface waves correspond well to sedimentary basins. At intermediate periods, we find a good correspondence to crustal thickness, but still see the effect of the deepest sedimentary basins. At long periods, we are primarily sensitive to upper mantle structure with fast cratons, slow convergence zones, and very slow ridges (Pasyanos, 2005).

Path coverage will be further improved in the future by the use of cross-correlation of ambient seismic noise to derive the Green function between two stations, and from which the dispersion characteristics can be derived. The benefits of this method in seismology have been dramatically demonstrated for southern California in Shapiro et al. (2005). Figure 1 shows cross-correlations from stations in the eastern Mediterranean using only one month of data. Even with this limited data, the Rayleigh wave signal is already starting to emerge and will become clearer as more data are stacked.

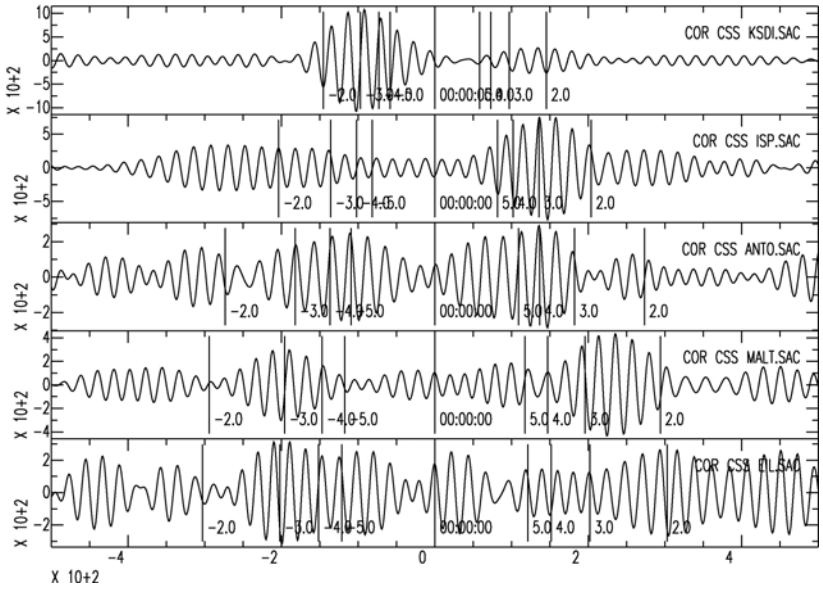

Figure 1. Cross-correlation waveforms between station CSS (Cyprus) and nearby stations KSDI (Kfar Sold, Israel), ISP (Isparta, Turkey), ANTO (Ankara, Turkey), MALT (Malatya, Turkey), and EIL (Eilat, Israel) between 20 and 25 secs derived from one month of data.

We have created high-resolution models for the Middle East and the YSKP region (Pasyanos, 2005). Figure 2 shows an example of our results from the Middle East for 15 second Rayleigh waves, which are sensitive to relatively shallow crustal structure. Here, we compare the results to a sediment thickness map and the results are excellent. Details like the extent of basins in the eastern Mediterranean, Persian Gulf, Mesopotamian Foredeep, and Caspian Sea are well resolved, as is the thin oceanic crust in the Red Sea.

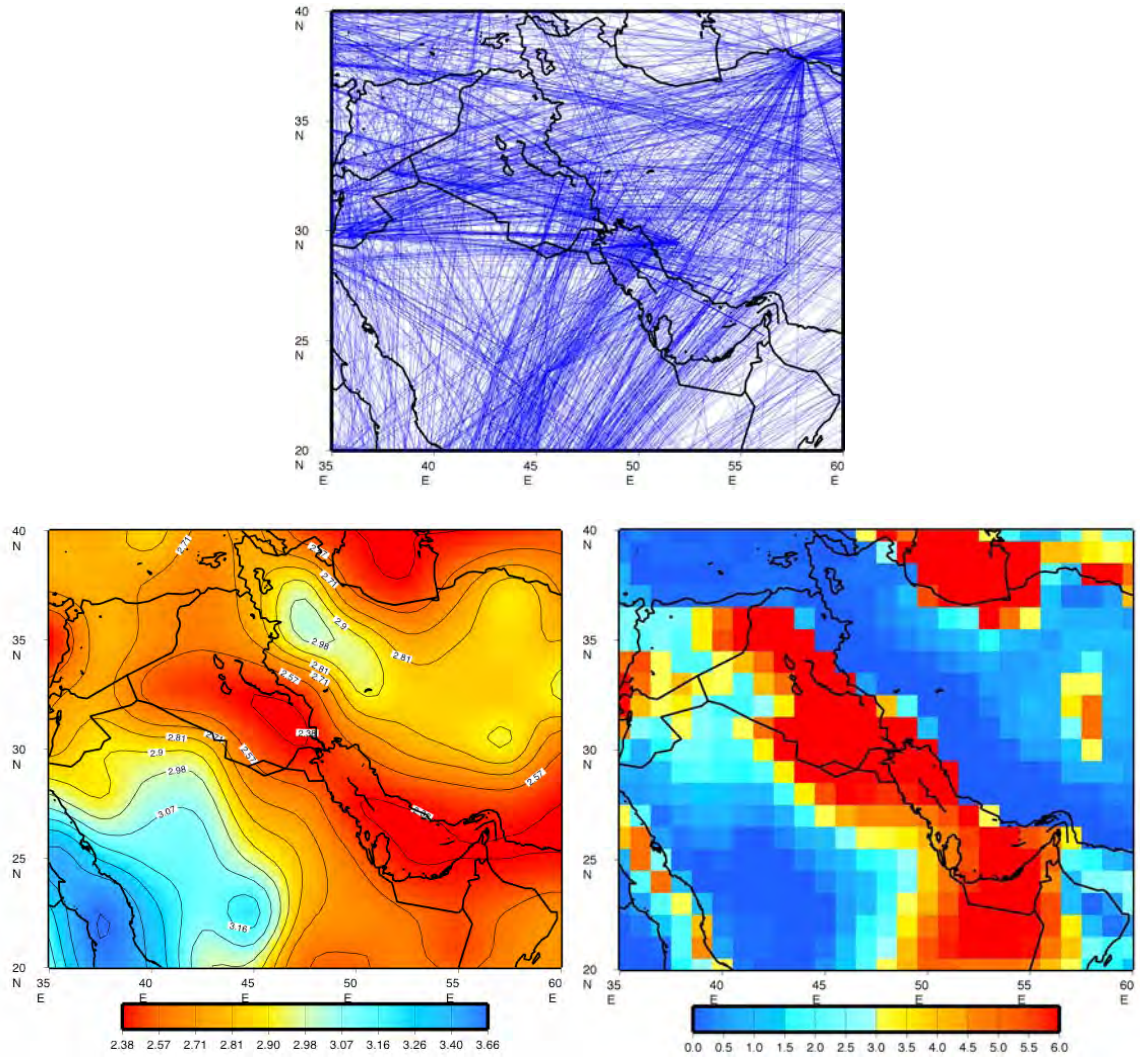

Figure 2. A path map of 15-second Rayleigh wave group velocities for the Middle East, followed by a tomographic model of 15-second Rayleigh waves and a comparison of the results to a sediment thickness map of the region (Laske and Masters, 1997). The color bar scale for the left figure is km/s (group velocity). The scale for the right figure is km (sediment thickness).

The surface wave results can be inverted either alone, or in conjunction with other data, to derive models of the local crust and upper mantle structure. By combining the surface wave data with other data, we can reduce the non-uniqueness inherent in the profile inversions performed using only surface wave data. In the next section, for example, we will be using the surface-wave data in combination with teleseismic receiver functions.

Another application of the group velocities is to construct phase-matched filters in combination with regional surface-wave magnitude formulas to improve the mb:Ms discriminant and extend it to smaller magnitude events. Phase-matched filtering has been shown to effectively winnow out any unwanted signals from the surface wave signal. An example of phase matched filtering is shown in Figure 3. The first example is from an event in eastern Turkey recorded at station HILS in Saudi Arabia. The top figure shows the original trace which shows body phases Pn and Pg, followed by a very large Lg phase coming in at a group velocity of about 3.5 km/s. The main surface-wave energy is followed by a second packet of surface

waves, and followed until the end of the trace by coda. The second trace shows the same event after the waveform has been phase-matched filtered using the tomography of Pasyanos (2005). The body waves including the large Lg phase are completely removed. In addition, the late-arriving multipathed surface waves are beaten down, as is the coda. This is a particularly good example of how using a phase-matched filter can improve our signal. The maximum amplitude surface wave without the filter would be energy arriving at 2.4 km/s, rather than the direct signal at 2.8 km/s. The bottom trace shows the residual signal that was filtered out by the phase-matched filter. Regional surface-wave magnitudes calculated using narrow-band filters (Russell, 2004) from the cleaned signal show a more consistent magnitude value between periods.

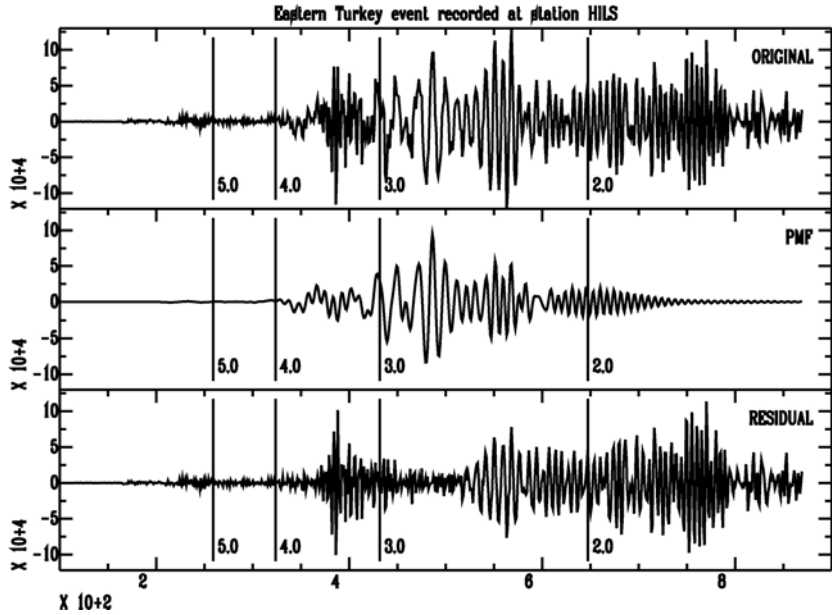

Figure 3. Waveform of an event in eastern Turkey recorded at station HILS in Saudi Arabia. The top trace shows the original waveform, the middle trace shows the waveform filtered using a phase-matched filter from the model of Pasyanos (2005), and the bottom trace shows the residual.

Receiver Function Profiles

We are also using receiver functions, in joint inversions with the surface waves, to produce profiles directly under seismic stations throughout the region. These two data types are complementary since receiver functions are sensitive to velocity contrasts and surface waves are sensitive to depth-averaged velocity. In a collaborative ROA with Penn State University, Ammon et al. have been focusing on stations throughout Western Eurasia and North Africa, while we have been focusing on Livermore deployments and cooperative ventures in the Middle East, including Kuwait, Jordan, Saudi Arabia, and the United Arab Emirates.

An example of a joint inversion is shown for station KBRS in Saudi Arabia. This station was selected as an example of a station which has a simple crustal but a complex lithospheric structure, resulting in models that cannot fit jointly the observed receiver functions and surface-wave group velocity dispersion curves. In this case, in order to produce realistic models that simultaneously fit the surface waves (both Love and Rayleigh) without significantly degrading the fit to the receiver functions, we need to introduce a more complicated upper mantle structure, having both lithospheric structure and anisotropy. The final model and fits to the teleseismic receiver functions and surface wave group velocity dispersion data are shown in Figure 4. A gradational Moho between 35 and 38 km is found in our best model. It was then necessary to

introduce a thin lithospheric lid and a low velocity zone in the upper mantle in order to match low velocities observed in the group velocity dispersion. A strong transverse isotropy (with SH > SV) is required in the upper mantle below Moho down to about 70-80 km in order to fit longer periods of Rayleigh wave group velocity dispersion. The profiles are also consistent with the tectonic setting of the region. In this region of the Arabian Peninsula, we find the thin sedimentary cover that would be expected for the Arabian Shield, a moderately thick crust, a lid indicating a 70 km thickness lithosphere over an asthenosphere with significantly slower shear wave velocity, and anisotropy consistent with mantle material laterally spreading away from the Red Sea Rift.

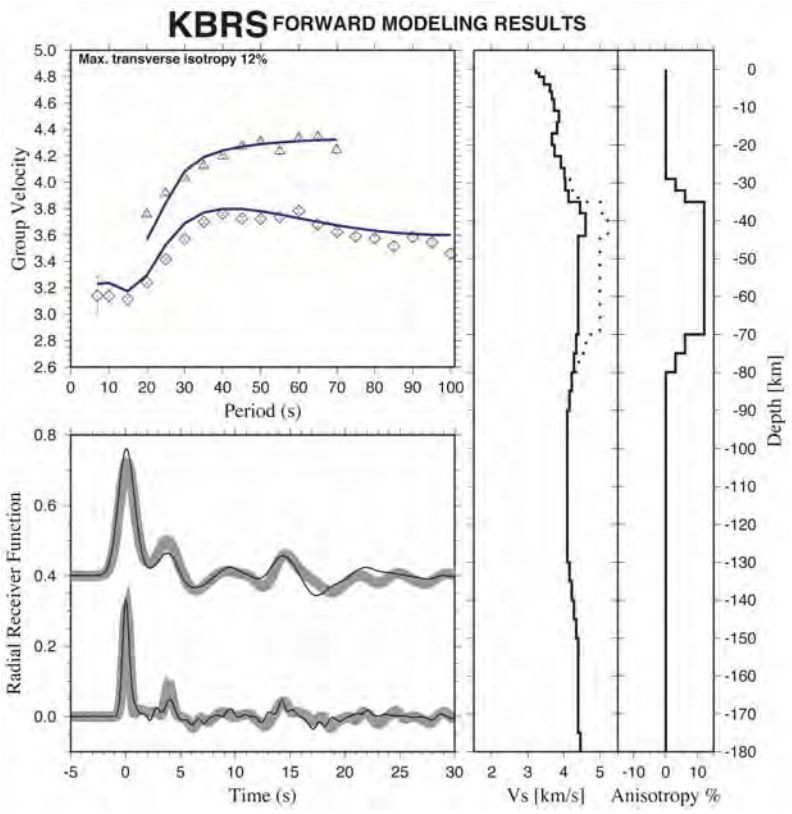

Figure 4. Joint inversion of receiver functions and surface waves to produce a velocity profile for station KBRS in Saudi Arabia. Upper left: symbols are surface-wave group velocity data points derived from surface-wave tomography, and solid lines represent a modeled dispersion. Lower left: Thick lines represent the observed receiver functions at two distinct frequency bands (for Gaussian parameter a=1.0 (top) and a=2.5 (bottom)), while thin solid lines are modeled receiver functions from the model shown on right. Right: final model of shear wave velocity as a function of depth. The dotted line shows Vsh where it differs from Vsv.

Regional Tomography Models

Regional tomography models can be used to predict the travel times of regional phases such as Pn and Sn. While details of the various methodologies vary, they all generally tomographically distribute the slowness along the upper mantle leg of the path, while either inverting or making some sort of correction for the crustal legs. The advantages of such a method is that the tomography can be used to help estimate travel times of these regional phases, even when no direct measurements have been made at a particular station. Due to the propagation path of these phases, however, the spatial coverage is generally limited to a relatively narrow swath around seismic areas within about 1500 km from events, making it of limited use in

aseismic regions. Another potential problem is that normalization in the tomography can dampen the full amplitude of the velocity anomalies.

Still, the utility of tomography is evident. A comparison of P-wave velocities in the upper mantle from both an *a priori* model and tomographic inversion is shown in Figure 5. While the two models generally show the same features (fast velocities beneath oceans, India, and the Former Soviet Union; slow beneath Red Sea, East African Rift, Tethys Belt; sharp contrast along the TTZ), there are obvious differences. Most notably, besides about a 0.04 km/s shift between the two models, there is considerable unmodeled variation in the tomography which does not exist in the *a priori* model. It is this variability that would be difficult to build into *a priori* type models. The application of these models, of course, is to predict these regional phases. The times derived by the models can be as a background model for empirical measurements or, where these don't exist, simply used as is.

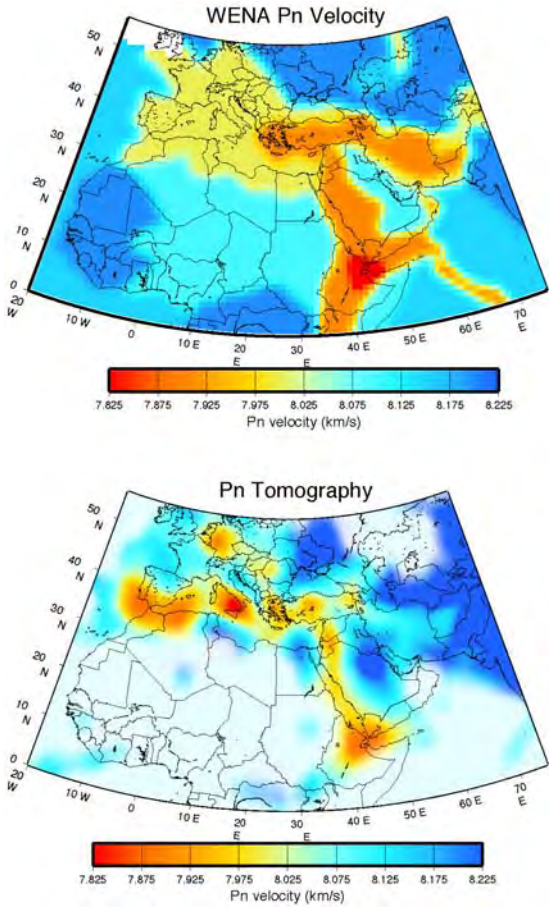

Figure 5. A comparison of uppermost mantle P-wave velocities from an *a priori* model and tomographic inversion. (a) The upper mantle velocities predicted by the WENA model. (b) The upper mantle velocities derived from the Pn tomography (Pasyanos et al., 2004).

Stochastic Geophysical Models

We have been exploring methodologies such as MCMC to generate data-driven stochastic models. In an effort to build seismic models that are most consistent with multiple seismic data sets, we have applied a new method known as the Stochastic Engine (SE). The SE uses MCMC to sample models from a prior distribution and test them against multiple data types in a staged approach to generate a posterior distribution of models.

While computationally expensive, this approach has several advantages over a single deterministic model. First, we are able to easily incorporate prior information on the model, such as the *a priori* geophysical models that were discussed earlier. Second, with this technique, we are able to reconcile different data types that can be used to constrain the model. We can also estimate the uncertainties of model parameters, properly migrating data uncertainties into model uncertainties. The method does not constrain models to be normally distributed, but instead allows non-Gaussian or multi-modal distributions. Finally, we can estimate uncertainties on predicted observable signals, such as would be required to apply this model as a correction surface.

We use this method to determine the crust and upper mantle structure of the Yellow Sea and Korean Peninsula (YSKP) region using surface wave dispersion data, body wave travel time data, and receiver functions. We have had great success using this approach. Where little or no data exist, the posterior model simply reflects the prior distribution. Where data exists, however, the model is driven by the data. Figure 6 shows a crustal thickness map and corresponding uncertainties, taken by calculating the mean and standard deviation of the posterior distribution. One can see the thinning associated with the oceanic crust of the Pacific Ocean and Sea of Japan. One can also see crustal thickening in the westernmost portion of our study area. We are in the process of improving the model by incorporating more data sets (i.e., gravity, amplitude information, waveforms, etc.) and increasing the resolution to 1 degree.

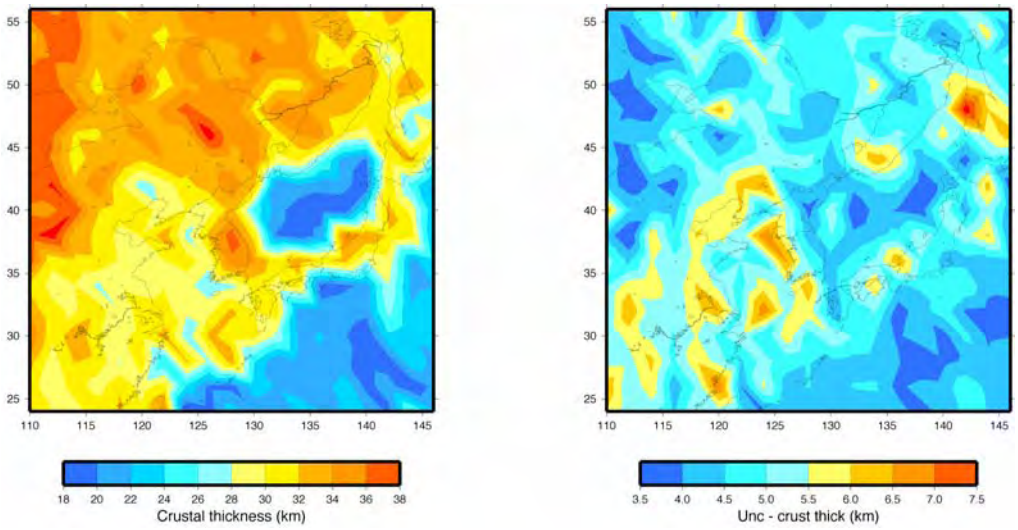

Figure 6. A crustal thickness map of the YSKP region determined using stochastic inversion methods, along with its associated uncertainties.

We also use this model to predict waveforms using a spectral element model (Komatitsch et al., 2002). Figure 7 shows a comparison of waveforms along a path from an event in the Liaodong Peninsula in China to station BJT in Beijing. Waveforms were calculated for the 1D PREM model (Dziewonski and Anderson, 1981), the CRUST2.0 (Bassin et al., 2000) model with S20RTS (Ritsema et al., 1999) mantle, the CUB2.0 model (Shapiro and Ritzwoller, 2002), and the mean MCMC model (Pasyanos et al., 2005). Unsurprisingly, the waveforms generated using the PREM model do not fit the data. The CRUST2.0 and CUB2.0 models both fit the early arrivals but neither model fits the late arriving energy. The MCMC model, however, which has thicker sediments along the profile, fits more of the waveform.

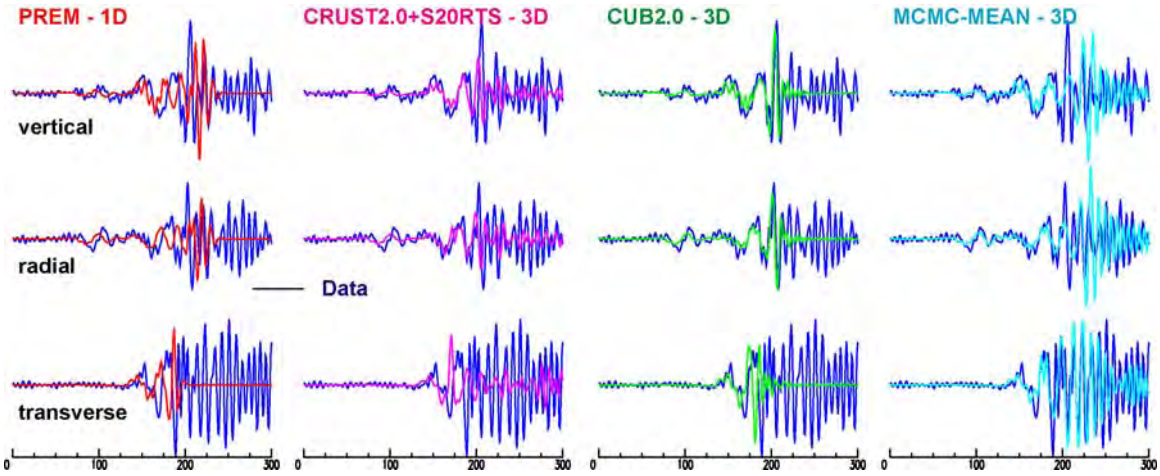

Figure 7. Waveforms for a path in eastern China generated using the spectral element method for models PREM (red), CRUST2.0 and S20RTS (magenta), CUB2.0 (green), and the MCMC method (cyan), and compared with data (blue).

In short, stochastic methods are an innovative technique for producing next-generation data-driven models. *A priori* models can be used as starting models for the inversion. Other model information such as surface wave dispersion measurements, teleseismic receiver functions, and regional body wave travel times (shown in the first three sections) can be included as additional constraints. Stochastic models have a number of advantages compared to traditional models, such as the ability to reconcile different types of geophysical data. An important component of this is the ability to predict new observables with proper uncertainties.

CONCLUSIONS AND RECOMMENDATIONS

Geophysical models are an important way of calibrating regions in the absence of direct measurements. Models can be a repository for a vast array of geological and geophysical datasets of all types—receiver functions, refraction profiles, tomographic inversions, travel time models, amplitude measurements, etc. This product integrates results from many sources and can be used to incorporate future results from current research.

Geophysical model research at LLNL has developed along a number of lines. We have developed a 3-D geophysical model for Western Eurasia and North Africa, along with sophisticated access tools, which are directly usable for generating a number of geophysical parameters of interest. The surface wave measurements and model for greater Eurasia, receiver functions throughout the region provide additional model constraints, and tomographic models can be used to predict regional travel times. We are now moving toward developing data-driven geophysical models that can use all of these results to produce reliable geophysical models.

REFERENCES

Bassin, C., G. Laske, and G. Masters, (2000), Current limits of resolution for surface wave tomography in North America, *EOS Trans AGU* 81: F897.

Dziewonski A.M., and Anderson D.L. (1981), Preliminary reference Earth model. *Physics of the Earth Planetary Interiors* 25: 297-356.

Johnson, M. and C. Vincent (2002), Development and testing of a 3-D velocity model for improved event location: a case study for the India-Pakistan region, *Bull. Seism. Soc. Amer.* 92: 2893-2910.

Komatitsch, D., J. Ritsema, J. Tromp (2002), The spectral-element method, Beowulf computing, and global seismology, *Science* 298: 1737-1742.

Laske, G. and T.G. Masters (1997), A global digital map of sediment thickness, *EOS Trans. AGU* 78: F483.

Pasyanos, M. E., W. R. Walter, S. E. Hazler (2001), A surface wave dispersion study of the Middle East and North Africa for monitoring the Comprehensive nuclear-test-ban Treaty, *Pure and Applied Geophysics* 158: 1445-1474.

Pasyanos, M. E., W. R. Walter, M. P. Flanagan, P. Goldstein and J. Bhattacharyya (2004), Building and testing an a priori geophysical model for western Eurasia and North Africa, *Pure and Applied Geophysics*, 161, 235-281.

Pasyanos, M.E. (2005), A variable-resolution surface wave dispersion study of Eurasia, North Africa, and surrounding regions, submitted to *J. Geophys. Res.*

Pasyanos, M.E., G.A. Franz, and A.L. Ramirez (2005), Reconciling a geophysical model to data using a Markov Chain Monte Carlo algorithm: An application to the Yellow Sea – Korean Peninsula region, submitted to *J. Geophys. Res.*

Ritsema, J., H. J. van Heijst, and J. H. Woodhouse (1999), Complex shear wave velocity structure imaged beneath Africa and Iceland, *Science* 286: 1925-1928.

Russell, D.R. (2004), Theoretical analysis of narrow-band surface wave magnitudes, AFTAC report AFTAC-TR-04-004, 42 pp.

Shapiro, N.M. and M.H. Ritzwoller (2002), Monte-Carlo inversion for a global shear velocity model of the crust and upper mantle, *Geophys. J. Int.* 151: 88-105, 2002.

Shapiro, N.M., M. Campillo, L. Stehly, and M.H. Ritzwoller (2005), High resolution surface wave tomography from ambient seismic noise, *Science* 307(5715): 1615-1618.

ASSESSING UNCERTAINTIES IN WAVEFORM MODELING OF THE CRUST AND UPPER MANTLE

Jay Pulliam and Mrinal K. Sen
University of Texas at Austin

Sponsored by Air Force Research Laboratory

Contract No. FA8718-04-C-0014

ABSTRACT

We developed and calibrated a synthetic seismogram code based on the reflectivity method for use in a distributed PC cluster and incorporated it into a global optimization algorithm for fitting seismic waveforms. Parallelization can be done either over frequencies or ray-parameters since each frequency or the ray-parameter component can be computed independently. There is very little communication overhead resulting in nearly linear speed-up in computation time with the number of processors used, so a larger cluster and/or faster processors will further increase computation speed significantly.

We applied the modeling code to observations of S, Sp, SsPmP, and SPL recorded for deep earthquakes located at distances of 31°–59° from stations of the China Digital Seismographic Network (CDSN) and focused on estimating uncertainties using the products of the broad search conducted by our variant of simulating annealing (SA). The SA variant used in our waveform-fitting process speeds up modeling by drawing each new model from a temperature dependent Cauchy-like distribution centered on the current model. This change with respect to SA has two fundamental effects. First, it allows for larger sampling of the model space at the early stages of the inversion and much narrower sampling in the model space as the inversion converges and the temperature decreases, while still allowing the search to escape from local minima. Second, each model parameter can have its own cooling schedule and model-space sampling scheme. In our case, each modeling run performs roughly a thousand iterations of forward calculations.

Multiple modeling runs can be used to obtain quick estimates of the posterior probability distribution (PPD) that give fairly accurate estimates of posterior model covariances and correlation, although individual variances may be underestimated. We used multiple simulated annealing runs to estimate the marginal PPD, the mean and posterior covariances and explored their utility in interpreting modeling results. The broad search of the model space conducted by simulated annealing, combined with analyses of sensitivity, resolution, and uncertainty, allows tradeoffs between model parameters to be evaluated, which helps build confidence in the final models.

OBJECTIVES

Our research focuses on developing and testing methods for determining event locations at regional distances (100-1000 km) using one or a few three-component, broadband seismographic stations. To be useful for discriminating explosions from earthquakes, focal depths must be determined accurately to within a few kilometers, yet the structure of the crust and upper mantle between the source and station strongly influences the arrival times and amplitudes of regional phases. Our first task, therefore, is to determine this structure. We will attempt to obtain a sufficiently accurate model of crustal structure beneath a given station by searching over a wide variety of crustal models to find the one whose synthetics best match the amplitudes and travel times of phases that arrive in the time window around the direct S phase, and which appear most strongly on the radial component seismogram. We use data from large-magnitude (6<Mb<7) deep events located at teleseismic distances for this purpose, for reasons discussed in detail below.

After structural models are in hand we propose to find focal depths by means of a waveform correlation technique. We will compute suites of synthetic seismograms for the candidate model corresponding to a given broadband station and, given data from small-magnitude regional events recorded at the same station, compute correlations between the suites of synthetic seismograms generated for a variety of distances and focal depths.

Case studies around the world, including application to "ground-truth" data in which focal depths are well constrained, are required in order to determine the range of applicability and usefulness of our event location strategy. Small magnitude events (2<mb<4) are rarely recorded at more than a few stations in many parts of the world, yet identifying these events is essential to monitoring nuclear explosions effectively. Our objective, therefore, is to develop and test methods for distinguishing between explosions and natural events in sparsely-instrumented parts of the world. Our strategy is to estimate hypocenter locations for small- and moderate-magnitude events using one or a few single broadband, three-component stations. Focal depth is a particularly helpful discriminating characteristic, if determined reliably.

BACKGROUND

The problem of finding earthquake locations using only a single three-component station, or a very sparse network of stations, has received a great deal of attention. Some authors, recognizing the greater difficulty in constraining focal depths, have focused on estimating event epicenters and origin times (e.g., Magotra et al., 1987; Roberts et al., 1989; Kedrov and Ovtchinnikov, 1990; Kim and Wu, 1997). Others have attempted to estimate not only focal depths but focal mechanisms, as well, via waveform modeling of regional events (Jimenez et al., 1989; Fan and Wallace, 1991; Zhao and Helmberger, 1994; Walter, 1993; Zhu and Helmberger, 1996). Frohlich and Pulliam (1999) review efforts to locate earthquakes using a single three-component station in detail. In contrast, the problem of determining earthquake focal depths with one or a few stations has received far less attention, yet obtaining accurate estimates of focal depths is important to tectonic interpretations of seismicity, to understanding seismic hazard, and to seismic monitoring of underground nuclear tests (National Research Council, 1997). If a seismic event were known reliably to have occurred at a depth greater than a few kilometers, one could confidently categorize that event as an earthquake rather than an explosion.

The most common approaches to determining focal depths utilize travel times (e.g., Douglas, 1967), which must be picked for the major seismic phases and then back-projected by a nonlinear or bootstrapped linear algorithm. A great deal of effort has been devoted to methods for picking arrival times automatically (Roberts et al., 1989; Saari, 1991). While these methods have proven useful for moderate to large magnitude events at far-regional and teleseismic distances, particularly for events that are deeper than a few tens of kilometers, they are prone to picking errors. These picking errors become relatively more important and more problematic for location procedures when dealing with small magnitude and shallow events. Furthermore, shallow events have little time separation between the downgoing, direct body wave phases and the upgoing, reflected ("depth") phases that are most useful for constraining focal depth. One must use high-frequency data to have any hope of identifying and picking distinct arrivals for these phases, which again complicates the picking process and increases the likelihood that errors will contaminate the location process. In some parts of the world, small-magnitude and relatively shallow events observed at regional distances typically have emergent rather than impulsive first arrivals, which renders travel time picking even more prone to errors. Lastly, reliable estimates of both epicenters and focal depths using travel times require redundancy, i.e., at least several and preferably many recordings from stations that are well-distributed with respect to azimuth around the event. But the great majority of earthquakes are small-magnitude, shallow events, which are much more likely than large events to be recorded by just one or a few seismographic stations. Locating

these small events accurately can be most useful for discriminating between nuclear explosions and earthquakes and can contribute a great deal to understanding regional tectonics.

Waveform modeling offers the best hope for constraining small-magnitude, shallow seismic events at regional distances with sparse observations. Ideally one would be able to match, and thereby determine the origin of, the time and amplitude of each arriving wave. Such a match is an unrealistic goal, in general, due to approximations required for tractability in modeling algorithms, to an incorrect or inadequately precise understanding of the crust and upper mantle in most regions, and to poor constraints on focal mechanisms and source time functions. While approaches such as finite difference methods offer hope for accurate and computationally feasible 3D modeling in the relatively near future, to be useful they will require far more precise and accurate velocity models than are currently available. Assuming that accurate 3D, or even 2D, modeling is currently out of reach, the question that arises is whether 1D modeling methods can be used in a strategy that minimizes the effects of laterally-varying structure and focal mechanism to constrain the focal depths of seismic events. Presenting and evaluating such a strategy are the goals of our research. Rather than matching direct and reflected pulse shapes, as do Goldstein and Dodge (1999) for larger magnitude (mb>=4.5) and more distant events, we seek to match some gross characteristics, such as the relative arrival times of a series of waves, as well as possible.

Producing 1D models that are sufficiently accurate to constrain focal depths of small events

Phases that arrive near the direct SV phase, including Sp (converted at the base of the Moho), SsPmP, and shear-coupled PL (SPL) waves, collectively sample the Earth's crust and upper mantle at oblique angles and therefore have the potential to produce an accurate lateral average of structural properties than teleseismic P waves. SPL waves essentially mimic the propagation characteristics of regional PL phases, with the important difference that the number of events available for modeling is often greater for relatively aseismic regions, since sources are located at teleseismic distances. SPL waves are sensitive to crust and upper mantle structure, including seismic velocity gradients, Vp/Vs, impedance contrast across the Moho, and layer thicknesses.

The conventional S phase (Figure 1) is the initial, relatively sharp and pulse-like arrival that signals the beginning of a wavetrain with generally longer periods and normal dispersion. The particle motion associated with the S phase is rectilinear and all three components of motion are in phase. The dispersive wavetrain that follows S exhibits prograde elliptical particle motion that is confined to the vertical plane. Oliver (1961) named this wavetrain "shear-coupled PL" because it is analogous to the PL wavetrain, which appears between P and S arrivals at regional distances. Oliver (1961) presented a theory, based on the observed group and phase velocity of SPL, that explained the phase as coupling between S and the fundamental leaking mode of Rayleigh waves in the crustal waveguide.

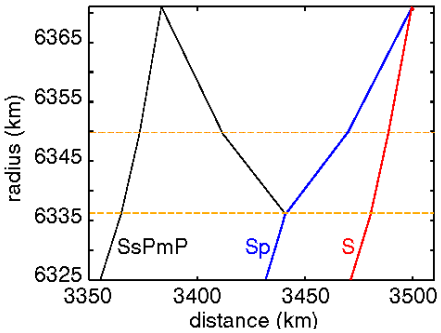

Figure 1. Typical raypaths for S, Sp, and SsPmP. These body wave phases provide constraints on crustal thickness, P and S velocities near the station.

According to this theory, shear energy generated by an earthquake (or explosion) travels through the Earth's mantle as a body wave, whereupon it impinges upon the Moho. Afterward a portion travels through the crustal waveguide as trapped P-waves and leaky SV-waves (Figure 2). The only difference between a PL phase, which is observed at regional distances from a source, and SPL phases, which are observed at teleseismic distances, is that SPL is generated by a shear wave impinging upon the Moho at regional distances from the observing station. In addition to producing SPL as it impinges on the Moho, a portion of the incident S wave converts to P as well, which then travels through the crust to arrive at the station as a precursor to S (Figures 1 and 3). This phase is called Sp and it has been used to model the crust by Jordan and Frazer (1975). Its sampling is much more localized to the station than is SPL's, making its sensitivity less representative of the broader region and more similar to that of P-coda

receiver functions. SsPmP arrives at the base of the crust as a shear wave, travels upward through the crust as a shear wave, converts to a P wave at its surface reflection and bounces once off the Moho as a P wave. Langston (1996), while demonstrating that it can be highly useful for regional crustal modeling, showed that SsPmP can arrive before or after direct S, with either larger or smaller amplitude, and can also distort the S arrival pulse. We will attempt to simultaneously model S, Sp, and SsPmP which essentially isolates differences to the P structure of the crust, for data collected for SPL modeling. Because receiver function methods typically deconvolve the vertical seismogram, which is most sensitive to compressional wave energy, from the radial seismogram, constraints on P velocity are essentially sacrificed in order to obtain clean records of shear phases. The data we propose to model will provide a valuable check of receiver functions, in that they constrain the bulk properties of the crust—average P velocity and

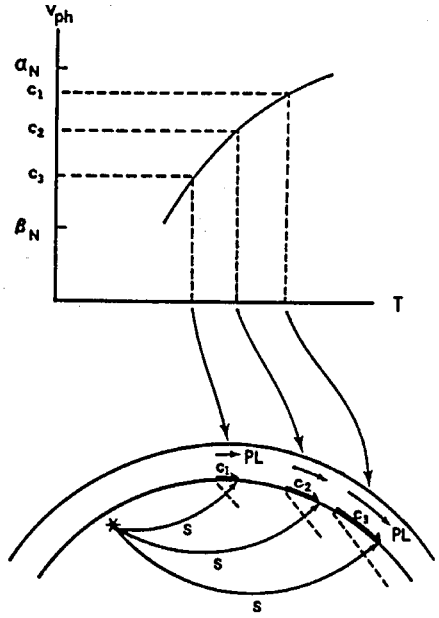

Excitation of *SPL*-waves with distance and corresponding period–phase velocity curve. α_N, β_N: velocities of *P*- and *S*-waves at the Moho, *T*: period, V_{ph}: phase velocity.

Figure 2. Propagation characteristics of shear-coupled PL phases (from Baag and Langston, 1985). Note that the distance of propagation of SPL, and therefore its sampling, depends on characteristics of the velocity structure, including the slope of velocities below the Moho and attenuation. The earliest-arriving and largest-amplitude SPL waves are those that have converted from S nearest to the station, so our modeling will weight local sampling more highly than distant sampling but the wavefield still averages structure laterally.

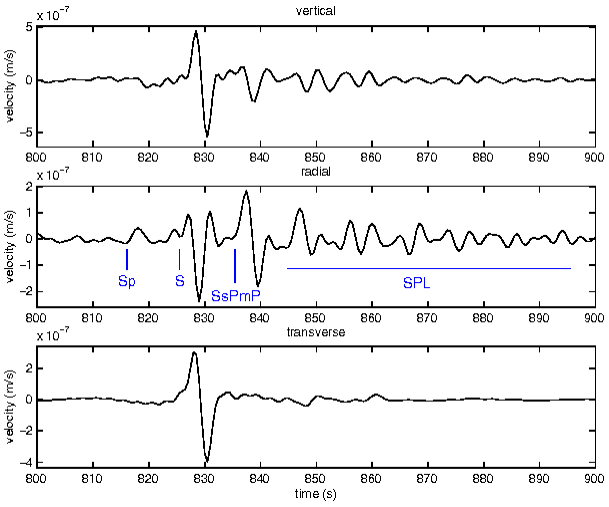

Figure 3. Depending on Earth structure and an earthquake's radiation pattern, the phases Sp, S, SsPmP, and SPL may appear prominently on the radial component seismogram at distances between 30° and 75°.

We are evaluating the usefulness of S, Sp, SsPmP (Figures 1 and 3), and shear-coupled PL (SPL) phases (Figures 2 and 3) for modeling crustal and upper mantle structure using real and synthetic data, developing a waveform inversion technique based on a novel implementation of the reflectivity method and global optimization algorithms, and applying this method to data recorded in China. We have made substantial progress in speeding up the synthetic seismogram computations to the point where a global optimization is feasible. The reflectivity calculation involves computation of reflectivity matrices for a stack of layers as a function of ray parameter (or wavenumber) and frequency. The computation of reflectivity responses for different ray parameters and frequencies are completely independent of each other. We took advantage of this independence to develop a reflectivity code that runs on parallel computer architectures. Our code loops over ray parameters, i.e., to each node we assign a certain number of ray parameters to compute. At the end, the master node assembles the partial responses and performs the inverse transformation to generate synthetic seismograms at the required azimuths and distances. We used MPI for message passing and ran our code on a PC cluster consisting of 16 nodes; each node is a 660MHz alpha processor with 8MB cache and 1GB of RAM. A Myrinet interconnect is used to communicate between nodes.

Figure 3 shows synthetic seismograms computed using our parallelized reflectivity code for a distance of 50° and an earthquake at 600 km focal depth. Since the reflectivity algorithm is "embarrassingly parallel" in that the response for each frequency or ray parameter can be computed on independent processors, without communication between processors, on a parallel machine computation speed increases nearly linearly with the number of processors. In a side-by-side comparison for various distances, source depths, and model complexity, our code matched results of the Fuchs-Muller code very well.

Our modeling method retains the time and cost advantages of P-coda receiver function methods but which uses types of data that are more appropriate for CTBT purposes: Shear-coupled PL phases (SPL), Sp phases converted at the Moho, and SsPmP. SPL samples the crust and upper mantle in the vicinity of a station most broadly compared to Sp, SsPmP and P and it emulates the propagation of regional phases, which reflect at more oblique angles (or are refracted by these layers) than are the more steeply arriving body phases typically used in receiver function modeling. In short, because of the data they use, the models produced by receiver function methods may be inadequate for the purposes of CTBT monitoring. These latter phases sample only a narrow cone beneath the station (e.g., Zhao and Frohlich, 1996). Modeled simultaneously (where they exist), SPL, Sp, and SsPmP offer the potential for producing azimuthally-dependent structural models.

We are pursuing this strategy because efforts to determine the locations of small, regional seismic events are hampered, in most parts of the world, by insufficient knowledge of the crust and upper mantle. Also, while focal depths are often a highly useful discriminant between explosions and earthquakes, their determination is quite sensitive to crustal structure. The most encouraging approaches to determining focal depths require precise modeling of seismic waveforms, particularly for small-magnitude events, in which travel time picks are relatively more prone to errors than for larger events. Yet, a precise modeling of waveforms at regional distances requires an accurate model of the crust and upper mantle along the propagation path between source and receiver.

RESEARCH ACCOMPLISHED

Results of the forward modeling code and the increase in computational speed that followed its parallelization, as well as examples of the optimization algorithm driven by simulated annealing, were reported previously. Here we will describe our efforts to assess the uncertainties associated with estimates of velocity structure using products derived from the global search.

Our modeling process is controlled by a global optimization algorithm called Very Fast Simulated Annealing (VFSA) (e.g., Sen and Stoffa, 1995). Simulated annealing (SA) is analogous to the natural process of crystal annealing when a liquid gradually cools to a solid state. The SA technique starts with an initial model m_0, with associated error or energy $E(m_0)$. It draws a new model m_{new} from a flat distribution of models within the predefined limits. The associated energy $E(m_{new})$ is then computed and compared against $E(m_0)$. If the energy of the new state is less than the energy of the initial state, the new model is accepted and it replaces the initial model. However, if the energy of the new state is higher than the initial state, m_{new} is accepted with the probability of $\exp\left(\left(E(\mathbf{m}_{new}) - E(\mathbf{m}_0)\right)/T\right)$, where T is a control parameter called temperature. This rule of probabilistic acceptance (called the Metropolis rule) allows SA to escape local minima. The process of model generation and acceptance is repeated a large number of times with the annealing temperature gradually decreasing according to a predefined cooling schedule. A variant of SA, called Very Fast Simulated Annealing (VFSA) speeds up the annealing process

by drawing new models from a temperature dependent Cauchy-like distribution centered on the current model. This change with respect to SA has two fundamental effects.

First, it allows for larger sampling of the model space at the early stages of the inversion (when "temperature" is high), and much narrower sampling in the model space as the inversion converges and the temperature decreases, while still allowing the search to escape from local minima.

Second, each model parameter can have its own cooling schedule and model-space sampling scheme. VFSA therefore allows for individual control of each parameter and the incorporation of a priori information. The model is parameterized in terms of layers, in which Vp, Vs, density, and layer thickness are free parameters.

In seismic inversion, more than one model can often explain the observed data equally well and trade-offs between different model parameters are common. It is therefore important not only to find a single, best-fitting solution but also to find the uncertainty and level of uniqueness of that solution. A convenient way to address these issues is to cast the inverse problem in a Bayesian framework (e.g., Tarantola, 1987; Sen and Stoffa, 1995) in which the posterior probability density function (PPD) is the answer to the inverse problem. "Importance sampling" based on a Gibbs sampler or a Metropolis rule (Sen and Stoffa, 1998) can be used effectively to evaluate the necessary multidimensional integrals and to estimate PPD, posterior mean, covariance and correlation matrices. The posterior covariance and correlation matrices quantify the trade-off between different model parameters. Sen and Stoffa (1995) showed that multiple VFSA runs with different random starting models could be used to sample models from the most significant parts of the model space. This "poor man's" importance sampling, which is computationally efficient, results in estimates that are fairly close to the values obtained by theoretically-correct Gibbs sampling.

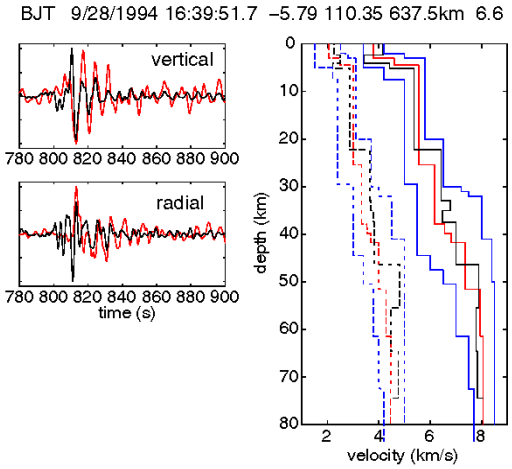

Figure 4. Optimization results after 600 iterations for fitting synthetics (black) to BJT vertical and radial records (red) of a deep earthquake in Indonesia. Best-fitting model (black), search bounds (blue), and receiver function model by Mangino et al. (1999) (red).

Figure 4 shows an example models produced for China using data from the China Digital Seismograph Network. For this example, depth zones A, B, and C in Figure 5 correspond to parameter correlations indicated by the same labels in Figure 6. Note that the thin, shallow layers in A are characterized by significant off-diagonal cross-correlations (trade-offs) with other parameters. This indicates that the data do not constrain these layers well. Also, the symmetric "variances" about the mean (actually 1 standard deviation) do not contain the best-fitting model at this depth, pointing to the non-linearity of the inverse problem. We defined the prior to be Gaussian, so the computed (posterior) variances are also symmetric, but the fact that the best-fitting model lies outside this distribution suggests that the true distribution is skewed. Zone B, in contrast, contains a low-velocity zone in Vs that appears to be well-constrained (Figure 5). There is no corresponding Vp low-velocity zone.

Results for Zone C suggest that the data do not place strong constraints on the model parameters at these depths, on the one hand. However, since the best-fitting model is pegged against the search limits for both Vp and Vs, we will widen the search limits and perform a greater number of VFSA iterations to explore this zone further.

CONCLUSIONS AND RECOMMENDATIONS

We are increasingly confident that S, SsPmP, Sp, and SPL phases, with their unique sensitivity to Earth structure, and the global search driven by simulated annealing offer strong constraints on P and S wave models of the crust, Moho, and upper mantle. However, the proof will be in its application to earthquake and/or explosion locations.

We intend to streamline the modeling method, from raw data to models, and to calibrate and evaluate its accuracy by locating earthquakes with well-constrained hypocenters from the Ground Truth Database in these models. In order to take advantage of the GTDB, we will need to apply the modeling method more broadly around the world. The streamlining—building a software front-end to take raw broadband data, associate it with an event, deconvolve instrument response, rotate into radial and transverse horizontal components, filter, window, and model—will allow us to evaluate both modeling and assessment tools more rigorously. Our medium-term goal, therefore, is to apply the method to additional data sets for which moderate-sized earthquakes have been located with confidence by others. Once we find several locations in which the method produces models that result in fairly accurate earthquake locations, we will compare the model uncertainty assessments that correspond to accurate earthquake locations to the assessments that correspond to the models used for poorly-located events. This comparison will, hopefully, provide insight into the usefulness of the PPD and covariance estimates and perhaps a calibration and a guide to their use.

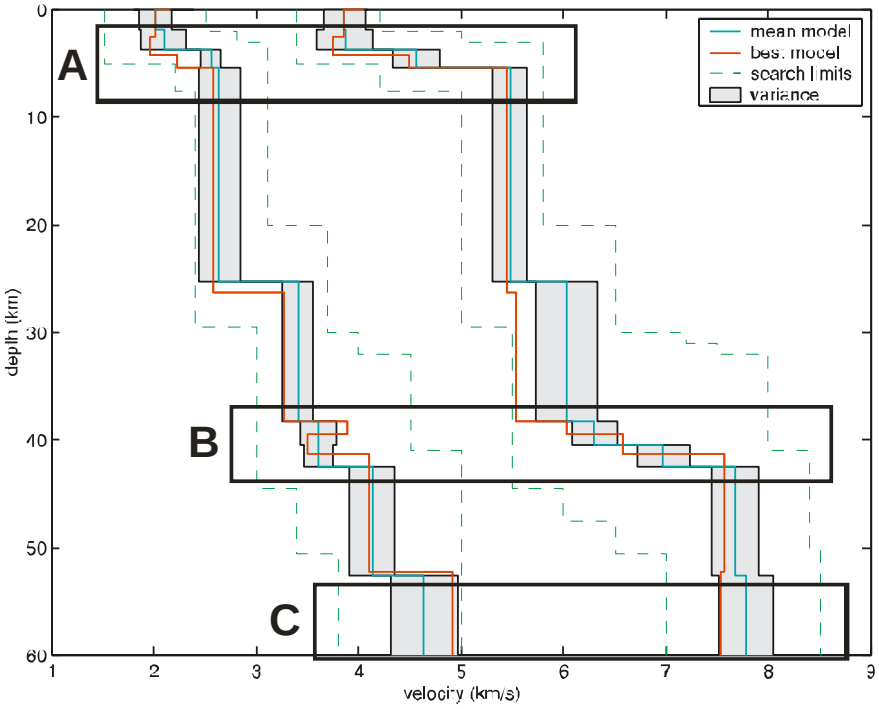

Figure 5. Mean (cyan) and best-fitting (red) models and variance of the optimization run shown in Figure 8. Search limits imposed by the operator at the outset are shown in green. Variances are only shown for Vs (left) and Vp (right).

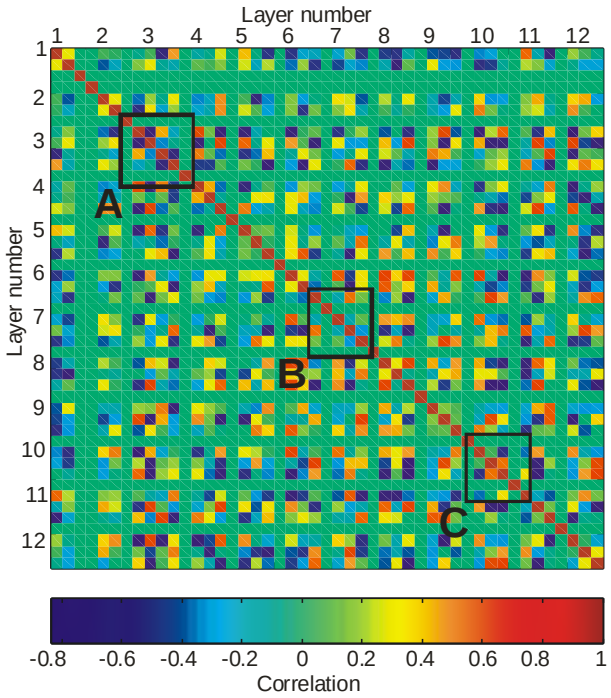

Figure 6. Parameter correlations computed for the optimization run shown in Figure 15. There are four independent parameters: Vp, Vs, layer thickness, and density, repeated in that order for 12 layers. The total of 48 parameters is shown here in color (left) and with a modified grayscale, in which zero correlation is white and perfect positive and negative correlations are both black (right).

REFERENCES

Baag, C. E. and C. A. Langston (1985), Shear-coupled PL, *Geophys. J. R. Astr. Soc.* 80: 363-385.

Beckers, J., S. Schwartz, and T. Lay (1994), *Geophys. J. Int*. 119, 574-594, 1994

Douglas, A. (1967). Joint hypocentral determination, *Nature*, 214, 47-48.

Dziewonski, A. M., Anderson, D. L. (1981), Preliminary reference Earth model, *Phys. Earth. Planet. Int.* 25: p. 297-356, 1981.

Fan, G. and T. Wallace (1991). The determination of source parameters for small earthquakes from a single, very broadband seismic station, *Geophys. Res. Lett.* 18: 1385-1388.

Frazer, L. N. (1977), Synthesis of shear coupled PL. *Ph.D. thesis*, Princeton University, 54 pp.

Frohlich, C., and J. Pulliam (1999). Single-station location of seismic events: A review, and a plea for more research, *Phys. Earth Planet. Int.* 113: 277-291.

Goldstein, P., and D. Dodge (1999). Fast and accurate depth and source mechanism estimation using P-waveform modeling: A tool for special event analysis, event screening, and regional calibration, *Geophys. Res. Lett.* 26: 2569-2572.

Grand, S. P., and D. Helmberger (1984), Upper mantle shear structure of North America, Geophys. *J. R. Astr. Soc.* 76: 399-438, 1984

Jimenez, E., M. Cara, and D. Rouland (1989), Focal mechanisms of moderate-size earthquakes from the analyusis of single-station three-component surface-wave records, *Bull. Seism. Am.* 79: 955-972.

Jordan, T. H., and L. N. Frazer (1975), Crustal and upper mantle structure from Sp phases, *J. Geophys. Res*. 80: 1504-1518.

Kedrov, O. K., and V. M Ovtchinnikov (1990), An on-line analysis system for three-component seismic data: Method and preliminary results, *Bull. Seism. Am.* 80: 2053-2071.

Kim, S. G. and Z. Wu (1997), Uncertainties of seismic source determination using a 3-component single station, *J. Phys. Earth* 45: 1-11.

Langston, C. A. (1996), The SsPmP phase in regional wave propagation, *Bull. Seism. Soc. Am.* 86: 133-143.

Magotra, N., N. Ahmed and E. Chael (1987), Seismic event detection and source location using single-station (three-component) data, *Bull. Seism. Soc. Am.* **77**: 958-971.

Mangino, S., K. Priestley, and J. Ebel, The receiver structure beneath the China Digital Seismograph Network Station, *Bull. Seism. Soc. Am.*, 89, 1053-1076, 1999

National Research Council (1997), Research Required to Support Comprehensive Nuclear Test Ban Treaty Monitoring, National Academy Press, Washington, D. C., 139 pp.

Oliver, J (1961), On the long period character of shear waves, *Bull. Seism. Soc. Am.* 51: 1-12.

Roberts, R. G., A. Christoffersson and F. Cassidy (1989). Real-time event detection, phase identification and source location estimation using single-station three-component seismic data, *Geophys. J.* 97: 471-480.

Saari, J. (1991). Automated phase picker and source location algorithm for local distances using a single three-component seismic station, *Tectonophysics*, 189: 307-315.

Sen, M., and P. L. Stoffa, 1995, *Global Optimization Methods in Geophysical Inversion*, Elsevier Science Publishing Company, The Netherlands.

Sen, M. K., and P. L. Stoffa, 1996, Bayesian inference, Gibbs' sampler and uncertainty estimation in geophysical inversion, *Geophysical Prospecting*, 44: 313-350.

Tarantola, A. (1987), *Inverse Problem Theory: Methods for Data Fitting and Model Parameter Estimation*, 613 pp., Elsevier, Amsterdam.

Walter, W. R. (1993). Source parameters of the June 29, 1992 Little Skull Mountain earthquake from complete regional waveforms at a single station, *Geophys. Res. Lett.* 20: p. 403-406.

Zhao, L. S., D. Helmberger, and D.V. Harkrider (1991), *Geophys. J. Int.* 105: 713-730.

Zhao, L. S. and C. Frohlich. Teleseismic body waveforms and receiver structures beneath seismic stations, *Geophys. J. Int.* 124: 525-540, 1996.

Zhu, L. and D.V. Helmberger (1996). Advancement in source estimation techniques using broadband regional seismograms, *Bull. Seism. Soc. Am*, 86: 1634-1641.

SHORT PERIOD SURFACE WAVE DISPERSION MEASUREMENTS FROM AMBIENT SEISMIC NOISE IN NORTH AFRICA, THE MIDDLE EAST, AND CENTRAL ASIA

Michael H. Ritzwoller[1], Nikolai M. Shapiro[1], Michael E. Pasyanos[2], Gregory D. Bensen[1], and Yingjie Yang[1]

University of Colorado at Boulder[1] and Lawrence Livermore National Laboratory[2]

Sponsored by National Nuclear Security Administration
Office of Nonproliferation Research and Engineering
Office of Defense Nuclear Nonproliferation

Contract Nos. DE-FC52-05NA26607[1] and W-7405-ENG-48[2]

ABSTRACT

We have begun to apply ambient noise surface wave tomography to broad-band seismic data obtained in North Africa, the Middle East, and Central Asia. The goal is to improve the calibration of surface wave propagation in aseismic areas.

The basic idea of the method is that ambient seismic noise contains a significant component of Rayleigh wave energy that is excited by oceanic microseisms and atmospheric forcing. Rayleigh wave Green functions can be extracted by computing cross-correlations between records by using observations over several days or months at pairs of seismic stations. Group velocities are then measured by applying frequency-time analysis to the waveforms emerging from the cross-correlations and traditional surface wave tomography is then performed.

The method was first systematically applied in California where cross-correlating one month of ambient seismic noise yielded hundreds of short-period (5 sec - 18 sec) surface-wave group-velocity measurements that have been used to construct tomographic images reflecting the principal geological units within California. More recently, we have applied the method at larger spatial scales and longer periods by computing cross-correlations and making surface-wave group velocity measurements for paths connecting more than one hundred broadband stations in North America. This is now producing thousands of broad-band group velocity measurements (10 sec - 150 sec) for stations separated by several hundred to a few thousands kilometers.

Here we present the results of the first application of the ambient noise measurement method to broadband seismic data located in North Africa, the Middle East, and Central Asia as a step toward calibrating the propagation of surface waves in this region.

OBJECTIVES

The objective of this research is to obtain short and intermediate period (7 - 30 sec) surface wave dispersion measurements from ambient seismic noise and use these measurements to produce dispersion maps for North Africa, the Middle East, and Central Asia. The ultimate purpose is to improve the calibration of surface wave propagation in aseismic areas and at short periods with particular emphasis on the monitoring and discrimination of small events using the Ms:mb discriminant.

RESEARCH ACCOMPLISHED

Background

Ambient seismic noise is excited by randomly distributed natural and artificial sources and, when considered over sufficiently long times, includes surface waves propagating in all directions. Ambient noise, therefore, contains information about surface wave propagation as well as the elastic structure of the crust and uppermost mantle. This information can be extracted by computing the two-point cross-correlation between noise records from each station pair. The relationship between the cross-correlation and the Green function of the wave propagating between the pair of stations is well established (Weaver and Lobkis, 2001a; Snieder, 2004). The use of ambient noise to extract Green functions has been applied successfully in a number of fields, including helioseismology (Duvall et al., 1993; Kosovichev et al., 2000; Rickett and Claerbout, 2000), ultrasonics (Weaver and Lobkis, 2001a, 2001b, 2002, 2003; Derode et al., 2003a, 2003b), exploration seismology (Schuster et al., 2004; Wapenaar, 2004), and marine acoustics (Roux et al., 2003).

In seismology, two types of signals have been considered to compose random wavefields and utilized to infer Green functions by cross-correlation. Most of the research using both types of random wavefields has been performed using data from North America. The first type of random wavefield is seismic coda, which results from multiple scattering of seismic waves from small-scale inhomogeneities. Campillo and Paul (2003) extracted fundamental-mode Rayleigh and Love waves by correlating coda waves following regional earthquakes in southern Mexico at stations separated by a few tens of kilometers. The second type of wavefield is ambient seismic noise excited by superficial sources such as ocean microseisms and atmospheric disturbances (Lognonne et al., 1998; Tanimoto, 1999; Roult and Crawford, 2000; Fukao et al., 2002). By correlating vertical records of ambient noise at stations separated by distances ranging from about 100 km to more than 2000 km, Shapiro and Campillo (2004) demonstrated that it is possible to extract fundamental mode Rayleigh waves at periods from about 7 sec to more than 100 sec. Similar proof-of-concept results, predominantly at periods below about 20 sec, have been established by Sabra et al. (2005a). Roux et al. (2005) have shown that at much shorter inter-station paths (several 10s of km) crustal P-waves near 1 Hz can also be extracted from cross-correlations. The method has been used to produce group velocity tomography maps between 7 and 20 sec period for Southern California by Shapiro et al. (2005) (see Fig. 1) and Sabra et al. (2005b).

Cross-correlating long time series to produce surface wave Green functions remains in its formative stages and the applications discussed above have been largely proof-of-concept experiments. It is clear, however, that this method possesses several key advantages over tradition surface wave tomography using teleseismic earthquakes. First, the cross-correlation method can be applied to relatively short paths between stations located in aseismic areas which improves resolution in areas that are well instrumented. Second, the new measurements can be extended to periods considerably shorter than 20 sec, which is important for monitoring small seismic events. Third, the new measurements are relatively unaffected by seismic source location and phase and, therefore, are relatively free of these potential sources of bias that affect traditional surface wave measurements. Fourth, the measurements are naturally repetitive and their uncertainties can be estimated by processing different time windows of the noise records.

Application on a Continental Scale Across North America

To date, the application of surface wave ambient noise tomography has been restricted to relatively small regions (notably Southern California) for periods below 20 sec. No results have been published yet on a continental scale or for periods above 20 sec. Even before USARRAY, broad-band data from 125 stations are available across or near

the United States (Fig. 2) from the Incorporated Research Institutions for Seismology (IRIS) Data Management Center (DMC) We are using these stations as a test-bed to develop the cross-correlation method on a continental scale. The fact that broad-band Green functions can be recovered from recordings at stations separated by up to several thousand km was first established by Shapiro and Campillo (2004). An example of cross-correlations for several period bands is shown in Figure 3 for a one month time series observed at two ground station network (GSN) stations (CCM - Cathedral Cave, MO; HRV - Harvard, MA).

The cross-correlograms can be used to measure group speeds between station pairs. Although we are compiling results at shorter and longer periods, we show results here only at 16 sec period. At present, our data set for the United States consists of cross-correlograms stacked over a four month period (Nov. 2003 - Feb. 2004). (Cross-correlograms for longer time series are being computed as this paper is being written.) Group speed measurements are obtained for both positive and negative lags on the cross-correlogram, corresponding to waves propagating in opposite directions between the two stations. In principle, the stations shown in Figure 2 could provide 7750 independent group speed measurements. We require, however, a level of consistency between positive and negative lag measurements and accept measurements only if the signal-to-noise is greater than 10. This reduces the number of acceptable measurements appreciably. For example, at 16 sec period the number of measurements reduces to 4508. These paths are shown in Figure 4a.

The 16 sec group speed measurements obtained on the paths shown in Figure 4a can be used as data in standard surface wave tomography (e.g, Barmin et al., 2001; Ritzwoller et al., 2002). Previous work resulted in a large data set of teleseismic group speed measurements (e.g., Ritzwoller and Levshin, 1998; Ritzwoller et al., 1998; Pasyanos et al., 2001) that has been used to produce a global shear velocity model of the crust and upper mantle (e.g., Shapiro and Ritzwoller, 2002). The 16 sec group speed map from this model (shown in Figure 4b) is used as the reference model for tomography based on more than 4500 group speed measurements obtained by the cross-correlation method. The reference map is then used as a background for the high-resolution tomography. The revised 16 sec group speed map obtained on a 1 ×1 degree grid across the US and adjacent regions is shown in Figure 4c. This map has much higher resolution than the reference map and displays significantly smaller features that in most cases are correlated with known structural features (such as a number of sedimentary basins across the US).

The research on short and intermediate period surface wave tomography from ambient seismic noise is continuing across the US as a guide to the development of the cross-correlation method on a continental scale. A particularly relevant area of further research involves subsetting the input time series to allow error estimates of the measured group speeds.

Preliminary Application Across Eurasia and North Africa

The North American data set is a test-bed for the application of ambient noise tomography to the coarser station coverage that exists on the larger scales of Eurasia. Work has begun to develop a similar data set across much of Eurasia and North Africa. The preliminary station distribution identified for use in this study is shown in Figure 5. The results presented here are for one-month time series acquired in Jan. 2004. At the time of writing, computation of cross-correlations for all stations in the one-month data set have not yet been completed so we show only sample results on the completed subset. The near term goal is to acquire data for all of 2004 and apply ambient noise tomography between 7 sec and 30 sec period.

Early results indicate that ambient noise Green functions across Eurasia have similar signal-to-noise properties as those acquired across North America. Cross-correlations in several pass-bands between stations in China for a single month of data are shown in Figure 6. Examples of typical receiver gathers are shown in Figure 7 for the band between 10 and 20 sec period.

Source of the Broad-Band Signal

More work needs to be done to understand the nature and variability of the ambient noise, although this is beyond the scope of the current contract. The source of ambient noise at periods below 20 sec is probably pretty well understood to be primary (12 - 18 sec) and secondary microseisms (6 - 9 sec) occurring in shallow waters in a several-hundred-km band offshore. The primary microseism results from the direct interaction between the oceanic

surface gravity wave and the seafloor through the exponential decay of pressure with depth. The secondary microseism results from the frequency doubling effect of the nonlinear wave-wave interaction between the incoming and reflected primary surface gravity waves. Although this source mechanism is understood generally, the spatial location and temporal (e.g., seasonal) variability of the source as well as how these waves will be observed across the region of study remains only dimly perceived as is the variation of these variables with wave frequency. More dimly perceived still is the source and nature of the ambient noise at periods longer than the primary microseism band. Presumably, at least until very long periods (i.e., above 150 sec), the source regions will be predominantly oceanic. Whether this is true and what the spatial and temporal distribution of sources are remains unclear. A truly informed application of the cross-correlation method will require the resolution of these questions.

CONCLUSIONS AND RECOMMENDATIONS

(1) Ambient noise surface wave tomography provides higher resolution tomographic images than traditional teleseismic surface wave tomography in regions where inter-station spacing is on average smaller than epicentral distances.

(2) The cross-correlation method yields broad-band Rayleigh wave Green functions on a continental scale both across North America and Eurasia.

Further work continues in the development of error estimates for the measured group speeds using data subsetting, in the development of a year-long data set (2004) for about 120 stations across Eurasia and North Africa, and in the application of ambient noise tomography to data sets from periods ranging from about 7 sec to 30 sec.

ACKNOWLEDGEMENTS

The data used in this work were obtained from the IRIS Data Management Center and include the Global Seismic Network (Butler et al., 2004), GEOSCOPE, and GEOFON data.

REFERENCES

Barmin, M.P., M.H. Ritzwoller, and A.L. Levshin (2001), A fast and reliable method for surface wave tomography, *Pure Appl. Geophys*. 158: (8), 1351 - 1375.

Butler, R., T. Lay, K. Creager, P. Earle, K. Fischer, J. Gaherty, G. Laske, B. Leith, J. Park, M. Ritzwoller, J. Tromp, and L. Wen (2004), The global seismic network surpasses its design goal, *Eos.* 85: (23).

Campillo, M. and A. Paul (2003), Long-range correlations in the diffuse seismic coda, *Science* 299: 547-549.

Derode, A., E. Larose, M. Tanter, J. de Rosny, A. Tourin, M. Campillo, and M. Fink (2003a), Recovering the Green's function from field-field correlations in an open scattering medium, *J. Acoust. Soc. Am*. 113: 2973-2976.

Derode, A., E. Larose, M., Campillo, and M. Fink (2003b), How to estimate the Green's function of a heterogeneous medium between two passive sensors? Application to acoustic waves, *Appl. Phys. Lett*. 83, 3054-3056.

Duvall. T.L., S.M. Jefferies, J.W. Harvey, and M.A. Pomerantz (1993), Time distance helioseismology, *Nature* 362: 430-432.

Fukao, Y., K. Nishida, N. Suda, K. Nawa, and N. Kobayashi (2002), A theory of the Earth's background free oscillations, *J. Geophys. Res*. 107: 2206, doi:10.1029/2001JB000153.

Kosovichev, A.G., T.L. Duvall, and P.S. Scherrer (2000), Time-distance inversion methods, *Solar Phys*. 192: 159-176.

Lognonne, P., E. Clevede, and H. Kanamori (1998), Computation of seismograms and atmospheric oscillations by normal-mode summation for a spherical earth model with realistic atmosphere, *Geophys. J. Int*. 135, 388-406.

Pasyanos, M.E., W.R. Walter, and S.E. Hazler (2001), A surface wave dispersion study of the Middle East and North Africa for monitoring the Comprehensive Nuclear-Test-Ban Treaty, *Pure Appl. Geophys*. 158(8), 1445 - 1474.

Rickett, J.E. and J.F. Claerbout (2000), Calculation of the Sun's impulse response by multi-dimensional spectral factorization, *Solar Phys*. 192, 203-210.

Ritzwoller, M.H. and A.L. Levshin (1998), Eurasian surface wave tomography: Group velocities, *J. Geophys. Res.* 103, 4839-4878.

Ritzwoller, M.H., A.L. Levshin, L.I. Ratnikova (1998), Intermediate period group velocity maps across Central Asia, Western China, and parts of the Middle East, *Geophys. J. Int*. 134, 315-328.

Ritzwoller, M.H., N.M. Shapiro, M.P. Barmin, and A.L. Levshin (2002), Global surface wave diffraction tomography, *J. Geophys. Res.* 107(B12), 2335.

Roult, G. and R. Crawford (2000). Analysis of 'background' free oscillations and how to improve resolution by subtracting the atmospheric pressure signal, *Phys. Earth Planet. Int.* 121, 325-338.

Roux, P., H.C., Song, and W.A. Kuperman (2003), Time-reversal using ambient noise as a probe source, *J. Acoust. Soc. Am.* 113, 2218.

Roux, P., K.G. Sabra, P. Gerstoft, W.A. Kuperman, and M.C. Fehler (2005), P-waves from cross correlation of seismic noise, *Geophys. Res. Lett*., submitted.

Sabra, K.G., P. Gerstoft, P. Roux, W.A. Kuperman, and M.C. Fehler (2005a), Extracting time-domain Green's function estimates from ambient seismic noise, *Geophys. Res. Lett.* 32, doi:10.1029/2004GL021862, 2005.

Sabra, K.G., P. Gerstoft, P. Roux, W.A. Kuperman, and M.C. Fehler (2005b), Surface wave tomography from microseisms in Southern California, *Geophys. Res. Lett*., in press.

Schuster, G.T., J. Yu, J. Sheng, and J. Rickett (2004), Interferometric/daylight seismic imaging, *Geophys. J. Int.* 157, 838-852.

Shapiro, N.M. and M. Campillo (2004), Emergence of broadband Rayleigh waves from correlations of the ambient seismic noise, *Geophys. Res. Lett.* 31, L07614, doi:10.1029/2004GL019491.

Shapiro, N.M. and M.H. Ritzwoller (2002), Monte-Carlo inversion for a global shear velocity model of the crust and upper mantle, *Geophys. J. Int.* 151, 88-105.

Shapiro, N.M. M. Campillo, L. Stehly, and M.H. Ritzwoller (2005), High resolution surface wave tomography from ambient seismic noise, *Science* 307(5715): 1615-1618.

Snieder, R. (2004), Extracting the Green's function from the correlation of coda waves: A derivation based on stationary phase, *Phys. Rev. E* 69, 046610.

Tanimoto, T. (1999), Excitation of normal modes by atmospheric turbulence: source of long-period seismic noise, *Geophys. J. Int.* 136, 395-402.

Wapenaar, K. (2004), Retrieving the elastodynamic Green's function of an arbitrary inhomogeneous medium by cross correlation, *Phys. Rev. Lett.* 93, 254301.

Weaver, R.L. and O.I. Lobkis (2001a), Ultrasonics without a source: thermal fluctuation correlation at MHz frequencies, *Phys. Rev. Lett.* 87, 134301-134304.

Weaver, R.L. and O.I. Lobkis (2001b), On the emergence of the Green's function in the correlations of a diffuse field, *J. Acoust. Soc. Am.* 110, 3011-3017.

Weaver, R.L. and O.I. Lobkis (2002), On the emergence of the Green's function in the correlations of a diffuse field: pulse-echo using thermal phonons, *Ultrasonics* 40, 435-439.

Weaver, R.L. and O.I. Lobkis (2003), Elastic wave thermal fluctuations, ultrasonic waveforms by correlation of thermal phonons, *J. Acoust. Soc. Am.* 113, 2611-2621.

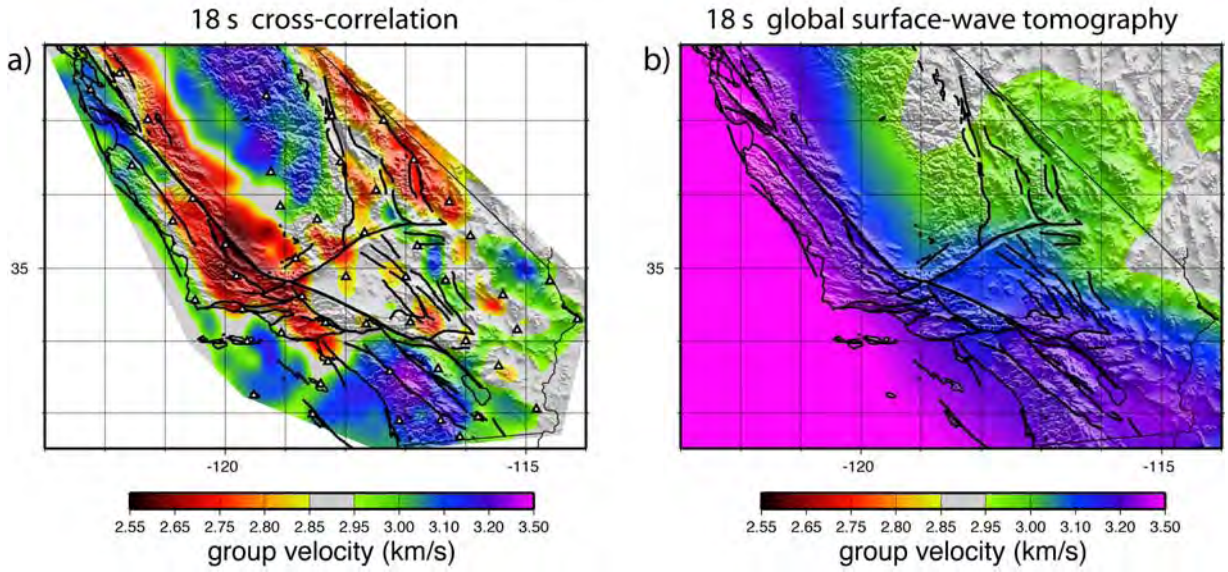

Figure 1. Ambient noise tomography compared with traditional global teleseismic tomography across Southern California. (a) The 18 sec group speed map on a 0.25 degree grid derived from group speeds measured on cross-correlations between 62 USARRAY Transportable Array stations. (b) The 18 sec group speed map derived from global teleseismic tomography, presented for comparison. Ambient noise tomography provides much better lateral resolution than traditional tomography, particularly in the context of a regional array.

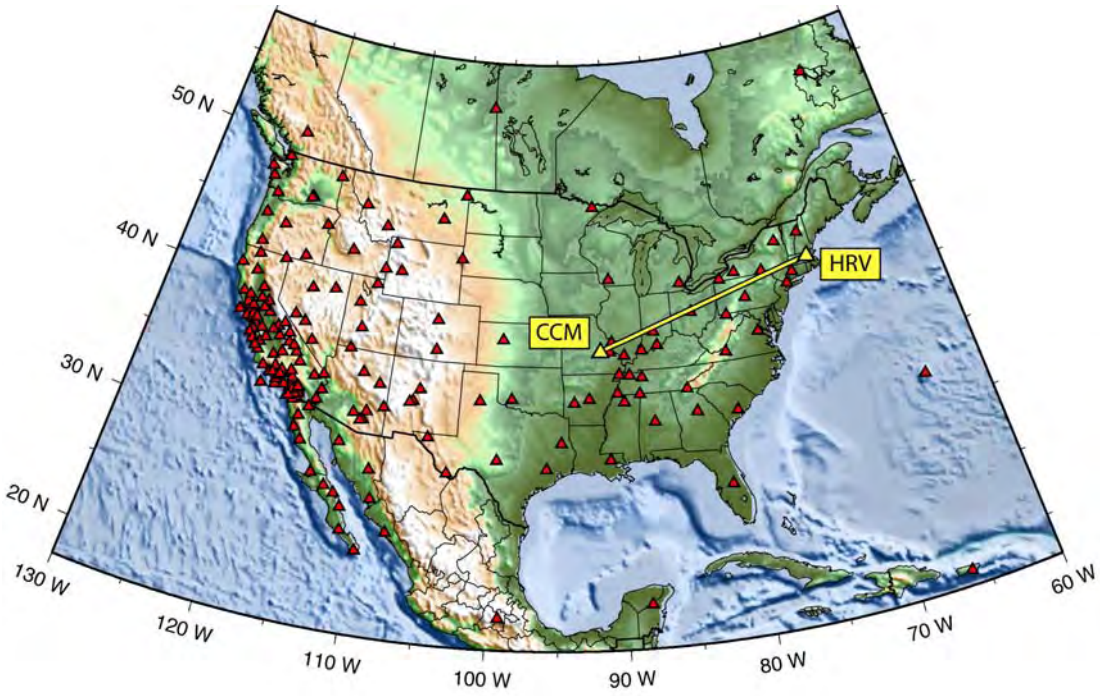

Figure 2. Current backbone network across the US. As a test-bed for continental scale tomography across Eurasia and North Africa, 125 broad-band stations (red triangles) are used within and surrounding the US. The path between GSN stations CCM (Cathedral Cave, MO) and HRV (Harvard, MA) is highlighted, and corresponds to the cross-correlations shown in Figure 3.

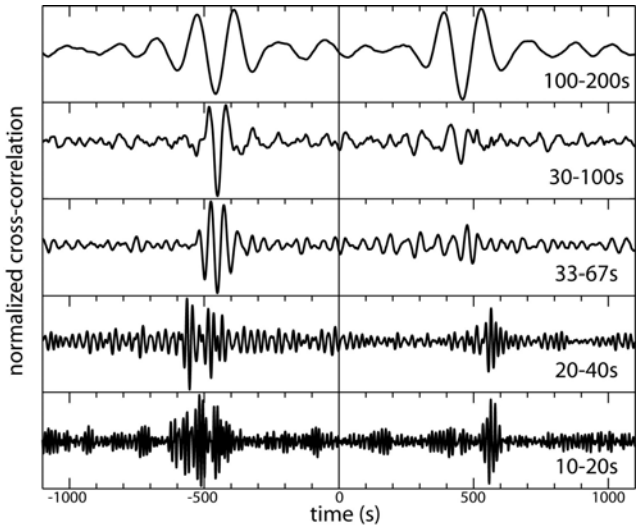

Figure 3. Broad-band cross-correlations between two North American GSN stations: CCM (Cathedral Cave, MO) and HRV (Harvard, MA). The cross-correlations are for 1 month of data from November, 2003. The time axis is the cross-correlation lag (in sec). In this case, positive lag corresponds to waves traveling from CCM to HRV and negative lag to waves from HRV to CCM. The pass band in each case is indicated.

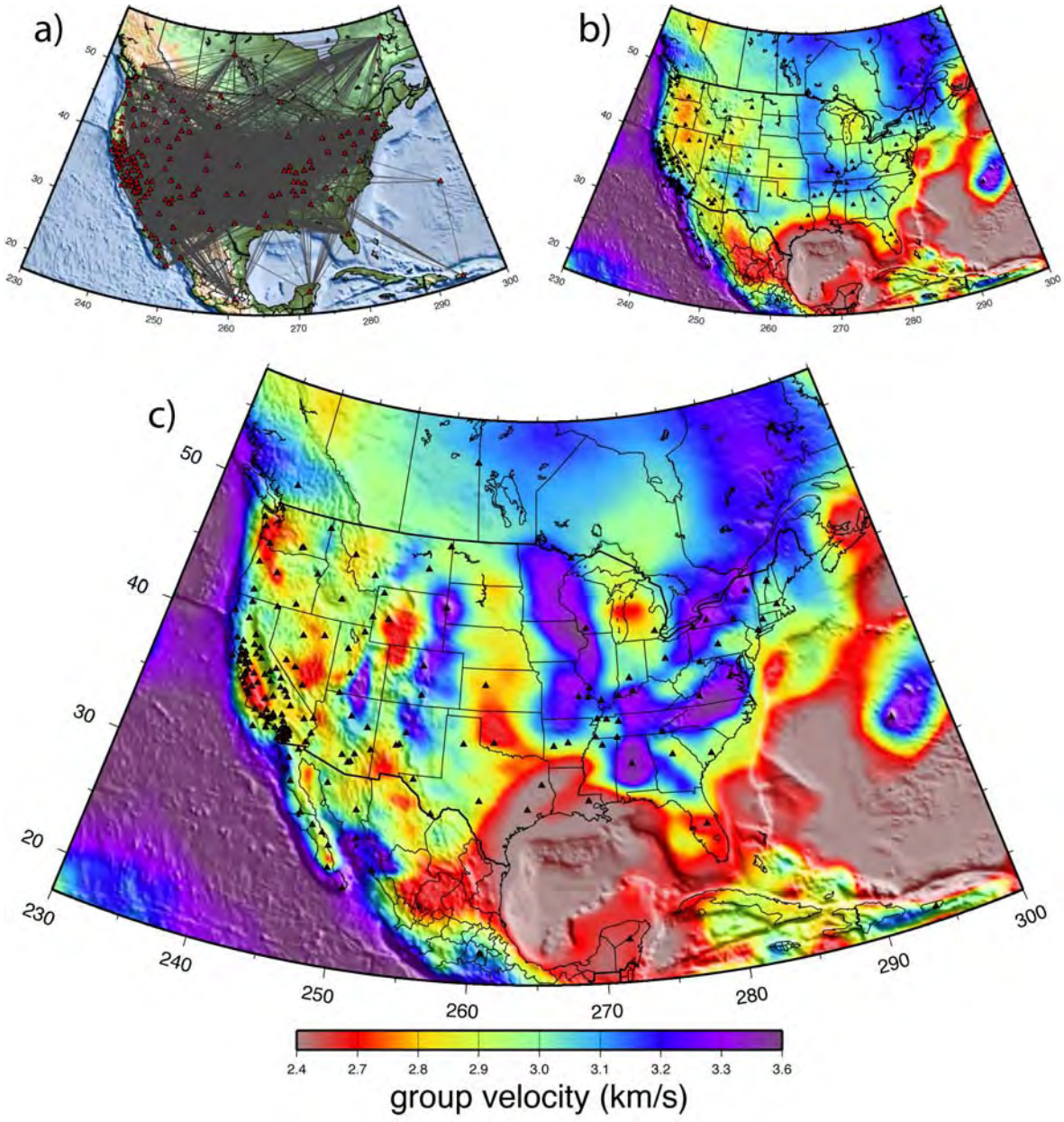

Figure 4. Results of ambient noise group speed tomography across the US at 16 sec period. (a) Coverage of the ~4500 paths composing the data set at 16 sec period. Each group speed measurement is obtained from a four month cross-correlation (Nov. 2003 – Feb. 2004) with a signal-to-noise ratio greater than 10. (b) The 16 sec group speed reference map is computed from the 3D shear velocity model of Shapiro and Ritzwoller (2002). This map is used as both a starting point and background model for the ambient noise tomography. (c) Results of ambient noise tomography using only the group speed measurement obtained from the four-month cross-correlations. The map is produced on a 1 degree grid across the region and provides a 65% variance reduction relative to the reference map in (b).

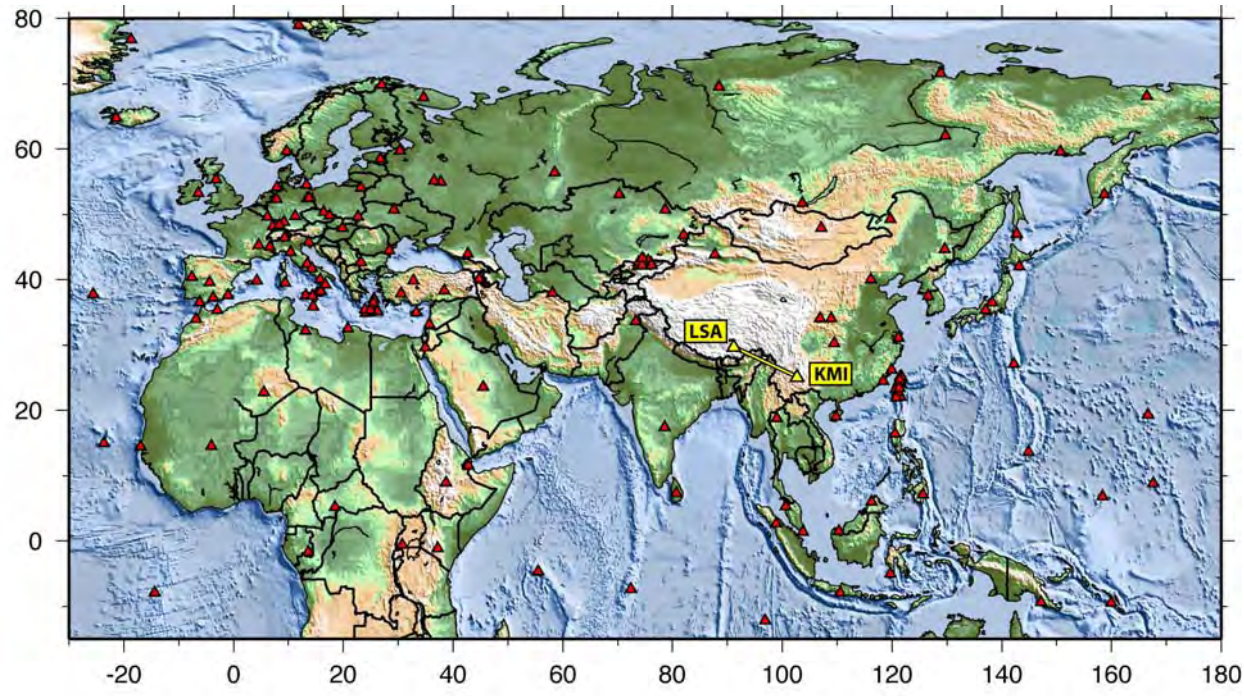

Figure 5. Broad-band stations (red triangles) to be used for tomography across Eurasia and North Africa. The path between GSN stations LSA (Lhasa, Tibet) and KMI (Kunming, China) is highlighted, and corresponds to the cross-correlations shown in Figure 6.

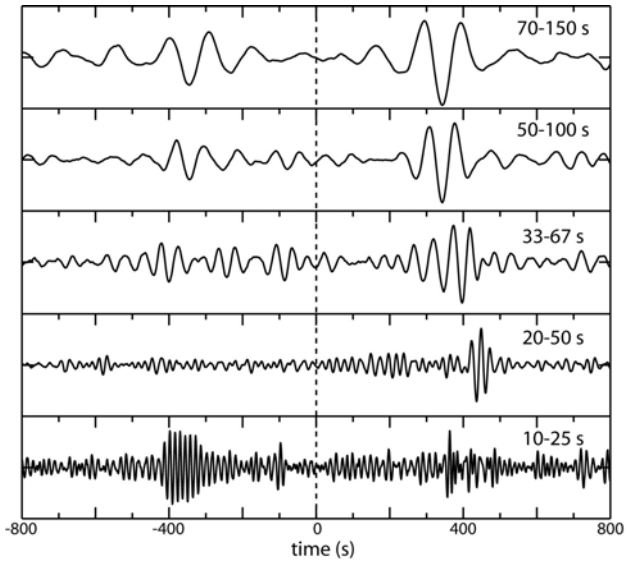

Figure 6. Broad-band cross-correlations between two Asian GSN stations: LSA (Lhasa, Tibet) and KMI (Kunming, China). The cross-correlations are for 1 month of data from January, 2004. The time axis is the cross-correlation lag (in sec). In this case, positive lag corresponds to waves traveling from KMI to LSA and negative lag to waves from LSA to KMI. Each pass-band is indicated.

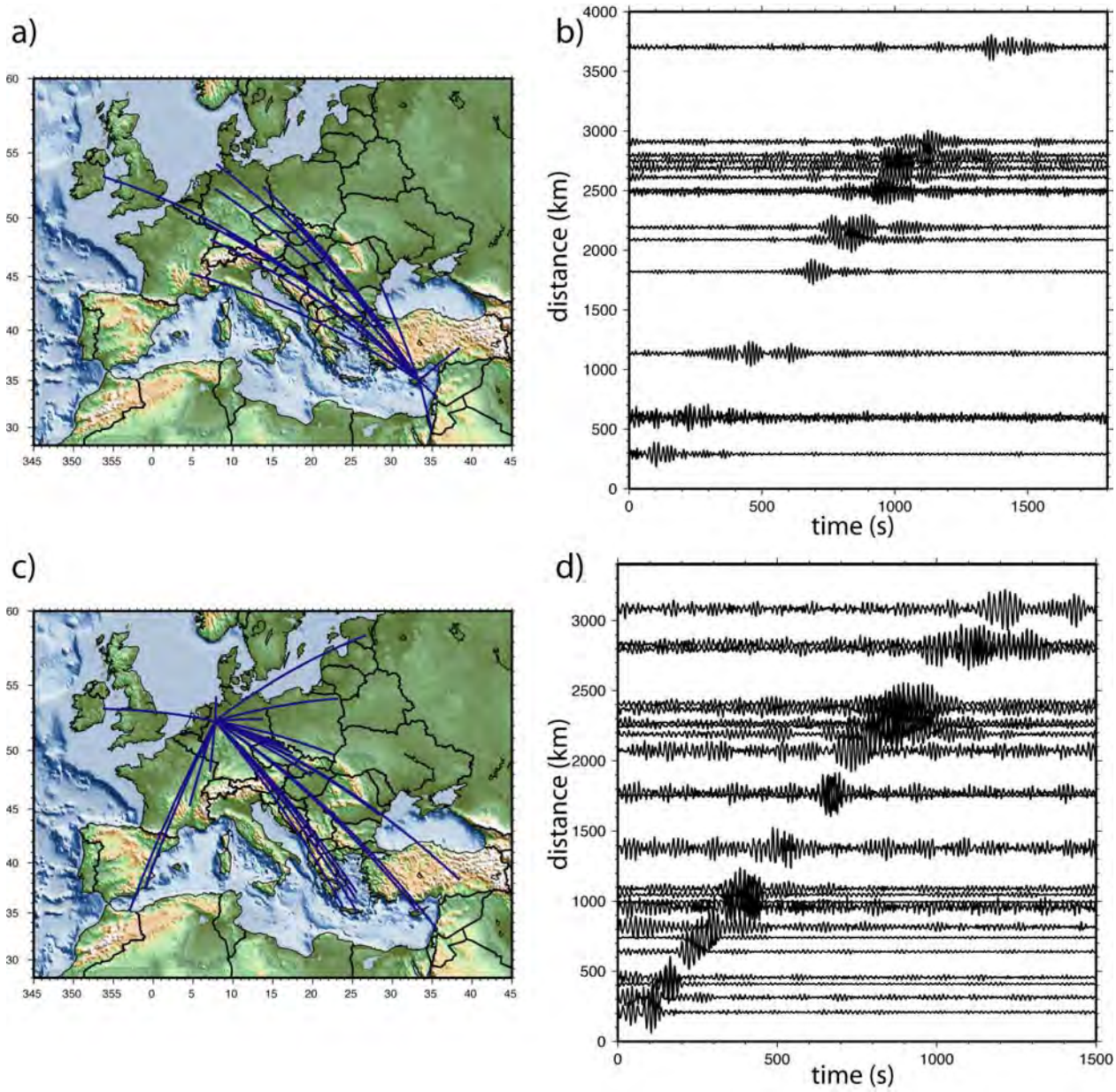

Figure 7. Example receiver gathers (record sections for particular stations) for one-month cross-correlations (Jan. 2004) bandpassed between 10 and 20 sec period for two European stations: CSS (Cyprus) and IBBN (N. Germany). (a) Paths between stations linked to CSS. (b) Receiver gather for station CSS. (c) Paths between stations linked to CSS. (d) Receiver gather for station IBBN. In (b) and (d) only positive cross-correlation lags are shown.

SOURCE AND PATH EFFECTS ON REGIONAL PHASES IN INDIA FROM AFTERSHOCKS OF THE JANUARY 26, 2001, BHUJ EARTHQUAKE

Arthur Rodgers [1], Paul Bodin[2], Luca Malagnini[3], Kevin Mayeda[1], and Aybige Akinci[3]

Lawrence Livermore National Laboratory[1], University of Memphis[2], and
Istituto Nazionale di Geofisica e Vulcanologia[3]

Sponsored by National Nuclear Security Administration
Office of Nonproliferation Research and Engineering
Office of Defense Nuclear Nonproliferation

Contract Nos. DE-FC52-03NA99512[2] and W-7405-ENG-48[1]

ABSTRACT

The January 26, 2001, Bhuj, India, M_W 7.6 earthquake was followed by an extensive aftershock sequence, including more than ten events with $M_W \geq 5.0$. Aftershocks were precisely located using available waveform data from temporary deployments and have been reported by Bodin and Horton (2004). As part of our previous research, we determined seismic moments and source spectra for nearly 900 events occurring during the aftershock deployment led by the University of Memphis and the United States Geological Survey (USGS). In the last year we have studied the attenuation of regional Lg phases from broadband waveforms for a small set of the largest aftershocks. The data were obtained from the Indian Meteorology Department (IMD), and the paths sample the subcontinent. Observed Lg spectra were modeled using the Magnitude Distance Amplitude Correction (MDAC) methodology of Walter and Taylor (2002). This method represents an observed regional phase Fourier amplitude spectrum in terms of a source and path correction. The theoretical source spectrum is based on the Brune (1970) model with modifications for non-constant stress-drop. The path effects include geometric spreading and attenuation for a frequency-dependent quality factor, $Q(f) = Q_0 f^g$, where f is frequency, Q_0 is the quality factor at 1 Hz, and g is the frequency exponent. For the available data we were able to compare theoretical source spectra, based on the estimated seismic moment and scaling parameters, with the estimated source spectra from local data, which is only slightly impacted by path propagation effects. Preliminary estimates of Lg attenuation indicate a frequency dependent quality factor model for the Indian sub-continent of $Q(f) = Q_0 f^{0.4}$, where Q_0 = 800-1000. The low attenuation for these paths is consistent with results from other stable continental regions. We will measure a complete set of amplitudes for all phases and estimate attenuation for the available paths.

OBJECTIVES

Discrimination of small, possibly decoupled, seismic events depends critically on high-frequency (0.5–16 Hz) phase amplitudes at regional distances (200–2000 km). We have determined ground truth seismic moments and source parameters from local recordings of aftershocks of the January 26, 2001, Bhuj, India, earthquake. The objective of this study is to use these data to estimate regional phase attenuation models for the Indian subcontinent and test methodologies for calibrating seismic moments and regional phase amplitudes.

RESEARCH ACCOMPLISHED

At last year's Seismic Research Symposium, we presented analysis of aftershocks of the January 26, 2001, Bhuj earthquake. These events, located in the state of Gujarat in western India, are shown in Figure 1. Using waveform data for aftershocks recorded by temporary deployments in the affected region, we reported locations, depths, focal mechanisms, seismic moments, and source spectra for a large event set spanning the time of our deployment (Bodin et al., 2004b). Our original plan was to use these ground truth source parameters to investigate the effect of source depth and focal mechanism on high-frequency regional phase amplitudes and discriminants. Unfortunately, there were no appropriate waveform data from openly available stations at regional distances (e.g., NIL, Nilore, Pakistan).

We were fortunate to obtain broadband three-component waveform data for 11 events from the nation-wide seismic network operated by the IMD. The IMD stations recorded broadband ground motions at 20 samples/second. These data include the mainshock and 10 aftershocks with $M_W \geq 5.0$. Unfortunately, we only have a source spectrum estimated from local data for one of the earthquakes. Several of these events were large enough to have centroid moment tensors (CMTs) from the Harvard CMT Project. Figure 2 shows the events, stations and paths for which we obtained IMD broadband waveforms.

Inspection of the high-frequency (0.5–8 Hz) regional waveforms showed that Lg propagates very strongly. Figure 3 shows a record section of the high-frequency vertical component data for one event.

We measured regional Lg Fourier amplitude spectra from the instrument corrected displacement waveforms, using a simple group velocity window (3.6–3.0 km/s) to isolate the phase. In order to quantitatively understand regional phase excitation and propagation in our study area, we model regional phase amplitude spectra with the MDAC (Taylor and Walter, 2002).

This methodology uses moment magnitudes, models of earthquake source spectra, geometric spreading, and attenuation to represent regional phase amplitude spectra. The MDAC equations represent an observed regional phase displacement spectrum, A(f), as a function of frequency, f, at distance, D, as a product of source, S(f), geometric spreading, G(D), apparent attenuation, q(D,f), site response, P(f), terms:

$$A(f) = S(f)\, G(D) q(D,f))\, P(f)\ . \qquad (1)$$

The source spectrum is based on the Brune (1970) model with modifications for non-constant stress-drop. The low-frequency level is directly proportional to the seismic moment. We use independent (and absolute) constraints on event size, from calibrated S-wave coda amplitude measurements (Mayeda et al., 2003; Bodin et al., 2004a, 2004b) or waveform modeling (e.g., Harvard CMT catalog). The source spectrum is then computed using a number of parameters, including the source and receiver elastic parameters and parameters controlling the scaling of corner frequency with moment. Geometric spreading is fixed to standard expressions. We typically use D^{-1} for Pn and Sn and $D^{-1/2}$ for Pg and Lg. Apparent attenuation is represented as:

$$q(D,f) = \exp\left[- D\, p\, f / \left[Q(f)\, U \right] \right] , \qquad (2)$$

where U is the velocity of the phase and attenuation is represented by the quality factor $Q(f) = Q_0\, f^g$.

For the present application we wish to model Lg amplitude spectra. We begin by using the seismic moment and reasonable values for the elastic parameters and source corner frequency scaling to compute the source spectrum. We fix the geometric spreading to $D^{-1/2}$ Lg. We then compare the observed spectra to the predictions from a suite of attenuation models. Figure 4 shows the observed spectra for the M_W 5.7 aftershock of January 28, 2001, and

predictions from several attenuation models. The observed spectrum is best fit by a model with Q_0 = 800–1000 and g = 0.4. This is in close agreement with a recent estimate of $Q(f) = 800f^{0.42}$ by Singh et al. (2004) from the Indian shield. And our estimate is also consistent with low attenuation within other stable continental regions.

CONCLUSIONS AND RECCOMMENDATIONS

The recently available broadband waveform data from the IMD allows us to estimate regional phase attenuation for paths crossing the Indian subcontinent. Preliminary estimates of Lg attenuation indicate a frequency dependent quality factor model of $Q(f) = Q_0f^{0.4}$, where Q_0 = 800–1000. Attenuation is low for these paths, consistent with stable continental regions. We will measure a complete set of amplitudes for all phases and estimate attenuation for the available paths.

REFERENCES

Bodin, P. and S. Horton (2004). Source Parameters and Tectonic Implications of Aftershocks of the M_W 7.6 Bhuj Earthquake of January 26, 2001, *Bull. Seism. Soc. Am.* 94: 818, 827.

Bodin, P., A. Akinci, L. Malagnini, K. Mayeda, and A. Rodgers (2004a), Seismic Sources and Wave Propagation in Western India, in *Proceedings of the 26th Seismic Research Review: Trends in Nuclear Explosion Monitoring*, LA-UR-04-5801, 1: pp. 221–226.

Bodin, P., L. Malagnini, and A. Akinci (2004b), Ground Motion Scaling in the Kachchh basin, India, Deduced from Aftershocks of the 2001 M_W 7.6 Bhuj Earthquake, *Bull. Seism. Soc. Am.* 94: 1658–1669.

Brune, J. (1970), Tectonic Stress and the Spectra of Seismic Shear Waves from Earthquakes, *J. Geophys. Res.* 75: 4997–5009.

Mayeda, K., A. Hofstetter, J. O'Boyle, and W. Walter (2003), Stable and Transportable Regional Magnitudes Based on Coda-Derived Moment-Rate Spectra, *Bull. Seism. Soc. Am*. 93: 224–239.

Singh, S. K., D. García, J. F. Pacheco, R. Valenzuela, B. K. Bansal, and R. S. Dattatrayam (2004), Q of the Indian Shield, *Bull. Seism. Soc. Am.* 94: 1564–1570.

Walter, W. and S. Taylor (2002), A Revised Magnitude Distance Amplitude Correction (MDAC2) Procedure for Regional Seismic Discriminants, Lawrence Livermore National Laboratory UCRL-ID-146882.

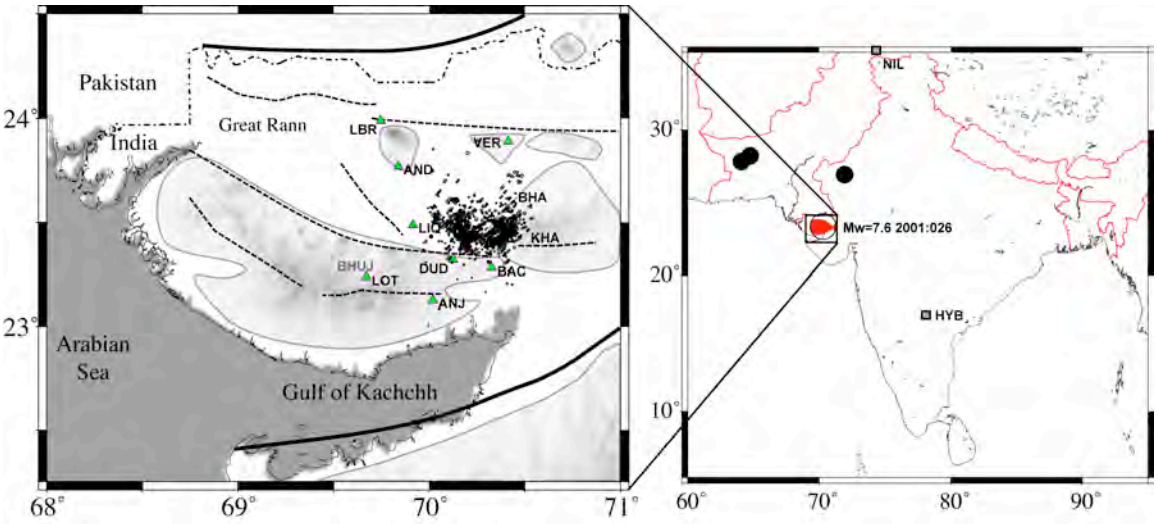

Figure 1. Map showing the January 26, 2001, Bhuj, India earthquake and aftershocks. On the right side is the USGS fault plane solution for the main shock, ground station network (GSL) seismic station NIL, and Geoscope station HYB and known nuclear test sites in Pakistan and India (black dots). The left side shows epicenters (circles) of aftershocks and the University of Memphis temporary network stations (green triangles) that were used to locate them precisely. Also shown are the locations of faults (dashed lines and bold solid lines) and uplifts (enclosed shaded regions).

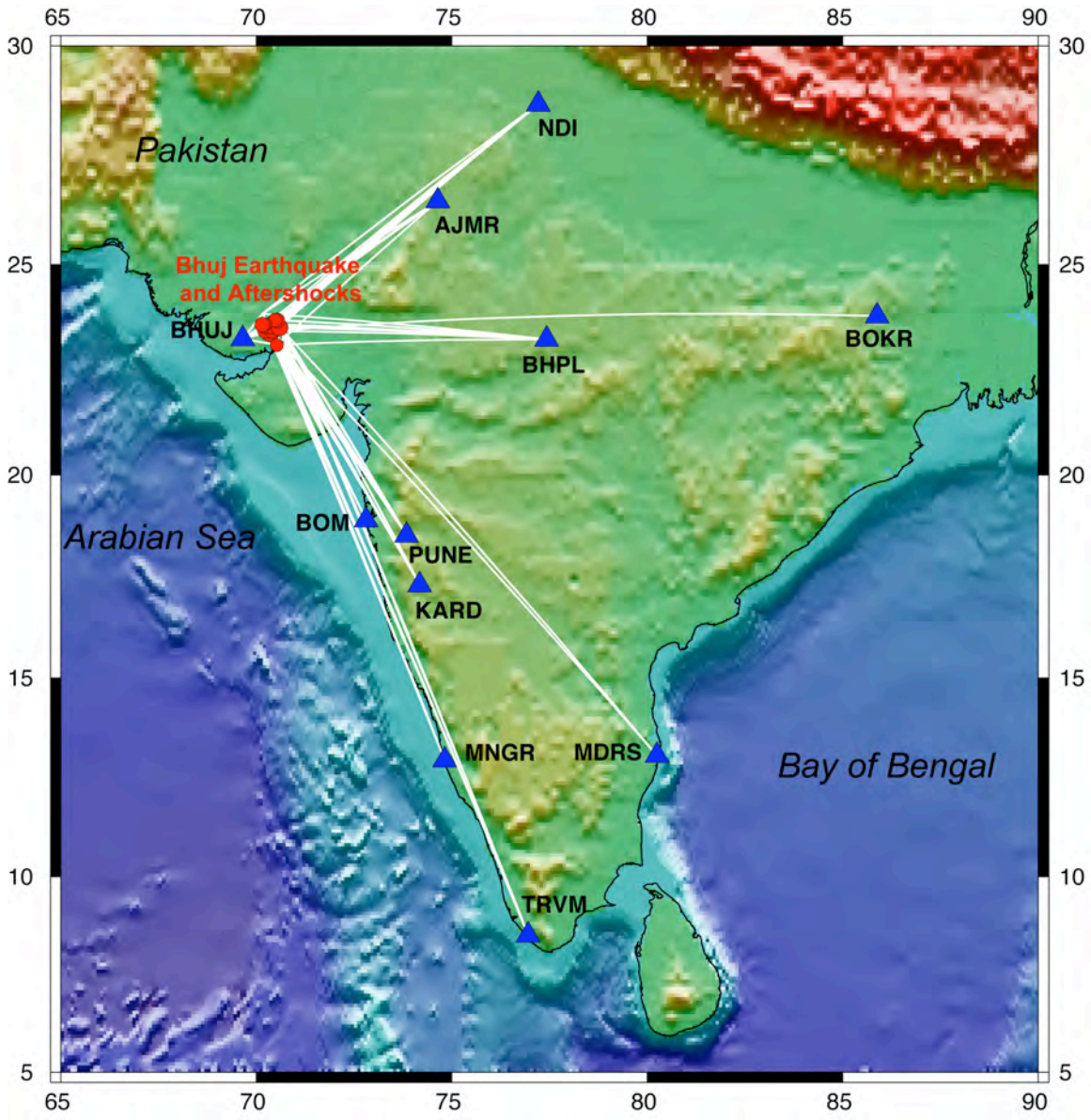

Figure 2. Map showing the 11 events (red circles, size is proportional to magnitude) for which we have broadband IMD waveforms. IMD stations are indicated by triangles and are labeled.

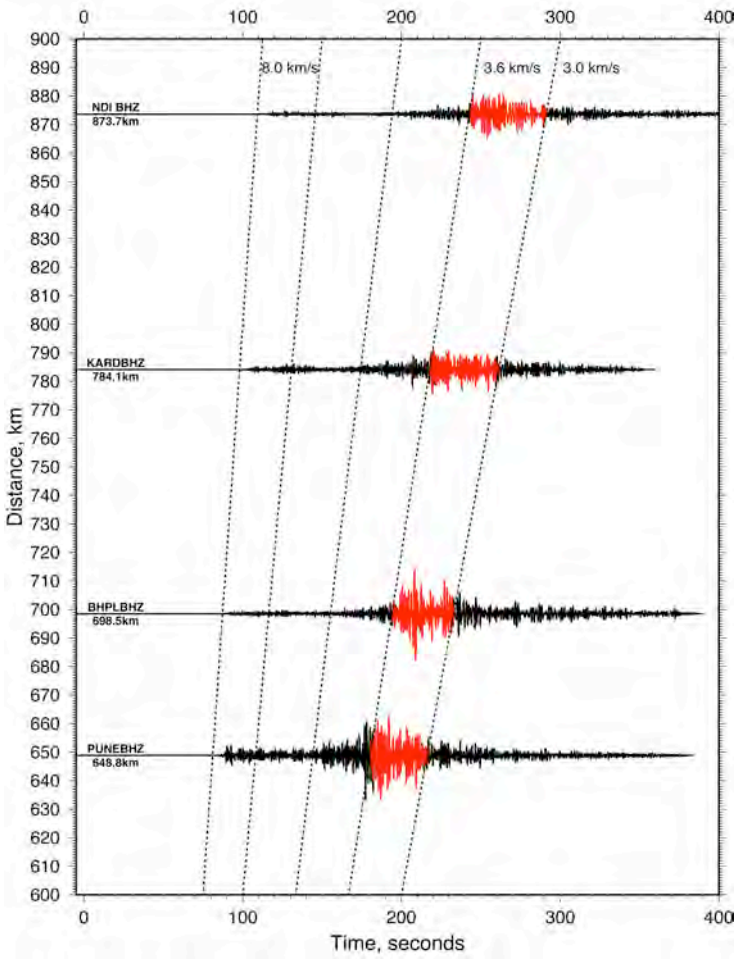

Figure 3. Record section of vertical component waveforms observed at the IMD stations. The Lg window (group velocities 3.6–3.0 km/s) is indicated by the red portion of the waveforms.

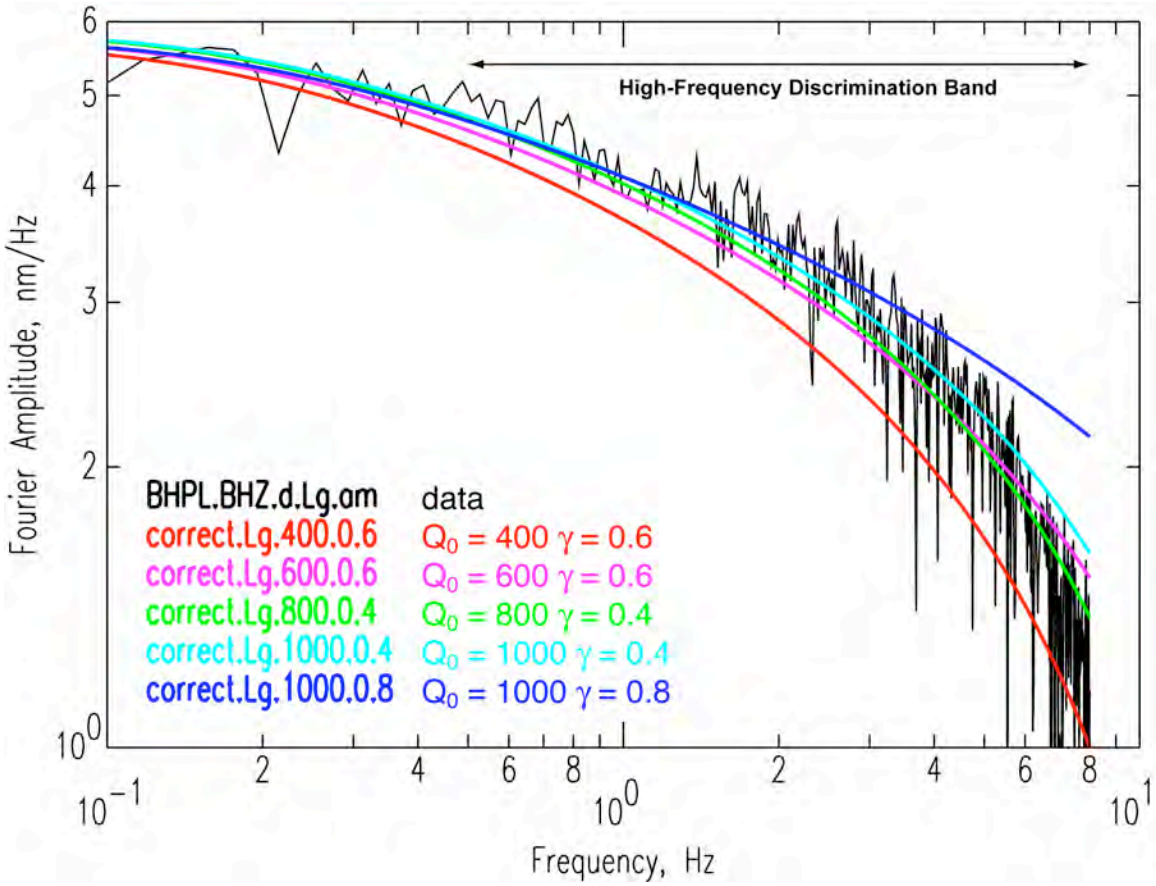

Figure 4. Observed Lg spectrum (black) and predictions of several attenuation models (colors). The observed spectrum is for the vertical component of station BHPL for the January 28, 2001, M_W 5.7 aftershock. Note that the observed spectrum is best fit in the discrimination band (0.5–8 Hz) with high quality factors of Q_0 = 800–1000 and g = 0.4.

DEVELOPMENT OF A JOINT REGIONAL BODY AND SURFACE WAVE TOMOGRAPHY METHOD

William L. Rodi[1] and Delaine T. Reiter[2]

Massachusetts Institute of Technology[1]
Weston Geophysical Corporation[2]

Sponsored by Air Force Research Laboratory

Contract No. FA8718-04-C-0027

ABSTRACT

Inadequately modeled Earth structures cause systematic biases in predictions of geophysical parameters such as the travel times and amplitudes of regional seismic phases. More accurate and reliable predictions of these quantities (especially in aseismic regions) are needed to improve nuclear monitoring efforts to detect, locate and discriminate regional events.

To specifically help improve regional location capabilities, Weston Geophysical Corporation and the Massachusetts Institute of Technology are collaborating on the development of a joint body-wave/surface-wave inversion method to derive self-consistent 3-D *P* and *S* velocity models for the crust and upper mantle. The method expands on our current *Pn* travel-time tomography algorithm, which uses finite-difference ray tracing to model body-wave travel times in 3-D Earth models. Surface-wave group delays (group travel times) are modeled in a two-step procedure. The first step calculates phase- and group-velocity dispersion curves at each point of a latitude/longitude grid, applying 1-D dispersion modeling to the velocity-depth profile for each point. The second step employs 2-D finite-difference ray tracing to the resulting phase-velocity maps, period by period, and then integrates the group-velocity maps along the derived ray paths to obtain group delays. The use of 2-D ray tracing accounts approximately for the non-great circle propagation of surface waves in 3-D Earth structures. Our inversion approach will follow these steps in reverse. Group-velocity maps will be fit to observed group delays along particular source-receiver paths, and the resulting group-velocity dispersion curve for each geographic grid point will be used to determine an updated velocity-depth profile for the point, using a 1-D inversion technique. Our approach uses the first-arrival body-wave travel times to directly update the 3-D *P* velocity structure.

Our progress to date includes the development of some of the key components of our method. These include 1) surface-wave modeling algorithms to create phase and group velocity maps as a function of period; 2) enhancement of our tomography algorithm to derive either 3-D velocity models (for body-wave inversion) or 2-D group-velocity maps (for surface-wave inversion); and 3) improvements in the underlying inversion methodology to allow for velocity bounds and spatially variable smoothness constraints. In addition, we have generalized the interfaces between the various modules of our system to facilitate the integration of body-wave and surface-wave inversion results into a unified 3-D Earth model.

We will apply our joint inversion method to a large region covering central and southern Asia. The body-wave data consist of travel times derived from the Engdahl, van der Hilst and Buland (EHB) bulletin for the years 1988 – 2004. The surface-wave data consist of measured group velocities from the University of Colorado research team, as well as measurements from previous and ongoing experiments in the region of study.

OBJECTIVES

To improve earth structure and associated monitoring efforts, Weston Geophysical Corporation and the Earth Resources Laboratory at the Massachusetts Institute of Technology are collaborating to develop a joint 3-D inversion technique that incorporates both body-wave travel times and Rayleigh-wave group velocity measurements to determine the full *P* and *S* velocity structure of the crust and upper mantle. Research objectives include the following:

- Extension of our current inversion codes to produce improved 3-D estimates of the *P* structure from first-arrival body-wave travel times;
- Development of a sequential inversion technique to jointly invert both body-wave travel times and Rayleigh-wave group velocities for 3-D *P* and *S* velocity structure;
- Estimates of the *P* and *S* model uncertainty; and
- Validation of the new model using a variety of techniques, including location calibration and full-waveform modeling.

We will apply the new technique to data from the broad region shown in Figure 1. The unique and innovative contribution that will result from this project will be an inversion methodology that combines regional body and surface wave data to constrain Earth structure. The application of this methodology to construct and validate a regional *P* and *S* model for southern and central Asia may directly impact nuclear monitoring capabilities and provide useful information for other seismologists.

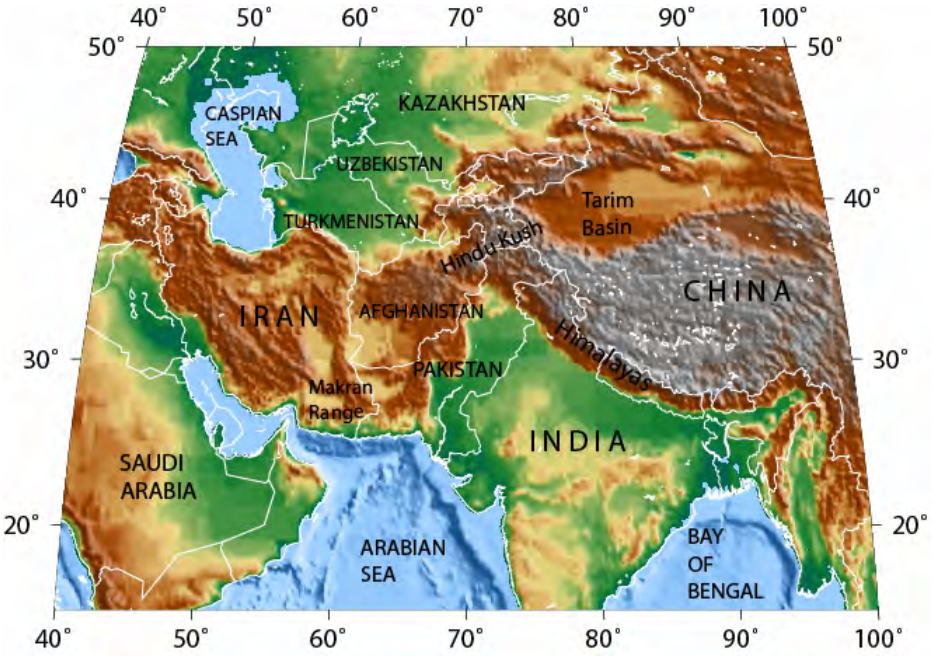

Figure 1. Map of study region.

RESEARCH ACCOMPLISHED

In the first year of the project we have focused on developing some of the core numerical techniques and software modules needed for our joint inversion approach. These have pertained mainly to the forward modeling method for surface-wave dispersion in 3-D Earth models, and the enhancements to the model parameterization and regularization employed in our underlying inversion algorithm. The next section describes our overall inversion approach and is followed by some specifics of the numerical techniques we have developed thus far.

Joint Inversion Approach

The starting point for this project was the regional travel-time tomography method developed by Reiter et al. (2005) and applied by them in India-Pakistan and by Murphy et al. (2005) in Russia and China. The method begins with a 3-D *P* velocity model for the crust and upper mantle, containing lateral variations both in velocity and in interface depths (e.g., the Moho). Forward modeling is performed with finite-difference ray tracing using the algorithm of Podvin and Lecomte (1991). The tomography method solves for an updated upper mantle *P* velocity based on *Pn* times observed from multiple earthquakes and stations in the model region. This earlier method restricts the velocity update in its parameterization by forcing built-in depth dependence. Essentially, the tomography solves for the velocity just below the Moho, and its difference from the initial model velocity at the same depth is extrapolated downward to a depth of 210 km and tapered linearly to zero between 210 km and 410 km. The free parameter in the inversion is thus a 2-D velocity function, latitude (θ) and longitude (φ).

This project is extending our original method by adding surface-wave dispersion data to the data set and the *S* velocity model to the inversion parameters. In addition, the velocity parameterization is more general, allowing full 3-D variation in the two unknown velocity functions: $v_P(\theta,\varphi,z)$ and $v_P(\theta,\varphi,z)$ (where *z* is depth).

For the time being, we are restricting the body-wave data to *Pn* travel times, and the surface-wave data to Rayleigh-wave group velocities at periods sensing upper mantle structure (periods greater than about 10 s). Accordingly, our method will initially solve for the 3-D velocity structure of the upper mantle between the Moho and the 410-km discontinuity, with the crustal velocities and crustal thickness held fixed to their initial (CRUST2.0) values. The techniques and software we are developing, however, will be sufficiently general to eventually accommodate additional data (e.g., *S* travel times, Love-wave dispersion, crustal body-wave phases, and a wider period band for dispersion) and additional model parameters (e.g., crustal velocities and Moho depth).

Given the initial focus of the project, one version of the methodology we are developing will perform body-wave and surface-wave inversion as separate procedures. That is, an inversion of *Pn* times will update v_P in the upper mantle and a separate inversion of Rayleigh-wave group velocities will update the upper mantle v_S (since the dependence of surface-wave dispersion on mantle *P* velocity is small). The two inversions will be coupled, however, through the prior information applied to the velocity functions. These will include smoothness constraints as well as prior upper and lower bounds on the velocity value at each point in the upper mantle. The bounds can be determined in part from bounds on Poisson's ratio, which would vary with depth and tectonic regime. In the surface-wave inversion, for example, bounds on v_S are implied by the current v_P model and the limits on Poisson's ratio. This will couple the body-wave and surface-wave inversions in a way that ensures consistency between the *P* and *S* velocity models. We plan to repeat the two inversions in an iterative process, which will solve the joint, nonlinear inverse problem.

Another key element of our approach is the factorization of the surface-wave inversion into two steps. In the first step, the group delays for the observed event-station pairs, for each frequency ω, are used to determine a group velocity map $u(\theta,\varphi,\omega)$. This inversion is effectively a 2-D tomography, performed frequency by frequency. The second step uses the resulting dispersion curve at each (θ,φ) to determine an *S* velocity-depth profile. This second step is a 1-D inversion performed separately for each latitude and longitude in the group velocity map, yielding collectively a 3-D velocity function $v_S(\theta,\varphi,z)$. This factorization was also done by Ritzwoller et al. (2002) and others and is compatible with the forward modeling method outlined in the next section.

The body-wave inversion will be a one-step, 3-D tomography that uses the observed *P* travel times over event-station paths to directly determine the 3-D velocity function $v_P(\theta,\varphi,z)$.

Forward Modeling of Surface-Wave Dispersion

Our approach for modeling surface wave dispersion in a 3-D Earth employs the same approximation used by Stevens and Adams (1999), Ritzwoller and Levshin (1998) and others, which states that the phase delay

($d^{ph}(\omega)$), or phase travel time, between an event and a station is obtained as an integral of the local phase velocity along a fixed travel path:

$$d^{ph}(\omega) = \int_{Path} \frac{ds}{c(\theta,\varphi,\omega)} \,. \qquad (1)$$

For each latitude/longitude point (θ,φ), $c(\theta,\varphi,\omega)$ is taken to be the dispersion response of the 1-D medium characterized by the velocity and density profiles at that point. For fixed frequency ω we refer to $c(\theta,\varphi,\omega)$ as a phase velocity *map*. Similarly, the *group* delay for the event-station pair is given by

$$d^{gr}(\omega) = \int_{Path} \frac{ds}{u(\theta,\varphi,\omega)} \,, \qquad (2)$$

where $u(\theta,\varphi,\omega)$ is the group velocity map. Typically the path integrations in Equations (1) and (2) are performed along the great circle connecting the source and receiver points (Woodhouse and Dziewonski, 1984). This is correct for a 1-D Earth model in which the local dispersion is the same at each latitude and longitude. However, lateral heterogeneities in the crust and upper mantle can cause both Rayleigh and Love waves to deviate laterally relative to the great-circle path. Many studies of regional and global surface wave propagation have observed off-great-circle path deviations. For example, Levshin et al. (1994) showed that regional structure in northern and central Eurasia caused significant departures from great-circle propagation, and recent studies by Cotte et al. (2000) demonstrated azimuthal deviations of up to 30° for surface waves between 20- and 40-second periods propagating in the French Alps.

A better approximation to phase and group travel times is found by integrating the phase and group slownesses along the minimum-time path through the frequency-specific, 2-D phase velocity map. Other researchers have used a paraxial, 2-D shooting, and finite-difference methods of raytracing to explore this approach (Ammon and Vidale, 1993; Bruneton et al., 2002; Kennett and Yoshizawa, 2002; Ritzwoller et al., 2002). We are using the Podvin-Lecomte ray-tracing technique (Podvin and Lecomte, 1991), as we do in body-wave modeling. In the body-wave application, we apply the Podvin-Lecomte (P-L) method to propagate first-arrival travel times from a given seismic station location through a 3-D medium to a 3-D grid of nodes, representing a grid of event hypocenters. The resulting 3-D travel-time grid can be interpolated to relevant event locations. Adapting the P-L ray tracer to 2-D dispersion modeling involves a multi-step process to obtain phase and group delays for various source-receiver paths. Here we illustrate these steps with our initial model, which consists of the CRUST2.0 3-D model (Bassin et al., 2000) tapered into the *iasp91* model (Kennett and Engdahl, 1991) at 210-km depth.

The first step of our modeling process is to compute the dispersion response for each geographic grid point of the 3-D Earth model, as determined by the 1-D velocity/density profile defined for each point. We perform these dispersion calculations using software adapted from a set of modal summation codes (Computer Programs in Seismology; Herrmann, 2002). Implicit in the use of these codes is an "Earth-flattening" transformation that corrects for the Earth's sphericity. We collate the output from these calculations at the frequencies of interest to produce a set of phase- and group-velocity maps, $c(x,y,\omega)$, and $u(x,y,\omega)$, respectively. Figure 2 shows the group-velocity maps (as percent deviation from the *iasp91* predicted group velocity) at periods of 10s, 15s, 20s, and 25s.

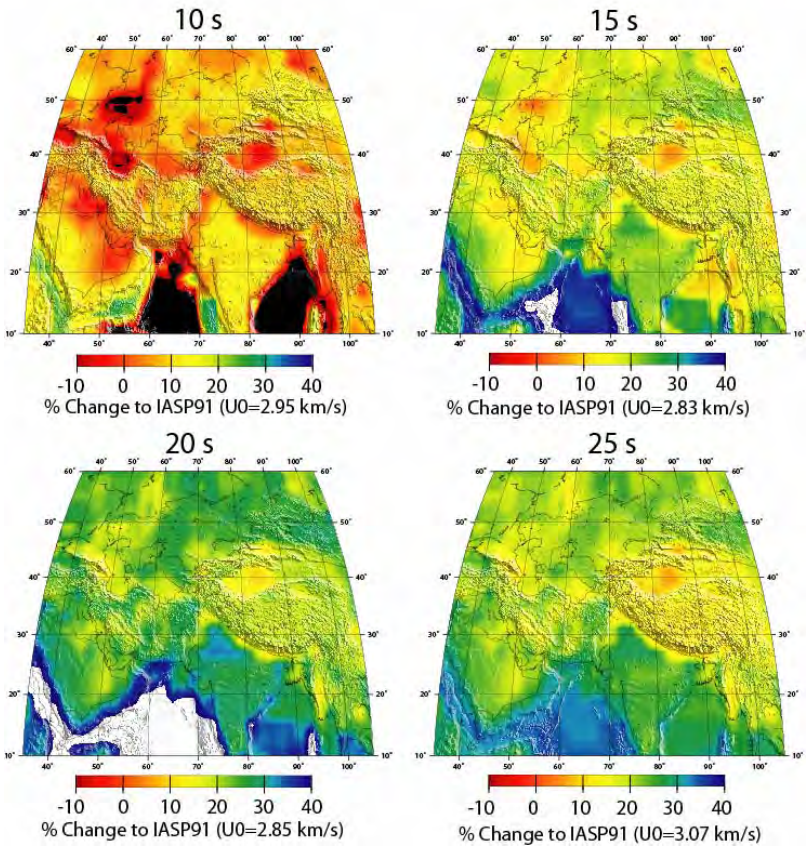

Figure 2. Initial model-predicted group velocities as a function of period, shown as a percent change from the constant (U0) velocity found using the 1-D *iasp91* model. The maps were generated using modal summation techniques at each nodal depth profile in the earth model.

The next step in the dispersion forward-modeling process is the calculation of phase-delay (or "phase-time") maps from the phase-velocity maps, using the P-L ray tracer. Our implementation of the P-L algorithm applies to flat Earth models represented by Cartesian grid of homogeneous velocity cells. Thus, on a station-by-station basis, we spatially interpolate each geographic phase velocity map onto a regular 2-D Cartesian grid based on a stenographic map projection. For example, Figure 3 shows the Cartesian phase-velocity maps that are generated from our initial model at periods of 10, 15, and 20 seconds for a 10-degree region around the station NIL (Nilore, Pakistan). In this example the Cartesian grid sampling was 10 km in *x* and *y*. (We are currently experimenting with the appropriate sampling interval to ensure travel-time prediction accuracy.) The regional variability of the velocity structure is clearly visible in the phase speed maps, where basins are delineated by low velocities and the Indian shield appears as a high in the southeastern corner of the maps. The strong low present in the southwest corner of the 10- and 15-second maps is the northeastern extreme of the Arabian Sea.

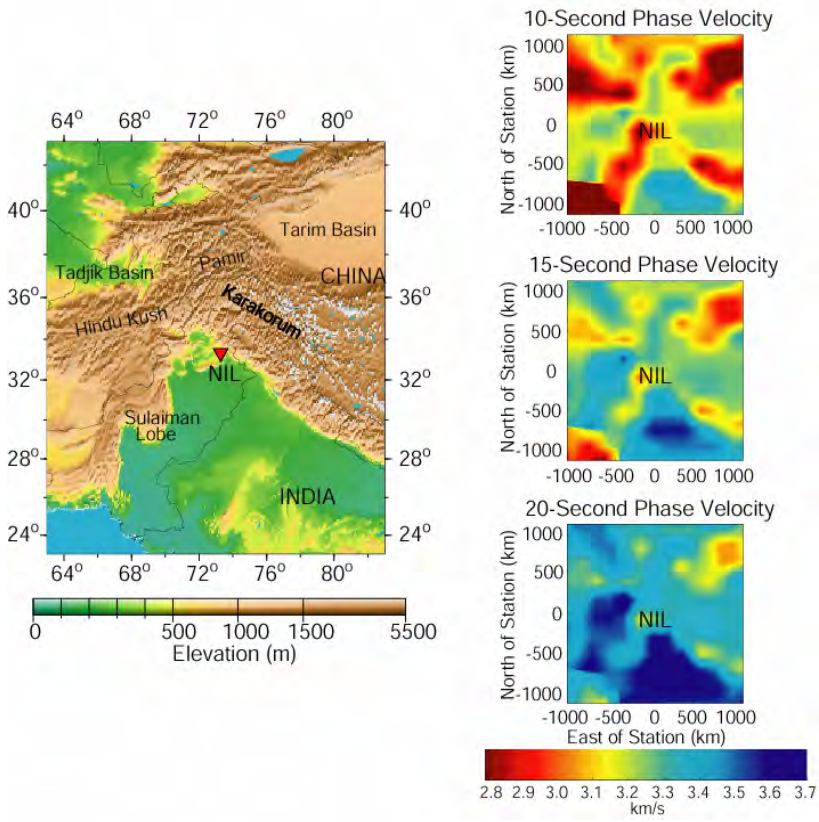

Figure 3. (Left) Topographic map of the NIL station and surrounding region out to 10° epicentral distance (Mercator projection). (Right) Cartesian maps of Rayleigh-wave phase velocities at 10-, 15-, and 20-seconds period based on our initial model. All phase-velocity maps are plotted on the same color scale.

For each station (and period), the 2-D version the P-L ray tracer creates a Cartesian grid of phase delays that represent the minimum travel time from the station location to each point in the Cartesian grid. The final step of our modeling process is to find the phase and group delays for the particular station/event pairs involved in the data set. For the phase delay, this is simply a matter of interpolating the calculated grid-point times to a particular event location (as transformed from geographic to Cartesian coordinates).

For the group delay, we must perform the integration indicated by Equation (2), where "*Path*" is taken to be the minimum phase-time ray path. In the P-L method, a ray path is represented by the sensitivities of the phase travel time to the phase velocities of cells, defined by

$$s_{lm}(\omega) = \frac{\partial d^{\,ph}(\omega)}{\partial c_{lm}^{-1}(\omega)}, \tag{3}$$

where ℓ and *m* index the cells of the 2-D Cartesian grid. The integral in Equation (2) is then approximated as

$$d^{\,gr}(\omega) = \sum_{\ell m} \frac{s_{\ell m}(\omega)}{u_{\ell m}(\omega)}. \tag{4}$$

We compute the cell sensitivities, $s_{\ell m}$, using an extension to the P-L code we used in our previous work (Reiter et al., 2005) to calculate sensitivities for body-wave travel times. The sensitivities of travel times to

cell slownesses are computed using recursive back-propagation of node-to-node and node-to-cell dependencies from any given receiver point (event position) toward the source (station position). Consistent with the underlying ray theory, the resulting sensitivities are concentrated along a trajectory of cells connecting the source and receiver points, and this trajectory defines the P-L version of a ray path.

In Figure 4 we depict the path sensitivities that are derived from the 20-second Rayleigh phase-speed map for a set of four events in the region surrounding NIL. The figure shows that out-of-plane (or non-great-circle path) propagation is present at the 20-second period for our 3-D initial model.

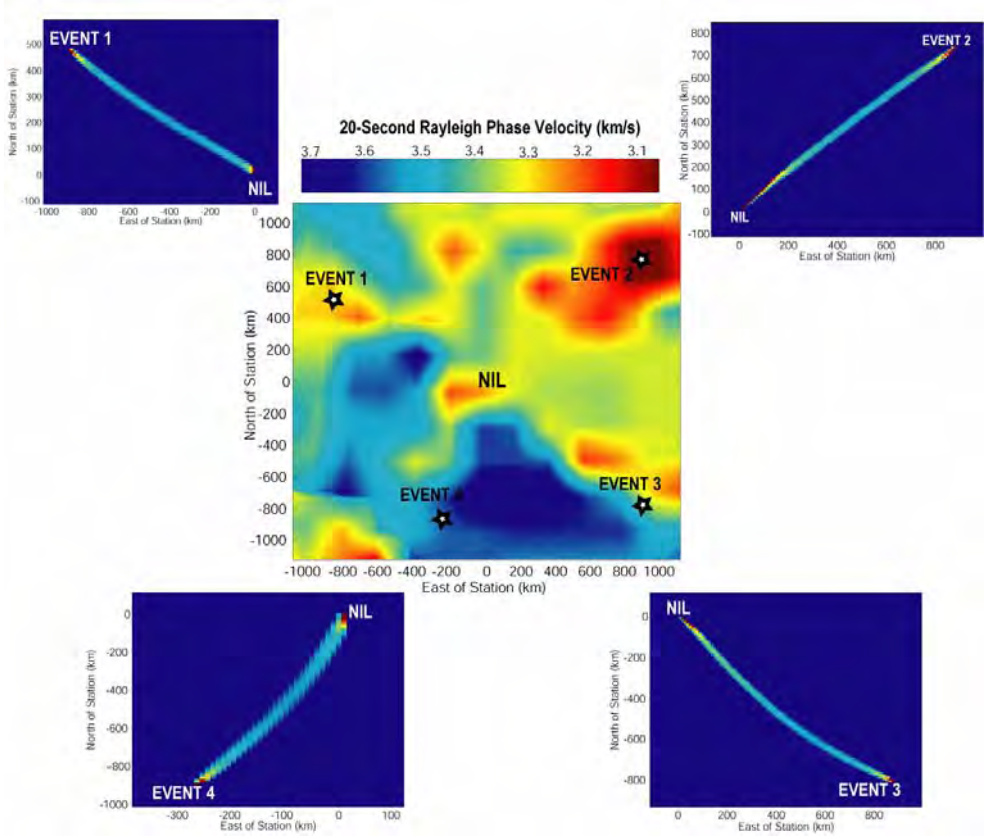

Figure 4. (Middle subplot) Phase velocity map at a period of 20 seconds surrounding station NIL. Plotted around the velocity map are four event positions, for which ray sensitivities have been calculated (each ray subplot is labeled according to its respective event). Note that the rays do not travel along great-circle paths.

Sensitivities are also needed to perform tomographic inversion, i.e., fitting group velocity maps to the group delays observed over particular paths. To create these, the $s_{\ell m}(\omega)$, defined on the P-L Cartesian grid, are transformed to sensitivities to the nodal values of the group velocity maps in geographic coordinates ($u(\theta,\varphi,\omega)$) using the inverse of the interpolation transformation that generated the Cartesian cell velocities.

Inversion Method

The inversion method used by Reiter et al. (2005) to estimate the *Pn* lid-velocity map, $v_{lid}(\theta,\varphi)$, was a regularized least squares technique. The inversion model function was taken to be the *Pn*-lid slowness:

$$m(\theta,\varphi) = \frac{1}{v_{lid}(\theta,\varphi)}, \tag{5}$$

and the solution to the inverse problem was defined as the function *m* that minimizes the objective function given by

$$\Psi = \sum_{ij} \left| d_{ij} - F_{ij}(m) \right|^2 / \sigma_{ij}^2 + \lambda\, S(m). \qquad (6)$$

In the first term, d_{ij} is the observed travel-time datum for the i^{th} event and j^{th} station; σ_{ij} is the standard deviation of the observational error in the datum; and F_{ij} is the forward modeling function for the datum (F_{ij} computes the Podvin-Lecomte travel time through the 3-D model extrapolated from v_{lid}). In the second term, *S(m)* is a stabilizing function which we set to

$$S(m) = \iint (\nabla^2 m)^2 \, d\theta \, d\varphi. \qquad (7)$$

This term serves to constrain the spatial roughness of *m*, with the regularization parameter, λ, controlling the strength of the constraint. We performed the minimization of Ψ by iterating over the linearized problem, in which each F_{ij} is replaced by its first-order expansion with respect to the current solution, as expressed with the sensitivities of F_{ij} to the nodal values of *m* that parameterize the model function.

In this project we are developing significant extensions of this inversion method. Here we describe three that we are implementing in the body-wave inversion step of our joint tomography method. First, the 2-D model function is being replaced with a 3-D function that provides explicitly for lateral and vertical *P* velocity variations in the upper mantle. Denoting the *P* velocity simply as *v*, the model function becomes

$$m(\theta, \varphi, z) = \frac{1}{v(\theta, \varphi, z)}, \qquad (8)$$

where *z* ranges between the Moho and the 410-km discontinuity. This replacement is facilitated by the fact that our earlier method derived the 2-D travel-time sensitivities to $1/v_{lid}$ from the 3-D slowness sensitivities, which are now used directly.

Second, our new method will apply hard bounds to the velocity function as a constraint on the minimization of Ψ. This is being done as follows: let the bounds be expressed as

$$v_-(x) \le v(x) \le v_+(x), \qquad (9)$$

where we let $x = (\theta,\varphi,z)$ for conciseness. We can satisfy this automatically with an appropriate transformation of the model function *m* to velocity. The transformation we are using at this time employs the error function (*erf*):

$$\frac{1}{v(x)} = \frac{1}{2}\left[\frac{1}{v_-(x)} + \frac{1}{v_+(x)}\right] + \frac{1}{2}\left[\frac{1}{v_-(x)} - \frac{1}{v_+(x)}\right] erf(\beta(x) m(x)), \qquad (10)$$

where $\beta(x)$ is a specified scaling parameter. Since the error function traverses -1 to 1 as *m* ranges from $-\infty$ to ∞, Equation (9) is obeyed without constraining *m* in the minimization of Ψ. A disadvantage of this technique is that the forward modeling functions, $F_{ij}(m)$, become nonlinear even for linearized (fixed ray) tomography. We are addressing this by using a *nonlinear* conjugate gradients technique to minimize Ψ.

The third extension of the tomography method we are in the process of implementing is the replacement of the stabilizing function with a more general form that is motivated by geostatistical concepts, as are used in kriging (e.g., Deutsch and Journel, 1998). The mathematical development of the new stabilizing function is described by Rodi et al. (2005) and Murphy et al. (2005). The functional form is given by

$$S(m) = \int m(x)\left[Dm\right](x)\, dx, \qquad (11)$$

where *D* is a specified differential operator. Our earlier method (Equation (7) took *D* to be the biharmonic (squared Laplacian) operator. An example of a geostatistically based *D* is

$$D = \frac{1}{8\pi\lambda^2\sigma_0^2}\left[\delta(x) - \lambda^2\nabla^2\right]^2. \qquad (12)$$

This operator treats *m(x)* as a stationary Gaussian random field with variance σ_0^2, correlation length λ, and a spatial correlation function of the exponential type (see Deutsch and Journel, 1998). We have implemented this and the larger class of differential operators considered by Rodi et al. (2005) using difference operators in spherical coordinates, consistent with the geographic model parameterization used in our tomography method. We are extending these operators to allow the geostatistical parameters (e.g., σ_0) to vary spatially, which provides a mechanism for varying the smoothness constraints in accordance with the ray coverage of the data set.

Joint Tomography Data Set

We will apply our joint inversion algorithm to a large database of first-arriving *P* and *S* travel times and fundamental-mode phase and group velocity measurements. Most of our data come from public sources, but we will also be incorporating travel-time and group velocity measurements from Weston's ongoing regional experiments.

The body-wave data set is composed of origin parameters and associated arrival times for a set of well-located seismic sources from the Engdahl et al. (1998; EHB) bulletin. We use several filtering criteria to limit the occurrence of residuals not related to velocity variations. These criteria include limitations on event depths, epicentral distances, and magnitudes. Distance and depth ranges are chosen to isolate waves propagating in the crust and upper mantle from faster, deeper traveling *P* waves. To ensure that an event's epicentral mislocation is no worse than 15 km for 85% of the events, we require the secondary azimuth gap (defined as the largest azimuthal gap filled by a single station) for a given event to be less than or equal to 130º (Bondár et al., 2004). To minimize the inherent picking error, we require the *P*-phase arrival times to be designated as impulsive and restrict the travel-time residuals with respect to the *iasp91* model to less than ±7 seconds.

The surface-wave database consists of phase- and group-velocity dispersion measurements from paths sampling our region of interest. We received our initial data set from the group at the University of Colorado at Boulder (Ritzwoller and Levshin, 1998). It comprises over 97,000 group velocity measurements at periods between 10 – 250 seconds. This database is especially rich in the short-period measurements that will constrain the crust and upper mantle portion of our model.

CONCLUSIONS AND RECOMMENDATIONS

Our first year's effort on this project has produced the overall design of the methodology we will use to perform joint body-wave and surface-wave regional tomography, which we are implementing in a set of integrated software modules for constructing calibrated 3-D Earth models and performing event location based on these models. Our initial focus on 3-D upper mantle *P* and *S* velocity structure in south/central Asia, inferred from *Pn* travel times and intermediate-period Rayleigh wave group velocities, is the natural extension of our earlier work on *Pn* tomography in India and Pakistan. The ultimate goal of the project, however, is to create a general capability for constructing full 3-D crust and upper mantle models for areas of monitoring interest around the world based on the available body-wave and surface-wave observations, including *P* and *S* travel times observed at local and regional distances, and regional Rayleigh and Love wave dispersion observed over a broad frequency band.

ACKNOWLEDGEMENTS

We are grateful to Dr. Bob Engdahl for providing updated versions of his event bulletin. We sincerely appreciate the extensive dispersion measurements provided by Prof. Mike Ritzwoller's group at the

University of Colorado. All maps were produced using the Generic Mapping Tools (GMT) data processing and display package (Wessell and Smith, 1991; 1995).

REFERENCES

Ammon, C. J. and J. E. Vidale (1993), Tomography without rays, *Bull. Seism. Soc. Amer*. 83: 509–528.

Bassin, C., G. Laske and G. Masters (2000), The Current Limits of Resolution for Surface Wave Tomography in North America, *EOS Trans AGU* 81: F897.

Bondár, I., E. R. Engdahl, X. Yang, H. A. A. Ghalib, A. Hofstetter, V. Kirichenko, R. Wagner, I. Gupta, G. Ekström, E. Bergman, H. Israelsson and K. McLaughlin (2004). Collection of a reference event set for regional and teleseismic location calibration, *Bull. Seism. Soc. Amer.* 94 1528–1545.

Bruneton, M., V. Farra, H. A. Pedersen and the SVEKALAPKO Seismic Tomography Working Group (2002), Non-linear surface wave phase velocity inversion based on ray theory, *Geophys. J. Int.* 151: 583–596.

Cotte, N., H. A. Pedersen, M. Campillo, V. Farra and Y. Cansi (2000), Off-great-circle propagation of intermediate-period surface waves observed on a dense array in the French Alps, *Geophys. J. Int.* 142: 825–840.

Deutsch, C. V. and A. G. Journel (1998), GSLIB: *Geostatistical Software Library and User's Guide*, 2nd ed., Oxford University Press, Inc., New York, 369 pp.

Engdahl E. R., R. van der Hilst, and R. Buland (1998), Global teleseismic earthquake relocation with improved travel times and procedures for depth determination, *Bull. Seism. Soc. Amer*. 88: 722–743.

Herrmann, R. B. (2002), *Computer Programs in Seismology*, Version 3.20, St. Louis University.

Kennett, B. L. N. and E. R. Engdahl (1991), Travel times for global earthquake location and phase identification, *Geophys. J. Int.* 105 429–465.

Kennett, B. L. N. and K. Yoshizawa (2002), A reappraisal of regional surface wave tomography, *Geophys. J. Int.* 150: 37–44.

Levshin, A. L., M. H. Ritzwoller, and L. I. Ratnikova (1994), The nature and cause of polarization anomalies of surface waves crossing northern and central Eurasia, *Geophys. J. Int*. 117: 577–590.

Murphy, J. R., W. Rodi, M. Johnson, D. D. Sultanox, T. J. Bennett, M. N. Toksöz, V. Ovtchinnikov, B. W. Barker, D. T. Reiter, A. M. Rosca, and Y. Shchukin (2005), Calibration of International Monitoring System (IMS) stations in central and eastern Asia for improved seismic event location, *Bull. Seism. Soc. Amer.* 95: 4.

Podvin, P., and I. Lecomte (1991), Finite difference computation of travel times in very contrasted velocity models: a massively parallel approach and its associated tools, *Geophys. J. Int.* 105: 271–284.

Reiter, D., W. Rodi, and M. Johnson (2005), Development of a tomographic upper-mantle velocity model beneath Pakistan and northern India for improved regional seismic event location, 95, 926–940.

Ritzwoller, M. H., and A. L. Levshin (1998), Eurasian surface wave tomography: Group velocities, *J. Geophys. Res.*, 103, B3, 4839–4878.

Ritzwoller, M. H., N. M. Shapiro, M. P. Barmin and A. L. Levshin (2002), Global surface wave diffraction tomography, *J. Geophys. Res*. 107**:** doi: 10.1029/2002JB001777.

Rodi, W., C. A. Schultz, G. Johannessen, and S. C. Myers (2005), Grid-search location methods for ground-truth collection from local and regional seismic networks, Final Technical Report to National Nuclear Security Administration, Dept. of Energy, Contract Nos. DE-FC03-01SF22397 and W-7405-ENG-48.

Stevens, J. L. and D. A. Adams (1999), Improved surface wave detection and measurement using phase-matched filtering and improved regionalized models, in *Proceedings of the 21st Seismic Research Symposium, Technologies for Monitoring the Comprehensive Nuclear-Test-Ban-Treaty*, Los Alamos National Laboratory document LA-UR-99-4700, Las Vegas, NV, 274–282.

Wessel, P. and W. H. F. Smith (1991). Free software helps map and display data, *Eos Trans. AGU* 72: 441, 445–446.

Wessel, P. and W. H. F. Smith (1995). New version of the Generic Mapping Tools released, *Eos Trans. AGU* 76: 329.

Woodhouse, J. H. and A. M. Dziewonski (1984), Mapping the upper mantle: three-dimensional modeling of Earth structure by inversion of seismic waveforms, *J. Geophys. Res*. 89: 5953–5986.

CALIBRATION OF 3D UPPER MANTLE STRUCTURE IN EURASIA USING REGIONAL AND TELESEISMIC FULL WAVEFORM SEISMIC DATA

Barbara Romanowicz, Mark Panning, and Ahyi Kim

Berkeley Seismological Laboratory, University of California, Berkeley

Sponsored by National Nuclear Security Administration
Office of Nonproliferation Research and Engineering
Office of Defense Nuclear Nonproliferation

Contract No.: DE-FC52-04NA25543

ABSTRACT

We present progress in the development of a new approach to develop and evaluate earth models at the regional scale that utilizes full waveform seismograms.

Adequate path calibrations are crucial for improving the accuracy of seismic event location and origin time, size, and mechanism, as required for Comprehensive Nuclear-Test-Ban Treaty (CTBT) monitoring. There is considerable information on structure in broadband seismograms that is currently not fully utilized. The limitations have been largely theoretical. The development and application to solid earth problems of powerful numerical techniques, such as the Spectral Element Method (SEM), has opened a new era, and theoretically, it should be possible to compute the complete predicted wavefield accurately without any restrictions on the strength or spatial extent of heterogeneity. This approach requires considerable computational power, which is currently not fully reachable in practice.

We have begun work on an approach that relies on a cascade of increasingly accurate theoretical approximations for the computation of the seismic wavefield to develop a model of regional structure for the area of Eurasia located between longitudes of 30 and 150 degrees E and latitudes of -10 to 60 degrees North. The selected area is particularly suitable for the purpose of this experiment, as it is highly heterogeneous, presenting a challenge for calibration purposes, but it is well surrounded by earthquake sources, and, even though they are sparsely distributed, a significant number of high quality broadband digital stations exist, for which data are readily accessible through the Incorporated Research Institutions for Seismology (IRIS) and the Federation of Digital Seismic Networks (FDSN).

The initial model is derived from a large database of teleseismic surface waveforms using well-developed theoretical approximations, the Path Average Approximation (PAVA) and Nonlinear Asymptotic Coupling Theory (NACT). Both approaches assume waveforms are only sensitive to structure along the great circle path between source and receiver, which is adequate for the development of a smooth velocity model.

We plan to refine this velocity model using a more accurate theoretical approach. We utilize an implementation of a 3D Born approximation, which takes into account the contribution to the waveform from single scattering throughout the model, including points situated outside of the great circle path. We perform verification tests of this approach for synthetic models and show that it can accurately represent the wavefield as predicted by numerical approaches such as SEM in several situations where approximations such as PAVA and NACT are insufficient.

The Born approximation will be used to perform an inversion of regional waveforms for a smaller subregion between longitudes 90 and 150 degrees E and latitudes 15 and 40 degrees N. The waveforms are a subset of the original dataset consisting of the source-receiver pairs contained within the region to avoid aliasing structure from outside the region into the model.

In future work, the model will be further refined using a novel inverse approach utilizing a regional implementation of the SEM code for calculation of the synthetic seismograms used in the inversion.

OBJECTIVES

The primary objective of this research is to develop and apply an approach to utilize increasingly advanced theoretical frameworks and numerical methods in order to obtain improved regional seismic structure calibration. Specifically, a large-scale regional Eurasian model will first be developed from a large dataset of seismic waveforms using the path-average approximation (PAVA) and Nonlinear Asymptotic Coupling Theory (NACT) (Li and Romanowicz, 1995), which are well-developed normal-mode based approaches which consider 1D and 2D waveform sensitivity respectively along the great-circle path between source and receiver. This model will then be refined in a smaller region using an implementation of Born single-scattering theory (Capdeville, 2005), which more accurately represents the 3D sensitivity of the seismic wavefield. Finally, we will utilize the Spectral Element Method (SEM), a numerical approach that accurately models both 3D and nonlinear effects (e.g., Faccioli et al., 1996; Komatitsch and Vilotte, 1998; Komatitsch and Tromp, 1999). To conserve computational resources for this step, we will restrict the use of spectral elements to the upper mantle by coupling to a normal mode solution (Capdeville et al., 2002) and applying appropriate boundary conditions. Additionally we plan to utilize a novel approach with stacked sources (Capdeville et al., 2003) to further speed computation.

A further objective of this research is to perform validation and improved calibration of the model described above using a variety of approaches and datasets, including ground truth datasets from the Knowledge Base. Specifically, we plan to apply teleseismic receiver function modeling, regional broadband data forward modeling, and surface wave group velocity measurements to test and improve the model using data not included in the original inversion.

This research can then serve as a proof of concept for applying a similar approach to the calibration of seismic structure in other regions of the Earth.

RESEARCH ACCOMPLISHED

A global dataset of surface wave waveforms crossing the region of interest was collected (Figure 1). We started from the existing waveform database that was collected at Berkeley over the last 10 years for the construction of global mantle tomographic models (Li and Romanowicz, 1996; Megnin and Romanowicz, 2000; Gung et al., 2003; Panning and Romanowicz, 2004). The goal was to complement this global database in the region of interest. After choosing data from 20 new events, and adding in the data from the existing dataset, we now have 38826 3-component waveforms from 393 events recorded at 169 stations. The data has been processed using an automated algorithm, which removes glitches, and checks for many common problems related to timing, poor instrument response, and excessively noisy windows. A weighting scheme has been applied to ensure even distribution of data across the region.

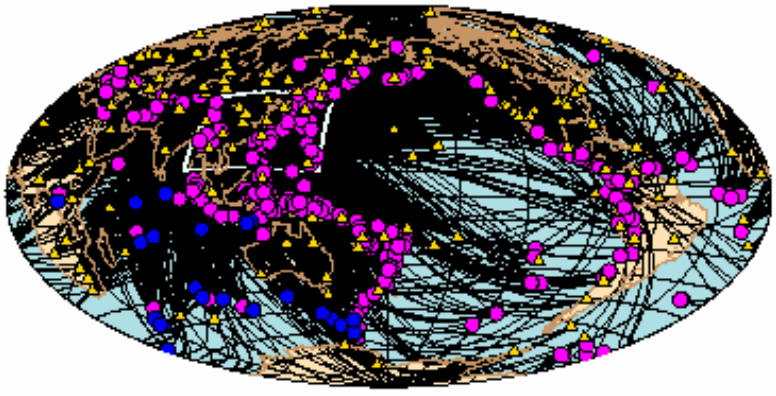

Figure 1. Source-receiver paths of waveforms included in the dataset. Receivers are shown as yellow triangles, events that are part of the previously existing waveform collection are shown by purple circles, and newly collected events are shown with blue circles. The region of interest is shown by the white rectangle.

Technical work continues on developing the theoretical and numerical approaches that consider 3D waveform sensitivity. Work is underway to adapt the SEM code, which will be used in the final inversion step to the regional case. Because coupling the SEM solution to a 1D mode solution at a spherical interface is a key feature of the coupled SEM (CSEM) code we plan to use, limiting the region to the upper mantle is easily accomplished using previously existing versions of the code and has been done. Limiting the 3D portion of the model to a selected region, however, requires larger changes to the code. Currently, work is underway to most efficiently integrate this into the code using the latest algorithms to apply boundary conditions at the boundaries of the region of interest for the SEM code. However, while preparation of that code continues, we have proceeded to develop a complementary 3D inversion approach, which incorporates many of the advantages of the CSEM inversion approach discussed in the proposal. As shown in Figure 2, very similar accuracy in defining the partial derivatives with respect to model parameters can be obtained using a 3D implementation of the Born (single scattering) approximation. We are adapting an implementation of this approach to be used for inverting our surface wave dataset. Because the Born approach is somewhat less numerically intensive than the CSEM-based inversion, an added benefit is that stacking of sources is no longer required, and therefore the waveforms can be divided into packets. Using packets is advantageous as it allows us to only use the highest quality data from the waveform dataset, while removing noisy portions of the seismograms.

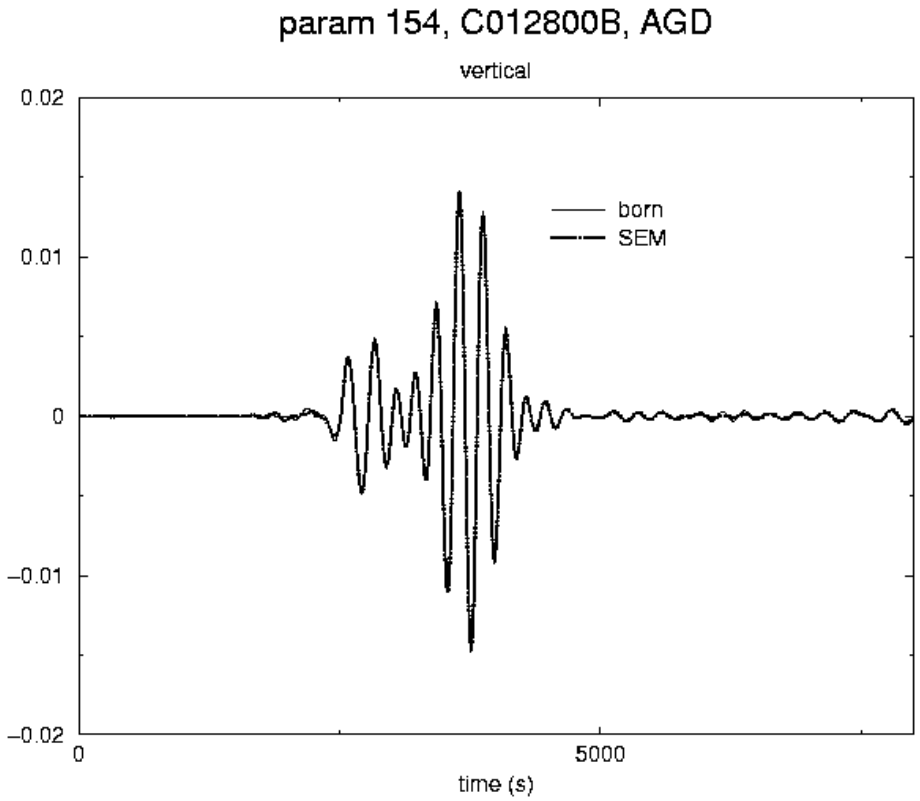

Figure 2. Comparison of partial derivative seismograms computed with SEM (dotted line) and normal modes Born approximation (solid line) for an epicentral distance of 92 degrees. The model parameter with respect to which partial derivatives are computed is between the source and the receiver, slightly off path.

To further test the effectiveness of the Born code, we have performed several tests which compare the Born code with other theoretical approximations. For example, for a case of a source-receiver path passing through a single slow anomaly centered at 220 km depth (Figure 3), all theoretical approaches produce seismograms consistent with

those predicted by CSEM. However, when the path passes just outside the anomaly (Figure 4), PAVA and NACT, which only consider structure along the great-circle path, do not accurately map the phase or the amplitude of the fundamental mode differential seismogram. NACT plus focussing (NACT+F), an additional theoretical approximation that also includes sensitivity to across-path derivatives of structure, and the Born code both do a better job of reproducing the CSEM data. Another slightly more realistic case to consider is when a path passes through both positive and negative velocity anomalies along the source-receiver path (figure 5), as would certainly occur for many source-receiver paths across Eurasia. In this case, PAVA sees nothing, as the two anomalies cancel out, while the 2D sensitivity of NACT predicts the amplitude but not the phase of the overtone phase (X1), or the fundamental mode (R1). NACT+F does a reasonable job of predicting the amplitude of the differential seismogram but does not match the phase well, particularly in R1. The Born code, on the other hand, correctly predicts the phase of the differential seismogram throughout, although it overpredicts the amplitude of the R1 portion of the seismogram.

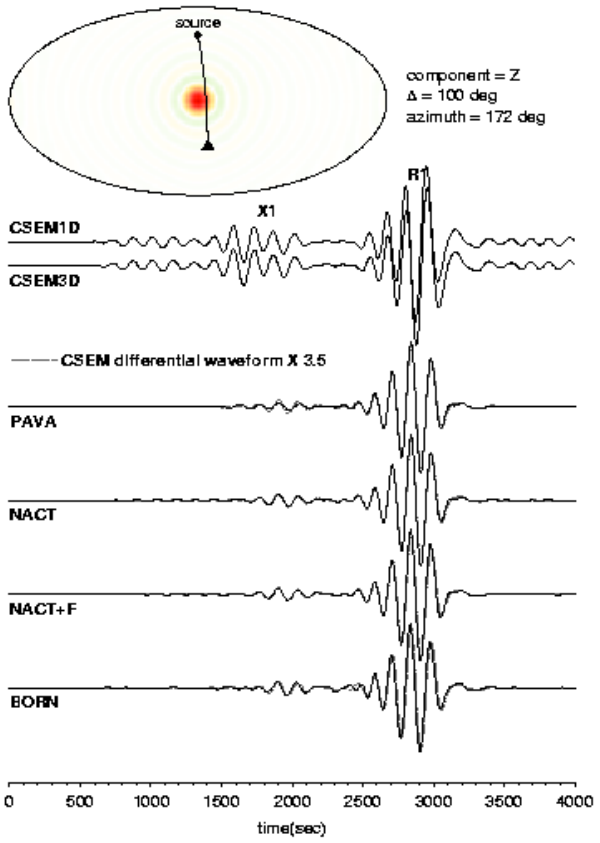

Figure 3. Comparison of performance of several mode-based approximations used in tomographic modeling. The map shows the source-receiver geometry and the velocity model, which consists of a ellipsoidal anomaly 5% slower than the background centered at 220 km depth. The top two traces are the SEM synthetics calculated from the 1D background model and the 3D model. The remaining traces show the differential waveforms obtained by subtracting the waveform produced by the 1D model. For each of the approximations shown, the differential SEM waveform is shown as a dotted line, and the waveform from the approximation. Results are shown for the PAVA, NACT, NACT plus a higher-order focusing approximation (NACT+F), as well as the 3D Born approximation.

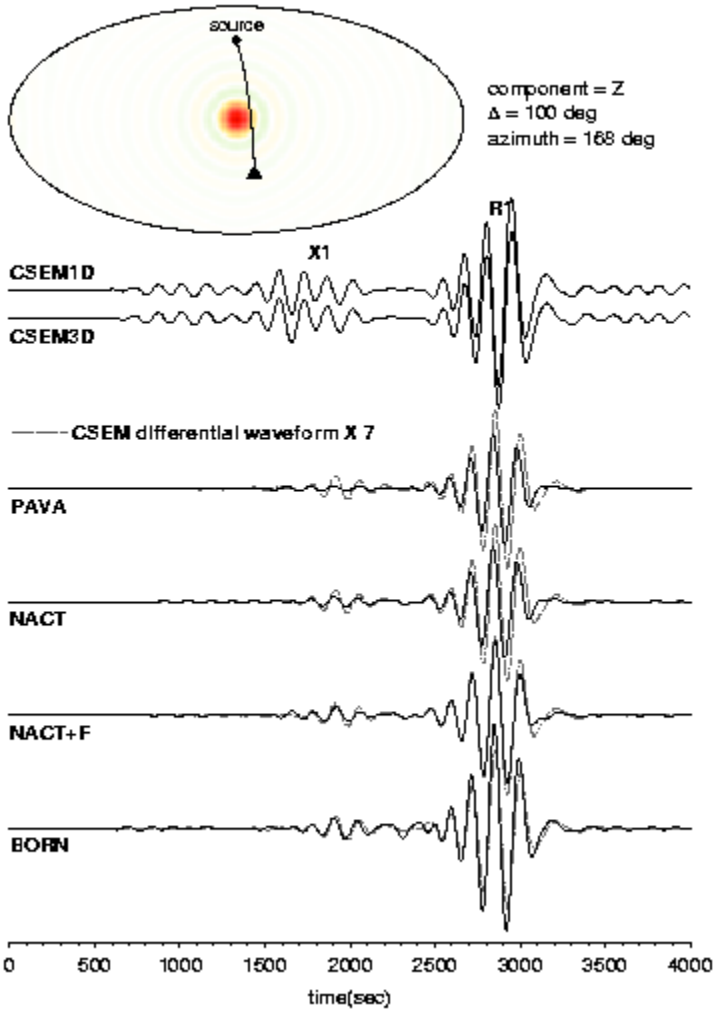

Figure 4. Same as Figure 3 for a path that passes slightly east of the anomaly.

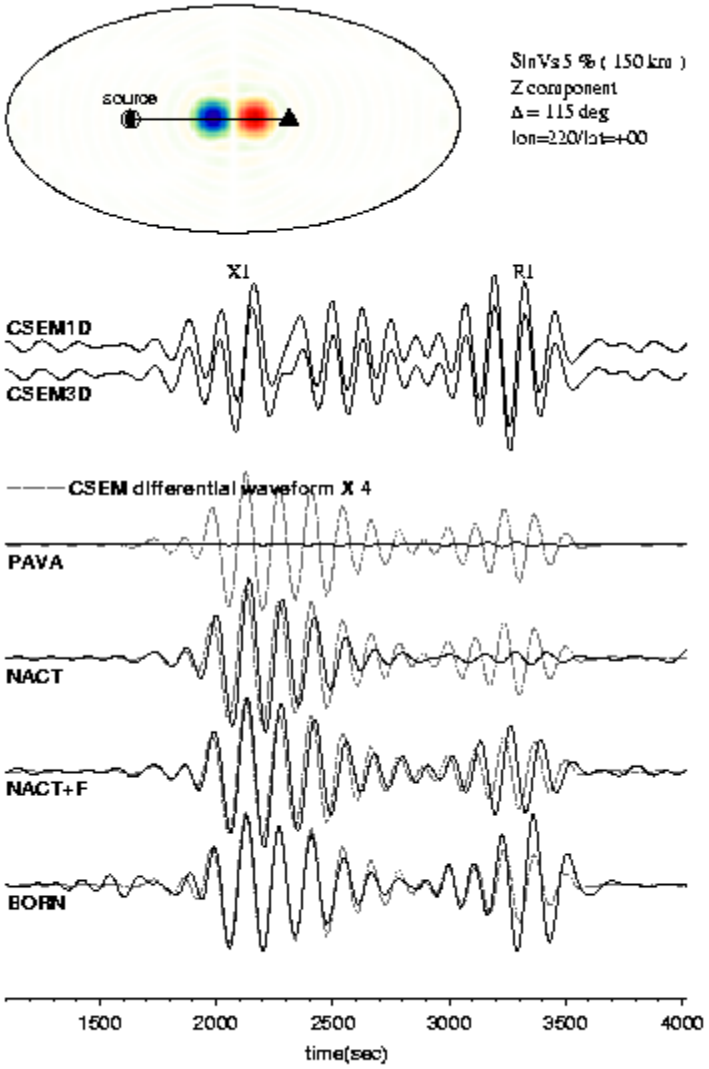

Figure 5. Similar to Figure 3 and 4, but for a model with two ellipsoidal anomalies of +/- 5% centered at 150 km depth and also using a realistic moment tensor source.

With the success of the Born code in predicting the 3D effects of structure in these particular paths, we have begun work to implement this theory into an inverse approach. The starting 3D S velocity model for this inversion will be based on our existing 3D global models. We have converted the global parameterization used in our global tomography to one based on local functions, specifically spherical splines. This parameterization is now available for inversions using the approximate NACT methodology to develop the first iteration model and is now also implemented for an inversion using the Born code.

CONCLUSIONS AND RECOMMENDATIONS

Using better theoretical and numerical approaches in regional tomographic modeling is very important for adequate seismic path calibration. Here a 3D implementation of Born scattering theory is shown to accurately model 3D effects for a few particular structures. Utilizing this theory in combination with the dataset of waveforms already gathered should allow for an improved model of Eurasian upper mantle velocity structure.

Further work on using SEM, a numerical approach which takes into account 3D and nonlinear effects, in an inversion should offer continued improvement of the model. Additionally, other approaches and datasets, including ground truth datasets from the Knowledge Base, teleseismic receiver functions, broadband waveform forward modeling, and surface wave group velocities allow for validation and improvement of the model.

ACKNOWLEDGEMENT

We would like to acknowledge Yann Capdeville for the use of his Born code and advice in the adaptation of this code to our project.

REFERENCES

Capdeville, Y., E. Chaljub, J. P. Vilotte, and J. P. Montagner (2002), Coupling the spectral element method with a modal solution for elastic wave propagation in global earth models, *Geophys. J. Int.* 152: 34–66.

Capdeville, Y., B. Romanowicz, and Y. Gung (2003), Global seismic waveform tomography based on the spectral element method, abstract, joint AGU/EGS/EUG Meeting, Nice, April 2003.

Capdeville, Y. (2005), An efficient Born normal mode method to compute sensitivity kernels and synthetic seismograms in the Earth, submitted to *Geophys. J. Int.*

Faccioli, E., F. Maggio, A. Quarteroni, and A. Tagliani (1996), Spectral-domain decomposition methods for the solution of acoustic and elastic wave equations, *Geophysics* 61: 1160–1174.

Gung, Y., B. Romanowicz, and M. Panning (2003), Anisotropy and lithospheric thickness, *Nature* 422: 707–711.

Komatitsch, D. and J. P. Vilotte (1998), The spectral element method: an effective tool to simulate the seismic response of 2D and 3D geological structures, *Bull. Seism. Soc. Am.* 88: 368–392.

Komatitsch, D. and J. Tromp (1999), Introduction to the spectral-element method for 3-D seismic wave propagation, *Geophys. J. Int.* 139: 806–822.

Li, X. D. and B. Romanowicz (1995), Comparison of global waveform inversions with and without considering cross branch coupling, *Geophys. J. Int.* 121: 695–709.

Li, X. D. and B. Romanowicz (1996), Global mantle shear velocity model developed using nonlinear asymptotic coupling theory, *J. Geophys. Res.* 101: 22,245–22,273.

Megnin, C. and B. Romanowicz (2000), The 3D shear velocity structure of the mantle from the inversion of body, surface and higher mode waveforms, *Geophys. J. Int.* 143: 709–728.

Panning, M. and B. Romanowicz (2004), Inferences on flow at the base of Earth's mantle based on seismic anisotropy, *Science* 303: 351–353

HIGH-RESOLUTION TOMOGRAPHIC MAPPING OF REGIONAL PHASE Q IN THE MIDDLE EAST

Eric Sandvol[1], Ekrem Zor[1], Jiakang Xie[2], and Brian J. Mitchell[3]

University of Missouri[1], Columbia University[2], and St. Louis University[3]

Sponsored by National Nuclear Security Administration
Office of Nonproliferation Research and Engineering
Office of Defense Nuclear Nonproliferation

Contract Nos. DE-FC52-03NA99518[1], DE-FC52-03NA99519[2], and DE-FC52-03NA99520[3]

ABSTRACT

To develop reliable discriminants for a given region, it is essential that source, station, and path effects be isolated. This is even more critical for paths through a region such as the Middle East, where both crustal and uppermost mantle attenuation are very high.

The most efficient method for developing path corrections for potential discriminants is to construct a frequency dependent Q model for the corresponding regional seismic phases Pn, Pg, Sn, and Lg. In Turkey and the surrounding regions, we have finished the collection and distillation of total regional waveforms of 55 stations from the Eastern Turkey Seismic Experiment (ETSE), the Western Turkey Regional Network (WTRN), the Midsea array of ETHZ, GEOFON, MEDNET, and GSN, using the IRIS data management center request tools. We have also used all available waveform data from the broadband stations of the KOERI network that have reliable instrument response information. We calculated 1760 Lg spectra from ~150 events. We obtained Lg Q values from 1151 two-station paths; we only used paths with interstation distances between 150 and 2000 km. Waveforms with complete Lg blockage and unstable values with standard deviations higher than 50% of the estimated Lg Q were excluded from the final data file for tomography. After this data reduction, we had a total of 715 two-station paths with good quality Lg Q and 209 two-station paths with Lg blockage. We expect to improve our tomographic image using the short period stations with this method.

We have found exceptionally low Q_0 values within both the eastern Anatolian plateau (~ 80 to 100) and the western Anatolian active extensional zone, especially the Menderes massif (~80 to 150). We also found low to normal Lg Q_0 values for the northern Arabian plate (~200 to 300) and part of the Taurus Mountains in western Anatolia. Resolution tests of 2^ox2^o cell size for our Lg-Q tomography indicate that we have very good resolution throughout much of the Anatolian plateau. We expect to improve on our existing coverage by including waveform data from the JSO (Jordanian Seismological Observatory) and the SNSN (Syrian National Seismic Network).

OBJECTIVE(S)

The objective of this study is to obtain laterally varying Q models for multiple regional waves, including Lg, Pg, and Pn, for the Middle East. We are developing Q models that have the highest possible lateral resolution. For some waves such as Lg and Pg, the resulting Q model will be in the form of a tomographic Q map; for other waves such as Sn, the resulting Q models may be region-specific--we will divide the Middle East into several sub-regions of constant Q. Blockage effects will be represented by low effective Q values in the models.

The difficulty associated with Q measurements

It is well known that the attenuation rate of regional waves, including the high-frequency Lg, Pg, Sn and Pn and the lower-frequency surface waves, is highly variable over major continents. Reliable knowledge of the lateral variation in regional wave attenuation rate, or its inverse, Q, is extremely important for event detection and identification in the nuclear monitoring program. The preferred way to acquire this knowledge is to conduct tomographic mapping of regional wave Q. However, in contrast to the wide success in seismic velocity tomography since the 1970s, there has been relatively little progress in Q tomography. The main obstacle is the difficulty in obtaining reliable measurements of Q: the observed amplitude of high-frequency waveforms is affected by a number of factors, including (1) possible non-isotropic source radiation patterns, (2) source spectra that may be only grossly described by a seismic moment and a corner frequency; (3) geometrical spreading terms caused by the wave front expansion which, in complex 3D Earth structures, may cause focusing and defocusing; and (4) potential site responses caused by local structural complications under the seismic stations. Effects of these factors are difficult to correct, causing biases in Q measurement.

The difficulty of precise Q measurement is clearly demonstrated by two examples involving the Lg phase. This first is given by Xie & Mitchell (1990), who list eight published Lg Q models for the Basin & Range Province. The 1 Hz Lg Q (Q_0) values in these models vary between 139 and 774, despite the area's being one of the best studied. The second is given by Fan and Lay (2003b), who list a number of previously and recently published models in Tibet. In these models, the Q_0 for the same sub-region (i.e., southern or eastern Tibet) ranges between 60 and 400. Because of these difficulties, the problem of measuring Q using regional waves has been a rapidly evolving research topic. Recently, progress has been made in mapping laterally varying regional wave Q structure, particularly through Q tomography. The primary reason for this progress is that the digital seismic database has grown rapidly, permitting the use of methods for measuring Q that are more precise but require abundant data and/or a specific pattern of path geometries. In the following sections, we will briefly summarize the work of various researchers, including both the Co-P.I.'s, on regional wave Q tomography.

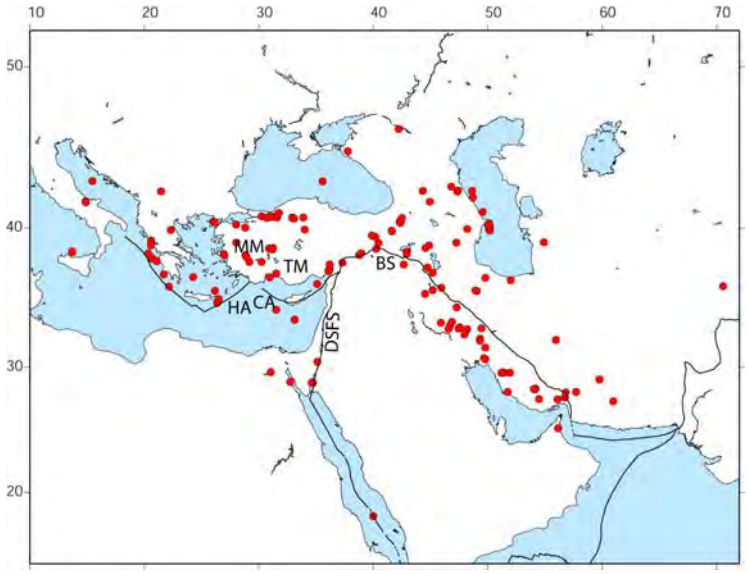

Figure 1. Seismic events used in our study of Lg Q and η. BS- Bitlis Suture; TM- Tauride Mountains; MM-Menderes Masif; DSFS-Dead Sea Fault System; CA-Cyprean Arc; HA-Hellenic Arc.

RESEARCH ACCOMPLISHED

Data Collection

A major component of this proposal is the acquisition and processing of new waveform data in the region. In order to successfully formulate a robust Q model for the four fundamental regional phases, we need to collect and construct a large waveform database for the Middle East. Given the large regions within the Middle East that are not accessible for a variety of reasons, this will continue to be an ongoing problem that we will address.

We have made agreements with scientists in several countries for them to share data for the Middle East. These new databases will greatly improve the existing ray coverage, especially the two station path coverage. Most significantly, we have reached a collaborative agreement with Kandilli Observatory and Earthquake Research Institute (KOERI) to exchange software and waveform data for Turkey. In Turkey and the surrounding regions, we have finished the collection and distillation of total regional waveforms of 55 stations from the Eastern Turkey Seismic Experiment (ETSE), the Western Turkey Regional Network (WTRN), the Midsea array of ETHZ, GEOFON, MEDNET, and GSN, using the IRIS data management center request tools. We have also used all available waveform data from the broadband stations of the KOERI network that have reliable instrument response information. We calculated 1760 Lg spectra from ~150 events. We obtained Lg Q values from 1151 two station paths; we only used paths with apertures greater than 150 km and less than 2000 km. Waveforms with a blocked Lg and unstable values with standard deviations higher than 50% from linear regression were excluded from the final data file for tomography. After this data reduction, we had total 715 two-station paths with good quality Lg Q and 209 two-station paths with zero Lg efficiency. We are still working on developing a method for the short period stations that do not have reliable instrument response. In order to accomplish this task, Dr. Eric Sandvol visited Dr. Jiakang Xie from Lamont Doherty National Laboratory and worked on the test data. We expect to improve our tomographic image using the short period stations with this method. We are still trying to obtain reliable instrument responses for the short period stations in our current database. We are also continuing to work on finalizing the JSO data.

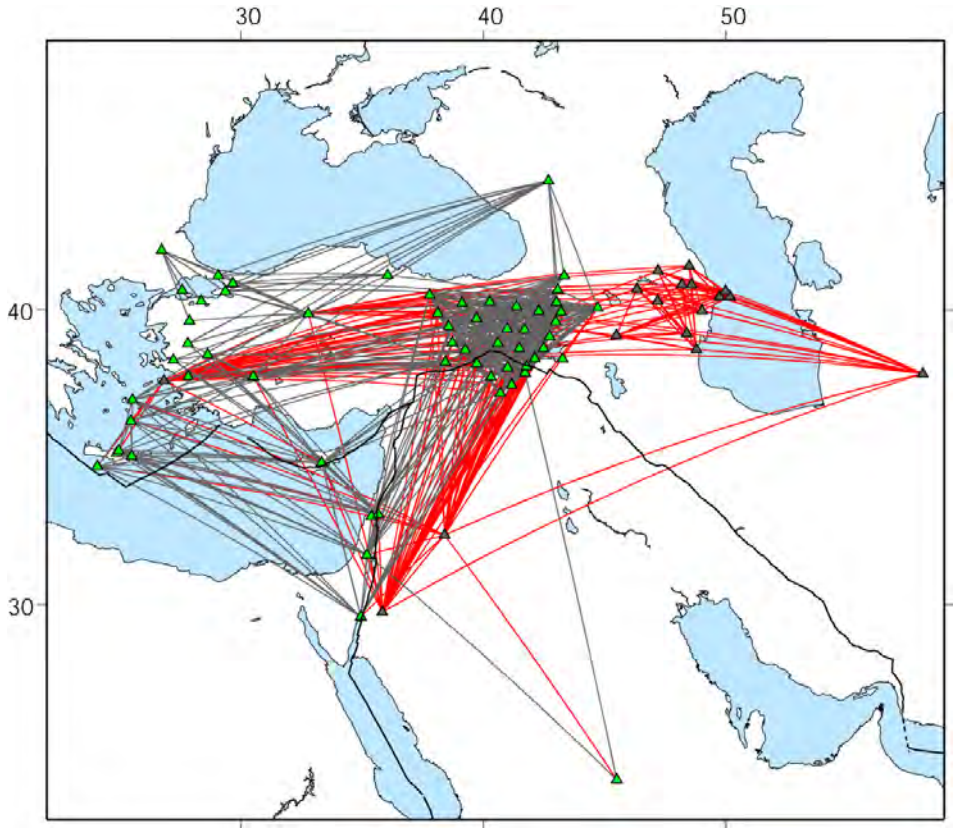

Figure 2. Existing (grey) and potential (red) two station paths for the Turkey and surrounding regions. We have determined reliable Q measurements for all existing paths.

Furthermore, we have begun to process data from the Azerbiajan Seismic Network (ASN). The ASN is composed of 10 broadband stations deployed throughout the Lesser Caucasus. We have begun to select waveforms for key events and analyze them. We have found that a large number of the seismic records that we have examined have little or no Lg energy.

We have also finished collecting waveform data from a number of temporary seismic networks in the Middle East, including the St. Louis University western Turkey Array. This array consisted of 4 broadband and 4 short period instruments running continuously for about a year starting in the fall of 2002. We are also utilizing the large waveform database from the 29-station ETSE broadband seismic network that ran from late 1999 to August 2001 and spanned much of Eastern Anatolia. ETSE in particular has provided us with excellent coverage throughout the eastern Anatolian plateau

Methodology

We are using or planning on using a number of methodologies to isolate the regional wave path attenuation (Q_0 and η) in the Middle East. In the following sections we outline each of the planned methods. Due to the rather non-uniform ray path coverage, we will need to apply different techniques depending upon the regional data availability. Figure 2 shows the two station paths that we have analyzed or plan to analyze in the near future. These paths were selected from data that were recorded during the operation of the ETSE array.

We have employed a two-station method for measuring Lg Q. This method cancels the source effect in Q measurement by using station pairs aligned with the source. Xie and Mitchell (1990) and Xie (2002a) used this method for measuring Lg Q, and presented rigorous error analyses. We have used event-station pairs that are aligned with 15 degrees of being on the same great circle path.

We have begun to collect data in order to examine regional waveform data using the event-pair spectral ratio method. This method was developed by Chun et al. (1987) to measure Pn Q and requires that regional waves (e.g., Lg) be recorded at two stations from two events; all must be located approximately on the same great circle. If this very restrictive recording condition can be met, then the method can simultaneously determine inter-station Q and the station site response**.** This method will then will allow us to incorporate data for which we cannot necessarily trust the instrument response information. For example, although we have instrument response information for many of the short period stations in the northern Middle East, the gain factors can be many orders of magnitude. The reverse two-station method will allow us to remove those stations that do not have reliable instrument parameters. The short period stations in the Middle East do not have reliable response data although our collaborators have provided us detailed gain values and instrument types**.** We are working to eliminate those waveforms with unreliable instrument response information by comparing a number of relative instrument response data.

Qualtiy Control

We have found that it is essential to carefully review our two-station Q measurements in order to ensure that the measurements are reliable. We have manually determined the appropriate frequency range used in the linear regression analysis used to estimate Q_0 and η. We also manually eliminated those two station spectral ratios that had: (1) large estimated uncertainties (larger than 50% errors), (2) large amounts of scatter in the spectral ratio, (3) a clearly nonlinear relationship between amplitude and frequency, or (4) a narrow frequency range (>0.5 Hz) over which the linear regression is determined. These quality control procedures help eliminate a substantial amount of scatter in our Q_0 and η determinations. The majority of our two station Q measurements are repeatable within the estimated errors.

We also chose to include those Q measurements with negative η values. We have found that even for negative values of η, the spectral ratios are very well behaved (i.e. decreasing linearly with decreasing frequency). We are currently working on developing a model of spatial variations in η across the northern Middle East in order to test whether there is any spatially coherent variation in η that would correlate with a tectonic or geologic boundaries such as the Arabian-Eurasian plate boundary.

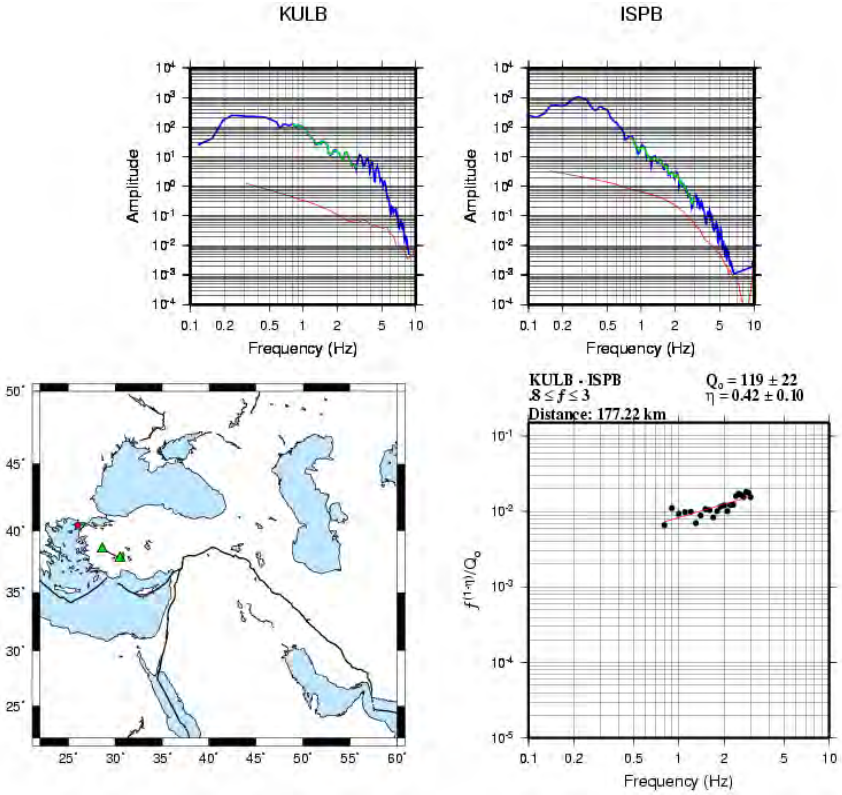

Figure 3. An example of a single Q measurement for a two-station path crossing the Menderes Massif in western Turkey. We have found low Lg Q values throughout most of the regions that are undergoing large amounts of crustal extension.

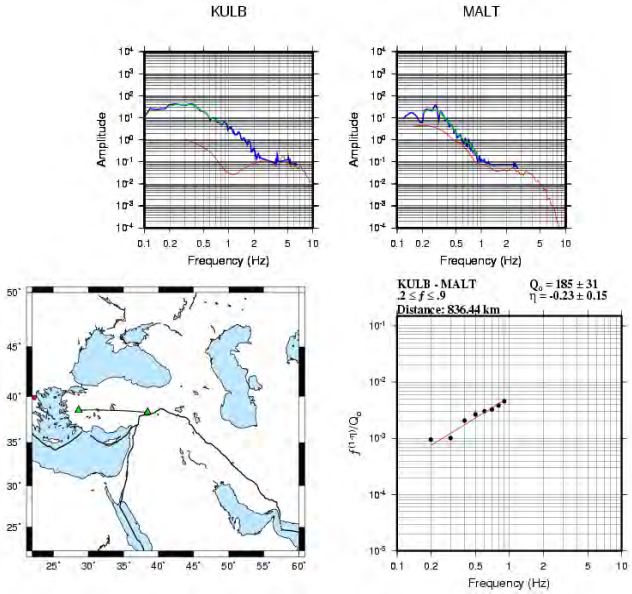

Figure 4. An example of a single Q measurement for a two-station path crossing the eastern Anatolian plateau.

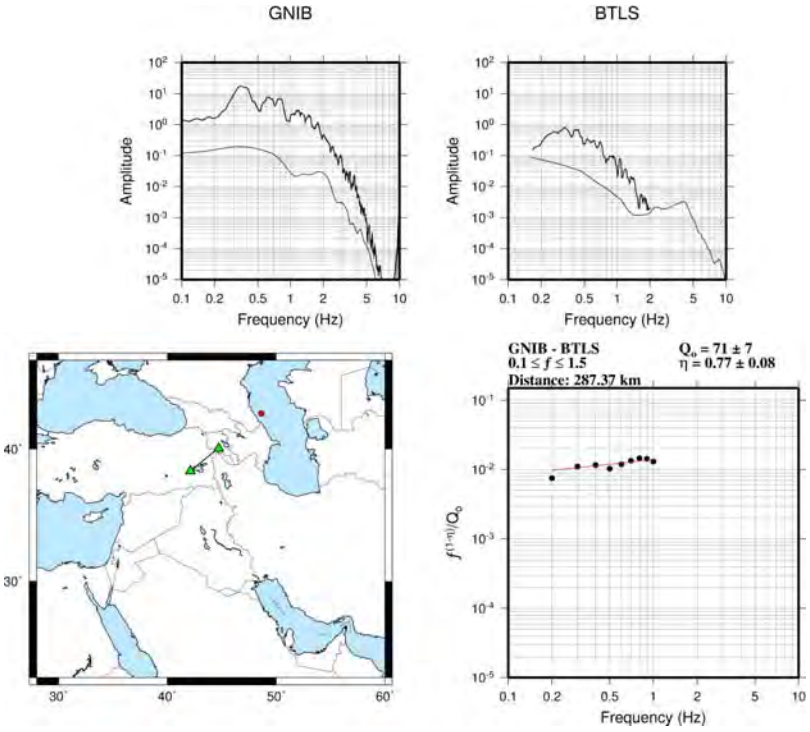

Figure 5. An example of a single Q measurement for a two-station path crossing the eastern Anatolian plateau. We have found exceptionally low Lg Q values throughout most of the Anatolian plateau.

Lg Q tomography for the Middle East

Figures 3, 4, and 5 illustrate some of the example measurements throughout the northern Middle East. We have finished developing a fully automated process of calculating spectra to apply a two-station method for measuring inter-station Q_0. We have taken these two station Q_0-values and developed a tomographic Q_0 model for Turkey and the surrounding region. We have tested several different tomographic algrorithms and found small variations between the different models (Figure 6).

We have found exceptionally low Q_0 values within both the eastern Anatolian plateau (~ 80 to 100) and in western including the Menderes Massif that is consistent with crustal melting. This is to some degree consistent with the Quaternary volcanism that is widespread throughout the Anatolian plateau. In fact, we observe relatively good correlation between very low Q values (less than 100) and the location of Holocene volcanism in the region. We also observe very low Q values in the western Anatolian active extensional zone, especially the Menderes massif (~80 to 150). We also found fairly normal Lg Q_0 values for the northern Arabian plate (~200 to 300), beneath Uludag and part of the Taurus Mountains in western Anatolia. It is important to note that all of the paths traversing the Taurides are east-west paths, so our results may be biased (Gok et al., 2000 observed Lg blockage for ray paths that are perpendicular to the strike of the Taurides).

We found low to normal Lg Q_0 values for the northern Arabian plate (~200 to 300). Variations in crustal structure across the Dead Sea Fault System and across the Palmyride fold and thrust belt do not appear to effect Lg propagation. Within the northernmost Arabian plate, near the Bitlis suture, we find low Q values that once again correspond well with the location of Holocene Volcanism. We observe very little attenuation for paths traversing western Arabian plate (Lg Q = 800) where there are few or no sediments. In eastern Arabia, Lg Q is substantially lower (~450). We also observe inefficient Lg propagation for the paths crossing the southeastern part of Aegean Sea (Figure 5).

In summary, we have found that our initial Lg Q tomography agrees to first order with our Lg/Pg ratio tomography in the region. We observe a good correlation between the high Q in the Arabian plate and the low Q in the Eurasian and Anatolian Plates. We also observe very high Lg Q values along the western Arabian plate and lower Q values within the eastern Arabian plate (Arabian platform).

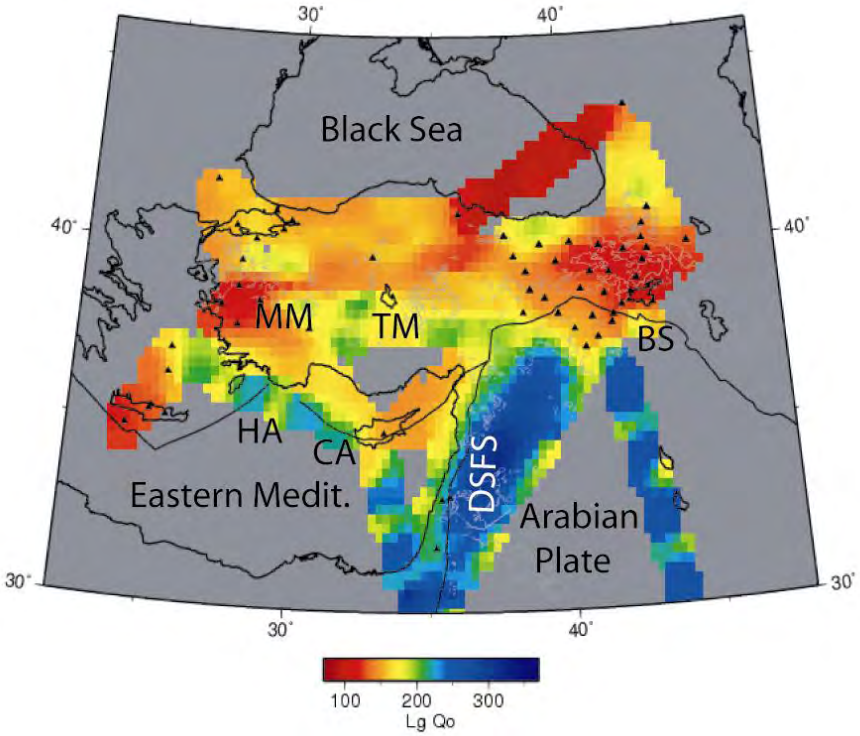

Figure 6. Preliminary Lg Q-tomography for Turkey and surrounding regions. BS- Bitlis Suture; TM-Tauride Mountains; MM- Menderes Masif; DSFS-Dead Sea Fault System; CA-Cyprean Arc; HA-Hellenic Arc.

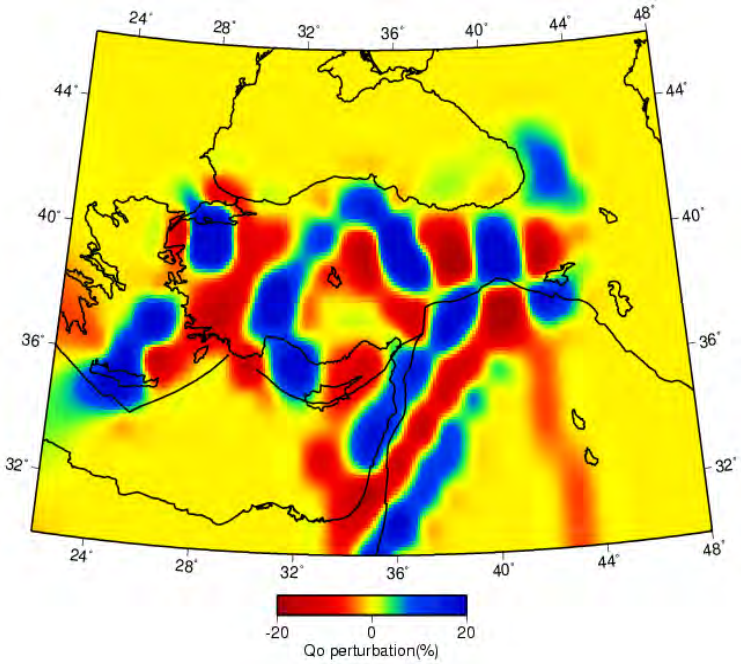

Figure 5. Checkerboard resolution of 2x2 cell for the preliminary Lg Q-tomography for eastern Turkey and the surrounding regions.

Resolution tests of 2x2 cell size for our Lg-Q tomography indicate that we have very good resolution throughout much of the Anatolian plateau. Currently, we cannot resolve details within much of the northern Arabian plate or the Dead Sea Fault System. We expect to improve on our existing coverage by including waveform data from the JSO (Jordanian Seismological Observatory) and the SNSN (Syrian National Seismic Network).

CONCLUSION(S) AND RECOMMENDATION(S)

We have found that in order to achieve sufficiently dense two station paths to cover the Middle East, it is necessary to integrate data from a variety of temporary and permanent, short period and broadband seismic stations. Using these large data sets it is possible to construct a reliable model for Lg Q throughout the northern portions of the Middle East and Dead Sea Fault System. We are currently in the process of calculating Q models for Pn, Pg, and Lg.

Clearly, one of the most challenging aspects of calculating Lg in the Middle East is the large number of blocked paths. Therefore it is critical to accumulate a large number of waveforms at local and near-regional distances in order to better constrain the Q in the very high attenuation zones such as the Eastern Anatolian plateau. Prior work has established the blockage zones, and these blocked paths will also be used to help create a robust attenuation model for the majority of the Middle East. It is therefore essential that more data be collected for these regions of exceptionally low Lg Q such as the lesser and possibly greater Caucasus and western Turkey.

After we finalize our Lg Q model we expect to include over 1200 two station paths using methods 1 and 2 in the last section or the Newton-like non-linear method for inversion with multiple co-located events. Lg Q_0 and η values measured using these methods are of very high quality since they are not subject to the trade-off between source and path parameters. Therefore in the tomographic inversion of laterally varying Q_0 and η values, the input Q_0 and η values along approximately 900 paths will be used to derive a more long-wavelength Q map for those regions of the Middle East with good two station path coverage.

We believe that it is essential to reconcile our two station Q measurements with those using alternative methods and coda based methods. We plan to apply available methods for Lg Q determination in order to better quantify the potential differences among the techniques. This should help build a more robust model for high frequency wave attenuation in the Middle East.

ACKNOWLEDGMENTS

We would like to thank Dr. Niyazi Turkelli both for providing data from the KOERI network and for assisting in the analysis of portions of the data. We would also like to thank Dr. Rob Mellors for providing data from the Azerbaijan Seismic Network and Dr. Arthur Rodgers for providing data from two Lawrence Livermore National Laboratory broadband stations in Jordan.

REFERENCES

Chun, K. Y., G. F. West, R. J. Kokoski, and C. Samson (1987), A novel technique for measuring Lg attenuation - Results from eastern Canada between 1-Hz to 10-Hz, *Bull. Seism. Soc. Am.* 77: 398-419.

Fan, G.-W., and T. Lay, 2003b. Strong Lg Attenuation in the Tibetan Plateau, *Bull. Seism. Soc. Am.*, in press.

Gok, R., N. Turkelli, E. Sandvol, D. Seber and M. Barazangi, Regional wave propagation in Turkey and surrounding regions, *Geophys. Res. Lett.* 27: No 3, 429-432, 2000

Hartse, H.E., S.R. Taylor, W. S. Phillips & G.E. Randall, 1997. A preliminary study of regional seismic discrimination in central Asia with emphasis on western China, *Bull. Seism. Soc. Am.* 87: 551-568.

McNamara, D.T., T. Owens and W. Walter, 1995. Observations of regional phase propagation across the Tibetan Plateau, *J. Gephys. Res.* 100: 22,215-22,229.

Mitchell, B.J., Y. Pan, J. Xie and L. Cong, 1997. Lg coda Q variation across Eurasia and its relation to crustal evolution, *J. Geophys. Res.* 102: 22767-22780.

Owens, T.J., and G. Zandt, 1997. Implications of crustal property variations for models of Tibetan plateau evolution,

Nature, 387: 37-43.

Patton, H.J., 2001. Regional magnitude scaling, transportability, and Ms:mb discrimination at small magnitudes. *Pure Appl. Geophys.*, 158: 1951-2015.

Phillips, W.S., G.E. Randall and S.R. Taylor, Path correction using interpolated amplitude residuals: An example from central China, *Geophys. Res. Lett.*, 25: 2729-2732, 1998.

Phillips, W.S., Empirical path corrections for regional phase amplitudes, *Bull. Seism. Soc. Am.*, 89: 384-393, 1999.

Phillips, W.S., H. E. Hartse, S. R. Taylor, and G. E. Randall, 2000. 1 Hz Lg Q Tomography in Central Asia, *Geophys. Res. Lett.*, 27, 3425-3428.

Rapine, R., J. Ni, J. Wu, and T. Hearn, 1997. Wave propagation in China and surrounding regions, Bull. Seismo. Soc. Am., 87: 1622-1636.

Rodgers, A., and S. Schwartz (1998). Lithospheric structure of the Qiangtang Terrane, northern Tibetan Plateau, from complete regional waveform modeling: evidence for partial melt, *J. Geophys. Res.*, 103: 7137-7152.

Sandvol, E., K. Al-Damegh, A. Calvert, D. Seber, M. Barazangi, R. Mohamad, R. Gok, N. Turkelli and C. Gurbuz C, 2001. Tomographic imaging of Lg and Sn propagation in the Middle East, *Pure Appl Geophys.*, 158: 1121-1163.

Sereno, T.J., 1989, Numerical modeling of Pn geometric spreading and empirically determination attenuation of Pn and Lg phases recorded in eastern Kazakhstan, Technical Report of Science Application International Corporation, SAIC 89//1555, San Diego.

Shin, T.C. and R.B. Herrmann, 1987, Lg attenuation and source studies using 1982 Miramichi Data, *Bull. Seism. Soc. Amer.***77**: (2) April, p. 366-383.

Tarantola, A., Inverse problem theory : methods for data fitting and model parameter estimation**,** Elsevier ; New York, NY, U.S.A.,1987

Taylor, S., Velasco, A., X. Yang, M. Maceria and W.S. Phillips, 2000. Bayesian tomography applied to seismic event identification problems, in *Proceedings of the 23rd. Seismic Research Review: Worldwide Monitoring of Nuclear Explosions,* LA-UR-01-4454, Vol. 1, pp. 440-447.

Taylor, S.R., Velasco, A.A., Hartse, H.E., Phillips, W.S., Walter, W.R.and A.J. Rodgers, 2002. Amplitude corrections for regional seismic discriminants, *Pure Appl. Geophys.* 159: 623-650.

Toiran, B.M., 2002. The New Cuban Seismograph Network, *Seism. Res. Lett.* 73: No. 4, 504-532.

Walter, W. R. and S. Taylor, 2002. A revised magnitude and distance correction (MDAC2) procedure for regional seismic discriminants, Lawrence Livermore National Laboratory UCRL-ID-246882.

Xie, J., 1993. Simultaneous inversion of source spectra and path Q using Lg with applications to three Semipalatinsk explosions, *Bull. Seismol. Soc. Am.*, 83, 1547-1562.

Xie, J., 1998. Spectral inversion using Lg from earthquakes: Improvement of the method with applications to the 1995, western Texas earthquake sequence, *Bull. Seismol. Soc. Am*. 88: 1525-1537.

Xie, J., 1999. Excitation and attenuation of regional waves from recent seismic events in China, *Proceedings of the 19th Annual Seismic Symposium on Monitoring a Comprehensive Test Ban Treaty,* Edited by U.S. DoD and U.S. DOE., Vol. 1, 323-332.

Xie, J., 2002a. Lg Q in the Eastern Tibetan Plateau, *Bull. Seism. Soc. Am*. 92: 871-876.

Xie, J., 2002b. The physical basis and improved criteria for the phase spectral ratio discriminants, *DTRA Final Report*, in review.

Xie, J. & B.J. Mitchell, 1990. Attenuation of multiphase surface waves in the Basin and Range Province, part I: Lg and Lg coda, *Geophys. J. Int.* 102: 121-137.

Zhu, T.F., K.Y. Chun & G.F. West, 1991. Geometrical spreading and Q of Pn waves: An investigative study in eastern Canada. *Bull. Seism. Soc. Am.* 81: 882-896.

DEVELOPMENT OF SURFACE-WAVE DISPERSION AND ATTENUATION MAPS AND IMPROVED METHODS FOR MEASURING SURFACE WAVES

Jeffry L. Stevens, Jeffrey W. Given, G. Eli Baker, and Heming Xu

Science Applications International Corporation

Sponsored by Air Force Research Laboratory

Contract No. FA8718-05-C-0023

ABSTRACT

The purpose of this new project is to optimize the procedures for measuring surface waves, particularly at regional and local distances. An important part of the project is the development of global regionalized dispersion and attenuation maps, with a particular focus on determining attenuation maps for Eurasia in the 8-15 second period band. This project follows earlier work to determine global earth models and dispersion maps using tomographic inversion of a very large data set. In this project, we are revising the procedure for performing tomographic inversion to incorporate scattering and diffraction. In addition to improving the dispersion models, this also provides a means to derive corrections for amplitude variations caused by heterogenous earth structure. We are assembling a data set of attenuation measurements through a combination of new measurements and existing measurements from other researchers, and performing tomographic inversions for Q structure. The inversion technique is very similar to that used for dispersion, using tomographic inversion of attenuation measurements to determine regionalized Q models which can then be used to generate attenuation maps at all frequencies (constrained by the frequency content of the data and background Q models).

We define a path corrected time-domain magnitude, which combines the time-domain narrow-band surface-wave magnitude procedure of Russell (2004) with the path corrected spectral magnitude of Stevens and McLaughlin (2001). Both the path corrected spectral magnitude and path corrected time-domain magnitude can be used reliably at any distance range, including regional and local distances. The earth structure and attenuation models described above are used to predict and correct for the amplitude variations along any source to receiver path. The procedure therefore results in an optimized surface-wave measurement procedure, which with good path corrections is valid at all distances. It is also valid at all frequencies with the caveat that frequency variations in source spectra must be taken into account if the procedure is used for Ms:mb discrimination.

OBJECTIVE

The objective of this project is to optimize the procedures for measuring surface waves, particularly at regional and local distances. An important part of the project is the development of global regionalized dispersion and attenuation maps, with a particular focus on determining attenuation maps for Eurasia in the 8-15 second period band.

RESEARCH ACCOMPLISHED

Overview

This is a new project and work to date has focused on implementing some of the procedures necessary to predict amplitude variations due to earth structure in a three-dimensional earth. An overview of the project is shown in Figure 1. In an earlier project we developed global, regionalized dispersion models that allow the phase and group velocity to be calculated between any two points on the earth. We did this by accumulating a large data set consisting of more than 1 million dispersion measurements derived by a number of researchers, and then inverting this data set to determine earth structure, which in turn is used to generate dispersion maps at all frequencies.

Figure 1. Overview of the surface wave dispersion and attenuation project.

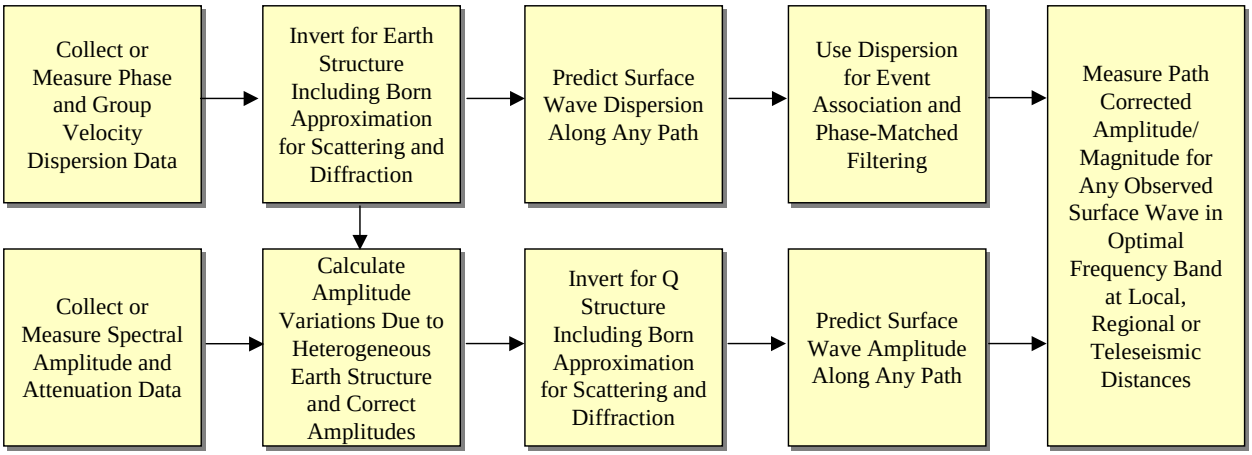

In the current project, we continue development of dispersion models, but incorporate into the modeling more complex phenomena caused by propagation in heterogeneous media including scattering and diffraction. The previous project modeled surface waves in a heterogeneous earth using the following approximations: 1) surface waves propagate along great circle paths, 2) surface-wave phase and group velocities and anelastic attenuation can be modeled using a path integral between source and receiver, and 3) energy is conserved with no mode conversion across material boundaries. This approximation is quite good for large parts of the world, but the unmodeled variations become important in regions of structural complexity.

A major emphasis of the project is the development of regionalized attenuation models. Our current model distribution includes attenuation maps as well as dispersion maps, but they are based on relatively generic models, and do not take into account attenuation differences between regions. The procedures that we developed for inversion of dispersion data for earth structure can also be applied to inversion of attenuation data for Q structure. The Q structures can then be used to predict attenuation between any two points on the earth.

Development of attenuation models is more difficult than development of dispersion models because it is more difficult to make attenuation measurements, and because amplitudes are more sensitive than dispersion to lateral variations in earth structure. Most of the measurements in our existing data set are group velocity measurements, which (except for very large events) can be derived accurately from single station measurements using the known origin time and location and the arrival times of different frequencies at the recording station. Phase velocities are more difficult to measure because they require either two station measurements or an assumption about the initial phase of the source. Attenuation measurements are more difficult yet, because they require either two station measurements or knowledge about the source amplitude and phase in order to determine the attenuation at the receiver point, and may also either require a correction or be unusable because of focusing/defocusing.

In the current project, we are developing a data set of attenuation measurements. We are requesting data from other researchers performing surface-wave attenuation studies, and will make additional measurements to augment these. We supplement these measurements with Q models that have been developed by other researchers where available. As with the dispersion modeling, we invert the attenuation measurements at all frequencies, together with existing Q models, for Q structure on a finite set of earth models, and then use these models to derive attenuation coefficients at all frequencies.

In addition to development of dispersion and attenuation models, we are developing improved procedures for surface wave measurement. This is particularly important at regional distances, where a traditional 20-second M_s measurement is difficult or impossible to make. There is a common misconception that surface waves cannot be measured at close distances, but in fact surface waves can be measured very close to the source and their highest signal to noise ratio is highest at the closest distances. The measurement threshold for surface waves can therefore be reduced significantly by making close in measurements; the difficulty is measuring the surface wave in a manner consistent with the measurement of more distant surface waves.

In our previous project we implemented and tested the use of path corrected spectral magnitudes. A path corrected spectral magnitude is the logarithm of the spectral amplitude of a (usually phase-matched filtered) surface wave divided by the Green's function of an explosion-generated surface wave along the same path. Doing this flattens the spectrum, and the path corrected spectral magnitude can then be determined by averaging the ratio over the optimum frequency band. The optimum frequency band depends on two things: the best signal-to-noise ratio and the best discrimination performance. At short ranges the signal-to-noise ratio is best at higher frequencies, but discrimination performance in general is better at lower frequencies. In our previous project we evaluated some of these tradeoffs and concluded that surface wave measurements for earthquake/explosion discrimination perform best at periods greater than 10 seconds.

In the current project we will be improving the path corrected spectral magnitude using the attenuation maps and amplitude corrections developed in this project. At very close distances (<5 degrees) surface wave attenuation is generally small and amplitude variations may result more from heterogeneous earth structure than from attenuation. We can test this by assessing whether the amplitude corrections developed from the earth models lead to more consistent measurements for these very short paths.

We are also developing an improved path corrected time-domain magnitude, which provides a way to measure a regionalized time-domain M_s that is consistent in value with a traditional time-domain M_s even at very close distances. This is accomplished by combining the path corrected spectral magnitude described above with a time-domain M_s procedure developed by Russell (2004). The Russell procedure is a path corrected time-domain magnitude for an earth average path. We can improve this by correcting for regional variations in earth structure and attenuation.

The inversion procedure for the 3D earth model

In our previous projects, we inverted a large volume of dispersion data for global earth structure. Global earth structure refers to a set of vertically layered earth models defined for each cell of a one-degree by one-degree grid of the earth. This procedure is summarized here, and in the following sections we show how it can be modified to include scattering and diffraction and modified to invert attenuation data for global Q structure. The relationship between dispersion and the shear wave velocities of the layers in the earth model is non-linear, so the shear velocities are estimated by an iterative least squares inversion procedure. At each step a system of equations is formed, augmented by additional equations of constraint, and then solved by the LSQR algorithm. The equations solved are

$$\begin{pmatrix} A \\ sH \\ \lambda I \end{pmatrix} \vec{\Delta x} = \begin{pmatrix} \vec{\Delta d} \\ -sH\vec{x} \\ \lambda\left(\vec{x}_C - \vec{x}\right) \end{pmatrix} + \vec{\varepsilon} \quad , \tag{1}$$

where $\Delta\mathbf{x}$ is the vector of adjustments to the shear wave slownesses of layers in each of the 577 model types. $\Delta\mathbf{d}$ is the vector of slowness differences between predicted and observed dispersion measurements. $\boldsymbol{\varepsilon}$ is the vector of residuals that remain after inversion (the inversion minimizes $|\boldsymbol{\varepsilon}|$). $\mathbf{x}$ is the vector of slownesses estimated in the previous iteration. The elements of the matrix **A** consist of partial derivatives of dispersion predictions with respect to shear wave slownesses in each layer. **H** is a difference operator that applies to vertically neighboring layers and has the effect of constraining the vertical smoothness of velocity profile. **H** applies to layers in the crust and upper mantle, but has explicit discontinuities at the crust/mantle boundary and at the base of surface sediments. The weighting of the smoothness constraint is **s** and can be a diagonal matrix (for variably weighted smoothing) or a scalar (constant smoothing). **I** is the identity matrix and $\boldsymbol{\lambda}$ weights the damping which constrains the norm of the difference between final slownesses and constraining model slownesses $\mathbf{x_c}$ (in this case a variant of the Crust 2.0 values). $\boldsymbol{\lambda}$ can be a scalar for constant damping, or a diagonal matrix for variable damping.

Correction for scattering and diffraction due to a realistic heterogeneous earth model

In our previous projects, we based the methodology for dispersion analysis and amplitude prediction on an approximation originally due to McGarr (1969) that uses propagation of surface waves along great circle paths with conservation of energy across material interfaces and no mode conversion. With these approximations, surface-wave propagation in a heterogeneous, anelastic structure takes the following form, separating source, path and receiver (notation follows Harkrider et al., 1994):

$$u_z(\omega, r, \varphi) = \frac{1}{\sqrt{a_e \sin\left(r/a_e\right)}} \sqrt{\frac{2A_{R_1}}{\pi\omega {c_1}^2}} \sqrt{c_2 A_{R_2}} \exp\left[i\left(\pi/4 - \omega r / c_p - \gamma_p r\right)\right] F_s(\omega, \varphi, h) \tag{2}$$

where ω is angular frequency, r is source to receiver distance, h is source depth, a_e is the radius if the earth, φ is azimuth, A_R is the Rayleigh wave amplitude function, c is phase velocity, γ is the attenuation coefficient, and the subscripts *1*, *2*, and *p* refer to parameters derived from the source region structure, parameters derived from the receiver region structure, and parameters which are defined by path averages, respectively. All source properties are contained in the function F_s. For an isotropic explosion source, the Rayleigh wave spectrum can be written

$$u_z(\omega, h_x, r) = M_0^{'} \frac{S_1^x(\omega, h_x) S_2(\omega) \exp[-\gamma_p(\omega) r + i(\varphi_0 - \omega r / c_p(\omega))]}{\sqrt{a_e \sin(r / a_e)}} \tag{3}$$

where φ_0 is the initial phase equal to -3π/4, S_1^x depends on the source region elastic structure and the explosion source depth, S_2 depends on the receiver region elastic structure. $M_0^{'} = \frac{3\beta^2}{\alpha^2} M_0$ where M_0 is the explosion isotropic moment. $M_0^{'}$ is defined this way so that the function S_1^x does not depend explicitly on the material properties at the source depth. (More details are given in Stevens and McLaughlin (2001) and Stevens and Murphy (2001)).

In our experience, this approximation works very well for modeling surface wave dispersion and amplitude over most of the world. In the current project, however, we are performing a more complete analysis including effects of scattering and diffraction. This is important for two reasons:

1) Some of the remaining residual in the global dispersion models is due to scattering and diffraction, and incorporation of these effects into our analysis will allow us to correct for them; and

2) To perform inversion of attenuation data for Q structure as described in the following section, we need to correct the amplitude for the effects of heterogeneous structure. The effect of heterogeneous structure on amplitude is stronger than on dispersion.

Modeling of scattering and diffraction is an active area of current research. Most of the research relevant to this project use variants of the single-scattering Born approximation to model the scattered wave field (Snieder, 1986). Zhou et al. (2004) summarize this work and derive sensitivity kernels for phase, amplitude, and arrival angle. The Born approximation models the observed surface wave at a receiver as a sum of a direct wave plus waves scattered from material inhomogeneities throughout the region. The sensitivity kernels show that the scattering and diffraction are largely confined to scatterers within the first Fresnel zone, which is defined by $k(\Delta' + \Delta'' - \Delta) < 3\pi/4$ where k is the wavenumber and Δ, Δ', Δ'' are the source to receiver, source to scatterer, and scatterer to receiver distances, respectively.

Ritzwoller et al. (2002) used a simplified version of the Born approximation to include diffraction in surface-wave tomography. They modeled the sensitivity kernel with a boxcar function the width of the Fresnel zone normal to the source to receiver path, then used an area integral over this region in place of the ray theory path integral for performing tomographic inversion. Yoshizawa and Kennett (2004) and Kennett and Yoshizawa (2002) use a similar technique with a narrower kernel that they believe to be more representative of realistic surface waves. Other recent papers on scattering and implications for surface-wave tomography include Spetzler et al. (2001, 2002).

Although the methods described above differ in detail, they are similar in practice and give similar results. That is, all the methods described predict the surface wave phase velocity by integrating slowness over an area approximately equal to the Fresnel zone with similar, although not identical, kernels. These techniques provide a straightforward way to incorporate scattering and diffraction into the inversion procedure described in the previous section. The matrix **A** in equation 1 is currently calculated using a path integral to calculate the phase velocity, with each element of the matrix corresponding to a piece of the path weighted according to the fraction of the path crossing a grid block and the sensitivity of the observable to the model velocity. This can be replaced by integration over the Fresnel zone area, which changes the weighting of each element and increases the number of elements corresponding to each ray. The matrix requires more time to calculate, but the inversion procedure is the same as in the ray-based tomographic inversion.

Inversion of attenuation data for Q structure

Inversion of attenuation data for Q structure can be accomplished using equation 4, which has the same form as equation 1 above:

$$\begin{pmatrix} A \\ sH \\ \lambda I \end{pmatrix} \overrightarrow{\Delta x} = \begin{pmatrix} \overrightarrow{\Delta d} \\ -sH\vec{x} \\ \lambda\left(\vec{x}_C - \vec{x}\right) \end{pmatrix} + \vec{\varepsilon} \qquad (4)$$

with the following changes:

1. The data are attenuation residuals instead of dispersion residuals. Attenuation estimates are derived from an existing Q model, and the differences between those and the observations are the data used in the inversion. Amplitude measurements are corrected for the effects of heterogeneous structure.

2. The matrix A is derived from derivatives of the attenuation coefficients with respect to model Q in each layer for the path-averaged inversion, and includes Born scattering sensitivity functions for the area integrals.

3. The constraining model is based on the best available Q models.

Note that equations 2 and 3 give the equation for the distance dependence of surface waves. In equation 5, we have rewritten this slightly to show how it is used in the inversion for attenuation. We have included the dependence on *r* in S_2 to show that it corresponds to the earth structure at the receiver location *r* (this provides a station dependent amplitude correction for local earth structure).

$$U(\omega, r) \sim \frac{\left|S_2(\omega, r)\right| \exp[-\gamma_p(\omega) r]}{\sqrt{a_e \sin(r / a_e)}} \tag{5}$$

The data used in equation 4, if derived, for example, from two stations along the same ray path, is calculated by taking the ratio of equation 5 evaluated at the two locations, and solving for γ_p. The amplitude measurements at both stations are corrected for heterogeneous structure effects prior to solving for γ_p.

Q models are much less well defined than the earth models used for the dispersion inversion. That is, for the dispersion inversion, we have a good background model developed from sediment maps, ocean depths, Crust 2.0, and the AK135 mantle model, but Q models are not known at the same level of detail. With the formulation of equation 4, however, we can include a generic background Q model augmented with better Q models for specific areas developed in other research projects. The generic model gives relatively distance-independent measurements at periods near and below 20 seconds. However, we expect to see much larger variations at the higher frequencies that are the primary focus of this study.

Optimization of surface wave measurement

Surface-wave measurements traditionally have been made by measuring a time-domain amplitude at a period near 20 seconds and then calculating a surface-wave magnitude M_s. This procedure is problematic at regional distances because the surface wave is not well dispersed and a distinct 20-second arrival may not be present. It is possible to measure time-domain amplitudes at higher frequencies with corrections (e.g., Marshall and Basham, 1972), however measurements may be inaccurate due to differences in dispersion caused by differences in earth structure. Stevens and McLaughlin (2001) suggested as an alternative replacing time-domain measurements with a path corrected spectral magnitude.

Path corrected spectral magnitudes

The path corrected spectral magnitude, $\log M_0$, is calculated by dividing the observed surface wave spectrum by the Green's function for an explosion of unit moment (see Equation 3) and taking the logarithm of this ratio, averaged over any desired frequency band. The path corrected spectral magnitude is defined as the logarithm of:

$$M_0^{'} = \left| U(\omega, r, \theta) \Big/ \left(\frac{S_1^x(\omega, h_x) S_2(\omega) \exp[-\gamma_p(\omega) r]}{\sqrt{a_e \sin(r / a_e)}} \right) \right| \tag{6}$$

where U is the observed surface-wave spectrum, and as above S_1^x depends on the source region elastic structure and the explosion source depth, S_2 depends on the receiver region elastic structure, and γ_p is the attenuation coefficient that depends on the attenuation integrated over the path between the source and receiver. All of the functions in Equation 6 are easily derived from plane-layered earth models, and allow the measurement to be regionalized to account for differences in earth structure at the source and receiver, and due to attenuation along the path.

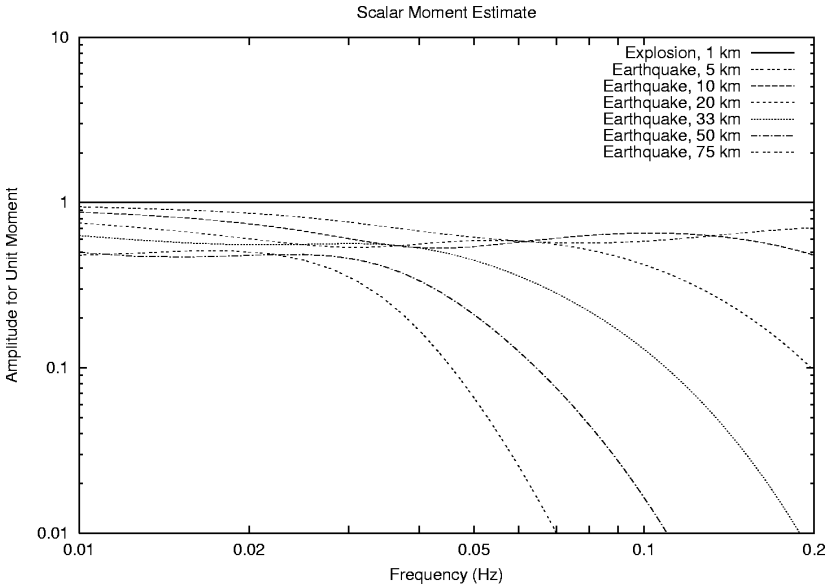

Figure 2. Path corrected spectra for an explosion and for earthquakes calculated for several depths. The path corrected explosion spectrum is flat over the entire frequency band (for perfect data and path correction), while the path corrected earthquake spectrum is flattened, but has some variation due to source mechanism and source depth.

The advantages of using $\log M_0$ instead of the traditional surface-wave magnitude M_s are that $\log M_0$ is insensitive to dispersion, independent of distance, works well at regional distances, and can be regionalized. Regionalized path corrected spectral magnitudes incorporate geographic variations in source excitation and attenuation. Furthermore, as discussed below, it can in principle be measured over different frequency bands to optimize the signal-to-noise ratio. M_s and $\log M_0$ share some limitations: spectra from earthquakes vary due to source mechanism and depth, and errors can occur if the measurement is made in a spectral dip or at high frequencies for a deep event (Figure 2).

Azimuthal variations in amplitude caused by focal mechanism also affect the amplitudes of both logM_0 and M_s. logM_0 can also be corrected for structural heterogeneity using the amplitude corrections described earlier.

Path corrected time-domain magnitudes

Russell (2004) proposed a new type of surface-wave magnitude $M_{s(b)}$ which differs from a traditional 20 second magnitude in that it uses a Butterworth filter to measure a time-domain amplitude in a narrow band around any desired frequency, and then applies a correction for the source function similar to the explosion source function used in the path corrected spectral magnitude described above. The main purpose of $M_{s(b)}$ is to allow surface waves to be measured at regional distances at higher frequencies. Bonner et al. (2004) showed that it gave consistent results in a test study. The magnitude is defined by

$$M_{s(b)} = \log\left(A_b\right) + \frac{1}{2}\log\left(\sin\Delta\right) + 0.0031\left(\frac{20}{T}\right)^{2.3}\Delta - 0.66\log\left(\frac{20}{T}\right) - \log\left(f_c\right) - 0.43 \qquad (7)$$

where A_b is the filtered amplitude, T is the measured period, and f_c is the Butterworth filter width. It is instructive to compare the terms in the Russell magnitude with the Rezapour and Pearce M_s and the path corrected spectral magnitude logM_0 described above. This is shown in Table 1.

Table 1. Comparison of time-domain and spectral magnitude measurement and correction terms

Magnitude Type	Amplitude Measure	Source	Receiver	Geometric Spreading	Attenuation	Dispersion	Filter	Norm
M_s	log(A/T)			$\frac{1}{2}\log\left(\sin\Delta\right)$	0.0046Δ	$\frac{1}{3}\log\Delta$		2.37
$M_{s(b)}$	$\log(A_b)$	$-0.66\log\left(\frac{20}{T}\right)$		$\frac{1}{2}\log\left(\sin\Delta\right)$	$.0031\left(\frac{20}{T}\right)^{2.3}\Delta$		$-\log\left(f_c\right)$	-0.43
$\log M_0$	$\log(A_s)$	$-\log(S_1)$	$-\log(S_2)$	$\frac{1}{2}\log\left(\sin\Delta\right)$	$\gamma_p\Delta$			

Note that each magnitude makes a slightly different set of corrections. logM_0 corrects for both source and receiver structure based on earth models at those locations and an explosion Green's function at the source. Similarly, $M_{s(b)}$ applies a source correction based on typical explosion source excitation. The Airy phase dispersion correction accounts for superposition of waves with similar group velocities, and is needed only in the time domain. $M_{s(b)}$ uses a Butterworth filter that is sufficiently narrow to avoid this problem. The filter correction corrects for the width of the Butterworth filter. The normalization for the two M_s measurements is chosen to make it consistent with historical M_s magnitudes at a chosen distance range. logM_0 has natural units of log moment and is not otherwise normalized; however, Stevens and McLaughlin (2001) showed that subtracting 11.75 makes logM_0 consistent with the Rezapour and Pearce M_s. Attenuation for M_s is an empirical correction based on a very large number of 20 second measurements. $M_{s(b)}$ similarly uses an empirical attenuation correction, but also includes an empirical correction for the change in attenuation with frequency. logM_0 uses attenuation calculated from earth (velocity, density, and Q) models along a source to receiver path. None of the magnitude measurements include any correction for scattering and diffraction.

A path corrected time-domain magnitude can be derived by combining the path corrected spectral magnitude with $M_{s(b)}$, using the source and path corrections from earth models to replace the empirical average corrections. We define the path corrected time-domain magnitude $M_{s(bp)}$ as:

$$M_{s(bp)} = \log\left(A_b\right) + \frac{1}{2}\log\left(\sin\Delta\right) + \gamma_p\Delta - \log\left(S_1\right) - \log\left(S_2\right) - \log\left(f_c\right) + C_{bp} \qquad (8)$$

where C_{bp} is a constant chosen to make $M_{s(bp)}$ consistent with historical magnitudes. Although equation 8 may appear more complicated than equation 7, the functions S_1, S_2, and γ_p are easily tabulated and stored in files, and a computer can quickly calculate them for any path based on a simple lookup table. There is substantial regional variation in these quantities that should be removed to ensure consistent measurements (examples of S_1, S_2, and γ for

continental and oceanic structures are shown in Stevens and McLaughlin, 1996). Another advantage of this approach is that it can ensure that f_c, which must be less than a minimum value calculated from the group velocity, is always set appropriately.

CONCLUSIONS AND RECOMMENDATIONS

We are implementing a procedure for optimizing the measurement of surface waves in the time and frequency domains using methods that model amplitude variations due to scattering and diffraction in addition to anelastic attenuation. Since the project started only recently it is premature to make specific conclusions or recommendations.

REFERENCES

Bonner, J. L., D. T. Reiter, D. G. Harkrider, and S. Russell (2004), Development of a time-domain, variable-period surface wave magnitude measurement procedure for application at regional distances, in *Proceedings of the 26th Annual Seismic Research Review, Trends in Nuclear Explosion Monitoring*, Los Alamos National Laboratory document LA-UR-04-5801, Orlando, FL, September 21-24, 2004.

Harkrider, D. G., J. L. Stevens, and C. B. Archambeau (1994), Theoretical Rayleigh and Love waves from an Explosion in Prestressed Source Regions, *Bull. Seism. Soc. Am.* 84: 1410–1442.

Kennett, B. L. N., and K. Yoshizawa (2002), A reappraisal of regional surface wave tomography, *Geophys. J. Int.* 150: 37– 44.

Marshall, P. D. and P. W. Basham (1972), Discrimination between earthquakes and Underground Nuclear Explosions Employing an Improved M_s Scale, *Geophys. J. R. astr. Soc*. 28: 431–458.

McGarr, A. (1969), Amplitude Variations of Rayleigh Waves – Propagation Across A Continental Margin, *Bull. Seism. Soc. Am.* 59: 1281–1305.

Ritzwoller, M. H., N. M. Shapiro, M. P. Barmin, and A. L. Levshin (2002), Global surface wave diffraction tomography, *J. Geophys. Res*. 107: 2335, doi:10.1029/2002JB001777.

Russell, D. R. (2004), Theoretical analysis of narrow-band surface wave magnitudes, AFTAC technical report AFTAC-TR-04-004.

Snieder, R. (1986), 3-D linearized scattering of surface waves and a formalism for surface wave holography, *Geophys. J. R. astr. Soc*. 84: 581–605.

Spetzler, J., J. Trampert and R. Snieder (2001), The effect of small-scale heterogeneity on the arrival time of waves, Geophys. J. Int., 145, 786–796.

Spetzler, J., J. Trampert and R. Snieder (2002), The effect of scattering in surface wave tomography, *Geophys. J. Int.* 149, 755–767.

Stevens, J. L. and K. L. McLaughlin (1996), Regionalized Maximum Likelihood Surface Wave Analysis, Maxwell Technologies Technical Report submitted to Phillips Laboratory, PL-TR-96-2273, SSS-DTR-96-15562, September.

Stevens, J. L. and K. L. McLaughlin (2001), Optimization of surface wave Identification and measurement, *Pure and Applied Geophysics* 158: 1547–1582.

Stevens, J. L. and J. R. Murphy (2001), Yield Estimation from surface wave amplitudes, *Pure and Applied Geophysics* 158: 2227–2251.

Yoshizawa, K., and B. L. N. Kennett (2004), Multimode surface wave tomography for the Australian region using a threestage approach incorporating finite frequency effects, *J. Geophys. Res*. 109: B02310, doi:10.1029/2002JB002254.

Zhou, Y., F. A. Dahlen and G. Nolet (2004), Three-dimensional sensitivity kernels for surface wave observables, *Geophys. J. Int.* 158: 142-168.

PREDICTING EXPLOSION-GENERATED *Sn* AND *Lg* CODA USING SYNTHETIC SEISMOGRAMS

Ileana M. Tibuleac[1], Anastasia Stroujkova[1], Jessie L. Bonner[1], and Kevin Mayeda[2]

Weston Geophysical Corporation[1] and Lawrence Livermore National Laboratory[2]

Sponsored by National Nuclear Security Administration
Office of Nonproliferation Research and Engineering
Office of Defense Nuclear Nonproliferation

Contract No. DE-AC52-05NA26610[1] and W-7405-ENG-48[2]

ABSTRACT

Recent examinations of the characteristics of coda-derived *Sn* and *Lg* spectra for yield estimation have shown that the spectral peak of the Nevada Test Site (NTS) explosion spectra is depth-of-burial dependent, and that this peak is shifted to higher frequencies for Lop Nor explosions at the same depths. To confidently use coda-based yield formulas, we need to understand and predict coda spectral shape variations with depth, source media, velocity structure, topography, and geological heterogeneity. Thus, we have undertaken a coda modeling study to predict *Sn* and *Lg* coda.

During the initial stages of this research, we have acquired and parameterized deterministic 6º x 6º velocity and attenuation models for the Nevada, Shagan, Degelen, Novaya Zemlya, and Lop Nor Test Sites. Near-source data are used to constrain density and attenuation profiles for the upper five km at several test sites. The upper crust velocity profiles are quilted into a background velocity profile at depths greater than five km. Topography from digital elevation models will eventually be incorporated into the model development. The models are parameterized for use in a modified version of the Generalized Fourier Method in two and three dimensions (GFM2D/3D). The new GFM algorithm will soon include a coordinate transform that allows for variable gridding in the upper few kilometers of the model and simulation of the topography at finer scales. The smaller grid size in the upper crust allows for an increase in the accuracy of the *Sn* and *Lg* synthetics.

We are modifying these models to include stochastic heterogeneities of varying correlation lengths within the crust and upper mantle. Two parameters—correlation length and fractional velocity perturbation of the heterogeneities—are used to construct different realizations of random media. Multiple runs with different realizations of stochastic velocity are needed to calculate average amplitude envelopes of the seismic traces for every set of the stochastic parameters. We will calibrate these parameters by matching synthetic earthquake *Sn* and *Lg* coda envelopes to local earthquakes with well-defined moments and mechanisms.

Once the deterministic and stochastic models have been generated, we will use GFM2D/3D to generate regional-distance synthetics for monopole explosions at depths ranging from 0.25 to 1 km for all test site models. We will then superimpose secondary source effects, such as spall and compensated linear-vector dipole (CLVD) sources, on the monopole synthetics. Finally, we will derive *Sn* and *Lg* coda spectra from the synthetics, estimate moments and yields from these spectra, and compare to observed data from each test site. If successful, this method may be used to estimate the *Sn* and *Lg* coda properties for yield estimation of explosions at historical test sites or for broad, uncalibrated regions where we will likely have little information on velocity structure.

OBJECTIVE

Our objective is to determine why the current mechanisms for *Sn* and *Lg* generation from explosions often produce stable coda magnitudes that are transportable between test sites. We aim to understand and predict *Lg* and *Sn* coda spectral shapes with variations in source depth, material properties, velocity structure, topography, and geological heterogeneity. We will use 2-D and 3-D modeling techniques to estimate synthetic explosion coda for five nuclear test sites as well as for regions without nuclear testing history.

RESEARCH ACCOMPLISHED

For sparse local and regional seismic networks and small events (< ~1 kt), one of the most stable and unbiased methods for yield and magnitude estimation is based on *Sn* and *Lg* coda envelopes (Mayeda, 1993). Coda-derived spectra have characteristics that require in-depth investigation so that any possible bias can be accounted for when lower bounds on yields are reported by U. S. monitoring agencies. For example, the peaks of coda-derived Nevada Test Site (NTS) and Lop Nor explosion spectra are depth-of-burial dependent; however, the peaks are shifted to higher frequencies at Lop Nor.

We are in the first phase of a research program in which we plan to compare observed local and regional *Sn* and *Lg* coda spectra to coda-derived source spectra for simulated explosions at the Nevada (NTS), Shagan (STS), Degelen (DTS), Novaya Zemlya (NZ), and Lop Nor (LN) test sites. We aim to develop a physical understanding of these data. We are currently developing a methodology consisting of 1) compilation and parameterization of deterministic material models for each test site; 2) addition of stochastic perturbations of variable correlation lengths to the deterministic model parameters; 3) calibration of stochastic variations at each test site using nearby earthquake data, and 4) calculation of 2-D/3-D synthetics for composite source models of varying depths and moments for each test site. Synthetic waveforms are created using a Generalized Fourier Method (GFM; Orrey et al., 2002). An illustration of our progress in developing this methodology is presented below with preliminary results for a simulated explosion at the Shagan Test Site.

1) Development of Velocity Models

Deterministic models. We are compiling deterministic velocity and attenuation models for the upper crust at five test sites (Table 1). Near-source data is used to constrain the *P*, *S*, density, and attenuation profiles for the upper 5 km at each test site. These upper crustal velocity profiles are "quilted" into a background velocity profile for each test site at depths greater than five km. We combine several background velocity models including the global 1°x1° models of Stevens and Adams (1999), the CRUST2.0 models of Bassin et al. (2000) and regionalized models (such as the regionalized background model for eastern Kazakhstan, Priestley et al., 1998). Each velocity model is parameterized for use in GFM2D/3D with a grid spacing of either 0.25 or 0.5 km.

Table 1. References for deterministic velocity and attenuation models for the upper crust at several test sites. Center coordinates of each test site are also listed.

Test Site	Abbreviation	References
Nevada Test Site (Pahute and Yucca) 37.148 N, 116.215 W	NTS	McLaughlin et al. (1983); Stump and Johnson (1984); Ferguson et al. (1994); Stevens et al., (1991); Mankinen et al. (2003); Benz et al., (1991)
Semipalatinsk (Shagan) 49.940 N, 78.862 E	STS	Bonner et al. (2001); Kazakh NNC Report (1996); Davis and Berlin (1992); Priestley et al. (1988)
Semipalatinsk (Degelen) 49.940 N, 78.048 E	DTS	Priestley et al. (1988); Belyashova et al. (2001)
Lop Nor 41.669 N, 88.703 E	LN	Kosarev et al., (1993); Burchin et al. (2001); Fisk, (2002); Waldhauser and Richards (2004).
Novaya Zemlya 73.335 N, 54.716 E	NZ	Kremenetskaya et al. (2001); Bowers (2002); Bungum et al. (2004)

Examples of 1D profiles of *P* and *S* velocity models of the five test sites are shown in Figure 1. The background velocity structure and the velocities in the upper crust are based on information provided by the references in Table 1. For example, the background velocity structure for the STS (left upper plot, dotted line) is based on a regional model for eastern Kazakhstan developed by Priestley et al. (1988). The velocities in the upper crust are based on borehole data (National Nuclear Center Nuclear Report) and *Rg* inversions (Bonner et al., 2001). The right upper plot shows a velocity profile at Pahute Mesa, at NTS. Examples of 1D profiles of *P* and *S* velocity models at the NZ and LN test sites are shown the lower plots of Figure 1. All models extend to 50 km in the horizontal direction and to at least 200 km in the vertical direction.

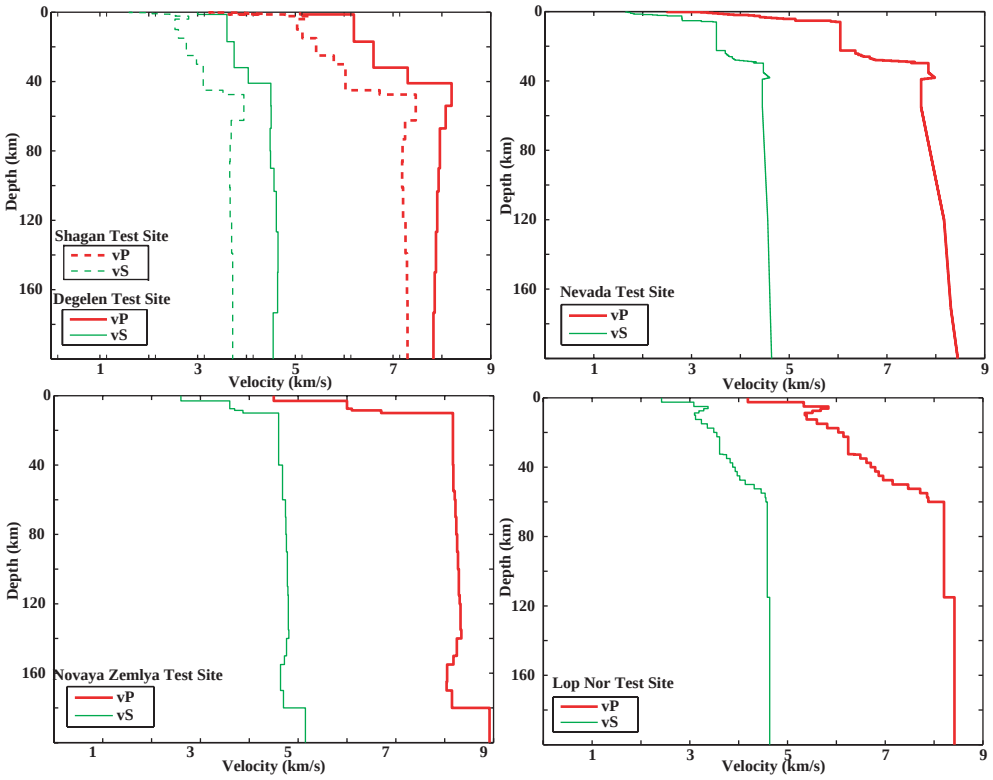

Figure 1. Examples of preliminary deterministic models for the Semipalatinsk (Shagan and Degelen) Test Sites (upper left plot), Nevada (upper right plot), Novaya Zemlya (lower left plot), and Lop Nor (lower right plot) test sites.

Stochastic models. The deterministic models are perturbed by adding random heterogeneities with predefined stochastic properties, obtained using the method of Frankel and Clayton (1986). A random number generator is used to create velocity perturbations at each point in the 2D or 3D deterministic velocity model. The random velocity perturbation field is then Fourier transformed to wave number space, filtered to achieve the desired spectrum (e.g., correlation distances), and transformed back to the velocity field. The perturbations are subsequently scaled to the desired amplitude and added to the 2D or 3D deterministic velocity field.

Three types of filters are commonly used to describe real geologic media: exponential, Gaussian, and von Karman (Table 2 and Figure 2). Velocity variations are well described by the von Karman self-similar autocovariance function (Frankel and Clayton, 1986; Levander and Hollinger, 1992; Pullammanappallil et al., 1997); therefore, we have chosen this function to describe our initial stochastic models.

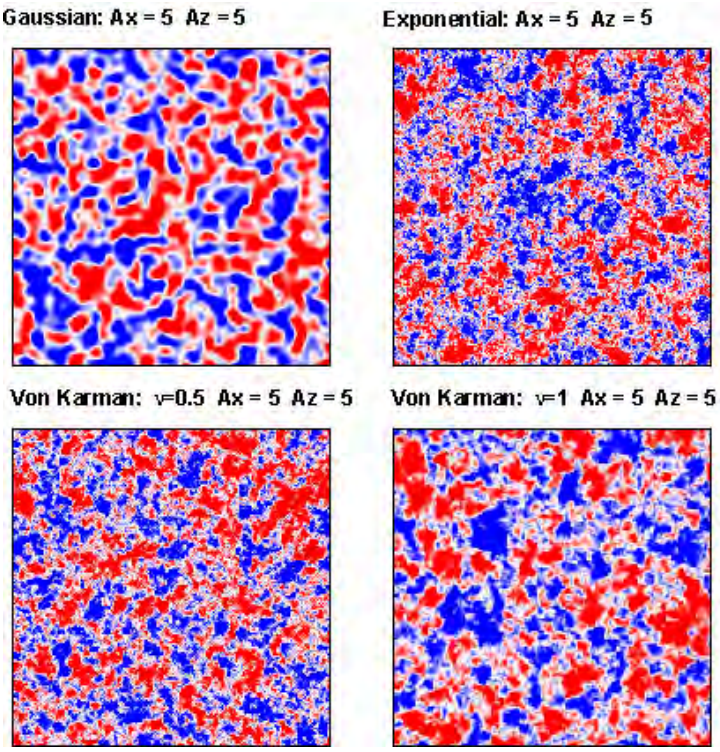

Figure 2. Random perturbation field examples obtained by using the filters listed in Table 2 on a 256 x 256 pixel block. The perturbations are scaled to the desired amplitude and added to the deterministic velocity field.

Table 2. Filters applied to the random perturbation field, where *a* is a characteristic correlation length of the medium and *v* is the Hurst number, related to the fractal dimension of the medium.

Filter	Spatial covariance function C
Gaussian	$C_g = \exp(-r^2 / 2a^2)$
Exponential	$C_e = \exp(-r / a)$
von Karman	$C_k = r^v K_v(r)$

To address the nonuniqueness inherent in our method, correlation functions for scattering at each test site are restricted to be within the bounds of the results from literature searches and satellite imagery correlation-length analyses. Nearby earthquakes with well-defined focal mechanisms can also be used, where available, to provide us with bounds on the scattering in our model.

Figure 3 is an example of this methodology applied to the Shagan velocity model shown in Figure 1, left upper plot. The correlation length for this model was chosen to be 1.5 km with 10% velocity variations.

2) Methodology illustration for an explosion at the Shagan Test Site

We superpose a 0.5 km deep explosion with a smaller Compensated Linear Vector Dipole (CLVD) source at a depth of 0.2 km, and present the results at a distance of 310 km. Figure 4 provides a comparison of the composite source synthetics (CLVD+Explosion Monopole) calculated using a model with and without random velocity variations (Figure 3). In the upper plot, we note that there are large high-frequency surface waves (> 2 Hz) that are typically not observed in regional data from explosions at the Shagan Test Site. The Q value used in the upper crust was less than 100; however, it did not decrease the amplitudes of these surface waves. But, adding the crustal heterogeneity (lower plot) *does* remove these surface waves by forward- and back- scattering the energy into the *Lg* coda. The synthetic seismogram in the lower plot of Figure 4 shows that coda resembling regional recordings can be generated using our methodology.

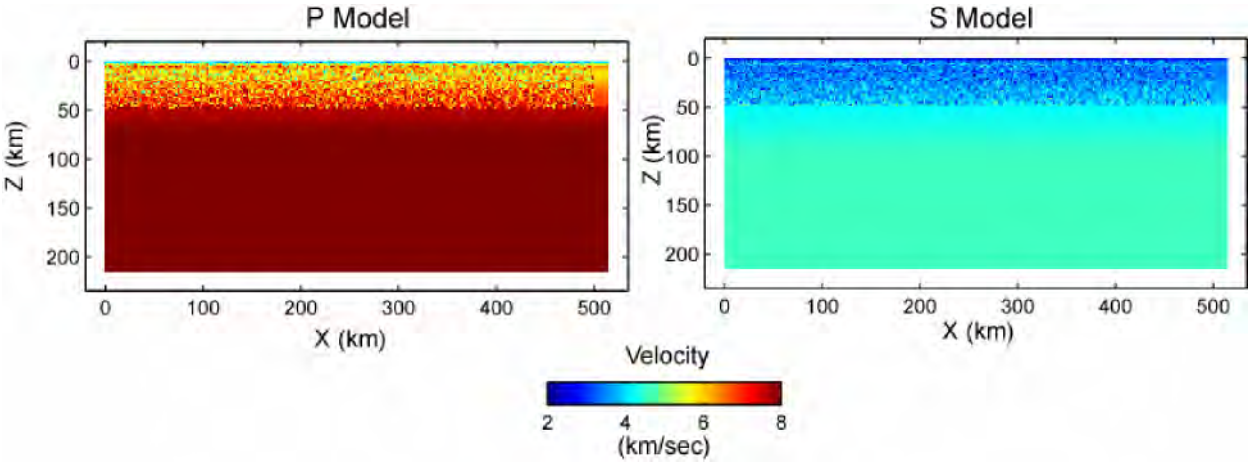

Figure 3. Example of combined deterministic and stochastic *P*- and *S*-wave models for the Shagan Test Site in Kazkahstan. The background velocity structure is shown in Figure 1, left upper plot, dotted line. Stochastic variations with correlation lengths of 1.5 km and 10% velocity perturbations were added using the methods of Frankel and Clayton (1986).

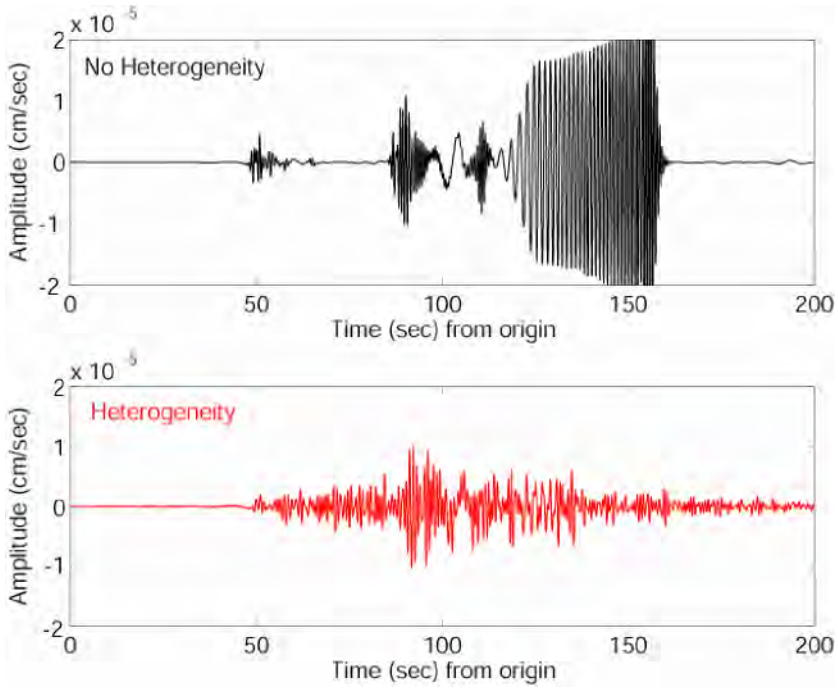

Figure 4. A comparison of synthetics for a composite explosion plus CLVD source in a Shagan test site velocity model without (upper) and with (lower) stochastic variations. In the lower plot, the *Lg* coda behaves very similarly to regional recordings of explosions at the Shagan Test Site.

Coda processing is performed using the coda software described in detail in Mayeda et al. (2003). An example of this processing as applied to the synthetic waveforms shown in Figure 4 is provided in Figure 5. While we show only the first 200 seconds of the synthetics in Figure 4, the analysis in Figure 5 is for 800 seconds of data. For the velocity model with no stochastic heterogeneities, we do not see appropriate coda behavior in the processing. The peaks associated with the *Lg* and *Rg* arrivals are observed, and then the amplitudes rapidly approach pre-event noise levels by 200 seconds after event origin. For the synthetics with stochastic heterogeneities, we observe appropriate coda behavior, as the amplitudes do not approach the background noise levels until 500 seconds after

the event origin. The coda behavior in different frequency bands is very similar to the lower-frequency type coda amplitude curves proposed for the Shagan test site by Phillips et al. (2004).

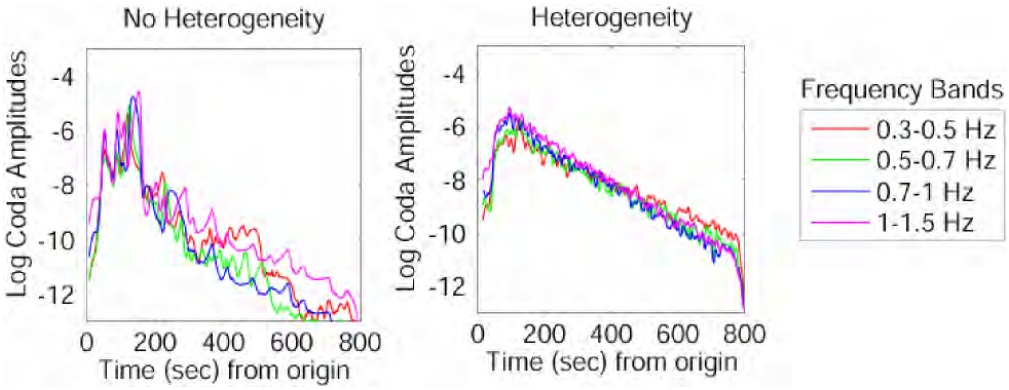

Figure 5. Examples of coda processing on synthetic seismograms without (left) and with (right) random velocity heterogeneities in the model. The coda amplitudes on the right are very similar to the type coda amplitude curves proposed for the Shagan Test Site by Phillips et al. (2004).

The next stage of modeling development will be the addition of topography. GFM2-D/3-D is undergoing modifications to include topography. We will use digital elevation models for all test sites in order to simulate *Rg* scattering from topography, which has been shown to be a primary constituent of explosion-generated shear waves. This scattering will contribute to the coda signatures for our synthetics. We will then systematically modify the random velocity heterogeneities to improve the match between the observed and synthetic data. 3D strip models will also be developed to examine scattering efficiency of 2-D media in comparison to 3-D simulations.

CONCLUSIONS AND RECOMMENDATIONS

In this paper we present preliminary results from a study which aims to develop a methodology for modeling *Sn* and *Lg* coda-derived source spectra for simulated explosions at the Nevada, Shagan, Degelen, Novaya Zemlya and Lop Nor test sites. Using synthetic seismograms at the Shagan Test Site we show that coda resembling regional recordings of explosions at the Shagan Test Site can be generated using a combination of deterministic and stochastic models.

In the future we will use GFM to propagate synthetics from compound explosion and CLVD sources to epicentral distances of up to 600 km in both 2D and 3D models. These waveforms will be used to generate coda-derived *Lg* and *Sn* spectra in order to estimate the magnitudes and yields for the synthetic events. We will compare the spectral peaks from different depths of burial and examine any similarities to observations. We will quantify possible biases in the yields between test sites and relate them to the choice of, or combination of, *Sn* and *Lg* mechanisms. Finally, we will use our techniques to estimate the *Sn* and *Lg* coda spectra for explosions in uncalibrated regions. We will use available earthquake data, digital elevation models, and satellite imagery to determine the properties of the stochastic models, so that explosion-generated coda spectra for uncalibrated regions can be estimated.

ACKNOWLEDGMENTS

We wish to thank Dr. Jeffrey Orrey for his continued support on the GFM2D/3D code. We express our gratitude to Heather Hooper for help editing this paper and to James Britton for help with ArcView figure plots.

REFERENCES

Bassin, C., G. Laske, and G. Masters (2000), Current limits of resolution for surface wave tomography in North America. *EOS Trans AGU.* 81: F897.

Belyashova, N. N., V. I. Shacilov, N. N. Mikhailova, I. I. Komarov, Z. I. Sinyova, A. V. Belyashov, and M. N. Malakhova (2001), On the use of calibration explosions at the former Semipalatinsk test site for compiling a travel-time model of the crust and upper mantle. *Pure Appl. Geophys.* 158: 193-209

Benz, H. M., Unger, J. D., Leith, W., and V. Ryaboy (1991), The Norilsk DSS Profile in Northern Siberia: Interpretation of the velocity structure and comparison with Basin and Range and New England profiling results, Abstracts of the 13'th Annual PL/DARPA Seismic Research Symposium, 85–100.

Bonner, J., D.C. Pearson, W.S. Phillips, and S.R. Taylor (2001), Shallow velocity structure of the Shagan River Test Site in eastern Kazakhstan. *Pure Appl. Geophys.* 158: 2017–2039.

Bowers, D. (2002), Was the 16 August 1997 Seismic Disturbance near Novaya Zemlya an Earthquake? *Bull. Seis. Soc. Am.* 92: 2400–2409.

Bungum, H., O. Ritzmann, J. Faleide, N. Maercklin, J. Schweitzer, W. Mooney, S. Detweiler, and W. Leith (2004), Development of a Three-dimensional Velocity Model for the Crust and Upper Mantle in the Barents Sea, Novaya Zemlya, Kara Sea and Kola-Karelia Regions, in *Proceedings of the 26th Annual Seismic Research Review on Nuclear Monitoring Technologies,* LA-UR-04-5801, Orlando, FL.

Burchin, B. G., A. Z. Mostinsky, A. A. Egorkin, A. L. Levhin, and M. H. Ritzwoller (2001), Isotropic and nonisotropic components of earthquakes and nuclear explosions on the Lop Nor Test Site, China, *Pure Appl. Geophys.* 158: 1497–1515.

Davis, P. A. and G. L. Berlin (1992), Geologic mapping of the Semipalintisk region using Land Sat thematic mapper and spot panochromatic data, LA-UR-92-310: 15.

Ferguson, J. F., A. H. Cogbill, and R. G. (1994), A geophysical-geological transect of the Silent Canyon caldera complex, Pahute Mesa, Nevada, *J. Geophys. Res.* 99: 4323–4339.

Fisk, M. D. (2002), Accurate locations of nuclear explosions at the Lop Nor Test Site using alignment of seismograms and IKONOS satellite imagery. *Bull. Seis. Soc. Am.* 92: 2911–2925.

Frankel, A. and R. W. Clayton (1986), Finite difference simulations of seismic scattering: implications for the propagation of short-period seismic waves in the crust and models of crustal heterogeneity. *J. Geophys. Res.* 91. (B6): 6465–6489.

Levander, S. A., and K. Hollinger (1992), Small-scale heterogeneity and large-scale velocity structure of the continental crust, *J. Geophys. Res.* 97: 8797–8804.

Kazakh NNC Report (1996), Unused vertical boreholes at the Balapan test field of the former Semipalantinsk test site: review of existing data on the boreholes geology and design, *National Nuclear Center of the Republic of Kazakhstan Report.*

Kosarev, G. L., Petersen, N. V. and L. P. Vinnik (1993), Receiver functions for the Tien Shan analog broadband network: contrasts in the evolution of structures across the Talasso-Fergana fault, *J. Geophys. Res.* 98: 4437–4448.

Kremenetskaya, E., V. Asming and F. Ringdal (2001), Seismic location calibration of the European Arctic, *Pure Appl. Geophys.* 158: 117–128.

Mankinen, E. A., T. G. Hildenbrand, C. J. Fridrich, E. H. McKee and C. J. Schenkel (2003), Geophysical setting of the Pahute Mesa-Oasis Valley region, Southern Nevada, Report 50, Nevada Bureau of Mines and Geology, University of Nevada: 12–13.

Mayeda, K. M. (1993),mb(*Lg*Coda): a stable single station estimator of magnitude, *BSSA,* 83: 851–861.

Mayeda, K., A. Hofstetter, J.L. O'Boyle, and W.R. Walter (2003), Stable and transportable regional magnitudes based on coda-derived moment-rate spectra, *Bull. Seis. Soc. Am.* 93: 224–239.

McLaughlin, KL, L. R. Johnson, LR and T.V. McEvilly (1983), Two-dimensional array measurements of near-source ground accelerations. *Bull. Seis. Soc. Am.* 73: 349–375.

Orrey, J. L., C. B. Archambeau and G. A. Frazier (2002), Complete seismic wavefield synthesis with a pseudospectral method: The Generalized Fourier Method, revised manuscript to be submitted to *Geophys. J. Int.*

Phillips, W., H. Patton, S. Taylor, H. Hartse, and G. Randall (2004), Calibration for coda based magnitude and yield, in *Proceedings of the 26th Annual Seismic Research Review on Nuclear Monitoring Technologies,* LA-UR-04_5801, Orlando, FL.

Priestley, K. F., G. Zandt, and G. E. Randall (1988), Crustal structure in Eastern Kazakh, USSR from teleseismic receiver functions. *Geophys. Res. Lett.* 15: 613–616.

Pullammanappallil, S., A. Levander, S. Larkin (1997), Estimation of crustal stochastic parameters from seismic exploration data, *J. Geophys. Res.* 102: 15,269–15,286.

Stevens, J. L. and D. A. Adams (1999), Improved methods for regionalized surface wave analysis. *Proceedings of the 21st Annual Seismic Research Symposium,* Las Vegas, NV.

Stevens, J. L., T. G. Berker, S. M. Day, K. L. McLaughlin, N. Rimer, and B. Shkoller (1991), Simulation of teleseismic body waves, regional seismograms, and Rayleigh wave phase shifts using two-dimensional, nonlinear models of explosion sources, *Explosion Source Phenomenology, Geophysical Monograph 65,* Copyright 1991, American Geophysical Union: 239–252.

Stump, B.W. and L. Johnson (1984), Near-field source characterization of contained nuclear explosions in tuff, *Bull. Seis. Soc. Am.* 74: 1–26.

Waldhauser, F. and P. G. Richards (2004), Reference events for regional seismic phases at IMS stations in China, *Bull. Seis. Soc. Am.* 94: 2265–2279.

P AND S WAVE VELOCITY STRUCTURE OF THE CRUST AND UPPER MANTLE UNDER CHINA AND SURROUNDING AREAS FROM BODY AND SURFACE WAVE TOMOGRAPHY

M. Nafi Toksöz, Robert D. Van der Hilst, Youshun Sun, and Chang Li

Massachusetts Institute of Technology

Sponsored by Air Force Research Laboratory

Contract No. FA8718-04-C-0018

ABSTRACT

The objective of this project is to use a combination of travel-time and surface wave tomography to obtain compressional and shear wave velocity distributions in the crust and upper mantle under China and surrounding areas.

The first phase of the study is directed at producing a P-wave velocity model based on travel-time tomography. Travel data from the Annual Bulletin of Chinese Earthquakes (ABCE) and the International Seismological Centre (ISC/EHB) are used. The tomographic inversion is carried out in two steps. First, the regional travel-time data from ABCE is used to obtain the crust/uppermost mantle (0 to 100 km depth) velocity model. A total of 345,000 P-wave regional travel times are used for the tomography. Two discontinuities (Conrad and Moho) are allowed in the inversion. The tomographic model provides three-dimensional (3-D) velocities in the crust and uppermost mantle, depth to the Moho, and detailed P_n velocities.

To extend the model deeper into the mantle through the upper mantle transition zone, ISC/EHB data for P and p^P phases are combined with the ABCE data. To counteract the "smearing effect," the crust and upper mantle velocity structure derived from regional travel times, as described above, are used for teleseismic tomography. A variable grid method based on ray density is used in the inversion. A 3-D P-wave velocity model extending to 1700 km depth is obtained.

The combined regional teleseismic tomography provides a high-resolution, 3-D P-wave velocity model for the crust, upper mantle, and transition zone. The crustal models correlate well with geologic and tectonic features. The mantle models show the images of current and past subduction zones. A surprising result is that the "roots" of some geologic features, such as the Sichuan Basin and Ordos Plateau, extend deep into the upper mantle.

OBJECTIVES

The primary goal of this project is to obtain compressional and shear wave velocity distributions in the crust and upper mantle under China and surrounding areas using a combination of travel-time and surface wave tomography. The first phase of the study is directed at producing a P-wave velocity model based on travel-time tomography.

RESEARCH ACCOMPLISHED

Introduction

China and the surrounding area is a seismically active and geologically complex region (Figures 1 and 2). More than 500 earthquakes with magnitudes (M) greater than 6.0 occurred in this region between January 1978 and May 2004 (Figure 1). From a geological point of view, there are four Precambrian platforms (Figure 1) in China and the surrounding area: the North China Block, the South China Block, the Tarim Basin and the Indochina Block. There are distinct basins (e.g., Sichuan and Ordos) filled with deep sediment.

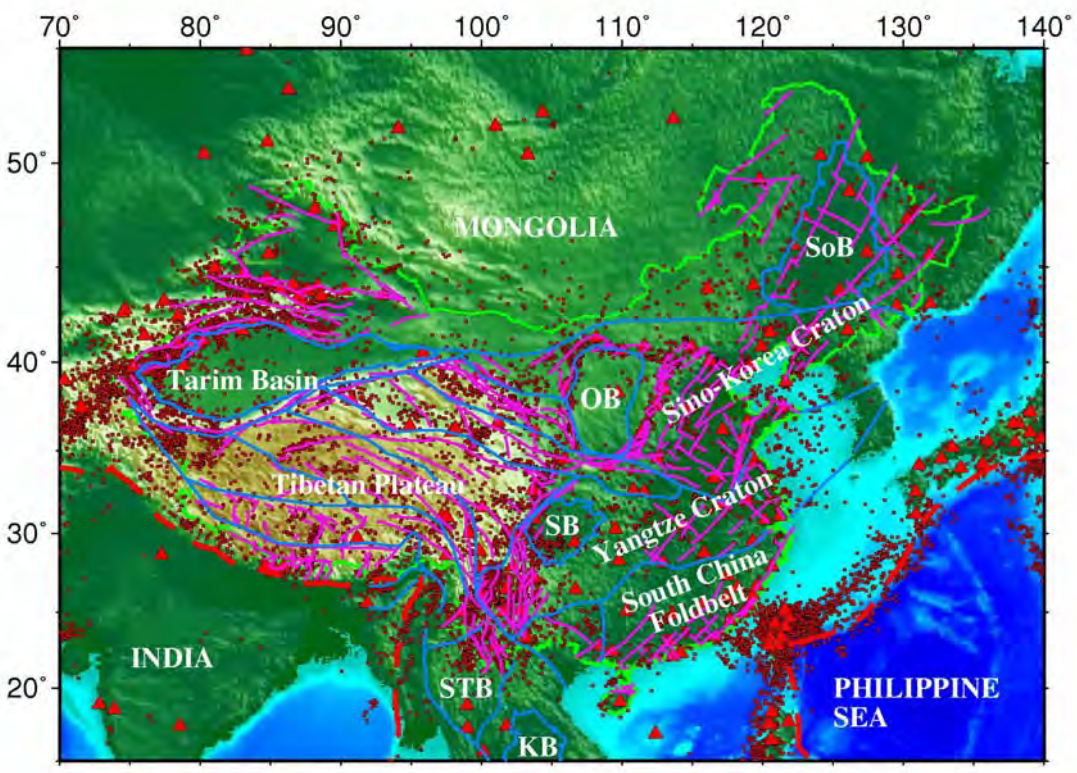

Figure 1. Locations of 512 earthquakes (M > 6.0 from January 1978 to May 2004), 220 stations, active faults and major tectonic boundaries in China and the surrounding area. Earthquake epicenters are shown in red dots and stations are shown in red triangles. The yellow line shows the boundary of China. Active faults in the China area are shown in purple lines and tectonic sutures are shown in blue lines, where SoB=Songliao Basin, OB=Ordos Basin, SB=Sichuan Basin, KB=Khorat Basin, STB=Shan Thai Block, and IB=Indochina Block.

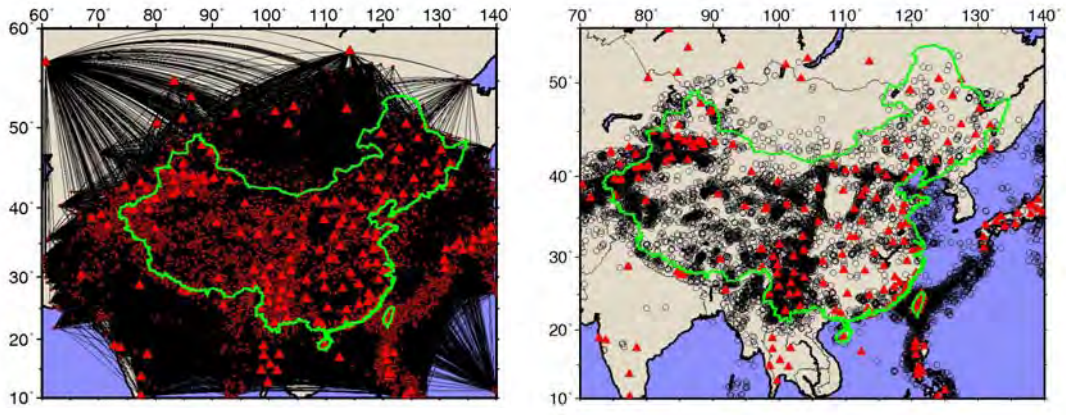

Figure 2. Left: Locations of 25,000 earthquakes, 220 stations, and 500,000 ray paths in China and the surrounding area. Earthquake epicenters are shown in black circles and stations are shown in red triangles. The green line shows the boundary of China. Right: Distribution of seismic stations and epicenters of selected earthquakes used in this study. A total of 16,572 events M 3.0 and greater are selected and plotted in black circles. All 220 stations are used and plotted in red triangles.

A high-resolution 3-D velocity model of China is necessary to provide accurate travel-times for reliable determination of earthquake locations. Large-scale models obtained by the teleseismic tomography technique generally cannot resolve vertical variations in the shallow structure. Regional models can be combined in order to cover a large area, but such models cannot guarantee smooth and consistent transitions between different regions. During the last several years, there have been many digital seismic stations installed in the China area (Figure 1). The large database of high-quality recorded arrival times provides an unprecedented opportunity to determine a detailed 3-D crustal structure under the region. Therefore, we introduce a method that constructs 3-D P-velocity models for the whole China area based on observed travel-time data.

The available P-wave velocity models of the crust and upper mantle in China and the surrounding area have been obtained using a variety of approaches. Some global models, such as CUB 1.0 (Shapiro and Ritzwoller, 2002) and the Science Application International Corporation 1° x 1° model (Stevens et al., 2001), were constructed from group and phase velocity dispersion measurements of surface waves. The global model CRUST 2.0 (Laske et al., 2001) was constructed from seismic refraction data and developed from the CRUST 5.1 model (Mooney, 1998) and a 1° x 1° sediment map (Laske and Masters, 1997). Although CRUST 2.0 was created by tomographic inversion, there are too few deep seismic soundings (DSSs) to provide enough refraction data for a detailed model. Regional models were constructed by Pn and/or Sn tomography (Ritzwoller et al., 2002; Hearn et al., 2004; Liang et al., 2004; Pei et al., 2004a), from surface waves (Wu et al., 1997, Lebedev and Nolet, 2003; Huang et al., 2003; Song et al.,1991; Zhu et al., 2002), and from P-wave travel-time tomography (Liu et al.,1990). The model of Liu et al. (1990) was constructed by regional and teleseismic tomography. The maximum and minimum grid spacings in the model of Liu et al. (1990) are 5° x 5° and 2° x 2°, respectively, in the horizontal direction, and 300 km and 45 km in the vertical direction. This model does not have the details for local and regional travel-time calculations and precise earthquake locations.

P-wave tomography has been performed in several local regions in China (Xu et al., 2002; Huang et al., 2002; Yu et al., 2003; Huang and Zhao, 2004; Sun and Liu, 1995; Zhu et al., 1990; Pei et al., 2004b). These models show detailed crustal structures only in a few regions. A detailed map for the whole China area remains to be developed.

In this study, we carry out the 3-D velocity tomography in two steps. First, we use the ABCE regional travel-time data to obtain the crust/uppermost mantle (0–100 km depth) velocity structure. Then, we extend the model deeper into the mantle through the transition zone using the ISC/EHB and ABCE data, and the shallow (1–100 km) velocity model from the first step.

Regional Travel-Time Data and 3-D Tomography

In this work, we use the earthquake phase data (first P-wave arrivals) from January 1990 to December 2003, found in the ABCE (IG-CSB, 1990-2003). There are 25,000 earthquakes, 220 stations, and 500,000 ray paths in China and the surrounding area in this database. Figure 2 shows earthquake epicenters, the stations, and the ray paths. We also incorporated special data such as 129 earthquakes with high-quality records and three quarry blast events (ground-truth events) from the Sichuan Province.

The study area is divided into parallelepipeds with a spatial size of 10 km x 10 km x 2 km. Among the earthquakes within each block, we select the event with the greatest number of first P-wave arrivals and the smallest hypocentral location uncertainty. As a result, our final dataset contains 16,000 events with more than 300, 000 ray paths. The ray coverage has a better (more uniform) distribution in the study area (Figure 2), thus it is more appropriate for tomographic study than the original dataset. Since most aftershocks occur in similar locations with smaller magnitudes and tend to produce larger reading errors for the phase arrivals than the main shocks, the final dataset contains the least number of aftershocks possible.

The starting model for the tomography is a 3-D model created with the adaptive moving window (AMW) method (Sun et al., 2004). The model assumes a layered crust and a one-layer uppermost mantle at each one degree intersection of longitude and latitude. The thickness and P-wave velocity of each layer are found from the observed travel-times. These 1° x 1° velocity profiles are quilted together with a suitable smoothing to obtain the starting model for the 3-D tomography. The model includes discontinuities such as the Conrad and the Moho. Although there is general consensus on the Moho (China Seismological Bureau, 1986; Zhang, 1998; Li et al., 2001; Hearn et al., 2004; Sun et al., 2004), the Conrad discontinuity is clear only in some regions of the study area, and therefore we only incorporate the Moho discontinuity in this study. Figure 3 shows the geometry of the Moho discontinuity as input into the 3-D tomography.

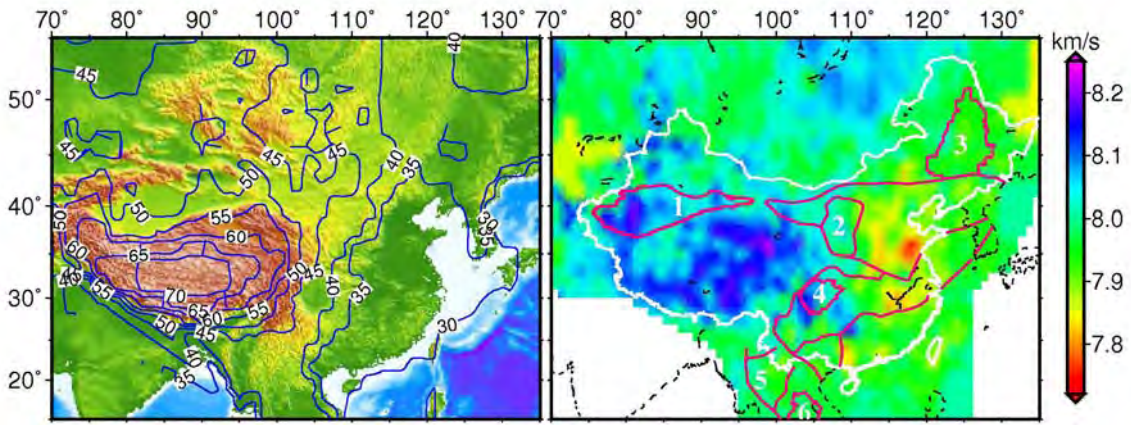

Figure 3. Depth distribution of the Moho discontinuities (left) and Pn velocities (right) in the present study area obtained by inverting the 1-D layered models from first arrivals of P-wave travel-time (Sun et al. 2004). The Moho depths are shown in contours. 1=Tarim Basin, 2=Ordos Basin, 3=Songliao Basin, 4=Sichuan Basin, 5=Shan Thai Block, and 6=Khorat Basin.

We used a modified version of the tomographic method of Zhao et al. (1992) to invert for the crustal and uppermost mantle velocity structure in China and the surrounding area. Zhao's method, described in detail in several papers (Zhao et al., 1992, 1994; Zhao, 2001), allows 3-D velocity variations everywhere in the model and can accommodate velocity discontinuities. The velocity structure is discretized using a 3-D grid. The velocity perturbation at each point is calculated by linearly interpolating the velocity perturbations at the eight surrounding (adjacent) grid nodes. Velocity perturbations at grid nodes are the unknown parameters for the inversion procedure. To calculate travel-times and ray paths accurately and rapidly, an efficient 3-D ray-tracing technique is employed to iteratively use the pseudo-bending technique (Um and Thurber, 1987) and Snell's law. Station

elevations and the sediment layers are taken into account in the ray tracing. The LSQR algorithm (Paige and Saunders, 1982) with a damping regularization is used to solve the large and sparse system of equations. The nonlinear tomographic problem is solved by iteratively conducting linear inversions.

Crust and Uppermost Mantle Velocity Models

The 3-D P-wave velocity models are shown at constant depths in Figure 4. At a depth of 40 km, low velocity (low-V) zones are visible in the western part of China, and high-velocity (high-V) zones exist in the eastern part. A clear dividing line appears around 105°E separating the east and west seismic zones in mainland China. At a depth of 60 km, the Tibetan plateau's thick crust is clearly outlined as a low-V zone. At a depth of 80 km, the root of the Tibetan plateau disappears, and high-V zones appear in the west and south part of the Tibetan Plateau. There are a few low-V zones sandwiched between the high-V zones. The deeper velocity slices (60 km and 80 km) with scattered low-V zones in eastern China indicate the presence of tectonic extension in the area. These results are consistent with those obtained by a joint inversion of the DSS data from multiple profiles (Li et al., 2001).

The Pn velocity image remains basically unchanged from the starting model. It has a high resolution in the whole study area (Figure 3). Pn velocities are low at the center of the Songliao Basin, but high under most of the Tarim Basin, the Sichuan Basin, and the Ordos Basin. This result is generally consistent with the recent Pn tomography by Pei et al. (2004a), Liang et al. (2004), and Hearn et al. (2004).

Velocity changes are visible across some of the fault zones such as the Sanjiang Folding Belt. Such a feature is visible from a depth of 10 km to a depth of 30 km, suggesting that some of the faults may have cut through the crust and reached to the middle or lower crust. No velocity contrast is visible across most of the faults, particularly in the middle to lower crust. Some features are associated with the basins.

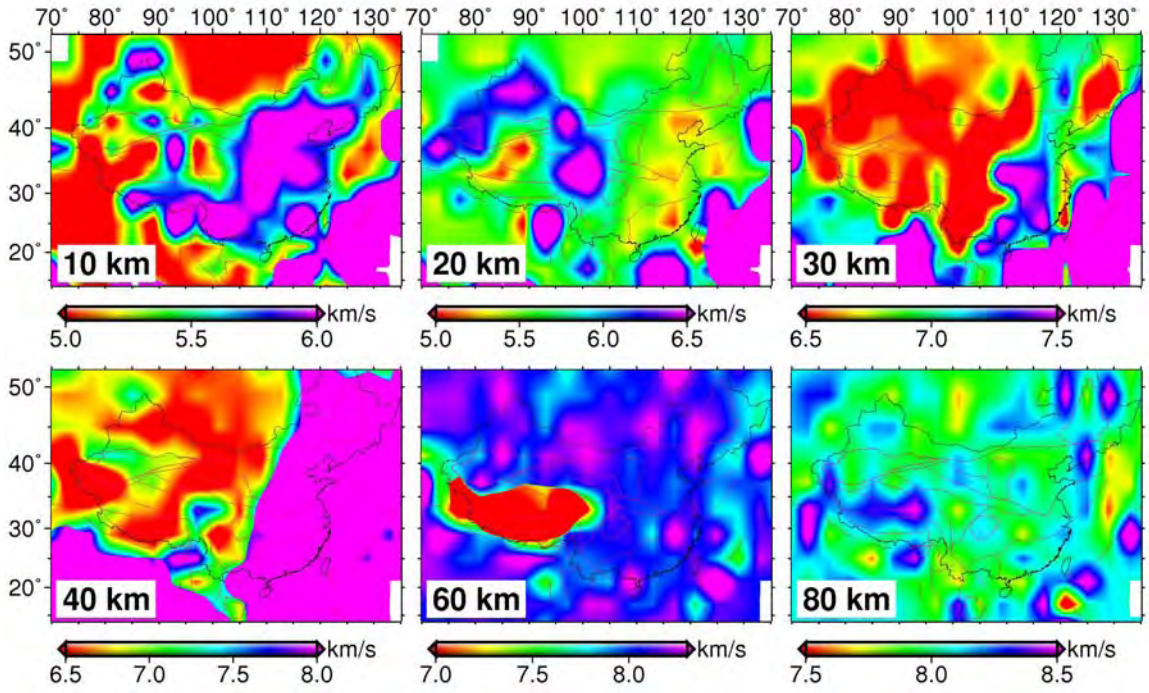

Figure 4. P-wave velocity image at each depth slice. The depth of each layer is shown at the lower-left corner of each map.

Validation with Ground Truth (GT) events

We test our 3-D model by relocating the GT events and comparing the results with known locations. Eleven GT events are the nuclear explosions in northwestern China from 1990 to 1996, recorded by stations in China and the surrounding area. Only P-wave travel-times are available in the dataset.

The GT events are closely clustered. Table 1 shows the parameters for these nuclear explosions (Sun, 2005). With our new P-wave velocity model for the crust and upper mantle in China and the surrounding area, we relocate the GT events using travel-time data recorded at stations within 20° epicentral distance. The relocation errors are also listed in Table 1. The three columns under "Error" are the hypocentral difference in kilometers between the reference hypocenters and relocations using the new 3-D P-wave model, 1-D average China model obtained from the 3-D model, and the AK135 global model.

The averaged hypocentral error of relocation is only 0.9 km with a standard deviation of 0.3 km for the new 3-D P-wave model. The mean hypocentral misfit is about 10 km if the averaged 1-D velocity in China is used, and about 20 km if the global AK135 model is used. Even though the GT events are located in northwestern China and most stations distributed in southern and eastern China, the small relocation errors clearly suggest that an accurate P-wave velocity model gives good event locations with limited azimuthal coverage.

Table 1: The eleven GT events in northwest China. The relocation errors (hypocentral) are listed in km. Events are relocated using our new P-wave model, the averaged 1-D model in China and the surrounding area, and the standard AK135 (global).

Event No.	Date (Y/M/D)	Time (H/M/S)	Latitude (degree)	Longitude (degree)	Error (km)		
					3D	1D	AK135
1	1990/05/06	07:59:59.25	41.5618	88.7183	0.4	6.2	18.9
2	1990/08/16	04:59:59.26	41.5392	88.7445	1.2	9.5	23.0
3	1992/05/21	04:59:59.06	41.5419	88.7678	0.8	8.7	18.4
4	1992/09/25	08:00:00.02	41.7167	88.3767	1.3	9.1	17.8
5	1993/10/05	01:59:57.92	41.5922	88.7035	1.1	9.3	19.1
6	1994/06/10	06:25:59.46	41.5271	88.7074	0.9	8.1	18.4
7	1994/10/07	03:25:59.44	41.5741	88.7256	1.1	7.7	19.6
8	1995/05/15	04:05:59.38	41.5545	88.7516	0.8	8.8	24.9
9	1995/08/17	00:59:59.35	41.5402	88.7533	0.7	9.2	18.8
10	1996/06/08	02:55:59.37	41.5780	88.6875	1.0	9.3	20.1
11	1996/07/29	01:48:59.62	41.7162	88.3757	0.6	8.4	21.5

Extension of P-wave Velocity Models into the Mantle

To extend the velocity models into the mantle, we add the teleseismic travel-time data. To minimize the "smearing effect" of the shallow structure or teleseismic tomography, we constrain the uppermost (top 100 km) of the model with that obtained from regional data as described in sections 2 and 3. The 1964-2004 ISC/EHB regional/teleseismic database includes 9.4 million travel-times for P, p^P, and PP phases (Li et al. 2005). For the tomographic inversion we use an adaptive parameterization of the grid based on ray sampling density, and iterative LSQR with norm and gradient damping (Li et al., 2005).

Examples of velocity cross sections for shallow and deep structure are shown in Figures 5 and 6, respectively. A continuum of lithospheric and mantle velocity structure provides the means for calculating accurate travel-times and for understanding the lithospheric mantle geodynamic processes.

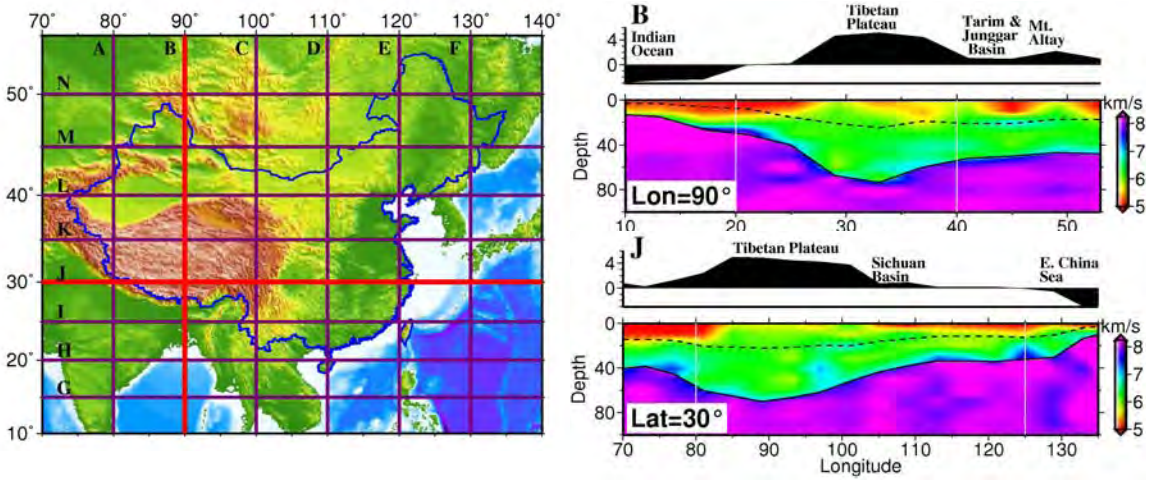

Figure 5. Vertical velocity profiles (right) of the crust and uppermost mantle. The selected profile locations are shown on the left.

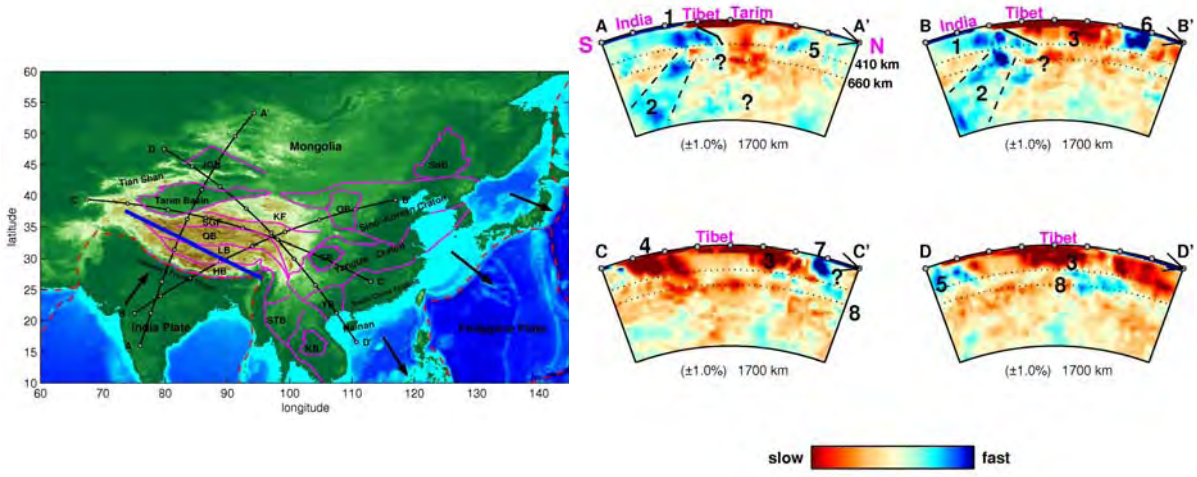

Figure 6. Vertical cross sections (right) of velocity image down to the mantle. The cross section locations are shown on the left.

CONCLUSIONS

Strong P-wave velocity variations of more than 10% found in the study area indicate the existence of significant structural heterogeneities in the crust and uppermost mantle in this region. The velocity models show the following features.

1. The seismic velocity images are characterized by block structures corresponding to geological features bounded by large fault zones. This region consists of a few geological structures: the North China Block including Songliao Basin, the South China Block, the Sichuan Basin, the Tarim Basin, and the Tianshan area. Those areas exhibit different patterns of velocity distribution in the tomographic images. The trend of velocity anomalies is consistent with the trend of regional tectonics.

2. A clear dividing line along the 105° parallel separates China into a low-V zone in the west and a high-V zone in the east at a depth of 40 km.

3. Our tomographic imaging has revealed significant velocity heterogeneities in the middle and lower crust.

4. Pn velocities are high under southern and eastern Tibet and under the Sichuan and Ordos basins.

The deeper velocity profiles show evidence of current and past subduction zones and other geodynamic processes. A surprising result is that the "roots" of some geologic features, such as the Sichuan Basin and Ordos Plateau, extend deep into the upper mantle.

REFERENCES

China Seismological Bureau, (1986), *Findings of Exploring the Crust and Upper Mantle Structure of China. Seismological Press*, 407 pp., Beijing (in Chinese).

Hearn, T. M., S. Wang, J. F. Ni, Z. Xu, Y. Yu, and X. Zhang, (2004), Uppermost mantle velocities beneath China and surrounding regions, *J. Geophys. Res. 109*, doi:10.1029/2003JB002874.

Huang, J., D. Zhao, and S. Zheng, (2002), Lithospheric structure and its relationship to seismic and volcanic activity in southwest China, *J. Geophys. Res. 107*, doi:10.1029/2000JB000137.

Huang, J., and D. Zhao, (2004), Crustal heterogeneity and seismotectonics of the Chinese capital region. *Tectonophysics, 385,* 159-180.

Huang, Z., W. Su, Y. Peng, Y. Zheng, and H. Li, (2003), Rayleigh wave tomography of China and adjacent regions, *J. Geophys. Res. 108*, doi 10.1029/2001JB001696.

Institute of Geophysics, China Seismological Bureau (IG-CSB), (1990-2003), *Annual Bulletin of Chinese Earthquakes (ABCE),* Seismological Publishing House, Beijing.

Laske, G., and G. Masters, (1997), A global digital map of sediments thickness (abstract), *EOS 78*, F483.

Laske, G., G. Masters, and C. Reif, (2001), CRUST 2.0: a new global crustal model at 2x2 degrees, http://mahi.ucsd.edu/Gabi/rem.dir/crust/crust2.html (last accessed July 2005).

Lebedev, S., and G. Nolet, (2003), Upper mantle beneath southeast Asia from S velocity tomography, *J. Geophys. Res. 108*, doi 10.1029/2000JB000073.

Li, C., R. van der Hilst, and M. N. Toksoz, (2005), Constraining P-wave velocity variation in the upper mantle beneath Southeast Asia, Submitted to PEPI.

Li, S., X. Zhang, and Z. Song, (2001), Three-dimensional crustal structure of the Capital area obtained by a joint inversion of deep seismic sounding data from multiple profiles, *Acta Geophys. Sin. 44*, 360-368 (in Chinese).

Liang, C., X. Song, and J. Huang, (2004), Tomographic inversion of Pn traveltimes in China, J. Geophys.Res. 109, B11304, doi:10.1029/2003JB002789.

Liu, F. T., H. Wu, J. H. Liu, G. Hu, Q. Li, and K. X. Qu, (1990), 3-D velocity images beneath the Chinese continent and adjacent regions, *Geophys. J. Int. 101*, 379-394.

Mooney, W. D., (1998), CRUST 5.1: a global crustal model at 5° x 5°, *J. Geophys. Res. 103*, 727-747.

Paige, C., and M. Saunders, (1982), LSQR: An algorithm for sparse linear equations and sparse least squares, ACM Trans. *Math. Software, 8*, 471.

Pei, S., Z. Xu, and S. Wang, (2004a), Discussion on origin of Pn velocity variation in China and adjacent region, *Acta Seismol. Sin. 26*, 1-10 (in Chinese).

Pei, S., Y. Chen, D. Zhao, A. Yin, J. Ning, and X. Chen, (2004b), Tomographic structure of east Asia and its geodynamic implication, Submitted to *J. Geophys. Res.*

Ritzwoller, M. H., M. P. Barmin, A. Villasenor, A. L. Levshin, and E. R. Engdahl, (2002), Pn and Sn tomography across Eurasia to improve regional seismic event locations, *Tectonophysics 358,* 39-55.

Shapiro, N. M., and M. H. Ritzwoller, (2002), Monte Carlo inversion for a global shear velocity model of the crust and upper mantle, *Geophys. J. Int. 151*, 88-105.

Song, Z. H., C. Q. An, G. Y. Chen, L. H. Chen, Z. Zhuang, Z. W. Fu, and J. F. Hu, (1991), Study on 3-D velocity structure and anisotropy beneath west China from the Love wave dispersion, *Acta Geophys. Sin. 34*, 694-707 (in Chinese).

Stevens, J. L., D. A. Adams, and G. E. Baker, (2001), Improved surface wave detection and measurement using phase-matched filtering with a global one-degree dispersion model, in *Proceedings of 23rd Seismic Research Review: Worldwide Monitoring of Nuclear Explosions,* LA-UR-01-4454, pp. 420-430.

Sun, Y., (2005), P- and S-wave tomography of the crust and uppermost mantle in China and surrounding areas, Ph.D. Thesis, Massachusetts Institute of Technology, Cambridge, Massachusetts.

Sun, R., and F. Liu, (1995), Crust structure and strong earthquakes in Beijing, Tianjin and Tanshan area, I. P wave velocity structure, *Acta Geophys. Sin. 38*, 599-607 (in Chinese).

Sun, Y., X. Li, S. Kuleli, F. D. Morgan, and M. N. Toksöz, (2004), Adaptive moving window method for 3-D P-velocity tomography and its application in China, *Bull. Seism. Soc. Am. 94*, 740-746.

Um, J., and C. Thurber, (1987), A fast algorithm for two-point seismic ray tracing, *Bull. Seism. Soc. Am. 77*, 972-986.

Wu, F. T., A. L. Levshin, and V. M. Kozhevnikov, (1997), Rayleigh wave group velocity tomography of Siberia, China, and vicinity, *Pure Appl. Geophys. 149*, 447-473.

Xu, Y., F. Liu, J. Liu, and H. Chen, (2002), Crust and upper mantle structure beneath western China from P wave travel-time tomography, *J. Geophys. Res., 107*, doi 10.1029/2001JB000402.

Yu, X., Y. Chen, and P. Wang, (2003), Three-dimensional P wave velocity structure in Beijing-Tianjin-Tangshan area, *Acta Seismol. Sin. 25*, 1-14.

Zhang, X., (1998), *Study of the Crust and Upper Mantle Structure in and Around the Zhangjiakou-Bohai Seismic Belt.* Active Fault Research (6), Seismological Press, Beijing.

Zhao, D., (2001), New advances of seismic tomography and its applications to subduction zones and earthquake fault zones: A review, *The Island Arc, 10*, 68-84.

Zhao, D., A. Hasegawa, and S. Horiuchi, (1992), Tomographic imaging of P and S wave velocity structure beneath northeastern Japan, *J. Geophys. Res., 97*, 19909-19928.

Zhao, D., A. Hasegawa, and H. Kanamori, (1994), Deep structure of Japan subduction zone as derived from local, regional and teleseismic events, *J. Geophys. Res., 99*, 223122329.

Zhu, J., J. Cao, X. Cai, Z. Yan, and X. Cao, (2002), High resolution surface wave tomography in east Asia and west pacific marginal sea, *Chinese J. Geophys., 45*, 679-698.

Zhu, L., R. Zeng, and F. Liu, (1990), 3-D P wave velocity structure under the Beijing network area, *Acta Geophys. Sin.*, 33, 267-277 (in Chinese).

TOWARDS A COMPREHENSIVE SEISMIC VELOCITY MODEL FOR THE BROADER AFRICA-EURASIA COLLISION REGION, TO IMPROVE NUCLEAR EXPLOSION MONITORING

S. van der Lee[1], A. Rodgers[2], M. Flanagan[2], M. Pasyanos[2], F. Marone[3], and B. Romanowicz[3]

Northwestern University[1], Lawrence Livermore National Laboratory[2], and UC Berkeley[3]

Sponsored by National Nuclear Security Administration
Office of Nonproliferation Research and Engineering
Office of Defense Nuclear Nonproliferation

Contract Nos. DE-FC52-04NA25541[1], W-7405-ENG-48[2], and DE-FC52-04NA25542[3]

ABSTRACT

We report on progress towards a new, comprehensive three-dimensional (3-D) model of seismic velocity in a broad region encompassing the Middle East, northern Africa, the Mediterranean Sea, the Levant, the Arabian Peninsula, the Turkish-Iranian Plateau, the Indus Valley, and the Hindu Kush. Our model will be based on regional waveform fits, surface wave group velocity measurements, teleseismic arrival times of S and P waves, receiver functions, and published results from active source experiments. We are in the process of assembling each of these data sets and testing the joint inversion for subsets of the data. Seismograms come from a variety of permanent and temporary seismic stations in the region. Some of the data is easily accessible through, for example, IRIS, while collection of other data is more involved. This work builds on ongoing work by Schmid et al. (2004, and manuscript in preparation).

In these proceedings, we highlight our data sets and their inferences, demonstrate the proposed new data-inversion modeling methodology, discuss results from preliminary inversions of subsets of the data, and demonstrate the prediction of arrival times with three-dimensional velocity models. We compare our preliminary inversion results with the results of Schmid et al., and the predicted arrival times to ground-truth data from the National Nuclear Security Administration (NNSA) Knowledge Base. Our data sets are simultaneously redundant and highly complementary. The combined data coverage will ensure that our three-dimensional model comprises the crust, the upper mantle, including the transition zone, and the top of the lower mantle, with spatially varying, but useful resolution.

The region of interest is one of the most structurally heterogeneous in the world. Continental collision, rifting and sea-floor spreading, back-arc spreading, oceanic subduction, rotating micro plates, continental shelf, and stable platforms, are just some of the region's characteristics. Seismicity and the distribution of seismic stations are also geographically heterogeneous. The crustal thickness ranges from near 20 to near 45 km under dry places in the Mediterranean region alone, which contains at least seven of the fourteen types of crust defined globally by Mooney et al. (1998). The S-velocity varies laterally by an entire 1 km/s over 1000 km within the uppermost mantle. On average the S-velocity is 50 to 150 m/s slower, between a depth of 150 km and the Moho, than global model IASPEI91. These lowered S velocities reflect the high amount of tectonic activity in the study region. In the transition zone,the S-velocity is roughly 150 m/s higher than IASPEI91. These heightened S velocities likely reflect the numerous fragments of oceanic lithosphere that subducted in the study region during geologically relatively recent times.

OBJECTIVES

Our primary objective is developing a new 3-D S-velocity model for the Middle East and Mediterranean region, including North Africa, southern Europe, and Arabia that

1) is resolved in aseismic regions,
2) is resolved throughout the upper mantle (to 660 km),
3) resolves laterally varying crustal thickness,
4) contains laterally varying vertical velocity gradients,
5) is simultaneously compatible with multiple data sets,
6) utilizes several recent, unique waveform data sets,
7) includes uncertainties of the model parameters.

These features would increase the model's ability to predict and calibrate regional travel times and waveforms, thereby providing improved event locations, focal mechanisms, and other event discriminants.

Secondly, we aim to convert the 3-D *S*-velocity model to a 3-D *P*-velocity model, using both literature on elastic properties (and their partial derivatives with temperature and pressure) of mantle rocks and empirical information provided by measured arrival times of teleseismic *P* and *P*ms waves. The corresponding *P*-wave model would provide an improved ability to locate seismic events.

The prediction and calibration of regional travel times and waveforms depends strongly on the methodology used to compute travel times and waveforms. Our third objective is to test the *S*-wave and *P*-wave models' ability to predict regional *P* and *S* travel times, deflect wave paths, and deform waveforms, and assess their effects first on the studied seismograms (travel times and waveforms) and subsequently on the 3-D models derived from these data.

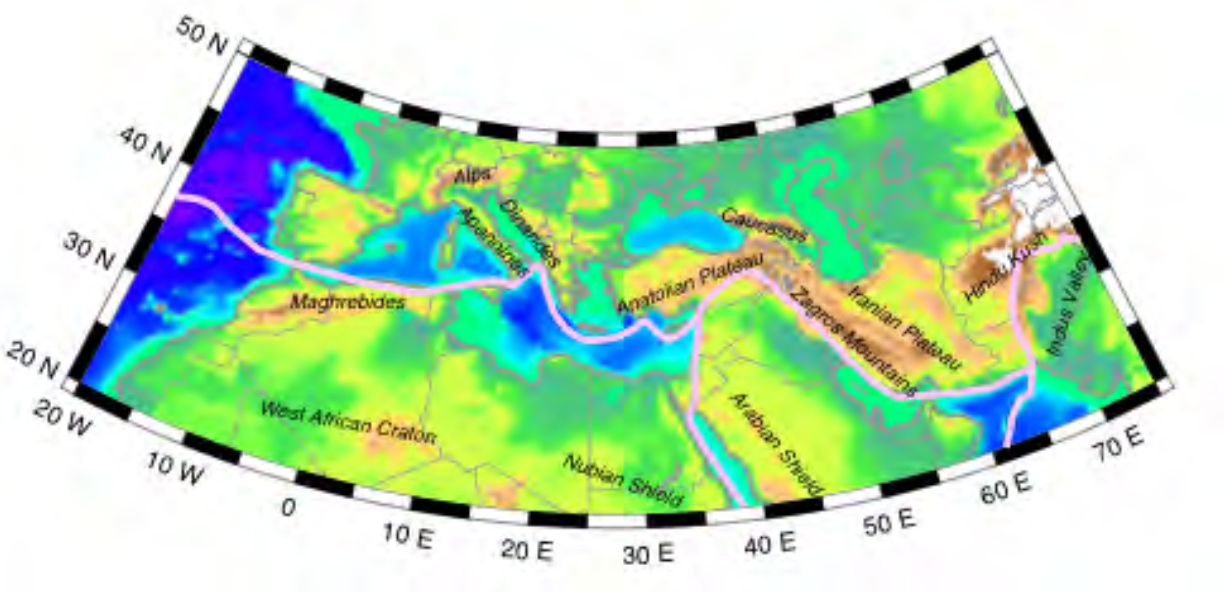

Figure 1. Topographic map of the study region. The pink line is the NUVEL1-A (DeMets et al., 1990) representation of the Eurasia-Africa-Arabia plate boundary.

The study region (Figure 1) is roughly centered around the Africa-Arabia-Eurasia triple junction. Two other triple junctions mark the western and eastern boundaries of the study region, with the Africa-Eurasia-North America junction at the Azores being just off the map in the west and the Arabia-Eurasia-Indian Plate junction at the edge of the study region to the east (Figure 1). The interaction of these six major tectonic plates with each other and with several microplates within a stretch as short as one quarter of the Earth's circumference makes this study region tectonically complex. The 3-D structure of the upper mantle and crust are correspondingly complex. More than half of the primary crustal types used by Mooney et al. (1998) for the construction of their global crustal model

CRUST5.1 are found in the study region. In many parts of the region the seismic *S*-velocity of the upper mantle strongly varies laterally and by large amounts (e.g. Pasyanos et al., 2001; Marone et al., 2004; Maggi and Priestley, 2005). We plan to capture various renditions of this structurally and tectonically complex part of the world in one model through the joint inversion of different types of seismic data. Predictions for seismogram characteristics (phase arrival times, amplitudes, dispersion) based on this new model are expected to match many of the observed characteristics and be useful for event discrimination. Simultaneously, the new model will refine our understanding of the structure and tectonics in the study region.

RESEARCH ACCOMPLISHED

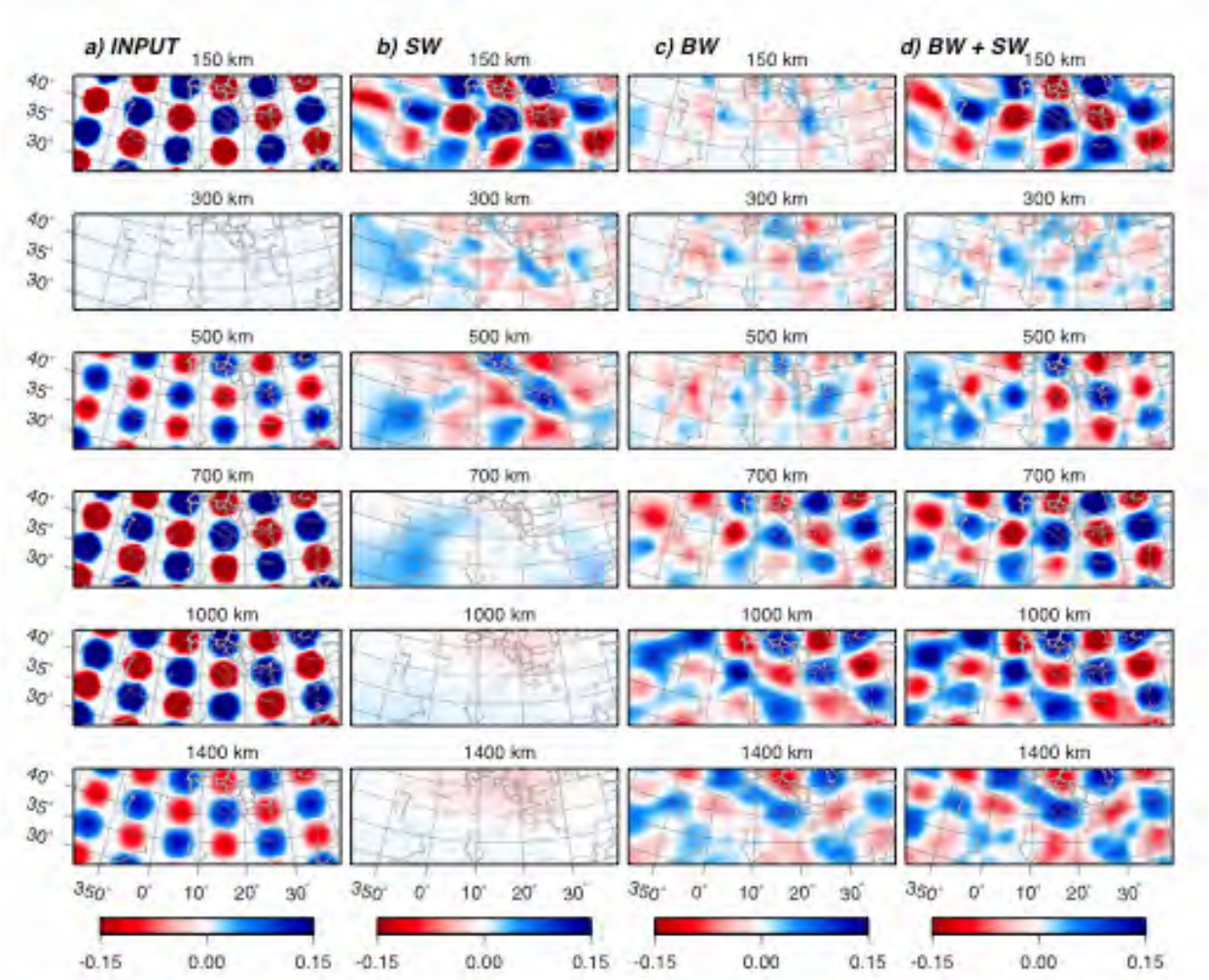

Figure 2. Joint-inversion resolution test for the western part of the study region. INPUT = hypothetical model, SW = resolved with regional waveforms only, BW = resolved with teleseismic *S* arrival times only, BW + SW = resolved by the joint inversion of both data sets.

Joint inversion

To achieve our primary objectives we are developing software than handles the joint inversion of constraints from regional waveform fits, teleseismic arrival times, receiver functions, and group velocities. We have completed the software for jointly inverting regional waveforms, receiver functions, and teleseismic arrival times. The joint inversion code has been tested on the teleseismic *S* arrival time data set of Schmid et al. (2004) and the data derived from regional waveform fitting from Marone et al. (2004). The results are encouraging, showing only a percent or two increase in the variance reduction obtained in the linear inversion of both data sets compared to their individual

inversions (Schmid et al., manuscript in preparation). The resolving power of the joint data sets, however, has increased dramatically (Figure 2). Figure 2 demonstrates the following: The teleseismic data add more lateral resolution to the regional waveform data, while the regional waveform data add more depth resolution to the teleseismic data. The resolved depth range of the combined data sets has doubled with respect to their individual depth ranges. The regional waveform data resolve the upper mantle more strongly while the teleseismic arrival times resolve the lower mantle more strongly. Where the two data sets overlap in spatial sensitivity, e.g.,in the transition zone (see the 500-km map in Figure 2), the resolving power of the combined data is superior to that of each of the data sets alone.

Example Waveform Fits

We have begun to fit the available waveform data in the Middle East using the non-linear inversion procedure employed by previous partitioned waveform inversion studies (Van der Lee and Nolet, 1997; Marone et al. 2004). Figure 3a shows the Middle East region and four events and paths for which we have estimated path-average structure. Earthquakes are indicated by their Harvard centroid moment tensor (CMT) solutions. These four paths sample some of the diversity of geologic/tectonic environments in the Middle East (Figure 1). The velocity structures were estimated using the average continental model MC35 (Van der Lee and Nolet, 1997), shown as the black line in Figure 3b, however we chose an appropriate crustal thickness for each path (in 5-km increments) based on a priori reported estimates. The inversion procedure estimates the perturbations to the starting model by non-linear optimization (Nolet et al.;1986; Nolet, 1990).

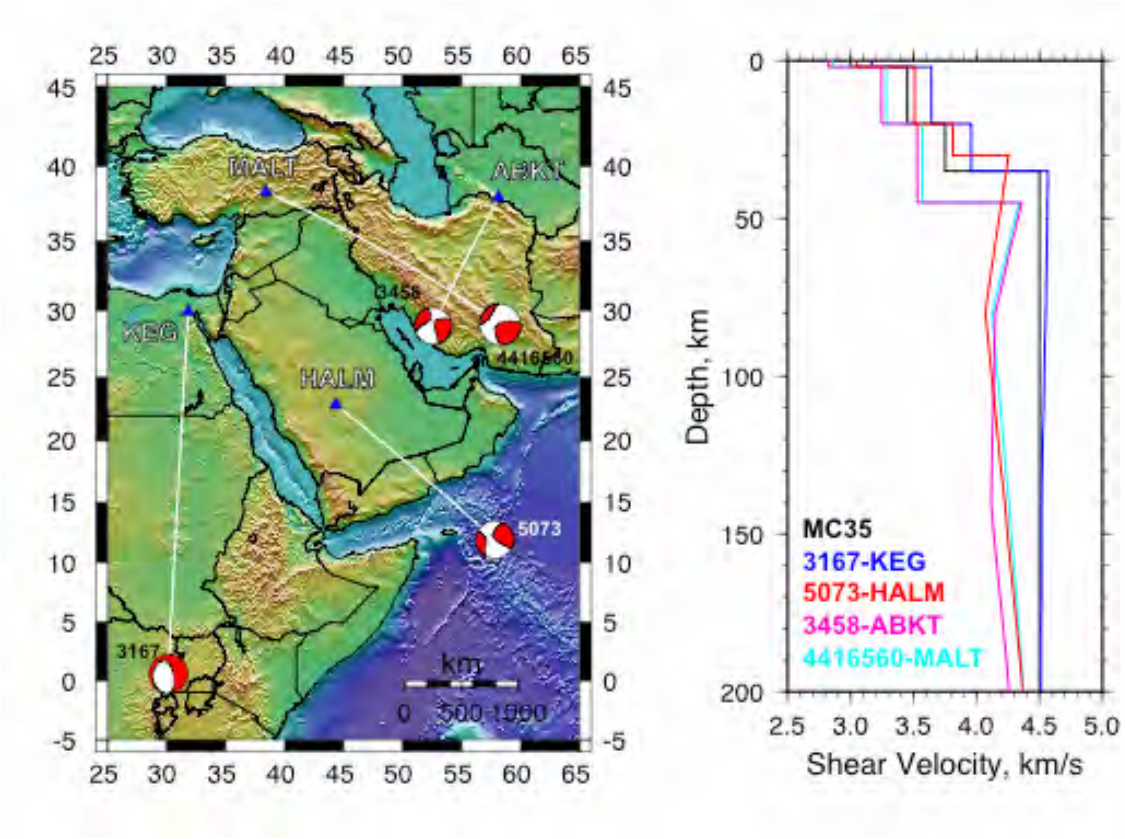

Figure 3. (a) Map of the Middle East showing four earthquakes and paths for which we fit waveforms. The events are indicated by their moment tensor and identified by their eventid (evid) number. Stations are shown as blue triangles. (b) Shear velocity profiles for the four paths shown in (a), color-coded by path (indicated by evid-station). The starting model, MC35, is shown in black.

The resulting shear-velocity profiles for these paths are shown in Figure 3b. These models show 1) faster crustal velocities and slightly faster mantle velocities for the Nubian shield (KEG); 2) lower velocities in the crust and upper mantle for the path crossing the Iranian Plateau (ABKT and MALT); faster crustal and low sub-Moho velocities path from the Owen Fracture Zone to the Arabian Shield (HALM). We discuss the fits and interpret the inferred structures in detail below.

The waveform fits are shown in Figure 4. These panels show the data (black) and synthetic seismograms for the starting model (red dashed) and final model (green). The starting model often predicts significant phase differences relative to the data for both the S- and Rayleigh waves. The path across the Nubian Shield (3167-KEG) is faster than the MC35 starting model. The crustal velocities along this path are quite high. This is consistent with fast crustal velocities in the Arabian Shield (e.g., Mokhtar and Al-Saeed, 1994; Sandvol et al., 1998; Rodgers et al., 1999; Julia et al., 2003; Al-Damegh et al., 2005). It is worth noting that the Red Sea broke up the Nubian-Arabian Shield and these provinces could have similar crustal petrologies. Both provinces have volcanics and it has been speculated that mafic intrusion may explain the higher crustal velocities. The inferred mantle velocities beneath the Nubian Shield are slightly faster than the starting model. However, reported mantle velocities beneath the Arabian Shield are lower than average (e.g., Mokhtar and Al-Saeed, 1994; Rodgers et al., 1999, Maggi and Priestley, 2005). Constraints on mantle velocities beneath the Nubian Shield will improve understanding of mantle dynamics associated with the opening of the Red Sea, including possible asymmetries across the axis of rifting.

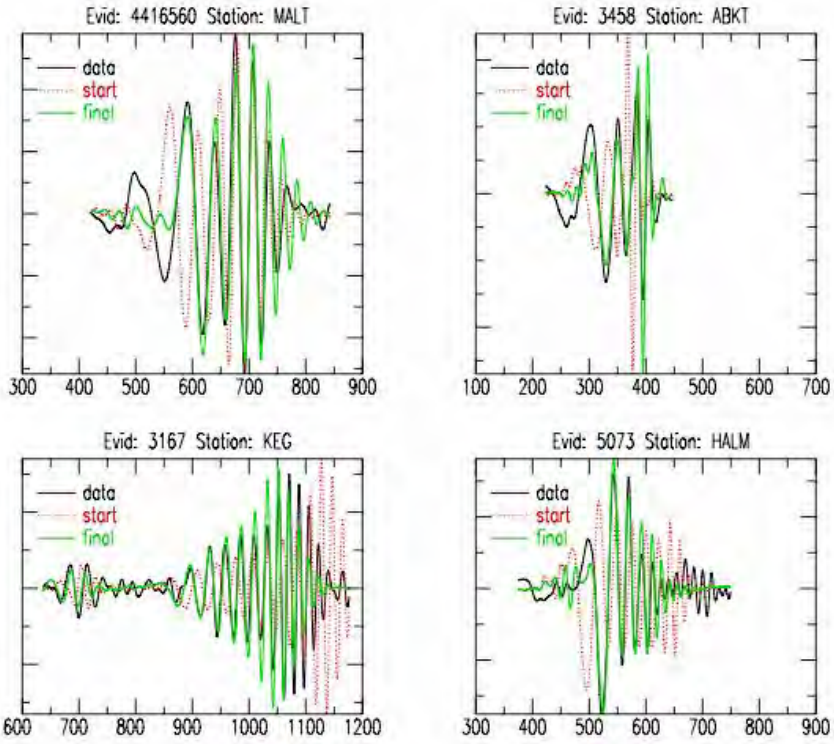

Figure 4. Fits for vertical component S- and Rayleigh waveforms for the four paths: (a) 4416560-MALT; (b) 3458-ABKT; (c) 3167-GNI; and (d) 5073-HALM. The waveforms are shown as observed (black), starting model (red dashed) and final (green). The frequency content of the data and synthetics is different for each fit but generally covers the band 0.006-0.04 Hz

The paths across the Iranian Plateau (3458-ABKT and 4416560-MALT) are fit with a model with 45-km crust, consistent with estimates of crustal structure in the Zagros Mountains (Hatzfeld et al., 2003). Estimated crustal

velocities in the Iranian Plateau are low, consistent with an orogenic crust. Mantle velocities beneath the Iranian Plateau are low, consistent with previous reports (e.g., Hearn and Ni, 1994; Al-Lazki et al., 2004; Maggi and Priestley, 2005). Note that this is a zone of high Sn attenuation, likely related to partial melt and shallow asthenospheric mantle (e.g., Kandinsky-Cade et al., 1981; Rodgers et al, 1997; Al-Damegh et al., 2004). The waveform fits for these paths are satisfactory for the Rayleigh wave, but the S-wave and higher-mode Rayleigh wave are not particularly well fit. This could result from Love wave energy that scattered onto the vertical component for the 4416560 (Dec. 26, 2003 Bam Iran) event. The radiation pattern for this event is nearly nodal for Rayleigh waves and thus maximal for Love waves. The long-period energy preceding the Rayleigh wave could be a quasi-Love wave due to anisotropy or multi-pathing.

The path from the Owen Fracture Zone to the Arabian Shield (5973-HALM) reveals low mantle velocities. This mixed oceanic-continental path was fit with a model with intermediate crustal thickness of 25 km. Mantle velocities are low, but this is not surprising given that the path passes through oceanic spreading centers along the Owen Fracture Zone and across the Gulf of Aden.

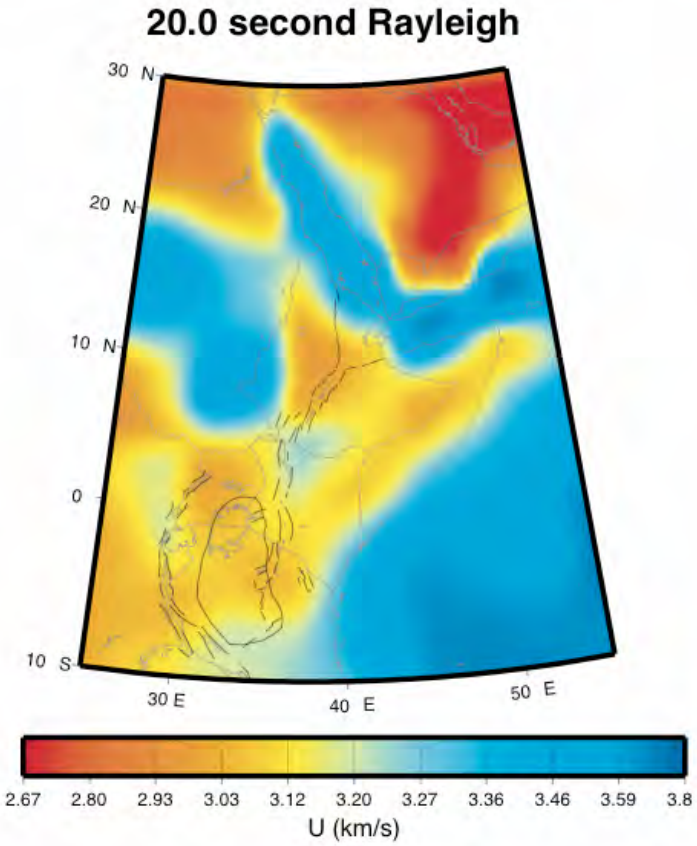

Figure 5. Inferred spatial variation in group velocity (U) for 20s Rayleigh waves.

Rayleigh group velocities

We have continued to measure group velocities of Rayleigh waves and use them to update previous group velocity maps (Figure 5). Twenty second Rayleigh waves are very sensitive to the crust, which is reflected in the stark group velocity contrast between the oceanic (and Red Sea) regions and the slower continental regions, with thicker crust (Figure 5). Pinpointing the cause of the group velocity differences within continental regions (Figure 5) awaits the analysis of the depth distribution of the *S*-velocity anomalies that give rise to the anomalous group velocities. The contrast between the Nubian Shield and Arabian peninsula in Figure 5 is, however, qualitatively consistent with the waveform fits (Figure 4) and their constraints on upper mantle structure (Figure 3), which show relatively high

velocity in the uppermost mantle between event 3167 and station KEG and relatively low velocities between event 5073 and station HALM. This consistency supports the anticipated benefits of a joint inversion.

Surface-wave group velocities can be reliably measured without knowledge of the event source mechanism. An important new source in the study region of data for such group velocity measurements is the MIDSEA data set (Van der Lee et al., 2001). Surface waves in the MIDSEA data have been analyzed for those events for which source mechanisms were available, but not yet for others.

Data transcription and conversion

The MIDSEA data are from a temporary PASSCAL-type experiment with an unusual mix of instrumentation and data formats. Conversion to a community-accepted exchangeable and complete data format (SEED) facilitates their analysis in a broader sense and into the future. A station list (Table 1) hints at the heterogeneity among stations and the data-processing procedures associated with each (Van der Lee et al., 2001). While data from some stations are already available in full SEED format at the IRIS or Geofon data centers, others lack continuity of records and/or response information, precluding them from conversion to SEED and the associated storage in a long-term accessible archive. We have transcribed and submitted the remainder of the MIDSEA data to the IRIS data management center (DMC) storage facilities and have assembled and tested a procedure to reliably convert the data to SEED format.

The quality of MIDSEA data is also heterogeneous. For some station location choices, environments that provided more security prevailed over environments providing better seismic recording ability. Many of the stations required 220 V AC, restricting the locations to existing facilities. None of the stations were telemetered, resulting in significantly delayed detection of normal problems with a station. The far and remote locations of the stations, relative to the project's headquarters, as well as international customs regulations and a limited budget, caused further delays in station repair in some cases. Some have been converted to permanent station sites. For example, stations MELI, GHAR, and MARJ are now permanent Geofon and CLTB is now a MedNet station.

Table 1. MIDSEA station information. COSEA stations, installed in the Azores (Van der Lee et al., 2001; Silveira et al., 2002), are excluded in this table. COSEA data are available at the IRIS DMC. MIDSEA station names are FDSN approved. * = station was moved a few 100 m

Station code	Latitude	Longitude	Elevation (m)	Approximate on date (dd.mm.yyyy)	Approximate off date (dd.mm.yyyy)	Data location and contact
CDLV	29.163	-13.444	37	07.06.1999	06.04.2001	IRIS, Van der Lee & Cabildo de Lanzarote
EBRE	40.823	0.494	36	17.06.1999	13.11.2000	IRIS, Van der Lee & Observatori de l'Ebre
POBL	41.379	1.085	550	14.11.2000	31.03.2003	University of Barcelona, Van der Lee & LEGEF
DUOK	44.113	14.932	115	16.07.1999	05.02.2001	IRIS, Van der Lee & University of Zagreb
HVAR	43.178	16.449	250	13.10.1999	08.02.2001	IRIS, Van der Lee & University of Zagreb
ITHO	37.179	21.925	400	23.10.1999	15.08.2001	IRIS, Van der Lee & NOA
KOUM	37.704	26.838	340	28.10.1999	15.08.2001	IRIS, Van der Lee & NOA
APER	35.55	27.174	250	03.11.1999	15.08.2001	IRIS, Van der Lee & NOA

Station code	Latitude	Longitude	Elevation (m)	Approximate on date (dd.mm.yyyy)	Approximate off date (dd.mm.yyyy)	Data location and contact
MELI	35.290	-2.939	41	17.12.1999	21.11.2001	Geofon, Van der Lee & ROA
GHAR	32.122	13.089	650	19.01.2000	10.11.2002	IRIS, Van der Lee & LCRSSS
MARJ	32.523	20.878	300	22.05.2000	17.10.2001	IRIS, Van der Lee & LCRSSS
ABSA	36.277	7.473	1025	18.07.2000	03.04.2002	IRIS, Van der Lee & CRAAG
CLTB	37.579	13.216	955	01.06.1999	30.09.2000	ORFEUS, Margheriti & INGV
SALI	38.564	14.833	360	01.06.1999	30.09.2000	ORFEUS, Margheriti & INGV
VENT	40.795	13.422	110	01.06.1999	30.09.2000	ORFEUS, Margheriti & INGV
DGI	40.318	9.607	343	29.07.1999	30.06.2000	University of Nice, Deschamps
GRI	38.822	16.420	525	15.07.1999	30.06.2000	University of Nice, Deschamps
MGR	40.138	15.554	297	14.07.1999	31.03.2001	University of Nice, Deschamps
SOI	38.073	16.055	300	15.07.1999	31.03.2001	University of Nice, Deschamps

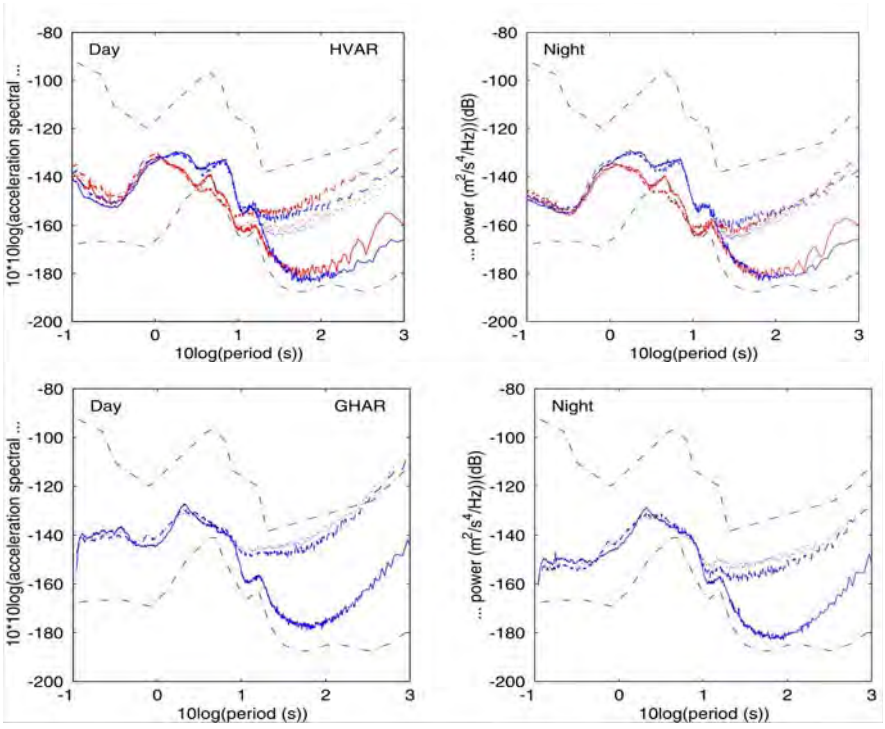

Figure 6. Acceleration spectral density of time series at two MIDSEA stations. Red and blue lines represent summer and winter, respectively. Solid and non-solid represent vertical and horizontal components, respectively. Grey dashed lines represent the Peterson high and low noise models. Earthquake records have not been removed from the time series.

Heterogeneity in MIDSEA data quality is illustrated in Figure 6. The spectral characteristics for two stations are extreme in that they both extend the Peterson noise model. The winter spectra for the horizontal components of station GHAR exceed the high noise model at the longest periods. The absence of this extreme during the night suggests that this might have something to do with human usage of the facility and its immediate environment that houses the seismometer. This seismometer was later moved to a vault. The summer spectra for HVAR are slightly below the low noise Peterson model at periods of several seconds. This illustrates the exclusiveness of the Hvar, Croatia, astronomical observatory that houses the station. Other time series spectra (not shown) demonstrate, among other issues, that the microseismic noise level is much higher in the Atlantic Ocean than in the Aegean Sea.

CONCLUSIONS AND RECOMMENDATIONS

The strength of a joint inversion of different types of seismic data lies in the various data sets being both redundant and complementary. The redundancy is needed to increase accuracy and to ensure that both data sets measure the same structural phenomena. The data sets need to be complementary to increase resolving power over a larger volume of mantle and crust and thereby reduce trade-offs, e.g.. between crustal thickness and uppermost mantle velocity, inherent in each type of seismic data set.

The broad consistency between seismic velocity anomalies inferred from teleseismic arrival times, Rayleigh wave group velocities, and regional waveforms shown here implies that these different types of data sets are at least in part redundant. The consistency further shows that the data sets record the same structural phenomena, despite differences in size and character between typical sensitivity kernels for each data set. This conclusion is further supported by an analysis of how teleseismic delay times depend on frequency (Schmid et al., 2004).

We have also shown that the teleseismic arrival times and the regional waveforms are highly complementary. The shared sensitivity, though different in character, of receiver functions and Rayleigh wave group velocities to crustal structure is anticipated to separate crustal effects on the observed data from mantle causes when included in the joint inversion.

Preliminary results from data analysis for the Middle East show that this part of the study region is slower on average than typical one-dimensional global velocity models. Marone et al. (2004) and Maggi and Priestley (2005) show that the same is true for the parts of the study region to the west and east, respectively. This allows for a fairly simple set of one-dimensional starting models, yielding a more uniform treatment of data recorded throughout the region. Our data analysis results are broadly consistent with results from the literature.

ACKNOWLEDGEMENTS

Christian Schmid produced Figure 2. Rick Benson helped with the conversion of the MIDSEA data to SEED format.

REFERENCES

Al-Damegh, K., E. Sandvol, A. Al-Lazki, and M. Barazangi (2004), Regional wave propagation (Sn and Lg) and Pn attenuation in the Arabian plate and surrounding regions, *Geophys. J. Int*. 157: 775–795.

Al-Damegh, K., E. Sandvol, and M. Barazangi (2005), Crustal structure of the Arabian plate: New constraints from the analysis of teleseismic receiver functions, *Earth. Planet. Sci. Lett*. 231: 177–196.

Al-Lazki, A., E. Sandvol, D. Seber, M. Barazangi, N. Turkelli, and R. Mohamad (2004), Pm tomographic imaging of mantle lid velocity and anisotropy at the junction of the Arabian, Eurasian and African plates, *Geophys. J. Int*. 158: 1024–1040.

DeMets, C., R. G. Gordon, D. F. Argus, and S. Stein (1990), Current plate motions, *Geophys. J. Int*. 101: 425–478.

Hearn, T., and J. Ni (1994). Pn velocities beneath continental collision zones: the Turkish-Iranian Plateau, Geophys. J. Int., 117: 273-283.

Julia, J., C. Ammon and R. Herrmann (2003). Lithospheric structure of the Arabian Shield from the joint inversion of receiver functions and surface wave group velocities, Tectonophysics, 371: 1-21.

Kadinsky-Cade, K., M. Barazangi, J. Oliver and B. Issacs (1981). Lateral variation in high-frequency seismic wave propagation at regional distances across the Turkish and Iranian plateaus, J. geophys. Res., 86: 9377-9396.

Hatzfeld, D., M. Tartar, K. Priestley and M. Ghafory-Astiany, Seismological constraints on the crustal structure beneath the Zagros Mountain belt (Iran), Geophys. J. Int., 155: 403-410.

Maggi, A. and K. Priestley (2005). Surface waveform tomography of the Turkish-Iranian Plateau, Geophys. J. Int., 160: 1068-1080.

Marone, F., S. van der Lee, and D. Giardini (2004), 3-D upper mantle *S*-velocity model for the Eurasia-Africa plate boundary region, Geophys. J. Int., 158: 109-130.

Mokhtar, T. and M. Al-Saeed (1994), Shear wave velocity structures of the Arabian Peninsula, Tectonophysics, 230: 105-125.

Mooney, W., G. Laske, and G. Masters (1998), CRUST5.1: a global crustal model at 5 x 5 degrees, J. Geophys. Res., 103: 727-747.

Pasyanos, M.E., W.R. Walter, and S.E. Hazler (2001), A surface wave dispersion study of the Middle East and North Africa for monitoring the Comprehensive Nuclear-Test-Ban Treaty, Pure appl. geophys., 158: 1445-1474.

Rodgers, A., J. Ni and T. Hearn (1997), Propagation characteristics of short-period Sn and Lg in the Middle East, Bull. Seism. Soc. Am., 87: 396-413.

Rodgers, A., W. Walter, R. Mellors, A. M. S. Al-Amri and Y. S. Zhang (1999), Lithospheric structure of the Arabian Shield and Platform from complete regional waveform modeling and surface wave group velocities, Geophys. J. Int., 138: 871-878.

Schmid, C., S. van der Lee, and D. Giardini (2004), Delay times and shear-wave splitting in the Mediterranean region, Geophys. J. Int., 159:275-290.

Silveira, G., S. Van der Lee, E. Stutzmann, L. Matias, D. James, P. Burkett, M. Miranda, L.M. Victor, J.L. Gaspar, L. Senos, S. Solomon, J.P. Montagner, and D. Giardini (2002), Coordinated seismic experiment in the Azores, ORFEUS Newsletter, 4: 10.

Sandvol, E., D. Seber, M. Barazangi, F. Vernon, R. Mellors, and A. Al-Amri (1998), Lithospheric seismic velocity discontinuities beneath the Arabian Shield, Geophys. Res. Lett., 25: 2873-2876.

Van der Lee, S., and G. Nolet (1997), Upper-mantle S-velocity structure of North America, J. Geophys. Res., 102:22,815-22,838.

Van der Lee, S., F. Marone, M. van der Meijde, D. Giardini, A. Deschamps, L. Margheriti, P. Burkett, S.C. Solomon, P.M. Alves, M. Chouliaras, A. Eshwehdi, A.S. Suleiman, H. Gashut, M. Herak, R. Ortiz, J.M. Davila, A. Ugalde, J. Vila, K. Yelles (2001), Eurasia-Africa Plate Boundary Region Yields New Seismographic Data, Eos Trans. AGU, 82: 637 645 646.

TOMOGRAPHIC MAPPING OF LG Q IN EASTERN EURASIA

Jiakang Xie[1], David Schaff[1], and Yunfeng Liu[2]

Lamont-Doherty Earth Observatory of Columbia University[1], University of Southern California[2]

Sponsored by Air Force Research Laboratory

Contract No. F19628-03-C-0122

ABSTRACT

Several thousands of Lg spectra have been collected in eastern Eurasia, from many seismic stations in China and its neighboring countries such as Mongolia, Russia, Khyrghistan, and Kazakhstan. Many spectra are recorded by pairs of two stations that are aligned with the sources, permitting estimates of inter-station Lg Q with either the standard two-station method, or the reversed two-station method of Chun et al. (1987). We select about 600 repeatedly sampled two-station paths with inter-station distances greater than 300 km to estimate Lg Q robustly. The estimated inter-station (Lg Q at 1 Hz) values are input to a back-projection algorithm to obtain a tomographic map of Q_0. Values of the mapped Q_0 vary laterally by about a factor of 10 across eastern Eurasia. Q_0 values are below or around 100 in much of the Tibetan Plateau, and are moderate (about 300-500) in eastern and central China. In regions of northeast China and the southeast coast of China, Q_0 values reach about 500 and are somewhat higher than in adjacent regions. Q_0 values generally increase northwards, to above 500 in Mongolia, Siberia, and eastern Europe. In two broad high latitude (>50 °N) regions in Siberia and eastern Europe, Q_0 values are larger than 800. The Q_0 map correlates well with the tectonic evolution history of eastern Eurasia, and is generally similar to the previous map of Q_0 developed using an Lg coda Q method. We are less confident on the individual power-law frequency dependence (η) values measured using the two-station methods because many spectral ratios are measured in relatively narrow frequency ranges, owing to the loss of high-frequency signals at the more distant stations. Often the highest available frequencies for the spectral ratio calculations are near 1 Hz. Nevertheless, there is a clear trend for the measured η values to be low. The mean η estimated over the 600 inter-station paths is about 0.2, with a spread (standard deviation) of about 0.3. These η values tend to be lower than the previously estimated values using Lg coda Q method, or a method of simultaneous inversion of source spectra and path Q. These previous estimates tend to have higher median values of about 0.4 to 0.5, but are obtained under idealized stochastic modeling which contain more assumptions than that used in the two-station methods.

OBJECTIVE

The objective of this research is to map lateral variations of regional wave Q in eastern Eurasia using data from various sources, including the IRIS DMC and other data centers. The regional waves to be used include Lg, Pg, Pn, Sn and long-period Rayleigh waves. The target is to develop regionalized Q models that have lateral resolutions as high as the data and methods permit. For some waves such as Lg and Pg, the resulting Q model will be in a form of a tomographic Q map; for other waves such as Sn, the resulting Q models may be region-specific by dividing eastern Eurasia into several (or more) subregions. The resulting Q models can be used for (a) estimating seismic source spectra, source energy radiation and seismic moments, (b) inferring source spectral scalings, stress drops and apparent stress of earthquakes; (c) inferring fundamental properties of the crust and upper mantle such as their temperature fields, and (d) evaluating the magnitude threshold of seismic events that can be recorded and studied using any set of seismic stations.

Because the Q models are of such fundamental and practical importance for scientific research and earthquake hazard mitigation, and because the new Chinese National Digital Seismic Network (CNDSN) has a large number of stations providing data to Chinese seismologists, the Lamont-Doherty Earth Observatory (LDEO) established a collaboration with the Data Management Center of the Chinese National Digital Seismic Network (DMC/CNDSN) through a mutually beneficial mode to generate high-quality Q models. A LDEO seismologist (Jiakang Xie) installs software on the DMC/CNDSN computers and trains the local personnel to collect and process regional wave spectra. Eventually the large number of regional wave spectra collected at the Incorporated Research Institution of Seismology (IRIS) Data Management Centers (DMC) by the LDEO, and at the DMC/CNDSN by the Chinese seismologists, will be merged and the seismologists from both LDEO and China will jointly invert these spectra to obtain Q models and source spectral scalings using high-frequency regional waves and long-period Rayleigh waves from eastern Eurasia.

RESEARCH ACCOMPLISHED

Background

The Lg is typically the most prominent short-period seismic phase observed over continental paths at distances greater than 200 km. Lg can be treated as a sum of higher mode surface waves, or multiple supercritically reflected S waves in the crust. The properties of Lg phase, such as its group velocity and Q, closely resemble those of the crustal average of shear waves. Whereas the Lg velocity varies by about 10% or less cross major continents, the Lg Q can vary by up to an order of magnitude. Such large variations are brought by the fact that Q is strongly affected by crustal properties such as fluid contents and temperature, both vary significantly from one region to another. Reliable measurements of Lg Q are difficult because the Lg amplitudes are affected by complications of source spectra and 3D velocity structures whose effects are difficult to fully account for, resulting in errors in Q measurement. Values of Q may be measured using the long duration of Lg coda under the assumption that coda is singly scattered Lg by crustal heterogeneities that are distributed stationarily (e.g., Mitchell, 1997). Values of the Lg coda Q can be measured with single seismograms and approximates those of Lg Q. There have been various attempts to measure Q using direct Lg waves (e.g., Philipps et al., 2000, 2002). Among methods of measuring Q using the direct Lg waves, the standard two-station method has the advantage in that it allows the source spectra to be canceled in Q measurements. The reversed two station method (Chun et al., 1987) further allows the cancellation of site responses. These methods, while being the most reliable, require restricted recording geometries and hence denser station and event coverages.

The eastern part of Eurasian continent that includes regions in and around China has a complex tectonic history. Currently the collision between Indian and Eurasian plates to the southwest results in the uplifting of the Tibetan plateau. The underthrusting of the Pacific plate from east is related to the extensions along the east coast of China. These processes provide the primary driving force of the current motions and deformations of a collage of blocks with diverse evolution histories. Timing of the last significant tectonic activity that modified the crustal blocks range between Paleozoic to current. Mitchell et al. (1997) found that the Lg coda Q values throughout Eurasia tend to correlate with the length of time that has elapsed since the last major tectonic activity. In the past decades, there have been a steady accumulation of digital Lg

waveforms from eastern Eurasia brought by the installation of various broad band seismic networks and the high seismicity in the region. In this paper we report a tomographic mapping of Lg Q in the region, obtained by applying the most reliable, two-station methods to about 6,000 recently collected Lg spectra.

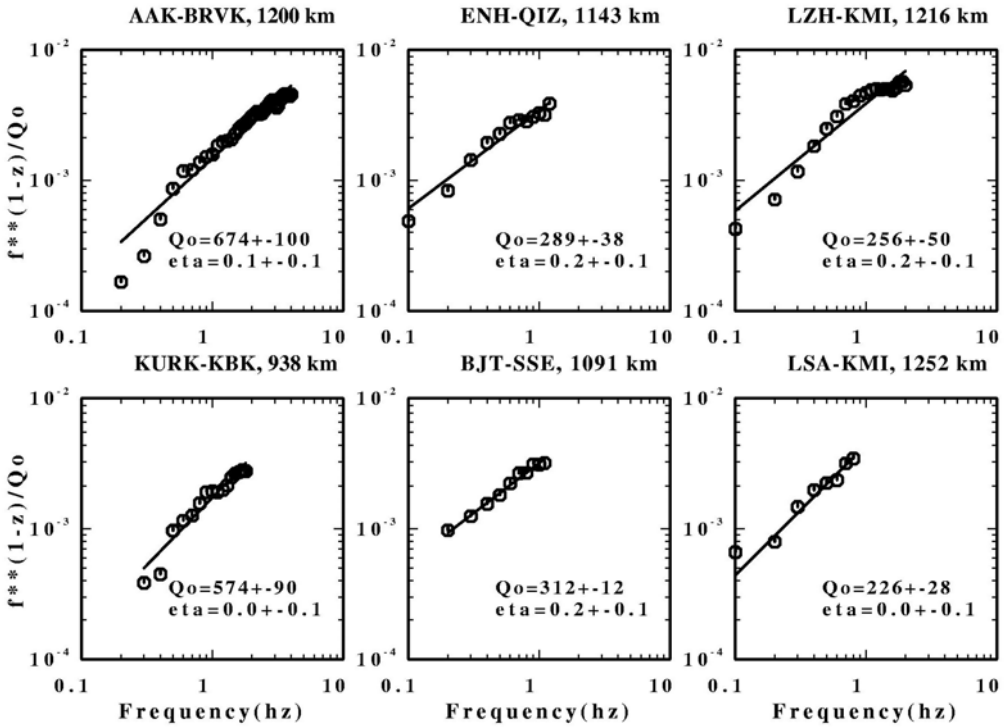

Figure 1. Average inter-station spectral ratios (circles) and the best fit Lg Q models (lines). Station codes, interstation distances and the estimated Q_0, η values are written in the panels. The first 3 ratios sample station-pairs from sources located in the same direction, so the standard two-station method (e.g., Xie et al., 2004) is used. The last 3 ratios sample station-pairs from sources located in opposite directions, so the method of Chun et al. (1987) is used.

Data and method of Q measurement

One hundred and sixty-two broad-band seismic stations are used in this study. The network affiliations include the Global Seismic Network (GSN) and various national or portable networks such as the Chinese National Digital Seismic network (CNDSN), the Kyrghistan and Kazakhstan seismic networks, and the three passive networks deployed in the Tibetan Plateau (e.g., Xie et al., 2004). Vertical component Lg waveforms from 186 events between 1988 and 2004 are retrieved from the DMC of IRIS and CNDSN. Most events are moderately sized (with magnitudes larger than 5.0). Fourier spectra of Lg are obtained using a well-established procedure (e.g., Xie et al., 2004). More than 6,000 Lg spectra are collected. From these, 5,787 pairs of spectra are selected from two stations that are (1) approximately aligned with at least one event, (2) separated far enough (> 250 km), permitting the use of the standard two-station method for Lg Q measurement. A subset of these spectral pairs further satisfies the criterion of the reversed two-station, two-event condition, permitting estimation of both inter-station Q free of site responses, and ratios of site responses (Chun et al., 1987). By examining the latter ratios we found that a few stations have non-unity site responses and/or erroneously documented instrument responses. These stations are screened out not in subsequent analysis. This results in 5,265 useful spectral ratios that collectively sample 594 inter-station paths. Average spectral ratios are calculated over these paths to estimate interstation Lg Q, which are assumed to follow the power-law frequency dependence ($Q=Q_0 f^{\eta}$ where Q_0 is Q at 1 Hz and η is the power-law frequency dependence). Typically, the lowest frequencies that yield usable spectral ratios are between 0.1 and 0.2 Hz. The highest usable frequencies are primarily controlled by the signal/noise ratio

threshold of 2 used in this study, and typically vary between about 1 and 2.5 Hz. Figure 1 shows examples of spectral ratios and the best fit Lg Q models.

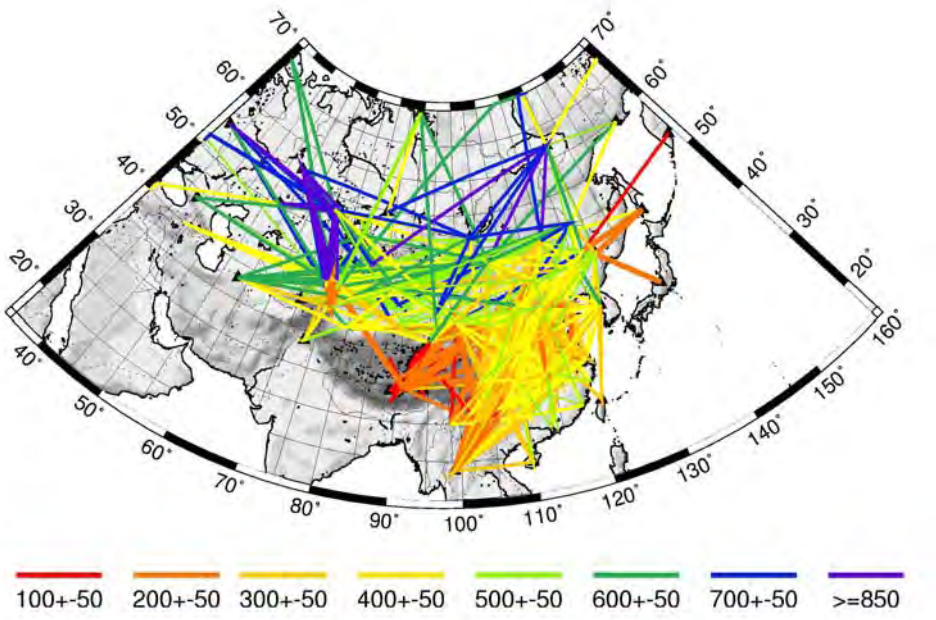

Figure 2. Two-station paths used in this study. Colors are coded to indicate Lg Q_0 values.

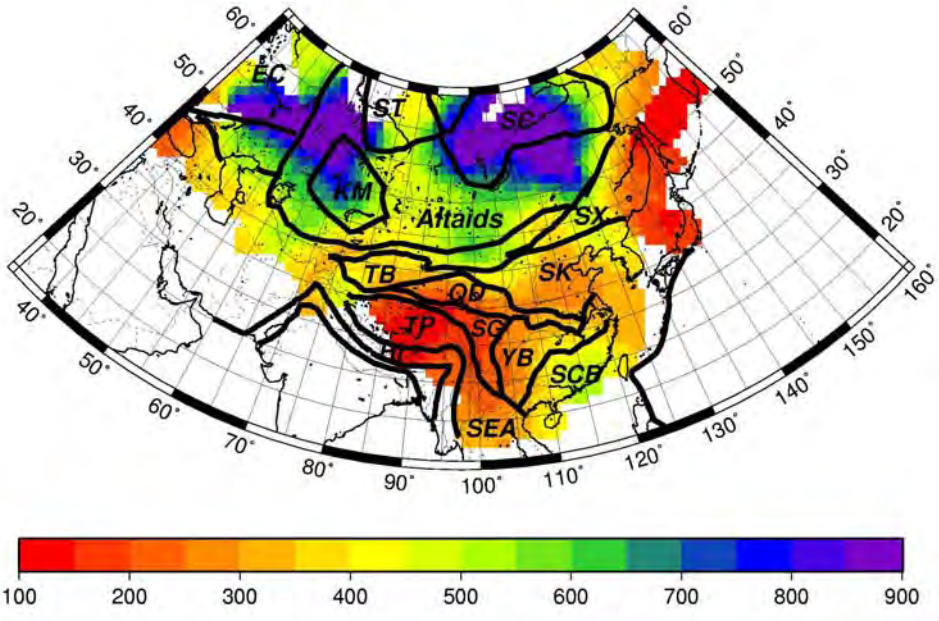

Figure 3. Lg Q_0 map for eastern Eurasia obtained in this study, and simplified tectonic boundaries (e.g., Mitchell et al., 1997; Wu et al., 1997; Hearn et al., 2004, Liang et al., 2004). Abbreviations are as follows: Tibetan Plateau (TP), Tarim Block (TB), Himalayas (HI), Songpan-Ganzi Belt (SG), Southeast Asia subplate (SEA), Yangtze block (YB), South China Block (SCB), Sino-Korean block (SK), Suolun-Xiamulun block (SX), Kazak Massif (KM), Siberia Craton (SC), Siberia Trap (ST) and Eastern Europe Craton (EC).

Result

Figure 2 shows the 594 two-station paths with colors to indicate the values of the Q_0 measurements. These values tend to be coherent at large scale and are input to a tomographic back-projection algorithm (e.g., Xie et al. 2004) to invert for the lateral variations in Q_0. To parameterize the spatially varying Q_0, the study area is divided into about 2,300 cells with constant Q_0 values and a size of 2 by 2 degrees. Figure 3 shows the resulting Q_0 model. The random errors and resolution associated with the model are estimated using the algorithm of Xie and Mitchell (1990) and Xie at el. (2004). The estimated random errors for the Q_0 model in Figure 3 is typically about 10-15%. The resolution, as measured by the point spread functions, varies between about 4 degrees in eastern China and about 10 degrees in higher latitudes (>=55°N).

The most striking low Q_0 region in Figure 3 is that in and around the Tibetan Plateau where Q_0 is at the level of 100 to 200. Toward east, Q_0 increases to about 300 in the Songpan-Ganzi Belt and Qaidam Basin, and to 350-550 in the Yangzi and south China blocks. To the north of these regions there is a band of moderate Q_0 regions (300-450) that covers the Tarim Block, the Ordos and the Sino-Korean Platforms. To the north of this band Q_0 increase with increasing latitude in the Altaids, to between about 400 and 600. Much of the Kazak Massif contains Q_0 values that are greater than 600. Variations of Q_0 in the northernmost regions can be resolved only at scales of about 10 degrees, with two broad regions of high Q_0 values of greater than 700, and up to 900, in the Siberian and Eastern Europe Cratons. Between these regions lies the Siberian Trap, a province that was affected by wide-spread volcanism and rifting in late Paleozoic-Mesozoic time. Values of Q_0 in the Trap are relatively lower (about 400-500) than in the Cratons. In general, Lg Q_0 values in Figure 3 exhibit a good correlation with the time length measured from the last major tectonic events that modified the blocks, as found by Mitchell et al. (1997) for Lg coda Q_0 values. The variations in Lg Q_0 in Figure 3 in the southern and eastern portions are more drastic than those of Lg coda Q_0, as would be expected if Lg coda is generated by an Lg-scattering process, which naturally smears out the spatial variations of Lg coda Q measurements.

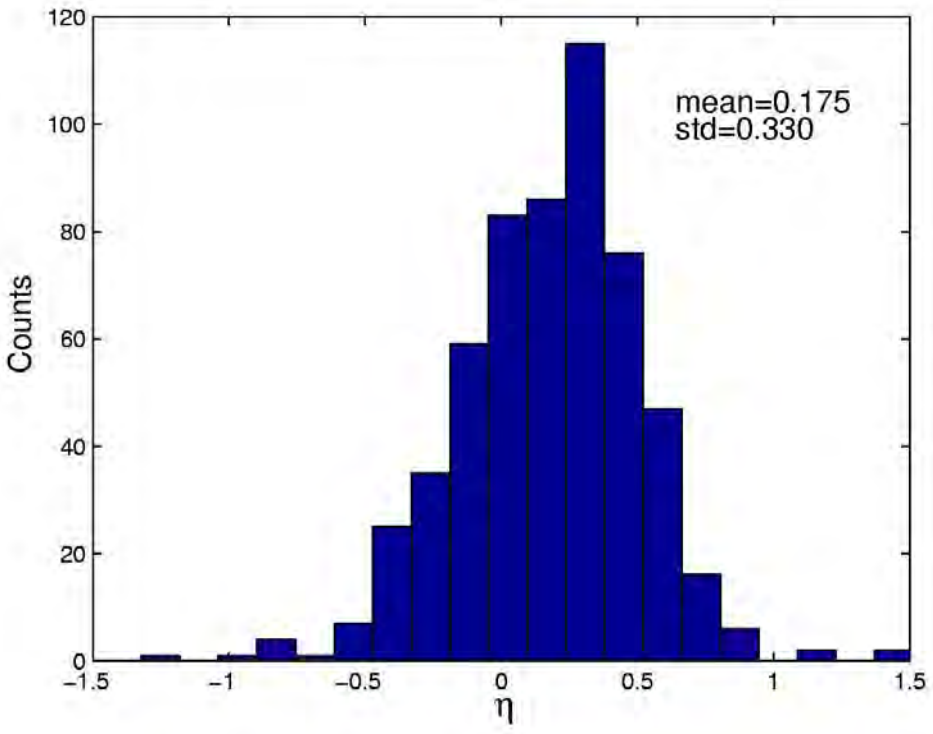

Figure 4. Distribution of the measured inter-station η values, with means and standard deviation indicated.

The frequency dependence (η) values are measured using the slopes of the logarithm of the inter-station spectral ratios (Figure 1). Ideally to measure η reliably, a wide frequency range between about 0.1 and a few Hz is desirable (Xie et al., 2004). Unfortunately, many spectral ratios used in this study are only available in relatively narrow frequency ranges between about 0.1 and 1 Hz owing to the rapid loss of high frequency signals at the more distant stations. We are, therefore, less confident at the measured η values for many individual paths. Figure 4 shows the histogram of the 594 η measurements, which allows us to examine their gross range. The mean and standard deviation of these η measurements are of 0.17 and 0.3, respectively, meaning the range of η is roughly between -0.1 and 0.5. The mean η of 0.17 is much lower than the mean η values of 0.4-0.5 obtained using Lg coda (Mitchell et al., 1997) or using a simultaneous inversion of source spectra and Lg Q (Xie et al., 1996). This discrepancy in measured η values may result from some systematic bias in the different measurement methods that are based on various assumptions. The coda Q method assumes a single, frequency independent scattering process. The simultaneous inversion of source spectra Q assumes an idealized, omega-squared source model. The two-station method assumes nothing about Lg scattering or source, but has a strict requirement of recording geometry which often leads to a large epicentral distances (> 1500 km) of the more distant stations. The assumptions of Lg scattering or omega-source model may not be perfectly valid, or η could tend to decrease with recording distance in addition to varying laterally (Xie et al., 1996). Assuming that the latter is not the case and η values measured in this study are not grossly biased, we may map the lateral variation of η spatially. Future research with more data should enable us to explore the cause of the η discrepancy.

CONCLUSIONS AND RECOMMENDATION

Thousands of Lg spectral ratios are collected from eastern Eurasia that includes China and surrounding regions. These ratios repeatedly sample Lg attenuation, or Q, over 594 two-station paths. Lateral variations of Lg Q are mapped using a tomographic inversion. The 1 Hz Lg Q (Q_0) varies between about 100 and 900. There is a general correlation between values of Lg Q_0 and the time length measured from the last major tectonic event that modified the crustal structure. The lowest Q_0 is found in the Tibetan plateau. Values of Q_0 increase to moderate numbers toward east and north. The highest Q_0 is found in broad regions that coincide with the Siberia and Eastern Europe Cratons. Values of Lg Q_0 are grossly compatible to those of Lg coda Q_0, measured using data, assumption and method that are different from those in this study. The power-law frequency dependence (η) values obtained in this study are systematically lower then those obtained previously using Lg coda. Resolving this discrepancy is important because path-corrections at high frequencies are critically dependent on accurately estimated η values. Future research with more data should enable us to explore the cause of the η discrepancy.

ACKNOWLEDGEMENTS

We thank Chuntao Liang, Xiaodong Song and Brian Mitchell for providing files of tectonic features of eastern Eurasia.

REFERENCES

Chun, K. Y., G. F. West, R.J. Kokoski and C. Samson (1987). A novel technique for measuring Lg attenuation - Results from eastern Canada between 1-Hz to 10-Hz, *Bull. Seism. Soc. Am*. 77: 398-419.

Hearn T. M., S. Y. Wang, J.F. Ni,, Z.H. Xu, Y.X. Yu and Zhang X.D. (2004). Uppermost mantle velocities beneath China and surrounding regions, *J. Geophys. Res*., 109: Art. No. B11301, doi:10.1029/2003JB002874.

Liang, C., X. Song, and J. Huang (2004). Tomographic inversion of Pn travel times in China, *J. Geophys. Res.* 109: B11304, doi:10.1029/2003JB002789.

Mitchell, B. J., Y. Pan, J. Xie and L. Cong, (1997). Lg coda Q variation across Eurasia and its relation to crustal evolution, *J. Geophys. Res*. 102: 22767-22780.

Phillips, W. S., Hartse H. E., Taylor S.R. and G.E. Randall (2000). 1 Hz Lg Q tomography in Central Asia, *Geophys. Res. Lett.* 27: 3425-3428.

Phillips, W. S. and H. E. Hartse (2002). Regional path calibration using multiple-station amplitude tomography. *Seism. Res. Lett.* 73: 228.

Wu F. T., A. L. Levshin and V.M. Kozhevnikov (1997). Rayleigh wave group velocity tomography of Siberia, China and the vicinity, *PAGEOPH* 149: 447-473.

Xie, J. and B. J. Mitchell (1990). A back projection method for imaging large scale lateral variation in Lg coda Q with application to continental Africa, *Geophys. J.* 100: 161-181.

Xie, J., L. Cong, and B. J. Mitchell, (1996). Spectral characteristics of the excitation and propagation of Lg from underground nuclear explosions in Central Asia, *J. Geophys. Res.* 101: 5813-5822.

Xie, J., R. Gok, J. Ni, and Y. Aoki (2004). Lateral variations of crustal seismic attenuation along the INDEPTH Profiles in Tibet from Lg Q inversion, *J. Geophys. Res.* 109: B10308, doi:10.1029/2004JB002988.

NEAR-SOURCE ENERGY PARTITIONING FOR REGIONAL WAVES IN 2D AND 3D MODELS, CONTRIBUTIONS OF S*-TO-LG AND P-TO-LG SCATTERING

Xiao-Bi Xie, Thorne Lay, and Ru-Shan Wu

University of California, Santa Cruz

Sponsored by Air Force Research Laboratory

Contract No. FA8718-05-C-0021

ABSTRACT

Regional seismic phases are now becoming of central importance for low-yield nuclear event size estimation and discrimination. However, the lack of fundamental understanding of the physics controlling regional wave energy partitioning remains a major concern for high-confidence applications of regional phases in nuclear monitoring. Due to the complex excitation and energy partitioning processes involved in regional phase formation, it is difficult to separate the contributions of different excitation mechanisms in the observed data. Given this situation, numerical simulations can play an important role for understanding the excitation of regional phases.

We develop innovative regional seismic wave numerical modeling procedures to enhance understanding of regional phase excitation and energy partitioning. Our approach is to separate the problem into consideration of near-source energy partitioning effects apart from long-range propagation effects. This is achieved by the "finite-difference modeling plus slowness analysis method". This method allows very fine 2D or 3D near source models to be used to investigate the near-source energy partitioning process. A localized slowness analysis tracks the energy partitioning instead of a time-consuming mode formation by long-distance propagator.

In this report, we focus on the frequency-dependent properties of the excitation and energy partitioning. A number of source and model parameters are calculated and examined for broad frequency ranges. As examples, *P-pS-Lg* conversion and *S**-to-*Lg* excitation in the presence of near-source scattering are tested as mechanisms for *Lg*-wave excitation. The numerical results reveal that the depth of the source and the depth of the scattering process have strong effects on the *P*-to-*S* conversion and partitioning of energy into trapped or leaking signals. The *Lg*-wave excitation spectra from these mechanisms are investigated. The contributions from the scattering process are separated from those of S*-wave. The modeling shows that *S**-to-*Lg* excitation is generally stronger for low frequencies and shallow source depths while *P*-to-*Lg* scattering is stronger for high frequencies. We also calculate the effect of near-source scattering on an explosion source in a 3D velocity model. The preliminary result shows that a few percent of random velocity fluctuation can generate considerable tangential waves which can be trapped in the waveguide to form the SH *L*g-wave.

OBJECTIVE

With the current emphasis on global monitoring for low-yield nuclear tests, regional seismic phases such as *Lg* have become very important for magnitude and yield estimation of underground nuclear tests. (e.g., Nuttli, 1986; Xie, et al., 1996; Patton, 2001). In addition, various *P*/*S*-type amplitude ratios for high-frequency regional phases (e.g., *Pn*/*Sn*, *Pn*/*Lg*, *Pg*/*Lg*, *Pg*/*Sn*) have become important for event discrimination (e.g., Taylor et al., 1989; Kim et al., 1993, 1997; Walter et al., 1995; Fisk et al., 1996; Taylor, 1996; Taylor and Hartse, 1997; Hartse et al., 1997; Fan and Lay, 1998a-c; Xie, 2002; Bottone et al., 2002). The applications of regional phases for yield estimation and event discrimination are largely based on empirical approaches, and while very promising in many cases, there are major questions about the nature of excitation of *S*-wave dominated phases such as *Lg*. Due to the complex excitation and energy partitioning processes associated with regional phases, it is difficult to empirically separate the contribution of individual energy partitioning mechanisms by analysis of data. Numerical modeling approaches are thus of great importance for investigating the excitation and propagation of regional phases (e.g., Wu, et al. 2000a, b; Bonner, et al., 2003; Stevens et al., 2003; Myers, et al., 2003, 2004).

Although there are continuing controversies about the dominant *P*-to-*S* transfer mechanisms affecting regional phases, most investigators agree that appreciable energy from explosion sources is converted to *S*-waves in the near-source region (e.g., Myers, et al., 2003). Several possible near-source energy excitation mechanisms have been proposed, including *P*-to-*Lg* scattering, *pS*-to-*Lg* conversion at the free surface, *Rg*-to-*Lg* coupling, *S**-to-*Lg* conversion, spall excitation of *S*, tectonic release and rock damage (e.g., Day and Mclaughlin, 1991; Gupta et al., 1992, 1997; Wallace, 1991; Gutowski, et al., 1984; Lilwall, 1988; Xie and Lay, 1994; Vogfjord, 1997; Johnson and Sammis, 2001). This project focuses on the near-source energy partitioning of regional phases in the environment prior to waveguide control on regional phase propagation. We develop the method based on 2D and 3D finite-difference simulation and local slowness analysis (FDSA method) to investigate energy partitioning right at the source region (Xie et al., 2005), while quantifying how energy will transfer into the long range propagation path, which is critical for comparisons with data. The underlying physical processes controlling the P-to-S conversion within several 10s of kilometers will be addressed. The excitation functions for different *Lg*-wave excitation mechanisms will be calculated as functions of frequency, source depth, and near-source structures

RESEARCH ACCOMPLISHED

P-*pS*-to-*Lg* and *P*-to-*Lg* Conversion

We first investigate the *P*-*pS*-to-*Lg* conversion caused by near-source lateral velocity variations and assess its effect on the explosion *S*-wave energy budget. For all numerical examples calculated in this paper, unless otherwise indicated, we use the horizontally layered Eastern Kazakh (EK) model (Priestley et al., 1988) as the background and modify it by adding random velocity fluctuations at different locations. In a horizontally layered model with overburden *P*-wave velocity larger than the upper mantle *S*-wave velocity, the free surface reflected *pS*-wave has a steep incidence angle and cannot be trapped in the crustal waveguide to form *Lg*. In this case, the energy transfer through *P*-*pS*-to-*Lg* coupling is almost zero. Although it is generally agreed that the existence of near-source lateral velocity variation can increase the *P*-to-*Lg* energy exchange, the detailed mechanism underlying this process is still not fully understood.

Figure 1 compares the simulated *P*-*pS*-to-*Lg* coupling in models with and without near surface lateral velocity variations. Figure 1a is for the EK-model. A shallow explosion source located at depth 0.5 km generates *P*, *pS* and *Rg* waves. Two-dimensional slowness analysis is conducted for selected phases in the wavefield and the results are shown together with the wavefield snapshot. The synthetic seismograms were bandpass filtered between 2.0 and 6.0 Hz before the slowness analysis. As can be seen from the result, the *P*-wave leads the wavefield and has a distinct slowness. Reverberations within the uppermost crust causes multiple parallel *pS* wavefronts with their horizontal slowness approximately equal to the overburdened *P*-slowness. The *pS* energy stays to the left of the upper-mantle *S*-slowness and there is no energy transferred from *P* to *Lg*. In Figure 1b, a shallow random velocity patch is added to the EK-model to test the effect of near surface scattering. The random patch has a 5% root mean square (RMS) velocity fluctuation (shown in the snapshot as a shaded area). The slowness analyses are conducted for *P*, *pS* and *pS*-coda. Although *P*- and early *pS*-waves are barely affected, the *pS*-coda clearly contains scattered energy with horizontal slowness to the right of the upper-mantle *S*-slowness.

Figure 2 investigates scattering taking place at deeper depths. The configuration of the source and model is similar to that used in Figure 1b, except the random patch with 3% RMS velocity fluctuation is added to the EK-model (shown in the snapshot as a shaded area). The 2D slowness analysis is conducted for selected phases in the wavefield and the results are presented in the figure. After passing through the random region, there is *P*-coda composed of scattered *P*- and *S*-waves generated from the direct *P*-wave. Although the early part of the *pS*-wave does not contribute to the trapped energy, its later part contains energy located to the right of the upper-mantle S-slowness which therefore will contribute to the trapped regional phases.

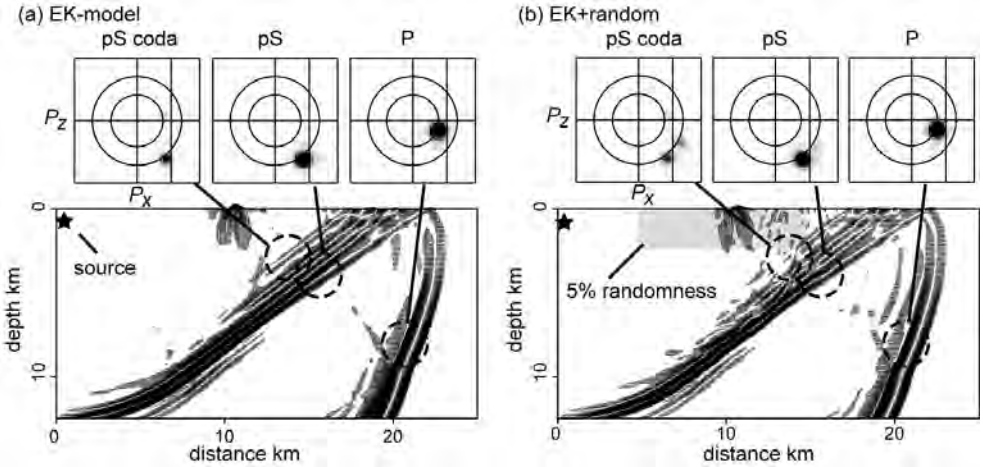

Figure 1. P-pS-to-Lg conversion due to shallow scattering. (a) is for the EK-model and (b) is for the EK-model with a shallow random patch. Details are given in the text.

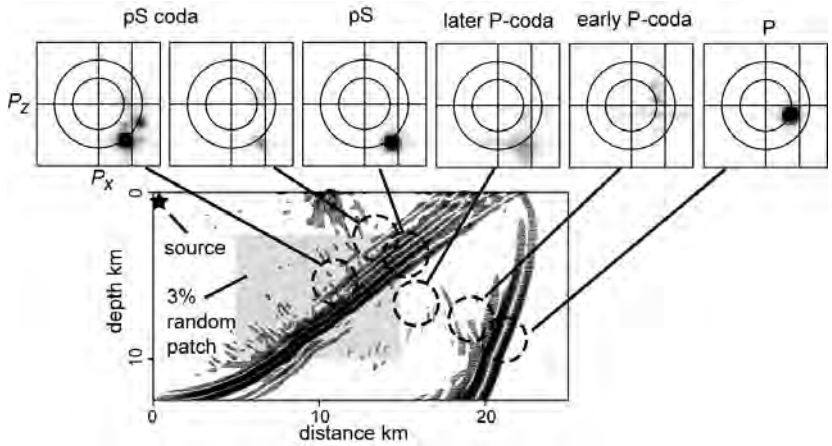

Figure 2. The P-pS-to-Lg conversion due to a deeper random patch. The slowness analysis for P, P-coda, pS and pS-coda are shown in the figure. Details are given in the text.

Figure 3 gives the energy distribution in the slowness-depth domain for different models where row (a) is for the EK-model and rows (b) and (c) are for the EK-model with 3% and 5% RMS fluctuations in a random patch like that used in Figure 2. The slowness analysis is conducted at a distance of 20 km and for depths between 0 and 12.5 km. As expected, with the EK-model no energy is seen beyond the upper mantle *S*-slowness, but after the lateral velocity variations are introduced, energy starts to build up to the right of the upper-mantle *S*-slowness. Two types of scattered energy can be found in the slowness-depth domain: weak but widely distributed *S* energy (indicated by the dashed ellipses) and scattered energy linked to the *pS*-wave (indicated by the dashed rectangles). Both types of energy satisfy the criterion $p_x \geq p_{S-mantle}$ and will contribute to the *Lg*-wave. The widely spread scattered *S*-wave is generated by the *P*-to-*Lg* coupling through volumetric scattering. The scattering process redistributes the angle spectrum of the original incident waves. Both volumetric scattering and scattering near the free-surface affect the general *P*-to-*Lg* conversion.

Contributions from the *S**-Wave

For shallow explosion sources, the *S**-wave may become a significant contributor to *Lg* (Gutowski, et al., 1984; Lilwall, 1988; Xie and Lay, 1994; Vogfjord, 1997). The amplitude of *S** can be large if the source depth is within a fraction of a wavelength from an interface. This makes its excitation highly dependent on the source depth and frequency. We investigate the contribution of the *S**-wave within the EK model. Figure 4 shows horizontal slowness analyses at a distance 35 km and for depths between 0 and 30 km. The time window is chosen between 11 to 13 s after the direct *P*-wave passes the receiver array. The synthetic seismograms are bandpass filtered between 1.0 - 5.0 Hz. The four rows from top to the bottom correspond to source depths 0.25 km, 0.5 km, 1.0 km, and 2.0 km, respectively. The major arrival is the down-going free surface reflected *pS*-wave, which has a horizontal slowness similar to the overburden *P*-slowness. As expected for a horizontally layered model, the *pS* energy stays to the left of the upper mantle *S*-slowness and has no contribution to the trapped regional phases. For shallow sources, the *Rg*-wave enters the array at about 12 s and its energy concentrates between 0 to 3 km, as can be seen on the upper right corners in the slowness-depth domain. For source depth of 2.0 km, the *Rg*-wave is very weak. The *S**-wave enters the array from a shallow depth and gradually merges with the *pS*-wave. The *S**-wave is strong for shallow sources and its amplitude decreases with increasing source depth. Very little *S** energy can be observed for source depths below 2 km. In the joint domains, the *S**-energy can be isolated and quantified even within a complicated wavefield, which is very difficult using remote surface synthetics. The dashed rectangles are the time-slowness-depth window used to locate the *S** energy. The energy from successive windows can be summed together to give the contribution of *S** to the trapped regional phases.

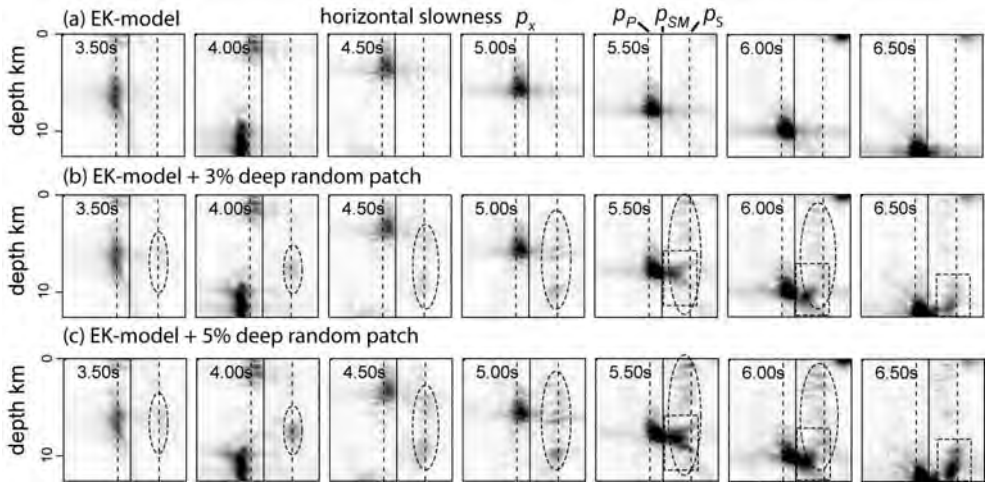

Figure 3. Energy distribution in depth and horizontal slowness domain for (a) the EK-model, (b) EK-model plus a 3% random patch and (c) EK-model plus a 5% random patch. The configuration of the source and model is same as that used in Figure 2. Energy circled by dashed rectangles is P-pS-to-Lg scattering and energy circled by dashed ellipses is P-to-Lg scattering.

The Frequency Dependent *Lg* Excitation Function

The frequency dependence of *Lg*-wave excitation is rooted in the underlying physical processes and is usually controlled by different characteristic scales. The excitation spectra from individual or joint mechanisms contributing to regional phases depict the frequency dependence of these processes. Frequency dependent *P*/*S* ratios will depend on the excitation functions of multiple phases. We use FDSA to quantify *Lg*-wave excitation spectra from *S**- and *pS*-waves. Figure 5 gives the *S**-to-*Lg* excitation spectra as functions of source depth and frequency. A series of bandpass filters is used to give responses at different frequencies. The vertical coordinate is the normalized relative energy $(E/E_0)^{1/2}$. Since the source spectrum has been taken away, the excitation function is the impulse response of the model to the source. The results clearly show that the *S**-to-*Lg* excitation is generally enhanced for lower frequency and shallow source depth. The major contribution comes from sources located above 1 km. For sources at depths below 1 km, only low-frequency energy below 1 Hz has significant contribution to *Lg*-wave excitation. However, the responses are also model dependent. For a model with a homogeneous crust (Figure 5a), the distribution has simple monotonic tendencies in both source depth and frequency. For the EK model (Figure 5b), the

excitation spectrum has a maximum at depth 1 km and a more complicated frequency dependence. This may reflect the fact that the EK model has an interface at 1 km depth.

To investigate the combined effect for *S**-wave and near-source scattering, we add shallow random velocity patches to the EK model. The random patch extends between distances of 5 to 25 km and depths of 0 to 2.5 km. Shown in Figures 6a and b are excitation spectra for random patches with RMS velocity fluctuations of 3% and 5%, respectively. The most prominent feature is the build up of high-frequency energy. The scattered energy increases with RMS velocity fluctuations. Figures 6c and d isolate the scattered energy by subtracting the excitation spectrum of the EK-model from the spectra for models with random velocity patches. Two types of energy can be identified within the frequency-depth domain. The high-frequency energy results from *P*-*pS*-to-*Lg* and *P*-to-*Lg* scattering. This energy is especially important for deeper sources to generate *Lg*-waves, since a deeper source generates little trapped energy in a horizontally layered model. The low-frequency energy concentrated at shallow source depths comes from *Rg*-to-*Lg* scattering.

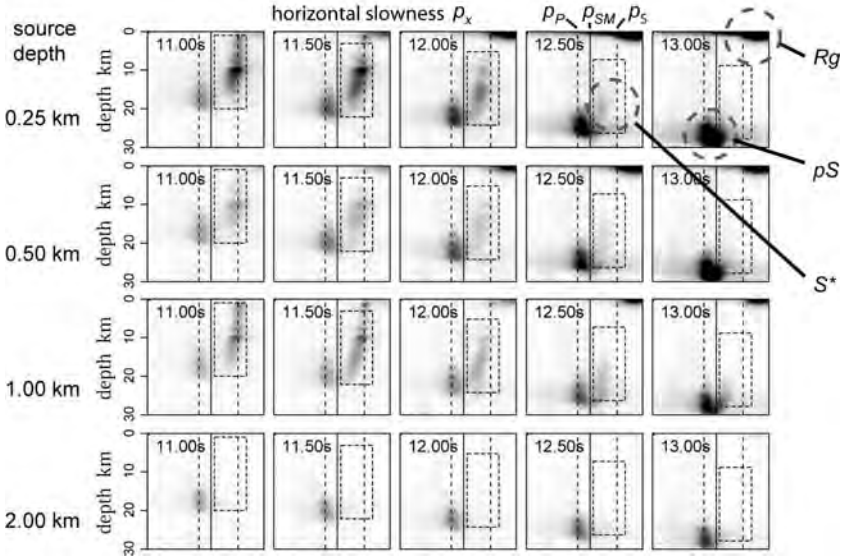

Figure 4. Slowness analysis for investigating S*-to-Lg conversion. Different rows are for different source depths. Dashed rectangles indicate the time-space-slowness windows used to pick the S* energy.

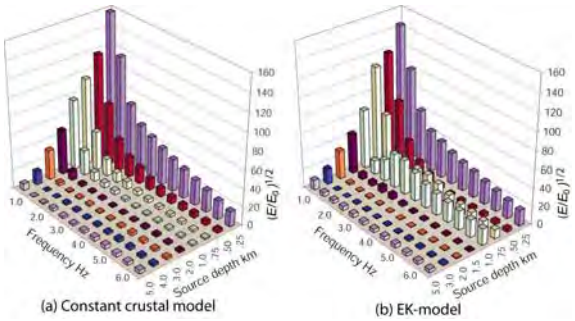

Figure 5. Normalized Lg excitation spectra for sources in different velocity models and at different depths with (a) a model with a homogeneous crust and (b) the EK-model.

Figure 7 gives the excitation spectra for the EK-model with deeper random patches. The random patch is located between distances 5 to 25 km and depths 7.5 to 10.0 km. Figures 6a and b give excitation spectra for random patches with RMS velocity fluctuations of 3% and 5%, respectively. Figures 7c and d give the isolated scattered energy. The scattered energy from the deeper random patches has little low-frequency content, which supports the interpretation that the low-frequency energy comes from the *Rg*-to-*Lg* scattering. The frequency dependent excitation spectra establish the relationship between the observations and the characteristics of sources and near-source structures. They provide the basis for evaluating the dominant mechanisms for *Lg*-wave excitation. Xie (2002) investigated the

Pn and *Lg* spectra from a group of explosions and found that the difference between these spectra requires a non-flat transfer function between the two phases. The *Lg*-wave excitation function obtained in this paper is the impulse response. Assuming that the *Pn* spectrum roughly represents the source spectrum, the excitation function obtained here approximates the *Pn* to *Lg* transfer function. Qualitatively, our excitation function explains the observations of Xie (2002) which require a non-flat *Pn* to *Lg* transfer function with an enhanced low-frequency excitation for *Lg*. To make a quantitative comparison, additional investigation is required.

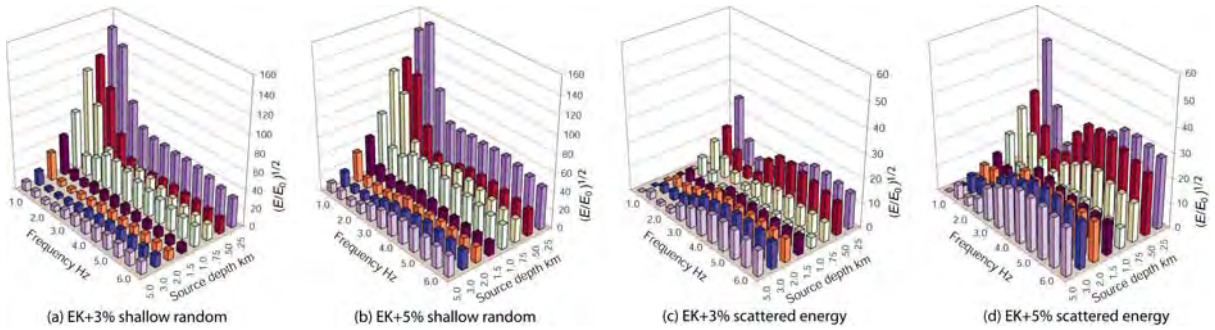

Figure 6. Normalized Lg excitation spectra for sources in the EK-model with shallow random patches, for (a) the EK-model with a 3% shallow random patch, (b) the EK-model with a 5% shallow random patch, (c) and (d) the isolated scattered energy in (a) and (b) respectively due to the random patches found by removing the energy for the layered models. Note different vertical scales are used for scattered energy.

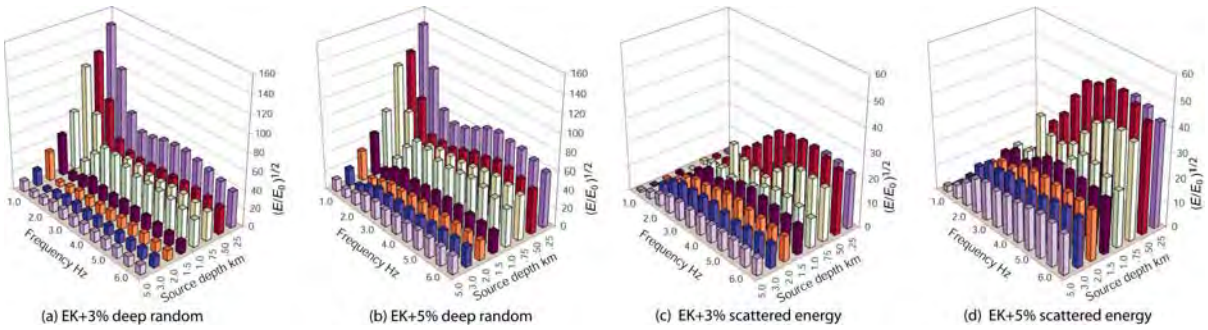

Figure 7. Normalized Lg excitation spectra for sources in the EK-model with deep random patches, for (a) the EK-model with a 3% deep random patch, (b) EK-model with a 5% deep random patch, (c) and (d) the isolated scattered energy in (a) and (b) due to the random patches.

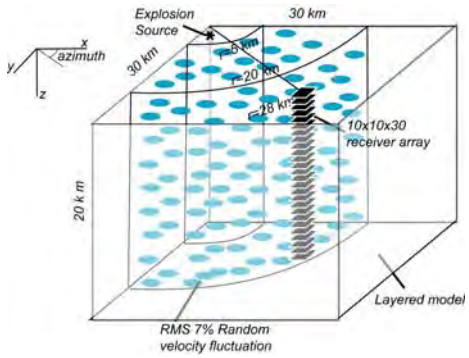

Figure 8. Cartoon showing the configuration of the 3D velocity model, source, and receiver array.

The 3D Slowness Analysis and the Excitation of SH Component

Although most Lg observations are taken from the vertical component of seismograms, the tangential component often has as much energy as the vertical component (e.g., Stevens, et al. 2003). Some researchers pointed out that at

the close range, clear SH energy comparable to that on the SV component can be observed and must be generated in the source region. Any Lg-wave excitation theory must provide an explanation for these observations. Since 2D geometry decouples the P-SV problem and the SH problem, it does not provide any information on the coupling between the source and SH component. We have conducted preliminary work to develop the 3D FDSA. A three dimensional velocity model is used to simulate the near source environment. The size of the model is 30 km × 30 km × 20 km, and the upper crust structure from the EK model is used as the background velocity. To test the effect of the heterogeneities on the P-S coupling, 7% RMS broadband random perturbation is added to P-, S-wave velocities and the density between two cylindrical surfaces around the z-axis. An eighth-order, staggered format 3D elastic finite difference code is used to generate synthetic seismograms. The grid interval used is 0.1 km. The explosion source is located at depth 0.5 km and the dominant frequency is about 3 Hz. A $10 \times 10 \times 30$ 3D receiver array is located at epicentral distance 28 km and azimuth direction 45 degrees (see Figure 8 for model configuration).

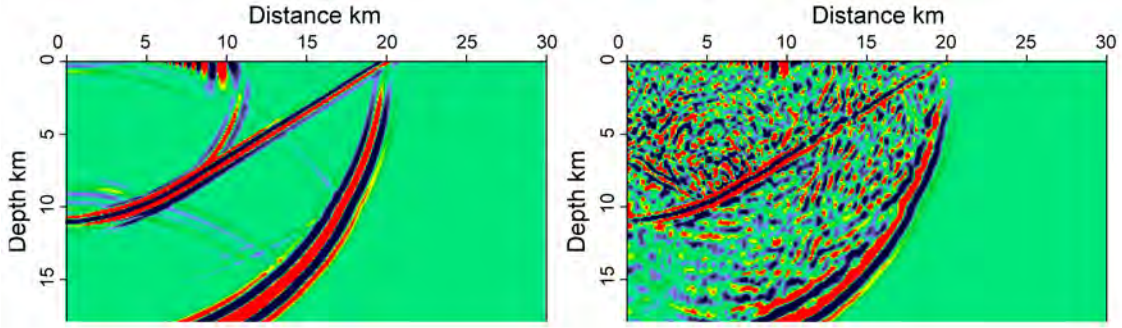

Firgure 9. Wavefield snapshot for the layered background model (left) and a laterally heterogeneous model with 7% RMS random fluctuations. Shown here is the vertical component of the displacement field.

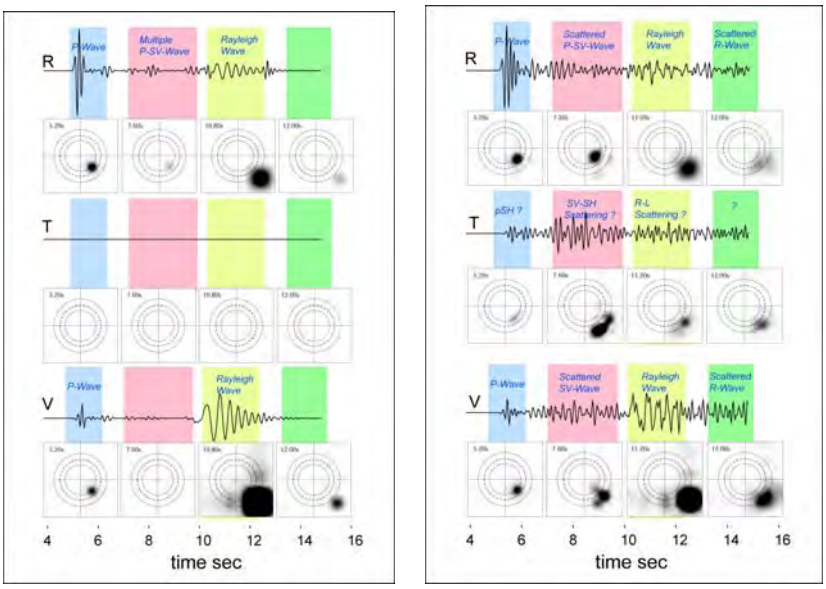

Figure 10. Comparison between synthetic seismograms and energy distribution in horizontal slowness domain for the layered velocity model (left panel) and velocity model with 7% RMS velocity fluctuations (right panel). Receivers are located at depth 1 km. All three components of the seismograms are normalized jointly but the slowness distribution for the radial component of the P-wave has been multiplied by a factor of 0.1. The P and Rayleigh waves can be clearly seen from the radial and vertical components. Note that the tangential component for the layered model is zero. For the random velocity model, scattered waves in both the tangential and vertical components can be seen. Note that much scattered energy falls outside of the upper mantle slowness (dashed line circle) and can be trapped into the crustal wave guide to form the Lg wave.

To investigate the effect of the random velocity perturbations, models both with and without the random fluctuations are calculated and their wavefield snapshots are shown in Figure 9. No surface roughness is included. Scattered energy appears in the model with random velocity fluctuations. Shown in Figures 10 are synthetic seismograms and the 2D horizontal slowness analysis from selected time windows for both the background and random models. The source depth is 0.5 km and receiver arrays are located at depth 1 km. For the background model (left panel), the P and Rayleigh waves can be clearly seen. Note the tangential component is zero. All three components of the seismograms are normalized jointly, but the slowness distribution for the radial component of the P-wave has been multiplied by a factor of 0.1. For the random model with 7% RMS velocity fluctuations (right panel), there are scattered waves in all three components including the tangential (SH) component. Much of the scattered energy falls outside of the upper mantle slowness (dashed line circle) and can thus be trapped into the crustal waveguide to form the regional phases.

Figure 11 gives the 2D horizontal slowness analysis for vertical and tangential components for the random velocity model. The receiver array is located at depth 7 km and epicentral distance 28 km. In the left panel for the vertical component, we can see that both P-wave (around 5.2 s to 5.6 s) and pS-wave (around 6.8 to 7.2 s) share the same slowness and will not contribute to the guided wave mode. Within the time window between 7.2 and 9.2 s, there is scattered P-SV energy propagating with a larger apparent horizontal slowness. The energy falls beyond the upper mantle S-wave slowness and will be trapped in the waveguide to form the P-SV Lg wave. In the right panel for the tangential component, there is considerable SH type scattered energy between 7.2 and 9.2 s with their slowness beyond the upper mantle S-wave slowness. The following features can be found from the results: (1) There is considerable SH energy excited due to the near-source lateral heterogeneities. (2) The SH energy appears to be generated through P-pS-SH or SV-SH since the SH component is relatively weak immediately following the P-wave front. The scattered energy has a broader azimuth range than the direct arrivals, which may provide a hint to reveal the actual scattering mechanisms. (3) Both SV and SH scattered energy can fall into the proper slowness region and form the crustal guided wave.

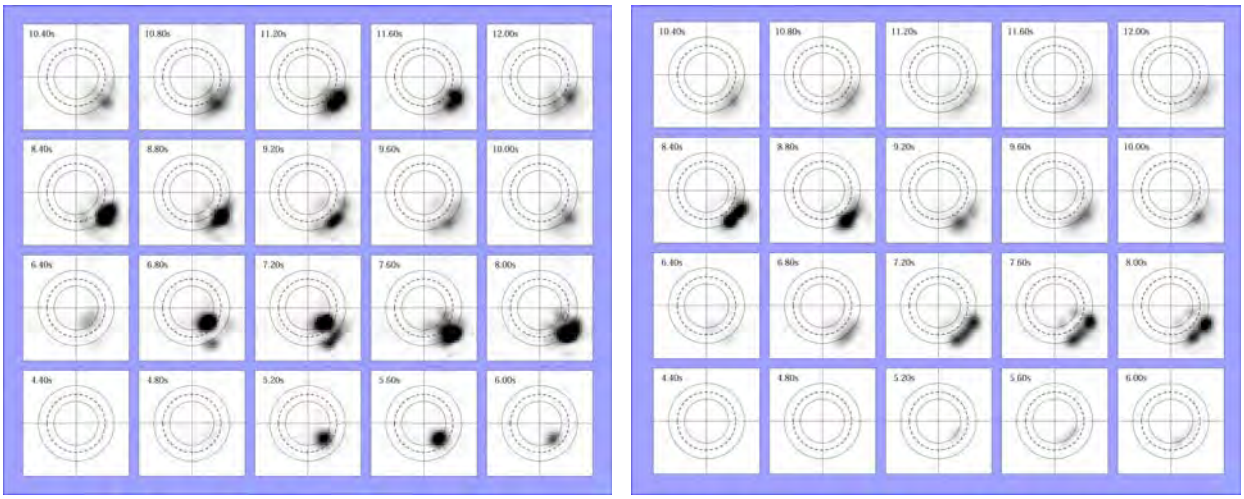

Figure 11. The wave energy distribution in the 2D horizontal slowness domain for the vertical (left) and tangential (right) components. The receiver array is located at epicentral distance 28 km and depth 7 km. Note the energy distribution outside of the upper mantle S-wave velocity.

CONCLUSIONS AND RECOMENDATIONS

A finite-difference modeling plus slowness analysis (FDSA) method has been developed to investigate near-source energy partitioning and *Lg*-wave excitation of explosive sources. The method has two major advantages. First, it allows us to study the near-source processes in multiple domains including space, time, slowness, and frequency. This provides an opportunity to isolate different mechanisms within the complex near-source environment. Second, the FDSA method can be applied at a close range, well before the *Lg*-wave is actually formed. It provides us with uncontaminated near-source information by calculating a relatively small velocity model with very fine near-source structures. Since this is a very efficient method, we can use it to investigate a broad frequency band and to test a

large number of source-model parameters. With this method, we investigated the contributions of *P-pS*-to-*Lg* conversion and *S**-to-*Lg* excitation using models with near-source random velocity fluctuations. The excitation functions of these mechanisms were also investigated. The contribution of *S**-to-*Lg* is concentrated at low frequencies and occurs for very shallow source depths. The contribution of *P-pS*-to-*Lg* coupling in the presence of near-source small-scale random heterogeneities is concentrated at high-frequencies.

The ability to handle a broad frequency band makes the FDSA an ideal tool to investigate excitation spectra and *P*/*S* type spectra ratios for different mechanisms and source-model parameters. The *Rg*-to-*Lg* scattering including the effect of uneven boundary topography should be included in future studies. We will further refine our 3D FDSA technique, systematically check the difference between the 2D and 3D simulations. This will help us to reevaluate the results of many previous simulations conducted on 2D models of both full-scale and near-source. It will also help us to select the problems that should be investigated using the 3D FDSA.

REFERENCES

Bonner, J. B., H. J. Patton, A. C. Rosca, H. Hooper, J. Orrey, M. Leidig, and I. Gupta (2003), Aspects of Rg and Lg generation from the Shagan depth of burial explosions, in *Proceedings of the 25th Seismic Research Review, Nuclear Explosion Monitoring: Building the Knowledge Base*, LA-UR-03-6029, 384–394.

Bottone, S., M. D. Fisk, and G. D. McCartor (2002), Regional seismic event characterization using a Bayesian formulation of simple kriging, *Bull. Seism. Soc. Am*. 92: 2277–2296.

Day, S. M. and K. L. McLaughlin (1991), Seismic source representations for spall, *Bull. Seism. Soc. Am*. 81: 191–201.

Fan, G. W. and T. Lay (1998a), Statistical analysis of irregular waveguide influences on regional seismic discriminants in China, *Bull. Seism. Soc. Am*. 88: 74–88.

Fan, G. W. and T. Lay (1998b), Regionalized versus single-station wave-guide effects on seismic discriminants in western China, *Bull. Seism. Soc. Am*. 88: 1260–1274.

Fan, G. W. and T. Lay (1998c), Statistical analysis of irregular waveguide influences on regional seismic discriminants in China: additional results for Pn/Sn, Pn/Lg and Pg/Sn, *Bull. Seism. Soc. Am*. 88: 1504–1510.

Fisk, M. D., H. L. Gray, and G. D. McCartor (1996), Regional discrimination without transporting thresholds, *Bull. Seism. Soc. Am*. 86: 1545–1558.

Gupta, I. N., W. Chan, and R. Wagner (1992). A comparison of regional phases from underground nuclear explosions at East Kazakh and Nevada Test Sites, *Bull. Seism. Soc, Am*. 82: 352–382.

Gupta, I. N., T. Zhang, and R. A. Wagner (1997), Low-frequency Lg from NTS and Kazakh nuclear explosions: observations and interpretations, *Bull. Seism. Soc. Am*. 87: 1115–1125.

Gutowski, P. R., F. Hron, D. E. Wagner, and S. Treitel (1984), S*, *Bull. Seism. Soc. Am*. 74: 61–78.

Hartse, H. E., S. R., Taylor, W. S., Phillips, and G. E. Randall, 1997, A preliminary study of regional seismic discrimination in central Asia with emphasis on western China, *Bull. Seism. Soc. Am*., 87: 551–568.

Johnson, L. R. and C. G. Sammis (2001), Effects of rock damage on seismic waves generated by explosions, *Pageoph*, 158: 1869–1908.

Kim, W. Y., V. Aharonian, A. L. Lerner-Lam, and P. G. Richards (1997), Discrimination of earthquakes and explosions in southern Russia using regional high-frequency three-component data from IRIS/JSP Caucasus Network, *Bull. Seism. Soc. Am*. 87: 569–588.

Kim, W. Y., D. W. Simpson, and P. G. Richards (1993), Discrimination of earthquakes and explosions in the eastern United States using regional high-frequency data, *Geophys. Res. Lett*. 20: 1507–1510.

Lilwall, R. C., (1988), Regional m_b:M_s, Lg/Pg amplitude ratios and Lg spectral ratios as criteria for distinguishing between earthquakes and explosions: a theoretical study, *Geophys. J. Int.*, 93: 137–147.

Myers, S. C., J. L. Wagoner, S. C. Larsen, A. Rodgers, K. Mayeda, K. D. Smith, and W. R. Walter (2003), Simulation of regional explosion S-phases (SIRES) project, in *Proceedings of the 25th Seismic Research Review, Nuclear Explosion Monitoring: Building the Knowledge Base*, LA-UR-03-6029, 117–124.

Myers, S. C., L. Preston, J. L.Wagoner, S. C. Larsen, K. D. Smith, and W. R. Walter, (2004), Simulation of regional explosion S-phases (SIRES) project, in *Proceedings of the 26th Seismic Research Review: Trends in Nuclear Explosion Monitoring*, LA-UR-04-5801, 124–133.

Nuttli, O. W. (1986), Yield estimates of Nevada Test Site explosions obtained from Lg waves, *J. Geophys. Res*. 91: 2137–2151.

Priestley, K. F., G. Zandt, and G. E. Randall (1988), Crustal structure in Eastern Kazakh, USSR from teleseismic receiver functions, *Geophys. Res. Lett*. 15: 613–616.

Patton, H. J. (2001), Regional magnitude scaling, transportability, and Ms:mb discrimination at small magnitudes, *Pageoph*, 158: 1951–2015.

Stevens, J. L., G. E. Baker, H. Xu, T. J. Bennett, N. Rimer, and S. M. Day (2003), The physical basis of Lg generation by explosion sources, in *Proceedings of the 25th Seismic Research Review, Nuclear Explosion Monitoring: Building the Knowledge Base*, LA-UR-03-6029, 456–465.

Taylor, S. R. (1996), Analysis of high frequency Pn/Lg ratios from NTS explosions and western U.S. earthquakes, *Bull. Seism. Soc. Am*. 86: 1042–1053.

Taylor, S. R., M. D. Denny, E. S. Vergino, and R.E. Glaser (1989), Regional discrimination between NTS explosions and western U.S. earthquakes, *Bull. Seism. Soc. Am*. 79: 1142–1176.

Taylor, S. R. and H. E. Hartse (1997), An evaluation of generalized likelihood ratio outlier detection to identification of seismic events in Western China, *Bull. Seism. Soc. Am*. 87: 824-831.

Vogfjord, K. S. (1997), Effects of explosion depth and earth structure on the excitation of Lg waves: S* revisited, *Bull. Seism. Soc. Am*. 87: 1100–1114.

Wallace, T. C. (1991), Body wave observations of tectonic release, in: S.R. Taylor, H.J. Patton and P.G. Richards (editors), *Explosion Source Phenomenology*, American Geophysical Union, 161–170.

Walter, W. R., K. M. Mayeda, and H. Patton (1995), Phase and spectral ratio discrimination between NTS earthquakes and explosions, Part I: Empirical observations, *Bull. Seism. Soc. Am.* 85: 1050–1067.

Wu, R. S., S. Jin and X. B. Xie (2000a), Seismic wave propagation and scattering in heterogeneous crustal waveguides using screen propagators: I SH waves, *Bull. Seism. Soc. Am*. 90: 401–413.

Wu, R. S., S. Jin and X. B. Xie (2000b), Energy partition and attenuation of Lg waves by numerical simulations using screen propagators, *Phys. Earth and Planet. Inter*. 120: 227–243.

Xie, J. (2002), Source scaling of Pn and Lg spectra and their ratios from explosions in central Asia: Implications for the identification of small seismic events at regional distances, *J. Geophys. Res.* 107: B7, 10.1029/2001JB000509.

Xie, J., L. L. Cong, characteristics of and B.J. Mitchell (1996), Spectral characteristics of the excitation and propagation of Lg from underground nuclear explosions in central Asia, *J. Geophys. Res.* 101: 5813–5822.

Xie, X. B. and T. Lay (1994), The excitation of Lg waves by explosions: A finite-difference investigation, *Bull. Seism. Soc. Am*. 84: 324–342.

Xie, X. B., Z. Ge ,and T. Lay (2005), Investigating explosion source energy partitioning and Lg-wave excitation using a finite-Difference plus slowness analysis method, submitted to *Bull. Seism. Soc. Am*.

TOWARD A RAYLEIGH WAVE ATTENUATION MODEL FOR EURASIA AND CALIBRATING A NEW M_S FORMULA

Xiaoning (David) Yang[1], Anthony R. Lowry[2], Anatoli L. Levshin[2], and Michael H. Ritzwoller[2]

Los Alamos National Laboratory[1] and University of Colorado at Boulder[2]

Sponsored by National Nuclear Security Administration
Office of Nonproliferation Research and Engineering
Office of Defense Nuclear Nonproliferation

Contract Nos. W-7405-ENG-36[1] and DE-FC52-05NA26608[2]

ABSTRACT

We are characterizing Rayleigh wave attenuation for Eurasia using tomographic inversion of surface-wave amplitude data. These attenuation models will be used to calibrate the regional surface-wave magnitude scale and to extend the teleseismic M_s-m_b event discriminant to regional distances. Our research is based on the successful proof-of-concept study conducted by the Los Alamos National Laboratory (LANL) researchers to develop a 20-s Rayleigh wave attenuation model for central and southeastern Asia. In order to minimize amplitude measurement errors caused by multipathing, focusing, and source uncertainty, LANL designed a measurement tool incorporating the phase-match filtering technique. The Surface Wave Amplitude Measurement TOOL (SWAMTOOL) proved effective in making reliable surface-wave amplitude measurements. A two-step inversion technique was employed using both two-station amplitude ratios and single-station amplitudes to better constrain the attenuation model.

In this study, we are developing shorter-period (10 – 18 s) attenuation models for Eurasia, covering geographical regions that increase in extent with period. At regional distances, the new M_s scale will most likely be measured at shorter periods and therefore requires shorter-period attenuation corrections. In order to make SWAMTOOL more suitable for measuring amplitudes at various periods more accurately, we have made modifications to improve its functionality. In addition to the existing ability of the tool to perform phase-match filtering and source parameter analysis, we added back-azimuth calculation using a cross-correlation technique. By comparing calculated back-azimuth with great-circle back-azimuth, we can assess whether the surface wave traveled along the great-circle path and, if not, the path deviation from the great circle. This information will help us to better identify the primary surface-wave arrival and better constrain the quality of the measurements. We also included pre-signal noise measurement in the tool. The noise level is used to identify the useful frequency band within which amplitude measurements have adequate signal-to-noise ratio.

We currently are collecting both two-station and single-station waveform data for measurement. We will collect data from permanent broadband and long-period stations in the region and from temporary PASSCAL deployments to improve data coverage, particularly at shorter periods.

OBJECTIVES

The objectives of the study are (1) to develop short-period (10–18s), two-dimensional (2-D) Rayleigh-wave attenuation models for Eurasia, along with associated uncertainty statistics through a tomographic approach, and (2) to calibrate Russell's (2004) M_s formula with these models for the same region.

RESEARCH ACCOMPLISHED

In order to apply M_s-m_b discriminant to regional-distance monitoring, a modified M_s formula using shorter-period (< 20) surface-wave amplitudes is required (Marshall and Basham, 1970; Russell, 2004). Because shorter-period surface waves are sensitive to the Earth's crust, the strong lateral material-property heterogeneity of the crust could result in large surface-wave amplitude scatter due to lateral attenuation variations. To reduce this scatter, we are developing short-period (10–18-s) 2-D surface-wave attenuation models for Eurasia through tomography, which can be used to account for 2-D path attenuation effects in regional M_s calculations.

Surface-Wave Measurement TOOL (SWAMTOOL)

The accuracy of surface-wave attenuation measurements is affected by uncertainties in source-parameter estimates and site responses and by medium elastic effects, with medium elastic effects such as multipathing, focusing, defocusing and off-great-circle paths being one of the principal sources of error (Mitchell, 1995; Selby and Woodhouse, 2000). As part of a previous 20-s surface-wave attenuation study, LANL researchers designed a Surface Wave Amplitude Measurement Tool (SWAMTOOL) to address some of these uncertainties (Yang et al., 2004). The measurement tool makes use of recently developed surface-wave group velocity models (Ritzwoller and Levshin, 1998; Levshin and Ritzwoller, 2003; Stevens et al., 2001; Levshin et al., 2003) to construct phase-matched filters (Herrin and Goforth, 1977) and applies these path-specific filters to the data before making amplitude measurements. The filtering process, along with the analysis of theoretical source radiation and spectra that is also part of the measurement tool, effectively reduced the bias caused by multipathing and focusing (Yang et al., 2004). We will use SWAMTOOL to make surface-wave amplitude measurements for this study.

To improve the functionality of SWAMTOOL, we have made several modifications to the tool. We added back-azimuth calculations to the tool using a cross-correlation technique (Chael, 1997). Vertical-component seismogram is first Hilbert transformed to shift its phase by 90° and then correlated with radial components for different azimuths between 0° and 360°. The azimuth at which the maximum correlation is obtained is designated as the measured back-azimuth. This azimuth is then compared with great-circle back-azimuth to evaluate the path direction of the surface wave. The back-azimuth information will help us better identify the primary surface-wave arrival and better constrain the quality of the measurements. For example, we can use back-azimuth calculations to differentiate incoming directions of successive surface-wave packets and therefore facilitate the identification of the primary surface-wave arrival.

We also added pre-signal noise measurement in SWAMTOOL. The noise level is used to identify the useful frequency band within which amplitude measurements have adequate signal-to-noise ratios (S/N). Amplitude measurements with adequate S/N will be retained for the tomographic inversion.

Other miscellaneous modifications include adopting a larger-area map display and adding the ability to distinguish single-station amplitude measurement and two-station amplitude ratio measurement automatically. Figure 1 is a screen snapshot of the improved measurement tool. A detailed description of the tool is provided in the figure caption. The example shown in the figure illustrates the effectiveness of the measurement tool in identifying and removing multipathing and focusing effects. It also shows the use of back-azimuth calculations in aiding the differentiation of the primary arrival from the multipathed arrival. If we move the cross-correlation window to bracket the second pulse in the cross-correlation, the difference between measured back-azimuth and great-circle back-azimuth changes from –7°to –2°, indicating a more deviated path for the second wave packet.

Surface wave data collection

We are currently collecting surface-wave waveform data to prepare for amplitude measurements. In the first stage of data collection we have concentrated on events that occurred in and around Eurasia 2000–2004.

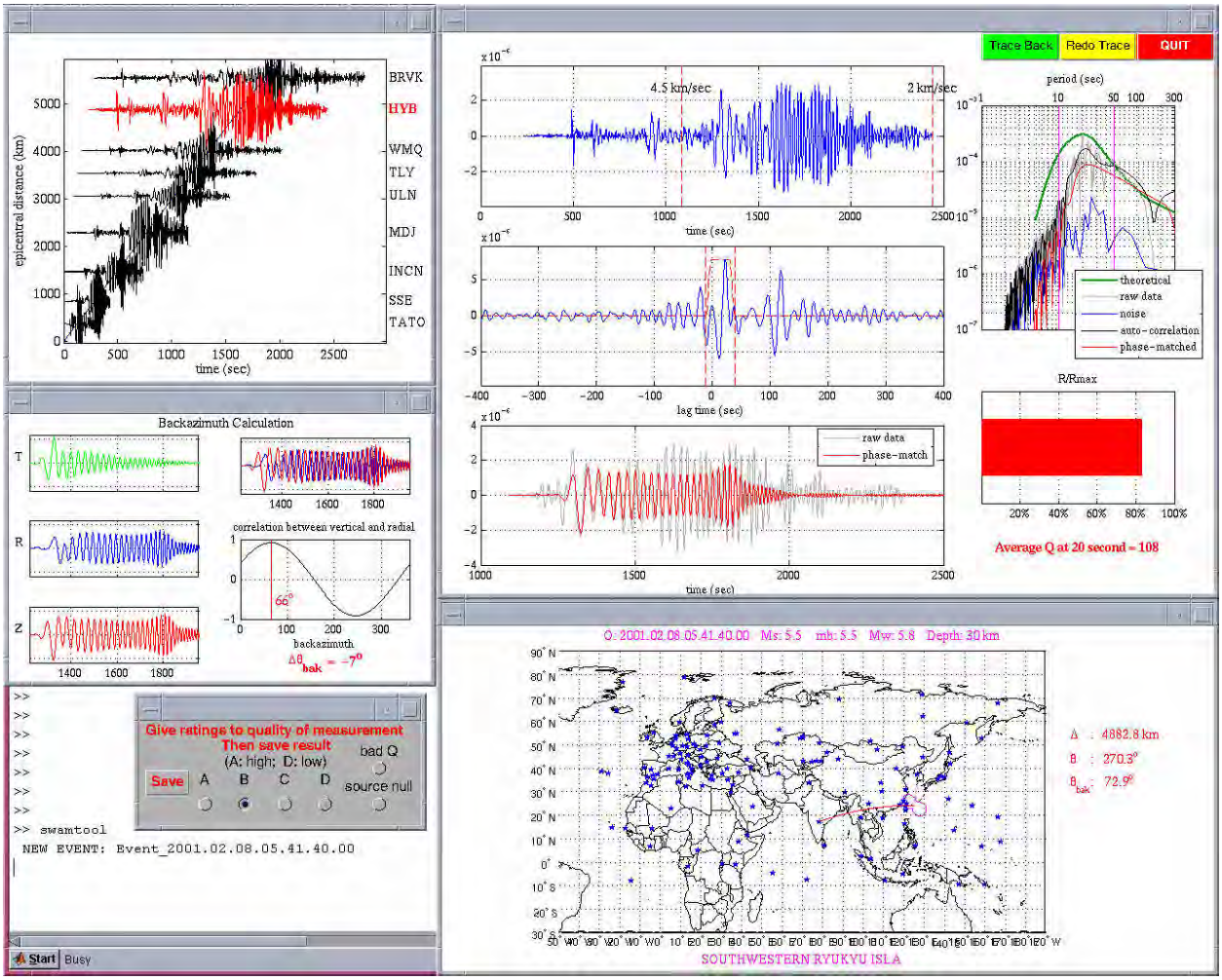

Figure 1. A snapshot of SWAMTOOL. In the upper-right window, the top-left plot shows the original seismogram. Cross-correlation between the seismogram and the phase-matched filter for this path is plotted in the middle, along with a window (red dashed line) isolating the primary arrival. The cross-correlation shows a clear second arrival indicating multipathing. The lower figure on the left in this window shows the phase-match filtered seismogram (red) and the original seismogram (gray). The plot on the upper right of the window shows the theoretical source spectrum, the original data spectrum, the smoothed data spectrum through auto-correlation, the phase-match filtered data spectrum, and the noise spectrum. The phase-match filtered spectrum is smooth and has a similar shape as the theoretical spectrum. Average attenuation at 20 s for this path is calculated and displayed at the lower-right corner of this window. The lower-right window displays the map of the study region. The theoretical source radiation pattern and the path for this trace are plotted for the purpose of evaluating whether the path is in a source radiation null direction. A quantitative estimate is displayed in the upper-right window, where the ratio between the amplitude of radiation in the path direction to the maximum amplitude is depicted as a percentage bar. Various source and path parameters are also displayed in the map window. Record section for this event is plotted in the upper-left window. The trace being analyzed is highlighted. Below the record-section window, results of back-azimuth calculation are displayed. In this window, different components of the data are plotted. The radial and vertical components are overlapped to assess their phase relationship. Comparison between measured back-azimuth and great-circle back-azimuth is displayed as the difference between the two azimuths. Finally, the analyst has an opportunity to assign a quality value to the measurement based on the information displayed on the screen.

We selected 486 events from the Harvard CMT Catalog (http://www.seismology.harvard.edu/CMTsearch.html) with $7.5 \geq M_s \geq 5.0$ inside the region from 10°S to 90°N and from 0°E to 160°E, and with the source depths less than 50 km. The map with the event distribution is shown in Figure 2.

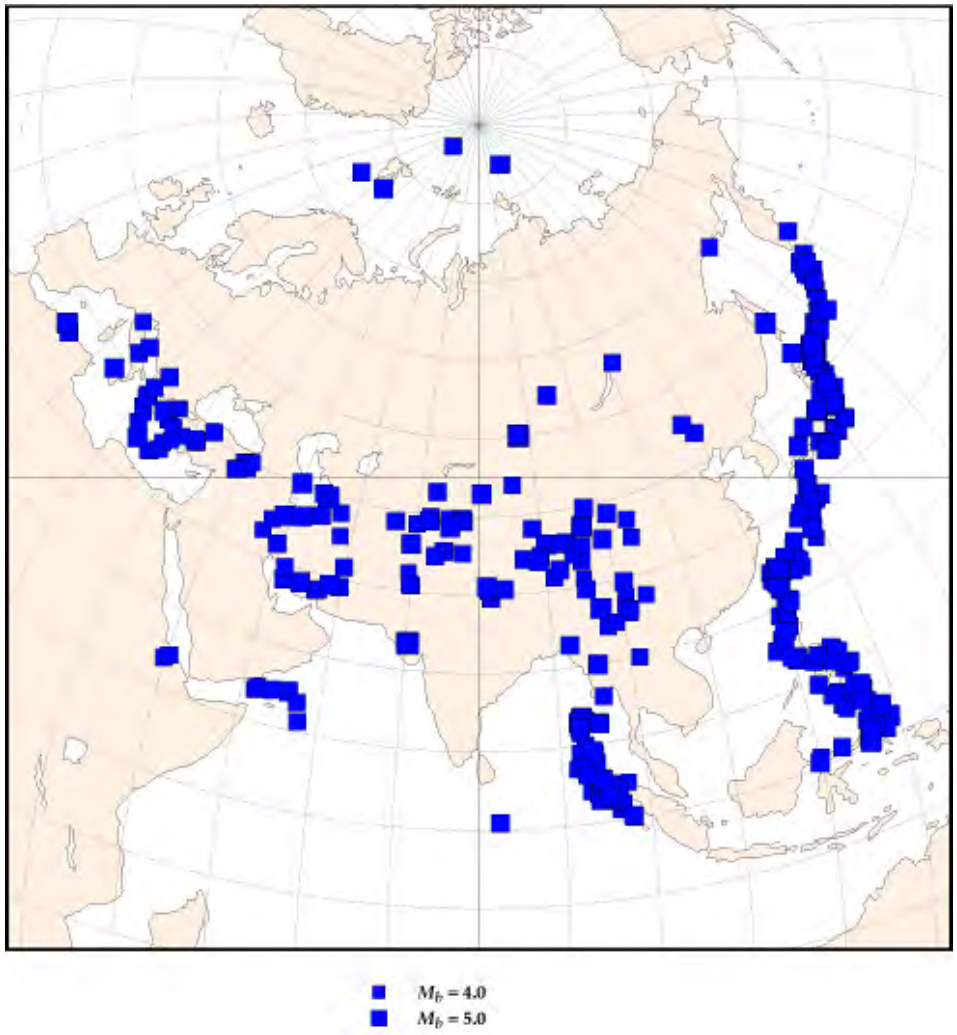

Figure 2. Events selected for first-stage surface-wave data collection.

Several global and regional broadband networks have existed in Eurasia during the considered time interval. These include Global Seismographic Network (GSN), International Monitoring System (IMS), GEOSCOPE, GEOFON, Mediterranean Seismic Network (MEDNET), China Seismological Digital Network (CDSN), Kyrgyz Seismic Network (KNET), Kazakhstan Seismic Network (KAZNET), and others. There have also been many temporary network deployments in the region, including close to 10 PASSCAL projects. Figure 3 shows the distribution of stations belonging to different networks across the region. Waveforms from these stations are available through IRIS DMC.

The waveform collection and preliminary waveform evaluation are now in progress. In addition to the events that we have selected, we also plan to collect waveforms for the events that occurred in 2005 and, if necessary, for smaller events between 2000 and 2005 with $M_s \geq 4.5$ or $m_b \geq 5.0$ if M_s is absent.

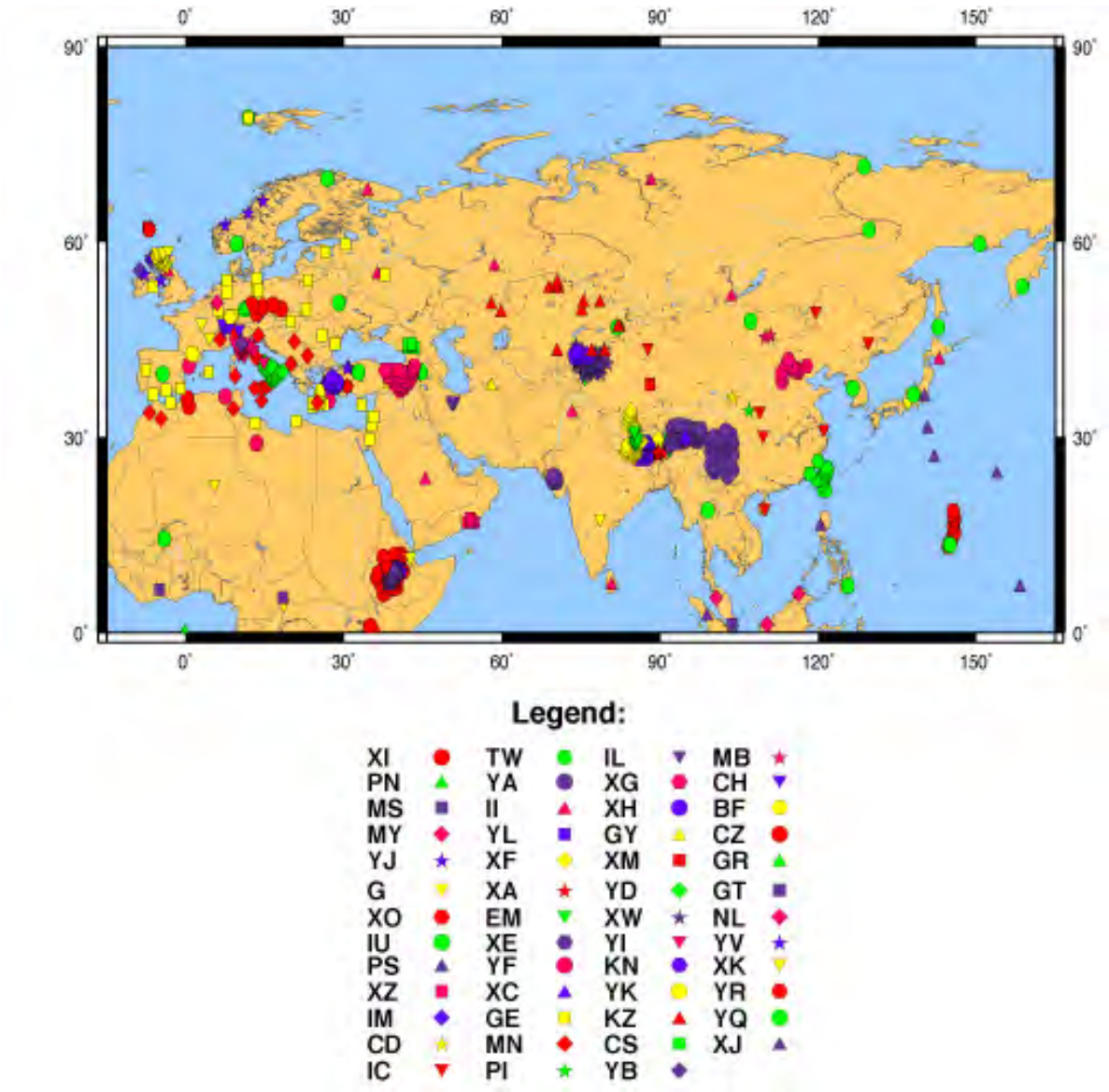

Figure 3. Station distribution for the data collection.

Calibrating Russell's M_s formula for Eurasia

The M_s formula proposed by Russell (2004) represents the latest development in regional surface-wave magnitude research. This formula requires amplitudes measured at variable periods as well as regional calibration for its parameterization. One approach of calculating magnitudes at variable periods is to make a suite of amplitude measurements at all periods within a frequency band and select the measurement that gives the maximum magnitude (Bonner et al., 2004). An alternative would be to calibrate, for a particular region, e.g., Eurasia, the optimum periods at which surface wave amplitudes yield the maximum magnitudes. These optimum periods will depend on variables such as path length, source size, location, depth, and the medium structure along the path. The mapping of the optimum periods as a function of these variables will provide important background information for M_s regionalization.

As the first step to investigating the regionalization of Russell's M_s formula for Eurasia, we measured the periods at which surface waves have the largest amplitudes from the amplitude dataset that LANL measured for the Asia 20-s surface-wave attenuation study (Yang et al., 2004). Figure 4 plots the period of the maximum surface-wave

amplitude as a function of source-receiver distance. The data show a large scatter reflecting the different source and path effects. There is also a tendency of increasing periods, as path lengths become longer. Nevertheless, the majority of the periods are below 20 s even for paths as long as close to 6000 km. Another observation is that even for the shortest paths considered, the periods are rarely below 10 s.

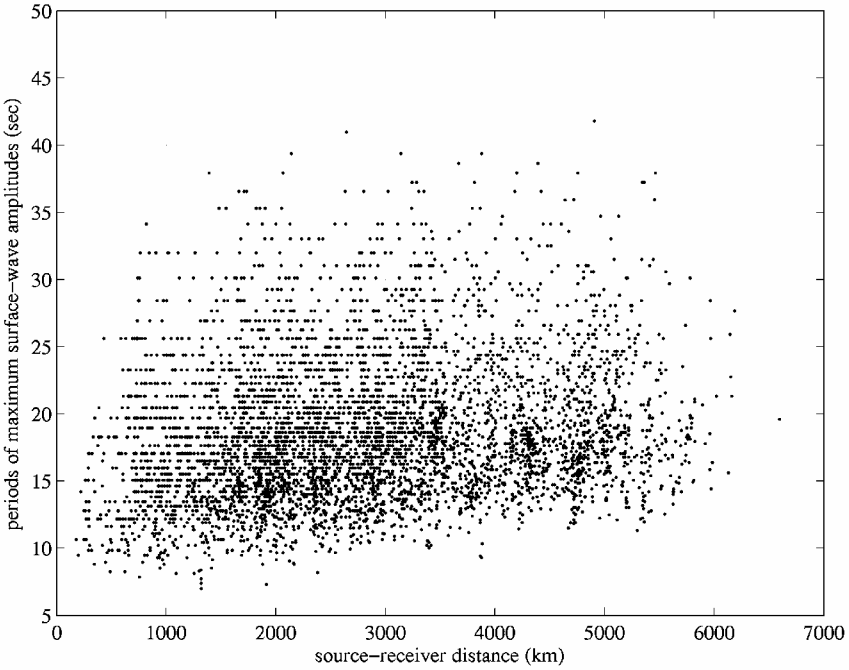

Figure 4. Periods of maximum surface-wave amplitudes from a data set of approximately 5200 measurements for the region of central and southeastern Asia.

CONCLUSIONS AND RECOMMENDATIONS

We have finished modification of the SWAMTOOL to include the back-azimuth calculation and noise measurement. This tool will be used for the short-period surface-wave amplitude and amplitude-ratio analysis and measurement. We have selected 486 events with CMT solutions for the study region to collect waveform data.

ACKNOWLEDGEMENTS

Surface-wave waveform data were obtained through IRIS DMC. Harvard CMT Catalog was used in the study. We thank Dr. Misha Barmin of CU-Boulder for his help in data collection and computer program setup. Review by Dr. Richard Stead of LANL is appreciated.

REFERENCES

Bonner, J. L., D. T. Reiter, D. G. Harkrider, and S. A. Russell (2004), Development of a time-domain, variable-period surface wave magnitude measurement procedure for application at regional distances, in *Proceedings of the 26th Seismic Research Review: Trends in Nuclear Explosion Monitoring*, Orlando, FL (Sept. 21–23, 2004), LA-UR-045801, Vol. 1: pp. 377–386.

Chael, E. P. (1997). An automated rayleigh-wave detection algorithm, *Bull. Seism. Soc. Am.* 87: 157–163.

Herrin, E. E. and T. T. Goforth (1977). Phase-matched filters: application to the study of Rayleigh Waves, *Bull. Seism. Soc. Am.* 67: 1259–1275.

Levshin, A. L. and M. H. Ritzwoller (2003). Discrimination, detection, depth, location, and wave propagation studies using intermediate period surface waves in the Middle East, Central Asia, and the Far East, technical report DTRA-TR-01-28, Defense Threat Reduction Agency, Fort Belvoir, Virginia, 120 pp.

Levshin, A. L., J. L. Stevens, M. H. Ritzwoller, D. A. Adams, and G. E. Baker (2003), Improvement of detection and discrimination using short period (7s-15s) surface waves in W. China, N. India, Pakistan, and Environs, Final Report, submitted to Defense Threat Reduction Agency, Fort Belvoir, Virginia, 49 pp.

Marshall, P. D. and P. W. Basham (1972), Discrimination between earthquakes and underground explosions employing an improved M_s scale, *Geophys. J. R. astr. Soc.* 28: 431–458.

Mitchell, B. J. (1995), Anelastic structure and evolution of the continental crust and upper mantle from seismic surface wave attenuation, *Rev. Geophys*. 33: 441–462.

Ritzwoller, M. H. and A. L. Levshin (1998), Eurasian surface wave tomography: group velocities, *J. Geophys. Res.* 103: 4839–4878.

Russell, D. R. (2004), Theoretical analysis of narrow-band surface wave magnitudes, technical report AFTAC-TR-04-004, Air Force Technical Applications Center, 36 pp.

Selby, N. D. and J. H. Woodhouse (2000), Controls on Rayleigh Wave amplitudes: attenuation and focusing, *Geophys. J. Int*. 142: 933-940.

Stevens, J. L., D. A. Adams and G. E. Baker (2001), Improved surface wave detection and measurement using phase-matched filtering with a global one-degree dispersion model, in *Proceedings of the 23rd Seismic Research Review: Worldwide Monitoring of Nuclear Explosions*, LA-UR-01-4454, Vol. 1: pp. 420-430.

Yang, X., S. R. Taylor and H. J. Patton (2004), The 20-S rayleigh wave attenuation tomography for Central and Southeastern Asia, *J. Geophys. Res.* 109, B12304, doi:10.1029/2004JB003193.

HIGH-RESOLUTION SEISMIC VELOCITY AND ATTENUATION STRUCTURE OF THE SICHUAN-YUNNAN REGION, SOUTHWEST CHINA, USING SEISMIC CATALOG AND WAVEFORM DATA

Haijiang Zhang[1], Clifford H. Thurber[1], and Xiaodong Song[2]

University of Wisconsin[1] and University of Illinois[2]

Sponsored by Air Force Research Laboratory

Contract No. FA8718-05-C-0016

ABSTRACT

One of the fundamental problems facing discrimination and location of earthquakes and explosions is creating accurate structure models for the crust and mantle. The routine practice of locating seismic events based on a one-dimensional velocity model inevitably introduces bias into locations. Using a high-resolution three-dimensional seismic velocity model significantly improves seismic event location accuracy and thus helps satisfy the goal of nuclear explosion monitoring. In addition to seismic event locations, seismic wave amplitudes are also important in discriminating between earthquakes and explosions. As seismic waves travel through an anelastic and heterogeneous medium, their amplitudes will be attenuated, and knowledge of the attenuation structure is vital to correct the distortion. This two-year project is to develop high-resolution models of the velocity and attenuation structure of the Sichuan-Yunnan region (latitudes ~97-108^{o}E and longitudes ~21-35^{o}N) that is located in southwest China using seismic catalog and waveform data. The Sichuan-Yunnan region lies in the transition zone between the uplifted Tibetan plateau to the west and the Yangtze continental platform to the east. This region has a very complicated geological structure and is one of the most active areas of continental earthquakes in the world.

There are four main components in this project: (1) using waveform alignment methods (waveform cross-correlation and bispectrum analysis) to obtain more accurate differential arrival times, (2) using regional scale adaptive-grid double-difference tomography to obtain detailed P- and S-wave velocity models of Sichuan-Yunnan region, (3) using the adaptive-grid "triple-difference" seismic attenuation method to determine the detailed attenuation structure for both Qp and Qs for this region, and (4) assembling a ground truth database.

Our first-year effort is to determine high-resolution velocity model of the Sichuan-Yunnan region using seismic catalog and waveform data. We will first collect catalog and waveform data from the China Seismological Bureau (newly named China Earthquake Administration), Sichuan and Yunnan provincial bureaus, and the IRIS data management center. We will then apply waveform alignment methods (waveform cross-correlation and bispectrum analysis) to obtain more accurate differential arrival times. Compared to conventional threshold-based waveform cross-correlation methods, our proposed methods have the ability to improve the quality and quantity of waveform-derived differential times through a rigorous bispectrum verification process. Finally we will develop and apply regional scale adaptive-grid double-difference tomography based on tetrahedral diagrams to determine high-resolution P- and S-wave velocity models. This method deals properly with the curvature of the Earth and has the ability to automatically adapt an inversion grid according to the data distribution. As a result, the tomographic system is more stable and the regions with higher density of data are more finely characterized. Our second-year effort will be more focused on developing and applying an adaptive-grid "triple-difference" seismic attenuation method to determine the detailed attenuation structure for both Qp and Qs and assembling a ground truth database for the region of size approximately 1300 km × 1000 km.

OBJECTIVES

The routine practice of locating seismic events based on a one-dimensional velocity model inevitably introduces bias into locations. Using a high-resolution three-dimensional seismic velocity model significantly improves seismic event location accuracy and thus helps satisfy the goal of nuclear explosion monitoring. In addition to seismic event locations, seismic wave amplitudes are also important in discriminating between earthquakes and explosions. As seismic waves travel through an anelastic and heterogeneous medium, their amplitudes will be attenuated, and knowledge of the attenuation structure is vital to correct the distortion. Our research program aims to develop high-resolution models of the velocity and attenuation structure of the Sichuan-Yunnan region (latitudes ~97-108^{o}E and longitudes ~21-35^{o}N) that is located in southwest China using seismic catalog and waveform data. This proposal falls in topic 2 (Seismic Calibration and Ground Truth Collection) in an effort to "develop models that calibrate earth velocity and attenuation structure." The Sichuan-Yunnan region lies in the transition zone between the uplifted Tibetan plateau to the west and the Yangtze continental platform to the east. This region has a very complicated geological structure and is one of the most active areas of continental earthquakes in the world.

Our research program consists of four components: (1) using waveform alignment methods (waveform cross-correlation and bispectrum analysis) to obtain more accurate differential arrival times, (2) using regional scale adaptive-grid double-difference tomography to obtain detailed P- and S-wave velocity models of Sichuan-Yunnan region, (3) using the adaptive-grid "triple-difference" seismic attenuation method to determine the detailed attenuation structure for both Qp and Qs for this region, and (4) assembling a ground truth database. In this paper, we will focus on our accomplishments under components 1 and 2.

RESEARCH ACCOMPLISHED

Background

The Sichuan-Yunnan region lies in an active transition zone between the Yangtze platform to the east and the Tibetan plateau to the west and is generally believed to have had its origin in the collision between the Indian plate and the Eurasian plate about 45 Ma ago. This continental collision led to active tectonic deformation on a larger-scale and created a high level of seismicity. There are seven major active seismic zones (belts) in this region including Longmen Shan, Xianshuihe, Anninghe, Xiaojiang, Red River, Lancang-Gengma, and Tengchong-Longling (Chan et al., 2001). Most, but not all, of the earthquakes in these belts are associated with fault zones that are identified at the surface. Obtaining a high-resolution seismic velocity model for this region and precise earthquake locations will help delineate fault zones at depth more clearly and facilitate their association with surface fault traces. Several magnitude 7 earthquakes occurred in this region in the last twenty years. Recent examples are the 1995 Mengnian earthquake (M=7.4) and the 1996 Lijiang earthquake (M=7.0). The auxiliary International Monitoring Station (IMS) station KMI is located in this region and China's nuclear test site Lop Nor is located about 1000 km to the northeast.

There have been some local to regional seismic tomography studies in this region. Chan et al. (2001) used both P and S arrival data from 4625 local and regional earthquakes recorded at 174 stations to determine a three-dimensional (3D) model of the crust. The horizontal grid spacing was 0.5 degrees between latitudes 25-34^{o}N and longitudes 97-105^{o}E. They found the crustal velocity was generally a bit slow with an average value of 6.25km/s and the crustal thickness had strong lateral variations between 38km and 65km and generally increased from southeast to northwest. Yang et al. (2004) conducted a simultaneous inversion to determine the velocity models and event locations using Pg and Sg picks on 193 stations from 9988 earthquakes during the period of 1992 to 1999. Their P-wave velocity model with a horizontal grid spacing of 1^{o} shows strong heterogeneity (contrast) across the faults. Liu et al. (2005) used a combination of 602 local and regional earthquakes and 102 teleseismic events to determine a 3D P-wave velocity model with a horizontal grid spacing of 0.5^{o} for this region. They imaged a relatively low-velocity anomaly over a large region at depths of 20 to 50 km that may indicate a mechanically weak north-south tectonic belt between Tibet and Eastern China.

Bispectrum Method

When two earthquakes have close hypocenters and share similar source mechanisms, they will generate similar waveforms. It is possible to obtain very accurate differential times from waveform data for such nearby events and use them to improve location results (e.g., Shearer, 1997; Rubin et al., 1999; Waldhauser and Ellsworth, 2002;

Schaff et al., 2002), or combine them with absolute arrival times to invert for high-quality 3D velocity structure (Zhang and Thurber, 2003). Such studies generally use a cross correlation (CC) technique to calculate the relative time delay between the waveforms of two events recorded at the same station. For very similar traces some researchers obtain a time delay to the sub-sample level by a weighted linear fitting of the cross spectral phase after first aligning the two waveforms with the CC-determined lag (Poupinet et al., 1984). The calculated time delay has an associated CC coefficient whose value may not be very high if the underlying signals are not time-delayed similar waveforms, or if the underlying time-delayed signals are contaminated by high levels of noise. It is hard to differentiate between these two possible causes, especially when many thousands or more waveforms are being analyzed automatically. Thus researchers often choose those time delay estimates with CC coefficients above a specified threshold. For example, Schaff et al. (2002) only select those time delays with CC values larger than 0.70 and mean coherences above 0.70.

The selection of an optimum threshold value is important but difficult. If it is set too high, then only a limited number of very accurate differential time data are available to constrain the relative positions of earthquakes. If the threshold value is set too low, then many unreliable differential time estimates are used which will negatively affect the relocation results. Du et al. (2004a) deal with this problem by computing additional estimates of the time delay with the bispectrim (BS) method. The BS method, which works in the third-order spectral domain, can suppress correlated Gaussian or low-skewness noise sources (Nikias and Raghuveer, 1987; Nikias and Pan, 1988). Du et al. (2004a) adopt this method to calculate two additional time delay estimates with both the raw (unfiltered) and band-pass filtered waveforms, and use them to verify (select or reject) the one computed with the CC technique using the filtered waveforms. Thus this BS verification process can reject unreliable CC time delay estimates and also can accept additional CC time delays even if their associated CC coefficients are smaller than a nominal threshold value if they pass the BS verification procedure.

We do not claim that the BS method always obtains a better time delay estimate than the CC technique. Rather, we use the BS time delay estimates to check the reliability of those computed with the CC technique. By applying two different methods that work in different spectral domains, we can improve the reliability of the selected time delays. The two BS time delay estimates do not always agree with each other because the characteristics of noise in the raw and filtered waveforms differ. Therefore checking the values of the CC time delay against both of them provides additional quality control.

Figure 1 shows four seismic waveforms (sampling rate=0.025s) from the Incorporated Research Institutions for Seismology (IRIS) Data Management Center recorded on the auxiliary IMS station KMI. These events are far apart from each other, up to several tens of kilometers away. But using the BS analysis, we are still able to extract the differential arrival times between event 19862792328 (top) and the other three events (19892630026, 19953311008, and 19953331916). The waveform correlation coefficients between the top waveform and the bottom three waveforms are 0.83, 0.80 and 0.71, respectively. The time window we choose here is 30 samples before and 97 samples after the preliminary P arrival picks. The results went through the BS verification process successfully. This example shows that we can obtain a substantial amount of waveform alignment data when we have access to local network waveforms.

Double-difference tomography

We have recently developed a double-difference (DD) seismic tomography method that makes use of both absolute and more accurate relative arrival times (Zhang and Thurber, 2003). DD tomography is a generalization of DD location (Waldhauser and Ellsworth, 2000); it simultaneously solves for the three-dimensional (3D) velocity structure and seismic event locations. DD tomography uses an evolving weighting scheme for the absolute and differential arrival times in order to determine the velocity structure from larger scale to smaller scale. This method yields more accurate event locations and velocity structure near the source region than standard tomography, which uses only absolute arrival times. It has the unique ability to sharpen the velocity image near the source region because of the combination of the higher accuracy of the differential time data and the concentration of the corresponding model derivatives in the source region. The latter results from the cancellation of model derivative terms where the ray paths overlap away from the source region.

To date, we have applied DD tomography to several synthetic datasets, to the Hayward fault dataset of Waldhauser and Ellsworth (2002) (Zhang and Thurber, 2003), to data from Parkfield, California (Thurber et al., 2004), and to data from northern Honshu, Japan (Zhang et al., 2004). The Hayward and Parkfield studies used a flat-earth version

of the DD tomography code (*tomoDD*) with pseudo-bending ray tracing (Um and Thurber, 1987), whereas the Japan study used a "sphere-in-a-box" version (*tomoFDD*) with finite-difference travel time calculations (Podvin and Lecomte, 1991). We have carried out synthetic tests with both versions. In all cases, we can see a "sharpening" of the velocity structure and/or a revelation of previously undetected features. Both the algorithms *tomoDD* and *tomoFDD* can use a nonuniform but regular inversion grid.

In the "sphere-in-a-box" version of DD tomography, the curvature of the Earth is explicitly taken into account. We note that the earth flattening transformation approach is only valid for 1D velocity models and not for 3D velocity models so that approach is not a viable one. Following Flanagan et al. (2000), we solve this problem by parameterizing a spherical surface inside a Cartesian volume of grid nodes. Figure 2a shows the case of putting the Earth into a cube so the curvature of the Earth can be taken into account. This scheme can be used for global seismic tomography. For regional seismic tomography, we are only interested in a part of the Earth and we can construct a rectangular box covering the portion of interest (Figure 2b and c). The coordinate center is placed at the surface of the Earth, positive X and Y-axes point to the direction of north and west, and the positive Z-axis points downward. The grid nodes above the Earth's surface (air nodes) are given the velocity for P waves traveling in air (Figure 2c). As a result, all the rays travel inside the Earth. Here we should emphasize that this version is still based on Cartesian coordinate system and not on a true spherical system.

Finite-difference ray tracing algorithms require a uniformly spaced velocity (or slowness) grid (Podvin and Lecomte, 1991). We interpolate the velocity values on the regular uniform grid nodes from non-uniform inversion grid nodes through trilinear interpolation. First we treat each station as a source and calculate travel times to all velocity nodes in the volume. The travel time from a station to each earthquake is interpolated from its 8 neighboring nodes through trilinear interpolation. The ray path from the earthquake to the station is found iteratively with increments opposite to the travel time gradient. The corresponding partial derivatives of travel times with respect to the slowness models are calculated by dividing the ray paths into small segments (Thurber, 1983).

Both the algorithms *tomoDD* and *tomoFDD* are based on a regular inversion grid. We recently developed an adaptive-mesh DD tomography method based on tetrahedral and Voronoi diagrams to automatically match the inversion mesh to the data distribution (Zhang and Thurber, 2005). Both tetrahedral and Voronoi diagrams have been shown to be powerful tools to represent spatial relationships in three dimensions and they allow a more flexible representation of the model. For example, model volumes of widely varying sizes with complex distributions are easily implemented, and it is more convenient to build parameterizations containing particular interfaces, on which the nodes can be distributed.

Linear and natural-neighbor interpolation methods can be derived for tetrahedral and Voronoi diagrams, respectively. Linear interpolation uses 4 tetrahedron nodes to interpolate the velocity/slowness values at any point and it has the advantage of calculating the interpolating basis functions easily and quickly. However, the linear interpolation function is not continuously differentiable, which is a desired property for some applications. In comparison, the natural-neighbor interpolation method interpolates the value at any point from its *n* natural neighbors. The natural-neighbor interpolation function guarantees continuity in first and second derivatives except at the nodes (Sambridge et al., 1995). Our algorithm allows the use of either approach.

We start the inversion from a regular inversion grid, equivalent to that of *tomoDD*. We randomly perturb the starting regular inversion grid by a very small amount (so that the nodes are not located on the same plane) in order to construct the tetrahedral or Voronoi diagram around these nodes using the Qhull algorithm (http://www.thesa.com/software/qhull/). We also construct a regular computational grid that remains fixed during the inversion, which can be the same as the starting regular inversion grid or finer. We trace rays between events and stations based on the current regular velocity grid. The rays between all the event and station pairs are saved for later use in defining the adaptive mesh. Using these rays, we find the partial derivatives of the travel times with respect to the model slowness parameters on the current inversion mesh. In the process, we calculate the derivative weight sum (DWS) values on the inversion mesh nodes (Thurber and Eberhart-Phillips, 1999). Threshold DWS values are set to add or remove nodes.

After this refining process, we obtain a new irregular inversion mesh, which cannot be guaranteed to be optimally data-adaptive. We construct a new tetrahedral or Voronoi diagram around the new irregular inversion mesh and recalculate the DWS values on all the nodes using the previously saved ray information. The threshold checking is repeated to determine the inversion mesh to be used for the current iteration of simultaneous inversion. Finally, a

new tetrahedral or Voronoi diagram is constructed and the partial derivatives of the travel times with respect to the new set of inversion mesh nodes are calculated for the construction of the seismic tomography equations. After each simultaneous inversion, the velocity values on the irregular inversion mesh nodes and the regular computational grid nodes are updated. For subsequent simultaneous inversions, the inversion mesh is again updated following the same procedure to better match with the ray distribution, which will change as the velocity model changes and hypocenters move.

Once the inversion mesh is set up and the partial derivatives of travel times with respect to the event locations and slowness model parameters are determined, we can construct the linear system of equations to solve for the event locations and slowness perturbations at the irregular mesh nodes in a similar way to the case of the regular inversion grid. Currently, we have finished the implementation of adaptive-grid scheme on the flat-model version of DD tomography (Zhang and Thurber, 2005). We are now in the process of implementing the adaptive-mesh scheme on the "sphere-in-a-box" version of DD tomography and will apply it to the Sichuan-Yunnan region, both as a whole and in the higher-resolution subregions we identify.

Preliminary result

At present, we have collected ~14800 catalog P and S picks from ~2080 events recorded on 63 stations covering a subregion of latitude 21^o to 30^o and longitude 96^o to 105^o (Figure 3). One part of the data is from the provincial bulletins compiled by the Yunnan and Sichuan Seismological Bureaus during the period of 1993 to 1997. Since this dataset was originally used by Liang et al. (2004) for Pn tomography in China, the distances between events and stations are generally greater than 1 degree. As a result, we only have ~3400 absolute P arrivals from ~800 events and ~60 stations. The other part of the data consists of P and S picks from the Annual Bulletin of Chinese Earthquakes (ABCE) during the period of 1990 to 2001, extracted from the dataset for China compiled by Sun (2005). We constructed ~73500 catalog differential times from event pairs within 40 km. In total, there are ~88000 catalog absolute and differential times for inversion, among which the number of P picks is twice that of S picks. The inversion grid spacing in the horizontal direction is 50 km and 5 km in the vertical direction (Figure 3). We start the inversion from a 1D velocity model and alternate between the simultaneous determination of velocity model and event locations and the determination of locations only.

The weighted root mean square (RMS) arrival time residual decreases from 37.348 s at the beginning of the inversion to 864 ms after the final iteration. Figures 4 and 5 show horizontal sections of P- and S-wave velocity models at a depth of 15 km and two cross-sections of P- and S-wave velocity models through latitudes of 23.6^o and 26^o, respectively. The inversion has revealed some interesting features of the region. The high plateau of the Southeastern margin of the Tibetan Plateau is remarkably well delineated by high crustal velocities (from ~22ºN to ~29ºN in latitude and from ~99ºE to ~103ºE in longitude) (Figure 4). The stable Yangtze Craton to the east has relatively low crustal velocity compared with the high plateau (Figures 4 and 5). To the west of longitude ~99^o, the western Yunnan and Myanmar regions also have relatively low crustal velocity, which correlates with the presence of a number of active volcanoes in the region (Figures 4 and 5) (Liang et al., 2004). Both horizontal slices and cross sections show strong lateral velocity heterogeneities, consistent with the nature of active fault zones in this region. Strong velocity contrasts are evident across major faults, such as Xiaojiang Fault and Red River Fault (Figure 5). The relocated earthquakes show relatively well-defined vertical linear features, corresponding to major faults at the surface (Figure 5). Recent application of DD location in this region (Yang et al., 2003) also showed that the relocated events are more concentrated near the fault zones using just the catalog differential data. We are confident that with much more local catalog data and new digital waveform data, we will be able to characterize the velocity structure at much higher resolution and obtain greatly improved earthquake locations.

CONCLUSIONS AND RECOMMENDATIONS

We have applied the "sphere-in-a-box" version of DD tomography code to a subregion of latitude 21^o to 30^o and longitude of 96^o to 105^o of the planned Sichuan-Yunnan study region using catalog picks. Both P- and S-wave velocity models show strong velocity heterogeneities, consistent with the nature of active transition zone between the Yangtze platform to the east and the Tibetan plateau to the west. Strong velocity contrasts are evident across some major fault zones and the relocated earthquakes show relatively well-defined vertical linear feature.

We are in the process of developing the adaptive-mesh "sphere-in-a-box" version of the DD tomography code and we are nearly finished with this task. Dr. Song is traveling in China in July to obtain more catalog picks and

waveform data. Once we have more data available, we can further improve the resolution of the velocity model and the accuracy of event locations in the Sichuna-Yunnan region.

ACKNOWLEDGEMENTS

We thank Megan Flanagan for allowing us to use her code in our "sphere-in-a-box" version of the DD tomography code. We are grateful to Youshun Sun for providing us his compiled picks for the Sichuan-Yunnan region.

REFERENCES

Chan, W. W., C. Y. Wang, and W. D. Mooney (2001), 3-D crustal structure in southwestern China, in *Proceedings of the 23rd Seismic Research Review: Worldwide Monitoring of Nuclear Explosions,* LA-UR-01-4454, Vol. I, pp. 12–20.

Du, W.X., C. H. Thurber, and D. Eberhart-Phillips (2004a), Earthquake relocation using cross-correlation time delay estimates verified with the bispectrum method, *Bull. Seismol. Soc. Am.* 94: 856–866.

Du, W., C. H. Thurber, M. Reyners, D. Eberhart-Phillips, and H. Zhang (2004b), New constraints on seismicity in the Wellington region of New Zealand from relocated earthquake hypocentres, *Geophys. J. Int*. 158: 1088–1102.

Flanagan, M. P., S.C. Myers, C. A. Schultz, M. E. Pasyanos, and J. Bhattacharyya (2000), Three-dimensional a priori model constraints and uncertainties for improving seismic location, in *Proceedings of the 22nd Annual DoD/DOE Seismic Research Symposium: Planning for Verification of and Compliance with the Comprehensive Nuclear-Test-Ban Treaty (CTBT),* Vol. 2, pp. 129-136.

Kim, W.-Y., D. P. Schaff, J. Zhang, F. Waldhauser, and P. G. Richards (2004), Evaluation of cross-correlation methods on a massive scale for accurate relocation of seismic events, *in Proceedings of the 26th Seismic Research Review: Trends in Nuclear Explosion Monitoring*, LA-UR-04-5801, Vol. 1, pp. 277–286.

Liang, C. T., X. D. Song, J. L. Huang (2004), Tomographic inversion of Pn travel-times in China, *J. Geophys. Res.* 109, B11304, doi:10.1029/2003JB002789.

Liu, Y., X. Xhang, J. He, F. Liu, and H. Sun (2005), Three-dimensional velocity images of the crust and upper mantle beneath the north-south zone in China, *Bull. Seismol. Soc. Am.* 95: 916–925.

Nikias, C. L., and R. Pan (1988), Time delay estimation in unknown Gaussian spatially correlated noise, *IEEE Trans. Acoust. Speech Signal Process* 36: 1706–1714.

Nikias, C. L., and M. R. Raghuveer (1987), Bispectrum estimation: A digital signal processing framework, *Proc. IEEE* 75: 869–891.

Podvin, P., and I. Lecomte (1991), Finite difference computation of travel times in very contrasted velocity models: a massively parallel approach and its associated tools, *Geophys. J. Int.*105: 271–284.

Poupinet, G., W. L. Ellsworth, and J. Frechet (1984), Monitoring velocity variations in the crust using earthquake doublets: An application to the Calaveras Fault, California, *J. Geophys. Res.* 89: 5719–5713.

Rubin, A. M., D. Gillard, and J. L. Got (1999), Streaks of microearthquakes along creeping faults, *Nature* 400: 635–641.

Sambridge, M., Braun, J., and McQueen, H. (1995), Geophysical parametrization and interpolation of irregular data using natural neighbours, *Geophys. J. Int.* 122: 837–857.

Schaff, D. P., and P. G. Richards (2004), Repeating seismic events in China, *Science* 303: 1176–1178.

Schaff, D. P., G. H. R. Bokelmann, G. C. Beroza, F. Waldhauser, and W. L. Ellsworth (2002), High-resolution image of Calaveras Fault seismicity, *J. Geophys. Res. 107,* 2186, doi:10.1029/2001JB000633.

Shearer, P. M. (1997), Improving local earthquake locations using the L1 norm and waveform cross correlation: application to the Whittier Narrows, California, aftershock sequence, *J. Geophys, Res.* 102: 8269–8283.

Sun, Y. (2005), P- and S-wave tomography of the crust and uppermost mantle in China and surrounding areas, PhD dissertation, Massachusetts Institute of Technology, 314 pp.

Thurber, C. H. (1983), Earthquake locations and three-dimensional crustal structure in the Coyote Lake area, central California, *J. Geophys. Res.* 88: 8226–8236.

Thurber, C., and D. Eberhart-Phillips (1999), Local earthquake tomography with flexible gridding, *Comp. & Geosci.* 25: 809–818.

Thurber, C., S. Roecker, H. Zhang, S. Baher, and W. Ellsworth (2004), Fine-scale structure of the San Andreas fault and location of the SAFOD target earthquakes, *Geophys. Res. Lett.* 31, doi:10.1029/2003GL019398.

Um, J., and C. H. Thurber (1987), A fast algorithm for two-point seismic ray tracing, *Bull. Seism. Soc. Am.* 77: 972–986.

Waldhauser, F. and W. L. Ellsworth (2000), A double-difference earthquake location algorithm: Method and application to the northern Hayward fault, CA, *Bull. Seismol. Soc. Am.* 90: 1353–1368.

Waldhauser, F., and W. L. Ellsworth (2002), Fault structure and mechanics of the Hayward Fault, California, from double-difference earthquake locations, *J. Geophys. Res.* 107: ESE 3-1-3-12.

Yang, Z., Y. Chen, Y. Zheng, and X. Yu (2003), Accurate relocation of earthquakes in central-western China using the double-difference earthquake location algorithm, Science in China (Series D), *Sci. China (D)* 46: 129–134.

Yang, Z.-X., X.-W. Yu, Y.-J. Zheng, Y.-T. Chen, X.-X. Ni, and W. Chan (2004), Earthquake relocation and 3-dimensional crustal structure of P-wave velocity in central-western China, *Acta Seismologica Sinica* 17: 20-30.

Zhang, H., and C.H. Thurber (2003), Double-difference tomography: method and application to the Hayward fault, California, *Bull. Seismol. Soc. Am.* 93: 1875–1889.

Zhang, H., and C. Thurber (2005), Adaptive mesh seismic tomography based on tetrahedral and Voronoi diagrams: Application to Parkfield, California, *J. Geophys. Res.* 110, B04303, doi:10.1029/2004JB003186.

Zhang, H., C. Thurber, D. Shelly, S. Ide, G. Beroza, and A. Hasegawa (2004), High-resolution subducting slab structure beneath Northern Honshu, Japan, revealed by double-difference tomography, *Geology* 32: 361–364.

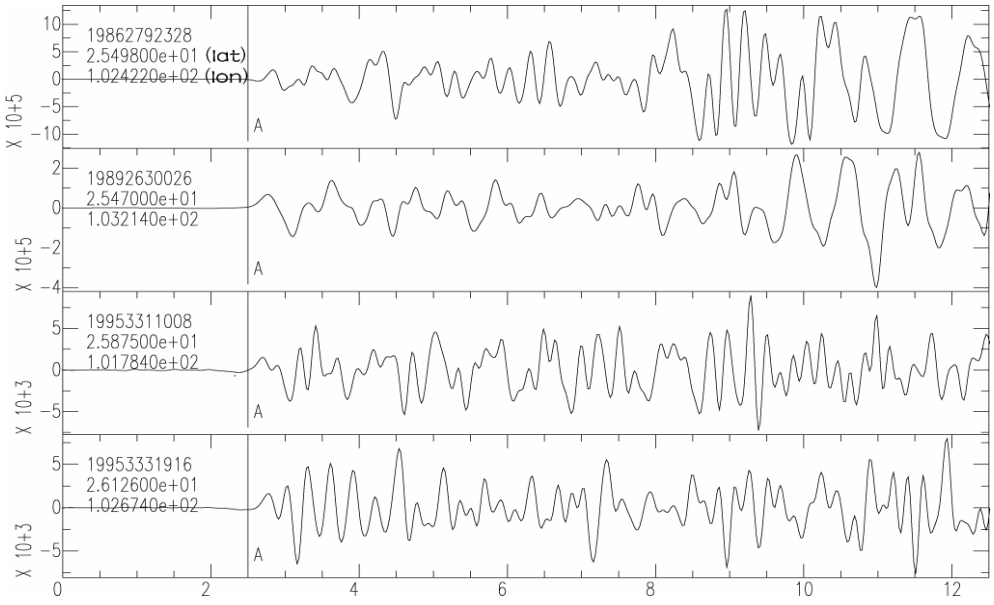

Figure 1. Seismic waveforms recorded on station KMI.

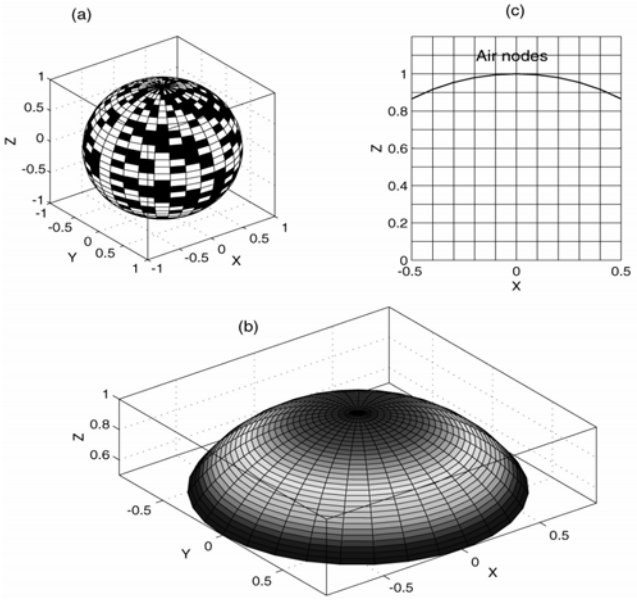

Figure 2. Grid setup for regional scale double-difference tomography. (a) The whole earth is inserted into a cubic box. (b) A rectangular box covers the region of interest. (c) The representation of (b) in the X-Z plane. The surface of the Earth is shown as a thick line. The regular grid is used for finite-difference ray tracing algorithm.

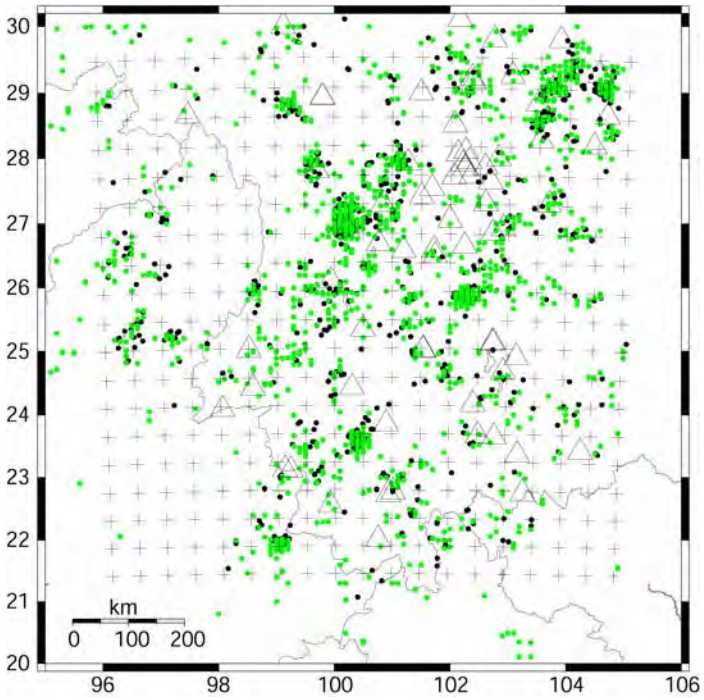

Figure 3. Event and station distribution map. Events and stations are indicated by dots and triangles, respectively. Black dots indicate events compiled by the Yunnan and Sichuan Seismological Bureaus, whereas green ones are from the Annual Bulletin of Chinese Earthquakes. Crosses are inversion grid nodes in the horizontal plane.

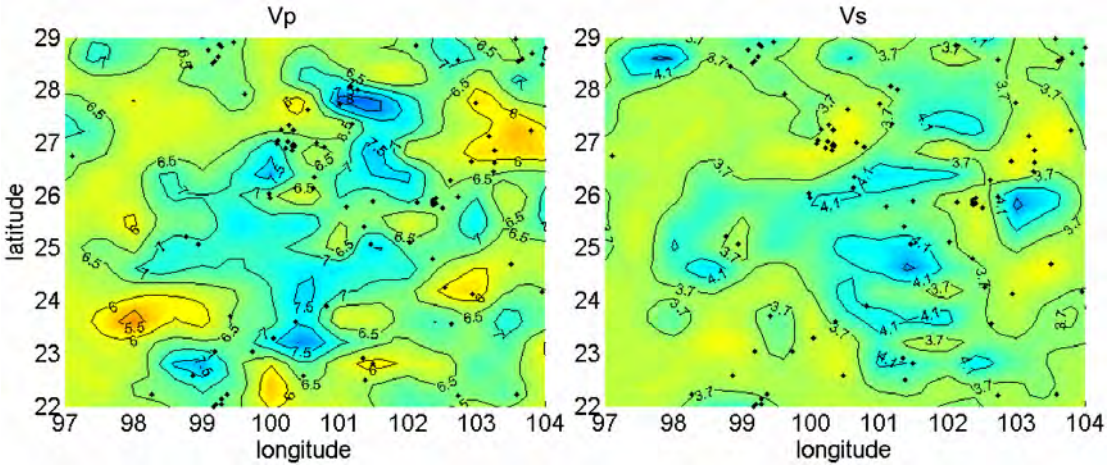

Figure 4. Horizontal sections of the P- and S-wave velocity models at a depth of 15 km. Blacks dots are seismic events within 2.5 km of this section.

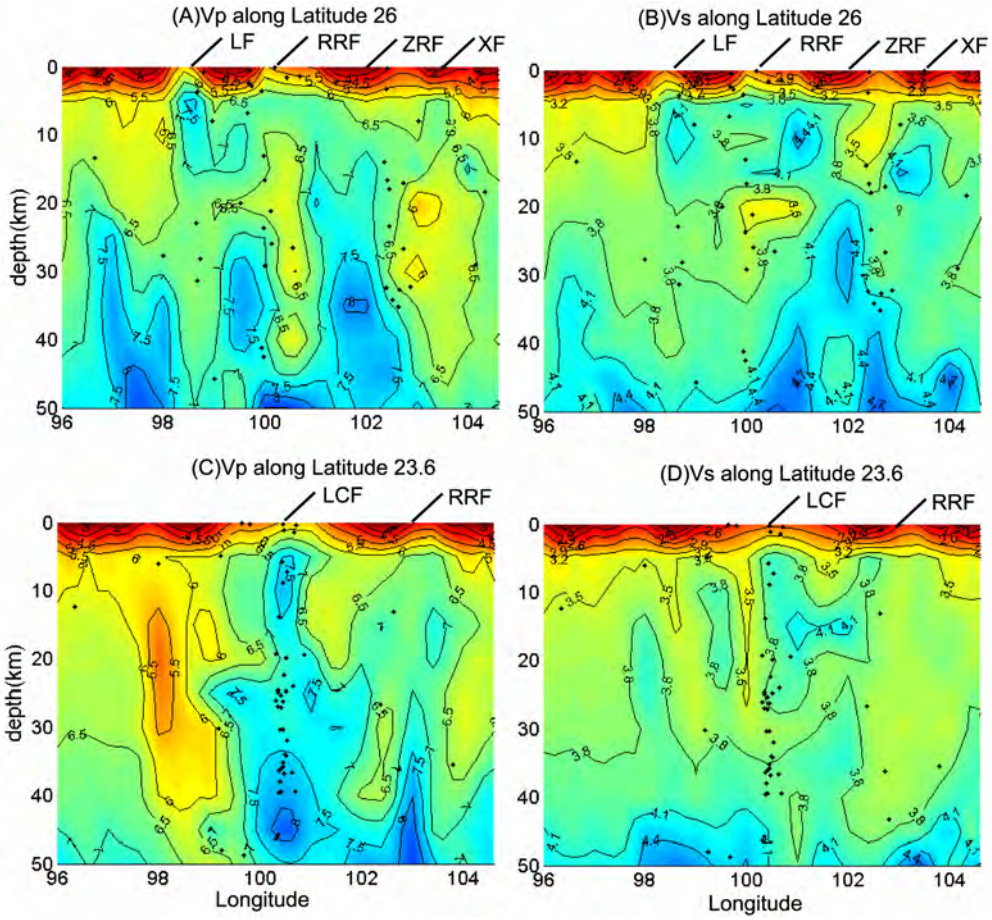

Figure 5. Cross-sections of P- and S-wave velocity models along latitudes 26° and 23.6°. LF - Longling Fault, RRF – Red River Fault, XF – Xiaojiang Fault, LCF – Lancang River Fault, ZRF – Zemu River Fault.

Seismic Event Detection and Location

A PRIORI EMPIRICAL CALIBRATION FOR MULTIPLE-EVENT LOCATION METHODS

Michael S. Antolik, Jason P. Erickson, Mark A. Tinker, Kevin D. Hutchenson,
Gordon D. Kraft, and Linda J. Owiesny

Quantum Technology Services, Inc.

Sponsored by Air Force Technical Applications Center

Contract No. F08650-01-C-0063

ABSTRACT

Multiple event location methods that explicitly solve for empirical path correction terms between the source region and receiver, such as Progressive Multiple Event Location, or PMEL (Pavlis and Booker, 1983), contain a singularity in the equations of condition that prevents the unique recovery of the path corrections and resolution of the absolute location of an event cluster. The standard practice for dealing with this singularity is to choose one event as a "calibration" event and to calculate the path corrections while holding its location fixed, or to use one or more master events. However, it is often the case that no independent information is available to constrain the locations of any of the cluster events, and the results obtained from the multiple event relocation may be highly dependent on the choice of calibration event. A significant improvement in these methods can be made, therefore, if an *a priori* test applied to data from an event cluster can aid in choosing a good calibration event.

In this paper we develop an *a priori* technique for selecting the best calibration events from a cluster and apply it to the PMEL method. We develop and test the technique using groundtruth data sets from nuclear test sites, mining blast data, and synthetic data. The procedure involves first the location of each member event independently using single event location (SEL) procedures, followed by the application of PMEL using each event as a calibration event. The results reveal a significant correlation between certain uncertainty parameters obtained from the SEL results and the mislocation (defined as the sum of the distances of all events in the cluster from groundtruth) obtained from PMEL. From the SEL parameters, we then define a calibration statistic (ϕ) that tends to have larger values for poor calibration events. ϕ is formed from a weighted sum of the deviations of the root-mean-square travel-time residual, the error ellipse strike, and the error ellipse eccentricity from the cluster mean of those quantities. The calibration statistic performs better than random chance in discriminating between acceptable and poor calibration events and performs about as well on the test data sets as with the development data set. It also works well using both teleseismic and regional phases.

The form of the dependence of PMEL mislocation on ϕ suggests that a critical value of ϕ can be used to identify poor calibration events. The best results are obtained with $\phi_{crit} = 0.25$. However, the best value of ϕ_{crit} can vary if the SEL uncertainty parameters (and, therefore, the ϕ-value) do not vary sufficiently between the member events of a cluster, and in some rare cases the correlation may break down. The level of scatter indicates that between 10–40% of the events in a cluster may be misclassified using this method, but in each case nearly all of the classification errors result from rejection of valid calibration events. The cost of making such an error is much less than using a calibration event that results in poor locations. The method also relies on having a sufficient number of member events within a cluster to calculate meaningful statistics, but the overall results suggest that this technique may aid the improvement of location estimates in regions that have not yet been calibrated.

OBJECTIVE

Multiple-event location algorithms are commonly used to jointly locate a set of clustered events while accounting for inaccuracies in the Earth model used to estimate the travel time along the source-receiver path. It is usually assumed that if the distance between the clustered events is small compared to the source-receiver distance, then the inaccuracies in the Earth model are the same for each event at all of the recording stations. Thus, by jointly locating the entire cluster, the necessary perturbations to the reference Earth model can be estimated and used to improve the accuracy of the resulting location estimates.

Two general types of multiple-event methods exist. The first is differencing methods such as Double Differences (DD) (Waldhauser and Ellsworth, 2000). These methods use residual differences between clustered events recorded at common stations to remove the effect of heterogeneity along the travel path. Although the DD method can in theory resolve the complete location of an event cluster (absolute location in space as well as correct relative locations between the events), the ability of the method to resolve absolute locations is subject to the same limitations as other multiple-event methods imposed by errors in the data and strong near-source velocity contrasts (Menke and Schaff, 2004; Michelini and Lomax, 2004). It also requires the presence of abundant nearby seismicity to achieve the most accurate relative locations.

The second general type of multiple-event method is the heterogeneity-based scheme where perturbations to the Earth model are explicitly solved for as part of the location process in the form of path correction terms. Examples of this type are the Joint Hypocenter Determination (JHD) method (Douglas, 1967) and the Progressive Multiple Event Location (PMEL) method (Pavlis and Booker, 1983). Both methods are effective in regions of sparse seismicity, and thus are quite useful in the nuclear explosion monitoring context. Unfortunately, they suffer from a singularity in the equations of condition that prevents the unique recovery of the path corrections and resolution of the absolute location of an event cluster. The standard method for dealing with this ambiguity is to choose one event whose location is very well known through independent means, and fix either the origin time or hypocenter location, or both. This allows the locations and origin times of all other events in the cluster to be tied to this calibration event, and the path corrections can then be uniquely determined.

The problem with this practice is that most often no independent information is available to constrain the locations of any of the events under consideration. Therefore, the choice of a calibration event becomes arbitrary. It also becomes problematic as to how to assess the uncertainty in the path corrections when estimating location error. Practical considerations usually mean that the *a priori* location estimates of the events in the cluster will differ in their quality, which may affect their utility as calibration events. The quality of these location estimates will depend on the station configuration that recorded each event, which may differ significantly, particularly if the time span of occurrence of the cluster is large. In addition, unless correlated relative arrival time picks have been made for the events, the random measurement error contained in the phase picks will most likely be different for each event. As a result, it has been found that the locations obtained for PMEL are often highly dependent on the particular choice of calibration event (Erickson et al., 2003). A significant step toward improvement of multiple-event location methods can be made, therefore, if an *a priori* test applied to data from an event cluster can aid in choosing the best calibration event. The main objective of this study is to investigate multiple-event location statistics and, if possible, to develop such a test.

Ideally, the "best" calibration event is that which places the locations of all events in a cluster closest to their actual, or "groundtruth," locations. If the groundtruth location is known for one or more events of the cluster, then the obvious choice for calibration is already made, assuming that errors in the data are small. Therefore, any test designed to determine the best calibration event must rely on a statistic which does not depend on knowledge of groundtruth. This statistic should also be readily determinable from the available data before the relocation is attempted.

In the following section, we develop and test a technique for identifying poor calibration events from within an event cluster for multiple-event location methods. We use several groundtruth data sets from nuclear explosion test sites and mining sites as well as synthetic data. We apply the technique to the PMEL method, although it is applicable to all multiple-event location methods that require the use of a calibration or master event to resolve the absolute cluster location. The PMEL method, as outlined by Pavlis and Booker (1983), differs from other

heterogeneity-based methods in that the path corrections and hypocenter parameters are determined separately in a two-step, iterative inversion process rather than simultaneously.

RESEARCH ACCOMPLISHED

Test Procedure

The test procedure applied to each data cluster consisted of two parts. In step 1, each member event was relocated using standard single-event location (SEL) procedures. The groundtruth locations were used as the initial seed locations. We then calculated various statistics from the results for each member event. These included the root-mean-square (RMS) travel time residual, the area of the resulting confidence error ellipse, and the eccentricity and orientation of this ellipse. In addition, we also examined attributes such as the origin time error estimated for each event, the number of defining phases, the azimuthal gap in the station distribution, and the average *a priori* data error, or *deltim* parameter, assigned to the phases. This *a priori* error is used for data weighting in the inversions and also for calculation of the hypocenter error ellipses.

In step 2, we relocated the cluster multiple times using the PMEL method, each time selecting a different event for calibration. We then calculated a statistic which quantifies the overall mislocation for the events in the cluster. The mislocation is defined as the horizontal distance between each event and the corresponding groundtruth location. We assumed that depth had independently been determined from other means and fixed the depths of the events to the surface in both steps. Examination of each event was then carried out to check for possible correlations between the statistics calculated in step 1, and the mislocation statistic calculated after step 2.

Development of the Calibration Discriminant

A natural choice to apply these tests is the group of nuclear explosions from the Lop Nor test site. Highly accurate groundtruth locations have been published based on satellite imagery for most of the 21 known explosions conducted at this site (Fisk, 2002). The magnitudes for these events are all large and they were well recorded at teleseismic distances. However, little or no regional phase data are available. We used a subset of 18 events dating from 1978 until 1996 having between 6 and 14 first-arriving *P* phases. The distance range of the data was between 14^o and 95^o. The phase picks were defined using a waveform correlation (Erickson et al., 2003) basis, and a varying *deltim* was assigned to the phase picks to best represent the estimated measurement error. In order to obtain a more diverse set of error ellipses in the single-event locations, the analyst-defined *deltim* values were used even though no attempt was made to account for model error.

No direct correlation could be found between the absolute size of the SEL error statistics and the PMEL mislocation statistic for the Lop Nor data. Figure 1 shows the size of the sum of the lengths of the mislocation vectors (normalized by the maximum for the cluster) plotted against the RMS travel time residual, the error ellipse size, the number of defining phases, and the average phase *deltim* from single-event location, when that event is used as a calibration event in PMEL. Although several choices for a mislocation parameter could be made, we found that there was virtually no difference between using the RMS length, the average length, and the sum of the mislocation vector lengths. We therefore discuss only the sum of the mislocation lengths in this study.

Several conclusions can be drawn from Figure 1. First, it can be seen that the majority of the events result in similar values of the mislocation statistic when used as calibration, but 6 of the 18 events result in a substantially larger mislocation. The median sum mislocation length in Figure 1 is 265 km, but the subset of 6 events with the largest mislocation values all have values exceeding 320 km. There is no relation between the number of defining phases used or the average *deltim* of an event and the mislocation statistic. This is somewhat surprising since these two parameters are often associated with location quality in standard single-event procedures. There is also no simple relation between the size of the travel time residual or the SEL error ellipse and the magnitude of mislocation. However, it is significant that 3 out of the subset of 6 events with the largest values of the mislocation statistic also have much larger SEL travel time residuals than the other events in the cluster. The other three events have RMS residual values lower than the average for the cluster. A similar pattern is seen in the area of the error ellipse, which is not unexpected since the SEL error ellipse size is partly determined by the size of the data residuals, in addition to the specific values of *deltim*.

Examining other variables, we find that all 3 of the events which have a large mislocation statistic but RMS residual values lower than the cluster average also have a SEL error ellipse whose strike differs from the cluster median by more than 20^o (Figure 2). The median error ellipse strike is about 80^o, and all but a handful of events cluster near this value. Of those events in this cluster, two belong to the above-mentioned subset of six events. These two events have among the largest values of RMS residual for the entire cluster. The other four events in this subset have SEL error ellipse strikes that differ from the median by a large value, only one of which also has a high RMS residual value (this event has both the highest normalized RMS residual and mislocation value for the entire data set). There is a clear correlation shown in Figure 2 between events having a large mislocation value and those having an SEL error ellipse whose orientation differs significantly from the cluster median. In addition, the correlation between the SEL RMS residual and the strike of the error ellipse is low, such that the combination of the two parameters enhance the capability of predicting whether a particular event will cause a large mislocation value when used as a calibration event for PMEL. The SEL error ellipse orientation is primarily a function of the station configuration, as well as the *a priori* data error (*deltim*). The data residuals, on the other hand, affect only the area of the ellipse. Thus it is not unusual for these two parameters to be uncorrelated.

Based on these results, we constructed a discriminant function from the SEL parameters designed to identify poor PMEL calibration events within a cluster. Figure 2 suggests that we need at least two parameters to do this. On further examination of the results, we chose three parameters; in addition to the two discussed above, we added a third (the eccentricity) which defines the shape or elongation of the SEL error ellipse. The Lop Nor data set also shows some correlation between the SEL ellipse eccentricity and the mislocation statistic, although it is not as strong as for the first two parameters. After examining the performance of discriminant functions involving various combinations of parameter weighting, we adopted the following as the calibration discriminant parameter ϕ:

$$\phi = \hat{r} + \frac{1}{2}\hat{s} + \frac{1}{2}\hat{e}, \tag{1}$$

where

$$\hat{r} = \frac{r - \bar{r}}{\max|r - \bar{r}|}, \quad \hat{s} = \frac{|s - \bar{s}|}{\max|s - \bar{s}|}, \quad \hat{e} = \frac{|e - \bar{e}|}{\max|e - \bar{e}|}, \tag{2}$$

and r, s, and e are the RMS residual in seconds, the strike of the SEL error ellipse, and the SEL error ellipse eccentricity, respectively. The overbars in equation (2) indicate the mean of that parameter over the cluster of events. Higher values of ϕ for an event tend to be associated with larger mislocation values when used as a calibration event. The variable $\hat{r}$ is defined so that only positive deviations of the RMS residual from the cluster mean cause an increase in ϕ, whereas any deviation of s and e from the cluster mean will do so. This is because there is no reason to expect that deviations in the orientation or elongation of the SEL error ellipse of one sign or the other will correlate more strongly with larger mislocation values, as indicated by Figure 2. Note that defining ϕ as in equation (1) means that it does not depend on the choice of confidence level or the number of degrees of freedom assumed in calculating the error ellipse (Jordan and Sverdrup, 1981). This is because although the area of the error ellipse depends on $\hat{r}$, it does not explicitly enter into equation (1). The possible range of values of ϕ is –1.0 to +2.0.

Figure 3 shows the mislocation statistic plotted against ϕ for the Lop Nor explosions. The horizontal red line represents an arbitrary threshold used to divide the data set into poor or valid calibration events for the purposes of evaluating performance of the discriminant. For this data set the division is easy to make because of the large separation between the poorest six events and the others in the cluster. However, for other data sets the application of this *a posteriori* threshold may not be as simple. The discriminant function does an excellent job of separating the subset of poor calibration events from the other events, although there is considerable scatter. The degree of success can be measured by the value of the squared point biserial correlation coefficient R^2, which is 0.37. The value of R^2 indicates how much of the variation in mislocation is explained by the variation in ϕ. To demonstrate that consideration of the error ellipse shape aids in the discrimination process, we show in Figure 4 the plot of $\hat{r}$ vs. the mislocation statistic. The correlation between $\hat{r}$ and mislocation is obviously less in this case, and the value of R^2 drops to 0.28.

Other Test Data Sets

The reliability of the calibration discriminant was verified by testing the process on two independent groundtruth data clusters. The first cluster consists of mining blasts from the Powder River, Wyoming, region. The second consists of Nevada Test Site (NTS) explosions. The 13 blasts in the mining data set were associated with particular coal mines in the region based on data from a local station (Erickson et al., 2003) at a distance of 1°. The location of each event within the particular mine is not known, however. The area of each mining site varies from a few 10s to about 100 km^2 (Erickson et al., 2003). Thus, the precision of the groundtruth locations is probably 5 km or better. Each event was located using a sparse array of regional stations, with 5 phases per event.

The discriminant function for the Wyoming data is plotted against the sum mislocation in Figure 5. The events do not separate as readily into two populations as in the previous case. The choice of a cutoff value for the mislocation statistic is therefore not as clear as for the Lop Nor data set, but should be made so that a sufficient number of events is defined as falling into both categories. Choosing 90 km as the threshold value identifies 7 of the 13 events as poor calibration events, and the resulting value of R^2 is nearly the same as for the Lop Nor data, 0.38. We also note that the use of $\hat{s}$ and $\hat{e}$ does not aid in discrimination in this case; in fact, $R^2 = 0.50$ when $\hat{r}$ is used as the only predictor variable. This is probably because the station configuration for all 13 events is identical, and the orientation and shape of the SEL error ellipses are determined only by the *deltim* parameter. Therefore, there is far greater similarity among the SEL error ellipses than for the Lop Nor data, which represent a much longer time span of occurrence and were recorded by a more diverse network of stations. In any case, it is evident that the size of the RMS residual is the most important indicator of the reliability of an event for calibration in both cases.

A diverse set of teleseismic, regional, and local phase data is available for NTS explosions. In order to better simulate a limited data scenario often encountered in monitoring situations, we restricted the analysis to first-arriving phases at far-regional distances (4–15°). All of the explosions date from the early 1990s. For this data set, all phases have a default *deltim* of 0.5 s. The results are shown in Figure 6. Because of the constant default *deltim* parameter, the SEL error ellipses are quite similar and most of the ϕ values cluster between 0.5 and 1.0. However, a similar dependence of ϕ on mislocation is observed as for the other data sets. A separation threshold of 130 km identifies 5 of the 17 explosions as poor calibration events, and $R^2 = 0.30$. The fact that ϕ is just as successful in identifying poor calibration events from independent data sets is encouraging.

Synthetic Experiment

Because the amount of data with knowledge of groundtruth is limited, it is desirable to examine the performance of the calibration discriminant using synthetic data. We derived a synthetic cluster of 17 events having direct *P* phases recorded at 8 stations. The tests were carried out using a different version of the data in each case. First, synthetic arrival times were calculated at each station using a 1-D reference Earth model, and the locations were derived using this same reference model. A constant model error was added to the phases for each station in addition to a random measurement error. We also varied the weighting, or *deltim*, assigned to each phase. Three types of weighting were used. The first type simply involved an equal default value of *deltim* for each phase. The second type added a random perturbation to *deltim*, while in the third type, the *deltim* assigned to each phase was correlated to the data residual for each phase, as measured by the combination of model and measurement error. This latter type of situation may arise when the analyst is assigning *deltim* values to a data set of phase arrivals that have a low signal-to-noise ratio.

The results of these tests, not shown for issues of space, generally validate the results obtained using real data. The correlation between ϕ and the PMEL mislocation generally increases with the diversity of the error ellipses. Similar correlations to the real data examples are obtained where the *deltim* values are not constant. The PMEL mislocation obtained using a particular event for calibration has little dependence on ϕ if the station distribution for all events is similar and the *deltim* values are constant.

Method for Selection of Calibration Events

Having calculated ϕ for a particular data set, the question remains as to how to identify an appropriate calibration event or events, since in most applications groundtruth information will not be available. The level of scatter observed in these experiments suggests that a restrictive criterion should be used. However, it is probably not advisable to simply choose the event having the smallest value of ϕ, because it is not likely that this event will produce the best results. In Figure 5, for example, the event having the smallest ϕ-value has the 5th largest mislocation of the entire cluster. Application of the discriminant function only means that it is likely that the events resulting in the largest mislocation for a given cluster will not be found among those events having the smallest ϕ-values. The reason this is true is because the location error is stable for small values of ϕ, but its variance increases considerably at large values of ϕ (Figs. 3, 5, 6).

The results suggest two possible approaches for selecting calibration events. The first is simply to select a calibration event from among the smallest *k*% of the ϕ-values. An appropriate value of *k* might be 10–30%, which for the test cases described in this report would amount to selecting from the 3–6 events with the smallest ϕ-values. One problem with this approach is that it becomes quite restrictive if the number of events in the cluster becomes small. In that case, however, the validity of the statistical method is reduced, and there may be only a small range of mislocation and ϕ-values across all of the events of the cluster. If a cluster involves only a handful of events with an identical station distribution, then it will most likely not be possible to use this method to limit the choice of calibration event.

Another obvious selection criterion is simply to define a cutoff value of ϕ (ϕ_{crit}) and choose from among those events having a smaller ϕ than the cutoff. The drawback of this approach is that a cutoff value appropriate for one cluster might not be appropriate for another. However, the test cases described in this study suggest that the best value of ϕ_{crit} may be fairly stable. This value appears to be $\phi_{crit} \sim 0.25$. Applying this cutoff value to the Lop Nor data (Figure 3) would divide the cluster into 7 events appropriate for calibration and 11 that are not. All six of the events that produce relatively large mislocation values have $\phi > 0.25$. However, 5 events from among the group with small mislocation values also have $\phi > \phi_{crit}$. Thus, we have made 5 classification errors out of 18, for an accuracy rate of 72%. Note, however, the cost of the two types of error is not the same, i.e., it is more serious to choose an event for calibration that results in large mislocation than it is to reject a valid event. With the knowledge that one-third of the events are poor choices for calibration, we would expect an accuracy level of 56% on the basis of random chance.

For the Powder River data, a cutoff ϕ-value of 0.25 results in an accuracy rate of 85% (Figure 5). In this case one of the 7 events identified as poor calibration events is misclassified, while only one valid event is misclassified. Since a cutoff mislocation value of 90 km divides the data set nearly in half, only slightly better than 50% success could be expected by random chance. Although the correlation between the two statistics is better if we define $\phi = \hat{r}$ (R^2 = 0.5), the classification accuracy rate does not improve if we use an appropriately adjusted value for ϕ_{crit}. In the case of Figure 6, although the correlation is good the uniform *deltim* results in a small range in ϕ-value for the events in the cluster. Consequently, a larger ϕ_{crit} of 0.5 would improve the classification accuracy to 76%, although even if ϕ_{crit} were chosen as 0.25 none of the five very poor events would be classified as valid. For nearly all of the synthetic test cases that do not use a uniform *deltim*, $\phi_{crit} = 0.25$ appears to be a good choice of cutoff value. However, we caution that it may be advisable to test this value using synthetic data for the particular station distribution represented in the real data before using it to select calibration events.

Rather than selecting one single calibration event, it might be assumed that selecting a combination of more than one, or even all, of the events classified as acceptable calibration events would be preferred. However, our tests indicate that unless very accurate *a priori* knowledge of the event locations is available, this is not the case. The reason is that when an event is selected for calibration of PMEL, its location is held fixed until the final iteration, when it is allowed to move. Therefore the tendency is that the final location of the calibration event will be very close to its initial location. If the initial location is poor, then it will be restrained from moving toward its groundtruth location. Figure 7 shows the results when different initial locations are used as the seed in the PMEL process, using the Powder River cluster. If the initial locations are groundtruth, then in addition to achieving a much smaller total mislocation in every case, the total mislocation decreases as more events are added as calibration events. On the other hand, if the locations from SEL are used as the seed, the quality of the locations deteriorates as

the number of calibration events is increased. Therefore, in most cases it is probably not true that using more than one calibration event will gain an advantage over using a single event.

CONCLUSIONS AND RECOMMENDATIONS

We have shown that parameters describing the size, shape, and orientation of the error ellipse derived from standard single-event location techniques correlate with the degree of location error when a particular event is used for calibration of the PMEL method. We have used the 95% confidence error ellipse in our calculations, but the results are applicable for any confidence level and for any degree of freedom used (e.g., Jordan and Sverdrup, 1981) in the error calculation. By using a weighted combination of these parameters, it is possible to separate potentially poor calibration events from the remainder of the events in a cluster, but it is not possible to identify the absolute "best" event. The results depend on the diversity of the single-event error ellipses (which is reflected in the range of values of ϕ for a cluster), but in most of the test cases the method performs much better than random classification of the events as either poor or valid calibration events. The applicability of the method is also dependent upon the number of events in a cluster, since it relies on a sufficient number of data points from which to draw meaningful conclusions. The method will produce the best results if accurate estimates of the measurement and modeling uncertainty (*deltim*) for each phase are available.

The correlation between the PMEL location error and the single-event error ellipse statistic (ϕ) appears to be very nonlinear, which suggests that it is appropriate to separate the two event classes (poor or valid) using a cutoff value of ϕ. This selection criterion produces good results because the mean location error from PMEL appears to be quite stable at small values of ϕ but then increases dramatically once a threshold value is exceeded. The best threshold value found from most of the tests is $\phi_{crit} \sim 0.25$. The level of scatter, both for real and synthetic data, indicates between 10% and 40% of the events in a cluster may be misclassified using this criterion. However, it is significant that the majority of classification errors result from the rejection of valid calibration events. The cost of making such an error is much lower than using a calibration event that results in poor locations.

The best cutoff value for ϕ is stable across a wide range of test conditions, but is somewhat dependent on the particular station distribution and the phase data weights. It may be possible to calibrate the value of ϕ_{crit} for the seismicity in a particular region by performing synthetic experiments that replicate the typical distribution of stations prior to applying this method. The method outlined in this report should aid in producing the most accurate location estimates possible in a region that has not been calibrated.

REFERENCES

Douglas, A. (1967), Joint epicenter determination, *Nature,* 215: 47-48.

Erickson, J., A. Ortiz, M. Tinker, L. Owiesny, K. Hutchenson, and G. Kraft (2003), *Seismic location methods and capabilities*, AFTAC/TT Technical Report, Patrick Air Force Base, FL.

Fisk, M.D. (2002), Accurate locations of nuclear explosions at the Lop Nor test site using alignment of seismograms and IKONOS satellite imagery, *Bull. Seism. Soc. Am*., 92: 2911-2925.

Jordan, T.H., and K.A. Sverdrup (1981), Teleseismic location techniques and their application to earthquake clusters in the south-central Pacific, *Bull. Seism. Soc. Am*., 71: 1105-1130.

Menke, W., and D. Schaff (2004), Absolute earthquake locations with differential data, *Bull. Seism. Soc. Am*., 94: 2254-2264.

Michelini, A., and A. Lomax (2004), The effect of velocity structure errors on double-difference earthquake location, *Geophys. Res. Lett*. 31: L09602, doi:10.1029/2004GL019682.

Pavlis, G., and J. Booker (1983), Progressive multiple event location (PMEL), *Bull. Seism. Soc. Am*., 71: 1753-1777.

Waldhauser, F., and W.L. Ellsworth (2000), A double-difference earthquake location algorithm: Method and application to the northern Hayward fault, *Bull. Seism. Soc. Am*., 90: 1353-1368.

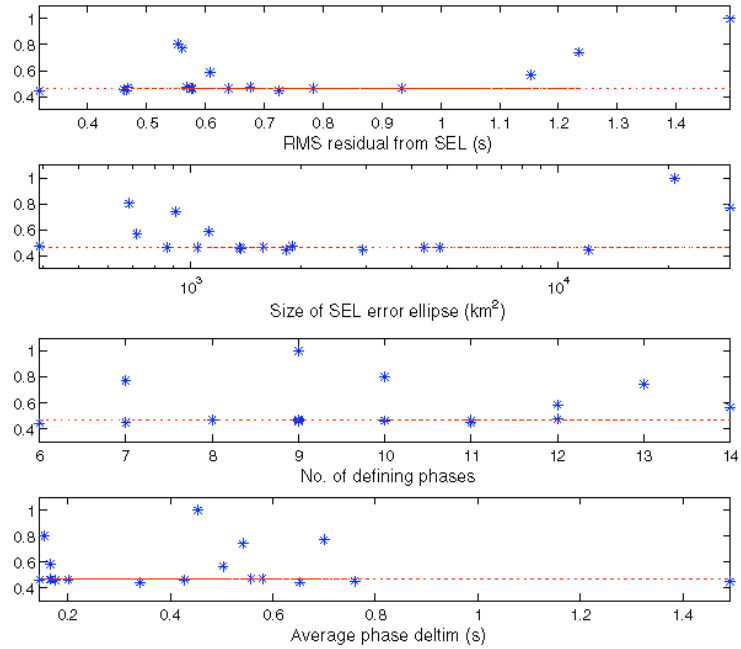

Figure 1. Mislocation normalized to cluster maximum plotted vs. SEL statistics for Lop Nor explosions. Each blue symbol represents one event, plotted at the mislocation value obtained when using that event as calibration for PMEL. The red line is the median mislocation for the cluster.

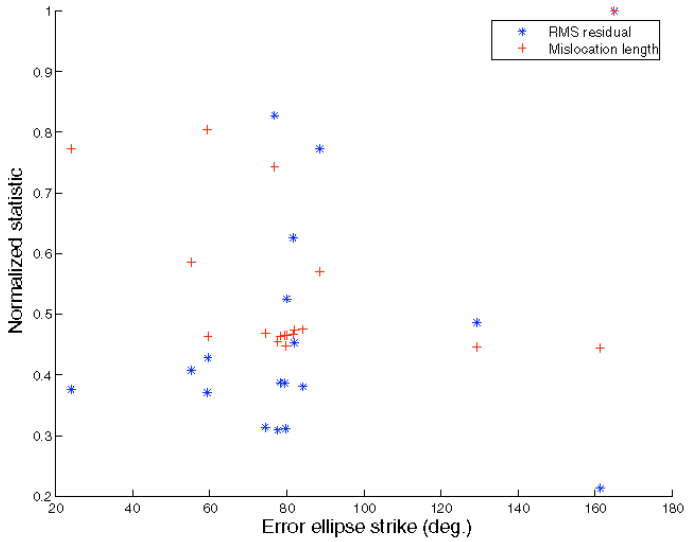

Figure 2. Normalized PMEL mislocation (red) and SEL RMS time residual (blue) for each event of the Lop Nor cluster plotted against the strike of the SEL error ellipse. The majority of events have an error ellipse strike near 80°.

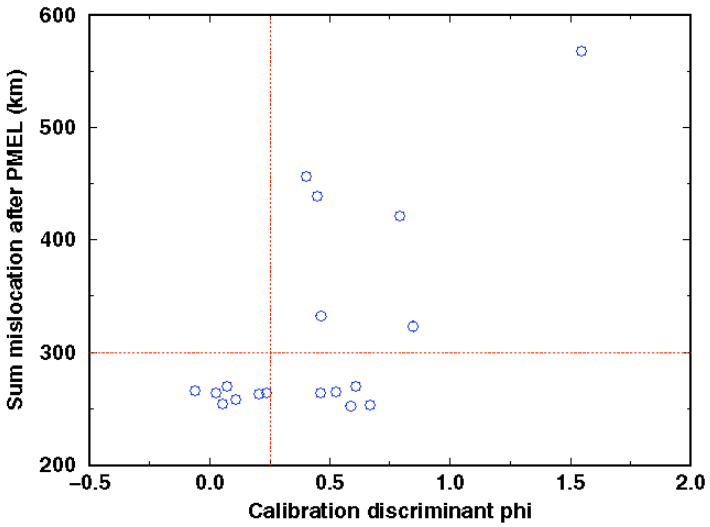

Figure 3. Relationship between the PMEL mislocation and the calibration discriminant function ϕ for the Lop Nor data. The horizontal line represents the *a posteriori* threshold applied to distinguish between good and poor calibration events, while the vertical line denotes $\phi_{crit} = 0.25$ (see text). Events that are correctly classified using these parameters lie in the lower-left and upper-right quadrants of the plot.

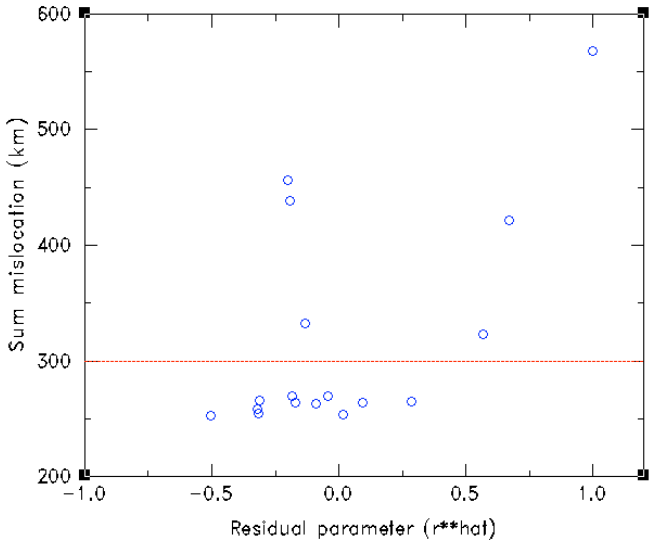

Figure 4. Relationship between the PMEL mislocation and the RMS residual parameter from equation (2) for the Lop Nor data. The correlation is lower than in Figure 3.

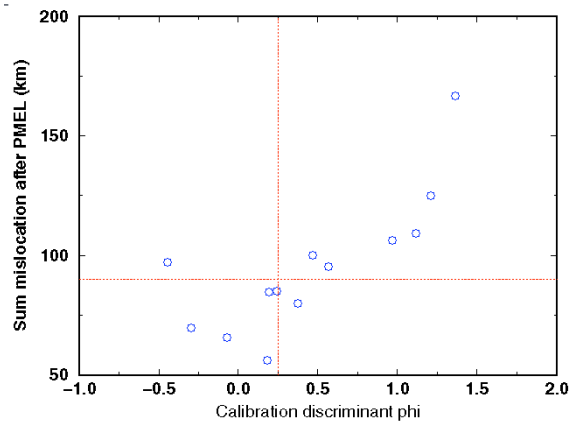

Figure 5. Same format as Figure 3 but showing results for the Powder River, WY, mining data.

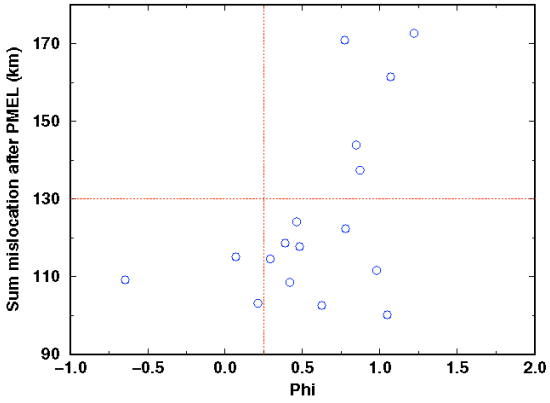

Figure 6. Same format as Figure 3 with results from the cluster at NTS. The discriminant values cluster in a narrow range of ϕ. The optimum ϕ_{crit} for this data is larger than 0.25.

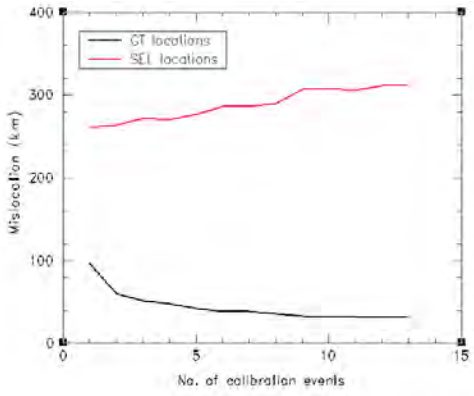

Figure 7. Results of applying different numbers of PMEL calibration events to the Wyoming mining blast data. The calibration events are applied in the order of increasing ϕ-value. The black curve was obtained using groundtruth as the initial seed locations and the red curve obtained using the individual SEL locations as seed. The total mislocation decreases as more calibrations are added if groundtruth is used but increases for the latter case.

GLOBAL GROUND TRUTH DATA SET WITH WAVEFORM AND IMPROVED ARRIVAL DATA

István Bondár[1], Ben Kohl[1], Eric Bergman[2], Keith McLaughlin[1], Hans Israelsson[1], Yu-Long Kung[1], Paul Piraino[1], and Bob Engdahl[3]

Science Applications International Corporation[1]
Global Seismological Services[2]
University of Colorado at Boulder[3]

Sponsored by Air Force Research Laboratory

Contract No. FA8718-04-C-0020

ABSTRACT

The main objective of the three-year research project is to produce a quality controlled global GT0-5 event set, accompanied with waveform and groomed arrival time data sets. Our efforts are directed toward developing and refining methodologies for generating new GT events through multiple event location analysis.

Multiple event location techniques, such as Hypocentroidal Decomposition (HDC) (Jordan and Sverdup, 1981; Engdahl et al., 2004), provide precise relative locations within an event cluster. However, the absolute locations could still be biased. In order to get accurate absolute locations, independent GT information is needed. We have developed a novel multiple-event location technique, Reciprocal Cluster Analysis (RCA), which combines local data with regional/teleseismic HDC results and uses local stations as GT0 constraints to obtain accurate absolute locations.

We have validated the HDC-RCA methodology using an event cluster of GT0 nuclear explosions and GT5 earthquakes which occurred within the Nevada Test Site (NTS). We demonstrated that the HDC-RCA method requires neither dense local networks, nor prior GT information. It relies on a few local stations, provided that the station centroid is inside the event cluster. We showed that absolute locations obtained from the HDC-RCA analysis are consistent with the true GT locations as RCA reduces the regional/teleseismic bias to less than 5 km. Monte Carlo simulations demonstrated that the RCA error ellipses are conservative estimates of the absolute location uncertainties. This allows us to identify GT5 events based on the semi-major axis of their error ellipses scaled to the 95% confidence level. Using this criterion, we identified 21 out of 24 GT events in the NTS cluster.

The size of the 95% confidence error ellipses is mainly driven by the reading errors. We utilize waveform cross-correlation to reduce reading errors, and possibly identify phases not reported in bulletins. Waveform correlation also offers a way to flag and correct phase identification errors. We follow a rigorous statistical approach by using the significance of the cross-correlation to assess the similarity of waveforms. Arrival times are automatically adjusted according to the optimal alignment derived from the waveform cross-correlation, thus resulting in accurate phase picks with reduced measurement errors.

We further demonstrate the potential of the HDC-RCA approach on selected event clusters (Chi-Chi, Taiwan; Afar triangle, Africa) and we are prepared to process candidate event clusters selected from an updated EHB (Engdahl et al., 1998) bulletin.

OBJECTIVE

The main objective of the research project is to produce new ground truth events of GT5 or better quality from an updated EHB (Engdahl et al., 1998) on a global scale. In order to achieve this goal we develop a novel method, the HDC-RCA analysis, which will allow us to identify new ground truth events without the reliance on dense local networks and prior GT information. To facilitate the HDC-RCA analysis, we develop a statistically robust waveform correlation technique to obtain a consistent set of refined arrival times with reduced measurement errors.

RESEARCH ACCOMPLISHED

During the first year of the project our primary focus was to develop, test and validate the methodologies we will use to generate new ground truth events using an updated EHB (Engdahl et al., 1998) bulletin. These include the Reciprocal Cluster Analysis (RCA), a novel multiple-event location method that combines local data with regional/ teleseismic HDC results and uses local stations as GT0 constraints to obtain accurate absolute locations, as well as a statistically solid waveform correlation technique to obtain a consistent set of refined arrivals with reduced measurement errors.

Reciprocal Cluster Analysis

Multiple-event location techniques provide precise relative locations within a cluster, but the absolute locations could still be biased due to unmodeled velocity heterogeneities in the Earth. In order to get absolute locations, modern multiple-event location techniques utilize independent GT information, such as existing reference events and InSAR data (e.g., Bondár et al., 2004; Engdahl et al., 2004), seafloor bathymetry (Pan et al., 2002), and active fault lines (Waldhauser and Richards, 2004), to estimate the mislocation vector between the true and apparent cluster centroid. Therefore, the availability of accurate independent GT information limits the applicability of multiple event location methods.

Reciprocal cluster analysis is a multiple-event location technique that combines local data with the regional/teleseismic HDC results to obtain accurate absolute event locations using the local stations as GT0 constraints. The HDC method, our choice for regional/teleseismic multiple-event location, is described in detail in Jordan and Sverdrup (1981) and Engdahl et al. (2004). While HDC uses stations in the distance range 3-90° to satisfy the underlying assumption of repeating ray paths, RCA utilizes stations from 0-150 km from the hypocentroid, thus introducing new information. In the RCA inversion we fix the *pattern* of relative hypocenters and origin times obtained from HDC, and locate the station centroid of the local stations, using the relative event locations as fictitious stations. The mislocation vector between the true and apparent station centroid represents the regional/teleseismic bias in the HDC relative locations. The entire cluster is then shifted so that the apparent and true station centroids coincide, thus yielding absolute event locations. Note that locating the station centroid is equivalent to locating the hypocentroid of the cluster using the local stations. The rationale behind exploiting the reciprocity principle is that typically there are many more events in a cluster than stations; therefore, locating the station centroid represents an overdetermined problem, better posed for the inversion. Moreover, local stations are generally poorly constrained by the events (they typically suffer from huge azimuthal gaps), thus solving directly for the station centroid yields a robust solution.

The cartoons in Figure 1 illustrate the HDC-RCA procedure. First we perform an HDC analysis using regional and teleseismic stations to obtain precise relative locations within an event cluster, then we select a subset of well-connected events and local stations. We require that a local station recorded at least four events and each event is recorded by at least three local stations. The connectivity constraints ensure that we can safely fix the pattern of both events and stations, an essential requirement in the RCA analysis. Applying the reciprocity principle implies that due to the uncertainties in the relative event locations we don't know where exactly our fictitious stations are. To account for this extra error term we propagate the relative event location uncertainties into the RCA error budget. Consequently, readings for events with large relative uncertainties are downweighted in the RCA inversion. The RCA inversion provides an uncertainty estimate on the centroid shift, which is propagated back to the relative uncertainties to obtain absolute location uncertainties. Finally, we shift the entire HDC cluster (including events that were not used in the RCA analysis) with the mislocation vector between the true and apparent station centroid to obtain accurate absolute event locations, and scale the absolute error ellipses to the 95% confidence level. Events with semi-major axis less than 5 km are then promoted to GT5 status.

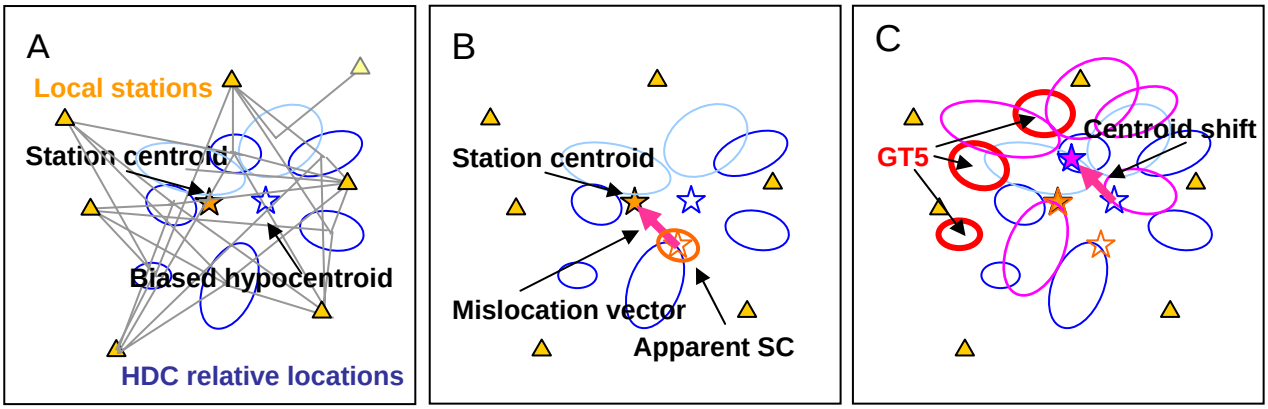

Figure 1. Illustration of the HDC-RCA analysis. A) Relative event locations and uncertainties obtained from the HDC analysis are shown in blue. Grey lines illustrate the connectivity of the cluster. Poorly connected events (light blue) and stations (light yellow) are not included in the RCA analysis. B) RCA inversion for the apparent station centroid. C) Centroid shift and GT identification.

Since RCA uses local stations to determine regional/teleseismic bias in the HDC locations, it is affected by local velocity heterogeneities. Synthetic tests showed that the local bias is bounded, as it requires 5-10% deviation from the iasp91 velocity model to build up more than 5 km bias at local distances. Using local velocity models further reduces the effect of local velocity heterogeneities.

We chose the Nevada Test Site (NTS) to validate the HDC-RCA analysis. NTS offers an ideal data set for testing and validating new algorithms as there is an abundance of GT events (both GT0 nuclear explosions and GT5 earthquakes), well-recorded at all distance ranges. Figure 2 shows our test data set selected from the SAIC ground truth database. It contains 24 GT events (10 GT0 nuclear explosions and 14 GT5 earthquakes) recorded by both local and regional/teleseismic stations. In this case we selected local stations within 50 km from the cluster centroid. Note that each event is recorded by only a subset of local stations, and while it appears a dense local network, it is also heavily unbalanced as with this local network none of the events satisfy the GT5 selection criteria of Bondár et al., (2004).

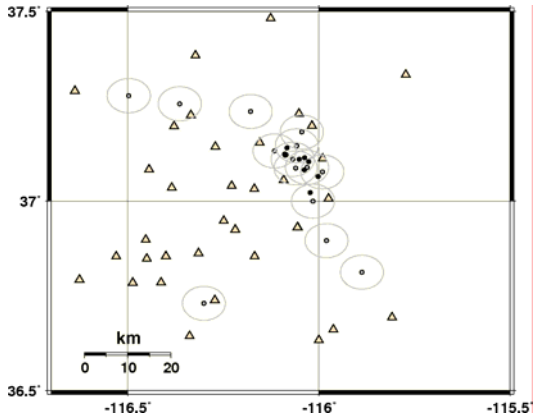

Figure 2. NTS test data set. GT0 nuclear explosions are shown as black dots, GT5 earthquakes are shown in grey, together with their 5 km uncertainty circle. Triangles indicate local stations within 50 km of the cluster centroid. Note that each event is located by a subset of local stations.

Instead of simply performing HDC on the raw data set, we first introduced an artificial bias using the Joint Hypocenter Determination (JHD, Dewey, 1972) by fixing the JHD master event to the wrong location. In this way we introduced artificial biases of 0.1° in the four cardinal directions. As a result, JHD not only perturbed the initial event locations for HDC, but more importantly, distorted the event patterns. HDC in each case removed the initial

bias, and produced nearly identical event patterns. However, the HDC hypocentroid still suffers from about 9.5 km bias. The application of RCA reduced this bias to 0.75 km. After the centroid shift, the mislocations of the GT0 events are all less than 5 km, and the absolute 95% confidence error ellipses overlap with the 5 km error circles of the GT5 earthquakes. Figure 3 shows the HDC-RCA analysis of the NTS cluster. While the locations from single-event locations using the same local network as with RCA are comparable to those obtained from the HDC-RCA analysis, the single-event location 95% confidence error ellipses are much larger, and thus none of the events could have been identified as GT5. On the other hand, with the HDC-RCA analysis we identified 21 out of 24 events as GT5. The remaining 3 events are contaminated by bad regional/teleseismic picks, resulting in large relative error ellipses.

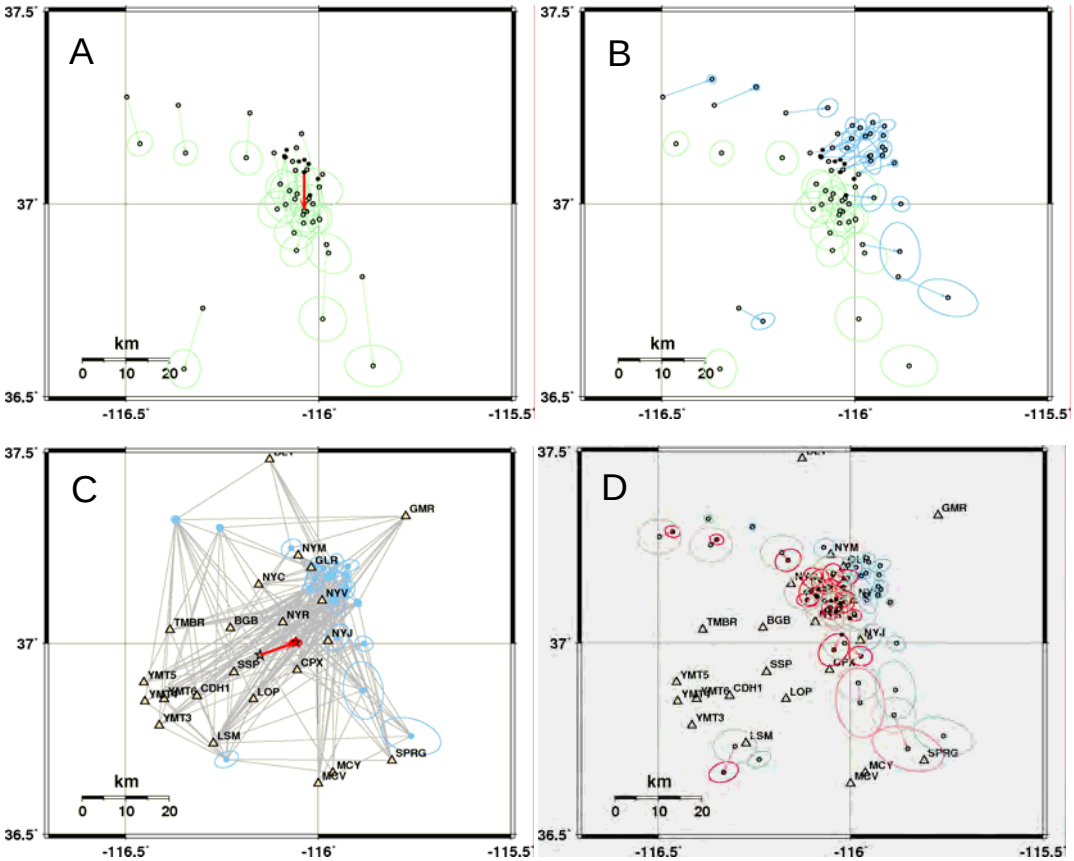

Figure 3. HDC-RCA analysis of the NTS test data set. GT0 nuclear explosions are shown as black dots, GT5 earthquakes are shown in grey. Triangles indicate local stations used in the RCA inversion. A) Initial locations (green) biased to the south by 0.1°. B) HDC relative event locations (blue). C) RCA inversion for the local station centroid. The red arrow indicates the mislocation between the true and apparent station centroid with which the entire cluster has to be shifted to obtain absolute locations. D) HDC-RCA absolute locations (red). The uncertainty in the centroid shift is propagated back to the relative uncertainties to obtain absolute location uncertainties. The absolute error ellipses are scaled to the 95% confidence level. Events with semi-major axes less than 5 km are promoted to GT5 status (bright red).

To validate the 95% confidence error ellipses obtained from the HDC-RCA analysis we performed Monte Carlo simulations using the NTS test data set. To test the sensitivity to errors in the event pattern we perturbed the relative event locations within their error ellipses and performed the RCA inversion. We also performed Monte Carlo simulations to test the effect of relative origin time and depth errors (assuming 0.2 s and 2 km depth errors, respectively). The results are shown in Figure 4. The blue error ellipse shows the uncertainty in the centroid shift scaled to the 95% confidence level, obtained from the RCA inversion using the unperturbed HDC results. The 95% error ellipse of the station centroid locations (red dots) from the Monte Carlo simulation is shown in red. The fact

that the RCA error ellipse encompasses the data cloud obtained from the Monte Carlo simulation indicates that the HDC-RCA error ellipses are conservative estimates of the absolute location uncertainties.

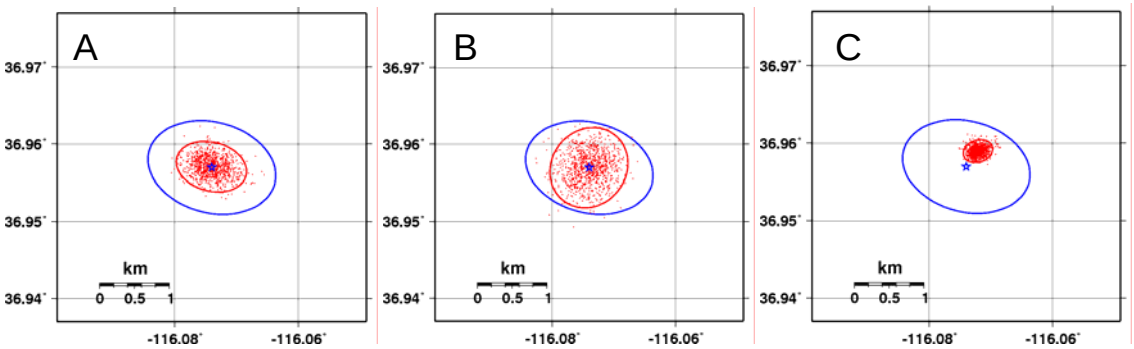

Figure 4. Monte Carlo validation of the RCA station centroid uncertainty estimate (blue). The 95% ellipses in red are derived from the data cloud (red) from the Monte Carlo simulation when A) the relative locations, B) origin times, C) depths were perturbed.

To test the robustness of results with respect to the number of local stations used in the RCA analysis we performed a bootstrap experiment on the NTS test data set. Figure 5 shows the mislocation vector between the true and apparent station centroid when only 1, 2, 3 and 4 stations are used to locate the local station centroid. Note that in the single-station case RCA degenerates to the single-event EvLoc location algorithm. The results show that once the number of local stations exceeds 3, RCA provides a robust estimate for the centroid shift. This implies that the application of RCA does not require dense local networks.

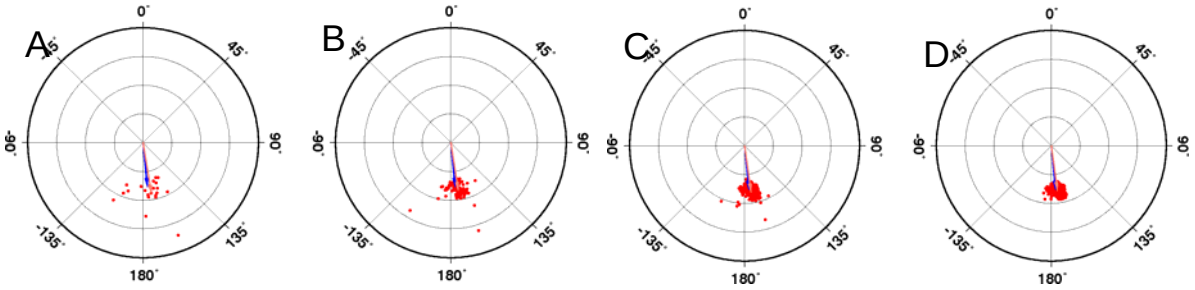

Figure 5. Station centroid mislocations (red) when only A) one, B) two, C) three, D) 4 stations are used in the RCA inversions. Concentric circles are drawn at every 10 km. The blue arrow indicates the station centroid mislocation vector when all stations were used.

We further illustrate the potential of the HDC-RCA analysis on two event clusters extracted from an updated EHB (Engdahl et al., 1998). The first example is the Chi-Chi, Taiwan aftershock sequence (Figure 6). In this cluster there are 11 events that satisfy the GT5 selection criteria of Bondár et al. (2004). We have identified 9 out of the existing 11 GT5 events, and produced 16 further GT5 events out of the 45 events used in the analysis. The HDC-RCA error ellipses overlap with the 5 km circles around the existing GT5 locations. The comparison with the Taiwan Central Weather Bureau locations shows that the HDC-RCA locations are also consistent with the local network solutions based on a local velocity model.

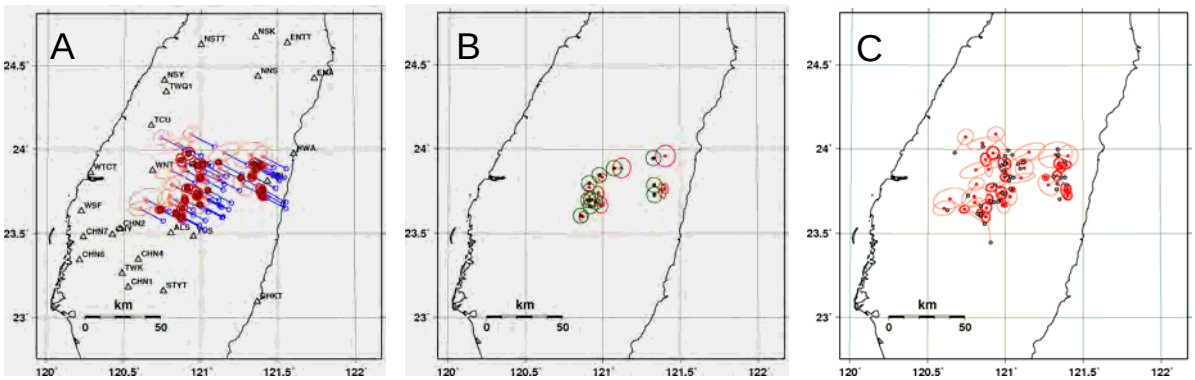

Figure 6. Chi-Chi aftershocks extracted from the EHB. A) HDC relative event locations (blue) and RCA absolute event locations (red). Events in bright red are identified as GT5. B) Comparison of prior GT5 events (green) with HDC-RCA locations (red). The HDC-RCA error ellipses overlap with the GT5 circles. C) Comparison of the Taiwan Central Weather Bureau local network locations (black) with the HDC-RCA locations (red).

Our second example is from the Afar triangle, Africa (Figure 7). In this case there is no prior GT information available. Nevertheless, with the HDC-RCA analysis we were able to identify 10 out of 18 events as GT5.

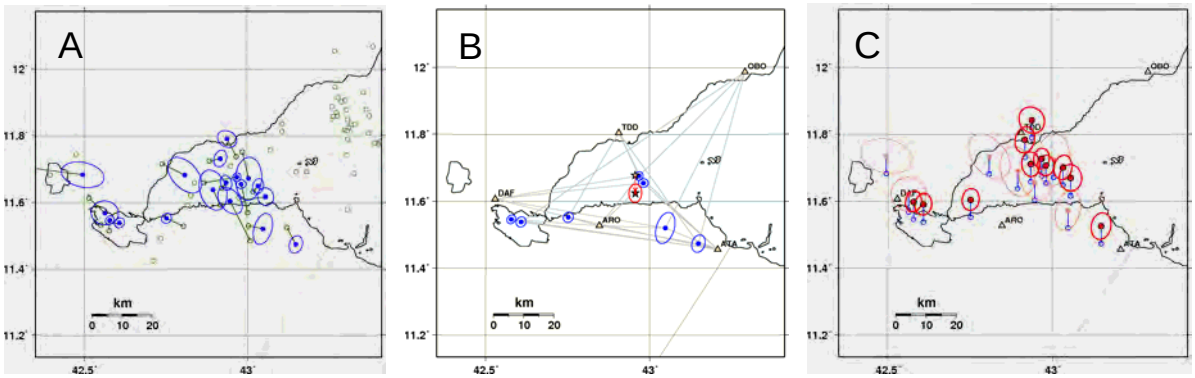

Figure 7. Djibouti cluster extracted from the EHB. a) HDC analysis. EHB locations are in green; HDC relative locations are in blue. b) RCA inversion. c) Centroid shift and GT5 (bright red) identification.

Waveform correlation

To obtain new GT5 events, the HDC-RCA methodology depends on the resulting semi-major axis of the 95% confidence ellipse being less than 5 km. The confidence ellipse is a combination of the uncertainty obtained for the station centroid in the RCA inversion and the relative location uncertainties obtained from the HDC analysis. The latter uncertainties are driven by measurement errors of regional and teleseismic phase arrivals. We employ waveform cross-correlation, which is now a proven technique for improving event locations at the local scale (Schaff et al., 2004, Shearer 1997, Thurber et al., 2003), to reduce the errors in regional and teleseismic arrival time measurements. These can in turn be fed back into the HDC-RCA analysis to obtain improved overall results.

To support the development of the methodology and to demonstrate the potential of waveform cross-correlation results to contribute to improved HDC-RCA analysis, we constructed a test dataset from events in the vicinity of the Nevada Test Site (NTS). We acquired waveform data from 595 events and 52 stations at regional and teleseismic distances with 2828 phase picks. Waveform data were acquired from the IRIS DMC and from the SMDC's archive of IMS stations and other arrays from the early 1990s through 2003 (Woodward et al., 2004).

One of the main issues we faced in this application was the very heterogeneous nature of the data set. It included broad-band three-component stations and short-period regional and teleseismic arrays with picks of regional P, teleseismic P and various secondary phases. To fully utilize these data we made three extensions to the cross-

correlation processing. We used correlation window lengths and filter bands that were phase and distance dependent. We performed the correlations on the individual channels of arrays and stations and performed a stack to obtain an array-based correlation trace. We made empirical measurement of the time-bandwidth product and used these measures to compute the statistical significance of the maximum of the correlation trace.

This last approach allowed us to replace the heuristic approach of using only those correlation results with a maximum above a given correlation threshold, typically 0.6 or 0.7. Consider that when cross-correlating noise or independent signals, Fisher's z-transform, defined as $z=\text{atanh}(r)$, has an asymptotic normal distribution with zero mean and variance, $\sigma^2=1/(N-3)$, where r is the correlation. N is the number of independent degrees of freedom which, in turn, depends on the time-bandwidth product (TB) and number of channels in the correlation stack, $N=2TB * N_{chan}$. The maximum of the correlation then follows an extreme value distribution and we compute the significance of the measured maximum from the cumulative of the extreme value distribution:

$$S = \left[\left(1+\text{erf}\left(\max(z)/\sqrt{2}\sigma_{eff}\right)\right)/2\right]^{2T_{window}\left(f_{high}-f_{low}\right)}. \qquad (1)$$

Our implementation involved using a time-domain convolution to compute the cross-correlation of the signals. We used a target window that was as much as 30 seconds longer than the template window in order to obtain cross-correlations of the template signal with uncorrelated pre-signal noise and uncorrelated coda + noise. We measured the variance of the distributions of the additional correlations to obtain an effective variance (σ^2_{eff}) used in the significance calculation. Further, we compared the variances before and after stacking the array elements to compute an effective number of channels (N_{eff}), which in turn allowed us to determine an effective time-bandwidth (TB_{eff}) product from $\sigma^2_{eff}=1/(2TB_{eff} * N_{eff}-3)$.

Figure 8 illustrates the strength of the significance test for a case where a seemingly low correlation (0.15) was found to be highly significant (0.995). These cases occur when low-SNR, long duration broadband signals (large TB_{eff}) and the full utility of an array (high N_{eff}) can be realized. Differential times were obtained from the cross-correlations by picking the lag of the maximum of the correlation with significance > 0.98. For reference, when using single channel correlations ($N_{chan}=1$), a 1 second window ($T=1$), filtered 1-10 Hz ($B=1$), a correlation threshold of 0.65 is equivalent to a significance threshold of 0.98. We inverted the measured differential times into refined absolute arrival times by using the expectation maximization algorithm to iteratively minimize the function

$$L(T;\tau) = \sum_{j=1,N}\sum_{i=1,N}\left|\tau_{ij}-\left(T_i-T_j\right)\right|^p w_{ij}\,, \qquad (2)$$

where τ_{ij} are the measured differential times and T_i are the absolute times. We used the normalized, z-transformed maximum correlations to weight the differential time measurements, $w_{ij} = \max(z_{ij})^2 / \sigma^2_{eff}$.

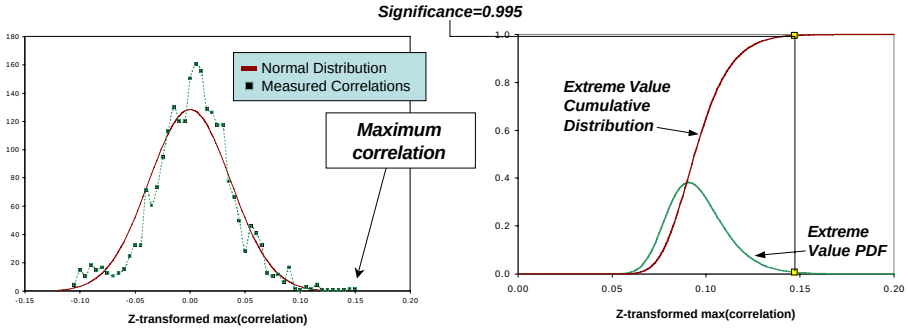

Figure 8. Example of the significance computation for a case where the maximum correlation (0.15) falls below the threshold typically used for screening correlation measurements. The significance is a measure of how much the maximum of the measured correlations (left panel, green squares) deviates from the expected maximum value (right panel, green line).

We cross-correlated all available data for the 595 events in the vicinity of NTS yielding more 400,000 correlations and differential times. After applying a significance threshold of 0.98 and inverting the differential times we obtained refined arrival times for 61% (1729 of 2828) of the arrivals. Figure 9 shows examples where the refined arrival times corrected mispicks in some cases of over 2 seconds. We found that 567 of the 595 events (95%) had at

least one arrival that was refined through our process. Of note is the fact that only about 30% of the arrivals would have been refined if we had used a threshold of 0.7 to screen out poor correlations. We plan to use the refined arrival times in the HDC analysis and evaluate the degree to which the HDC relative locations are improved by using improved arrivals.

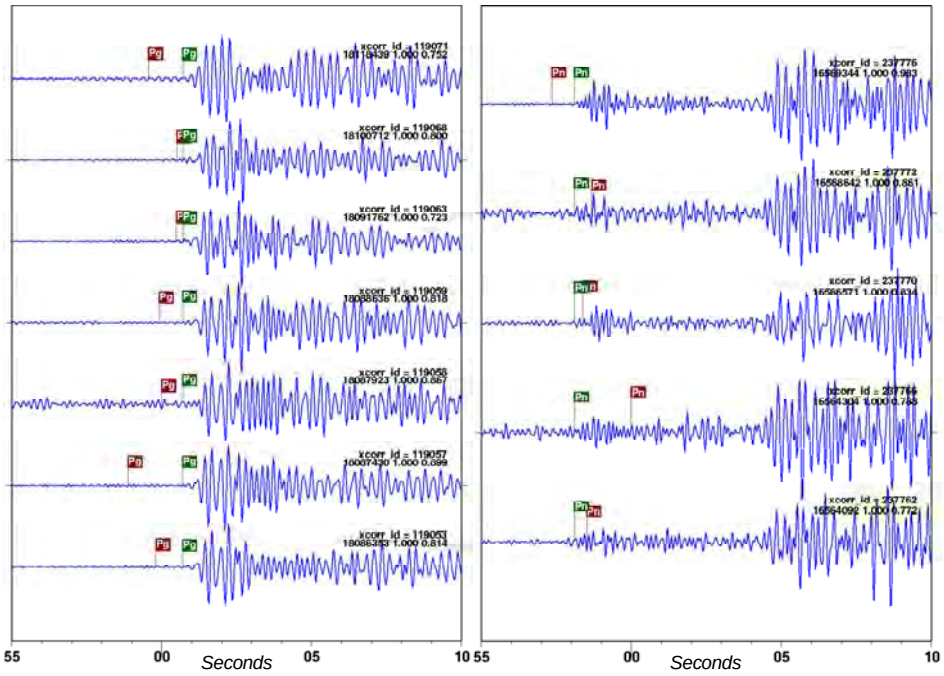

Figure 9. Arrivals and waveforms for selected phases that were refined (green flags) through the use of waveform cross-correlation. This example shows how mispicks (red flags) as large as 2 seconds were identified and corrected.

CONCLUSIONS AND RECOMMENDATIONS

We have developed a novel multiple event location technique that exploits local data to determine the regional/teleseismic bias in the HDC relative event locations. The basic idea is to fix the relative event location pattern obtained from HDC and locate the station centroid of local stations by invoking the reciprocity principle. The mislocation vector between the apparent and true (a GT0 constraint) station centroid is a robust estimate of the regional/teleseismic bias with which the entire event cluster is shifted to obtain accurate absolute locations. We have validated the method using the NTS cluster. We have demonstrated that the HDC-RCA analysis reduces the regional/teleseismic bias to less than 5 km, and that the absolute event locations are consistent with the true GT locations. We have shown that the HDC-RCA 95% confidence error ellipses are conservative estimates of the absolute location uncertainties, which allows us to promote events to GT5 status based on the semi-major axes of their 95% confidence error ellipses. The HDC-RCA analysis requires neither dense local networks nor independent GT information to produce GT5 (or better) events. Only a few stations are necessary, provided that the station centroid is inside the event cluster and has sufficient ray coverage.

We are in the process of developing applicability criteria similar to those of Bondár et al., (2004), which would guarantee that the HDC-RCA analysis produces GT5 events from a cluster. We have already identified a set of candidate metrics:

- The secondary azimuthal gap on the local station centroid defined by the events is less than a threshold;
- The local station centroid satisfies the GT5 selection criteria of Bondár et al., (2004);
- The azimuthal gap of event-station pairs, when collapsed to the origin, is less than a threshold (metrics on ray coverage)

We will perform further Monte Carlo and bootstrap experiments to refine and validate the above criteria.

We will use an updated EHB (Engdahl et al., 1998) bulletin to form event clusters for the HDC-RCA analysis. Figure 10 shows the locations of potential HDC-RCA clusters, where there are at least 5 shallow events recorded by at least 10 stations at the HDC (3-90°), and by at least 4 stations in the RCA (0-150 km) distance range.

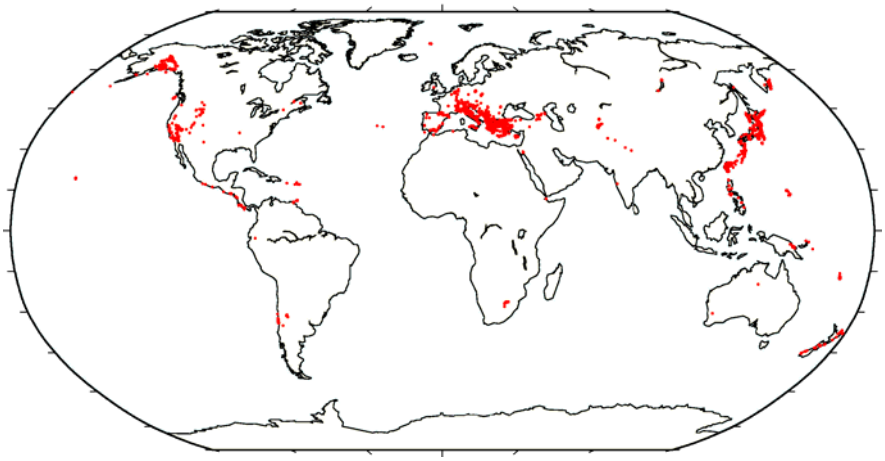

Figure 10. 1546 potential HDC-RCA clusters identified in an updated EHB bulletin.

We have developed a robust statistical framework for the waveform correlation technique, which takes advantage of arrays by stacking the correlation traces at the array elements, and more importantly, uses the significance of the maximum correlation, instead of an arbitrary threshold on the correlation coefficient, to establish a measure of similarity between waveforms. Using a significance threshold of 0.98 allows us to refine the absolute arrival times of twice as many picks as with a correlation threshold of 0.7. We will incorporate the improved waveform correlation technique in the HDC-RCA analysis.

ACKNOWLEDGEMENTS

We thank the Taiwan Central Weather Bureau for providing the local network locations of the Chi-Chi aftershock sequence.

REFERENCES

Bondár, I., S.C. Myers, E.R. Engdahl, and E.A. Bergman (2004). Epicentre accuracy based on seismic network criteria, *Geophys. J. Int.* 156: 1-14, doi: 10.1046/j.1365-246X.2004.02070.x.

Bondár, I., E.R. Engdahl, X. Yang, H.A.A. Ghalib, A. Hofstetter, V. Kirichenko, R. Wagner, I. Gupta, G. Ekström, E. Bergman, H. Israelsson, and K. McLaughlin (2004). Collection of a reference event set for regional and teleseismic location calibration, *Bull. Seism. Soc. Am.* 94: 1528-1545.

Dewey, J.W. (1972). Seismicity and tectonics of Western Venezuela, *Bull. Seism. Soc. Am.* 62: 1711-1751.

Engdahl, E.R., E.A. Bergman, S.C. Myers, and F. Ryall (2004). Improved ground truth in Southern Asia using in-country data, analyst waveform review and advanced algorithms, *Proc. 26th Seismic Research Review: Trends in Nuclear Explosion Monitoring*, LA-UR-04-5801, Orlando, FL, Sept. 21-23, 2004, Vol. 1, 257-266.

Engdahl, E.R., R.D. van der Hilst, and R.P. Buland (1998). Global teleseismic earthquake relocation with improved travel times and procedures for depth determination, *Bull. Seism. Soc. Am.* 88:722-743.

Jordan, T.H. and K.A. Sverdrup (1981). Teleseismic location techniques and their application to earthquake clusters in the south-central Pacific, *Bull. Seism. Soc. Am.* 71:1105-1130.

Pan, J., M. Antolik, and A.M. Dziewonski (2002). Locations of mid-oceanic earthquakes constrained by seafloor bathymetry, *J. Geophys. Res*. 107:B11, 2310, EPM 8 1-13, doi: 10.1029/2001JB001588.

Schaff, D.P., G. H. R. Bokelmann, W. L. Ellsworth, E. Zanzerkia, F. Waldhauser and G. C. Beroza (2004). Optimizing correlation techniques for improved earthquake location, *Bull. Seism. Soc. Am.* 94:705-721.

Shearer, P. M. (1997). Improving local earthquake locations using the L1 norm and waveform cross correlation: Appli-cation to the Whittier Narrows, California, aftershock sequence, *J. Geophys. Res.* 102: 8269-8283.

Thurber, C. H., W-X Du, H. Zhang and W.J. Lutter (2003). Methods for improving seismic event location processing, *Proc. 25th Seismic Research Review Review - Nuclear Explosion Monitoring: Building the Knowledge Base,* LA-UR-03-6029, Vol. 1, 342-351.

Waldhauser, F. and P.G. Richards (2004). Reference events for regional seismic phases at IMS stations in China, *Bull. Seism. Soc. Am.* 94: 2265-2279.

Woodward, R., M. Bahavar and R. North (2004). Data resources to support nuclear explosion monitoring research, *Proc. 26th Seismic Research Review: Trends in Nuclear Explosion Monitoring,* LA-UR-04-5801,Orlando, FL, Sep. 21-23, 2004, Vol. 2, 790-799.

IMPROVED EVENT LOCATION UNCERTAINTY ESTIMATES

István Bondár, Keith McLaughlin, and Hans Israelsson

Science Applications International Corporation

Sponsored by Air Force Research Laboratory

Contract No. FA8718-05-C-0018

ABSTRACT

While many studies aimed to reduce location bias by introducing improved travel-time corrections, little effort was devoted to the complete estimation of location uncertainties, despite the fact that formal error ellipses are often overly optimistic. Since most location algorithms assume that the observations are independent, correlated systematic errors due to similar ray paths inevitably result in underestimated location uncertainties. Furthermore, the tails of real seismic data distributions are heavier than Gaussian. The main objectives of this project are to develop, test and validate methodologies to estimate location uncertainties in the presence of correlated, systematic and non-Gaussian errors. Particular attention will be paid to robust and transportable models of a travel-time covariance matrix.

The characterization of the full covariance matrix will separate and estimate non-Gaussian, heavy-tailed distributions of measurement and model errors and take into account the correlation due to systematic errors. We will characterize measurement errors as a function of signal parameters, such as phase, distance and amplitude. To achieve this goal we will perform fully controlled experiments by using known signals, scaled down to several magnitude levels and embedded in clean noise (Kohl et al., 2004). We will estimate the correlation structure in the data using various variogram models. To estimate non-linear dependence structures in the data that are not captured by the full covariance matrix, we will apply the theory of copulas, a quickly growing field of statistics to describe tail dependence. Based on the copula theory we will develop a hypothesis test, independent of formal uncertainties, to assess the reliability of the error ellipses obtained from the classical approach using the full covariance matrix.

During the first year of the project preliminary methodologies will be developed, tested and demonstrated on a limited set of event clusters. For validation purposes we use event clusters with GT0-2 events. Our primary choice is therefore the Nevada Test Site (NTS) where an abundance of GT0 nuclear explosions, well-recorded in all distance ranges, is available. The NTS cluster allows us to simulate sparse, unbalanced networks by using subsets of stations. We will also use the Lop Nor, China nuclear explosions (well-recorded teleseismically but with sparse regional networks) and the Lubin, Poland mining explosions (recorded by dense but unbalanced regional networks) to demonstrate the applicability of our methodologies.

OBJECTIVES

The objectives of this project are to develop methodologies to estimate location uncertainties in the presence of correlated, systematic model errors; to characterize measurement errors as a function of signal parameters such as phase and signal-to-noise ratio; and to describe the total error budget in the case of non-linear, non-Gaussian dependence structure. The improved understanding of the complete error budget will be applied to non-linear location estimators to make location programs more robust in the presence of correlated errors and outliers. The resulting error budgets will lead to more robust estimates of location uncertainty. A hypothesis test (independent of formal uncertainty estimates) will be developed to assess the reliability of location uncertainty estimates.

RESEARCH ACCOMPLISHED

The assumption of independent error processes prevails in most modern location algorithms, despite the fact that the problem arising from inadequate representation of systematic bias has been known to seismologists since the advent of modern instrumental seismology. A classic example is the Longshot nuclear explosion (29 October 1965, Amchitka). Herrin and Taggart (1968) showed that a large number of arrivals traveling along similar ray paths through an unmodeled oceanic subducting slab introduced location bias. If unrecognized, correlated systematic errors result in unrealistic error ellipses with degraded coverage (true locations do not lie within the ellipses) and introduce location bias. To further illustrate our motivation to consider the correlation structure in the data, we performed a constrained bootstrapping (Yang et al., 2004) experiment on the 7 October 1994 Lop Nor, China nuclear explosion. The explosion is considered GT1 (Fisk, 2002) and recorded by some 600 stations at teleseismic distances. As Figure 1a indicates, the station distribution is far from azimuthally uniform; and is dominated by the networks in California, Japan and Europe. Figure 1b shows the trajectory of the mislocation vector with increasing number of stations. As more and more stations contribute to the solution the location is driven away from the GT1 location. Since the location algorithm does not account for correlated travel-times along similar ray paths, the relative importance of the Californian and European stations steadily increases, resulting in ever more increasing location bias. As the information carried by the network geometry is exhausted relatively early, adding more stations merely increases data redundancy and increases bias. Furthermore, as shown in Figure 1c, the area of the 90% coverage ellipse monotonically decreases with increasing number of stations. This is because the off-diagonal elements of the covariance matrix are ignored assuming independent errors. Hence, it is guaranteed that the error ellipse will not cover the true location once a sufficiently large number of correlated systematic errors contribute to the solution.

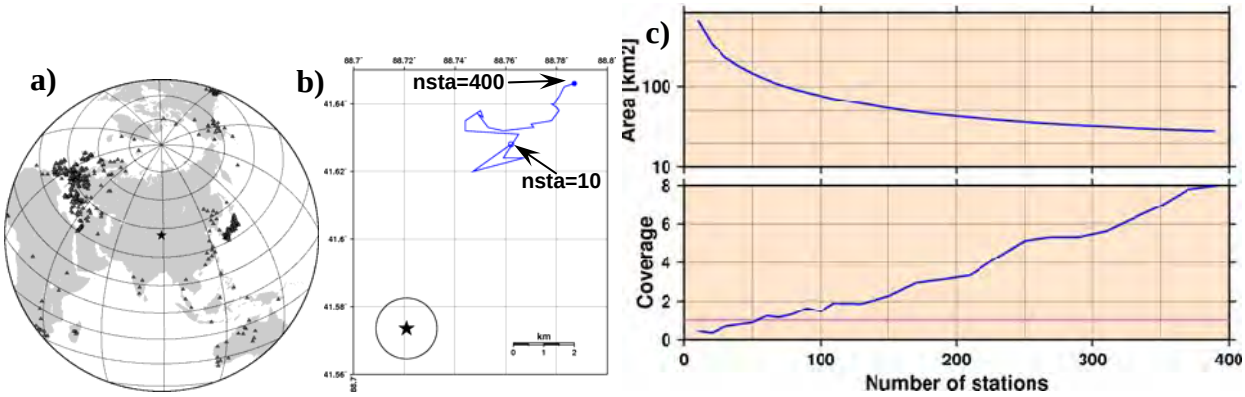

Figure 1. a) Teleseismic station distribution for the 7 October 1994 Lop Nor, China nuclear explosion. b) Trajectory of location bias from 10-station subnetworks (open circle) to 400-station subnetworks (full circle). The star denotes the GT1 location of the nuclear explosion. c) Area of error ellipse (top) and actual ellipse coverage (bottom) with respect the number of stations. If the coverage parameter is larger than one, the true location falls outside the error ellipse.

In this project we focus on the treatment of correlated errors, with non-Gaussian, non-zero-mean, heavy-tailed skewed distributions of reading errors. We will employ variogram analysis of observed residuals to estimate the correlation structure in the data. We will estimate the full covariance matrix by fitting variogram models to empirical station-station variograms using fixed ground truth events and event clusters, as well as event-event variograms for fixed stations. Note that estimating the correlation structure through variogram analysis is essentially

the same process that is used to construct empirical travel-time correction surfaces by kriging (Schultz and Myers, 1998; Myers and Schultz, 2000; Rodi, 2003). We will retain the information derived for the correlation structure offered by the variogram analysis to construct a full covariance matrix.

Chang et al (1983) have shown that incorporating the full covariance matrix in the location algorithm is straightforward. The correlation structure implies that linear combinations of station residuals may exist. This can be taken into account by diagonalizing the covariance matrix, thus reducing the dimensionality of the problem. The estimated location error ellipses then necessarily become larger, reflecting the reduction in the equivalent number of uncorrelated observations. We apply a methodology developed by McLaughlin et al. (1988) that transforms the empirical correlation matrix, derived from variogram analysis, so that it becomes positive definite, with positive eigenvalues and unit diagonal elements.

Data sets

To validate the methodologies developed during the course of the project we will rely on high quality, GT0-2 event clusters. Our primary choice is the Nevada Test Site (NTS) data set (Figure 2), which contains a large number of GT0 events, well recorded in all distance ranges. The NTS data set will allow us to perform Monte Carlo and bootstrap experiments using subsets of events and stations to investigate the effect of systematic errors due to unbalanced networks.

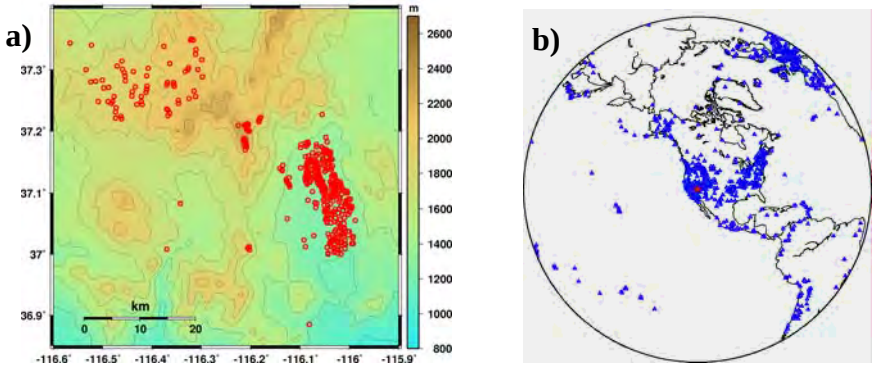

Figure 2. Nevada Test Site (NTS) data set. a) 401 GT0 underground nuclear explosions at Pahute Mesa and Yucca Flat. b) Station distribution in the 0-90° distance range.

The second data set we identified is the GT1-2 underground nuclear explosions at the Lop Nor Test Site (Figure 3). These events are well-recorded at teleseismic distances, but by only a sparse regional network.

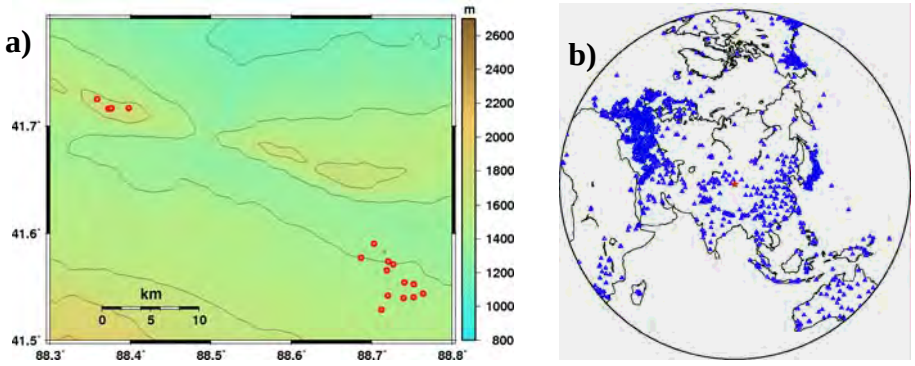

Figure 3. Lop Nor Test Site data set. a) 17 GT1-2 underground nuclear explosions. b) Station distribution in the 0-90° distance range.

Our third data set constitutes the Lubin, Poland GT1-2 mine events (Figure 4). These are recorded by a sparse teleseismic network, and with a dense, but heavily unbalanced, regional network.

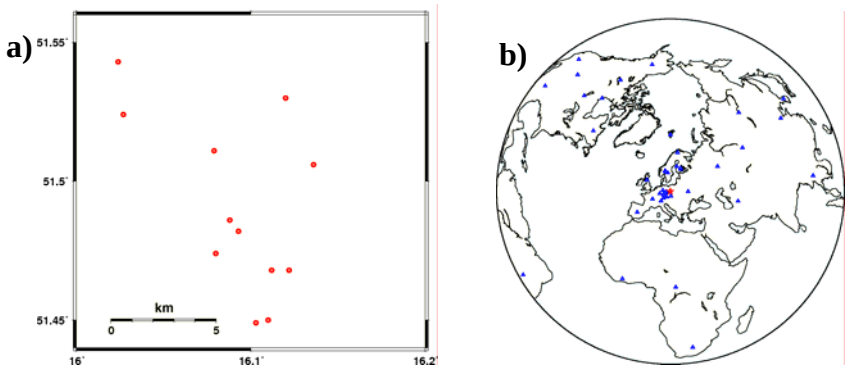

Figure 4. Lubin, Poland data set. a) 12 GT1-2 mine events. b) Station distribution in the 0-90° distance range.

Preliminary analysis of measurement errors

Errors of arrival times are usually assumed to be Gaussian in seismic event location algorithms. It has long been realized, however, that distributions of picking errors are skewed; for example, errors in arrival times of weak signals, picked by both seismic analysts and automatic algorithms, are frequently biased late (Buland, 1986). With improved travel time models being developed, accurate descriptions of picking error distributions and their dependence on signal characteristics, such as SNR and dominant frequency, become more important for location error estimates. Douglas et al. (2005) emphasize the effect of SNR on measurement errors.

The lack of "true" onset times makes the estimation of the error distribution difficult. Consistency of independent readings of seismic analysts is sometimes used as a baseline or “true” onset. However, such "true" onset times based on analyst consistency cannot escape the element of subjectivity in manual readings. Moreover, standard errors of manual picks of about 0.2 s for impulsive phases have been reported (Leonard, 2000). In this project we will use seismic events with ground truth (GT0-2) locations and origin times as well as controlled experiments as a basis for estimating statistical characteristics of picking errors.

An example of using ground truth information is shown by the box plot in Figure 5, which shows the errors in Pn arrival time picks at the station PRI (Priest, CA) from GT0 underground nuclear explosions at the Yucca Flat, Nevada Test Site. The bias in the picking errors gradually increases with decreasing magnitudes and becomes 1s or larger below mb=4.5. Notice also the increased scatter in the errors as the magnitudes become smaller, which indicates the increasing uncertainty in analyst picks as clean onsets fade away with decreasing signal-to-noise ratio.

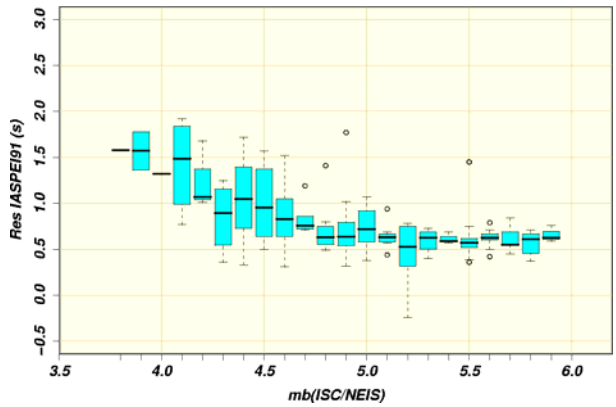

Figure 5. Picking errors of Pn arrival times at the station PRI from GT0 underground nuclear explosions at Yucca Flat, Nevada Test Site as a function of magnitude. Residuals are calculated relative to the IASPEI91 predictions from the known origin times.

Unfortunately, GT0 event clusters are not always at our disposal to investigate the effect of decreasing SNR on arrival time picks. To overcome this problem, we follow the methodology of Kohl et al (2004, 2005) which uses

known signals scaled to various magnitude levels and embedded in clean background noise. Since we know exactly where the embedded signals are and that they are not contaminated by other signals (hence the notion of clean noise), the procedure allows us to design controlled experiments.

An example of using signals embedded at known times in clean background noise for estimating picking error characteristics is given in Figure 6. The example shows picking errors of an automatic algorithm (DFX) for P signals at FINES from large underground nuclear explosions at the Lop Nor Test Site, scaled down to varying sizes and embedded in clean noise. Figure 6a shows how the bias or lateness of the picks sets in for SNR around 6-7 and continues to increase with decreasing SNR, much like the effect illustrated in Figure 5. The QQ plot (quantiles of observed picking errors plotted against Gaussian quantiles) in Figure 6b indicates that picking errors of signals at various SNR ranges exhibit varying means and variances (Rodi, 2004) and deviate from the normal distribution even at high SNR levels.

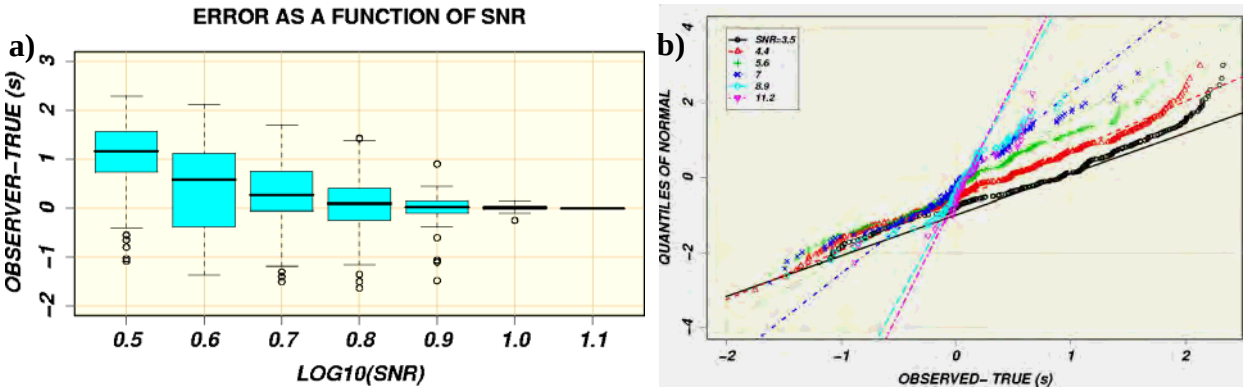

Figure 6. Picking errors of an automatic algorithm obtained for signals, scaled down to various amplitudes and embedded in clean background noise, at the FINES array. a) Reading errors become biased as SNR decreases. b) Reading errors at various SNR levels. If the errors were Gaussian, the observed picking errors (symbols) would align with the normal quantiles (lines).

We will use the methodology outlined above to obtain improved models of observational errors with respect to phase and to account for the effect of signal-to-noise ratio on the residuals when constructing the full covariance matrix.

Non-linear dependence structure

Estimating the full covariance matrix will allow us to account for correlated systematic errors in regions where the bias is unknown (uncalibrated). However, the linear Gaussian approach has its limitations. The full covariance matrix approach implies that the observations are described by a multivariate Gaussian distribution, which can only account for linear correlation structures. Non-linear dependence structures may exist in the data that are not captured by the correlation matrix. Every location algorithm, either linearized or non-linear, minimizes a misfit function, which is typically expressed as the sum of powers of weighted residuals. The inherent assumption is that the likelihood function can be written as the product of individual probability density functions of the observations – that is, the observations are independent. If the observations are dependent, the joint distribution is no longer the mere product of the marginal distributions; and the negative logarithm of the likelihood function can no longer be written as the simple sum of powers of weighted residuals.

Constructing the likelihood (i.e. the joint probability density) function in the general case often proves to be very difficult, and this is exactly why location algorithms make the somewhat unsupported assumption of independent error processes. Sklar's theorem (1959) offers a way to construct the joint distribution function of continuous multivariate random variables. The theorem states that if H is an n-dimensional joint distribution function with marginal cumulative distributions $F_1,\ldots,F_n$, then there exists a unique copula function C such that $H(x_1,\ldots,x_n) = C(F_1(x_1),\ldots,F_n(x_n))$, where $u_i = F_i(x_i)$ denotes the probability integral transformations of x_i. Thus, the copula is the joint cumulative distribution function of the order statistics of the univariate marginal distributions.

The converse of Sklar's theorem is also true, and it implies that we can link together univariate distributions of any type with any copula in order to get a valid multivariate distribution. If F_i^{-1} denotes the inverse of the marginal distribution functions, then there exists a unique copula such that $C(u_1,\ldots,u_n) = H(F_1^{-1}(u_1),\ldots,F_n^{-1}(u_n))$. The separation of the dependence structure from the marginals is apparent in the form of the likelihood function:

$L(x_1,\ldots,x_n;p) = c(F_1(x_1),\ldots,F_n(x_n);\vartheta)\prod_i f_i(x_i;p)$, where $c(u_1,\ldots,u_n;\vartheta) = \dfrac{\partial^n C(u_1,\ldots,u_n;\vartheta)}{\partial u_1\ldots\partial u_n}$ denotes the copula density function; p and ϑ stand for the model and copula parameters, respectively. Hence, a copula is a function that joins or 'couples' a multivariate distribution function to its one-dimensional marginal distribution functions. For a detailed discussion of copulas see Joe, (1997) and Nelsen (1999). The basic idea behind the copula formalism is to separate dependence and marginal behavior between elements of multivariate random vectors.

Using Sklar's theorem, one can construct multivariate distributions with arbitrary margins. For simplicity, we consider bivariate distributions. A great many examples of copulas can be found in the literature and most of the copulas are members of families with one or more real parameters. When the joint multivariate distribution is Gaussian with a covariance matrix Σ, the likelihood function can be written as

$$L(x_1,\ldots,x_n;p) = \frac{1}{(2\pi)^{n/2}\sqrt{\det\Sigma}}\, e^{-\frac{1}{2}(\mathbf{x}-\mu)^T\Sigma^{-1}(\mathbf{x}-\mu)} = c^G(\Phi_1(x_1),\ldots,\Phi_n(x_n);\Sigma)\prod_i f_i(x_i;p)$$

Hence, the copula formalism offers a way to develop a hypothesis test: if the best fitting copula to the data is the Gaussian copula, then the full covariance matrix adequately describes the dependence structure and provides a reliable estimate for the location uncertainty.

Variogram models with copulas

To illustrate the power of the copula approach, we apply the copula formalism to derive variograms for the NTS data set. Copulas of the form $C(u,v) = \varphi^{-1}(\varphi(u)+\varphi(v))$ are called Archimedean copulas, where φ is a convex, decreasing function with domain (0,1] and range [0,∞) such that $\varphi(1) = 0$. The function φ is called the generator function, which uniquely determines an Archimedean copula. Table 1 lists the most frequently used one-parameter Archimedean copulas. For a more complete set of Archimedean copulas see Nelsen (1999).

Table 1. One-parameter Archimedean copulas

Copula	$C(u,v)$	$\varphi(t)$	α	Limits	Kendall's τ
Clayton	$\max\left(\left[u^{-\alpha}+v^{-\alpha}-1\right]^{-1/\alpha},0\right)$	$\dfrac{(t^{-\alpha}-1)}{\alpha}$	$(0,\infty)$	$C_0=\Pi$ $C_\infty=M$	$\dfrac{\alpha}{\alpha+2}$
Ali-Mikhai-Haq	$\dfrac{uv}{1-\alpha(1-u)(1-v)}$	$\ln\dfrac{1-\alpha(1-t)}{t}$	$[-1,1)$	$C_0=\Pi$	$\dfrac{3\alpha-2}{3\alpha}-\dfrac{2(1-\alpha)^2}{3\alpha^2}\ln(1-\alpha)$
Gumbel	$\exp\left(-\left[(-\ln u)^\alpha+(-\ln v)^\alpha\right]^{1/\alpha}\right)$	$(-\ln t)^\alpha$	$[1,\infty)$	$C_1=\Pi$ $C_\infty=M$	$1-\dfrac{1}{\alpha}$
Frank	$-\dfrac{1}{\alpha}\ln\left(1+\dfrac{(e^{-\alpha u}-1)(e^{-\alpha u}-1)}{e^{\alpha}-1}\right)$	$-\ln\dfrac{e^{-\alpha t}-1}{e^{-\alpha}-1}$	$(-\infty,\infty)\setminus\{0\}$	$C_{-\infty}=W$ $C_0=\Pi$ $C_\infty=M$	$1-\dfrac{4}{\alpha}\left[D_1(-\alpha)-1\right]$ $D_1(-\alpha)=\dfrac{\alpha}{2}+\dfrac{1}{\alpha}\int_0^\alpha\dfrac{t}{e^t-1}dt$
Joe	$1-\left[(1-u)^\alpha+(1-v)^\alpha-(1-u)^\alpha(1-v)^\alpha\right]^{1/\alpha}$	$-\ln\left[1-(1-t)^\alpha\right]$	$[1,\infty)$	$C_1=\Pi$ $C_\infty=M$	No closed form

Since φ is a function of the copula parameter α, identifying φ is equivalent to identifying the Archimedean copula itself. Genest and Rivest (1993) described a procedure to identify the form of φ from a sample of bivariate observations. The procedure is based on generating the intermediate (unobserved) random variable $\omega_i = F(x_i, y_i)$ that has a distribution function $K(t) = P(\omega_i \le t)$. Thus, $K(t)$ is the cumulative distribution function of the pseudo-observations ω_i, or in other words, the multivariate probability integral transformation of $F(x,y)$ (Genest and Rivest, 2001; Genest et al., 2002; Nelsen et al., 2003). This distribution function is related to the generator of an Archimedean copula through the expression $K(t) = t - \varphi(t)/\varphi'(t)$.

Thus, to identify the best fitting copula, we

1. Estimate Kendall's τ from the sample by the non-parametric estimate
   $\tau_n = \frac{2}{n(n-1)} \sum_{i<j} sign\left((x_i - x_j)(y_i - y_j)\right)$
2. Construct a non-parametric estimate of $K(t)$
   a. $\omega_i = \frac{\sum_j 1(x_j < x_i, y_j < y_i)}{n-1}, \quad i = 1, \ldots, n$
   b. $K_n(t) = \frac{\sum_i 1(\omega_i \le t)}{n}, \quad 0 < t < 1$
3. Construct a parametric estimate of $K_\varphi(t)$
   a. Use τ_n to get an initial estimate of α_n
   b. Use α_n to estimate $\varphi_n(t)$
   c. Use $\varphi_n(t)$ to estimate $K_\varphi(t)$ using the relationship $K_\varphi(t) = t - \varphi(t)/\varphi'(t)$
   d. Refine α so that it minimizes $\sum \left| K_n(t) - K_\varphi(t) \right|$

Repeat step 3 for several choices of φ and select the best fitting copula.

The copula formalism offers an elegant way to construct the conditional probability distributions and derive quantile regression curves of *y* subject *x* (Frees and Valdez, 1998). The *p*-th quantile regression curve is defined as $y_p = F_2^{-1}(v_p)$ where v_p is the solution of the equation $C(v_p \mid u) = \frac{\partial C(u, v_p)}{\partial u} = p$. Setting *p* to 0.5 yields the median regression curve of *y* subject to *x*.

Because of the well-known local upper-mantle velocity heterogeneity at the NTS site (e.g. Cormier, 1987; Lynnes and Lay, 1988) we treat Pahute Mesa and Yucca Flat separately. We use robust statistics (*smad*) to estimate the variance of residual differences as a function of station separation for fixed events. Using the copula framework allows us to derive strictly data-driven models of variograms, (i.e. we are not forcing any a priori models, such as the commonly used exponential or spherical models), which still yield closed formulas. We define the variogram as the median regression curve of *smad* with respect to station separation, and we derive the median regression from the best fitting copula.

Figure 7 shows the Pn median regression curves for Pahute Mesa and Yucca Flat. Note that in both cases the best fitting copula is identified as the Clayton copula, with a slightly different parameter: 0.56 and 0.35, respectively. The difference in the copula parameters for Pahute Mesa and Yucca Flat may also account for the SNR dependence in the residuals, as signals from Yucca Flat explosions have typically lower SNR than those from Pahute Mesa.

For the Clayton copula, solving $C(v_p \mid u) = u^{-\alpha-1}\left(u^{-\alpha} + v_p^{-\alpha} - 1\right)^{-(\alpha+1)/\alpha} = p$ for v_p we obtain

$$v_p = \left(1 + u^{-\alpha}\left(p^{-\alpha/(\alpha+1)} - 1\right)\right)^{-1/\alpha}.$$

The Clayton copula exhibits lower tail dependence, conveniently describing the fact that with decreasing station separation the residual differences become increasingly correlated.

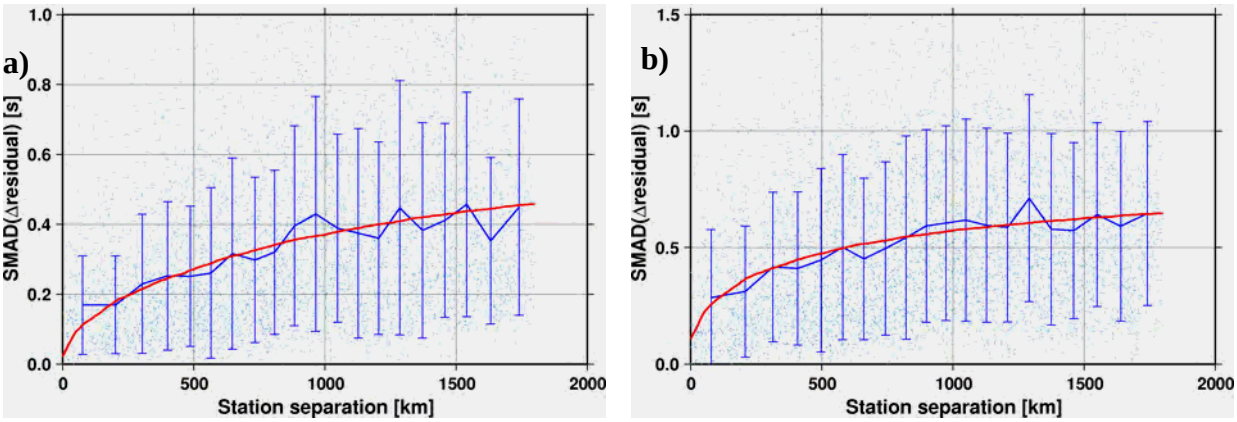

Figure 7. Variogram estimation for Pn phases at Pahute Mesa (a) and Yucca Flat (b). The thick blue line connects the median smad values at every 5-percentile worth of data; the red line shows the median regression curve derived from the best fitting copula.

CONCLUSIONS AND RECOMMENDATIONS

We have identified the data sets we will use to test and validate the methodologies developed in the course of the project. These include the NTS GT0 and Lop Nor GT1-2 underground nuclear explosions, as well as the GT2 mining events in Lubin, Poland.

We have developed preliminary methodologies to obtain improved models of reading errors and deriving the full covariance matrix from variograms. We have also developed a method to transform the empirical covariance matrix so that it becomes a positive definite matrix.

We have developed a data-driven methodology, based on copula theory, to obtain robust estimates of variogram models.

During the first year of the project we concentrate our efforts to develop, test and validate methodologies, and demonstrate their applicability on a limited set of event clusters.

REFERENCES

Buland, R. (1986). Uniform reduction error analysis, *Bull. Seism. Soc. Am.* 76: 217-230.

Chang, A.C., R.H. Shumway, R.R. Blandford and B.W. Barker (1983). Two methods to improve location estimates – preliminary results, *Bull. Seism. Soc. Am.* 73: 281-295.

Cormier, V.F. (1987). Focusing and defocusing teleseismic P waves by known three-dimensional structure beneath Pahute Mesa, Nevada Test Site, *Bull. Seism. Soc. Am.*, 77, 1688-1703.

Douglas, A., J.B. Young, D. Bowers and P.D. Marshall (2005). An analysis of P travel times for Nevada Test Site explosions recorded at regional distances, *Bull. Seism. Soc. Am.* 95: 941-950.

Fisk, M. (2002). Accurate locations of nuclear explosions at the Lop Nor test site using alignment of seismograms and IKONOS satellite imagery, *Bull. Seism. Soc. Am.* 92: 2911-2925.

Frees, E.W. and E.A. Valdez (1998). Understanding relationships using copulas, *North Am. Actuarial J.* 2: 1-25.

Genest, C., L-P. Rivest (1993). Statistical inference procedures for bivariate Archimedean copulas, *J. Am. Stat. Assoc.* 88: 1034-1043.

Genest, C. and L-P. Rivest (2001). On the multivariate probability integral transformation, *Statistics & Probability Letters* 53: 391-399.

Genest, C., J-F. Quessy and B. Rémillard (2002). Test of serial independence based on Kendall's process, *Canadian J. Statistics* 30: 1-21.

Herrin, E., and J. Taggart (1968). Source bias in epicenter determination, *Bull. Seism. Soc. Am.* 58: 1791-1796.

Joe, H. (1997). *Multivariate models and dependence concepts*, Chapman and Hall, London.

Kohl, B., T. J. Bennett, I. Bondár, B. Barker, W. Nagy, C. Reasoner, and J. Hanson (2004), Development of a network data set for evaluating detection and network processing performance, in *Proceedings of the 26th Seismic Research Review: Trends in Nuclear Explosion Monitoring*, LA-UR-04-5801, Vol. 2, pp. 725-734.

Kohl, B., T.J. Bennett, I. Bondár, B. Barker, W. Nagy, C. Reasoner, H. Israelsson and P. Piraino (2005). Development of a network data set for evaluating detection and network processing performance, in *Proceeding of the 27th Seismic Research Review: Trends in Nuclear Explosion Monitoring*, Palm Springs, CA.

Leonard, M. (2000). Comparison of manual and automatic onset time picking, *Bull. Seism. Soc. Am.* 90: 1384-1390.

Lynnes, C.S. and T. Lay (1988). Analysis of amplitude and travel-time anomalies for short-period P-waves from NTS explosions, *Geophys. J. Int.* 92: 431-443.

McLaughlin, K.L., R.H. Shumway and T.W. McElfresh (1988). Determination of event magnitudes with correlated data and censoring: A maximum likelihood approach, *Geophys. J. Int.* 95: 31-44.

Myers, S.C. and C.A. Schultz (2000). Improving sparse network seismic location with Bayesian kriging and teleseismically constrained calibration events, *Bull. Seism. Soc. Am.* 90: 199-211.

Nelsen, R.B., J.J. Quesada-Molina, J.A. Rodriguez-Lallena and M. Ubeda-Flores (2003). Kendall distribution functions, *Statistics & Probability Letters* 65: 263-268.

Nelsen, R.B. (1999). *An introduction to copulas*, Lecture Notes in Statistics 139, Springer Verlag, New York.

Rodi, W., S.C. Myers and C.A. Schultz (2003). Grid-search location methods for ground-truth collection from local and regional seismic networks, in *Proceedings of the 25th Seismic Research Review - Nuclear Explosion Monitoring: Building the Knowledge Base*, LA-UR-03-6029, Vol. 1, pp. 311-319.

Rodi, W.L. (2004), Error analysis in the joint event location/seismic calibration inverse problem, in *Proceedings of the 26th Seismic Research Review: Trends in Nuclear Explosion Monitoring*, LA-UR-04-5801, Vol. 1, pp. 307-316.

Schultz, C.A., S.C. Myers, J. Hipp and C.J. Young (1998), Nonstationary Bayesian kriging: A predictive technique to generate spatial corrections for seismic detection, location and identification, *Bull. Seism. Soc. Am.* 88: 1275-1288.

Sklar, A. (1959), Fonctions de repartition à *n* dimensions et leurs marges, *Publ. Inst. Statist. Univ. Paris* 8: 229-231.

Yang, X., I. Bondár, J. Bhattacharyya, M. Ritzwoller, N. Shapiro, M. Antolik, G. Ekström, H. Israelsson and K. McLaughlin (2004), Validation of regional and teleseismic travel-time models by relocating GT events, *Bull. Seism. Soc. Am.* 94: 897-919.

GROUND TRUTH EVENTS, MAGNITUDE SCALE, VELOCITY MODELS AND TRAVEL TIME CORRECTION SURFACES FOR NORTHEASTERN AFRICA

Richard A. Brazier[1], Margaret Benoit[1], Yongcheol Park[1], Andrew A. Nyblade[1], and Michael Pasyanos[2]

Penn State University[1] and Lawrence Livermore National Laboratory[2]

Sponsored by National Nuclear Security Administration
Office of Nonproliferation Research and Engineering
Office of Defense Nuclear Nonproliferation

Contract Nos. DE-FC03-02SF22500[1] and W-7405-ENG-48[2]

ABSTRACT

Determining accurate seismic locations with representative uncertainty estimates is of fundamental importance to ground-based nuclear explosion monitoring. This project has developed a catalog of reference events (ground truth) in the northeast African area of interest where reference event coverage is exceptionally poor. The results of this project will enable the seismic monitoring community to enhance their operational capability to monitor for nuclear tests in North Africa and the Middle East by increasing their ability to accurately locate and identify seismic events in these regions.

The collection of ground truth events for northeastern Africa has been achieved using broadband seismic data from regional PASSCAL networks in Ethiopia, Kenya and Tanzania, as well as broadband data from primary and auxiliary International Monitoring System stations in the region. Accurate event locations for twenty-two M>3.5 events are reported. For events in Tanzania, focal mechanisms have been obtained by modeling P and SH polarities and amplitude ratios in a grid search method. Epicenters have been constrained by using P and S arrival times, and focal depths have been constrained by waveform modeling of regional and local depth phases. Most of the earthquakes occur on either the western or eastern branch of the East African Rift, and the mechanisms obtained are all normal or strike-slip. For events in Ethiopia, epicentral locations have been obtained using only P arrival times. Eleven events from Ethiopia and one from Tanzania meet either the GT5 local and/or the GT20 regional criteria of Bondar et al. (2004).

Within this project, several other efforts have been undertaken to improve monitoring capabilities in northeastern Africa. A Bayesian kriging method has been used with the well located events to construct regional travel-time correction surfaces. Group velocity measurements from many thousand station-event pairs for 10-60 second Rayleigh and Love waves have been measured, and these measurements have been inverted to produce group velocity maps of northeastern Africa, and new models of crust and uppermost mantle structure in southern Ethiopia and northern Kenya. A new local magnitude scale for Ethiopia has also been developed.

OBJECTIVE

The objectives of this project are to provide 1) a reference catalog of accurately located earthquakes for northeastern Africa, 2) a local magnitude scale for Ethiopia, 3) improved velocity models of the crust and upper mantle for northeastern Africa, and 4) new travel time correction surfaces.

INTRODUCTION

Determining accurate seismic locations with representative uncertainty estimates is of fundamental importance to ground-based nuclear explosion monitoring. In this project, we have developed a catalog of reference events (ground- truth [GT]) for northeastern Africa where reference event coverage is exceptionally poor due to the limited station coverage by historic networks. The catalog will enable the seismic monitoring community to enhance their operational capability to monitor for nuclear tests in North Africa and the Middle East by increasing their ability to accurately locate and identify seismic events in these regions.

Earthquakes in northeastern Africa provide a principal source of ground truth for North Africa and the Middle East. The earthquakes of interest are associated with the northern and central portions of the East African Rift System (Figure 1). Since there are very few earthquakes within North Africa proper or within large parts of the Middle East that can be used to develop a set of ground truth, naturally occurring events in northeastern Africa take on an added importance for improving monitoring capabilities in the region.

The development of GT for North Africa and the Middle East has in the past been limited not only by the lack of appreciable seismicity but also by a dearth of seismic stations throughout most of Africa. This situation is now changing. We operated regional seismic networks in Ethiopia and Kenya comprised of 27 and 11 broadband stations, respectively, between 2000 and 2002, and several years ago (1994-1995) we operated a similar network of 20 broadband seismic stations in Tanzania. The broadband waveforms recorded by these networks, together with waveforms from primary and auxiliary IMS stations in the region, provide a rich data set that can be used to accurately locate earthquakes and determine origin times and source mechanisms.

Accurate event locations for twenty-two M>3.5 events are reported. For events in Tanzania, focal mechanisms have been obtained by modeling P and SH polarities and amplitude ratios in a grid search method. Epicenters have been constrained by using P and S arrival times, and focal depths have been constrained by waveform modeling of regional and local depth phases. Most of the earthquakes occur on either the western or eastern branch of the East African Rift, and the mechanisms obtained are all normal or strike-slip. For events in Ethiopia, epicentral locations have been obtained using only P arrival times. Eleven events from Ethiopia and one from Tanzania meet either the GT5 local and/or the GT20 regional criteria of Bondar et al. (2004).

Within this project, several other efforts have been undertaken to improve monitoring capabilities in northeastern Africa. A Bayesian kriging method has been used with the well located events to construct regional travel-time correction surfaces. Group velocity measurements from many thousand station-event pairs for 10-60 second Rayleigh and Love waves have been measured, and these measurements have been inverted to produce group velocity maps of northeastern Africa, and new models of crust and uppermost mantle structure in southern Ethiopia and northern Kenya. A new local magnitude scale for Ethiopia has also been developed.

BACKGROUND INFORMATION

The locations of the broadband seismic experiments, together with the geology and topography of East Africa, are shown in Figure 1. The geology of the region is comprised of an Archean craton (the Tanzania Craton, Figure 1) surrounded by Proterozoic mobile belts. The rift faults of the Cenozoic East African rift system have developed mainly within the Proterozoic mobile belts, forming a rift system that begins with the Main Ethiopian Rift intersecting the Red Sea and the Gulf of Aden at the Afar triple junction continuing southwest through Kenya and splitting into two branches (Western rift and Eastern rift) around the Tanzanian Craton.

The broadband seismic experiment in Tanzania was conducted in 1994 and 1995 and consisted of 20 seismic stations deployed for a year in two skewed arrays; one oriented more or less east-west, and the other northeast-southwest. The experiment was designed so that structure beneath the Archean Tanzania Craton and the terminus of

the Eastern Rift in northern Tanzania could be imaged with seismic data from local, regional and teleseismic earthquakes. Information about the station configuration, recording parameters and other details of the field deployment has been reported by Nyblade et al. (1996).

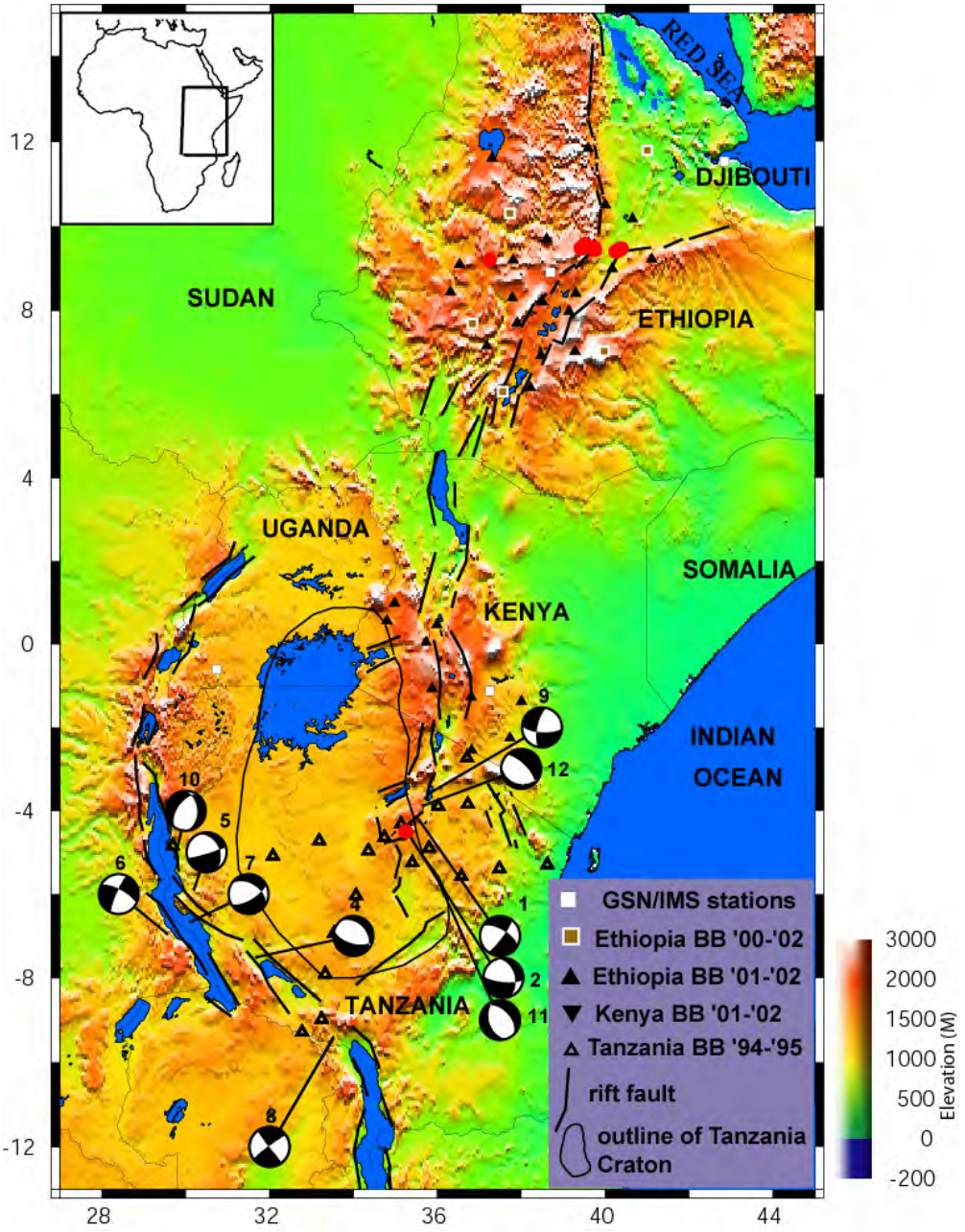

Figure 1. Topographic map of East Africa showing the Ethiopian and East African plateaus (regions with > 1000 m elevation), the outline of the Archean Tanzania craton, the major rift faults of the East African rift system, focal mechanisms and locations for our GT events (red circles), and the location of broadband seismic stations.

In the other broadband seismic experiments, seismic stations consisting of broadband sensors, 24-bit data loggers, 4 Gbyte hard disks, and GPS clocks were deployed in regions of Ethiopia and Kenya safe for traveling (Figure 1). The stations were spaced 50 to 200 km apart and were located to optimize the recording of teleseismic body and surface

waves that sample upper mantle structure beneath the Eastern Rift. For East Africa, the major source regions for teleseismic earthquakes are the Hindu Kush/Pamir region to the northeast and the Fiji/Tonga subduction zones to the east. Additional criteria used for site selection included access to bedrock, security, and year-round road conditions.

Installation of the Ethiopian stations was completed in two phases. During March 2000, five stations were installed around the periphery of the network, and then one year later (March 2001) an additional 20 stations were installed to densify the network (Figure 1). All 25 stations were removed from the field in March 2002. Installation of the Kenyan stations took place during July and August 2001, and all 10 of the stations were removed in July 2002. Two data streams were recorded, a 1 sample/sec continuous stream and a 20 sample/sec continuous stream, yielding a data volume of 21 Mbytes per station per day. Data recovery for the Ethiopian stations was nearly 90%, and it was about 70% for the Kenyan stations.

EVENT LOCATIONS

Event locations have been obtained for several events in Tanzania with magnitudes $\geq$ 3.7 and in Ethiopia with magnitudes > 2.4 that were well recorded by the Tanzania and Ethiopia regional networks. The locations were obtained using P and S arrival times for events in Tanzania, P arrival times for events in Ethiopia, a regional velocity model for the crust and upper mantle constrained by previous studies, and the event location code HYPOELLIPSE (Lahr, 1993). The P and S onset times were individually handpicked to within 0.1 seconds. The velocity model in Table 1 was used in event location in Tanzania. Crust and uppermost mantle in East Africa has been studied in detail by many authors using refraction surveys, receiver functions, surface waves, regional waveforms and Pn tomography. From these studies, it is clear that crustal and uppermost mantle structure in Tanzania is fairly uniform in the Precambrian terrains away from the rift valleys proper (Last et al., 1997; Brazier et al., 2000; Nyblade, 2002; Langston et al., 2002; Fuchs et al. 1997 and references therein). Only minor differences in crustal thickness (2-5 km), mean crustal velocity (0.1-0.2 km/s), and uppermost mantle P velocities (0.1 – 0.2 km/s) are found between the various stations of the Tanzania network, and these differences introduce very small uncertainties in the event locations. For locating events in Ethiopia, we used station dependent velocity models determined by Dugda et al. (2005).

TABLE 1. Crust and uppermost mantle seismic structure for Tanzania and Ethiopia, East Africa.

	V1 (km/s)	V2 (km/s)	Poisson's Ratio	Moho Depth (km)	Mean crustal Vp (km/s)	Pn (km/s)
Tanzania	5.84	7.09	0.25	38	6.5	8.3

V1= uppermost crustal velocity; V2=lowermost crustal velocity

Table 2 summarizes the event origin times and locations, and the uncertainties from Hypoellipse associated with the locations. All of the events are well recorded on at least 11 stations. A number of the events are within a few tens of kilometers of a station and none are more than a few hundred kilometers from a station. The magnitude estimates for the Tanzania events comes from using the maximum surface wave amplitude and the local magnitude scale for East Africa determined by Langston et al. (1998). Magnitudes for events in Ethiopia given in Table 2 come from a new local magnitude scale given below.

Focal mechanisms for the Tanzania events have been determined using polarities and amplitude ratios of local and regional P and S phases in a grid-search technique (Snoke et al., 1984) and are plotted in Figure 1 and listed in Table 3. The focal mechanisms were then used with a wavenumber integration algorithm (Kennett, 1983) to compute full synthetic seismograms for several stations at several depths. The synthetics were compared against the data and regional depth phases such as pPn, sPn and PmP were identified to constrain the source depths. An example is shown in Figure 2 and a complete description in Brazier et al. (2005). In addition, eleven events from Ethiopia and one from Tanzania meet either the GT5 local and/or the GT20 regional criteria set by Bondar et al., (2004) and are listed in Table 4.

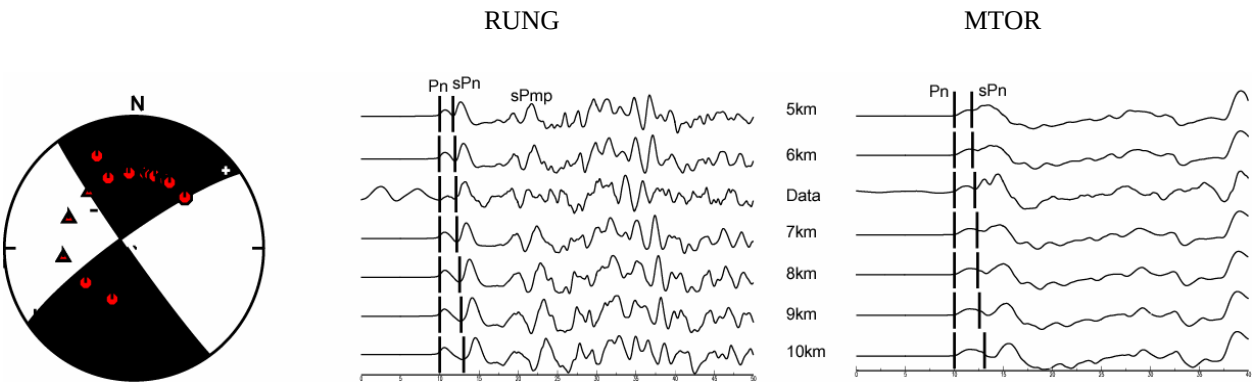

Figure 2 Vertical displacement waveforms and focal mechanisms from the November 16 1994, Mbeya event (No. 8: in Table 2) recorded at RUNG ($\Delta = 248$ km) and MTOR ($\Delta = 480$ km) and synthetics for source depths between 5-10 km. Traces are aligned on Pn and depth phases sPn and sPmp are noted. Circles are compressional first motions; triangles are dilatational first motions.

TABLE 2. Locations for earthquakes in East Africa, from July 1994 to June 1995, recorded by the Tanzania Broadband Seismic Experiment and from April 2000 to March 2002 by the Ethiopian Broadband Experiment.

Ev	yr:mo:day:hr:min:sec	Lat.	Lon.	Dep	M	N	Gap	RMS	Smaj	Az	Smin	Sez
1	94:07:20:11:32:04.09	-4.225	35.585	29	4.5	19	133	1.52	0.25	-106	0.40	0.47
2	94:08:17:03:23:32.68	-4.448	35.585	13	3.7	20	71	4.05	0.22	-105	0.31	0.52
4	94:09:05:04:08:54.83	-7.502	31.700	15	4.1	18	174	0.54	0.38	-50	0.55	2
5	94:09:30:01:36:53.14	-5.920	29.890	26	4.5	16	229	1.13	0.55	-40	1.18	1.4
6	94:11:12:12:17:57.73	-6.939	29.552	18	5.3	23	94	2.13	0.31	-40	0.36	2
7	94:11:12:20:16:58.19	-6.652	30.135	8	4.7	17	211	1.29	0.39	-26	0.73	2
8	94:11:16:01:08:05.78	-9.424	33.513	7	4.5	20	150	3.6	0.29	-52	0.54	0.97
9	94:11:27:04:20:53.71	-4.084	35.828	11	4.0	15	146	2.28	0.29	-112	0.48	0.7
10	94:12:25:04:25:35.97	-5.173	30.580	29	4.2	11	150	1.48	0.67	22	4.98	2
11	95:01:29:00:23:33.29	-5.033	35.923	9	4.1	11	111	3.51	0.31	-111	0.53	1.04
12	95:02:12:16:37:33.85	-3.879	35.670	34	4.5	13	215	0.56	0.36	-107	0.96	2
13	01:07:13:22:34:15.21	9.426	40.270		3.0	20	90	2.17	0.23	-56	0.31	0.55
14	01:06:26:22:22:07.36	9.394	40.391		3.3	17	99	2.30	0.26	-78	0.40	0.69
15	01:06:23:20:00:24.18	9.413	40.254		3.5	19	89	2.93	0.23	-67	0.35	0.66
16	01:06:26:22:32:19.97	9.434	40.339		3.5	18	89	2.20	0.25	-66	0.36	0.71
17	01:05:23:01:16:11.41	9.465	39.410		3.4	24	61	2.13	0.19	-47	0.28	0.5
18	01:11:11:21:05:22.89	9.511	39.691			10	71	0.58	0.32	-71	0.36	0.66
19	01:11:11:22:32:42.83	9.442	39.722			22	43	1.83	0.21	-67	0.25	0.49
20	01:11:11:22:38:04.17	9.487	39.727		3.7	22	45	1.47	0.21	-60	0.25	0.82
21	01:11:27:21:35:36.86	9.477	39.705		2.4	14	68	1.63	0.27	-51	0.30	0.64
22	01:12:13:02:14:40.67	9.497	39.705		3.0	16	63	1.58	0.24	-63	0.29	0.58
23	01:05:12:02:06:42.39	9.507	39.710		2.7	15	61	1.06	0.27	6	0.28	0.60

Dep = depth in km.
M = magnitude. Magnitudes for Tanzanian events are based on the ML scale from Langston et al. (1998), and the new scale presented in this text for events in Ethiopia
N = number of stations used in the event location.
Gap = azimuth range in stations.
RMS = Rms error in arrival times.
Smaj, Smin, Sez, Az = dimensions (in kms) and orientation of the error ellipse. For this study, the numbers in the table are for a 68% confidence level.

Table 3. Focal mechanisms for events in Table 2

Ev.	Strike (deg)	Dip (deg)	Rake (deg)
1	301	64	-11
2	335	35	-10
4	318	36	-63
5	335	36	-10
6	204	80	-20
7	303	46	-35
8	143	88	-5
9	93	69	-22
10	215	55	-65
11	162	43	-71
12	316	68	-77

Table 4 GT level for events in Table 2

Event	Gap	Secondary Gap	No. stations < 2.5 deg.	No. stations Between 2.5 and 10 deg.	No. stations < 30km	GT level
2	71	133	12	8	1	GT5
13	90	103	9	11	0	GT20
14	99	105	5	12	0	GT20
15	89	100	7	12	0	GT20
16	89	101	5	13	0	GT20
17	61	85	14	10	1	GT5/20
18	71	120	10	0	1	GT5
19	43	80	12	10	0	GT20
20	45	86	12	10	1	GT5/20
21	68	104	11	4	1	GT5
22	63	100	11	5	1	GT5
23	61	101	12	3	1	GT5

Secondary Gap = azimuth range in stations with one station omitted.

LOCAL MAGNITUDE SCALE

We have developed a new magnitude scale following Richter's (1958) method, based on the seismograms recorded by Wood-Anderson instruments with period T_0 = 0.8 sec, magnification = 2800 and damping = 0.8. The local magnitude M_L is defined as:

$$M_L = \log A - \log A_0 + S \qquad (1)$$

where A is the trace maximum amplitude observed on the horizontal components of the seismogram; A_0 is an empirically determined distance curve with assumption that when the maximum amplitude of 1 mm is observed at a distance of 100 km, M_L = 3.0; S is an empirically determined station correction. Following Hutton and Boore (1987), the distance-correction curve can be written as:

$$\log A_{ij} = -n\log\left(r_{ij}/100\right) - K\left(r_{ij} - 100\right) - 3.0 \qquad (2)$$

Where n and K are parameters related to the geometrical spreading and attenuation; A_{ij} is the horizontal maximum amplitude of the i^{th} event observed at the j^{th} station; r_{ij} is the distance from the epicenter of the i^{th} event to the j^{th} station. Combining equations (1) and (2):

$$-n\log\left(r_{ij}/100\right) - K\left(r_{ij} - 100\right) + M_{Li} - S_{jk} = \log A_{ijk} + 3.0, \qquad (3)$$

where M_{Li} is the local magnitude of the i^{th} event and S_{jk} is the correction for the j^{th} station on the k^{th} component. Based on equation (3), the parameters *n*, *K*, local magnitude M_L and station correction S can be solved using the

generalized inversion method (Aki and Richards, 1980), as several investigators have done before (Hutton and Boore, 1987; Langston et al., 1998). We inverted for 58 station factors and 2 model parameters, n and K. All the stations are in a similar region, and therefore we assume the station factors average to zero. This is added as a constraint to the system of equations.

As opposed to Langston et al. (1998), we performed the inversion in a single step calculating all 60 parameters at once, avoiding the convergence issues of an iterative method. The inversion included 446 events and nearly 6000 amplitudes, yielding values $n = 0.60812$ and $K = 0.00036301$. The magnitude scale for Ethiopia in comparison to the Tanzania local magnitude scale (Langston et al., 1998) has high attenuation. The Tanzania scale needed a equivalent motion stipulation at 17 km as opposed to 100 km to avoid the attenuation effect. The ML residuals are normally distributed with no outliers. The residuals are also linearly distributed when plotted against distance. Details of the inversion and local magnitude scale can be found in Brazier et al. (manuscript in prep.).

VELOCITY MODELS

To improve regional velocity models for the study area, we have made surface wave dispersion measurements for both Love and Rayleigh group velocities using a multiple narrow-band filter technique. Combined with thousands of other measurement made in the broader regional area (Pasyanos et al., 2001), we have performed a high resolution group velocity tomography of northeastern Africa. Surface wave tomography results can be seen in Figure 3 for 10 to 60 second period Rayleigh waves. These maps have been inverted for crustal and upper mantle structure using a grid search approach (Benoit, 2005). Results are shown in Figure 4.

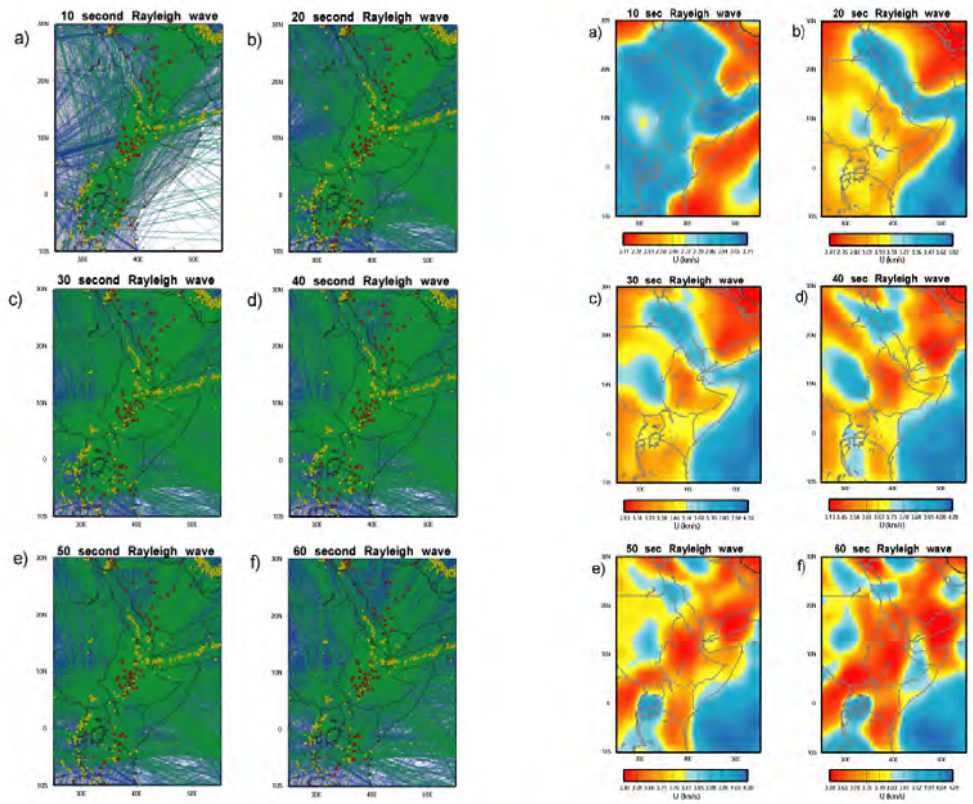

Figure 3. Path locations and results of the tomography for 10 to 60 second Rayleigh waves

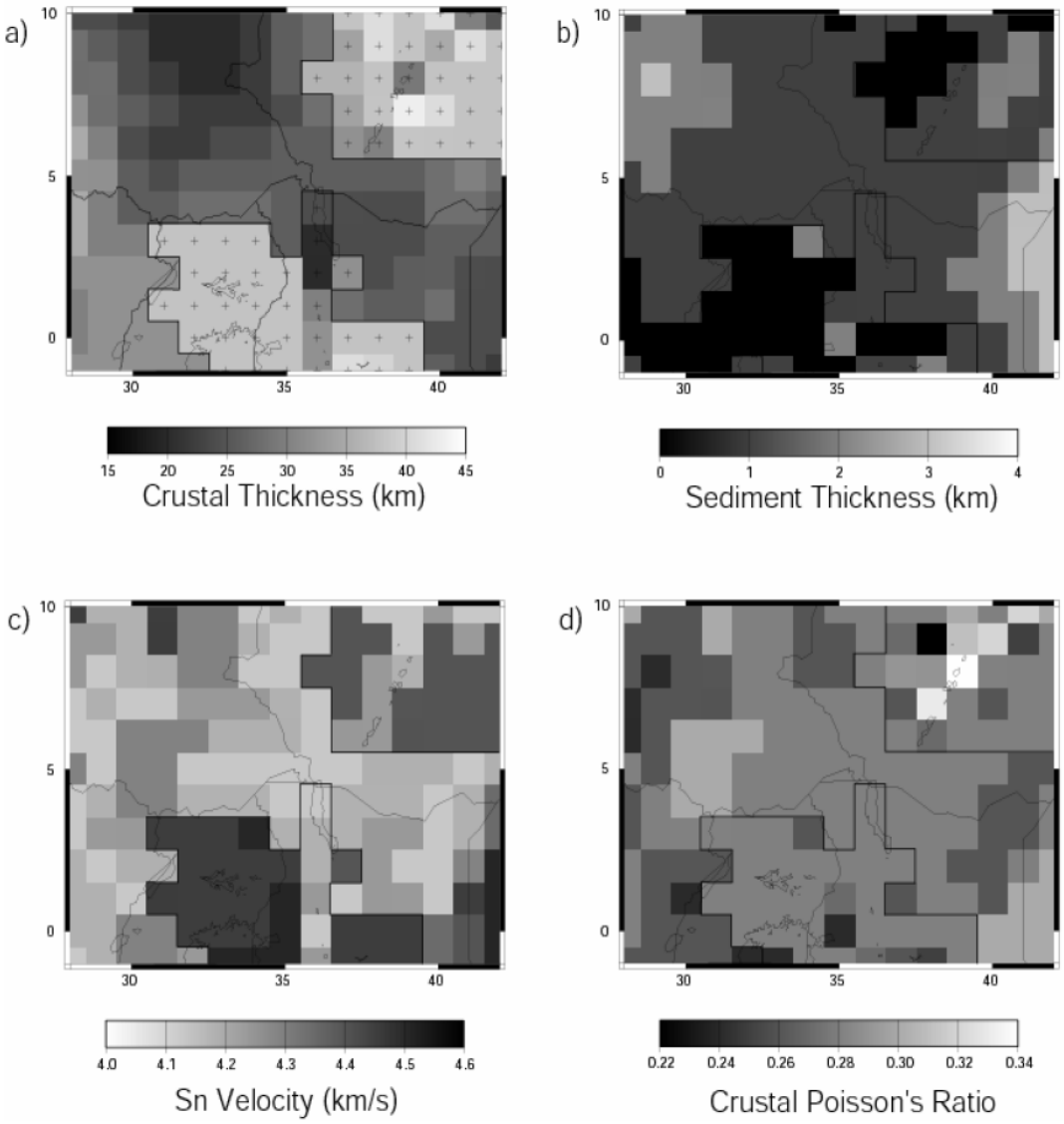

Figure 4. Crustal structure constructed from the surface wave tomography

TRAVEL-TIME CORRECTION SURFACES

To expand the catalog of events in northeastern Africa, we have taken the GT events from Table 2 and used them along with teleseimic GT15-25 events (Engdahl et. al., 1998) as calibration events to construct travel-time correction surfaces using the kriging method of Schultz et al. (1998, 1999) and Myers and Schultz (2000). P-wave results for station BGCA can be seen in Figure 5. P and S correction surfaces have been developed for stations DBIC, BOSA, LBTB, and TAM.

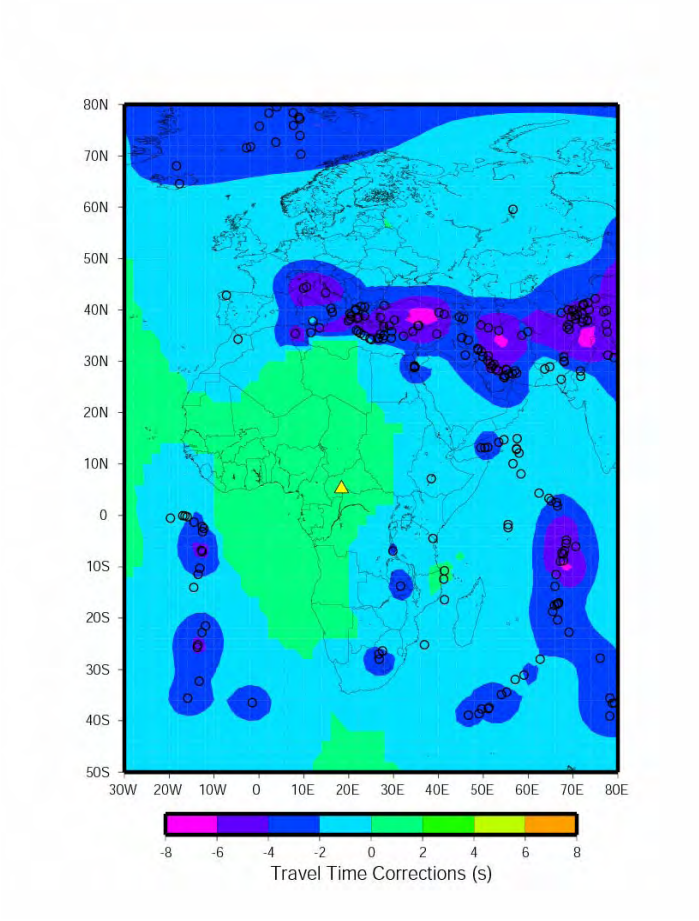

Figure 5 P wave traveltime correction surface for BGCA in the Central African Republic.

REFERENCES

Aki, K., and P.G. Richards (1980). Quantitative Seismology: Theory and Methods, Vols. 1 and 2. San Francisco: W.H. Freeman.

Benoit, Evidence for crustal thinning in the low lying region between the Ethiopian and East African plateau from modeling Rayleigh waves, *Ph.D. Thesis, Pennsylvania State University.*

Bondar, I, S.C. Myers, E. R. Engdahl and E.A. Bergman (2004), Epicentre accuracy based on seismic network criteria *Geophysical Journal International* 156: 3, 483-496.

Brazier, R., A.A. Nyblade, C. A. Langston, and T.J. Owens (2000), Pn velocities beneath the Tanzania Craton and adjacent rifted mobile belts, East Africa, *Geophys. Res. Lett.* 27: 2365-2368.

Brazier, R., A.A Nyblade and J. Florentin (2005), Focal mechanisms and the stress regime in NE and SW Tanzania, East Africa, *Geophys. Res. Lett.*, accepted.

Dugda, M. and A.A. Nyblade (2005), Determination of Crustal Parameters in the South-Eastern part of Djibouti by Receiver Function Analysis: New Insights for the Nature and Origin of Crust in the Afar Depression, *Submitted , Geol. Soc. Of Lon. Special Volume on EAR.*

Engdahl, E. R., R. D. Van der Hilst and R.P. Buland (1998), Global teleseismic earthquake relocation with improved travel times and procedures for depth determination. *Bull. Seis. Soc. Am.* 88: 722-743.

Fuchs, K., Altherr, B., Muller, B., and Prodehl, C. (1997), Structure and dynamic processes in the lithosphere of the Afro-Arabian rift system, *Tectonophysics*, 278, 1-352.

Hutton, L.K. and D.M. Boore (1987). The M_L scale in southern California, Bull. Seis. Soc. Am., **77**, 2074-2094.

Kennett, B.N.L., and E. R. Engdahl (1991), Travel times for global earthquake location and phase identification, *Geophys. J. Int.* 105: 429-465.

Kennett, B.N.L., Seismic wave propagation in stratified media, *Cambridge University Press*, 1983.

Lahr, J.C. (1993), Hypoellipse, a computer program for determining local earthquake hypocentral parameters, magnitude and first motion pattern, U.S. Geological Survey Open File Report 89-116.

Langston, C.A., R. Brazier, A.A. Nyblade, and T. J. Owens (1998), Local magnitude scale and seismicity rate for Tanzania, East Africa, *Bull. Seis. Soc. Am.* 88: 712-721.

Langston, C.A., A.A. Nyblade, and T. J. Owens (2002), Regional wave propagation in Tanzania, East Africa, *J. Geophys. Res.* 107: 10.1029.

Last, R., A.A. Nyblade, C.A. Langston, and T.J. Owens (1997), Crustal structure of the East African plateau from receiver functions and Rayleigh wave phase velocities, *J. Geophys. Res.* 102: 24469-24483.

Myers, S., and C. Schultz (2000), Improving sparse network seismic location with Bayesian kriging and teleseismically constrained calibration events, *Bull. Seis. Soc. Am.*, 90, 199-211.

Nyblade, A.A., C. Birt, C. A. Langston, T .J. Owens, and R. J. Last (1996), Seismic experiment reveals rifting of craton in Tanzania, *Eos Trans. AGU, 77*, 517-521.

Nyblade, A. A. (2002), Crust and upper mantle structure in East Africa and the origin of Cenozoic extension, magmatism and plateau uplift, in *Magmatic Rifted Margins*, edited by M. Menzies, C. Ebinger and S. Klemperer, Geological Society of America special paper 362-0, in press.

Pasyanos, M. E., W. R. Walter, and S. E. Hazler (2001), A surface wave dispersion study of the Middle East and North for monitoring the Comprehensive Nuclear-Test-Ban Treaty, *Pure and Applied Geophysics*, 2001.

Schultz, C., S. Myers, J. Hipp, and C. Young (1999), Nonstationary Bayesian kriging: a predictive technique to generate spatial corrections for seismic detection, location and identification, *Phys. Earth. Planet. Int.* 113: 321-338.

Schultz, C., S. Myers, J. Hipp, and C. Young (1998), Nonstationary Bayesian kriging: a predictive technique to generate spatial corrections for seismic detection, location and identification, *Bull. Seis. Soc. Am.* 88: 1275-1288.

Snoke, J. A., J. W. Munsey, A. G. Teague, and G. A. Bollinger (1984) A program for focal mechanism determination by combined use of polarity and SV-P amplitude ratio data, *Seismological Society of America, Eastern Section, 56th annual meeting, Earthquake Notes* 55: (3), pp.15.

GROUND TRUTH OF AFRICAN AND EASTERN MEDITERRANEAN SHALLOW SEISMICITY USING SAR INTERFEROMETRY AND GIBBS SAMPLING INVERSION

Benjamin A. Brooks[1], Francisco Gomez[2], Eric A. Sandvol[2], and Neil Frazer[1]

University of Hawaii[1] and University of Missouri[2]

Sponsored by Air Force Research Laboratory

Contract No. F19628-03-C-0107[1, 2]

ABSTRACT

Our study focuses on the further development and application of a technique to combine Synthetic Aperture Radar Interferometry (InSAR) and Gibbs Sampling (GS) inversion methods to provide ground-truth data (at GT5 or better levels) for small, shallow earthquakes in remote areas such as North Africa and the Eastern Mediterranean region. In general the analysis comprises three phases: (1) production of the interferogram, (2) inversion of the ground displacements for hypocentral location, and (3) combination with seismological data and analysis.

We are making significant progress on assembling a catalog of InSAR-based GT5 events for the region. Currently we have positively identified events in interferograms with spatial coverage in the north (Morocco), central (Zaire), and south (South Africa) of the African continent. In addition, the Bam, Iran earthquake is an excellent test-bed event for which there are both ascending and descending interferograms and numerous broadband records. Azimuth offset analysis will allow a three-dimensional (3-D) displacement field to be calculated and analyzed in conjunction with the seismic waveform data. We are also currently working on more than 15 candidate events throughout the region.

For the candidate events, interferogram production can prove to be a challenge due to temporal and geometric decorrelation effects. The short timescales of apparent temporal decorrelation has come as somewhat of a surprise, however, as many of the North African regions are desert areas where previous experience suggested that correlation should be very good. Alternative processing strategies comprising more aggressive filtering strategies show promise in retrieving usable data from some of these images.

We have collected a number of broadband waveforms for both the 2003 Bam earthquake and the 1999 South Africa seismic event and we are beginning our comparison of InSAR hypocentral locations with locations derived from seismic waveform modeling. We are actively working on a joint inversion of waveform and InSAR data. This is a highly multiparametric inversion that likely will include estimates of more than 15 parameters. Combining the Gibbs sampling method and parallel computation will likely allow this process to be accomplished with reasonable temporal latency.

OBJECTIVES

Our research focuses on delivering 5-km ground-truth (GT5) or better locations for seismic events in North and East Africa and the eastern Mediterranean region using Synthetic Aperture Radar Interferometry (InSAR) geodesy. InSAR, combined with elastic dislocation modeling, is an emerging tool for acquiring GT information in remote areas (Begnaud et al., 2000; Lohmann et al., 2002). Our work will provide much-needed GT events for a large region currently covered by a very small number of GT5 events. In addition, by applying Gibbs Sampling (GS) (Brooks and Frazer, 2005), a powerful non-linear inversion method, to the problem of inverting InSAR data for earthquake characteristics, the posterior probability distributions for our estimated source parameters will reflect accurate treatment of data variance. This will allow GT event parameters to be compared quantitatively with one another and to be used, for instance, as prior distributions for kriging-based interpolation efforts (Schultz et al., 1998). The general methodology is one that will be of use to the entire monitoring community engaged in regional calibration.

RESEARCH ACCOMPLISHED

Interferometry

To date we have identified coseismic signals in interferograms from 3 events spanning the African continent and 1 event in Iran. We are currently processing data from another 7 candidate events in the region and have ordered data for a number of other events. Below we give overviews of the interferometric results.

GT Event 1: Bam, Iran; 26 December, 2003; M_W 6.5

The Bam event is an excellent one to use as a test bed for the InSAR source parameter technique because of the large amounts of available InSAR and seismic waveform data, and because of the event's relatively clean signal. Previously (Brooks et al., 2004), we reported on our preliminary processing and analysis of the descending interferogram. Mean values from the preliminary GS results indicate that the earthquake accommodated ~2.75 meters of right-lateral strike-slip and negligible dip-slip on an ~north-south striking, 60° east-dipping fault with dimensions of ~10 x 10 km and an upper edge at ~2500 meters depth. Standard deviations of location parameters (dx, dy, the upper left corner of the dislocation) are of the order of 400 meters. These results are similar to recently published analyses (Fialko et al., 2005).

For additional constraints on the earthquake solution, we are in the process of calculating offset estimates in the azimuthal (along-track) direction from comparing before and after amplitude images (Fialko et al., 2001). This technique is of lesser precision than traditional interferometry, but it should provide displacement estimates with ~5-cm precision in an orthogonal direction to the line-of-sight view of the interferogram and allow a 3-D displacement field (albeit one with a non-orthogonal basis) to be computed. Our intent is to then perform a joint InSAR-waveform inversion with the broadband data we have collected (see below).

GT Event 2: Welkom, South Africa; 23 April, 1999; M_L 4.5

For different reasons than the Bam event, the Welkom event (Doyle et al., 2001) is also an excellent test-bed example for the InSAR source parameter technique. Primarily, it was an extremely small event at least an order of magnitude smaller than previously imaged ones. In addition, the seismicity was due to a well-documented rock burst in the Matjhabeng mine that resulted in the deaths of 2 mine workers.

In Figure 1a we show an ERS-2 descending interferogram spanning the time from 4 October 1998 to 19 September 1999. Although regional coherence is poor, locally coherence is good enough to clearly identify fringes associated with the event. Our preliminary GS analysis shows the event to be well constrained, particularly the important ground-truth (GT) location parameters of x, y, z centroid location (Figure 1b). The marginal distributions for the length and width of the rectangular dislocation, however, exhibit interesting behavior (Figure 1b). They are noticeably skewed towards very small values (<100 meters) and suggest that the source may be best characterized as a point source. This may suggest that the assumption of a shear dislocation for this event is invalid and so we are currently exploring whether other parameterizations (i.e., point sources) are more appropriate for this event.

GT Event 3: N. Morocco; 24 February, 2004; M_w 6.5

For this earthquake, we have produced two differential interferograms from a descending view (baselines of 75 m and 320 m, spanning 14 months and 5 months, respectively) (Figure 2). The interferograms were quite noisy, but strong filtering has improved the spatial coherence. However, coherence in the vicinity of the epicenter is quite low, probably owing to damage and temporal decorrelation. As a result, for additional constraints we are also exploring the possibility of using azimuth amplitude offsets for this event as described above. Data in an ascending view have also been ordered for this earthquake. In addition, we will also use co-seismic displacements from 3 nearby global positioning system (GPS) sites for further control on the solutions. As part of this process, we developed a considerably more rigorous filtering scheme than we have previously used.

In some cases, iterative application of an adaptive spectral filter has helped to remove "white" noise from interferograms and improve coherence. The effectiveness of the filter depends, in part, on the size of the fast Fourier transform (FFT) window used for the spectral analysis. Larger FFT windows can be used if the topographic phase contribution is effectively removed—if it is not, severe artifacts result. Repeated application of the filter also creates coherence, although the data are significantly smoothed. We have focused on improved baseline estimates and modeling of topographic phase prior to filtering. Although a strong filter may smooth interferometric fringes and produce local errors in the unwrapped interferograms, the overall interferogram can be unwrapped sufficiently well for a very accurate baseline estimate. With this new, accurate baseline estimate, we perform another iteration of modeling and removing the topographic phase from the original interferogram, followed by filtering and phase unwrapping.

GT Event 4: E. Zaire; 11 December, 1995; M_W 5.7

Figure 3 shows a preliminary ERS-1 interferogram from the region of the Zaire event with the region containing what we believe to be the fringes associated with the event. The International Seismological Centre (ISC)-located epicenter is ~40 km to the southeast of this location along the right edge of the image. We base this preliminary assessment on the elliptical pattern of fringes representing close to 2 full cycles of phase difference. The other smaller features with semi-elliptical patterns do not exhibit similarly steep phase gradients and we believe they are likely atmospheric artifacts.

Seismic Waveform Analysis

To date, we have collected a number of broadband waveforms for both the 2003 Bam earthquake and the 1999 South Africa seismic event. We have collected only broadband waveforms in order to be able to utilize the longer period energy (greater than 10 seconds) to obtain the optimal source parameters. We have also chosen to focus on local and regional seismic waveforms for this data analysis because these stations provide the best constraints on the hypocentral location parameters. For the Bam earthquake we have found 25 three component broadband seismograms with excellent signal to noise ratios within 30 degrees of the event. For the South Africa event we have found 7 regional broadband seismograms. We show five selected broadband waveforms for the South Africa event plotted as a function of distance (Figure 4)

We are beginning our comparison of InSAR hypocentral locations of the Bam earthquake and the 1999 South Africa seismic event with locations derived from seismic waveform modeling. This comparison will allow us to assess the quality of the seismically derived hypocentral locations relative to those of the InSAR results. Ultimately, our integration of InSAR data and travel time data will also lead to more robust and reliable GT events. In order to accomplish this goal, we will utilize long period vertical and radial seismograms along with existing crustal and upper mantle lid models to find optimal location parameters. To model the observed seismograms we will use the reflectivity method of Randall (1994), which takes advantage of all possible reflections, refractions and conversions at all interfaces.

This will be done using well-developed double-couple grid search methods (Walter, 1992). Three-component long-period (from 20 up to 50–100 seconds) waveforms are fit to synthetics for an appropriate velocity model by

systematically searching over depth, strike, dip and rake. The seismic moment is solved for each parameter combination. The optimal solution provides the minimum misfit to the observed waveforms. We will also compare our regional waveform modeling with the locations from the Harvard Centroid Moment Tensor (CMT) studies. An example of the approach we will use is shown in Figure 5.

CONCLUSIONS AND RECOMMENDATIONS

We are making progress on realizing a significant catalog of InSAR-located GT events for the African continent and the Eastern Mediterranean region. Our analyses further demonstrate the utility of InSAR for GT efforts. The combination of the InSAR data with seismic waveform data in joint inversions will certainly allow for even tighter GT constraint for the events.

A practical issue stems from the uncertainty in reported epicenter locations. In some of these regions, this uncertainty is large enough that the events could be outside of the initially ordered SAR scenes. If data from the sensing platforms were more freely available, then the temporal bottleneck involved in ordering data and evaluating whether they contain the seismic event would be alleviated.

REFERENCES

Begnaud, M. L., A. A. Velasco, and L. K. Steck (2000), Utilizing Results from InSAR to Develop Seismic Location Benchmarks and Implications for Seismic Source Studies, in *Proceedings of the 22nd Annual DoD/DOE Seismic Research Symposium: Planning for Verification of and Compliance with the Comprehensive Nuclear-Test-Ban Treaty (CTBT)*, 2: pp. 25–32.

Brooks, B. and L. N. Frazer (2005), Importance Reweighting Reduces Dependence on Temperature in Gibbs Samplers: An Application to the Coseismic Geodetic Inverse Problem, *Geophys. J. Int.* 161: 12–21.

Brooks, B. A., N. Frazer, F. Gomez, and E. A. Sandvol (2004), Ground Truth of African and Eastern Mediterranean Shallow Seismicity Using SAR Interferometry and GIBBS Sampling Inversion, in *Proceedings of the 26th Seismic Research Review: Trends in Nuclear Explosion Monitoring*, LA-UR-04-5801, 1: pp. 237–46.

Doyle, G. S., R. J. Stow, and M. R. Inggs (2001), Satellite Radar Interferometry Reveals Mining Induced Seismic Deformation in South Africa, in *Geoscience and Remote Sensing Symposium, 2001. IGARSS '01*, pp. 2037–39, IEEE 2001 International.

Fialko, Y., D. Sandwell, M. Simons, and P. A. Rosen (2005), Three-Dimensional Deformation Caused by the Bam, Iran, Earthquake and the Origin of Shallow Slip Deficit, *Nature*, 435: 295–299.

Fialko, Y., M. Simons, and D. Agnew (2001), The Complete (3-D) Surface Displacement Field in the Epicentral Area of the 1999 Mw7.1 Hector Mine Earthquake, California, from Space Geodetic Observations, *Geophys. Res. Lett.* 28: 3063–3066.

Lohmann, R. B., M. Simons, and B. Savage (2002), Location and Mechanism of the Little Skull Mountain Earthquake as Constrained by Satellite Radar Interferometry and Eeismic Waveform Modeling, *J. Geophys. Res.* 107: 2118.

Randall, G. (1994), Efficient Calculation of Complete Differential Seismograms for Laterally Homogeneous Earth Models, *Geophys. J. Int.* 118: 245–254.

Schultz, C., S. Myers, J. Hipp, and C. Young (1998), Nonstationary Bayesian Kriging: Application of Spatial Corrections to Improve Seismic Detection, Location and Identification, *Bull. Seism. Soc. Am.* 88: 1,275–1,288.

Walter, W. (1992), Source Parameters of the June 29, 1992 Little Skull Mountain Earthquake from Complete Regional Waveforms at a Single Station, *Geophys. Res. Lett.* 20: 403–406.

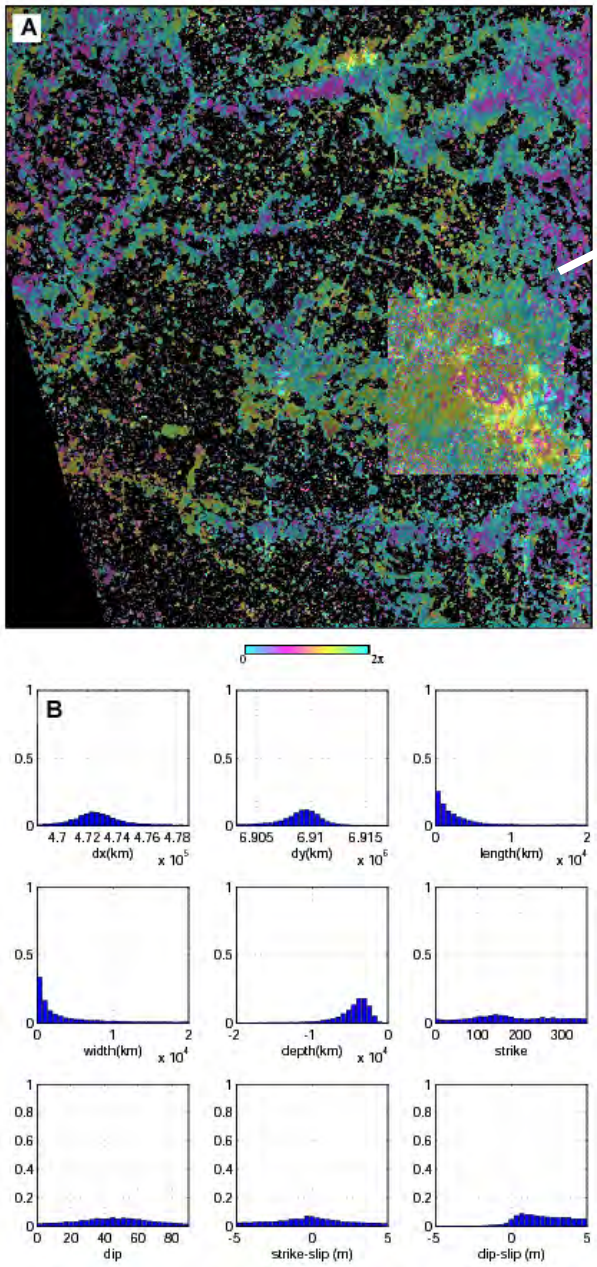

Figure 1. A) ERS-2 descending interferogram spanning the time from 4 October, 1998-19 September, 1999. The arrow demonstrates fringes associated with the 23 April 1999 earthquake. B) Results of Gibbs Sampling inversion for earthquake source parameters presented as marginal probability distributions.

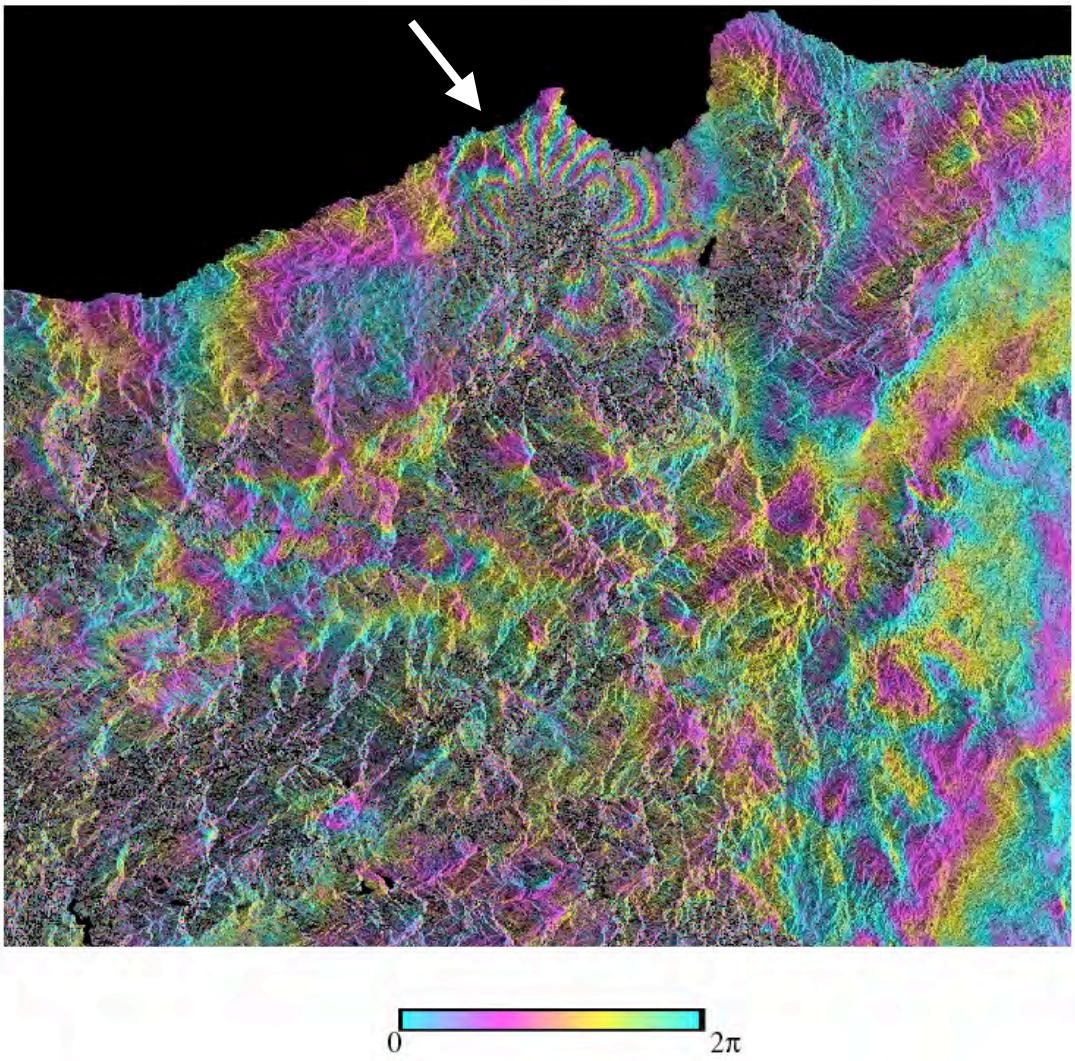

Figure 2. Envisat descending interferogram in flipped radar coordinates with a 14-month temporal baseline and a 75-m perpendicular baseline. The arrow demonstrates fringes associated with the 24 February 2004 earthquake.

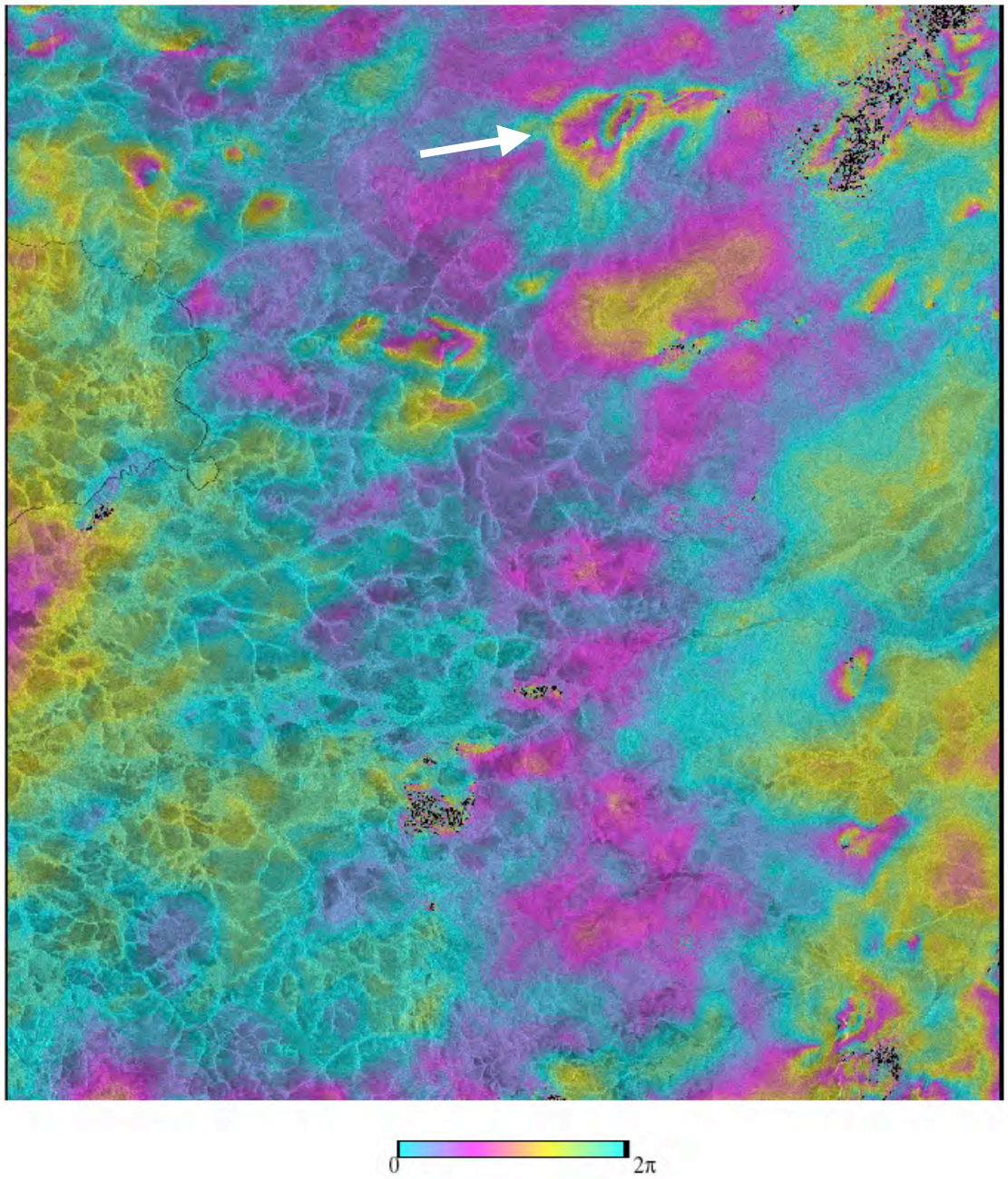

Figure 3. ERS-1 descending interferogram in flipped radar coordinates with a 35-day temporal baseline and a 235-m perpendicular baseline. The arrow demonstrates fringes likely associated with the 11 December 1995 earthquake.

.

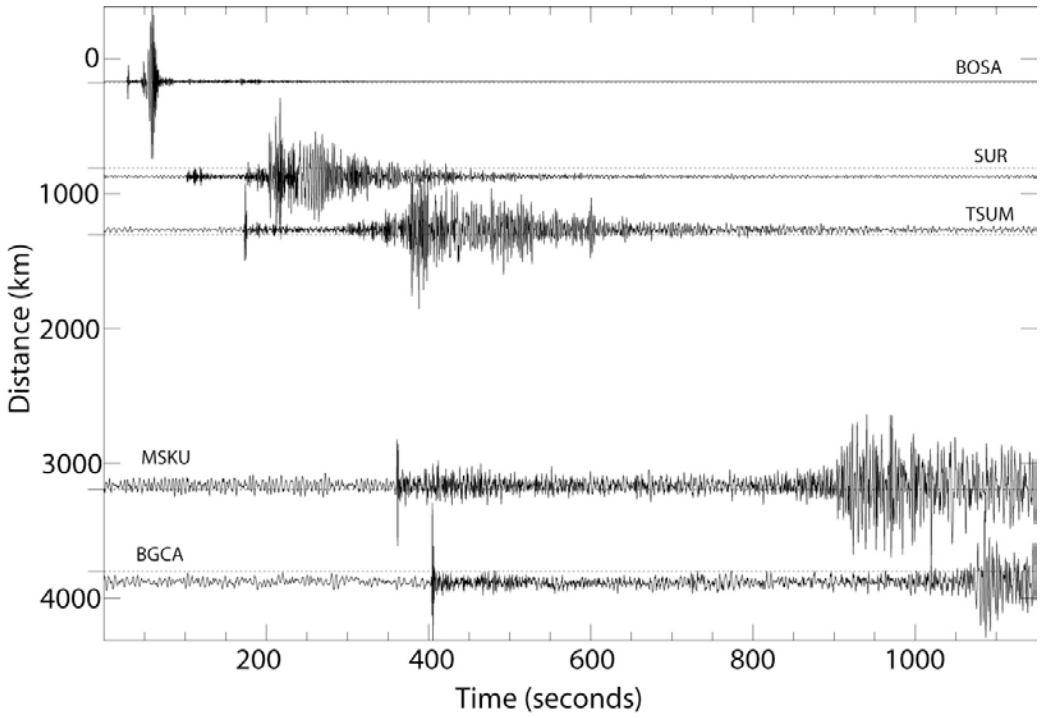

Figure 4. A record section plot of the 22 April 1999 seismic event in South Africa.

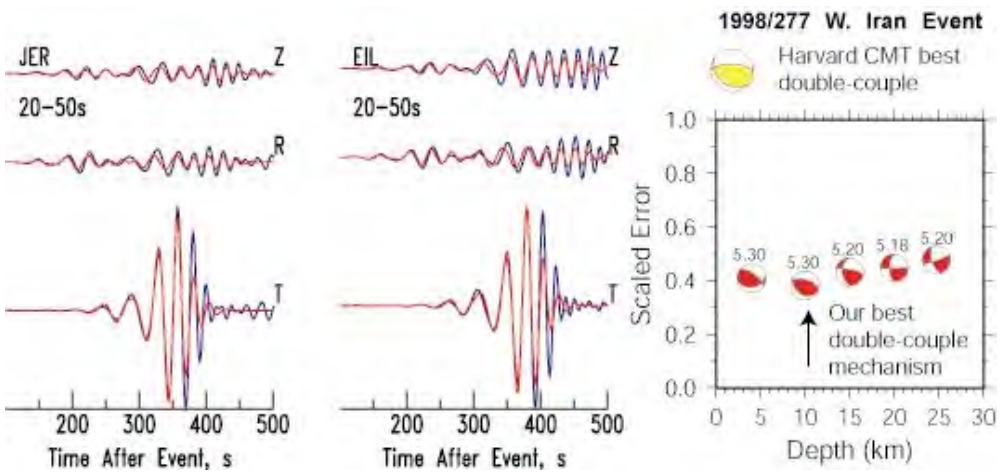

Figure 5. An example of the waveform fit for source parameters of the 1998/277 western Iran event. We used the multiple station grid search (based on Walter, 1992) for optimal double couple mechanism, depth and seismic moment. Observed and synthetic three-component waveforms were filtered 20–50 s. Good agreement with the Harvard CMT gives us confidence to apply these methods to other events with good signal-to-noise ratios in this pass band. (Courtesy Arthur Rodgers)

UTILIZING PRIOR INFORMATION FOR DEPTH TO IMPROVE SEISMIC EVENT DISCRIMINATION

Deborah K. Carlson[1], Kelly Kane[2], Rick Schult[2], Sandy Ballard[3], Chris Young[3], and Dale Anderson[1]

Pacific Northwest National Laboratory[1], Air Force Research Laboratory[2], and Sandia National Laboratories[3]

Sponsored by National Nuclear Security Administration
Office of Nonproliferation Research and Engineering
Office of Defense Nuclear Nonproliferation
and
Air Force Research Laboratory

Contract No. DE-AC06-76RLO 1830

ABSTRACT

We have developed and tested a novel algorithm for estimating the depth of a seismic event in order to improve the discrimination of events. Information from the algorithm can be incorporated into a statistically based discrimination framework to determine the source of an event. The depth estimation approach differs from currently used algorithms, which use non-linear regression techniques, by using Bayesian techniques to incorporate constraints, or prior information about the depth of an event. We demonstrate this proof-of-concept algorithm with first arriving P-waves and their associated modeled travel times. The likelihood is constructed with Gaussian errors. Depth may be constrained with a skewed distribution if characteristics of the waveforms from an event indicate that bounds on depth are appropriate. For instance, the *Rg* phase is present in a waveform only when an event is shallow. A high confidence *Rg* phase in one or more defining waveforms can lead one to assume a shallow-skewed prior distribution for the depth parameter.

OBJECTIVE

For many seismic events, depth and origin time are the hypocentral parameters that are most poorly constrained because of the source-receiver geometry imposed by the Earth. It is not unusual for current location algorithms to return event solutions that fit the data very well and yet have event depths that are above the surface of the earth (so called "air quakes") or well below the known limits of seismicity for a given area. The solutions are statistically valid in that the confidence bounds are large enough to encompass more realistic depths the specified percent of the time, but they are unsatisfying to seismologists. The effect of repeatedly seeing such unreasonable depth estimation is to develop a mistrust of the depth determinations in general, even when depth may be well constrained. What is needed is a means to flexibly incorporate a priori information about acceptable depth distributions. This will better constrain the hypocentral depth estimates when they are poorly controlled by the data, and let the data control the depth estimate when the data have good depth control. Our research has developed an algorithm that shows promise in achieving these depth estimation properties.

The single event hypocenter location model is

$$t_i = \tau + T_i(\mathbf{s}) + \varepsilon_i \, , \; i=1,2,\ldots,n \qquad (1)$$

where t_i is the arrival time at the i^{th} station, τ is the event origin time, T_i is the travel time from the event located at $\mathbf{s} = [x, y, z]^T$ to the i^{th} station, and $\varepsilon_i \sim$ iid $N(0, \sigma^2)$.

Regardless of the solver used to estimate **s**, it is possible with the non-linear regression formulation to estimate z as a negative number (an airquake), or to get an unreasonably large estimate of the depth given known seismicity. One approach to correcting an air quake is to simply set negative estimates of z to zero (the surface). Our efforts focused on the incorporation of constraints on z in the non-linear regression formulation. Fully mature research will provide

a general mathematical framework that allows one to incorporate constraints (or whatever prior information exists) into the estimation problem for all of the parameters.

The research and development presented here assumes the origin time is known without error. Additionally, we have assumed no prior information on latitude or longitude, (y, x). Two different prior distributions for depth were considered: the first a uniform distribution, which assumes equal probability for all possible depths within a reasonable range; the second a shallow-skewed distribution which assigns the greatest probability to very shallow depths.

The test case for this proof-of-concept effort is an event near the coast of Japan whose hypocenter estimation has been difficult to obtain with commonly used location algorithms. The dataset consists of first arriving P waves. Figure 1 shows the 14 locations of stations which observed this event.

RESEARCH ACCOMPLISHED

Mathematical Formulation

The general Bayesian equation is $p(\mathbf{s}|\mathbf{t},\theta) \propto \pi(\mathbf{s}|\theta)\, f(\mathbf{t}|\mathbf{s})$. Here f is the likelihood, which we assume to be Gaussian, and π is the prior distribution; $\mathbf{s}$ represents the vector of parameters, $\mathbf{t}$ is the vector of observed arrival times, and θ is the vector of hyperparameters in the prior distribution defined by physical-basis constraints. Ultimately we are interested in the distribution of the depth given the data, or $p(z|\mathbf{t},\theta)$. For the model given in Equation (1), the parameters are $\mathbf{s} = [x, y, z]^T$, and σ^2. Because we assume that origin time is known without error, τ is not considered a parameter, but a known value. Future work will incorporate τ as an unknown parameter. We can rearrange Equation (1) so that

$$\varepsilon_i = t_i - \tau - T_i(\mathbf{s}),\ i = 1, 2, ..., n.$$

Now the likelihood can be written

$$f(x, y, z, \tau, \sigma) = \prod_{i=1}^{n} \Phi\left(\frac{t_i - \tau - T_i(x, y, z)}{w_i \sigma} \right),$$

where $\Phi(\cdot)$ is the Gaussian cumulative distribution function (CDF). The w_i are weights associated with a data quality measure, such as *deltim* in SeaLoc or signal-to-noise.

The prior distribution, $\pi(\mathbf{s}|\theta)$, is specified as the product of individual priors $\pi(x|\theta)$, $\pi(y|\theta)$, $\pi(z|\theta)$ so that $\pi(\mathbf{s}|\theta) = \pi(x|\theta)\ \pi(y|\theta)\ \pi(z|\theta)$. While this independence-of-priors formulation might be a simplification, we have used it in our proof-of-concept effort.

We have considered two prior distributions for depth: the first a uniform distribution; the second a beta distribution with parameters selected to give the highest probability to shallow depths. The hyper parameters for the beta distribution define a density with the mode at approximately 3 km deep (Figure 2 shows this distribution). Longitude and latitude are constrained with a uniform distribution over a reasonable range of coordinates.

Results

Results are presented graphically for both prior distributions on z and using the uniform priors for x and y (Figures 3 and 4). The results are “standardized”. This standardization is not that of proper probability density construction; however it results in a common scale for the plots. Depths between 0 and 110 km, by 5 km are presented. The figures show only the interesting subset of depths for each z prior distribution.

The least-squares solution is shown as a reference point in each plot as a black dot. The least-squares solution for depth is 100 km. The posterior mode solution is shown by a black asterisk on the depth plot where it occurs.

Under a uniform prior for depth, the maximum posterior density is at 50 km (Figure 3). Not surprisingly, when a shallow-skewed prior is used, the maximum density is at a much shallower depth, 10 km (Figure 4). The mode

travels from the northeast to the southwest as the depth increases; if a fixed (x, y) location were selected, the non-linear behavior of the travel times would be evident as curved contours across depth. With both priors, the mode of the posterior is achieved at a location southeast of the least-squares location estimate.

CONCLUSIONS AND RECOMMENDATIONS

Our proof-of-concept work has demonstrated that a Bayesian formulation of depth estimation can provide physical-basis constraints on the estimate. Next steps include

- seismicity studies to asses the implications and veracity of the new hypocenter locations derived from the developed Bayesian algorithm
- the calculation of the marginal distribution (integrating constant) in order to estimate highest posterior density (HPD) regions, which are analogous to confidence regions, for the location parameters,
- the incorporation of the origin time as an unknown parameter,
- research to determine the influence of the prior distribution on depth when a deep-skewed prior is utilized,
- characterization of the hypocenters for a simulated set of data where the true hypocenter is known, and
- sensitivity analysis with regard to the number of data points needed to overcome the prior distribution.

REFERENCES

Ballard, S. (2004), Seismic event location: dealing with multi-dimensional uncertainty, model non-linearity, and local minima, in *Proceedings of the 25th Seismic Research Review—Nuclear Explosion Monitoring: Building the Knowledge Base*, LA-UR-03-6029, Vol. 1, pp. 193-202.

Carlin, B. .P and T. A. Louis (2000), *Bayes and Empirical Bayes Methods for Data Analysis.* Chapman and Hall, New York.

Kennett, B. L. N. and E. R. Engdahl (1991), Traveltimes for global earthquake location and identification, *Geophy. J. Int.* 105, 405-465.

Kennett, B. L. N., E. R. Engdahl, and R. Buland. (1995), Constraints on seismic velocities in the Earth from traveltimes, *Geophys. J. Int.* 122: 108-124.

Lay, T. and T. C. Wallace (1995), *Modern Global Seismology*, Academic Press, San Diego.

Robert, C. P. and G. Casella (1999), *Monte Carlo Statistical Methods*, Springer, New York.

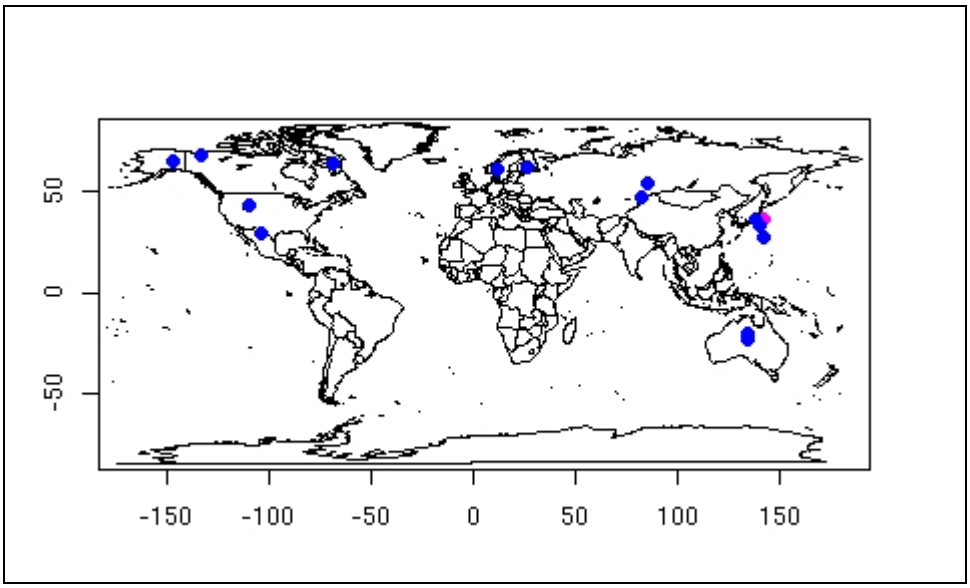

Figure 1. Map showing the estimated location of the event via (pink) least-squares and the stations which observed it (blue).

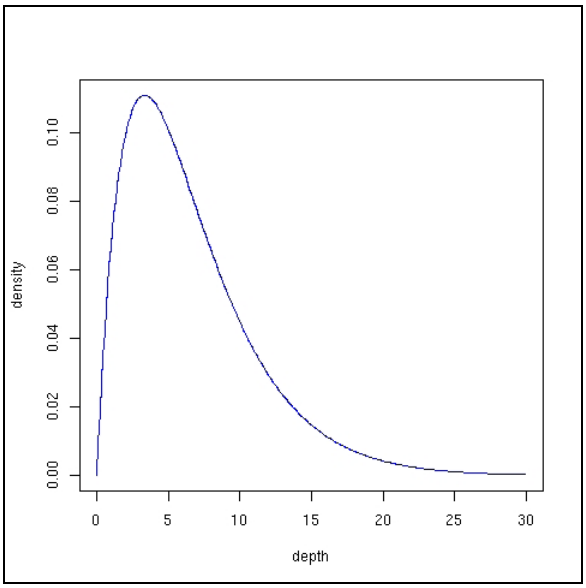

Figure 2. Shallow-skewed beta distribution for the depth parameter.

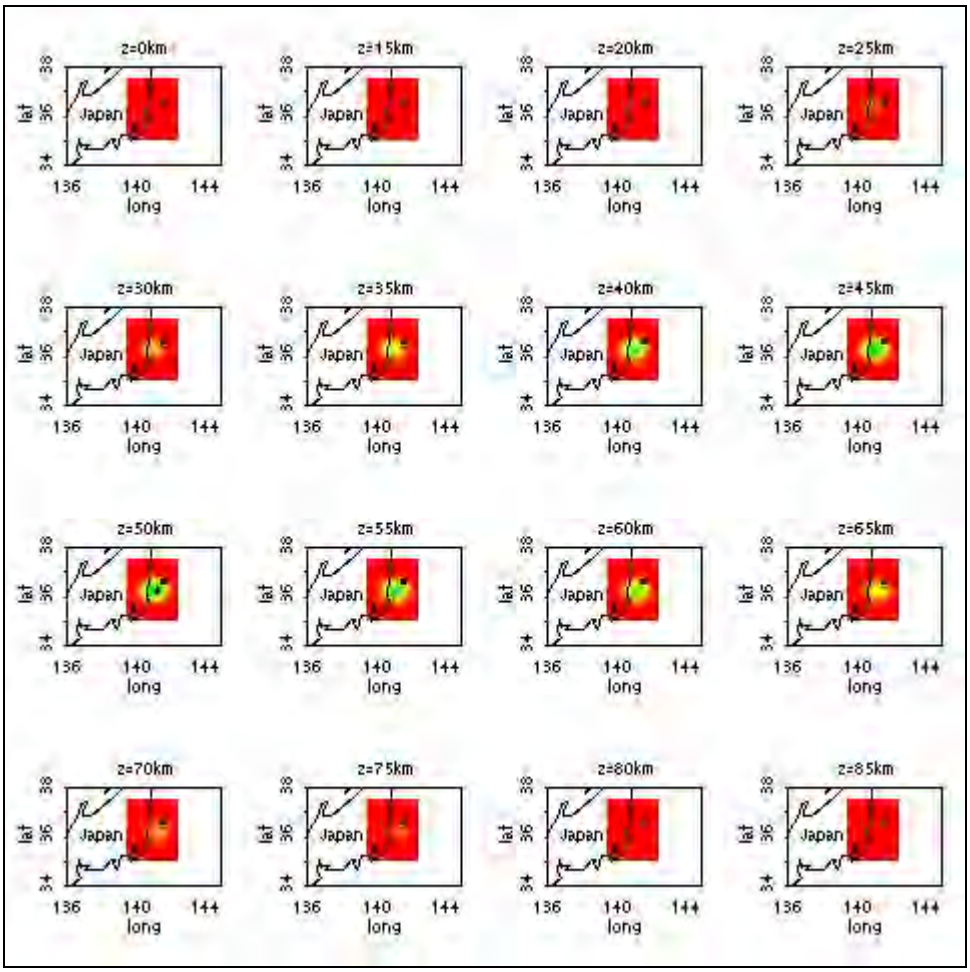

Figure 3. Standardized posterior probabilities for a subset of depths when a uniform prior distribution is used. Yellow to green colors indicate high probabilities.

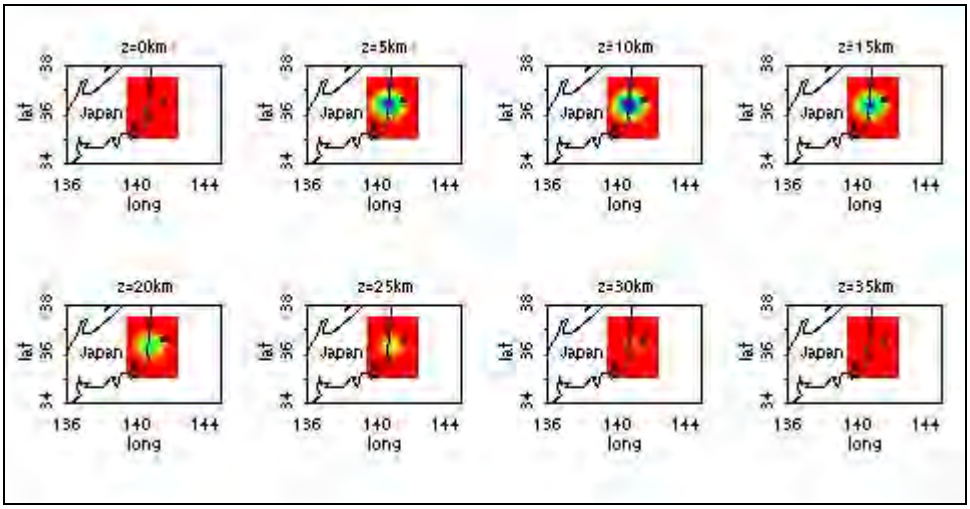

Figure 4. Standardized posterior probabilities for a subset of depths when a shallow-skewed prior distribution is used. Yellow to green to blue indicate high probabilities.

IMPROVED GROUND TRUTH IN SOUTHERN ASIA USING IN-COUNTRY DATA, ANALYST WAVEFORM REVIEW, AND ADVANCED ALGORITHMS

Eric R. Engdahl[1], Eric A. Bergman[1], Stephen C. Myers[2], and Floriana Ryall[2]

University of Colorado[1] and Lawrence Livermore National Laboratory[2]

Sponsored by National Nuclear Security Administration
Office of Nonproliferation Research and Engineering
Office of Defense Nuclear Nonproliferation

Contract No. DE-FC52-03NA99516[1] and W-7405-ENG-48[2]

ABSTRACT

We continue to improve the relative and absolute accuracy of locations for recent large earthquakes through analyzing clusters of earthquakes simultaneously with the Hypocentroidal Decomposition (HDC) method of multiple event relocation. Absolute locations of such clusters are calibrated with reference (or ground truth) event information from local, aftershock deployments or from nonseismic (e.g., InSAR) constraints, which provides independent evidence for the absolute location of one or more of the cluster events. We have used both local network data and InSAR analysis of co-seismic ground deformation for this purpose. There is also potential for using mapped fault zones to provide some constraint on absolute locations. When both location and origin time can be calibrated for a cluster through use of reference event information, we are able to estimate the true travel times to all reporting stations. These estimates are the basis for improved models of the crust and upper mantle, which in the future will permit far more accurate routine earthquake locations using regional seismic data.

Much development work has been done on the HDC code as it is applied to the ground truth problem, with emphasis on statistical rigor and robustness. One focus has been on an improved algorithm for shifting of the cluster hypocentroid to best fit the available ground truth data. We also now include the uncertainties of the ground truth data in this process, which yields more accurate estimates of the uncertainties of the final estimates of absolute (calibrated) locations. The other main focus has been on phase identification. A method based on probability density functions has been implemented, but much additional work is needed for full functionality. An improved (more robust) method for estimating empirical reading errors from cluster residuals has been implemented. Developmental aspects of this work are described.

We have established arrangements for gathering and assessing potential ground truth data and phase arrival-time data for events of interest from local and regional stations in Iran. Many new ground truth (GT5) events are now being obtained as an ongoing activity, and validation of these events is in progress. In addition, we have been able to obtain and apply waveform data and phase readings from digital stations. Example waveforms are shown. For events of interest these data are supplemented with regional and teleseismic phase arrival times carefully read by an expert analyst from seismograms in the waveform data base at Lawrence Livermore National Laboratory (LLNL).

Collaborative efforts continue with scientists at Cambridge and Oxford Universities on seismotectonic applications of cluster analysis and development of new ground truth constraints from geological and remote-sensing (InSAR) data. An example of one such an effort is the analysis of the 2002 Avaj (Changureh) earthquake sequence. A large main shock was followed by a number of smaller events, and a cluster of 17 events was formed. Analysis of the smaller events in the cluster was facilitated by analyst-reviewed phase readings and phase arrival times from stations in Iran. Results using the new HDC developmental code and these new data are shown along with some associated waveforms from digital stations.

OBJECTIVES

This research seeks to improve the database of ground truth information and velocity models useful for calibration in southern Asia with the following objectives: (1) Aggressive pursuit of in-country data acquisition, especially the collection of ground truth at GT5 level or better for events of magnitude 2.5 and larger recorded by dense local networks, including associated velocity models; (2) expanded analyst review of relevant regional waveforms for ground truth events by the comprehensive re-picking of phase arrival times from all available waveforms, with special attention to the regional phases Pg, P*, Pn, Sg, S* and Sn; and (3) application of advanced algorithms, such as those used for multiple event relocation, to refine and validate all available ground truth data, to achieve the optimal selection of data for analysis, to better understand the uncertainties of the results, and to handle the error budget as realistically as possible.

RESEARCH ACCOMPLISHED

Recent Developments of the Hypocentroidal Decomposition Method of Multiple Event Relocation for Application to Ground Truth Studies

Confidence Ellipses for Cluster Vectors

A review of the algorithm used in the hypocentroidal decomposition (HDC) code to derive confidence ellipses for cluster vectors (relative locations relative to the hypocentroid) led to modifications that make it more sensitive to the error budget of individual events. This algorithm was not fully developed in Jordan & Sverdrup (1981), and the HDC code originally used an approach that was based on the equivalent procedure for the hypocentroid. This approach had the effect of averaging the error budget over all events for scaling the ellipses. With more careful choices of parameters, confidence ellipses for "average" events change little, while confidence ellipses for "bad" events become larger (sometimes significantly), and those for very good events become slightly smaller. For ground truth work, in which the emphasis is on very well constrained events, there is little practical difference, but the new method is clearly more rigorous. There is no change to the estimates of cluster vectors themselves.

As shown in Figure 1, the effect of this change is seen primarily for the poorest-located events in a cluster, which tend to have larger confidence ellipses with the new algorithm. In the worst cases, an event located with a small number of readings that have large residuals, the difference can be a factor of 2 or 3 in area.

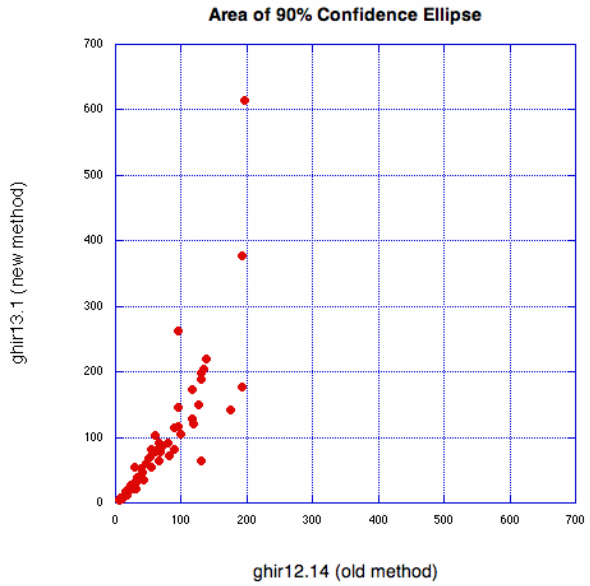

Figure 1. Comparison of the area of the 90% confidence ellipses with old and new algorithms (see text) for cluster vectors of the Ghir cluster.

Robust estimation of reading errors

One of the significant advances in location accuracy that HDC makes possible is the ability to make empirical estimates of reading error for individual station-phase combinations, based on the spread of path-corrected, normalized residuals. In the past, we made these estimates from the standard deviation (SD) of the residuals. Now we use a robust estimate of scale, "Sn," which does not need an estimate of central location and does not assume symmetric distributions (Croux and Rousseuw, 1992). The algorithm for Sn includes correction factors that make it nearly unbiased even at small sample sizes. A comparison of reading errors estimated from the same cluster data by SD and Sn in Figure 2 shows the expected effect of outliers, which cause excessively large estimates of SD. Sn is not so sensitive to outliers. Conversely, SD will yield unrealistically small estimates of spread when there are a small number of readings that happen to be close to one another. Sn is less sensitive to this situation.

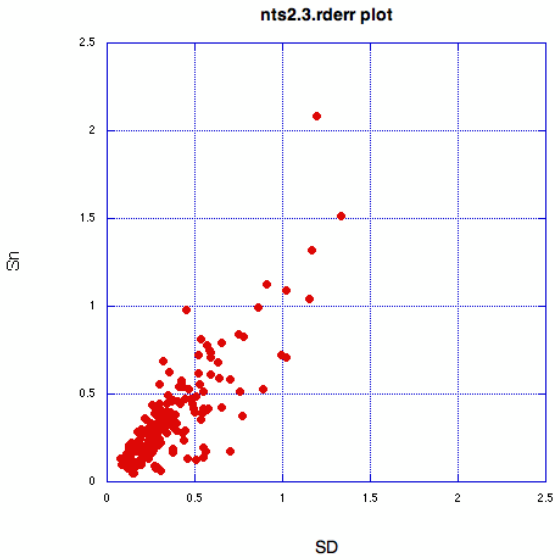

Figure 2. Comparison of empirical reading errors estimated by standard deviation and the robust Sn estimator.

GT Shifting Algorithm

In our ground truth work, we shift the cluster hypocentroid (which is biased by the use of an average global travel time model) to best fit a subset of cluster events with independently known locations. Formerly, we assumed that the ground truth data were all perfectly known. If there were more than one ground truth event, we averaged the shift vectors, ignoring the differing uncertainties of the associated cluster vectors. We now take into account the uncertainty of both the ground truth locations and the cluster vectors in this process.

Weighted Shift Vector

An estimate of the covariance matrix for the GT must be supplied. It can be derived from a single-event location procedure or derived from plausible uncertainties of a geographic estimate such as InSAR analysis of ground deformation. Because the cluster vector and GT are completely independent, their covariance matrices simply add. Each estimate of the shift vector (GT-HDC) is weighted inversely to the area of the 90% confidence ellipse of the combined (HDC+GT) estimation process. Origin time and depth calibration (if relevant) are handled in an equivalent univariate method.

Uncertainty of Ground Truth Calibration

To estimate the uncertainty of the estimated "calibration shift" needed to bring the hypocentroid into optimal alignment with GT data, we add the combined HDC+GT covariance matrices, inversely weighted according to the area of the equivalent 90% confidence ellipses. This yields a covariance matrix that can be added to those of the

cluster vectors and scaled to yield final estimates of the uncertainty of the calibrated absolute locations of all cluster events.

Phase Association

The clusters analyzed by HDC for our GT work have normally been preprocessed in a reviewed EHB (Engdahl et al., 1998) single-event algorithm which re-associates (or re-identifies) readings with phases in the ak135 model. Some additional editing of phase associations has been done by hand within the HDC processing. The EHB process utilizes a probabilistic method to associate readings with depth phases. As shown in Figure 3, the probability density functions (PDFs) for the phases of interest are determined from prior studies. For each reading, the relative probability of association with each depth phase is calculated, and a random number is generated to determine which phase is actually selected, with the appropriate probability. The HDC code has now adopted this approach to phase association for all readings. The algorithm operates on reading groups (all readings from a given station for an event), not individual readings. Phase association is done when data are first read and after the first iteration. If phase association is done after each iteration, even a few unpredictable changes in phase association can prevent convergence.

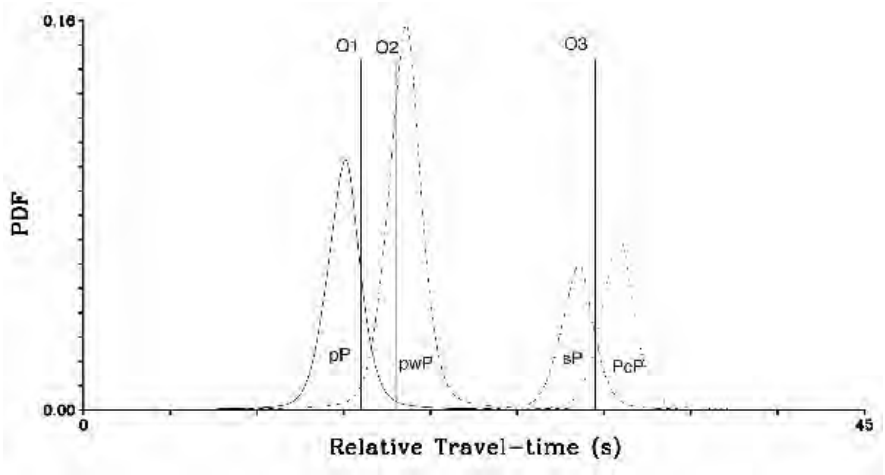

Figure 3. Example of EHB-style probabilistic phase association applied to depth phases.

Rule Set for Phase Association

A set of rules is being developed to incorporate seismological knowledge into this process. The basic idea is that the PDF approach is applied to all theoretical phases (ak135) within a large window (±10 s for P phases, ± 15 s for S phases and unidentified) around the observed arrival, but rules are used to eliminate some phases from consideration. The current rule set is as follows:

1) The initial reading of a station group is normally forced to associate with the first-arriving phase at that distance. This requirement is relaxed if the first reading is an S phase, if the theoretical first arrival would be Pdiff (these are often PKP phases), or if the first reading is very late with respect to the predicted arrival time. Such readings are not allowed to associate as depth phases.

2) A reading can only be associated with secondary arrivals of the same type (P or S, ignoring depth legs), if the phase type can be determined from the original dataset.

3) The first S reading is associated with the first-arriving S phase in ak135 at that distance. If the residual is large, however, an attempt is made to associate it with Lg (not in the ak135 model). If that fails, the reading is turned loose to associate with any eligible secondary phase using the PDF algorithm.

4) Association as a depth phase is only allowed if the corresponding parent phase has been associated.

5) An Lg phase identified by the operator is not automatically re-associated. Other secondary phases (S-type, unidentified, or P-type measured from horizontal components) may be associated with Lg. Lg is only a possible phase for association at distances less than 20° and for sources less than 35 km deep.

Remaining Issues

Estimates of the probability density functions for some phases as a function of source depth and epicentral distance are available, but much work remains to be done. At present, the algorithm operates with identical PDFs for all phases. This cannot be improved incrementally—PDFs for all phases of interest must be updated at the same time to avoid introducing unwanted weighting of different phases. As our suite of GT-calibrated events grows, we will analyze the associated readings to derive more appropriate PDFs for phases of interest.

Ground Truth Data

Critical to our ground truth data discovery and acquisition process are collaborative arrangements that have been made with key organizations in southern Asia. These arrangements are built on exchanges that are mutually beneficial to the parties involved, usually based on our applying advanced techniques to refine locations of the host country's natural seismicity in return for access to in-country ground truth information. These arrangements provide a forum for gathering and assessing potential ground truth data, and collecting waveform and phase reading data for events of interest from local and regional stations. We are also in contact with several groups developing ground truth locations from InSAR-detected ground displacement and other satellite-based location methods that provide important constraints independent of seismic observations. Much new ground truth information is now being obtained from these sources as an ongoing activity. Validation of these data is in progress (Table 1 and Figure 4).

Validation through critical examination of the data and procedures that were used in the local network or InSAR location of a proposed ground truth event is an *internal* process. It is certainly of great value and, in some cases, adequate to guarantee ground-truth levels of accuracy. In many cases, however, an internal validation process of local network locations is highly susceptible to unavoidable uncertainties in the arrival time data and the local velocity structure. For example, there can be undocumented timing errors in the local network, incorrect station locations, incorrectly picked or mis-associated arrivals, and unrealistic estimates of reading error. A very difficult problem in many regions is the specification of a sufficiently accurate velocity structure for the local network location. Investigators rarely have enough information to control all these factors in a validation exercise, and a certain amount of faith is ultimately required in adding such events to a ground truth data set. Therefore, an *external* validation process, one that utilizes other information as a crosscheck on the reported or derived (using HYPOSAT) local network location, is highly desirable. We use HDC, a powerful algorithm for multiple event relocation, as a tool for discovery and validation of ground truth data. HDC is applicable in situations in which several candidate ground truth events and/or InSAR signals are located in a limited region, and in cases where other seismic activity in the area can be localized to known faults and other geologic features. The essence of the validation process is to compare the relative locations in space and time of events based on their ground truth locations, and the relative locations revealed by HDC. An added bonus of the validation process is the generation of additional ground truth events that are of GT5 quality. Although preliminary validation results are already available for nearly all these ground truth data, final results remain pending for most as we await analyst reviewed arrival-time picks and releases of International Seismological Centre (ISC) and United States Geological Survey (USGS) phase data for the more recent events.

Table 1. Ground Truth Data

Name	Date	Origin	Latitude	Long.	Depth	Mag.	Source	Status
Boroujen	78 07 03	01 35 25.9	31.702	51.193	25.1	4.3 (mb)	Local Net	Pending
Tabas	78 10 09	16 04 38.2	33.340	57.283	8.0	4.6 (mb)	Local Net	Validated
	78 10 12	15 01 39.4	33.362	57.334	8.0	4.9 (mb)	Local Net	Validated
Korizon	79 12 02	21 09 34.1	34.047	59.669	4.0	4.1 (mb)	Local Net	Pending
	79 12 11	02 16 58.1	34.023	59.684	4.9	4.4 (mb)	Local Net	Pending
	79 12 16	22 35 35.1	34.094	59.491	5.1	5.0 (mb)	Local Net	Pending
Rudbar	90 07 24	07 27 16.6	36.651	49.769	12.0	4.3 (mb)	Local Net	Pending
Fork	90 11 21	03 42 34.6	28.315	55.498	12.0	4.6 (mb)	Local Net	Pending
Gorgan	91 10 17	15 41 48.1	36.156	53.367	22.0	4.3 (ML)	Local Net	Pending
	91 10 17	19 16 25.6	35.948	53.358	22.0	4.0 (ML)	Local Net	Pending
Sefidabeh	94 02 23	08 02 02.5	30.870	60.520	7.0	6.1 (Mw)	Fit to InSAR	Validated
	94 02 23	11 54 30.6	30.837	60.510	9.0	5.5 (Mw)	Ground	
	94 02 23	22 45 15.5	30.902	60.470	9.0	5.3 (mb)	Displacement	
	94 02 24	00 11 10.1	30.881	60.473	9.0	6.3 (Mw)		
	94 02 26	02 31 08.8	30.817	60.530	9.0	6.1 (Mw)		
	94 02 28	11 13 51.5	30.884	60.527	7.0	5.6 (Mw)		
	94 03 02	14 57 16.9	30.882	60.470	9.0	4.5 (mb)		
Firuzabad	94 03 07	00 57 22.1	29.028	52.678	9.4	4.1 (mb)	Local Net	Pending
Bastak	97 05 05	15 11 52?	27.130	53.881	5.2	5.4 (Mw)	InSAR	Pending
	97 09 18	14 52 52?	27.083	53.492	3.5	5.0 (Mw)	InSAR	Pending
Buyin-Zahradeg	97 06 07	20 29 47.3	36.170	50.480	8.0	3.9 (mb)	Local Net	Pending
Chakhu	97 06 20	12 57 32?	32.28?	60.00?	2.0	5.6 (Mw)	InSAR	Pending
Sahlabad	98 04 10	15 00 50?	32.25?	60.02?	6.7	5.8 (Mw)	InSAR	Pending
Ghir	97 12 26	01 05 32.9	28.109	53.467	13.1	4.2 (mb)	Local Net*	Validated
	97 12 26	05 08 00.1	28.088	53.468	15.0	4.1 (mb)	Local Net*	Validated
	99 04 30	04 19 59.9	27.870	53.628	4.1	5.3 (Mw)	InSAR	Validated
Kerman	98 03 14	19 40 29?	30.14?	57.59?	9?	6.6 (Mw)	InSAR	Pending
	81 08 10	21 29 19.1	30.107	57.688	17.0	4.1 (mb)	Local Net	Pending
	81 08 20	19 02 08.7	30.170	57.473	12.8	4.6 (mb)	Local Net	Pending
Zagros	98 10 18	10 02 39?	28.6777	54.245	1.4	4.5 (Mw)	InSAR	Pending
Tabriz	99 08 19	04 33 11.3	38.513	46.559	10.1	4.5 (mb)	Local Net	Pending
Avaj	02 07 03	19 24 39.2	35.731	49.026	7.4	4.3 (mb)	Local Net*	Validated
Alborz	03 06 21	15 00 01.3	35.498	52.661	?	4.5 (mb)	Local Net	Pending
	03 06 22	03 39 09.1	35.471	52.730	?	4.3 (mb)	Local Net	Pending
Bam	04 01 11	05 06 02.8	28.908	58.287	10.0	4.1 (mb)	Local Net	Pending
Baladeh	04 05 29	09 23 48.3	36.466	51.365	14.2	4.7 (mb)	Local Net	Pending
	04 05 30	19 27 00.7	36.390	51.631	7.4	4.4 (mb)	Local Net	Pending
	04 06 07	04 01 20.7	36.427	51.511	7.3	4.3 (mb)	Local Net	Pending
	02 04 08	18 30 52.1	36.513	51.937	8.5	4.1 (mb)	Local Net	Pending
Zarand	05 02 22	02 25 22.1	30.774	56.736	14.1	5.7 (mb)	Local Net	Pending
	05 05 14	18 04 54.8	30.806	56.991	14.1	5.4 (mb)	Local Net	Pending

* HYPOSAT Location

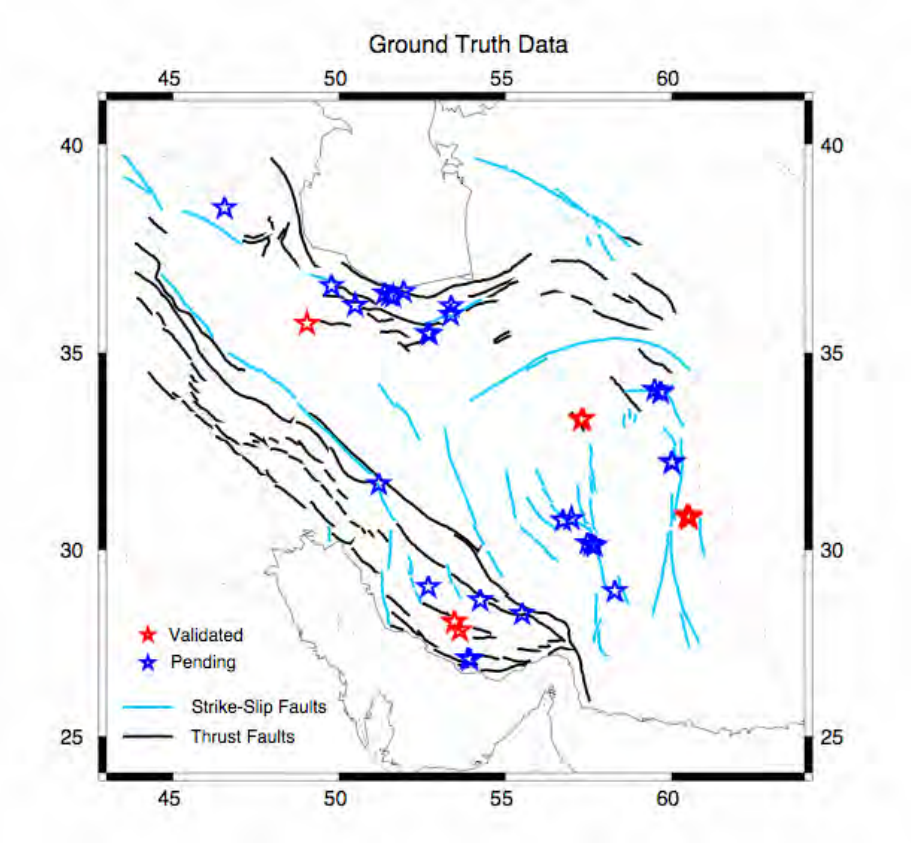

Figure 4. Ground truth data that have been validated or for which validation is pending.

Validation of Ground Truth Data

The HDC method for validation yields improved accuracy for both the relative and absolute locations of clustered earthquakes. The gist of the method is to use a multiple-event relocation method with regional and teleseismic phase arrival times to constrain relative locations of clustered earthquakes and then to calibrate the absolute location of the cluster by obtaining independent information on the absolute location of one or more members of the cluster. For each cluster, there is independent information on location that helps to calibrate the absolute locations. The Avaj cluster shown here, extracted from our new catalog of phase data for events in Iran, will illustrate our approach to this important problem. The HDC analysis includes further refinement of the data set by making empirical estimates of readings errors and using these estimates to help identify outliers. These steps yield significant improvements in accuracy and resolution for the relocations. Of course, the main benefit of HDC analysis is to largely remove the biasing effects (path anomalies) of lateral heterogeneity in the Earth, which permits much better resolution of the relative locations of cluster earthquakes.

In developing ground truth databases, we have previously depended almost entirely on arrival time picks reported in the catalogs of international agencies, such as the ISC and the USGS's National Earthquake Information Center (NEIC). While these picks have proven to be quite useful in the analysis of clustered ground truth events, where the statistical properties of source-station path anomalies can be determined, reading errors are often large and, of course, the picks cannot be confirmed. We address that deficiency by expanded analyst review of relevant waveforms that can be acquired for ground truth events in all countries of southern Asia. Our expanded analyst reviews will include the comprehensive repicking of phase arrival times from all available waveforms, with special attention to the regional phases Pg, P*, Pn, Sg, S*, and Sn. The product will be improved databases for all existing and newly discovered ground truth events of magnitude 2.5 and larger in southern Asia, including isolated single events in regions that are difficult or impossible to access. Through analyst review of waveform data, we will be able to update and replace catalog picks with analyst picks not only for new events but also for ground truth events in clusters that we already have studied. The goals will be to expand, further refine, and reduce the uncertainties

(better statistics) in station path anomalies to those clusters, to eliminate or minimize reliance on catalog picks, and to restate the scale length of lateral heterogeneity in the region.

Avaj (Changureh): Calibration Using Aftershock Survey Data and Comparison with Geological Mapping and Remote Sensing Data

The cluster consists of the June 22, 2002, Mw 6.4 Changureh mainshock, aftershocks, and several earlier events, 17 events in total. The result of our HDC analysis of the Changureh earthquakes is shown in Figure 5. The relative locations of events are plotted with respect to the hypocentroid or geometrical center of the cluster vectors that describe the relative locations.

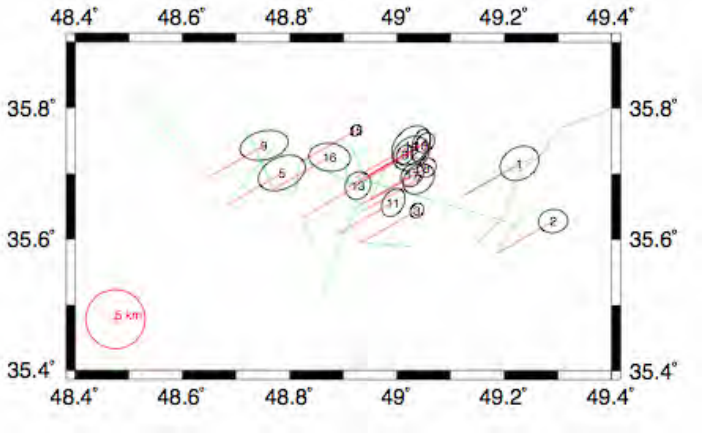

Figure 5. Relocated epicenters of the Avaj cluster. 90% confidence ellipses for relative locations (cluster vectors) are shown. Line to each event shows change in location from starting (EHB single event) location. Green segment is the change due to HDC analysis, red segment is the shift required to bring the cluster into agreement with the ground truth data for this cluster (event 12). Variable gray lines are rivers.

The Changureh mainshock (#3) is at the southeastern edge of the 1992 seismic activity. Events 1 and 2 are from 1967 and 1984. These results support a fault model in which rupture initiated in the southeast end of the rupture zone and propagated unilaterally to the northwest for 20-25 km (Walker et al., 2005). This finding would be consistent with the source time function duration of about 5 seconds, derived from body wave modeling by the Cambridge group.

We obtained arrival time data for one of the cluster events (#12) from an aftershock study by a group of IIEES scientists and also a crustal model derived from the aftershock study of Changureh (Farahbod, personal comm.). We relocated the event using the HYPOSAT code of Schweitzer (2001) and used this location to calibrate the absolute location of the HDC cluster. The mislocation vector is rather typical of those we have found in southern Asia, 10.8 km at an azimuth of 60°, with an origin time shift of -1.87 seconds.

Regional Path Anomalies and In-Country Seismograms

We use the calibrated cluster arrival time data to infer empirical path anomalies (relative to the global model ak135) from the Avaj source region to surrounding seismic stations. Figure 6 shows the results for Pn and P phases at regional distances. There is broad consistency of path anomalies at most azimuths. The early arrivals at stations in Saudi Arabia reflect propagation across the Arabian shield. The path anomalies can be the result both of variations in bulk velocity and differences in ray paths caused by lateral heterogeneity.

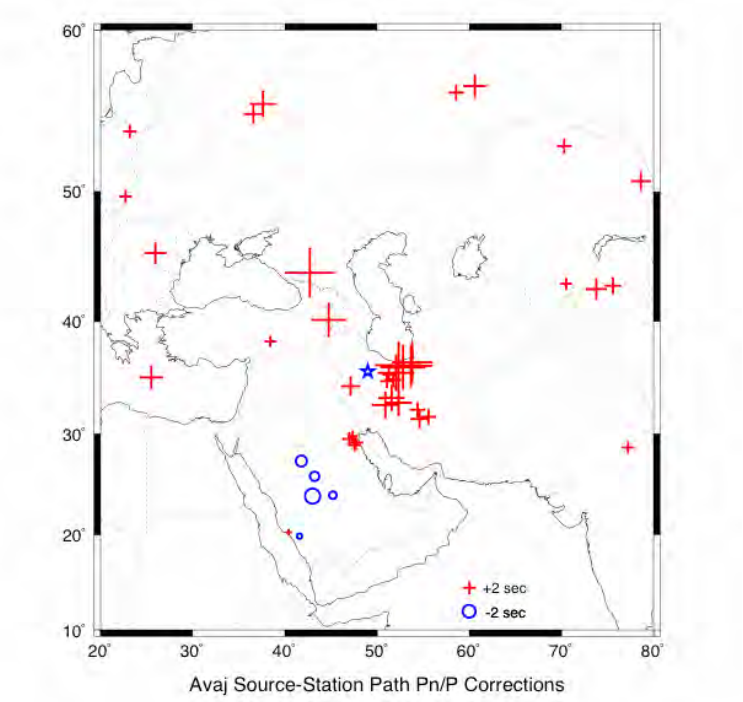

Figure 6. Empirical path anomalies (relative to ak135) for Pn and P phases from Avaj (star).

Figure 7 is a location map of digital stations that have operated or are currently operating in Iran. Stations of the Iranian Seismological Telemtry Network (ISTN) are separated into sub-networks whose data are compiled into a single database of phase data and waveforms. Example waveforms extracted from this database for the Avaj cluster are displayed in Figure 8.

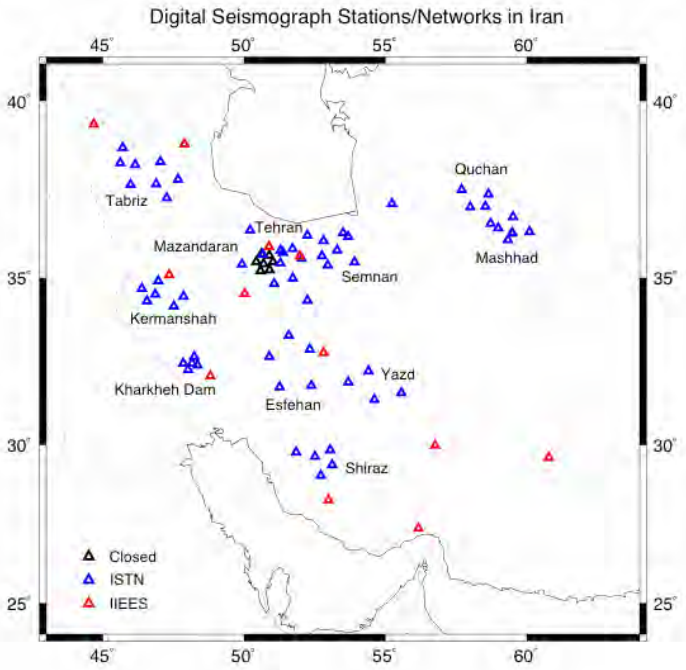

Figure 7. Digital seismograph stations that have operated or are presently operating in Iran.

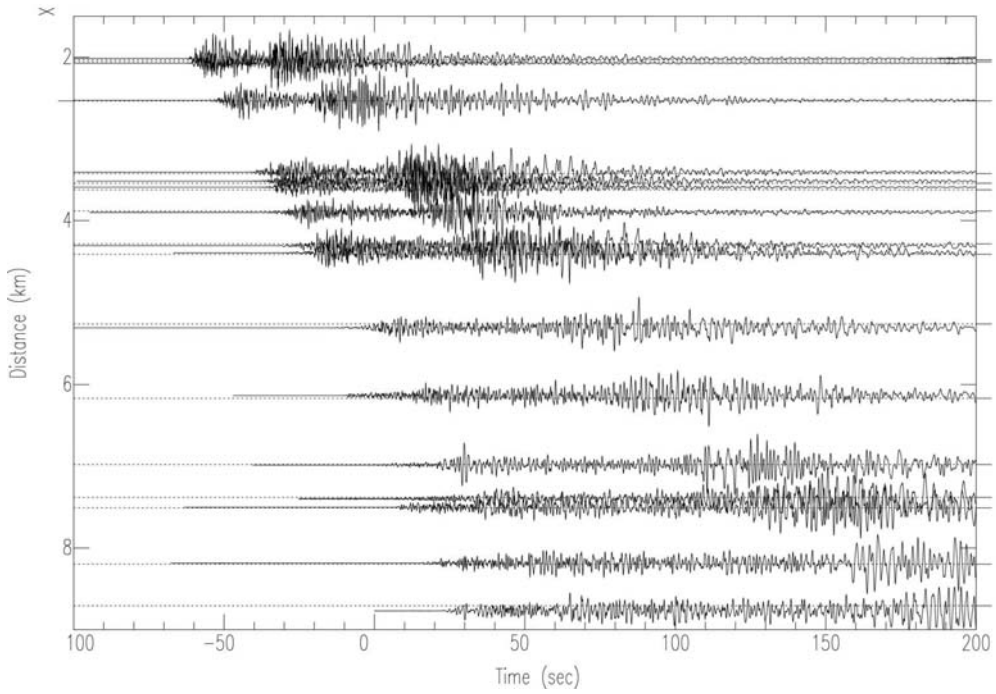

Figure 8. Sample record section of ITSN regional seismic stations, for the Avaj mainshock.

CONCLUSION(S) AND RECOMMENDATION(S)

We have developed several new ground truth events in southern Asia, based on detailed multiple event relocation and use of reference events, both from local seismic network data and from InSAR data. The use of analyst-reviewed picks is extremely helpful in some circumstances, and the practice should be expanded. The greatest value comes from having the analyst read seismograms from stations that were not reported in the standard global catalogs. We are continuing to develop resources for local network data inside Iran and expect these efforts to lead to new ground truth events and resulting data on empirical path anomalies that will substantially improve location capabilities in this region.

ACKNOWLEDGEMENTS(S)

We are grateful to Eric Fielding, Richard Walker and James Jackson at Bullard Laboratories, Cambridge University, for providing data, figures, and advice used in this study.

REFERENCE(S)

Croux C., and P. J. Rousseuw (1992),Time efficient algorithms for two highly robust estimators of scale, *Computational Statistics, V1*, Dodge and Whittaker, ed., *Physica-Verlag, Heidleberg*: 411–428.

Engdahl, E. R., R.D. Van der Hilst and R.P. Buland (1998), Global teleseismic earthquake relocation with improved travel times and procedures for depth determination, *Bull. Seism. Soc. Amer.*, v. 88: 722–743.

Jordan, T.H. and K.A. Sverdrup (1981), Teleseismic location techniques and their application to earthquake clusters in the south-central Pacific, *Bull. Seis. Soc. Amer.*, 71, 1105-1130.

Schweitzer, J. (2001), HYPOSAT - an enhanced routine to locate seismic events, *Pure appl. geophys*. 158: 277–289.

Walker, R. T., E. Bergman, J. Jackson, M. Ghorashi, and M. Talebian (2005), The 2002 June 22 Changureh (Avaj) earthquake in Qazvin province, northwest Iran: epicentral relocation, source parameters, surface deformation and geomorphology, *Geophys. J. Int.*, 160: 707–720.

GROUND-TRUTH EVENT LOCATIONS USING CROSS-CORRELATED SEISMIC PHASES AND SATELLITE IMAGERY

Mark D. Fisk[1] and Stephen C. Myers[2]

ATK Mission Research[1] and Lawrence Livermore National Laboratory[2]

Sponsored by National Nuclear Security Administration
Office of Nonproliferation Research and Engineering
Office of Defense Nuclear Nonproliferation

Contract Nos. DE-FC52-03NA99515[2] and W-7405-ENG-48[2]

ABSTRACT

Efforts are described to establish ground-truth (GT) locations of industrial blasts in South Korea that can be used to calibrate seismic travel times. Our approach is to apply waveform cross-correlation and master-event location techniques to obtain precise relative locations of event clusters, and use high-resolution satellite imagery to associate the clusters to observed surface features of blasting activity. Currently, eight clusters of blasts have been analyzed using cross-correlated seismic phases (Pn, Pg, and/or Lg), mainly recorded by KSRS and INCN, to estimate relative locations of events within each cluster. Seven clusters have been fixed to specific sites, based on examination of surface features in IKONOS satellite imagery. Another cluster has been located relative to a nearby fixed cluster, but has not yet been associated with surface features in imagery. Efforts so far have resulted in 133 GT events. Four events are categorized as GT0, 100 as GT1, 18 as GT2, and 11 as GT5 or better. An important ramification of this research is that very precise relative location estimates (i.e., within hundreds of meters) can be obtained for small explosions using as few as three seismic phases recorded by only two stations, if the phases are aligned properly, despite very large azimuthal gaps (e.g., 290 to 340 degrees) for most of these events. Implications of these results are discussed with regard to (1) location performance for small explosions using limited seismic data; and (2) extensive applicability of this technique to establish valuable ground-truth location information for clusters of surface blasts in many other regions.

OBJECTIVE

The objective of this effort is to establish ground-truth (GT) locations of industrial blasts on the Korean Peninsula and in China that can be used to calibrate seismic travel times and thereby improve the accuracy of location estimates in such regions. This is difficult (or impossible) to accomplish using seismic data alone, since international stations are very sparse and relevant local networks generally do not provide data to foreign researchers. Thus, additional information, such as space-based imagery, must be used to ascertain GT locations. Our approach is to collect seismic data for relevant blasts, apply waveform cross-correlation and master-event location techniques to obtain precise relative locations of event clusters, and use high-resolution satellite imagery to associate these clusters to visible surface features of blasting activity.

RESEARCH ACCOMPLISHED

As part of previous research and development efforts by Science Applications INternational Corporation (SAIC) and ATK/MR (Barker et al., 2004; Kohl et al., 2004), 219 seismic-acoustic (SA) events, presumably blasts in a larger listing by Che (2002, personal communication), were processed to automatically cross-correlate Pg and Lg phases among the events at KSRS (Wonju seismic array, Republic of Korea). Nearest-neighbor cluster analysis was applied to the geometric mean of Pg and Lg maximum cross-correlation values to form 10 main clusters from 195 of the 219 events. Eventually, the cross-correlation and cluster analyses were applied to 628 events on the Korean Peninsula, of which 408 events were formed into 28 clusters, the first 10 correspond to the initial set of clusters. All but 4 of these 28 clusters include at least one member listed as an SA event by Che (2002, personal communication). These data were used as a starting point for this effort.

Currently, eight clusters of industrial blasts on the Korean Peninsula have been analyzed using cross-correlated Pn, Pg, and/or Lg phases mostly recorded by KSRS and INCN (seismic station near Inch'on, Republic of Korea) to estimate relative locations of events in these clusters. Seven of these clusters have been fixed to specific sites, based on surface features in IKONOS imagery. Another cluster has been located relative to a nearby fixed cluster, but surface evidence of these blasts has not yet been found in imagery. The analyses and results are illustrated below for a couple of cases in South Korea, and some concluding remarks are provided. Other clusters have also been analyzed partially; however, due to limited signal-to-noise ratio (SNR) mainly at INCN, seismic data from one or more additional stations are needed in order to obtain locations estimates using cross-correlated arrival times.

Master-Event Location Analysis

As a starting point for this work, the small stars in Figure 1 represent preliminary location estimates of events in South Korea from Barker et al. (2004), color-coded by membership in a given cluster. The circles correspond to additional events that were not assigned to any of the 28 clusters. Note that cross-correlated arrival times were not used to estimate these locations. Spatial dispersion within clusters is mostly due to variations of automatic phase picks and/or phase identification errors for the more obvious outliers. A significant number of these events were located using arrival time, azimuth, and slowness data from KSRS only. The large stars in Figure 1 correspond to location results obtained under this effort, using cross-correlation and master-event analyses, and shifted to GT locations, based on examination of satellite imagery.

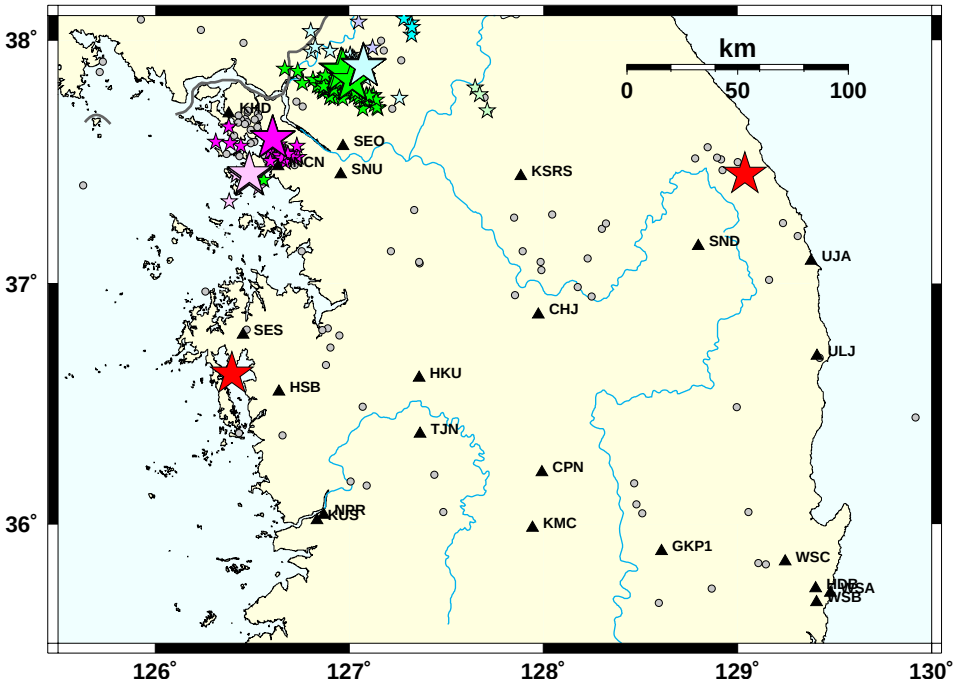

Figure 1. The small stars depict preliminary location estimates of events in South Korea from Barker et al. (2004) that were assigned to a cluster, based on nearest-neighbor cluster analysis of Pg and Lg cross-correlations. The large stars represent the GT location results obtained thus far under this effort. Stars are color-coded by membership in a given cluster.

In the analyses below, the cross-correlated arrival time offsets for Pg and Lg at KSRS were used to automatically align relative phase picks among events. All picks were reviewed and refined interactively in *geotool* and additional arrivals at KSRS and INCN were picked. Data from CHNAR and some Korean Meteorological Agency (KMA) stations are available for some events, but presently not for enough events at common stations to be very useful in the following analysis. As an example, Figure 2 (left) shows KS31/bz seismograms, filtered in the 2-8 Hz band, for four events. Figure 2 (right) illustrates the similarity of Lg phases for two of the events. This allows for very precise relative phase picks, which lead to precise relative locations of the events.

A master event was then selected for each cluster and their epicenters fixed, based on surface evidence of blasting activity in IKONOS satellite imagery and other considerations, discussed below. Fixing the epicenter and depth, *LocSAT* was used to estimate the origin time and travel-time residuals (relative to IASPEI91) of each master event. These residuals were then used to correct the travel times of corresponding phases/stations for the other events in the same cluster and *LocSAT* was used to estimate their epicenters and origin times, with all depths fixed at the surface. This is the same procedure that was used by Fisk (2002) to obtain very accurate locations of underground nuclear explosions at the Lop Nor test site. Case-specific details are described below.-

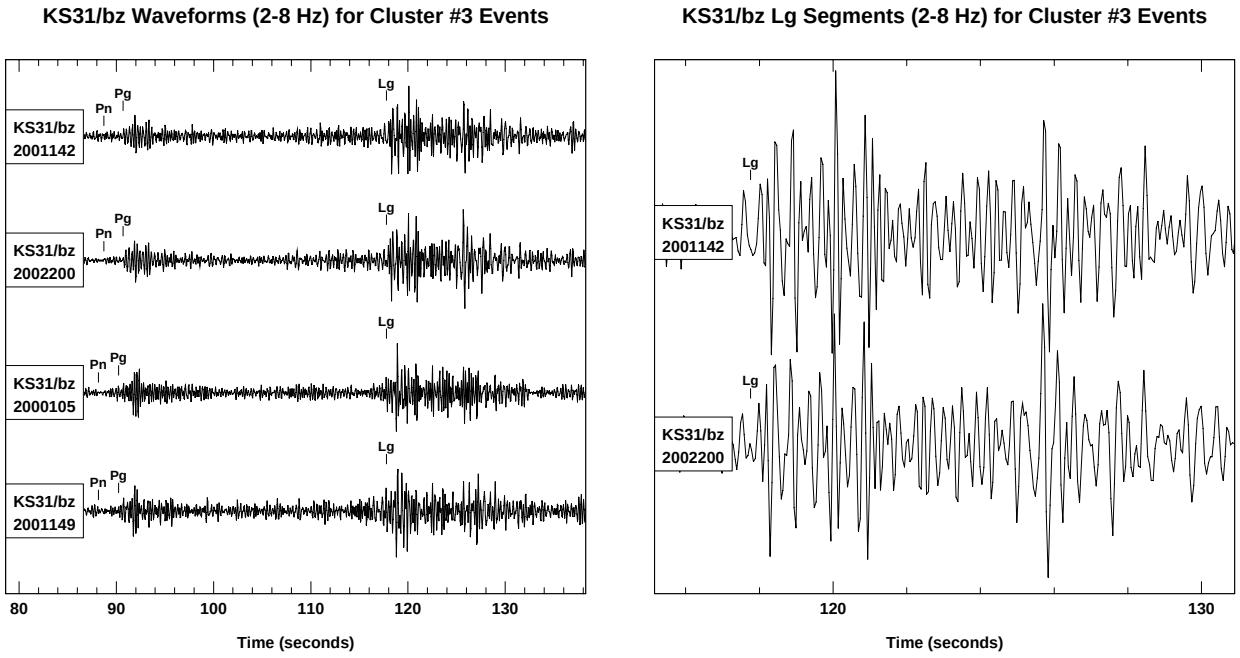

Figure 2. Example of KSRS (KS31/bz) waveforms filtered in the 2 to 8 Hz band for four selected mining blasts (left) and Lg waveform segments for two of the mining blasts (right), showing the similarity of Lg phases.

Example #1: Quarries in South Korea

As noted by Stump et al. (2002), numerous blasts to the south of CHNAR correspond to hard rock mines (quarries) in South Korea, and most of these shots use modest amounts of explosives and are delay-fired. Seven main clusters of seismic-acoustic events were formed by Barker et al. (2004) for this general area, although only two clusters (#2 and #4) currently include enough events with sufficient SNR at two or more stations (mainly KSRS and INCN) to allow application of the master-event analysis. Access to CHNAR data for these events would allow improved accuracy of the solutions and application of the analysis to additional clusters. Figure 3 shows the preliminary locations estimates of these events (small stars), the GT solutions obtained (large red stars), and footprints of satellite imagery used. Since clusters #2 and #4 are separated by less than about 10 km, both clusters were analyzed simultaneously to ensure consistent seismic phase picks (Pg and Lg at KSRS and INCN) and relative locations among the events in the two clusters. Matching the pattern of relative locations of these clusters to a pattern of surface features in the satellite imagery also helps to confirm the uniqueness of the absolute locations.

Figure 4 shows a dendrogram of the nearest-neighbor linkage for 123 events in clusters #2 and #4, using the geometric mean of Pg and Lg maximum cross-correlation values at KSRS as a similarity measure. The analysis forms two to four subclusters of events, depending on the similarity value at which the dendrogram is cut. It is not clear how much the variations in cross-correlations are due to spatial separation, variations in blasting practices, and/or SNR, but the cross-correlations for all combinations of these event pairs range from less than 0.05 to greater than 0.86.

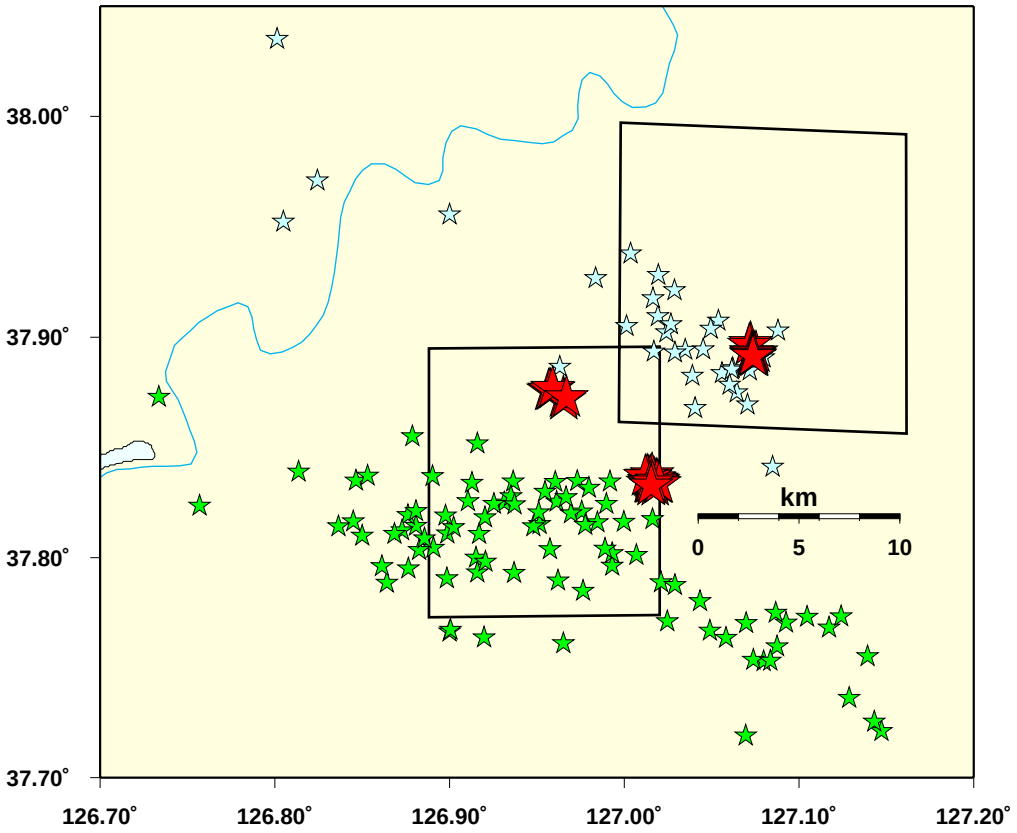

Figure 3. Preliminary location estimates of events assigned to clusters #2 (green stars) and #4 (blue stars), as in Figure 1. The large red stars represent the GT location results obtained for these events. The two rhombi indicate the footprints of satellite imagery that are shown in Figures 5 and 6.

Stump (2004, personal communication) provided the GT location and origin time for a shot on September 26, 2000. However, available data for this event are currently limited to KSRS. In order to utilize the GT0 information, the location and origin time of the 2000/09/26 shot were fixed and the travel time residuals for Pg and Lg at KSRS were computed. Another event on 23 June 2001 was found with high waveform cross-correlation at KSRS to the GT event. Making the assumption that these events are closely located, the epicenters of both events were fixed at the same location and the relative Pg and Lg arrival times at KSRS were used to estimate the origin time of the June 23, 2001, shot. With depth, epicenter, and origin time of this event fixed, this allows the travel time residuals for Pg and Lg at KSRS and INCN to be computed. Based on this procedure, the June 23, 2001 shot was then used as the master event to locate the other events in clusters #2 and #4. Note that the GT information could be used more straightforwardly if CHNAR data become available for the September 9, 2000, GT event and one or more of the other events. Nevertheless, the absolute location accuracy of the master event is well within one km and the origin time is estimated to be consistent relative to the GT information provided by Stump (2004).

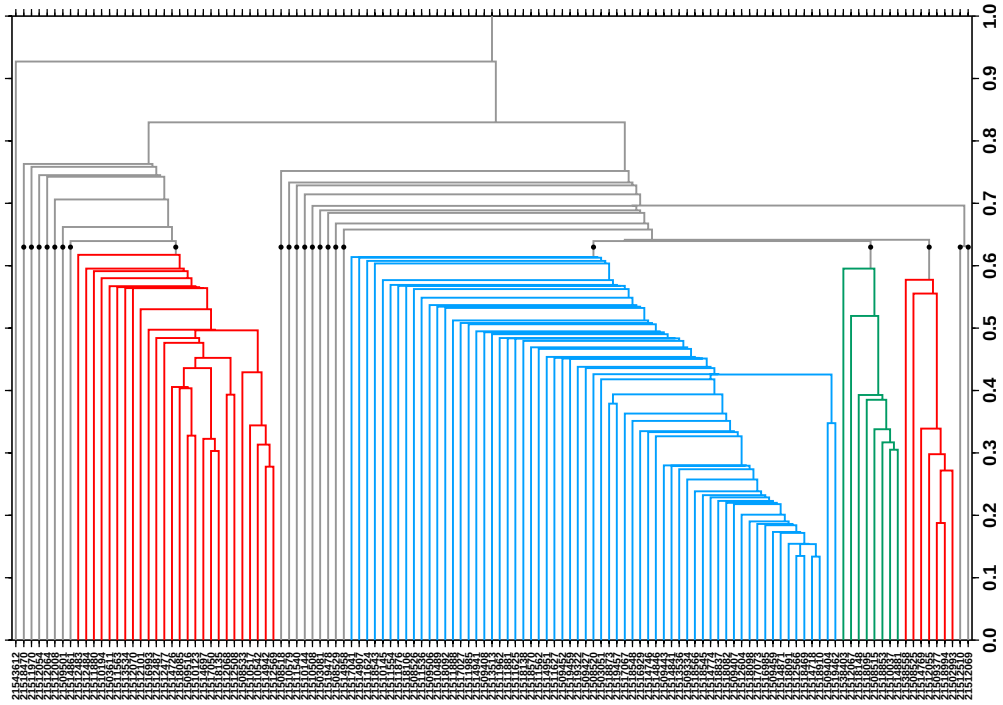

Figure 4. Dendrogram of nearest-neighbor cluster analysis for clusters #2 and #4, showing distinct subclusters. The axes represent the orid and one minus the maximum cross-correlation.

Origin times and epicenters were estimated for 41 blasts of cluster #2, using mostly arrival times of Pg and Lg at KSRS and Lg at INCN (some larger blasts also have Pg picks at INCN), relative to the June 6, 2001, master event. Figure 5 depicts these location estimates (red stars) on an IKONOS image containing a prominent quarry in South Korea. The majority of blasts are associated with this quarry. Eight of the events form two small subclusters of blasts that appear to be associated with a water reservoir approximately six km to the northwest of the quarry. The locations of these eight events are within one km of apparent dam-like features at two ends of the reservoir. The reliability of these solutions is still being investigated. The solutions of the other 32 quarry blasts are well within one km of the master event and visible quarry features, and their origin times are also fairly well constrained by the GT information and procedure above. Thus, these events are categorized as GT1.

Origin times and epicenters were also estimated for 25 blasts of cluster #4, using arrival times for Pg and Lg at KSRS and Lg at INCN and the June 6, 2001, shot of cluster #2 as the master event. Figure 6 depicts these location estimates (red stars) on an IKONOS image containing a small quarry about 8 to 9 km to the northeast of the quarry seen in Figure 5. Location estimates of 22 blasts are within 135 meters of each other and three other blasts are located about 500 meters to the north. These latter three blasts also appear as a fairly distinct subcluster in the dendrogram of the cluster analysis. The location estimates of all 25 blasts are well within one km of the quarry, and their origin times should also be fairly well constrained by the GT information and procedure described above. Thus, these events are also categorized as GT1. It is remarkable that the precise relative locations for these events in clusters #2 and #4 were estimated using only 3-4 phases at 2 stations with azimuthal gaps greater that 260 degrees.

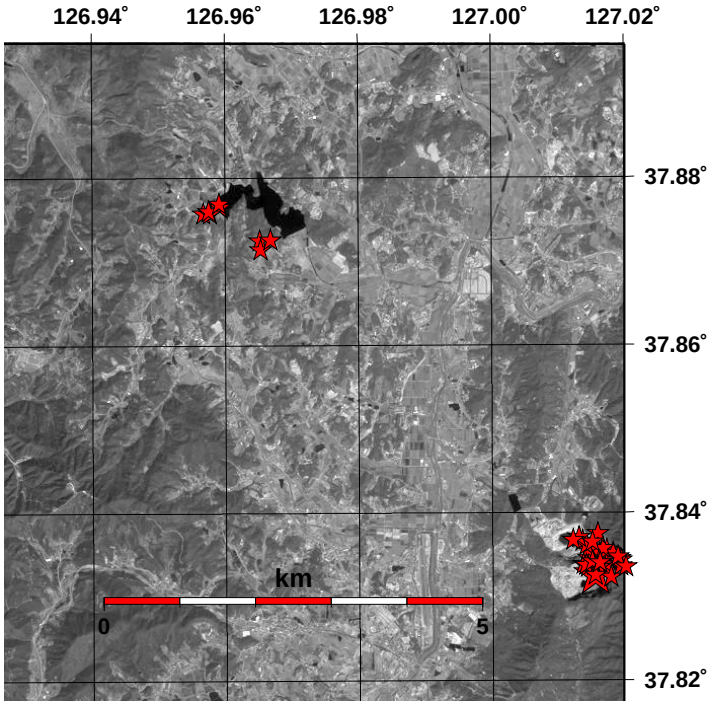

Figure 5. Location estimates of cluster #2 blasts (red stars) on an IKONOS image containing a quarry in South Korea. The main cluster of blasts is associated with the quarry and two small subclusters of blasts appear to be associated with a water reservoir about 6 km to the northwest of the quarry.

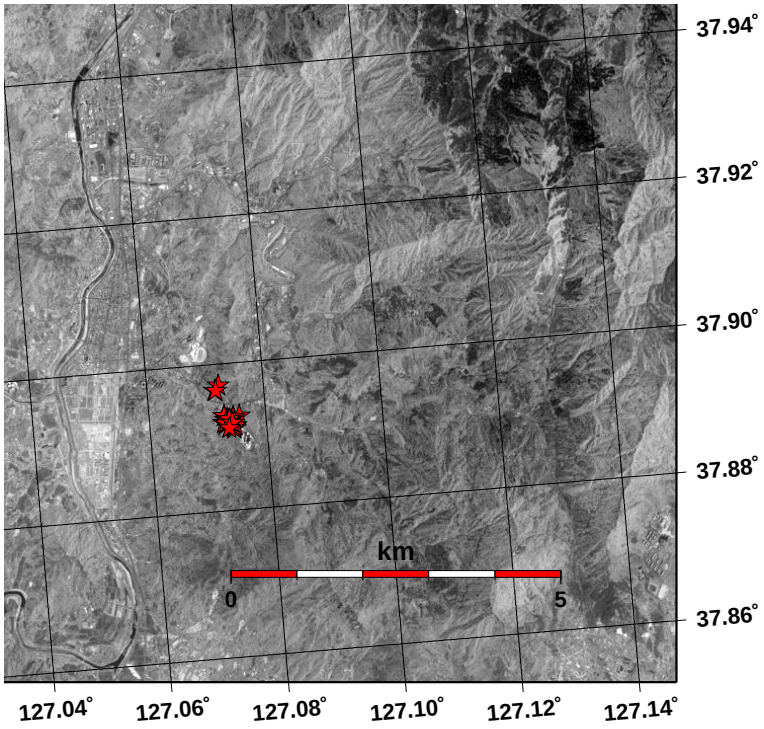

Figure 6. Location estimates of cluster #4 blasts (red stars) on an IKONOS image containing a small quarry in South Korea about 8 to 9 km northeast of the quarry shown in Figure 5.

Example #2: Inch'on International Airport

Numerous blasts were used in the construction of an international airport near Inch'on, Republic of Korea (e.g., Stump et al., 2000, 2001, 2002), such as to flatten topographic features. Many of these blasts produced clear seismic signals at KSRS, INCN, CHNAR, and other stations, and infrasonic signals at CHNAR. In this analysis, two clusters of events were located using Pg and Lg phases at KSRS and INCN (3-4 defining phases with azimuthal gaps of 289 to 343 degrees). Seismic and GPS instruments were deployed locally to record two blasts on April 6 and 7 2000. Stump (2004, personal communication) provided their GT locations and origin times. The blast on April 7, 2000, is used as the master event, with its epicenter, depth, and origin time constrained to the GT information provided. Epicenters and origin times were estimated for eight blasts that are part of a cluster of shots used to level an island at the airport and for nine additional blasts located relative to the April 7, 2000, master event at the airport site.

Figure 7 shows the location estimates of the events in both clusters and an IKONOS image of the airport that provides visible evidence of surface blasting slightly west of the estimated epicenters (red stars). In fact, the entire image is shifted slightly west relative to the event locations and coastline data, presumably due to a minor image registration error of ~200 meters. Regardless, the two blasts on 6-7 April 2000 are categorized as GT0, based on information from Stump (2004), and the location estimates of the other six nearby events are within 535 meters and are considered to be GT1. The other nine events form a relatively tight cluster about 20 km to the northeast of the cluster at the airport (blue stars in Figure 7). IKONOS imagery have been examined to find surface features associated with these blasts on the mainland, but unsuccessfully so far. Independent analysis of backazimuth estimates from two infrasound arrays (Barker *et al.*, 2004) corroborates the relative location of this cluster obtained here using cross-correlated seismic data. The GT quality of these solutions is still under investigation, but appears to be GT5 or better.

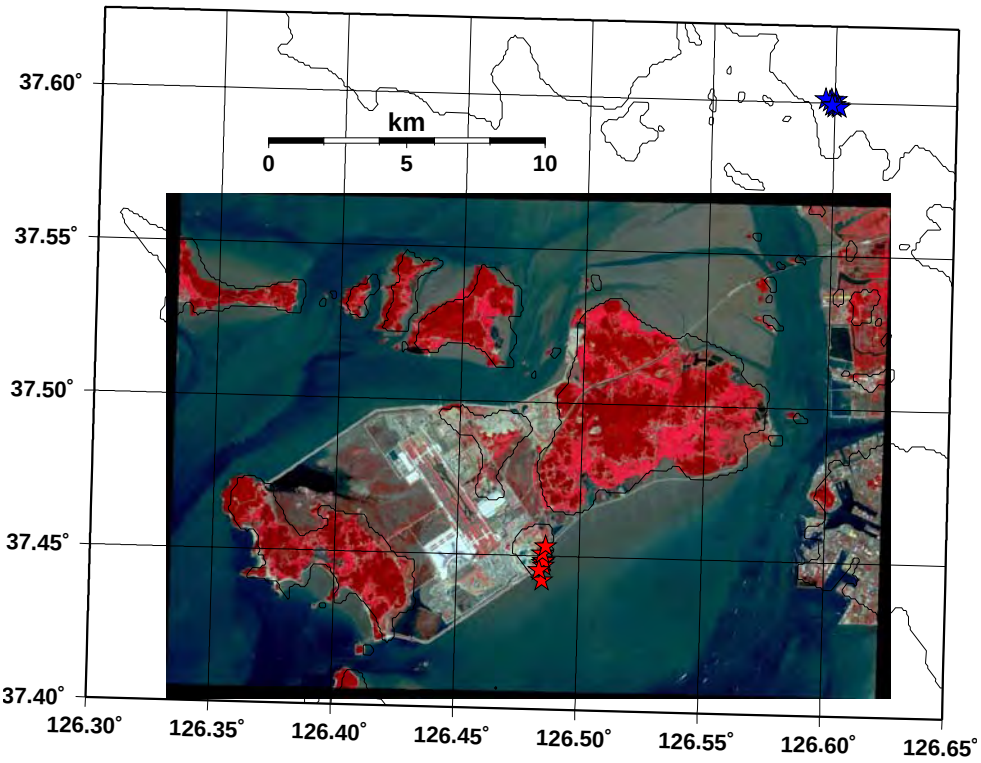

Figure 7. Location estimates of two clusters of blasts, separated by about 20 km, near the Inch'on International Airport, Republic of Korea, using a master event (7 April 2000) at the airport.

CONCLUSIONS AND RECOMMENDATIONS

Efforts thus far have produced 133 GT events for the Korean Peninsula. Four events are categorized as GT0, 100 as GT1, 18 as GT2, and 11 as GT5 or better. The examples shown above illustrate the analysis procedures and typical results, although the other cases do not have *a priori* GT information. Although further work is being pursued to improve the GT quality of some of these solutions, the existing results are suitable to help calibrate travel times of seismic phases for this region and to evaluate the performance of location capabilities. Dr. Myers has independently reviewed these results and reproduced location estimates to within the stated accuracies of the solutions.

Figure 8 shows histograms of the number of defining phases and azimuthal gaps for the 133 event locations obtained in this study. Most of the solutions used four or fewer defining phases at two stations with almost all azimuthal gaps greater than 260 degrees. (Solutions for five events also included cross-correlated seismic phases recorded by numerous KMA stations.) Indeed, a remarkable outcome of this study is that very precise relative location estimates (i.e., within hundreds of meters) can be obtained for small blasts using only 3 to 4 seismic phases recorded by as few as 2 stations, if the phases are properly aligned (i.e., cross-correlated), despite very large azimuthal gaps of 260 to 340 degrees for most of these events, using only KSRS and INCN. A couple of clusters were located relative to master events that were 8 to 20 km away and the relative location estimates were found to be within 1 to 2.5 km from evidence of blasting in IKONOS imagery. This surprisingly high degree of accuracy for locations relative to more distant master events may be due to the fairly homogeneous geological structure of the Korean Peninsula (e.g., Stump et al., 2002), and is not expected to be as good in more heterogeneous regions.

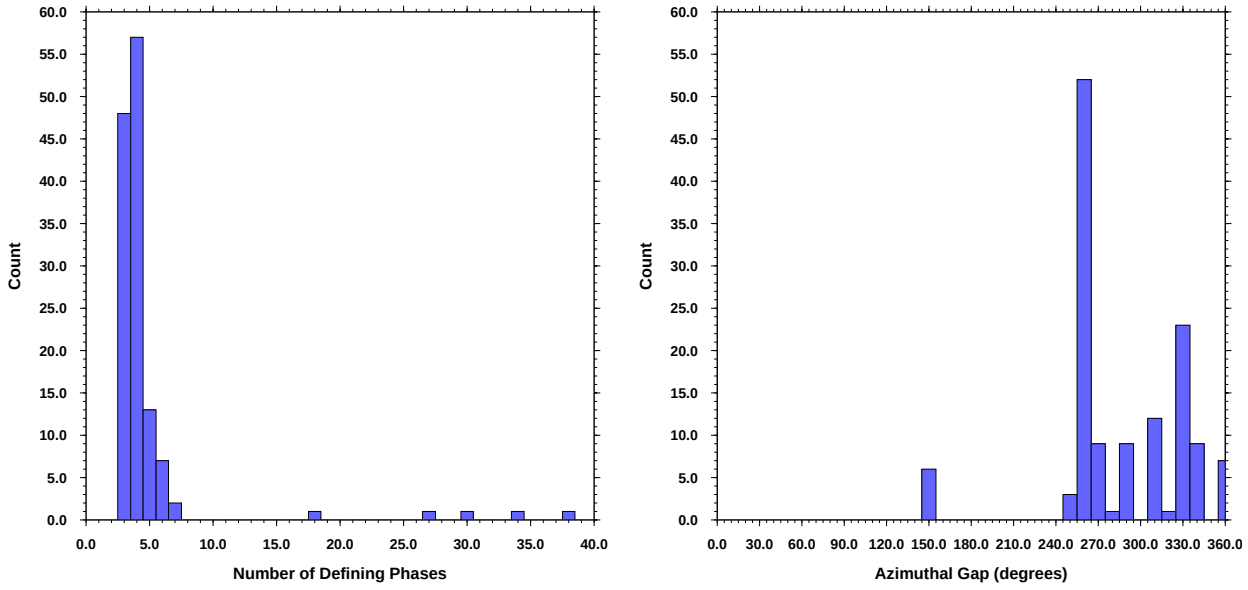

Figure 8. Histograms of the number of defining phases (left) and azimuthal gaps for the relative event locations estimated for the 133 GT events.

Preliminary examination of location performance, based on *default* processing methods using *LocSAT* and IASPEI91 travel time curves, and comparison to the GT solutions, indicates mislocations up to 35 km, median mislocation of about 8 km, median error ellipse area of about 1400 km^2, and coverage of the GT epicenters by about 90% of the error ellipses. These results are probably biased better than might be expected for a broader set of typical events on the Korean Peninsula because the 133 events with GT solutions that were used in this assessment were typically ones

with the highest SNR. Future plans include assessing location performance for all events in the various clusters (regardless of whether they were relocated by the methods described above), evaluating the performance of regional travel time curves, and separating the contributions to location errors that come from arrival time measurement errors and those that are due to travel time biases.

This study also demonstrates that high-resolution satellite imagery is very useful to obtain accurate absolute locations in the absence of other GT information or other forms of data to constrain the true locations. These results are very encouraging for continued successful and extensive application of these techniques to many other clusters of mining and other industrial blasts to establish valuable GT information. Future plans include applying these procedures to clusters of mining blasts in China.

ACKNOWLEDGMENTS

We are grateful to Professor Brian Stump of SMU for providing valuable information regarding mines and instrumented blasts and Dr. Ben Kohl of SAIC for providing seismic data and discussions regarding event clusters and imagery. We also acknowledge the IRIS Data Management Center for seismograms from INCN.

REFERENCES

Barker, B., T. Bennett, I. Bondár, M. Fisk, B. Kohl, H. Israelsson, K. McLaughlin, W. Nagy, M. Skov, J. Stevens, X. Yang, B. Zuzolo (2004). Application of Advanced Seismo-Acoustic Technologies to Regional Monitoring of North Korea, B. Kohl (editor), SAIC-04/2200.

Fisk, M. D. (2002) Accurate locations of nuclear explosions at the Lop Nor test site using alignment of seismograms and IKONOS satellite imagery, *Bull. Seism. Soc. Am.* 92: 2911-2925.

Kohl, B., I. Bondár, M. Fisk, T. Bennett, B. Barker, J. Stevens, W. Nagy, Keith McLaughlin, H. Israelsson, X. Yang, and M. Skov (2004) Use of Sparse Networks for Characterizing Events in the Korean Peninsula in *Proceedings of the 26th Seismic Research Review: Trends in Nuclear Explosion Monitoring,* LA-UR-04-5801, Vol 2, pp. 725-734.

Stump, B. W., C. Hayward, S. M. House, M.-S. Jun, and J.-S. Jeon (2000), A Small Aperture Seismo-Acoustic Array: Signal Assessment, in *Proceedings of the 22nd Annual Seismic Research Symposium: Planning for Verification of and Compliance with the Comprehensive Nuclear-Test-Ban Treaty (CTBT),* Vol. 3, pp. 281-290.

Stump, B. W., M.-S. Jun, C. Hayward, J.-S. Jeon, I.-Y. Che, S. M. House, and T.-S. Kim (2001). Assessment of Seismic and Infrasound Signals in Korea with Ground Truth, in *Proceedings of the 23rd Annual DTRA/ NNSA Seismic Research Review: Worldwide Monitoring of Nuclear Explosions,* LA-UR-01-4454, Vol. 1, pp. 431-439.

Stump, B. W., S. M. McKenna, C. Hayward, and T.-S. Kim (2002) “Seismic and Infrasound Data and Models at Near-Regional Distances” in *Proceedings of the 24th Seismic Research Review – Nuclear Explosion Monitoring: Innovation and Integration,* LA-UR-02-5048, Vol. 2, pp. 572-581.

REPRESENTING KRIGED TRAVEL TIME CORRECTION SURFACES WITH OPTIMAL TESSELLATIONS

James R. Hipp, Sanford Ballard, Marcus C. Chang, and Lee A. Jensen

Sandia National Laboratories

Sponsored by National Nuclear Security Administration
Office of Nonproliferation Research and Engineering
Office of Defense Nuclear Nonproliferation

Contract No. DE-AC04-94AL85000

ABSTRACT

Enhancing the accuracy and performance characteristics of event location is critical to seismic monitoring, during both the event association processing and event characterization stages. Recently, methods to compute the base model path-correction for travel time, azimuth, and slowness have been improved using the Bayesian Kriging approach.

The current Bayesian Kriging approach has proven to be a near ideal technique for providing robust estimates for path corrections, including both value (travel-time, azimuth, slowness, magnitude, etc.) and associated error, at specific interpolation locations on the Earth. However, due to the nature of the matrix inversion process, it has proven to exhibit less than desirable performance qualities when even moderate numbers of ground-truth events are involved in the calculation. For this reason, methods that yield the desired result with nearly equivalent accuracy, but with much higher performance, have been sought.

We have implemented one such method where an optimal tessellation representation of the Bayesian Kriging value and error surface is generated in-lieu of using the Bayesian Kriging approach directly. The new approach interpolates locally on the tessellation using natural-neighbor interpolation. The tessellation is optimized in a pre-processing step to minimize the difference between the true Kriged path-correction surface and the approximate tessellated surface. The technique uses successive triangle sub-division steps to sub-divide existing triangles into four new, smaller, triangles thereby reducing the difference between the true and approximate surface with each successive sub-division. The sub-division terminates when a preset absolute error tolerance is achieved as prescribed by the executing client. Mesh smoothing techniques are employed to ensure high-quality triangle formation following each sub-division step.

One draw-back to this approach is that data load times can increase significantly over that required by the Bayesian Kriging model. This limits the practicality of this approach to a server based application supplying requesting clients with interpolation results using a load-once run-many calculational approach. On the other hand, observed calculation times have improved by significant factors (and in some instances several orders of magnitude) over the Bayesian matrix inversion technique. In general, the amount of improvement depends strongly on the number of ground-truth events used in the Kriging approach, but is affected only slightly by the number of node points that comprise the tessellation.

This report presents performance comparisons between tessellated and Kriged representations including accuracy of representation and data load times required to initiate interpolation. The comparisons are calculated using the LocOO event location software to perform a series of benchmark location calculations.

OBJECTIVES

Obtaining an accurate location is one of the most important tasks in assessing any geo-seismic event. For large, well-recorded events, high-quality seismic locations can be obtained using global one-dimensional travel time models such as IASPEI91 (Kennett and Engdahl, 1991) or ak135 (Kennett et al., 1995). This is both because teleseismic distance paths have most of their lengths in the deeper, laterally homogenous parts of the Earth, and because whatever deviations do occur tend to be averaged out if the azimuthal coverage is good.

However, as the size of the event decreases and fewer stations detect the event, global one-dimensional models do not work as well and resulting mislocations can be large. Further, if the location error associated with the model is not properly accounted for in the location algorithm, then the associated confidence ellipses calculated for many smaller events do not actually contain the true locations as often as the calculated confidence would indicate.

Recently, Kriging methods have been employed to both enhance location estimates while simultaneously improving the associated error estimate (Shultz et al., 1998). These Kriged travel-time path corrections have significantly improved location estimates while simultaneously enhancing the associated accuracy of the estimate.

Unfortunately they come with a rather significant computational cost. The Bayesian Kriging method requires the inversion of a square matrix whose size is equivalent to the square of the number of ground-truth observations used in the kriging calculation. The inversion solution time is proportional to the cube of the number of ground-truths. The elements of the matrix are position dependent and force a new inversion calculation for each new interpolation location. With observation counts routinely composed of several hundred to a few thousand observations, Kriging calculation solution times are easily one or two orders of magnitude more costly than standard base model evaluations.

In order to alleviate this computational bottleneck, we propose an alternative data representation which can maintain both the path correction estimate and associated error to within a user specified tolerance. This new tessellated representation trades the computational inefficiency of Kriging with memory resource availability to achieve performance that is more consistent with the traditional one-dimensional velocity models mentioned above.

RESEARCH ACCOMPLISHED

Optimal Tessellation

We propose an approach where an optimal spherical geometry tessellation of well-shaped triangular elements is developed as an alternative representation for one or more Kriged surfaces. By optimal we mean a triangular tessellation whose nodal density and distribution characteristics are designed to meet a user specified absolute error tolerance with the original Kriged surface(s). The tolerance is specified such that the absolute value of the difference between the Kriged representation and the tessellated representation is less than the absolute error tolerance everywhere within the Kriged representation domain. With this definition we can produce an alternative data representation that matches the original Kriged, or true, surface, while ensuring that the tessellation is not over-refined with unnecessary nodes. This approach will minimize the amount of storage required to store the alternative data representation while guaranteeing that the error condition is met.

Obviously, in order to determine the difference between a true (Kriged) surface and a tessellated surface we must have a means of interpolating the tessellated surface. Many methods exist to interpolate a spherical geometry tessellation. Representatives include linear, natural-neighbor (Watson, 1992; Sambridge et al., 1995), or moving least-squares (Levin, 1998), as examples of increasing interpolation complexity, respectively.

Generally all of these methods are local interpolation techniques and only require a small subset of triangles that immediately surround the interpolation location to perform the calculation. The linear approach only requires data associated with the three nodes of the triangle that actually contains the interpolation location. The natural-neighbor interpolant requires data from the nodes of natural-neighbor triangle simplex, which are the triangles whose circum-circles (circles that pass through all three nodes of a triangle) contain the interpolation point. The natural-neighbor

interpolation technique requires that the tessellation be a Delaunay representation (Delaunay, 1934), which is a set of triangles whose maximum angles have been minimized. The moving least-squares technique can use any local set of data, but generally the natural-neighbor simplex is a good choice. The moving least-squares technique finds a set of coefficients that minimize a standard least-squares functional (usually a polynomial) where the functional is weighted with a set of position dependent basis functions whose value is zero near the boundary of the local simplex but maximally large near the interpolation location.

The linear approach is the fastest, of course, but lacks smoothness and 2nd order differentiability conditions. The natural-neighbor approach has conditions similar to bi-linear or quasi-quadratic smoothness but is not differentiable at the tessellation nodes. The moving least-squares technique is continuous and infinitely differentiable everywhere, but takes the longest to evaluate.

For purposes of this paper we have selected the natural-neighbor technique to illustrate the optimal tessellation and to compare its performance to the Kriged surface approach. Regardless of the approach each method requires that a search of the containing triangle be accomplished before the interpolation calculation. This is the same for either interpolation method and tends to take on the order of $O(\sqrt{N})$ per search (Lawson, 1977), where N is the number of nodes (or triangles, which is generally twice the number of nodes in a spherical geometry tessellation). This value is precise for an equally spaced grid but is only an average taken over a set of random search locations for a tessellation possessing a variable node density whose nodal distribution is completely unstructured.

Tessellation Construction

Before discussing performance issues associated with optimal tessellations we need to briefly describe how they are assembled. Optimal tessellations are constructed in a set of three staged processes which include: 1) initial mesh construction and densification; 2) mesh accuracy refinement; 3) and mesh decimation. The first step is used to arrive at an initial construction that is reasonably dense where excessive surface curvature is expected, but not overly refined where there is no curvature. For Kriged path correction surfaces the primary curvature occurs around the observation points while very little curvature is found at distances that are 10 or 15% greater than the Kriged surface observation correlation range. This means that a technique that builds well shaped triangles that are coarse at distances far from the Kriged ground-truth observations, but increases the nodal density to a prescribed maximum around the ground-truths can be used to construct the initial mesh. Figure 1 illustrates such a configuration for an arbitrary set of ground-truth observations. Notice the high-density node distribution located around the ground-truths (blue points) which is gradually reduced, beginning at a preset distance from the ground-truth, to a coarser density at distances further away. This method has proved very effective for defining an initial guess for a specific optimal tessellation.

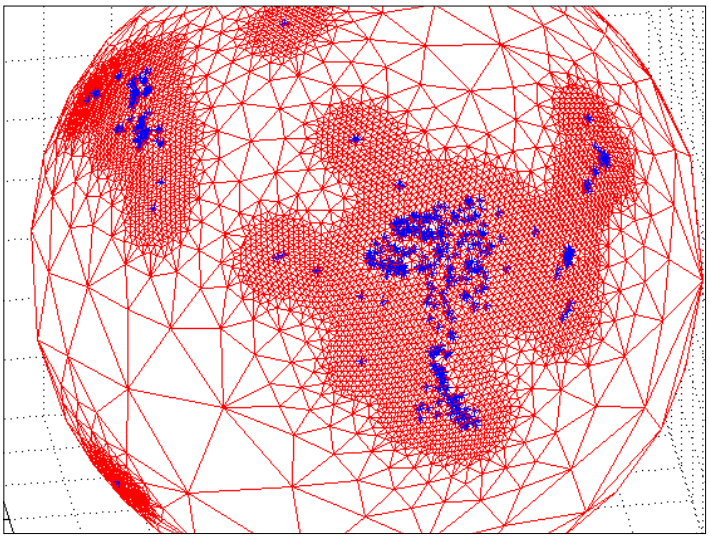

Figure 1. Initial Tessellation Construction

After the initial mesh has been constructed we can begin the accuracy refinement stage. In the accuracy refinement stage each triangle is interpolated in a sub-divided fashion at several internal points and compared with the true surface which is interpolated at the same locations. If the change in value of a surface attribute that is undergoing refinement exceeds the user defined relative sub-division error criteria across a sub-divided triangle, then the sub-triangle is sub-divided further and the algorithm is recursively called to continue the comparison on all of its' subdivided components. This process continues until the relative change in the value across the surface for a sub-triangle is less than a user prescribed relative error. If the relative error criteria is met then the algorithm returns (recursively) with the maximum discovered error for the triangle undergoing refinement.

Figure 2 illustrates the typical error distribution across a triangle during the accuracy refinement stage. Figure 2a depicts the true surface while Figure 2b shows the tessellated approximation. The absolute value of the difference between the two surfaces is shown in Figure 2c. These figures depict a typical triangle undergoing its first refinement. Since the natural-neighbor interpolator is exact at the nodes the surface difference always goes to zero at those locations and maximizes somewhere near the edge midpoints or in the interior of the triangle.

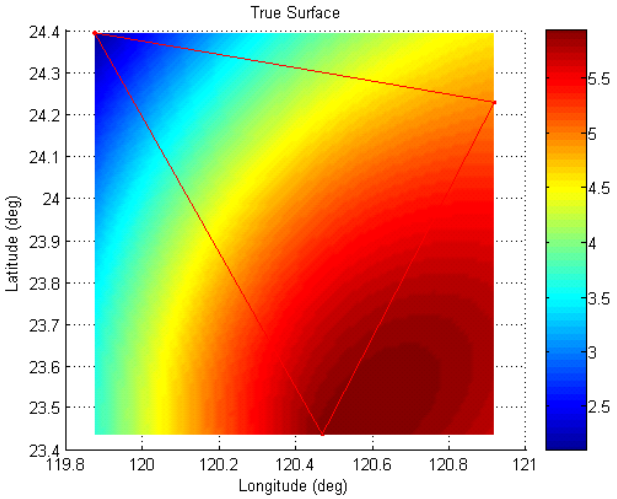

Figure 2a

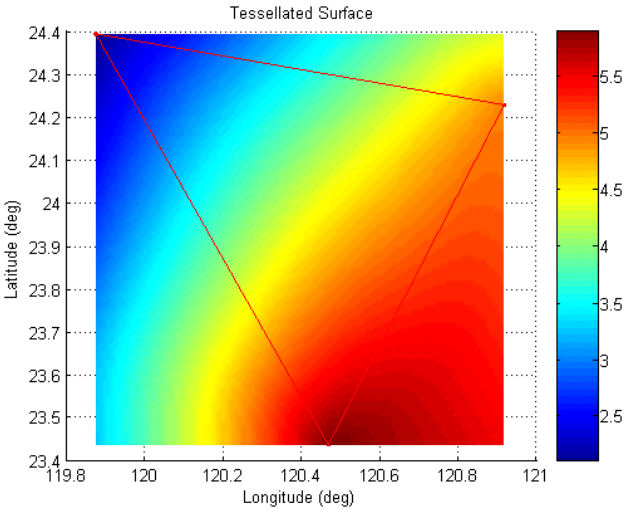

Figure 2b

If at any point during the refinement the error exceeds the user defined absolute error for a specific Kriged surface within the triangle undergoing refinement then the algorithm exits and the triangle is marked for refinement. When all triangles have been checked for refinement those that have been marked are sub-divided and the resulting new nodes are added to the tessellation and smoothed. Then the refinement process is repeated for all newly formed triangles and their immediate adjacent neighbors. The refinement process continues until no more triangles are in need of refinement. Figure 3 shows the previous dense mesh after having had 42 separate surfaces refined onto the initial grid. The resulting tessellation has approximately 144,000 nodes and was refined to an absolute error specification of .01 seconds between the true surface value and its tessellated equivalent.

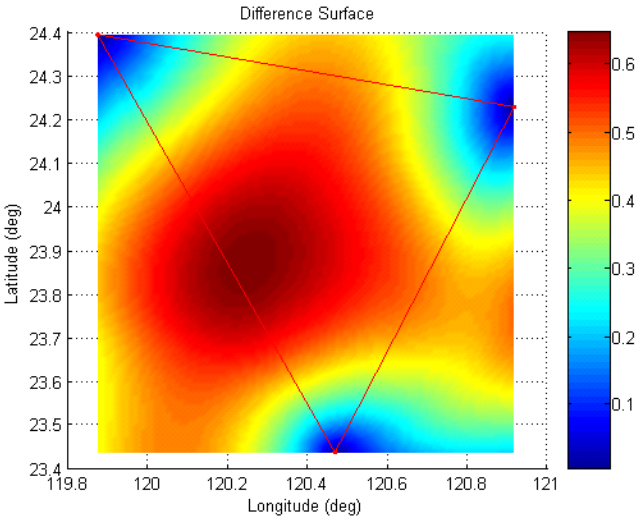

Figure 2c

The final construction stage is the decimation stage. Here any triangles that were never refined during the previous stage are checked to see if they are overly accurate. This is accomplished by removing the triangle (and generally, any associated neighbors) and testing to see if the new coarser set of triangles meets the absolute error criteria. If they do then the process is repeated. If they do not then the previous assembly of triangles is restored and marked as refined. This continues for all triangles that are undergoing decimation inspection until none remain.

The final resulting tessellation guarantees that all attributes undergoing refinement onto the tessellation can be interpolated to within the user defined absolute error criteria.

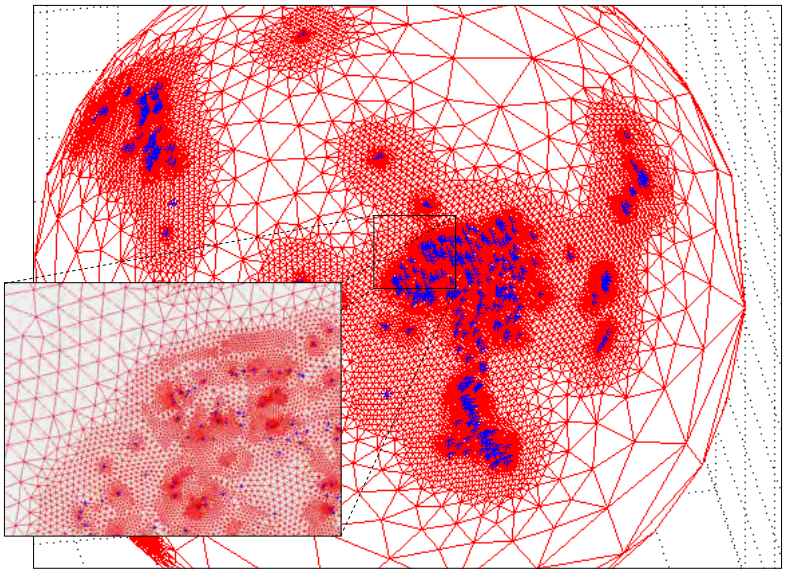

Figure 3. Final Refined Tessellation

Performance Considerations

Now that we have defined an optimal tessellation and briefly described how to construct them we can begin to examine some of their performance issues. We shall begin by defining the run-time behavior of the natural-neighbor tessellation interpolator using a triangle-walk searcher. This behavior can be characterized by the expression

$$t_I = c_{tw}\sqrt{N_N} + c_{iw} + c_{iws} \qquad (1)$$

where t_I is the average time to interpolate a single location in any arbitrary tessellation, c_{tw} is the triangle-walk proportionality constant that gives the walk time as a function of the square-root of the local node density (or the total node count, N_N, if equally spaced on average), c_{iw} is the interpolation weight calculation time, and c_{iws} is the interpolation weight sum. Note that the walk time is an average assessment over many interpolations. Any specific walk may encompass a wide range of triangle traversals, including zero traversals if the beginning triangle contained the interpolation point, or very many traversals if the interpolation point lies far away from the initial triangle. The specific triangle-walk time is directly proportional to the number of triangles traversed. Since this varies each time we interpolate we use an average assessment to determine the interpolation performance. Understanding that this is not the specific time per interpolation is crucial later when we describe the benefit derived from the operational nature of the locator relative to our interpolation problem.

The interpolation weight calculation is a locally constant time process. On average approximately 4 to 7 nodes will participate in any arbitrary interpolation. The interpolation weight sum is simply the sum of the surface values assigned to the participating nodes times the weight determined for each node. Since the participating node count is effectively constant the weight sum is also.

To demonstrate the rough performance of the natural-neighbor tessellation interpolator we have constructed a synthetic data set of three separate tessellations with 1000, 3100, and 10000 nodes, respectively. We have defined 31

separate surfaces (station phase pairs of travel time corrections) on to each tessellation. With these tessellations we shall interpolate a random set of interpolation locations to assess the performance of the natural-neighbor interpolator.

The interpolations were performed for over 22,000 randomly generated locations in the region of ground-truth influence within the synthetic data set. The same set of 22,000 locations was used in all interpolations. Each surface was interpolated at the 22,000 locations over 6 separate independent executions of the test software. The six sets of results were then averaged to produce a single average value for the time spent in the triangle-walk, in the triangle-walk and node weight calculation, and to perform the entire end-to-end interpolation yielding the final interpolation result. From these pieces of data we can find the time to perform the weight calculation by subtracting the walk time from the walk + weight calculation. Similarly, the weight-sum calculation can be found by subtracting the walk + weight time from the total interpolation time. The total interpolation time, the weight-sum calculation time, the weight calculation time, and the walk time were then plotted as a function of the three evaluated node densities. Also, the proportionality constant for the walk time was found by dividing the walk time by the square root of the total node count. Table 1 and Figure 4 below show the results.

Table 1. Interpolation Results

Avg. Node Count	Load & Initialization	Triangle Walk	Walk + Weight	Total Interpolation Time	Weight Calculation	Weight Sum Calculation	c_{tw}
977.71	0.014317	6.96E-06	2.83E-05	2.97E-05	2.14E-05	1.36E-06	2.22E-07
3134.45	0.043051	1.31E-05	3.51E-05	3.64E-05	2.2E-05	1.25E-06	2.35E-07
10114.5	0.149752	2.42E-05	4.68E-05	4.81E-05	2.26E-05	1.35E-06	2.41E-07

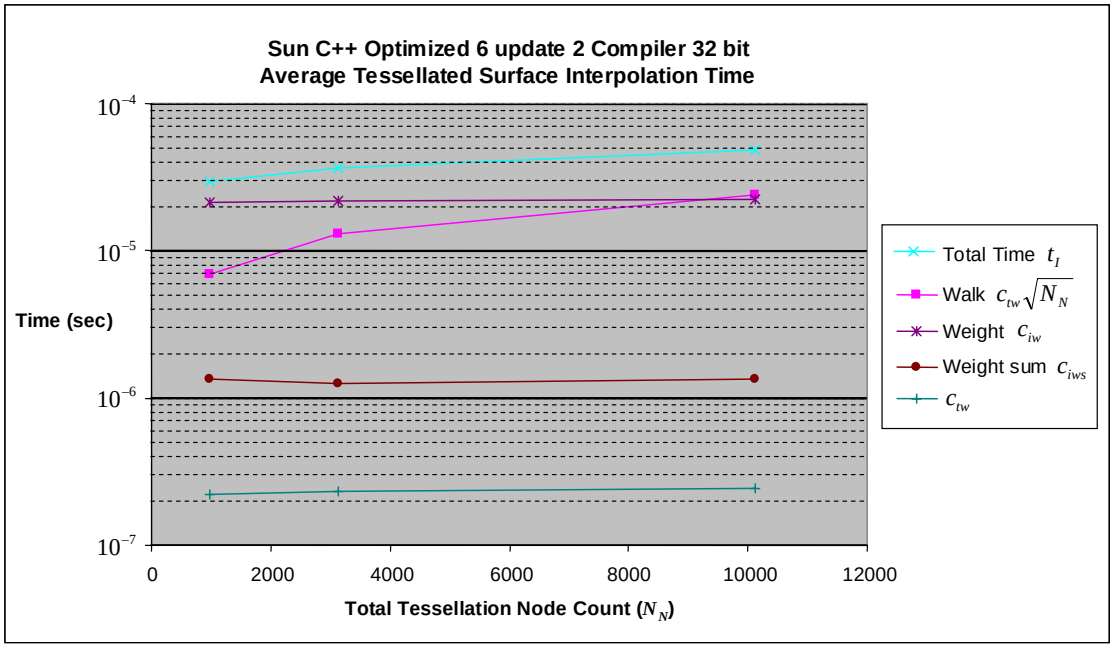

Figure 4. Natural-neighbor interpolation component breakdown illustrating the walk, weight, and weight-sum calculation times.

The load times were not displayed in the figure but average about 1.5 seconds per 10000 nodes loaded.

We can use the data developed from Figure 4 above to show the interpolation time over a broader range of nodes. This can be compared to the times determined for both base model evaluation and for the Kriging interpolation. First we shall describe how the base model interpolation times were defined and then we shall examine the Kriging times.

The base model interpolations were performed for over 16,000 randomly generated locations in two regions for the distance and depth dependent base models. The first region's set of data ranges from 0° to 180° distance and 0 to 400 km depth, covering teleseismic ranges, while the second region ranged from 0° to 20° distance and 0 to 5 km depth, to represent regional evaluation. The same two sets of 16,000 locations, one for both regions, were used in all interpolations. Each base model was interpolated at the 16,000 locations, in both regions, over 6 separate independent executions of the test software. The six sets of results were then averaged to produce a single average set of assessments. The minimum, maximum, and average for all 237 base models (IASPEI91 and ak135 evaluated for all available phases) were determined. The IASPEI91 P phase was also reported considering its general importance in overall location calculations. These were then consolidated into a single minimum, maximum, average, and IASPEI91 P phase evaluation time. The results included an average base model evaluation time of 6.81 $\times 10^{-5}$ sec within a range of 1.18×10^{-5} to 2.03×10^{-4} sec. The average IASPEI91 P phase evaluation was 2.01×10^{-5} sec. The wide range is caused by the different interpolation scenarios within the base model algorithm. Some base models have coarser tables yielding slightly faster results. Some have large regions that are undefined requiring extrapolation using the rational spline approximation, which can be very slow to evaluate. The end result is a factor of approximately 20 from the minimum to maximum base model evaluation times.

The Kriging interpolations were performed for the same set of over 22,000 randomly generated locations used by the tessellated surface tests in Figure 4. The Kriged surfaces were interpolated for all 31 stations (P phase only) and averaged together. The interpolation test was performed in 6 separate independent executions and the subsequent results were then averaged to give a single value of 9.09×10^{-4}sec. We know that this time is dominated by the cube of the number of ground-truths used to define the region, which for these Kriged surfaces, was approximately 100. However, the effective number of ground-truths used per interpolation was recorded for purposes of delineating these performance tests and was found to be on average 61 ground-truths per evaluation of the 22,000 interpolation locations. Using the cubic performance requirement for the Kriging solution we can determine that an effective ground-truth count of less than 17 would be required to enable Kriging with a performance equivalent to the IASPEI91 P phase base model evaluation.

Figure 5 illustrates the time to interpolate a single tessellated surface as a function of the tessellation node count. The base model and Kriging results are also shown for comparison.

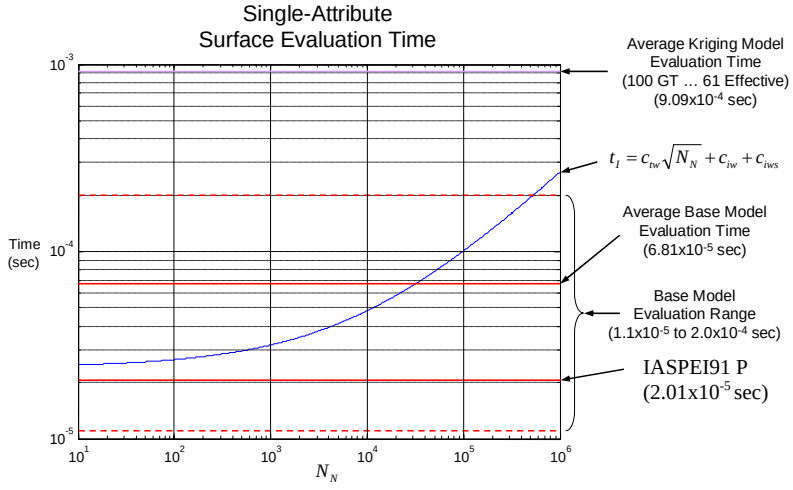

Figure 5. Single-attribute surface evaluation time given as a function of average node count. Base model and Kriged evaluations are also shown for comparison.

The fact that a tessellated surface can map more than a single attribute allows us to ask the question whether having one tessellation with many or all surface attributes assigned might not be a more efficient solution than many tessellations with only one attribute assigned per tessellation. Is there sufficient operational separation between steps that may allow us to take advantage of the fact that the first two costly steps are purely spatial (triangle search and

weight calculation) and only the highly efficient last step (weight-attribute sum) requires knowledge of the attribute information?

We can answer this question by examining the previous expression for the run-time behavior of the natural-neighbor interpolation method. Let the number of interpolation attributes be denoted by N_{AI}. Since the containing triangle search and subsequent weight calculation only needs to be performed once in order to evaluate the resulting interpolation for all attributes the previous expression for the run-time behavior of the natural-neighbor interpolation can be rewritten as

$$t_I = c_{tw}\sqrt{N_N} + c_{iw} + N_{AI}c_{iws}\,. \qquad (2)$$

Notice that only the last constant is affected by the extra calculation for the additional surface attributes. The value for that constant is slightly more than a micro-second ($1.3e^{-6}$). If we have, for example, a tessellation with 100 surface attributes mapped to its nodes, then from Figure 5 we see that the total solution time for surface with 100,000 nodes will climb from $1.0e^{-4}$ seconds to approximately $2.0e^{-4}$ seconds. That's only a factor of two for an additional 99 surface attribute evaluations. An equivalent number of IASPEI91 P phase base model evaluations will jump from 2.0×10^{-5} seconds to approximately 2.0×10^{-3} seconds. This result suggests that huge time savings can be recovered by saving multiple surface attributes onto the nodes of individual tessellations.

The previous discussion neglected the significant impact that many tessellations with a few attributes, or a few tessellations each with many attributes, can have on storage requirements and subsequent data load times. In the next section we shall examine the impact of both load time and run time for a more realistic set of tessellations that have large numbers of nodes with multiple surface attributes assigned to each. These comparisons will be accomplished using the Sandia National Laboratories' event location tool LocOO (Ballard, 2003), which will incorporate the effects of realistic software overhead into the results shown above.

Locator (LocOO) Specific Performance Comparison

To demonstrate the effect of the timing difference between using tessellations versus Kriging in an actual event location application, we set up a test using a synthetic data set developed for general purpose testing of path correction surfaces. The data set consists of 126 synthetic seismic events with 31 P wave travel time observations associated with each event. There are path corrections available for each of the 31 observations.

For this test, we compared the time it took to 1) load the model information from the file system into memory, 2) locate a set of events and 3) unload the model information from memory, using 5 different run conditions: 1) base model information only, 2) path corrections calculated using Kriging, 3) path corrections calculated based on a 24,000 node tessellation, 4) a 68,000 node tessellation and 5) a 226,000 node tessellation. Note that the time required to perform all data input/output functions is excluded from this analysis.

In the first run of the test, we located only one of the events in the data set. The results are illustrated in Figure 6.

In this scenario, the amount of time spent actually computing the event location was small compared to the time required to load and unload the model. A comparison of the base model and Kriged path corrections with the tessellated interpolation for the 226K tessellation shows that 90%, 50% and 99.8% of the time was spent loading and unloading the model information, respectively. The total time required by the 226K tessellation was 25 times greater than the total time required by the Kriging-only solution.

In the second run of the test, 126 events were located (see Figure 7). In this case, the models were only loaded/unloaded once but 126 events were located using the model while it was in memory. In this scenario, tessellation performed much better than Kriging only case because it took approximately 10 times longer to compute each location using Kriging as compared to any of the other models.

The bottom line is that if the location software is operated in a mode where it loads a model, computes a location and then unloads the model, Kriging may be a better option unless only small tessellations (a few thousand nodes) are involved. On the other hand, if the location software can be operated in a mode where the model is loaded once and many locations are computed, then a tessellation interpolation can significantly outperform Kriging.

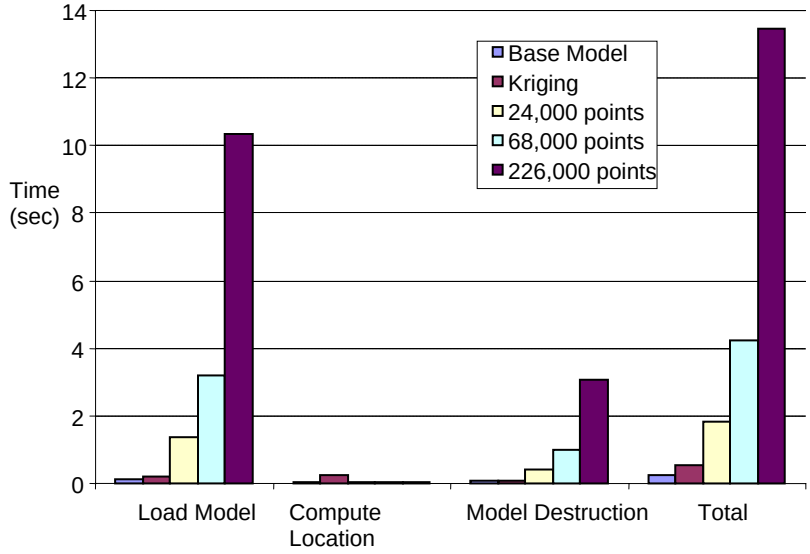

Figure 6. Time required performing various subtasks of a seismic event location calculation when locating single seismic events.

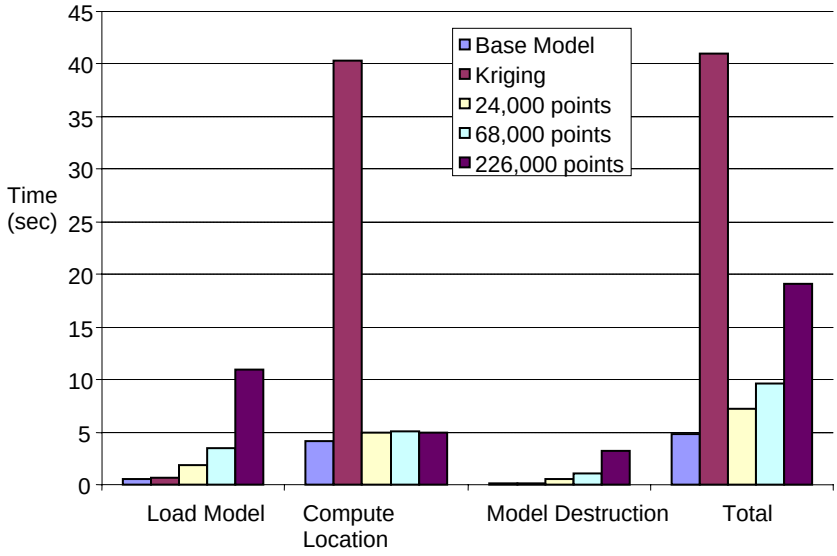

Figure 7. Time required performing various subtasks of a seismic event location calculation when locating 126 seismic events.

CONCLUSIONS AND RECOMMENDATIONS

In summary, the use of an optimal spherical geometry tessellation for representing Kriged path corrections surfaces can far surpass Kriging interpolation performance, and for multiple surface attributes assigned on the same tessellation, the method can be as fast as or faster than standard base-model evaluations. Further, this is true for tessellations with as many as 250,000 nodes and more than 60 surface attributes mapped to the tessellation. The primary problem with the tessellation approach concerns data storage and data load times which can be excessive. As long as sufficient storage is available and the operational use of the software is of the form of load-once and interpolate-many, then this method can be substantially faster than typical Kriging approaches.

ACKNOWLEDGEMENTS

We would like to thank Mark Harris and David Gallegos for thoughtful reviews. Their comments have improved the manuscript.

REFERENCES

Ballard, S. (2003). Seismic event location: Dealing with multi-dimensional uncertainty, model non-linearity and local minima, in *Proceedings from the 25th Seismic Research Review—Nuclear Explosion Monitoring: Building the Knowledge Base*, LA-UR-03-6029, Vol. 1, pp. 193-202.

Delaunay, B.N., (1934), Sur la Sphere Vide, Bull. Acad. Science USSR VII: Class. Sci. Math., 793-800.

Kennett, B.L.N., and E.R. Engdahl (1991). Traveltimes for global earthquake location and phase identification. *Geophys. J. Int.* 105: (2), 429-465.

Kennett, B.L.N., E.R. Engdahl, and R. Buland (1995). Constraints on seismic velocities in the earth from travel time. *Geophys. J. Int*. 122, 108-124.

Lawson, C.L. (1977). Software for C1 surface interpolation, in Mathematical Software III, J. Rice (ed). Academic Press, New York.

Levin, D. (1998), The Approximation Power Of Moving Least-Squares, *Mathematics Of Computation* 67: 224, 1517-1531, October 1998.

Sambridge, M., J. Braun, and H. McQueen (1995). Geophysical parameterization and interpolation of irregular data using natural neighbors, *Geophys. J. Int*., 122: (3), 837-857.

Schultz, C., S. Myers, J. Hipp, and C. Young (1998), Nonstationary Bayesian Kriging: Application of Spatial Corrections to Improve Seismic Detection, Location and Identification, *Bull. Seism. Soc. Am*., 1275-1288.

Watson, D. F., (1992). *Contouring: A Guide to the Analysis and Display of Spatial Data*, Pergamon, ISBN 0-08-040286-0, 321 pp.

EVALUATION OF CROSS-CORRELATION METHODS ON A MASSIVE SCALE FOR ACCURATE RELOCATION OF SEISMIC EVENTS

Won-Young Kim, Paul G. Richards, David P. Schaff, Felix Waldhauser, and Jian Zhang

Lamont-Doherty Earth Observatory of Columbia University

Sponsored by Air Force Research Laboratory

Contract No. F19628-03-C-0129

ABSTRACT

We are evaluating a method of locating seismic sources (earthquakes, explosions) based on the use of waveform cross-correlation (WCC) measurements instead of using the conventional measurements of seismic wave arrival time (phase picks). WCC measurements have been demonstrated to be 10 to 100 times more accurate, where they can be used. The principal issue we are exploring is the extent to which a significant fraction of seismicity can be located using WCC measurements. In this second year of the project we have focused on studies of intraplate seismicity in New Madrid (Central United States) and Charlevoix (Eastern Canada). We have also compared our results for these regions, with the results for a separately-funded project to study the seismicity of Northern California.

Datasets have been assembled from scratch working in conjunction with regional network operators. For New Madrid, three datasets have been acquired. The first is from stations of the network originally installed by Otto Nuttli and his colleagues at St. Louis University. This is an archive of 51,541 phase picks, associated with events from 1974 to 1998. The second is a waveform archive, associated with 42 PANDA stations, 918 events, and 17,598 phase picks for events from October 1989 to August 1992. The third is also a waveform archive, associated with 85 stations, 614 events, and 16,461 events from January 2000 to October 2003, obtained from the Center for Earthquake Research and Information (CERI) network, operated by the University of Memphis. We are currently processing the data from this station network for an additional time period, from 1995 to 1999, specifically in order to associate the waveforms with phase pick information and bulletin locations. It may be noted that several of the station locations operated by St. Louis University are the same as those used by CERI, and thus we expect to be able to present a unified picture of New Madrid seismicity for a period of about thirty years from 1974. Preliminary WCC results of the PANDA network indicate that about 76% of 809 relocated events have five or more P-wave cross-correlations ($CC \geq 0.7$). Similar statistics have been acquired for CERI data at New Madrid. Both PANDA data and CERI allow the identification of clearly defined lineations (faulting), previously identified but not seen so well in the traditional bulletin locations.

For Charlevoix, using data acquired from the Geological Survey of Canada, we have now relocated 2272 events using phase-pick data and waveform data from a 46-station network that had just eight stations close to the seismicity. Here we find that only 5% of the events had five or more P-wave cross-correlations ($CC \geq 0.7$). In the north-east part of this region, fault structures can clearly be seen in cross sections of the relocated seismicity.

We also comment on the results of a seismicity study of Northern California, for which 95% of 225,000 events cross-correlate at 4 or more stations. In general, we conclude that the benefits of using cross-correlation methods and multi-event relocation analysis are so substantial, that they should be considered for application to the work of routine bulletin publication.

The basic reason for a much lower percentage of Charlevoix events cross-correlating, is the paucity of stations close in to the seismicity.

OBJECTIVE

We are evaluating a method of locating seismic sources (earthquakes, explosions) that is based on the use of waveform cross-correlation (WCC) measurements instead of using the conventional measurements of seismic wave arrival time. WCC measurements are ten or a hundred times more accurate, where they can be used. The principal issue we shall explore is the extent to which a significant fraction of seismicity can be located using WCC measurements.

RESEARCH ACCOMPLISHED

We have completed and published waveform-based studies of the seismicity of China (Schaff and Richards, 2004ab), and are currently conducting such studies for New Madrid, Central United States; Charlevoix, Eastern Canada; and, in a separate study not funded by the Air Force Research Laboratory (AFRL) of Northern California. About 10% of the earthquakes in China, as monitored at far regional distances, cross-correlated. In the next subsection, we briefly report preliminary results for New Madrid and Charlevoix, and summarize key differences between these two regions, and a recent study of Northern California. Because there are significant differences in the fraction of seismic events that can be located precisely by modern methods (i.e., using relative arrival times measured accurately by waveform cross-correlation, followed by application of a multi-event relocation algorithm such as “double difference”) in each region, we then discuss in a separate subsection the likely causes of these differences. Further discussion of these results has recently been submitted for publication (Richards et al., 2005).

Preliminary relocations for New Madrid and Charlevoix, and their differences from Northern California

We are studying the seismicity of the New Madrid region, Central United States, for three different eras of station deployment. Data consists of phase picks as well as waveforms. The first era, is from 1974 to about 1998 when personnel at St. Louis University operated analog stations and used traditional phase pick methods (over 52,000 phase picks). The second era is associated with the operation of a PANDA network by the Center for Earthquake Research Information (CERI) of the University of Memphis, from October 1989 to August 1992 (42 stations, 918 events, 17,598 phase picks). The third era is also associated with CERI, but utilizing a different network (up to 85 stations, about 1000 events) from 1994 to October 2003. In this short paper we show only one example of relocations for New Madrid. Thus, Figure 1 shows relocation of 809 events monitored by the New Madrid PANDA network: 616 (76%) of these events cross-correlated (with $CC \geq 0.7$) at 5 or more stations; 695 (86%) at 4 or more stations; and 735 (91%) at 3 or more stations. The two cross-sections in Figure 1 show a fault plane dipping to the west, with dip that steepens to the south.

We are studying the seismicity of the Charlevoix region, Eastern Canada, from January 1988 to December 2003 involving 27,976 events with 33,423 phase picks recorded at 46 stations operated by the Geological Survey of Canada. Although we have waveforms from many of these stations, as we shall see in a later section we find that only 8 of these stations, close to the source region, are the basis for almost all the successfully cross-correlated waveforms. Many of these stations are 100s to 1000s of km away and record only the larger events. Figure 2 shows the relocation of 2272 events: only 242 of them (5%) cross-correlated (with $CC \geq 0.7$) at 5 or more stations; 622 (25%) at 4 or more stations; and 1439 (57%) at 3 or more stations. These preliminary relocations, as well as the original bulletin locations for this region, indicate that active faulting is simpler and more clearly defined in the northeastern part of the zone, compared to more complex features in the southwestern part. Cross-section 2–2´ shows a fault dipping about 50º to the southeast, whereas the other cross-section shows a fault dipping more steeply, at about 75º.

It may be noted that the percentage of events whose waveforms cross-correlate at enough stations to apply modern methods of event location differs significantly between New Madrid (higher %), and Charlevoix (lower %). Schaff and Waldhauser (2005) have described results from an application of cross-correlation methods to process the complete digital seismogram data base for Northern California to measure accurate differential times for correlated earthquakes observed at common stations. Their results are even better than those for New Madrid. Their waveform database includes about 15 million seismograms from 225,000 local earthquakes between 1984 and 2003. A total of 26 billion cross correlation measurements were performed on a 32-node (64 processor) Linux cluster. All event pairs with separation distances of 5 km or less were processed at all stations that recorded the pair. A total of about 1.7 billion P-wave differential times had cross correlation coefficients (CC) of 0.6 or larger. The P-wave differential

times are often on the order of a factor of ten to a hundred times more accurate than those obtained from routinely picked phase onsets. 1.2 billion *S*-wave differential times were measured with CC > 0.6, a phase not routinely picked at the Northern California Seismic Network because the onset of *S*-phases is often obscured by *P*-wave coda. These results show a surprisingly high degree of waveform similarity for most of the Northern California catalog, which is very encouraging for improving earthquake locations. For about 95% of the events, waveforms have CC values that are greater than 0.7 for at least four stations with one or more other events. 90% of the events meet this criterion at eight or more stations, and 82% of the events in the catalog cross-correlate at twelve or more stations. Even tectonically complicated zones exhibit these favorable statistics, such as Long Valley Caldera and Geysers Geothermal Field, where mechanisms are quite variable. Apparently, as long as the earthquake density is high enough there is a high probability that at least one other event occurs nearby with a similar focal mechanism, enabling very precise relative locations.

For the four regions we have examined, China was studied with far-regional signals and the other three regions were studied with local stations. Yet we found significant differences, in that about 85% of New Madrid events could be relocated with modern methods (using waveform cross-correlation), and 95% of Northern California events; but only about 25% of Charlevoix events. In the next sub-section we comment further on these differences and discuss underlying causes.

Comparisons, to explore the applicability of wave-based methods in different seismic regions

Figure 3 shows a map for each of three regions: part of Northern California (around the Calaveras fault); New Madrid; and Charlevoix. The Figure shows relocated events and the stations at which cross-correlated signals are found. Note that primarily seven of the Charlevoix stations cross-correlate. The other stations of the network in Eastern Canada are at greater distance, and typically can contribute only phase picks plus just a few correlations to the location of Charlevoix events. These maps all share the same distance scale, and it is interesting that New Madrid and Northern California have approximately the same station density (about one station per 100 sq. km) and distances between stations (about 12 km) whereas Charlevoix is a factor of two smaller in density and a factor of two greater in station distance. From the station plot for Charlevoix it is easy to see why a criterion of “4 or more” or “5 or more” stations is hard to achieve for the events: first, because greater epicentral distances are involved to reach four stations, and second because at least half the stations had to record the event with good signal-to-noise ratio (SNR) and high similarity. This may not happen, due to radiation pattern, etc. Four out of 38 stations at New Madrid is much easier to achieve. It appears that increasing the number of stations near Charlevoix would increase the percentage of events that cross-correlate in that region.

Figure 4 shows distributions of event depth and magnitude for the three regions. Here we see that while the magnitude distributions are more or less similar, the Charlevoix events tend to be deeper than both California and New Madrid by 5 km or more. Since depths as well as epicentral distances (see Fig. 3) are greater for many of the Charlevoix events, it is likely that fewer stations would have good SNR, and hence fewer stations would cross-correlate. Concerning earthquake densities, it is of interest that New Madrid and Charlevoix have about the same value (around 1 earthquake per sq. km), whereas Northern California (or at least the Calaveras fault) has about 160 events per sq. km (for the time periods studied). The inter-event separations are likewise similar for New Madrid and Charlevoix (averaging about 2 km), as shown by the distributions depicted in Figure 5, whereas for the Calaveras fault it is only about 100 m.

Figure 6 shows the distribution of cross-correlation values with distance. These curves tend to flatten out beyond 2 km, and similar results are obtained for Northern California. It is for this reason that the scientifically most interesting results of streaks and repeating events in Northern California can be documented — because most of the good correlations are for inter-event separations of less than 2 km. For New Madrid and Charlevoix, where many of the nearest neighbors are 2 km away or more, we expect lower CC values and less collapsing of structures into clusters, except for a few isolated clusters with higher CCs.

Differences in the number of cross-correlation measurements per event pair are mainly controlled by the number of available stations. In both the Charlevoix and the New Madrid region 90% or more of the events correlate with at least one other events at one station. That number decreases to 10% for the Charlevoix and 76% for the New Madrid region when 5 or more correlation measurements per event pair are considered. This difference reflects the availability of stations with digital waveforms. The Charlevoix network consists effectively of only 8 stations which provided digital waveforms for cross correlation, while the Panda network includes 38 such stations.

CONCLUSIONS AND RECOMMENDATION

Cross-correlation measurements for earthquakes in the New Madrid seismic zone (NMSZ) and the Charlevoix seismic zones (CSZ) indicate that a much higher number of events (about 85%) correlate in the NMSZ, compared to only 5 to 25% of the events that correlate in the CSZ. The reason for this discrepancy may be due to: differences in the network geometry and number of stations; differences in the type and diversity of faulting associated with the events; the variation of geophysical properties in general; and the degree of structural heterogeneity in particular, within the areas of investigation; or a combination of all.

We recommend that for regions of high seismicity within which a high percentage of events cross-correlate at enough stations to achieve precise relocations, consideration be given to a wholly different paradigm for event location — namely, a framework in which events are located using cross-correlation measurements obtained from relevant portions of the waveform, rather than using phase picks.

ACKNOWLEDGEMENTS

We greatly appreciate the assistance of the Geological Survey of Canada, and personnel at St. Louis University and the University of Memphis. In particular we thank Drs. David McCormack and Jim Lyons at the Geological Survey of Canada, Ottawa, who helped us assemble phase and waveform data from earthquakes in the Charlevoix region. We thank Drs. Jer-Ming Chiu of CERI, University of Memphis and Jiakang Xie at Lamont-Doherty who helped us to acquire phase and waveform data from the PANDA New Madrid deployment. We also thank Drs. Mitch Withers at CERI, University of Memphis for New Madrid seismic network data and Robert Herrmann at St. Louis University for the Central Mississippi Valley seismic bulletin.

REFERENCES

Chiu, J. M., A. J. Johnston, and Y. T. Yang (1992). Imaging the active faults of the central New Madrid seismic zone using PANDA array data, *Seism. Res. Let.* 63: 375–393.

Richards, P. G., F. Waldhauser, D.P. Schaff, and W.-Y. Kim (2005). The applicability of modern methods of earthquake location, submitted to *Pure and Applied Geophysics*.

Schaff, D. P., and P. G. Richards (2004a). Lg-wave cross correlation and double-difference location: application to the 1999 Xiuyan, China, sequence, *Bull. Seism. Soc. Amer.* 94: 867–879.

Schaff, D. P., and P. G. Richards (2004b). Repeating seismic events in China, *SCIENCE* 303: 1176–1178.

Schaff, D. P., and F. Waldhauser (2005). Waveform cross-correlation based differential travel time measurements at the Northern California Seismic Network, submitted to *Bull. Seism. Soc* .

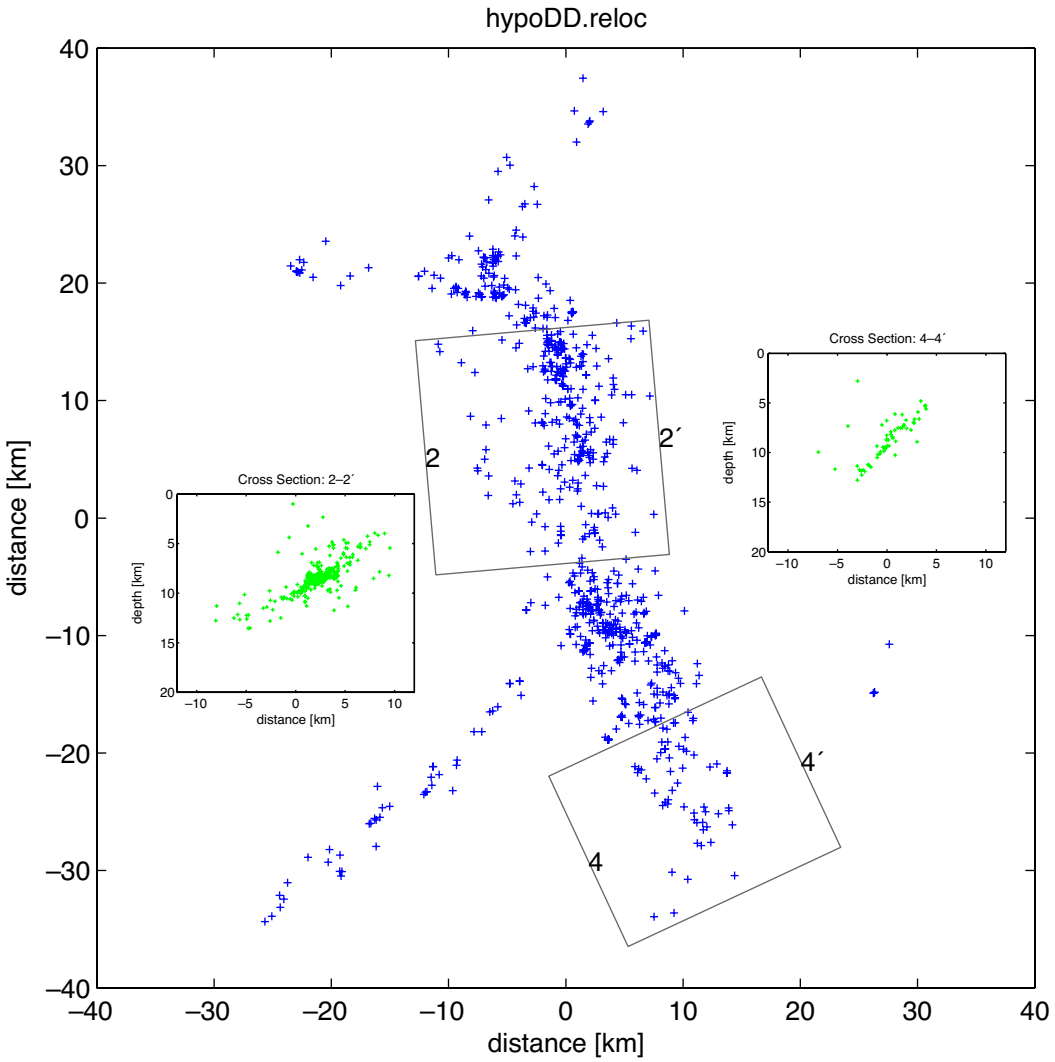

Figure 1. Relocation of 809 seismic events in the New Madrid region of te central United States from October 1989 to August 1992, using 42 stations of a PANDA network (see Chiu et al. 1992). This application of the double-difference algorithm was based upon phase pick pairs and cross-correlations, in each case using P-waves and S-waves. We have also obtained such relocations for the later period during which the University of Memphis operated a larger network of stations.

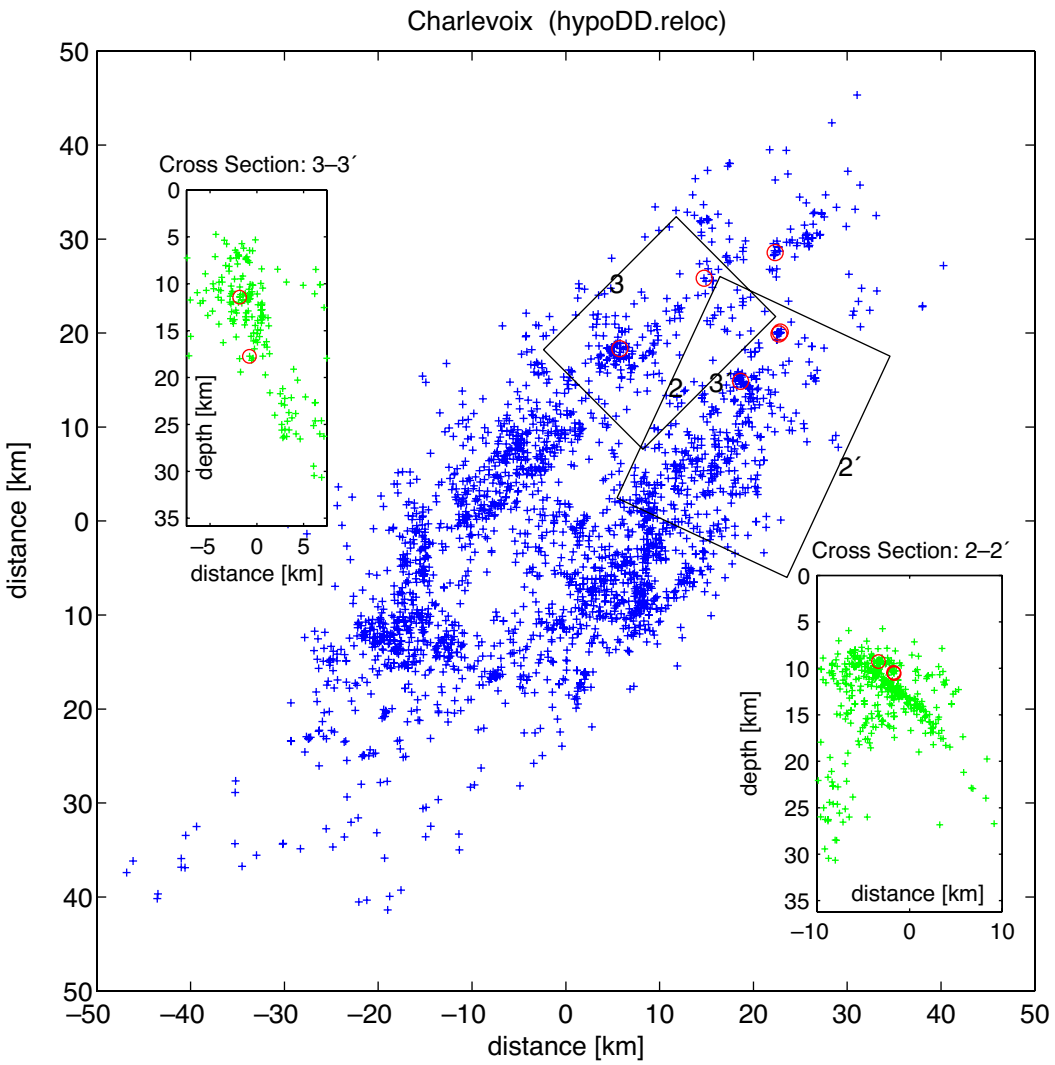

Figure 2. Relocation of 2242 events in the Charlevoix region of Eastern Canada from January 1988 to December 2003, using 46 stations operated by the Geological Survey of Canada. Red circles denote events of magnitude 4 or larger.

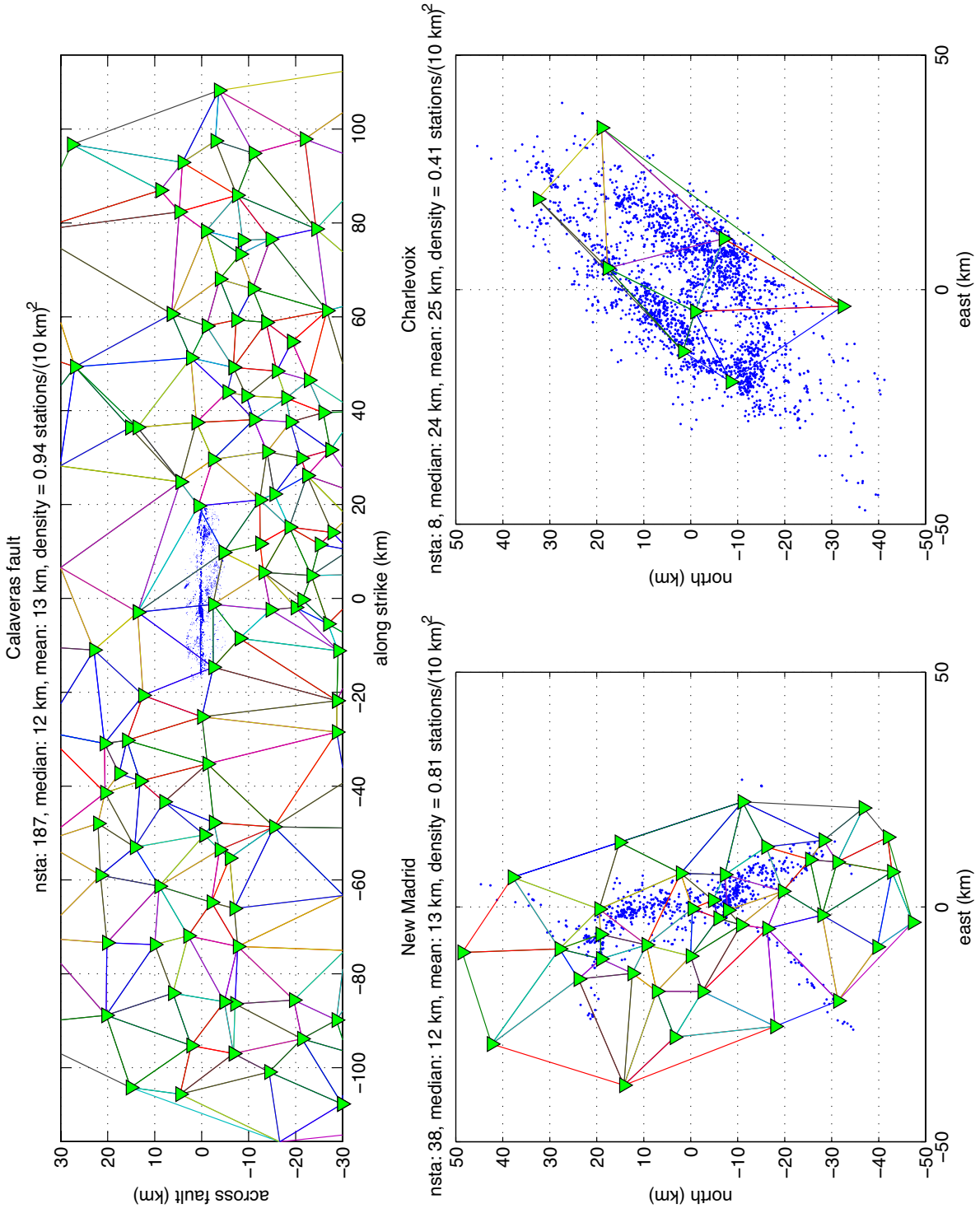

Figure 3. Station distance and density (Delaunay tessellation). Charlevoix has about half the station density of the Calaveras and New Madrid regions.

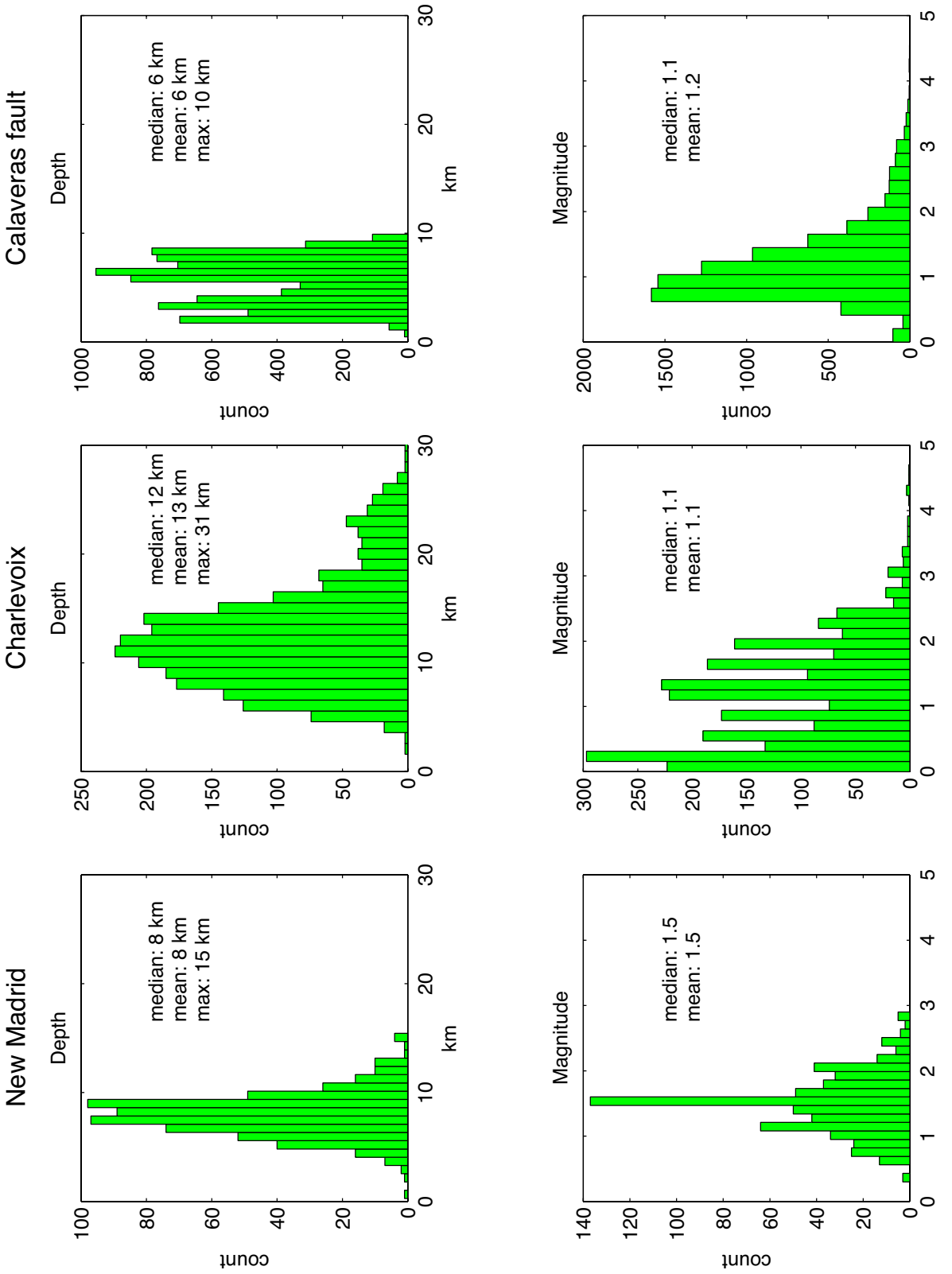

Figure 4. Depth and magnitude distributions, for three different regions of seismicity.

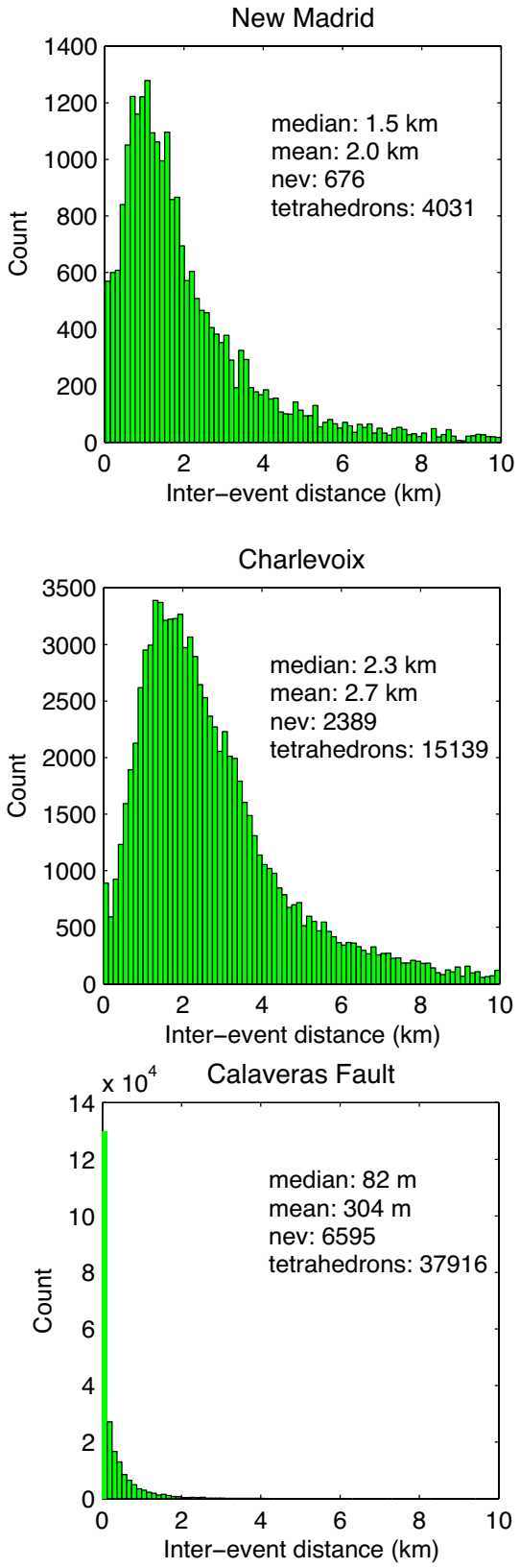

Figure 5. Distribution of nearest natural neighbor distances (based on 3-D Delaunay tessellation).

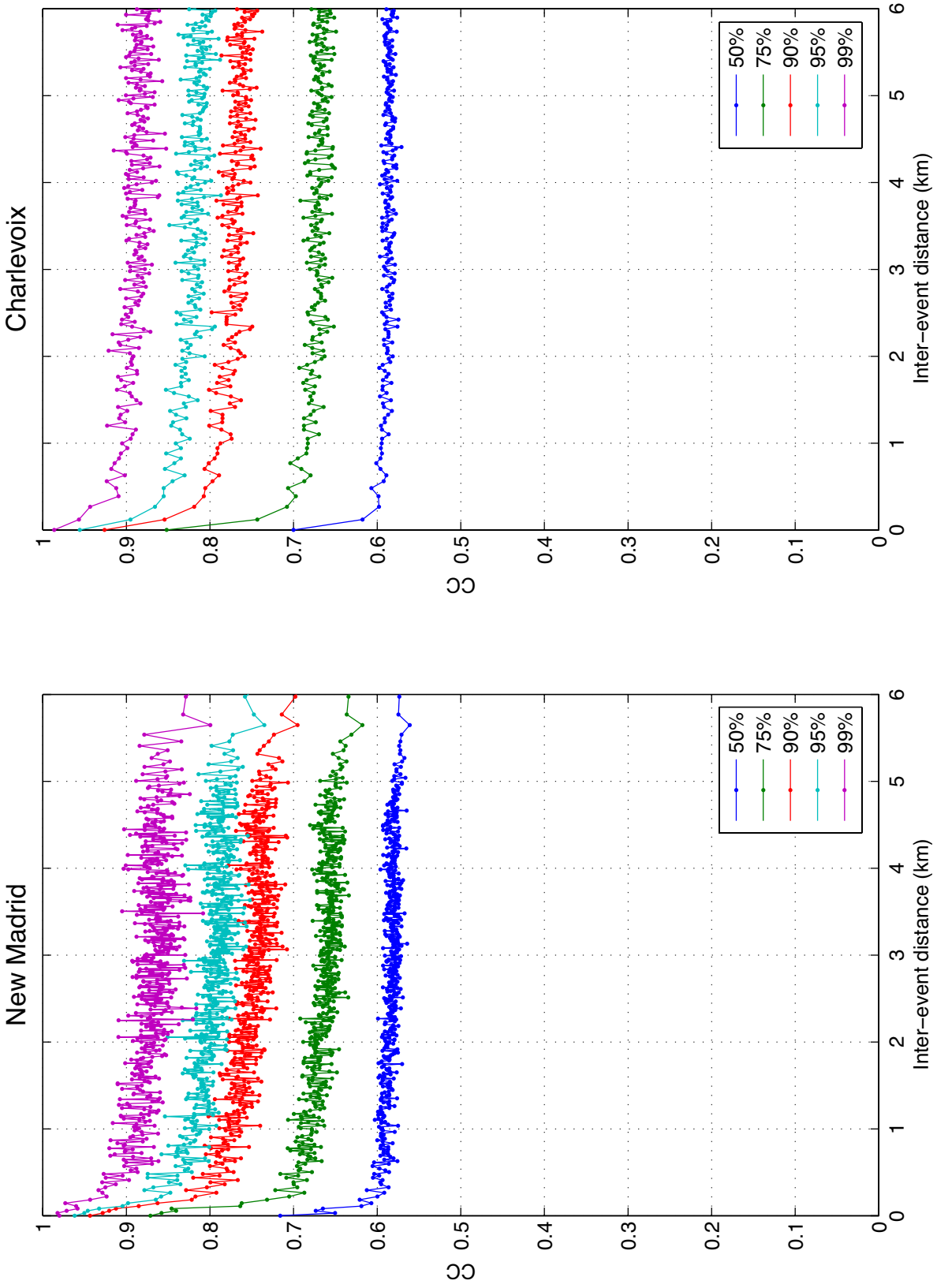

Figure 6. Distribution of cross-correlation values (CC) with distance

GROUND TRUTH IN CENTRAL ASIA FROM IN-COUNTRY NETWORKS

Gaspar Monsalve[1], Anne F. Sheehan[1], Thomas de la Torre[1], Charlotte Rowe[2], and Michael Begnaud[2]

University of Colorado at Boulder[1] and Los Alamos National Laboratory[2]

Sponsored by National Nuclear Security Administration
Office of Nonproliferation Research and Engineering
Office of Defense Nuclear Nonproliferation

Contract Nos. DE-FC52-04NA25544[1] and W-7405-ENG-36[2]

ABSTRACT

We improve regional velocity structure and the database of seismic event ground truth (GT) information for central and southern Asia using data from a recent broadband seismic experiment in the Himalayas and the southern Tibetan Plateau, supplemented by local network data and other regional data. GT events can be used to calibrate station-centric correction surfaces and increase the ability to accurately locate and identify seismic events in these regions. In central Asia, limited station coverage results in poor reference-event coverage. The Himalayan Nepal Tibet Seismic Experiment (HIMNT) consisted of 29 broadband STS2 seismometers deployed in eastern Nepal and southern China (2001–2003). The data set is unique, with many stations in remote and difficult to access locations. GT coverage is sparse, and no permanent stations exist in most of the area covered by our network.

We have examined the entire continuous HIMNT seismic data set and have located >1600 regional and local events with magnitudes between 1 and 5.5. Initial hypocenters were determined using *a priori* one-dimensional (1D) velocity models and a weighted least squares location algorithm. We further refined the earthquake hypocenters using double-difference schemes and iterative three-dimensional (3D) velocity tomography with earthquake relocation. We have applied joint inversion routines to the >1600 earthquakes to solve simultaneously for hypocenters and seismic velocity structure. The code VELEST was used to determine best fitting 1D velocity models for the Himalayas and the southern Tibetan Plateau. We have found high velocities in the Tibetan lower crust and low Vp/Vs in the upper crust beneath the Tibetan Plateau. We also found a >15-km difference in crustal thickness between the Lesser Himalaya and the Tibetan Plateau. Receiver function analysis further constrains the crustal thickness variations. This large velocity heterogeneity over a small lateral distance makes a 3D velocity model important for determining accurate hypocenters. The code SIMUL2000 was then used to determine 3D velocity structure and iteratively relocate events in the new 3D velocity model. Earthquake hypocenters delineate several distinct groupings that correlate with collision zone tectonics. Crustal earthquakes show alignments with depths <25 km along the Himalayan Front's region of highest relief. Clusters of upper mantle earthquakes are found beneath the High Himalaya, in the Tethyan Himalaya, and beneath southern Nepal. We observe earthquake hypocenters over a range of depths, beneath Nepal from near-surface to 65 km deep and beneath the Tibetan Plateau from near-surface to 90 km deep. Although events cluster with depth, there are no large depth-distribution gaps.

Developing our GT catalog includes supplementing HIMNT data with other network data, along with moment tensor and source parameter analysis of GT events, with particular attention to depth control. We determined focal mechanisms using waveforms and first motions from 17 of the largest, best-recorded local earthquakes during the HIMNT experiment. We used a regional waveform moment tensor inversion method and first-motion polarities obtained from HIMNT, Nepal Department of Mines and Geology (DMG), and the Program for Array Studies of the Continental Lithosphere (PASSCAL) network deployed in Bhutan (2001–2003). Waveform solutions were obtained using HIMNT, Bhutan PASSCAL, and GSN (Lhasa) data. We performed a grid search over source depth to examine the sensitivity of the moment tensor solution to event depth and to find the best fitting source depth. We performed inversions using a range of passbands. Crosschecking focal mechanisms from full waveform moment with first-motion solutions revealed good agreement. We found that normal faulting with extensional axes trending E-W is common in the Tibetan Plateau's upper crust and that many earthquakes occur beneath the Moho, most having strike-slip mechanisms with compressional axes trending NW-SE to NE-SW. The new GT events can be used to calibrate station-centric correction surfaces and increase the ability to accurately locate and identify seismic events in these regions.

OBJECTIVES

The goals of this project are (1) to contribute to the database of GT seismic events in central Asia using data from the HIMNT network and other regional seismic data and (2) to determine detailed seismic body-wave velocity models for the portion of central Asia covered by the HIMNT network.

RESEARCH ACCOMPLISHED

HIMNT deployment

The HIMNT was a National Science Foundation PASSCAL deployment in Nepal and Tibet during 2001–2003 (Figure 1). HIMNT was the first broadband seismic experiment to cover the plains of southern Nepal, the Lesser and Greater Himalaya, and the Southern Tibetan Plateau simultaneously. The HIMNT experiment included the deployment of 29 three-component broadband seismic stations, which recorded continuously at a sample rate of 40 sps. Although the project primarily has tectonic objectives, the high-quality data collected is ideal for GT data for monitoring purposes. HIMNT stations were installed with approximately 40–50 km station spacing, covering a two-dimensional area approximately 300 km wide east-west by 300 km north-south (Figure 1). This geometry is well suited for both event location and seismic velocity structure projects. Station locations were dictated strongly by logistics, with some stations only accessible by air or by a several-day hike on foot.

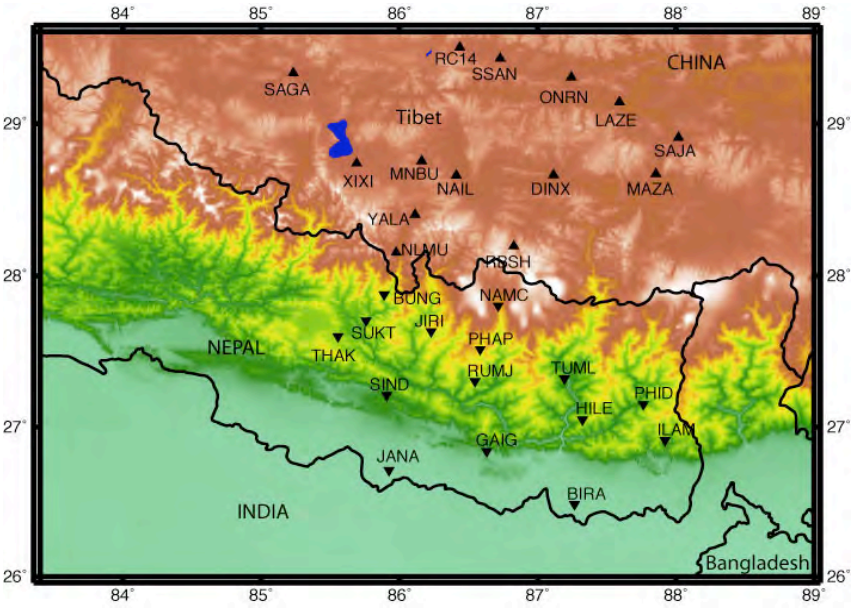

Figure 1. Topographic map with broadband seismic stations of the 2001–2003 Himalayan Nepal Tibet PASSCAL Seismic Experiment.

Initial locations

After identifying times for all the first P- and S-wave arrivals from the HIMNT continuous data set of seismograms, hypocenters were determined for 1651 local earthquakes. Earthquake hypocenters were first determined using the ANTELOPE software of Boulder Real Time Technologies. In particular, we used the ANTELOPE routine dbgenloc, which utilizes a weighted least-squares method using a three-layer *a priori* velocity model in order to determine earthquake hypocenters given first arrival travel times. All travel time arrivals were used in the hypocentral inversion, and each event was located individually. Weight was assigned to every arrival according to the length of the error window given to the pick and the event-station distance. Local magnitudes were calculated for all the earthquakes and ranged from 1 to 5.5. Moment magnitudes were also calculated for a subset of earthquakes with high-quality seismograms for which full waveform moment tensor inversions were performed. Comparison of these two kinds of independently estimated magnitudes shows a good agreement between the two, though the local magnitudes are on average larger by one-fifth of a magnitude unit compared to the moment magnitudes (Figure 2).

Figure 3 shows a magnitude-frequency diagram for our network, which can be used to estimate our detection threshold and catalog completeness. The relatively uniform slope of the magnitude-frequency curve indicates that our HIMNT earthquake catalog is complete for events with magnitudes greater than 2.5. Event detection is not complete for events of magnitude <2.5, although many events of this size have been detected and located. Most of the earthquakes in our HIMNT catalog are not found in the global catalogs. Since the lateral variation of the velocity structure in the north-south direction is very significant in the study area, we used two different velocity models (dashed lines in Figure 4), one for the Sub-Himalaya and Lesser Himalaya (Pandey et al., 1995) and one for the southern Tibetan Plateau (Cotte et al., 1999). For earthquakes near the boundary between these two areas, the location was performed using the model corresponding to the volume through which the seismic waves predominantly propagated.

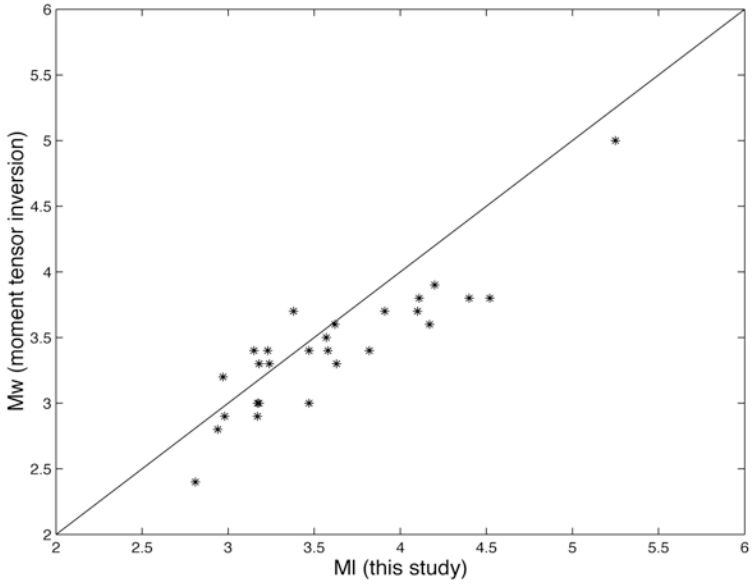

Figure 2. Comparison between local magnitudes and moment magnitudes calculated through full waveform moment tensor inversion for a subset of earthquakes. The reference line has a slope of 1 and goes through the origin.

Improved velocity model and earthquake locations

The program VELEST (Kissling, 1995) was used to invert simultaneously for earthquake locations and 1D velocity structure using the arrival time data, the initial earthquake locations and a starting velocity model. After many runs with different starting models and control parameters, two velocity models, one for the Himalayas and the other for the southern Tibetan Plateau, were selected on the basis of minimum root mean square (RMS) misfit and some *a priori* information obtained from previous studies (Sapin et al., 1985; Pandey et al., 1995; Galve et al., 2002). Figure 4 shows the improved velocity models for the Himalaya of Nepal and the southern Tibetan Plateau. Using this improved velocity model, all the local earthquakes were then relocated. Figure 5 shows a map view with the earthquake relocations. Events beneath the Himalayan front show an alignment on the region of highest relief. Clusters of upper crustal earthquakes in the north part of the network are mainly related to normal faults and grabens in the southern Tibetan Plateau. A group of lower crust and upper mantle earthquakes is found beneath the Lesser Himalaya of Nepal, possibly related to the magnitude 6.5 08/20/1988 Udayapur earthquake (Pandey et al., 1999). There is also a NW-SE stripe of earthquakes in the lower crust and upper mantle beneath the Southern Tibetan Plateau and the High Himalayas. A receiver function analysis (Schulte-Pelkum et al., 2005) shows that the Moho is at most 50 km below sea level beneath the Lesser Himalaya and 75 km below sea level beneath the southern Tibetan Plateau, indicating that some of the earthquakes we located are in the upper mantle. Depths range from surface to around 65 km below sea level in the Lesser and Sub-Himalaya and from surface to around 90 km below sea level in

the High Himalaya and the southern Tibetan Plateau. No evident gaps in depth are found among the located earthquakes.

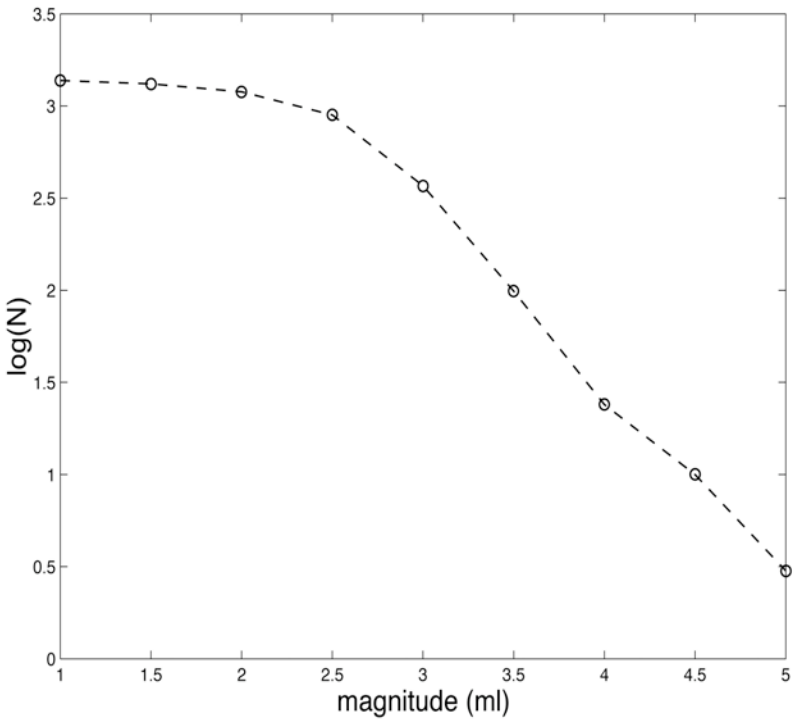

Figure 3. Magnitude-frequency diagram for events detected and located in HIMNT network. Logarithm of the number of events greater than a certain magnitude is plotted on the vertical axis. The uniform slope for magnitudes greater than 2.5 indicates that our catalog is complete for this range of magnitudes.

From the obtained models and the observed changes in velocity with depth, it is clear that the crust is >15 km thicker in the Tibetan Plateau than it is in the Lesser Himalaya. This greater thickness is also suggested by the receiver function analysis carried out by Schulte-Pelkum et al. (2005). These variations in crustal thickness suggest the existence of a large lateral heterogeneity in the study region, pointing out the need to invert for a 3D velocity model. A subset of 539 high-quality earthquakes was used as input to the program SIMUL2000, which relocates these earthquakes and finds a 3D velocity distribution using a damped least-squares inversion (Thurber, 1983). The study region is parameterized as a rectangular grid of nodes; SIMUL2000 iteratively inverts for P-wave velocity (Vp) at each node, P-wave velocity to S-wave velocity ratio (Vp/Vs) and earthquake location. The 1D velocity models obtained from VELEST were used as a starting model for the 3D inversion, and a succession of inversions going from coarse to finer grids was performed. The final grid has a mean node separation of about 40 km in the horizontal direction near the center of the network and 15 km in the vertical direction.

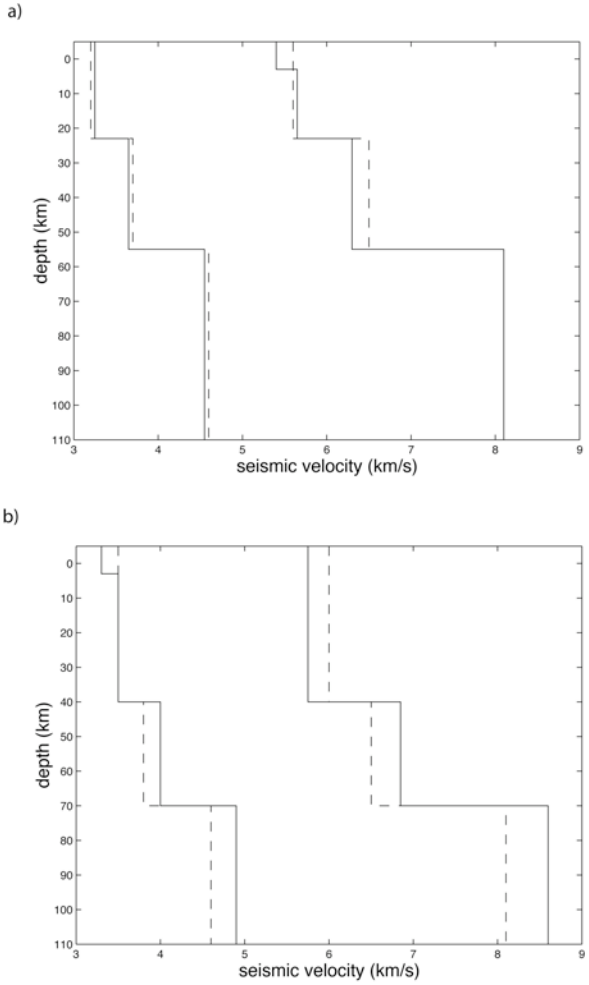

Figure 4. The 1D velocity models used for preliminary locations (dashed lines) and the minimum-error model found with VELEST (solid lines). Layer boundaries kept fixed. (a) Results for the Lesser Himalaya (Nepal) part of the array. Initial model by Pandey et al (1995). (b) Results for the Tibetan Plateau part of the array. Initial model by Cotte et al. (1999).

Figure 6 shows the results for Vp (6a) and Vp/Vs (6b) as horizontal slices at six different depths. Among the robust features resulting from these inversions are low values of Vp/Vs in the upper crust beneath the southern Tibetan Plateau, high P-wave velocities in the lower crust beneath the Tibetan Plateau, and high upper-mantle velocities beneath the High and Tethyan Himalayas.

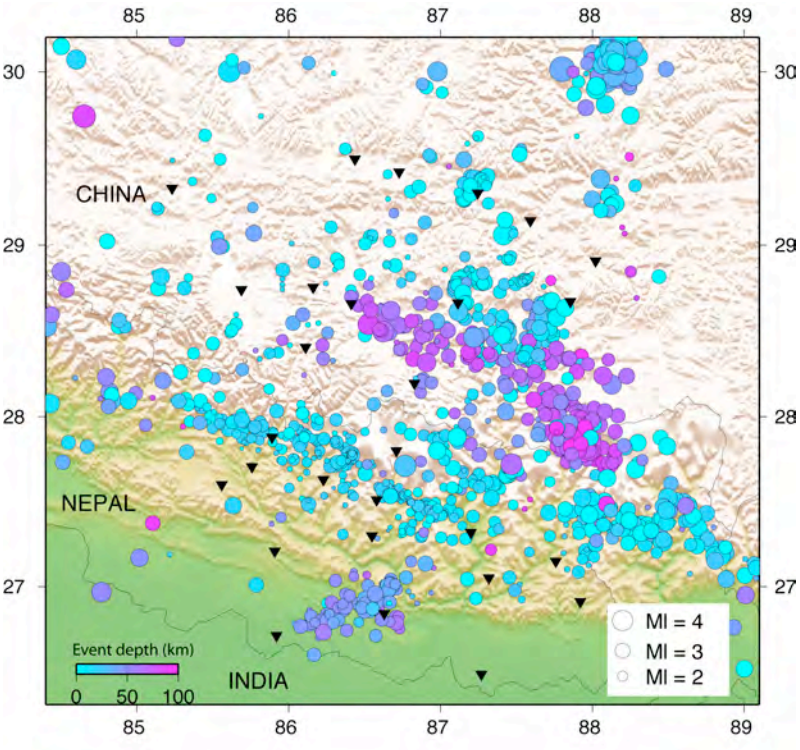

Figure 5. Map view of earthquake locations after refining the velocity model using VELEST. The event symbol size is scaled by magnitude. Earthquakes are color scaled by depth in kilometers. Inverted triangles show HIMNT station locations. (The only stations plotted are the ones with data used here.)

Moment tensor and Source Parameter Analysis

We used the moment tensor inversion method of Ammon and Randall (Ammon and Randall, 1994; Randall et al., 1995; Stich et al., 2003) to calculate the deviatoric moment tensor solutions for 17 high-quality earthquakes, using data collected from the HIMNT experiment, the Bhutan PASSCAL network (Velasco, personal communication, 2004) and the Global Seismic Network (GSN, station LSA). We calculated Green's functions using two 1D velocity models, one for the Himalayas and the other for the Tibetan Plateau. The whole waveform was modeled in each inversion. We performed a grid search over depth at 5-km increments and over several overlapping bandpass ranges. The depths of minimum misfit between the data and the synthetics are in good agreement with the depths obtained by travel time inversion. Figure 7 shows observed and synthetic seismograms for a representative event, along with misfit versus depth curves calculated using several bandpasses. We also calculated first-motion focal mechanism solutions to compare to the full waveform moment tensor solutions. First motions were obtained from HIMNT data, seismograms collected from the Bhutan PASSCAL network, and the permanent short-period single-component network of the Nepal DMG.

Figures 8 and 9 illustrate the focal mechanisms in map view and cross-section respectively, along with HIMNT seismicity described in the earlier section. The moment tensor solutions for the shallow events in the southern Tibetan Plateau indicate east-west extension. Under the Himalayas, from the mid crust to the Moho, east-west extension is also present. At Moho depths and below, under the High and Tethyan Himalayas, earthquakes show normal faulting changing to strike-slip. We observed a shift in the focal mechanisms at Moho depths that indicates a change in the maximum stress through the lower crust to the upper mantle from vertical to a NW-SE/NE-SW direction.

Our GT catalog will include many of the events with moment tensor solutions. The source parameters will be provided for the GT events, and we have paid particular attention to the issue of depth control. Our waveform moment tensor solutions are improved by supplementing HIMNT data with Bhutan and GSN data, and first motion mechanism solutions use data from HIMNT, Bhutan, and the Nepal DMG network. We performed a grid search

over source depth to examine the sensitivity of the moment tensor solution to event depth and to find the best fitting source depth. Inversions were performed using a range of passbands, and sensitivity to frequency was explored. Focal mechanisms from full waveform moment tensor inversions were crosschecked with first motion solutions, and good agreement was found.

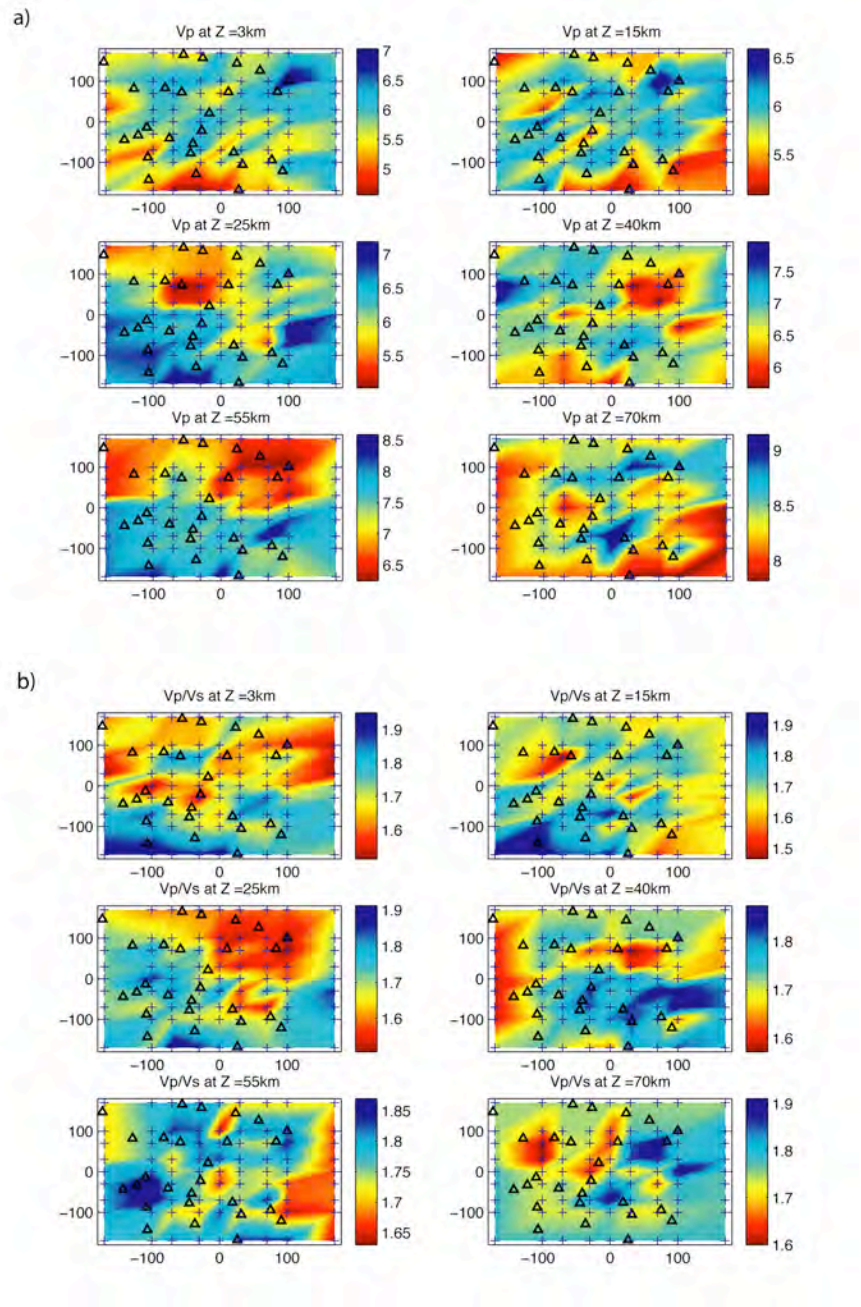

Figure 6: Horizontal depth slices through a 3D tomography model from the application of SIMUL2000 to HIMNT P- and S-wave travel times. (a) P-wave velocity (Vp) in km/s. (b) P-wave to S-wave velocity ratio (Vp/Vs). Crosses denote inversion nodes. Black triangles represent station locations.

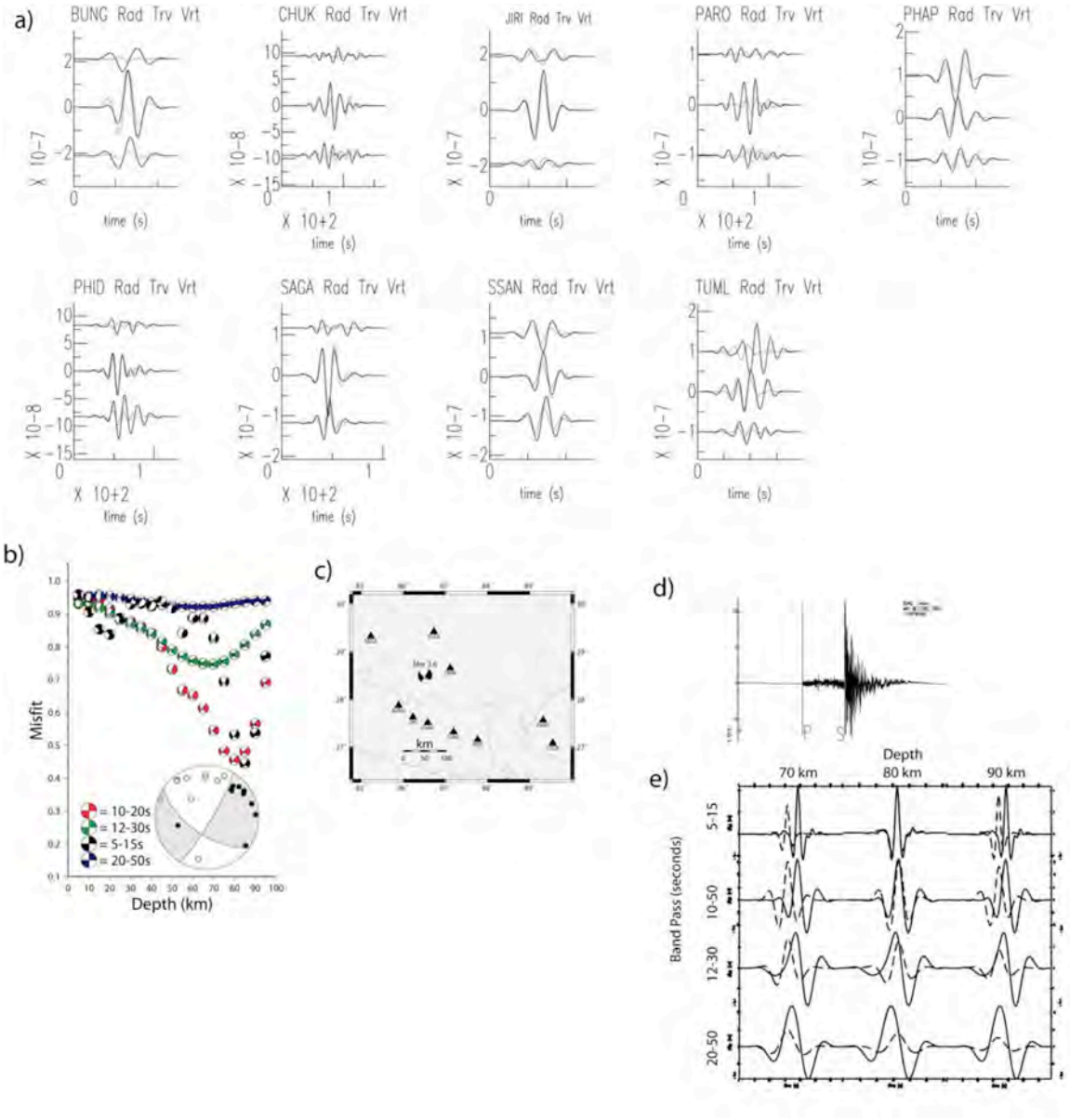

Figure 7. Full waveform moment tensor inversion of event located at 28.5N 86.5E, depth 81 km. (a) Synthetic (dashed) and observed (solid) waveforms (10–20 s bandpass). Synthetic was calculated for the minimum misfit solution at 80 km. (b) Misfit versus depth curves for four different waveform bandpass intervals. The inset shows first-motion polarity points plotted on the best solution from moment tensor inversion. The black circles are compressions; the white circles are dilatations. The best waveform solution occurs using the 5-15 s and 10-20 s bandpass interval for an 80–85 km source depth. (c) Station locations and the best moment tensor solution plotted at event location. (d) Observed seismogram at station BUNG transverse component with P and S picks. Note the lack of surface wave energy. (e) Synthetic versus observed seismogram for synthetics calculated using source depths of 70, 80 and 90 km. Observed seismograms for bandpass intervals 5-15 s, 10-20 s, 12-30 s and 20-50 s.

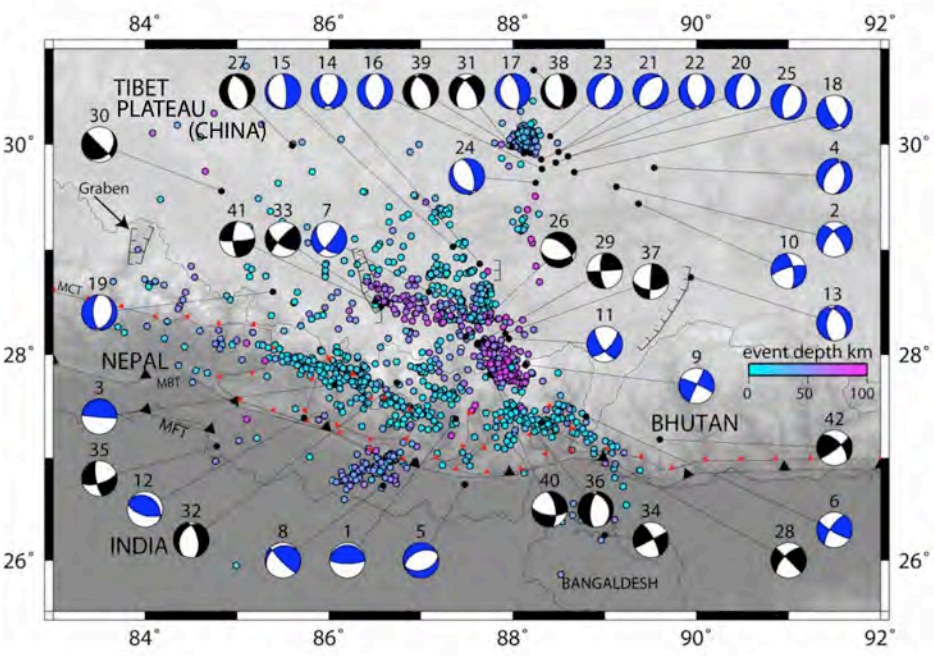

Figure 8. Focal mechanisms from HIMNT and previous studies plotted with HIMNT seismicity from October 2001 to April 2003. Seismicity (shown as small colored circles) is color coded by depth. HIMNT focal mechanisms are shown in black. The blue focal mechanisms are from the Harvard Centroid Moment Tensor catalog and from previously published solutions (Baranowski et al., 1984; Chen et al., 1981; Chen and Yang, 2004; Molnar and Chen, 1983; Ni and Barazangi, 1984; Zhu and Helmberger, 1996). Faults shown include MCT, Main Central Thrust; MBT, Main Boundary Thrust; and MFT, Main Frontal Thrust.

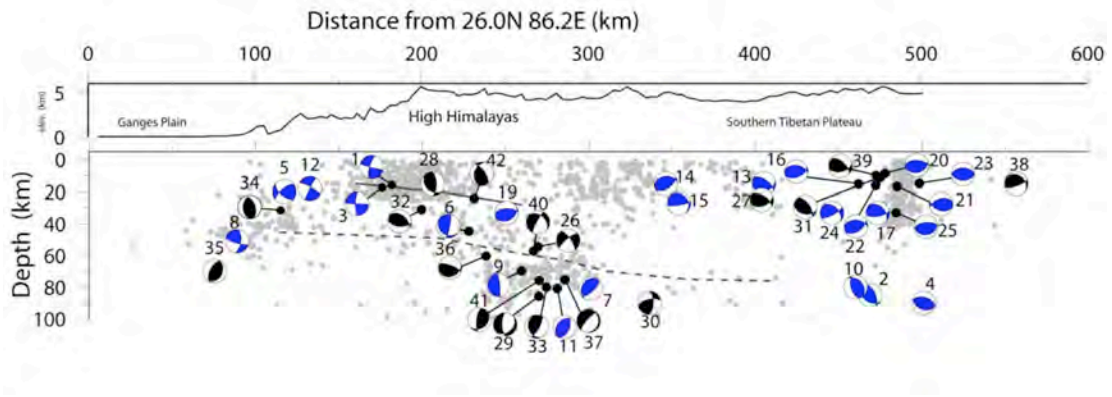

Figure 9. Cross-section from 26.0N 86.2E azimuth 018 showing HIMNT seismicity and focal mechanisms from HIMNT and other studies. The dashed line indicates the Moho, and the solid line marks the top of the Indian Plate (Schulte-Pelkum et al., 2005). Regional topography is plotted above the seismicity. Focal mechanism colors are as in Figure 8.

CONCLUSION

Using in-country networks contributes to GT location determination in central Asia, which is important for validating regional velocity models and correction surfaces. Examining data from the HIMNT network indicates a wealth of high-quality events not available in global catalogs. Important steps toward the determination of precise earthquake locations, source parameters and velocity structure have been taken. Such events are of utility for GT as well as for regional velocity structure and will contribute to the National Nuclear Security Administration knowledge base.

REFERENCES

Ammon, C. J. and G. E. Randall (1994, last updated July 2001), Moment Tensor Inversion, http://eqseis.geosc.psu.edu/~cammon/HTML/MTinvDocs/mtinv01.html (2005).

Baranowski, J., J. Armbruster, L. Seeber, and P. Molnar (1984), Focal Depths and Fault Plane Solutions of Earthquakes and Active Tectonics of the Himalaya, *J. Geophys. Res.* 89 (NB8): 6918–6928.

Chen, W. P., J. L. Nabelek, T. J. Fitch, and P. Molnar (1981), An Intermediate Depth Earthquake beneath Tibet—Source Characteristics of the Event of September 14, 1976, *J. Geophys. Res.* 86 (NB4): 2863–2876.

Chen, W. P., and Z. H. Yang (2004), Earthquakes beneath the Himalayas and Tibet: Evidence for Strong Lithospheric Mantle, *Science* 304: 1949–1952.

Cotte, N., H. Pedersen, M. Campillo, J. Mars, J. F. Ni, R. Kind, E. Sandvol, and W. Zhao (1999), Determination of the Crustal Structure in Southern Tibet by Dispersion and Amplitude Analysis of Rayleigh Waves, *Geophys. J. Int.* 138: 809–819.

Galve, A., M. Sapin, A. Hirn, J. Diaz, J. C. Lepine, M. Laigle, J. Gallart, and M. Jiang (2002), Complex Images of Moho and Variation of Vp/Vs across the Himalaya and South Tibet from a Joint Receiver-Function and Wide-Angle Reflection Approach, *Geophys. Res. Lett.* 29: 35-1–35-4.

Harvard Centroid Moment Tensor Catalog, www.seismology.harvard.edu/CMTsearch.html (2005).

Kissling, E. (1995), Program VELEST User's Guide—Short Introduction, www.sg.geophys.ethz.ch/aes/aes-html/**velest**.html .

Molnar, P., and W. P. Chen (1983), Focal Depths and Fault Plane Solutions of Earthquakes under the Tibetan Plateau, *J. Geophys. Res.* 88: 1180–1196.

Ni, J. and M. Barazangi (1984), Seismotectonics of the Himalayan Collision Zone—Geometry of the Underthrusting Indian Plate beneath the Himalaya, *J. Geophys. Res.* 89: 1147–1163.

Pandey, M. R., R. P. Tandukar, J. P. Avouac, J. Lave, and J. P. Massot (1995), Interseismic Strain Accumulation on the Himalayan Crustal Ramp (Nepal), *Geophys. Res. Lett.* 22: 751–754.

Pandey, M. R., R. P. Tandukar, J. P. Avouac, J. Vergne, and T. Heritier (1999), Seismotectonics of the Nepal Himalaya from a Local Seismic Network, *J. Asian Earth Sci.* 17: 703–712, 1999.

Randall, G. E., C. J. Ammon, and T. J. Owens (1995), Moment Tensor Estimation Using Regional Seismograms from a Tibetan Plateau Portable Network Deployment (1995), *Geophys. Res. Lett.* 22: 1665–1668.

Sapin, M., X. Wang, A. Hirn, and Z. X. Xu (1985), A Seismic Sounding in the Crust of the Lhasa Block, Tibet, *Ann. Geophys.* 3: 637–648.

Schulte-Pelkum, V., G. Monsalve, A. Sheehan, M. R. Pandey, S. Sapkota, R. Bilham, and F. Wu (2005), Imaging the Indian Subcontinent beneath the Himalaya, *Nature* 435: 1222–1225, doi:10.1038/nature03678.

Stich, D., C. J. Ammon, and J. Morales (2003), Moment Tensor Solutions for Small and Moderate Earthquakes in the Ibero-Maghreb Region, *J. Geophys. Res*. 108.

Thurber, C. H. (1983), Earthquake Locations and Three-Dimensional Crustal Structure in the Coyote Lake Area, Central California, *J. Geophys. Res.* 88: 8226–8236.

Zhu, L. P. and D. V. Helmberger (1996), Intermediate Depth Earthquakes beneath the India-Tibet Collision Zone, *Geophys. Res. Lett*. 23: 435–438.

MULTIPLE-EVENT LOCATION USING THE MARKOV-CHAIN MONTE CARLO TECHNIQUE

Stephen C. Myers, Gardar Johannesson, and William Hanley

Lawrence Livermore National Laboratory

Sponsored by National Nuclear Security Administration
Office of Nonproliferation Research and Engineering
Office of Defense Nuclear Nonproliferation

Contract No. W-7405-ENG-48

ABSTRACT

The goal of next-generation seismic location is to ascertain a consistent set of event locations and travel-time corrections through simultaneous analysis of all relevant data. Towards that end, we are developing a new multiple-event location algorithm that utilizes the Markov-Chain Monte Carlo (MCMC) method for solving large, non-linear inverse problems. Unlike most inverse methods, the MCMC approach produces a suite of solutions, each of which is consistent with seismic and other observations, as well as prior estimates of data and model uncertainties. In the MCMC multiple-event locator (MCMCloc), the model uncertainties consist of prior estimates on the accuracy of each input event location, travel-time prediction uncertainties, phase measurement uncertainties, and assessments of phase identification. The prior uncertainty estimates include correlations between travel-time predictions, correlations between measurement errors, and the probability of misidentifying one phase for another (or bogus picks). The implementation of prior constraints on location accuracy allows the direct utilization of ground-truth events in the location algorithm. This is a significant improvement over most other grid multiple-event locators (GMEL is an exception), for which location accuracy is achieved through post-processing comparisons with ground-truth information. Like the double-difference algorithm, the implementation of a correlation structure for travel-time predictions allows MCMCloc to operate over arbitrarily large geographic areas. MCMCloc can accommodate non-Gaussian and multi-modal pick distributions, which can enhance application to poorly recorded events. Further, MCMCloc allows for ambiguous determination of phase assignments, and the solution includes the probability that phases are properly assigned. The probabilities that phase assignments are correct are propagated to the estimates of all other model parameters. Posteriori estimates of event locations, path corrections, pick errors, and phase identifications are made through analysis of the posteriori suite of acceptable solutions.

We test the MCMC locator on a regional data set of Nevada Test Site nuclear explosions. Event locations and origin times are known for these events, allowing us to tests the features of MCMCloc against a true ground truth (GT0) data set. Preliminary tests suggest that MCMCloc provides excellent relative locations (similar to other algorithms), and excellent absolute locations when constraints from one or more ground truth event are included. Tests also include realistic phase misidentification, where phase assignments are switched for phases that arrive within a few seconds of one another. We find that MCMCloc is a promising method for simultaneously locating large, geographically distributed data sets. Because we allow for input of prior knowledge on many aspects of the data set, MCMCloc is ideal for combining trusted and lesser-quality data.

OBJECTIVES

Traditionally, multiple event locators simultaneously determine the optimal, relative location for a geographically clustered set of events (e.g., Douglas, 1967; Dewey, 1971; Jordan and Sverdrup, 1981; Pavlis and Booker, 1981). These methods work best when there is substantial overlap in the network of stations that recorded each event and inter-events distances are short relative to event/station distances. These conditions allow for robust estimation of a travel-time correction for each station/phase pair and the determination of relative event locations. In a recent effort Waldhauser and Ellsworth (2000) expand the applicability of multiple-event methods to larger geographic regions by allowing for spatially varying travel-time corrections. Myers and Schultz (2000) also use spatially varying travel-time corrections but with a modeled correlation structure, thus approximating a multiple-event result with a single-event algorithm. Each method has it advantages and challenges. The HypoDD method of Waldhauser and Ellsworth (2000) employs an ad hoc correlation structure, so the transition between relative and absolute location is based on a static preset parameter. Also, the location estimates are determined by iteratively inverting a system of linear equations, requiring approximately exponential growth in computational power as the number of observations grows. Therefore, application to very large problems can become computationally restrictive. In the case of travel-time corrections based on Bayesian Kriging, Myers and Schultz, 2000 demonstrate that single-event locations can closely match multiple event estimates. Because the application is through a single-event location algorithm, application to large data sets is "embarrassingly" parallel. However, development of a self-consistent set of correction surfaces for each station and phase is time intensive for the analyst. Also, the correction surface method is not applicable to the local-distance case, where slowness changes rapidly with event depth.

In this study we introduce a new multiple-event method that uses the Markov-Chain Monte Carlo (MCMC) method for solving large inverse problems. The new method (MCMCloc) allows us to simultaneously estimate event location, travel-time correction, pick precision, and phase identification. We present a brief outline of the forward problem, the statistical framework for assessing data fit, and a "first cut" example application to the Nevada Test Site (NTS) data set of nuclear explosions with known source parameters.

RESEARCH ACCOMPLISHED

The MCMC method and its applicability to seismic location

In single-event location, where the full space of potential locations can be interrogated, grid-search and related methods have a proven record of performance (Billings et al., 1994; Rodi et al., 2003, Lomax, 2005). However, for multiple-event location the full-combination of potential solutions quickly out strips even modern computational capabilities. Markov Chain Monte Carlo (MCMC) is particularly well suited to characterize (albeit not fully explore) the multiple-event solution space, because it is a "smart" search through a potentially enormous space, and the efficiency of the search can be further improved by taking advantage of prior information about each event location (and other parameters).

The MCMC approach, while not new to geophysics (e.g., Shapiro and Ritzwoller, 2002; Pasyanos et al., submitted), has not to our knowledge been used in multiple event locations. General overviews of MCMC can be found in, for example, Gilks et al. (1996) and Gelman et al. (2004). At its core, the MCMC technique is a Markovian proposal process, meaning that a new parameter configuration (i.e., hypocenters, arrival-time measurement errors, travel-time corrections, and phase assignments) is made by modifying the current configuration. The series of configurations is referred to as a chain. The new configuration is, by design, consistent with prior parameter constraints. A configuration is kept as a potential solution if predictions based on that configuration (e.g., travel-time predictions) are within prescribed uncertainties of observed data (Figure 1). The MCMC approach is distinct from traditional (linearized) inversion techniques that return a point for each location with an associated confidence ellipsoid. The MCMC solution for each event location is a cloud of points that defines a probability density function. The "best" or "most probable" location and a confidence region can be derived from the non-linear probability distribution.

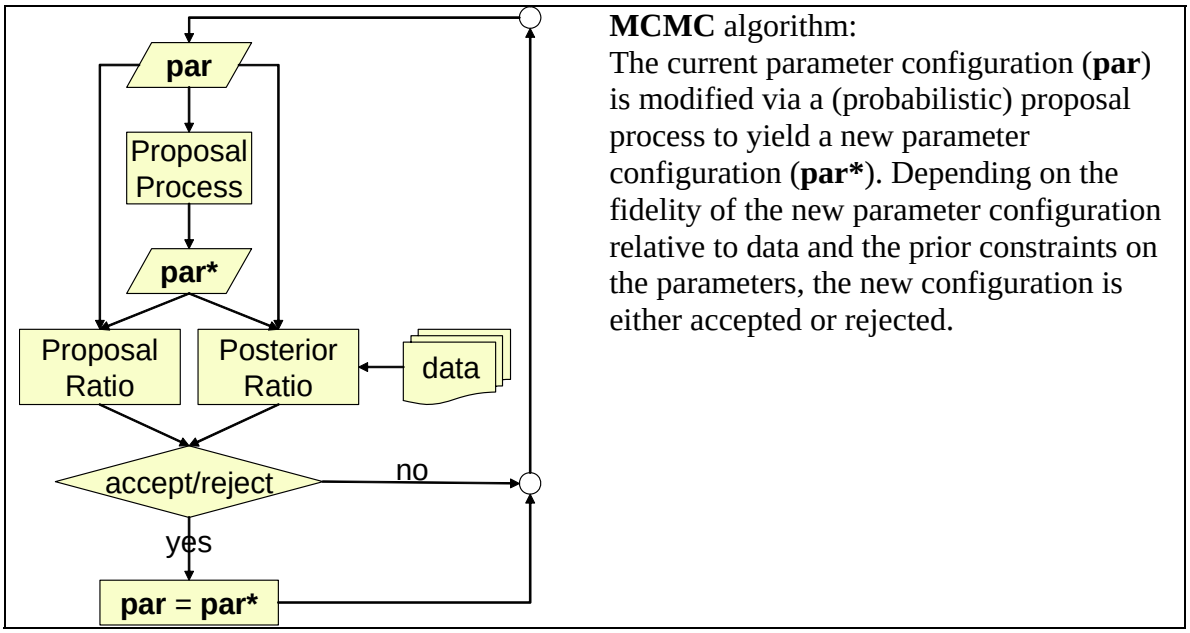

Figure 1. Flow chart depicting the proposal and assessment of parameter configurations in the MCMC inversion procedure.

Formulation of the MCMCloc forward problem

We have developed a new location algorithm (MCMCloc) with the MCMC solver at its core. In MCMCloc the seismic location forward problem is by dividing into 3 components.

1. Hypocenter-Model: Conditional distribution of event location parameters given prior estimates and resulting fit to data.
2. Data-Model: Conditional distribution on the observed data given the true configuration of arrival-times and phase assignments (akin to pick error but now includes phase assignments).
3. Prediction-Model: Conditional distribution for the true arrival-times and phase assignments given a particular configuration of event locations (path corrections).

Component (1) is the traditional location inversion problem, allowing for constrains on hypocenter parameters. Any hypocenter component of any event can be constrained using any specified probability density function. The default is a flat prior (no constraint). Component (2) is a model of observational error. We extend traditional assessments of observation error – random measurement or "pick" error – to include the chance that phase assignments may be incorrect and the chance that any datum may be altogether bogus. Component (3) accounts for errors in travel-time prediction. The model for travel-time predictions can be quite general for MCMCloc, but in this initial implementation it is simply a static adjustment to the travel-time curve for each phase.

MCMCloc iteratively modifies each *component* of the forward model (as defined above). That is, MCMCloc alternates between proposing a new *component* of the solution. Therefore, MCMCloc will propose one of the following: (a) a new hypocenter model, (b) a new data model, (c) or a new travel time prediction model. Choosing a succession of components that are modified can greatly speed convergence.

In order to ensure coverage of the solution space, multiple chains are generated independently. Each chain is run for an initial burn-in period after which the chain continues for additional adaptive training that fine-tunes the proposal process. The multiple chains are merged to form a global distribution.

Example Application

We relocated 9 nuclear tests at the Nevada Test Site (NTS) (Walter et al., 2003) for demonstration purposes (Figure 2). The hypocenter is known for each event, providing unambiguous assessment of location accuracy. For this demonstration we locate using Pn, Pg, and Lg arrival times. The number of observed phases for each event ranges from 7 (3 stations) to 23 (8 stations), with a total of 128 arrivals for the 9 events.

The prior distribution for the hypocenter parameters (lat, lon, depth, time) was taken to be multivariate normal, with depth log-transformed. The travel-time model is IASP91 (Kennett and Engdahl, 1991), which is known to result in location bias of ~5km for the NTS explosion data set (Anderson and Myers, 2005). The travel-time error-model is, in this instance, very simple: a travel-time shift for each phase (with a normal prior on the travel-time shift parameters). The travel-time residual model (pick error) was taken to be normal, with independent variance for each station and phase. More specifically, $\log[\mathrm{Var}(i,j,k)] = A(k) + B(j)$, where $\mathrm{Var}(i,j,k)$ is the variance associated with the i-th event, the j-th station, and the k-th phase, and $A(k)$ and $B(j)$ are phase- and station-specific parameters, respectively.

We consider three test cases:

1. A vague prior on all parameters and phase-assignments assumed correct (standard relative location).
2. A strong (narrow) prior for the hypocenter parameters of two events and phase-assignments assumed correct (relative location with two fixed locations).
3. A strong (narrow) prior for the location parameters of two events, phase-assignments *not* assumed correct. In this instance, three Pn/Pg phase-assignments were switched and 10 sec was added to another three Pg arrival times (i.e., corrupted data).

Case 1

Figure 3 shows a map of epicenter posterior distributions for the 9 events. For well-observed events, the posterior distribution is relatively tight around the true location. As expected, for poorly observed events the distribution is wider and the mean of the distribution is not centered on the known location. However, it is important to note that the distribution still covers the true event location for the most poorly observed events. The “mass” of the origin time posterior distributions was generally within 1 second of the true origin-time (not shown). Instances with broad origin posterior distributions still covered the known value. Posterior distributions for event depth were broad (not shown), owing to inherent uncertainties. The depth distributions, although broad, included the true depth in all cases. The phase-specific variance parameter was largest for Lg and smallest for Pn. As a result Pn arrivals get considerable more weight that Lg arrivals. In other words, the uncertainty in measuring the Lg arrival overwhelms the increased sensitivity due to the slow Lg velocity. Lastly, we find a considerable variation in the station-specific variance parameters (pick error), which is likely the result of better quality signals at some stations that results in high-precision arrival-time measurements.

For comparison purposes, we show conventional relative locations in Figure 4. Conventional relative methods assume a static travel-time adjustment for each station/phase pair. Unfortunately, addition of the station/phase parameters comes at the cost of lost resolution in absolute location accuracy, and in this case epicenters are displaced to the east of the known locations. Our choice of a simple travel-time adjustment is, in this instance, beneficial because location accuracy is maintained. In the near future, we plan to extend the simple travel-time correction model to include station/phase terms; however, our plan is for a hierarchic approach in which adjustments to the travel-time curve are made first, followed by station/phase specific adjustments. The station/phase terms will include spatial correlation, which will allow application over an arbitrarily large area. Using this general approach we aim to maintain as much accuracy as possible, while introducing the terms that improve relative location precision.

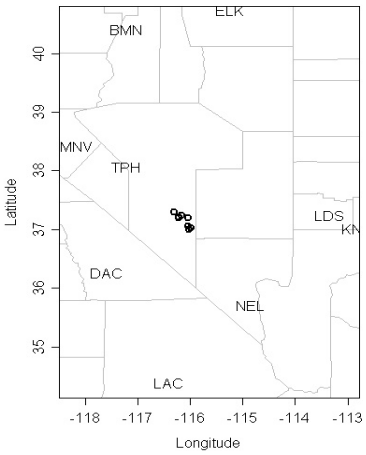

Figure 2. Test event (circles) and stations (shown as station abbreviations) for the regional test case.

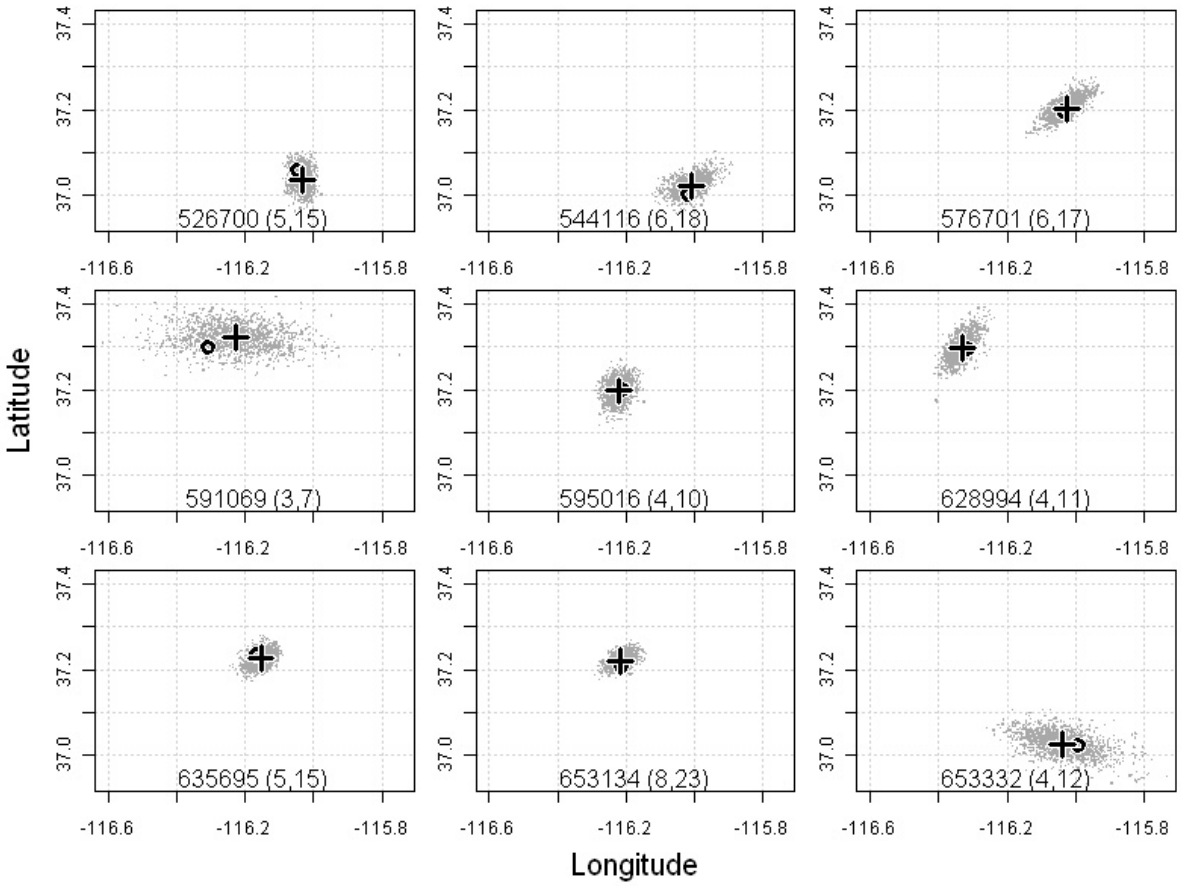

Figure 3. Epicenter posterior distribution of the 9 events in case 1 (relative locations). Each panel shows the distribution of a single event. Each gray dot is an epicenter realization that was "accepted" by MCMCloc. Black circles show the true location of the event, and black crosses show the posterior average (mean) location. The bottom of each panel shows an event identification number along with the number of stations observing the event and the total number of observed phases in parentheses.

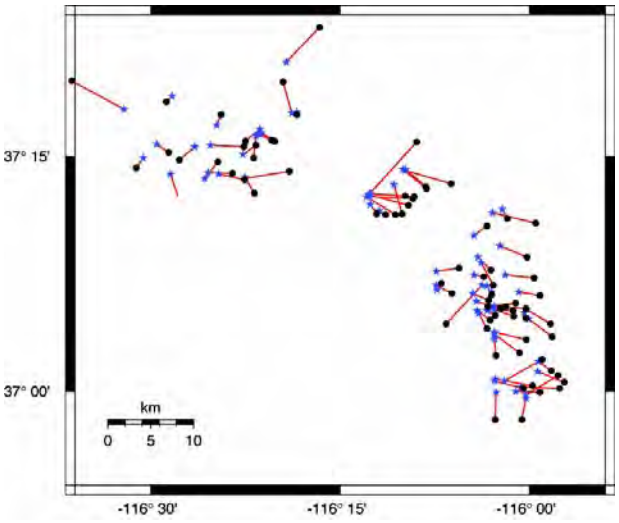

Figure 4. Relative locations of the full NTS set of explosions using a conventional relative location method. Blue stars are the known location and black dots are estimated epicenters. Note the eastward bias of ~5 km. (From Anderson and Myers, 2005).

Case 2

Figure 5 shows epicenter posterior distributions when two events are constrained to the known location (tight priors). Because locations in case 1 are excellent, there is not a large visual difference between Figures 3 and 5, but closer inspection shows slightly tighter posteriors in case 2, as expected. Posterior epicenter distributions in case 2 tighten because the travel-times are "calibrated" with more certainty by the two constrained events.

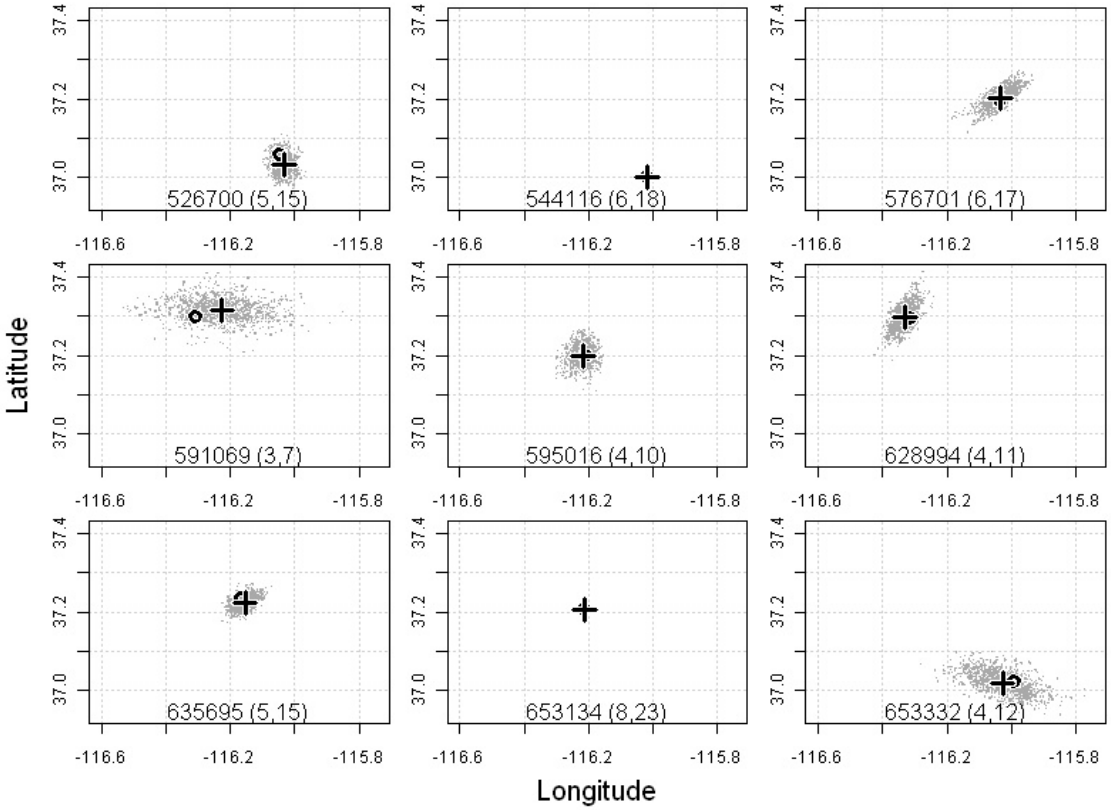

Figure 5. Latitude-longitude location posterior distribution of the nine events in case 2. See Figure 3 for caption.

Case 3

In this case, Pg/Pn phase-assignments are switched for events numbers 628994, 576701, and 635695. The confusion of Pg and Pn is presented only to demonstrate the capabilities of MCMCloc, as this mistake may not be realistic for most data sets. Pn and Pg phases arrive within 6, 10, and 1 second of one another for these event numbers, respective to the listed order above. For the same events, we also delayed 3 Lg arrivals by 10 seconds (not at the same stations for which phase-assignments were switched). Hence, for example, event 628994 has 11 phases at 4 stations. Of those 11 observations, Pn and Pg phase names were switched at one station and one Lg observation was delayed by 10 seconds (i.e., 3 out of 11 observation were corrupted).

In case 3 the phase-assignments were viewed as a model parameter with a prior based on the analyst's phase assignment. Phase assignments were sampled in MCMCloc, and posteriori assessments of the phase assignments were made. In addition to allowing for phase mislabeling in our model, we also allow for bad data. Bad data are reassigned to the "X" phase label.

Figure 6 shows the epicenter posterior plot for case 3. The most striking difference between Figures 6 and 3 is event 591069, which had no data corrupted in case 3. The change in event 591069 is the result of corrupted data from one station whose weight was decreased by the data corruption.

For the mislabeled phases (Pn and Pg switched), the marginal posterior phase-assignments are reported in Table 1. Unfortunately, in our test run we inadvertently set the probability of the correct phase assignment to 99%. We find that our prior was too "tight"; MCMCloc diligently followed the tight prior by maintaining the input phase assignment; however, it is interesting that MCMCloc reported a significant probability that the tampered arrivals are bogus.

Table 1. Assigned phase (rows) with posterior probability of phase assignment (columns). In each of these cases, Pn and Pg phase assignments were reversed. Each column shows the posterior probability for assigning a given arrival observation (labeled by O[X], where X is the observed phase-label) to the three possible phase-labels (P[Lg], P[Pg], P[Pn]), plus the 'bogus' label (P[NA]) – each column should sum up to 1. Recall that the observed Pg (O[Pg]) are actually Pn and the observed Pn are Pg. As can be seen, where the phase mislabeling occurred, the observation tends to be removed.

628994 to KNB	576701 to BMN	635695 to TPH
O[Lg] O[Pg] O[Pn]	O[Lg] O[Pg] O[Pn]	O[Lg] O[Pg] O[Pn]
P[Lg] 0.888 0.000 0.000	P[Lg] 0.958 0.000 0.000	P[Lg] 0.882 0.003 0.000
P[Pg] 0.000 0.706 0.038	P[Pg] 0.000 0.975 0.002	P[Pg] 0.000 0.000 0.013
P[Pn] 0.000 0.000 0.000	P[Pn] 0.000 0.000 0.000	P[Pn] 0.000 0.000 0.961
P[NA] 0.112 0.294 0.962	P[NA] 0.042 0.025 0.998	P[NA] 0.118 0.997 0.026

The marginal posteriori phase-assignments for the arrivals that were corrupted by 10 seconds are reported in Table 2. The posterior phase assignment suggests that corruption of the Lg arrival time does not call for its removal. Although it may be unexpected, 3 instances of 10 second error in this data set is consistent with the overall posterior distribution of Lg arrival-time uncertainty. In this instance, MCMCloc pointed out a flaw in our perception that such a large arrival time error would be inconsistent with other observations. We note, however, that MCMCloc down weighted the Lg phase considerably, and the location estimates were minimally affected by the Lg data.

Table 2. Assigned Phase (rows) with posterior probability of phase assignment. In each of these cases 10 seconds was added to the Pg arrival time. See table 1 caption for more detail.

628994 to NEL	576701 to ELK	635695 to NEL
O[Lg] O[Pg] O[Pn]	O[Lg] O[Pg] O[Pn]	O[Lg] O[Pg] O[Pn]
P[Lg] 0.949 0.000 0.000	P[Lg] 0.783 0.000 0.000	P[Lg] 0.939 0.000 0.000
P[Pg] 0.000 0.947 0.000	P[Pg] 0.000 0.922 0.000	P[Pg] 0.000 0.979 0.000
P[Pn] 0.000 0.000 0.979	P[Pn] 0.000 0.000 0.979	P[Pn] 0.000 0.000 0.972
P[NA] 0.051 0.053 0.021	P[NA] 0.217 0.078 0.021	P[NA] 0.061 0.021 0.029

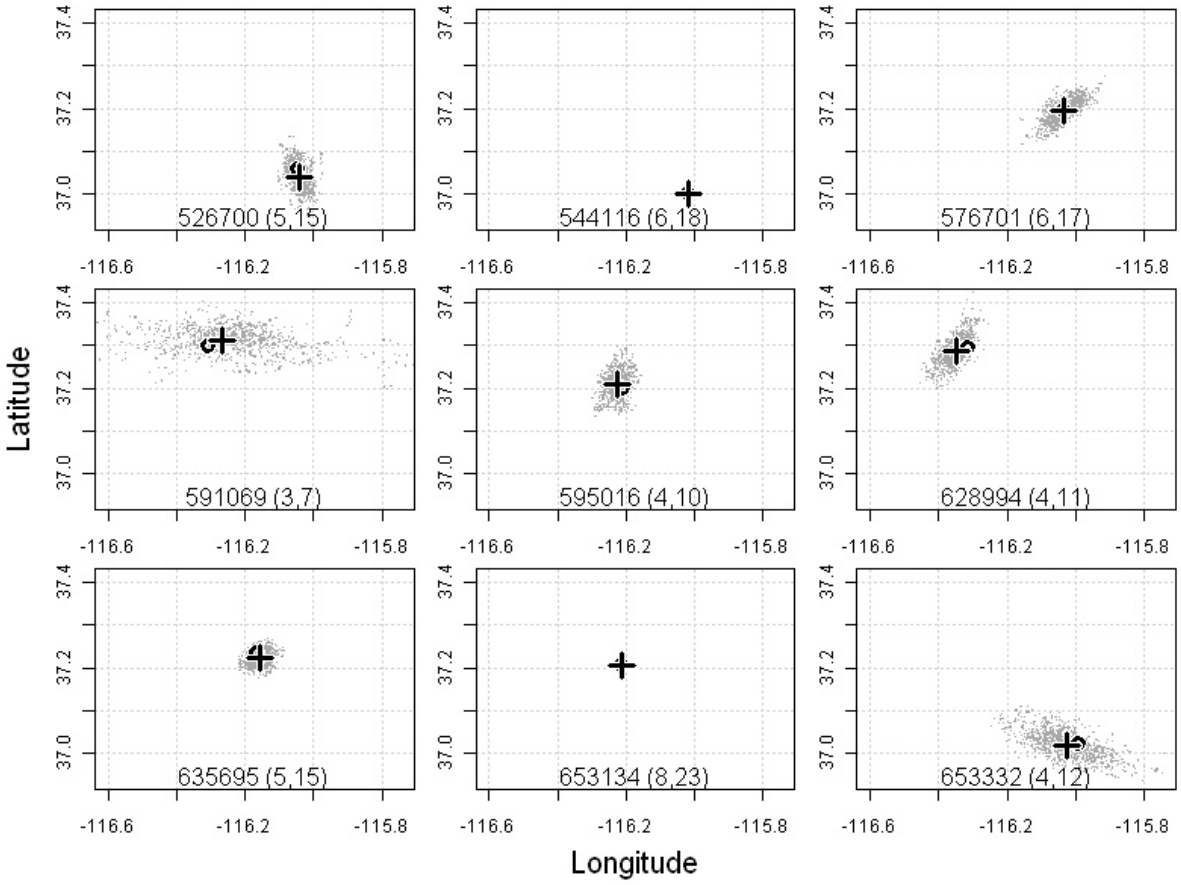

Figure 6. Epicenter posterior distribution of the nine events in case 3. See Figure 3 for caption.

CONCLUSIONS AND RECOMMENDATIONS

We have developed a multiple-event location algorithm (MCMCloc) that employs the Markov Chain Monte Carlo method for solving large, non-linear inverse problems. The MCMC method is an efficient way to probe large model spaces, and it enables us to execute a smart search over the numerous combinations of model parameters. The introduction of prior constraints on model parameters further improves the efficiency of the parameters search and (like conventional techniques) helps to improve the accuracy of parameter estimates.

The MCMCloc forward model is divided between event location, travel-time prediction, and arrival time data. The most novel aspect of the MCMCloc forward model is the introduction of phase assignments into the arrival time model component. Therefore, we assess the likelihood that phases are properly named in the location algorithm. Although MCMCloc is in its formative stage, we find that inclusion of the phase assignment into the list of unknowns is desirable, and can lead the user to discover flaws in the data set. Further, MCMCloc tests for "bad" data that do not match any known arrival. Bad data may be removed from some instances of the solution or, if the data are persistently bad, they will be removed from every solution.

We test MCMCloc on a 9-event subset of the NTS nuclear explosions (Walter et al., 2003). We find that our preliminary version of MCMCloc outperforms conventional relative location methods. By implementing travel-time corrections in a hierarchic fashion in which travel-time curves are adjusted first, we find a distinct improvement in absolute location accuracy. In the case where 2 events are used to calibrate surrounding locations, we do not find a notable difference in absolution location error, but we do see smaller uncertainty bounds. In our last example, we demonstrate the ability of MCMC loc to reassign phase names and identify questionable data. This feature, while still in need of tuning, shows promise for automating the tedious task of grooming travel-time data sets.

ACKNOWLEDGEMENTS

We have benefited from many conversations with Bill Rodi on the subject of seismic location. Thanks also to Bill Walter for leading the effort to compile and quality control the NTS data set.

REFERENCES

Anderson, M., and S.C. Myers (2005), Assessment of regional-distance location calibration using a multiple event location algorithm, *In preparation for Bull. Seism. Soc. Am.*

Billings, S.D., B.L.N Kennett, M.S. Sambridge (1994), Hypocenter location: genetic algorithms incorporating problem-specific information, *Geophys. Jour. Int.* 118: 693-706.

Dewey, J.W. (1971), Seismicity and tectonics of western Venezuela, *Bull. Seism. Soc. Am*. 62: 1711-1751.

Douglas, A. (1967), Joint epicenter determination, *Nature* 215: 47-48.

Jordan, T.H., and K.A. Sverdrup (1981), Teleseismic location techniques and their application to earthquake clusters in the south-central Pacific, *Bull. Seism. Soc. Am.* 71: 1105-1130.

Kennett, B.L.N., and E.R. Engdahl (1991), Traveltimes for global earthquake location and phase identification, *Geophys. Jour. Int.*, 105, 429-465.

Lomax, A. (2005), NLLoc - Non-linear, earthquake location program, http://alomax.free.fr/nlloc/.

Myers, S.C., S.C. Schultz (2000), Improving sparse network seismic location with Bayesian kriging and teleseismically constrained calibration events *Bull. Seism. Soc. Am*., 90: 199-211.

Pavlis, G.L, and J.R. Booker (1983), Progressive multiple event loction (PMEL), *Bull. Seism. Soc. Am*. 73: 1753-1777.

Pasyanos, M.E., G.A. Franz, and A.L. Ramirez (2005), Reconciling a geophysical model to data using a Markov Chain Monte Carlo algorithm: An application to the Yellow Sea - Korean Peninsula region, submitted to J. Geophys. Res.

Rodi, W., S. Myers, and C. Schultz (2003), Grid-Search Location Methods for Ground-Truth Collection from Local and Regional Seismic Networks, in *Proceedings of the 25th Seismic Research Review—Nuclear Explosion Monitoring: Building the Knowledge Base,* LA-UR-03-6029, Vol. 1, pp. 311-319.

Shapiro, N. and M. Ritzwoller (2003), Monte-Carlo inversion for a global shear-velocity model of the crust and upper mantle, *Geophys. J. Int.* (2002) 151, 88–105.

Waldhauser F, Ellsworth WL (2000), A double-difference earthquake location algorithm: Method and application to the northern Hayward fault, California *Bull. Seism. Soc. Am*., 73: 1753-1777.

Walter, W.R., K. D. Smith, J. L. O'Boyle, T. F. Hauk, F. Ryall, S.D. Ruppert, S.C. Myers, M. Anderson, and D.A. Dodge (2003), Improving The Fundamental Understanding Of Regional Seismic Signal Processing With A Unique Western United States Dataset, *Proceedings of the 25th Seismic Research Review - Nuclear Explosion Monitoring: Building the Knowledge Base*, LA-UR-03-6029, Vol. 1, pp. 486-494.

IMPROVED REPRESENTATION AND CALCULATION OF BASE MODEL TRAVEL TIMES USING THE PARAMETRIC GRID LIBRARY

Paul C. Reeves, Sanford Ballard, James R. Hipp, Christopher J. Young,
Daniel S. Myers, and Breanna Ammons

Sandia National Laboratories

Sponsored by National Nuclear Security Administration
Office of Nonproliferation Research and Engineering
Office of Defense Nuclear Nonproliferation

Contract No. DE-AC04-94AL85000

ABSTRACT

Efficient and accurate event location is critical to nuclear event monitoring, during both the event association processing and event characterization stages. Computation of predicted (i.e., base model) travel times, slowness values, and their spatial derivatives is a core component of these calculations. Common base model algorithms represent travel time using a standard, rectilinear, two-dimensional (distance, depth) lookup table for each seismic phase. The values used are typically computed as a preprocess using ray theory, with dummy values inserted into the table at distance/depth points beyond where the seismic phase is observed.

Linearized least-squares event location algorithms require computing the expected travel times for each observed phase at each iteration of the hypocenter calculation. Using the lookup tables, travel time values are computed using a high-order interpolation scheme so spatial derivatives of travel time can be computed. These are needed by the location algorithm to formulate the gradient of the predicted travel time with respect to event location, which is used to iteratively move towards a minimum-residual solution. Second derivatives of travel time with respect to event location are needed whenever slowness observations are used. When a hypocenter lies outside the valid distance/depth range of a given phase, then extrapolation of information from valid regions is required. Together, these calculations comprise the vast majority of the computational effort involved in seismic event location (See Hipp et al., 2005).

We present results demonstrating the potential weakness of this method if spatial discretization is too coarse. We also show the danger of computing slowness from the numerical derivative of travel time with respect to distance. These problems arise due to discontinuities in the travel time surface where different branches cross and/or where different phases arise.

We present two alternate representations to standard, rectilinear lookup tables, that overcome the problems that arise from discontinuities. They represent the two-dimensional lookup table on an optimized, irregular, triangular grid whose density is proportional to the curvature of the travel-time field. One uses a single gridded region to represent a particular seismic phase, while the other uses sub-regions representing particular branches or phases in order to eliminate discontinuities. This representation should provide fast numerical performance while achieving high accuracy.

We also advocate pre-computing all relevant values (travel time, travel time error, slowness, *dtt/dz*, *dsh/dz*, *dsh/d*Δ, and model error) as a preprocess, including extrapolation beyond the valid region for the phase. This will allow simple bilinear interpolation and minimize significantly the amount of on-the-fly calculations, both of which will increase speed. The preprocessing can be done at high resolution to provide improved accuracy.

OBJECTIVES

Fast earthquake location algorithms are required for nuclear explosion monitoring. These are typically supported with simple one-dimensional earth velocity models such as IASPEI91 (Kennett and Engdahl, 1991) or ak135 (Kennett et al., 1995). Calculations of predicted travel time values are facilitated with two-dimensional (distance-depth), rectilinear lookup tables for each phase of interest (e.g., LocSAT [Bratt and Bache, 1986; Nagy, 1996]). The alternative, ray tracing or ray theory methods (e.g., TauP [Crotwell et al., 1999]), are currently too slow for operational purposes.

Lookup tables offer both representational and numerical advantages. They are easy to use and can require negligible memory if discretization is coarse. For gradient descent location algorithms, a four-by-four patch of neighboring points may be used to support bicubic interpolation which yields travel time and its first and second spatial derivatives. If slowness observations are used in the solution formulation, then slowness predictions are often supplied as the numerical derivative of travel time with respect to distance.

Despite these advantages, this representation poses significant risk if spatial discretization is too coarse. Fine discretization can address accuracy problems, but degrades computational speed and inefficiently utilizes memory. We discuss these issues below and present an alternative representation that could provide both accuracy, efficiency, and speed through optimal tessellation and natural neighbor interpolation using the Parametric Grid Library (Hipp et al., 1999, 2005)

RESEARCH ACCOMPLISHED

Figure 1 shows computed travel-times for the “first” P phase throughout its defined source depth and distance range based on the IASPEI91 velocity model (Kennett and Engdahl, 1991). The data for the plot was generated using TauP Toolkit (Crotwell et al., 1999), which is commonly used to populate travel time lookup tables. The surface appears to be smooth and well behaved except at the jump between Pdiff and PKIKP at 114º; however, there are subtle discontinuities along any given depth where different branches intersect. These can be seen in Figure 2, which presents a complete set of P-phase travel time curves for an event at 28 km depth. There are triplications arising from the velocity discontinuities at 410 and 660 km depth that show up near 20º, but in practice they are not distinguished since they are too difficult to pick on a seismogram. The discontinuity at the Pdiff – PKIKP transition is apparent, and there is also a small range near 145º where the PKPab branch arrives before PKIKP (a.k.a. PKPdf). The “first” P table (Figure 1) uses the earliest arriving phase. Pdiff is an exception due to its weak signal, so PKIKP and PKPab are substituted for Pdiff where they exist.

Representing “first” P phase travel times in a lookup table would appear benign at first glance. However significant errors can result if spatial resolution is too coarse. Figure 3 and 4 show the difference between the look up table-predicted and TauP travel times using a common spatial discretization for the lookup table (black points) and libloc’s bicubic interpolation algorithm (Nagy, 1996; Nagy, 2001). The algorithm does an excellent job at the grid points, as expected, with errors increasing in proportion to the distance from grid support. This yields a “quilted” appearance. Discrepancies between the interpolated and TauP travel times become substantial near triplications caused by velocity discontinuities in the IASPEI91 velocity model at depths of 210, 410 and 660 km. These discrepancies are evident in the distance range of 10° to 30° in Figures 3 and 4. These anomalies occur because the supporting four-by-four grid straddles the triplication and is unable to accurately represent the discontinuous derivative of travel time with respect to position at the triplication.

While the problems at depth may be of lesser concern to the monitoring community, there are still problematic areas near the surface. Figure 4 is a detail of Figure 3 at shallower depth that shows how travel time prediction errors persist even within the crust, exceeding ±1 second in some areas. The largest errors occur near zero distance where the upgoing p is the first arrival. The discretization fails to capture its concave shape and the discontinuity with downgoing P. The Pdiff – PKIKP transition at distances of 114° is also problematic, as expected, as is the area where PKPab arrives first (around 148°). These problems are all symptomatic of the coarse discretization, which is, in fact, much finer at the shallow depths shown here.

Figures 5 and 6 show details of the travel time curve (Figure 2) together with predicted values where the p phase arrives first (Figure 5) and where the P phase triplications arrive (Figure 6). The 1º table discretization completely

misses the p phase (Figure 5), so the predictions fail to capture its concave shape at distances less than about 0.7°. Figure 6 shows the how the discretization and cubic spline undershoot the triplications within the P phase.

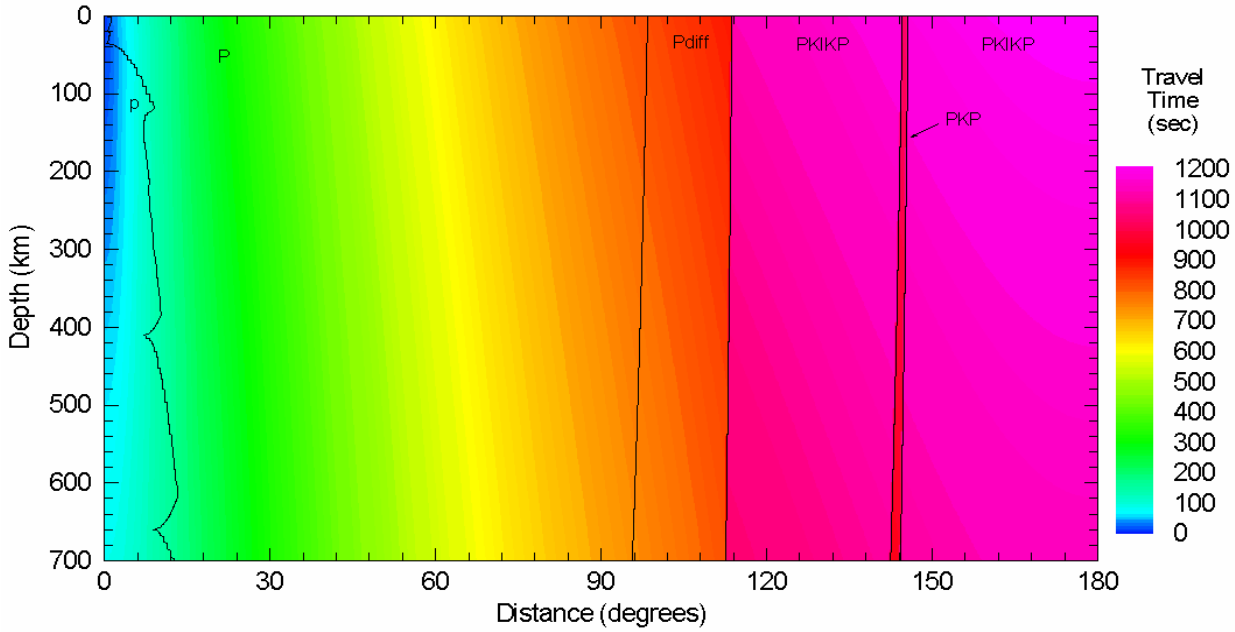

Figure 1. "First" P-phase travel times computed with TauP. Spatial resolution is 0.36° in distance and 5 km in depth.

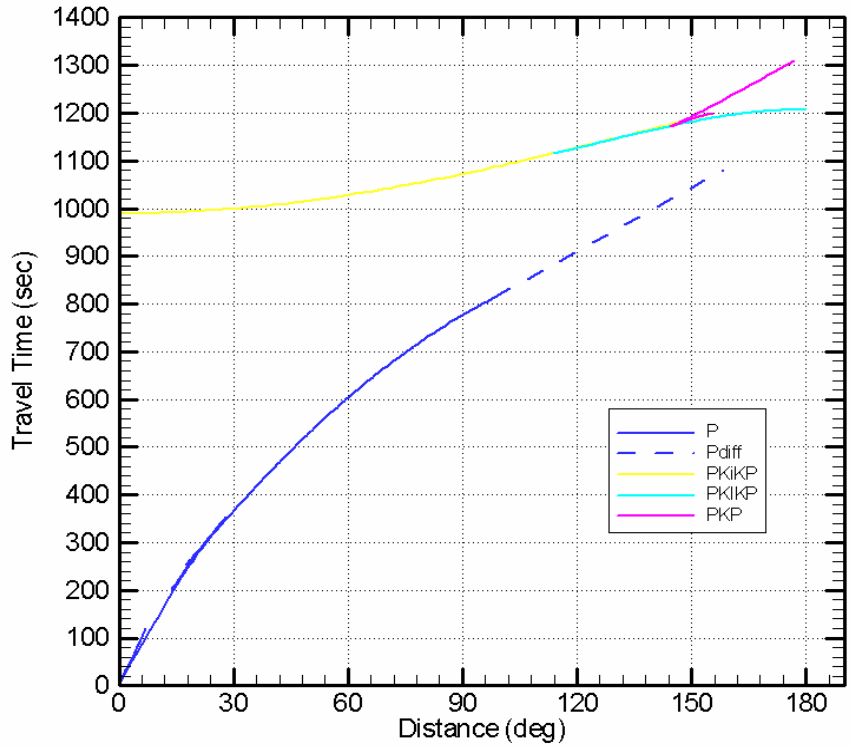

Figure 2. "First" P-phase travel time curve at a depth of 28 km. All phases and triplications are shown.

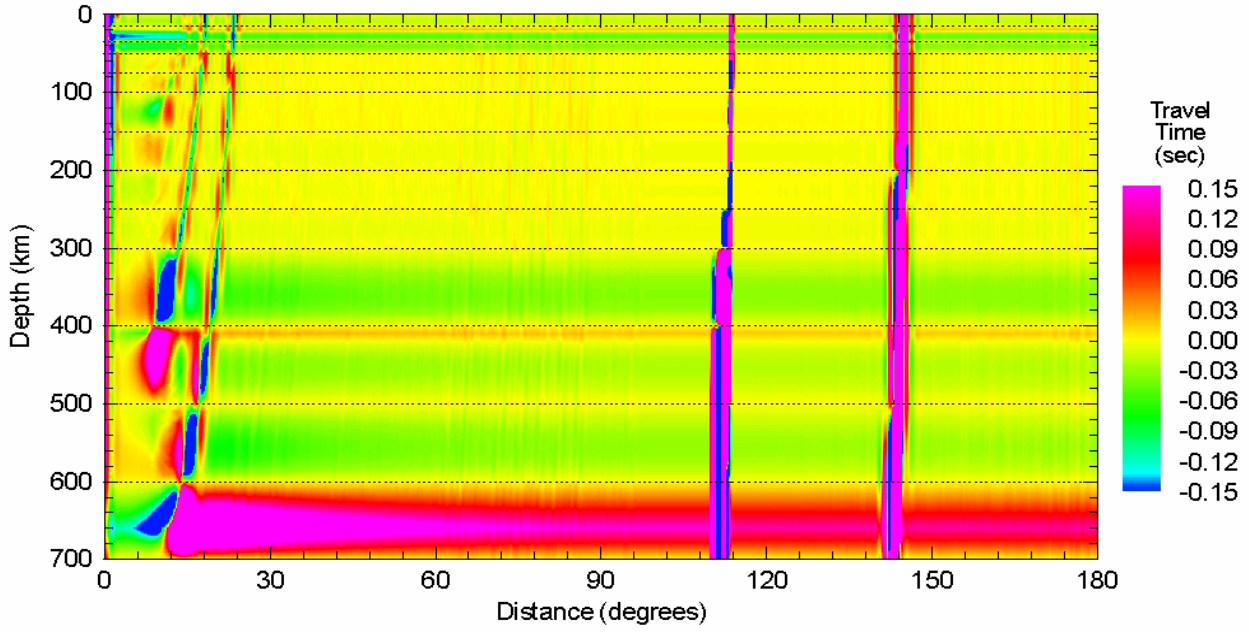

Figure 3. Difference between the TauP and libloc computed travel time values using a standard travel time table discretization (shown as black points).

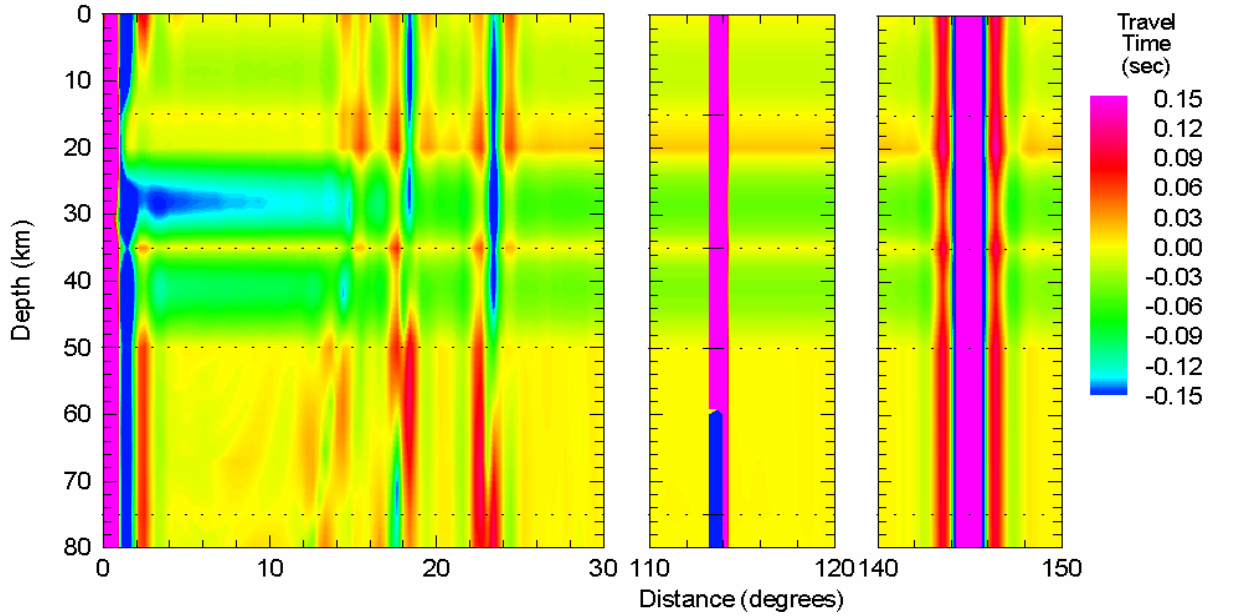

Figure 4. Detail of the difference between the TauP and libloc computed travel-time values. Data Between 30°-110° and 120°-140°have been omitted to better highlight problematic areas.

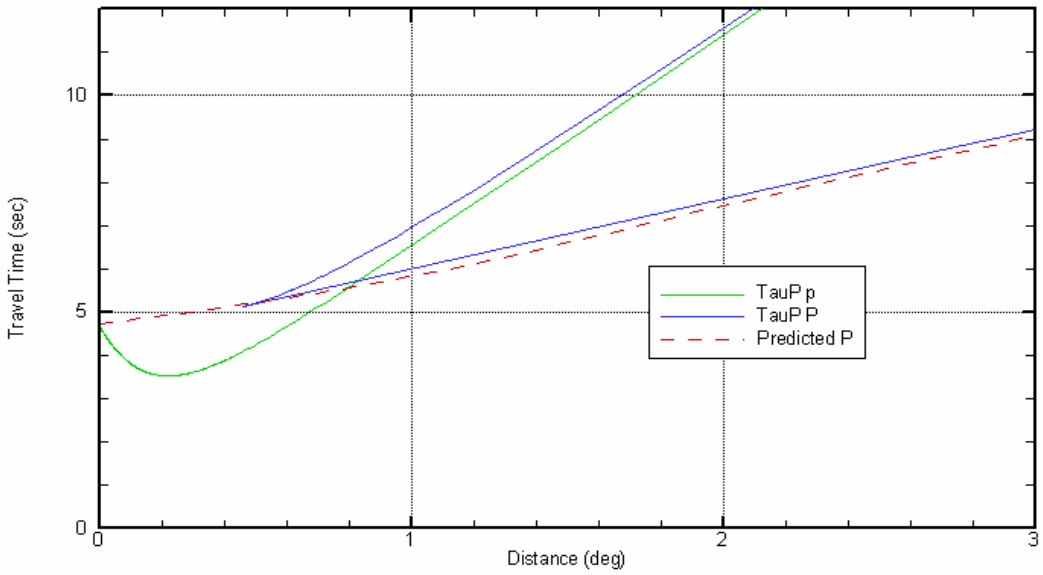

Figure 5. Reduced travel time as a function of distance at a depth of 28 km. With Predicted P discretization of 1º, the p phase is missed entirely, resulting in a discrepancy of more than 1 second at very close distances.

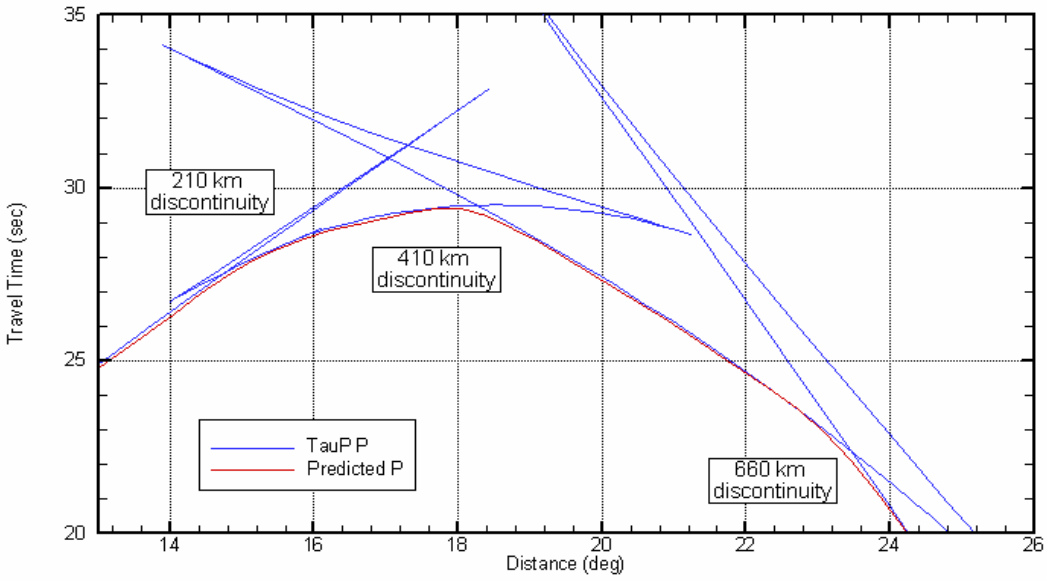

Figure 6. Reduced travel time as a function of distance at a depth of 28 km, emphasizing the triplications arising from the 210 km, 410 km, and 660 km velocity discontinuities. Note the discrepancies between the predicted first arrivals very close to the triplications.

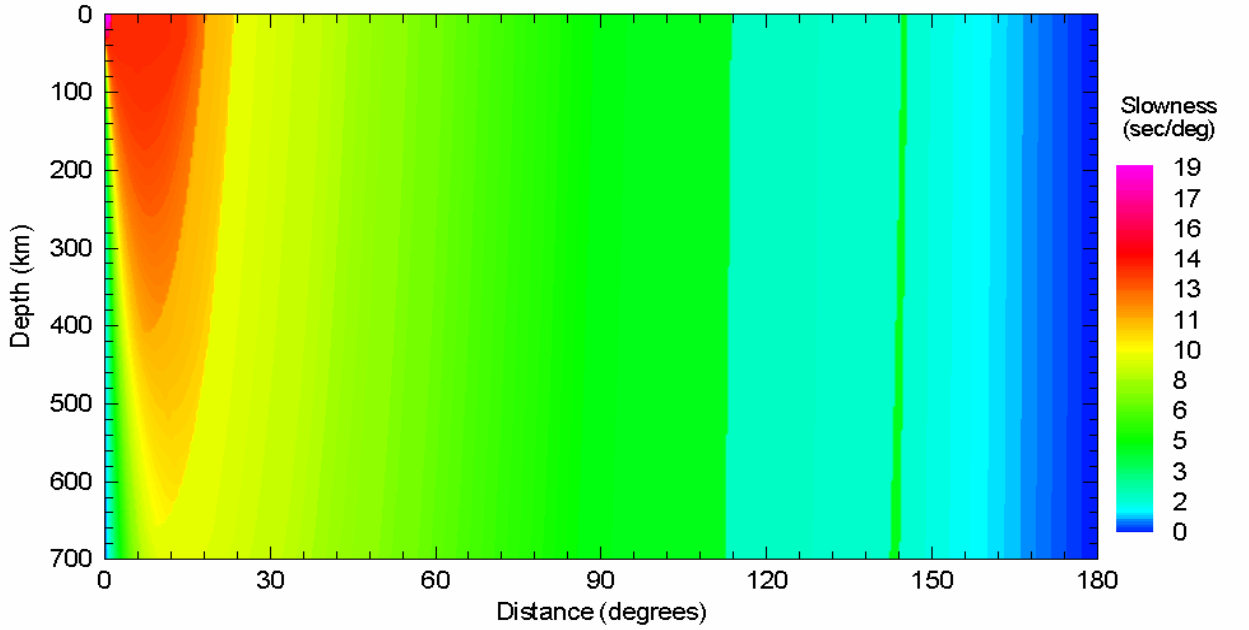

Figure 7. "First" P-phase slowness values computed with TauP. Spatial resolution is 0.36° in distance and 5 km in depth.

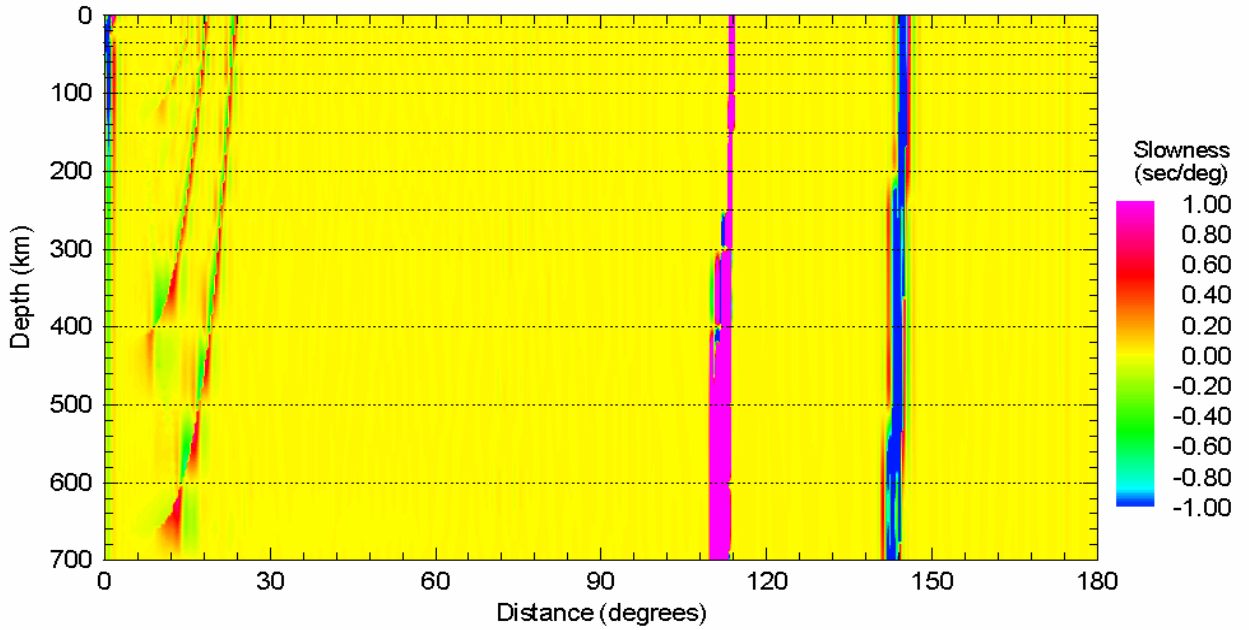

Figure 8. Difference between the TauP and libloc computed slowness values using a standard travel time table discretization (shown as black points).

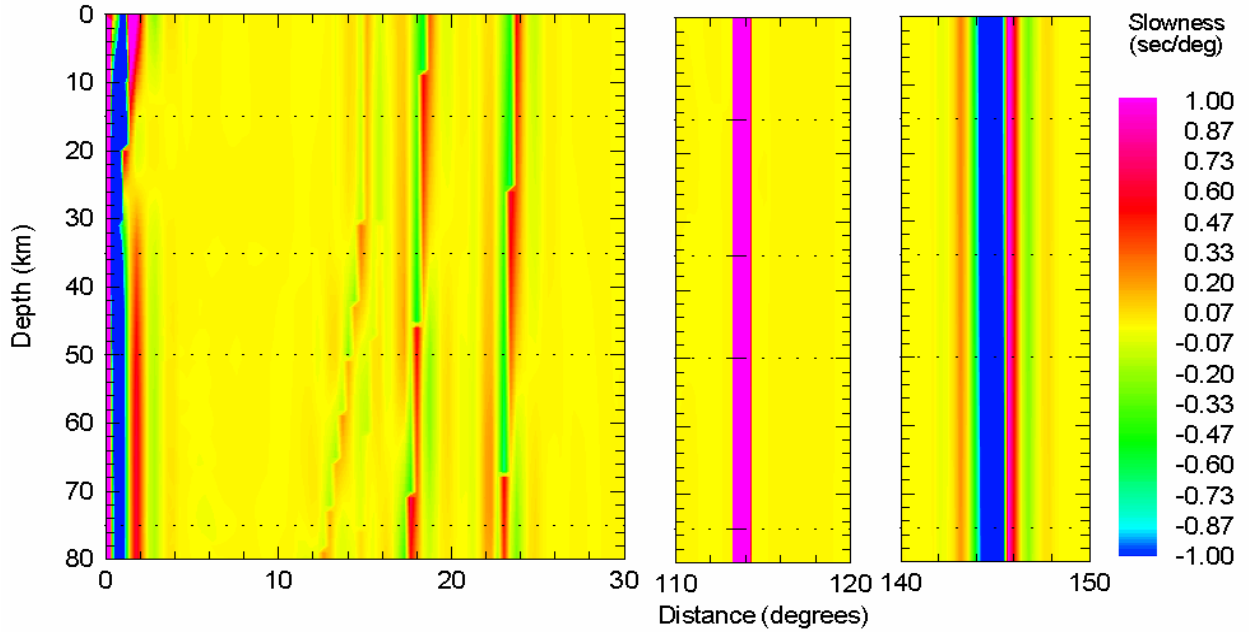

Figure 9. Detail of the difference between the TauP and libloc computed slowness values. Data between 30º-110º and 120º -140º have been omitted to better highlight problematic areas.

Results for slowness, when computed as the numerical derivative of travel time with respect to distance, are even more striking. Figure 7 displays the TauP computed slowness, while Figures 8 and 9 show the difference between look up table predictions and TauP using the same discretization as above.

Again we see problems along triplications, but the pattern is now asymmetric with under-predictions to the left and over-predictions to the right of the triplications. Unlike travel time predictions, slowness predictions are degraded throughout the depth profile, because the error is proportional to the grid spacing in the distance direction and does not vary with depth. Consequently, the magnitude of the slowness prediction errors exceeds 10% in places, even at the surface. This has significant implications with respect to phase identification and event locations involving slowness observations.

Our studies indicate that the use of coarsely gridded lookup tables can lead to significant errors in predicted travel time and slowness values, and undoubtedly affects computed spatial derivatives as well. Likewise, a coarse discretization is unable to represent the lateral boundaries of the valid phase ranges. We can expect these problems to be manifested as (a) poor event locations and (b) larger location uncertainties, whenever an observation falls into the poor prediction region. It is not clear how these problems impact model error. In addition, if the numerical derivative of travel time with respect to distance is used to support slowness predictions, then the current formulation can be expected to yield slowness prediction errors of several percent. This problem should also be expected to impact predicted event locations and confound phase identification during association.

We intend to explore two categories of modification to the current implementation that could significantly improve both accuracy and computational performance:

A) slowness values should also be represented as a table lookup with values derived directly from TauP. High-accuracy derivatives (*dtt/dz*, *dsh/dΔ*, and *dsh/dz*) should also be precomputed and represented on the lookup table. This would then allow us to use a lower order interpolation scheme, which would be faster. Values beyond the valid phase region should be pre-extrapolated to eliminate costly on-the-fly calculations. We anticipate that all values (travel time, slowness, model error and derivatives) could be represented on the same support grid, thereby amortizing lookup costs. These modifications would reduce significantly the numerical cost of supporting location calculations, while improving accuracy.

B) Ellipticity corrections are also phase-specific and require the calculation of three coefficients that vary with distance and depth. These are normally computed via a lookup table. We recommend using the same grid as (A) to further amortize lookup costs.

C) An alternative lookup-table discretization should be developed. We intend to investigate three possible approaches, which we present here in order of increasing complexity.

Approach 1: Rectilinear Grid with Fine Discretization

The simplest approach would be to refine the lookup table while maintaining a simple, rectilinear grid. In particular, the grid would need to be refined about the triplications. However, because the triplications are not always aligned with the grid, this would lead to over sampling in some areas. While this approach would require no algorithm modifications to perform interpolations, the memory requirements would probably increase by an order of magnitude. Likewise, the numerical cost of table lookup (via bisection) would also increase. As noted above, the values of interest are smooth and well-behaved except near the discontinuities, so a fine discretization would be inefficient in regions where the bicubic spline performs well.

Approach 2: Single-Region Model with Optimal Grid Sampling

An alternative approach would be to abandon rectilinear sampling. Instead, an optimal tessellation could be developed using algorithms already implemented in the Parametric Grid Library for the support of path correction calculations (see Hipp et al., 2005). Recent upgrades allow it to tessellate a region with a uniform triangular grid and then refine and decimate the grid until a desired level of accuracy is obtained. This yields an irregular triangular grid suitable for natural neighbor interpolation using the points of the triangle containing the interpolation point [e.g., Lawson, 1977; Sambridge et al., 1995]. For the problem at hand, the grid should be fine in and around discontinuities with coarser support in between. Interpolation supported by an irregular triangular grid requires first determining which triangle contains the point in question, which we propose to accomplish by a walking triangle search. This operation is $O(\text{Sqrt } N_t)$, where N_t is the number triangles in the table (Lawson, 1977). This compares favorably with two passes of $O(\log_2 N_n)$ for bisection of a rectilinear grid, where N_n is the number of nodes in a given direction, so long as the grid doesn't become too refined.

This method should provide accuracy to any desired level while also minimizing memory usage, but it is difficult to know in advance how computationally expensive the triangle lookup will be since we do not know how many triangles the representation will require. If the discretization becomes too fine near the discontinuities, then this could hinder a single-region approach.

Approach 3: Multi-Region Model with Optimal Grid Sampling

A more complex approach would involve a multi-region representation similar to how travel time path corrections are represented by the Parametric Grid Library (Hipp et al., 2005). Regions defining a given branch or phase would be individually tessellated and assembled to form a master lookup table. This would yield a series of overlapping meshes, each of which would be optimally sampled. Because there would no longer be discontinuities within any region, each could be accurately modeled with a relatively coarse mesh, thereby minimizing memory usage. Table lookup would proceed as follows: first the region containing the point of interest would be determined, then triangle lookup would be performed in that region's mesh as in the single-region model. Because of the coarseness of the regional discretization and the two-step lookup process, lookup should be much faster than a single-region optimal sampling. Interpolation would proceed via natural neighbor interpolation (e.g., Lawson, 1977; Sambridge et al., 1995). In summary, this representation should yield (1) arbitrary accuracy, (2) optimal memory usage, and (3) fast lookup.

Figure 10 shows this method schematically. The bottom portion shows three regions of support for the lookup table. The regions overlap and represent individual branches and/or regions where different phases arrive first. Crossovers are depicted in red. The upper portion shows the corresponding travel time curve at zero depth. When an interpolation is required, the first arrival's lookup table data is used, in this case, that of region B.

This representation could be used to construct a "global" first P table that combines compressional phases p, P, Pdiff, etc. This would be done by combining phase-specific regions within which a given phase is expected to be the first arrival. These phase-specific regions could be further sub-divided into sub-regions as necessary to capture finer branch regions.

CONCLUSIONS AND RECOMMENDATIONS

In summary, the use of a rectilinear grid for representing travel time tables fails to capture the discontinuities of the surface and can lead to significant travel time and slowness prediction errors. An optimal tessellation scheme, either single or multi-region, could overcome these problems while maintaining numerical efficiency. Further efficiencies could be gained by pre-computing spatial derivatives and ellipticity correction coefficients and by pre-extrapolating values for lookup tables for phases having a limited valid range. As a final comment, it should be noted that Approaches 2 and 3 introduce discontinuous spatial derivatives, thereby impacting any gradient descent method. Consequently, a location algorithm designed to handle nonlinearities (e.g., Ballard, 2003) will be required if it is to be supported by such high-fidelity base models.

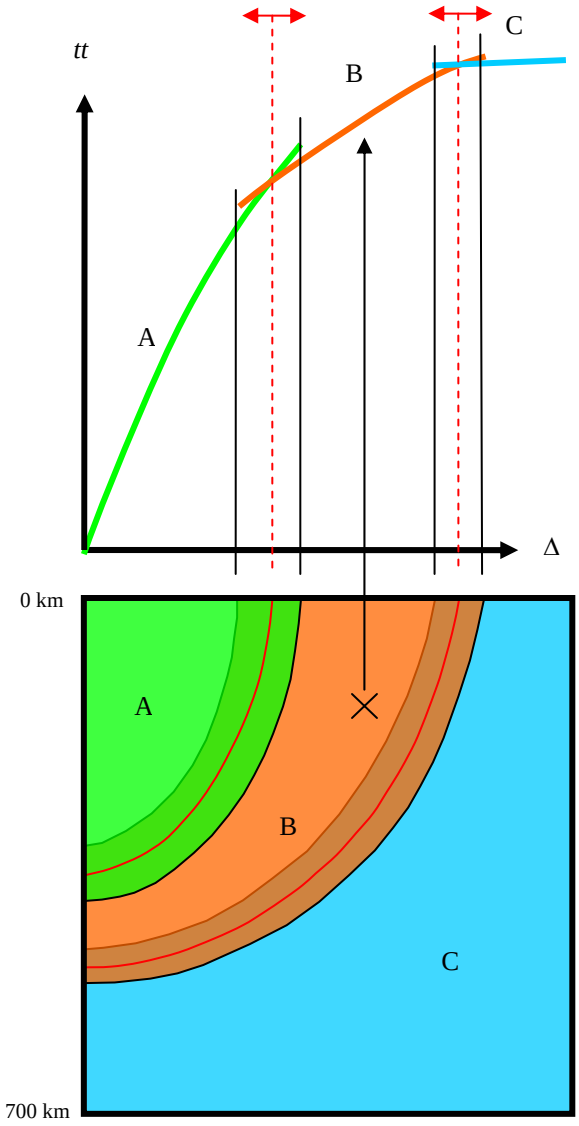

Figure 10. Depiction of a multi-region model with optimal grid sampling. Top: Travel time curve at zero depth showing how different branches or phase regions of the travel time curve support calculations. Bottom: Regions supporting calculations for various branches.

ACKNOWLEDGEMENTS

We would like to thank Mark Harris and David Gallegos for their thoughtful reviews. Their critiques and suggestions have improved the manuscript.

REFERENCES

Ballard, S. (2003). Seismic event location: Dealing with multi-dimensional uncertainty, model non-linearity and local minima, in *Proceedings from the 25th Seismic Research Review—Nuclear Explosion Monitoring: Building the Knowledge Base*, LA-UR-03-6029, Vol. 1, pp. 193-202.

Bratt, S.R. and T.C. Bache (1988). Locating events with a sparse network of regional arrays. *Bull Seism. Soc. Am.* 78: (2), 2019-2035.

Crotwell., H. P., T.J. Owens, and J. Ritsema (1999). The TauP Toolkit: Flexible seismic travel-time and ray-path utilities. *Seismological Research Letters* 70: (2), 154-160.

Hipp, J.R., C.J. Young, S.G. Moore, E.R. Shepherd, C.A. Schultz, and S.C. Myers (1999). Parametric Grid Information in the DOE Knowledge Base: Data Preparation, Storage, and Access, Sandia National Laboratories, SAND99-2277.

Hipp, J.R., S. Ballard, M.C. Chang, and L.A. Jensen (2005). Representing kriged travel time correction surfaces with optimal tessellations, this issue.

Kennett, B.L.N., and E.R. Engdahl (1991). Traveltimes for global earthquake location and phase identification. *Geophys. J. Int*. 105: (2), 429-465.

Kennett, B.L.N., E.R. Engdahl, and R. Buland (1995). Constraints on seismic velocities in the earth from travel time. *Geophys. J. Int*. 122: 108-124.

Lawson, C.L. (1977). Software for C1 Surface Interpolation, in *Mathematical Software III*, J. Rice (ed). Academic Press, New York.

Nagy, W. (1996). New travel-time handling facilities at the IDC: Functionality, testing and implementation details. Science Applications International Corporation, Technical Report, SAIC-96/1179.

Nagy, W. (2001). International Data Centre Documentation: Event Location Software. Science Applications International Corporation, Technical Report, SAIC-01/3010.

Sambridge, M., J. Braun, and H. McQueen (1995). Geophysical parameterization and interpolation of irregular data using natural neighbors, *Geophys. J. Int*. 122: (3), 837-857.

IMPROVED DEPTH-PHASE DETECTION AT REGIONAL DISTANCES

Delaine Reiter and Anastasia Stroujkova

Weston Geophysical Corporation

Sponsored by National Nuclear Security Administration
Office of Nonproliferation Research and Engineering
Office of Defense Nuclear Nonproliferation

Contract No. DE-FG02-03ER83820

ABSTRACT

The accurate estimation of the depth of small, regionally recorded events continues to be an important and difficult monitoring research problem. In previous studies we have focused on the extraction of depth phases from body waves using cepstral techniques, with greater success at teleseismic rather than regional distances. To further enhance the accuracy of regional focal depth estimation, other waveform characteristics that are sensitive to depth must be exploited. The primary goal of our current research project is to develop a synergistic tool that combines different methodologies to estimate the depth of regional seismic events. The three methods we are incorporating include: a) improved depth-phase detection in the complex *Pn* coda of regional seismograms; b) sparse-network locations with Monte Carlo confidence regions on focal depth; and c) surface-wave inversions for depth and focal mechanism. We have chosen to apply these three methods rather than full-waveform modeling of the regional seismograms, primarily because the observables used in these methods are significantly easier to measure and model.

As part of our research project we have focused on understanding the propagation characteristics of regional depth phases and developing robust methods to routinely detect them. To accomplish this goal, we have computed synthetic seismograms for regional events observed at regional and teleseismic arrays in Asia. For each of these events, we varied the input velocity model, focal mechanism, and source depth. In addition to waveform modeling, we have applied array-processing techniques to derive accurate estimates of phase velocities, azimuth, and coherence as a function of time in the *Pn* wavetrain. These studies indicate that cepstral depth-phase detection results should be accompanied by estimates of the focal mechanism, phase velocities and back azimuths to help eliminate false detections.

We have also continued research on improvements to the cepstral processing technique, known as the Cepstral F-Statistic Method (CFSM) that we have employed in the past (Bonner et al., 2002). The application of cepstral ‘liftering’ (or filtering in the log spectrum domain) is a topic of active research, as is robust denoising of the array waveforms prior to application of the cepstral technique. One denoising method that is showing some promise is semblance filtering of the array waveforms. This method measures phase coherence that can then be used to filter or ‘weight’ the array element data.

Improved regional depth-phase detections combined with depth estimates measured from other waveform observables will provide the Air Force Technical Applications Center (AFTAC) with increased confidence that an event is either deep enough to be ruled out as a nuclear explosion or shallow enough to require further analysis using regional discriminants such as M_S:m_b or *Lg/P* ratios. Our goal is to develop an analysis tool that can be used on a special-event basis to improve the US government’s ability to correctly classify events as either man-made explosions or naturally-occurring earthquakes.

OBJECTIVES

The primary goal of our project is the development of a synergistic tool that combines three different technologies to estimate the depth of regional seismic events. These methods include 1) improved depth phase detection in the complex *Pn* coda of regional seismograms; 2) sparse-network hypocenter locations with associated Monte-Carlo confidence regions; and 3) surface-wave spectral amplitude inversions for depth and moment magnitude. In the first year of the project we have focused on the first of these methods: improved depth-phase detection. To accomplish this we have conducted multiple modeling exercises using standard 1-D and 2-D modeling codes to examine the effects that different focal mechanisms and velocity structures have on the frequency, relative amplitudes, and travel times of regional depth phases. We also continue to test and add further capabilities to the Cepstral F-Statistic Method (CFSM) (Bonner et al., 2002), which is designed to determine the delay time between *pPn* and/or *sPn* and the primary *Pn* arrival. Finally, we are investigating innovative filtering techniques to enhance regional depth phases in the *Pn* coda, and we report on a promising method that utilizes semblance-based weighting on array element data.

RESEARCH ACCOMPLISHED

Synthetic Studies of Regional Depth-Phase Characteristics

We conducted a series of synthetic modeling experiments using a variety of focal mechanisms and velocity structures to better understand the amplitudes and travel times of *Pn* and its associated depth phases, *pPn* and *sPn*. Our specific purpose in these exercises was to determine if the CFSM, which relies on observable energy in the depth phases to robustly estimate the depth-phase delay time (*pPn-Pn* or *sPn-Pn*), will be successful at regional distances. In this paper we show examples from two events observed at the Kazakhstan arrays, MKAR (Makanchi) and KKAR (Karatau), noting that we are also studying other events at several arrays in central and southeastern Asia. Figure 1a) shows the event, along with the published Harvard Central Moment Tensor (CMT) solution and the positions of the MKAR and KKAR arrays.

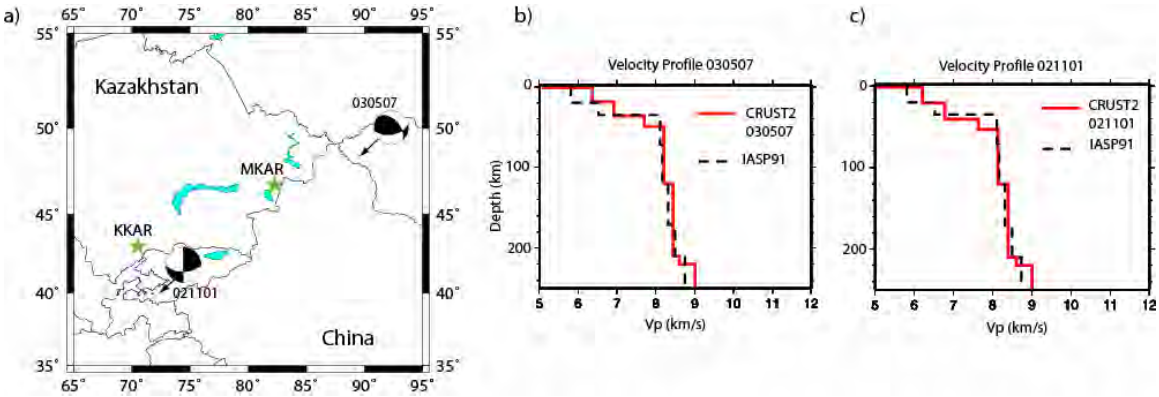

Figure 1. Locations and models for events examined in this paper. a) Event locations and published Harvard CMT solutions for events in Mongolia (05/07/03) and Kyrghystan (11/01/02); b) regional 1-D velocity profile for Event 030507 interpolated from the CRUST2.0 velocity model (Bassin et al., 2002); c) same as b) but for Event 021101. The IASPEI91 average global 1-D model is shown for comparison in both b) and c).

To generate the synthetics, we used the wavenumber integration code from the Computer Programs in Seismology (Herrmann, 2002; CPIS), which requires a 1-D layered velocity structure for input. We selected an appropriate regional profile from the CRUST2.0 velocity model (Bassin et al., 2002), merging the two sediment layers together and appending the regionalized upper mantle (RUM) model for the upper mantle structure (Gudmundsson and Sambridge, 1998). The V_p structures used in the modeling are shown in Figure 1b) and 1c), along with their comparison to the IASPEI91 global model (Kennett and Engdahl, 1991).

We calculated waveform synthetics, holding the focal mechanism and velocity structure constant and varying the event depth. For example, in Figure 2 we show the synthetic calculations for event depths Z=2, 6, 10, 14, 18, 22 and 30 km at MKAR for Event 030507. The depth phases are clearly seen in the synthetics, with *sPn* having significantly larger amplitude. This amplitude increase is not seen in the data (lower panel) and appears to be a quirk of the wavenumber integration method. Overall, our modeling for this and other events indicates that differences in focal depth only slightly change the relative amplitudes of *Pn*, *pPn* and *sPn* (the first three significant arrivals in the synthetics).

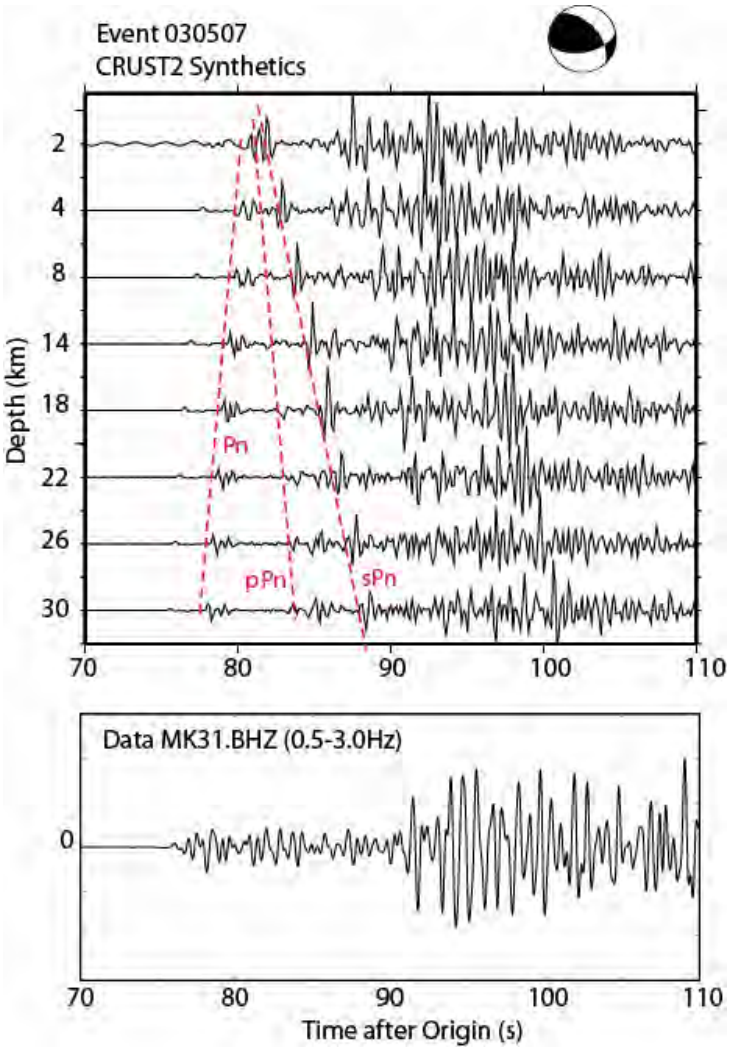

Figure 2. Top: Synthetic calculations for Event 030507, using the Harvard CMT focal mechanism, the velocity model shown in Figure 1c) and varying the depth. The *Pn* arrival, its depth phases, and *Pg* are marked by dotted lines. Bottom: The vertical component of the broadband instrument installed at the MKAR array.

Next, we calculated synthetics in which we held the event depth constant and varied the focal mechanism. We chose an arbitrary depth of 6 km, since the synthetics show similar characteristics for all depths as a function of focal mechanism. Our results indicate that differences in focal mechanism play the dominant role in the amplitude relationships and frequency content of *Pn* and its depth phases. For example, in Figure 3a) we present the results for strike-slip mechanisms. For this type of mechanism, the orientation of the nodal planes changes only the absolute amplitudes, which preserves the relative amplitudes between *Pn*, *pPn* and *sPn*. However, the amplitudes of the depth phases are much more sensitive to the dip-slip

component of the mechanism, as shown in Figure 3b; in fact, for many focal mechanisms there is no appreciable depth-phase energy. The results of these modeling exercises confirmed that an estimate of the focal mechanism must be part of a regional depth-phase detection methodology, since it will provide an indication of whether the depth phases will have appreciable amplitudes in the *Pn* coda.

Finally, we have observed that mid-crustal refractions (e.g., *Pb*) can interfere with the depth phases, particularly at shorter distances (Δ < 3.5-4°). Some areas we studied in central Asia do exhibit this type of arrival, which means that the presence of such phases should be identified through array processing to eliminate them from contention as regional depth phases. In fact, the application of cepstral processing for depth phase delays at distances shorter than approximately 4° is difficult, due to the interference of upper and mid-crustal secondary phases at nearly the identical travel times as the depth phases.

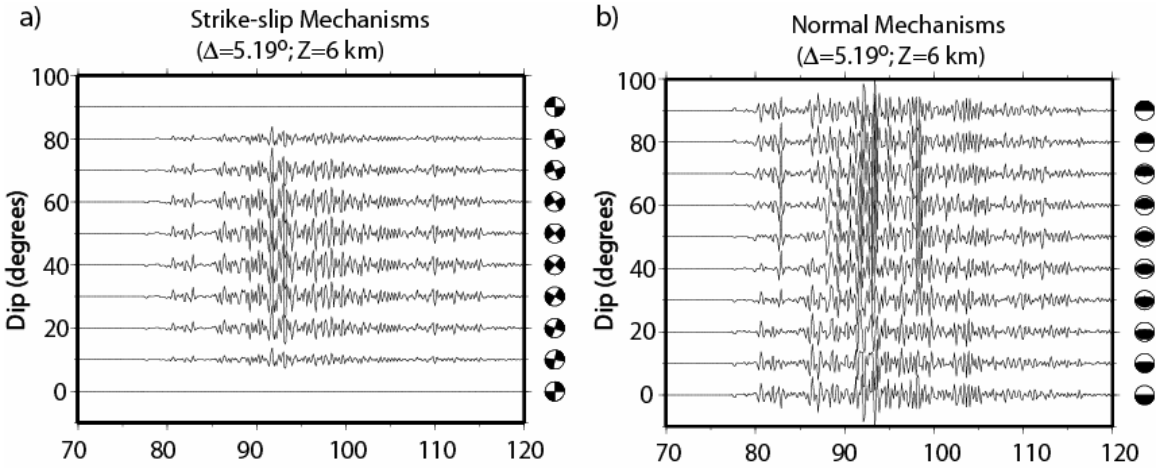

Figure 3. Synthetic waveforms demonstrating the effects that focal mechanisms have on the *Pn* arrival, its depth phases, and later coda arrivals. a) Strike-slip mechanisms for an earthquake at 6-km depth, at the same distance as MKAR from Event 030507 (Δ=5.19°); b) normal mechanisms for the same distance and focal depth.

The Cepstral F-Statistic Method: Liftering to Improve Delay Estimates

In previous work (Bonner et al., 2002), we presented a focal-depth estimation method using a cepstral F statistic (the CFSM) that provides a statistical estimate of the significance of peaks in a stacked cepstrum. We calculate the power cepstrum, as defined by Bogert et al. (1963), as the Fourier transform of the log spectrum of a windowed time signal. The classic paper by Bogert et al. (1963) also introduced the concept of liftering as part of cepstrum computation. Liftering is literally linear filtering of the log spectrum, and its purpose is to emphasize the periodic component of the log spectrum (rather than the spectral envelope), thereby enhancing the detectability of echoes. Researchers in speech analysis noted that by applying a low-pass lifter to the cepstrum, they could extract low-quefrency components that were indicative of the resonance structure of the vocal tract (Noll, 1967). The application of liftering to seismic data, however, is more problematic (Childers et al., 1977), because of the inherent noisiness and limited bandwidth in the data. We are investigating the benefits and limitations of liftering in the log spectra of regional seismic array data, specifically to determine the potential improvement to focal depth estimates using the CFSM.

Liftering is useful in the CFSM in two ways; first, we can use it to eliminate low-quefrency values (i.e., low delay times). In Figure 4, we illustrate the use of liftering in the CFSM. Figure 4 is a typical display of the output from the CFSM; in the top panel, we show the beam cepstrum (summed cepstra across the array) and the total cepstrum (cepstrum of the mean array log spectrum). In the lower panels, we show the calculated F statistic along with the 95% confidence line (see Bonner et al. (2002) for more details on the CFSM). All peaks above the confidence line can be considered ‘significant’; however, not all of them have any physical meaning. We always look for confirmation of peaks in the beam and total cepstrum to accompany peaks in the F statistic. As we illustrate in Figure 4, without the use of liftering (Figure 4a), it is

difficult to interpret low-quefrency cepstral values, since noise from the early cepstrum dominates the F-statistic delay-time estimate. In the past, we restricted analysis of the final cepstral estimates to quefrency values above 2.5 seconds, which meant that we could only evaluate event depths greater than approximately 15 km. With the use of liftering (Figure 4b) we can specify the precise number of seconds to eliminate in the final cepstral estimate. Currently, we lifter out the first .9 seconds of the cepstrum in the CFSM; however, we continue to test to determine the most appropriate value.

Cepstral liftering also allows us to set the length of window to retain in the final cepstral calculation, so that we can define the exact delay-time window that we are most interested in. This allows the user to input a much longer analysis window of raw data from the seismogram, which presumably contains the reflected phases of interest and their later-arriving multiples. Then, through liftering, the final log spectrum has high-frequency 'chatter' eliminated prior to the final FFT. We currently limit the output delay-time (quefrency) window to 13 seconds, theorizing that interesting depth phase reflections for most events at regional distances will occur within 13 seconds of the *Pn* (first) arrival. The 13-second limit is equivalent to restricting the search to depth-phase delays from events up to approximately 14° away in epicentral distance with depths up to 40 km (using theIASPEI91 model).

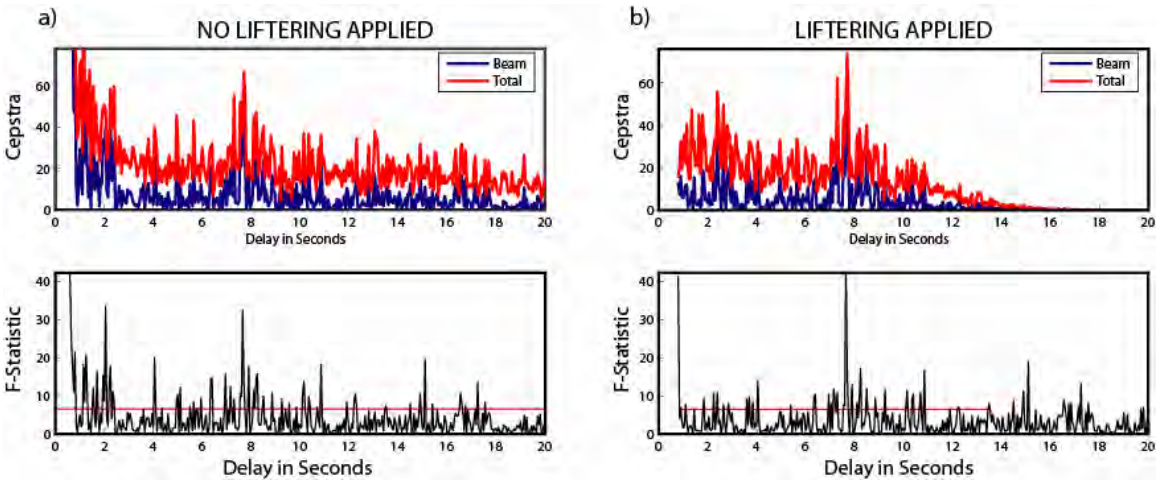

Figure 4. a) An example of an application of the CFSM to the MKAR data for Event 021101 in which no liftering has been applied. b) The same data as in a), except liftering has been performed in the log spectrum domain between the equivalent of .9 and 13 seconds. Note the diminished amplitudes in the low delay times (1-6 seconds), which is due to the removal of high-frequency noise in the log spectrum domain. When we incorporate liftering, we also do not interpret cepstral peaks above 13 seconds.

Improved Filtering and Enhancement of Regional Depth Phases

During the first year of the project, we investigated methods that could be used to enhance or isolate the depth phases in regional data. One method that is showing promise involves semblance weighting of the first arrival and its coda. We judge a filtering method's usefulness by comparing the performance of the CFSM before and after a particular filtering technique is applied to the data.

Semblance Weighting. A convenient measure of coherence across a seismic array is provided by semblance (Taner and Koehler, 1969). Semblance weighting is commonly used in exploration geophysics to enhance small but coherent arrivals in reflection data. The semblance between L traces of an array for i^{th} time index is defined as

$$S_i = \frac{\sum_{w=-W/2}^{W/2}\left[\sum_{j=1}^{L} y_j(i+w)\right]^2}{N\sum_{w=-W/2}^{W/2}\sum_{j=1}^{L}\left[y_j(i+w)\right]^2}, \quad (1)$$

where L is the number of traces, j is the trace for which the semblance weighting is applied, and $y_j(i)$ is the sample of the seismic trace. The stacking is performed over a time gate W, which for stability reasons should be larger than the period of the phase being filtered. The semblance is always positive and ranges between 0 and 1. It is close to unity for coherent events and approaches $1/N$ otherwise.

If the array is beamed along linear distance-arrival time (i.e., $X - T$) trajectories, defined by horizontal ray parameters, then the semblance can be estimated along the same trajectories. In this case, an appropriate time shift must be added to the sample number i. Semblance weighting of the seismic traces can then be performed along these trajectories:

$$y_j^s(i) = S_i y_j(i) \quad (2)$$

In Figure 4 we show examples of semblance weighting applied to data from the MKAR and KKAR arrays for the 021101 Kyrghystan event. The upper panels of Figure 4a and 4b show the semblance values along the beamed seismogram as a function of back azimuth with a color scale ranging from 0.1 (magenta) to 1 (red). The maximum semblance value indicates an apparent azimuth of arrival for each arriving phase. A dashed horizontal line shows the positions of the International Seismological Centre (ISC) bulletin's back azimuth for comparison. In the bottom panels of Figures 4, we show the array beams before (black lines) and after (red lines) semblance weighting. The semblance weighting was performed along the $X - T$ trajectories using the direction of the apparent azimuth of the first arrival and the slowness derived from V_p (as shown in the figures). The predominant effect of the semblance weighting procedure for this example is the reduction of amplitudes for incoherent arrivals.

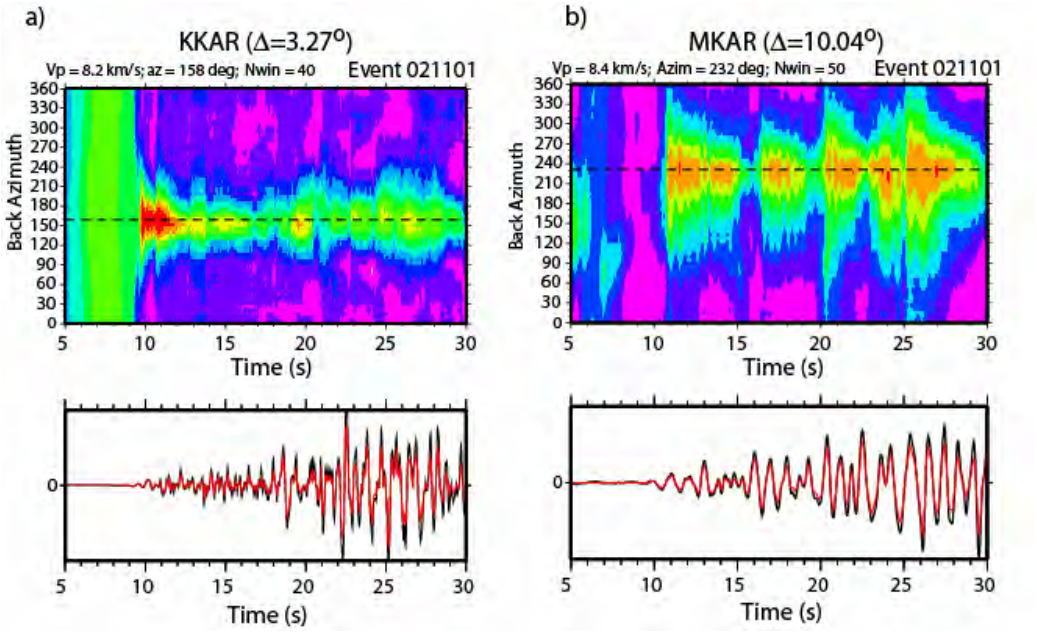

Figure 5. a) Semblance processing for Event 021101 recorded at KKAR. Top panel shows semblance as a function of back azimuth, assuming V_p = 8.2 km/s. b) Same for MKAR, with V_p = 8.2 km/s.

Another example of semblance weighting is shown in Figure 5 for Event 030507. In this case there is a considerable difference (about 20º) between the published and inferred back azimuths for the *Pn* arrival. This may be explained by either significant inhomogeneity in the crust or changes in Moho depth between the earthquake and the array.

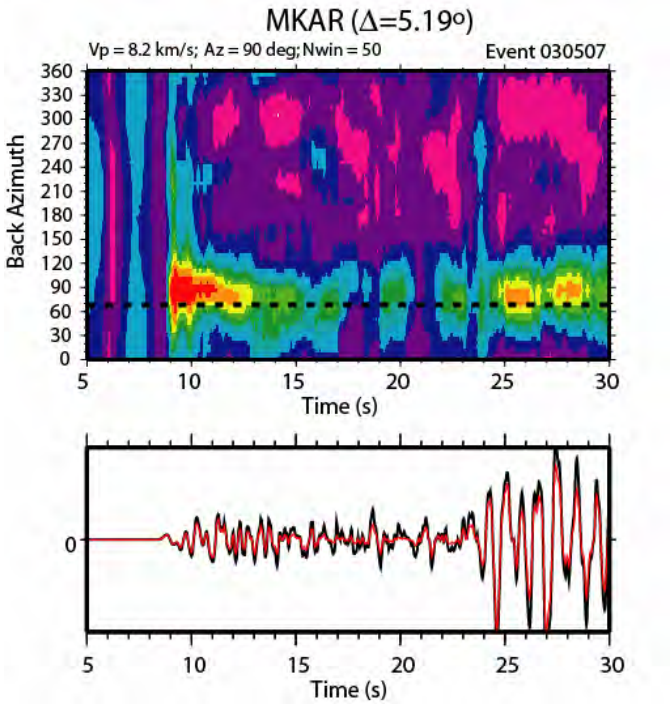

Figure 6. Semblance processing for Event 030507, assuming V_p = 8.2 km/s. The azimuth estimated by semblance for the MKAR array is nearly 20° greater than the one published by the ISC.

Application of Semblance Weighting to the CFSM. We are currently testing the effectiveness of the semblance weighting method as a pre-filtering method for the CFSM. For example, we show the results of applying the CFSM to the MKAR data from Event 021101 in Figure 7. Figure 7a) shows the unfiltered individual array waveforms in the top panel (we note that element MK09 was not available for this event) and the cepstral analysis results in the bottom two panels. Figure 7b) shows the same results for the semblance-weighted array data. It is somewhat difficult to see significant changes between the unfiltered and semblance-weighted array waveform data, but the changes in the cepstral quantities are significant. In particular, the unfiltered data has significantly larger peaks in the beam and total cepstrum at delay times between 2-6 seconds than do the results the semblance-weighted data. Also, the peak at approximately 7.5 seconds in the CFSM results is more pronounced with the semblance-weighted data. We have observed the low delay-time effects for many applications of the CFSM using unfiltered and semblance-weighted data. Another example of this type of behavior, albeit not as pronounced is shown in Figure 8, in which we performed the same analysis for Event 021101 with the KKAR data.

The results from the cepstral analyses of the KKAR and MKAR data for Event 021101 are quite different from each other. KKAR is at a distance of 3.27° for this event, and travel-time predictions using the model in Figure 1c) indicate that the secondary crustal phases *Pb* and *PnPn* should arrive very close to the *Pn* depth phases (*pPn* and *sPn*). The KKAR cepstral analysis reflects this muddied succession of arrivals, with no isolated and prominent peaks in the beam or total cepstrum, or in the F-statistic. On the other hand, the MKAR cepstral analysis reveals a clear peak (or possibly double peak) near 7.5-8.0 seconds delay time. At a focal depth of 15 km, this peak corresponds to the delay times for the *sPn* and *PnPn* phases, which arrive at nearly the same time following *Pn* at this distance (10.04°). The ISC bulletin lists focal depths from various agencies for this event that range from 10-33km, and teleseismic depth phase constraints fixed the

depth to be 10.4 ± 1.88 km. Our results are within range of that depth, given the limited regional array data we analyzed for the event. Finally, array analysis (not shown here) of the MKAR and KKAR data using a robust cross-correlation technique (Tibuleac and Herrin, 1997) confirms our cepstral analysis.

CONCLUSIONS AND RECOMMENDATIONS

The first year of this project was focused on improving the regional capabilities of the CFSM. Several conclusions can be drawn from this work: First, the proper application of the CSFM should be accompanied by an estimate of the focal mechanism of the event (even a preliminary one) and an array analysis of phase slowness, travel time and azimuth. Second, the application of liftering in the log spectrum prior to final calculation of the cepstrum can reveal hidden details in the quefrency (delay time) domain that are not apparent. In the next year we will attempt to confirm the usefulness of liftering for regional seismic data. Finally, pre-filtering array data using a semblance-weighting technique appears to reduce noise in the CSFM results.

During the next year, we will complete the development and testing of a multi-objective optimization technique to estimate regional focal depths. This technique will incorporate depth estimates made from regional surface waves, depth-phase detections in the Pn coda and possibly sparse-network hypocenter locations. We believe that the synthesis of results from multiple data types will be required for the successful estimation of depth at regional distances.

ACKNOWLEDGEMENTS

We are grateful to Drs. Jessie Bonner and Ileana Tibuleac for advice and discussion related to many of the topics discussed in this paper. All maps were produced using the Generic Mapping Tools (GMT) data processing and display package (Wessell and Smith, 1991; 1995).

REFERENCES

Bassin, C., G. Laske and G. Masters (2000), The Current Limits of Resolution for Surface Wave Tomography in North America, *EOS Trans AGU* 81, F897.

Bogert, B. P., M. J. R Healy, and J. W. Tukey (1963), The quefrency analysis of time series for echoes: Cepstrum, pseudo-autocovariance, cross-cepstrum, and saphe cracking, in *Time Series Analysis*, M. Rosenblatt, Ed., Ch. 15: 209–243.

Bonner, J. L., D. T. Reiter, and R. H. Shumway (2002), Application of a cepstral F-statistic for improved depth estimation, *Bull. Seism. Soc. Am* 92, 1675–1693.

Childers, D. G., D. P. Skinner, and R. C. Kemerait (1977), The cepstrum: a guide to processing, *Proceedings of the IEEE* 65: 1428–1443.

Gudmundsson, O. and Sambridge, M. (1998), A regionalized upper mantle (RUM) seismic model, *J. Geophys. Res.* 103: 7121–7136.

Herrmann, R. B. (2002), *Computer Programs in Seismology* Version 3.20, St. Louis University.

Kennett, B. L. N., and E. R. Engdahl (1991), Travel times for global earthquake location and phase identification, *Geophys. J. Int*. 105: 429–465.

Noll, A.M. (1967), Cepstrum pitch determination, *J. Acoust. Soc. Am*. 41: 293–309.

Taner, M. T., and F. Koehler (1969), Velocity spectra – digital derivation and applications of velocity functions, *Geophysics* 34: 859–881.

Tibuleac, I.M., and E. T. Herrin (1997), Calibration studies at TXAR, *Seism. Res. Lett.* 68: 353–365.

Wessel, P., and W. H. F. Smith (1991). Free software helps map and display data, *Eos Trans. AGU* **72**: 441, 445–446.

Wessel, P., and W. H. F. Smith (1995). New version of the Generic Mapping Tools released, *Eos Trans. AGU* 76: 329.

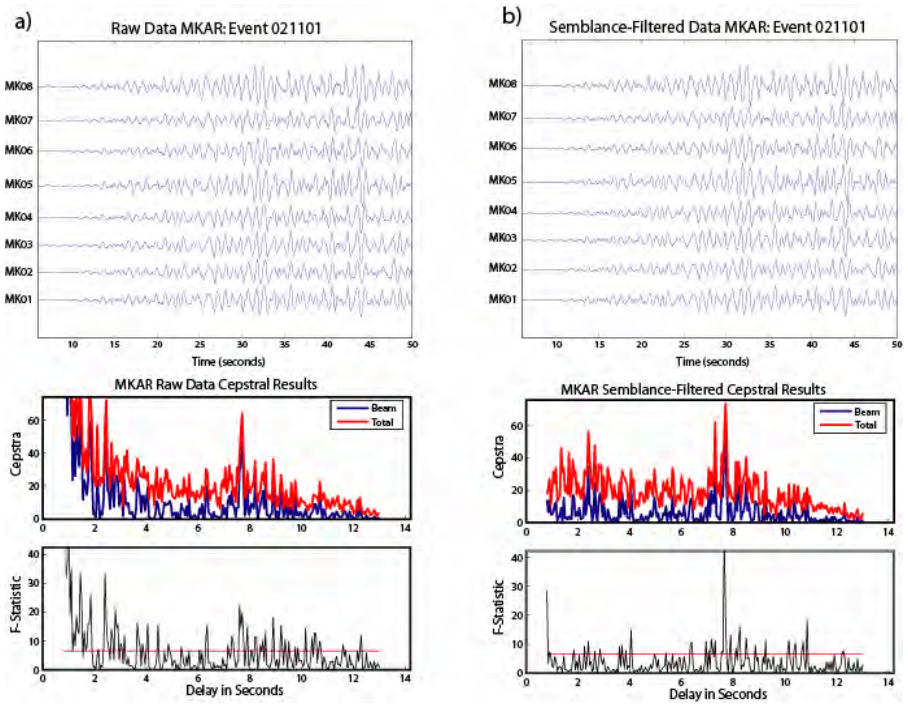

Figure 7. Event 021101: Comparison of the CFSM for unfiltered and semblance-weighted MKAR data. a) Top panel shows the unfiltered array data, middle and bottom panels show the results from the CFSM; b) same as a) but with semblance-weighted data input to the CFSM.

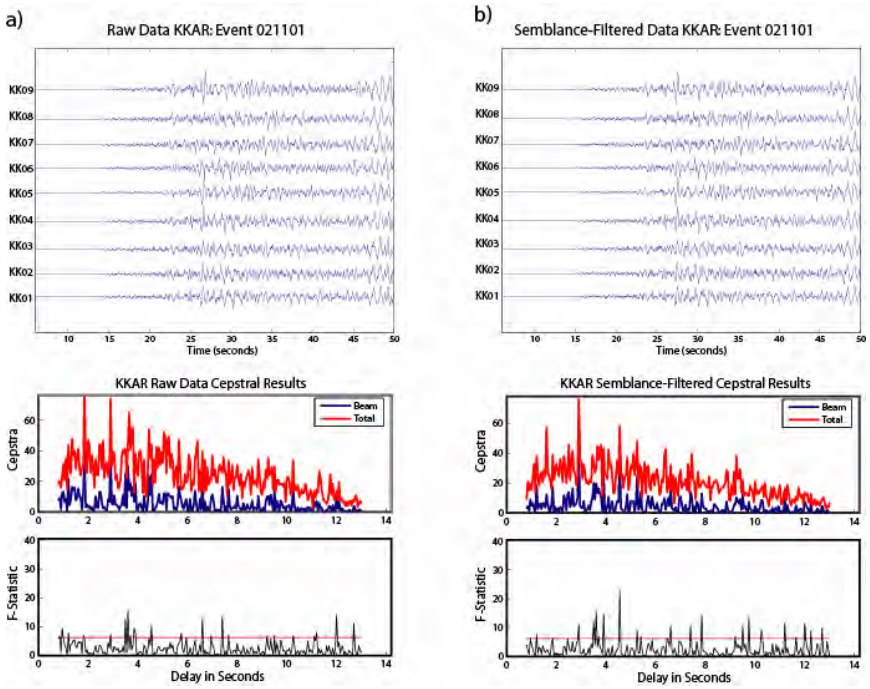

Figure 8. Event 021101: Comparison of the CFSM for unfiltered and semblance-weighted KKAR data. a) The top panel shows the unfiltered array waveforms, and the middle and bottom panels provide results from the CFSM; b) same as in a) but with semblance-weighted data used as input to the CFSM.

ADAPTIVE WAVEFORM CORRELATION DETECTORS FOR ARRAYS: ALGORITHMS FOR AUTONOMOUS CALIBRATION

Frode Ringdal[1], Steven J. Gibbons[1], and David B. Harris[2]

NORSAR[1] and Lawrence Livermore National Laboratory[2]

Sponsored by National Nuclear Security Administration
Office of Nonproliferation Research and Engineering
Office of Defense Nuclear Nonproliferation

Contract Nos. DE-FC52-05NA26604[1] and W-7405-ENG-48[2]

ABSTRACT

Correlation detection is a relatively new approach in seismology that offers significant advantages in increased sensitivity and event screening over standard energy detection algorithms. The basic concept is that a representative event waveform is used as a template (i.e., matched filter) that is correlated against a continuous, possibly multichannel, data stream to detect new occurrences of that same signal. These algorithms, therefore, are effective at detecting repeating events, such as explosions and aftershocks at a specific location.

We present evidence that correlators can be used to lower detection thresholds by 0.5 to 1 magnitude units over standard energy detection algorithms. Thus, they offer roughly the same enhancement in detection performance that is achieved by replacing single sensors with arrays. This enhancement can be achieved *in addition to* the sensitivity increase afforded by arrays.

The fact that correlators are specific to individual sources makes them attractive as event classifiers. This feature can be exploited to construct efficient screens for mining explosions or earthquake aftershocks. This major research topic is addressed in this project.

In principle, the deployment of correlation detectors against seismically active regions could involve very large numbers of very specific detectors. To meet this challenge, we are examining two strategies:

- use of *subspace detectors*, an extension of correlators, which allows representation and detection of signals exhibiting some range of variation, and
- autonomous calibration of many (subspace and correlation) detectors in a flexible, adaptive detection framework, subject to analyst review.

Because array-based correlation detectors are new to seismology, a significant amount of research on how to tune these detectors is needed to inform later calibration efforts that will arise if they are adopted for operational use.

We have begun to explore these issues through a series of representative case studies drawn from important monitoring problems involving detection of weak sources and effective screening of mining explosions and earthquake swarms and aftershocks. We focus upon two geographical regions for these case studies: (a) the European Arctic and (b) Central Asia, using available arrays and seismic networks in and near these regions. Examples of such case studies are presented.

OBJECTIVE

The overall objective of this proposed three-year study is to develop and test a new advanced, automatic approach to seismic detection using waveform correlation, with special application to seismic arrays. The principal goal is to develop an adaptive processing algorithm. By this we mean that the detector is initiated using a basic set of reference ("master") events to be used in the correlation process, and then an automatic algorithm is applied successively to provide improved performance by extending the set of master events selectively and strategically. These additional master events are generated by an independent, conventional detection system. A periodic analyst review will then be applied to verify the performance and, if necessary, adjust and consolidate the master event set.

RESEARCH ACCOMPLISHED

Introduction

Correlation detection is a relatively new approach in seismology that offers significant advantages in increased sensitivity and event screening over standard energy detection algorithms. The basic concept is that a representative event waveform is used as a template (i.e., matched filter) that is correlated against a continuous, possibly multichannel, data stream to detect new occurrences of that same signal. These algorithms, therefore, are effective at detecting repeating events, such as explosions and aftershocks at a specific location. Matched filters have been used for decades in radar, sonar, and communications processing to detect occurrences of weak signals in background noise (van Trees, 1968). The principal unique features in the seismological application are the following:

- that the signal to be detected is obtained empirically, and is not under the control of the system designer,
- for arrays, the template is multichannel (i.e., the correlator cannot be factored into separate spatial and temporal components) as a consequence of the strong scattering and multipathing experienced by seismic waves, and
- the template is strongly a function of the specific source location, mechanism, and excitation time history.

Correlators use the fine spatial and temporal structure of the signal to produce exquisitely sensitive detection algorithms. We present evidence that correlators can be used to lower detection thresholds by 0.5 to 1 magnitude units over standard energy detection algorithms. Thus, they offer roughly the same enhancement in detection performance that is achieved by replacing single sensors with arrays (Figure 1). This enhancement can be achieved *in addition to* the sensitivity increase afforded by arrays. This remarkable additional capability is a consequence of the fact that array correlators add the exploitation of temporal signal structure to the exploitation of spatial structure currently afforded by array beamforming. Array correlators also provide a means of compensating signal decorrelation across an array (or indeed network) aperture, allowing a type of high-frequency, spatially coherent beamforming across a very large aperture. The sensitivity of correlators is a consequence of their very specific waveform templates, a fact which also imposes certain limitations:

- confinement to very small geographical footprints (typically 1-2 wavelengths at the dominant signal frequency)
- confinement to events that exhibit very little variation in source characteristics, such as the source mechanism and time history.

Subspace detectors generalize correlators by continuously matching the (multichannel) data stream against an optimal linear combination of a collection of waveform templates. The signal subspace basis (i.e. waveform templates) can be chosen to represent the variability observed in a particular source as a consequence of spatial, mechanism, or temporal variation of the source.

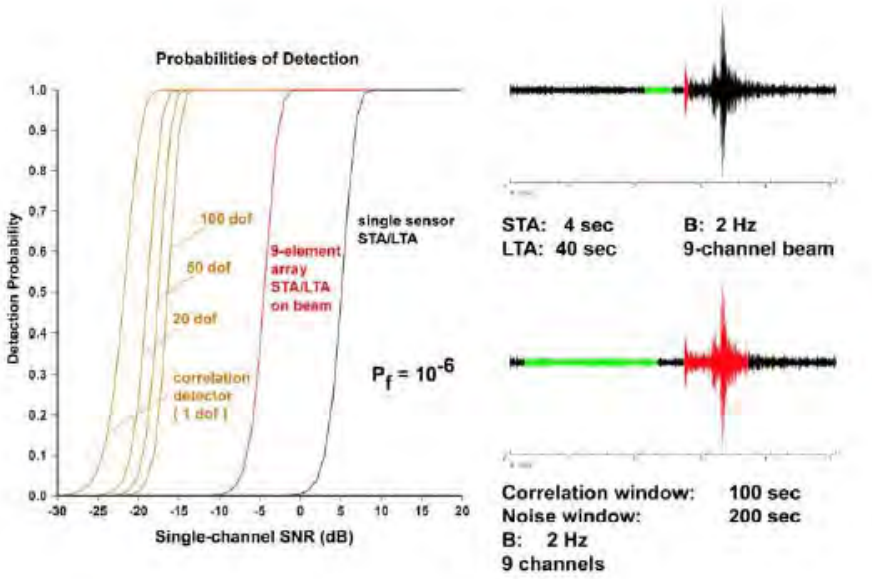

Figure 1. Comparison of theoretical detection performances of simple energy detectors and the class of correlation detectors (including subspace detectors). The suite of curves to the left show probabilities of detection at a fixed (low) false alarm probability of 10^{-6} and at varying signal-to-noise ratios for a variety of detectors. To the far right of this suite of curves is the detection probability curve for a single sensor using a short-term average/long-term average (STA/LTA) algorithm and a characteristically small window duration (4 sec) usually chosen to detect individual phases; note that it has a threshold above SNR=1 (0 dB). The next curve to the left is the detection probability for an STA/LTA detector operating on an 9-sensor array beam, assuming perfect signal coherence. To the far left is the detection probability for a correlator operating on a 9-sensor array and a 100-second detection window (correlation detection allows the coherent collection of signal energy over large windows). Intermediate are a suite of curves for subspace detectors of varying dimension degrees of freedom (dof) that could be chosen to represent a degree of signal variability. Note that all correlators exhibit an increase in performance comparable to or exceeding that afforded by replacing a single sensor with an array.

Since correlation detectors are relatively new to seismology, significant work is required as to how to tune these detectors in order to inform subsequent calibration efforts that will arise as and when they are adopted for operational use. Issues that will arise include the following:

- How many detectors are required to cover a particular source region?
- What distribution of events (number of events, magnitude range, range of source locations) is required to calibrate a detector?
- How are tuning parameters (such as signal duration, bandwidth, number of channels) optimized in order to maximize the probability of detection at a fixed false alarm rate?
- What is the optimal dimension of a subspace detector given the trade-off between false-alarm rates, detection probability, enhanced geographical coverage, and insensitivity to variation in source mechanism and time history?
- Is it possible to devise an autonomously operating framework which can continuously spawn and update correlation detectors (under analyst review) as new sources become active?
- Is it more efficient to deploy a large number of correlators or a small number of subspace detectors to cover a given geographical region?

All of these issues are to be addressed through a series of representative case studies drawn from important monitoring problems involving the detection of weak sources and the effective screening of mining explosions and earthquake swarms and aftershocks. Examples of such case studies are presented in this paper.

Detecting small chemical explosions

NORSAR has recently applied array-based waveform cross-correlation techniques to detect small chemical explosions in Sweden, with considerable success (Gibbons and Ringdal, 2004, Stevens et al., 2004). This work was initiated under a Defense Threat Reduction Agency (DTRA)-funded joint project with Science Applications International Corporation (SAIC). Between 1986 and 1989, a total of 11 chemical explosions were carried out in two underground chambers at a site in Älvdalen, central Sweden. Explosions with yields 10, 1000, and 5000 kg were performed in each of the two chambers, one with size 300 m^3 and one with size 200 m^3. The signals from these events were sought in order to provide a comparison with a later series of explosions in a different chamber at the same site; it was, however, not known at which times these events had taken place.

To detect the signals from the Älvdalen explosions for which the origin time was unknown, we developed a procedure using array correlation which proved highly successful. The basic procedure was as follows:

1. select a reference event among the known explosions and a seismic array for which data exists both for the reference event and the time period in which the sought-after event was known to have occurred
2. select a frequency band with an optimum SNR
3. for each individual channel, correlate the filtered signal from the reference event against the data stream containing the sought-after signal
4. sum (i.e., beamform) the single channel correlation traces
5. apply a standard power detector to the beam

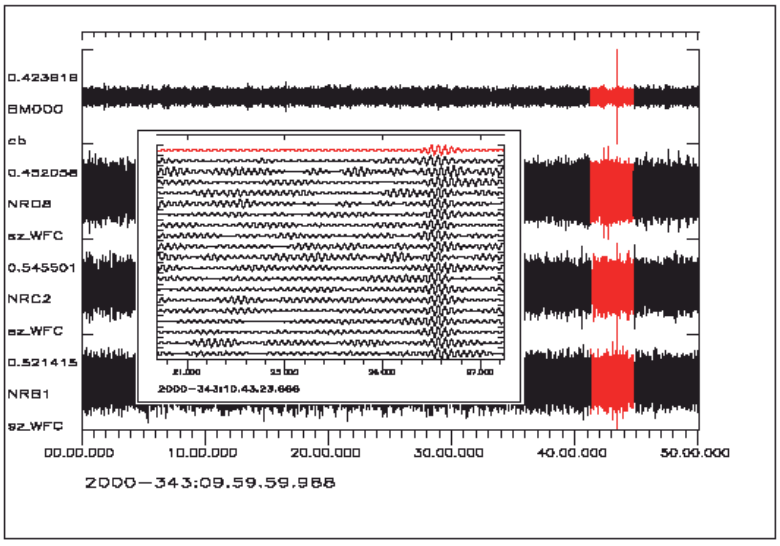

Figure 2. Example of detecting a small chemical explosion by cross-correlation. The source was a detonation of 500 kg TNT within an underground chamber with volume 1000 m^3 at a distance of 142 km from the NORES array. The master event was a 10000 kg detonation in the same chamber 5 days later. The waveforms were filtered within a narrow frequency band (14.0 - 18.0 Hz), which was necessitated by the high-frequency nature of these signals. Note the high SNR gain on the top trace, which is the beam of the individual correlation traces.

All of the explosions of 1000 kg and more were detected by this procedure using NORES and NORSAR array data. In addition, we succeeded in detecting an explosion with a yield of only 500 kg TNT which we knew had taken place but had been entirely unable to detect the signals using conventional processing. A significant aspect of the correlation detector is the low false alarm rate. To test the reliability of the procedure, the detector was run on NORSAR array data over selected time-segments totalling over one year; the process triggered 5 times only, each time corresponding to a confirmed event at Älvdalen. No event at this site of which the authors are aware has failed to be detected by this procedure, and on no occasion did the test produce a detection without there having been a confirmed explosion at the site.

Detecting rockbursts in the Barentsburg mine, Spitsbergen

Detecting sequences of earthquakes and rockbursts is an obvious application of the waveform correlation technique. We present an illustrative example, which clearly demonstrates the power of the approach. This example is from the Barentsburg mine in Spitsbergen, using data from the Spitsbergen array at approximately 50 km from the mine (see Figure 3). Since Kola Regional Seismological Center operates two in-mine seismic stations in Barentsburg, we have been able to verify that for selected time periods during which we had access to the in-mine data, the events in this swarm (see Figure 4) are in fact real and located in or near the mine. This reconfirms the ability of the array correlation detector to operate at a high sensitivity combined with a low false alarm rate.

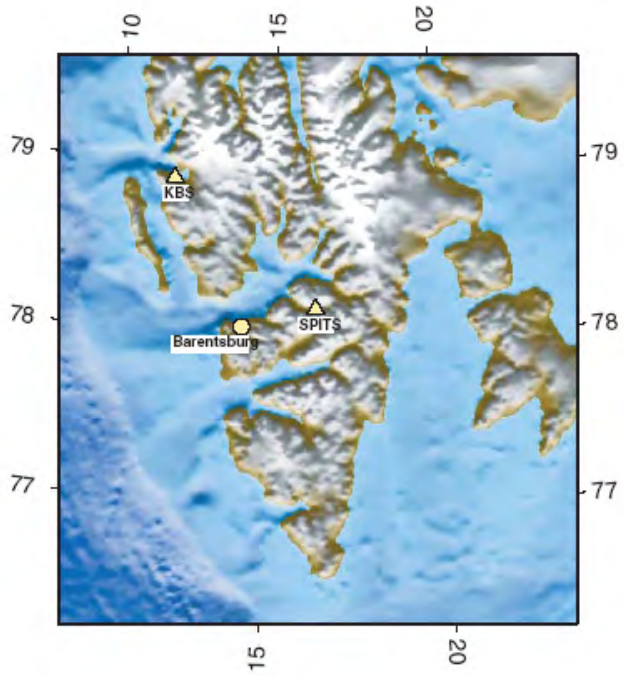

Figure 3. Locations of the Spitsbergen seismic array and the Barentsburg coal mine on Svalbard. The distance between the array and the mine is approximately 50 km.

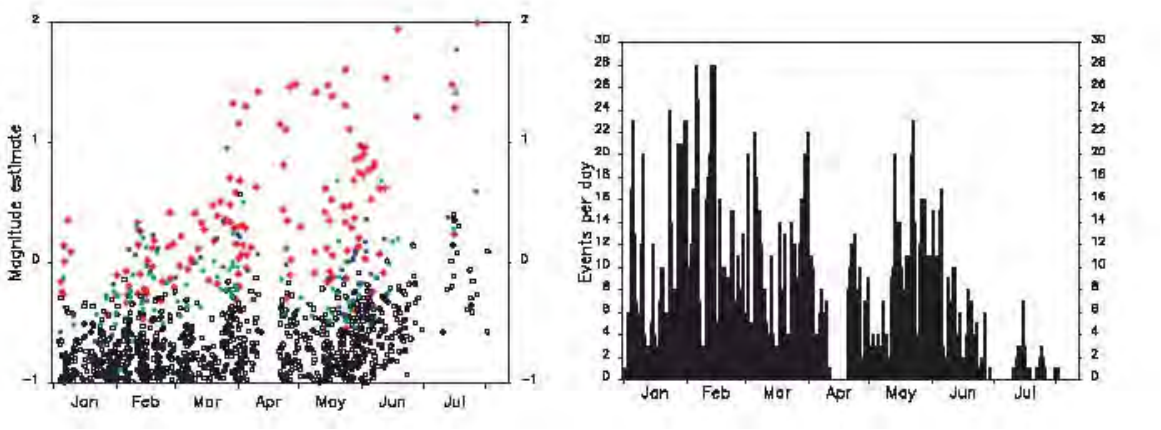

Figure 4. Sequence of waveform correlation detections of events assumed to come from the Barentsburg coal mine on Svalbard. A fatal rockburst occured on July 27, 2004, and data from the Spitsbergen array (at a distance of approximately 50 km) was searched for similar waveforms using the signal from this $m_b = 2.0$ event (filtered between 3.0 and 6.0 Hz) as the master waveform. A total of 7378 detections were made on the correlation beam between January 1, 2004, and August 12, 2004, the majority of which were discarded automatically based on the results of f-k analysis (Gibbons and Ringdal, 2005). The plots illustrate the 1578 events which, following manual examination, were deemed likely to come from the mine. The histogram (right) illustrates the frequency with which these events occured, which is known to correspond well with activity at the mine. The other panel (left) displays the magnitude estimated from the waveform correlation for these events, scaled to the master event which has been fixed at 2.0. Black circles indicate correlation detections which were not detected using traditional processing on the SPI array. Red symbols indicate correlation detections for which both a P and S detection with a suitable slowness estimate and arrival time were measured. Blue symbols indicate that only a suitable P detection was made, and green symbols indicate that only an S detection was made.

Array processing

In the Älvdalen study, we found that beamforming on correlation traces is particularly effective in suppressing noise while preserving the "signal" (i.e., the correlation peak). While standard array beamforming requires coherent signals and incoherent noise, the "correlation beamforming" requires only that the noise be incoherent; the requirement for spatially coherent signals is replaced by a requirement of similarity between the detected and master waveform. Thus, even across the NORSAR array, the correlation traces line up perfectly with no loss in the beamforming. This applies regardless of frequency. For example, in detecting the Älvdalen explosions, we applied a filter of 14-18 Hz, as illustrated in the preceding section (Figure 2).

When applying waveform correlation over a small aperture array, correlation detections can occur when two unrelated incoming wavefronts exhibit a coincidental degree of similarity over a short time-window. It can be demonstrated that the correlation traces emulate a plane wavefront traversing the array with a slowness approximately equal to the difference between the slownesses of the two correlating data segments. It is therefore possible to perform f-k analysis on the correlation traces; a clearly non-zero slowness at the time of the maximum correlation almost guarantees the occurrence of a false alarm since the correlating wavefronts come from different directions. In our processing of the Barentsburg sequence, we have used the f-k results to effectively screen out such false alarms.

Subspace detectors

Waveform correlators, including the multichannel correlator just described frequently provide exquisitely sensitive detectors of repetitive signals from geographically compact sources. However, it is often (even usually) the case that repeating sources exhibit a degree of variability in the signals that they generate. Variability can be caused by the

events from the source being distributed over a region of small, but nonetheless nonvanishing extent (such as the aperture of an aftershock sequence). Signal diversity also can be caused by variations in the source time history (as is frequently the case with ripple-fired mining explosions) or the source mechanism. It is desirable to develop detectors that are tolerant of signal diversity while still achieving much of the sensitivity of correlation detectors.

Subspace detectors (Scharf and Friedlander, 1994) are a generalization of waveform correlators that provide a flexible mechanism for trading diversity in signal representation for detector sensitivity. Subspace detectors add an uncertain signal model to the usual formulation of the detection problem. In detection problems, a window is scanned continuously along a data stream, and, for each window position, a test of two alternative hypotheses is carried out: H_0, that the window contains noise only, and H_1, that the window contains signal plus noise. In the subspace detector formulation, the signal being sought is assumed to be a linear combination of orthonormal basis functions. The basis functions are known, but the coefficients are not and must be estimated continuously as the window is scanned along the data stream. The coefficients are chosen to maximize the correlation between the linear combination of basis functions and the data in the detection window. This step-wise optimization feature provides subspace detectors with the flexibility required to deal with source variability.

The problem of subspace detector design is to find a low-dimension collection of waveform basis functions that spans the range of signals anticipated for a source. An empirical procedure for accomplishing this objective is outlined in Figure 5. In this approach to subspace design, a collection of waveforms from events defining the expected variation of the source is assembled, the waveforms are aligned as columns in a data matrix, and the waveform basis is constructed from a singular value decomposition (SVD) of the data matrix. The dimension of the waveform basis can be determined by counting the significant singular values in the SVD. Alternatively, it is possible to calculate the probabilities of detection and false alarm under an assumption of uncorrelated, normally-distributed background noise. Then the optimum dimension can be found to maximize the probability of detection for a fixed false alarm rate (Neyman-Pearson criterion). In Figure 5, the events defining the source are assembled by clustering a large collection of events detected with an STA/LTA algorithm on the basis of waveform correlation. The events from a single cluster are assumed to arise from a single source

This procedure has been tested numerous times on mining explosions, earthquake swarms, and aftershocks. The following example, drawn from detection of the San Ramon, California, swarm of 2002, indicates that subspace detectors can provide an increase in performance over waveform correlators when properly designed. Figure 6 shows the location of the swarm and two stations used in the example. Event waveform data from the broadband station KCC, 240 kilometers from the swarm, was used to construct a correlator and several subspace detectors to compare detection performance. A cluster of 19 events detected with an STA/LTA algorithm was used to design subspace detectors; the waveform of the largest event (an ML 3.9 event) was used in a correlator. The subspace detectors and the correlator were multichannel algorithms, using all three channels of the three-component broadband station.

The distributions by magnitude of the detections made by the correlator and a 9-dimension subspace detector are shown in Figure 7. The Berkeley Seismological Laboratory (BSL) catalog was used for ground truth on the swarm events. The histograms show that the correlator missed some of the high magnitude events, but the subspace detector captured all events down to duration magnitude (Md) 1.5.

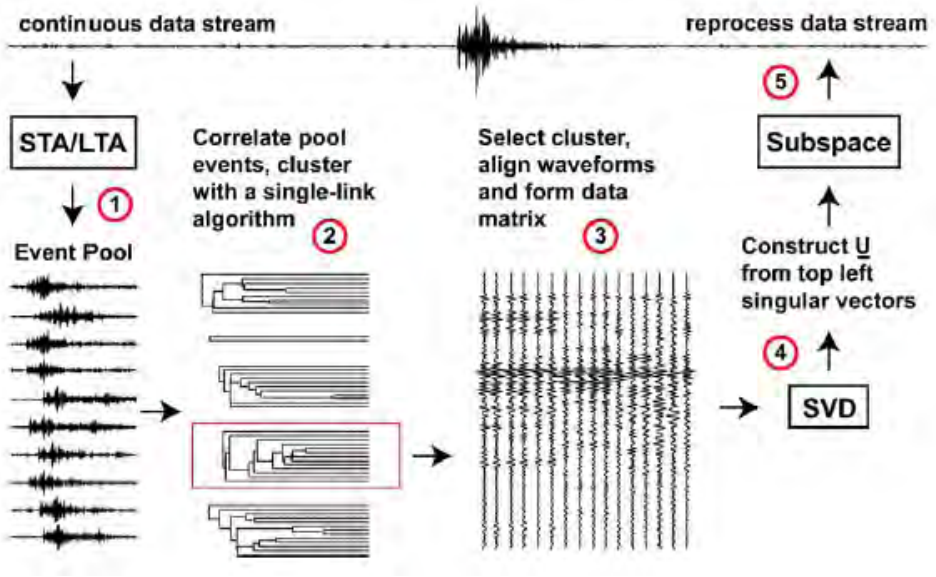

Figure 5. A "bootstrap" procedure for designing and applying subspace detectors empirically to reduce the detection threshold for a specific source with five steps.

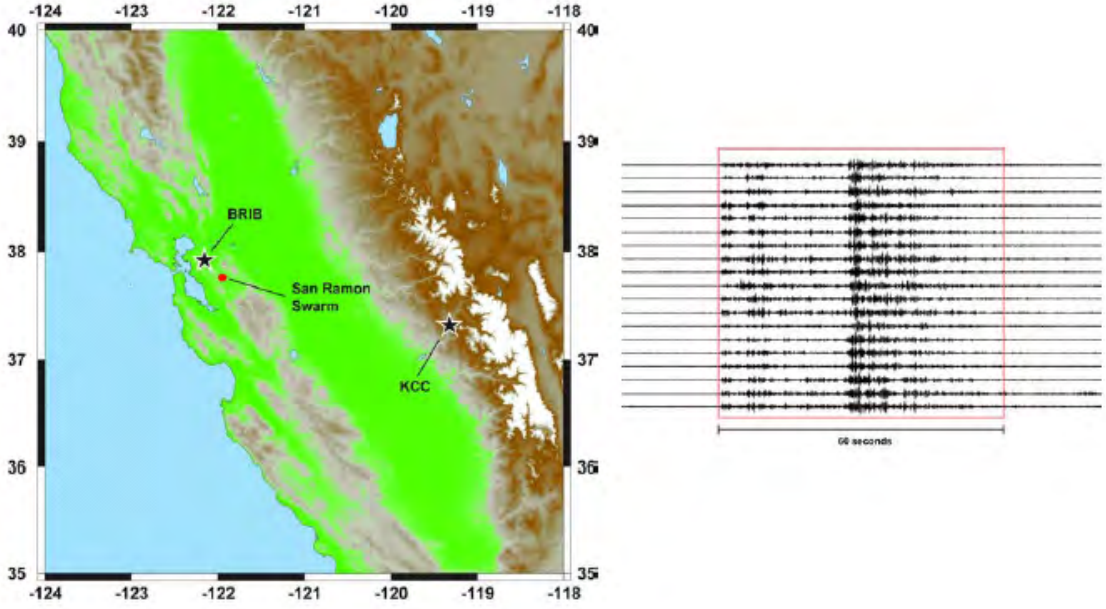

Figure 6. The 2002 San Ramon, California, swarm provided a convenient test of subspace detector design and performance. Data from two Berkeley Digital Seismic Network broadband stations (KCC, BRIB) were used in the test example to implement the detector and help assess its performance. At right are the waveforms of the 19 events used to develop subspace detectors and a correlator. A degree of signal variation is evident in the waveforms.

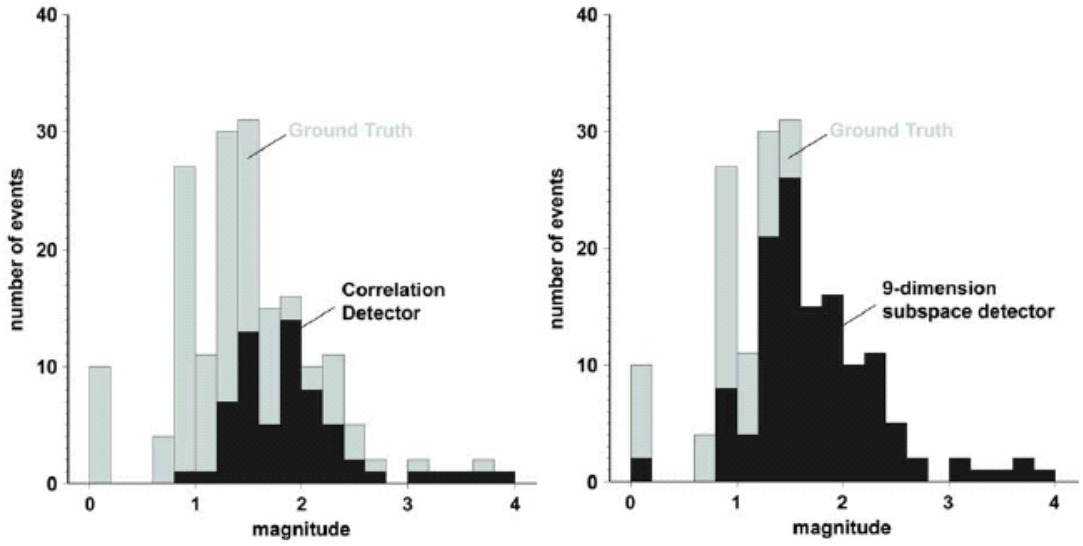

Figure 7. A 9-dimension subspace detector detected twice as many San Ramon swarm events as the correlation detector when both were operated at the same theoretical false alarm rate. The histograms above com pare the distribution of detections by magnitude to the ground truth event distribution obtained from the BSL catalog. The subspace detector has a threshold around Md 1.5 at 240 kilometers range.

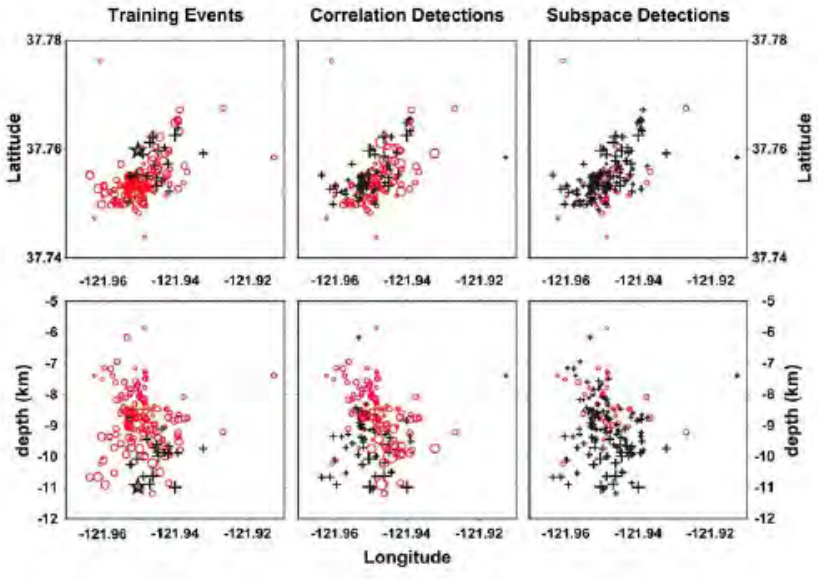

Figure 8. Subspace algorithm detections have broader spatial distribution than the correlator detections, but both miss a large fraction of the shallower events in the sequence. The maps above show the distribution of San Ramon sequence events in latitude and longitude (top maps) and in longitude and depth (bottom maps). The maps at left show the distribution of master events used in the design of the correlator (star) and subspace detectors (star and crosses).

Plots of the spatial distribution of the detected events are shown in Figure 8. These show that the subspace detectors are sensitive to events over a wider geographic footprint than the correlator based upon a single event waveform. The reason for this effect is clear from the spatial distribution of the events used to design the subspace detector (left column of Figure 8): these form a more complete sampling of the geographic distribution of events in the swarm.

One of the interesting questions to be addressed in this proposed project is whether subspace detectors provide more efficient detection and lower detection thresholds than multibeam correlators (or vice versa). These two approaches essentially provide different representations for the source: the first by constructing a minimal waveform basis for the signals to be detected and the second by using a bundle of individual waveform correlators to represent a diverse source.

CONCLUSIONS AND RECOMMENDATIONS

The project is still in an initial stage. We expect that the work will result in the development of a new advanced, automatic approach to detection/location using array processing in combination with waveform correlation. Based on the promising preliminary results described in this paper, we expect that the application of the method will result in significantly improved detection of low-magnitude events, combined with a low false alarm rate at sites for which adequate calibration information is available.

While it is not our purpose to develop an operational system at this point, the project is intended to provide automatic algorithms that will facilitate future implementation in an operational environment.The overall purpose is to develop practical methods that can be implemented into operational monitoring, and that will be useful for improving the quality of automatic bulletins and for reducing the routine workload of the analysts. Among the products of our research will be examples of clusters of events that are guaranteed to produce effective correlation detectors, including “correlation templates” in selected cases.

The development of correlation detectors is challenging because of the large number of sources that surround many stations, requiring distinct dedicated detectors. The number of detectors required is compounded by the fact that the detailed structure of signals may change over time for many of these sources, requiring detector updates. We plan to address these problems by automating the correlation detector development to the extent possible, under analyst review. The framework that we propose to develop is intended to allow exploration of a number of different strategies for autonomous detector development.

REFERENCES

Gibbons, S. J., and F. Ringdal (2004), A waveform correlation procedure for detecting decoupled chemical explosions, *Semiann. Tech. Summary,* NORSAR Sci. Rep. 2-2004, Kjeller, Norway, pp 41–50.

Gibbons, S. J., and F. Ringdal (2005), The detection of rockbursts at the Barentsburg coal mine, Spitsbergen, using waveform correlation on SPITS array data, *Semiann. Tech. Summary,* NORSAR Sci. Rep. 1–2005, Kjeller, Norway, pp 35-48.

Scharf, L. L. and B. Friedlander (1994), Matched subspace detection, *IEEE Transactions on Signal Processing*, 42 (8): 2146–2157.

Stevens, J., Rimer, N., Xu, H., Murphy, J., Barker, B., Gibbons, S., Lindholm, C., Ringdal, F., Kværna, T., and I. Kitov (2004), Analysis and simulation of cavity-decoupled chemical explosions, in *Proceedings of the 26th Seismic Research Review, Trends in Nuclear Explosion Monitoring*, LA-UR-04-5801, Vol. 1: pp. 495–502.

van Trees, H. L. (1968), Detection, Estimation, and Modulation Theory. New York: John Wiley & Sons, Inc.

RESEARCH IN REGIONAL SEISMIC MONITORING

F. Ringdal[1], S. J. Gibbons[1], T. Kvaerna[1], V. Asming[2], Yu. Vinogradov[2], S. Mykkeltveit[1], and J. Schweitzer[1]

NORSAR[1] and Kola Regional Seismological Center[2]

Sponsored by Air Force Technical Applications Center

Contract No. F08650-01-C-0055

ABSTRACT

This project represents a continuing research effort aimed at improving seismic monitoring tools at regional distances, with emphasis on the Barents/Kara Sea region, which includes the former Novaya Zemlya test site. The tasks comprise development and improvement of detection, location and discrimination algorithms as well as experimental on-line monitoring using tools such as regional generalized beamforming and Threshold Monitoring (TM). It also includes special studies of mining events, for which detailed ground truth information is being provided by the Kola Regional Seismological Centre (KRSC). These studies are documented in the NORSAR Semiannual Technical Summaries. In this paper, we present three of these investigations in more detail.

The first topic is the use of the large-aperture NORSAR array for automatic processing of regional phases. Such processing is notoriously difficult, due to the low coherency across the large array of the high-frequency regional phases, and has not been successfully implemented in the past. We have recently completed a new processing system for incorporating regional seismic phases detected by the large NORSAR array into the generalized beamforming process currently in use at NORSAR for on-line automatic detection and location of seismic events in the European Arctic. The system employs a multitaper method to calculate continuous spectra of the waveforms and detects changes in spectral content consistent with regional phases propagating across the array. It represents a significant im provement over previous processing systems for this large array, and opens up interesting possibilities for improved automatic detection and location using local or regional networks.

The second topic is a continued study of combining seismic and infrasonic recordings for detection and characterization of seismic events at local and regional distances. We present results from an analysis of several recent surface explosions in the Kola peninsula near the Norwegian border. These explosions were carried out for the purpose of destroying old ammunition, and generated unusually strong infrasonic signals in addition to seismic signals. Not unexpectedly, the infrasonic signals were well recorded on the infrasound array in Apatity, but more interestingly, they were also clearly recorded on the seismic sensors at the ARCES and Apatity arrays (both at about 250 km distance from the source area). We used the recordings to make a location estimate based upon the infrasonic detections (on the seismic sensors) at these two arrays, and found that the locations matched closely the locations obtained through standard seismic data analysis. This indicates an interesting potential for joint two-array infrasonic processing, and this concept will be further developed once the International Monitoring Station (IMS) infrasound array near ARCES has been established (expected in 2006).

The third topic concerns an initial investigation of the potential of obtaining improved detection of small seismic events by the use of waveform correlation in conjunction with array processing. We present examples on the power of the array-based correlation technique, demonstrating that waveform correlation could be used to detect the small aftershock (mb=2.5) following the 16 August 1997 Kara Sea event, not only at the Spitsbergen array (distance 1100 km), but even at the large NORSAR array situated more than 2300 km from the epicenter. We also discuss some other potential applications of this technique, which we will develop further over the next three years in a separate joint research project with Lawrence Livermore National Laboratory (LLNL).

OBJECTIVE

This work represents a continued effort in seismic and infrasonic monitoring, with emphasis on studying earthquakes and explosions in the Barents/Kara Sea region, which includes the former Russian nuclear test site at Novaya Zemlya. The overall objective is to characterize the seismicity of this region, to investigate the detection and location capability of regional seismic networks and to study various methods for screening and identifying seismic events in order to improve nuclear explosion monitoring capability. Another objective is to carry out special studies of mining events, for which detailed ground truth information is being provided by the Kola Regional Seismological Centre (KRSC).

RESEARCH ACCOMPLISHED

Introduction

NORSAR and the Kola Regional Seismological Centre (KRSC) of the Russian Academy of Sciences have for many years cooperated in the continuous monitoring of seismic events in North-West Russia and adjacent sea areas. The research has been based on data from a network of sensitive regional arrays in northern Europe. This regional network, which comprises stations in Fennoscandia, Spitsbergen and NW Russia provides a detection capability for the Barents/Kara Sea region that is close to mb = 2.5 (Ringdal, 1997).

The research carried out during this effort is documented in detail in several contributions contained in the NORSAR Semiannual Technical Summaries. In the present paper we will limit the discussions to some recent results of interest in the general context of regional monitoring of seismic events in the European Arctic.

Developing NORSARs regional processing system

NORSAR has for a number of years carried out processing and analysis of seismic events in the European Arctic, using the regional array network in Fennoscandia and NW Russia. The regional processing system at the NORSAR Data Center comprises the following steps:

- Automatic single array processing, using a suite of bandpass filters in parallel and a beam deployment that covers both P- and S-type phases for the region of interest.
- An STA/LTA detector applied independently to each beam, with broadband f-k analysis for each detected phase in order to estimate azimuth and phase velocity.
- Single-array phase association for initial location of seismic events, and also for the purpose of chaining together phases belonging to the same event, so as to prepare for the subsequent multiarray processing.
- Multi-array event detection, using the generalized beamforming approach (Ringdal and Kværna, 1989) to associate phases from all stations in the regional network
- Interactive analysis of selected events, resulting in a reviewed regional seismic bulletin, which includes hypocentral information, magnitudes and selected waveform plots.

Until recently, the large aperture NORSAR array in southern Norway has not been incorporated in this process, since a sufficiently reliable regional processing system has not been available for an array this size. The NORSAR array was designed in the late 1960s to detect low-yield underground nuclear explosions at teleseismic distances (Bungum et. al., 1971). The instruments, covering an aperture of approximately 100 km, were spaced to minimize the coherency of microseisms and thus provide an optimal signal-to-noise (SNR) gain for teleseismic signals between 0.5 and 2.0 Hz using classical beamforming with suitable steering parameters. After 1980, the focus in nuclear explosion monitoring turned towards the observation and interpretation of regional seismic phases and this motivated the development of the NORES regional seismic array and numerous subsequent arrays based upon this design (Mykkeltveit et al., 1990). The generalized beamforming system provides fully automatic event locations by the association of phase detections made by the network of regional seismic arrays in Fennoscandia and Spitsbergen and

the absence of detections from the NORES array (since June 2002) has led to a substantially worse detection and location capability for southern and western Norway.

A spatial reconfiguration of the NORSAR array to facilitate the processing of high-frequency regional phases using traditional regional array processing methods has been deemed undesirable because of the exciting possibilities which the large aperture NORSAR array represents in terms of detection of low-magnitude events using full waveform methods and because of the unique opportunity to study the variation of site effects over this large heterogeneous region. The vast majority of underground nuclear explosions occurred before most of the regional arrays were built and the 35 year long database of high quality digital seismic data from the NORSAR array provides a unique and invaluable reference.

Traditional array processing methods are entirely inadequate to process high-frequency regional phases over the NORSAR array due to the signal incoherence. The low attenuation in Fennoscandia means that many regional signals are best observed at high frequencies; signals become incoherent over the NORSAR subarrays (aperture of the order 10 km) above approximately 3 Hz. It was noted many years ago by Ringdal et al., 1972, however, that high-frequency signals could be detected with a high SNR over the NORSAR array despite the incoherence of the actual waveforms by forming incoherent beams with the envelopes of filtered waveforms.

Attempts to estimate propagation parameters from such a procedure have subsequently failed due to the very different time-histories recorded at the different sites. The multitaper method of Thomson (1982) facilitates the calculation of low-variance estimates for the amplitude density spectrum, *A(f)*, over relatively short time windows and recent improvements in CPU power mean that it is now trivial to compute running "spectrograms" (i.e., *A(f)* as a continuous function of time) in real-time for the entire NORSAR array. In particular, the function

$$D(f,t) = \log_{10}(A(f)_{t+}) - \log_{10}(A(f)_{t-}) \qquad (1)$$

measures the ratio between the energy in a time-window immediately following time *t* and the energy in a time-window immediately prior to time *t*. Figure 1 shows the functions *A(f,t)* and *D(f,t)* for two channels of the NORSAR array for a regional event. The *D(f,t)* function reaches a maximum value in the vicinity of the phase arrival time with variation determined by how emergent the signal is and how the amplitude at each site varies with time. However, the form of the *D(f,t)* function is a far more stable indicator of the arrival of a phase than the SNR of a waveform filtered in a given frequency band. Under the traditional power detectors of the kind proposed by Freiburger (1963), frequency bands are chosen a priori and are not necessarily optimal for a given signal; the *D(f,t)* function only attains significant values for the frequencies at which an SNR is observed. A time window length of 3.0 seconds was deemed ideal for the identification of regional phases at NORSAR; the sought after phases generally have a frequency content between 2.0 and 16.0 Hz and this length of time window is generally sufficient to ensure that the maximum value comes close to the phase onset time even for quite emergent signals.

These functions of time and frequency can be beamformed in the same way as seismograms using the plane-wave delays appropriate for regional phases. Although the NORSAR array is too large for the true validity of such propagation models, the deviations from plane waves generally cancel out under the beamforming process resulting in a
maximum value which typically fits the arrival time at the NB200 central array element with a surprising consistency. Eventually, the plane-wave time delays employed during the current experimental phase will be replaced by calibrated time delays. The detection process is executed by calculating a scalar function of time which is a mean of *D(f,t)* in a frequency band appropriate for the anticipated phase. Following a detection reduction algorithm, the slowness of the detected phase is estimated by beamforming the differentiated spectrograms on a dense grid; the slowness results for the northern Norway event displayed in Figure 1 are shown in Figure 2. For each of the phases shown, the slowness estimate is close to that anticipated from the reviewed event location.

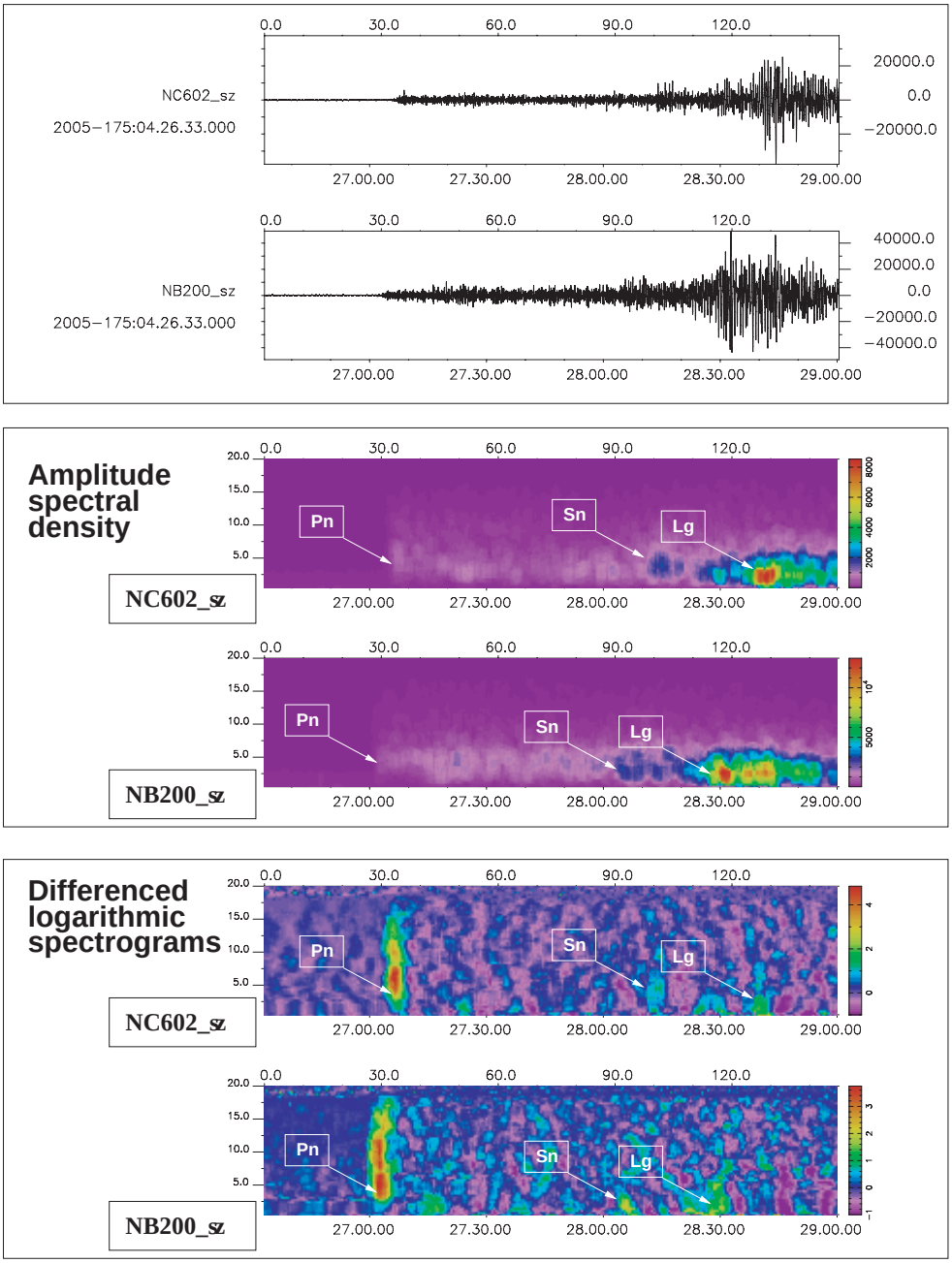

Figure 1. Seismograms from two elements of the NORSAR array (top panel) for an earthquake in northern Norway (distance approximately 610 km) with corresponding spectrograms, *A(f,t)*, (center panel) and the function $D(f,t) = \log_{10}(A(f)_{t+}) - \log_{10}(A(f)_{t-})$ (lower panel). The secondary phases exhibit relatively poor spectral contrast on single channel spectrograms. This contrast is improved greatly by beam forming these functions using the appropriate delay times. The large number of array sites and large intersite distances mean that features which are not observed at a majority of sites at the appropriate times are rarely detected.

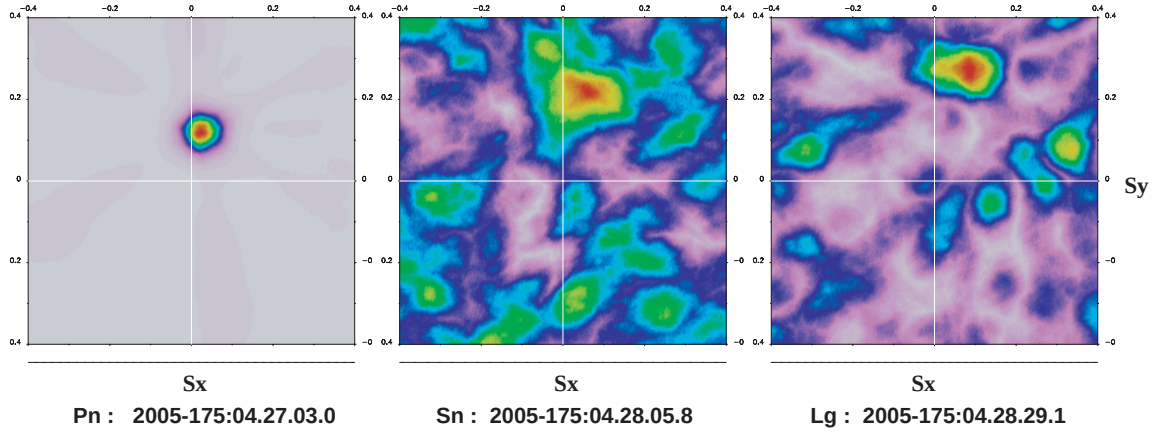

Figure 2. Slowness estimates from the large aperture NORSAR array for the Pn, Sn, and Lg phases from the North Norway event on June 24th 2005, using spectrogram beamforming at the times indicated. The automatic location estimate incorporating these phase detections, together with detections from the regional arrays in Fennoscandia, is found on http://www.norsar.no/NDC/bulletins/gbf/2005/GBF05175.html

Such detections from the NORSAR array have been incorporated in the generalized beamforming system since March 16, 2005, and, despite the unconventional method employed, have contributed significantly to the automatic detection capability in this region and have reduced considerably the analyst workload. Since operations began, an average of 40 detections per day have been registered for regional, far regional and some teleseismic events. Most teleseismic events are
missed since the waveforms are bandpass filtered above 1.8 Hz; such signals are captured by the traditional processing of the NORSAR array. Although the number of detections made is far smaller than for the regional arrays, the large aperture of the array, combined with a conservative detection threshold, ensures that almost all detections are the result of genuine regional phases and the vast majority are subsequently associated with phases from the regional arrays. Local Rg detections which can often dominate the detection lists from the other arrays are not made since such phases would not excite all seven subarrays at times consistent with regional body waves or Lg phases. Given that the energy contrast is so low for many coda phases, few are detected using this process; beamforming with the appropriate steering parameters on a coherent array is required to achieve a sufficient SNR for detection. This is regrettable in that the rich information available to a regional array is lost, but, for the multi-array phase association (generalized beamforming), the absence of many coda detections has meant that the NORSAR array contributions have in many cases provided the best constraints on the solution since the detections made are almost inevitably the first P- and first S- phases at these sites.

Combined seismic-infrasonic processing

We have continued our studies of combining seismic and infrasonic recordings for detection and characterization of seismic events at local and regional distances, following up the work of Vinogradov and Ringdal (2003). We present results from an analysis of five recent surface explosions in the Kola Peninsula near the Norwegian border. These co-located explosions were carried out for the purpose of destroying old ammunition, and generated unusually strong infrasonic signals in addition to seismic signals. Not unexpectedly, the infrasonic signals were well recorded on the infrasound array in Apatity, but more interestingly, they were also clearly recorded on the seismic sensors at the ARCES and Apatity arrays (both at about 250 km distance from the source area). Figure 3 shows selected seismometer recordings from the ARCES array for one of the explosions, with the seismic waves and the sound waves indicated on the figure.

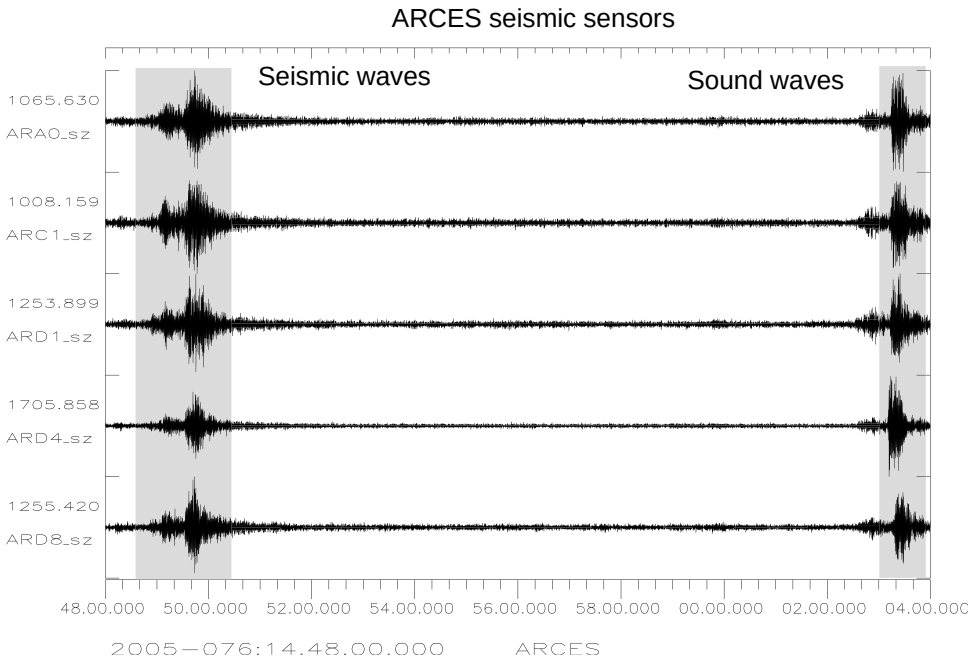

Figure 3. ARCES waveforms for one of the explosions discussed in the text. Note the clear recording of both the seismic P and S waves and the sound waves, which appear about 14 minutes later.

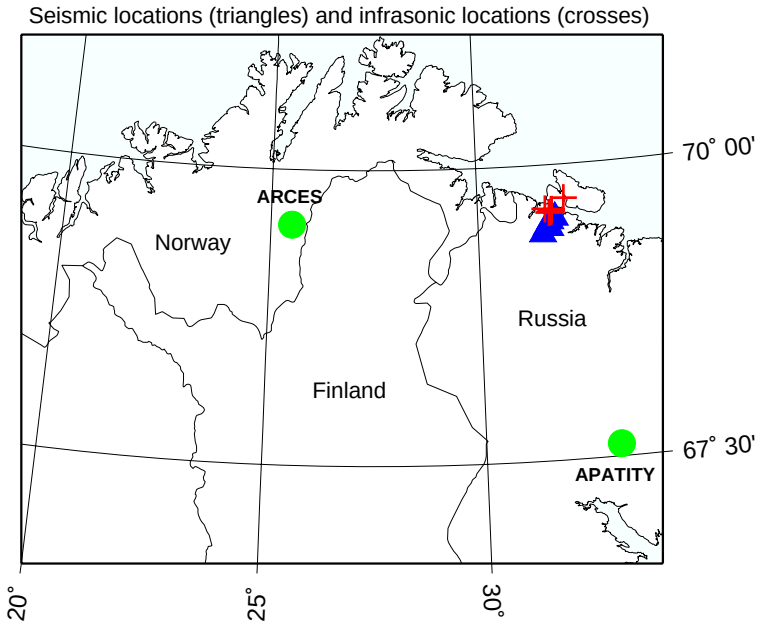

Figure 4. The map shows results from locating the five explosions described in the text. The triangles are locations based on standard interactive analysis of the seismic data from the ARCES and APATITY arrays, whereas the crosses are locations obtained using only the estimated azimuths of the sound waves recorded by the two arrays.

Although we do not know the exact coordinates of the explosion site, we used this opportunity to investigate the stability of azimuth estimates of sound waves, using various subconfigurations of the ARCES array. It turned out that the estimates were very stable, even for the smallest subset of the array (the four-element A-ring, with a diameter of about 300 m). The estimates ranged from 82 to 86 degrees, with no significant change in the stability with the size of the selected array subset. For the 3-element APATITY infrasound array, (diameter 300 m), the estimates were likewise stable, ranging from 346 to 351 degrees.

We used the estimated azimuths (from the infrasonic waves) for the two arrays to locate the five events, and com pared the recordings to those obtained using standard seismic analysis. As can be seen from Figure 4, the locations match quite closely. This indicates an interesting potential for joint two-array infrasonic processing, and this concept will be further developed once the IMS infrasound array near ARCES has been established (expected in 2006).

Array-based waveform correlation

We have carried out an initial investigation of the potential of obtaining improved detection of small seismic events by the use of waveform correlation in conjunction with array processing. As an example of the power of using arrays in the waveform correlation process, we describe briefly some results from detecting an aftershock of the well known Kara Sea event of 16 August 1997. This small aftershock (mb=2.5), occurred about 4 hours after the main event, and was detected by only one IMS station (the Spitsbergen array) by conventional processing (see map in Figure 5). This array is situated about 1280 km from the event, and had several P-phase detections with a relatively low SNR, but no S-phase detection. The event could therefore not be located automatically, and was identified as an aftershock through careful analyst inspection.

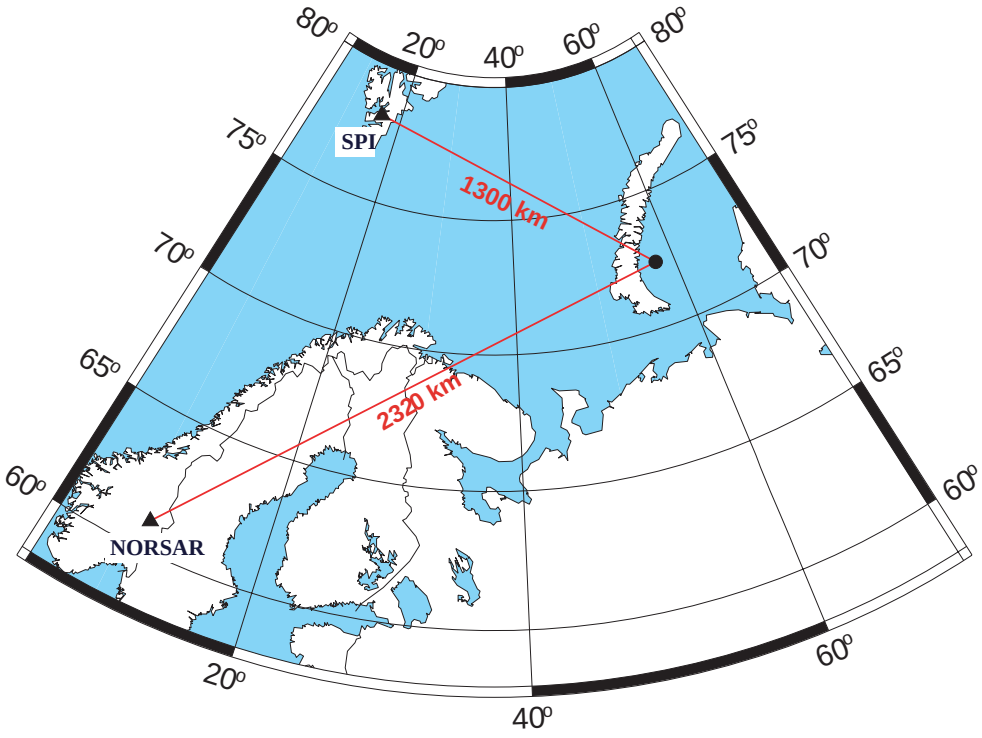

Figure 5. The location of the NORSAR and Spitsbergen arrays in relation to the site of the 16 August 1997 Kara Sea events (main shock of mb=3.5 and aftershock of mb=2.5).

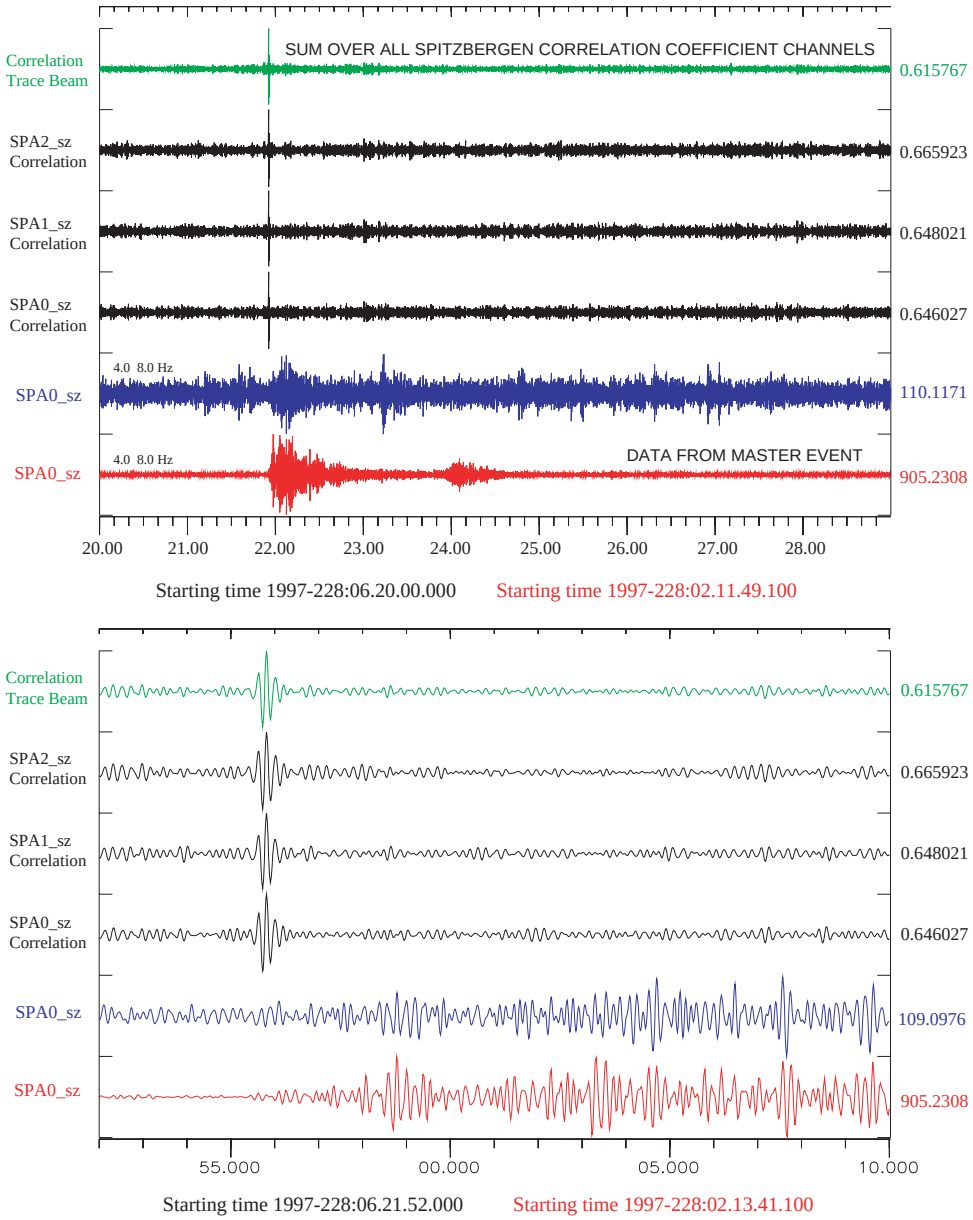

Figure 6. Detection of an aftershock from the 16 August 1997 Kara Sea event using waveform correlation on the short period vertical channels of the Spitsbergen array. Each channel was bandpass filtered between 4.0 and 8.0 Hz and a 60 second long data segment was extracted from the master event signal (shown in red for SPA0 sz) with the first master event data segment beginning at 1997-228:02.13.44.913. The data containing the presumed aftershock was filtered in the same band (shown in blue for SPA0) and a trace of fully normalized correlation coefficients was calculated for each channel. The green channel is the summation of the 9 correlation coefficient traces. A clear peak is observed on the correlation beam at a time 1997-228:06.21.55.815. The lower panel is a zoom-in of the upper panel.

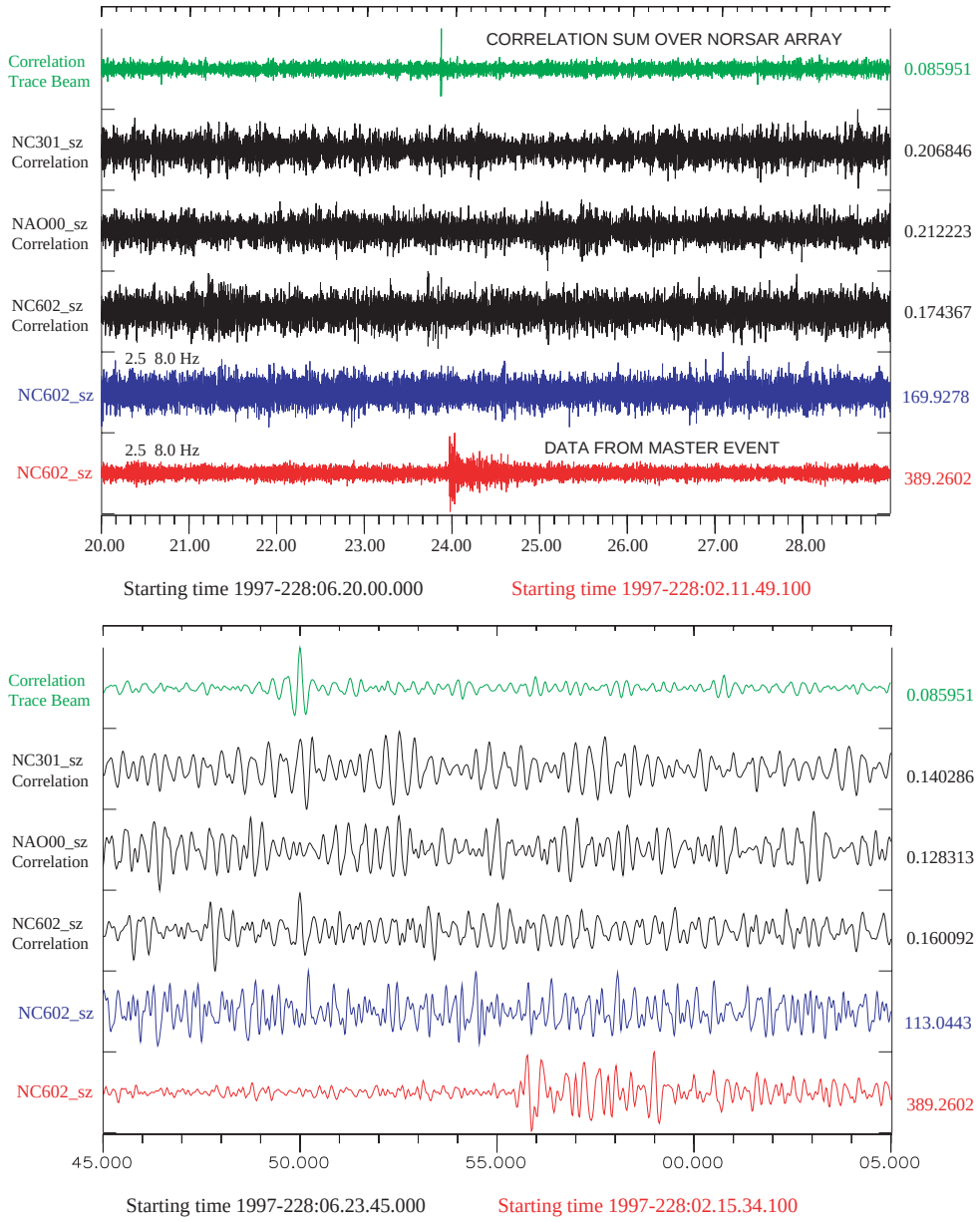

Figure 7. Detection of the Kara Sea event aftershock by waveform correlation using the NORSAR array. The frequency band applied in this calculation is 2.5 - 8.0 Hz. The 60 second long time windows containing the master event signal are staggered by several seconds to account for the significant time delays across the array; the first master event time-window begins at 1997-228:02.15.39.087 for instrument NC301. The signal at this far more distant array is buried in the noise to a far greater extent than at SPI and in no filter band could this signal be detected with a conventional STA/LTA detector. While the SPI signal is very coherent over the array in the frequency band for which the SNR is optimal facilitating a reasonable SNR gain by conventional beamforming; this is not the case for the NOA signal. In contrast to the correlation displayed in Figure 3, the individual sensor correlation traces do not indicate clear simultaneous maxima. However, the beam (formed by applying the appropriate tim e-shifts to the individual correlation traces) displays a clear peak at time 1997-228:06.23.49.999.

We applied an array correlation procedure to both the small-aperture Spitsbergen array and the large-aperture NORSAR array (at a distance of more than 2300 km), using the main event as a master waveform. The results for the small aftershock are shown in Figures 6 and 7. Both figures show very distinct correlation peaks for the aftershock, and thee timing of these peaks is indicative of two co-located events. The Spitsbergen array (Figure 6) has clear peaks both for the individual sensors and on the beam. The results from the large NORSAR array (Figure 7) are even more impressive, and illustrate one of the main strengths of the correlation/beamforming process; the individual correlation traces are coherent across the array even when the actual waveforms are not. The correlation/beamforming process therefore provides an SNR gain far greater than that achieved by conventional beamforming. In fact, the event cannot even be seen on the NORSAR individual sensor correlation traces, whereas it is clearly visible on the beam of these traces.

CONCLUSIONS AND RECOMMENDATIONS

We have implemented a new processing system for incorporating regional seismic phases detected by the large NORSAR array into the generalized beamforming process currently in use at NORSAR for on-line automatic detection and location of seismic events in the European Arctic. The system represents a significant improvement over previous processing systems for large arrays, and we recommend that this method be further developed for im proving automatic detection and location using local or regional networks.

We have obtained some interesting results when comparing location estimates based on seismic and infrasonic recordings of surface explosions at local and regional distances. Using ARCES and Apatity array recordings of a set of explosions near the Norwegian-Russian border, we have found that the infrasonic locations (using azimuths only) match closely the locations obtained through standard seismic data analysis. This indicates an interesting potential for joint two-array infrasonic processing, and we recommend that this concept be further developed once the IMS infrasound array near ARCES has been established (expected in 2006).

We have documented a significant potential of obtaining improved detection of small seismic events by the use of waveform correlation in conjunction with array processing. We have demonstrated that waveform correlation could be used to detect the small aftershock (mb=2.5) following the 16 August 1997 Kara Sea event, not only at the Spitsbergen array (distance 1100 km), but even at the large NORSAR array situated more than 2300 km from the epicenter. We recommend that further studies be undertaken on potential applications of this technique, which we will develop further over the next three years in a separate joint research project with LLNL

REFERENCES

Bungum, H., E. S. Husebye and F. Ringdal (1971). The NORSAR array and preliminary results of data analysis, *Geophys. J. R. Astr. Soc.* 25: 115-126.

Freiburger, W. F.(1963). An approximation method in signal detection, *Quart. J. App. Math.* 20: 373-378.

Mykkeltveit, S., F. Ringdal, T. Kværna and R. W. Alewine (1990). Application of regional arrays in seismic verification research, *Bull. Seism. Soc. Am.* 80: 1777-1800.

Ringdal, F. (1997): Study of low-magnitude seismic events near the Novaya Zemlya nuclear test site, *Bull. Seism. Soc. Am.* 87: No. 6, 1563-1575.

Ringdal, F. and T. Kværna (1989). A multichannel processing approach to real time network detection, phase association and threshold monitoring, *Bull. Seism. Soc. Am.* 79: 1927-1940.

Ringdal, F., E. S. Husebye and A. Dahle (1972). Event detection problems using a partially coherent seismic array, NORSAR Tech. Rep. 45, Kjeller, Norway.

Thomson, D. J. (1982). Spectrum Estimation and Harmonic Analysis, *Proc. IEEE*, 70: 1055-1096.

Vinogradov, Yu. and F. Ringdal (2003). Analysis of infrasound data recorded at the Apatity array, *Semiannual Technical Summary 1 July - 31 December 2002*, NORSAR Sci. Rep. 1-2003, Kjeller, Norway.

ERROR ANALYSIS IN THE JOINT EVENT LOCATION/SEISMIC CALIBRATION INVERSE PROBLEM

William L. Rodi

Massachusetts Institute of Technology

Sponsored by Air Force Research Laboratory

Contract No. F19628-03-C-0109

ABSTRACT

The goal of this project is to develop new mathematical and computational techniques for analyzing the uncertainty in seismic event locations, as induced by both observational errors and errors in the travel-time model used in the location process. The analysis is being done in the context of the multiple-event inverse problem, in which the locations of multiple events are inferred jointly with travel-time corrections for the event-station paths. The premise is that one of the events is the target of the location uncertainty analysis while the others are calibration events that serve to constrain the path corrections within some level of error. Performing uncertainty analysis on the coupled location/calibration inverse problem takes implicit account of how errors in the inferred path corrections affect the location of the target event and, conversely, how errors in the calibration event locations affect the path corrections.

To date, the project has addressed the case in which travel-time corrections are parameterized as a simple time term for each station/phase combination in the data set. Under this assumption, the first year's effort resulted in a scheme for computing a confidence region on the target event location, in a fully nonlinear sense, that reflects the total uncertainty in all of the parameters of the joint location/calibration problem. These "multiple-event'" confidence regions are computed with a two-step procedure: (1) generating a map of the likelihood function on a grid encompassing the best fitting location of the target event, and (2) performing a Monte Carlo simulation to determine a confidence level for each value of likelihood in the map. Each step requires repeated solution of the multiple-event inverse problem, making the method very computationally intensive. A major focus of the project has been to speed up the method, which was achieved last year by simplifying the second step (Monte Carlo simulation) and has been addressed in the current year by designing better grids for the first step (likelihood mapping) and by making the underlying grid-search single-event location algorithm that both steps use more efficient. Additional accomplishments of the current year were (1) a technique for computing multiple-event confidence regions that are based on the traditional Gaussian/linear assumptions, which provide a useful baseline for evaluating the fully nonlinear confidence regions, and (2) incorporating the ability to apply "soft'" constraints on location parameters and travel-time corrections in the form of prior probability distributions, as an alternative to the hard constraints used previously. This paper illustrates these new capabilities using data from the Nevada Test Site.

OBJECTIVE

The objective of this project is to develop new mathematical and computational techniques for quantifying the errors in seismic event locations, including the effects of observational errors and errors in the travel-time forward model. Our approach associates the latter, or *model errors*, with the uncertainty in path travel-time corrections that have been inferred from calibration data. We thus analyze event location uncertainty in the context of the joint location/calibration inverse problem, whereby arrival time data from multiple events and stations are used to simultaneously locate the events and estimate calibration parameters that underlie the travel-time corrections. One of the multiple events is taken to be a new event under investigation while the remaining events are calibration events. Calibration parameters can be, for example, explicit travel-time corrections for paths, travel-time correction surfaces, or a 3D velocity model that generates travel-time corrections via ray tracing. A complete error analysis that considers the errors in all the unknown parameters—the location of the new event, the locations of non-GT0 calibration events, and the calibration parameters—accounts for the key sources of error in the new event location, including picking errors in the observed arrival times for the new *and* calibration events, and errors in the calibration event locations.

We are addressing this joint inverse problem with numerical techniques, like grid search and Monte-Carlo simulation, that lift key limitations of analytic approaches to uncertainty analysis in large inverse problems. These limitations include the restriction to Gaussian data errors, the necessity of using a linear approximation to the travel-time forward model, and restricted mechanisms for incorporating *a priori* constraints on the unknowns (notably, Gaussian prior distributions). Moreover, analytic approaches typically provide only Gaussian descriptions of location uncertainty, such as variance matrices and confidence ellipses, which may inadequately characterize uncertainty when Gaussian/linear assumptions are violated.

RESEARCH ACCOMPLISHED

Summary of Approach

Rodi (2004) presented the mathematical formulation of the joint location/calibration inverse problem and maximum-likelihood uncertainty approach that are the basis for this project. To summarize, we write the joint inverse problem as

$$d_{ij} = T_j(\mathbf{x}_i) + t_i + c_{ij} + e_{ij} \qquad (1)$$

where i indexes each of m seismic events and j indexes each of n station/phase combinations that have been observed from one or more of the events. Then, d_{ij} denotes the arrival time observation for the ith event and jth station/phase ((i,j)th path); $\mathbf{x}_i$ and t_i are the origin parameters (hypocenter and time, respectively) of the ith event; T_j is a model-based travel-time function for the jth station/phase; c_{ij} is a correction to this function for path (i,j); and e_{ij} is an observational error. This equation holds only for the paths (i,j) for which data have been observed. The unknown parameters of the joint location/calibration inverse problem are the event hypocenters and origin times, $\mathbf{x}_i$, t_i, $i = 1,\ldots,m$, and the path travel-time corrections, c_{ij}. The joint location/calibration problem is often referred to as the *multiple-event location* problem.

To date, this project has focused on the "basic" multiple-event location problem, in which the path corrections are assumed to be event-independent (see Jordan and Sverdrup, 1981; Pavlis and Booker, 1983):

$$c_{ij} = a_j. \qquad (2)$$

The calibration parameters then comprise a time term, a_j, for each station/phase pair in the data set. Other ways of parameterizing path corrections include reciprocal correction functions (Rodi et al., 2003) and velocity models, and these will be addressed later in the project.

Our approach to uncertainty analysis is based on likelihood functions, which quantify how well any given values for the parameters agree with the observed data. The likelihood function is determined by the assumed probability

distribution of the observational (picking) errors in the data, e_{ij}. We have assumed that these errors are statistically independent and that each has a *generalized Gaussian* probability distribution of order p (Billings et al., 1994). For basic multiple-event location, this error model implies a likelihood function, L, given by

$$-\log L = \mathbf{const} + \sum_{ij} \log \sigma_{ij} + \frac{1}{p} \sum_{ij} \frac{1}{(\sigma_{ij})^p} \left| d_{ij} - T_j(\mathbf{x}_i) - t_i - a_j \right|^p . \quad (3)$$

In this paper we will assume the data standard errors, σ_{ij}, are known *a priori*. The task of maximizing L with respect to the event location and calibration parameters is equivalent to minimizing an l_p norm (to the pth power) of the data residuals, as given by the last term of equation (3). The case of Gaussian errors coincides with $p = 2$.

In previous projects we have developed an algorithm called GMEL (grid-search multiple-event location) for maximizing the likelihood function in equation (3). GMEL solves jointly for the location parameters of the events, $\mathbf{x}_i$ and t_i, and the travel-time correction terms of the station/phase combinations, a_j. It accepts prior constraints on all the parameters in the form of upper and lower bounds on each unknown parameter (e.g. $a_j^{\min} \le a_j \le a_j^{\max}$). Bounds on an event epicenter take the form of a maximum epicentral distance from a specified geographic point. The algorithm used by GMEL is described in Rodi et al. (2002).

Location confidence regions

Our approach to uncertainty analysis in the joint location/calibration (multiple-event location) inverse problem extends the formulation of Rodi and Toksöz (2001) for the single-event location problem, i.e. the special case in which there is one event ($m = 1$) and the path corrections (c_{1j}) are assumed known. We can summarize the approach for both problems as follows. Let the vector **p** contain the subset of unknown problem parameters on which a confidence region is desired, and let the vector **q** contain the remaining "hidden" parameters. For example, **p** may be the hypocenter of the first event, i.e. $\mathbf{p} = \mathbf{x}_1$. In single-event location, **q** would then be simply the origin time of the event: $\mathbf{q} = (t_1)$. In the multiple-event location problem, however, **q** contains t_1, all the other event locations and the travel-time corrections:

$$\mathbf{q} = (t_1, \mathbf{x}_2, t_2, \ldots, \mathbf{x}_m, t_m, a_1, a_2, \ldots, a_n). \quad (4)$$

To address the uncertainty in the *epicenter* of event 1, as another example, we would move its depth, z_1, from **p** to **q**. Let **d** denote the vector of relevant arrival time observations: the d_{ij} in the multiple-event problem, or d_{1j} in the single-event problem. We can write the likelihood function for both problems as $L(\mathbf{p},\mathbf{q};\mathbf{d})$.

A confidence region on **p** is defined in terms of a test statistic, $\tau(\mathbf{p},\mathbf{d})$, which compares the likelihoods that are achieved with **p** fixed to a particular value and with **p** free to vary (within prior bounds). In each case **q** is free to vary within its bounds. Let us define the (negative) log-likelihood function relevant to **p** as

$$\Lambda(\mathbf{p},\mathbf{d}) = -\log \max_{\mathbf{q}} L(\mathbf{p},\mathbf{q};\mathbf{d}). \quad (5)$$

The test statistic is then defined as

$$\tau(\mathbf{p},\mathbf{d}) = \Lambda(\mathbf{p};\mathbf{d}) - \min_{\mathbf{p}'} \Lambda(\mathbf{p}';\mathbf{d}) \equiv \Lambda(\mathbf{p},\mathbf{d}) - \Lambda(\mathbf{p}^*;\mathbf{d}) \quad (6)$$

where $\mathbf{p}^*$ is the maximum-likelihood solution for **p**. A confidence region on **p** at confidence level β (e.g. β =90 %) is the locus of points satisfying

$$\tau(\mathbf{p},\mathbf{d}) \le \tau_\beta \quad (7)$$

where τ_β is a critical value of the probability distribution of $\tau(\mathbf{p},\mathbf{d})$, as induced by the errors in **d**.

Confidence region algorithm

This project is developing a numerical algorithm for computing multiple-event confidence regions appropriate for Gaussian or non-Gaussian errors and accounting for the nonlinearity of the forward travel-time model and the effects of nonlinear parameter constraints (e.g. hard bounds). The algorithm is a two-step procedure:

1. *Likelihood mapping*: $\Lambda(\mathbf{p};\mathbf{d})$ is evaluated on a dense grid in **p**-space, centered on $\mathbf{p}^*$. For example, the likelihood map is a function of the epicenter of event 1 when an epicenter confidence region is sought.

2. *Monte Carlo simulation*: $\tau(\mathbf{p}^*,\mathbf{d}^{syn})$ is evaluated for many realizations of synthetic data, $\mathbf{d}^{syn}$.

The likelihood map from Step 1 is converted to a map of $\tau(\mathbf{p},\mathbf{d})$, using equation (6). The results of Step 2 are used to estimate the critical statistic τ_β. The results of both steps can then be combined into a map of the confidence region, as defined in (7). Rodi (2004) and Rodi and Toksöz (2001) describe these two steps in more detail.

Both steps of this procedure entail maximizing the likelihood function with respect to **q**, or both **p** and **q**, many times. In multiple-event location, each maximization entails solving for multiple event locations and travel-time corrections, resulting in a very computationally intensive algorithm. Our early implementations of the procedure required up to one hour of CPU time, on a 2.4 Ghz Xeon processor, to perform each step for *epicenter* confidence regions on the Nevada Test Site (NTS) events discussed below. Rodi (2004) discussed how Step 2 (Monte Carlo simulation) is sped up tremendously (less than 1 minute of CPU time) with the use of a reasonable approximation; namely, that τ_β does not depend on the constraints applied to **q**. The speed-up of Step 2 is thus achieved by holding the calibration event locations fixed. This cannot be done in Step 1, however.

In the current year, we have made several improvements to our location uncertainty approach. These include further increases in algorithm speed, achieved by improving the underlying single-event grid-search algorithm used by GMEL, and by using more efficient grids in Step 1 of the multiple-event confidence region algorithm. More significantly, we have developed some new capabilities that provide a means for evaluating our uncertainty results. The next sections describe and demonstrate these new capabilities.

Quadratic Approximations

Expanding the log-likelihood function, Λ in equation (5), in a second order Taylor series around the maximum-likelihood solution, $\mathbf{p}^*$, provides a quadratic approximation to this function. Denoting the approximation as Λ_2 (and hiding the explicit dependence on **d**) we have

$$\Lambda_2(\mathbf{p}) = \Lambda(\mathbf{p}^*) + \mathbf{g}(\mathbf{p}^*)^T(\mathbf{p}-\mathbf{p}^*) + \frac{1}{2}(\mathbf{p}-\mathbf{p}^*)^T\mathbf{H}(\mathbf{p}^*)(\mathbf{p}-\mathbf{p}^*) \qquad (8)$$

where $\mathbf{g}(\mathbf{p}^*)$ denotes the gradient vector of Λ with respect to **p**, and $\mathbf{H}(\mathbf{p}^*)$ denotes the Hessian matrix of Λ, both evaluated at $\mathbf{p} = \mathbf{p}^*$. The gradient and Hessian exist for any exponent of the error distribution greater than 1, $p > 1$, as long as the travel-time forward functions, $T_j(\mathbf{x})$, have finite first and second derivatives. Additionally, if each component of $\mathbf{p}^*$ lies between its prior bounds, we have $\mathbf{g}(\mathbf{p}^*) = 0$. Referring to equation (6), the test statistic resulting from the quadratic approximation to Λ then becomes

$$\tau_2(\mathbf{p}) = \frac{1}{2}(\mathbf{p}-\mathbf{p}^*)^T\mathbf{H}(\mathbf{p}^*)(\mathbf{p}-\mathbf{p}^*) \qquad (9)$$

When the data errors are Gaussian ($p = 2$) and if second derivatives of the travel-time functions can be ignored, the approximation is exact: $\Lambda_2 = \Lambda$ and $\tau_2 = \tau$. Moreover, the probability distribution of τ_2 is known analytically, i.e., $2\tau_2$ is chi-squared distributed with k degrees of freedom, where k is the number of target parameters (dimensionality of **p**). Under these circumstances, a confidence region on **p** is the ellipsoid given by

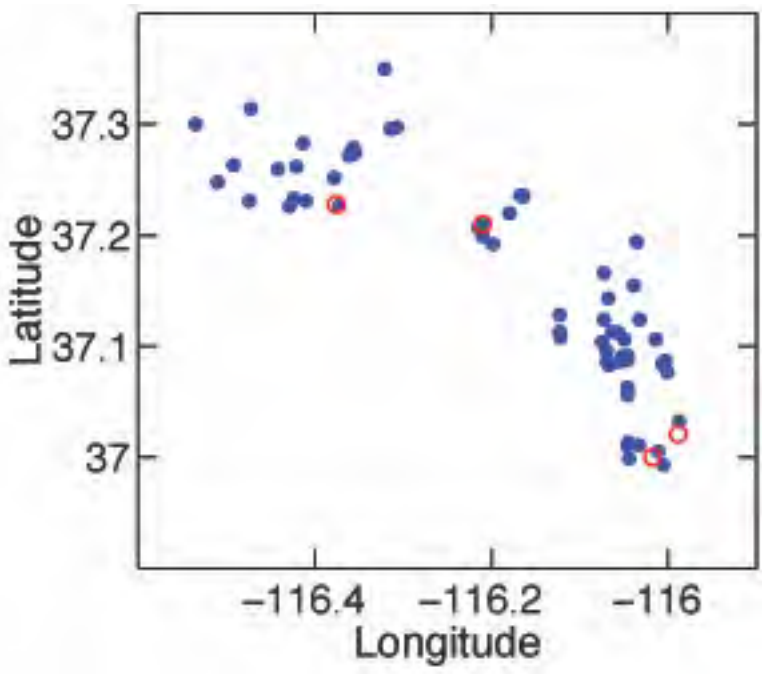

Figure 1. GT0 locations of 71 NTS explosions used for testing our uncertainty algorithm. The event shown as a red circle near 37.2°N, 116.2°W is a well-recorded explosion at Rainier Mesa that was constrained as a GT event in our tests. The other three red circles are a Pahute Mesa explosion and two Yucca Flat explosions for which multiple-event confidence regions were computed.

$$\left(\mathbf{p}-\mathbf{p}^*\right)^T \mathbf{H}\left(\mathbf{p}-\mathbf{p}^*\right) \le \chi_k^2(\beta) \tag{10}$$

where the right-hand side is the critical value of the chi-squared distribution for the confidence level β. (This result was first obtained by Evernden, 1969). In this case, the confidence region is concisely described by the ellipsoid axis lengths and orientations, which are easily obtained from the eigenvalue decomposition of **H**.

Event location algorithms typically calculate the confidence ellipsoids of equation (10) by constructing the Hessian analytically from the first derivatives of the travel-time forward functions, ignoring second derivatives and thus nonlinearity of the forward problem. When computing single-event confidence regions, GMEL computes ellipse parameters for epicenters using this same technique. The technique could also be applied to multiple-event confidence regions, but the Hessian calculation becomes much more difficult. This is because analytic computation of the Hessian with respect to **p** requires the computation, and inversion, of the full Hessian with respect to **p** and the hidden parameters **q**. In single-event location there are few hidden parameters (e.g. just origin time) but in multiple-event location there are many, as indicated in equation (4).

Therefore, we have developed a numerical technique for computing the Hessian of Λ with respect to **p**. The technique entails sampling Λ at a small number of points in *p*-space near **p***, and then approximating **H** with finite second differences of the sample values. Computing Λ at each grid point requires maximizing the likelihood with respect to the hidden parameters, i.e. solving a multiple-event location problem. The computations are thus like those done in Step 1 of our general confidence region algorithm. However, only a few grid points are involved instead of the dense grid required to map Λ.

While ellipsoidal, multiple-event confidence regions derived from the quadratic approximation are only exact for Gaussian errors and when nonlinearity is negligible, GMEL computes them in all situations to provide a comparison to the more general confidence regions obtained with our two-step algorithm described above.

Examples with Nevada Test Site data

We are testing our new uncertainty analysis techniques on regional seismic arrival times from Nevada Test Site explosions, for which precise locations and origin times are known. The data set was generated by Lawrence Livermore National Laboratory (LLNL) (see Walter et al., 2003). To date, our tests have used only a subset of the Pn arrivals, obtained by removing two stations (TPH and DAC) that are within 1.5° of most of the explosions, as well as events with fewer than 4 arrivals and stations with fewer than 2 arrivals. The resulting subset comprises 548 Pn picks from 71 events and 38 stations. Figure 1 shows the GT0 locations of the 71 events.

Confidence regions were computed for three of the events having relatively few arrivals: an event from the Pahute Mesa testing area and two from Yucca Flat. These events are shown as red circles in Figure 1. When considering each of these three events in turn, the remaining 70 events were treated as calibration events. Only one of the calibration events, however, was assigned a finite GT accuracy: a well-recorded Pahute Mesa explosion (20 Pn arrivals), which is also shown as a red dot in Figure 1. The GT level of this event was varied in the experiments: GT0, GT2 or GT5. The 69 other calibration events help to constrain the unknown travel-time corrections (a_j) even though no prior information on their locations is used. The corrections themselves were assigned hard bounds of ±5 sec, which is effectively unconstrained. All event depths were fixed to their true values in these tests. Furthermore, the origin times of the events, including the ground-truth calibration event, were unconstrained. The tests were done with the IASP91 travel-time tables as the forward model. Picking errors were assumed to be Gaussian with a standard deviation of 0.325 sec.

Figure 2 compares single-event and multiple-event confidence regions for the three target events. The single-event regions (left panels) are smaller because they assume that the path travel-time corrections are known exactly (zero). In multiple-event location, in contrast, the corrections are estimated jointly with the event locations. The multiple-event confidence regions (right panels) account for the additional location uncertainty induced by uncertainty in the estimated corrections. The multiple-event confidence regions in Figure 2 assume the ground-truth event at Rainier Mesa is GT0. Therefore, the multiple-event confidence regions do not account for any location uncertainty for the GT event.

The ellipse plotted on each panel of Figure 2 is the 90% confidence ellipse computed under the quadratic approximation, using the new likelihood differencing technique described above. We see that, for both the single-event and multiple-event cases, the ellipses match the numerically computed 90% confidence regions (blue areas) quite closely. This indicates, first of all, that in these cases the effects of nonlinearity are small. Secondly, it indicates that our differencing method for calculating the Gaussian/linear confidence ellipses is accurate. For the single-event case, in fact, the ellipses derived from the likelihood-differenced Hessian matrix are virtually identical to those derived from the analytically computed Hessian (the traditional approach; see Flinn, 1965).

Figure 3 compares multiple-event confidence regions for the same three target events, obtained with different assumptions about the location accuracy of the GT calibration event at Rainier Mesa. The left panels are the same as the right panels in Figure 2 (GT0 case). The center panels assume the GT event is GT2, while the right ones assume it is GT5. We see that, as expected, the confidence regions become larger as the assumed accuracy of the GT event location worsens. We also see that the Gaussian/linear 90% confidence ellipses (black circles) depart increasingly from the numerically computed 90% regions (blue areas) as the GT accuracy degrades. This implies that the effects of nonlinearity become more important as the location error increases.

We note that the GT2 and GT5 cases in Figure 3 used a hard constraint on the GT calibration event. In the GT2 case, for example, the GT event location was constrained to be within a 2 km radius of the known (GT0) location of the event. The next section compares this to the use of soft bounds on locations.

Soft Constraints on Locations and Corrections

In the current year, we also enhanced GMEL to allow “soft'” constraints on parameters as an alternative to hard bounds. The soft constraint on a given parameter takes the form of a prior probability distribution, which multiplies the likelihood function implied by the arrival data (as in Bayesian inference methods). We take the prior

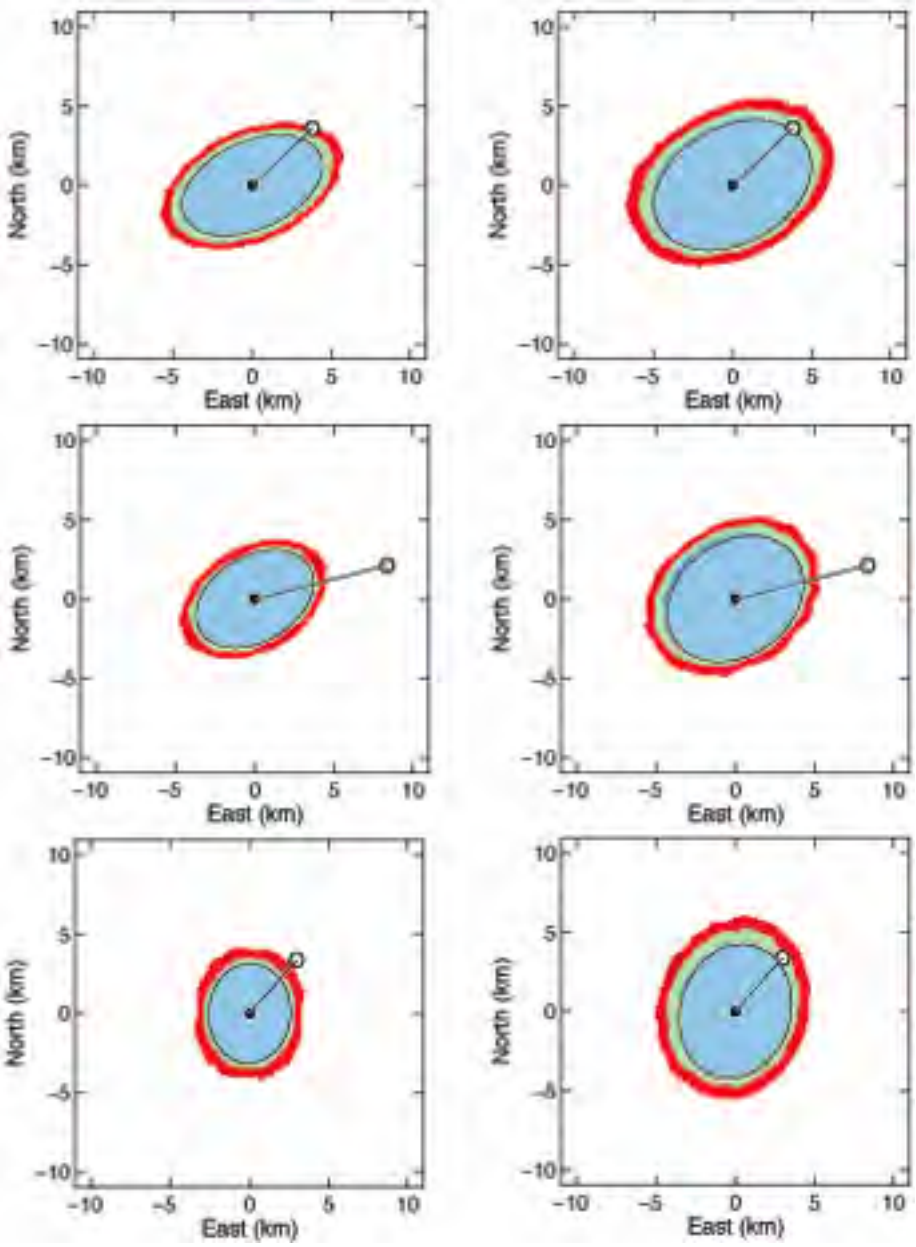

Figure 2. Epicenter confidence regions for three NTS events. *Top:* a Pahute Mesa explosion with 6 Pn arrivals. *Center:* a Yucca Flat explosion with 7 Pn arrivals. *Bottom:* a Yucca Flat explosion with 8 Pn arrivals. The frames on the left show *single*-event confidence regions (path travel-time corrections assumed known). The frames on the right show *multiple*-event confidence regions (path corrections unknown), computed with one well-recorded Rainier Mesa explosion constrained to be a GT0 event. Confidence regions are shown for 90, 95 and 98% confidence (blue, green and red, respectively). In each frame the black circle marks the maximum-likelihood solution for the event and the white circle is its GT0 location (from Walter et al., 2003). The ellipse in each frame is the 90% confidence ellipse determined under the Gaussian/linear approximation.

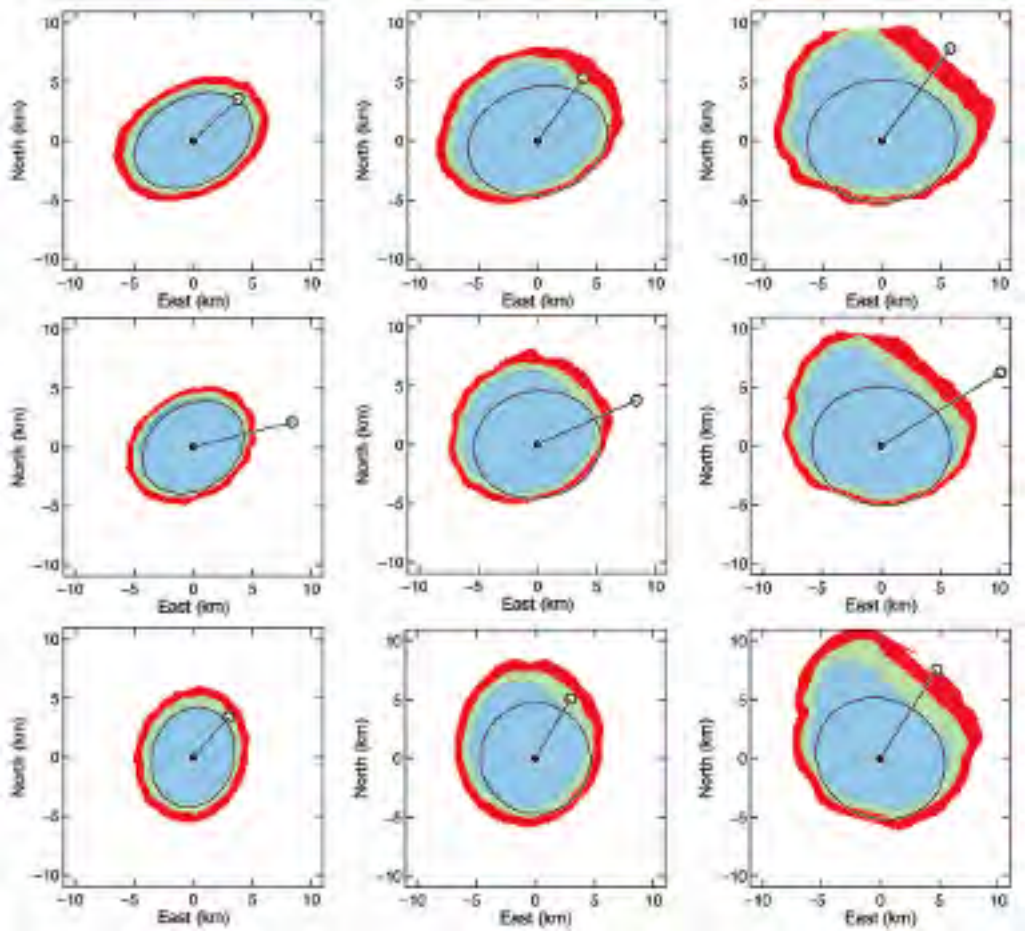

Figure 3. Multiple-event confidence regions for three NTS events (one at Pahute Mesa, two at Yucca Flat) computed with different GT levels for the ground-truth event at Rainier Mesa: GT0 (left), GT2 (center) and GT5 (right). The events are ordered from top to bottom the same way as in Figure 2, and plotting conventions are the same as in that figure.

distributions on parameters to be of the generalized Gaussian type, as we assume for the data errors. Thus, for example, a soft constraint on a travel-time correction, a_j, adds a term to the log-likelihood function of the form

$$\Lambda\left(a_j; a_j^0\right) = \frac{1}{p(\sigma_j)^p}\left|a_j - a_j^0\right|^p . \tag{11}$$

The constraint is thus specified with a parameter prior mean $\left(a_j^0\right)$, standard error (σ_j) and order of the generalized Gaussian (p). The epicentral latitude (θ_i) and longitude (ϕ_i) of an event are constrained jointly by adding the prior log-likelihood given by

$$\Lambda\left(\theta_i, \phi_i; \theta_i^0, \phi_i^0\right) = \frac{1}{p(\sigma_i)^p}\left[X\left(\theta_i, \phi_i; \theta_i^0, \phi_i^0\right)\right]^p \tag{12}$$

where X denotes the epicentral distance function.

As now implemented, each type of parameter can have a different distribution order p, which in turn can be different from that assigned to the data errors. When $p = 2$, the prior distribution on a parameter is Gaussian. As p increases, the distribution becomes "boxier", and the parameter constraint approaches the use of hard bounds.

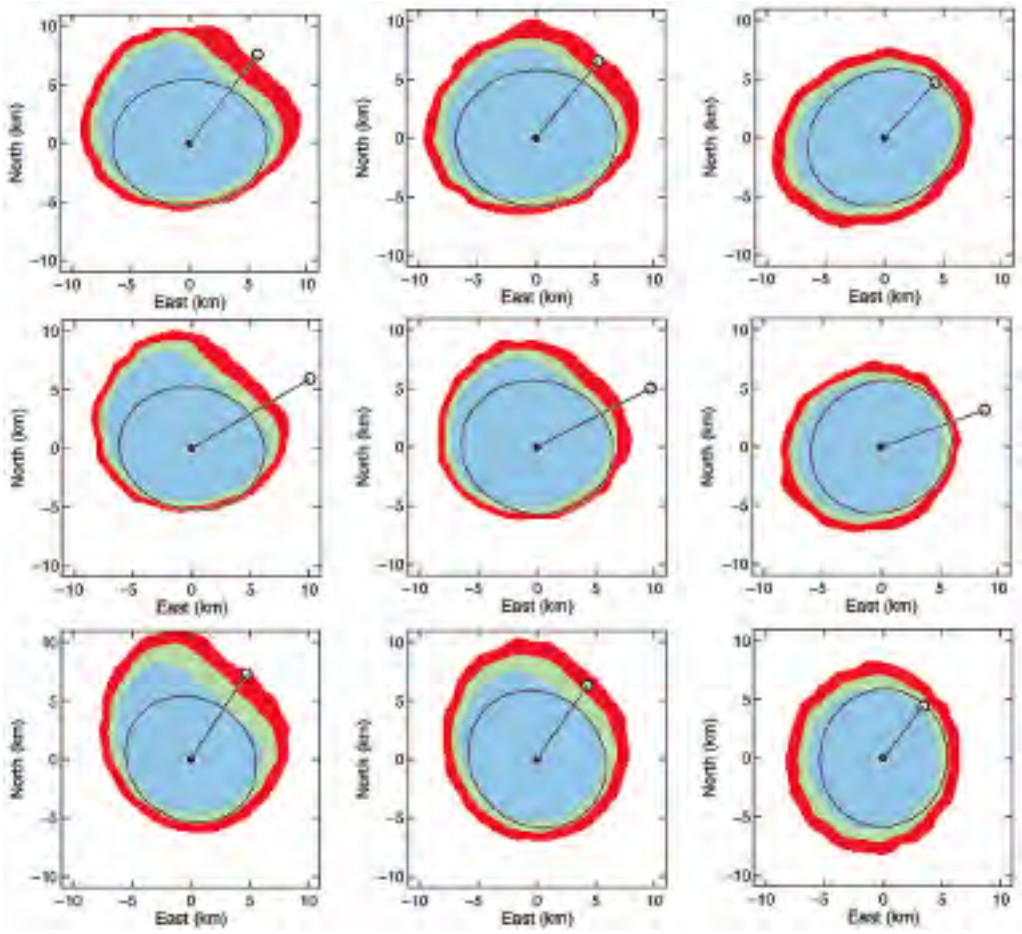

Figure 4. Multiple-event confidence regions for the three NTS events, computed using soft constraints on the location of the GT event. Three values of the order of the prior distribution are compared: p = 20 (left), p = 5 (center) and p = 2 (right). In each case, the prior distribution corresponded to a GT5 constraint at 90% confidence. Plotting conventions are the same as in Figures 2 and 3.

Examples with Nevada Test Site data

Figure 4 shows multiple-event confidence regions for the three target events we have been considering, computed using soft, instead of hard, GT constraints on the well-recorded Rainier Mesa event. Three values of the prior distribution order p in equation (12) were used: 20 (left frames), 5 (center) and 2 (right), corresponding to three levels of "hardness" of the GT location constraint. All the results in Figure 4 took the GT event to be GT5, which means that the 5 km circle surrounding the prior location contains 90% of the prior probability distribution.

The confidence regions in the left column of Figure 4 look similar to the right column of Figure 3 because p = 20 generates a very boxy prior distribution and the GT constraint is essentially a hard GT5 bound. As the constraint is softened (center and right columns), we see that the numerical confidence become more elliptical. For p = 2, they are not very different from the Gaussian/linear approximations. We can thus identify the non-ellipticity of confidence regions seen in the examples of this paper mainly with the use of hard constraints on GT event locations.

CONCLUSIONS AND RECOMMENDATIONS

We have made significant progress in the development of numerical techniques for event location uncertainty analysis in the framework of the joint location/calibration inverse problem, which considers the effects of both picking and model errors on event location errors. The techniques compute "multiple-event" confidence regions without need of the convectional assumptions of Gaussian errors and linearity of the forward problem. An important

accomplishment of the current year, ironically, was the development of a simple, efficient technique for computing multiple-event confidence regions *under* the Gaussian/linear assumption, for these provide the opportunity to evaluate our more general approach. The numerical experiments performed thus far, using data from the Nevada Test Site, indicate that Gaussian/linear confidence ellipses are an adequate description of the errors in event *epicenters* when Gaussian probability distributions are used for both the observational error model and prior constraints on event locations. The implication is that nonlinearity of the travel-time forward model does not invalidate the approximation. It remains to be seen whether this holds for hypocentral confidence regions and focal depth confidence intervals, which we have discovered to be quite susceptible to travel-time nonlinearity in the single-event location problem.

While we made good progress on improving the computational efficiency of our general uncertainty method, it is not yet clear whether it will be a practical tool for routine analysis, especially when more complex parameterizations of travel-time corrections are considered (e.g., correction surfaces). If not, the method will still be a valuable laboratory instrument for studying the limitations of approximate confidence regions. We point out that our technique for computing elliptical approximations to location confidence regions is quite efficient and, since it involves similar computations as the more general method (sampling the likelihood function on a grid), it is possible that a hybrid of the two techniques could be a practical approach to routine nonlinear, non-Gaussian analysis of event location uncertainty.

ACKNOWLEDGMENTS

I wish to thank Steve Myers of LLNL, who provided the NTS explosion data set.

REFERENCES

Billings, S.D., M.S. Sambridge and B.L.N. Kennett (1994), Errors in hypocenter location: picking, model and magnitude dependence, *Bull. Seism. Soc. Am., 84*, 1978-1990.

Evernden, J.F. (1969), Precision of epicenters obtained by small numbers of world-wide stations, *Bull. Seism. Soc. Am.* 59: 1365-1398.

Flinn, E.A. (1965), Confidence regions and error determinations for seismic event location, *Rev. Geophys.* 3*:* 157-185.

Jordan, T.H. and K.A. Sverdrup (1981), Teleseismic location techniques and their application to earthquake clusters in the south-central Pacific, *Bull. Seism. Soc. Am., 71*,1105-1130.

Pavlis, G.L, and J.R. Booker (1983), Progressive multiple event location (PMEL), *Bull. Seism. Soc. Am.* 73: 1753-1777.

Rodi, W. (2004), Error analysis in the joint event location/seismic calibration inverse problem, in *Proceedings of the 26th Seismic Research Review, Trends in Nuclear Explosion Monitoring*, LA-UR-04-5801, Vol. 1, pp. 307-316.

Rodi, W. and M.N. Toksöz (2001), Uncertainty analysis in seismic event location, in *Proceedings of the 23rd Seismic Research Review, Worldwide Monitoring of Nuclear Explosions*, LA-UR-01-4454, Vol. 1, pp. 324-332.

Rodi, W., E. R. Engdahl, E. A. Bergman, F. Waldhauser, G. L. Pavlis, H. Israelsson, J. W. Dewey and M.N. Toksöz (2002), A new grid-search multiple-event location algorithm and a comparison of methods, in *Proceedings of the 24th Seismic Research Review—Nuclear Explosion Monitoring: Innovation and Integration*, LA-UR-02-5048, Vol. 1, pp. 403-411.

Rodi, W., S.C. Myers and C.A. Schultz (2003), Grid-search location methods for ground-truth collection from local and regional seismic networks, *Proceedings of the 25th Seismic Research Review—Nuclear Explosion Monitoring: Building the Knowledge Base*, LA-UR-03-6029, Vol. 1, pp. 311-319.

Walter, W.R., K.D. Smith, J. L. O'Boyle, T.F. Hauk, F. Ryall, S.D. Ruppert, S.C. Myers, M. Anderson, and D.A. Dodge (2003), Improving the fundamental understanding of regional seismic signal processing with a unique western United States dataset, in *Proceedings of the 25th Seismic Research Review—Nuclear Explosion Monitoring: Building the Knowledge Base*, LA-UR-03-6029, Vol. 1, pp. 486-494.

GROUND TRUTH LOCATIONS USING SYNERGY BETWEEN REMOTE SENSING AND SEISMIC METHODS-APPLICATION TO CHINESE AND NORTH AFRICAN EARTHQUAKES

C. K. Saikia[1], H. K. Thio[2], D. V. Helmberger[2], G. Ichinose[1], and C. Ji[2]

URS Group, Inc.[1] and California Institute of Technology[2]

Sponsored by National Nuclear Security Administration
Office of Nonproliferation Research and Engineering
Office of Defense Nuclear Nonproliferation

Contract No. DE-AC52-03NA99505

ABSTRACT

The primary objective of this study is to establish ground truth (GT) locations of moderate to large magnitude earthquakes ($4.5<M_w<8$) occurring in China and North Africa using synergy between seismic and synthetic aperture radar interferometric methods. To this end, we have completed relocating earthquakes occurring in China and North Africa. In our last report, we have shown initial results from the Tibet (Manyi) earthquake (97/11/08, origin time 10h02m, latitude 35.069 E, longitude 87.325 N, preliminary determination of epicenters [PDE]; and $M_w = 7.5$) and its large aftershock (01/03/05, origin time 15h50m, latitude 34.369 N, longitude 86.902 E, and $M_w = 5.7$). We obtained the location of the mainshock by inverting surface deformation obtained by processing the satellite data and teleseismic waveforms together.

In this study, we have investigated the sensitivity of the method to location of the rupture initiation due to a variation in depth and along its strike direction. Our results show that for large earthquakes such as the Manyi mainshock, the waveforms remain insensitive, but the objective function that is used for the error analysis may still resolve the location. Using this new location, we estimated source-specific station corrections (SSSCs) for stations of the Chinese New Digital Station Network (CNDSN), using travel times obtained from the Chinese earthquake catalog. Using these SSSCs, we relocated many earthquakes occurring in its proximity for which we have travel times from the Chinese earthquake catalogs at common stations. Similar relocation was also done using travel times for earthquakes occurring in northeastern China (98/01/10, origin time 03h50m, latitude 41.11 N, longitude 114.55 E, and $M_w = 5.7$). We have also processed satellite data for several earthquakes that occurred in North Africa and ground deformation could be observed for two, one in Algeria (99/12/12, origin time 1h36m56.24s, latitude 35.32ºN, longitude 1.281ºW, h = 4.4 km, $M_w = 5.6$. National Earthquake Information Center [NEIC]) the other in Tunisia (97/03/20, origin time 18h02m17.98s, latitude 34.0046ºN, longiude 8.24ºE, h = 13.6 km, $M_w = 5.0$, International Seismological Centre [ISC]). Using both satellite and seismic data together, we established their new locations as follows: (a) Algerian event: latitude 34.963ºN and longitude 1.209ºW and (b) Tunisia event: latitude 34.0263ºN and longitude 8.288ºE. Using these relocations, we estimated SSSCs at stations that recorded these events and used the SSSCs at common stations to relocate many small earthquakes that occurred in their neighborhood.

OBJECTIVES

One of the most important problems in seismic monitoring is in determining GT locations so that the events can be used for calibration. Usually, large explosions provide the best GT location with error on the order of 1 km, but they are limited and one must rely primarily on earthquake data to extend the geographical coverage. Geodetic data, in the form of Synthetic Aperture Radar Interferometry (InSAR) measurements, provide much needed help in this process under some circumstances. The overall goal of this on-going study is to utilize geodetic data to establish high quality locations for shallow and moderate-sized earthquakes in Asia and North Africa in conjunction with seismic methods to validate GT location results. The work concentrates on events in North Africa (Algeria, Libya, Morocco, and Egypt), southwest Asia (Iraq and Iran, including China), and the Korean Peninsula. One of the major objectives of this study is to develop schemes to ascertain the location of rupture initiation on a given fault associated with large earthquakes. In this presentation, we will discuss earthquakes occurring in China, which have potential to become candidates for such GT events.

RESEARCH ACCOMPLISHED

November 8, 1997 (M_w 7.6) Tibet (Manyi) Mainshock

Our initial thrust here is in development of schemes that integrate both seismic and satellite data to establish the GT locations of large earthquakes. Earthquakes of magnitude greater than 6 at shallow depths provide strong co-seismic deformation that is easily discernable in satellite data, but unfortunately are difficult for establishing their epicenters. As pointed out in our previous report (Saikia et al., 2004), co-seismic deformation can be inverted for a dislocation fault model and the seismic data can then be inverted for a dislocation fault model and used to establish the time delays of these slip elements on the fault.

In our last report, we demonstrated the resolving power of InSAR in conjunction with seismic data for the November 8, 1997, M_w 7.6 Mayni (Tibetan) earthquake. This event occurred along the Kunlun fault as shown in Figure 1. The fault that ruptured has been studied by Tapponier and Molnar (1977) and a portion of it ruptured earlier in 1973. Three epicenters for the main event were reported; two based on the teleseismic data (centroid moment tensor, United States Geological Survey [USGS]) and one based on the regional travel time data as published by the Chinese Seismological Bureau, Beijing. The fault breakage outlined in Figure 1 is discussed in Peltzer et al. (1999).

We used a waveform inversion procedure developed by Ji et al. (2002a, b), which uses wavelet transforms to model the P and S data. The slip model developed based on the teleseismic P waves assuming the location from the CNDSN as a rupture initiation point, including the linear strike orientation (W18°N) of the inferred fault, is displayed in the top Figure 2. The middle panel shows the asperity established from the satellite data, and the bottom panel shows when both surface deformation from the satellite data and teleseismic waveforms were inverted jointly.

The top panel in Figure 3 shows the geo-coded interferogram obtained by combining three separate geo-coded interferograms that resulted from processing satellite data over the entire length of the Kunlun fault. Satellite data came from three tracks, namely 305, 33, and 26. The star shows the epicentral location taken from the CNDSN catalog and is off from the fault that is clearly demarcated in the satellite data. The fault is a steeply dipping fault and its hypocenter should remain almost on the fault track. The bias in the CNDSN location is due to the station distribution as the majority of the CNDSN stations were located in the southwest quadrant of the epicenter.

During the last Seismic Research Review (SRR) meeting, we showed a complex slip model obtained from the combined inversion of the satellite data and teleseismic waveforms that produced a very good fit to all data (bottom panel in Figure 2), but its major feature is similar to the slip model developed based on the satellite data alone. In this presentation, we therefore present results that were further carried out in regards to the sensitivity of the location that is inferred based on our method. Figure 4 (left panel) shows the sensitivity of the teleseismic waveforms for four different hypocenters along the strike of the fault by keeping the depth fixed. Similarly, we also varied the depth of the event, but kept the epicentral location fixed and results are shown in Figure 4 (right panel). For each case, the error estimate is displayed at the upper left corner of each inversion result. Clearly, if we were to compare only the waveforms, it would have been difficult to constrain the location; however, the objective function (Saikia et

al., 2004) used to define the best fit converges to the same location that was obtained by the synergy between the InSAR and seismic methods.

Next, we fixed its hypocenter and used travel times from all Chinese stations (station locations were earlier provided by Dr. Paul G. Richards, Lamont Doherty Observatory) and a local velocity model to estimate the origin time of the event, thus establishing its best location that has the following parameters: origin time 10h02m50.69s, 35.295ºN, 87.5084ºE.

March 5, 2001, (M_w 5.7) Tibet Aftershock

During the 26th SRR meeting, we showed modeling of the teleseismic waveforms for this earthquake indicating that its depth is less than 6 km rather than a depth of 38.9 km reported in the ISC catalog. Regional waveform modeling also suggested a depth consistent with the teleseismic data. Therefore, we hoped to obtain satellite data for this earthquake and use it to relocate the event in conjunction with the seismic data. Although the archive of the satellite database indicated that satellite data were acquired, we could not locate them at EURIMAGE and further study could not be pursued.

January 10, 1998 (M_w 5.7) Northeast China Earthquake

Its surface deformation was also presented in the last SRR meeting. Using the location that was obtained from the surface deformation from the satellite data and depth that was obtained from the seismic waveform modeling, we were able to establish its origin time using travel times collected from 85 CNDSN stations within 30° of the event. Based on this new reliable location, we estimated the SSSCs at all CNDSN stations, which in turn we have used to relocate events that occurred in its vicinity.

North Africa: Events in Algeria and Tunisia

Figure 5 shows locations of four events for which we processed satellite data to find their surface deformation. Of the four events, we were able to find surface deformation for two events, one in Algeria (99/12/12, origin time 17h36m56.24s, latitude 35.32ºN, longitude 1.281ºW, h = 4.4 km, NEIC, Mw 5.6) the other in Tunisia (97/03/20, origin time 18h02m17.98s, latitude 34.0046ºN, longitude 8.24ºE, h = 13.6 km, Mw = 5.0, ISC). Several other events occurred in the same location of the Algerian event. By analyzing both the satellite and seismic data as before, we were able to establish their high quality locations. The relocation parameters for the Algerian event are as follows: origin time 17h36m49.30s, latitude 34.963º, longitude 1.209ºE, and depth 5 km. The Tunisia event has the following parameters: origin time 18h02m14.98s, latitude 34.0623ºN, longitude 8.288ºE. and a depth of 2–4 km. Note that depths are based on both the regional and teleseismic waveform analysis. Figure 6 shows the unwrapped interferogram (bottom panel) for the Algerian event. The surface deformation observed in the interferogram (top panel) is noisy, making it difficult to form the geo-coded interferogram. Nonetheless, it was possible to ascertain the location of the event based on the InSAR interferogram shown in the top panel with a GT5 (ground truth) type of the location uncertainty. As before, we used the relocation of this event to calculate the SSSCs at both regional, far-regional, and teleseismic stations, which were in turn used to locate the other earthquakes in its neighborhood (Table 1). Figure 7 shows the geo-coded interferograms for the Tunisia event, which can be seen as a bull's eye formation of fringe pattern inside each rectangle. For this event, we found two sets of satellite data that could be processed and the event could be observed in both of them.

CONCLUSIONS AND RECOMMENDATAIONS

The overall objective of this three-year project is to concentrate on events in North Africa (Algeria, Libya, Morocco, and Egypt), southwest Asia (Iraq and Iran, including China), and the Korean Peninsula. However, this study is primarily focused on the earthquakes occurring in China because of the availability of travel-time data from the Chinese network stations. This study shows that the travel-time data from the CNDSN have great promise for analyzing both the seismic and satellite data together towards establishing GT locations for some moderate-sized Chinese earthquakes (M_w>5.5).

So far, we have established SSSCs for stations located in China using travel times from their earthquake catalog. Thus, we are successful in relocating many events that have occurred in their neighborhood.

Even though the success in North Africa is only 50% in delineating surface deformation in satellite data, we have established reliable (GT5 type) locations for two critical events, one in Algeria and the other in Tunisia. Both these events allowed us to compute SSSCs for nearby events.

REFERENCES

Ji, C., D. J. Wald, and D. V. Helmberger (2002a), Source description of the 1999 Hector Mine, California earthquake, Part I: wavelet domain inversion theory and resolution analysis, *Bull. Seismol. Soc. Am.* 92: 1192–1207.

Ji, C., D. J. Wald, and D. V. Helmberger (2002b), Source description of the 1999 Hector Mine, California Earthquake, Part II: Complexity of Slip History, *Bull. Seismol. Soc. Am.* 92: 1208–1226.

Ji, C., D. V. Helmberger, D. J. Wald, and K. F. Ma (2003), Slip history and dynamic implications of the 1999 Chi-Chi Taiwan, Earthquake, *J. Geophys. Res.* 108: (B9): 2412. doi:10,1029.2002JB001764.

Peltzer, G., F. Crame, and G. King (1999), Evidence of non-linear elasticity of the crust from the Mw 7.6 Manyi (Tibet) Earthquake, *Science* 286: 272–276.

Saikia, C. K., R. Lohman, G, Ichinose, and M. Simons (2003), Ground truth location using a synergy between InSAR and seismic methods, in *Proceedings of the 25th Seismic Research Review—Nuclear Explosion Monitoring: Building the Knowledge Base*, LA-UR-03-6029, Vol.1, pp. 324–333.

Saikia, C. K, C. Ji, G. A. Ichinose, D. V. Helmerger, A. O. Konca, and M. Simons (2004), Ground truth locations using synergy between remote sensing and seismic methods—application to Chinese earthquakes, in *Proceedings of the 26th Seismic Research Review: Trends in Nuclear Explosion Monitoring*, LA-UR-04-5801,Vol. 1, pp. 328-337.

Tapponier, P. and P. Molnar (1977), Active faulting and tectonics in China, *J. Geophys. Res*. 82: 2905–2930.

Table 1. Relocation Parameters of Earthquakes That Occurred in the Proximity of the Algerian Event. (Relocations are after the SSSCs were applied.)

Date	Origin Time Hr:mn:ss	Latitude (ºN)	Longitude (ºE)	Erx (km)	Ery (km)	RMS (sec)	H (km)
02/12/01	08:38:02.09	35.410	-0.981	35.9	21.2	0.59	-
	08:37:56.80	35.173	-0.783	27.0	16.2	0.37	2.8
00/08/23	00:42:01.19	35.158	-1.300	14.5	8.3	0.40	93
	00:41:54.10	35.081	-1.184	10.3	6.0	0.24	18
00/05/23	12:26:27.73	35.579	-1.442	11.5	6.8	0.39	0.2
	12:26:25.99	35.454	-1.290	12.4	7.1	0.37	2.0
00/01/02	07:05:43.10	35.465	-1.399	89.9		0.82	
	07:05:43.8	35.669	-1.451	9.8		0.47	
00/01/06	11:56:14.93	35.798	-1.734	22.6		0.69	39.8
	11:56:04.00	35.468	-1.403	15.6		0.36	
00/01/27	14:43:27.03	35.328	-1.449	13.2		**0.40**	
	14:43:29.60	35.019	-1.118	19.1		**0.54**	
00/03/18	01:29:07.86	35.434	-1.431	18.5		0.54	1.2
	01:29:03.92	35.317	-1.293	8.6		0.21	1.2
00/07/30	01:05:13.31	35.301	-1.372	10.4		0.67	0.0
	01:05:10.23	34.947	-1.100	6.3		0.34	40.0
99/12/25	21:23:14.04	35.145	-1.326	16.0		**0.38**	
	21:23:08.77	34.935	-1.114	14.8		**0.41**	
99/12/23	00:48:19.41	35.615	-1.415	7.8		**0.46**	0.0
	00:48:07.24	34.993	-0.822	15.3		**0.53**	0.0
99/12/22	18:14:19.76	35.359	-1.426	16.4	9.4	0.52	38.3
	18:14:08.30	34.973	-1.163	15.5	8.6	0.35	1.2
99/12/22	18:32:49.12	35.355	-1.198	12.5		0.75	8.8
	18:32:42.31	35.101	-1.367	7.9		0.49	0.0
97/12/19	15:32:21.98	35.388	-0.871	8.1		0.44	
	15:32:18.54	35.316	-0.736	22.8		0.39	
95/11/21	00:25:10.67	35.522	-0.951	7.6	5.1	0.78	0.0
	00:24:56.86	34.798	-0.253	8.1	11.5	0.29	0.0
95/06/05	09:29:36.57	35.462	-2.478	10.8		0.81	
	09:29:27.45	34.909	-2.345	24.4		0.43	

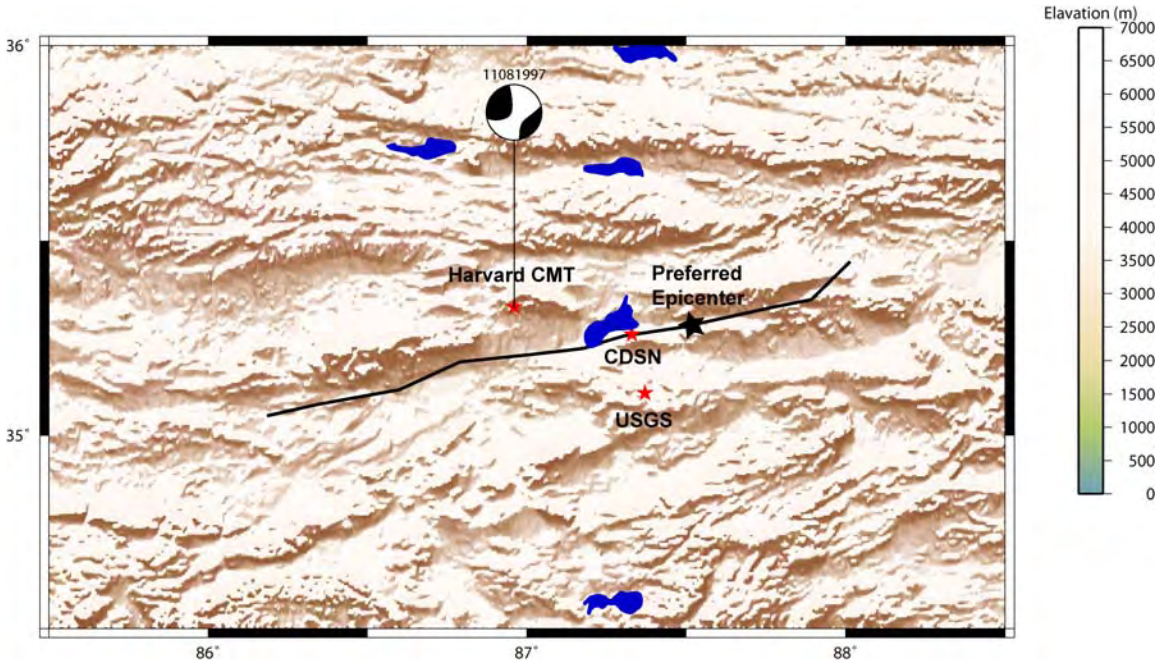

Figure 1. Map with proposed epicenters in red along with our preferred location for the November 8, 1997, Tibet (Manyi) earthquake. The fault breakage is indicated with the heavy dark line.

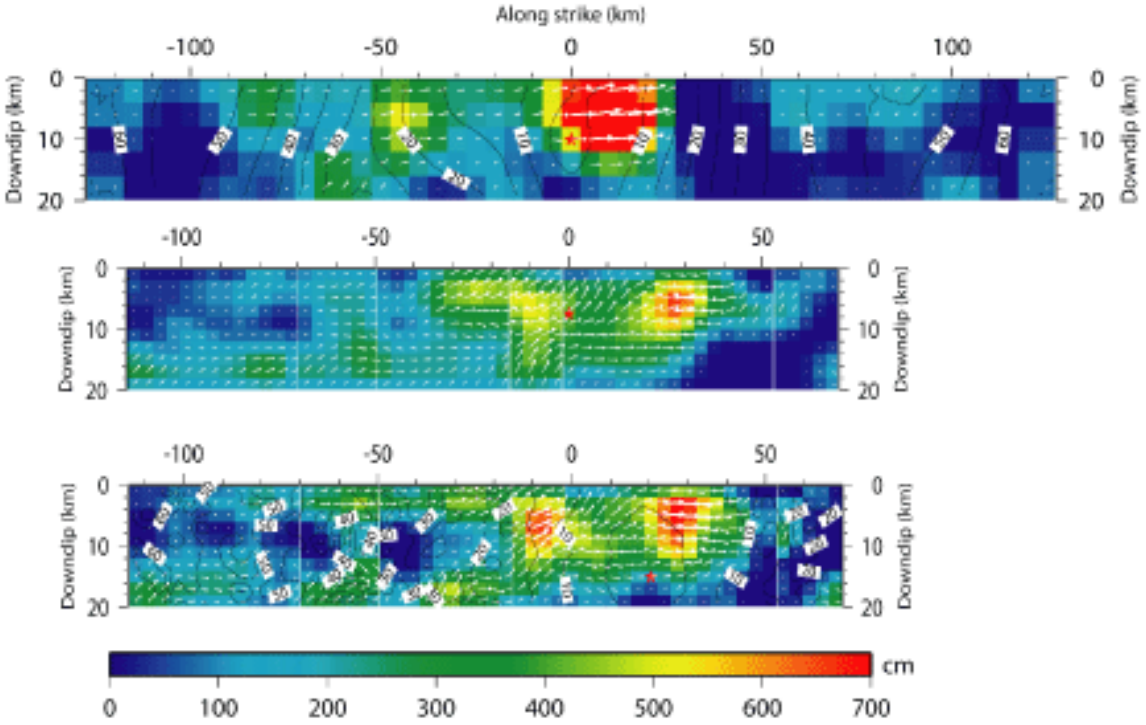

Figure 2. Three panels of slip distributions: top (teleseismic waveforms only), middle (geodetic only, InSAR), and bottom (combined teleseismic and InSAR). Contour lines are included indicating the positions of the rupture front as a function of time after onset. Note that the location of the CDSN epicenter has been shifted 20 km to the right in the bottom panel.

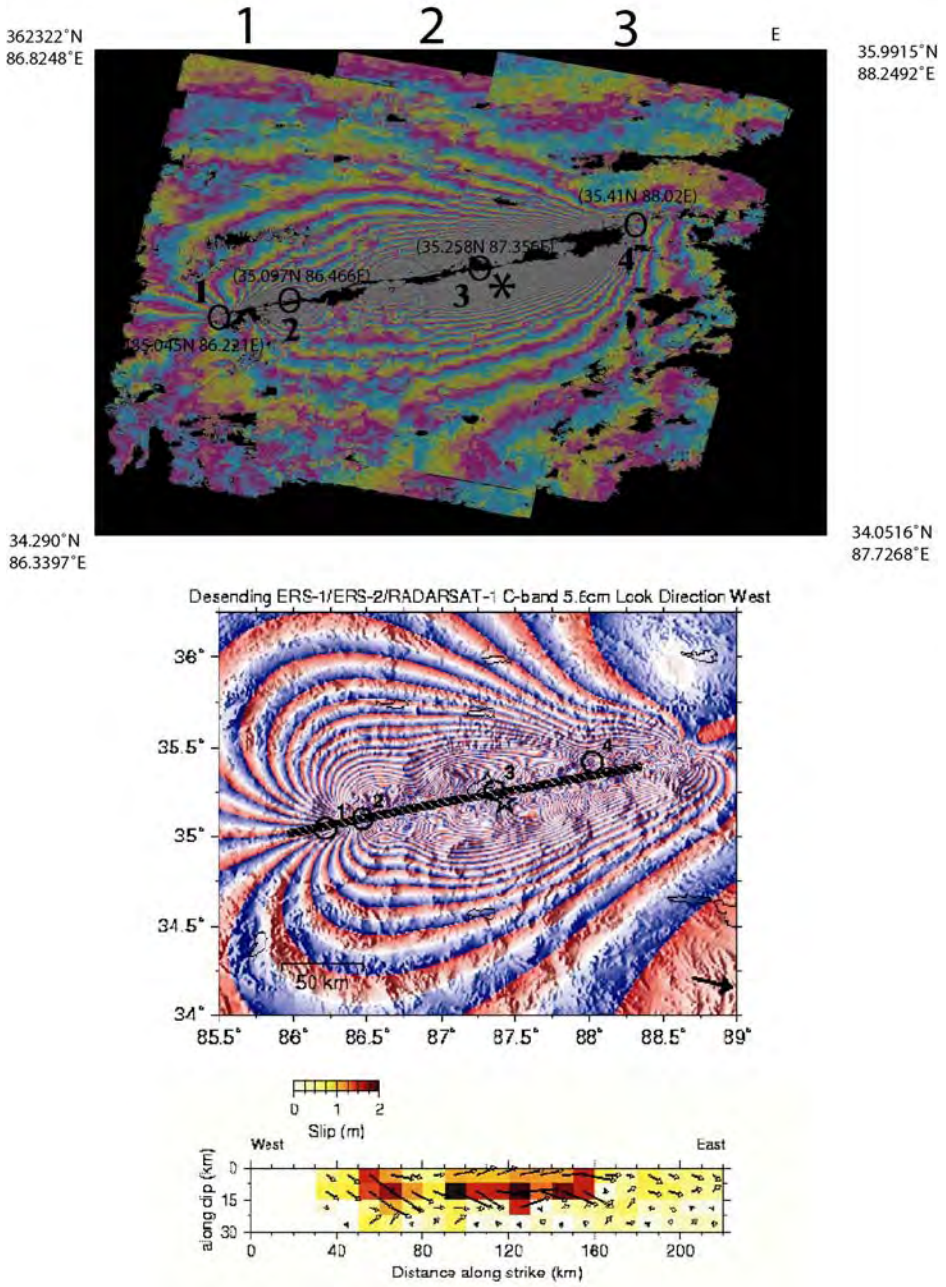

Figure 3. The top panel shows the geo-coded interferograms formed by joining three separate geo-coded interferograms obtained by processing satellite data to cover the entire Kunlun fault. The middle panel shows predicted interferogram using the slip model (bottom panel) obtained by inverting the teleseismic waveform alone. There is an overall match in the fringe pattern match seen in the observation.

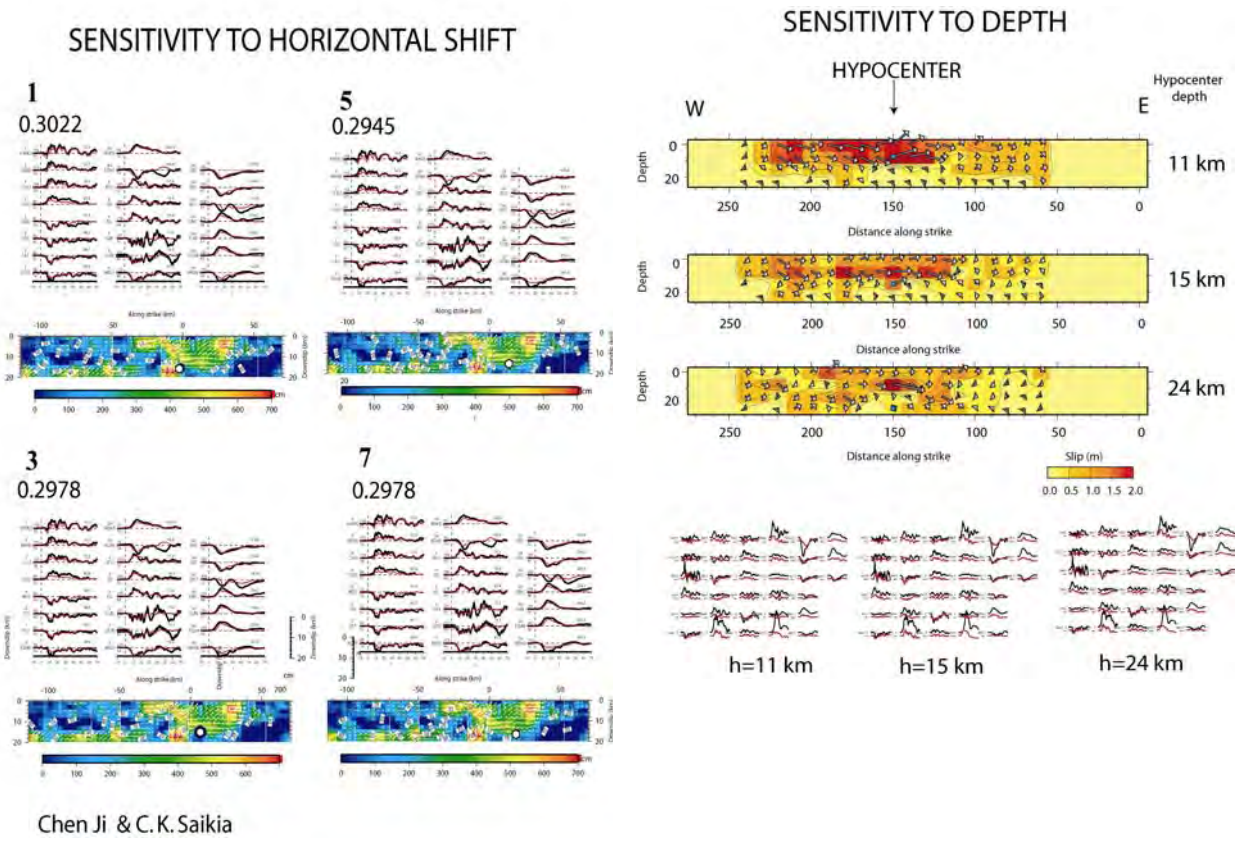

Figure 4. Sensitivity analysis of the teleseismic waveforms to various locations of the hypocenter. The left panel shows the comparison of the observed (black lines) and predicted (red lines) seismograms when the hypocenter was placed at a fixed depth, but at different locations along the strike of the fault. For each case, both InSAR deformation and teleseismic waveforms were jointly inverted. The right panel shows the same for the variation only in depth, but for the teleseismic data. Clearly, teleseismic waveform fit alone cannot distinguish one set of data comparison to the other set of the data comparison. However, the case 5 (left panel) appears to be the global minimum, which is obtained based on the objective function discussed in Saikia et al. (2004).

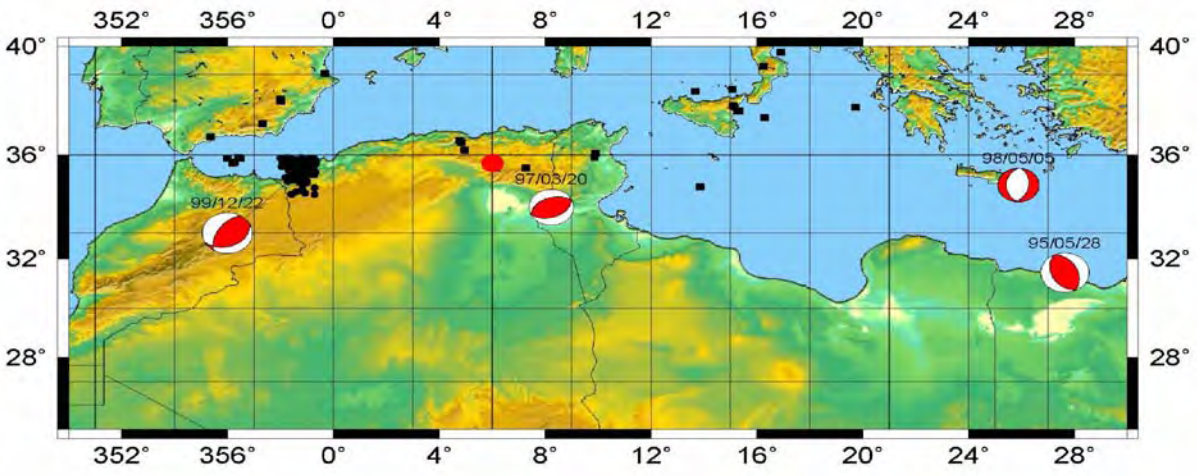

Figure 5. We processed satellite data for events lying within Northern Africa. Of the four events analyzed here, we were able to identify surface deformation in the case of two events. As expected, these events are shallow. These shallow depths were confirmed by modeling both seismic and InSAR data separately.

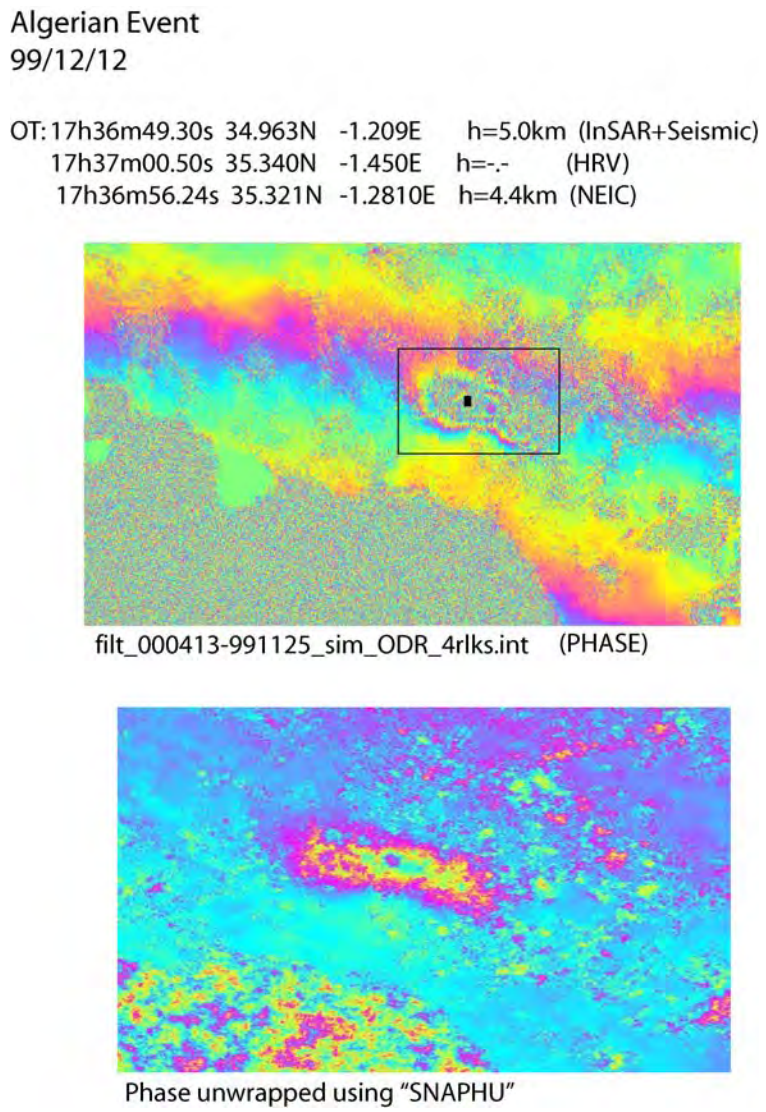

Figure 6. Interferogram processed using the satellite data for the December 12, 1999, Algerian earthquake. It was difficult to unwrap this interferogram by the routine ROI_PAC phase unwrapping schemes. We used a separate code "SNAPHU" to unwrap the phase, which is shown in the bottom panel

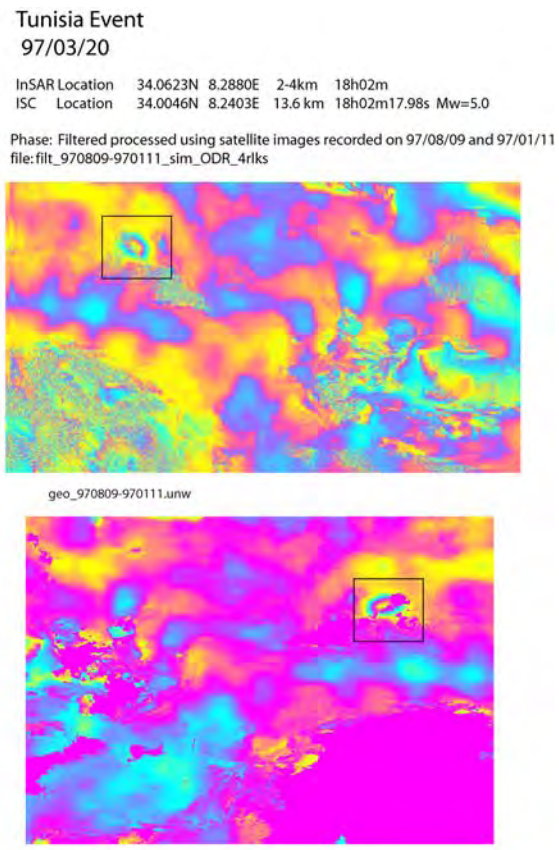

Figure 7. Two geo-coded interferograms for the March 20, 1997, Tunisia event processed using the satellite data acquired from EURIMAGE. The event can be seen in both the interferograms. The DEM was used from the SRTM database.

SEISMIC SOURCE LOCATIONS AND PARAMETERS FOR SPARSE NETWORKS BY MATCHING OBSERVED SEISMOGRAMS TO SEMI-EMPIRICAL SYNTHETIC SEISMOGRAMS

David H. Salzberg, Karen E. Votaw, and Margaret E. Marshall

SAIC Ocean Sciences Division

Sponsored by Air Force Research Laboratory

Contract No. FA8718-05-C-0019

ABSTRACT

The purpose of this study is to demonstrate the feasibility of full-waveform earthquake location using semi-empirical synthetic waveforms and received data from two or more regional stations.

Matching observed waveforms with synthetic waveforms has been used for some time in ocean acoustics to provide robust tracking of underwater sources in bearing, range and depth using synthetic pressure fields (e.g., Baggeroer et al., 1993). In such matched field processing, the pressure time series recorded by a dense array of hydrophones is steered using the synthetic pressure field predicted for a known environment. This approach is ideally suited for the ocean environment since the medium properties are well constrained. In contrast, the properties of the solid earth are not known at the detail required to perform matched field processing on seismic arrays for source location on a global scale. Matched waveform processing for seismic source locations has only been successfully applied when the overall velocity is well constrained (e.g., Pulliam et al., 2000).

Our method overcomes the uncertainty in the velocity models by generating semi-empirical synthetic seismograms. Empirical and semi-empirical approaches for modeling waveforms have been used to model waveforms from large events using smaller events as Green's functions (Wu, 1978). However, this approach breaks down when the two events are neither co-located nor have similar mechanisms. Others use semi-empirical synthetic seismograms, i.e., synthetic seismograms convolved with empirically determined source time functions, to estimate the ground motion of hypothetical events to assess earthquake hazards (e.g., Summerville et al., 2000). Salzberg (1996) developed a semi-empirical technique for fundamental mode surface waves which allows synthetic seismograms to be computed when the reference event is at a different location and has a different mechanism.

Our approach is to find the semi-empirical synthetic seismogram computed that best matches the observed seismic waveforms across a dense grid of possible locations. For each grid location, two or more waveforms are compared for a known moment tensor using the semi-empirical synthetic waveforms. The resulting minimum in the residual at the grid points yields the optimal location.

OBJECTIVE(S)

The objective of the research is to provide a method that gives accurate locations and source mechanisms using a sparse regional network when two or more seismic stations record the event. Tests using synthetic waveforms indicate that location accuracy on the order of 300-500 km^2 and depth uncertainty of less than 5 km can be obtained with recordings from only two stations low pass-filtered at 0.5 Hz. Since the fundamental constraint in matched waveform processing is the increasing incoherence between the complete waveforms with distance, sensor separation can be used to simulate event separation. Thus, examining full waveform correlations from a seismic array should provide a separate estimate of the ability to resolve the source location.

Methodology

SAIC is implementing a matched waveform approach to locate seismic events using a sparse regional network.

Matching observed waveforms with synthetic waveforms has been used for some time in ocean acoustics to provide robust estimates of underwater source locations in range, bearing and depth (Baggeroer et al., 1993) using synthetic pressure fields. In such matched field processing, the pressure time series recorded at each element of a tightly spaced an array of hydrophones correlated with the synthetic pressure field. The variation is the wave field resulting from interference patterns may be unique to the source location. By searching over a grid of potential sources, the optimal source location is identified by the maximum in correlation. This approach is ideally suited for the ocean environment since the medium properties are well constrained.

In contrast, the properties of the solid earth are not known at the detail required to perform matched field processing on seismic arrays for source location on a global scale. However, matching synthetic waveforms has been effectively applied in seismology to techniques such as inversion of the source and inversion of velocity models (Burdick and Langston, 1977). Waveform matching for source properties has been limited to regions with well constrained velocity models such as teleseismic body-waves which travel mostly in the lower mantle (Langston, 1981), long period surface waves (Romanowicz, 1981), and normal modes (Dziewonski et al., 1981). In these three examples, most of the energy propagates within the lower mantle. However, matched waveform processing for source locations, has only been successfully applied when the overall velocity is well constrained (Pulliam et al., 2000).

SAIC‘s method overcomes the uncertainty in the velocity models by generating semi-empirical synthetic seismograms. Empirical and semi-empirical approaches for modeling waveforms have been used to model waveforms from large events using smaller events as Green’s functions (Wu, 1978). This approach, however, breaks down if the two events are neither co-located nor have similar mechanisms. Others (e.g., Summerville et al., 2000) use semi-empirical synthetic seismograms, i.e., synthetic seismograms convolved with empirically determined source time functions, to estimate the ground motion of hypothetical events to assess earthquake hazards. Salzberg (1996) developed a semi-empirical technique for fundamental mode surface waves which allowed synthetic seismograms to be computed when the reference event is at a different source location and has a different mechanism. This technique provided coherent surface-waves at periods as short as 15 seconds, and allowed for the determination of moment tensor source mechanisms for small events (M > 4.7).

SAIC’s approach is to find the semi-empirical synthetic seismogram computed across a dense grid of possible locations that best matches the observed seismic waveforms. For each grid location, two or more 3-component waveforms are inverted for the moment tensor using the semi-empirical synthetic waveforms. The resulting minimum in the residual (χ^2 norm) from the moment tensor inversion results at the grid points yields the optimal location. .

Semi-Empirical Synthetics

When comparing the synthetic waveform with real data, a match is not possible unless the velocity model is well defined. Furthermore, errors in the synthetic waveforms translate into errors in the resolved location

and source parameters. Consequently, the primary limitation in matched waveform processing is the ability to produce high-fidelity simulations based on an idealized environmental model. One approach that can be used to improve the quality of the synthetic waveforms is to empirically determine the propagation portion of the synthetic waveform, yet still use the theoretical excitation (Salzberg, 1996; Velasco et al., 1994). These semi-empirical Green's Functions can be used to characterize the seismic wavefield recorded from sources in a reasonably homogeneous source region at a seismic station or array.

Semi-empirical Green's Functions are unnecessary if the source-to-receiver velocity structure is known perfectly, as full waveform synthetic seismograms are sufficient for matched waveform processing. However, only high-quality approximations of the velocity model can be determined. As such, any synthetic waveforms generated will only approximate the observed waveform written as:

$$observed\ (t) = u(t) * \Delta u(t) \tag{1}$$

where * represents the convolution operation, u is the synthetic waveform, and Δu is the mismatch of the data and synthetic represented as a filter. Δu corresponds to a systematic bias caused by model mismatch and an incoherent portion caused by random noise. The systematic portion of Δu can be written as:

$$\Delta u\ (\omega) = \Delta p(\omega) \cdot \Delta x(\omega) \tag{2}$$

where Δp is the mismatch caused by inaccuracies in the propagation, and Δx is the mismatch in the source excitation. The synthetic waveform, u, can be written as (Mendiguren, 1977):

$$u(r,\theta,h,\omega) = P(r,\omega) \cdot s(\omega) \cdot \sum_{i=1}^{5} H_i(\omega,\theta,h) \cdot m_i \tag{3}$$

where u is the far-field displacement, s is the source function, P is the propagation from source to receiver, H_i is the excitation function corresponding to m_i, and m_i is the ith element of the moment tensor. Transferring Equation (1) into the frequency domain, and combining with Equations (2) and (3) can be combined to represent the observed seismogram as:

$$observed(\omega) = P(r,\omega) \cdot \Delta p(\omega) \cdot \left[s(\omega) \cdot \sum_{i=1}^{5} H_i(\omega,\theta,h) \cdot m \right] \cdot \Delta x(\omega) \tag{4}$$

In this formulation, the propagation term is mathematically separable from the source terms which include the moment tensor, excitation, and time functions. After deconvolving the source terms from the reference waveforms of known source mechanism, location, and depth, the source-to-receiver propagation is isolated as:

$$P(r,\omega) = \frac{reference(\omega)}{\left[s(\omega) \cdot \sum_{i=1}^{5} H_i(\omega,\theta,h) \cdot m_i \right] \cdot \Delta x(\omega) \cdot \Delta p(\omega)} \tag{5}$$

If a second event occurs close to the first event, then it reasonable to assume that the propagation from the second event to the receiver will be similar to the first event. The reference waveform can then be transferred to the mechanism and depth of the new waveform by substituting the empirical propagation determined in Equation (5) into observed waveform formulation in Equation (4). This result gives new waveform as

$$new(\omega) = \frac{reference(\omega)}{\left[\tilde{s}(\omega)\cdot\sum_{i=1}^{5}\tilde{H}_i(\omega,\theta,\tilde{h})\cdot\tilde{m}_i\right]\cdot\Delta\tilde{x}(\omega)\cdot\Delta\tilde{p}(\omega)}\cdot\left[\sum_{i=1}^{5}H_i(\omega,\theta,h)\cdot m_i\right]\cdot\Delta x(\omega)\cdot\Delta p(\omega) \tag{6}$$

where ~ over a variable indicates the reference waveform.

Accurate knowledge of the source moment tensor and excitation terms implies that the Δx terms are approximately 1. Furthermore, since the two events are in close proximity and assumed to have the same propagation, or $\Delta\tilde{p} = \Delta p$. Thus the new semi-empirical synthetic waveform is:

$$new(\omega) = \frac{reference(\omega)}{\left[\tilde{s}(\omega)\cdot\sum_{i=1}^{5}\tilde{H}_i(\omega,\theta,\tilde{h})\cdot\tilde{m}_i\right]}\cdot\left[\sum_{i=1}^{5}H_i(\omega,\theta,h)\cdot m_i\right] \tag{7a}$$

$$new(\omega) = \frac{reference(\omega)}{synthetic_{reference}(\omega)}\cdot synthetic_{new}(\omega) \tag{7b}$$

Conceptually, the formulation in (7b) assumes that the mismatch between the reference waveform and its synthetic waveform is identical to the mismatch between the new waveform and its corresponding synthetic waveform.

Examples

Two clusters from central and southern California were studied. This region was selected due to the quality of the catalog locations (GT2 or better), and the large number of regional stations. This particular study focuses on the Parkfield and Hector Mine events using data from two regional stations (TUC and ELK). In preliminary tests, semi-empirical Green's Functions and derived synthetics were computed on a 0.02^o x 0.02^o x 2 km grid, assuming that the reported focal mechanisms were correct. The results are listed Table 1.

Parkfield Event of Sept. 30, 2004 18:54:28

The reference event used for Parkfield was the 29-Sep-2004 17:10:04 aftershock. The match between the semi-empirical synthetic waveforms computed at each grid pint (.02 x .02 degree grid, 2 km in depth) and the observed waveforms indicates the optimal source location (upper left). As shown in Figure 1, this location is within 5 km of the ground-truth location, and a significant improvement over a location 11 km from ground truth reported by the CTBTO IDC. However, the event was also within 8 km of the location of the reference event. The optimal depth at each horizontal grid point, shown in Figure 2, was determined by finding the depth of the minimum residual at each point. However, this shows considerable variability , at the minimum residual shown in the upper right, where the optimal depth of 12 km is close to the ground truth depth of 10.43 km. In Figure 3, the observed waveform shows an excellent agreement to the semi-empirical synthetic waveform ().

Hector Mine Event of October 16, 1999 17:38

Matching the waveforms the Hector Mine aftershock relative to another Hector Mine Aftershock of October 22 at 16:08:48 yields an optimal source location which is within 8 km of the ground-truth location even though the event was 50 km from the reference event (Figure 4). In this case, the CTBTO PIDC system did not locate this event.

CONCLUSION(S) AND RECOMMENDATION(S)

In this preliminary study, we have demonstrated the ability to accurately locate events by matching semi-empirical synthetic waveforms to observed data using two regional broad-band stations. Assumptions implicit in the analysis are that the source mechanism for the event is known and there is a reference event available to generate the semi-empirical synthetic waveforms. In both cases listed in the table below, the two-station optimal location was within 8 km of ground-truth. Of particular importance is that our solution was closer to the ground truth location than the IDC REB solution.It should be noted that we accomplished these results using a global earth structure and published source mechanisms. After incorporating more appropriate regional velocity models and refined source inversions, the accuracy and robustness of the technique should improve significantly.

RESEARCH ACCOMPLISHED

- Refined Methodology; tested in 3-D for Parkfield and Hector Mine Aftershocks
- Collected Data for 218 Events in Southern and Central California (Figure 5)
- Reviewed the available data to identify those with usable signals

Work in the next 12 months:

- Measure the Group Velocity Curves or all reviewed waveforms
- Cluster the event to common group velocity curves at each station
- Define a set of master/reference events for each cluster
- Determine the 1-d path specific velocity models
- Generate Semi-Empirical Synthetics for the grid spacing
- Execute to grid search

ACKNOWLEDGEMENTS(S)

All waveform data was obtained from the IRIS DMC. The IDC event locations were from the SMDC Monitoring Research Web Page.

REFERENCE(S)

Aki, K. and P. G. Richard, (1980), *Quantitative Seismology: Theory and Methods, Volume 1*, W. H. Freeman and Company.

Baggeroer, A. B., W. A. Kuperman, and Peter N. Mikhalesky (1993), An Overview of Matched Field Methods in Ocean Acoustics, *IEEE Journal of Ocean Engineering*, 18: 401–424.

Dziewonski, A. M., A. T. Chou, and J. H. Woodhouse (1981). Determination of Earthquake Source Parameters from Waveform Data for Studies of Global and Regional Seismicity, *J. Geophys. Res.* 86: 2825–2852.

Herrmann, R. H. and C. A. Ammon, (2002) Computer Programs in Seismology: Surface Waves, Receiver Functions and Crustal Structure.

Kanamori, H., and J. W. Given (1982), Use of Long-Period Surface Waves for Rapid Determination of Earthquake Source Parameters 2. Preliminary Determination of Source Mechanisms of Large Earthquakes (M_S > 6.5) in 1980, *Phys. Earth and Planetary Int.* 30: 260-268.

Kennett, B., and Engdahl, E. (1991), Traveltimes for global earthquake location and phase identification, *Geophys. J. Int.* 105: 429–465.

Langston, C. A. (1981), Source Inversion of Seismic Waveforms: The Konya, India Earthquake of September 13, 1967, *Bull. Seism. Soc. Am* 71**:** 1–24.

Langston, C.A., and D. V. Helmberger (1975), A Procedure for Modeling Shallow Dislocation Sources, *Geophys. Journ. R. A. S*. 42: 117–130.

Lay, T. and T. C. Wallac (1995), *Modern Global Seismology*, Academic Press, San Diego, California.

Mendiguren, J. A. (1977), Inversion of Surface Wave Data in Source Mechanism Studies, *J. Geophs. Res.* 78: 889–894.

Patton, H. J. and G, Zandt (1980), Seismic Moment Tensors of Western U. S. Earthquakes and Implications fir the Tectonic Stress Field, *J. Geophys. Res.* 85: 821–848.

Press, W. H., B. P. Flannery, S. A., Teukolsky, and W.T. Vetterling (1986), *Numerical Recipes: The Art of Scientific Computing*, Cambridge University Press, Cambridge, England.

Pulliam, J. , C. Frohlich, and B. Phillips (2000), Single Station Event Location:
Epicentral Distance, Bearing, and Focal Depth, DOE Seismic Research Symposium.

Salzberg, David. H. (1996), *Simultaneous inversion of moderate earthquakes using body and surface waves: methodology and applications to the study of the tectonics of Taiwan,* Ph.D. Thesis, The State University of New York at Binghamton, Binghamton, NY.

Savage, B. J. Chen, and D. V. Helmberger (2003), Seismic Velocity Variations beneath the Southern Sierra Nevada and the Walker Lane, *J. Geophs. Res.* 108: 2325–2341.

Summerville, P. R. Graves and N. Collins (2000), Ground Motions for Site Response Estimates – 1906 Earthquake, Technical Report to the Pacific Earthquake Engineering Research Center.

Velasco, A.A., C.J. Ammon, and T. Lay (1994), Recent Large Earthquakes Near Cape Mendocino and in the Gorda Plate: Broadband Source Time Functions, Fault Orientations and Rupture Complexities, *J. Geophys. Research* 99: 711–728.

Wu, F. T. (1978), Prediction of String Ground Motion Using Small Earthquakes, *Proceedings of the 2nd International Conference on Microzonation,* National Science Foundation, San Francisco, CA, 701–704.

Table 1. The relocated event locations compared with catalog events.

Time	Name	GT Lat	GT Lon	GT Depth	WF Lat	WF Lon	WF Depth	Error	IDC Lat	IDC Lon
2004/09/30 18:54	Parkfield	35.9885	-120.5387	10.43	35.96	-120.54	12	3.2	36.0283	-120.4298
1999/10/16 17:38	Hector Mine	34.43	-116.252	N/A	34.36	-116.26	14	7.8	N/A	N/A

Figure 1. Map Minimum Residual for the Parkfield test Case

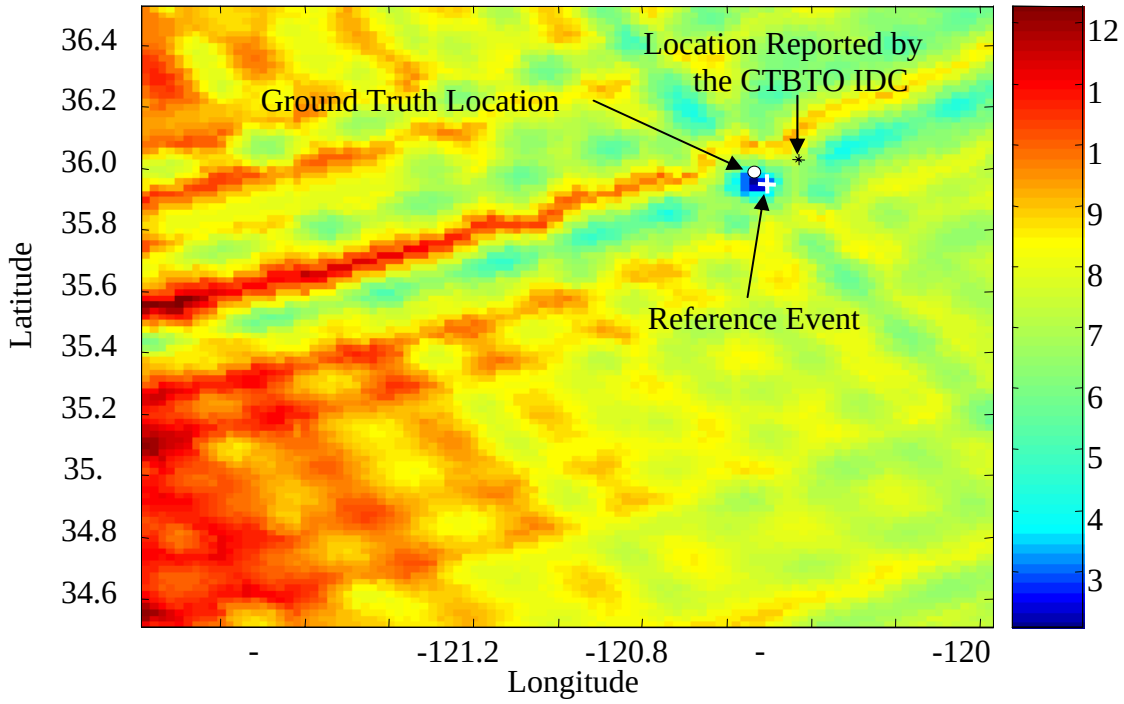

Figure 2. Residual vs. Depth for the Parkfield test Case

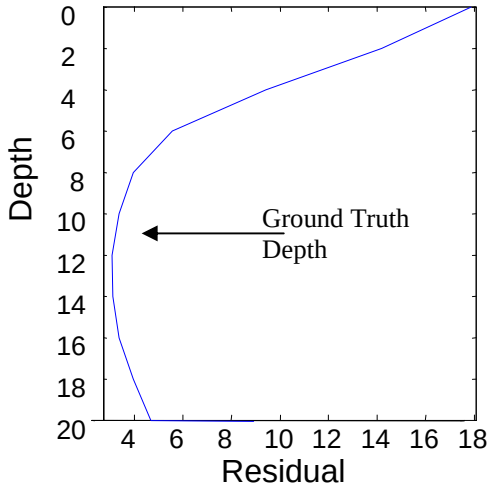

Figure 3. Comparison of Data and Synthetic for Parkfield Test Case

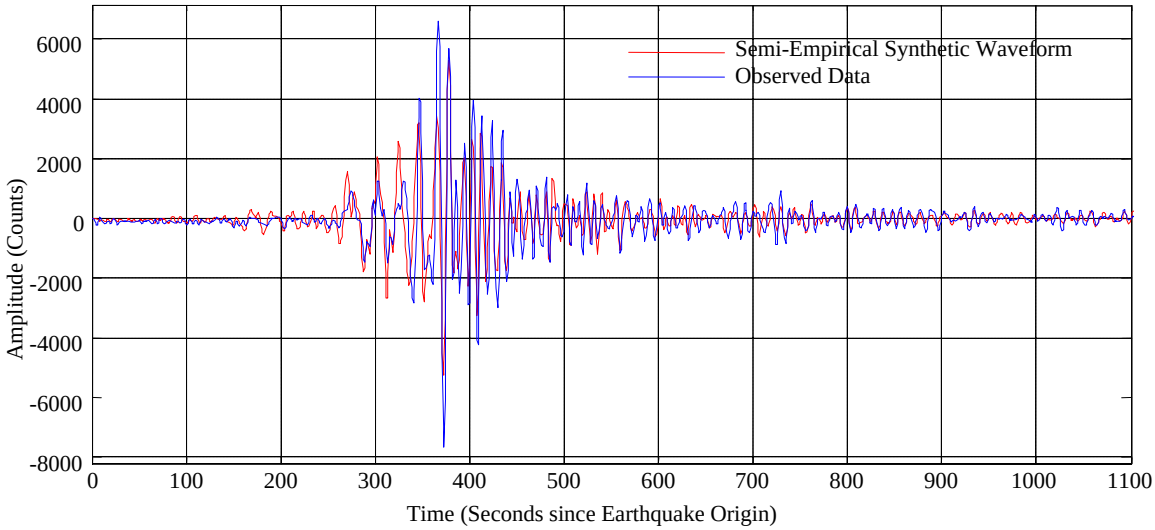

Figure 4. Map Minimum Residual for the Hector Mine test case

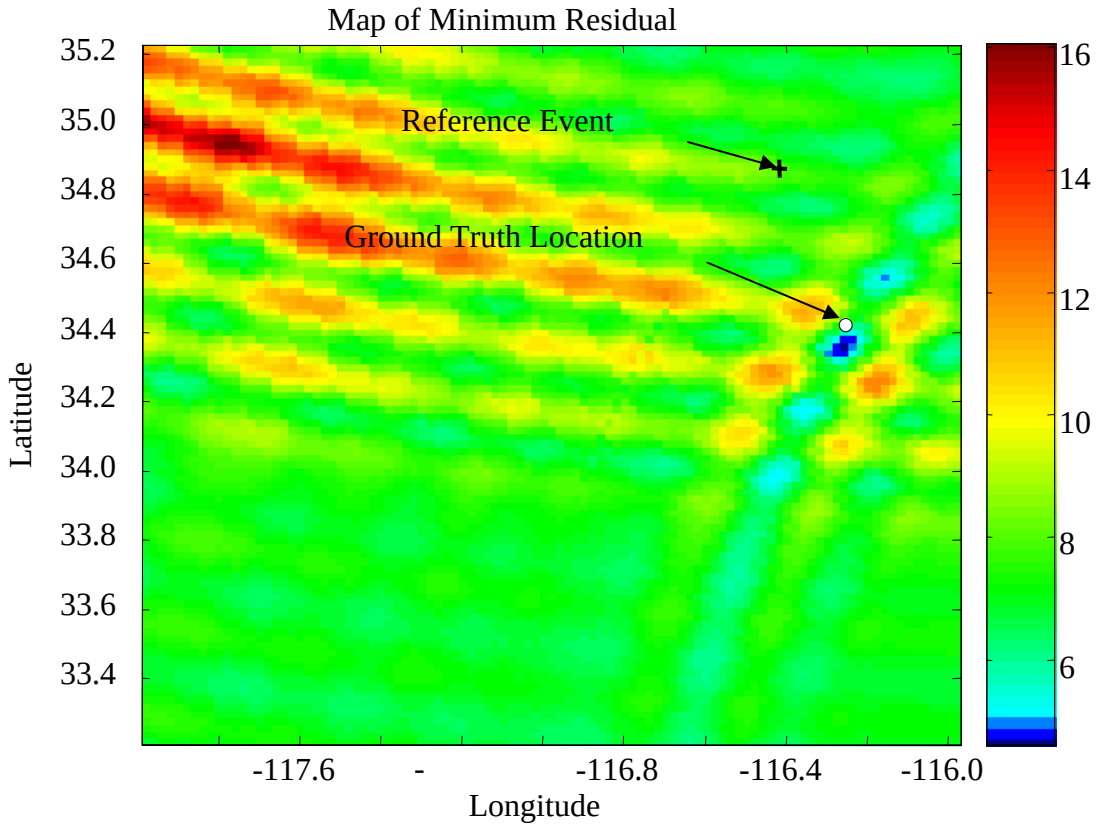

Figure 5. Event groupings in the study

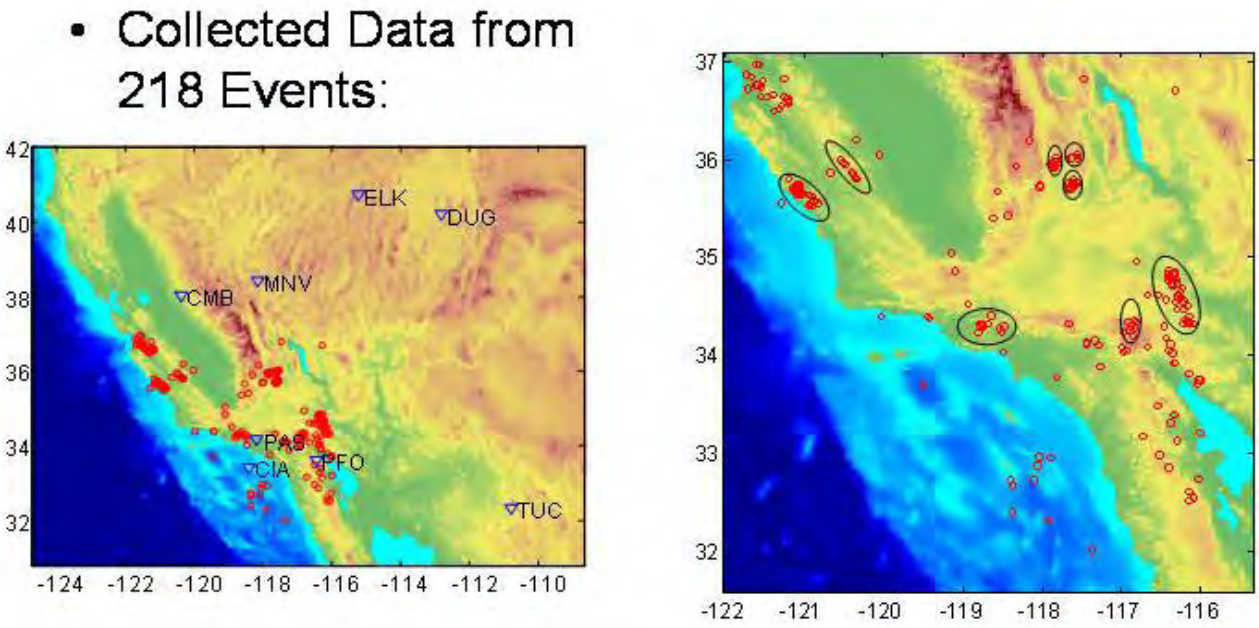

ADVANCES IN MIXED SIGNAL PROCESSING FOR REGIONAL AND TELESEISMIC ARRAYS

Robert H. Shumway

Department of Statistics, University of California, Davis

Sponsored by Air Force Research Laboratory

Contract No. FA8718-04-C-3010

ABSTRACT

This project is aimed at applying recently modified array signal processing techniques to the problem of detecting and estimating mixtures of signals observed on teleseismic and regional arrays. We are developing new techniques for enhancing both signal detection and estimation of azimuth and phase velocity parameters. In particular, we seek an automated detection procedure that sequentially isolates signals in an unknown mixture and provides estimators and confidence intervals for both the propagation parameters and the number of signals.

The methodology is an extension of the standard F-detector which is well known to be based on a nonlinear regression model that tests for the presence of a single signal as a function of slowness parameters. Formulating the multiple signal model as a test of hypothesis for the presence of the most recently added signal, we are able to develop a sequential procedure analogous to stepwise multiple regression by adding signals until no further additions are statistically significant. Both the sequential F-tests and versions of AIC and squared error are monitored to arrive at the final model. A frequency domain bootstrap procedure provides estimators for the standard errors of the estimated velocities and azimuths of the component signals.

Current tests of the methodology have focused on a verifiable mixture of two simultaneously occurring earthquakes observed at the United States Atomic Energy Detection System (USAEDS) long-period seismic array in Korea and a contrived short-period mixture of two regional events. Conventional methods such as single-signal F, MUSIC and high resolution detectors arrive at the incorrect azimuths for this data whereas the multiple-signal F-detector finds the correct number of signals and identifies their propagation characteristics.

OBJECTIVES

This project is aimed at applying recently modified array signal processing techniques to problems involving single and multiple signals observed on teleseismic and regional arrays. We are focused on Topic 3 (Seismic Detection, Location and Discrimination) with particular emphasis on proposing "new techniques to enhance signal detection and parameter estimation (e.g., azimuth, phase velocity) in strongly heterogeneous media".

Specifically, we are developing the sequential F-statistic as a method for off-line or on-line processing of signals in the presence of possible interfering signals or noises. We are evaluating the statistical performance of the detectors as well as the accuracy of estimated velocities and azimuths of the component signals. Deconvolutions of the component signals will be included. The sequential method as well as current methods will be tested on a test-bed of data obtained from AFTAC to determine the best procedures for on-line detection and off-line analysis.

RESEARCH ACCOMPLISHED

Several algorithms such as the sequential F-detector considered here and the multiple signal characteristic (MUSIC) algorithm are available that offer promise for handling array data with low signal-to-nose ratios and contamination from interfering signals. In this project, we are investigating the performance of currently available algorithms on teleseismic and regional data containing mixed signals in order to demonstrate the superior performance of the sequential F-statistic. A sequential analysis of power using the F-statistic is employed that estimates the correct number of signals and their velocities and azimuths. This is contrasted with results using conventional f-k estimators that do not handle the mixed signal case.

Approaches to detecting signals on arrays all focus on the basic model that expresses the observed channel as sums of delayed signals and a unique noise process. The delays are functionally dependent on velocity and azimuth if the signals are propagating plane waves and this is the assumption that is usually made. Methods that are commonly in use for analyzing such data when a single signal is assumed to be present can be roughly categorized as (1) beam-forming and plotting the power as a function of slowness, which can be converted to estimators of velocity and azimuth, (2) beam-forming converted to an F-statistic by dividing by an estimator of the noise power (see Shumway, 1983, 1999, Shumway et al., 1999, Blandford, 2002,a,b) (3) Capon's estimator (see Capon, 1969), (4) Multiple Signal Characteristic (MUSIC)(Schmidt, 1979, Stoica and Nehorai, 1989) and (5) cross correlation (Tribuleac and. Herrin, 1997). Only the MUSIC estimator listed above seems to be at all appropriate for analyzing the mixed signal case.

In the first year of this contract, we have concentrated on developing the multiple signal F-detector as an improvement over conventional detectors such as those given above or the currently favored ratio of short term to long term mean squares (STA/LTA). Technical difficulties in applying the Cramer lower bound approach to getting the variances has necessitated the use of the frequency domain bootstrap (Paparoditis, E. and D.N. Politis, 1999) as an alternative. Software (mul_sig_sl, mul_boot_sl) now computes the detection results along with standard deviations and confidence intervals for velocity and azimuth from the bootstrap distribution for data containing an arbitrary number of signals. Empirical results indicate that the distribution is approximately normal but this is not necessary for the validity of the bootstrap confidence intervals. Analysis capabilities have been expanded to include the ability to generate simulated data containing multiple signals at varying signal-to-noise ratios using the software *array_sim*.

Two Examples

Conventional methods such as (1)-(5) above, have met with varying degrees of success when they have been applied in practice to cases where there are known interfering signals. We illustrate some of the pitfalls by considering the two events in Figure 1. The left panel of Figure 1 shows three of six channels containing a mixture of two simultaneously occurring earthquakes, one from the south of Africa and the other from the Philippine, observed at the USAEDS long-period seismic array in Korea. The correct back-azimuths for these events are 226 degrees and 198 degrees. Yet, simple time delay estimation for this event gives a back-azimuth of 203 degrees, which is close to

the second signal. A second example illustrates the simulation capability of the current software and shows a contrived mixture of two regional events, also observed at the Korean Seismic Array (KSAR). The right panel of Figure 1 shows the two component signals and the mixture of the two at azimuths 198 and 231 degrees with additive white Gaussian noise with standard deviation .05.

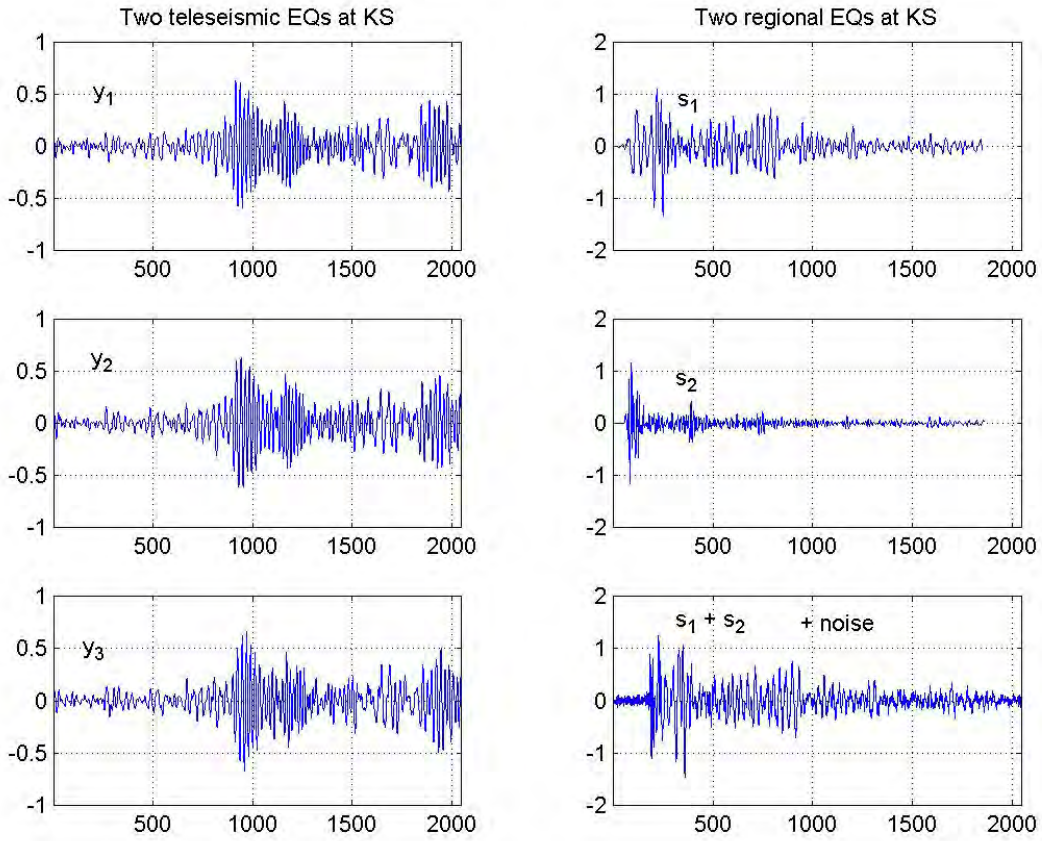

Figure 1. Left column contains three of six channels from a known mix of two EQ's at teleseismic distances. Right column has a single simulated channel of 18 total channels with a known mixture of two closely spaced regional events (s1 and s2) with added white noise.

Analysis with conventional detectors

Figure 2 shows estimated velocities and azimuths for the teleseismic mixture using the methods 1)-5). Note that methods (1) and (2), shown as (a) and (c), are based on the slowness coordinates that maximize beam power. The F-detector divides the beam power by an estimator of the noise power computed over the signal window and has that advantage as well of being distributed as an F-statistic that is independent of signal and noise nuisance parameters. The beam power, however, depends on the unknown noise spectrum and is only distributed proportionally to a chi-squared statistic, making it less suitable as a detector. Both statistics lead to an azimuth of 203 degrees which is well off the azimuths (226, 198) of the two known components. In this case the estimated azimuth is midway between the two known azimuths although this is not typical. Equating measured time delays from cross correlations to the theoretical slowness parameters and solving yields similar results, namely, an azimuth of of 204 degrees and a velocity of 3.7 km/sec.

The Capon (1969) estimator is based on the inverse of a quadratic form that matches the unknown wave-number vector with the inverse of the estimated spectral matrix. Both the Capon and multiple signal estimator (MUSIC) of

Schmidt (1979, see also Stoica and Nehorai, 1989) expressed in terms of the eigen vectors and eigen values of the spectral matrix and have expectations that get large when the correct slowness vector is matched. They are both

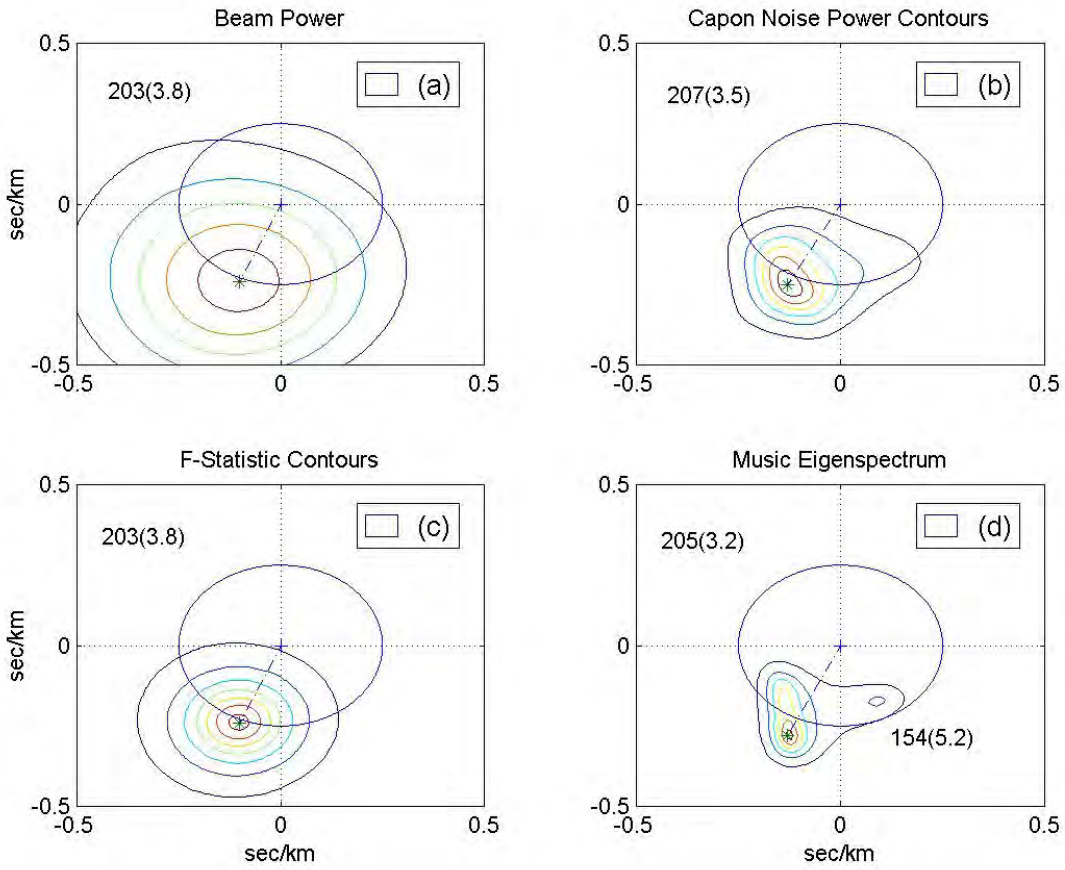

Figure 2. Slowness plots for four conventional detectors applied to the mixture of two long period signals known to be at azimuths 226 and 198 degrees. Estimated azimuth (velocity) pairs are given on each plot.

based on the assumption that the signal is stochastic and perfectly correlated with an additive uncorrelated noise. Again the estimators, shown as (b) and (d), are rather far off at azimuths of 205 and 207 degrees, a gain, essentially midway between the two correct values. Both show mild evidence of a second signal in the 150 degree range. This is of interest even though it is at the wrong azimuth because the sequential F-detector shown later on finds the two correct azimuths plus a third azimuth at 130 degrees, indicating that azimuth as a third statistically significant contributor. The MUSIC estimator here was based on assuming a two-signal source and was adapted to arrays by Shumway (2002) for the infrasound problem.

Analysis of the regional mixture on the right-had side of Figure 1 showed similar results although the single signal F-statistic focused on the first signal at 198 degrees, the correct azimuth of the second signal. The Capon and MUSIC detectors showed the primary maximum at 201 degrees and 197 degrees respectively, with some distortion indicating a possible additional signal at around the correct azimuth of the second signal at 226 degrees; the estimated velocities of 9.6 and 6.1 obtained with the MUSIC estimator were somewhat off. Hence, the simulated data gave a better result for the MUSIC detector and we conclude that this estimator offers some promise. Measured time delays gave an azimuth of 199 degrees and a velocity of 7.9 km/sec, focusing again on the first signal.

Analysis with the multiple signal F-detector

The analysis of multiple signals involves considering a succession of nonlinear regression models written in the frequency domain with parameters expressed in terms of slowness. Beginning with the single signal model with an estimated set of slowness coordinates, we consider an alternative model with two signals. The likelihood ratio test for a two-signal model against a single-signal model yields a monotone function of an F-statistic. The numerator is the difference between the error power under the two-signal model and the error power under the single signal model and represents the reduction in power possible from the added signal. This reduction is scaled by the noise power under the full model and a function of the number of parameters and the error degrees of freedom. The sequential fitting of more signals continues one at a time until no more added signals are statistically significant. The final estimated velocities and azimuths are those that obtain under the best model.

Standard errors and confidence intervals for velocities and azimuths are computed using the frequency domain bootstrap of Paparoditis and Politis (1999) adapted to the non-linear regression case under the multiple signal model. This involves reconstructing the frequency domain observations from the regression model evaluated at the maximum likelihood estimators for slowness. The residuals from this model will be roughly independent and constitute the basic re-sampling population. To reconstruct a bootstrap sample of the data, draw a sample of these residuals with replacement and use the non-linear regression model to reconstitute a pseudo-sample of the observed data. The estimated and velocity and azimuth computed from this pseudo-sample constitute the firs pair of estimated parameters. Repeat the above procedure a large number of times (500) and retain the estimators. The sampling distribution of these estimators yields the standard deviations and the 95% confidence intervals shown in Tables 1-4 below.

Table 1. Analysis of Power for long period mixture. Sequential F-Tests.

Source	Added Power	F-Statistic	P-Value	% Power
First Signal	396	35.8	0	86
Second Signal	43	4.9	.0000	95
Third Signal	14	2.5	.0003	98
Fourth Signal	3	0.5	.1183	99

Table 2. Estimated velocities and azimuths for single-signal and best model for long period mixture. True azimuths are 226 and 198 degrees respectively. Confidence intervals are from the bootstrap distribution.

Model	Azimuth(Velocity)	Standard Errors	95% Confidence Intervals
Single Signal	203(3.85)	1(.04)	(200, 206) (3.8, 3.9)
Signal 1	200(3.5)	2(.05)	(196, 203) (3.4, 3.6))
Signal 2	223(3.9)	2(.05)	(218, 228) (3.8, 4.0)
Signal 3	130(4.0)	2(.05)	(125, 133) (3.8, 4.1)

Tables 1 and 2 show the results of the sequential F-tests applied to the long period event and give the confidence intervals resulting from the best model. Note that the first signal identified at azimuth 203 degrees accounts for 85% of the total power and still gives an estimated azimuth midway between the two known azimuths of the mixture. The F-detector is highly significant. Adding a second signal to the model increases the percentage of power accounted for substantially and still yields a highly significant F. Testing for the third signal again produces a highly significant F-statistic and increases the power accounted for to 98%. Finally, testing for a fourth potential component accounts for a minimal increase in power and the P-value of about .12 is not significant at any useful level. Table 2 shows the estimated azimuths for the three component signals as 200, 223, and 130 degrees. The first two match up well with the known values but the third has not been identified from alternate records as a real seismic signal. Possibly, this third signal is a coherent noise source, and we have not investigated pure seismic noise sources for this phenomenon. A second concern is the small size (6 elements) of the array in relative to the large number of potential signals.

Tables 3 and 4 below give the comparable results for the regional mixture. Here, the two signals known to be present come in strongly at reasonable azimuths (199, 229) and the confidence intervals include the true values. The first two signals account for 99% of the power and the addition of a potential third signal leads to a non-significant F-statistic with a P-value of .32.

Table 3. Analysis of Power for regional mixture. Sequential F-Tests.

Source	Added Power	F-Statistic	P-Value	% Power
First Signal	482	378	0	96
Second Signal	17	28	.0000	99
Third Signal	.3	.3	.32	99

Table 4. Estimated velocities and azimuths for single-signal and best model for contrived regional mixture. True azimuths are 198 and 231 degrees respectively. Estimators shown are for a single signal model and for a double signal model.

Model	Azimuth(Velocity)	Standard Errors	95% Confidence Intervals
Single Signal	198.3(8.1))	.40(.02)	(197.5, 199.1) (8.04, 8.10)
Signal 1	199.2(8.2)	.2(.01)	(198.8, 199.6) (8.09, 8.12))
Signal 2	229.9(8.0)	.8(.04)	(228.4, 231.3) (7.94, 8.09)

CONCLUSIONS AND RECOMMENDATIONS

We have refined the statistical properties of the proposed sequential F-statistic testing procedure and shown that it will give correct velocities and azimuths in both known and contrived mixtures. The frequency domain bootstrap as applied to the nonlinear regression model will yield satisfactory estimates for variances and confidence intervals. Recommendations for additional research are summarized in 1-5 below.

1. **Deconvolution of component signals and testing on limited data:** Deconvolving the signal mixtures into their component parts should lead to improved estimators for magnitudes of the separate events. The softward *mul_decon* is being debugged and tested for this purpose.

2. **Further simulations:** We are continuing to apply the sequential F-detector and the velocity and azimuth estimation procedures to signals embedded in noise at different signal-to-noise ratios.

3. **Analysis of other events:** We are planning on applying the sequential F-statistic to larger test bases of teleseismic and regional data.

4. **Coherent noise sources.** Of interest is testing the single and multiple signal detectors on coherent noise sources and on mixtures of signals in the presence of coherent noise. The assumption at present is that most noise sources propagate at some velocity and are directional in nature. In this case, they will appear as additional signals and produce *false signals* similar to those plaguing the single-signal detectors.

5. **Online monitoring:** The sequential procedure is somewhat sensitive to the locations of the start values for nonlinear optimization of the multiple signal slowness vector. We need to investigate parameters such as these start values as well as lengths of time windows for a time varying online procedure. An automatic version of the current procedure would begin in the slowness quadrant corresponding to the likely location of the test and proceeds by searching adjacent quadrants first.

ACKNOWLEDGEMENTS

Gene Smart and Jon Clauter of AFTAC have graciously provided the data used in this analysis as well as valuable insights into potential methods of analysis. In particular, the previous work of Smart (1972, 1976) on FK analysis forms the basis for the sequential F-detector.

REFERENCE(S)

Blandford, R. R. (2002a). Detection and azimuth estimation by infrasonic arrays as a function of array aperture and signal coherence. *AFTAC-TR-02-007*, Air Force Technical Applications Center, Patrick AFB, FL 32925-002.

Blandford, R. R. (2002b). A plan of development for detection systems for seismic and infrasound arrays. *AFTAC-TR-02-005*, Air Force Technical Applications Center, Patrick AFB, FL 32925-002.

Capon, J. (1969). High-resolution frequency-wavenumber spectrum analysis. *Proc. IEEE* 57: 1408-1418.

Paparoditis, E. and D. N. Politis (1999), The local bootstrap for periodogram statistics, *J. Time Series Analysis* 20: 193-222.

Schmidt, R.O (1979), Multiple emitter location and signal parameter estimation. *Proc. RADC Spectral Estimation Workshop*, 243-258. Rome, Italy.

Shumway, R.H.(1983), Replicated time series regression: An approach to signal estimation and detection. *Handbook of Statistics Vol. 3*, Chapt. 18, 383-408, Time Series in the Frequency Domain. D.R. Brillinger and P.R. Krishnaiah ed., North Holland.

Shumway, R.H., S.E. Kim and R.R. Blandford (1999). Nonlinear estimation for time series observed on arrays. Chapter 7, Ghosh ed. *Asymptotics, Nonparametrics and Time Series*, 227-258. New York: Marcel Dekker.

Shumway, R.H. (2002), Detection and location capabilities of multiple infrasound arrays. Final Scientific Report. *DTRA01-00-C0082*, Preprint available from author.

Smart, E. (1972), FKCOMB, A Fast General-Purpose Array Processor, *Seismic Array Analysis Center*, Teledyne Geotech, 20 December, 1972.

Smart, E. (1976), Linear high-resolution frequency-wavenumber analysis. PhD Dissertation, *Southern Methodist University*.

Stoica, P. and A Nehorai (1989), Music, maximum likelihood, and Cramer-Rao lower Bound. {\it IEEE Trans. Acoustics, Speech and Signal Processing}, 37, 720-741.

Tribuleac, I. M. and E. T. Herrin (1997), Calibration studies at TXAR. *Seis. Res. Lttrs* 68: 353-365.

Pn TOMOGRAPHY AND LOCATION IN EURASIA

Lee Steck[1], Scott Phillips[1], Charlotte Rowe[1], Michael Begnaud[1], Kevin Mackey[2], Kazuya Fujita[2], and Hans Harste[1]

Los Alamos National Laboratory[1] and Michigan State University[2]

Sponsored by National Nuclear Security Administration
Office of Nonproliferation Research and Engineering
Office of Defense Nuclear Nonproliferation

Contract No. W-7405-ENG-36

ABSTRACT

We are exploring the use of Pn tomography for improving seismic event location in Eurasia. Toward this end, we have developed a new approach based on travel-time differences for two stations recording the same event. The premise of the station-differencing method is that by using travel-time differences among station pairs, the effect on the inversion of location errors inherent in the bulk of seismic bulletin origins can be significantly reduced. This permits the use of events previously discarded due to large location uncertainty, providing additional needed travel-time constraints in areas with sparse data coverage. The ability to include these lower-quality events in the inversion significantly expands our available constraints and enhances the quality of the tomographic results. We have applied our method to the preliminary Annual Bulletin of Chinese Earthquakes (ABCE), yielding a map of Pn velocity perturbations and station delay terms. This map is similar in character to earlier, single-ray tomography results, although the perturbations from our differential method tend to be more smoothly varying within tectonic provinces. Preliminary location tests using the tomographic Pn results show improvement over IASPEI91-based locations on the order of 30%. We intend to compare travel times from our study to those of previous research efforts to assess relative strengths of different approaches. We also plan to extend our study by applying our new method to the Michigan State University (MSU) eastern Russia database. Station differencing can also be used to perform quality control on seismic catalogs themselves, helping to identify bad phase arrival picks, stations with intermittent timing errors, and other sources of erroneous travel-time information. Results from an inversion for timing errors reveal questionable performance for some ABCE stations, as well as 10, 20, and 60 s timing residuals that may arise from typographical errors.

OBJECTIVE(S)

The objectives of this study are to improve location calibration through the use of velocity models derived from Pn tomography and to develop methods for catalog quality control. Our approach in both cases is based on the use of station differencing of travel-time residuals, implemented to extract useful information from plentiful but poor quality ground-truth data.

RESEARCH ACCOMPLISHED

Interstation Arrival Time Differences

The premise for our work is that the difference between regional arrival times from one seismic event to a pair of receivers is insensitive to source location (Figure 1). Therefore, poorly located events may still provide useful information on regional seismic wave propagation. This premise is subject to some geometric constraints, such as the region between the two stations where sensitivity to location is high. Figure 2 illustrates the sensitivity to event location for a pair of stations in China. For this figure, event locations were perturbed in three dimensions using 200 realizations of 20 km Gaussian random noise. The sensitivity is plotted as the logarithm of the root-mean-square time differences between the true location and the perturbed locations. From this figure it is clear that there are large regions within regional distances where sensitivity to 20 km mislocation is low. The rings at 1700 and 2000 km correspond to triplications arising from gradient changes in the upper mantle. Interstation differences have been widely used to eliminate source effects from seismic studies, going back to Brilliant and Ewing (1954) for determination of Rayleigh wave group velocity and Aki et al. (1977) for teleseismic travel-time inversion for upper mantle structure. In this paper we present only a brief outline of our approach to inverting regional travel-time residual differences for Pn velocity. For full details, see Phillips et al. (2005).

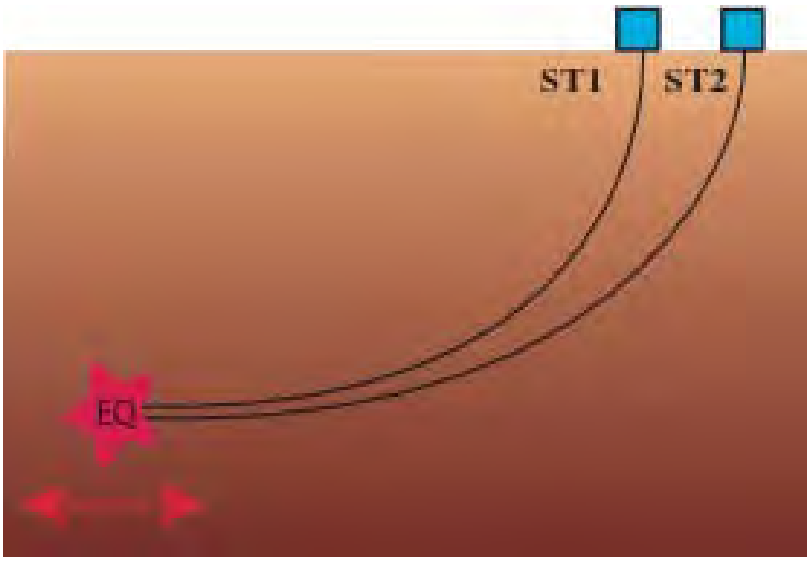

Figure 1. Cartoon showing the relationship between a regional seismic event and two observing stations. Interstation travel-time differences are insensitive to event mislocation, with some geometric constraints (after Rowe et al., 2003).

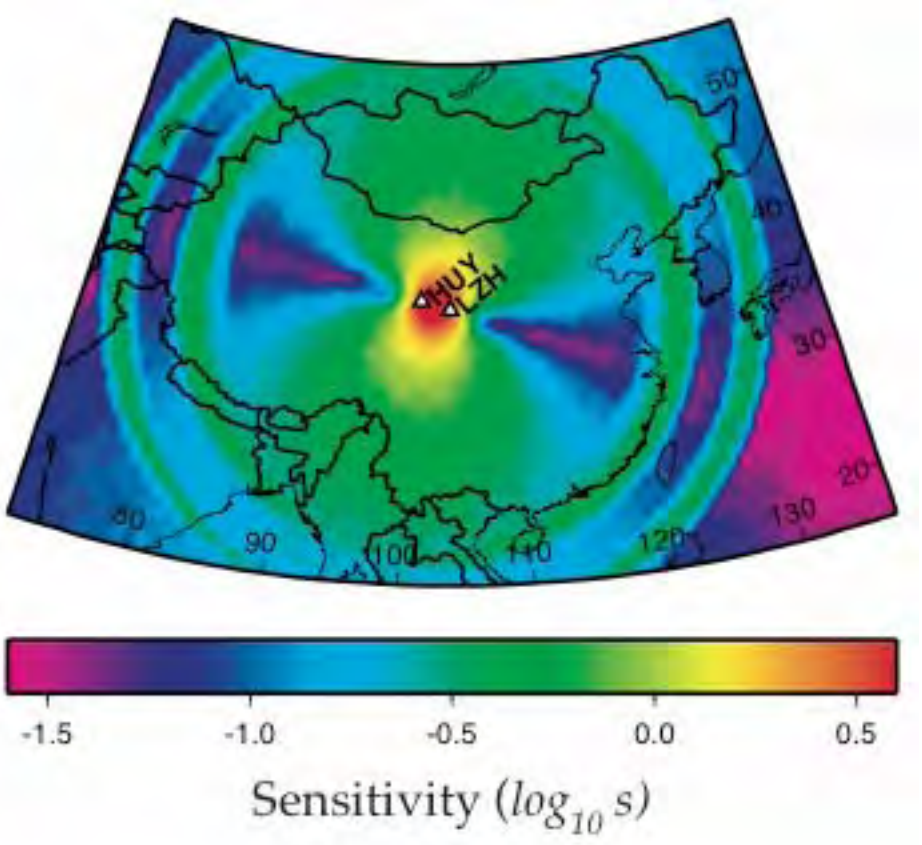

Figure 2. Sensitivity of interstation travel-time residual differences to geographic position for stations HUY and LZH in China.

Pn Tomography Results for China and Location Performance

To study the Pn propagation characteristics of China, we use the Annual Bulletin of Chinese Earthquakes (ABCE) (Lee et al., 2002). We began by relocating the ABCE catalog using IASPEI91. We then select data for events with depth < 50 km, distances between 1.6° to 20°, horizontal 95% confidence errors < 100 km, and travel-time residuals < 7.5 s. This resulted in nearly 1.5 million arrival time differences. To ensure stability, these data were limited to event locations whose sensitivity **S**, as shown in Figure 2, was less than or equal to 1.6s ($\log_{10}$**S**≤0.2s). Lastly, median smoothing was applied over a 0.5 ° grid, requiring at least 5 data points per cell. The resulting dataset consisted of 20,415 high quality time differences for 133 stations and 2819 events. An example of data for the station pair LZH/XAN is shown in Figure 3. These data are then inverted to produce Pn velocity perturbations and site terms for each station. Pn velocity variations and site terms are shown in Figure 4, top and bottom, respectively.

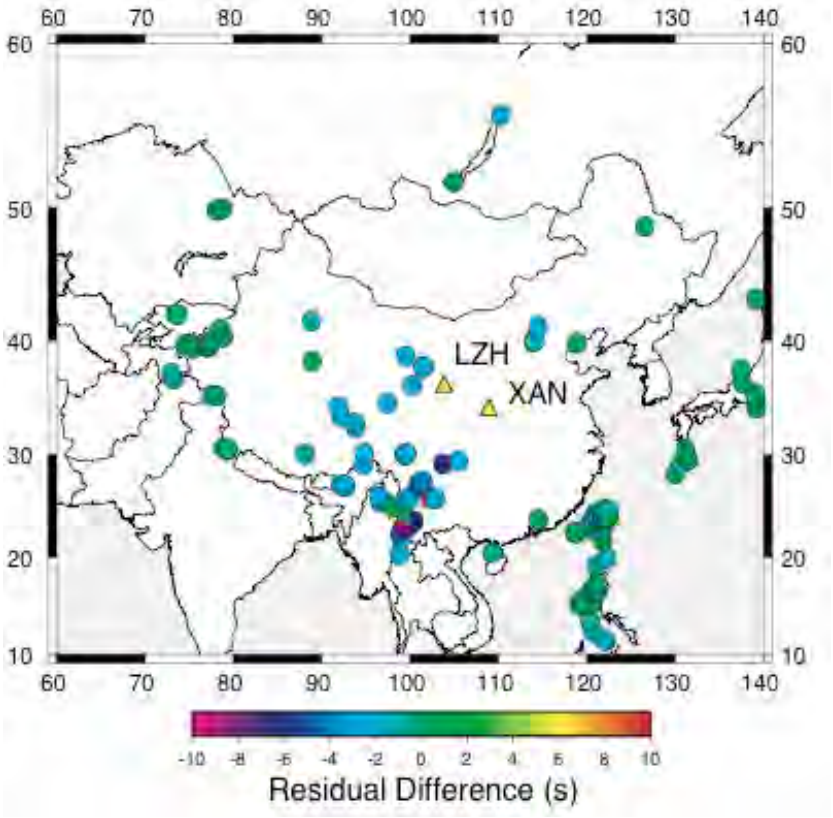

Figure 3. Travel-time residual difference data for station pair LZH/XAN (after Rowe et al., 2003).

The velocity variations we observe (Figure 4a) are qualitatively similar to those of previous studies (Hearn et al., 2004; Liang et al., 2004). Velocity is high across western China, particularly beneath the Sichuan (E), Tarim (F), Junggar(G), and Qaidam (H) basins, all areas of competent media associated with relatively undeformed, accreted micro-continents. Velocity is low across eastern and southeast China and Indochina, suggesting higher mantle temperatures. We also see low velocities in Mongolia, north-central and eastern Tibet (A), the Qilian Shan (C), and the western Tian Shan (B). Site delays are low (early) across east and southeast China and generally increase towards western China. Large delays (Figure 4b) seen for stations around the Bohai Sea (D) are not likely due to crustal thickness; rather, they appear to reflect upper mantle effects as noted by Hearn et al. (2004).

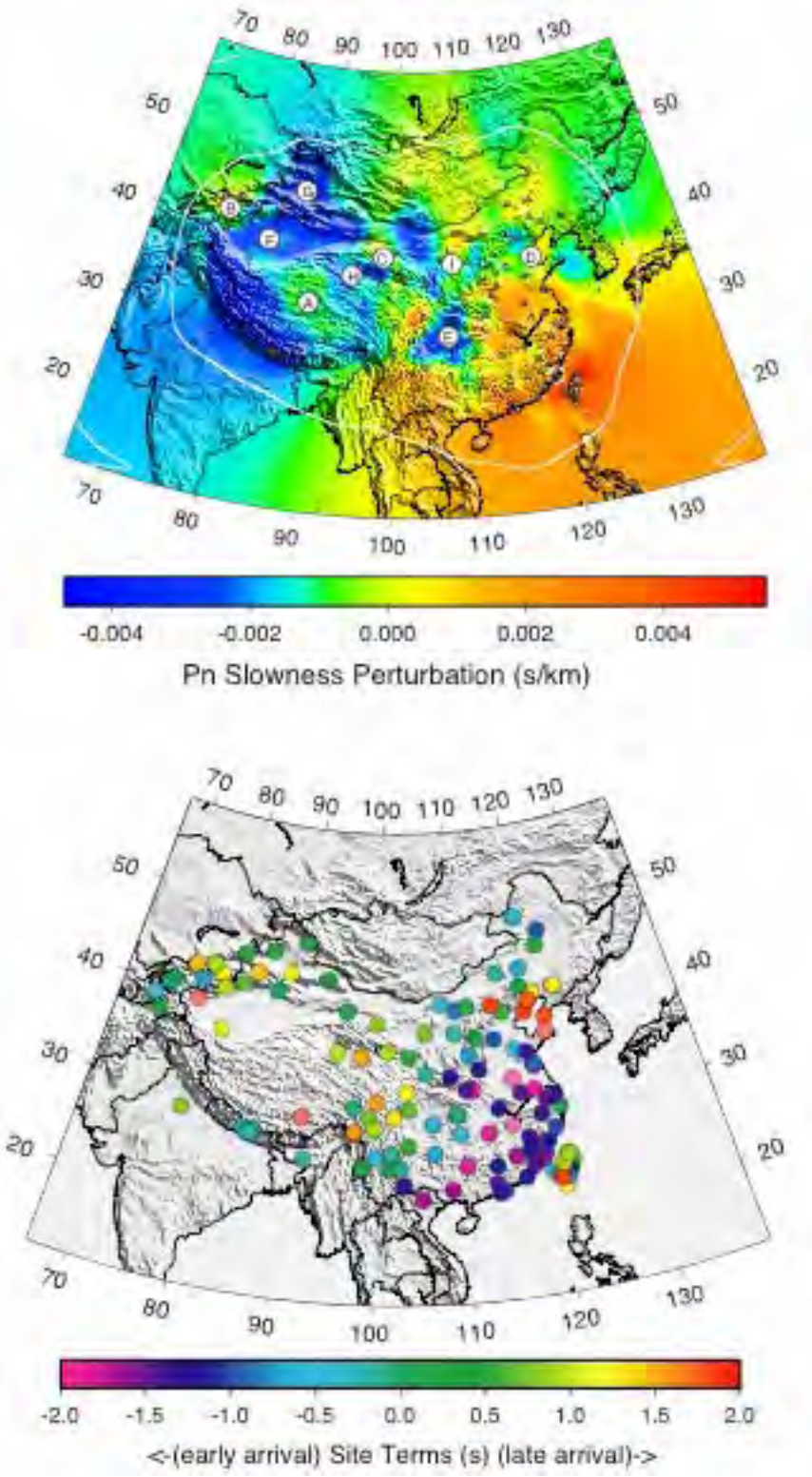

Figure 4. (Top) Pn velocity variations across China from tomographic inversion of travel-time differences. (Bottom) ABCE station site terms from the same areas (from Phillips et al., 2005).

To test the inversion results we integrated travel times calculated from the Pn perturbations and station corrections into the Knowledge Base Calibration Integration Tool (KBCIT) and created Pn travel-time correction surfaces for the ABCE stations. We then used these stations to relocate nuclear tests at the Chinese Test Site with and without corrections to the IASPEI91 model (Figure 5). Use of corrections results in a 30% improvement in location accuracy. There is a bias in both relocation sets that may reflect poor resolution in our model through Tibet, where station coverage is sparse. Future work in this area will involve using merged data for the China region from the National Nuclear Security Administration (NNSA) Knowledge Base, including as many stations and events as possible.

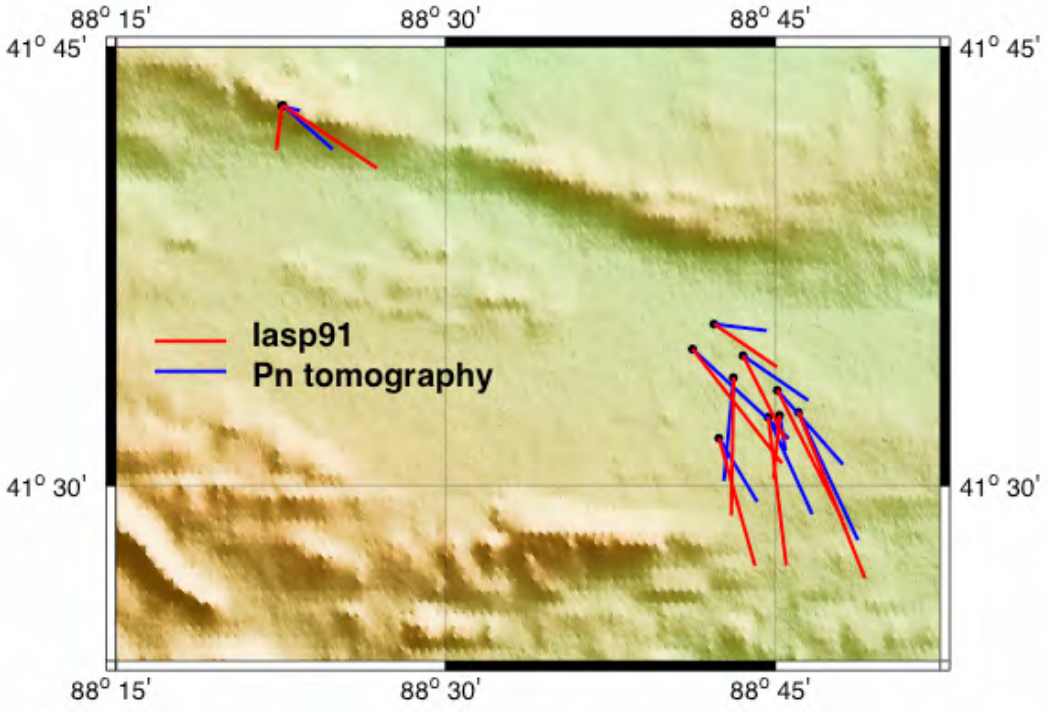

Figure 5. (Top) Pn velocity variations across China from tomographic inversion of travel-time differences. Black dots are satellite locations from Fisk (2002). Red lines connect uncorrected locations to the Fisk locations; blue lines are for the corrected relocations using Pn tomography results.

Pn Tomography of Eastern Russia – a Progress Report

We are beginning to compile a dataset for Pn tomography of the MSU Eastern Russia Database. We have identified over 100,000 event-station-station triplets that fall within 1.6° to 20° with depths < 50 km. These are for 53 stations and nearly 8200 events. Inversion runs are currently in progress and results should be available by the time of this year's Seismic Research Review.

Catalog Quality Control

In addition to its potential for improving tomographic images of velocity perturbations, travel-time differences can be used to assess the quality of travel times and station performance. An expected stable time difference that is anomalous relative to neighboring events indicates that one or both arrival times are poorly determined. We have developed a simple inversion that compares all stable pairs and assigns error estimates to individual arrival times. Results from this inversion are shown in Figures 6 and 7 (Rowe et al., 2004).

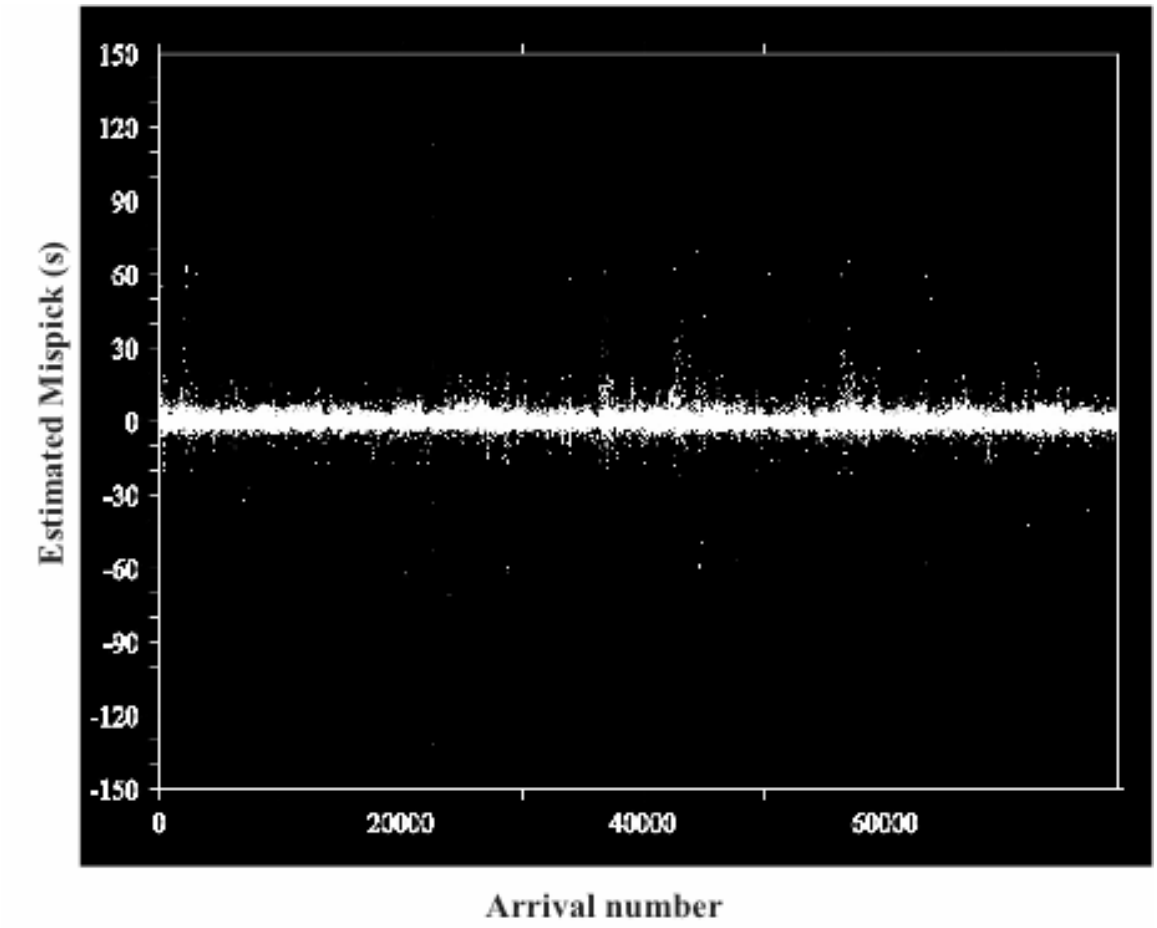

Figure 6. Inversion results for quality control of the ABCE catalog (from Rowe et al., 2004).

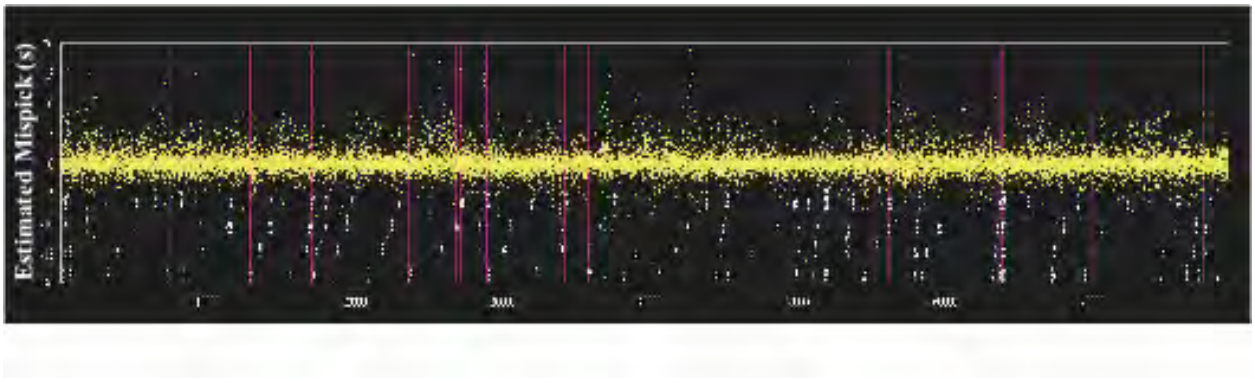

Figure 7. The same data as in the previous figure, but sorted by station and time with estimated mispick limited to +/- 20 s (from Rowe et al., 2004).

CONCLUSIONS AND RECOMMENDATIONS

We find that event/station-pair time differences have several valuable uses. This approach should be further investigated for both regional tomography efforts and for quality control studies of seismic catalog data. Correction surfaces from Pn tomography in China improve location accuracies at the Chinese test site by about 30% over those from the IASPEI91 global travel-time model.

ACKNOWLEDGEMENTS

Many of the plots in this document were made with Generic Mapping Tools (Wessel and Smith, 1991). Also, we thank Paul Richards for providing access to the ABCE data.

REFERENCES

Aki, K., A. Christoffersson, and E. S. Husebye (1977), Determination of the three-dimensional seismic structure of the lithosphere, *J. Geophys. Res.* 82: 277–296.

Brilliant, R. M., and M. Ewing (1954), Dispersion of Rayleigh waves across the U.S., *Bull. Seismol. Soc. Am.* 44: 149–158.

Fisk, M. D. (2002), Accurate locations of nuclear explosions at the Lop Nor test site using alignment of seismograms and IKONOS satellite Imagery, *Bull. Seismol. Soc. Am.* 92: 2911–2925.

Hearn, T. M., S. Wang, J. F. Ni, Z. Xu, Y. Yu, and X. Zhang (2004), Uppermost mantle velocities beneath China and surrounding regions, *J. Geophys. Res.* 109: B11301, doi:10.1029/2003JB002874.

Lee, W. H. K., H. Kanamori, P. C. Jennings, and C. Kisslinger (Eds.) (2002), *International Handbook of Earthquake and Engineering Seismology* [CD-ROM], Elsevier, New York.

Liang, C., X. Song, and J. Huang (2004), Tomographic inversion of Pn traveltimes in China, *J. Geophys. Res.* 109: B11304, doi:10.1029/2003JB002789.

Phillips, W. S., C. A. Rowe, and L. K. Steck (2005), The use of interstation arrival time differences to account for regional path variability, *Geophys. Res. Letts.* 32: L11301, doi:10.1029/2005GL022558.

Rowe, C. A., W. S. Phillips and L. Steck, 2003, Relative constraints on correction surfaces for more effective use of low-order ground truth, *EOS Trans. Amer. Geophys. U.* 84: (46) Fall meeting Suppl., Abstract S21D-0332.

Rowe, C. A., W. S. Phillips and L. K. Steck, 2004, Differential travel-time residual analysis for improved site correction and catalog quality, and insights into laterally-varying earth structure in China / East Asia, *EOS Trans. Amer. Geophys. U.*, 85: (47) Fall meeting Suppl., Abstract S11B-1019.

Wessel, P. and W.H.F. Smith (1991), Free software helps map and display data, *EOS Trans. Amer. Geophys. Union* 72: 441, 445–446.

CRUSTAL AND MANTLE STRUCTURE BENEATH EASTERN EURASIA FROM FINITE FREQUENCY SEISMIC TOMOGRAPHY (FFST)

Ting Yang[2], Yang Shen[2], and Xiaoping Yang[1]

Science Applications International Corporation[1] and University of Rhode Island[2]

Sponsored by Air Force Research Laboratory

Contract No. FA8718-05-C-0017

ABSTRACT

An accurate, high-resolution 3-D earth model is crucial to the seismic calibration for nuclear monitoring. We use the newly developed Finite Frequency Seismic Tomography (FFST) approach to construct the crustal and mantle structure beneath eastern Eurasia. Traditionally, travel times of seismic waves are calculated based on the ray theory, which is valid strictly for infinite-frequency waves. Observed seismic waves, however, are finite frequency signals. As a result of scattering and diffractive effects, travel times of realistic finite frequency waves are sensitive to 3-D structure around the geometrical rays, and the travel time shifts caused by heterogeneities diminish gradually from the heterogeneities to receivers - a phenomena named the wave front healing. The ray theory ignores this ubiquitous effect of the propagation of realistic seismic waves. Tomographic inversions based on it, therefore, tend to underestimate the magnitudes of heterogeneities. The newly developed FFST utilizes the 3-D Born-Fréchet sensitivity kernels of the travel times of finite-frequency seismic waves. The new method accounts for the wave front healing, off-ray scattering and other non-geometrical diffraction phenomena, and significantly improves the resolution of the velocity heterogeneity.

In addition to the new methodology, we will use a more comprehensive data set than in previous studies to construct the new earth model beneath eastern Eurasia. We will collect data from the publicly accessible sources e.g., Incorporated Research Institutions for Seismology (IRIS), Global Seismographic Network (GSN), the Program for the Array Seismic Studies of the Continental Lithosphere (PASSCAL), and International Monitoring System (IMS) stations. Efforts will also be made to collect data sets from other networks in the region such as the Japanese Broadband Seismograph Network (F-net), the Japanese International Seismic Network (JISNET in Indonesia), and the Taiwan Broadband Seismic Network. Access to other unique sources including permanent and portable seismic stations throughout the study area further improves the station coverage over eastern Eurasia.

This is the beginning of a three-year effort to improve seismic calibration in eastern Eurasia. We will first develop a 3-D FFST velocity model using body waves, along with model uncertainties. Travel time corrections and modeling error surfaces will be derived and applied to relocating ground truth (GT5) events. The final model will be developed using joint body and surface waves. From the 3D velocity models, we will also simulate the full wave propagation in the transition zone. To facilitate data integration, a project database and a web-based tool are being implemented.

OBJECTIVES

We will develop a new generation of high-resolution P and S velocity models that are based on the recent wave propagation theory for realistic, finite-frequency seismic waves using both public and unique data sets. We will derive frequency-dependent travel time corrections and uncertainty estimates for eastern Eurasia, and validate the model and event location improvement using ground truth (GT) data. Three-dimensional (3D) full waveform simulations will be carried out to model wave propagation through the transition zone and seismic anisotropy.

RESEARCH ACCOMPLISHED

Previous Studies

Eastern Eurasia is one of the most tectonically complex regions in the world due to the India-Eurasia collision and subsequent extensive lithospheric deformation. While the evolution history of continental lithosphere has been well recognized (Briais et al., 1993), the fine structure associated with the complicated deformation in this region is far from clear, and deep mantle processes that accompanied shallower lithosphere deformations are poorly understood. An accurate, high-resolution 3D earth model for this region is needed to improve seismic calibration for nuclear monitoring. Efforts have been made in developing and applying regional and teleseismic models for this purpose (Johnson and Vincent, 2002; Antolik et al., 2003; Ritzwoller et al., 2003; Richards et al., 2003; Yang et al., 2004).

Many seismic imaging studies have already been conducted in Eastern Eurasia and adjacent west Pacific area. Most of regional studies covering a large area of eastern Eurasia are based on surface wave observations (e.g. Wu et al., 1994; Ritzwoller et al., 1998; Curtis et al., 1998; Zhu et al., 2002; Lebedev and Nolet, 2003). While there are extensive short–period body wave tomographic studies performed along the subduction zone of the pacific plate in western Pacific (Van der Hilst et al., 1991; Fukao et al., 1992; Windiyantoro and Van der Hilst, 1997; Bijwaard et al., 1998; Zhao et al., 2000), only limited body wave travel-time tomographic studies have been conducted within the eastern Asia continent. The resolutions in those studies were limited by the relatively sparse seismic stations in the earlier work (Liu et al., 1989), or only limited to small regional (Pei et al., 2005) and local (Liu et al., 1989; Xu et al., 2001; Huang and Zhao, 2004) areas. There are also several studies using Pn waves to obtain the crustal thickness and uppermost mantle structure beneath the great China region (e.g., Sun et al., 2004; Liang and Song, 2004).

Finite Frequency Seismic Tomography

Almost all global and regional tomographic models, including the ones for Eastern Eurasia, are based on the geometrical ray theory (e.g. Dziewonski, 1984; Grand, 1994; Van der Hilst et al., 1997), which assumes that the seismic waves have an infinite frequency band, and the arrival time of a body wave depends only on the velocity along the geometrical ray path between the source and receiver. In fact, observed seismic waves are finite frequency signals, and their travel times are sensitive to a 3-D volume around the geometrical ray and subjected to wavefront healing, scattering and other diffractive effects. As a result, the travel time shifts are affected by wavefront healing for velocity heterogeneities with dimensions smaller than the width of the Fresnel zone (Nolet et al., 2000; Hung et at., 2000; Baig et al., 2004), and tomography based on ray theory, therefore, tends to underestimate the magnitude of velocity heterogeneities. In contrast, the 3-D Born-Fréchet travel-time sensitivity kernels (Marquering et al., 1999; Dahlen et al., 2000; Hung et al., 2000; Zhao et al., 2000) account for the wavefront healing, off-ray scattering and other non-geometrical diffraction phenomena. By using waveform cross-correlation, the kernel can provide better measurements of the travel time shifts caused by velocity anomaly for finite frequency seismic waves. Thus the seismic imaging technology based on this 3-D sensitivity kernel can significantly improve the resolution of the velocity heterogeneity. The 3-D kernel theory has been successfully applied to regional (Hung et al., 2004; Shen and Hung, 2004) and global (Montelli et al., 2004) seismic tomography. A comparison of the velocity models beneath Iceland showed that the finite-frequency tomography significantly improves the resolution of the velocity structure beneath the Iceland hotspot (Hung et al., 2004).

The general formula for the inverse problem, after parameterization of the model function on a spatial grid of nodes, can be expressed as a concise matrix form for discrete inverse problem:

$$d_i = A_{il} m_l \qquad (1)$$

For teleseismic regional tomography, d_i represents the *i*th relative travel time delay, and m_l is velocity anomaly at the *l*th grid node. The difference between ray-based and kernel-based tomography is in A_{il}. In traditional tomography, A_{il} is the difference of the total path lengths throughout a specific volume that contributes to the *l*th node between the two arrivals in the *i*th paired relative travel time measurement. In 3-D kernel-base inversion problem, however, A_{il} is the differential value of the integrated volumetric kernels contributing to the *l*th node (Hung et al., 2004). In order to make the sparse equation solvable, the smoothness regularization is usually needed in the ray-based inversion problem. In finite-frequency seismic tomography (FFST), however, the 3-D broad Born-Fréchet kernel itself provides physical smoothness constraints. So, only a simple norm damping is needed to avoid the *ad hoc* smoothness enforcement.

In FFST, the relative travel-time delays are frequency dependent because seismic waves with different frequency contents sample different volumes of the velocity structure (Dahlen et al., 2000; Hung et al., 2004). To take advantage of the broadband nature of the seismic records, the broadband waveforms can be filtered into several narrower frequency band signals, each of which can constrain a different volume of the velocity heterogeneity, and therefore has different relative travel-time shifts. Figure 1 shows an example of frequency dependent relative travel-time delays at several GSN seismic stations in eastern Eurasia. Another advantage of this feature of FFST is the microseism and other noise having known frequency contents that can be easily isolated from the signals.

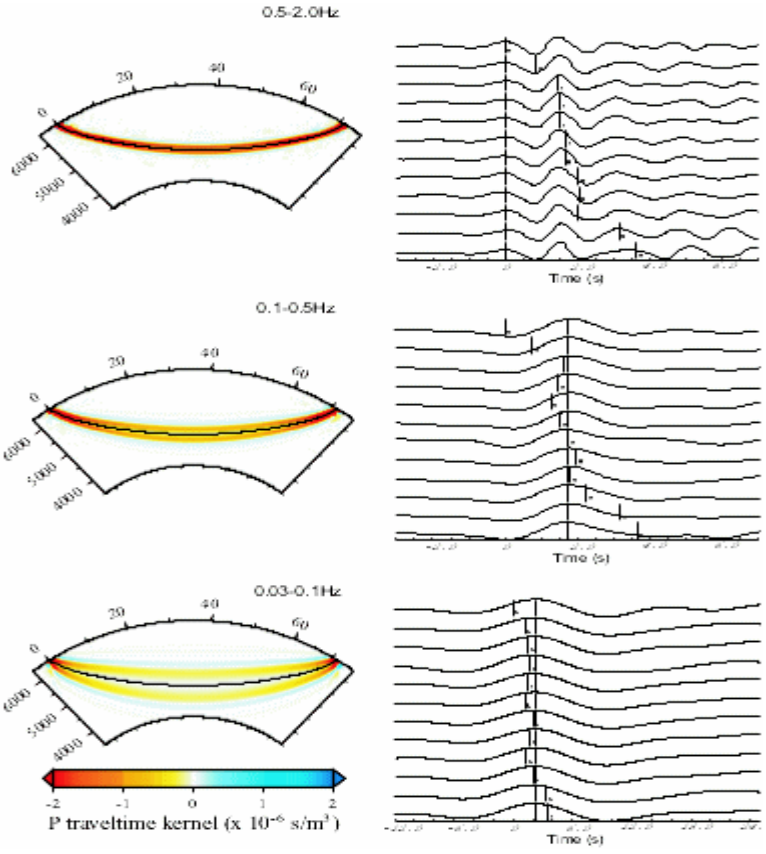

Figure 1. (Left) A comparison of Born-Fréchet kernels for travel-time of teleseismic P phases, measured by cross-correlation of the observed waveforms with the synthetics in three frequency bands: 0.5-2.0, 0.1-0.5 and 0.03-0.1 Hz. (Right) Example of frequency-dependent P arrivals observed at 12 GSN stations from one earthquake. Broadband pulses have been bandpass-filtered at the three frequencies. The waveforms are aligned according to the time picks of the multi-channel cross-correlation method. The vertical bars mark the relative travel-time shifts used to align the waveforms.

Data Set and Inversion

The resolution of seismic models depends on the underlying theory and the data sets used in inversion. In addition to the new seismic imaging technology that integrates realistic, finite-frequency body and surface waves in a self-consistent way, we will collect and utilize a more comprehensive data set than in previous studies to construct the new earth model beneath eastern Eurasia.

As the first step of the three-year effort, we are collecting data from IRIS, GSN, PASSCAL, and IMS stations, the Japanese F-net and JISNET and Taiwan Broadband Seismic Network, as well as unique sources including permanent and portable seismic stations throughout the study area. Figure 2 shows the stations in the study region with broadband data. So far we have obtained an initial data set of broadband waveforms for events in eastern Eurasia since 2000. It includes all GSN stations within the study region in 2000-2004, Taiwan stations in 2000-2004, and JISNET stations in 2000-2001.

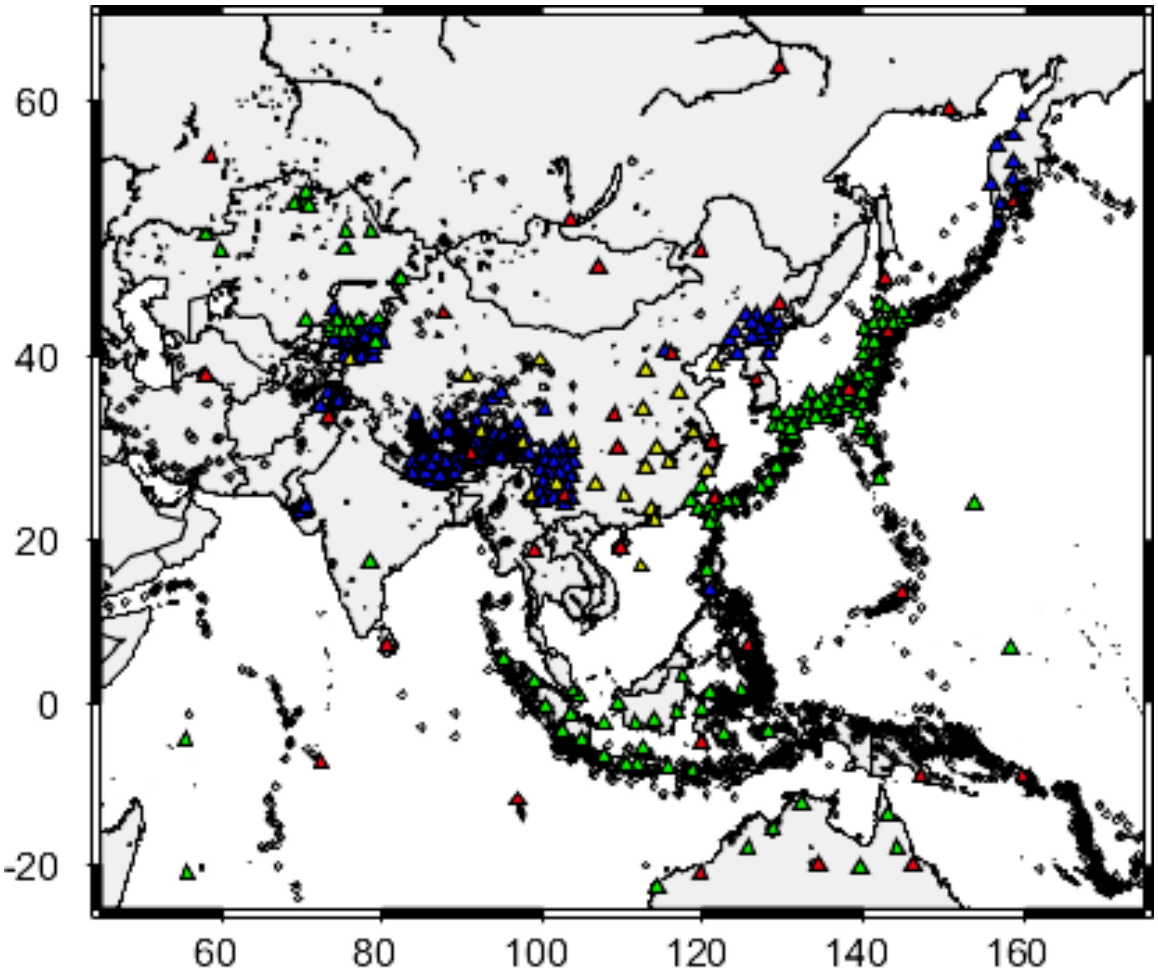

Figure 2. Triangles mark the locations of broadband seismic stations in Eastern Eurasia (red: GSN stations; blue: PASSCAL stations; yellow: part of the CNDSN; green: other permanent or long-term seismic networks). Data from some of the PASSCAL stations will be available only in the later half of this project. Circles represent earthquakes with magnitude greater than 5.0 during the period of 2000-2003.

We have developed an automated waveform cross-correction routine, and processed P waves from global earthquakes (2001-2004) with magnitude greater than 5.5 recorded by the GSN stations in eastern Eurasia and selected stations in Taiwan. In addition to the direct P arrival, we will also use other complementary phases, including the depth phase pP, surface-bounce phase PP (with bouncing point within the study region), and the

steeply incident core phases PKP and PKIKP. Figure 3 shows the distribution of global and regional earthquakes used in our preliminary model.

In processing data, to isolate the microseism and utilize the high dynamic range of the seismic records, we filter the broadband waveforms of the P waves in high, intermediate and low frequency bands (0.5-2.0, 0.1-0.5, and 0.03-0.1 Hz, respectively). We specify a threshold value of the signal to noise ratio of 20 for automated data selection in each frequency band and inspect each selected record visually for consistency. The relative travel time delays of the arrivals in each frequency band for each event are measured by multi-channel cross-correlation (VanDecar and Crosson, 1990).

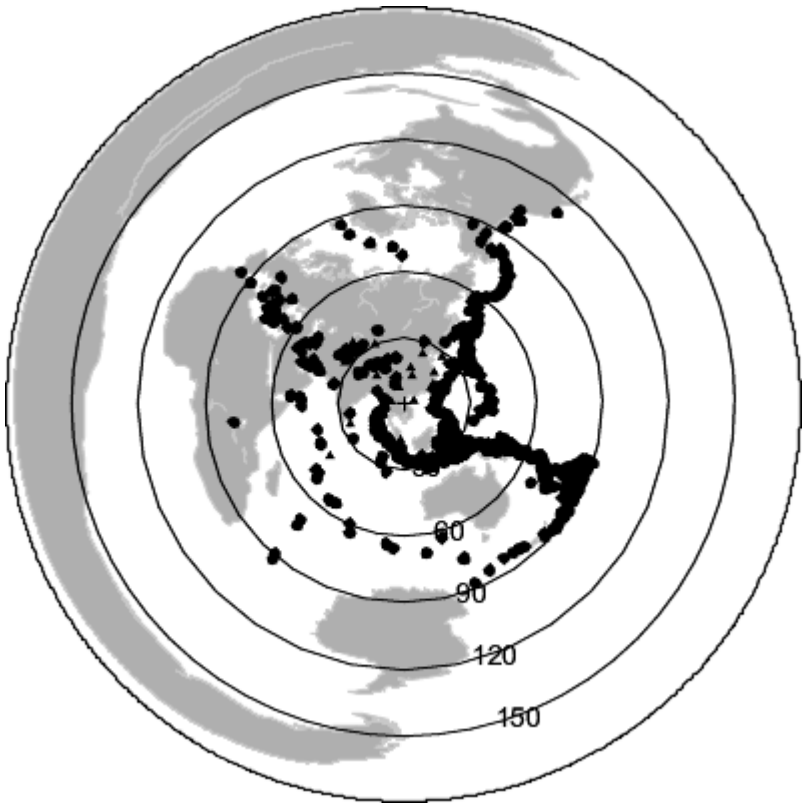

Figure 3. Location of the earthquakes with useful P phases (solid circles) and GSN stations (triangles) in the study region.

The norm damping factor of the inversion is determined by the trade-off analysis of model roughness versus variance reduction (Menke, 1989). An additional free term at each station was added into the inversion to absorb the time shifts due to the lateral variation in station elevation and velocity anomalies at shallow depths, which cannot be constrained due to the lack of crossing rays. The inversion of the massive matrix is approximated by the iterative solution of the LSQR algorithm (Paige et al., 1982).

Preliminary Results

Figure 4 shows the sampling density from high-, intermediate-, and low-frequency P waves from teleseismic earthquakes recorded by the GSN stations. The sampling density is the diagonal values of the product of the Gram matrix in equation 1 and its transpose (Hung et al., 2004). By examining the sampling, we can find where the model space is expected to be well resolved and where additional earthquake-station paths or phases are needed to obtain an adequate sampling of the velocity structure beneath the study region. As shown in Figure 4, direct P arrivals provide a good coverage in the depth range of 400 - 1500 km. There exist large coverage gaps in the shallow upper mantle and crust due to the sparse GSN station distribution.

We note that so far only a small fraction of the available data sets has been used in this preliminary result. The other data sets being collected (e.g., CNDSN, IRIS, PASSCAL, IMS and JISNET) will fill most of the blanks in Figure 4, especially beneath the Eurasia continent. The depths phase pP, surface multiple phase PP, and regional arrivals will provide resolution for the shallow structure. PKP and PKIKP phases will provide coverage in the deep mantle and vertical ray paths that cross with other phases in the shallower mantle. We also note that surface waves, which sample the crust and shallow mantle, will be used in joint tomography of finite-frequency body and surface waves to obtain the 3-D shear-wave velocity structure.

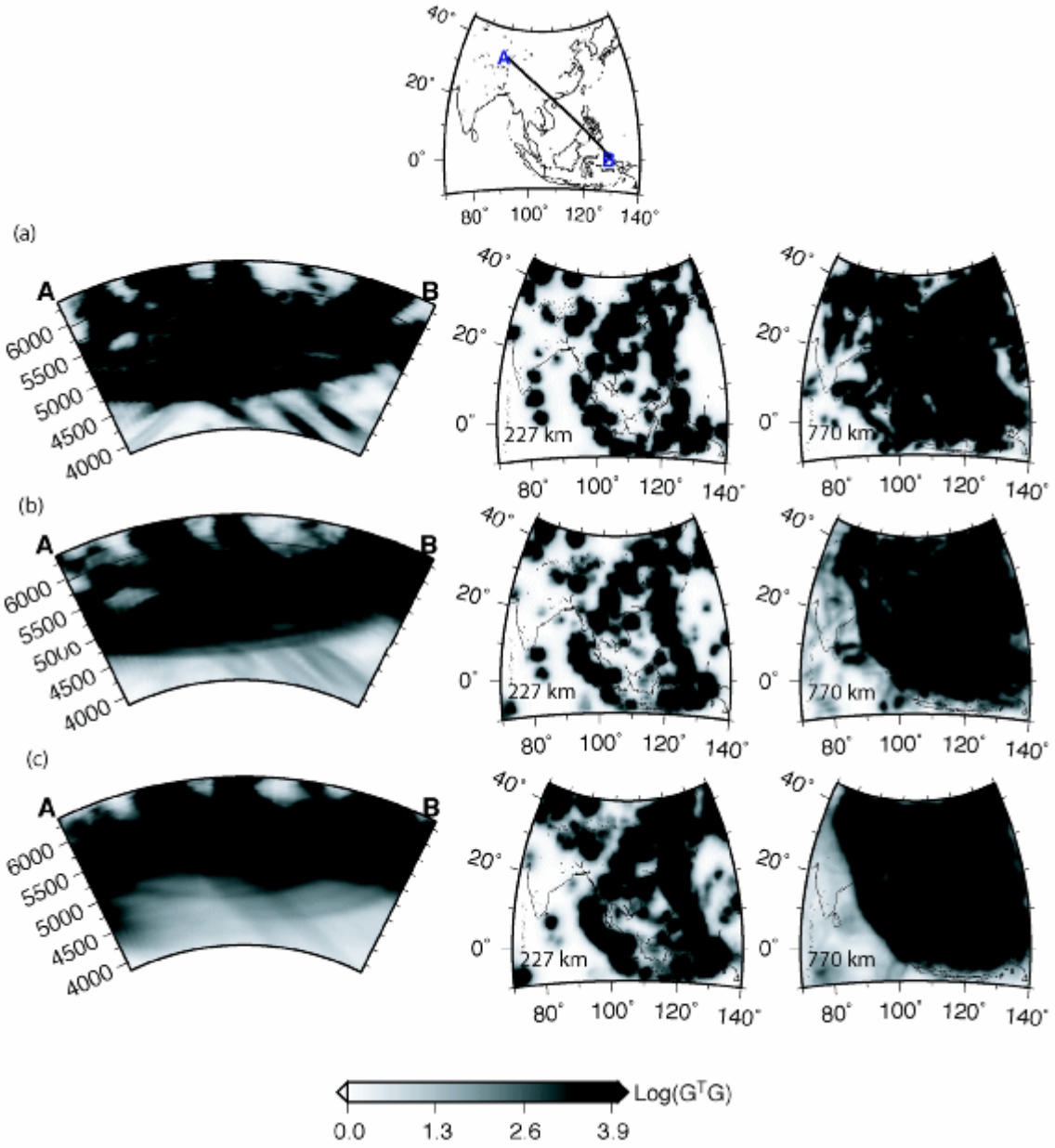

Figure 4. Sampling of the model space by 3D sensitivity kernels of P waves with (a) the high-frequency band (0.5-2 Hz), (b) intermediate frequency band (0.1 -0.5 Hz), and (c) low-frequency band (0.03 -0.1 Hz). The line AB in the map view marks the location of the vertical profile. The horizontal slices are at 227 and 770 km depth.

Because of the relatively narrow "banana-doughnut" sensitivity kernels of high-frequency P waves (Figure 1), the sampling of high-frequency P waves (Figure 4a) resembles that in ray theory. At intermediate and low frequencies,

the broad sensitivity kernels provide a more smooth coverage of the structure (Figures 4b and 4c). FFST will combine the sensitivity kernels in all frequency bands.

Project Database and Web-based Tool

We have created a project database to integrate data sets collected for model construction and validation. The database will include a large amount of waveforms as well as ground truth (GT) data with event location uncertainty within 5 km. It is an Oracle relational database using the core NNSA schema with some modifications. We have implemented the fundamental principles of the database management system (DBMS) to obtain an Entity-Relationship diagram (Figure 5).

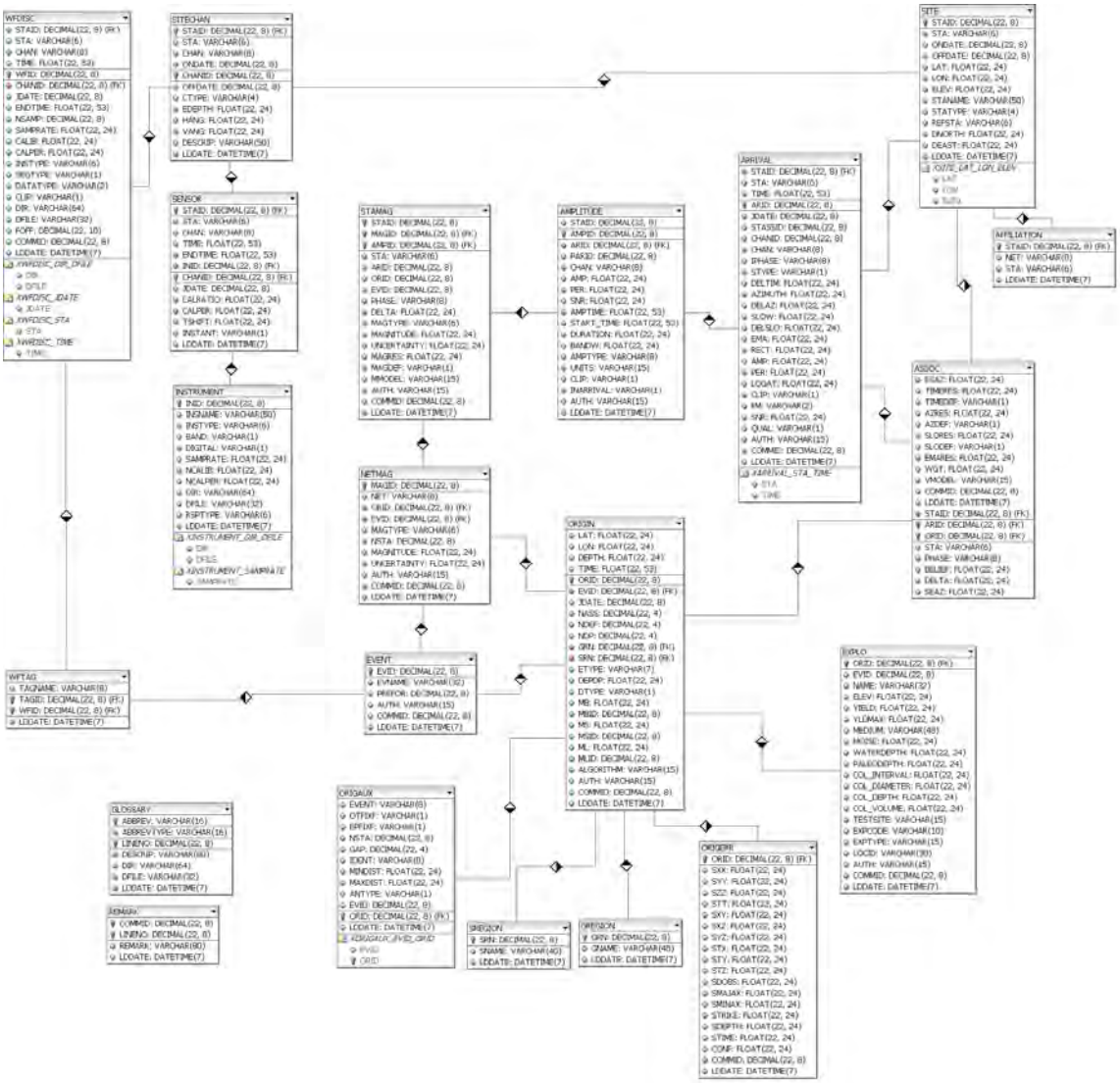

Figure 5. E/R diagram for the project database.

As data are being collected by the team members in this project, they are integrated and stored in the project database. To facilitate efficient data integration and access, a Science Applications International Corporation (SAIC) existing web-based tool is being implemented for use by the project. Figure 6 shows the interface developed under SAIC support. This tool will enable the distributed team members to remotely upload data directly into the database besides other functionalities such as search.

Figure 6. Web-based tool for use in data integration and data access.

CONCLUSIONS AND RECOMMENDATIONS

In this three-year project we will improve seismic calibration for nuclear explosion monitoring in eastern Eurasia using our recently developed FFST. The 3-D, finite-frequency kernels account for wavefront healing and other finite-frequency effect of wave diffraction. In addition to the new methodology, we will use a more comprehensive data set than in previous studies to construct the new earth model beneath eastern Eurasia.

Preliminary tomographic inversions using finite-frequency kernels have demonstrated significant improvement in resolution compared to those based on ray theory. Initial data processing using teleseismic earthquakes recorded by the GSN stations in eastern Eurasia demonstrates that 3-D finite-frequency sensitivity kernels yield a more smooth and uniform sampling than in ray theory, which improves tomographic inversions. The mantle in the 400-1500 km depth range is well sampled by the direct teleseismic P arrivals. The initial results show that additional phases (e.g., pP, PP, PcP, PKP) as well as regional arrivals are essential to imaging the shallow (<400 km depth) and deep (>1500 km) velocity structure.

The 3D velocity models will be used in seismic calibration in Eurasia. We will develop frequency-dependent travel time corrections and uncertainties, and used them in relocating GT events for validating the model and event location improvement. From the 3D velocity model we will also simulate 3D full wavefield for modeling wave propagation through the transition zone.

REFERENCES

Antolik, M., Y. Gu, G. Ekstrom, and A. Dizwonski (2003), J362D28: a new joint model of compressional and shear velocity in the Earth's mantle, *Geophys. J. Int.* 153: 443–466.

Baig, A.M., F. A. Dahlen, and S.-H. Hung (2004), Traveltimes of waves in three-dimensional random media, *Geophys. J. Int.* 153: 467–482.

Bijwaard, H., W. Spakman, and E. R. Engdahl (1998), Closing the gap between regional and global travel time tomography, *J. Geophys. Res*. 103: 30,055–30,078.

Briais, A., P. Patriat, and P. Tapponnier (1993), Updated interpretation of magnetic anomalies and seafloor spreading stages in the South China Sea: Implications for the Tertiary tectonics of Southeast Asia, *J. Geophys. Res*., 98, 6299–6328.

Curtis, A., J. Trampert, R. Snieder, and B. Dost (1998), Eurasian fundamental mode surface wave velocities and their relationship with tectonic structures, *J. Geophys. Res.* 103: 26,919–26,947.

Dahlen, F. A., S.-H. Hung, and G. Nolet (2000), Fréchet kernels for finite frequency traveltimes-I. Theory, *Geophys. J. Int.* 141: 157–174.

Dziewonski, A.M (1984)., Mapping the lower mantle: determination of lateral heterogeneity in P velocity up to degree and order 6, *J. Geophys. Res.* 89: 5929–5952.

Fukao, Y., M. Obayashi, H. Inoue, and M. Nenbai (1992), Subducting slabs stagnant in the mantle transition zone, *J. Geophys. Res.* 97: 4809–4822.

Grand, S.P. (1994), Mantle shear structure beneath the Americas and surrounding oceans, *J. Geophys. Res.* 99: 11591-11621.

Huang, J. and D. Zhao (2004), Crustal heterogeneity and seismotectonics of the region around Beijing, China, *Tectonophysics* 385: 159-180.

Hung, S.-H., F. A. Dahlen, and G. Nolet (2000), Fréchet kernels for finite frequency traveltimes—II. Examples, *Geophys. J. Int.* 141: 175–203.

Hung, S-H ,Y. Shen, and L.-Y. Chiao (2004), Imaging seismic velocity structure beneath the Iceland hot spot: A finite frequency approach, *J. Geophy. Res.* 109: doi: 10.1029/2003JB002889.

Johnson, M., and C. Vincent (2002), Development and testing of a 3D velocity model for improved event location: a case study for the India-Pakistan region, *Bull. Seism. Soc. Am.* 92: 2893–2910.

Lebedev, S. and G. Nolet (2003), Upper mantle beneath Southeast Asia from S velocity tomography, *J.Geophys. Res*. 108: B1, 2048, doi: 10.1029/2000JB000073.

Liang, C., X. Song, and J. Huang (2004), Tomographic inversion of Pn travel times in China, *J. Geophys. Res* 109 : B1,1304, doi:10.1029/2003JB002789.

Liu, F., K. Qu, H. Wu, et al. (1989), Seismic tomography of the Chinese continent and adjacent region, *Chinese J. Geophys*. 32: (3), 281–291.

Marquering, H., F. A. Dahlen, and G. Nolet (1999), Three dimensional sensitivity kernels for finite-frequency traveltimes: The banana-doughnut paradox, *Geophys. J. Int.* 137: 805–815.

Menke, W. (1989), *Geophysical data analysis: Discrete Inverse Theory*, Academic, San Diego, Calif.

Montelli, R., G. Nolet, G. Masters, F. A. Dahlen, E. R. Engdahl, and S.-H. Hung (2004), Finite-frequency tomography reveals a variety of plumes in the mantle, *Science* 303: 338–343.

Nolet, G. and F. A. Dahlen (2000), Wave front healing and the evolution of seismic delay times, *J. Geophys. Res.*, 105, 19,043–19,054.

Paige, C.C., and M. A. Saunders (1982), LSQR: An algorithm for sparse linear-equations and sparse least-squares, *Trans. Math. Software* 8: 43–71.

Pei, S., Y.J. Chen, D. Zhao, A. Yin, J. Ning and X.F. Chen (2005), Tomographic structure of East Asia: 1. No fast (slab) anomalies beneath 660-km discontinuity, *J. Geophys. Res.*, Submitted.

Richards, P., J. Armbruster, V. Burlacu, V. Cormier, M. Fisk, V. Khalturin, W.-Y. Kim, I. Morozov, E. Morzova, C. Saikia, D. Schaff, A. Stroujkova, and F. Waldhauser (2003), Seismic location calibration for 30 International Monitoring System stations in eastern Asia: finite results, in *Proceedings of the 25th Seismic Research Review- Nuclear Explosion Monitoring: Building the Knowledge Base*, LA-UR-04-5801, Vol. 1, pp. 280-290.

Ritzwoller, M. H., A.L. Levshin (1998), Eurasian surface wave tomography: group velocities, *J. Geophys. Res., 103,* 4839-4878.

Ritzwoller, M., N. Shapiro, A. Levshin, E. Bergman, and E.R. Engdahl (2003), The ability of a global 3-D model to locate regional events, *J. Geophy. Res.* 108: 2353, ESE9-1-ESE9-24.

Shen, Y., and S.-H. Hung (2004), Ridge-like upwelling in the uppermost lower mantle beneath eastern Africa from finite-frequency seismic tomography, *Eos Trans. Am. Geophys. Union* 85:47, U41A–0720.

Sun, Y., X. Li, S. Kuleli, D. Morgan, and N. Toksoz (2004) Adaptive moving window method for 3D P-velocity tomography and its application in China, *Bull. Seis.Soc. Am.* 94: (2), 740–746.

Van der Hilst, R. D., E. R. Engdahl, W. Spakman, and G. Nolet (1991), Tomographic imaging of subducted lithosphere below northwest Pacific island arcs, *Nature,* 353: 37–43.

Van der Hilst, R. D., Widiyantoro, S. and Engdahl. E.R. (1997), Evidence for deep mantle circulation from global tomorgpahy *Nature* 386: 578–584.

VanDecar, J. C., and R. S. Crosson (1990), Determination of teleseismic relative phase arrival times using multi-channel cross-correlation and least squares, *Bull. Seism. Soc. Am.* 80: 150–169.

Widiyantoro, S., and R. van der Hilst (1997), Mantle structure beneath Indonesia inferred from high-resolution tomographic imaging, *Geophys. J. Int.* 130: 167–182.

Wu, F., and A. Levshin (1994), Surface wave tomography of east Asia, *Phys. Earth Planet. Inter.* 84: 59–78.

Xu, Y.G. (2001), Thermo-tectonic destruction of the archaean lithospheric keel beneath the Sino-Korean Craton in China: Evidence, timing and mechanism. *Phys. And Chem. of Earth Part A: Solid Earth and Geodesy,* 26: 747–757.

Yang, X., I. Bondar, J. Bhattacharyya, M. Ritzwoller, N. Shapiro, M. Antolik, G. Ekstrom, H. Israelsson, and K. McLaughlin (2004), Validation of regional and teleseismic travel time models by relocating ground truth events, *Bull. Seism. Soc. Am.* 94: 897–919.

Zhao, D., Y. Fukao, and T. Seno (2000), A plume-like slow anomaly under the subducting Pacific slab beneath central Japan, *Eos Trans. Am. Geophys. Union* 81:22, W137.

Zhao. Li., T. H. Jordan, and C. H. Chapman (2000), Three-dimensional Fréchet differential kernels for seismic delay times, *Geophys, J. Int*. 141: 558–576.

Zhu, J., J. Can, X. Cai, Z. Yan and X. Cao (2002), High resolution surface wave tomography in east Asia and west Pacific Marginal Sea, *Chinese J. of Geophys.* 45: 679_698.

Seismic Identification and Source Characterization

EVENT IDENTIFICATION FRAMEWORK FOR TELESEISMIC AND REGIONAL DISCRIMINANTS

Dale N. Anderson[1], Deborah K. Carlson[2], Gordon D. Kraft[2], Frederick R. Schult[3], Steven R. Taylor[4], and William R. Walter[5]

Pacific Northwest National Laboratory[1], Quantum Technology Services Incorporated[2], Air Force Research Laboratory[3], Los Alamos National Laboratory[4], and Lawrence Livermore National Laboratory[5]

Sponsored by National Nuclear Security Administration
Office of Nonproliferation Research and Engineering
Office of Defense Nuclear Nonproliferation

Contract No. DE-AC06-76RLO1830

ABSTRACT

Seismic monitoring for nuclear explosions answers three questions: Where is the seismic event located? What is the source type for the event? If an explosion, what is the yield of the event? Under the Threshold Test Ban Treaty (TTBT), treaty verification involved a seismic analysis processing seismograms of strong events, whose path was largely in the mantle, that is, teleseismic events. This paper reviews the seismic/mathematical development of a general event identification framework. This framework is extensible to include both regional and teleseismic discriminants.

The developed framework consists of two fundamental steps, or components. First, for each discriminant (teleseismic or regional) a probability model is formulated under a general null hypothesis of explosion characteristics. The veracity of the hypothesized model for each discriminant is measured with a calculation that is exactly, or analogous to, a p-value and ranges between zero and one. A value near zero indicates inconsistency with explosion characteristics, and a moderate to large value indicates consistency with explosion characteristics. The hypothesis test formulation ensures that seismic phenomenology is tied to the interpretation of the p-value.

In the second component, the p-values are transformed into standardized discriminants that also possess predictable statistical properties. They also range between zero and one, their interpretation is analogous to that of p-values, and they are approximately Gaussian. Therefore, established Gaussian discrimination methods can be used to formulate a unified decision from standardized discriminants.

The framework components are modular, and the mathematics to aggregate standardized discriminants is operationally independent of the construction of discriminant hypothesis tests. To develop and integrate new discriminants into the framework 1) the seismic theory of the discriminant must be integrated into an appropriate probability model, 2) a hypothesis test must be formulated from the model with an explosion characteristics null hypothesis and, 3) the result of the test must be summarized as a p-value calculation. The aggregation mathematics does not need to change when new discriminants and/or source types are added.

OBJECTIVES

This research and development effort provided a mathematical statistics formulation of established teleseismic discriminants, mapped these discriminants to a p-value calculation and constructed a general mathematical framework for teleseismic discrimination using p-values that is fully extensible to regional discriminants.

RESEARCH ACCOMPLISHED

Four core teleseismic discriminants are depth from travel time (TT), presence of long-period surface energy (LP), depth from reflective phases (PP), and polarity of first motion (FM). The mathematical statistics formulation of these follows, all under a general null hypothesis of H0: explosion characteristics.

TT Discriminant. Elements of location estimation as discriminants are intuitive and logically simple. For example, the combined costs and limitations of mining and drilling technology make deep underground nuclear explosions (deeper than 5 km or 10 km) very unlikely. Also, underground nuclear tests have associated support infrastructure or hole/tunnel construction. These illustrations indicate how epicenter and depth estimation contribute to event identification. The TT discriminant is mathematically formulated with the hypotheses H0: Depth $\leq \xi$ and HA: Depth $> \xi$. If H0 is true, then a test statistic, based on the sum of squares of fit, can be derived from non-linear regression theory that has an approximate F distribution with degrees of freedom equal to 1 and n–4. Here, n is the number of defining stations used in the hypocenter estimation. However, the hypotheses H0 and HA have directionality, that is, a test is needed that determines if H0: Depth $\leq \xi$ is consistent with the data. If H0 is true, then the statistic T = sign(depth estimate–ξ)Sqrt(F) has a central Student's T-distribution with n–4 degrees of freedom. Large values of T are inconsistent with H0 because the F statistic measures adequacy of fit under H0. The p-value is simply the right tail probability of a central Student's T-distribution calculated from the observed value of T. A small p-value implies a large observed T, which leads to the inference inconsistent with H0. A large p-value implies a small observed T, which leads to the inference consistent with H0 (Figure 1).

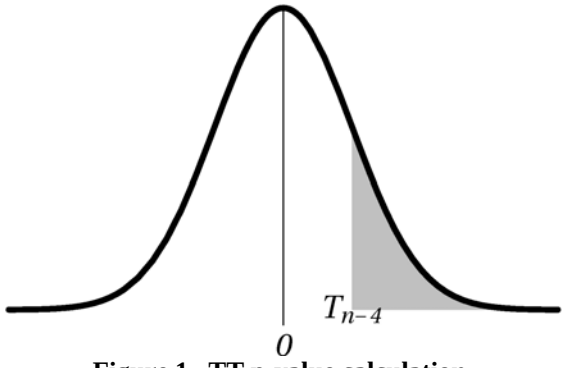

Figure 1. TT p-value calculation.

LP Discriminant. The body-wave magnitude (mb) versus surface-wave magnitude (Ms) discriminant is based on the physics that an earthquake excites relatively more surface-wave energy than a single-shot explosion. This means the ratio of Ms to mb generally will be larger for an earthquake than for an underground explosion with equivalent body-wave energy. In practice, this discriminant is formed from the difference of network average of surface-wave and body-wave magnitudes. Subtracting the historical average of this difference, when the seismic source is an explosion and then dividing by the standard error gives standard z-score statistic. The common variance for mb and Ms in the standard error is calculated from historical data and is assumed known. From established statistical theory, the test statistic z has a standard Gaussian distribution. Extreme negative values of z are inconsistent with H0; therefore, the p-value is simply the left tail probability of a standard Gaussian distribution calculated from the observed value of z. A small p-value, calculated from an extreme negative value of Z, leads to the inference inconsistent with H0. A large p-value implies consistency with H0 (Figure 2).

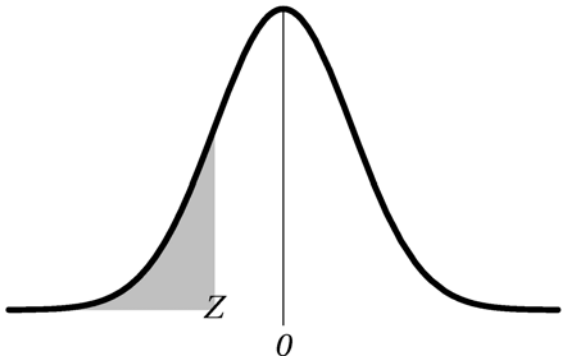

Figure 2. LP p-value calculation.

PP Discriminant. A reliable depth estimate can be obtained from the difference in arrival times of the compression waves P and pP. The P-wave travels directly from a seismic disturbance to a seismometer. In contrast, the pP-wave is a reflected P-wave that travels from the seismic disturbance to the earth's surface before being reflected to a seismometer. The time difference between the arrival of P and pP-waves (Δt) is a function of the depth of the seismic source and the epicentral distance from the source to the seismometer. This difference is predominantly dependent on the depth of a seismic disturbance when the focus is less than approximately 100 km deep.

For an event, stepout (denoted as r) is the observed change in Δt from the nearest station to the farthest station. Estimation of focal depth with reflected wave arrival times requires an a priori epicenter estimate. Physical phenomenology indicates it is highly unlikely that observed reflected waves of high quality (good signal-to-noise ratio and azimuthal distribution) could exhibit stepout if those waves were not correctly associated depth waves. Scenarios where this claim fails includes events that are analyzed with an inadequate earth model or spurious associations. Should the observed values of Δt for the closest and most distant seismometers be significantly and systematically different, then stepout is indicated, which implies that the event is deep.

Developing a mathematical formulation of the PP discriminant, and associated hypothesis H0 and p-value, requires that mathematical statistics theory yield obeisance to physical basis. The mathematical statistics formulation of the PP discriminant is a compound probability distribution of two measurements - the number of observed depth phases (number of observed pP) from an event, and a measurement of stepout. The number of observed pP is modeled with a Poisson distribution - appropriate because this number is rare under the null hypothesis. Stepout given a number of observed pP is modeled with statistical methods to relate Stepout to epicentral angle.

The null hypothesis is H0: No observed pP (Explosion Characteristics). Inconsistency with H0 is indicated when the number of observed pP is large or when observed stepout is large. The mathematical formulation of PP will give a small p-value when good-quality depth phases are seen; however, solid inconsistency with H0 requires observed stepout. For example, the formulation provides solid inconsistency with H0 with only two observed pP and strong stepout. In contrast, many observed pP with weak stepout indicates only marginal inconsistency with H0. The p-value calculation for the PP discriminant is illustrated in Figure 3.

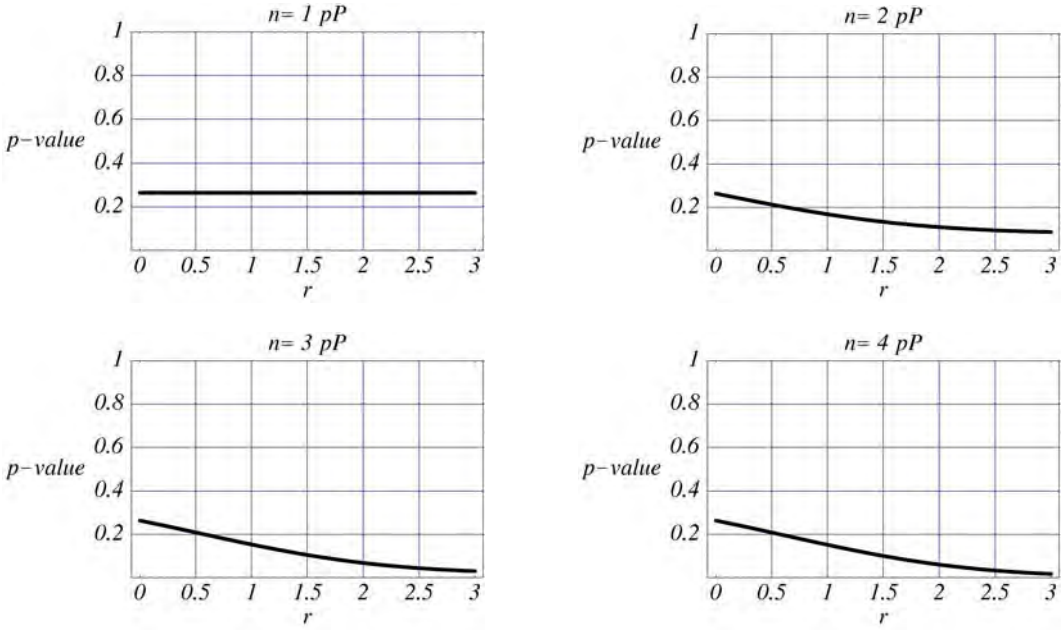

Figure 3. PP p-value calculation.

FM Discriminant. Polarity of first motion, as a discriminant, is based on the fact that an underground or underwater nuclear detonation produces mostly P-wave energy. Excluding pathological cases, a seismogram from an explosion exhibits the initial earth movement of the P-wave as upward or positive, regardless of the location of the seismometer. In contrast, an earthquake is caused by relative movements of adjacent blocks of the earth due to tectonic forces. This movement creates P-waves with opposite initial movements in different directions. Across a well-dispersed global seismic monitoring network, the initial P-waves from an earthquake will appear positive at some stations and negative at others. As a discriminant, if the polarity of first motion is negative at some stations, then the seismic disturbance is unlikely to be an explosion. If the polarity of first motion is positive at all stations, then the seismic disturbance might be the result of an explosion. The ambiguity under unanimous positive first motion is potentially caused by an inadequate distribution of seismic stations, that is, no earthquake P-waves with negative first-motion polarity travel to areas with seismic network coverage, or poor signal-to-noise ratio (inability to observe the P-wave signal because it is too small compared to background noise). A clear limitation of this discriminant is its dependence on the accurate identification of the first arrival of a seismic disturbance. In addition, shallow earthquakes of a type that produce vertical uplifts (thrusts or reverse mechanisms) often radiate energy with exclusively positive polarity. The first motion from some seismic disturbances is often difficult to distinguish from background noise. If the true onset of a seismic disturbance is poorly estimated, then the polarity of the first motion may be incorrectly assigned. For these reasons, the FM discriminant is only used as an explosion rejecter.

With adequate signal-to-noise at each station, the polarity of first arrival can be accurately identified with high probability (even with good signal-to-noise, first arrival polarity can be hard to identify in some instances). Uncertainty in identifying first arrival polarity motivates a mathematical statistics construction of the FM discriminant. The null hypothesis is H0: The source mechanism is single-point explosive. Under H0, the probability of positive first motion at a station is composed of two component probabilities; the probability of positive first motion from the source, and the probability that first motion polarity is correctly determined given positive first motion from the source. Under H0, the first component, the probability of positive first motion from the source, equals one. There may be pathological cases where this is not true; however, they are assumed to be negligible for this development. The second component probability is governed by many factors including signal-to-noise, analyst training and experience, and accurate P arrival pick. For this development, only signal-to-noise is considered in the determination of the second component probability, and with good signal-to-noise at all stations, this probability is modeled as a constant. This reasoning is succinctly summarized as P(+ first motion observed at a station)=P(+ first motion from source) × P(first motion polarity correctly identified | + first motion from source)=1 × θ. From this

formulation, there will be a positive first motion (or not) at each station -- a binary random variable with P(+ first motion observed at a station)= θ. Assume that stations are probabilistically independent. Therefore, for M stations forming an event, the number of stations (N = n) under H0 that have positive first motion has a binomial distribution with parameters M and θ. For observed N = n, the FM p-value is simply the binomial cumulative distribution function.

The parameter P(+ first motion observed at a station) = θ will be near one under H0, and so a large number of stations with positive first motion will give a large p-value, leading to the inference consistent with H0. However, note again that the FM discriminant cannot offer confirmatory evidence for an explosion unless the station constellation fully covers the focal sphere. Illustrative plots of p-value versus the number of stations (N=n) that have positive first motion are given in Figure 4 for a suite of values M.

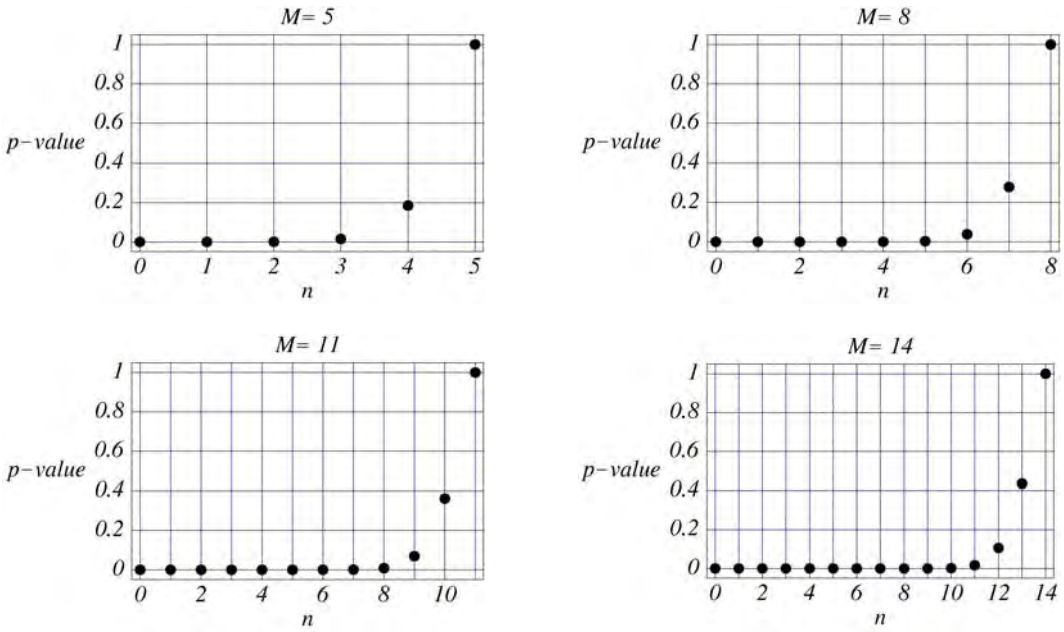

Figure 4. FM p-value calculation.

Regularized Discriminant Analysis-based Framework for Seismic Event Identification. Regularized Discriminant Analysis (RDA) (Friedman 1989) is fundamentally a Gaussian likelihood-based method. It therefore simplifies to a Mahalanobis distance as the basis for identification. For inputs into a general RDA-based discrimination framework, p-values are transformed into standardized discriminants that possess predictable statistical properties. Like p-values they range between zero and one, their interpretation is analogous to that of p-values, and they are approximately Gaussian. At an intuitive level, the Mahalanobis distance is very clear and appealing -- it measures the membership of a suite of standardized discriminants in source distributions (see Figure 5). In doing this membership analysis, the Mahalanobis distance accounts for the potentially different covariances that sources may have. RDA naturally grounds source identification as an empirical analysis, yet it is model-based.

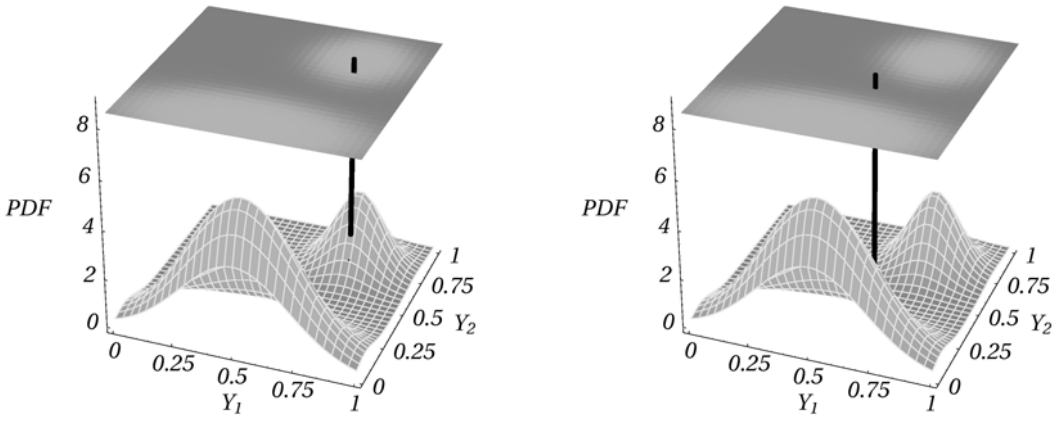

Figure 5. Illustrations of RDA source membership.

Inherent in the RDA identification approach is the concept that events that differ from historical source data are flagged for further analysis. This means that an event with individual p-values that strongly indicate explosion can be flagged for further analysis if, in the aggregate, the standardized discriminants are inconsistent with a historical explosion model. This property of RDA also implies that unusual natural events may be flagged for further analysis. Events that are in fact natural, yet inconsistent with all sources may be a new source type and appropriately merit further analysis. However, these events may be clear earthquakes from an inspection of individual p-values.

RDA is remarkably robust in its performance and offers a parametric transition between Linear Discriminant Analysis (LDA) and Quadratic Discriminant Analysis (QDA). It provides an operational identification solution even in settings with minimal calibration data. It is model-based, yet requires its parameters to be calibrated with data, and this balance implies that RDA will not over-fit calibration data. It provides the mathematics to perform identification in cases with missing discriminants. RDA offers the flexibility to include standardized discriminants that are co-linear.

CONCLUSIONS AND RECOMMENDATIONS

A mathematical framework for teleseismic discrimination has been completed. Teleseismic discriminants have been appropriately formulated for inclusion in the framework. The framework is mathematically extensible to regional discriminants. The framework should be calibrated and populated with regional discriminants.

REFERENCES

D. N. Anderson, S. R. Taylor, and K. K. Anderson (1999), Discrimination information in phase amplitude thresholds with application to Western China regional data, *Bulletin of the Seismol. Soc. Am.* 89: (3), 648-656.

D. N. Anderson and S. R. Taylor (2002), Application of regularized discrimination analysis to regional seismic event identification," *Bulletin of the Seismological Society of America* 92: 2391-2399.

L. Dumbgen and L. Homke (2000), *P-Values for Discriminant Analysis*. Preprint series: Schriftenreihe der Institute fuer Informatik/Mathematik, Bericht A-00-14, University of Lubeck, Germany.

P. J. DiPillo (1976), The application of bias to discriminant analysis, *Communications in Statistics - Theory and Methods A* 5(9):843-854.

P. J. DiPillo (1977), Further application of bias to discriminant analysis, *Communications in Statistics - Theory and Methods A* 6: (10):933-943.

P. J. DiPillo (1979), Biased Discriminant Analysis: Evaluation of the Optimum Probability of Misclassification, *Communications in Statistics - Theory and Methods A* 8: (14):1447-1457.

J. H. Friedman (1989), Regularized Discriminant Analysis, *Journal of the American Statistical Association* 84: 165-175.

E. A. Maharaj (2000), "Clusters of Time Series," *Journal of Classification* 17: 297-314.

R. K. Smidt and L. L. McDonald (1976), *Ridge Discriminant Analysis*. University of Wyoming Department of Statistics, Technical Report No. 108, Laramie, Wyoming.

DISCRIMINATION OF SMALL EVENTS USING REGIONAL WAVEFORMS: APPLICATION TO SEISMIC EVENTS IN THE US AND RUSSIA

Marie D. Arrowsmith[1], Stephen J. Arrowsmith[2], Brian Stump[1], and Michael Hedlin[2]

Southern Methodist University[1] and University of California at San Diego[2]

Sponsored by National Nuclear Security Administration
Office of Nonproliferation Research and Engineering
Office of Defense Nuclear Nonproliferation

Contract Nos. DE-FC52-03NA99510[1] and DE-FC52-03NA99511[2]

ABSTRACT

Historically, event identification has focused on the task of separating earthquakes and explosions. This approach was adequate for large events observed at teleseismic distances since there are few other types of manmade sources large enough to be observed. However, with the availability of high-quality regional data, smaller events (m_b 3.5 and below) that include many manmade sources are observed. The present challenge of seismic-event identification now includes the task of categorizing not only earthquakes and single-fired explosions (nuclear or chemical), but also mining explosions, underground mining collapses, and rock bursts.

In order to investigate smaller, mining-related events, we have assembled a comprehensive database of earthquakes and mining events. This database consists of events in both the United States (US) and Russia and includes ground-truth data for several different kinds of mines (iron, copper, and coal in the US and coal in Russia). The US portion of the database comprises 128 stations (which include broadband three-component stations as well as regional short-period arrays, such as the Pinedale Seismic Array [PDAR]). The station distribution within the United States allows for good azimuthal coverage around three mining districts in Wyoming, Minnesota and Arizona. Nearly 72,000 waveforms were collected for 800 mining events and 400 earthquakes. The Russian portion of the database includes approximately 17,000 waveforms from five stations for 830 mining events and 260 earthquakes. The mining events were identified seismically by the Siberian Branch of Geophysics and co-locate well with known coal mines within the Altai-Sayan region of Russia. Additionally, through cooperation with Los Alamos National Laboratory (LANL) and Lawrence Livermore National Laboratory (LLNL), we have access to many additional prior events in both Russia and the US.

We have been using this extensive database to develop discrimination tools that specifically consider the physical processes that accompany mining explosions and what makes them unique from earthquakes and other types of explosions for categorization purposes. In order to test the tools, we focus on mining events in the Powder River Basin of Wyoming as well as nearby earthquakes. The discrimination tools we are currently testing, both individually and combined, include magnitude and distance corrected (MDAC) amplitude ratios, time-varying spectral analysis, and infrasound. Ultimately, we hope to incorporate cluster analysis and M_S:m_b in order to generate a combined discriminant, which confidently and effectively identifies small mining events.

OBJECTIVES

During the past year we have made progress on three key tasks. These include: (1) Development of a comprehensive ground-truth database; (2) Quality review of a subset of data for testing discriminants; and (3) Identification and testing of discriminants.

Development of a comprehensive ground truth database. In order to characterize the source mechanism of mining related events against a large background of natural seismicity, a ground truth database of different types of mine blasts in varying geological regions is essential. Additionally, this data should be supplemented with earthquake data that span a range of magnitudes and depths. Finally, such a database should utilize the NNSA Knowledge Base schema to allow for easy integration with other NNSA database products. We present the results of our database development that meet these standards.

Quality review of a subset of data for testing discriminants. A high-quality training dataset is necessary to apply discriminants and understand their behavior before extending their use to a larger dataset. The training dataset should feature mining events and earthquakes of different sizes consistently recorded at various regional stations, with well determined magnitudes and regional phase arrival times. We have chosen to build a training dataset for events recorded at the Pinedale Seismic Array, PDAR. This allows us to determine discrimination techniques that fully utilize the capabilities of small, regional arrays. Focusing on (coal) mining events recorded at PDAR allows us to apply our techniques to the coal mining regions of Russia.

Identification and testing of discriminants. Various types of discriminants have been successful at characterizing certain types of mining events in various regions (Stump et al., 2002). Determining a set of discriminants that confidently identify mining events from other types of events, regardless of blasting practice employed and the geological structure surrounding the mine, is critical. To address this problem, we are initially investigating three discriminants: amplitude ratios, time varying spectral estimation, and presence of infrasound.

RESEARCH ACCOMPLISHED

Development of a Comprehensive Ground Truth Database

We have focused on database development in two main regions: the United States (US) and Russia. In the US, we have obtained ground truth data from three mining districts that employ different mining practices to accommodate the extraction of a variety of materials. The first is the Powder River Basin in northeast Wyoming. This region has active surface coal mines. Contact with mines in the area has provided a catalog of 295 mining events for which we have approximate origin times, blast types, and approximate yields. The second mining district, in southeast Arizona, features porphyry copper where mining explosions are used to fracture rock for ore extraction. Through collaborative experiments with the mines, a catalog of 129 mining events has been derived and features detailed information on origin time, yield, and shot geometry (number of holes, shot delay time, and hole locations within mine). The third district comprises the taconite mines of northwestern Minnesota. Collaboration with local mines has yielded a catalog of 379 events featuring origin time, location within the mine, yield, shot delay times, and number of shots per blast.

The mining data have been supplemented with earthquake data as closely co-located as possible to each of three mining districts. In the Powder River Basin, catalogs derived from the University of Utah, the Montana Bureau of Mines and Geology, and the United States Geological Survey, preliminary determination of epicenters (USGS PDE) feature 213 earthquakes ranging in size from $M_L = 2.0$ to $M_L = 4.9$ at depths ranging from zero to 27 km, where most of the events are concentrated in the upper two to three km of the crust. The 87 earthquakes in the Arizona region were obtained from the USGS PDE and range in size from $M_L = 2.5$ to $M_L = 5.5$ at depths identified as upper- to mid-crustal (one to ten km). Finally, 119 earthquakes in the Minnesota mining region were obtained from the Canadian Geological Survey's earthquake bulletin. They range in size from $M_L = 1.1$ to $M_L = 4.7$ and are identified as mid-crustal (depths fixed at either five or 18 km). Figure 1 illustrates both the earthquakes and explosions gathered for the US portion of the study.

Data were obtained for these events via the Incorporated Research Institution for Seismology (IRIS) and the US National Data Center (NDC). A total of 128 unique stations from a range of both permanent network (e.g., Global Seismic Network [GSN]) and temporary deployments provide high-quality broadband and short-period data with

good azimuthal coverage around the three mining districts of interest. For the Powder River Basin events, 38 seismic stations (which include PDAR) have recorded data for some or all of the events in the dataset. In the Arizona district, 41 seismic stations have recorded data for some or all of the events. Finally, in the Minnesota district, 58 stations provide data for some or all of the events. This comprehensive station coverage has provided nearly 72,000 waveforms comprising the US portion of the dataset. Figure 2 shows the station coverage in the US.

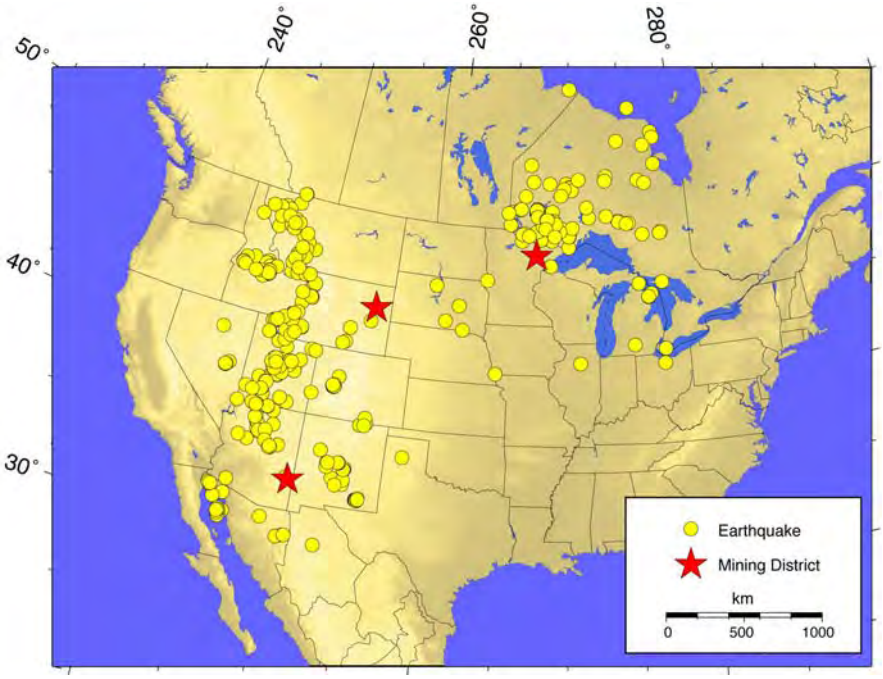

Figure 1. Earthquakes and explosions in the US portion of the database. Mining events in each of the three districts are initially given a single location, causing them to plot at a single point.

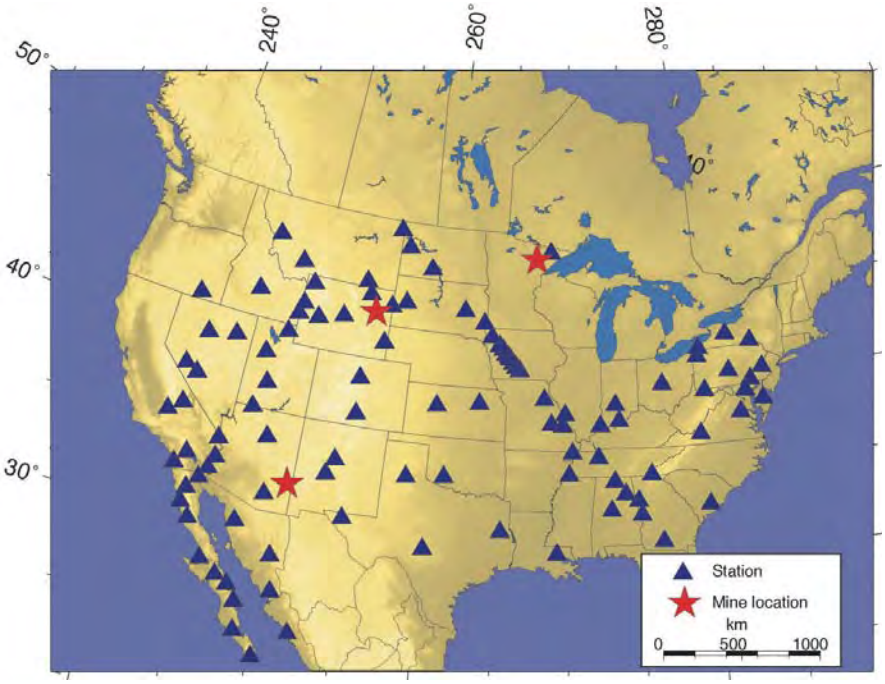

Figure 2. Station coverage for the US portion of the database. There are a total of 128 unique stations; several of the stations recorded data for more than one mining district.

Collaborative efforts with the Siberian Branch of the Russian Academy of Sciences Institute of Geophysics ("The Institute"), as facilitated by Vitaly Khalturin, has yielded a catalog of mining explosions and nearby earthquakes in the Altai-Sayan mining district in the Kuzbass region of Russia (Hedlin et al., 2004). The Institute administers the Altai-Sayan Seismological Expedition (ASSE) network; data analysts at The Institute use seismic location information from this network as well as blasting logs provided by local mines to quantify events as either mine blasts or earthquakes. Their efforts have resulted in the compilation of a catalog of 833 mining events and 263 earthquakes. Little information is known about the mining events, other than their co-location with active coal mines in the area. Magnitude estimates have been determined by The Institute and converted to approximate m_b measurements. These range in size from m_b = 3.1 to m_b = 3.8. The earthquakes range in magnitude from m_b = 3.1 to m_b = 5.6. Data were obtained for these events via IRIS and the PIDC for five stations in the Altay-Sayan area, which amounts to approximately 16,500 waveforms. Figure 3 illustrates the station coverage and events collected for the Russian portion of the database.

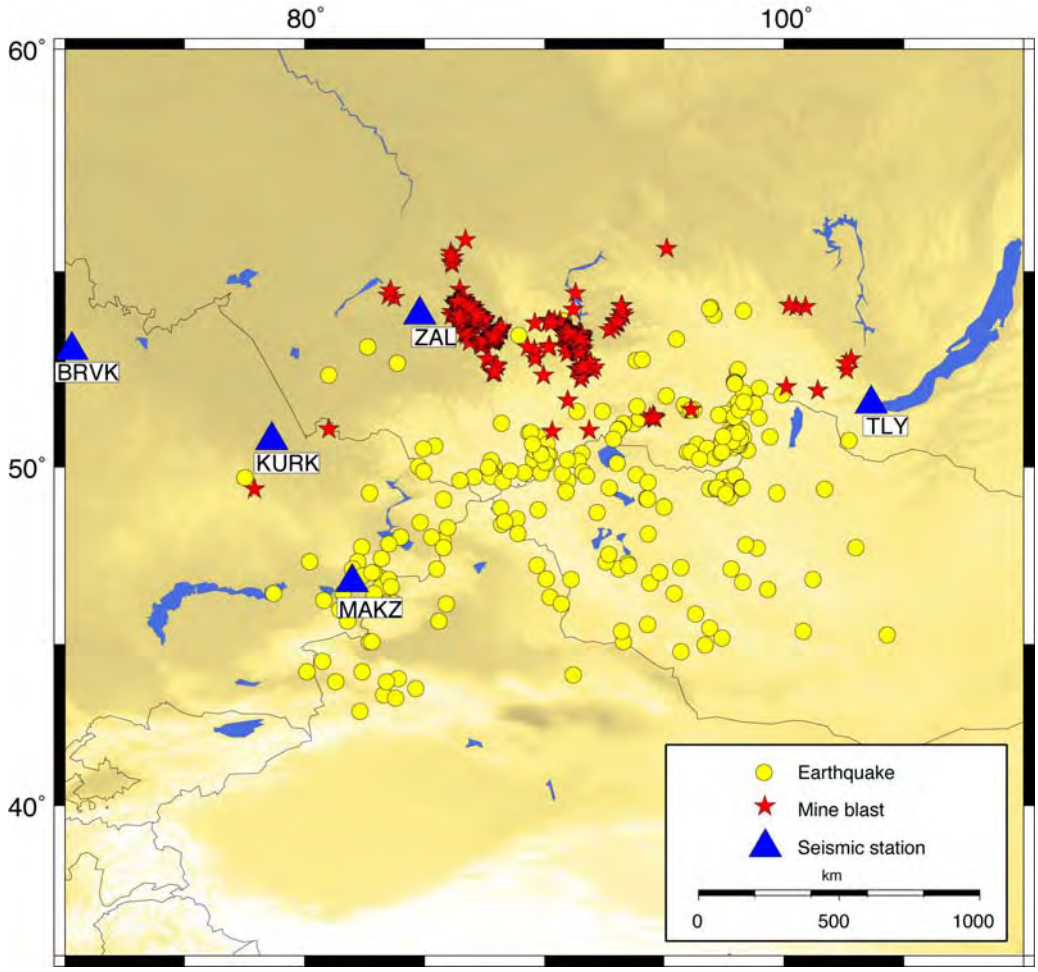

Figure 3. Earthquakes and explosions in the Russian portion of the database. The five stations for which data were obtained are also shown.

Figure 4 gives a statistical summary of the data we have collected thus far. In addition to the database we have developed, we have also integrated data collected by both LLNL and LANL for various projects. To complement our US dataset, Bill Walter and his colleagues at LLNL have provided us with their Western US database featuring earthquakes, mining related events, and nuclear explosions recorded at the Nevada Test Site (NTS) (Walter et al., 2003). To complement our Russian dataset, Julio Aguilar-Chang at LANL has provided us with an additional 12,700 waveforms recorded at 57 stations for 552 events in the Altai-Sayan area.

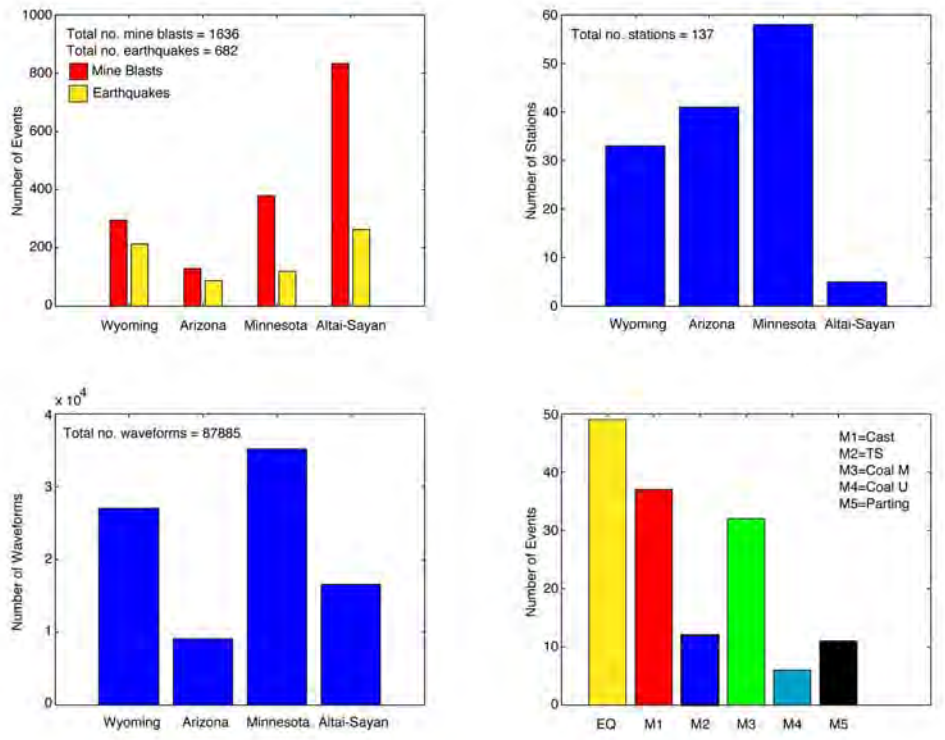

Figure 4. Summary of the US and Russian database. The top left graph illustrates the total number of mine blasts and earthquakes in the dataset for the four mining regions (Wyoming, Arizona, and Minnesota in the US and the Altai-Sayan in Russia). The top right graph shows the number of stations for which we have collected data. The bottom left graph shows the total number of waveforms collected for each of the four regions. Finally, the bottom right figure summarizes the types of events (see Table 1) featured in the subset database we are using for initial analysis (Powder River Basin, Wyoming).

Quality Review of a Subset of Data for Testing Discriminants

In order to begin testing of discriminants on small, mining-related events, we have chosen to focus on a subset of the larger database collected. We have reviewed over 300 events recorded at the PDAR in Wyoming. PDAR is 367 km from one of the largest coal mines in the Powder River Basin for which we have detailed ground-truth data. These data includes origin information as well as information about the blast types utilized by this mine (Table 1). It may be necessary to include additional event types, for example blast anomalies where a significant portion of the blast array detonates simultaneously.

Table 1. Blast types for a large coal mine in the Powder River Basin, Wyoming.

Blast Type	Description	Min Yield (lbs)	Max Yield (lbs)
Cast Overburden	Overburden is casted and removed into adjacent empty pit.	300,000	2,500,000
TS Overburden	Blasts in overburden material to be excavated by shovels loading into trucks.	100,000	600,000
Coal – Main	Blasts in the main coal seam, which is 60 - 70 ft in thickness.	20,000	200,000
Coal – Upper	Blasts in the upper coal seam, which is 10 ft in thickness.	2000	10,000
Parting	Blasts of waste material layer between the upper and lower coal seam, ranging from 0 to 40 ft in thickness.	200	500

Of the events reviewed in the Wyoming region, there were 98 mine blasts that could confidently be associated with the origin and location information in the database and that generated enough signal to be seen at PDAR. Additionally, there were 49 earthquakes that generated sufficient signal to be recorded at PDAR. The bottom right graph in Figure 4 summarizes the number of different blast types contained in the subset database. Earthquake locations relative to the mine location and to PDAR are shown in Figure 5.

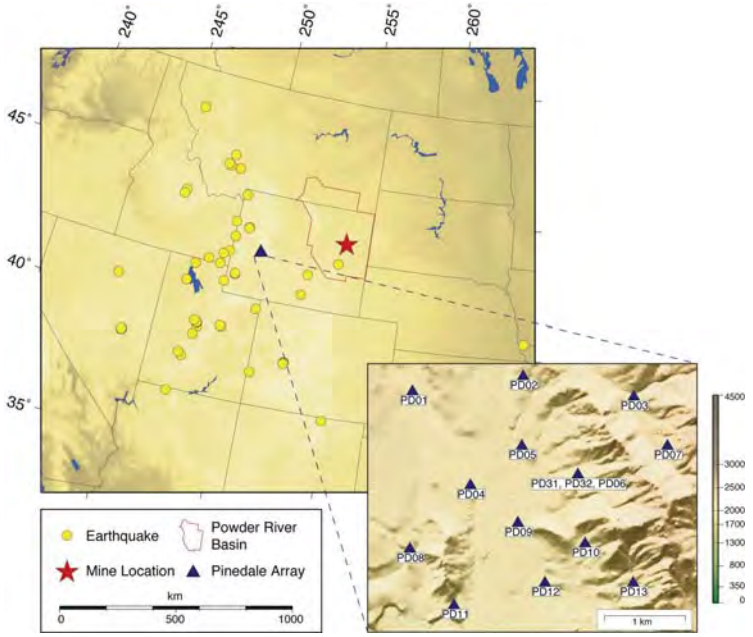

Figure 5. The subset of data used for testing the discriminants, illustrating earthquakes recorded at PDAR for the period 01/04 through 01/05 and the geometry of PDAR.

Identification and Testing of Discriminants

Amplitude Ratios using MDAC Corrected Amplitudes

Amplitude ratios have been used to successfully discriminate earthquakes from single-fired explosions, and discrimination power is greatly enhanced when path and source corrections are applied. We apply these same tools to mining explosions. In order to characterize the behavior of phase, spectral, and cross-spectral ratios for the types of events (Table 1) recorded at PDAR, we employ the use of the MDAC procedure. This procedure removes magnitude and distance trends in regional phase amplitudes using an earthquake source model and allows for maximum flexibility in the later construction of discriminants (Taylor et al., 2002). Using a velocity model determined by Prodehl and Lipman (1989) for the northern Rocky Mountains, regional phases (P_n, P_g, and L_g) were picked on elements of PDAR. Root mean square amplitude measurements were made using the frequency-domain procedure outlined in Hartse (2001) in six frequency bands commonly used for discrimination (0.5-1.0 Hz, 1.0 -2.0 Hz, 2.0-4.0 Hz, 4.0-6.0 Hz, 6.0-8.0 Hz, and 8.0-10.0 Hz). Because the MDAC procedure corrects for differences in source size, an estimate of m_b is necessary before applying the corrections. We have used the m_b(Pn) formula for the Western US, as described in Denny *et al.* (1987) to calculate magnitudes for each of the events in the subset, which range from m_b = 2.5 to m_b = 4.5.

The results of applying the MDAC corrections using parameters unique to the Western US are shown in Figure 6. Historically, high frequency Pg/Lg has been used to discriminate mine blasts (Stump et al., 2002). For the set of events featured here, that discriminant does not appear to be successful. Examination of selected waveforms shows great variability in both the earthquake and explosion populations in terms of relative Pg/Lg. The large variation in relative amplitudes for the mine blasts suggests that more study is needed to quantify how and why similar source types (e.g., cast blasts) are seismically different. Variations in the earthquake relative amplitudes due to path effects may be an indication that calibration studies are needed to improve the results of amplitude discrimination in this region. Examination of other ratios yields similar variability trends, although the Pn(1-2 Hz)/Pn(6-8 Hz) discriminant (Figure 7) shows promise in discriminating cast blasts (red) from earthquakes (yellow).

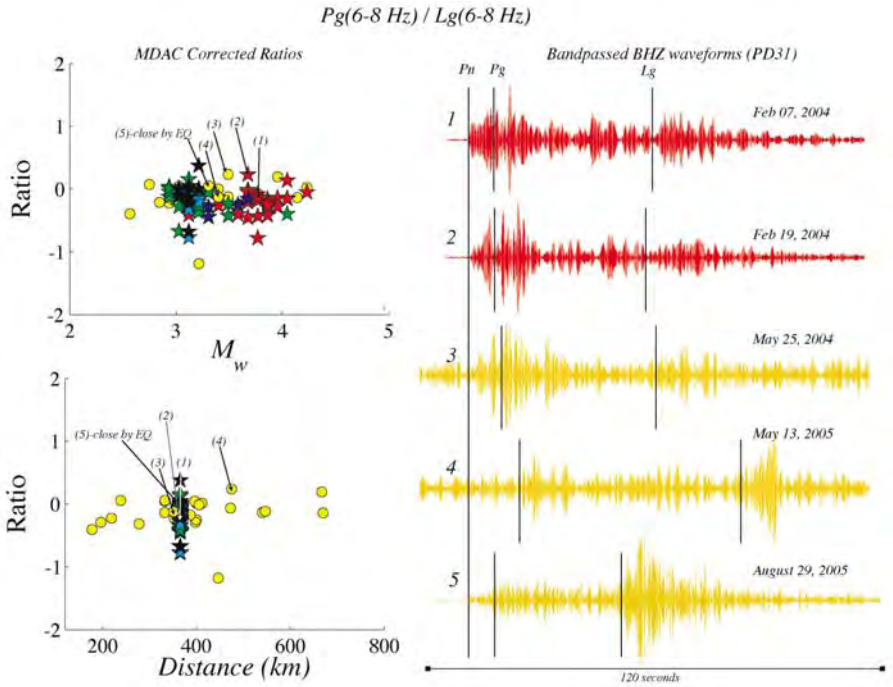

Figure 6. High frequency Pg/Lg discriminant values as a function of Mw and distance. Selected waveforms are shown for two cast blasts (red) and three earthquakes (yellow). Events passing an SNR of 2 for Pn and Pg and 1.3 for Lg are shown. Each point is colored by event type using the scheme in Figure 4.

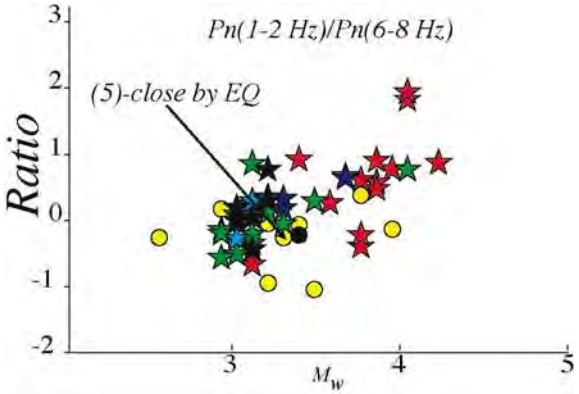

Figure 7. Pn(1-2 Hz)/Pn(6-8 Hz) ratio, which is a promising discriminant for Wyoming cast blasts.

Time-Frequency Discriminant

The time-frequency discriminant is based on spectrograms of recorded events. The discriminant exploits the fact that delay-fired mine blasts exhibit time-independent spectral modulations (Hedlin, 1989). Such spectral modulations are thought to be caused by either the dominant inter-shot or inter-row time spacing, or by the duration of the entire set of blasting depending on the individual delays and bandwidth of the observational data.

Figure 8 illustrates the time-frequency discriminant methodology using an example delay-fired mine blast. For each event, a spectrogram is computed for every component of each sensor that recorded it. The spectrograms are computed in time windows that begin at the first arrival (Pn or Pg) and extend through the Lg wave coda. Each spectrogram is reduced to binary form by filtering each spectral estimate with two running-average filters that comprise different window lengths, and then differencing the two filtered spectra (Figure 8). Locally high and low spectral values are then replaced 1 and 0 respectively and then the mean is removed.

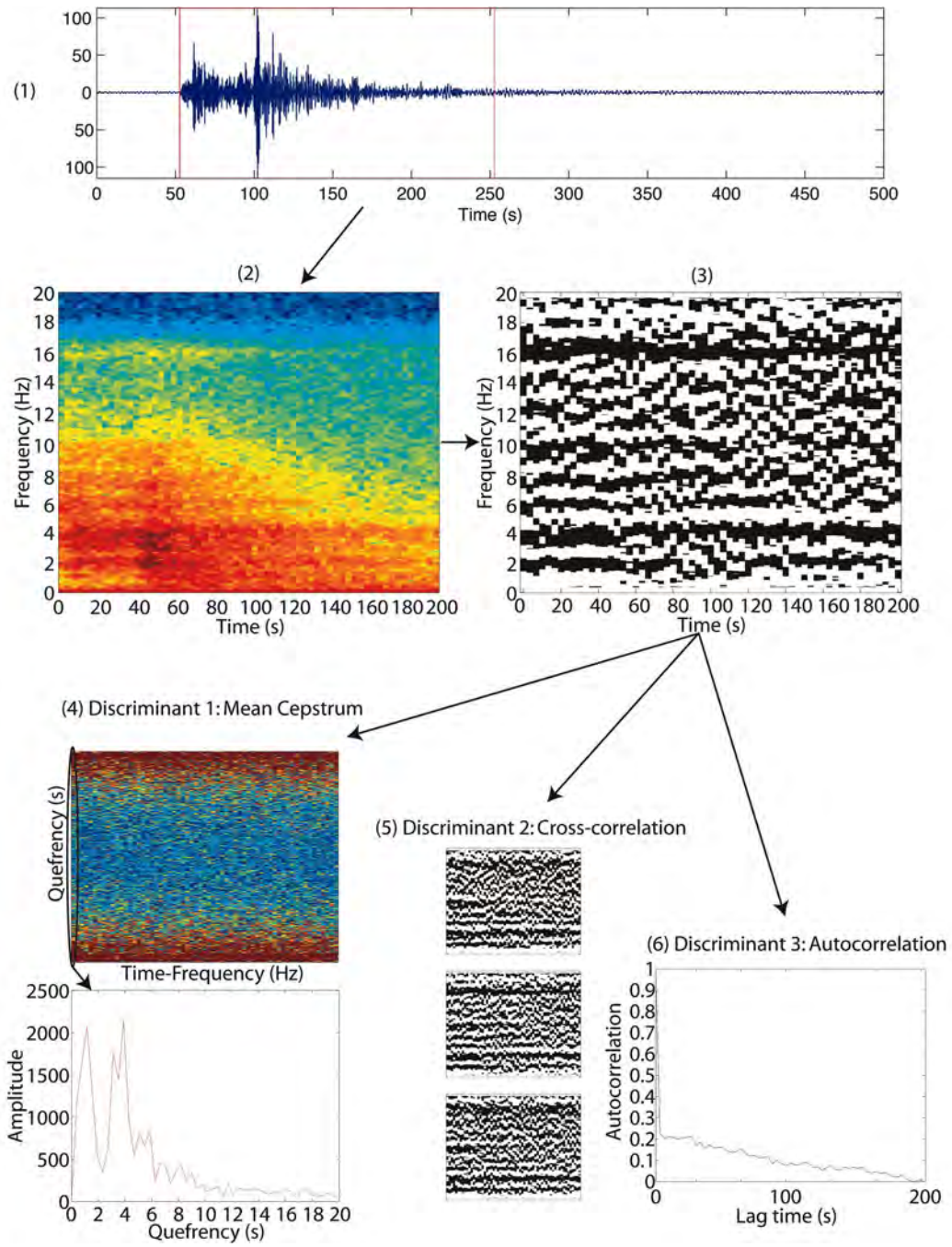

Figure 8. Flowchart that aids in explaining the time-frequency discriminant methodology using an example recording of a ripple-fired mine blast. (1) Input trace, with the red box showing the first arrival time of P energy through the Lg coda (window used for processing). (2) Spectrogram of input trace. (3) Binary spectrogram computed from input spectrogram in (2), showing clear evidence of time independent spectral scalloping. (4) 2D Cepstrum and 1D Cepstrum at zero time-frequency, showing clear evidence of cepstral peaks related to the time independent spectral scalloping. (5) Cross-correlation discriminant is computed using additional 2 traces of a 3-component recording. The additional 2D binary sonograms are shown to illustrate the clear correlation in spectral banding on the different components. (6) The autocorrelation is computed at a range of lag times and the mean is taken as a third discriminant.

Following Hedlin (1998) three different sets of discriminants are then computed, based on the binary spectrograms (Figure 8). The first discriminant is the mean cepstral value. This discriminant is evaluated by calculating the 2D cepstrum of each binary spectrogram and then retaining that part of the 2D cepstrum that reflects energy that is periodic in frequency but independent of time. For three-component seismometers the estimates from each of the individual components are stacked. This exploits the fact that cepstral structure should correlate on all 3 components for delay-fired mine blasts, but should be uncorrelated for earthquakes and single-fired mine blasts as long as a time independent spectral structure isn't acquired during propagation. A further two discriminants (Figure 8) exploit the fact that time independent spectral modulations should correlate on all 3 components (Cross-correlation) and that they should be time independent (Autocorrelation).

Figure 9 shows the mean cepstral values obtained for each class of event in the picked Wyoming dataset using the time-frequency discriminant method outlined above. We observe a clear separation between earthquakes (yellow) and the largest mining events (Cast blasts, red), with poorer separations for the smaller mining events. Similar results are obtained for the other two time-frequency discriminants: cross-correlation and autocorrelation. The methodology requires an a priori choice of a number of free parameters (e.g., filtering parameters for creating the binary spectrograms) and further work is required to train the algorithm to optimize the separation of earthquakes and each class of mine blasts separately. Although our initial results are very encouraging, different choices of filtering parameters for each class of mining event may result in an improved separation from earthquakes.

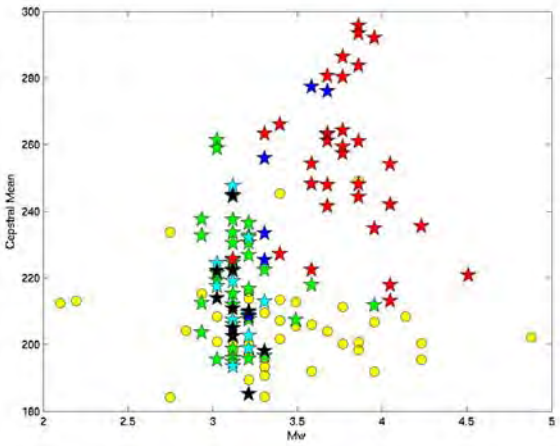

Figure 9. Mean cepstral value versus Mw for each event in the picked Wyoming dataset. Each point is colored by event type using the scheme in Figure 4.

Infrasound Discriminant

We will test using infrasound as an additional discriminant in Wyoming using Pinedale Infrasound Array (PDIAR) data. The premise behind this discriminant is that mine blasts are more efficient generators of infrasound than earthquakes, owing to their location on the free surface. Therefore, infrasound has potential to be an effective depth discriminant. For each event in the database, we will search for an associated infrasound signal with a consistent arrival time and backazimuth. Signal detection will be performed using the Progressive Multichannel Cross Correlation method. We will evaluate whether the presence (or absence) of an infrasound signal may then be used as a separate discriminant in our suite of discriminants.

CONCLUSIONS AND RECOMMENDATIONS

Using a subset of data in the Powder River Basin and surrounding area, we have tested two discriminants: amplitude ratios and time-frequency estimation. Initial results for the amplitude ratios show great variation in relative amplitudes for both earthquakes and mine blasts, making discrimination difficult using traditionally successful ratios (e.g., Pg/Lg (6-8 Hz)). Other ratios show better results, but further study is needed. Future work in this area will focus on gathering more information on individual blasts from the mines to ascertain conditions that lead to amplitude variability. Additional study on regional earthquakes will be useful to determine how path effects are influencing the outcome of this discrimination method. Initial results for the time-frequency method are very

promising, showing good separation between cast blasts and earthquakes, as well as some of the smaller mining events. Future work in this area will focus on refining filtering parameters and using all array elements to improve discrimination performance. We will also determine how to optimally combine each of the discriminants in order to maximize performance. Figure 10 illustrates a first order look at how utilizing more than one discriminant can increase population separation (cast blasts [red] discriminate well from earthquakes [yellow]). Finally, we plan to extend our analysis to include data collected in the Altai-Sayan coal mining regions in Russia; that dataset allows for the opportunity to test the transportability of the discriminants utilized in the Powder River Basin.

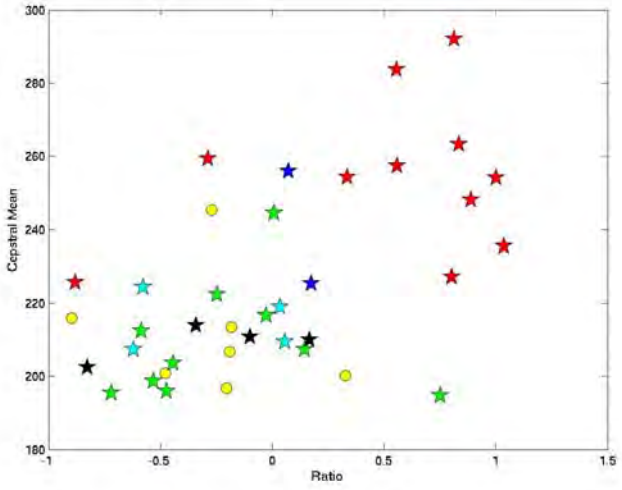

Figure 10. Combined results of the amplitude ratio discriminant featured in Figure 7 and the cepstral mean discriminant featured in Figure 9.

ACKNOWLEDGEMENTS

We wish to thank Steve Taylor at LANL for providing access to MDAC codes and data; Julio Aguilar-Chang at LANL for assembling additional data to supplement our database; Bill Walter at LLNL for giving us access to his Western US database; and the IRIS Data Management Center (DMC) for providing much of the data utilized in this study.

REFERENCES

Denny, M.D., S.R. Taylor, and E.S. Vergino (1987). Investigation of mb and Ms formulas for the Western United States and their impact on the Ms/mb discriminant, *Bull. Seism. Soc. Am.* 77: 987–995.

Hartse, H. E. (2001), A comparison of time- and frequency-domain amplitude measurements, in *Proceedings of the 23rd Seismic Research Review, Worldwide Monitoring of Nuclear Explosions,* Los Alamos National Laboratory document LA-UR-01-4454, Vol. 2, pp. 181-189.

Hedlin, M., B. Stump, S. Arrowsmith, and M. Renwald (2004), A Comparative Test of Seismic Discriminants for Mining Explosions, in *Proceedings of the 26th Seismic Research Review, Trends in Nuclear Explosion Monitoring,* LA-UR-04-5801, Vol. 1, pp. 407-416.

Hedlin, M. A. H. (1998), A Global Test of a Time-Frequency Small-Event Discriminant, *Bull. Seism. Soc. Am.* 88: 973–988.

Hedlin, M. A. H. , B. Minster, and J. Orcutt (1989), The Time-Frequency Characteristics of Quarry Blasts and Calibration Explosions Recorded in Kazakhstan, U.S.S.R., *Geopys. J. Int.* 99: 109–121.

Prodehl, C. and P.W. Lipman (1989), Crustal structure of the Rocky Mountain region, in Pakiser, L.C., and Mooney, W.D., *Geophysical Framework of the continental United States*: Boulder, Colorado, Geological Society of American Memoir 172, 249–284.

Stump, B., M.A.H. Hedlin, D.C. Pearson, and V. Hsu (2002), Characterization of Mining Explosions at Regional Distances, *Reviews of Geophysics*, 40: (4), 1011, doi:10.1029/1998RG000048.

Taylor, S. R., A. A. Velasco, H. E. Hartse, W. S. Phillips, W. R. Walter, and A. J. Rodgers (2002), Amplitude corrections for regional seismic discriminants, *Pure. App. Geophys.*, 159, 623-650.

Walter, W., K. Smith, J. O'Boyle, T. Hauk, F. Ryall, S. Ruppert, S. Myers, M. Anderson, and D. Dodge (2003), Improving the Fundamental Understanding of Regional Seismic Signal Processing with a Unique Western United States Dataset, in *Proceedings of the 25th Seismic Research Review*: *Nuclear Explosion Monitoring: Building the Knowledge Base*, Los Alamos National Laboratory document LA-UR-03-6029, pp. 486–494.

APPLICATION OF A TIME-DOMAIN, VARIABLE-PERIOD SURFACE WAVE MAGNITUDE MEASUREMENT PROCEDURE AT REGIONAL AND TELESEISMIC DISTANCES

Jessie Bonner[1], David Russell[2], David Harkrider[1], Delaine Reiter[1], and Robert Herrmann[3]

Weston Geophysical Corporation[1], Air Force Technical Applications Center[2], and St. Louis University[3]

Sponsored by Air Force Research Laboratory

Contract No. DTRA01-01-C-0080

ABSTRACT

Russell (2003) developed a time-domain method for measuring surface waves with minimum digital processing, using zero-phase Butterworth filters. For applications over typical continental crusts, the proposed magnitude equation for zero-to-peak measurements in millimicrons is

$$M_S(VMAX) = log(a_b) + \frac{1}{2} log(sin(\Delta)) + 0.0031\left(\frac{20}{T}\right)^{1.8}\Delta - 0.66\, log\left(\frac{20}{T}\right) - log(f_C) - 0.43 \qquad (1)$$

where

$$f_C \le \frac{0.6}{T\sqrt{\Delta}}.$$

To calculate M_s(VMAX), the following steps should be taken:

a. Determine the epicentral distance in degrees to the event Δ and the period *T*.
b. Calculate the corner filter frequency f_c using the inequality above.
c. Filter the time series using a zero-phase, third-order Butterworth band-pass filter with corner frequencies $1/T$-f_c, $1/T$+f_c.
d. Calculate the maximum amplitude a_b of the filtered signal and calculate M_s(VMAX).

We demonstrate the capabilities of the method using applications to three different datasets. The first application utilizes a dataset that consists of large earthquakes in the Mediterranean region. The results indicate that the M_s(VMAX) technique provides regional and teleseismic surface-wave magnitude estimates that are in general agreement except for a small distance dependence of -0.002 magnitude units per degree. We also find that the M_s(VMAX) estimates are less than 0.1 magnitude unit different than those from other formulas applied at teleseismic distances such as Rezapour and Pearce (1998) and Vaněk et al. (1962).

In the second and third applications of the method, we demonstrate that measurements of M_s(VMAX) versus m_b provide adequate separation of the explosion and earthquake populations at the Nevada and Lop Nor Test Sites. At the Nevada Test Site, our technique resulted in the misclassification of two earthquakes. We also determined that the new technique reduces the scatter in the magnitude estimates by 25% when compared to our previous studies using a calibrated regional magnitude formula. For the Lop Nor Test Site, we had no misclassified explosions or earthquakes; however, the data were less comprehensive.

A preliminary analysis of Eurasian earthquake and explosion data suggests that similar slopes are obtained for observed surface-wave data at m_b < ~5. These results suggest that the discrimination of explosions from earthquakes can be achieved at lower magnitudes using the Russell (2005) formula and the M_s(VMAX) measurement technique.

OBJECTIVES

Russell (2005) developed a time-domain method for measuring surface waves with minimum digital processing, using zero-phase Butterworth filters. The method can effectively measure surface-wave magnitudes at both regional and teleseismic distances at variable periods between 8 and 25 seconds. For applications over typical continental crusts, the magnitude equation is

$$M_S(VMAX) = log(a_b) + \frac{1}{2}log(sin(\Delta)) + 0.0031\left(\frac{20}{T}\right)^{1.8}\Delta - 0.66\,log\left(\frac{20}{T}\right) - log(f_c) - 0.43 \qquad (2)$$

where a_b is the amplitude of the Butterworth-filtered surface waves (zero-to-peak in nanometers) and

$$f_c \le \frac{0.6}{T\sqrt{\Delta}}$$

is the filter frequency of a third-order Butterworth band-pass filter with corner frequencies $1/T$-f_c, $1/T$+f_c. At the reference period T=20 seconds, the equation is equivalent to von Seggern's formula (1977) scaled to Vaněk et al. (1962) at 50 degrees. For periods $8 \le T \le 25$, the equation is corrected to T=20 seconds, accounting for source effects, attenuation, and dispersion.

To calculate M_s(VMAX), the following steps should be taken:

a. Determine the epicentral distance in degrees to the event Δ and the period T.
b. Calculate the corner filter frequency f_c using the inequality above.
c. Filter the time series using a zero-phase, third-order Butterworth band-pass filter with corner frequencies $1/T$-f_c, $1/T$+f_c.
d. Calculate the maximum amplitude a_b of the filtered signal and calculate M_s(VMAX).

The objective of this paper is to present the results of applying the Russell (2005) formula at teleseismic and regional distances for variable-period data. First, we applied the formula to a large earthquake dataset to demonstrate the analysis method and to determine if the regional and teleseismic magnitudes are unbiased with respect to each other. We compare the resulting magnitudes from the Russell equation with estimates from the Vaněk et al. (1962) and Rezapour and Pearce (1998). Then, we used the formula to estimate surface-wave magnitudes for explosions and earthquakes in Eurasia and North America to examine if we can improve discrimination performance.

RESEARCH ACCOMPLISHED

We applied the Russell (2005) formula and our M_s(VMAX) technique to three different surface-wave datasets. For the first application of the formula, we estimated surface-wave magnitudes for several large earthquakes in the Mediterranean region of Europe. For the second and third applications, we estimated M_s(VMAX) for earthquakes and explosions in North America and Eurasia, respectively. And finally, we examined all of the data in Eurasia to determine the performance of the M_s-m_b discriminant when our magnitude estimation techniques are used.

Mediterranean Region

We applied the Russell (2005) formula and M_s(VMAX) measurement technique to earthquakes in the Mediterranean region to determine if a) we obtain consistent magnitudes at regional and teleseismic distances and b) our M_s estimates match those obtained using the Vaněk et al. (1962) and Rezapour and Pearce (1998) formulas.

Data. We developed a database of broadband vertical component recordings of 34 earthquakes that occurred in the Mediterranean region of Europe (Figure 1). For this pilot study, we focused on larger events (mb > 5.4) with depths of 50 km or less. These restrictions ensured adequate signal-to-noise ratios for the surface waves recorded at regional and teleseismic distances. The data were acquired from the Incorporated Research Institutions for Seismology (IRIS) and consisted of global and regional networks in the study region. The data were all transformed

from counts to displacement in nanometers using the Seismic Analysis Code command "transfer" and the SEED response files. The data were decimated from their original sampling rates (> 20 samples/second) to approximately 1 sample/sec for the surface-wave analysis. Down sampling increases the analysis speed and eliminates digital filter problems associated with narrow-band filtering, as discussed in Appendix B of Russell (2005).

Figure 1. Test dataset of events in the Mediterranean region and stations used to test the Russell (2005) formula and M_s(VMAX) measurement technique.

Results. Our first objective in this exercise was to determine if there is a distance dependence in the formula and measurement technique. As mentioned in the introduction of this manuscript, previous research has been unsuccessful at finding a single, variable-period formula valid at both regional and teleseismic distances.

We performed a distance analysis on all 34 events of our test database similar to the one performed in the lower plot of Figure 2. In order to compare events of different magnitudes, we removed the mean magnitude from each event's analysis. Figure 2 shows the results, which include 1,348 M_s(VMAX) magnitude estimates from the events shown in Figure 1. Our objective was to test the formula for a predominance of continental paths; thus, data are at distances less than 70 degrees. A linear regression of the mean-removed magnitude estimates with increasing distance shows a small (0.002 magnitude unit [mu] per degree) decrease in magnitudes. The standard deviation for the regression analysis is 0.21 mu). This suggests that if an event had an M_s(VMAX) magnitude estimate of 6.0 measured at a distance of 5 degrees, the magnitude estimated at a distance of 60 degrees would be ~5.89. This difference is well within the scatter typically observed for surface-wave magnitude estimates resulting from focal mechanisms and path effects.

Because M_s(VMAX) is a variable-period technique, we also examined the periods at which the estimates were formed (Figure 3). There is a general increase in the number of measurements in each bin from shorter to longer periods. This increase is reassuring, since it is consistent with past studies which found that the best period range to measure M_s is between 17 and 23 seconds.

We observe an edge effect associated with ending the surface-wave magnitude analysis at 25 seconds. There are two explanations for this behavior. Because of the spectral shape of earthquakes, they will tend to select longer periods, especially when the events are deeper than the upper crust. In addition, because of the nature of surface wave propagation, we would expect to see a general trend of longer-period measurements with increasing distances. This trend is related to the rapid attenuation of shorter-period amplitudes compared with the longer periods at longer epicentral distances. In Figure 3, we plotted the distances and periods at which the magnitudes were estimated. The plot shows that for the magnitudes estimated at periods of 10 seconds or less, the corresponding epicentral distances were less than 30 degrees. From 10 to 18 seconds, we note a general increase in the cut-out distance from 30 to 60 degrees. For periods greater than 18 seconds, we note that the cut-out distance continues to increase but is less

constrained by the available data. The results in Figure 3 suggest that the formula is behaving as we intended. It also hints that the analysis could be improved by increasing the long-period limit to periods greater than 25 seconds.

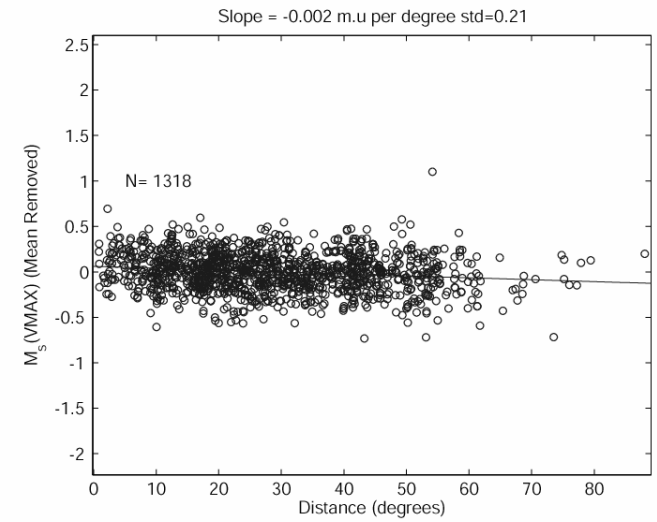

Figure 2. Regression of mean-removed M_s(VMAX) magnitude estimates for the 34 events in Figure 1 with distance. There is a very small decrease in magnitude units (0.002 m.u. per degree) with increasing distance.

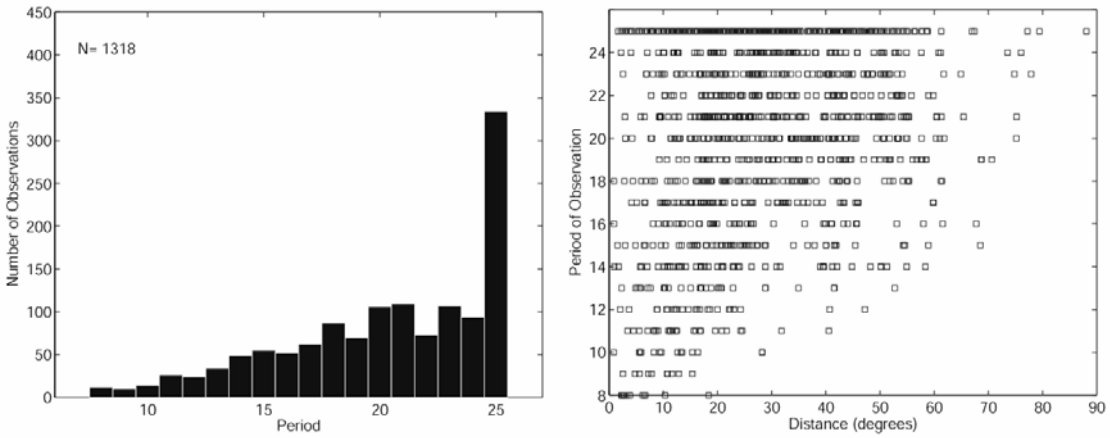

Figure 3. (Left). Bins showing the periods used to estimate the M_s(VMAX) magnitudes at 1348 different station-source pairs. (Right). Comparison of the periods of the M_s(VMAX) estimates compared with the epicentral distance.

As a final step in the analysis of the events in Figure 1, we compared our M_s(VMAX) estimates with magnitude estimates published by the United States Geological Survey (USGS) and the International Data Center (IDC) in Vienna and to the M_w estimates obtained from Harvard's Centroid Moment Tensor (CMT) analysis. The results are shown in Figure 4. We note that the USGS uses the Vaněk et al. (1962) formula, while the IDC uses the Rezapour and Pearce (1998) formula. We performed a fixed slope (slope=1) regression of the M_s(VMAX) estimates against the results from the other organizations to determine the offset between the estimates. The results indicate that the M_s(VMAX) is -0.03 and 0.05 magnitude units different than the Vaněk et al. (1962) and Rezapour and Pearce (1998) formulas, respectively. Differences of this size for all three comparisons are well within the scatter of the observations. Also, the right subplot of Figure 4 shows that the M_s(VMAX) and M_w estimates are approximately equal for $6.0 < M_w < 7.2$.

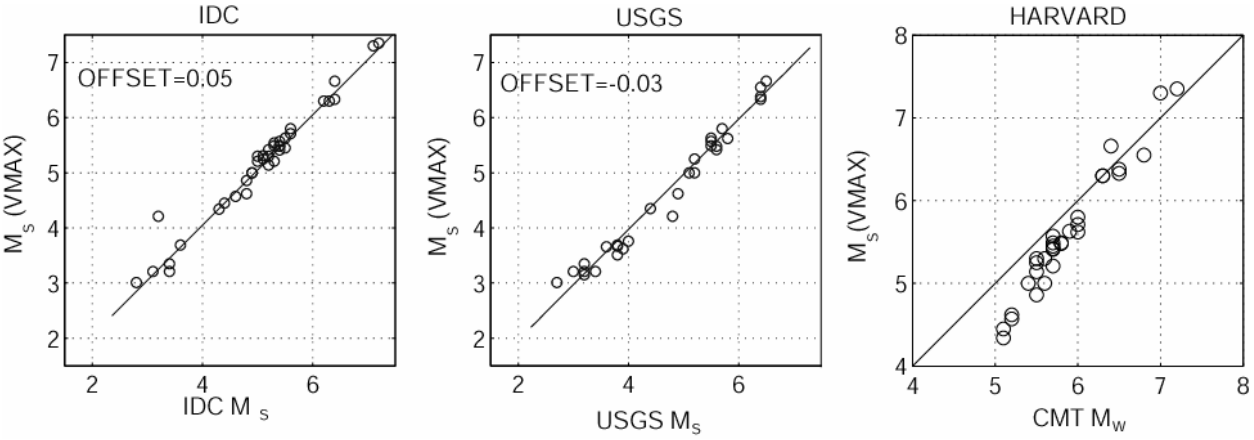

Figure 4. (Left). Fixed slope (slope=1) regression of M_s(VMAX) network-average magnitudes versus the IDC M_s for the Mediterranean events. (Middle). Fixed slope (slope=1) regression of M_s(VMAX) network-average magnitudes versus the USGS M_s. (Right). Comparison of the M_s(VMAX) network-average magnitudes versus the Harvard CMT M_ws.

Nevada Test Site Earthquake and Explosion Discrimination.

Next, we examined the performance of the Russell (2005) formula and M_s(VMAX) measurement technique on earthquake and explosion discrimination at the Nevada Test Site in the western United States (Figure 5). Figure 6 shows the regression of the M_s (VMAX) versus the Denny et al. (1987; 1989) m_b for both the earthquake and explosion populations in our test dataset (Figure 5). The best-fitting regression lines are plotted as solid lines, and the slope and intercepts for the lines are presented in the left subplot. The populations plotted in Figure 6 suggest that M_s and m_b will be fitted well by linear regressions, with approximately equal slopes assumed for the earthquake and explosion populations. While we did observe slightly different slopes in the regression analyses for the two populations, we believe that this is due to inadequate sampling of earthquakes at m_b magnitudes greater than 5.2. Our dataset does not present any evidence that the two populations are converging at smaller magnitudes, although other M_s-m_b studies (Stevens and McLaughlin, 2001) suggest that convergence does occur. The classification equation based on the parallel-slope assumption becomes

$$d = M_s(\text{VMAX}) - 1.3m_b \qquad (3)$$

where d is the decision value. We chose to use the explosion slope, as we believe that it is better constrained with the available data, and synthetic studies suggest (Bonner and Herrmann, 2004) that it does not change with increasing magnitude. If d < -2.30, the event will reside in the explosion population. We note that this does not require the event to be a nuclear explosion, as additional testing is needed to ensure the event is shallow enough to be a candidate explosion. If d > 2.30, the event falls into the earthquake classification. We misclassified two earthquakes in the explosion population. In our previous studies based on 7-second data (Bonner et al., 2003), we misclassified four earthquakes as explosions.

Lop Nor Test Site Earthquake and Explosion Discrimination.

In our third application of the Russell (2005) formula and M_s(VMAX) measurement technique, we examined earthquake and explosion discrimination at the Lop Nor nuclear test site in China (Figure 7). As shown in Figure 8, we regressed the M_s (VMAX) versus the USGS m_b for both the earthquake and explosion populations in our test dataset. The best-fitting regression lines are plotted as solid lines. The slope and intercepts for the lines are presented in the left subplot.

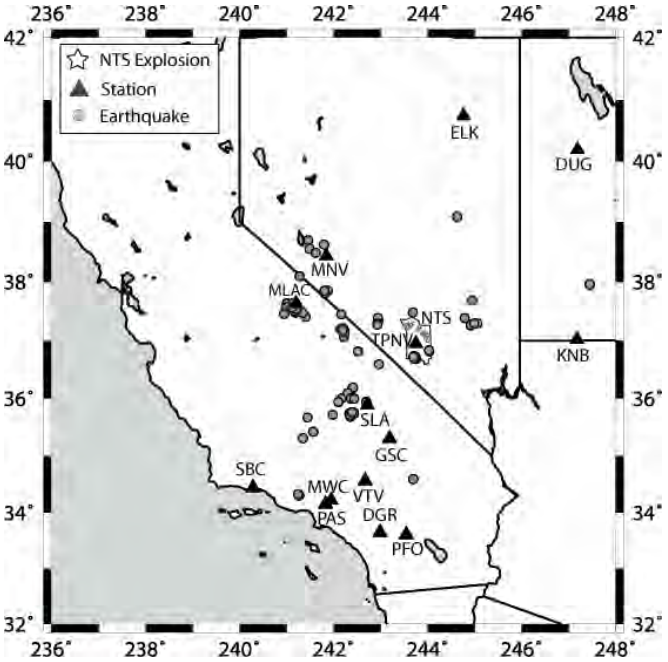

Figure 5. Test dataset consisting of NTS explosions recorded on the LNN dataset together with western United States earthquakes recorded on at least one LNN station and other regional networks.

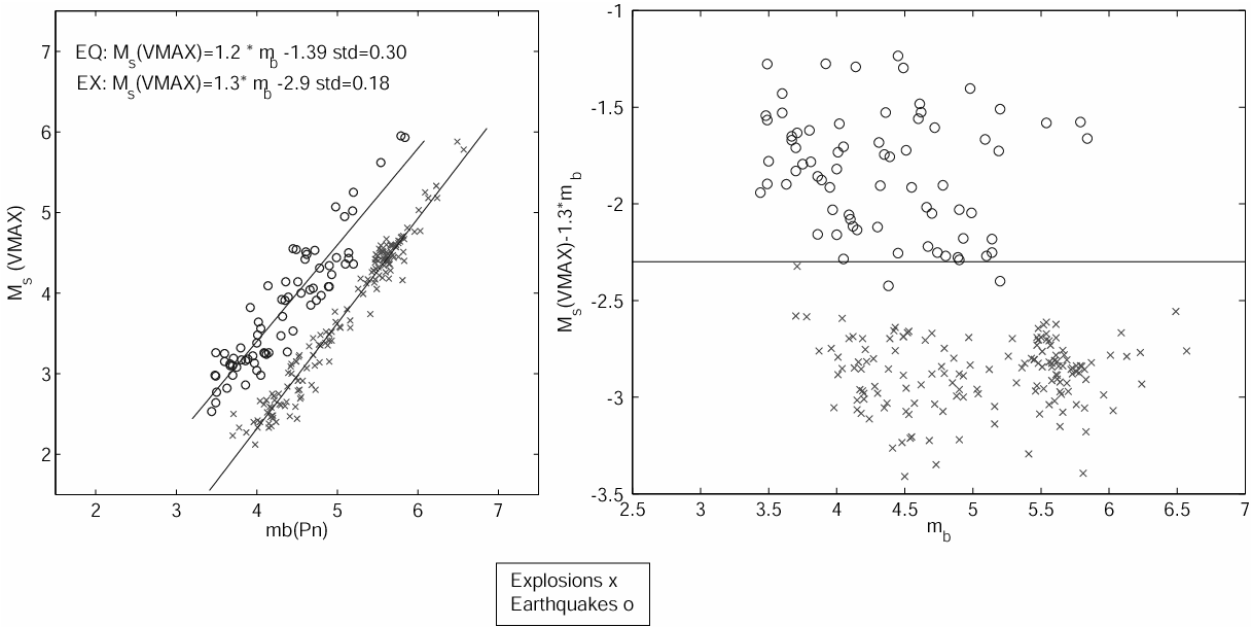

Figure 6. Discrimination results for M_s (VMAX) at the Nevada Test Site. Left: M_s (VMAX) vs. m_b for western United States earthquakes and nuclear explosions. Right: Linear discrimination of the two datasets showing the decision line for classifying an event as a possible nuclear explosion. If d=M_s (VMAX) – 1.3m_b is less than -2.45, the event may be an explosion, and additional analysis will be required to prove the event is not a deep and/or anomalous earthquake.

The slopes for the earthquake and explosion data were 1.0 and 1.2, respectively. Again, there is no evidence suggesting that the populations are converging at smaller magnitudes. We used the slope for the explosions to compute a linear discriminant analysis. As a result, we developed the following classification equation:

$$d = M_s(\mathrm{VMAX}) - 1.2m_b, \quad (4)$$

where d is the decision value. If d < -2.6, the event will reside in the explosion population and requires additional processing prior to being classified as a candidate explosion. If d > -2.6, the event falls into the earthquake classification. We note that no Lop Nor explosions or earthquakes were misclassified using the VMAX magnitude estimation technique with the Russell (2005) surface-wave magnitude scale. However, we have fewer events for this region than we did for the NTS comparison.

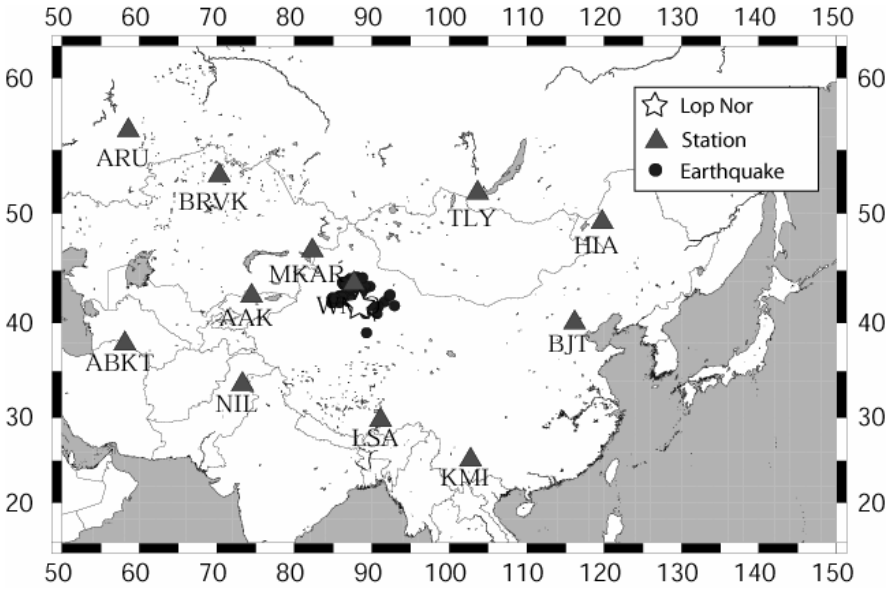

Figure 7. Test dataset consisting of Lop Nor explosions recorded on regional and near-teleseismic stations (triangles) together with western Chinese earthquakes (solid circles).

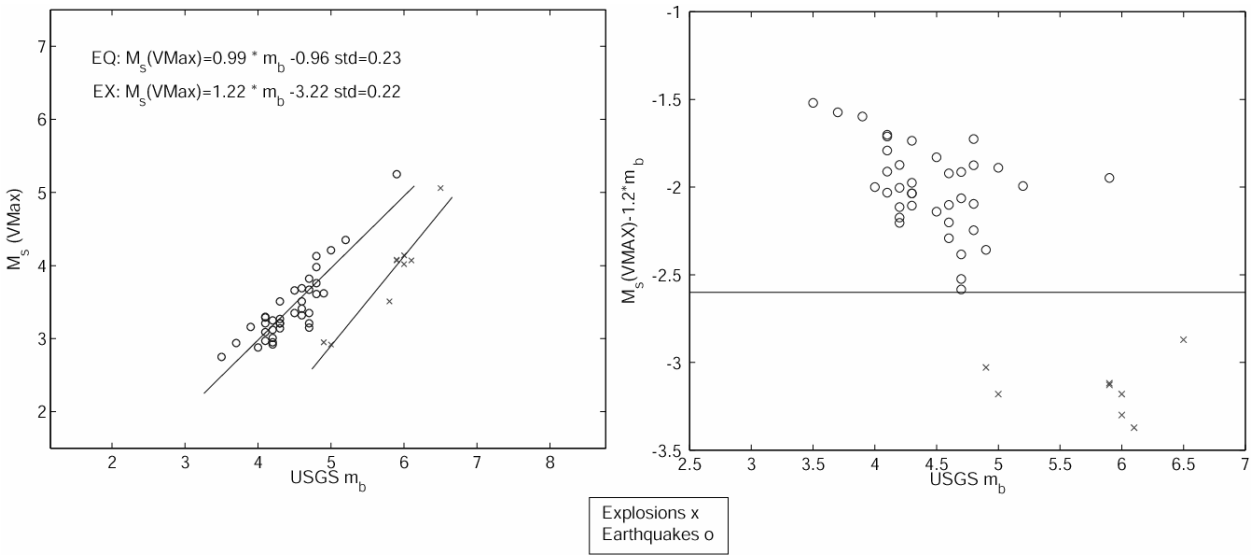

Figure 8. Discrimination results for M_s (VMAX) at the Lop Nor Test Site. Left: M_s (VMAX) vs. m_b for northwestern China earthquakes and nuclear explosions at Lop Nor. Right: Linear discrimination of the two datasets showing the decision line (-2.6) for classifying an event as a possible nuclear explosion.

Eurasian Results

There is a general disagreement among researchers in the nuclear monitoring community as to how well the M_s—m_b discriminant performs at small-to-intermediate body-wave magnitudes. Some researchers believe that the available M_s—m_b datasets suggest that the two populations converge at smaller magnitudes (e.g., Stevens and McLaughlin, 2001). These researchers believe that the population convergence is caused by earthquake and explosion sources that become phenomenologically similar at smaller magnitudes. Lambert and Alexander (1971) determined that the earthquake and explosion populations at the Nevada Test Site are characterized by parallel M_s vs. m_b curves, with slopes of 1 and a difference of 0.82 magnitude units based on linear regression fits. Alexander (2002; personal communication) suggests that any convergence at the smaller magnitudes is related to depth and not the phenomenology behind explosion and earthquake sources.

To determine whether depth or source phenomenology is responsible for converging M_s—m_b behavior at smaller magnitudes, we pooled all of our Eurasian M_s(VMAX) estimates. We also calculated M_s(VMAX) for 11 additional nuclear explosions in Eurasia and combined them with the Lop Nor explosions from Figure 8. Figure 9 shows the M_s(VMAX) estimates from all these data plotted versus USGS m_b.

Because of corner frequency effects for earthquakes and m_b measurement procedures, there should be a change in slope for regressed M_s(VMAX) vs m_b near m_b = 5 (Nuttli, 1983). As shown in Figure 9, the slope for the best-fit regressions above m_b = 5 is 1.46 with a standard deviation of 0.21 magnitude units. The slope for the regressions below m_b = 5 is 0.94, which is similar to the slope determined for the observed explosion data (1.04). With the current dataset, we cannot rule out the possibility that a single line with slope equal to 1.54 can fit all of the earthquake data. In fact, the correlation coefficients for single-line or two-line fits are essentially the same (R^2 > 0.85). If the earthquake data were fit with a single line, we would see convergence of the populations near m_b = 3.5, which agrees with Stevens and McLaughlin (2001).

However, if we focus on the two-line case, the slopes for our earthquake and explosion populations at m_b values < 5 are similar to the Lambert and Alexander (1971) results. Additionally, we observed 0.90 magnitude units separation between the two populations at m_bs below 5, while Lambert and Alexander (1971) noted a difference of 0.82 magnitude units, based on the fitted regression lines for their NTS earthquakes and explosions. Differences between the theoretical and observed slopes above m_b > 5 may be related to the difficulties of measuring body-wave magnitudes for large events. While more data will be required to finalize the two-slope hypothesis, these preliminary results suggest that the discrimination of explosions from earthquakes can be achieved at lower magnitudes using the Russell (2005) formula and the M_s(VMAX) measurement technique.

Murphy et al. (1997) determined an event screening relationship based on M_s—m_b estimates. For USGS estimated m_b, the screening criterion is

$$M_s = 1.25\, m_b - 2.60. \qquad (5)$$

We plotted the Murphy et al. (1997) criterion in Figure 9 as the dashed line and note that two of the earthquakes fall below this line. More importantly, none of our explosions plotted above this line.

CONCLUSIONS AND RECOMMENDATIONS

The Russell surface-wave magnitude formula and the M_s(VMAX) measurement technique provide a new method for estimating surface-wave magnitudes. There are several benefits to the new method. First, the technique allows for time domain measurements of surface-wave amplitudes, giving an analyst the ability to visually confirm that the pick is correct and is an actual surface wave. Also, it allows for surface-wave magnitudes to be measured at local and regional distances where traditional 20-second magnitudes cannot be used. And these magnitudes are not biased with respect to teleseismic estimates using the same M_s(VMAX) measurement technique. Additionally, the application of narrow-band Butterworth-filtering techniques appropriately handles Airy phase phenomena that prior to this study, had to be accounted for using Marshall and Basham's (1972) empirical corrections. Finally, because the method is variable period and not restricted to near 20-seconds period, the analyst is allowed to measure M_s where the signal is largest. The new method has been successfully tested on three research datasets, and the results

suggest that the method can be used to screen out a large percentage of small earthquakes at $m_b < 5$. Thus, we are currently implementing the technique for operational testing.

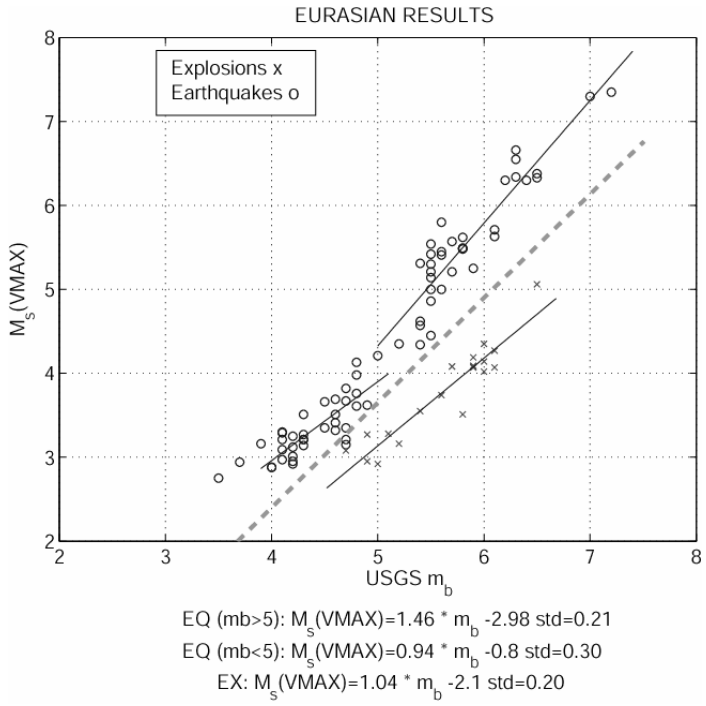

Figure 9. M_s—m_b relationships for all Eurasian earthquake and explosion data for which an M_s (VMAX) was estimated during this study. The body wave magnitudes are all from the United States Geological Survey. We split the earthquake data at m_b = 5 based on corner frequency effects for earthquakes and m_b. The earthquake and explosion populations both have slopes that are approximately 1 for m_b < 5 and are separated by an average of 0.90 magnitude units. The dashed line is the Murphy et al. (1997) criterion for event screening.

REFERENCES

Alexander, S. S. 2002, Seismic monitoring for underground nuclear explosions, in Science, Technology and National Security, Majumbar, S. K., Alexander, S. S., Rosenfeld, L. M., Rieders, M. F., Miller, E. W., and A. I. Eds., The Pennsylvania Academy of Sciences, Easton, PA 18042, 267pp.

Bonner, J., D. Harkrider, E. T. Herrin, R. H. Shumway, S. A. Russell and I. M. Tibuleac (2003). Evaluation of short-period, near-regional M_s scales for the Nevada Test Site. *Bull. Seism. Soc. Am.* 93: 1773–1791.

Bonner, J. and R. B. Herrmann (2004), A Synthetic M_s—m_b study. Weston Geophysical Scientific Report. 20p.

Denny, M.D., S. R. Taylor, and E.S. Vergino (1987), Investigation of m_b and M_s formulas for the western United States and their impact on the M_s/m_b discriminant, *Bull. Seism. Soc. Am.* **77**: 987–995.

Denny, M.D., S. R. Taylor, and E.S. Vergino (1989), Erratum: Investigation of m_b and M_s formulas for the western United States and their impact on the M_s/m_b discriminant, *Bull. Seism. Soc. Am.* 79: 230.

Herrmann, R. B. (2004), Computer programs in seismology Version 3.30, St. Louis University.

Lambert, D.G. and S.S. Alexander, (1971), Relationship of body and surface wave magnitudes for small earthquakes and explosions, SDL Report 245, Teledyne Geotech, Alexandria, VA.

Marshall, P.D. and P.W. Basham (1972), Discrimination between earthquakes and underground explosions employing an improved M_s scale, *Geophys. J. R. Astr. Soc.* 29: 431–458.

Murphy, J. R., B. W. Barker, and M. E. Marshall, (1997), Event screening at the IDC using the Ms/mb discriminant. Maxwell Technologies Final Report. 23 p.

Nuttli, O.W. (1983). Average seismic source-parameter relations for mid-plate earthquakes. *Bull. Seism. Soc. Am.*, 73: 519–535.

Rezapour, M., and R.G. Pearce (1998), Bias in surface-wave magnitude M_s due to inadequate distance correction, *Bull. Seism. Soc. Am.* 88: 43–61.

Russell, D.R. (2005), Development of a time-domain, variable-period surface wave magnitude measurement procedure for application at regional and teleseismic distances. Part I—Theory. Submitted to *the Bull. Seism. Soc. Am.*

von Seggern, D. (1977), Amplitude distance relation for 20-Second Rayleigh waves, *Bull. Seism. Soc. Am.* 67**:** 405–411.

Stevens, J. L. and K.L. McLaughlin (2001), Optimization of surface wave identification and measurement, in *Monitoring the Comprehensive Nuclear Test Ban Treaty: Surface Waves*, eds. Levshin, A. and M.H. Ritzwoller, *Pure Appl. Geophys.* 158: 1547–1582.

Vaněk, J., A. Zatopek, V. Karnik, Y. V. Riznichenko, E. F. Saverensky, S. L. Solov'ev, and N. V. Shebalin (1962), Standardization of magnitude scales, *Bull. (Izvest.) Acad. Sci. U.S.S.R., Geophys. Ser.* 2: 108.

SOURCE PHENOMENOLOGY EXPERIMENTS IN ARIZONA

Jessie L. Bonner[1], Brian Stump[2], Mark Leidig[1], Xiaoning Yang[3], Rongmao Zhou[2], Tae Sung Kim[2], William R. Walter[4], Aaron Velasco[5], Chris Hayward[2], Diane Baker[3], C. L. Edwards[3], Steven Harder[5], Heather Hooper[1], Travis Glenn[2], Cleat Zeiler[5], Rengin Gok[4], James Britton[1], and James F. Lewkowicz[1]

Weston Geophysical Corporation[1], Southern Methodist University[2], Los Alamos National Laboratory[3], Lawrence Livermore National Laboratory[4], and University of Texas at El Paso[5]

Sponsored by National Nuclear Security Administration
Office of Nonproliferation Research and Engineering
Office of Defense Nuclear Nonproliferation

Contract Nos. DE-FC03-02SF22638[1], 021364[2], FIA-02-048-A001[3], L-9783[4], and 26-8210-14[5]

ABSTRACT

The Source Phenomenology Experiments (SPE) were conducted at mines in northeastern and southeastern Arizona in the summer of 2003. The Arizona experiments have resulted in an important dataset for the nuclear monitoring community by providing data to address a number of source parameter issues. We designed, detonated, and recorded ten single-fired explosions at a copper mine in southeast Arizona and nine single-fired explosions in a northern Arizona coal mine. The single-fired explosions ranged in size from 200 to ~33000 lbs. of a mixture of Ammonium Nitrate Fuel Oil (ANFO) and emulsion explosives. Delay-fired mining explosions at each mine were also recorded. The explosions were recorded by hundreds of seismic instruments deployed at local and regional distances in addition to permanent regional broadband stations.

Using this large dataset, we developed velocity models of the Black Mesa basin, Colorado Plateau, and southern Arizona for moment tensor inversion. Detailed refraction surveys were conducted at the mine test sites in order to determine the *P*- and *S*-wave velocities of the test beds and layer thicknesses. We used local single-component geophones (Texans) and regional broadband stations to study the *P*-wave velocity structure of the upper crust. *Rg* dispersion curves were extracted from the single-component local (<15 km) data and we inverted the data for *S*-wave velocity structure of the test pit region and upper crust. We also performed a joint inversion of surface wave dispersion and receiver functions to constrain the structure of the middle and lower crust.

By inverting near-source broadband data, we developed time-dependent source moment tensors for several explosions detonated during the SPE. The results show that isotropic components dominate the moment tensors, especially for the contained explosions. Vented explosions have moment-tensor spectra that are more peaked than those of fully contained explosions. Moment tensors of cast blasts show a certain amount of longer-period later-arriving energy for off-diagonal components, which is responsible for most of the shear energy generated.

We examined the regional discrimination of the SPE shots relative to normal production mining explosions, natural earthquakes, and previous nuclear tests at the Nevada Test Site. The discrimination analysis includes identifying and picking the onset times of the regional phases *Pn*, *Pg*, and *Lg*, making amplitude measurements in a variety of passbands, normalizing those measurements for the effects of source and path using the Magnitude and Distance Amplitude Correction (MDAC) methodology, and calculating *Pg*/*Lg* ratios for each event. We find that the MDAC-corrected SPE shots fall in the middle of the nuclear explosion population with very little variation due to the differing shot conditions. Thus for particular discriminants at several regional stations, the SPE shots and mining explosions are good surrogates for nuclear explosions, and the differences in depth of burial and single versus multiple shot have only a small effect on the discriminant measures. We are extending this analysis to other regional stations (e.g., ANMO, TUC, WUAZ; regional profile stations) and other discriminants to more completely examine the discrimination relationship of the SPE shots to production shots, earthquakes and nuclear tests.

OBJECTIVES

We have continued research on the large dataset collected during the Source Phenomenology Experiments (SPE) in Arizona. The goal of the project is to understand the phenomenology differences that affect various types of explosions and improve the discrimination of earthquakes and chemical and nuclear explosions. In this paper, we discuss the continued work on: 1) the inversion of near-source data for source moment tensors, 2) the effects of yield and confinement on source functions, and 3) the development of regional discriminants. These objectives are supported by the development of detailed site, local and regional velocity models for the regions involved.

RESEARCH ACCOMPLISHED

Experiment Location and Design

In September 2003, we detonated and recorded ten single-fired explosions at a copper mine in southeastern Arizona and nine single-fired explosions in a northern Arizona coal mine. The single-fired explosions ranged in size from 200 to ~33000 lbs. of a mixture of ANFO and emulsion explosives. Delay-fired mining explosions at each mine were also recorded. Additionally, we carried out detailed refraction surveys in and around the source region to define local material properties. Figure 1 shows the mine locations and the stations deployed to record the explosions.

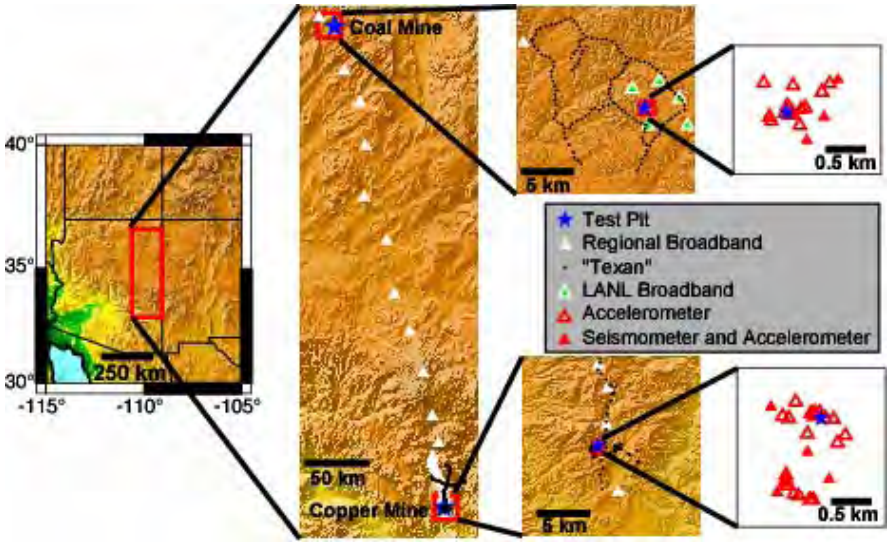

Figure 1. Location maps for the SPE mines and stations deployed.

Velocity Structure

The development of a detailed velocity and attenuation structure for the coal mine in northern Arizona is discussed in the Seismic Research Review paper by Leidig *et al.* (2004) and also in Leidig *et al.* (in review). The explosion medium at the coal mine was determined to be slow and indicative of highly-fractured, dry sedimentary rock. Leidig *et al.* (2004) also discusses the development of a velocity model for the copper mine in southern Arizona. Below is a further discussion of the velocity model for the copper mine.

Detailed refraction surveys were conducted at the copper mine test site in order to determine the *P*-wave velocities (V*p*) of the test bed. The structure consisted of a shallow (4-5.5 m) weathered layer (0.58 < V*p* < 0.67 km/sec), a second layer (~18 m with 2.44 < V*p* < 3.05 km/sec), and faster velocities at greater depths (V*p* > 4.57 km/sec). The refraction studies are described in detail in Hayward et al. (2004). The velocities of the emplacement media in this granite porphyry are significantly faster than the limestone test pit at the coal mine.

The compressional-wave velocity was further constrained using the first arrivals of *P*- waves recorded on a north-south line of Texans north of the copper mine. A *P*-wave velocity structure of two layers over a halfspace, with velocities estimated to be 4.55, 5.21, and 6.07 km/s respectively, was inferred from the travel-time curves. The corresponding layer thicknesses were calculated to be 0.15 km and 3.38 km, using the relationship between velocity, critical distance, and intercept time (Dobrin, 1960).

The dispersion curves of the *Rg* phase recorded on the N-S broadband station profile were used to provide shear wave velocity constraints for our model. The dispersion curves show a systematic variation, implying the existence of a strong lateral variation in the velocity structure around the mine (Figure 2a). It is believed that the variation is caused by a change from a granodiorite body (faster dispersion curves) located in the source region (0-7 km in Figure 2b) to deformed sedimentary rocks (slower dispersion curves). The velocity models produced from differential inversion of these dispersion curves are tabulated in Kim and Stump (in preparation).

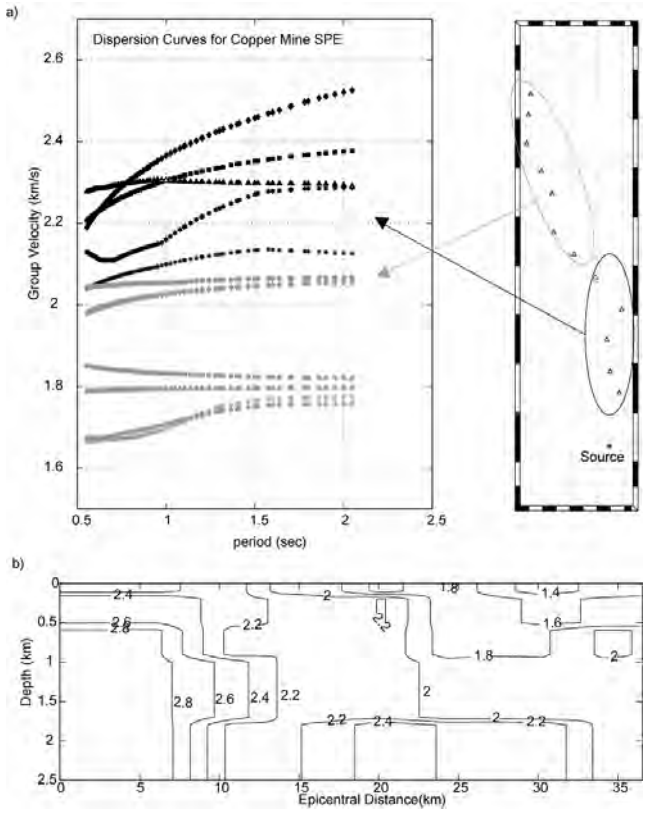

Figure 2. Shear wave velocity data for the source region at the copper mine. a) Short-period, fundamental-mode Rayleigh wave (*Rg*) group velocity dispersion curves from broadband recordings showing possible lateral variations in shear-wave velocity structure. b) Differential inversions of the dispersion curves showing changes in the structure with increasing distance from the sources.

Moment Tensor Inversion

We used the Leidig et al. (in review) velocity model from northern Arizona in moment tensor inversions of shots 3 (fully contained), 4 (partially contained), and 9 (uncontained cast shot without delays between holes). The moment-rate tensors all show strong isotropic characteristics (Figure 3). The acausal appearance of the shot 9 moment tensors was possibly caused partly by the point-source approximation that is not as accurate for cast blasts as for contained shots. Further information can be extracted from the moment-rate tensor spectra in Figure 4. Although shots 3 and 4 were of about the same size, their diagonal moment-tensor component spectra are not quite the same. Shot 3 (Figure 4, left) has larger amplitudes (a factor of about 1.7) and lower corner frequency than that of shot 4 (Figure 4, center; 13 Hz vs. 16 Hz). Spectra of diagonal moment-tensor components of shot 4 are more peaked, possibly due to stronger spall. For shot 9 (Figure 4, right), a considerable amount of Myz energy is seen in the frequency band between 1 and 6 Hz. There is also enhanced Mzz energy in this frequency band. Figure 5 shows the bandpass

filtered (1-6 Hz) moment-rate tensors of shots 3 and 9. There is a clear signal enhancement in the Myz component of shot 9 (Figure 5, right) compared with shot 3 (Figure 5, left). The Myz signal is lower frequency than that of the initial pulse and may also be delayed in time. This could indicate that the signal was generated by the bench material cast into the pit.

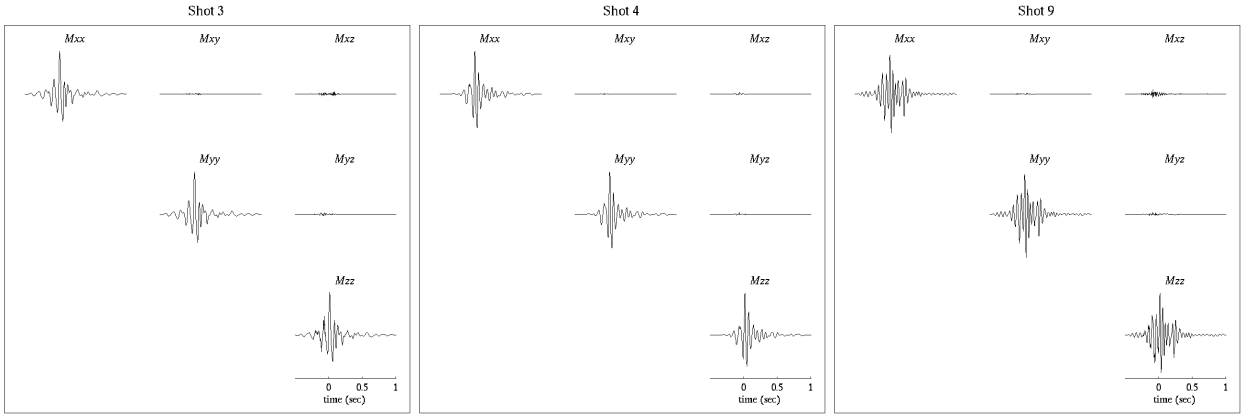

Figure 3. Moment tensor inversion results for shot 3 (left), shot 4 (center), and shot 9 (right).

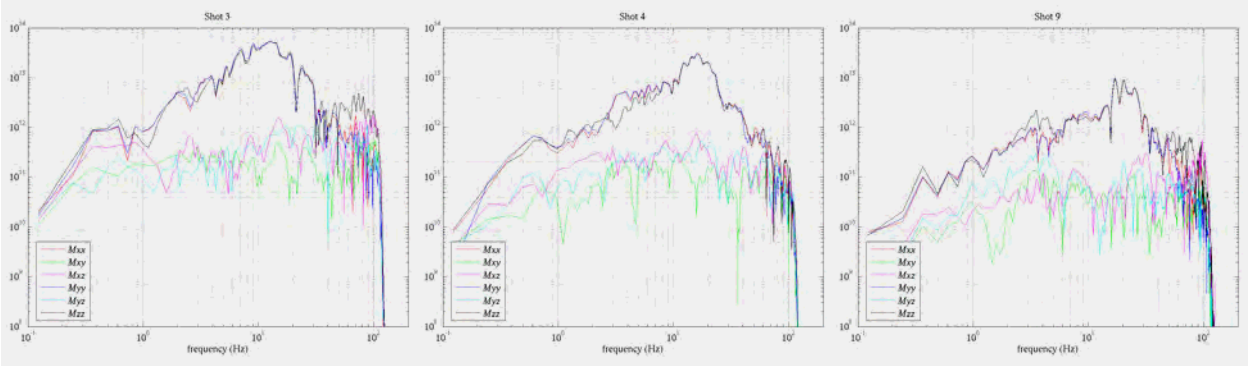

Figure 4. Moment-rate tensor spectra for shot 3 (left), shot 4 (center), and shot 9 (right).

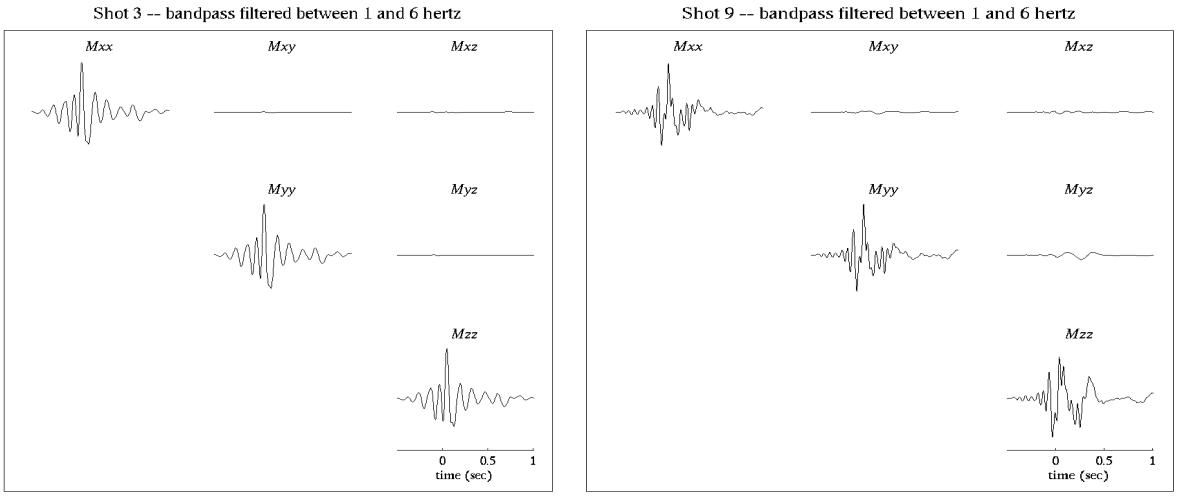

Figure 5. Moment tensor inversion results for shot 3 (left) and shot 9 (right), both bandpass filtered between 1 and 6 Hz.

Although the amplitude of the Myz component of shot 9 is only about 7% of the diagonal components, it can generate a much larger percentage of shear energy. Figure 6 plots synthetic seismograms calculated using the shot 9 source at an azimuth of zero degrees and a distance of approximately 5 km. The transverse component amplitude generated by the off-diagonal moment tensor is about 30% of the *P*-wave amplitude generated by the explosive source.

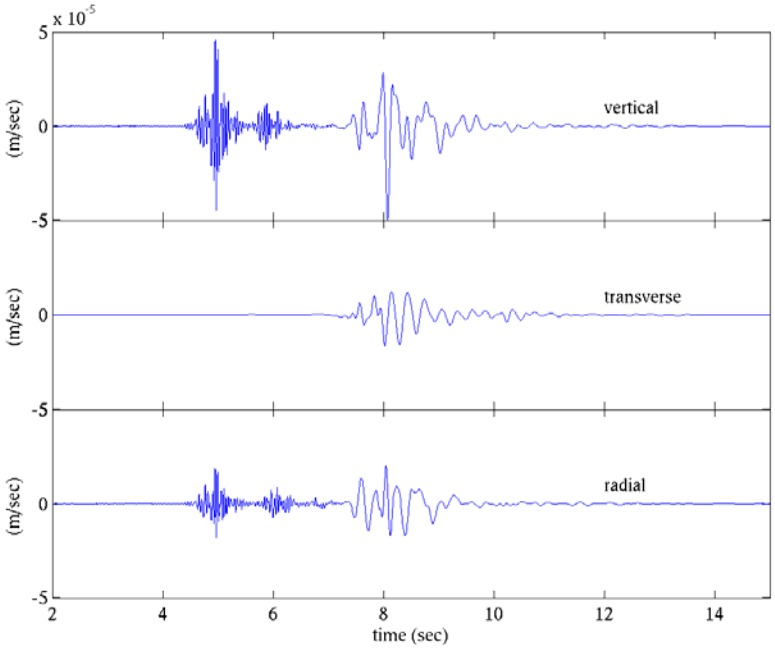

Figure 6. Synthetic seismograms based on the moment tensors for shot 9.

Effects of Yield and Confinement

Research on the effects of yield and confinement at the copper mine was initially reported on by Leidig et al. (2004). The following provides an update to this research at the southern Arizona copper mine. In Figure 7, the effects of yield are quantified at various station distances by comparing the spectral ratios for shots with the same confinement and different explosive size. In general, the spectral ratios at all distance ranges are similar in shape and amplitude indicating a common source scaling with distance.

The effects of confinement have been studied by comparing the spectral ratios for shots with identical yield and the results are presented in Figure 8. The spectral ratios of twice depth to free face for 13600 and 1700 lbs. shots are relatively flat at all frequencies. They indicate a reduction of coupling on the free face shots of ~2-4. Similar reduced coupling is also found by comparing the data from the twice burden and free face shots. These results suggest that the failure of the free face results in a reduction in seismic energy at all distances ranges.

Source modeling. Figure 9 presents the comparison of the predicted spectral ratios from the Mueller-Murphy granite model source function (dotted lines) with the shots of twice depth (Figure 7a). The *P*-wave velocity model (V*p*=3.048 km/s) of the source materials was based on the in-mine refraction survey assuming Poisson medium for shear wave velocity and density=2.2 gm/cc. The model matches the observed data to 6 Hz, above which the observed ratios begin to increase.

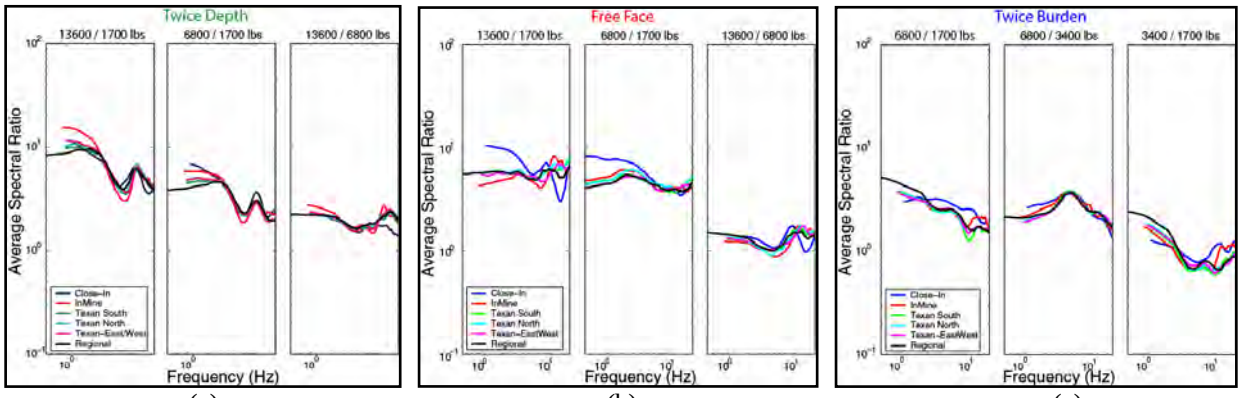

(a) (b) (c)

Figure 7. Spectral ratios of shots with same confinement and different yield, (a) twice depth; (b) free-face; and (c) twice burden.

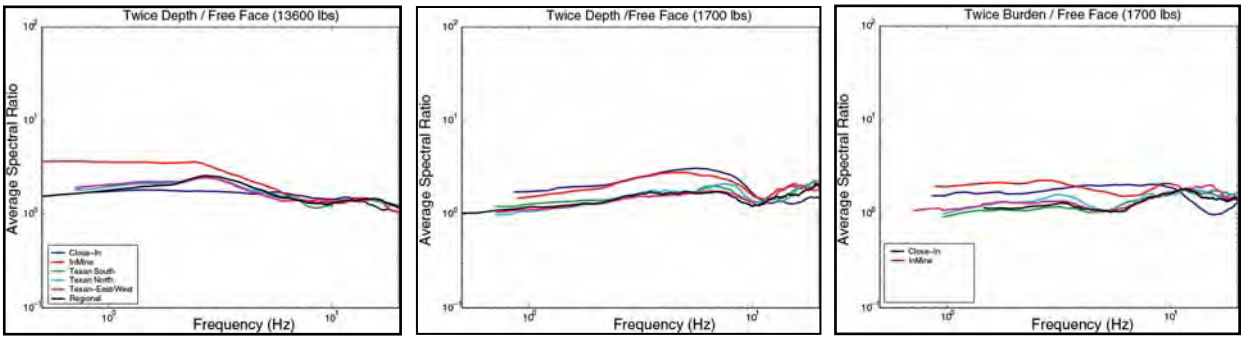

(a) (b) (c)

Figure 8. Spectral ratios of shots with same explosive size and different confinements, (a): twice depth / free face (13600 lbs); (b) twice depth / free face (1700 lbs); and (c) twice burden / free face (1700 lbs).

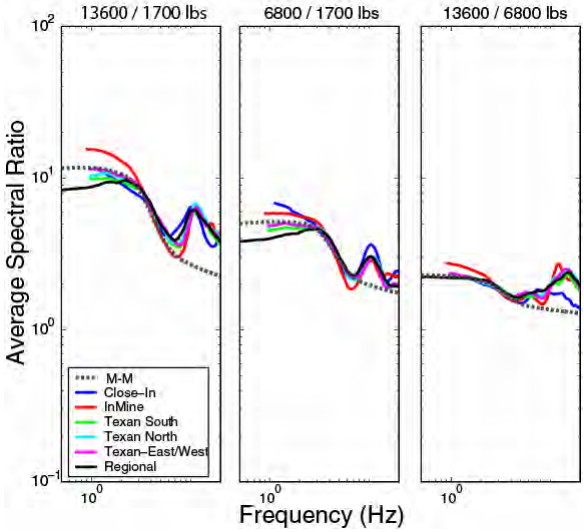

Figure 9. Comparison of the predicted spectral ratios from the Mueller-Murphy granite model (dotted line) with twice depth shots.

Effects of Confinement on Short-Period Surface Waves. Hooper et al. (2004) reported research on the excitation of short-period, fundamental mode Rayleigh waves (*Rg*) by explosions, using SPE data collected from the network of vertical component geophones. This research has continued, and we have explored the effects of confinement on the generation of *Rg* from explosions.

Results show important differences between the *Rg* amplitudes of confined and unconfined explosions that need to be understood in order to develop discriminants for mining explosions. *Rg* energy and frequency content are dependent upon explosive weight and confinement, and unconfined explosions generate less energy than equivalent confined explosions due to decoupling effects. We calculated empirical decoupling factors, which provide a first-order estimate of the frequency-dependent decoupling caused by the lack of confinement. The decoupling factors are calculated by taking the ratios of observed and theoretical spectral ratios from the explosions:

$$\frac{\text{Observed Ratio}}{\dfrac{\text{CONFINED EXPLOSION}}{\text{UNCONFINED EXPLOSION}}} \Big/ \frac{\text{Theoretical Ratio}}{\dfrac{\text{CONFINED EXPLOSION}}{\text{CONFINED EXPLOSION}}}$$

The observed confined explosion is shot 3, and shots 4-9 are unconfined. The theoretical spectral ratios are based on Mueller-Murphy sources (all confined) simulating the same shots.

The chemical decoupling factors for unconfined shots vary from 1 to 10 at frequencies between 0.5 and 8 Hz, indicating that unconfined explosions generate up to 10 times less *Rg* energy than confined explosions (Figure 10). For this reason, unconfined mining explosions cannot be simulated using a Mueller-Murphy (1971) source without including an empirical chemical decoupling factor such as those described above. Additionally, studies of a small, overburied shot indicate that some *Rg* excitation effects are not being adequately modeled by the Mueller-Murphy source and the available medium-dependent properties (Hooper et al., in review).

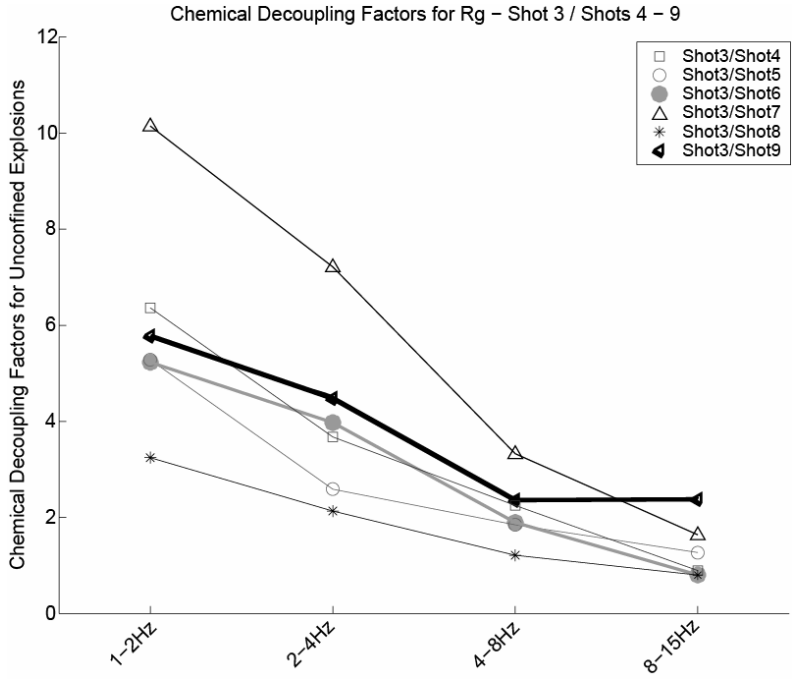

Figure 10. Chemical decoupling factors (observed ratio / theoretical ratio) calculated for the shot 3 (confined) / shots 4-9 (unconfined) ratios for *Rg* for various frequency bands. These chemical decoupling factors are mainly due to the differences between the unconfined and confined sources.

Regional Discrimination

We have started to examine the regional discrimination behavior of the SPE shots relative to normal production mining explosions, natural earthquakes, and previous nuclear tests at the Nevada Test Site. Examples of the regional seismograms from the northern Arizona coal mine SPE shot 3 are shown in Figure 11. The discrimination analysis includes identifying and picking the onset times of the regional phases *Pn*, *Pg*, and *Lg*, making amplitude measurements in a variety of passbands, normalizing those measurements for the effects of source and path using the Magnitude, Distance, and Amplitude Correction (MDAC) methodology (Walter and Taylor, 2002), and calculating *Pg/Lg* ratios for each event. Figure 12 shows the results at station KNB (Kanab, Utah) for six of the northern Arizona coal mine SPE shots (diamonds) and production mining explosions (triangles), compared with a set of nuclear tests (stars) and western U.S. earthquakes (circles). We find that the MDAC-corrected SPE shots fall in the middle of the nuclear explosion population with very little variation due to the differing shot conditions. Thus for this particular discriminant at this station, the SPE shots and mining explosions are good surrogates for nuclear explosions, and the differences in depth of burial and single versus multiple shot have only a small effect on the discriminant measures. We are extending this analysis to other regional stations (e.g., ANMO, TUC, WUAZ; regional profile stations) and other discriminants to more completely examine the discrimination relationship of the SPE shots to production shots, earthquakes and nuclear tests.

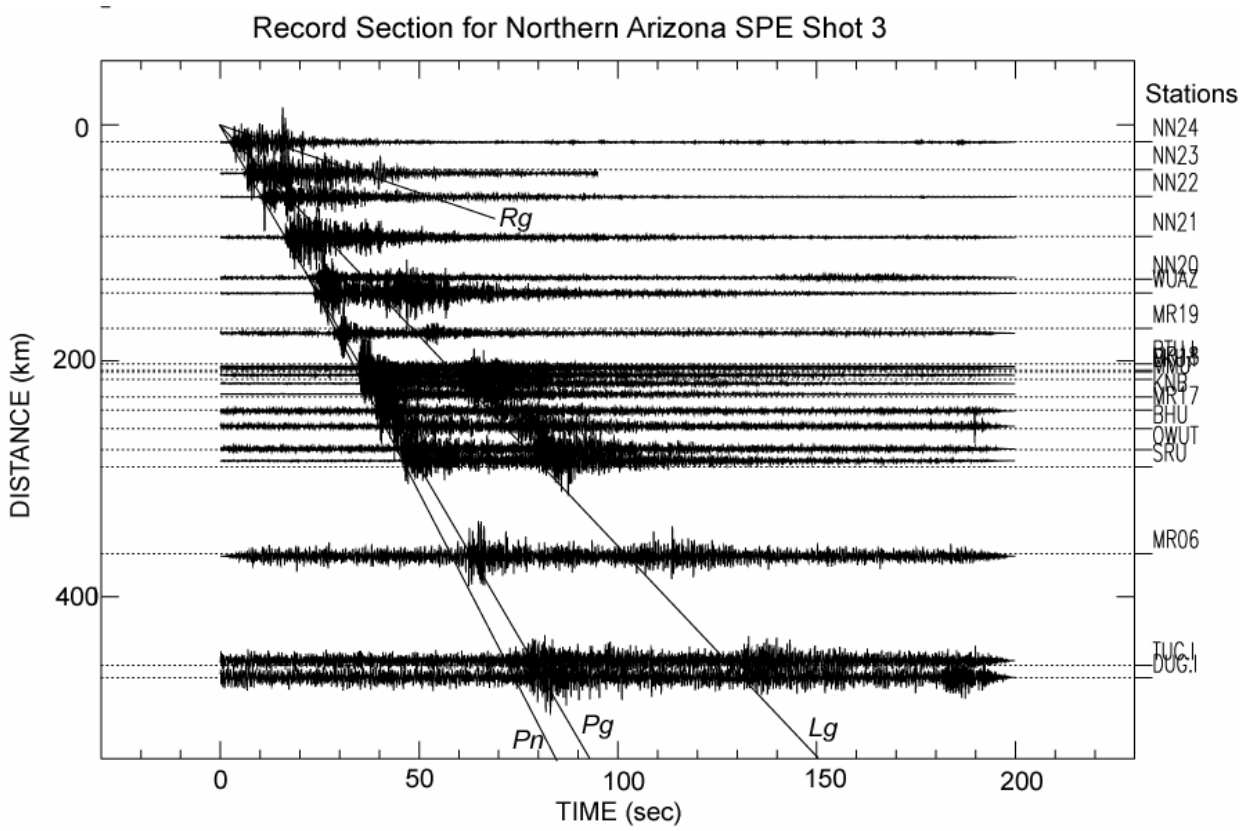

Figure 11. Record section of near-regional data recorded from SPE shot 3 at the coal mine in northern Arizona. *Pn*, *Pg*, and *Lg* are the prominent arrivals at regional distances. At local distances, we note a prominent 1 Hz *Rg* arrival; however, it is highly attenuated in the upper crust of the Colorado Plateau.

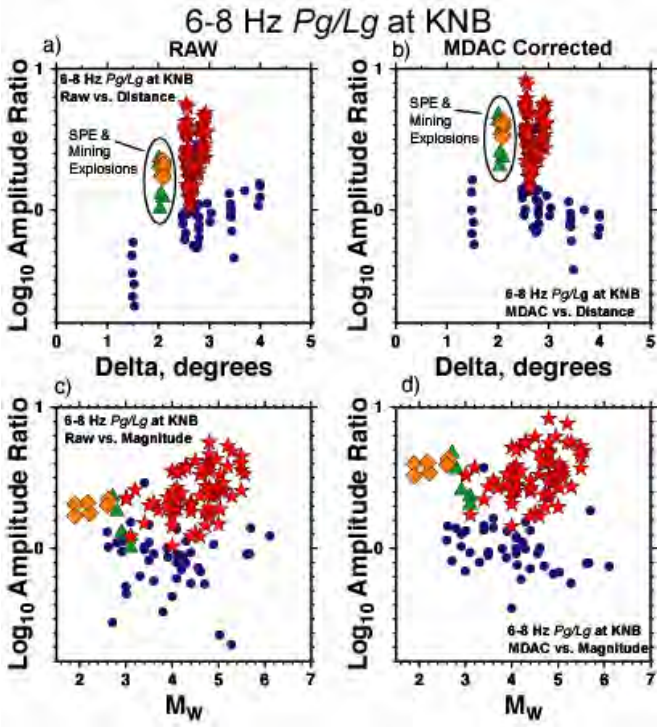

Figure 12. Comparison of six SPE shots from the northern Arizona coal mine (diamonds) with production shots at the same mine (triangles) at station KNB using the 6-8 Hz *Pg/Lg* discriminant (e.g. Walter et al., 1995). The ratios are plotted as either raw (a and c) or MDAC-corrected (b and d) amplitude ratios as a function of distance (a and b) or moment magnitude (c and d). The SPE shots show less variability and have similar values to the mean of the nuclear tests (stars), making them possible surrogates in this discriminant case. Earthquakes are plotted as circles.

Regional coda envelopes provide very stable single station estimates of source spectra (e.g., Mayeda et al. 2003). Here we have calibrated the paths based on Colorado Plateau earthquakes. For each station we can then examine the differences in source spectra as determined from the coda (Figure 13). The differences in source spectral shape due to depth and confinement are quite subtle. Between the two mines the hard rock copper site shows less 6-8 Hz energy than the coal mine. This is clear in the comparison of similar size (12,000 and 13,600 lbs) and depth (30 and 33 m) events. This difference causes the copper mine to have larger low/high spectral-ratios discriminant values than we observe for the coal mine.

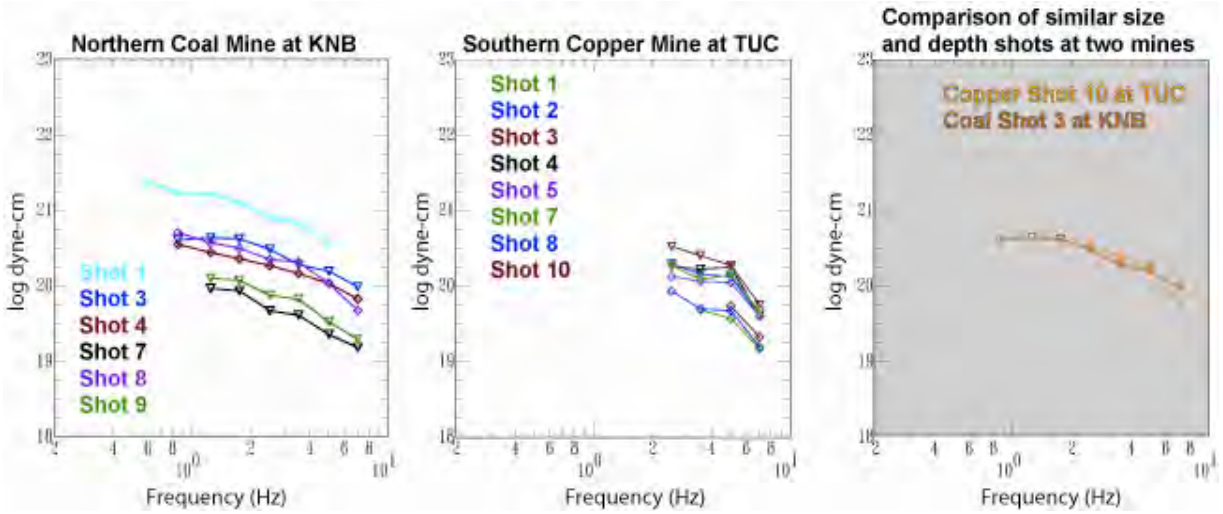

Figure 13. Source spectra for shots at the northern Arizona coal mine and the southern Arizona copper mine.

CONCLUSIONS AND RECOMMENDATIONS

The Arizona SPE experiments have resulted in an important dataset for the nuclear monitoring community. The 19 dedicated single-fired explosions and multiple delay-fired mining explosions were recorded by one of the most densely instrumented accelerometer and seismometer arrays ever fielded, and the data have already proven useful in quantifying confinement and excitation effects for the sources. It is very interesting to note that we have observed differences in the phenomenology of these two series of explosions resulting from the differences between the relatively slow (limestone) and fast (granodiorite) media. We observed differences at the two SPE sites in the way the rock failed during the explosions, how the *S*-waves were generated, and the amplitude behavior as a function of confinement. Our consortium's goal is to use the synergy of the multiple datasets collected during this experiment to unravel the phenomenological differences between the two emplacement media. The results so far suggest that the single-fired explosions are surrogates for nuclear explosions in higher frequency bands (e.g., 6-8 Hz *Pg*/*Lg* discriminants).

ACKNOWLEDGEMENTS

We express our sincere thanks to all involved and to those who helped support the Source Phenomenology Experiments. This research would not have been possible without the tremendous support of the front office, engineers, and miners of the mines used in this study. We slowed their production schedules, yet they were always gracious and wonderful hosts. We thank Darlene McEwand, John Sandru, Aaron Hirsch, and the University of Nevada Las Vegas for teaching us how to bury a Texan. We thank the Navajo Nation for allowing us to place instruments on their lands. In addition, we thank IRIS PASSCAL for their help on this project. We also wish to thank Mr. Mike Rosenthal for his support in obtaining variances for the largest explosions.

REFERENCES

Dobrin, M. B., (1960), *Introduction to Geophysical Prospecting*. 2nd edition, McGraw-Hill Book Co, Inc., New York.

Hayward, C., R.-M. Zhou and B. Stump, (2004), QuickLook Report: 2004 January Morenci Refraction Experiments and Morenci Refraction Interpretation, February 2004, Southern Methodist University.

Hooper, H., H. Patton, J. Bonner, and M. Leidig, (2004), Using short-period surface waves to model source phenomena, in *26th Seismic Research Review: Trends in Nuclear Explosion Monitoring*, LA-UR-04-5801, Vol. 1, pp. 417-426.

Hooper, H., J. L. Bonner, and M. Leidig, (in review), Effects of confinement on short-period surface waves: Observations from a new dataset. Submitted to *Bull Seism. Soc. Am.*

Kim, T.S. and B.S. Stump (in preparation). Upper crustal velocity structure around the Morenci copper mine from Pg and Rg phases.

Leidig, M., J. Bonner, and D. Reiter, (in review), Development of a velocity model for Black Mesa, Arizona and the southern Colorado Plateau from multiple datasets, Submitted to the *Bull. Seism. Soc. Am.*

Leidig, M., B. Stump, J. Bonner, C. Hayward, A. Velasco, D. Baker, H. Hooper, W. Walter, X. Yang, R. Zhou, C.L. Edwards, M. Renwald, and J. Lewkowicz (2004). Source phenomenology experiments in Arizona, *Proceedings of the 26th Seismic Research Review: Trends in Nuclear Explosion Monitoring*, LA-UR-04-5801, Vol. 1, pp. 427-438.

Mayeda, K., A. Hofstetter, J.L. O'Boyle, and W.R. Walter (2003), Stable and transportable regional magnitudes based on coda-derived moment-rate spectra, *Bull. Seism. Soc. Am*. 93: 224–239.

Mueller, R.A., and J.R. Murphy, (1971), Seismic characteristics of underground nuclear detonations. *Bull. Seism. Soc. Am*., 61: 1675–1692.

Walter, W.R., K.M. Mayeda, and H.J. Patton, (1995), Phase and spectral ratio discrimination between NTS earthquakes and explosions, Part 1, Empirical Observations, *Bull. Seism. Soc. Am*. 85: 1050.

Walter, W. R. and S. R. Taylor (2002), A revised magnitude and distance amplitude correction (MDAC2) procedure for regional seismic discriminants. Lawrence Livermore National Laboratory UCRL-ID-146882.

ENERGY PARTITIONING FOR SEISMIC EVENTS IN FENNOSCANDIA AND NW RUSSIA

Hilmar Bungum[1], Tormod Kvaerna[1], Svein Mykkeltveit[1], Nils Maercklin[1], Michael Roth[1], Ketil Astebol[1], David B. Harris[2], and Shawn Larsen[2]

NORSAR[1] and Lawrence Livermore National Laboratory[2]

Sponsored by National Nuclear Security Administration
Office of Nonproliferation Research and Engineering
Office of Defense Nuclear Nonproliferation

Contract Nos. DE-FC03-02SF22636[1] and W-7405-ENG-48[2]

ABSTRACT

We address the problem of energy partitioning at distances ranging from very local to regional for various kinds of seismic sources, and are now in the last year of this three-year effort. On the small scale we have focused on analysis of observations from an in-mine network of 16-18 sensors in the Pyhäsalmi mine in central Finland. This analysis has been supplemented with 3-D finite difference wave propagation simulations to investigate the physical mechanisms that partition seismic energy in the near source region in and around the underground mine. On the local and regional scale (20-220 km) we have targeted events from the region offshore Western Norway where we have both natural earthquake activity as well as frequent occurrence of underwater explosions carried out by the Norwegian Navy.

Since the previous reporting of this project at the 2004 Seismic Research Review (Bungum et al., 2004), we have extended the finite difference simulations in the 3-D geological model of the Pyhäsalmi mine. This model, which encompasses a geologic volume 500 meters in each direction, includes 3-D representations of the ore bodies, excavated regions, tunnels, and voids. The model is discretized on both 2 and 4 meter grids making it possible to simulate seismic energy up to 100-200 Hz. We perform a variety of sensitivity tests to determine the mechanisms that produce shear energy in an underground mine environment. For example, we conduct a suite of 15,000 (2-D) explosive source simulations to quantify the influence of source location on the amplitude of generated shear energy. In fact, most of the shear energy appears to be generated within 10-20 meters from the source (at frequencies of 50 Hz). Examination of waveforms reveals that both geologic heterogeneity and the structural influences of the mine are contributors to the near-source generation of shear energy. There is some suggestion that the effects of geologic inhomogeneity are significant early in the wavetrain, whereas the mine structure is likely to produce scatter and be more significant later in the waveforms. As a validation measure, the synthetic waveforms are compared with observed data from single and multi-component instruments located in the mine. The simulated data match the amplitude and character of the observed waveforms particularly well, especially at frequencies at and below 50 Hz. This suggests that we can reliably infer energy partitioning phenomena based on these simulations.

A database of underwater explosions and earthquakes from the region offshore Western Norway, recorded at seven selected stations of the National Norwegian Seismic Network (NNSN), were analyzed for differences in the S/P amplitude ratios. In order to separate the path and source effects for the two event populations, we have investigated the station, distance, and frequency dependencies of the recorded data in detail. The results indicate that the mean S/P amplitude ratios for both underwater explosions and natural events vary from station to station but are, in general, higher for natural events. For frequencies above 3 Hz, the difference in S/P ratios between explosions and natural events is higher than for lower frequencies. However, the distributions of S/P ratios for explosions and natural events overlap in all analyzed frequency bands. Thus, for individual events in our study area, S/P amplitude ratios can assist the discrimination between an explosion or a natural event, but other measures such as spectral analysis should be included in the interpretation.

OBJECTIVE

The main objective of this project is to increase the (nuclear) explosion monitoring effectiveness through improved understanding of basic earthquake and explosion phenomenology. What this entails is detailed characterization and understanding of how the seismic energy is generated from these phenomena (including simple and complex explosions and rockbursts, i.e., stress release in mines, and ordinary tectonic earthquakes, all at different depths and in different geological environments) and how this energy is partitioned between P and S waves. Specific questions are:

- How is the generation and partitioning of seismic energy affected by properties such as source region medium and overburden, the local structure, and the surrounding tectonic structure?
- What are the significant measurable effects of the partitioning of the seismic energy into various regional P and S phases, especially at higher frequencies?
- What is the physical basis for a measurable property, such as magnitude, that can be directly related to the yield of a fully coupled explosion, and how can emplacement conditions affect the observations?

RESEARCH ACCOMPLISHED

We are now in the last year of a three-year project that started on 30 September 2002 (Bungum et al., 2003, 2004), which is a collaboration between NORSAR (as the lead organization) and Lawrence Livermore National Laboratory (LLNL). During the last year we have addressed the problem of energy partitioning at distances ranging from very local to regional for various kinds of seismic sources. On the small scale we have focused on analysis of observations from an in-mine network of 16-18 sensors in the Pyhäsalmi mine in central Finland. This analysis has been supplemented with 3-D finite difference wave propagation simulations to investigate the physical mechanisms that partition seismic energy in the near source region in and around the underground mine. On the local and regional scale (20-220 km) we have targeted events from the region offshore Western Norway where we have both natural earthquake activity as well as frequent occurrence of underwater explosions carried out by the Norwegian Navy.

3-D finite difference modeling

We have investigated physical mechanisms that partition seismic energy in the near source region by performing modeling studies of the Pyhäsalmi mine in Finland in comparison with observations. Our recent efforts have focused on the quantification of shear energy generation as a function of source location within the mine. In particular, we performed over 15,000 2-D finite-difference wave propagation simulations of the mine using an explosive (purely compressional source) positioned at different locations within the mine. We have examined the generation of shear energy as a function of source position relative to mine heterogeneities such as ore bodies and excavated regions (voids).

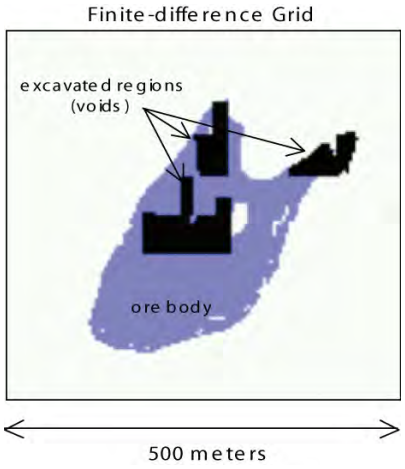

Figure 1. 2-D vertical cross section through the Pyhäsalmi mine. Blue represents high velocity ore. Black represents excavated portions of the mine. White represents the background geology.

Figure 1 shows a 2-D model cross section through the central portion of the Pyhäsalmi mine. This 2-D representation was extracted from a 3-D model of the mine. The horizontal and vertical dimensions are 500 meters. The model is discretized on a 4 meter finite-difference grid.

The E3D finite-difference wave propagation code (Larsen & Schultz, 1995; Larsen & Grieger, 1998) and the 2-D mine model are used to perform several thousand seismic simulations. A purely compressional (explosive) 50 Hz point source is used to drive the simulations. An example of one such simulation is shown in Figure 2.

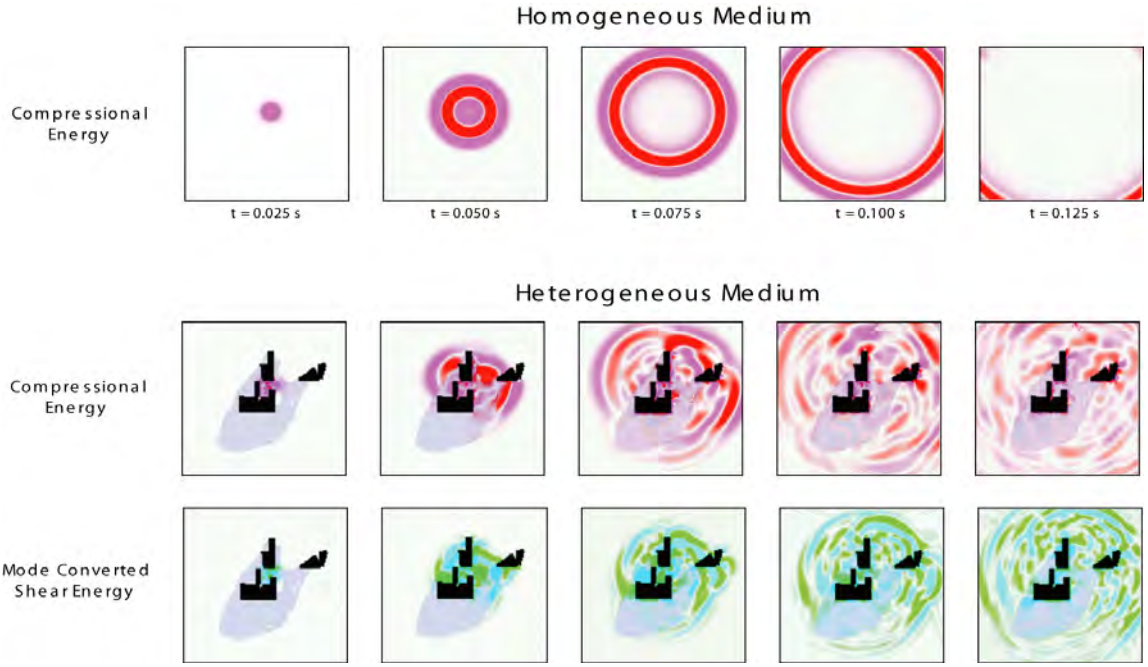

Figure 2. Simulations illustrating generation of shear energy due to an explosive source near the center of the heterogeneous Pyhäsalmi mine.

In this case, the source is located slightly off from the center of the finite-difference grid. The figure shows the seismic wavefield at multiple time snapshots for a simulation using the heterogeneous 2-D model. For reference, an equivalent simulation is performed in a homogeneous model. Red and red-blue represent compressional energy (P potential) and green and green-blue represent shear energy (S potential) at various time snapshots. Because the source is purely compressional and there are no heterogeneities in the model, no shear energy is generated in the homogeneous model. However, significant shear energy is generated in the real model. This energy is generated as the compressional waves interact with both the excavated regions of the mine (voids) and with the heterogeneity in the mine (ore body). The shear energy amplitude is comparable to that of the compressional energy.

Figure 3 illustrates the method used here to quantify the generation of shear energy. For any given source position, we compute the amount of shear and compressional energy that leaves the near-source region in an “energy flux box” near the edge of the finite-difference grid. Paraxial absorbing boundary conditions are applied to the grid boundaries so little energy is reflected back into the model. More precisely, we compute the maximum shear amplitude and the maximum compressional amplitude at each point along the flux box. We then determine the S/P ratio at each point and average these ratio’s to estimate of total shear energy generated within the model. While this method is ad hoc and does not include issues such as the duration of the compressional and shear wavefields, it does provide a first order estimate for how much shear energy is being generated for an explosive source at any given location within the model.

We have performed 15,376 2-D simulations similar to the one shown in Figure 2 and Figure 3. The source is located at a different grid point for each simulation. The results from these simulations is illustrated as the S/P ratio map shown in Figure 4. Each point within this map represents the amount of shear energy that is generated from a source located at that point using the S/P ratio method described above and in Figure 3. Red indicates source locations that promote the generation of shear energy. White indicates source locations where minimal shear energy is generated.

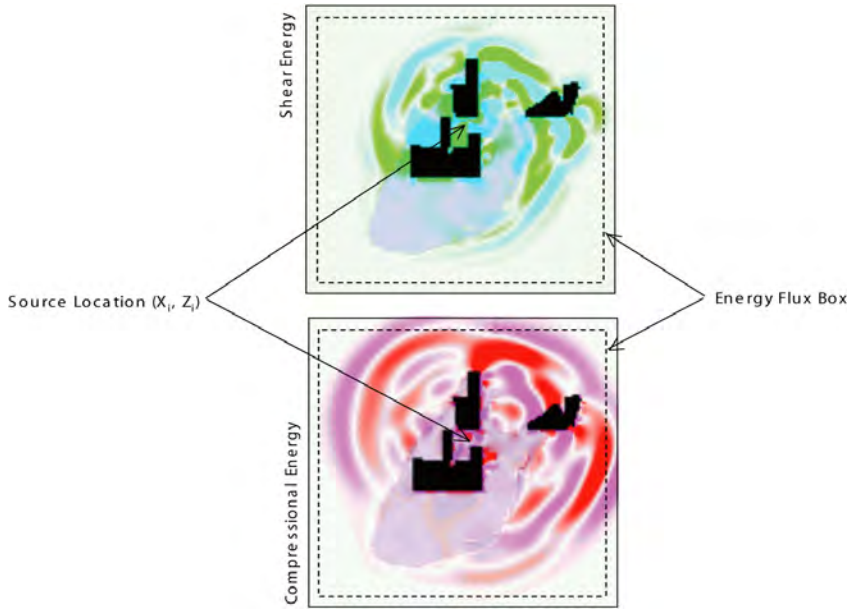

Figure 3.
Figure illustrating the method used here to quantify the generation of shear energy. P and S energy leaving the source region (flux box) can be quantified to determine how much shear energy is generated for a source at any given location.

Figure 4 suggests that shear energy is more likely to be produced when a source is located near geologic heterogeneity or a structural boundary. In fact, for these simulations, significant shear energy is most often generated when the source is located 10 - 20 meters from a natural or engineered interface. This corresponds to approximately 1 - 2 seismic wavelengths at the simulated frequency of 50 Hz.

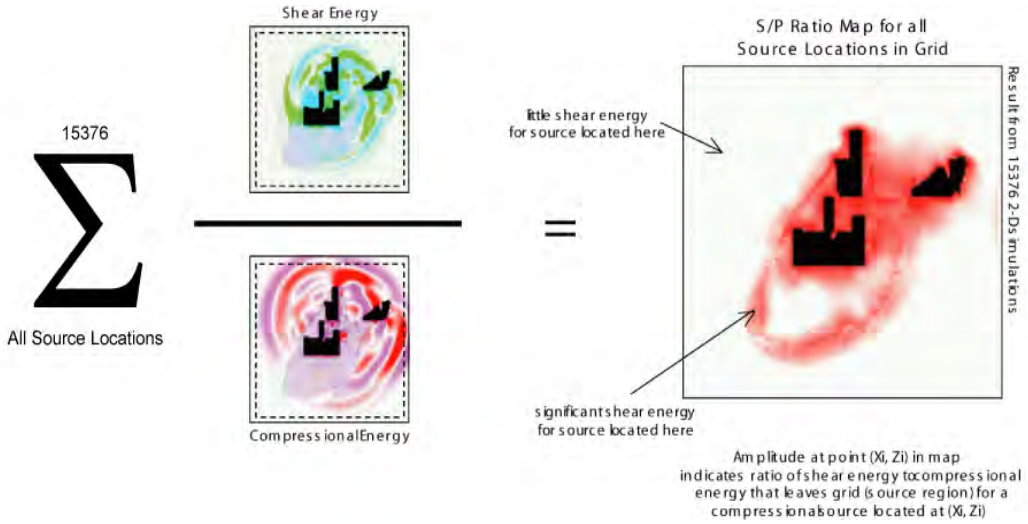

Figure 4. **Figure illustrating the method used here to quantify the generation of shear energy in the Pyhäsalmi mine. Each point within the map represents the amount of shear energy (S/P ratio) that is generated from an explosive source located at that point.**

We have performed two other sets of 15,376 simulations. In one case, only the excavated or mined-out portions of the mine are included in the 2-D model. In the other case, only geologic heterogeneities (e.g., ore body) are included in the model. The S/P ratio maps for each simulation set, along with the result for the full mine model, are shown in Figure 5. For better clarity, we also have scaled the two new S/P ratio maps and these are shown at the bottom of Figure 5.

The results from Figure 5 are somewhat puzzling. When the ore body is excluded from the model, the S/P ratio map suggests that more shear energy is generated for those sources located near excavated portions of the mine. When the excavated portions of the model are excluded, the S/P ratio map suggests that shear energy generation for sources located near the ore boundary is smaller. We have no ready explanation for this behavior. It may be that shear energy generation is non-linearly coupled to the presence of both geologic and engineered heterogeneities. It also may be true that the excavated regions are responsible for the bulk of the mode converted shear energy. This would not be too surprising since there is a stronger impedance contrast with the excavated voids than there is with geologic ore. However, further study is needed.

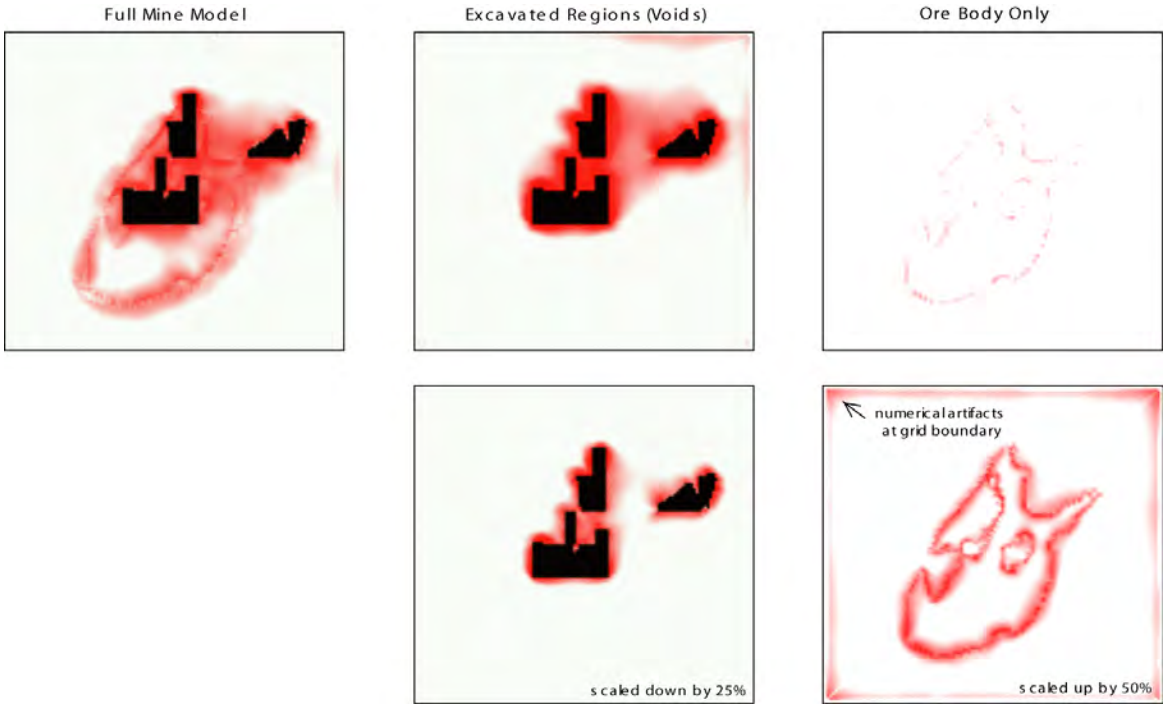

Figure 5. S/P ratio maps for different geological components of the Pyhäsalmi mine. Again, each point within the map represents the amount of shear energy (S/P ratio) that is generated from an explosive source located at that point.

The results of these modeling exercises suggest that significant shear energy generation is more likely to occur when a source is located within 1 - 2 seismic wavelengths of a natural or engineered heterogeneity. This corresponds to 10 - 20 meters for a 50 Hz source in a typical mine environment. In addition, large excavated regions of a mine may be more influential for the production of mode converted shear energy.

Energy partitioning for seismic events near the coast of Western Norway

We have addressed the question of how seismic energy is partitioned between P and S waves at regional distances between 20 and 220 km. We have chosen to target events from the region offshore Western Norway where we have both natural earthquake activity as well as frequent occurrence of underwater explosions carried out by the Norwegian Navy.

The data base for this study are seismic phase arrival times, source locations, and waveform data of natural events and underwater explosions recorded at seven selected three-component stations in Western Norway between 1997 and 2004 (Figure 6). The seismic stations are part of the permanent National Norwegian Seismic Network (NNSN), and the data were provided by the University of Bergen (UiB). The selected source region is located around 60 °N, 5° E, where both event types, earthquakes and explosions, occur.

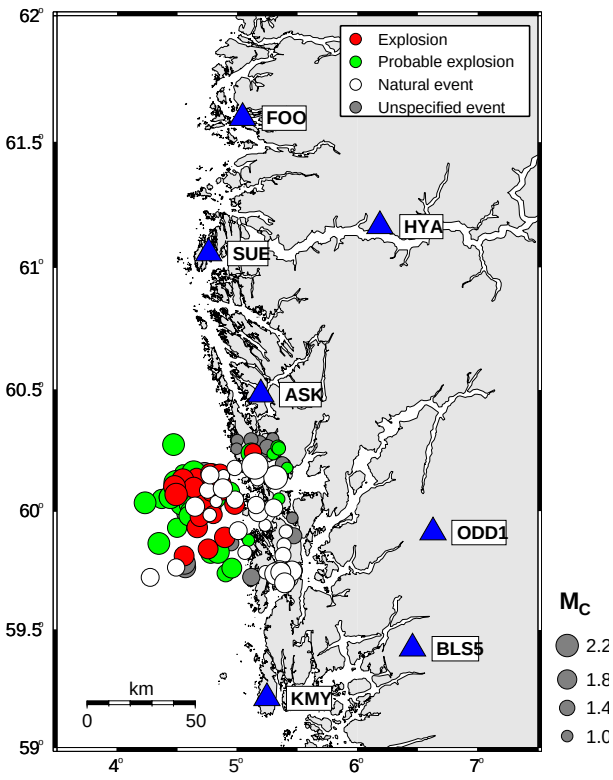

Figure 6. Seismic three-component short-period stations (triangles) and events used for this study: ASK = Askøy, BLS5 = Blåsjø, FOO = Florø, HYA = Høyanger, KMY = Karmøy, ODD1 = Odda, and SUE = Sulen.

At UiB, all events are classified as one of four main classes: explosions (E), probable explosions (P), natural events (N), and unspecified events. Typically, the explosions are detonations in the water column and confirmed by or related to the Norwegian Navy (Haakonsvern). Coda magnitudes of all events are mainly in the range 1.0 < Mc < 2.3. Explosions usually occur at daytime. A peak at daytime in the temporal distribution of unspecified events suggests that many of these events are also explosions.

Whereas the initial database contains many confirmed explosions, only a few events in our source region are classified as natural earthquakes. Therefore, we analyzed signals and amplitude spectra of previously unspecified events in order to find more natural events for our study. The judgement was based on the fact that explosions in the water column are typically characterized by reverberations, which appear in amplitude spectra as distinct notches. Figure 7 shows vertical-component seismograms and spectra of two events, an explosion (left) and a natural event (right). The more continuous shape of the spectrum of the natural event is clearly visible. For our study we added those originally unspecified events to the set of natural ones that show a similar spectral behavior and no evidence of reverberations as seen in the example on the left. Additional constraints on the reclassification of unspecified events into natural events were that they occurred during nighttime, and that the resulting population of natural events should have a flat time-of-day distribution. After this reclassification procedure we ended up with 49 earthquakes and 24 explosions (see Figure 6).

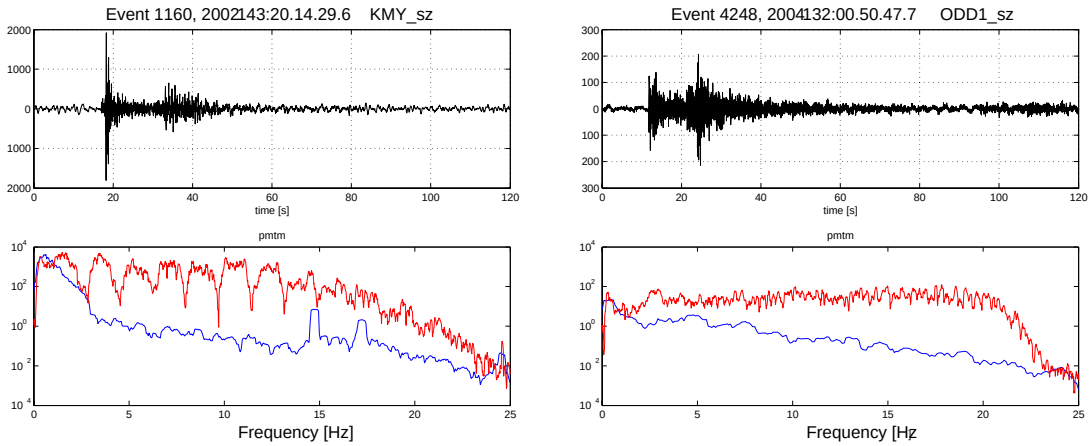

Figure 7. Vertical component seismograms and amplitude spectra of an explosion (left) and a natural event (right). Signal spectra (red) are calculated in a 60 s time window starting at the P onset and using the Thomson multitaper method (Thomson, 1982), and for noise spectra (blue) the time windows covered the time period from the origin time to 2 s before P, which were the noise data segments available in the UIB database.

The first step of the data analysis was to determine azimuth and incident angle of the P-phase using polarization analysis on bandpass-filtered data between 2 and 8 Hz. The analysis time window was 3 s long starting at the P arrival time determined by UiB. In general, calculated azimuths deviate from theoretical (geometric) values by just a few degrees. With the calculated azimuths and incident angles the data are rotated into the ray coordinate system (L, Q, T) for subsequent processing and analysis. The incidence angles and azimuths calculated from the P phases may not be optimal for the S-waves, but we do not consider this to have any significant effect on the estimates of the S/P ratios.

Figure 8 shows bandpass filtered (2-8 Hz) seismograms for two events recorded at two different stations, KMY (top) and SUE (bottom). The panels on the left show a confirmed explosion and those on the right a natural event. At the bottom of each panel are the original traces in the ZNE system, and on top the rotated ones (LQT). Here, differences in S/P amplitude ratios are clearly visible.

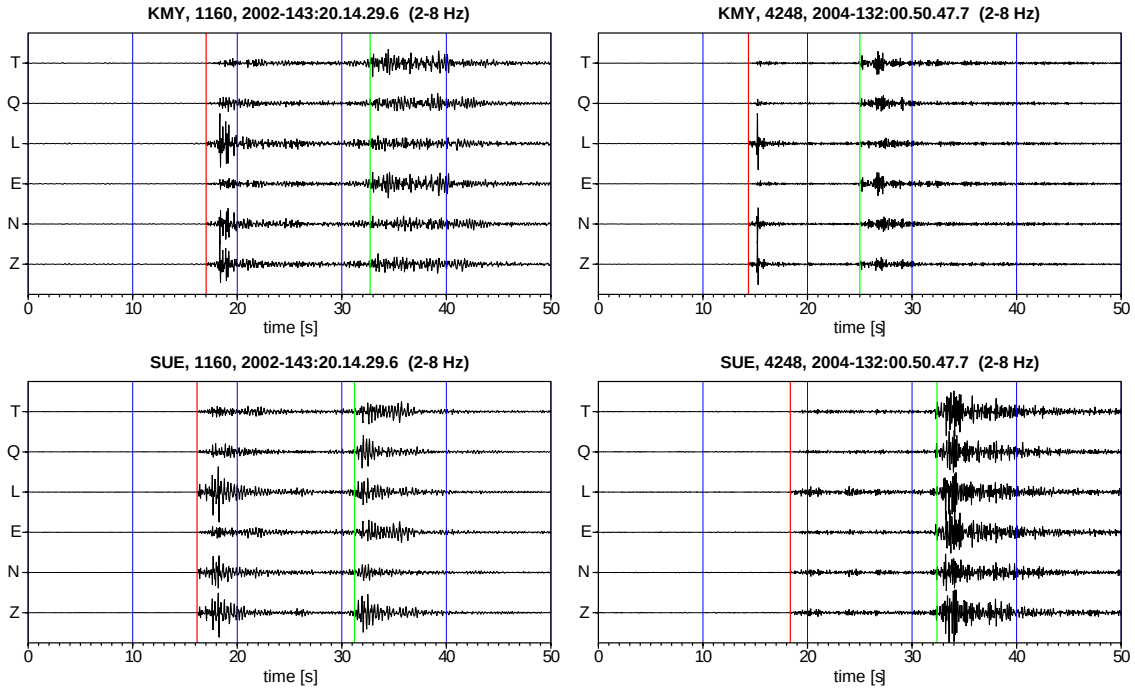

Figure 8. Three-component seismograms (2-8 Hz) recorded at the two stations KMY and SUE (see Figure 6). The time axis is relative to the origin time given on top of each panel, and red and green lines indicate the P and S onsets, respectively. Left: confirmed navy explosion (Haakonsvern), and right: natural event.

We measured S/P amplitude ratios for the two event sets in eight 1-octave passbands ranging from 1.0-2.0 to 12-24 Hz. The P amplitude was taken to be the maximum amplitude on the L component in the time window from the P onset to 0.5 s before the S onset. The S amplitude was taken to be the maximum in the orthogonal QT plane (vector sum of the Q and T components) in a 10 s time window starting at the S onset.

Figure 9 shows the distribution (histograms) of S/P amplitude ratios for all the explosions (red) and natural events (black outline) recorded at all seven stations. The abscissa (S/P ratios) is logarithmic, i.e., positive values indicate higher S than P amplitudes. The histograms for explosions exhibit a clear trend to lower S/P amplitude ratios (higher P energy) with increasing frequency, whereas the values for natural events cover a wider range and do not show such a trend.

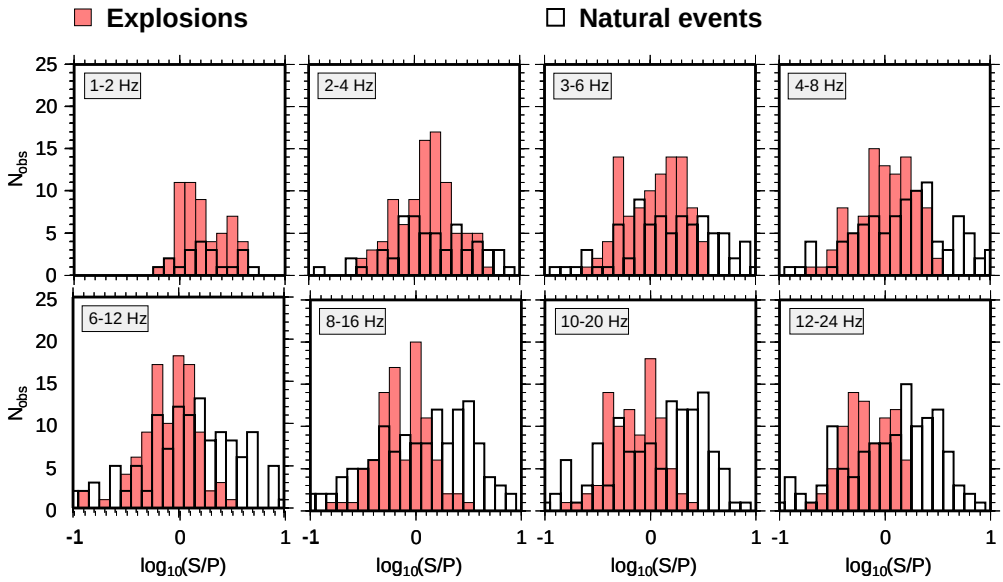

Figure 9. Histograms of S/P amplitude ratios (logarithm) for all explosions (red) and natural events (black outline).

The overall dependencies of the S/P amplitude ratios on frequency band, the source-receiver distance (20-220 km) to the different stations, as well as the S/P ratio variations with distance for individual events were investigated. Except for the trend that the average S/P ratios for explosions are generally lower than for natural events, we could not find any pronounced distance dependency.

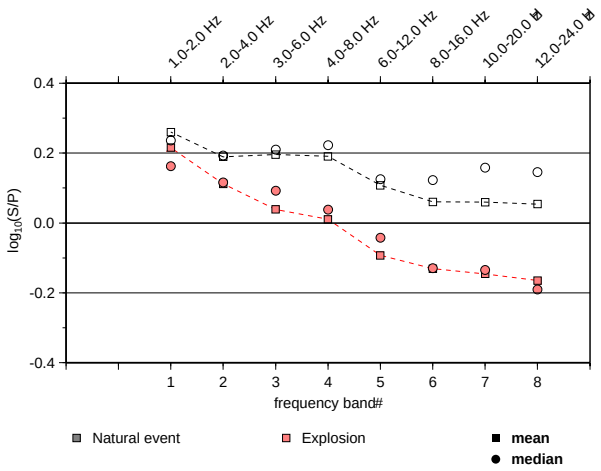

Figure 10. Mean and median S/P amplitude ratios (logarithm) for different event sets as a function of frequency band.

As seen from Figure 10, the explosions show generally decreasing S/P amplitude ratios with increasing frequency. Furthermore, explosions are characterized by higher P energy relative to S at high frequencies. S/P ratios are higher for natural events than for explosions above about 3 Hz. However, the distributions of S/P ratios for explosions and natural events overlap significantly in all analyzed frequency bands.

This may be partly related to path or site effects at different stations. This is illustrated in Figure 11 which shows measured S/P ratios and corresponding mean values for explosions and natural events recorded at four selected stations. Both absolute S/P ratios and the shape of S/P as a function of frequency differ from station to station. But at an individual station, e.g., BLS5 (bottom panels), S/P ratios for natural events seem to be better separated from those for explosions than in a combined analysis for all stations.

In order to get a better understanding of the mechanisms behind the observed S/P ratios there are additional factors that need to be investigated. Such factors are the directivity of the earthquakes sources, mixing of Pn, Pg and Sn, Sg in the measurement of S/P ratios, depth effects of the earthquake sources, and S-wave generation from underwater explosions in regions with strong topography.

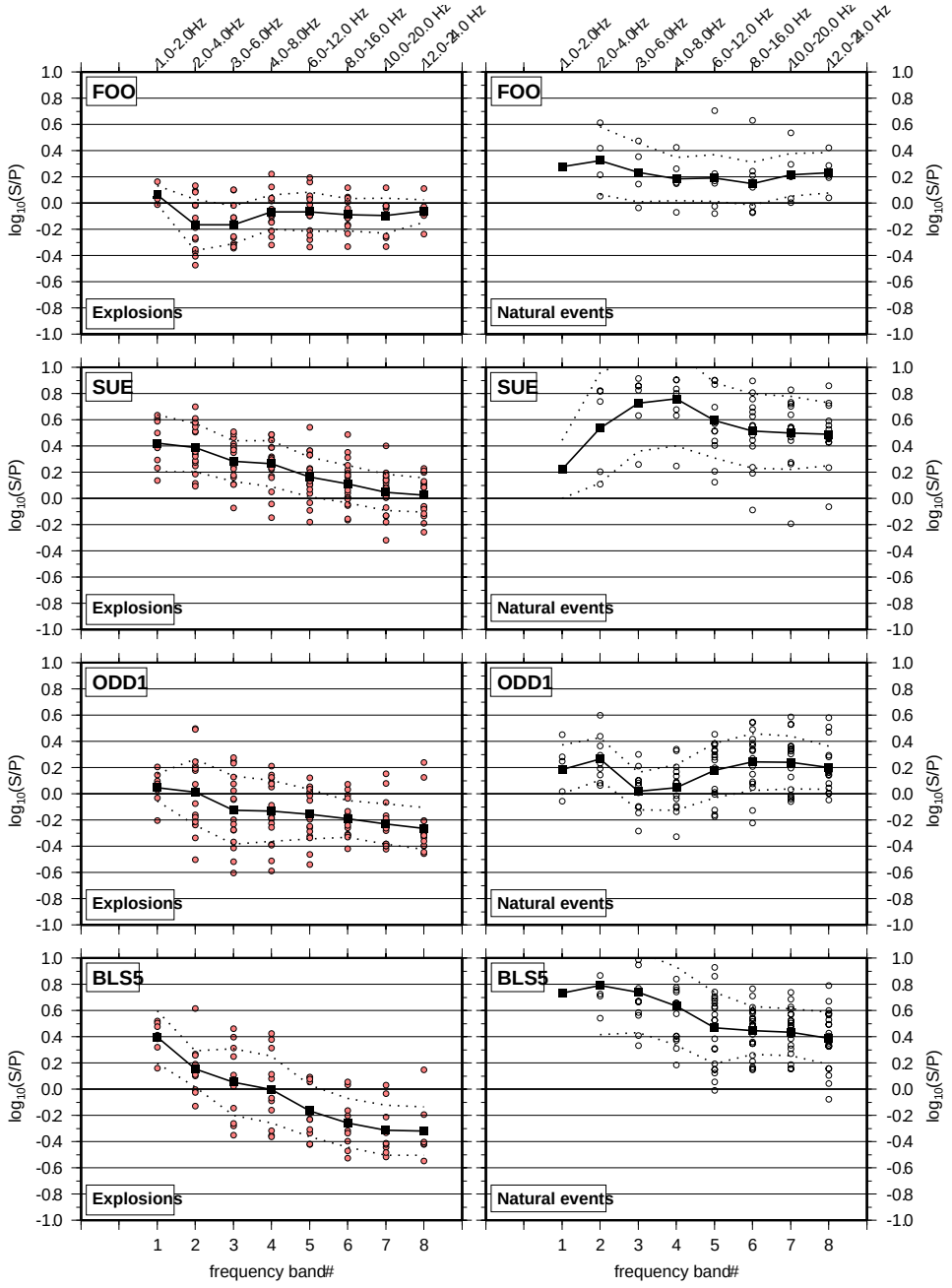

Figure 11. S/P amplitude ratios (logarithm) for explosions (left) and natural events (right) recorded at individual stations. Mean values are plotted as black squares and solid lines, and dashed lines indicate the standard deviation.

CONCLUSIONS AND RECOMMENDATIONS

One of the most significant results from this project has been the demonstration of the strong influence of the in-mine structures on the generation of S-waves from explosions. Through numerical modeling we have found that shear energy generation is particularly prevalent when the source is located near a geologic or structural boundary of the mine. Comparisons with in-mine observations from the Pyhäsalmi mine have further confirmed the reliablity of the waveform simulations. These findings are also in accordance with the results from the more conceptual study of Toksöz et al., 2004.

The strong influence of the near source structure in the generation of shear energy may explain the difficulty in using S/P ratios as reliable discriminants between explosive sources and rockbursts in mines.

We have also investigated the partitioning of S and P energy from earthquakes and underwater explosions occurring in the same region offshore western Norway. Although the earthquakes show generally larger S/P ratios than the explosions, there is a large scatter in the observations. Due to the absence of near-source recordings, these results are quite inconclusive with respect to the path effects involved in the generation of shear energy.

If the structures in the vicinity of explosion sources in general actually give rise to a significant amount of shear energy, we may have an explanation for the difficulty in using S/P ratios for reliable event discrimination. Our recommendation for further studies on energy partitioning between P- and S-energy would be to conduct controlled experiments with good near source recordings, combined with 3-D waveform modelling in both conceptual and realistic structures.

REFERENCES

Bungum, H., T. Kvaerna, S. Mykkeltveit, M. Roth, K. Astebol, D.B. Harris and S. Larsen (2003). Energy partitioning for seismic events in Fennoscandia and NW Russia, in *Proceedings of the 25th Seismic Research Review - Nuclear Explosion Monitoring: Building the Knowledge Base*, LA-UR-03-6029, Vol. 1, pp. 394-404.

Bungum, H., T. Kvaerna, S. Mykkeltveit, M. Roth, V. Oye, K. Astebol, D.B. Harris and S. Larsen (2003), Energy partitioning for seismic events in Fennoscandia and NW Russia, in *Proceedings of the 26th Seismic Research Review - Nuclear Explosion Monitoring: Trends in Nuclear Explosion Monitoring*, LA-UR-04-5801, Vol. 1, pp. 394-404.

Larsen, S. C. and C. A. Schultz (1995). ELAS3D: 2D/3D elastic finite-difference wave propagation code. *UCRL-MA-121792*, 18 p.

Larsen, S., and J. Grieger (1998). Elastic Modeling Initiative, Part III: 3-D *Computational Modeling, Soc. Expl. Geophys. Confer. Proceed.*, 68, 1803-1806, and Lawrence Livermore National Laboratory Technical Report UCRL-JC-130224.

Thomson, D.J. (1982). Spectrum Estimation and Harmonic Analysis. *Proc. IEEE*, 70, No. 9, 1055-1096.

Toksöz, M.N., X. Li, M. Krasovec and S. Chi (2004). Characterization of an Explosion Source in a Complex Medium by Modeling and Wavelet Domain Inversion, in *Proceedings of the 26th Seismic Research Review - Nuclear Explosion Monitoring: Trends in Nuclear Explosion Monitoring*, LA-UR-04-5801, Vol. 1, pp.503-512.

MODELING AND EMPIRICAL RESEARCH ON ENERGY PARTITIONING OF REGIONAL SEISMIC PHASES USED FOR EXPLOSION MONITORING

Mark D. Fisk[1], Thorne Lay[2], and Steven Taylor[3]

ATK Mission Research[1], University of California, Santa Cruz[2], and Los Alamos National Laboratory[3]

Sponsored by National Nuclear Security Administration
Office of Nonproliferation Research and Engineering
Office of Defense Nuclear Nonproliferation

Contract Nos. DE-AC52-04NA25536[1], DE-FC52-04NA25537[2], and W-7405-ENG-36[3]

ABSTRACT

We are investigating energy partitioning of local and regional seismic phases, focusing on geophysical causes of their frequency dependence and variances, mechanisms of P-to-S conversion, different scattering effects for P and S phases that affect their complexity, and implications for reliable and defensible use of P/S discriminants. For empirical studies, we are using large data sets consisting of Pn, Pg, Sn and Lg spectra and time-domain measurements at frequencies from 0.1 to 10 Hz, and correcting for geometrical spreading, attenuation, and magnitude, so that the variability and frequency dependence of individual phases may be assessed. Objectives are to quantify these aspects for explosions and earthquakes near the Lop Nor, Semipalatinsk, Novaya Zemlya, and Nevada test sites, and assess whether consistent patterns emerge. We plan to interpret empirical observations in terms of geophysical mechanisms by using complex elastic-screen simulations, spanning relevant spectral content (0.1 to 10 Hz) for distances of at least 0 to 600 km, using realistic models with multi-scale heterogeneity, rough Moho, topography, and other boundaries.

Preliminary efforts have focused on examining spectral scaling as a function of source size and frequency-dependent P/S discrimination performance for nuclear explosions and selected earthquakes near the Lop Nor test site in China. Network-averaged relative spectra for given phases (using nearby events of various sizes) are compared to theoretical relative spectra using a modified Brune (1970) model for earthquakes and a Mueller and Murphy (1971) model [MM71] for explosions in granite. Spectral contributions of surface reflected phases are also considered. Some preliminary observations are as follows. First, a modified Brune model, with corner frequency scaling as seismic moment to the -1/4 power, seems to adequately predict spectral scaling for the earthquakes examined. Evidence that Pn, Sn and Lg from earthquakes scale fairly similarly with source size suggests that frequency dependence of P/S discrimination performance is not primarily due to earthquake source mechanisms. Second, a modified MM71 model, that treats surface-reflection interference, provides reasonably good fits up to about 4 Hz to empirical spectral ratios of P and Pn waves for Lop Nor explosions, if they are suitably averaged over stations and azimuths. Spectral interference effects due to surface reflections appear to be significant for teleseismic and regional phases. For Lop Nor explosions between mb 4.7 to 6.5, the main effect of destructive interference occurs between about 0.7 to 2.5 Hz. Frequency-dependent discrimination performance of Pn/Sn and Pn/Lg appears to be mainly due to differences in corner frequencies of P and S waves and spectral overshoot for explosions, as observed by Xie and Patton (1999). Enhanced relative energy of Sn and Lg is observed at frequencies below about 2 Hz for the shallower 1996/07/29 tunnel shot, relative to the 1996/06/08 shaft shot, as compared to MM71. It appears that corner frequencies, depth of burial, and interactions with the free surface all have significant impacts, to varying degrees, on the frequency dependence of P/S discriminants for explosions. Path and station effects that impact the variability of regional phases are being explored.

OBJECTIVES

This is a 3-year contract to investigate energy partitioning of local and regional seismic phases to better understand geophysical causes of the variability and frequency dependence of P/S discriminants. We are analyzing large data sets of Pn, Pg, Sn and Lg spectra and time-domain measurements at frequencies from 0.1 to 10 Hz, and correcting for geometrical spreading, attenuation, and magnitude, so that the variability and frequency dependence of individual phases may be assessed. Objectives are to quantify these aspects for explosions and earthquakes near the Lop Nor, Semipalatinsk, Novaya Zemlya, and Nevada test sites, and assess whether consistent patterns emerge. We plan to interpret empirical observations in terms of geophysical mechanisms by using complex elastic-screen simulations, spanning relevant spectral content (0.1 to 10 Hz) for distances of at least 0 to 600 km, considering realistic models with multi-scale heterogeneity, rough Moho, topography, and other boundaries.

RESEARCH ACCOMPLISHED

Preliminary efforts have focused on spectral modeling of Pn, Sn, and Lg phases for nuclear explosions and selected earthquakes near the Lop Nor test site in China. This initial study region has the benefit of including many nearby explosions and earthquakes that were recorded by numerous regional stations, allowing much of the path variability to be averaged out to better examine source characteristics. Network-averaged relative spectra (using nearby events of different sizes) are compared to theoretical relative spectra, using a modified Brune (1970) model for earthquakes and a Mueller and Murphy (1971) model [MM71] for explosions in granite. Spectral contributions of surface reflected phases are also considered. Below we describe the earthquake and explosions models, present some example of spectral scaling, and draw some conclusions regarding near-source mechanisms that affect P/S discrimination.

Brune Earthquake Source Model

The Brune (1970) model is used here to represent the source spectral function for earthquakes. For a particular phase type, ξ (P or S), the spectrum is given by

$$S_\xi(f) = \frac{M_0 R_{\theta\phi}(\xi)}{4\pi\sqrt{\rho_s \rho_r v_s(\xi)^5 v_r(\xi)}[1 + (f/f_c(\xi))^2]} \quad , \tag{1}$$

where M_0 is the seismic moment, $R_{\theta\phi}$ is the radiation pattern coefficient for P or S waves, ρ_s and ρ_r are the source and receiver medium densities, v_s and v_r are the source and receiver medium velocities for P or S waves, and f_c is the source corner frequency. For this study, the parameters in Table 1 of Taylor et al. (2002) are used for the radiation pattern coefficients, densities, and velocities. For a Brune (1970) dislocation source, the corner frequency is given by

$$f_c(\xi) = c_\xi v_s(\xi)\left(\frac{\sigma_b}{M_0}\right)^{1/3} \quad , \tag{2}$$

where σ_b is the stress drop and c_ξ is a constant that can depend on phase type. In the following, $c_P = 0.41$ and $c_S = 0.49$ are used. Taylor et al. (2002) discuss observations by Cong et al. (1996), Nuttli (1983), and Mayeda and Walter (1996) suggesting that the scaling of corner frequency as event moment (M_0) to the -1/4 power is more appropriate than -1/3 scaling for earthquakes in central Asia and the western U.S. This departure from cube root scaling can be viewed as a result of non-constant stress drop. Following Walter and Taylor (2002), non-constant stress drop may be treated by defining the apparent stress drop for a given event moment, M_0, as

$$\sigma_b = \sigma_b^{(0)}\left(\frac{M_0}{M_0^{(0)}}\right)^{\psi} , \tag{3}$$

where $\sigma_b^{(0)}$ is the stress drop at a reference moment $M_0^{(0)}$. This formulation of the apparent stress drop provides appropriate units for any scaling exponent ψ. Values of $\psi = 0$ and $\psi = 1/4$ correspond to corner frequency scaling with moment to the -1/3 and -1/4 powers, respectively. Although there are some trade-offs, the parameters $\sigma_b^{(0)}$, $M_0^{(0)}$, and ψ may be fit to data. Setting $\log M_0^{(0)} = 15.0$ Nm and restricting $0 < \psi < 0.25$, the best fit obtained for the Lop Nor earthquakes presented below is for $\psi = 0.21$ and $\sigma_b^{(0)} = 3.58 \times 10^6 \mathrm{N/m}^2$.

Mueller/Murphy Explosion Source Model

Mueller and Murphy (1971) represented the radial stress by a Heaviside step function and an exponentially decaying term, $\sigma_{rr} = -(P_0 + P_1 \exp(-\omega_1 \tau))U(\tau)$, for the pressure profile acting at the elastic radius. Under this assumption, the far-field amplitude spectrum (without geometrical spreading term) is given by (e.g., Denny and Johnson, 1991)

$$|S(\omega)| = \frac{\gamma P_p R_e \sqrt{\omega^2 + (\omega_1 P_0 / P_p)^2}}{\rho_s v_s(P) \sqrt{\omega^2 + \omega_1^2} \sqrt{(\omega_0^2 - \gamma\omega^2)^2 + \omega_0^2 \omega^2}}, \quad (4)$$

where $\sqrt{\gamma} = v_s(P)/2v_s(S)$, R_e is the elastic radius, proportional to $W^{1/3}(\rho g h)^{-0.417}$ for granite (from empirical studies), h is the depth of burial, and the corner frequency is $\omega_0 = v_s(P)/R_e$. Mueller and Murphy (1971) inferred that the peak pressure is 1.5 times the overburden, i.e., $P_p = P_0 + P_1 = 1.5\rho g h$, and assuming incompressibility, $P_0 = (4\mu/3)(R_c/R_e)^3$, where empirical studies indicate that $R_c = cW^{0.29}h^{-0.11}$ for granite. This model is used with source medium density and velocities inferred from geological borehole samples at the LNTS reported by Matzko (1994). The density is set at 2620 kg/m^3, and the P and S wave velocities (all in units of m/s) are set at 5300 and 3300 for explosions shallower than 500 m and 5600 and 3500 for the explosions deeper than 500 m. Murphy and Barker (2001) showed that their Shagan River model for explosions in granite (with $\omega_1 = 0$) provides reasonable interpretation of P wave spectra for LNTS explosions between mb 5.0 to 6.2, although they found it necessary to increase the source medium velocities by about 30% for larger/deeper explosions to fit the corner frequency.

As described by many authors (e.g., Lay, 1991; Murphy and Barker, 2001; and references therein), surface reflections, interpreted as pP, can significantly affect amplitudes of teleseismic P at frequencies of destructive and constructive interference. As noted by these authors, this effect is complicated by nonlinear spallation processes. Thus, the relative amplitudes and delay times of pP phases cannot be predicted simply by linear reflection (i.e., the relative amplitudes are generally much lower and the delay time longer than predicted by linear theory), nor are the reflections purely impulsive signals. Nevertheless, the contribution of pP to the observed P wave amplitude spectrum is modeled by

$$\left| \frac{P(\omega) + pP(\omega)}{P(\omega)} \right| = \sqrt{1 + A^2 - 2A\cos(\omega t_0)}, \quad (5)$$

where A is the relative amplitude of pP to P and t_0 is the pP delay time. These parameters cannot be estimated from simple linear reflection theory, but may be estimated directly from network-averaged P wave spectra.

Examples of Relative Spectra and Model Fits

Using the ratio of spectra of a given seismic phase for two nearby events recorded by the same station has the benefit that the majority of path (including attenuation), instrument response, and other station effects are canceled out. Thus, the use of relative spectra, when averaged over numerous stations with good azimuthal coverage, is expected to provide a fairly good estimate of the far field relative source spectra. It is particularly useful to consider nearby events with substantially different source sizes to highlight differences in spectral behavior. For investigation of regional phase spectra, it is most useful to also consider more recent events that were recorded by up to 17 regional stations in

Kazakhstan, Kyrgyzstan, Pakistan, and Russia, most of which were installed (or disseminated data) after mid 1994. LNTS explosions that best meet these criteria are the 1996/07/29 tunnel shot (mb 4.7) and the 1996/06/08 shaft shot (mb 5.8). A drawback is that these events were separated by about 30 km and the emplacement conditions were different. Two shaft shots on 1993/10/05 (mb 5.8) and 1992/05/21 (mb 6.5) are also considered below, although these events have recordings by only 5 common regional stations, all of the Kyrgyzstan network (KNET). The 1999/01/27 (mb 3.95) and 1999/01/30 (mb 5.40) earthquakes are very useful to study because they occurred very close to each other and the LNTS (Figure 1), they both have similar depths of about 20 km, based on well-constrained depth-phase solutions, and the difference in their magnitudes is sufficient to examine effects of source size on the relative spectra.

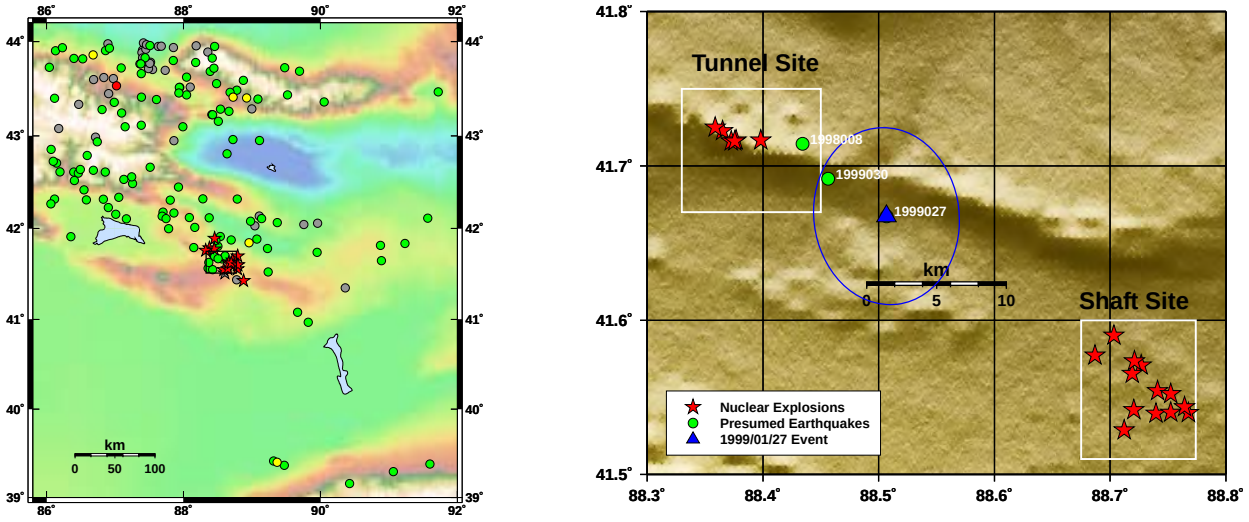

Figure 1. Maps showing locations of nuclear explosions and 156 regional earthquakes considered in this study.

Figure 2 shows network-averaged (using 13 to 17 common stations) relative spectra of Pn, Sn and Lg phases for the pairs of explosions in 1996 and earthquakes in 1999. It also shows the relative spectra of teleseismic P waves for the explosions, using 33 common stations and arrays. Spectra were restricted to a signal-to-noise ratio (SNR) of at least 2.5, and at least 3 stations with adequate SNR are required to contribute to the network average at a given frequency. Last, Figure 2 shows the theoretical relative spectra based on Mueller/Murphy (MM71) and Brune models. Yields and depths of 3 kT and 240 m for the 1996/07/29 shot and 70 kT and 480 m for the 1996/06/08 shot were used. Moments for the earthquakes were computed using $\log M_0 = 1.5 M_W + 16.05$ (Hanks and Kanamori, 1979) and estimates of $M_W = 4.38$ and $M_W = 5.69$ for the 1999 earthquakes. Some observations from Figure 2 include:

- The relative spectra of Pn, Sn and Lg for the earthquakes are all very similar over frequencies of 0.6-3.0 Hz. Variations for different phases outside this frequency range are not very dramatic. Relative spectra for all phases are fairly consistent with the modified Brune model using corner frequency scaling as moment to the -1/4 power.
- Network-averaged P (magenta) and Pn (solid red) relative spectra for the 1996 explosions agree surprisingly well. This is likely achieved because of averaging over many teleseismic or regional stations with fairly good azimuthal coverage. Similarities in the P and Pn relative spectra, including the minimum at about 2 Hz and the local maxima at about 1.2 and 3.5 Hz, suggests that these curves represent relative source characteristics. Significant deviations of these curves from the MM71 curve are explored below.
- Network-averaged Sn (solid green) and Lg (solid blue) relative spectra for the explosions exhibit very significant differences from the P and Pn curves, predominantly at frequencies below about 2 Hz, indicating that Sn and (even more so) Lg energy are enhanced at these lower frequencies for the smaller/shallower explosion in a man-

ner inconsistent with predictions by the MM71 model for P waves. Hypotheses of Rg-to-S scattering and spall effects have been investigated to explain this behavior, which is also observed at other test sites.

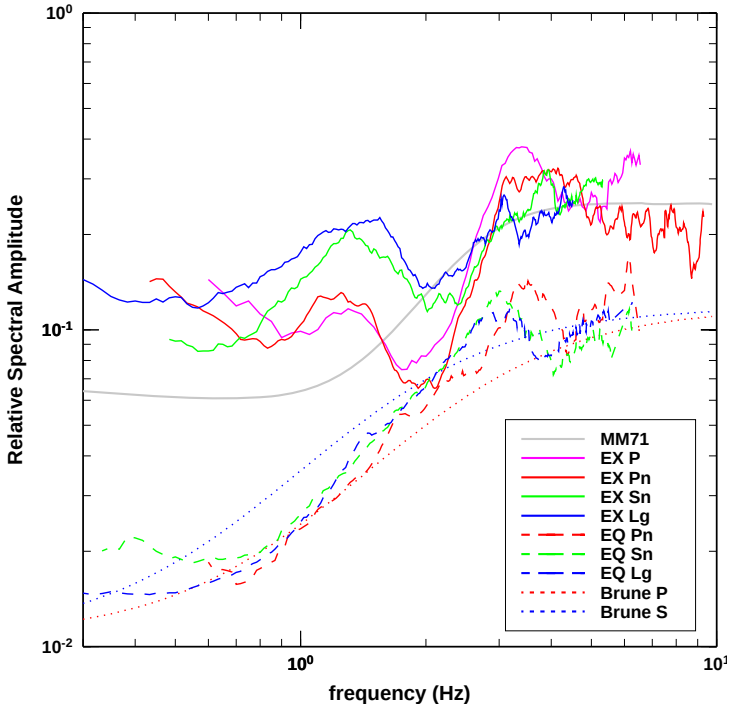

Figure 2. Relative spectra for two 1996 explosions and two 1999 earthquakes (smaller over larger). The legend associates the various curves with theoretical and empirical relative spectra for various events and phase types.

To explore deviations of the P and Pn relative spectra from MM71, Figure 3 shows the result of fitting pP parameters (black curve, MM71 P+pP) to the network-averaged teleseismic P relative spectra (solid magenta) for the 1996 shots. The dotted magenta curves represent the 90% confidence interval of the network-averaged P spectral ratio, indicating considerable variability. The relative amplitudes and delay times are estimated to be 0.49 and 0.47s for the July tunnel shot and 0.13 and 0.90s for the June shaft shot, which are consistent with the range of values obtained for tunnel and shaft shots for LNTS explosions prior 1993 (Murphy, 2005). Treating pP interference accounts for the majority of deviations from the MM71 (P only) model from about 0.8 to 3.5 Hz. The first local maximum in the spectral ratio corresponds to constructive interference for the smaller shot in the numerator. The first local minimum corresponds to constructive interference for the larger shot in the denominator. Differences in theoretical and empirical curves below about 0.6 Hz is likely due to inadequate overshoot in the model used here. The green curves in Figure 3 show spectral ratios for the two 1996 explosions for Pn at MAK (left) and P at EKA (right), which exhibit even more pronounced frequency-dependent departures from the MM71 P-only model. Comparison of these two plots illustrates that these pronounced variations can be observed for both regional and teleseismic phases. Such strong variations at individual stations are often reduced considerably by network averaging because the pP relative amplitudes and delay times vary from one station to another as functions of many geophysical effects, including take-off angle and asymmetric nonlinear spall effects (Murphy, 2005). There are undoubtedly other effects that have not been treated here.

Figure 4 shows similar relative spectra for the 1993/10/05 (mb 5.8) shot to the 1992/05/21 (mb 6.5) shot, both at the shaft site. Yields and depths of 75 kT and 650 m for the 1993 shot and 650 kT and 1000 m for the 1992 shot were used to fit the data. This suggests that the 1993 shot may have been slightly overburied, although there is currently no conclusive evidence. The yield and depth of the 1992 event are consistent with current estimates. The pP relative

amplitudes and delay times are estimated to be 0.42 and 0.69s for the 1993 shot and 0.15 and 1.34s for the 1992 shot. Estimates of pP parameters by Murphy (2005) for the 1992 shot are 0.29 and 1.18s. Modest differences in these estimates could be due to the use of different stations and processing methods.

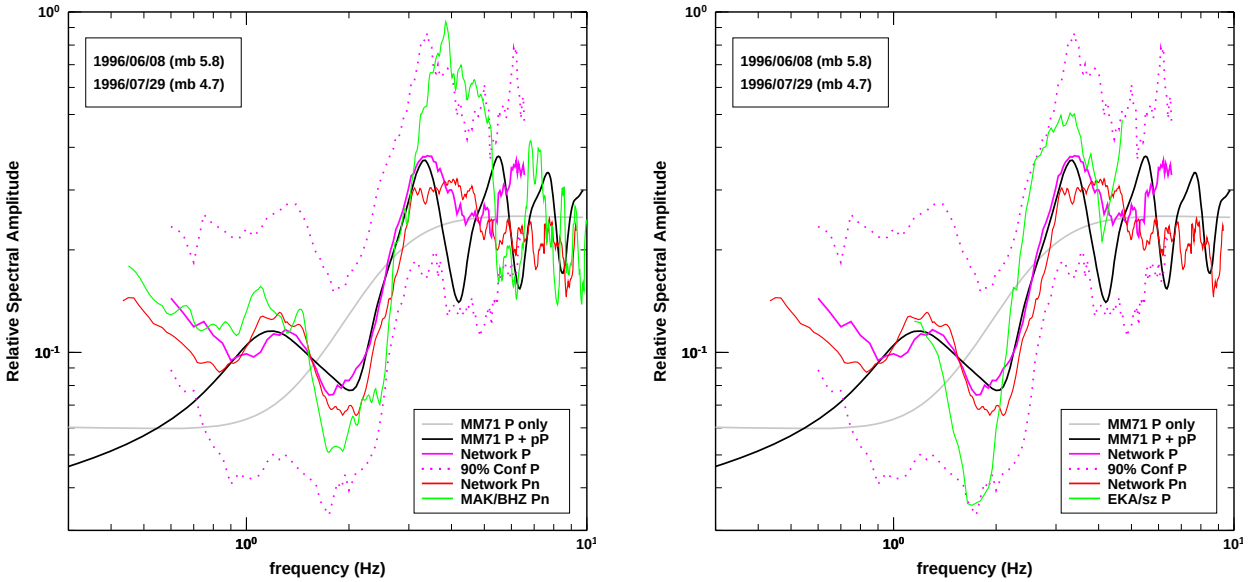

Figure 3. Empirical and model P and Pn relative spectra for the 1996/07/29 and 1996/06/08 LNTS explosions. The green curves represent the relative spectra of Pn at MAK (left) and P at EKA (right).

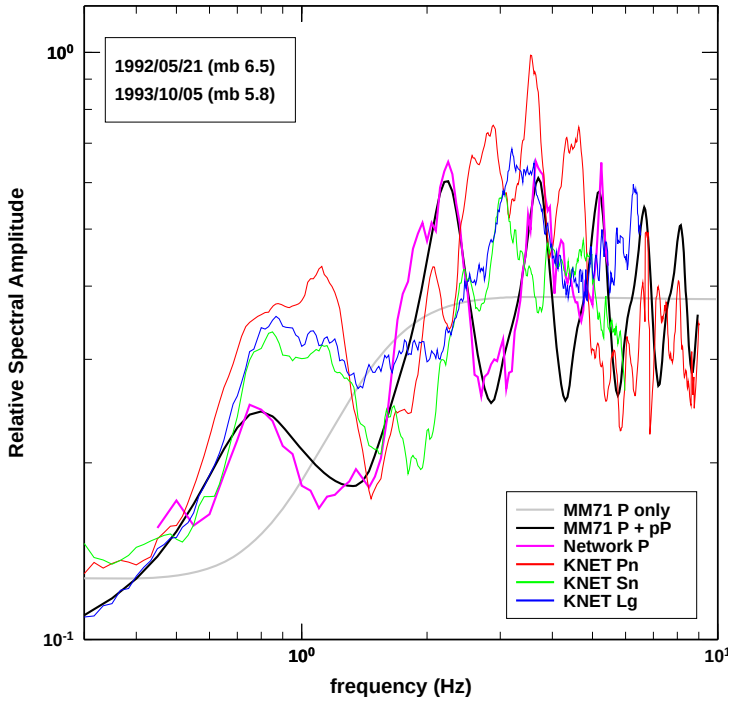

Figure 4. Model and empirical P, Pn, Sn, and Lg relative spectra for the 1993/10/05 to 1992/05/21 LNTS shots.

Figure 4 shows that the MM71 (P+pP) model fits the network-averaged P spectral ratio reasonably well from about 0.5 to 4.0 Hz. It also shows the Pn spectral ratio (red curve) averaged over 5 KNET stations with common recordings

of these two shots. Agreement between the Pn and P spectral ratios is not very good in this case, likely because only 5 stations with little azimuthal coverage are available. Nevertheless, some similar qualitative frequency dependence can be observed in both spectral ratios (e.g., common local maxima at about 0.7 Hz). Last, the Sn and Lg relative spectra in Figure 4 do not exhibit enhanced energy at lower frequencies compared to the Pn relative spectra (contrary to the effect observed in Figure 2 for the smaller/shallower 1996/07/29 tunnel shot).

Implications for Regional P/S Discriminants

To investigate regional P/S discrimination performance, we compare empirical spectral ratios of Pn/Sn and Pn/Lg to model predictions. In this case, differential attenuation of P and S waves must be treated. The attenuation coefficients estimated by Taylor et al. (2002) for station MAK are used here. Figure 5 shows Pn/Sn and Pn/Lg spectral ratios at MAK for the 1996 explosions and the 1999 earthquakes. The smaller events have less bandwidth because of the SNR threshold of 2.5. The solid and dashed gray curves show predictions of the modified Brune model for the 1999/01/30 and 1999/01/27 earthquakes. The shapes of these curves are due to differential attenuation of P and S phases and different P and S corner frequencies as functions of moment. Model spectral ratios for the earthquakes (gray curves) provide relatively good fits to the data, although there is no evidence in this case, nor some other studies (e.g., Walter and Taylor, 2002) that P/S is systematically lower for smaller earthquakes. The solid and dashed black curves show MM71 predictions for the explosions assuming the same source model for all phases, but with Sn and Lg corner frequency lower than for Pn by a factor of $v_s(S)/v_s(P)$. Differences in P/S spectral values between the two shots are due to differences in P and S corner frequencies (as suggested by Xie and Patton, 1999) as functions of yield and pP interference effects (cf. Figure 2). The offset between the gray and black curves is largely due to the ratio of P and S velocities in the Brune model. That is, the ratio of earthquake P/S spectral amplitudes at zero frequency is given by

$$\frac{S_P(0)}{S_S(0)} = \frac{R_{\theta\phi}^{(P)}}{R_{\theta\phi}^{(S)}}\left[\frac{v_s(S)^5 v_r(S)}{v_s(P)^5 v_r(P)}\right]^{1/2}. \qquad (6)$$

Using values from Taylor et al. (2002) of $R_{\theta\phi}^{(P)} = 0.44$ and $R_{\theta\phi}^{(S)} = 0.60$ for the average radiation pattern terms and $v_s(P) = 6100$, $v_r(P) = 5000$, $v_s(S) = 3526$, $v_r(S) = 2890$ (all in units of m/s) for the source and receiver P and S medium velocities, the expression in (6) equals 0.14. For comparison, the dotted black curves in each plot represent the P/S spectral ratios for explosions, assuming the same MM71 model (and corner frequencies) for P and S waves.

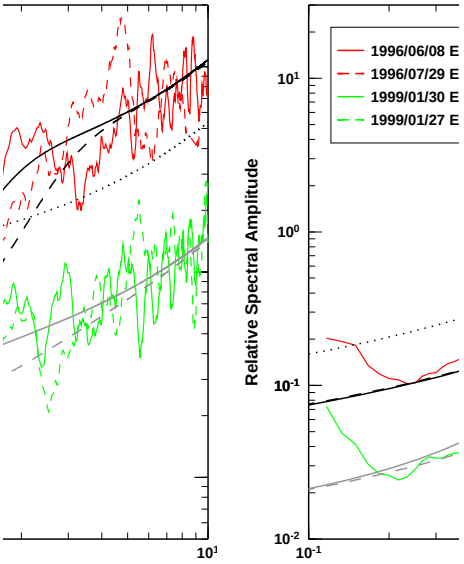

Figure 5. Empirical and model Pn/Sn (left frame) and Pn/Lg (right frame) spectral ratios for MAK BHZ recordings of the two 1996 explosions and two 1999 earthquakes at the LNTS.

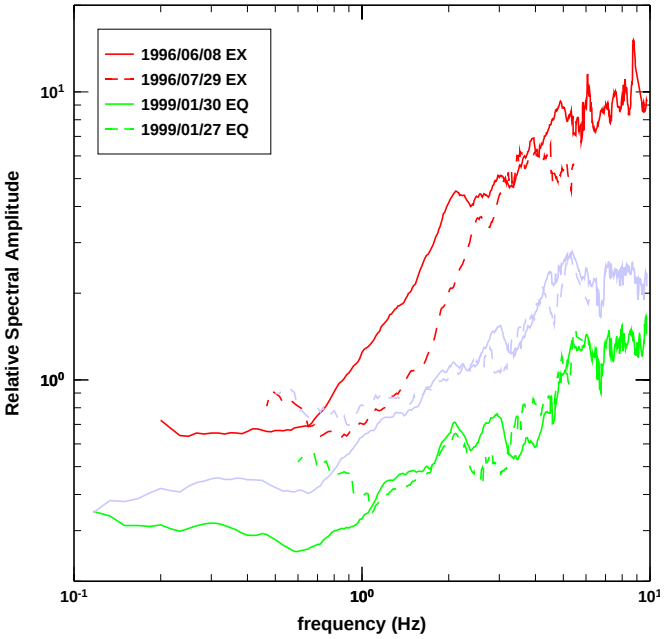

Figure 6. Network-averaged Pn/Sn spectral ratios for two 1996 LNTS explosions and two 1999 earthquakes with time windows that include (blue curves) or exclude (green curves) depth phases.

As an aside, Figure 6 shows that reflected phases can also affect P/S discriminants for earthquakes. Depicted are network-averaged Pn/Sn spectral ratios for the 1996 explosions and 1999 earthquakes at LNTS. The light blue curves represent the spectral ratios for earthquakes using a default velocity window for Pn (6.8 to 8.2 km/s), while the green curves are for a time window that excludes at least sPn at all stations. The results are yet to be corrected for station-dependent attenuation and site effects, but this does not affect the general conclusion regarding the potential impact of depth phases from earthquakes on Pn measurements, which can significantly affect P/S discrimination performance.

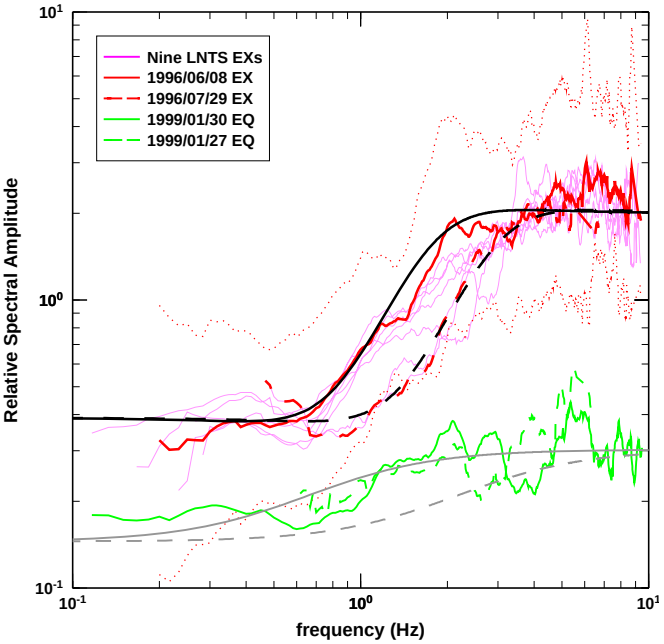

Figure 7. Network-averaged Pn/Sn spectral ratios, corrected for attenuation and station effects, for nine LNTS explosions and two 1999 earthquakes. Theoretical predictions of Pn/Sn ratios are shown for the 1996 shots and 1999 earthquakes (black and gray curves). The dotted red curves represent

As an example of recent results, Figure 7 shows Pn/Sn spectral ratios for nine LNTS explosions with regional data (magenta curves), the 1996 shots (red curves), and the 1999 earthquakes (green curves), using

preliminary attenuation and station corrections, and then network averaging. Model predictions are shown for the 1996 explosions and 1999 earthquakes (black and gray curves, respectively), which seem to adequately represent the data and indicate that the main effect of frequency-dependent P/S discrimination performance is due to different corner frequencies of P and S waves and stronger spectral shapes (including overshoot) for explosions than earthquake spectra. Note that we increased the explosion Pn corner frequencies by 30%, as was done by Murphy and Barker (2001), to obtain the model results. Also shown is the 90% confidence interval of Pn/Sn for the 1996/06/08 shot (dotted red curves), which illustrates the considerable variability of Pn/Sn spectral ratios at the various stations. We plan to investigate this variability using numerical simulations, and these source model parameterizations, during subsequent phases of this contract.

CONCLUSIONS AND RECOMMENDATIONS

Although these preliminary results are anecdotal at this point, and subject to revision after further investigations, there are some interesting observations. First, the modified Brune (1970) source model with corner frequency scaling as moment to -1/4 power seems to adequately predict spectral scaling for the earthquakes considered here and past observations in central Asia by several authors. Relative spectra of Pn, Sn, and Lg exhibit fairly minor differences over a frequency range of about 0.5 to 5.0 Hz, suggesting that the frequency dependence of P/S discrimination performance is not primarily due to earthquake source mechanisms, although the relative P and S wave velocities near the source are expected to affect P/S discrimination performance at all frequencies. As an ancillary comment, windows used to measure first P amplitudes for earthquakes should be designed to exclude depth phases, if possible.

Second, the modified MM71 P+pP model provides reasonably good fits up to about 3-4 Hz to empirical spectral ratios of P and Pn for LNTS explosions, if they are suitably averaged over stations and azimuths. Spectral effects of pP interference can be significant for teleseismic and regional phases. For LNTS explosions between mb 4.7 to 6.5, the main effect of destructive pP interference occurs between roughly 0.7 to 2.5 Hz. This cause of weak P amplitudes in this frequency range has been discussed at length by Lay (1991) and others, typically in the context of teleseismic P waves. Note that a relative pP amplitude of 0.5 produces a range of variations from the P-only MM71 model by a factor of three. It is interesting that the relative amplitudes of pP are the largest for the 1996/07/29 tunnel shot (A = 0.49) and the 1993/10/05 shaft shot (A = 0.48), which seems to have been somewhat overburied. Note that the average pP relative amplitudes estimated by Murphy and Barker (2001) and Murphy (2005) for LNTS explosions between 1976 and 1992 are 0.50 for the tunnel shots and 0.18 for the shaft shots. It is tempting to speculate that the tunnel and overburied shots may have produced much weaker spallation, leading to stronger (more linear) reflections of pP. This effect, along with strong enhancement of regional S waves in this frequency range for smaller/shallower shots may contribute to poorer regional P/S discrimination at frequencies below about 3 Hz. However, as noted by Xie and Patton (1999), frequency-dependent performance of regional P/S discriminants appears to be primarily due to differences in corner frequencies of P and S waves and spectral shape (including overshoot) for explosions.

As shown in the Lop Nor Advanced Concept Demonstration (e.g., Bahavar et al., 2004), Pn/Sn discrimination results using 3-component records in the 4-6 Hz band are all very comparable for nine actual nuclear explosions (mb 4.7 to 6.5) and simulated explosions scaled down to mb 3.0. There is no evidence, empirically or theoretically, that this should not be true for P/S measurements above the Pn corner frequency for explosions, where discrimination performance seems to saturate. However, at lower frequencies there is evidence that explosions can have enhanced S wave energy relative Pn, leading to poorer discrimination. Note that the Brune and MM71 models we used here both predict that the ratio of asymptotic high-frequency to low-frequency limits of P/S behave according to the ratio of the P to S corner frequencies squared. Using the geologic parameters considered here for LNTS, the ratio of asymptotic limits of high-frequency to low-frequency P/S is about 2 for earthquakes and about 5 for explosions (cf. Figure 7). Much more work is needed to examine this behavior for other regions and many more events, but a geophysical

understanding of frequency-dependent P/S discrimination performance seems attainable, which could be utilized to predict performance, on average, for regions with sufficient geologic information. Encouraging results thus far are (1) a better understanding of why P/S discriminants do not perform as well at lower frequencies and (2) that application of regional P/S discriminants should be limited to frequencies above the Pn corner frequency for explosions, which can be computed, at least in principle, if adequate information is available regarding the explosion yield, depth, and near-source geology. Considerably more work is required to understand regional phase variability due to path (scattering) and station effects.

Future plans include (1) analysis of more earthquakes near Lop Nor; (2) application of numerical simulations to explore geophysical path and station effects on the variability of individual phases for LNTS events, using the source model parameterizations developed thus far; and (3) similar investigations at other nuclear test sites. More work is certainly needed to better understand source excitation and scattering effects for regional S waves from explosions.

ACKNOWLEDGMENTS

We are grateful to Howard Patton, Jiakang Xie, and Gary McCartor for many useful discussions.

REFERENCES

Bahavar, B., B. Barker, G. Beall, I. Bondar, D. Brumbaugh, M. Fisk, J. Hanson, H. Israelsson, B. Kohl, Y.-L. Kung, J. Murphy, R. North, V. Oancea and J. Stevens (2004). Seismic calibration of Lop Nor, China test site region for improved regional monitoring, Editor J. Bennett, Science Applications International Technical Report, SAIC-04/2208.

Brune, J. N. (1970). Tectonic stress and the spectra of seismic shear waves from earthquakes, *J. Geophys. Res.*, **75**, 4997-5009.

Cong, L., J. Xie and B. J. Mitchell (1996). Excitation and propagation of Lg from earthquakes in central Asia with implications for explosion/earthquake discrimination, *J. Geophys. Res.*, 101, 27,779-27,789.

Denny, M. D. and L. R. Johnson (1991). The explosion seismic source function: models and scaling laws reviewed, *Explosion Source Phenomenology, Geophysical Monograph*, 65, 1-24.

Hanks, T. and H. Kanamori (1979). A moment-magnitude scale, *J. Geophys. Res.*, 84, 2348-2350.

Lay, T. (1991). The teleseismic manifestation of pP: problems and paradoxes, *Explosion Source Phenomenology, Geophysical Monograph*, 65, 109-125.

Matzko, J. R. (1994). Geology of the Chinese nuclear test site near Lop Nor, Xinjiang Uygur Autonomous Region, China, *Engineering Geology*, 36, 173-181.

Mayeda, K. and W. R. Walter (1996). Moment, energy, stress drop, and source spectra of Western United States earthquakes from regional coda envelopes, *J. Geophys. Res.*, 101, 11,195-11,208.

Mueller, C. S. and J. R. Murphy (1971). Seismic characteristics of underground nuclear detonations Part I: seismic spectrum scaling, *Bull. Seism. Soc. Am.*, 61, 1675-1692.

Murphy, J. R. and B. W. Barker (2001). Application of network-averaged teleseismic P-wave spectra to seismic yield estimation of underground nuclear explosions, *Pure and Appl. Geophys., Special Edition on Monitoring the Comprehensive Nuclear-Test-Ban Treaty: Source Processes and Explosion Yield Estimation*, 158, 2123-2171.

Nuttli, O. W. (1983). Average seismic source-parameter relations for mid-plate earthquakes, *Bull. Seism. Soc. Am.*, 73, 519-535.

Taylor, S. R., A. A. Velasco, H. E. Hartse, W. S. Phillips, W. R. Walter, and A. J. Rodgers (2002). Amplitude corrections for regional seismic discriminants, *Pure and Appl. Geophys., Special Edition on Monitoring the Comprehensive Nuclear-Test-Ban Treaty: Seismic Event Discrimination and Identification*, 159, 623-650.

Walter, W. R. and S. R. Taylor (2002). A Revised Magnitude and Distance Amplitude Correction (MDAC2) Procedure for Regional Seismic Discriminants: Theory and Testing at NTS, *UCRL-ID-146882, LA-UR-02-1008*.

Xie, J. and H. J. Patton (1999). Regional phase excitation and propagation in the Lop Nor region of central Asia and implications for P/Lg discriminants, *J. Geophys. Res.*, 104, 941-954.

USING GROUND TRUTH EXPLOSIONS FOR STUDYING SEISMIC ENERGY GENERATION AND PARTITIONING INTO VARIOUS REGIONAL PHASES

Yefim Gitterman, Vladimir Pinsky, and Abraham Hofstetter

Geophysical Institute of Israel

Sponsored by Air Force Research Laboratory

Contract F19628-03-C-0124

ABSTRACT

During the first year of the project numerous data were collected to study empirical features of seismic energy generation (especially for S waves from explosions) for different seismic sources; and how this energy is partitioned between P, S, and surface waves, in specific geological conditions and tectonic settings of the Middle East. The sources include experimental land and underwater explosions, military detonations, and routine quarry blasts, for which Ground Truth information (GT0) and blast design parameters were collected. Some earthquakes were included in the database, for comparative waveform analysis.

We analyzed quantification of the source coupling for contained (with different scaled depth), single-fired, chemical experimental explosions observed at regional stations. An extensive dataset was collected from selected seismic events recorded by national network short-period, and International Monitoring System (IMS) broadband stations in Israel (EIL, MMAI) and Jordan (ASF), providing different characters of S-waves at regional distances up to 390 km. Based on the charge-weight explosion series conducted in Sayarim Valley (June 2004), similar power law scaling parameters for charge weight were determined for the amplitude of each of the dominant regional phases: P (0.93), S (0.87) and Rg (0.93).

A series of experimental shots of 0.5, 2, and 20 tons ANFO, and 0.5 ton TNT, in large diameter boreholes was conducted at the basalt quarry Beit-Alpha in Northern Israel in June 2005. The shots provided data for the yield-dependent analysis of regional waveforms, similar to the Sayarim experiment (June 2004), but in a different geological environment. The seismic effect of different explosives (ANFO and TNT) was also examined for close and remote stations.

Data collected for simultaneous ground truth explosions were used for analysis of the magnitude dependence on charge weight. The relation for underwater explosions was validated, and the equation for land shots was modified with a scaling factor similar to the magnitude upper limit for sources of known yield in hard rocks.

We started to evaluate and analyze S/P maximum amplitude and energy ratios for selected events. Existing Geological Institute of Israel (GII) software for visualization and preliminary processing of accelerograms and seismograms was modified and adapted for the project goals, including SEISPECT (analysis of spectra and spectral ratios), and AIST (waveform analysis of different data formats). Appropriate software for S/P amplitude and energy ratio estimation was developed. We estimated and analyzed S/P maximum amplitude and energy ratios for selected events in different time and frequency bands (0.5-3, 3-6 and 6-9 Hz), against distance and charge weight (averaged over recorded stations). The results demonstrate clear dependencies of the S/P ratios on distance and yield. The S/P maximum amplitude ratio calculated in different spectral bands shows a potential for identification of explosion seismic sources.

OBJECTIVES

The main objectives of the project are: 1) conduct of experimental single-fired explosions of special design; 2) determination and verification of empirical source scaling relationships estimating the dependence of seismic wave parameters on different source features; 3) quantifying coupling and specific seismic source features, including energy generation and partitioning into various regional phases.

RESEARCH ACCOMPLISHED

Collection of data and Ground Truth information.

During the first year of the project an initial dataset was collected to study empirical features of seismic energy generation (especially for S waves from explosions) for different seismic sources; and how this energy is partitioned between P and S waves, in specific geological conditions and tectonic settings of the Middle East. The sources include experimental explosions (mostly in single boreholes), strong routine quarry blasts and a military detonation, where GT0 and blast design parameters were collected.

Sayarim charge weight series. A series of three experimental explosions (S1-S3) of variable charge (ANFO explosives) was conducted in the Sayarim Valley near Eilat, Israel (Figure 1, Table 1). The largest single-fired shot of 32.5 tons, in 11 large-diameter (60-70 cm) boreholes of ~20 m depth, was designed as a large-scale land calibration explosion for a MERC project aimed at improving regional velocity models for calculating regional travel times and calibration of an IMS station (MMAI at Mt. Meron). Two smaller explosions of 0.3 ton and 2 tons were conducted at the same site, in single boreholes of the same depth and diameter, thus providing (together with the calibration shot) a series for the yield-dependent analysis of regional waveforms. The large hole diameter resulted in smaller linear charge size (approaching near-spherical form) and in more explosive concentration for the largest shot. Geologically the area is a graben filled by Quaternary alluvial conglomerates, underlain by consolidated rocks. Clear signals were observed for the largest shot at MMAI (r~350 km).

For comparison of data obtained with other observations, ANFO charges were converted to TNT equivalent (Table 1). We also calculated the scaled (burial) depth, characterizing seismic energy generation and surface effects (Table 1): $\hat{h}$ (m/kg$^{1/3}$)=H(m)/(W, kg)$^{1/3}$=0.01H(m)/(W, kT)$^{1/3}$
where H=depth, W=charge weight in kg or kT.

Mehola and MERC experimental shots. A number of experimental explosions were conducted in October 2004 (Figure 1). Two shots in single holes of large diameter (80 cm) and various depth (Mehola experiment, shots M1A, M1B, Table 1) were conducted. Explosion M1A produced anomalously small amplitudes relative to M1B, which was of similar charge but placed in a hole full of water and using a large (250 kg) TNT booster. Field observations, video and close-in records from M1A suggest that the explosives did not completely detonate, resulting

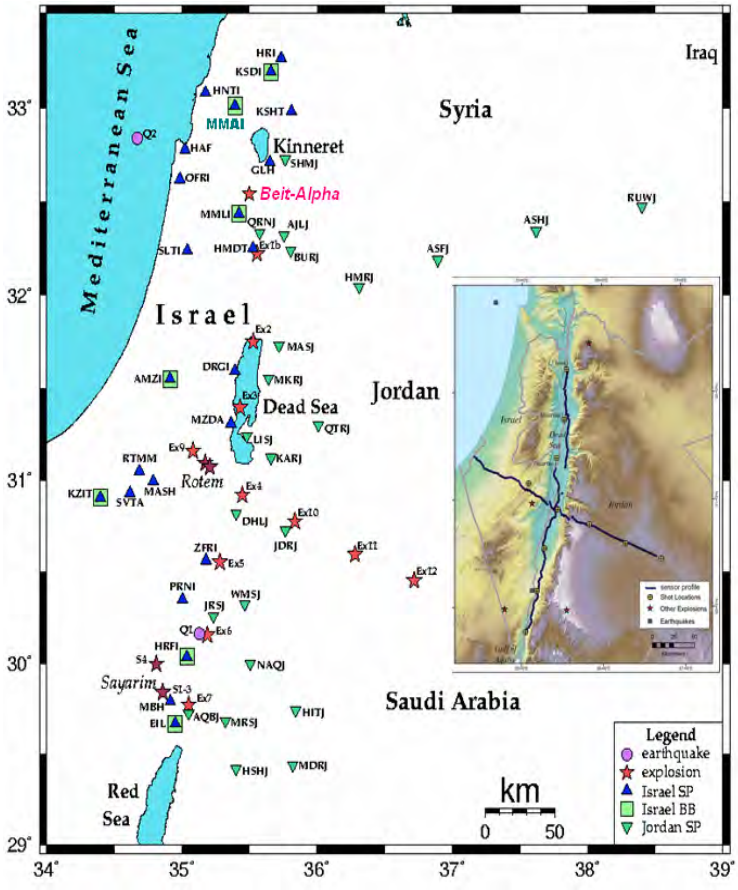

Figure 1. Location of selected seismic events and observed seismic stations (on the insertion - two profiles of ~800 IRIS SP sensors deployed in October 2004).

in reduced seismic signals (see below).

Other explosions were carried out in a MERC project (ten Brink et al., 2004): two underwater shots in the Dead Sea, and land detonations in single holes, in dry or water-saturated media, in different geological and tectonic settings in Israel and Jordan on both sides of the Dead Sea Fault zone. IRIS blast boxes provided detonations at pre-determined times. Ground Truth (GT0) information was collected for all the explosions, with broad variety of blast design parameters, charge geometry, geological settings, and shot media (Gitterman et al., 2005).

Beit-Alpha experiment. GII recently conducted (June 6, 2005) a series of experimental explosions at Beit-Alpha basalt quarry, Lower Galilee (Figure 1, Table 1), in boreholes of large diameter (0.5-0.55 m) at depth of ~15 m, drilled in the cover basalt flow, weathered and cracked in the subsurface layer. The largest shot Bα4 of 20 tons, designed as a large-scale land calibration explosion, was executed as a MERC project, complementary to the Southern Sayarim shot S3 of 32.5 tons of similar design. The local magnitude was M_L~2.6; clear signals were observed at BB EIL (322 km).Three smaller shots of 0.5 ton ANFO, 0.5 ton TNT and 2 tons ANFO in boreholes of the same design, together with the large explosion, provided a series for yield-dependent analysis of regional waveforms, similar to the Sayarim experiment, but in a different geological environment. The two 0.5 ton shots were fully contained, whereas the two larger shots were poorly contained, resulting in reduced magnitudes. Preliminary analysis shows a small (~4-5%) increase in signal vector amplitude and energy for the TNT shot comparing to the ANFO shot (at BB station MMLI, r~13 km), less than expected.

Table 1. Parameters of experimental shots conducted in the project and large quarry/military blasts collected.

Ex. No.	Date	Lat. Lon.	Origin Time, GMT	M_L	ANFO charge, kg	TNT equiv., kg	Hole depth, m	Scaled depth, m/kg$^{1/3}$	No. of holes	Comments
S1	13.06.04	29.84334 34.85866	12:20: 01.192	-	300	262	20	3.05	1	fully contained, no crater
S2	15.06.04	29.84244 34.85860	11:49: 39.349	2	2000	1635	20	1.40	1	partially contained, crater R~13-14m)
S3		29.84188 34.85851	13:00: 01.493	3	32500 (single ~3000)	26860 (2442)	17-20.5	1.11	11	poorly contained, non-symm. craters
M1A	20.10.04	32.22269 35.55644	11:15: 00.0	-	3000(?) henamit	-	25	1.5	1	partially detonated, fully contained
M1B			12:15: 00.0	2.4	3000 henamit	-	35	2.2	1	water-filled hole, fully contained
Bα1	06.06.05	32.54499 35.46868	10:05: 01.422	1.5	500	-	14.7	1.5	1	fully contained
Bα2		32.54506 35.46850	10:30: 01.604	1.5	-	500	16	1.7	1	
Bα3		32.54522 35.46883	11:00: 01.330	1.4	2000 (1000)	-	14.7-15.5	1.0-1.1	2	poorly contained
Bα4		32.54549 35.46914	12:00: 01.532	2.6	20000 (1000)	-	14-16	1.0-1.2	20	
R1	25.04.04	31.093 35.173*	9:15:18.5*	2.7	13278	-	3-7	~1-1.5	211	ripple-fired blasts at Rotem quarry
R2	22.07.04	31.072 35.207*	9:54:46.9*	2.9	~15000	-	-	-	-	
S4	07.06.04	29.991 34.798*	15:06: 28.4*	2.5	-	~10000	surface shot in 0.5-1m deep trench at Sayarim range			

* estimated from records of Israel Seismic Network (ISN)

All the experimental explosions were observed at the dense network of SP and BB stations in Israel, including IMS and CNF stations. For some strong events records and phase data from Jordan and Lebanon were collected.

Large controlled land blasts and selected earthquakes. We also collected GT information and records for three large land quarry/military blasts conducted in 2004 (Table 1). Specific feature of these sources is the unusually high seismic energy released, shown by high local magnitude M_L values estimated from ISN observations. The Rotem quarry blast R2 of 15 tons (ANFO) in several dozen holes with many delays produced a seismic event with

magnitude 2.9, very close in magnitude to Sayarim shot S3 of 32.5 ton in 11 holes (located ~120 km to the South), that yielded magnitude ~3.0. Likewise, the military shot S4 of ~10 ton of TNT, intended to destroy out-dated ammunition, in a trench open to the air, produced a significant magnitude of 2.5, and clear seismic signals are observed up to 160 km, along with very strong acoustic waves. Some earthquakes, recorded in the same period and co-located with the explosion sources, were included in the project database for comparative waveform analysis (see Figure 1).

Near-source observations.

An extensive dataset of high-quality records was acquired from ETNA accelerometers, installed mainly at 0.1-0.5 km from the explosions, and portable short-period 3C seismic stations deployed at a distance range of 1-15 km.

Seismic source complexity for the Sayarim explosion S3 conducted in 11 boreholes was observed at the closest accelerometer. Two wave groups separated by ~0.2 sec were found on all three components (Figure 2); the first group is like the signal from single-hole shot S2. The accelerogram is similar to near-field strong-motion data from the Lyaur explosions with delayed detonations in multiple rows (Negmatullaev et al., 1999). All borehole charges were detonated simultaneously, but due to the hole spacing, the distance difference from the closest and remotest charges to station ACC3 was ~60-70 m, and the time shift could reach ~0.2 sec (assuming S-wave velocity ~300-350 m/s).

We estimated attenuation of Peak Ground Acceleration (PGA) with distance for the vertical component and the vector. The PGA data are fit with the power relation: $\mathbf{PGA_{(cm/s/s)} = a*r_{(m)}^{-b}}$. Similar attenuation factors $\boldsymbol{b_i}$ were obtained for all three Sayarim explosions (Figure 2), therefore we applied an average fixed value $\boldsymbol{b}$=1.74 to estimate the scale coefficients $\boldsymbol{a_i}$, used for estimation of the yield W scaling relation: $\mathbf{PGA \sim W^{0.58}}$.

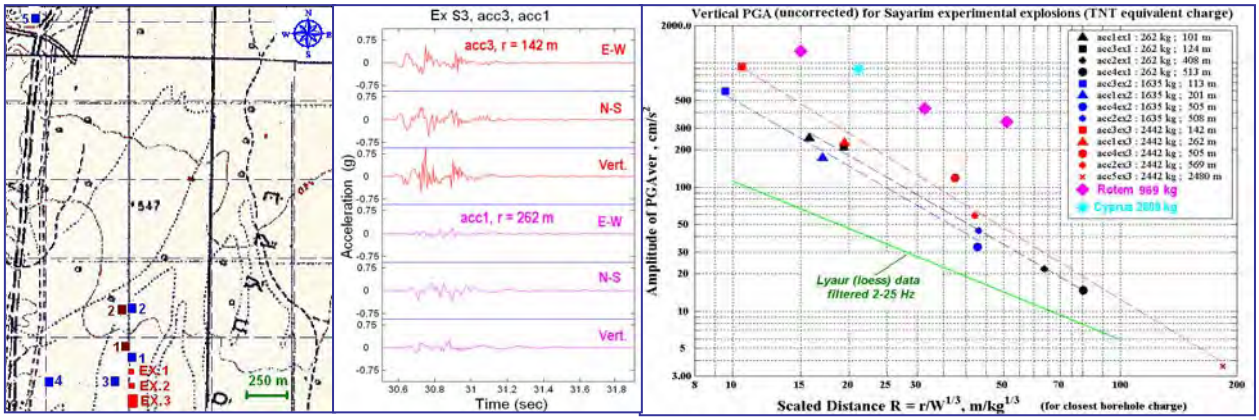

Figure 2. Location of Sayarim shots and accelerometers (left), sample records of the two closest ETNA (center) and data analysis (right): attenuation of vertical peak accelerations vs scaled distance for different shots and geological settings. For two multiple-hole shots (S3 and Rotem 25ton) we used single-hole charge.

Using the scaled distance $R=r/W^{1/3}$ (instead of distance r,m) reduced but did not remove the offset of the three attenuation lines. The discrepancy is caused by different scaled depths and the large total charge for S3. The amplitudes of the 3 Sayarim shots (in dry alluvium/conglomerates) are higher than values for blasts in loess (Negmatullaev et al., 1999), and lower than for shots in consolidated sediments (Rotem) and hard rock (Cyprus) (Gitterman et al., 2004).

Near-source seismic data were used to investigate the characteristics of the anomalous single-fired shot M1A, that produced small amplitudes (as mentioned above, Table1), and to estimate a detonated charge equivalent, similar to the case of two partially detonating blasts in the Wyoming experiment (Stump et al., 2003). Spectral ratios for the pair (M1A and fully detonated M1B) were calculated using data from the portable short-period 3C seismic station #1 in the near-source area (r=3 km) (Figure 3).

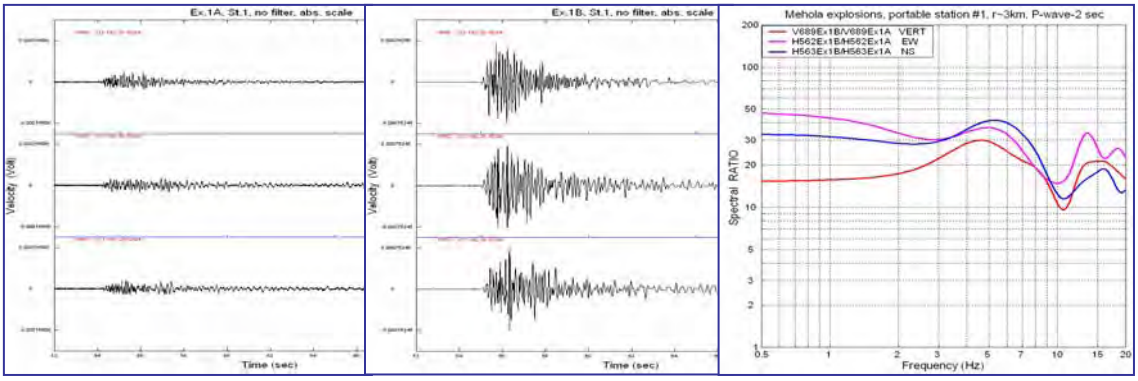

Figure 3. Seismograms and spectral ratios of P-waves for the two Mehola shots at portable 3C seismic station #1 (EW - about transverse) (analyzed by SEISPECT software).

The roughly flat ratio in the low-frequency range suggests that the explosion M1A was reduced by a factor of ~20, resulting in a detonated charge equivalent W~150 kg. An observed decrease of the spectral ratios at ~7-8 Hz can be related to the estimated corner frequency for the strong shot M1B of 3 tons, close to the value f_c~9 Hz from an empirical corner frequency-yield relation for single-fired contained explosions (Gitterman et al., 2004):

$$f_c = 266*W^{-0.4161}$$

S-wave character at close and remote stations.

Different detonation features and a water component in one of the boreholes may have caused different S-wave character for the Mehola explosions (Figure 4), rather than different borehole depth: S-wave amplitudes for the weak M1A are comparable with the P-waves, whereas for the strong M1B shot the S-wave is negligible. We note that S-waves are more pronounced on velocigrams than on accelerograms (Figure 5). Preliminary estimates from strong-motion data (Figure 5) showed velocities of ~1380 m/s for P-waves, and ~300 m/s for S-waves, corresponding satisfactorily to the geology of the area, Quaternary alluvium deposits.

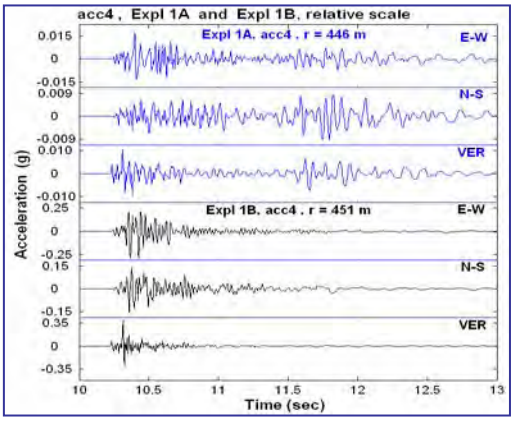

Figure 4. Different S-wave character for the two Mehola explosions recorded at ~450 m (relative scale).

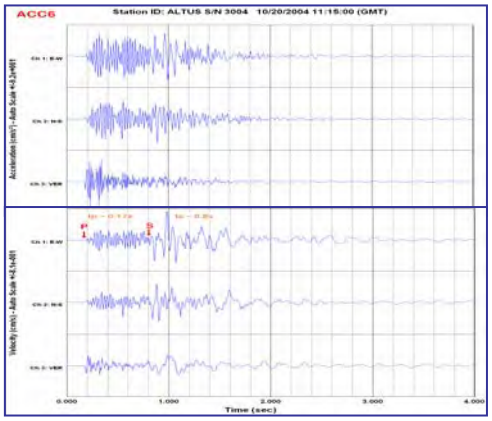

Figure 5. Velocity transform (bottom) of acceleration at ACC6 (top) emphasizes the S-wave for shot M1A (distance 235 m).

Distinctive S-waveforms and S/P amplitude ratios were observed at vertical network SP stations from two experimental explosions of similar design (1 ton in a single hole) in Jordan (Ex.7) and Israel (Ex.9) conducted in the MERC project, in October 2004 (see Figure 6). The Jordanian shot produced strong dominant amplitude P-waves and significant surface wave energy (at some close stations), but a clear S-phase was not observed. The Israeli explosion showed considerable S-waves and S-coda amplitudes and energy, and unexpectedly weak P-waves. The difference between the Jordan and Israel explosion recordings may be related to different geological settings in the

near-source area, and location in diverse tectonic units separated by the Dead Sea Transform zone, where the shots were located (Figure 1), as well as different features of the explosion design.

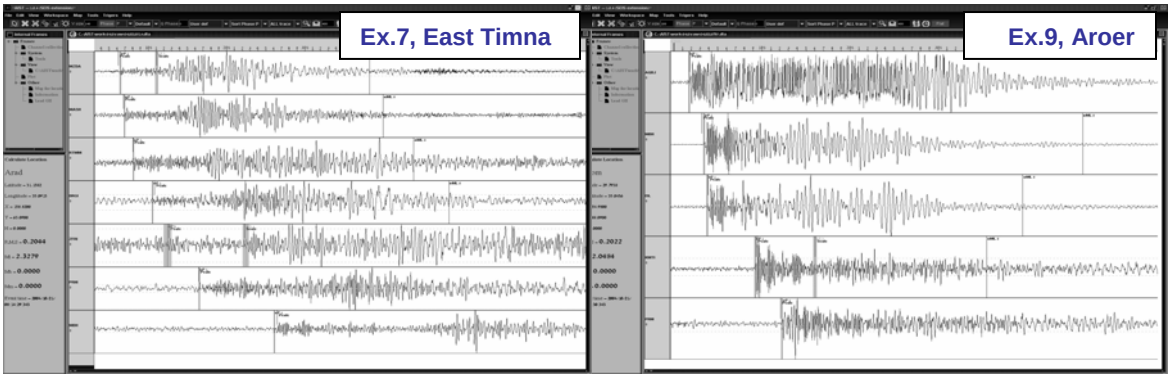

Figure 6. Sample of distinct S-waves for two explosions of similar design (charge 1 ton in a single hole), observed at ISN stations (analyzed by AIST software).

Peak Amplitude scaling.

All three experimental explosions of the Sayarim charge-weight series were well recorded at IMS BB station EIL (r~20 km), providing data for source-scaling analysis. Inspection of the waveforms observed on the 3C record (Figure 7) allows identification of regional phases P, S and Rg (surface waves).

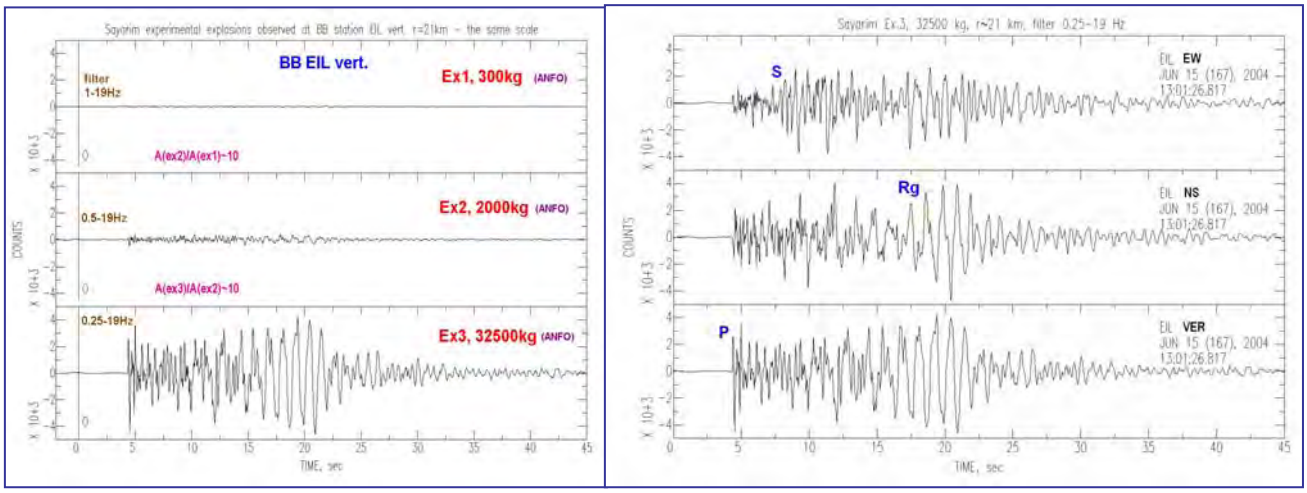

Figure 7. Vertical record of the Sayarim series at EIL (absolute scale, left) and 3C record of shot S3 (right).

Vertical Peak Amplitudes (VPA, micron/sec) were measured for each of the phases and plotted against charge weight for shots S1-S3 (Figure 8). TNT equivalent charges were used (Table 1) and for the multiple-hole explosion S3 the total charge was taken.

The data for each phase are fit with the power law equation:

$$VPA_{(mic/sec)} = A * W_{(kg)}^{B} \quad (1)$$

An r.m.s. procedure provided estimates of ***A*** and ***B*** for each of phases P, S and Rg (see Figure 8): similar power law scaling parameters were determined for each of the dominant regional phases.

Power law fits to each phase demonstrate little difference between the source yield scaling parameter ***B*** for the different phases P (0.93), S (0.87) and Rg (0.93). The ***B***-values obtained are in close agreement with the scaling parameter of Vergino and Mensing (1983) for Pn waves from nuclear explosions in Nevada, and Stump et al. (2003)

for Pn, Pg, and Lg regional phases (0.84-0.91) from chemical explosions in Wyoming. The ***A*** value depends on distance and site conditions and for station EIL is comparable for all three phases, similar to estimations of Stump et al. (2003) for Pg and Lg phases.

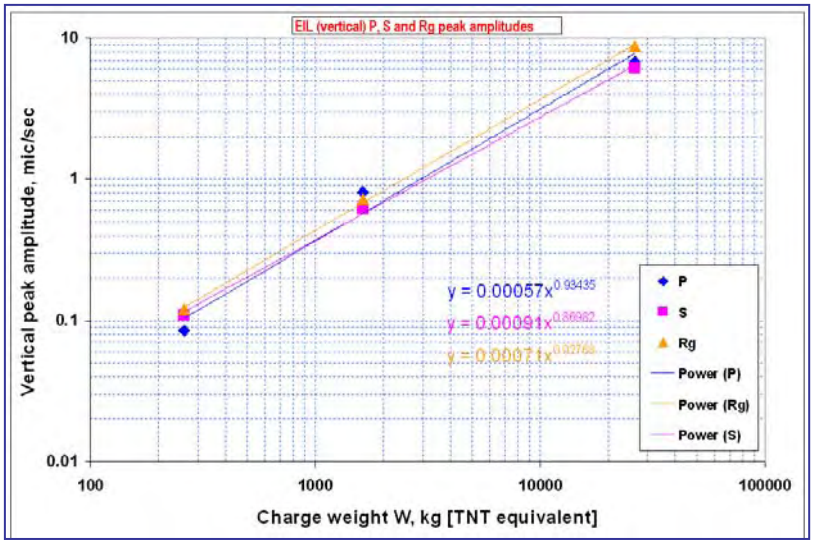

Figure 8. Peak vertical amplitude source scaling for different wave phases at local distances (EIL at ~21 km).

Magnitude scaling.

We used Ground Truth data of simultaneous explosions conducted for the project (Table 1) for analysis of magnitude dependence on charge weight. Some other experimental land and underwater shots conducted previously by GII in DSWA/DTRA projects (Gitterman et al., 2002, 2003) and in the MERC project in October 2004 were also included. The analysis results are shown in Figure 9, where the observation values and different curves fit for simultaneous shots are presented for comparison. Three of the curves were developed earlier for different types of explosive seismic sources:

a) Under-Water Explosions (UWE) includes calibration and experimental shots in the Dead Sea conducted by GII (Gitterman, 1998): M = 0.285 + log10 (W, kg). Two recent experimental shots in the Dead Sea (October 2004), correspond well to previous data and the fit curve (1).

b) Upper limit of magnitude for known yield sources in hard rocks (Khalturin, 1998): M=2.45+0.73*log10(W, ton). All values for the land explosions are below the curve (2).

c) Single-fired commercial blasts at Israel quarries, including a limited dataset (Gitterman, 1998): M = -1.42 + 0.99*log10(W, kg). New data for experimental simultaneous land explosions demonstrate a slightly different curve (3), therefore we developed a new equation fitting the observed data:
M = -0.2937 + 0.7327*log10 (W, kg) (4)
Note, the estimated scaling parameter (the curve slope) 0.7327 is very similar to the upper limit curve (2).

Analysis of the results leads to the following conclusions:

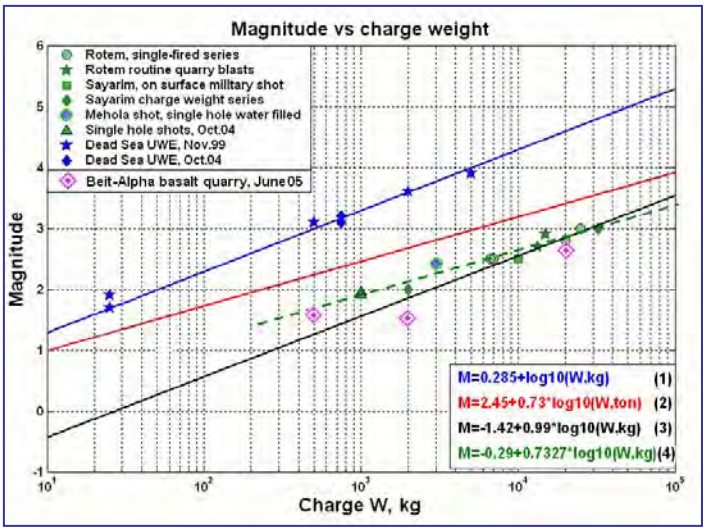

Figure 9. Magnitude vs charge for collected single-fired explosions and quarry blasts in Israel and Jordan

1) Comparison of local magnitude values for Sayarim explosions (June 2004) with the Rotem series data (Gitterman et al., 2002) conducted in consolidated rocks (caolin) with a special design of concentrated near-spherical charges does not show any significant magnitude difference. As shown from regional observations, significant seismic strength was achieved (M_L~2 for S2 and M_L~3 for S3) in spite of the non-consolidated media, dry alluvium, commonly considered low-coupling material (e.g. US Congress, 1988), and shallow burial depth that caused poorly contained explosions (scaled depth 1.1-1.4 m/kg$^{1/3}$).

2) Three large land quarry/military blasts conducted in 2004 (see Table 1) showed unusually large seismic energy release, shown by high local magnitude M_L values estimated from Israel network observations. The Rotem quarry blast R2 of 15 ton ANFO in several dozen holes with delays produced a seismic event with magnitude 2.9, very close to the energy produced by the Sayarim large experimental simultaneous explosion of 32.5 ton ANFO in 11 holes (located ~120 km to the South) that yielded magnitude ~3.0.

3) Likewise, the military explosion of ~10 ton of TNT, intended to destroy out-dated ammunition, in a trench and open to the air, produced a significant magnitude 2.5, and clear seismic signals are observed up to 160 km, along with very strong acoustic waves.

4) The Dead Sea underwater shots in October 2004 with charges of 750 kg of TNT at 50 m agree well with the previously developed curve (1) for UWE with less-energetic explosives "Henamon" at a larger depth of 70 m.

5) The Beit-Alpha explosions were conducted after the new magnitude-charge curve (4) was developed. An anomalously low seismic effect for the 2-ton shot Bα3 is seen, evidently resulting from poor containment observed clearly on the video-record, due to locally fractured basalt rocks. Three other shots fit curve (4).

Software development.

To evaluate and analyze S/P maximum amplitude and energy ratios for selected events, existing GII software for visualization and preliminary processing of accelerograms and seismograms was modified and adapted for the project goals, including SEISPECT (analysis of spectra and spectral ratios), and AIST (waveform analysis of different data formats). Software application samples are shown in Figures 3 and 6. Appropriate programs for S/P amplitude and energy ratio estimation were also developed (see below).

S/P maximum amplitude ratios in different frequency bands.

Different amplitude and spectral ratios for different wave phases are used for discrimination purposes (see e.g., review of Blandford, 1995, and more recent research of Walter et al., 2004). We analyzed the S/P maximum amplitude ratio in different frequency bands, using software (Kurpan, 2004) based on SEISPECT program. As a case study we used four explosions in the Sayarim area. Seismograms at Israel Seismic Network (ISN) vertical stations were filtered in three spectral bands: 0.5-3 Hz (low filter), 3-6 Hz (medium filter) and 6-9 Hz (high filter), and maximum amplitudes were measured in windows 3-5 sec after the P and S arrivals. A wide band filter (0.5-12 Hz) including the whole recording frequency range is also used in the analysis.

The S/P maximum amplitude ratios obtained for different ISN stations, presented in Figure 10, do not show a clear dependence on distance and frequency band. If the ratio values for a fixed shot are averaged over the stations, then two tendencies can be observed: a decrease with charge (especially for the low and medium filters) and higher ratios for the lower frequency band (Figure 11). Note that the explosion S4 of 10 tons TNT on surface is consistent with three other borehole ANFO shots located in the same area.

The S/P parameter shows a potential for identification of explosion seismic sources and discrimination between earthquakes and explosions, and will be tested on other explosions and earthquakes.

Estimating energy partitioning for observed phases.

A number of programs and scripts were developed to calculate seismic energy of different regional phases observed on seismograms As a case study we used the large (32.5 tons) explosion S3 (Table 1) and applied the processing procedure. As a first effort we analyzed signals in a broad frequency range, with a filter applied to the records.

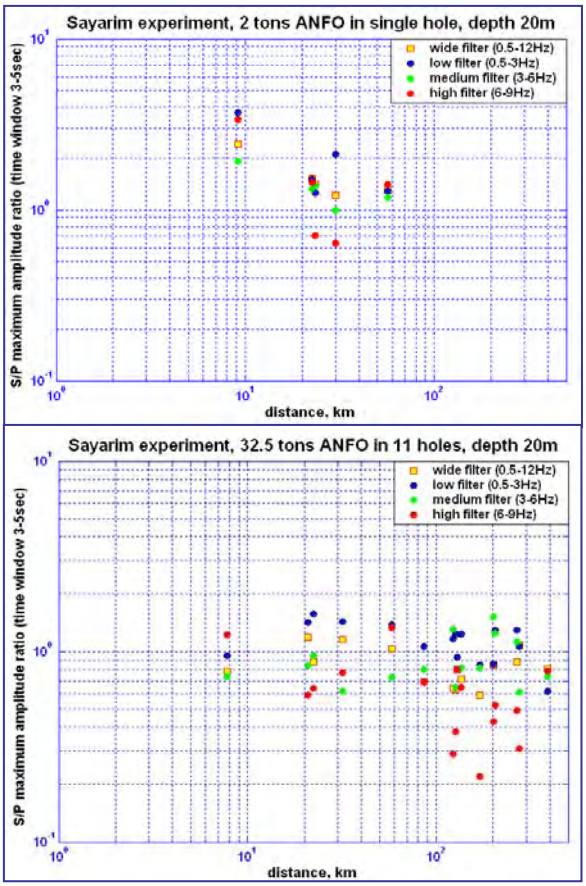

Figure 10. S/P maximum amplitude ratios vs distance for observations at different SP ISN stations from single-fired explosions S2 (up) and S3 (down) in Sayarim area.

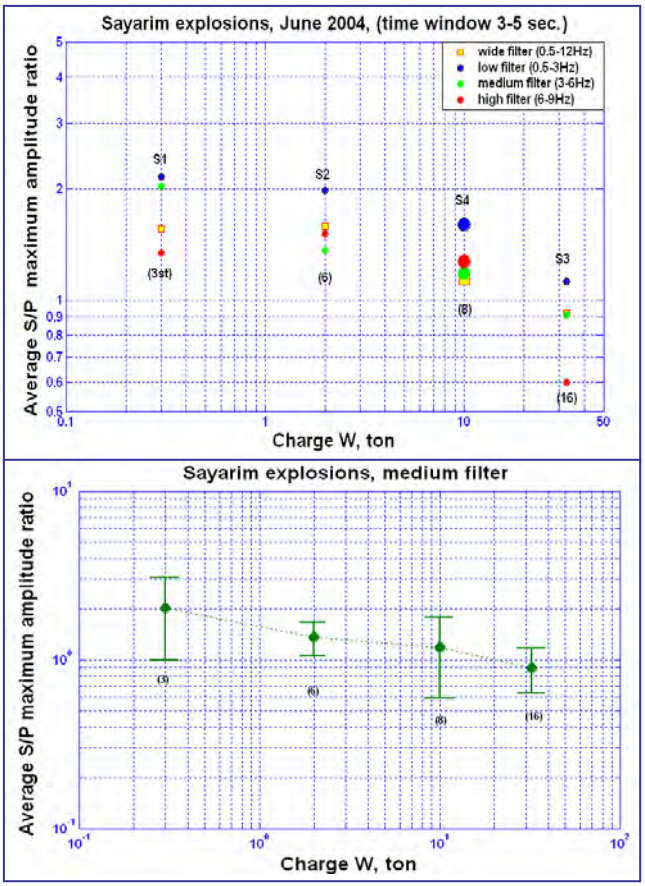

Figure 11. S/P maximum amplitude ratios vs charge averaged for different ISN stations for Sayarim explosions (up); mean and standard deviation estimations for the medium filter (3-6Hz) (down). Number of processing stations (in) is also shown.

Considering the recording range for ISN short-period stations, and observed frequencies for local distances and magnitudes, we can say that seismic energy was calculated for unfiltered signals. The analysis was focused on four portions of the signal: 1) All the signal – 60 seconds from the P phase start; 2) P-waves – 2 seconds after the P arrival; 3) S-waves – 2 seconds after the S arrival; 4) surface waves – starting 2.5 sec after the S-arrival to twice the S-arrival lapse time. The P and S first arrival times are computed from the local 1D velocity model.

The seismic waveform energy was computed as sum of squares of amplitudes over the specified time interval for two groups of data separately: 3C network short period and BB stations, and vertical component stations (see the map in Figure 1). For the 3C stations amplitudes are the square root of the sum of the squared component amplitudes. The results of computations for the 6 available 3C stations are presented in the Figures 12 and 13. The stations range from 21 km (EIL) up to 187 km (AMZI). Energy partitioning for the 3C stations is shown in Figure 13 as percent of the total energy computed in the [P arrival, P+60 sec] time intervals (Figure 12). The estimates show that the energy in 3C motion is larger in the S time interval relative to the P time interval and undulates within 10%. The surface waves accommodate most of the signal energy, and increases with distance.

Energy of P waves on vertical channels is dominant over S wave energy. Surface waves annex almost all the seismic energy of the signal at larger distances. The stations used in the analysis range from 8 to 388 km.

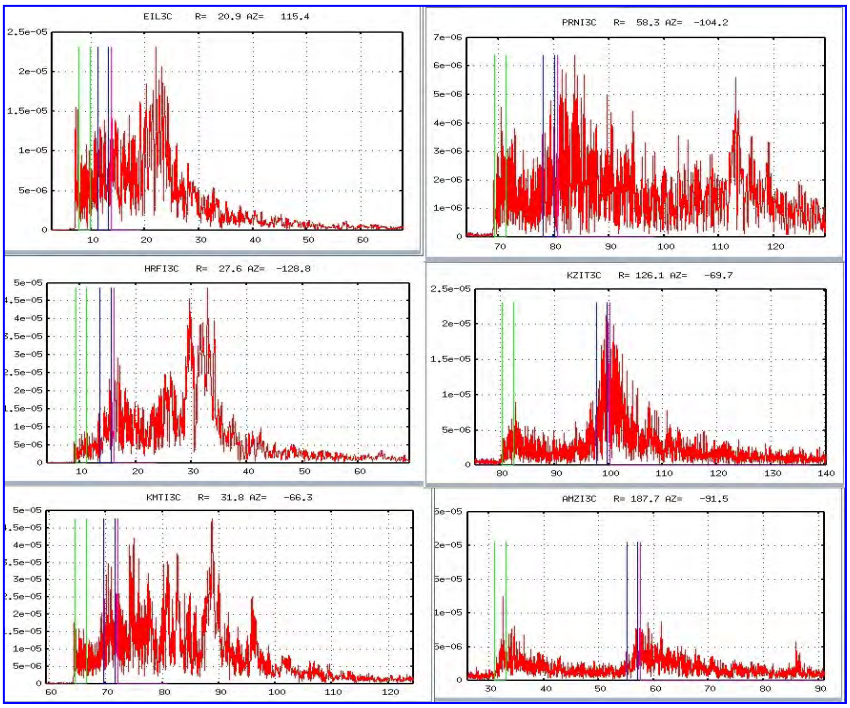

Figure 12. Amplitudes (m/sec) versus time (sec) for six 3C stations (3 BB and 3 SP stations) (shot S3). Vertical lines mark time intervals for energy computation.

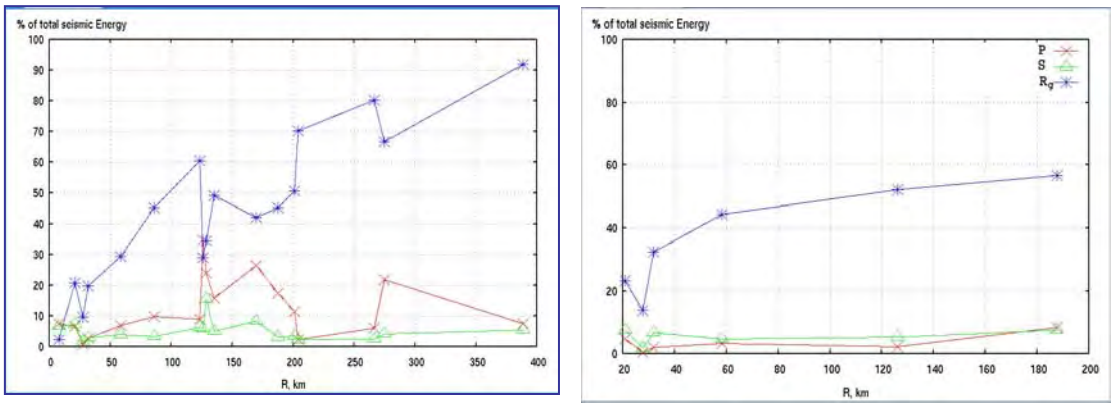

Figure 13. Energy partitioning between P, S and Rg (surface waves) versus distance from the largest Sayarim explosion S3 for sixteen vertical stations (left) and six 3C stations (right)

CONCLUSIONS AND RECOMMENDATIONS

A project event database was created to study empirical features of seismic energy generation and partitioning between P and S waves. Selected explosions present a broad variety of design features, charge weight, burial depth, source rocks and geological settings.

A number of experimental single-fired explosions were conducted and numerous 3C and vertical observations were acquired beginning from the near-source zone at ~0.1 km (by accelerometers) to near-regional distances ~390 km (by seismic stations of local networks in Israel and Jordan).

GT parameters and local seismic stations records were collected for several large controlled quarry and military blasts. The events were recorded by SP and BB instruments, and seismic arrays, including IMS stations. Preliminary analysis showed a diversity of regional phases P, S, and Rg.

To fulfill project goals existing software was modified and new programs and scripts were developed. As a case study analysis the computer procedures were applied to the Sayarim experimental explosion series of variable charge weight. Preliminary results show definite tendencies in dependency of S/P maximum amplitude and energy ratios on distance and yield. The S/P ratios in different frequency bands, averaged over network stations, show a potential for identification of explosion seismic sources and discrimination between earthquakes and explosions. Source scaling estimations based on BB records at local distances of the same series show similar yield scaling parameters (0.87-0.93) for different regional phases. The power law parameter values are in close agreement with the constants for nuclear explosions in Nevada and chemical explosions in Wyoming.

Application of the spectral ratio procedure to data collected from some experimental explosions provided estimates of the corner frequency-charge weight relation, and the equivalent yield of a partially detonated explosion.

The analysis will be continued for other events from the dataset and new planned experimental shots to validate the results obtained.

REFERENCES

Blandford, R.R. (1995), Regional seismic event discrimination, in: E.S. Husebye and A.M. Dainty (Eds.), *Comprehensive Test Ban Treaty, NATO ASI Series, Series E: Applied Sciences* - Vol. 303, 689-719.

Gitterman, Y. (1998), Magnitude-yield correlation and amplitude attenuation of chemical explosions in the Middle East, *Proceedings of the 20th Annual Seismic Research Symposium on Monitoring a CTBT,* Vol. 1, pp. 302-311.

Gitterman, Y., V. Pinsky, A. Shapira, M. Ergin, D. Kalafat, G. Gurbuz, and K.Solomi (2002), Improvement in detection, location and identification of small events through joint data analysis by seismic stations in the Middle East/Eastern Mediterranean region, in *Proceedings of the 24th Seismic Research Review—Nuclear Explosion Monitoring: Innovation and Integration*, LA-UR-02-5048, Vol. 1, pp. 271-283.

Gitterman, Y., V. Pinsky, A. Shapira (2003), Improvements in Monitoring the CTBT in the Middle East by the Israel Seismic Network, Final Report, Rep. DTRA-TR-01-35, October 2003, 196 pp.

Gitterman, Y., V. Pinsky, K. Solomi, R. Hofstetter, C. Gurbuz, and M. Ergin (2004), Using ground truth events for travel time calibration and studying seismic energy generation and partitioning into various regional phases, in *Proceedings of the 26th Seismic Research Review, Trends in Nuclear Explosion Monitoring*, LA-UR-04-5801, Vol. 1, pp. 61-72.

Gitterman, Y. and V. Pinsky (2005), Seismic energy generation and partitioning into various regional phases from different seismic sources in the Middle East region, *Annual Report No.1, GII Report No. 542/123/05(2).*

Kurpan J. (2004), Discrimination of seismic events in Israel recorded by national seismic network, M. Sc. Thesis, *Tel-Aviv University*, supervisors Prof. Z. Ben-Avraham and Dr. Y.Gitterman.

Negmatullaev S.Kh., M.I. Todorovska, M.D. Trifunac (1999), Simulation of strong earthquake motion by explosions – experiments at the Lyaur testing range in Tajikistan. *Soil Dynamics and Earthquake Engineering* 18 (1999), 189–207.

Stump, B., D.C. Pearson and V. Hsu (2003), Source scaling of contained chemical explosions as constrained by regional seismograms, *Bull. Seism. Soc. Am*. 93: 1212-1225.

ten-Brink, U., Al-Zoubi, A., Rybakov, M. and Rotstein Y. (2004), Integrated geophysical study of the Dead Sea rift for hazard assessment and mineral resources. MERC program of U.S. AID, Grant No. TA-MOU-01-M21-012.

U.S. Congress (1988), Office of Technology Assessment, Seismic Verification of Nuclear Testing Treaties, OTA-ISC-361 (Washington, DC: U.S. Government Printing Office, Chapter 6, May 1988).

Vergino, E.S., and R.W. Mensing (1983), Yield estimation using regional m_bP_n, *Bull.Seism.Soc.Am.* 80: 1200–1206.

Walter, W. R., K. M. Mayeda, A. J. Rodgers, S. R. Taylor, D. A. Dodge, E. Matzel and M. D. Ganzberger (2004), Regional Seismic Identification Research: Processing, Transportability and Source Models, *Proceedings of the 26th Seismic Research Review: Trends in Nuclear Explosion Monitoring* , LA-UR-04-5801, Vol. 1, pp. 513-523.

SOURCE ARRAY ANALYSIS ON THE COMPOSITION OF REGIONAL WAVES FROM BALAPAN EXPLOSIONS IN THE NEAR-SOURCE REGION

Tae-Kyung Hong and Jiakang Xie

Lamont-Doherty Earth Observatory of Columbia University

Sponsored by National Nuclear Security Administration
Office of Nonproliferation Research and Engineering
Office of Defense Nuclear Nonproliferation

Contract No. DE-FC52-03NA99514

ABSTRACT

Regional seismic waves from 67 historic underground nuclear explosions (UNEs) in the Balapan test site of Kazakhstan, recorded at station Borovoye (BRV), are studied with a source array analysis under the reciprocity theorem. The source array data are used to conduct a frequency-slowness power spectra (FSPS) analysis to determine the phase composition of the plane wave fields in the near source region. Since station BRV is equipped with short-period instruments with flat displacement responses above 1 hz, our analysis is limited to high-frequencies above about 0.5 Hz. Source locations and the origin times are obtained from geodetic measurements, a scaling law between event magnitudes and depths, and a calibrated Pn travel time curve. Between frequencies of 0.5 and 3.0 Hz, the *Pn* slowness power spectra are concentrated at a phase velocity (v_h) of 8.0 km/s. The expected Sn window contains two dominant phases, a scattered P wave with a v_h around 7.1 km/s and a mantle shear wave with v_h of 4.8 km/s. The *Lg* waves are coherent between 0.5 and 2.0 Hz, with a dominant v_h of 4.2 km/s. The Rg wave at frequencies between 0.5 and 0.8 Hz is dominantly composed of a coherent fundamental mode Rayleigh wave with a v_h of 3.0 km/s. At higher frequencies (>0.8 Hz), this coherent Rayleigh wave is not observed in the Rg window due to attenuation during wave propagation.

The difference between the phase velocities of Lg and Rg implies that the dominant waves composing Lg and Rg are originated differently in the source region. The dominant wave field in the near source region that eventually becomes regional Lg wave is coherent and has an *SmS*-type of slowness. If a near source Rg-to-Lg scattering is primarily responsible for the Lg excitation, we are expected to observe either a strong peak in the FSPS concentrated near the Rg slowness (slower than 3.0 km/s at frequencies higher than 0.8 Hz), or multiple peaks in the FSPS with reduced amplitudes. The former FSPS pattern is observed if the scattered Rg wave exists in a form of a plane wave in the near source region. The latter pattern is expected if the scattered Rg waves exist in a form of non-planar waves or multiply superposed plane waves. Neither of the two patterns are observed. We therefore infer that for our data set, a Rg-to-Lg scattering does not seem to dominate the Lg excitation process. It is also found that the strength of shear waves contained in the expected Sn window varies with local geology much more than does the strength of Lg. Since the Sn is enriched in its high-frequency (>1 Hz) content as compared to the Lg, this observation suggests that the local geology influences shear wave excitation at high frequencies more than at lower frequencies. We plan to investigate the spectral characteristics of regional wavefields from UNEs of various test sits to infer the best-fit source model.

OBJECTIVES

The objective of this research project is to understand how regional P (Pn, Pg) and S waves (Sn, Lg) are generated by UNEs using regional clustered UNEs that were recorded at single stations. The single-station records can be treated as array records under a reciprocal theorem. Hundreds of clustered UNEs in central Asia and Nevada between the 1970s and 1990s were recorded at common regional stations. The waveforms of the source array records provide dense time-space domain sampling of the wavefields in the near source region.

A FSPS analysis is applied to the source-array records to explore the phase composition of regional waves from UNEs as they leave the sources. In each frequency band we estimate the powers of various wavelets, including direct body and surface waves and scattered/multipathed waves. Improved depth and yield estimates can be determined in the course of the study. In the next stage, we examine whether each previously proposed mechanism for regional wave excitation is compatible to observed phase composition. Best-fit or dominant excitation mechanisms and best-fit spectral models for regional waves from UNEs will be presented. Using the best-fit models, we shall develop scalings of these parameters with event magnitudes and depths, and explore the dynamic relations among all these parameters and testing styles, local structures, and geological environments.

RESEARCH ACCOMPLISHED

Under a reciprocal theorem, velocity seismograms from these clustered explosion sources can be treated as seismograms at an array of fictitious strain meters buried at the source locations, recording a single force acting at the station location [Spudich and Bostwick, 1987; Xie et al., 1996]. We apply a frequency-wave number technique to the source array seismograms, and investigate the phase composition of regional waves recorded at the BRV in Kazakhstan as they leave the source region.

Data acquisition and assembly of ground truth information

Short-period displacement records at BRV for UNEs at the Balapan nuclear test site between 1968 and 1989, are analyzed and shown in Figure 1. The sampling intervals of the data are 0.032 s and 0.096 s . The records display high signal-to-noise ratios (S/N>50 dB) between 0.5 and several Hz. The epicentral distances vary between 680 and 697 km. The event magnitudes (m_b) are between 4.8 and 6.2, with 58 out of the total 67 events having magnitudes larger than 5.5 (Marshall et al., 1985; Kim et al., 2001). High-precision hypocentral locations of the UNEs are measured geodetically, with uncertainties of less than 200 m (NNCRK, 1999; Thurber et al., 2001). Precise ("ground truth") origin times and depths of burial are available for 10 UNEs between 1985 and 1989 (Adushkin et al., 1997). For all UNEs, teleseismically determined origin times are also available from multiple sources, such as the International Seismological Centre (ISC) and Thurber et al. (2001).

Estimation of scaling relationships among depth, yield, and magnitude

Groundtruth information on the depths and origin times of most Balapan UNEs are not available. To estimate the depths of the UNEs used in this research project, we calibrate the scalings among the body-wave magnitudes (m_b), the yields in kilo-ton (Y), and the depths in meter (H) of those Balapan UNEs whose ground truth depths and/or yields are available. These scalings are then used to estimate H values of all other events from their m_b values. Several authors [e.g., Bocharov et al., 1989; Spivak, 1996; Adushkin et al., 1997 information presented at Seismological Society annual meeting, April, 1992] provided Y and m_b values of 19 Balapan explosions. The magnitudes (m_b) of Balapan nuclear explosions are given in Marshall et al. [1985] and Kim et al. [2001]. Using these values we obtain a relationship (Figure 2)

$$m_b = 0.753 \cdot \log(Y) + 4.428. \qquad (1)$$

This relationship is very similar to that obtained by Ringdal et al. (1992).

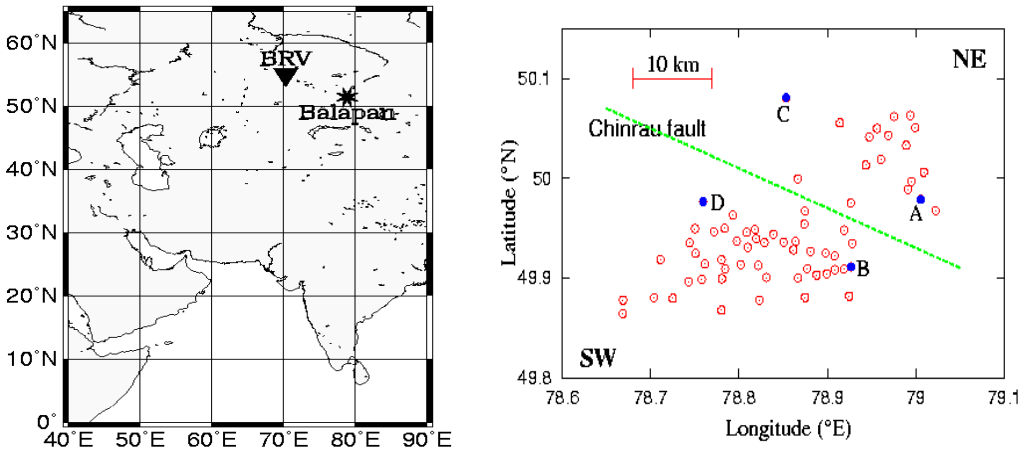

Figure 1. Maps showing locations of the Borovoye observatory (BRV) and the Balapan nuclear test site (left), and locations of nuclear explosions in the test site (right). The explosion sources can be grouped into NE (18 events) and SW subregions (49 events) according to the velocity and geological structure. The dotted line dividing the Balapan region approximately delineates the Chinrau fault. Time records from four representative events (A,B,C,D) are given in Fig. 7.

An empirical scaling between the yield and depth of burial is given in a form of cube-root rule in the Balapan test site [Khalturin, 2004, personal communication; also cf. Lay et al., 1984]:

$$H = c \cdot \sqrt[3]{Y}, \qquad (2)$$

where H is the depth of burial in meters and c is a constant . Thus, using the given scaling relationships and available groundtruth values of H, we estimate the scaling relationship between m_b and H by

$$m_b = 2.25 \cdot \log(H) - 0.10. \qquad (3)$$

From the m_b-H relationship, we calculate the unknown depths of burial.

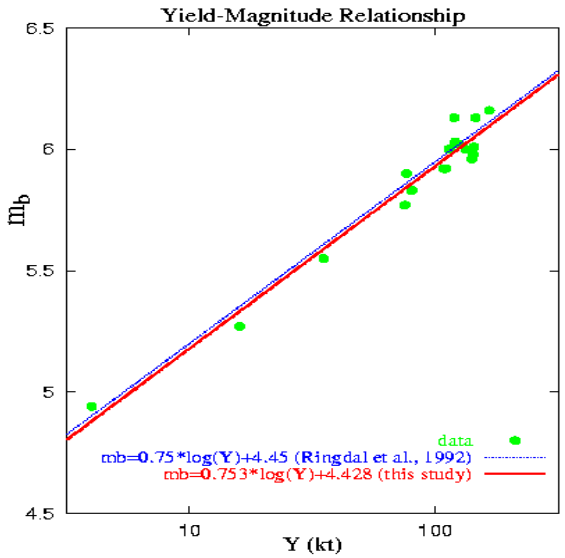

Figure 2. A linear relationship between yield (Y) and body-wave magnitude (m_b) obtained in this study. The refined relationship is very close to the previous result of Ringdal et al. (1992).

Frequency-slowness power spectra (FSPS) analysis

We analyze FSPS of source-array records using a conventional frequency-wave number (F-K) technique to study the phase velocities of the waves in source region. In the original (true) geometry, the analysis yields the phase composition of the wavelets leaving the explosion sources. The slowness power spectrum (P_c) at angular frequency ω and wave number **k** (= ω**s** , where **s** is the slowness vector) is determined by

$$P_c(\omega\mathbf{s},\omega) = \left|U(\omega\mathbf{s},\omega)\right|^2, \qquad (4)$$

where U is the double-Fourier transform of the waveforms $u(\mathbf{r},t)$ recorded at location **r** in the reciprocal geometry. When a seismic wave is approximately nondispersive in a finite frequency range, coherent power spectral features can be enhanced by stacking the $P_c(\omega\mathbf{s}, \omega)$ over frequencies (ω) [Spudich and Bostwick, 1987]:

$$P_w(\mathbf{s}) = \frac{1}{N}\sum_{j=1}^{N} P_c(\omega_j\mathbf{s},\omega_j)\cdot\frac{1}{m_j}, \qquad (5)$$

where N is the number of discrete frequencies, ω_j is the jth angular frequency, P_W is the stacked slowness power spectrum, and m_j is a normalization (whitening) factor. P_W indicates the relative strength of a plane wave leaving the source region in a finite frequency range. The pre-whitening normalization removes the effect of non-flat responses of the instrument and wave propagation [Spudich and Bostwick, 1987] which are virtually the same for all records.

Phase composition

We do FSPS analysis on a slowness-azimuthal angle domain with a discrete slowness interval of 0.05 s/km and a discrete azimuthal angle interval of 1°. In Fig. 3, the slowness power spectrum of Pn waves has a maximum value at horizontal slowness (s_h) of 0.125 s/km, which corresponds to P waves travelling in the uppermost mantle with a phase velocity (v_h) of 8.0 km/s [Quin and Thurber, 1992]. For the Pn phase velocity, the uncertainty introduced by the discrete domain is ±0.17 km/s. The azimuth of the maximum power is 303° which agrees with the great-circle azimuths of events (302.2° - 304.5°).

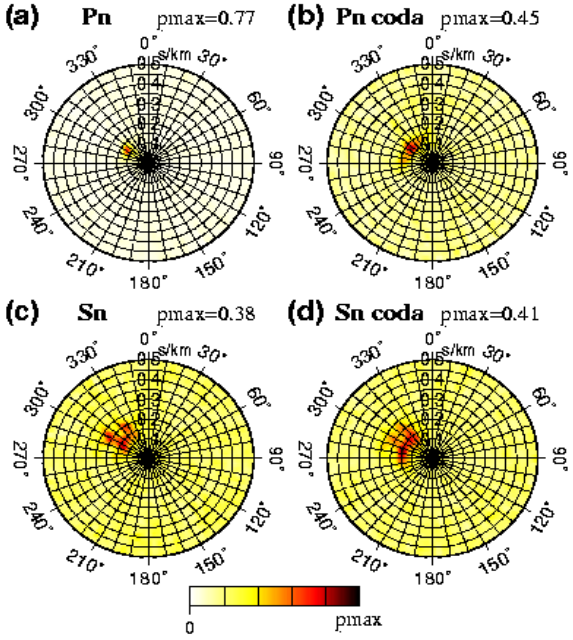

Figure 3. Slowness power spectra of (a) Pn, (b) Pn coda, (c) Sn, and (d) Sn coda. The event lapse-time windows for Pn, Pn coda, Sn, and Sn coda are 92 to 96 s, 125 to 130 s, 162 to 170 s, and 178 to 186 s, respectively. The frequency band used is 0.5 to 3.0 Hz. The annotation of pmax refers to the maximum power shown in the individual plot. This corresponds to the "pmax" shown in the color bar of the figure.

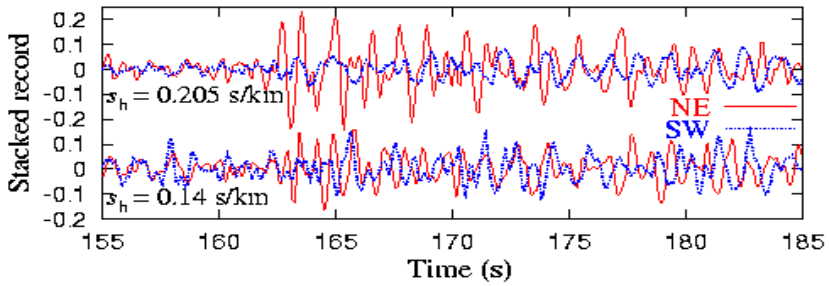

Figure 4. Slant-stacked seismograms of Sn window along horizontal slowness (s_h) of 0.205 and 0.14 s/km that are two dominant phases in the window. The stronger Sn at the NE subsite is mainly caused by enhancement of the phase with an s_h of 0.205 s/km.

The slowness power spectrum of the expected Sn window, which spans group velocities between about 4.0 and 4.3 km/s, exhibits two dominant phases with s_h of 0.14 and 0.205 s/km, respectively (Fig. 3(c)). The phase with s_h of 0.14 s/km (v_h=7.1 km/s) spreads into multiple azimuths, implying that it is composed of multiple forward scattered lower crustal (Pg) waves. The phase with s_h of 0.205 s/km (v_h=4.8 km/s) is the shear wave propagating in the uppermost mantle. The scattered Pg phase displays a comparable energy level to the Sn phase (Fig. 4). This implies that a strong lateral velocity heterogeneity or topography variation must be present along the Pg ray path in the near source region. The complexity of Sn phase is discussed more in a following subsection.

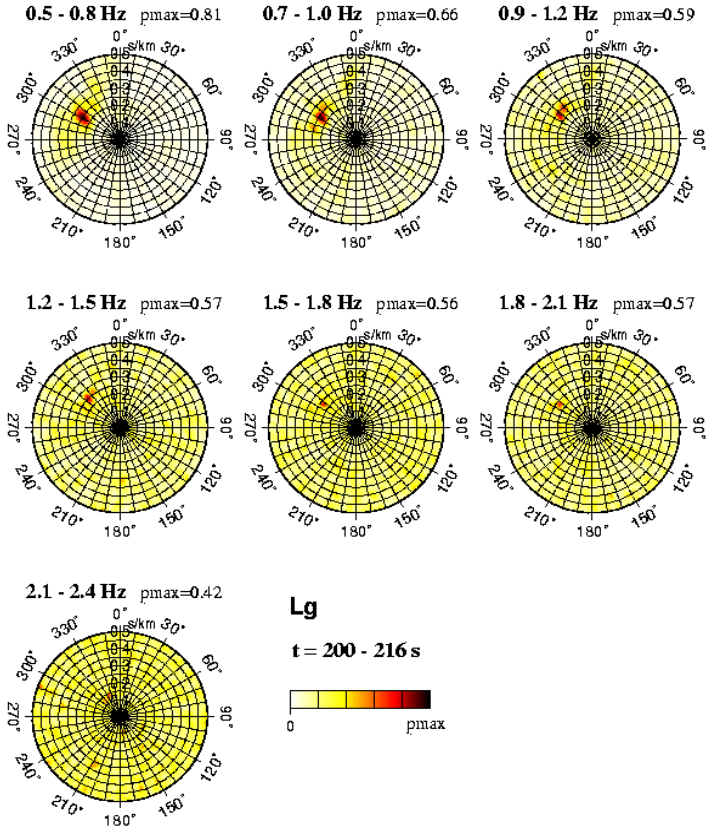

Figure 5. Slowness power spectra of the Lg window in various frequency bands. The dominant phase with phase velocity of 4.2 km/s is observed in frequency range between 0.5 and 2.0 Hz, above which the coherency in slowness power spectra degrades.

The phase velocities of Pn and Sn coda are similar to those of Pn and Sn (Figure 3). But, the azimuthal distributions of the maximum slowness power spectra of the coda are wider than those of the Pn and Sn . This indicates that the waves constituting the coda tend to undergo forward scattering in the near source region. The azimuthal span of slowness power spectra of coda increases with time, indicating that the scattered rays tend to increasingly deviate from the great-circle azimuth toward later coda.

The Lg waves are composed of crust-guided shear waves, with group velocity of 3.0 to 3.6 km/s [e.g., Kennett, 2002]. The dominant phase in the expected Lg window has a v_h of 4.2 km/s at frequencies up to 2.0 Hz (Fig. 5). This phase velocity is typical of Lg observed in conventional receiver array analysis [e.g., Der et al., 1984]. The coherency of the phase in the Lg window degrades at frequencies above 2.0 Hz.

In time window where fundamental mode Rayleigh (Rg) wave is expected, the dominant signal frequency is around 0.2 to 0.8 Hz. The dominant phase velocity in that window is 3.0 km/s at frequencies between 0.5 and 0.8 Hz, and appears to increase gradually with frequency (Fig. 6); it reaches 4.0 km/s at frequencies between 0.9 and 1.2 Hz, and 5.7 km/s at frequencies between 1.3 and 1.6 Hz. At frequencies above 1.6 Hz, the coherency in the slowness power spectra decrease drastically owing to a lack of coherent high-frequency energy. These observed high phase velocities ($v_h \geq 4.0$ km/s) at frequencies higher than 0.8 Hz are too high for Rg wave. These high phase velocities suggest that the Rg wave is attenuated out at these high frequencies, leaving the dominant signals to be those from forward-scattered higher mode or mantle *S* waves. The absence of Rg at high frequency is confirmed by a multiple filter analysis [Herrmann, 2002].

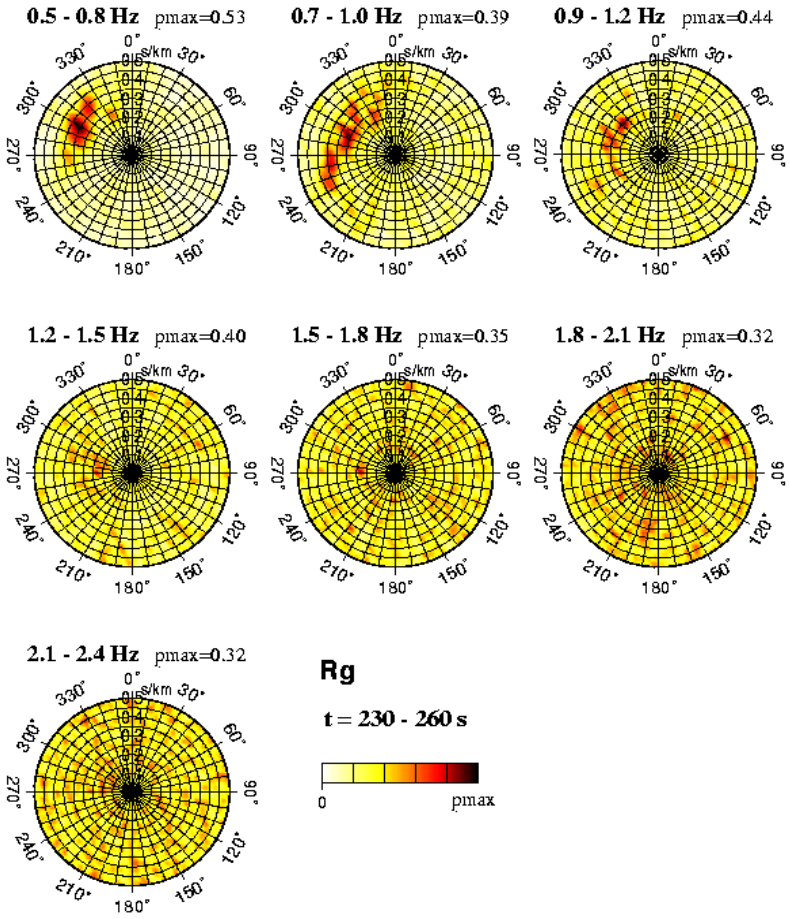

Figure 6. Slowness power spectra of the expected *Rg* window for various frequencies. The phase velocity of Rg is 3.0 km/s at frequencies between 0.5 and 0.8 Hz, which is the dominant frequency range of coherent *Rg* signal. Phases at higher frequencies appear to be scattered Lg and body waves with higher phase velocities. Note the coherency generally degrades with frequency.

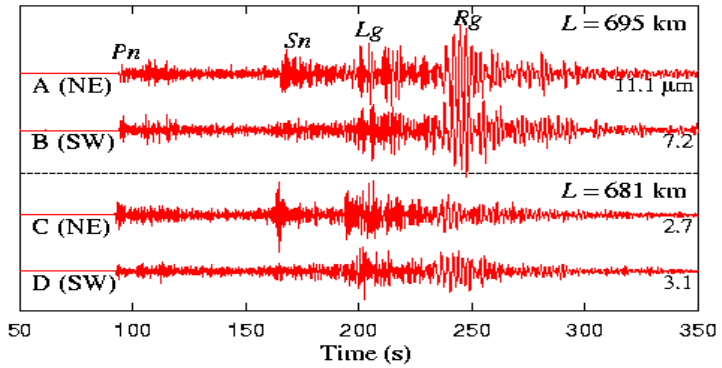

Figure 7. BRV seismograms from four events (A,B,C,D) in Fig. 1 (b). The seismograms are normalized for Lg waves. The reference Lg amplitudes for normalization are presented at the ends of records. Strong Sn waves are observed in the seismograms from the NE subsite that has a slower velocity structure, while the Sn waves are rather weak in the records from the SW subsite with a faster velocity structure.

In Figure 7, we show records at four locations (A, B, C, D in Figure 1(b)) with epicentral distances of about 695 and 681 km. The selected pairs of records are from events with similar magnitudes (m_b): the m_b of A and B are 6.01 and 5.86, and those of C and D are 5.29 and 5.45, respectively. The variation of Rg amplitudes with m_b is obvious in the figure. It is well known that the strength of Rg is dependent on both the size of explosion (m_b) and the depth of burial. In Figure 7, on the other hand, the Lg amplitudes are less variable than the Rg amplitudes.

In a hypothesis that Rg-to-S scattering is a dominant mechanism for Lg generation, Lg is expected to have the same dominant phase velocity as Rg at the same frequencies. If the scattered Rg waves are present in a form of plane waves in the near source, a strong peak in the FSPS concentrated near the Rg slowness should be observed. On the other hand, if the scattered Rg waves exist in a form of non-planar waves or multiply superposed plane waves, multiple peaks with reduced magnitudes in the FSPS are expected. However, we observe that the Lg slowness power spectra is concentrated at a phase velocity of an SmS (v_h=4.2 km/s) in frequencies between 0.5 and 2.0 Hz, while the phase composition in the Rg window varies with frequency. A coherent and dispersive fundamental mode Rayleigh wave with v_h of 3.0 km/s is observed below 0.8 Hz (Figs. 6, 7). The fundamental mode Rayleigh wave is not observed at high-frequencies (> 0.8 Hz) since it is attenuated out during the regional-distance (around 690 km) propagation. The distinct difference in FSTS composition between Lg and Rg implies that Rg-to-S scattering does not appear to be a dominant mechanism for Lg excitation of our data set.

Effects of source site geology on shear waves

We split the data set into two sub-groups according to event locations and local geology (Figure 1(b)). The shear wave velocity of uppermost crust at the NE subregion is about 0.4 km/s lower than the SW subregion (Bonner et al., 2001). We find that the phase compositions from the two subgrouped data exhibit a clear difference in the expected Sn window (Figure 8). The slowness power spectrum for the slower-velocity NE subregion is dominated by a strong shear-wave energy with an s_h of 0.205 s/km. On the other hand, shear-wave energy is relatively weak for the higher-velocity SW subregion. Raw seismograms from the two subregions are compared in Fig. 7. A striking feature is that the records from the NE subregion have strong and impulsive Sn waves, while those from SW region have weak Sn waves (see also, Fig. 8).

We also examine the relative amplitudes of shear wave and scattered Pg waves using a slant-stack technique. We stack the waveforms in the expected Sn window along the two dominant slownesses (s_h) of of 0.14 and 0.205 s/km (Figure 4). The stacked records show that the strong Sn energy from the NE subsite is largely caused by the larger amplitudes of the mantle shear wave propagating with an s_h of 0.205 s/km. On the other hand, the amplitude of the shear wave from the SW subsite is weaker as it becomes comparable to that of the scattered Pg wave with an s_h of 0.14 s/km.

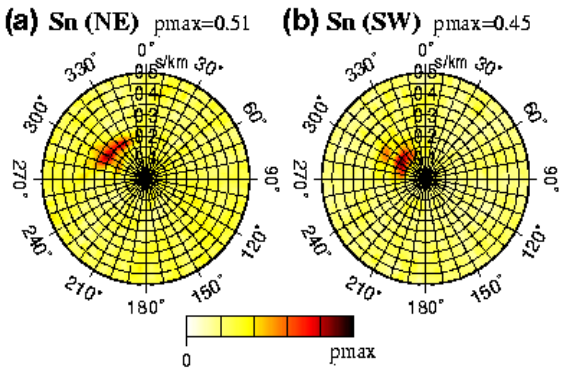

Figure 8. Slowness power spectra of the expected *Sn* window for data sets from two subsites ((a) NE, (b) SW) which were divided according to the velocity structure. The NE subsite has a lower velocity structure than the SW subsite. The *Sn* window used is between 162 and 170 s. The frequency band used is 0.5 to 3.0 Hz.

The amplitude of the Lg waves is less variable with the source locations than the Sn in Fig. 7. The spectra of Sn are enriched between about 1 and 3 Hz as compared to Lg spectra. Apparent corner frequencies of Sn are 2 to 3 times higher than those of Lg. This is consistent with the substantial report of Xie (2002) that different regional waves exhibit different source corner frequencies from UNEs. These observations suggest that the efficiency of shear wave excitation by UNEs may be dependent on source site geology in a frequency-variable manner: shear wave excitation may be more variable at higher frequencies. This scenario is consistent with a physical consideration that the excitation of shear waves with shorter wavelengths is more affected by the shallow source zone geological structures.

CONCLUSIONS

We investigated the near-source phase composition of regional seismic waves leaving underground nuclear explosions at the Balapan test site by applying a slowness power spectral analysis to source array records under a reciprocal theorem. The dominant Pn phase velocity (v_h) is about 8.0 km/s. The energy in the expected Sn window is composed of scattered crustal Pg wave with a v_h of 7.1 km/s and the mantle shear waves with a v_h of 4.8 km/s. The Lg wave in a frequency range between 0.5 and 2.0 Hz has a phase velocity of 4.2 km/s that is typical for super-critically reflected crustal S waves. On the other hand, the expected Rg window is dominated by a fundamental mode Rayleigh wave with a v_h of 3.0 km at frequencies below 0.8 Hz. Above 0.8 Hz the phase coherency degrades drastically owing to a strong attenuation of Rayleigh wave during propagation. From the comparison of slowness power spectral composition between Lg and Rg, the Rg-to-S scattering mechanism does not appear to be a dominant mechanism for the Lg excitation from Balapan UNEs.

The geology of the source region appears to play an important role on the strength of mantle shear wave in the expected Sn window. In that window, slower near surface velocity in the source region seems to enhance shear waves. On the other hand, the strength of Lg waves is much more robust with varying source region geology. The Lg window generally contains lower frequency content relative to the Sn window. The observation implies that source region geology tends to make stronger influence on the strength of higher-frequency shear waves. The study is currently being expanded to other UNE records (e.g., Delgelen test site records) for comparisons with the observations from the Balapan records.

ACKNOWLEDGEMENTS

We thank Howard Patton, Paul Richards and Bill Menke for fruitful comments on the study, Won-Young Kim for information on data and instrument response, Vitaly Khalturin for information on nuclear explosions at Kazakhstan.

REFERENCES

Adushkin, V. V., V. A. An, V.M. Ovchinnikov, and D.N. Krasnoshchekov (1997), A jump of the density on the outer-inner core boundary from the observations of PKiKP waves on the distance about 6 degrees, *Doklady Akademii Nauk* 354: (3), 382-385.

Bocharov, V. S., Zelentsov, S. A., and Mikhailov, V. I. (1989), Characteristics of 96 underground nuclearexplosions at the Semipalatinsk test site, *Atomnaya Energiya* 67: 210-214, (in Russian).

Bonner, J. L., D. C. Pearson, W. S. Phillips, and S. R. Taylor (2001), Shallow velocity structure at the Shagan River test site in Kazakhstan, *Pure Appl. Geophys*. 158: 2017-2039.

Der, Z., M. E. Marshall, A. O'Donnell, and T. W. McElfresh (1984), Spatial coherence structure and attenuation the *Lg* phase, site effects, and interpretation of the *Lg* coda, *Bull. Seism. Soc. Am.* 74: 1125-1148.

Herrmann, R.B. (2002), *Computer Programs in Seismology*, ver3.30, Saint Louis University.

Kennett, B. L. N. (2002), *The Seismic Wavefield*, Volume II, Interpretation of Seismograms on Regional and Global Scales, Cambridge University Press, New York.

Kim, W.-Y., P. G. Richards, V. Adushkin, and V. Ovtchinnikov (2001), Borovoye digital seismogram archive for underground nuclear tests during 1966-1996, Technical Report, Lamont-Doherty Earth Observatory of Columbia University.

Lay, T., D. V. Helmberger, and D. G. Harkrider (1984), Source models and yield-scaling relations for underground nuclear explosions at Amchitka Island, *Bull. Seism. Soc. Am.* 74 (3): 843-862.

Marshall, P. D., T. C., Bache, and R. C., Lilwall (1985), Body wave magnitudes and locations of Soviet underground nuclear explosions at Semipalatinsk Test Site, *AWRE Report*, No. O 16/84, H.M. Stationery Office, London.

NNCRK (1999), Technical Report, Proceedings of the Workshop on IMS Location Calibration, contributed by the National Nuclear Centre of the Republic of Kazakhstan, Oslo, Jan 1999.

Quin, H. R. and C. H. Thurber (1992), Seismic velocity structure and event relocation in Kazakhstan from secondary *P* phases, *Bull. Seism. Soc. Am.* 82, 2494-2510.

Ringdal, F., P. D. Marshall, and R. W. Alewine (1992), Seismic yield determination of Soviet underground nuclear explosions at the Shagan River test site, *Geophys. J. Int.* 109: 65-77.

Spivak, A. A. (1996), Aftershocks of underground nuclear explosions, *Geoecology* N6: 27-42, (In Russian).

Spudich, P. and T. Bostwick (1987), Studies of the seismic coda using an earthquke cluster as a deeply buried seismograph array, *J. Geophys. Res.* 92: (B10), 10,526-10,546.

Thurber, C., C. Trabant, F. Haslinger, and R. Hartog (2001), Nuclear explosion locations at the Balapan, Kazakhstan, nuclear test site: the effects of high-precision arrival times and three-dimensional structure, *Phys. Earth Planet. Inter.* 123: 283-301.

Xie, J. (2002), Source scaling of *Pn* and *Lg* spectra and their ratios from explosions in central Asia: Implications for the identification of small seismic events at regional distances, *J. Geophys. Res.* 107: (B7), 2128, doi:10.1029/2001JB000509.

Xie, J., L. Cong, B.J. Mitchell, and J.-M. Chiu (1996), Complexities in high-frequency seismic waveforms due to three-dimensional structure in the New Madrid Seismic Zone, *J. Geophys. Res.* 101: (B3), 5751-5778.

IMPROVING M_s ESTIMATES BY CALIBRATING VARIABLE PERIOD MAGNITUDE SCALES AT REGIONAL DISTANCES

Heather Hooper[1], Ileana M. Tibuleac[1], Michael Pasyanos[2], and Jessie L. Bonner[1]

Weston Geophysical Corporation[1] and Lawrence Livermore National Laboratory[2]

Sponsored by National Nuclear Security Administration
Office of Nonproliferation Research and Engineering
Office of Defense Nuclear Nonproliferation

Contract Nos. DE-AC52-04NA25547[1] and W-7405-ENG-48[2]

ABSTRACT

One of the most robust methods for discriminating between explosions and earthquakes is the relative difference between the body-wave (m_b) and surface-wave (M_s) magnitudes for a seismic event. Most M_s formulas have been developed for teleseismic distances and for Rayleigh waves in the period range of 17-23 seconds. For small-to-intermediate yield explosions recorded at regional distances, the amplitudes for Rayleigh waves in this period range may be below background noise levels; however, shorter period surface waves (< 15 sec) may still be extracted and processed using phase match filtering. Thus, calibrated and transportable formulas, which allow for estimation of M_s at regional distances at the period of maximum amplitude (between 8 to 25 seconds) are required to lower the M_s thresholds for small earthquakes and explosions. Additionally, these calibrated formulas may be able to significantly reduce the variance in M_s estimates for larger events in the region.

For small events, detection of a Rayleigh wave is often difficult to achieve; thus we are attempting to develop an automated method for surface wave detection and magnitude estimation. First, Rayleigh phases are identified using a detector modeled after the Chael (1997) automatic teleseismic Rayleigh-wave detection method; however, we have modified the detector for regional distance and for 8-25 sec period applications. The modifications include: 1) application of six zero-phase Butterworth filters centered on periods of 9, 12, 15, 20, 22 and 25 seconds; 2) calculation of the covariance matrix for rotated waveforms; and 3) addition of three new weights of the detection function; two for planarity and one for group velocity verification. We have tested the detector on United States Geological Survey (USGS)-located events from eastern and southern Asia. Second, variable-period magnitude formulas are applied, including the new M_s (VMAX) technique (Bonner et al., 2005), on surface waves extracted by automated phase-match filtering. Information for phase match filtering is provided by updated regional tomographic group velocity models of Eurasia, which we are attempting to extend to periods of 10 seconds or less in southern Asia.

OBJECTIVES

Developing a methodology for calculating surface wave magnitudes that is valid at both regional and teleseismic distances, applicable to events of variable sizes and signal-to-noise ratios (SNR), calibrated for variable structure and propagation, and easy to automate in an operational setting is an important monitoring goal. Our objectives are to create such a methodology, and to use it to lower M_s estimation and detection thresholds. We hope that the method will provide a seamless tie between M_s estimation at regional and teleseismic distances.

Our methodology includes the following:

- Extending the geographic coverage of existing group velocity tomography maps to our entire study area, as well as extending the maps to periods of 10 seconds or less,
- Using a semi-automated Rayleigh wave detector to verify that the waveforms contain fundamental-mode Rayleigh waves,
- Using the updated group velocity maps and automated phase match filtering to extract the surface waves from the waveforms,
- Using a variable-period maximum amplitude M_s formula based on Russell (2005) to calculate M_s,
- Calibrating that formula and others for regional distance applications at a number of stations in the study area, and
- Developing empirical and theoretical M_s threshold maps of the study area.

We are in the first stages of this project, which includes updating our group velocity models for Eurasia, developing the Rayleigh detector, developing a phase match filtering routine, and performing preliminary calculations of M_s.

RESEARCH ACCOMPLISHED

Updates to Group Velocity Models

Global and regional group velocity models serve an important function for nuclear monitoring efforts using surface wave analysis. The models serve as input into automated processing routines that can extract small amplitude surface-wave arrivals (e.g., Herrin and Goforth, 1977; Stevens and McLaughlin, 2001), thus lowering M_s detection thresholds. Recent efforts in developing these models have focused on the shorter periods (Levshin et al., 2002; Pasyanos et al., 2003; Taylor et al., 2003).

One region of nuclear monitoring interest which is poorly constrained in current group-velocity tomographic maps is southern Asia. The current coverage is mainly composed of dispersion data from the GEOSCOPE station HYB in Hyderabad, India, along with a few recordings from stations at PUNE (western India), PALK, and a few other open data sources. However, the geometry of the sources and limited stations is such that there are relatively few crossing paths, which are needed to improve the resolution of the models.

Using data collected in southern Asia, we have increased our understanding of the group velocity structure in this region. This has included incorporating the data and results from Mitra et al. (in review) into our models. Mitra et al. used one-dimensional path-averaged dispersion measurements for 1001 source-receiver paths to produce tomographic images between periods of 15 and 45s (Figure 1). Testing of the group velocity models demonstrates that the average resolution across the region ranges from 5 to 7.5 degrees for the periods used in this study.

We are also working to extend our group velocity models of Eurasia to lower periods. Using short period data from stations in India, we are completing new tomographic inversions in order to extend the models to periods of 10 seconds or less. These short-period observations are needed to improve the automated phase match filtering of surface waves.

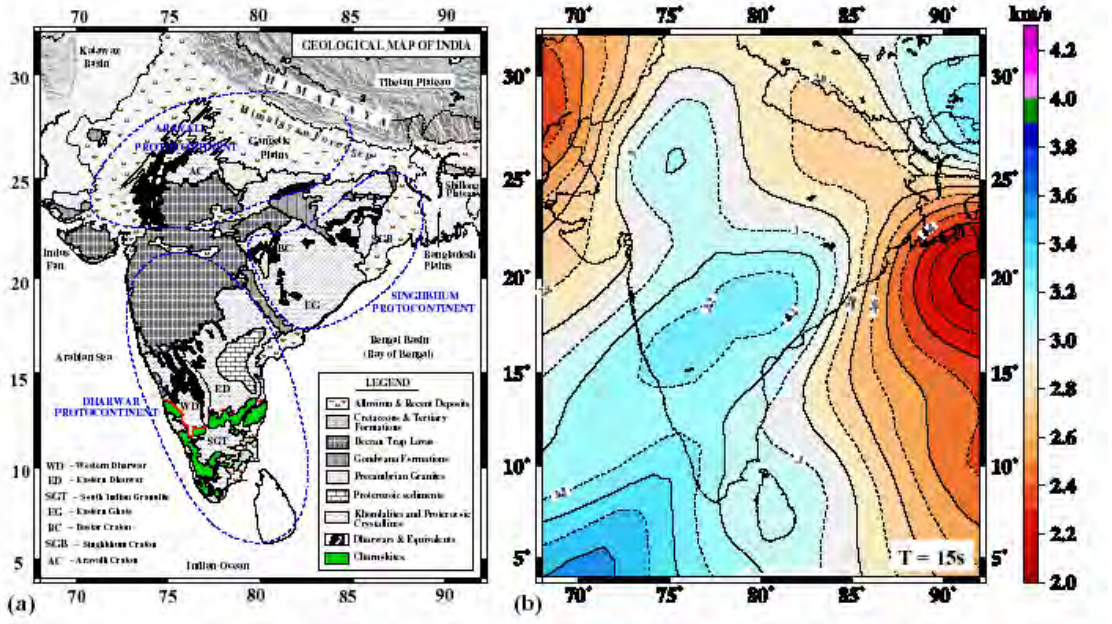

Figure 1. A comparative plot of (a) the geology and tectonics of southern Asia and (b) the tomographic group velocity at a period of 15 seconds, after the work of Mitra et al. (in review). These data have been incorporated into our models of southern Asia and Eurasia.

Semi-Automatic Rayleigh Wave Detection Method

To estimate variable-period (8 to 25 second) regional surface-wave magnitudes, we must first identify Rayleigh-wave phases. We use a semi-automatic detector, similar to an *Rg* detection algorithm developed by Tibuleac *et al.* (2004) and modeled after the Chael (1997) automatic teleseismic Rayleigh-wave detection method. We have modified the detector for regional distance and for 8-25 second period applications. The modifications include: 1) Application of six zero phase Butterworth narrow band filters centered on periods of 9, 12, 15, 20, 22 and 25 seconds. One of these periods is chosen by the analyst to estimate the back azimuth; 2) Calculation of the covariance matrix for rotated waveforms; and 3) Addition of three new weights of the detection function: two for planarity and one for group velocity verification. We have observed that selection of an appropriate frequency band is essential for back azimuth accuracy and for regional Rayleigh wave identification.

We have tested the detector on 154 USGS-located events (Figure 2) with a magnitude range of $3 < m_b < 5.2$, recorded between Jan. 2000 and Dec. 2001 at the WMQ (Urumqi, Xinjiang, China) seismic station, located at 43.8211 N, 87.695 E. Out of 154 analyzed events, an analyst identified 140 Rayleigh phases (91%). For an acceptable back azimuth error of 45 degrees, 121 (86% of the analyst-accepted events) were detected automatically. Three events (2%) were false alarms. 19 events (14%) were automatically rejected. Figure 3 shows the detector performance. The mean Rayleigh back azimuth residual (Figure 3, left plot) was -3.5 degrees, with a sample standard deviation of 15.7 degrees. Most of the Rayleigh phases that were not detected automatically but were confirmed by the analyst (open circles in Figure 3), show back azimuth residuals between 45 and 90 degrees, and are located 400 to 500 km from the station. Analyst-detected Rayleigh arrivals with an estimated detection angle up to 90 degrees off the great circle path are observed when Love waves overlap the Rayleigh waves (Figure 4, upper plots). For this reason our acceptable automatic back azimuth error (45 degrees) was larger than in other studies (Selby, 2001). The semi-automatic routine we have developed can detect Rayleigh phases from events with body-wave magnitude larger than 3, arriving from distances between 250 and at least 1500 km. Further work is needed to address the Rayleigh-Love phase interference as well as integration of multiple filtering in an entirely automatic algorithm. Figures 4 and 5 show an example of the detector output for an m_b=4.5 earthquake that occurred on March 17, 2000, 01:20:39.6, 844.3 km from WMQ, at 40.82 N, 78.24 E, with a depth of 51.8 km, and a back azimuth of 250 degrees.

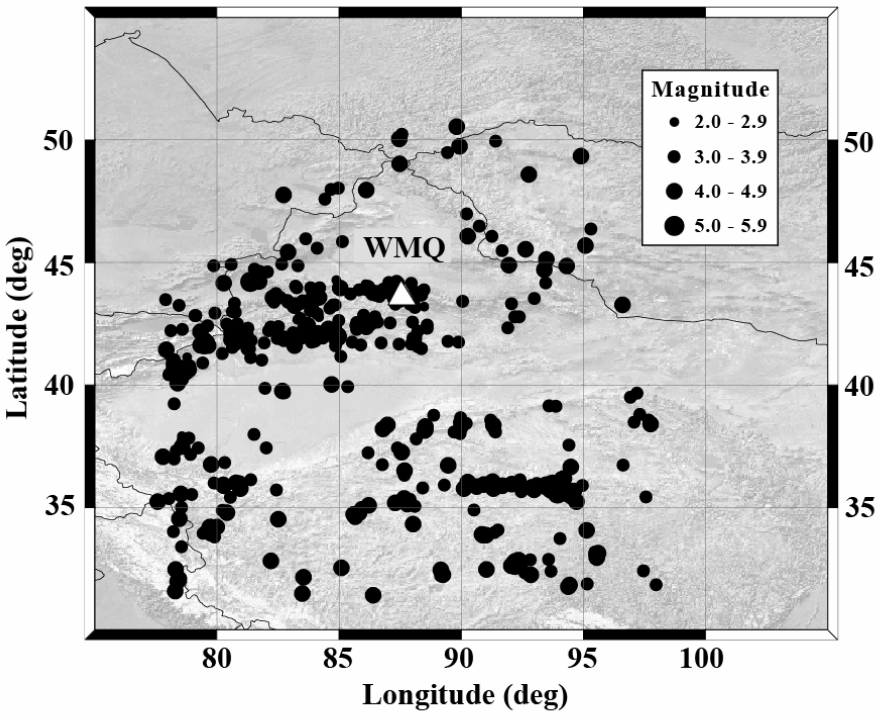

Figure 2. Locations of the events and of the WMQ seismic station.

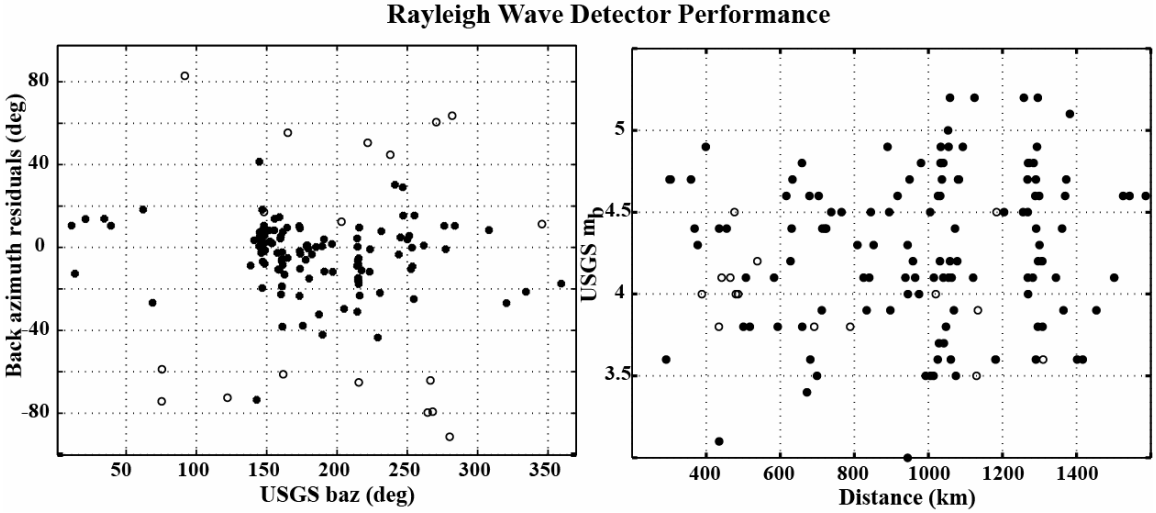

Figure 3. (Left) Back azimuth residuals as a function of USGS back azimuth. The residuals are calculated as the difference between detector-estimated and USGS-estimated back azimuth. Dots represent automatic detections, while open circles represent analyst detections that were rejected automatically. (Right) Detector performance as a function of event epicentral distance and USGS body-wave magnitude. Symbols are the same as in the left plot.

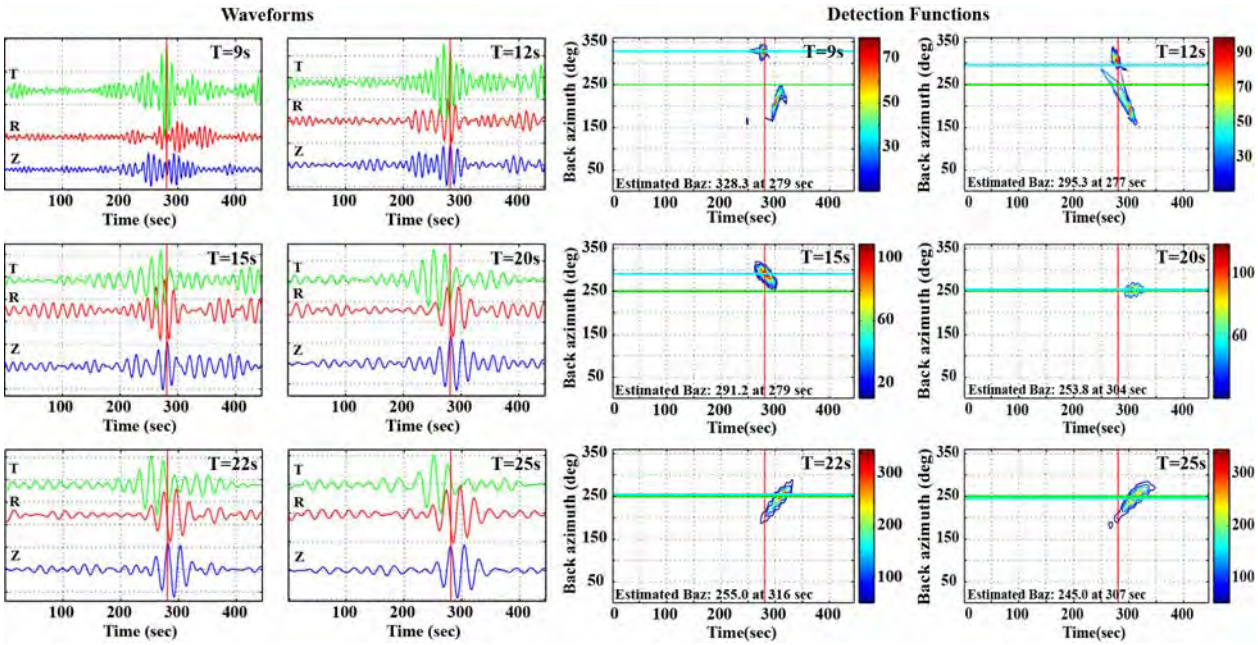

Figure 4. Example of detector output for an m_b=4.5 earthquake that occurred on March 17, 2000, 01:20:39.6, 846.6 km from WMQ, at 40.82 N, 78.24 E, with a depth of 51.8 km, and a back azimuth of 250 degrees. (Left) Waveforms rotated to the USGS-estimated back azimuth and filtered using six zero-phase Butterworth filters centered on periods of 9, 12, 15, 20, 22 and 25 seconds. Rayleigh phases arrive at a time lag of approximately 250 seconds. (Right) Detection function values as a function of time and back azimuth for the filtered waveforms shown at left. The green line represents the USGS-estimated back azimuth, and the cyan line represents the detector-estimated back azimuth. The detector-estimated back azimuths vary from the USGS values by up to 50 degrees for filters centered on 9, 12 and 15 second periods. This effect is caused by the simultaneous arrival of large-amplitude Love phases with the Rayleigh phases at those periods. The vertical red lines represent a group velocity of 3km/s.

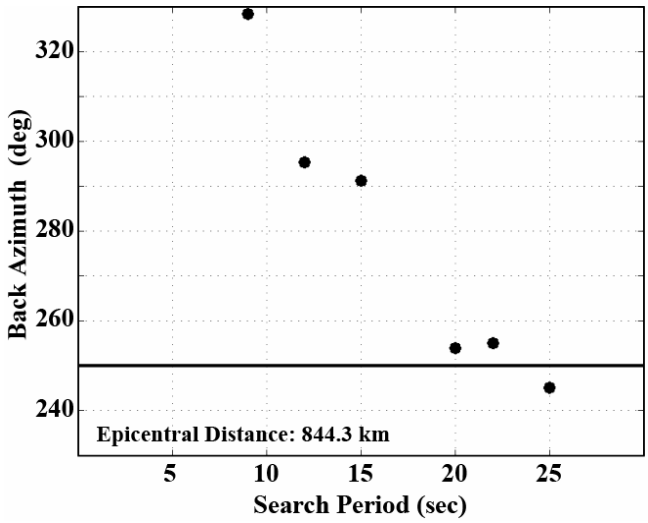

Figure 5. An example of detector-estimated back azimuth variation as a function of the filter center period for the event shown in Figure 4. The black line represents the back azimuth to the USGS location (250.07 degrees). Better back azimuth estimates are achieved when the Rayleigh waves do not overlap the Love wave train.

Phase Match Filtering

We use phase match filtering (PMF) (Herrin and Goforth, 1977; Herrmann, 2004) to extract the surface waves from the seismograms. We use the group velocity dispersion curves obtained from the group velocity tomographic maps (discussed above) for each event-station path to find and apply a filter that has approximately the same phase as the Rayleigh wave signal of interest. This technique improves the signal-to-noise ratio for the extracted surface waves by compressing the dispersed surface-wave signals and removing the effects of microseismic noise, multipathing, body waves, higher-order surface waves, and coda (Pasyanos et al., 1999). Figure 6 shows an example of phase match filtering for the m_b=4.5 sample event shown in Figures 4 and 5.

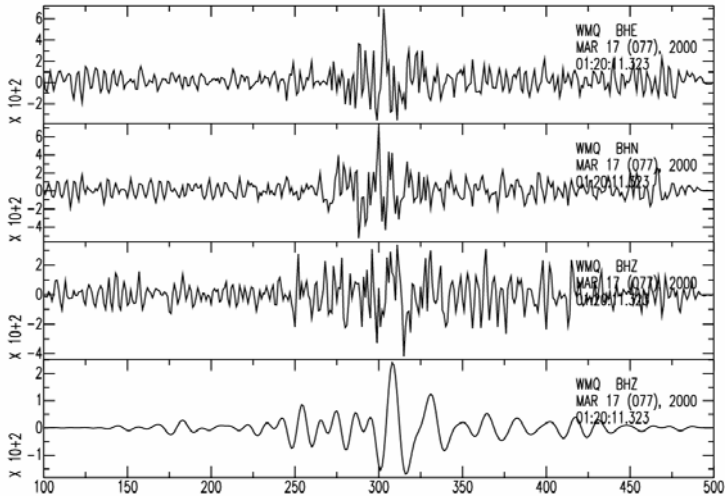

Figure 6. Three-component data from the sample event shown in Figures 4 and 5. The top three panels show the east, north and vertical components of the data. The bottom panel shows the vertical component after phase match filtering. The Rayleigh wave begins at approximately 250 seconds.

M_s Estimation

At regional distances, surface-wave trains are not well dispersed and are often characterized by a pulse-like shape with dominant periods ranging from 5 to 12 seconds. Thus, it is difficult, and for small events often impossible, to determine an M_s as it was originally defined for 17 to 23 second Rayleigh waves. An M_s scale that can incorporate variable periods is required to examine the performance of the M_s-m_b discriminant for small events recorded at regional distances. The maximum amplitude variable-period methodology that we are developing, which includes an M_s formula based on Russell (2005), will reduce the variance at large magnitudes and increase the detection and applicability thresholds, as well as avoid problems associated with depth as long as the event is within the crust or upper mantle.

After phase match filtering has extracted the surface waves of interest, the next step is to measure the amplitudes of the Rayleigh waves in the various frequency bands. The choice of the filtering method is very important to our goal of reducing the variance in the M_s estimates. Building on the work of Yacoub (1983) and Russell (2005), we use a "comb" method in which 18 Butterworth narrow band-pass filters are applied at center periods of 8 to 25 seconds. The filters are applied to the autocorrelation function output of the phase match filtering method, thus helping to remove the effects of Airy phases and dispersion. Figure 7 shows an example of these "comb" filters applied on the previously discussed sample event for both phase match filtered (right) and non-phase match filtered (left) data.

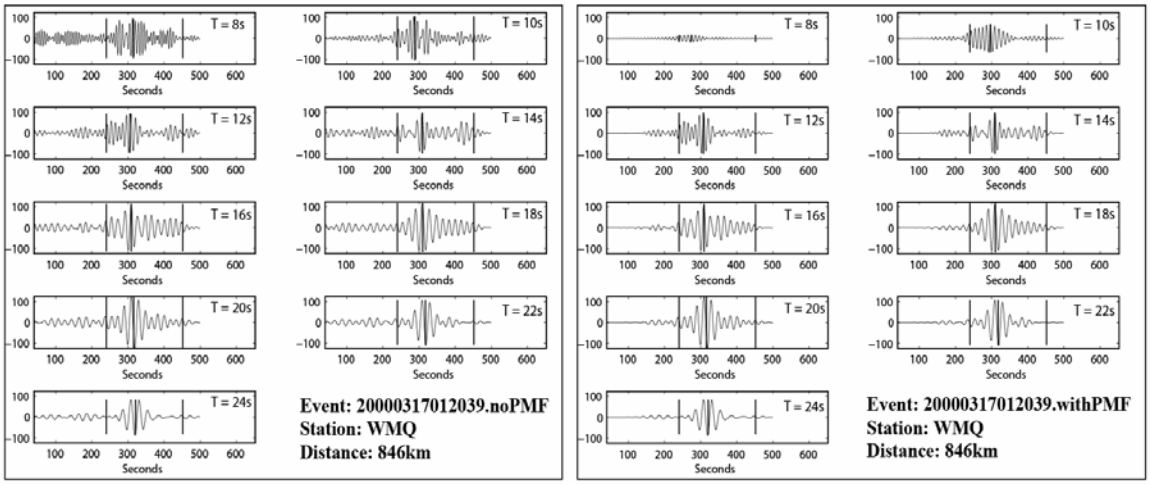

Figure 7. Data from the sample event shown in Figures 4-6. (Left) Narrow-band Butterworth "comb" filters applied to data that have not been PMF'd. (Right) The same filters applied to data that have undergone PMF'ing. Since this event is fairly large and close to the station, with a good signal-to-noise ratio, the PMF doesn't make much difference.

Our M_s program automatically chooses the period of maximum amplitude, but if the signal-to-noise ratio is low, it asks the analyst to check the pick. The analyst can then approve the program's pick, choose a different period, or eliminate the station from the analysis. One of the reasons that this analysis is done in the time domain is that it allows the analyst to visually confirm that the chosen amplitude corresponds to the fundamental mode, and not to possible multipathing or leakage that can contribute to the PMF results, or noise that obscures the Rayleigh phase. Once the period of maximum amplitude is chosen, an M_s is calculated. A mean and standard deviation of the M_s for each station is then calculated. Figure 8 shows the final output of the program for the sample event, for both phase match filtered (right) and non-phase match filtered (left) data.

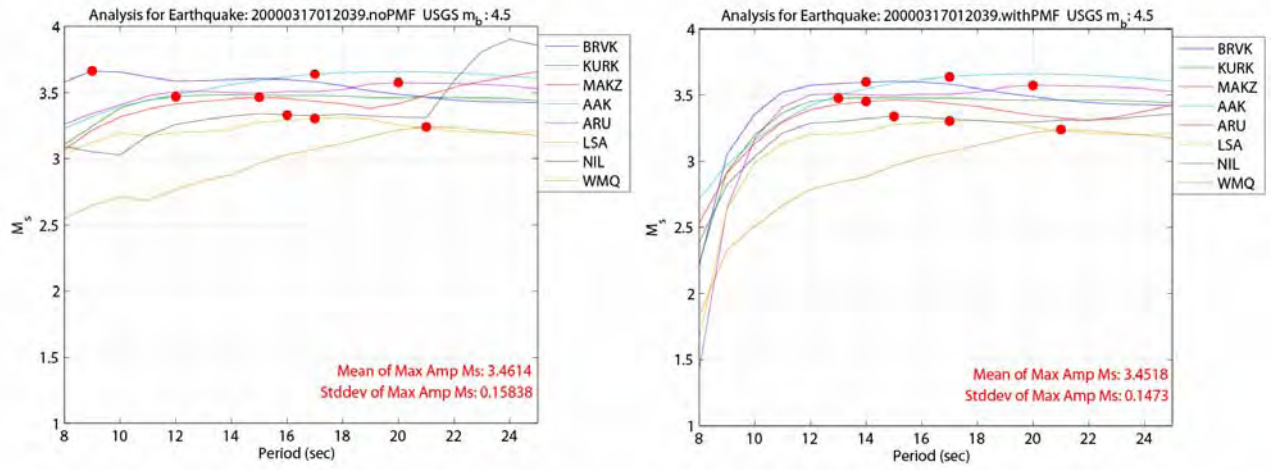

Figure 8. Final output of the M_s program for the sample event shown in Figures 4-7. (Left) The individual M_s estimates for the non-PMF'd data, as well as the mean M_s and standard deviation. (Right) The individual M_s estimates for the PMF'd data, as well as the mean M_s and standard deviation. Since this event is fairly large and close to the station, with good signal-to-noise ratio, the PMF doesn't make much difference in the final result. It did, however, reduce the variance and improve the M_s estimation at a few stations. The red dots are the maximum amplitude Ms for each station.

Pasyanos et al. (1999) show that use of the phase match filter generally results in a very slight lowering of the measured M_s, with the greatest change seen for $m_b < 5.0$. Preliminary results from this research show the same effect. In larger magnitude events, the use of the PMF has little or no effect on M_s: using 72 events with IDC $m_b \geq 3.4$, we found a mean M_s residual between the non-filtered data and the filtered data of 0.0363, with a sample standard deviation of the residual of 0.051. The standard deviation of the final M_s is generally close for the filtered and non-filtered data as well (Figure 9, right plot), although the difference between them is smaller for higher-magnitude events. When we extend our analysis to smaller events (IDC $m_b < 3.5$), we expect the PMFing to have a much greater effect on the standard deviation. One effect that was very noticeable in our preliminary study was that the use of the PMF filter often allows us to use more stations in the M_s analysis for a given event (Figure 9, left plot), by improving the signal-to-noise ratio for noisy stations which would otherwise have to be discarded from the analysis.

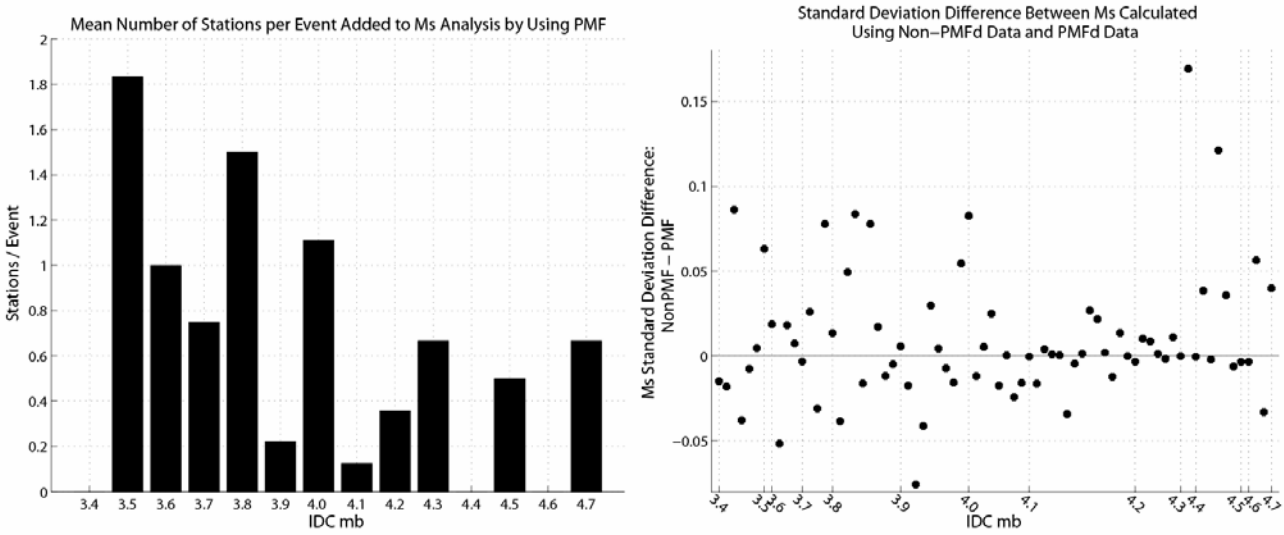

Figure 9. (Left) PMF'ing the data can improve the SNR at noisy stations, which often allows us to use more stations in the M_s analysis, particularly for smaller-magnitude events. To show this effect, we subtracted the number of stations used in the M_s analysis without PMF from the number of stations used with PMF for each event (for a total of 72 events), binned the events according to IDC m_b, and divided by the number of events in each bin. (Right) The difference in the M_s standard deviation between data that have not been PMF'd and data that have been PMF'd.

Figure 10 shows the M_s results for all 72 events analyzed thus far, with IDC $m_b \geq 3.4$, depth < 50km, and event-station distances from 200 to 4000 km. The solid diagonal line is the event screening equation $M_s = 1.25m_b - 2.2$ from Murphy et al. (1997). Note that all but two of the events fall above the discrimination line.

CONCLUSIONS AND FUTURE WORK

During the initial phases of this research project, we have extended the geographic coverage and lowered the periods of existing group velocity tomography maps in southern Asia. We have developed both a semi-automated Rayleigh wave detector and an automated phase match filtering routine which allow us to verify that Rayleigh phases are present and extract them from the waveforms. We have had success in the preliminary application of these new research products, along with the Russell (2005) surface wave formula, to a Eurasian dataset of events with $m_b < 5$.

In future phases of this research, we will calibrate the Russell (2005) and other magnitude formulas for regional distance applications. We will apply them, as part of our new methodology, to estimate M_s for earthquakes, quarry blasts, and explosions in Eurasia and southern Asia. We will also develop empirical and theoretical M_s threshold maps, based on the use of these calibrated, variable-period formulas and improved signal processing techniques. The new M_s thresholds will be compared with methods currently used in nuclear explosion monitoring to quantify any significant improvements obtained by using short-period surface waves.

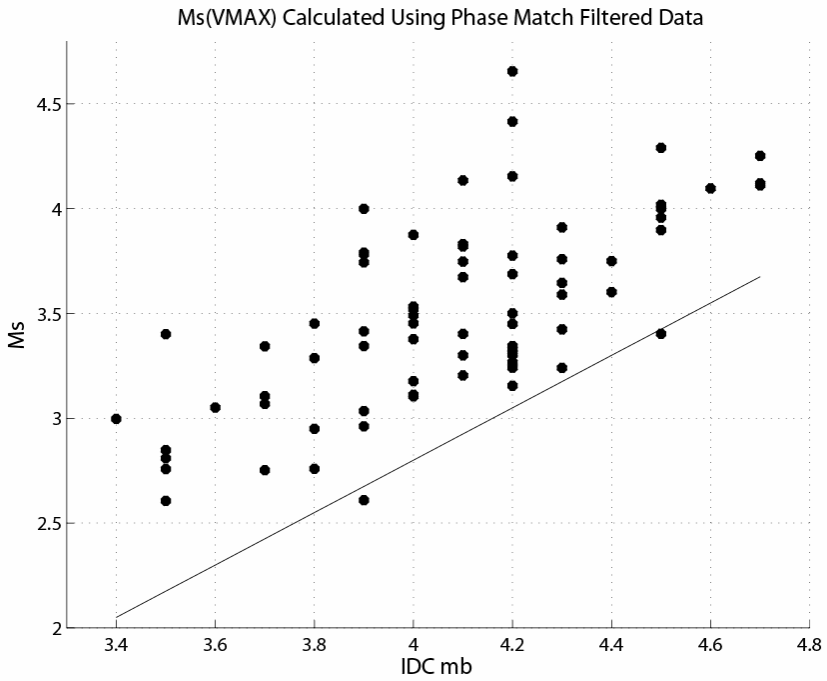

Figure 10. M_s results for all 72 events analyzed thus far, with IDC $m_b \geq 3.4$, depth < 50km, and event-station distances from 200 to 4000 km. The diagonal line is the event screening line from Murphy et al., 1997.

ACKNOWLEDGEMENTS

Thanks to Anastasia Stroujkova for insightful comments and ideas on improving the Rayleigh detector.

REFERENCES

Bonner, J. L., D. Russell, D. G. Harkrider, D. T. Reiter, and R. B. Herrmann (2005), Application of a time-domain, variable-period surface wave magnitude measurement procedure at regional and teleseismic distances – Part II: Application and M_s-m_b Performance, submitted to *Bull. Seism. Soc. Am.*

Chael, E. P. (1997), An Automated Rayleigh-Wave Detection Algorithm, *Bull. Seism. Soc. Am.* 87: 157–163.

Herrin, E.T. and T. Goforth (1977), Phase-match filtering: application to the study of Rayleigh Waves, *Bull. Seism. Soc. Am*. 67: 1259–1275.

Herrmann, R. B. (2004), *Computer programs in seismology*, St. Louis University.

Levshin, A., J. Stevens, M. Ritzwoller, and D. Adams (2002), Short-period (7s to 15s) group velocity measurements and maps in Central Asia, in *Proceedings of the 24th Seismic Research Review - Nuclear Explosion Monitoring: Innovation and Integration*, LA-UR-02-5048, Vol. 1, pp. 97–106.

Marshall, P.D. and P.W. Basham (1972), Discrimination between earthquakes and underground explosions Employing an Improved M_s Scale, *Geophys. J. R. Astr. Soc*. 29: 431–458.

Mitra, S. K. Priestley, V. K. Gaur, S. S. Rai, and J. Haines (in review), Variation in group velocity dispersion and seismic heterogeneity of the Indian Lithosphere, submitted to *Geophys. J. Int.*

Murphy, J. R., B. W. Barker, and M. E. Marshall (1997), Event screening at the IDC using the M_s/m_b discriminant, Maxwell Technologies Final Report, 23 p.

Pasyanos, M.E., W. R. Walter, S. R. Ford and S. E. Hazler (1999), Improving m_b:M_s discrimination using phase matched filters derived from regional group velocity tomography, in *Proceedings of the 21st Seismic Research Symposium - Technologies for Monitoring the Comprehensive Nuclear-Test-Ban Treaty*, LA-UR-99-4700, Vol. 2, 565–571.

Pasyanos, M., W. Walter, and M. Flanagan (2003), Geophysical models for nuclear explosion monitoring, in *Proceedings of the 25th Seismic Research Review - Nuclear Explosion Monitoring: Building the Knowledge Base*, LA-UR-03-6029, Vol. 1, 125–129.

Rezapour, M., and R.G. Pearce (1998), Bias in Surface-Wave Magnitude M_s Due to Inadequate Distance Correction, *Bull. Seism. Soc. Am*. 88: 43–61.

Russell, D.R. (2005), Development of a time-domain, variable-period surface wave magnitude measurement procedure for application at regional and teleseismic distances. Part I – Theory, submitted to *Bull. Seism. Soc. Am*.

Selby, N. D., (2001), Association of Rayleigh Waves using back azimuth measurements: application to test ban verification, *Bull. Seism. Soc. Am.* 91: 580-593.

Stevens, J. L. and K.L. McLaughlin (2001), Optimization of Surface Wave Identification and Measurement, in Monitoring the Comprehensive Nuclear Test Ban Treaty: Surface Waves, eds. Levshin, A. and M.H. Ritzwoller, *Pure Appl. Geophys*. 158: 1547–1582.

Taylor, S., X. Yang, W. Phillips, H. Patton, M. Maceira, H. Hartse, and G. Randall (2003), Regional event identification research in Eastern Asia, in *Proceedings of the 25th Seismic Research Review - Nuclear Explosion Monitoring: Building the Knowledge Base*, LA-UR-03-6029, Vol. 1, 476–485.

Tibuleac, I. M., J. Britton, D. B. Harris, T. Hauk, H. Hooper and J. L. Bonner (2004), Detection methods for mining explosions in Southern Asia, in *Proceedings of the 26th Seismic Research Review: Trends in Nuclear Explosion Monitoring*, LA-UR-04-5801, Vol. 1, 366–374.

Yacoub, N. K. (1983), Instantaneous amplitudes: A new method to measure seismic magnitude, *Bull. Seism. Soc. Am*. 73: 1345–1355.

POSSIBLE EFFECTS OF FROZEN ROCK ON EXPLOSIVE COUPLING

Mark Leidig[1], Jessie Bonner[1], Roger Hansen[2], Vladimir Romanovsky[2], Stephen Brown[3], Randy Martin[3], and Jim Lewkowicz[1]

Weston Geophysical Corp.[1], University of Alaska at Fairbanks[2], and New England Research Inc.[3]

Sponsored by Air Force Research Laboratory

Contract No. FA8718-04-C-0026

ABSTRACT

Weston Geophysical Corporation, University of Alaska at Fairbanks, and New England Research, Inc., have formed a consortium to test the effects of explosions in frozen rock. Laboratory studies have demonstrated that frozen rock is significantly stronger than unfrozen rock, and it has been hypothesized that this increased strength can significantly alter seismically estimated yield. Our consortium is planning a series of explosive tests to determine the seismic variations between detonating explosives in frozen and unfrozen rock. The information derived from the proposed research will provide a thorough test of the hypothesis. It will also provide important results for application in regions where explosions can be detonated in permafrost conditions.

The experiment will be conducted near Fairbanks, Alaska, where abrupt lateral boundaries on discontinuous permafrost exist. For a proper assessment of amplitude variations, the shots need to be in close proximity to effectively remove path effects. We will detonate a series of small, repeated explosions ranging in size from 2 to 500 lbs. of explosives. The explosives will be placed at approximately 20–30 m depth in regions of frozen and unfrozen rock and will be recorded on a near-source network of 18 accelerometers and velocity seismometers. Scaling studies have been conducted to determine the proper distance for recording stations and expected ground shaking. Over 120 seismometers will be deployed between 1 and 15 km from the explosions. Several stations of the Alaska Earthquake Information Center network are in close proximity and AFTAC's ILAR and ALPA seismic arrays are within 100 km; thus, the explosions should be recorded by an extensive regional network.

Initial 10-m borehole temperature measurements indicate frozen (-0.5°C) and unfrozen (1.5°C) rock can be found within 300 m of each other. A refraction velocity survey will be conducted across the test site prior to blasting. Immediately following this, the explosive boreholes will be drilled and temperature logged, and then the frozen rock experiments will be conducted.

OBJECTIVES

Weston Geophysical Corp., the University of Alaska at Fairbanks, and New England Research, Inc., have formed a consortium to conduct the Frozen Rock Experiments (FRE) in central Alaska to characterize the variations in ground motion scaling and coupling for explosions in frozen and unfrozen rocks. The experiment will help quantify the variations in estimated seismic yield of explosions in frozen rock due to changes in coupling. The consortium has spent the previous year planning the experiment and in the next phase will detonate and record the explosions on approximately 150 near-source and local stations deployed specifically for the experiment. The data will also be recorded on permanent regional stations of the Alaska Earthquake Information Center (AEIC) network and nearby Air Force Technical Applications Center (AFTAC) arrays. In the final phase, we will analyze the data to quantify the source function variations for equal yield explosions detonated in frozen and unfrozen rocks.

RESEARCH ACCOMPLISHED

Experiment Background

A critically important aspect of nuclear test monitoring is yield estimation. United States monitoring agencies must be able to accurately estimate yields for nuclear explosions detonated in regions of monitoring concern. If frozen-rock emplacement conditions create a circumstance favorable for biased yields, data must be available such that any bias can be accounted for when the yield is estimated. Prior studies (Mellor, 1971) have established that frozen-rock properties are considerably different from unfrozen-rock properties. Moreover, it has been hypothesized that these altered properties may be sufficient to cause significant variations in seismic coupling, which in turn, significantly alter seismic yield estimates.

Sammis and Biegel (2004) have noted that an increase in low-temperature uniaxial strength is related to the ice in the initial pores and cracks. The ice increases the apparent coefficient of sliding friction on these initial cracks. Since the strengthening is strain-rate dependent, for nuclear explosions, the full strengthening should occur near 0°C. This is important given that our experimental test site region has frozen ice in the cracks at temperatures of -0.5°. It may be necessary to use nonlinear modeling using the damage mechanics models proposed by Sammis and Beigel (2004) and Ashby and Sammis (1990) to effectively model the amplitudes for explosions detonated in frozen rock.

Experiment Location

We will conduct the experiment near Fairbanks, AK (Figure 1) because that region contains both frozen and unfrozen rock. Temperature logging in 10 m wells has found 2° C unfrozen rock approximately 300 m from -0.5° C frozen rock. Figure 2 shows temperature profiles of a monitoring well in permafrost near the test site. The data indicates the ground is frozen between 15 and at least 70 m depth. This area is also well located to permanent regional seismic stations and will allow for relatively easy placement of near-source and local instruments to record the experiment.

Explosion Design

In planning the FRE explosions, we considered local vibration requirements. In addition, it is critical that the explosions be fully confined and rock fracturing be contained to completely frozen or unfrozen rock, depending on the type of shot. Every attempt will be made to use a charge depth equivalent to a typical scaled depth for nuclear tests if possible. Drilling and temperature logging will be conducted immediately prior to the tests to determine the thickness of the frozen and unfrozen rock and to ensure we use the proper charge weights and emplacement depth. Initial analysis indicates using a maximum charge weight of 500 lbs. of ammonia nitrate fuel oil (ANFO) and an emplacement depth of 20–30 m. These values will be refined after final temperature logging of the site. Table 1 lists the planned shots of the experiment. We will detonate a series of explosions with increasing charge weight to observe the variations between frozen and unfrozen explosions as a function of yield. The frozen and unfrozen explosions will be detonated within 300 m of each other to minimize effects of the travel path and emplacement medium.

Table 1. Planned Frozen Rock Experiment Explosions

Shot Number	Charge Weight (lbs.)*	Charge Depth* (m)	Rock Condition
1	100	20	Frozen
2	200	25	Frozen
3	500	30	Frozen
4	100	20	Unfrozen
5	200	25	Unfrozen
6	500	30	Unfrozen

*Initial planning. Actual weight and depth may vary to comply with regulations and rock conditions.

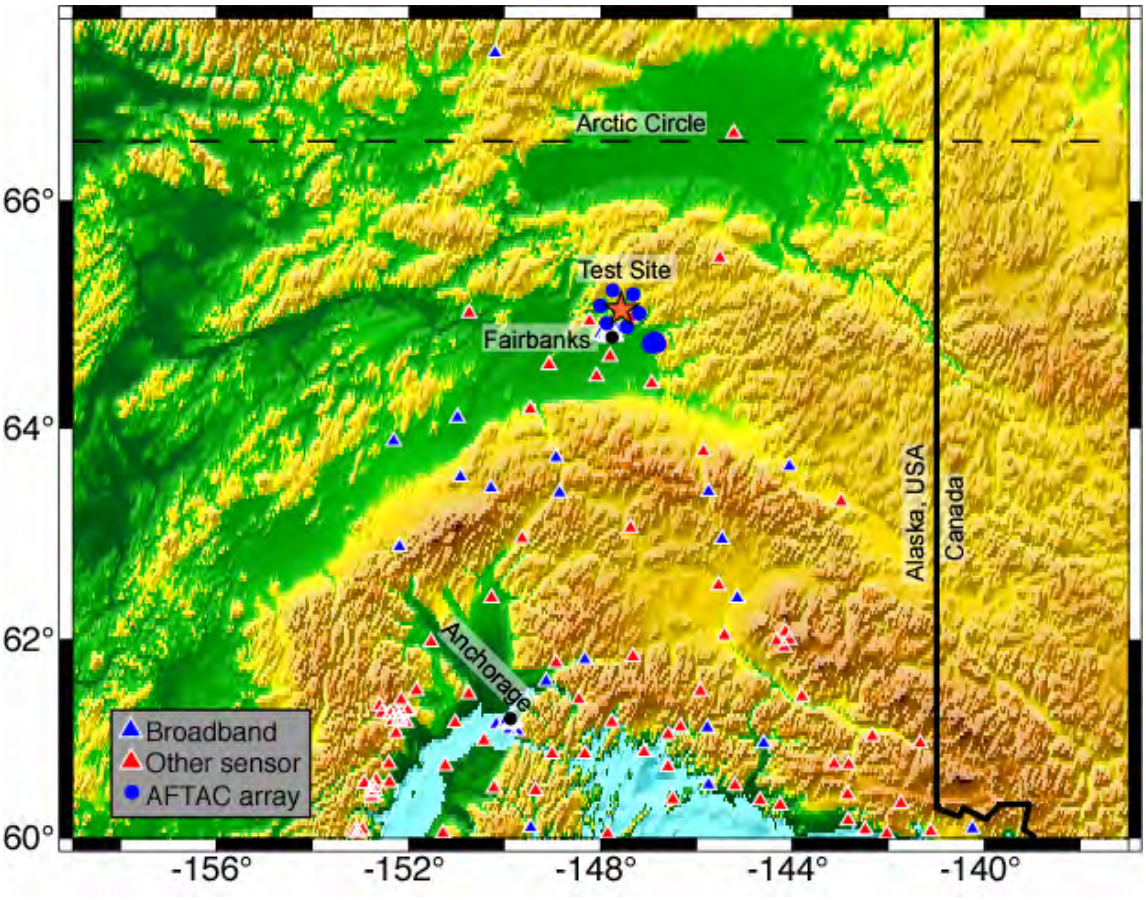

Figure 1. Location map of the test site region (star) and nearby seismic stations.

Station Deployment

We will deploy approximately 150 seismic stations within 15 km of the test site. These sensors include high g accelerometers, vertical component Texans, short-period seismometers, and broadband seismometers. Over 400 sensors of different types are permanently deployed across Alaska. An accelerometer will be placed within 5 m of each explosion to acquire an accurate origin time. In order to determine the proper station distance for the remaining stations, we examined signal quality from the Source Phenomenology Experiment (SPE) in September 2003 (Bonner et al., 2005) and modeled expected ground shaking for the FRE. The planned shot sizes for the FRE are approximately an order of magnitude smaller than the SPE shots, yet the SPE explosions, including the 233 lbs.

calibration shot, provide a guide to determine the proper explosion to station distance and prevent damage to nearby structures.

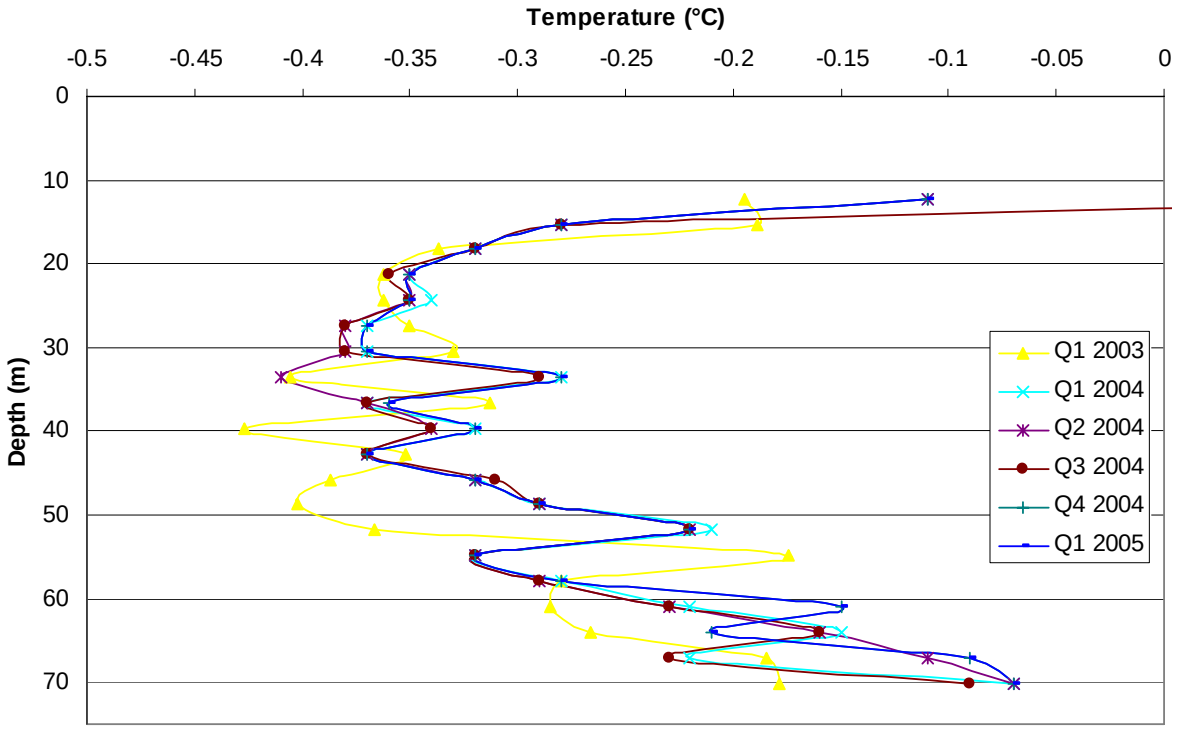

Figure 2. Temperature logs of a permafrost monitoring well near the frozen rock test site.

Peak Velocity. In order to determine the amount of shaking expected, we followed the analyses of Stump (2003) for the SPE project. The peak velocities for different shot sizes and distances were calculated using models developed by various published authors (summarized in Leidig, 2004). The Fuis et al. (2001) model with distance scaling was chosen as the most realistic based on observations from the SPE data. The peak velocity equation is

$\text{Log}(v) = -1.9277\text{Log}(r) - 0.3411\ (\text{Log}(r))^2 + 0.8119\ \text{Log}(w) - 3.1249$, where v is velocity, r is distance, and w is charge weight.

The peak velocities were calculated and plotted in Figure 3 for 100, 200, 500, 1,000, and 5,000 lbs. shots. Our largest planned explosion is 500 lbs., though.

Peak Acceleration. Nearby structures and equipment can be damaged by large ground accelerations. Following Stump (2003), peak accelerations were calculated by multiplying the peak velocity by $2\pi f_c$, where f_c is the corner frequency. Stump determined f_c to be approximately 35 Hz for a 1,800 lbs. shot and then used a cube root scaling relationship for other shot sizes. The corner frequencies for the shot sizes used in the FRE study are listed in Table 2. In Figure 4, we plot the peak accelerations from the velocities plotted in Figure 3.

Station Locations. The appropriate station distances are listed in Table 3. Figure 5 shows an example of how we might deploy the broadband and Texan seismometers based on terrain accessibility, azimuthal coverage, and appropriate station to explosion distance. The near-source accelerometer and short-period instrument placement is shown in Figure 6. This configuration will allow us to extensively record both the frozen and unfrozen tests without having to redeploy stations between tests. Hundreds of permanent stations are already deployed at regional distances.

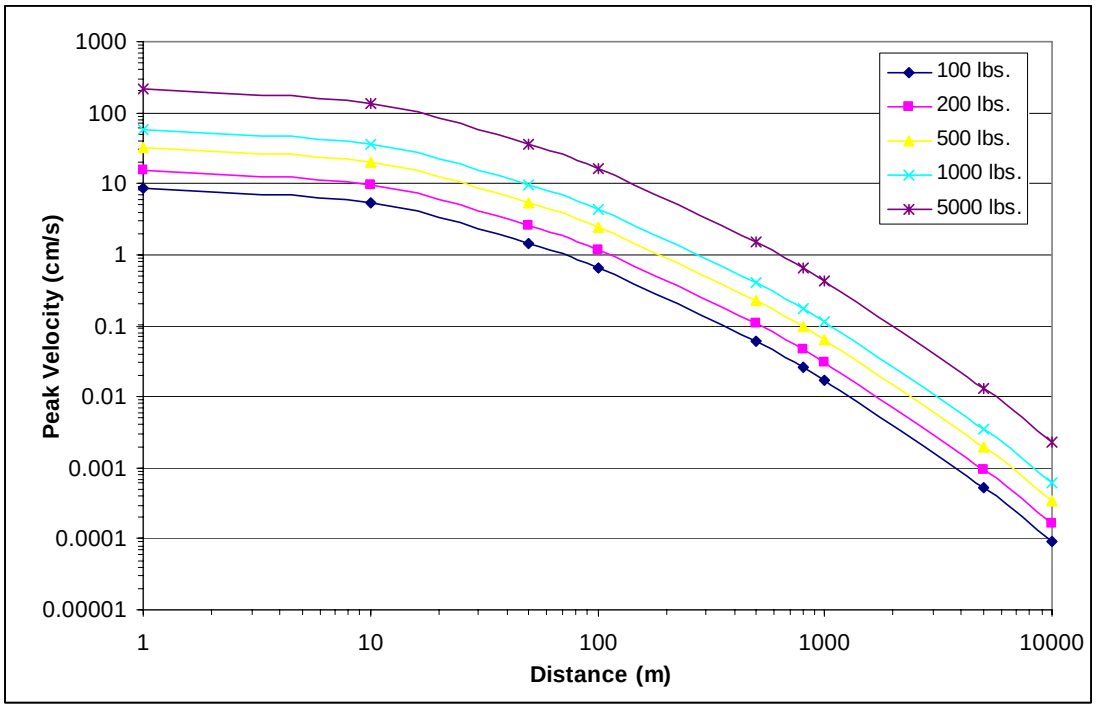

Figure 3. The peak velocities calculated for shots of various sizes using the Fuis et al. (2001) model.

Table 2. Corner Frequency as a Function of Shot Size

Shot Size (lbs.)	Corner Frequency (Hz)
100	91.7
200	72.8
500	53.6
1,000	42.6
5,000	24.9

Table 3. Instrument Distances for the FRE

Instrument	Distance Range
100 g accelerometer	< 20 m
25 g accelerometer	10 - 50 m
1 g accelerometer	> 100 m
Texan seismometer	1-12 km
Broadband seismometer	1-100 km

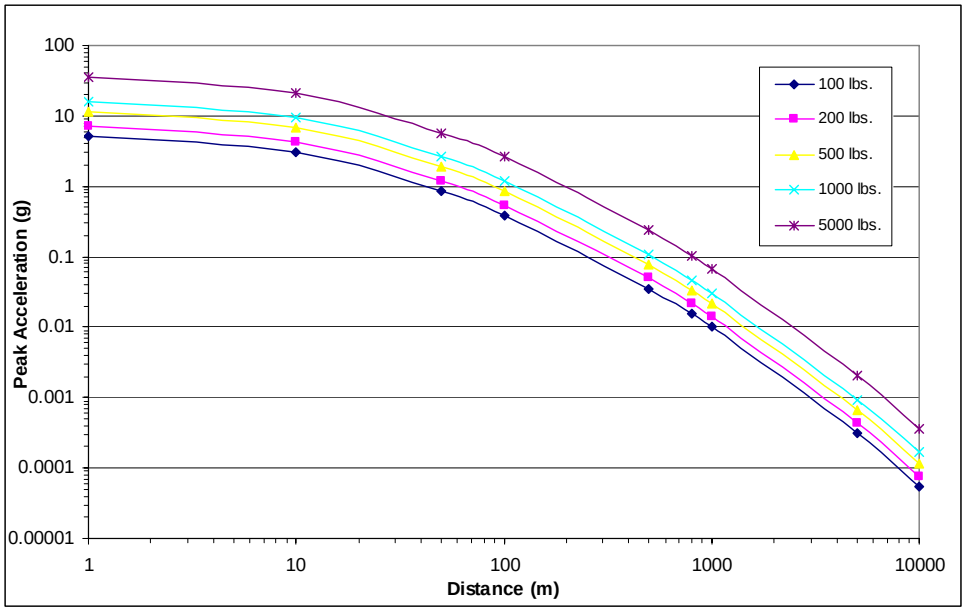

Figure 4. The peak accelerations calculated from the Fuis et al. (2001) model for a range of shot sizes.

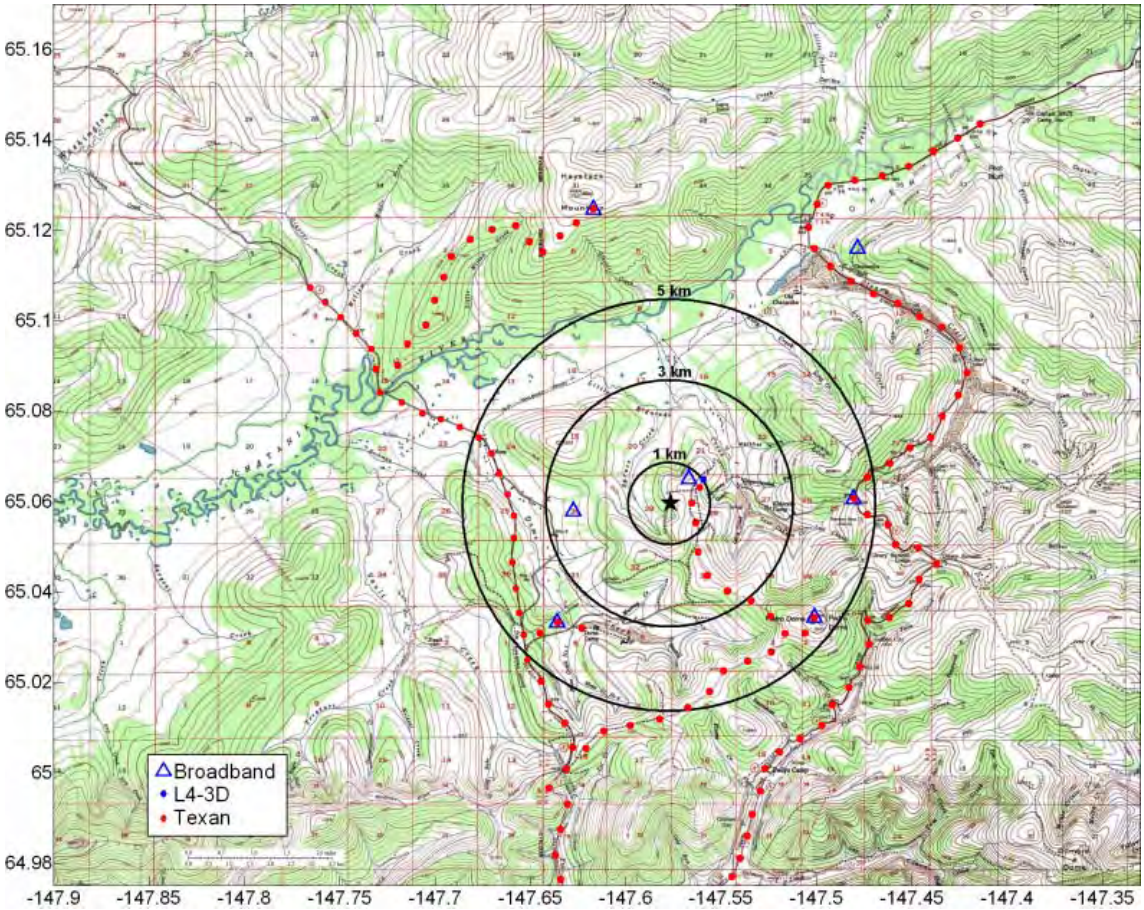

Figure 5. An example station deployment map showing how we could deploy seismometers.

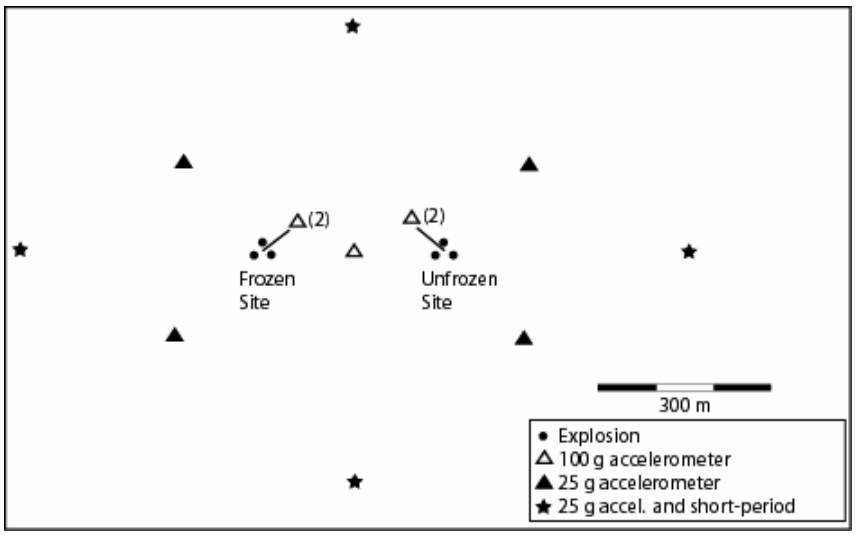

Figure 6. Near-source deployment of accelerometers and short-period instruments to adequately record both the frozen and unfrozen explosions without redeploying the stations in between tests.

CONCLUSIONS AND RECOMMENDATIONS

A series of single-fired explosions will be conducted in Alaska to advance the understanding of phenomenology and estimated yield differences from explosions in frozen and unfrozen rock. We may choose to conduct the experiments in the spring of 2006 so that the frozen rock will extend closer to the surface and be as cold as possible. Upon completion of the testing, our consortium will analyze videographic and seismic data to quantify the variations from near-source to regional distances.

REFERENCES

Ashby, M. F., S. and C. G. Sammis (1990), The damage mechanics of brittle solids in compression, *Pure appl. Geophys*, 133: 489–521.

Bonner, J. L., B. Stump, M. Leidig, R. Zhou, T. S. Kim, W. R. Walter, A. Velasco, C. Hayward, D. Baker, S. Harder, H. Hooper, T. Glenn, J. Britton, X. Yang, J. F. Lewkowicz, W. S. Blomberg, B. Greschke, S. Azevedo, and G. Gettamy (submitted March, 2005), Preliminary report on source phenomenology experiments in Arizona, *Seismological Research Letters*.

Fuis, G. S., J. M. Murphy, D. A. Okaya, R. W. Clayton, P. M. Davis, K. Thygesen, S. A. Baher, T. Ryberg, M. L. Benthien, G. Simila, J. T. Perron, A. K. Yong, L. Reusser, W. J. Lutter, G. Kaip, M. D. Fort, I. Asudeh, R. Sell, J. R. Vanschaack, E. E. Criley, R. Kaderabek, W. M. Kohler, and N. H. Magnuski (2001), Report for borehole explosion data acquired in the 1999 Los Angeles Region Seismic Experiment (LARSE II), Southern California: Part I, Description of the survey, United States Geological Survey Open-File Report 01-408.

Leidig, M. (2004), Frozen rock scaling study: Station deployment and shaking limits, Weston Geophysical Corp.

Mellor, M., (1971), Strength and deformability of rocks at low temperatures, Hanover, NH, Cold Regions Research and Engineering Laboratory (CRREL), U. S. Army Corps of Engineers, *Research Report 294*.

Sammis, C. and R. Biegel, (2004), Mechanics of strengthening in crystalline rock at low temperatures: a preliminary assessment, in *Proceedings of the 26th Seismic Research Review: Trends in Nuclear Explosion Monitoring*, LA-UR-04-5801, Vol. 1, pp. 475-484.

Stump, B. W. (2003), Near-source scaling estimated for the Morenci and Black Mesa single-fired experiments, Quarterly report no. 4 for Source Phenomenology Experiments, Contract no. DE-FC03-02SF22638/A000.

2-D PATH CORRECTIONS FOR LOCAL AND REGIONAL CODA WAVES: A TEST OF TRANSPORTABILITY

Kevin M. Mayeda[1], Luca Malagnini[2], W. Scott Phillips[3], William R. Walter[1], Douglas S. Dreger[4], and Paola Morasca[5]

Lawrence Livermore National Laboratory[1]; Istituto Nazionale di Geofisica e Vulcanolgia, Roma[2]; Los Alamos National Laboratory[3]; University of California, Berkeley[4]; and University of Genova[5]

Sponsored by National Nuclear Security Administration
Office of Nonproliferation Research and Engineering
Office of Defense Nuclear Nonproliferation

Contract Nos. W-7405-ENG-48[1] and W-7405-ENG-36[3]

ABSTRACT

Reliable estimates of the seismic source spectrum are necessary for accurate magnitude, yield, and energy estimation. In particular, how seismic radiated energy scales with increasing earthquake size has been the focus of recent debate within the community and has direct implications for earthquake source physics studies as well as hazard mitigation. The one-dimensional (1-D) coda methodology of Mayeda et al. (2003) has provided the lowest variance estimate of the source spectrum when compared against traditional approaches that use direct S-waves, thus making it ideal for networks that have sparse station distribution. The 1-D coda methodology has been confined mostly to regions of approximately uniform complexity. For larger, more geophysically complicated regions, two-dimensional (2-D) path corrections may be required. We will compare performance of 1-D versus 2-D path corrections in a variety of regions. First, the complicated tectonics of the northern California region coupled with high quality broadband seismic data provide for an ideal “apples-to-apples” test of 1-D and 2-D path assumptions on direct waves and their coda. Next, we will compare results for the Italian Alps using high frequency data from the University of Genova. For northern California, we used the same station and event distribution and compared 1-D and 2-D path corrections and observed the following results: (1) 1-D coda results reduced the amplitude variance relative to direct S-waves by roughly a factor of 8 (800%); (2) Applying a 2-D correction to the coda resulted in up to 40% variance reduction from the 1-D coda results; (3) 2-D direct S-wave results, though better than 1-D direct waves, were significantly worse than the 1-D coda. We found that coda-based moment-rate source spectra derived from the 2-D approach were essentially identical to those from the 1-D approach for frequencies less than ~0.7 Hz; however, for the high frequencies ($0.7 \le f \le 8.0$ Hz), the 2-D approach resulted in inter-station scatter that was generally 10-30% smaller. For complex regions where data are plentiful, a 2-D approach can significantly improve upon the simple 1-D assumption. In regions where only 1-D coda correction is available it is still preferable over 2-D direct wave-based measures.

OBJECTIVE

The motivation behind this study was to test the averaging nature of coda waves in a region that is laterally complicated. Recently the coda methodology of Mayeda et al. (2003) was applied to micro-earthquake data sets from two sub-regions of northern Italy (i.e., west Alps and northern Appenines). Since the study regions were small, ranging between local-to-near-regional distances, the simple 1-D path assumptions used in the coda methodology worked very well. However, the lateral complexity of this region would suggest that a 2-D path correction might provide even better results, especially when paths traverse larger distances and complicated regions. The structural heterogeneity of northern Italy makes the region an ideal test area to apply a 2-D Q tomography technique and test the transportability of the 2-D methodology of Phillips et al. (2003). We will compare our results with those derived from direct waves as well as some recent results from northern California.

RESEARCH ACCOMPLISHED

Coda waves are the scattered waves that follow the geometrical arrival, often referred to as the “direct waves.” The 1-D methodology of Mayeda et al. [2003] has been successfully applied in a variety of tectonic settings where the assumption of a radially symmetric path correction was sufficient (e.g., Eken et al., 2004; Morasca et al., 2005). In general, this resulted in inter-station amplitude scatter that was 3-to-4 times smaller than the traditional approach using direct S, Lg, and surface waves.

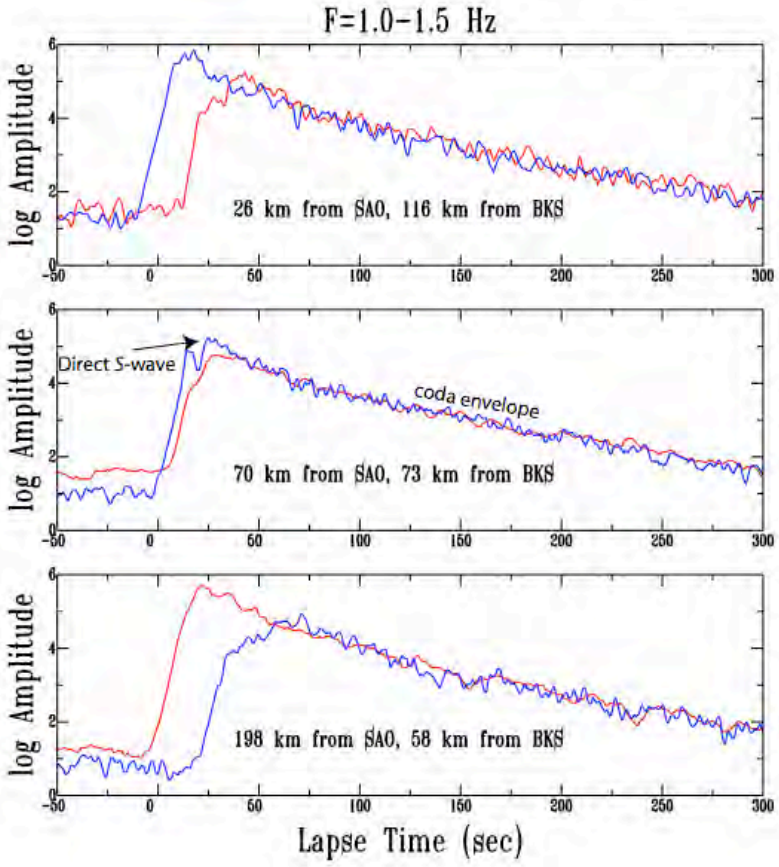

Figure 1. Example envelopes (*f*=1.0-1.5 Hz) for three events located in the San Francisco Bay region recorded at stations SAO (blue) and BKS (red), part of the Berkeley Digital Seismic Network (BDSN). At this range of distances, the scattered S-waves or "coda" is homogeneously distributed in the crust.

Figure 1 illustrates a unique property of coda waves that has been the basis of numerous studies over the past several decades, namely that the coda approaches a homogeneous distribution in space and time behind the expanding direct-wave front. In this example we show three panels of three events that are recorded at station BKS and another station, SAO, located ~140 km to the southeast. The three events were chosen such that one was relatively close to BKS, the other roughly in between, and the last event was close to SAO. In all panels we see that the coda envelope levels are approximately the same, independent of the source-station distance. This is in sharp contrast to the direct waves (S and L_g), which differ significantly in amplitude because of attenuation, geometrical spreading, and radiation pattern. Whether one believes in single or multiple scattering, isotropic or non-isotropic scattering, the observational evidence clearly shows that the crust tends to homogenize the coda energy at local-to-near-regional distances (e.g., Aki, 1969).

The previous example is in a region that is generally uniform, dominated by structures related to the coast ranges. In larger, more laterally complex regions there may be a need to extend the 1-D approach to account for 2-D variations

in structure, especially at frequencies above ~1 Hz. Phillips et al. (1998) showed that 2-D interpolated path corrections could reduce variance in regional direct phases and coda amplitudes, with the most dramatic effect on direct L_g. Recently, Phillips et al. (2003) have applied a 2-D amplitude ratio tomography to data in central Asia by assuming that the coda envelope amplitude could be idealized as if it were a direct wave, which is valid for the short segments of the early coda that they used. They performed a tomography to invert for 1/Q along the path, and through the choice of damping parameter and geometrical spreading, they in effect distributed the attenuation over an area, not unlike what has been previously assumed in the single-scattering model of Aki (1969) where the attenuation is attributed to an ellipsoidal volume.

Coda Measurements

The coda methodology is described in detail by Mayeda et al. (2003) so we give only a short, qualitative review here. The coda method is based upon narrowband amplitude measurements taken simultaneously from the envelope ranging from several tens of seconds up to hours depending on the frequency band and event magnitude (e.g., Mayeda and Walter, 1996). A coda envelope amplitude measurement significantly reduces the variance associated with 3-D path heterogeneity, random interference, and source heterogeneity, all of which more strongly affects the direct waves.

To form the envelopes, the horizontal velocity waveforms for each event were narrow bandpassed for 13 frequency bands ranging between 0.03 and 8.0 Hz. Envelopes were formed for each component, $\log_{10}$ averaged for additional stability then smoothed. The coda envelopes for each frequency band can be idealized with the following equation,

$$A_c(f,t,r) = W_o(f)\cdot S(f)\cdot T(f)\cdot P(r,f)\cdot H(t-t_s)\cdot(t-t_s)^{-\gamma(r)}\exp\left[-b(r)\cdot(t-t_s)\right] \quad , \qquad (1)$$

where f is the center frequency, r is the epicentral distance in kilometers, t is the time in seconds from the origin time, t_s is the S-wave travel time in seconds, W_o represents the S-wave source, S is the site effect, T represents the S-to-coda transfer function effect, P includes the distant-dependent effects of geometrical spreading and attenuation, H is the Heaviside step function, $\gamma(r)$ and $b(r)$ are the distance-dependent coda shape factors that control the coda envelope shape. For simplicity, we have set $\gamma = 0.2$ noting that this parameter only controls the early part of the coda immediately following the direct arrival which is more influenced by source radiation pattern. Since we are fitting the coda over large amounts of time, the exponential term $b(r)$ is the most important parameter as it controls the majority of the coda envelope shape. However for the purpose of generating synthetics we set W, S, T, and P to unity. The coda shape parameters and velocity of the peak S/L_g-wave arrival were fit as a function of distance using the form of a hyperbola,

$$\left[\text{e.g., } b(r) = b_0 - \frac{b_1}{b_2 + r}\right] \quad . \qquad (2)$$

1-D Coda

The empirical 1-D path correction for coda has the property of being roughly constant up to a certain critical distance then falls off with increasing distance. This phenomenon has been observed with local and regional data (e.g., Figure 1) where the path term P in Equation 1 can be written as

$$P(r,f) = \left[1 + \left(\frac{r}{p_2}\right)^{p_1}\right]^{-1} \quad , \qquad (3)$$

where p_1 controls the amplitude decay beyond the critical distance p_2. We used common recordings using 6 station pairs that sample the region and then grid searched over p_1 and p_2 and tabulated the interstation scatter for each frequency band. The choice of frequency-dependent path correction for the entire region was based upon the path parameters p_1 and p_2 that gave the lowest average interstation standard deviation between our 6 station pairs.

1-D Direct Waves

For every coda amplitude that was measured we also measured the corresponding peak envelope amplitude of the direct wave (e.g., S, L_g or surface waves). As done previously with the coda, we applied a grid search using the direct wave amplitudes to estimate the best value of Q. Through numerical simulation Yang (2002) showed that regional, peak envelope amplitudes decay roughly as 1/*r* so we have adopted the following formulation where the direct wave amplitude at distance *r* and frequency *f* is,

$$A(r,f) = A_0 \cdot S(f) \cdot \frac{1}{r} \cdot e^{-\left[\frac{\pi f}{\beta Q_\beta}\right]} \quad , \tag{4}$$

where A_0 is the source term, S is the site effect, β is the S-wave velocity (set to 3.5 km/sec), and Q_β is the S-wave quality factor. We then solved for the best value of Q that minimized the scatter between the same 6 station pairs that were used for the coda path corrections. The averaged S-wave Q follows the form, $Q(f) = 129\, f^{0.57}$ for frequencies between 0.3 and 8.0 Hz.

2-D Corrections

For testing 2-D attenuation we elected to use amplitude ratios taken between two or more stations that recorded the same event. This avoids solving for or applying initial estimates of source terms, which results in much higher resolution images and lowers residual variance. This is simply the tomographic extension of popular methods such as the reversed two-station method (e.g., Chun et al., 1987) or the station-pair-event-pair method (e.g., Shih et al., 1994; Fan and Lay, 2003), both used to obtain a single *Q* for a sampled region. We must assume that the source radiates isotropically, which is generally true for L_g and coda, and thus, allows cancellation of source terms for rays that take off along different azimuths. We apply the following amplitude ratio formulation:

$$A_{ij} - \langle A_{ij} \rangle_j = S_i - \langle S_j \rangle_j + (\mathrm{P}_k\, dx_{ijk}\, a_k - \langle \mathrm{P}_k\, dx_{ijk}\, a_k \rangle_j) \log_{10}(e) \quad , \tag{5}$$

where *A* represents $\log_{10}$ amplitude after correction for assumed 1/*r* spreading, *i, j, k,* indices represent site, source and path discretization, respectively, *S* represents $\log_{10}$ site terms, the *dx* are path lengths through a discretized region of the Earth, *a* is the discretized attenuation coefficient ($a_k = \omega/2Q_k c$) and the P_k represent ray path sums. The $\langle\rangle_j$ represent averages taken over all ray paths or sites associated with event *j*. The equation is obtained from (4) taking the average for event *j*, then removing the average. The source term becomes source minus the average source for event *j*, which is taken to be zero. Implementation requires sources recorded at multiple stations, as an event recorded at a single station will result in a null equation. This is a standard technique for removing source effects from an inverse problem (e.g., Aki and Richards, 1980). The equation is linear and can be solved easily using sparse matrix methods. We apply first-difference regularization (smoothness constraints) to the attenuation model and require that the site terms sum to zero to account for the non-uniqueness associated with the relative nature of the problem.

We used the same data set as in the 1-D case and assumed a cell dimension of 0.1 degree. First of all, we found that the coda results loosely followed the direct wave results in that the Q's in the coast ranges were low relative to the Sierra Nevada region (Figure 2). The main difference was that the coda results rarely varied by more than a factor of 2 across the region, whereas the direct waves varied by upwards of 4-to-5 times. As expected, the direct wave Q's were more sharply defined than the coda results which is likely the result of the natural smoothing of coda waves.

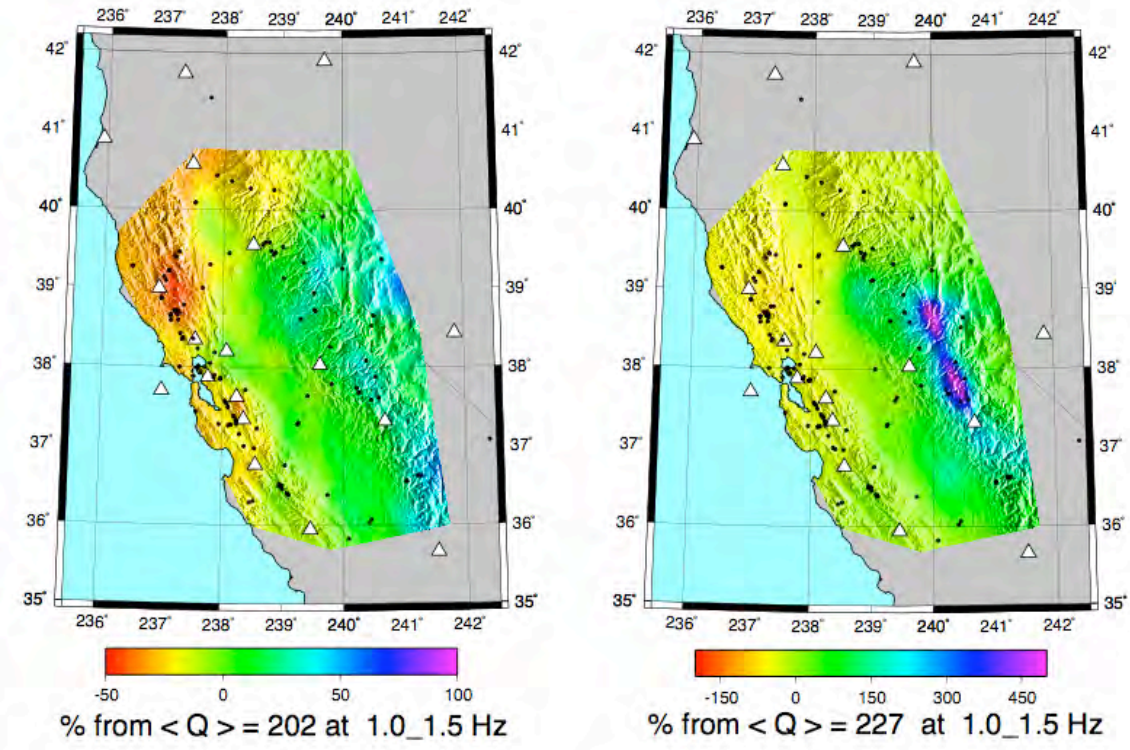

Figure 2. (a) For the 1.0–1.5 Hz case we observe coda attenuation is highest near the coast ranges and low in the Sierra Nevada region. (b) Same as in Fig. 2a except for the direct wave case. Triangles represent broadband stations and solid black circles are events used in the study. The colored portion of the map was determined by a 1-degree checkerboard test and delineates the region where we have good resolution.

COMPARISONS

We compared distance-corrected amplitudes at multiple pairs of stations to assess the performance of the four different approaches. In general, the average interstation standard deviation for the 1-D coda slowly increases from ~0.08 at 0.05–0.1 Hz to ~0.22 at 6–8 Hz whereas the scatter for 1-D direct waves resulted in an average interstation scatter that is generally a factor of 2-to-3 larger, or roughly 800% larger in variance (Figure 3). The 2-D coda results were roughly 2 times lower in scatter than 2-D direct *S*-wave results, and surprisingly the 2-D direct wave results were still much worse than the 1-D coda results. Finally, the 2-D coda results did improve the scatter relative to the 1-D case, reducing the variance by roughly 40%.

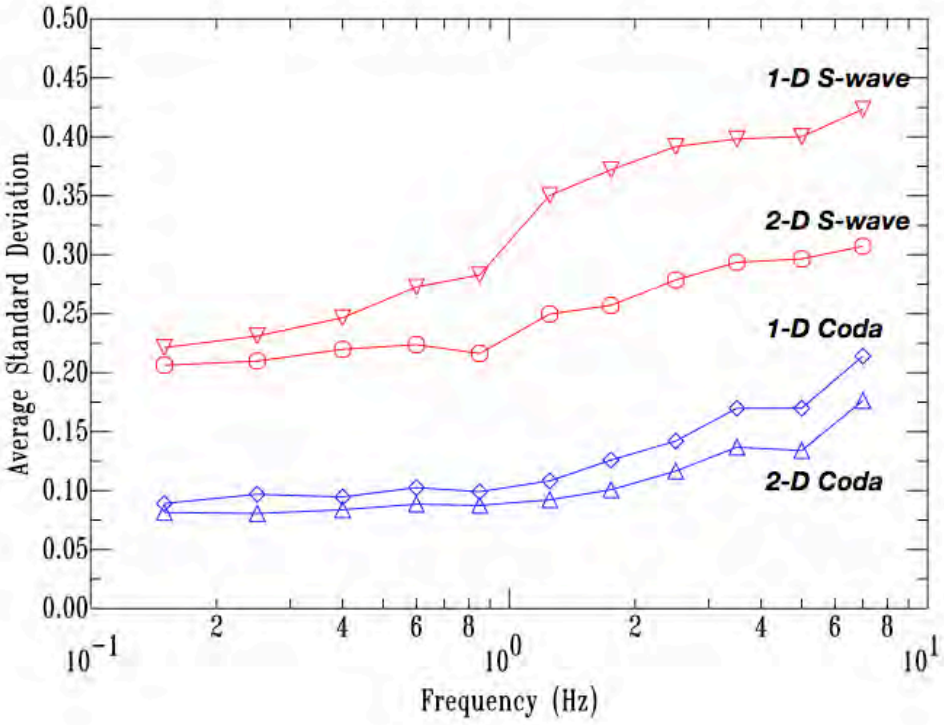

Figure 3. Averaged interstation standard deviation using 45 station pairs as a function of frequency. We see that 1-D coda are significantly less scattered than either of the direct S-wave results.

Although the coda amplitudes are corrected for frequency-dependent path effects, they still carry the S-to-coda transfer function as well as site effects that must be removed in order to obtain a moment-rate spectrum that has absolute units (e.g., dyne-cm). Again we refer the reader to Mayeda et al. (2003) for the calibration details. As found in other regions, coda-derived M_W's from a single station were in excellent agreement with the network-averaged values. We also applied a similar transformation to remove the site effect for the direct waves and their averaged M_W's were also in good agreement. Figure 4 summarizes results of all four methods using the M_W 5.0 Napa earthquake of September 3, 2000, as an example. Though more scattered, the average of the direct wave spectra is very similar to the individual coda spectra, thus proving the point that a single-station coda spectra is equivalent to a network average using direct waves. The stability of the coda-derived spectra is remarkable considering they are derived from different azimuths and distances, mixing local S-wave, regional L_g, and surface wave codas.

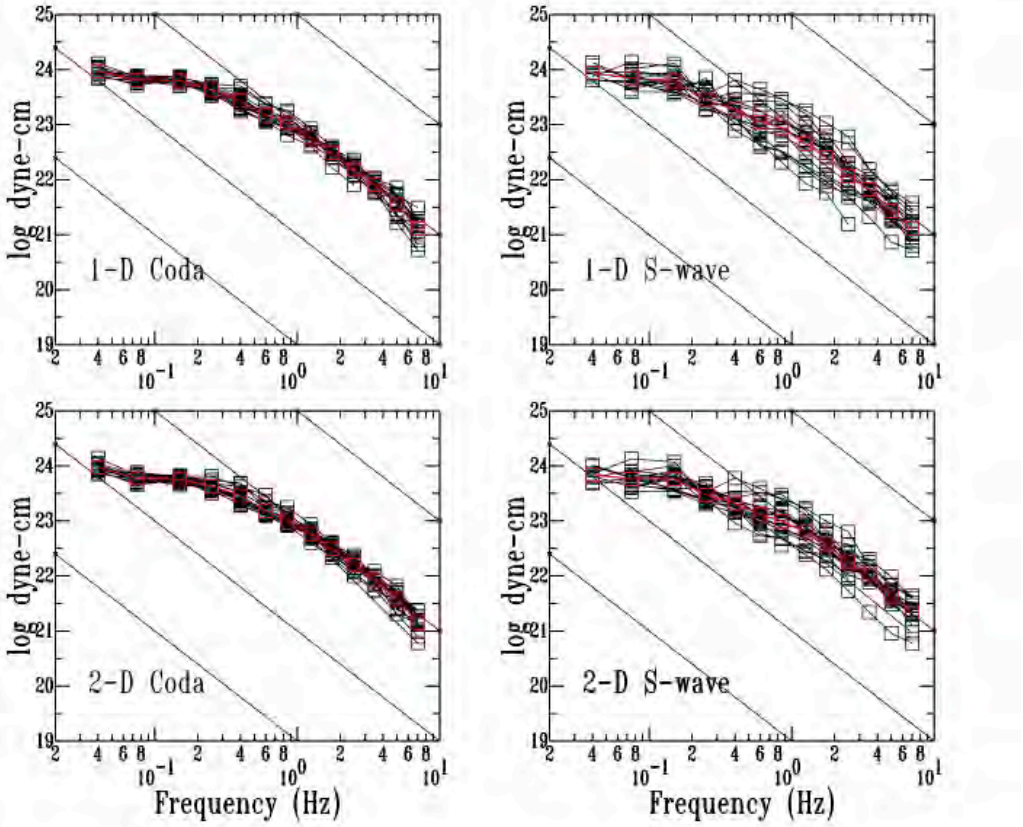

Figure 4. Moment-rate spectra for the M_W 5.0 Napa earthquake of September 3, 2000. Black lines represent individual station spectra and red lines represent the average. Stations are situated at a variety of azimuths and range between a few 10's of kilometers to over 400 kilometers.

In addition to stable single station estimates of M_W, the coda spectra shown in Figure 4 can also be used to obtain reliable estimates of the radiated energy (E_R) (e.g., Mayeda and Walter, 1996; Mayeda et al., 2005). Ide and Beroza (2001) reviewed a number of scaled energy $\tilde{e}$ ($=E_R/M_0$) studies from around the world and concluded that the large scatter did not support $\tilde{e}$ changing as a function of increasing M_0. We found dramatic regional differences in $\tilde{e}$ for events with the same M_W. For example, events in and around the Geysers have anomalously low corner frequencies and low $\tilde{e}$ in sharp contrast to events in the Gilroy and Sierra Nevada regions which have much larger corner frequencies and larger high frequency amplitudes. This finding could not be explained by low Q in the Geysers region and points to a difference in rupture dynamics for these events. This illustrates the potential problem of combining $\tilde{e}$ for events over a broad region because the scatter of $\tilde{e}$ could make resolving scaling variations impossible. Instead, it may be more prudent to look for scaling in earthquake sequences or smaller geographical regions to avoid undo scatter (e.g., Mayeda et al., 2005).

Transportability to Northern Italy

To test the transportability of the method, we selected the same events and stations for both coda and direct S-waves in northern Italy (see Figure 5). We compared direct and coda waves using 1-D and 2-D attenuation corrections showing that the 2-D method provides more stable results than the 1-D approach for the same phase. However, when we compare direct and coda waves, we notice that the simple 1-D attenuation corrections applied to coda measurements result in more stable source spectra than those obtained using the 2-D parameters applied to direct waves. The same trend is observed for northern California, although the standard deviations are slightly larger than those in Italy for the frequency range 0.7–8.0 Hz. Moreover, we obtain a lower Q for the coda when we correct

using the 2-D attenuation. Since the study area is quite small because of the data and station distribution, for the future we will add more events and stations from other networks to enlarge the study area and better understand the relation between attenuation and geological structures.

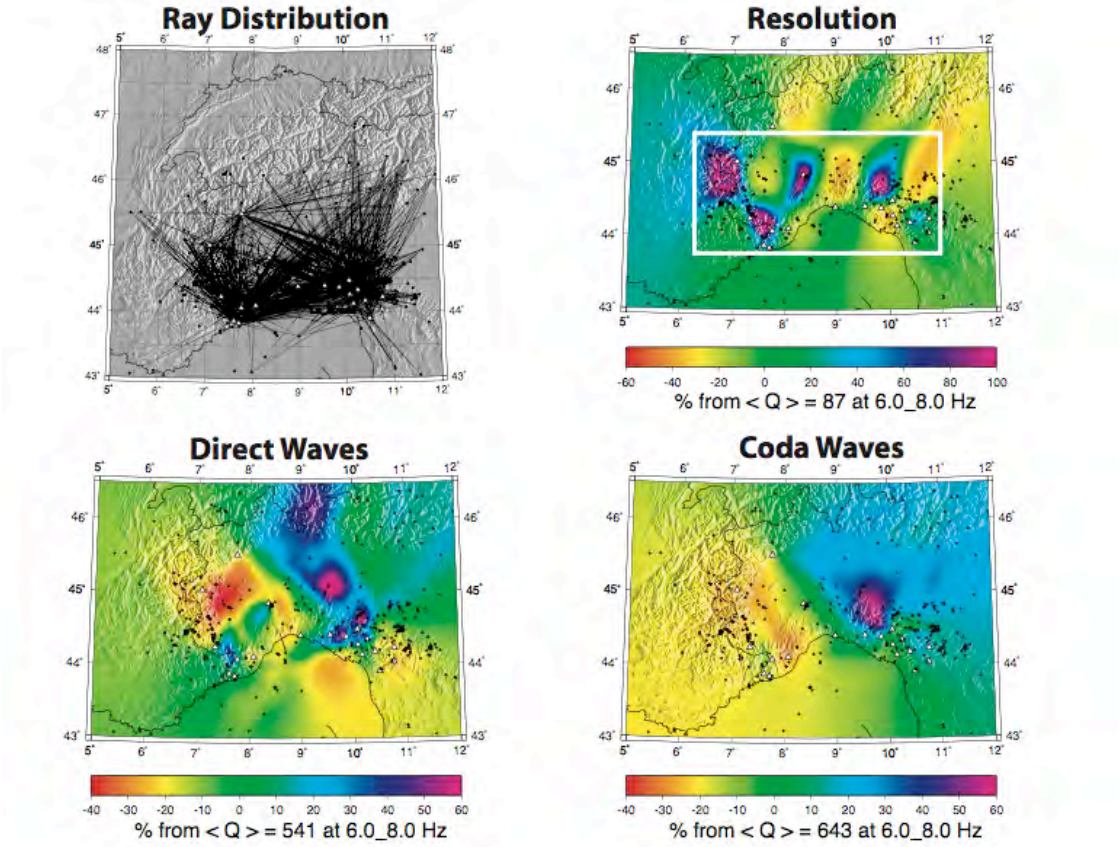

Figure 5. (a) Path map showing event and station distribution of the case of 6–8 Hz in northern Italy. (b) Result of checkerboard test using cells of 0.75 degree by 0.75 degree. White rectangle shows the region for which we believe we have good resolution. (c) The 2-D inversion results for direct waves show finer scale features. (d) Results for coda waves are smoother than those in Figure 5c but result in much lower inter-station variance, similar to California.

CONCLUSIONS AND RECOMMENDATIONS

We showed that the 2-D coda tomography methodology of Phillips et al. (2003) worked well for both northern California and northern Italy. The purpose of this study was not to exhaustively calibrate both regions for 2-D attenuation. Our goal was to perform an "apples-to-apples" test of 1-D versus 2-D path corrections using the same event and station distribution. We wanted to test the extent to which 2-D path corrections for direct waves and coda waves improved upon simple 1-D assumptions. We found that in spite of the complex structure of the region, 1-D coda results performed very well. Though additional variance reduction was obtained when we applied 2-D path corrections to the coda (~40%), these were relatively minor and come at the expense of adding ~15 degrees of freedom. Comparing direct S-wave results, we found significant variance reduction for 2-D versus 1-D results, by as much as 200% at frequencies above 1 Hz. In spite of many more degrees of freedom, the 2-D direct wave results still performed significantly worse than the simple 1-D coda. The 2-D approach for coda may be more useful in the case when there are longer path lengths and/or more significant lateral changes in crustal structure and thickness. For the northern California region however, 1-D results were perfectly adequate to derive stable source spectra and related parameters for coda.

The calibration resulted in excellent agreement with the Berkeley Seismological Laboratory's (BSL) long-period waveform-based moment magnitude estimates (~3.5< M_w <6.5). Coda-based moments have the advantages that M_w's can be measured reliably with as few as one station and for events that are too small to be waveform modeled. This last point is important because it extends the BSL's capability of computing M_w for events in the M_w 2 range throughout the footprint of the BDSN. We demonstrate in this study that the simple assumptions of frequency-dependent, 1-D path corrections are perfectly adequate for on-shore events in the northern California region.

ACKNOWLEDGEMENTS

L. Malagnini was partially funded by the Ministero dell'Universita' e della Ricerca Scientifica, MIUR, under project FIRB, Prot. RBAU013NRZ.

REFERENCES

Aki, K. (1969), Analysis of Seismic Coda of Local Earthquakes as Scattered Waves, *J. Geophys. Res*. 74: 615–631.

Aki, K., and P.G. Richards (1980), *Quantitative Seismology*, W. H. Freeman, San Francisco.

Chun, K.-Y., G. F. West, R. J. Kokoski, and C. Samson (1987), A Novel Technique for Measuring Lg Attenuation: Results from Eastern Canada between 1 to 10 Hz, *Bull. Seism. Soc. Am*. 77: 398–419.

Eken, T., K. Mayeda, A. Hofstetter, R. Gök, G. Örgülü, and N. Turkelli (2004), An application of the coda methodology for moment-rate spectra using broadband stations in Turkey, *Geophys. Res. Lett*. 31: 11, L11609.

Fan, G. W. and T. Lay (2003), Strong Lg Wave Attenuation in the Northern and Eastern Tibetan Plateau Measured by a Two-Station/Two-Event Stacking Method, *Geophys. Res. Lett.* 30: 1530.

Ide, S and G. C. Beroza (2001), Does Apparent Stress Vary with Earthquake Size? *Geophys. Res. Lett.* 28: 3349–3352.

Mayeda, K., R. Gök, W. R. Walter, and A. Hofstetter (2005), Evidence for Non-Constant Energy/Moment Scaling from Coda-Derived Source Spectra, *Geophys. Res. Lett.* Doi:10.1029/2005GL022405.

Mayeda, K., A. Hofstetter, J. L., O'Boyle, and W. R. Walter (2003), Stable and Transportable Regional Magnitudes Based on Coda-Derived Moment-Rate Spectra. *Bull. Seismol. Soc. Am.* 93: 224–239.

Mayeda, K. and W. R. Walter (1996), Moment, Energy, Stress Erop, and Source Spectra of Western United States Earthquakes from Regional Coda Envelopes. *J. Geophys. Res.* 101: 11, 195–208.

Morasca, P., K. Mayeda, L. Malagnini, and W. R. Walter (2005), Coda-Derived Source Spectra, Moment Magnitudes, and Energy-Moment Scaling in the Western Alps, *Geophys. J. Int.* 160: 263–275.

Phillips, W. S., G. E. Randall, and S. R. Taylor (1998), Regional Phase Path Effects in Central China, *Geophys. Res. Lett.* 25: 2729–2732.

Phillips, W. S., H. J. Patton, C. M. Aprea, H. E. Hartse, G. E. Randall, and S. R. Taylor (2003), Automated Broad Area Calibration for Coda Based Magnitude and Yield, in *Proceedings of the 25th Seismic Research Review—Nuclear Explosion Monitoring: Building the Knowledge Base*, LA-UR-03-6029, 1: pp. 437–444.

Shih, X. R., K.-Y. Chun, and T. Zhu (1994), Attenuation of 1–6 s Lg Waves in Eurasia, *J. Geophys. Res.* 99: 23859–23874.

Yang, X. (2002), A numerical investigation of Lg geometrical spreading, *Bull. Seismol. Soc. Am.,* 92, 3067–3079.

A SCALING ANALYSIS OF FREQUENCY DEPENDENT ENERGY PARTITION FOR LOCAL AND REGIONAL SEISMIC PHASES FROM EXPLOSIONS

John R. Murphy[1], Brian W. Barker[1], and Jamil Sultanov[2]

Science Applications International Corporation[1] and Institute for Dynamics of the Geospheres[2]

Sponsored by Air Force Research Laboratory

Contract No: FA8718-04-C-0030

ABSTRACT

It has long been recognized that seismic identification of underground nuclear tests with $m_b < 4$ will have to be based largely on discriminants which are effective in the regional distance range. Research conducted over the past 20 years has demonstrated that the most reliable of the regional discriminants considered to date are those based on high-frequency spectral ratios of the amplitudes of the seismic shear phases Sn and Lg to those of the corresponding direct P phases Pn and Pg. While much observational evidence supporting the general applicability of these regional discriminants has now been accumulated, a problem remains in that there is currently no deterministic model of shear wave generation by explosions which has been shown to be quantitatively consistent with the wide range of Sn and Lg observations from explosion sources. Consequently, extrapolation of these discrimination criteria to previously untested locations and source conditions is still subject to considerable uncertainty. The technical objectives of this research program are to determine frequency dependent source scaling relations for the regional phases Pn, Pg, Sn and Lg through statistical analyses of data recorded from underground explosions at the Semipalatinsk, Novaya Zemlya, Lop Nor and Nevada Test Site (NTS) nuclear test sites, and to apply these derived scaling relations to a quantitative evaluation of the plausibility of various proposed physical source mechanisms for the regional shear phases Sn and Lg observed from underground explosion sources.

During the first year of this program, the study effort has been focusing on analyses of regional seismic data recorded from explosions at the Degelen Mountain and Balapan testing areas of the Semipalatinsk test site. For this purpose, digital data recorded at the Borovoye Geophysical Observatory in North Kazakhstan from selected Semipalatinsk explosions is being supplemented by parametric data collected from over 20 stations of the former Soviet Union's permanent seismic network to better constrain the relative source excitation levels of the various regional seismic phases. Data from an initial sample of 23 Degelen explosions of known yield and depth of burial have now been compiled and analyzed. The yield range of these explosions extends from about 1 to 100 kt, and thus provides a good basis for quantitatively evaluating the frequency-dependent source scaling of the regional P and S wave data recorded from these explosions. Digital data recorded from these explosions at the Borovoye station have been carefully previewed by an experienced analyst and systematically edited to remove the numerous spikes and data dropouts which could contaminate any quantitative spectral analyses. These broadband Borovoye data, recorded at a range of about 650 km, show strong short-period Sn and Lg arrivals relative to the corresponding initial P phases. Spectral analyses of these data indicate large Lg/Pn ratios out to about 3 Hz, above which the Lg spectral amplitude level decreases quite rapidly to the P coda level at about 5 Hz. The observed Sn spectral amplitude levels are also greater than those of P out to about 3 Hz but decrease less rapidly than those of Lg at higher frequencies, showing spectral amplitude levels above the P coda level out to 10 Hz. The Sn/Pn and Lg/Pn spectral ratios corresponding to this sample of Degelen explosions have been statistically analyzed to derive yield scaling exponents as a function of frequency. Both of these regional phase spectral ratios show some modest yield dependence in the 1-3 Hz band but no statistically significant yield dependence at the higher frequencies used for discrimination. These observations place strong constraints on the possible S wave source generation mechanisms for these explosions. Regional phase peak amplitude data measured from recordings at some 22 Soviet network stations from Degelen explosions have also been statistically analyzed to test for any significant azimuthal dependence of the corresponding Sn/Pn and Lg/Pn peak amplitude ratios. No statistically significant azimuthal dependence has been found for either of these regional phase amplitude ratios, which provides another important constraint on the range of plausible mechanisms of S wave generation from these explosions. These source scaling analyses are currently being extended to encompass data from a representative sample of Balapan explosions in an attempt to better constrain the regional S-wave generation mechanisms for Semipalatinsk explosions.

OBJECTIVES

The technical objectives of this research program are to determine frequency dependent source scaling relations for the regional phases Pn, Pg, Sn, and Lg through statistical analyses of data recorded from underground explosions at the Semipalatinsk, Novaya Zemlya, Lop Nor, and Nevada Test Site (NTS) nuclear test sites, and to apply these derived scaling relations to a quantitative evaluation of the plausibility of various proposed physical source mechanisms for the regional shear phases Sn and Lg observed from underground explosion sources. The ultimate objective is to improve U.S. operational monitoring capability by providing a quantitative framework which can be used for confidently evaluating expected regional event discrimination performance as a function of the ranges of explosion source size and emplacement conditions which must be considered in global nuclear monitoring.

RESEARCH ACCOMPLISHED

A number of focused research studies have been conducted in recent years in attempts to better define the source of the S-waves observed from underground nuclear explosions, particularly as they relate to the generation of the Lg regional phase which has come to play a central role in the identification and yield estimation of small explosions. In early studies of the seismic waves generated by underground nuclear explosions, it was generally assumed that the observed S-waves were produced by linear conversion of the primary explosion P-waves by the layered geology in the source region and along the propagation path between the source and the receiver. However, it was soon recognized that relatively strong S arrivals were also observed on the transverse components of motion at regional distances and this necessitated the addition of a nonisotropic scattering mechanism to the simple linear conversion model. Subsequent deterministic simulations of the Lg phases produced by point source explosions in planar multilayered approximations of the crustal waveguide raised further questions regarding the plausibility of the linear P to S conversion mechanism in that isotropic explosions in high velocity source media such as granite were predicted to generate very little Lg energy (Jih and McLaughlin, 1988).

These inconsistencies prompted intensive searches for alternate sources of Lg which generally focused on either scattering of the Rg phase induced by the isotropic explosion into Lg (e.g., Gupta et al., 1991, 1997) or on direct generation of S and Rg waves by the non-isotropic components of the explosion source associated with spall and other nonlinear interactions of the primary explosion source with the overlying geology and free surface (e.g., Stevens et al., 1991, 2003). Although significant theoretical and observational evidence has been marshalled to support the plausibility of both of these hypothetical sources of Lg, problems remain in that neither seems completely consistent with the wide range of Lg observational data which is currently available (Stevens et al., 2003). For example, it has been observed that Lg amplitude level correlates remarkably well with the known yields of underground explosions over broad source regions, and this fact seems difficult to reconcile with the Rg-scattering hypothesis. Moreover, both of these proposed sources would predict a pronounced dependence of Lg excitation on source depth, and this seems inconsistent with the results of Nuttli (1986) and others who have obtained reliable Lg-based yield estimates for very deep explosions, including the U.S. Peaceful Nuclear Explosion (PNE) RULISON which was detonated at a scaled depth more than six times larger than the nominal NTS containment depth. It follows that additional research is needed to identify potential sources of explosion S and Lg phases which satisfy all available constraints.

One potentially powerful constraint on the source of S-waves from explosions is provided by their frequency-dependent scaling as a function of explosion yield, depth of burial and source medium, relative to the well-documented scaling of the associated direct P-wave phases. That is, since it is well established that the scaling of the direct P-waves observed from explosions can be explained to first order by a simple isotropic source model (Mueller and Murphy, 1971), the degree to which the scaling of secondary regional phases such as Sn and Lg is similar to that of the corresponding Pn phases provides direct evidence of any significant departures from the isotropic source model. Thus, while a scaling analysis in itself will not specifically identify a physical mechanism for Lg generation, it will nonetheless provide powerful quantitative constraints which would have to be met by any proposed source mechanism.

One example of this approach was provided by Murphy et al. (2001), who analyzed the source scaling characteristics of regional phase data recorded at the Borovoye Geophysical Observatory in North Kazakhstan from a sample of 21 Soviet PNE events of known yield and depth of burial. On the basis of prior experience (e.g., Mueller

and Murphy, 1971), it was assumed that the explosion seismic source, $S(\omega)$, could be approximated as a product of the form

$$S(\omega) \sim W^{n(\omega)} h^{m(\omega)} \qquad 1$$

where W and h are the explosion yield and depth of burial, respectively, and $n(\omega)$, $m(\omega)$ are the associated frequency-dependent scaling exponents. The source scaling exponents estimated from a covariance statistical analysis of the observed Borovoye PNE regional phase spectral amplitude data are displayed as a function of frequency in Figure 1 for Pn and the four secondary regional phases P_{coda}, Pg, Sn and Lg. It can be seen from this figure that the source scaling exponents for all these regional phases are fairly similar over the frequency band from 0.5 to 5.0 Hz, particularly for the yield-scaling exponents. The depth scaling exponents do however show some consistent differences between phases (e.g., Lg versus Pn) over significant portions of this frequency range which could be indicative of differences in source mechanism. Unfortunately, Murphy et al. (2001) concluded that the formal uncertainty in these derived scaling exponents is too large to be able to conclude with high confidence whether these inferred depth scaling differences are statistically significant. This lack of resolving power is at least partially due to the fact that these PNE events were widely dispersed throughout the territories of the former Soviet Union and, consequently, propagation path variability made it difficult to estimate the source scaling exponents with high accuracy. In the present program we are minimizing such propagation path variability by analyzing data recorded at specific stations from multiple explosions at fixed nuclear weapons test sites. This should allow us to more precisely define any consistent differences in the source scaling of the various regional phases, which, in turn, will provide much improved quantitative constraints on proposed source mechanisms for the secondary regional shear phases Sn and Lg.

The initial focus of this study has been on the analysis of broadband digital data recorded at the Borovoye station from underground nuclear explosions of know yield and depth of burial which were conducted at the Degelen Mountain area of the former Soviet Semipalatinsk test site. The vertical component data recorded at this station from 20 such Degelen explosions are plotted as a function of apparent group velocity, in order of increasing yield, in

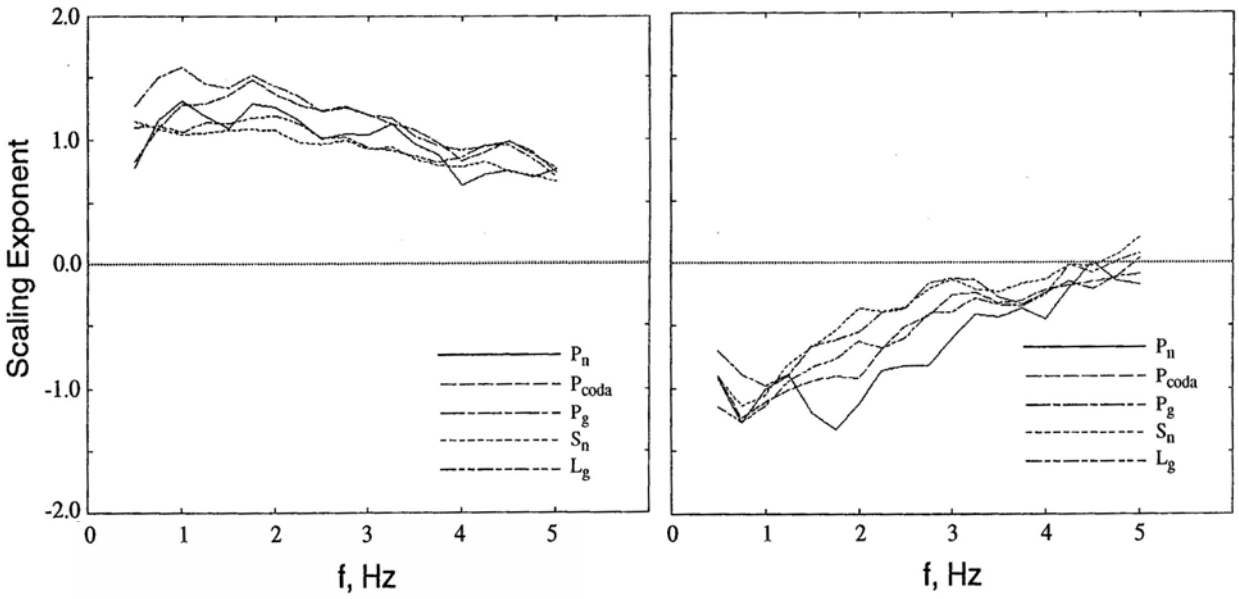

Figure 1. Comparison of yield (left) and depth (right) frequency-dependent scaling exponents determined for the different regional phases recorded at Borovoye from the selected Soviet PNE events.

Figure 2. It can be seen that this sample of explosions encompasses a range of yields extending from 1.1 to 78 kt. Moreover, these data, recorded at a distance of about 650 km, show evidence of strong short-period Sn and Lg relative to the corresponding Pn phases. These digital data have been carefully previewed by an experienced analyst and systematically edited to remove the numerous spikes and data dropouts which could contaminate any subsequent quantitative spectral analyses.

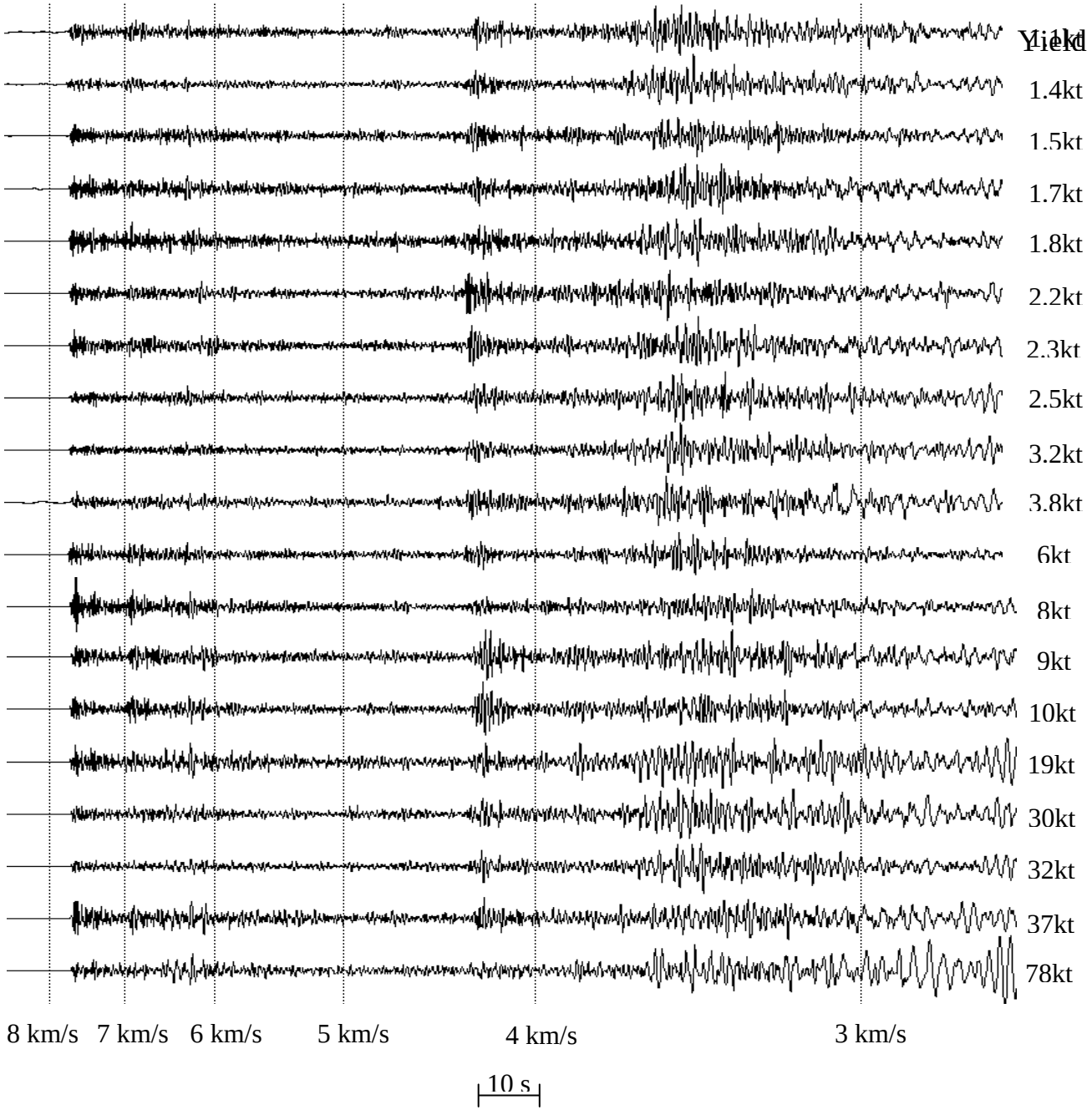

Figure 2. Vertical component digital data recorded at the Borovoye Station ($\Delta \approx 650$ km) from a sample of Degelen Mountain nuclear explosions of known yield and depth of burial. The data are plotted as a function of apparent group velocity and in order of increasing yield.

The Borovoye data of Figure 2 have been processed to obtain estimates of the different regional phase spectra for each event. In the first step of this processing, the data for each explosion were bandpass filtered using a Gaussian comb of filters spaced at intervals of 0.25 Hz between 0.5 and 10 Hz, where each filter is characterized by a Q value of $6f_c$, with f_c the filter center frequency. Filters of this type have been used by us (Murphy et al., 2001) and a number of other investigators in previous studies and have been found to provide spectral estimates which are useful for purposes of seismic analyses. Figure 3 shows an example of filter outputs encompassing this frequency range for the 1.8 kt Degelen Mountain explosion of October 4, 1989, where the selected time windows for the Pn, Sn and Lg regional phases are indicated. It can be seen that these data indicate large Lg/Pn ratios out to about 2 Hz, above which the Lg spectral amplitude level decreases quite rapidly to the P coda level at about 5 Hz. The observed Sn spectral amplitude levels are also greater than those of Pn out to about 3 Hz but decrease less rapidly than those of Lg at higher frequencies, showing spectral amplitude levels above the P coda levels out to 10 Hz. For purposes of the source scaling analysis, the spectral amplitude levels at each filter center frequency were estimated by computing RMS values from the instrument corrected filter outputs in each of the designated regional phase time windows.

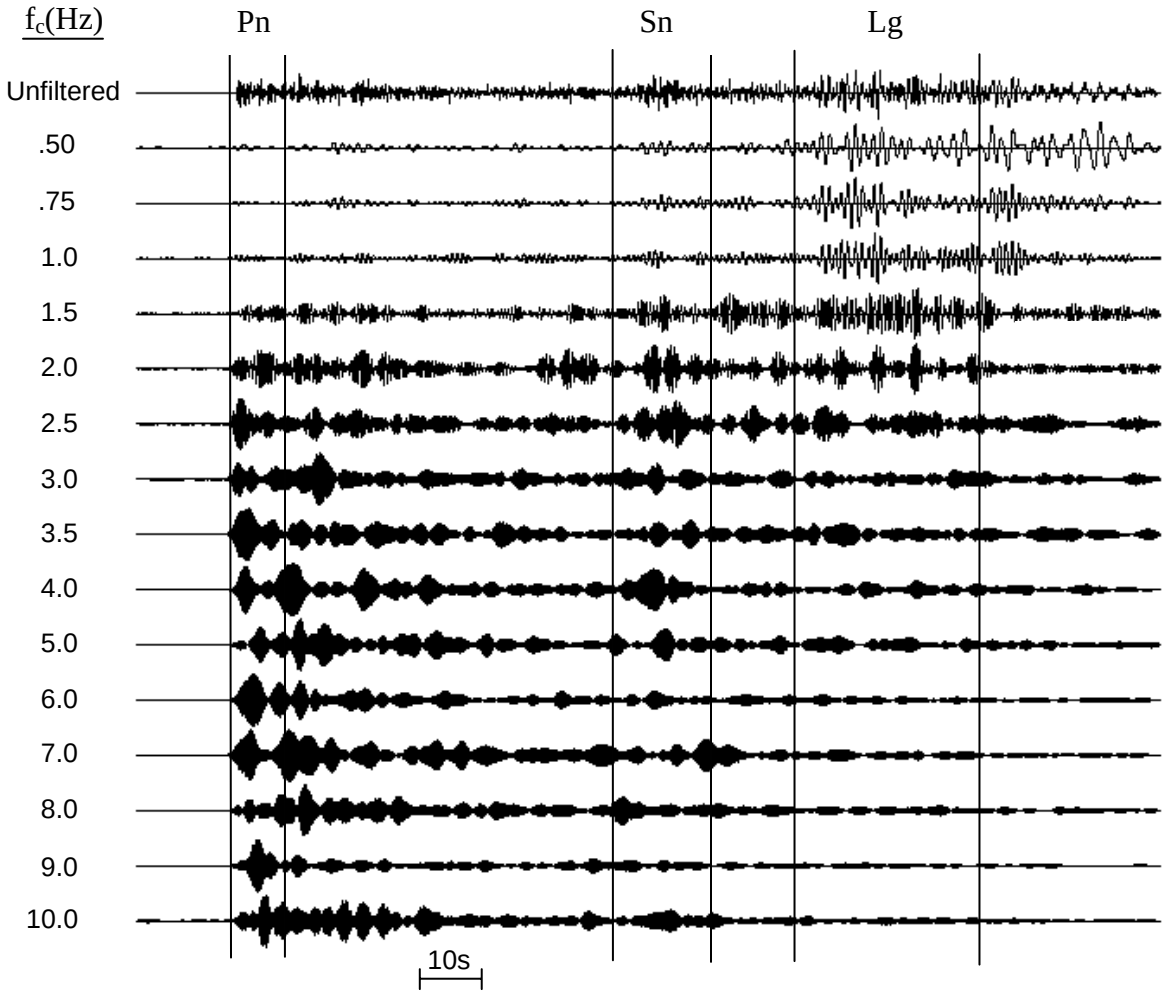

Figure 3. Bandpass filter processing results for the Borovoye recording of the 1.8 kt Degelen Mountain nuclear explosion of October 4, 1989.

An initial yield-scaling analysis has been conducted using the regional phase spectral ratios Sn/Pn and Lg/Pn. That is, the observed Degelen spectral amplitude data were statistically analyzed using an assumed yield-scaling relation of the form

$$\frac{\mathrm{Sn}(\omega)}{\mathrm{Pn}(\omega)} \sim W^{n(\omega)} \qquad 2$$

and a corresponding relation for the Lg/Pn spectral ratio. The resulting yield-scaling exponents are displayed as functions of frequency in Figure 4. Now if the frequency-dependent yield-scaling for the secondary phases Sn and Lg are the same as that for Pn, then the scaling exponents for these ratios would not be significantly different from zero. In fact, the inferred yield-scaling exponents are quite small ranging only from about –0.25 to +0.10, which indicates that the ratios vary by less than a factor of 3 over the nearly two orders of magnitude range in yield encompassed by this sample of Degelen Mountain explosions. More specifically, the scaling exponents differ significantly from zero at the 95% confidence level only in the narrow frequency range from about 1 to 3 Hz. Note that the estimated scaling exponents for the Lg/Pn ratio are effectively zero above 5 Hz, consistent with our previous observation from Figure 3 that the Lg spectral amplitude appears to drop to the P coda level at about this frequency. It follows that, in the higher frequency ranges used for regional discrimination purposes, these source scaling results are not inconsistent with an Sn, Lg generation mechanism with a linear, frequency independent conversion of direct P-wave energy.

A corresponding analysis of the dependence of these Degelen regional phase spectral ratios on source depth is complicated by the fact that our sample of known yield explosions encompasses only a limited depth range from 83 to 332 m, corresponding to a scaled depth range which extends only from 62 to 101 m/kt$^{1/3}$. Consequently, it is not possible to estimate statistically robust source depth scaling relations at this time. However, qualitative comparisons of the observed ratios indicate that any systematic differences in the source depth dependencies between Sn, Lg, and Pn must be quite small, at least over this limited range in depth. This fact is illustrated for Sn in Figure 5 which shows comparisons of observed Sn/Pn ratios which sample the available ranges of depth and scaled depth. It can be seen that these observed ratios are essentially identical over the sampled ranges of depth and scaled depth, consistent with a source depth scaling for Sn which must be very similar to that for Pn. Similar conclusions apply to the corresponding observed Lg/Pn spectral ratios.

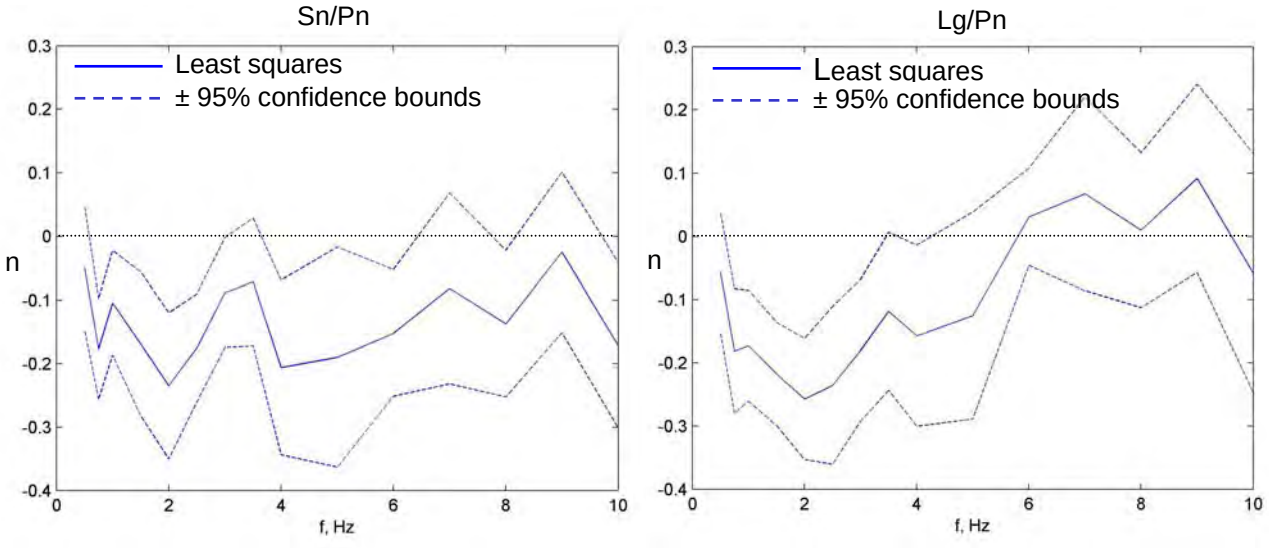

Figure 4. Estimated yield-scaling exponents as a function of frequency for the Sn/Pn (left) and Lg/Pn (right) regional phase spectral ratios for Degelen Mountain explosions.

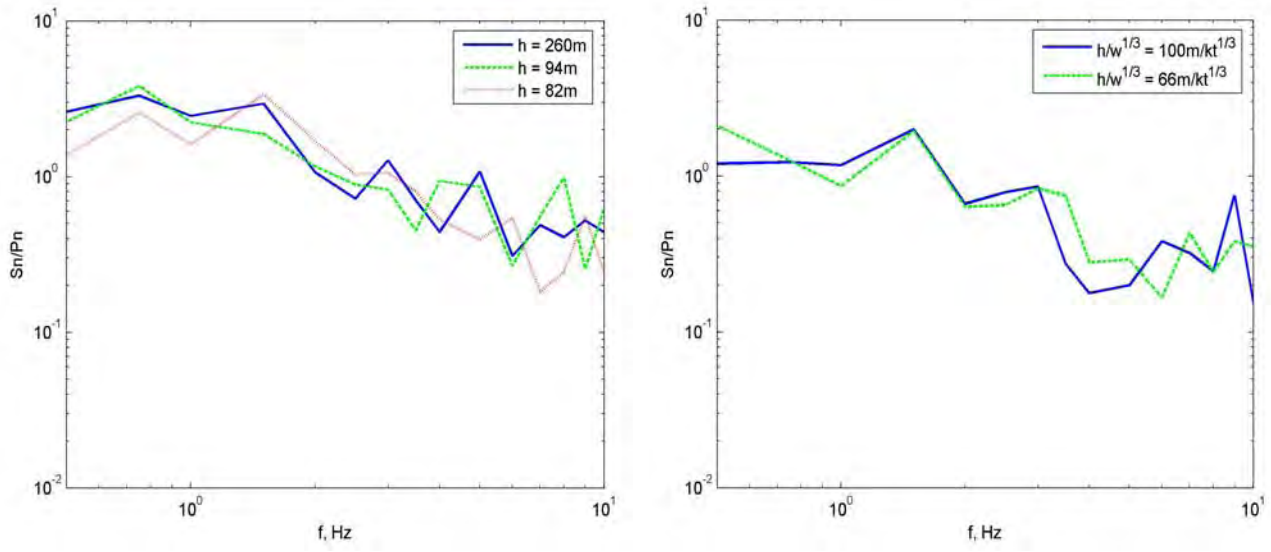

Figure 5. Comparison of observed Degelen Mountain explosion Sn/Pn spectral ratios as a function of source depth (left) and scaled depth (right).

One limitation of the above analysis is that it is based on a single station at a fixed azimuth and thus provides no bounds on possible azimuthal variations in the Pn, Sn, and Lg seismic source functions. Unfortunately, the available digital regional data from Degelen explosions are not adequate to address this issue. As an alternative, regional phase peak amplitude data measured from Degelen explosion analog recordings at some 22 Soviet network stations have also been statistically analyzed. Although such data provide no diagnostic information on possible frequency-dependent effects, they do permit us to examine possible azimuthal effects in the short-period band extending from about 1 to 3 Hz. Figure 6 shows the average observed Degelen explosion Sn/Pn and Lg/Pn peak amplitude ratios at each of the 22 stations, plotted as a function of source to station azimuth. These results indicate that any azimuthal variations in the seismic source functions of these regional phases must be fairly small relative to the single station variability at a fixed azimuth, at least in the short-period band sampled by these data.

Sn/Pn and Lg/Pn peak amplitude ratios for 23 Degelen explosions recorded at Soviet network station AAB ($\Delta \approx 730$ km) are plotted as a function of event m_b value in Figure 7. It can be seen that these observed peak amplitude ratio values show no obvious systematic dependence on m_b. That is, these observations at a station at a very different azimuth (i.e., 180° versus 310°) are generally consistent with the Borovoye results which indicated a weak dependence of the regional phase spectral ratios on explosion yield.

CONCLUSIONS AND RECOMMENDATIONS

During the first year of this investigation the research has focused on seismic source scaling analyses of regional Pn, Sn, and Lg phase data recorded from underground nuclear explosions at the former Soviet Semipalatinsk test site. Digital data recorded at the Borovoye station from a sample of Degelen Mountain explosions of known yield and depth of burial have now been processed and analyzed to define regional phase spectra over the frequency range

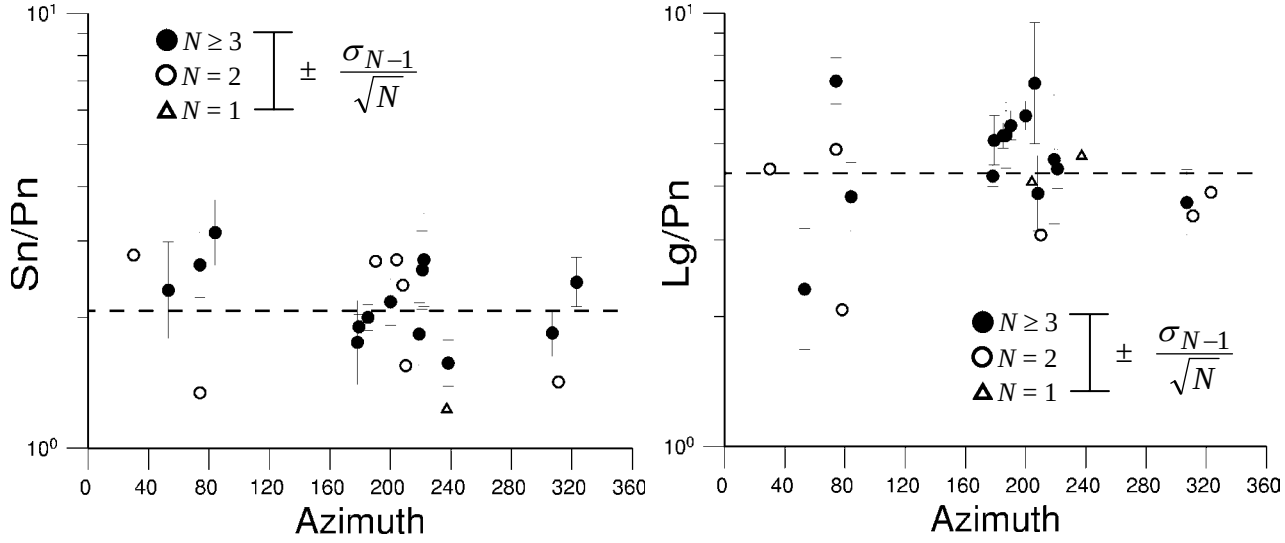

Figure 6. Average observed Degelen Mountain explosion Sn/Pn (left) and Lg/Pn (right) peak amplitude ratios as a function of source to station azimuth for Soviet permanent network stations.

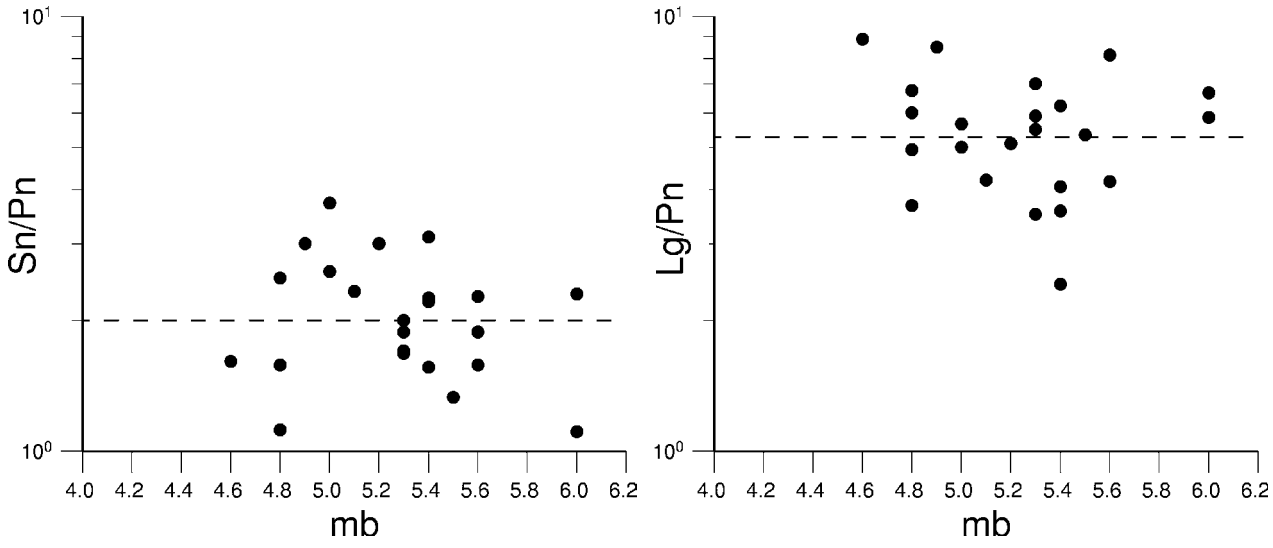

Figure 7. Degelen Mountain explosion Sn/Pn (left) and Lg/Pn (right) peak amplitude ratios as a function of mb at the Soviet permanent network station AAB.

from 0.5 to 10 Hz. Results of yield scaling analyses of the corresponding Sn/Pn and Lg/Pn spectral ratio data were found to be consistent with an Sn, Lg source generation mechanism which is compatable with a linear, frequency independent conversion of direct P wave energy from the explosion, at least in the higher frequency ranges used for regional discrimination. Moreover, it has been found that these observed regional phase spectral ratios are essentially independent of source depth over the limited range in depth sampled by these Degelen explosions, consistent with source depth scaling relations for the Sn and Lg phases which must be very similar to that for Pn. These source scaling analyses are currently being extended to encompass explosions at the Balapan area of the Semipalatinsk test site.

REFERENCES

Gupta, I. N, T. W. McElfresh, and R. A. Wagner (1991), Near-source scattering of Rayleigh to P in teleseismic arrivals from Pahute Mesa NTS shots, in *Explosion Source Phenomenology, AGU Geophysical Monograph* 65, ISBN 0-87590-031-3: 151–159.

Gupta, I. N., T. Zhang, and R. Wagner (1977), Low-frequency Lg from NTS and Kazakh nuclear explosions – observations and interpretations, *Bull. Seism. Soc. Am*., 87: 1115–1125.

Jih, R. S., and K. L. McLaughlin (1988), Investigation of explosion generated SV Lg waves in 2-D heterogeneous crustal models by finite-difference method, report No. AFGL-TR-88-0025.

Mueller, R. A. and J. R. Murphy (1971), Seismic characteristics of underground nuclear detonations, I: seismic spectrum scaling, *Bull. Seism. Soc. Am*. 61: 1675–1692.

Murphy, J. R., I. O. Kitov, B. W. Barker and D. D. Sultanov (2001), Seismic source characteristics of soviet peaceful nuclear explosions, monitoring the Comprehensive Nuclear-Test-Ban Treaty, in *Source Processes and Explosion Yield Estimation, PAGEOPH Topical Volume*, Birkhauser, 2077–2101.

Nuttli, O. W. (1986), Yield Estimates of Nevada Test Site Explosions Obtained from Seismic L_g Waves, *J. Geophys. Res*., 91: 2137–2151.

Stevens, J. L., T. G. Barker, S. M. Day, K. L. McLaughlin, N. Rimer, and B. Shkoller (1991), Simulation of teleseismic body waves, regional seismograms, and Rayleigh Wave Phase Shifts using two-dimensional nonlinear models of explosion sources, *Explosion Source Phenomenology, AGU Geophysical Monograph* 65, ISBN 0-87590-031-3: 239–252.

Stevens, J. L., G. E. Baker, H. Xu, T. J. Bennett, N. Rimer, and S. M. Day (2003), The physical basis of Lg generation by explosion sources," in *Proceedings of the 25th Seismic Research Review – Nuclear Explosion Monitoring: Building the Knowledge Base*, LA-UR-03-6029, Vol. 1, pp. 456-466.

REGIONAL MAGNITUDE RESEARCH SUPPORTING BROAD-AREA MONITORING OF SMALL SEISMIC EVENTS

Howard J. Patton and W. Scott Phillips

Los Alamos National Laboratory

Sponsored by National Nuclear Security Administration
Office of Nonproliferation Research and Engineering
Office of Defense Nuclear Nonproliferation

Contract No. W-7405-ENG-36

ABSTRACT

Los Alamos National Laboratory has a long-standing magnitude research project in support of regional yield estimation and source discrimination. In recent years, this project has developed magnitude-yield scaling relationships based on regional P and S phases and coda waves to improve capabilities to monitor nuclear explosions over broad areas and at low yields. Essential to this development is a better understanding of the transportability of scaling relationships for explosions conducted in different media and for regional phase propagation through different geologic structures. Due to the great variability of regional seismograms, the methods developed for broad-area monitoring must be adaptable to different phases and different frequency bands. These requirements pose a significant challenge from a practical standpoint and from the standpoint of an underlying physical model, which any broad-area method must have to be ultimately successful.

A significant finding of our past research is that the scaling is not the same for magnitudes based on P and S waves. This finding has been documented extensively in previous papers and Seismic Research Review (SRR) presentations for 1 Hz magnitudes showing that mb(P) and mb(Pn) scale at higher rates with yield than do mb(Lg) and the logarithm of apparent Lg coda source amplitudes (ACSA). We have also found that the scaling slopes of mb(Lg) and log (ACSA) are identical, supporting claims of a common source mechanism(s) of Lg and Lg coda waves from explosions. These results have important implications for yield estimation and discrimination, as well as our understanding of S wave generation mechanisms for explosions. The latest observations will be summarized in this paper on plots of one amplitude measure versus another (e.g., mb(Pn) versus log (ACSA), etc.) for test sites around the world. Comparisons for Nevada Test Site (NTS) explosions provide evidence that coupling effects cancel on such plots leaving behind clear indications of scaling differences.

In the past few years, our research has started to characterize the scaling behaviors of regional phases across frequency bands of interest for broad-area monitoring. These include bands both higher and lower than 1 Hz, and phases Pn, Lg and their associated codas. Log (ACSA) for 1.5-2.0 and 2.0-3.0 Hz bands show scaling rates as low as the results for 1 Hz if not lower. In this paper we present our latest observations of multi-band scaling observations for regional P and S waves. These observations are complimented by coda source spectra which display spectral peaking unlike earthquake spectra. This work is forming the observational basis from which to draw insights for improving yield-estimation and discrimination methodologies and for establishing a physical model to support these monitoring functions.

OBJECTIVE

We seek to improve yield estimation and seismic discrimination capabilities for broad areas and small events through the development of regional magnitude methodologies and data sets for direct phases and coda waves. One way our research advances the state of the art in nuclear explosion monitoring is to characterize the scaling behavior and transportability of regional magnitudes based on path-corrected amplitudes using advanced calibration techniques.

RESEARCH ACCOMPLISHED

In recent years, we have witnessed exciting technical advances showing great promise to increase the precision of seismic yield estimates and extend Ms-mb discrimination to small magnitudes through the use of amplitudes measured off regional seismograms. With these advances has come an extraordinary change in the measurements we rely upon since they are often based on the amplitudes of shear phases (Lg, Sn) and codas following those phases, and to a lesser degree on the compressional phases that explosions excite with great efficiency. This is because shear phases are usually the largest on regional seismograms and hence are the best recorded as source sizes decrease and noise levels increase, an important consideration for the ability to do low-yield monitoring. The reliance upon regional shear phases represents a paradigm change from the way seismologists monitor nuclear explosions at teleseismic distances, and this change is a driver for much new innovative research in our community today.

A significant component of the research in this project is directed at characterizing the scaling behavior of regional magnitudes over a broad yield range and in different frequency bands in order to address the challenges confronted by monitoring small events in broad areas. Much of this work is focused on coda waves following Lg, and in the process, we are forming an observational basis from which to draw new insights for improving yield estimation and extending Ms-mb to smaller magnitudes. Equally important is the need to develop a physical model for shear-wave generation by underground explosions and to lay a theoretical foundation supporting the empirical methods employed for regional monitoring. These scaling observations provide important constraints that future models must satisfy.

The ability to estimate yields and discriminate seismic events especially at small magnitudes depends in large part on the energy partitioning between P and S phases and the manner in which the phases scale with yield or source size (e.g., the yield or magnitude dependence of energy partitioning). Another important consideration is the portability of seismic measurements across broad areas, as scatter between areas could be a sign that path effects are not being completely corrected for in our measurements or it could be a sign of intrinsic source effects. This is one reason that so much research has been invested in the calibration of regional path effects, and the development of tomographic models for 1- and 2-D path corrections. In many areas of monitoring concern, these models are nearing a maturity where we are confident that the path effects are effectively and completely removed. We believed this to be so for the corrected amplitudes used to measure magnitudes in this study.

In our project, much effort has been spent on developing methodologies to estimate regional magnitudes and building magnitude data bases of historic explosions in Asia, as well as at the Nevada Test Site (NTS) where so much ground truth information is known. Over the years, our efforts, joint with Livermore's, have investigated coda amplitudes of Lg and Sn waves, tied to seismic moment through an innovative calibration method (Mayeda and Walter, 1996), for purposes of yield estimation, and the results of this work have shown great promise. The corrected coda measurements are referred to as "apparent coda source amplitudes" (ACSA) with units of Nm, and they are measured through a bank of narrowband filters with set bandwidths, the most extensively studied so far being 1.0-1.5, 1.5-2.0, and 2.0-3.0 Hz bands. More bands exist at frequencies below and above these, but to date we have been able to develop yield scaling relationships for these three bands and to study some aspects of their transportability.

A remarkable finding in the results for Lg and Sn 1.0-1.5 Hz ACSA is a difference in scaling compared to teleseismic mb(P), where 1 Hz P wave amplitudes appear to scale with yield at a faster rate than coda amplitudes of Lg and Sn waves. Similar differences have been noted for mb(Lg) and mb(Pn) observations of NTS explosions for the traditional 1 Hz short-period passband defined by the World-Wide Standard Seismographic Network response (WWSSN) (Patton, 2000). In this paper, we will review some of these observations and discuss their implications for the source and our ability to estimate yield and discriminate seismic events. This work is ongoing, and we are currently extending our investigations to other frequency bands and a broader range of yields by incorporating new observations for small explosions.

Here we show a series of scaling results plotting the seismic magnitude of one wave type against the magnitude of another. This has the benefit of reducing many effects related to source coupling, as the first illustration shows. Figure 1 is a plot of mb(Pn) against teleseismic mb(P) for NTS explosions fired on Yucca Flats and in Rainier Mesa. Yucca Flats explosions were detonated in dry and water-saturated tuffs and in dry alluvium. Rainier Mesa explosions exhibit coupling variables due to perched water tables, and explosions in dry alluvium generally couple poorly due to their low material strength. Nevertheless, the scatter plot shows that all observations plot uniformly around the line of equality. This is due to the fact that coupling variations caused by gas porosity and material strength cause near-equal perturbations to the amplitudes of P and Pn waves. Thus, such perturbations tend to move the data points in Figure 1 on trajectories parallel to a line of unit slope. Other effects must be the cause of the scatter, and background seismic noise is a likely candidate judging from the increasing scatter at small magnitudes. The amplitudes of Pn waves are often small, and teleseismic P are difficult to record for small explosions at such great distances. Thus, there are strong practical reasons for using regional shear phases to monitor at small magnitudes.

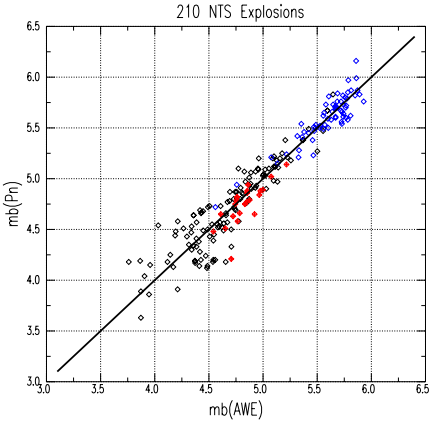

Figure 1. Regional mb(Pn) versus teleseismic mb(P) reported by Blacknest, Atomic Weapons Establishment (AWE). Blue, Yucca below water table; black, Yucca above; red, Rainier Mesa.

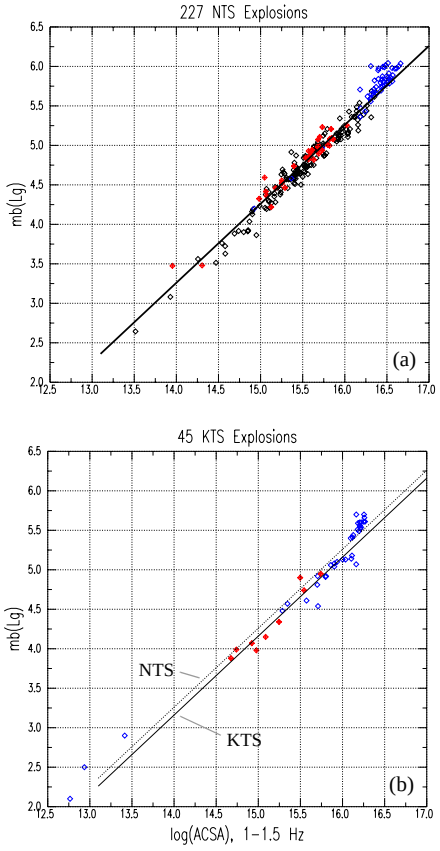

Figure 2. mb(Lg) versus log(ACSA) based on Lg coda waves. Color coding for NTS explosions is the same as in Figure 1. For KTS, blue are explosions at Balapan, while red are Degelen Mountain shots.

The next scaling plots compare mb(Lg) with log(ACSA) for Lg coda wave amplitudes in the 1.0-1.5 Hz band. Figure 2a is a plot of NTS explosions, and Figure 2b is for explosions at the Kazakhstan Test Site (KTS) at Semipalatinsk. KTS observations utilized waveforms from the Borovoye archive (Kim *et al*., 2000), as well as waveforms of regional stations for explosions in the late 80's. We include three 25-ton chemical explosions from the 1997 Depth of Burial (DOB) experiment in Figure 2b, and other chemical explosions will be included on future plots to better characterize the scaling at small yields. Note that Degelen explosions were conducted in tunnels as were Rainier Mesa explosions, while shots at Balapan and on Yucca Flats are in vertical shafts.

It may not come as a complete surprise that the scaling of log(ACSA) for Lg coda waves is very similar to the scaling of mb(Lg) judging from the good agreement of the observations with scaling relationships for a unit slope (lines in Figure 2). This suggests that the generation mechanisms of S waves by explosions are common to both Lg and Lg coda waves (also for Sn waves, as indicated by other results). There is a sign at large yields that the observations bend upward as if log(ACSA) is saturating before mb(Lg). This appears to be a bandwidth issue since Lg amplitudes were measured through a WWSSN short period response characterized by gradual frequency roll-offs, while the narrowband filters used for coda measurements have rapid fall-offs on both shoulders of the response (two-pass Butterworth filter with four poles, i.e., 48 db/octave). Thus the Butterworth filters cut off energy at both high and low frequencies before the WWSSN response does. This illustrates the care with

which comparisons should be made for observations taken with different frequency responses, and in subsequent plots, we avoid comparisons at large magnitudes.

Coupling variations are also mitigated on the plots in Figure 2 for the same reasons they are in Figure 1. On the other hand, the scatter is reduced considerably for Lg and Lg coda waves. This is due in part to better signal-to-noise conditions, but it should be mentioned that Lg and Lg coda observations are all based on data from the Livermore NTS Network, while the network used for teleseismic mb measurements changed station composition from event to event, and this is a source of additional scatter. It is also worth pointing out that the emplacement style, whether in tunnels or in vertical shafts, has little impact on these comparisons, both at NTS and KTS.

Of significance is the very good comparison between the scaling relationships for NTS and KTS explosions in Figure 2 (see lines plotted for NTS and KTS in Figure 2b). This suggests two rather important findings. First is the effectiveness of our path calibrations for correcting Lg and Lg coda wave amplitudes in regions of contrasting geologies, one characterized by the extensional tectonics of the Basin and Range in western U. S. and the other by the continental collision of southern Asia and compressive tectonics. The second finding reinforces our conclusion about the commonality of Lg and Lg coda-wave source generation for NTS and KTS explosions. Thus it appears that the amplitude perturbations caused by S-wave mechanisms are of the same strength for Lg and Lg coda so that the trajectories of data points on our plots are parallel to a line of unit slope, just as they are for coupling perturbations. This finding does not provide any information about the size of the perturbations at the respective test sites, which is of importance for transportability. Information about the size is inferred from the next set of scaling plots.

Figure 3 shows regional and teleseismic mb plotted against log(ACSA) for NTS and KTS explosions. At this stage in our research we have far more observations for NTS (274 combined mb(P) and mb(Pn) measurements), but more measurements for Asian explosions will be available in the near future to better resolve the scaling behavior. At the present time, our KTS data set numbers 89 explosions including three chemical shots, two from the Omega series in the tunnels of Degelen Mountain and one from the DOB experiment. All of these chemical explosions were uncontained bursts with significant cratering effects. Such phenomenology introduces a degree of uncertainty into our interpretations of the scaling relationships, as does the scatter of observations for nuclear explosions at Degelen.

Amplitude scaling differences between mb(P) and log(ACSA) for Lg coda waves are apparent in the NTS observations. The slope of the line plotted in Figure 3a indicates P amplitudes scale 13% faster than Lg coda amplitudes in log space, consistent with the scaling results of mb(Pn) and mb(Lg) (Patton, 2000). It is important to note that the difference in amplitude scaling is not a reflection of the actual difference in yield scaling for P and Lg coda waves because containment practices will also introduce systematics affecting the amplitude scaling. Our investigations of NTS explosions have shown that log(ACSA) decrease with depth of burial, a surrogate for yield, at roughly twice the rate of P log amplitudes. This will tend to reduce the slope of the data as plotted in Figure 3. Such effects further highlights our concern with the KTS observations, since the chemicals were underburied, a rare occurrence at NTS, and the nuclear explosions were conducted by the former Soviet Union with containment practices that differed considerably from those followed by the U. S..

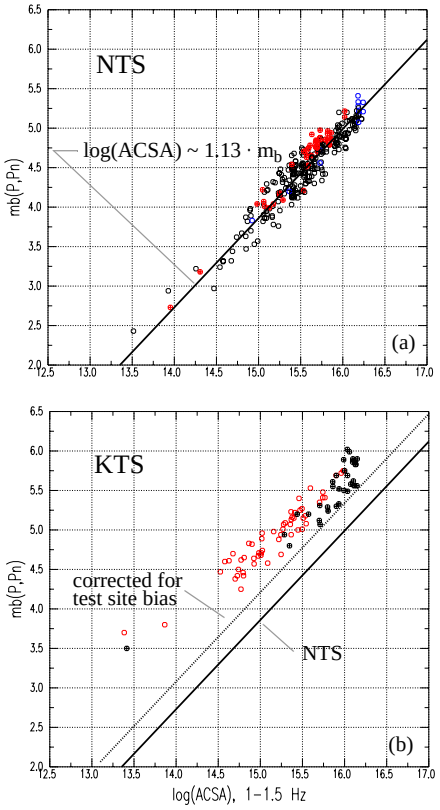

Figure 3. mb(P), mb(Pn) versus log(ACSA) based on Lg coda waves. Color coding is the same as in Figures 1&2. No relationship is shown for KTS shots due to limited observations at small yields.

One significant result in Figure 3 is the large offset between the NTS and KTS observations. This offset is not about to change with the addition of new observations at small yields that we are currently working on. The effectiveness of

path corrections for log(ACSA) measurements was already noted above in regard to Figure 2b, where the good agreement between NTS and KTS scaling results implies that path effects have been removed from Lg and Lg coda wave amplitudes. For mb however, it is well known that a regional bias in western U. S. reduces the teleseismic magnitude of NTS explosions by as much as 0.4 mu. This also applies to mb(Pn) since the mb(Pn) scale for western U. S. was calibrated against mb(P) observations for earthquakes and explosions (Denny et al., 1987; also note that the equality line goes directly through the magnitude observations in Figure 1). Correcting the mb observations for test site bias brings the NTS relationship into better agreement with the KTS observations, but it still does not account for the entire offset (see Figure 3b).

The effect of material properties on P-wave amplitudes is related to the factor $[1/(\rho\alpha^3)]^{0.5}$ (Stevens and Day, 1985). For nominal P velocities (α) and densities (ρ) of media at the Yucca and Balapan test areas, the relative amplitudes of P waves are predicted to be ~0.3 mu larger for NTS explosions. If corrections for this effect were made to the NTS relationship, the offset would increase, shifting the relationship downward to nearly its original position in Figure 3b. On the other hand, we argue that material effects are also present in the Lg observations, and if they are of similar size, material properties will have little net effect on the offset. In any case, an offset remains between the corrected NTS relationship and the KTS observations, and this is an indication of source and/or propagation effects yet to be accounted for in the observations. The explanation we favor is seismic wave scattering close-in to the explosion, where the scattering environment is stronger at NTS compared to KTS, and the amplitudes of S waves generated by P-to-S or Rg-to-S scattering are larger than the amplitudes generated by KTS explosions for the same yield. This is plausible in light of the contrasts in local geology and structural heterogeneity for NTS and KTS test sites. Furthermore, our path corrections will not account for these effects since the calibration data are based on earthquakes. Under this scenario, the entire offset in Figure 3b is caused by the NTS log(ACSA) observations being shifted to the right more than the KTS observations as a result of significant differences in the strength of near-field scattered wavefields at the two test sites. If this scenario is true, the implications for transportability are readily apparent.

We are also characterizing amplitude and yield scaling relations as a function of frequency. Figure 4 compares the amplitudes of 2-3 Hz log(ACSA) with those in the 1-1.5 Hz band. Observations of small chemical explosions detonated at Balapan as part of an emplacement hole closure project supported by the U. S. Department of Energy through the U. S. Defense Special Weapons Agency are plotted on this figure. Log(ACSA) in the 2-3 Hz band show signs of saturation for apparent moments greater than 10^{14} Nm. We will compare the scaling of Pn amplitudes with ACSA for Lg coda waves in different frequency bands on our poster to ascertain what these data reveal about scaling behaviors at frequencies above 1 Hz.

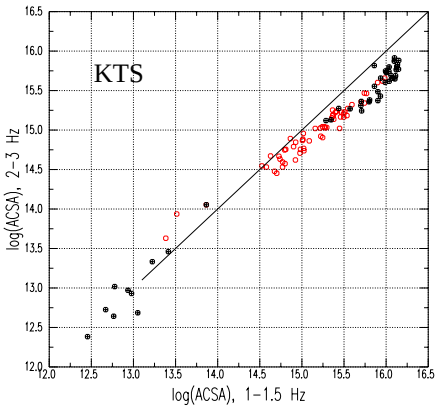

Figure 4. 2-3 Hz log(ACSA) versus 1-1.5 Hz log(ACSA). Color coding is the same as Figure 2b.

CONCLUSIONS AND RECOMMENDATIONS

The magnitude research project at Los Alamos National Laboratory is focused on improving yield estimation and seismic discrimination capabilities for broad areas and small events through the development of regional magnitude methodologies and data sets for direct phases and coda waves. A significant component of the research characterizes the scaling behavior of regional magnitudes over a broad yield range and in different frequency bands in order to address the challenges confronted by monitoring small events in broad areas. We have summarized some explosion results of this research in this paper, but much more research is needed to characterize observations in different frequency bands and for different seismic phases including coda waves.

REFERENCES

Denny, M. D., S. R. Taylor, and E. S. Vergino (1987), Investigation of mb and Ms formulas for the western United States and their impact on the Ms/mb discriminant, *Bull. Seism. Soc. Am.* 77: 987-995.

Kim, W.-Y., P. G. Richards, V. Adushkin, and V. Ovtchinnikov (2001), Borovoye digital archive for underground nuclear tests during 1966-1996, data report on the web at http://www.ldeo.columbia.edu/res/pi/Monitoring/Data/brv_exp_archive.html, Borovoye Archive for UNT (information product in PDF).

Mayeda, K. and W. R. Walter (1996), Moment, energy, stress drop, and source spectra of western United States earthquakes from regional coda envelopes, *J. Geophys. Res*. 101: 11, 195-11, 208.

Patton, H. J. (2000), M_s:m_b relationships for small magnitude events: Observations and physical basis for m_b based on regional phases, in *Proceedings of the 22nd Seismic Research Review: Planning for Verification of and Compliance with the Comprehensive Nuclear-Test-Ban Treaty (CTBT)*, LA-UR-00-2436, Vol. 2, pp. 293-300..

Stevens, J. L., and S. M. Day (1985). The physical basis of mb:Ms and variable frequency magnitude methods for earthquake/explosion discrimination, *J. Geophys. Res*. 90: 3009-3020.

EXPLOSION SOURCE PHENOMENA USING SOVIET TEST ERA WAVEFORM DATA

Tatyana G. Rautian[1], Vitaly I. Khalturin[1], W. Scott Phillips[2], and Paul G. Richards[1]

Lamont-Doherty Earth Observatory, Columbia University[1], and Los Alamos National Laboratory[2]

Sponsored by National Nuclear Security Administration
Office of Nonproliferation Research and Engineering
Office of Defense Nuclear Nonproliferation

Contract Nos. DE-FC52-03NA99513[1] and W-7405-ENG-36[2]

ABSTRACT

During the nuclear testing era, the former Soviet Union carried out extensive observations of underground nuclear explosions, recording both their own shots and those of foreign nuclear states. Between 1961 and 1989, the Soviet "Complex Seismological Expedition" deployed seismometers at time-varying subsets of over 150 sites to record explosions at regional distances from the Semipalatinsk and Lop Nor test sites and from the shot points of peaceful nuclear explosions. This data set included recordings from broadband, multi-channel ChISS[1] seismometers that produced a series of band-limited outputs, which could then be measured to perform spectral studies. Quantitative, pre-digital era investigations of high-frequency source scaling relied on this type of data (e.g., Aki and Chouet, 1975; Rautian and Khalturin, 1978; Tsujiura, 1978). To augment data sets of Central Asia explosions, we have measured and compiled ChISS coda envelopes for Semipalatinsk events recorded at Talgar, now Kazakhstan. In addition, we have compiled regional, direct phase measurements for ChISS recordings at Talgar, Garm, Zerenda, and Novosibirsk. The Talgar coda data were used to construct an average scaling law of coda spectra for Semipalatinsk explosions, presented in last year's contribution. The ChISS envelope data have been integrated into coda processing at Los Alamos National Laboratory (LANL) by applying ChISS filter bands to modern, digital data from central and east Asia, for purposes of yield calibration. The difference in manual versus digital measurement methods are captured in site terms that are higher by up to 0.5 $\log_{10}$ units for ChISS data, relative to modern Talgar data due to the measurement of peak, rather than mean envelopes. After correction for site and path effects, ChISS amplitudes compare well to measurements from the Borovoye archive for events in common. Direct wave measurements have been used to construct spectra for Semipalatinsk explosions, and will be used to explore the behavior of regional phase amplitudes with shot point and emplacement condition. For example, we see a marked difference in the complexity of P phases, quantified by Pn/P2 ratios, where P2 is a secondary P phase, between Balapan and Degelen source regions.

[1] ChISS is the Russian abbreviation for multichannel spectral seismometer. In this instrument the signal from the seismometer is passed through a system of bandpass filters and recorded on photo paper. ChISS instruments have from 8 to 16 channels in the frequency range from 100 sec to 40 Hz. We used data mostly from 8 channel instruments in the range of 0.3 to 40 Hz.

OBJECTIVE

Our objective is to augment the collection of seismic recordings of central Asia underground nuclear tests and test-site earthquakes using ChISS data collected between 1961 and 1989, and to integrate these data into processing schemes currently in use with modern digital data. This will greatly increase the numbers of events used in explosion source scaling, yield estimation, and event identification studies.

RESEARCH ACCOMPLISHED

1. The ChISS Instrument

The ChISS instrument is a real-time, spectral-analyzing seismic recording system, designed by K.K. Zapolsky in the early 1950s. It produced band-passed traces in several (usually 7-10) frequency channels over a broad range from 100 sec to 40 Hz.

Any description of signal in the time domain, and its frequency content, is limited by an uncertainty principle that relates the time interval dt over which a frequency component f_0 endures in the time domain to a frequency band of width df (centered on f_0) within which the Fourier spectrum has significant amplitude in the frequency domain: df is inversely proportional to dt. If we want an accurate measure of the strength of the f_0 component, it appears we need a long time interval, dt, in order to have a small value of df. Although this gives detailed information on the amplitude spectrum, we have no information about its variation within the interval dt.

The filters used in the ChISS system are chosen to optimize the trade-off between time and frequency. Zapolsky used frequency bands of width df that are just half the center frequency fc of each filter (see Figure 1). They allow measurement of spectral amplitude for time intervals of duration 2/fc in each case (that is, for each filter), and enable an optimized description of the frequency content of the seismic signal as a function of time.

Four civilian ChISS recording sites were established by the Soviet Union in the region surrounding the Semipalatinsk test site (Figure 2). The components of a ChISS system are the seismometer, calibration device, amplifier, filter bank and galvanometer along with a photo-paper recording device. Instrument calibration was accomplished in the following manner. Each seismometer had an excitation coil with a separate magnet to input the calibration signal. The frequency of the calibration electric signal was slowly decreased in time from the high end of the highest frequency filter to the low end of the lowest frequency filter. The shape of the response to this signal on the seismogram exactly corresponds to the frequency response of the seismometer-filter-galvanometer system. The impulse response consists of 1.5-2 periods (3-4 extrema). Such a short transition guarantees minimal distortion of the initial seismic signal and stabilizes the envelope shape. Filters used in ChISS systems are characterized by the low and high band limits (at 0.7 maximum magnification), f1 and f2, the central frequency, fc, the absolute band width, df=f2-f1, and the relative band width, (f2-f1)/fc.

The ChISS filter parameters are shown in Tables 1 and 2. Parameters were changed in September 1973 when the system was improved to include two sets of filters for independent short-period (ShP) and long-period (LP) seismometers, as well as independent systems of calibration and recording. The LP and ShP ChISS instruments employ Soviet SKD and SKM seismometers, respectively. Two identical ChISS filters, with central frequency 0.62 Hz, are output from both systems. The calibration signal was recorded daily on each ShP ChISS seismogram and once a week on LP ChISS seismograms. Responses for the ShP system are plotted in Figure 1. Examples of LP system seismograms from the ChISS station at Zerenda (ZRN) are given in Figure 3.

Table 1. Early ChISS parameters.

f1-f2 (Hz)	fc (Hz)	Width
0.27-0.40	0.32	0.4
0.54-0.84	0.67	0.45
1.1-1.7	1.36	0.45
2.3-3.6	2.9	0.45
4.6-7.1	5.7	0.45
9.2-14	11.3	0.45

Table 2. Standard ChISS parameters.

LP/ShP	f1-f2 (Hz)	fc (Hz)	Width
LP	0.05-0.1	0.07	0.7
LP	0.1-0.2	0.14	0.7
LP	0.2-0.4	0.28	0.5
LP	0.5-0.8	0.62	0.5
ShP	0.5-0.8	0.62	0.5
ShP	1.0-1.6	1.25	0.5
ShP	2.0-3.2	2.5	0.5
ShP	4.0-6.4	5.0	0.5
ShP	8.0-13.0	10.0	0.5

2. Explosion Data

The Talgar (TLG) ChISS station began operating in September 1961. It recorded almost all Soviet underground nuclear tests (UNTs) from the Semipalatinsk test site (STS), including the first two STS UNTs on Oct. 11, 1961, and Feb. 2, 1962, until the final tests in 1989.

For this study, we manually measured coda envelopes of 178 TLG ChISS records of 124 UNTs (nm/s) and entered the data into electronic form. More than 500 coda envelopes were analyzed from channels between 0.08 Hz and 5 Hz. Further details of the coda measurements can be found in our previous contribution (Rautian et al., 2004). In addition, we measured ChISS peak amplitudes for regional phases from 226 UNTs at the four ChISS stations, on multiple band channels, including two gain levels for certain records, and entered into electronic form. The measured phases were Pn, P2 (secondary Pn arrival), Pg, Sn, Li, Lg1, Lg2, Lg3 (various Lg peaks) and Rg, and we recovered 1753, 1439, 1469, 1430, 91, 1305, 1368, 1265, and 542 measurements for each phase, respectively, totaling 10,662 measurements overall. We also obtained measurements for a small number of chemical explosions and for the March 20, 1976, Semipalatinsk earthquake.

3. ChISS Measurement

To manually obtain the coda envelope from a photo paper record, one must choose each individual moment of time to measure. We choose measurement times such that monotonically decreasing amplitudes are obtained. Strict adherence to this rule enhances repeatability, which we have verified by comparing measurements obtained independently by two analysts. Further testing has shown that measurements from the ShP and LP systems in the common, 0.62 Hz, channel are the same.

The accuracy of manual measurements of ChISS envelopes depends on amplitude. The accuracy is lower for small amplitudes (below 1-2 mm) and large amplitudes (over 50-70 mm). We estimate that amplitudes less than 1 mm can by measured with error on the order of the amplitude itself. Therefore we eliminate all data below this level. The difficulty with large amplitudes is that waveforms from neighboring channels can overlap. Channels are recorded side by side and are separated by 70 mm; thus, amplitudes larger than 40-50 mm overlap. From our experience, measurement quality depends on brightness of the record. We keep the large amplitudes in our data set, which allows future decisions on their use on a case-by-case basis. This decision can be made comparing with smaller amplitude envelopes as the coda shapes are expected to be the same.

Occasionally, errors result from mistakes in measuring calibration levels. In such cases, both coda and phase amplitudes have the same discrepancy for that channel. This cannot be seen in individual envelopes, but is revealed in the spectra of individual events and in correlations between amplitude and magnitude. Such comparisons have been made to control the quality of the ChISS data sets.

4. Integration into Coda Processing

Talgar ChISS coda have been integrated into coda processing at LANL by applying ChISS filter bands (Tables 1 and 2) to digital data from central and east Asia, including digital seismograms from the Borovoye archive, STsR-TSG recording system (Kim and Ekstrom, 1996). Talgar envelopes were used in their raw form, under the assumption that differences in measuring envelopes manually and automatically would be consistent and would then

be absorbed in frequency dependent site terms. To evaluate the Talgar ChISS coda results, we compared path-corrected coda amplitudes with common events recorded at Borovoye (Figure 4). Results show offsets that we attribute to measurement method (Figure 5), and show scatter that is very tight (standard deviation of differences less than 0.2, often less than 0.1). These levels compare favorably with those observed between modern digital stations (standard deviation 0.1 or less). The Talgar ChISS results can be used in yield calibration studies.

5. Phase Amplitude Data

We have completed and quality controlled lists of amplitudes for regional phases for Semipalatinsk explosions recorded at four ChISS stations. Sample spectra for a variety of phases are shown in Figure 6 for a number of events that include the first and second Soviet underground tests, October 11, 1961, and February 2, 1962, respectively. We also show comparisons between spectra of events from the same adits (Figure 7). These comparisons will help us understand effects of near source damage on regional signals (these show very little effect) and, in the absence of such effects, will give us bounds on repeatability, after possible source scaling effects are accounted for. Discriminant ratios can also be studied using these data and an example of the behavior of cross-phase discriminants with frequency is shown in Figure 8. Finally, variation of discriminants with shot location and emplacement conditions can be studied. We show the variation of P2/Pn ratios, a measure of P complexity, in Figure 9, demonstrating marked differences between the Balapan and Degelen source regions, as well as coherent variations across the Degelen area. We suspect these variations are due to wave propagation effects.

CONCLUSIONS AND RECOMMENDATIONS

We have manually measured coda envelopes from Talgar ChISS analog records for 124 STS explosions that occurred between 1961 and 1988. These data have been used to study the composition of the coda for the STS-Talgar path, define coda limits, estimate coda attenuation and construct a scaling law of explosion spectra (see previous year's contribution: Rautian et al., 2004). The coda data have been integrated into LANL coda calibration procedures. The ChISS data have been tested for consistency with existing Borovoye digital data from events recorded in common, and are suitable for use in yield calibration work. Phase amplitude measurements for Semipalatinsk explosions have also been collected, entered, and quality controlled. Examples of spectra are given, including spectra for events in the same adits. These data will be useful for studying variations in discriminant ratios that might result from shot point location or emplacement conditions. The distribution of a P complexity measurement for Talgar shows strong shot location dependence, thought to result from a wave propagation effect.

REFERENCES

Aki, K., and B. Chouet, (1975). Origin of coda waves: attenuation, and scattering effects. *J.Geophys.Res*. 80: 3322-3342.

Kim, W. Y., and G. Ekstrom, (1996). Instrument responses of digital seismographs at Borovoye, Kazakhstan, by inversion of transient calibration pulses, *Bull. Seism. Soc. Am*. 86: 191-203.

Rautian, T. G, and V. I. Khalturin, (1978). The use of the coda for determination of the earthquake source spectrum. *Bull. Seism. Soc. Am*. 68: 923-948.

Rautian, T. G., V. I. Khalturn, W.S. Phillips and P.G. Richards, (2004). Explosion source phenomena using Soviet test era waveform data, in *Proceedings of the 26th Seismic Research Review: Trends in Nuclear Explosion Monitoring*, LA-UR-04-5801, Vol. 1, 457-466.

Tsujiura, M., (1978). Spectral analysis of the coda waves from local earthquakes. *Bull. Earthquake Res. Inst*. 53: 1-48.

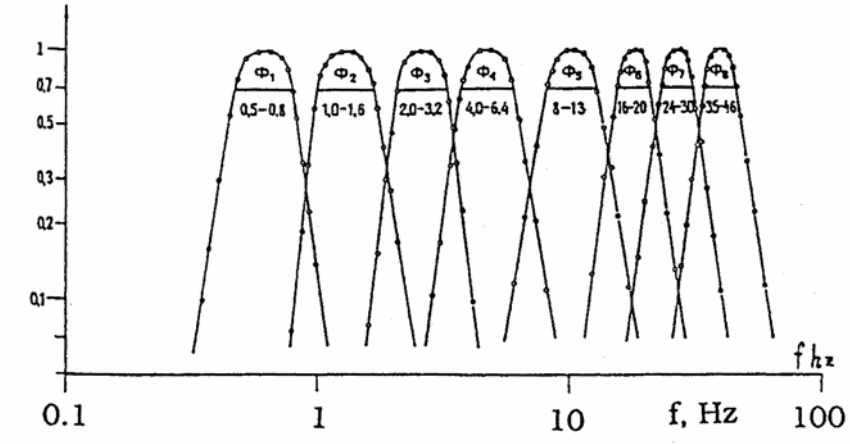

Figure 1. Short period ChISS response.

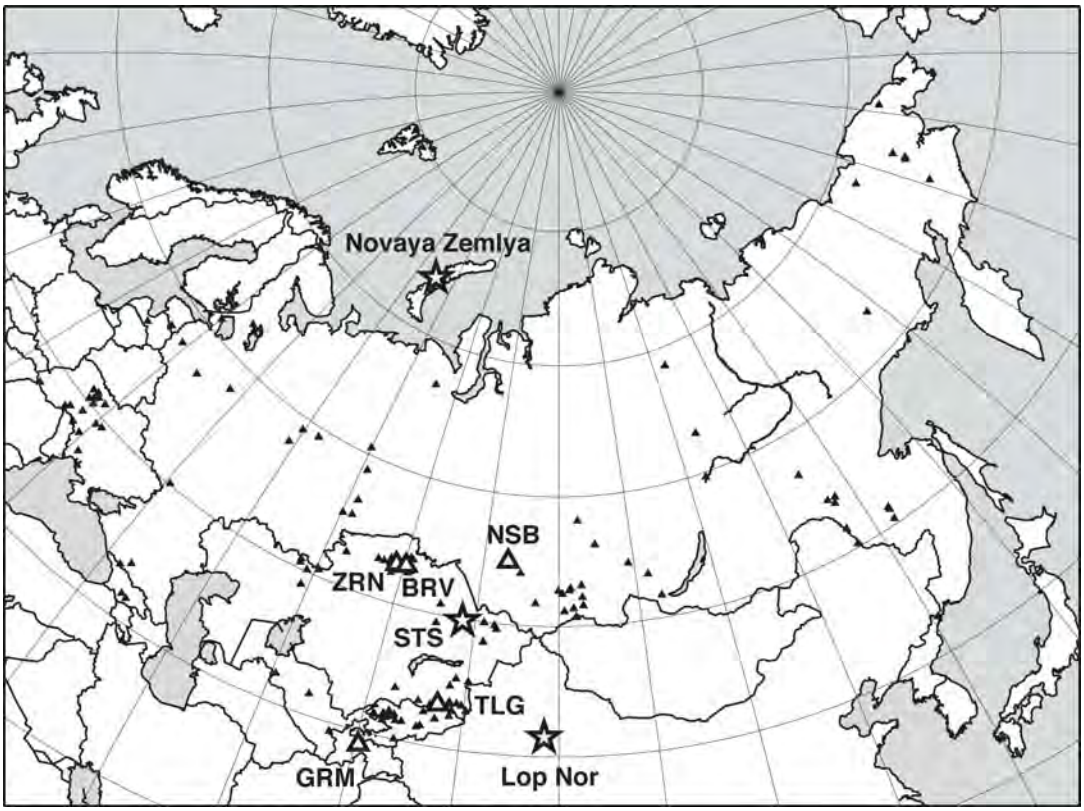

Figure 2. Map of Soviet stations and Asia test sites. Four ChISS stations and the Borovoye site are represented by large triangles, other Complex Seismological Expedition stations, by small triangles. Test sites are represented by stars.

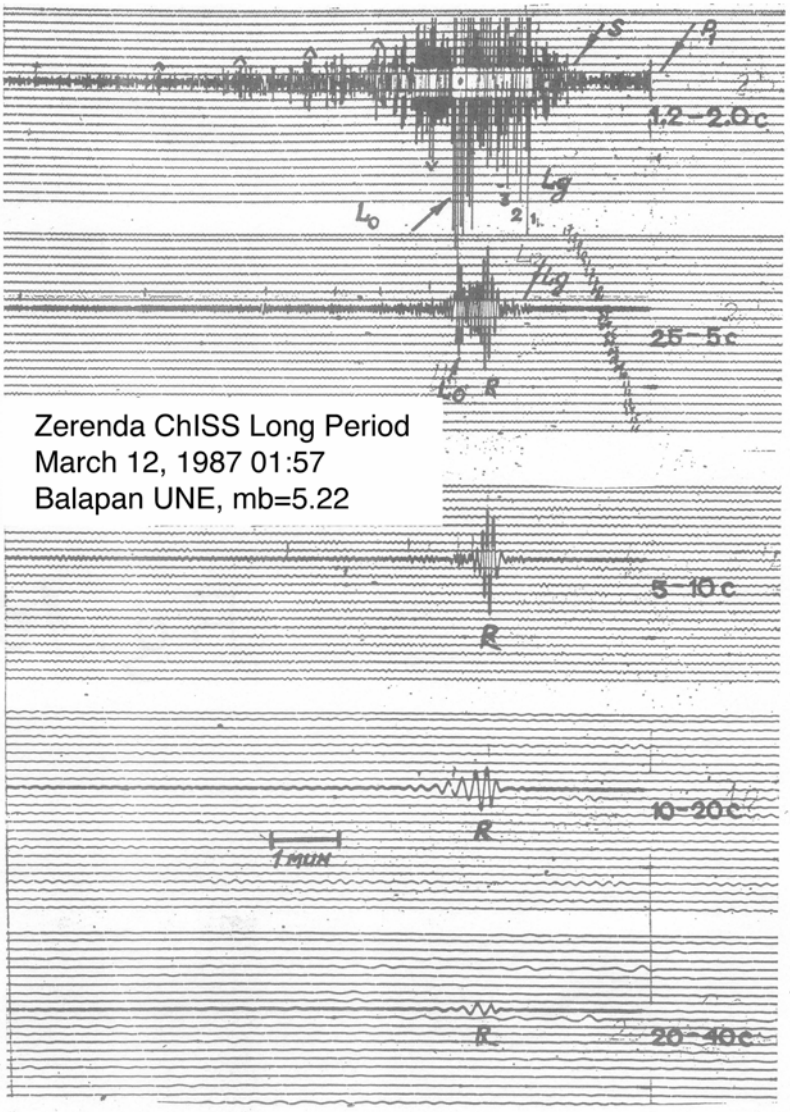

Figure 3. Long period ChISS seismograms from Zerenda. Time runs right to left.

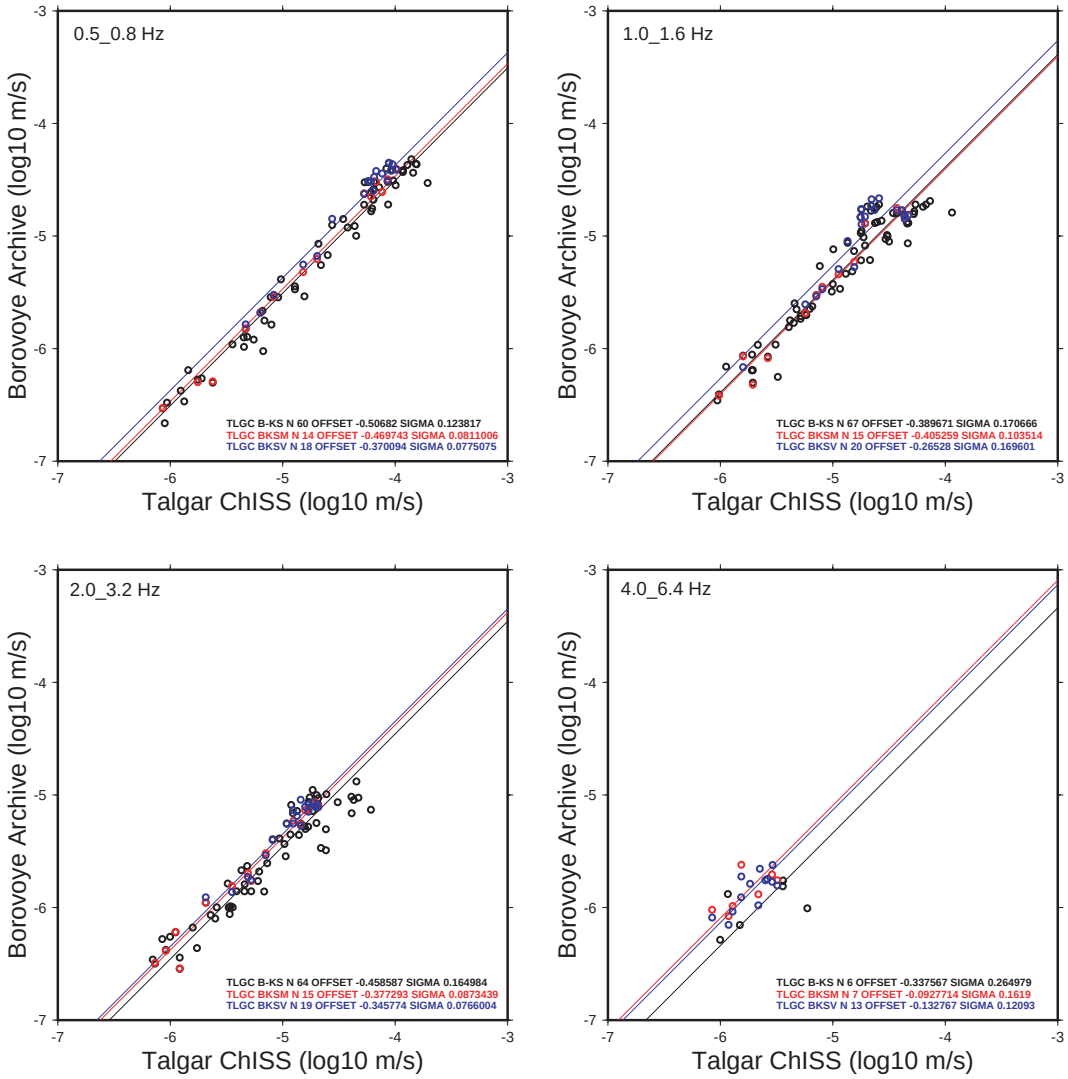

Figure 4. Comparison of path-corrected spectra between Talgar ChISS and Borovoye Archive stations.

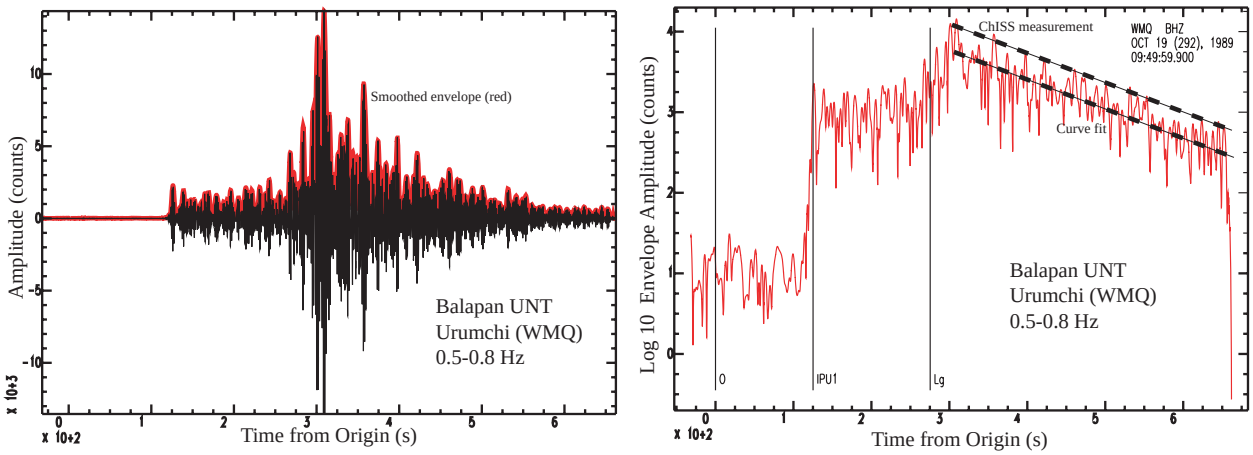

Figure 5. Example of offset resulting from ChISS measurement technique. This offset is absorbed in the site term when integrated into magnitude-yield processing for Asia. The calculation was performed in counts.

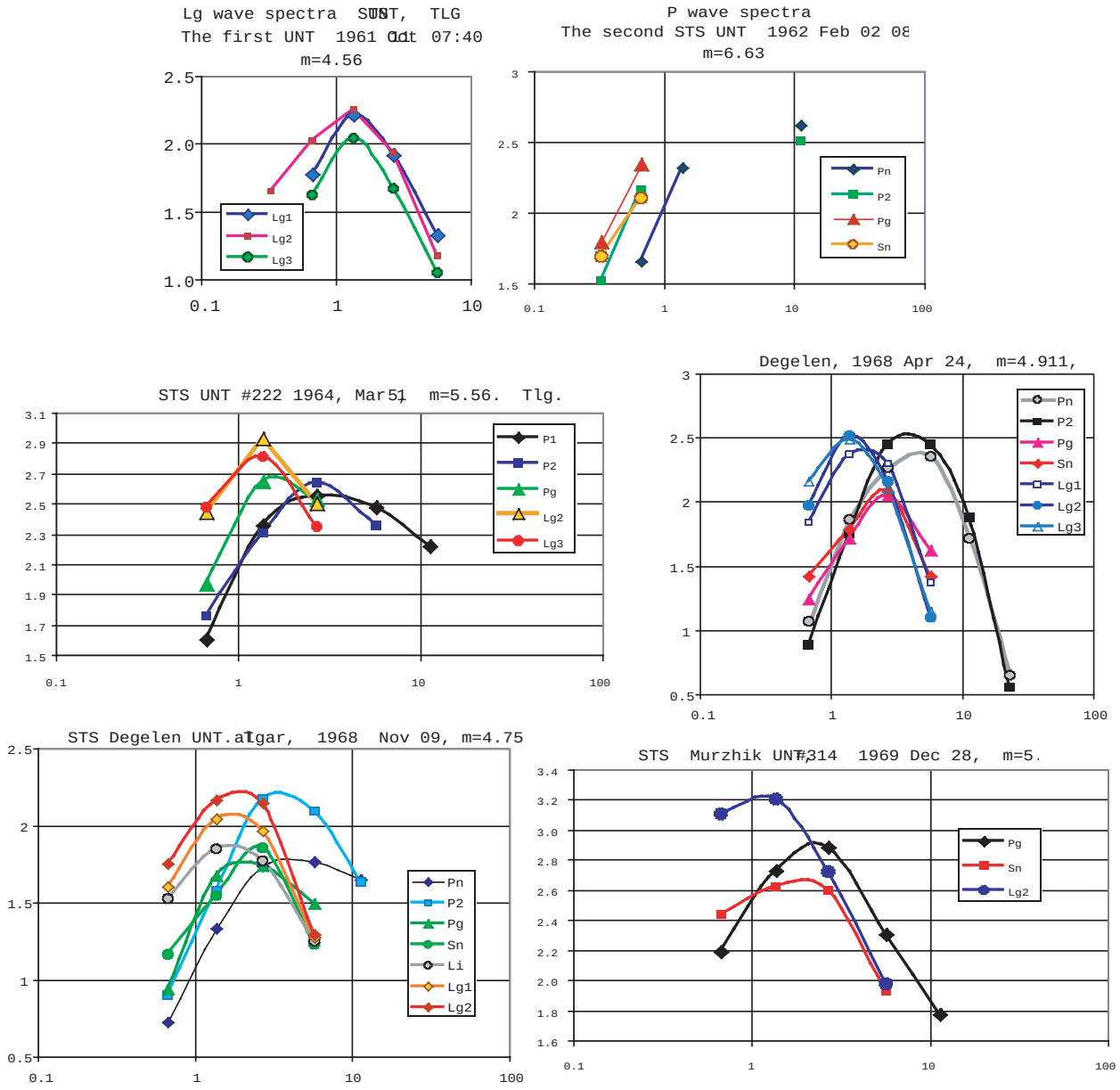

Figure 6. Examples of ChISS spectra (nm/s) for regional phases. Frequency in Hz.

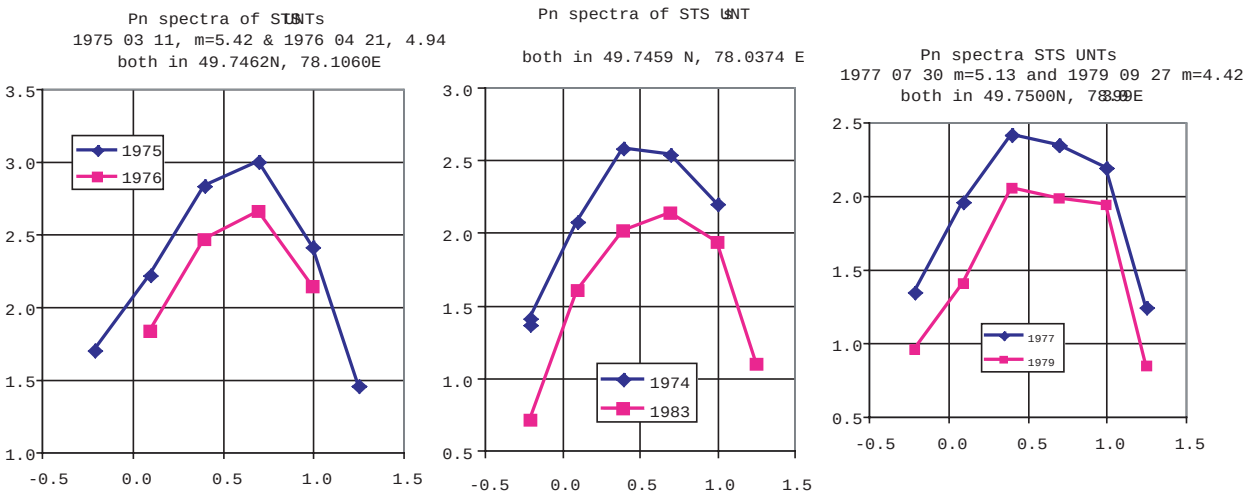

Figure 7. Examples of ChISS spectra (nm/s) for events in the same adit. Log10 frequency (Hz) is shown.

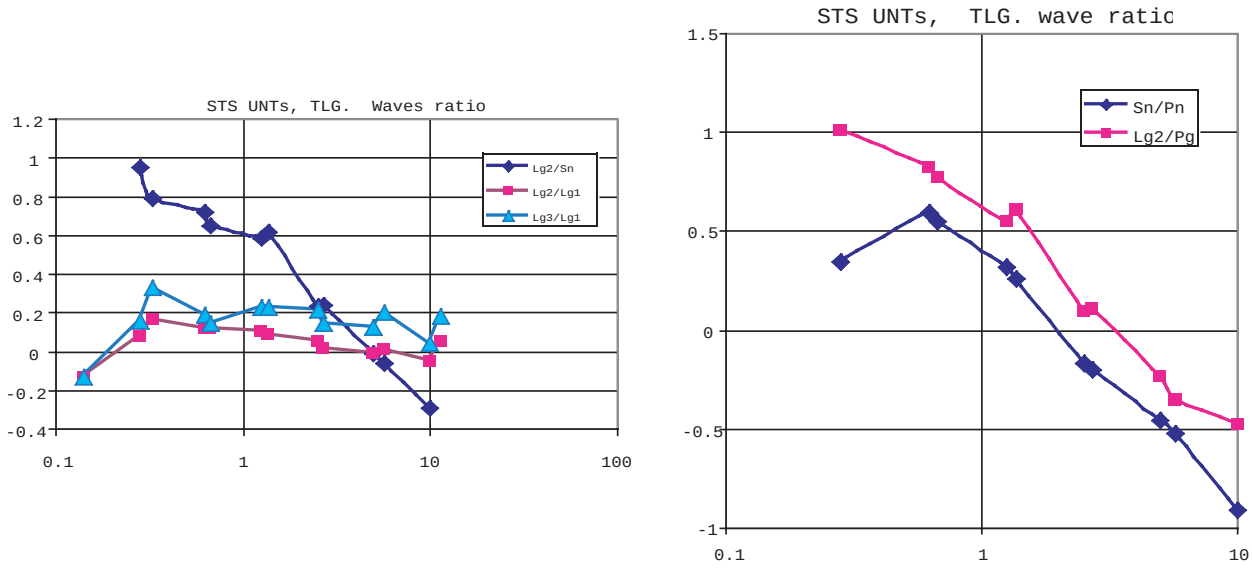

Figure 8. Spectral ratios versus frequency (Hz) for Semipalatinsk events.

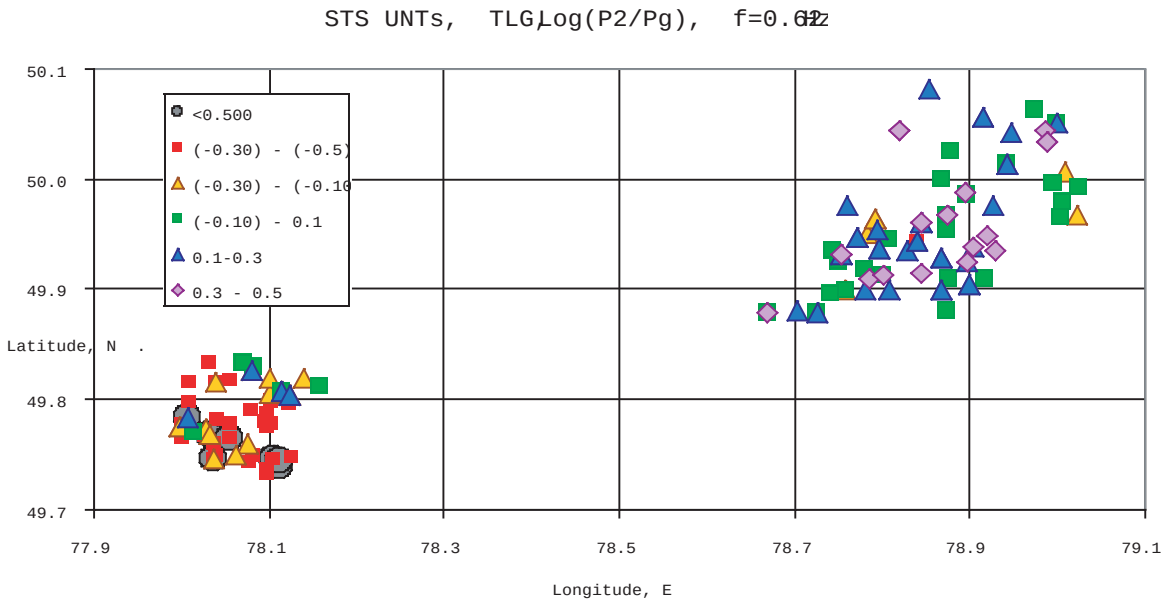

Figure 9. Geographical variation of the P2/Pg phase ratio for Balapan and Degelen events.

SEISMIC SOURCE CHARACTERIZATION AND ENERGY PARTITIONING FROM IN-MINE AND REGIONAL BROADBAND DATA IN SOUTH AFRICA

Eliza B. Richardson[1], Andrew A. Nyblade[1], William R. Walter[2], Kevin Mayeda[2], and Lindsay Lowe[2]

Penn State University[1] and Lawrence Livermore National Laboratory[2]

Sponsored by National Nuclear Security Administration
Office of Nonproliferation Research and Engineering
Office of Defense Nuclear Nonproliferation

Contract Nos. DE-FC03-02SF22673[1] and W-7405-ENG-48[2]

ABSTRACT

Mining-induced seismicity provides an important link between man-made and natural tectonic processes because it includes both fresh-fracturing events that are directly triggered by excavation and blasting, as well as events dominated by frictional slip which are analogous to tectonic earthquakes. These two types of events have distinguishable characteristics, such as different spatio-temporal clustering patterns, as well as different spectral signatures. Some previous studies using local in-mine data indicated that the fresh-fracturing events often have isotropic (explosional) moment tensors. Being able to differentiate the two types of events at regional and teleseismic distances is important for seismic verification studies.

We are studying a dataset of M > 2.5 mining-induced events that occurred between 1997 and 1999 in the Far West Rand gold-mining region of South Africa, approximately 80 km southwest of Johannesburg. The depth range of these events is 1.5 - 4 km; they were recorded locally by five networks of 109 three-component geophones installed at depth throughout the active mining environment. These events were also recorded at regional distances by a two-year PASSCAL deployment of 80 broadband stations.

Using a spectral method, we have calculated source parameters for these events from the in-mine recordings, including seismic moment, stress drop, corner frequency and energy. Larger stress drops are found than for frictional events, although the latter generally have larger seismic moments. S/P wave amplitude ratios are lower for fracturing events as well, which can be an indication of isotropic components of the source. From spectral analysis, scaling relations, and statistical analysis of the characteristic length scales between sequential frictional events, we confirm earlier estimates of the critical slip length (D_c ~ 100 microns) and critical patch size (R_c ~ 10 m). We believe these dimensions represent the nucleation size of events in this hard-rock mine environment.

We have inverted for the moment tensors of 15 events from the Far West Rand gold-mining region of South Africa that range in size from 1.0 < M < 3.2. These events occurred at 1-4 km depth and were recorded locally by four networks of 102 three-component geophones installed at depth throughout the active mining region as well as by a two-year PASSCAL deployment of 80 broadband seismometers. The moment tensors of the 15 events are consistent with purely double-couple solutions. In addition, we studied several events in the range 1 < M < 2 whose poor signal-to-noise ratio on the regional recordings prevented reliable moment tensor inversions. We presume that these events also have double-couple mechanisms based on their similar P/S amplitude ratios in comparison to the 15 well-characterized events. Therefore, we find little evidence in our data for seismic events with isotropic (explosional) mechanisms, at least down to the M = 1 level.

The broad southern Africa region offers the opportunity to examine variability in regional phase discriminants, such as high frequency P/S, which may be caused by unusually shallow depth events. We used a set of larger events (M>3.5) throughout the region to determine average source characteristics for the region and attenuation characteristics for each of the regional phases (Pn, Pg, Sn and Lg). We also determined moment magnitudes for these events using regional seismic coda envelopes. After correcting for source and path effects we find large variation in 6-8 Hz P/S ratio values (Pn/Lg, Pg/Lg and Pn/Sn). We are studying the behavior of these P/S values in terms of depth and focal mechanism effects.

OBJECTIVES

Mining-induced seismicity not only occurs at scales between those in the laboratory and those on tectonic faults, but can be recorded at the depth of seismic nucleation using in-mine seismometers, thus creating an excellent "natural laboratory" in which to study the physics of earthquake rupture. At present most gold mines in the Witwatersrand basin of South Africa use sophisticated underground arrays of geophones and accelerometers to record over 1,000 events per day. The extensive seismicity recorded at moment magnitude $M_w > 2$ provides a unique dataset to develop and test methods of discrimination between natural seismicity, mining tremors, and other industrially-related events such as chemical explosions. These $M_w > 2$ mining-induced events are large enough to be recorded on the in-mine arrays, as well as regionally by broadband seismometers. Therefore, locations, magnitudes, and focal mechanisms may be accurately determined from the high-frequency local data while regional phase propagation and energy partitioning may be studied via regional recordings. Another feature of this dataset is the variety of focal mechanisms as some mine events are purely double-couple shearing events whereas others have significant isotropic components (McGarr, 1992).

As the mines develop the technology to remove ore from deeper and deeper within the crust, larger stresses accumulate, producing higher rates of seismicity. Characterization of these events in terms of comparisons to other types of seismicity, both natural and man-made is important for building a comprehensive knowledge base of crustal seismic activity as well as for the pure science of earthquake physics and nucleation. In this study we seek to determine seismic source characteristics as well as moment tensors for a variety of mining-induced events in order to construct a catalog of "typical" large mining-induced events that can be used for source discrimination purposes as well as energy partitioning studies of the southern African crust.

RESEARCH ACCOMPLISHED

Source parameters

We have assembled a dataset of large ($M_w > 1.4$) mining-induced events from four gold mines in the Far West Rand region. The locations of these events were determined by operators at the mines via a ray-tracing algorithm based on body wave arrival times (Mendecki, 1993, 1997). This method incorporates a layered velocity model based on geologic units that have been determined by underground surveying and mapping as well as surface-based refraction profiles and borehole log data. The wavespeeds and location procedures have been verified by test blasting, so location uncertainties are typically on the order of 10-20 m for events of $M_w > 2$.

Using the spectral method developed by Andrews (1986) and adapted by Richardson & Jordan (2002) for use with in-mine seismic recordings, we have calculated source parameters for fourteen events that occurred in 1999, and 23 events from 1998 (see Table 1). Each of the events in this study were recorded by at least ten stations. In order to determine source parameters, we median-stacked each event's spectra and integrated the results up to the Nyquist frequency to determine S_D, the integral of the displacement power spectra (see Equation 6 of Andrews, 1986}), S_V, the integral of the velocity power spectra (see Equation 7 of Andrews, 1986), and A^2, the acceleration power spectral level (see Equation 19 of Andrews, 1986). These are used to determine the source parameters radiated energy (E), seismic moment (M_0) , and static stress drop ($\Delta\sigma$) as follows:

$$E = 4\pi\rho v S_V \tag{1}$$

$$M_0 = \frac{8\pi\rho v^3 S_D^{(3/4)}}{\Re S_V^{(1/4)}} \tag{2}$$

$$\Delta\sigma = \frac{2\pi f_0 \rho A^2}{C\Re} \tag{3}$$

in which the corner frequency is found by

$$f_0 = \left(\sqrt{S_V / S_D}\right) / 2\pi. \tag{4}$$

In the previous equations, ρ is the rock density, which has been determined experimentally at the mines, v is wavespeed, $\Re$ is a constant based radiation pattern, and C is also a small constant. An advantage of this method is that the exponent of the spectral rolloff is not a fixed parameter as in the case of fitting spectra with a Brune-type curve. Because our data is band-limited, there is an upper limit to the radiated energy we can determine (Ide & Beroza, 2001). However, in practice the underestimation of energy for this dataset is very small (approximately 5%) since typical corner frequencies for the events in this study are generally 1/5 to 1/10 of the Nyquist frequency (Richardson & Jordan, 2002).

In the following table, event dates and times are listed as yyyymmddhhmmss (The event times are local to the mines. Subtract two hours to get GMT time). Event locations are given by their latitude (°N), longitude (°E), and depth (meters below datum). It should be noted that event depths are referenced to the origin or "datum" of the Z axis of the local mine coordinates. This datum is a reference point in Johannesburg, and is 250 m above ground level and about 1800 m above sea level in the Carletonville Mining District where these events occurred (Figure 1). Seismic moment M_0 is in Nm, magnitude M_w is moment magnitude (Hanks & Kanamori, 1979), energy E is given in Joules, corner frequency f_0 is in Hz, and static stress drop $\Delta\sigma$ is in MPa.

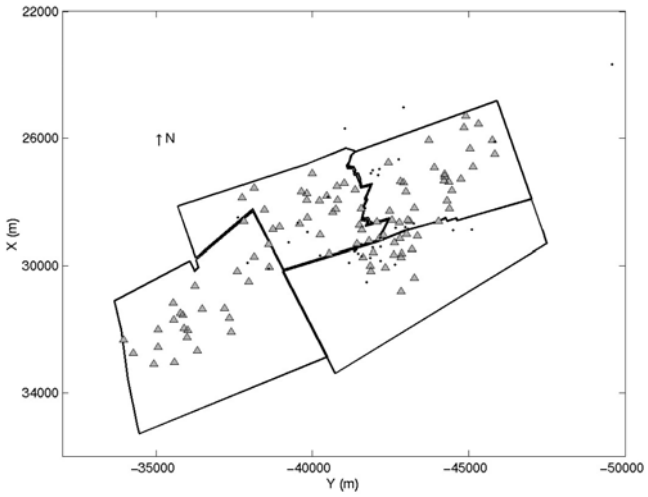

Figure 1. Map view of the lease areas of four mines in the Carletonville district (in mine coordinates). There are 102 three-component stations installed at depth (triangles). Dots represent the epicenters of large mining-induced events for which spectral source parameters were calculated (see Table 1) in this study.

Table 1. Source parameters of mining-induced events determined by in-mine array data. Events in bold are those for which moment tensors have been determined.

Event	Lat	Lon	Depth	M_0	M_w	E	f_0	$\Delta\sigma$
19980111144841	-26.401	27.411	2338	1.4e13	2.7	5.5e8	15.8	5.87
19980220050356	-26.429	27.430	3694	7.8e13	3.2	1.0e10	12.9	20.00
19980328134551	-26.437	27.417	2729	1.2e13	2.7	2.8e8	16.6	3.65
19980329051801	-26.435	27.422	2587	2.2e13	2.8	4.9e8	16.3	3.46
19980331135629	-26.439	27.380	2053	2.2e13	2.8	2.1e8	9.3	1.47
19980404190603	-26.430	27.399	2047	1.1e13	2.7	1.8e8	14.6	2.51
19980420170707	-26.395	27.430	2273	2.8e13	2.9	1.6e9	13.8	8.76
19980420194749	-26.412	27.422	1925	2.5e13	2.9	9.1e8	14.8	5.72
19980502123739	-26.414	27.419	1955	2.2e13	2.8	4.9e8	11.9	3.43
19980508103233	-26.440	27.427	2661	1.1e13	2.6	1.8e8	12.1	2.46
19980622162025	-26.439	27.423	2588	1.3e13	2.7	3.4e8	15.2	4.01
19980708212049	-26.434	27.416	2553	1.2e13	2.7	3.9e8	14.8	4.83
19980727135740	-26.427	27.419	2409	2.5e13	2.9	4.3e8	9.5	2.73
19981002194336	-26.432	27.423	2569	1.0e13	2.6	1.3e8	10.2	1.90
19981007192539	-26.420	27.406	3123	2.0e13	2.8	1.3e9	16.9	10.30
19981019200410	-26.436	27.416	2505	1.3e13	2.7	2.0e8	10.5	2.40
19981021044841	-26.434	27.420	2613	1.0e13	2.6	1.3e8	11.5	2.00
19981023160058	-26.437	27.420	2745	3.1e13	2.9	7.1e8	8.7	3.50
19981027090946	-26.426	27.377	2989	1.2e13	2.7	3.6e8	15.2	4.72
19981102163835	-26.427	27.434	2552	2.5e13	2.9	6.2e8	10.4	3.90
19981110172424	-26.404	27.459	2770	1.2e13	2.7	3.1e8	15.0	4.10
19981119170822	-26.414	27.422	2268	1.1e13	2.6	3.0e8	13.3	4.20
19981223093859	-26.433	27.393	3375	2.8e13	2.9	1.1e9	12.8	5.94
19990103155836	**-26.412**	**27.420**	**1748**	**1.1e13**	**2.6**	**1.2e7**	**12.1**	**0.87**
19990118102526	**-26.420**	**27.446**	**3422**	**9.0e11**	**1.9**	**9.4e6**	**27.3**	**0.80**
19990118112405	**-26.420**	**27.446**	**3443**	**2.0e11**	**1.4**	**1.1e6**	**36.1**	**0.68**
19990118200717	**-26.415**	**27.422**	**2039**	**2.9e12**	**2.2**	**1.9e7**	**15.9**	**0.51**
19990118213352	**-26.409**	**27.429**	**2879**	**9.1e12**	**2.6**	**1.6e7**	**15.0**	**1.00**
19990201194832	**-26.428**	**27.406**	**3137**	**4.8e12**	**2.4**	**3.4e7**	**13.6**	**0.53**
19990202123021	**-26.435**	**27.415**	**2582**	**1.2e13**	**2.7**	**3.2e7**	**13.6**	**3.00**
19990203221201	**-26.423**	**27.363**	**2638**	**1.4e12**	**2.0**	**1.5e7**	**23.4**	**1.98**
19990205025535	**-26.420**	**27.417**	**2991**	**4.3e12**	**2.3**	**5.8e7**	**17.6**	**1.37**
19990205175933	**-26.420**	**27.363**	**2686**	**3.1e11**	**1.6**	**5.0e6**	**44.3**	**3.07**
19990205205457	**-26.463**	**27.362**	**2558**	**2.9e12**	**2.2**	**3.1e7**	**18.5**	**0.96**
19990209154922	-26.477	27.329	2738	6.6e11	1.8	3.1e5	10.7	0.19
19990209195821	**-26.401**	**27.418**	**1618**	**4.2e13**	**3.0**	**9.2e8**	**9.3**	**3.20**
19990216053511	**-26.429**	**27.432**	**3761**	**1.2e13**	**2.7**	**9.2e6**	**10.4**	**0.56**
19990226143150	**-26.397**	**27.387**	**1981**	**4.5e12**	**2.4**	**2.2e6**	**12.3**	**0.53**
19990309161938	-26.435	27.415	2464	1.1e13	2.6	6.8e7	8.1	0.99
19990310023001	-26.429	27.428	2651	1.0e13	2.6	1.7e8	14.9	2.50
19990318193538	-26.428	27.396	395	4.6e13	3.1	1.5e9	11.5	5.20
19990703111216	-26.169	27.497	3099	2.2e13	2.9	1.8e8	18.5	10.60
19990709200228	-26.395	27.413	7235	5.5e13	3.1	9.7e8	8.7	4.00
19990718173016	-26.393	27.403	3823	7.0e13	3.2	1.2e9	8.6	4.80
19990907150924	-26.386	27.446	3634	4.0e13	3.0	2.7e9	13.0	10.90
19990923132820	-26.386	27.452	4028	4.1e13	3.0	1.5e9	13.3	10.30

Moment tensors of selected events

We determined moment tensors for events that covered a range of magnitudes, depths, and locations to provide as much variation as possible in composing a catalog of "typical" large mining-induced events. Some events are also part of foreshock-mainshock-aftershock sequences. We followed the method outlined in Ammon et al. (1998) and calculated regional Green's functions, then inverted for the moment tensors using broadband data from the Kaapvaal PASSCAL deployment. Since we used the PASSCAL data alone, we obtained independent measurements from those of the in-mine array data previously used to determine the source parameters (see Table 1). A comparison of event magnitudes as calculated by the spectral method using only the in-mine array data with magnitudes determined as part of the moment-tensor inversion is shown in Figure 3. By only using eight nearby stations for the inversions (see Figure 2), we will be able to use the more distant stations for regional phase amplitude analysis; therefore, the results of the two studies will be independent of each other.

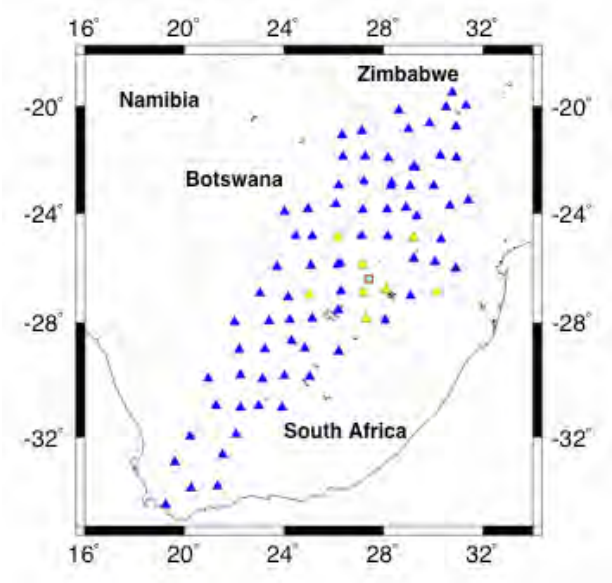

Figure 2. Map of southern Africa showing locations of the Kaapvaal Craton PASSCAL deployment (triangles). Yellow triangles are the stations used in the moment tensor inversions. The small red box is the area shown in detail in Figure 4.

To compute regional Green's functions, we used a simple 45-km thick crustal half-space for the velocity model based on the results of receiver function analysis of the crustal structure of the Archean craton by Nguuri et al. (2001). This study determined that crustal thickness ranged from approximately 41-50 km across the area covered by the stations used in our moment tensor inversions. We used wavespeed and density values determined experimentally by the mines (P = 6.1 km/s, S = 3.65 km/s, ρ = 2.7g/cm^3).

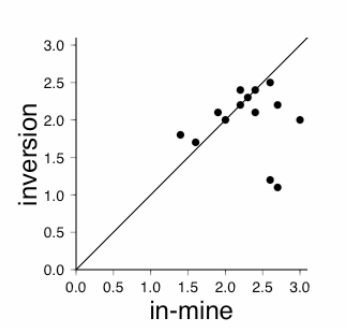

Figure 3. Comparison between moment magnitude as determined by the spectral analysis using in-mine seismic data and that determined through the moment tensor inversion using the broadband data. The 1:1 line is drawn for reference.

The results of the moment tensor inversions are given in Table 2. These are fully deviatoric tensors. We allowed the moment tensors to have some isotropic component in the inversion, but none were significantly isotropic. It has been shown that S/P-wave amplitude ratios of mining-induced events are often smaller for events with significant isotropic components when compared with purely double-couple events of approximately the same moment (Cichowicz et al., 1990; Gibowicz et al., 1991). Therefore, using the in-mine recordings, we calculated high-frequency (> 10 Hz) S/P-wave amplitude ratios of several other events between $1 < M_w < 2$ whose signal-to-noise ratios were not good enough to perform moment tensor inversions using broadband data. The S/P-wave amplitude ratios were not significantly different than those of the double-couple events for which we determined moment tensors, and therefore we do not expect significant isotropic components of the source down to at least $M_w = 1$. It should be noted that the previous studies involving S/P-wave amplitude ratios were conducted with events of $M_w < 0$.

The fourteen events for which we determined moment tensors ranged in size from $1.4 < M_w < 3.0$ and ranged in depth from 1.6 km to 3.8 km. This depth range is typical of the larger mining-induced events in the Carletonville district. We do not observe any significant trend in type of faulting with either depth or event size (see Figure 4). The events in this study so far show two major modes of failure: normal faulting and strike-slip faulting. It is surprising to find such a large population of strike-slip events in this group, as the vast majority of faults observed underground have measurable offsets consistent with normal motion alone. There are several possibilities for this apparent discrepancy. Not all seismogenic faults are directly visible underground, therefore there may be an historical bias in favor of normal faults because of observational limitations. In addition, the faults observed underground have yet to be studied in detail to determine whether all fault offset is due to seismic activity, or whether there is some creep. For example, do faults creep in a normal sense, but release seismic energy in a strike-slip or dip-slip pattern? Strike-slip motion is inherently difficult to discern when there is only limited visible access and when the displacement is not large enough to juxtapose different formations. There has been little in the way of detailed analysis of fault cores taken from depth; therefore sense of motion has been assumed, but may in fact be a relic of ancient fault activity that predates the active mining. It may also be that these moment tensors, which were determined by surface broadband data alone are not accurate, although the waveform fits are generally good. An obvious next step in this analysis will be to perform a joint inversion using in-mine data for moment tensor analysis. In addition, S-wave data could be included in the moment-tensor inversions.

Table 2. Moment tensors of mining-induced events

Event	M_{xx}	M_{xy}	M_{xz}	M_{yy}	M_{yz}	M_{zz}
19990103155836	-0.273E-03	-0.268E-02	0.230E-02	-0.583E-02	0.222E-02	0.611E-02
19990118102526	0.623E+00	-0.121E+01	0.179E-01	-0.152E+01	0.552E+00	0.896E+00
19990118112405	0.832E+00	-0.275E+01	-0.352E-02	-0.166E+01	-0.306E+00	0.828E+00
19990118200717	-0.132E+01	-0.169E+01	0.256E-01	0.239E+01	-0.965E-01	-0.107E+01
19990118213352	-0.382E+00	-0.185E+00	-0.166E-01	0.616E+00	-0.406E+00	-0.233E+00
19990201194832	0.186E -01	0.151E+00	-0.140E+00	0.112E+00	-0.273E+00	-0.131E+00
19990202123021	-0.118E+00	-0.320E-01	-0.143E-01	0.275E+00	-0.193E-01	-0.157E+00
19990203221201	-0.188E+01	-0.154E+01	-0.125E-01	0.363E+01	0.884E-01	-0.175E+01
19990205025535	0.135E+01	0.194E+01	-0.961E-01	-0.240E+01	0.309E+00	0.106E+01
19990205175933	0.738E+00	-0.674E+00	-0.229E-01	-0.123E+01	0.135E+00	0.496E+00
19990205205457	0.408E+00	0.895E+00	-0.760E-01	-0.965E+00	0.318E+00	0.557E+00
19990209154922	-0.610E+00	-0.143E+01	0.560E-01	0.121E+01	-0.242E+00	-0.603E+00
19990216053511	0.353E-02	-0.130E-02	-0.270E-02	-0.360E-02	0.155E-02	0.738E-04
19990226143150	0.406E-02	-0.919E+00	-0.456E-01	0.190E+00	0.275E+00	-0.194E+00

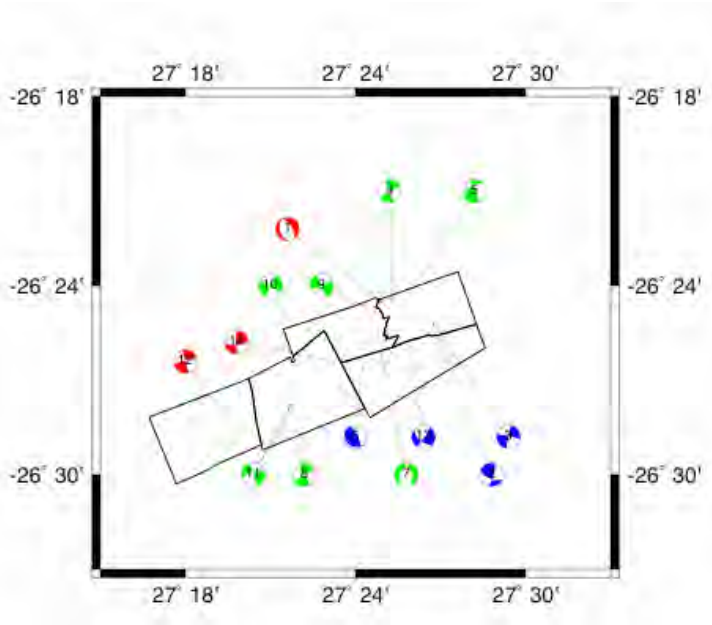

Figure 4. Map view of the lease areas of five mines in the Carletonville district with locations and focal mechanism (FC) diagrams of the events for which moment tensors have been determined. Events are labeled in chronological order (The FC labeled "1" is 19990103155836, and the FC labeled "14" is 19990226143150, etc.). Red FCs denote events whose depths are between 1-2 km, green FCs are for events between 2-3 km and blue FCs show events whose depths are between 3-4 km.

Regional P/S amplitude measurements

In order to obtain geometric spreading, attenuation and coda amplitude corrections for the permanent International Monitoring Station (IMS) stations in southern Africa (BOSA, LBTB, SUR), we picked Pn, Pg, Sn, and Lg arrivals for all events of M > 2.5 in the Lawrence Livermore National Laboratory (LLNL) database from 1998 – 2004. We then culled this dataset to events of M > 3.5 to perform the station calibrations. We determined coda M_w for these events as well based on the well-studied large event of October 30, 1994 (e.g. Bowers, 1997). The locations of these M > 3.5 events are shown in Figure 5.

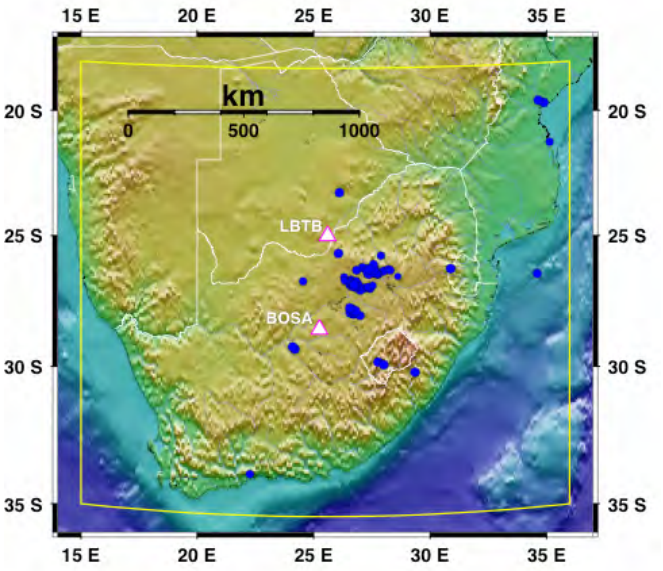

Figure 5. Map of southern Africa showing the location of M > 3.5 events (blue circles) used to determine regional geometric spreading, attenuation, and coda amplitudes for comparison with the target events in our database. Permanent stations BOSA and LBTB are white triangles.

We next used the coda M_w's for these events to remove distance and magnitude trends from the high frequency discrimination amplitude ratios (see Figure 6). This dataset spans a narrow range of frequency and magnitude, so no trend is readily apparent in the raw measurements of amplitude ratios with respect to magnitude (compare the bottom two plots in each set of quad plots in Figure 6). The magnitude and distance amplitude correction (MDAC) removes the significant trend with respect to source-receiver distance (compare the top two plots in each set of quad plots in Figure 6) in the amplitude ratios at this frequency band.

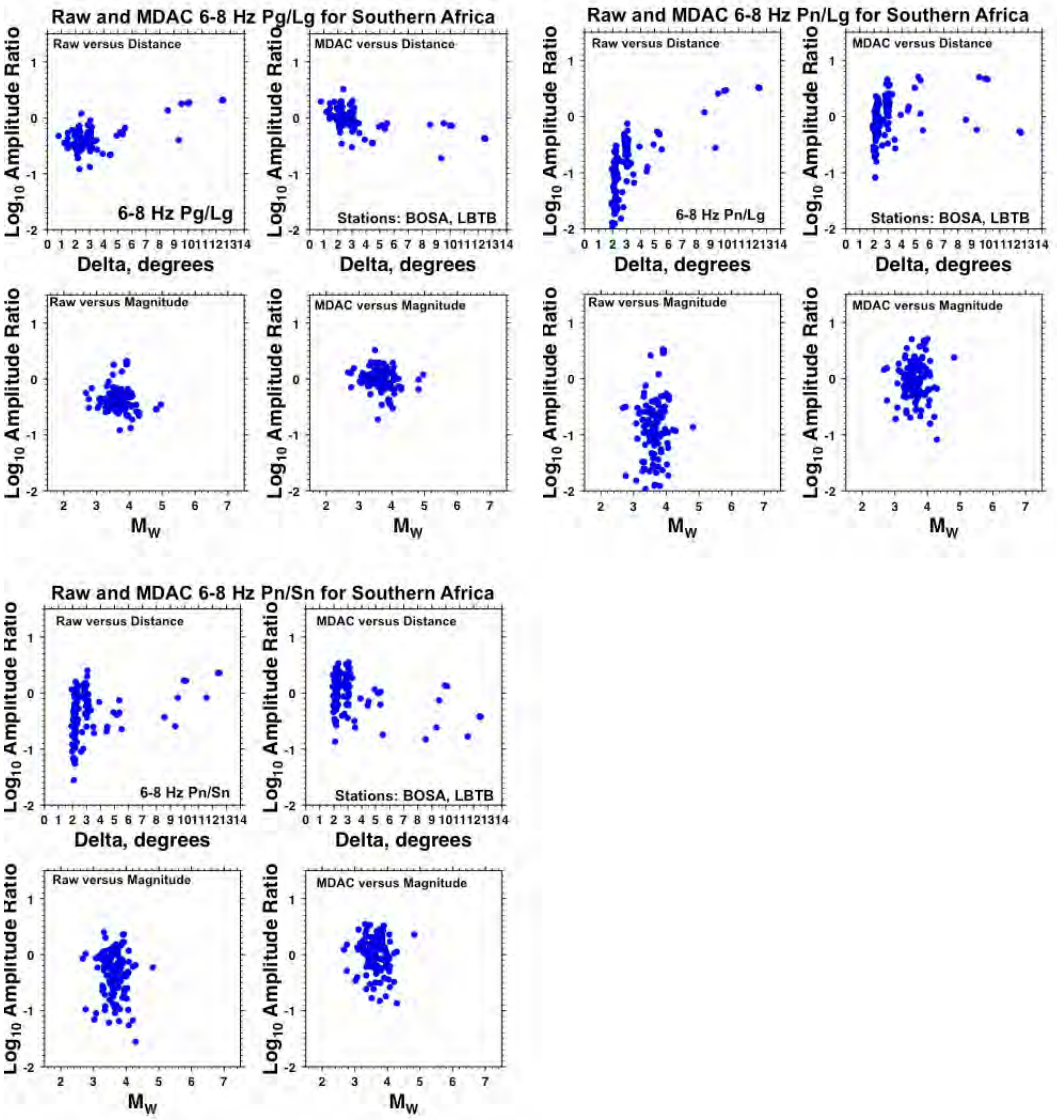

Figure 6. Regional P/S amplitude ratios at 6-8 Hz for the events in Figure 5. Each set of quad plots shows raw measurements (left) and measurements whose amplitudes have been corrected for magnitude and distance (right) for a given amplitude ratio as a function of source-receiver distance (top) and as a function of magnitude (bottom). The first set of quad plots is for the ratio Pg/Lg, the second is for the ratio Pn/Lg, and the third is for Pn/Sn.

Many prior studies have shown that high frequency P/S ratios have the potential to discriminate earthquakes from explosions (e.g., Walter et al. 1995, Battone et al. 2002), particularly after correcting for source and path effects (e.g., Taylor et al. 2002). The range of high frequency P/S values in Figure 6 is fairly large, even after correcting for source and path effects. We want to understand the source of this variability and suspect that some of it comes from the presence of mine-related seismicity, which has very shallow depths and potentially a greater range in focal mechanism, as compared with ordinary tectonic events. To examine the effects of depth and mechanism on P/S ratios and other regional discriminants, we plan to determine the regional phase amplitudes of the mine-related events in Table 1, and Table 2 where depth and focal mechanism, respectively, have been independently determined. We will estimate the coda moment magnitudes and use the source and path corrections as determined from the larger background events shown in figures 5 and 6. We also plan to determine some additional depths and focal mechanisms for a few of the larger events shown in Figure 5 that are amenable to regional waveform modeling.

CONCLUSIONS AND RECOMMENDATIONS

We have calculated source parameters for 46 mining-induced events of $M_w > 1$ and inverted for the best-fitting moment tensors for 14 events and do not find any significant isotropic components of the source for any of the events studied. This supports the hypothesis that large mining-induced failures occur by shearing of pre-existing planes of weakness under frictionally-controlled conditions (i.e., high normal stress) and that these events are physically analogous to natural tectonic earthquakes. A surprising number of strike-slip mechanisms were determined, in contrast to normal faulting, which was expected. There have been few thorough studies of the source characteristics of these events to date with which to compare our results. Therefore, we must continue to determine more moment tensors, and we must incorporate the in-mine data in a joint inversion for the moment tensors. The next step in the characterization of these mining-induced events is to take the ground-truthed depth and mechanism data and combine this with the MDAC-corrected data to look for depth and focal mechanism trends. We also plan to determine more accurate locations and mechanisms for some of the larger tectonic events in the LLNL database so that we will obtain two separate datasets whose origins are known (tectonic and mining-related).

ACKNOWLEDGEMENTS

We thank Chuck Ammon for lending us his expertise in calculating local and regional Green's functions.

REFERENCES

Ammon, C. J., R. B. Herrmann, C. A. Langston and H. Benz (1998), Source parameters of the January 16, 1994 Wyomissing Hills, Pennsylvania earthquakes, *Seism. Res. Letters* 69: 261-269.

Andrews, D. J. (1986), Objective determination of seismic source parameters and similarity of earthquakes of different size, in *Earthquake Source Mechanics*, S. Das, J. Boatwright, C.H. Scholz, eds, vol. 6 of Geophysical Monograph *Am. Geophys. Union* 37: 259-267.

Battone, S., M. D. Fisk and G. D. McCarter (2002), Regional Seismic-Event Characterization Using a Bayesian Formulation of Simple Kriging, *Bull. Seism. Soc. Am*. 92: 2277-2296.

Bowers, D. (1997), The October 30, 1994 seismic disturbance in South Africa: Earthquake or large rockburst?, *J. Geophys. Res*. 102: 9843-9857.

Cichowicz, A., R. W. E. Green, A. van Zyl Brink, P. Grobler and P. I. Mountfort (1990), The space and time variation of micro-event parameters occurring in front of an active stope, in *Rockbursts and Seismicity in Mines*, ed. C. Fairhurst, 2: 171-175.

Gibowicz, S. J., R. P. Young, S. Talebi, and D. J. Rawlence (1991), Source parameters of seismic events at the Underground Research Laboratory in Manitoba, Canada: Scaling relations for events with moment magnitude smaller than –2, *Bull. Seism. Soc. Am*. 81: 1157-1182.

Hanks, T.C. and H. Kanamori (1979), A moment magnitude scale, *J. Geophys. Res*. 84: 2348-2350.

Ide, S. and G. C. Beroza (2001), Does apparent stress vary with earthquake size?, *Geophys. Res. Lett.* 28**:** 3349-3352.

Mendecki, A. J., ed., *Seismic Monitoring in Mines*, Chapman and Hall, 1997.

Mendecki, A. J. (1993), Real time quantitative seismology in mines, Keynote lecture in *Proceedings of the 3rd International Symposium on Rockbursts and Seismicity in Mines*, ed. By R. P. Young, Balkema, Rotterdam, pp. 1141-1144.

McGarr, A. (1992), Moment tensors of ten Witwatersrand mine tremors, *Pure Appl. Geophys.* 139**:** 781-800.

Nguuri, T. K., J. Gore, D. E. James, S. J. Webb, C. Wright, T. G. Zengeni, O. Gwavava, J. A. Snoke, and Kaapvaal Seismic Group (2001), Crustal structure beneath southern Africa and its implications for the formation and evolution of the Kaapvaal and Zimbabwe cratons, *Geophys. Res. Lett*. 28, pp. 2501-2504.

Richardson, E. and T.H. Jordan (2002), Seismicity in deep gold mines of South Africa: Implications for tectonic earthquakes, *Bull. Seism. Soc. Am*. 92, pp. 1766-1782.

Taylor, S., A. Velasco, H. Hartse, W. S. Philips, W. R. Walter, and A. Rodgers, (2002). Amplitude corrections for regional discrimination, *Pure. App. Geophys*. 159, 623-650.

Walter, W. R., K. Mayeda, and H. J. Patton (1995), Phase and spectral ratio discrimination between NTS earthquakes and explosions Part 1: Empirical observations, *Bull. Seism. Soc. Am.* 85, 1050-1067.

DEVELOPING MULTIPLE-FREQUENCY DISCRIMINANTS FOR USE WITH REGIONAL CODA-AMPLITUDE MEASUREMENTS

C. K. Saikia[1], K. Mayeda[2], L. Zhu[3], and R. B. Herrmann[3]

URS Group, Inc.[1], Lawrence Livermore National Laboratory[2], and Saint Louis University[3]

Contract Nos. DE-AC52-04NA225545[1], DE-FC52-04NA25546[3], and W-7405-ENG-48[2]

ABSTRACT

This is a collaborative study involving three institutions to investigate the feasibility of employing regional coda-wave amplitude measurements in multiple narrow pass bands for the purpose of discriminating small, regionally recorded seismic events. The motivation comes from previous studies that have shown that regional, single-station coda-magnitude estimates are more stable and accurate than any direct phase measure to date (e.g., Mayeda et al., 2003a,b). Typically, the source amplitude estimates derived from the coda have inter-station variances on the order of 0.07 log amplitude units; hence the method is excellent for regions with sparse station coverage. The method has been tested over large geographic regions spanning both local and regional distances for the purpose of magnitude estimation (e.g., Phillips et al., 2003; Mayeda et al., 2003, Eken et al., 2003; Morasca et al., 2003). In terms of the discrimination, only a preliminary study using coda waves was performed on Nevada Test Site (NTS) explosions and earthquakes in the study by Walter et al. (2003). Due to the nature of the coda, path and azimuthal source-radiation effects are averaged over, making coda amplitudes insensitive to local structure, in sharp contrast to direct regional phases such as Pn, Pg, and Lg. Calibrated to seismic moment (M_0), or moment magnitude (Mw), coda-derived source spectra provide a means to obtain moment estimates from smaller or more distant events, which cannot be analyzed with conventional waveform or spectral source-inversion techniques because of signal-to-noise limitations.

So far, we made progress in obtaining M_0 and M_w of small magnitude earthquakes that have occurred in Korea and China using regional seismograms recorded by the in-country stations. Tying M_w (coda magnitude) to M_w (moment magnitude) also provides a physical measure of event size, which is unbiased, i.e., transportable. However, shallow events (h <3 km) of all source types have pronounced peaks in their spectra in the 0.2–1.0 Hz range, relative to normal-depth earthquakes due to the Rg-to-S conversion. These source-spectra differences need to be accounted for to make direct coda-amplitude comparisons with normal-depth earthquakes, particularly for discrimination purposes. Without doing so, shallow events will tend to have their long-period source spectrum overestimated. To facilitate M_w (coda magnitude) vs. M_w (moment magnitude) comparison, we established focal mechanisms, depths and seismic moments for a small subset of earthquakes occurring in the Korean Peninsula and in its adjoining eastern and western seas. Similar studies have also been undertaken for estimating M_o(seismic moment) and M_w(moment magnitude) for Chinese earthquakes by modeling regional seismograms. We have also completed a study related to earthquakes in southwestern United States (US). Thus, we have established accurate source depth and seismic moments needed for the calibration of the regional coda amplitude in our study region. To add to our dataset, we have also collected regional waveforms recorded by stations of three temporary PASSCAL networks operated in Nepal, Bhutan, and Nanga Parbhat so that decay of the coda amplitudes can be calibrated to many regions of the world.

OBJECTIVE

The objective of this study is to investigate how to best employ multiple-frequency coda-amplitude measurements to identify source type, i.e., discriminate seismic events. To do so, we take advantage of the known differences in coda source-spectra characteristics between normal depth earthquakes and shallow events, particularly explosions. To this end, our objective is to apply the analysis to events occurring in the southwest US and then calibrate the Korean Peninsula, China, Nepal, and Nanga Parbhat by analyzing regional seismograms. That work requires estimating seismic moment (M_o) and moment-magnitude (M_w) from small magnitude earthquakes.

We make coda-amplitude measurements and compare them with those measured from the Lg waves (Figure 1) (Mayeda et al., 2003a,b). This illustrates that coda methodology works well, including across the tectonic regions. Data plotted in this example were obtained by applying the method to broadband data from 50 earthquakes ($4.0<M_w<7.6$) distributed over the entire region of Turkey. The upper left panel shows distance corrected-coda amplitude measurements from the stations ISP and ISKB using signals in the frequency band 0.1–0.2 Hz. The direct Lg waves amplitude measurements in the same frequency band between these two stations are shown in the right. Clearly, the direct Lg wave amplitude measurements have larger scatter in the range of 0.27 to 0.45. This indicates that the inter-station scatter in the distance-corrected coda-amplitude measurements is remarkably 3-to-4 times lower than those obtained from the distance-corrected direct Lg waves. Once we complete the entire data collection, the objective is to undertake a similar study to establish how well inter-station coda amplitude behaves relative to Lg waves in our study region.

RESEARCH ACCOMPLISHED

Figure 2 shows the distribution of stations of the KMA and KIGAM seismic networks in the Korean Peninsula, including the locations of 171 earthquakes that occurred in and around the Korean Peninsula. We have collected regional seismograms from these events and organized and binned them according to magnitude. Although the seismic networks have many stations, we have waveforms from only a limited number of stations for each event. Using these regional data, our team member Prof. R. B. Herrmann has determined focal mechanisms, depths, and seismic moments of nine earthquakes ($3.4<Mw<3.8$). The modeling study is still on-going, and we are selecting events that have suitable seismograms for the purpose.

We also collected regional seismograms recorded by the stations of the Chinese National Digital Seismic Network (CNDSN, Figure 3). This network had started several years ago by the Chinese Seismological Bureau and covers the entire mainland China. Seismograms from some events are available to our team member who is modeling regional seismograms to develop crustal models for different parts of China. The top panel in Figure 4 shows the epicenter of a M_w 5 aftershock of the 2001 Kunlun earthquake. Triangles represent the locations of the nearby stations of the CNDSN. The bottom panel in the figure shows an example of the on-going modeling study where the solid dark traces correspond to the recorded seismograms, and thin red traces on top of the dark traces correspond to the synthetic seismograms predicted using the best fitting focal mechanism. Here we show the P_{nl} seismograms in the first two columns and the long-period surface waves of the vertical, radial, and tangential components in the next three columns, respectively. The velocity model used in the inversion was taken from the Tibet region. The top number beneath each waveform pair (data and synthetic) for each segment represents the time shift that is allowed in fitting the data. The bottom number corresponds to the estimate of the cross-correlation coefficient between the two data traces times 100. So far, regional seismograms from 15 events have been successfully modeled and their seismic moment (M_o) and moment-magnitude (M_w) have been tabulated.

Because of the restrictive nature of the Chinese data set Dr. Zhu himself visited URS Group, Inc., to measure the coda and Lg amplitudes at multiple frequency bands as previously selected by Dr. Kevin Mayeda of Lawrence Livermore National Laboratory. To this end, we have completed an analysis of events recorded at stations HTA, HTG, KSH, and WUS. Figure 5 shows examples of the envelopes processed at different frequency bands that have been used in the measurement of the coda amplitude.

In addition to these data, we have collected regional waveforms from the Nanga Parbhat PASSCAL experiment in northern Himalaya. Researchers at Lamont Doherty Observatory have already determined the locations of many of the events recorded by this network and we used their catalog to download seismograms from the IRIS database.

The events have occurred in the Himalayan mountain region and are recorded between 250 and 500 km by multiple stations. Because of the complex geology of the region, we expect these data to provide a good test bed for testing the robust behavior of the coda-wave measurements vs the Lg wave amplitude measurements.

We have also employed a modified version of Mayeda et al. (2003a,b) coda-magnitude method in which an additional distance term is incorporated into the empirical magnitude relationship. This was applied to a dataset compiled for events occurring in the southwestern United States. Figure 6 is a map showing the stations and events used. Unlike the multiple bands, we used only one passband that of a worldwide station network short-period instrument, and measured the coda magnitude instead of the coda amplitude. The upper-left panel in Figure 7 compares single-station (PAS) M_w (coda) values to those determined from the waveform and spectral inversion source studies; a fairly small standard error of 0.09 is achieved. The upper-right and lower-left panels provide inter-station M_w comparisons. The lower-right panel shows network averaged M_w (coda) vs. the best estimate of M_w from source inversion studies. There is a slight depression in M_w(coda) values for the larger (M_w>6.5) events, which is believed to be due to post-corner-frequency spectral fall-off in the coda measurements.

CONCLUSIONS

The on-going study investigates the feasibility of employing regional coda-wave amplitude measurements in multiple narrow pass bands for the purpose of discriminating small, regionally recorded seismic events. Collection of data for this purpose is a continued effort and we have collected a major amount of data from different tectonic areas, including the main focus regions in Korea and parts of China. So far, we have completed waveform modeling to establish seismic moment and moment-magnitude (M_w) for several earthquakes from Korea and China.

REFERENCES

Eken, T, K. Mayeda, A. Hofstetter, R. Gok, N. Turkelli, and G. Orgulu (2003), An Application of the Coda Methodology for Moment-Rate Spectra Using Broadband Stations in Turkey, submitted to *Geophys. Res. Lett.*

Hartse, H. W., W. S. Phillips, M. C. Fehler, and L. S. House (1995), Single-Station Spectral Discrimination Using Coda Waves, *Bull. Seism. Soc. Am.* 85: 1464–1474.

Mayeda, K., A. Hofstetter, J. O'Boyle, and W. R. Walter (2003a), Stable and Transportable Regional Magnitudes Based on Coda-Derived Moment-Rate Spectra, *Bull. Seism. Soc. Am*. 93: 224–239.

Mayeda, K., T. Eken, A. Hofstetter, N. Turkelli, J. O'Boyle, G. Orgulu, and R. Gok (2003b), Moment Magnitude Calibration for the Eastern Mediterranean Region from Broadband Regional Coda Envelopes, in *Proceedings of the 25th Seismic Research Symposium—Nuclear Explosion Monitoring: Building the Knowledge Base*, LA-UR-03-6029, Vol. 1, pp. 420–427.

Morasca, P., K. Mayeda, L. Malagnini, and W. R. Walter (2003), Coda-Derived Source Spectra, Moment Magnitudes, and Energy-Moment Scaling in the Western Alps, submitted to *Geophy. J. Int.*

Phillips, W. S., H. J., Patton, C. M. Aprea, H. E. Hartse, G. E. Randall, and S. R. Taylor (2003), Automated Broad Area Calibration for Coda Based Magnitude and Yield, in *Proceedings of the 25th Seismic Research Review—Nuclear Explosion Monitoring: Building the Knowledge Base*, LA-UR-03-6029, Vol. 1, pp. 437–444.

Walter, W. R., M. E. Pasyanos, A. J. Rodgers, K. M. Mayeda, and A. Sicherman (2003), Regional Body-Wave and Surface-Wave Tomography Models to Improve Discrimination, in *Proceedings of the 25th Seismic Research Review—Nuclear Explosion Monitoring: Building the Knowledge Base*, LA-UR-03-6029, Vol. 1, pp. 495–503.

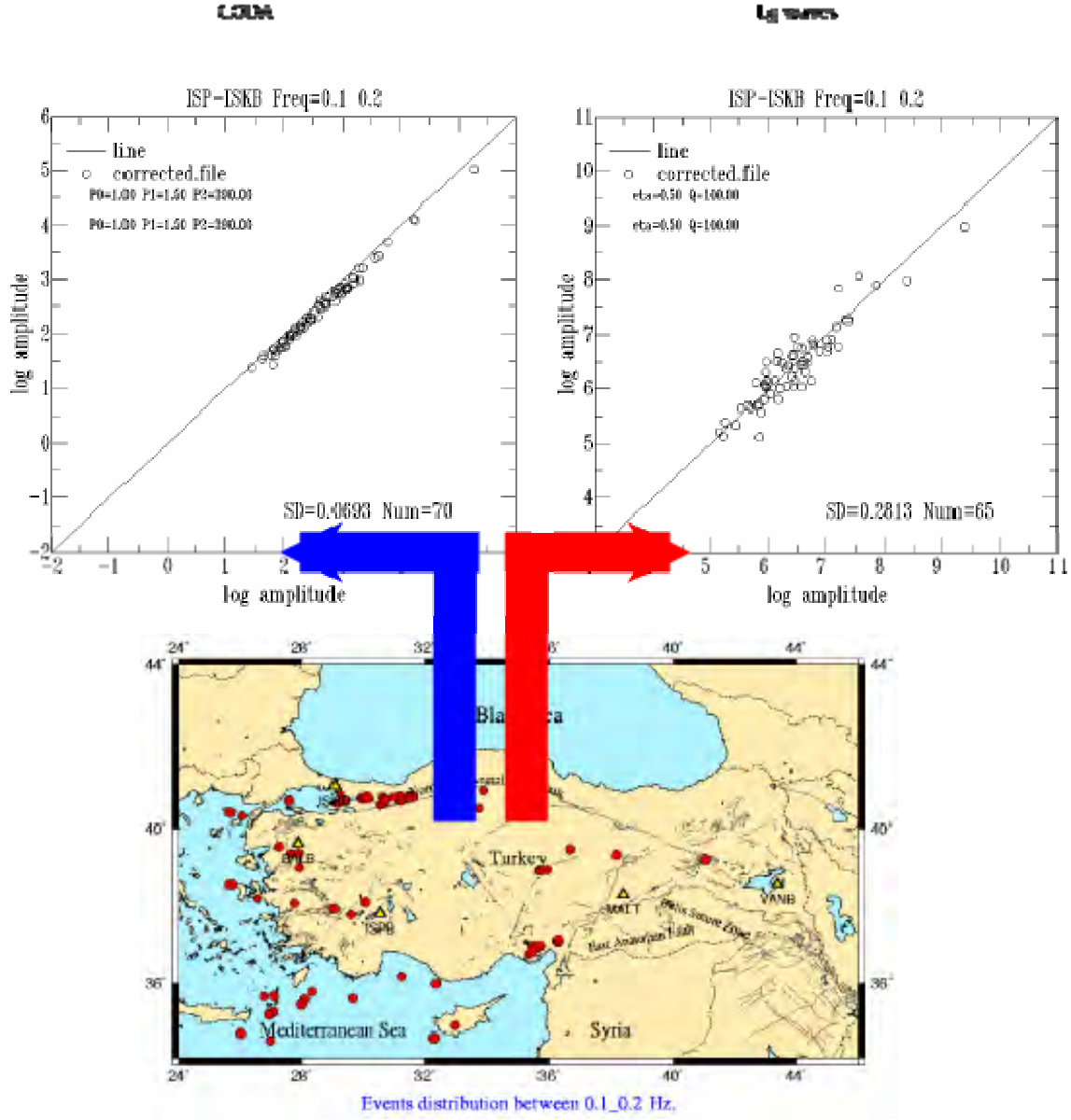

Figure 1. Illustration of transportability of the coda method. Plotted are the measurements of the distance-corrected coda amplitude (upper left panel) and direct Lg wave amplitudes (right panel) at stations ISP and ISKB in the frequency band 0.1–0.2 Hz. The inter-station standard deviation results show that coda amplitudes at this frequency band are four times more stable than distance corrected direct Lg waves using common events in the map shown at the bottom (taken from Mayeda et al., 2003).

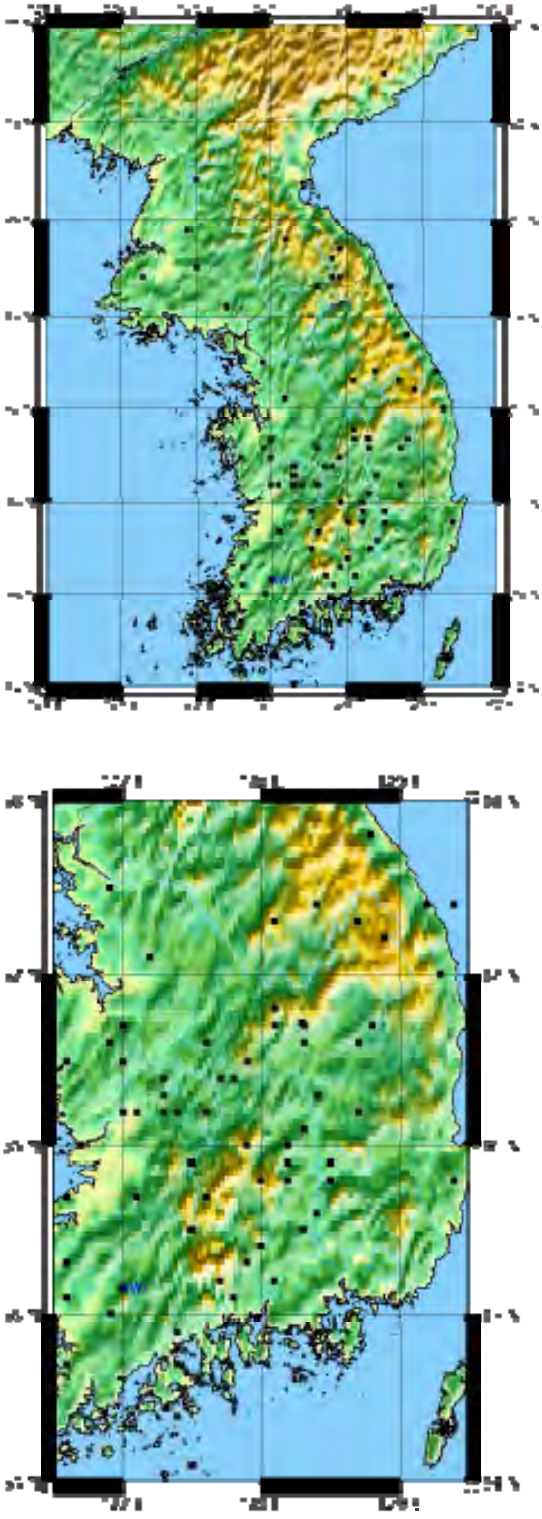

Figure 2. Map in the upper panel shows the event locations from which regional seismograms recorded by the KMA and KIGAM network stations (shown by solid squares, lower panel) have been archived. Seismograms have already been transformed to the necessary format for further processing.

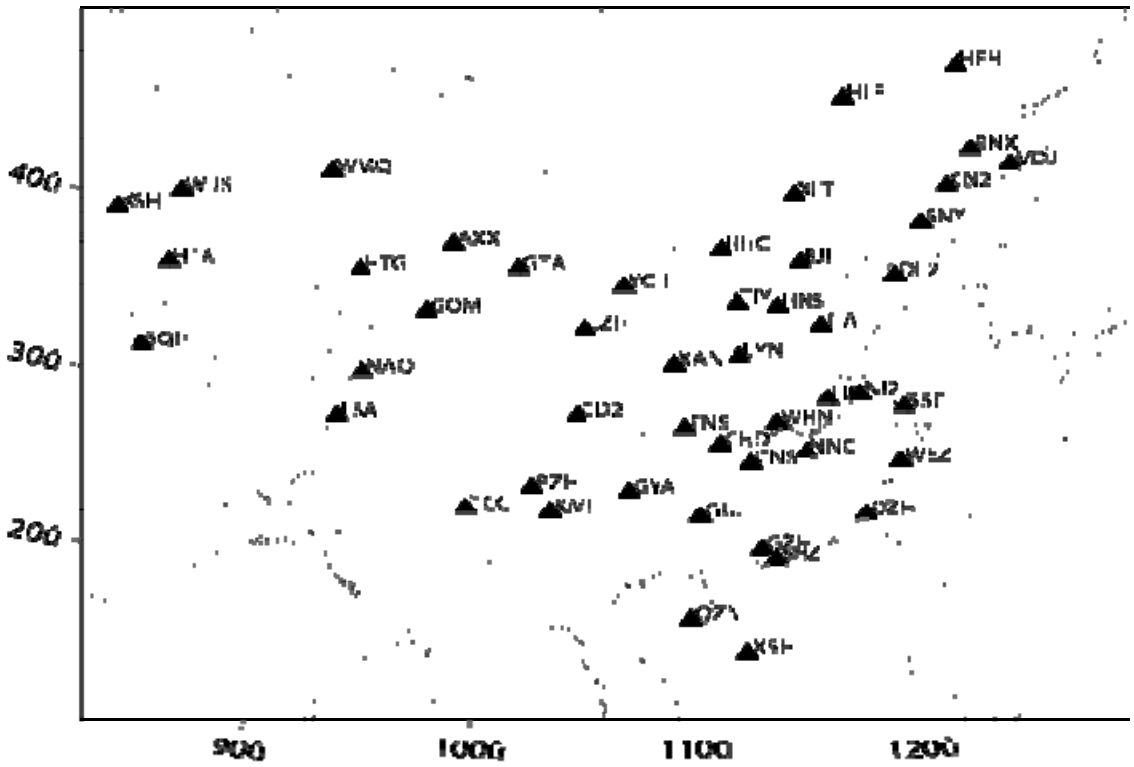

Figure 3. Station map of the CNDSN. Regional seismograms from this network have currently been modeled by our team member who is working collaboratively with the in-country scientists to investigate the crustal model in different parts of China. Using these data, seismic moment (M_o) and moment-magnitude (M_w) of many events have also been determined.

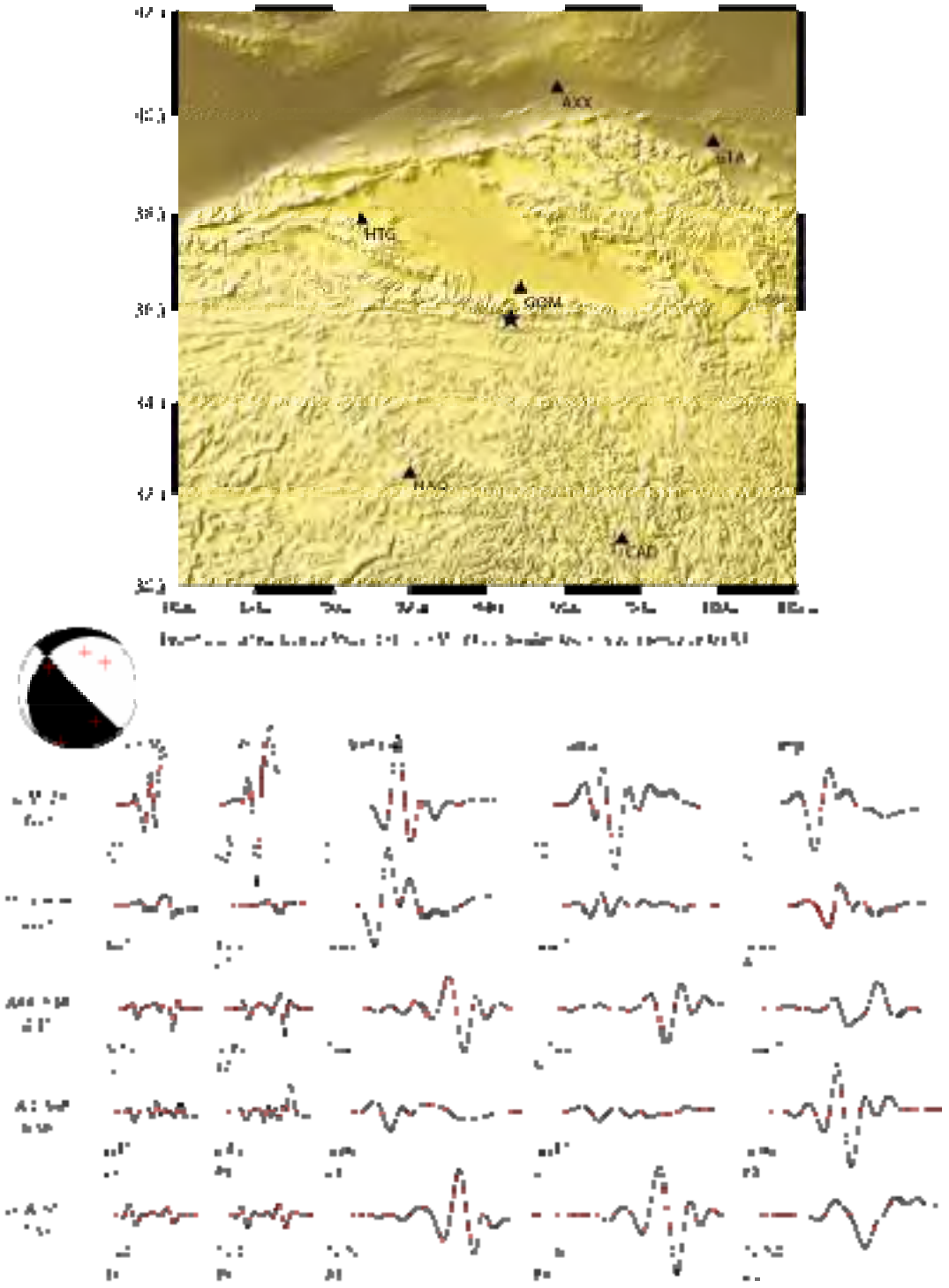

Figure 4. In top panel, the star represents the epicenter of a M_w 5 aftershock of the 2001 Kunlun earthquake. Triangles are the nearby CNDSN stations. The bottom panel shows modeling of the regional P_{nl} and surface wave seismograms yielding accurate focal parameters, seismic moment, and moment magnitude (M_w).

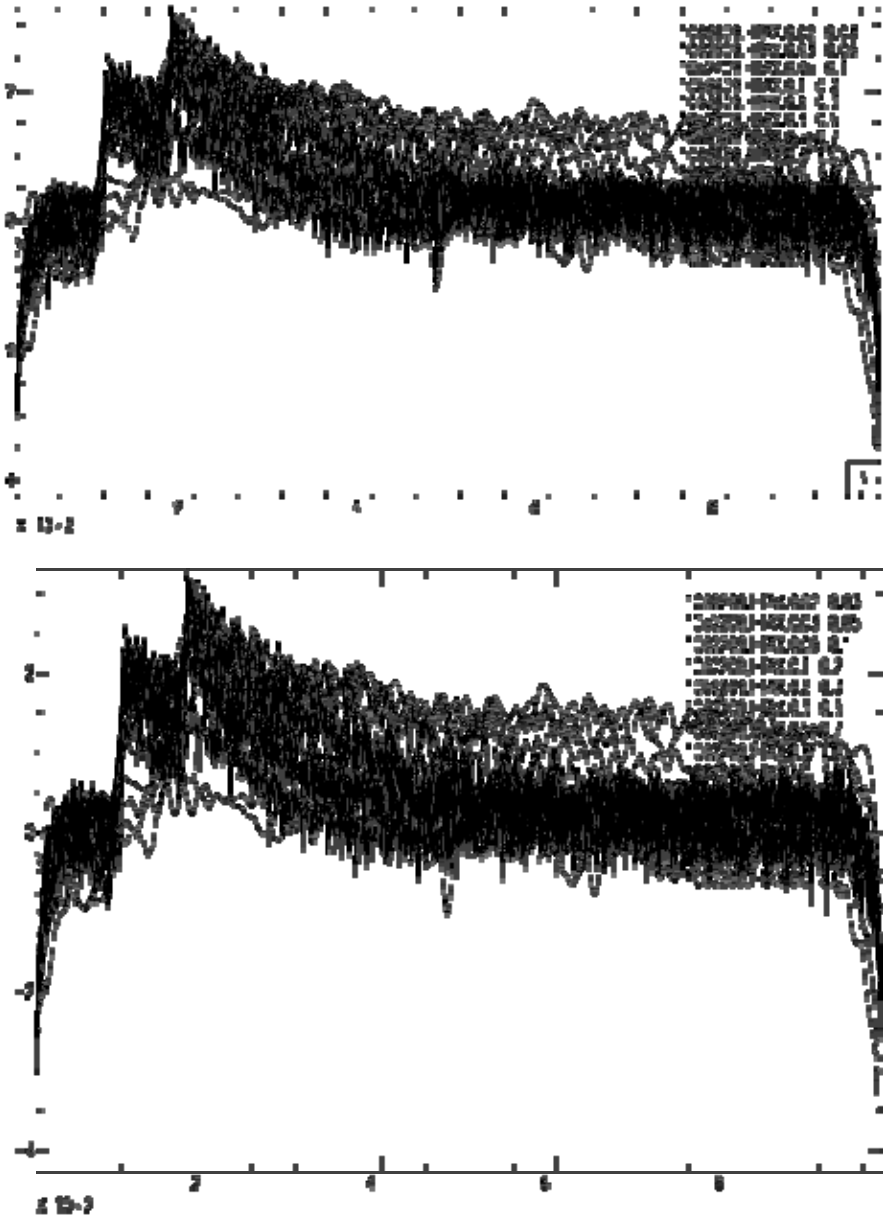

Figure 5. Envelopes processed using regional seismograms recorded at CNDSN station HTA at 14 different frequency bands from two separate events. Clearly, these envelopes show a straight-line decay between 2 and 4 Hz over which the coda magnitude can be measured.

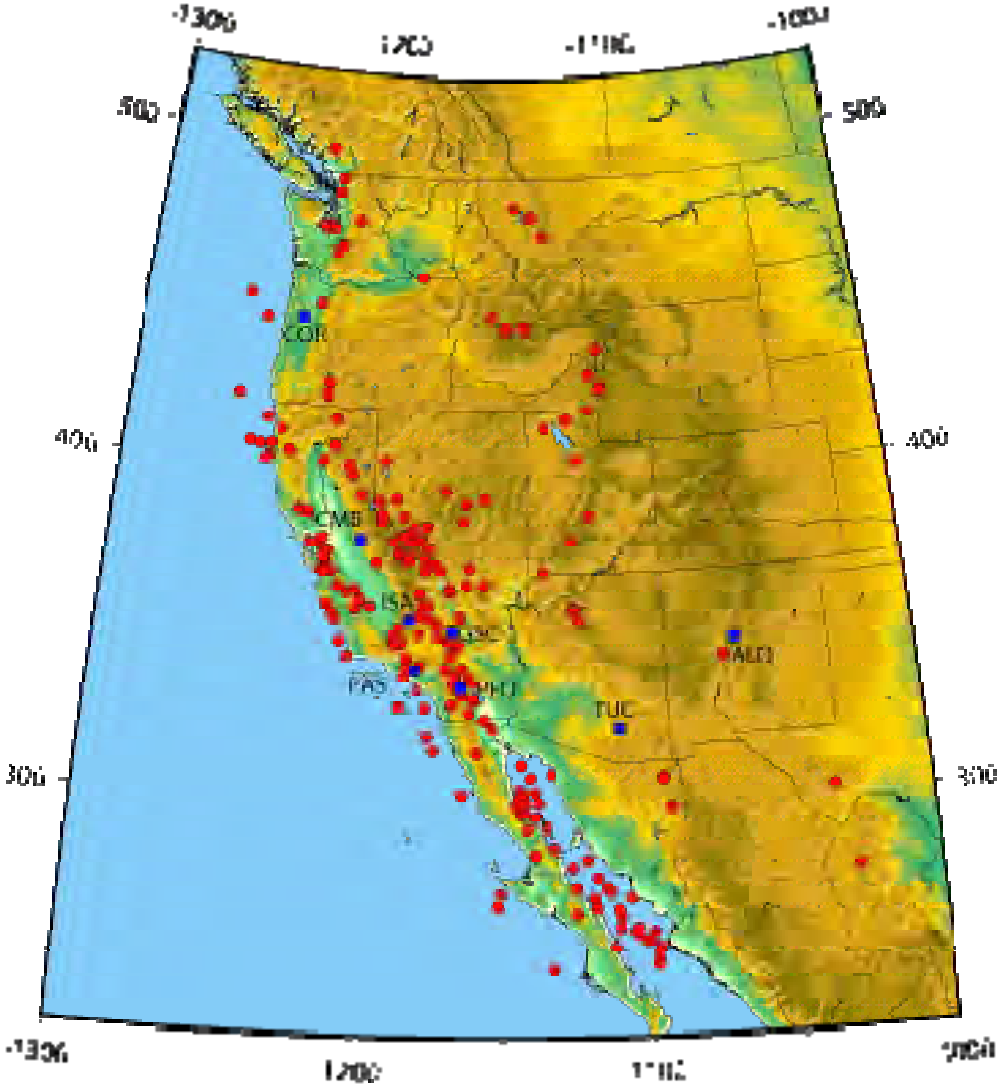

Figure 6. Map of the southwestern United States and bordering regions, showing the stations (blue squares) and earthquakes (red circles) used in a study to compare inter-station M_w (coda magnitude) and M_w (station-specific coda magnitude) vs M_w (moment-magnitude).

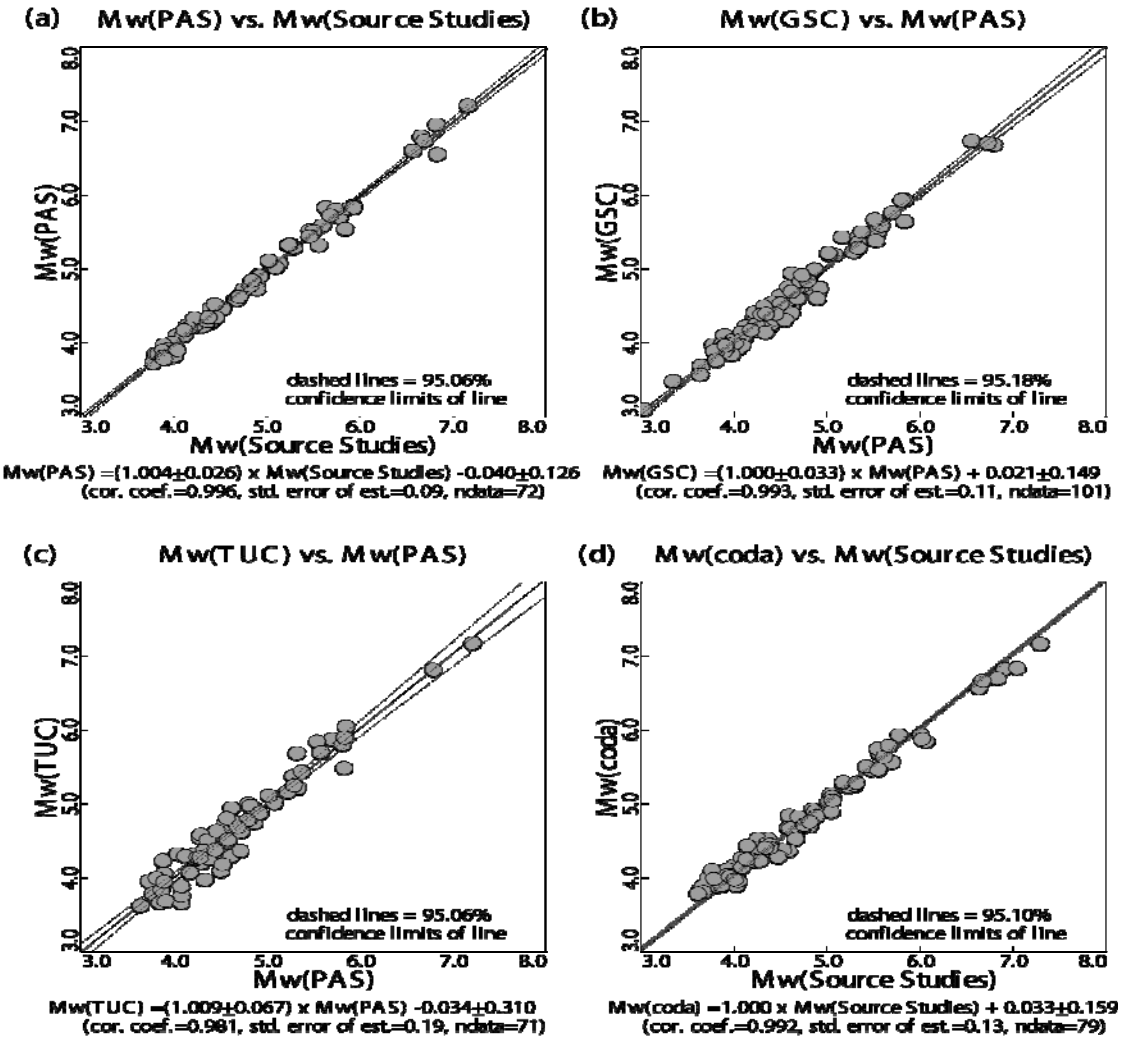

Figure 7. M_w(coda) results for (a) single-station (PAS) vs M_w (source studies), (b) inter-station M_w(coda) comparison for two relatively nearby stations GSC and PAS, (c) inter-station M_w(coda) comparison for two distance stations TUC and PAS, and (d) network averaged M_w(coda) vs M_w (source studies). M_w (source studies) is the moment-magnitude estimated using waveform modeling.

SEISMIC RADIATION FROM EXPLOSIONS IN FROZEN CRYSTALLINE ROCK

Charles G. Sammis and Ronald L. Biegel

University of Southern California

Sponsored by Air Force Research Laboratory

Contract No. FA8718-04-C-0012

ABSTRACT

When water in the cracks of low-porosity crystalline rock freezes, it affects the mechanical properties of the rock mass in two important ways. First, by immobilizing some cracks and bridging (and thus shortening) others, it reduces the average size and density of the initial cracks. O'Connell and Budiansky (1974) showed that a small reduction in this product of the average size of cracks times their volume density can produce a large increase in the elastic moduli of the rock. Second, ice in the cracks increases the fracture strength of the rock. Sammis and Biegel (2004) showed that this strengthening may be attributed to an increase in the effective coefficient of static friction for sliding on the cracks. By applying the micromechanical damage mechanics developed by Ashby and Sammis (1990), they were able to explain the strong temperature dependence of this strengthening in terms of the increase in the flow stress of the ice asperities with decreasing temperature below the freezing point. At the lowest temperatures, the strength of granite increased by a factor of 2 while the strength of limestone increased by a factor of 4. Since the Sammis and Biegel friction model is based on the flow stress of ice in the cracks, and this flow stress also depends on the strain-rate, these large increases in strength can be achieved at temperatures near the freezing point of water at high strain-rates in the explosion source. We used the "equivalent elastic medium model" for an explosive source developed by Johnson and Sammis (2001) to explore the effect of an increase in both elastic stiffness and compressive strength on the amplitude of far-field seismic radiation. An increase in the elastic moduli produces a decrease in the far field amplitudes. This is not surprising since it is well known that the apparent yield of an explosion decreases as the inverse of the shear wave velocity in the source rock. An increase in the coefficient of static friction, and consequent increase in compressive strength, also reduces the amplitude of the far-field seismic radiation. Our conclusion is that an explosion in frozen rock should have a smaller apparent yield than the same explosion in rock at temperatures above the freezing point. The effect should be larger in limestone than in granite.

OBJECTIVES

The objectives of this research program are to:

1. Build the micromechanical damage mechanics developed by Ashby and Sammis (1990) into source models for underground explosions.
2. Use this model to explore the influence of site effects such as rock type, ground water saturation, permafrost, and depth of burial on the seismic signature generated by the explosion.
3. Use this model to help interpret laboratory measurements and field experiments.
4. Explore the possibility that secondary radiation generated by the damage contributes to the regional seismic phases.

RESEARCH ACCOMPLISHED

Introduction

The Soviet test site at Novaya Zemlya at $73°$ North latitude lies well above the Arctic Circle. Rock at this site is probably below the freezing point of water to considerable depth. Permafrost thickness is greatest in non-glaciated polar regions like Siberia, where a record depth of 4900 feet to the permafrost base has been reported. Permafrost thickness in arctic Canada has been estimated to exceed 3000 feet and in arctic Alaska it may exceed 2000 feet. The question has therefore arisen as to how frozen water in cracks and pores might affect the seismic signature of an underground explosion.

Last year, Sammis and Biegel (2004) interpreted uniaxial compressive and tensile strength data on frozen rock from Mellor (1973) using the micromechanical damage model developed by Ashby and Sammis (1990). In this model, sliding on preexisting cracks in rock induces additional fracture damage and ultimate failure. The effect of ice in the damage model is to increase the effective coefficient of sliding friction on the preexisting cracks thus inhibiting the generation of new damage and strengthening the rock. In addition to strengthening, the damage model was also able to explain some of the subtler phenomenology in the frozen rock data such as the differences between porous and crystalline rock and the progressive strengthening observed to occur as the temperature was lowered from $0°\,\mathrm{C}$ to $-150°\,\mathrm{C}$.

We now use the "equivalent elastic medium source model" developed by Johnson and Sammis (2001) to investigate the effects of frozen water in the cracks of crystalline rock on the seismic radiation from an underground explosion.

The Mechanical Effects of Ice in the Cracks of Crystalline Rock

When water in the cracks of crystalline rock freezes, it affects the mechanical properties in two ways: 1) it increases the elastic moduli and 2) it increases the strength. Both effects can be understood in the context of the micromechanical damage mechanics developed by Ashby and Sammis (1990).

The Effect of Ice on the Elastic Properties

In the Ashby and Sammis (1990) damage mechanics, the size and density of fractures in crystalline rock are characterized by a single parameter called damage. The initial damage, before loading, is defined as

$$D_0 = \tfrac{4}{3}\,\pi\left(a\cos\chi\right)^3 N_V \qquad (1)$$

where a is the half-length of the cracks, N_V is the number of cracks per unit volume, and χ is an angle describing their orientation (see Figure 1).

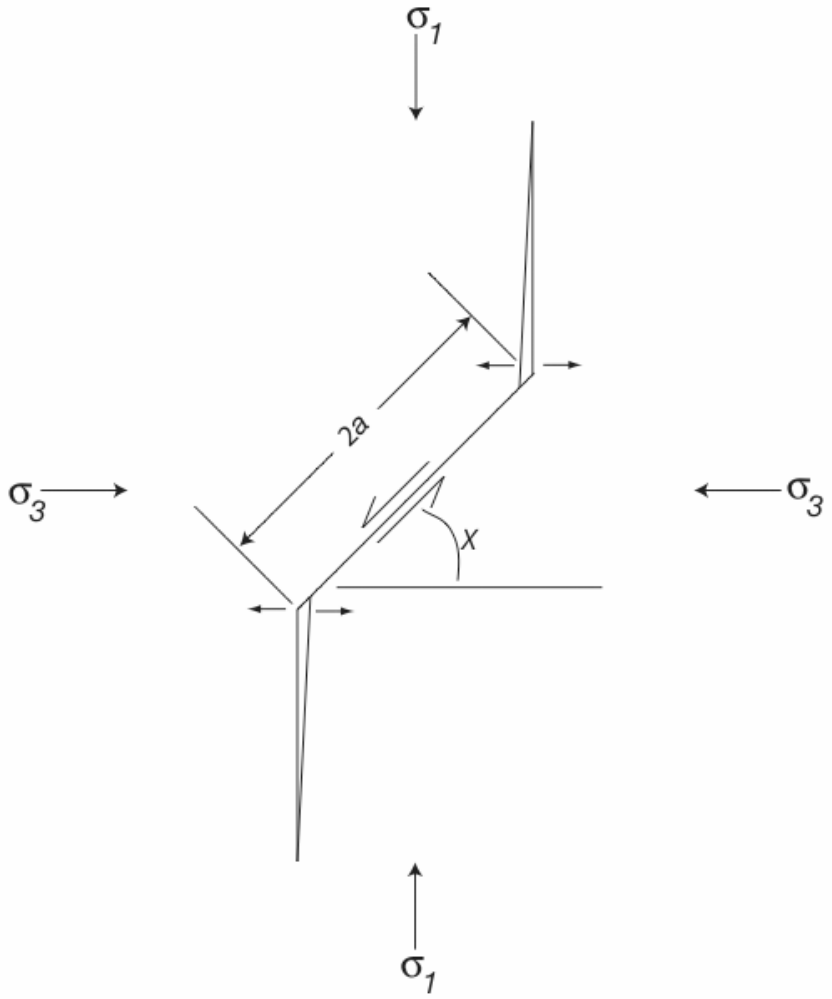

Figure 1. Crack geometry used in the Ashby and Sammis (1990) damage mechanics. Sliding on an inclined crack of length 2*a* nucleates tensile wing-cracks at its ends. Interaction between such cracks in an array of *Nv* cracks per unit volume leads to failure and fragmentation.

The effect of ice in the inclined crack in Fig. 1 is to either totally immobilize it, thus reducing Nv in eqn. (1), or, if saturation is not total, to form ice bridges thus reducing *a* in eqn. (1). The net effect of both is to reduce the initial damage *Do*.

The elastic moduli of rock are extremely sensitive to *Do*. Figure 2, from O'Connell and Budiansky (1974) shows the effect of changing *Do* on the P and S wave velocities in dry and water saturated rock. Note that the x-axis in Fig.2 is $\varepsilon = N\left\langle a^3 \right\rangle$ where *N* is the number of cracks per unit volume and *a* is the half-length of the crack. Comparison with eqn. (1) shows that ε can be written in terms of the initial damage as

$$\varepsilon = \frac{3}{4\pi}\left(\frac{1}{\cos\chi}\right)^3 D_o \approx 0.68 D_o \qquad (2)$$

The effect of freezing water in the cracks is to move to the left (toward lower damage) on the curves in Figure 2. This will produce an increase in elastic wave velocity. The effect is larger for S waves than for P waves in saturated rock.

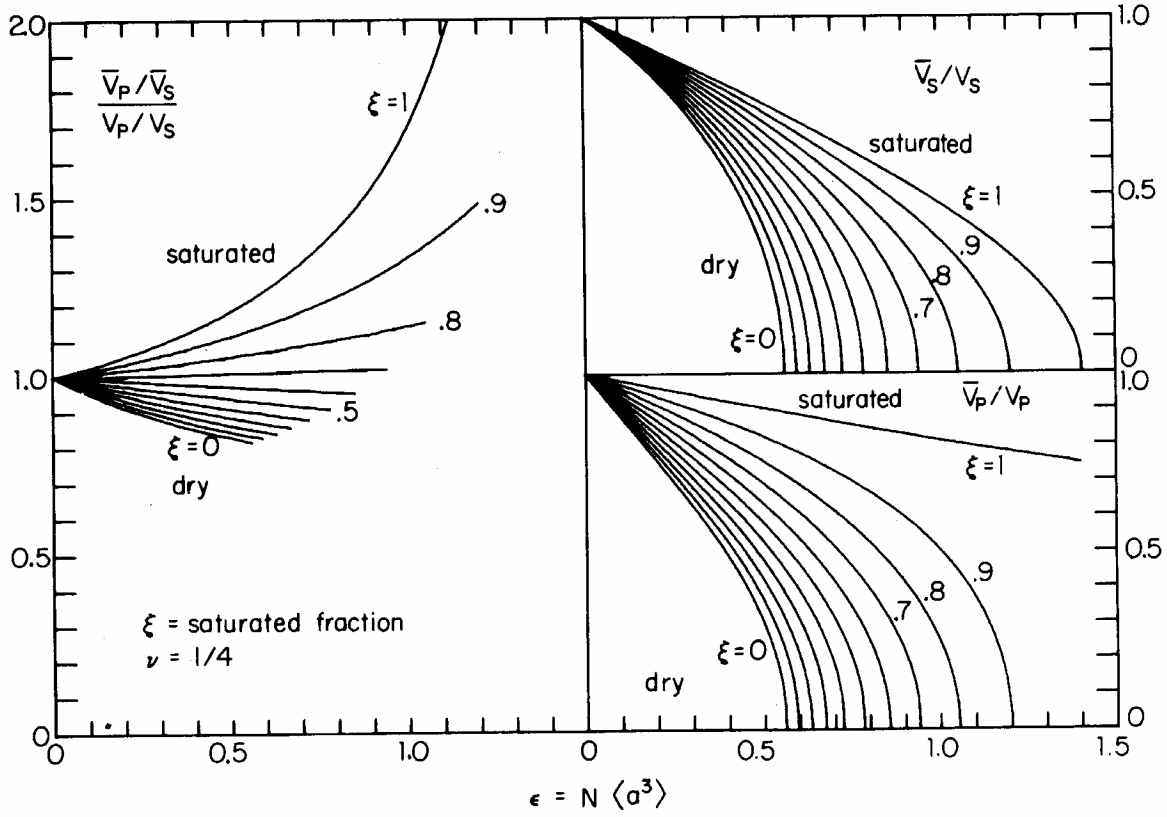

Figure 2. The effect of fractures on the elastic wave velocities in wet and dry rock (from O'Connell and Budiansky, 1974). The crack density parameter ε is closely related to the damage parameter in the Ashby and Sammis (1990) damage mechanics, differing only by a constant (see eqn. 2).

The Effect of Ice on the Strength

Sammis and Biegel (2004) used the Ashby and Sammis (1990) damage mechanics to explain measurements by Mellor (1973) of the uniaxial strength of saturated rock as a function of temperature from 20 to –197°C. They found that Mellor's data for the compressive strength (replotted here as Fig. 3) could be fit by the Ashby-Sammis model if the coefficient of friction in the sliding cracks is temperature dependent. The required temperature dependence is shown in Figure 4. Sammis and Biegel (2004) then showed that a simple Bowden and Tabor (1950, 1964) asperity model consisting of a combination of rock and ice asperities could explain the temperature dependence of the coefficient of static friction in Figure 4 using the known temperature dependence of the creep strength of ice.

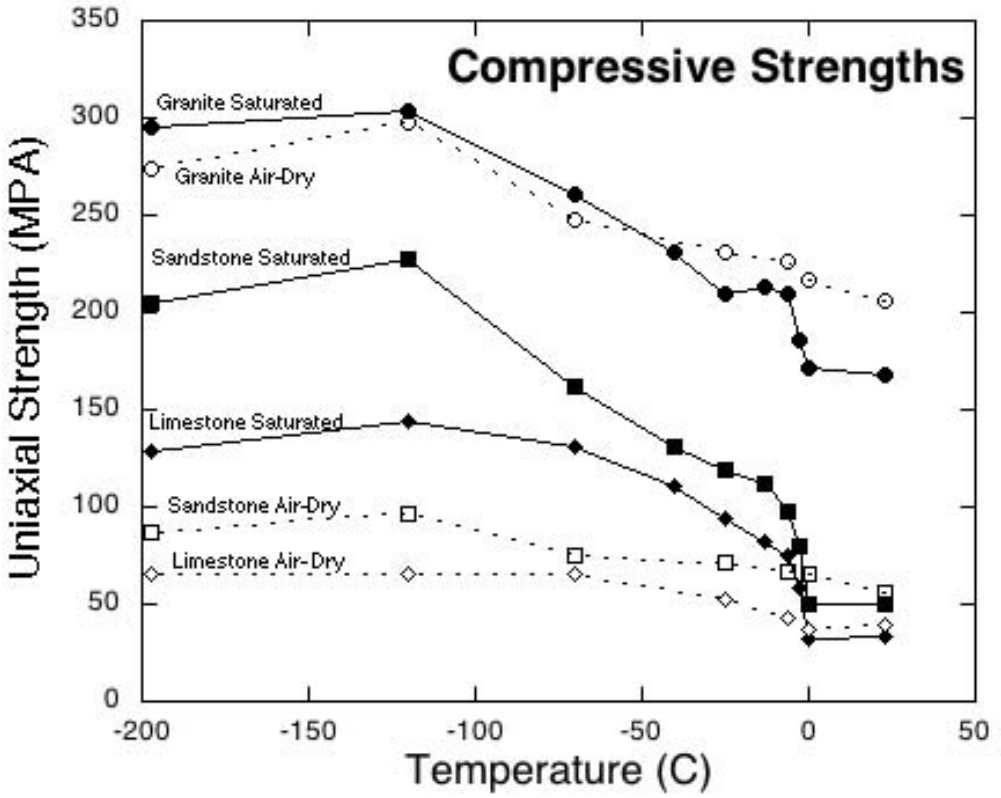

Figure 3. Strength of granite, limestone, and sandstone in uniaxial compression at low temperatures from Mellor (1973). Note that the strengths of saturated and air-dry granite samples are nearly the same at all temperatures indicating that the thin cracks in granite are saturated under air-dry conditions (From Sammis and Biegel, 2004).

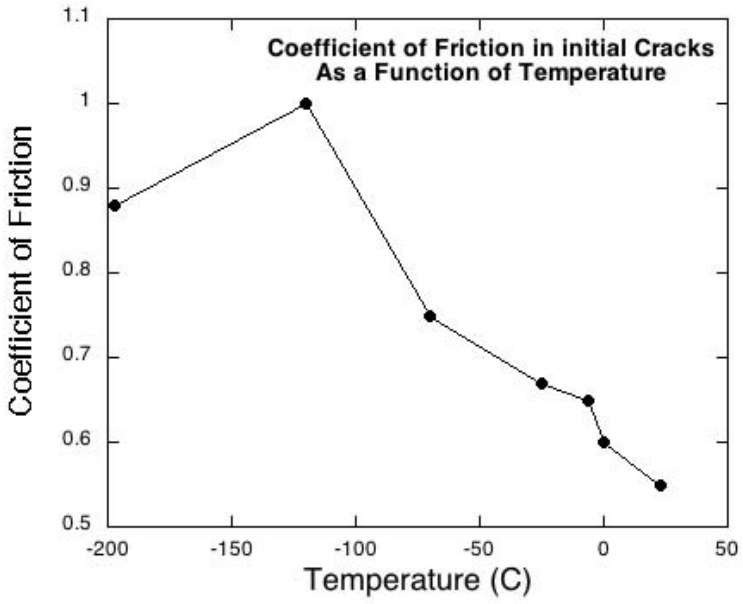

Figure 4. Coefficient of friction on starter cracks required if the damage mechanics model is to explain the increase in compressive strength at low temperatures in Fig. 3 (From Sammis and Biegel, 2004).

The Effects of Ice in the Cracks of Crystalline Rock on Seismic Radiation from an Explosion

In order to model the effect of ice on the damage generated by an explosion and on the seismic radiation, we require the principal stresses generated by the explosion as a function of distance and time. This is made difficult by the existence of the nonlinear processes between the cavity radius and the effective elastic radius, beyond which the assumptions of ordinary linear elasticity are valid. Sophisticated computer codes have been developed which include hydrodynamic effects, shock waves, and nonlinear equations of state (see, for example, Rodean, 1971; King et al., 1989; Glenn, 1993; Glenn and Goldstein, 1994, for discussion and further references). We use here an approximate method to calculate the stresses surrounding an explosion that is based on the equivalent elastic method developed by earthquake engineers to model the nonlinear behavior of soils that that occurs during strong ground motion. The central idea is to make the material properties a function of the stress in the outward propagating pressure pulse and then to adjust these material properties in an iterative process until the appropriate values are present at all distances from the source. In effect, the nonlinear stress-strain behavior is approximated by a series of linear relationships that change with the level of stress. The present formulation, described by Johnson (1993), relates density and bulk elastic properties to the peak pressure and shear and anelastic properties to the maximum shear strain.

The details of this model are published in Johnson and Sammis (2001) and will not be repeated here. In that paper we modeled the 1 kt chemical explosion detonated in September 1993 as part of the Non-Proliferation Experiment (NPE) (see Denny, 1994). The results of this simulation and attendant damage calculations are summarized in the next section.

Simulation of the NPE Explosion

The first objective in modeling the 1993 NPE event was to check the ability of the equivalent elastic method to simulate the stress field around an explosion. As illustrated in Figure 5 the model gives reasonable values for the peak velocity as a function of distance out to about one kilometer beyond which the model predicts slightly higher velocities than those observed. The calculated waveforms were also comparable to those observed except for a bit of excessive reverberation.

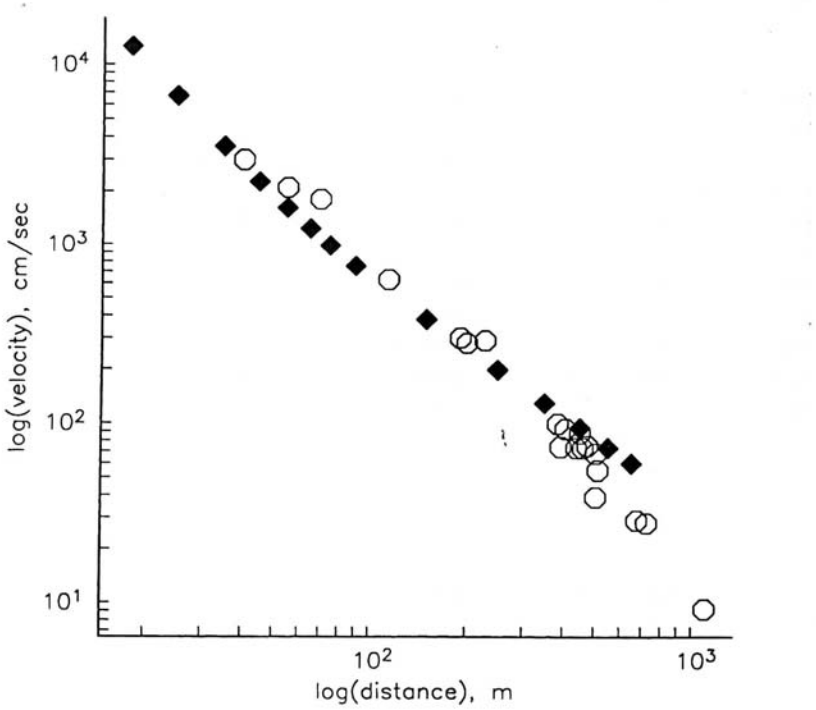

Figure 5. Measured and calculated peak velocities for the NPE explosion. The open symbols are observations taken from Smith (1994) and Olsen and Peratt (1994), while the filled symbols were calculated with the equivalent elastic method (from Johnson and Sammis, 2001).

Having established that the equivalent elastic method gives a good approximation to the observed motions close to the NPE explosion, we now ask how these results would change if we increased the P and S wave velocities, the coefficient of friction, and the strength to simulate the mechanical properties if the cracks were filled with ice.

Figure 6 shows the effect of increasing the coefficient of friction on the radial distribution of fracture damage in the non-linear source region. For the higher coefficient of friction, damage is suppressed close in and enhanced further out. This is because the stresses do not fall off as fast with distance due to the smaller damage close in. Radial cracks are thus expected to extend out an additional 10 meters in the frozen rock (about an additional 20%).

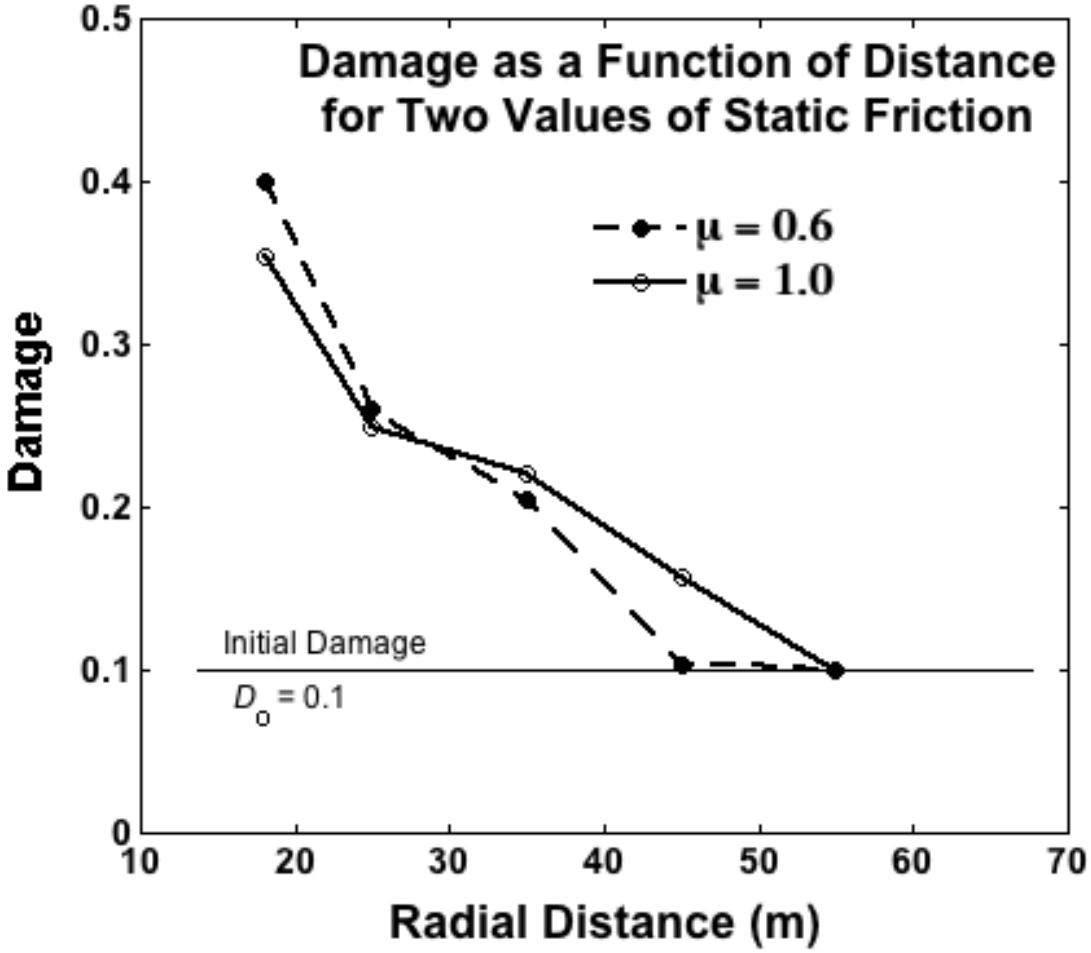

Figure 6. The effect on the radial distribution of damage when the coefficient of static friction is increased from μ = 0.6 to μ = 1.0 in the NPE simulation by Johnson and Sammis (2001).

Figure 7 shows the effect of increasing the compressive strength on the radial distribution of damage. In the equivalent elastic source model the compressive strength is expressed as a reference strain defined as

$$\varepsilon_r = \frac{\tau_{\max}}{\mu_o} \qquad (3)$$

In Figure 7, the reference strain is doubled (corresponding to ice in granite) and multiplied by 4 (corresponding to ice in limestone). The effect is very similar to that of increasing the coefficient of static friction – there is more damage and it extends an additional 10 meters.

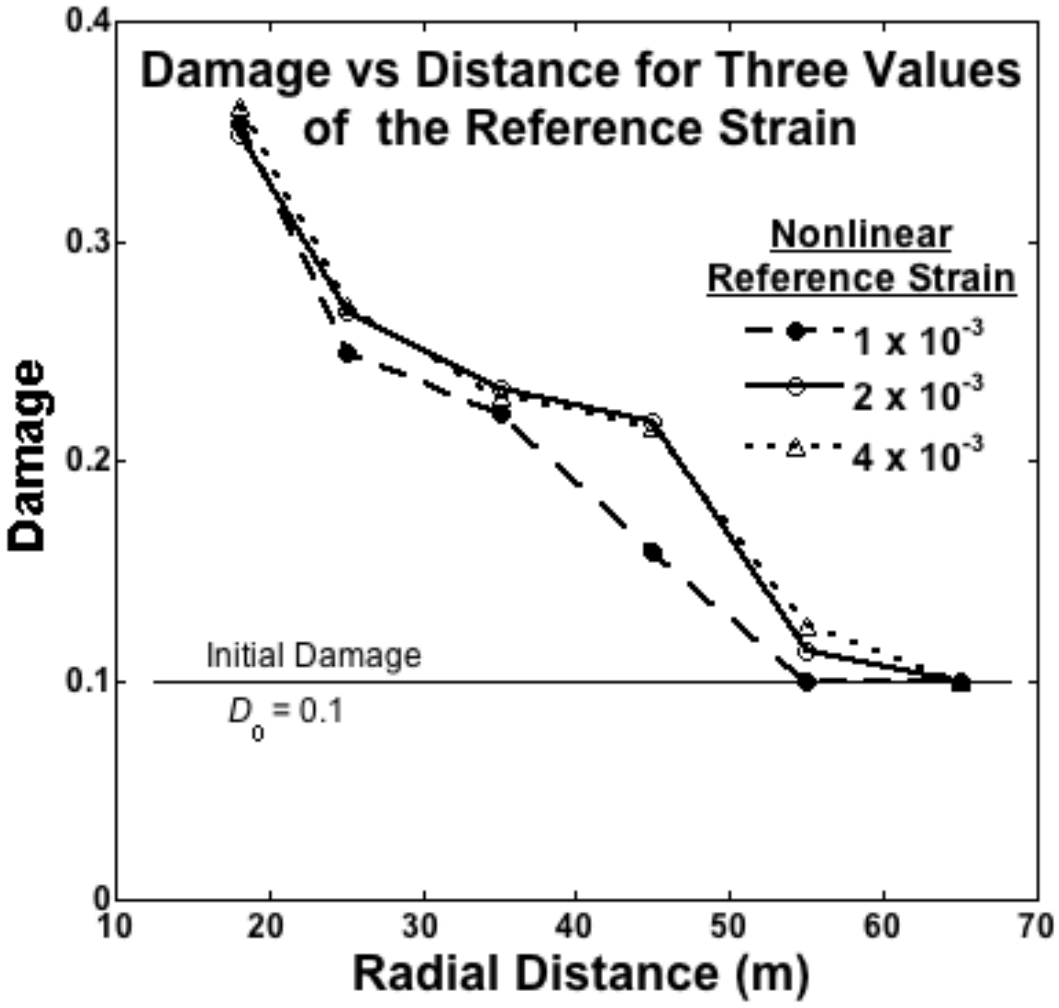

Figure 7. The effect on the radial distribution of damage when the non-linear reference strain is increased by factors of 2 and 4 in the NPE simulation by Johnson and Sammis (2001). This is equivalent to increasing the compressive strength by a factor of 2 (simulating ice in granite) and 4 (simulating ice in limestone).

Figure 8 summarizes the effect of ice in the cracks on the amplitude of seismic radiation in the far-field. As argued above, ice is expected to increase the initial wave velocities and the strength of the source rock. These ice-induced changes all decrease both the amplitude and reduced velocity potential in the linear elastic regime.

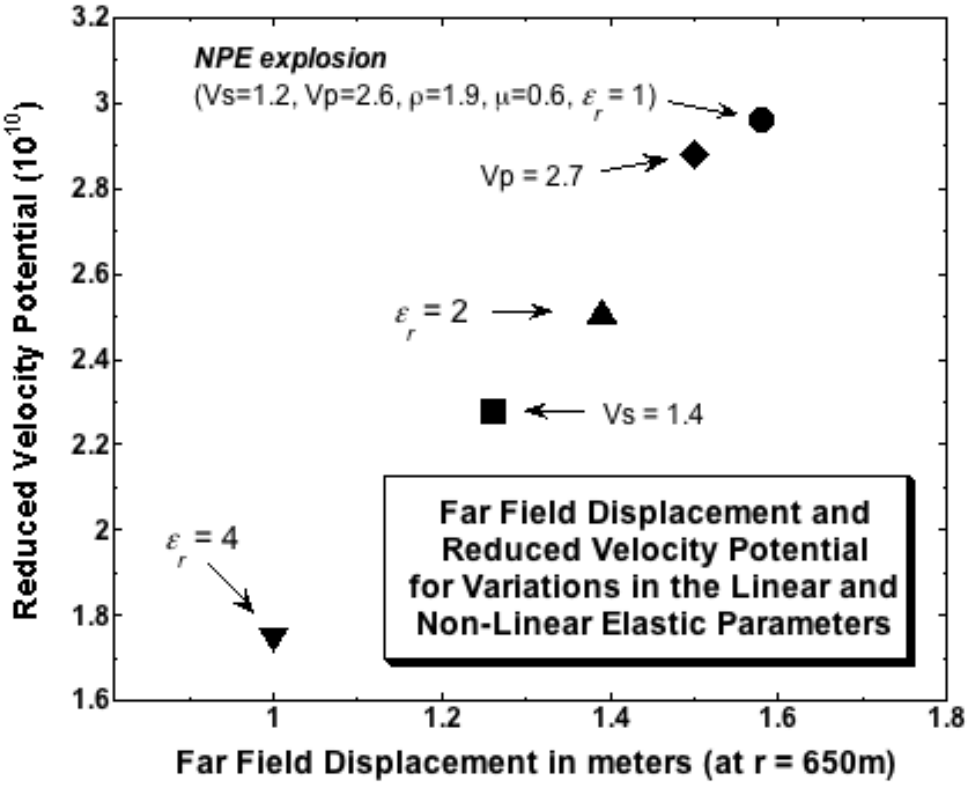

Figure 8. The effect of ice in the cracks on the reduced velocity potential and far-field displacement. The solid circle is the velocity potential and displacement at a radial distance of 650 m from the NPE explosion calculated by Johnson and Sammis (2001). The other symbols show the effect of changing either the initial velocity or strength of the rock. Note that effect of increasing either the initial seismic velocity or the strength is to reduce the amplitude of the seismic radiation in the far field making the explosion appear smaller than an equivalent explosion in rock above the freezing temperature of water.

CONCLUSIONS AND RECOMMENDATIONS

Inclusion of the mechanical effects of ice in the cracks of crystalline rock into the explosion source formulated by Johnson and Sammis (2001) has led to the following conclusions:

1. The increase in elastic wave velocities associated with ice in the cracks will decrease the seismic amplitudes in the far field resulting in an apparently smaller yield.

2. The increase in compressive strength caused by ice in the cracks will also decrease seismic amplitudes in the far field, also resulting in an apparently smaller yield.

3. At high loading rates, as in an underground explosion, the strength of granite is expected to increase by a factor of about 2, while that in limestone by a factor of about 4.

The following recommendations are based on the analysis in this paper and last year's analysis of the frozen rock data (Sammis and Biegel, 2004).

1. The uniaxial data from Mellor (1973) should be supplemented with a full set of triaxial data in granite at low temperatures. Uniaxial data typically shows large experimental scatter, mostly because the strength is extremely sensitive to the initial flaw distribution in the absence of confining stress. A set of triaxial data would allow a more comprehensive assessment of the extent to which the damage model can represent the strength of rock at low temperatures.

2. The triaxial data set should be supplemented with measurements of the coefficient of friction as a function of temperature under saturated and air-dry conditions. These measurements can be made either on saw-cut samples as part of the triaxial set of experiments, or in Jim Dieterich's double-shear apparatus at the United States Geological Survey laboratory in Menlo Park, California.

3. Both the triaxial measurements and friction measurements should be performed at different strain-rates to further test the hypothesis that the strengthening is associated with ice asperities.

4. Seismic velocities should be measured in frozen and thawed rock at the same field location as part of any pending field study of explosions in frozen rock.

5. The equivalent elastic source model of Johnson and Sammis (2001) should be improved to make the non-linearity depend explicitly on the damage. This non-linearity is now given by an analytic approximation that depends only on the peak stress (or, equivalently, on the reference strain).

ACKNOWLEDGEMENTS

We thank Professor Lane Johnson for many helpful discussions and for computational assistance with the equivalent elastic medium source model.

REFERENCES

Ashby, M. F. and C. G. Sammis (1990), The Damage Mechanics of Brittle Solids in Compression, *Pure appl. Geophys*: 133, 489-521.

Bowden, F. P. and D. Tabor, (1950), *The Friction and Lubrication of Solids. Part I*, Oxford: Clarenden Press.

Bowden, F. P. and D. Tabor (1964), *The Friction and Lubrication of Solids. Part II*, Oxford: Clarenden Press,.

Denny, M. D. (1994), Introduction and Highlights, in *Proceedings of the Symposium on the Non-Proliferation Experiment (NPE): Results and Implications for Test Ban Treaties*, M. D. Denny (editor), CONF-9404100, Department of Energy.

Glenn, L. A. (1993), Energy-density effects on seismic decoupling, *J. Geophys. Res.* 98: 1933-1942.

Glenn, L. A. and P. Goldstein (1994), Seismic decoupling with chemical and nuclear explosions in salt, *J. Geophys. Res.*: 99, 11,723-11,730.

Johnson, L. R. (1993), Wave propagation near explosive sources, PL-TR-93-2118, Phillips Laboratory, 22 pp.

Johnson, L. R. and C. G. Sammis (2001), Effects of rock damage on seismic waves generated by explosions, *Pure Appl. Geophys.*: 158: 1869-1908.

King, D. S., B. E. Freeman, D. D. Eilers, and J. D. Johnson (1989), The effective yield of a nuclear explosion in a small cavity in geologic material: enhanced coupling revisited, *J. Geophys. Res.:* 94, 12,375-12,385.

Mellor, M. (1973), Mechanical properties of rocks at low temperatures, *Second International Conference on Permafrost*, National Academy of Sciences, Washington, D.C., 334-343.

O'Connell, R. J. and B. Budiansky (1974), Seismic velocities in dry and saturated cracked solids, *J. Geophys. Res.* 79: 5412-5426.

Olsen, K .H. and A. L. Peratt (1994). Free-field ground motion for the non-proliferation experiment: preliminary comparisons with nearby nuclear events, in *Proceedings of the Symposium on the Non-Proliferation Experiment (NPE): Results and Implications for Test Ban Treaties*, M. D. Denny (editor), CONF-9404100, Department of Energy.

Rodean, H.C. (1971), Nuclear-Explosion Seismology, U.S. Atomic Energy Commission, TID-25572, 156 pp.

Sammis, C.G. and R.L. Biegel (2004). "Mechanics of strengthening in crystalline rock at low temperatures: a preliminary assessment," in *Proceedings of the 26th Seismic Research Review: Trends in Nuclear Explosion Monitoring*, Orlando, FL (Sept. 21–23, 2004), LA-UR-04-5801.

Smith, C. W. (1994), NPE - close-in stress and motion measurements, in *Proceedings of the Symposium on the Non-Proliferation Experiment (NPE): Results and Implications for Test Ban Treaties*, M. D. Denny (editor), CONF-9404100, Department of Energy.

SOURCE PARAMETERS OF SEISMIC EVENTS IN A COAL MINE IN INDIA

C. Srinivasan, C. Sivakumar, and R. N. Gupta

National Institute of Rock Mechanics

Sponsored by Coal India, Ministry of Mines, Government of India.

Contract No. WOS052121

ABSTRACT

Longwall mining is one of the most widely used mining methods in underground coal mining. Longwall mining results in a large volume of coal being taken from underground; this changes the stress distribution and causes roof strata to deform and fracture near the working face. As a result many microseismic events and roof falls are observed. Microseismic monitoring in mines is a unique technique to locate the high stress zone areas which ultimately lead to the occurrence of roof falls.

The Integrated Seismic System from South Africa was used to monitor strata behavior in real time during longwall mining operation at the Rajendra longwall mine of South Eastern Coal Fields Limited (SECL) in India. The geophones were installed through boreholes at different depths covering the area of the longwall face in three dimensions and the data were recorded continuously in real time at the central computer system on the surface. Analysis of the seismic events revealed that the local magnitudes of these events were between -3.4 and 0.5, seismic moment varied between 1.4xE+05 and 3.6xE+09 Nm, seismic stress drop between 0 and 39.93 bars, Brune radius between 3 and 16.5m, apparent stress between 0 and 8.61 bars, radiated energy between 1.0E-03 and 9.2E+07 Joules, and predominant frequency between 10 and 500 Hz. After the coal mine face advances a certain distance, the strata behind the face typically caves in. If the roof does not cave, the entire mass of strata may detach from the layer above and try to rest on the powered supports, leading to failure and ground control problem. To help mitigate the situation, blasts were detonated behind the face after every 30 m of face advance. The quantity of explosives used was from 400 to 1500 kg. The source parameters of the blasts were obtained. Local magnitudes of these events were between -0.8 and 1.8, seismic moment varied between 7.1xE+07 and 8.5xE+10 Nm, seismic stress drop between 3.10 and 556 bars, Brune radius between 2.7 and 34.62 m, apparent stress between 2.27 and 326 bars, radiated energy between 5.4xE+02 and 9.2E+07 Joules and predominant frequency between 20 and 250 Hz. The details are discussed in this paper.

OBJECTIVES

The longwall technique is one of the most productive and safest mining operations. There were difficulties in the past when longwall technology was first introduced in many coal mines. This was due to incomplete understanding of the mechanism of caving. The characterization and understanding of strata behaviour immediately above the extraction panel is important for effective mine design.

India was the world's fourth largest (presently 3rd) coal producer in 1997. The international longwall census report notes that early efforts in longwall mining in India were poorly implemented, but experience, better equipment specification and improved infrastructure have increased the chances of success. Today in India, there are examples of moderately successful mechanized longwall faces, which produce on an average 1500 Mt per day. Powered support longwall technology contributes nearly 50% of the global production of coal from underground mines and is the most prevalent methodology in the leading coal producing countries, as reported by Mehta et al. (2003).

The longwall technique was introduced in India during the 1960s and powered support longwall mining was introduced in the1970s. In most longwall faces, the main problem was caving of the roof strata. This was mainly due to the presence of massive sandstone which is generally difficult to cave and caves in dynamically and violently. At present, instrumentation used in the longwall panel includes convergence measurement, leg pressure monitoring, stress and strain measurement; this will give only site specific information and only at the final stages of caving. These techniques and methods were found to be insufficient because of their limitations in locating high stress zones which ultimately result in roof collapses. The microseismic technique has been tried in one of the longwall faces at Rajendra Longwall mine of (SECL).

A Science and Technology project entitled "Monitoring of Strata Behaviour During Longwall Coal Mining Using Microseismic Monitoring Technique and Estimates of Caving Height" was undertaken jointly by SECL and NIRM at Rajendra Colliery (Sivakumar et al., 2004). The introduction of modern digital seismic systems to the mines and progress in the theory and methods of quantitative seismology enabled the implementation of real time monitoring to quantify rock mass response to mining in a better manner as reported by Mendecki and Van Aswegan (2001). During the period of microseismic monitoring several thousands of microseismic & roof fall events were recorded. Blasting was carried out on the surface of the working panel through drilled boreholes to release the buildup of stresses and avoid overload on the powered support. All the blasts during the monitoring period were recorded and analyzed. The source parameters of microseismic events, roof falls and induced blasts are discussed in this paper.

RESEARCH ACCOMPLISHED

Project site

Rajendra underground mine is operated by SECL and is situated in the Sohagpur area of Rewa Coal fields. It is located in the Western Part of the Sohagpur Area in the District of Shahdol in Madhya Pradesh between 23^0 08' 12'' and 23^0 10' 10'' North and 81^0 28' 05'' & 81^0 30' 50'' East. It is about 8

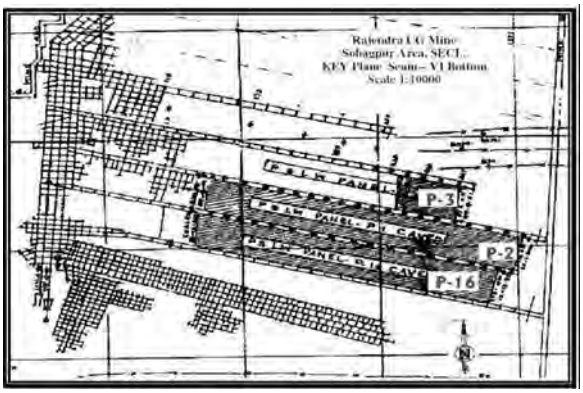

Figure 1. Plan showing the Rajendra Longwall underground Coal mine.

km from Burhar Railway station. The Area is close to the workings of the Burhar-Dhanpuri group of collieries. Figure 1 shows the location of longwall panel P-2 where investigations were undertaken.

Geology of the site

The coal bearing area is largely covered by the younger Supra-Barakars formation and is chiefly composed of grayish-white coarse-grained sandstone, a few coal seams are carbshale. The recent/sub-recent formation is alluvium with a lithology of soil and alluvium. The Upper Cretaceous age Lemeta formation has a lithology of reddish & greyish sandstone & modular limestone. The Triassic age Supra-Barakars formation has a lithology of pink, buff and red sand stone & shales. The Lower Permian age Barakars formation has a lithology of coarse to medium grain sandstone, subordinate shale & coal seams. The bottom seam VI is 1.30m to 4.75m thick and is presently being worked at the longwall Rajendra coal mine.

Mine workings

Rajendra underground mine was initially planned to be worked by Board and Pillar but due to the large demand for the high quality coal, the Powered Support Longwall Technique (PSLW) of coal mining was introduced. The details of PSLW panel-P2 are given below.

Working Height	: 2m to 3m
Length of face	: 150m
Length of Panel	: 1000m
Coal available	: 0.54 MT (3.1m thick)

The panel-P2 where the bottom seam is extracted lies at a depth of 68m to 74m below the surface. The roof of the seam consists of alluvium, sandstone and shale.

Instrumentation and monitoring systems

At Rajendra Colliery P-2 longwall face the microseismic monitoring system Integrated Seismic System (ISS) procured from South Africa was installed. The ISS system has sophisticated hardware and powerful software features for data acquisition and data analysis. The system was developed around network technology and built using distributed Data Acquisition Units (DAS) with central access to an online data processing system. Figure 2

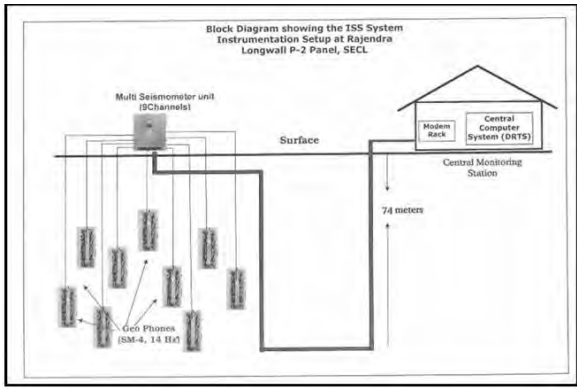

Figure 2. Block diagram of ISS instrumentation setup.

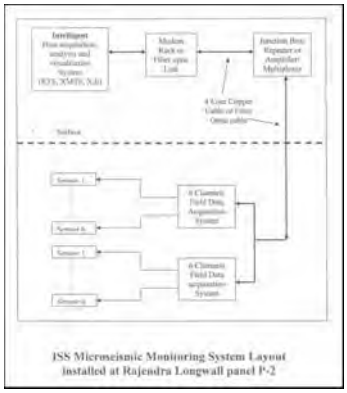

Figure 3. Block diagram of ISS monitoring system.

illustrates the block diagram of the ISS system used at Rajendera mine. The geophones were installed from the surface through boreholes, ahead of the face, behind the face and at the Main gate and the Tailgate. A total of 8 geophones at a time covering a volume of 200m length, 150m width and 75m depth were connected to the ISS system.

The ISS system consisted of 18 uni-axial geophones which were deployed in boreholes drilled from surface. The 18 uni-axial geophones were installed in three phases, 8 at each phase, replacing the unusable geophone sets which

were buried in the goaf from time to time as the face advanced. These sensors were installed at boundaries of the roof strata at a different depths varying from 36m to 67m and covering about 150 to 200m in length and 150m in width (face of the panel) on the surface. The cables from all geophones were brought to a junction box situated in the middle of the panel on the surface and connected to a MS-9 data acquisition unit, housed in a moveable metal box to protect it from environmental conditions. This box was shifted from time to time with the face advancement of every 200m. The central computer was situated about 3 km away from the MS-9 microseismic unit; the area in-between is inaccessible on surface. A borehole was drilled from the surface to the underground workings (74 m) at the end of the panel into the tailgate and a two pair twisted armored annealed copper cable was used for data transmission. The cable was brought out to the surface from the ventilation shaft, which was close by the central computer monitoring station. This cable connected to a modem and to an HP Kayak Xu 800 workstation through a RS232 port on a communication board placed in the PCI slot. The central computer was capable of setting and changing the data acquisition parameters of the MS-9 unit and received the data collected on demand once an event was detected by satisfying the prerequisite conditions (e.g., trigger levels on a number of channels). The ISS microseismic monitoring system layout installed at Rajendra mine is shown in Figure 3.

Analysis

Source parameters extracted from the waveforms of microseismic events, roof falls, and blasts were local magnitude, seismic moment, seismic stress drop, Brune radius, apparent stress, radiated energy and predominant frequency. The energy release during fracture and frictional sliding was due to the transformation of elastic strain into inelastic strain. Seismic energy is proportional to the integral of the squared velocity spectrum in the far field and can be derived from recorded waveforms. Seismic moment is a scalar that measures the co-seismic inelastic deformation at the source. Stress drop estimates the stress release at the seismic source. The comparison of radiated seismic energies for seismic events of similar moment provides information about the stress change in the source areas. The ratio of radiated seismic energy to seismic moment multiplied by rigidity is called apparent stress and is recognized as a model independent measure of the stress change at the seismic source, as described by Mendecki (1997).

Signal characteristics

A typical microseismic signal picked up by the ISS system is shown in Figure 4. The seismogram is a graph of velocity of ground motion versus time at the location of the sensor. The background noise level is within ± 0.01mm/sec., the microseismic signal is superimposed on this background level. The frequency content of the signal was 200 Hz, duration 0.56 sec and the maximum amplitude recorded was at frequency 83.33 Hz. Depending on the distance, direction and source medium, the signals were picked up with different onsets, frequencies, durations and amplitudes. Low frequencies in the seismogram indicates soft strata (predominantly sandstone), whereas in the case of hard sandstone signals with high frequencies were observed.

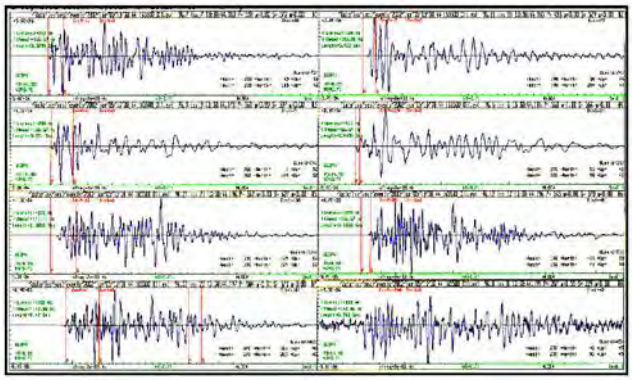

Figure 4. Microseismic signal recorded by ISS monitoring system.

Examples of three types of microseismic signals that were recorded during the longwall monitoring at Rajendra Mine are shown:

a) High frequency and short duration (Figure 5.)
b) Low frequency and long duration (Figure 6.)
c) Between low & high frequency and duration (Figure- 7.)

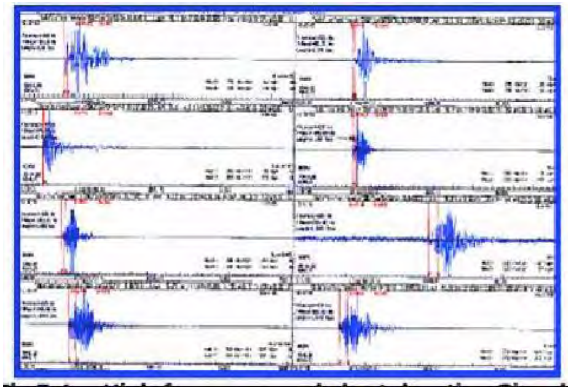

Figure 5. Microseismic signal (High Frequency and short duration)

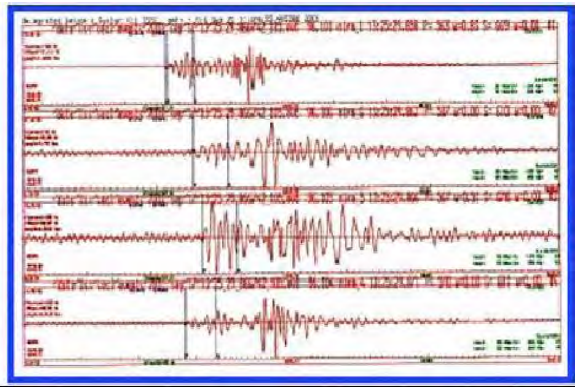

Figure 6. Microseismic signal (Low Frequen and long duration)

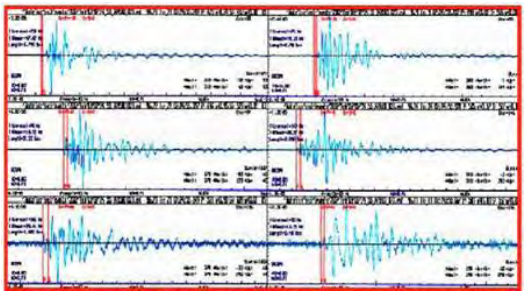

Figure 7. Microseismic signal (In between high and low frequency and duration.)

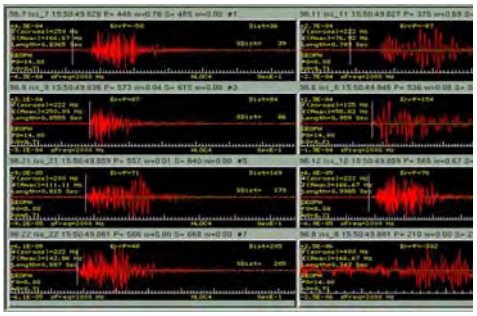

Figure 8. Seismogram of Roof Fall on 18-11-2001 at 20:39:52 Hrs.

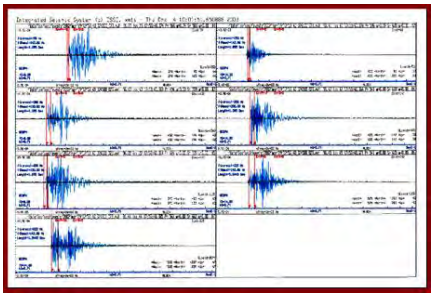

Figure 9. Blast signal recorded on 19-03-2002 at 12:53:40 Hrs.

In order to monitor the panel P-2 (1200m length x 150m width x 75m depth) very closely, the whole panel was divided into smaller segments of 200 to 300m in length and populated with 8 to 14 sensors (geophone stations). The network was shifted with a new set of geophones as the face advanced.

The microseismic events associated with longwall mining, roof falls (Figure 8) and blasts (Figure 9) were recorded at the Rajendra mine. The recorded waveforms were used to compute the source parameters. These events were recorded by a minimum of five geophones in the network and their locations are available. The events were located within an accuracy of less than 5 m. STA and LTA criteria were used to detect and record the events in real time. Signal characteristics are shown in Table-1. These parameters are site specific, depending on the strength of the rock mass and the stress profile at the time of recording.

Table 1. Details of Source Parameters computed from Rajendra mine.

Sl. No.	Source Parameters	Microseismic events	Roof falls	Blasts
1	Amplitude in m/sec	10^{-06} --10^{-05}	10^{-06} -- 10^{-04}	10^{-04} --10^{-02}
2.	Magnitude	-4.0 -- 0.0	-3.0 -- 0.5	-0.8 -- 1.8
3	Seismic Energy Joules	$1.9X10^{02}$ -$1.6X10^{04}$	$1X10^{-03}$ -- $1X10^{05}$	$5.4X10^{02}$ --$9.2X10^{07}$
4	Seismic Moment in Nm	$8.9X10^{07}$ - $7.3X10^{08}$	$1X10^{05}$ -- $4X10^{09}$	$7.1X10^{07}$ --$8.5X10^{10}$
5	Apparent stress in Bars	0.64 -- 3.33	0 -- 8.0	2.27 -- 326
6	Static stress drop in Bars	2.16 -- 10.58	0 -- 40	3.0 -- 556
7	Source radius in m	3.66 -- 6.25	3.0 –16.5	2.0 -- 34
8	Predominant Frequency. Hz	37 -- 500	10 -- 330	21 --250

Blasts

Blasting was carried out on the surface of the working panel through drilled boreholes for every 30m interval in the goaf area to release the build up of stresses in the center of the panel. This helped avoid overload and the possibility of an air-blast. The microseismic monitoring system recorded all the blasts during the monitoring period. Several seismic parameters were obtained by analyzing the blast data, such as magnitude, source radius, static stress drop, corner frequency and predominant frequency. After blasting many roof falls occurred. From their time of occurrence, location and other details it was possible to understand the result of blasting. Continuous monitoring of stress levels before and after blasting helped to carry out blasting and further helped to optimize blasting. The correlation of blasting with computed source parameters and other details are explained below. A typical induced blast signal is shown in Figure-9. The details of blasts are listed in Table 2. The effects of blasting on the mine strata were explained by Srinivasan et.al (2004). The magnitudes of blasts recorded were in the range of –0.8 to 1.8 on the local magnitude scale

Table 2. Details of Induced Blastings carried out at Rajendra mine.

Date / Time	Explosives in Kgs.	Local Magnitude	Seismic Moment	Energy in Joules
21.10.01 / 20:27:15	1500	1.3	2.1 E+10	6.4E+06
21.10.01 / 20:37:22	1500	1.4	3.5E+10	1.1E+07
27.10.01 / 23:20:59	1425	1.8	8.5 E+10	9.2 E+07
06.11.01 / 16:57:34	1500	1.2	1.4 E+10	5.1 E+06
15.11.01 / 16:00:39	872	1.2	2.1 E+10	4.9 E+06
23.11.01 / 20:47:16	462	0.3	1.5 E+09	6.3 E+04
30.11.01 / 19:47:40	563	-0.6	1.2 E+08	1.3 E+03
13.12.01 / 13:51:23	450	1.2	2.8 E+10	1.8 E+06
31.12.01 / 13:50:40	700	1.2	3.1 E+10	2.1 E+06
16.01.02 / 18:46:49	400	0.4	3.4 E+09	5.6 E+04
19.01.02 / 15:23:15	1300	0.4	2.6 E+09	1.2 E+06
31.01.02/15:24:12	1050	1.1	1.7E+10	2.2E+06
11.03.02/20:13:12	122	0.2	1.6E+09	3.8E+04
15.03.02/13:35:21	233	0.6	4.1E+09	3.3E+05
19.03.02/12:53:40	350	-0.3	3.9E+08	4.9E+03
23.03.02/13:08:23	347	0.9	7.6E+09	1.2E+06
14.04.02/14:39:23	275	0.0	5.3E+08	3.0E+04
09.05.02/15:53:01	391	0.7	5.0E+10	8.8+04

Magnitude and source radius

Fracturing in rock took place due to a blast near the source; this is quantified by the radius of the spherical volume which was fractured. Table 1 gives an indication of the fracturing radius for different blasts. It was observed that the source radius increased as the magnitude of the blasts increased. The magnitude of the blast depends on the quantity

of explosive used as shown in Table 2. Although there is a clear increasing trend between magnitude and explosive used, there is scatter in the magnitude up to 600Kg of explosives used. The scatter is caused by blasts of the same quantity of explosive giving rise to different magnitudes and different fracture radii. Especially with the use of explosive up to 600Kg of explosive the fracturing taking place in the rockmass varies between 2.5m to 10.25m radius. The fracturing created due to blasts depends on the stress regime at the time of the blast, the distance of the blast from the longwall face, and the strength and hardness of the roof (sandstone layer).

Stress levels before and after blasting

In order to understand blasts and their effects on the longwall strata, the energy index versus time before and after blasts was examined. Energy index is a measure of the stress regime in the rock during blasts. Out of many blasts recorded only two blasts are shown as examples below to show the effect of blasting seen in real time.

Blast 1 (27.10.2001 at 23:20:54 Hrs.)

It was observed that one hour before this blast the stress level showed an increasing trend indicating build up of stress and after the blast within 20 minutes the stress level dropped indicating release of stress, as seen in Figure 10.

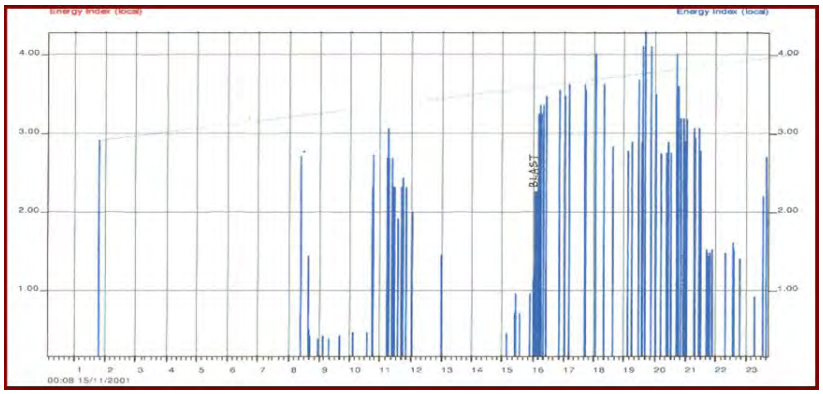

Figure 10. Stress level before and after Blast 1.

Blast 2 (31.12.2001 at 23:20:54 Hrs.)

One hour before the blast there was high stress level, as can be seen in Figure 11. The stress level came down within two hours after the blast and gradually decreased further.

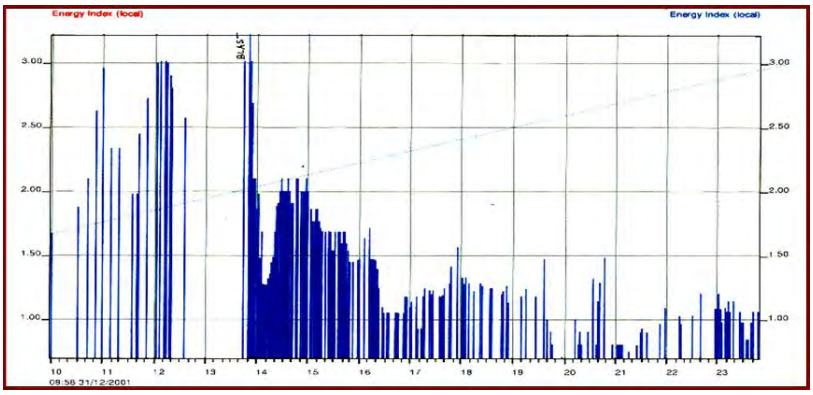

Figure 11. Stress level before and after the Blast 2.

The ISS system used at the Rajendra mine captured all information pertaining to ground strata behaviour during the period of monitoring. The data obtained were number of microseismic events along with the source parameters of individual events. Plotting different source parameters against time gave clear indication of high stress zones and

unstable conditions developing in strata which ultimately resulted in ground failure. The locations of microseismic events plotted on the plan view of the mine gave the location of cluster of events and contours gave an indication of high stress. The high stress zone ultimately resulted in roof falls endangering the safety of men and machinery. To avoid major problems, blastings were used. The details are described below.

High stress zone

Longwall mining results in a large volume of coal being taken out from underground in relatively a short period. This causes changes in stress, roof strata deformation and fractures near the working face. Behind the face supports the fractured roof strata are encouraged to collapse in a controlled manner by blasting. Carrying out blasting at the right time and right location is important to get optimum results of the induced caving technique. There is no conventional monitoring available to obtain scientific information on location and time to carry out blasting. The microseismic technique provides appropriate scientific information in real time in this respect. Figure 12 shows the contour plot of the stress zone before blasting on 21.2.02. The high stress zone is concentrated towards the tailgate side. By identifying the high stress zone area the location that needs to be blasted and the approximate time is obtained. Blasting was carried on 21.02.02 at 10:30 hrs. After the blast the high-stress-zone area has disappeared and development of a fresh zone in another area is seen in Figure 13.

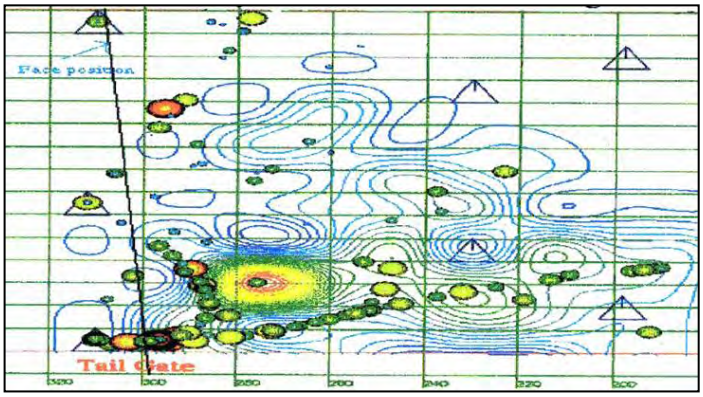

Figure 12. High stress zone before Blasting on 21.02.2002.

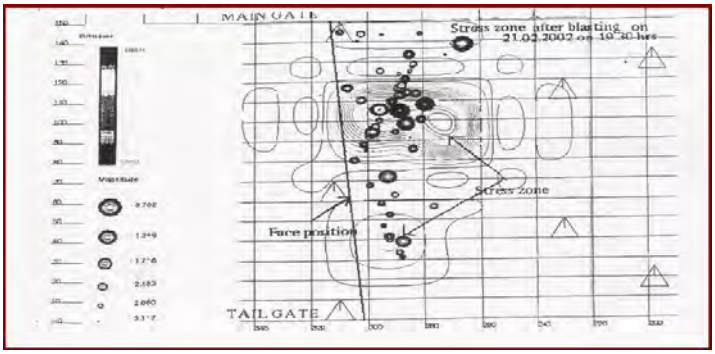

Figure 13. High stress zone after Blasting on 21.02.2002.

Discussion

Microseismic emissions are generated by deformation and cracking of rock around an opening inside a mine. The typical characteristics of these microseismic event patterns is shown to be of diagnostic value in sensing in advance roof fall that invariably follow such events. The source parameters of microseismic events are found to be less than those of roof falls in terms of amplitude, seismic energy, seismic moment, apparent stress, stress drop, source radius and magnitude, whereas the predominant frequency is higher for microseismic events compared to roof falls and blasts. The source parameters of blasts are higher than microseismic events and roof falls except for the predominant frequency, where it is less than microseismic events and roof falls.

Blasting was carried out from the surface of the working panel through drilled boreholes for every 30m interval in the goaf area to release the build up of stresses. A microseismic monitoring system recorded the blasts during the monitoring period. Source parameters obtained after analyzing the waveform data were magnitude, seismic moment, radiated energy, source radius, static stress drop, corner frequency, and predominant frequency. These seismic parameters helped understand the effects of each blast with respect to quantity of explosives used and stress levels before and after every blast. These results will help in the future to take decisions regarding the time and location to carry out blasts and to optimize the quantity of explosive. The stress levels in the various locations of strata before and after the blast can be quantified.

CONCLUSIONS AND RECOMMRNDATIONS

The microseismic investigation carried out at Rajendra colliery has obtained source parameters of microseismic events, roof falls and blasts. Brune's simple dislocation model has been used to compute the source parameters. The computed source parameter values of blasts are found to be higher than the values obtained for roof falls and microseismic events, except in the case of predominant frequency content where it is lower. The effects of blasting on strata can be identified using stress concentration zones. The results are listed below:

1. Various seismic parameters quantified for microseismic events, roof falls and blasts are local magnitude; radiated energy, seismic moment, apparent stress, source radius and seismic stress drop showing an increasing trend with respect to magnitude of blast; corner frequency showing a decreasing trend.

2. The magnitudes of blasts recorded were from -0.8 to 1.8.

3. The extent of fractures (source radius of fracture) was from 3.296m to 34.627m.

4. The predominant frequency recorded was from 22Hz to 250Hz.

5. The duration of blast vibration was from 0.5sec to 4.5 Sec.

6. Blasts have induced microseismic events within two hours after the blast and the stress level before and after blasts can be quantified.

7. One may delineate high stress zone and know the time to carry out a blast

8. The above information can be used for optimization of the blast.

9. The above information has helped to better understand the performance and effects of induced blasts carried out at Rajendra Colliery.

10. Discrimination of man-made and natural seismic events is possible.

ACKNOWLEDGEMENTS

The present project was carried out under a grant received from the Department of Coal, Ministry of Mines, Government of India and implemented jointly by South Eastern Coalfields Limited, Bilaspur and National Institute of Rock Mechanics, Kolar Gold Fields. We express our sincere thanks to CMPDI and SECL for sanctioning the project and providing the financial support. Finally, the support and help of all those staff of NIRM and SECL directly or indirectly helped to complete the project is also thankfully acknowledged. Sincere thanks to AOARD, Tokyo for financial support extended under WOS which enabled to present the paper in the 27th Seismic Research Review Symposium. We are highly grateful to Dr. Anton M. Dainty, AFRL/VSBYE for his technical support and scientific interaction. Mr. Y. Ahnoch Willy is specially thanked for his assistance in preparation of this paper.

REFERENCES

Mendeki, A. J. and Van Aswegan, G. (2001), *Seismic monitoring in mines. - Selected terms and definitions*, Chapman and Hall, London.

Mendecki, A. J.(Ed). (1997), *Seismic Monitoring in Mines*, Chapman and Hall, London.

Mehta, S. R. and S. Dasgupta (2003), Why Longwall in India has not succeeded as in other developing country like China, Vol.84: IE(I), Journal -MN.

Sivakumar, C., C. Srinivasan and R. N.Gupta (2004), Completion report-2004- Coal S&T project MT-116 " Monitoring strata behaviour during Longwall Mining using Microseismic monitoring Technique and Estimation of Caving Height".

Srinivasan, C., C.Sivakumar and R.N.Gupta (2004), Study of Induced Blasting effect on the longwall roof strata at Rajendra Colliery using Microseismic technique in MGMI International Conference on Future of Indian Mineral Industry challenges and opportunities ,Kolkatta, India. 17-18th September 2004.

THE PHYSICAL BASIS OF THE EXPLOSION SOURCE AND GENERATION OF REGIONAL SEISMIC PHASES

Jeffry L. Stevens, G. Eli Baker, Heming Xu, and Theron J. Bennett

Science Applications International Corporation

Sponsored by Air Force Research Laboratory

Contract No. FA8718-04-C-0025

ABSTRACT

The objective of this project is to determine the source physics and corresponding generation and evolution of local and regional seismic waves from nuclear explosions. In particular, we want to explain the source of the explosion-generated Lg phase. In a previous project we identified the following contributing sources to Lg: surface reflected pS that is trapped in the crust, S*, scattered Rg, and shear waves directly generated by non-spherical source elements. Our goal now is to quantify the contribution of each to Lg under different source conditions. To this end we have performed work in several complementary areas.

The Russian Institute for the Dynamics of the Geospheres (IDG) has provided yield and depth information for 11 Degelen and 4 Balapan explosions. They have digitized records on their near regional stations (50-100 km distance) for all four Balapan explosions and one of the Degelen explosions. They have also provided near source peak particle velocities, rise times, and positive pulse duration measurements from ten Degelen nuclear explosions. These explosions were all conducted in high velocity media (>5 km/sec P velocity) and therefore place important constraints on the Lg generation problem. The Balapan near regional data provides a contrast with existing near regional Degelen explosion data. As the source media are similar while the near source topographies differ, these data may be useful in distinguishing the role of topography in near source scattering. The new near field measurements and near regional records provide an opportunity to track differences between Balapan and Degelen regional records back to their source.

In a closely related analysis, to assess whether the amount of shear waves generated is affected by source depth and/or scaled depth, we examine the regional phase amplitudes of 13 Degelen explosions with known yields and source depths. The events range from 20% to 50% underburied. Preliminary analysis shows similar $\log_{10}$ amplitude vs. $\log_{10}$ yield curves for the initial Pn, the entire P wavetrain, Sn, Lg, and Lg coda. The slope of those curves varies with frequency, ranging from approximately 0.84 at 0.6 Hz to 0.65 at 6 Hz. We perform nonlinear source calculations to complement these observations, aimed at determining constraints on the relative size of CLVD and explosion sources.

We have also examined recordings of historical co-located decoupled and tamped explosions at Azgir in the former Soviet Union, utilizing all 3 components of data and focusing on differences in shear wave generation between the explosions. The relative S to P wave amplitude appears similar at low frequencies, but is much greater above 8 Hz for the tamped explosion, although interpretation is complicated by the frequency dependence of the decoupling. The tamped explosion also has clear Sn at regional distances. No similar records were available for the decoupled explosion. The tamped explosion, at 64 Kt and 987 m depth in salt, was 2 times overburied. Even if it were tamped, the 10 Kt decoupled explosion would have been nearly 4 times overburied. Wavenumber synthetic seismograms show that generation of the observed shear waves by a spherical explosion source is implausible, even in very complex source structure. We plan to perform nonlinear source calculations to assess the possibility of non-spherical source terms, at the surface and at an interface between the salt and overlying sediments.

Finally, we model scattering of Rg into Lg for known source areas and compare resulting synthetics with regional data. We use an approximation based on modal scattering of fundamental mode Rg into higher mode Lg, using as constraints estimates of Rg decay rates from Degelen and deep seismic sounding explosions. The goal of this analysis is to quantify the contribution of Rg to Lg in different areas with different earth structures.

OBJECTIVE

The objective of this project is to determine the source physics and corresponding generation and evolution of local and regional seismic waves from nuclear explosions. This is a joint project between Science Applications International Corporation (SAIC) and IDG in Moscow, Russia.

RESEARCH ACCOMPLISHED

Introduction

We are in the first year of a new project to determine the source physics and corresponding generation and evolution of local and regional seismic waves from nuclear explosions. This is a joint project between SAIC and IDG in Moscow, Russia. The project continues work initiated under two previous projects: 1) a joint project between SAIC and IDG to digitize and analyze a large data set of near field (35-900 meters) and near regional (10-100 km) waveforms from Degelen mountain explosions (Stevens et al., 2003; and 2) a project to determine the source of explosion-generated Lg using numerical modeling and data analysis (Stevens et al., 2004b).

In the previous joint project, IDG provided an exceptional historical data set of 192 near field and near regional records of 23 Degelen mountain nuclear explosions. In the current project, IDG is providing near field measurements from 26 Degelen Mountain explosions, and near regional waveforms from 10 Balapan explosions, together with explosion yields and depths where available for each event. We are using the near regional data from Degelen and Balapan to assess the evolution of different seismic phases over this distance range, the variability of seismic phases, and the differences in source function and regional waveforms due to differing media at the two test sites. We are also using IDG data from the Degelen test site to investigate the effect of explosions located close enough together that the first explosion could have affected the rock properties near the second explosion. Previous studies of Lg generation have been dominated by studies of Nevada Test Site (NTS) explosions because of the availability of data and good control on source media and explosion yields. The data and information provided by IDG are particularly important because they relate to nuclear explosions in high velocity source media, and in a region of interest.

Lg consists of shear waves trapped in the crust and observed at regional distances. It is important to treaty monitoring because 1) Lg amplitudes have been found to correlate with explosion yield better than other phases; and 2) Lg spectral characteristics and Lg/P spectral ratios are important regional discriminants. However, without a clear physical understanding of the source of Lg, use of these procedures in uncalibrated areas is questionable and errors are likely.

In the previous Lg generation project, we made considerable progress in understanding explosion-generated shear waves by quantifying and numerically reproducing features of observations of shear waves generated under different source conditions. In the current project, we are trying to quantify the results and determine the implications for the transportability of explo`sion yield estimation and discrimination. We are using the large data set of local and regional signals from nuclear explosions collected under the previous contract, combined with the new Russian data, to improve our understanding of the explosion source and to assess the contributions of different mechanisms for generation of Lg under different source conditions.

A simple point explosion generates no shear waves, so the Lg phase is generated entirely by non-spherical components of the source and conversions through reflections and scattering. The most important contributors to the Lg phase are:

- P->S conversion at the free surface and other near source interfaces.
- S waves generated directly by a realistic distributed explosion source including nonlinear effects due to the free surface and gravity.
- Rg scattering to Lg.

Each of these sources is sensitive, in different ways, to source region structure, near regional path characteristics, source depth, scaled depth, and yield. For example, Lg generated by P->S conversion depends on the source region velocity relative to the mantle velocity; S waves generated by the source are sensitive to scaled depth; Lg generated by Rg scattering depends on source depth and the near regional scattering rate. These effects can be quantitatively modeled and constrained by known information about the source and source region.

In addition to source and near source effects, Lg is affected by scattering and conversion along the travel path. The most important effects are:

- S->S scattering that changes the orientation and direction of the near source P-to-S converted waves, affecting the extent to which they are trapped in the crust.
- Randomization of the components of Lg.

Both effects tend to homogenize the observations of Lg. For example, S waves generated by P->S conversion at the free surface in a high velocity structure leak to the mantle, but S->S scattering reduces this effect by changing the ray direction and allowing more S to be trapped. Randomization of Lg orientation reduces differences between the components. In addition to the effects listed here, a variety of other scattering modes including P->S conversion along the path and Lg scattering also contribute to Lg and Lg coda.

Our goal in this project is to quantify the contribution of each of the major source mechanisms for Lg, determine the amount of variation in each with changes in source region structure, near regional path characteristics, source depth, scaled depth, and yield, compare predictions with data, assess the effects of path contributions to Lg, and evaluate the implications of the results for discrimination and explosion yield estimation.

New data from IDG

IDG is providing data and related information from the Soviet nuclear test program. To date, they have delivered the data listed in Table 1, including near field tabular data of particle velocity and rise time from 10 Degelen explosions, near regional seismic records from one Degelen and four Balapan explosions, and the explosion yields and depths for these events. Figure 1 shows an example of the data.

Table 1. Data collected by IDG

Date	Yield (kt)	Depth (m)	Site	Rock Type
1961/10/11	1.16	141	D	G
1962/02/02	16.9	265	D	G
1964/06/06	1.05	75	D	G
1964/11/16	23	203	D	QP
1965/02/04	17	262	D	G
1965/02/04	1.0	126	D	G
1965/09/17	10	148	D	QP
1966/02/13	109-125	343	D	QP
1967/12/08	12.5	166	D	QP
1968/09/29	75	358	D	QP
1985/07/20	76	466	D	
1988/04/22	2	---	B	
1988/09/14	140	651	B	
1989/01/22	108	580	B	
1989/02/12	74	572	B	

D stands for Degelen
B stands for Balapan
G stands for Granite
QP stands for Quartz Porphyry

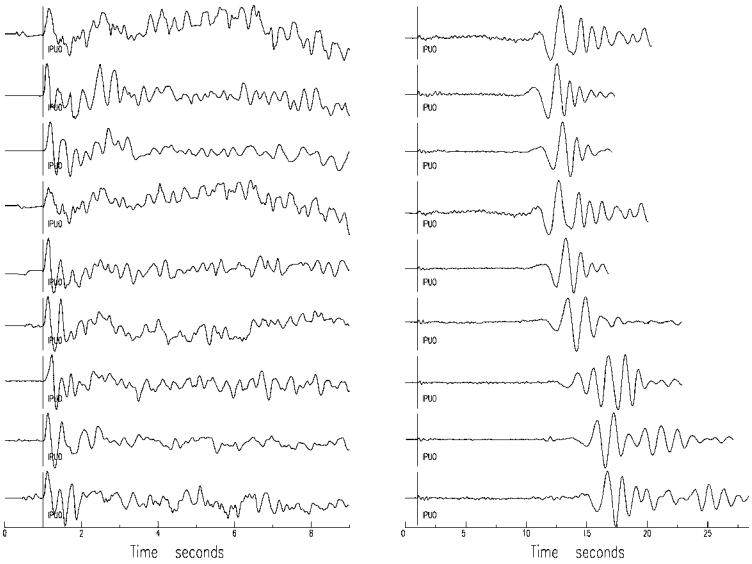

Figure 1. Vertical component records, from 58 to 88 km distance, of the 1989/01/22 Balapan explosion. Rg dominates (right), so initial segments of the records cut off before the Rg arrival are also plotted (left). Unlike most of the Degelen explosions, there is no clear S-wave phase between the P and Rg.

Numerical modeling of the explosion source

One of the major contributors to generation of shear waves by explosions is the effect of the free surface and gravity. This causes a very substantial vertical asymmetry in the source. We are investigating the effect of depth, scaled depth, and material properties on generation of shear waves from a realistic explosion source. Figure 2 shows regions of nonlinear deformation and cracking from two nonlinear source calculations, and Figure 3 shows waveforms calculated for these calculations. The calculations were performed in a structure with material properties

appropriate for the Degelen test site at the same depth (300 meters) but for different yields (31 kt and 112 kt) and therefore different scaled depths. Normal containment depth is approximately 122 $W^{1/3}$ meters where W is yield in kilotons, so the explosions are both underburied at 78% and 51% of normal scaled depth, respectively.

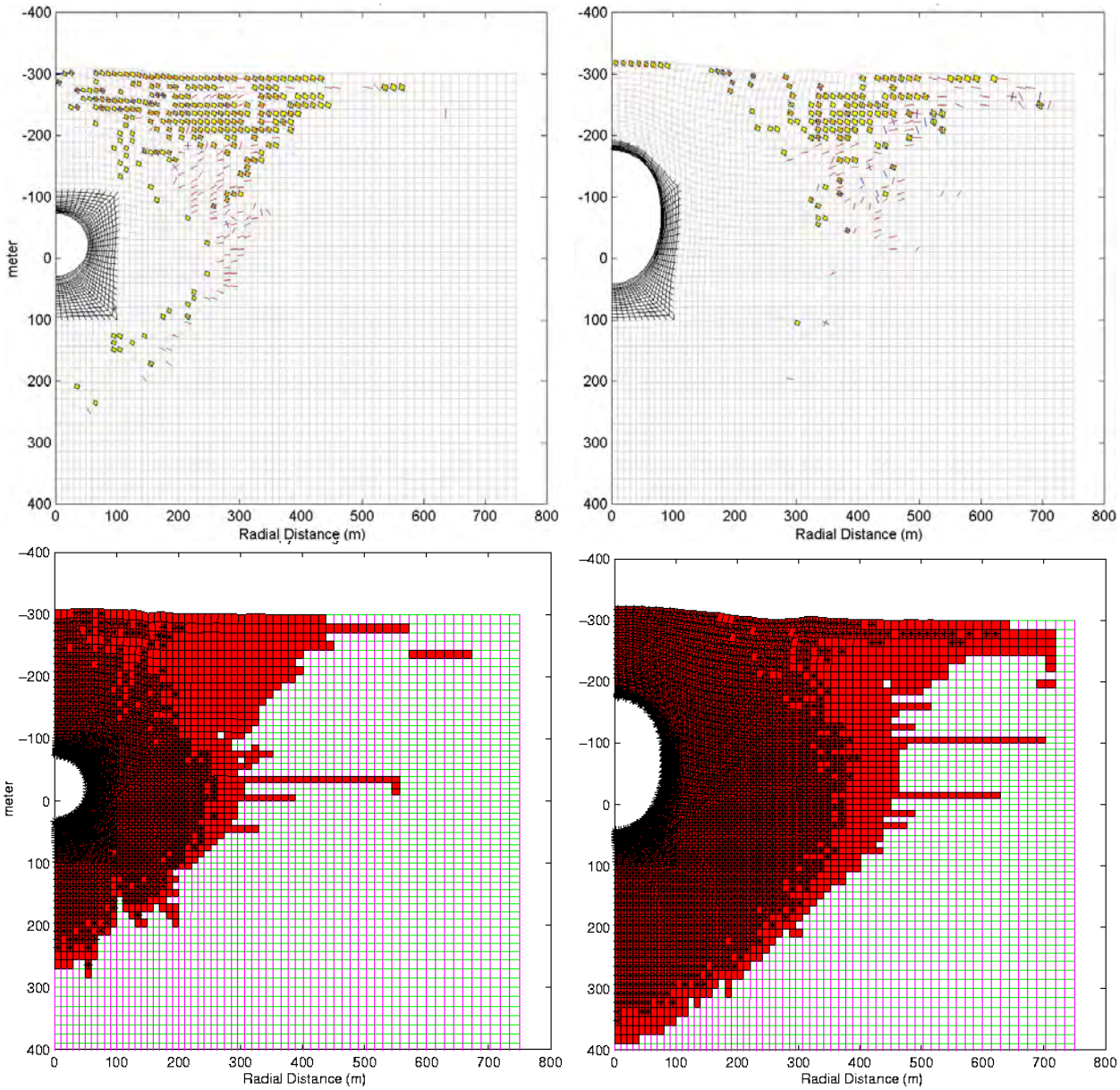

Figure 2. Near source permanent deformation due to cracking (upper) and yielding (lower) for explosions in a granite halfspace, at 78% (left) and 51% (right) of source depth. In the cracking images, yellow squares indicate hoop cracks, and red and blue lines indicate radial and in-plane tangential cracking respectively. Grid lines in both plots were initially straight. Their positions shown above represent the permanent displacement after the explosions.

Note the strong distortion of the cavity by the larger event. Both events generate strong S phases, and the Lg to P ratios are similar. This suggests that S generation is both strong and relatively independent of scaled depth for normal to underburied explosions. However, as we showed previously (Stevens et al., 2004b), generation of S does decrease for overburied explosions. All of the Degelen explosions that we analyzed are underburied, while the Balapan explosions that we will be analyzing are more commonly normally or slightly overburied.

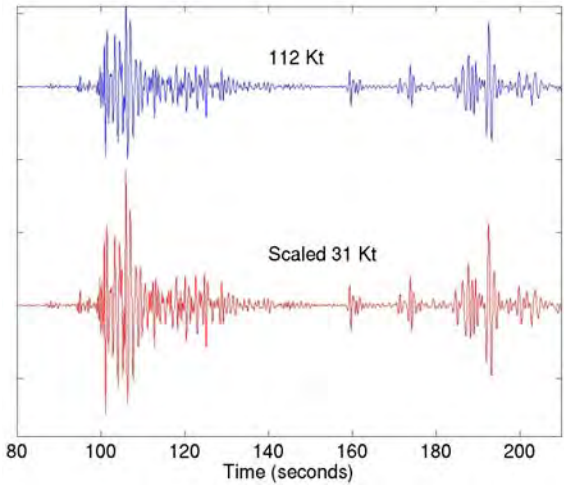

Figure 3. Seismograms calculated from the 112kt (top) and 31 kt (bottom) calculations at a distance of 650 km. The 31 kt seismogram has been scaled by a factor of 112/31.

Amplitude vs. yield, depth, and extent of underburial for 14 Degelen Mt. explosions recorded at BRVK

We examined 41 vertical component seismograms recorded at BRVK (650 km) of 14 Degelen nuclear explosions for which there exist reported yields. Thirteen of the events also have a reported depth. The multiplicity of recordings on 8 different types of instruments provides redundancy and so improves confidence in correlations. We measured amplitudes of Pn (first 5 seconds), the entire P wavetrain (first break to 5.4 km/s group velocity), Sn (first 10 seconds after the picked arrival time), Lg (3.6 to 3.0 km/s), and Lg coda (3.0 to 2.5 km/s). Amplitudes were converted to microns using reported gains and response curves at the frequency of observation.

There are consistent offsets between the amplitudes recorded on different instruments, reflecting systematic errors in reported gains of some, or all, instruments. The slope of the $\log_{10}$ amplitude vs. $\log_{10}$ yield curves for each instrument type are similar for each phase and frequency, so we use the amplitudes of all the phases and a constant slope of the $\log_{10}$ amplitude vs. $\log_{10}$ yield curve for each frequency to determine offsets of each instrument. These offsets were used to correct $\log_{10}$ amplitude measurements from all other instruments to that of the KS instrument, which was the most common. The corrections are approximately 3% to 5% of the individual $\log_{10}$ phase amplitudes, and should aid in detecting trends in amplitude with yield, source depth, or source depth relative to scaled depth.

Log_{10} amplitude vs. $\log_{10}$ yield curves were calculated using all 41 records, and again for just the 26 records made with the 4 instruments (KS, SBU-V, SKM, and SVKSMt) that had the most recordings and the most consistent amplitude offsets relative to other records. Figure 1 shows the slopes of those curves for a range of frequencies. Many of the explosions had multiple recordings, so at each frequency, a single amplitude was determined for each phase based on the median of the amplitudes after corrections to the KS instrument. That provided up to 14 amplitudes for each phase for comparison with yield. These values were bootstrapped 1000 times. The colored squares in each plot represent the median slope of all the bootstrapped outcomes. The confidence bounds represent the 25^{th} and 75^{th} percentiles, and are generally smaller for the P-wave measurements than for the S wave phases. The ratio of Lg signal to pre-Lg noise amplitudes dropped below 1.5 above 2.4 Hz. Figure 2 shows examples of the data on which the above analysis is based, the $\log_{10}$ amplitudes at 0.6 and 2.4 Hz of the each phase vs. $\log_{10}$ yield.

The slope of the $\log_{10}$ amplitude vs. $\log_{10}$ yield curve as a function of frequency, based on all phases and all recordings, with weighting for data quality, is $s = 0.855 - 0.034*f$, where s is slope and f is frequency. This provides a slope of 0.84 at 0.6 Hz, and a slope of 0.65 at 6 Hz. Various weightings of the data produce similar relationships.

Lg coda is larger than the P phases at low frequency, but much smaller at high frequency. This may mirror a change in its composition. At low frequency it stands out in the seismogram and is likely composed of similar waves to Lg that could be modeled as higher-mode surface waves. At higher frequencies, its amplitude is monotonically decreasing with time and is more like typical coda, commonly considered to be composed of multiply scattered

shear waves. The entire P wavetrain is made up of Pn and Pg. Their relative contributions vary from low frequency, where both appear significant, to high frequency where Pn appears to dominate.

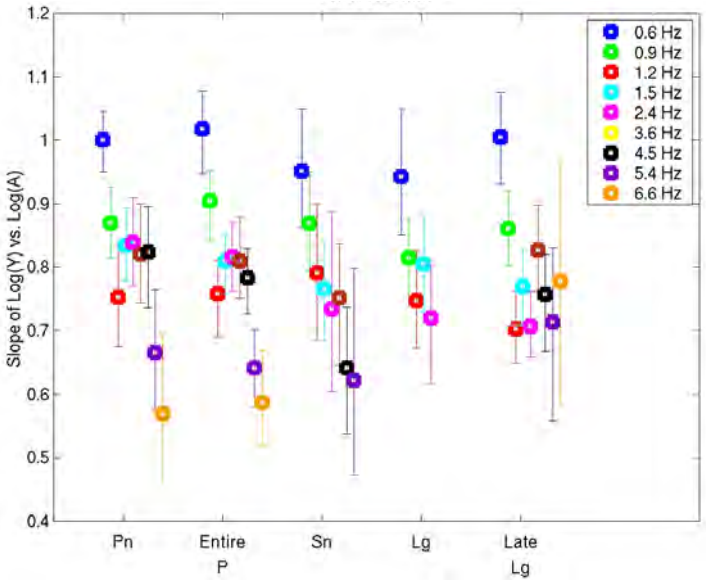

Figure 4. Slopes of the $\log_{10}$ amplitude vs. $\log_{10}$ yield curves for each phase and for a range of frequencies, using all 41 records available.

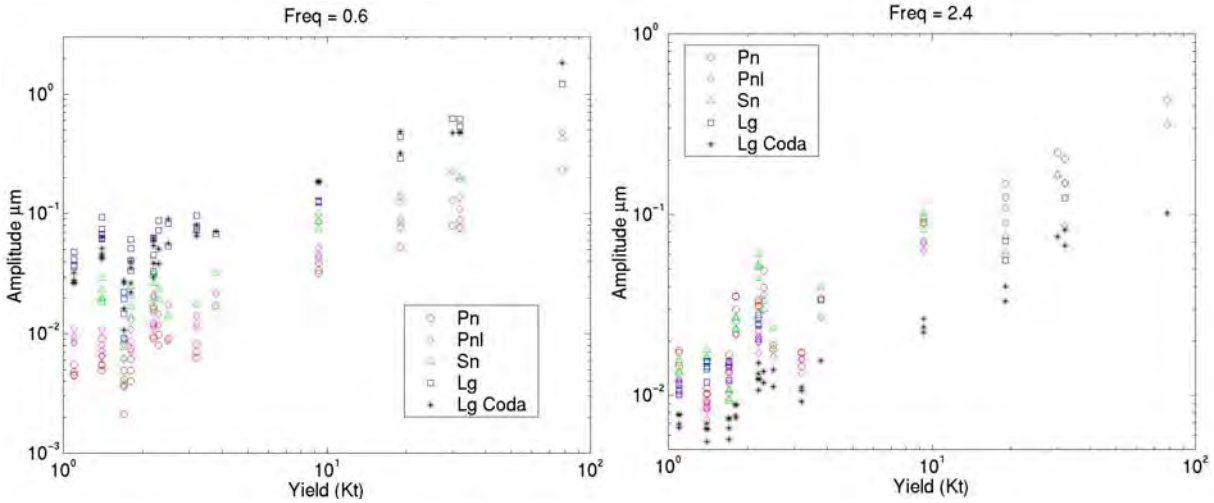

Figure 5. amplitude vs. yield curves for each phase at 0.6 Hz (left) and 2.4 Hz (right). The slopes are all similar, but the shear wave curves are higher at 0.6 Hz and the P wave curves are higher at 2.4 Hz.

For each phase, we determined an amplitude-yield relation using the same predicted slope of the $\log_{10}$ amplitude vs. $\log_{10}$ yield curve, s= 0.855 - 0.034*f, but with a different intercept determined for each phase. Residual amplitudes for each phase were then compared with depth, the extent to which the event was underburied, and yield. No statistically significant dependence is apparent between amplitudes of any of the phases and depth, yield, or extent of underburial. No strong dependence is apparent between ratios of the different phases and the parameters, although Lg/Lg Coda ratios at 1.1 Hz, and Sn/Pn ratios at 2.4 and 3.7 Hz appear to decrease slightly with depth and yield. More data are necessary to determine whether this observation can be substantiated.

Table 2 shows the median of the yield residuals for each phase with 2 smad error bounds on the median, for a range of frequencies. This is based on a common set of recordings for each phase. We use only those records with signal-to-noise ratio greater than 1.5 for all phases for the first 4 frequencies, and for Pn, the entire P wavetrain, Sn, and Lg coda at the higher frequencies (where Lg drops below the pre-Lg noise level). Pre-event noise is used to assess S/N

for Pn, Pnl, and Lg Coda. Pre-Sn and pre-Lg windows are used to assess S/N for those two phases. The yield errors are smallest for the entire P wavetrain, except for the 3 highest passbands, where the coda based estimate is more accurate. Below 1 Hz, Lg and Sn yield estimates have at least twice the error of the P wavetrain. They are closer in accuracy at 1.2 and 1.5 Hz, and the Lg error is comparable at 2.4 Hz.

Table 2. Median Log_{10} yield errors +/- 2 SMAD.

Hz	npts	Pn	Pnl	Sn	Lg	Lg Coda
[1]0.6	32	0.10±0.05	0.07±0.03	0.18±0.10	0.18±0.08	0.12±0.05
0.9	18	0.11±0.10	0.05±0.04	0.13±0.05	0.10±0.07	0.07±0.04
1.2	27	0.19±0.09	0.08±0.05	0.13±0.07	0.11±0.06	0.12±0.05
1.5	24	0.11±0.08	0.07±0.04	0.12±0.07	0.11±0.06	0.12±0.05
2.4	22	0.15±0.09	0.09±0.06	0.22±0.14	0.09±0.05	0.11±0.07
3.6	34	0.08±0.05	0.06±0.03	0.12±05	*	0.10±0.05
4.5	34	0.10±0.05	0.09±0.04	0.16±0.08	*	0.08±0.04
5.4	29	0.13±0.08	0.12±0.07	0.14±0.08	*	0.06±0.03
[1]6.6	23	0.12±0.08	0.12±0.08	0.07±0.06	*	0.09±0.07

[1] 0.6 Hz is at or below the low frequency corner of most of the instruments, and 6.6 Hz is at the upper end of most of the known response curves, so the calibrations applied to these measurements may be less accurate than those at the intermediate frequencies.
* insufficient signal at common instruments over a large yield range

Rg-to-Lg scattering

We are attempting to model Rg to Lg scattering using a mode conversion model constrained by observations in different regions. Observations provide the Rg decay rate, a critical parameter in the modeling. Modeling results will be compared with Lg waveforms. We anticipate that widely varying decay rates in Eurasia vs. the western U.S. will lead to different Rg-to-Lg predictions. For example, Rg is observed at 650 km from the larger Degelen explosions (e.g., Figure 6), while it is difficult to distinguish Rg at local distances to NTS explosions. The near field Degelen and Balapan records, and Deep Seismic Sounding data will provide Rg decay rate values in Eurasia. A previous upper bound calculation (Stevens et al., 2004b) based on instantaneous scattering of all Rg into higher modes in an NTS structure, found that scattered Rg most strongly affects late Lg (later than 3 km/s) at frequencies below 1 Hz.

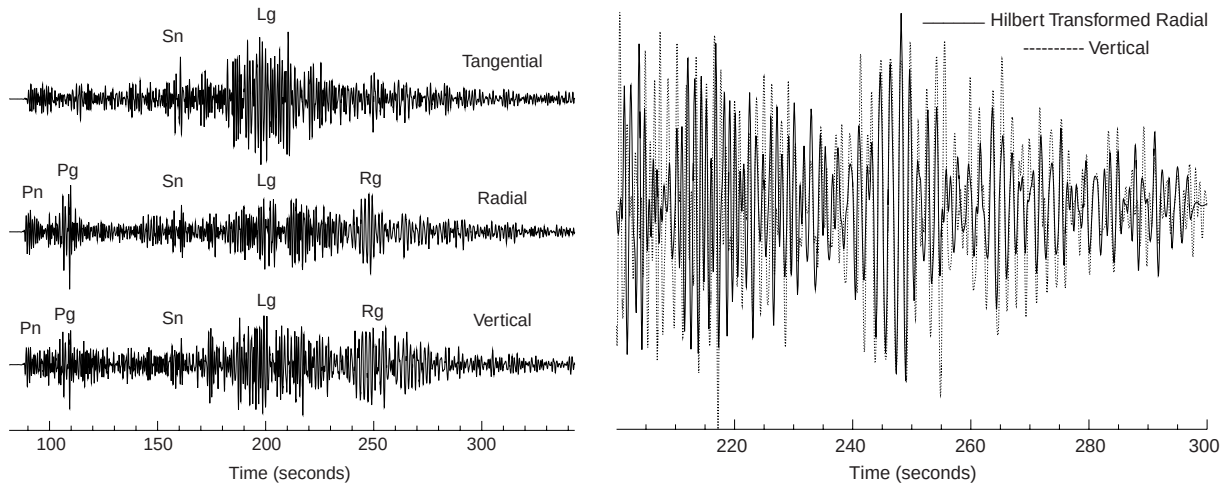

Figure 6. 3-component records (left) of a 90 Kt Degelen explosion on 4/25/1971, recorded at 651 km, at 0.5 Hz to 1 Hz. The vertical and Hilbert transformed radial seismograms (right) from 3.26 to 2.17 km/sec group velocities overlay from 240 seconds (~2.7 km/sec) onward, confirming identification of Rg in that window.

We model Rg to Lg scattering under the assumption that Lg is generated by a distribution of surface scatterers and that all energy scattered from Rg is converted to Lg. We make the following assumptions:

1) The explosion may be a complex source, but has a known source function and is located at the origin.
2) Scattering occurs on the earth's surface and can be modeled as generated by a distribution of vertical point sources.
3) No energy is lost in scattering.

All scattering is from Rg to higher modes. We neglect secondary scattering and scattering to leaky phases. We therefore consider that the scattered Rg consists of waves from a cylindrical distribution of point forces at the location of the propagating Rg phase (Figure 7), and that the scattered Rg goes into higher modes. These are optimistic assumptions and should be regarded as providing an upper bound on Lg generated by Rg scattering.

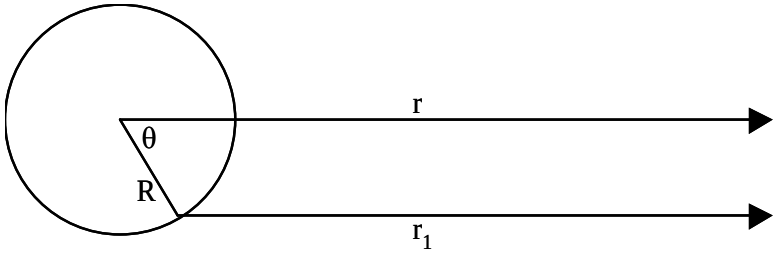

Figure 7. Rg propagates from the origin to radius R where it is scattered to Lg.

The vertical displacement from the initial Rg wave u_z^0 has the form

$$u_z^0(\omega,z,r) = A_0(\omega)G_s(r)\exp(-ik_0 r - \gamma_0 r)E_2(k_0,z)/\sqrt{r}\ , \tag{1}$$

where k_0 is the wave number ω/c, ω is the angular frequency, z is the depth, E_2 is the Rayleigh wave vertical displacement eigenfunction which is normalized to 1 at the free surface z=0, and A_0 is amplitude spectrum which depends on characteristics of the source and source region earth structure. γ_0 is the intrinsic attenuation function of Rg. G_s is a function that represents the attenuation of Rg due to scattering. The radial displacement has a similar form with E_2 replaced by the radial eigenfunction E_1. The kinetic energy T in the mode at location r is given by

$$T_0 = \tfrac{1}{2}\omega^2 \int_0^\infty \rho(|u_z|^2 + |u_r|^2)dz = \pi\omega^2 G_s^2(r)\exp(-2\gamma_0 r)|A_0(\omega)|^2 I_1^0\,, \tag{2}$$

where I_1^0 is the energy integral on the left with the superscript indicating the fundamental mode. I_1 is the notation used by Takeuchi and Saito (1972) for this integral.

If part of u_z^0 is converted to a sum of higher modes u_z^1 at point R, we have

$$u_z^1 = \iint dR d\theta \sum_{i=1}^{N} S(\omega,R)\alpha_i(\omega)\exp(-ik_0 R - ik_i r_1 - \gamma_i r_1)E_2^i(k_i,z)/\sqrt{r_1}\,, \tag{3}$$

where α_i are modal coefficients corresponding to a vertical point force and S is the excitation function related to the energy transfer. Assuming azimuth independence of scatterers and neglecting small differences in attenuation and geometric spreading between r and r_1, we get:

$$u_z^1 = \frac{2\pi}{\sqrt{r}}\sum_{i=1}^{N}\alpha_i(\omega)\exp(-\gamma_i r - ik_i r)E_2^i(k_i,z)\int_0^\infty dR J_0(k_i R)\exp(-ik_0 R)S(\omega,R) \tag{6}$$

where J_0 is the Bessel function. The converted wave has a total energy of

$$T^1 = 4\omega^2\pi^3\sum_{i=1}^{N}|\alpha_i(\omega)^2|\,I_1^i\exp(-2\gamma_i r)\left|\int_0^\infty dR J_0(k_i R)\exp(-ik_0 R)S(\omega,R)\right|^2 \tag{7}$$

The Rg energy loss rate due to scattering at R is

$$\frac{dT_0}{dR} = 2\pi\omega^2|A_0(\omega)|^2 I_1^0 G_s\frac{dG_s}{dR}\exp(-2\gamma_0 R) \tag{8}$$

The total energy available for conversion to Lg is the integral of this equation. To determine the dynamic solution for Rg to Lg scattering, we equate the energy lost from Rg to the energy gained by Lg at each point R. Equation 8 represents the Rg energy loss and the derivative of equation 7 represents the energy gain, so

$$4\omega^2\pi^3\sum_{i=1}^{N}\left|\alpha_i(\omega)^2\right|I_1^i\left|\int_0^R dRJ_0(k_iR)\exp(-ik_0R)S(\omega,R)\right|^2=-\int_0^R\frac{d}{dR}T_0dR \qquad (9)$$

The right hand side of this equation can be calculated for each point given a form for G_s, for example $\exp(-\gamma_s R)$. Equation 9 can be solved for small kR:

$$S(\omega,R)=\frac{1}{2\pi}\frac{\sqrt{\gamma_s(\gamma_s+\gamma_0)}B(\omega)\exp(-2\gamma_sR-2\gamma_0R)}{\sqrt{1-\exp(-2\gamma_sR-2\gamma_0R)}},\ B(\omega)=\left(\left|A_0(\omega)\right|^2 I_1^0\Big/\sum_{i=1}^{N}\left|\alpha_i(\omega)\right|^2 I_1^i\right)^{1/2} \qquad (10)$$

Equation 9 is an integral equation for S, which can be solved numerically, starting with equation 10 for small R, and then used to calculate Lg using (6). Our plan is to calculate Rg-to-Lg scattering using this technique for a range of earth structures and scattering rates.

Shear wave generation by Azgir tamped and decoupled explosions

On December 22, 1971, a 64 Kt tamped nuclear explosion at 987 m depth in salt created a 38 m horizontal radius by 33 m vertical radius cavity in salt at the Soviet Azgir test site. On March 29, 1976, A 10 kt explosion was detonated in the cavity and was recorded at 4 of the same 3-component stations that had recorded the tamped explosion. We examine differences in shear waves between records, which can be attributed to differences between the sources. The most useful set of records are at 17.8 km, where distinct P, S, and Rg phases can be identified.

The tamped and decoupled explosions overlay nearly identically at 0.2 to 0.5 Hz (not shown), where a very slow Rg phase dominates. This provides a constraint on sediment thickness and velocity in our modeling. Up to ~3 Hz, the tamped and decoupled seismograms are very similar (Figure 8). At higher frequencies however, the tamped explosion generates much more shear wave energy. This suggests different mechanisms for shear wave generation at low and high frequencies, shared by both tamped and decoupled explosions at low frequencies only.

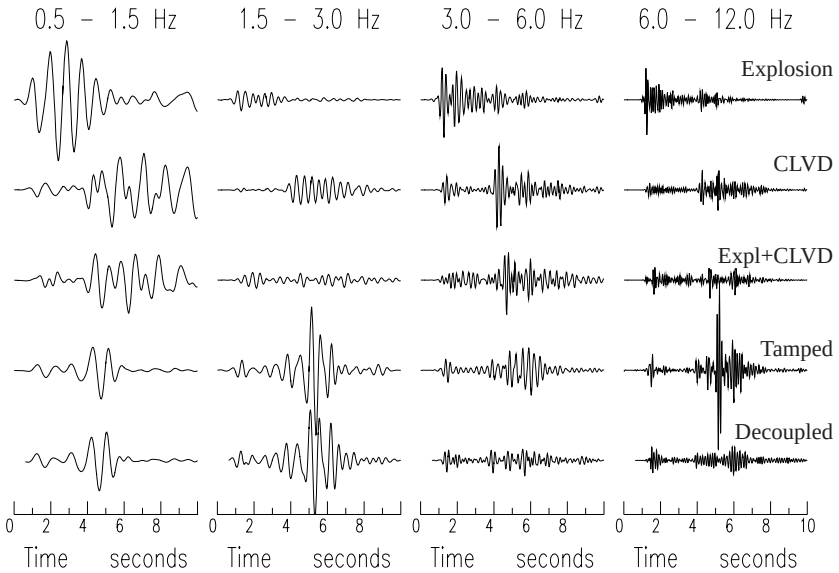

Figure 8. Vertical seismograms at 17 km from synthetic spherical explosion source and compensated linear vector dipole (CLVD) calculations (upper two traces), the sum of those two (middle), and the tamped and decoupled explosions in 4 passbands. Each of the synthetics is scaled by the P-wave rms amplitude of the sum of the explosion and CLVD source, in each passband, and the tamped and decoupled records are scaled by their P-wave rms amplitude.

To determine whether the S-wave observations can be easily modeled with a spherical point explosion in a reasonable velocity structure, and if not, how large an S-wave source the data require, we calculated wavenumber synthetic seismograms for spherical explosion and CLVD sources for a number of models. The models range from a very simple homogeneous salt dome, to a complex, strongly layered model based on the velocity structure for a

7/21/84 explosion at the Lira test site (Murphy et al, 2001), which is north of Azgir. That structure is strongly layered, with highly variable Poisson's ratio. The explosion was in salt at 987 m depth. The sediment thickness was modified to match the observed large, slow Rg. The deeper structure is from the Stevens et al. (2004a) global earth model from surface waves. The fine details of this model are not important, as it would be impossible to uniquely determine the structure from the data, but are simply chosen to allow us to most easily compare the observed P and S phases with the synthetics, by ensuring similar timing, while assessing whether the complex structure can produce the secondary phases observed in the explosion data. We place the CLVD at 650 m depth within a salt layer, rather than in the one of the much higher velocity anhydrite layers. For the range of complex models used here, the observed S-waves were not produced by conversion from a spherical point explosion.

CONCLUSIONS AND RECOMMENDATIONS

Analysis of Degelen nuclear explosion records from BRVK at 650 km indicates that Pn, the entire P wavetrain (Pn through 5.4 km/s, Sn, Lg (3.6 to 3.0 km/s), and Lg coda (3.0 to 2.5 km/s) vary similarly with yield. Their yield dependence can be well fit by the relation slope = 0.855 - 0.034*f, where f is frequency. Amplitudes of Lg coda (3.0 to 2.5 km/s) and the entire P wavetrain (Pn arrival to 5.4 km/s) generally correlate with yield more accurately than do Lg or Sn. There is no apparent dependence of any phase amplitudes on depth, or the extent to which an event is underburied. Non-linear source calculations predict this observation, despite significant differences in the nature of the permanent deformation around cavities of 20% and 50% underburied explosions. We intend to perform similar analysis of Balapan records, for which we have obtained new yield and depth information.

IDG has delivered near source tabular data for 10 historical Degelen nuclear explosions, local seismic records from 4 Balapan and 1 Degelen explosion, and yields and depths the events. We intend to perform more detailed analyses as the dataset increases in size. The near source tabular data will permit exploration of the effect of previous nearby explosions on rock strength and pulse shape. The local measurements, and new depth and yield information, will permit a more detailed assessment of the relationships between the phase amplitudes of local and regional records and source depths, yields, and depth/scale depth ratios for a greater range of values than has previously been possible.

We have derived a solution for the dynamic problem of Rg-to-Lg scattering in which the loss of energy at a point R is directly converted to Lg, and are preparing to perform calculations for different regions, where Rg decay rates will constrain the calculations, and results can be compared with regional Lg observations.

Analysis and modeling of local seismic records indicates that below ~3 Hz, tamped and decoupled explosions generate very similar shear waves in size (relative to P) and shape, whereas the S/P ratio of the decoupled explosion records decreases and that of the tamped explosion increases dramatically at higher frequencies. This suggests that a similar mechanism generates the low frequency shear waves from both tamped and decoupled explosions, while a mechanism not present in the decoupled explosion generates the high frequency shear waves for the tamped explosion.

REFERENCES

Murphy, J. R., I. O. Kitov, B. W. Barker, and D. D. Sultanov (2001), Seismic source characteristics of Soviet peaceful nuclear explosion, *Pure and Applied Geophysics*, 158: 2077–2101.

Stevens, J. L., N. Rimer, H. Xu, G. E. Baker and S. M. Day (2003), Near field and regional modeling of explosions at the Degelen Test Site, SAIC final report to DTRA, SAIC-02/2050, January.

Stevens, J. L., D. A. Adams, G. E. Baker, M. G. Eneva and H. Xu (2004a), Improved surface-wave dispersion models, amplitude measurements, and azimuth estimates, in *Proceedings of the 26th Seismic Research Review: Trends in Nuclear Explosion Monitoring*, LA-UR-04-5801, Vol. 1, pp. 170-180.

Stevens, J. L., G. E. Baker, H. Xu, T. J. Bennett, N. Rimer and S. M. Day (2004b), The Physical Basis of Lg Generation by Explosion Sources, SAIC Final Report submitted to the National Nuclear Security Administration under contract DE-FC03-02SF22676, December.

Takeuchi, H., and M. Saito, (1972), Seismic surface waves, *Methods Comput. Phys*. 11: 217–295.

REGIONAL EVENT IDENTIFICATION RESEARCH IN EASTERN ASIA

Steven R. Taylor, Howard J. Patton, Xiaoning (David) Yang, and Monica Maceira

Los Alamos National Laboratory

Sponsored by National Nuclear Security Administration
Office of Nonproliferation Research and Engineering
Office of Defense Nuclear Nonproliferation

Contract No. W-7405-ENG-36

ABSTRACT

We describe ongoing studies of broad-area, regional-event identification in Eastern Asia. The goal of our work is to provide a framework that allows for accurate identification, operational transparency, and clear reporting to nontechnical decision makers. The underlying methodologies need to have a clear physics basis packaged in a sound statistical framework having proper uncertainty estimates. We are developing regional surface-wave discriminants (e.g., m_b - M_s) through a suite of focused studies. The 20-second m_b-M_s discriminant is one of the most reliable and best understood methods for identifying underground nuclear explosions. To extend the discriminant to lower magnitude thresholds at regional distances it is necessary to perform the M_s measurement at shorter periods. Although shorter period Rayleigh wave measurements have lower detection thresholds than those at 20 seconds, they are more influenced by the effects of earthquake depth causing overlap of earthquake and explosion populations. We present a technique using a probability of detection model (PXD) to estimate the probability that a surface wave detection came from an underground explosion. The key to the method is the development of a simple analytic model used to predict the maximum expected amplitude probability distribution (upper tail) from an underground explosion of a given size recorded at a specified distance. For a given sensor we can define the probability of detection given that the source was an explosion. Using Bayes' Rule we can then determine the probability that the signal detection originated from an explosion. Using a hypothesis test, we can compute the conditional probability (represented as a *p* value) that the detected signal originated from an explosion. We show results of the signal detection formulation using short period Rayleigh waves from earthquakes and explosions in Eurasia and compare to the traditional m_b-M_s at different periods. For a set of earthquakes and explosions recorded at WMQ measured at 6 – 12 seconds period, false alarm rates are reduced from 28% for m_b-M_s to 18% using the probability of detection model.

For our regional m_b – M_s work, multi-frequency surface wave magnitudes M_s have been measured for earthquakes and explosions in southern Asia using the methodologies of Marshall and Basham (1972) and Russell (2004) using regional and far-regional seismograms. Five frequency bands with center periods of 20, 16, 12, 10, and ~7 sec were chosen, and the final M_s corresponds to the band giving the largest M_s or the largest amplitude. In either case, M_s from both methods show good correlation with independently determined seismic moments for the earthquakes. Due to the narrowband filtering criteria used in the Russell method, no corrections for dispersion are necessary and this offers practical advantages over other methods requiring such corrections. We have developed surface-wave attenuation tomographic maps for central and southeast Asia. These maps can be used in the reformulation of regional M_s calculations with two-dimensional (2-D) path corrections to reduce station-magnitude scatter and network-magnitude bias. Compared with one-dimensional (1-D) distance corrections, the use of 2-D attenuation models for path corrections in M_s calculations reduced the station-magnitude scatter by 16% to 18% on the average.

Another component of these studies involved evaluation and refinement of existing surface-wave slowness tomographic models at shorter periods (6 seconds and above) for central Asia. Rayleigh-wave group-velocity dispersion curves are used to compute high-resolution, 0.5-degree cell size, slowness tomographic maps. Using our high-resolution tomographic maps of western China, we investigate the shear velocity structure beneath the Tarim and Junggar basins. Preliminary results show high upper-mantle shear velocities that are usually interpreted as old, cold, thick lithospheric blocks and differences in shear velocities between eastern and western Tarim. To obtain a 3D model and improve resolution, we divide into 1º x 1º cells the entire region comprising the Tarim basin, the Tien Shan, and the Junggar basin. We develop an inversion technique to invert the dispersion curves for all the 1º x 1º cells simultaneously imposing some geophysical constraints such as the gravity anomalies in the region.

OBJECTIVE

The objective of this work is to provide methodologies and calibration parameters for robust regional-event identification at reduced magnitude thresholds.

RESEARCH ACCOMPLISHED

A Probability of Detection Method for Reducing Short Period $m_b - M_s$ False Alarm Rates

The 20-second teleseismic m_b-M_s discriminant is one of the most reliable and best understood methods for identifying underground nuclear explosions. However, at lower magnitudes and regional distances, detection of 20-second surface waves can be very difficult. Short period (SP) Rayleigh waves (6-12 seconds) generally show lower detection thresholds than 20 second Rayleigh waves used to construct $m_b - M_s$ discriminants. The Rayleigh waves from earthquakes are typically expected to be greater than those from explosions because of the shear energy radiated from the faulting process. However, short period surface waves are more strongly affected by earthquake depth resulting in much scatter in the traditional $m_b - M_s$ discriminant. We have developed a technique using a probability of detection model (PXD) to estimate the probability that a surface wave detection came from an underground explosion (Taylor and Patton, 2005). The key to the method is the development of a simple analytic model to predict the maximum expected amplitude probability distribution (upper tail) from an underground explosion of a given size recorded at a specified distance.

The detection classifier can be applied when there is a signal detection, $A_o > N_o$ and the observed amplitude is greater than the maximum expected amplitude, $A_o > A_x^\alpha$ (Equation 1). The right portion of Figure 1 shows an enlargement of the magenta box in the left portion of Figure 1 and illustrates the conditions under which the detection classifier is applicable. It is important to note that the maximum expected amplitude from the explosion can also be greater than the noise as illustrated by the red dashed line. Thus, the PXD method can be applied under the detection conditions

$$D \in \left\{A_o > \max\left(N_o, A_x^\alpha\right)\right\}. \tag{1}$$

Next, for each sensor we define the probability of detection given that the source was an explosion

$$P(D \mid X) = 1 - \int_{-\infty}^{\max\left(N_o, A_x^\alpha\right)} f_x(A)dA = 1 - F_x\left(\max\left(N_o, A_x^\alpha\right)\right). \tag{2}$$

Using Baye's Rule we can determine the probability that the signal detection was from an explosion

$$P(X \mid D) = \frac{P(D \mid X)P(X)}{P(D)}. \tag{3}$$

where $P(X)$ is the prior probability that an explosion occurred and $P(D)$ is derived from a probability of detection curve for the signal of interest. For this study we set *P(X)* and *P(D)* to be equal.

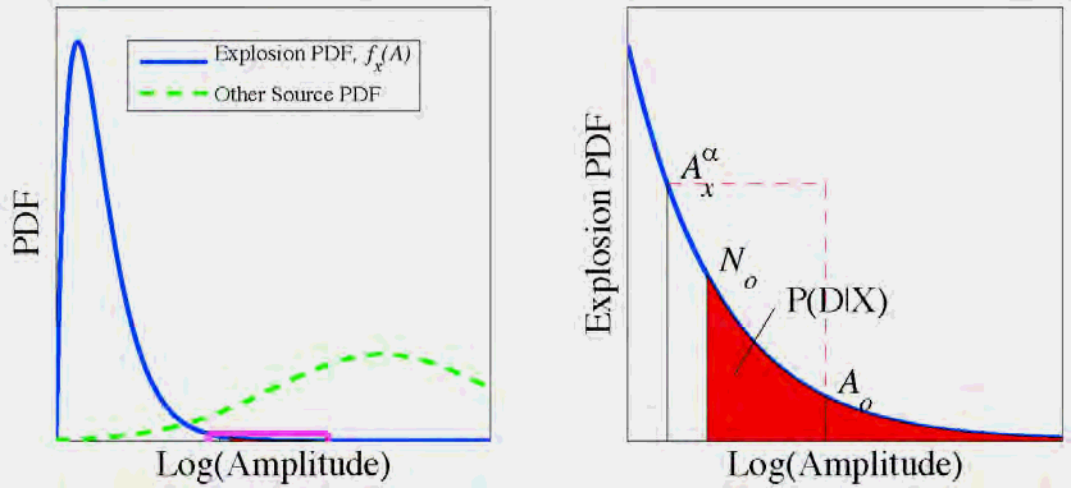

Figure 1. Left: Schematic illustration of expected Probability Density Functions (PDFs) for explosions and another benign source type (e.g. earthquakes). Right: Blowup of magenta box in left figure showing high amplitude tail of explosion PDF and measurements discussed in text. Note that the maximum expected amplitude can also be greater than the noise for the PXD method to be applicable under the detection conditions of Equation 1; $D \in \left\{A_o > \max\left(N_o, A_0^\alpha\right)\right\}$ **as indicated by the dashed red line.**

The next step in the procedure is to develop a simple analytic model to predict the maximum expected amplitude from an explosion of a specified size and distance. The vertical fundamental mode Rayleigh wave displacement spectrum for a step function explosion at depth zero is (Aki and Richards 1980; eq. 7.151)

$$\left|u_z^R(r,\omega)\right| = -\frac{r_2}{8\omega c U I_1}\sqrt{\frac{2}{\pi kr}}\left\{kr_1 + \frac{dr_2}{dz}\right\}M_0^x \tag{4}$$

where $I_1 = \frac{1}{2}\int_0^\infty \rho\left(r_1^2 + r_2^2\right)dz$ is the energy integral and r_1 and r_2 are the radial and vertical displacement eigenfunctions, respectively, r is the range, ω is the angular frequency, c is the phase velocity, U is the group velocity, k is the wavenumber and M_0^x is the explosion moment. For a Poisson solid ($\mu = \lambda$) half space, $c = U = 0.92\beta = 0.5308\alpha$ and it can be shown that $r_1 = 0.4227$, $r_2 = -0.6204$, $dr_2/dz = -0.1410k$ and $I_1 = 0.6205(\rho/k)$. Thus, Equation 8 simplifies to

$$\left|u_z^R(r,\omega)\right| = \frac{0.6461 M_0^x}{\rho\alpha^{7/2}\sqrt{Tr}} \tag{5}$$

where T is the period. Using the shorthand $\left|u_z^R(r,\omega)\right| = A_s(T)$ and taking the base 10 logarithm of Equation 5 gives

$$\log A_s(T) = \log M_0^x - \frac{1}{2}\log Tr - \log \rho\alpha^{7/2} - 0.1897 \tag{6}$$

Next, we will add three new terms to Equation 6, the first representing the maximum expected contribution to the Rayleigh wave amplitude for tectonic release (or other secondary sources), a second term converting spectral amplitude to peak-to-peak (P-P) amplitude and an attenuation operator.

Thus after adding the tectonic release term and the conversion from spectral amplitude to P-P and an attenuation operator Equation 6 becomes

$$\log A_{pp}(T) = \log M_0^x - \frac{1}{2}\log Tr - \frac{\pi \log e}{Q(T)U(T)T} r - \log \rho \alpha^{7/2} + \log A_T - \frac{1}{2}\log \frac{T_w}{B} + \log A_{pp/rms} - 0.1897 \quad (7)$$

where $\log A_{pp/rms}$ is the conversion from RMS to P-P amplitude. From the attenuation term in Equation 7 it is evident that attenuation and group velocity tomography can be used in the estimation of the maximum expected amplitudes.

To illustrate the PXD method, we selected a data set of 6 to 12 second period Rayleigh wave P-P amplitude measurements from station WMQ in western China. The dataset and measurements are described in Hartse et al., (1997). The P-P measurements were converted to M_s using Rezapour and Pearce (1998). We next assess the performance of the short-period single station $m_b - M_s$ discriminant at WMQ by basically following a similar but simplified methodology of that outlined by Fisk et al., (2002). To do this we assign a critical value of $m_b - M_s$ to be that of the lowest explosion below which all events are declared earthquake. A histogram of the $m_b - M_s$ values at WMQ is shown in Figure 2. The critical value in this case is set to be $m_b - M_s = 0.61$ resulting an estimated false alarm rate, $P(X|Q) = 0.283$ (or 28.3%). Note that this value of $P(X|Q)$ is higher than the approximate value of 20% in Fisk et al., (2002). Of course, none of the explosions are misclassified, $P(Q|X) = 0$. Interestingly, using PXD by itself as an earthquake identifier, 78% of all events are assigned a p value resulting in a false alarm rate of 22% that is better than $m_b - M_s$ alone for this dataset.

Figure 3 shows the results of the PXD analysis portrayed on an $m_b - M_s$ plot versus m_b and distance (using snr cutoff of 2). We have taken some liberties with our probabilistic notion, but in the figure $P(X|Q)$ indicates calling an event an explosion when it is actually an earthquake (false alarm), $P(Q|X)$ indicates calling an event an earthquake when it is in fact an explosion (missed explosion), and $P(Q|Q)$ and $P(X|X)$ are correctly classified earthquake and explosions, repectively. $P(X|X)$ actually means that an explosion was not assigned a p value. For the PXD method the $P(X|Q)$ is reduced from 28.3% down to 18.6%.

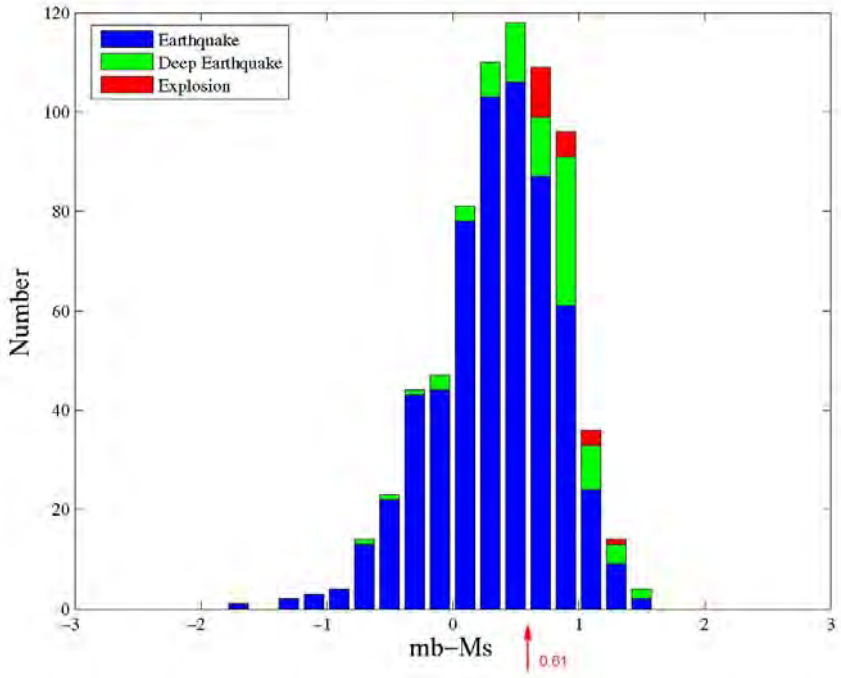

Figure 2. Histogram for $m_b - M_s$ data. Critical point for $m_b - M_s$ discriminant test set to 0.61 (the lowest explosion value).

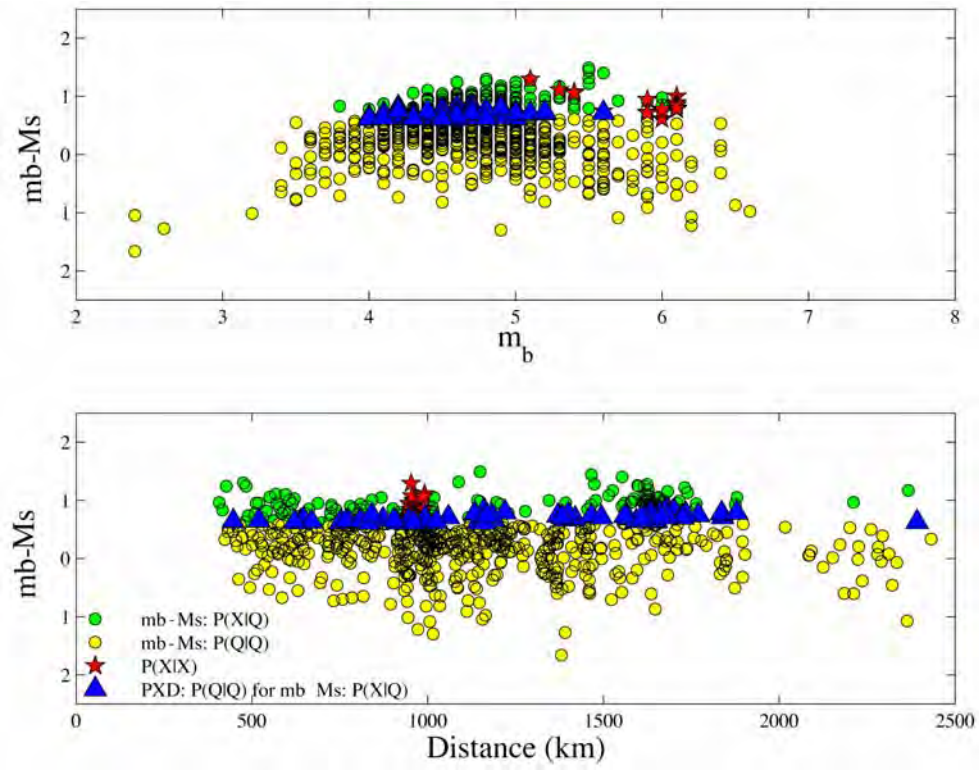

Figure 3. Comparison of $m_b - M_s$ and PXD results (see text for details).

Regional $m_b - M_s$

The M_s work reported on in this paper is part of LANL's development and evaluation of regional $m_b - M_s$ data sets for key stations and monitoring areas in Asia to ascertain their discrimination capabilities at small magnitudes. Traditionally M_s is measured in the 20 s passband, but regional-distance applications offer the promise to lower the magnitude threshold that M_s can be measured through the implementation of multi-frequency M_s methodologies coupled with better corrections for propagation effects of intermediate-period (20-7 s) surface waves. New M_s methodologies (e.g., Russell, 2004) and tomographic inversions of surface wave group velocities and attenuation coefficients in Asia (e.g., Levshin and Ritzwoller, 2003; Yang et al., 2004) have advanced the state-of-the-art to where regional M_s calibrations should yield fruitful results for future discrimination studies.

In this application, five passbands were selected for measuring multi-frequency M_s, and these passbands had center periods of 20, 16, 12, 10, and 8 s. M_s was calculated in two ways: (1) the well-known method due to Marshall and Basham (1972), and (2) a new method due to Russell (2004). The Marshall and Basham M_s formula is

$$M_s = \log(A) + B'(\Delta) + P(T) \tag{8}$$

where A is the maximum amplitude in nm measured off the displacement Rayleigh wave train, $B'(\Delta)$ is a distance correction accounting for spreading on a sphere, dispersion, and absorption, and P(T) is an additional dispersion correction, T is wave period in s, U group velocity in km/s, and Δ distance in degrees. The Russell M_s formula is taken from Eq. 57 of the 2004 report

$$M_{s(b)} = \log(a_b) + \frac{1}{2}\log(\sin(\Delta)) + 0.0031\left(\frac{20}{T}\right)^{2.3}\Delta - 0.66\log\left(\frac{20}{T}\right) - \log(f_c) - 0.43 \tag{9}$$

where f_c is the corner frequency of a three-pole, two-pass Butterworth filter used to filter the displacement Rayleigh wave train before measuring the maximum zero-to-peak amplitude, a_b, in nm. The Butterworth filter is designed to minimize the effects of dispersion by choosing an f_c such that $f_c \le 0.6/T\sqrt{\Delta}$, where the minimum value of G (see Eq. 44 of the 2004 report) is ~0.6 for most continental paths and wave periods, 8 < T < 25 s. In the case of Marshall and Basham M_s (M-B M_s), the corner frequencies of the Butterworth filters were held fixed and correspond to the following period ranges: 23-17, 19-13, 14-10, 12-8, and 9-5. The corner frequencies f_c for the Russell M_s (DR M_s) are dynamic in the sense that they depend on path length, as well as center period.

We processed 365 seismic waveforms recorded at four stations (BRVK, MAKZ, MK31, and WMQ) from 111 earthquakes and 56 explosions distributed in southern Asia for the most part. Both long-period (1 s/s) and broadband (40 s/s) channels were used. Waveforms from the Borovoye Archive (Kim et al., 2001) are for the DS seismometer system with 20-s natural period and ~3-s sampling rate. Forty-nine of the 111 earthquakes have seismic moment M_o estimates from regional studies of Ammon et al. (2003). The remaining earthquakes are those with usable surface waves from the ENSCO dataset. The vast majority of explosions are from the Semipalatinsk test site. Three-component waveforms were corrected for instrument response and rotated to the great-circle path. The following describes the processing steps taken to measure amplitude and period used in the M_s formulas. The processing begins by filtering the displacement waveforms into five passbands, and proceeds to operate independently on each of the filtered waveforms. For particle motion processing, the product of the Hilbert-transformed radial component with the vertical component is taken, and the absolute value of the resulting time series is passed through a band-reject filter to obtain a smooth envelope function where the largest amplitudes correspond to times consistent with Rayleigh particle motion. This envelope function is converted to a unit boxcar trace using an amplitude threshold set to 1/2 the maximum value of the envelope time series. For group velocity processing we chose to apply group velocity windowing, where time windows were computed using slowness predictions from tomographic models developed for Eurasia (Ritzwoller and Levshin, 1998; Stevens et al., 2001; Levshin and Ritzwoller, 2003) on a path-by-path basis. Minimum and maximum slowness values were found for the frequency band in question, and these values were adjusted to account for uncertainty in the predicted estimates. The measurement window corresponds to a time range consistent with Rayleigh particle motion and the tomographic predictions of Rayleigh group arrivals. An amplitude measurement for M_s is legitimate only on that portion of the waveform lying inside a measurement window. A few simple rules were used to construct the measurement window from the particle motion and group velocity windows discussed above. If there is no intersection between the arrival time window and a particle motion window, the result is a "null" trace and no amplitude measurement is made.

The final M_s were determined from either maximum magnitude or maximum amplitude criteria. In the case of M-B M_s, a magnitude was computed for each of the four utilized passbands, and the band yielding the largest magnitude was selected. The DR M_s is based on the passband with the largest amplitude. No attempt was made to compute network M_s from the limited number of stations calibrated so far. Further testing of our M_s measurements was performed by (1) comparing M-B M_s with DR M_s, (2) comparing M_s with independently determined log M_o, and finally (3) plotting M_s versus m_b. M-B M_s versus DR M_s for all 365 seismic waveforms plot with unit slope showing that the two sets of M_s values scale identically, as we would expect. DR M_s are on average 0.23 magnitude units (mu) larger than M-B M_s. This difference would have been even larger if the final M-B M_s had been computed from maximum amplitude, like DR M_s was, instead of maximum magnitude.

The correlation plots of DR M_s against log M_o are shown in Figure 4. One plot is for DR M_s based on maximum amplitude and the other is for DR M_s based on maximum magnitude. Assuming a slope of 1.0, the root-mean-squared residual scatter about the line is 0.25 mu and 0.27 mu, respectively. Thus there is not a reason to favor maximum amplitude over maximum magnitude based on these results. For reference, M-B M_s has an RMS scatter of 0.27 mu, very similar to DR M_s. A plot of DR M_s versus m_b for earthquakes and explosions in Figure 5. As expected, for a given M_s explosions have larger m_b than earthquakes do. For these single-station M_s measurements, the earthquake population shows much more scatter than the explosion population. This is due to variations in source radiation patterns and path effects since the earthquakes are located over a much wider area than the explosions, the majority being detonated at the Semipalatinsk test site. Another source of scatter for the earthquakes is focal depth, with deep earthquakes less efficient exciting surface waves than shallow ones. While the scatter is great and many earthquakes may not have reliable depth determinations, there appears to be some tendency for deeper earthquakes to have smaller M_s for their m_b.

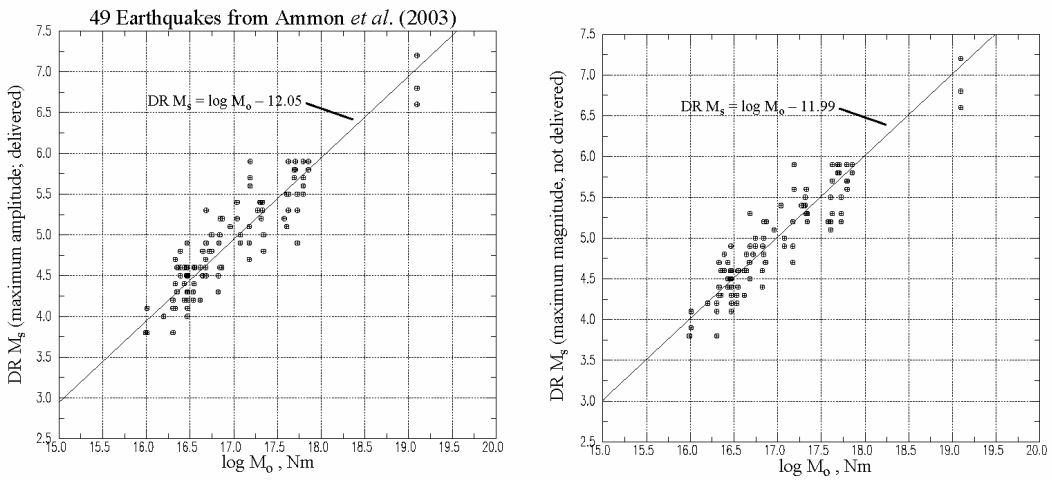

Figure 4. Plots of DR M_s versus log M_o. The left plot is for DR M_s based on maximum amplitude, while the right plot is DR M_s based on maximim magnitude.

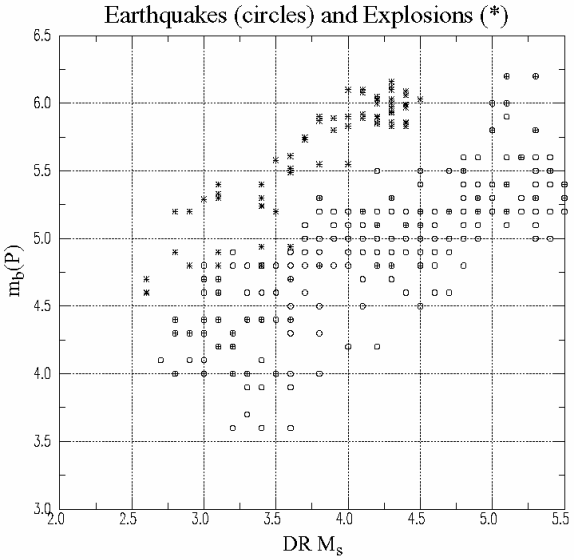

Figure 5. M_s -m_b plot for selected earthquakes and explosions in Asia. Deep earthquakes (> 50 km) are plotted as circles with a cross enclosed. m_b are catalog values for earthquakes and non-Semipalatinsk explosions. Atomic Weapons Establishment m_b are used for Semipalatinsk explosions.

Application of Rayleigh-Wave Slowness Tomography to the Determination of the Shear-Velocity Structure of Central Asian Basins

We investigate the shear velocity structure of the crust and upper mantle beneath two main central Asia sedimentary basins from surface wave velocity inversions. We have developed short-period (6 to 30 s) high-resolution, half-degree cell size, slowness tomographic maps of fundamental mode Rayleigh waves for a region in northwestern China (Maceira et al., 2005). We extended the computation of the tomographic maps to longer periods up to 100 s. Our computed Rayleigh wave slowness tomography models show unprecedented resolution that reveals greater geologic detail than has previously been achieved using surface waves, and which give us insight into the shear-velocity structure of the crust underlying this part of Asia.

We used these slowness models to predict group velocity dispersion curves along 13 specific paths through the Tarim basin, western China. Using an iterative, stochastic, least square inversion technique (Herrmann, 1988), we inverted the group velocity dispersion curves for the 1D shear velocity structure profiles. Figure 6 shows the

velocity profile resulting from one of the inversions. The fit to the data is very good. Placing all the resulting profiles together, we can get a 2D image of the shear velocity versus depth, which clearly shows differences between the east and west Tarim basin (Figure 7). The same type of study for the Junggar basin, northwest China, shows a simpler image with high upper-mantle shear velocities that are usually interpreted as old, cold, thick lithospheric blocks.

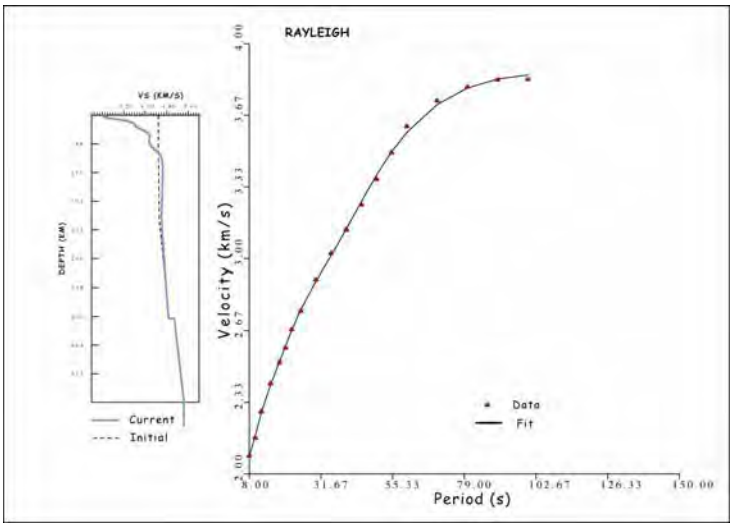

Figure 6. Schematic diagram showing 1D shear-velocity profile for a specific path along the Tarim basin (left) and the fit to the Rayleigh wave dispersion measurements used for the specific inversion (right).

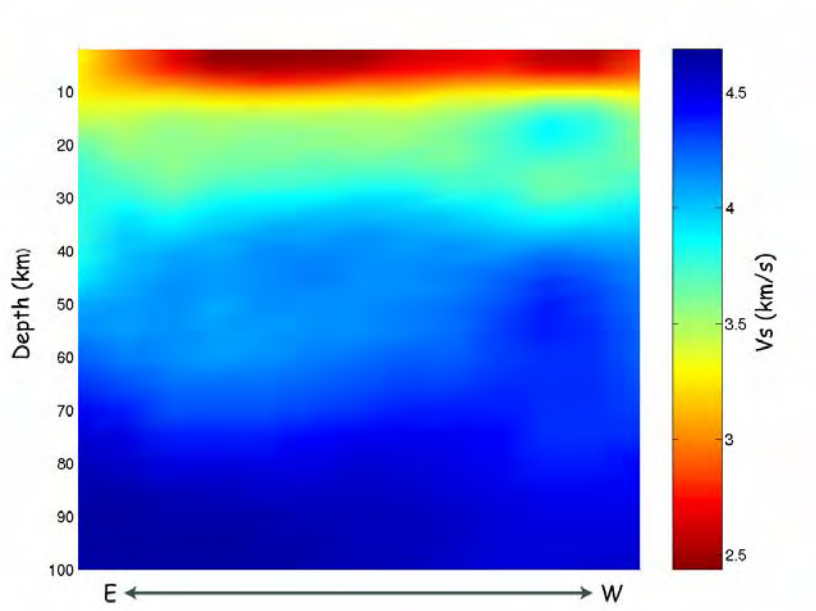

Figure 7 2D image of the shear velocity versus depth along an east-west direction through the Tarim basin. Differences between east and west Tarim are evident not only on the surface but also deeper into the lower crust and upper mantle.

To obtain a 3D model and improve resolution, we now divide into 1º x 1º cells the entire region comprising the Tarim basin, the Tien Shan, and the Junggar basin. Figure 8 shows different images of the 3D model when we invert the dispersion curves for all the cells simultaneously. We are right now working on the developing of a new

inversion technique, which will allow us to jointly invert surface wave dispersion measurements and gravity anomalies observations in the region. Improved knowledge of the shear velocity structure of these two sedimentary basins is of fundamental importance for understanding and posing constraints on possible models of geodynamic evolution. Furthermore, the improved 3D shear velocity model will help in the better location determination of epicenters applicable to different seismological studies.

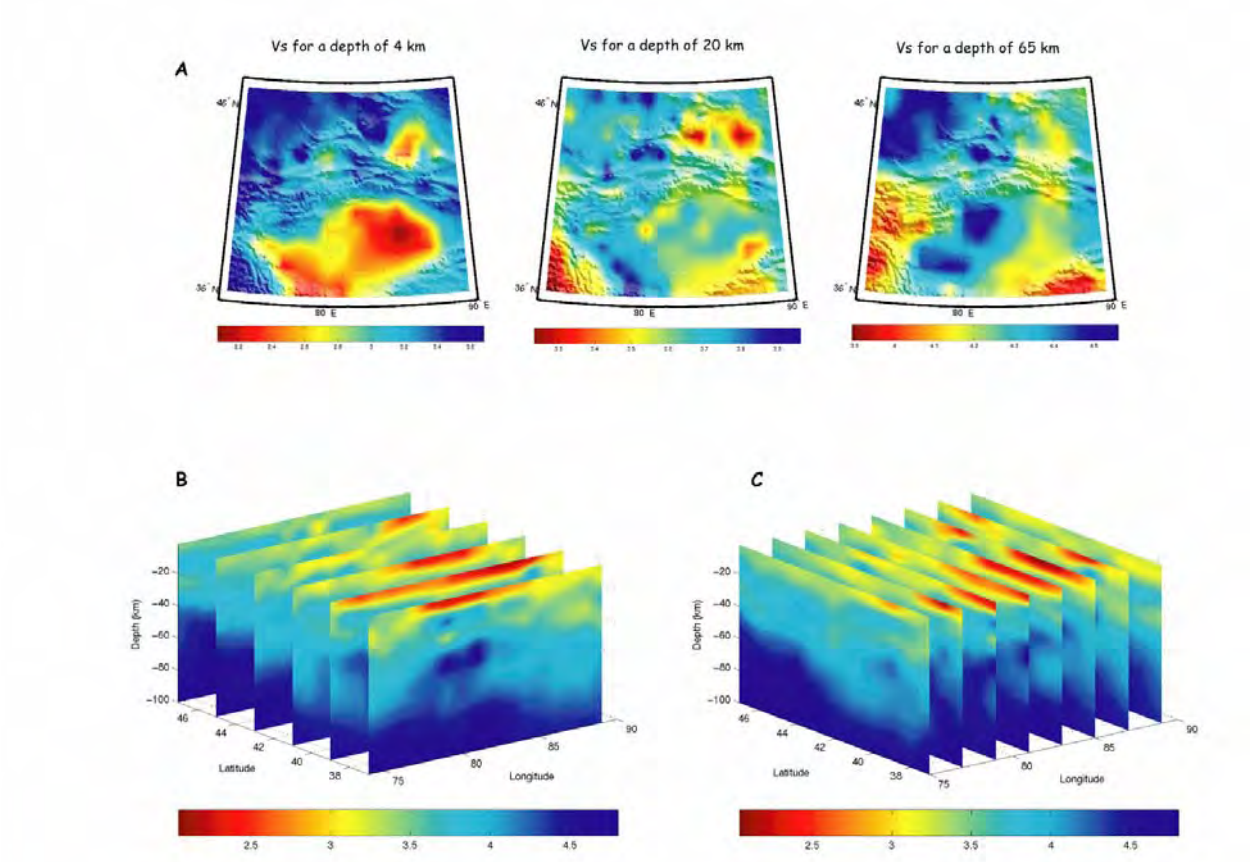

Figure 8 3D shear velocity model for the region in northwestern China comprising the Tarim basin, the Tien Shan, and the Junggar basin. A) shear velocity model slices at 4, 20, and 65 km depth; B) shear velocity model plotted at different latitudes; C) shear velocity model plotted at different longitudes. Note that the color scale is different for each image.

CONCLUSIONS AND RECOMMENDATIONS

Event identification studies in Eastern Asia involve development of algorithms for constructing discriminants as well as applying the algorithms for station calibration. Our research outlined in this paper has focused on regional seismic discrimination using regional $m_b - M_s$ discriminants and MDAC corrected amplitudes. Our ongoing work in the development of regional $m_b - M_s$ discriminants will build upon the surface-wave attenuation model and short-period surface-save slowness maps that we have developed.

REFERENCES

Aki, K. and P. G. Richards. *Quantitative Seismology. Theory and Methods,* W.H. Freeman and Co., New York, NY, 1980.

Ammon, C., G. Randall, and J. Julia (2003). Improving estimates of depth, magnitude, and faulting parameters of earthquakes in central Asia, in *Proceedings of the 25th Seismic Research Review—Nuclear Explosion Monitoring: Building the Knowledge Base*, LA-UR-03-6029, Vol. 1, pp. 24-33.

Fisk, M.D., D. Jepsen, and J.R. Murphy, Experimental seismic event-screening criteria at the Prototype International Data Center (2002), *Pure. App. Geophys*., 159, 865-888.

Hartse, H.E., S.R. Taylor, W.S. Phillips, and G.E. Randall (1997), Regional event discrimination in central Asia with emphasis on western China, *Bull. Seism. Soc. Am.*, 87, 551-568.

Herrmann R. B. (1988), Surface wave inversion program, *Computer Programs in Seismology*, Vol. IV, Saint Louis University, Saint Louis, Missouri.

Kim, W.-Y., P. G. Richards, V. Adushkin, and V. Ovtchinnikov (2001). Borovoye digital archive for underground nuclear tests during 1966-1996, Data report on the web at http://www.ldeo.columbia.edu/res/pi/Monitoring/Data/brv_exp_archive.html, Borovoye Archive for UNT (information product in PDF).

Levshin, A. L. and M. H. Ritzwoller (2003). Discrimination, detection, depth, location, and wave propagation studies using intermediate period surface waves in the Middle East, Central Asia, and the Far East, Technical Report DTRA-TR-01-28, 120 pp., Defense Threat Reduction Agency, Fort Belvoir, Virginia.

Maceira, M., S.R. Taylor, C.J. Ammon, X. Yang, and A.A. Velasco (2005), High resolution surface wave slowness tomography in central Asia, *J. Geophys. Res*., 110, B06304, doi:10.1029.

Marshall, P. D. and P. W. Basham (1972). Discrimination between earthquakes and underground explosions employing an improved Ms scale, *Geophys. J. R. Astr. Soc.* 28: 431-458.

Rezapour, M. and R. G. Pearce (1998), Bias in surface-wave magnitude M_s due to inadequate distance corrections, *Bull. Seismol. Soc. Am.* 88: 43-61.

Ritzwoller, M. H. and A. L. Levshin (1998), Eurasian Surface Wave Tomography: Group Velocities, *J. Geophys. Res.* 103: 4839-4878.

Russell, D. R. (2004). Theoretical analysis of narrow-band surface wave magnitudes, AFTAC-TR-04-004, Air Force Technical Applications Center, Patrick Air Force Base, FL.

Stevens, J. L., D. A. Adams, and G. E. Baker (2001), Improved surface wave detection and measurement using phase-matched filtering with a global one-degree dispersion model, in *Proceedings of the 23rd Seismic Research Review: Worldwide Monitoring of Nuclear Explosions*, LA-UR-01-4454, Vol. 1, pp. 420-430.

Taylor, S.R. and H.J. Patton (2005), A probability of detection method for reducing short period $m_b - M_s$ false alarm rates, Los Alamos National Laboratory, *LA-UR-05-0236*, submitted to *Bull. Seism. Soc. Am.*

Yang, X., S.R. Taylor, and H.J. Patton (2004), 20-sec Rayleigh-wave attenuation tomography for central and southeast Asia, *J. Geophys. Res*. 109: B12.

CHARACTERIZATION OF AN EXPLOSION SOURCE IN A COMPLEX MEDIUM BY MODELING AND WAVELET DOMAIN INVERSION

M. Nafi Toksöz, Shihong Chi, Yang Zhang, Edmond Sze, and Rongrong Lu

Massachusetts Institute of Technology

Sponsored by Air Force Research Laboratory

Contract No. F19628-03-C-0126

ABSTRACT

Explosions often are conducted in complexes with chambers, tunnels, and shafts used for access and instrumentation. These structures can act as strong scatterers of seismic waves and complicate the radiation patterns from explosions. The objectives of this project are (1) to study the effects of these near-source scatterers on seismic waves radiated from explosions, and (2) to use a wavelet domain based moment-tensor inversion scheme to determine “explosive” and “multi-couple” components of the source.

The modeling of seismic waves from an explosive source near a strong scatterer, such as a tunnel, is done using a finite-difference code. The code is developed for realistic earth models including (1) free surface, (2) heterogeneous structure, (3) surface topography, and (3) seismic attenuation. In addition, a perfectly matched layer (PML) was incorporated into the code to improve the absorption at the boundaries. Forward modeling using the 3-D finite-difference code was conducted with an explosive source and a tunnel in a layered half-space. Calculations were carried out for (1) a reference model without a tunnel, and (2) a model with a finite length horizontal tunnel. The calculations show P to P and P to S scattering and a complicated radiation pattern. P to S scattering is amazingly strong and the tunnel acts as a virtual shear wave source. Because of shallow depth, surface waves dominate the seismograms and significant SH waves are generated by the presence of the tunnel.

The effects of wave scattering due to various topographical features are investigated. Realistic and smooth topographic features do not contribute much to scattering. However, features with sharp gradients or corners, such as a mesa or canyon, act as strong scatterers of seismic waves, especially of surface waves.

To determine the properties of a complex source, such as an explosion and a tunnel, we evaluated the effectiveness of two approaches. The first is a wavelet domain moment tensor inversion. Synthetic seismograms are used to test the performance of moment tensor inversion and its ability to separate the volumetric and shear components of the source. The method is well suited for sparse networks. With good azimuthal coverage, the moment tensor shows significant shear components in the presence of a scatterer. Second, we tested the applicability of the time reversed acoustics (TRA) approach for detecting the presence of a tunnel near the source. In this approach, the recorded seismograms are time-reversed and sent back into the earth at each station. The back-propagating wavefields focus at the source. The P wave focuses strongly at the explosion and the S wave at the tunnel. TRA has great potential for determining the seismic source properties.

OBJECTIVES

An explosive source in a laterally homogeneous layered half-space generates P, SV, and Rayleigh waves, but not SH or Love waves. However, seismograms from a large number of explosions show nonisotropic radiation patterns for P- and Rayleigh waves, and prominent SH and Love waves. The near-source contribution to nonisotropic radiation of P-, Rayleigh waves, and SH wave generation by an explosion can be attributed to one or more of several mechanisms: tectonic strain energy released by the explosions; the shape of the explosion cavity; scattering from surface topography; and near source scattering. The objective of this research is to study the role of scattering from near source structures such as tunnels, shafts, adits, and surface topography for contributing to the generation of complicated radiation patterns and SH waves from explosions. In addition, the study will test the performance of moment tensor inversion to separate the isotropic (i.e., explosion) and multi-couple components of the source as an aid to seismic discrimination.

RESEARCH ACCOMPLISHED

A three-dimensional (3-D) finite difference program was developed to model wave propagating and scattering in heterogeneous media. The program utilizes a variable grid implemented through a grid-stretching technique. A rotated staggered grid scheme is also implemented to handle arbitrary topography and high contrast interfaces in the media. The code is parallelized to run on a computer cluster. Calculations are conducted for 3-D modeling with an explosive source and a finite length tunnel in the earth with free surface and topography. The calculations show P to P and strong P to S scattering as well as a complicated radiation pattern when an explosive source is placed near a tunnel. A new wavelet-domain moment tensor inversion with the calculated seismograms shows that the equivalent source has a double couple component, but the isotropic component still dominates. The time reversed acoustics (TRA) approach is capable of detecting the presence of a tunnel near the source and shows great potential for determining the seismic source properties.

Modeling by the Finite Difference Approach

Various calculations were carried out for an explosive source. Figure 1 shows the 3-D geometry of the model with an explosive source and a finite length, horizontal, cylindrical tunnel, in a two-layer earth model. Simulation is also conducted without the tunnel. The dimensions of the model in the x, y, and z directions are 6,000 m, 6,000 m, and 400 m, respectively. The thicknesses of the first and second layers are 300 and 100 meters, respectively. PML absorbing boundaries are placed at five sides of the model to eliminate spurious reflected waves from the boundaries. The top of the model is the free surface. An explosion source with a center frequency of 10 Hz is placed at 100 m depth. The length and radius of the cylindrical tunnel are 50 m and 15 m, respectively. The axis of the tunnel is parallel to the y axis, as shown in Figure 1.

The elastic properties of the formations and tunnel are as follows. In the first layer, the formation compressional and shear wave velocities and density are 3000 m/s, 1700 m/s, and 2300 kg/m^3, respectively. In the second layer, the formation compressional and shear wave velocities and density are 4000 m/s, 2300 m/s, and 2800 kg/m^3, respectively. Inside the tunnel, we assume an acoustic velocity of 340 m/s and a compressed air density of 200 kg/m^3.

The receiver array with 100 m spacing forms a grid on the free surface. The first row of Figure 2 shows the x and z components of the seismograms along the x axis (velocity fields) when the tunnel is absent. Due to multiple reflections between the free surface and the layer boundary, P-, S-, and surface waves are generated and the wavefield becomes complicated. When the tunnel is present near the explosion source, strong scattering occurs. The seismograms in the second row of Figure 2 show that the strong shear waves are scattered from the tunnel. To demonstrate the effect of scattering, we subtract the seismograms with an explosion only from those with the explosion plus the tunnel. The third row of Figure 2 shows the scattered waves. These show that the scattered S waves are much larger than the scattered P waves.

The azimuthal variation of seismograms and scattering to SH waves due to the tunnel are demonstrated by showing the recordings at a circular array of points at the surface. Figure 3a shows the seismogram traces when a tunnel is

present near the explosion. Figure 3b shows the scattered wavefields only, obtained by subtracting the wavefields due to an explosion only. Note the strong lobate azimuthal distribution of the SH waves.

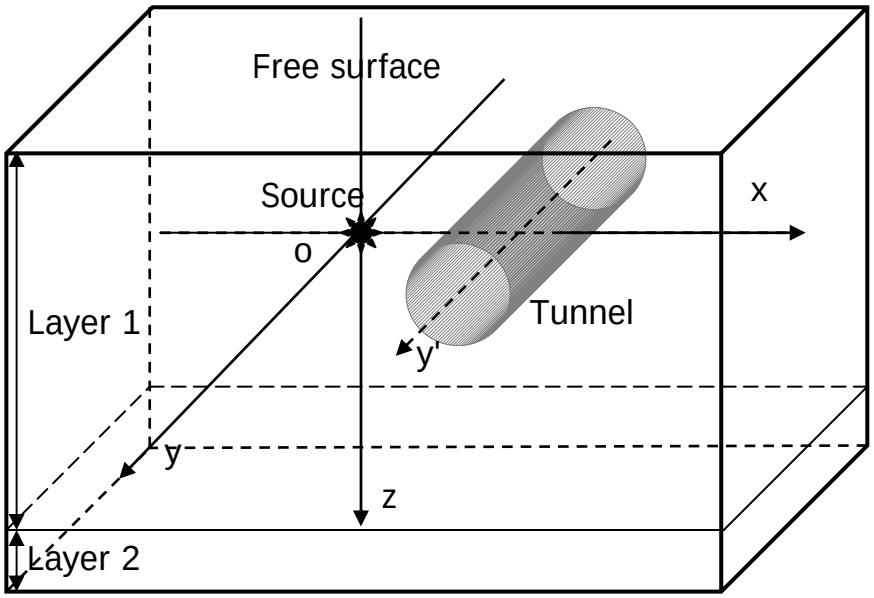

Figure 1. The geometry diagram of the tunnel model. The explosion source is located at 100 meter deep. A cylindrical tunnel is set 30 m away from the source, with radius of 15 m and length of 50 m. Its symmetric axis is parallel to the y axis. The receivers are set on the free surface. The distance between the adjacent receivers in x or y axis direction is 100 m.

Scattering due to topography

We study the effects of different topographic features on propagation and scattering of seismic waves from explosion sources at shallow depth. In the following calculations, we use a pressure Kelly wavelet with center frequency of 10 Hz as an explosion source. The formation compressional and shear wave velocities and density are 3000 m/s, 1700 m/s, and 2300 kg/m^3, respectively. A detailed study of topographic effects was carried out by Stevens (2004).

We first study the effect of a hill on wave propagation. The hill is 300 m high and 2000 m wide. A tunnel is placed 100 meters below the free surface, as shown in Figure 4a. An explosion source is also placed at the same depth. The configuration of the cylindrical tunnel is the same as shown in Figure 1. Figure 4b compares waveforms for a flat free surface model and a free surface with a hill. We see that the presence of the hill does not affect the direct body waves, but affects the surface waves.

To show the effects of topographic features with high slopes, we compare the snapshots of wavefields in the earth with a flat free surface (Figure 5a), in earth with a hill (Figure 5b) and in earth with a mesa (Figure 5c). In all cases, the explosive source is at a depth of 100 m. Both the hill and the mesa are small features: 50 m high and 100 m wide. Note that for the 10 Hz center frequency source, the dominant P wavelength is 300 m and the dominant S-wavelength is 170 m. The snapshots in Figure 5 are a 2-D model. The top row shows the divergence and the bottom the curl of the wavefield. P-and S-waves are clearly separated. Both the hill and the mesa act as strong scatterers for the S- and surface waves. Both forward and backward scattering are observed. Even though the general patterns are similar for the hill and the mesa, scattering due to the mesa, especially at the corners, is more prominent.

Source Characterization: Detection of a Scatterer

Forward modeling of the seismic radiation from an explosive source near a tunnel showed the effects of scattering from the tunnel, especially the strong P to SV and SH scattering. In this section, we investigate two methods of determining the properties of the composite explosion-scatterer source from the seismograms. The first method is

wavelet domain moment tensor inversion. The second is based on time-reversed acoustics (TRA). Both methods assume some knowledge of the Green's function, either calculated from a model of the structure, or determined empirically.

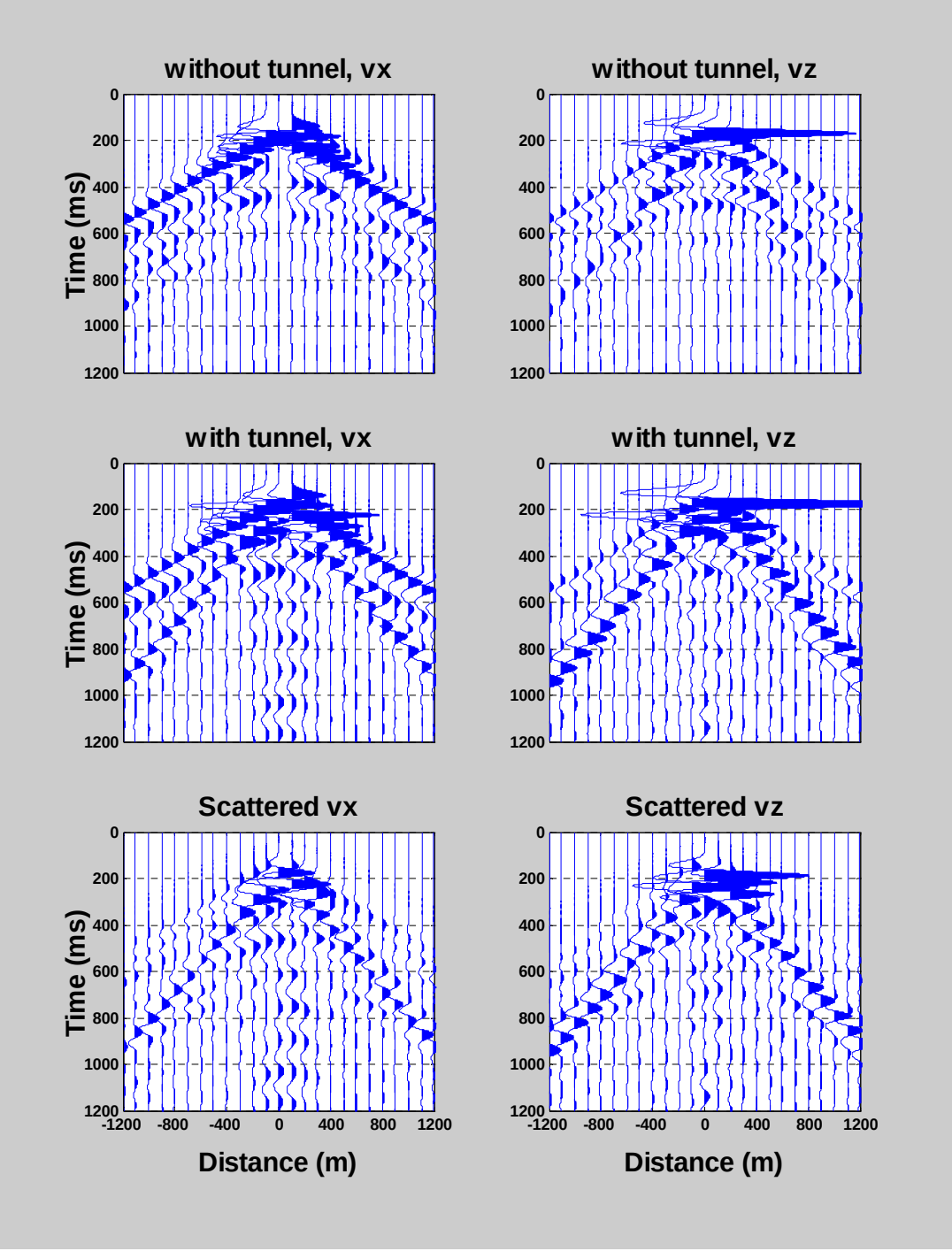

Figure 2. Comparison of the x and z components of the velocity fields at the free surface in the absence and the presence of the tunnel. Respective scattered velocity fields of the x and z components, obtained by subtracting row 1 from row 2, are also shown in the last row of this figure.

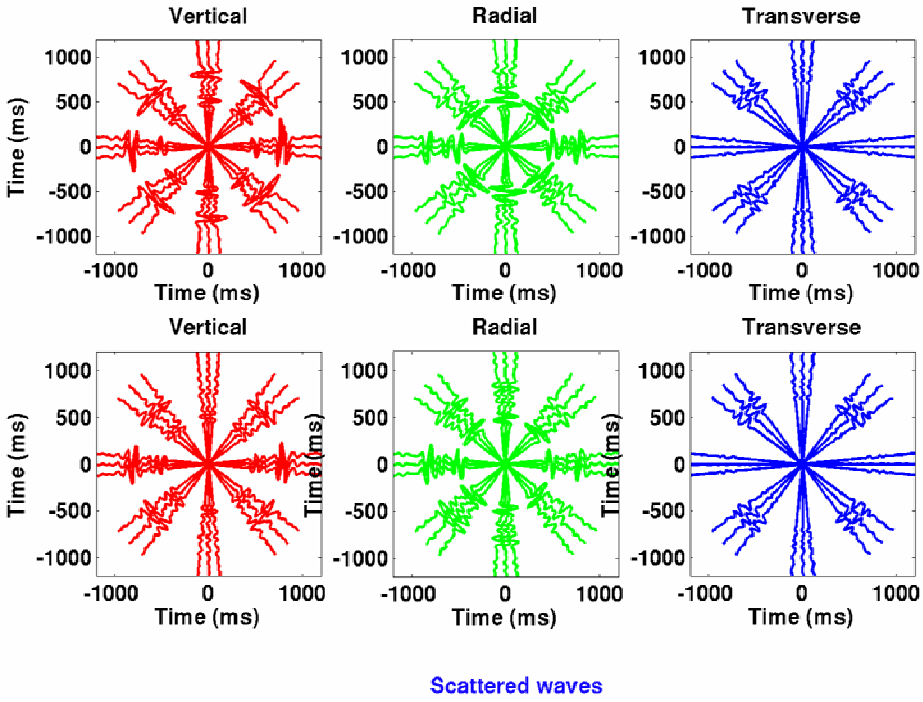

Figure 3. Three components of the recorded wavefields at 1 km offset of different azimuths. a) Free surface with tunnel near the explosion. b) Scattered wave only.

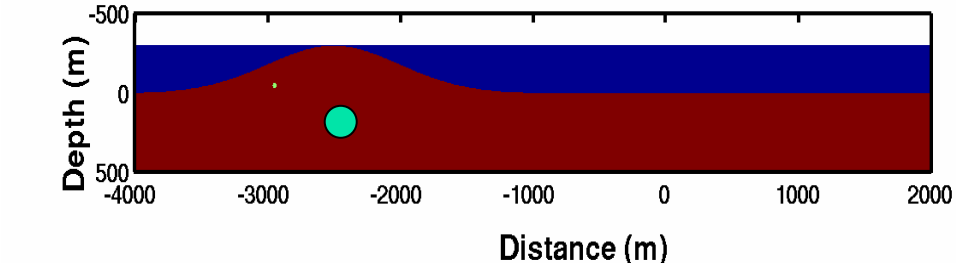

Figure 4a. Model for an explosion and a tunnel under a broad hill.

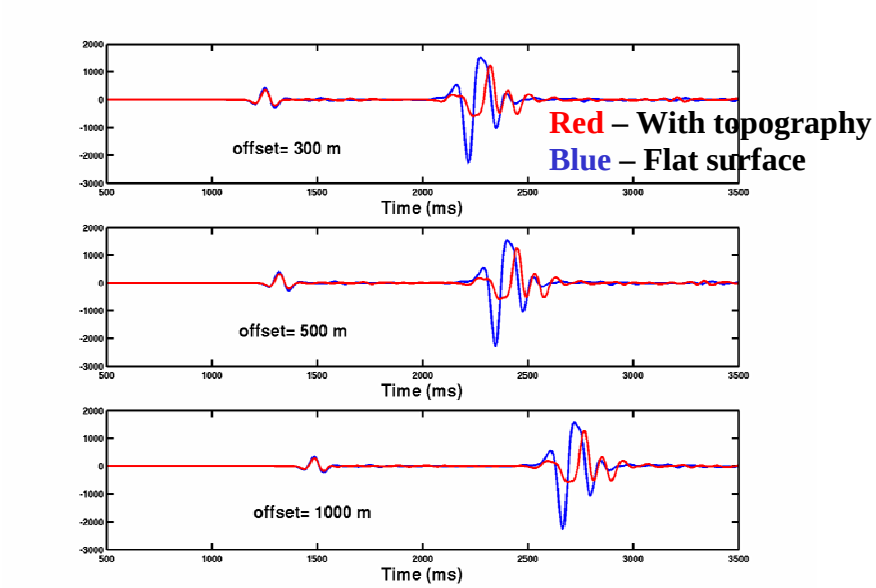

Figure 4b. Comparison of waveforms for an explosion/tunnel under a flat free surface and under a hill.

Moment Tensor Inversion

We used synthetic seismograms to test the performance of the wavelet-domain moment tensor inversion method to separate the explosion component from that of the scatterer. The method involves the representation of the source time function and the seismograms in terms of wavelets (Sze and Toksoz, 2005). The inversion is done in a wavelet domain.

To test the method we use a set of finite-difference, synthetic seismograms calculated for the explosion/tunnel source geometry shown in Figure 1. Figure 6a shows the results of the wavelet-domain moment tensor inversion. Figure 6b shows the fit to the waveform. The wavelet-domain inversion method was able to retrieve the explosive source, indicated by the large isotropic components and zero deviatoric components before 0.05 s. The effect of scattering from the tunnel is the late shear event at around 0.15 s (Figure 6a). The fit to the waveforms is excellent (Figure 6b). The moment of the explosion is about two times that of the multi-couple moment due to scattering from the tunnel.

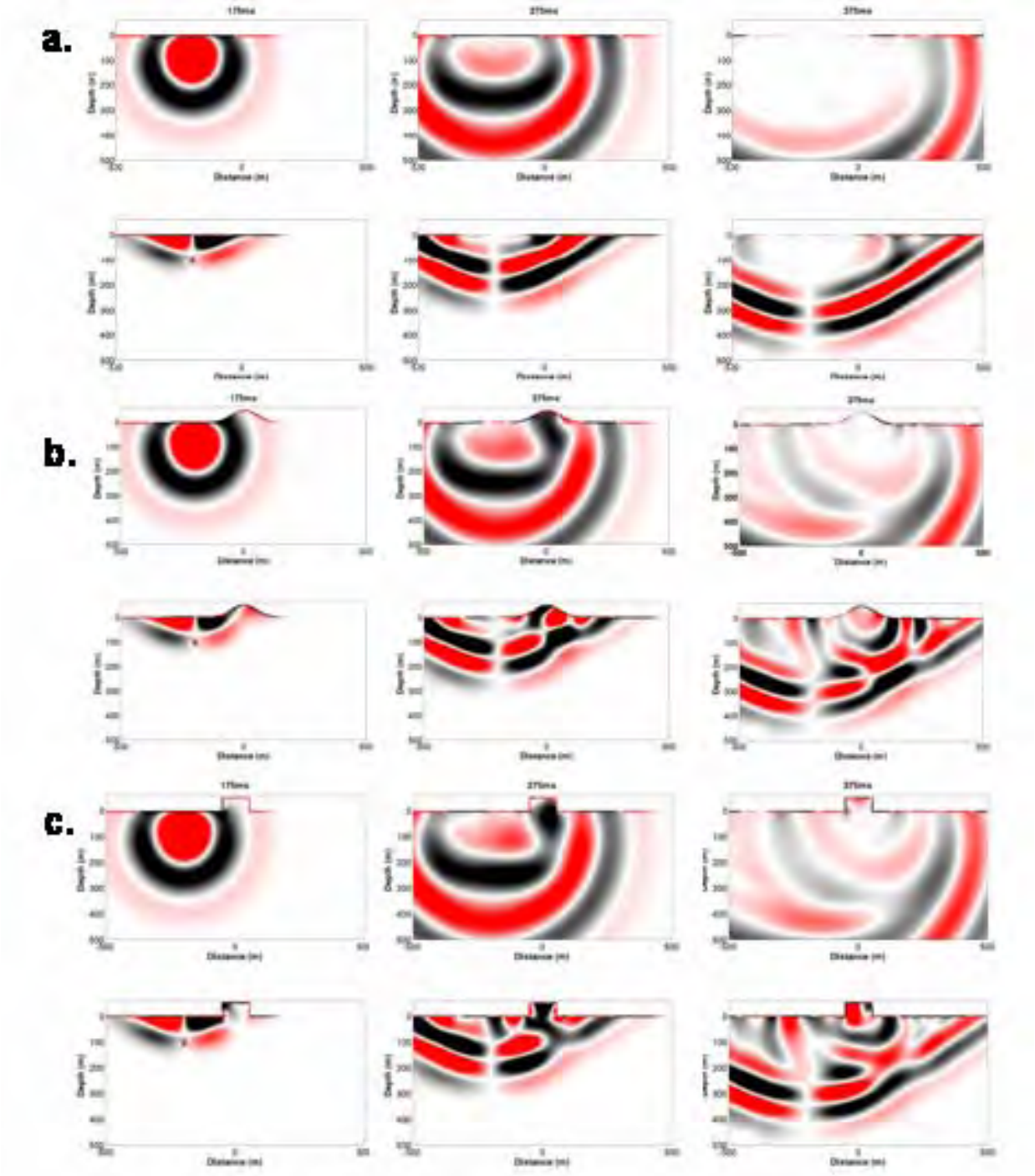

Figure 5. Snapshot of the divergence (upper panel) and curl (lower panel) of the wavefield from an explosion in the earth with (a) a flat surface, (b) a hill, (c) a mesa. Note the strong scattering due to the corners of the mesa.

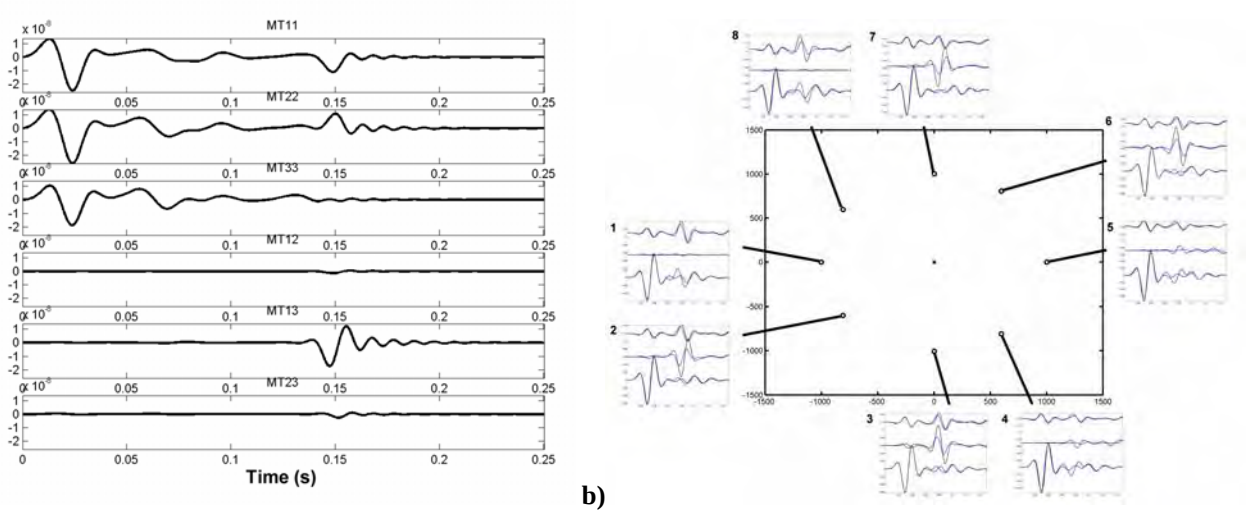

Figure 6: a) The results of wavelet-domain moment tensor inversion for an explosion with tunnel. Some anomalous components of M11, M22 and M13 showed up at a later time (~0.15 s) but the inversion was still able to retrieve large isotropic components (M11, M22, M33) and zero deviatoric components (M12, M13, M23) in the beginning. b) Fitting of waveforms (blue) by the wavelet-domain inversion to the synthetic data (black) of an explosion with tunnel. Data from eight stations (circles) surrounding the explosion (cross) were used for the inversion. At each station traces are (top to bottom) vertical, tangential and radial components.

Source and Scatterer Imaging Using Time Reversed Acoustics

According to the TRA concept, acoustic waves recorded at several stations when time-reversed and put back into the medium, propagate and focus at the original source (Fink, 1993, 2001; Song and Kupperman, 1999; Derode et al., 2000; Lu and Toksöz, 2004). The concept is illustrated schematically in Figures 7a, and 7b. To demonstrate the applicability to seismic source characterization, we conducted two numerical experiments. In each experiment, seismic waves generated by a source in heterogeneous media were calculated using the finite difference code. Then these seismograms were time reversed and "pumped" back into the medium.

Figure 8 shows the geometry of the first experiment where an explosion source is placed in a layered medium and recorded by a circular array of receivers. Note that the source is off-centered. Figure 9 shows, through a series of snapshots, the convergence of the waves to the source.

The next example is for an explosion that is located near a tunnel. Synthetic seismograms calculated by the finite difference code are recorded at 18 surface stations. The TRA methodology is applied to these recorded seismograms by first reversing them in time and then applying them as sources at the top of the same 3D elastic model. Figure 10 shows snapshots of the back-propagated wavefield at four different times. The left column shows the horizontal component of motion, the middle column shows the divergence of the wavefield (the P-wave energy), and the right column shows the curl of the wave field (the shear wave energy). The star indicates the location of the source and the circle shows the outline of the tunnel. The recorded length of the data used for back propagation is 0.4595 s. The top row of snapshots is 0.2995 s and the subsequent frames shown are at 0.3775 s, 0.4405 s, and 0.494 s. The bottom row of snapshots, at 0.4595 s, is the zero source time. Clearly seen in the bottom row at the original model time is the convergence of the P-wave energy at the source position in the left and middle figures. The shear wave energy converges to the tunnel, the source of the P to shear wave conversion, at a back propagation time of 0.4405 s. The difference, between 0.4595 and 0.4405 s, is due to travel of the P waves to the tunnel and scattering at the tunnel.

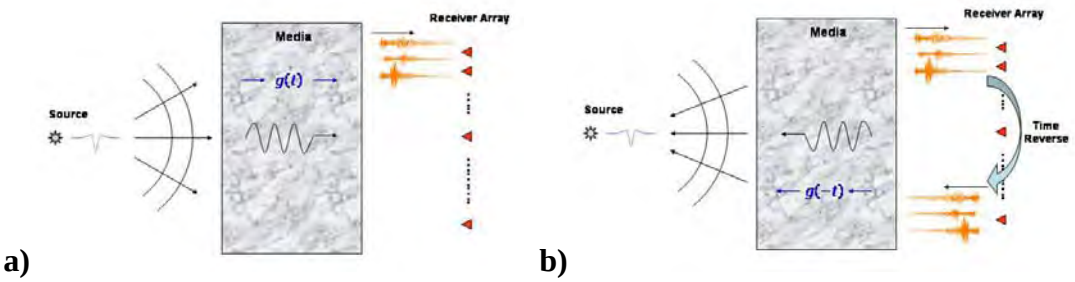

Figure 7. a) Schematic showing energy from a seismic source propagating through a medium with many scatterers, and being recorded at the stations denoted by red triangles. The yellow traces represent the recorded seismograms. The recorded traces are created by a convolution of the source function, s(t), with the appropriate transfer function, $g_j(t)$. b) Schematic showing the TRA process on the data recorded as Figure 7a. First the recorded seismograms (top yellow traces) are reversed in time (bottom yellow traces) and pumped back into the medium at the station locations. The energy reverses its path through the medium and converges upon the original source position.

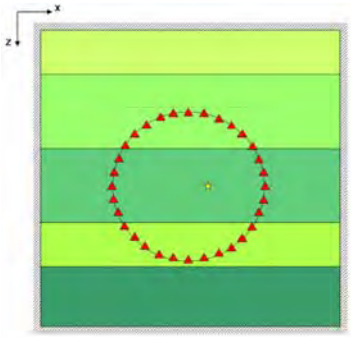

Figure 8. Simple 2D layered earth model with seismic source located at the yellow star, and a ring of receivers, each indicated by a red triangle.

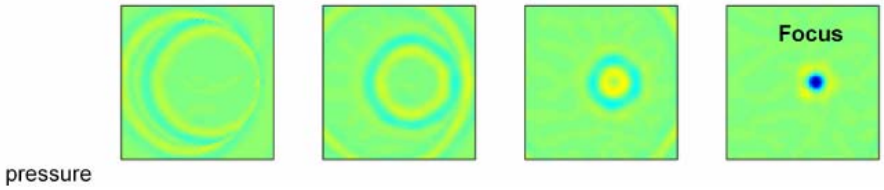

Figure 9. Progressive snapshots of the wavefield (recorded by the receivers in Figure 8) propagated backward in time. The fourth frame corresponds to zero time.

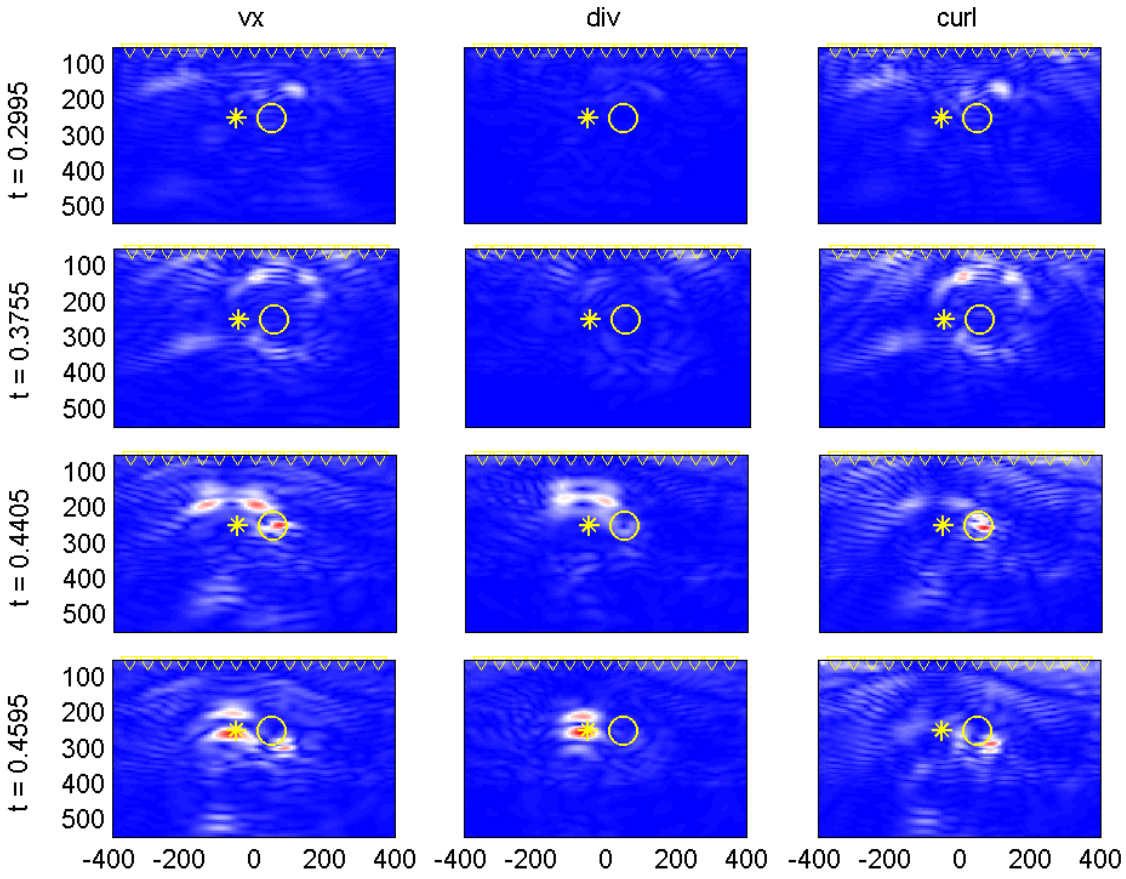

Figure 10. Snapshots of back propagated records for an explosion (star) located next to an air filled tunnel (circle). The left column shows the vertical component of motion, the middle column shows the divergence of the field (P wave energy only), and the right column shows the curl of the field (shear energy only). The bottom row represents zero time in the original forward model.

CONCLUSIONS

1. A tunnel near an explosion acts as a strong scatterer. P to S scattering is much stronger than P to P scattering. Some energy is scattered into SH waves. **2.** Surface topographic features act as scatterers. Overall, scattering from topography is small compared to that of tunnels. The smooth topography effect on scattering is relatively small. Sharp topographic features (e.g., mesas) cause strong scattering of the surface waves. **3.** For explosion identification, wavelet-based moment tensor inversion recovers the relative strengths of the explosion and the scatterer source. **4.** TRA methodology has the potential of determining seismic source properties with good resolution.

REFERENCES

Derode, A., Tourin, A., and Fink, M. (2000), Limits of time-reversal focusing through multiple scattering: long range correlation, *J. Acoust. Soc. Am.* 107: 2987-2998.

Fink, M. (1993), Time reversal mirror, *J. Phys. D*, 26, 1330-1350.

Fink, M. (2001), Time reversed acoustics, *Rev. of Progress in Quant. Nondestruct. Eval.* 20: 3-15.

Lu, R. and Toksöz, M. N. (2004), Finite-difference simulations of time reversed acoustics in a layered earth model, *MIT Earth Resources Laboratory, Industry Consortia Annual Report.*

Song, H., and Kuperman, W., (1999), Iterative time reversal in the ocean, *J. Acoust. Soc. Am.* 105: 3176-3184.

Stevens, J.L., G.E. Baker, H. Xu, T.J. Bennett, N. Rimer, and S. Day (2004), The physical basis of Lg generation by explosion sources, SAIC Final Report, NNSA, Contract No. DE-FC03-02SF22676.

Sze, E.K.M. and M.N. Toksoz (2005), Wavelet-domain inversion for earthquake source parameters, submitted to *Bull. Seismol. Soc. Am.*

REGIONAL SEISMIC DISCRIMINATION OPTIMIZATION WITH AND WITHOUT NUCLEAR TEST DATA: WESTERN U.S. EXAMPLES

William R. Walter, Kevin M. Mayeda, Rengin Gok, Arthur J. Rodgers, Alan Sicherman, Tracy Hickling, Doug Dodge, Eric Matzel, Mike Ganzberger, and Veronica Parker

Lawrence Livermore National Laboratory

Sponsored by National Nuclear Security Administration
Office of Nonproliferation Research and Engineering
Office of Defense Nuclear Nonproliferation

Contract No. W-7405-ENG-48

ABSTRACT

The western United States (U.S.) has abundant natural seismicity, historic nuclear explosion data, and widespread mine blasts, making it a good testing ground to study the performance of regional source-type discrimination techniques. We have assembled and measured a large set of these events to systematically explore how to best optimize discrimination performance. Nuclear explosions can be discriminated from a background of earthquakes using regional phase (Pn, Pg, Sn, Lg) amplitude measures such as high frequency P/S ratios. The discrimination performance is improved if the amplitudes can be corrected for source size and path length effects. We show good results are achieved using earthquakes alone to calibrate for these effects with the magnitude and distance amplitude correction (MDAC) technique (Walter and Taylor, 2002). We show significant further improvement is then possible by combining multiple MDAC amplitude ratios using an optimized weighting technique such as linear discriminant analysis (LDA). However, this requires data or models for both earthquakes and explosions. In many areas of the world regional distance nuclear explosion data are lacking, but mine blast data are available. Mine explosions are often designed to fracture and/or move rock, giving them different frequency and amplitude behavior than contained chemical shots, which seismically look like nuclear tests. Here we explore discrimination performance differences between explosion types, the possible disparity in the optimization parameters that would be chosen if only chemical explosions were available and the corresponding effect of that disparity on nuclear explosion discrimination.

There are a variety of additional techniques in the literature also having the potential to improve regional high frequency P/S discrimination. We explore two of these here: three-component averaging and maximum phase amplitude measures. Typical discrimination studies use only the vertical component measures and for some historic regional nuclear records these are all that are available. However, S-waves are often better recorded on the horizontal components and some studies have shown that using a three-component average or a vertical-P/horizontal-S or other three-component measure can improve discrimination over using the vertical alone (e.g., Kim, et al., 1997; Bowers, et al., 2001). Here we compare the performance of vertical and three-component measures on the western U.S. test set.

A complication in regional discrimination is the variation in P- and S-wave propagation with region. The dominantly observed regional high frequency S-wave can vary with path between Sn and Lg in a spatially complex way. Since the relative lack of high frequency S-waves is the signature of an explosion, failing to account for this could lead to misidentifying an earthquake as an explosion. The regional P phases Pn and Pg vary similarly with path and also with distance, with Pg sometimes being a strong phase at near regional distances but not far regional. One way to try and handle these issues is to correct for all four regional phases but choose the phase with the maximum amplitude. A variation on this strategy is to always use Pn but choose the maximum S phase (e.g., Bottone et al., 2002). Here we compare the discrimination performance of several different (max P)/(max S) measures to vertical, three-component and multivariate measures. Our preliminary results show that multivariate measures perform much better than single ratios, though transportability of the LDA weights between regions is an issue. Also in our preliminary results, we do not find large discrimination performance improvements with three-component averages and maximum phase amplitude measures compared to using the vertical component alone.

OBJECTIVES

Monitoring the world for potential nuclear explosions requires characterizing seismic events and discriminating between natural and man-made seismic events, such as earthquakes and mining activities, and nuclear weapons testing. We continue developing, testing, and refining size-, distance-, and location-based regional seismic amplitude corrections to facilitate the comparison of all events that are recorded at a particular seismic station. These corrections, calibrated for each station, reduce amplitude measurement scatter and improve discrimination performance. We test the methods on well-known (ground truth) data sets in the U.S. and then apply them to the uncalibrated stations in Eurasia, Africa, and other regions of interest to improve underground nuclear test monitoring capability.

RESEARCH ACCOMPLISHED

As part of the overall National Nuclear Security Administration's Ground-Based Nuclear Explosion Monitoring Research and Engineering program, we continue to pursue a comprehensive research effort to improve our capabilities to seismically characterize and discriminate underground nuclear tests from other natural and man-made sources of seismicity. To reduce the monitoring magnitude threshold, we make use of regional body and surface wave data to calibrate each seismic station. Our goals are to reduce the variance and improve the separation between earthquakes and explosion populations by accounting for the effects of propagation and differential source size.

Western U.S Data Corrected for Magnitude and Distance Effects

We have been re-examining the large database of the western U.S. underground nuclear tests and earthquakes we assembled under a prior year broad agency announcement award (Walter et al., 2003). This western U.S. nuclear explosion data covers a wide range of depths and material properties and has excellent ground truth information (Springer et al., 2002). This is unlike the situation in most of the world where regional recordings of nuclear tests are scarce and discrimination optimization needs to be done in their absence. In addition we have chemical explosions recorded at the same stations from the Arizona Source Phenomenology Experiment (AZSPE). The AZSPE carried out dedicated single shot chemical explosions under a variety of depth and confinement conditions in two mining regions, a soft rock coal mine and a hard rock copper mine (see Bonner et al., 2005, this Proceedings). These mining regions also routinely detonate ripple-fired production blasts that can be observed at regional distances. The availability of both nuclear and chemical explosions lets us examine the differences in optimization and performance of the two source types relative to the earthquakes. The locations of the data and stations discussed in this paper are shown in Figure 1.

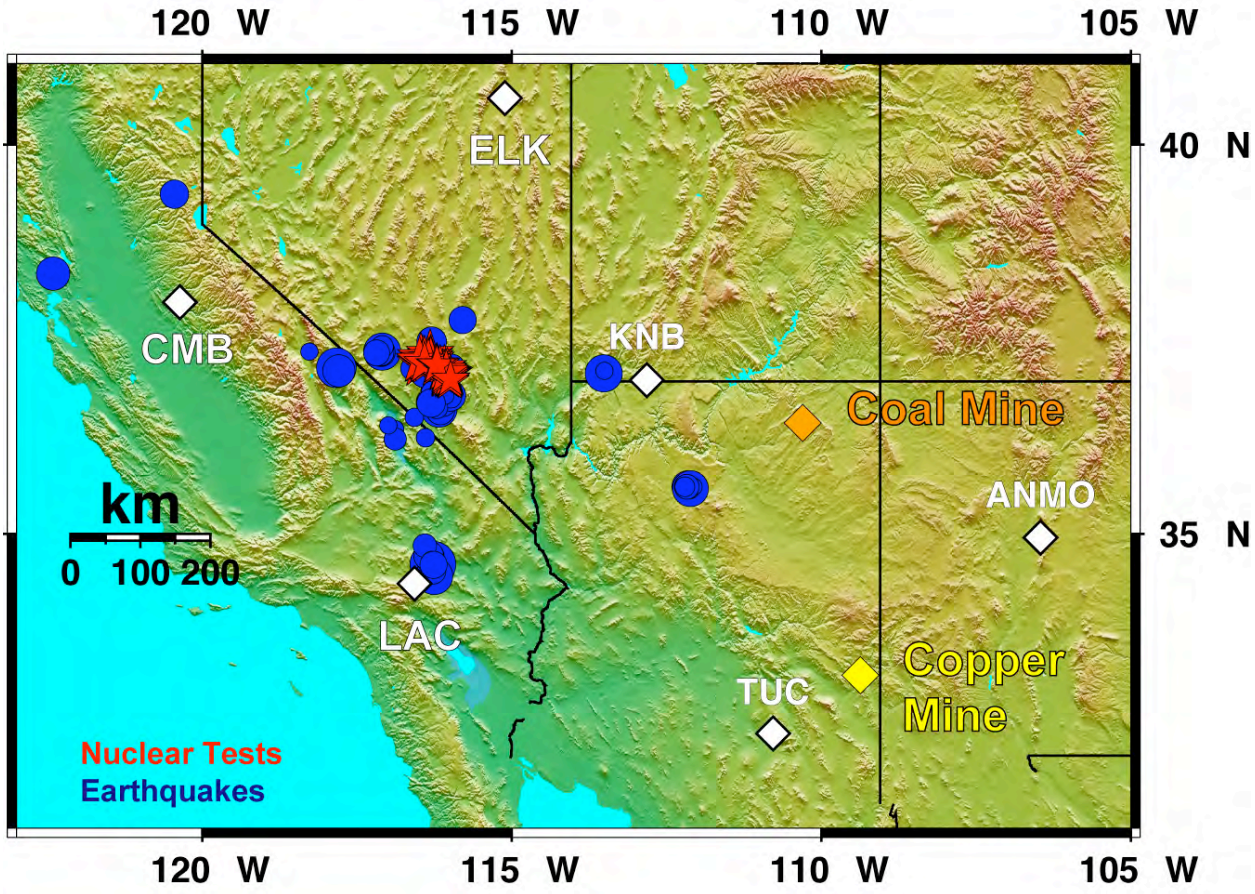

Figure 1. Map showing the location of earthquakes, historic nuclear explosions, mining explosions and stations discussed in this paper.

Effective earthquake-explosion discrimination has been demonstrated in a broad variety of studies using ratios of regional amplitudes in high-frequency (primarily 1- to 20-Hz) bands (e.g., Walter, et al., 1995; Taylor, 1996; Hartse et al., 1997; Rodgers and Walter, 2002; Taylor et al., 2002; Battone et al., 2002; and many others). When similar-sized earthquakes and explosions are nearly co-located, we can understand the observed seismic contrasts, such as the relative P- to S-wave excitation, in terms of depth, material property, focal mechanism and source time function differences. However, it is well known that path propagation effects (e.g. attenuation, blockage) and source scaling effects (e.g., corner frequency scaling with magnitude) can make earthquakes look like explosions and vice versa. We have developed a technique called MDAC (Walter and Taylor, 2002) that can account for these effects with proper calibration. We use the earthquakes alone to determine the MDAC parameters such as geometrical spreading, frequency dependent Q and the average apparent stress. After calibration the MDAC formulation provides expected spectral amplitudes as a function of phase, magnitude and distance. These can then be subtracted from the actual observations. For earthquakes the corrected data should exhibit a close zero mean, and a magnitude and distance detrended population. Explosions should have significant non-zero mean residuals, leading to improved discrimination. We show the results of a low to high frequency Lg spectral ratio before and after MDAC correction in Figure 2.

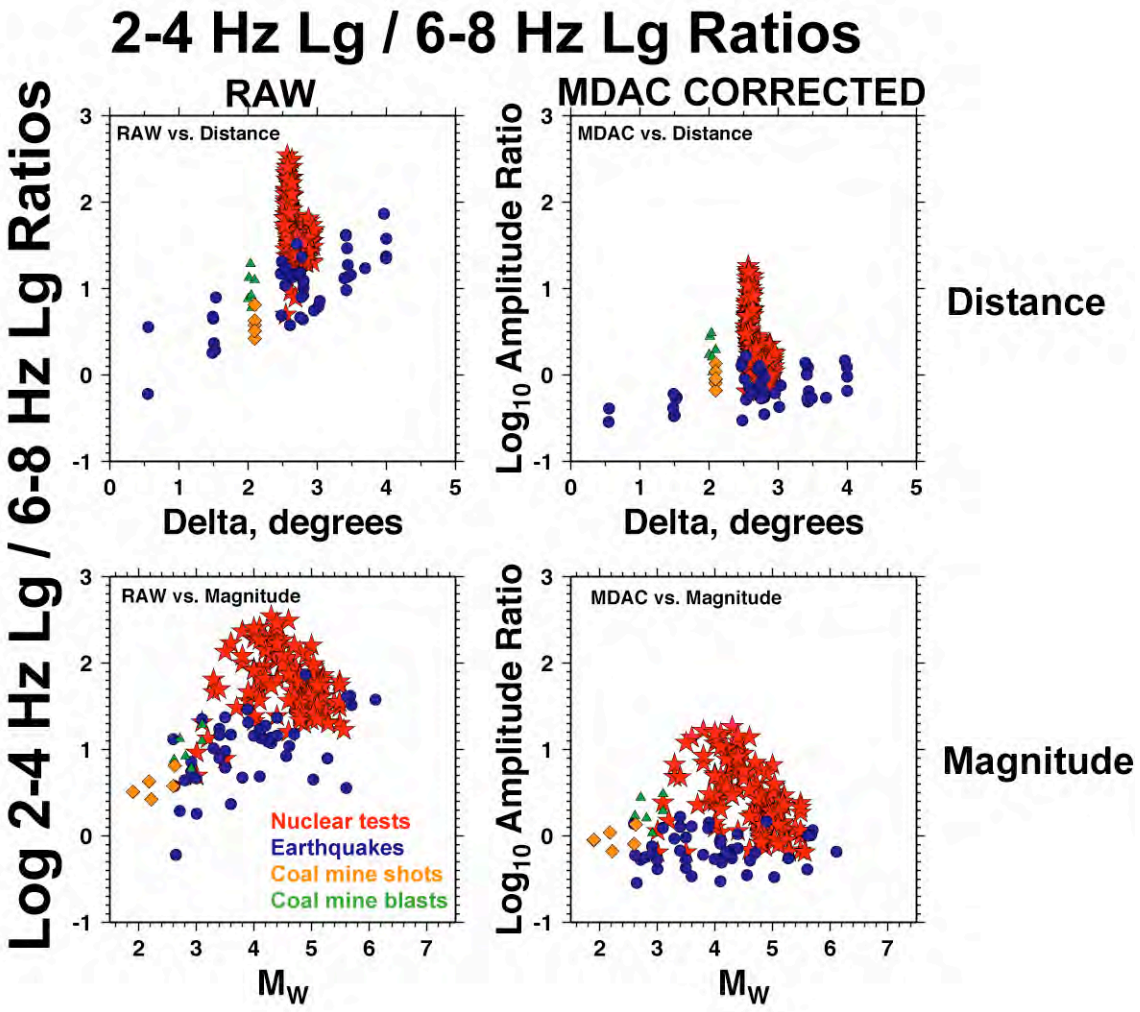

Figure 2. Western U.S earthquakes (blue circles), nuclear explosions (red stars), northern Arizona coal mine dedicated shots (orange diamonds) and regular production mine blasts (green triangles) for the discriminant ratio of (2–4 Hz Lg)/(6–8 Hz Lg) at station KNB. The left-hand side shows raw data as a function of distance (top) and magnitude (bottom). The right-hand side shows MDAC corrected data. Note that strong distance and magnitude trends apparent in the raw data are removed by MDAC, improving discrimination.

After the MDAC correction we can explore optimal combinations of particular regional discriminants (e.g., Taylor, 1996). We use LDA to find the optimal coefficients to combine the measurements. As an example of this we show in Figure 3 a combination at station KNB of three different regional phase and spectral ratios. The metric of performance we use is the equiprobable point, which provides a measure of the overlap of the earthquake and explosion populations. It is the point on a receiver operating characteristic (ROC) tradeoff curve where the error rates are equal. For example an equiprobable point of 0.1 implies that 10% of the earthquakes are misclassified as explosions and 10% of explosions are misclassified as earthquakes. In practice, one might choose a decision line with unequal error rates, such as by picking a low probability of misclassifying an explosion. The equiprobable point provides a single numerical measure of performance that is much more intuitive than other measures such as Mahalanobis distance, though it can be related to that measure.

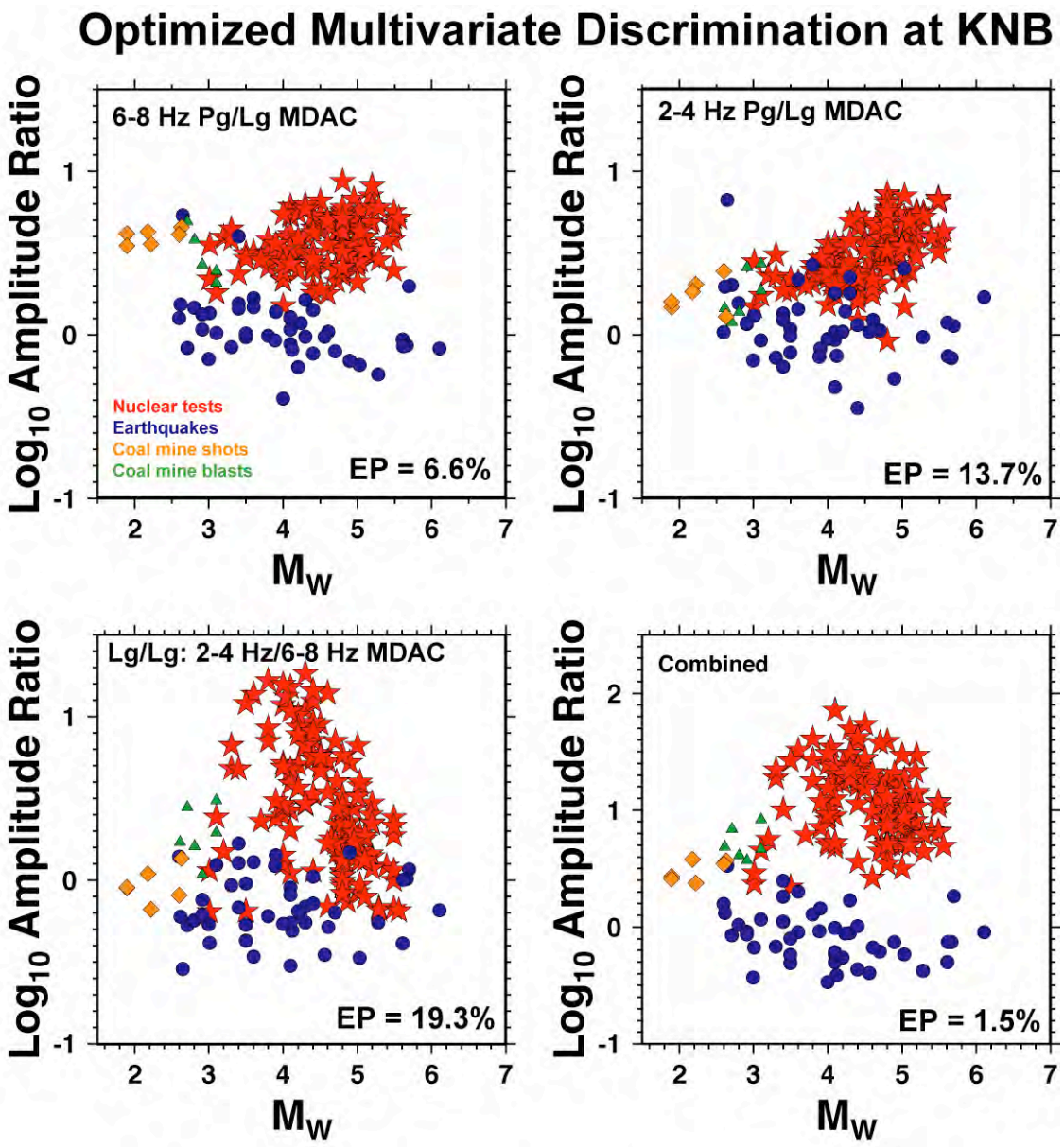

Figure 3. We show nuclear explosion discrimination from earthquake performance at station KNB for three different regional phase ratios after MDAC corrections were applied. In the lower right we combine these three ratios using an optimal set of weights determined using LDA to get a dramatic increase in performance. The combination is 0.71 (6–8 Hz Pg/Lg) + 0.88 (2–4 Hz Pg/Lg) + 0.57 (2–4/6–8 Hz Lg/Lg). This shows how optimally combining even mediocre discriminants can improve the performance of very good discriminants because new information always helps. Note that the mine shots track the nuclear tests for the P/S ratios but not for the low to high Lg ratio. Using the mine shots to obtain LDA weights would degrade the nuclear explosion discrimination performance.

A very interesting result demonstrated in Figure 3 is that by adding together several different mediocre discriminant measures using LDA coefficients we can greatly improve performance. In fact, using LDA we can always improve performance by adding another discriminant measure because it provides new information. In practice we have found that after combining about three to five different regional amplitude ratios using LDA, further improvement by adding additional measures is limited as the new measures do not provide much new information. We have found significant improvements by using LDA to combine measures for all the stations

where we have done such analysis, covering a wide variety of regions. The challenge is that the best few discriminant measures and their optimal LDA coefficients vary from region to region in ways we do not yet fully understand, complicating transportability from region to region.

The two different types of chemical explosions (single contained shots versus ripple fired production blasts) show some interesting similarities and differences to the nuclear explosions. They all have similar high frequency P/S ratios as shown in Figure 3. However, in looking at regional seismic coda derived spectra (e.g., Mayeda and Walter, 1996; Mayeda et al., 2003) in Figure 4 we find the production shots have steeper spectral decay between 1–8 Hz and this accounts for the differences we see in the low to high frequency ratios. For this reason it is clear that doing an LDA analysis on the production chemical explosions and the earthquakes would produce different coefficients and discrimination performance. This is an area of research we are actively exploring.

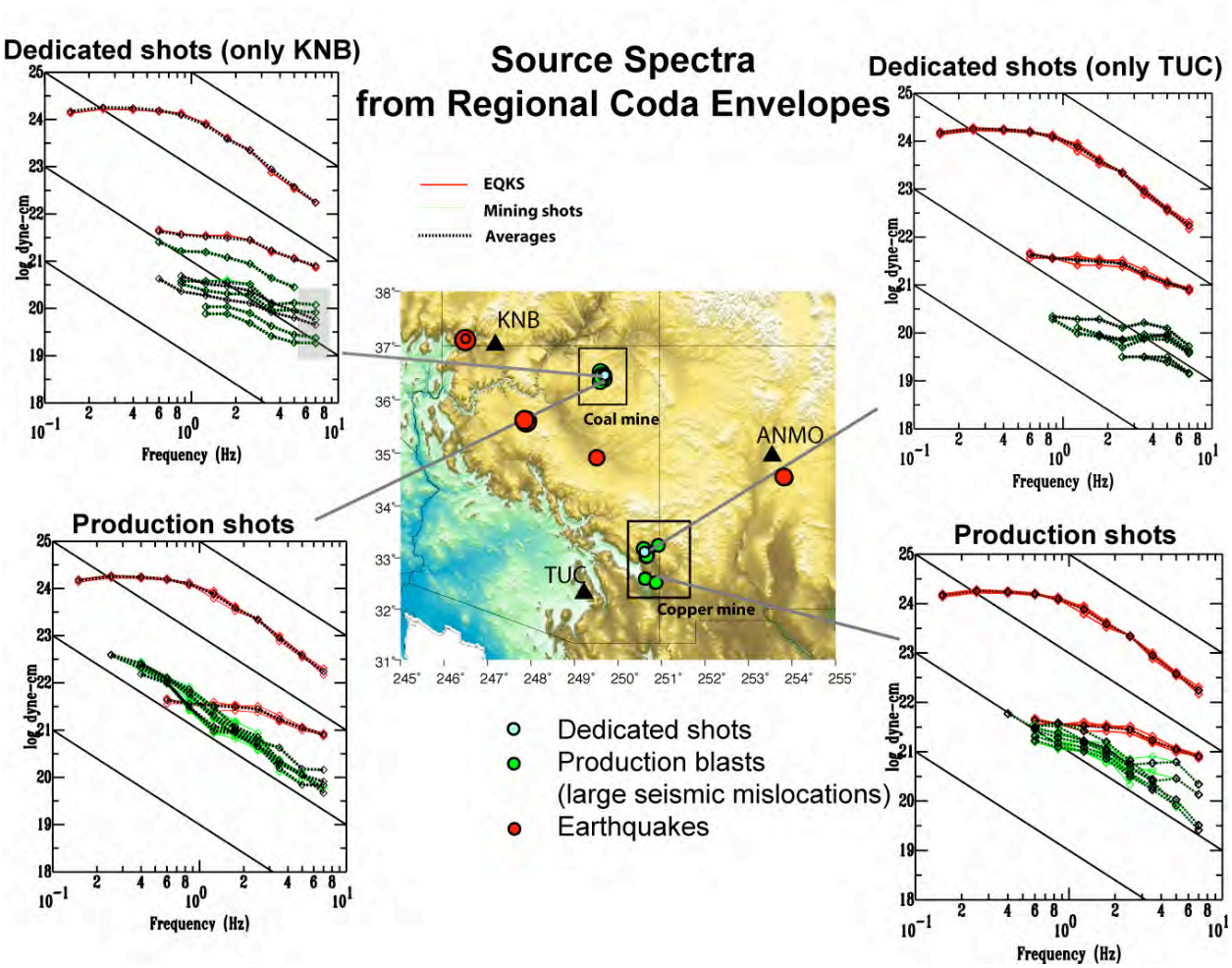

Figure 4. Regional coda envelope derived S-wave spectra of earthquakes (red) and dedicated single shot chemical explosions (light blue) and normal mine production explosions (green). The coda calibrations were done using the Colorado Plateau earthquakes shown. Left-hand side plots show the coal mine region single shots at top and ripple-fired production shots below. Similar plots for the copper mine region are shown on the right-hand side. Note that most of the ripple-fired shots have much steeper spectral falloff than the single shots.

Vertical Component Versus Three-Component

When three-component instruments are available the S-waves are often more clearly observed with larger amplitude on the horizontal components. Similarly, the P-waves often are more clearly observed with larger amplitude on the vertical component. For this reason a variety of studies have suggested that P/S ratio discrimination can be improved if all three components are used (e.g., Kim et al., 1997; Bowers et al., 2001). There are a variety of ways to make the measures, such as vertical P and horizontal S and rotation of the horizontals to radial and transverse and then using vertical and radial P and transverse S; but the simplest way is to average all three components together. In the prior study of Kim et al. (1997) the simple average did not perform much worse than the more sophisticated ways of separating out the P-SV and SH waveform components. Here we compare the performance of vertical and three-component measures on the western U.S. test set. We compare the vertical alone to the three-component average for 6–8 Hz Pg/Lg at station ELK in Figure 5 for a western U.S. set of earthquakes and nuclear explosions. The improvement in discrimination performance is modest. We are repeating these tests at other stations and using several different ways of doing the measures.

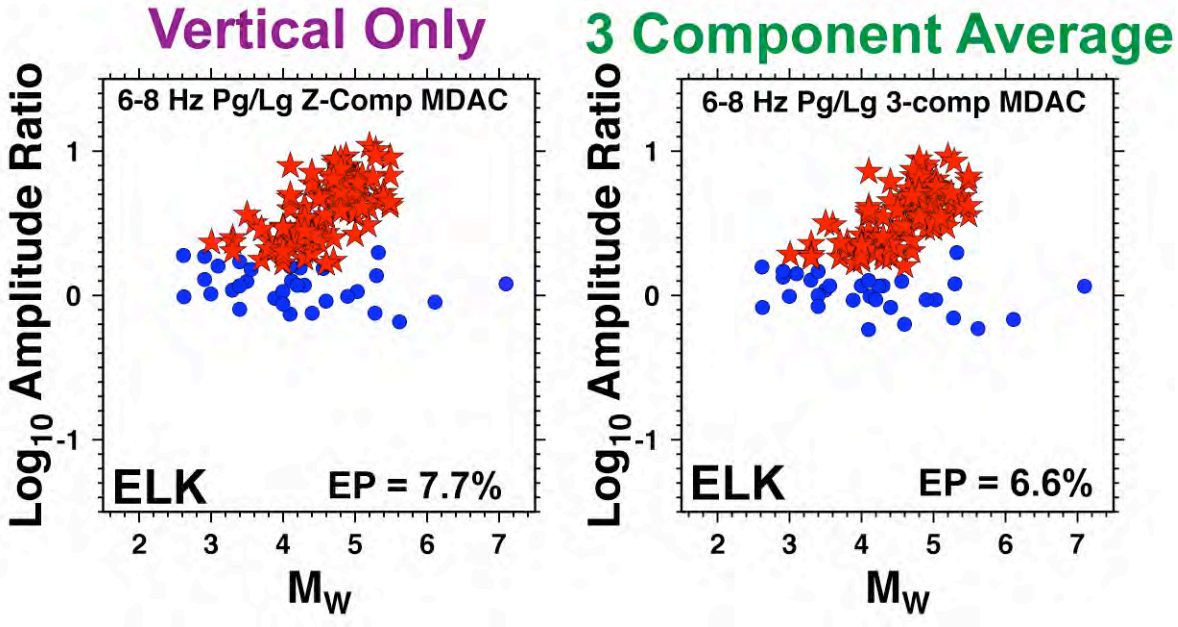

Figure 5. Here we use the same set of earthquakes and explosions at station ELK to test the improvement provided by measuring the 6–8 Hz Pg/Lg discriminant by averaging all three components (right-hand side) versus just using the vertical component (left-hand side). The improvement both in the scatter plot and as measured quantitatively by the equiprobable value is modest.

Maximum P and Maximum S

A complication in regional discrimination is the variation in P- and S-wave propagation with geophysical province. The dominantly observed regional high frequency S-wave can vary with path between Sn and Lg in a spatially complex way. Since the relative lack of high frequency S-waves is the signature of an explosion, failing to account for this could lead to misidentifying an earthquake as an explosion. The regional P phases Pn and Pg vary similarly with path and also with distance, with Pg sometimes being a strong phase at near regional distances but not far regional. One way to try and handle these issues is to correct for all four regional phases

but choose the phase with the maximum amplitude. A variation on this strategy is to always use Pn but choose the maximum S phase (e.g., Bottone et al., 2002).

An important point in using maximum amplitude methods or any regional discrimination technique is that separate source, path and site effects still need to be determined for each of the four phases that might be used. The mantle phases Pn and Sn have geometrical spreading and attenuation parameters which tend to be quite different from crustal Pg and Lg phases, so one still needs to know which of the phases is giving the maximum amplitude to make the appropriate correction. For this reason the maximum amplitude techniques require the same amount of calibration effort as the traditional fixed phase ratio methods. The main operational advantage of maximum amplitude methods is simplicity in plotting all the results together rather than trying to form an optimal combination or discarding measurements when a phase is not present due to blockage or attenuation below the noise level.

The question of whether using a maximum amplitude measure will help or hurt discrimination performance depends on the style of variation of the regional phase amplitudes in the area. We show examples in Figure 6 of 6–8 Hz P/S ratios where the maximum (Pn, Pg) to maximum (Sn, Lg) measure would improve or worsen discrimination performance relative to a straight Pg/Lg measure. If the number of events where performance is hurt are small relative to the number where performance is helped, than the maximum amplitude measure will do better than the single ratio.

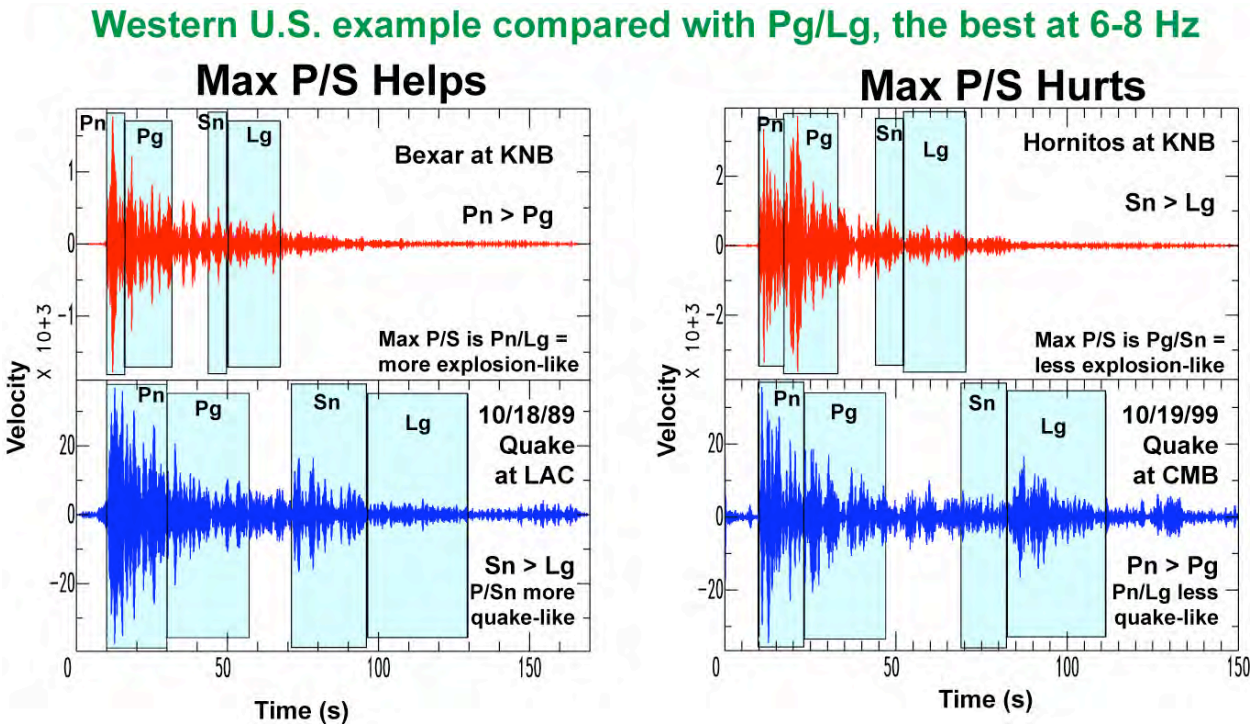

Figure 6. This figure demonstrates how using a maximum P from Pn or Pg and/or a maximum S from Sn and Lg can help or hurt the discrimination of event relative to just using a single ratio such as Pg/Lg. Here we show an example nuclear explosion and an example earthquake seismogram for each of the possible cases. The comparison is to 6-8 Hz Pg/Lg, which is the best 6-8 Hz P/S ratio. At the upper left we show an example where using the maximum P, in this case Pn, makes the explosion event more explosion-like, helping the discrimination process. In contrast, on the upper right we show a case where using the maximum S, in this case Sn, makes the explosion more earthquake-like. We show similar behavior for earthquakes in the bottom half of the figure.

Here we compare the discrimination performance of several different (max P)/(max S) measures to vertical, three-component and multivariate measures. Figure 7 shows the results in terms of the equiprobable value for several different 6–8 Hz P/S ratios combining the results from four stations in the western U.S. First it is clear that the MDAC corrections improve the discrimination performance of all the different P/S ratios. Second we note that the simple Pg/Lg ratio has better overall performance than the Pn/Maximum (Sn, Lg) technique. Given the uncertain results of which phases will have the maximum amplitude for a given event-station path, and the remarkable improvements available using LDA combinations demonstrated in Figure 3, we believe that in practice it makes the most sense to measure standard ratios of the major observed regional phases and then form LDA combinations. For example in the western U.S. we would expect that 6–8 Hz Pg/Lg, as the best single measure in combinations with other measures involving major observed phases such as 6–8 Hz Pn/Lg, will provide the best overall performance, as was demonstrated in Figure 3.

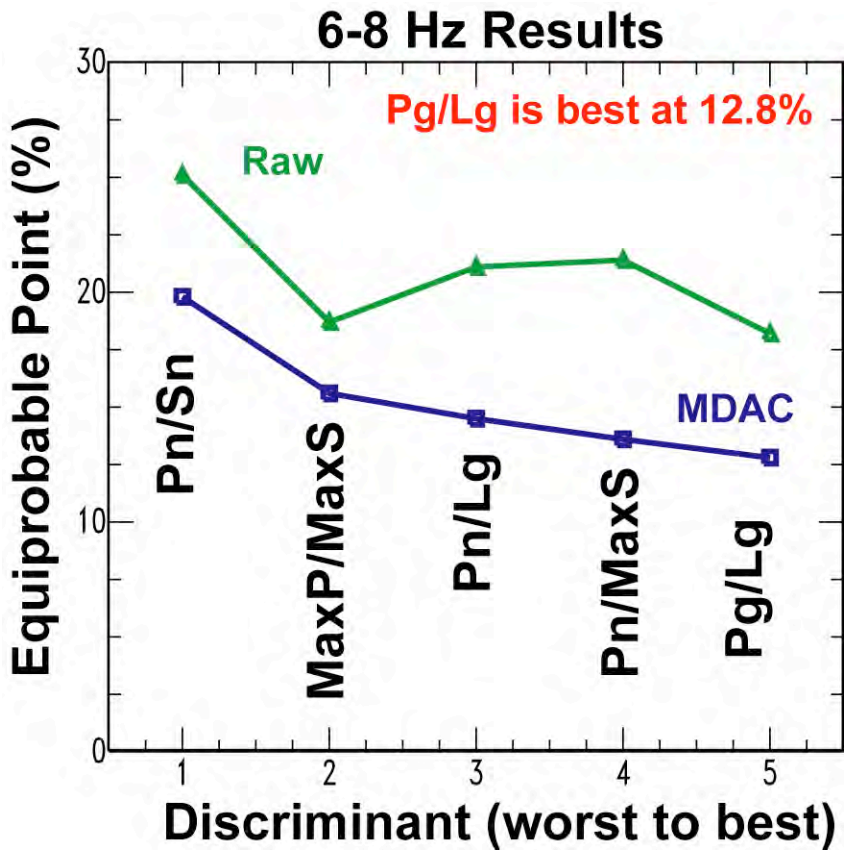

Figure 7. We combined data from four stations (CMB, ELK, KNB, LAC) to evaluate discriminant performance using equiprobable value as a metric. Equiprobable value is the level when the earthquake and explosion misidentification rates are equal, so the lower the number the better. We tried a variety of 6–8 Hz measures including taking the max (Pn, Pg) and max (Sn, Lg) and found Pg/Lg does the best. Note that the MDAC corrections significantly improve performance for all discriminants.

CONCLUSIONS AND RECOMMENDATIONS

Regional discrimination algorithms require calibration at each seismic station to be used for nuclear explosion monitoring. We have developed a revised MDAC procedure to remove source size and path effects from regional body-wave phases. This allows the comparison of any new regional events recorded at a calibrated station with all available reference data and models. This also facilitates the combination of individual measures to form multivariate discriminants that can have significantly better performance.

ACKNOWLEDGEMENTS

We thank Stan Ruppert, Terri Hauk and Jennifer O'Boyle for loading and maintaining the Lawrence Livermore National Laboratory (LLNL) database.

REFERENCES

Battone, S., M. D. Fisk and G. D. McCarter (2002), Regional Seismic-Event Characterization Using a Bayesian Formulation of Simple Kriging, *Bull. Seism. Soc. Am*. 92: 2277–2296.

Bowers, D., P. D. Marshall, and A. Douglas (2001), The Level of Deterrence Provided by Data from the SPITS Seismometer Array to Possible Violations of the Comprehensive Test Ban in the Novaya Zemlya Region, *Geophys, J. Int.* 146: 425–438.

Hartse, H., S. R. Taylor, W. S. Phillips, and G. E. Randall (1997), A Preliminary Study of Regional Seismic Discrimination in Central Asia with an Emphasis on Western China, *Bull. Seism. Soc. Am.* 87: 551–568.

Kim, W.-Y., V Aharonian, A. L. Lerner-Lam, and P. G. Richards (1997), Discrimination of Earthquakes and Explosions in Southern Russia Using Regional High Frequency Three-Component Data from the IRIS/JSP Caucasus Network, *Bull. Seism. Soc. Am.* 87: 569–88.

Mayeda, K. M. and W. R. Walter, (1996), Moment, Energy, Stress Drop and Source Spectra of Western U.S. Earthquakes from Regional Coda Envelopes, *J. Geophys. Res*. 101: 11,195–11,208.

Mayeda, K., A. Hofstetter, J. L. O'Boyle, and W. R. Walter (2003). Stable and Transportable Regional Coda Magnitudes Based on Coda-Derived Moment Rate Spectra, *Bull. Seism. Soc. Am.* 93: 224–239.

Rodgers, A. J. and W. R. Walter (2002), Seismic Discrimination of the May 11, 1998, Indian Nuclear Test with Short-Period Regional Data from Station NIL (Nilore, Pakistan), *Pure Appl. Geophys.* 159: 679–700.

Springer, D. L., G. A. Pawlowski, J. L. Ricca, R. F. Rohrer, and D. K. Smith (2002), Seismic Source Summary for All U.S. Below-Surface Nuclear Explosions, *Bull. Seism. Soc. Am.* 92: 1806.

Taylor, S. (1996), Analysis of High-Frequency Pg/Lg Ratios from NTS Explosions and Western U.S. Earthquakes, *Bull. Seism. Soc. Am.* 86: 1042–1053.

Taylor, S., A. Velasco, H. Hartse, W. S. Philips, W. R. Walter, and A. Rodgers (2002), Amplitude Corrections for Regional Discrimination, *Pure. App. Geophys*. 159: 623–650.

Walter, W. R., K. Mayeda, and H. J. Patton (1995), Phase and Spectral Ratio Discrimination between NTS Earthquakes and Explosions Part 1: Empirical Observations, *Bull. Seism. Soc. Am.* 85: 1050–1067.

Walter, W. R. and S. R. Taylor (2002), A Revised Magnitude and Distance Amplitude Correction (MDAC2) Procedure for Regional Seismic Discriminants, Lawrence Livermore National Laboratory report UCRL-ID-146882.

Walter, W. R., K. D. Smith, J. L. O'Boyle, T. F. Hauk, F. Ryall, S. D. Ruppert, S. C. Myers, M. Anderson, and D. A. Dodge (2003), Improving the Fundamental Understanding of Regional Seismic Signals with a Unique Western

United States Dataset, in *Proceedings of the 25th Seismic Research Review—Nuclear Explosion Monitoring: Building the Knowledge Base*, LA-UR-03-6029, 1: pp. 486–494.

STUDY OF REGIONAL BROADBAND WAVES FROM EARTHQUAKES AND MAN-INDUCED EVENTS IN NE CHINA

Rong-Mao Zhou[1], Brian W. Stump[1], and Christopher T. Hayward [1]
Zhi-Xian Yang[2], and Yun-Tai Chen [2]

Southern Methodist University[1] and China Seismological Administration[2]

Sponsored by Air Force Research Laboratory

Contract No. DTRA01-02-C-0003

ABSTRACT

We investigate the use of intermediate period surface wave magnitude, M_s, and high-frequency body wave magnitude, m_b, from regional mining explosions for event discrimination using techniques originally intended for teleseismic observations but modified for regional application. The magnitudes, M_s and m_b were estimated for an event that occurred in an iron mine in China (QianAn Explosion) with explosive yield of 1.3 kiloton and were compared to similar estimates from four kiloton-size mining explosions in Wyoming, USA. These magnitude estimates for mining explosions were compared to values from previous studies that included earthquakes and contained, single-fired explosions (Stevens and Day, 1985; Bonner et al., 2003). Although the previous studies examined mostly larger events, the Wyoming and China mining events plot in or near the earthquake population. Data from an anomalous Wyoming event, a blast in which a failure of the timing system caused a large portion of the blast pattern to simultaneously detonate, plots within the explosion population with m_b 4.4. The simultaneous detonation of a large portion of the blast array increased the body wave magnitude but had little effect on surface wave amplitudes. The actual values of M_s and m_b suggest that the surface waves generated by long-time-duration mining explosions can make them appear earthquake like. The data from the single anomalous shot indicates that if a significant part of the total explosives is simultaneously detonated the event will fall into the explosion population.

We continue data acquisition at 10 stations around the Beijing area and moved five stations into the Haicheng area, the second proposed study area. Following the Haicheng network installation, two local events occurred approximately 165 km southwest of the network with magnitude M_L 2.8 and 3.3 on August 25, 2004. These data illustrate the value of low noise sites in conducting regional studies of moderate sized events.

Finally, the complementary nature of Chinese digital station data to our study is demonstrated by some selected events. Observations from the QianAn explosion illustrate the value of these permanent three-component stations to our network observations providing improved event location and source characterization.

OBJECTIVES

The deployment of the broadband seismic network operated by the Southern Methodist University (SMU) and the Institute of Geophysics, China Earthquake Administration (IGCEA, formerly IGCSB) has been completed. The current operating network includes 10 stations around the Yanqing-Huailai Basin, NW of Beijing and five stations in the Haicheng, NE China (Figure 1). The seismic data has been archived into the IRIS DMC database. The goals of this collaborative study between SMU and IGCEA are to develop a database of earthquakes and man-induced events; to refine event locations in Yanqing-Huailai Basin and Haicheng area; to understand source characterization of natural and man-induced events; and to separate source and propagation path effects at regional distances.

Beijing and Haicheng are two regions of historical natural and man-induced seismicity as well as a seismic hazard. The region includes the site of the first successful earthquake prediction in 1975 near Haicheng and the great Tangshan earthquake in 1976. The broadband seismic network provides near-source and regional coverage for the study area. Data from this network has been used to constrain the preliminary velocity structure around Beijing (Zhou, 2004) and investigate event discrimination for mining explosions (Zhou et al., 2004).

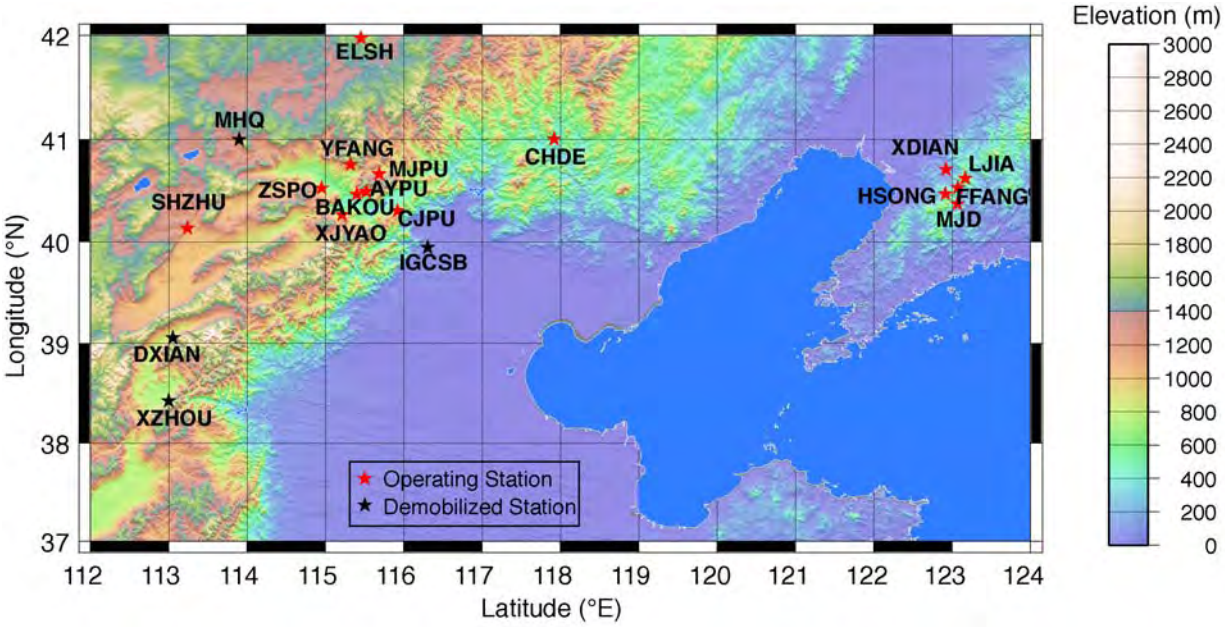

Figure 1. Map of the SMU-IGPCEA Broadband Seismic Network (Operating stations: red stars; Demobilized stations: black stars).

RESEARCH ACCOMPLISHED

The Completion of Deployment of the Broadband SMU-IGCEA Network

The deployment of the broadband SMU-IGCEA network was proposed in two phases. In Phase I, we deployed stations around the Yanqing-Huailai basin, and extended the network into the Haicheng area in Phase II. We continue data acquisition at 10 stations around the Beijing area. At the beginning of August, 2004, the group at IGCEA demobilized three stations at XZHOU, DXIAN and MHQ and installed five stations in Haicheng, Liaoning Province, the second proposed study area. The current SMU-IGCEA Broadband Seismic Network is summarized in Figure 1.

Data Archive

Data is archived locally at each site. Periodic visits to the sites provide the opportunity to retrieve the data where it is stored on a Sun Ultra 10 at IGCSB, Beijing. Data is transferred to SMU by disk exchange. All data from Phase 1 has

been converted to SEED format and archived at the Data Manage Center at the Incorporated Research Institutions for Seismology (IRIS DMC). Data through September 2004 from Phase II were also been converted to SEED format and archived at IRIS DMC. The group at IGCEA has collected the data for September 2004 to May 2005 and will ship them to SMU. We are anticipating conversion and storage in July 2005.

M_s:m_b Discriminant of Mining Explosions

Comparing M_s and m_b values for earthquakes and nuclear explosions has proven to be a successful teleseismic discriminant (Stevens and Day, 1985) since for a common body wave magnitude, earthquakes are more efficient than explosions in generating surface waves. The theoretical understanding of this relationship is related to the source function of the two event types, the materials surrounding the source, and the source depth.

M_s in these teleseismic studies was defined for Rayleigh waves (Gutenberg, 1945) with periods near 20 s for events recorded at epicentral distances greater than 20°. Marshall and Basham (1972) suggested that M_s determination may be extended to smaller events and shorter periods with a path correction, which can be estimated from the quantification of dispersion curves for intermediate period surface waves. Application of such estimates to the explosion waveforms and the determination of regional body wave magnitudes provides for the investigation of such measures as discriminants between earthquakes and explosions.

We investigate the use of intermediate period surface wave magnitude, M_s, and high frequency body wave magnitude, m_b, from regional mining explosions for event discrimination. The magnitudes, M_s and m_b were estimated for the event occurred in an iron mine in China with explosive 1.3 kiloton and compared to the results of four kiloton-size mining explosions in Wyoming, USA (Zhou et al., 2004). For the events in Wyoming, we use the Denny et al. (1987) body wave magnitude formula which was specifically developed for the Western US from an extensive database of earthquakes and nuclear explosions at or near the Nevada Test Site. We use the formula for stable continent to estimate m_b for the QianAn event(Evernden, 1967).

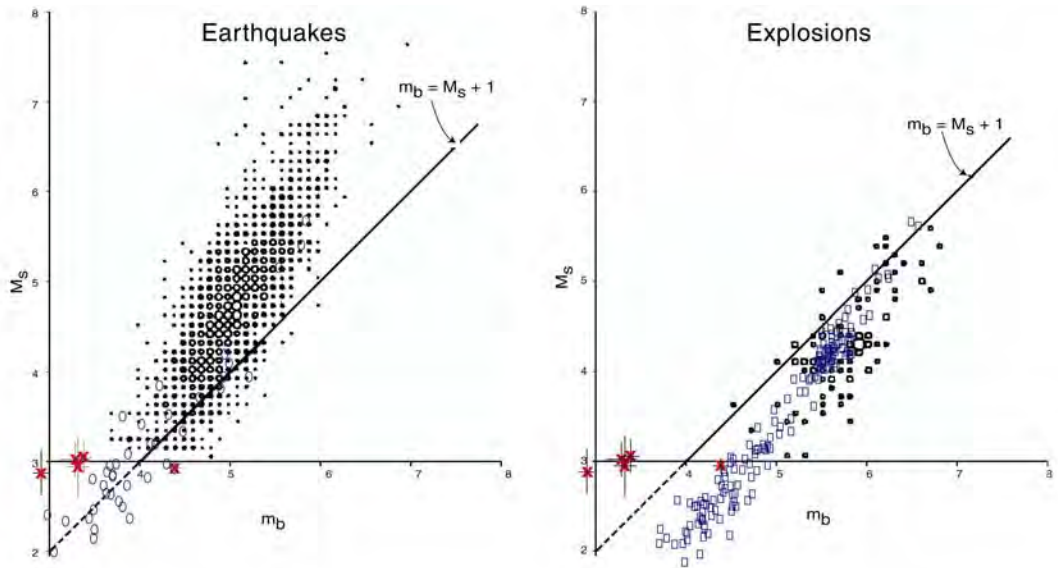

Figure 2. The m_b : M_s plots for earthquakes (left) and explosions (right). Original figures are from Stevens and Day (1985) superposed with results from Bonner *et al.* 2003 (blue ellipses for earthquakes and blue rectangles for explosions) and our results (red x) with the standard deviations in gray.

Figure 2 presents the M_s and m_b results from our study with the comparison to two previous studies that included earthquakes and contained single-fired explosions (Stevens and Day, 1985; Bonner et al., 2003) and examined mostly larger events than those in this study. All of our events fall at the very smallest magnitude range of the Stevens and Day study. Since the events are small, all of the estimates are based upon regional observations, whereas the Stevens and Day (1985) observations are primarily teleseismic. Despite these significant differences it is interesting to compare results. Except for the anomalous event (96214), all of our mining blasts plot in the

earthquake population, a result consistent with the robust intermediate period surface waves generated from these events.

The one anomalous event (96214) had about the same surface wave magnitude as the other events but the body wave magnitude is almost one full magnitude unit higher moving it into the explosion population. The only difference between this event and the other four is the time over which the explosion was detonated with a significant part of the explosive array being nearly simultaneously detonated.

Figure 3 presents the vertical component raw data for event 96214 recorded at PD31, a broadband seismic station of the permanent IMS array PDAR, and the filtered seismograms with frequency bandwidth of 0.0625 ~ 0.25 Hz, and 1.0 ~ 16.0 Hz. The spectral composition of event 95236, a single-fired explosion (22,700 kg) detonated at the same mine on 24 Aug., 1995 (Stump et al., 2003) and the normal production shot event 96201 are also presented in Figure 3. Figure 3(d) shows that the waveform characteristics of this anomalous event at high frequency (1 ~ 16 Hz) matches those from the single-fired explosion. In addition, the comparison illustrates that the cast shots generate intermediate surface waves and the single-fire explosion does not. The simultaneous detonation of a large portion of blast array increased the body wave magnitude but had little effect on surface wave amplitudes. The actual values of M_s and m_b suggest that the surface waves generated by long duration mining explosions can make them appear earthquake like. The data from a single anomalous shot indicates that if a significant part of the total explosives is simultaneously detonated the event will fall into the explosion population.

The source duration was estimated from the design delay times in the explosions as 4.4, 3.2, 3.6 and 5.6 s for 96201, 96214, 96215 and 97226, respectively. Zhou and Stump (2004) illustrated the source duration contribution to the fundamental Rayleigh wave in their Figure 20. This comparison here also suggests that the time function of mining and single-fired explosion may play a critical role in the performance of this discriminant.

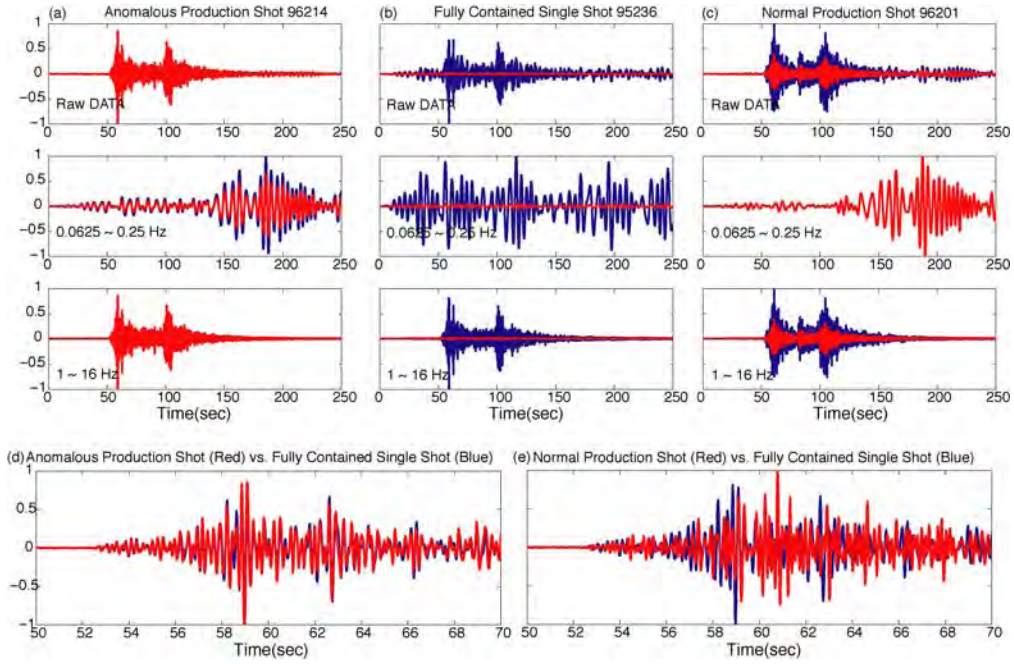

Figure 3. Spectral composition (raw data and band-pass filtered with bandwidth 0.0625 ~ 0.25Hz; 1 ~ 16Hz) of event 96214 – anomaly (a), event 95236 – single-fired (b), event 96201 – normal (c) recorded at PD31. In each sub-panel, the seismogram in blue is normalized by the maximal amplitude of each event and the red seismogram is normalized by the maximal amplitudes of the three events in the same frequency band; (d) compares 20 s of filtered P wave data (1 ~ 16 Hz) for event 96214 – anomaly (red) and event 95236 – single-fired (blue); and (e) for event 96201 – normal (red) and event 95236 (blue).

Seismograms Modeling

Fundamental mode, intermediate period Rayleigh waves generated by the five mining explosions are utilized to constrain the crustal structure of Wyoming (Zhou and Stump, 2004) and NE China (Zhou, 2004). Group velocities of fundamental mode Rayleigh waves were estimated using the Multiple Filter Analysis technique and refined with Phase Matched Filtering. A least square inversion technique was used to invert group velocity dispersion curves for the shallow shear-wave velocity structure. The 1-D structure model along the path to KRET and BJT is presented in Figure 4.

The 96201 blast in Wyoming consisted of 7 rows and 620 decked shots with a total yield of 2,065,412 kg, the largest explosion of those documented in 1996. The inter-shot delay was 35 ms and the inter-row delays ranged from 200 to 275 ms. Multiple charges were detonated in the same hole with different times in a decked charge. In this event, each hole contained two charges separated by 50 to 200 ms. Although the number of shots in each row varied from 85 to 93, for simplicity we assumed each row had 89 shots. The synthetic seismograms were calculated using MineSeis (Yang, 1998). The algorithm assumes the linear superposition of signals from identical single-shot sources composed of isotropic and spall components. Both shooting delays and location differences among individual shots are taken into account in calculating delays of superposition, although the Green's function is assumed to change slowly so that a common Green's function is used for all the single shots. The reflectivity method has been used to calculate the Green's functions.

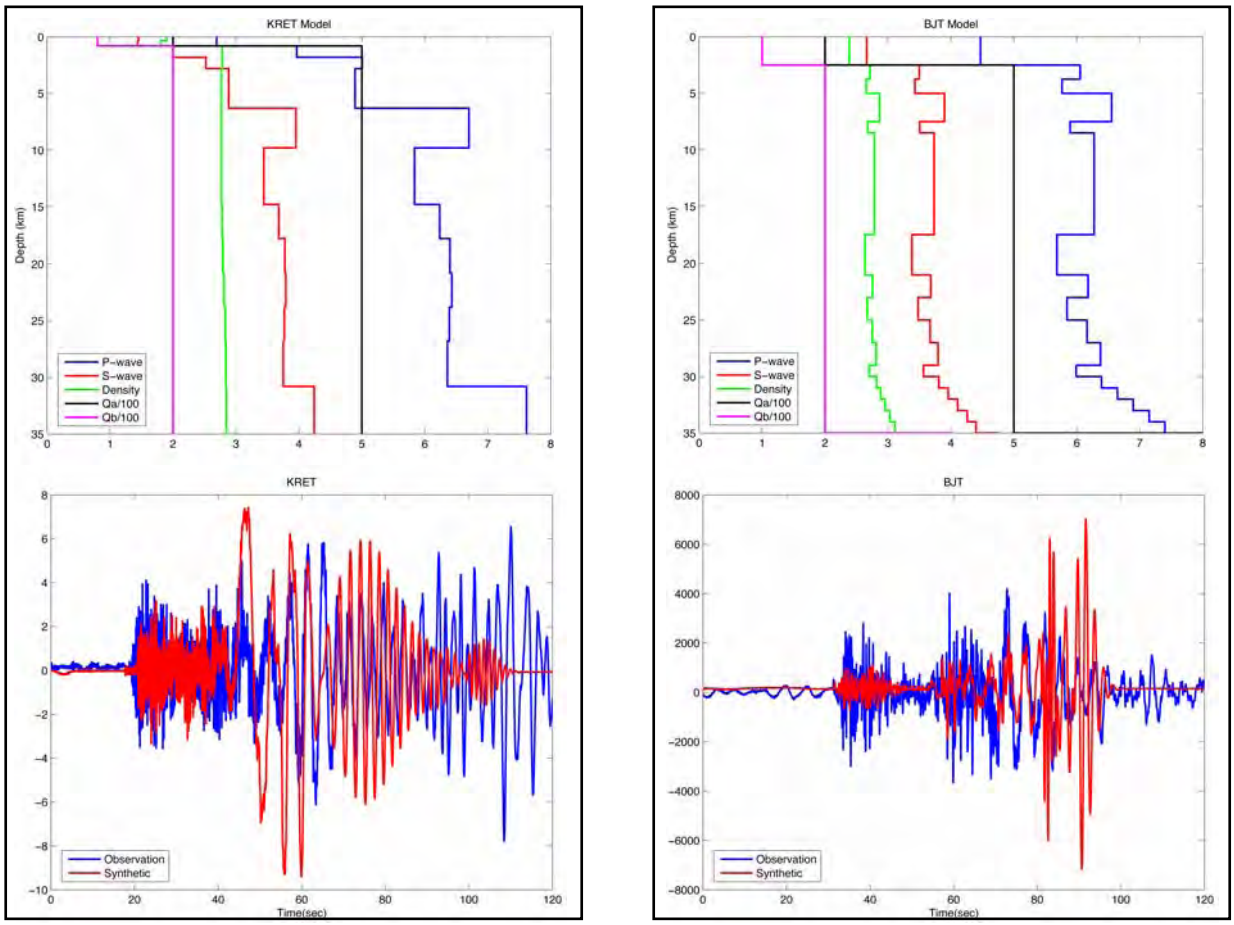

Figure 4. The comparison of synthetic (red) with observational seismograms (blue) at KRET (left) and BJT (right).

The ground truth information for the QianAn explosion is somewhat more limited. The explosion used a total of 1.3 kilotons of explosives designed to move a volume of rock 450 x 150 x 100 m. The source was constructed of 21 individual explosions detonated over 1.3 s. Since the exact dimensions of the spatial and temporal dimensions of the source were unknown the 21 explosions were equally distributed in space and time for seismogram synthesis.

The synthetic seismograms at KRET and BJT are shown in Figure 4 and compared with the observational seismograms. The arrival times of high frequency body waves and long period surface waves match with the observations. And KRET gives a better fit of the P/Lg ratio than the BJT because we have only limited ground truth information for QianAn event, rather than the detailed designed pattern for Wyoming as described earlier. The synthetics and the observations illustrate the strong contribution of the intermediate surface waves in both Wyoming and China. The synthetic study indicates that the presence of these surface waves is strongly dependent upon the relatively long temporal duration of the source for these of mining explosions.

This comparison between synthetic seismograms and observation illustrates the importance of the detail propagation path and ground truth information, the data interpretation, and source characterization.

DATA

Yanqing-Huailai Basin Area

Within the Yanqing-Huailai Basin and surrounding area (Figure 5), earthquake risk and propagation path assessments are important because of the historical seismicity and the large population in Beijing and other big cities in this region. Numerous underground mines here regularly experience rock bursts and collapses resulting in the disruption of mining operations, injury, and occasionally death. An understanding of these man made events can lead to a mitigation of these effects as well.

Historically, two large earthquakes occurred in Yanqing-Huailai area. One was the Huailai earthquake with M_s 6.5 on September 8, 1337; the other one was the Shacheng earthquake with M_s 6.75, near Shacheng on July 12, 1720 (open circles in Figure 5). On July 20, 1995, a M_L 4.1 earthquake occurred in the Yanqing-Huailai Basin (white dot in Figure 5) followed by approximately 450 aftershocks (Chen et al., 1998).

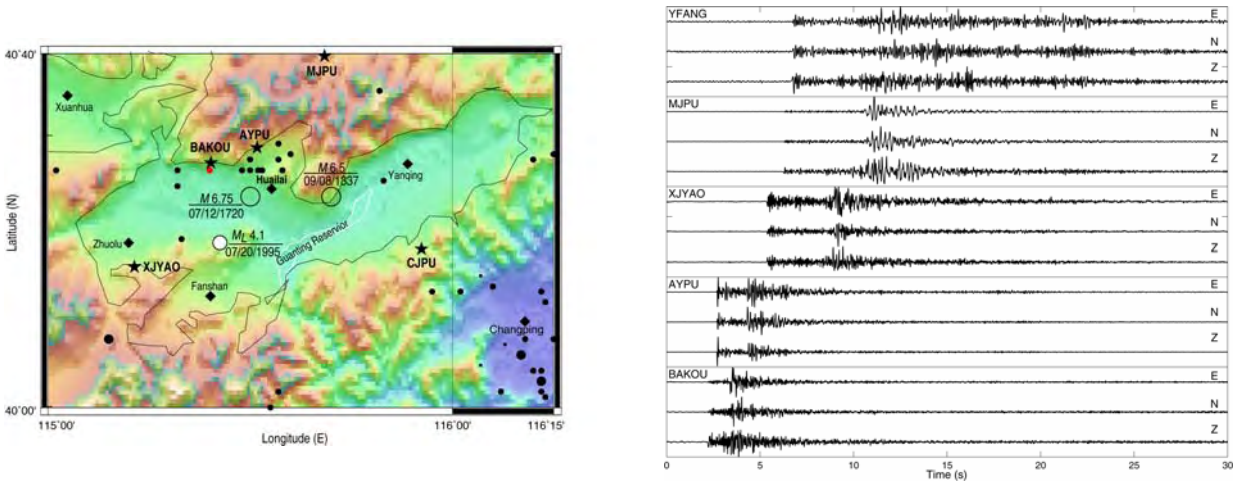

Figure 5. Left: Seismicity map (solid circles) of Yanqing-Huailai Basin. Stations of the SMU-IGCEA Huailai Seismic Network are designated as stars. Open circles are locations of two historical earthquakes in 1337 and 1720. The white dot is the epicenter of a M_L 4.1 earthquake on July 20, 1995. Diamonds are towns in the area. Right: Seismograms of the Huailai M_L 1.4 earthquake on January 2, 2003 (the epicenter location is a red dot in left figure).

Man-induced earthquakes occur approximately once a day and include both mining blasts and underground collapses and rock bursts inside the basin (Zhou et. al., 2003). Signals recorded by the SMU-IGCEA Network from events within a few kilometers of the stations often result in repeated signals the analysis of which will help understanding the source and local propagation path characteristics over a broad frequency range.

According to the report from the Hebei Seismic Information Network (*http://www.eq-he.ac.cn*), a magnitude M_L 1.4 earthquake occurred at 40.45°N, 115.4°E on January 2, 2003 (red dot in the left panel of Figure 5). The right panel of Figure 5 shows records of the three components (East: E; North: N and Vertical: Z) of this event at five stations; the records clearly show the good signal-to-noise ratio at all stations. The waveform differences between paths reflect the local geological settings. The short period (1-2 s) surface waves indicate the shallow epicentral depth (5km).

Haicheng Area

The 1975 Haicheng Earthquake, the first predicted in China, occurred in this region and motivates an interest to understand seismicity for hazard reduction. The Haicheng area is also rich in natural resources such as iron, lead, zinc, coal, oil and natural gas. Mining activities related to resource recovery provide additional sources of seismic waves.

Following the Haicheng network installation, two local events occurred approximately 165 km southwest of the network with magnitude M_L 2.8 (UTC 13:11:0.67) and 3.3 (UTC 13:19:9.6) on August 25, 2004. Four of the five new stations recorded these two events (MJD experienced a power failure). Figure 6 presents the seismograms for these two events at four stations. These data illustrate the value of low noise sites in conducting regional studies of moderate sized events.

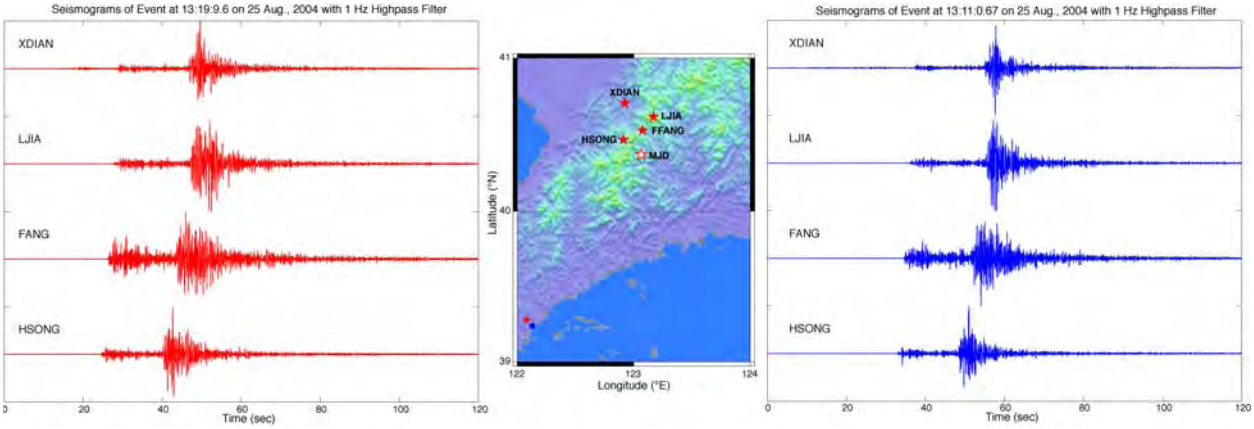

Figure 6. Map of the stations (red stars) and epicenters of two local events (dots) on August 25, 2004 with the seismograms (left: M_L 2.8 red dot; and right: M_L 3.3, blue dot).

CONCLUSIONS AND RECOMMENDATIONS

An important component of this study is the development of detailed source information for selected events, e.g., the QianAn explosion. In this case, detailed data on the location, amount of explosives, and detonation information were provided and used in the modeling and analysis of this unique event (Zhou et al., 2004). We propose to develop similar information for additional events with the cooperation of IGCEA.

Additional ground truth will be acquired for events that occur within or near the two focus areas of our current deployment, Huailai-Yanqing Basin and Haicheng Area. Five broadband stations are closely spaced in each of these areas of significant earthquake activity. These near-source observations can be used to provide source locations of GT10 or GT5 quality as well as source characterization to high frequencies unaffected by regional attenuation. This characterization can then be used to assess propagation path effects to the remaining regional stations.

In the currently deployed regional network, stations are self-contained with local data storage. Because the SMU-IGCEA network is in two widely separated areas (Huailai-Yanqing Basin and Haicheng) and some stations require substantial travel time, it is difficult and expensive to make frequent visits to retrieve data. During the winter it is impossible to visit some of the remote stations. This inability to retrieve frequent data updates has led to data recovery problems since a broken station is not detected for several months. It imposes a substantial load on the analysts, since data arrives in batches of many Gigabytes and substantially lengthens the time required to repair problems, since the instrument turnaround time is so long. The delay in data also makes it difficult to collect ancillary data including news reports and regional seismic data and non-detected segments that may be unarchived. We propose to add real-time telemetry to selected stations to alleviated a number of these problems.

Stump et al. (2004) suggest that the addition of an infrasound array to existing seismic stations can provide additional constraints for source characterization. The addition of infrasound sensors to an existing site can be accomplished for a small incremental installation and operation cost. The combined analysis of seismic and infrasound signals can provide unique constraints on sources near the solid earth – atmosphere boundary (Stump et al., 2004). A variety of man induced and natural events will add to our understanding not only of the source but also the effects of atmospheric propagation as well. We will integrate the seismo-acoustic observations with data from three new proposed infrasound upgrades in China in order to facilitate these source and propagation path studies.

ACKNOWLEDGEMENTS

Equipment for the study was supplied by the PASSCAL Instrumentation Center. We would like to thank Xiang-wei Xu, Shi-yu Bai, and Xiang-tong Xu at the Institute of Geophysics, China Earthquakes Administration, and Mary Templeton at Incorporated Research Institutions for Seismology (IRIS/PASSCAL) Instrument Center for their help with network installation and data collection.

REFERENCES

Bonner, J. L., D. G. Harkrider, E. T. Herrin, R. H. Shumway, S. A. Russell, and I. M. Tibuleac (2003), Evaluation of short-period, near-regional M_s scale for the Nevada Test Site. *Bull. Seism. Soc. Am.* 93**:** 1773–1791.

Chen, Y.-T., X.-T. Xu, X.-W. Yu and P.-D. Wang (1998). Observations and interpretation of seismic ground motion and earthquake hazard mitigation in Beijing area, *South China Journal of Seismology* 18: 2–8 (in Chinese).

Denny, M.D., S.R. Taylor, and E.S. Vergino (1987). Investigation of mb and Ms formulas for the Western United States and their impact on the Ms/mb discriminant, *Bull. Seism. Soc. Am.* 77: 987–995.

Evernden, J. F. (1967), Magnitude determination at regional and near-regional distances in the United States, *Bull. Seism. Soc. Am.* 57: 591–639.

Gutenberg, B. (1945), Amplitudes of surface waves and magnitudes of shallow earthquakes, *Bull. Seism. Soc. Am.* 35: 3-12.

Marshall, P. D. and P. W. Basham (1972), Discrimination between earthquakes and underground explosions employing an improved M_s scale, *Geophys. J. R. Astr. Soc.* 28: 431–458.

Stevens, J. L. and S. M. Day (1985), The physical basis of m_b:M_s and variable frequency magnitude methods for earthquake/explosion discrimination, *J. Geophys. Res.* 90**:** 3009–3020.

Stump, B. W., D. C. Pearson and V. Hsu (2003), Source scaling of contained chemical explosions as constrained by regional seismograms, *Bull. Seism. Soc. Am.* 93**:** 1212–1225.

Stump, B., M.-S. Jun , C. Hayward , J.-S. Jeon , I.-Y. Che, K. Thomason, S. House and J. McKenna, 2004, SMALL APERTURE SEISMO-ACOUSTIC ARRAYS: *Design, Implementation and Utilization, Bul. Seismo. Soc. Am.* 94**:** 220–236.

Zhou, R.-M., B. W. Stump, Y.-T. Chen, C. Hayward, Z.-X. Yang, M. Templeton, X.-W. Yu, S.-Y. Bai and X.-T. Xu (2003). Network installation in the Yanqing-Huailai Basin and preliminary study of natural and man-induced events. *Proceedings of the 25th Seismic Research Review —Nuclear Explosion Monitoring: Building the Knowledge Base*, LA-UR-03-6029, Vol. 2, pp. 504–513.

Zhou, R.-M. and B. W. Stump (2004). Rayleigh Waves Generated by Mining Explosions and Upper Crustal Structure Around the Powder River Basin, Wyoming. *Bull. Seismo. Soc. Am.* 94**:** 1410–1429.

Zhou, R.-M., B. W. Stump and C. T. Hayward (2004). M_s:m_b discrimination study of mining explosions in Wyoming, USA and Qianan, China. *Proceedings of the 26th Seismic Research Review: Trends in Nuclear Explosion Monitoring*, LA-UR-04-5801, Vol. 1, pp. 541–550.

Zhou, R.-M. (2004). Intermediate period surface waves from mining explosions for crustal structure and source studies: application in the Western USA and Northeast China. *Ph. D. Dissertation*, Southern Methodist University, pp 240.

Yang, X.-N. (1998). MineSeis – A Matlab GUI program to Calculate Synthetic Seismograms from a Linear, Multi-Shot Blast Source Model, *Proceedings of the 20th Annual Seismic Research Symposium on Monitoring a Comprehensive Test Ban Treaty*, September, 1998, LA-UR-98-1486, 755–764.

Hydroacoustic Monitoring

2005

Proceedings of the
27th Seismic Research Review:
Ground-based Nuclear Explosion Monitoring Technologies

Vol. II

To view these Proceedings online, visit
https://www.nemre.nnsa.doe.gov/review2005

Proceedings of the 27th Seismic Research Review: Ground-based Nuclear Explosion Monitoring Technologies

September 20–22, 2005

Rancho Mirage, California

Volume II

Hydroacoustic Monitoring
Radionuclide Monitoring
Infrasound Monitoring
Data Processing and Analysis

Approved for Public Release; further dissemination unlimited.

National Nuclear Security Administration

LA-UR-05-6407

AIR FORCE RESEARCH LABORATORY

Table of Contents - Volume II

4. Hydroacoustic Monitoring 713

4-01 **Blackman, D. and C. de Groot-Hedlin**
Acoustic Propagation Through the Antarctic Convergence Zone – Calibration Tests for the Nuclear Test Monitoring System 715

4-02 **Bowman, J., J. Hanson, and D. Jepsen**
An Active-Source Hydroacoustic Experiment in the Indian Ocean 722

4-03 **Matzel, E., A. Ramirez, and P. Harben**
Model-Based Hydroacoustic Blockage Assessment and Development of an Explosive Source Database 733

4-04 **Pulli, J. and Z. Upton**
Azimuthal Dependence of Hydroacoustic Blockage at Diego Garcia and Implications for Discrimination 740

4-05 **Upton, Z., J. Bhattacharyya, J. Pulli, S. Shah, and M. Collins**
Improving the Physical Understanding of Hydroacoustic Blockage: Statistical and Model Based Studies 749

5. Radionuclide Monitoring 759

5-01 **Biegalski, S. and O. Ezekoye**
Design of Aerosol Sampler to Remove Radon and Thoron Progeny Interference from Aerosol Samples for Nuclear Explosion Monitoring 761

5-02 **Biegalski, S., K. Biegalski, and D. Haas**
Development of the Spectral Deconvolution Analysis Tool (SDAT) to Improve Counting Statistics and Detection Limits for Nuclear Explosion Radionuclide Measurements 770

5-03 **Cooper, M., A. Carman, J. Hayes, T. Heimbigner, C. Hubbard, K. Litke, J. McIntyre, S. Morris, M. Ripplinger, and R. Suarez**
Improved β-γ Coincidence Detector for Radioxenon Detection 779

5-04 **Hennig, W., H. Tan, W. Warburton, and J. McIntyre**
Digital Pulse Shape Analysis with Phoswich Detectors to Simplify Coincidence Measurements of Radioactive Xenon 787

5-05 **Hull, E., H. Miley, R. Pehl, C. Aalseth, and T. Hossbach**
Segmentation of the Outer Contact on P-type Coaxial Germanium Detectors 795

5-06 **Seifert, C., J. McIntyre, K. Antolick, A. Carman, M. Cooper, J. Hayes, T. Heimbigner, C. Hubbard, K. Litke, M. Ripplinger, and R. Suarez**
Mitigation of Memory Effects in Beta Scintillation Cells for Radioactive Gas Detection 804

6. Infrasound Monitoring 815

6-01 **Christie, D., B. Kennett, and C. Tarlowski**
Detection of Regional and Distant Atmospheric Explosions at IMS Infrasound Stations 817

6-02 **Gibson, R. and D. Drob**
Infrasound Propagation Calculation Techniques Using Synoptic and Mesoscale Atmospheric Specifications 828

6-03 **Norris, D., R. Gibson, J. Bhattacharyya, and R. Whitaker**
Development of Advanced Propagation Models and Application to the Study of Impulsive Infrasonic Events at Various Ranges 838

6-04 **ReVelle, D.**
Additional Infrasonic Studies of Earthquakes and Mining Blasts Discrimination 845

6-05 **Walker, K., M. Zumberge, J. Berger, and M. Hedlin**
An Improved Method for Determining Infrasound Back Azimuth with Optical Fiber Sensors 855

6-06 **Woodward, R., H. Israelsson, I. Bondár, K. McLaughlin, J. Bowman, and H. Bass**
Understanding Wind-Generated Infrasound Noise 866

7. Data Processing and Analysis 877

7-01 **Akers, P. and K. Wilbanks**
Robust Remote Seismic Station 879

7-02 **Begnaud, M., R. Stead, J. Aguilar-Chang, and H. Hartse**
Optimizing Data Access and Availability for Seismic Calibration Research 888

7-03 **Buckley, S., P. Vincent, and D. Yang**
New Ground Truth Capability from InSAR Time Series Analysis 898

7-04 **Hart, D., B. Merchant, J. Harris, and C. Young**
The 2005 MatSeis and NNSA Seismic Regional Analysis Tools 907

7-05 **Kohl, B., T. Bennett, I. Bondár, B. Barker, W. Nagy, C. Reasoner, H. Israelsson, and P. Piraino**
Development of a Network Data Set for Evaluating Detection and Network Processing Performance 917

7-06 **Kvaerna, T., S. Gibbons, F. Ringdal, and D. Harris**
Integrated Seismic Event Detection and Location by Advanced Array Processing 927

7-07 **Ruppert, S., D. Dodge, A. Elliott, M. Ganzberger, T. Hauk, and E. Matzel**
Enhancing Seismic Calibration Research Through Software Automation and Scientific Information Management 937

7-08 **Woodward, R., M. Skov, M. Bahavar, G. Davis, and Y. Kung**
Data and Tools to Support Nuclear Explosion Monitoring Research and Development 946

7-09 **Young, C. and S. Ballard**
A Potential New Nuclear Explosion Monitoring Schema 956

Acronyms, etc. 967

Acronym - Definition 969

Station Code - Location and/or description 973

ACOUSTIC PROPAGATION THROUGH THE ANTARCTIC CONVERGENCE ZONE – CALIBRATION TESTS FOR THE NUCLEAR TEST MONITORING SYSTEM

Donna K. Blackman and Catherine de Groot-Hedlin

University of California San Diego

Sponsored by Army Space and Missile Defense Command

Contract No. W9113M-05-1-0019

ABSTRACT

We plan to carry out a series of calibration shots within and to the south of the Antarctic convergence zone (ACZ). The seagoing experiment will be one component of an already scheduled and funded multi-disciplinary expedition in the Southern Ocean. Hydrophone stations of the International Monitoring System (IMS) will record the calibration shots, and the observed source-receiver travel times will allow us to document the scale of the source location errors associated with hydroacoustic propagation through the strong oceanographic gradients of the convergence zone, and determine the transmission losses for sound crossing the convergence zone. In addition, apparent back azimuths to the source will be determined and, together with the travel times, compared to predictions of acoustic propagation models. Environmental parameters within the models will be varied systematically to assess how each change affects the predicted travel times, azimuths, and transmission loss. These findings will be related to our calibration shots specifically and will also be of general import, in terms of quantifying of the types of source characterization uncertainties that arise for hydroacoustic propagation across high oceanographic gradient zones. Physical parameters that will be considered include ocean temperature and salinity, seafloor variability (depth and sediment thickness), and sea surface roughness (waves) in the region where the sound channel breaches the surface.

The planned seagoing voyage departs Australia, crosses the ACZ along the way to the Davis Antarctic Station, and crosses the zone again on return to Hobart, Australia. We predict that the travel path between the calibration source site and at least one of the IMS receivers will be unblocked by seafloor topography along the entire ship track. We plan to use 4-lb US Navy signals underwater sound (SUS) charges, which generate broadband signals. These small explosive devices have been used for defense and research purposes in the ocean for several decades. Although other acoustic sources might be preferable, conditions in the Southern Ocean preclude the use of more sophisticated systems that require a calm-moderate sea state for safe operation.

Our experiment is designed as a one-time case. The calibration shots will be conducted along transects that each take about a week. Therefore, we will obtain essentially a snapshot of the ACZ and our signals will document the travel times and losses for the corresponding structure. The idea behind this type of experimental plan is that we can document the scale of the errors that arise due to uncertainty in ACZ structure. This will allow us to characterize how well an unknown event in the Southern Ocean could be located. The combination of our measurements with post-cruise modeling will allow us to assess the magnitude of various factors that contribute to the determined uncertainties. In summary, our experiment is designed to answer the following questions:

- *How does propagation through the ACZ affect travel times and apparent source-receiver azimuths?*

- *How does propagation through the ACZ affect the signal strength?* Parabolic equation modeling confirms that acoustic propagation is ducted north of the ACZ boundary, and surface-limited south of it. An unresolved question is whether acoustic energy is lost due to the strong gradient in ocean sound speeds at the ACZ boundary, or whether energy is lost due to scattering at the rough sea surface in the region south of the boundary.

- *How does source depth affect the transmission loss and travel times for source within the ACZ?* At a few sites, more than one charge will be deployed; trigger depths for successive charges will be varied between 200-100m below the sea surface so that variations due solely to source depth can be assessed.

OBJECTIVES

We have recently been funded to conduct a series of hydroacoustic calibration shots that will be used to compare observed signal propagation time and direction to that predicted by numerical models for paths crossing the (ACZ). A calibration experiment is needed because ocean temperature and salinity gradients across the ACZ are not sufficiently well characterized to predict how travel times may be affected by seasonal and annual variation in the structure of the zone, and propagation models are insufficient to fully handle the complexity of propagation across the ACZ. Our calibration signals will propagate to IMS hydrophones in the Indian Ocean from a series of Southern Ocean sites located along ship transects from 48°S-62°S. Comparison between the signal source locations determined using techniques that are standard for nuclear test monitoring and the known source locations will indicate the level of uncertainty in current methods. In addition, analysis of transmission loss between the sources and the receivers will be used to assess the influence of variation in oceanographic properties, sea surface conditions, and sea floor depth along the propagation paths.

Precise source times and locations are critical for calibrating trans-ACZ travel times to the IMS hydrophone stations. While there are natural sources that yield acoustic signals generated south of ACZ that are observed at IMS stations, for example, icequakes (Talandier et.al., 2002) and earthquakes, their event times and locations must be inferred from model-dependent calculations; ground truth information on exact event time or location is not available. Furthermore, many of these naturally occurring events do not generate strong signals in the bandwidth of interest (30-100 Hz).

We are in the process of finalizing the seagoing plan; at this time it still looks likely that we will join one of the 05/06 field season voyages run by the Australian Antarctic Division (AAD). A candidate voyage track enroute to Davis Antarctic Station and back is shown in Figure 1. The path between the calibration source sites and at least one, preferably more, of the IMS receivers must not be blocked by sea floor topography. This is the case to the Cape Leeuwin and Diego Garcia IMS stations for much of the area 85°E-135°E; paths to the Crozet IMS station will include some loss during propagation over Kerguelen Plateau, for sources east of 80°E (Figure 1), but paths for sources further west will be unblocked.

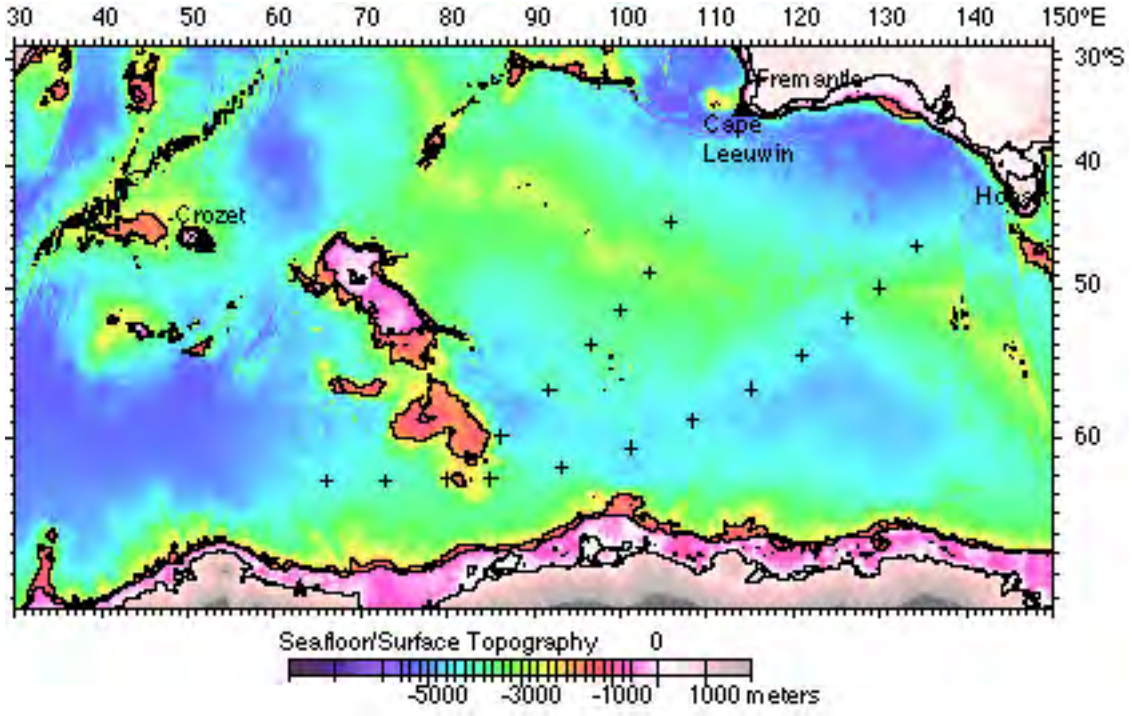

Figure 1 sketch of possible calibration source sites across the ACZ. Seafloor depth (color), IMS hydrophone stations (triangle; Diego Garcia off the map to the North), tentative source sites: +. The transects shown here correspond to Voyage 3 of the AAD field season for 05/06 austral summer.

We plan to use 4-lb US Navy SUS charges for our acoustic source. Although other acoustic sources might be preferable, conditions in the Southern Ocean preclude the use of more sophisticated systems that require calm-moderate sea state for safe operation. Source trigger depths will be varied between 200 and 1000 m below the sea surface. The SUS signal is broadband and the output level of a 4-lb charge is listed as 276 dB re 1 μPa. The energy density flux is estimated to be about 6 dB greater than that for the 1.8 lb charges used for our prior work (Urick, 1983). At a few sites, more than one charge will be deployed; trigger depths for successive charges will be varied so that path effects are constant and variations due solely to source depth can be assessed.

The calibration shots will be conducted along transects through the ACZ that each take about a week and are separated by up to a few weeks (while other scientific activities are completed near the Antarctic station). Therefore, we will obtain essentially two snapshots of the ACZ and our signals will document the travel times and losses for the corresponding structure.

RESEARCH ACCOMPLISHED

We have analyzed transmission paths to the IMS receivers. For most paths, there is some ridge or plateau that projects at least partly into the oceanic sound channel and will probably strip away the highest order modes. Sites will therefore be selected prior to the cruise based on predictions of optimal signal to noise ratios at each IMS station. An example is shown in Figures 2 and 3. Figure 2 shows the environmental models from a potential site near 60°S, 101°E to each IMS hydrophone at which we anticipate signals can be detected. The axis of the sound channel shoals significantly toward the polar ocean and the upper part of the waveguide breaches the surface. Thus, even for relatively unblocked paths, part of the transmission would be surface limited (that is rays would be reflected from the sea surface) for sources within the ACZ. Propagation to H04W is at least partially blocked by the Kerguelen plateau, and would furthermore be surface limited for the entire path.

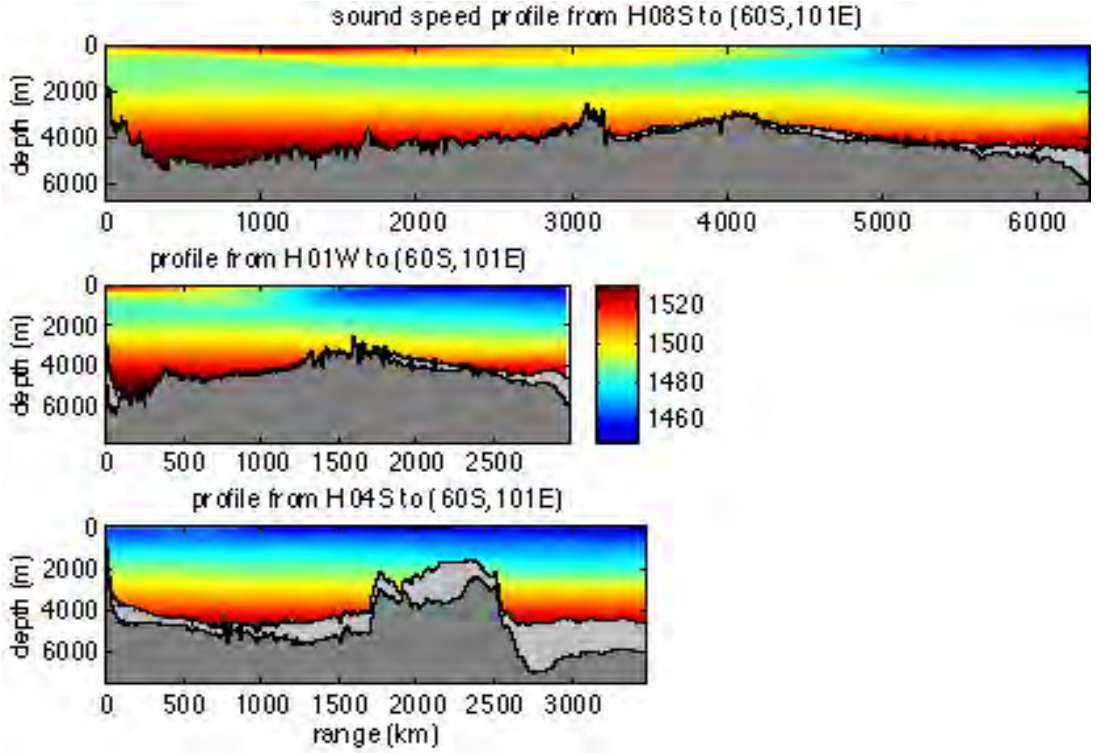

Figure 2. Ocean sound speed (m/s) profiles for paths between a potential source site (at 60.5°S, 101° E) and three IMS hydrophone stations. Dark gray is hard (basement) rock, light gray is a sediment layer (thicknesses from www.ngdc.noaa.gov/mgg/sedthick/sedthick.html). Sea floor characteristics affect transmission loss (TL) computations as sound mainly reflects from basement rock but is absorbed and attenuated by sediments.

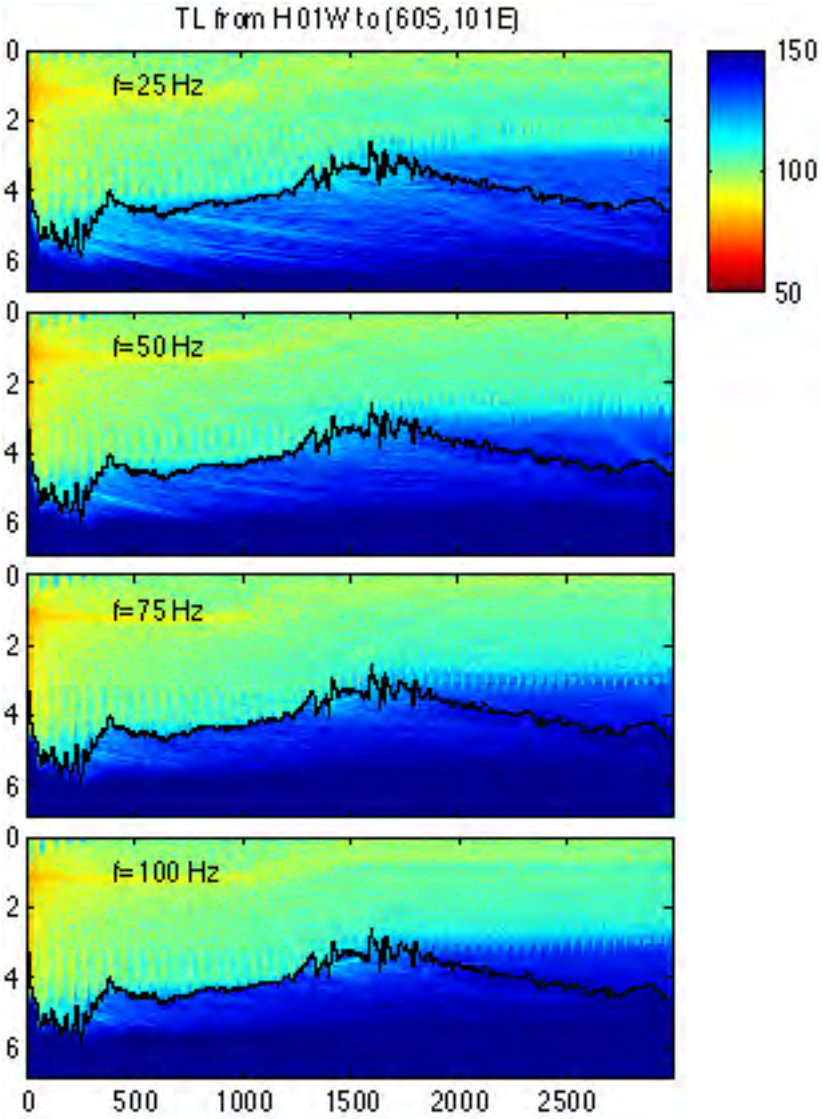

Figure 3. Predicted TL (dB) between the hypothetical source site and H01. Source and receiver are switched, so a series of trial trigger depths can be estimated using a single calculation per frequency. Propagation is surface limited where sound channel breaches the surface. Most the energy is confined within about 2.5 km of the surface, about the minimum seafloor depth along the travel path.

Figure 3 shows predicted acoustic transmission losses (TL) along a path from a H01W hydrophone to the potential site location near 60°S, 101°E, for several frequencies. These were computed using the acoustic parabolic equation (PE) modeling algorithm described in (Collins, 1993). By reciprocity, the source and receiver locations may be interchanged. Therefore, by computing acoustic transmission losses for a source at the hydrophone position, we only need to run the algorithm once in order to estimate the losses for a series of trial shot depths. For example, Figure 3 shows the expected transmission loss for a sweep of ranges (along profile) and depths (vertical axis) for a source located at the H01W hydrophone, near Cape Leeuwin. By reciprocity, a source fired at any point along the profiles would yield the identical transmission loss at H01W. Thus Figure 3 implies that any source fired within approximately 2000 m of the sea surface would yield relatively low transmission losses at the H01W hydrophone; deeper sources would be much more severely attenuated. It is worth noting that the shots fired in the Heard Island experiment (Heaney et al., 1991; Munk et al., 1988) had even longer propagation paths through the Antarctic Convergence zone, and were detected at Bermuda on unfiltered records; thus even with our much smaller shots, we might be able to detect signals with careful processing.

Note that the transmission losses computed above represent best-case scenarios because the propagation modeling assumes a mirror-flat sea surface, which reflects, with phase reversed, all in-coming hydroacoustic energy. Furthermore, the PE equation modeling does not take into account back-scatter at the ACZ transition zone. More realistically, when acoustic propagation is surface limited the transmission is adversely affected by sea surface roughness, which scatters incoming energy. Sea surface roughness depends strongly on weather conditions along the travel path and throughout the Southern Ocean. The faster the wind, the longer it blows in one direction, and the greater the fetch, the bigger the waves. The contribution of sea surface roughness to transmission loss should therefore be seasonally and storm dependent. Wave height information derived from satellite data will allow us to assess the contribution of sea surface roughness to losses for each source-receiver path. Figure 4 (from https://www.fnmoc.navy.mil/ PUBLIC/) is a map of wave height and wind direction for the Indian Ocean, indicating a large storm moving across the region in which are shots will be fired. In general the sea surface roughness is greatest south of 40°S, especially in winter.

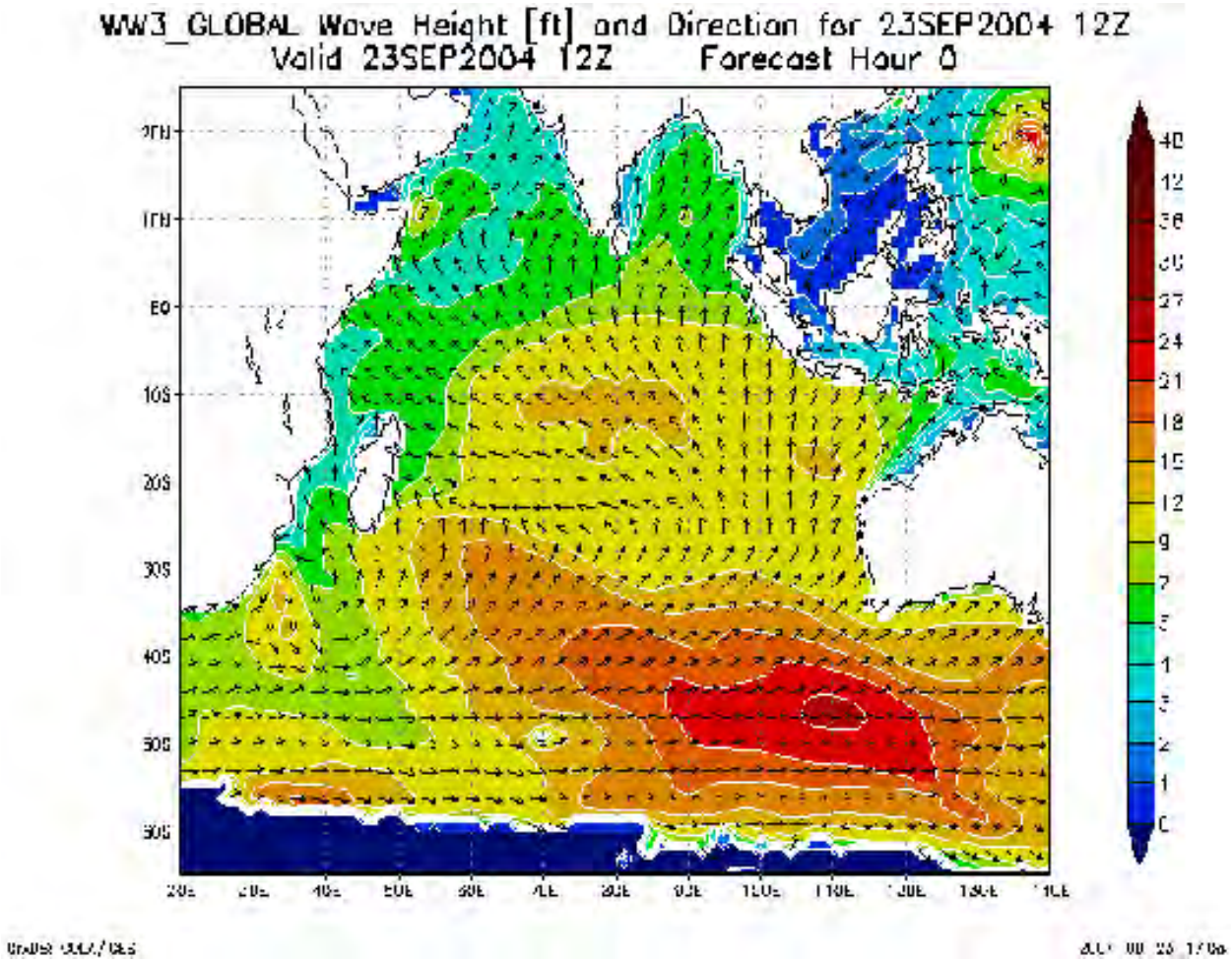

Figure 4. a) Wave height (0 to 50 ft, blue to brown) and wind direction (arrows), from www.fnmoc.navy.mil/ PUBLIC. These daily data will allow us to assess sea surface roughness along the propagation paths.

The effect of sea surface roughness is most pronounced at high frequencies. In Brekhovskikh and Lysanov (1991), it is shown that at a rough boundary, the modified reflection coefficient in the specular direction (ie the direction predicted by Snell's law) is given by

$$R' = R(\theta) \exp(-P^2/2),$$

where $$P = 2 k \sigma \cos(\theta),$$

R(θ) is the reflection coefficient for the equivalent smooth surface as a function of incidence angle θ, k is the wave number of the sound, θ is the angle of incidence of the sound wave at the boundary, and σ is the rms displacement of the rough surface from its average position. The reflection coefficient at a rough surface therefore depends on acoustic wavelength, and thus frequency. In Figure 5, the absolute value of the reflection coefficient is plotted as a function of frequency for several rms displacement values. For a perfectly smooth sea surface, the reflection coefficient has an absolute value of 1, that is, the energy is totally reflected in the specular direction. As the ratio of the roughness to the acoustic wavelength increases, more energy is scattered in the ocean channel. The dash-dot lines represent values for normal incidence at the sea surface and thus represent maximal scattering. More realistic values for the angle of incidence at the sea surface can be derived from the TL example shown in Figure 3. As indicated there, most of the rays have turning points within the top 2.5km. Using Snell's law, and the ocean sound speed profile data near (60S, 101E), we find that the angle of incidence at the sea surface would range from 80° to 76° for turning points from 1km to 2.5km depth. The solid lines in Figure 5 represent values for angles of incidence of 75°; the specular reflection coefficient increases significantly at grazing incidence. Using the result that, in a medium with a constant velocity gradient a ray path follows the arc of a circle, we can also find the approximate distance between surface reflections for the example shown in Figure 3. This distance varies from about 25km for a ray with a turning point at 1km depth, to about 40km for a ray that turns at 2.5km depth.

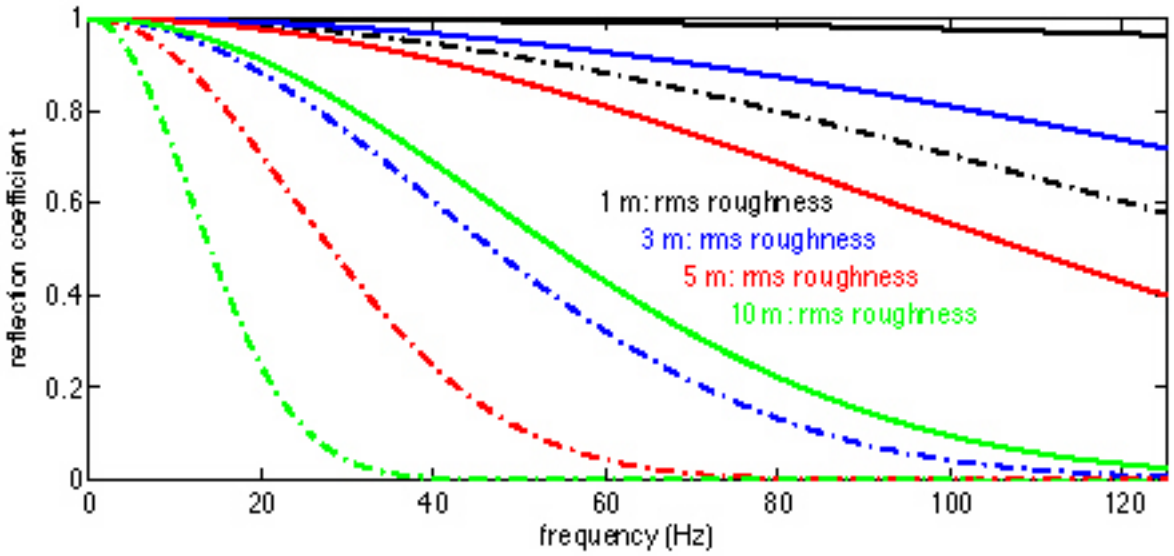

Figure 5. Specular reflection coefficients as a function of frequency at a rough seasurface. The values are shown for several sea states: black indicates 1m rms roughness (calm seas), blue indicates 3m rms roughness (a moderate seastate), red indicates heavy seas (5m rms roughness) and green indicates very heavy seas (10m rms roughness). The dash-dot lines are the values for normal incidence on the sea surface, which correlates to maximum scattering. The solid lines are the reflection coefficients for a 75° angle of incidence, which is a more realistic value as discussed in the text.

Given the number of surface reflections for a particular path and the specular reflection coefficients shown in Figure 5, it might seem straightforward to compute the additional transmission losses that result from scattering at the rough sea surface. However, it should be noted that much of the energy scattered at the rough surface may end up propagating to the receiver anyway; scattering mainly results in dispersing the energy out into a broader beam about the specular direction. Acoustic energy is lost if it is scattered downward into the sea floor, or into a direction away from the receiver. The amount of transmission loss attributable to sea surface roughness is thus not easily predicted; our experimental design will allow us to place observational constraints on acoustic transmission losses due to sea surface scattering.

The rest of our work in this first period of the study has been in experimental planning. We have completed the initial review stages for joining an Australian Antarctic Division voyage. The final stage of environmental review is currently underway, with preliminary assessment indicating that we will not be required to file for a permit (which would probably delay the experiment 1 year). We are working with the expedition leader to determine whether we can join the ship in Hobart or Fremantle, and have cleared most of the SUS shipment/handling issues for the latter.

The voyages under consideration would provide source signals in either late October/November 2005 or late February/early March 2006.

CONCLUSIONS AND RECOMMENDATIONS

We have designed a relatively inexpensive, logistically feasible experiment that will allow us to determine source-receiver travel time and azimuth errors that are characteristic of autumn (or summer) conditions across a range of polar front acoustic propagation paths. This is the type of information required to assess the location capabilities of the IMS for possible Southern Ocean nuclear tests. The main results that we will obtain are:

- Quantify travel-time errors associated with limited accuracy in ACZ characterization.
- Compute location uncertainties for Southern Ocean events, based on these errors.
- Assess the scale at which various physical parameters contribute to this uncertainty.

One-season results will document the scale of such errors. Given this knowledge it will be possible to address whether additional efforts are justified to more fully document, for example, early versus late season, annual, or source-receiver path differences that could be developed into a database for events from specific time/space regions for the Southern Ocean.

REFERENCES

Brekhovskikh, L.M. and Yu. P. Lysanov (1991), *Fundamentals of Ocean Acoustic*s, in *Wave Phenomena 8,* 2nd ed., Springer- Verlag.

Collins, M.D. (1993), A split-step Padé solution for the parabolic equation method, *J. Acoust. Soc. Am*. 93: 1736–1742.

Heaney, K.D., W.A. Kuperman, and B.E. MacDonald (1991), Perth-Bermuda sound propagation (1960): Adiabatic mode interpretation, *J. Acoust. Soc. Am.*, 90: 2586–2594.

Munk, W.H., W.C. OReilly, and J.L. Reid (1988), Australia-Bermuda sound transmission experiment (1960) revisited, *J. Phys. Oceanog.*, 18: 1876–1898.

Talandier, J., O. Hyvernaud, E.A. Okal, P.-F. Piserchia (2002), Long-range detection of hydroacoustic signals from large icebergs in the Ross Sea, Antarctica, *Earth. Plan. Sci. Lett.* 203: 519–534.

Urick, R.J. (1983), *Principles of underwater sound*, McGraw-Hill, New York.

AN ACTIVE-SOURCE HYDROACOUSTIC EXPERIMENT IN THE INDIAN OCEAN

J. Roger Bowman[1], Jeffrey A. Hanson[1] and David Jepsen[2]

Science Applications International Corporation[1] and Geoscience Australia[2]

Sponsored by Army Space and Missile Defense Command

Contract No. W9113M-05-C-0138

ABSTRACT

The purpose of this project is to improve hydroacoustic discrimination of underwater events. The central element will be an explosive-source experiment conducted in the Indian Ocean offshore of Western Australia. We expect to conduct the experiment sometime in the middle of 2006. We will analyze high-frequency signals using data from hydrophone stations of the International Monitoring System (IMS). This is a joint project between the Science Applications International Corporation (SAIC) and Geoscience Australia. A feasibility study has been conducted that indicates the proposed experiment can be conducted economically and within existing environmental regulations.

The project will consist of three phases. The first phase will be experiment design, planning, and modeling. We will refine our preliminary designs (including finalizing the experiment site and defining the pattern, sizes, and deployment depths for shots) by analyzing high-frequency propagation and reflection losses using previously recorded data from natural and man-made sources. We will plan the logistics for execution of the experiment and will prepare and support applications for all required government permits.

We examined recordings of two explosions in the Bay of Bengal on May 5, 2004, to help guide the experiment design. These events are identified as explosions based on their high-frequency content and spectral scalloping. Bubble pulses are seen for direct arrivals at the four hydrophone triads examined and for reflected signals at three of the triads. The direct arrivals have consistent delay times with an average of 37.3 and 14.5 msec for the first and second events, respectively. Assuming the yield is the same for the two explosions, which have similar amplitudes, we infer that the second explosion is three times as deep as the first.

The second project phase will execute the field experiment itself. We will assemble personnel, equipment, explosives, and a marine vessel at the port of debarkation and transit to the experiment site. We will then deploy and detonate explosive charges and measure shot parameters.

In the third project phase, we will analyze and interpret data from the IMS hydrophone stations. We will improve knowledge of underwater event discrimination by determining the loss of high-frequency energy during reflection from coastlines and during propagation across partially blocked portions of the ocean's sound channel. We will also establish the ability to characterize events using reflected arrivals.

The principal products of this project will be the following:

- Unique ground-truth data set from in-water explosions comprising accurate source parameters and waveforms from IMS hydrophone stations
- Quantitative estimates of high-frequency reflection and propagation efficiency of hydroacoustic energy under different conditions
- Comparison between observed reflection and propagation loss and theoretical models

OBJECTIVES

This project is designed to improve discrimination of underwater seismic events and improve location of hydroacoustic sources in or just above the water column. Improvement in discrimination will be achieved by empirically quantifying and theoretically modeling high-frequency (greater than 30–50 Hz) loss of hydroacoustic energy propagating in the Sound Fixing and Ranging (SOFAR) channel from reflections off coastlines and interaction with bathymetric obstacles along path. We will also use variations in the observed residual amplitudes to identify important environmental factors that most impact high-frequency transmission loss. We will localize coastal reflector locations that will allow for better prediction of the reflected wave field. We will examine the robustness and accuracy of measuring bubble pulses from reflected or highly attenuated signals.

RESEARCH ACCOMPLISHED

We selected the Indian Ocean for this experiment because three hydrophone stations of the International Monitoring System have been installed in that ocean basin (Figure 1) and because abundant earthquakes along the mid-ocean ridges and the Java trench provide natural, surrogate sources to complement the planned explosions (Hanson and Bowman, 2005b). Our experiment will complement the earlier experiments conducted by the Scripps Institution of Oceanography and Lawrence Livermore National Laboratory (LLNL).

In 2001 Scripps and LLNL conducted the first calibration experiment in the Indian Ocean since the new IMS hydrophone stations began operating (Blackman et al., 2004). The experiment was a preliminary test to use various nonexplosive sources, such as airgun arrays and imploding glass spheres, as calibration events. The experiment ran an ocean transect from the Seychelles Islands to Perth, Australia, with 11 locations at which various sources were tested. They conducted a similar calibration experiment in 2003, crossing the Indian Ocean basin from Cape Town, South Africa to the Cocos-Keiling Islands using 2-kg SUS charges in addition to imploding spheres (Blackman et al., 2003; Harben et al., 2004). Both experiments provided data useful for many calibration needs. However, the sources used have limited ability to evaluate station effectiveness or processing approaches as a whole, because the signals generated do not allow for robust coherent processing and evaluation of large explosion discriminates. The chief reason for this is the low signal-to-noise (SNR) received levels at lower frequencies (less than20 Hz). The proposed experiment, with larger sources, will provide higher SNR across the spectrum, including at lower frequencies suitable for coherent signal processing. Our experiment will complement the earlier experiments, because it will produce signals better suited for processing with the large-aperture triad arrays and should also produce observable high-frequency reflected energy.

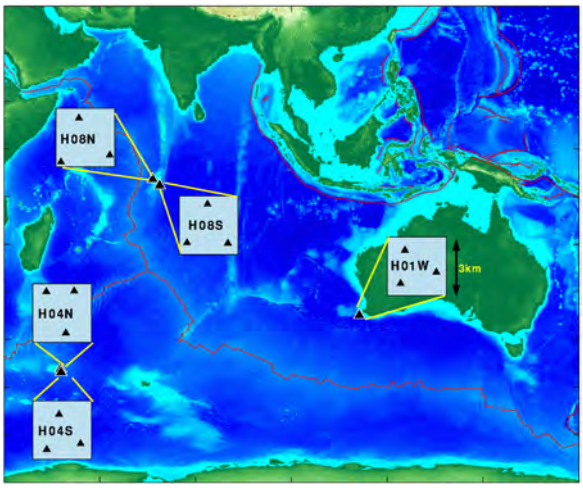

Figure 1. Seafloor bathymetry map with Indian Ocean hydrophone triad stations. There are five triads: Cape Leeuwin, Australia (H01W), Diego Garcia Island North and South (H08N, H08S), and Crozet Island North and South (H04N, H04S). Two elements at Crozet are not currently operational.

Experiment design and plans. We conceived the Indian Ocean experiment with limited geographical scale so that it could be executed with modest, commercially available resources and so that environmental regulations could be addressed in a single jurisdiction. Our preliminary design considers important logistical and practical constraints. These include

- Choice of port,
- Time of year,
- Maximum range from port,
- Maximum total amount of explosives, and
- Maximum source depth.

These logistical considerations are discussed below. Our preliminary designs considered two ports in Western Australia, Fremantle and Dampier (Figure 2). Fremantle is the principal port of Western Australia, near Perth. A ship out of Fremantle would likely be a fishing vessel. This port would have the advantages of accessibility and shorter transit to the experiment site than Dampier. Dampier is the principal town servicing the oil and gas industry in the offshore Northwest Shelf oil fields. A ship out of Dampier would more likely be a vessel designed for exploration or oil field servicing. Such a ship could probably better handle and carry more explosives, but ship time would be more expensive, and the experiment would require a longer transit. We selected Dampier as the base for the experiment because we were able to identify suitable ships to conduct the experiment there, but not in Fremantle.

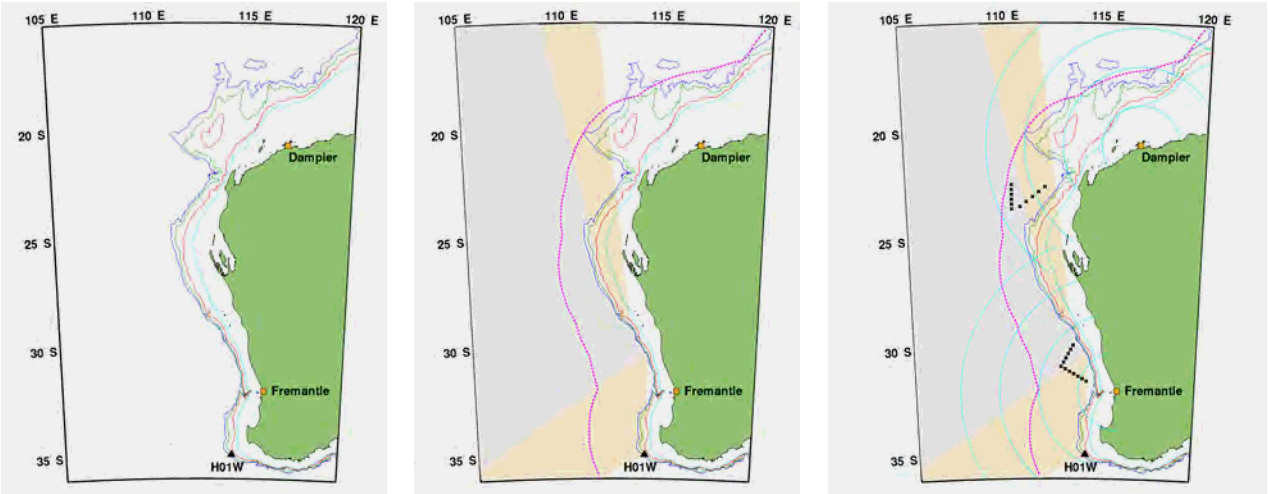

Figure 2. Bathymetry on the western continental slope of Australia. a) Contours are placed at 500-m intervals covering depths of 500 to 2000 m; the red contour represents a depth of 1000 m. b) Grey depicts areas with relatively clear paths to the three hydrophone stations. Beige represents the area with paths that intersect significant shallow waters to one or more stations. The blockage is based on approximate bathymetric boundaries and does not include small seamounts. The map also includes an approximation of the Australia's Exclusive Economic Zone (dashed line). c) Two potential experiment layouts. The black crosses represent shot locations. Semi-circles indicate distances from each port in steps of 200 km.

Related to the choice of home port is the maximum range from port. Our preliminary design constrains this range to 800 km. This is based on a 6-day cruise, allowing 3 days of round-trip transit time and 3 days of conducting the actual experiment. The range will also be affected by the state of the sea, and we anticipate conducting the experiment during the summer months to minimize chances of large swells.

Most vessels expected to be available for charter operate principally within Australia's Exclusive Economic Zone (EEZ). The boundary of the EEZ is shown in purple in the right panel of Figure 2. For these vessels, travel into international waters would require a ship to carry more insurance and a larger crew, thus increasing the experiment's cost. Our preliminary designs have thus been constrained to lie within Australia's EEZ. However, we retain the option during the design and planning phase to enter international waters if our scientific objectives cannot be met otherwise.

Portable explosives magazines available in Western Australia have maximum capacity of 500 kg. Some vessels could only accommodate a single magazine, whereas a larger vessel from Dampier might be able to carry two or more. Our preliminary designs assume a maximum of 1000 kg of explosives available for the experiment. The experiment layout will likely consist of approximately a dozen shot locations. The shots will be arranged to provide variations in direct path blockage and to provide a variety of event/reflector/station geometries. Various depths and shot sizes will be used to achieve desired SNR levels across different frequency bands while maximizing the total number of shots. The individual shot sizes will range from 20 to 80 kg.

We anticipate lowering explosives with a cable, and therefore, there is a practical limit on the maximum depth at which the sources may be deployed. Our preliminary design assumes a maximum source depth of 400 m. Important scientific considerations to be determined during the detailed experiment design include the following:

- Signal transmission loss to IMS stations
- Water depth
- Source yield and depth

Each of these scientific considerations is discussed here. The left panel in Figure 2 shows the bathymetry surrounding Western Australia that is less than 2000 m deep. In the center panel of Figure 2, an approximate boundary of the EEZ is shown, and a two-tone shading is used to indicate areas that have relatively clear paths to all three hydrophone stations (gray) and areas that are partially blocked to one or more stations (beige). Here, a clear path is defined as not crossing shallow waters (less than 1000 m) over a significant portion of the path length. Partially blocked paths are defined as paths with a significant portion that crosses shallow water to one or more stations. The shading does not take into account small features such as mid-ocean seamounts that will cause localized blockage.

Our preliminary designs constrain the experiment to deep-water locations (greater than 4000 m) to avoid complicating the direct arrival from near-source reverberations and/or reflections. Because the explosions are planned to occur at depth (i.e., in the sound channel), we do not have to rely on near-source bathymetry to horizontally scatter acoustic energy. This will simplify our analysis and make reflected energy easier to distinguish.

Source characteristics for an explosion are dependent on yield and depth. A small explosion (e.g., a 2-kg. SUS charge) might be enough to produce observable signal levels at high frequencies for the direct arrival. However, a larger explosive yield is needed to produce sufficient energy in the low-frequency bands and to produce observable high-frequency reflections. The left panel in Figure 3 shows source level (SL) as a function of depth for different size explosions. Near the surface, the SL is nearly constant with depth, but below a "corner," SL decreases rapidly with depth. Keeping sources shallow produces the largest source levels, but because of the sound channel (Figure 4), deeper sources will suffer less transmission loss. Thus, there is an optimal depth that maximizes the received levels for a given frequency band for a given yield. The right panel in Figure 3 shows preliminary predicted SNR at the Diego Garcia South triad for two frequency bands.

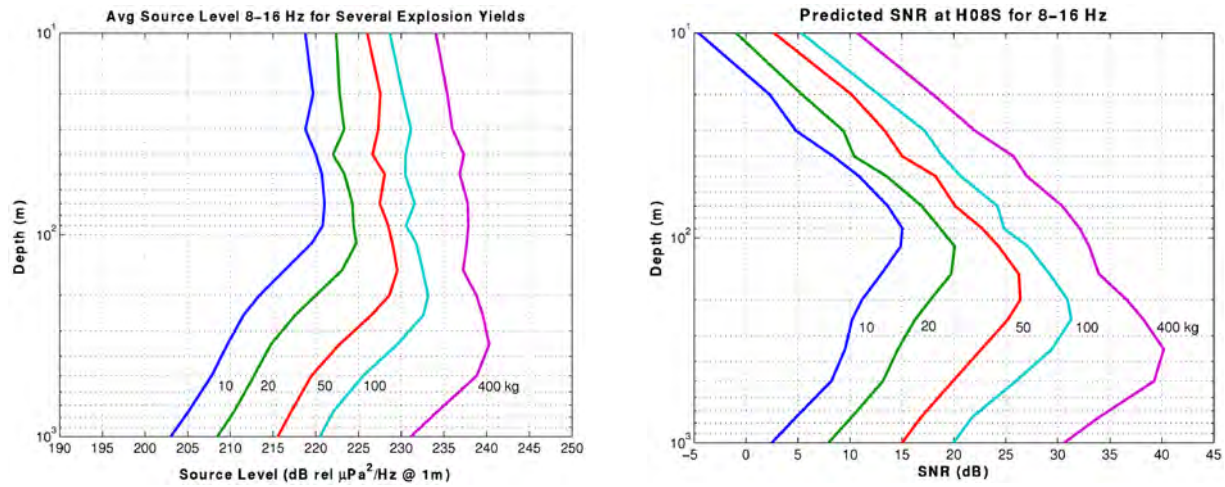

Figure 3. The predicted average SL and SNR for a suite of different yield explosions in the 8–16 Hz band. Near the surface, the source level is approximately constant with depth. Below some critical depth, which is a function of frequency and yield, the SL rapidly decreases. The SNR is predicted for Diego Garcia using the source level, an average noise level at Diego Garcia South, and a predicted transmission loss. The source level and transmission loss are functions of depth and display maxima that vary with yield and frequency. This estimation does not include any processor gain, which will effectively increase the SNR level in all the curves. Higher frequencies will have larger SNR because the explosives produce more high-frequency energy, and the ambient noise at the hydrophone stations is lower at the higher frequencies.

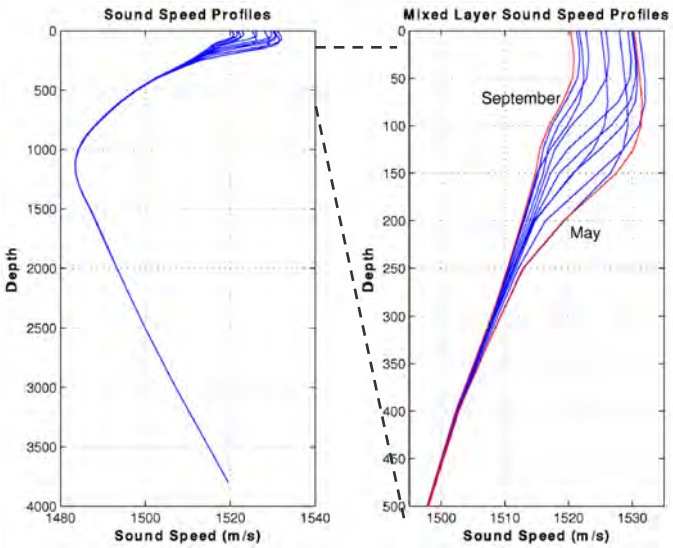

Figure 4. Sound speed profiles at the experiment location that were considered near Fremantle for each month of the year. The right panel is an enlargement of the left panel and shows the upper 500 m. For efficient long-range propagation the shots need to be below the mixed layer, which is the layer at the ocean's surface where the sound speed is nearly constant with depth. This is deepest in May (over 100 m) and shallowest in September (about 50 m). This thickness can vary from year to year.

Experiment phases. The project consists of three phases. We are currently in the first phase, which involves experiment design, planning, and modeling. We will refine our preliminary designs (including finalizing the experiment site, and defining the pattern, sizes, and deployment depths for shots) by analyzing high-frequency propagation and reflection losses using previously recorded data from natural and man-made sources. We will plan the logistics for execution of the experiment and will prepare and support applications for all required government permits.

The second project phase will execute the field experiment itself. We will assemble personnel, equipment, explosives, and a marine vessel at the port of debarkation and transit to the experiment site. We will then deploy and detonate explosive charges and measure shot parameters.

In the third project phase, we will analyze and interpret data from the IMS hydrophone stations. We will improve knowledge of underwater event discrimination by determining the loss of high-frequency energy during reflection from coastlines and during propagation across partially blocked portions of the ocean's sound channel. We will also establish the ability to characterize events using reflected arrivals.

Anticipated products. These are the principal products of this project:

- Unique ground-truth data set from in-water explosions comprising accurate source parameters and waveforms from IMS hydrophone stations
- Quantitative estimates of high-frequency reflection and propagation efficiency of hydroacoustic energy under different conditions
- Comparison between observed reflection and propagation loss and theoretical models

Explosion observations. Historical and recent recordings of underwater explosions have guided the design of our experiment in the Indian Ocean. Large underwater explosions are uncommon, so it is important to fully exploit those that have been well recorded. Here we present examples of explosions in the Indian Ocean in 2003 and 2004 recorded on IMS hydrophone stations and in the Pacific Ocean in 1996 recorded on the legacy Wake Island hydrophone station.

Figure 5 shows a spectrogram for two 2-kg SUS charges from the Scripps/LLNL 2003 Indian Ocean experiment (Blackman et al., 2003; Harben et al., 2004). The SUS charges produced impulsive signals with fairly large SNR at high frequency. Time delays across the hydrophones of the H08S triad are consistent with back azimuths to the sources, but because of the limited frequency range of the signal and the 2-km spacing of the hydrophones, coherent processing is not effective. This makes it difficult to identify reflections (if present at all) or to precisely estimate signal-back azimuth. Bubbles pulses are not evident in these signals (Figure 5), which is due to the small source and deep detonation. Our experiment will complement the earlier experiments, because it will produce signals better suited for processing with the large-aperture triad arrays. Our experiment should also produce signals that include observable high-frequency reflected energy.

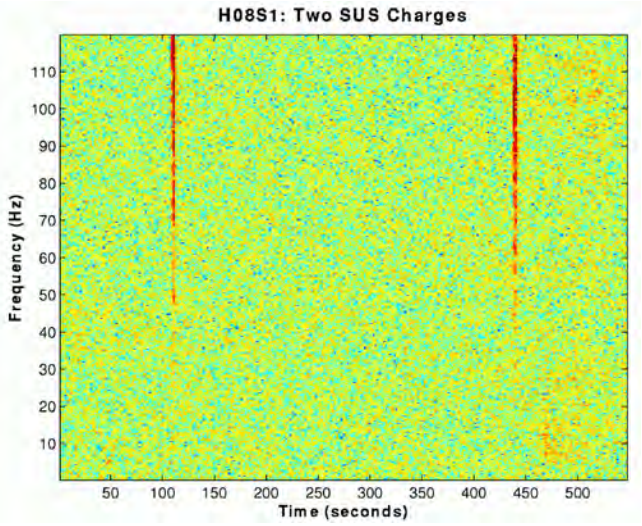

Figure 5. Spectrogram from H08S1 for two sources from the 2003 Indian Ocean experiment (Blackman et al., 2003). Sources were 1300 km south of H08S at depths of 915 m and 610 m, respectively. The signals have high SNR above 60 Hz and negligible energy below 30 Hz.

Figure 6 illustrates the high-frequency energy for an explosion of 20 kg at 3000 km distance in the Pacific Ocean. For large amplitude signals, this high-frequency content can be used to discriminate underwater explosions from other sources. (For smaller amplitude signals, the high-frequency content may also result from other

causes, such as ice cracking at the Antarctic margin [Hanson and Bowman, 2005a] or air guns used for seismic reflection surveys [Blackman et al., 2004]).

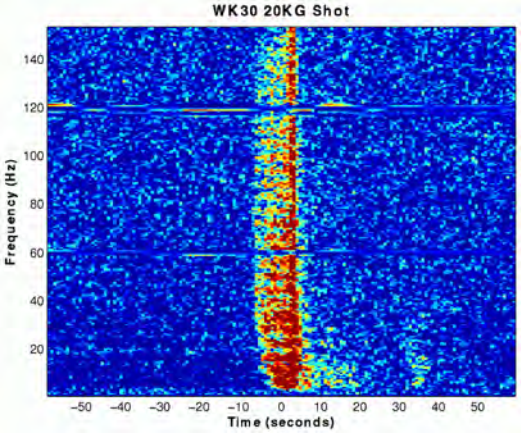

Figure 6. Spectrogram of a 20-kg explosion recorded at the WK30 hydrophone near Wake Island (Brumbaugh and Le Bras, 1998). Note the abundant energy content at frequencies up to 150 Hz. A faint signal 30 seconds after the main arrival at frequencies of 10-20 Hz is interpreted as a reflection, possibly off the Japanese coastline, based on cepstral analysis.

An important question for nuclear test monitoring is whether reflected signals, or the lack thereof, can be used for discrimination of underwater events. This question reduces to how much signal bandwidth and how much coherent signal is preserved upon reflection that can be used for discrimination. Figure 7 shows the spectra for direct and reflected signals from a submarine earthquake and a 400-kg explosion. The direct signal from the earthquake does not have sufficient high-frequency energy to determine whether such energy is preserved upon reflection. To answer this question will require high-frequency sources, such as the explosive sources proposed for our experiment.

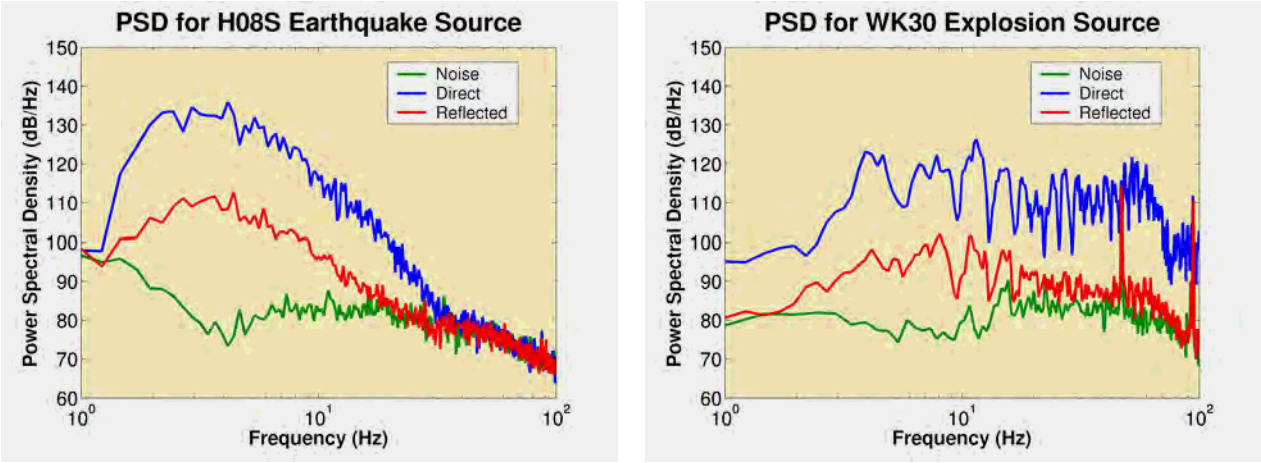

Figure 7. Spectra of direct and reflected signals from an earthquake (left) and a 400-kg explosion (right). The m_b 5.9 earthquake occurred along the Java trench and was recorded at Diego Garcia (H08S). The explosion was part of a Japanese refraction experiment in 1996 that was recorded at the Wake Island hydrophone station (WK30). Note that the refraction experiment was designed to propagate the hydroacoustic energy vertically and not horizontally over ocean basin distances. Our experiment will more efficiently transmit the energy into the SOFAR channel.

Two explosions in the Bay of Bengal were well recorded by IMS hydrophone stations on May 5, 2004 (Graeber and Firbas, 2005; Spiliopoulos and Jepsen, 2005; see Table 1). These were interpreted as explosions based on their high-frequency content and spectral scalloping. The two explosions were separated by about 45 minutes. Spectrograms at H01W for the two explosions in Figure 8 show that the direct signal, at 1800 seconds in these plots, is broadband, with energy from 5 Hz to more than 120 Hz. For the first event (left panel), a second signal is seen clearly 50 seconds after the direct arrival in the frequency band 10 to 80 Hz. For the second event (right panel), a weaker signal is seen at the same time in the frequency band 30 to 80 Hz. These are interpreted as reflected signals. A weaker signal around 1820 seconds is also likely to be a reflected signal.

Table 1. Attributes of Bay of Bengal explosions (Graeber pers. comm., 2005).

Time	Latitude	Longitude
2004 May 5 1528:04 UT	10.14	89.07
2004 May 5 1616:46 UT	10.01	89.50

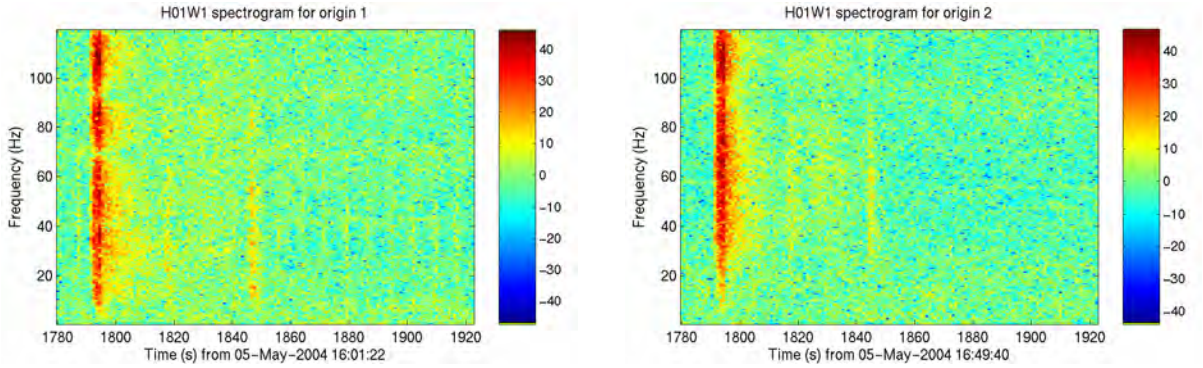

Figure 8. Spectrograms from H01W1 of Bay of Bengal events on May 5, 2004, at 1528 (left) and 1616 (right) UT. The direct signal near 1800 seconds has high signal-to-noise from 10 to 120 Hz for both events. The reflected signal near 1850 seconds is stronger for the first event, particularly between 10 and 60 Hz, but also seen for the second event between 30 and 60 Hz. A weaker signal near 1820 seconds may also be a reflection.

Analysis using all three triad elements provides an estimate of the arrival of coherent energy from any azimuth. For the first event, coherent energy is seen arriving at 1800 seconds from 327.9° and at 1850 seconds from 352.0°. We interpret these to be direct and reflected signals, respectively. The weaker signal at 1820 seconds did not have sufficient signal strength for estimation of its azimuth. Using the arrival time of the signals and the azimuth of arrival, the reflection point can be estimated (Hanson, et al., 2002; Hanson and Bowman 2005a). This is shown in Figure 9 for the larger reflection observed at Cape Leeuwin. The yellow circle indicates the explosion location estimated from the direct arrivals. The white square is the estimated reflector location using the measured back azimuth, the arrival time, and the event location. The reflection point coincides with the 1000 m bathymetric contour surrounding the Australian continental shelf. Reflections are also observed at H04N and H08S.

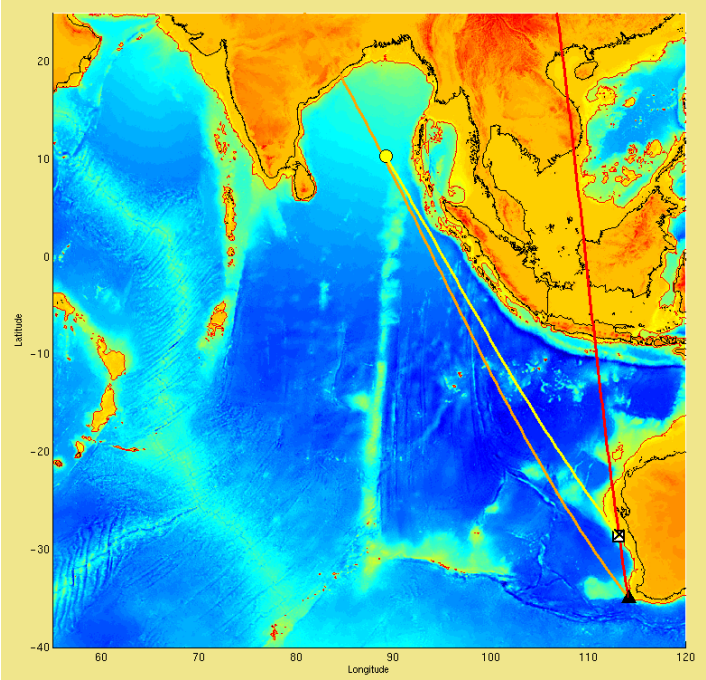

Figure 9. Reflector location from the first Bay of Bengal event on May 5, 2004, at 1528 UT observed at H01W (black triangle) in Australia. The orange line extending northwest from H01W shows the back-azimuth of the direct signal based on coherent triad processing. The red line extending north from the station shows the back-azimuth of the reflected signal. The yellow circle shows the location estimate derived from the direct arrivals. The square with a cross shows the estimated reflection point using the back-azimuth and arrival time of the reflected signal. It coincides with the 1000-m bathymetry contour (thin red surrounding landmasses) providing confidence that it is a true reflection.

The results of spectral and bubble-pulse analysis for the first Bay of Bengal event for four hydrophone stations are shown in Figure 10. For H01W (upper left panel), results are shown for both the direct and reflected arrivals. Similar spectral scalloping is seen for each of the stations. The direct signal is above the noise level from 5 to 120 Hz for H01W, H04N, and H08S. The low-freqency noise increases dramatically at H04S and obscures the signal below 10 Hz. The reflected signal at H01W is 5 to 10 dB above the noise level from 5 to 50 Hz but converges with the noise near 90 Hz. The bubble-pulse analysis uses an estimate of the autocorrelation. The first peak with a lag greater than zero corresponds to the first bubble pulse. The direct arrivals have consistent delay times with an average of 37.3 msec. This corresponds to about nine samples for these hydrophones. The reflected signals have autocorrelations that agree with the direct arrivals but are not as distinct. This is due to their lower SNR and limited bandwidth. The second explosion has an average delay of 14.5 msec, which corresponds to only four samples.

The bubble-pulse period can be used to determine a depth/yield trade-off curve. This is shown for the two explosions in Figure 11. The amplitudes of the two explosions are very similar. Assuming the yield is the same for the two explosions, the second explosion would have to be thee times as deep as the first. This is consistent with the observed frequency content of the signals. The first explosion has more low-frequency energy and less high-frequency energy than the second explosion as predicted from Figure 3. Depths between 50 and 1000 m correspond to yields from less than 1 kg to 100 kg. A transmission loss analysis could be conducted to constrain the yield, and consequently the depth, of the sources.

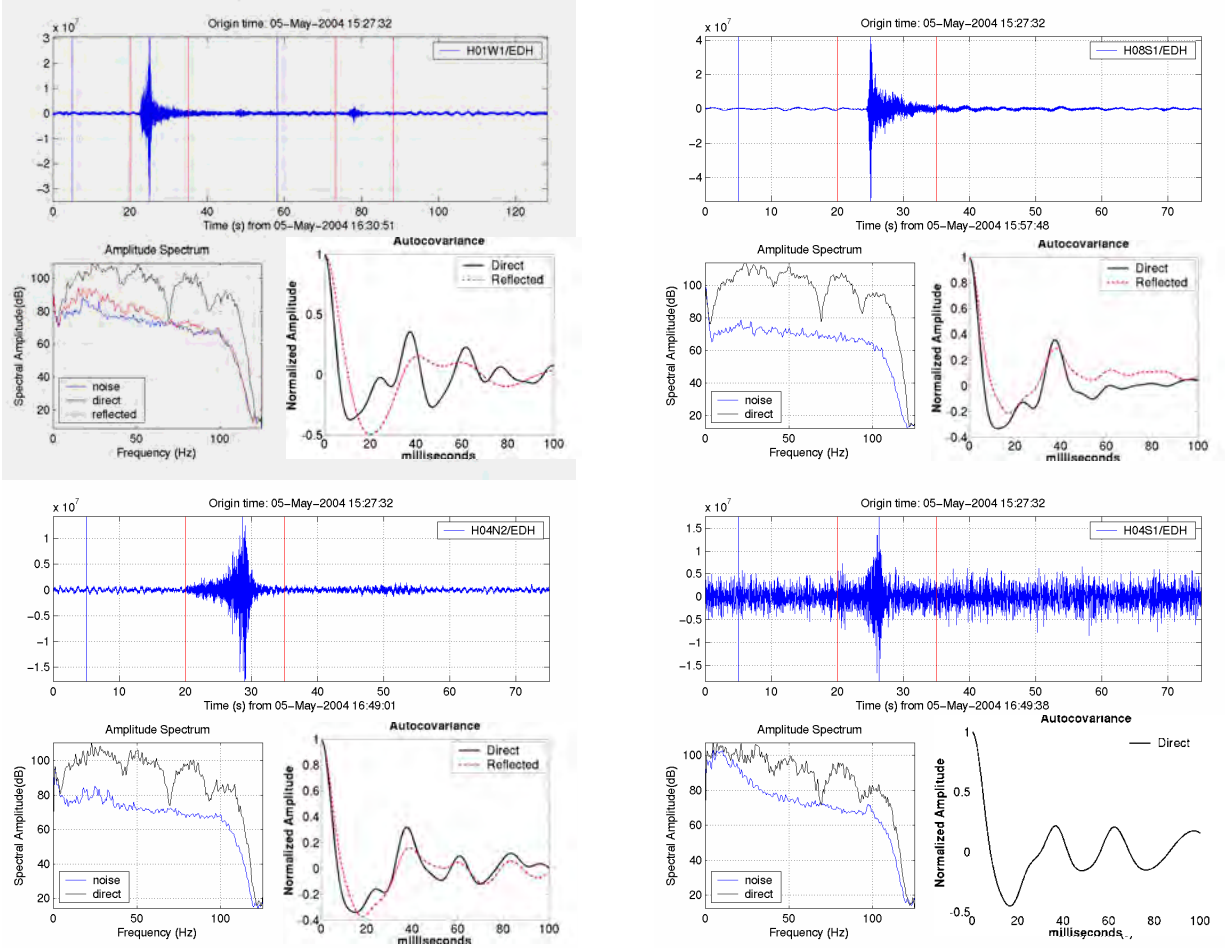

Figure 10. Spectral and bubble-pulse analysis of the first Bay of Bengal event on May 5, 2004 at 1528 UT. Clockwise from upper left, the stations are H01W, H08S, H04S, and H04N. For each station, the figure shows the unfiltered hydrophone waveforms, the amplitude spectrum, and autocovariance. Vertical red lines in the waveform plots represent the windows used for the signal spectra, while the blue vertical lines show the start of the noise windows, which end at the first vertical red line in each trace plot.

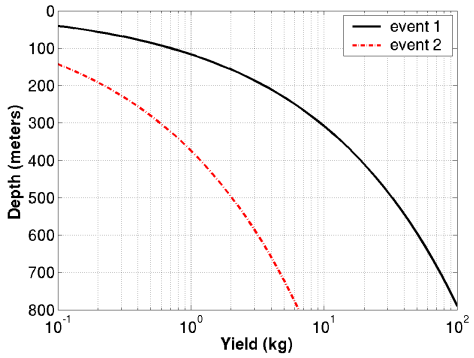

Figure 11. Depth/yield trade-off for the bubble-pulse delay times observed for the two explosions. The delay times are 37.3 and 14.5 msec for the first and second explosions, respectively. If the yields of the two explosions are equivalent, then the depth of the second explosion is approximately three times deeper than the first.

CONCLUSION AND RECOMMENDATION

A modest, but strategically important, experiment is being planned for next year off the western coast of Australia. The experiment is designed to quantify frequency dependent attenuation of partially blocked and reflected signals. A candidate port has been selected, Dampier. Preliminary shot locations have been selected that provide a variety of unblocked and partially blocked paths to the various hydrophone stations in the Indian Ocean. Numerous logistical and scientific issues with concern to the experiment have been or are being addressed.

Observations from previous experiments and sources of opportunity indicate that modest size explosives are effective in producing broadband signals with sufficient energy to have observable reflections. The frequency content of the signals is a function of depth and yield. Bubble-pulse periods can be used to identify reflected signals. Reflections with sufficient low-frequency energy can be located via coherent array processing. We conclude that moderate size explosions offshore of Western Australia will be effective in determining the loss of high-frequency energy during reflection from coastlines and propagation across partially blocked portions of the ocean's sound channel.

ACKNOWLEDGEMENTS

We thank Colin Reasoner for analysis of the 2004 Bay of Bengal explosions.

REFERENCES

Blackman, D.K., J.A. Mercer, R. Andrew, C.D. de Groot-Hedlin, and P. Harben (2003), Indian Ocean calibration tests: Cape Town-Cocos Keeling, in *Proceedings of the 25th Seismic Research Review–Nuclear Explosion Monitoring: Building the Knowledge Base*, Vol. 2, 517-523.

Blackman, D.K., C. de Groot-Hedlin, P. Harben, A. Sauter, and J.A. Orcutt (2004), Testing low/very low frequency acoustic sources for basin-wide propagation in the Indian Ocean , *J. Acoust. Soc. Am.*: 116, 2057.

Brumbaugh, D. and R. Le Bras (1998), Hydroacoustic signals from a ground-truth data set of marine explosions, SAIC Report, SAIC-98/3008.

Graeber, F. and P. Firbas (2005), Recent developments in hydroacoustic data processing at the IDC, Hydroacoustic Workshop, Victoria, BC, May 1-5, 2005.

Hanson, J., J.R. Bowman, J.R., and G. Beall (2002), An advanced concept demonstration for monitoring the Indian Ocean, in *Proceedings of the 24th Seismic Research Review–Nuclear Explosion Monitoring: Innovation and Integration*, Vol. 2, pp. 632-642.

Hanson, J.A. and J.R. Bowman (2005a), Methods for monitoring hydroacoustic events using direct and reflected T waves in the Indian Ocean, *J. Geophys. Res*., in press.

Hanson, J.A. and J.R. Bowman (2005b), Indian Ocean Ridge seismicity observed with a permanent hydroacoustic network, *Geophys. Res. Lett*., *L06301*, 10.1029/2004GL021931.

Harben, P.E., E. Matzel, D.K. Blackman, and D. Clarke (2004), Hydroacoustic blockage calibration for discrimination: Results from 2003 Indian Ocean cruise, and imploding sphere calibration source development, in *Proceedings of the 26th Seismic Research Review: Trends in Nuclear Explosion Monitoring*, Vol. 2, pp. 553-559.

Spiliopoulos, S. and D. Jepsen (2005), Studies in the Indian Ocean: Preliminary phase identification and synergies with the seismic network, Hydroacoustic Workshop, Victoria, BC, May 1–5, 2005.

MODEL-BASED HYDROACOUSTIC BLOCKAGE ASSESSMENT AND DEVELOPMENT OF AN EXPLOSIVE SOURCE DATABASE

Eric Matzel, Abe L. Ramirez, and Philip E. Harben

Lawrence Livermore National Laboratory

Sponsored by National Nuclear Security Administration
Office of Nonproliferation Research and Engineering
Office of Defense Nuclear Nonproliferation

Contract No. W-7405-ENG-48

ABSTRACT

We are continuing the development of the Hydroacoustic Blockage Assessment Tool (HABAT) which is designed for use by analysts to predict which hydroacoustic monitoring stations can be used in discrimination analysis for any particular event. The research involves two approaches (1) model-based assessment of blockage, and (2) ground-truth data-based assessment of blockage. The tool presents the analyst with a map of the world, and plots raypath blockages from stations to sources. The analyst inputs source locations and blockage criteria, and the tool returns a list of blockage status from all source locations to all hydroacoustic stations. We are currently using the tool in an assessment of blockage criteria for simple direct-path arrivals. Hydroacoustic data, predominantly from earthquake sources, are read in and assessed for blockage at all available stations. Several measures are taken. First, can the event be observed at a station above background noise? Second, can we establish backazimuth from the station to the source? Third, how large is the decibel drop at one station relative to other stations? These observational results are then compared with model estimates to identify the best set of blockage criteria and used to create a set of blockage maps for each station. The model-based estimates are currently limited by the coarse bathymetry of existing databases and by the limitations inherent in the raytrace method. In collaboration with BBN Inc., the Hydroacoustic Coverage Assessment Model (HydroCAM) that generates the blockage files that serve as input to HABAT, is being extended to include high-resolution bathymetry databases in key areas that increase model-based blockage assessment reliability. An important aspect of this capability is to eventually include reflected T-phases where they reliably occur and to identify the associated reflectors.

To assess how well any given hydroacoustic discriminant works in separating earthquake and in-water explosion populations it is necessary to have both a database of reference earthquake events and of reference in-water explosive events. Although reference earthquake events are readily available, explosive reference events are not. Consequently, building an in-water explosion reference database requires the compilation of events from many sources spanning a long period of time. We have developed a database of small implosive and explosive reference events from the 2003 Indian Ocean Cruise data. These events were recorded at some or all of the IMS Indian Ocean hydroacoustic stations: Diego Garcia, Cape Leeuwin, and Crozet Island. We have also reviewed many historical large in-water explosions and identified five that have adequate source information and can be positively associated to the hydrophone recordings. The five events are: Cannikin, Longshot, CHASE-3, CHASE-5, and IITRI-1. Of these, the first two are nuclear tests on land but near water. The latter three are in-water conventional explosive events with yields from ten to hundreds of tons TNT equivalent.

OBJECTIVE

The objective of this research is to enhance discrimination capabilities for events located in the world's oceans. Two research and development efforts are needed to achieve this: 1) improvement in discrimination algorithms and their joint statistical application to events, and 2) development of an automated and accurate blockage prediction capability that will identify all stations and phases (direct and reflected) from a given event that will have adequate signal to be used in a discrimination analysis. The strategy for improving blockage prediction in the world's oceans is to improve model-based prediction of blockage and to develop a ground-truth database of reference events to assess blockage. Currently, research is focused on the development of a blockage assessment software tool. The tool is envisioned to develop into a sophisticated and unifying package that optimally and automatically assesses both model and data based blockage predictions in all ocean basins, for all National Data Center (NDC) stations, and accounting for reflected phases (Pulli et al., 2000). Currently, we have focused our efforts on the Diego Garcia, Cape Leeuwin and Crozet Island hydroacoustic stations in the Indian Ocean.

RESEARCH ACCOMPLISHED

We have continued the development of the Hydroacoustic Blockage Assessment Tool (HABAT) which employs a model-based approach to assess blockage from source events to hydroacoustic monitoring stations. HABAT is a stand-alone, platform independent, JAVA tool which allows the user to predict which hydroacoustic monitoring stations can be used in discrimination analysis for any particular event. The code uses the HydroCAM output "path", travel time and attenuation files as input. The "path" files can be either source-centered, indicating the area illuminated by the source, or station-centered, indicating the area visible to the station. The user then defines a series of points of interest, typically stations for the source-centered path case, or potential sources for the station-centered case.

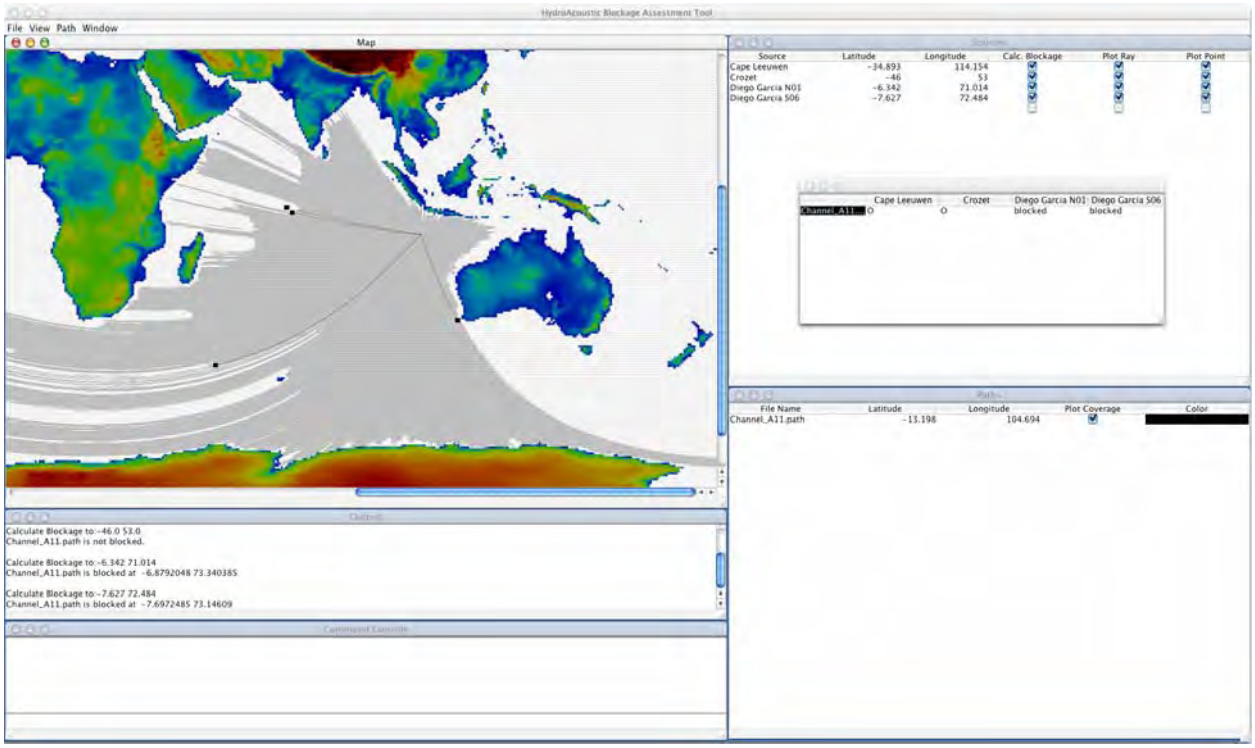

Figure 1. The HABAT tool user interface, showing the coverage map for source (A11) to the Cape Leeuwin, Crozet Island, Diego Garcia North, Diego Garcia South hydroacoustic stations in the Indian Ocean.

The user interface to the blockage assessment tool is shown in Figure 1. The tool is divided into several panels, including a scalable map of all input sources and monitoring stations with optional plotting of the coverage estimate, raypaths, travel time and attenuation contours. In the example above, a coverage map for source location (A11) from

the 2003 Indian Ocean cruise is plotted, along with raypaths between the source and the Indian Ocean stations (Diego Garcia, Cape Leeuwin, and Crozet Island). The panel below the map shows an assessment of blockage to each station from a given source in list format. The rightmost panels are editable tables of station point locations (top) and source path locations (bottom). The tool provides an analysis for specific user-specified blockage criteria given in depth cutoff criteria. A 1,000 m cutoff criteria, for example, means that a specific source-receiver path is considered blocked if bathymetry above 1,000 m is encountered anywhere along the path. The coverage estimate shown in Figure 1 was based on the simple assumption that the source is blocked if the bathymetry cuts the sound channel axis. For that criteria, the prediction is that the source will be blocked at both Diego Garcia North and South, but visible at Cape Leeuwin and Crozet.

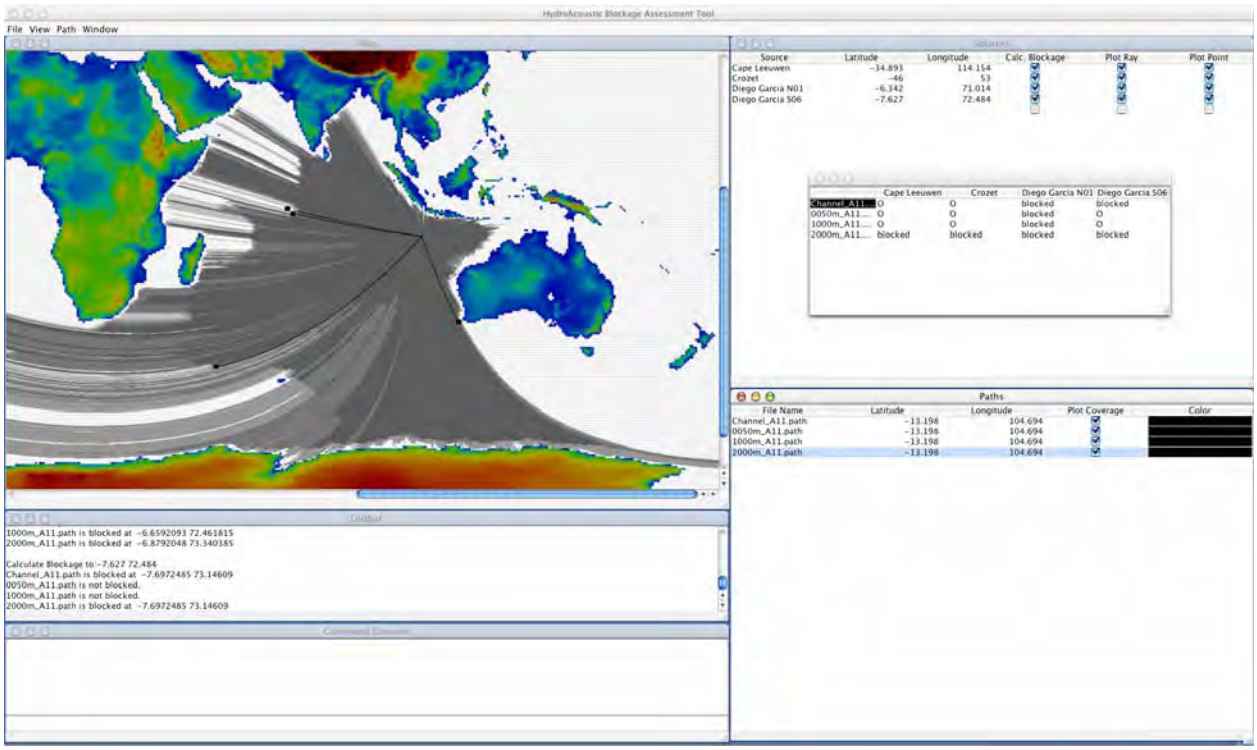

Figure 2. The user interface showing coverage maps for multiple blockage criteria. Source (A11) to Cape Leeuwin, Crozet Island, Diego Garcia North, Diego Garcia South.

Figure 2 shows the how the blockage prediction changes for based on different blockage criteria. In this case, path files produced by HydroCAM were based on a number of cutoff criteria from 2,000 m to sea level. In general, more blocked paths are predicted with deeper cutoff criteria. The tool is written so that an analyst can interact with multiple files simultaneously, allowing for comparison and analysis of multiple sources, stations, and blockage criteria. The coverage maps, raypaths, station and source locations can all be plotted and evaluated together or individually as desired.

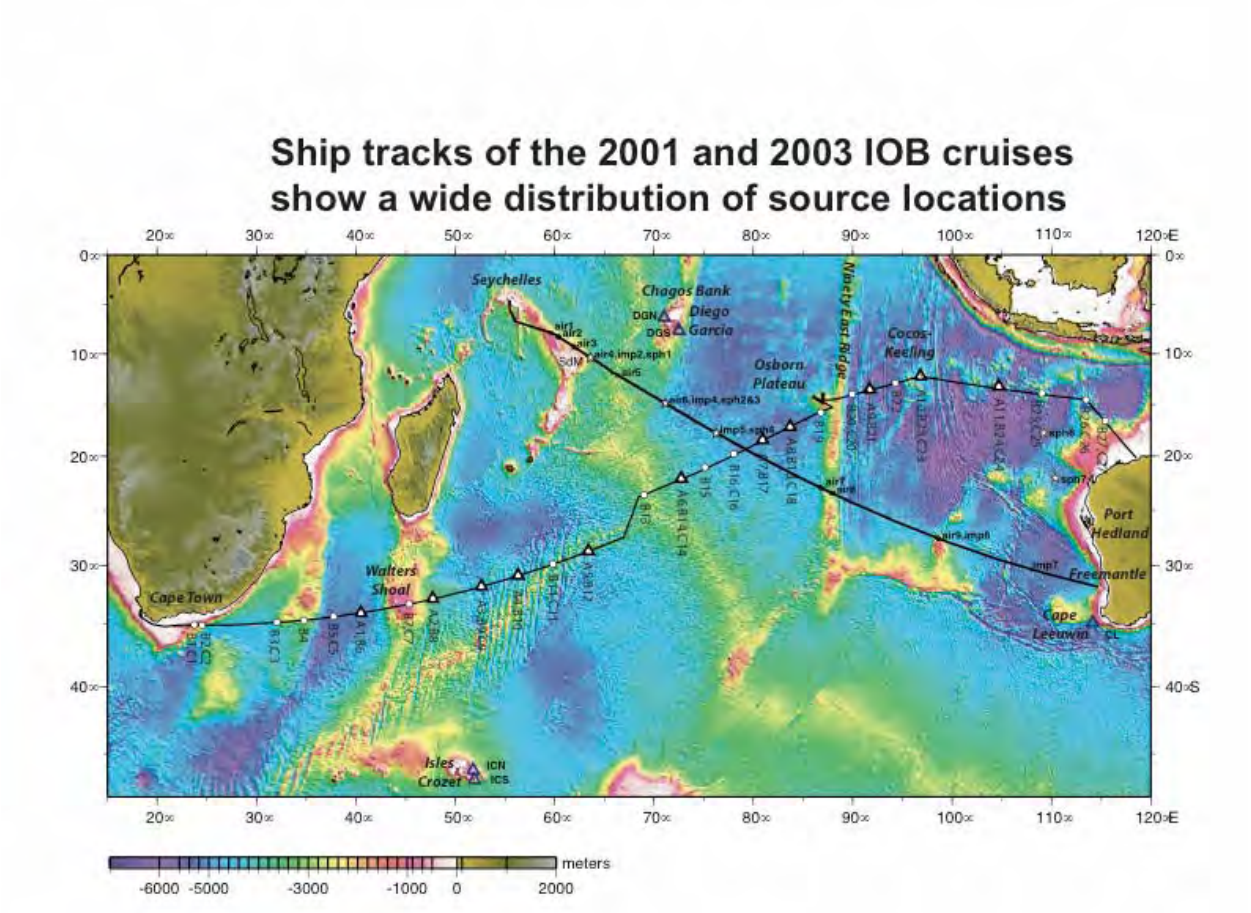

Figure 3. The Indian Ocean basin map shows the ship track of the 2001 cruise (Seychelles –Freemantle) and the 2003 cruise (Cape Town – Darwin) and the locations of all SUS, sphere, and airgun sources.

In order to evaluate blockage criteria we need to compare the model-based estimates to actual measurements. We've begun to address this using data from the 2003 Indian Ocean cruise. The 2003 cruise sailed along a track from Cape Town, South Africa to Darwin, Australia (Harben et al., 2004; Figure 3). The experiment resulted in 13 ground truth events which were detected at 1 or more of the hydroacoustic stations, including 40-50 individual waveforms of both SUS and imploding sphere sources. We measured the spectra from each of the explosive source charges at each of the Indian Ocean stations (Diego Garcia North and South, Cape Leeuwin, and Crozet Island). Figure 4 shows the observation of the SUS source from location A07 at stations DGN and DGS. Note that the signal spectra exceeds pre-event noise levels for both stations at frequencies above 30 Hz., and that the true and measured source-receiver backazimuths match within a few degrees, verifying that this source was detected at both stations. Because a non-detection of a source could be due either to blockage along the source-receiver path or attenuation of the signal over distance, it's helpful to have measurements at several stations to compare with one another. DGN and DGS are an excellent pair of stations to evaluate blockage criteria, because they are located close to one another, but are in a region with significant bathymetric features which result in very different blockage predictions for each. Thus, an event which is observed at one site should be observed at the other, unless there is a true blockage along the path. This allows us to evaluate blockage as a function of frequency and bathymetry. This is illustrated in Figure 5 for the SUS source from location A11.

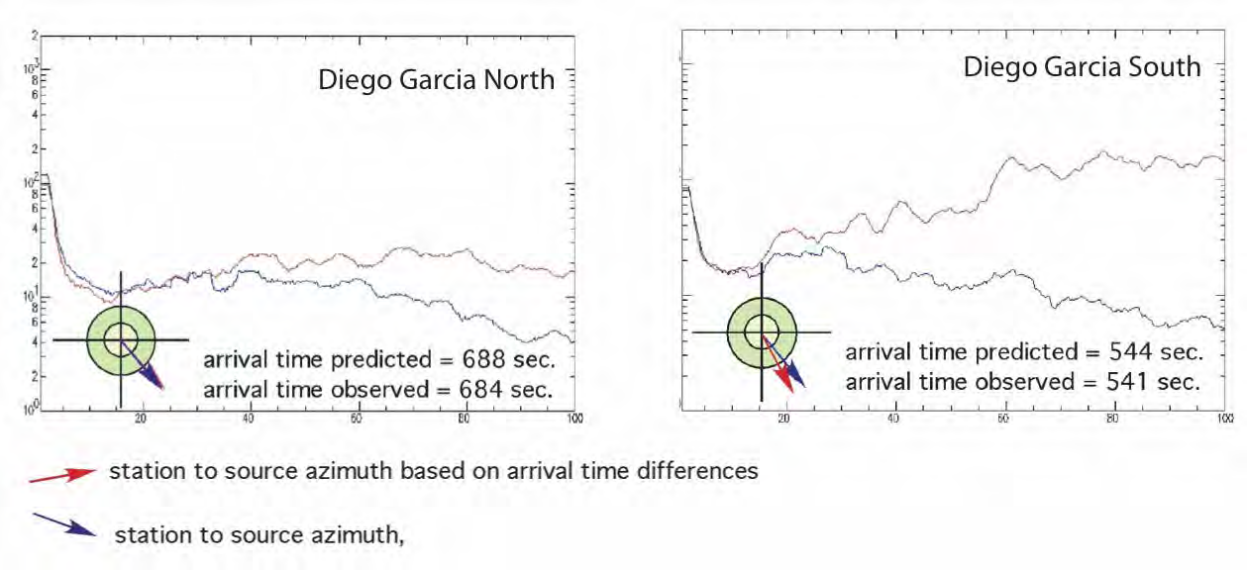

Figure 4. Spectra of the signal (red) and pre-event noise levels (blue) for the A07 SUS charge source at the Diego Garcia North and South hydroacoustic monitoring stations. The horizontal scale is frequency in Hz.

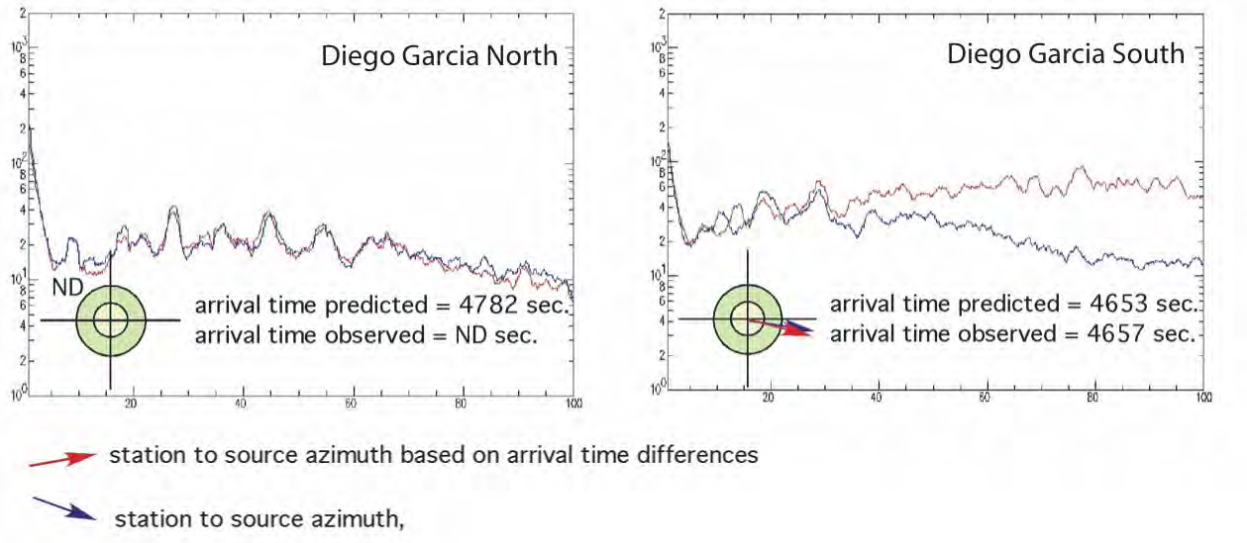

Figure 5. Spectra of the signal (red) and pre-event noise levels (blue) for the A11 SUS charge source at the Diego Garcia North and South hydroacoustic monitoring stations. The horizontal scale is frequency in Hz.

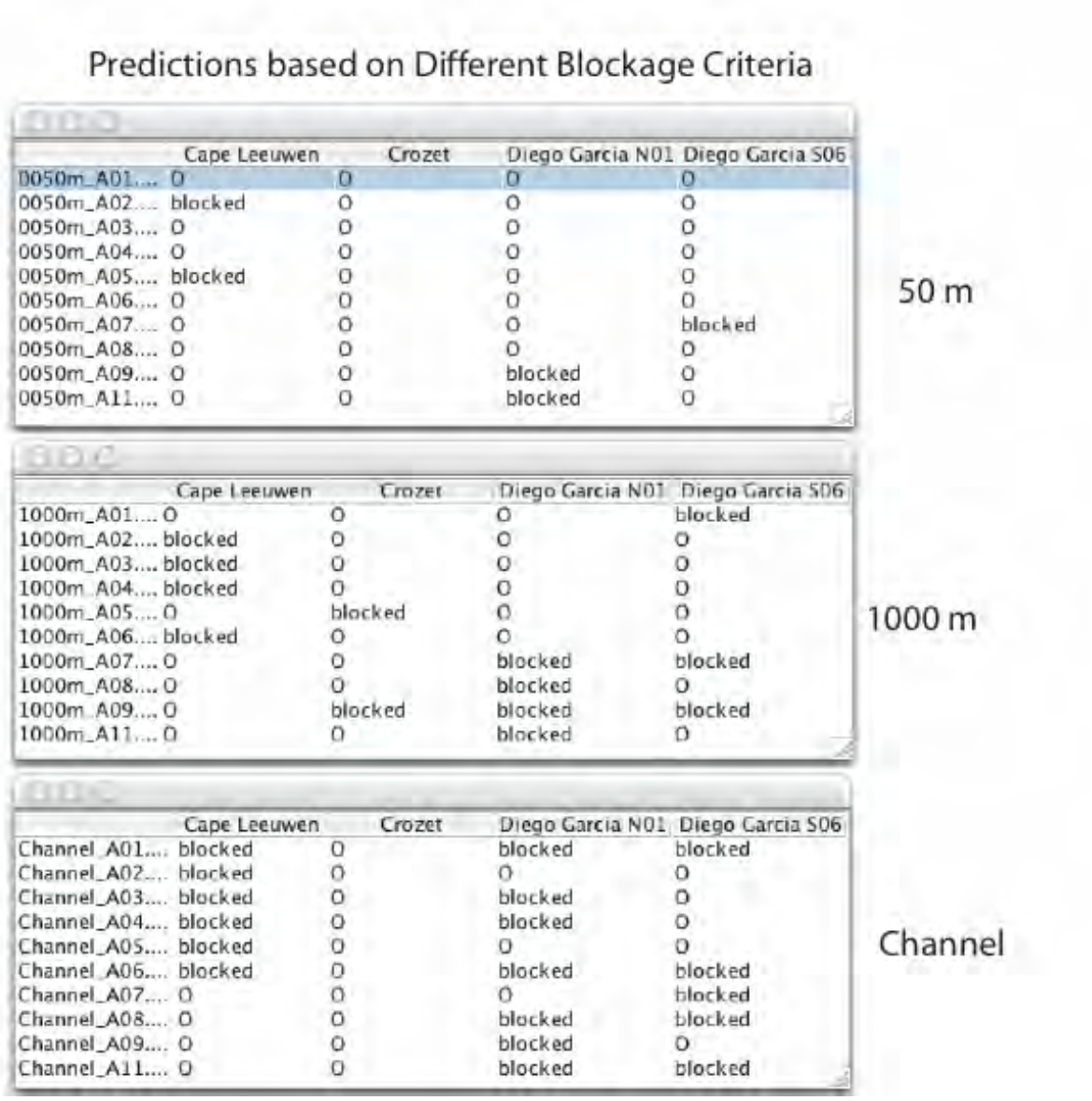

	Cape Leeuwen	Crozet	Diego Garcia N01	Diego Garcia S06
0050m_A01....	0	0	0	0
0050m_A02....	blocked	0	0	0
0050m_A03....	0	0	0	0
0050m_A04....	0	0	0	0
0050m_A05....	blocked	0	0	0
0050m_A06....	0	0	0	0
0050m_A07....	0	0	0	blocked
0050m_A08....	0	0	0	0
0050m_A09....	0	0	blocked	0
0050m_A11....	0	0	blocked	0

	Cape Leeuwen	Crozet	Diego Garcia N01	Diego Garcia S06
1000m_A01....	0	0	0	blocked
1000m_A02....	blocked	0	0	0
1000m_A03....	blocked	0	0	0
1000m_A04....	blocked	0	0	0
1000m_A05....	0	blocked	0	0
1000m_A06....	blocked	0	0	0
1000m_A07....	0	0	blocked	blocked
1000m_A08....	0	0	blocked	0
1000m_A09....	0	blocked	blocked	blocked
1000m_A11....	0	0	blocked	0

	Cape Leeuwen	Crozet	Diego Garcia N01	Diego Garcia S06
Channel_A01....	blocked	0	blocked	blocked
Channel_A02....	blocked	0	0	0
Channel_A03....	blocked	0	blocked	0
Channel_A04....	blocked	0	blocked	0
Channel_A05....	blocked	0	0	0
Channel_A06....	blocked	0	blocked	blocked
Channel_A07....	0	0	0	blocked
Channel_A08....	0	0	blocked	blocked
Channel_A09....	0	0	blocked	0
Channel_A11....	0	0	blocked	blocked

Figure 6. Blockage predictions based on various blockage criteria: (top) bathymetry < 50 m, (middle) bathymetry < 1000 m, (bottom) bathymetry cuts the sound channel axis. The names A01-A11, in the first column, refer to the source locations from the Indian Ocean cruise experiment

Figure 6 shows the several blockage predictions for the 2003 Indian Ocean Experiment sources (A01-A11) to each of the Indian Ocean hydroacoustic stations: Cape Leeuwin, Crozet, Diego Garcia North (DGN), and Diego Garcia South (DGS). Note the significant differences in the source-receiver path blockage predictions. For example, the predictions for DGN range from nearly all unblocked given the least restrictive criteria (top) to nearly all blocked given the most restrictive criteria (bottom). The actual observations are shown in Figure 7 and listed for simplicity merely as “observed” or “no-detection”. Note that none of the simple ray-based blockage criteria match all the observations. For example, DGN is best matched by the most restrictive “bathymetry cuts Channel axis” criteria: only 2 of the sources (A2 and A7) were well observed. On the other hand that criteria is far too restrictive for the nearby station DGS. Notice also, that even the least restrictive criteria predict that the path from A07 to DGS will be blocked although, in actuality, it is well observed (Figure 4). This prediction error is due to a small feature roughly 100 km from the station and is the result of the ray based nature of the calculation.

Measured

	Cape Leeuwen	Crozet	Diego Garcia ...	Diego Garcia ...
A1	ND	O	–	–
A2	O	ND	O	ND
A3	ND	ND	ND	ND
A4	ND	O	ND	O
A5	ND	O	ND	ND
A6	O	O	ND	O
A7	O	O	O	O
A8	O	O	?	O
A9	O	O	ND	O
A11	O	O	ND	O

Figure 7. Indian Ocean Experiment – source observations. (ND) no detection. (O) observed source. (?) possible detection. (–) no data. The names A1-A11, in the first column, refer to the source locations from the Indian Ocean cruise experiment. Compare to the estimates in Figure 6.

CONCLUSIONS AND RECOMMENDATIONS

We are continuing the development of the Hydroacoustic Blockage Assessment Tool and using it in conjunction with Indian Ocean data to derive a set of blockage criteria. The fundamental objective is to provide a robust prediction about which hydroacoustic monitoring stations can be used in discrimination analysis for any particular event. Currently, we are limited by the small set of ground-truth data and the limitations of ray theory in defining path-stop conditions. It is apparent that blockage is not a simple phenomenon, but as we continue to collect network data we should be able to develop coverage, propagation and attenuation maps for each of the hydroacoustic stations and develop the basic criteria for establishing blockage in the ocean at large.

REFERENCES

Harben, P. E., E. Matzel, D. K. Blackman, and D. Clarke (2004), Diego Garcia Reflections and Implosion Source Development, in *Proceedings of the 26th Seismic Research Review: Trends in Nuclear Explosion Monitoring*, LA-UR-04-5801, Vol. 2, pp. 553-562.

Pulli, J.J., Z. Upton, R. Gibson, J. Angell, T. Farrell, and R. Nadel (2000), Characterization of Reflected Arrivals and Implications for Hydroacoustic Test-Ban-Treaty Monitoring, *BBN Tech. Memor.* W1380.

AZIMUTHAL DEPENDENCE OF HYDROACOUSTIC BLOCKAGE AT DIEGO GARCIA AND IMPLICATIONS FOR DISCRIMINATION

Jay J. Pulli and Zachary M. Upton

BBN Technologies

Sponsored by Army Space and Missile Defense Command

Contract No. W9113M-05-C-0136

ABSTRACT

An understanding of hydroacoustic blockage around bathymetric features serves many purposes in ocean monitoring. These include the planning of station placement, estimation of network detection thresholds, and the evaluation of evasion scenarios. Our early estimates of hydroacoustic blockage in the Indian Ocean (Pulli and Upton, 2001) utilized ray based propagation models and binary blockage estimates based on a variety of environmental criteria. These models predicted, for example, that T-waves from events along the Sumatran Arch would not be seen at the north array of Diego Garcia. However, once actual data were accumulated for the Diego Garcia arrays, observations showed that paths that were predicted to be blocked were actually attenuated, often by approximately 30 dB. Possible mechanisms for this process include diffraction around the island, refraction, and perhaps acoustic-to-seismic-to-acoustic conversion.

In order to better under the azimuthal and frequency dependence of blockage around Diego Garcia, we have accumulated a dataset of earthquake sources located around the atoll and recorded by both the north and south arrays. The goal is to assemble a virtual array of sources for high-resolution studies. For example, events to the west of Diego Garcia include those occurring along the Carlsberg Ridge and Chagos Archipelago. A typical blockage value from the north to the south arrays is approximately 30 db. To the east of Diego Garcia, the recent sequence of events along Sumatra provides a vast amount of data for analysis. Blockage estimates here are about 25 dB. To the south of Diego, events along the Mid-Indian Ridge are used. For each event, the spectrum of the T-wave recorded on the north and south arrays is measured and compared.

To understand the implications of these measurements for detection and discrimination, we combine these measurements with our studies of T-wave amplitudes (sound pressure levels) versus seismic magnitude (Pulli et al., 2005). These studies indicate a near-linear trend of 15 dB/Mw. Broadband background noise levels at Diego North are approximately 90–95 dB and at Diego South they are 95–100 dB. Combining these measurements with an average blockage value of 30 dB, we estimate that blocked signals from events along the Sumatran arch can still be detected if the event is at least magnitude 4.5. Spectral decay of T-waves averages 1.5 dB/Hz above 1 Hz. Hence, by 30 Hz, the high frequencies of the blocked signals at the minimum detection level will be below the noise. Discriminants based on the ratio of high-frequency to low-frequency energy will thus not work for these small events. However, bubble-pulse frequencies are typically lower than 10 Hz, so cepstral parameters may still be able to separate underwater explosions from nonexplosions using these low amplitude blocked signals.

OBJECTIVES

The overall objective of this effort is to improve our understanding of the effects of bathymetric blockage and reflection on hydroacoustic signals and to use this understanding to assess the effects on hydroacoustic signal discrimination. The specific tasks include the following:

- A study of the azimuthal and frequency dependence of blockage at Diego Garcia using virtual arrays of earthquake sources surrounding the atoll.
- The identification of prominent bathymetric reflectors in the Indian, Atlantic and Pacific Oceans using both contemporary and historic hydroacoustic data.
- The selection of a specific source-reflector-receiver scenario which will be used to model and analyze the reflection process; this effort is being conducted in conjunction with Lawrence Livermore National Laboratory.
- An analysis of the effects of blockage and reflection on the hydroacoustic discrimination process.

RESEARCH ACCOMPLISHED

Introduction

During the first few months of this effort, we have focused on the task of determining the azimuthal and frequency dependence of blockage at Diego Garcia. An understanding of hydroacoustic blockage around bathymetric features serves many purposes in ocean monitoring. These include the planning of station placement, estimation of network detection thresholds, and the evaluation of evasion scenarios. Our early estimates of hydroacoustic blockage in the Indian Ocean (Pulli and Upton, 2001) utilized ray based propagation models and binary blockage estimates based on a variety of environmental criteria. However, once actual data were accumulated and analyzed for the Diego Garcia arrays, observations showed that the blockage process was more complicated and could not be predicted by these simple models. Possible mechanisms for this process include diffraction around the island, refraction, and perhaps acoustic-to-seismic-to-acoustic conversion.

In order to better understand this process, our approach is to make blockage measurements at nearly all angles around the archipelago. To make these measurements, we are utilizing a ground-truth database of seismic events in the Indian Ocean that we have accumulated during the time period of 2000–2005 (we continue to accumulate ground truth events as they occur). This database now includes nearly 200 events (see Figure 1). Many events were added during 2005; most of these events occurred along the nearly 1000-km long aftershock zone of the December 26, 2004, Sumatra earthquake, which provides a high degree of azimuthal resolution to the east. The current azimuthal coverage for our database is shown in Figure 2.

To estimate the blockage function, we isolate the T-wave signal for each event at both the north and south array elements, then compute it's spectrum around the mode-1 arrival (peak amplitude of the signal train, window lengths typically 16 or 32 seconds; the time series are first detrended and a 30% cosine taper is applied before the FFT is computed). The spectra are then averaged over the three array elements for the north and south arrays. We define the blockage function as the difference in the spectral amplitudes between the north and south arrays. These measurements can then be utilized in other studies that are attempting to model the blockage process using an adiabatic mode parabolic equation model (AMPE) (Upton et al., 2005).

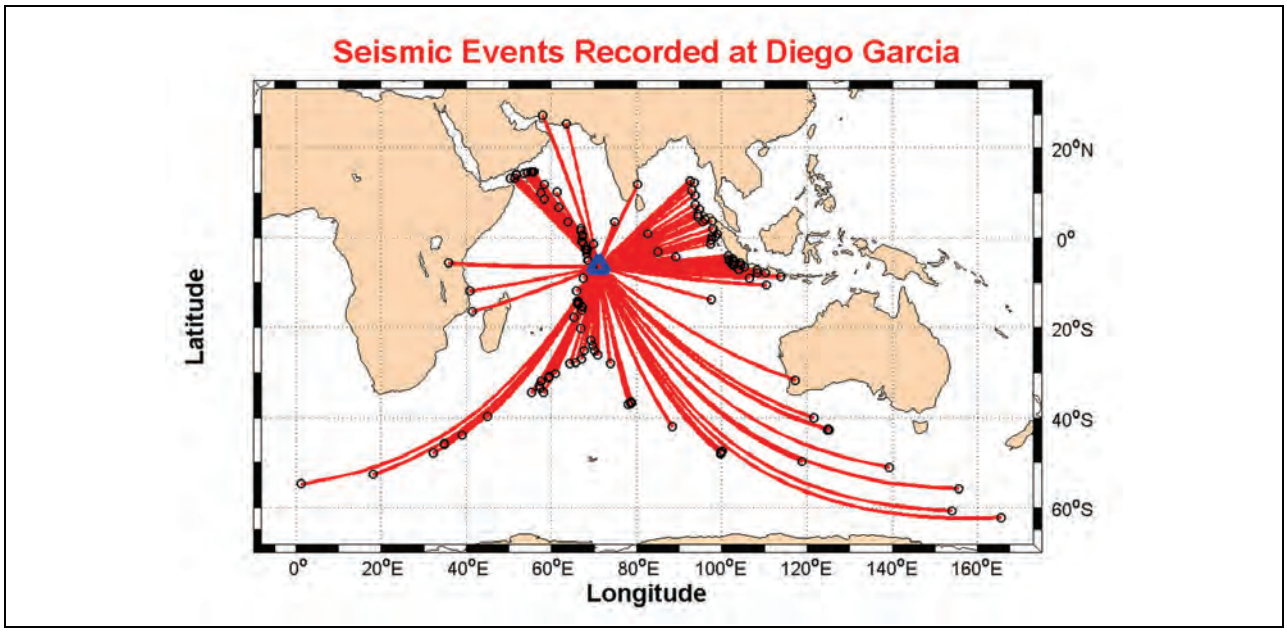

Figure 1. Locations of events in the Indian Ocean used to measure the azimuthal and frequency dependence of blockage at Diego Garcia.

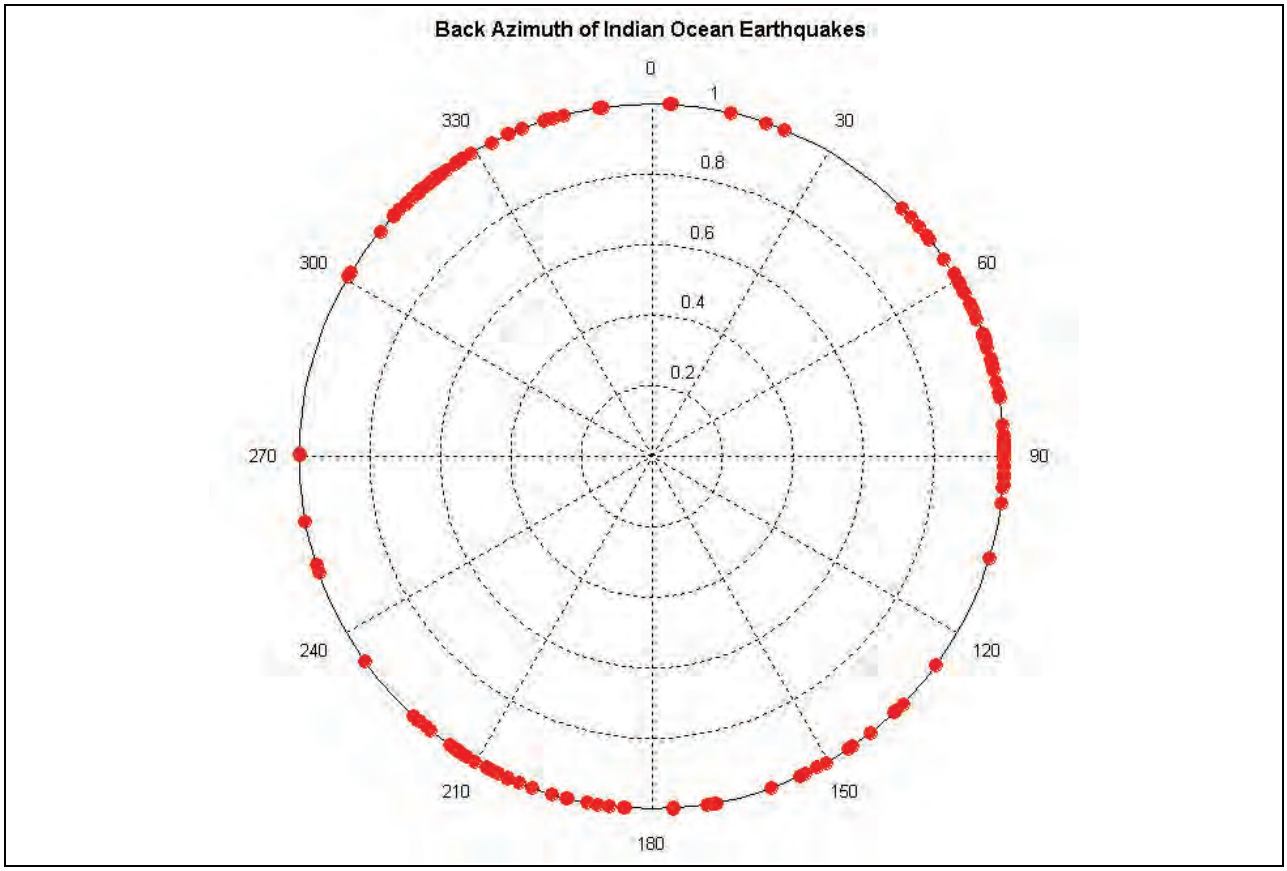

Figure 2. Azimuthal coverage of events and blockage estimates at Diego Garcia.

Examples of Blockage at Diego Garcia – East and West Sources

We now illustrate some blockage measurements at Diego Garcia using signals from the east and west of the atoll. The first example uses the T-wave signals generated by the great Sumatran earthquake of December 26, 2004. Hydroacoustic waveforms for this event recorded at Diego Garcia are shown in Figure 3. In this case, the T-wave signal at the north array is partially blocked by the atoll. In Figure 4, we show the spectra of these T-waves, and the estimate of the blockage function is approximately –32 dB over the frequency band of 5–40 Hz.

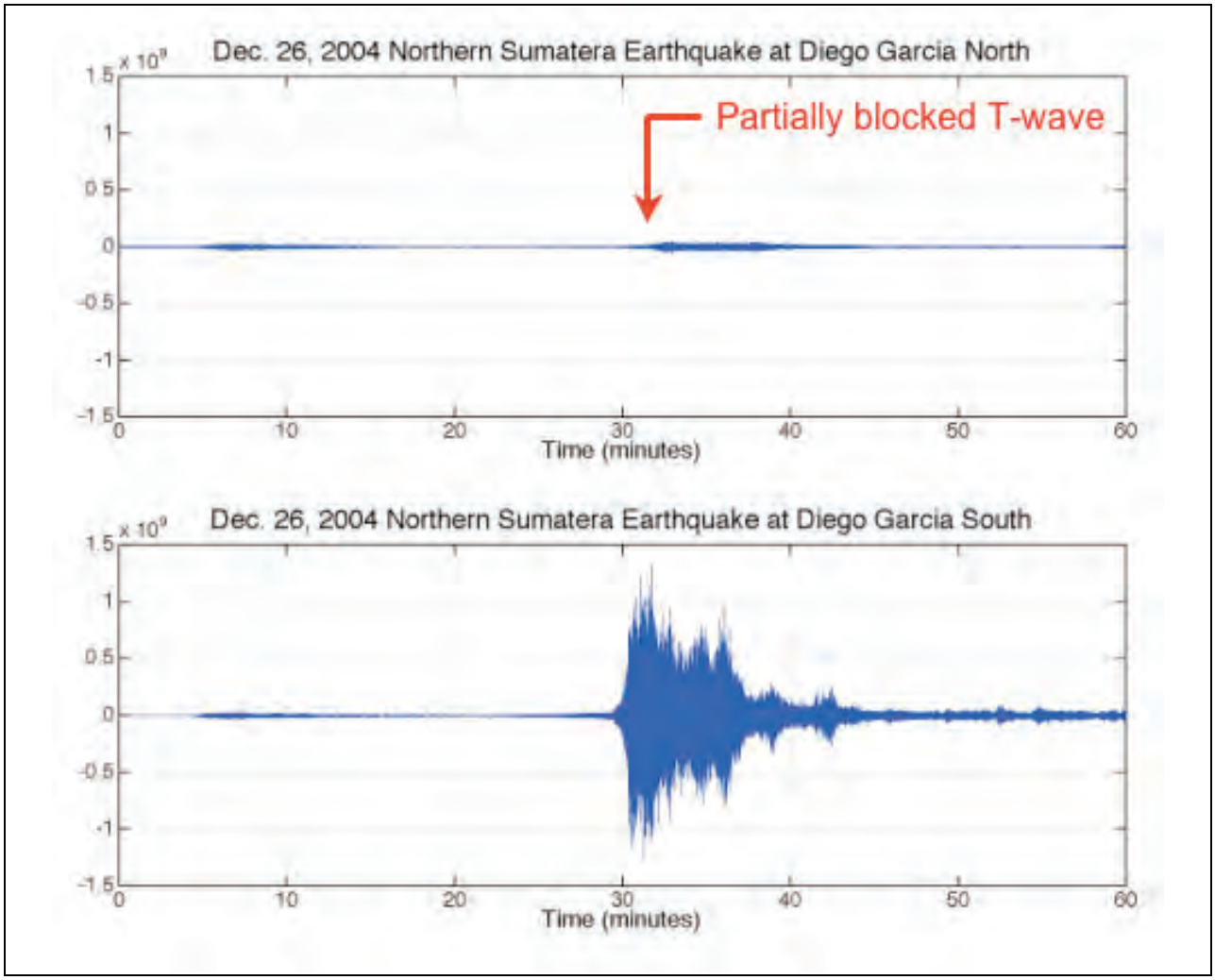

Figure 3. Hydroacoustic waveforms for the December 26, 2004, Sumatra earthquake recorded at Diego Garcia North (top) and South (bottom). The T-wave signal at the north station is partially blocked, but because the event was so large, the signal-to-noise ratio of the partially blocked signal is also large and enables an accurate measurement of blockage.

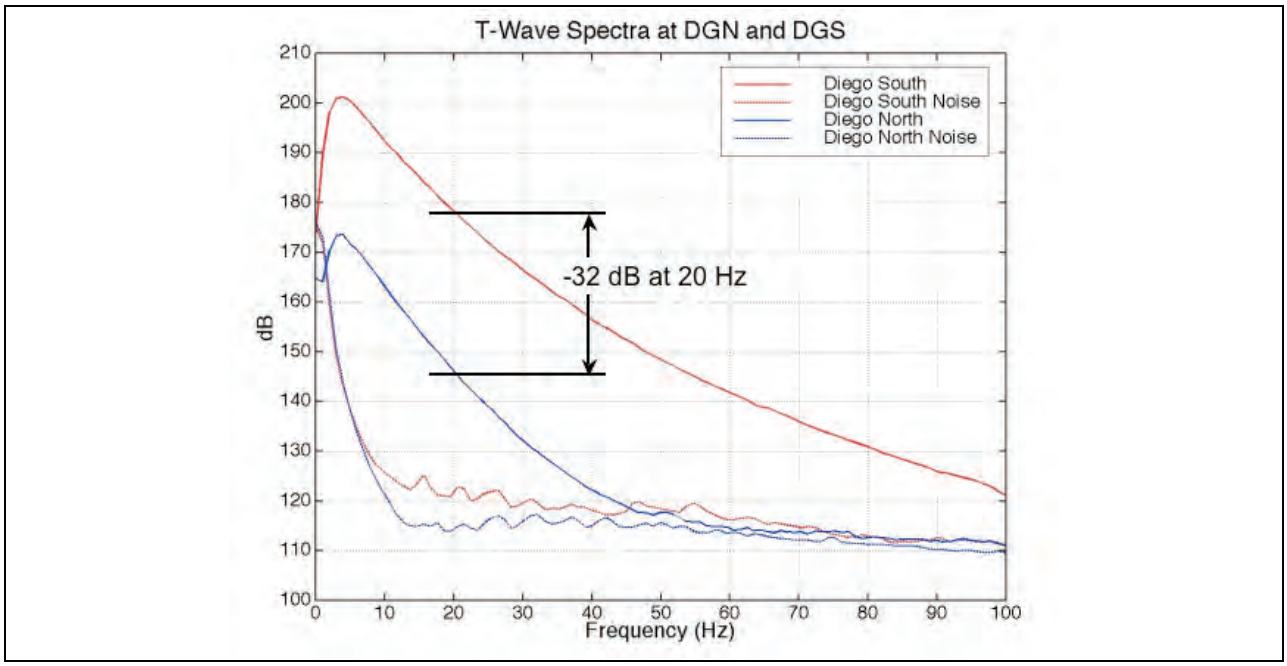

Figure 4. Spectra of T-waves for the December 26, 2004, Sumatra earthquake recorded at Diego Garcia north and south arrays. There is a near-constant –32 dB difference in the signals (blockage) as a function of frequency.

Our second example is from the west of Diego Garcia; the event occurred on July 25, 2002, on the Chagos Archipelago. T-waves from this event at Diego Garcia are shown in Figure 5. Here we see the opposite effect from what was shown previously; here, the south station is partially blocked. The spectra of the T-waves are shown in Figure 6. From this direction, the blockage is approximately –20 db, lower than from the opposite side.

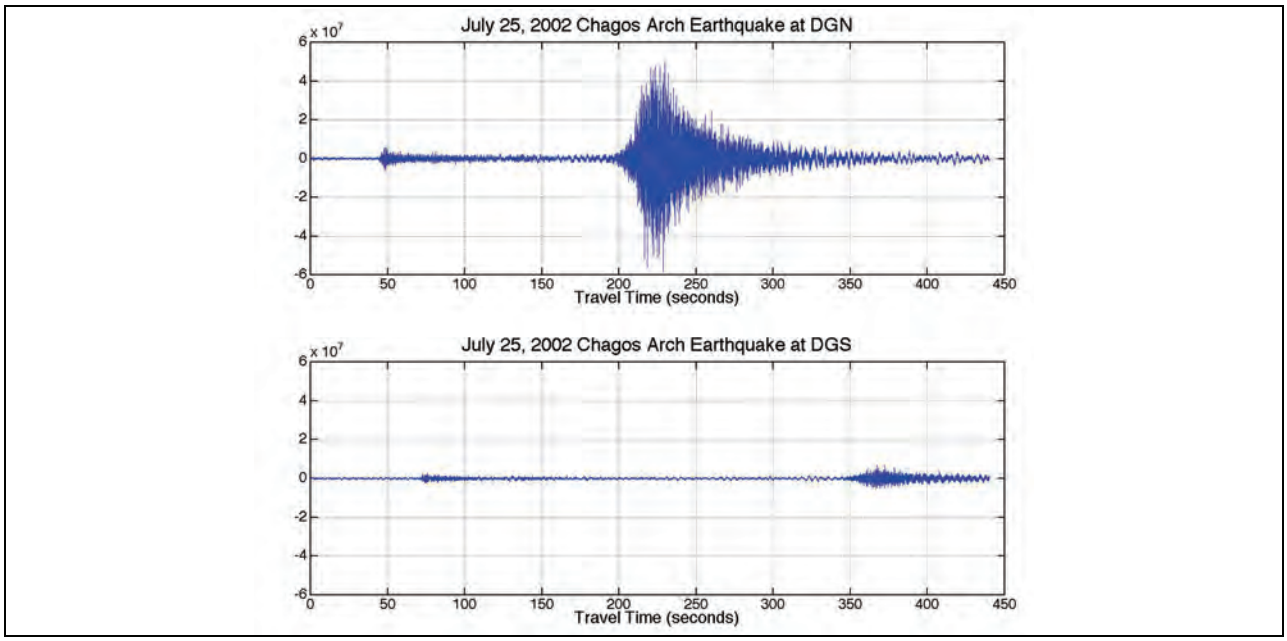

Figure 5. Hydroacoustic waveforms for the July 25, 2002, earthquake on the Chagos Archipelago, recorded at Diego Garcia North (top) and South (bottom). The T-wave signal at the south station is partially blocked.

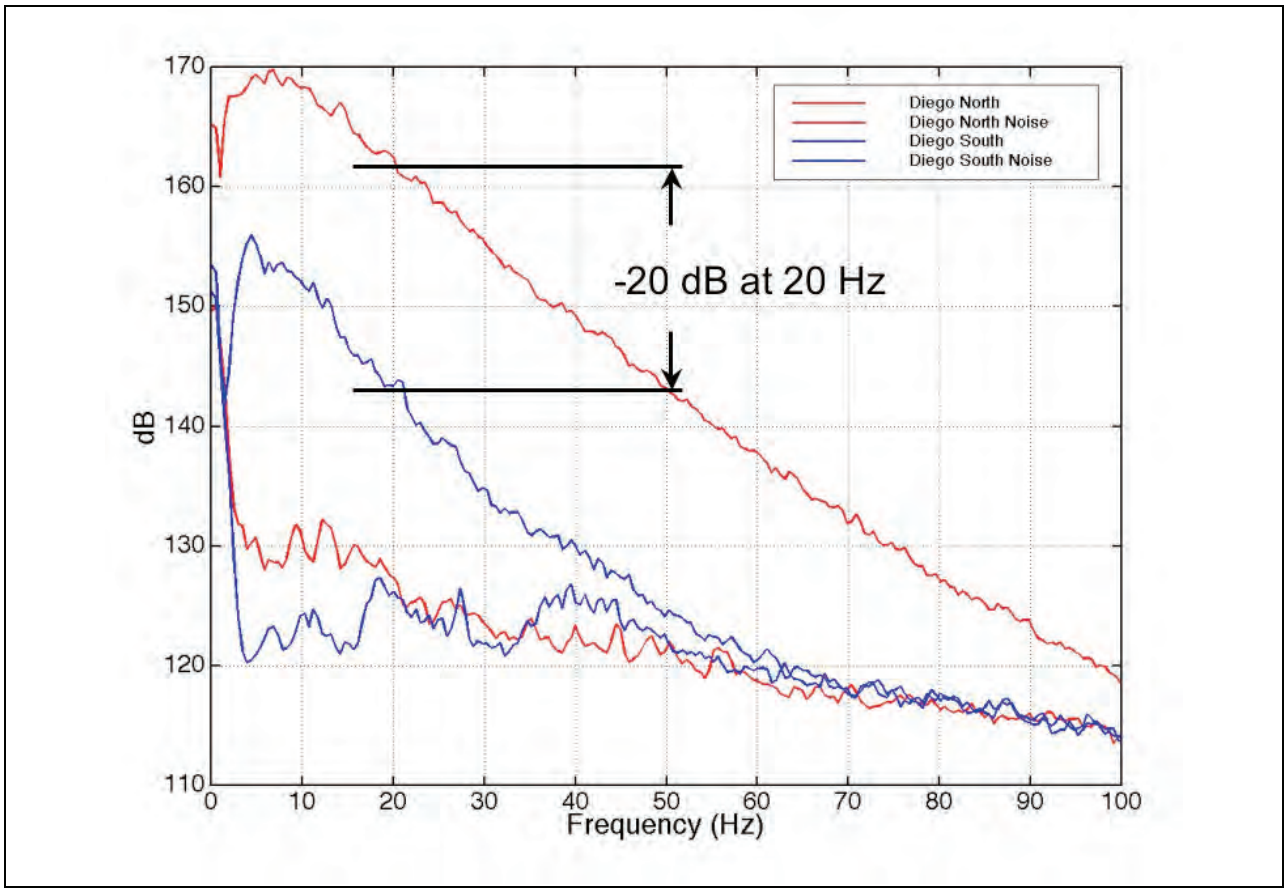

Figure 6. Spectra of T-waves for the July 25, 2002, Chagos Archipelago earthquake recorded at Diego Garcia north and south arrays. There is a near-constant –20 dB difference in the signals (blockage) as a function of frequency. Blockage in this direction (west-to-east) is lower than in the east-to-west direction.

Azimuthal Dependence

To date, we have performed the high-resolution blockage estimates using a group of earthquake sources in the Sumatra area. A map of these events is shown in Figure 7. For now, we have grouped the events into three categories: northern, central, and southern Sumatran events. The computed blockage functions for these three areas are shown in Figure 8. The general trend is for the blockage to decrease from north to south. For the northern group of events, the blockage averages 30 dB. For the central events, the blockage averages 26 dB. For the southern events, the blockage averages 23 dB.

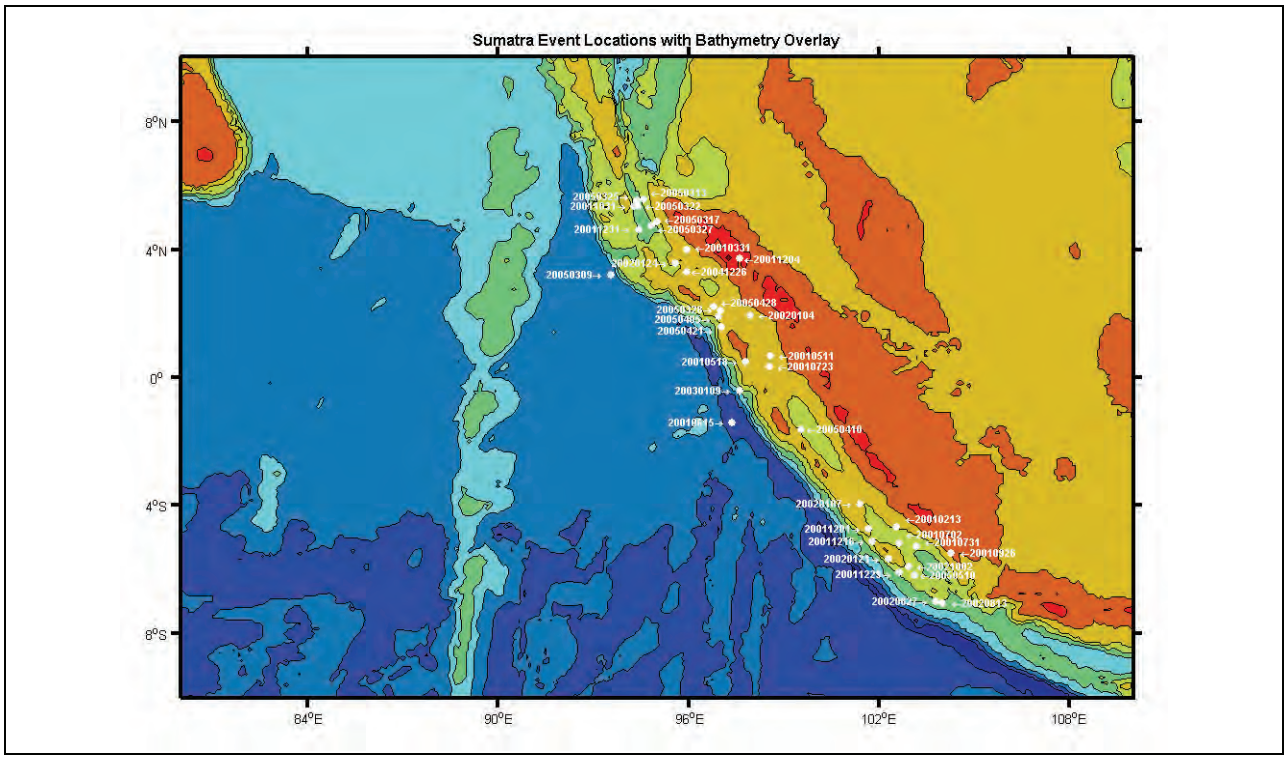

Figure 7. Map of events in the Sumatra area used to study the azimuthal dependence of blockage.

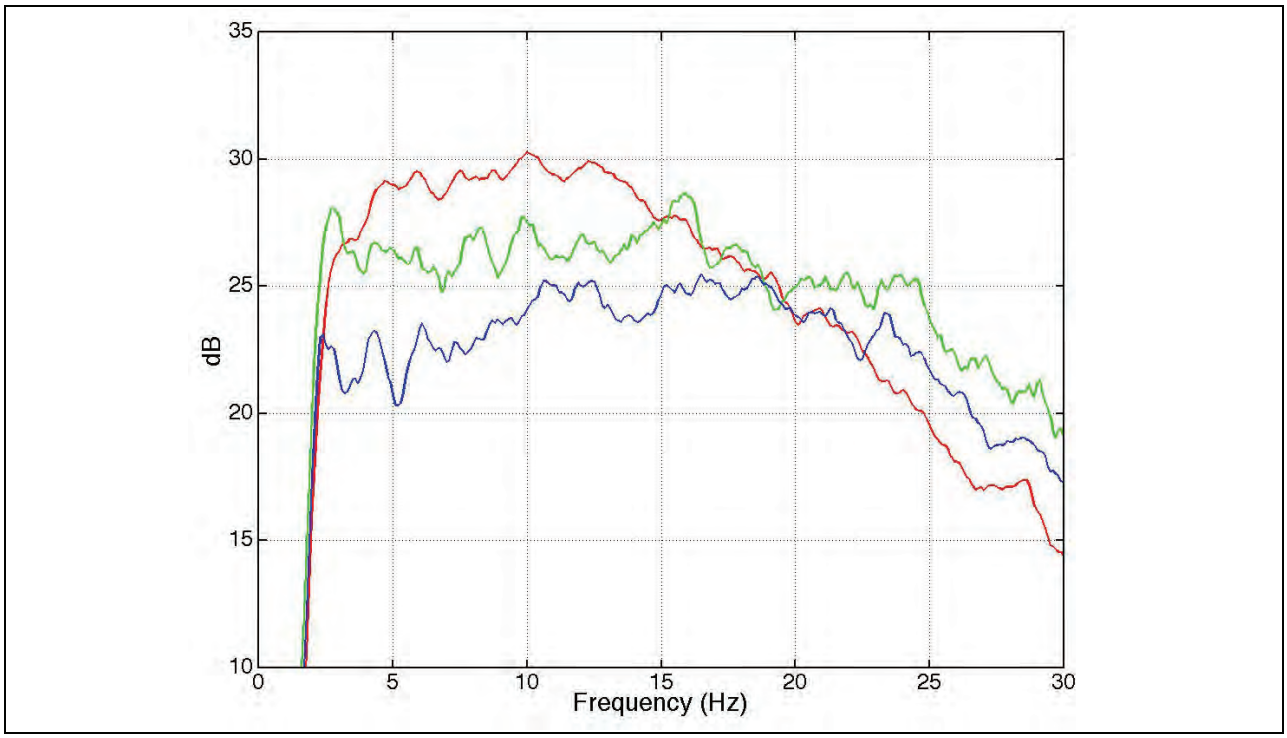

Figure 8. Blockage functions for events in the northern (red), central (green), and southern (blue) source zones of Sumatra.

Implications for Hydroacoustic Discrimination

To understand the implications of these measurements for detection and discrimination, we combine these measurements with our studies of T-wave amplitudes (sound pressure levels) versus seismic magnitude (Pulli et al., 2005). These studies indicate a near-linear trend of 15 dB/Mw. Broadband background noise levels at Diego North are approximately 90–95 dB and at Diego South they are 95–100 dB. Combining these measurements with an average blockage value of 30 dB, we estimate that blocked signals from events along the Sumatran Archipelago can still be detected if the event is at least magnitude 4.5. Spectral decay of T-waves averages 1.5 dB/Hz above 1 Hz. Hence, by 30 Hz, the high frequencies of the blocked signals at the minimum detection level will be below the noise. Discriminants based on the ratio of high-frequency to low-frequency energy will thus not work for these small events. However, bubble-pulse frequencies are typically lower than 10 Hz, so cepstral parameters may still be able to separate underwater explosions from nonexplosions using these low-amplitude blocked signals. These in-water sources have a relatively higher signal amplitude since the acoustic energy is directly coupled and is not going through the seismic-to-acoustic conversion process of T-waves.

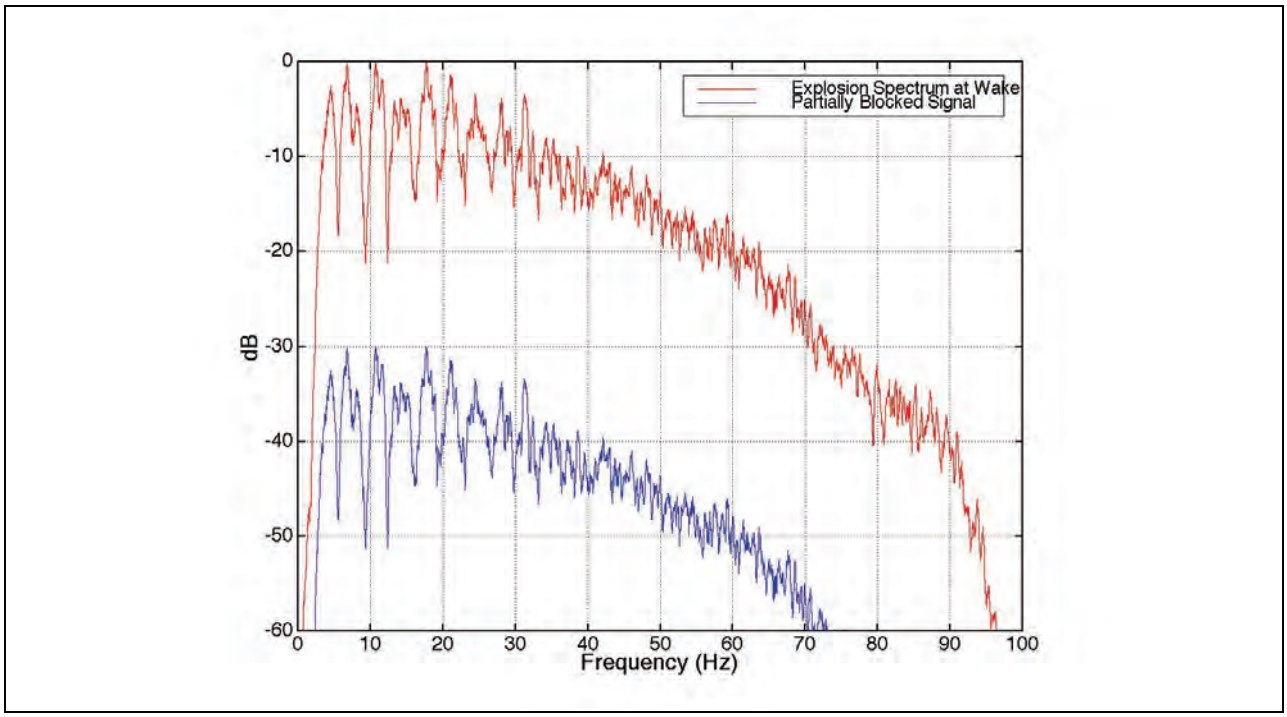

Figure 9. Hydroacoustic recording of the IITRI underwater explosion made at Wake Island (red). Note the bubble pulse and water reverberation effects in the signal below 30 Hz. The blue curve indicates the same spectrum attenuated by a 30 dB blockage function. Since signal levels are higher for in-water explosions than for sub-sea earthquakes, even blocked signals should be relatively easy to discriminate if their signal-to-noise ratio is at least 40 dB.

CONCLUSIONS AND RECOMMENDATIONS

During the first few months of this study, we have established the azimuthal dependence of blockage around Diego Garcia. In the examples shown in this paper, east-to-west, the blockage is approximately –30 dB, whereas from west-to-east the blockage is –20 dB. We also see azimuthal variations over small azimuth swaths, such as from the Sumatra area. Over the course of this program, we will evaluate the blockage's azimuthal dependence and endeavor to databases showing the complex bathymetric structure of the Chagos Archipelago. A full 360-degree survey will be presented later in this effort.

ACKNOWLEDGEMENTS

Most of the data for this project are being obtained from the Air Force Technical Applications Center. Additional assistance by Joydeep Bhattacharyya, Mathew Coryea, and Sheila Shah of BBN Technologies is also appreciated.

REFERENCES

Pulli, J.J. and Z. Upton (2001), Hydroacoustic blockage at Diego Garcia: models and observations, in *23rd Seismic Research Review; Worldwide Monitoring of Nuclear Explosions*, Jackson Hole, WY (Oct. 2–5).

Upton, Z.M., J. Bhattacharyya, J. J. Pulli, S. Shah and M. Collins (2005), Improving the physical understanding of hydroacoustic blockage: statistical and model-based studies, in *Proceedings of the 27th Seismic Research Review: Ground-Based Nuclear Explosion Monitoring Technologies*, Palm Springs, CA (Sept 20–22).

IMPROVING THE PHYSICAL UNDERSTANDING OF HYDROACOUSTIC BLOCKAGE: STATISTICAL AND MODEL BASED STUDIES

Zachary M. Upton[1], Joydeep Bhattacharyya[1], Jay J. Pulli[1], Sheila Shah[1], and Michael Collins[2]

BBN Technologies[1] and Naval Research Laboratory[2]

Sponsored by National Nuclear Security Administration
Office of Nonproliferation Research and Engineering
Office of Defense Nuclear Nonproliferation

Contract No. DE-AC03-02SF22560

ABSTRACT

The hydroacoustic network of the International Monitoring System (IMS) is a sparse set of only eleven stations. This network relies on the efficient propagation of acoustic energy in the natural underwater waveguide called the sound fixing and ranging (SOFAR) channel. Sound traveling in the channel that encounters an island or seamount must either diffract, scatter, or be translated into seismic energy. When signals from a source are observed from the opposite side of one of these obstructions, they have likely been affected by all of these processes. In past studies, we have shown that ray-based models with a simple, binary blockage condition (i.e., blocked or not blocked) will not suffice for accurate prediction of blockage (Pulli and Upton, 2001). Recently, we have accumulated a set of over 150 events in the Indian Ocean that allowed for an initial assessment of blockage based on recorded data at Diego Garcia (H08).

U.S. Department of Energy (DOE) researchers at Lawrence Livermore National Laboratory have designed a Hydroacoustic Blockage Analysis Tool (HydroacousticBAT) that combines model predictions from the Hydroacoustic Coverage Assessment Model (HydroCAM) and observations from data. The tool will be used to assess ramifications of blockage on the detection and discrimination capability of the hydroacoustic network.

Our current efforts in understating hydroacoustic blockage are focused on improving HydroCAM's modeling capability and interpolating data observations to advance the HydroacousticBAT. The first step in this effort is to characterize amplitude variations in recorded data across the Indian Ocean. This information is essential both for calibrating hydroacoustic propagation and testing modeling techniques. We will present results from an interactive analysis of the signal and noise amplitudes over the 2 – 100 Hz frequency range.

Secondly, a model of blockage, including the effects of diffraction and acoustic-seismic-acoustic energy conversion at islands is required to ensure that we understand the physical processes that produce amplitude variation with blockage in the recoded data. This study describes the initial implementation of an adiabatic mode parabolic equation (AMPE) model for HydroCAM that accounts for these physical processes. We will present initial modeling results and compare it with observations.

Finally, the sparse geographical coverage of the long-range hydroacoustic paths in this region lends itself readily to the well-established Kriging technique, which uses a statistical framework to robustly interpolate between observed values. We will show preliminary models of amplitude variations across the Indian Ocean region, as a function of frequency, in this presentation.

OBJECTIVES

The primary objective of this work is to improve Air Force Technical Applications Center (AFTAC) and Department of Energy (DOE) understanding of hydroacoustic blockage by advancing the modeling capabilities of the Hydroacoustic Coverage Assessment Model (HydroCAM) and using established extrapolation techniques to provide an empirical prediction of blockage to the DOE Hydroacoustic Blockage Analysis Tool (HydroacousticBAT).

We have designed an interactive method to make frequency-dependent measurements of signal amplitude for each of the events in our 150+ event database at Diego Garcia. These observations allow us to compare data observations to model predictions and to calibrate propagation characteristics around Diego Garcia. To improve the modeling capability of HydroCAM, we have obtained the Adiabatic Mode Parabolic Equation (AMPE) model and evaluated its applicability to the blockage problem. This model includes the effects of diffraction and acoustic to seismic to acoustic conversion. We are adapting this model to the environmental databases and software platform used in HydroCAM. We will use the above observations and Bayesian Kriging techniques to extrapolate empirical amplitude measurements into areas where events of opportunity are not available.

RESEARCH ACCOMPLISHED

Amplitude Measurements

To better understand the effects of blockage, BBN has accumulated an event database in the Indian Ocean of more than 150 events recorded at Diego Garcia. In earlier efforts, we compared these data to ray-based blockage models and demonstrated that binary (blocked or not blocked) prediction of blockage was not appropriate, and that future studies needed to account for diffraction and other physical effects that might allow a signal to be detected after interaction with a seamount or island (Pulli and Upton, 2001). Figure 1 shows the origin locations of the database events, with ray paths (regardless of blockage) to Diego Garcia.

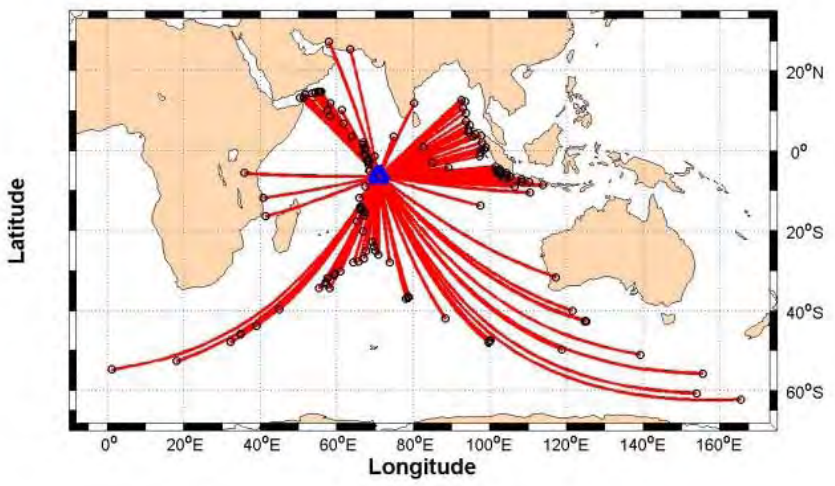

Figure 1. Ray-based blockage predictions for H08N (left) and H08S (right).

In the current study, we are focused on understanding the physical processes of blockage through data analysis and modeling. To gain a uniform set of observations for the ground truth dataset, we have measured the signal and noise levels at the North and South arrays at Diego Garcia. These measurements are valuable in validating models, feeding data extrapolation processes like Kriging, and studying amplitude variations with source magnitude, distance, mechanism, and depth.

To identify the correct earthquake arrival in a signal window, HydroCAM's GlobeRay model (Farrell, et al. 1997) was used to predict acoustic travel time from the event origin to the array at Diego Garcia. This estimate did not

account for the difference in location between earthquake origin and seismic-to-acoustic conversion point, but it was sufficient for identifying the earthquake arrival. Signal and noise level estimates were made for each event in the database by manually picking a signal window and noise window. The signal window was chosen to incorporate the peak (low-order mode) signal energy. The noise window was picked sufficiently far away from signal arrivals to eliminate source effects. An example of the window selection is shown in Figure 2. Both the signal and noise power spectra were computed for both the North and South stations using these chosen windows.

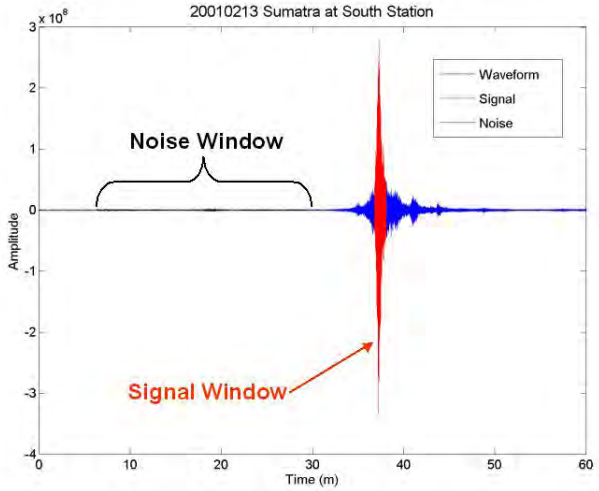

Figure 2. Waveform with signal (red) and noise (black) windows shown after manually choosing them at H08S

One result of these measurements is source and noise spectra. A spectral comparison for the Great Sumatran Earthquake (December 26, 2004, magnitude 9.3) is shown in Figure 3 at 20 Hz. The North station measurement shows a 32 dB difference in signal level over the South station. The difference between the stations for this event is similar to the spectra received from other events in nearby regions of Sumatra.

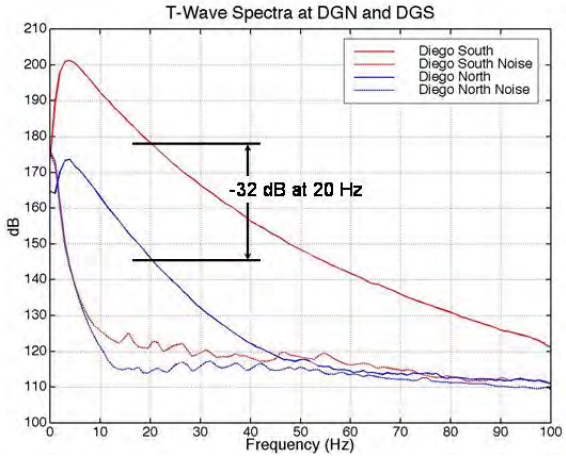

Figure 3. Spectral comparison for the December 26, 2004, Great Sumatran Earthquake recorded at H08N (blue) and H08S (red).

Signal level measurements for the event database are shown in Figure 4 at 20Hz for both the North and South stations (depicted as red triangles). As expected, the signal amplitude detections originating from the Mid Indian Ridge are higher amplitude at the North Station and those originating from Sumatra are higher at the South station. These general results are consistent through a range of frequencies (5Hz–60Hz). Comparison between the stations provides information as to the attenuation of the signals due to the archipelago.

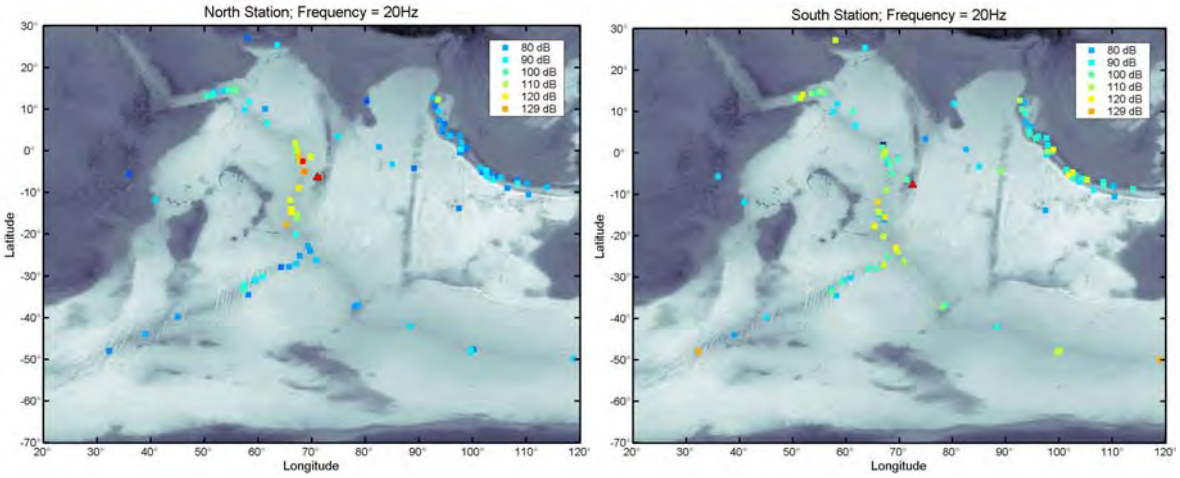

Figure 4. Amplitude estimates at 20Hz for the 150+ events in the ground truth event database at H08N (left) and H08S (right).

In the next few sections, we present analysis of dataset-scale variation in signal amplitudes with frequency, depth and magnitude of the events. The goal of this analysis is to remove some of the source effects from our analysis of blockage.

Frequency Dependence of Signal Amplitudes

We show the large-scale variation of signal and noise with frequency, as recorded at H08N and H08S, in Figure 5. We have combined all of our amplitude measurements in this case, thereby suppressing possible amplitude variations due to changes in signal blockage, source magnitude, source-receiver distance, etc.

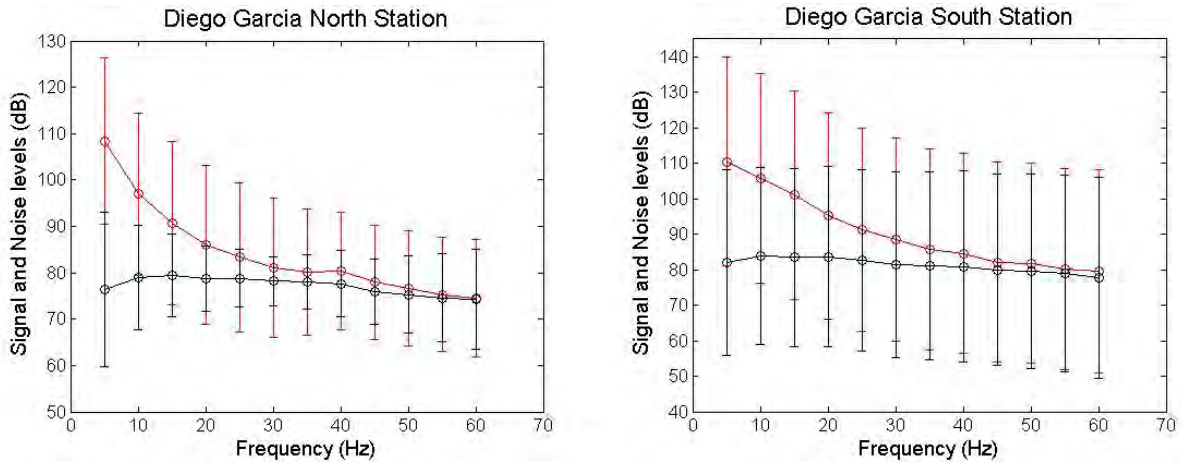

Figure 5. Variation of signal and noise with amplitude for Diego Garcia North and South stations from recorded data. The scatter of the data, shown as the standard deviation of the estimate at each frequency, is shown. It is clear that the signal levels decrease monotonically with frequency while the noise spectra do not show such variations. On average, for our dataset, the signal and noise levels are slightly higher at the South station.

Frequency dependence of SNR

Figure 6 shows a comparison of the large-scale variation of SNR at H08N and H08S. The amplitudes primarily differ within a frequency band of 10-30 Hz.

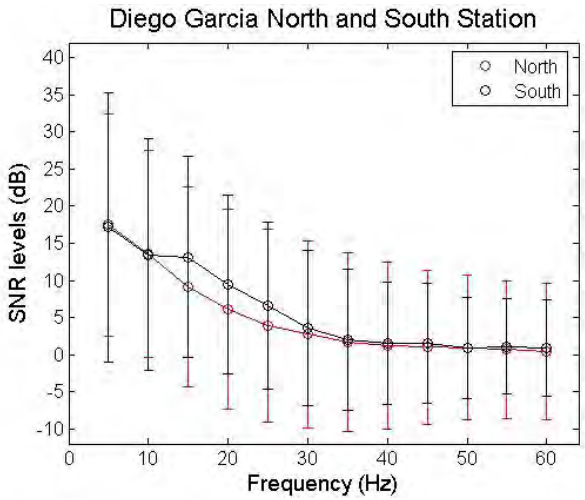

Figure 6. Variation of SNR with frequency for Diego Garcia North (H08N) and South (H08S) arrays for our dataset. On average, the amplitudes differ significantly only within frequencies of 10-30 Hz.

Variation of signal amplitude with event depth

One of the outstanding issues of hydroacoustic propagation is the location of the T-phase conversion region. One of the factors that can affect this location is the depth of the seismic source, as that would control the incidence angle at the crust-water interface. In this section, we investigate the large-scale variation of signal spectra with source depth for events recorded at H08N and H08S. We note that for a significant number of the events in our database, the source depth is known only to a default value, i.e., 10 km or 33 km, depending on the catalog. To decrease the sensitivity of our analysis to such values, we have divided our event into two subsets, deep (depth > 40 km) and shallow. Figure 7 shows the variation of signal amplitude and SNR, with frequency and source depth.

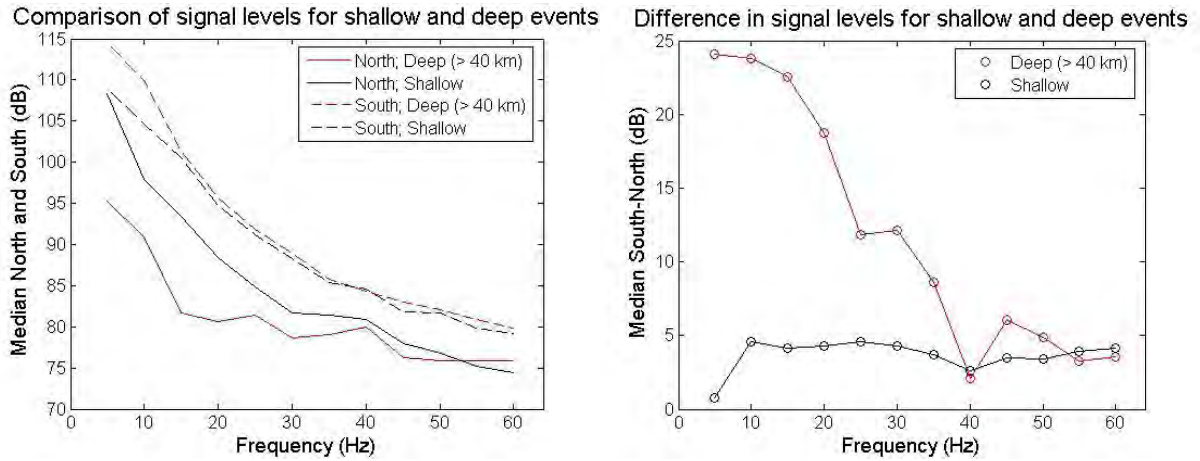

Figure 7. Variation of signal amplitude and SNR with frequency and earthquake source depth. We note that though the event depth does not affect the amplitudes significantly for the southern station (H08S), shallow events have a larger amplitude at H08N up to frequencies of about 35 Hz. The SNR for the deep events is significantly larger at the South station; however, we do not observe this difference for the shallow events. Some of the aforementioned amplitude variations might be accounted for by the differences in typical source depths, sometimes specific to regions, with blocked or unblocked paths.

Variation of signal blockage with frequency

We define blockage as those observations for which the amplitude differs by more than 10 dB between the North and South stations, for a particular frequency. Figure 8 shows the locations of the events for the blocked paths at 20 Hz; a positive value signifies blockage on the North station. We note that the signal is preferentially blocked at the North station from events near Sumatra, the Carlsberg Ridge and the Mid-Indian ridge. Alternately, events located close to the North station are mostly blocked at the South. Next, we separate the paths which are blocked at either the North or the South stations and estimate the variation with frequency.

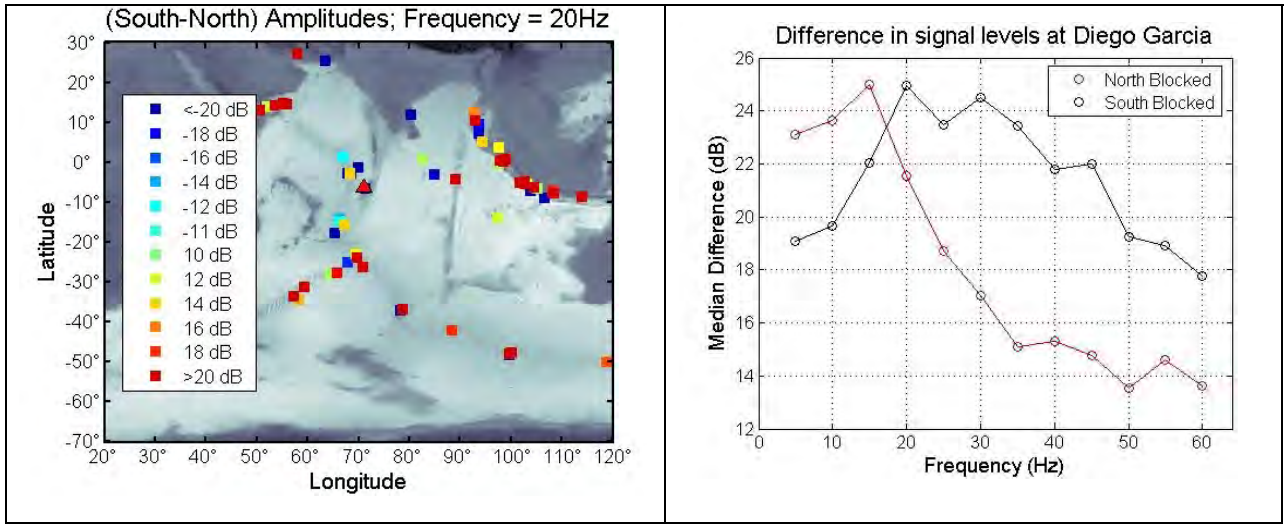

Figure 8. Variation of blocked path with source location (left) and signal frequency. Signals are preferentially blocked at the North station (H08N).

These amplitude measurements will be used to validate new blockage modeling techniques. In addition, we will use these measurements in the Kriging extrapolation process.

Geospatial Analysis of Signal Amplitudes

Robust predictions of amplitudes of hydroacoustic T-phases are essential in nuclear monitoring. In this study, we are augmenting our group's earlier theoretical estimates with measurements from Ground Truth data. These measurements, described above, can be used to map out the spatial variation of the amplitudes recorded at H08N and H08S, as a function of the source locations. However, as is obvious from the map in Figure 1, the geographical distribution of our dataset is inadequate for ocean basin analysis of spatial variation. To use such a sparse dataset to extract robust amplitude predictions, we will use the well-established kriging technique, which allows us to combine the information from our measured and predicted amplitude estimates. Using kriging, we obtain both the amplitude and its formal error on a grid of geographical locations. Using a separate test dataset, we now in turn can evaluate the validity of our kriged model. As an initial analysis step for kriging, here we show the variation of observed amplitude with source-receiver distance, at a set of frequencies (Figure 9).

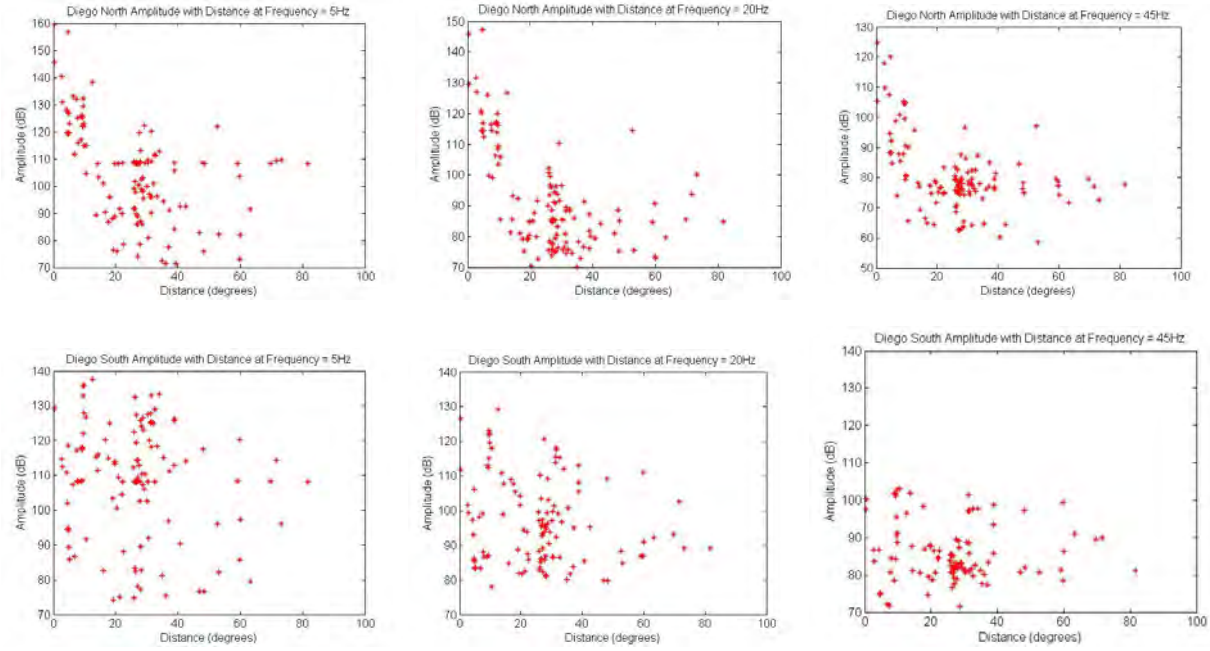

Figure 9. Amplitude distribution with distance and frequency at H08N and H08S.

Blockage Modeling

Prior ray-based modeling did not include the effects of diffraction over and around bathymetric features nor acoustic-seismic-acoustic through the bathymetric feature. The goal of this part of our research is to improve HydroCAM's modeling capability by implementing a model that accounts for the diffraction process. Following a search of published literature, we have obtained the Adiabatic Mode Parabolic Equation (AMPE) model (Collins, 1993) from the Naval Research Laboratory and evaluated its applicability to the blockage problem in nuclear explosion monitoring. The preliminary evaluation of this model is shown here.

The AMPE model merges modal modeling theory with the parabolic equation to predict acoustic propagation in three dimensions in a manner that is efficient for long-range propagation studies in the frequency band of interest for nuclear explosion monitoring (0-150Hz). As the name implies, the model assumes that the environment varies slowly over the horizontal path such that energy does not transfer between modes of the depth-separated wave equation. Each modal coefficient is calculated using the Parabolic Equation (PE) method to solve the acoustic wave equation in latitude and longitude. The model accounts for azimuthal coupling, and therefore horizontal diffraction. (Collins et al., 1995).

Shown here is a model of a source to the East of Diego Garcia, along the same back-azimuth as the origin of the Great Sumatran Earthquake of December 26, 2004. The spectra of that event, recorded at the hydrophones of Diego Garcia, are shown in Figure 3. The output of the AMPE model is in terms of transmission loss (TL), so the difference in TL between the South and North stations at a given frequency should compare directly with the difference in spectral levels between the two tripartites at that same frequency. Figure 10 shows the modeling scenario, plotted on top of the Sandwell and Smith 2-minute bathymetry in the area. Note that there are a number of shallow features along the Chagos Archipelago that could interfere with sound traveling in the SOFAR channel. Figure 11 shows cross sections of bathymetry along straight-line paths from the source location to the centroid of each tripartite. The AMPE model is currently configured to use the DBDB5 5-minute resolution bathymetry, so cross sections are shown for both databases. Note that, for the path to H08N, the DBDB5 bathymetry shows a large subsurface (~100m depth) bathymetric feature along the straight line path, while the Sandwell and Smith bathymetry shows that feature at the surface.

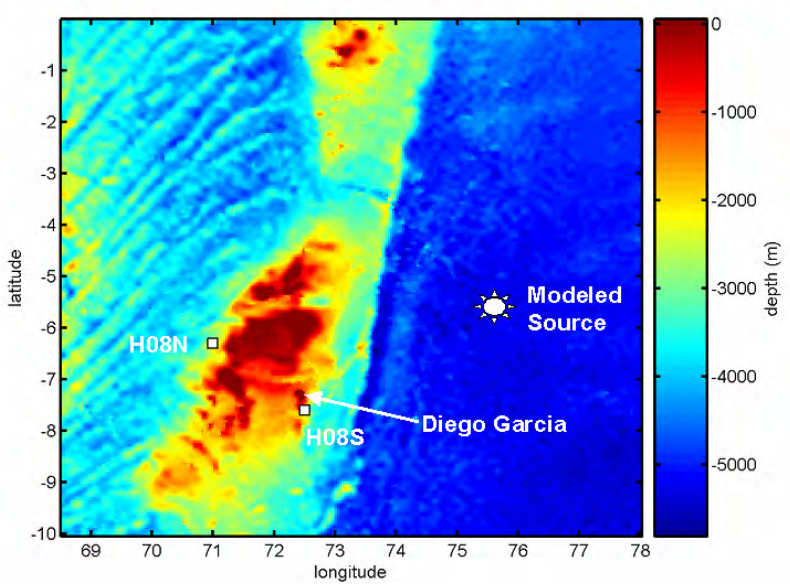

Figure 10. Sandwell and Smith 2-minute resolution bathymetry near Diego Garcia. H08N and H08S station locations are shown as white boxes.

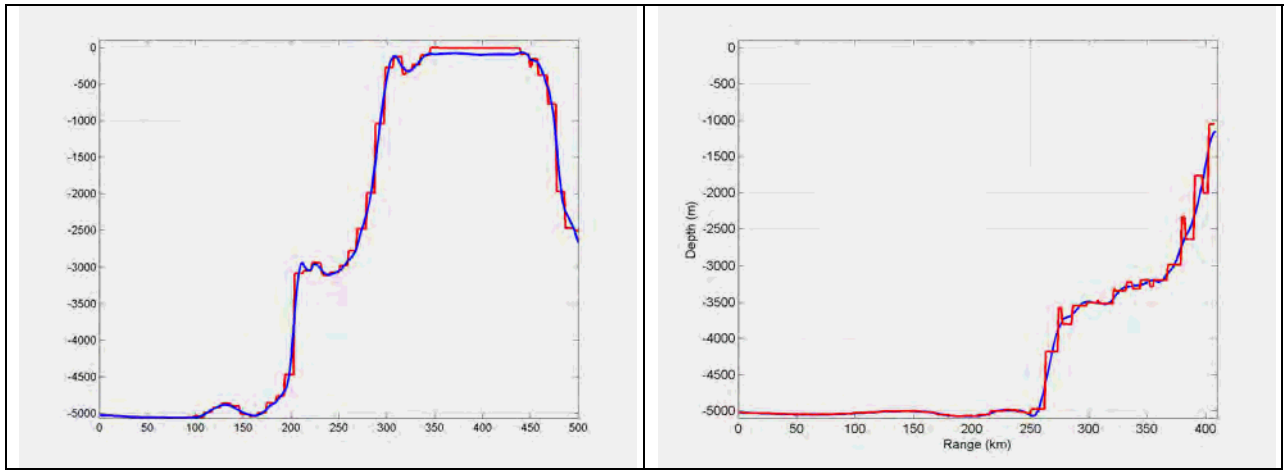

Figure 11. Bathymetric cross sections from the model source location to H08N (right) and H08S (left). DBDB5 data are shown in blue and Sandwell and Smith data are shown in red. Ranges of zero are at the source location while the end of the range axis is the hydrophone location.

Figure 12 shows the output of the AMPE model at 5 Hz. There is a distinct horizontal diffraction pattern around the gross shape of the bathymetry of the Chagos Archipelago. Attenuation between the South and North tripartites is predicted to be over 50 dB, substantially more than the 35 dB shown in Figure 3. In contrast, at 10 Hz, it appears that diffraction over and/or transmission through the features of the archipelago may dominate the propagation prediction. In this case, the approximately 40 dB difference in TL between the two stations is a much closer match to the data shown in Figure 3.

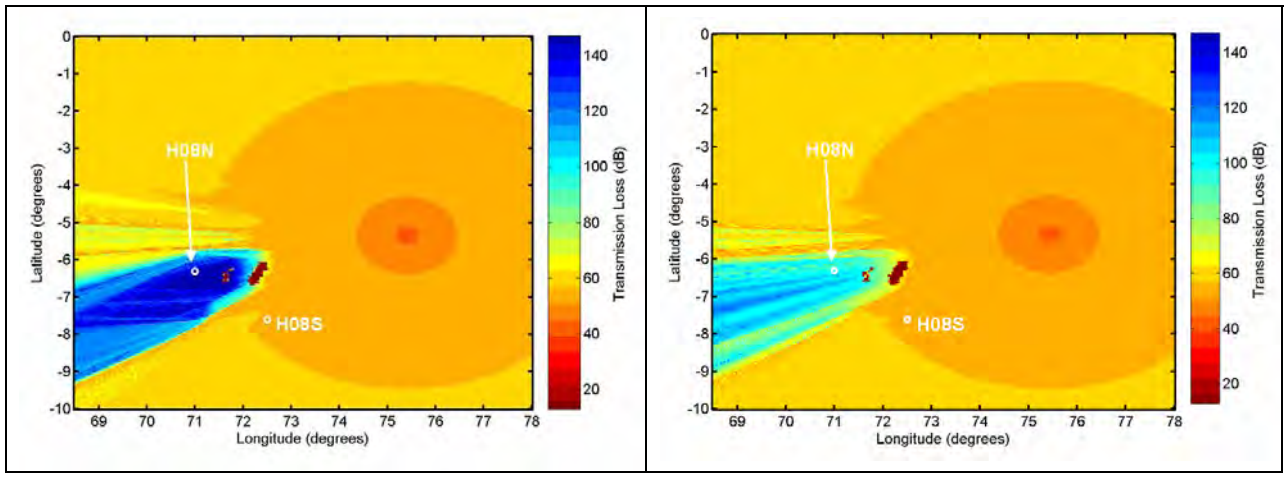

Figure 11. AMPE propagation prediction at 5 Hz (left) and 10 Hz (right).

These preliminary model results will be studied and advanced over the coming months to further understand the output of the AMPE model, the physics of diffraction at the Chagos Archipelago and the use of this model in the context of nuclear explosion monitoring. For example, higher resolution environmental data (bathymetry, sound velocity, etc.) will be integrated into the model. Also, it will be used to predict diffraction and transmission effects from a variety of azimuths. Amplitude measurements will be used to refine and validate the model.

CONCLUSION(S) AND RECOMMENDATIONS

Through a regimen of data analysis and modeling, we are coming to a deeper understanding of the complexity of the blockage issue. For the 150+ earthquake event database, we have measured signal and noise amplitudes and conducted some large-scale analysis to understand source effects on amplitude. Further study is required to completely understand the variation of source amplitudes with event depth, magnitude, azimuth, source mechanism, etc. In the coming months, we will apply Bayesian Kriging techniques to this data in order to predict the spatial effects of bathymetry on signal amplitudes.

We have identified and conducted a preliminary analysis of the (AMPE) model. This model demonstrates potential in the modeling of diffraction and transmission effects on signal amplitude. Initial modeling demonstrates frequency dependence on the physical process of blockage. This model will be integrated into HydroCAM in the next few months. Further study is required to refine the model for nuclear monitoring use, integrate the model into HydroCAM, and thoroughly evaluate the physical process of blockage.

REFERENCES

Bhattacharyya J., A. Rodgers, J. Swenson, C. Schultz, W. Walter, W. Mooney and G. Clitheroe (2000), LLNL's regional model calibration and body-wave discrimination research in the Former Soviet Union using peaceful nuclear weapons (PNEs), in *22nd Annual DoD/DOE Seismic Research Symposium*, Vol. 1, pp. 3-12..

Collins, M. D. (1993), The Adiabatic Mode Parabolic Equation, *J. Acoust. Soc. Am*. 94: (4), pp. 2269-2248

Collins, M. D., B. E. McDonald, K. D. Heaney, and W. A. Kuperman (1995), Three-dimensional effects in global qacoustics. *J. Acoust. Soc. Am*. 97: (3), pp. 1567-1575

Farrell, T., K. LePage, C. Barklay, J. Angell, M. Barger (1997), Users Guide for the Hydroacoustic Coverage Assessment Model (HydroCAM). BBN Technical Memorandum W1309

Fisk, M. S. Bottone, G. McCartor (2000), Regional seismic event characterization using a Bayesiean Kriging Approach, in *22nd Annual DoD/DOE Seismic Research Symposium*, Vol. 1, pp. 23-34.

Pulli, J.J., Z.M. Upton (2001), Hydroacoustic blockage at Diego Garcia: models and observations, in *Proceedings of the 23rd Seismic Research Review: Worldwide Monitoring of Nuclear Explosions*, Vol. 2, pp. 45-54.

Rodgers, A., W. Walter, C. Schultz, S. Myers, and T. Lay (1999), A Comparison of Methodologies for Representing Path Effects on Regional P/S Discriminants, */Bulletin of the Seismological Society of //America/* 89:394-408.

Radionuclide Monitoring

DESIGN OF AEROSOL SAMPLER TO REMOVE RADON AND THORON PROGENY INTERFERENCE FROM AEROSOL SAMPLES FOR NUCLEAR EXPLOSION MONITORING

S. R. Biegalski and O. A. Ezekoye

The University of Texas at Austin

Sponsored by Army Space and Missile Defense Command

Contract No. W9113M-05-1-0016

ABSTRACT

An aerosol sampler is being designed to physically separate aerosols containing radioactivity from natural origin from aerosols containing radioactivity produced in a nuclear weapons explosion. Studies show that aerosols with natural activity have an aerodynamic diameter in the range of 0.1 to 1 μm. In contrast, atmospheric nuclear explosions produce radioactive aerosols with aerodynamic diameters less than 0.1 μm. Surface nuclear explosions produce a bimodal distribution of radioactive aerosol particles. The first group of particles in a surface explosion is produced by spontaneous nucleation and is very similar in distribution to that of the atmospheric explosion. These particles do not combine with material from the ground entrained within the explosion and have aerodynamic diameters less than 0.1 μm. The second group of particles from a surface explosion contains admixed particles entrained in the explosion and has particles with aerodynamic diameters greater than 1 μm. These differences in aerosol sizes are quite fortuitous because they allow aerosol aerodynamic diameter to be utilized as a physical property to separate aerosols of natural origin from those produced in a nuclear explosion.

The benefits of this aerosol sampler are clear for nuclear explosion monitoring. Since aerosols with natural radioactivity are the primary contributors to background in gamma-ray spectroscopy of the aerosol filters, separation of the natural radioactivity from the aerosol samples will result in detection limit improvements. Not only will the background be reduced, but the air filters will not require significant decay times between collection and the start of the gamma-ray spectrum acquisition. For locations where radon and thoron levels are high, these detection limit improvements will be significant. In addition, the aerosol size provides information that may be utilized to distinguish between a surface explosion and an atmospheric explosion. This information is not available from the aerosol samplers currently in use for nuclear explosion monitoring. The capabilities of the U.S. nuclear explosion monitoring system will be significantly enhanced with this aerosol sampler.

OBJECTIVE(S)

Background

The United States has maintained an interest in nuclear explosion monitoring since the Trinity test shot at Alamagordo, New Mexico on July 16, 1945. In August 1948, the U.S. Air Force created the Office of Atomic Energy-1 (AFOAT-1), giving it responsibility for managing the Atomic Energy Detection System (AEDS) discovering foreign atomic tests and other nuclear-weapons related activities (Ziegler and Jacobson, 1995). The AFOAT-1 would later be renamed the Air Force Technical Applications Center (AFTAC). The initial monitoring was based off of atmospheric aerosol collection from airplanes during transoceanic flights. The first USSR nuclear test conducted at the Semipalatinsk nuclear test site on August 29, 1949, and was subsequently observed by the United States through this atmospheric monitoring (Rhodes, 1995; Ziegler and Jacobson, 1995).

These first nuclear explosion tests were easily observed by aerosol collection. The aerosols were measured on the on the opposite side of the world for up to a month after the explosion (Perkins et al., 1995). Nuclear explosion monitoring became more difficult after the Limited Test Ban Treaty (LTBT) in 1963. The LTBT prohibited atmospheric testing by the signatories and nuclear weapons testing consequently moved underground. While the underground testing did contain significant portions of the fission products, many tests vented and released substantial radioactive material. Nuclear explosion monitoring focused on new technologies to monitor the underground tests. The aerosol collection stations were upgraded to enhance detection limits. Noble gases (e.g., Xe) have a higher probability for release from underground explosions, so noble gas monitoring was adopted into the nuclear explosion monitoring efforts. Additional focus was also given to seismic monitoring that could precisely determine the time of the event, accurately determine the location of the explosion, and estimate the yield.

The United States currently maintains a program to look for nuclear explosions (Welch, 1997). Atmospheric radionuclide monitoring is one technology among the many that are used. The atmospheric monitoring efforts consist of aerosol monitoring and noble gas monitoring. This proposal will focus on a way to improve the detection capability of the aerosol monitoring stations.

Aerosol Collection and Measurement

Current aerosol monitoring stations are stationary and work by filtering a large volume of air at flow rates between 500 and 1000 m^3 hr^{-1}. A nominal collection methodology is to collect the air filter for 24 hours, allow the radionuclides on the filter paper to decay for 24 hours, and then acquire a gamma-ray spectrum of the air filter is for 24 hours. The total turnaround time for a sample collection, decay, and gamma-ray spectrum acquisition is 72 hours.

Natural background radiation is one of the main factors that inhibit the detection of nuclear weapons debris through aerosol monitoring. Figure 1 shows an example of an aerosol filter gamma-ray spectrum exhibiting signal from just natural radionuclides. The presence of these natural radionuclides in the gamma-ray spectrum raises the Compton continuum and decreases the detection capability for radionuclides resulting from nuclear weapons tests.

The main contributors to the natural radiation spectrum are thoron progeny, radon progeny, ^{40}K (a primordial radionuclide), and ^{7}Be (produced through cosmic-ray interactions in the atmosphere). Specifically, ^{208}Tl, ^{212}Bi, and ^{214}Bi cause the majority of the Compton continuum in the rage most fission products are expected to be measured (300 to 1300 keV). Thus, the concentrations of these radionuclides in an aerosol sample directly affect the detection limits for fission products. In the thoron decay series, ^{212}Pb is the longest lived progeny with a half-life of 10.6 hours. In the radon decay series, ^{214}Pb is the progeny to be noted with a half-life of 26.8 minutes (Willeke and Baron, 1993). In order to decrease the Compton continuum contributions from thoron and radon progeny, air filters are normally allowed to decay for up to 24 hours. While ^{210}Pb has a half-life of 22 years, it does not contribute significant Compton continuum interference due to its low energy gamma-ray.

The relationship between detection limit and the concentration of thoron progeny is shown in Figure 2. The figure shows the relationship between ^{140}Ba minimum detectable concentration (MDC) as calculated by the Currie method (Currie, 1968) and ^{212}Pb concentration. The concentrations of ^{212}Pb, ^{212}Bi, ^{212}Po, and ^{208}Tl reach a state of equilibrium during the decay period after sample collection. Therefore, the relationship shown in Figure 2 represents

the combined effect of thoron progeny on ^{140}Ba MDC. Likewise, the MDC for ^{140}Ba (main gamma-ray energy at 537 keV) should be considered illustrative of other radionuclides that have gamma-rays in the same energy region.

Figure 2 shows ^{212}Pb concentrations ranging up to 0.02 Bq m^{-3}. These concentrations are actually quite moderate in comparison to regions of the world that have high thoron concentrations. For example, ^{212}Pb atmospheric aerosol concentrations in Europe range up to 0.1 Bq m^{-3} (Gäggeler, 1995). This is a factor of five higher than what was observed in Charlottesville, Virginia during the measurement period from November 18, 2000 to January 21, 2001. For the range shown in Figure 2, the relationship between ^{140}Ba MDC and thoron concentration appears linear. However, the relationship is actually a function of the square root of the Compton continuum at the point of the ^{140}Ba primary gamma-ray line. Therefore, extrapolation of this relationship to higher ^{212}Pb concentrations is difficult. The conclusion should be that the adverse effect of local thoron concentrations can be much worse than what is shown with the data from Charlottesville, VA.

Detection limit improvements may also be seen if the sample decay time is shortened. The 24 hour decay time is currently needed in the sampling methodology to allow for decay of the short-lived radon and thoron progeny. This consequently reduces the magnitude of the Compton continuum. While this is advantageous for detection of radionuclides with half-lives longer than a few days, the detection of shorter-lived radionuclides is depreciated by the 24 hour decay time. Many radionuclides of interest to nuclear explosion monitoring fall into the category of having a half-live less than 24 hours (e.g., ^{91}Sr, ^{93}Y, ^{97}Zr, ^{99m}Tc, ^{133}I, ^{135}I, ^{156}Sm and ^{157}Eu). By removing the natural radioactivity from the aerosol sample, the gamma-ray spectrum acquisition may start with no need for decay time after the end of the sample collection. In fact, gamma-ray spectrum acquisition could be conducted during aerosol collection without significant interference from natural radioactivity. A reduction in decay time would result in a detection limit improvement for nearly all radionuclides of interest for nuclear explosion monitoring.

The MDC for a given radionuclide may generally be calculated as shown in equation 1 (Biegalski and Biegalski, 2001). This formula assumes that the radionuclide is not a daughter involved in a complex decay chain.

$$MDC = \frac{L_D \lambda^2}{\varepsilon I_\gamma F \left(1 - e^{-\lambda t_c}\right)\left(e^{-\lambda t_d}\right)\left(1 - e^{-\lambda t_a}\right)} \quad (1)$$

where

L_D is the detection limit
ε is the detector efficiency
I_γ is the radionuclide gamma-ray yield
λ is the radionuclide decay constant
t_c is the aerosol collection time
t_d is the sample decay time
t_a is the gamma-ray spectrum acquisition time

This formula may be utilized to calculate the MDC achieved by shortening the decay time. Table 1 shows the factor improvements expected from a reduction in decay time from 24 hours to 0, 1, and 4 hours. These improvements are directly related to the radionuclide half-life. The shortest-lived radionuclide in this example, ^{99m}Tc, would receive more than a factor of 15 improvement in MDC with a reduction in decay time from 24 hours to 0 hours. These factors assume that all other factors in equation 1 remain constant for the comparison. Due to the time-dependent dynamics of the Compton continuum structure these values should be referred to as only rough estimates.

The combination of reduced Compton continuum and reduced decay times will produce significant MDC improvements for the detection of aerosols containing nuclear explosion debris. Reduction in MDC by a factor of 3 may be expected for high radon and thoron days at locations like Charlottesville, VA. Far greater improvements may be expected for sampling locations with much higher radon and thoron concentrations. Reduction in decay time will also result in improvements for radionuclides with half-lives on the order of one day or less. Depending on the radionuclide and the decay time, this improvement will reduce the MDC by a factor ranging between 2 and 15. The combination of these effects could easily result in a factor of six improvement in MDCs for various radionuclides of interest. Factors above ten would be realistic for station locations that have high radon and thoron levels.

Aerosol Size of Natural Radioactive Aerosols and Radioactive Aerosols from Nuclear Explosions

In order to improve the detection capability for ground-based aerosol collection systems, it is advantageous to physically separate the natural radioactive aerosols from the radioactive aerosols produced in a nuclear explosion. Figure 3 is an illustration of the size range that these aerosol particles may be categorized in. Separation of the natural radioactive aerosol particles by size will allow for significant improvements to be made in ground based aerosol detection system MDCs for nuclear explosion debris.

Work published by Grundela and Porstend (2004) show that the majority of aerosol particles containing thoron progeny lie in the size range between 0.1 μm and 1.0 μm. The measurements were made with an on-line alpha cascade impactor for many natural radionuclides. The results for ^{212}Po and ^{218}Po are very similar and their consistency illustrates that all thoron progeny likely fall within this aerosol size range. While these data are specific to the aerosols collected in Göttingen, Germany, the results are similar to those found in other studies for thoron progeny (Bondietti et al., 1987).

Storebø (1974) published an extensive study on the aerosol size distributions of debris from nuclear explosions. For an atmospheric explosion, nearly all the aerosol particles fall below the 0.1 μm mark for cases where the vapor mixing ratio is 10^{-4} or less. For surface explosions, the particles are generated in a bimodal distribution. The first group of particles in a surface explosion is produced by spontaneous nucleation and is very similar in distribution to that of the atmospheric explosion. These particles do not combine with material from the ground entrained within the explosion and have aerodynamic diameters less than 0.1 μm. The second group of particles from a surface explosion contains admixed particles entrained in the explosion and has particles with aerodynamic diameters greater than 1 μm. An underground nuclear explosion may be categorized as a surface explosion with a high initial surrounding concentration. The data provided in the Storebø (1974) publication is consistent with aerosols collected in Sweden from the September 26, 1976 Chinese nuclear explosion (De Geer et al., 1978), an above-ground test performed at Lop Nor in the range of 20-200 kt.

Water surface and underwater bursts were not included in the study by Storebø (1974). Glasstone and Dolon (1977) state that the particles entering the atmosphere from a sea burst consist mainly of salts and water drops. When dry, these particles are very small and light. As a result, it may be assumed that a water surface or underwater burst will produce aerosol particles with size similar to those produced in an atmospheric explosion. However, during transport the hygroscopic nature of the seal salt particles may cause the particles to grow if they enter a region with high humidity.

RESEARCH ACCOMPLISHED

Research has been initiated to design an aerosol sampler that will selectively remove aerosols in the 0.1 to 1 μm range. Many different designs exist for aerosol samples to separate a particle by size. These designs are largely based off the inertia of the particles as they are pulled through the sampler. In a curved flow field inertia makes the particle trajectories deviate from the flow streamlines (Willeke and Baron, 1993). The particles that deviate from the flow streamlines are then removed from the air flow and consequently collected. The two main designs used for aerosol separation by size are the cyclone design and the impactor design. In a cyclone, particles are removed from the air flow by the centrifugal force. In general, a cyclone does not yield as sharp a cutoff in particle size as an impactor (Willeke and Baron, 1993). For this reason, the impactor design if preferred for this project.

By combining several single-stage impactors in a series, a multistage impactor may be constructed. Each stage within the impactor would collect particles with a specific inertial range. The first stage would collect the particles with the most inertia (largest particles) and subsequent stages would collect smaller particles. This is achieved by decreasing the nozzle diameter in each successive stage.

Figure 4 shows how the aerosol sampler will collect aerosol particles in three separate stages. The first stage will contain the largest aerosol particles with an aerodynamic diameter greater than 1 μm (second group of particles from surface nuclear explosions). The second stage will collect aerosol particles with an aerodynamic diameter between 0.1 μm and 1 μm (aerosols of natural origin). The third stage will collect aerosol particles with an aerodynamic diameter less than 0.1 μm (aerosols from atmospheric nuclear explosions and the first group of particles produced in

a surface explosion). To increase the volumetric flow through the sampler, a grid of cascade impactors as shown in Figure 4 will likely be utilized in the prototype sampler.

This sampler will result in the majority of the natural radioactivity being deposited on the Stage 2 filter. The Stage 1 and Stage 3 filters will contain the aerosols in the size region produced during nuclear explosions. A number of scenarios are possible for gamma-ray spectrum acquisition. One scenario would be to acquire a gamma-ray spectrum for the Stage 1 and Stage 3 filters with no decay time after collection. A second gamma-ray spectrum of the Stage 1, 2, and 3 filters could be collected after 24 hours of decay. Experiments will have to be conducted to determine the optimum methodology, but it should be clear that all aerosol material is collected with this sampler and will be available for subsequent analysis. This sampler will in no situation reduce the detection capabilities for aerosols from nuclear explosions.

The flow field for these computations will be found from using a commercial computational fluid dynamics (CFD) package (Fluent 6.1). The CFD solver has been benchmarked to solve transport equations in complex geometries. Our most recent study used this software tool to investigate aerosol transport in a smoke detector geometry. The user defined function (UDFs) for the smoke detector analysis will be modified to analyze the impactor design in the proposed project. The CFD simulations will be used to determine both the streamline behavior through the impactor plates as well as to determine how close to the theoretical value of $\sqrt{St_{50}} \approx 0.49$ our system can be designed.

CONCLUSIONS AND RECOMMENDATIONS

Within the next year, The University of Texas at Austin will complete the design and construction of this prototype aerosol sampler. Testing will be conducted to verify the aerosol cut-off diameters achieved by the sampler. Environmental sampling with confirm the size range of the natural aerosols. Once the prototype sampler has been fully tested, an effort will be placed to design a modification to allow size separation in the aerosol samplers currently deployed by the U.S. Government for nuclear weapons test monitoring.

REFERENCESS

K. M. F. Biegalski and S. Biegalski (2001), Determining detection limits and minimum detectable concentrations for noble gas detectors utilizing beta-gamma coincidence systems, *J. Radioanal. Nucl. Chem.*, 248 (3), 673.

E. A. Bondietti, C. Papastefanou, and C. Rangarajan (1987), Aerodynamic size associations of natural radioactivity with ambient aerosols, in *Radon and is Decay Products-Occurrence, Properties and Health Effects*, ed. P. K. Hopke. ASC-Symposium Series 3131, 397.

L A. Currie (1968), Limits for Qualitative and Quantitative Detection, *Anal. Chem.* 40: 586.

Lars-Erik De Geer, Rune Arntsing, Ingemar Vintersved, Jan Sisefsky, Siv Jakobsson, Jan-Ake Engstrom (1978). Particulate Radioactivity, Mainly from nuclear explosions, in air and precipitation in Sweden mid-year 1975 to mid-year 1977, FOA Report, FOA-C—40089

H. W. Gäggeler (1995). Radioactivity in the Atmosphere, *Radiochemica Acta*, 70/71: 345.

S. Glasstone and P. J. Dolan (1977), *TheEffects of Nuclear Weapons, 3rd Edition*, United States Department of Defense and the United States Department of Energy.

M. Grundela and J. Porstend (2004), Differences between the activity size distributions of the different natural radionuclide aerosols in outdoor air, *Atmos. Env.* 38: 3723.

Perkins, Miley, Hensley, Abel (1995). Airborne Radionuclides of Concern and Their Measurement in Monitoring a Comprehesive Test Ban Treaty, PNL-SA-25481.

R. Rhodes (1995), *The Making of the Atomic Bomb*, Simon & Schuster, New York.

P. B. Storebø (1974), Formation of Radioactivity Size Distributions in Nuclear Bomb Debris, *Aerosol Sci.* 5: 557.

M. Welch (1997), AFTAC Celebrates 50 Years of Long Range Detection, *AFTAC Monitor*.

K. Willeke and P. A. Baron (1993), *Aerosol Measurement: Principles Techniques and Applications*, Van Nostrand Reinhold, New York.

C.A. Ziegler and D. Jacobson (1995), *Spying Without Spies: Origin of America's Secret Nuclear Intelligence Surveillance System*, Praeger.

Table 1. Estimated Improvement in MDC Resulting from Decay Time Reduction (assuming all other factors equal).

Nuclide	Half-life (hr)	Factor Improvement in MDC Resulting from Decay Time Reduction From 24 Hours		
		0 hr Decay	1 hr Decay	4 hr Decay
^{91}Sr	9.63	5.6	5.2	4.2
^{93}Y	10.18	5.1	4.8	3.9
^{97}Zr	16.91	2.7	2.6	2.3
^{99m}Tc	6.01	15.9	14.2	10.0
^{133}I	20.8	2.2	2.2	1.9
^{135}I	6.57	12.6	11.3	8.2
^{156}Sm	9.4	5.9	5.5	4.4
^{157}Eu	15.18	3.0	2.9	2.5

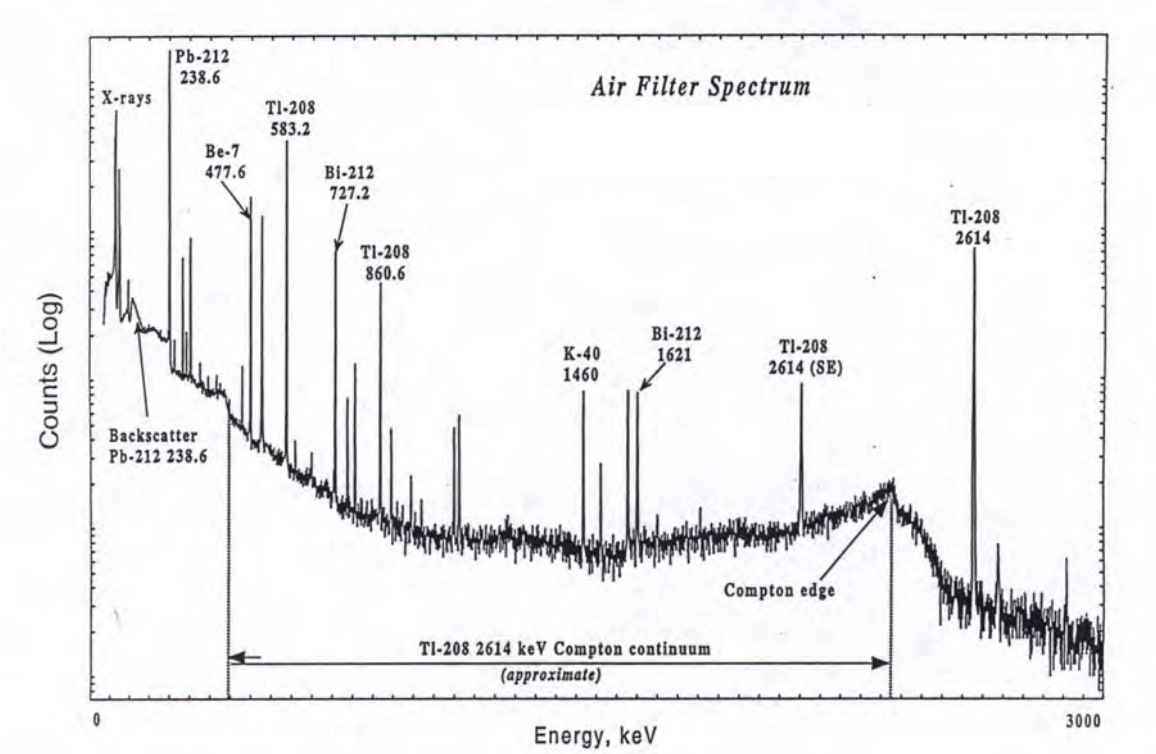

Figure 1. Gamma-ray spectrum of air filter acquired on a HPGe detector (24 hour collection, 24 hour decay, and 24 hour spectrum acquisition).

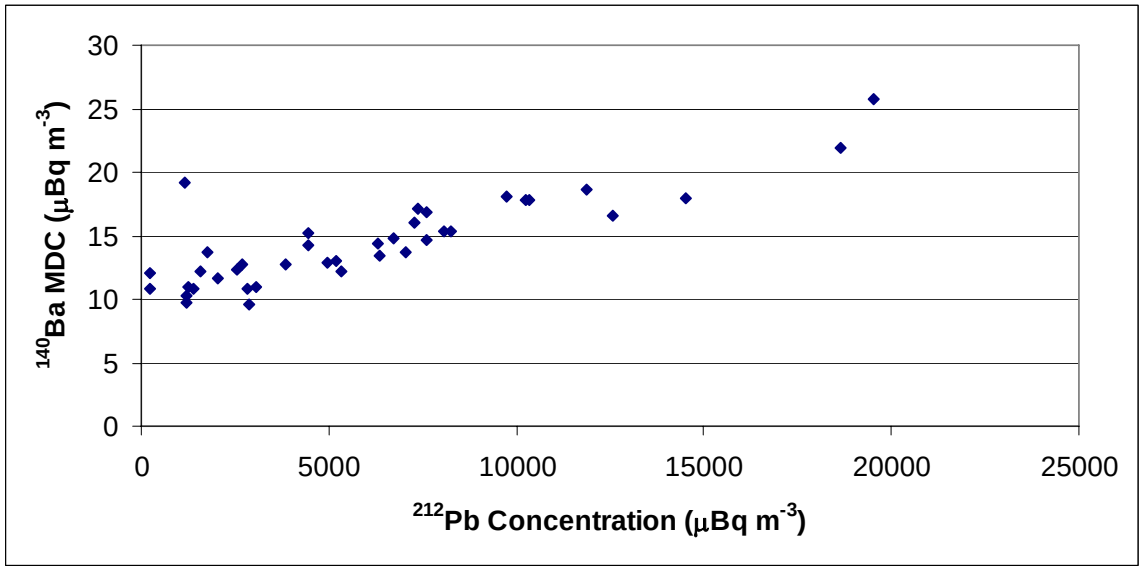

Figure 2. Relationship between ^{140}Ba minimum detection limit and ^{212}Pb concentration for aerosol sampling station in Charlottesville, VA, USA. The collection, decay, and gamma-ray spectrum acquisition periods were 24 hours each. These samples were collected November 18, 2000 to January 21, 2001.

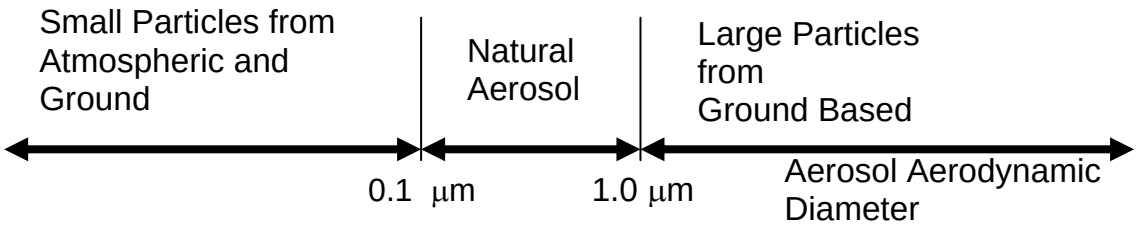

Figure 3. Size range of aerosol particles from natural sources and nuclear explosions.

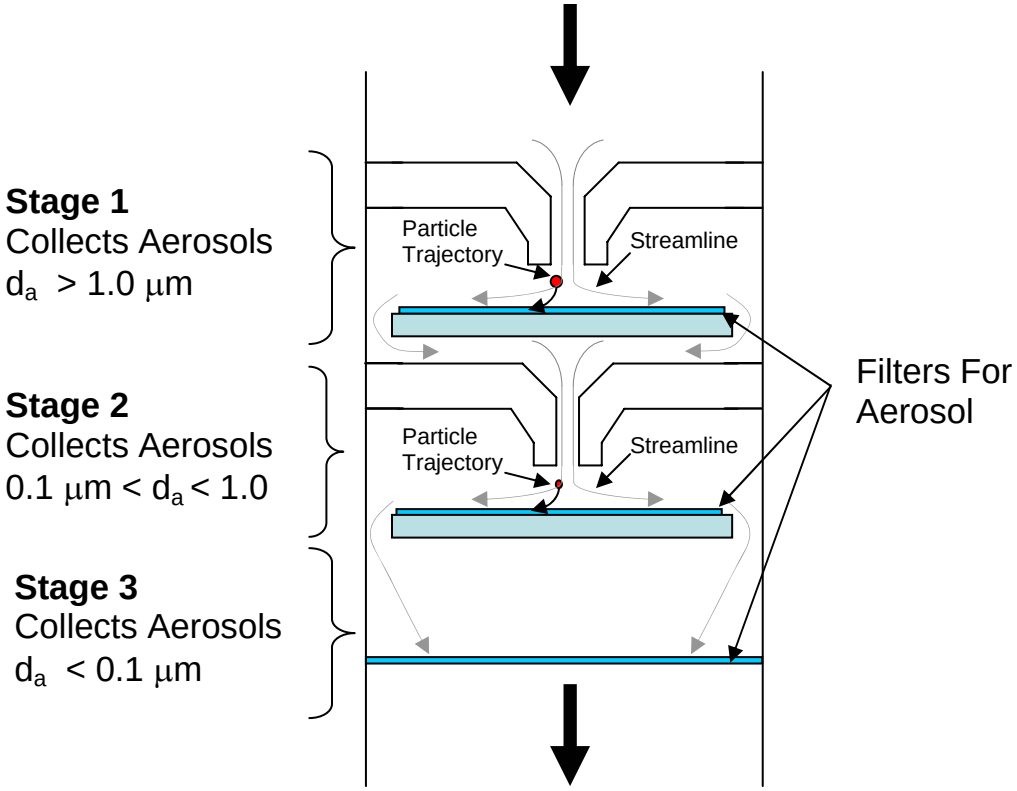

Figure 4. Three stage impactor.

DEVELOPMENT OF THE SPECTRAL DECONVOLUTION ANALYSIS TOOL (SDAT) TO IMPROVE COUNTING STATISTICS AND DETECTION LIMITS FOR NUCLEAR EXPLOSION RADIONUCLIDE MEASUREMENTS

S. R. Biegalski, K. M. Foltz Biegalski, and D. A. Haas

The University of Texas at Austin, Austin, TX 78712

Sponsored by Army Space and Missile Defense Command

Contract No. W9113M-05-1-0017

ABSTRACT

The Spectral Deconvolution Analysis Tool (SDAT) is being written to improve counting statistics and detection limits for nuclear explosion radionuclide measurements. SDAT will utilize spectral deconvolution spectroscopy techniques to analyze both β–γ coincidence spectra for radioxenon isotopes and high-resolution High Purity Germanium (HPGe) spectra that are utilized for aerosol monitoring. Spectral deconvolution spectroscopy is an analysis method that utilizes the entire signal deposited in a gamma-ray detector rather than the small portion of the signal that is present in one gamma-ray peak. Counting statistics are improved by utilizing the entire detector response and the deconvolution algorithm directly handles interferences between radionuclides. This method shows promise to improve detection limits over classical gamma-ray spectroscopy analytical techniques.

The Multiple Isotope Comparison Analysis (MICA) algorithm was developed previously to demonstrate the concept for this technique for β–γ coincidence spectra utilized for radioxenon analysis. These spectra are difficult to analyze by the classical peak analysis technique due to spectral interferences among the radioxenon isotopes as well as the interferences between radon progeny and the radioxenon isotopes. The deconvolution algorithm unravels the interferences and utilizes the complete signal from each radionuclide. While the MICA algorithm has demonstrated its utility for the analysis of β–γ coincidence spectra, additional developments are necessary before this technique reaches a point where it may be applied in an operational environment. SDAT will incorporate the complete functionality of the MICA algorithm, will add in spectral weighting functions to reduce the analytical residual, and will include the ability to analyze high-resolution HPGe spectra with the deconvolution method.

A significant portion of this work will involve the development of calibration methods for both radioxenon and high-resolution HPGe systems. Proper calibrations of the detection systems are especially necessary for application of the spectral deconvolution spectroscopy algorithm. The detector response from each radionuclide of interest must be individually determined. The University of Texas TRIGA reactor will be utilized to irradiate a fission product generator for production of xenon isotopes for calibration. Fission products will also be generated for calibration and testing of the SDAT algorithm for HPGe spectra. Calibrations will be conducted through experimental measurements and will also be supported through Monte Carlo N-Particle Extended (MCNPX) modeling.

OBJECTIVE(S)

Background

Spectral deconvolution algorithims have been investigated for use on the analysis of β-γ coincidence spectra from the Automated Radioxenon Sampler/Analyzer (ARSA) (Biegalski and Biegalski, 2004). The ARSA was initially developed by Pacific Northwest National Laboratory (PNNL) for the purpose of monitoring atmospheric radioxenon levels for nuclear explosion monitoring (Bowyer, 1998). This system utilizes a β-γ coincidence spectroscopy system that acquires energy dispersive data on both the beta energy and photon energy axes. The initial software program written at the Center for Monitoring Research to analyze the ARSA data was *rms_xanalyze* (Biegalski, 2001). This algorithm is based on a Region of Interest (ROI) approach similar to most high-resolution gamma spectroscopy algorithms, but applied in two dimensions. The main problem arising with the *rms_xanalyze* algorithm is that not all the physics of the problem are taken into account (such as ^{135}Xe contributions in the E_γ = 30 keV region), which can result in negative net counts or higher than necessary false positive detection rates for some radioxenons. To improve the data processing for such β-γ coincidence data, work has been underway on a new software algorithm that incorporated all known physics and reduced the uncertainties involved in the results.

The new software involves the deconvolution of a sample signal into the contributions from each isotope. Detector-specific responses for each possible isotope are used in the deconvolution. The responses can be generated using actual radioisotope sources counted on the detector, or they can be created using modeling techniques like the MCNPX code. The geometry and materials of the detector must be known to produce good response files. Because only five different isotopes are detected in xenon samples, deconvolving a sample is not highly complex. Deconvolution of nuclear spectroscopy data is not a new concept (Prettyman et al., 1995). What makes this research unique is that this methodology is applied to 3-D β-γ coincidence data.

Required Input Data

The detector response for a sample consists of a 255 x 255 matrix of numbers. Each entry represents the number of counts registered in a certain $E\gamma$, E_β bin. Each row represents a γ-channel bin and each column represents a β-channel bin. We will refer to this structure as a histogram. Other information contained in the sample file includes calibration information and other sample characteristics, e.g., the sample Xe gas volume from which the total sampled atmospheric volume is calculated.

It is the sample histogram that will be deconvolved into individual isotopic responses using the MICA concept to determine atmospheric activity concentrations for each radioxenon of interest. To do this, however, we must have calibrated histograms of all the possible individual signals that can make up a sample histogram. These histograms should have the same size and calibration characteristics as the sample histogram in addition to good counting statistics. Therefore, we need the following detector response matrices with their associated activities:

$$\left[^{131m}Xe\right]_{255x255},\ \left[^{133m}Xe\right]_{255x255},\ \left[^{133}Xe\right]_{255x255},\ \left[^{135}Xe\right]_{255x255},\ \left[^{214}Pb\right]_{255x255},\ \text{and}$$
$$\left[DETBKG\right]_{255x255}. \quad (1)$$

Each detector response histogram can be generated using a detector modeling program like MCNPX or acquired by counting a calibration source on the detector. Since the ARSA has four beta detector cells, the above detector response histograms would need to be generated or acquired for each beta cell. In addition, the energy, resolution, and efficiency calibrations have to be determined for each beta cell. With all of this information at hand, and knowing in which detector cell the sample was counted, the following algorithm can be applied to a sample for determining the atmospheric radioxenon concentrations.

Concentration Calculation

First, the detector response histograms and sample histogram are vectorized, i.e., the 255 x 255 matrices are converted into column vectors of dimension 65025x1. This is done by appending each histogram row onto one another, and then transposing the resulting row matrix, i.e.,

$$\begin{aligned}
&\left[{}^{131m}Xe\right]_{255\,x255} \rightarrow \left[{}^{131m}Xe\right]_{65025\,x1}, \\
&\left[{}^{133m}Xe\right]_{255\,x255} \rightarrow \left[{}^{133m}Xe\right]_{65025\,x1}, \\
&\left[{}^{133}Xe\right]_{255\,x255} \rightarrow \left[{}^{133}Xe\right]_{65025\,x1}, \\
&\left[{}^{135}Xe\right]_{255\,x255} \rightarrow \left[{}^{135}Xe\right]_{65025\,x1}, \\
&\left[{}^{214}Pb\right]_{255\,x255} \rightarrow \left[{}^{214}Pb\right]_{65025\,x1}, \\
&\left[DETBKG\right]_{255\,x255} \rightarrow \left[DETBKG\right]_{65025\,x1}, \\
&\left[SAMPLE\right]_{255\,x255} \rightarrow \left[SAMPLE\right]_{65025\,x1}.
\end{aligned} \tag{2}$$

The separate vectorized detector response histograms are then assembled into a response matrix like so:

$$\left[\left[{}^{131m}Xe\right]_{65025\,x1}\ \left[{}^{133m}Xe\right]_{62025\,x1}\ \left[{}^{133}Xe\right]_{62025\,x1}\ \left[{}^{135}Xe\right]_{62025\,x1}\ \left[{}^{214}Pb\right]_{62025\,x1}\ \left[DETBKG\right]_{62025\,x1}\right]_{62025\,x6} \tag{3}$$

This results in a two-dimensional matrix with 65,025 rows and six columns, i.e.,

$$\left[\mathrm{Re}\,sponse\right]_{65025\,x6} = \begin{bmatrix} X & X & X & X & P & D \\ e & e & e & e & b & E \\ 1 & 1 & 1 & 1 & 2 & T \\ 3 & 3 & 3 & 3 & 1 & B \\ 1 & 3 & 3 & 5 & 4 & K \\ m & m & & & & G \end{bmatrix}_{65025\,x6} \tag{4}$$

The response matrix is related to the vectorized sample histogram by the following equation:

$$\left[\mathrm{Re}\,sponse\right]_{65025\,x6}\ \left[Coefficients\right]_{6\,x1} = \left[Sample\right]_{65025\,x1} \tag{5}$$

The coefficient matrix holds the multipliers needed for multiplying the activities associated with each of the detector response histogram to obtain the sample activities for each isotope in the sample. This is a classic over-determined system of equations. The non-negative least squares solution was chosen to solve for $[\text{Coefficients}]_{6x1}$ in this problem (Lawson and Hanson, 1974). This method was chosen over the standard least squares solution since all the components of the $[\text{Coefficients}]_{6x1}$ matrix should be greater than or equal to zero.

This same analysis methodology may be applied to HPGe detector spectra as well. However, the library for the HPGe spectra needs to be much larger than for the ARSA spectra since there are significantly more component possibilities. Generation of the HPGe library is possible through individual measurement of each radionuclide of interest or through modeling of the detector with MCNPX.

RESEARCH ACCOMPLISHED

The research accomplished to date falls into two categories. The first category is the writing of the SDAT tool for the spectral analysis. The second category is the detector model generation in MCNPX that will be used to create simulated detector spectra.

SDAT Development

The SDAT development has been initiated in a Matlab environment. Spectral files and library files are stored as text files. SDAT reads these into the code as matrices. The deconvolution is performed via the Matlab least squares routine. Testing has been performed with both the standard least squares routing and the non-negative least squares routine that forces the solution to yield positive results. Both methods have produced the same results for our test spectra.

A spectral gain shifting algorithm has also been written in Matlab for SDAT. This algorithm is necessary to match the gain of the sample spectra with the gain of the library spectra. It may be used for either β–γ coincidence spectra or for HPGe γ spectra. For the β–γ coincidence spectra, the β energy calibration is treated as a second-order polynomial and the γ energy calibration is treated as a first-order polynomial. For the HPGe γ spectra, the energy calibration is treated as a fourth-order polynomial. The code takes the original energy calibrations and then determines transfer coefficients by taking into account the new energy calibration and the number of channels in the spectrum. If the code performs a negative gain shift (condenses data into a fewer number of channels), then the channels at the end of the spectrum are filled with zeros.

Work has also begun on a spectral weighting function algorithm. This algorithm weights parts of the spectrum according to their importance during the deconvolution. This algorithm helps reduce the residual of the deconvolution process and potentially improves the method detection limits. Currently the weighting process is binary: important regions of the spectrum are given a weight of one and unimportant regions of the spectrum are given weights of zero. A quality control routine is being worked on that will alert users if an unanticipated signal is being down weighted.

MCNPX Model Development

MCNPX has been chosen as the code to be utilized for generating the detector models. The reason for choosing MCNPX over MCNP is due the MCNPX's new mesh tallies, coincidence tallies, and plotting capabilities. New detector models have been generated that use the macrobody feature available in MCNPX.

Figure 1 illustrates the photon flux modeled in β–γ coincidence detector model with ^{133}Xe in the top cell. The model simulates the ARSA detector currently being utilized in the Provisional Technical Secretariat Noble Gas Experiment. The detector has four gas cells surrounded by two NaI(Tl) crystals. The beta flux from ^{133}Xe generated from this model is shown in Figure 2. Its first goal will be to qualitatively compare the data generated via the MCNPX model to data collected from the ARSA in China (shown in Figure 3). Initial testing was conducted with the coincidence tallies available in MCNPX, but they do not appear useful for this problem. A post-MCNPX algorithm will be generated to generate the coincidence spectra.

A MCNPX model has also been developed for a HPGe detector. This model is based off of a TennElec closed-end coaxial cylindrical detector with a crystal of diameter 59.5 mm and length of 59 mm. Figure 4 shows an example of this detector model. The model has been used to generate gamma-ray spectra and detector efficiency curves. Initial comparisons show a good correlation to data obtained directly from the detector.

CONCLUSION(S) AND RECOMMENDATION(S)

The work reviewed above had just begun. The SDAT software is still in its infancy state and a significant level of testing is required to optimize the spectral deconvolution algorithm. Data for the SDAT calibration libraries will be generated both through MCNPX models and through experiment. MCNPX models have been developed for both the $\beta-\gamma$ coincidence detector for noble gas detection and the HPGe detector for γ-ray spectroscopy. Work on obtaining fission product spectra through real measurements has not started.

REFERENCE(S)

K. M. F Biegalski and S. Biegalski (2001). Determining detection limits and minimum detectable concentrations for noble gas detectors utilizing beta-gamma coincidence systems, *J. Radioanalytical Nucl. Chem.*, 248: (3), 673.

K.M. Foltz Biegalski (2001). Automatic Analysis Algorithm for Radionuclide Pulse Height Data from Beta-Gamma Coincidence Systems, *J. Radioanalytical Nucl. Chem.* 248: (3), 663.

T.W. Bowyer (1998). Xe Radionuclides, Atmospheric: Monitoring in Encyclopedia of Environmental Analysis and Remediation, editor: R. A. Meyers, John Wiley & Sons, Inc.

G. Knoll (1989) *Radiation Detection and Measurement, 2nd Edition*, John Wiley & Sons, New York.

C.L. Lawson and R.J. Hanson (1974). Solving Least Squares Problems, Englewood Cliffs, N.J., Prentice-Hall, 1974.

T.H. Prettyman, R.A.Cole, R.J. Estep, G.A.Sheppard (1995). A Maximum-Likelihood Reconstruction Algorithm for Tomographic Gamma-Ray Nondestructive Assay, *Nucl.Inst .Meth. Phys. Res. A* 356: 470.

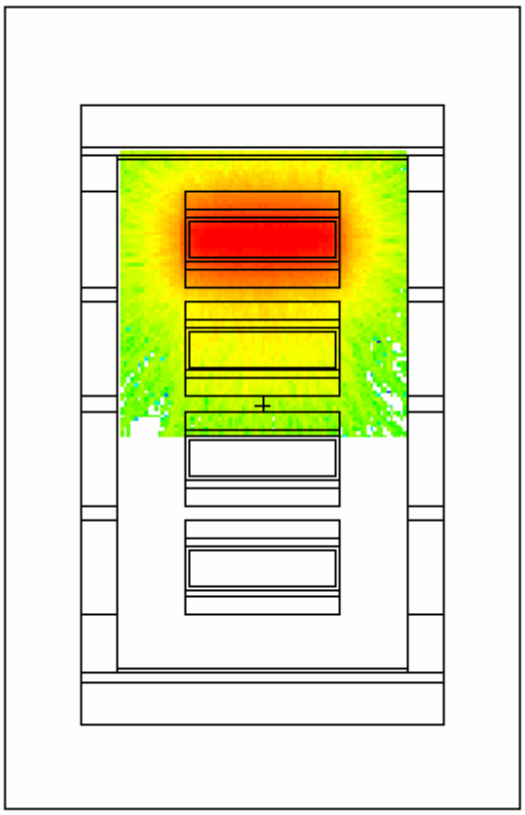

Figure 1. Map of photon flux from ^{133}Xe source in top chamber of β–γ coincidence detector MCNPX model.

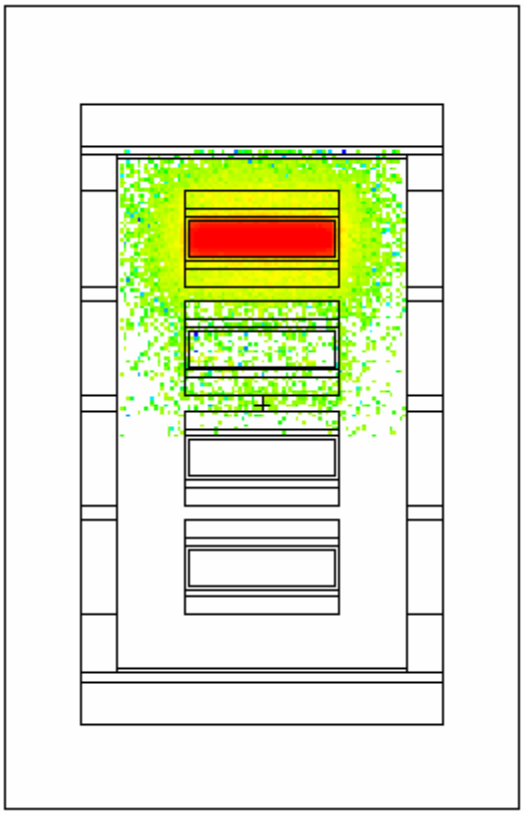

Figure 2. Map of beta flux from ^{133}Xe source in top chamber of β–γ coincidence detector MCNPX model.

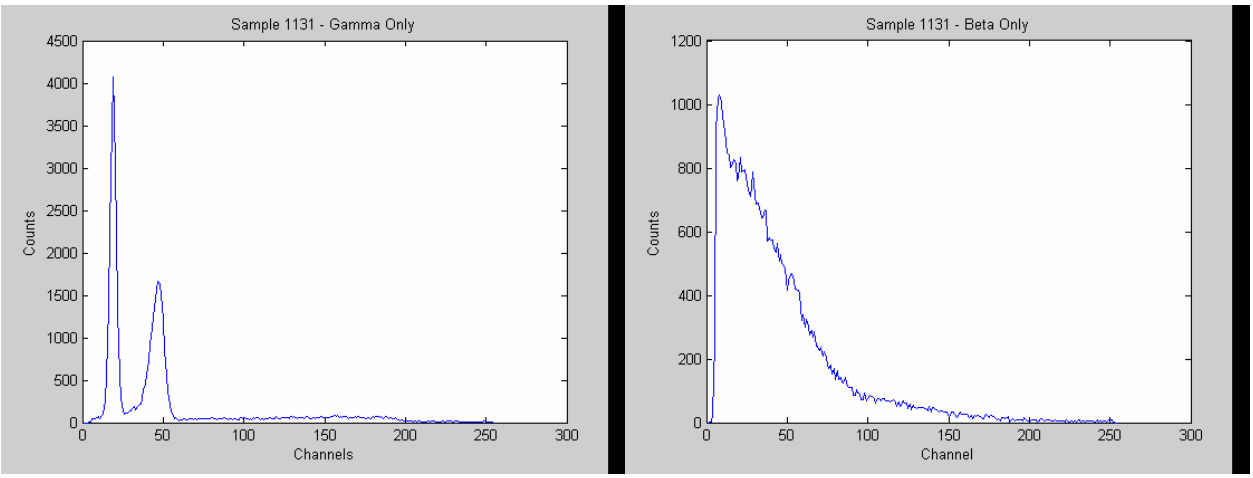

Figure 3. β and γ spectra generated from ARSA in China.

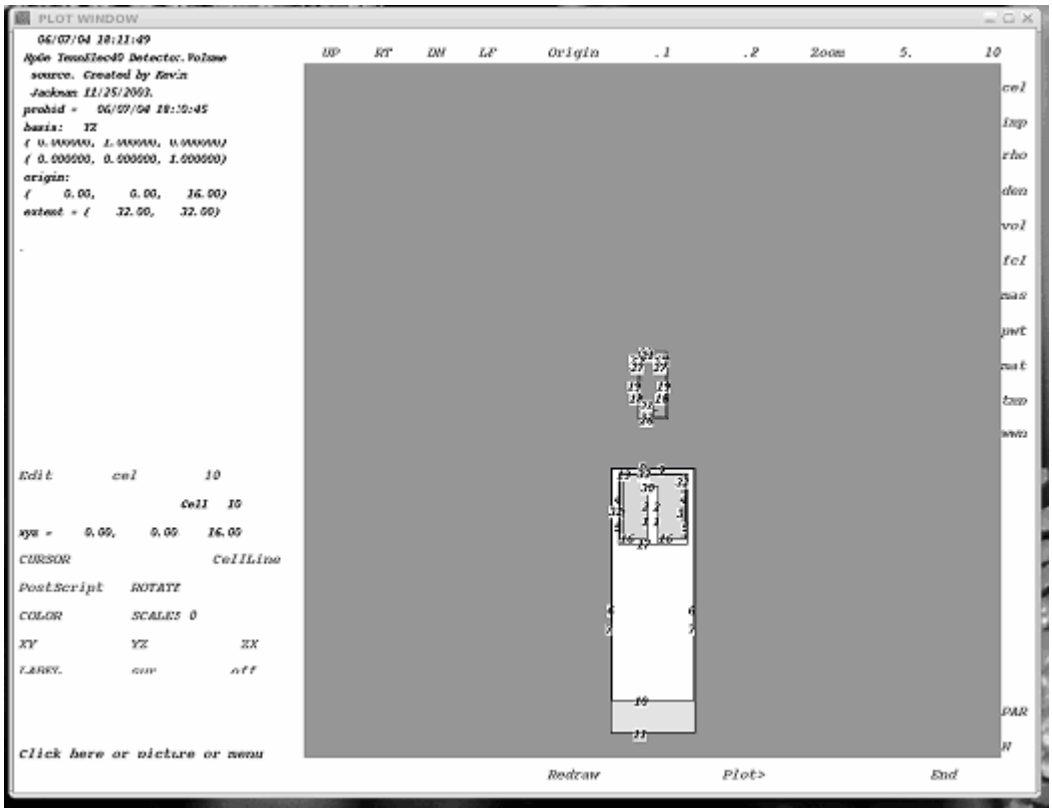

Figure 4. HPGe detector model.

IMPROVED β-γ COINCIDENCE DETECTOR FOR RADIOXENON DETECTION

Matthew W. Cooper, April J. Carman, James C. Hayes, Tom R. Heimbigner, Charles W. Hubbard, Kevin E. Litke, Justin I. McIntyre, Scott J. Morris, Michael D. Ripplinger, and Reynold Suarez

Pacific Northwest National Laboratory

Sponsored by National Nuclear Security Administration
Office of Nonproliferation Research and Engineering
Office of Defense Nuclear Nonproliferation

Contract No. DE-AC06-76RL01830

ABSTRACT

The Automated Radioxenon Analyzer/Sampler (ARSA), built by Pacific Northwest National Laboratory (PNNL), can collect and detect several radioxenon isotopes. ARSA is very sensitive to ^{133}Xe, ^{131m}Xe, ^{133m}Xe and ^{135}Xe due to the compact high efficiency β-γ coincidence detector it uses. For this reason it is an excellent treaty monitoring and environmental sampling device. Although the system is shown to be both robust and reliable, based on several field tests, it is also complex due to a detailed photomultiplier tube gain matching regime. This complexity is a problem from a maintenance and quality assurance/quality control (QA/QC) standpoint. To reduce these issues a simplified β–γ coincident detector has been developed. A comparison of three different well detectors has been completed. In addition, a new plastic scintillator gas cell was constructed. The new simplified detector system has compared favorably with the original ARSA design in spectral resolution and efficiency and is significantly easier to setup and calibrate.

OBJECTIVES

Monitoring radioactive releases from nuclear explosions is a major component of the International Monitoring System [1]. As part of the international effort to develop monitoring equipment PNNL developed and deployed two automated units. The first system developed was the Radionuclide Aerosol Sampler/Analyzer (RASA), which has been deployed at over 30 locations. The RASA collects airborne radioactive particulate debris on filters, which are then counted with a high purity germanium (HPGe) detector [2]. The second system, the Automated Radioxenon Analyzer/Sampler (ARSA)[3], measures radioxenon isotopes by directly collecting and processing air samples. The radioxenon isotopes are generated in nuclear fission, and the isotopic ratios can be used to distinguish the xenon generated in power reactors from that generated in nuclear explosions. The specific isotopes are identified and measured using either the β-γ coincidences or the conversion electron (CE) and x-ray coincidences [4].

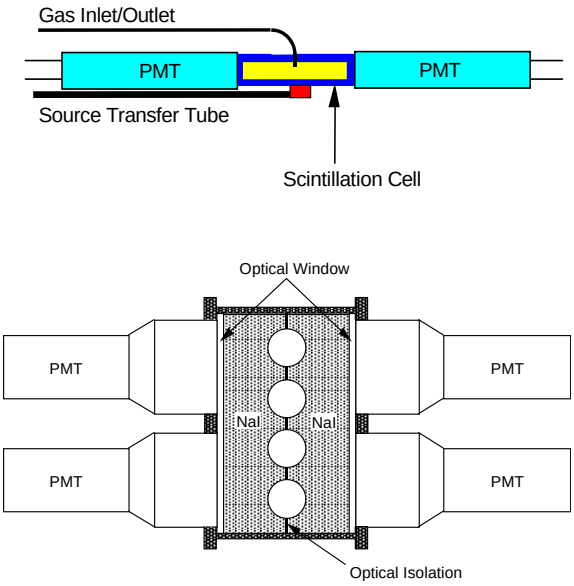

Figure 1. Upper schematic is a representation of the plastic scintillation gas cell with photo-multiplier tubes (PMT), gas transfer line and calibration source transfer tube. The lower schematic is a diagram of the NaI(Tl) γ detector. Plastic scintillator β cells occupy the four holes in the NaI(Tl) detectors. These holes extend all the way through the detector.

In the ARSA, a low background NaI(Tl) detector measures the photon energy and a plastic scintillation gas cell (Figure 1) detects the charged particles. The optimum CE and β energy resolution is achieved by viewing the 5 cm long gas cell on either end by gain matched 15-mm photo-multiplier tubes (PMT). The gas cell has a nearly 100% efficiency due to 4π coverage, although there is a small loss due to the low energy of the β coming from ^{133}Xe and ^{135}Xe as well as the standard losses associated with light transmission in a scintillator. The gas cells are enclosed in four transverse NaI(Tl) wells, which provide very good solid angle coverage for emitted γ- and x-rays while still maintaining a compact unit. The two independent NaI(Tl) crystals allow rejection of multiple scatter and background events; however gain matching the PMTs is also difficult and time consuming. To eliminate gain matching, the number of PMTs can be reduced. However, given a reduction in the PMT number, it is still necessary to maintain a large solid angle (>3.5π coverage) for β-γ nuclear emissions, an adequate energy resolution, a robust scintillation material for field use, and minimal attenuation of x-rays and low energy γ–rays.

Experimental Apparatus

The new design uses a single well detector to detect the x-rays and γ-rays, along with a single PMT gas cell to detect the β and CE emissions. The first diagram in Figure 2 is a rendering of the complete 4 gas cell detector assembly, which includes individual CsI(Na) wells, gas cells, surrounding copper, and 2.5 cm thick lead cave. The well detectors are tightly packed to help reject both cosmic-rays and ambient γ-rays in the same fashion as the original ARSA detector. The second diagram shows the internal layout of the gas cell and PMT with a high-voltage tube base. The gas cell is 28 mm long by 18 mm in diameter with 2 mm thick plastic scintillation walls and a rounded end. A stepped plastic end-cap closes the gas cell and a small hole provides for a thin gas transfer tube. This redesign accomplished several critical goals, which include: simplified calibration, increased robustness, and increased efficiency. The reduction in the initial setup calibration efforts is directly attributed to each of the four γ-ray detectors being able to be calibrated independently. The new detector is more robust since each cell is separate from the others, which in effect eliminates the effect a poor energy or resolution response from a defective PMT has on the other detectors. Finally, the overall detection efficiency has improved with the increase of the solid angle of detection. The gas cell energy resolution was maintained, despite the reduction to one PMT, by using a larger PMT and by rounding the ends of the gas cells.

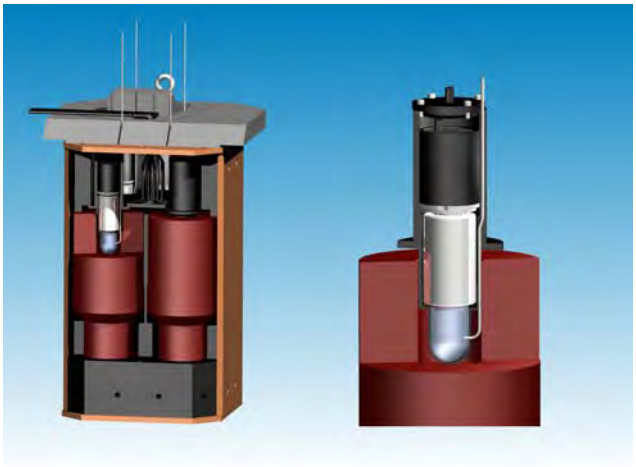

Figure 2. Schematic of four well detectors with gas cells, inside of 1" lead cave. The second schematic is the redesigned gas cell with PMT and tube base. The cell extends 5.5 cm into the CsI(Na) wells to provide the same solid angle coverage as the ARSA gas cells.

RESEARCH ACCOMPLISHED

γ-ray Detectors

Using the new design, studies were performed to replicate and possibly enhance the performance of the γ-ray and gas cell β detectors. Furthermore, a new more robust scintillation material was sought to replace the NaI(Tl). Cesium Iodide doped with Na or Tl were two obvious choices. Cesium Iodide has comparable density, detection efficiency, energy resolution, light output, and timing characteristics with NaI(Tl) but is much more robust. Three well detectors, a NaI(Tl), a CsI(Tl and a CsI(Na), were procured differing only in the material [5]. The crystal sizes were a right cylinder 7.6 cm long by 8.13 cm in diameter, with a 3.1 cm wide by 5.1 cm deep well. The three well detectors were initially compared for resolution and relative efficiency. The 7.5 cm diameter PMTs were optically matched to maximize the total response for the characteristic wavelength emission of each type of crystal. Initial studies included energy response linearity, energy resolution, and efficiency across a wide range of x-ray and γ energies. Figure 3 shows the spectrum obtained with the CsI(Tl) using a multi-line γ-ray standard from Amersham©. The linearity of the energy calibration was excellent for the three detectors, however the CsI detectors were markedly better

across the entire range, see Table 1. The ^{137}Cs γ line at 661.7 keV was used to compare the resolution and efficiency for the three detectors.

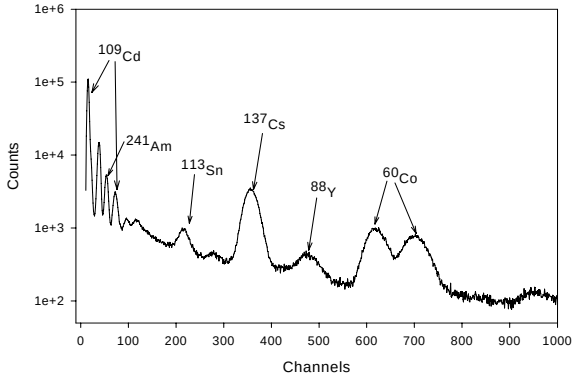

Figure 3. Histogram of the CsI(Tl) response using an Amersham© radiological standard. The energy range covers the 22 keV x-ray from ^{109}Cd to the double peaks at 1179 keV and 1332 keV of ^{60}Co. Each peak was fit with a Gaussian using SigmaPlot© to determine the peak centroid and the peak width.

Table 1. γ Detector Comparison

Parameters	γ Detector Material		
	NaI(Tl)	CsI(Na)	CsI(Tl)
Quadratic term / linear term	7.4×10^{-4}	5.8×10^{-5}	1.7×10^{-4}
Resolution @ 661.7 keV (%)	6.7 ± 0.1	8.7 ± 0.1	9.5 ± 0.1
Relative efficency @ 661.7 keV (%)	24.2 ± 1.0	28.3 ± 1.2	28.1 ± 1.4
Density (g/cm^3) [5]	3.67	4.51	4.51
Primary decay time (ns) [5]	230	630	1000

As expected, the NaI(Tl) had the best resolution of the three detectors due to the better optical matching of the PMT to the NaI(Tl) scintillation light emissions. The primary x-rays and γ-rays of interest are at 30 keV, 80 keV and 250 keV, which have large enough energy separations that the CsI crystals were more than adequate for good resolving power between the peaks. Also expected is the increase in efficiency seen by the two CsI crystals. They have densities that are ~ 23% greater than NaI and the average electron density is ~20% greater.

Gas Cell Detectors

The ARSA gas cells need to discriminate between the two conversion electrons of ^{133m}Xe and ^{131m}Xe and the β distributions from ^{133}Xe (see Table 2 for the primary decay paths for each of the radioxenons). The original ARSA gas cells had two PMTs looking at either end of the 1.5 cm x 5 cm right cylinder cell with 1.2 mm thick walls. By gain matching photo-tubes, a 25-30% resolution for the 129 keV CE can be achieved. A major requirement for the new simplified scintillator gas cell was that it needs to attain a similar resolution to the ARSA beta cells. The material choices for the gas cells were limited to materials that were non-hygroscopic, had good charged particle energy resolution, were robust, and were sufficiently thin such that the walls did not attenuate the 30 keV x-rays from ^{133}Xe, ^{131m}Xe and ^{133m}Xe. The ARSA detector employed BC-404 scintillating plastic shaped into hollow tubes with stepped end caps to complete a gas tight cell [5]. The new gas cell has slightly thicker walls and end cap and were molded into a concave shape. This design allows for only one PMT to be used on the plastic scintillator. Light is refocused from the rounded end back towards the single PMT. The overall dimensions were 2 mm thick and 28 mm long. A larger PMT was used to maximize the use of the sensitive central portion of the PMT where the conversion efficiency is highest. To enhance the internal reflection of light back towards the PMT the gas cell was wrapped in two layers of Teflon tape. The effect of the Teflon tape can clearly be seen in Figure 4

which shows the response of the plastic gas cell to a ^{36}Cl β source. Several β sources were used for this study and only the ^{36}Cl is shown to illustrate the additional light collection that the Teflon provides.

Table 2. Dominant Decay Modes of the Radioxenon Isotopes [a].

Isotope	^{131m}Xe	^{133}Xe	^{133m}Xe	^{135}Xe
Half-life (days)	11.84	5.24	2.19	0.38
Primary γ-ray energy (keV)	163.9	81.0	233.2	249.8
γ-ray abundance (%)	1.96	37	10.3	90
X-ray energy (keV)	30	31	30	31
X-ray abundance (%)	54	48.9	56.3	5.2
β-particle endpoint energy (keV)	346	905		
β-particle abundance (%)	99	96		
Conversion electron energy (keV)	129	45	199	214
Conversion electron abundance (%)	60.7	54	63.1	5.7

[a] From Ref. [6].

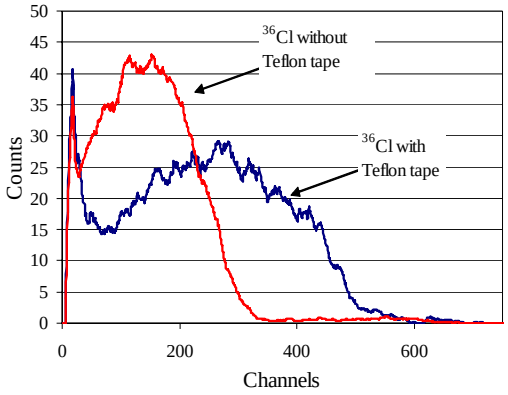

Figure 4. Response of the new gas cell with and without the Teflon tape wrapping. It is clear that the addition of the Teflon reflector provides a significant increase in the total light collected by the PMT. The source used is ^{36}Cl with a β end point energy of 1142 keV. The full energy is unlikely to be deposited because the 2 mm thick plastic has a stopping power of ~ 450 keV.

β-γ Coincidence Measurements

Two tests were performed using the new gas cell and three well detectors to compare performance characteristics between the different detector types. The first test uses Compton scattering of the 662 keV peak from ^{137}Cs to generate β-γ coincidences in the detector, see reference 8 for an in-depth description of the technique. The second technique uses well-aged radioxenon from a commercial medical isotope supplier. This source has both ^{133}Xe and ^{131m}Xe, the metastable is a contaminate at very low relative levels compared to the ^{133}Xe after several months the metastable has decayed much less and is therefore more abundant and easily discernable in the mixed source. The initial source strength (174 MBq) is far too high to use and aging has the effect of decreasing the ^{133}Xe activity down to useable levels.

Compton Scattering Technique Using ^{137}Cs

The use of Compton scattering of γ-rays is a very successfully technique and provides a method of β-energy and energy resolution calibration that can be done quickly and in the case of the ARSA system automatically and remotely. It provides a reliable method to compare detector response over an extended period. It also allows gain shifts in PMT and relative efficiency declines to be measured and tracked. The technique allows a more direct measurement than using β sources because the γ-rays illuminate the entire

gas cell, therefore eliminating much of the position dependence of the source. The typical β sources illuminate only the material directly in front of the source. Assuming only Compton scatter occurs (low atomic numbers in the plastic prevent gamma-ray absorption from occurring with any measurable frequency), the maximum energy transfer to an electron is 477 keV. Within the β-γ coincidence plane all electron energies from 0 to 477 keV would be populated. Figure 5 is a 2-dimensional β-γ histogram that clearly shows the Compton electrons that are scattered in the plastic of the gas cell and scattered γ-ray. The diagonal line is along constant energy when the γ energy is added to the β energy: $E_\beta + E_\gamma = 662$ keV.

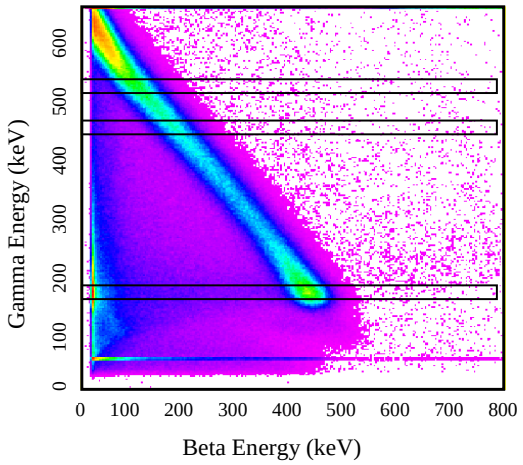

Figure 5. This plot shows the 2-dimensional β-γ coincidence histogram using a ^{137}Cs source. The diagonal feature is a constant energy line from the 662 keV γ-ray from ^{137}Cs and indicates Compton scattering. The γ endpoint is at 662 keV and the β end point is at 477 keV. Intermediate values can be used to define the β energy scale and the resolution of the gas cell.

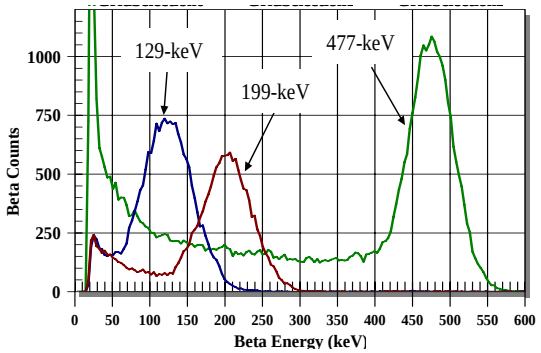

Figure 6. Highlighting narrow regions in the β-γ histogram (Figure 5) at the appropriate γ energies gives a projection along the β axis that is centered at the CE energies of ^{131m}Xe, ^{133m}Xe and the Compton scatter end point energy of 477 keV for the 662 keV γ from ^{137}Cs.

This correlation gives the β energy scale when the γ energy scale is calculated using the Amersham© source. It also allows the determination of the β energy resolution from ~ 15 keV all the way up to 477 keV. Figure 6 shows the results of this analysis for the Compton scattered equivalent CE energies of ^{131m}Xe and ^{133m}Xe as well as the Compton scattering endpoint. The fit of the Gaussian peaks along the constant energy line is an indication of how linear the detector response is. In the ARSA gas cell,

comparable linearity was achieved only by tedious and time consuming PMT matching and taking the geometric sum of the response of the two PMTs. The overlap between the 129 keV and 199 keV peaks is ~10%. While it is possible to determine through peak fitting routines the counts in each of these peaks, it would be beneficial if this overlap were reduced further. The β energy resolution for the new detector using one PMT is equivalent to the ARSA detector using two. Thus there is no loss of detector performance.

Radioxenon Response

The use of aged medical ^{133}Xe gives a direct measure of the β energy and resolution as well as providing the complete response of the β-γ coincidence detector. Figure 7 shows the 2-dimensional β-γ coincidence spectrum that was obtained after injecting a well aged ^{133}Xe sample with ^{131m}Xe as a contaminate. The plot shows the two regions for ^{133}Xe highlighted. The ^{131m}Xe shows up as a dark spot in the 30 keV x-ray region. The inset shows the projection of the data to the γ-axis and indicates the excellent separation between the x-ray and γ-ray response. The 30 keV x-rays of the ^{133}Xe and the ^{131m}Xe are indistinguishable along this axis and show the power of using the β energy and CE energy in coincidence. Figure 8 shows the projection of the two regions on the β axis. The 80 keV region is a pure ^{133}Xe β distribution with no CE interferences. The x-ray region has two CE, one at 45 keV for the ^{133}Xe (small peak) and the more prominent CE is centered at 129 keV and is from the decay of 131mXe. The resolution of this peak is 0.248 ± 0.031, which is in very good agreement with the ARSA detector.

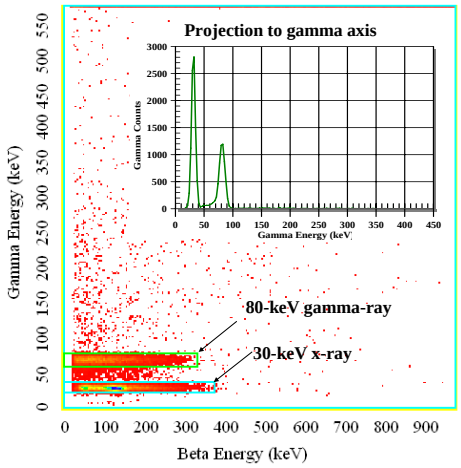

Figure 7. This plot shows the 2-dimensional beta-gamma coincidence histogram of a ^{133}Xe plus ^{131m}Xe gas. The two regions for ^{133}Xe are highlighted and the ^{131m}Xe shows up as a dark spot in the x-ray region. The inset shows the projection of the data to the γ-axis and indicates the excellent separation between the x-ray and γ-ray response.

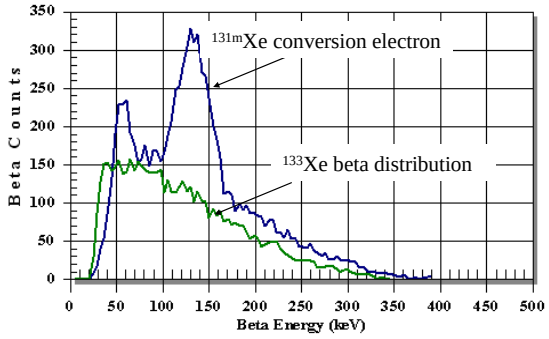

Figure 8. The projection of the two regions marked in Figure 7 are indicated above. The γ-ray region is a pure 133Xe β distribution with no CE interferences. The x-ray region has two CE, one at 45 keV for the ^{133}Xe (small peak) and the more prominent CE is centered at 129 keV and is from the decay ^{131m}Xe. The resolution of this peak is 0.248 ± 0.031, which is in good agreement with the ARSA detector.

CONCLUSIONS AND RECOMMENDATIONS

The optimal replacement well detector was determined to be CsI(Na), because it has good mechanical properties and better efficiency than the NaI(Tl). It also has a time decay constant that is closer to that of NaI(Tl) than the longer CsI(Tl), so it has less impact on the readout electronics. Likewise, the gas cell redesign gives comparable results in linear energy response and resolution to the multi-PMT configuration. The new geometry also has helped to reduce the energy calibration time and complexity and now can be done using automated operation and analysis routines. The failure of one detector has a much lower impact on the other detectors due to the new design.

Two future studies that are needed before a true replacement detector can be fielded in the ARSA units are the effect the close pack detector design has on vetoing cosmic-rays and an extended period of testing under field conditions.

The new detector design is much easier to calibrate and allows in-field replacement of a single unit. Initial studies indicated that the well design maintains both radioxenon detection efficiency and γ-ray energy resolution. Furthermore, the design has the potential to be an excellent replacement β-γ coincidence detector system for the fielded ARSA system.

REFERENCES

[1] Operational manual for radionuclide and the international exchange of radionuclide data, preparatory commission for the Comprehensive Nuclear-Test-Ban-Treaty Organization, CTBT/WGB/TL-11/5/Rev. 4, (1999).

[2] Miley, H. S, R. J. Arthur., E. A. Lepel, S. L. Pratt, and C. W. Thomas (2001). "Evaluation of fission product isotopes for field or laboratory detection", *Jour. Radioanalytical Chemistry*, Vol. 248-3, pp. 651-656, June.

[3] Hayes, James C., Keith H. Abel, Theodore W. Bowyer, Tom R. Heimbigner, Mark E. Panisko, Paul L. Reeder, Justin I. McIntyre, Robert C. Thompson, Lindsay C. Todd, Ray A. Warner (1999). Operations of the automated Radioxenon sampler/analyzer - ARSA, in the *Proceedings of the 21st Seismic Research Sumposium: Technologies for Monitoring the Comprehensive Nuclear-Test-Ban Treaty*, LA-UR-99-4700, Vol. 2, pp. 249-260.

[4] Bowyer, T. W., J.I. McIntyre, and P. Reeder (1999). High sensitivity detection of Xe isotopes via β-γ coincidence counting, in the *Proceedings of the 21st Seismic Research Sumposium: Technologies for Monitoring the Comprehensive Nuclear-Test-Ban Treaty*, LA-UR-99-4700, Vol. 2, pp. 231-241.

[5] Saint Gobain© website, http://www.bicron.com/

[6] Browne, E., and R.B. Firestone (1986). *Table of Radioactive Isotopes*,Wiley, New York.

DIGITAL PULSE SHAPE ANALYSIS WITH PHOSWICH DETECTORS TO SIMPLIFY COINCIDENCE MEASUREMENTS OF RADIOACTIVE XENON

W. Hennig[1], H. Tan[1], W. K. Warburton[1], and J. I. McIntyre[2]

XIA LLC[1] and Pacific Northwest National Laboratory[2]

Sponsored by National Nuclear Security Administration
Office of Nonproliferation Research and Engineering
Office of Defense Nuclear Nonproliferation

Contract No. DE-FG02-04ER89121

ABSTRACT

The Comprehensive Nuclear-Test-Ban Treaty establishes a network of monitoring stations to detect radioactive xenon in the atmosphere from nuclear weapons testing. One such monitoring system is the Automated Radioxenon Sampler/Analyzer (ARSA) developed at Pacific Northwest National Laboratory, which uses a complex arrangement of separate beta and gamma detectors to detect beta-gamma coincidences from the xenon isotopes of interest. The coincidence measurement is very sensitive, but the large number of detectors and photomultiplier tubes requires careful calibration. Simplifying this coincidence measurement system while maintaining its performance is the objective of the research described here.

It has been suggested that beta-gamma coincidences could be detected with only a single photomultiplier tube and electronics channel by using a phoswich detector consisting of optically coupled beta and gamma detectors (Ely, 2003). In that work, rise time analysis of signals from a phoswich detector was explored as a method to determine if interactions occurred in either the beta or the gamma detector or in both simultaneously. However, this approach was not able to detect coincidences with the required sensitivity or to measure the beta and gamma energies with sufficient precision for radioxenon monitoring.

In this paper, we present a new algorithm to detect coincidences by pulse shape analysis of the signals from a BC-404/CsI(Tl) phoswich detector. Implemented on fast digital readout electronics, the algorithm achieves clear separation of beta only, gamma only and coincidence events, accurate measurement of both beta and gamma energies, and has an error rate for detecting coincidences of less than 0.1%. Monte Carlo simulations of radiation transport and light collection were performed to optimize design parameters for a replacement detector module for the ARSA system, obtaining an estimated coincidence detection efficiency of 82-92% and a background rejection rate better than 99%. The new phoswich/pulse shape analysis method is thus suitable to simplify the existing ARSA detector system to the level of a single detector per sample chamber while maintaining the required sensitivity and precision to detect radioxenon in the atmosphere.

OBJECTIVE

The Comprehensive Nuclear-Test-Ban Treaty establishes a network of monitoring stations to detect radioactive xenon in the atmosphere from nuclear weapons testing. One such monitoring system is the Automated Radioxenon Sampler/Analyzer (ARSA) developed at Pacific Northwest National Laboratory (Reeder, 1998). The ARSA system consists of a pair of large NaI(Tl) scintillator crystals holding four cylindrical fast plastic scintillator (BC-404) cells which are optically isolated from the NaI(Tl). The cells are filled with the xenon gas to be counted, which decays by emitting gamma rays or X-rays in coincidence with beta particles or conversion electrons. The plastic scintillator is meant to absorb all beta particles and conversion electrons, while the longer range gamma rays and X-rays will mainly be absorbed in the NaI(Tl) scintillator. Each BC-404 cell and each NaI(Tl) crystal is coupled to a pair of photomultiplier tubes (PMTs) and is read out by independent electronic channels. The sensitivity for detecting xenon isotopes is greatly increased by requiring coincidence between the signals from the PMTs coupled to the NaI(Tl) and the signals from the PMTs coupled to the BC-404.

While obtaining high coincidence detection efficiency and resolutions of about 25% for characteristic 80keV gamma rays, the current ARSA system design results in significant operational complexity. The principle of time based coincidence, while effective in suppressing the background, requires separate signals from the NaI(Tl) and the BC-404, i.e., separate PMTs and readout electronics. In particular, the 12 PMTs require careful gain matching and calibration, and as the PMT gains change with time, voltage and temperature, the system easily drifts out of calibration.

To improve the current ARSA system a new concept for coincidence measurements was explored previously (Ely, 2003) based on rise time analysis of signals from a phoswich detector. The phoswich detector consisted of a 0.04 inch thick CaF_2(Eu) crystal (decay constant 940ns) optically coupled to a 2x2 inch NaI(Tl) crystal (decay constant 250ns) and was read out by a single PMT. The CaF_2(Eu) is used as the beta detector to absorb beta particles and conversion electrons and the NaI(Tl) acts as the gamma ray detector to absorb gamma rays and X-rays. By integrating the signal from the PMT in a charge integrating preamplifier and acquiring pulse waveforms with a fast digital pulse processor, the scintillator in which radiation interacted could be determined by the signal rise times. While this method of pulse shape coincidence detection worked well to distinguish CaF_2(Eu) only events and NaI(Tl) only events, coincident events in both scintillators were not easily identified by this algorithm and/or choice of scintillators and it was deemed challenging to separate the individual gamma and beta contributions with any precision.

In this paper, we describe an improved method to detect coincidences with a phoswich detector and single channel of readout electronics. The method uses the signal directly from the phoswich detector, without a charge integrating preamplifier, and determines the scintillator(s) in which the interaction occurred by analyzing the signal over characteristic time periods, thus detecting coincidences. Applied to radioxenon monitoring, the method provides beta-gamma coincidence detection and energy measurement of both beta and gamma energies with a greatly simplified measurement setup.

RESEARCH ACCOMPLISHED

1. Development of Pulse Shape Analysis with Prototype Phoswich Detector

The pulse shape analysis algorithms were developed using a prototype phoswich detector consisting of a 1” diameter by 1” thick CsI(Tl) crystal optically coupled to a 1” diameter, 1-mm thick disk of the plastic scintillator BC-404 on the front end. The detector was illuminated with a variety of solid sources or Xe and Rn gas enclosed in small plastic bags. Using an XIA Pixie-4 digital spectrometer directly connected to the PMT coupled to the detector, we acquired waveforms of the detector signals and found the three basic types of events shown in Figure 1: a) slow rising and slow falling pulses corresponding to interactions only in the CsI, b) very fast pulses with high amplitude corresponding to interactions only in the BC-404, and c) combinations of the previous cases corresponding to coincident interactions in both scintillators. Limiting the signal bandwidth of the Pixie-4 analog front end reduced the amplitude of the fast BC-404 signals without affecting the slower, low amplitude CsI signals. A single channel could thus accommodate the highest beta particle energies expected from the radioxenon decays while still obtaining sufficient precision for low amplitude X-ray signals.

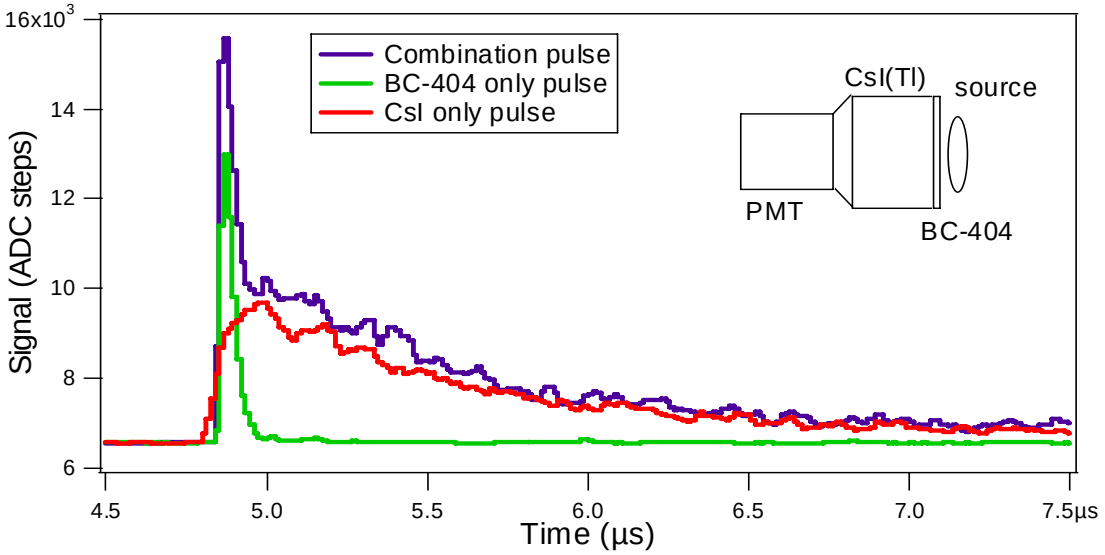

Figure 1: Pulse waveforms from the prototype phoswich detector (shown in insert). There are three types of events: CsI only pulses, BC-404 only pulses and combination pulses depositing energy in both parts of the phoswich detector.

Analyzing the acquired waveforms off-line, we calculated the signal rise time and various filter sums over different regions of the waveform for each acquired pulse. These properties allowed a clear distinction of the three event types described above and thus can be used to detect coincidences between the gamma and beta radiation from the samples. The properties can further be used to calculate the energies deposited in each part of the phoswich detector and display events in 2D energy scatter plots as shown in Figure 2. In the graph, CsI only events fall on the vertical axis (plastic energy is zero) and plastic only events fall on the horizontal axis (CsI energy is zero). Coincidence events form two horizontal bands, corresponding to 30 keV X-rays or 81 keV gamma rays in coincidence with betas of varying energy. Note that the 30 keV X-ray coincidence events are also well separated from the beta-only events.

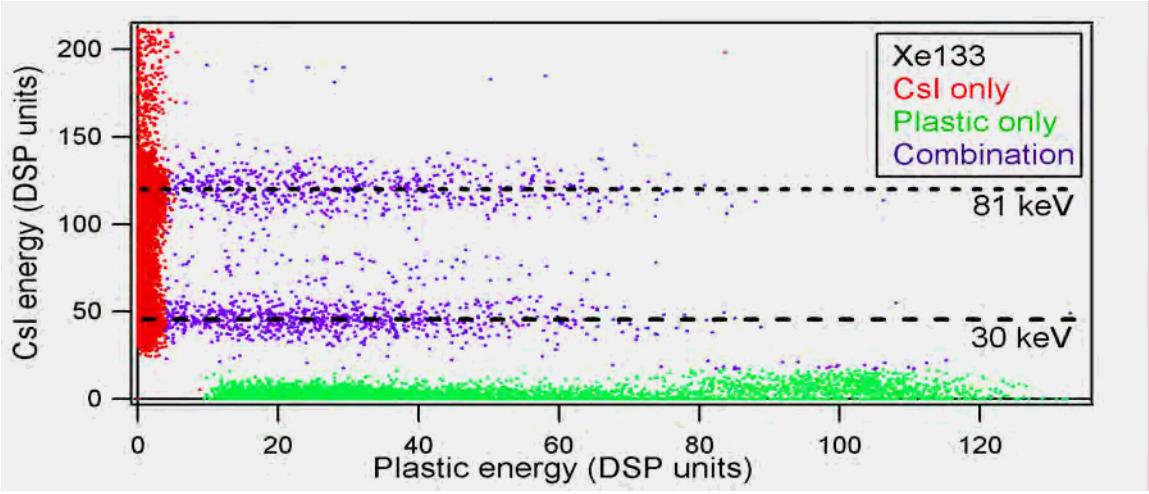

Figure 2: Energy scatter plot for ^{133}Xe colored by event type. CsI only events fall on the vertical axis, plastic only events fall on the horizontal axis, and coincidence events form horizontal bands at characteristic X-ray or gamma ray energies (fixed photon energy deposited in the CsI and varying beta energy deposited in the BC-404).

By defining thresholds for the rise time and energy values, the three event types can be separated and binned into separate energy histograms as shown in Figure 3. The energy resolution at the 81keV peak is 16.9% for Eco, the energy deposited in the CsI in CsI only events, and 17.1% for Ecb, the energy deposited in CsI in coincidence events, which is significantly better than resolutions achieved with the current ARSA detector. The energy resolution is good enough to resolve even the 52 keV Iodine escape peak in both Eco and Ecb. In experiments with ^{60}Co, we obtained resolutions of 5.2% for Eco and 5.4% for Ecb for the 1.3 MeV peak. This is comparable to resolutions routinely achieved with a standard CsI detector and demonstrates that our pulse shape algorithms do not degrade energy resolution compared to standard pulse processing methods.

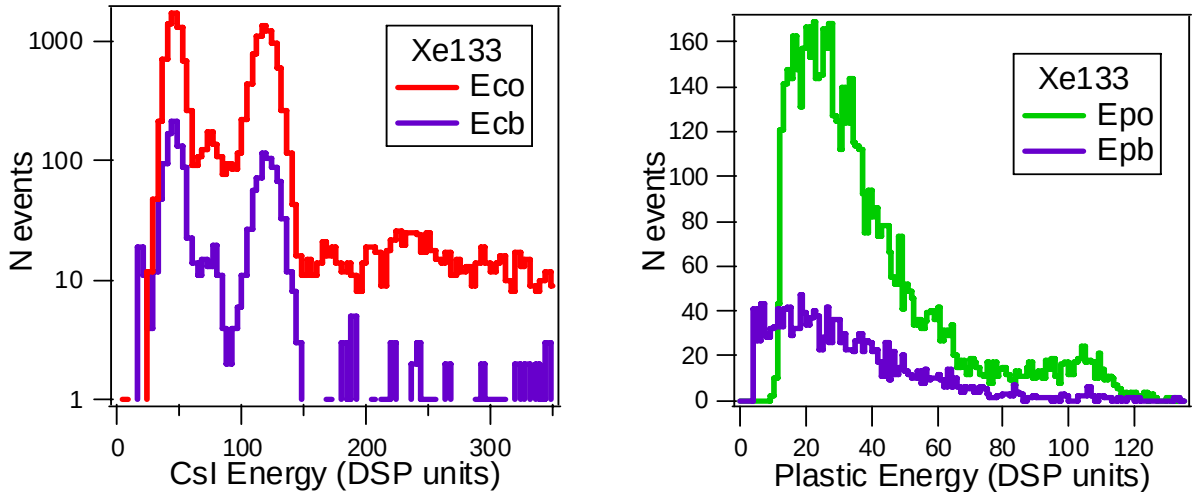

Figure 3: Energy histograms for ^{133}Xe formed by projecting the data of Figure 2 onto the two energy axes. The left graph shows the energy deposited in the CsI for CsI only events (Eco) and combination events (Ecb). The right graph shows the energy deposited in the plastic for plastic only events (Epo) and combination events (Epb).

The error rate of the algorithm was estimated from measurements with ^{241}Am which emits alpha particles and X-rays in coincidence. In the setup shown in Figure 1, the algorithm classified 30% of detected events as BC-404 only events and 3.5% as coincident events. When an Al shield was inserted between source and detector to stop all alpha particles, the fraction of BC-404 only events and coincident events dropped to 0.2% and 0.1%, respectively. Since there can be no true coincidences without the alpha particles, the measured 0.1% must be either random coincidences, scattering of a single X-ray from one scintilator to the other, or non-coincident events wrongly classified as coincident by the algorithm. As a worst case estimate, we can thus determine that the algorithm wrongly classifies events as coincidences at a rate of less than 0.1%.

2. Monte Carlo Simulations of Phoswich Well Detector for Radioxenon Monitoring

While the prototype detector was sufficient to develop the algorithms for detecting coincidences and measuring individual energies with good precision in a single channel of electronics, it has very low coincidence detection efficiency since at least half of the beta radiation and the gamma radiation will be emitted away from the detector. Using Monte Carlo simulations of light collection and radiation transport, we therefore studied a phoswich well detector design in which a BC-404 cell holding the radioxenon will be enclosed in a 3” cylinder of CsI, see Figure 4.

2.1. Light Collection Simulations

The unusual geometry of the phoswich well detector will affect the uniformity of light collection in the detector. We therefore carried out Monte Carlo simulations of the light collection for the geometry of the proposed detector, the test detector, and other geometries using Monte Carlo code DETECT2000. Figure 5 shows the distribution of light collection efficiency in the 3” prototype detector with a reflectivity of 0.95 or 0.99 for the diffusive reflector on the outer surface of CsI. We found that placing a structure inside the CsI crystal somewhat degrades the uniformity of

the light collection efficiency, especially if the coating on the outside of the CsI crystal has a low reflection coefficient. From the volume-weighted probability distribution of the light collection efficiency, we estimate that the energy resolution of mono-energetic gamma rays, due only to the non-uniformity of the collection efficiency in the crystal, increases from 2.4% without a cell to 2.9% with a spherical cell and 3.8% with a cylindrical cell (for the conservative estimate of the reflectivity, i.e. 0.95). Optimizing uniformity thus requires minimizing of the number of interfaces, paying careful attention to their shape, and maximizing the reflection coefficient of the reflector on the outside of the CsI crystal. However, compared to a typical measured resolution of ~7% at 662 keV (resulting from photostatistics, crystal non-uniformities and energy non-linearities), the effects of the embedded cell are small. Adding these numbers in quadrature, we anticipate the phoswich detector energy resolution to not worsen significantly at the lower energies from the Xe isotopes due to effects of light collection arising from either the inclusion of the BC-404 cell or its specific geometry, provided that the reflectivity is kept high and the cell is not unreasonably shaped.

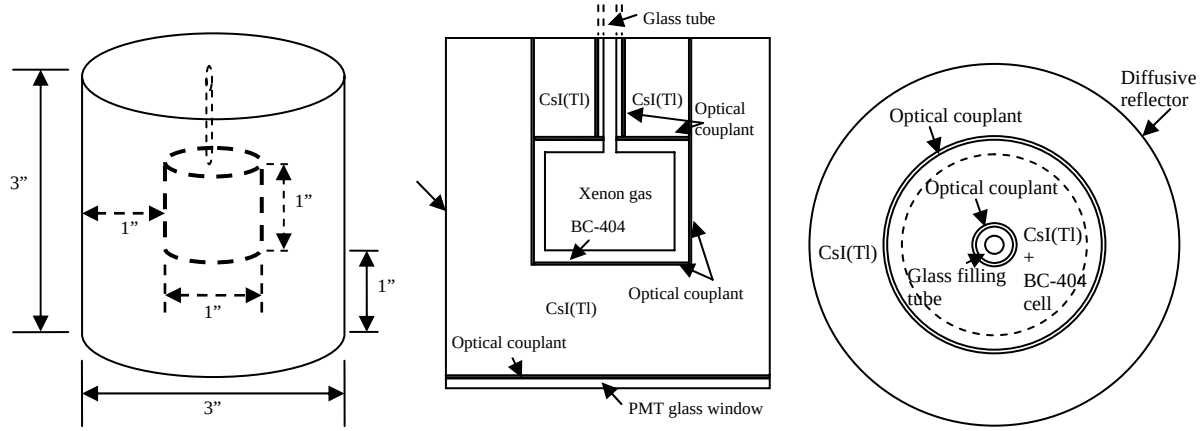

Figure 4: Geometry the phoswich well detector. The outer 3” × 3” cylinder is the CsI(Tl) crystal. Embedded inside is the 1” × 1” BC-404 counting cell whose wall thickness may be up to 5 mm. The counting cell contains the xenon gas which is fed into the cell through the slender tube. Left: sketch of the detector size; middle: side view of the detector; right: top view of the detector.

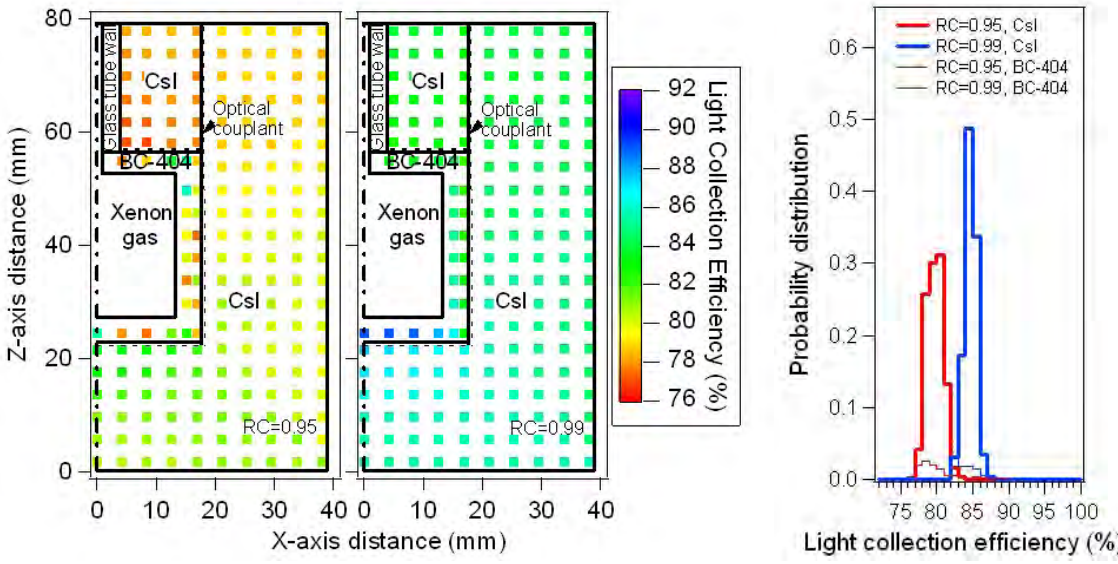

Figure 5: Geometric distribution of light collection efficiency in the prototype detector. The left figures are distributions of light collection efficiency in the prototype detector with two typical outer reflectors (reflection coefficient = 0.95 and 0.99, respectively). The right figure is the volume-weighted probability distribution of light collection efficiency.

2.2. Radiation Transport Simulations

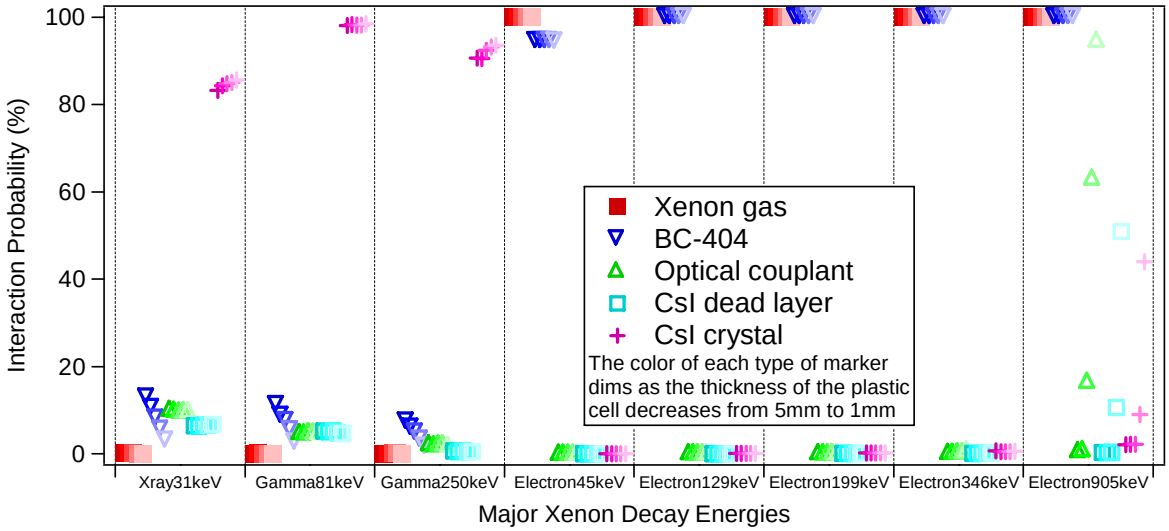

Figure 6: Interaction probability of major radioxenon decay energies in each component of the phoswich well detector for radiation emitted from the center of the counting cell. The thickness of the BC-404 cell varied from 5mm to 1mm.

Monte Carlo simulations of the radiation transport in the phoswich detector were performed to determine optimum values of design parameters and to estimate the coincidence detection efficiency. Using Monte Carlo code PENELOPE, several characteristic energies of gamma rays, X-rays, beta particles and conversion electrons from radioxenon were simulated for the well detector and also for the prototype detector to compare the simulation to the experiments. The simulations showed that most beta particles or conversion electrons will be absorbed in the BC-404 and most X-rays or gamma rays will be absorbed in the CsI, as intended (see Figure 6). A small fraction of high energy gamma rays will escape from the detector, and a small fraction of low energy beta particles will be absorbed in the xenon gas, i.e., they will not be detected. The thickness of the BC-404 cell has to be adjusted to compromise between preventing betas from reaching the CsI (thicker wall) and reducing the chance of photons interacting with the plastic (thin wall). A wall thickness of 2-3 mm is a good compromise.

Table 1. Probabilities (in %) of simultaneous interactions of characteristic gamma rays and beta particles from ^{133}Xe in the phoswich well detector. Only events where betas interact with the BC-404 only and gammas interact with the CsI only (bold) are coincidence events with good energy measurement.

	beta not interacting	**beta interacting with BC-404 only**	**beta interacting with CsI only**	**beta interacting with both BC-404 and CsI**
gamma not interacting	0.0	1.5	0.0	0.0
gamma interacting with BC-404 only	0.0	0.3	0.0	0.0
gamma interacting with CsI only	0.0	**92.6**	0.0	0.5
gamma interacting with both BC-404 and CsI	0.0	5.1	0.0	0.0

The interaction probabilities of the characteristic energies were then used to estimate the coincidence detection efficiency. For example, 81 keV gamma rays and 346 keV beta particles may be taken to represent the coincidence radiation from ^{133}Xe. Each has a certain probability to interact a) not at all, b) with BC-404 only, c) with CsI only, or d) with both BC-404 and CsI. The products of the probabilities for the altogether 16 combinations are shown in Table 1. Only events where betas interact with the BC-404 only and gammas interact with the CsI only are coincidence events with good energy measurement, shown in bold in Table 1. For ^{133}Xe, the estimated coincidence detection efficiency of the well detector is thus 92.6%, for other xenon isotopes of interest it is about 82%.

Table 2. Probability of external background gamma rays to interact with the phoswich well detector, obtained from simulations. Only events directly aimed at the center of the detector were simulated; estimated to be 1/27th of the overall background. The numbers shown have thus to be divided by 27 to obtain the overall background coincidence rate.

Gamma Energy (MeV)	not interacting	interacting with BC-404 only	interacting with CsI only	interacting with both BC-404 and CsI	interacting with both, < 250keV deposited in CsI
0.583	8.66%	0.22	88.95	2.17	0.86
1.461	24.20	0.49	73.05	2.26	0.82
2.614	30.18	0.48	66.87	2.47	0.68
5	32.35	0.14	64.33	3.18	0.22
10	29.08	0.05	65.55	5.32	0.07
20	23.22	0.01	66.70	10.07	0.01

To estimate the rejection ratio of the well detector, interactions of background radiation were also simulated. Table 2 shows the interaction probabilities for gamma rays with representative energies, coming from a single external location and directed towards the center of the detector. Of the simulated gamma rays, a majority interacts with CsI only and will thus be rejected by the pulse shape analysis. About 2-10% of simulated events interact with both scintillators and will be categorized as coincidences, but only 0.9-0.01% will deposit less than 250 keV in the CsI, the maximum gamma-ray energy from the xenon decay chain, i.e. most of the background coincidences can be rejected by a simple energy cut. In addition, the radiation will in practice be coming from a multitude of locations around the detector and most of the radiation will not be directed towards the BC-404 cell, only interacting with the plastic if scattered towards the center. Therefore, as a very crude estimate, we assume that the simulation represents only the fraction of the background radiation equal to the volume fraction of the BC-404 cell in the detector, and that the rest will not interact will the BC-404 cell at all. The simulated events thus represent only 1/27th of the background radiation, and the not simulated events will be rejected by the pulse shape analysis. This means that overall the background rejection ratio for the phoswich well detector is greater than 99.9% in the energy range of interest.

CONCLUSION

In summary, we developed an algorithm to detect beta-gamma coincidences in the signals from a BC-404/CsI(Tl) phoswich detector, using a single channel of readout electronics. The algorithm achieves clear separation of beta only, gamma only and coincidence events, accurate measurement of both beta and gamma energies, and has an error rate for detecting coincidences of less than 0.1%. Monte Carlo simulations of radiation transport and light collection were performed to optimize design parameters for a replacement detector module for the ARSA system, obtaining an estimated coincidence detection efficiency of 82-92% and a background rejection rate better than 99%. The new phoswich/pulse shape analysis method is thus suitable to simplify the existing ARSA detector system to the level of a single detector per sample chamber while maintaining the required sensitivity and precision to detect radioactive xenon in the atmosphere.

ACKNOWLEDGEMENTS

We would like to thank the PNNL ARSA development team headed by Theodore Bowyer for valuable information and insight on radioxenon collection, as well as Michael Momayezi from Bridgeport Instruments for his support in this research.

REFERENCES

Reeder, P.L., T.W. Bowyer, and R.W. Perkins, (1998) Journal of Radioanalytical and Nuclear Chemistry, Vol. 235, No. 1-2 (1998) 89-94

Ely, J. H., C.E. Aalseth, J. C. Hayes, T. R. Heimbigner, J. I. McIntyre, H. S. Miley, M. E. Panisko, and M. Ripplinger, (2003), Novel Beta-Gamma Coincidence Measurements using phoswich detectors, in *Proceedings of the 25th Seismic Research Review – Nuclear Explosion Monitoring: Building the Knowledge Base*, LA-UR-03-6029, Vol. 2, pp. 533-541.

SEGMENTATION OF THE OUTER CONTACT ON P-TYPE COAXIAL GERMANIUM DETECTORS

Ethan Hull [1], Harry Miley [2], Richard Pehl [1], Craig Aalseth [2], and Todd Hossbach[2]

PHDs [1] and Pacific Northwest National Laboratory[2]

Sponsored by National Nuclear Security Administration
Office of Nonproliferation Research and Engineering
Office of Defense Nuclear Nonproliferation

Contract Nos. DE-AC05-RLO1830[1] and DE-FG-02-05ER84157[2]

ABSTRACT

Arrays of segmented germanium detectors are needed for low-level gamma-ray counting facilities. Applications of such user facilities include characterization of low-level radioactive samples and the search for rare events like neutrinoless double-beta decay. Coaxial germanium detectors having segmented outer contacts can provide the next level of sensitivity improvement for these low-background measurements. The segmented contact allows advanced pulse-shape analysis measurements that decrease the measured background. Currently, such detectors are very expensive and available only after relatively long lead times. Advances in segmentation technology will reduce fabrication costs and improve availability of these detectors for the low-level counting community.

For similar reasons, segmentation research also extends to applications of interest to the nuclear explosion monitoring community. Large segmented p-type coaxial detectors could serve as the gamma-ray spectrometers on instruments such as the Radionuclide Aerosol Sampler/Analyzer (RASA). These detectors will provide a more sensitive, lower background, measurement than currently available with unsegmented p-type coaxial detectors. In addition to more sensitive spectroscopy, the position resolution within a segmented germanium detector can be used to determine the impinging direction of incident gamma rays. This directional sensitivity can be used to futher reduce background by separating the directions of interest from directions contibuting only to background. Furthermore, the directional sensitivity can help locate an intense source of gamma rays at a distance.

The conventional contacts used to fabricate germanium detectors are boron-implanted p+ and the lithium-diffused n+ contacts. Boron-implanted contacts are thin (~1000 Å) and can be segmented. Lithium-diffused contacts are thick (~ 0.5 mm) and very difficult to segment. For pulse-shape analysis using a coaxial detector, the outer detector contact must be segmented. Consequently, the outer contact must be a segmented boron-implanted p+ contact forcing the bulk detector material to be n-type germanium. Because of electron trapping limitations, n-type germanium detectors of sufficient quality for large-diameter coaxial detectors are far more difficult and expensive to produce than p-type germanium. This project shall research alternatives to the thick lithium n+ contact to allow the use of p-type germanium as the material for segmented coaxial detectors. Amorphous germanium contacts pose a possible solution. Amorphous contacts are being researched as an alternative to lithium-diffused contacts. The thin (~1000 Å), easily segmented, amorphous germanium contact naturally lends itself to fine segmentation of the n+ contact.

OBJECTIVES

Funding for this program has only just begun. This paper is a brief on the work to be done and the motivation for that work.

Germanium detector arrays are needed for low-level counting facilities. The practical applications of such user facilities include characterization of low-level radioactive samples. In addition, the same detector arrays can also perform important fundamental physics measurements including the search for rare events like neutrinoless double-beta decay (Miley et al. 1991, Miley et al. 1990, Majorance Collaboration White Paper, 2003). Coaxial germanium detectors having segmented outer contacts will provide the next level of sensitivity improvement in low-background measurements. The segmented outer contact allows performance of advanced pulse-shape analysis measurements. These techniques can be used to discriminate between multiple Compton-scattered gamma-ray events and single-point beta-decay events. Recently, such techniques have been demonstrated with Clover detectors at Los Alamos National Laboratory and confirming simulations done at Pacific Northwest National Laboratory, Lawrence Berkely National Laboratory, and Oak Ridge National Laboratory. Because of their complexity, the segmented coaxial detectors are expensive and available only after relatively long lead times. Improved detector segmentation techniques would be both important and timely. Such technological advances will reduce fabrication costs and improve availability of these detectors for the low-level counting community. These highly sensitive detectors are also useful for nuclear explosion monitoring in systems such as the RASA.

Currently, the fabrication of a segmented coaxial germanium detector requires an n-type germanium crystal for the detector. Depleting a coaxial detector with a reasonable bias voltage requires the rectifying (p^+n or n^+p) junction to be at the outside diameter of the detector. For an accurately segmented coaxial detector, the outer contact must be segmented. The n-type (reverse-electrode) germanium coaxial detectors are needed because the boron-implanted (p+) outer contact is the more conveniently segmented conventional contact. However, p-type (conventional-electrode) coaxial detectors are more desirable for a number of reasons. P-type coaxial detectors are significantly less expensive and have better gamma-ray energy resolution than n-type coaxial detectors. Fundamentally, this is due to the presence of electron-trapping sites found in even the best detector-quality germanium. A small percentage of the electrons arising from gamma-ray interactions in the detector are trapped before reaching the electron-collecting contact. The charge is trapped for a sufficient duration that it is not included in the processed signal for that event. The resulting pulse-height deficits cause broadening of gamma-ray peaks. The magnitude of energy-resolution degradation from electron trapping is strongly dependent on the geometry of the detector. In detectors of coaxial geometry, the charge carriers collected on the inner contact are responsible for inducing most of the total signal from gamma-ray interactions occurring in most of the volume of the detector. In n-type coaxial detectors, electrons are collected on the inner contact. Consequently, the gamma-ray energy resolution of n-type coaxial detectors is degraded by even small amounts of electron trapping. On the other hand, the spectroscopy of p-type detectors of coaxial geometry relies more heavily on the collection of holes on the inner contact. As a result, electron trapping causes much less resolution degradation in a p-type coaxial detector than in an n-type coaxial detector. This allows a greater percentage of grown detector-grade germanium crystals to be used in the fabrication of p-type coaxial detectors having excellent energy resolution. The lesser importance of electron trapping also allows fabrication of larger-diameter p-type coaxial detectors. Thus fewer detectors are needed to make an array of a given total volume. It is important to note that electron trapping is still relatively poorly understood and difficult to control in the growth of detector-quality germanium. Any large-scale low-level counting facility employing segmented coaxial detectors would benefit greatly, both technically and financially, from the use of p-type coaxial detectors. These segmented detectors will also be quite useful as ultrasensitive gamma-ray detectors for nuclear explosion monitoring.

Currently, the segmentation of the required outer Li-diffused n+ contact of a p-type coaxial detector is a nontrivial operation. The outer contact of a p-type coaxial detector is conventionally made using a rather thick (as much as ~ 1-mm thick) lithium-diffused layer as the hole-injection barrier. Thick lithium-diffused contacts are very rugged and reliable but require rather drastic techniques for segmentation. The current state-of-the-art involves cutting through the lithium-diffused layer with a saw to segment the contact. Although it can work, such detector fabrication techniques are expensive, time-consuming, and mechanically cumbersome. In the event that a saw-cut lithium contact does not successfully function, successive fabrication attempts may prove very difficult. Accommodating the saw-cut grooves during the subsequent fabrication attempts may be sufficiently complicated to compel regrinding the crystal diameter or even starting over again with a new crystal. In addition, such saw cuts can cause charge-

collection and surface-channel problems in the vicinity of the grooves between the segments. Grooves often result in effectively “dead” germanium near the grooves. The initial saw cuts and electronically dead germanium consume valuable germanium detector volume, resulting in a decrease in sensitivity.

Suffice it to say that better outer coaxial contacts must be researched to replace the conventional saw-cut segmented thick lithium-contact. This must be accomplished to make segmented p-type coaxial detectors viable. In this age of photolithographic techniques capable of fabricating millions of transistors on a square inch, we believe that more elegant contacting and segmentation solutions can be found for germanium detectors. There are other contact technologies with the potential to provide hole-injection barriers that are more easily segmented than thick lithium-n+ contacts. This study seeks to determine the best solution for producing segmented hole-injection barrier contacts on p-type germanium detectors.

We will investigate alternative techniques for making segmented hole-injection barrier contacts in lieu of conventional thick lithium-diffused n+ contacts. Amorphous germanium contacts represent one possible alternative. We will fabricate many small planar detectors (~ 4-mm thick, ~30-mm diameter) having a boron-implanted p+ contact as the electron-injection barrier and segmented amorphous germanium contacts as the hole-injection contacts. Amorphous germanium contact technology naturally lends itself to the simple fabrication of finely segmented germanium detectors (Luke et al. 1992, Hull et al. 2002, Hull et al. 2003). Our commercial research facility in Livermore, California, is specifically designed to fabricate and test many germanium detectors in rapid succession. We will study the rectification and segmentation of amorphous germanium contacts with a focus on the hole-injection barrier. Fabrication parameters will be optimized to make reliable segmented amorphous germanium contacts having the largest possible hole-injection barrier height. Our fabrication techniques will then be demonstrated by fabricating a segmented p-type pseudocoaxial detector. The detector will serve to demonstrate the viability of this approach for making segmented p-type coaxial detectors.

Segmented planar germanium detector technology is our specialty. We believe that the best way to approach the fabrication of segmented coaxial detectors is to first understand the fabrication processes for planar detectors. With the fundamental physics and technology well in hand, the technology can be extended to accommodate the nonplanar geometry issues arising in coaxial detector fabrication. We are familiar with the complexities of cooling, connecting, and instrumenting germanium detectors systems having many detector segments on a single wafer of germanium. This program will benefit our planar germanium detector efforts as well as provide coaxial detector technology for nuclear explosion monitoring.

RESEARCH ACCOMPLISHED

This project will establish the viability of fabricating p-type coaxial detectors with segmented outer contacts. The outer contact of a p-type coaxial detector must prevent the injection of holes into the detector. The commonly used hole-injection barrier is a thick lithium-diffused n+ contact. Lithium-diffused contacts are extremely rugged and reliable but they are thick and difficult to segment. This difficulty makes them unsuitable for the fabrication of segmented p-type coaxial detectors. This study will evaluate the viability of amorphous germanium contacts as replacements for thick lithium-diffused contacts.

One of the central points to be addressed is the rectification ability of the amorphous germanium contact. The contact must function as the outer contact of a large-diameter p-type coaxial detector. This means the contact must prevent hole injection into the detector. The most important property of a detector contact is its ability to prevent charge injection while maintaining a high electric field throughout the volume of the detector. In large coaxial detectors, it is not uncommon to have electric fields of ~ 3000 V/cm. The high electric field is important for good charge collection over long distances (~ 4 cm). The hole-injection barrier formed by the amorphous germanium contact must be demonstrated to be consistently capable of suppressing hole injection to the extent needed in large-diameter coaxial detectors. At common operating temperatures (~ 85 K), hole injection from the amorphous germanium contact should not cause more than a few tens of picoamperes of leakage current while withstanding electric fields on the order of 3000 V/cm. In addition, the contact must be sufficiently rugged to withstand temperature cycles between liquid-nitrogen temperature and room temperature. Excessive leakage current is undesirable because it causes electronic noise in the detector.

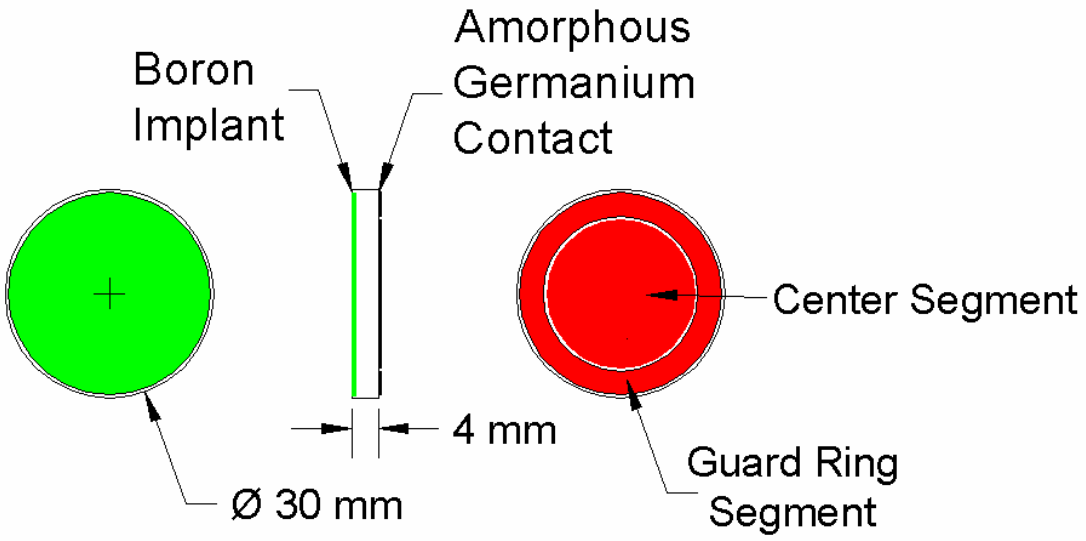

Figure 1. A drawing shows the test detector structure. One side of the detector is a boron-implanted p+ contact while the other side is a segmented amorphous germanium contact. The amorphous germanium contact is divided into center and guard-ring segments.

Small p-type planar test detectors will serve as the basis for studying the rectification properties of the contacts. Many such detectors will be fabricated and tested in rapid succession to find the best detector fabrication parameters and techniques. Making many detectors provides meaningful statistics and makes trends in performance easily visible. Our detector research system at PHDs is set up for the fabrication and testing of several detectors each day. The p-type test detectors will be 4-mm thick and approximately 30 mm in diameter. Figure 1 shows a diagram of one of the test detectors. One side of the detector will be boron implanted to form a p+ electron-injection barrier. The boron implant will be done by a local area implantation shop, Core Systems in Sunnyvale, CA. We will then sputter-deposit an amorphous germanium layer on the other side of the detector, providing the hole-injection barrier. Finally, a layer of aluminum will be evaporated over the amorphous germanium. A shadow-mask ring will be placed on the amorphous germanium side during the aluminum evaporation to provide electrically separate center and guard-ring segments of the detector. When finished, the detectors will look like the drawing in Figure 1.

After the detectors are fabricated, they will be placed in one of our test cryostats, cooled, and tested. Negative-bias voltage will be applied to the boron-implanted contact. The center and guard-ring segments of the amorphous germanium contact will be grounded separately through charge-sensitive preamplifiers. The preamplifiers provide separate leakage-current measurements from the center and guard-ring contacts. The leakage current will be measured as a function of bias voltage. These measurements, known as I(V) measurements, serve as an indication of the success of the fabrication process.

This detector contact structure has been chosen to facilitate the study of the hole-injection barrier formed by the amorphous germanium contact. The boron-implanted contact forms a well-understood, very large electron-injection barrier having a height of the entire germanium band gap, 0.7 eV. The amorphous germanium contact forms either a hole- or electron-injection barrier of approximately half the height of the crystalline-germanium band gap (Hansen and Haller, 1977). Because the boron-implanted electron-injection barrier is so much larger than the amorphous germanium hole-injection barrier, hole injection from the amorphous germanium contact will dominate the leakage current of the detector. Figure 2 shows band diagrams of two different detector structures. On the left side of the figure is a standard p^+-p-n^+ structure. On the right side of the figure is our innovative p^+-p-αGe structure. The standard p-n^+ junction forms a hole-injection barrier height equal to the germanium band gap, 0.7 eV. Our proposed

structure uses an amorphous contact to form the hole-injection barrier. The amorphous germanium barrier height is somewhat smaller than the barrier formed by a p-n junction. The actual height of the amorphous germanium hole-injection barrier can be adjusted by changing fabrication parameters during the sputter deposition process. However, the specific relationship between the sputter-deposition parameters and the height of the hole-injection barrier is not quantitatively known. Understanding this relationship is a central goal of this project. This will facilitate fabrication of the largest possible amorphous-germanium hole-injection barrier for segmented outer contacts of p-type coaxial detectors.

The amorphous-germanium hole-injection barrier height will be measured as a function of fabrication parameters. To measure the barrier height, the I(V) of detectors will be measured as a function of operating temperature. The detector I(V) will be measured in the 83^{o}K to 120^{o}K temperature range. The test cryostat will be outfitted with a variable-temperature stage of the style described in (Pehl et al., 1989). By applying power to a zener diode on the variable-temperature detector stage of the cryostat, the temperature of the detectors can be set and held constant at any temperature between 83^{o}K and 423^{o}K. As described below, making these I(V,T) (leakage current as a function of voltage and temperature) measurements gives us the hole-injection barrier height formed by the amorphous germanium contact. After the barrier height has been determined for a particular set of detectors, the contacts will be etched off and the same set of germanium wafers will be made into new detectors. This is another advantage of the amorphous germanium contact. Along with ease of fabrication and segmentation, the contact may be easily refabricated, if necessary, with minimal loss of germanium volume. If the contact does not function the first time, the process can be repeated with only the loss of a few tens of microns of germanium during etching.

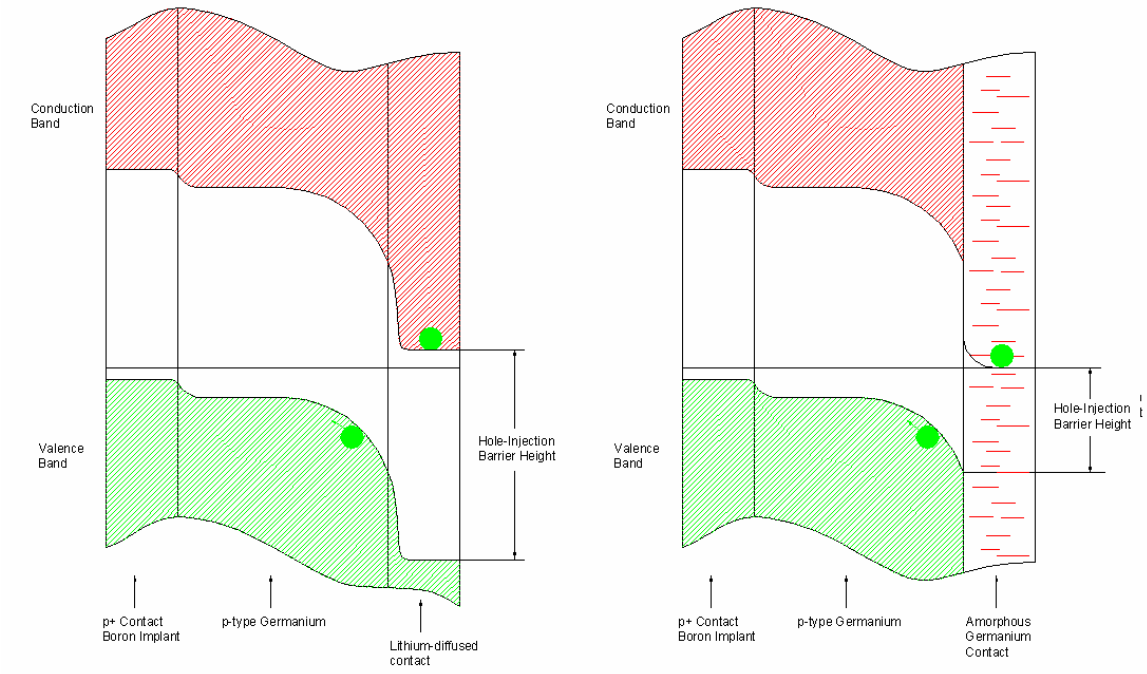

Figure 2. The left-hand energy band diagram shows the standard p+-p-n+ electrode structure used in most commercially available germanium detectors. The right-hand diagram shows our proposed innovative electrode structure that relies on the amorphous germanium contact to provide a hole-injection barrier.

The amorphous contact has recently been understood in terms of a long existent amorphous-crystalline heterojunction model (Hull 2004) (Dohler and Brodsky, 1984). A barrier height and a Fermi-level density of states N_f characterize the reverse-biased properties of the amorphous-crystalline heterojunction. The leakage-current density follows the expression:

$$j = j_\infty \exp(-\{\varphi - [(\varepsilon_0\varepsilon_{Ge}/N_F)^{1/2}(V+V_{depl})/d]\}/k_BT). \quad (1)$$

The expression is for a fully depleted planar detector of thickness d. The applied voltage is V and the depletion voltage is V_{depl}. The matrix element j_∞ is taken to be a constant determined by experiment.

Like a Schottky barrier, the amount of leakage current thermionically ionized over the amorphous-germanium hole barrier is proportional to $\exp(-\varphi/k_BT)$. The barrier height, φ, is of paramount importance. Increasing the barrier height from .35 eV to .40 eV reduces the amount of thermionically emitted leakage current by a factor of ~ 2000 at 80 K. In fact, our calculations predict that a hole-injection barrier ~.42 eV is sufficiently high that thermionic emission over the barrier is no longer the dominant source of leakage current. As the hole-injection barrier height increases toward ~.42 eV, the dominant source of leakage current becomes thermal generation in the bulk germanium rather than the contact. Thermal excitations generate free electron-hole pairs from generation-recombination sites at the mid-band-gap position throughout the bulk germanium (Pehl et al., 1973). If the hole-injection barrier height can be increased to .42 eV or greater, there will be effectively no measurable difference between the rectifying properties of an amorphous-germanium hole barrier and lithium-diffused n+ contact!

The density-of-states (N_f) term in the leakage-current expression determines the amount of electric-field dependent barrier lowering. In typical cases, the electric field lowers the barrier enough to increase the thermionically emitted leakage current over the barrier by a factor of ~ 2 from 100 V/cm to 3000 V/cm. Although the original barrier height is a much more important term, it would also be advantageous to also maximize the density of states to decrease the electric-field dependent barrier lowering.

The matrix element j_∞ is a constant to be determined by measurement. This matrix element differs somewhat from the temperature dependent A^*T^2 matrix element for Schottky barriers. The parameter A* is the Richardson constant. The temperature dependence of the Schottky matrix element arises from calculable transition probabilities from extended states in the metal contact to extended states in the crystalline material. The comparable matrix element for the amorphous-crystalline heterojunction is not readily calculable because it involves transitions from localized states on the amorphous side of the junction to extended states on the crystalline side of the junction. Experimentally, j_∞ does indeed appear to be a constant with respect to temperature. It will be interesting to understand the fabrication parameters affecting j_∞. If possible, j_∞ will be minimized to lower the leakage current.

The contact parameters N_f, φ, and j_∞ will be determined by fitting the I(V,T) curves to our expression for leakage-current density. Together, these three parameters fully characterize the rectifying electronic properties of the amorphous germanium contact. By making many detectors under different sputter-deposition conditions, we will understand the relationship between fabrication parameters and the contact parameters.

In the past, we have made detectors that rely on amorphous germanium contacts for both hole- and electron-injection barriers. We usually deposit identical contacts on both sides of the germanium wafer. If the same contact is made on both sides of a detector, a symmetric barrier is formed. This would be comparable to mirroring the amorphous-germanium contact in Figure 2 onto both sides of the crystalline piece of p-type germanium. When a bias voltage is applied to such a detector, the contact at the higher potential will rectify as a hole-injection barrier while the other side forms an electron-injection barrier after full depletion of the carriers in the bulk. In such a situation, the sum of the hole-and electron-injection barriers is equal to the band gap, .7 eV. A large hole-injection barrier, say .42 eV, would result in a small electron-injection barrier, .28 eV. A relatively large amount of electron-injection current would result. For the purpose of making our strip detectors, we usually want both hole- and electron-injection barriers to be approximately the same size, ~ .35 eV. The work proposed here is different. Here we need to maximize the barrier for just one sign of charge injection - hole injection. An improved understanding of the parameters affecting the type and height of the charge-injection barrier formed by the amorphous germanium contact will be of great practical importance in the fabrication of segmented contacts for p-type coaxial detectors. In addition, such an understanding stands on its own as an interesting piece of semiconductor physics.

CONCLUSIONS AND RECOMMENDATIONS

After many different fabrication parameters have been studied with the planar test detectors, we will choose the best method and make a more elaborate detector to evaluate the optimum fabrication technique for a coaxial-like detector. The detector will have 8 segments. It will be called MJ1. Figure 3 shows a drawing of MJ1. This detector will be a small p-type pseudocoaxial detector. It will be approximately 4 cm in diameter and 2 cm thick. The crystal will be ground into a right cylinder with one end having a rounded edge as shown in the drawing. The electron-injection barrier will be a small boron implanted spot in the middle of the larger flat surface of the detector. The outer diameter and rounded top of the detector is the sputtered amorphous-germanium hole-injection barrier contact. The amorphous germanium contact will be segmented into eight elements or pixels.

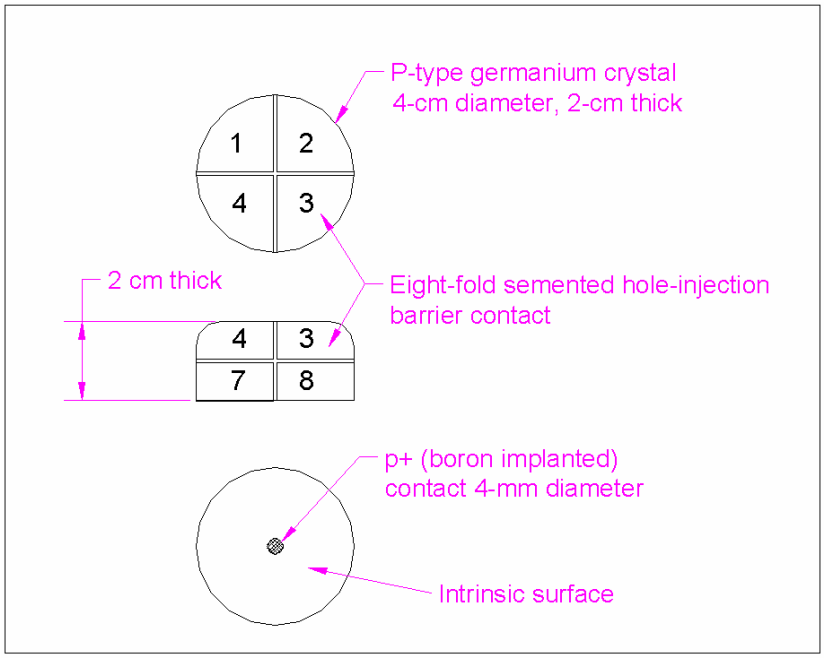

Figure 3. A technical drawing shows the segmented p-type pseudocoaxial detector (MJ1) having a segmented outer hole-injection barrier contact. Successful development of this detector is a key step in the establishment of amorphous germanium contacts as viable hole-injection barriers on p-type coaxial detectors.

Once the detector is functioning it will serve as a demonstration of the viability of the amorphous germanium contact for the hole-injection barrier on a segmented p-type coaxial detector. The detector performance will be evaluated. Later in the project, larger more sensitive segmented p-type coaxial detectors will be fabricated for low background highly sensitive gamma-ray detectors. These detectors will be ideal candidates for nuclear explosion monitoring systems such as the RASA.

REFERENCES:

Miley, H, S., R. J. Arthur, R. L. Brodzinski, W. K Hensley, J. H. Reeves, and F. T. Avignone (1991), Low Background Detectors for Exotic Physics Experiments, *Proceedings of the 4th International Workshop on Low Temperature Particle Detectors*.

Miley, H. S., F. T. Avignone, R. L. Brodzinski, J. I. Collar, and J. H. Reeves (1990), Suggestive Evidence for the 2-Neutrino Double-Beta Decay of Ge- 76. *Physical Review Letters* 65: (25), 3092-95.

Majorana Collaboration White Paper, The Majorana Zero-Neutrino Double-Beta Decay Experiment, LA-UR-2003-7709 and P. N. NL-14420. November 3, 2003, http://majorana. pnl. gov/MajoranaWhitePaper. pdf

Luke P. N., C. P. Cork, N. W. Madden, C. S. Rossington, M F. Wesela (1992), Amorphous Ge bipolar blocking contacts on Ge detectors, *IE. E. E Trans. Nucl. Sci.* 39(4), 590

Hull E. L., M. T. Burks, C. P. Cork, W. Craig, D. Eckels, L. Fabris, A. Lavietes, P N. Luke (With Madden, R. H. Pehl, K. P. Ziock) (2002), A germanium orthogonal strip detector system for gamma-ray imaging, AIP Conference Proceedings, *Unattended Radiation sensor systems for remote application*, 632**,** Washington, DC, 118.

Hull E. L. (2003). Germanium Detectors for Gamma-Ray Imaging, In *Radiation Detection Technologies Program, R & D Portfolio*, Eds. Spears DP and Alonzo GM, Albuquerque, NM, Dec 9-11, 22.

Hansen W. L., E. E. Haller (1977). Amorphous germanium as an electron or hole blocking contact on high-purity germanium detectors, *IE. E. E Trans. Nucl. Sci*. 24: (1) (1977), 61.

Pehl R. H., N. W. Madden, D. F. Malone, C. P. Cork, D. A. Landis, J. S. Xing, D. L. Friesel 1989). A variable temperature cryostat that produces in situ cleanup of germanium detector surfaces. *IE. E. E Trans. Nucl. Sci*. 36(1), 190-193.

Hull E. L., R. H. Pehl (Accepted for publication September 13, 2004). Amorphous germanium contacts on germanium detectors, *Nucl. Instr. and Meth*.

Döhler G. H. and M. H. Brodsky (1974). Amorphous-crystalline heterojunctions, in *Tetrahedrally Bonded Amorphous Semiconductors*, in American Institute of Physics, Eds. Brodsky, Kirkpatrick, and Weaire, New York (1974), 351-356.

Pehl R. H., E. E. Haller, and R. C. Cordi (1973). Operational Characteristics of Germanium Detectors at Higher Temperatures, *IE. E. E Trans. Nucl. Sci.,* 20, 494.

Döhler G. H. and M. H. Brodsky (1974). Amorphous-crystalline heterojunctions, in *Tetrahedrally Bonded Amorphous Semiconductors*, Eds. Brodsky M. H., Kirkpatrick S, Weaire D, NY, 351-356.

Hansen W. L., E. E. Haller (1977). Amorphous germanium as an electron or hole blocking contact on high-purity germanium detectors, IE. E. E *Trans. Nucl. Sci*. 24: (1), 61.

Hull E. L. (2003). Germanium Detectors for Gamma-Ray Imaging, In *Radiation Detection Technologies Program, R & D Portfolio*, Spears D. P. and Alonzo G. M., Eds, 22.

Hull E. L., M. T. Burks, C. P. Cork, W. Craig. D. Eckels, L. Fabris, A. Lavietes, P. N. Luke, N. W. Madden, R. H. Pehl, K. P. Ziock (2002). A germanium orthogonal strip detector system for gamma-ray imaging, AIP Conference Proceedings, 632**,** *Unattended Radiation Sensor Systems for Remote Application,* 118.

Hull E. L., R. H. Pehl (Accepted for publication September 13, 2004). Amorphous germanium contacts on germanium detectors, *Nucl. Instr. and Meth*.

Luke P. N., C. P. Cork, N. W. Madden, C. S. Rossington, M. F. Wesela (1992). Amorphous0 Ge bipolar blocking contacts on Ge detectors, IE. E. E *Trans. Nucl. Sci*. 39: (4), 590.

Majorana Collaboration White Paper, The Majorana Zero-Neutrino Double-Beta Decay Experiment, LA-UR-2003-7709 and P. N. NL-14420. November 3, 2003, http://majorana. pnl. gov/MajoranaWhitePaper. pdf

Miley, H. S., R. J., Arthur, R. L. Brodzinski, W. K. Hensley, J. H. Reeves, and F. T. Avignone (1991). Low Background Detectors for Exotic Physics Experiments, in *Proceedings of the 4th International Workshop on Low Temperature Particle Detectors.*

Miley, H. S., F. T. Avignone, R. L. Brodzinski, J. I. Collar, and J. H. Reeves (1990). Suggestive Evidence for the 2-Neutrino Double-Beta Decay of Ge- 76. *Phys. Rev. Let*. 65: (25), 3092-95.

Pehl R. H., E. E. Haller, and R. C. Cordi, Operational Characteristics of Germanium Detectors at higher Temperatures, *IE. E. E*

Pehl R. H., N. Madden, D. Malone, C. Cork, D. Landis, J. Xing, D. Friesel (1989), A variable temperature cryostat that produces in situ cleanup of germanium detector surfaces, *IE. E. E Trans. Nucl. Sci*. 36: (1), 190-193.

MITIGATION OF MEMORY EFFECTS IN BETA SCINTILLATION CELLS FOR RADIOACTIVE GAS DETECTION

Carolyn E. Seifert, Justin I. McIntyre, Kathryn C. Antolick, April J. Carman, M.W. Cooper, James C. Hayes, Tom R. Heimbigner, Charles W. Hubbard, Kevin E. Litke, Mike D. Ripplinger, and Reynold Suarez

Pacific Northwest National Laboratory

Sponsored by National Nuclear Security Administration
Office of Nonproliferation Research and Engineering
Office of Defense Nuclear Nonproliferation

Contract No. DE-AC05-76RL01830

ABSTRACT

Detection of radioactive noble gases can provide definitive evidence of a nuclear explosion at large stand-off distances. The Automated Radioxenon Sampler/Analyzer (ARSA) developed at Pacific Northwest National Laboratory (PNNL) measures the relative concentrations of xenon isotopes using a β-γ coincidence system. Typically, a set of plastic scintillating cells are surrounded by a NaI(Tl) scintillator. The cells are evacuated and the background count rate is measured before the cell is filled with sampled air. Any radioxenon present in the air emits β particles, which are detected in the plastic cell, as well as coincident γ rays, which are detected in the NaI(Tl). When a sample count is finished, the cell is again evacuated, and another background count is taken before measuring the next air sample. Previous tests of the ARSA system have shown that latent radioactivity remains in the plastic cells after evacuation of the gases, leading to a "memory effect" in which the background count rate is dependent on the sample history. The increased background results in lower detection sensitivity.

Two possible solutions to the memory effect are explored in this work: depositing a thin layer of metal on the plastic cell ("metallization"), and using an inorganic scintillating cell composed of yttrium aluminum perovskite (YAP). In both cases, the presence of inorganic material at the surface is intended to inhibit the diffusion of gases into the cell walls.

In the metallization experiments, several different metals (Al, Cu, chrome) were deposited on plastic cells using electron beam lithography. The light collection performance of the cells was evaluated using standard sealed γ-ray sources and compared to a bare plastic cell. The aluminized cell demonstrated comparable light collection performance and good adhesion to the plastic and was chosen for further studies.

The aluminized cell, YAP cell, and bare plastic cell were each placed in the void of a CsI(Na) well counter and injected with radioactive xenon and radon. β-γ coincidence measurements were taken before, during, and after injection of radioactive gases. The YAP cell demonstrated little or no observable memory effect, while the aluminum-coated plastic cell showed reduced latent radioactivity relative to the bare cell as expected. Although the memory effect results for the YAP cell are promising, the wall thickness is too large for the escape of the xenon x-rays into the gamma-ray detector, which is required for radioxenon detection. This paper discusses the measurement details and provides recommendations for further research and optimization.

OBJECTIVE

The Automated Radioxenon Sampler/Analyzer (ARSA) system detects and measures the relative concentrations of radioxenon isotopes, seeking a definitive signature of nuclear explosions. A full description of the ARSA system is given elsewhere (Bowyer 1998), and only a brief synopsis will be given here. The system collects and processes air samples, filtering out particulates and unwanted elements. The xenon is separated and pumped into scintillating plastic cells for β detection, which are surrounded by NaI(Tl) γ-ray detectors. The radioxenon isotopes are detected by operating the β and γ-ray detectors in coincidence. Isotopic ratios of xenon can be determined by the signatures observed in the β-γ coincidence spectrum (Reeder 1998). Specific isotopic ratios indicate the occurrence of a nuclear explosion.

In ARSA field tests, a memory effect was observed wherein the β-γ coincidence system would measure latent radioactivity in the gas cells after they had been evacuated. Not all of the radioactivity could be pumped out of the system (McIntyre 2001). Corrections for this increased background were successfully applied, but the sensitivity of the system was poorer than what could be obtained if there were no memory effect.

The objective of this work is to test two possible methods for mitigating the memory effect in the gas cell used for detection of radioactive xenon. The first technique involves depositing a metal on the interior surface of the β cell, which should inhibit the adhesion of the gas to the cell walls and the diffusion of noble gases into the cell walls. The second method uses an inorganic, rather than plastic, scintillator to detect β radiation, which should have a similar effect as the metal. The experimental methods and results are discussed in the paper, and a recommendation is provided for future designs.

RESEARCH ACCOMPLISHED

Metallization Experiments

Aluminum, chrome, and copper were all tested as surface treatments for the scintillation cells. Al and Cu were evaporated at a rate of 9 Å/s onto the plastic under vacuum conditions using an electron-beam chamber at the Environmental Molecular Sciences Laboratory (EMSL) at PNNL. Chrome was deposited thermally in the same chamber. The total thickness of the metals was estimated to be roughly 1 μm in all cases. Shown in Figure 1 is a copper coated cell. The outside of the cell remains uncoated, as seen on the endcap in the figure.

The scintillation cells used in this experiment are not the original design for ARSA, which had cylindrically shaped scintillators with two photomultiplier tubes (PMTs) embedded in NaI(Tl) blocks. Cooper et al. present concurrently with this work the modifications—including the new bullet-shaped cell design—used to improve the reliability of ARSA system (Cooper 2005). In this experiment, the new cell design is used.

Figure 1. Photograph of copper-coated plastic scintillating gas cell and endcap for detection of β radiation. Only the interiors of the cell and endcap are metallized.

To test the light collection capability of the metallized cells, we examined the energy spectra from several γ-ray sources placed near the endcap. The endcap (by itself) was optically coupled to a photomultiplier tube, and both were placed inside a light-tight housing. γ-ray sources were placed individually against the outer wall of the housing, and the resulting energy spectra are recorded using an Ortec DART connected to a laptop computer. Due to the low atomic numbers of the elements present in the endcap, very little photoabsorption occurs in the scintillator. Almost all observed interactions are due to Compton scatter, which results in a continuum not unlike β energy spectra. The endpoints of these distributions are the Compton edges, which occur at a known energy for a given γ-ray energy.

Figure 2 shows the comparison between observed distribution endpoints and known Compton edge energies. The data follow a 2nd-order polynomial trend. For a thick detector, one would expect a linear trend between the energy of the scattered Compton electron and the observed channel number. However, higher energy electrons can escape from the β cell before losing all their energy. Therefore, for high-energy electrons the amplitudes of the pulses from the β cell are reduced compared to the amplitude corresponding to the full energy of the electron.

The chrome and copper data show a reduced channel number compared with the other endcaps, indicating less light collection. This is not surprising, given that the visible light reflectivities of chrome (~0.6) and copper (~0.4) are much smaller than that of aluminum (~0.95) (*CRC Handbook*). Thus, more light is reflected at the aluminum surface back into the scintillator for possible collection at the PMT than for the other metals. Additionally, copper specifically is a poor choice of metal not only for its selective frequency absorption characteristics (i.e. what gives copper its unique color) but also because it was easily peeled from the surface of the cell. During cell evacuation and filling, it is likely that some of the copper would flake off and cause a blockage in the gas transfer system. No such fragility was observed with the aluminized cell.

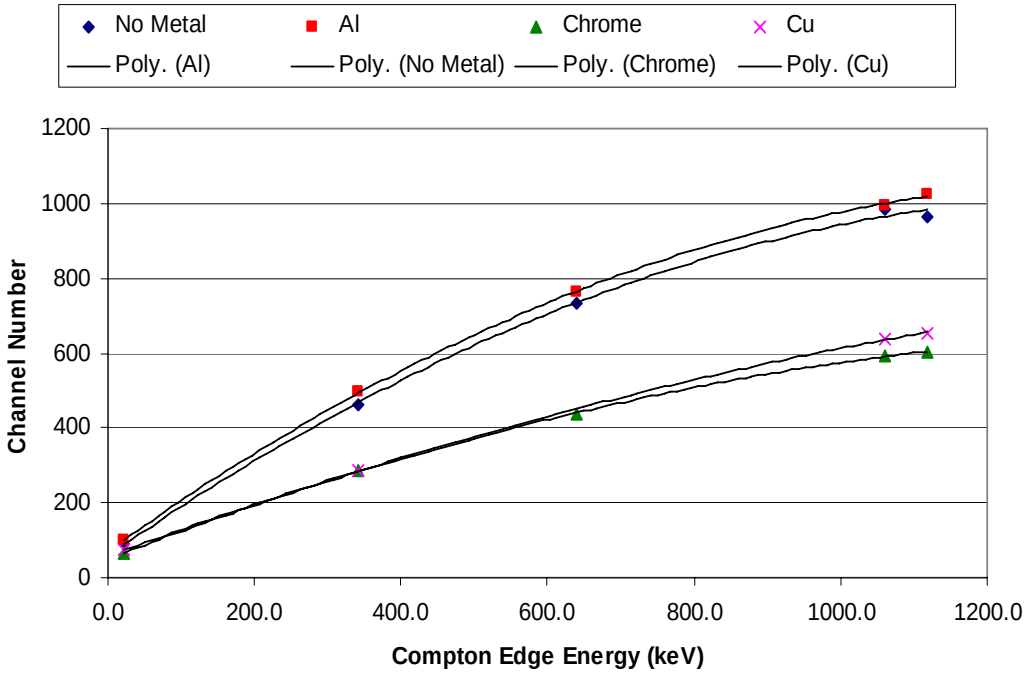

Figure 2. Comparison of observed Compton edge channel numbers with known energies for the different metallization schemes. The data follow 2nd-order polynomials.

The aluminum and bare cells were then fully assembled and sealed with optical cement. The cells were wrapped in Teflon tape to improve light collection efficiency, were coupled to a PMT, and were again placed inside a light-tight housing. The γ-ray measurements were repeated for the two cells, and the results are given in Figure 3. Again the performance of the aluminum coated cell was similar to that of the bare cell, except that the light output was slightly higher. The total light output of the fully assembled cells was about twice that of the endcaps alone. The γ-ray measurements demonstrate that aluminum is a good choice for metallization and does not result in any loss of signal in the β cell.

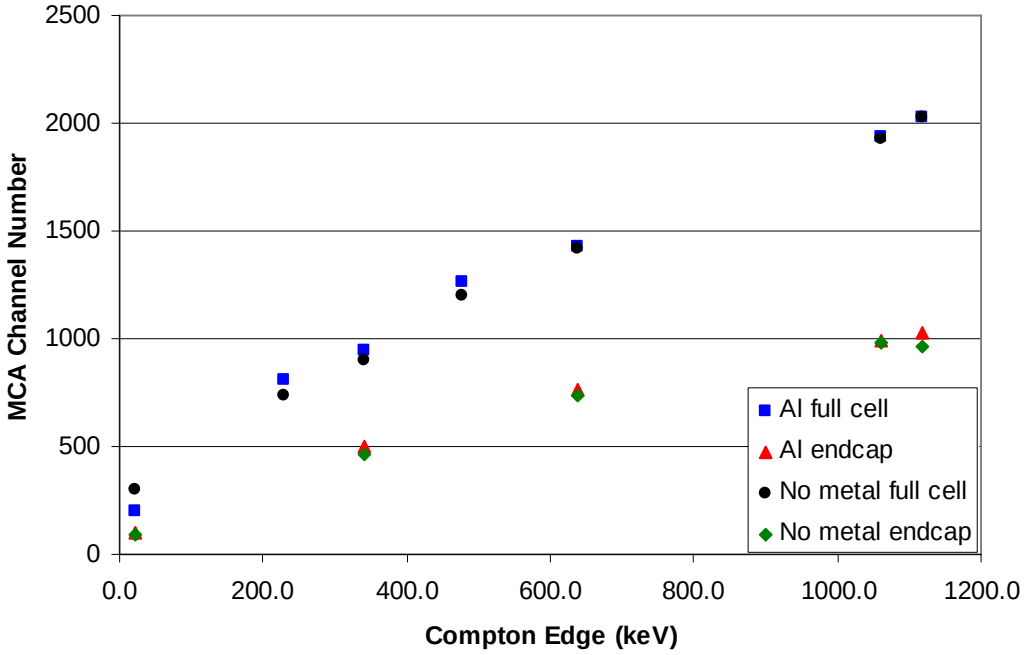

Figure 3. Comparison of observed Compton edge channel numbers with known energies for the endcaps and fully assembled bare and aluminum-coated cells.

Radioactive Xenon Measurements

To test the memory effect of the scintillations cells, radioactive gas measurements were performed. The bare plastic cell and aluminum-coated plastic cell were tested along with an inorganic scintillator cell composed of yttrium aluminum perovskite (YAP). Stainless steel gas tubes were inserted into the cells and secured in place with optical cement and then opaque epoxy. The β cell housings were placed in the void of a CsI(Na) well detector, and the assembly was encased in black polyethylene. The detectors were placed in a 4-inch-thick lead cave with a 0.25-inch-thick copper lining to reduce ambient background from cosmogenic and environmental radioactive sources.

Radiation measurements were taken before, during, and after exposure to radioactive gases in the following manner. The cells were evacuated using a vacuum pump, typically resulting in pressures of a few mTorr. Background data were taken for 24 hours. Because the cells tend to leak up to atmospheric pressure over the course of one day, they were again pumped to low pressures before the radioactive gas was injected. Again, data were taken for 24 hours. The cell was then pumped and flushed with ambient air three times before a final 24-hour background measurement was performed. This procedure was used for both radioxenon and radon measurements.

Figure 4 shows the 2-D β-γ coincidence spectrum for the bare cell injected with radioxenon. There are two main γ-ray peaks, corresponding to the 81 keV γ ray from Xe-133g and 30 keV x-ray emitted from all xenon isotopes. The β spectrum is the sum of contributions of the electron energies from Xe-131 (129 keV conversion electron (CE)), Xe-133m (199 keV CE), and Xe-133g (346 keV max β energy). A detailed discussion of this spectrum is provided by Reeder (Reeder et al. 1998).

If the β cells exhibited no memory effect, then the count rate after pumping the gas out of the cell should be the same as that in the background measurement before gas injection. Two xenon regions, shown in Figure 4, are defined, and the count rates in each region are compared with and without the gas present. The count rates are corrected for the observed background. The results for each detector type are given in Table 1. The bare cell demonstrated a very large count rate even after the cell was evacuated. Previous estimates of the memory effect were about 5% for a bare cell with radioxenon (McIntyre 2001), and the observed rates may be artificially high due to a malfunctioning vacuum pump.

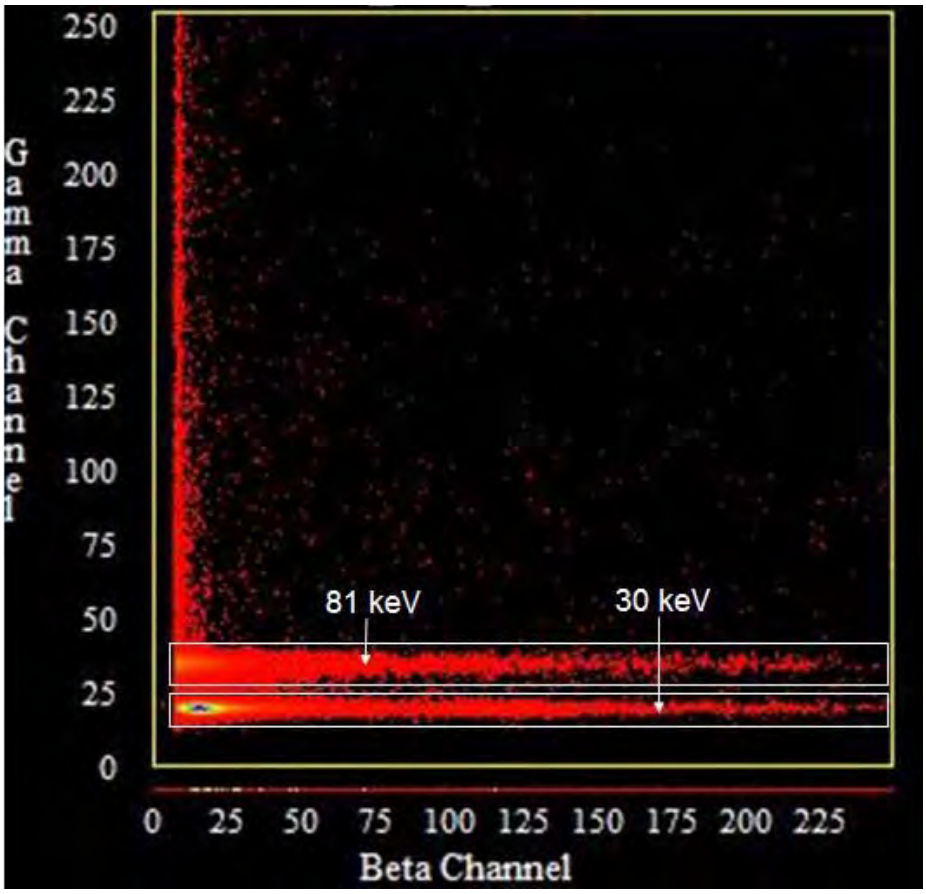

Figure 4. β-γ coincidence spectrum for aluminum-coated cell injected with radioxenon. Rectangular "xenon regions" are defined for further quantitative evaluation.

Table 1. Percent of Xenon Count Rates Observed after Evacuation of Gas Cell in 30 keV and 81 keV Regions of Xenon β-γ Coincidence Spectrum

	30 keV	81 keV
Bare	94 ± 4 %	80 ± 7%
Aluminized	7.8 ± 0.2%	8.1 ± 0.4%
YAP	Not observed	8 ± 2%

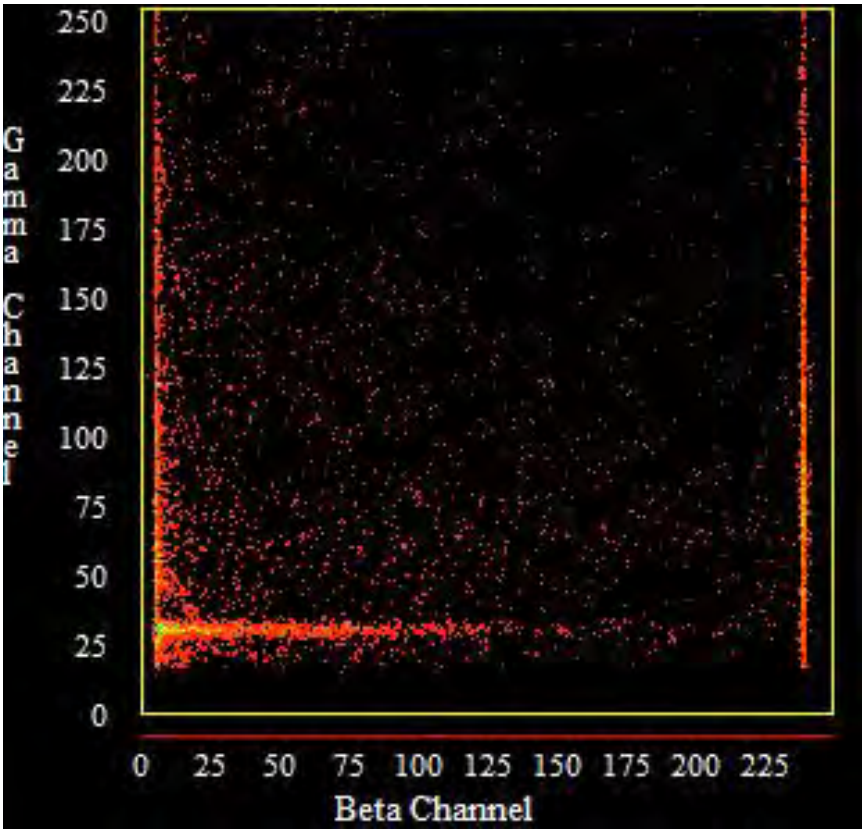

Figure 5. β-γ coincidence spectrum for YAP cell injected with radioxenon. Only the 81 keV γ-ray peak is visible in the spectrum.

It is important to note that the β-γ coincidence spectrum for the YAP cell consists of only one γ-ray peak, as seen in Figure 5. Because the YAP cell has a much higher effective atomic number than the plastic scintillator, the 30-keV x-rays from Xe are more likely to be absorbed in the β cell directly and will not reach the CsI(Na) detector to initiate a coincidence. Also visible in Figure 5 is a bright line corresponding to high β energies; this is actually overflow in the multi-channel analyzer. The high-energy electrons that enter the cell walls from the gas deposit more of their energy in the YAP cell than in the plastic cell due to the higher stopping power of YAP. The analyzer puts these high-energy counts in the last few β channels. In addition, despite the calculated 8±2% effect shown in Table 1, the γ-ray spectrum shows very little evidence of latent radioactivity, as seen in Figure 6. There is an elevated background shelf, but no evidence of a peak in the 81-keV vicinity. This is unlike the aluminized cell, for which two small peaks are visible in the γ-ray spectrum data taken after the cell was evaculated (not shown).

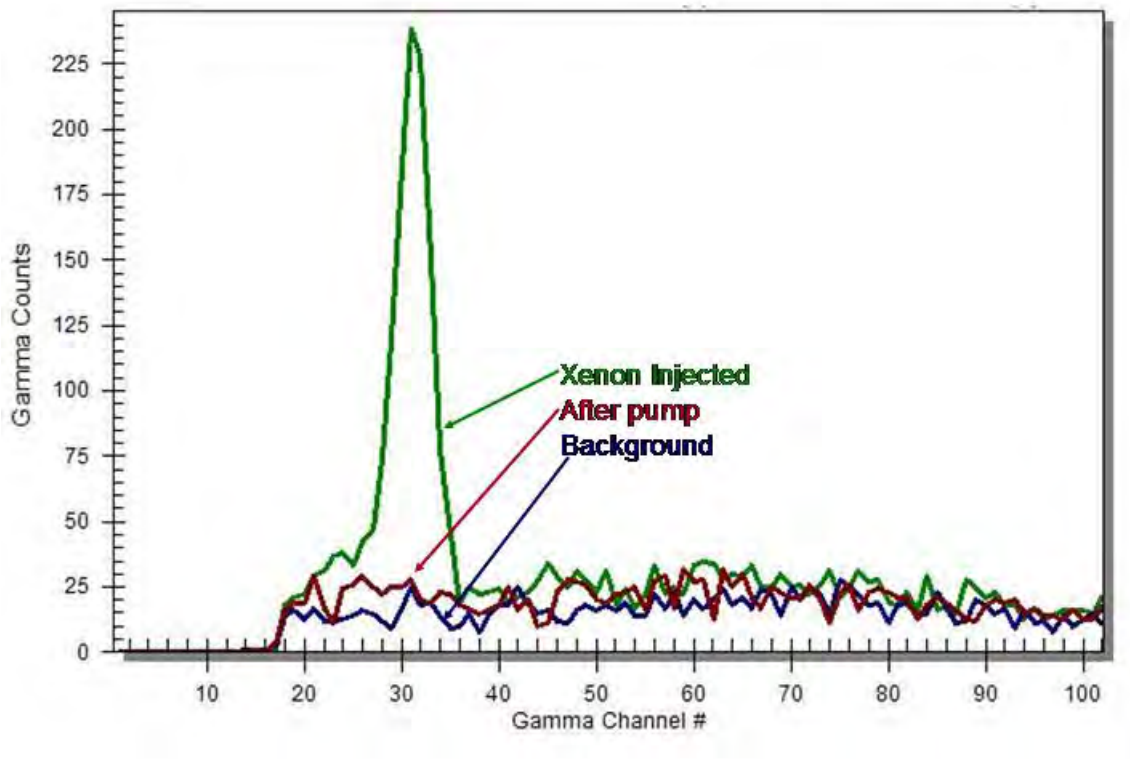

Figure 6. β-gated γ-ray spectrum using YAP cell with xenon injected.

Radioactive Radon Measurements

The ARSA system is designed to measure radioxenon, and the presence of radon isotopes can be detrimental. The atmospheric concentration of ^{222}Rn is ~ 10 Bq/m^3, which is 10^5 times greater than the desired sensitivity level of ^{133}Xe in the ARSA system (Bowyer 1998). Furthermore, not all of the ^{222}Rn is filtered from the air in the gas separations process—only about 99.98% of the radon is removed (McIntyre 2001). In terms of the memory effect, the influence of radon is significant. Unlike the Xe isotopes, which decay to stable or long-lived nuclides, the Rn daughters have very short half-lives (on the order of seconds or minutes), and thus have a relatively high activity. Because the Rn daughters are not noble gases, they are likely to adhere to the cell walls and not be pumped out of the cell, which leads to a higher latent activity from radioactive contaminants in the cells after evacuation than if the sample consisted only of xenon. This was confirmed by previous measurements: the memory effect for radon is larger than that for xenon (McIntyre 2001). With the β-γ coincidence method, simply having extra radioactivity would not in itself be detrimental. However, ^{222}Rn decays to ^{214}Pb and ^{214}Bi, which have γ- and x-rays that interfere with the 81 keV and 250 keV γ rays from ^{133g}Xe and ^{135g}Xe, respectively.

In the past, corrections have been made to account for the memory effect due to the radon impurities in the gas (McIntyre 2001). A system in which there is no memory effect for radon—or at least reduces the magnitude of such an effect—would result in a higher sensitivity for radioxenon. Thus, we performed the radioactive gas experiments using radon on each of the three detector types to measure the improvement, if any, compared with the bare cell.

Shown in Figure 7 is the β-γ coincidence spectrum for the bare cell. There are several γ-ray energies observed in coincidence with β or CEs from the radon daughters. These correspond to the 352 keV, 295 keV, and 242 keV γ-rays from ^{214}Pb, as well as x-rays from ^{214}Pb and ^{214}Bi between 75 to 90 keV. Figure 8 shows a comparison of the β-gated γ-ray spectra for radon and xenon for the bare cell. The interference at 81 keV is clearly seen.

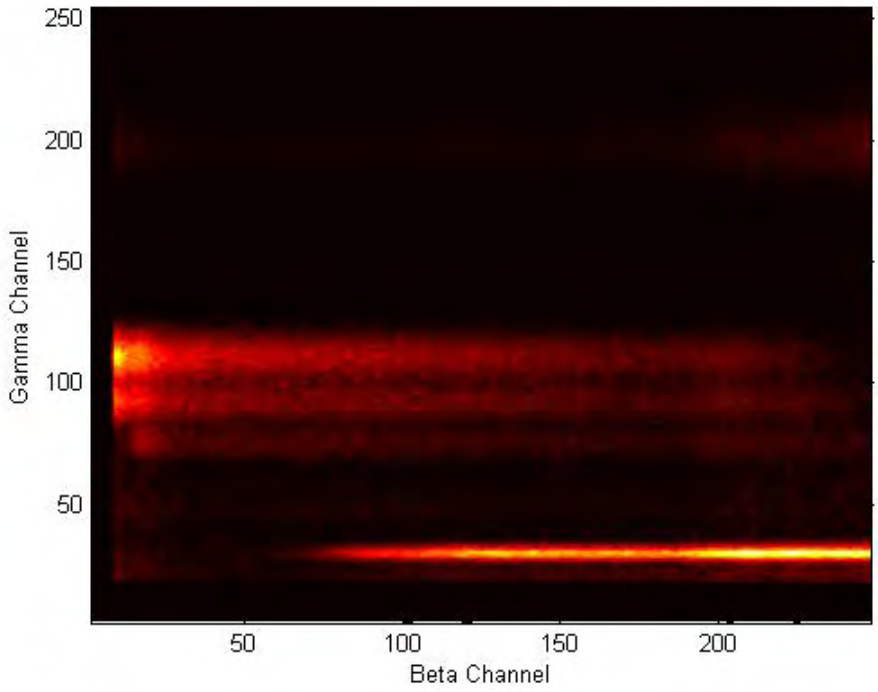

Figure 7. β-γ coincidence spectrum for bare cell injected with radon.

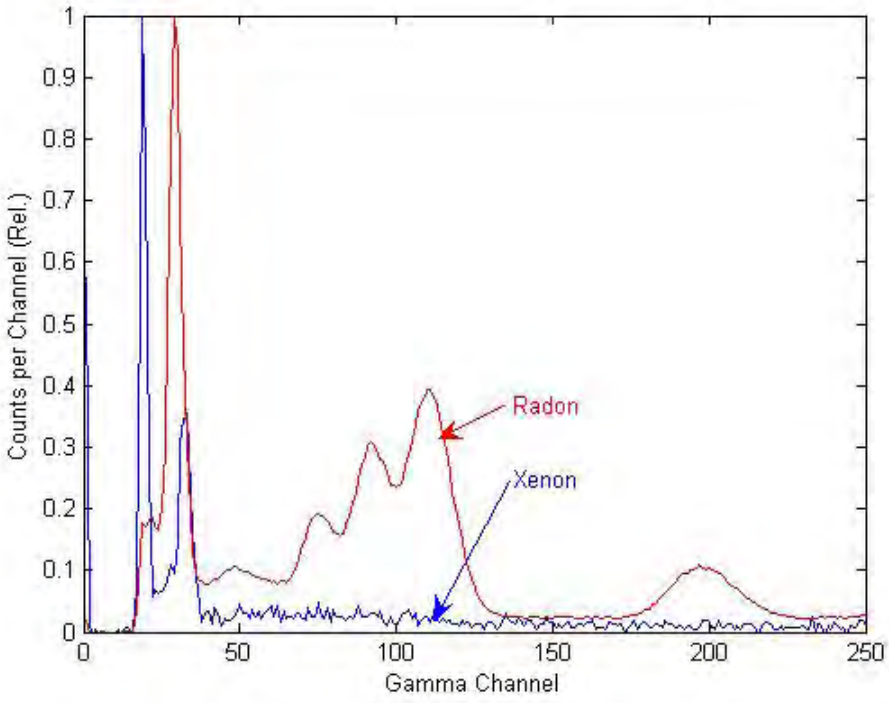

Figure 8. Normalized β-gated γ-ray spectra for radon and xenon injection in a bare cell. Note the overlap in signatures at 81 keV (γ channel 34).

For the radon measurements, the comparison of the total count rate before and after the radon-filled cell is evacuated is used as a measure of the memory effect. Corrections must be made in the count rates to account for the decay of ^{222}Rn (half-life of 3.8 days) during the two 24-hour measurements. Consider the following. The number of counts C observed between times t_1 and t_2 for a source with activity $A(t)$ is given by

$$C = \varepsilon \int_{t_1}^{t_2} A(t)dt \,, \tag{1}$$

for a constant detection efficiency ε. The main contribution of the ^{222}Rn chain to the β-γ coincidence spectrum will be from ^{214}Pb and ^{214}Bi. The radionuclides in the chain that alpha decay do not produce a coincidence signature in the detectors, and the ^{214}Bi daughter, ^{214}Po quickly alpha decays to ^{210}Pb, which has a half-life (23 years) that is long compared to the acquisition time. Thus,

$$C = \varepsilon \int_{t_1}^{t_2} \left[A_{Pb}(t) + A_{Bi}(t)\right]dt \,. \tag{2}$$

The activities $A_{Pb}(t)$ and $A_{Bi}(t)$ can be calculated using the Bateman equation for radioactive decay. Furthermore, the activities are directly proportional to the amount of radon present at $t=0$, $N_{Rn}(0)$:

$$A_i(t) = N_{Rn}(0)\, f_i(t) \,, \tag{3}$$

where i indicates ^{214}Pb or ^{214}Bi. Therefore, the initial amount of radon can be estimated from the observed count rates, estimated detection efficiency, and decay functions $f_i(t)$:

$$N_{Rn}(0) = \left[\frac{C}{\varepsilon \int_{t_1}^{t_2} \left[f_{Pb}(t) + f_{Bi}(t)\right]dt} \right]. \tag{4}$$

The estimated amount of radon at $t=0$ is calculated for the data collected before and after the evacuation of the cell. The ratio of the two estimates yields a measure of the radon remaining in the cell after evacuation, and thus is a measure of the memory effect. Because ratios of the radon estimates are used, the detector efficiency term cancels.

The integrand in the equations above, dubbed the “total effective activity”, is shown in Figure 9. Also plotted in Figure 9 is the evaluated integral for $t_1=0$ and t_2 plotted on the horizontal axis. This is the effective number of disintegrations that have occurred until t_2. The vertical scales on both graphs are relative; the use of ratios allows us to neglect the absolute value of these functions.

To appropriately correct the data, the measured counts are first background subtracted to yield the measured counts C. Then, Equation (4) is evaluated (neglecting the efficiency term) using the number of disintegrations function in Figure 9, and the estimated initial amounts of radon are determined. The ratio of radon estimates after and before evacuation is calculated for each detector type, and the results are given in Table 2.

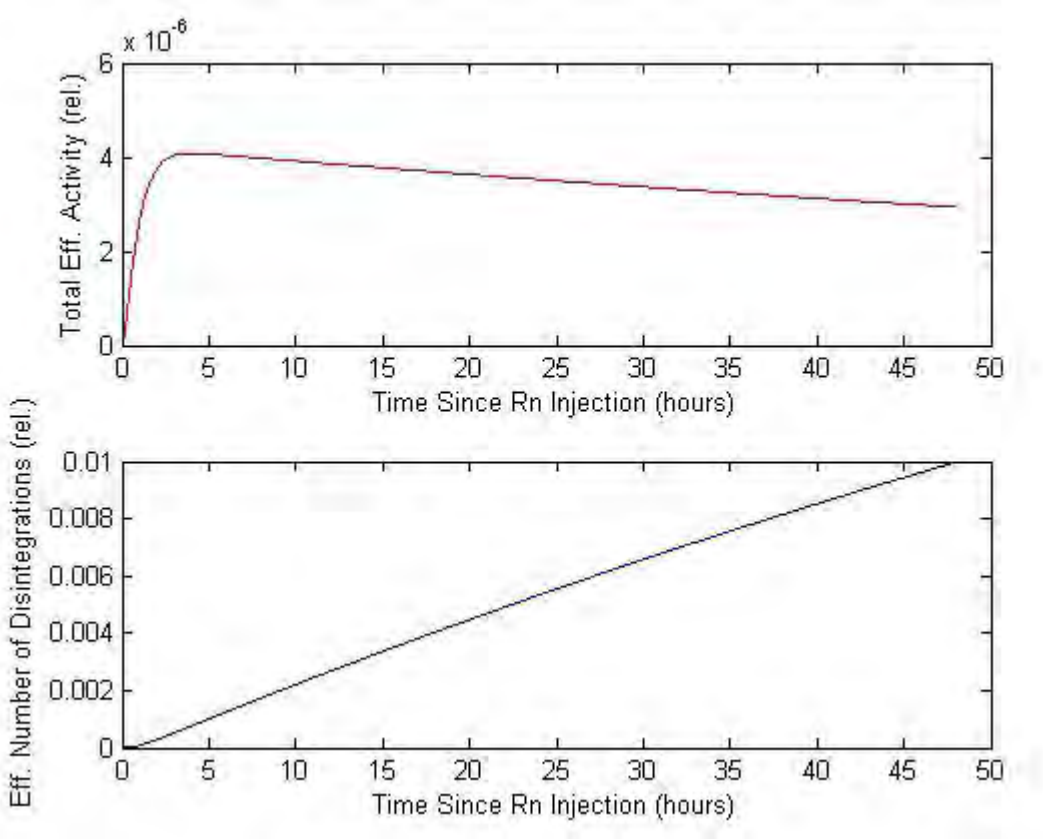

Figure 9. a) Total effective activity—the sum of ^{214}Bi and ^{214}Pb activities as a function of time after ^{222}Rn injection. b) Effective number of disintegrations from ^{214}Pb and ^{214}Bi as a function of time after injection.

Table 2. Memory Effect Estimates for Radon-Injected Gas Cells

	Memory Effect
Bare	19.6%
Aluminized	13.5%
YAP	1.8%

The estimated effect for the bare cell was approximately 20%, which is similar to numbers previously reported for the ARSA system and is much less than determined in this work for Xe. This indicates a possible vacuum pump malfunction during the xenon experiments. Actual cell pressures were not monitored during every experiment. The aluminized cell showed an increase in the memory effect for radon compared with xenon, as expected. Also, the aluminum coating on the cell did have the desired effect—there was an observed reduction in latent activity relative to the bare cell for radon. The YAP cell demonstrated surprisingly good performance in the radon experiment. Very little radon was observed in the cell after the experiment.

There were a few strange features observed in the data. The acquisition software is capable of tracking the count rates as a function of time. There was an initial coincidence count rate decrease due to the decay of the radon daughters that remained in the cell after evacuation. This is expected. However, later, in both the aluminized and

bare cells, there were anomalous changes in the count rate that cannot be accounted for. The rates were not measured for the YAP cell. These same features exist also for the β singles and γ singles count rates. It is unclear what caused these rate changes or if they affect the spectroscopic data in the β-γ coincidence spectrum. Further measurements are required to determine the cause of this behavior.

CONCLUSIONS AND RECOMMENDATIONS

The radon data clearly demonstrate that using an inorganic surface on the β cell reduces the memory effect from gases remaining in the cells after evacuation. Depositing aluminum on the surface of the plastic cell reduced the memory effect from 20% to 14%. This could lead to better ARSA performance. The YAP cell performed extremely well in both the xenon and radon measurements. With additional optimization of the cell wall thickness (less than 2mm) the YAP cell will provide excellent beta detection while allowing the low energy x-rays to pass through for detection in the surrounding NaI(Tl). In addition, the present configuration of the YAP cell may be more appropriate as a β detector when higher energy γ rays are detected, such as with radon.

While not discussed in this paper, the energy resolution of the YAP is far superior to the energy resolution of the plastic. Additional testing using a thin walled YAP cell will be able to exploit this energy resolution in detecting the 129-keV and 199-keV conversion electron energies of ^{131m}Xe and ^{133m}Xe respectively. Additional studies are continuing on the three cells considered in this paper and a thin walled version of the YAP cell will be available during FY 06 to investigate both the x-ray attenuation issue and the enhanced energy resolution properties.

REFERENCES

Bowyer, T.W., K.H. Abel, C.W. Hubbard, A.D. McKinnon, M.E. Panisko, R.W. Perkins, P.L. Reeder, R.C. Thompson, and R.A. Warner (1998). Automated separation and measurement of radioxenon for the Comprehensive Test Ban Treaty, *Journal of Radioanalytical and Nuclear Chemistry*, 235: 1-2: 77–81.

Cooper, M.W., A. J. Carman, J.C. Hayes, T.R. Heimbigner, C.W. Hubbard, K.E. Litke, J.I. McIntyre, S.J. Morris, M.D. Ripplinger, and R. Suarez (2005), Improved β-χ coincidence detector for radio-xenon detection, in current Proceedings.

CRC Handbook of Chemistry and Physics, Editor D.R. Lide (2001), 12: 153.

McIntyre, J. I., K. H. Abel, T. W. Bowyer, J. C. Hayes, T. R. Heimbigner, M. E. Panisko,P. L. Reeder, R. C. Thompson (2001), Measurements of Ambient Radioxenon levels using the Automated Radioxenon Sampler/Analyzer (ARSA), *Journal of Radioanalytical and Nuclear Chemistry*, 248: 3, 629–635.

Reeder, P.L., and T.W. Bowyer (1998), Xe isotope detection and discrimination using beta spectroscopy with coincident gamma spectroscopy, *Nuclear Instruments and Methods in Physics Research*, A408: 582–590.

Infrasound Monitoring

DETECTION OF REGIONAL AND DISTANT ATMOSPHERIC EXPLOSIONS AT IMS INFRASOUND STATIONS

Douglas R. Christie, Brian L. N. Kennett, and Chris Tarlowski

Australian National University

Sponsored by Air Force Research Laboratory

Contract No. FA8718-04-C-0032

ABSTRACT

Work is proceeding rapidly on the establishment of the 60-station infrasound component of the International Monitoring System (IMS). This is a fairly sparse network. The average distance between stations is about 2500 km for stations located in continental land mass areas and up to about 4500 km for stations that monitor the vast open ocean areas of the Southern Hemisphere. A good understanding of the detection capability for small nuclear explosions located in the distance range from 1000 to 4500 km is clearly essential. At the present time, the properties of explosion-generated infrasonic signals observed in this distance range remain poorly understood. This is especially true for explosions with yields of a few kilotons or less due to a lack of well-documented digitally recorded events. It is worth noting that there have been surprisingly few observations in the last decade of infrasonic waves from surface mining explosions and other impulsive sources located at distances beyond 1500 km. This may indicate that currently used detection procedures do not reliably detect infrasound from surface explosions with yields of a few kilotons or less when the distance to the source is large. This initial investigation is therefore focussed on a study of the properties of regional and distant explosion-generated infrasonic waves observed at two neighbouring IMS infrasound monitoring stations, IS07 Warramunga and IS05 Hobart in Australia. The primary goal of this investigation is to delineate any possible problems that may reduce detection efficiency for regional and distant surface explosions and to determine procedures that will enhance the detection of explosions at distances in the range from 1000 to 4500 km.

A wide variety of infrasonic events has been detected at IS07 and IS05 ranging from impulsive short-lived signals generated by mining and volcanic explosions to continuous signals associated with storms over the open oceans around Australia, air flow over high mountains and auroral activity. The morphology and frequency content of observed infrasonic signals indicate that many of the detected short-lived signals are generated by local sources. The properties of continuous infrasonic signals and signals from local sources will not be described here. Instead, this study is concerned with the observed properties of relatively long-period infrasonic waves from regional and distant sources and the influence that these properties have on global detection capability for small nuclear explosions. In particular, this investigation is concerned with a study of the observed properties of signals from regional and distant mining explosions, distant bolides and distant volcanic explosions.

.

OBJECTIVE

The main objective of this research in to identify potential problems with the detection of infrasound generated by distant atmospheric explosions and to determine procedures that will improve detection capability for explosions at distances that are comparable with the spatial separation of monitoring stations in the global IMS infrasound network. The vast open ocean areas of the Southern Hemisphere are particularly difficult to monitor since monitoring stations must be located at sites that are often separated by more than 3500 km. This research is therefore focused on a study of infrasound detection capability at typical IMS monitoring stations for infrasonic signals generated by explosions located at distances in the range from about 1000 to 4500 km.

RESEARCH ACCOMPLISHED

Introduction

The global IMS infrasound monitoring network is a 60-station network of array stations distributed as uniformly as possible over the surface of the globe. The average separation between stations located in continental land mass areas is about 2500 km. In contrast, the average spacing between stations that surround the vast open ocean areas of the Southern Hemisphere is greater than 3500 km. Since the minimum acceptable requirement of the IMS network for nuclear explosion monitoring is two-station detection capability for a 1 kiloton explosion located at any point on the globe, individual IMS infrasound stations need to be able to reliably detect 1-kiloton explosions at ranges of up to 3000 km or more. Upper atmospheric winds have a very beneficial influence on the propagation of infrasound when propagation is directed along the direction of the stratospheric winds. This means that detection capability for nuclear explosions will generally be very good at monitoring stations located downwind from the source in the direction of the stratospheric winds. Detection capability will be significantly reduced, however, when the monitoring station is located either upwind from the source or normal to the direction of the stratospheric winds. In this case, detection will usually be restricted to thermospheric arrivals. In this regard, we note that very few well-documented observations have been reported in recent years of infrasound from surface explosions at distances beyond 1500 km. The initial research summarized here is part of a more extensive program that is focused on a detailed investigation of the detection, location and discrimination of infrasonic signals under a wide range of conditions at IMS infrasound stations in the Southern Hemisphere.

Much of the work in recent years on the monitoring of small atmospheric nuclear explosions has been concerned with the detection of relatively high-frequency infrasonic waves in the passband from about 0.5 to 2 Hz. The emphasis on this particular passband has been motivated primarily by: a) problems with the construction of noise reducing systems that are effective at low frequencies, b) the recognition that infrasound from small nuclear explosions may be detectable in the 0.5 to 2 Hz passband, c) the problem of separating coherent explosion signals from a background of coherent microbarom signals in the passband from 0.1 to 0.5 Hz passband, and d) at higher frequency, concern with potential spatial aliasing and signal coherence problems. It is generally agreed (see, e.g., Blandford 1997, 2004) that detection of infrasound from small nuclear explosions at distances of up to at least 1000 km will usually be optimum in a passband around 1Hz. While it is clearly important to have good monitoring capability in the passband from 0.5 to 2.0 Hz, this passband may not be the best detection passband if the source is located at greater distances or if propagation is confined by the upper wind structure to a thermospheric waveguide. Indeed, the higher frequencies may be eroded away completely at larger distances with the result that it may not be possible to detect infrasound from a distant nuclear explosion at any frequency above 0.5 Hz. The problem of the loss of the higher frequency signal components from distant sources is particularly relevant to the problem of monitoring the vast open ocean areas of the Southern Hemisphere.

The potential difficulties in detecting infrasound from distant explosions will be illustrated here by observations recorded at two IMS infrasound stations in Australia. The main detected events that we use to illustrate this problem have been chosen because they are located a distances beyond 1000 km and because they include an example of signal detection along a propagation path that is perpendicular to the stratospheric winds.

Infrasound monitoring stations in Australia

Australia is host to a total of four IMS infrasound monitoring stations on Australian territory and an additional station (IS03 Davis Base) located in Antarctica. Two of these stations, IS05 Hobart in Tasmania and IS07 Warramunga in the Northern Territory, are in operation and certified. The construction of a third station, IS04

Shannon, located in the southwestern corner of Australia, is nearly finished and this station should be in operation and certified by October 2005. This station is expected to play an important role in the monitoring of the South Indian and Southern Oceans. The forth station in this regional network, IS06 Cocos Islands, will be installed in 2006 and the station at Davis Base will be established in the following year.

The location of the infrasound monitoring stations in Australian, the source location of two of the analyzed events and the location of the main open-cut mining areas in Australia are shown on the map in Figure 1. The average distance between the three infrasound monitoring stations located on the Australian mainland is about 2730 km. All of the observations used in this study were recorded at IS05 and IS07.

Figure 1. Map of the Australian region showing the locations of infrasound monitoring stations IS04, IS05 and IS06, the locations of the main open-cut mines, the locations of the nearest active volcanoes (dark red circles) in the area to the north of Australia, the location of the explosive eruption of Manam Volcano in Papua New Guinea on 27 January 2005, and the location of the New South Wales (NSW) bolide on 5 December 2004.

The characteristics of IS05 Hobart and IS07 Warramunga differ significantly. IS05 is located on the southeastern side of Tasmania at latitude 42.5 ºS in a fairly sparse eucalyptus forest, about 20 km from the coast of the South Pacific Ocean. The station is partially sheltered from the ambient winds by the surrounding forest, but noise levels over the array tend to vary widely from site to site at all times of day. The station is also subject to infrasonic noise generated by surf activity along the eastern margin of Tasmania and to high levels of microbarom noise associated with intense storms over the Southern Ocean. IS07 is located at latitude 19.9 ºS in the arid interior of Australia. Long grass and a few small trees and bushes provide some shelter from the ambient winds, but wind noise levels tend to be fairly high during the daytime and much lower at night when the upper winds are decoupled from the surface by an intense nocturnal radiation inversion. Thermal mixing due to convection is extreme at Warramunga and the well-mixed daytime boundary layer can extend to a height of two km or more. In contrast with IS05 Hobart, IS07 Warramunga is subject to highly nonlinear gravity wave disturbances in the form of large amplitude solitary waves and internal bore waves (see e.g., Christie, 1989; Brown and Christie, 1998). These mesoscale disturbances are significant because they generate turbulence and local wind squalls that increase background noise levels at IS07. Highly nonlinear gravity waves propagate over great distances in Northern Australia on the deep nocturnal boundary layer inversion. They are a commonly occurring feature at Warramunga, but they seldom, if ever, occur at IS05 Hobart.

As can be seen in Figure 2, the array configuration at IS07 differs substantially from the array configuration at IS05. The array response for each of these stations is fairly good, but not ideal. The overall apertures of the two arrays are comparable and each array contains a smaller aperture sub-array (H1, H2, H3 and H4 at IS07 and H6, H7 and H8 at IS05), which significantly improves the array response and helps to minimize the influence of spatial aliasing (Kennett et al., 2003).

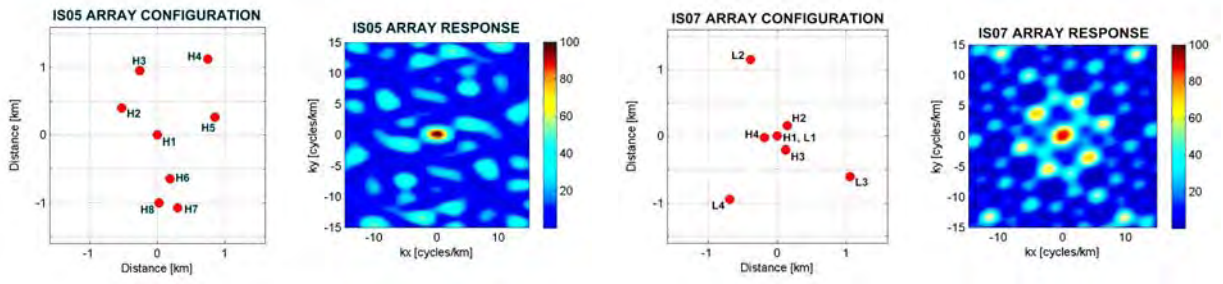

Figure 2. Array configuration and response of IS05 Hobart (left) and IS07 Warramunga (right).

Detection of distant explosions

Numerous studies have been reported in recent years (see, e.g., Sorrells et al., 1997; Stump et al., 2002; Sarker and Kim, 2002) of the use of seismic and infrasound data recorded simultaneously at the same site as a means to improve discrimination and location estimates for surface mining explosions. This has proven to be an effective procedure when mining explosions are located at regional distances. These investigations are, however, usually limited to source distances of less than 800 km. A survey of the detection of small mining blasts in the Western United States at infrasonic arrays operated by the Los Alamos National Laboratory at ranges of up to 880.5 km is described as part of a discrimination study in ReVelle et al. (2004). There appear to be very few reports of the detection of infrasound from large mining explosions at distances beyond 1000 km. A brief description of the detection at IS07 Warramunga of infrasonic waves generated by a large open-cut coal mining explosion in the Bowen Basin (see Figure 1) at a distance of 1520 km is given in Christie (2004). In this regard, we note that the Australian IMS stations are almost ideally located for long-range studies of infrasound generated routinely by large open-cut mines located on the Australian mainland and in other areas to the north of Australia.

Very well documented observations of infrasound signals generated by the Watusi surface explosion experiment on 28 Sept. 2003 at the Nevada Test Site have been reported by Bhattacharyya et al. (2003) and Whitaker et al. (2003). Infrasonic signals from this relatively small test explosion (0.019 kT of TNT equivalent) were clearly detected at a number of stations in the Western United States at distance of up to 883 km and also at IS10 Lac du Bonnet in Canada at a range of 2165 km. All observations appear to be consistent with a thermospheric propagation path. No signals were detected at IS57 (390 km) and TXIAR (1440 km), both located to the south of the explosion. Brown et al. (2003) have also described infrasound signals from small test explosions (5000 and 27000 kg) at the Woomera facility in South Australia. Signals from both explosions were clearly recorded at two stations located at distances of 467 and 476 km to the east and north of the source. Clear signals (probably thermospheric) were also recorded from the larger explosion at IS07 Warramunga, 1257 km to the north. Norris and Gibson present a detailed comparison of wave propagation modeling results with observations of infrasound at a range of 1579 km at IS31 Aktyubinsk in Kazakstan from a large train car explosion in Newyshabur in Iran on 18 Feb. 2004. The observations were made in a passband extending from 0.5 to 3 Hz. The observed signals probably correspond to propagation in a thermospheric waveguide, but stratospheric or mixed stratospheric /thermospheric propagation cannot be ruled out. These authors also note that this event was observed at a range of 4078 km at IS34 in Mongolia, but no details are given.

It is now recognized that infrasound generated by high altitude bolide explosions in an elevated waveguide will leak to the surface by scattering from large scale inhomogeneities and may be detectable at monitoring stations located at great distances from the source. The first outstanding example of the long-range detection at IMS stations of infrasound from a high altitude bolide was the unexpected observation of signals at a distance of 10800 km at IS26 Freyung in Germany from a large bolide explosion (~ 10 kT) over the Pacific Ocean between California and Hawaii at a height of 28.5 km on 23 April 2001 (see, e.g., Brown and Gault, 2001; Garces et al., 2004). There have been several other reports of the long-range detection of infrasound from high-altitude bolides since this initial

observation in 2001. McCormack (2004) has recently described and interpreted observations from a particularly interesting bolide explosion that occurred on 3 Sept. 2004 over the Atlantic Ocean side of the Antarctic ice shelf. This relatively large event (estimated yield is 33 ± 17 kT) was detected at IS27 Neumayer, Antarctica (1090 km), IS55 Windless Bight, Antarctica (3720 km), IS35 Tsumeb, Namibia (5400 km), IS17 Dimbokro, Ivory Coast (7000 km), and IS26 Freyung, Germany (13000 km). Weak signals from this event were also recorded at IS05, Hobart (7055 km) (Brown, 2005, private communication). However, failure to detect signals from this event at many other IMS infrasound monitoring stations, including IS07 Warramunga (8990 km), suggests that the propagation of energy away from this rapidly moving source was highly anisotropic. It is also worth noting that all observed signals from this event were detected only in the long-period passband from 0.03 to 0.1 Hz.

Observations

We now consider the results of a study of infrasound observations at IS05 Hobart and IS07 Warramunga from two significant explosive events located at large distances from each monitoring station. The first event is a series of explosions generated by the sudden eruption of Manam Volcano on the northern side of Papua New Guinea on 27 January 2005. The second event corresponds to a bolide explosion on 5 December 2004, over the east coast of New South Wales in southeastern Australia. Both events were clearly detected at IS05 and IS07, but the characteristics of the signals recorded at each station differ considerably. Details relating to the detection of each of these events are given in the following table.

Table 1. Station and source parameters for the detection of infrasound from Manam Volcano and the New South Wales bolide.

	Manam Volcano	New South Wales Bolide
Source location	4.10 ºS, 145.06 ºE	31.7 ºS, 152.6 ºE
Source time	~ 14:00 27 Jan. 2005 UT (00:00 28 Jan. 2005 LT)	18:15 5 Dec. 2004 UT (04:15 6 Dec. 2004 LT)
Distance to IS05	4261 km	1270 km
Back azimuth from IS05	355.8 º	22.5 º
Distance to IS07	2103 km	2260 km
Back azimuth from IS07	35.0 º	126.0 º

The sudden eruption of Manam Volcano started at around 14:00 UT (midnight local time) on 27 January 2005 and continued as a series of violent explosions for a period of about two hours. Signals from this large event were detected at the two operating IMS stations in Australia (IS05 and IS07) and also at IS55 Windless Bight in Antarctica at a distance of 8303 km and IS53 Fairbanks, Alaska at a distance of 9358 km (Wilson and Olson, 2005). The signals detected at IS55 and IS53 were long-period signals with maximum power in the passband from 0.03 to 0.10 Hz. The observations at IS05 show that the higher frequency components above 0.1 Hz have also vanished completely at a range of 4261 km. In contrast, higher frequency components were detected up to a frequency of at least 3 Hz at IS07 at a range of 2103 km. The signals detected at IS07 and IS05 are illustrated in Figures 3 and 4 for frequency passbands spanning the range from 0.01 to 9 Hz. No signals were detected at IS05 at frequencies above 0.1 Hz. The passband from 0.1 to 0.5 Hz at IS05 was completely dominated by coherent microbarom signals from severe storms in the Southern Ocean. In contrast to the observations at IS05, higher frequency components were observed at IS07 at frequencies above 0.1 Hz, but the best signal-to-noise ratio occurs in the longer period passband from about 0.03 to 0.07 Hz. It is also interesting to note that signals from the eruption of Manam Volcano were clearly detected in a background of microbarom signals in the passband from 0.1 to 0.5 Hz. Hobart is located almost due south of Manam Volcano. In the case of IS05, the absence of higher frequency signals can be attributed to the greater distance to the source and also to the rapid attenuation of higher frequencies in a thermospheric waveguide.

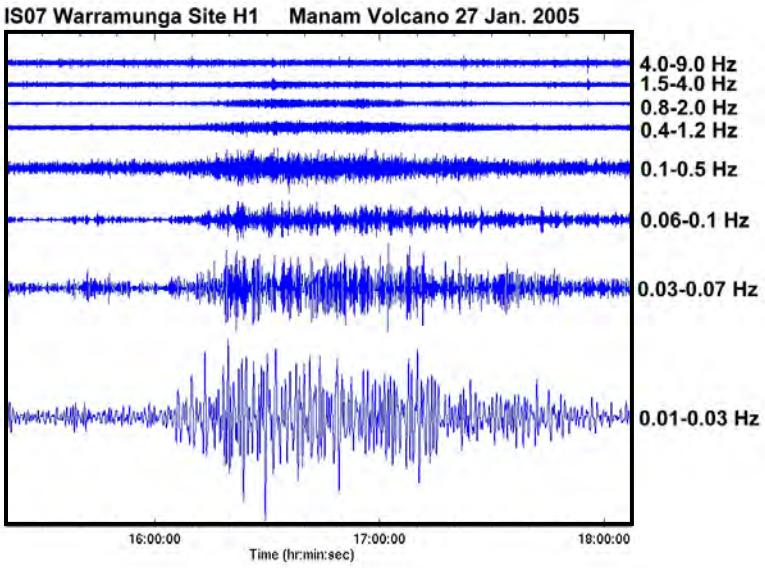

Figure 3. Bandpass filtered signals recorded at IS07 Warramunga from the explosive eruption of Manam Volcano on the north side of Papua New Guinea on 27 Jan. 2005.

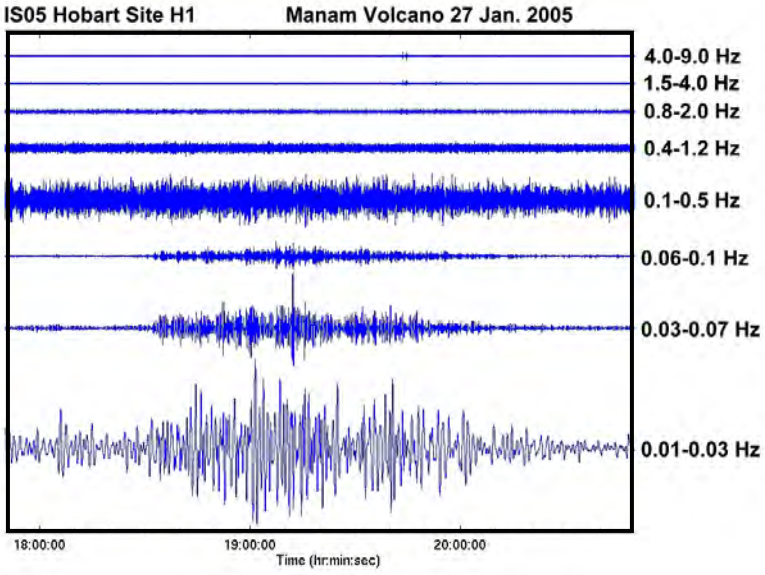

Figure 4. Bandpass filtered signals recorded at IS05 Hobart from the explosive eruption of Manam Volcano on 27 Jan. 2005.

A comparison of the high- and low-frequency signals from the eruption of Manam observed at IS07 Warramunga and the longer period signals observed at IS05 Hobart is given in Figures 5 and 6. As can be seen from these examples, large signal-to-noise ratios were observed at both IS05 and IS07 for longer period signals. The signal-to noise ratio observed in the 1 Hz passband (0.5 –2.0 Hz) at IS07 is also quite large. It might appear, at first glance, from the high frequency results presented in Figure 5, that high-frequency signals from Manam Volcano observed at a distance of 2103 km would be easily detected in the routine automatic processing of data at IS07. However, an examination of the high frequency data shows that the degree of correlation of the higher frequency signals from Manam is very small between the array elements in the large aperture main array (L array). The spatial coherence of the higher frequency Manam signals is much higher between array elements in the small aperture sub-array (H-array) and this partial degree of coherence between elements in the small array does in fact allow these higher

frequency signals to be detected by the routine data processing algorithms. However, the average Fisher F-statistic found in the high-frequency analysis is much smaller than the average F-statistic found in the analysis of long-period data. The significance of these results is discussed below.

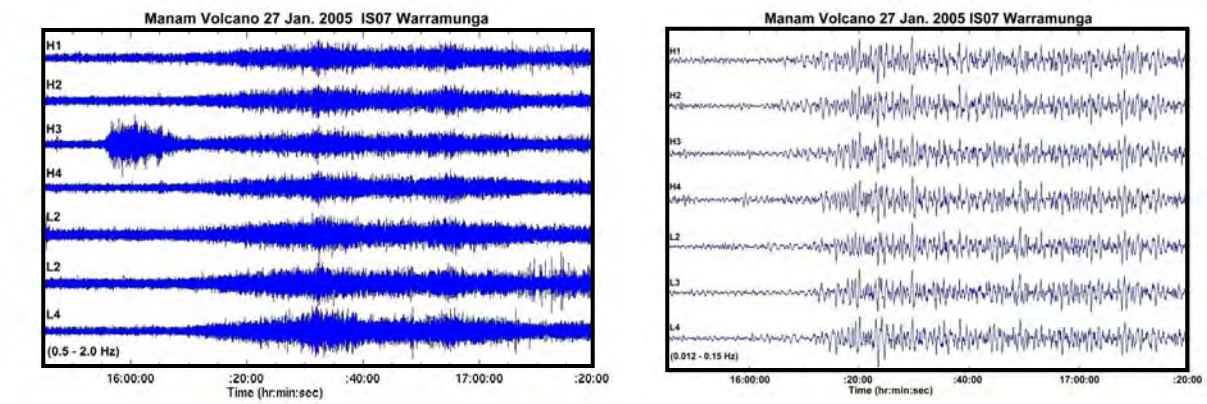

Figure 5. High-frequency (left) and low-frequency (right) infrasonic signals observed at IS07 Warramunga from the explosive eruption of Manam Volcano on 27 January 2005.

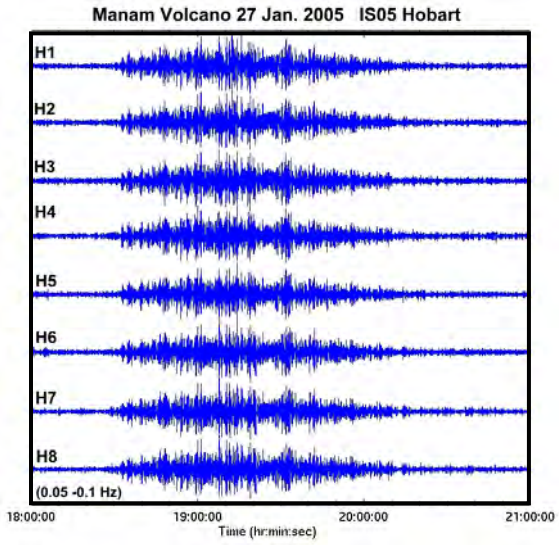

Figure 6. Low-frequency 0.05 to 0.1 Hz passband filtered infrasonic signals observed at IS05 Hobart from the explosive eruption of Manam Volcano on 27 January 2005.

A second example of the long-range detection of infrasonic waves at both IS05 Hobart and IS07 Warramunga is presented in Figures 7 to 9. In this case, the observed signals were generated by an early morning bolide explosion over the east coast of New South Wales at about 18:15 on 5 Dec. 2004 UT (04:15 AM on Dec. 6 local time). This event was widely reported in the media. From the media reports, it appears that this event was accompanied by a number of separate explosions and this appears to be supported by the observed infrasonic signatures at IS05 and IS07. Again, infrasound was detected at both IS05 and IS07 over a wide range of frequencies. This is illustrated in Figures 7 and 8 for data filtered in a number of passbands between 0.03 and 9.0 Hz. As in the case of infrasound detections from Manam, the high level of noise due to coherent microbarom waves precluded any detection of the bolide signals at IS05 in the passband from 0.1 to 0.5 Hz. Signals from the bolide were, however, easily detected in the 0.1 to 0.5 Hz passband during the automatic processing of data from IS07 Warramunga. The observations at IS05 and IS07 also differ in that signals were detected at IS05 at longer periods in the low-frequency passband from 0.05 to 0.1 Hz. There is no trace of any longer period energy below 0.1 Hz in the observations at IS07. Finally, we note that the signal-to-noise ratio in all passbands (including the very high frequency passband from 4 to 9 Hz) is

significantly larger for observations recorded at IS05 than it is at IS07. These results are somewhat puzzling since both stations are located at roughly the same distance from the source (2103 km for IS07 and 2260 km for IS05). Furthermore, the stratospheric wind component along the propagation path is higher for the path to IS07 than it is to IS05. Failure to detect any signals in the 0.1 to 0.5 passband at IS05 can be attributed to the high levels of coherent microbarom signals in this passband.

The main result of interest here is similar to that found for the detection of signals from Manam Volcano. The degree of signal coherence between array elements in the larger aperture sub-array at each station is found to be significantly smaller than the degree of coherence between array elements in the small aperture sub-array. This means that automatic detection in the higher frequency passbands is almost entirely the result of the partial coherence between array elements in the smaller aperture sub-array. It should be emphasized, however, that signal-to-noise ratios and the degree of signal coherence decrease fairly rapidly for frequencies above 1Hz.

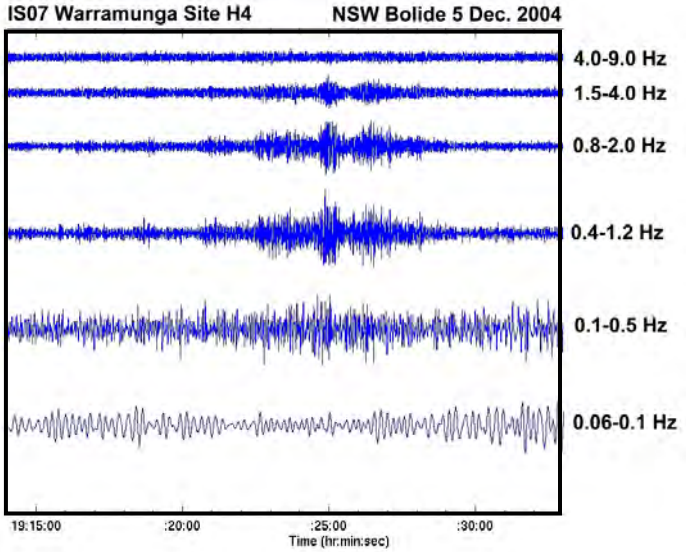

Figure 7. Bandpass filtered signals recorded at IS07 Warramunga from the New South Wales Bolide on 5 Dec. 2005. No detectable signals were found at frequencies below 0.1 Hz.

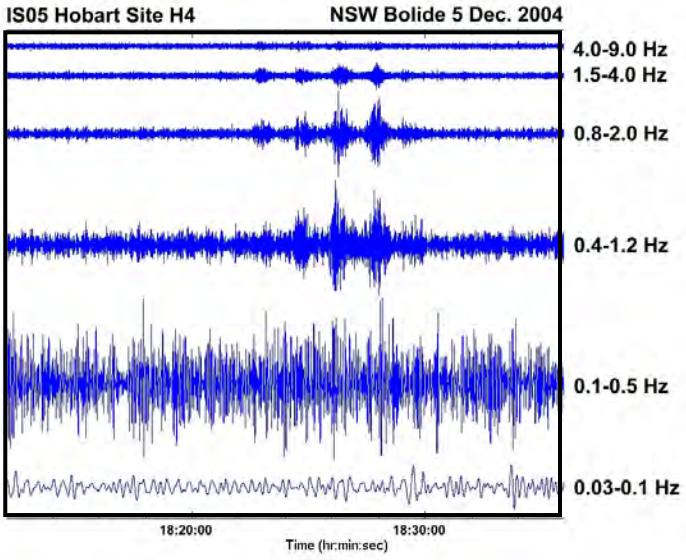

Figure 8. Bandpass filtered signals recorded at IS05 Hobart from the New South Wales Bolide on 5 Dec. 2005. Signals were detected above and below the microbarom passband (0.1 to 0.5 Hz).

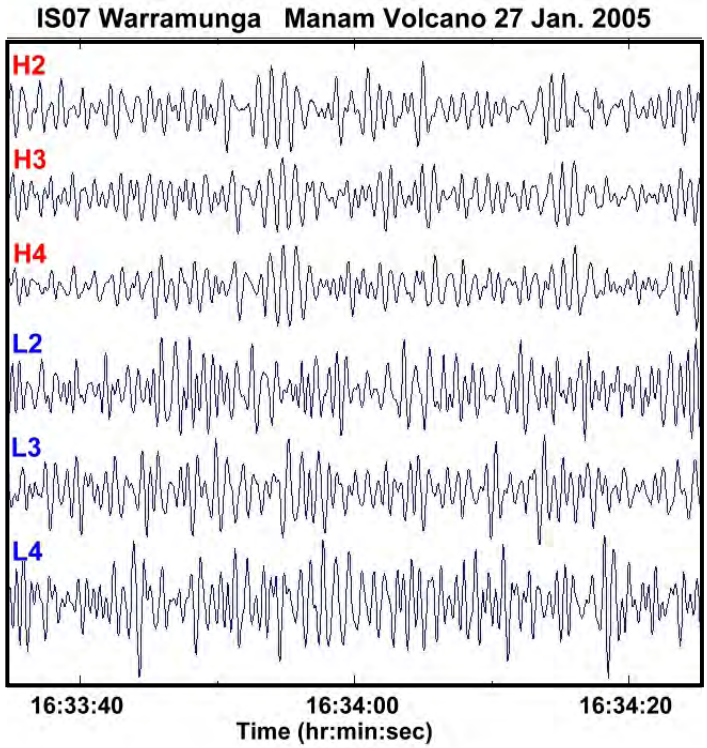

Figure 9. Detailed comparison of signals from the Manam eruption recorded at IS07 in the 0.8 to 2.0 Hz passband. H2, H3 and H4 are separated by about 380 m. L2, L3 and L4 are separated by about 2 km.

Discussion

A good understanding of the spatial coherence of infrasonic signals as a function of frequency and source distance is clearly important to the design of reliable infrasound monitoring stations. Mack and Flinn (1971) developed a model for spatial coherence as a function of source distance and frequency from observations of relatively long-period signals from very large explosions at a large aperture array. Blandford (1997, 2000, 2004) has carried out a sophisticated design study based on an extrapolation of the Mack and Flinn model to determine an optimal design for IMS type infrasound monitoring arrays. The optimal design depends on the accuracy of the extrapolation to much higher frequencies and smaller aperture arrays. There have been several attempts in recent years (see e.g., Blandford, 1997, 2000 and 2004; Armstrong, 1998; McCormack, 2002) to accurately measure the spatial correlation of infrasonic waves from smaller explosions at higher frequencies and sensor separation distances that are of interest to the detection of smaller nuclear explosions. There seems to be a tendency for the observed coherences to be somewhat higher than those predicted by an extrapolation from the results of Mack and Flinn, but accurate measurements have proven to be quite difficult and the errors on the reported results are significant. Further work needs to be undertaken in this area.

The observations presented above show that the higher frequency components in explosion-generated infrasonic signals decay fairly rapidly with distance from the source and may not be detectable at frequencies above 0.5 Hz at distances that are comparable with distances between array elements in the global IMS infrasound monitoring network. These results also indicate that detection of signals from distant explosions may be limited at higher frequencies due to a decrease in the degree of spatial coherence between array elements in the monitoring array. The loss in signal coherence in the 0.8-2.0 Hz detection passband between widely separated array elements can be seen in the comparison shown in Figure 9 for data recorded at array elements H2, H3 and H4 with an average sensor separation of about 380 m with the data recorded at array elements L2, L3 and L4 with an average sensor separation of about 2.06 km. As can be seen from Figure 9, the observed signals have a fairly high degree of coherence between elements in the H-array and a much smaller degree of coherence between elements in the L-array. The addition of the central element H1 in the small aperture array significantly improves detection capability in the 0.8 to

2.0 Hz passband. The potentially serious limitations imposed on signal detection by the reduction in spatial coherence of higher frequency signals can be summarized by the detection parameters presented in the following table for signals from Manam Volcano recorded on large and small aperture sub-arrays at IS07. Signal detection fails completely on the large array at all frequencies above 0.8 Hz and is only marginal for frequencies in the 0.4-1.5 Hz band. Signal detection is also marginal on the small aperture array in the highest frequency passband 1.5-4.0. The analysis of signals from the New South Wales bolide and signals from other distant sources gives essentially the same results.

Table 2. Detection parameters for infrasound signals from Manam Volcano recorded at IS07 on a small aperture triangular sub-array (H1, H2 and H3 with an average separation of 380 m) and a large aperture triangular sub-array (L1, L2 and L3 with an average separation of 2.06 km).

Frequency Band	Sub-Array	Maximum F-statistic	Average F-statistic	Comment
1.5-4.0 Hz	H1, H2, H3	19.0	~ 7	Marginal detection
	L1, L2, L3	-	~ 2.5	Not detected
0.8-2.0 Hz	H1, H2, H3	44.3	~ 15	Good detection
	L1, L2, L3	-	~ 2.5	Not detected
0.4-1.5 Hz	H1, H2, H3	31.7	~ 15	Good detection
	L1, L2, L3	10.1	~ 3.5	Marginal detection
0.1-0.5 Hz	H1, H2, H3	45.1	~ 22	Good detection
	L1, L2, L3	24.6	~ 14	Good detection
0.03-0.1 Hz	H1, H2, H3	70.4	~ 40	Good detection
	L1, L2, L3	136.3	~ 60	Good detection

CONCLUSIONS AND RECOMMENDATIONS

It is clear, from the results presented here, that the loss of signal coherence may seriously reduce detection capability at higher frequencies for infrasound signals from sources that lie at distances beyond 1000 km. This result has particular relevance for IMS monitoring stations that have only four widely separated array elements. Attenuation of higher frequency signals over long propagation paths may also rule out any possibility of signal detection in the higher frequency passbands when the distance to the source is large. This is an especially important factor when propagation is confined to a thermospheric waveguide. The essential conclusions are as follows:

a) Infrasound monitoring stations should have both large and small aperture sub-arrays in order to eliminate spatial aliasing and signal coherence problems at higher frequency and to ensure accurate azimuthal measurements.
b) Automatic data processing should be carried out in passbands that span both high and low frequencies.

ACKNOWLEDGEMENTS

We thank David Brown for many valuable discussions and for assistance with the detection algorithm.

REFERENCES

Armstrong, W. T. (1998), Comparison of infrasound correlation over differing array baselines, in *Proceedings of the 20th Annual Seismic Research Symposium*, pp. 543–554.

Bhattacharyya, J., H. E. Bass, D. P. Drob, R. W. Whitaker, D. O. ReVelle, and T D. Sandoval, (2003), Description and analysis of infrasound and seismic signals recorded from the Watusi explosive experiment, September 2002, in *Proceedings of the 25th Seismic Research Review, Nuclear Explosion Monitoring: Building the Knowledge Base,* LA-UR-03-6029, Vol. 2, pp. 587–596.

Blandford, R. R. (1997), Design of Infrasonic Arrays. Air Force Technical Applications Center Report, AFTAC-TR-97-013.

Blandford, R. R. (2000), Need for a small subarray at IMS infrasound stations – Implications of shuttle and S. Pacific nuclear signals, in *Proceedings Infrasound Workshop*, Passau, Germany.

Blandford, R. R. (2004), Optimal infrasound array design for 1kt atmospheric explosions, *Proceedings Infrasound Technology Workshop*, Hobart, Australia.

Brown, D. J. and D. R. Christie (1998), Fully nonlinear solitary waves in continuously stratified incompressible Boussinesq fluids, *Phys. Fluids*, 10, 2569–2586.

Brown, D. J. and A. Gault (2001), Observations and preliminary analysis of the northern Pacific infrasonic event, April 23, 2001, *CMR Tech. Rep.* CMR-01/09, 21 May.

Brown, D. J., C. Collins and B. Kennett (2003). The Woomera infrasound and seismic experiment, September-October 2002, in *Proceedings Infrasound Technology Workshop*, La Jolla, California.

Christie, D. R. (1989), Long nonlinear waves in the lower atmosphere, *J. Atmos. Sci*., 46, 1462–1491.

Christie, D. R. (2004), Observations of infrasound in central Australia, in *Proceedings Infrasound Technology Workshop*, Hobart, Australia.

Garces, M., H. Bass, D. Drob, C. Hetzer, M. Hedlin, A. Le Pichon, K. Lindquist, R. North, and J. Olson (2004). Forensic studies of infrasound from massive hypersonic sources, EOS, *Trans. Am. Geophys. Union*, 85, 433.

Kennett, B. L. N., D. J. Brown, M. Sambridge, and C. Tarlowski (2003). Signal parameter estimation for sparse arrays, *Bull. Seism. Soc. Am.*, 93, 1765–1772.

Mack. H. and E. A. Flinn (1971), Analysis of the spatial coherence of short-period acoustic-gravity waves in the atmosphere, *Geophys. J. R. Astr. Soc*., 26, 255–269.McCormack, D. (2002), Towards characterization of infrasound signals, in *Proceedings Infrasound Technology Workshop*, De Bilt, The Netherlands

McCormack, D., W. N. Edwards, and P. G. Brown (2004), Multi-station detection of infrasound from the September 3rd, 2004 bolide, in *Proceedings Infrasound Technology Workshop*, Hobart, Australia.

Norris, D. and R. Gibson (2004), Validation studies using a TDPE propagation model and near real-time atmospheric specifications, in *Proceedings Infrasound Technology Workshop*, Hobart, Australia.

ReVelle, D. O., R. W. Whitaker, J. P. Mutschlecner, and M. D. Renwald (2004), Discrimination of earthquakes and mining blasts using infrasound, in *Proceedings of the 26th Seismic Research Review, Trends in Nuclear Explosion Monitoring*, LA-UR-04-5801, Vol. 2, pp. 670–679.

Sarker, G and W. -Y. Kim (2002), Analysis of infrasound signals from Ekibastuz mining blasts at Kurchatov, Kazakstan, in *Proceedings of the 24th Seismic Research Review-Nuclear Explosion Monitoring: Innovation and Integration*, LA-UR-02-5048, Vol. 2, pp. 814–822.

Sorrells, G. G., E. T. Herrin, and J. L. Bonner (1997), Construction of regional ground truth databases using seismic and infrasound data, *Seis. Res. Let*., 68, 743–752.

Stump, B. W., S. M. McKenna, C. Hayward, and T. -S. Kim (2002), Seismic and infrasound data and models at near-regional distances, in *Proceedings of the 24th Seismic Research Review- Nuclear Explosion Monitoring: Innovation and Integration*, LA-UR-02-5048, Vol. 2, pp. 572–581.

Whitaker, R. W., T. D. Sandoval and J. P. Mutschlecner (2003), *Proceedings of the 25th Seismic Research Review-Nuclear Explosion Monitoring: Building the Knowledge Base*, LA-UR-03-6029, Vol. 2, pp. 646–654.

Wilson, C. R. and J. V. Olson (2005), I53US and I55US Signals from Manam Volcano, Inframatics, 9, 31-35.

INFRASOUND PROPAGATION CALCULATION TECHNIQUES USING SYNOPTIC AND MESOSCALE ATMOSPHERIC SPECIFICATIONS

Robert G. Gibson[1] and Douglas P. Drob[2]

BBN Technologies[1], Naval Research Laboratory[2]

Sponsored by U.S. Army Space and Missile Defense Command

Contract No. W9113M-05-C-0132

ABSTRACT

Numerical modeling of infrasound propagation is necessary to support accurate infrasound source location and phase identification. Predicting the details of infrasound propagation relies both on propagation models that capture the fundamental physical processes and on characterization of the propagation medium, namely the global atmosphere from the ground to altitudes above 100 km. The accuracy of propagation modeling depends in part on the fidelity of the atmospheric characterization. The analysis tool kit InfraMAP (Infrasound Modeling of *A*tmospheric *P*ropagation) integrates infrasound propagation models and environmental representations, including near-real-time atmospheric updates, such as the output from numerical weather prediction models that supplement the baseline climatological characterization of temperature, wind and air composition. These capabilities allow infrasound researchers to investigate critical propagation phenomena, conduct sensitivity studies, and compare results of numerical modeling with observed signals. Recent efforts aim to evaluate and quantify the propagation improvements attainable using global and synoptic specifications that characterize the relevant atmospheric physics more fully than climatological models.

Global synoptic models provide specifications that are well-suited for use in long-range propagation predictions. Further investigation of infrasound propagation phenomenology on a regional basis and development of suitable tools for studying regional events are necessary. Thus we investigate combining accurate, high-resolution regional atmospheric specifications with infrasound propagation modeling codes. Mesoscale models, which focus on the meteorology of a specific region, can better account for and resolve important meteorological phenomena relevant to regional and local infrasound propagation. By investigating realistic spatial and temporal atmospheric models at a range of resolutions, we seek insight into the appropriate spatial and temporal scales that are necessary for achieving improved infrasound predictions at the relevant frequencies. Approaches are being developed to assess performance of candidate techniques for incorporating mesoscale atmospheric models and terrain specifications with propagation models and to evaluate the benefits. Evaluation of propagation model performance using synoptic and mesoscale atmospheric specifications utilizes observed infrasound events with known ground truth.

RESEARCH OBJECTIVES

In order to advance the state of the art for high-fidelity infrasound predictions, it is necessary to develop both propagation models and atmospheric characterizations that capture more of the fundamental physics that affect infrasound. The overall objective of this effort is to improve understanding of the effects of atmospheric dynamics on the propagation of infrasound, thus improving infrasonic source localization, phase identification, and discrimination. This will be accomplished by developing and analyzing advanced atmospheric specifications for use with propagation models and applying them in comparison studies using ground truth infrasound events. Specific objectives include:

- Comparing ground truth observations to propagation predictions using existing atmospheric specifications and propagation models. This will include sensitivity studies using the Naval Research Laboratory (NRL) Ground-to-Space (G2S) specification at various resolutions and statistical uncertainty studies to address atmospheric model biases and error budgets.
- Developing a multi-resolution, regional environmental specification capability, based on the NRL-G2S framework, for use in propagation calculations. This will include assimilation of mesoscale atmospheric models that provide high resolution meteorological information on local and regional scales.
- Comparing ground truth observations to propagation predictions using the newly developed regional specifications that incorporate mesoscale atmosphere and terrain elevation.
- Investigating effects of including variable terrain elevation in ray-tracing propagation predictions.
- Developing research products that are useful for improving nuclear explosion monitoring capability.

This work discusses recent progress in providing accurate atmospheric specifications for ground-based nuclear explosion monitoring via infrasound. The propagation properties of infrasound in the atmosphere are driven, in part, by the atmosphere, which has significant spatiotemporal variations. Therefore, in order to accurately relate regional infrasound propagation calculations to microbarograph array observations, the use of adequate atmospheric specifications is required. If the initial conditions for an infrasound propagation calculation (e.g., source altitude and surface conditions) or specifications of the intervening medium are specified inaccurately, then erroneous estimates of ducting heights, travel times, and amplitudes will result. In shifting away from current climatological characterizations, a great deal of complexity is introduced into atmospheric specification. This complexity arises from the natural variability of the atmosphere over all heights. For long-range propagation the time scale of interest ranges from several hours to a month over horizontal scales of roughly 500 km.

Recent work by Drob et al., 2003 has provided a simple framework to account for this complexity over certain height ranges. The NRL Ground to Space (NRL-G2S) semi-empirical spectral model combines numerous sparse datasets using global spectral methods to specify the details of the entire atmosphere for infrasound propagation calculations. The environmental modeling system includes important latitudinal, longitudinal, and hourly variability as given by available historical and near-real-time operational data such the Navy Operational Global Atmospheric Prediction System (NOGAPS) and the National Oceanic and Atmospheric Administration (NOAA)-National Center for Environmental Prediction Global Forecast System (NCEP-GFS) and the NRLMSISE-00 and HWM-93 (Hedin et. al., 1996, Picone et al., 2002) empirical upper atmospheric models, derived from historical databases.

Recent advances in the infrasound analysis tool kit InfraMAP (Infrasound Modeling of Atmospheric Propagation) allow new options for specifying the propagation environment by incorporating the output from numerical weather prediction models to supplement the baseline climatological characterization of temperature, wind and air composition (Gibson and Norris, 2003). InfraMAP modules enable integration of propagation models with near-real-time atmospheric characterizations including NRL-G2S, as described above, and NOGAPS. These synoptic specifications are used with infrasound propagation models in order to improve predictions compared to those based on climatology. However, observed infrasound phases have not been well predicted by state-of-the-art propagation models for several ground truth events (e.g., Bhattacharyya et al., 2003). Therefore, modeling advances that address the fundamental physical processes that affect infrasound are required. Also required, in parallel, are advances in specification of the propagation environment that address fundamental atmospheric physics at appropriate spatial and temporal scales and that can be utilized to improve the performance of advanced propagation models. This

paper discusses recent research that will result in improved accuracy and understanding of the underlying physics of infrasound propagation calculations for nuclear explosion monitoring at regional and local ranges.

RESEARCH ACCOMPLISHED

A Regional Scale Atmospheric Model for Infrasound Propagation Calculations

The recent national trend in numerical weather prediction (NWP) is to move away from larger scale global numerical prediction systems such as NOGAPS and NCEP-GFS toward regional or mesoscale weather prediction systems such as the Navy Coupled Ocean and Atmosphere Mesoscale Prediction System (COAMPS^{TM}) and the Weather Research and Forecasting Model (WRF) (e.g., Hodur, 1997; Skamarock, 2004). The idea here is that by focusing only on the meteorology and data from a specific geographic region, these systems can better resolve important meteorological phenomena such as down-slope winds, surface roughness, soil moisture, and cloud physics. In addition these modeling systems include complete three-dimensional data assimilation systems comprised of data quality control, analysis, initialization, and forecast model components. Additional features of these models include globally relocatable grids with user-defined resolutions and dimensions, nested grids, options for idealized or real-time simulations, and source code that allows for portability between a number of different mainframes and workstations.

Physics-based constraints must be employed to assimilate the available meteorological observations (e.g., surface temperature/winds, radiosonde profiles, and satellite temperature sounding) into these systems in order to produce three-dimensional (3d) weather data cubes for weather forecasting. These models solve the time-dependent non-hydrostatic equations for momentum, non-dimensional pressure perturbation, potential temperature, turbulent kinetic energy, and the mixing ratios of water vapor, clouds, rain, ice, and snow. The models contain detailed parameterizations for boundary layer processes, precipitation, and radiation physics. The resulting three-dimensional data grids typically extend from the surface to 35 km and have horizontal resolutions ranging from 10 to 20 km. Examples of some currently available operational model domains from mesoscale models are shown in Figure 1.

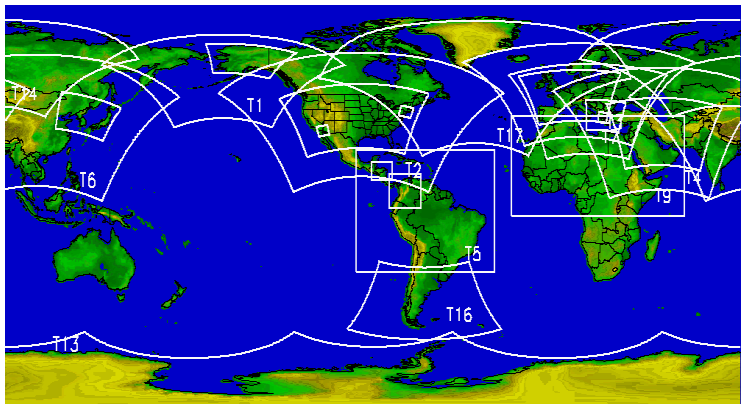

Figure 1. Example model domains for standard operational mesoscale models.

Mesoscale model outputs are typically provided 4 times daily (00/06/12/18Z), but can also be staggered at 00/12Z and 06/18Z, and may include specialized ultra-high resolution nested sub-domains. The Defense Modeling and Simulation Office (DMSO) Master Environmental Library (MEL) maintains online archives of COAMPS data extending back to 1998 for several domains of interest including CONUS, Korea, South West Asia, and Europe. Within the NRL all of the resources needed to generate COAMPS outputs for other regions of interest and times for infrasound research are available. In addition, WRF model initialization fields and source codes are similarly available independently from NOAA, Air Force Weather, and the National Center for Atmospheric Research.

Unfortunately for infrasound propagation calculations, mesoscale models are limited to tropospheric altitudes (< 35 km). Above this altitude the weather systems are dominated by globally coherent planetary waves and vertically propagating tides. These waves and tides become uncoupled from the local influences of tropospheric water vapor, the oceans, and topography, all of which dictate much of the meteorology in the lower atmosphere. Thus the

dynamics of the stratosphere and mesosphere cannot be accurately modeled on regional scales. Therefore global NWP models that extend into the stratosphere and beyond are still needed for accurate infrasound propagation calculations. In addition, these models are required to initialize and specify the time dependent mass flux conditions at the boundaries of the mesoscale model domains. Routine development and operation of global stratospheric numerical weather models are well established at the National Aeronautics and Space Administration (NASA) Goddard Space Flight Center, which operates the GEOS-4 model, as well as at the European Center for Medium Range Weather Forecasting (ECMWF). Recent NRL research and development efforts geared at operational implementation of a stratospheric and mesospheric numerical weather prediction model, NOGAPS-α (McCormack et al., 2004; Coy et al., 2005), may benefit the ground-based nuclear monitoring research community in the near future.

Much like the trend in numerical weather prediction modeling, a recent trend in national nuclear monitoring efforts is toward technologies for regional propagation modeling capability in order to improve source detection and classification. There are, therefore, good reasons to develop a regional G2S atmospheric specification capability that takes advantage of and supplements existing operational mesoscale models. First, by staying in step with current trends in operational meteorology, our effort will ensure that future infrasonic monitoring systems will be able to take advantage of the most up-to-date environmental information available. Second, the conformally mapped rectangular grids provided by the mesoscale specification systems will be easier to transform into the spectral domain and merge with similarly gridded and transformed subsets of the Stratospheric NWP data and HWM/MSIS upper atmospheric empirical models.

In the current G2S system (Drob et al., 2003) global vector spherical harmonic transforms are required because of coordinate system singularities at the poles, while conformally mapped regional specifications can be spectrally decomposed, stored, and easily manipulated with simpler 2-D Fourier transforms. This will make client-side reconstruction of the merged atmospheric models for infrasound propagation calculations more straightforward, although some of the same fundamental issues of optimal resolution and interpolation remain. During the ongoing effort, we will develop subroutines that enable improved propagation modeling via incorporation of mesoscale specifications into InfraMAP, and we will investigate the vertical and horizontal resolution required in an atmospheric specification to accurately calculate relevant infrasonic observables. Figure 2 shows how the regional high-resolution G2S framework will be constructed for use in developing an improved understanding of the physics needed to improve national capabilities for infrasound monitoring.

Terrain elevation has been identified as a potentially important issue for infrasound propagation calculation (Drob, et al., 2003). At regional distances the earth is not a locally flat, perfectly reflecting surface for infrasound waves. This is particularly important for propagation modeling over mountainous regions where steep terrain can create shadowing, diffraction, and scattering effects. Many regions of concern contain mountainous areas, which may provide protection against infrasonic detection of clandestine nuclear tests. Furthermore, terrain adds to the complexity of the characterization of winds near the earth's surface. In order to represent complex fluid interaction over variable topography, mesoscale models such as COAMPS and WRF contain detailed terrain models. These systems also contain information on land use, roughness scales, vegetation and soil type that may also be useful for infrasound propagation modeling work. Therefore, another advantage to adapting a regional/mesoscale framework for the G2S model is that inherent to COAMPS and WRF outputs are complete representations of the relevant topographical features that can be simultaneously included along with the environmental specifications for infrasound propagation model calculations. We intend to address issues associated with propagation over variable terrain, so that the atmosphere and the terrain can be evaluated on a consistent spatial scale. Issues to be addressed include: correctly accounting for altitude above mean sea level when evaluating the various atmospheric characterizations; characterizing near-surface winds in the vicinity of rapidly varying terrain such as mountain ranges and islands; consistently modeling ground reflections using physically valid assumptions; and determining spatial length scales that are appropriate for evaluating terrain elevation and slope at infrasonic frequencies of interest. InfraMAP currently incorporates ETOPO 5-minute topography for environmental display purposes but not in propagation calculations. The HARPA ray-tracing model can readily support propagation calculations over variable terrain elevation (Jones et al., 1986). In addition to obtaining the source codes and supplemental data sets needed to run the COAMPS and WRF models locally for infrasonic research and development activities, we have obtained the 30-arc-second (1 km) global Digital Elevation Model (DEM) from the National Geophysical Data Center (Hastings and Dunbar, 1998).

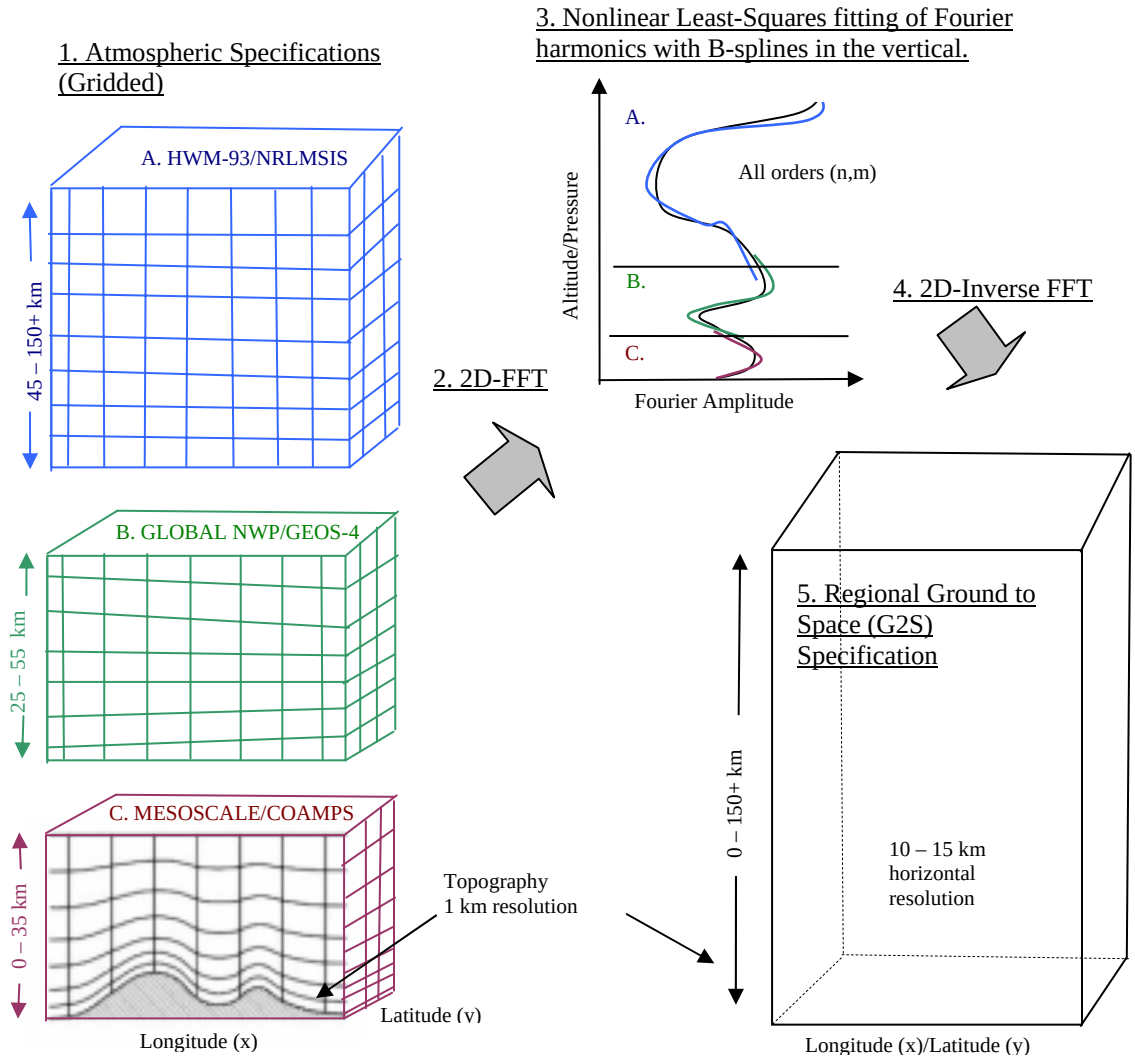

Figure 2. The regional high resolution atmospheric specification framework for infrasound propagation calculations.

At regional distances there are a number of open scientific questions concerning the characterization of infrasonic arrivals at ranges of 50 to 350 km that cannot always be explained by classical ray methods. One specific example is in the observed arrivals at the NVIAR array during the Watusi experiment conducted on September 28, 2002 (Bhattacharyya, 2003). Along with an investigation into the breakdown of classical ray theory, accurate regional specifications of the near field environmental conditions are needed to address the scattering of infrasound off of internal wave structures and topography to explain the observed phenomena. The development of high-resolution regional-scale G2S specification capabilities, begun in the work presented here, will be able to support future calculations and investigations of these aspects of infrasound propagation via advanced propagation models that more fully capture the relevant fundamental physics of a propagating infrasonic wavefront. Recent model developments include a Fourier-synthesis time-domain parabolic equation (TDPE) model [Norris, 2004]. Other researchers are investigating application of 3-d, finite-difference, time-domain techniques (FDTD) to local and regional scale infrasound propagation; initial applications of the FDTD supported by existing low resolution G2S capabilities were recently reported by Collier et al. (2004) and Symons et al. (2004).

A recent ground truth event that demonstrates the value of the G2S atmospheric specification is the 18-Feb-2004 train car explosion in Neyshabur, Iran, which was observed at two International Monitoring System (IMS) infrasound arrays, I31KZ (1579 km to the north) and I34MN (4078 km to the east). Detailed results of analysis and

modeling have been recently presented by Gibson and Norris, 2004. At I31KZ, the explosion signal was observed to have travel times ranging from 5200 to 5835 sec. The observed azimuth deviation (from the great circle) was -7.9 deg. Ray-tracing calculations were made using both climatology and G2S. The predicted travel times that are consistent with the observation are shown in bold, with those rows shaded. Significantly higher zonal wind velocities and effective sound speeds are predicted between approximately 30-50 km altitude using G2S. This difference is sufficient to define a stratospheric duct using G2S that is not predicted using climatology. Furthermore, the predicted azimuth deviation using G2S is approximately 95% of the observed value, compared with less than 60% using HWM and MSIS. In this case, near-real-time specifications significantly improve both travel time and azimuth predictions compared to climatology.

Further understanding is required of the strengths and weaknesses of existing propagation calculation techniques. Ongoing work will include detailed propagation case studies using G2S and other atmospheric characterizations for a set of ground truth events selected from a body of available data. Comparisons between models and data will be conducted not only using ray-tracing but also using other modeling techniques. By investigating realistic spatial and temporal atmospheric models at a range of resolutions, we desire to gain insight into the appropriate spatial and temporal scales that are necessary for achieving improved infrasound predictions at the relevant frequencies. We intend to assess performance of candidate techniques for incorporating mesoscale (regional) atmospheric models and terrain specifications with propagation models and evaluate the benefits.

A Predicted Annual Time Series of Infrasonic Observables

This research effort includes comparison studies and sensitivity studies to assess the improvements in predicting travel times and back-azimuths (for event location) and phase identification (for localization and association) that are attainable with synoptic and/or mesoscale predictions. A goal of the studies is to test the accuracy and applicability of the infrasound predictions, and to obtain a realistic estimate of the model error budget. Previous efforts at calibrating travel times have focused on stratospheric or thermospheric paths. Typically, these times have been estimated using only a ray-theoretic approach with simple, seasonal atmospheric parameterizations. Ongoing studies in this effort will be focused on developing new understanding of propagation at local and regional ranges.

A number of researchers have suggested and demonstrated that infrasound propagation characteristics vary significantly on a day-to-day basis as the result of natural variability of the lower atmosphere (e.g., Garces et al., 2002; LePichon et al., 2002; Drob et al., 2003). This was recently illustrated with one year of continuous volcanic observations by LePichon et al. (2005). Drob et al., 2003, calculated acoustic ray-turning heights, single skip travel times, ranges, and velocities using a simple ray-tracing code, comparing both the HWM-93/NRLMSISE-00 and G2S models. These initial calculations were limited to only 25 days in January 2003, but clearly illustrated the value added by operational NWP data. These calculations have now been expanded with new ray tracing capabilities to evaluate the impact of time dependent meteorological phenomena on infrasound propagation over an entire year. Travel time, arrival azimuth, and apparent phase velocity of the infrasonic signals from a series of fictitious calibration explosions at White Sands Missile Range (WSMR) are calculated for a number of regionally located infrasound stations. These forward calculations are performed for a total of 1460 (365 x 4) simulated explosions occurring at 6-hour intervals for the entirety of 2004.

For each of the hypothetical events, a dense quiver of rays that spans elevation angles of ± 50º, and ± 7.5º of true azimuth at .01º intervals was shot toward one of fourteen receivers. In addition, novel pruning techniques based on simple heuristics at intermediate ray turning points are used to terminate integration of rays that have no chance of reaching a detector. Those rays that eventually land within ± 0.75 km of a station are deemed detectable. A check of the numerical stability of the detected eigenrays was then performed by integrating these backwards in time from the receiver to the source. Results shown here are for a series of hypothetical infrasound calibration sources 50 km over WSMR in the spirit of the calibration experiment outlined in Herrin et. al., 2004.

Figure 3 shows the time series of travel time predictions for two of the hypothetical stations, one located 463 km ENE of the source at a bearing of 79º (panel A) and the other located at distance of 405 km WSW of the source at a bearing of 207º (panel B).

The calculations indicate that during the northern hemisphere winter months when the stratospheric winds at mid latitudes blow from west to east, stratospheric ray paths are possible in the eastward downwind direction (A) Figure

3. During the summer months there is a reversal in the stratospheric wind direction from east to west, again resulting in stratospheric ray paths in the westward downwind direction (B) Figure 3. It is well known to the atmospheric science community that stratospheric winds and planetary wave activity in the winter hemisphere are highly variable compared to those in the summer hemisphere. This stratospheric wave variability can result in changes of order 100 sec in travel times over a 5 day period. During the summer months when the stratospheric wind is relatively quiescent, travel times are predicted to remain relatively constant. The calculations also show that the seasonal change in stratospheric winds near the source altitudes (50 km) results in the formation of a second thermospheric ray path which has a reflection height near 130 km. In reality these arrivals will likely not be observed, as classical molecular attenuation was neglected. Finally, the detection time series reveals fine splitting of travel times on the order of 50 seconds over a 24 hour period due to the effects of migrating tides in the mesosphere and lower thermosphere driven by solar heating. When considering the significance of these tidal influences it is important to note that no realistic day-to-day variations of the diurnal and semidiurnal solar migrating tidal amplitudes are included in the G2S (HWM-93) model, only slowly varying seasonal variations. Furthermore, tidal amplitudes may be underestimated by a factor of 2 in amplitude (Drob and Picone, 2000). Because the HWM/MSIS models form the basis for the specification of winds and temperatures for the G2S model above 60 km, any biases or errors above this region will impact calculation of travel times and azimuth deviations for thermospheric phases, regardless of the model selected.

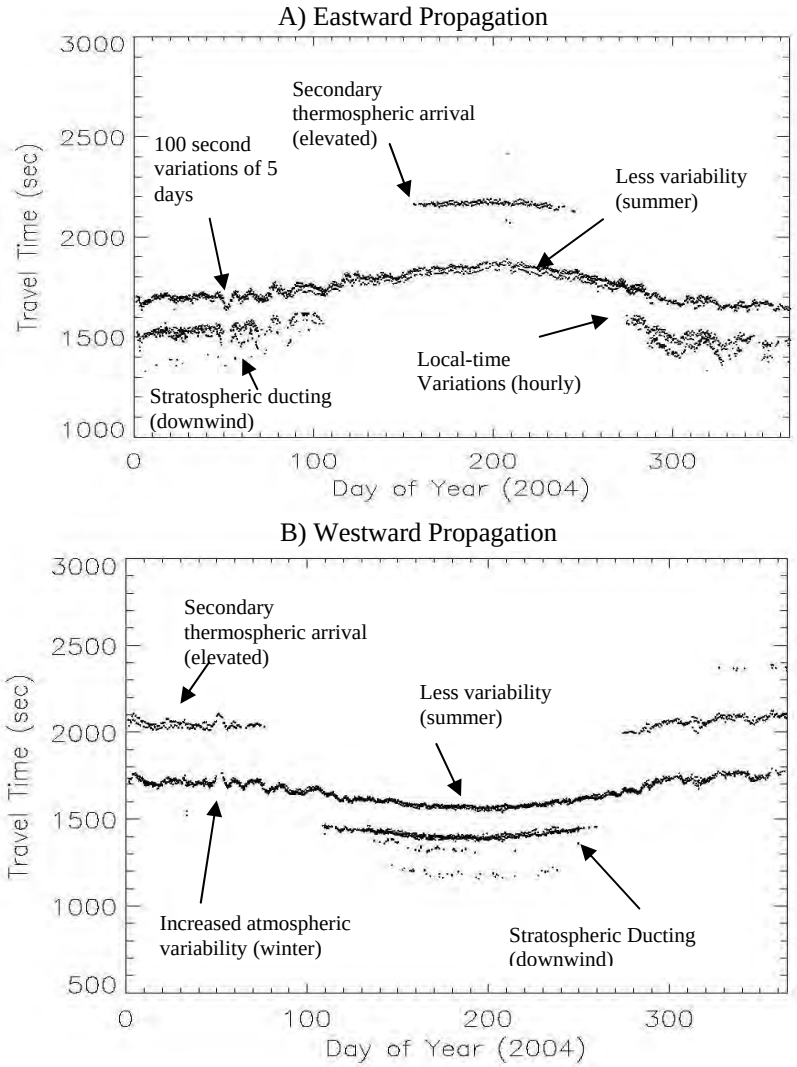

Figure 3. Predicted travel times for two hypothetical stations, one located 463 km ENE of the source at a bearing of 79º (A) and the other located 405 km WSW of the source at a bearing of 207º (B).

Figure 4 shows the predicted azimuth deviations for two stations, one located almost due east of the source at a range of 639 km and bearing of 89º (A), and the other located to the SSE at a distance of 525 km with a bearing of 149º (B). Again large daily variations in the predicted azimuth deviations resulting from the significant tropospheric and stratospheric wintertime synoptic scale wave activity are observed. Apparent azimuth deviations for a typical source-to-receiver configuration may vary by as much as 5.0° over a 5 day period (A, B). In addition the seasonal variation in the apparent azimuth for meridionally oriented source to receiver configurations can range from greater than 7.5° in the winter months to -5.0° in the summer as the result of atmospheric winds (B). The reason for the observed asymmetry is that the stratospheric wind jet is lower and stronger in the winter as compared to the summer, combined with the fact that the tropospheric jet stream is always predominantly eastward. Finally, the predicted hourly variations are on the order of ± 2.5°. Similar variations of volcanic infrasound over a one year period were observed by LePichon et al. (2005). The G2S model showed dramatic improvement over the HWM model in predicting the observations, however significant errors in azimuth deviation of on the order of 3.0° occurred during certain time intervals. Wind corrections of up to 50 m/s in the 65-to-120 km region of the G2S/HWM model were needed to bring the predicted azimuths in line with the observations.

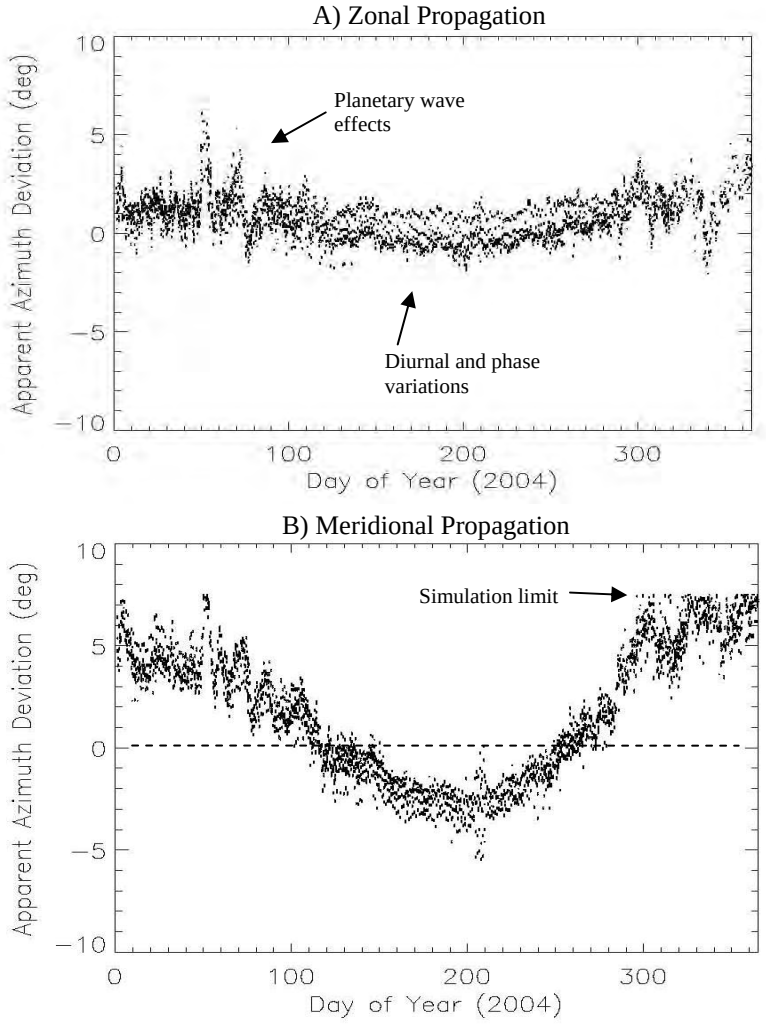

Figure 4. Predicted azimuth deviations for two stations, one located 639 km away at a bearing of 89° from the source (A) and the other located 525 km away at a bearing of 149° from the source (B).

CONCLUSIONS AND RECOMMENDATIONS

Synoptic specifications are used with infrasound propagation models in order to improve predictions compared to those based on climatology. However, observed infrasound phases have not been well predicted by state of the art propagation models for several ground truth events. Therefore, modeling advances that address the fundamental physical processes that affect infrasound are required. Also required, in parallel, are advances in specification of the propagation environment that address fundamental atmospheric physics at appropriate spatial and temporal scales and that can be utilized to improve the performance of advanced propagation models.

Study of long range events will improve understanding of the strengths and weaknesses of global synoptic specifications. Mesoscale atmospheric models and terrain databases, used to improve characterization of the lower regions of the atmosphere, will enable improved understanding of local and regional propagation of infrasound signals. Study of local and regional events will improve understanding of the importance of mesoscale phenomena.

One of the important aspects of the work is to consider the uncertainties introduced by the various physical assumptions and environmental specifications that relate the infrasonic observable back to source characteristics. The significance of these assumptions and uncertainties must be compared to uncertainties in the measurement techniques and statistics of the ground truth event database. Assumptions about the spatiotemporal resolution of environmental specifications can be further quantified deterministically in this line of research. There are a number of known biases and irresolvable atmospheric phenomena that also need to be considered in the evaluation of the performance of infrasonic monitoring systems.

For infrasound applications, G2S is meant to replace the HWM-93/NRLMSISE-00 empirical models as the next generation semi-empirical atmospheric specification tool. Since G2S incorporates HWM/MSIS predictions at high altitudes, the adjustment or updating of the current HWM-93/NRLMSISE-00 internal model coefficients is a high priority, due to known issues regarding tidal predictions in the models.

ACKNOWLEDGEMENTS

The authors would like to thank the National Aeronautics and Space Administration (NASA) Goddard Space Flight Center, Global Modeling and Assimilation Office (GSFC-GMAO), and the NOAA National Centers for Environmental Prediction (NCEP) for making their meteorological products available for this research. Partial funding support for Dr. Drob from the Office of Naval Research for basic scientific research to investigate the possible use of infrasound for remote sensing of upper atmospheric wind parameters led to a number of important technical advances that were both enabled and subsequently applied to this research.

REFERENCES

Bhattacharyya, J., H. Bass, D. P. Drob, R. Whitaker, D. Revelle, and T. Sandoval (2003), Description and Analysis of Infrasound and Seismic Signals Recorded from the Watusi Explosive Experiment, on September 28, 2002, in *Proceedings of the 25th Seismic Research Review - Nuclear Explosion Monitoring: Building the Knowledge Base*, Tucson, Arizona, LA-UR-03-6029: Vol. 2, pp. 587-596.

Collier S.L., D.H. Marlin, N. P. Symons, D. F. Aldridge, D. K. Wilson, E. G. Patton, P. P. Sullivan, V. E. Ostashev, and D. P. Drob (2004), Acoustic Wave Propagation in Complex Atmospheric Environments: Third Year Results, in *Proceedings of the Meeting of the Military Sensing Symposia (MSS) Specialty Group on Battlefield Acoustic & Seismic Sensing, Magnetic & Electric Field Sensors*, Laurel, MD.

Coy L, D. E. Siskind, S. D. Eckermann, J. P. McCormack, D. R. Allen, and T.F. Hogan (2005), Modeling the August 2002 Minor Warming Event, *Geophys. Res. Lett.* 32: (7): Art. No. L07808.

Drob, D. P., J.M. Picone, and M. Garces (2003), Global Morphology of Infrasound Propagation, *J. Geophys. Res.* 108: (D21): Art. No. 4680.

Drob, D. P. (2003), Detailed Specifications of the Atmosphere for Infrasound Propagation Modeling, in *Proceedings of the 25th Seismic Research Review - Nuclear Explosion Monitoring: Building the Knowledge Base*, LA-UR-03-6029: Vol. 2, pp. 605-616.

Drob D.P., and J.M. Picone (2000), Statistical Performance Measures of the HWM-93 and MSISE-90 Empirical Atmospheric Models and the Relation to Infrasonic CTBT Monitoring, in *Proceedings of the 22nd Annual DoD/DOE Seismic Research Symposium: Planning for Verification of and Compliance with the Comprehensive Nuclear-Test-Ban Treaty (CTBT)*, New Orleans, LA, no.07-03, 8 pages.

Garces, M., C. Hetzer, K. Lindquist, and D. P. Drob (2002), Source Location Algorithm for Infrasonic Monitoring, *Proceedings of the 24th DTRA/NNSA Seismic Research Review - Nuclear Explosion Monitoring: Innovation and Integration*, LA-UR-02-5048, Vol. 2, pp. 755-765.

Gibson, R. and D. Norris, (2003), Integration of InfraMAP with near-real-time atmospheric characterizations and applications to infrasound modeling, *Proceedings of the 25th Seismic Research Review - Nuclear Explosion Monitoring: Building the Knowledge Base*, LA-UR-03-6029, Vol. 2, pp. 638-645.

Gibson, R. and D. Norris, (2004), Integration of InfraMAP Software with Near-Real-Time Atmospheric Characterizations, Final Report to AFRL under Contract DTRA01-01-C-0084.

Hastings, D.A. and P.K. Dunbar (1998), Development & Assessment of the Global Land One-km Base Elevation Digital Elevation Model (GLOBE), *International Society of Photogrammetry and Remote Sensing | Commission IV | Symposium in September, 1998, ISPRS Archives*, Vol.32, number 4, pp. 218-221.

Hedin, A. E, E. L. Fleming, A. H. Manson, F. J. Schmidlin, S. K. Avery, R. R. Clark, S. J. Franke, G. J. Fraser, T.Tsuda, F. Vial, and R. A. Vincent (1996), Empirical wind model for the upper, middle, and lower atmosphere, *J. Atmos. Terr. Phys*. 58: 1421-1447.

Herrin, E.T., P.W. Golden, P. Negraru, H.E. Bass, G.S. Hunter, W.L. Andre, J.V. Olson, D.L. Osborne, M.A. Garces, M.A. Hedlin , K. Hoffman (2004), Infrasound calibration experiments at White Sands Missile Range: Planning and preparations, in *Proceedings of the 26th Annual Seismic Research Review: Trends in Nuclear Explosion Monitoring*, LA-UR-04-5801, Vol. 2, pp. 645-653.

Hodur, R.M. (1997), The Naval Research Laboratory coupled ocean/atmosphere mesoscale prediction system (COAMPS), *Month. Weather Rev.*, 125 (7): 1414-1430.

Jones, M. J., J. P. Riley, and T. M. Georges, 1986: A Versatile Three-Dimensional Hamiltonian Ray-Tracing Program for Acoustic Waves in the Atmosphere above Irregular Terrain, NOAA Special Report, Wave Propagation Laboratory, Boulder, CO.

Le Pichon, A., M. Garces, E. Blanc, M. Barthelemy, and D. P. Drob (2002), Acoustic Propagation and Atmosphere Characteristics Derived from Infrasonic Waves Generated by the Concorde, *J. Acoust. Soc. of Amer.* 111: (1), 629-641.

Le Pichon, A., E. Blanc, D.P. Drob, S. Lambotte, J.X. Dessa, M. Lardy, P. Bani, S. Vergniolle (2005), Infrasound Monitoring of Volcanoes to Probe High-altitude Winds, *J. Geophys. Res.* 110: No. D13, D13106, 10.1029/2004JD005587.

McCormack J.P., S.D Eckermann., L. Coy, D.R. Allen, Y.J. Kim, T. Hogan, B. Lawrence, A. Stephens, E.V. Browell, J. Burris, T. McGee, C.R. Trepte, (2004), NOGAPS-ALPHA modeling simulation of stratospheric ozone during the SOLVE2 campaign, *Atmos. Chem. and Phys.* 4: 2401-2423.

Norris, D., 2004: Time-domain modeling techniques and the study of infrasound propagation, in *Proceedings of the 26th Seismic Research Review*: *Trends in Nuclear Explosion Monitoring*, LA-UR-04-5801Orlando, FL.

Picone, J. M., A. E. Hedin, D. P. Drob, and A. C. Aikin, (2002), NRLMSISE-00 Empirical Model of the Atmosphere: Statistical Comparisons and Scientific Issues, *J. Geophys. Res.* 107: (A12), art. no.-1468.

Gropp W., E. Lusk, N. Doss and A. Skjellum (1996), A high-performance, portable implementation of the {MPI} message passing interface standard, *Parallel Computing* 22: 6, 789-828.

Skamarock W.C. (2004), Evaluating mesoscale NWP models using kinetic energy spectra, *Mon. Weather Rev.* 132 (12): 3019-3032.

Symons N.P., D.F. Aldridge, D.H. Marlin, D.K. Wilson, E.G. Patton, P.P. Sullivan, S.L. Collier, V.E. Ostashev, and D. P. Drob (2004), 3D Staggered Grid Finite-Difference Simulation of Sound Refraction and Scattering in Moving Media, in *Proceedings of the 11th International Symposium on Long Range Sound Propagation*, Fairlee, VT.

DEVELOPMENT OF ADVANCED PROPAGATION MODELS AND APPLICATION TO THE STUDY OF IMPULSIVE INFRASONIC EVENTS AT VARIOUS RANGES

David Norris[1], Robert Gibson[1], Joydeep Bhattacharyya[1], and Rodney Whitaker[2]

BBN Technologies[1] and Los Alamos National Laboratory[2]

Sponsored by Army Space and Missile Defense Command

Contract No. W9113M-05-C-0135[1]

ABSTRACT

Advanced propagation modeling of infrasound includes the application of Parabolic Equation (PE) and Nonlinear Progressive wave Equation (NPE) models. In this study, the effects of several PE approximations are evaluated in the context of long-range infrasonic propagation. Specifically, the focus is on quantifying the following: phase errors resulting from different split-step Fourier (SSF) implementations, solution stability with respect to step size, and prediction sensitivity to the choice of reference sound speed. The tradeoff between improved performance gain and increased computational loading will be considered. In addition, the expected improvements of applying the NPE will also be addressed.

The study will include comparison of PE waveform predictions with measurements from infrasonic events. These comparisons are of interest in assessing the PE modeling performance, applicability, and limitations. Waveform predictions are made by integrating the continuous-wave PE model into a Fourier-synthesis Time-domain PE (TDPE).

OBJECTIVES

The objective of this research is to improve our ability to understand and characterize infrasonic propagation. This objective will be accomplished by developing advanced propagation models and applying them in comparison studies with ground truth datasets of various infrasonic events.

Through these efforts, the driving mechanisms affecting the measured waveforms will be identified, and the prediction performance of the new models will be quantified. These advances will ultimately improve event localization capabilities. More robust prediction of infrasonic arrivals, for example, those that reach the ground through diffraction, more accurate travel-time predictions, and more robust amplitude predictions will improve localization. Variability bounds placed on travel time and amplitude predictions will provide physics-based predictions that will greatly improve the accuracy of confidence bounds placed around event localizations. In addition, these advances will support discrimination between various infrasonic impulsive events. Waveform synthetics will be generated and compared with measurements, and the physical processes relevant to different sources studied.

Modeling

Advanced propagation models are proposed in areas that will support an improved understanding of the propagation and an improved ability to predict travel times, amplitudes, other waveform metrics, and associated uncertainty bounds.The specific modeling advances are listed in the left column of Table 1.They will focus on diffraction, variability, terrain, and nonlinear effects. Specifically,

- Ray tracing capabilities will be advanced by integrating a diffraction model for shadow zone regions;
- Variable terrain will be integrated into PE and TDPE models;
- Atmospheric density gradients and their effect on refraction will be modeled and evaluated;
- Small-scale atmospheric variability characterizations will be integrated into the PE and TDPE models;
- A version of the Nonlinear Progressive Equation (NPE) model will be developed that addresses the nonlinearities associated with a weak shock front.

Ground Truth Datasets

A repository of ground-truth datasets will be created and maintained, consisting of both nuclear and non-nuclear events. Additional data will be compiled from archived Nevada Test Site (NTS) records that are becoming available, and new events of opportunity will also be used. The ground truth datasets will be used to compare arrival times, amplitudes, and other waveform metrics with model predictions. The comparison studies will leverage state of the art environmental characterizations that are now available, including near real-time formulations.

Model Validation

As the propagation modeling advances are developed they will be applied to study Ground Truth events. The main goals of these model validation studies are to:

- Quantify the accuracy and applicability of the model predictions
- Estimate of the uncertainty associated with the modeling predictions, including contributions from both the modeling assumptions and unresolved atmospheric structure.
- Identify the relevant physical mechanism affecting the propagation for specific ranges and source types

These test goals will be met by laying out the framework for the validation, developing an event list from which the tests will be performed, and listing the hypotheses to be tested. In Table 1, the validation framework and expected benefit is summarized for each propagation modeling advance.

Table 1. Framework for evaluation of modeling advances.

Modeling Advancement	Relevant physical mechanism	Validation Criteria	Benefit
Extended ray predictions	Diffraction in elevated duct	Signal detection; Travel time estimation; Azimuthal deviation	Improved detection, association and localization
TDPE Variable terrain	Terrain shadowing/focusing	Signal amplitude; Travel time estimation;	Improved detection and localization
Propagation variability	Scattering/Diffraction from atmospheric inhomogeneities	Signal amplitude and its variance; signal duration; Travel time variance; azimuthal variation	Improved synthetics for discrimination; improved confidence bounds on localizations
Ambient density gradient	Density-driven refraction	Travel time	Improved detection and localization
Non-linear effects	Weak-shock effects on refraction, diffraction, dissipation, and ground interaction	Signal amplitude; Signal duration; Travel time estimation; Azimuthal deviation	Improved synthetics for discrimination; Improved localization and detection

RESEARCH ACCOMPLISHED

Propagation Modeling and Comparisons

As part of the task to advance the PE and TDPE propagation models, including the integration on ambient density gradient effects, work has begun on quantifying the effect of algorithm approximations on long-range predictions. The baseline PE model uses the split-step Fourier (SSF) algorithm (Jensen et al., 1994). Figures 1 and 2 illustrate the difference between the wide-angle and narrow-angle implementations for thermospheric propagation predictions at 2 Hz. A significant difference can be seen in the first bounce range. It is 320 km for the standard-angle approximation and 230 km for the wide-angle version. The closer arrival of energy in the latter case can be attributed to the ability to model the high angle propagation that reaches 115 km and above in the thermosphere.

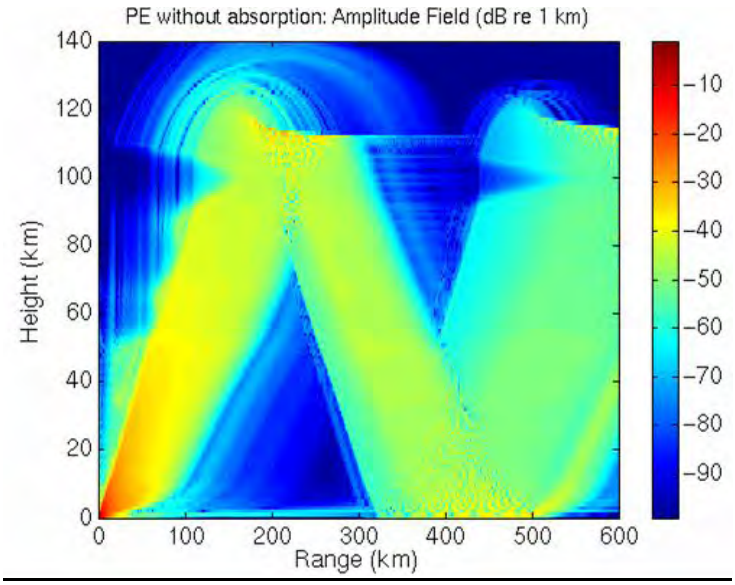

Figure 1. PE model prediction at 2 Hz using the narrow-angle approximation.

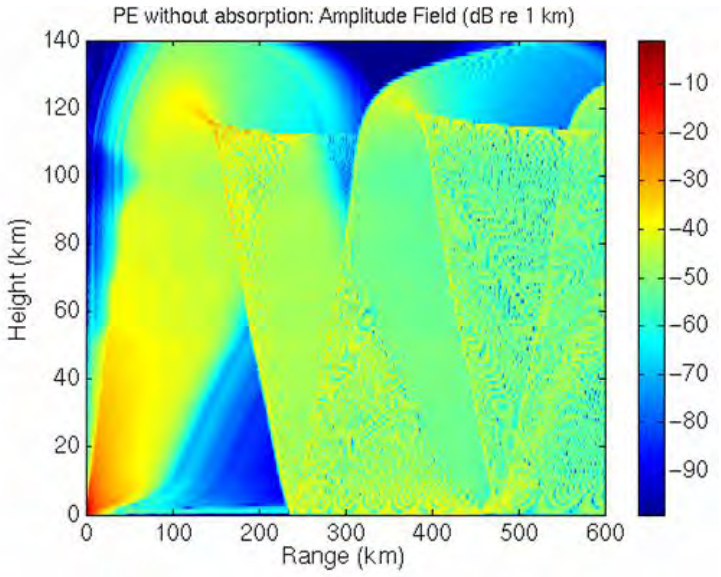

Figure 2. PE model prediction at 2 Hz using the wide-angle approximation.

Waveform predictions can be made from Fourier synthesis implementations of the wide-angle PE model [Nghiem-Phu and Tappert, 1985].The train car explosion in Neyshabur, Iran on 18-Feb-2004 is a ground-truth event that provides a good opportunity for model to data comparisons. This event was observed at the International Monitoring System (IMS) array Kazakhstan (I31KZ).The range was 1579 km and the observation had a 10-minute and 35-second duration. Figure 3 shows the observed waveform and TDPE prediction through a NRL-G2S characterization of the atmosphere. There is general agreement in arrival time and shape, although the predicted waveform arrives approximately 100 seconds before the observation.

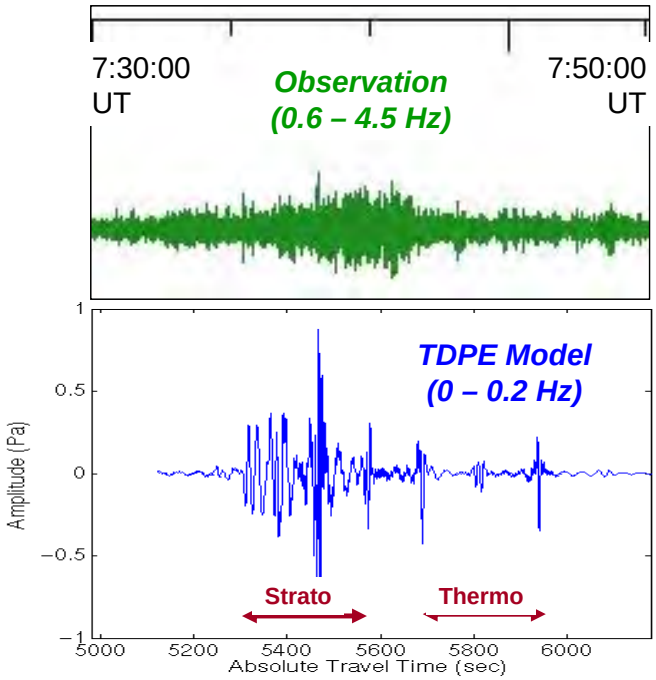

Figure 3. Comparison between TDPE prediction and measured wavefrom recorded at I31KZ from train car explosion in Neyshabur, Iran, 18-Feb-2004, 06:07 UT.

Ground Truth Database Compilation

Over the last several years, the members of the BBN and Los Alamos National Laboratory (LANL) teams have been developing such a dataset that span different propagation ranges and event types. Moreover, we have obtained GT information from our international colleagues for several global events and from published GT studies (Blinkhorn and McCormack 2003; Israelsson et al., 2003; O'Brien et al., 2003; Bass et al., 2003).

Our current GT dataset contains 102 events for which we have source and receiver information and recorded waveforms. These dataset can be broken up into the following source types, with the number of events in the parenthesis: Aircraft (3),Bolide (15), Chemical Explosion (12), Earthquake (2), Gas Pipe Explosion (2), High Altitude Nuclear Explosion (2), Microbarom (3), Mine Explosions (28), Near-Surface Nuclear Explosion (16), Space Shuttle Re-entry (4), Rocket Launch (9), Static Motor Test (1), and Volcano (5).

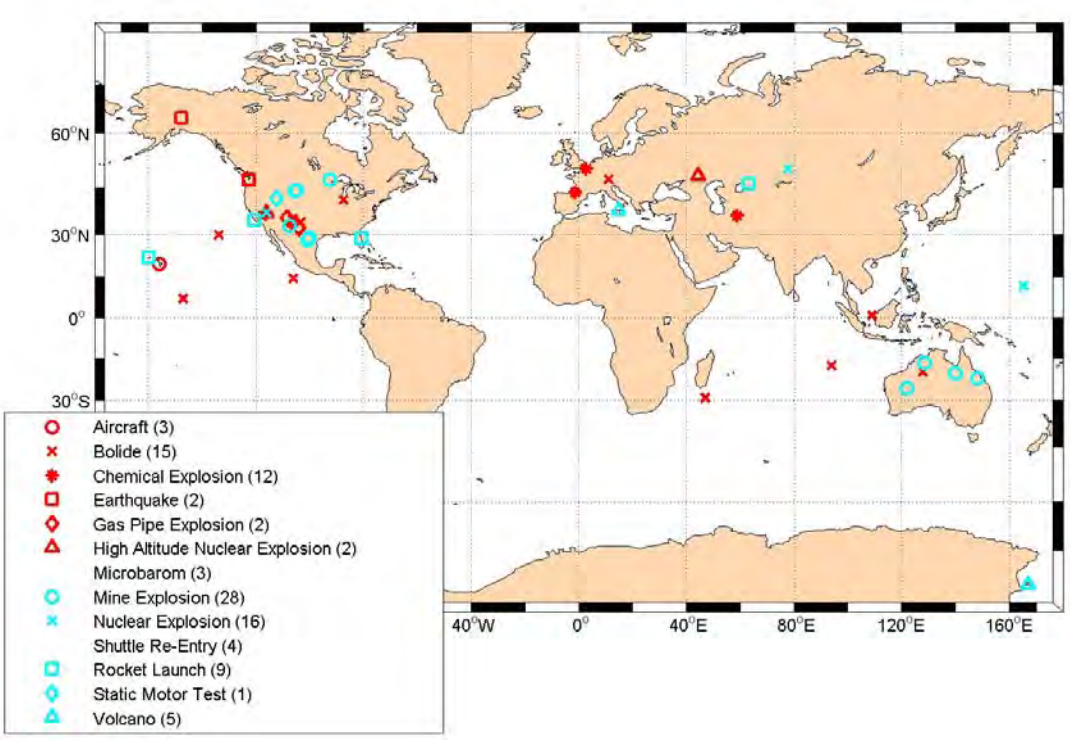

Figure 4. Geographical distribution of ground truth events, with received waveforms, available to us for this project. We list the event types and the number of events in each source category in the attached table. We do not show the locations of similar sources within the same area, e.g., events in the same mining region or test site, and events which have a large source location uncertainty like microbaroms and shuttle re-entry.

The geographical distribution of these events is given in Figure 4.The distance range of the observations range from about 20 km (Mt. Erebus to I55US) to more than 10,000 km (Pacific Bolide to IS26).The richness of spatial sampling and source types is apparent and will allow us to thoroughly evaluate the model predictions over multiple scenarios. We should note that some of the abovementioned sources, e.g., microbaroms and rocket re-entries, are not impulsive events. However, they will be available as secondary events for evaluation, if appropriate.

The ground truth dataset includes data from a Sandia National Laboratory (SNL) and LANL project, which involves digitizing infrasound records from atmospheric explosions carried out in the continental United States in the 1950s (Chael and Whitaker, 2004).Currently, this project has digitized nine events over a range of yields and heights, including underground, near surface, and high-altitude tests and from test sites in Bikini Atoll and NTS. For the larger events, detected signals are distinct at frequencies between 0.5–3.0 Hz; for the smaller events (<20 kT), higher

frequencies are observed. The smaller yield, higher frequency events are more compatible with current array configurations and monitoring goals, and therefore they will be the primary focus.

Software Tools

Over the last several years, state of the art atmospheric and propagation modeling capabilities have been integrated into the tool kit Infrasonic Modeling of Atmospheric Propagation (InfraMAP). InfraMAP has been developed by BBN for use by researchers and analysts active in the study of infrasonic propagation and monitoring. The tool kit is composed of propagation models and upper-atmospheric characterizations, integrated to allow for user-friendly model execution and data visualization. It can be applied to predict travel times, bearings, amplitudes, and waveforms for a wide range of man-made and natural infrasonic events. InfraMAP also provides the ability to define a local network of stations and compute event localizations and associated error ellipses from station measurements and propagation predictions.

Currently, InfraMAP is used by approximately 50 researchers within government laboratories, universities, and industry. The most recent version includes near-real-time atmospheric modeling capabilities (Gibson and Norris, 2004).

CONCLUSIONS AND RECOMMENDATIONS

We anticipate that the results of this research effort will improve state of the art capabilities in accurately predicting infrasonic propagation parameters and assessing the influence of fundamental physical processes. Recent improvements in environmental characterization, particularly with near-real-time model, enable the ability to generate high-fidelity, global environmental fields for a specific event time. Advanced model developments described here will fully leverage these existing atmospheric capabilities in prediction performance. Specific areas of improvement are given below.

Increased applicability of ray models. Ray modeling will be extended in the regions beyond an elevated duct through integration of a diffraction model. This advancement will enable ray predictions and localizations in scenarios that currently cannot be addressed.

Determination of terrain effects. New versions of the PE and TDPE models will provide waveform predictions over variable terrain. This capability will improve predictions capabilities by accounting for terrain blockage, travel time, and amplitude effects.

Quantification of small-scale atmospheric effects. Integrating small-scale atmospheric structure into PE and TDPE models will predict the associated impact on waveform structure. Uncertainty bounds of travel time predictions will improve confidence in error bounds placed on localization prediction.

Prediction of nonlinear propagation effects. By developing the NPE model, predictions that include nonlinear effects can be made. Comparing the results of linear and nonlinear models with measurements will identify the significant nonlinear processes. Predictions improvements in travel time, amplitude, and other waveform characteristics will be achieved, depending on the nonlinear mechanisms at work.

Increase in model applicability. Through careful comparison of model predictions with ground-truth datasets, an assessment can be made as to model performance. Strengths and weaknesses of the models can be delineated and recommendations established as to an analyst's course of action with respect to which models to apply for specific scenarios and ranges of interest.

REFERENCES

Bass, H., M. Garcés, M. Hedlin, G. D'Spain, J. Olson, C. Wilson, D. Osborne, G. Herrin, P. Golden, R. Whitaker, D. Revelle, and J. Bhattacharyya (2003), Infrasound monitoring of atmospheric events, in *Proceedings of the 25th Seismic Research Review—Nuclear Explosion Monitoring: Building the Knowledge Base*, LA-UR-03-6029, Vol. 2, pp. 577-586.

Blinkhorn, J. and D. McCormack (2003), GINA – A Global INfrasound Archive, *AGU Fall Meeting*, San Francisco, CA.

Chael, E. and R. Whitaker (2004), Infrasound Signal Library,in *Proceedings of the 26th Seismic Research Review: Trends in Nuclear Explosion Monitoring,* LA-UR-04-5801, Vol. 2, pp. 618-623.

Gibson, R. and D. Norris (2004), Integration of infrasound propagation models and near-real-time atmospheric characterizations, in *Proceedings of the 26th Seismic Research Review: Trends in Nuclear Explosion Monitoring,* LA-UR-04-5801, Vol. 2. pp. 635-644.

Israelsson, H., J. Bhattacharyya, D. Brown, and A. Gault-Galjan (2003), Analysis of basic infrasonic signal features of explosions and other events in the atmosphere, SAIC Technical Report SAIC-03-3012.

Jensen, F. B., W. A. Kuperman, M. B. Porter, and H. Schmidt (1994), *Computational Ocean Acoustics*, AIP Press, New York.

Nghiem-Phu, L. and F. Tappert (1985). Parabolic equation modeling of the effects of ocean currents on sound transmission and reciprocity in the time domain, *J. Acoust. Soc. Am.* 78: 642-648.

O'Brien, M., M. Bahavar, E. Baker, M. Garcés, C. Hetzer, H. Israelsson, C. Katz, C. Reasoner, and J. Stevens(2003). Detection of infrasonic events using a sparse global network of infrasound stations, *Infrasound technology Workshop*, La Jolla, Ca.

ADDITIONAL INFRASONIC STUDIES OF EARTHQUAKES AND MINING BLASTS DISCRIMINATION

Douglas O. ReVelle

Los Alamos National Laboratory

Sponsored by National Nuclear Security Administration
Office of Nonproliferation Research and Engineering
Office of Defense Nuclear Nonproliferation

Contract No. W-7405-ENG-36

ABSTRACT

We have continued to examine earthquake and mining blast data to search for infrasonic detections using Los Alamos (LANL) infrasound arrays. During this past year, we examined all of the remaining earthquakes that were located at regional-scale, great-circle distances (< 1500 km) from the LANL DLIAR array. Once again, we have determined that about one of every nine earthquakes (generally between local seismic magnitudes 3 and 4) were detectable infrasonically. Although both stratospheric and thermospheric returns were generally evident, > ~58 % of all earthquakes or > ~ 55 % for all mining blasts only had thermospheric returns. The goal of this research is to be able to distinguish between earthquakes and small mining blasts using discriminants established using either infrasound or in conjunction with seismic data. The proposed discriminants include (1) amplitude correction for range (normalized) and amplitude-corrected for Stratospheric wind speed effects, but without application of these wind speed effects for thermospheric arrivals, (2) fast Fourier transform (FFT) power spectral analysis differences, (3) seismic R_g phases, i.e., as a fundamental depth discriminant over short propagation ranges.

OBJECTIVE

We will present the results of our analyses of earthquake-generated infrasonic signals from mining blast explosions. In this follow-up study, we will focus attention only on regional detections of small earthquakes and mining blasts (with local seismic magnitudes generally < 4 at ranges < 1500 km). The ultimate goal in this work is to establish reliable discriminants for distinguishing earthquakes from mining blasts for infrasonic and seismic detections made over regional propagation distances.

RESEARCH ACCOMPLISHED

A study of small earthquakes and small mining blasts was undertaken as an extension of last year's initial work on this subject. The latter study is still a work in progress, but will be briefly summarized. Data for the location and times of small earthquakes and mining blasts in the western US from 2000 to 2002 were assembled with the help of Professor B. Stump (SMU, Dallas, TX) and from a United States Geological Survey (USGS) website. Over 300 earthquakes and over 425 mining blasts were assembled for a subsequent infrasonic search for coherent signals with the requisite great-circle back azimuth, signal velocity and amplitude in order to be designated as having been detected at a single array. For mining blasts we demanded a much closer agreement between observations and processed data than we did for the small earthquakes. Because other researchers have shown that the epicenter need not be the source of the strongest infrasonic waves, we chose to use a weaker azimuth constraint on the deduced infrasound back azimuth from earthquakes (Le Pichon et al., 2003). The great-circle back azimuth deviations and all key associated parameters for the infrasonically detected earthquakes are summarized in Table 1. They are all generally < ~20° (but with one event ~34.5° away from the great-circle azimuth), fully consistent with previous studies for the larger earthquakes (ReVelle et al., 2004, Mutschlecner and Whitaker, 2005). Similarly, this information is listed for the mining blast shots in Table 2, where it can be observed that the great-circle azimuth deviations are usually much smaller, < ~5°, with a few exceptions. All infrasonic amplitudes and standard deviations listed have been revised from our single-channel analyses done last year. Amplitudes (in Pa) are generally averages of all four-signal channels within the 0.5 to 3-Hz passband. Occasionally, only three data channels were available, and these averages have been reported if they were deemed reliable. Amplitudes are also reported for each infrasonic return (phase). The various phases considered are listed in the footnotes in each of the two tables.

The new study emphasized regional-scale detection of small earthquakes and mining blasts, while the earlier study emphasized regional and teleseismic detection of much larger earthquakes. In order to proceed with the domain of very small sources, we wanted to establish a set of reasonable search criteria. Thus our new emphasis was to use the larger earthquakes as a guide for the successful detection of smaller events.

The approach used in our semiautomatic "nominal" data processing analysis for small events was to set various single-array selection criteria as follows (for infrasound signals whose duration above the prevailing background noise level was > 30-45 seconds, that were nominally band-pass filtered from 0.5 to 3.0 Hz using a Butterworth filter of order 2, initially for 20-s Hanning data windows with 50 % overlap between windows on a standard slowness plane consisting of 61 × 61 points):

i) A minimum cross-correlation threshold for > 3 consecutive data windows was set: $r_{min}^2 = 0.50$.

ii) A specific limit of allowable array trace speeds, V_{trace}: $0.28 \le V_{trace} \le 0.75$ km/sec. Equivalent slowness limits, S, in middle latitudes: 200 sec/degree ≤ S ≤ 400 sec/degree.

iii) A specific limit of allowable observed signal velocities, V_{sig} : $0.14 \le V_{sig} \le 0.36$ km/sec.

iv) A maximum deviation of the great-circle back azimuth from source to observer was set. This value was ± 25° for earthquakes and ± 5° for mining blasts for regional distances <1500 km.

v) Observed microbarom back azimuths were also determined for all events in order to be confident that the observed signals were not microbarom related "bursts" (< ~15 % of the final detections were removed because of this added constraint). With this effort a new microbarom identification/location tool, MCBAROM, was designed to reliably determine any

changes in the relevant back azimuths and speeds of microbaroms over about a 10-minute time window throughout the periods of interest (typically data blocks of one hour were used).

In MCBAROM, the plane wave, great-circle back azimuth was initially determined (for a data processing window duration of 500 seconds for a one-hour data interval) by first isolating the very stable long-period side of the microbarom band (using upper and lower frequencies of 0.150 and 0.125 Hz respectively). This allowed great-circle back azimuths to be determined that were generally in good agreement in middle latitudes with seasonally averaged wind speeds, i.e., easterly in summer and westerly in winter, etc. (Donn and Rind, 1972). Next, using the approach of Rind and Donn (1975), we were able to compute the stratospheric wind speed (temporally and spatially averaged values at an average height of ~50 km) by assuming a geometrical acoustics approach that relied on the constancy of the characteristic velocity generated at the source for a horizontally stratified, range-independent, steady-state atmosphere. In addition, by limiting microbarom trace velocities to values < ~ 0.50 km/s, we were successfully able to separate thermospheric microbarom arrivals from the desired stratospheric type. Assuming a sound speed at the turning height (from a model or direct observations), regular determinations of the wind speed at the turning height are possible from knowledge of the trace velocity of the microbaroms (Rind and Donn, 1975).

In all cases where detections were declared, a comparison was made between the Matseis/InfraTool, plane-wave, great-circle back azimuth and standard seismic f-k (frequency wavenumber) slowness plane approach in order to confirm all of our detections that were made using InfraTool. In addition, examinations of the spectrograms (frequency versus time as a function of acoustic power) often allowed an independent confirmation of the detections if the signal time period was not too “noisy.”

After a semiautomatic detection was established for the searched events, either the data window size and/or the degree of overlap between data windows or the upper and lower band-pass frequency limits were systematically varied in order to refine the search. This approach took substantial amounts of time and needs to be automated, especially as the degree of overlap between data windows approaches large values.

So far in our data processing search, we have examined ~183 earthquakes and ~55 mining blasts using only the LANL array, DLIAR. Histogram distributions of the number of events versus local seismic magnitude and the number of events versus source-observer range for both earthquakes and mining blasts are plotted in Figures 1a to 1d. Of these 183 earthquakes, a total of 20 infrasonic detections were made with a high degree of certainty, while for the mining blasts a total of 16 high quality detections were made from a search of ~55 events in a similar local seismic magnitude range. Figure 2a illustrates infrasonic detection is illustrated of a small, shallow earthquake (# 102) that occurred on 12/01/2000 (local seismic magnitude 3.0, depth = 6.0 km). The corresponding MCBAROM tool results for the plane wave, back azimuth of microbaroms during this time interval are plotted in Figure 2b. The corresponding standard seismic f-k analysis for this infrasonic earthquake detection yielded a back azimuth of 270 ° (compared to 269 ° from InfraTool) with a corresponding slowness of 320 sec/deg.

A geographic summary of these infrasonic detections is given in Figure 3 where it is noted that for earthquakes, a repetition of source locations is clearly evident (in Idaho and in the CA-Baja region for example). In Figure 3, we have plotted the locations of both types of sources that we have detected at the DLIAR array as well as the locations of the other LANL infrasound arrays in the western US (with the exception of the Pinedale array at the Pinedale Seismic Research station in Wyoming). It can also be seen in Figure 3 that we may have the chance to detect these same sources at more than one infrasound array, a task which we will attempt after all events in our 2000-2002 database have been initially examined at DLIAR. Part of the reason for our success in detecting small mining blast relative to earthquakes is a result of the source ground-coupling factor and also the fact that the mining blast source is very near the Earth’s surface. Earthquakes have two fundamentally different faulting mechanisms, only one of which is expected to generate significant infrasonic signals. In addition however, earthquake sources can also be at great depths. Since the generation of infrasound is fundamentally related to the up-down part of the source ground motion, deeper earthquakes are generally not expected to generate significant infrasound. The deepest source that has been detected infrasonically so far was 13.8 km, while others were detected closer

to the earth's surface. Eventually we will examine all of our infrasonic earthquake detections in terms of both their depth and faulting mechanisms, etc.

We also examined our detections in terms of establishing possible discriminants between small mining blast and earthquakes. We are currently examining earlier predictions of wind-corrected infrasonic amplitude versus local seismic magnitudes that were developed for larger sources at generally longer ranges to determine if we can establish a similar regression curve for use in the small source-size range. Additional discriminants currently being investigated include the following:

i) Separate analyses of the relationship between infrasonic amplitudes from earthquakes and from mining blasts (as normalized for range and corrected for stratospheric wind effects) versus the local seismic magnitude have been made. In the case of thermospheric arrivals, wind corrections are not made; however, because for such returns wind speeds are generally << than the local sound speed at such large heights and do not limit the ducting possibilities.
ii) PSD (power spectral density) analysis of differences between earthquakes and mining blasts.
iii) Seismic R_g phases for separating earthquake signals from mining blasts over short-range shallow propagation paths, i.e., as a fundamental depth-discriminant concept.

In the coming year, we will continue to pursue all of these activities and develop a conceptual framework for the reliable discrimination of infrasonic signals from earthquakes from those from mining blasts.

CONCLUSIONS AND RECOMMENDATIONS

We have examined a fairly wide range of small earthquake and mining blast magnitudes and distances. For large earthquakes, we previously determined that a relationship exists between the wind-corrected and range-normalized infrasonic amplitude and the local seismic magnitude, and we wish to determine if this relationship is still applicable for smaller magnitude sources. If a similar regression line can be established for small sources over regional detection distances, at least one physical discriminant can be readily developed for separating mining blast shots from earthquakes. This discrimination tool will be a very important development since a very large number of both types of sources occur annually worldwide. Our general conclusions at this time for the current set of processed results are the following:

1) Durations of earthquakes are generally much larger than those of the mining blast shots, with the exception of the mining blast shot at Newcastle, Wyoming on 2/26/2001 (total duration > 4 min).
2) The earthquake detections are generally "cleaner," i.e., the standard deviation of the recorded amplitudes averaged over all available data channels, is generally much smaller with respect to the average value.
3) Our concentration of work efforts next year will be entirely on mining blast shots and this should help to clarify the current situation and further our efforts to reliably discriminate between these source types.

REFERENCES

Donn, W. L. and D. Rind (1972), Microbaroms and the temperature and wind of the upper atmosphere, *J. Atmos. Sci*. 29, 156-172.

Le Pichon, A., M. Aupetit, E. Blanc, Y. Cansi, J. Guilbert, S. Lambotte and J. Plantet (2003), Six-years review of infrasound monitoring at the French NDC, Invited Abstract U32C-01, American Geophysical Union Annual Fall Meeting, San Francisco.

Mutschlecner, J. P. and R. W. Whitaker (2005), Infrasound from earthquakes, *J. Geophys. Res*. 110: D01108.

ReVelle, D. O., R. W. Whitaker, J. P. Mutschlecner and M. Renwald (2004), Discrimination of earthquakes and mining blasts using infrasound, in *Proceedings of the 26th Seismic Research Review—Trends in Nuclear Explosion Monitoring*, LA-UR-04-5801, Vol. 2, pp. 669-679.

Rind, D. and W. L. Donn (1975), Further use of natural infrasound as a continuous monitor of the upper atmosphere, *J. Atmos. Sci*. 32: 1694-1704.

Webb, W. L. (1964), Stratospheric solar response, *J. Atmos. Sci*. 21: 582-591.

Young, H.D. (1962), *Statistical Treatment of Experimental Data,* McGraw-Hill Book Co., Inc., 172 pp.

Table 1: Summary: Regional Scale Earthquake Detections- DLIAR infrasound array (*)

Earth-quake	Date: mm/dd/yy	General Location	Time: UT	Local Seismic magnitude and depth: km	Range km- along great circle path	G.C. (**) back azimuth: (BA): °	ΔBA: (***): °	Raw amp. Pa: 4 channel average value ± stand. dev.	Signal velocity: km/s and phase type(s) (*****)
# 17	2/29/00	CA-NV	22:08	4.1, 0.0	1013.2	268.0	3.5 -7.5	0.032 ±0.012 0.014 ±0.006	0.32, S 0.24, Th
# 42/44	5/26/00	WY	21:58	4.0, 5.0	711.8	351.0	-3.8	0.092 ±0.018	0.22, Th
# 85	11/10/00	MT	19:14	4.0, 2.1	1243.9	338.5	10.1 -12.5	0.038 ±0.014 0.025 ±0.015	0.28, S 0.14, Slow Th
# 102	12/01b/00	S. NV	00:01	3.0, 6.0	778.2	269.0	-2.7 -6.2	0.014 ±0.004 0.009 ±0.003	0.29, S 0.20, Th
# 177	9/04/01	CO	12:45	4.0, 5.0	206.9	47.2	2.2	0.031 ±0.002	0.29, S
# 191	10/08a/01	E. Idaho	13:47	3.6, 0.1	1140.4	328.9	2.6 34.5 (??)	0.007 ±0.001 0.055 ±0.004 (??)	0.28, S 0.14, Slow Th
# 192	10/08b/01	NV	05:37	4.6, 0.0	1018.4	302.7	12.7	0.008 ±0.003	0.22 Th
# 206	12/09/01	W. AZ-Sonora	01:42	4.5, 10.0	901.8	239.7	-2.7	0.026 ±0.007	0.26 Th
# 207	12/12/01	MT	11:17	3.0, 5.6	1122.3	333.9	3.0	0.013 ±0.002	0.22, Th
# 208	12/13/01	W. Idaho	05:42	3.2, 5.0	1251.5	323.0	-6.4 -13.8	0.020 ±0.009 0.013 ±0.003	0.31, S 0.25, Th
# 221	01/04e/02	CA-Baja	19:38	3.3, 7.0	885.4	242.9	21.3	0.079 ±0.012	0.31, S
# 222	01/04f/02	E. Idaho	13:11	3.2, 5.0	908.2	329.2	-8.0	0.007 ±0.002 (****)	0.16, Slow Th
# 225	01/08/02	UT	17:26	3.2, 8.2	592.1	281.1	1.8	0.046 ±0.006	0.20 Th
# 230	01/22/02	W. Idaho	08:31	3.7, 5.0	1160.8	322.5	16.7	0.015 ±0.002	0.30, S
# 239	02/22/02	CA-Baja	19:32	5.5, 7.0	916.3	242.0	-3.6	0.069 ±0.011	0.29, S
# 242	03/19/02	Gulf of CA	22:14	4.1, 10.0	935.3	225.0	-10.6	0.118 ±0.017	0.27, S
# 264	05/11/02	UT	06:30	3.0, 9.2	800.5	323.4	4.2	0.042 ±0.016	0.24, Th
# 265	05/14/02	Central CA	05:00	4.9, 7.7	1370.0	270.5	-16.4	0.052 ±0.004	0.14 Slow Th
# 278	07/15/02	CA-NV	20:18	4.1, 13.0	1089.7	275.3	-1.8 18.1	0.061 ±0.015 0.061 ±0.016	0.31, S 0.16, Slow Th
# 279	07/23/02	E. Idaho	08:17	3.0, 5.0	864.0	329.3	8.2	0.016 ±0.004	0.18, Slow Th

(*): Final regional earthquake detection list at DLIAR: All marginal detections have been removed. The removal of events was finally decided on the basis of too brief a signal duration, a back azimuth too close to the prevailing microbaroms back azimuth (available from MCBAROM), or too small an r^2 value, etc.

The amplitude computations were made using Δp (Pa) = $0.5 \cdot \Delta S_{p\text{-}p}$(cm) · {2.5 Pa/V} · S(V/cm), where S is the scale factor for each individual microphone channel and $\Delta S_{p\text{-}p}$ is the individual channel maximum signal amplitude (peak-to-peak value). Symmetry of the total amplitude about the origin was assumed, so that the zero-to peak-value was calculated to be one half of the maximum total signal amplitude.

(**): InfraTool great-circle, back azimuth Towards the USGS source location from the DLIAR array.

(***): Plane-wave, back azimuth deviation from the great-circle path back to the infrasonic source

ΔBA = Computed great-circle back azimuth – observed standard seismic f-k back azimuth

(****): Marginal amplitude measurement at very low S/N ratio

(*****): Infrasonic phases are L: Lamb, T: Tropospheric, S: Stratospheric, Th: Thermospheric and Slow Th: Slow Thermospheric returns.

Table 2: Mining Blast Infrasound Detections Summary: (∗)

Mining blast shot location	Date mm/dd/yy	Time: UT	Local Seismic Magnitude	Range: km- along great-circle path	G.C. (∗∗), back azimuth (BA): °	Δ BA (∗∗∗): °	Raw amp. Pa: 4 channe average value ± stand. dev.	Signal velocity: km/s and Arrival phase type(s) (∗∗∗∗∗)
Newcastle,WY	2/26/01	21:09	3.5	871.0	7.9	0.80	0.027 ±0.013	0.28, S
Craig, CO	2/28b/01	23:06	3.3	510.7	344.8	16.4	0.010 ±0.006	0.34, L
Safford, AZ	3/22/01	19:19	3.2	417.2	221.2	1.4 -5.7	0.074 ±0.024 0.383 ±0.243 (??)	0.30, S 0.15, Slow Th
Gillette, WY	3/27/01	21:17	3.1	880.5	6.5	-2.3 -17.9 (∗∗∗∗)	0.054 ±0.013 0.029 ±0.012	0.35, L 0.17 Slow Th
Gillette, WY	4/01/01	20:10	3.1	880.5	6.5	6.5	0.022 ±0.005	0.32, S
Gillette,WY	4/25a/01	20:04	3.2	880.5	6.5	-3.4	0.025 ±0.016	0.31, S
Safford, AZ	4/25b/01	22:13	3.4	417.2	221.5	-3.8	0.015 ±0.007	0.28, S
Safford, AZ	4/30/01	18:50	3.1	417.2	221.5	-5.6 -20.6 (??)	0.017 ±0.013 0.024 ±0.016 (??)	0.25, Th 0.17, Slow Th
Gillette,WY	5/12/01	20:02	3.3	880.5	6.5	1.5	0.015 ±0.009	0.14, Slow Th
Sheridan,WY	6/19/01	19:03	3.1	1039.9	359.2	-0.80	0.037 ±0.022	0.32,T/S
Rock Springs,WY	6/26/01	21:38	3.2	674.9	341.9	7.3	0.012 ±0.005	0.22, Th
Craig, CO	6/27/01	18:14	3.5	510.7	344.8	1.3	0.090 ±0.040	0.14, Slow Th
Gillette, WY	7/04/01	18:18	3.4	880.5	6.5	-1.6	0.074 ±0.018	0.28, S
Craig, CO	7/07/01	22:04	3.5	510.7	344.8	-1.2	0.080 ±0.025	0.21, Th
Rock Springs,WY	7/11/01	17:16	3.3	674.9	341.9	-4.7	0.072 ±0.031	0.24, Th
Craig, CO	8/18/01	13:58	3.3	510.7	344.8	-2.9 -2.4	0.008 ±0.003 0.012 ±0.004 (?)	0.26, Th 0.11, Slow Th

(∗): This list is not final yet, since numerous mining blast shots still need to be evaluated infrasonically.

The amplitude computations were done using: Δp (Pa) = $0.5 \cdot \Delta S_{p\text{-}p}$(cm) · {2.5 Pa/V} · S(V/cm) where S is the scale factor for each individual microphone channel and $\Delta S_{p\text{-}p}$ is the individual channel maximum signal amplitude (peak to peak value). Symmetry of the total amplitude about the origin was also assumed so that the zero to peak value was calculated to be one half of the maximum total signal amplitude.

(∗∗): Infra_Tool great-circle, back azimuth: Towards the USGS source location from the DLIAR array.

(∗∗∗): Plane wave, back azimuth deviation from the great-circle path back to the infrasonic source: ΔBA = Computed great-circle back azimuth – observed standard seismic f-k back azimuth

(∗∗∗∗): Using Infra_Tool's back azimuth for this Slow Th phase, Δ BA = 1.6 °. The reason for this discrepancy is not yet understood.

(∗∗∗∗∗) Infrasonic phases are L: lamb, T: tropospheric, S: stratospheric, Th: thermospheric and Slow Th: Slow thermospheric returns

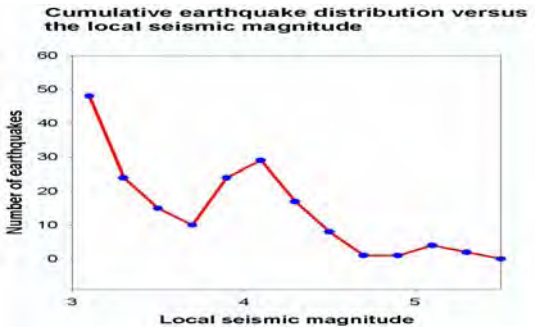

Figure 1a. Number of earthquakes versus local seismic magnitude.

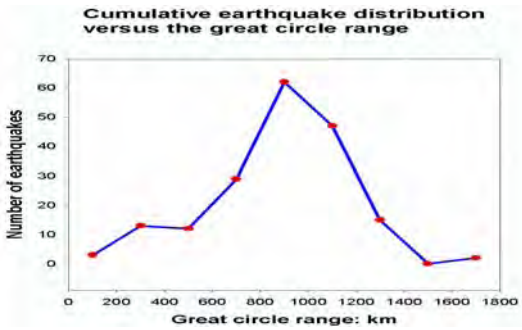

Figure 1b. Number of earthquakes versus source-observer range.

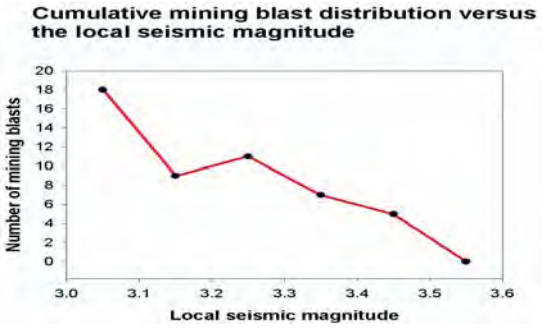

Figure 1c. Number of mining blasts versus local seismic magnitude.

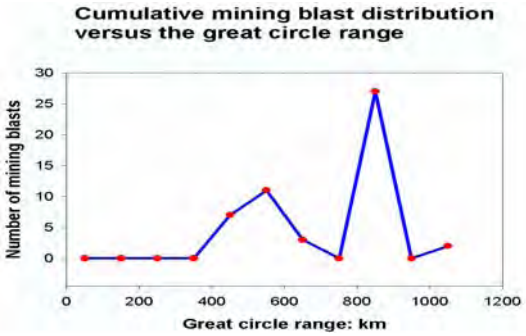

Figure 1d. Number of mining blasts versus source-observer range

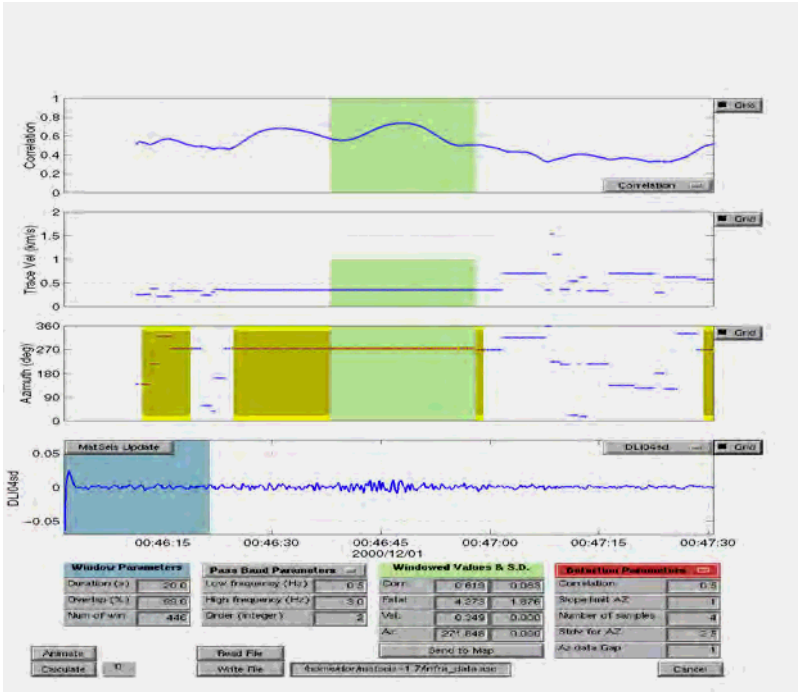

Figure 2a. Matseis signal processing and analysis: Infrasonic detection of earthquake (# 102) of 12/01b/2000. Averaged pair-wise cross-correlation, trace velocity, back azimuth, and a single-channel time series versus pressure amplitude.

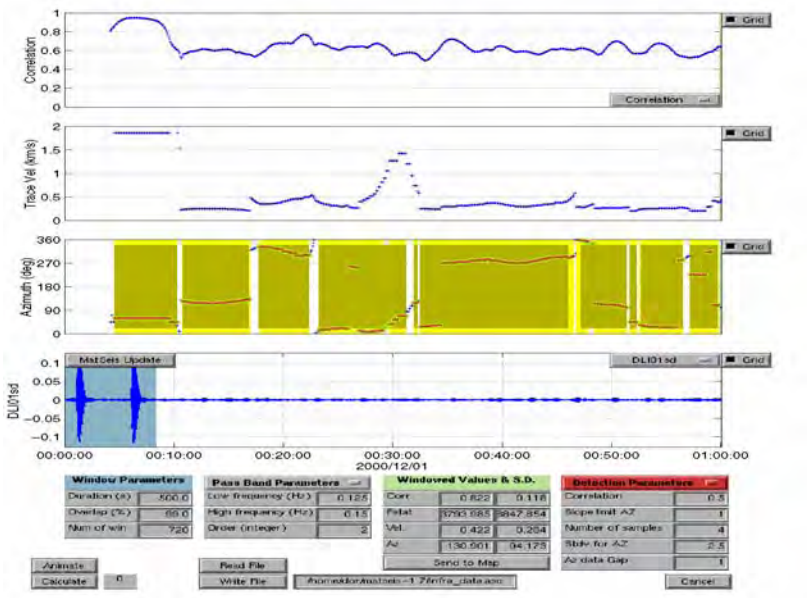

Figure 2b. Matseis signal processing and analysis: detection results during the same time interval as for earthquake (# 102) of 12/01b/2000 in Figure 1a. Averaged pair-wise cross-correlation, trace velocity, back azimuth, and a single-channel time series versus pressure amplitude.

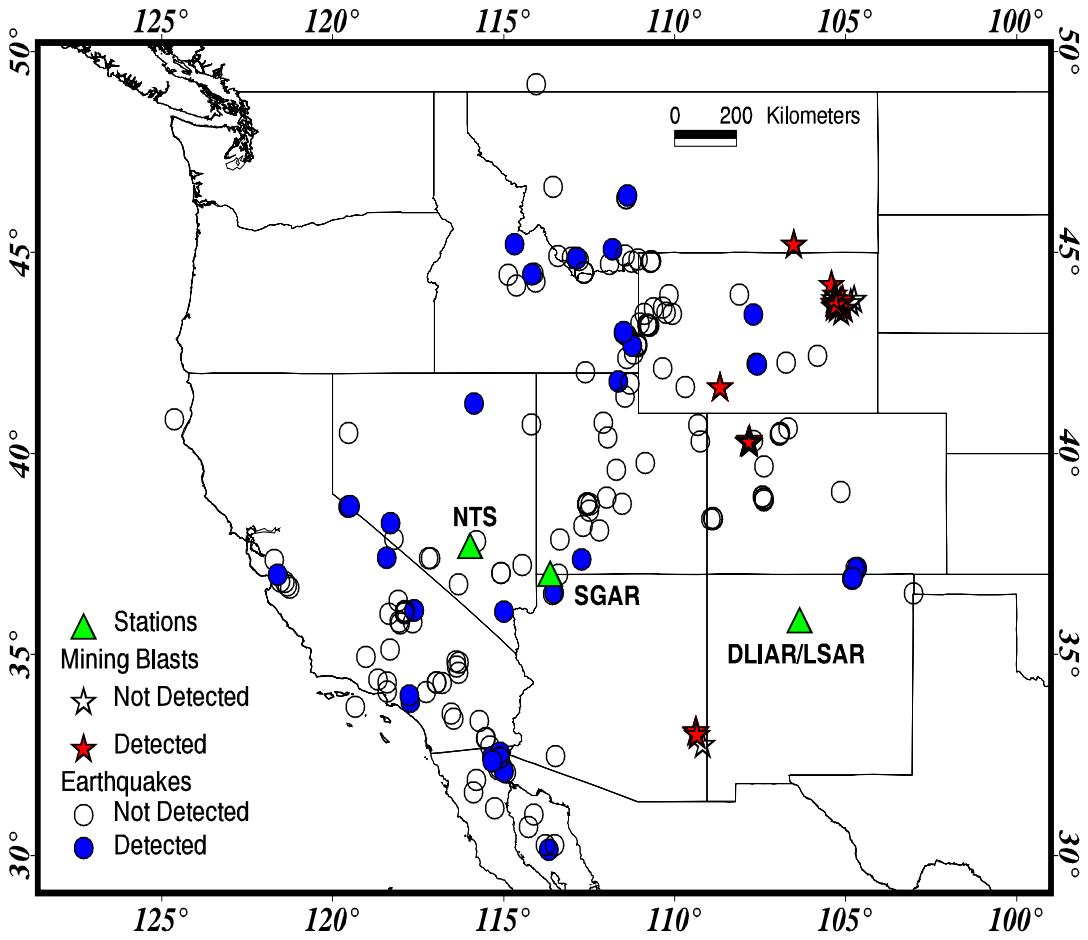

Figure 3. Spatial summary: infrasonic detections of small earthquakes and mining blasts.

AN IMPROVED METHOD FOR DETERMINING INFRASOUND BACK AZIMUTH WITH OPTICAL FIBER SENSORS

Kristoffer Walker, Mark Zumberge, Jonathan Berger, and Michael Hedlin

University of California, San Diego

Sponsored by US Army Space and Missile Defense Command

Contract No. W9113M-05-1-0020

ABSTRACT

Optical Fiber Infrasound Sensors (OFIS) are long compliant tubes wrapped with optical fiber that interferometrically measure the pressure variation along the length of the tube. Because each sensor averages spatially along the path of the tube, the response of the straight-line OFIS to the pressure variation is a function of the orientation of the OFIS relative to the back azimuth (BAZ) and incidence angle (INC) of the incoming wave. We have exploited this property with three 89-m-long OFIS having their azimuths separated by 120° and their centers separated by 77 m and have found that they can resolve the BAZ of most subhorizontal arrivals having good signal-to-noise ratio. We find a very good match between the BAZ determined from our technique and those determined from the same signals recorded on the co-located I57US microphone array using the Progressive Multichannel Cross-Correlation technique (RMS = 7°). We have also determined that a multi-arm OFIS can resolve the INC of the incoming signal.

OBJECTIVES

Optical Fiber Infrasound Sensors (OFIS) detect acoustic signals in the infrasound band (below 20 Hz), which propagate approximately in the horizontal plane. We defer a detailed instrument description to Zumberge et al. (2003). In general, a fiber is split into two fibers that are helically wrapped around a sealed, compliant tube in such a way that for an ambient pressure variation, the tube deforms and changes the optical path length difference *l* between the two fibers (Figure 1). The fibers are recombined and connected to a photodetector. The change in the path length difference is measured interferometrically by illuminating the photodetector with a 1310-nm laser. A lock-in amplifier is used to calculate the derivative of the fringe signal *y* while modulating the path length difference *l* by a small fraction of a wavelength at several hundred kHz with a piezoelectric crystal. When plotted against each other, the two fringe signals (*y* and *dy/dl*) trace out an ellipse. The angle swept out by the ellipse is empirically related to the pressure in real time at 200 Hz (Zumberge et al., 2004).

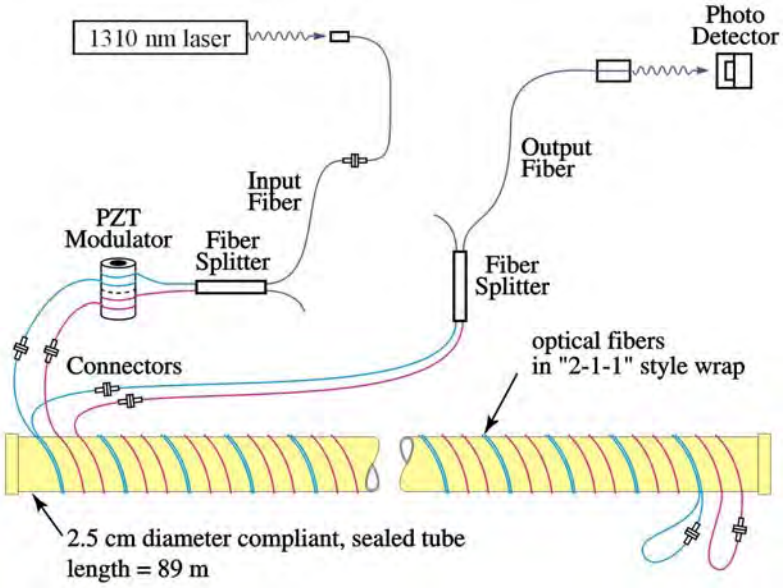

Figure 1. Schematic of one of four Optical Fiber Infrasound Sensor (OFIS) arms that are operating at PFO (I57US).

A multi-arm OFIS has several advantages over other infrasound sensors such as pipe and hose arrays. It is relatively inexpensive to build, deploy, and maintain. It is also easy to deploy, and requires much less space, making it highly portable (Figure 2). There is also evidence that in low-wind conditions, the noise floor of the OFIS is lower than the pipe and hose arrays for frequencies down to 1 Hz.

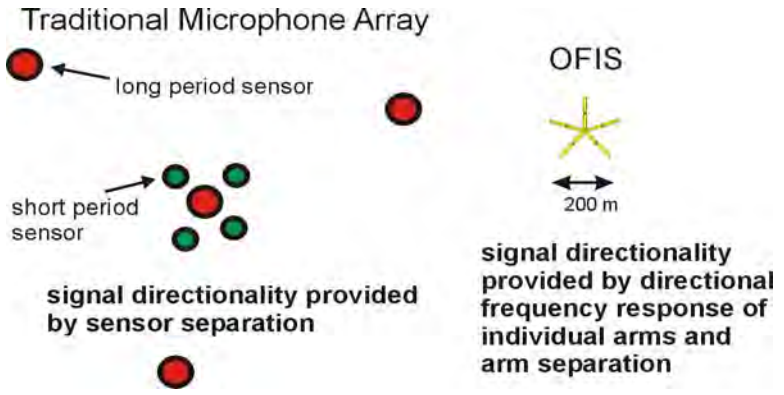

Figure 2. A typical International Monitoring System (IMS) infrasound array and a multi-arm OFIS shown to scale.

The objective of this research is determine if a ~200 m aperture multi-arm OFIS can be made to perform at least as well as a much larger (~1000-2000 m aperture) microphone array. In this paper, we (1) determine the number of OFIS and optimum configurations that are necessary to resolve the back azimuth of infrasound signals, (2) develop a generic technique for estimating back azimuths using an *n*-arm OFIS, (3) test the technique by comparing back azimuths estimated from synthetic signals and real signals recorded by a three-arm OFIS at Piñon Flat Observatory (PFO, I57US) in the southern California high desert, and (4) describe sensor uptime problems and solutions.

RESEARCH ACCOMPLISHED

Sensor Directivity

The response, *R*, of an OFIS relative to a point detector is a function of the orientation of the signal propagation with respect to the length of the OFIS:

$$R = \mathrm{sinc}\left(\frac{L\pi f}{V_a}\cos(\theta)\right) \quad (1)$$

where *f* is frequency, *L* is the length of the OFIS, V_a is the sound speed at the Earth's surface, and θ is the angle between the incident ray path and the OFIS.

$$\theta = \cos^{-1}(\cos(\theta_b)\sin(\theta_i)) \quad (2)$$

where θ_b is the back azimuth, and θ_i is the incidence angle. For typical telesonic infrasound signals, θ_i is approximately 90° (horizontal), and $\theta = \theta_b$. Figure 3a shows a polar plot of *R* as a function of angle from the long axis of the OFIS for three typical infrasound signal frequencies (assuming θ_b = 90°).

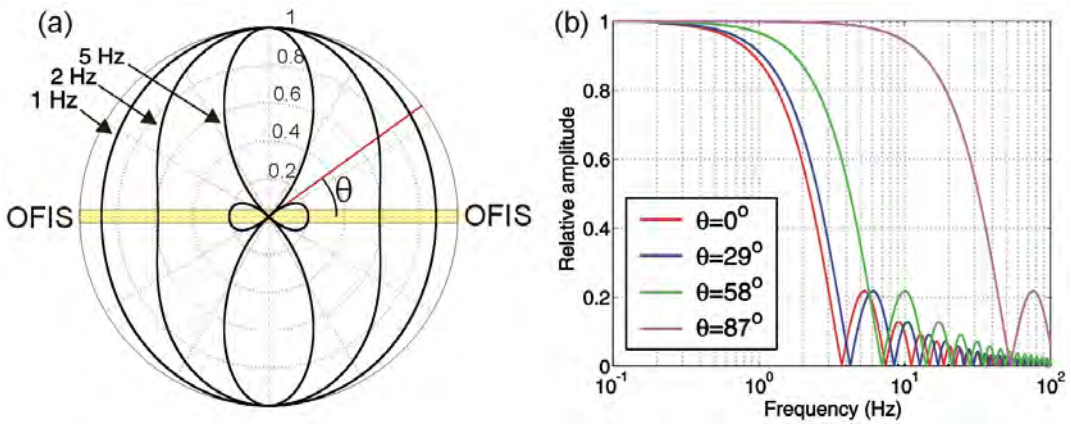

Figure 3. Frequency response *R* for an 89-m long OFIS at V_a = 340 m/s as a function of frequency and angle θ (eqns. 1-2).

The response *R* varies remarkably as a function of frequency, OFIS length, and acoustic velocity (Figure 3b). The phase of *R* is linear with respect to frequency, and corresponds to a static shift in the time domain. Therefore, if the back azimuth for a signal with a significant bandwidth is known, one can deconvolve *R* in frequency space from the recorded signal S_r to determine the actual signal waveform $S_w = S_r / R$.

Two-Arm OFIS

Because the response function is known for all signal orientations, one can record the signal of interest on two sensors with different orientations and "invert" for the signal by means of a grid search.

Algorithm

The recorded OFIS signal $S_r = f(S_w, \theta, V_a, L)$, where only S_w and θ are the unknowns. One can therefore estimate S_w and θ if one records the signal on two OFIS with different orientations (Figure 4)

$$S_{r1} = f(S_w, \theta) \qquad (3)$$

$$S_{r2} = f(S_w, \theta)$$

We do this by a substitution grid search, i.e., using S_{r1} to predict ${S_w}^p$, and then ${S_{r2}}^p$ for possible signal orientations

$${S_{r2}}^p = {S_w}^p R_2 = (S_{r1}/R_1)R_2. \qquad (4)$$

We can make the assumption (although not required) that the incidence angle θ_i = 90° and perform a grid search over only trial θ_b (between 0° and 90° from the OFIS 1 azimuth in 1° increments) to minimize the L2 misfit between S_{r2} and ${S_{r2}}^p$. However, the resolution power and accuracy is better when we minimize the sum of the L2 misfits between S_{r1} and ${S_{r1}}^p$ and S_{r2} and ${S_{r2}}^p$. The resolution is also much better if we perform a full grid search over trial θ_b and θ_i. We can perform the deconvolution in the frequency domain by using the water-level technique to avoid numerical instability; i.e., we raise all near-zero amplitudes in the denominator frequency spectrum to a "water level" of 1% of the maximum amplitude (e.g., Langston, 1979). We also can calculate formal 2σ error bars using the technique of Silver and Chan (1991), which assumes the misfit function is the sum of squares of a random chi-squared noise process.

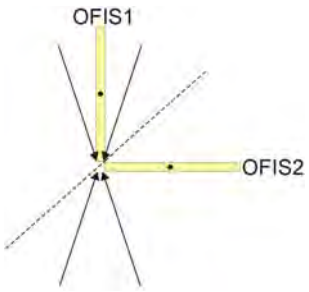

Figure 4. Layout of a two-arm OFIS in the 2-90 configuration. The dashed line is the plane along which arriving signals cannot be distinguished (azimuth of ambiguity). The arm centers are separated by 63 m to distinguish between the complementary set of 4 possible orientations from which arriving signals have identical shapes.

The configuration that offers the best signal orientation resolution for a two-arm OFIS is two arms separated by 90°, with their centers separated by at least 63 m. We call this the 2-90 configuration. Because an OFIS integrates the change in pressure along the length of the tube, one cannot determine the quadrant from which a signal originates (Figure 4). Any angle from OFIS 1 is part of a complementary set of four angles from which an incoming signal has identically recorded shapes on both OFIS. To get around this ambiguity for the 2-90 configuration, we exploit the fact that the two OFIS are separated by 63 m, and perform a cross-correlation during each trial θ_b to find the optimum time separation between S_{r2} and ${S_{r2}}^p$ before calculating the misfit. Then for the optimum θ_b, we check

the corresponding *dt*, which determines from which of the four angles it originated assuming θ_i = 45-90°. The resulting misfit function contains misfits from the optimally time-shifted S_{r2} and $S_{r2}{}^{p}$.

The angle halfway between both OFISs is an angle for which the recorded signals on both OFISs should be identical (Figure 4). We term this special angle the angle of ambiguity because one cannot resolve between it, its 180° complement, or a signal from directly above (θ_i = 0°).

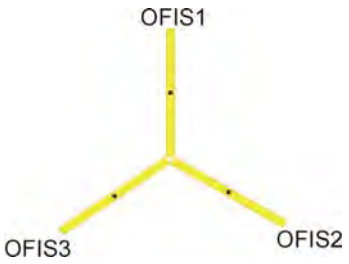

Figure 5. Layout of a three-arm OFIS in the 3-120 configuration. The arm center separations of 77 m eliminate any ambiguities in the arriving signal orientation.

Three-arm OFIS

The three-OFIS algorithm can easily be extended and applied to an *n*-arm OFIS. Our misfit function becomes the sum of the L2 misfits between the various predicted and observed OFIS recorded signals (sum of n^2 misfits). This requires much more CPU time. As a consequence, such an algorithm should be programmed in assembly language for real-time applications and optimized Fortran for research applications.

Testing the Algorithm on Synthetic and Real Data

The results of testing the algorithm for a two-arm OFIS in a 2-90 configuration were presented by Walker et al. (2004). They found that using the technique above, synthetic and recorded infrasound signals at PFO (spring 2004; I57US) when compared with those obtained by the co-located, 1.4-km wide microphone array (Hedlin et al., 2003) using the Progressive Multichannel Cross-Correlation algorithm (PMCC) (Cansi, 1995) suggest that a 2-90 OFIS is generally capable of resolving the back azimuth of signals that have a good signal-to-noise ratio, although there were a significant number of inaccurate measurements. In this section we report the results of testing a two-arm OFIS with a 120° azimuth separation (2-120 configuration) and a three-arm OFIS with a 120° separation (3-120). We calculate the resolution kernels using synthetic signals as well as compare recorded OFIS signal orientations to those determined using the PMCC method. We perform the analysis by (1) assuming horizontally traveling signals and searching only over the trial back azimuth, and (2) searching over both trial back azimuth and incidence angle. Due to the major increase in CPU time required for the additional search over incidence angle for a three-arm OFIS, we were required to convert our original Matlab algorithm into Fortran, although we developed a generic Matlab user interface.

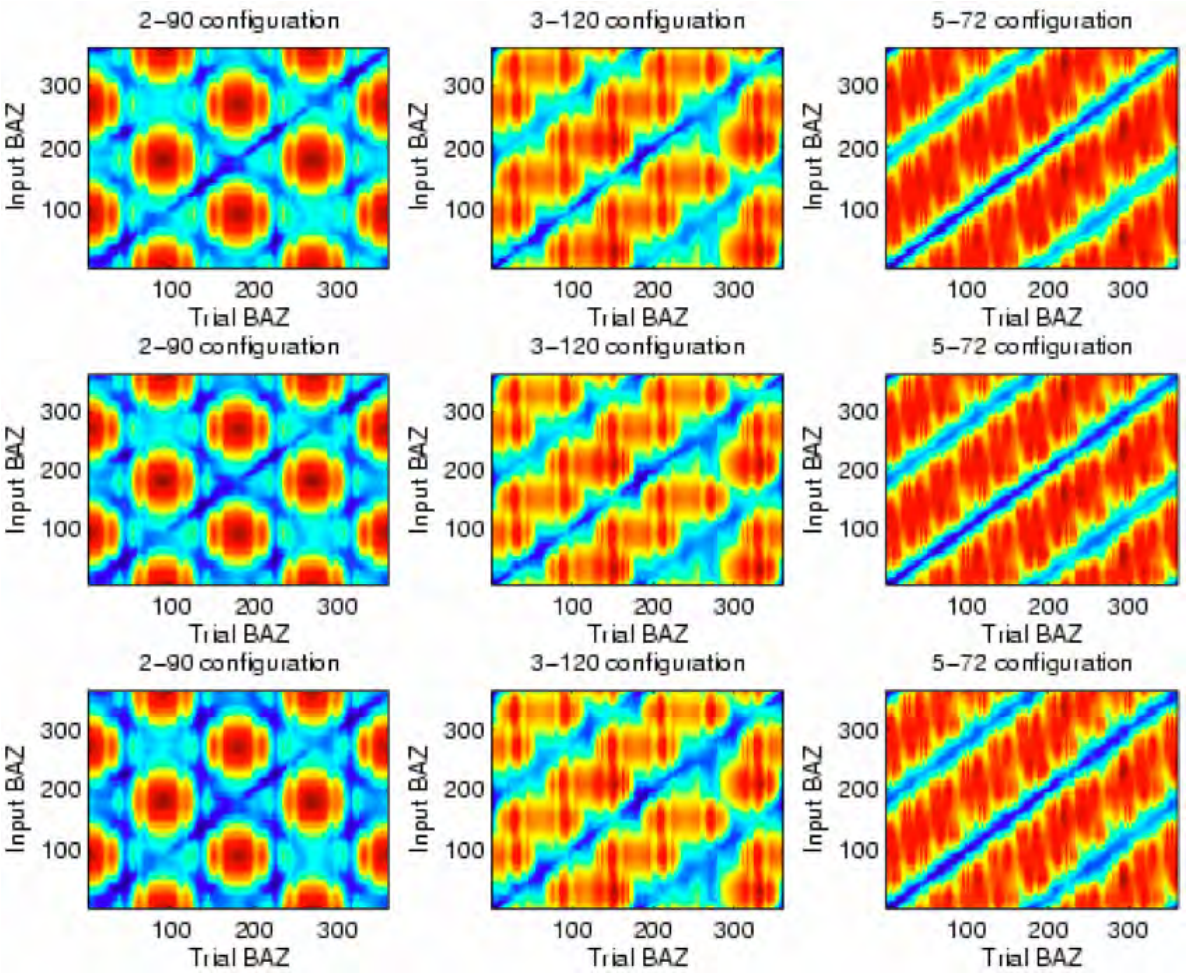

Figure 6. Resolution kernels of various OFIS configurations as a function of the trial back azimuth and the input back azimuth. These kernels were calculated using one of several possible algorithms, some of which are better than others.

Figure 6 compares the resolution kernels for the 2-90, 3-120, and 5-72 configurations (columns) at various input noise levels (rows). We created each 2D plot by generating synthetic waveforms for each input back azimuth assuming horizontally propagating signals. For each of these waveforms, the algorithm calculated the misfit function between the predicted and "observed" OFIS waveforms as a function of the trial back azimuth. Color indicates the log of the misfit: blues are lows and indicate the algorithm-determined back azimuth. In the ideal case, one expects to see a single blue line intersecting the origin with a slope of unity.

The most apparent feature for the 2-90 configuration plots are the complementary set of 4 orientations that yield similar misfit lows for most input back azimuths. For the input back azimuth of 45° (azimuth of ambiguity), one cannot determine between that orientation and its 180° complement.

2-120 configuration 3-120 configuration

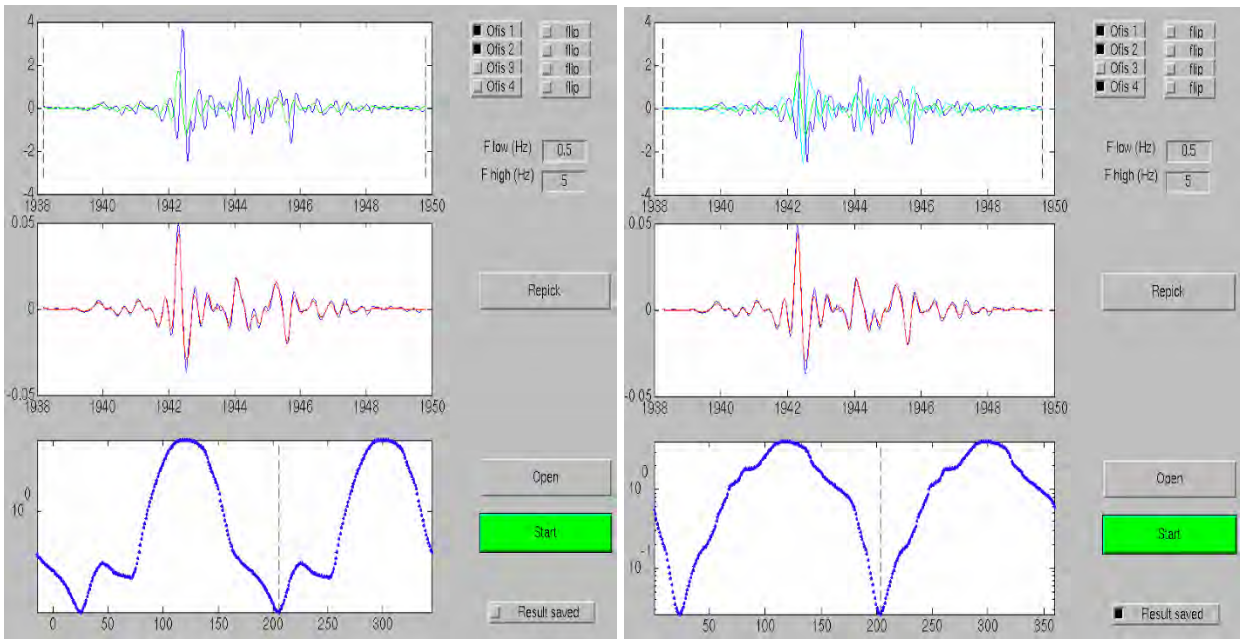

Figure 7. Characteristic plots for analyzing a signal recorded at PFO with a PMCC-determined back azimuth of 204° for a 2-120 (left) and 3-120 (right) configuration. The top plot shows the recorded OFIS signals as a function of time. The middle plot shows the optimum predicted and observed OFIS 1. The lower plot shows the log plot of the misfit as a function of the trial back azimuth. The vertical dashed line indicates the optimum OFIS-determined back azimuth. The misfits are identical in these plots because an unusual timing problem restricted our use of relative timing information, although we were still able to determine the correct hemisphere from which the signal arrived.

The situation is much better for the 3-120 configuration, as the correct resolution region (central blue line) is more consistent in size and shape. Although the azimuth of ambiguity problem is resolved, you can see to either side of the central blue line is a lighter blue line. Although present in the 2-90 results as well, these lines become distinctly visible now and represent the 180° complement of the set of 4 complementary orientations described above. Distinguishing between the true and 180° complement orientation for all configurations is strictly a function of the OFIS center separation. Therefore, the farther apart the centers, the warmer the colors of those lines.

The 5-72 configuration is nearly ideal in that the resolution region is quite consistent in size and shape. A 6-60 configuration would yield a nearly identical result. As with the 3-120 configuration, the 180° complement lines are clearly visible, although they are not mistaken for the true solution (colors are the log of misfit).

For all configurations, the noise level does not greatly affect the resolution kernel. This is intuitive because we are adding white noise to the synthetic waveforms before applying our preprocessing band pass filter and subsequent OFIS transfer functions *R*. Therefore, the spectral differences are not being greatly affected. The kernels would likely change considerably as a function of noise level if the noise was due to an acoustic source or if wind noise is spatially coherent over tens to hundreds of meters distance, which previous field experiments suggests is not.

During spring 2005, we recorded 24 signals of unknown origin at Piñon Flat Observatory on a 2-120 and 3-120 multi-arm OFIS configuration. Figure 7 shows the misfit functions for one of these signals for each configuration. Although both configurations resolve the correct back azimuth of 204°, the misfit function is more precise for the 3-120 configuration.

(a) (b)

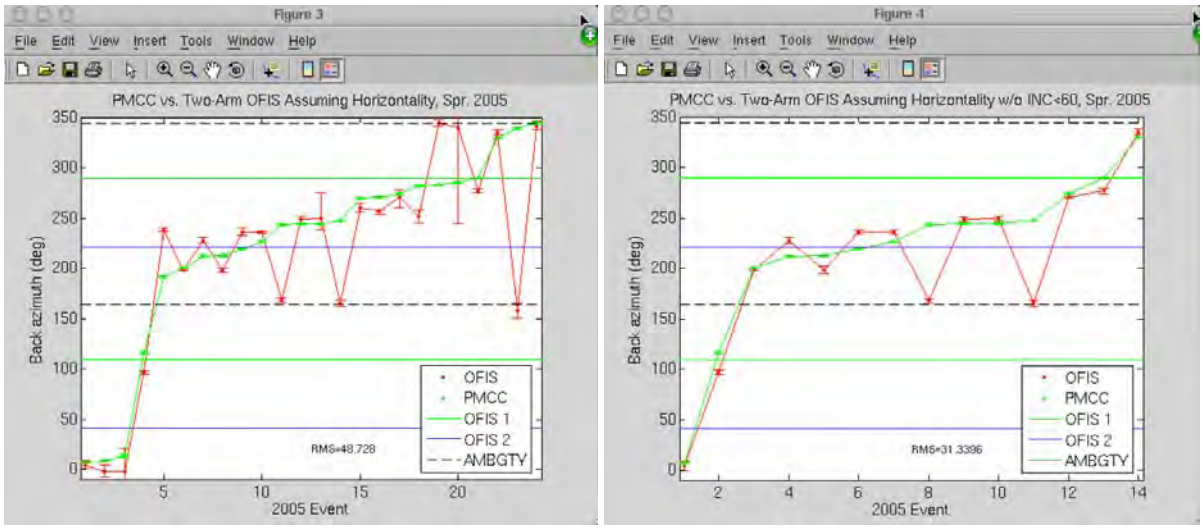

Figure 8. Comparison of the 2-120 OFIS and the I57US (PMCC) back azimuths determined for signals recorded during spring 2005. Events are sorted by PMCC back azimuth. (a) Results for all 24 signals. (b) Subset of signals for which the OFIS-determined incidence angle was 60-90°. PMCC was only permitted to search between θ_i = 60-90°.

We determined the true signal orientation by the co-located, 1.4-km aperture I57US microphone array using the PMCC method. Only 5 elements were operating during this time, so the accuracy of the reference signals is not well known. We also only allowed PMCC to search for signals with incidence angles θ_i = 60-90°. When we compare the back azimuths determined by PMCC and the 2-120 configuration assuming horizontally traveling signals, we see that there is considerable scatter with an RMS error of 49° (Figure 8a). However, when we use our algorithm with the 3-120 configuration, we identified many signals for which the θ_i<60°. Figure 8b shows the subset of 2-120 and PMCC back azimuths for θ_i>60°. This more valid comparison yields an RMS error of 31°. Better results were generally obtained with the 2-90 configuration (Walker et al., 2004).

A 3-120 configuration yields much better results (Figure 9a). By simply assuming horizontally traveling signals, the RMS error was reduced by half to 16°. By only considering those signals with θ_i = 60-90°, the RMS error is further reduced to 9° (Figure 9b). The RMS error decreases to 7° when we use the back azimuths determined during the full search over trial θ_b and θ_i (Figure 9c).

The results in Figure 9 suggest that incidence angle is a very important quantity that should not be ignored if back azimuth accuracy is desired. These results also raise the question of how well incidence angle is resolved. Figure 10 shows a color plot of the misfit as a function of back azimuth and the incidence angle for a nearly horizontally traveling signal and one with a moderate incidence angle. A single orientation is not well resolved in (b), which may be due to a fast moving source (e.g., meteor), a signal with a narrow bandwidth, or a poor resolution of incidence angle for that particular signal orientation. A resolution kernel as a function of the incidence angle and configuration must be further investigated. The distinct separation between orientations in (b) may be due to the PMCC limit of θ_i = 60-90°.

(a) (b)

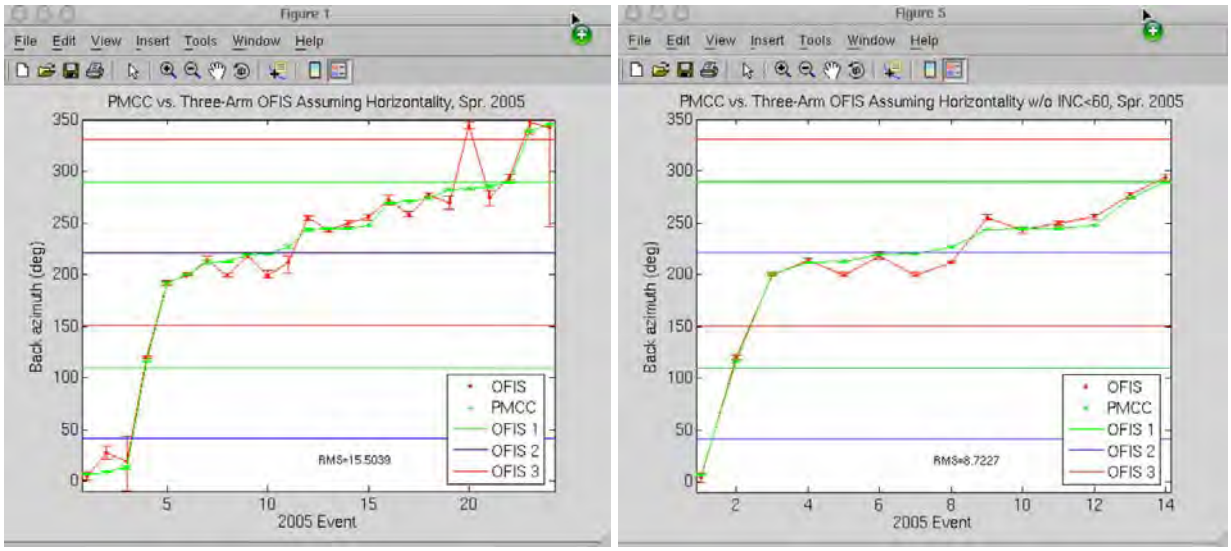

(c) (d)

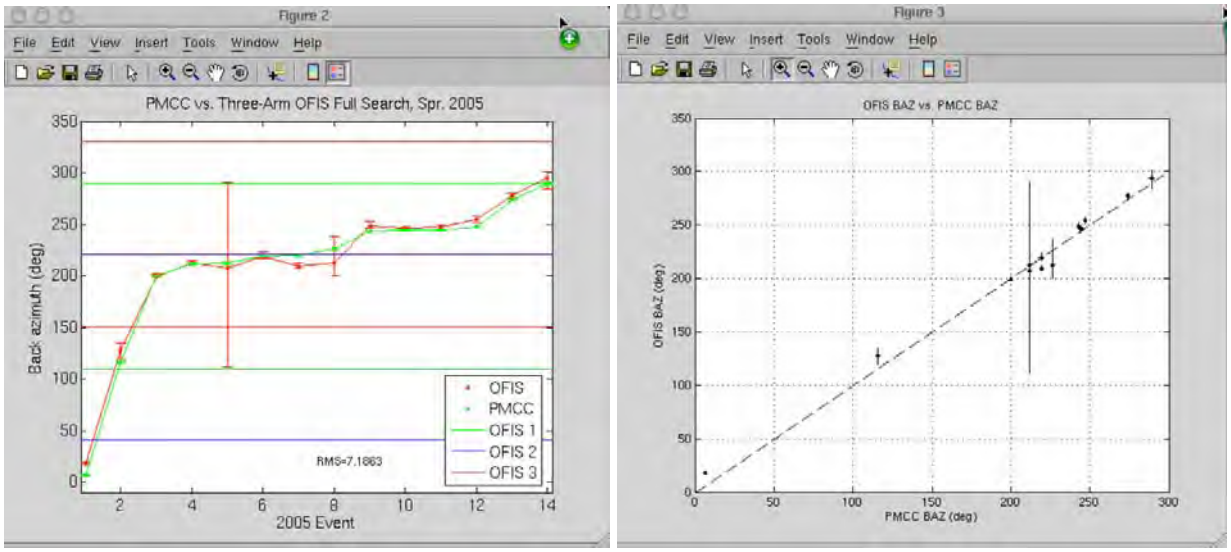

Figure 9. Comparison of 3-120 OFIS and I57US (PMCC) back azimuths. Shown are (a) all results assuming horizontally traveling signals, (b) subset of (a) for signals with θ_i = 60-90°, (c) same events as in (b) but using back azimuths determined during full search over θ_b and θ_i, and (d) plot of OFIS back azimuth in (c) versus PMCC back azimuth.

The results in Figure 9 suggest that a three-arm OFIS in a 3-120 configuration can determine the back azimuth and incidence angle of an incoming signal. The close similarity to back azimuths determined via the PMCC method, the results in Figure 10, and the limited number of I57US elements used raises the question of the accuracy of our PMCC results. Walker et al. (2004) found that the orientation of each OFIS to within 0.3°. They also performed an analysis on the I57US orientation by using PMCC to analyze the signals of 16 known regional mine-blast events from θ_b = 280-340°, and found that the theoretical θ_b matched those from PMCC within 10°. It is therefore possible that the OFIS back azimuths and incidence angles are more accurate than those provided by PMCC.

(a) (b)

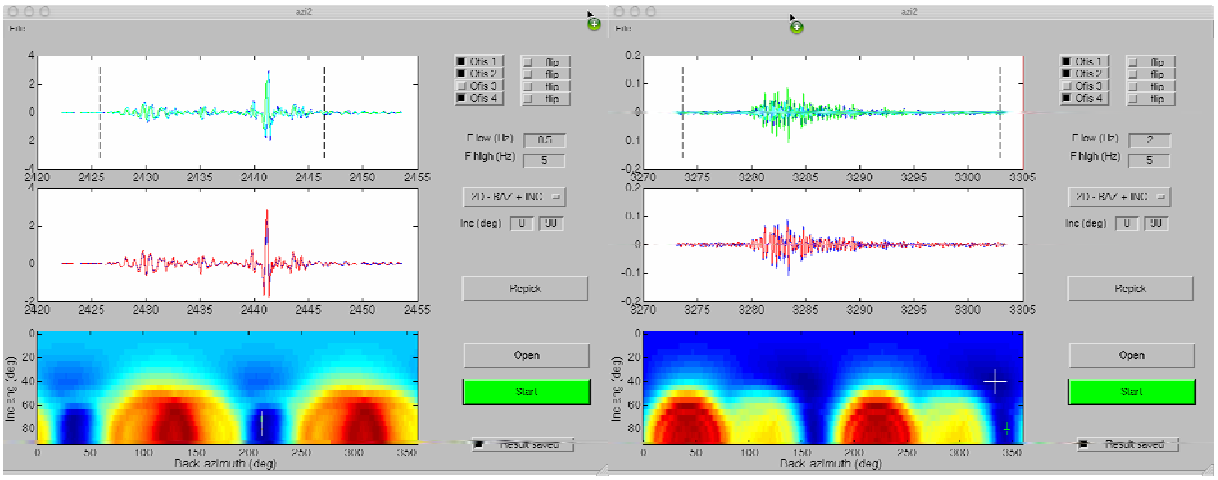

Figure 10. Resolution of incidence angle and source motion for signals of unknown origin for a 3-120 configuration. Shown are results of a full search over trial θ_b and θ_i for a nearly horizontally traveling signal (a) and one with a moderate incidence angle (b). Axes are as in Figure 7, except the lower plot shows the log of the misfit (blues are lows) as a function of trial θ_b and θ_i. The white and green pulses indicate the OFIS- and PMCC-determined signal orientations, respectively.

Figure 9d shows that most of our results were for signals from the western hemisphere. Ideally one needs to repeat such a study at a field site with a larger variety of known source locations.

Problems and Solutions that Affect OFIS Uptime

There are two problems that we have identified that affect OFIS uptime. The first and most problematic is that due to differential polarization change of the split laser beam in the two fibers wrapped around the OFIS. The fringe signal *y*, which is necessary to recovering the pressure change, is created by the interference between the recombined laser beams from each of the two fibers wrapped around the OFIS. This interference is associated with the change in the differential optical-fiber path length. In order to obtain *y* the laser in the two fibers must have the same polarization when they are recombined just before the photodetector. If one of the fibers has a polarization that is orthogonal to the other, no interference will occur and the fringe signal will not develop. We have confirmed that the difference in the polarization between the two fibers changes greatly as a function of OFIS temperature. This is especially a problem during the hot summer months.

Our OFIS prototype tube is black. Consequently, it heats up greatly in the sun. When clouds pass overhead, it cools off. At times the polarizations would become mutually orthogonal, sometimes several times per hour. We found that covering the tube with a white polyvinyl chloride (PVC) outer covering eliminates a great deal of OFIS temperature fluctuation and subsequent differential polarization change. However, ambient air temperatures still greatly affect this. We experimented with an alternative solution using a polarization scrambler. This instrument rapidly changed the input polarization and we applied a low-pass filter on the photodetector output. Unfortunately the polarization was changing too greatly for this technique to work.

We also experimented with a diversity detector. In this solution, one uses a series of polarizing beam splitters to recombine the two fibers along three different polarization angles. Each recombined beam goes to a photodetector. We confirmed that this technique with two recombined beams/photodetectors works by visually monitoring the two ellipses in the field during the course of a day. When one ellipse began to collapse, the other ellipse got bigger. This is currently our preferred method for dealing with polarization change, and we are in the process of evaluating a variation of this solution that will enable us to work with only one composite ellipse (rather than two or three).

The other problem we encountered is spiking in the pressure data. The problem is the worst beginning at sunset when the outside temperature begins to fall rapidly, but continues well into the early morning of the following day.

We have identified the source to be creaking between the fiber and OFIS silicone tube. This creaking has been demonstrated in the laboratory, and occurs when the grip of the fiber around the tube is loosening. Such a situation occurs most evenings at sunset when the falling temperature cools the tube causing it to shrink. This problem is far worse on OFIS arms that we have moved in the field from their originally deployed position. We twisted a problem OFIS arms to tighten the grip between the fiber and the silicone. This greatly reduced the spiking problem, although itchanged the calibration factor (and possibly calibration consistency along the OFIS). We believe a pressurized OFIS silicone tube at ~1 psi above the ambient will be enough to eliminate the spiking problem and preserve the consistency in calibration.

CONCLUSIONS AND RECOMMENDATIONS

We confirm that three OFIS arms with angular separations of 120° and centers separated by 77 m are fully capable of resolving the back azimuth of telesonic infrasound signals that have a good signal-to-noise ratio with the algorithm we present above. Tentative results also suggest that a 3-120 configuration can also resolve the orientation of signals with moderate incidence angles, although this needs to be confirmed by additional analyses. For two OFIS arms, an angular separation of 90° provides better back azimuth (and probably incidence angle) resolution and a faster algorithm speed than for an angular separation of 120°. We suggest that a five-arm OFIS with arms laying on the ground, azimuth separations of 72°, and an aperture of 200 m provides the best resolution in back azimuth and incidence angle for infrasound signals with a central frequency of 2-5 Hz.

Our results are highly significant because they indicate that a multi-arm OFIS, acting as a directional antenna, is capable of providing the same directional information as an array of conventional rosette filters while covering much less space. Conventional arrays rely on time delays between elements to determine θ_b and θ_i, requiring significant separation between elements (several hundreds to thousands of meters) to produce time differences. The OFIS reliance on directional frequency response (and to a less extent time delays) provides the same information within a more localized area (Figure 2)—a significant advantage when space is at a premium (e.g., on island sites) and maintenance costs are high.

ACKNOWLEDGEMENTS

We are indebted to Matt Dzieciuch, Petar Durdevic, and Pat Walsh and for their time and effort in software/hardware development and field work. We thank the US Army Space and Missile Defense Command for sponsoring this project (Contract No. W9113M-05-1-0020).

REFERENCES

Cansi, Y. (1995), An automatic seismic event processing for detection and location: the P.M.C.C. method, *Geophys. Res. Lett*. 22: 1021.

Hedlin, M.A.H., B. Alcoverro, and G. D'Spain (2003), Evaluation of rosette infrasonic noise-reducing spatial filters, *J. Acoustic. Soc. Am.* 114: 1807.

Langston, C.A. (1979), Structure under Mount Rainer, Washington, inferred from teleseismic body waves, *J. Geophys. Res.* 84: 4749.

Silver, P.G., and W.W. Chan (1991), Shear-wave splitting and subcontinental mantle deformation, *J. Geophys. Res.* 96: 16, 429.

Walker, K.T., S. Arrowsmith, J. Berger, M. Hedlin, and M. Zumberge (2004), Resolving infrasound signal back azimuths with arrays of optical fiber sensors, in *Proceedings of the 26th Seismic Research Review*: *Trends in Nuclear Explosion Monitoring*, LA-UR-04-5801, Orlando, FL, 680-687.

Zumberge, M.A., J. Berger, M.A.H. Hedlin, E. Husmann, and S. Nooner (2003), An optical fiber infrasound sensor: A new lower limit on atmospheric pressure noise between 1 and 10 Hz, *J. Acoust. Soc. Am.* 113: 2474.

Zumberge, M.A., J. Berger, M.A. Dzieciuch, and R.L. Parker, (2004), Resolving quadrature fringes in real time, *Applied Optics* 43: 771-775.

UNDERSTANDING WIND-GENERATED INFRASOUND NOISE

Robert Woodward[1], Hans Israelsson[1], István Bondár[1],
Keith McLaughlin[1], J. Roger Bowman[1], and Henry Bass[2]

Science Applications International Corporation[1]
National Center for Physical Acoustics, University of Mississippi[2]

Sponsored by Army Space and Missile Defense Command

Contract Nos. DASG60-03-C-0009[1] and DASG60-99-C-0018[2]

ABSTRACT

We have analyzed wind-generated pressure noise at infrasound stations to better understand the mechanisms of noise generation and possible strategies for mitigating the effects of this noise. Wind and microbaroms are the dominant sources of noise on infrasound stations. Both can cause false signal detections as well as obscure real signals. We have investigated in detail the observed wind and pressure characteristics at International Monitoring System infrasound stations. By understanding better the relationship of wind and pressure, we can design signal detection algorithms which mitigate the impact of wind-generated noise.

We analyzed variations in wind speed and pressure noise over long periods of time (up to two years). The goal of this analysis is to better understand seasonal, diurnal, or other variations in these quantities so that we may better understand their relationship. We see that the ambient pressure noise is highly variable by season, time of day, station and site type. The pressure noise is correlated to horizontal wind speed above a threshold value, and this threshold varies by station and is often between 0.5-1.5 m/s.

We have computed pressure spectra for time periods with different average wind speeds and see relatively consistent spectra, particularly when these spectra are displayed as a function of frequency normalized by wind speed. Wind speed spectra calculated for time periods of relatively high wind speeds often have slopes around -5/3, a characteristic of so called Kolmogorov turbulence. Wind turbulence can vary substantially at the stations, with periods of low winds often having the highest turbulence. Individual stations show substantial variations in wind turbulence as a function of wind direction, which may be related to the terrain and vegetation at the infrasound station.

We have considered two primary approaches to characterizing the relationship between wind and pressure variations. First, we develop an empirical model for pressure noise as a function of wind speed. We find a clear relationship between wind speed and pressure, which varies by station and frequency band. The empirical model is characterized by the slope of the pressure-wind relationship and shows a clear distinction (change in slope) between low- and high-wind regimes, though the wind speed at which this change occurs varies by station. We assess the ability of this model to predict root-mean-square (RMS) pressure variations based on observations of wind. For test cases the standard error of predictions was 3db or less for frequency bands above 0.5 Hz and wind speeds above 1.5 m/s. A key variable is the time varying nature of the empirical model. We also seek to understand how long it takes to characterize the wind speed-to-pressure relationship and to determine how frequently it must be updated.

We have used a statistical framework for our second approach to characterizing the wind speed-pressure relationship. We analyze extreme values of wind and noise (i.e. the tails of the distributions of these observations) via copula functions. The copula function analysis lets us characterize the joint probability distribution of wind and pressure variations. By understanding this relationship, we can estimate the probability that large values of pressure are due to wind. This relationship can ultimately be used to design signal detectors with a constant false alarm rate (for wind-induced false alarms) by dynamically adjusting detection thresholds based on wind speed.

OBJECTIVES

Our objective has been to improve our understanding of the underlying physical processes responsible for noise at infrasound stations, particularly wind-generated noise. We then leverage this understanding to develop noise mitigation strategies.

RESEARCH ACCOMPLISHED

Data

We have used data from virtually all current infrasound stations (Figure 1). All of these stations are arrays consisting of 4 to 9 elements. Twenty-nine stations are part of the International Monitoring System (IMS) network, and five are experimental stations. The stations contain different combinations of microbarometer, digitizer, and wind filter design, as well as different array geometries. Data are obtained from the data archive operated by the Research and Development Support Services (RDSS) project of the US Army Space and Missile Defense Command's Monitoring Research Program (MRP)

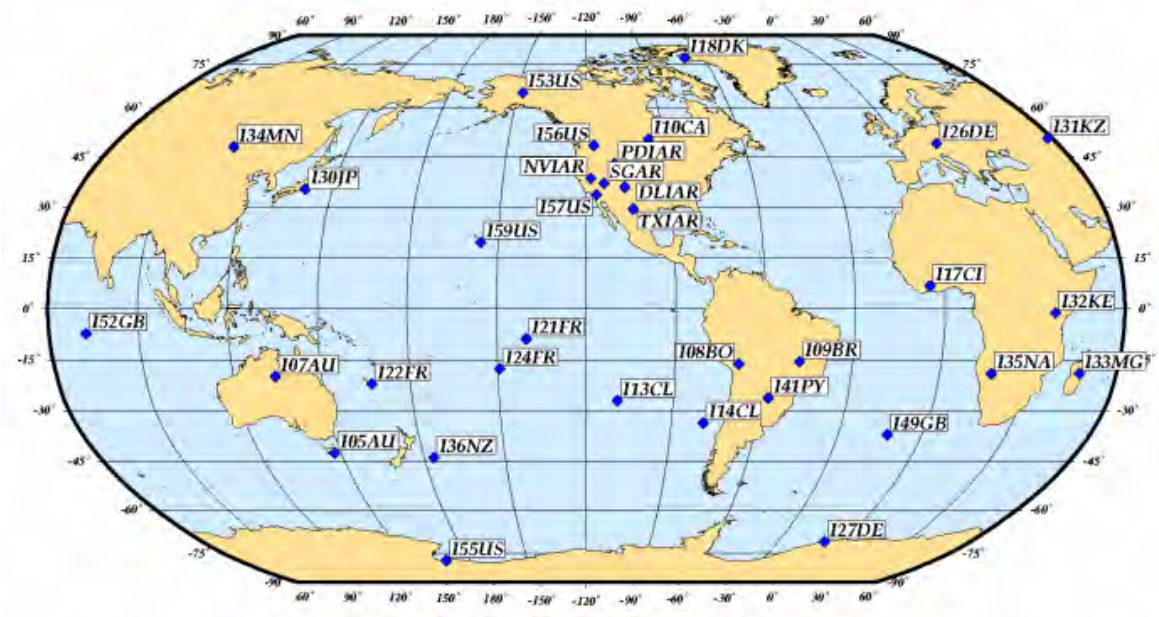

Figure 1. Map showing a superset of the infrasound stations used in our analyses.

Infrasound Noise

In order to characterize the ambient noise, power spectral density was measured at 28 stations (Figure 1) using the approach of Bowman et al. (2004a, b, 2005a, b). Data were analyzed from January 20, 2003 through December 31, 2004, from 21 consecutive 3-minute segments of data taken four times daily, beginning at 06:00, 12:00, 18:00, and 24:00 local time, resulting in 1,476,309 spectral estimates. Three-minute windows were used to minimize smoothing of the amplitude distributions, while permitting estimation of the longest periods of interest. Spectra were calculated using *geotool* (Coyne and Henson, 1995) and the method of overlapping fast Fourier transforms. A Hanning taper was applied to the outer 10% of each data window. Spectra were corrected by *geotool* for instrument responses in the RDSS data archive database.

Power Spectral Density (PSD) for noise in four seasons and at four times of day are shown in Figure 2 for station I57US at Piñon Flat, California. All spectra calculated for each time and season interval are plotted as yellow lines, the median for each interval as a black line, and the 5^{th} and 95^{th} percentiles of the distribution as red lines. Green lines show the median of all spectra for all times and seasons for 15 stations having a complete year of data, and thus serve as references for comparison among time and season intervals and among stations. At any time, season and frequency the PSD varies by four to five orders of magnitude. Seasonal and diurnal variations are evident among the subplots. For example, the median noise level is similar to the network median at 6 AM in spring, but is almost an

order of magnitude lower at the same time in summer, and is an order of magnitude higher in the same season at noon. Plots similar to those in Figure 2 are provided for nearly all current infrasound stations (28 in all) in Bowman et al. (2005b).

Relationship of Micropressure and Wind

It is well known that infrasound noise increases as wind speed near the sensor increases. For example, Figure 3 illustrates wind-induced noise due to diurnal variations at I08BO, Bolivia. The large amplitudes on the micropressure channels due to wind can cause false signal detections. Conversely, the wind-generated noise can reduce signal coherence across the array and result in no detections at all, particularly for detection algorithms which exploit the across-array coherence of signals.

We have characterized the gross relationship between noise and horizontal wind speed at all stations having wind speed data. Wind speeds are calculated for the same time intervals used for the ambient noise analysis reported above (Bowman, 2005a, b). This provides nearly a million simultaneous micropressure and wind speed observations.

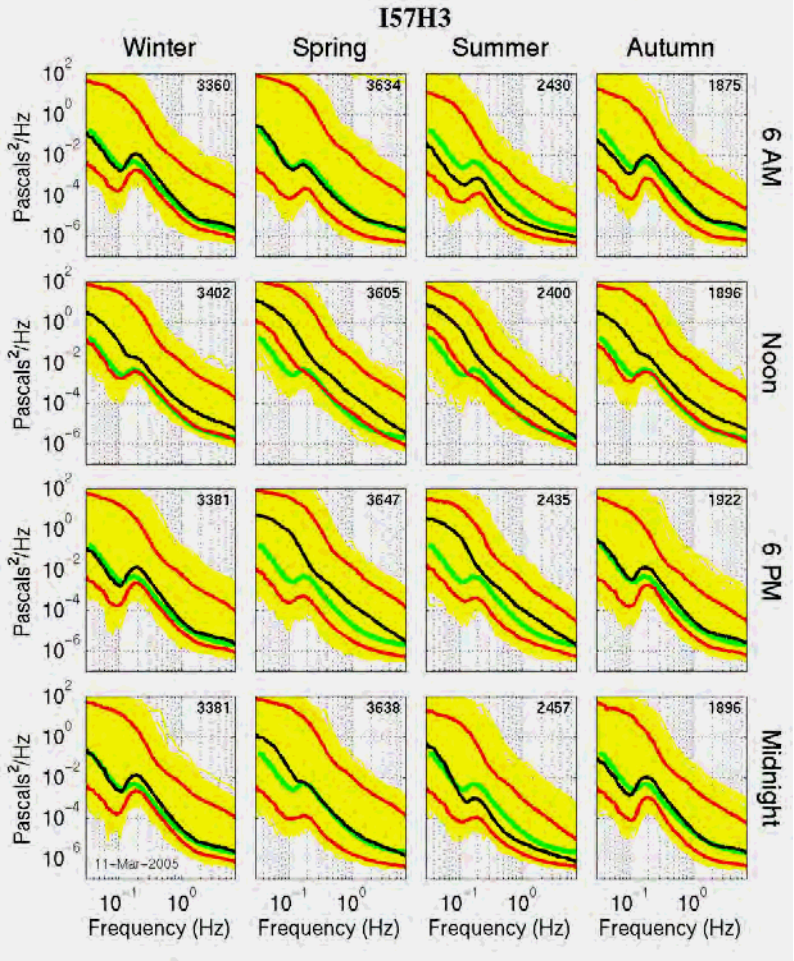

Figure 2. Power Spectral Density for I57US (I57US), Piñon Flat, California. The number of spectra in each plot is shown in the upper right. The rows group plots by time intervals, the columns group plots by seasons.

Figure 4 shows a comparison of noise at 0.2 Hz versus wind speed for several stations. Similar plots for a larger set of 22 stations which have wind speed data are provided in Bowman et al. (2005b). Examining the noise versus wind speed observations for all 22 stations indicates there is wide variability in the range of wind speeds and the range of associated micropressure fluctuations. The most basic observation from this analysis is that noise at most stations

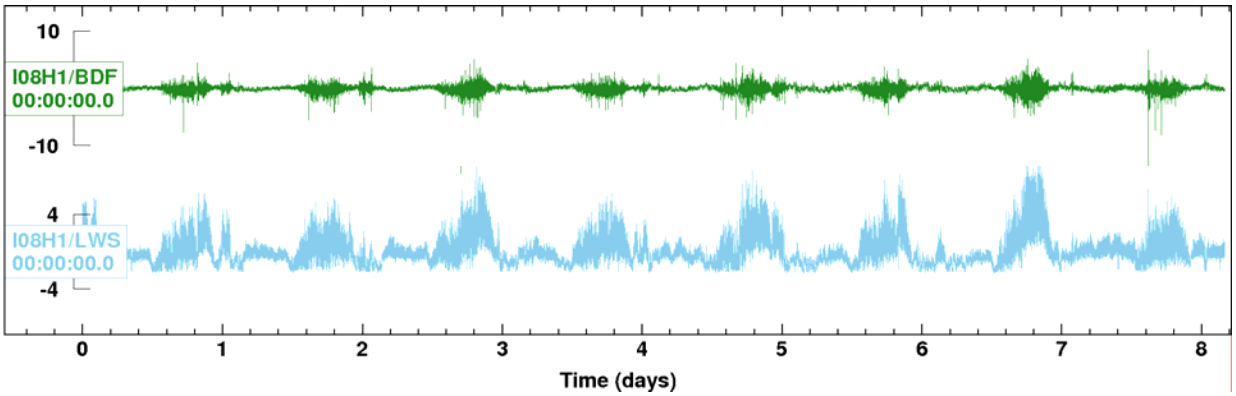

Figure 3. Micropressure data (top trace) and wind speed (bottom trace) at I08BO between May 1 and 8, 2005. Note how the micropressure noise levels increase with increasing wind speed.

increases gradually up to some wind threshold, and then increases more rapidly at higher wind speeds. Note that at stations I55US (shown in Figure 4) and I27DE (not shown) in Antarctica this wind threshold is at a higher value, possibly due to the fact that the wind filters at these stations are buried in snow at least part of the year. The relationship between infrasound noise at 1 Hz and wind speed is similar to that at 0.2 Hz (Bowman et al., 2005b).

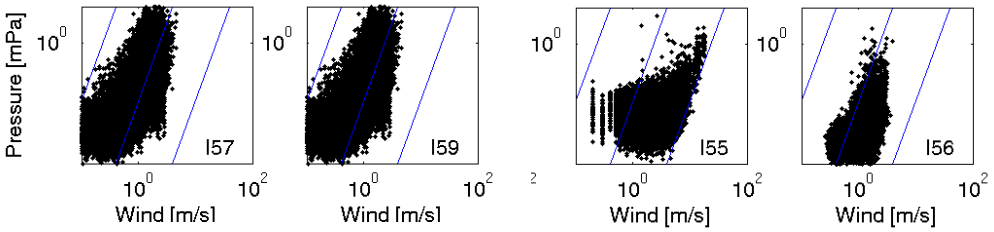

Figure 4. Relationship between ambient infrasound noise at 0.2 Hz and horizontal wind speed, on log-log scales. The blue reference lines are spaced in decade intervals in wind speed and aid in comparison among plots. Vertical groupings of data points for I55 are the result of truncation of wind speed to integer values (in m/s) for part of the observation period.

Wind and Micropressure Power Spectra

We have investigated the micropressure and wind speed power spectra in greater detail using a representative subset of IMS stations: I08BO, I17CI, I18DK, I22FR, I24FR, I31KZ, I33MG, I34MN, and I35NA (Israelsson and McLaughlin, 2005). For these analyses we used a data window of 3 min. for consistency with ambient noise spectral calculations reported above (Bowman et al., 2005a).

Figure 5 (top) shows averaged wind speed spectra at I08BO at wind speeds between 3-7 m/s. The drop off rate of the scaled spectra for I08BO have a slope of approximately -5/3 (heavy dashed lines in the diagrams) predicted for Kolmogorov turbulence of the inertial regime. Further, the spectra for different wind speeds, when scaled by wave-number (frequency/wind speed), collapse into a narrow spectral density range (Figure 5, bottom). Similar results were obtained for stations I24FR and I35NA, while the slopes of spectra for I31KZ and I34MN clearly deviated from -5/3 throughout the wave-number range. The wave-number intervals with slopes ~ -5/3 correspond to wavelengths between 10-100 m.

The IMS stations analyzed here are equipped with two types of wind sensors, cup anemometers (Campbell) and ultrasonic sensors (Gill). The overall shape of average wind spectra at the five stations with cup anemometers are similar, whereas there is more variation in shapes among average spectra at the four stations using ultrasonic sensors. The power spectra for stations with cup instruments tend to flatten out at high frequencies for low wind speeds less than about 2 m/s, which might be caused by inertia of the instruments.

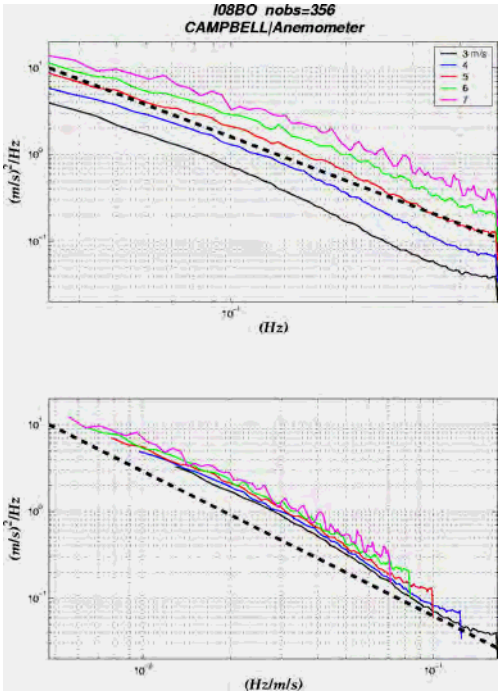

Figure 5. Comparison of power spectra for wind speed fluctuations at different wind speeds (3-7 m/s) at station I08BO as a function of frequency (top) and as a function of wave-number (bottom). The heavy dashed lines have a slope of -5/3

Power spectra of micropressure are binned by mean wind speed, followed by stacking of spectra in each bin on a daily basis. The stacking reduces the scatter in the data and was motivated by the pronounced diurnal variation of the wind speed at most of the stations. Figure 6 shows averaged micropressure power spectra, as a function of frequency (top) and as a function of frequency/wind speed, (bottom), for wind speeds between 3 to7 m/s. The dashed lines in the lower panel of Figure 6 has a slope of -7/3, which is expected in the inertial range of turbulence from dimensional analysis, although this drop off in power with wave-number is not generally agreed upon (Shields, 2005). When plotted as a function of wave-number the spectra lie closer together at low wave-numbers between about 0.01-0.04 m^{-1}, where the spectra drop off with a slope of approximately -7/3. Similar results were obtained for I18DK, I34MN, and I35NA. Wave-numbers between 0.01 and 0.04 m^{-1} correspond to wavelengths between 25-100 m, in which range wind spectra for I08BO drop off with a slope around -5/3. This suggests that the I08BO spectra at low wave-numbers, for both wind and micropressure, are in qualitative agreement with standard models for the inertial subrange of turbulence for the two stations.

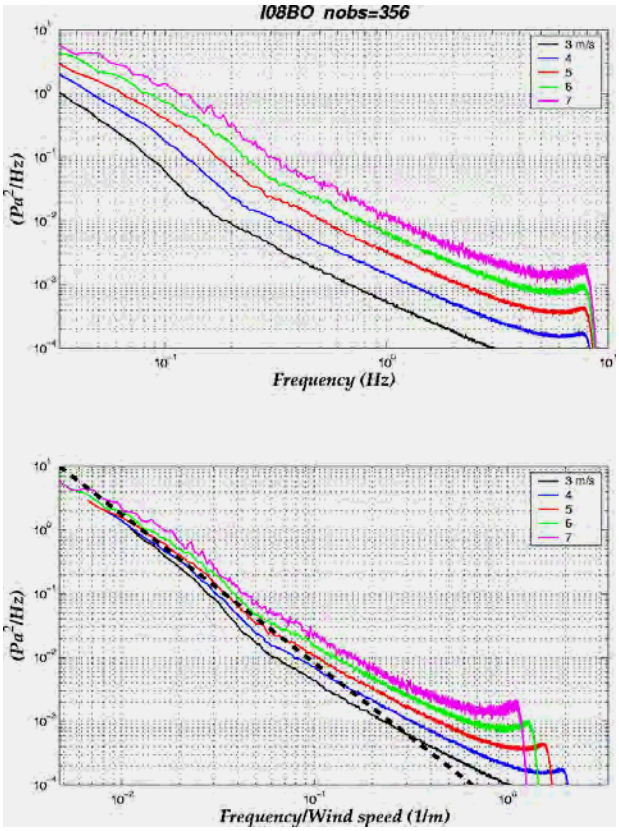

Figure 6. Comparison of power spectra for micropressure for different wind speeds (3-7 m/s) at station I08BO as a function of frequency (top) and as a function of wave-number (bottom). The heavy dashed line is provided for reference and has a slope of -7/3.

Prediction Using Empirical Relationship of Micropressure and Wind

As noted earlier, sudden large amplitudes on micropressure recordings can be due to signals or noise from wind gusts. In this section we attempt to exploit the high correlation between micropressure and wind speed to predict micropressure amplitudes from wind speed. Such predictions would allow us to identify features in the micropressure record that are explained by wind (potential false alarms) and features that cannot be explained by the wind (potential signals).

For these predictions we calculated RMS amplitudes of micropressure recordings in six non-overlapping one octave frequency bands (0.01-0.05, 0.05-0.10, 0.10-0.5, 0.5-1.0, 1-2, and 2-4 Hz) using a data window of 600 s with a 50% overlap between consecutive windows. In addition, the mean wind speed and its NS and EW components were calculated along with the RMS of the wind speed fluctuations for the same data windows. Figure 7 shows the logarithm of RMS micropressure as a function of the logarithm of average wind speed, for station I08BO. The logarithmic transformation enhances resolution at low wind speeds. We use locally robust regression to estimate the relationship between RMS micropressure and wind, and this is shown by the dashed line in Figure 7.

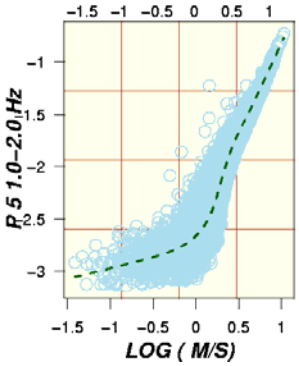

Figure 7. RMS micropressure (1-2 Hz band) as a function of average wind speed at I08BO. The data points represent the logarithms of RMS micropressure and wind measurements.

A comparison of the estimated RMS (1-2 Hz) micropressure and mean wind speed relationships for nine different stations are shown in Figure 8. The estimates have similar slopes at high wind speeds, and large variation at low wind speeds where the levels are affected by the microbarom levels.

In prediction experiments we used data for the first half of the month to estimate relations between micropressure and wind. The estimates were then used to predict RMS micropressure amplitudes during the second half of the month. Figure 9 shows an example of time domain micropressure predictions. Predicted RMS amplitudes in the frequency band 1-2 Hz at I08BO during the second half of October 2004 are compared with the actual amplitudes and the mean wind speed. The predictions were based on a relation between RMS amplitudes and mean wind speed estimated with locally robust regression from observations during the first half of October 2004. The traces for mean wind speed, observed and predicted RMS amplitudes (three bottom traces) are quite similar with a clear diurnal variation. The ratio of the predicted-to-observed pressures (in dB) is plotted in the top trace and the difference (predicted – observed) in the trace below. The ±3dB error levels are marked as dashed lines on the top trace. The errors, just like the wind speed and RMS amplitudes, show a diurnal variation. The relative errors (see top trace) are generally larger during periods of low wind speeds during local night time than during local day time with high wind speeds. The magnitude of the errors (e.g. second trace from top) is greatest in the day time.

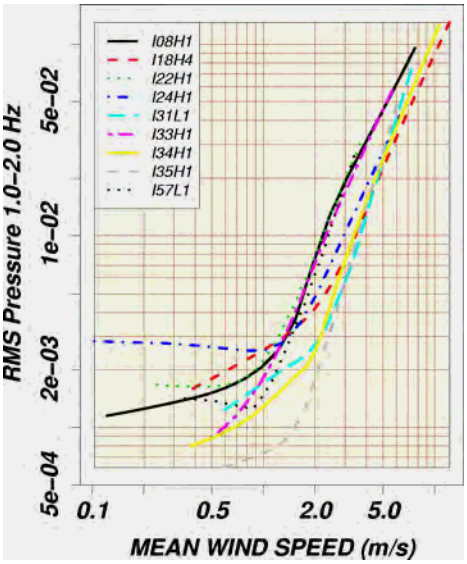

Figure 8. Estimated relations between RMS micropressure (1-2 Hz) and mean wind speed for October 2004.

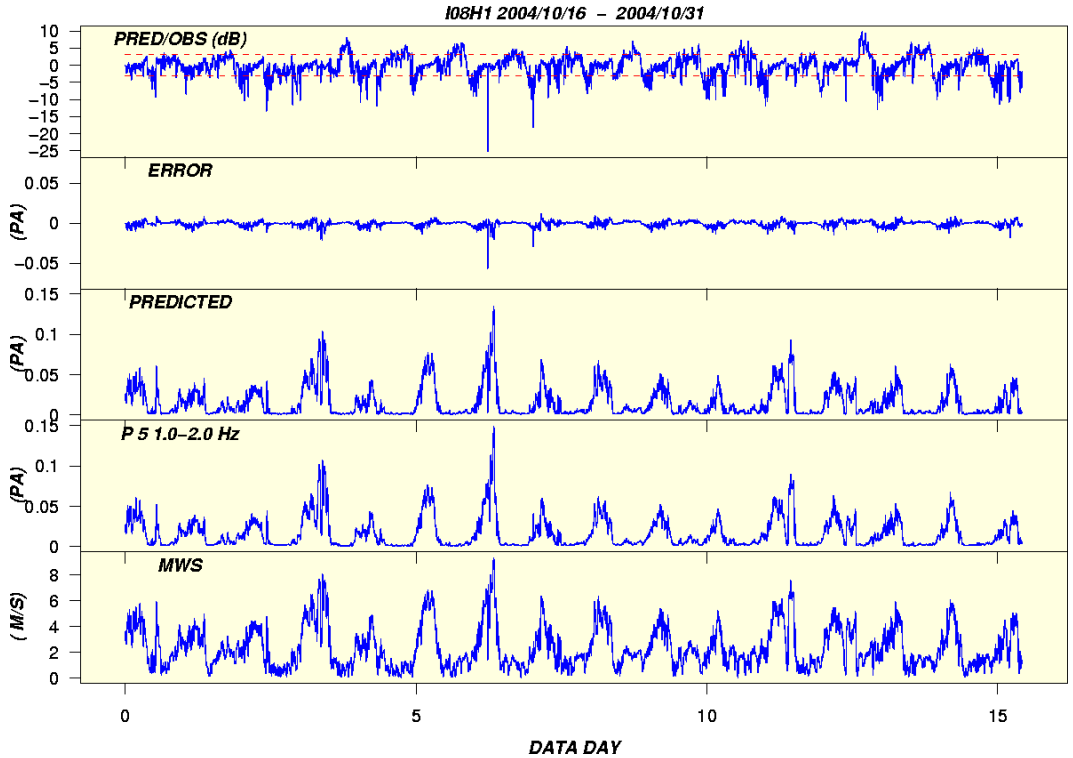

Figure 9. Comparison of observed and predicted RMS amplitudes (1-2 Hz) at I08BO during Oct 16-31, 2004. The traces for mean wind speed (bottom trace), observed RMS amplitudes (2nd trace from bottom), and predicted amplitudes (3rd trace from bottom) are quite similar. A clear diurnal variation is obvious in the ratios of predicted/observed amplitudes (top trace) and amplitudes errors, observed-predicted, (2nd trace from top).

The dependence of prediction error on wind speed indicates that the estimated standard errors are generally larger at lower wind speeds where the relation between wind and micropressure is less well defined and is subject to changes

in the microbarom level. For the same reason errors near the microbarom peak are also larger. Further discussion of these results, as well as polynomical-based regression results, can be found in Israelsson and McLaughlin (2005).

Prediction Using Statistical Relationship of Micropressure and Wind

As the above discussion makes clear, the relation between wind and micropressure is non-linear – at low wind speeds micropressure variations are less dependent on the wind, while at higher wind speeds the micropressure variations are dominated by wind-induced effects. In other words, the wind-micropressure relation exhibits tail-dependence structure. A weakness of standard regression analysis, as used in the preceding section, is that it cannot cope well with tail-dependence structures. As an alternative, we apply copula theory, a non-linear statistical framework to study non-Gaussian, non-linear dependence structures. Copula theory allows us to form the joint probability distribution of wind and micropressure, from which we can derive non-linear regression curves at any given percentile level. The quantile regression curves could eventually serve as design curves for a constant false alarm rate (CFAR) detector.

A copula is a function that joins or 'couples' a multivariate distribution function to its one-dimensional marginal distribution functions. For a formal framework of copulas see Joe (1997), Nelsen (1999), and Drouet-Mari and Kotz (2001). The basic idea behind the copula formalism is to separate dependence and marginal behavior between elements of multivariate random vectors. For simplicity, we consider bivariate copulas. A great many examples of copulas can be found in the literature and most of the copulas are members of families with one or more real parameters. One important class of copulas is the normal or Gaussian copula. Another important class of copulas is the Archimedean copulas. We discuss the various copulas in much greater detail in Bondár (2005), and confine our discussion here to the use of the Gumbel copula, in the Archimedean class. Note that the Gumbel copula is also an extreme value copula, and exhibits positive upper tail dependence.

We have determined the 50% and 95% quantile regression for the micropressure channel at I08H1 versus a variety of wind, or wind derived quantities, including wind speed, longitudinal wind speed, mean wind speed, and the Bernoulli trace. We generate the 'Bernoulli' trace from the average wind speed and the radial (longitudinal) wind component as $w_{avg} * (w_r - w_{avg})$. This formula follows from Bernoulli's principle, which states that for a laminar flow, small variations in air pressure are proportional to the full derivative of wind speed: $dp \sim w*dw$ where dw denotes the wind fluctuation. While Bernoulli's principle ignores turbulence, it might still serve as a good approximation for the micropressure variations.

In our regressions we used data for each day in the data set shown in Figure 3 and considered a range of copulas. Using the Gumbel copula we obtain good quantile regression fits to the micropressure and Bernoulli data, so we limit the following discussion to these particular results. Furthermore, to facilitate the copula formalism, we work with the envelopes of the various traces.

Figure 10 shows the corresponding quantile regression curves obtained from the Gumbel copula and the micropressure and Bernoulli trace data. The value of copula parameter α and the misfit between the empirical and theoretical K(t) distributions are given in the legends. In some cases (e.g. May 7) the copula fitting procedure suggested that micropressure variations are independent from the wind. This is most likely related to data problems due to the inertia of anemometers at low wind speeds (calms), and to the insufficient sampling of the distribution tails. In order to measure tail dependence, the data set should be large enough to provide a representative sample from the tails of the

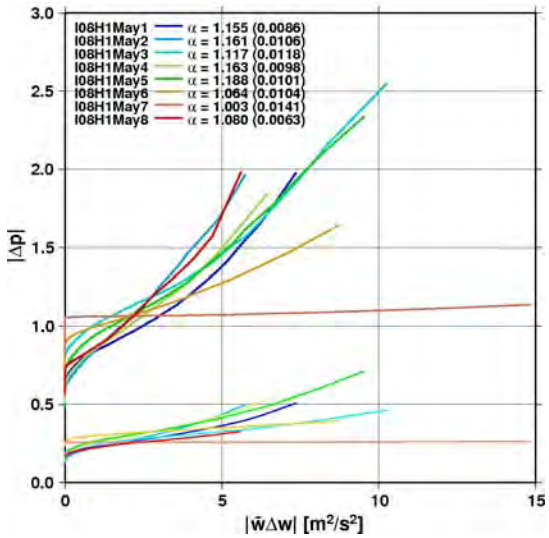

Figure 10. Median and 95% quantile regression curves (lower and upper curves, respectively) of absolute micropressure variations subject to Bernoulli trace at I08BO between May 1 and 8, 2005 derived from the Gumbel copula.

marginal distributions. Furthermore, true signals may contribute to the tails; hence the data set used to derive the regression curves subject to wind should avoid periods with infrasonic signals.

We used the quantile regression curves obtained for I08BO on May 1, 2005 to predict absolute micropressure variations for the rest of the days. Figure 11 shows the absolute micropressure and the Bernoulli traces for May 1, 2005. The green lines in Figure 11 are detections reported by the International Data Centre (IDC), based on use of the Progressive Multi-Channel Correlation (PMCC) algorithm (Cansi, 1995). Unlabeled PMCC detections indicate noise detections. This day should be suitable dfor deriving regression curves, since PMCC made only two signal detections (labeled green lines) on this day.

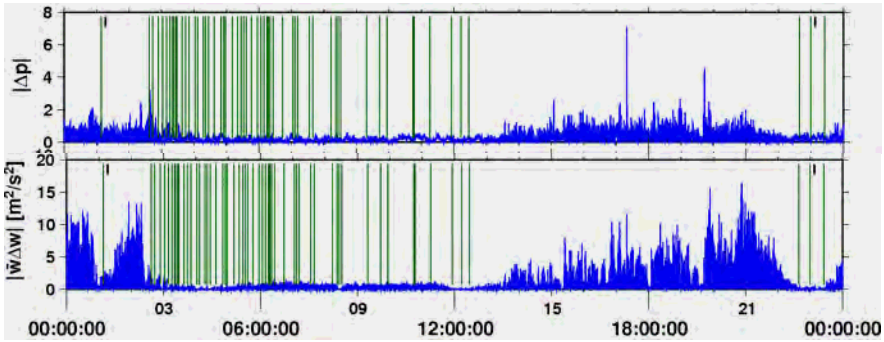

Figure 11. Absolute micropressure (top) and Bernoulli traces (bottom) at I08H1 on May 1, 2005. Green lines denote PMCC detections; unlabeled detections are noise detections.

Figure 12 shows the absolute micropressure variations and the predictions, based on the Bernoulli trace, for May 2-8, 2005 at I08H1, predicted from the corresponding Gumbel quantile regression curves from May 1, 2005. Note that the 95% quantile regression is interpreted such that 95% of the times the absolute micropressure variation is below the 95% quantile regression. If the micropressure variation exceeds this threshold, then it is not explained by the wind.

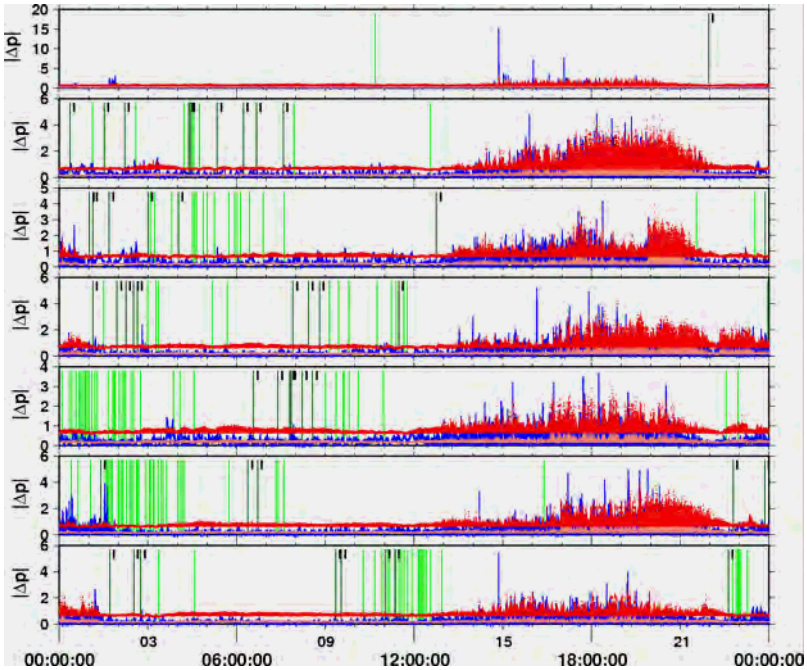

Figure 12. Absolute micropressure (blue) at I08H1 for May 2 to 8, 2005 (bottom to top), with predictions from the Gumbel median (light red) and 95% (dark red) quantile regressions. Regressions based on the micropressure and Bernoulli traces on May 1, 2005. Green lines indicate PMCC detections reported by the IDC.

We are only able to characterize the low frequency micropressure versus wind relations due to the low sample rates used for the wind sensors at IMS stations. Thus, during calm periods, although for most cases the micropressure variations appear to be explained by the wind, the coherence across the array may be carried in higher frequency bands, allowing PMCC to make detections. Similarly, the peaks above the 95% quantile curves could indicate data

problems and may not be coherent in the whole infrasonic frequency band. Nevertheless, there are instances when the micropressure fluctuations persistently exceed the 95% quantile curves without producing PMCC detections. These may indicate missed signals. A more comprehensive discussion of these results, as well as our overall application of a statistical approach to predicting micropressure variations from wind observations, can be found in Bondár (2005).

CONCLUSIONS AND RECOMMENDATIONS

In this study we focused on developing and validating the methodology to characterize the relations between wind and micropressure. We have demonstrated the practical value of wind measurements for understanding the structure of infrasonic noise.

We applied a common methodology to estimate the ambient infrasound noise. This investigation took advantage of the availability of infrasound data on the rapid-access RDSS data archive. These analyses indicate that the median noise amplitude at a given station and frequency may vary by two orders of magnitude depending on time of day or season and may vary among the stations by a factor of about 15 at 0.2 Hz and about 40 at 1 Hz. Ambient noise clearly increases with horizontal wind speed, particularly above a threshold wind speed (which varies among stations). To ensure that the full range of inter-station variability in the noise-wind relationship is captured we recommend that ambient noise at new stations be estimated as data become available. Further, all of the results described here are critically dependent on accurate station parametric (e.g. amplitude and phase response) and environmental (e.g. vegetation at site) metadata. We recommend continued efforts to compile and maintain these metadata.

We found that the overall dependence of micropressure on the mean wind speed is similar for all frequencies and mean wind speeds. At low wind speeds, less than about 1 m/s, there is only a moderate increase in micropressure as the wind speed increases. At high wind speeds, above 2 m/s or so, the micropressure increases rapidly with increasing wind speed. For wind speeds above about 2 m/s the effect of the wind on the micropressure is much larger than that of microbaroms at the stations studied here.

The close correlation between micropressure power spectra and wind speed motivated experiments to predict micropressure amplitudes in the time domain from the mean wind speed. Such predictions can serve to assess the probability that high amplitude micropressure signals are generated by wind gusts or by other sources. We presented two methods for making predictions based on independent estimates of micropressure and wind speed relations. In the first method, we used locally robust regression to model the relationship of mean speed to micropressure based on data from a two week period. We then applied this relationship to data during the subsequent two weeks. The micropressure predictions based on the regression estimates gave similar results for micropressure during wind speeds above 1.5 m/s, with standard errors of less than 3dB for RMS amplitudes in six frequency bands covering frequencies between 0.05 – 4 Hz.

In our second method for making estimates of micropressure from wind speed observations we used a statistical methodology, based on copula theory. We found that the dependence structure of micropressure variations is best described by the Gumbel copula that belongs to the family of Archimedean copulas. The tail-dependence structure described by the Gumbel copula fits the observations well. That is, infrasonic noise becomes dominated by local winds when wind speeds exceed a threshold level. The copula formalism allows us to construct the conditional probability distribution of absolute micropressure subject to wind statistics, and derive quantile regression curves at any given percentile level. The quantile regression curves can serve as design curves for a constant false alarm rate detector, as well as quantify the probability of a detection being a real signal.

In order to derive a robust estimate of the quantile regression curves, the data set must be large enough, preferably void of true signals, to provide sufficient sampling of the tails of the marginal distributions. Our experience shows that at least one day of data is required to get reasonable estimates. The quantile regression curves can then be used to predict micropressure fluctuations for other periods. We found that among the wind statistics we investigated (horizontal wind speed, longitudinal wind speed, average wind speed and Bernoulli trace) the Bernoulli trace offers the most conservative predictions.

The promising results for predicting micropressure from wind speed, as reported here, should be pursued further. For example, we can take azimuth and temporal variations into account, and consider refinements of the regression and statistical models. Issues to consider include investigating the coherence structure of the wind field propagating across the array, investigating the pressure-wind dependence structure at frequencies above 1 Hz, and considering the longitudinal/transverse component of the wind. The systematic application of the regression and copula methodologies to all IMS infrasound stations was beyond the scope of this work. A more comprehensive analysis will be particularly enlightening, given that the IMS infrasound stations are deployed in widely varying environments, with different types of spatial filters.

REFERENCES

Bondár, I. (2005). Statistical Analysis of Wind-generated Infrasound Noise, SAIC Technical Report, in preparation.

Bowman, J.R. (2005a). Meteorological Conditions at Infrasound Stations, *Inframatics*, 9.

Bowman, J.R. (2005b). Meteorological Conditions at Infrasound Stations, SAIC Technical Report SAIC-05/3000.

Bowman, J.R., G.E. Baker, and M. Bahavar (2004a). Infrasound Station Ambient Noise Estimates, SAIC Technical Report SAIC-04/3003.

Bowman, J.R., G.E. Baker, and M. Bahavar (2004b). Infrasound Station Ambient Noise Estimates, Proceedings of the 26th Annual Seismic Research Review, Orlando, FL, 608-617.

Bowman, J. R., G. E. Baker, and M. Bahavar (2005a). Ambient Infrasound Noise, *Geophys. Res. Lett.*, *32*, L09803, doi:10.1029/2005GL022486.

Bowman, J.R., G. Shields, G.E. Baker, and M. Bahavar (2005b). Infrasound Station Ambient Noise Estimates and Models, SAIC Technical Report SAIC-05/3001.

Cansi, Y. (1995). An Automatic Seismic Event Processing for Detection and Location: The PMCC Method, *Geophys. Res. Lett.*, **22**, 1021-1024.

Coyne, J. and I. Henson (1995). Geotool Sourcebook: User's Manual, Teledyne Brown Engineering, Scientific report. no. 1, 01.

Drouet-Mari, D. and S. Kotz (2001). *Correlation and Dependence*, Imperial College Press, London.

Israelsson, H. and K. McLaughlin (2005). Empirical Prediction of Wind Generated Noise at Infrasound Stations, SAIC Technical Report, in preparation.

Joe, H. (1997). *Multivariate Models and Dependence Concepts*, Chapman and Hall, London.

Nelsen, R.B. (1999). *An Introduction to Copulas*, Lecture Notes in Statistics **139**, Springer Verlag, New York.

Shields, F. D. (2005). Low-frequency Wind Noise Correlation in Microphone Arrays, *J. Acoust. Soc. Am.*, 117: 3489-3496.

Data Processing and Analysis

ROBUST REMOTE SEISMIC STATION

Paul B. Akers and Kevin B. Wilbanks

Geotech Instruments, LLC

Sponsored by National Nuclear Security Administration
Office of Nonproliferation Research and Engineering
Office of Defense Nuclear Nonproliferation

Contract No. DE-FG02-04ER83966

ABSTRACT

The United States government sponsors and supports various programs to monitor nuclear explosions through seismic, hydroacoustic, and infrasound data collection stations. These stations are typically deployed in remote areas all over the world. However, current remote data acquisition station technology is limited by (1) poor data quality and reliability and (2) high installation, operation, and maintenance costs. This project was initiated to begin the development of a new generation of compact, remote, seismic data acquisition hardware and software using advanced low power electronics, packaging, and power source technologies. It specifically addresses the problems of data quality and data communications reliability and will reduce deployment, operational, and maintenance costs.

This paper describes the work conducted in Phase I of this project that investigated new technologies and evaluated the feasibility of using these technologies to successfully achieve this project's goals. Specifically Phase I investigated the following: (1) new low power high-resolution analog-to-digital converter (ADC) devices and configurations, (2) overall size and power reduction using low power highly integrated miniaturized components, (3) integrated most of the major subsystems of the station into a single electronics package, (4) new low power satellite and wireless commutations options, and (5) advanced power supplies such as fuel cell technologies. Phase I found that due to the convergence of these technologies driven by the consumer mass market, it was feasible to develop a much improved seismic data acquisition platform for future needs.

Continuing forward into Phase II, this project will result in a working prototype system for a new generation of robust remote seismic stations that will integrate the technologies investigated in Phase I. Using the conceptual designs developed in Phase I, prototype hardware and software will be designed, fabricated, and tested in Phase II. This project specifically pertains to land based borehole seismic data collection stations, however the concepts developed are equally applicable to surface vault type seismic, hydroacoustic, and infrasound data collection stations.

In addition to national security and nonproliferation applications, the hardware and software developed in this project will be directly applicable to commercial earthquake, strong motion, infrasound, and hydroacoustic data acquisition and monitoring. By providing high quality reliable data, more data will be available for monitoring and study activities that should bring about advances in these areas. Also, by providing lower overall installation, operation, and maintenance costs, more stations should be able to be fielded with higher productivity. All of this will improve seismic data acquisition coverage and monitoring capabilities that in turn will improve the assessment of nuclear nonproliferation and seismic hazards and reduce the associated risk of each.

OBJECTIVE

The United States government sponsors and supports various programs to monitor nuclear explosions by means of seismic, hydroacoustic, and infrasound data collection and analysis. These data collection stations are typically deployed in remote areas to remove them from culturally generated noise signals. Also, to perform their monitoring functions, they may need to be located in politically sensitive areas. These requirements give rise to several problems encountered with past and current station designs. These include the following:

- High installation, operation, and maintenance costs.
- High physical profile because of the equipment and infrastructure required to support the station.
- Low reliability of intrasite data communications in remote areas as well as communications back to a central data collection center.
- Power availability, consumption and generation.

The objective of this Small Business Innovation Research (SBIR) Phase I grant was to research and assess the feasibility of using current and emerging new technologies to develop a new generation of Robust Remote Seismic Station (RRSS) hardware and software to mitigate these current shortcomings. The working goals for this new generation of equipment are as follows:

1. High quality 24-bit or better data.
2. Remove the need for a central hub data collection point by having the individual stations connect directly to a global or wide-area network (GAN/WAN) to eliminate a large physical presence and cost. It also removes a large power requirement and a possible single point of failure.
3. Very low power (<5 W peak, <1 W average at each seismic station).
4. High level of integration to reduce size and provide a very low physical profile.
5. Direct low power low Earth orbit (LEO) satellite communication to “Internet in the sky.”
6. Two-week persistent data buffer in case of communications outages.
7. Autonomous power operation (off the grid).
8. One-year operation between servicing.

Specifically, Geotech Instruments, LLC (Geotech) performed research in the following areas:

- **High Quality Data**: Using new low power analog signal conditioning and high-resolution delta-sigma ($\Delta\sum$) ADC techniques to deliver high quality, low noise seismic data.

- **Size and Power Reduction**: Using low power surface mount electronics and miniaturized packaging technologies to reduce overall size and power requirements.

- **Integration**: The integration of the electronics modules into one borehole installable instrument package to allow the physical profile of the station to be reduced. By minimizing the total number of components and instrument packages, cabling and interconnects was minimized thus reducing installation, operation, and maintenance costs significantly. The ultimate goal was to achieve a near zero maintenance system that could be quickly deployed by inexperienced personnel. The system would be plug and play requiring few if any field configuration or adjustments.

- **Communications**: Using new low power and low cost satellite and wireless communications to connect each station directly back to a data center removing the need for a remote central data hub. This eliminated problems encountered with intrasite communications and a possible single point of failure. Eliminating the central hub also reduces installation, operation and maintenance costs. Data from the new seismic station will be delivered in standard CD 1.1 formats and protocols to maintain compatibility with and preserve the investment in current data center processing hardware and software.

- **Advanced Power Supplies**: Using new fuel cell technology as the power source for the station. By significantly reducing the power consumption of the station from current levels, new smaller power source options can be used. This allows for a large reduction in the installation, operation, and maintenance costs associated with the power subsystem.

RESEARCH ACCOMPLISHED

High Quality Data

The Phase I goals in this area were to investigate:

- Reduction of system induced analog noise.
- New lower power, low noise analog front-end components.
- New lower power, high-resolution ADC components.
- Discrete ΔΣ ADC and digital signal processor (DSP) processing methods.
- Matching sensors, analog front-end, and ADC for optimized performance.

Prior to proposing this SBIR program, Geotech's standard 24-bit data acquisition products were its line of D-Series instruments. These instruments used 1st generation ΔΣ ADC chips. The total power requirements for a three channel ADC (analog front-end, ΔΣ modulator and DSP finite impulse response [FIR] filter) was 1630 mW and required 43.7 sq in. of printed circuit (PC) board space.

Development of Geotech's newest line of 24-bit data acquisition products, the SMART-24™, and this SBIR program proposal phase and Phase I activities occurred concurrently. In this effort, 2nd generation ΔΣ ADC and analog front-end chips were designed in and evaluated. In this hardware, the total power requirements for a three channel ADC (analog front-end, ΔΣ modulator and DSP FIR filter) was drastically reduced to 258 mW and required only 13.5 sq in. of PC board space. It was also found that this generation of devices was significantly less sensitive to induced noise from the digital portions of the hardware (see Figure 1). This greatly reduced the amount of isolation, shielding and special PC board layout required to obtain good performance results. A 3–6 dB improvement in dynamic range was also achieved.

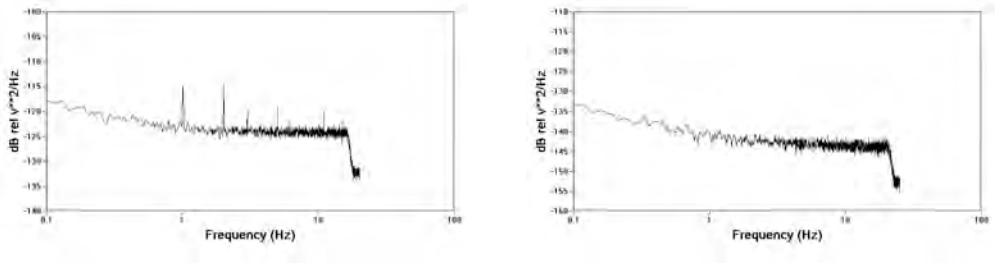

Figure 1. Input terminated noise of a 1st generation ADC (left, showing a small amount of digitally induced integer hertz noise) and a 2nd generation ADC (right, showing no digital pickup).

In evaluating this design further, it was found that additional improvements can be made by optimizing power supply voltages, matching the ADC to the sensor and by moving the DSP FIR filtering functions into underutilized field-programmable gate array (FPGA) and DSP processor resources that are consuming power but not being used effectively. This could reduce the power and PC board space even further to 150 mW and 4.7 sq in., respectively. These results are summarized in Table 1.

Table 1. Three Channel ΔΣADC Power and PC Board Space Requirements.

	1st Gen. ΔΣ ADC	2nd Gen. ΔΣ ADC	SBIR 3rd Gen. ΔΣ ADC
Analog Front End	940 mW	99 mW	75 mW
ΔΣ Modulator	630 mW	99 mW	75 mW
DSP Filter	60 mW	60 mW	N/A
Total Power	**1630 mW**	**258 mW**	**150 mW**
Board Space	43.7 $in.^2$	13.5 $in.^2$	4.7 $in.^2$

In addition, Geotech is currently cooperating with various vendors in the development of new 24-bit ΔΣ ADC devices that will be available in the late 2005 and 2006. These devices promise to further reduce power, board space and cost while improving the dynamic range performance and they will be evaluated more fully in Phase II of this project as they become available.

Discrete ΔΣ ADC topologies were also reviewed and studied in Phase I that have the potential to push ADC resolution past the 24-bit barrier. This evaluation will continue under Phase II where prototype circuits will be designed, built, and tested.

Size and Power Reduction

The Phase I goals in this area were to investigate the following:

- Reduction of PC board size using new miniaturized components (see Figure 2).
- Reducing power requirements to a minimum.

Given recent advancements in both miniaturized and low-power integrated circuits driven by the wireless phone, personal digital assistant (PDA), and digital camera industries, smaller, more-compact low-power electronics can be designed. While FPGAs typically use more quiescent power, the overall power requirement is lower if 1.8-V I/O, peripherals and System on a Programmable Chip (SoPC) modules can be used and integrated into a larger device. Many of the peripheral building blocks, DSPs, and microcontrollers used in Geotech's current SMART-24™ system can be integrated into a single FPGA to significantly reduce size and overall power. This reduced size will result in an overall reduction in cost, power, physical size, and weight. Currently, Geotech's borehole digitizers have a 3.5-in. diameter and are roughly 26 in. long. The reduction in size will result in a new generation of borehole digitizers, which will be targeted at a 3.5-in. diameter and a length of 8 in. This reduction in size will reduce the weight by an estimated 75%–80%.

Figure 2. This figure shows a 70% reduction in PC board size from a 1st generation ADC (left) to a 2nd generation ADC (right). Another 50% reduction in size is anticipated going to a new 3rd generation of ADC.

Hardware developed in Phase II of this program will be the building block for Geotech's next generation surface digitizer to replace the SMART-24™ instruments carrying forward Geotech's intellectual property and innovations respected around the world. This investment in intellectual property will allow Geotech to advance its hardware platform as newer, faster, and lower-power integrated circuits come to market; all this with maximum portability via very high speed integrated circuit hardware description language design tools and methodologies. FPGAs where selected over application-specific integrated circuits (ASICs) because of a more rapid migration to newer technology and programmability. By letting the FPGA industry invest time and money into the semiconductor devices, Geotech can stay 2 to 3 years ahead of the ASIC based competition. The current borehole digitizer contains nine boards and consumes 188 sq in. of board space. Under this program, the next generation borehole digitizer is targeted for two boards and a 39-sq-in. area.

This integration of SoPCs onto a single FPGA will allow Geotech to lay the foundation for an integrated ΔΣ ADC, which could expand the range of the current 24-bit digitizers beyond the 24-bit limit. Having the core instantiated

internal to the FPGA, the ΔΣ ADCs and ΔΣ DACs can be dynamically scaled for lower speed ADCs and DACs. In seismology, sometimes 24-bit resolution is excessive. Lower resolution customers could benefit by the power savings of a 16-bit or 20-bit system; all this without investing in changes to the hardware design. Also, multiple 10-bit and 12-bit ΔΣ ADCs and ΔΣ DACs can be instantiated for state-of-health (SOH) type digital signaling.

Integration

The Phase I goals in this area were to investigate the following:

- Overall station size reduction to reduce its physical profile.
- The integration of components into a single package.
- Providing simple installation and user-friendly operation.
- Near zero maintenance and configuration, easy to identify failures and to repair.

Reduced PC board size requirements allow for more components of the station to be integrated into a single package. This will allow the pre-amplifiers, global positioning system (GPS) receiver, and data authentication to all be integrated into a single digitizer package with fewer boards and interconnects. This in turn will increase reliability and lower manufacturing and maintenance costs. Reducing the number of total components and interconnections will allow for a smaller overall physical profile of the station. Stations will be installed in such a way so that only the GPS and communications antennas are exposed to reduce its above ground profile (see Figure 3).

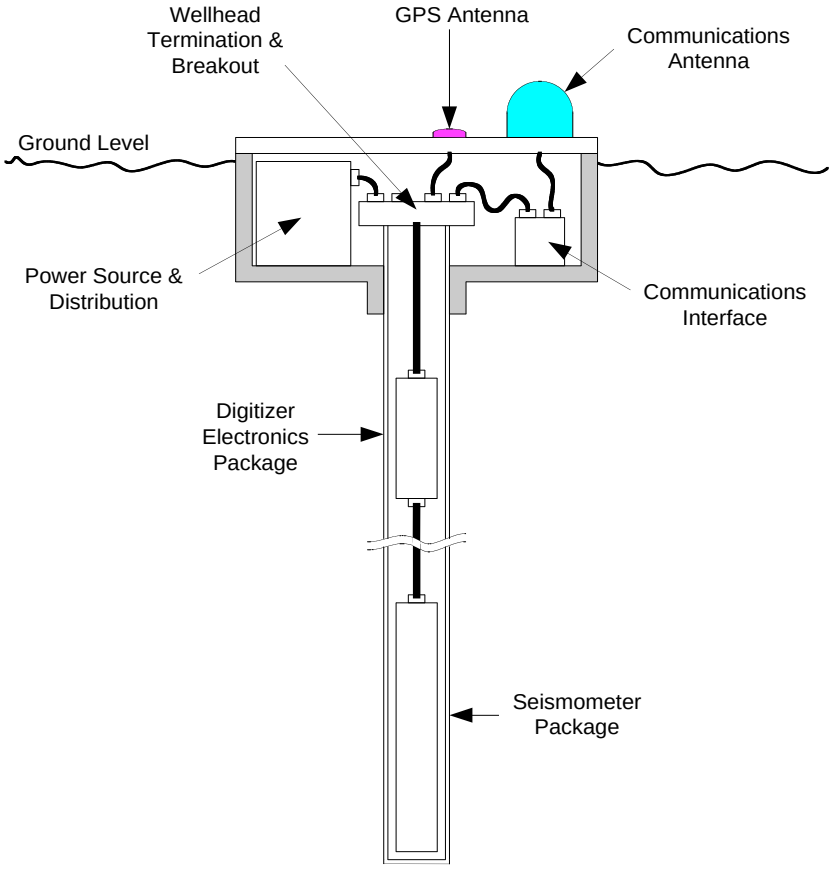

Figure 3. Typical RRSS system integration.

Because the individual stations can connect directly to a network, the need for a central data hub in an array is removed. This eliminates a large installation, maintenance, and power cost from the system. The use of SMART-24™ plug and play technology in the digitizer allows it to automatically detect the components connected

to it and to take the appropriate configuration actions. HTTP web, Telnet, and FTP access to each station allows for easy setup and operation remotely without special user software. Software updates can be accomplished remotely over the network connection.

The stations will be designed with a one-year service interval in mind. SOH monitoring and logging allows the system to remotely notify the user in the event of any out of range conditions.

Communications

The Phase I goals in this area were to investigate the following:

- Direct satellite network communications.
- Short haul wireless network communications.
- Methods of data compression and error recovery.

Satellite communications at this time consist mainly of two types; geosynchronous earth orbit (GEO) and LEO, as shown in Figure 4.

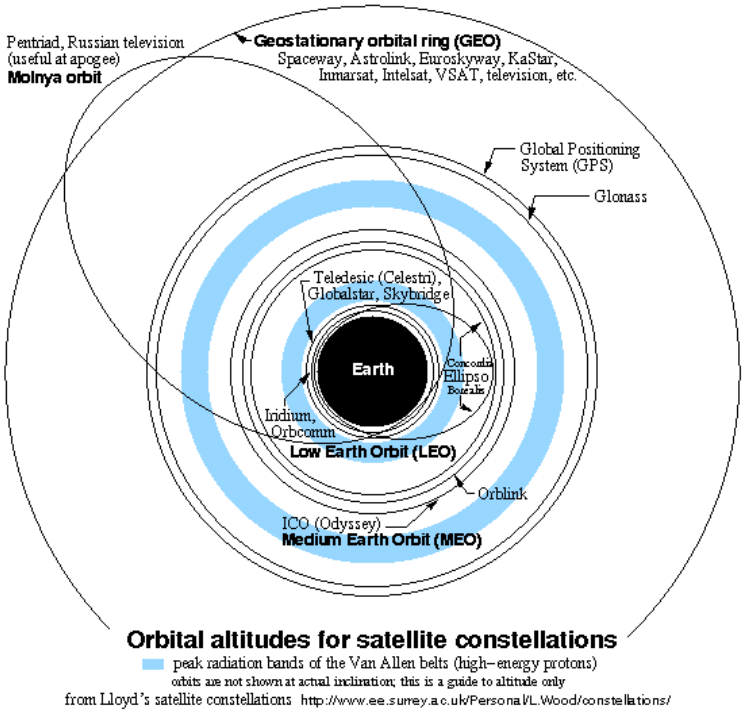

Figure 4. Satellite constellations and orbits.

GEO satellites can provide large coverage with a few satellites (but poor coverage in the polar regions) and can provide high data rates. However, they generally require a relatively large dish antenna, have large power consumption, and have large transmission delays to cope with. Examples of GEO systems are very small aperture terminal (VSAT) systems from various providers and Inmarsat.

Geotech currently provides VSAT solutions to its customers and has an on site VSAT link for testing. However, VSAT would not be the ideal solution for this project due to its large antenna and power requirements.

Inmarsat Broadband Global Area Network (BGAN) service is an interesting option for a GEO system since it only requires a small flat panel antenna (similar in size to a small laptop computer) making it much more portable and easy to setup. It can provide data rates up to 432 Kbps, but current data terminal modems require high power at around 50 W. However, as the BGAN service is rolled out for global coverage in 2005 and 2006, smaller lower power data terminals should become available.

LEO satellites provide the advantages of small omni-directional antennas, lower power operation, negligible transmission delays, and full earth coverage (including the polar regions). However, because of LEO, satellite positions in the sky are not fixed and many more satellites are required for full coverage. Since the satellites are constantly moving, complex satellite signal switching and routing are also required. This all makes the cost of a LEO system far more than a GEO system causing them to be less economically viable. Many LEO systems have been proposed but few have made it off the ground (Teledesic being the most ambitious to have failed and gone out of business). Of those that have, only Iridium and Globalstar have potential application to this project. Two systems, Skybridge and S2Com, are still on the drawing board and hold great promise to provide true "DSL Internet in the sky" if they are launched in the next few years.

Iridium began with great fanfare in the late 1990s, but quickly fell into bankruptcy. Iridium has been reborn and currently provides voice and data services globally. There are several low power (<2 W) original equipment manufacturer (OEM) data modems available for iridium, but data rates are limited to the 2400–9600 bps range.

Globalstar also provides voice and data service at 9600 bps. However, because it uses a simpler "bent pipe" architecture, its ground stations limit its coverage. Coverage is currently provided to North America, South America, Europe, Australia, and most of Asia. Low-power OEM data modems and small antennas are also available for the Globalstar system.

Geotech is currently fielding wireless local-area network (WiLAN) solutions for connecting stations to the network at data rates from 1.5 to 11 Mbps over distances of 20 miles.

With its SMART-24^{TM} instruments, Geotech has implemented and tested the following communications related technologies:

- TCP/IP based stack and transport providing error recovery and retransmission.
- CD 1.1 continuous data format providing error recovery, data buffering, and retransmission.
- Data compression providing up to 6:1 compression (low noise, 2-3:1 typical with high seismic background level).

The decision was made to not integrate the data modem directly into the digitizer package, but to rather provide standard ethernet and serial interfaces to a communication subsystem. Since at this time there is no universal communication solution to meet all needs, this provides the most flexible solution to allow any TCP/IP based solution to be used now and in the future as the need and technology presents itself.

In analyzing the communication requirements of a typical seismic data acquisition station with three channels running at 40 sps with authentication and compression turned on, the minimum required bit rate was found to be 9600 bps to account for data, commands, and protocol overhead at a ten second data frame interval. Larger data frame intervals do not appreciably increase transmission efficiency as shown in Table 2 and Figure 5. In Phase II of this project, Geotech will purchase and test various communication solutions that meet this requirement.

Table 2. Communication bandwidth requirements at various data frame intervals. This assumes three channels at 40 sps with 2:1 data compression and 50% overhead for command and protocol requirements.

Data Frame Size (sec)	No Compression (bps)	2:1 Compression (bps)
1	18048	14208
10	8716	4876
20	8198	4358

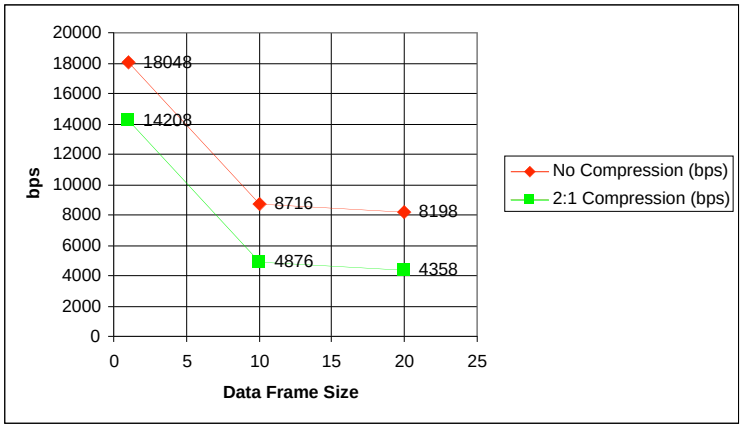

Figure 5. Communication bandwidth requirements at various data frame intervals. This assumes three channels at 40 sps with 2:1 data compression and 50% overhead for command and protocol requirements.

Advanced Power Supplies

The Phase I goal in this area was to investigate advanced power supply alternatives. Several fuel cell technologies are in the final stages of research and are developing into the first generation of fuel cell products. Four of these fuel cells technologies are direct methanol fuel cells (DMFCs), proton exchange membrane fuel cells (PEMFCs), direct ethanol fuel cells (DEFCs), and microbial fuel cells (MFCs). While each fuel cell technology has its own unique advantages, each also has disadvantages. MFCs are in a very infant stage and are not a viable option for the near future. While PEMFC has the highest energy density, the logistics of transporting and long-term storage of the hydrogen fuel eliminate PEMFC as a viable solution. In PEMFCs, converting H_2 energy to electric energy can be obtained at around 50%. If long-term storage and transportation issues are resolved in the next few years, this option could be revisited. DMFCs and DEFCs are the two promising options for near term implementation.

Figure 6. These are examples of 1st generation fuel cell products currently emerging onto the market.

The first generation of DMFC units will be released in 2005. Interest in DMFC (mainly due to the portability of the methanol fuel source) has accelerated the development of these units. Methanol can be transported similar to petroleum products. An estimated 10 gal. of methanol can run a 5-W station for one full year without refueling. This is roughly half the size of a fuel tank on a full sized American automobile. The weight of 10 gal. of methanol is approximately 66 lb, and that amount of methanol takes roughly 1.33 cu ft of space. This weighs less than and is much smaller than a solar panel. The only byproducts of a DMFC are water and CO_2.

Methanol does have some hazardous properties, while ethanol on the other hand does not. Ethanol has half the energy of methanol and would require a 20-gal. tank for storage of a year supply of ethanol. Ethanol is also transported as a liquid. A major disadvantage in using ethanol would be vandalism. Since ethanol is the consumable

portion of an alcoholic beverage, great care would need to be taken to secure the storage facility. DEFCs are considered an emerging fuel cell technology. Since ethanol is generated with renewable fuel sources, this is an interesting technology to consider even for the near future.

With pros and cons evaluated for each fuel cell technology, DMFC seems to be the most viable option for the near future. The following positives outweigh any of the negatives:

- 1st generation available in 2005.
- Fuel is readily available.
- 10 gal. (1.33 cu ft) needed for 1-year operation (66 lb).
- Byproducts are H_20 and CO_2

As DMFCs rapidly mature, they are slated to be the preferred fuel cell technology for small portable devices. At <5 W, a completely operational seismic station would be considered a small device. A typical laptop computer consumes 30–50 W. The first generation of DMFCs requires a lead-acid battery for startup.

With enough forethought, the installation can be adapted to support DMFCs in the initial implementation and DEFCs as the technology advances.

CONCLUSION AND RECOMMENDATION

With the convergence of the development of Geotech's new SMART-24™ instruments and this SBIR Phase I effort, Geotech has developed, implemented, and proven several technologies relating to this SBIR effort including the following:

- A 2nd generation 24-ADC with better performance and much lower power.
- Matching of sensors and ADC to improve performance.
- SMART-24™ technology for "plug and play" operation.
- TCP/IP connectivity making the instruments true "Internet appliances" with HTTP Web, Telnet, and FTP access.
- Standard data formats with CD 1.1 and error recovery.
- Data compression.
- Remote software updates via the Internet.
- Reliable VSAT satellite communications.

These advancements are already implemented in Geotech's new instruments and are in use by customers in the field.

Consumer mass market products (cell phones, PDAs, MP3 players, etc.) are propelling the push for smaller, low power components that will allow for further significant reductions in size and power of these instruments. At the same time there are now some viable options for low power satellite and wireless communications that were not previously available. New and faster communications options are also on the horizon and will become available in the next few years. Advanced power sources such as fuel cell technology are maturing with many products coming on line in the next year or so. For these reasons, Phase I of this project has shown that it is not only feasible, it is the ideal time to push forward and continue the development of a RRSS into Phase II.

OPTIMIZING DATA ACCESS AND AVAILABILITY FOR SEISMIC CALIBRATION RESEARCH

Michael L. Begnaud, Richard J. Stead, Julio Aguilar-Chang, and Hans E. Hartse

Los Alamos National Laboratory

Sponsored by National Nuclear Security Administration
Office of Nonproliferation Research and Engineering
Office of Defense Nuclear Nonproliferation

Contract No. W-7405-ENG-36

ABSTRACT

The Ground-based Nuclear Explosion Monitoring Research & Engineering (GNEM R&E) program has made recent advances in optimizing data access and availability for seismic calibration research. Some of the most challenging tasks of maintaining functional and accessible data warehouses are the development of software to automate the continuous and up-to-date population of the database, the quality control (QC) needed to resolve data conflicts, the synchronization of database tables between unclassified and classified warehouses, and the integration of all data sources into a cohesive database for delivery to the Knowledge Base (KB).

One important challenge in using large data warehouses is the simple and efficient access to the vast holdings within them. Web-based tools have become important assets that address this problem. We have developed web-based tools that enable researchers to do tasks such as track the progress of seismic analysis, access information about stations, origins, and waveforms, view contextual information on a map, handle logistical tasks (i.e., assignment of unique identifiers, track the description and resolution of data problems identified through quality controls), and gain fast access to database metadata (e.g., schema descriptions).

Advances in easy access to metadata are supporting many of the higher-level efforts in quality control, automation, and web access. The first of these is the documentation of the seismic calibration schema using a database schema. This schema is designed to represent all of the detailed table and field information that, up until recently, has been available only in text-based documents. Such information in database form has immediate application to a wide variety of efforts involving the database. (e.g., table creation and quality control, software tools). Another advance in using metadata, with a more narrow application, has been the creation of bulletin descriptive tables. These tables describe the sources of bulletin data that have been imported into the data warehouse, as well as provide a means to track individual data elements to the corresponding lines of text in the original document.

As data become more voluminous and complex, QC has become an increasingly visible and important issue regarding the Knowledge Base. Improvements in QC procedures are helping researchers and data managers to more readily identify complex quality problems. The outcome is consistent research products resulting from improved data upon which those products are based. As we understand the QC problem in more detail, we have begun to automate the process of applying QC to large datasets.

Calibration efforts by Los Alamos National Laboratory (LANL) researchers require working with three separate data warehouses that are physically unable to communicate with each other: two are within LANL; one is located at a remote site. While it is relatively simple to add new data to all warehouses, it is difficult to capture changes made in one and then propagate them to the other two. We have recently developed a procedure based on database triggers to capture these changes. These triggers capture all update, insert, and delete operations against a predefined set of tables. Periodically, the information captured by these triggers is moved to the other environments and executed, thus keeping the warehouses synchronized.

OBJECTIVE(S)

The GNEM R&E program has made recent advances in applying data warehouses to seismic calibration research. Some of the most challenging tasks of maintaining functional data warehouses are the development of software to easily access the contents of the data warehouse, the QC needed to resolve data conflicts, the synchronization of database tables between local and remote warehouses, and the integration of all data sources into a cohesive database for delivery to the (KB). This paper is a brief introduction to the wide range of data management technical issues that we face everyday and the future work needed to fully address all aspects of managing and handling vast amounts of data in a data warehouse that is used in nuclear explosion monitoring research.

RESEARCH ACCOMPLISHED

Web Technology Access to Data Warehouses

As data gathering techniques continue to improve and general data availability increases, the GNEM R&E data warehouses will acquire more data than is readily accessible using the standard SQL command-line interface. One of the challenges is to develop a simple, yet efficient way to view the contents of our data warehouses to assist researchers in developing their calibration products.

Web-based tools provide an efficient, yet easy way to access data from the Oracle GNEM R&E databases. In addition to viewing the seismic data itself, we have developed web pages to interact with database schema viewing and development, handle logistical tasks (i.e., assignment of unique identifiers, tracking of database problems and data requests from researchers, etc.), and view metadata contents (e.g., glossary). The LANL GNEM R&E intranet web technology interface has been operational for over a year and has been extremely useful for accessing data quickly. Recent improvements include being able to generate an origin query, viewing quick, interactive maps of queried data, and implementing a data request system for researchers. Figure 1 is a view of the starting LANL GNEM R&E home page.

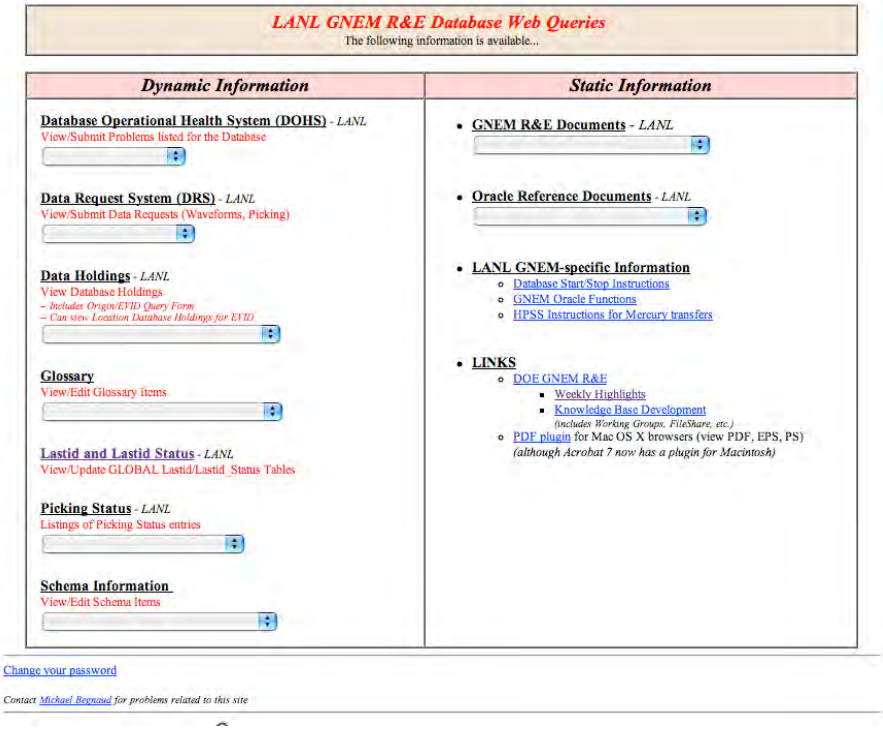

Figure 1. LANL GNEM starting web page. From this page, users can access seismic database entries, glossary and schema information, logistical data, and GNEM-related internal pages.

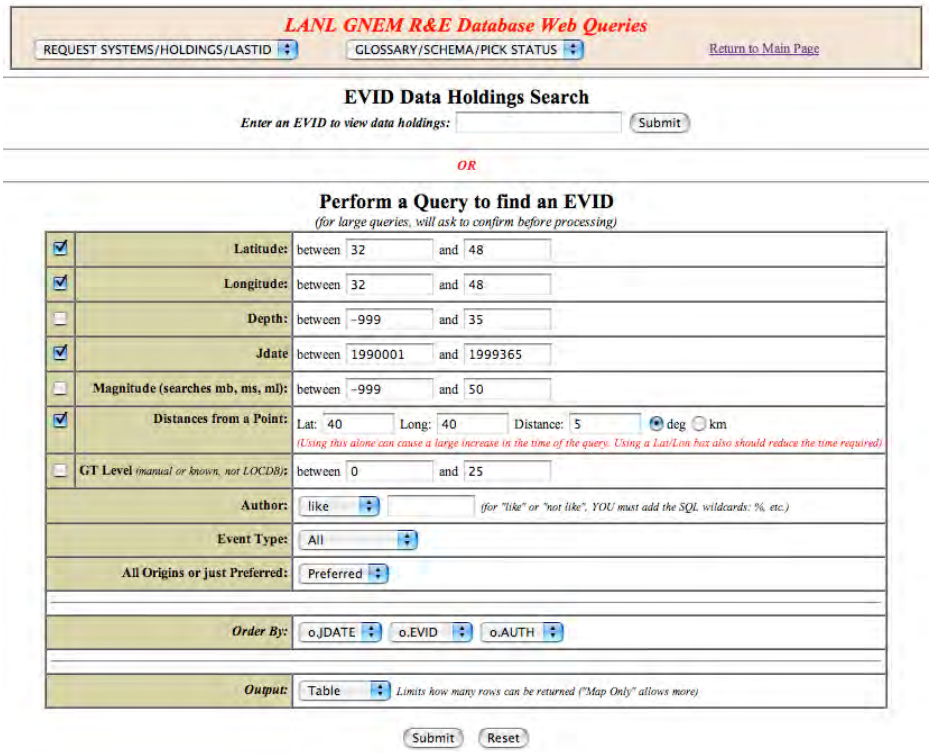

Figure 2. Event query page. Users can enter an EVID directly or perform an origin query. Selected parameters shown were used to generate a query producing results in Figure 3 and Figure 4.

Because of the need for LANL GNEM R&E team members to access data from remote locations, we implemented username/password access as well as Secure Socket Layer (SSL) 128-bit encryption for our internal web technology data access. Within LANL, users are granted access by a browser-standard basic username/password authentication. Outside LANL, users must first use a LANL-authorized cryptocard to gain web access behind the LANL firewall before proceeding to the username/password screen.

Seismic Data Holdings

The GNEM R&E database schema generally follows the National Nuclear Security Administration (NNSA) structure (Carr, 2005). This structure is mostly centered around events which are built with origins, associations, arrivals, waveforms, etc. Using an Event Identification number (EVID), a user can generally access all the data available for that event. Database users can either enter an EVID directly, or enter parameters for an origin query. Parameters include latitude/longitude, depth, julian date, magnitude, distance from a point, ground-truth value, author or authority, general event type (earthquake, explosion, mining), and all origins or just preferred (Figure 2). Users can request an output HTML table (Figure 3) or just gather data on the web server to produce a map (Figure 4).

In the table output view (Figure 3), a user will see origin information as well as the known ground-truth level. The AUTH and ETYPE fields have cross-referenced links to a glossary table. Clicking one of these links shows the definition of the field information. In the map output view (Figure 4), users can interactively view the results of the origin (or other) queries.

When an EVID is selected from the table output, a new screen appears with an initial summary of available data for that EVID (Figure 5). The web scripts determine if waveform segments, pick status entries, and location database entries exist for that event. Buttons are highlighted for those types available. Since there can be multiple origins for an event, the web page displays each origin and highlights buttons if arrivals, magnitudes, and amplitudes exist for that origin. Users can quickly navigate all data associated with an EVID.

In addition to the EVID-based data holdings, users can query for site-related information, by station abbreviation, reference station, or by entering a manual query (Figure 6). For a single site, the relevant SITE, AFFILIATION, SITECHAN, SENSOR, and INSTRUMENT information are displayed.

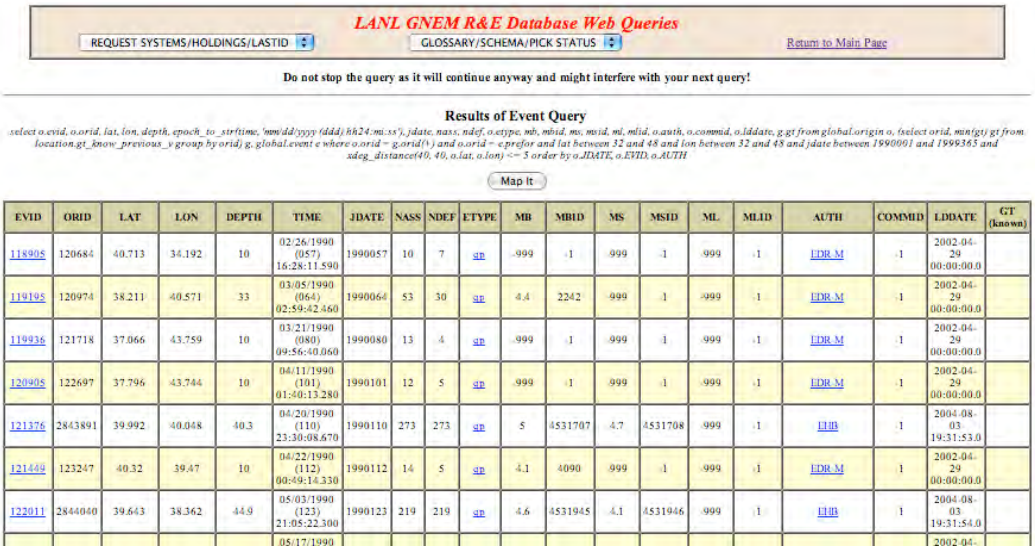

LANL GNEM R&E Database Web Queries

REQUEST SYSTEMS/HOLDINGS/LASTID | GLOSSARY/SCHEMA/PICK STATUS | Return to Main Page

Do not stop the query as it will continue anyway and might interfere with your next query!

Results of Event Query

Map It

EVID	ORID	LAT	LON	DEPTH	TIME	JDATE	NASS	NDEF	ETYPE	MB	MBID	MS	MSID	ML	MLID	AUTH	COMMID	LDDATE	GT (known)
118905	120684	40.713	34.192	10	02/26/1990 (057) 16:28:11.590	1990057	10	7	sp	.999	-1	.999	-1	.999	-1	EDR_M	-1	2002-04-29 00:00:00.0	
119195	120974	38.211	40.571	33	03/05/1990 (064) 02:59:42.460	1990064	53	30	sp	4.4	2242	.999	-1	.999	-1	EDR_M	-1	2002-04-29 00:00:00.0	
119936	121718	37.066	43.759	10	03/21/1990 (080) 09:56:40.060	1990080	13	4	sp	.999	-1	.999	-1	.999	-1	EDR_M	-1	2002-04-29 00:00:00.0	
120905	122697	37.796	43.744	10	04/11/1990 (101) 01:40:13.280	1990101	12	5	sp	.999	-1	.999	-1	.999	-1	EDR_M	-1	2002-04-29 00:00:00.0	
121376	2843891	39.992	40.048	40.3	04/20/1990 (110) 23:30:08.670	1990110	273	273	sp	5	4531707	4.7	4531708	.999	-1	EHB	-1	2004-08-03 19:31:53.0	
121449	123247	40.32	39.47	10	04/22/1990 (112) 00:49:14.330	1990112	14	5	sp	4.1	4090	.999	-1	.999	-1	EDR_M	-1	2002-04-29 00:00:00.0	
122011	2844040	39.643	38.362	44.9	05/03/1990 (123) 21:05:22.300	1990123	219	219	sp	4.6	4531945	4.1	4531946	.999	-1	EHB	-1	2004-08-03 19:31:54.0	
					05/17/1990													2002-04-	

Figure 3. Partial results of table output for origin query using parameters from Figure 2. Users may select the EVID at left to view specific data (origins, arrivals, netmags, etc.) for that event. Other terms are cross-referenced with glossary tables, giving the definition of the term.

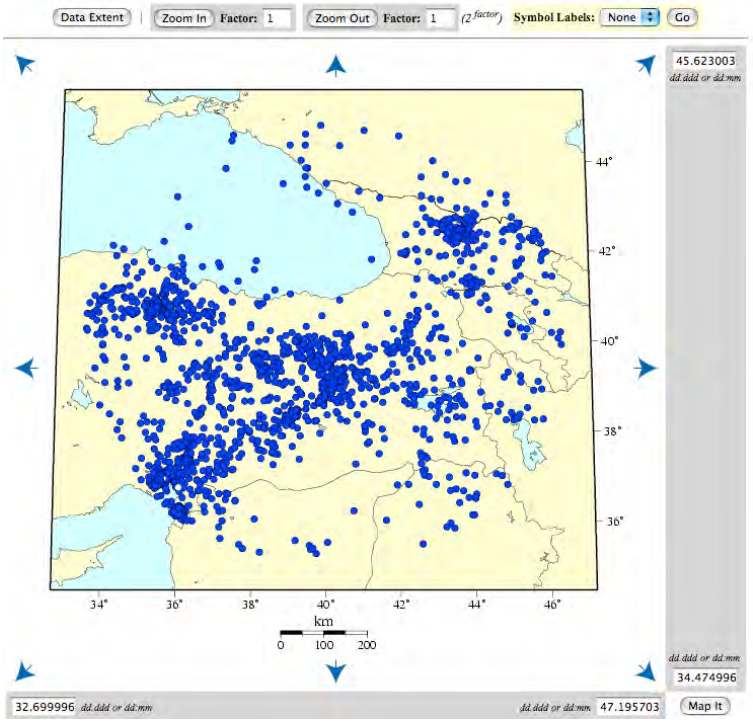

Figure 4. Interactive map of origins produced from query in Figure 2. Users can zoom in or out, set the bounds of the map, and translate the view. Labels can also be turned on or off.

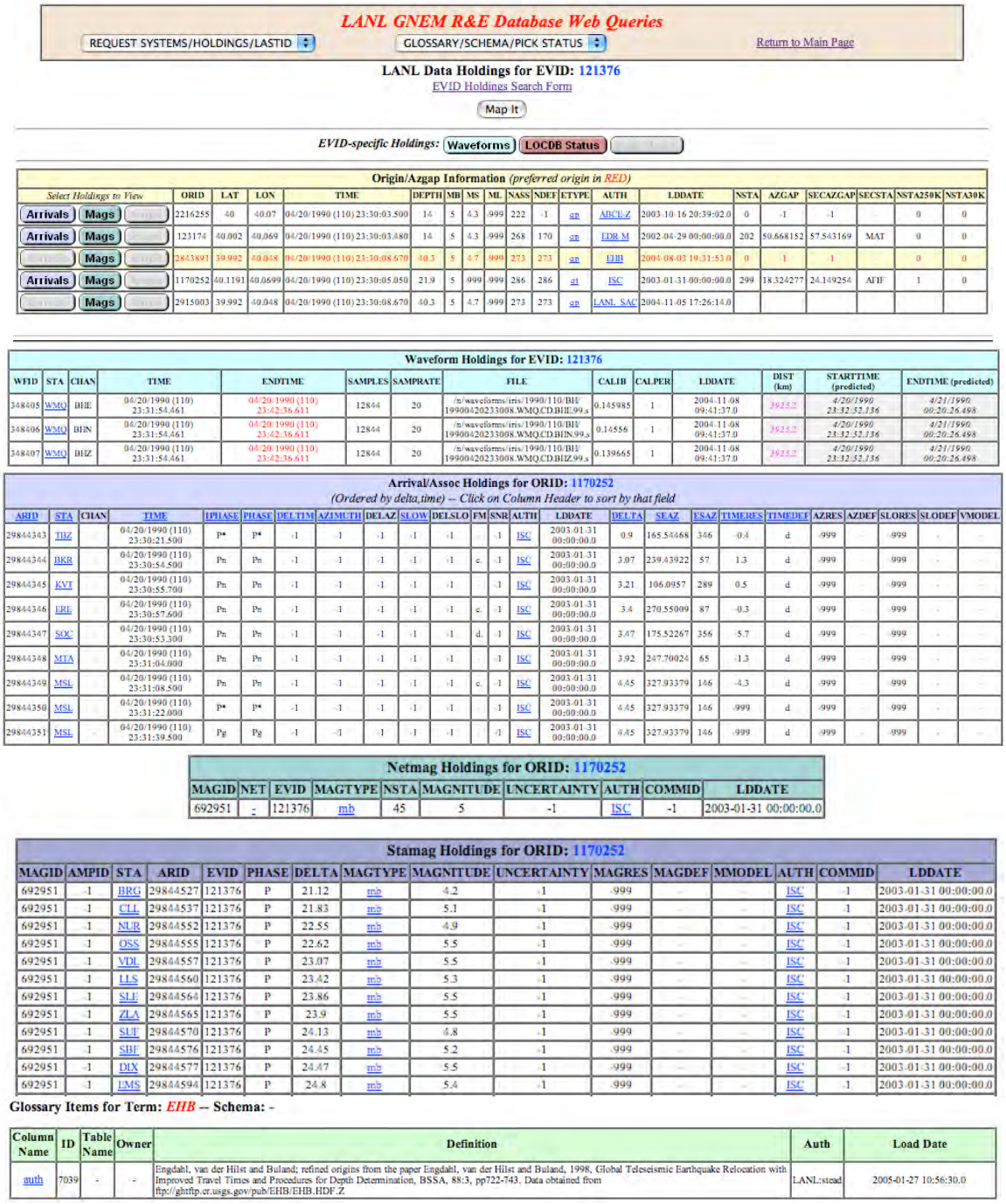

LANL GNEM R&E Database Web Queries

REQUEST SYSTEMS/HOLDINGS/LASTID | GLOSSARY/SCHEMA/PICK STATUS | Return to Main Page

LANL Data Holdings for EVID: 121376

EVID Holdings Search Form

Map It

EVID-specific Holdings: Waveforms | LOCDB Status

Origin/Azgap Information *(preferred origin in RED)*

Select Holdings to View	ORID	LAT	LON	TIME	DEPTH	MB	MS	ML	NASS	NDEF	ETYPE	AUTH	LDDATE	NSTA	AZGAP	SECAZGAP	SECSTA	NSTA250K	NSTA30K
Arrivals Mags	2216255	40	40.07	04/20/1990 (110) 23:30:03.500	14	5	4.3	999	222	-1	sp	ABCE,Z	2003-10-16 20:39:02.0	0	-1	-1		0	0
Arrivals Mags	123174	40.002	40.069	04/20/1990 (110) 23:30:03.480	14	5	4.3	999	268	170	sp	EDR M	2002-04-29 00:00:00.0	202	50.668152	57.543169	MAT	0	0
Mags	2843891	39.992	40.048	04/20/1990 (110) 23:30:08.670	40.3	5	4.7	999	273	273	sp	EHB	2004-08-03 19:31:53.0	0	1	1		0	0
Arrivals Mags	1170252	40.1191	40.0699	04/20/1990 (110) 23:30:05.050	21.9	5	999	999	286	286	at	ISC	2003-01-31 00:00:00.0	299	18.324277	24.149254	AFIF	1	0
Mags	2915003	39.992	40.048	04/20/1990 (110) 23:30:08.670	40.3	5	4.7	999	273	273	sp	LANL SAC	2004-11-05 17:26:14.0						

Waveform Holdings for EVID: 121376

WFID	STA	CHAN	TIME	ENDTIME	SAMPLES	SAMPRATE	FILE	CALIB	CALPER	LDDATE	DIST (km)	STARTTIME (predicted)	ENDTIME (predicted)
348405	WMQ	BHE	04/20/1990 (110) 23:31:54.461	04/20/1990 (110) 23:42:36.611	12844	20	/n/waveforms/iris/1990/110/BH/19900420233008.WMQ.CD.BHE.99.s	0.145985	1	2004-11-08 09:41:37.0	3923.2	4/20/1990 23:32:52.136	4/21/1990 00:20:26.498
348406	WMQ	BHN	04/20/1990 (110) 23:31:54.461	04/20/1990 (110) 23:42:36.611	12844	20	/n/waveforms/iris/1990/110/BH/19900420233008.WMQ.CD.BHN.99.s	0.14556	1	2004-11-08 09:41:37.0	3923.2	4/20/1990 23:32:52.136	4/21/1990 00:20:26.498
348407	WMQ	BHZ	04/20/1990 (110) 23:31:54.461	04/20/1990 (110) 23:42:36.611	12844	20	/n/waveforms/iris/1990/110/BH/19900420233008.WMQ.CD.BHZ.99.s	0.139665	1	2004-11-08 09:41:37.0	3923.2	4/20/1990 23:32:52.136	4/21/1990 00:20:26.498

Arrival/Assoc Holdings for ORID: 1170252

(Ordered by delta,time) -- Click on Column Header to sort by that field

ARID	STA	CHAN	TIME	IPHASE	PHASE	DELTIM	AZIMUTH	DELAZ	SLOW	DELSLO	FM	SNR	AUTH	LDDATE	DELTA	SEAZ	ESAZ	TIMERES	TIMEDEF	AZRES	AZDEF	SLORES	SLODEF	VMODEL
29844343	TIIZ		04/20/1990 (110) 23:30:21.500	P*	P*	-1	-1	-1	-1	-1		-1	ISC	2003-01-31 00:00:00.0	0.9	165.54468	346	-0.4	d	999		999		
29844344	BKR		04/20/1990 (110) 23:30:54.500	Pn	Pn	-1	-1	-1	-1	-1	c.	-1	ISC	2003-01-31 00:00:00.0	3.07	239.43922	57	1.3	d	999		999		
29844345	KVT		04/20/1990 (110) 23:30:55.700	Pn	Pn	-1	-1	-1	-1	-1		-1	ISC	2003-01-31 00:00:00.0	3.21	106.0957	289	0.5	d	999		999		
29844346	ERE		04/20/1990 (110) 23:30:57.600	Pn	Pn	-1	-1	-1	-1	-1	c.	-1	ISC	2003-01-31 00:00:00.0	3.4	270.55009	87	-0.3	d	999		999		
29844347	SOC		04/20/1990 (110) 23:30:53.300	Pn	Pn	-1	-1	-1	-1	-1	d.	-1	ISC	2003-01-31 00:00:00.0	3.47	175.52267	356	-5.7	d	999		999		
29844348	MTA		04/20/1990 (110) 23:31:04.000	Pn	Pn	-1	-1	-1	-1	-1		-1	ISC	2003-01-31 00:00:00.0	3.92	247.70024	65	-1.3	d	999		999		
29844349	MSL		04/20/1990 (110) 23:31:08.500	Pn	Pn	-1	-1	-1	-1	-1	c.	-1	ISC	2003-01-31 00:00:00.0	4.45	327.93379	146	-4.3	d	999		999		
29844350	MSL		04/20/1990 (110) 23:31:22.000	P*	P*	-1	-1	-1	-1	-1		-1	ISC	2003-01-31 00:00:00.0	4.45	327.93379	146	999	d	999		999		
29844351	MSL		04/20/1990 (110) 23:31:39.500	Pg	Pg	-1	-1	-1	-1	-1		-1	ISC	2003-01-31 00:00:00.0	4.45	327.93379	146	999	d	999		999		

Netmag Holdings for ORID: 1170252

MAGID	NET	EVID	MAGTYPE	NSTA	MAGNITUDE	UNCERTAINTY	AUTH	COMMID	LDDATE
692951	-	121376	mb	45	5	-1	ISC	-1	2003-01-31 00:00:00.0

Stamag Holdings for ORID: 1170252

MAGID	AMPID	STA	ARID	EVID	PHASE	DELTA	MAGTYPE	MAGNITUDE	UNCERTAINTY	MAGRES	MAGDEF	MMODEL	AUTH	COMMID	LDDATE
692951	-1	BRG	29844527	121376	P	21.12	mb	4.2	-1	999			ISC	-1	2003-01-31 00:00:00.0
692951	-1	CLL	29844537	121376	P	21.83	mb	5.1	-1	999			ISC	-1	2003-01-31 00:00:00.0
692951	-1	NUR	29844552	121376	P	22.55	mb	4.9	-1	999			ISC	-1	2003-01-31 00:00:00.0
692951	-1	OSS	29844555	121376	P	22.62	mb	5.5	-1	999			ISC	-1	2003-01-31 00:00:00.0
692951	-1	VDL	29844557	121376	P	23.07	mb	5.5	-1	999			ISC	-1	2003-01-31 00:00:00.0
692951	-1	LLS	29844560	121376	P	23.42	mb	5.3	-1	999			ISC	-1	2003-01-31 00:00:00.0
692951	-1	SLE	29844564	121376	P	23.86	mb	5.5	-1	999			ISC	-1	2003-01-31 00:00:00.0
692951	-1	ZLA	29844565	121376	P	23.9	mb	5.5	-1	999			ISC	-1	2003-01-31 00:00:00.0
692951	-1	SUF	29844570	121376	P	24.13	mb	4.8	-1	999			ISC	-1	2003-01-31 00:00:00.0
692951	-1	SBF	29844576	121376	P	24.45	mb	5.2	-1	999			ISC	-1	2003-01-31 00:00:00.0
692951	-1	DIX	29844577	121376	P	24.47	mb	5.5	-1	999			ISC	-1	2003-01-31 00:00:00.0
692951	-1	LMS	29844594	121376	P	24.8	mb	5.4	-1	999			ISC	-1	2003-01-31 00:00:00.0

Glossary Items for Term: *EHB* -- Schema: -

Column Name	ID	Table Name	Owner	Definition	Auth	Load Date
auth	7039	-	-	Engdahl, van der Hilst and Buland; refined origins from the paper Engdahl, van der Hilst and Buland, 1998, Global Teleseismic Earthquake Relocation with Improved Travel Times and Procedures for Depth Determination, BSSA, 88:3, pp722-743. Data obtained from ftp://ghtftp.cr.usgs.gov/pub/EHB/EHB.HDF.Z	LANL:stead	2005-01-27 10:56:30.0

Figure 5. View of EVID-specific data holdings page and several data frames, including a glossary definition. Buttons are highlighted if data are available for that data type. From this page, arrivals, magnitudes (netmag, stamag), and amplitude data can be viewed for the different origins. Users can also view a map of the different origins and stations with waveforms.

Schema Documentation

A major effort in making database metadata available is the documentation of the seismic calibration schema using a database schema. This schema is designed to represent all of the detailed table and field information that, up until recently, has been available only in text-based documents. These documents include versions of the NNSA KB core schema, NNSA KB custom schema, and the United States National Data Center (USNDC) schema documents. The portions that are most needed as readily available metadata are also the portions most amenable to adaptation into

database tables themselves: the table descriptions and the column description. Four tables are used to describe schema information: TABDESCRIPT, COLASSOC, COLDESCRIPT, and GLOSSARY. We have also developed a web technology interface to view and edit the schema and glossary information (Figure 7). The schema tables have been accepted as the schema documentation for the GNEM R&E program and are now used by Sandia National Laboratories for complete schema documentation (Carr, 2005). In addition, many of the KB tools developed by Sandia depend on these schema database tables.

TABDESCRIPT provides a basic description of the table, identifies that table with a particular documented schema, and provides a reference in the database to connect the fields that may be associated with the table.

The COLDESCRIPT table not only provides the description of a column but also provides metadata such as NA values, units, and ranges in useful forms. Most numeric ranges have been properly translated into *nmin*, *nminop*, *nmax*, and *nmaxop*. Each operation is relative to the value in the column; that is, 'column *nminop nmin*' and 'column *nmaxop nmax*'. If both are set, then both must apply (implied 'and'). A range type of 'defined' means the value of the column is limited to a short set of predefined values. A 'finite set' is a limited but long or not pre-defined set of values. A 'reference set' is limited to the values in a particular table (as given in *reftab*). Using these fields properly can completely and precisely define the various field ranges.

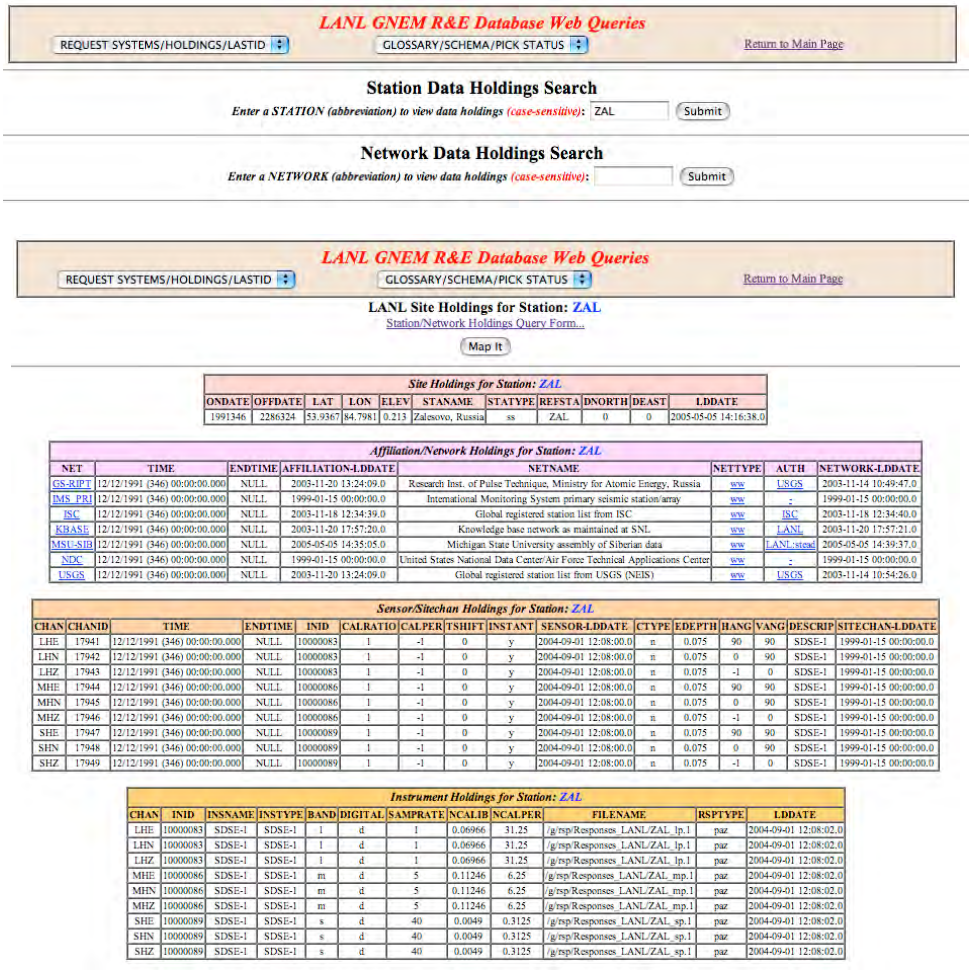

LANL GNEM R&E Database Web Queries

REQUEST SYSTEMS/HOLDINGS/LASTID | GLOSSARY/SCHEMA/PICK STATUS | Return to Main Page

Station Data Holdings Search

Enter a STATION (abbreviation) to view data holdings (case-sensitive): ZAL Submit

Network Data Holdings Search

Enter a NETWORK (abbreviation) to view data holdings (case-sensitive): Submit

LANL GNEM R&E Database Web Queries

REQUEST SYSTEMS/HOLDINGS/LASTID | GLOSSARY/SCHEMA/PICK STATUS | Return to Main Page

LANL Site Holdings for Station: ZAL

Station/Network Holdings Query Form...

Map It

Site Holdings for Station: ZAL

ONDATE	OFFDATE	LAT	LON	ELEV	STANAME	STATYPE	REFSTA	DNORTH	DEAST	LDDATE
1991346	2286324	53.9367	84.7981	0.213	Zalesovo, Russia	ss	ZAL	0	0	2005-05-05 14:16:38.0

Affiliation/Network Holdings for Station: ZAL

NET	TIME	ENDTIME	AFFILIATION-LDDATE	NETNAME	NETTYPE	AUTH	NETWORK-LDDATE
GS-RIPT	12/12/1991 (346) 00:00:00.000	NULL	2003-11-20 13:24:09.0	Research Inst. of Pulse Technique, Ministry for Atomic Energy, Russia	ww	USGS	2003-11-14 10:49:47.0
IMS_PRI	12/12/1991 (346) 00:00:00.000	NULL	1999-01-15 00:00:00.0	International Monitoring System primary seismic station/array	ww	-	1999-01-15 00:00:00.0
ISC	12/12/1991 (346) 00:00:00.000	NULL	2003-11-18 12:34:39.0	Global registered station list from ISC	ww	ISC	2003-11-18 12:34:40.0
KBASE	12/12/1991 (346) 00:00:00.000	NULL	2003-11-20 17:57:20.0	Knowledge base network as maintained at SNL	ww	LANL	2003-11-20 17:57:21.0
MSU-SIB	12/12/1991 (346) 00:00:00.000	NULL	2005-05-05 14:35:05.0	Michigan State University assembly of Siberian data	ww	LANL:stead	2005-05-05 14:39:37.0
NDC	12/12/1991 (346) 00:00:00.000	NULL	1999-01-15 00:00:00.0	United States National Data Center/Air Force Technical Applications Center	ww	-	1999-01-15 00:00:00.0
USGS	12/12/1991 (346) 00:00:00.000	NULL	2003-11-20 13:24:09.0	Global registered station list from USGS (NEIS)	ww	USGS	2003-11-14 10:54:26.0

Sensor/Sitechan Holdings for Station: ZAL

CHAN	CHANID	TIME	ENDTIME	INID	CALRATIO	CALPER	TSHIFT	INSTANT	SENSOR-LDDATE	CTYPE	EDEPTH	HANG	VANG	DESCRIP	SITECHAN-LDDATE
LHE	17941	12/12/1991 (346) 00:00:00.000	NULL	10000083	1	-1	0	y	2004-09-01 12:08:00.0	n	0.075	90	90	SDSE-1	1999-01-15 00:00:00.0
LHN	17942	12/12/1991 (346) 00:00:00.000	NULL	10000083	1	-1	0	y	2004-09-01 12:08:00.0	n	0.075	0	90	SDSE-1	1999-01-15 00:00:00.0
LHZ	17943	12/12/1991 (346) 00:00:00.000	NULL	10000083	1	-1	0	y	2004-09-01 12:08:00.0	n	0.075	-1	0	SDSE-1	1999-01-15 00:00:00.0
MHE	17944	12/12/1991 (346) 00:00:00.000	NULL	10000086	1	-1	0	y	2004-09-01 12:08:00.0	n	0.075	90	90	SDSE-1	1999-01-15 00:00:00.0
MHN	17945	12/12/1991 (346) 00:00:00.000	NULL	10000086	1	-1	0	y	2004-09-01 12:08:00.0	n	0.075	0	90	SDSE-1	1999-01-15 00:00:00.0
MHZ	17946	12/12/1991 (346) 00:00:00.000	NULL	10000086	1	-1	0	y	2004-09-01 12:08:00.0	n	0.075	-1	0	SDSE-1	1999-01-15 00:00:00.0
SHE	17947	12/12/1991 (346) 00:00:00.000	NULL	10000089	1	-1	0	y	2004-09-01 12:08:00.0	n	0.075	90	90	SDSE-1	1999-01-15 00:00:00.0
SHN	17948	12/12/1991 (346) 00:00:00.000	NULL	10000089	1	-1	0	y	2004-09-01 12:08:00.0	n	0.075	0	90	SDSE-1	1999-01-15 00:00:00.0
SHZ	17949	12/12/1991 (346) 00:00:00.000	NULL	10000089	1	-1	0	y	2004-09-01 12:08:00.0	n	0.075	-1	0	SDSE-1	1999-01-15 00:00:00.0

Instrument Holdings for Station: ZAL

CHAN	INID	INSNAME	INSTYPE	BAND	DIGITAL	SAMPRATE	NCALIB	NCALPER	FILENAME	RSPTYPE	LDDATE
LHE	10000083	SDSE-1	SDSE-1	l	d	1	0.06966	31.25	/g/rsp/Responses_LANL/ZAL_lp.1	paz	2004-09-01 12:08:02.0
LHN	10000083	SDSE-1	SDSE-1	l	d	1	0.06966	31.25	/g/rsp/Responses_LANL/ZAL_lp.1	paz	2004-09-01 12:08:02.0
LHZ	10000083	SDSE-1	SDSE-1	l	d	1	0.06966	31.25	/g/rsp/Responses_LANL/ZAL_lp.1	paz	2004-09-01 12:08:02.0
MHE	10000086	SDSE-1	SDSE-1	m	d	5	0.11246	6.25	/g/rsp/Responses_LANL/ZAL_mp.1	paz	2004-09-01 12:08:02.0
MHN	10000086	SDSE-1	SDSE-1	m	d	5	0.11246	6.25	/g/rsp/Responses_LANL/ZAL_mp.1	paz	2004-09-01 12:08:02.0
MHZ	10000086	SDSE-1	SDSE-1	m	d	5	0.11246	6.25	/g/rsp/Responses_LANL/ZAL_mp.1	paz	2004-09-01 12:08:02.0
SHE	10000089	SDSE-1	SDSE-1	s	d	40	0.0049	0.3125	/g/rsp/Responses_LANL/ZAL_sp.1	paz	2004-09-01 12:08:02.0
SHN	10000089	SDSE-1	SDSE-1	s	d	40	0.0049	0.3125	/g/rsp/Responses_LANL/ZAL_sp.1	paz	2004-09-01 12:08:02.0
SHZ	10000089	SDSE-1	SDSE-1	s	d	40	0.0049	0.3125	/g/rsp/Responses_LANL/ZAL_sp.1	paz	2004-09-01 12:08:02.0

Figure 6. Site query and information pages for a single station (ZAL). In addition to standard site information, affiliation, sitechan, sensor, and instrument data are also displayed. Users may also plot a map of the site.

The COLASSOC table associates a given COLDESCRIPT with a TABDESCRIPT. The table will have multiple columns (column positions 1 through the total number, in order), and columns can appear in multiple tables. The column type will define the basic function of the field in the database (i.e., primary key, unique key, descriptive data, measurement data, administrative data). *Key* allows key columns to be identified with respect to the table: the reference table for the key, or a table in which the key is foreign. These keys are primarily numerical identifiers. Keyschema is used when the reference table is part of a separate schema.

The GLOSSARY table serves two purposes: The first is to simply define generic strings used in various description fields, primarily acronyms and abbreviations. The second is to serve as the reference table for 'defined' range types and 'finite set' range types. A given definition can apply in all circumstances (column_name, table_name, owner and schema are all not set), which is a generic definition, or it can apply to increasingly selective subsets of columns, tables, owners, and schemas. For 'defined' and 'reference set' range types in COLDESCRIPT, the complete permitted set of values will be found in GLOSSARY, one entry for each value (values are found in the name column), and *column_name* will always be set for these.

Having such schema information in database form has proven beneficial to a wide variety of efforts involving the database, both specific to Los Alamos, and across NNSA. This schema for table description metadata is a key contribution to the web-based database documentation discussed in this paper. It is also the foundation for automated QC efforts at LANL (see below). The schema tables have changed slightly over the past year, in response to experience using it at LANL and elsewhere. The tables provide immediate advantages in the maintenance of the schema descriptions, such that they can be easily checked for errors, quality, and completeness. The use of the TABDESCRIPT, COLDESCRIPT, and COLASSOC tables is becoming fairly well established. The GLOSSARY table has more recently seen greater use and has proven helpful in QC of text fields and in finding full descriptions of various text-based values such as phase names or authors (e.g., "just what is SPdifKS?", "is there a reference for "SIB:AT62"?").

Logistical Information

The LANL web technology access not only displays seismic and schema information, but has interfaces to allow researchers to handle logistical tasks such as requesting waveform, picking, and catalog data, submitting problems encountered with the database, and viewing identifier values for database primary key fields. Both of these functions

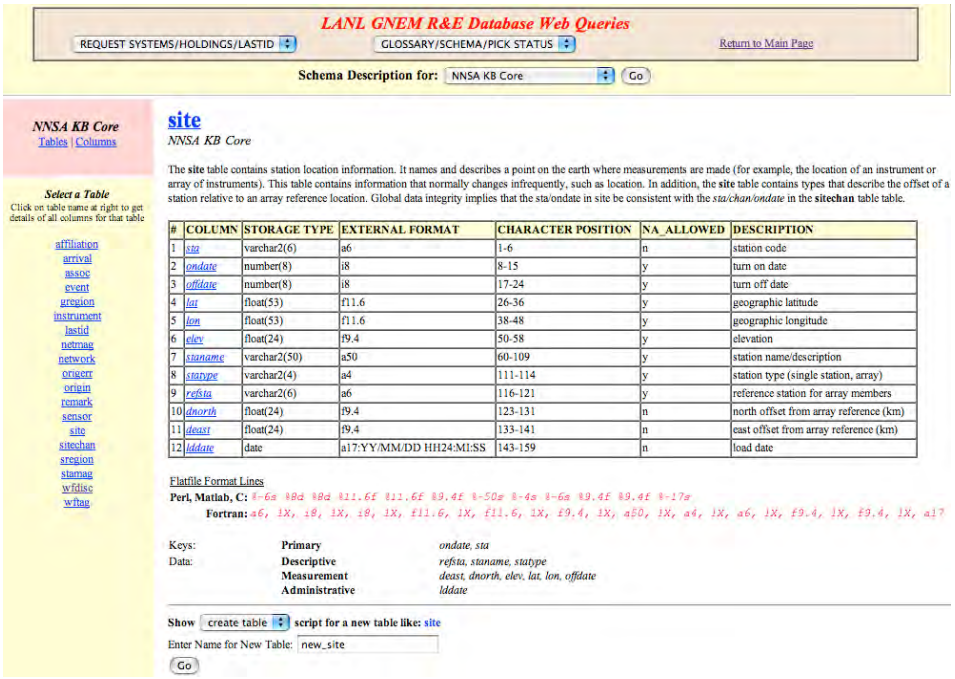

Figure 7. View of schema web page. Any schema can be displayed with links pointing to table descriptions as well as individual column descriptions. Other web pages are also used to directly edit the schema information.

enable tracking of pending and completed data requests and listed database problems.

For the new Data Request System (DRS) (Figure 8), users can request that waveform, arrival picks, or catalog data be acquired for use in their research projects. Requests are entered into the system, logging who made the request along with the request details, and notifications are automatically sent to members of the LANL Data Management Team. A member of the team then accepts the request, retrieves the data, and sets the status of the request to "Completed." During this process, the person who originally made the data request is automatically notified of changes in status or comments from the "Acceptor." This formal method for data requests allows tracking of researcher needs and reduces instances of miscommunication.

Quality Control and Assurance

As data become more voluminous and complex, QC has become a challenging and extremely interesting issue to consider when developing content for the KB. In particular, because of recent advances in tools that access KB data, researchers have been able to make more efficient use of this large volume of data but have also found inconsistencies in applying the data to their research efforts. Improvements in QC procedures are helping researchers and data managers to more readily identify complex quality problems. The outcome is improved research products resulting from improved data upon which those products are based. QC is handled in a wide variety of ways at the present, and much effort is being made to better structure this procedure and automate as much of it as is practical to do so.

There are three main categories of QC: manual, tool-assisted, and automated. Improvements in manual QC are occurring constantly as a wider variety of issues are captured and understood. But this kind of QC is the least transportable and repeatable. The next step is to capture the tracking and resolution of QC problems in various simple tools, usually case-specific scripts. Tool-assisted QC is more transportable and repeatable, since the script serves as documentation of procedures but it still requires case-by-case modification and application. Automated QC is preferred and cannot happen without there first being a fairly comprehensive understanding of the problem.

The best approach to automated QC is to document exactly what the database should be and reject anything that does not conform. This approach is why the database descriptive schema discussed above has been a valuable tool in automated QC. This cannot address all QC issues (for example, QC of waveforms), but will handle the bulk of the information in the database. LANL now has an automated process that can be configured to run a very comprehensive QC against a wide variety of data sets that may be incorporated into the KB. Since it is based on the content of the schema tables (i.e., TABDESCRIPT, COLASSOC, COLDESCRIPT, GLOSSARY), it can readily handle the addition of new custom tables for particular data sets. It produces a comprehensive QC report that greatly speeds the identification of problems that need to be addressed. This was of great help, for example, in preparing the recently delivered Siberian dataset, which was a highly heterogeneous collection of data from a wide variety of sources. The process is based on the schema tables, uses a simple parameter file, and implements single-column and single-table tests, two-table joins, and the notorious "wftag"-type join. It also extends these tests and joins using a special database table called COMPLEXJOIN, that permits a wide variety of complex relationships including

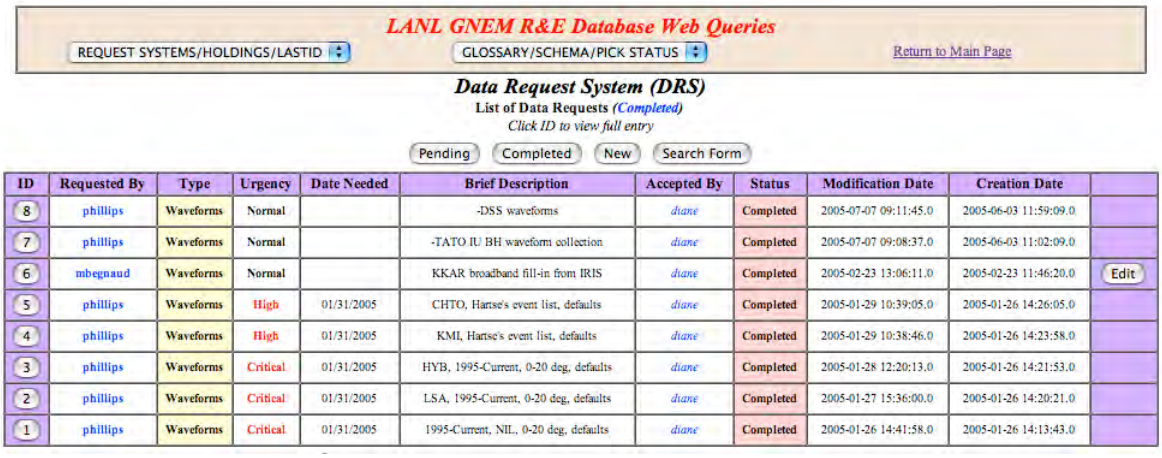

Figure 8. Data Request System page showing "Completed" requests.

grouping relationships (i.e., comparing origin.nass to assoc), multi-table joins (ex: comparing wfdisc.instype to instrument.instype), and computations (i.e., comparing origin.time to origin.jdate). Future development in this area will examine the possibility of automating the repairs, in addition to just the QC. In general, QC remains a large problem and GNEM R&E is making new and unique contributions toward resolving this important problem.

Bulletin Descriptive Tables

An advance in using schema information for QC has been the creation of bulletin descriptive tables. These tables describe the sources of bulletin data that have been imported into the data warehouse, as well as providing a means to track individual data elements to the corresponding lines of text in the original document. There are two tables involved: BULLETIN and BULLASSOC. The BULLETIN table contains one entry for each individual bulletin, with columns *dir* and *dfile* pointing to the text file on the system that contains the bulletin. It also has a *bullid* column that is unique to each bulletin. The other information in the table describes the bulletin, including format. The BULLASSOC table has one line for each data object extracted from the bulletin (origins, arrivals, magnitudes, etc.) It links the *bullid* and the *id* of the extracted object and provides the line number in the bulletin corresponding to the object. These tables have immediate use in QC. First, they allow problematic objects to be traced directly to the corresponding file and line number. Second, they can be used to extract the entire contents of a single bulletin from the integrated database when the need to remove or replace the data from a particular bulletin arises.

Segmenting Continuous Waveforms

Over the years LANL has acquired segmented and continuous waveforms from many different sources in formats such as SEED, SAC, CSS (with accompanying WFDISC lines), GSE, and SEGY. To make these data readily available to researchers, we have developed a PERL code that uses a database interface (the “PERL DBI”) to assemble user-specified, event-based wave segments into SAC files. We call this code "wfdisc2sac.pl", because it requires a database WFDISC line description of each waveform that might be cut and transformed into SAC format.

For the case of SEED data handling, wfdisc2sac.pl calls the executable “rdseed”. To run the code, a user builds a list of EVIDs that correspond to events of interest and specifies a list of desired stations and channels. The user can also specify desired time window lengths of the final SAC waves based on Jeffreys-Bullen travel-time tables. If ORIGIN, SITE, and ARRIVAL tables are available, wfdisc2sac.pl will use the PERL DBI to query these tables and find information to populate the newly created SAC header fields. To prevent accidental recutting of segments already listed in the LANL WFDISC table, an option is available to check for existing segments prior to attempting a fresh cut on continuous data. A second PERL code builds WFDISC flat file lines that can be immediately inserted into the WFDISC table.

Database Synchronization - Capturing and Propagating Data Changes

Calibration efforts by LANL researchers require the use of three separate databases that are physically unable to communicate with each other: two within LANL, and one at a remote site. Because of the lack of direct communication between these databases, maintaining data synchronization between them is difficult. The content of these databases is such that some data are common to all the databases, some data are common between only two of the databases, while some data are allowed to exist only at the remote location. While it is relatively simple to add new data to all databases, it is difficult to capture changes such as updates or deletes made in one and then propagate them to the other two.

We have recently developed a procedure based on database triggers to capture changes made to core database tables. This procedure has been in place for about one year, and results to date have been satisfactory. The changes being monitored on the predefined set of tables are data inserts, updates, and deletes. This process is referred to as Capture Data Changes (CDC). The acronym, as well as the fundamental idea, is similar to Oracle’s Change Data Capture method of implementing the incremental recording of data changes. The main difference between Oracle’s implementation and LANL’s is that our method does not depend on a particular version of the Oracle Relational Database Management System (RDBMS). Oracle’s CDC method is directly tied to a specific application that must be installed, configured, and run against an Oracle 9i database. Our procedure is entirely based on database triggers, which are available on any version of the Oracle RDBMS; thus, our implementation is not tied to any particular version of the Oracle database and can be implemented on any platform.

The concept is simple. Database triggers are created against a predefined set of tables to be monitored. These triggers fire upon insert, update, or delete operations against these tables. The triggers capture unique information about a row being inserted, deleted, or updated. Our implementation of capturing only the information needed to uniquely identify a changed row in a table leads to significant disk space savings.

An interesting by-product of our synchronization procedure is that we not only capture unique information about the rows being modified in the tables being monitored, but we also capture the modification date and the name of the database user who made the modification to each row. This information, together with the built-in database auditing capabilities that can be enabled at the table level, can serve the secondary purpose of providing a security audit trail to be able to answer questions regarding changes made to critical production data.

The synchronization operation between the source database and the two target databases is a manual process at this time. The synchronization operation starts after a predetermined number of changes have occurred in the source database tables. A special set of tables is created from the unique information captured by the triggers that contain the table structure and changed rows of data from the source tables that will be used to replace the outdated information in the target databases. The second and final step of the synchronization process is done on the target databases, both at LANL and at the remote location. First, we delete from and insert rows into the target tables. The rows to be deleted in the target databases are the rows that were either updated or deleted from the original source tables. In this step, the decision was made to replace the entire row when an update occurred in the source table, rather than try to make a column-by-column comparison to only update specific columns in the target table. The latter choice would be costlier in terms of computer resources.

CONCLUSIONS AND RECOMMENDATIONS

Developing web technology interfaces to handle common database queries has allowed LANL researchers to access data more readily and efficiently. Specific information for seismic events can be retrieved quickly with ties to relevant information. Utilizing protected web interfaces allows users to view data remotely and helps in synchronizing data retrieval and processing tasks. We are continually finding new reasons and ways to securely access the database through the web. Future web technology development includes tracking processing steps for waveforms, picking, amplitudes, etc., as well as improving QC checks. In addition, we are working on better methods for viewing and interacting with waveform and map data via a web interface.

QC has become an increasingly visible and important issue regarding the KB, as data have become more voluminous and complex. Improvements in QC procedures will help researchers and data managers to more readily identify complex quality problems. The outcome is improved research products resulting from improved data upon which those products are based.

The process of CDC shows great promise. It is expected that we have not encountered all possible use cases, and modifications to the process will need to be made and perhaps auxiliary tables or triggers will need to be created. This process has been in place for about one year and it appears to be successful. Many of the steps involved in synchronizing local and remote databases are manual, and direct interaction with the databases is needed throughout the process. Future work includes the automation of many of the synchronization steps and the incorporation of appropriate quality control checks to ensure that the synchronization between databases was successful.

ACKNOWLEDGEMENTS

The authors wish to acknowledge LANL personnel who have made important contributions in the past and those who continue to make vital contributions to the development and maintenance of the LANL research data warehouse: Diane F. Baker, Marian D. Peters, W. Scott Phillips, George E. Randall, James T. Rutledge, and Steven R. Taylor,

REFERENCES

Carr, D. (2005), *National Nuclear Security Administration Knowledge Base Core Table Schema Document*, Sandia National Laboratories report SAND2002-3055.

NEW GROUND TRUTH CAPABILITY FROM INSAR TIME SERIES ANALYSIS

Sean M. Buckley[1], Paul Vincent[2], and Dochul Yang[1]

University of Texas at Austin[1] and Lawrence Livermore National Laboratory[2]

Sponsored by National Nuclear Security Administration
Office of Nonproliferation Research and Engineering
Office of Defense Nuclear Nonproliferation

Contract Nos. DE-FC52-03NA99566[1] and W-7405-ENG-48[2]

ABSTRACT

We demonstrate that next-generation interferometric synthetic aperture radar (InSAR) processing techniques applied to existing data provide rich InSAR ground truth content for exploitation in seismic source identification. InSAR time series analyses utilize tens of interferograms and can be implemented in different ways. In one such approach, conventional InSAR displacement maps are inverted in a final post-processing step. Alternatively, computationally intensive data reduction can be performed with specialized InSAR processing algorithms. The typical final result of these approaches is a synthesized set of cumulative displacement maps.

Examples from our recent work demonstrate that these InSAR processing techniques can provide appealing new ground truth capabilities. We construct movies showing the areal and temporal evolution of deformation associated with previous nuclear tests. In other analyses, we extract time histories of centimeter-scale surface displacement associated with tunneling. The potential exists to identify millimeter per year surface movements when sufficient data exists for InSAR techniques to isolate and remove phase signatures associated with digital elevation model errors and the atmosphere.

OBJECTIVES

The goal of this study is to assess new satellite SAR data and InSAR processing techniques for improvements to current remotely-sensed ground truth collection capability for determining seismic source location, depth and characterization. Specifically, we are

- applying InSAR time series analysis to sets of European Remote Sensing Satellite (ERS) and Envisat radar interferograms and
- using InSAR results to constrain geophysical source modeling to improve determinations of seismic source location, depth, and mechanism.

RESEARCH ACCOMPLISHED

This paper presents results from the application of an InSAR time series technique in which a linear inversion is applied to a database of interferograms to produce a sequence of interferograms which show cumulative deformation relative to a reference start date. We present results for two sites of interest: Lop Nor, China, nuclear test site and London, UK, underground tunnels. In both cases, we detect a time evolution of displacement signals that would not be possible using standard processing techniques. The new time series allow for more detailed analyses of the location and time history of subtle deformation signals and provide more accurate ground truth information from the same InSAR dataset.

Methodology

The goal is to obtain deformation measurements at each of the SAR acquisition dates for a set of interferograms overlapping in time and exhibiting generally good coherence. The result is a history of cumulative deformation relative to a user-selected SAR reference date.

This InSAR time series problem can be formulated as a linear system of equations (Usai, 2001; Schmidt and Bürgmann, 2003):

$$Ax = b\,, \qquad (1)$$

where b is an array of input interferogram displacements, x is the estimated cumulative deformation at each of the SAR acquisition dates, and A is a matrix relating the measurements to the parameters to be estimated. A single output date is associated with a column in A. The rows correspond to the input interferograms with the measured displacement assumed to be the difference between the estimated cumulative subsidence values between two image dates. Specifically, each row of A contains the following integer values: +1 at the interferogram reference date, –1 at the interferogram secondary date, and zeros for all other dates.

We find the solution x to the linear system through singular value decomposition. To address error propagation, error estimates associated with each of the input interferograms can be computed by summing the phase noise and Digital elevation model (DEM) error variances. Errors of the estimated displacements x are then computed as the square root of the main diagonal elements of the output covariance matrix:

$$\operatorname{cov} x = \left(V\Lambda^{-1}U^T\right)\operatorname{cov} b\left(V\Lambda^{-1}U^T\right)^T \qquad (2)$$

where $A = U\Lambda V$ is the singular value decomposition. The decomposition is readily obtained from any number of computational software packages.

The InSAR time series analysis examples presented in the next two sections were performed as an InSAR post-processing procedure. In other words, conventional differential InSAR processing was followed by an inversion of the geocoded displacement maps. Some other approaches, e.g., permanent scatterer analysis, require specialized intermediate processing steps to generate the final time series. Our post-processing strategy is motivated by a desire

to make best use of any number of conventional InSAR software packages and provide a means to easily extend the analysis of a study site when additional data is obtained.

Lop Nor, China Nuclear Test Site

InSAR data processing began with image formation for 15 SAR data acquisitions spanning 1996-1999 (Table 1). One hundred and five initial interferograms were created from the possible image-pair combinations. The maximum spatial and temporal baselines were 327 meters and 1191 days. The initial interferograms were evaluated and several discarded due to decorrelation. A mosaic of Shuttle Radar Topography Mission (SRTM) 3-arcsecond digital elevation model data was used to remove the topographic phase variations from the remaining interferograms.

The InSAR processing resulted in 101 geocoded maps consisting of radar line-of-sight displacements at 3-arcsecond horizontal postings. Errors corresponding to each output product pixel were assumed to come from two sources: phase noise associated with interferogram decorrelation and DEM errors. Phase standard deviations were calculated from the correlation coefficient, and a 10-meter SRTM one-standard deviation height error was used for time series error analysis. Atmospheric phase variations are also superimposed on the displacement measurements.

The 101 geocoded displacement and corresponding error maps were inverted to arrive at a time series of 14 synthetic displacement maps, one at each of the radar acquisition dates (Table 1, Figure 1). The 19960730 and 19980804 images are noticeably afflicted with atmospheric artifacts. Time series plots of several features of interest were extracted (Figure 2) and show ground motion both toward and away from the radar.

Figure 1 shows a time series of cumulative deformation observed of the Lop Nor, China, nuclear test site relative to a start date of January 1, 1996. Each frame represents cumulative deformation from the reference date (1/1/96) to the date labeled in the frame (e.g., the first frame labeled 960416 represents the cumulative deformation between Jan. 1, 1996 and April 16, 1996). The top row of frames shows no significant deformation occurring between 1/1/96 and 5/21/96. A deformation signal is suspected in the first frame of the second row (960730), but this frame is also contaminated with significant atmospheric noise. In the second frame of the second row, there is much less atmospheric noise, and the suspected deformation signal remains. This demonstrates how the time series helps identify and confirm suspect deformation signals. We know from published literature that there was an underground nuclear test conducted in the vicinity of the InSAR signal on 96/06/08 (Waldhauser et al., 2004). We are comparing these signals with those from the Nevada Test Site (Vincent et al., 2003) to learn more about the effect of rock type, etc. on the surface deformation signals from underground nuclear tests to be in a better position to use InSAR to help identify potentially clandestine nuclear test activities.

London, UK Underground Tunnels

We began our analysis of London with 31 SAR acquisitions distributed over the period 1992-2001 (Table 1). Due to the carefully controlled nature of the ERS-1 and ERS-2 orbits over Europe, we found all 465 potential SAR data pairs to have spatial baselines suitable for interferometry. We were able to visually inspect and remove initial interferograms with significant atmospheric variability associated with the 19960816, 19970801, 19971219, and 19990319 SAR acquisitions. SRTM DEM data was used to remove the topographic phase signature from interferograms with spatial baselines less than 200 meters. After performing consistency checks between combinations of interferograms, 211 3-arcsecond radar line-of-sight displacement maps were inverted using the InSAR time series approach previously discussed.

Figure 3 shows our time series results for London, UK, where a subsidence signal increases linearly with time over an underground utility tunnel owned by London Electric Company. Figure 4 shows a plot of the deformation time series associated with a single pixel in the deformation maps. A linear trend of indicates ongoing subsidence from 1993 through 2001. This tunnel is known to be 60 feet underground in a thick clay layer, which suggests that a soil creep dynamic may be responsible for the observed linear subsidence with time. We are currently working on a soil creep finite element model to simulate this creep process. The ability to identify the rate of subsidence with time is critical for accurate simulations of the subsurface processes causing the observed signals. We are also working on modeling similar tunnels in solid and fractured rock that have nonlinear deformation with time, as well as damage zones above past underground nuclear tests, e.g., Vincent et al. (2003).

CONCLUSIONS

InSAR time series approaches provide an organizational framework for the use and interpretation of InSAR deformation products resulting from anything more than a handful of SAR images. We have applied one such approach to two sites of interest: Lop Nor, China, and London, UK. Our results show detailed temporal and spatial information not easily obtained from the tens of displacements maps generated with conventional InSAR processing. The Lop Nor time series shows surface deformation appearing at the time of a known underground nuclear test as well as other interesting features that are under further investigation. The London time series shows the appearance and steady increase of subsidence with time associated with a known underground tunnel. The new observations afforded by InSAR time series analysis provide more detailed ground truth information which can be used to produce more accurate, time-dependent deformation models and better constrain seismic and aseismic subsurface sources of deformation. This information can ultimately help location and identification studies if a sufficient number (>10) of SAR image acquisitions are available.

ACKNOWLEDGEMENTS

We thank Krishnavikas Gudipati at UT-Austin for developing the InSAR linear inversion software used in this analysis. ERS original SAR data were provided by the European Space Agency copyright 1993-2000. Additional data purchases were made by the WInSAR consortium with funding from the National Aeronautics and Space Administration, United States Geological Survey, and the National Science Foundation.

REFERENCES

Schmidt, D. A. and R. Bürgmann (2003), Time-dependent land uplift and subsidence in the Santa Clara valley, California, from a large interferometric synthetic aperture radar data set, *J. Geophys. Res.* 108: (B9), 2416, doi:10:1029/2002JB002267.

Usai, S. (2001), A New Approach for Long Term Monitoring of Deformations by Differential SAR Interferometry, Ph.D. Dissertation, Delft University of Technology, The Netherlands.

Vincent, P., S. Larsen, D. Galloway, R. Laczniak., W. Walter, B. Foxall, and J. Zucca (2003), New signatures of underground nuclear tests revealed by satellite radar interferometry., *Geophy. Res. Let.*, 30: 2141.

Waldhauser, D., D. Schaff, P. G. Richards, W. Y. Kim (2004), Lop Nor revisited: underground nuclear explosion locations, 1976-1996, from double-difference analysis of regional and teleseismic data, *Bull Seim. Soc. Am*. 94, 1879-1889.

Table 1. Dates of SAR acquisitions used in Lop Nor and London InSAR time series analysis. Four London SAR acquisitions were discarded because they contained noticeable atmospheric artifacts.

Lop Nor

Date	Days Since Reference Date
19960101	0000
19960102	0001
19960205	0035
19960416	0106
19960520	0140
19960521	0141
19960730	0211
19970401	0456
19970819	0596
19971202	0701
19980106	0736
19980421	0841
19980804	0946
19980908	0981
19990406	1191

London

Date	Days Since Reference Date
19920505	0000
19920609	0035
19920818	0105
19920922	0140
19930209	0280
19930803	0455
19950413	1073
19950727	1178
19950831	1213
19950901	1214
19960816	Not used
19960920	1599
19970103	1704
19970314	1774
19970523	1844
19970627	1879
19970801	Not used
19971009	1983
19971114	2019
19971219	Not used
19980123	2089
19980403	2159
19990319	Not used
19990702	2614
19991015	2719
19991224	2789
20000127	2823
20000128	2824
20000407	2894
20001103	3104
20010112	3174

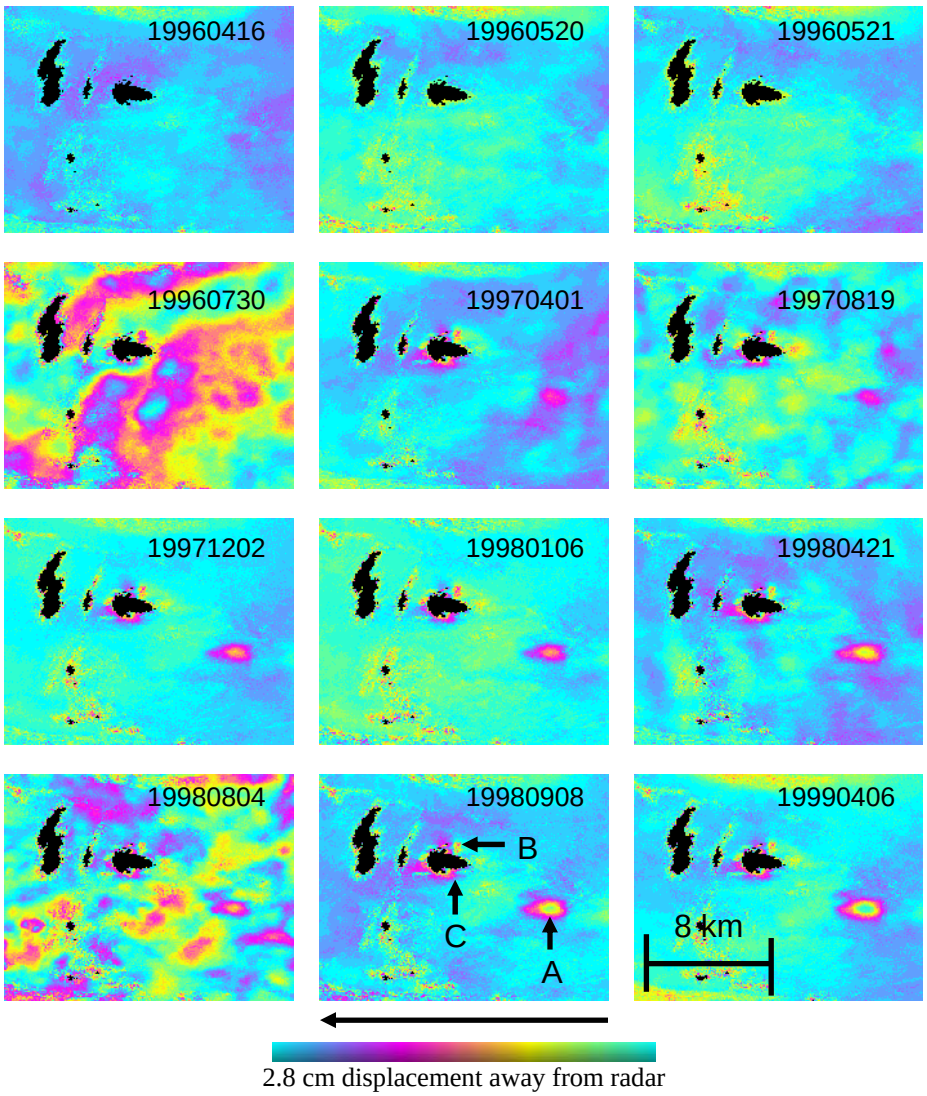

Figure 1. Maps of cumulative displacement since January 1, 1996 for Lop Nor. One cycle through color wheel represents 2.8 cm of radar line-of-sight displacement. The 19960730 and 19980804 images are noticeably afflicted with atmospheric artifacts.

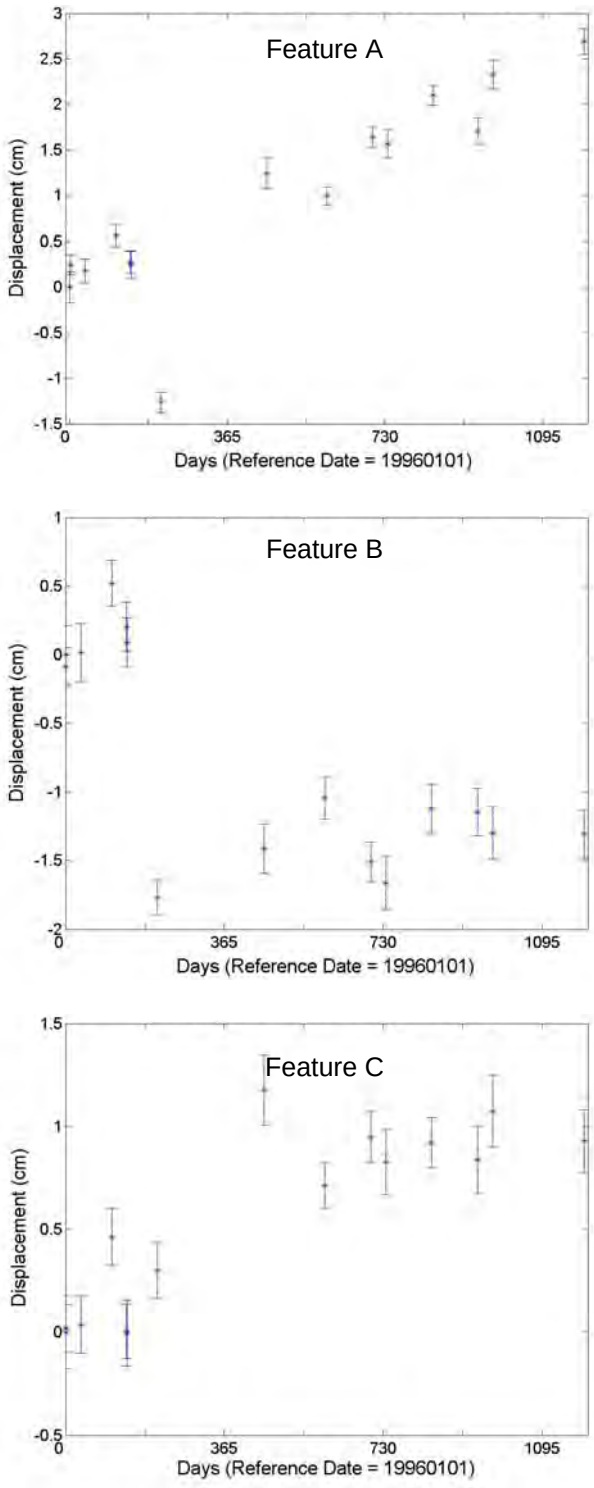

Figure 2. Cumulative displacement along radar line-of-sight since January 1, 1996 for features identified in previous figure. Positive (negative) displacement represents movement toward (away from) radar. Error bars correspond to one standard deviation for interferogram phase noise and SRTM DEM error variances propagated through inversion.

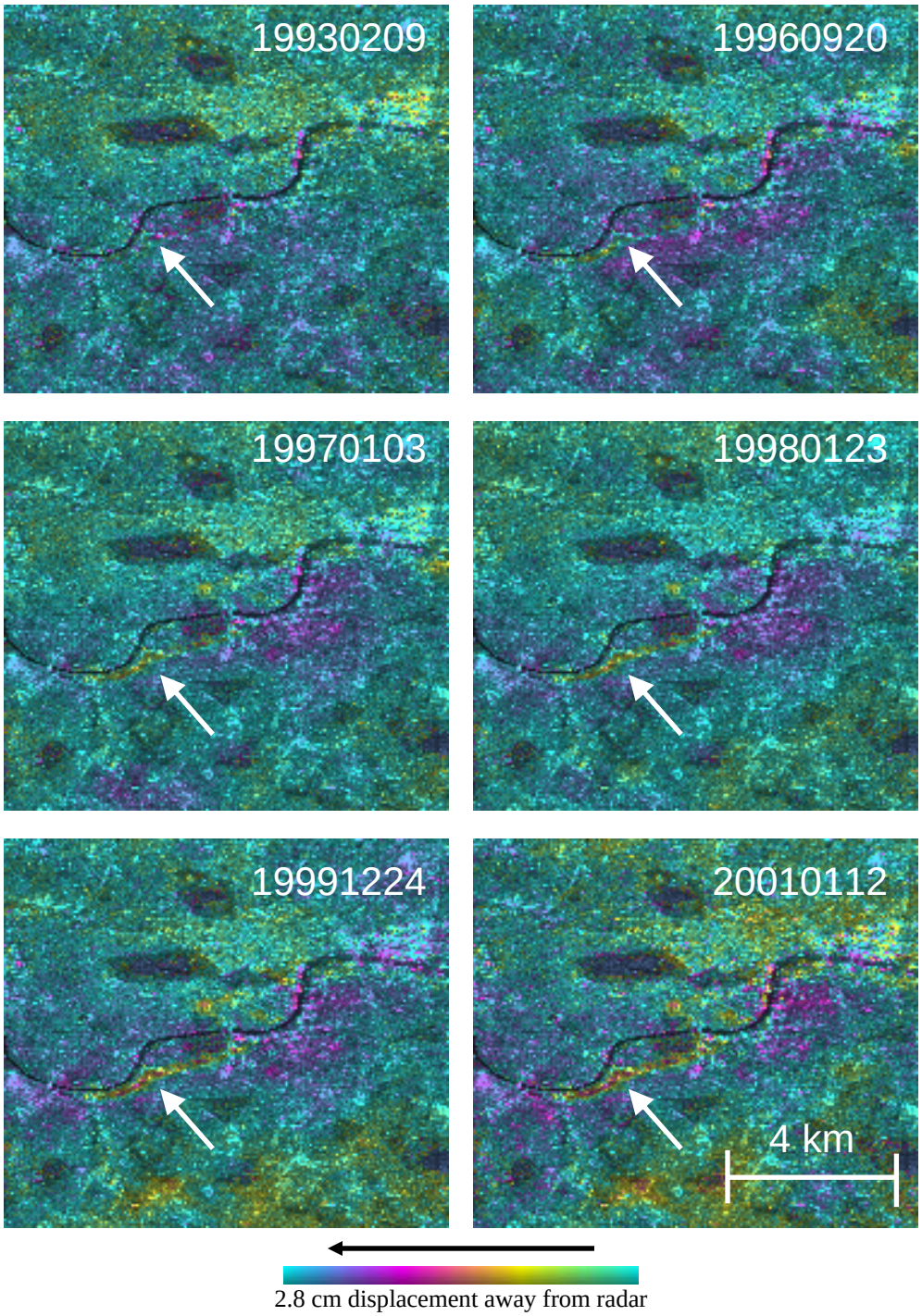

Figure 3. Maps of cumulative displacement since May 5, 1992 for London tunneling area. One cycle through color wheel represents 2.8 cm of radar line-of-sight displacement.

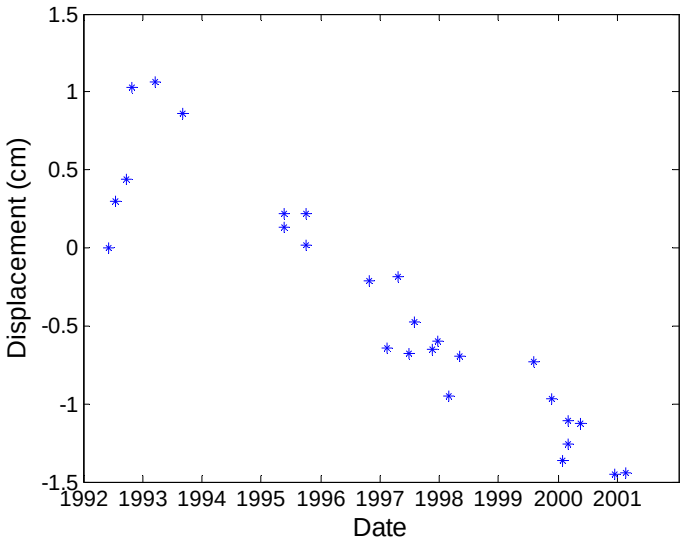

Figure 4. Cumulative displacement along radar line-of-sight since May 5, 1992 for London tunneling area identified by arrow in previous figure. Positive (negative) displacement represents movement toward (away from) radar.

THE 2005 MATSEIS AND NNSA SEISMIC REGIONAL ANALYSIS TOOLS

Darren M. Hart, B. John Merchant, J. Mark Harris, and Christopher J. Young

Sandia National Laboratories

Sponsored by National Nuclear Security Administration
Office of Nonproliferation Research and Engineering
Office of Defense Nuclear Nonproliferation

Contract No. DE-AC04-94AL85000

ABSTRACT

In continuing to support the National Nuclear Security Administration (NNSA) Knowledge Base (KB), we developed a set of prototype seismic regional analysis tools (MatSeis, EventID Tool, CodaMag Tool, PhaseMatch Tool, and Infra Tool) to facilitate evaluation of new KB data products, and we continue to maintain and improve these tools. A brief description of the latest versions of MatSeis and the regional analysis tools are given below. MatSeis has been extended to use the FISSURES data handling interface (DHI) client FISSURES-Matlab-Interface (FMI) to connect to both the Northern and Southern California data centers located at Berkeley and Caltech, respectively. A routine was built to support instrument response file download and to automatically perform waveform conversion from counts to nanometers. In addition, both SENSOR and INSTRUMENT flatfile database tables are now exportable through the "waveform write" function. For PhaseMatch Tool, a new method has been added to select station-event pairs for dispersion curve calculations. The user is presented with a list of available stations for a given event, and by selecting from the list, a great circle path is highlighted and the dispersion curve presented. Infra Tool now has the ability to remove a specified signal (i.e., signal-subtraction) from its analysis, in an attempt to detect secondary signals. Preliminary results demonstrate complete removal of the specified signals, allowing for further analysis of residual FK plane. Work is continuing in this area to refine methodology and increase user functionality. For CodaMag Tool, the station-specific MDAC source spectrum and S-wave corner frequency are computed and displayed for reference on the moment spectrum determined by modeling the coda magnitude. Also, Mw is read from any available sources (i.e., STAMAG, NETMAG and DISCRIM_DATA) and displayed as an internal consistency check. For EventID Tool, the amplitude measurement type was switched to the time-domain RMS (TRMS) method, and we have also implemented linear discrimination analysis (LDA), and developed a new tool for computing integrated attenuation maps for a user specified location. In this paper, each of the aforementioned additions are described in greater detail with regard to usage and where relevant, their underlining theory.

OBJECTIVE

MatSeis and the regional analysis tools continue to provide an excellent prototyping environment in which promising seismic analysis techniques can be implemented and evaluated quickly and with relatively little effort. These products are now all fairly mature, but development on them continues in response to the research results from our co-workers at LANL and LLNL and to feedback from our users at other institutions.

RESEARCH ACCOMPLISHED

The following sections describe the latest versions of MatSeis, and the regional seismic analysis tools – PhaseMatch Tool, Infra Tool, CodaMag Tool and EventID Tool.

MatSeis

The main MatSeis graphical window is a standard time vs. epicentral distance plot that can display waveforms, arrivals, origins, and travel time curves. The user can interact with this display by clicking directly on the displayed objects, by using the buttons along the bottom, by using the menus along the top, or by typing commands at the Matlab prompt. MatSeis is predominantly written as Matlab m-file functions, which are organized in a set of directories according to the general purpose of each. However, the package also includes a set of compiled C functions and Java objects. Typically the compiled code is introduced where performance of an m-file is too slow (e.g., FK calculations) or cumbersome (e.g., managing the waveform, arrival, origin, and travel time objects). For a more detailed description of the features in MatSeis, see Hart and Young (2004).

MatSeis continues to be available to the public from the NNSA NEM R&E website (https://www.nemre.nnsa.doe.gov/cgi-bin /prod /nemre/matseis.cgi). We have introduced a new method for tracking downloads of MatSeis that allows us to compile a list of registration information provided by users and create maps of user locations. Our first map of this type is shown in Figure 1, detailing the broad distribution of MatSeis, especially in Western Europe and the east coast of the United States.

Data Center Access

For the last several versions, MatSeis has been reading data from two standard sources: Java database connectivity (JDBC) compliant database tables (e.g., Oracle) and flatfile database tables, each following the NNSA Core Schema (Carr, 2002). In a recent collaboration with University of Washington and IRIS DMC, MatSeis is now able to read data directly from suitably equipped data centers, across the internet. This is possible through FISSURES DHI client services and the DHI client FISSURES-MATLAB-INTERFACE (FMI). Initially, work was done to connect to the IRIS DMC event, network and seismogram server. Once these connections were established and tested, work proceeded to connect to other data centers that were running the same FISSURES DHI client services. These data centers are the Northern California Earthquake Data Center (NCEDC) located at the University of California – Berkeley and the Southern California Earthquake Data Center (SCEDC) located at the California Institute of Technology. Our main goal in this task was to establish connections to the seismogram and network servers for the retrieval of waveform and instrument response data. Over time, the connections were established and routines were developed to use the FMI client as the backbone for download. Once this basic capability was available in MatSeis, we were then able to work on more detailed use cases. One of these was the conversion of retrieved waveforms from counts to nano-meters (nm). In this use case, the user sets up a time-window based query, start time and duration, and specifies the network, station, channel and location code desired for download. The provided information is used by the data center to search its holdings and reply with the number of waveforms that met the provided criteria. The user can use the received information about available holdings to further restrict which waveforms to download, by specifying limits in latitude/longitude coordinates or by distance/azimuth. In the end the user will select to retrieve the waveforms. Once the waveforms are retrieved, the user is prompted to decide whether waveform calibration is desired. If it is, then a list is built of the waveforms network(s), station(s), channel(s) and

location codes and used in querying the data center's network server for the instrument response files. The available instrument response files are then downloaded, saved to disk and then used to calibrate the waveforms to a specific frequency based on the waveform's associated channel type (e.g., UHZ calibration frequency equals 0.004 Hz, BHZ calibration frequency equals 1.0 Hz and HHZ calibration frequency equals 10.0 Hz). The downloaded instrument response files from a data center's network server are in SEED format and are based on the number of stage filters used by the instrument. The final step in this process was to build up routines for generating flatfile tables for SENSOR and INSTRUMENT so the instrument response associations would be available for future use. With these routines in place, a nearly complete set of flatfile database tables (e.g., arrival, assoc, instrument, lastid, netmag, origerr, origin, sensor, site, sitechan, and wfdisc) and data directories (i.e., /resp and /w) can be generated, upon export, after event processing during a MatSeis session.

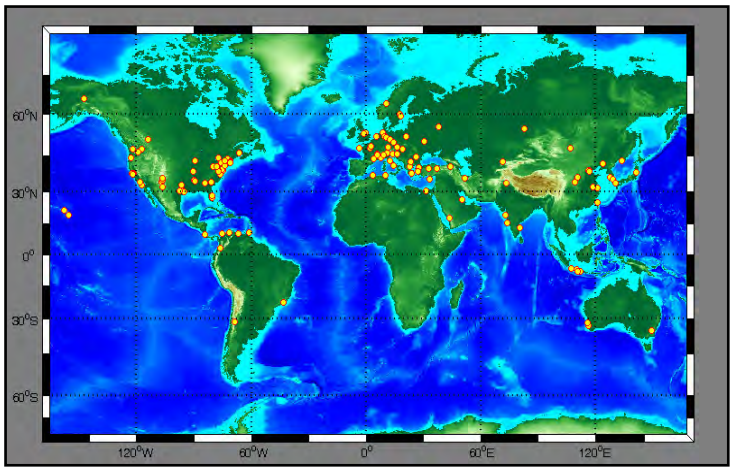

Figure 1. Map of locations for 167 separate MatSeis downloads from December 2004 through July 2005.

Phase Match Tool

PhaseMatch Tool is a waveform analysis interface launched from MatSeis that allows the user to calculate the predicted surface wave dispersion for a given source to receiver path by ray tracing through a model, and then use the model dispersion to generate and apply a matched filter (Herrin and Goforth, 1977). The tool allows the user to view the observed waveform, the model dispersion, the predicted waveform, the cross-correlation of the predicted and observed waveforms, and the match-filtered waveform. The user can control the frequency range of the model dispersion used, as well as the time limit of the portion of the cross-correlated waveform from which the match-filtered waveform is taken. Once a satisfactory filtering has been achieved, the user can send either the observed waveform or the filtered waveform to the MatSeis amplitude measurement widget -- Measure Tool -- to measure surface wave amplitudes. These amplitudes can then be used to determine event magnitude, which in turn can be used as part of an mb/Ms discriminant.

The new surface wave analysis features are part of the LR Path Tool, which we designed as a companion tool to Phase Match to allow the user to examine the dispersion models they are using. By loading an event and set of stations into MatSeis, launching the LR Path Tool and selecting the new button "Set to Map GC", MatSeis takes the selected origin and station list and builds the great circle paths for event-station pairs and presents them in MapTool. Then generates a listbox with station information (i.e., great circle object

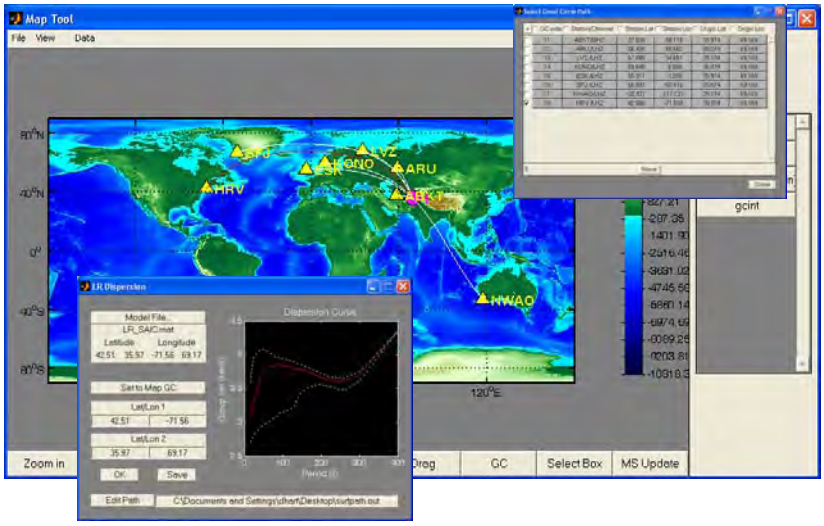

Figure 2. New LR Path Tool. The list of loaded stations is presented and the LR dispersion curve is updated based on station to event path.

index, station channel name, great circle path endpoint coordinates). After selecting a station from the list, the tool computes and displays its dispersion curve. Figure 2 illustrates the set of windows used while working with the new LR Path Tool.

Coda Magnitude Tool

CodaMag Tool is a waveform analysis interface launched from MatSeis that allows the user to calculate magnitudes and source spectra for an event of interest by fitting empirical decay functions to narrow-band coda envelopes of a given phase (currently Lg). The technique was developed by Mayeda and has been described in detail in several papers (Mayeda, 1993; Mayeda and Walter, 1996; Mayeda et al., 1999; Mayeda et al., 2003). The tool consists of two displays. The main one shows the calculated moment spectrum and the derived magnitudes. The second display, launched from the first, shows how the spectrum was derived. The user can adjust the Lg arrival window, examine the fit between the observed and synthetic envelopes, and control which frequency bands are used for the magnitude calculations. The various required parameters (frequency bands, groups velocity windows, decay curves, etc.) are read from parameter files unique to each station.

New features to version 1.10 include display of theoretical source moment–rate spectrum and S-wave corner frequency to help evaluate the quantities derived from the data. For computing the CodaMag theoretical source moment-rate spectrum, we started with the spectral shape defined by Brune (1970) given in Equation 1.

$$S(w) = \frac{So}{1 + (\frac{w}{w_c})^2} \qquad \text{Equation 1.}$$

Where S_0 is the zero frequency spectral level and w_c is the angular corner frequency. Since the moment-rate spectrum is required to have a zero frequency spectral level equal to the moment (M_0), the term S_0 in equation 1 is substituted with the moment, yielding Equation 2, which is the moment-rate spectrum plotted in CodaMag Tool.

$$\text{moment-rate spectrum}(w) = \frac{Mo}{1 + (\frac{w}{w_c})^2} \qquad \text{Equation 2.}$$

For calculation of the S-wave corner frequency we use the formulation by Walter and Taylor (2002), using station specific Magnitude-Distance Amplitude Correction (MDAC) parameters. Figure 3 shows a screen-shot of version 1.10 of CodaMag Tool, illustrating the new features of the tool.

The upcoming work on CodaMag Tool will include displaying values of Mw retrieved from different internal database sources (i.e. STAMAG, NETMAG and DISCRIM_DATA tables) to help evaluate the accuracy of coda magnitude calibration for a given station, multiple-band yield estimates by region, reading processing parameters from database tables, and storage of the processing parameters in database tables.

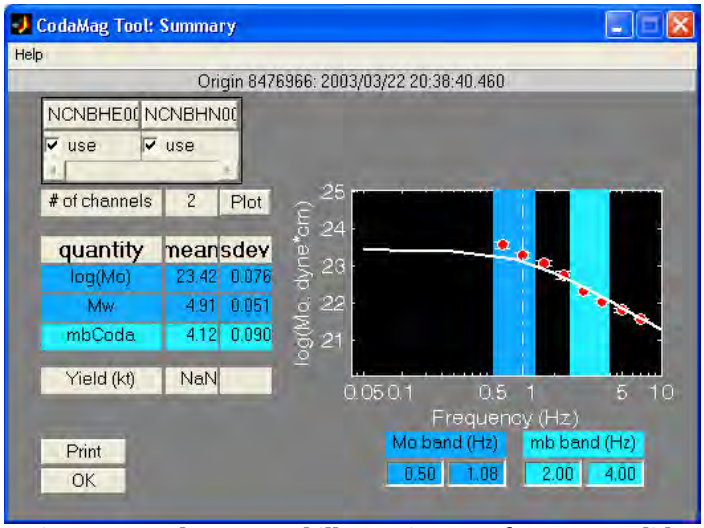

Figure 3. CodaMag Tool illustrating new features. Solid white line is the moment-rate spectrum, and vertical white dashed line is the S-wave corner frequency (f_{cS} = 0.84 Hz). Processing parameters provided by Kevin Mayeda of Lawrence Livermore National Laboratory.

Event Identification Tool

EventID Tool is a waveform analysis interface launched from MatSeis that allows the user to categorize an event of interest (i.e. explosion or earthquake) using spectral ratios of standard regional arrivals (see Hartse et al., 1997; Walter et al., 1999). This is a station-calibrated technique, and researchers must provide a set of station-specific calibration parameters that are stored in a set of database tables and assessed by the tool when processing an event of interest. The tool consists of three displays. The main display plots the phase ratio for the current event against a backdrop of the same ratio for archived events (if available) that have already been identified (event types are indicated with different symbology). The user can choose different phases and/or frequency bands to ratio to try to improve the separation of the earthquake and explosion populations, and the display will immediately update. A second display shows the user a plot of an "MDAC-o-gram" (i.e. the MDAC corrected measurements at all of the phase/frequency combinations) for the current event along with all of the archived events. This can be useful in deciding which ratio will yield the best separation. If there are questions about the amplitude measurements themselves, a third display can be brought up, and the user can easily examine group velocity windows for the phases and change them if necessary. If they are changed, the measurements will automatically be re-made and the ratios will be updated in the main display.

Version 1.10 of EventID Tool supports both time and frequency domain amplitude measurement types, as defined in the custom schema for DISCRIM_DATA (i.e. FREQ and TRMS). It also implements the linear discrimination analysis (LDA) technique, can run validation scripts, and can generate path-integrated attenuation (Q) maps. We describe these new features below.

In previous versions of EventID Tool, amplitude measurements were made in the frequency domain (i.e. FREQ f_t_type measurements), while the reference events were being read from the database based on their time-domain (i.e. TRMS f_t_type measurements) counterparts. In theory, the measurements are equivalent, but in practice, slight differences are observed, so a consistent method of amplitude measurement was desired. The tool will now compute both measurement types for the current event, and comparisons can be made using the MDAC-o-gram, as shown in Figure 4. Future work will focus on allowing more flexibility within the tool for switching between measurement types, both for validation and operational purposes. For a more detailed description of the TRMS and FREQ measurement techniques see Rogers et al. (2002).

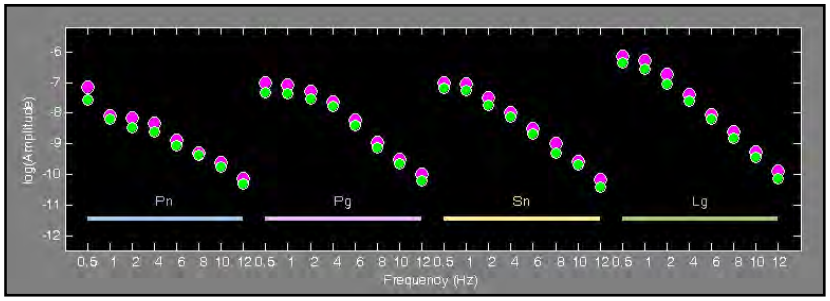

Figure 4. Plot demonstrating log(amplitude) measurement types FREQ (green) and TRMS (magenta) across 8 frequency bands (0.5-1 Hz, 1-2 Hz, 2-4 Hz, 4-6 Hz, 8-10 Hz, 10-12 Hz and 12-16 Hz). In the case shown here, the log residual differences (i.e. TRMS-FREQ) had a standard deviation of 0.113 about the mean of 0.211 for Pn, 0.066 about the mean of 0.207 for Pg, 0.057 about the mean of 0.194 for Sn and 0.067 about the mean of 0.207 for Lg.

For evaluation of the LDA technique, new controls were added to implement this method as unobtrusively as possible without interfering with the existing single-ratio discriminant capability. As seen in Figure 5, the previous methods for selecting phase, spectral and cross-spectral ratios are located just above the new section for selecting and editing a LDA string. The user controls the active method by selecting from a radio-button, "on" or "off", switch. Upon selecting one of the discrimination methods the other methods controls are disabled ensuring that the tool and user are clear as to the desired functionality. There are many ways to implement LDA within the tool; we anticipate further work on refining this interface based on feedback from users.

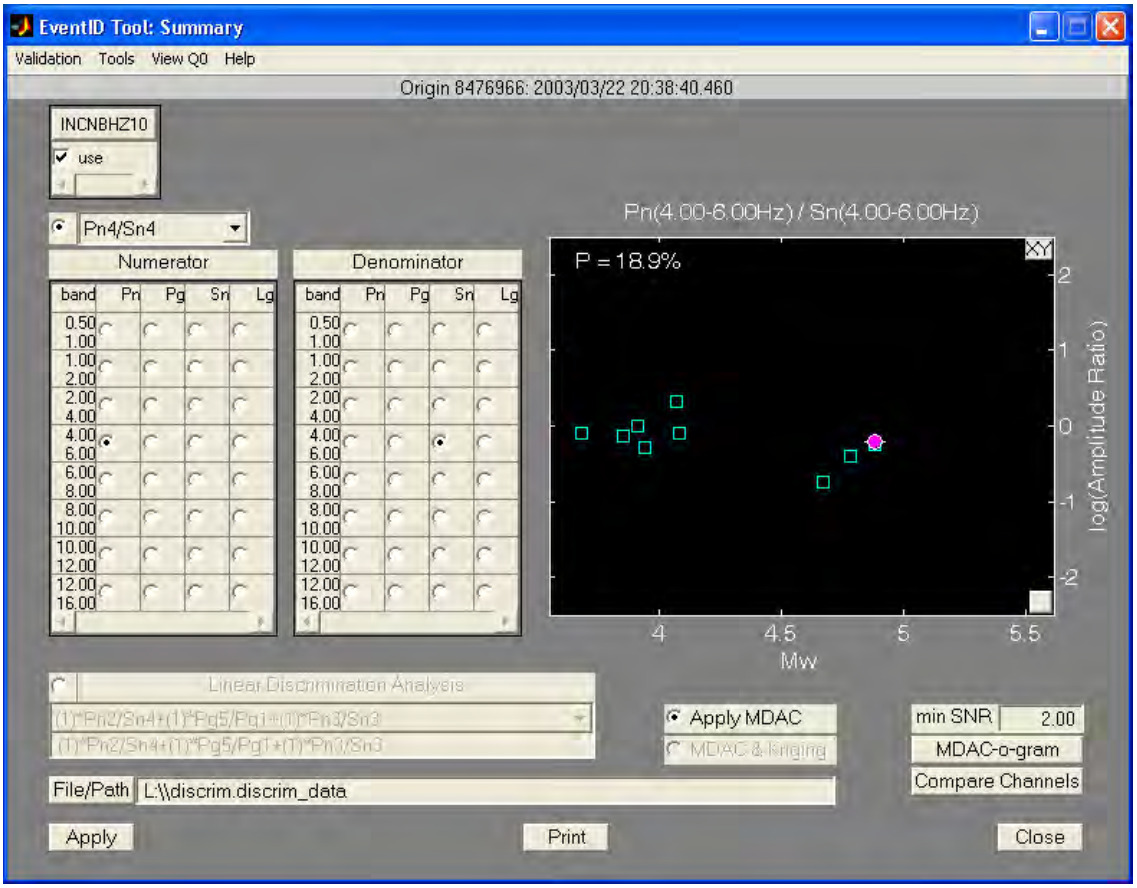

Figure 5. EventID Tool. Minor layout changes have been made to allow for new LDA controls. Menus have been added for selection of other new feature, e.g., validation methods, Q model viewer tool. Processing parameters were provided by Bill Walter of Lawrence Livermore National Laboratory. A hypothetical LDA string is shown to demonstrate the format intended for use by the tool.

To help researchers quickly validate ever larger numbers of calibrated stations, we have introduced a new capability into the tool. A routinely used script for product validation was modified to handle an abundant number of cases that the data products might fall within. The output from the validation script provides useful numerical analyses for an event that has been delivered in the DISCRIM_DATA database table and was processed by the tool using data from DISCRIM_PARM, MDAC_FI and MDAF_FD. Comparisons are separately made between the reference event and tool processed event, for both the MDAC corrected and uncorrected log(amplitude) measurements, providing residuals for evaluation of measurement consistency. Other useful information is also output; e.g., station and channel name, event type, start and end time for phase processing windows. Additional possible output variables may be added if requested.

To better understand the effects of attenuation observed at a station for events occurring at different source points, a new tool was developed to quickly build path-integrated Q maps using the 2D Q models that are included with some calibrated stations. A path-integrated Q map consists of taking an existing tomography grid of Q values, defining a point of interest within the Q tomography grid (in this case the station of interest), defining a path-integration grid for the integration to take place over, and then computes the path-integrated Q values for the great-circle paths between the station and each of the path-integration grid points. An example path-integrated Q map is shown in Figure 6, for station ARA0 of the ARCESS array, using a 1Hz Pn Q tomography model.

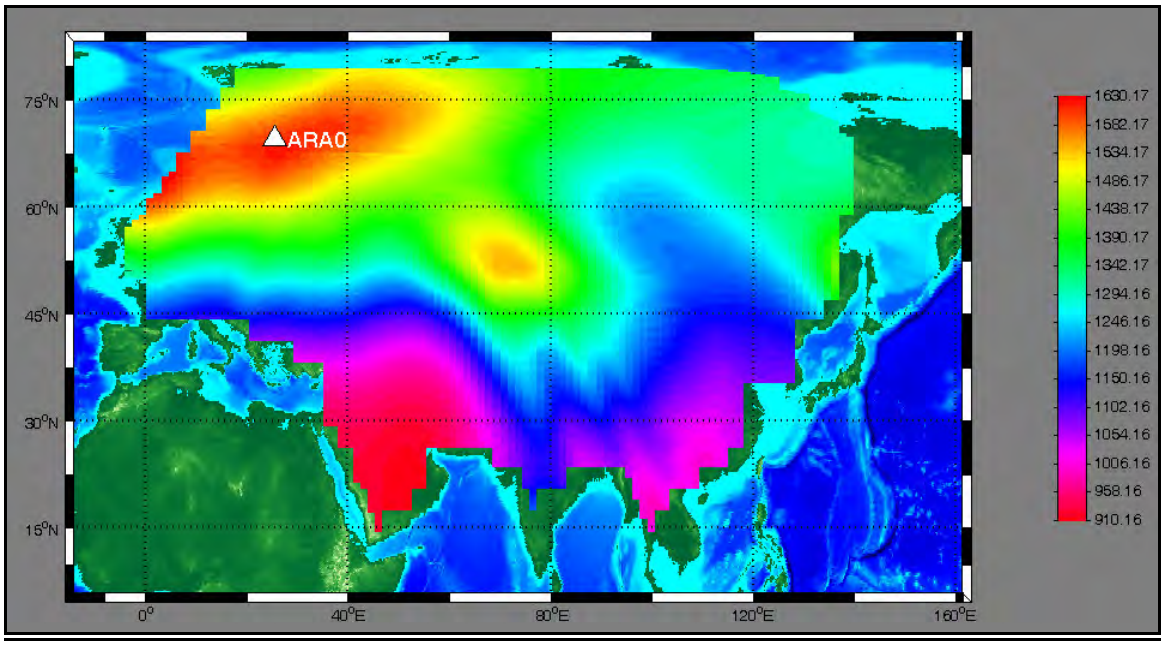

Figure 6. Pn path-integrated Q0 map station ARA0. A grid increment of 0.66 degree in both latitude and longitude was used. Q0 map used to construct this plot was provided by Steve Taylor of Los Alamos National Laboratory.

Infra Tool

Research and evaluation is currently underway to extend Infra Tool for 1) detection of imbedded secondary signals, and 2) removal of a constant noise source from infrasound array data. For the first task a signal-subtraction technique is used for removal of the primary source of correlated signal power from the FK plane for each window step when processing a segment of data. Our implementation of signal-subtraction is done by beamforming the infrasound array to the azimuth and slowness defined by the peak correlated power in the FK plane, then subtracting the beam from each array element and re-computing the FK on the beam-subtracted waveforms. After signal subtraction, the residual FK plane will have a new point of peak correlated power from which detection criteria (Hart, 2004) can be used to determine if secondary signals are present. For the second task of constant noise source jamming, we use a fixed azimuth and slowness for beamforming and the residual FK plane is again searched for signals meeting the detection criteria. Our purpose is to provide functionality to remove a constant noise source (e.g., microbaroms), or any peak correlated power observed in the FK plane (e.g., chemical explosion or artillery blasts). A new GUI, shown in Figure 7, was designed and built to control the signal-subtraction processing. Features in the new GUI include methods to switch between fixed source jamming and peak correlation, a switch to turn ‘on’ and ‘off’ results from non-signal-subtraction, and a switch for applying or not applying the signal subtraction method. Work continues on developing evaluation plots of the technique for the user to review for validity of the method.

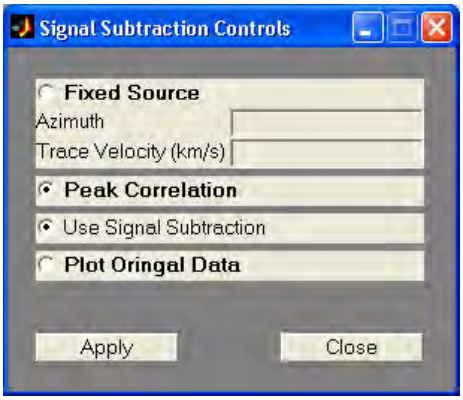

Figure 7. New graphical user interface for the signal-subtraction method planned for Infra Tool. Select fixed source and add specific azimuth and trace velocity values for the fixed noise source jamming method, or choose the peak correlation method. Select the Use Signal Subtraction to turn "on" and "off" the signal-subtraction processing routine. By selecting the Plot Original Data, the results from non-signal subtraction are displayed for comparison.

As an example, we show results from processing using the standard method and signal-subtraction for peak correlated power removal and secondary signal detection in Figures 8 a and b. Figure 8a shows that the standard processing method clearly detects two pulses with start times of 1998/10/20 21:56:20 and 1998/10/20 22:01:00 and durations 3.3 minutes and 2.5 minutes, respectively. The average azimuth of these pulses is 289.2 degrees. Figure 8b shows the signal-subtraction results of the initial peak correlated power obtained by the standard processing method. In this case three detections are made and each occurs at the approximately same azimuth, 327.2 degrees. These are likely refracted wavefronts from local topography near the infrasound station of the primary pulses detected with the standard processing method.

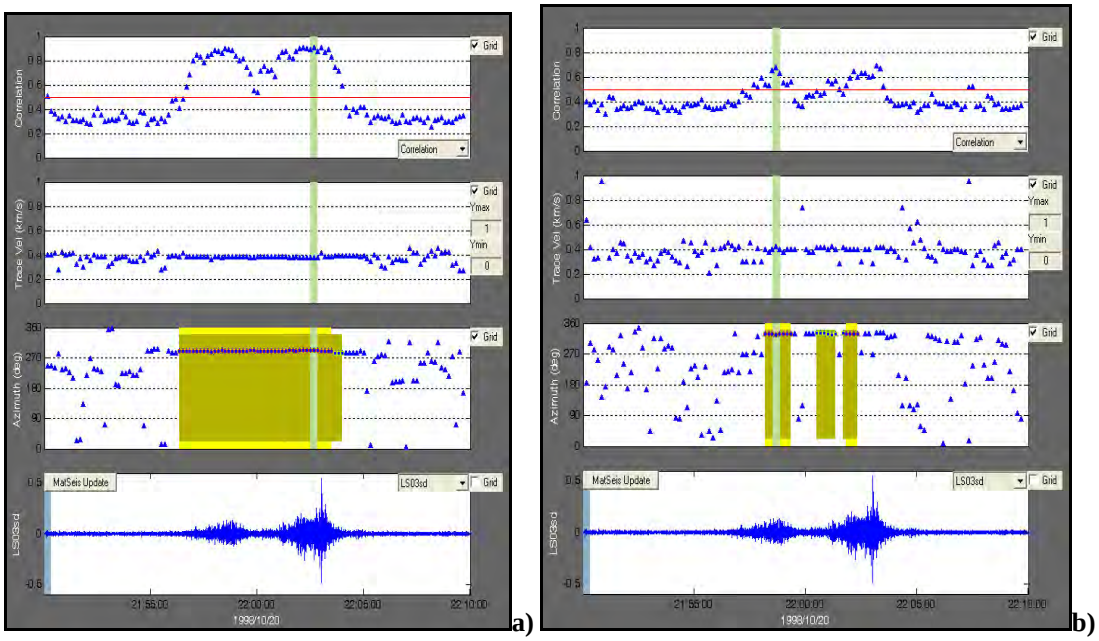

a) b)

Figures 8a and 8b. Demonstration of signal-subtraction technique for removal of peak correlated power and secondary signal detection. A waveform segment with start time 1998/10/20 21:50:00 and 20 minute duration was chosen for the Los Alamos Infrasound Array (LSAR). Waveforms were bandpass filtered at 1-3 Hz (bottom displays of both panels) and processed using 20 second moving window with 50% overlap. Detection threshold criteria were set to: correlation > 0.5, slope limit in azimuth < 1.0 degrees, Number of samples 4 (i.e. 80 second LTA), standard deviation in azimuth < 2.5 and azimuth data gap 0. a) Standard processing results, with associated detection windows. Detection window statistics: average correlation 0.8 ± 0.097, trace velocity 380 m/s ± 7 and azimuth 289.2 ± 2.0. b) Signal-subtraction results for removal of peak correlated power, with associated detection windows. Detection window statistics: average correlation 0.566 ± 0.105, trace velocity 399 ± 20 m/s and azimuth 327.2 ± 1.8. Data obtained from the U.S. Army Space and Missile Defense Command (SMDC) Monitoring Research website Infrasound database of ground truth events.

CONCLUSIONS AND RECOMMENDATIONS

In this paper, we have highlighted some of the more significant changes in the past year in MatSeis and the MatSeis-based regional analysis tools. In the coming year and beyond, we expect to continue to modify the tools in response to user feedback, with the ultimate goal of building a well-integrated, user-friendly, and powerful regional analysis environment.

The official 1.9 version of the basic MatSeis package is available to all from the GNEM R&E web site: https://www.nemre.nnsa.doe.gov/cgi-bin/prod/nemre/matseis.cgi, with MatSeis version 1.10 planned for release in November 2005.

Matlab and the Signal Processing Toolbox are required to run MatSeis. MatSeis will run on Sun workstations, Windows PC's, and Linux PC's. MatSeis should run on other supported Matlab platforms as well, but the C code will need to be re-compiled.

ACKNOWLEDGEMENTS

We thank all of the MatSeis users who have helped us to debug and improve the software, particularly our colleagues at LANL and LLNL.

REFERENCES

Carr, D. (2002), National Nuclear Security Administration Knowledge Base Core Table Schema Document, Sandia National Laboratories, SAND2002-3005 (available at http://www.nemre.nn.doe.gov).

Hart, D. M. (2004), Automated Infrasound Signal Detection Algorithms Implemented in MatSeis – Infra Tool, Sandia Technical Report SAND2004-1889.

Hart, D. M. and Chris J. Young (2004), MatSeis User Manual version 1.9, https://www.nemre.nnsa.doe.gov/prod/nemre/fileshare/matseis_manual.pdf.

Hartse, H. E., Taylor, S. R., Phillips, W. S., and G. E. Randall (1997). A preliminary study of regional seismic discrimination in central Asia with emphasis on western China, *Bull. Seism. Soc. Am*. 87: 551-568.

Herrin, E. and T. Goforth (1977). Phase-matched filters: application to the study of rayleigh waves, *Bull. Seism. Soc. Am.* 67: 1259-1275.

Mayeda, K. (1993). Mb(LgCoda): a stable single station estimator of magnitude, *Bull. Seism. Soc. Am*. 83: 851-861.

Mayeda, K. and W. R. Walter (1996). Moment, energy, stress drop, and source spectra of western United States earthquakes from regional coda envelopes, *J. Geophys. Res.* 101: 11,195-11,208.

Mayeda, K., R. Hofstetter, A. J. Rodgers and W. R. Walter (1999). Applying coda envelope measurements to local and regional waveforms for stable estimates of magnitude, source spectra, and energy, *21st Annual Seismic Research Symposium on Monitoring a CTBT*, Vol I, pp. 527-533.

Mayeda, K., A. Hofstetter, J. L. O'Boyle and W. R. Walter (2003). Stable and Transportable Regional Magnitudes Based on Coda-Derived Moment-Rate Spectra, *Bull. Seism. Soc. Am.* 93: 224-293.

Rogers, A. J., T. Lay, W. R. Walter, and K. M. Mayeda (1997). Comparison of Regional Phase Amplitude Ratio Measurement Techniques, *Bull. Seism. Soc. Am.*, 87, 1613-1621.

Walter, W. R., A. J. Rodgers, A. Sicherman, W. Hanley, K. Mayeda, S. C. Myers and M. Pasyanos (1999). LLNL's regional seismic monitoring research, *21st Annual Seismic Research Symposium on Monitoring a CTBT*, Vol I, pp. 294-302.

Walter, W.R. and S. R. Taylor (2002), A Revised Magnitude and Distance Amplitude Correction (MDAC2) Procedure for Regional Seismic Discriminants: Theory and Testing at NTS, Lawrence Livermore National Laboratory, Livermore CA, report: UCRL-ID146882 and Los Alamos report: LA-UR-02-1008.

DEVELOPMENT OF A NETWORK DATA SET FOR EVALUATING DETECTION AND NETWORK PROCESSING PERFORMANCE

Benjamin Kohl, Theron J. Bennett, István Bondár, Brian Barker, Walter Nagy, Colin Reasoner, Hans Israelsson, and Paul Piraino

Science Applications International Corporation

Sponsored by Army Space and Missile Defense Command

Contract No. DASG60-03-C-0009

ABSTRACT

Practical implementations of new or improved monitoring technologies, such as signal detectors, network phase association algorithms, location and event identification methods, rely on quantitative assessments of performance such as detection probabilities and false alarm rates. These types of performance metrics are typically obtained through experiments using data sets constructed from archival data records. However, such experimental data sets implicitly contain signal and event recordings from numerous unknown sources (e.g., small earthquakes not reported in published local, regional, or teleseismic bulletins) potentially contaminating the data set and complicating the interpretation of processing results. Furthermore, they are only representative of events and station network characteristics contained during the time interval of the archival data. Our objective is to develop an experimental network data set in which all the target signal and event detections are known and ultimately to extend those results to represent expected network data from potential surrogate events and stations, which may not be included in the historical archive. To achieve this objective, we have been developing the framework for synthesizing a database including continuous waveform data for a network of seismic and infrasound stations relevant to nuclear explosion monitoring which contains signals from actual events, scaled to various sizes, and embedded in a variety of background noise.

Our initial focus for this study has been a large region in southern Asia (15°-45°N 50°-115°E). We have identified a network of 51 core seismic and infrasound stations, most useful for monitoring this region; and we have been collecting waveform data from those stations to represent background noise and signals from historical nuclear explosions as well as earthquakes and seismo-acoustic sources. In constructing the data for background noise, we are seeking to form long, continuous waveforms of detection-free clean noise spanning several days into which we can then embed real event signals and signals which have been scaled down on the basis of source scaling predictions to magnitudes representing lower levels. Formation of clean noise waveforms has required meticulous analysis to exclude time-windows with phase arrivals predicted from global and regional seismic bulletins as well as phases picked by standard signal detectors. Resulting noise segments have been carefully merged together to produce several days of continuous clean noise waveforms while maintaining basic noise attributes with respect to overall level and seasonal, weekly, and diurnal variations. From our effort to date, we have generated clean noise waveforms of two-days duration, as well as reversed noise waveforms of similar duration, for 42 of the seismic stations.

We have assembled the seismic signal waveforms from 6 underground nuclear explosions and approximately 100 well-recorded earthquakes with high signal-to-noise ratio (SNR) which occurred in southern Asia along with seismo-acoustic signals from 23 mine blasts and one bolide recorded by infrasound stations in Mongolia and Kazakhstan. We have been testing and employing frequency-dependent explosion (e.g., Mueller/Murphy) and earthquake (e.g. Brune with both inverse cube- and quad-root corner frequency dependence on moment) source scaling models to scale down the large, high-SNR events to small events covering a range of yields/magnitudes approaching the monitoring thresholds. In addition to describing target events for analyzing monitoring performance, the scaling/embedding process is also being used to represent potential sources of regional and teleseismic clutter signals, which increases processing complexity (while continuing to maintain control of the contributing sources) and provides a more realistic background condition than the clean noise scenario. Preliminary event detection experiments are quantifying the systematic time, amplitude and azimuth measurement biases that can be expected from low-SNR detections. Methodologies for analyzing the performance of the infrasound stations for monitoring seismo-acoustic events from the southern Asia source region are also being assessed.

OBJECTIVES

Our objective is to develop an experimental network data set in which target signal and event detections are known, as well as having realistic distributions of false or "clutter" detections and background noise characteristics. We are utilizing a variety of actual nuclear explosion, earthquake, mine blast and infrasonic event recordings and developing scaling and embedding algorithms to yield continuous waveforms with numerous target events at or near the detection threshold in southern Asia. This will allow for detection, location and identification experiments utilizing the known characteristics of small events under realistic background noise and seismicity conditions. The background noise, scaled signals, embedded waveforms and relevant meta-data from this effort are available to the monitoring research community via the mechanisms of the Research and Development Support Services (RDSS) web site (http://www.rdss.info/, Woodward et al. 2005).

RESEARCH ACCOMPLISHED

The basic framework for the comprehensive network data set was developed previously (Kohl et al., 2004) and is depicted in Figure 1. It involves taking well-recorded, high signal-to-noise ratio (SNR) signals, scaling them down to various sizes based on source theory and embedding them in a variety of background noise conditions. We are scaling and embedding nuclear explosion, earthquake, seismo-acoustic (e.g., mine blast) and infrasonic event recordings at levels spanning the detection threshold.

We assembled a background noise library of two days of continuous detection-free clean noise, two days of reversed clean noise and fours days of whole background noise for a core network of 42 stations. We constructed a signal library from 6 nuclear explosions, over 100 earthquakes, 23 mine blasts and one bolide. We developed source scaling models for nuclear explosions and earthquakes and scaled the nuclear explosion records and earthquakes to equivalent m_b ranging from 1.8 to 4.5. We embedded the scaled signals several hundred times in varying noise conditions and conducted a number of signal detection experiments yielding Receiver Operating Characteristic (ROC) curves and quantitative assessments of arrival time, azimuth and amplitude biases as a function of SNR for selected stations. We continue to develop scaling models for infrasound signals and plan on conducting experiments to demonstrate the utility of this approach to assess network processing performance.

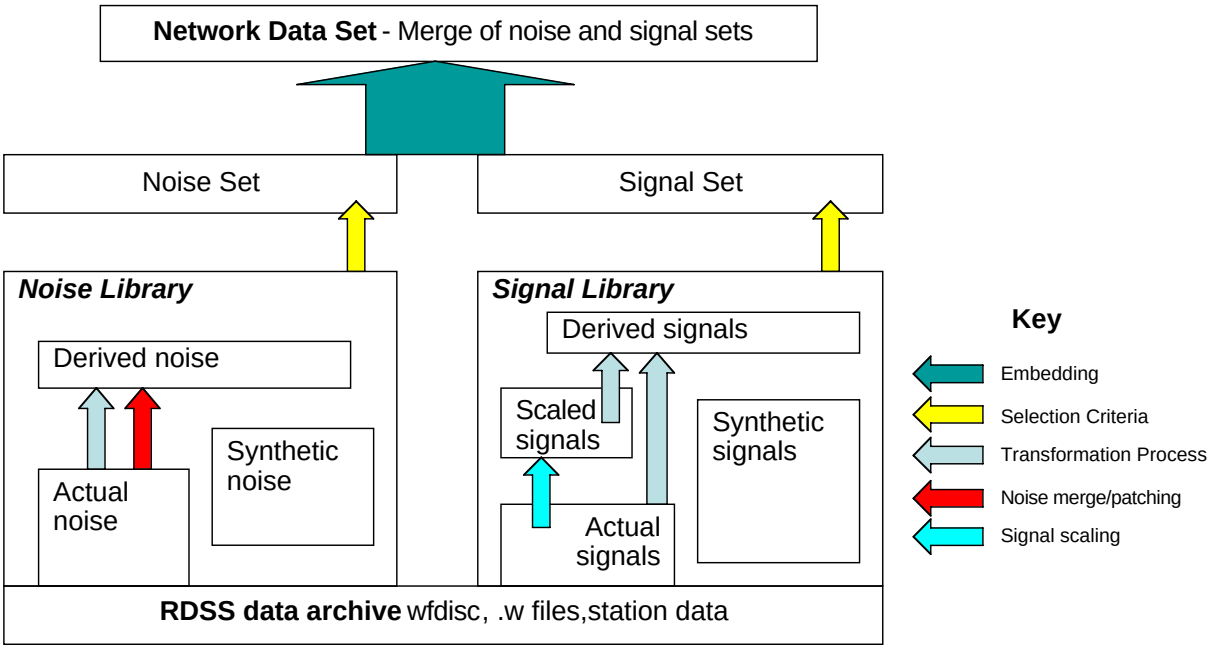

Figure 1. Basic framework for constructing a network data set for systematic testing and evaluation of new or improved monitoring technologies. Scaled signals from a variety of sources are embedded in a variety of noise conditions to construct a data set in which target detections have been characterized.

Noise and Signal Library

In the past year we completed the construction of three background noise datasets for a network of 42 stations useful for building experimental data sets for testing monitoring capabilities in southern Asia (15°-45°N 50°-115°E). The first of these data sets (clean-noise, two days) was constructed by stitching together detection free segments. To insure that the stitched clean-noise realistically represented actual noise, including known seasonal and diurnal variability, we first assembled a set of reference spectra for each station and channel spanning the range of variability for each station (Figure 2). For example, for stations that exhibited strong diurnal variability in the noise levels, we computed a separate reference spectrum for every hour of the day. Only those detection-free segments derived from the same hourly span, *and* whose spectra matched the reference spectra were used. To minimize the effects of the merging process we used 10 to 120 second tapers at the ends and overlapped neighboring segments. All the channels of stations and arrays were merged consistently in time to retain the noise coherency characteristics originally present in the data.

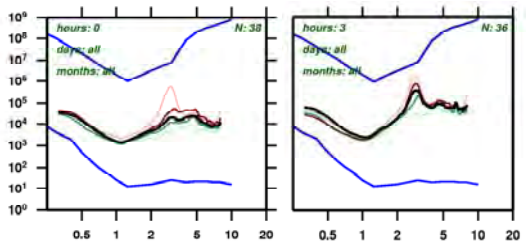

Figure 2. Example reference spectra for hours 0 and 3 for the CM16 element of CMAR.

The second noise dataset (reversed, two days) was constructed by simply time-reversing the clean background noise, thus also yielding two days of continuous noise. The third noise dataset (whole-background) was constructed by simply extracting four days of raw continuous data (June 1998). This third dataset is analogous to what is normally used in signal processing experiments. As a quality control measure, and to establish a baseline background detection rate, we ran standard signal processing (DFX) against the clean noise. Despite the fact that the clean noise was constructed from detection-free segments, low-level detections were still made against the clean and reversed noise. On average the detection rate against the clean-noise was 20% of that against whole-background noise and reversed noise had a detection rate of about 30% of the whole-background noise. Figure 3 shows the waveform and the spectrogram of a waveform stitched from detection-free segments.

In the past year we assembled a signal library from the waveforms of 6 historical nuclear explosions, more than 100 earthquakes, 23 mine blasts and one bolide that occurred in central and southern Asia. We are computing a wide variety of signal characteristics (e.g. Figure 4) on the original event records, and the scaled signals.

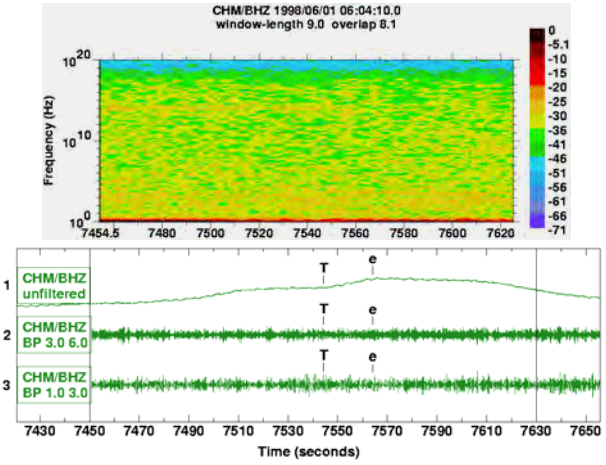

Figure 3. Spectrogram of merged clean-noise around a stitching boundary (marked start – "T" and end – "e" markers).

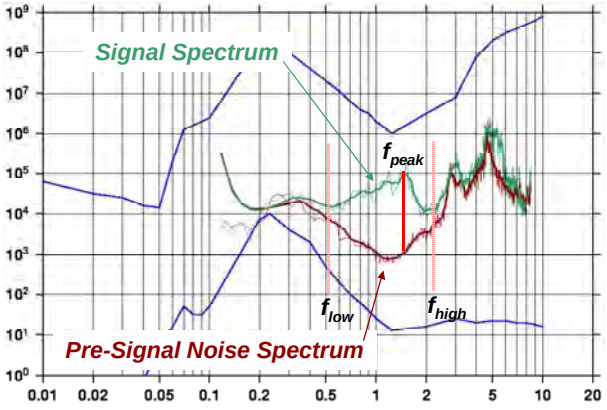

Figure 4. Schematic showing the signal bandwidth and peak-frequency measurements routinely computed for the signal library.

Explosion and Earthquake Scaling

One of the principal objectives of this project is to provide realistic assessments of monitoring performance for smaller events for which the signal detections from station networks are often incomplete. To better understand the factors affecting this performance for our southern Asia study area, we have been using source scaling theory to scale the signals from larger events. This scaling introduces a frequency-dependent change in signal amplitudes.

For explosion scaling we have been using the Mueller-Murphy (MM) model which has been validated over the years for a range of explosion observations (Mueller and Murphy, 1971; Murphy 1977). Alternative models (e.g., vonSeggern and Blandford, 1972) would be expected to produce very similar predicted behavior. The MM model is formulated in terms of explosion yield (W) and provides an expression of the P-wave spectrum as a function of source media properties, explosion yield, depth, and empirical constants corresponding to different geologic emplacement media. For southern Asia we use the explosion scaling relations for granite, which worked well for nuclear explosions at Semipalatinsk and Lop Nor test sites. For scaling the explosions in terms of body-wave magnitude m_b, we use the relation $m_b = 4.45 + 0.75 \log W$, which has been previously validated for these test sites, to convert to yields. Our MM model results were verified by comparing observations of Pn spectral ratios from nearly co-located nuclear explosions with the predictions based on the source scaling theory. Some of these comparisons showed very good matches, although in other cases there appeared to be corner frequency differences, which may require future modifications to some of the model parameters.

To test the explosion scaling model, we applied the MM scaling procedures to scale the signals recorded on a network of regional and teleseismic stations from 6 southern Asia underground nuclear explosions, down from their original magnitudes ($4.5 \le m_b(\text{REB}) \le 6.0$) to a range of lower magnitudes ($m_b(\text{REB}) = 4.5$ and in 0.1 magnitude unit steps from 4.0 m_b(REB) to 1.8 m_b(REB)). We then applied standard IDC processing to the scaled signals to measure initial P amplitudes and associated periods, which would be used for computing station magnitudes. The results are presented in Figure 5a, in which we plot the observed magnitude differences at each stations, $\log A_i/T_i$(original unscaled) – $\log A_i/T_i$(scaled) where i is a station index, versus the target m_b difference, m_b(original for the network) – m_b(target for the network). Obviously the ideal result would be for the observed magnitude difference at each station to equal the target magnitude difference, and this is achieved quite well in the explosion scaling measurements in Figure 5a. The observations are scattered around a line with a slope approximately equal to 1.0. With the exception of a few outliers related to data quality issues, the scatter in the observations is less than half of a magnitude unit, and the least-squares linear fit to the observations is 1.02 with only a slight bias indicated at the largest target magnitude differences. Thus we conclude that the MM explosion scaling procedure appears to be performing as expected over a fairly large range of magnitudes.

For earthquake scaling, we began with a Brune ω^2-source model. For this model the corner frequency is proportional to velocity of the source medium and inversely proportional to a source dimension term, which scales with moment. In scaling the earthquake signals, we consider both cube-root (as indicated in original models by Brune 1970, Hanks and Bakun 2002) and quad-root (as suggested by Mayeda and Walter 1996 amongst others) for

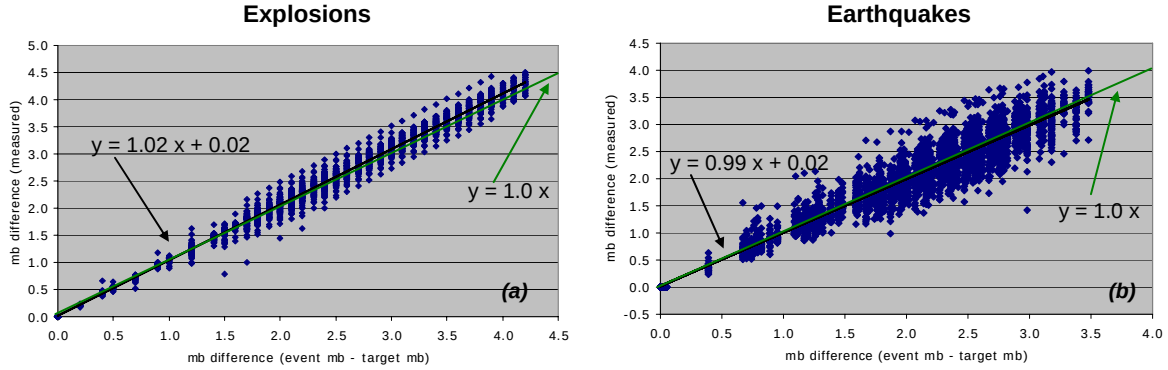

Figure 5. Results of magnitude differences for P and Pn signals measured from routine processing of the observations from 6 southern Asia nuclear explosions scaled using MM explosion source scaling (a) and from 17 southern Asia earthquakes scaled using our preferred cube-root earthquake model (b).

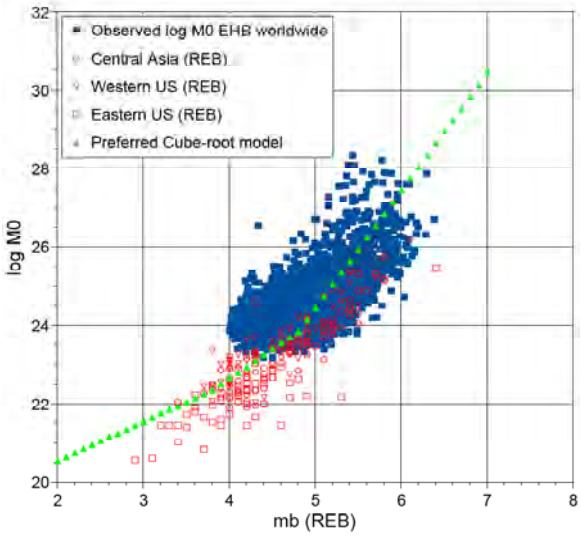

Figure 6. Log M0 versus mb(REB) for a large global earthquake sample reported by EHB and elsewhere.

corner frequency dependence on seismic moment. Our analyses to date focus on the model with cube-root corner frequency dependence. In the earthquake model we followed the approach of Hanks and Bakun (2002), using the definition of moment magnitude, M_w, to establish the relationship to source moment – i.e., $\log M_0 \equiv 1.5\, M_w + 16.05$. We began with a simple linear model for relating M_w to m_b. We drew upon observations from the global EHB (Engdahl et al. 1998) earthquake sample for large events (m_b(REB) > 4) along with observations from smaller events for selected areas reported by Patton (2001), which were adjusted to equivalent REB m_b's (assuming $m_b \approx m_b$(REB) + 0.3). Although the data scatter (Figure 6) would appear to permit a linear M_w-vs-m_b model (i.e. essentially a straight-line relationship between $\log M_0$ and m_b), the implied effects on spectral behavior are not realistic. In particular, for small events with magnitudes measured from signals with frequencies below the corner frequency, a one unit change in m_b should correspond to a factor of ten change in M_0. To meet this objective we would need to have $M_w \propto 2/3 m_b$ – i.e. $\log M_0 \propto 1.0 m_b$. The observations in Figure 6 cannot support such a slope over magnitudes $3 \le m_b(\text{REB}) \le 6$. We, therefore, decided to investigate a model for which the M_w-vs-m_b relationship is nonlinear; Taylor et al. (2002) reached a similar conclusion and developed a model only slightly different from those described below. In particular, we sought to determine an earthquake model for which $\log M_0$ scales directly as the m_b difference for small events, produces $M_w \approx m_b$ over some intermediate range in magnitude, and has M_w greater than m_b for larger events (where we know m_b is saturated).

As a preliminary validation test to further constrain our earthquake model, the earthquake scaling relations were used to scale down the signals from selected samples of large southern Asia earthquakes which were well recorded at regional and teleseismic stations. Just as for the scaled explosion signals above, we compared the A/T measurements from the scaled P and Pn signals to the target values for the earthquakes, m_b(REB) = 2.5 – 4.5. When this scaling model was applied to the signals from 17 southern Asia earthquakes, the A/T measurements were in very good agreement with the expectation (Figure 5b). There appears to be very little indication of bias in the results; the slope of the least-squares straight line fit to the observations is 0.99 and the intercept is 0.02. Scatter about the line is about 0.7 magnitude units, only slightly greater than the scatter seen in the corresponding explosion measurements. We conclude that the cube-root model combined with our $\log M_0 - m_b$ relation (Table 1), provides a reasonable procedure for scaling the southern Asia earthquakes. We are continuing to look at additional validation with spectral ratios (e.g., Figure 7) from nearly co-located events and to evaluate alternatives, including an earthquake model with quad-root corner frequency dependence.

Table 1: Preferred moment-vs-m_b relationship

$\log M_0 - m_b$ relation for cube-root model	
$\log M_0 = m_b$(REB) + 18.55	m_b (REB) ≤ 3.8
$\log M_0 = 1.5\, m_b$ (REB) + 16.65	3.8 ≤ m_b (REB) ≤ 4.8
$\log M_0 = 3.0\, m_b$ (REB) + 9.45	m_b (REB) ≥ 4.8

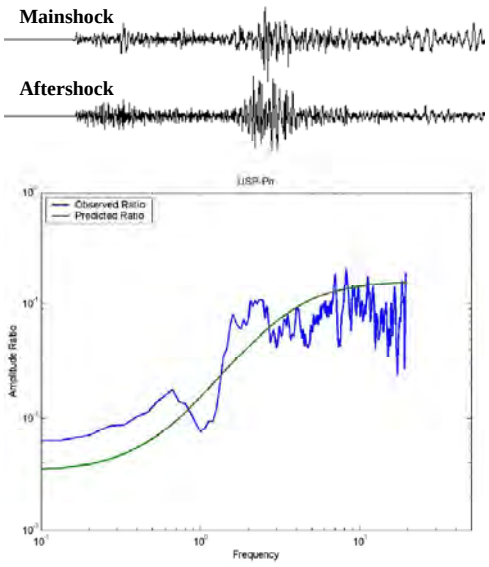

Figure 7. Spectral ratio of a mainshock/aftershock pair in southern Asia, showing good agreement with the cube-root model (green).

Signal Processing Experiments

Controlled experiments with the embedded data offer several opportunities for evaluating algorithms for station signal processing with regard to signal detection as well as estimation of signal parameters. We give examples below with results from initial seismic signal processing experiments. Test data sets were constructed from background noise and scaled signals for three stations: CMAR, FINES, NIL. Signals scaled to magnitudes between m_b =1.8 - 4.5 in increments of 0.1 magnitude units (m.u.) from three large and similar (m_b ~ 5.5) underground nuclear explosions at the Lop Nor test site were embedded in noise of different types – whole background, clean, and reversed clean. The test data sets were processed with DFX signal detection and parameter extraction programs with configurations currently employed at the IDC.

Signal Detection Probabilities

Detection probabilities as a function of m_b were calculated as the ratio of the number of detected signals/total number of embedded signals of magnitude m_b. Figure 8 compares the probabilities for the three stations as a function of m_b. The probability curves are in reasonable agreement with a Gaussian cumulative distribution functions with mean values corresponding to the 50% detection probability threshold, and the standard deviation is a measure of noise amplitude variation. The data in Figure 8 thus support the common assumption of network detection simulations that incremental detection probabilities as a function of m_b can be approximated by cumulative Gaussian distribution functions (Kvaerna and Ringdal, 1999).

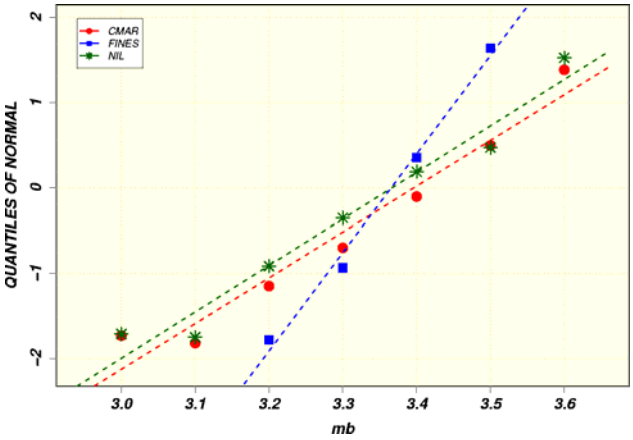

Figure 8. Detection probabilities as a function of m_b for the stations CMAR, FINES, and NIL. A Gaussian scaling is used for the detection probabilities on the vertical axis so that true Gaussian data would follow a straight line. The data points for the detection probabilities follow the fitted lines closely suggesting a that the detection probability as a function of m_b can be approximated with a cumulative Gaussian distribution.

False alarm rates

Estimates of false alarm rates from the rates of unassociated detections become uncertain when based on observations of real data; such unassociated detections include detections of signals from events of unknown origin as well as detections triggered by signal coda. Clean noise, free of signals, can provide a more robust estimate of the false alarm rate, that is unbiased both due to signals of unknown origin and due to coda detections.

In Table 2 we compare the false alarm rates of the three types of noise samples. The false alarm rates for clean and clean-reversed noise with no embedded signals represent genuine false alarms of the detector configuration, whereas for the real noise data some portion of the detections are from signals of seismic events. The number of detections of the whole background noise data that could be associated (using a 4 second allowance for initial P) with seismic events in the ISC database was small (< 10%). The ISC reported close to 200 worldwide events/day for the time period analyzed here, but its event catalog is incomplete for small events. Furthermore, secondary phases or coda detections were not considered in the association, so total detection rates, with ISC associations subtracted, still overestimate the actual false alarm rate. The difference is most striking for NIL, for which the unassociated rate of the clean noise is about a factor of eight lower than that for the real data, while this factor is around 5 for FINES and a little more than 2 for CMAR.

Table 2. Daily Unassociated Detection Rates for Different Noise Types

Station	Clean[1]	Reversed Clean	Whole Background
CMAR	190 | 37	160 | 29	411
FINES	20 | 6	30 | 6	165
NIL	62 | 7	85 | 3	507

1. The two numbers represent the number of unassociated detections in clean noise with no embedded signals/number of additional unassociated detections when signals were embedded.

With signals embedded in the clean noise the false alarm or unassociated rate goes up slightly due to additional coda detections that normally would have been assumed to be false alarms. The rates of such additional unassociated detections are also given in Table 2. The median of this increase in false alarm or unassociated rates when signals are embedded for the clean and reversed clean noise is about 20%.

ROC curves

The performance of a signal detector is often defined by the so-called Receiver Operating Characteristic, ROC, which describe the trade-off between signal detection probability and false alarm probability (Van Trees, 1968). Using scaled signals embedded in clean noise affords the opportunity to construct ROC curves, which is difficult, if not impossible, to do from real data. An example of an ROC curve constructed from detection experiments with the array FINES is shown in Figure 9. The histograms to the left show the distributions of the logarithm of the short term/long term averages (sta/lta), or SNR, for noise (red) and for signals (plus noise) (in blue) of the same size (m_b=3.30). Note that the histograms for the signals include data for signals that were not detected. SNR values for undetected signals could be calculated because of their known embedding times. Gaussian curves draped on the histograms show reasonable agreement with the empirical SNR distributions for both noise and signal data. The detector triggers if the SNR is above a preset threshold and the default threshold used in the processing experiment is marked as a vertical dashed line (green) to the right. A significant portion of the SNR distribution for the explosion signals is below the threshold and hence went undetected. If the threshold were lowered to, e.g., the mean of the SNR distribution (black dashed line to the left marked "NEW THRESHOLD"), the probability to detect an explosion signal would increase significantly (to 50%) without significantly increasing the probability of triggering on noise, or of a false alarm.

In the right diagram the two Gaussian distributions for noise and signal detection probabilities were combined to a standard ROC curve. The “default” and the "new" thresholds are marked showing that by lowering the threshold the false alarm probability would not change much, whereas the detection probability would go up from less than 20% to 50%. It should be noted that the data in Figure 9 represent beam forming with steering of a single beam that is optimum for FINES and the Lop Nor test site.

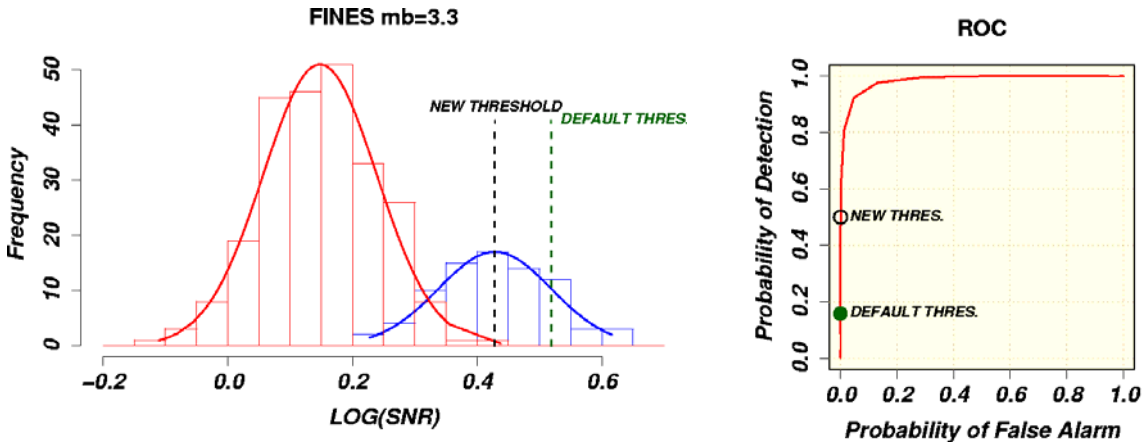

Figure 9. The histograms in the left diagrams for SNR (log scale) of noise (red) and of signals (blue) are used to construct the ROC curve in the right diagram. The default threshold used in the detection experiment is marked as a green dashed line in the left diagram and as a filled dot in the ROC curve. The ROC curve shows that lowering the default threshold (marked as “NEW THRES” in the diagrams) has little effect on the probability of false alarm, but would increase the probability of detection from less than 20% to 50%.

Estimation of Signal Parameters

Apart from detection the processing algorithm that we use (DFX) estimates signal parameters that characterize a detection, such as time of arrival, SNR, amplitude, and for arrays, slowness vector. With the ground truth of the characteristics of embedded signals, the distributions of errors in parameter estimates can be estimated with accuracy. Figure 10 summarizes some statistics of estimation errors in amplitude/period ratios (to the left) and

azimuths of slowness vectors (to the right) for the DFX algorithm for experiments with FINES. The boxplot to the left shows that the automatically estimated amplitude/period ratio becomes increasingly positively biased with decreasing SNR of the detected signal. The bias at the threshold of the detector (log SNR=0.5) is, on average, about 0.3 m.u. The bias is probably caused by low frequency noise that the automatic algorithm cannot account for as the amplitude/period ratios for the downscaled signals were unbiased prior to embedding in the noise (see Figure 5). The bias raises the question whether amplitude/period measurements at low SNR should be used uncorrected for magnitude estimation.

The errors in azimuth estimates (right diagram in Figure 10) grow fast with decreasing SNR. A bias is not as clearly defined as for the amplitude/period ratios, but the scatter increases drastically as indicated by the widening of the boxes which represent 50% of the data around the median. The dashed red lines outline the 50% limits of the azimuth uncertainty (measurement errors) assigned by the automatic algorithm, which clearly underestimates the spread of the actual azimuth errors at low SNRs around 4 and below. An analysis of the empirical distributions of the amplitude and azimuths errors revealed that they are well represented by a Gaussian for all SNRs.

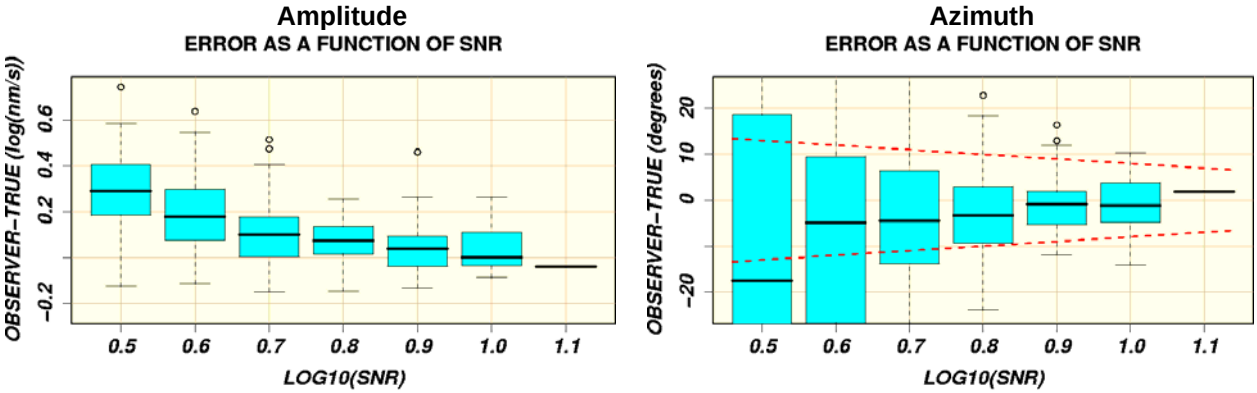

Figure 10. Errors in amplitude/period ratios (left) and azimuth (right) of the automatic DFX algorithm for signals embedded in clean noise of the array FINES. The boxplots show the errors as a function of log SNR; the dashed lines for azimuth in the boxplot to the right outline the 50% limits of errors assigned by the automatic algorithm (measurement errors).

Seismo-Acoustic Event Database and Scaling

Detection of infrasound signals from seismo-acoustic events (e.g., mine blasts) can provide valuable insights into a variety of research topics, such as infrasound propagation, seismic vs. acoustic coupling and the effects of wind-generated noise on infrasound detection. It is our objective to provide to the nuclear monitoring research community a controlled data set where scaled infrasound signals are embedded in a variety of noise conditions. This will be particularly useful for evaluations of detection algorithms. Currently evaluations with respect to variations in ambient noise are dependent on finding data sets where signals from known sources are detected in a variety of noise conditions. Given the current dearth of such infrasound ground truth, a comprehensive evaluation of infrasound detection capabilities using actual recordings is difficult.

We are following the same basic methodology for infrasound that we used for seismic data (described above). Namely, we are building a background noise database from historical recordings, collecting high-SNR infrasound signals from known sources, applying a source scaling function to the recorded data, and embedding the scaled signals in the background noise. In contrast to nuclear explosion or earthquake source theory, general theoretical models cannot be used to predict the scaling of infrasound signals from mine blasts. This is in large measure due to the fact that differing mine practices, acoustic coupling and other local conditions vary immensely from mine to mine and region to region. Therefore we are following an empirical approach to assess the scaling of infrasound signals and limiting the scope of the scaled and embedded data. We are building the data set such that each scaled/embedded event represents effectively the same source and meteorological conditions as the original event, with only the signal amplitude (by no more than one order of magnitude) and the ambient noise conditions varying.

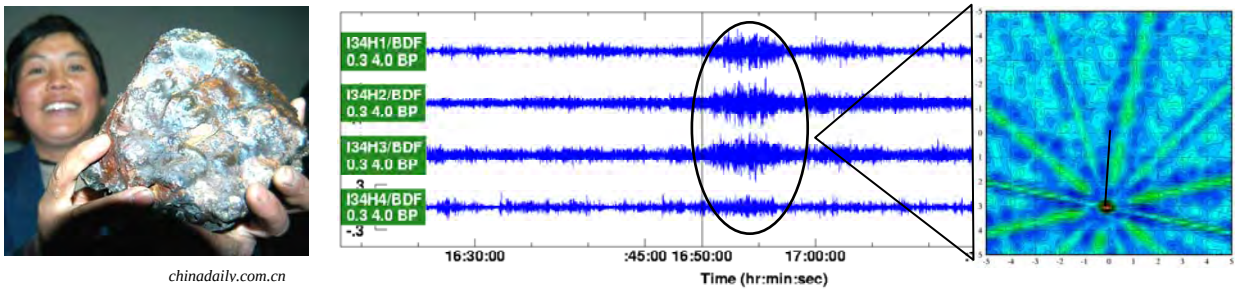

chinadaily.com.cn

Figure 11. Bolide near Lanzhou, China on December 11, 2004 recorded on the IMS infrasound array I34MN and reported in the local media.

We obtained seismo-acoustic recordings (seismic and infrasonic signals from the same source) from 23 mine blasts (c) and 1 bolide (Figure 11) in central Asia for inclusion in our signal library. The mine-blast data offer an opportunity to look for evidence of non-linear source scaling in the infrasound data. b shows a section of 9 infrasound signals recorded at I31KZ for mines at ranges between 50 and 400 km. Traces 1 and 3 originating from the same mine, however, had signal amplitudes differing by a factor of about 10. Similarly traces 2 and 4, again originating from the same mine, had signal amplitudes differing by a factor of about 3. In both cases, spectra ratio comparisons showed that the signals scaled approximately linearly with frequency, consistent with the visual similarity of the waveforms. Thus, based on this admittedly limited data set we are proceeding with a linear scaling function and embedding these in a variety of noise conditions.

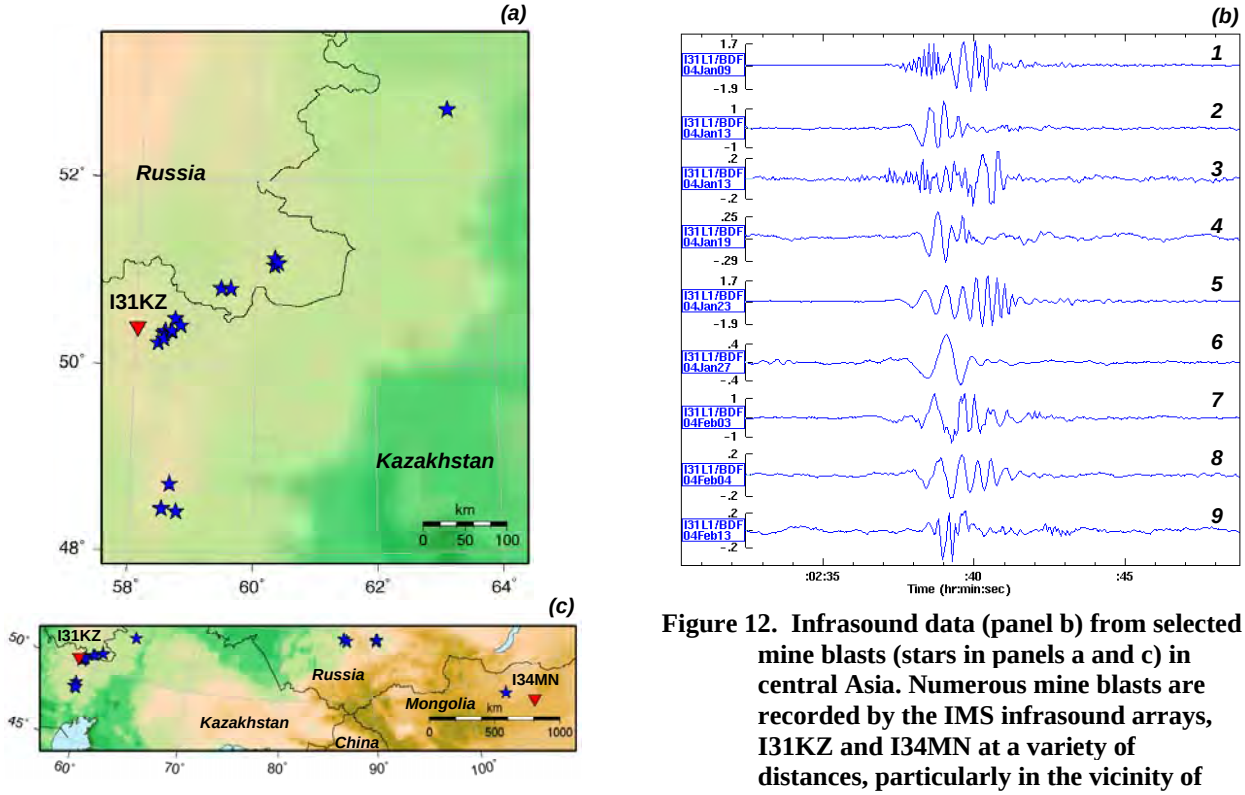

Figure 12. Infrasound data (panel b) from selected mine blasts (stars in panels a and c) in central Asia. Numerous mine blasts are recorded by the IMS infrasound arrays, I31KZ and I34MN at a variety of distances, particularly in the vicinity of I31KZ (panel a).

CONCLUSIONS AND RECOMMENDATIONS

We developed a network data set where scaled signals were embedded in varying background noise conditions, including carefully constructed clean noise. Analysis of reprocessed scaled data show that both a Mueller-Murphy model for nuclear explosions, and modified Brune model with cube-root corner frequency scaling and an empirical $\log M_0$-m_b relation for earthquakes, give consistent amplitude scaling for events in southern Asia.

The detection experiments we executed illustrate some of the benefits that using an embedded data set can provide for assessment of signal detection and characterization algorithms. We found clear evidence for an amplitude bias for low SNR signals and that measurement uncertainties for azimuth probably underestimate the error at low SNR. In general we conclude that experiments with an embedded data set can:

- Validate assumptions for detection probabilities underlying network simulations of real data
- Provide accurate estimates of station detection probability as a function of source strength
- Provide unbiased estimates of false alarm rates
- Accurately map ROC curves for relative assessment of signal detectors and detector configurations
- Estimate the statistical characteristics of errors of signal parameters such as arrival times, slowness vectors, and signal amplitudes.

The background noise, scaled signals, embedded waveforms and relevant meta-data from this effort are available to the monitoring research community via the RDSS web site (http://www.rdss.info/, Woodward et al. 2005).

REFERENCES

Brune, J. N. (1970), Tectonic stress and spectra of seismic shear waves from earthquakes, *J. Geophys. Res.* 75: 4997-5009.

Engdahl, E.R., R. van der Hilst & R. Buland (1998), Global Teleseismic Earthquake Relocation with improved Travel Times and Procedures for Depth Determination, *Bull. Seism. Soc. Am.*, 88: 722-743.

Hanks, T. C., and W. H. Bakun (2002). A bilinear source-scaling model for M-logA observations of continental earthquakes, *Bull. Seism. Soc. Am.* 92: 1841-1846.

Kohl, B., T. Bennett, I. Bondár, B. Barker, W. Nagy, C. Reasoner, and J. Hanson (2004), Development of a Network Data Set for Evaluating Detection and Network Processing Performance, in *Proceedings of the 26th Seismic Research Review: Trends in Nuclear Explosion Monitoring*, LA-UR-04-5801: Vol. 2, pp. 725-734.

Kværna, T. and F. Ringdal (1999), Seismic Threshold Monitoring for Continuous Assessment of Global Detection Probability, *Bull. Seism. Soc. Am.*, 89: 946-959.

Mayeda, K., and W. R. Walter (1996), Moment, energy, stress drop, and source spectra of western United States earthquakes from regional coda envelopes, *J. Geophys. Res.* 101: 11,195-11,208.

Mueller, R. A., and J. R. Murphy (1971), Seismic characteristics of underground nuclear detonations, part 1: seismic spectrum scaling, *Bull. Seism. Soc. Am.* 61: 1675-1692.

Murphy, J. R. (1977), Seismic source functions and magnitude determinations for underground nuclear detonations, *Bull. Seism. Soc. Am.* 67: 135-158.

Patton, H. J. (2001), Regional magnitude scaling, transportability, and MS:mb discrimination at small magnitudes, *PAGEOPH* 158: 1951-2015.

Taylor, S. R., A. A. Velasco, H. E. Hartse, W. S. Phillips, W. R. Walter, and A. J. Rodgers (2002), Amplitude corrections for regional seismic discriminants, *PAGEOPH* 159: 623-650.

Van Trees, H. L., (1968), *Detection, Estimation and Modulation Theory*, John Wiley and Sons.

vonSeggern, D. H. and Blandford, R. (1972), Source time functions and spectra for underground nuclear explosions, *Geophys. J.* 31: 8-97.

Woodward, R., M. Skov, M. Bahavar, G. Davis and Y.-L. Kung (2005), Data and tools to support nuclear explosion monitoring research and development, in *Proceedings of the 27th Seismic Research Review: Ground-Based Nuclear Explosion Monitoring Technologies*, in current Proceedings.

INTEGRATED SEISMIC EVENT DETECTION AND LOCATION BY ADVANCED ARRAY PROCESSING

T. Kvaerna[1], S. J. Gibbons[1], F. Ringdal[1], and D. B. Harris[2]

NORSAR[1] and Lawrence Livermore National Laboratory[2]

Sponsored by National Nuclear Security Administration
Office of Nonproliferation Research and Engineering
Office of Defense Nuclear Nonproliferation

Contract Nos. DE-FC52-03NA99517[1] and W-7405-ENG-48[2]

ABSTRACT

We have developed a prototype system for the automatic monitoring of seismic events from sources of interest using regional seismic arrays. The aim of such a system is to provide significantly improved location estimates for low-magnitude events compared with current automatic approaches, combined with a low false alarm rate. The system is a generalization of an algorithm developed under a pilot project to monitor events from the Kovdor mine in NW Russia using only the ARCES regional array at a distance of 300 km, applying carefully calibrated processing parameters based upon previous observations of confirmed events at the site of interest. The new automatic system is therefore suited, but not restricted, to the single array case. We have applied the process to the Fennoscandian arrays and the arrays in Kazakhstan.

As an initial step, every detection at each of the stations employed is reprocessed in two stages: firstly, the onset time is re-estimated using an autoregressive method and, secondly, the slowness is estimated using broadband f-k analysis in several predetermined fixed frequency bands. The slowness observed can vary considerably from one frequency band to another and the frequency band providing the most stable estimates for repeated observations from a given source varies greatly from site to site. For the local and regional events considered, frequencies below 2 Hz rarely provide useful slowness estimates for the Fennoscandian arrays due to the strong background noise. Frequencies above 4 Hz were not used in the reprocessing of the Kazakhstan data due to signal incoherence over the arrays.

The automatic monitoring system is based upon two types of templates: a site template that lists which phases are anticipated at which stations at which times, and a template for each phase specifying a permissible range of slowness and azimuth observations. In order to calibrate the templates required to identify phase arrivals from events at a given site, a dataset of confirmed events is required. For the mining regions on the Kola Peninsula of NW Russia, lists of confirmed industrial blasts were obtained for many different mines, allowing an extensive study of variability of slowness estimates in various frequency bands for each anticipated phase. Such ground truth information was not available for the Swedish mining regions or industrial explosions in Kazakhstan. However, given a small number of events known to have occurred at different sites, lists of events guaranteed to have occurred in the near vicinity of these master events have been generated by performing waveform correlation on signals from likely candidate events.

Conventional f-k analysis and beamforming assume a plane wavefront which is coherent across the array; this assumption breaks down due to refraction and scattering, leading to energy loss in beamforming and bias in slowness estimates. In matched field processing, the plane-wave steering vectors are replaced with empirical steering vectors estimated from observations of phases from events in the region to be monitored. An efficient suite of calibration software has been developed in this project to filter suites of waveforms from training event sets into a large number of narrow bands and to estimate matched field steering vectors for each band. We present an example whereby a set of steering vectors was calibrated for the Pn-phase at ARCES from compact underground explosions at the Kirovsk mine. In the 7.8-12.5 Hz frequency band, the matched field beam captures a factor of 2 more energy than the conventional beam and, when filtered above 10 Hz, the factor is closer to 3.

OBJECTIVE

This two year collaboration between NORSAR and Lawrence Livermore National Laboratory (LLNL) has explored improvements to the automatic detection and location of seismic events using regional arrays. At the heart of the study has been the calibration of processing parameters for the detection and location of events from a specific region using observations of previous ground truth events at the sites of interest. The goal is to attribute, with a high degree of confidence, automatically located events to active mines or areas with known recurring seismicity. The study has examined sites in Fennoscandia and Kazakhstan using the seismic arrays in these regions.

The signals at a given array station, resulting from a set of events from a site with recurring seismicity, are likely to display common characteristics which may be exploited in order to identify subsequent events from the same region. A template describing the measurements which can be anticipated at a given station at a given time can be used to judge whether or not a detected signal is the likely result of an event from the site of interest. Such templates must be calibrated by investigating the variability of measurements made from events confirmed to have taken place at the sites; such calibrations have been the main focus of this investigation. We have, in addition, explored the potential of applying advanced new “matched field” array processing methods in order to compensate for array processing loss due to refraction and scattering, thus enhancing array gain at high frequencies.

RESEARCH ACCOMPLISHED

Introduction

The ARCES regional array in northern Norway is a primary International Monitoring Station (IMS) seismic station within a few hundred kilometers of many active mining regions, both in north-west Russia and northern Sweden (Figure 1). Signals from routine industrial explosions at these sites in fact dominate the ARCES detection lists and their identification and location require considerable analyst time. Fully automatic event locations at NORSAR are currently provided using the Generalized Beamforming (GBF: Kværna and Ringdal, 1989) system which associates detected phases from the entire network of regional arrays. The collection of ground truth data from mining explosions on the Kola Peninsula (under the DOE funded contract “Ground-Truth Collection for Mining Explosions in Northern Fennoscandia and Russia”; Harris et al., 2003) has provided an excellent opportunity to assess the current state of the automatic event detection and location procedures and to examine approaches for improving it.

The ground truth information for the mining regions on the Kola Peninsula provides the origin times of shots from 13 mines from the four distinct Russian mine clusters color-coded in the upper panel of Figure 1. The corresponding colored symbols in the lower panel of Figure 1 indicate the fully automatic locations from the GBF system for the confirmed events from these mines between October 1, 2001, and September 30, 2002. It is immediately apparent that the distances between the automatic location estimates and the true locations vary enormously. In particular, given a single one of these automatic locations for a recently detected event, it is impossible to ascribe the signal to any of the sources shown without performing a full time-consuming manual analysis upon the signal. The most significant reasons for the large variance of location estimates from the GBF system are the following:

- Azimuth and slowness estimates are performed on data filtered in a frequency band which varies from detection to detection. The frequency band is set in order to optimize the signal-to-noise ratio (SNR) and it is demonstrated in Kværna et al. (2004), the extent to which the slowness estimates for the same set of events become more stable when estimated in fixed frequency bands.
- Many of the events have complicated firing sequences which can lead to an incorrect association of phases. For instance, if two similar blasts follow within seconds of each other, it is possible that an S-phase from the second shot may be associated with the P-phase from the first shot leading to a location estimate at too great a distance. Other combinations of incorrect coda phase associations can lead to similar spurious location estimates.
- The GBF system follows somewhat empirically determined rules which help to determine which of several candidate sources (hypocenter and origin time) is the most likely to have produced a given set of phases. A single trial hypocenter which corresponds to a large number of phases may score more highly than, for example, two hypotheses for different events which would give a more accurate description of the cause of the detected phases.

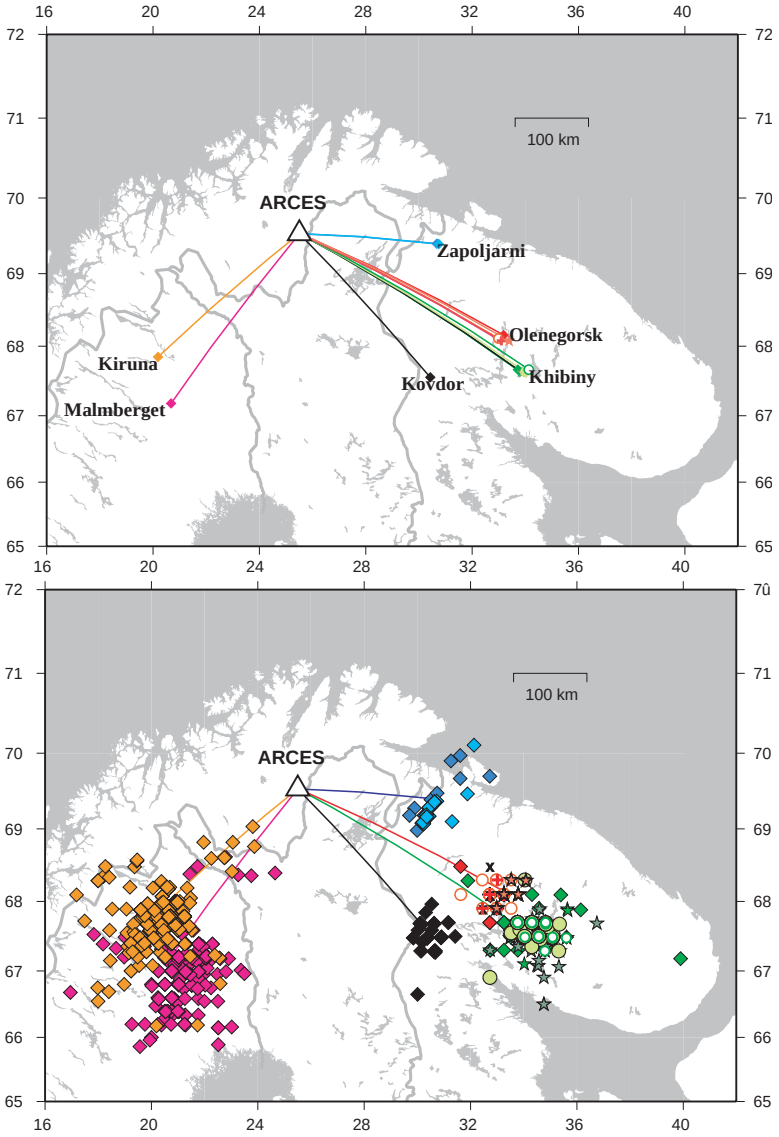

Figure 1. Location of the ARCES regional array in relation to mining regions in northern Sweden and on the Kola Peninsula, Russia (top panel) and automatic event locations using the NORSAR GBF system for events known to have occurred at the sites indicated (lower panel).

Under a pilot project, a fully automatic system for the identification and location of events occurring at, and in the close vicinity of, the Kovdor mine in north west Russia, using only the ARCES regional array, was developed. The details of this procedure are provided by Gibbons, Kværna, and Ringdal (2005). Fundamental to this system is the consistency provided by slowness measurements in a fixed frequency band of a given phase from a given site. If, for a given detection, a slowness estimated from broadband f-k analysis in a fixed frequency band falls within the narrow confines of a template calibrated from the observations of previous events, we can immediately form a hypothesis that an event at our monitored site occurred at the indicated time. We subsequently test this hypothesis by examining whether or not slowness measurements in time-windows fixed relative to the hypothetical origin time are consistent with the existing body of observations from that site. Gibbons, Kværna and Ringdal (2005) demonstrate that the single array automatic location estimates are a significant improvement on the existing automatic solutions and are comparable to multi-array analyst locations. The greatest difficulty encountered in this study was the problem in the identification of secondary phases (usually the result of complicated source time histories) which led to many events which could not be located in this manner; these events had to be filed for analyst review.

The goal of the current project has been to construct an integrated framework in which the philosophy behind the single array monitoring system of Gibbons, Kværna and Ringdal (2005) could be generalized to a range of different source regions and seismic arrays. The ground truth collection project had also acquired information on a very large number of events from the Zapoljarni, Olenegorsk, and Khibiny mining regions (Figure 1). These mining clusters present an additional complication in that several mines operate within short distances of each other; the inter-mine separation is not generally large enough for a single array at a distance of several hundred kilometers to be able to differentiate between two sites from a slowness measurement alone, but it is sufficiently large for the fixed time-window scheme of the Kovdor monitoring process to be compromised.

For other sites, such as the Kiruna and Malmberget mining regions in northern Sweden, there exists the problem that we do not possess ground truth data on routine explosions which are necessary in order to calibrate the templates. The approximate times of the daily routine detonations were however known for both sites which made it possible to identify very likely events and perform a careful analyst location for each of these. With a few master events for each mine, large numbers of events were subsequently identified using a correlation detection algorithm as being almost certain to have originated within a few hundred meters of the master events. The detected events which corresponded to reasonably high correlation coefficients and which displayed a satisfactory signal-to-noise ratio were selected to build up the databases of events assumed to originate from these source regions. All the orange and magenta symbols in the lower panel of Figure 1 were identified in this way.

Calibrating the event and phase templates

Given a sufficiently large set of events from the sites for calibration, it is necessary to identify properties of the resulting wavefields which provide the most stable characteristics for the subsequent identification of new events. The most stable property is almost always the slowness estimate for the initial P-arrival from each event; this is demonstrated clearly in Figure 8 of Kværna et al. (2004). It also emerges that the frequency band which provides the most stable slowness estimates for a given event population varies greatly (c.f. Figure 6 of Kværna et al., 2004). For the Zapoljarni mines, for example, the 2-4 Hz frequency band gave a far smaller spread of slowness estimates than other frequency bands whereas, for the Khibiny mines, the 4-8 Hz frequency band gave the most consistent estimates.

This raises the question of how a “likely candidate phase” should best be identified and, given the results from the processing of the Kola ground truth mining events, it was deemed that the best procedure would be to perform broadband f-k analysis in a wide range of fixed frequency bands for every detection made by the arrays. In this way, a detection list could simply be scanned by a number of “trigger templates” each examining the frequency band (or set of frequency bands) which provided the best slowness estimates for the target phase. It would be sensible to construct a trigger template for an initial P-arrival from a Zapoljarni event that would be activated when a slowness estimate in the 2-4 Hz band fell within the permitted bounds (obtained from the set of training events) and a trigger template for a P-phase from a Khibiny event which would test the slowness in a higher frequency band. Experience has however shown that it is advisable to provide a few alternative trigger combinations since the optimal frequency band may give a spurious slowness estimate as a result of, for example, an interfering signal. It was found to be helpful to generate panels displaying the slowness estimates and corresponding beams for each of the fixed frequency bands to allow an “at-a-glance” assessment of the quality of each detection. An example of such a panel is displayed in Figure 5 for a regional phase arrival at one of the arrays in Kazakhstan.

It was also demonstrated by Kværna et al. (2004) that autoregressive onset time estimates frequently provided far better estimates than amplitude-only-based methods and so a two-stage reprocessing system was activated for each array in which we first obtain the best possible arrival time estimate and then obtain the slowness estimates in each of the specified frequency bands. This reprocessing procedure can be performed for an arbitrarily specified time and can consequently be applied to any form of detection. It is currently applied for every conventional detection from each of the regional arrays which supply data to NORSAR. However, it could conceivably also be applied to correlation detections, detections from matched-field processing, or simply at times for which there is reason to suspect that an arrival of interest may have occurred.

On each occasion that a trigger template is activated, an event hypothesis is formed for the site region for which the activated template is calibrated. Each such calibrated site has a corresponding “site template” listing the phases which ought to be observed whenever an event at that site occurs. Each of these phases corresponds to a “phase template”

stating at which time the phase should be observed, which range of slowness values are consistent with the phase in a specified set of frequency bands, how large an SNR should be observed to support the assumption that the phase has indeed arrived at the stated time, and which range of autoregressive arrival time estimates are acceptable under the considered event hypothesis. The following section considers an automatic event detection algorithm using the very simplest form available for site templates: a single P-phase and a single S-phase recorded at a single array.

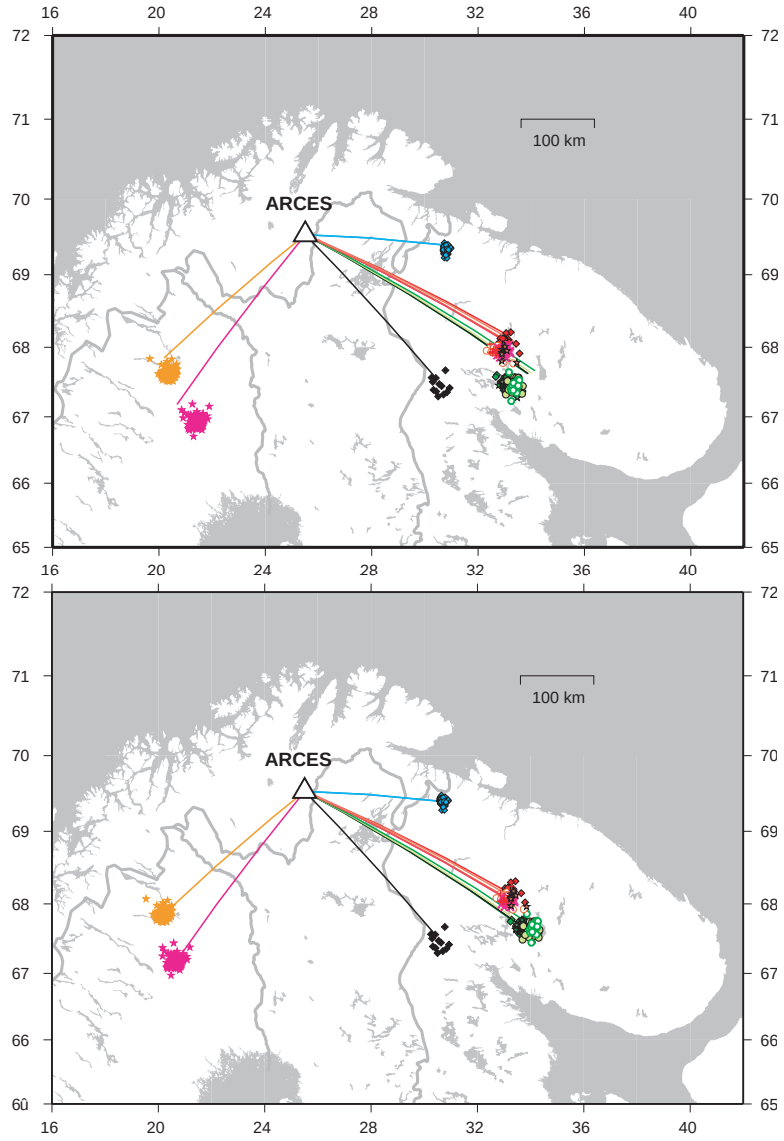

Figure 2. Locations of the events in the lower panel of Figure 1 based upon the site-specific location algorithms with slowness and azimuth estimated in fixed frequency bands selected for each site, and phase onset times estimated by autoregressive methods. The upper panel features the locations made without systematic slowness and travel-time corrections in the location procedure and the lower panel features locations made applying corrections. Note that not all of the events shown in Figure 1 are included in these figures since events which fail to match required components of the templates are excluded prior to the location procedure. Each event which is located showed sufficient evidence of belonging to the geographical region represented by the template; this essentially eliminates the possibility of events being located at large distances from the target sites. Locations are made using the HYPOSAT algorithm (Schweitzer, 2001) using only the Pn and Sn phase arrivals at the ARCES array (Pg and Sg for the Zapoljarni mines).

A template-based event location procedure

For each of the mining regions displayed in Figure 1, a site template was formulated listing two anticipated phases: the initial P-arrival at ARCES (which would be used to trigger an event hypothesis) and the first S-arrival (only used to confirm an event hypothesis). The first S-arrival at ARCES is Sn for all of the sites shown except for the Zapoljarni mines for which the Sg-phase is the first secondary phase to arrive. The slowness bounds for each of the phase templates were set according to the variability observed for the sets of training events (see Kværna et al., 2004). Since an initial P-arrival at ARCES from one of the Khibiny mines would not permit the system to exclude the possibility that the phase originated from one of the other Khibiny mines, it was decided that a site-template would be set up for each one of the mines, and all would trigger for an initial P-phase from any one of the Khibiny sites. Each of the site templates would differ in the initial setting of the time-window for the examination of the secondary phases but, unlike the Kovdor monitoring process (Gibbons, Kværna and Ringdal, 2005) in which slowness estimates were only performed in time-windows fixed relative to the initial P-arrival, we allow here a small deviation through a limited number of iterations. In practice, this means that we measure the slowness in a time-window fixed relative to the initial P-arrival, then form a beam steered by these parameters, measure a new autoregressive onset time, then confirm that the new time falls within a permissible time-window and that the slowness measured at the new time falls within the accepted range. The new slowness is subsequently used to form a new beam and the procedure is repeated. If, at any stage, a test is failed then the event hypothesis is rejected (or at least filed for analyst review); this will limit how far from the specified site template the solution can deviate but should permit a location to be found even if the event is a short distance away from the exact site for which the site-template was tuned.

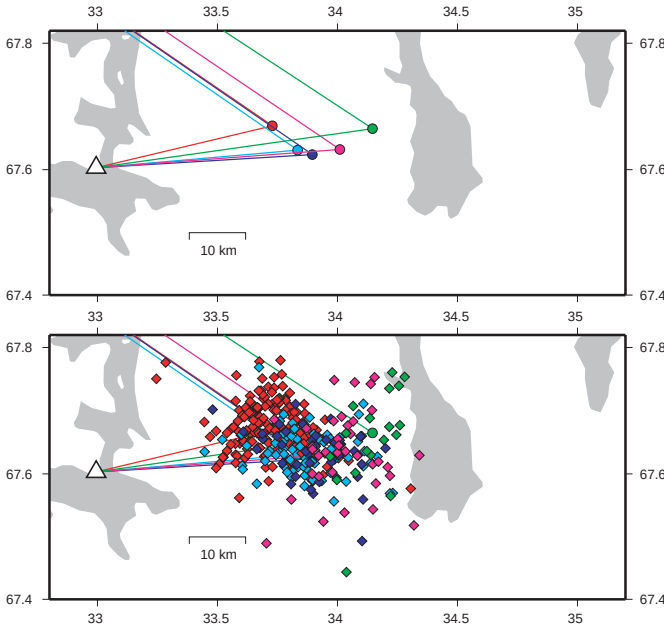

Figure 3. Zoom-in view of the locations of the mines of the Khibiny Massif near the town of Apatity in NW Russia (upper panel) together with automatic, single-array locations of confirmed events from these mines between October 2001 and September 2002 (lower panel). All locations are made using HYPOSAT using only the Pn and Sn phases only from the ARCES array at a distance of approximately 410 km to the North West. The triangle indicates the location of the Apatity array (not used in these locations) and the colored lines indicate the shortest routes from the mines to the seismic arrays.

Figure 2 shows the automatic event locations obtained for the events shown in the lower panel of Figure 1 using the slowness and azimuth estimates obtained from the frequency bands specified in each of the phase templates and phase arrival times measured by the autoregressive onset estimates. This figure indicates the vast improvement to the location estimates afforded by this controlled process and also the importance of applying slowness and travel-time corrections to the solution prior to calling a location algorithm. If the azimuth measured in the most stable frequency band is interpreted directly as being the geographical backazimuth, large systematic biases (of up to 50 km) can be

introduced. In fact, the Kovdor mine is unique among these mining regions in that the systematic azimuthal bias for this site can essentially be ignored; the systematic azimuth bias for the other sites is often of the order of 5 degrees.

Not every event from the mining regions was able to be located using this single-array, two phase site template algorithm. Many events were excluded for having failed a test (a slowness estimate which was not consistent with a phase template or an arrival time estimate which did not fall within the permissible range or which displayed too low an SNR). In particular, many events from the Kovdor mine failed this two-phase algorithm due to the failure of the Sn phase to record an acceptable slowness value in the pertinent time-window; this is often caused by a low amplitude, emergent Sn phase compounded by complicated firing sequence. Gibbons, Kværna, and Ringdal (2005) improve the number of events located by also considering the far stronger Lg phase. An alternative strategy would be to attempt to detect phase arrivals at a different station, which would reduce the importance of detecting a secondary phase.

Figure 3 shows a zoom-in of the calibrated single-array locations for the mines on the Khibiny massif. While the events from the Kirovsk mine (red symbols) cluster to the West and events from the Norpakh mine (green symbols) cluster to the east, as would be hoped from the source locations, we see that this single array process is unable to resolve these populations. This limit of location resolution is consistent with that experienced by Gibbons, Kværna, and Ringdal (2005) for the Kovdor mine. However, even without use of the nearby Apatity array, this location algorithm is probably sufficiently good to provide a preliminary clustering of events which can then undergo a full waveform source identification procedure.

Application of calibrated array processing to data from Kazakhstan

Like Fennoscandia, Kazakhstan is a region containing several seismic arrays and large numbers of routine industrial explosions. Figure 4 shows the locations of the arrays together with reviewed bulletin locations of events over a one month period for which at least one regional phase was recorded at the Akbylak array. It is clear from this distribution that a large number of events cluster around small regions which coincide with the locations of mines.

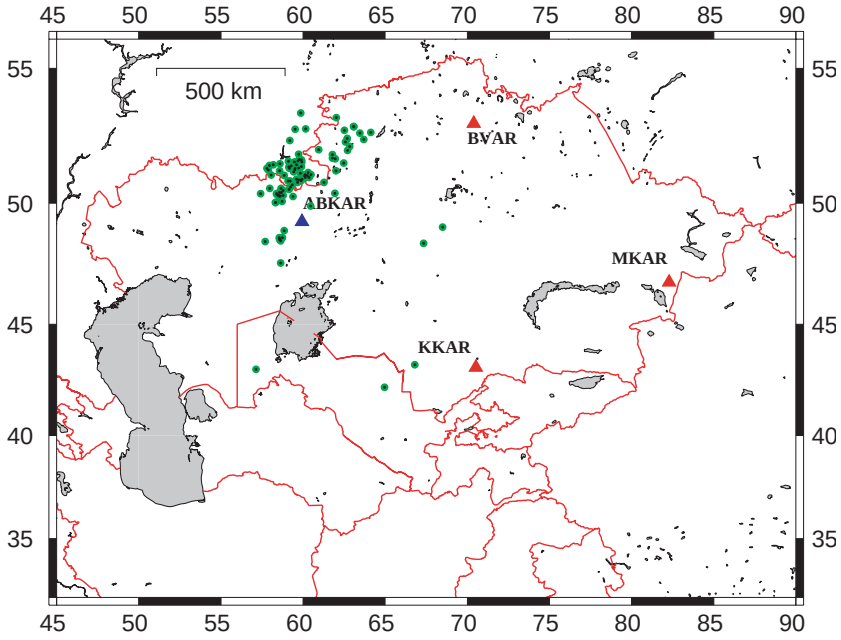

Figure 4. Locations of the four 9-element arrays in Kazakhstan together with locations from the Kazakhstan NDC reviewed event bulletin of all events during May 2004 for which regional phases were recorded at the Akbylak array (ABKAR). Also shown are the arrays at Borovoye (BVAR), Makanchi (MKAR), and Karatau (KKAR).

While ground truth information for the mining sites is not yet available, it appears that the waveform-correlation bootstrapping approach applied to the Swedish mining regions may also be applied here. Many of the analyst-located events in the Kazakhstan bulletin occur within a small geographical region at times at which the mines are known to conduct routine explosions. When the waveforms are filtered in a sufficiently low-frequency band, many events are observed to show a high degree of waveform semblance indicating a small separation between the source regions.

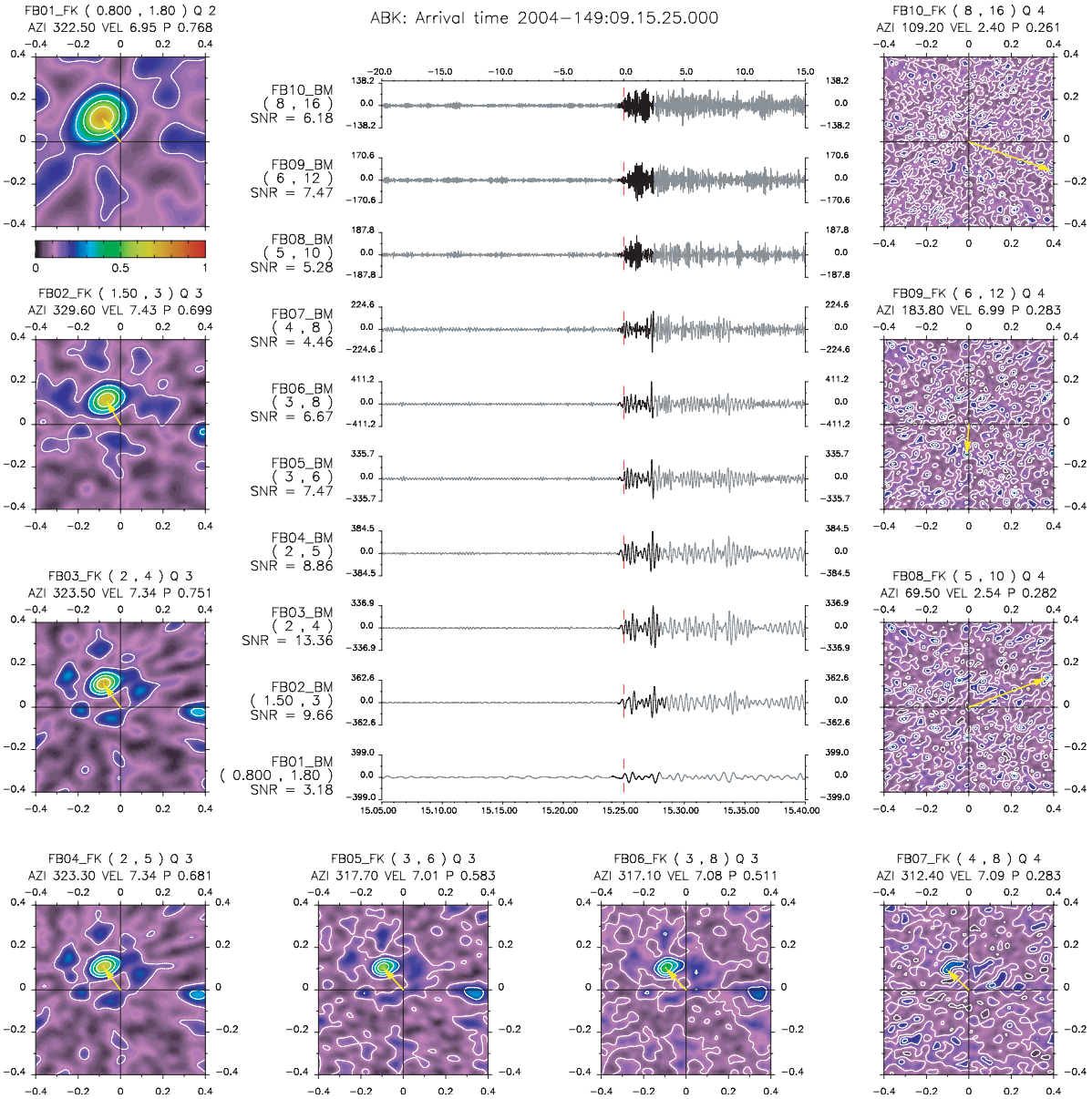

Figure 5. Slowness and azimuth estimates in a predetermined set of fixed frequency bands for a first P-arrival from regional event at a distance of approximately 150 km from the Akbylak array in Kazakhstan.

It appears that the events in the clusters identified so far exhibit a similar "slowness and azimuth as a function of frequency band" to that observed at ARCES (see Figure 5). However, the frequency bands in which regional signals are best observed are very different at the arrays in Kazakhstan from those in Fennoscandia. For ARCES and the other Fennoscandian arrays, frequencies below 2 Hz are essentially unusable for regional signals because of the high-microseismic noise. The SNR for most of the mining explosions simply improves as the frequency increases and

the optimal analysis frequency band is a trade-off between SNR and coherence. In Kazakhstan, the low frequencies do allow good observations of regional phases and the frequency bands above 4 Hz for these arrays do not give good slowness estimates due to signal incoherence. The set of fixed frequency bands for the reprocessing is therefore chosen accordingly.

Compensation for array loss using matched-field processing

Classical beamforming transforms the incident waveforms using steering vectors which are set according to the assumption of a plane-wavefront. Array loss occurs when the coherence of the waveforms is diminished or the plane-wavefront assumption is otherwise violated due to diffraction or scattering. It has already been noted that many of the signals of interest exhibit the best (single channel) SNR at high frequencies for which beamforming is ineffective due to low waveform semblance. A method of compensating for such array loss by replacing the theoretical steering vectors with empirical steering vectors calibrated from measurements of the wavefield structure, the so-called "matched-field processing" method, has already been employed successfully in the field of underwater acoustics (Baggeroer et al., 1993). The steering vectors are calculated as the eigenfunctions of sample covariance matrices obtained from narrow-band filtered waveforms from populations of events known to have come the same source location.

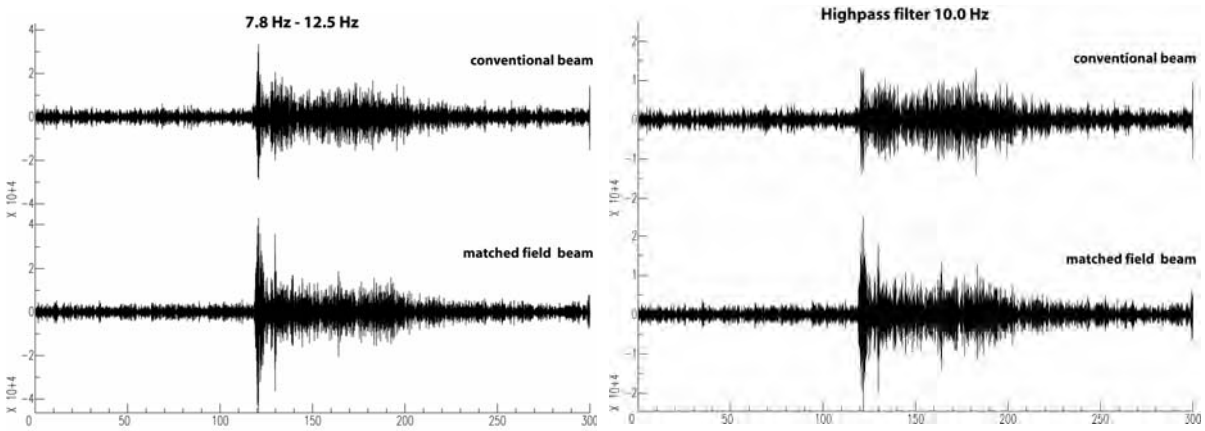

Figure 6. A comparison of conventional and emprical matched field Pn beams using the ARCES array for signals generated by a confirmed compact underground explosion at the Kirovsk mine on the Khibiny massif. A low-frequency array geometry was used here to illustrate the possible gains of matched field processing in situations where signals are only partially coherent. The matched field beam captures between and 3 and 5 dB more Pn energy depending on the frequency band considered.

These calibrations can be applied by performing narrow-band filtering upon an incoming data-stream and beamforming the resulting waveforms using the empirical steering vectors. Figure 6 illustrates the improvement in the SNR on the matched-field beam over a conventional beam for a Pn arrival from a Khibiny massif event. The effect may be even greater for high-frequency regional signals on the arrays in Kazakhstan for which loss of coherence at high frequencies presents a serious problem.

CONCLUSIONS AND RECOMMENDATIONS

We have designed a framework for the automatic monitoring of seismic events from sites of interest using regional seismic arrays. Under the current automatic detection and event location algorithms employed at NORSAR and elsewhere, slowness and azimuth estimates are calculated using broadband f-k analysis in frequency bands which are determined on a detection by detection basis in order to capture the best possible part of the signal. Whereas this generally leads to the best SNR it also leads to a demonstrable variability in automatic event location estimates (Figure 1) which necessitates a costly manual event location procedure for every such signal detection. Under the system proposed here, each detection is reprocessed by performing f-k analysis in each of several fixed frequency bands. This has the advantage that, since the fixed band slowness estimates are typically more stable for events from any given site and that the optimal frequency band varies from site to site, candidate detections can be readily picked

out by a process which detects slowness estimates in a specified band (or combination of bands) which fall within a given set of calibrated bounds. Each time such a candidate phase detection causes a trigger, a full process testing a site template can be initiated which tests any appropriate combination of phases at any appropriate combination of stations. For each time of an anticipated arrival, a new fixed-band slowness estimate is initiated together with an arrival time determination procedure. We have demonstrated that, even in the case of a single array with a two-phase site template, the fully automatic location estimates provide a great improvement over the existing solutions. We have also demonstrated the need to correct for systematic bias in direction and travel time measurements in the location procedure.

The most time consuming and difficult part of this procedure is in the calibration of templates for events known to have originated from a given site. This has been facilitated in this study by the provision of ground truth information from operators of the mines in NW Russia and the application of waveform correlation procedures elsewhere. To conclude this project, we will examine the effectiveness of such a procedure for sites of recurring seismicity in Kazakhstan.

ACKNOWLEDGEMENTS

We are grateful to Vladimir Asming and colleagues at the Kola Regional Seismological Center in Apatity, Russia, for collecting ground truth information from the Russian mine-operating companies as to the sites and times of routine industrial explosions. We would also like to thank staff at the Kazakhstan NDC for providing data from the Kazakhstan array network together with automatic and reviewed event bulletins.

REFERENCES

Baggeroer, A. B., W. A. Kuperman, and P. N. Mikhalevsky (1993), An overview of matched field methods in ocean acoustics, in *IEEE Journal of Oceanic Engineering*, 19(4): 401-424.

Gibbons, S. J., T. Kværna and F. Ringdal (2005), Monitoring of seismic events from a specific source region using a single regional array, in *J. Seismol.* (in press).

Harris, D. B., F. Ringdal, E. O. Kremenetskaya, S. Mykkeltveit, J. Schweitzer, T. F. Hauk, V. E. Asming, D. W. Rock and J. P. Lewis (2003), Ground-truth collection for mining explosions in Northern Fennoscandia and Russia, in *Proceedings of the 25th Seismic Research Review - Nuclear Explosion Monitoring: Building the Knowledge Base*, LA-UR-03-6029, Vol. 1, pp. 54-63.

Kværna, T., S. J. Gibbons, F. Ringdal, and D. B. Harris (2004), Integrated Seismic Event Detection and Location by Advanced Array Processing, in *Proceedings of the 26th Seismic Research Review - Trends in Nuclear Explosion Monitoring*, LA-UR-04-5801, Vol. 2, pp.742-751.

Kværna, T. and F. Ringdal (1989), A multichannel processing approach to real time network detection, phase association and threshold monitoring, in *Bull. Seism. Soc. Am.* 79: 1927–1940.

Schweitzer, J. (2001), HYPOSAT - An enhanced routine to locate seismic events, in *Pure Appl. Geophys*. 158: 277-289.

ENHANCING SEISMIC CALIBRATION RESEARCH THROUGH SOFTWARE AUTOMATION AND SCIENTIFIC INFORMATION MANAGEMENT

Stanley D. Ruppert, Douglas A. Dodge, Annie B. Elliott, Michael D. Ganzberger, Teresa F. Hauk, and Eric M. Matzel

Lawrence Livermore National Laboratory

Sponsored by National Nuclear Security Administration
Office of Nonproliferation Research and Engineering
Office of Defense Nuclear Nonproliferation

Contract No. W-7405-ENG-48

ABSTRACT

The National Nuclear Security Administration (NNSA) Ground-Based Nuclear Explosion Monitoring Research and Engineering (GNEM R&E) program has made significant progress enhancing the process of deriving seismic calibrations and performing scientific integration with automation tools. We present an overview of our software automation and scientific data management efforts and discuss frameworks to address the problematic issues of very large datasets and varied formats utilized during seismic calibration research. The software and scientific automation initiatives directly support the rapid collection of raw and contextual seismic data used in research, provide efficient interfaces for researchers to measure and analyze data, and provide a framework for research dataset integration. The automation also improves the researchers ability to assemble quality controlled research products for delivery into the NNSA Knowledge Base (KB). The software and scientific automation tasks provide the robust foundation upon which synergistic and efficient development of GNEM R&E program seismic calibration research may be built.

The task of constructing many seismic calibration products is labor intensive and complex, hence expensive. However, aspects of calibration product construction are susceptible to automation and future economies. We are applying software and scientific automation to problems within two distinct phases or “tiers” of the seismic calibration process. The first tier involves initial collection of waveform and parameter (bulletin) data that comprise the “raw materials” from which signal travel-time and amplitude correction surfaces are derived and is highly suited for software automation. The second tier in seismic research content development activities includes development of correction surfaces and other calibrations. This second tier is less susceptible to complete automation, as these activities require the judgment of scientists skilled in the interpretation of often highly unpredictable event observations. Even partial automation of this second tier, through development of prototype tools to extract observations and make many thousands of scientific measurements, has significantly increased the efficiency of the scientists who construct and validate integrated calibration surfaces. This achieved gain in efficiency and quality control is likely to continue and even accelerate through continued application of information science and scientific automation.

Data volume and calibration research requirements have increased by several orders of magnitude over the past decade. Whereas it was possible for individual researchers to download individual waveforms and make time-consuming measurements event by event in the past, with the terabytes of data available today, a software automation framework must exist to efficiently populate and deliver quality data to the researcher. This framework must also simultaneously provide the researcher with robust measurement and analysis tools that can handle and extract groups of events effectively and isolate the researcher from the now onerous task of database management and metadata collection necessary for validation and error analysis. Lack of information-management robustness or loss of metadata can lead to incorrect calibration results in addition to increasing the data-management burden. To address these issues, we have succeeded in automating several aspects of collection, parsing, reconciliation, and extraction tasks, individually. Several software automation prototypes have been produced and have resulted in demonstrated gains in efficiency of producing scientific data products. Future software automation tasks will continue to leverage database and information-management technologies in addressing additional scientific calibration research tasks.

OBJECTIVES

The National Nuclear Security Administration (NNSA) Ground-Based Nuclear Explosion Monitoring Research and Engineering (GNEM R&E) program has made significant progress enhancing the process of deriving seismic calibrations and performing scientific integration with automation tools. We present an overview of our software automation efforts and framework to address the problematic issues of very large datasets and varied formats utilized during seismic calibration research and the attributes required to construct next-generation data acquisition. The scientific automation engineering and research will need to provide the robust hardware, software, and data infrastructure foundation for synergistic GNEM R&E program calibration efforts. The current task of constructing many seismic calibration products is labor intensive and complex, hence expensive. However, aspects of calibration-product construction are susceptible to automation and future economies. Data volume and calibration research requirements have increased by several orders of magnitude over the past decade. We have succeeded in automating many of the collection, parsing, reconciliation, and extraction tasks, individually. Several software automation prototypes have been produced and have resulted in demonstrated gains in efficiency of producing scientific data products. In order to fully exploit voluminous real-time data sources and support new requirements for time critical modeling, simulation, and analysis, a more scalable and extensible computational framework will be required.

RESEARCH ACCOMPLISHED

The primary objective of the Scientific Automation Software Framework (SASF) efforts is to facilitate development of information products for the Ground-Based Nuclear Explosion Monitoring Research and Engineering (GNEM R&E) regionalization program. The SASF provides efficient access to, and organization of, large volumes of raw and derived parameters, while also providing the framework to store, organize, integrate and disseminate information products for delivery into the National Nuclear Security Administration Knowledge Base (NNSA KB). The current framework supports integration, synthesis, and validation of the various different information types and formats required by each of the seismic calibration technologies (Figure 1). For example, the seismic location technology requires parameter data (site locations, bulletins), and time-series data (waveforms) and produces parameter measurements in the form of arrivals, gridded geospatially registered corrections surfaces and uncertainty surfaces through the use of various tools and information-processing frameworks (relational databases (RDBs), Geographical Information Systems (GISs), and associated product and data visualization and data management tools (e.g., RBAP, KBALAP, KBCIT, DM).

These information-management and scientific automation tools are used together within specific seismic calibration processes to support production of tuning parameters for the United States Atomic Energy Detection System operated by the Air Force (Figure 2). The calibration processes themselves appear linear (Figure 2), beginning with data acquisition and extending from reconciliation, integration, and measurement and simulation to construction of calibration / run-time parameter products. Efficient production of calibration products, however, requires extensive synergy and synthesis not only between data-types (Figure 1), but also between measurements and results derived from the different calibration technologies (e.g., Location, Identification, Detection) (Figures 1 and 2). Even with successful implementation of automation within many of the individual steps, the current infrastructure will not scale to handle order-of-magnitude additional data or extend to handle time-critical data acquisition or analysis. This lack of scalability and flexibility limits efficient production and delivery of run-time calibrations to the operational seismic monitoring pipeline (Figure 2, bottom) as a large manual effort is still required to acquire and integrate streaming (10–20 GB/day) signals with associated metadata. This synergy and synthesis between complex tools and very large datasets is critically dependent on having a scalable and extensible unifying framework. These requirements of handling large datasets in diverse formats and facilitating interaction and data exchange between tools supporting different calibration technologies led to an extensive scientific automation software engineering effort to develop an object-oriented database-centric framework (Figure 3) as a unifying foundation.

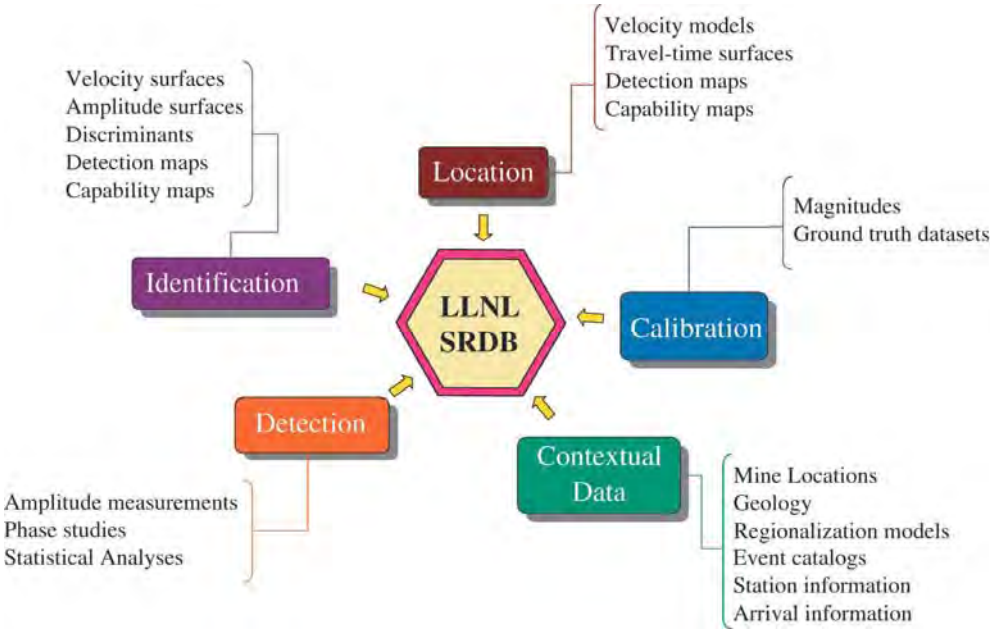

Figure 1. The Scientific Automation Software Framework provides a unifying framework for contextual/reference data and information products.

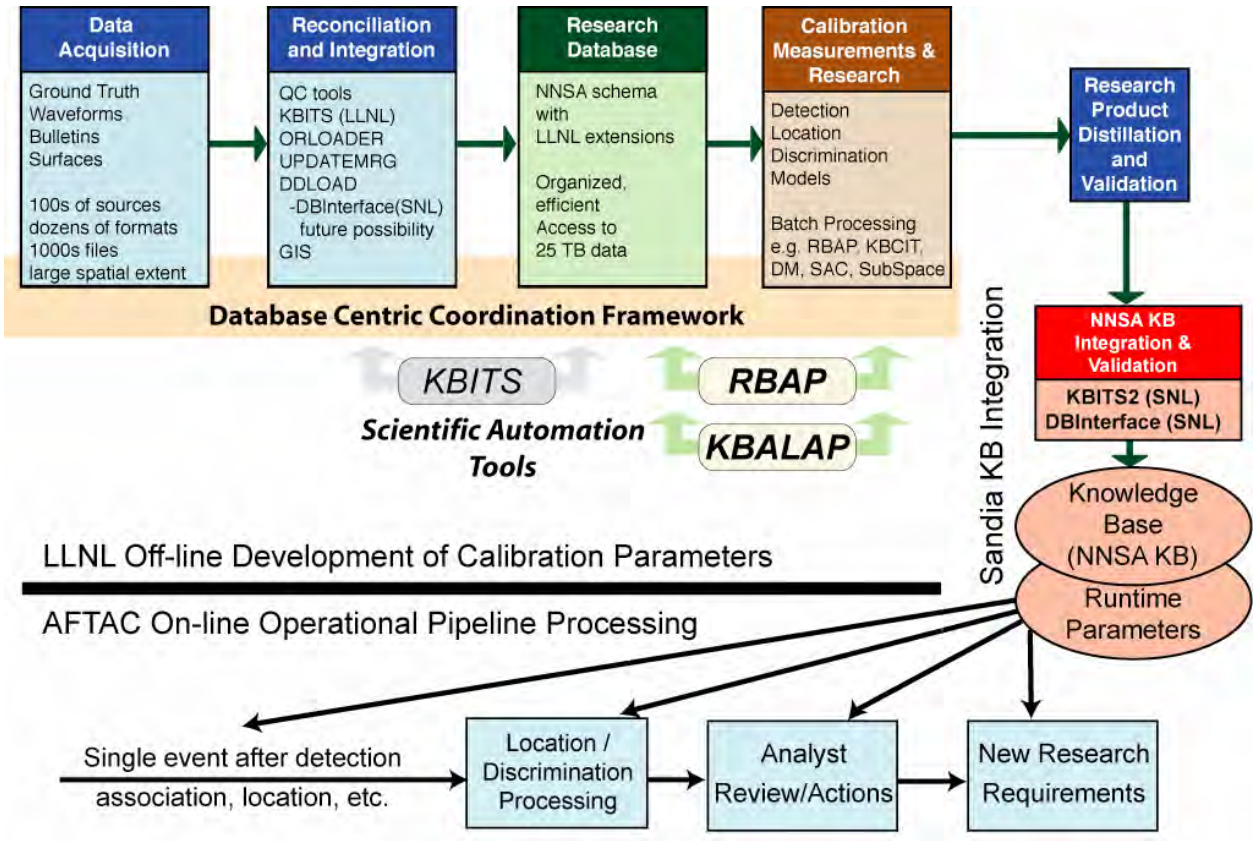

Figure 2: Summary of the processes of data collection, research, and integration within the LLNL calibration process that result in contributions to the NNSA KB. The relationships of the current LLNL calibration tools, scientific automation tools, and database coordination framework to those involved in the assembly of the NNSA KB are delineated.

Scientific Automation Software Tools

Information products created using the Lawrence Livermore National Laboratory (LLNL) Seismic Research Database (SRDB) may be grouped under two major categories or tiers: Tier 1 - primary data products, and Tier 2, derived products. In order to calibrate seismic monitoring stations, the LLNL SRDB must incorporate and organize the following categories of primary and derived measurements, data, and metadata:

Tier 1: Contextual and Raw Data
Station Parameters and Instrument Responses
Global and Regional Earthquake Catalogs
Selected Calibration Events
Event Waveform Data
Geologic/Geophysical Datasets
Geophysical Background Model

Tier 2: Measurements and Research Results
Phase Picks
Travel-time and Velocity Models
Rayleigh and Love Surface Wave Group Velocity Measurements
Phase Amplitude Measurements and Magnitude Calibrations
Detection and Discrimination Parameters

Automating Tier 1

Corrections and parameters distilled from the calibration database provide needed contributions to the NNSA KB for the Middle East/North Africa/Western Europe (ME/NA/WE) region and will improve capabilities for underground nuclear explosion monitoring. The contributions support critical functions in detection, location, feature extraction, discrimination, and analyst review. Figure 2 outlines the processes of data collection, research, and integration within the LLNL calibration process that result in contributions to the NNSA KB and the relationship of the LLNL calibration tools to those involved in the assembly of the NNSA KB or within the AFTAC operational pipeline. Within the major process steps (data acquisition, reconciliation/integration, calibration research, product distillation) are many labor intensive and complex steps. The previous bottleneck in the calibration process was in the reconciliation/integration step (Figure 2). This bottleneck became acute in 1998, and the KBITS suite of automated parsing, reconciliation, and integration tools for both waveforms and bulletins (ORLOADER, DDLOAD, UpdateMrg) was developed. The KBITS suite provided the additional capability required to integrate data from many data sources and external collaborations. Data volumes grew from the 11,400 events / 1 million waveforms in 1998 to the 6 million events / 70 million segmented waveforms and terabytes of continuous data today (e.g., Ruppert et al., 1999, Ruppert et al., 2004). This rapid increase in stored parameters soon led to new bottlenecks hindering rapid development and delivery of calibration research.

Automating Tier 2

As the number of data sources required for calibration increased in number and source location, it became clear that the manual and labor-intensive process of humans transferring thousands of files and unmanageable metadata could not keep the KBITS software fed with data to integrate, nor could the seismic research efficiently find, retrieve, validate, or analyze the raw parameters necessary to effectively produce seismic calibrations in an efficient manner. Significant software engineering and development efforts were applied to address this critical need to produce software aids for the seismic researcher. Two scientific automation tool prototypes (RBAP, KBALAP) (Figure 2) are under development for seismic location and seismic identification calibration tasks.

Both of these prototypes include methods and aids for efficiently extracting groups of events and waveforms from the millions contained in the SRDB and making large numbers of measurements with metadata in a batch mode. The concept of event sets (groups of related seismic events or parameters that can be processed together, e.g., either station centric or event centric) was introduced as previous SAC scripts and macros could not scale to the task.

The KBALAP Program

The Knowledge Base Automated Location Assessment and Prioritization (KBALAP) program is a set of database services and a client application that combine to efficiently produce location ground truth (GT) data that can be used in the production of travel time correction surfaces and as part of the preferred event parameters used by other tools in our processing framework.

The part of KBALAP that runs as a database service is responsible for evaluating bulletin and pick information as it enters the system to identify origin solutions that meet predefined GT criteria with no further processing, and to identify events that would likely meet a predefined GT level if a new origin solution were produced using available arrivals. The database service is also responsible for identifying events that should have a high priority for picking based on their existing arrival distribution and the availability of waveform data for stations at critical azimuths and distances.

The interactive portion of KBALAP has three principal functions. These are

- interactive production of GT origins through prioritized picking and location,
- interactive specification of GT-levels for epicenter, depth, origin time, etype, and
- batch-mode location of externally-produced GT information.

The first of these capabilities allows the user to view epicenters and GT information on a map based on selection criteria input by the user. The user can select any GT or potential GT event and observe the distribution of stations with picks and stations with available waveforms. The user can select any station with available waveforms and open a picker with any current picks displayed. There the user can adjust existing picks, add new picks, mark bulletin picks as unusable, and relocate the event. A new GT level is calculated, and the user can choose to accept that origin solution and GT level or continue working with other stations.

The interactive GT entry mode of KBALAP allows the user to retrieve information about a specific event and add or update that event's GT parameters. The program can also create a new event with a GT level for cases where epicenter, time, depth and magnitude GT data are available. Similarly, the batch mode part of the program allows specification of flat files containing GT data for events already in the database.

The RBAP Program

The Regional Body-wave Amplitude Processor (RBAP) is a software tool to help automate the process of making amplitude measurements of regional seismic phases for the purpose of calibrating seismic discriminants at each station. RBAP generates station-centric raw and Magnitude Distance Amplitude Correction (MDAC) corrected Pn, Pg, Sn and Lg amplitudes along with their associated calibration parameters (e.g., phase windows, MDAC values, reference events, etc.) in database tables. It strictly follows the Working Group (WG) 2 standardized processing described in the MDAC White Paper (Walter et al., 2003) and it replaces the original collection of scripts described by Rodgers (2003). RBAP has a number of advantages over the previous scripts. It is much faster, significantly easier to use, scales more easily to a larger number of events and permits efficient project revision and updating through the database.

RBAP integrates the functions of the modules in the previous LLNL scripts into a single program that is designed to perform the amplitude measurement task efficiently and to require a minimum effort from the users for managing their data and measurements. For well-located events with pre-existing analyst phase picks, the user reviews for quality control and then generates all the amplitudes with just a few mouse clicks. For events needing more attention, the user has complete control over the process (e.g., window control, ability to mark bad data, define regions, define MDAC parameters, and define the events to be used in the overall calibration process). RBAP shortens the time needed by the researcher to calibrate each station while simultaneously allowing an increase the number of events that can be efficiently included. RBAP is fully integrated with the LLNL research database. Data are always read directly from the appropriate tables in the research database rather than from a snapshot, as was done in the previous system. All RBAP result tables have integrity constraints on the columns with dependencies on data in the LLNL research database. This design makes it very difficult for results produced by RBAP to be stale and also ensures that as the research database expands, RBAP automatically becomes aware of new data that should be processed. RBAP initial users will be LLNL WG 2 members working on Integrated Research Products for FY04.

Some RBAP Key Features

• *Based on WG 2 Standardized Algorithm*
-RBAP is built on the WG 2 standardized body-wave amplitude measurement algorithms documented in the "MDAC White Paper" (Walter et al., 2003). Its results are completely consistent with the last version of the LLNL scripts (Rodgers, 2003) that were vetting in the February 2003 WG 2 exercise between LLNL, LANL, and AFTAC.

• *Fast and Efficient Calibration*
RBAP is self-contained and optimized for station-centric body-wave processing. "Good" events can be handled with just a few mouse clicks. The researcher has direct control over key calibration parameters within the tool such as phase amplitude windows and migration, marking bad segments, defining distinct geophysical regions, event types to process, etc. We expect RBAP to provide roughly a factor of 5 increase in calibration speed compared with the original scripts, enabling us to calibrate more stations, with more events per station.

• *Project Management*
RBAP is designed so that a calibration project can be put down for a day, month, or year, and easily picked up, by the same researcher or a new one. All processing metadata are saved and events are easily tracked as processed, unprocessed, or outside the current project definitions. This allows a researcher to efficiently work through a huge data list without repetition and to easily identify and incorporate new events as they become available in the database.

• *Utilizes Database for Up-to-Date results*
RBAP can draw on the latest calibration parameters being generated by other working groups, such as the most recent phase picks, relocations, magnitudes, instrument response information, or event type ground truth.

• *Batch Processing*
RBAP is designed to allow simple batch updating of the amplitude results, whether the change is small (e.g., one-event is relocated) or large (instrument response is changed, affecting all events).

Database Centric Coordination Framework

As part of our effort to improve our efficiency, we have allowed researchers to easily share their results with one another. For example, as the location group produces GT information, that information should become available for other researchers to use. Similarly, phase arrival picks made by any qualified user should also become immediately available for others to use. This concept extends to the sharing of information about data quality. It should not be necessary for multiple researchers to have to repeatedly reject the same bad data. Rather, once data are rejected because of quality reasons, they should automatically be excluded from processing by all tools. We are implementing this system behavior using database tables, triggers, stored procedures, and application logic. Although we are at the beginning of this implementation, we have made significant progress over the last year with several kinds of information sharing using the new Database Centric Coordination Framework. These are discussed below.

Significant software engineering and development efforts have been applied successfully to construct an object-oriented database framework that provides database-centric coordination between scientific tools, users, and data (Figure 3). A core capability this new framework provides is information exchange and management between different specific calibration technologies and their associated automation tools such as Seismic Location (e.g. KBALAP), seismic identification (e.g., RBAP), and data acquisition / validation (e.g., KBITS). A relational database (ORACLE) provides the current framework for organizing parameters key to the calibration process from both Tier 1 (raw parameters such as waveforms, station metadata, bulletins, etc.) and Tier 2 (derived measurements such as ground-truth, amplitude measurements, calibration and uncertainty surfaces etc). Efforts are underway to augment the current relational database structure with semantic graph theory structured queries for handling complex queries.
Seismic calibration technologies (location, identification, etc.) are connected to parameters stored in the relational database by an extensive object-oriented multi-technology software framework (Figure 3, middle) that include elements of schema design, stored procedures, real-time transactional database triggers, and constraints, as well as

coupled Java and C++ software libraries to handle the information interchange and validation requirements. This software framework provides the foundation upon which current and future seismic calibration tools may be based.

Sharing of Derived Event Parameters

We have long recognized the inadequacies of the CSS3.0 origin table to serve as a source of information about the "best" parameters for an event. One origin solution may have the best epicenter but poor information on other parameters.

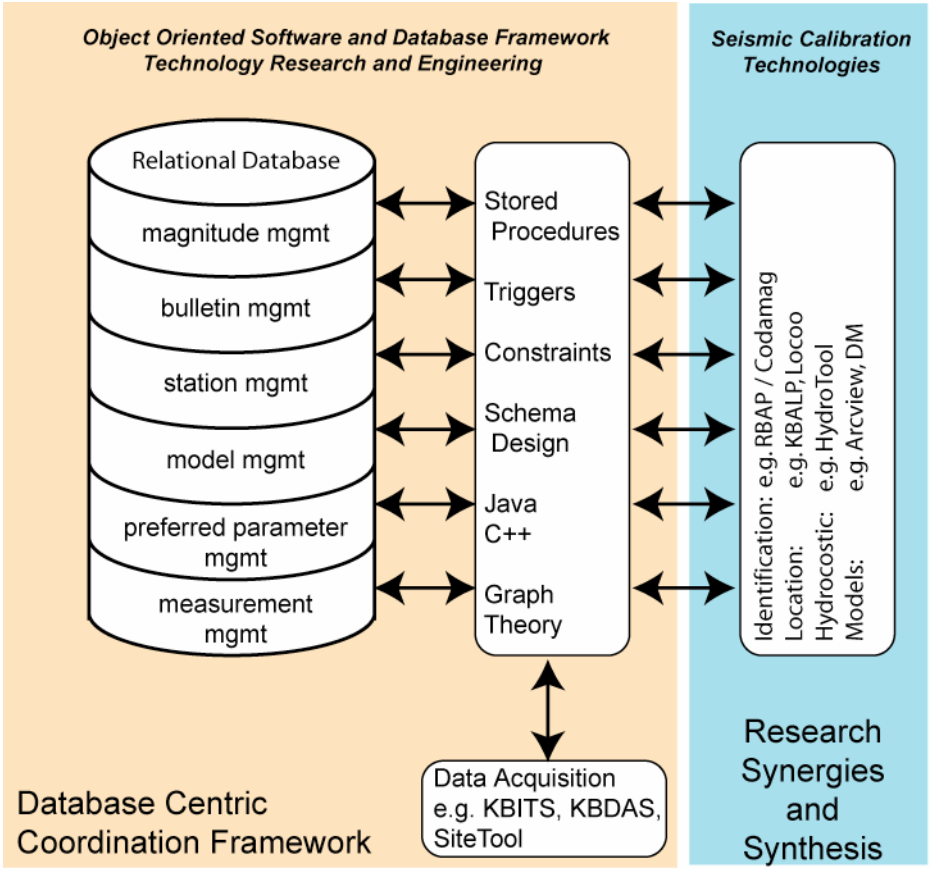

Figure 3. Overview of the Database Centric Coordination Framework that provides the enabling information technology to allow synergy and synthesis of data and calibration technologies for the efficient production of calibration deliverables.

Another may have the correct event type but be poor in other respects, and so on. We had discussed producing origin table entries, with our organization as the author, but that approach has difficulties. Different groups would have responsibility for different fields in the origin. Because their information would not be produced in synchronization, we would always have to be either updating the preferred origin or producing new preferred origins. Also, there would be difficulties in tracking the metadata associated with each field of the preferred origin. Our solution was to create a set of new tables and associated stored procedures and triggers that collectively maintain the "best" information about events.

Enhancements to Efficiency through Cluster-Based Computing

We have begun to leverage scalable and reconfigurable cluster computing resources to improve the efficiency of our computational infrastructure. Just as the database-centric approach to information management provided important gains in efficiency, we needed to move to a different computational paradigm to provide the computational power

necessary during calibration production and research. We have begun developing a set of flexible and extensible tools that are platform independent and parallelizable. These research tools will provide an efficient data processing environment for all stages of the calibration work flow, from data acquisition through making measurements to calibration surface preparation. This scalable and extensible approach (Figure 4) will result in more coupled and dynamic work flow in contrast to the linear work flow of the past, and allow more interaction between data, model creation, and validation processes.

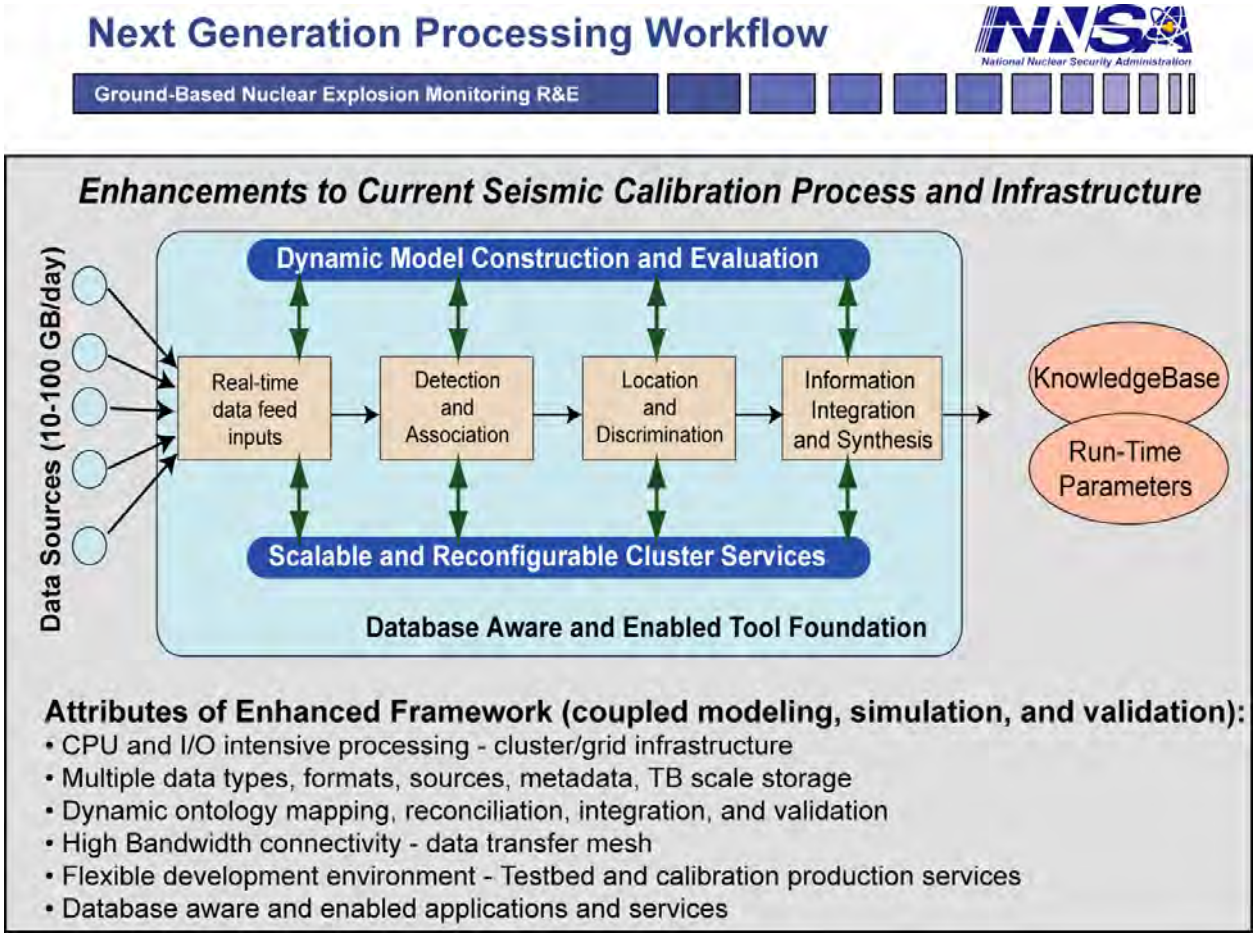

Figure 4. Overview of the cluster based calibration workflow under design and development.

Initial development and modification of existing codes and algorithms of the cluster based computing environment, has yielded significant efficiency improvements in RBAP and other measurement tools. Modification of RBAP to incorporate threads to isolate computationally intensive operations has provided a more interactive and responsive environment for the researcher and has laid the ground work for moving the threads to cluster-based computing resources. Other areas under investigation for taking advantage of cluster resources are for waveform correlation and subspace detector work, in addition to providing the ability to efficiently perform large-scale event relocations to evaluate ground truth and model calibrations.

CONCLUSIONS AND RECOMMENDATIONS

We present an overview of our software automation efforts and framework to address the problematic issues of very large datasets and varied formats utilized during seismic calibration research and the attributes required to construct next-generation data acquisition. By combining both a database centric information management system coupled with scalable and extensible cluster-based computing, we have begun to leverage a high-performance computational framework to provide increased calibration capability. These new software and scientific automation initiatives

could directly support our current mission, including rapid collection of raw and contextual seismic data used in research, providing efficient interfaces for researchers to measure/analyze data, and providing a framework for research dataset integration. The initiatives would improve time-critical data assimilation and coupled modeling/simulation capabilities necessary to efficiently complete seismic calibration tasks. The scientific automation engineering and research will need to provide the robust hardware, software, and data infrastructure foundation for synergistic GNEM R&E program calibration efforts.

ACKNOWLEDGEMENTS

We acknowledge the assistance of the LLNL computer support unit in implementing and managing our computational infrastructure. We thank Jennifer Aquilino and Laura Long for their assistance in configuration and installation of our Linux cluster.

REFERENCES

Ruppert, S., T. Hauk, J. O'Boyle, D. Dodge, and M. Moore (1999), Lawrence Livermore National Laboratory's Middle East and North Africa Research Database, in *Proceedings of the 21st Seismic Research Symposium: Technologies for Monitoring The Comprehensive Nuclear-Test-Ban Treaty*, LA-UR-99-4700, Vol. 1, pp. 234-242, Las Vegas, NV.

Ruppert, D. Dodge, A. Elliott, M. Ganzberger, T. Hauk, E. Matzel, and F. Ryall (2004), Enhancing seismic calibration research through software automation, in *Proceedings of the 26th Seismic Research Review: Trends in Nuclear Explosion Monitoring*, LA-UR-04-5801,Vol. 2, pp. 780-789, Orlando, FL.

DATA AND TOOLS TO SUPPORT NUCLEAR EXPLOSION MONITORING RESEARCH AND DEVELOPMENT

Robert Woodward, Michael Skov, Manochehr Bahavar, Geoff Davis, and Yu-Long Kung

Science Applications International Corporation

Sponsored by Army Space and Missile Defense Command

Contract No. DASG60-03-C-0009

ABSTRACT

The nuclear explosion monitoring research and development (R&D) community can access raw data and unique research databases using state-of-the-art data browsing and selection tools as part of the Research and Development Support Services (RDSS) project operated by the United States (US) Army Space and Missile Defense Command Monitoring Research Program.

The waveform data archive maintained by the RDSS provides direct and immediate access to 100% of the data in the archive. A high-speed spinning disk mass-storage system is used to store all the waveforms in the archive (roughly 12 Tb of seismic, hydroacoustic and infrasound waveforms from over 300 locations worldwide). Every waveform in the archive can be directly and instantly accessed, making it possible to provide data users with a range of new tools and services that go beyond traditional data center functions. User interaction with the data archive is provided through several mechanisms, including a web-based, "e-commerce-like," interface. This web-based interface allows users to visually browse data (waveforms) or data products (e.g., bulletins), select data or data products to be placed in a "shopping cart," and then provides the capability to manage and download the selected objects. A waveform viewer runs under a standard web browser and provides the capability to display multiple traces, perform filtering, zooming, and scrolling. Any waveform in the entire data archive can be viewed using this tool. The user can select waveforms from the display for subsequent download. A download manager then provides the ability to download the various products a user has selected during a session (or sessions—the download manager can manage product selections made during multiple sessions). Any data in the archive can be downloaded in either CSS3.0 or SAC formats.

The waveform data archive also supports data intensive computing by providing direct access to all data files in the archive via RDSS servers. Users who load software on these servers can perform experiments on any desired cross-section of the waveform archive, with no need to "stage" data. Further, it is not necessary to make special modifications to scientific software, since the data are stored in the archive in a common, analysis ready format. An example of a recent large-scale, data intensive experiment was the analysis of ambient noise at infrasound stations. This experiment required computing noise values at multiple infrasound stations, at multiple times per day, for every day of a 2-year period. Over a million discrete (noncontiguous) time series were analyzed for this study.

The RDSS also provides a range of value-added R&D databases, which are a significant resource for the US R&D community. These databases are accessible through interactive, web-based tools and bring together a wide range of open-source data into individual, well-organized packages. For example, the recently expanded infrasound database draws on a unique collection of waveforms (many of which are not archived anywhere else) from infrasound arrays operated by the Department of Energy, the International Monitoring System, and other organizations. These data go back to 1995, and include data from sites on every continent. The database includes acoustic recordings of a variety of natural and man-made events, as well as historical recordings of atmospheric nuclear explosions. The seismic R&D databases include the Nuclear Explosion Database, an exhaustive collection of metadata and waveforms from nuclear tests; the Ground Truth Database, containing a wide range of carefully selected and quality-controlled events for ground-truth (GT) levels of 0 to 15 km; and region-specific databases for the Lop Nor, China, region and the Arctic region.

In this paper we provide a summary of the major RDSS data assets and resources. We provide examples and descriptions of the types of data and metadata in each database, and provide information on how these resources can be accessed.

OBJECTIVE

The objective of the RDSS is to support the nuclear explosion monitoring research and development community with a wide range of data, state-of-the-art data access tools, and value-added datasets.

RESEARCH ACCOMPLISHED

During the current contract we have pursued initiatives in three primary areas with the goal of extending existing resources or developing new resources which will provide direct benefit to the nuclear explosion monitoring R&D community. First, we have expanded and improved the waveform archive, concentrating especially on creating a high-speed archive and new access tools which fully exploit the capabilities of the new system. Second, we have improved our existing, value-added R&D databases and have created several new databases. Third, we have developed new tools, using an application service provider model, to provide remote users with access to sophisticated R&D software. In the following sections we describe these developments in greater detail.

Waveform Archive and Data Access

The RDSS maintains a large archive of waveform data from seismic, hydroacoustic, and infrasound stations. Data in the archive go back to 1995 (earlier for some stations) for stations distributed worldwide (Figure 1).

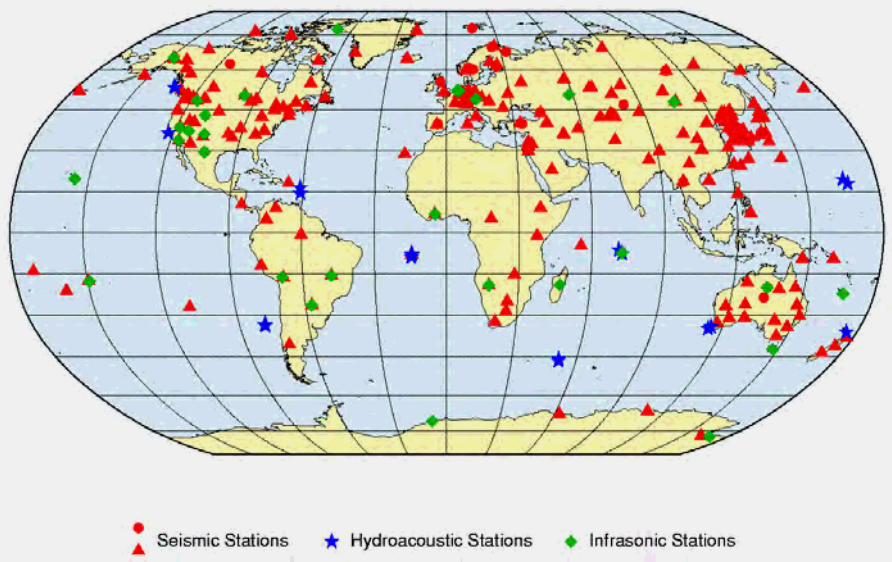

Figure 1. Seismic arrays (circles) and three-component stations (triangles) and hydroacoustic and infrasonic arrays (stars and diamonds, respectively) for which waveform data are available from the RDSS archive. For many of these stations and arrays the data are continuous over periods of several years.

The waveform archive now exceeds 14 Tb of data. The entire data archive is hosted on a spinning-disk mass storage system (RAID disk farm). This system provides access to the entire archive that is at least two orders of magnitude faster than its predecessors and makes very large scale experiments and data visualizations possible.

The RDSS website is continuously enhanced to improve data access for the research community. During the past year we have initiated work to integrate the suite of tools and interfaces available on the web site into an "e-commerce-like" interface. The goal of this effort is to provide a unifying theme for all user interactions (i.e., data selection, data downloads, etc.) with the site that is based on concepts familiar from e-commerce (on-line shopping) websites. The goal of this web model is to allow users to visually browse data (waveforms) or data products (e.g., bulletins), select data or data products to be placed in a "shopping cart," and then provide the capability to manage and download the selected objects.

We have substantially improved the web-based waveform viewing capability. Last year we introduced an online waveform viewing capability which allowed users to view any waveform in the entire data archive. This capability has been extended to provide mult-itrace support and enhanced waveform display control. The updated waveform

viewer (Figure 2) allows users to simultaneously view multiple channels of data from a single station or to view data channels from different stations. The waveform tool is not intended as an analysis tool, but rather as a waveform browser to streamline the process of locating, previewing, selecting, and acquiring waveforms of interest. However, basic scroll, zoom and filter functions are available. The waveform viewer is accessed through a standard web browser—no special installations or modifications on the user's (client's) machine or web browser are required.

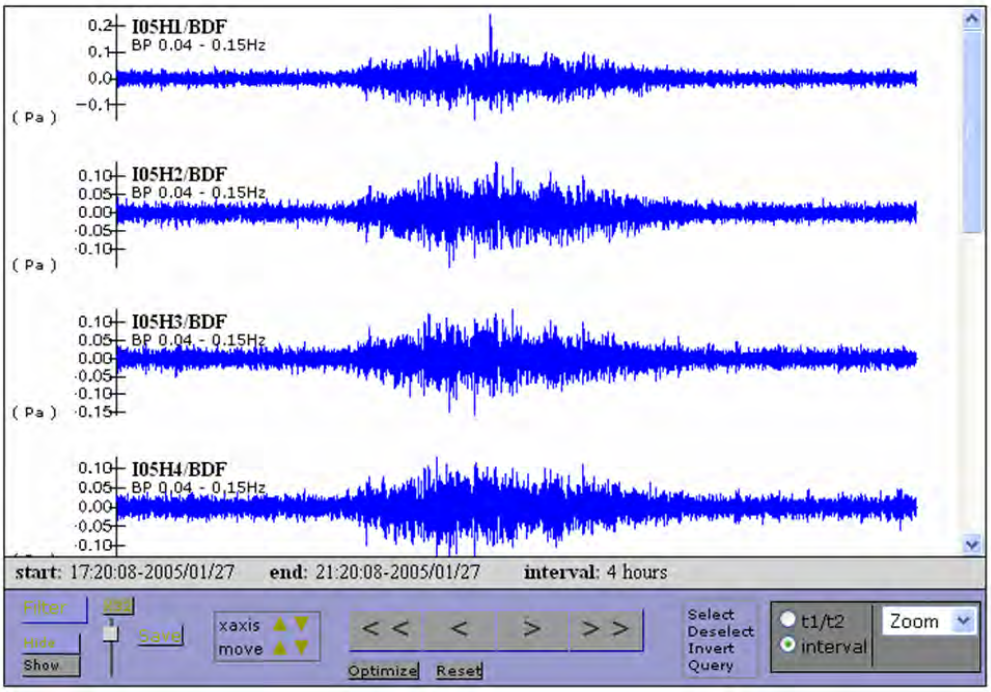

Figure 2. The web-based data viewing tool provides easy access to all data in the archive. Data on display are from station I05AU in Australia and show signals from the eruption of a volcano on Manam Island at approximately 38° distance. The data have been bandpass filtered between 0.04 and 0.15 Hz.

Once the desired data have been identified, the user "selects" these data (equivalent to placing items in a shopping cart on an e-commerce website). Data selections are stored in a private folder for later review, revision, and download (Figure 3). User preferences for data format and delivery method are recalled automatically, greatly reducing the effort required to obtain waveform data. For example, both CSS3.0 and SAC formats are available for waveform data. Multiple data selections may be packaged together into a single download and once the content of a particular data package is defined, the user may return to browsing while the data are collected and converted to the user's preferred format. A given data package may be downloaded more than once and prior downloads are recorded in a history folder, freeing researchers from the need to maintain permanent data warehouses on their computer.

An enhanced waveform data location service is in development as a replacement for the existing General Data Extractor (GDE) web service. Like the existing GDE, this tool will permit users to locate waveform data based on event information and other constraints such as group velocity limits and preferred station and channel selections. The replacement tool is enhanced to provide integration with both the new private folder infrastructure and the improved waveform browser—enabling the user to preview GDE-based waveform selections as well as manage selections via the user's private data folder.

A major goal in the development of these new tools is to support collaborative research by distributed research teams. Research teams might identify and define relevant data sets to be shared by members of the team. These data selections would then be available to any team member at any time without each individual requiring a personal copy of all data. Researchers would need only to download to their personal workstations those data subsets relevant to the current task. These downloaded data could be removed and replaced with other research team data as needed, freeing each team member from managing individual data sets.

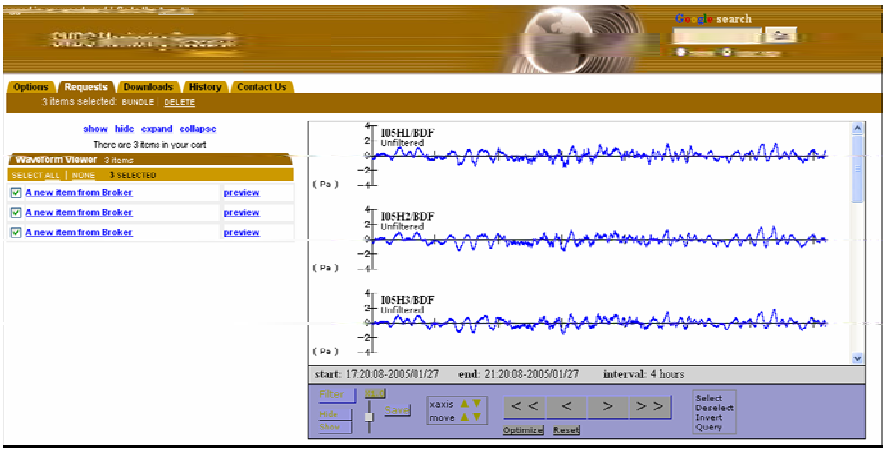

Figure 3. Using the data download manager, the user can review data in a "shopping cart." In this example, the data selected with the waveform viewing tool (e.g., the data shown in Figure 2) are being reviewed prior to downloading (note that in this view the data are shown unfiltered).

In addition to the new web-based data access tools described above, we provide backward compatibility for existing tools, such as the e-mail based *AutoDRM* software. In many cases the performance of these existing tools is greatly improved because of the quick response times of the spinning-disk mass-storage system.

Data-Intensive Computing

It is possible to perform massive, data-intensive experiments directly on the data in the archive. This is possible since the archived data are written on the mass-storage system in an analysis ready format (CSS3.0). The data can be read directly by application software—making it possible to perform experiments on any desired cross section of data in the archive, with no need to "stage" data in advance.

Recent studies of infrasound ambient noise (Bowman et al., 2005a, b) provide an excellent example of the types of data-intensive computations facilitated by the high-speed mass-storage system. To characterize ambient infrasound noise, power spectral density was measured for 28 of the 34 infrasound stations shown in Figure 4. Data were analyzed from January 20, 2003, through December 31, 2004, from 21 consecutive 3-minute segments of 20 sample per second data taken four times daily, beginning at 06:00, 12:00, 18:00, and 24:00 local time. This required computing power spectra for 1,476,309 data segments (Figure 5), comprising approximately 5.3 billion data samples. In a companion study (Bowman, 2005a, b), average meteorological conditions (wind speed, wind direction, temperature, and absolute pressure) were calculated for the same 3-minute windows at 21 of the IMS stations. This computation utilized approximately three million data segments.

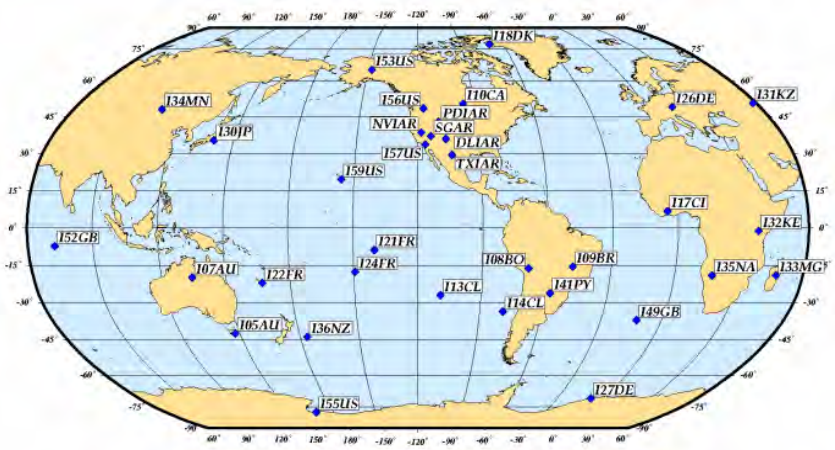

Figure 4. Data from 34 current infrasound stations are in the RDSS data archive.

The RDSS has a special server configuration to provide data intensive computing capability to the nuclear explosion monitoring R&D community. Remote users access a server which has direct (read-only) file access to the entire spinning-disk mass-storage system. Users essentially upload their code to the server rather than download data. The UNIX server is equipped with compilers, database access, and local storage for writing the results of computations. The user's code runs on the server and can read any waveform data in the archive (all data files are in CSS3.0 format). Researchers interested in utilizing this service should contact the RDSS.

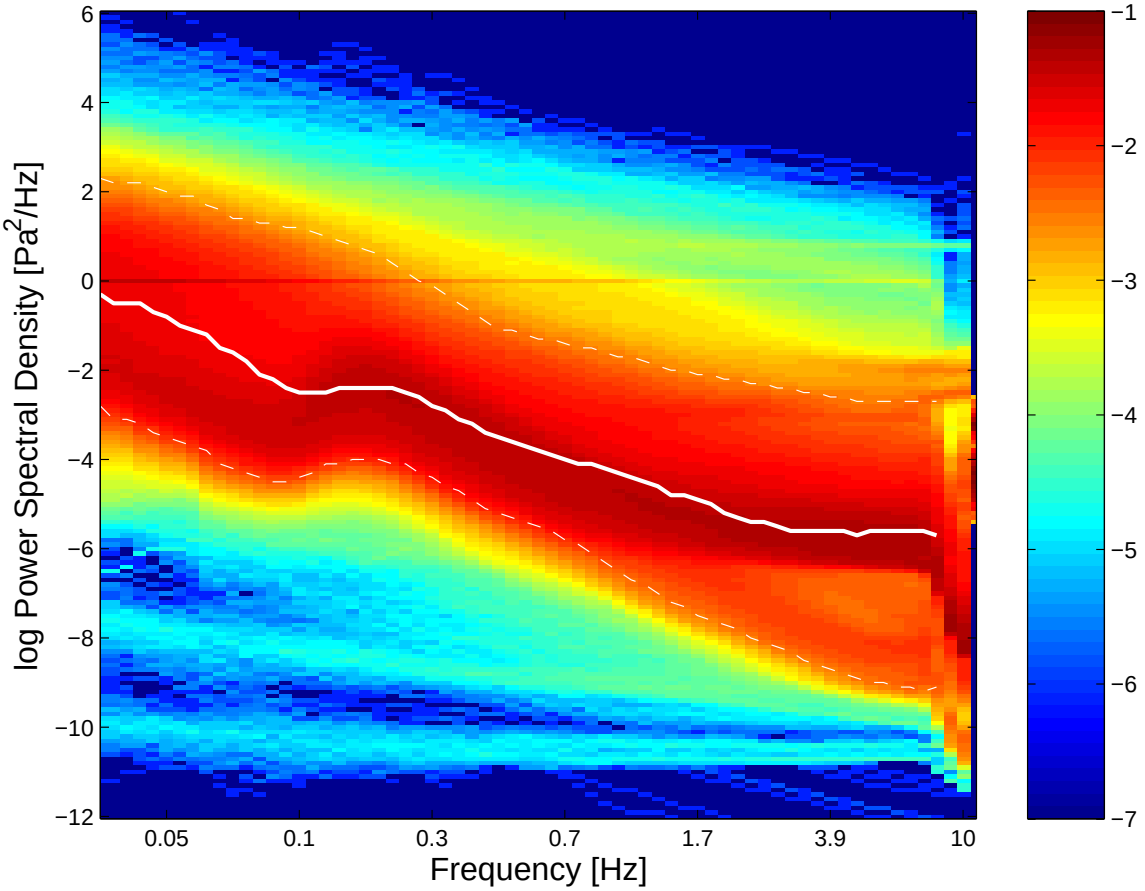

Figure 5. Probability density function of Power Spectral Density (PSD) for all time intervals at 25 infrasound stations. About 1.4 million spectra are binned in intervals of 0.1 log PSD. The color scale is proportional to the log of the number of spectra that fall within each bin. The solid white line shows the all-time network median for 15 stations having data for 1 year or longer, and the lower and upper dashed white lines show the low- and high-noise models, respectively (figure from Bowman et al., 2005b).

Value-Added Databases

The RDSS provides value-added R&D databases which are a significant resource for the US R&D community (Table 1). The data (waveforms and/or arrivals) included in these databases are extracted from the general RDSS waveform archive (described above) as well as from a wide variety of other open sources. The careful compilation of data, along with relevant metadata, is typically a challenging and time-consuming task. However, the resultant data sets provide unique, value-added resources which can support studies in nuclear explosion detection, location, and identification. We describe several of the value-added databases below. Users are encouraged to visit the Monitoring Research Program's RDSS web pages (http://www.rdss.info) for more details on all of the value-added databases described in Table 1.

Table 1. Summary of value-added research databases available through the RDSS.

Database	Description
Infrasound	Acoustic recordings from natural and man-made events, including atmospheric nuclear explosions. Data suitable for detection and source classification studies.
Nuclear Explosion	A vast compilation of seismic and infrasound recordings and arrival data from underground, underwater, and atmospheric nuclear explosions.
Ground Truth	Seismic phase arrival data for GT0 through GT15 events.
Lop Nor	Seismic waveforms (~100 GB) and phase arrival data for events and stations in the Lop Nor, China region. Includes recordings of larger nuclear explosions which have been scaled down to smaller yields and embedded in background noise. Provides multiple source location estimates obtained from different open sources. See Kohl et al. (2002).
Arctic Region	Seismic waveforms and phase arrival data for events and stations in the Arctic region. Provides multiple source location estimates obtained from different open sources.
Network Data Set	Database of event and waveform data for seismic and infrasound stations to support evaluation of detection and network processing performance.

The infrasound database has been significantly expanded during the past year. The database contains waveforms from infrasound arrays operated by the Department of Energy, the International Monitoring System, and other organizations (many of which are not archived anywhere else). The 34 infrasound arrays for which continuous data are currently in the database are shown in Figure 4. These data holdings go back to 1995 and include data from sites on every continent. The database also includes a research component, which contains recent and historic acoustic recordings of a variety of natural and man-made events, including atmospheric nuclear explosions (Table 2 and Figure 6). The signals in the infrasound database are suitable for a variety of signal detection and source characterization studies, such as the examination of such issues as seasonal propagation variability.

Table 2. Summary of events in the Infrasound Research Database. Numbers in black indicate current database holdings. Numbers in red represent data recently added, and numbers in blue indicate events to be added (i.e., in the queue).

Event Source Type	Events	Events with Arrivals	Arrivals	Station Waveforms
Nuclear explosion	63 (31) (8)			250 (110)
Chemical explosion	14 (4) (2)	10 (1)	17 (2)	26 (6)
Gas pipe explosion	3 (1)	2	3	5 (2)
Mine explosion	5 (5) (13)	5 (5)	7 (7)	5 (5)
Rocket launch	7	7	10	10
Bolide	19 (7) (8)	10	18	43 (19)
Rocket reentry	4	4	7	7
Volcano	29 (3)	1	1	29
Earthquake	3 (15)	3	4	4
Aircraft (not sonic boom)	1	1	1	1
Auroral wave	48	–	–	48
Gravity wave	5	–	–	5
Microbarom	29	–	–	29
Mountain wave	49	–	–	49
Unknown	18	14	14	18
Total	297 (48) (49)	57 (6)	82 (9)	529 (142)

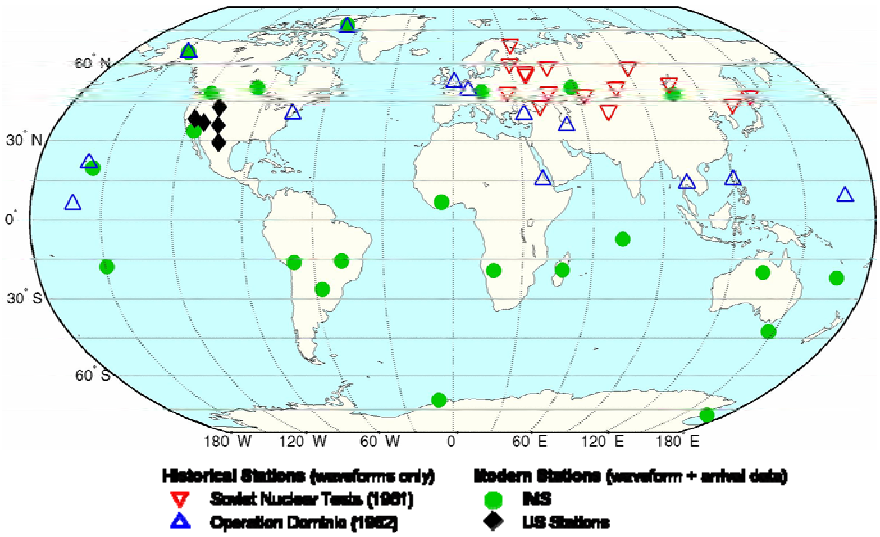

Figure 6. The Infrasound Research Database contains waveform data from a variety of historic and current station locations.

The Network Data Set (Kohl et al., 2005) provides a comprehensive database for evaluating detection and network processing performance. This "synthesized" network data set provides the means to evaluate signal processing algorithms on a large data set which has completely known characteristics. The data set utilizes seismic and infrasound signals from actual events. The signals are scaled to various sizes and embedded in clean background noise. Figure 7 shows the locations of the stations and events currently in the Network Data Set.

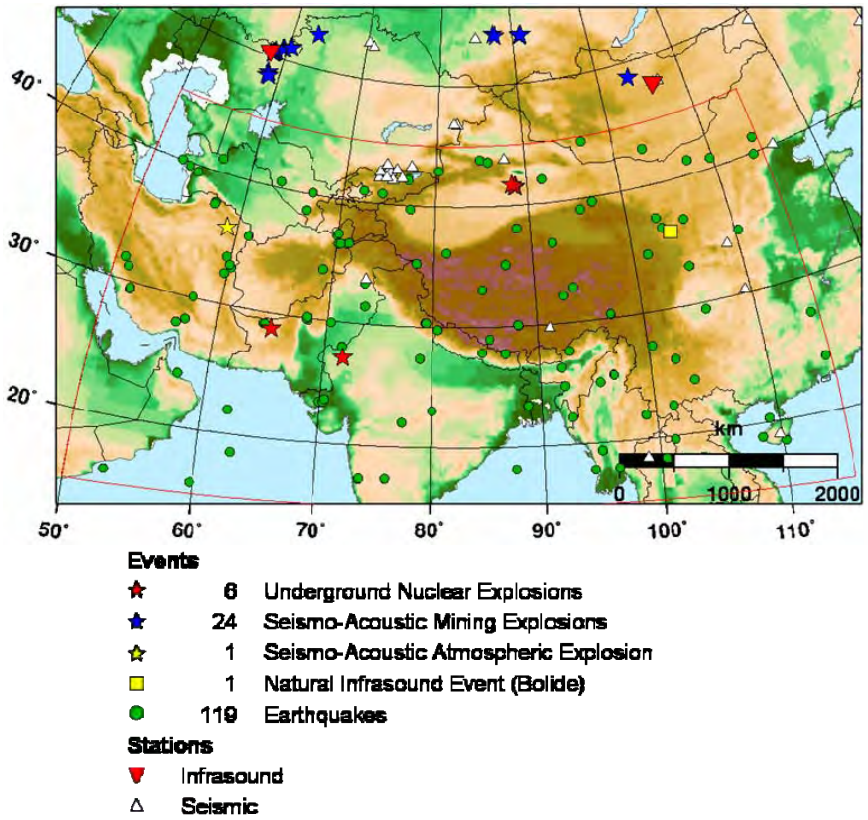

Figure 7. Locations of events and stations currently in the Network Data Set.

The Nuclear Explosion Database contains information on all reported nuclear explosions in the atmosphere, underground and underwater since the first nuclear explosive device was set off in 1945. The database gives the most accurate and complete unclassified information on time and place of both announced and presumed nuclear explosions and provides, whenever available, information on explosion yield, depth and shot medium (Table 3). In addition, the database contains a large archive of seismic (and some infrasound) recordings from about one-third of the explosions (Figure 8).

The explosion database was originally compiled in 1997 and has subsequently been maintained and updated. It currently holds data for 2041 explosions. The list of explosions in the data base was derived from more than 40 different data sources with information reported by both official, such as Department of Energy (DOE/NV-209, 2000), and non-official organizations and appearing in a variety of publications. A detailed description of the database has been compiled by Yang et al. (2000, 2003) and Bondár et al. (2001).

Table 3. Locations of stations for which nuclear explosion waveforms (seismic or infrasound) or arrival data are included in the Nuclear Explosion Database.

Explosion Environment	Total Number of Explosions	Number of Explosions with:				
		Shot Depth/ Height	Yield	Shot Medium	Arrival data	Waveforms
Underground	1516	632	1035	457	608	739
Underwater	10	7	9			1
Atmosphere	515	110	452		7	25

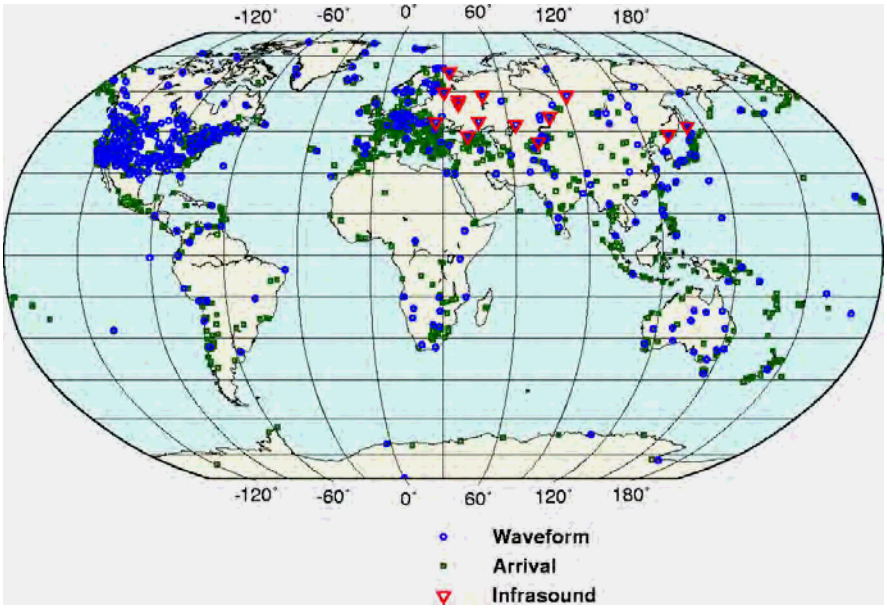

Figure 8. Locations of stations for which nuclear explosion waveforms (seismic or infrasound) or arrival data are included in the Nuclear Explosion Database.

The Ground Truth Database contains a collection of events of GT quality to support location calibration studies. The database includes nuclear and chemical explosions, mine blasts, rock bursts and earthquakes of global coverage. The earthquakes in the database all have shallow focus (less than 40-km focal depth), since deep earthquakes are of lesser interest from a nuclear monitoring point of view. Every event is accompanied with arrival data as well as references to document the source of information.

The events in the Ground Truth Database are distributed globally, though they are dominantly in the northern hemisphere (Figure 9). The database currently holds 13,379 GT0-15 events (Table 4) with some 900,000 associated phases (of which some 810,000 are defining) recorded at 3,771 stations. Residuals in the bulletins refer to IASP91 (Kennett and Engdahl, 1991) predicted travel times with the source fixed to the GT locations. Note that the categories GT7 and GT11 stand for events promoted to GT status after performing multiple event location on an event cluster. For details see Bondár et al. (2004), Engdahl and Bergman (2001), and Engdahl et al. (2002). The GT15 events (Pan et al., 2002) are included only to provide coverage on mid-oceanic ridge events in the mid-Atlantic ridge, the Carlsberg ridge and the Gulf of Aden.

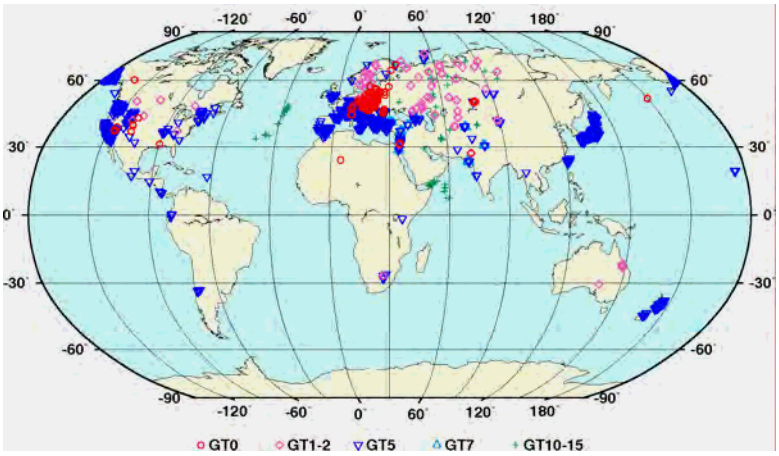

Figure 9. Locations of events in the Ground Truth Database.

Table 4. Summary of Ground Truth Database holdings, by source type and GT level.

Source	GT0	GT1-2	GT5	GT7	GT10	GT11	GT15	Total
Nuclear explosion	428	359	23	-	26	-	-	836
Chemical explosion	155	44	1	-	-	-	-	200
Mine blast, rock burst	-	141	58	-	-	-	-	199
Earthquake	-	-	11596	324	12	183	29	12144
Total	583	544	11678	324	38	183	29	13379

CONCLUSIONS AND RECOMMENDATIONS

We have described a variety of resources which are available to the US nuclear explosion monitoring research and development community.

A vast quantity of data is available to users via the spinning disk mass-storage system. New tools have been developed which make it possible to visually browse any waveform in the entire data archive. The waveform viewer runs under any standard web browser and provides the ability to view multiple channels of data from one or more stations. Data can be selected via the waveform viewer or with other tools. Selected data can then be downloaded via the data download manager, which provides user-specific configuration and download management.

The mass-storage system also supports data intensive computing experiments. Application software can access data directly from the mass-store—facilitating experiments which require large volumes of data from any combination of stations and time windows. Researchers interested in remotely accessing the data intensive computing infrastructure should contact the RDSS (e.g., via the website).

A wide range of value added databases have been produced. These databases represent unique assemblies of waveform data, arrival and event data, and metadata. The databases are all available on-line and provide valuable resources for use in detection, location, and identification studies.

We recommend that researchers in the nuclear explosion monitoring R&D community visit the MRP websites to learn more about the MRP's RDSS resources. The MRP maintains both an open website (http://www.rdss.info) and a restricted access website (at https://www.rdss.info; access limited to US government-authorized researchers).

ACKNOWLEDGEMENTS

We thank the members of the US Infrasound Team for making available high-quality data from the research stations and International Monitoring System stations which they operate.

REFERENCES

Bowman, J. R. (2005a), Meteorological Conditions at Infrasound Stations, *Inframatics*, 9.

Bowman, J. R. (2005b), Meteorological Conditions at Infrasound Stations, SAIC Technical Report SAIC-05/3000.

Bowman, J. R., G. E. Baker, and M. Bahavar (2005a), Ambient Infrasound Noise, *Geophys. Res. Lett.*, 32: L09803, doi:10.1029/2005GL022486.

Bowman, J. R., G. Shields, G. E. Baker, and M. Bahavar (2005b), Infrasound Station Ambient Noise Estimates and Models, SAIC Technical Report SAIC-05/3001.

Bondár, I., E. R. Engdahl, X. Yang, H. A. A. Ghalib, A. Hofstetter, V. Kirichenko, R. Wagner, I. Gupta, G. Ekström, E. Bergman, H. Israelsson, and K. McLaughlin (2004), Collection of a Reference Event Set for Regional and Teleseismic Location Calibration, *Bull. Seism. Soc. Am.* 94: 1528–1545.

Bondár, I., X. Yang, R.G. North, and C. Romney (2001), Location Calibration Data for CTBT Monitoring at the Prototype International Data Center, *Pure Appl. Geophys.* 158: 19–34.

DOE/NV-209 (2000), United States Nuclear Tests, July 1945 through September 1992, Rev. 15.

Engdahl, E. R. and E. A. Bergman (2001), Validation and Generation of Reference Events by Cluster Analysis, in *Proceedings of the 23rd Seismic Research Review: Worldwide Monitoring of Nuclear Explosions*, LA-UR-01-4454, Vol. 1, pp. 205–214.

Engdahl, E., E. Bergman, M. Ritzwoller, N. Shapiro, and A. Levshin (2002), A Reference Event Data Set for Validating 3-D Models, in *Proceedings of the 24th Seismic Research Review—Nuclear Explosion Monitoring: Innovation and Integration*, LA-UR-02-5048: 261–270.

Kennett, B. and E. R. Engdahl (1991), Travel Times for Global Earthquake Location and Phase Identification, *Geophys. J. Int.* 105: 429–465.

Kohl, B., R. North, J. R. Murphy, M. Fisk, and G. Beall (2002), Demonstration of Advanced Concepts For Nuclear Test Monitoring Applied to the Nuclear Test Site at Lop Nor, China, in *Proceedings of the 24th Seismic Research Review—Nuclear Explosion Monitoring: Innovation and Integration*, LA-UR-02-5048, Vol. 1, pp. 302–312.

Kohl, B., T. J. Bennett, I. Bondár, B. Barker, W. Nagy, C. Reasoner, H. Israelsson, P. Piraino (2005), Development of a Network Data Set for Evaluating Detection and Network Processing Performance, in current Proceedings.

Pan, J., M. Antolik, and A. Dziewonski (2002), Locations of Mid-Oceanic Earthquakes Constrained by Sea-Floor Bathymetry, *J. Geophys. Res.* 107: 2310, doi:10.1029/2001JB001588.

Yang, X., R. North, and C. Romney (2000), CMR Nuclear Explosion Database (Revision 3), CMR Technical Report CMR-00/16.

Yang, X., R. North, C. Romney, and P. Richards (2003), Worldwide Nuclear Explosions, in *International Handbook of Earthquake and Engineering Seismology*, Vol. 81B, W. H. Lee, H. Kanamori, P. Jennings, and C. Kisslinger, Eds., Academic Press.

A POTENTIAL NEW NUCLEAR EXPLOSION MONITORING SCHEMA

Christopher J. Young and Sanford Ballard

Sandia National Laboratories

Sponsored by National Nuclear Security Administration
Office of Nonproliferation Research and Engineering
Office of Defense Nuclear Nonproliferation

Contract No. DE-AC-04-94-AL85000

ABSTRACT

Relational database schemas are widely used in nuclear explosion monitoring applications (Carr, 2004) and they work well for many aspects of monitoring, but have some limitations that can only be addressed through fundamental redesign. In this paper we present a new seismic schema that captures all of the information in the current core schema, but is better normalized, more extensible, and provides a better basis for next generation seismic monitoring research and system development.

Past modifications of the core schema have typically been minor, avoiding significant changes to the existing tables because software that interfaces with them may have to be modified also. Introducing custom tables is equally problematic and similarly avoided. In the short term, keeping the original tables makes sense because software modifications can be expensive. For conducting new seismic monitoring research and developing next generation monitoring software systems, however, keeping the current table structure can become a significant impediment.

Using the Object Role Modeling (ORM) component of Visio Enterprise Architect Edition, and starting from the basic object fact relationships, we have developed a data model and resultant schema that supports many-to-many event-to-origin relationships, completely captures complex model prediction information, properly records array membership, and properly normalizes network magnitude storage, to name just a few features. By using the Visio tool, we are assured that our resultant schema is highly normalized, that all tables are linked with settable primary, foreign and unique keys, and that important constraints are enforced within the database via stored procedures. The resulting schema favors efficiency and maintainability, but ease of interaction with the information in the database can still be achieved through the use of views. We have made great efforts to make our design easily extensible without modifying the schema, but should modifications be required they can be made easily through the ORM model. Because we include the ORM as part of the schema design, there is no confusion in our schema about why a table or column is included: every feature of the schema can be related directly back to a simple fact statement that can be validated by any seismic monitoring domain expert. To verify the accuracy of our new schema, we have developed sql scripts to set up the old schema tables as views of the new tables.

Our initial development has focused on seismic monitoring, but we have made efforts to keep the schema as generic as possible so that it can be used to capture similar types of information for other ground-based monitoring technologies (e.g., hydroacoustic and infrasound). Should our proposed schema be chosen for use with real monitoring systems, large amounts of old-format data would need to be converted to the new schema. We show in this paper how this would be done with a simple custom utility.

OBJECTIVE

The basic table structure of the seismic schema currently used for nuclear explosion monitoring was developed more than 15 years ago (Anderson et al., 1990) and has changed very little since then (Carr, 2004). We have had many years of experience with this schema, both using it to hold data as well as designing increasingly sophisticated software to interface with it. For most basic purposes, the schema works well, but our work with developing the NNSA Knowledge Base has produced a list of problems that is both too long and of too fundamental a nature to address with simple fixes to the current tables. In particular, we think that the current design has become an impediment to modern software design practices (e.g., object oriented coding) that rely on a well-designed schema architecture with settable primary and foreign keys. We believe that a fundamental redesign of the core monitoring schema is in order and present our first attempt at that in this paper. Our ultimate goal is to develop a schema that efficiently and accurately captures as much of the monitoring domain as possible and that will extend well with data sets and techniques yet to be developed. For our design, we used the ORM component of Visio Enterprise Architect Edition, and started from the basic object fact relationships (e.g., "an origin has zero or more arrivals"). By using the Visio tool, we are assured that our resultant schema is highly normalized, that all tables have settable primary, foreign and unique keys, and that important constraints are enforced within the database via stored procedures.

RESEARCH ACCOMPLISHED

The core tables are often divided into "Primary" and "Lookup," and we will do the same here. Lookup tables are those that contain static information (i.e., information related to networks, stations, etc.). Primary tables are those that contain dynamic information associated with a given candidate explosion event: location, time, magnitude, which stations recorded it, various amplitude measurements, etc.

To help clarify the discussion below, we introduce the following conventions: table names are in **boldface**, and **c**olumn names are *italicized*.

Primary Tables

Figure 1 shows the Entity Relationship Diagram for the primary tables, with only the key columns (primary = PK, foreign = FK, and unique = UK) shown to simplify. To make our schema more easily understood by those familiar with the current schema, where tables are analogous to tables in the existing schema we have used the same name. Note, however, that none of the tables are exactly the same and some differ significantly, as we discuss below.

Events

An event can be thought of as the highest level object captured by the primary tables (i.e., every other object can ultimately be tied to an event). In the current schema, the **Event** table groups together one or more origins (hypothetical locations), one of which is the preferred origin. However, no origin can be part of more than one event; that is, in the current schema, event-to-origin is one-to-many. This is problematic for a data archive like the NNSA Knowledge Base where events (origin groupings) may have been put together by more than one author. The current design is limiting in another way as well. When multiple origins are relocated simultaneously using location algorithms such as Joint Hypocenter Determination, origin groupings need to be defined. For these reasons, we choose to instead model the event-to-origin relationship as many-to-many, which introduces an additional association table (**EvorAssoc**) that has foreign keys pointing to each of the tables it links. The many-to-many relationship also implies that the **Event** primary key *evid* is no longer needed as a column in the new **Origin** table. With our new association table, an origin can be linked to an arbitrary number of events.

Origins

We have made numerous changes to the **Origin** table for our new schema. Related to the location information represented by an origin, we introduce 3 new tables designed to store specialized information. **AzGap** stores information about station azimuthal coverage, **ModSource** stores information about the source of models used to predict observations, and **RefLocation** stores information about reference locations that an origin may be associated

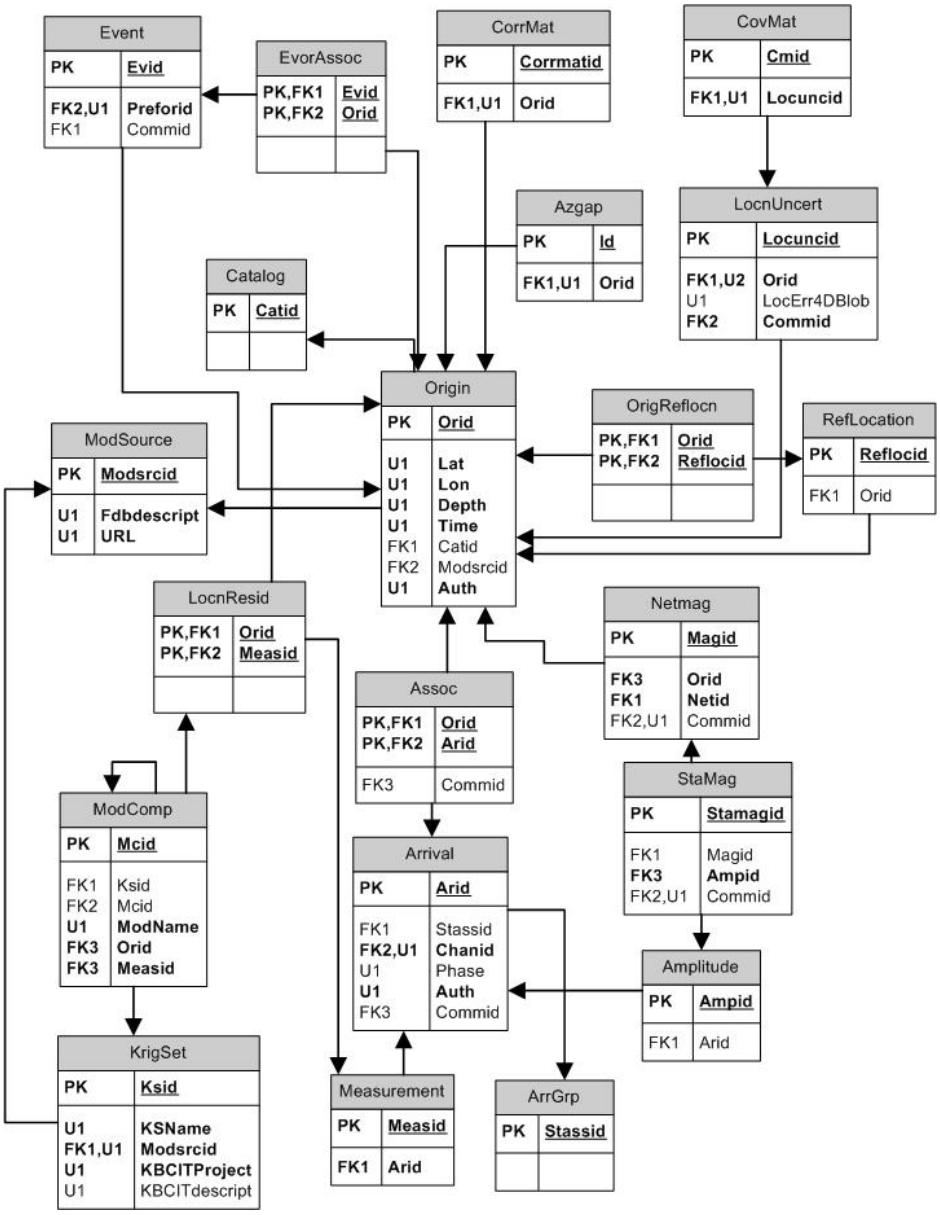

Figure 1. Entity Relationship Diagram (ERD) for the primary tables.

with (e.g., test sites). The **AzGap** ties one-to-one with a specific origin, so this table has *orid* as a foreign key pointing to the **Origin** table. The same **ModSource** information may be used for more than one origin, so this is a one-to-many relationship and hence *modsrcid* (the primary key for **ModSource**) is a foreign key column in the **Origin** table. An origin can have more than one reference location and vice versa, so this is a many-to-many relationship and an association table (**OrigReflocn**) is introduced in the new schema to link **Origin** and **RefLocn**.

Frequently, origins come from specific catalogs, so we have introduced a new **Catalog** table to capture information about the catalogs, including *name*, *description*, and *rank* (*rank* is used to determine which origin in an event is the preferred one). Because **Catalog** to **Origin** is a one-to-many relationship, *catid* (the **Catalog** primary key) is added as a foreign key in the new **Origin** table.

For magnitude information, the changes are all deletions. The current **Origin** table has *mb*, *mbid*, *ms*, *msid*, *ml*, and *mlid*. These ids are all foreign keys to *magid* in the current **Netmag** table, but this is unnecessary because the

Netmag to **Origin** relationship in the current schema is many-to-one, implying that a given origin could have any number of network magnitudes but each network magnitude is related to only one origin (thus *orid* is a foreign key column in **Netmag**). A simple query of **Netmag** by *orid* and *magtype* can fetch mb, ms, or ml values, so these do not need to be stored in **Origin**. Thus, 3 foreign keys in the current **Origin** that point to specific types of magnitudes (*mbid*, *msid*, *mlid*) in **Netmag** are redundant, as are the values associated with them (*mb*, *ms*, *ml*), so we remove all of these in the new schema. If there are multiple network magnitudes of the same type for the same origin, then it might be desirable to designate one of these as the preferred one. To implement this, we have added a new column "*is preferred*" to **Netmag**.

Arrivals

An arrival, also sometimes referred to as a "pick" or "detection," is the fundamental, station/phase-specific observation. Many types of measurements can be made for a given arrival, and one of the most fundamental problems we have found with the current schema is that the information for arrivals is very poorly normalized. An arrival may have travel time, azimuth, and/or slowness observation types measured for it, and the current **Arrival** table has columns to capture information for all three. This is inefficient in that it is very common that not all three types will be measured, so several columns are typically nulled. Further, for each observation type, the basic data to be stored (quantity and uncertainty) are the same, so the columns are highly redundant. Finally, we observe that if another fundamental observation type were deemed to be useful to measure for arrivals, additional columns would have to be added to the **Arrival** table.

We address all of these problems in our new schema by removing the measurement information from **Arrival** and putting it into its own table called **Measurement**. Each measurement has an *obstype*, a *quantity*, an *uncertainty*, and is tied to **Arrival** by the foreign key *arid*. Rows are added to this table only if a particular observation type has been made for an arrival, and there is no limit on how many could be added for a given arrival. In the future, if some new type of observation relevant to an arrival is deemed to be important, the information can be added to the existing tables without having to change the basic structure of any tables.

A further arrival normalization problem occurs with the many amplitude measurements that may be made for a given arrival (peak-to-trough, zero-to-peak, RMS, etc.). The current **Arrival** table has single columns for *amp* and *per*, so these are quickly used. This problem has long been recognized and extension tables have been introduced to capture multiple amplitude measurements per arrival. The USNDC P2B2 schema (Oo et al., 2003) introduces an **Amplitude** table that we have adapted almost exactly for our new schema. This is a generic table with *arid* as a foreign key, so an arbitrary number of amplitude measurements can be made for any arrival. With this table as part of the new schema, we drop the old amplitude support columns in the current **Arrival** table (*amp*, *per*, *SNR*).

Arrivals Linked to Origins

We believe the association of arrival information with origins is also fundamentally flawed in the current schema. Currently, the **Arrival** table and **Origin** tables are linked with a many-to-many relationship via the **Assoc** table. On a high level, that is correct, but if we examine the relationship in more detail, problems emerge.

First, an arrival can be associated with an origin in two ways, and this is not well-modeled. An arrival can simply be tied to an origin in a general sense (it corresponds to a seismic wave caused by the origin), or it can be part of the process that was used to locate the origin. The latter is the reason for the *timdef, azdef, slodef* columns in the current **Assoc** table. The problem with the current schema is that these two types of information are both put in the same table (**Assoc**). Thus, **Assoc** has columns that are often nulled if an arrival is not used for location at all or is used only for travel time, azimuth, or slowness. Further, as was discussed for the current **Arrival** table, the information recorded in **Assoc** for each type of observation (defining, residual value, and weight) is the same, so the columns are redundant. Finally, though the **Assoc** table might have all three current observation types as defining, and hence using a model to drive location, there is only one column (**vmodel**) to capture the model information, which could easily be different for each observation type. A further problem with the current **Assoc** table is that there is only one *wgt* column when in fact separate weight columns are needed for each observation type. Omission of the weight information for azimuth and slowness observations in the **Assoc** table makes it impossible to recompute the sum squared weighted residuals of the observations associated with an origin if there are any defining azimuth or slowness observations. This is a major flaw since the sum squared weighted residuals are the quantity minimized by the location algorithm that produced the origin to which the assoc entry is linked.

To fix these problems, we made several significant changes. First, we split the information in the current **Assoc** table into two new tables: **Assoc** and **LocnResid**. The new **Assoc** table is basically a subset of the old **Assoc** table, with all the columns relating to locating the origin removed. Retained are columns to hold basic information such as station-to-event distance and azimuth, etc. The removed information is put into the **LocnResid** table, which is a many-to-many link between **Origin** and **Measurement**. This makes sense because the location information is all related to measurements (travel time, azimuth, and slowness) made from the arrival, not the arrival itself. The **LocnResid** table is fully generic, suited to holding information for travel time, azimuth, slowness, or any new observation types that might be introduced in the future.

LocnResid has separate rows for each observation type, so the problem with being limited to a single weight entry and model designation for all observation types is eliminated. Our new schema goes further than this, however, and is able to fully capture the complexity of location models. For many years, the models used for location have actually been composed of a base model plus a set of corrections (elevation, ellipticity, path correction, etc.), so specifying a single model has long proven problematic. Further, in the latest models emerging from location calibration research, the single resultant models developed for a given station/phase are actually composites of several region-specific models blended together. To capture all of this complexity requires a heavily genericized set of tables that can handle arbitrary hierarchies of complexity and we think we have achieved this in our new schema. We capture any of the various model components (base model total or by region, various corrections total or by region) in the new **ModComp** table. **ModComp** has a foreign key pointing to **LocnResid**, so it is easy to find the model components that go with any measurement-origin combination. The hierarchy of model components (e.g., the total base model may come from blending base models from two regions) is captured by endowing the **ModComp** table with a foreign key pointing to itself. To find out if a model component has subcomponents (children), all that is necessary is to query for **ModComp** rows that point to that row. This hierarchy can be extended to as many levels as desired, though we have had no reason to go beyond two (total and regional subcomponents).

To capture the information about the actual source of the models used for a given location (i.e.. file name and location, brief description), we have introduced a new table **ModSource**. Based on our knowledge of the current location models being developed and those anticipated in the future, we expect that all of the model information used to locate an event will come from the same source, so we tie this table to **Origin** rather than **ModComp**. The relationship between **ModSource** and **Origin** is one-to-many, so this introduces the primary key from **ModSource** (*modsrcid*) as a foreign key column in the new **Origin** table.

Currently, only state-of-the-art location algorithms account for correlation between observations, which has been shown to significantly affect both the calculated locations and the uncertainty estimates in some cases (Chang et al., 1983). We have introduced tables to capture this information in the new schema. The individual correlation values are stored in the **CorrEl** (correlation element) table that links together two rows from the **Measurement** table. **CorrEl** rows are in turn grouped into a correlation matrix via the **CorrMat** table. The **CorrMat** table has a one-to-many relationship with **Origin** (i.e., *orid* is a foreign key in **CorrMat**).

Location Uncertainty

As almost no candidate explosion locations are known with perfect accuracy, properly capturing the location uncertainty is essential. The current schema does this with the **Origerr** table, which is a simple extension to the **Origin** table (i.e. it has the same primary key—*orid*—and so just adds additional columns related to location uncertainty). This table captures the full covariance matrix, the one-dimensional (1D) time uncertainty, 1D depth uncertainty and the two-dimensional (2D) horizontal uncertainty ellipse. Three-dimensional (3D) and four-dimensional (4D) uncertainty information is not stored by the current schema. We have introduced separate tables for each type of uncertainty information (**LocErr1D**, **LocErr2D**, **LocErr3D**, **LocErr4D**). The covariance matrix information is stored in its own table (**CovMat**).

Magnitude

We discuss network magnitudes in the Origin section above. Station magnitude measurements are captured in the new **Stamag** table, which is fairly similar to the current **Stamag** table. The changes in this case are deletions. The current **Stamag** table contains numerous redundant convenience columns (*evid*, *orid*, *arid*, *sta*, and *phase*) that can be obtained via joins with other tables, and we have removed these from the new table. If using these joins to access this information proves cumbersome and/or degrades performance significantly, we may reintroduce some of these

fields. We have also given the new **Stamag** its own simple primary key (*stamagid*) rather than the current composite primary (*magid*, *sta*), to make it easier to set up foreign keys pointing from other tables to this one.

Lookup Tables

Figure 2 shows the Entity Relationship Diagram for the lookup tables. Again, to make our schema more easily understood by those familiar with the current schema, where tables are analogous to tables in the existing schema we have used the same name. Also again, however, note that none of the tables are exactly the same and some differ significantly, as we discuss below.

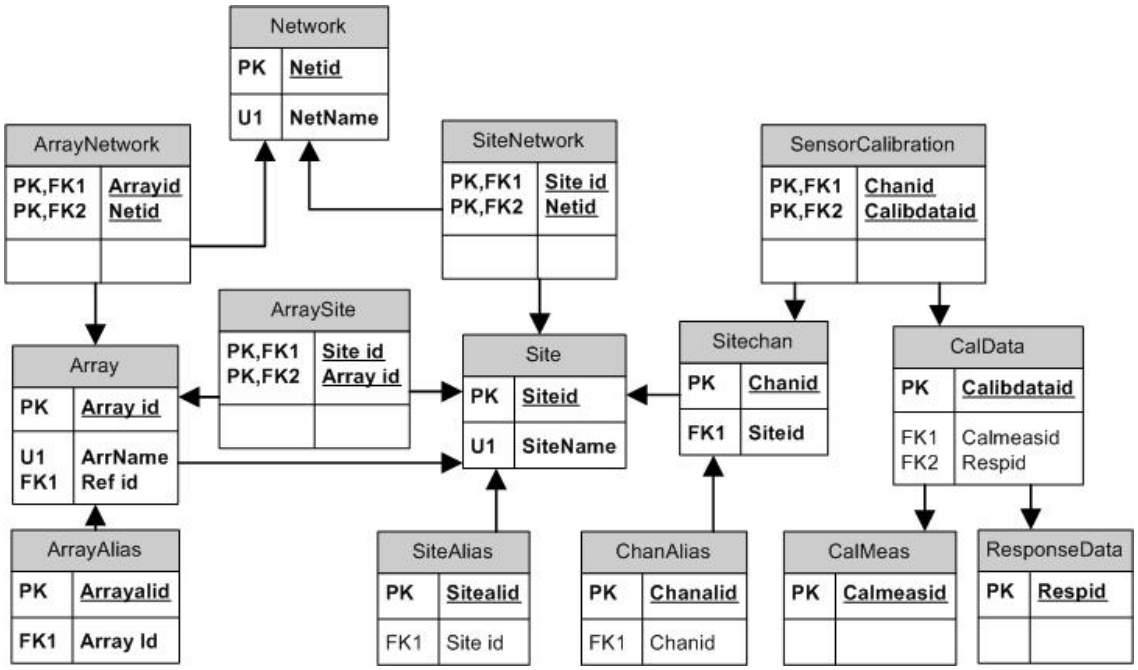

Figure 2. Entity Relationship Diagram (ERD) for the lookup tables.

Network

The top level object for the lookup tables is a network, so we begin there. Our **Network** table is very similar to the current table, except that we add *starttime* and *endtime* to capture the time period during which a network is operational.

Sites

In the current schema, the **Site** table captures the information about the name and location of where seismic instrumentation has been deployed, and we do essentially the same thing. There are however, a few important differences between the new and current **Site** tables. First, we introduce a simple primary key (*siteid*) for the new **Site** table to make it less cumbersome to create foreign keys to point to this table (the current primary key is *sta*, *ondate*). Second, we remove the array-specific columns (*dnorth*, *deast*, *refsta*) from the **Site** table. Storing these in Site is both inefficient because many sites are not part of arrays, and confusing.

Site Groupings into Networks

In the current schema this is done with the **Affiliation** table, and we use a similar table, though we give it a different name—**SiteNetwork**—due to the way we choose to handle arrays. Also, we add *starttime* and *endtime* columns to capture the period during which a site was part of a network. Note that **Network** to **Site** is a many-to-many relationship, so **SiteNetwork** has foreign keys pointing to the primary keys of each of these tables (*netid*, *siteid*).

Arrays

In the current schema, an array is treated just like a network, and so networks of arrays are captured with hierarchies of networks. Though some see this as clever and efficient, we have found it to be confusing and inefficient. In the current schema, for a given array, all elements, including the name given to the array center or beam position (e.g., NORSAR), are rows in the **Site** table. The fact that they are all part of the same array is supposed to be captured in two ways (but seldom is). First, all are given the same *refsta* value in **Site**, which should be the name of the array itself. Second, the array is added as a row to the **Network** table and **Affiliation** rows are added to tie each element to the array. A row is then added to the **Affiliation** table to tie the array to a **Network** (e.g., IRIS). Because the latitude, longitude information stored with each site may not be accurate enough for array processing (e.g., FKs), offsets relative to the array center are stored in the **Site** table (*dnorth*, *deast*). As pointed out above, this is inefficient because all site rows carry these columns, even though most sites are not array elements. A further problem is that if a site is to be used as an element of more than one array (easily done given that arrays are virtual entities) only one set of offsets can be stored.

In our new schema, we take a much more direct approach and model arrays according to the simple fact statements "arrays consist of one or more sites" and "zero or more arrays may be associated with a network." In our approach, there is an **Array** table that captures the basic information about the array (e.g., name, and a foreign key pointing to **Site** to indicate which site position is the center or beam position). **Array** to **Site** is a many-to-many relationship, so a new association table **ArraySite** is introduced. This is the table where the offsets (*dnorth*, *deast*) are stored, as well as the *starttime* and *endtime* of each site's membership in the array (which is not captured at all in the old schema). The many-to-many array membership in networks is captured with another association table, **ArrayNetwork**. Again, this table has *starttime* and *endtime* columns to capture the period of membership for each array in a network.

Channels

Each site is composed of one or more seismic instruments to record the motion of the Earth. Information about each instrument deployed at a site is captured in the current schema with the **Sitechan** table, and our **Sitechan** table is nearly identical. One important difference is that we explicitly model the one-to-many relationship between **Site** and **Sitechan** by giving our **Sitechan** table a foreign key pointing to the primary key in **Site** (*siteid*). We use *starttime, endtime* columns in **Sitechan** to record the operational period for the particular channel, which may be different from the *starttime, endtime* appropriate for the site as a whole.

Aliases

A further source of confusion with lookup information not captured by the current schema is that arrays, sites, and channels can all have aliases (i.e., synonyms). For example, a short period vertical channel may be SHZ or SZ. The fact that such names are equivalent is not captured in the current schema, and this can lead to errors when using data. We fix the problem by introducing a set of very similar tables (**ArrAlias**, **SiteAlias**, **ChanAlias**) to link the various aliases to the "true" name. Each of these tables has *starttime* and *endtime* columns to capture the duration of the alias.

Mapping the Current Schema to the New Schema

Should our proposed schema be chosen for use with real monitoring systems, large amounts of old-format data would need to be converted to the new schema. This is easily done, as we show in Figure 3 for a few of the key tables.

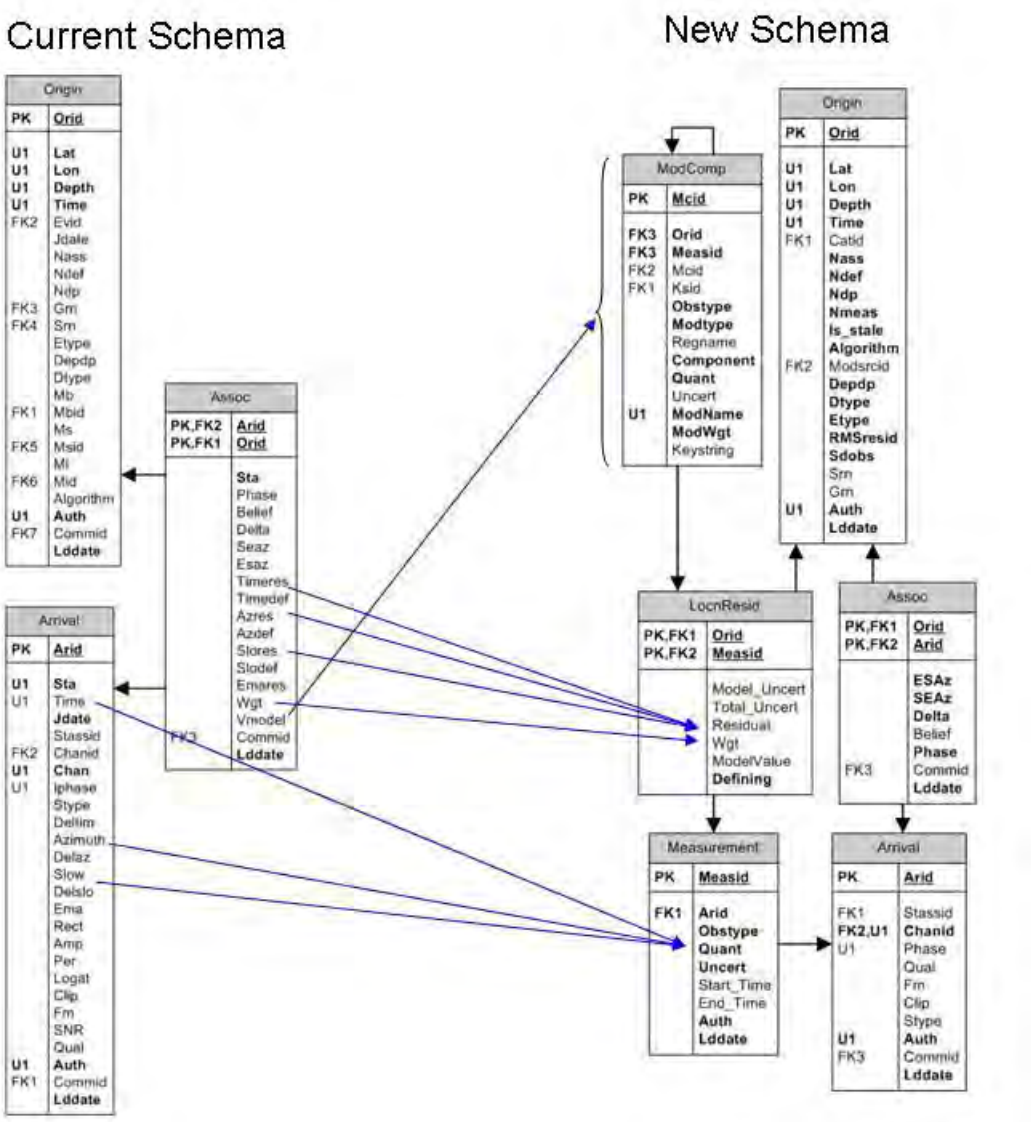

Figure 3. Remapping current schema tables to new schema tables.

In this example, we show how an origin and associated arrivals used for location would be converted from the current schema to the new schema. Much of the information in the current **Arrival** table (*phase*, *qual*, *fm*, etc.) would map directly to the new **Arrival** table. Travel time, azimuth, and slowness observations and estimated uncertainties (*time*, *deltim*, *azimuth*, *delaz*, *slow*, and *delslo*), however, would be mapped to separate rows in the new **Measurement** table. Information from the current **Assoc** table would be mapped to 3 tables in the new schema: **Assoc**, **LocnResid**, and **ModComp**. Residual values for travel time, azimuth, and slowness (*timeres*, *azres*, *slores*) would be mapped to separate rows in the **LocnResid**. The same would be true for the weights for each observation type, except that the current schema only stores one of these (*wgt*), so we would have to specify which observation weight to map to in the new schema. The woefully inadequate *vmodel* column in the current **Assoc** table essentially gets remapped to the entire **ModComp** table, though there is not enough information available for historic events to properly populate the new table. Presumably the string in *vmodel* could be mapped to *modname* in the **ModComp** table. The remaining information in the current **Assoc** table (*esaz*, *seaz*, *phase*, *belief*) maps directly to corresponding columns in the new **Assoc** table.

Similar remaps can be made for the rest of the information in the current schema, and using these remaps we have written some simple scripts to translate information archived in the old format schema into the new schema.

Unfortunately, by using the current schema in the first place, some critical information was never stored properly (e.g., detailed information about the models used for location), so the new tables will not be fully populated for historical data. There is still a gain in doing the translation because the new schema is more efficient and more amenable to code development, but the full benefit of our data model can only be realized when it is used from the start to archive data.

CONCLUSIONS AND RECOMMENDATIONS

We have designed a new database schema to manage information related to nuclear explosion monitoring that captures all of the information stored with the current schema but overcomes many of the problems with the current design. Guiding principles to which we sought to adhere in our design include

- all tables that store fundamental quantities (**Origin**, **Arrival**, **Site**, etc.) should have single, numeric, primary keys;
- having columns that are very frequently null in a table is to be avoided whenever possible; and
- the schema should form a cohesive, integrated entity with settable primary, unique and foreign keys.

Our design

- allows **Origins** to be grouped together in multiple different ways to reflect **Events** defined by different researchers/institutions and to allow the definition of groups of **Origins** that were located simultaneously using Joint Hypocenter Determination;
- properly normalizes magnitude information;
- adds tables that document the source of earth model information and the various components that constitute the predictions of observed quantities;
- defines the **Measurements** made on an **Arrival** separately from the **Arrival** itself, thereby reducing redundancy and enhancing extensibility;
- associates **Measurements** with **Origins** using **Residuals** in addition to the currently defined association between **Origin** and **Arrival**; and
- defines **Sites**, **Arrays** and **Networks** in a way that is more intuitive and that promotes discipline.

Our schema is backward-compatible with the current schema in that it is possible to capture all information stored in the current schema, and views of the new schema can be constructed which allow current software to access information stored in the new schema.

ACKNOWLEDGEMENTS

We thank Richard Stead, Julio Aguilar-Chang, Stan Ruppert, Dorthe Carr, and Mark Harris for countless discussions about problems associated with the current schema and how they should be fixed.

REFERENCES

Anderson, J., W. Farrell, K. Garcia, J. Given, and H. Swanger (1990), Center for Seismic Studies Database: Version 3.0 Structure, SAIC document.

Carr, D. (2004), National Nuclear Security Administration Knowledge Base Core Table Schema Document, Sandia National Laboratories, SAND2002-3005.

Chang, A. C., R. H. Shumway, R. R. Blandford, and B. W. Barker (1983), Two Methods to Improve Location Estimates—Preliminary Results, *Bull. Seismol. Soc. Am.* 73: 281–295.

Oo, K., D. Irons, A. Henson, and C. Morency (2003), Database Design Description (DBDD) Phase 2, Rev C, United States National Data Center (US NDC), SAIC-01/3047 (REV C).

Acronyms, etc.

Acronyms, etc.

Acronym	Definition
2-D, 2D, 3-D, 3D	two-dimensional, three-dimensional, etc.
ABCE	Annual Bulletin of Chinese Earthquakes
ACD	Advanced Concept Demonstration
AFRL	Air Force Research Laboratory
AFTAC	Air Force Technical Applications Center
AK135	seismic travel time model
ANFO	Ammonium Nitrate Fuel Oil
ANOVA3	analysis of variance code
ArcView	commercial GIS software (used in Knowledge Base)
ARSA	Automated Radioxenon Analyzer/Sampler
ASSE	Altai-Sayan Seismological Expedition
ATOC	Acoustic Thermometry of the Ocean Climate
BB	broad band
BDSN	Berkeley Digital Seismic Network
Be-7	beryllium-7
CANC	Correlated data Adaptive Noise Canceling
CauSIN	Caucasus Seismic Information Network
CDSN	Chinese Digital Seismic Network
CEA	Commissariat à l'Energie Atomique (French bulletin)
ChISS	Russian abbreviation for multichannel spectral seismometer
CLVD	Compensated Linear Vector Dipole
CMT	Harvard Centroid Moment Tensor
CodaMag	tool to implement magnitude calculations (Mayeda, 1993; Mayeda and Walter, 1996)
CORBA	Common Object Request Broker Architecture (data communications tool)
CRUST2.0	crustal model (Bassin et al., 2000)
CTBT	Comprehensive Nuclear-Test-Ban Treaty
CTBTO	Comprehensive Nuclear-Test-Ban Treaty Organization
CU	University of Colorado
CUB2.0	3D global models (Shapiro et al., 2002)
CU-Boulder	University of Colorado, Boulder
DB24	Geotech Remote Digitizer
DD	double-difference
DMC	Data Management Center
DOB	depth of burial
DoD	Department of Defense
DOE	Department of Energy
DOF	degrees of freedom
DOS	Department of State
DSS	deep seismic sounding
DTRA	Defense Threat Reduction Agency
EDR	Earthquake Data Reports
EHB	Engdahl, E.R., van der Hilst, R. & Buland, R., 1998. Global teleseismic earthquake relocation with improved travel times and procedures for depth determination, Bull. Seismol. Soc. Amer., 88, 722-743
EM	electro magnetic
ERL	Earth Resources Laboratory
ERS	European Remote Sensing (satellites)
ESRI	Environmental Systems Research Institute

Acronyms, etc.

Acronym	Definition
ESRI	Environmental Systems Research Institute (makers of ArcInfo, ArcIMS, ArcGIS, etc. [http://www.esri.com/company/about/history.html]
ETOPO5	terrain model
ETTC	Empirical Travel Time Corrections
EventID	tool to implement event discrimination (Hartse et al., 1997; Walter et al., 1999)
EvLoc	location software
FSPS	frequency-slowness power spectra
Fstat, F-stat	F-statistic
FSU	Former Soviet Union
GBF	generalized beamforming
GDAIS	General Dynamics Advanced Information Systems
GII	Geophysical Institute of Israel
GIS	Geographical Information System
GMEL	grid multiple-event location or multiple-event location algorithm
GSEL	grid single-event location or single-event location algorithm
GSN	ground station network
GT	ground-truth
GUI	graphic user interface
Guralp CMG-3T	3-component broadband seismometer
HDC	hypocentroidal (or hypocentral) decomposition
HIMNT	Himalayan Nepal Tibet Seismic Experiment
HPGe	High Purity Germanium
HydroCAM	Hydroacoustic Coverage Assessment Model
HypoDD	hypo double-difference
Hz	hertz
IASPEI	International Association of Seismology and Physics of the Earth's Interior
IASPEI91	standard earth model
IDC	International Data Center
IDG	Russian Institute for the Dynamics of the Geospheres
IKONOS	satellite-based imagery acquisition systems, 4m multispectral and 1m panchromatic
IMS	International Monitoring System
INDEPTH II, III	experiments
InfraMAP	Infrasound Modeling of Atmospheric Propagation
InSAR	Interferometric Synthetic Aperture Radar
IRIS	Incorporated Research Institutions for Seismology
IRP	integrated research product
ISC	International Seismological Centre
ISTC	International Science and Technology Center
JAXB	Java Architecture for XML Binding
JHD	Joint Hypocenter Determination
KACST	King Abdulaziz City for Science and Technology
KB	Knowledge Base
KBCIT	Knowledge Base Calibration Integration Tool
KIGAM	Korean Institute of Geology and Mining or Korea Institute of Geosciences and Mineral Resources
KLD	Karhunen-Loéve decomposition
KMA	Korean Meteorological Administration
KOERI	Kandilli Observatory Earthquake Research Institute

Acronyms, etc.

Acronym	Definition
KRSC	Kola Regional Seismological Centre
LANL	Los Alamos National Laboratory
LBNL	Lawrence Berkeley National Laboratory
LDA	linear discriminant analysis
Lg	regional seismic near surface shear phase
LLNL	Lawrence Livermore National Laboratory
LOCOO	LOCator Object Oriented (program code)
Matlab	commercial software application
MatSeis	seismic analysis package developed by SNL using Matlab
mb	body wave magnitude
MCMC	Markov Chain Monte Carlo
Md	duration magnitude
MDAC	magnitude and distance amplitude corrections
MDAC2	Magnitude and Distance Amplitude Correction procedure (Walter and Taylor, 2002)
ME/NA/WE	Middle East/North Africa/Western Europe
MFA	Multiple Filter Analysis
MIT	Massachusetts Institute of Technology
MOU	Memorandum of Understanding
Ms	surface wave magnitude
MSE	mean squared error
MSIS	thermospheric atmospheric model
MSISE	total atmospheric model
MU	magnitude unit
Mw	Moment Magnitude
NA-22	Office of Nonproliferation Research and Engineering
NCEDC	Northern California Earthquake Data Center
NEIC	National Earthquake Information Center
NEM R&E	Nuclear Explosion Monitoring Research and Engineering
NK ATD	North Korea Advanced Technology Demonstration
NNSA	National Nuclear Security Administration
NOAA	National Oceanic and Atmospheric Administration
NOGAPS	Navy Operational Global Atmospheric Prediction System
NRL	Naval Research Laboratory
NTS	Nevada Test Site
OFIS	Optical Fiber Infrasound Sensors
ORB	object request broker
ORLOADER	software package
PANDA	CERI's portable network - The PANDA stations were deployed in the central New Madrid seismic zone during October 1989 - August 1992.
PASSCAL	IRIS program that manages seismic equipment
PDE	Preliminary Determination of Epicenters
PDF	Portable Document Format
Pg	local and regional seismic phase
PGL	Parametric Grid Library
PhaseMatch	tool that implements match filtering to isolate surface waves (Herrin and Goforth, 1977)
PMCC	Progressive Multichannel Cross-Correlation
PMEL	Progressive Multiple Event Location or Pacific Marine Environmental Laboratory
PMF	Phase Matched Filtering

Acronyms, etc.

Acronym	Definition
Pn	regional seismic compressional phase
PNE	peaceful nuclear explosions
PNNL	Pacific Northwest National Laboratory
PPD	posterior probability distribution
PREM	Preliminary Reference Earth Model (Dziewonski and Anderson, 1981)
PrepCom	Preparatory Commission
PS362	3D global models (Antolik et al., 2002)
PSDs	Power Spectral Densities
PSU	Penn State University
P-wave	primary wave
Q	Q Factor
QDA	quadratic discriminant analysis
RASA	Radionuclide Aerosol Sampler Analyzer
RBAP	Regional Body-wave Amplitude Processor
RDB	relational database
RDSS	Research and Development Support Services
REB	Reviewed Event Bulletin
REFTEK or RefTek	72a 24-bit data recorder
RELOC	software
rftn96	program suite for determining crustal structure
RMS	root mean square (errors)
RUM	mantle velocity model
SA	seismic-acoustic or simulating annealing
SAC	Seismic Analysis Code
SAIC	Science Applications International Corporation
SAN2000B	SAIC Authenticator/Formatter
SASCs	Slowness-Azimuth Station Corrections
SBSO	Serialized Binary Stream Object
SDAS	Seismic Data Acquisition System
SDI	Spatial Data Interface (application)
SLU	Saint Louis University
SMDC	Space Missile Defense Command (Army)
Sn	regional seismic shear phase
SNR	signal-to-noise ratio
SNU	Seoul National University
SP	Short Period
SPOT	high-resolution imagery products are 10m panchromatic
SRD	System Requirement Document or Secret Restricted Data
SRDB	Seismic Research Database
SSS	Sensor Site Subsystem (AFTAC)
SSSCs	source-specific station corrections or site-specific station corrections
STS-2	Streckeisen seismometer model STS 2
surf96	program suite for determining crustal structure
SUS	stationary uncorrelated scattering or signals, underwater sound
SVD	singular value decomposition
S-wave	secondary wave
TM	threshold monitoring

Acronyms, etc.

Acronym	Definition
TPC	tactical pilotage chart
T-phase	hydroacoustic phase
UCB	University of California, Berkeley
UCSD	University of California, San Diego
UNE	underground nuclear explosions
UNR	University of Nevada, Reno
USGS	United States Geological Survey
USNDC	United States National Data Center
UWE	underwater explosions
VELEST	software program
VEXTool	Viewing and EXtraction Tool
VMAX	Variable-Period, Maximum Magnitude Estimation
WCC	waveform cross-correlation
WG	working group
WINPAK3D	P-wave velocity model for India and Pakistan
WWSSN	World Wide Standard Seismograph Network
YSKP	Yellow Sea – Korean Peninsula

Station Code	Location and/or description
AAK	Ala-Archa (Kyrgyzstan)
AKTO	Aktyubinsk Auxiliary Seismic Station
ANMO	Albuquerque
APA	Apatity station (array)
ARCES	seismic array in northern Norway
ARS	Arshan
AS049	auxilliary seismic IMS station #49 on Mount Merron, Israel
BJI	Beijing (Baijiatuan; Peking)
BRAR	seismic array in Belbasi, Turkey
BRVK	Borovoye auxiliary seismic station
CHG	Chiang Mai
CHNAR	Chulwon (seismo-acoustic array)
CMB	Columbia College
DUG	Dugway
EIL	Elat (Eilat) (seismic)
ELK	Elko
FINES	seismic array in southern Finland
GEOFON	global seismic Broadband Digital Network; Potsdam; Germany
Geoscope	global Seismic broadband network; France
H01	Cape Leeuwin
H08	Diego Garcia
HFS	Hagfors
HLR	Highlands Ranch (closed)
ISP	Isparta
KAZ	Karuizawa
KEV	Kevo regional station
KMI	Kunming
KNB	Kanab
KNET	Kyrgyz Broadband Seismic Network

Acronyms, etc.

Station Code	Location and/or description
KSAR	seismic array in Wonju, Korea
KURK	Kurchatov Auxiliary Seismic Station
LAC	Landers
LSA	Lhasa (Tibet, China)
LVZ	Lovozero regional station
LZH	Lanzhou
MAG	Magadan
MAKZ	Maqanshy (Makanchi)
MALT	Malatya
MEDNET	MedNet digital seismic broadband network; Italy
MNA	Mina
MRNI	Mount Meron (old seismic station that has been replaced by AS049)
NEW	Newport
NIL	Nilore
NORES	seismic array in southern Norway
NRIS (NRI)	Noril'sk
NVAR	seismic array in Mina, Nevada
OBN	Obninsk seismic station
PDY	Peleduy seismic station
PFO	Pinon Flat Observatory
PS38	seismic array in central Saudi Arabia
SEY	Seymchan
SPITS	seismic array in Spitsbergen
SSE	Sheshan
TIXI (TIK)	Tiksi
TLY	Talaya seismic station
TUC	Tucson
ULN	Ulaanbaatar, (Mongolia)
WMQ	Urumqi (Wulumuchi) seismic station
XAN	Xi'an (Hsian)
YAK	Yakutsk
YKA	seismic array in Yellowknife, Canada
ZAL	Zalesovo

SOFAR Channel	a layer of water deep in the ocean (near Bermuda it's around 1000 m deep) where the speed of sound is at a minimum. Sound waves can get caught in this channel and travel hundreds of kilometers. The SOFAR channel is formed by the interplay between changes in ocean temperature and pressure with increasing depth. Temperature and pressure are the two main factors that determine the speed of sound in the ocean.